NASA TECHNICAL MEMORANDUM

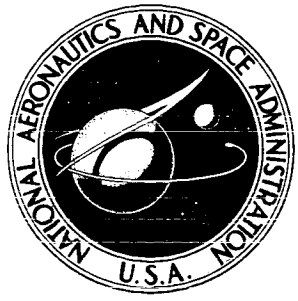

NASA TM X-2440

NASA TM X-2440

PROCEEDINGS OF THE NATIONAL SYMPOSIUM ON NATURAL AND MANMADE RADIATION IN SPACE

E. A. Warman, Editor

Held at
Las Vegas, Nevada
March 1-5, 1971

NATIONAL AERONAUTICS AND SPACE ADMINISTRATION • WASHINGTON, D. C. • JANUARY 1972

1. Report No.	2. Government Accession No.	3. Recipient's Catalog No.
NASA TM X-2440		

4. Title and Subtitle	5. Report Date
PROCEEDINGS OF THE NATIONAL SYMPOSIUM ON NATURAL AND MANMADE RADIATION IN SPACE	January 1972
	6. Performing Organization Code
7. Author(s)	8. Performing Organization Report No.
E. A. Warman, Editor	
	10. Work Unit No.
9. Performing Organization Name and Address	
Aerojet Nuclear Systems Company P. O. Box 13070 Sacramento, California 95813	11. Contract or Grant No.
	13. Type of Report and Period Covered
12. Sponsoring Agency Name and Address	Technical Memorandum
National Aeronautics & Space Administration and U.S. Atomic Energy Commission Washington, DC 20546 Washington, DC 20545	14. Sponsoring Agency Code

15. Supplementary Notes

Proceedings of National Symposium on Natural and Manmade Radiation In Space held at the Frontier Hotel Las Vegas, Nevada, March 1-5, 1971

16. Abstract

This document contains the manuscripts of 140 technical papers delivered in 24 separate sessions of the National Symposium on Natural and Manmade Radiation in Space, which was held in Las Vegas, Nevada in March, 1971. These proceedings reflect an interdisciplinary topical theme concentrating on most aspects of radiation in space. A strong radiobiological representation is included in addition to discussions of radiation transport, detection and shielding. The bases for analytical predictions of naturally occurring space radiation are explored along with some reports of space radiation measurements. The radiation aspects of space nuclear power and space nuclear propulsion systems are reviewed.

17. Key Words (Suggested by Author(s))	18. Distribution Statement
Space radiation, radiobiology, radiation shielding, radiation detection, space nuclear propulsion, space nuclear power, radiation effects, radiation dosimetry, nuclear reactors	Unclassified - Unlimited

19. Security Classif. (of this report)	20. Security Classif. (of this page)	21. No. of Pages	22. Price*
Unclassified	Unclassified	1,035	$10.00

*For sale by the National Technical Information Service, Springfield, Virginia 22151

THE SYMPOSIUM ORGANIZATION

ORGANIZATION AND PROGRAM COMMITTEE

E. A. Warman, Aerojet Nuclear Systems Company - General Chairman

A. Reetz, Jr., NASA Office of Advanced Research and Technology

P. G. Johnson, NASA/AEC Space Nuclear Systems Office

C. McCallum, NASA/AEC Space Nuclear Systems Office

R. A. Hartman, NASA Office of Manned Space Flight

M. R. Fleishman, NASA/AEC Space Nuclear Systems Office

J. I. Vette, NASA Goddard Space Flight Center

SYMPOSIUM ACTIVITIES COMMITTEE

All members from host organization: Aerojet Nuclear Systems Company

E. A. Warman	Chairman
F. R. Basque	Finance and Registration Chairman
L. A. Safford	Arrangements Chairman
H. Blue	Publications
R. L. Clothier	Hotel and Exhibitor Liaison
J. Bodley	Tickets and Functions
B. Dietrick	Local Arrangements
T. Ross	Publicity and Press

FOREWORD

The National Symposium on Natural and Manmade Radiation in Space was held at the Frontier Hotel in Las Vegas, Nevada, March 1-5, 1971. The initial plans for the Symposium were formulated with the intention of structuring a meeting similiar in content to previous symposia on Protection Against Radiations in Space which were held at Gatlinburg, Tennessee in 1962 and 1964. There were, however, two main differences between the Las Vegas and Gatlinburg meetings: First, the scope of the Las Vegas Symposium was enlarged to include papers related to manmade radiation sources associated with space nuclear propulsion systems and isotopic and reactor space electric power systems. Second, at Las Vegas more emphasis was placed on the operational aspects of radiation problems in space.

The Symposium was sponsored by the National Aeronautics and Space Administration and the U.S. Atomic Energy Commission. Co-sponsors of the meeting were the Aerospace and the Shielding and Dosimetry Divisions of the American Nuclear Society and the Sacramento Section of the American Institute of Aeronautics and Astronautics. The Aerojet Nuclear Systems Company of Sacramento, California served as the host organization for the symposium.

The symposium provided an excellent interdisciplinary forum for the discussion of radiation in space, including radiobiologists, dosimetrists, radiation shielding and radiation effects experts, and space scientists involved in the measurement of the space radiation environment. The large response from the radiobiology community to participate in the meeting was especially rewarding as the papers in that area were most interesting and provided the highlight of the symposium.

The symposium was attended by approximately 300 scientists and engineers who came to hear a total of 140 technical papers in 24 sessions over a four-day period. Three special plenary sessions of invited papers were held during the mornings of the first three days; the afternoons of these days and the entire fourth day were devoted to concurrent sessions of both invited and contributed papers. In addition an excellent luncheon talk was presented by a special guest speaker each of the four days of the symposium. The speakers were: Milton Klein, Manager of the NASA/AEC Space Nuclear Systems Office; Dr. Russell C. Drew of the Office of Science and Technology, Executive Office of the President; Dr. Douglas Grahn, Associate Director, Division of Biological and Medical Research, Argonne National Laboratory, and Dr. Charles Berry; M.D., Director of Medical Research and Operations, NASA Manned Spacecraft Center. Mr. Klein discussed the status of the NERVA program and the possible impact of current decisions to reduce the funding support for the program. Dr. Drew's luncheon address, "Where Do We Go From Here?" was directed to the future development and plans for the nation's space activities. Dr. Grahn, reporting as Co-Chairman of the National Academy of Sciences' Radiobiological Advisory Panel, summarized the panel's findings and recommendations regarding nuclear radiation protection guides and constraints for manned space missions. Dr. Berry reviewed the medical aspects of the Apollo XIV flight and discussed some of the less publicized operational aspects of manned missions.

The complete manuscripts of the papers delivered at the symposium are included in these proceedings. In general, papers are grouped within the session in which they were presented at the symposium. In the addendum to the proceedings are two papers which arrived too late to be listed in the proceedings proper. Also in the addendum is a special report by Dr. Philip K. Chapman and his associates on the investigation of cosmic ray induced eye flashes as witnessed by the Apollo XIV astronauts.

Arthur Reetz, Jr.
NASA Headquarters
Washington, D.C.

TABLE OF CONTENTS

PLENARY SESSION I
SPACE NUCLEAR SYSTEMS AND APPLICATIONS
CHAIRMAN: R. E. SCHRIEBER (TECHNICAL ASSOCIATE DIRECTOR-LOS ALAMOS SCIENTIFIC LABORATORY)

SESSION II.1
NUCLEAR PROPULSION SYSTEMS: RADIATION ASPECTS OF VEHICLE DEFINITION STUDIES
CHAIRMAN: D. SAXTON (NASA-MARSHALL SPACE FLIGHT CENTER)

SESSION II.2.
NUCLEAR POWER SYSTEMS: SNAP REACTOR SHIELDING
CHAIRMAN: C. McCALLUM (SPACE NUCLEAR SYSTEMS OFFICE-NASA/AEC)

SESSION II.3.
NATURAL SPACE RADIATION SHIELDING
CHAIRMAN, A. REETZ, JR. (OFFICE OF ADVANCED RESEARCH AND TECHNOLOGY - NASA)

SESSION II.4.
SPACE RADIATION DOSIMETRY
CHAIRMAN: T. PARNELL (MARSHALL SPACE FLIGHT CENTER)

PLENARY SESSION III
NATURAL SPACE RADIATION
CHAIRMAN: J.I. VETTE (DIRECTOR, NATIONAL SPACE SCIENCE DATA CENTER, GODDARD SPACE FLIGHT CENTER)

SESSION IV.1.
RADIOBIOLOGY: SOME HUMAN RESPONSES TO RADIATION EXPOSURE
CHAIRMAN: V. P. BOND, M.D. (ASSOCIATE DIRECTOR - BROOKHAVEN NATIONAL LABORATORY)

SESSION IV.2.
SPACE OPERATIONS IN THE PRESENCE OF MANMADE RADIATION
CHAIRMAN: P.G. JOHNSON (SPACE NUCLEAR SYSTEMS OFFICE-NASA/AEC)

SESSION VI.2.
RADIATION TRANSPORT AND SHIELDING: BASIC PHYSICS DATA
CHAIRMAN: C. PRESKITT (GULF RADIATION TECHNOLOGY)

SESSION VI.3.
NATURAL SPACE RADIATION: GEOMAGNETIC TRAPPED RADIATION BELTS
CHAIRMAN: J.W. KELLER (OFFICE OF SPACE SCIENCE AND APPLICATIONS-NASA)

SESSION VI.4.
RADIATION EFFECTS AND DOSIMETRY
CHAIRMAN: W. ROSE (GENERAL DYNAMICS/FORT WORTH)

SESSION VII.2.
RADIATION TRANSPORT AND SHIELDING: APPLICATIONS OF MONTE CARLO TECHNIQUES
CHAIRMAN: M.O. BURRELL (MARSHALL SPACE FLIGHT CENTER)

SESSION VII.3.
NATURAL SPACE RADIATION: INSTRUMENTATION AND BACKGROUND EFFECTS
CHAIRMAN: H. D. HENDRICKS (LANGLEY RESEARCH CENTER)

SESSION VII.4.
SPACE OPERATIONS IN THE PRESENCE OF NATURAL SPACE RADIATION (INCLUDING LIGHT FLASHES)
CHAIRMAN: R. HARTMAN (OFFICE OF MANNED SPACE FLIGHT-NASA)

SESSION VIII.3.
ATMOSPHERIC AND SUPERSONIC TRANSPORT RADIATION ENVIRONMENT
CHAIRMAN: J. MCLAUGHLIN (AEC HEALTH AND SAFETY LABORATORY)

SESSION VIII.4.
SPACE RADIATION DOSIMETRY
CHAIRMAN: M.D'AGOSTINO (GRUMMAN)

PLENARY SESSION I
SPACE NUCLEAR SYSTEMS AND APPLICATIONS

CHAIRMAN: R. E. SCHRIEBER
TECHNICAL ASSOCIATE DIRECTOR
LOS ALAMOS SCIENTIFIC LABORATORY

SPACE NUCLEAR PROPULSION SYSTEMS AND APPLICATIONS

FRANCIS C. SCHWENK

AEC/NASA Space Nuclear Systems Office

The basic principles of the operation of a nuclear rocket engine are reviewed along with a summary of the early history. In addition, the technology status in the nuclear rocket program for development of the flight-rated NERVA engine is described, and applications for this 75,000-pound-thrust engine and the results of nuclear stage studies are presented. Advanced research and supporting technology activities in the nuclear rocket program are also summarized.

INTRODUCTION

In presenting a paper on Space Nuclear Propulsion Systems and Applications for this National Symposium on Natural and Man-made Radiation in Space, I am going to assume that general remarks describing a nuclear rocket engine would give a valuable perspective for this distinguished audience of specialists in many fields. In addition, I will review the nuclear rocket program and discuss the use of the NERVA nuclear rocket engine in space flight missions.

Let me summarize a few important points before discussing details. For 15 years or so, the nuclear rocket program has been engaged in providing the necessary technology for development of the initial nuclear engine for flight. This engine is known as NERVA. Based on a successful technology program, the development of NERVA was initiated in 1969 and received limited funding for two fiscal years, 1970 and 1971. At this time in history, March 1, 1971, the budget for FY 1972 proposed by the Administration contains a rather low funding level for the nuclear rocket program, and the NERVA program and other important activities must be cut back substantially. It is important to realize that development of the NERVA engine is to be continued. Although maintained at a much reduced pace, we will try to retain some of the program capability and to make progress on essential areas of a very important, versatile, and useful propulsion system for a variety of space missions of the future. The budgetary problem stems from the limited resources allocated for advanced technology activities and the Space program and the need for funds in near term missions. This situation is summed up by a statement released by George Low, Acting NASA Administrator: "There is a need for the NERVA program. This need exists because nuclear propulsion represents a major breakthrough in the efficiency of space propulsion; and because many advanced space missions depend on this. But there is not a need to proceed with the full development of NERVA now. There are many programs that must be done before the capabilities represented by NERVA can be used -- these are the programs that are in our budget for FY 1972."

DESCRIPTION OF THE NUCLEAR ROCKET ENGINE

The essential features of a nuclear rocket engine system are shown in figure 1. After the liquid hydrogen propellant is pumped from storage in the rocket vehicle, it flows through the double-walled jet nozzle and the reflector to cool these components. Appropriately designed passages guide the hydrogen through the turbine to drive the pump, through an internal shadow shield, and through the hot fuel elements of the solid reactor core. Fuel elements, containing uranium-235, are heated by the energy released during fission. This energy is transferred to the hydrogen which is accelerated to high velocities as it flows through the jet nozzle to produce the desired thrust.

Nuclear rockets offer performance advantages over chemical rockets because a nuclear rocket has a specific impulse approximately two or more times that of a high-energy chemical system. While nuclear rocket engines are heavier than equivalent-thrust chemical rockets and while the propellant tankage of a nuclear stage tends to be larger because of the use of the low-density hydrogen propellant, these penalties do not compromise the gains derived from the high specific impulse of nuclear rockets. In general, the net effect is a nuclear advantage of about 50% or more per stage for missions of moderate energy and over 100% for high-energy missions. These gains are possible for the initial nuclear rocket engine; greater gains can be expected with advanced propulsion concepts.

This description of a nuclear rocket engine highlights certain important features that have set the course for the program to date. In order to achieve the

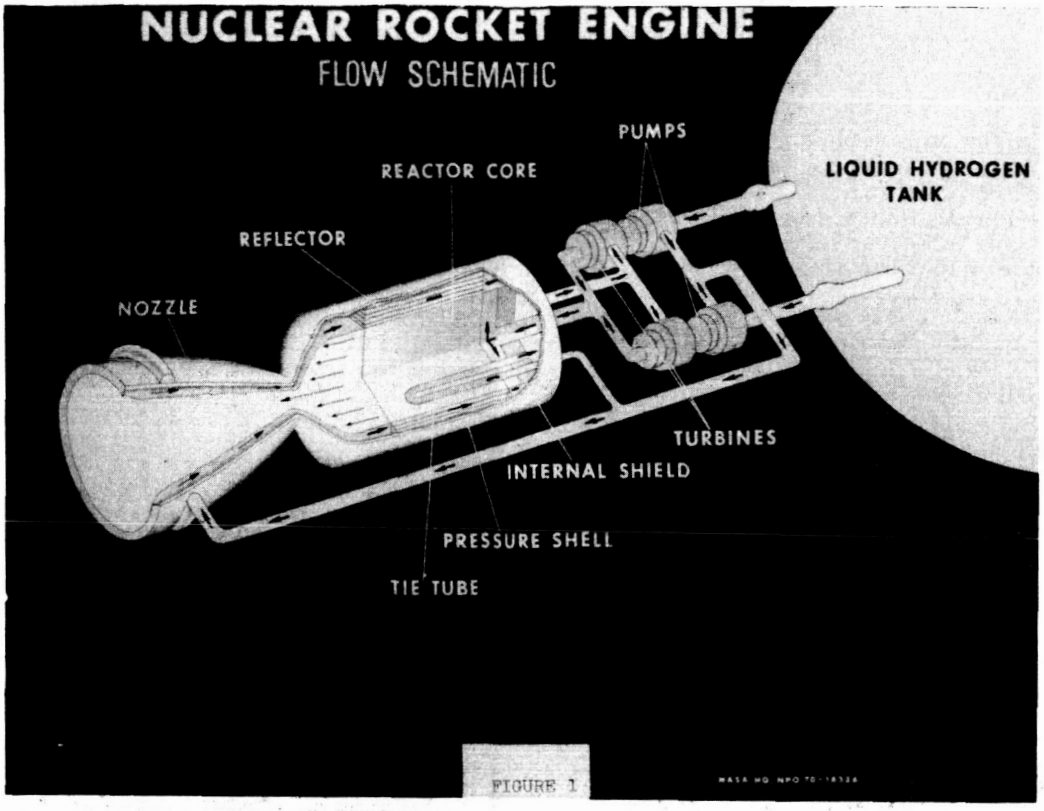

FIGURE 1

desired high specific impulse, the reactor must heat hydrogen to very high temperatures, approximately 4000°F for a specific impulse of 825 seconds. (Rocket engines that consume hydrogen-oxygen propellant can reach specific impulse values of 460 seconds.) Therefore, the rocket reactor must be constructed of a high temperature material having an appropriately low neutron absorption cross-section. The reactor must be compact to conserve weight; however, the structural design must permit the extraction of large quantities of power from the mass of the reactor. To gain some perspective as to the magnitude of the reactor design problem, consider that a rocket reactor produces 1500 Megawatts in a volume not much larger than an office desk. During every minute of operation, the reactor heats a 3-ton-per-minute flood of hydrogen from a temperature of -300°F to 4000°F. At operating conditions the reactor material glows with a white heat like that of the filament in an incandescent lamp.

The material initially chosen for this rigorous service in a rocket reactor is graphite. This material has desirable nuclear properties and, more importantly, retains mechanical strength at extremely high temperatures. Graphite, at the elevated temperatures required, reacts readily with hydrogen at a rate that would completely destroy the reactor in a few minutes unless some form of corrosion protection is provided. The necessary protection is supplied by metal carbide coatings that allow required reactor lifetimes to be achieved in tests at rated conditions as shall be discussed.

In addition to a high performance reactor, the nuclear rocket program had to pioneer in cryogenic engineering, development of liquid hydrogen turbopumps, fabrication of rocket nozzles and, generally, unite liquid rocket engine technology with nuclear technology to provide the basis for NERVA engine development.

HISTORY

Having described a nuclear rocket engine, we can now move on to a brief history of the program which has provided the basis for development of a flight-rated nuclear rocket engine. Additional information on the operation of the nuclear rocket and the history of the program are contained in reference 1.

Program Initiation & Technology Phases

A joint AEC-Air Force nuclear rocket program, known as ROVER, was initiated in 1955 at the AEC's Los Alamos Scientific Laboratory and Lawrence Radiation Laboratory as a result of an interest in considering nuclear rockets for long-range missiles. When it was decided that nuclear rockets were not required for missiles, the nuclear rocket program was continued for later application to space missions. In March 1957, the Los Alamos Scientific Laboratory (LASL) was selected as the single AEC laboratory for the nuclear rocket program and Lawrence Radiation Laboratory was assigned the responsibility for research on nuclear ramjet propulsion.

In October 1958, upon the establishment of the National Aeronautics and Space Administration, Air Force responsibilities for ROVER were transferred to the new agency in keeping with the dominant space role expected for nuclear rockets. The NASA Administrator stated the view that the ROVER program should proceed as fast as the technology would allow and NASA continued the development, initiated by the Air Force, of the hydrogen turbopump required for the KIWI reactor tests. (The name KIWI was taken from the flightless bird, Apteryx australis, of New Zealand, because these reactors were not intended for flight systems.)

The program initiation phase of the nuclear rocket program was highlighted by the KIWI-A series of proof-of-principle reactor tests conducted at the Nevada Test Site by LASL. Figure 2 shows the size of the KIWI-A reactor in relation to other reactors designed at LASL. These tests were as follows:

1959 - KIWI-A Reactor: Operated for 5 minutes at a power level of 70 Megawatts at high temperature.

1960 - KIWI-A Prime: Operated for 3 minutes at 85 Megawatts.

KIWI-A3: Operated for 5 minutes at 100 Megawatts.

The KIWI-A series of reactor tests gave data on reactor design and control and demonstrated the value of carbide coatings for protection of graphite from corrosion against the hot hydrogen propellant.

Another important step was the establishment in 1960 of the joint AEC-NASA Space Nuclear Propulsion Office for management of all nuclear rocket propulsive activities in both agencies. The name of this organization was changed to the Space Nuclear Systems Office in 1970 in recognition of its expanded responsibility for nuclear power as well as propulsion.

In May 1961, President John F. Kennedy, in an announcement that established the Apollo program as a national goal, recommended development of nuclear rocket propulsion technology and requested Congress to add $30 million to the FY 1962 ROVER program budget. The NERVA (Nuclear Engine for Rocket Vehicle Application) project was born and NASA and AEC awarded a contract to Aerojet-General and Westinghouse for the development of the Los Alamos KIWI-B reactor into a NERVA nuclear rocket engine for flight applications.

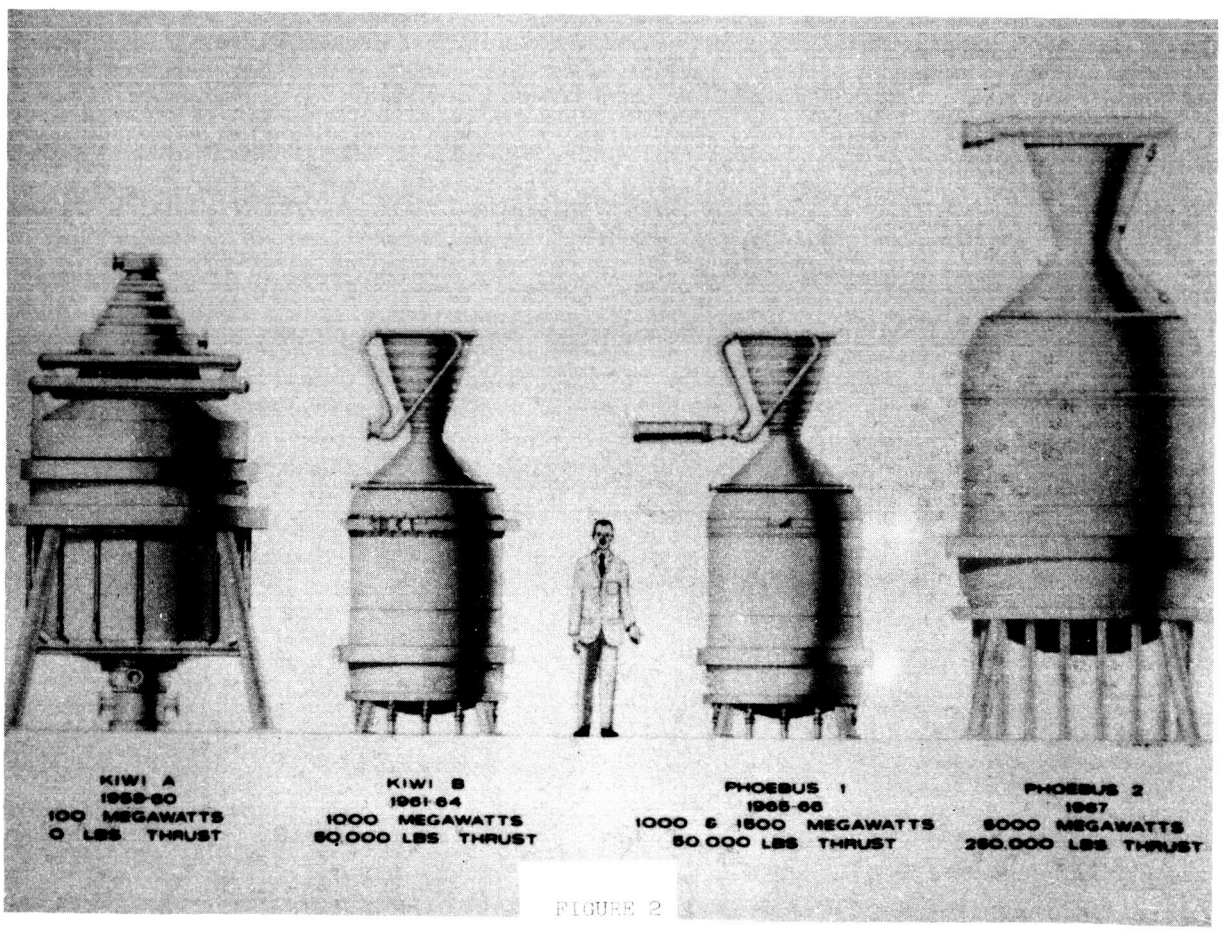

FIGURE 2

Late in 1961 the first of the KIWI-B series of reactors was tested at the Nuclear Rocket Development Station (NRDS) by LASL. This series of reactors was intended to examine, more specifically, design features that would be required in a flight system and to obtain experience with operation on liquid hydrogen. A second KIWI-B reactor test, KIWI-B1B, showed that rocket reactors could be stably operated with liquid hydrogen at high pressures, high-power levels and high-flow rates. This test was followed by a test of a flight-type reactor designated KIWI-B4A which suffered a structural failure later proven to be caused by mechanical vibrations induced by the flow of hydrogen in the reactor core. Further "hot" reactor testing was postponed until solutions to these structural problems were found as demonstrated by the recent history of the nuclear rocket program.

In the early 1960's a set of objectives was established to define the needed output for a program to establish the basic technology of the nuclear rocket. These objectives of the technology phase of the program are shown in figure 3. In the reactor area we had two sets of objectives. The first set was to achieve 760-seconds of specific impulse (Isp) with an endurance of an hour at 1100 Megawatts power. In addition, we set goals of higher performance to be achieved, if technology permitted, of up to 825-seconds Isp and increases in endurance, power-density and power-level up to more than 4000 Megawatts. The engine system objectives encompassed the total known needs for operational characteristics, control and performance. In addition we had to assure that necessary non-nuclear technology, in such things as pumps, valves and other hardware was available. In August of 1969, we completed this program when the tests of a ground experimental engine (to be discussed later) fulfilled its objectives.

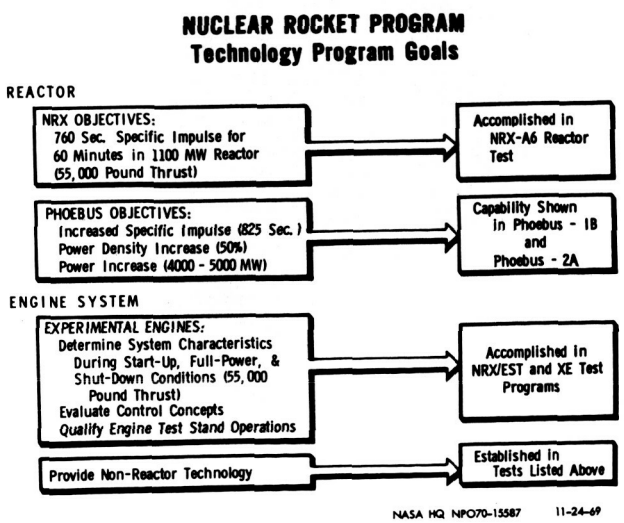

FIGURE 3

Since the end of 1963, the nuclear rocket program has operated successfully 10 reactors, a breadboard engine system labeled NRX/EST, and a ground-experimental engine (XE). Figure 4 is a list of major test events in this program. Among the 10 different reactors were reactors operated at 500, 1100, 1500, and 4200 Megawatts of thermal power, covering a spectrum of design possibilities. As shown on figure 5, the testing program has accumulated more than 14 hours of operation, of which, over four were at or near full design power. Restart was demonstrated in reactor tests; the NRX/EST was started 10 times, the XE, 28 times. Fuel-element performance, as demonstrated in the laboratory, has been extended from 1964's 10-minutes endurance to a point at which now several elements have operated 600 minutes with 60 cycles. As a result of these efforts, the reliability and operational stability of nuclear rockets have been shown to be very high, with a successful record of operations as planned. In the process of gaining this experience, large amounts of design data have been accumulated and varying design concepts examined.

Ground Experimental Engine (XE) Technology

In addition to reactor activities, the technology program also has had the objective of understanding the characteristics of an integrated engine system. This aim was partly accomplished in the breadboard-engine system test program (NRX/EST) conducted in 1966 in reactor Test Cell A at the Nuclear Rocket Development Station and completed with the testing of the Ground Experimental Engine (XE) using the Engine Test Stand, ETS-1, at NRDS.

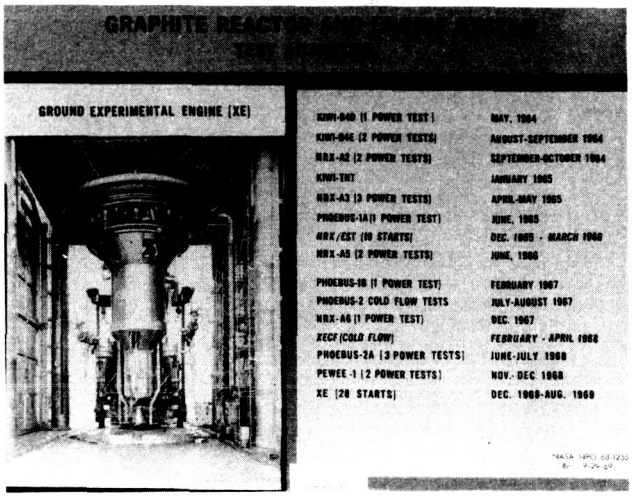

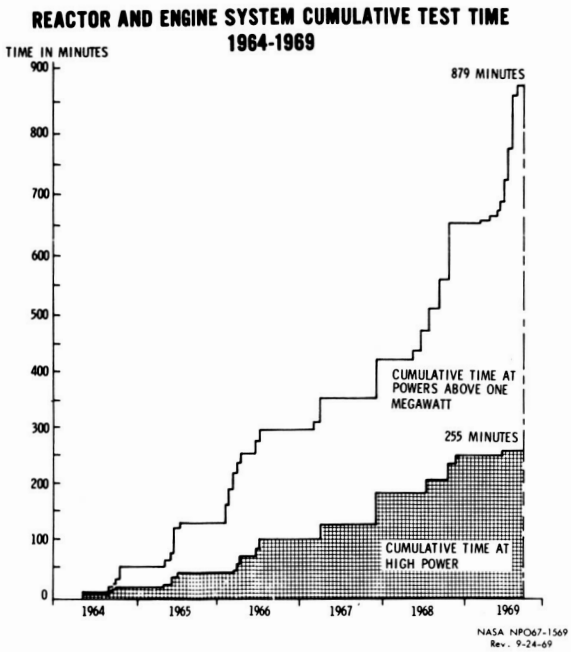

FIGURE 5

Figure 6 is a comparison of the XE configuration with that of the breadboard-engine system test (NRX/EST). The fundamental characteristics of both these systems are the same; the reactor, turbine, pump, nozzle, lines and valves are quite similar. However, in the XE engine, these components are arranged in a configuration closer to that of a flight system, and the use of a closely-coupled liquid-hydrogen run tank and the operation in a partially evacuated test compartment are new aspects of the XE test in ETS-1. All of these features reflect a closer simulation of the conditions which are expected to play a role in NERVA development.

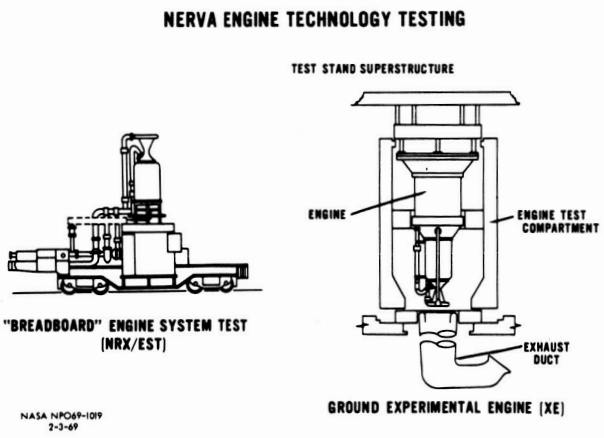

FIGURE 6

The actual configuration of XE is shown in figure 7 which is a photograph taken of the engine in the test stand, ETS-1, at NRDS. An internal view of the XE engine is shown on figure 8. It illustrates the test stand adapter and propellant shutoff valve, the upper subassembly including the turbopump, and the lower subassembly including the reactor, nozzle and various lines. Finally, to complete the configuration of test equipment, figure 9 is a recent photograph of ETS-1 showing the engine test compartment, side shields, run tank and exhaust duct.

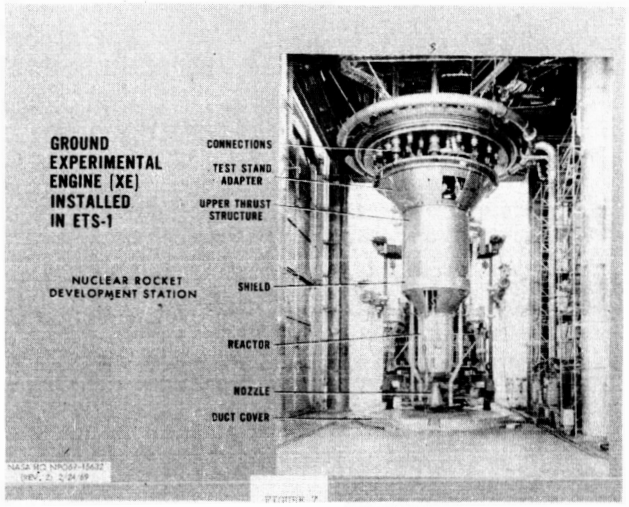

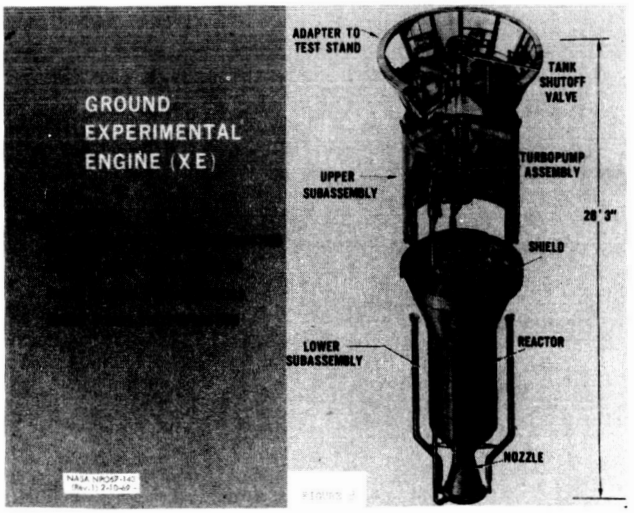

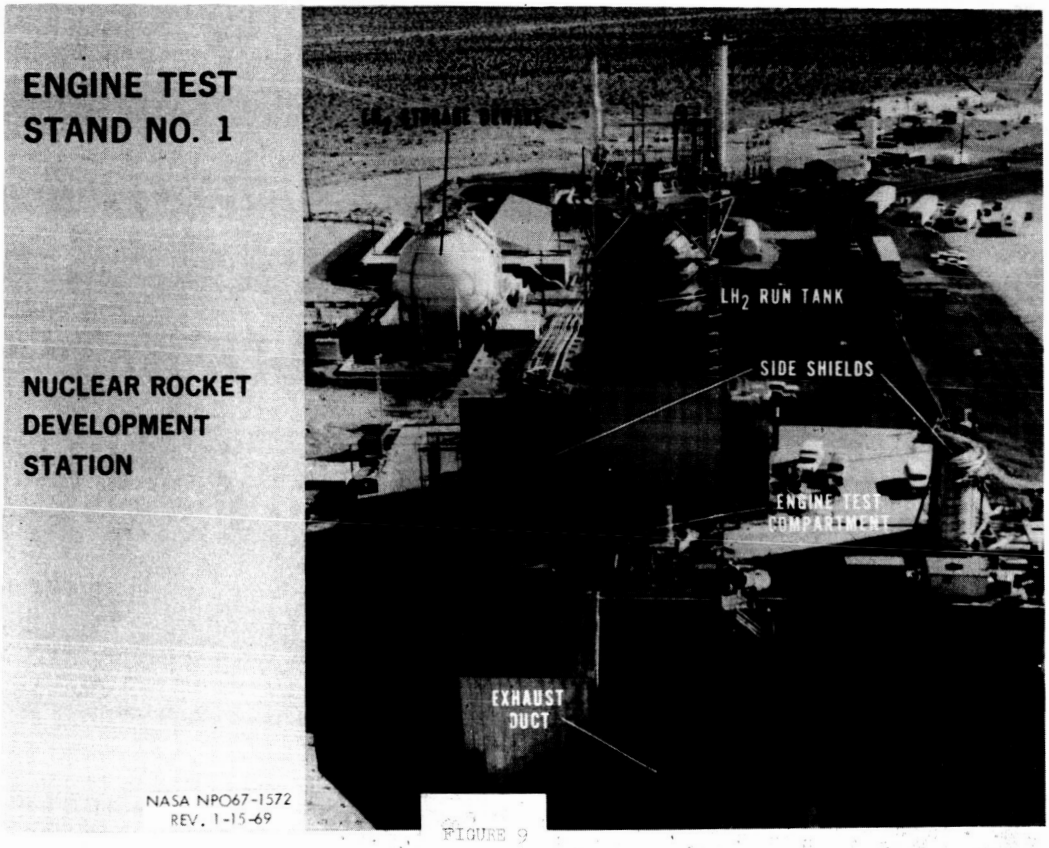

FIGURE 9

On August 28 of 1969, the XE experimental nuclear rocket engine was put through its last two test operations. These tests were high impulse start-ups to determine how the engine could be brought to power while maintaining an exit gas temperature as high as possible to minimize the impulse lost while the engine is at low power. These tests, the final in the XE engine series, made a total of 28 tests on this engine in the period beginning March 20, 1969. The total operating time was just under four hours at various power levels in a test program summarized in figure 10. During this period of time, we had only one significant component failure and that component was replaced to permit continuation of the test program.

During the XE engine series, the operation of ETS-1, a unique test facility capable of testing nuclear rocket engines in a down-firing attitude, was also demonstrated. The two special conditions which made the operation of ETS-1 of more than normal difficulty compared to chemical rocket test stands were (1) the high radiation fields surrounding the test stand, which made it necessary to operate the entire stand remotely and restricted subsystems to those capable of operating reliably in radiation fields, and (2) the down-firing of an engine with a pure hydrogen exhaust under conditions of near vacuum startup. The XE test

GROUND EXPERIMENTAL ENGINE (XE) TEST SUMMARY

TEST PERIOD, 3/20/69 - 8/28/69

EXPERIMENTS CONDUCTED

STARTUP INVESTIGATIONS	15
PERFORMANCE CHARACTERISTICS AT HIGH POWER	6
ENGINE DYNAMIC PERFORMANCE	10
FACILITY EVALUATION	4

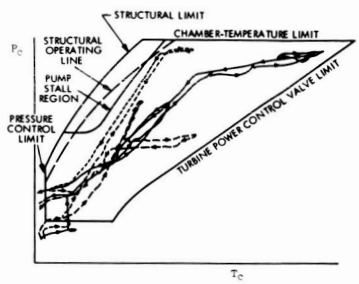

SUMMARY - 28 TEST OPERATIONS,
3 HOURS 48 MINUTES OF OPERATION

NASA NPO70-826
(Rev. I) 1-30-70

FIGURE 10

series was an excellent test for the ETS-1 facility. The tests exercised the facility over the full range of its capabilities. Experience was gained in remotely replacing radioactively "warm" components, and in operations involving the full range of control dynamics for the test stand as well as the engine.

In summary, from the data gathered during the XE series and the preceding tests, we have learned a great deal about how to design a reliable flight engine. We have also demonstrated that the nuclear rocket is basically a highly reliable, safe, and predictable engine.

NERVA ENGINE DEVELOPMENT

During the past year the design of the NERVA engine has proceeded on schedule. We have completed the baseline design and have nearly completed the formal design review. The design baseline and specifications for the overall engine and nuclear subsystem have been thoroughly documented in accordance with the strict systems engineering approach being employed.

The resulting overall engine design is pictured in a photograph of the engine mock-up on figure 11 and the cutaway drawing on figure 12. The thrust will be 75,000 pounds and the specific impulse 825 seconds. The engine will be highly reliable and safe in operation due to the use of very conservative design and employment of a high degree of redundancy in the moving parts such as valves and turbines. The endurance goal is 10 hours and the engine will be capable of many start and stop cycles, based on the requirements of an orbit-to-orbit shuttle mission with a reusable nuclear stage.

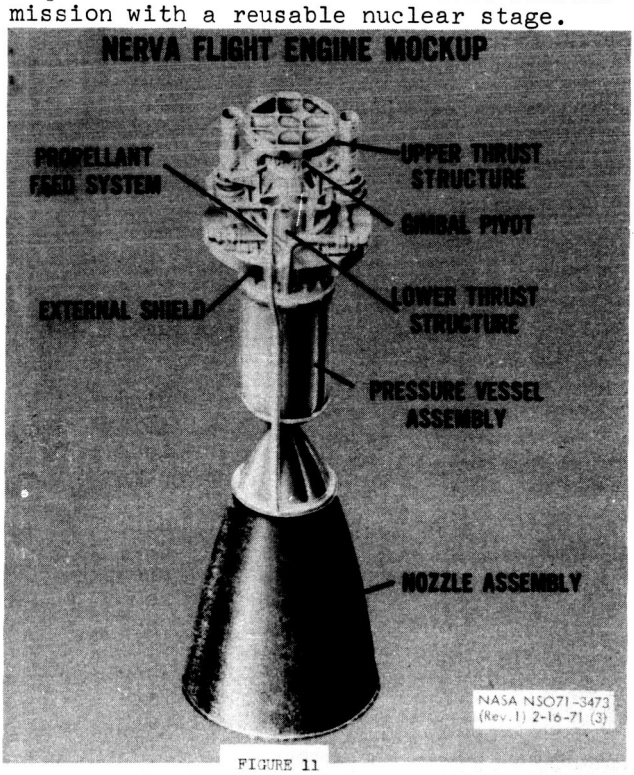

FIGURE 11

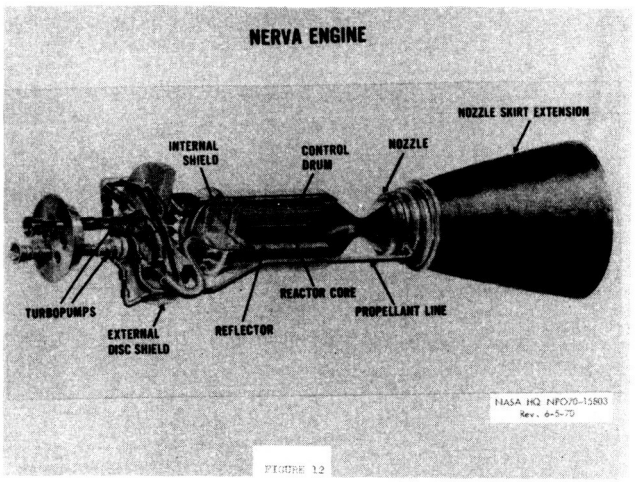

FIGURE 12

Figure 13 illustrates the systems engineering approach being used for the NERVA engine design. The design starts with the establishment of requirements and then in orderly sequence proceeds through the steps of developing functional requirements, allocating those requirements to specific components or systems, conducting design and trade studies to select designs which meet the requirements, developing designs of both the overall system and the components based on the selected concepts, and producing specifications and extensive engineering data to provide the baseline for the development of the engine. All of the activities shown on this chart with the exception of detailed component design and development are finished or scheduled to be finished this fiscal year.

With the completion of the overall design we are now in a position to intensify efforts on detailed design of the components and to release long lead-time material procurements and fabrication actions. Because of budget limitations, progress can only be made on some of the most critical of the development hardware items, including the turbopump, the nozzle extension, the reactor fuel elements and support system and the evaluation and characterization of vital materials in radiation and other applicable environments. These components will be fabricated and test programs to evaluate some of them will be started in FY 1972. In this manner, some technical progress will be made and a capability will be retained which will permit resumption of the full development program when that becomes possible.

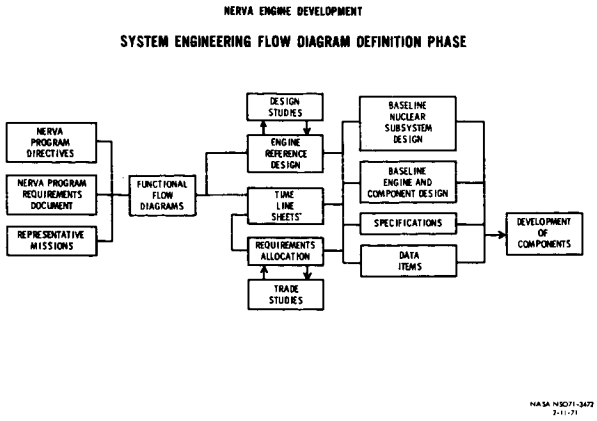

FIGURE 13

NERVA APPLICATIONS

The NERVA engine is the only practical propulsion system which can be made available to meet the requirements of many missions in prospect for the 1980's. The report of the President's Space Task Group proposed a space transportation system to cut the cost of access to space. One element of this system is a space shuttle to deliver payloads at low cost to an orbit about the Earth. The other major element is a NERVA-powered nuclear stage to go beyond the orbital range of the space shuttle. The high specific impulse of the NERVA engine, with the potential for further performance growth, makes it a flexible, economical propulsion system for a wide range of applications.

When it becomes appropriate to resume manned lunar exploration after the Apollo program is completed, a system with the capability of the NERVA engine will be needed to transport men and equipment to and from the moon (figure 14). The NERVA-propelled nuclear stage could provide transportation of automated spacecraft for exploration of the surfaces of Mars, Venus, Mercury, some of the moons of Jupiter and certain asteroids. The return of samples to the Earth will be possible in some cases. In addition, the nuclear stage could send spacecraft on fast trips to the distant planets, reducing trip times by several years in comparison to other propulsion units. Another application would likely be to move large payloads between low and synchronous orbits or from one orbital plane to another. It is expected that at least some of these missions will occur early in the 1980's. In fact, it is possible that nearly all complex missions beyond those in low orbit could be planned around the use of the NERVA stage in much the same manner that the space shuttle is considered to be the launch vehicle for virtually all purposes.

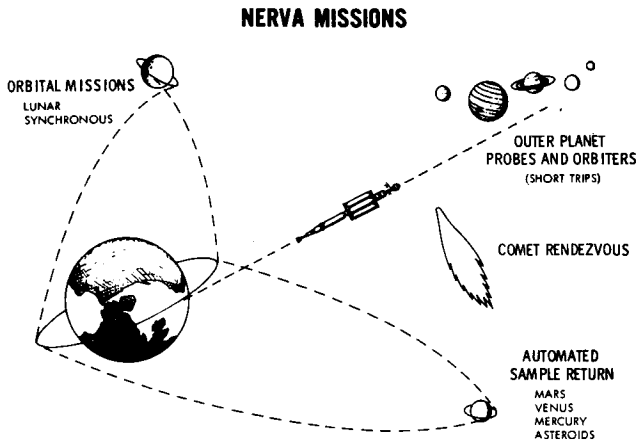

FIGURE 14

Nuclear Stage Definition Studies

In order to provide information on nuclear stages needed for mission analysis, engine design, and program planning, studies are conducted under contract to define the characteristics of a complete system for use with the NERVA engine. Illustrative of this work are the sketches (figure 15) of the various nuclear stage configurations under study. These range from the single, large-tank version to the cluster of multiple small tanks each one sized to fit within the cargo bay of the orbiter stage of the space shuttle.

The configurations on the left side of figure 15 show how shielding considerations affect stage design. The long conical aft bulkhead provides added distance between the source of radiation and a detector at the payload end of the stage and eliminates the scattering centers that would be present in a conventional ellipsoidal aft bulkhead. The modular tank concepts achieve desired distance and tank geometry through proper arrangement of the tanks. Vehicles with large single propellant tanks could be launched into Earth orbit with the Intermediate-21 or an equivalent disposable launch vehicle

NUCLEAR STAGE CONCEPTS

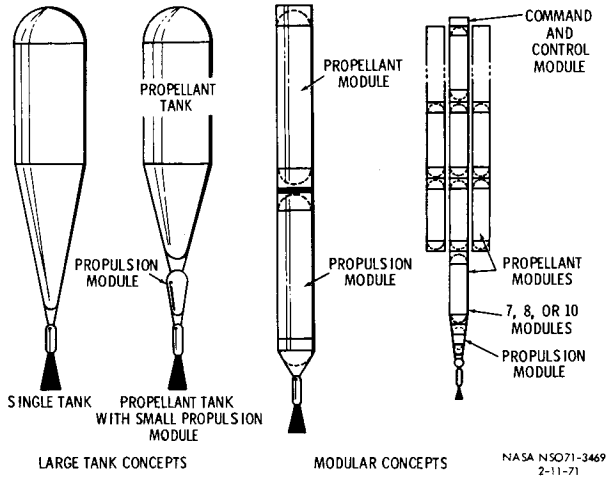

FIGURE 15

and then reloaded with propellant by space shuttle flights. Other nuclear vehicle configurations might be launched by the space shuttle (figure 16). These modular vehicles launched the the shuttle are particularly versatile since the size of the vehicle can be changed to fit many types of lunar and planetary science missions by varying the number of propellant modules.

LAUNCH CONCEPTS FOR NUCLEAR STAGES

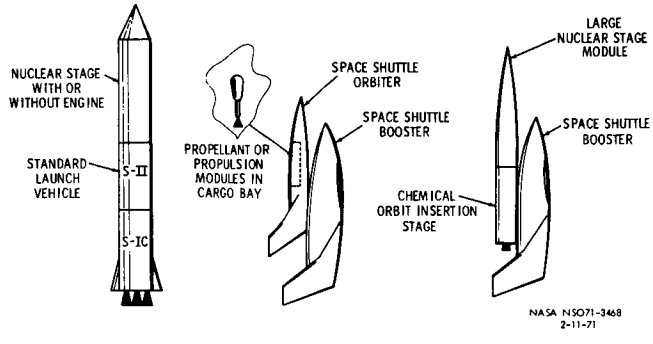

FIGURE 16

Lunar Shuttle Applications

A typical use of the nuclear vehicle in the reusable orbit-to-orbit mode would be in support of manned lunar operations in which lunar stations or bases, equipment and supplies are delivered from Earth orbit to the lunar vicinity and personnel are rotated on a regular basis. A nuclear vehicle with a usable propellant capacity of 305,000 pounds (8 propellant modules) would support a minimum manned lunar program with an average of six flights per year. A two-stage chemical vehicle capable of supporting the same lunar program would require a total usable propellant of 520,000 pounds; the corresponding Earth-orbit departure weight would be nearly 705,000 pounds.

Solar System Exploration With NERVA Engine and Stage

The nuclear stage concept formed by assembling shuttle-launched propellant tanks has some interesting prospects for conducting missions to explore the solar system with automated spacecraft. First, the system could be made available to perform prospective energetic missions in the early 1980's. Second, the nuclear stage could be tailored to suit the mission requirements of payload and energy by choosing the number of propellant tanks needed. Third, the NERVA engine could be operated at high specific impulse since short operating times would be required. Fourth, additional performance gains can be achieved by disposing of propellant tanks as they are emptied. The sum of all these features is a propulsion system that is flexible and economical with the capability to perform a range of missions, including very demanding ones.

One mission we have examined is the return of samples from the surface of Mars by means of an automated spacecraft. A nuclear stage configuration consisting of 5 propellant tanks can deliver a payload of 35,000 - 65,000 pounds into orbit around Mars. This payload would allow 160-240 pounds of material to be selected by roving vehicles from two or three different locales of the Martian surface for return to Earth. The mission duration would be about 600 days.

Studies of sample return missions from other bodies in the solar system are in process or planned. Preliminary results show that this nuclear stage could make it possible to recover samples of the Venusian atmosphere (if not the surface), of the surface of Mercury, and of many asteroids.

Another interesting application for the reusable nuclear stage would be to deliver orbiting automated laboratories to the distant planets. A preliminary study of such missions shows that the NERVA-propelled stage of only 4 propellant tanks could carry 4000 pounds of payload to an orbit about

Jupiter on a trajectory that consumes only 500 days of travel time. The short trip time of the nuclear rocket is preferred for the sake of an increase in probability of mission success and to speed the return of data to the scientific investigators.

Short trips to the planets beyond Jupiter would also be much desired. The NERVA-propelled stage could deliver about 4000 pounds of spacecraft to Neptune in approximately 6.5 years on a direct flight and in 4.8 years with an assist from a Jupiter swingby, a performance capability comparable to a 100-kilowatt electric propulsion system having a specific weight in the range of 30 kilograms per kilowatt.

In addition to this propulsion capability, it appears that the NERVA engine could also be designed, if desired, to provide 15 to 25 kilowatts of electrical power for long periods of time. A study managed by Marshall Space Flight Center has described a technique for generating this much power from the NERVA reactor with only relatively straightforward modifications in the basic engine and with little or no extension of power-conversion technology. In the power-generating mode, the NERVA reactor would be operated at low power levels (100 kilowatts) and low temperatures. A separate flow-loop through the reflector region would carry the energy from the reactor to a power conversion unit. In addition to providing power, this kind of system would reduce and simplify the after-heat removal from the NERVA reactor following operation in the high-power, rocket-engine mode.

SUPPORTING AND ADVANCED TECHNOLOGY

The nuclear rocket program continues to fund research and advanced technology activities aimed at realizing the full potential of nuclear energy for space propulsion. Some of this work extends the technology of solid-core nuclear rocket engines to high levels of specific impulse and power density. Other activities are providing a base of technology for development of a nuclear stage, and studies are conducted to define characteristics and capabilities of nuclear stages. A program of applied research and engineering studies is conducted to evaluate the feasibility of advanced nuclear propulsion concepts including both fission and fusion reactions as sources of energy.

Advanced Propulsion Concepts

While NERVA represents a major advancement in space propulsion, nuclear energy can potentially provide even greater improvements in performance of space missions beyond that possible with NERVA. In technical terms, nuclear processes yield the highest known specific energy (energy per mass of reactants) releases. Theoretically, nuclear energy could produce a specific impulse of 1 million seconds; however, there are major technical problems that prohibit the attainment of the ultimate in performance. The existence of this vast potential for nuclear propulsion stimulates programs to extend technology and to explore the feasibility of new concepts for utilizing nuclear energy to the maximum practical extent.

Structural limitations associated with solid fuel elements restrict the specific impulse of NERVA-type systems to 1000 seconds. For many years, the nuclear rocket program has conducted research and studies to ascertain the feasibility and performance potential of nuclear fission reactors in which the fuel is in the gaseous state and for which the potential specific impulse is as high as 5000 seconds. These systems are classed as gas-core nuclear rockets. Two concepts are receiving attention at this time, the coaxial flow and light-bulb reactors.

The coaxial flow reactor consists of a large nearly spherical cavity surrounded by a moderator-reflector system (figure 17). Vaporized uranium would be centered in the cavity, held there by the action of the hydrogen propellant flowing through the porous walls of the cavity. Heat generated in the fissioning uranium plasma would be transferred to the hydrogen by thermal radiation. The light-bulb reactor consists of several cylindrical cavities each containing a transparent wall of fused silica used to separate the gaseous uranium from the hydrogen propellant (figure 18). (In contrast to the coaxial concept, no uranium would be carried away with the hydrogen stream.) Thermal radiation must pass through the transparent wall in order to heat the hydrogen to desirable temperatures.

COAXIAL-FLOW GAS-CORE NUCLEAR ROCKET

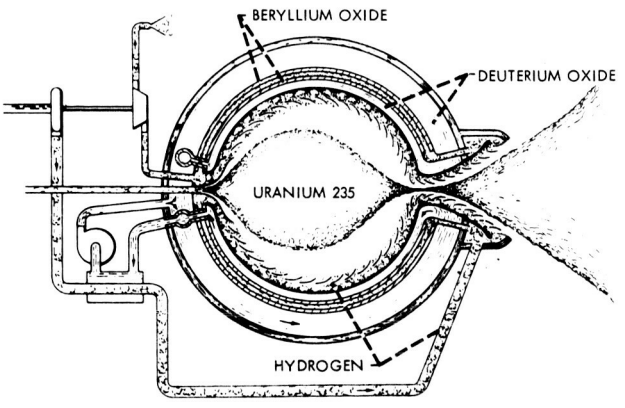

NASA NPO 70-878
1-26-70

FIGURE 17

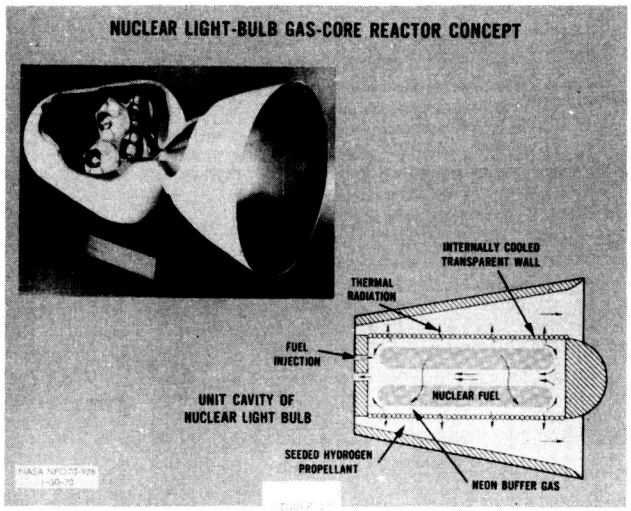

In both concepts, we are dealing with very difficult questions of feasibility, and there are a number of NASA-sponsored research programs involved in getting answers. While this work is broad in scope it is limited to studies of fundamental problems. Basic studies are conducted to define the emission and absorption of thermal radiation in uranium and hydrogen plasmas at high temperatures and pressures. The use of ultra-fine particles to "seed" hydrogen to make it opaque is the subject of experimental programs and considerable effort is devoted to providing electrically-heated plasmas hot enough to explore thermal problems of gas-core reactors. Other research includes fluid mechanics, radiation-effects on transparent materials, system analysis, and stability of high-density plasmas.

Progress in these gas-core programs has been encouraging within the context of the limited funding applied in this area. Some of this progress is as follows. Plasmas have been produced with equivalent radiating temperatures hotter than the Sun. In a small but significant first step, seeded hydrogen has been heated for the first time in a laboratory by thermal radiation alone to temperatures in excess of 40000°R. Small scale tests of a coaxial flow reactor configuration have been conducted with induction-heated plasmas, and a porous wall, and vaporization of a solid to simulate formation of a uranium plasma. In the area of systems studies, analyses have shown a coaxial-flow gas core reactor may be capable of achieving a specific impulse in the range of 5000 seconds.

Other concepts besides these gas core reactors are being studied in the nuclear rocket program. This past year we initiated a small program to investigate a dust-bed reactor concept and its potential for a high-power density. A unit such as this would be useful in applications where high-thrust and moderate engine weight are essential. In addition, we began sponsorship of some research at the Lewis Research Center into that area of plasma physics related to the production of propulsive thrust from a controlled fusion reaction. This step appeared appropriate in view of the progress reported recently in the fusion research programs throughout the world.

Recently reported advancements in pulsed-lasers and predictions that fusion plasmas could be produced thereby have generated interest in this form of energy production. LASL has begun studies and research into the means by which a laser-ignited fusion reaction could be applied to propulsion and power generation. Indications are that high specific impulses could be produced at high thrust levels.

It is not possible to say at this time, as we can for the NERVA engine, whether any of the advanced systems described above can be successfully developed. The technology is extremely difficult. In spite of these difficulties, we are of the opinion that research into the feasibility of all these advanced concepts should continue at a modest level of funding. Through support of this research, breakthroughs may be stimulated or we may find the job in some areas to be less difficult than now expected. Even if this does not happen, the very nature of these advanced propulsion concepts places the research at the frontiers of technology in high temperature plasmas, radiant heat transfer, lasers, fluid mechanics, materials, etc. The output of this research will be beneficial in many areas even if a new propulsion capability is not produced.

REFERENCE

1. Corliss, W.R. and Schwenk, F.C.: Nuclear Propulsion for Space. United States Atomic Energy Commission Division of Technical Information. Library of Congress Catalog Card Number 67-61704, 1971.

SPACE NUCLEAR POWER SYSTEMS

by

R. T. Carpenter

AEC/NASA Space Nuclear Systems Office

Abstract

Space nuclear power systems have been, are being and will be developed for use in those particular spacecraft applications for which nuclear power systems offer unique advantages over solar and/or chemical space power systems. Many of these advantages are discussed relative to the past and future applications of nuclear power systems in our space program. Both isotopic and reactor heated space electrical power units are described in an attempt to illustrate their operating characteristics, spacecraft integration aspects, and factory-to-end of mission operational considerations. Much experience has been gained with nuclear space power sources which have been flown. This experience is being used to guide current developments to make those units more attractive for operational use.

The status of technology developments in nuclear power systems is presented. Some projections of these technologies are made to form a basis for the applications of space nuclear power systems to be expected over the next 10-15 years.

I. Introduction

Some of the major sources of manmade radiation in space which you will hear much more about in the next few days are the nuclear power sources being used or expected to be used in non-propulsive nuclear space power systems. In the next few moments I will describe various space nuclear power systems which are designed to produce electricity for spacecraft payloads. Nuclear heat sources are also being developed which will be used for thermal power applications in space to provide thermal control and/or process heat for various spacecraft. The space nuclear electric power program, which I will discuss, does not include these thermal power applications except, possibly, in the case where waste heat from the heat-to-electricity conversion equipment is used to provide thermal control for the spacecraft.

Some examples of purely thermal applications of nuclear (only isotope) sources in space include the radioisotope heaters used on the Experimental Scientific Experiment Package left on the moon by the Apollo 11 crew or the isotope heater used on the Russian lunar rover (Lunokhod-1) where the nuclear heat maintains the electronics at a survivable temperature during the long, cold lunar night. The electrical power for the two missions is provided by solar cells during the lunar daytime. Another thermal control source is the radioisotope heater unit planned for use on Pioneer spacecraft. A typical process heat application is the use of an isotope heater with the life support/waste management system which can regenerate potable water from body wastes in manned space vehicles. As you can readily conclude, these thermal sources are being omitted here not because they are unimportant, but because of the short time I have and because what I will cover in terms of nuclear heat sources for electrical power systems is generally applicable to thermal power sources for use in space.

So, nuclear space power systems, as used through the remainder of this paper, refer to the combination of a nuclear heat source and a heat-to-electricity power conversion subsystem for the production of electrical power in space. Two types of heat sources are used: Radioisotopes, which generate heat by their own spontaneous decay; and reactors, which derive their heat from the controlled fission process.

As you will see, there is more than one isotope and several types of nuclear reactors which can be used in space power systems. There are many different types of power conversion concepts which have been developed for use with these nuclear heat sources. My intent here is to concentrate on those systems which have survived the elimination process rather than dwell on why certain other systems are not being pursued in this program. We have lots of ways of building these systems which are good enough; but, because of budgets and other constraints, we attempt to build a few versatile systems using what we consider the best available technology and try to advance the state-of-the-art at the same time we are building systems to fly.

II. General Applications

Space nuclear power systems have been, are being, and will be developed for use with those particular spacecraft applications for which nuclear electric power systems are attractive as listed in Figure 1.

Typical missions which have these conditions are shown on Figure 2 and include planetary missions to Jupiter and beyond or missions of extended duration on the surfaces of the planets or the moon. These missions require the use of nuclear power. In addition, high performance electric propulsion missions require the use of nuclear reactor power systems. The requirements of these few types of missions dictate the need for the development of space isotope and reactor power systems. The selection of these nuclear or non-nuclear power systems for those many missions which can be done with competitive chemical and/or solar power systems are made on the basis of superior mission capabilities, spacecraft integration, technology readiness, cost effectiveness, and other mission program considerations.

There is no question that there will be a continuing need for nuclear power in space which will increase as the space missions become more ambitious in the future. Therefore, the space nuclear electric power program conducted by the AEC and NASA will provide isotope heated power systems in the lower range and reactor heated power systems in the higher power range as dictated by the mission needs.

Figure 1

CONDITIONS UNDER WHICH
NUCLEAR POWER SYSTEMS ARE ATTRACTIVE

* LACK OF SUNLIGHT
* HIGH RADIATION FIELDS
* LOW CROSS-SECTIONAL AREA
* HIGH POWER LEVEL & LONG LIFE
* HEAT REQUIRED IN PAYLOAD
* EXTREME TEMPERATURES
* DENSE METEORITE FIELDS

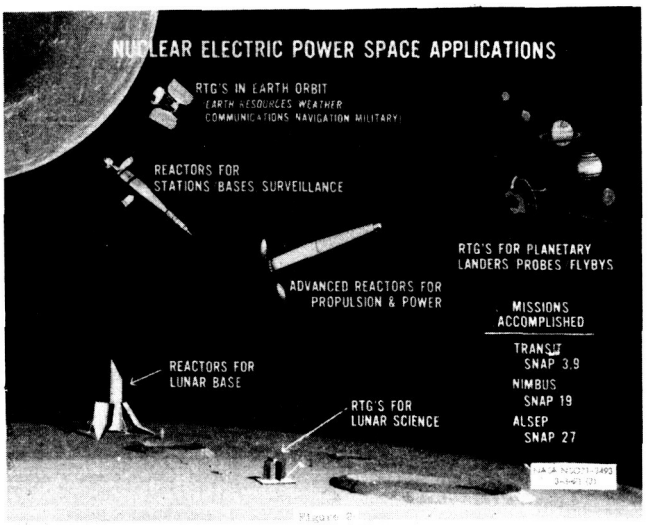

III. Systems in Use

The first use of nuclear power in space was the SNAP-3A launched on the Transit 4A Navy Navigation Satellite in June 1961. This 2.7 watt, Plutonium-238 fueled, 5 pound, PbTe thermoelectric generator paved the way for a series of nuclear power systems which have been launched in the past ten years as listed in Figure 3. SNAP-3A is still operating as are all the isotope units which have been successfully launched.

All of the isotope power systems launched to date have used PbTe thermoelectric converters and Pu-238 heat sources (see Figure 4). Pu-238 was selected for space use primarily because of its long half-life (87.5 years) and its low radiation levels. As larger heat sources were used, the aerospace nuclear safety philosophy changed from burn-up in the atmosphere to intact reentry which forced an evolution of fuel forms and heat source designs. Plutonium metal was used in SNAP-3A and SNAP-9A; PuO_2 microspheres were used in SNAP-19 and SNAP-27. The introduction of the oxide increased the neutron levels of the sources, but provided a higher melt temperature, lower inhalation hazard, and less soluble or reactive fuel form.

Summary of Space Nuclear Power Systems
Launched by U. S. A. (1960-1971)

System	Mission	Launch Date	Fate
SNAP-3A	TRANSIT-4A	6/29/61	Successfully achieved > 1000 year orbit.
SNAP-3A	TRANSIT-4B	11/15/61	Successfully achieved > 1000 year orbit.
SNAP-9A	TRANSIT-5BN-1	9/28/63	Successfully achieved > 1000 year orbit.
SNAP-9A	TRANSIT-5BN-2	12/5/63	Successfully achieved > 1000 year orbit.
SNAP-9A	TRANSIT-5BN-3	4/21/64	Failed to achieve orbit, burned up on reentry.
SNAP-10A	SNAPSHOT	4/3/65	Successfully achieved ~ 2,300 year orbit.
SNAP-19B2	NIMBUS-B-1	5/18/68	Failed to achieve orbit, retrieved from ocean floor.
SNAP-19B3	NIMBUS-III	4/14/69	Successfully achieved ~ 3000 year orbit.
SNAP-27	APOLLO-12	11/14/69	Successfully placed on lunar surface.
SNAP-27	APOLLO-13	4/11/70	Failed to reach moon, returned to Pacific Ocean.
SNAP-27	APOLLO-14	1/31/71	Successfully placed on lunar surface.

Figure 3

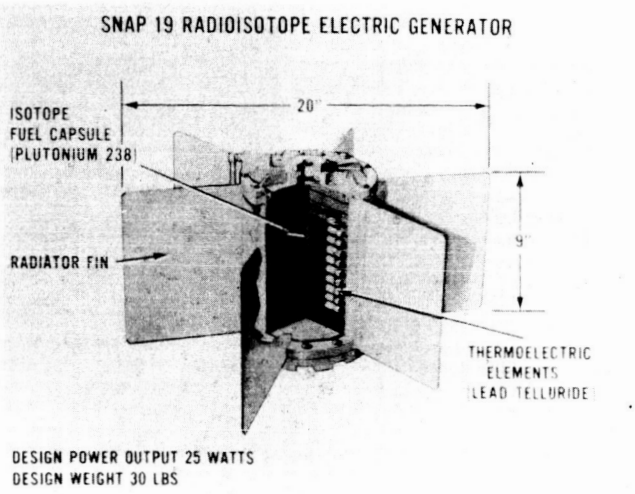

Figure 5

Figure 4

Space Isotopic Power Systems

System	Power (watts)	Weight (lbs.)	Converter	Fuel Form	Fuel Quantity (curies)	Safety Philosophy
SNAP-3A	2.7	4.6	2N/2P PbTe	Pu-238 Metal	1,800	Fuel Burn-Up
SNAP-9A	25	27	2N/2P PbTe	Pu-238 Metal	16,000	Fuel Burn-Up
SNAP-19B1	30	30	2N/2P PbTe	PuO_2-238 Microspheres	34,000	Capsule Burn-Up Fuel Dispersal
SNAP-19B2	30	30	2N/2P PbTe	PuO_2-238 Microspheres	34,000	Intact Reentry
SNAP-19B3	30	30	2N/3P PbTe	PuO_2-238 Microspheres	37,600	Intact Reentry
SNAP-27	63	68	2N/3P PbTe	PuO_2-238 Microspheres	44,500	Intact Reentry

NIMBUS III SPACECRAFT
WITH SNAP-19 RADIOISOTOPE THERMOELECTRIC GENERATOR

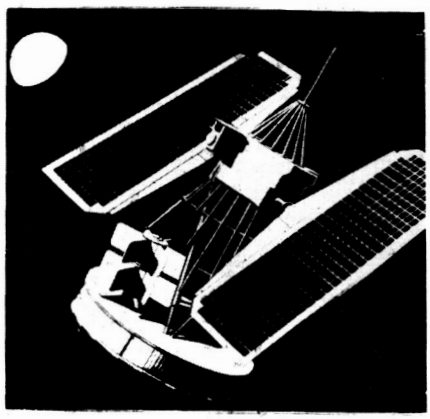

SNAP-19 CHARACTERISTICS

Launched	April 1969
No. of Units	2
Initial Power	56 Watts
Fuel	Pu 238
Weight	59 Pounds
Lifetime	1 Year

Figure 6

Figure 5 shows a cutaway view of SNAP-19 to illustrate the generator configuration used in all of these isotope systems where the heat is generated in a central heat source, about 5% of it is converted to electricity as it passes through the static thermocouples and the rest is radiated away to space. Figure 6 shows the two SNAP-19's on the Nimbus 3 weather satellite which are still supplementing the main solar cell/battery power system.

Figure 7 shows the SNAP-27 being deployed on the moon to provide the total power to the Apollo Lunar Surface Experiments Packages. The Apollo 12 and Apollo 14 stations are both working very well. In fact, if the first SNAP-27 powered station had not lasted well beyond its design life of one year, we would not be getting the added benefits of two simultaneous stations on the moon which we are now receiving.

ALSEP/SNAP-27 DEPLOYMENT

APOLLO 12 - NOVEMBER 1969

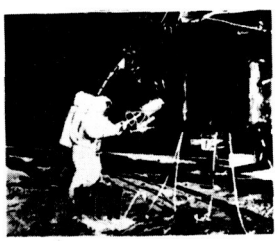

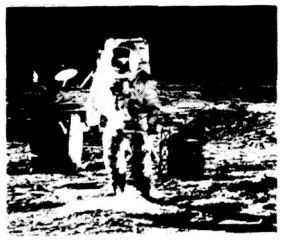

SNAP-27
SYSTEM CHARACTERISTICS

INITIAL POWER	73 Watts
LIFETIME	1 Year
FUEL	Pu 238
WEIGHT	
FUELED GENERATOR	43.5 lbs.
FUEL CASK	25.2 lbs.

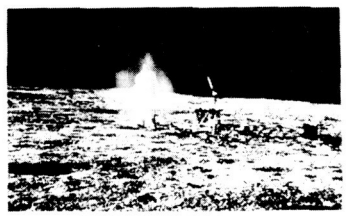

Figure 7

The radiation levels from SNAP-19 and SNAP-27 are shown in Figure 8. The predominant emissions from these sources are the neutrons from spontaneous fission and the Alpha-neutron reactions with the light elements in the fuel, such as oxygen and impurities. You can see that measurements made on SNAP-27 after about two years shows a factor of two increase in gammas which is due to a build-up of gamma emitting products such as thallium-208. The gamma level from Pu-238 can be 7 or 8 times higher after 15 to 20 years.

Radiation Levels for SNAP-19 and SNAP-27
(Dose Rate at 1 meter)

		Neutrons (mrem/hr)	gammas (mrem/hr)	Total (mrem/hr)
SNAP-19B (630w., PuO_2 microspheres)				
Capsule 402/432	Side	39	2.8	41.8
	End	27	1.3	28.3
			(2.5×10^7 n/sec)	
Capsule 453/454	Side	37	3	40
	End	26	1.8	27.8
			(2.4×10^7 n/sec)	
SNAP-27 (1480 w., PuO_2 microspheres)				
Capsule No. 4	Side (6/68)	99	7	106
	(8/70)	97	16	113

Figure 8

The first reactor power system used in space was the SNAP-10A launched in 1965 (see Figure 9). This reactor operated successfully for 43 days at which time it was inadvertently shut-down due to a failure in the voltage regulator. This 500 watt, SiGe thermo-electric system was powered by a 40 Kwt Uranium-Zirconium-Hydride reactor which has been the cornerstone for the technology in space reactor power systems. The radiation levels for the SNAP-10A flight configuration are shown in Figure 10. The reactor systems require shielding tailored to the pay-load requirements, as will be illustrated later.

SNAP 10A SYSTEM & CYCLE

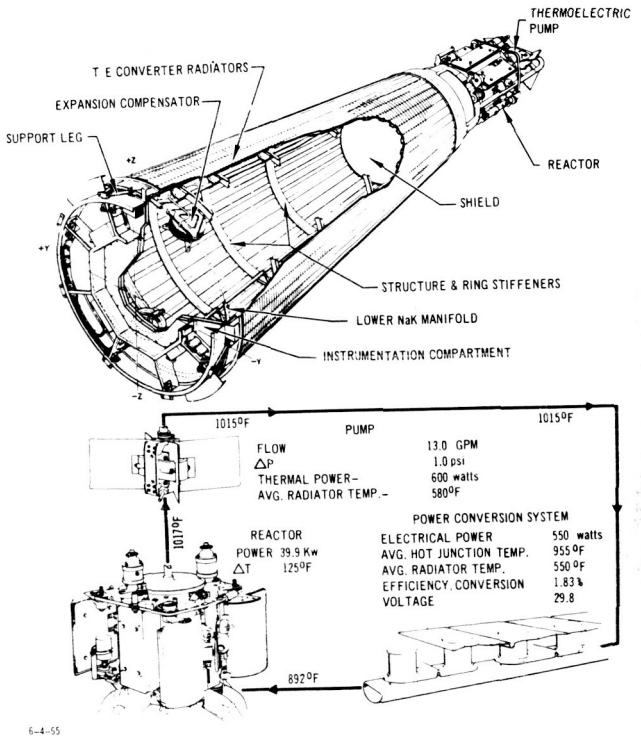

Figure 9

IV. Isotope Power Systems Under Development

Flight Systems

Three near-term missions for which radioisotope thermoelectric generators (RTG's) are now being developed are shown in Figure 11. The primary reasons RTG's are to be used on these missions are: For Transit-long life and resistance to radiation levels expected at this orbital altitude; for Pioneer - independence of solar flux and resistance to radiation to be encountered on the way to Jupiter; and for Viking - independence of the environment on the surface of Mars. Fueled ground test units have been built for Transit and Pioneer and flight systems will soon be built.

SNAP 10A NPU AGENA RADIATION LEVELS

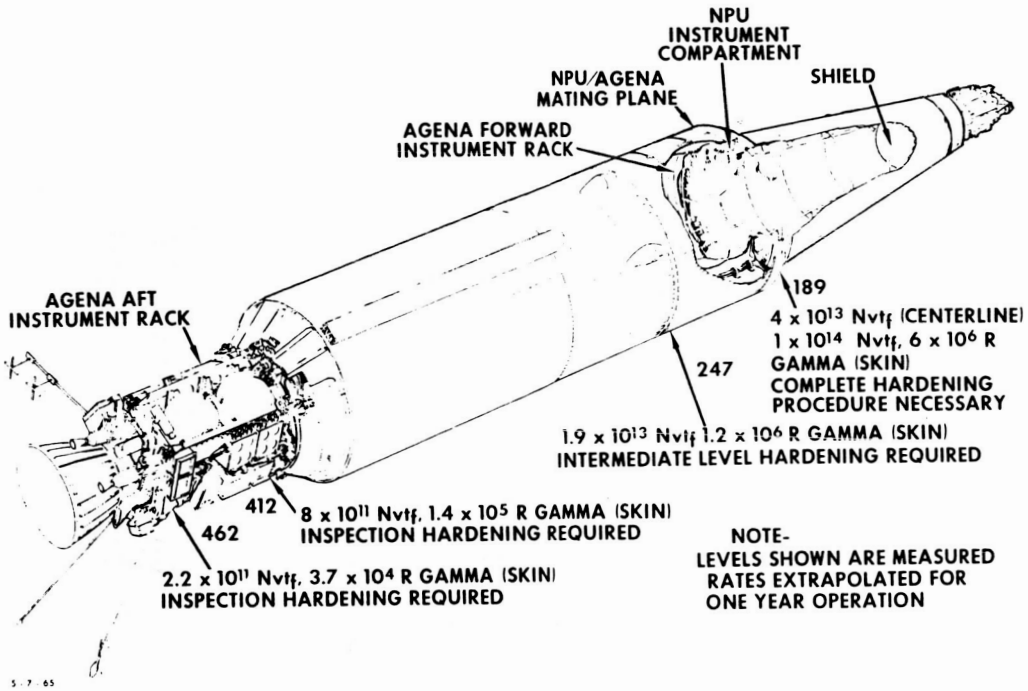

Figure 10

RADIOISOTOPE THERMOELECTRIC GENERATORS
MISSION COMMITMENTS

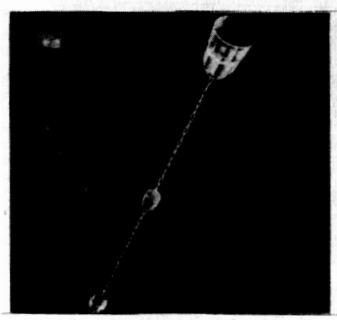

TRANSIT

PIONEER

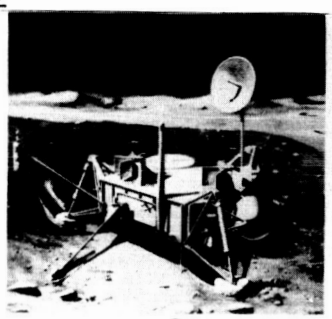

VIKING

PROGRAM	OBJECTIVE	AGENCY	LAUNCH SCHEDULE	POWER REQUIREMENT	LIFETIME	SELECTED PWR. SUPPLY
TRANSIT	NAVIGATIONAL SATELLITE	NAVY (DOD)	Classified	30 WATTS EOL	5 YEARS	TRANSIT RTG
PIONEER (F & G)	JUPITER FLYBY	NASA	1972 &1973	120 WATTS	3 YEARS	FOUR SNAP-19's (Modified)
VIKING	MARS SOFT LANDER	NASA	1975	70 WATTS	2 YEARS	TWO SNAP-19's (Modified)

Figure 11

The Transit RTG, shown in Figure 12, is 24 inches in diameter and about 18 inches high. It is to be mounted directly on the satellite so as to provide up to 100 watts of heat to the satellite to help maintain fairly constant temperatures in the electronics of the payload as it passes into and out of the shadow of the earth. The RTG is to produce 37 watts at BOL and 30 watts after 5 years. It is fueled with 850 watts of Pu-238. Heat is radiated from the heat source to the light-weight 2N/3P PbTe Isotec panels which operate between 752 and 288°F. The total weight, including the mounting cone, is about 30 pounds.

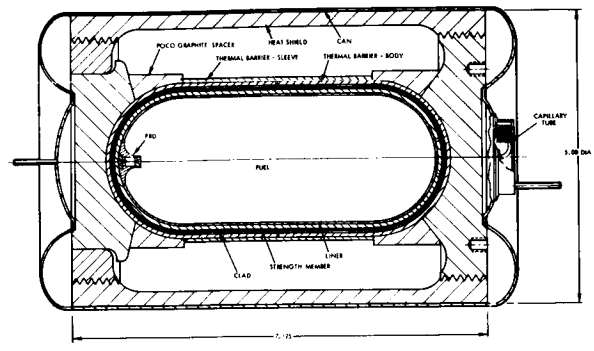

Figure Transit Heat Source

TRANSIT RADIOISOTOPE THERMOELECTRIC GENERATOR

SYSTEM CHARACTERISTICS	
POWER LEVEL	
BOL	37 WATTS
EOL	30 WATTS
LIFETIME	5 YEARS
FUEL	Pu 238
WEIGHT	27 Lbs.
CONVERTER	ISOTEC
SAFETY	IMPACT CAPSULE SURVIVAL

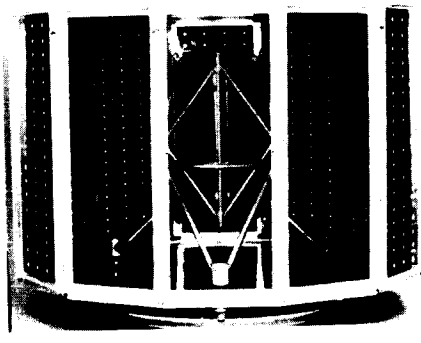

Figure 1

The heat source, which is designed to contain the fuel during reentry and impact, is shown in Figure 13; it weighs about 14 pounds. The fuel, a plutonium oxide-molybdenum cermet (PMC), is contained in layers of refractory and noble metals surrounded by graphite for protection from reentry heating. The assembly is canned in a thin superalloy to prevent deterioration of the materials in the heat source while exposed to air before launch and to maintain a back pressure of gas in the gaps to minimize operating temperatures in space.

The Pioneer RTG is a modified SNAP-19, shown in Figure 14. It is 15.8 inches across the fins, 11.1 inches high, and weighs 29.2 pounds. It is fueled with 645 watts of PMC and produces 38 watts at BOL or 30 watts after 3 years or at Jupiter encounter. The thermoelectric converter employs 2N/TAGS materials operating between 950 and 3500F. The Pioneer RTG is filled with a cover gas and welded shut. The heat source for Pioneer, shown in Figure 15, is made of almost identical materials as that for Transit. The reentry protection design is somewhat different because of the size constraints of the SNAP-19 heat source (3.5 inches across the flats by 6.75 inches long) and the more severe heating environments of the possible Pioneer mission aborts which could lead to super-orbital reentry. Since the generator is sealed, no can is used around the heat source. The heat source weighs 11.3 pounds.

PIONEER (MODIFIED SNAP19) RADIOISOTOPE THERMOELECTRIC GENERATOR

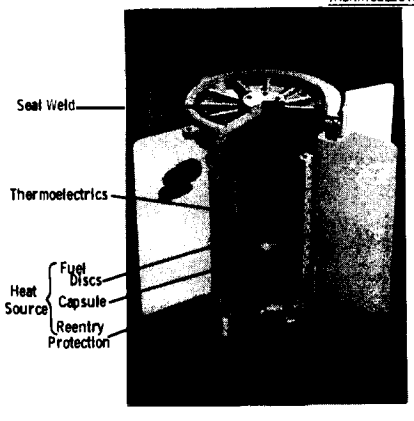

System Characteristics

Number of Generators	4
Power Level (per Gen.)	
BOL	38 watts
EOL	30 watts
Lifetime	3 Years
Fuel	Pu-238
Weight (per Gen.)	29 lbs.
Converter	SNAP 19
Safety	Impact Capsule Survival

Launch Schedules

FEB. - MAR.	1972
APR.	1973

Figure 14

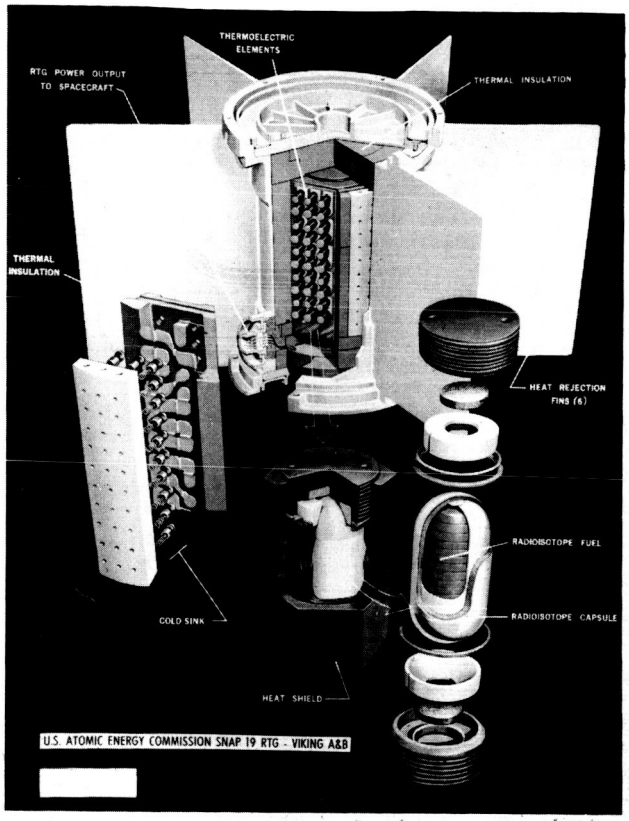

Figure 15

The generators to be used on Viking are similar to the Pioneer RTG's. The fuel loading will be 675 watts to get 35 watts after 2 years and the thermal design (fin length and housing thickness) will be tailored to the Viking mission environment.

An enlarged cross section of the PMC fuel is shown in Figure 16. The PMC is made from PuO_2 particles 105-250 micrometers in size which are coated with about 3 micrometers of molybdenum, as shown on the left. These are pressed into discs 2.14 inches by 0.2 inch thick which produce 40 watts each. The PMC is 17.5% Mo and has a power density of 3.5 watts/cc, and is shown on the right.

The radiation levels which have been measured for the Transit and Pioneer capsules are given in Figure 17. The average neutron activity in this PMC fuel ranges from 3.29×10^4 - 4.5×10^4 n/Sec./GM Pu-238, even though it is made from oxygen enriched in O-16. It can be improved by using a $MoCl_5$ coating process in place of the MoF_6 process, as will probably be explained in detail in Section VIII-2 on Thursday afternoon. Using a neutron activity of 4×10^4 N/SEC/GM Pu-238, the neutron flux on the Pioneer spacecraft (3 meters away) is calculated to be about 28 N/SEC/Cm^2 or 1.8×10^9 N/Cm^2 over the 2-year mission.

PLUTONIUM-MOLYBDENUM - CERMET

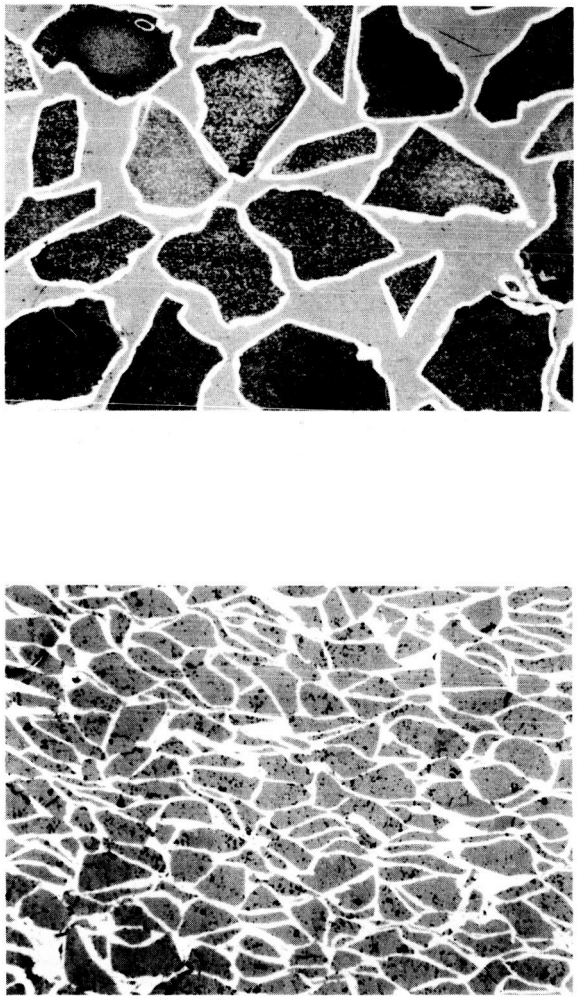

Figure 16

For higher powered applications, such as the two shown in Figure 18, the Multi-Hundred Watt (MHW) modular RTG is being developed. The Grand Tour missions to three different outer planets are good examples of the unique capability of RTG's. These missions require on the order of ten times as much power for mission lifetimes up to twice as long as any other mission to date with very tight constraints on size and weight to explore a region of space where we have never been before.

Radiation Levels from
PMC Capsules for Transit & Pioneer

Bare Capsule	Neutrons (n/sec)	Dose Rate (mrem/hr) at 1 meter Neutrons	gammas	Total
Transit TF-1 (950 w)	5.43×10^7	80	2.6	82.6
Pioneer PF-1 (645w)	5.15×10^7	70.9	3	73.9
Pioneer PF-2 (645w)	4.26×10^7	58.3	2.7	63
Pioneer PF-3 (645w)	3.77×10^7	53	1.5	54.5
Pioneer PF-4 (645w)	3.73×10^7	53	1.6	54.6

Capsule in Cask	Total Dose Rate at Surface (mrem/hr)			
Transit TF-1	123-166	30.3	0.9	31.2
Pioneer PF-4	330-410	27	0.7	27.7
Multiplication Factor in fuel:	1.24 to 1.32			
Capsule neutron Count:	3.29×10^4 - 4.5×10^4 n/sec/gm Pu-238			

Figure 17

The thermal design uses radiative coupling between the heat source and the thermocouples. This allows for some flexibility in heat source design. The reference insulation is refractory metal foils with ceramic separators. The very high operating temperatures of the MHW RTG and the safety goals, to withstand the environments of any launch vehicle and any mission and still remain intact after reentry and impact, require a more advanced heat source design. One of the designs being considered for MHW is shown in Figure 20. This heat source is 6.85 inches in diameter by 15.0 inches long, and it weighs over 40 pounds. It maximizes the use of graphitic and ceramic materials and shapes to bring the fuel through reentry and impact.

The heat source design will not be frozen until late this year. One of the changes in MHW may be in the fuel. Pure PuO_2 is being considered as a replacement for the PMC. With 2200 watts, or 66,000 curies, per module, the Grand Tour spacecraft will require an inventory of 8800 watts, or 264,000 curies of Pu-238. This will be a neutron source of about 1.6×10^8 N/SEC (based on 10,000 N/SEC/GM Pu-238) to be reckoned with.

MULTI-HUNDRED WATT RADIOISOTOPE GENERATOR APPLICATIONS

LINCOLN EXPERIMENTAL SATELLITE

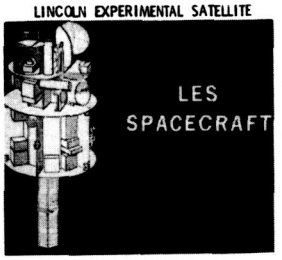

OUTER PLANET SPACECRAFT

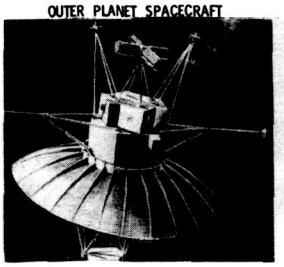

PROGRAM	OBJECTIVE	AGENCY	LAUNCH SCHEDULE	POWER REQUIREMENT	LIFETIME	SELECTED POWER SUPPLY
LES	SPACE COMMUNICATION	DOD (Air Force)	MID-1970's	220-300 W(e)	5 YEARS	TWO MHW RTG's
GRAND TOUR	UNMANNED OUTER PLANETARY EXPLORATION	NASA	1977 & 1979	300-500 W(e)	>9 YEARS	FOUR MHW RTG's

Figure 18

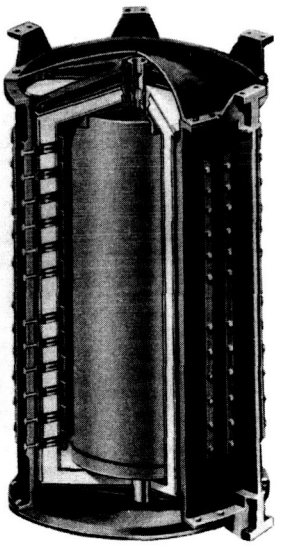

MULTI-HUNDRED WATT
RADIOISOTOPE THERMOELECTRIC GENERATOR

Power Level	145 W(e)
Weight	75 pounds
T/E Material	SiGe
Fuel	Pu-238
Safety	Qualified to Composite Mission Environment

Figure 19

The MHW RTG (or module) is shown in Figure 19. It will produce at least 145 watts at BOL from 2200 watts of Pu-238. It is 11 inches in diameter by about 21 inches high and weighs about 75 pounds. The thermoelectric converter employs 80% GeSi Airvac thermocouples operating at 1832°F (or higher) in a Be housing which is sealed for operation in air.

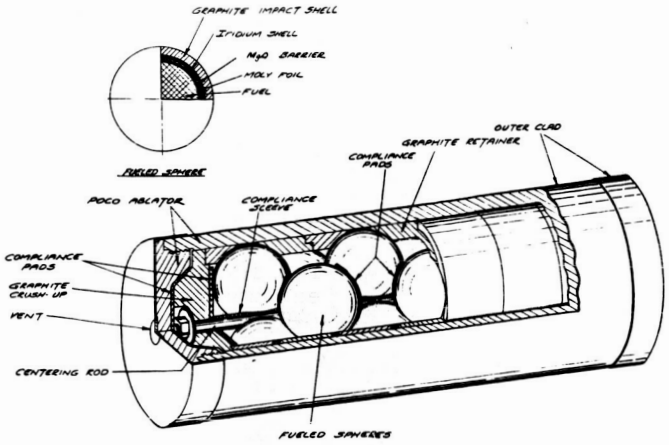

MHW Reference Heat Source Design

Figure 20

If Curium-244, another long-lived alpha emitter, were used in the MHW, the power to weight ratio would be increased about 10-15%. Cm-244 has a higher power density than Pu-238 because of its shorter half-life (~18 years) and a promise of about 1/5 the cost per thermal watt (see Figure 22). The penalty to be paid with Cm-244 which is of interest here is the higher neutron count due to spontaneous fission (approximately 1000 times higher for Cm-244 than for Pu-238). This could influence the use of Cm-244 fueled systems on radiation sensitive scientific payloads and manned missions.

Future Systems

Some improvements in these current flight systems can be projected for future systems to make them more attractive for some applications. The MHW SiGe RTG can be cascaded with the PbTe or TAGS Isotec panels similar to those used on the Transit RTG to provide a higher power, a wider useful power range, and more efficient use of the fuel meaning lower cost and radiation levels per electrical watt. A drawing of such a cascaded RTG is shown in Figure 21. This cascaded RTG would produce over 200 watts at 9-10% efficiency at over 2 watts/pound with the same Pu-238 heat source.

LONG-LIFE ISOTOPE FUELS TECHNOLOGY
PLUTONIUM-238 AND CURIUM-244

	Pu-238	Cu-244
POWER DENSITY (microspheres, thermal watts/cc	2.7	13.5
FUEL COST ($ per thermal watt)	650 TODAY 500 OBJECTIVE	500 TODAY 100 Pu-RECYCLE
WEIGHT (lb per thermal kw)*		
Small Heat Sources (2 kwt) Without shield	15	5
25 kwt Heat Source w/Reentry Vehicle Without shield	120	32
With manned shield Crew at 3 meters	170	320
Crew at 15 meters	130	100 - 120

* Including re-entry protection

DUAL STAGE MHW-RTG SEALED DESIGN

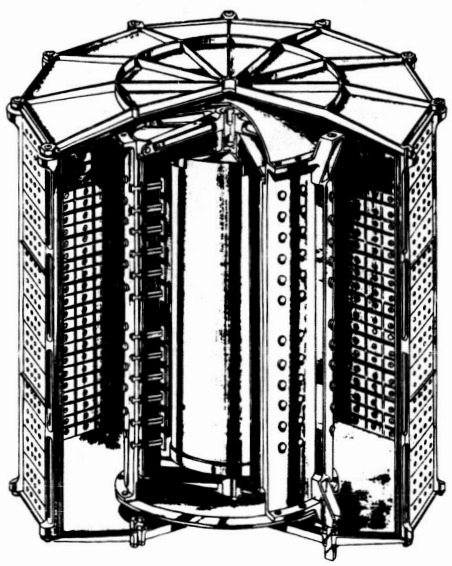

Figure 21

For power levels above that which is practical with the MHW, above 1 Kw, more efficient power conversion technologies are being considered for isotope power systems. These are the static thermionic system and the dynamic Brayton system. Design studies have been completed on a 110 watt Cm-244 fueled thermionic module. This program was an outgrowth of the SNAP-13 Thermionic generator development which was completed in 1965. These studies have shown that thermionic modules in the 200-500w range offer a module efficiency about twice that of thermoelectric and a specific power of about 4 watts/pound - also about twice as good as for thermoelectric generators. The thermionic generator is also smaller in

size because of the high radiator temperature. This feature makes thermionic generators very attractive for missions close to the sun or on the surface of the inner planets where high ambient temperatures are experienced. To achieve these advantages, the high power density fuel, Cm-244, must be used and the heat source operating temperatures must be in excess of 3000°F. Quite a bit more development work must be done in isotope thermionic generators to demonstrate their operating performance and lifetimes. This development activity is currently being deferred due to budgetary constraints.

The use of the dynamic Brayton cycle allows efficiencies as high as 25-28% at heat source temperatures comparable to those for the MHW in the power range of 2-10 Kw. It can use Pu-238 or Cm-244. The Brayton conversion machinery has been under development at NASA's Lewis Research Center for several years. An electrically heated system (minus the radiator) has been tested for over 2500 hours and the combined rotating unit is still undergoing a life test after some 5000 hours, most of which has been unattended. A joint NASA-AEC program is underway to conduct an isotope-heated test of the system under simulated space conditions.

The isotope heat source assembly for the Brayton system is shown in Figure 23. An array of heat sources, probably based on the MHW technology, are carried in a reentry vehicle which provides double protection during reentry mishaps and maximizes the chances of recovery of the large isotope inventory. A 12.5 Kw power system, which has been studied for use on the manned orbital space station, would contain 52.8 Kw (thermal) or 1.6 Megacuries of Pu-238 at beginning of life. The reentry vehicle, including the isotope heat sources, would be about 8 feet in diameter and would weigh about 3900 pounds. The total 12.5 Kw system would weigh about 6,000 pounds or about 2 watts/pound. This type of system is especially attractive for low orbit, man-tended spacecraft which can be launched and recovered by the planned space shuttle.

V. Reactor Power Systems

At very high power levels, 5 Kw and up, the nuclear reactor heated power systems come into play. Space applications expected to require such high power levels are shown in Figure 24. These include unmanned satellites (communication and military uses), manned earth orbital space stations or

HEAT SOURCE REENTRY VEHICLE ASSEMBLY

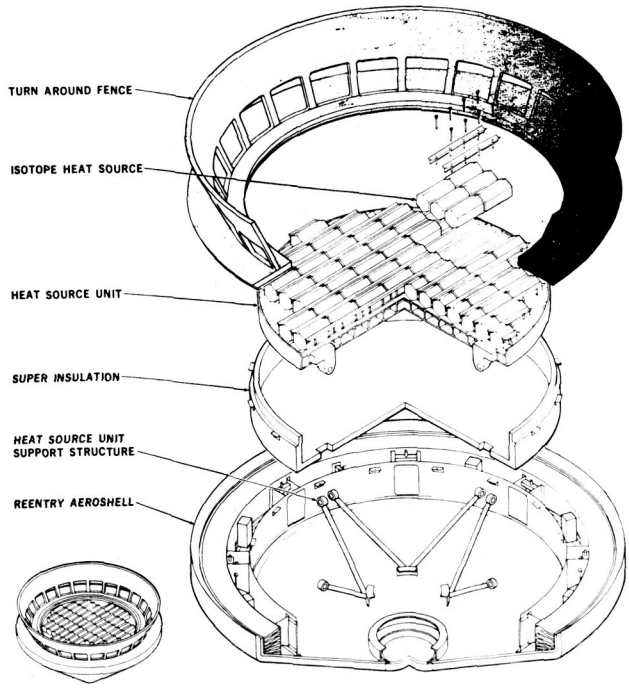

Figure 23

bases and lunar orbit stations or lunar bases which require auxiliary power levels up to 100 Kw. These requirements can be met with the uranium-zirconium-hydride reactor in combination with either thermoelectric or Brayton power conversion systems. To meet the requirements for nuclear electric propulsion missions, which cannot be done any other way, a more advanced space reactor system will be required which has a specific weight of about 50 pounds/Kw at power levels greater than 100 Kw.

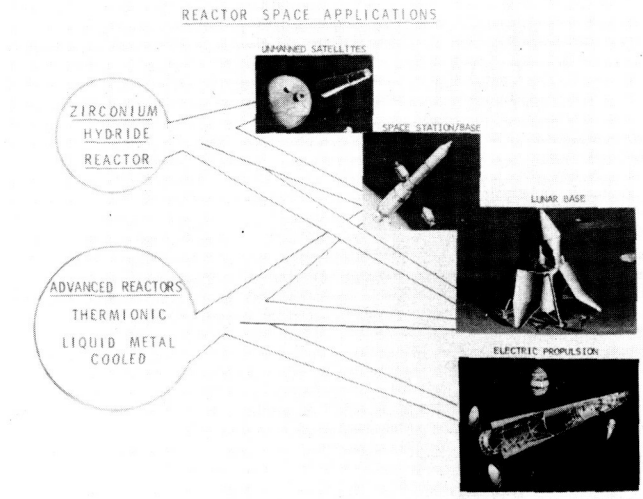

Figure 24

The uranium-zirconium-hydride (UZrH) reactor program (see figure 25) has three main threads of effort - the reactor technology, the thermoelectric power conversion system (PCS) technology, and the large Brayton PCS technology. The UZrH reactor technology extends the capability which was first flight demonstrated in SNAP-10A. Work being performed has the goals of a long-lived (5 year) reactor which will provide 100-600 Kw of heat at operating temperatures between 1000 and 1200°F. The UZrH reactor design is shown in Figure 26 where the SNAP-8 development reactor is compared with the long lived reference design with the new reflectors that allow for smaller shield weights in a manned mission. The reference reactor is about 36 inches high and 22 inches in diameter.

ZIRCONIUM HYDRIDE REACTOR SPACE POWER SYSTEMS

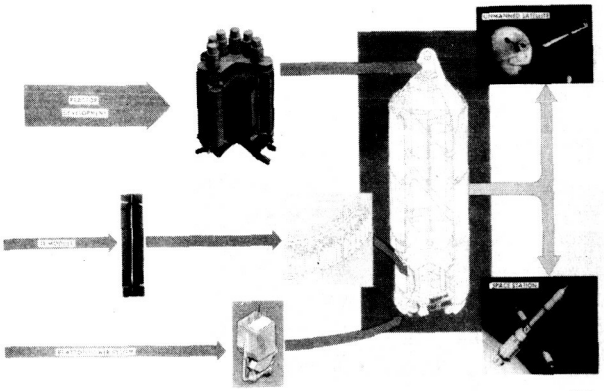

ZIRCONIUM HYDRIDE REACTOR DESIGNS

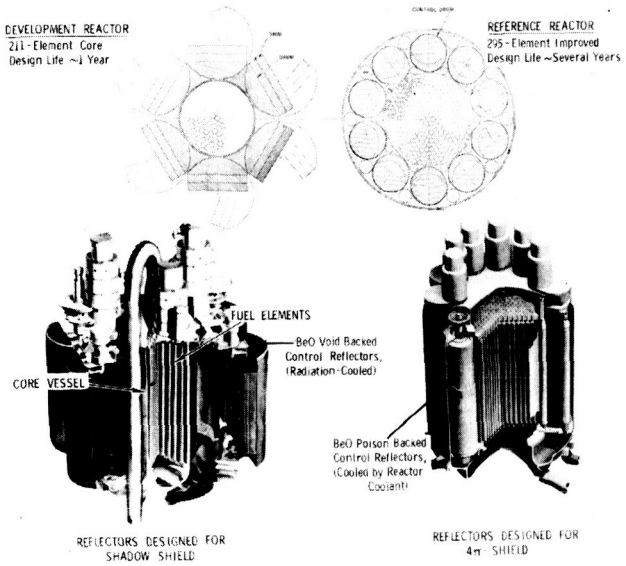

The UZrH reactor (using the number of fuel elements and reflector design sized for the job) in combination with the tubular compact converter thermoelectric modules is very attractive for 5-20 Kw unmanned satellite applications in terms of size, weight, and costs. A two-loop system (see figure 27) can be used for unmanned missions because the activated NaK coolant in the primary loop does not have to be shielded. For manned missions, a split shield, 3-loop system is used to allow the PCS to be maintainable by the astronauts. The UZrH-Brayton power system requires 3 loops because of the need for NaK and gaseous working fluids on the hot-side of the PCS.

Studies are going on considering the use of UZrH-TE systems in unmanned satellites in the late 1970's. Work is also progressing on a large Brayton PCS for demonstration with a UZrH reactor for higher powered missions, such as the space station, to be flown in the 1980's.

REACTOR-SPACE POWER
SYSTEM SCHEMATICS

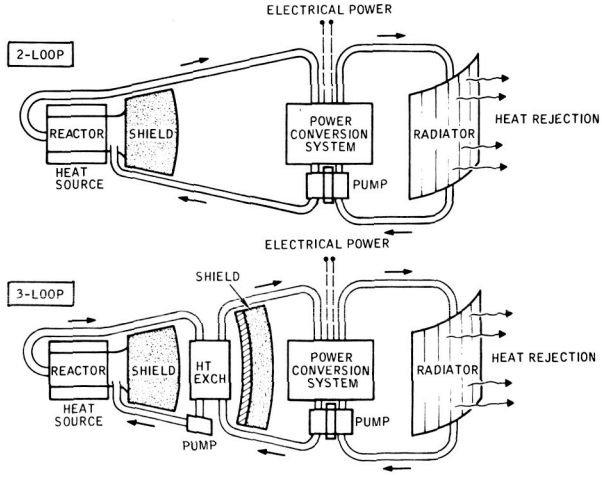

The UZrH reactor technology also forms a building block for moving on to the advanced thermionic reactor (see Figure 28) which is required for nuclear electric propulsion missions, such as Halley's Comet rendezvous. The key element of the thermionic reactor is the thermionic fuel element (TFE) which is tested in a UZrH moderated reactor and will be clustered to make a fast.

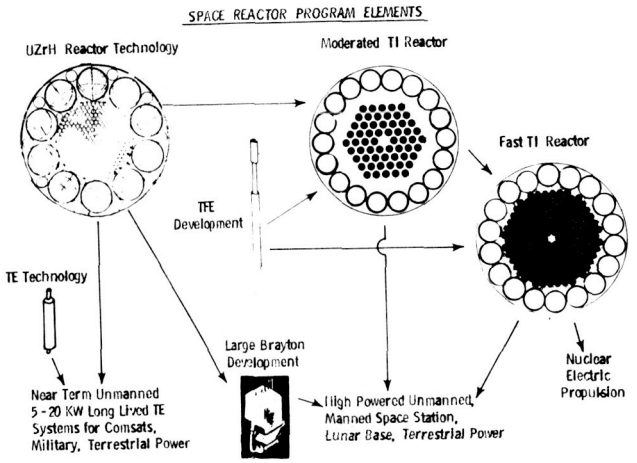

Figure 29

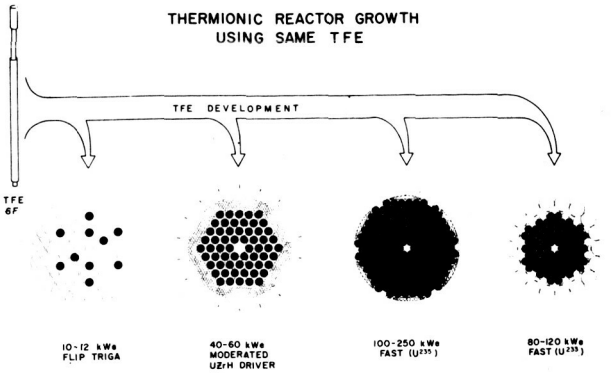

Figure 30

thermionic reactor (shown in Figure 29). Each TFE contains 6-10 thermionic diodes in series. The fuel is inside the diode and the electricity is formed directly in the TFE itself. This same TFE technology is the basis for a series of advanced reactors shown in Figure 30. The use of TFE's in a moderated UZrH driver reactor would provide useful static power systems which overlap the power range of the UZrH-Brayton power system. An attractive feature of this reactor is that the only very high operating temperature encountered are in the TFE itself. The emitter temperature is about 3100°F. The coolant outside the TFE is at the same 1000-1200°F where the UZrH reactor operates. This allows much higher radiator temperatures and therefore smaller radiators than the UZrH reactor power systems using the thermoelectric or Brayton PCS. In addition only one or two coolant loops are required because the PCS is in the reactor core (see Figure 31). Currently the thermionic reactor program effort is concentrating on the development of the TFE and the first full sized TFE is built and awaiting test in the TRIGA reactor.

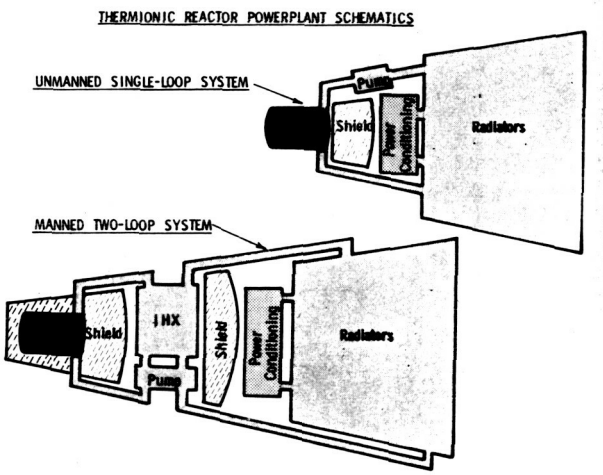

Figure 31

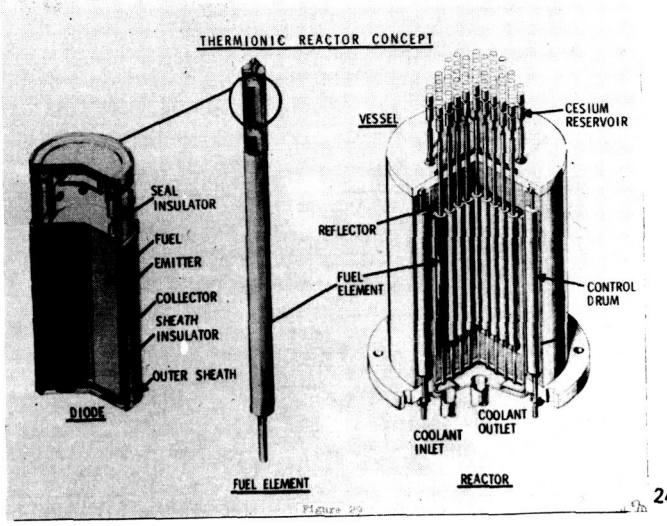

Figure 32

The other advanced space reactor technology concept which is being pursued as an alternative to the thermionic reactor for greater than 100 Kw type systems is the Advanced Liquid Metal Reactor. This is a fast reactor which will operate at 1800°F or higher and will be cooled by molten lithium metal. The attractive features of such a high temperature reactor are that it is applicable to many different types of power conversion and to many different high powered missions (see Figure 32). The current efforts are directed primarily toward the materials development and neutronic measurements, such as the fast critical experiment.

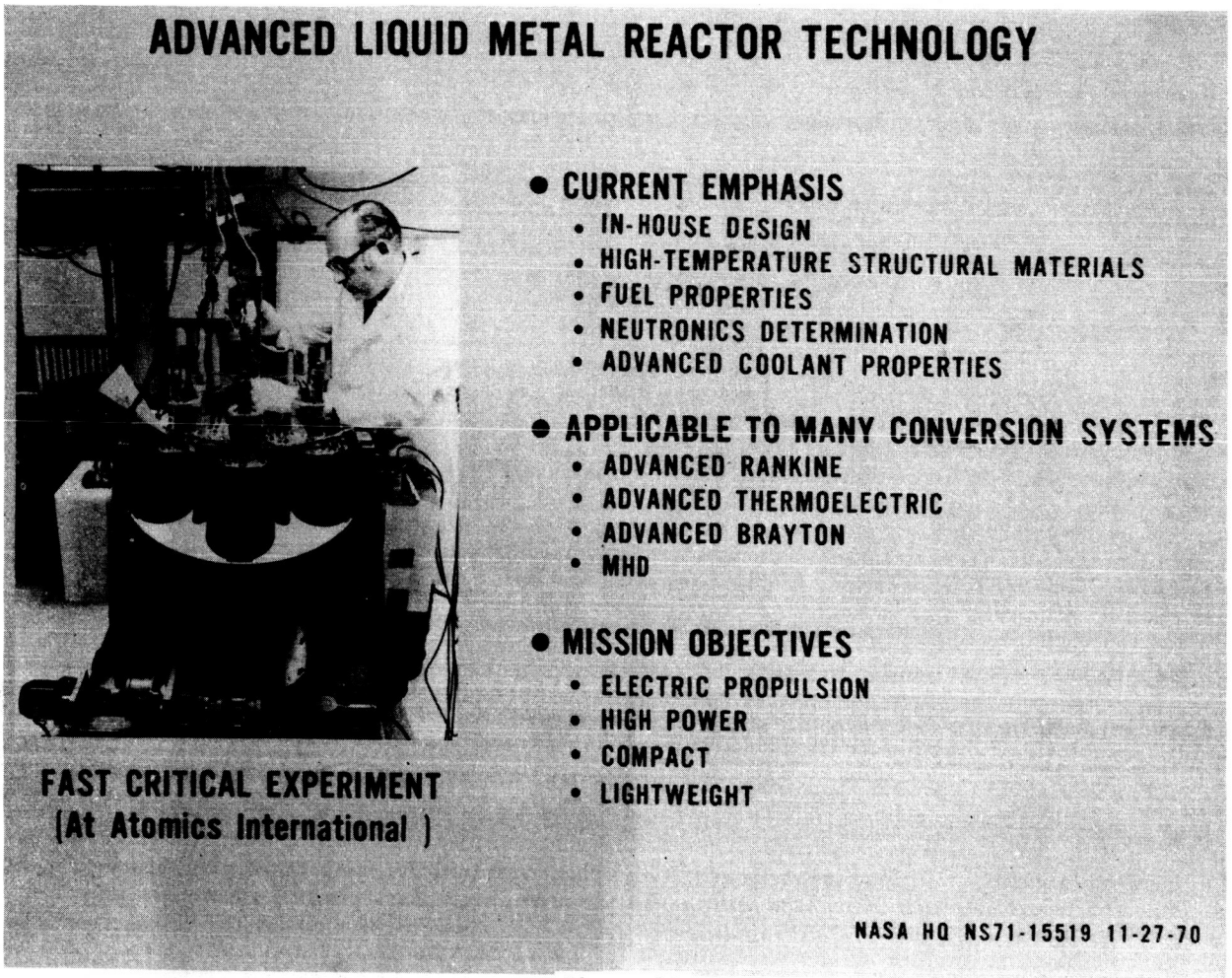

Figure 32

VI. Conclusions

I have attempted to describe the current and foreseeable radiation sources that are or will be in space as the result of the use of nuclear space power systems. Our primary concern over radiation in space is due to our plans to conduct more numerous and ambitious operations in space. To do that one needs electrical power which can be, and in some cases can only be, provided by nuclear power and radiation sources.

NUCLEAR APPLICATIONS IN MANNED SPACE STATION

W. A. Brooksbank, Jr.
Manager, Space Station Program, MSFC

G. J. Sieren
Systems Engineer, Space Station Task Team, MSFC

ABSTRACT

Current and future NASA Space Station studies will place a great deal of emphasis on economical systems which can start small and grow as the station itself grows. Space Station Electrical Power Systems based on nuclear sources will have to be increasingly adaptable to the lower power ranges to be competitive with other systems, while at the same time exploiting their inherent growth capability. Power growth capabilities as high as three of four-to-one will be required to meet the needs of a space station which is initially manned with a small crew and grows incrementally to a large station capable of accommodating a very complex experiment program.

The zirconium hydride reactor, coupled to a thermo-electric or Brayton conversion system, and the Pu 238 isotope/Brayton system, are considered to be the viable nuclear candidates for the Modular Space Station Electrical Power System.

This paper reviews the basic integration aspects of these nuclear electrical power systems, including unique requirements imposed by the buildup and incremental utilization considerations of the modular station. Also treated are the various programmatic aspects of nuclear power system design and selection.

INTRODUCTION

Nuclear devices of various types have played an important role in numerous NASA space missions over the last decade. These applications have ranged from use of nuclear materials to measure heat shield ablation during early nose cone reentry tests, to the relatively large and complex SNAP 27 generator used on the Apollo moon missions.

In the late sixties a new and prime candidate for the use of nuclear power appeared on the horizon. This application has been studied under the various names of Manned Orbiting Laboratory (MOL), Manned Orbital Research Laboratory (MORL), Earth Orbiting Space Station (EOSS) and, lately, simply the Space Station. In January 1971 NASA formally completed the Phase B (Preliminary Design) study of the 33-foot diameter Space Station. This station, with a 10-year lifetime, 1975-78 initial operating capability (IOC), 12-man crew, and 25-30 Kwe power requirement, was a prime candidate for the application of nuclear electric power, and the two parallel Phase B studies emphasized definition of the large isotope and reactor power systems in addition to solar array system.

Several factors influenced NASA to discontinue effort on the 33-foot diameter station and turn instead to the concept of an evolutionary modular space station consisting of several modules delivered to orbit by the space shuttle and assembled on-orbit to form an integrated space station. Among these factors were the suspension of Saturn V production, increased shuttle utilization and the overriding consideration of minimizing funding for the space station in the early years of the program.

In addition to meeting the requirement for low initial funding, the modular concept also lends itself well to early use of the station through incremental manning. Although the modular station concepts now under study have the capability of growing to the equivalent capability of the 33-foot diameter space station, they are intended for manning and limited experimental work at the intermediate levels of three and six man crews. Thus, the six-man modular station has come to be known as the Initial Space Station (ISS); the twelve-man version is known as the Growth Space Station (GSS); and the three-man version if known as the Initial Space Station with incremental manning. Representative modular stations are shown in Figures 1, 2 and 3.

The two primary areas of interest for nuclear applications are the electrical power generating system and the process heat generating subsystem of the environmental control and life support (EC/LS) system. The electrical power system (EPS) will be treated in more detail below. Before discussing these applications, however, it is useful to review the mission requirements of the modular space station as they affect the selection of subsystems for which nuclear applications are candidates.

INITIAL SPACE STATION (ISS) WITH INCREMENTAL MANNING

- 1978 – 1982
- 13 KWe
- 3 MAN CREW
- 75% GPL
- 2.7 KWe FOR EXPERIMENTS

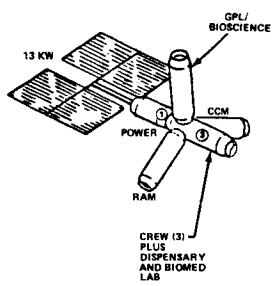

FIGURE 1

GROWTH SPACE STATION (GSS)

- 1984
- 41 KWe
- 12 MAN CREW
- 100% GPL
- 6.8 KWe FOR EXPERIMENTS

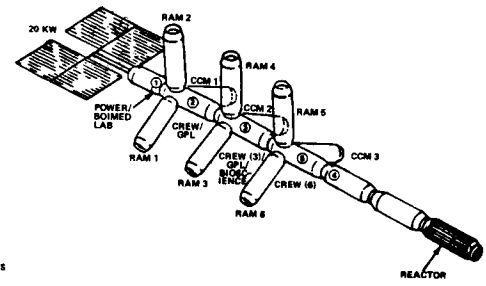

FIGURE 3

INITIAL SPACE STATION (ISS)

- 1982 – 1984
- 21 KWe
- 6 MAN CREW
- 100% GPL
- 4.4 KWe FOR EXPERIMENTS

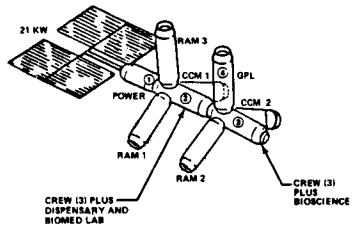

FIGURE 2

MODULAR SPACE STATION REQUIREMENTS

A minimum cost ISS which in addition minimizes early development costs yet meets the mission requirements and is designed to allow efficient expansion to at least the equivalent capabilities of the 12-man, 33-foot diameter station is a primary consideration. Although the IOC date for the ISS is later than for the original 33-foot station, thus allowing more time for development of technology, the cost constraints imply less optimistic technology advancements over this period, thereby reducing the development risk that can be tolerated. The 10-year mission lifetime constraints imposed on the 33-foot space station have now been broken into time periods at various manning levels. One timeline under study retains the 3-man level for four years, 6 men for two years, and finally reaches 12 men in 1984. With a maintenance philosophy permitting the addition or replacement of entire modules, subsystem lifetimes are less related to mission lifetimes. It is conceivable that mission lifetime will exceed ten years, depending only on how much of the NASA Blue Book experiment program NASA is able to accomplish and funding available. Even with an indefinite mission lifetime and the capability for module return/refurbishment, long life subsystems will still be required, but this constraint is somewhat softer than it was for the 33-foot station.

Mission flexibility, in terms of one design accommodating a variety of missions such as polar, synchronous, lunar and low earth orbits, has been reduced for the modular space station program. This implies that development costs for the station will be written off against a smaller number of missions and tends to favor those subsystem approaches which have a lower non-recurring to recurring ($\frac{NR}{R}$) cost ratio.

The space shuttle has a significant impact on the modular space station program. Besides module weight and volume constraints, the shuttle has a direct impact on such things as resupply, maintenance philosophy, and even subsystem selection. The degree of EC/LS loop closure is a strong function of the cost per pound for delivering expendables and other supplies to orbit. High resupply costs tend to favor subsystems with low resupply requirements. Current values being used for maintenance launch cost vary from $140 to $250 per pound delivered to orbit.

The requirement for artificial-g, which was a particularly strong configuration and subsystems selection driver on the 33-foot station, has not been retained in the modular space station program.

In the 33-foot diameter space station study, commonality meant commonality of the space station structures, subsystems, etc., to those of the fifty-man space base and the Mars interplanetary mission. As it is being developed in the modular station study, commonality has a dual meaning: commonality of structures and subsystems of the modular space station with those of the research and applications (RAM) experiment modules and the crew/cargo module; and, secondly, structural and assembly level commonality between the various modules of the modular space station itself.

The requirement for flexibility in crew manning level imposed on the modular space station results in a variable electrical power requirement. Figure 4 shows an early estimate of power required at various times in the mission. As compared to the 33-foot station, the electrical power requirements have increased due to the dispersed configurations of the modular space station, revised Blue Book experiment electrical power requirements, and changes in subsystems requirements such as limiting the cabin CO_2 partial pressure to 3 MM of mercury as opposed to 4 MM. The 1984 12-man growth version of the modular space station, although equivalent to the 12-man, 33-foot diameter station in its ability to conduct experiments, will likely have an electrical power requirement in excess of 40 Kwe.

The 33-foot station was somewhat limited in radiator area available, and was only marginally capable of satisfying both the EC/LS and primary electrical power system requirements without utilizing more extreme measures such as deployable radiators. The large amount of surface area available on the modular stations relieves this problem.

POWER REQUIREMENTS

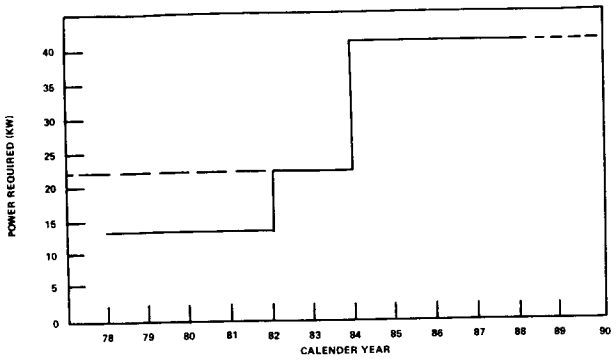

FIGURE 4

Aerospace nuclear safety, while still an important consideration, has been shown in the recently completed 33-foot space station Preliminary Safety Analysis Report (PSAR) to have a less significant impact than previously anticipated. Although the systems sized were one-to-two orders of magnitude larger than present systems, it has been shown that the mission risk attributable to these large systems can be reduced to the level of that for systems previously flown.

These are the mission requirements for the modular space station, summarized in Figure 5. They exert a strong influence on subsystems selection and design.

MODULAR SPACE STATION
REQUIREMENTS SUMMARY

- COST
  - DEVELOPMENT
  - TOTAL PROGRAM
- DEVELOPMENT RISK
- MISSION FLEXIBILITY
- SPACE SHUTTLE COMPATIBILITY
- ZERO-G
- MISSION LIFETIME
  - ISS (INCREMENTAL MANNING)
  - ISS
  - GSS
- COMMONALITY
- POWER LEVEL

FIGURE 5

CANDIDATE POWER SYSTEMS/GROWTH OPTIONS

The applicability of nuclear power candidates to the modular space station will now be examined. Due to the intimate relationship between the issue of which of the candidate systems to consider and the growth options that exist for each candidate, these subjects will be discussed together. Furthermore, past studies have indicated that from the standpoint of vehicle integration, the real issue in nuclear electrical power system definition and comparison is the energy source itself, and that the choice of a power conversion system is somewhat of a second order consideration. Nevertheless, certain energy source/conversion system combinations have classically been linked together, as shown in Figure 6. The growth options for these electrical power systems are shown in Figure 7. Based on considerations of lowest initial development cost, development risk, initial and maintenance launch weight, and general suitability in satisfying the mission requirements, only Options 1 to 3 have been retained for further consideration in the modular space station study.

MODULAR SPACE STATION
POWER SYSTEM CANDIDATES

- SOLAR ARRAY
- ISOTOPE – BRAYTON
- REACTOR – THERMOELECTRIC
- REACTOR – BRAYTON

FIGURE 6

Option 1 typically uses a minimally sized array for the ISS in the 1978-82 period, but with booms, structures, gimbal drives, etc., sized to accommodate a slightly larger array with which it could be replaced for the 1982-84 period. Two of these arrays, one at each end of the station, provide the required power for the 12-man GSS in Option 1. Option 3 would typically start (1978-84) as in Option 1. In the period 1982-84, however, a 20-40 Kwe reactor system would replace one of the arrays and the other array would be retained as the backup system. In this option the solar array backup system pays its way, so to speak, by providing primary power for a period of time and its development cost as a backup to the nuclear reactor need not bias the nuclear system cost comparison.

POWER SYSTEM
GROWTH OPTIONS

OPTION	INCREMENTAL MANNING (3)	ISS (6)	GSS (12)
1	SA →		
2	SA →		IB
3	SA →		Rx/TE OR Br SA BACKUP
4	IB →		
5	Rx/TE OR Br SA BACKUP →		

FIGURE 7

Option 2 is considered to be a somewhat unlikely candidate whose position could only be improved upon by significant changes in mission requirements such as reinstatement of artificial-g requirements or the requirement for commonality with some other mission for which it is desired, such as the Mars interplanetary mission.

With this initial selection of power systems and growth options as a function of modular station buildup, the evaluation process can continue by the application of tradeoff criteria such as those derived for electrical power system evaluation in the 33-foot space station study, to each specific option. However, it is beyond the scope of this dissertation to evaluate these criteria for each power system. Rather, we would prefer to make selected comments about how the various options fit into the modular space station program.

MODULAR STATION ELECTRICAL POWER SYSTEMS

Solar Array/Battery System: It is pertinent to the present discussion to evaluate the technical and programmatic implications of the use of a solar array system on the initial modular space station and to evaluate the by-product benefits to a later, add-on nuclear system. The solar array/battery system is significant since, if used as a primary power system on the initial station, it may serve as the backup electrical power system when a nuclear reactor is added, provided that the end-of-life output of the array is sufficient. The characteristics of this system are shown in Figure 8. Such a system might cost from $40 to $100 million dollars, with the low end of the range corresponding to a rigid Skylab-type array and the upper estimate resulting from advanced,

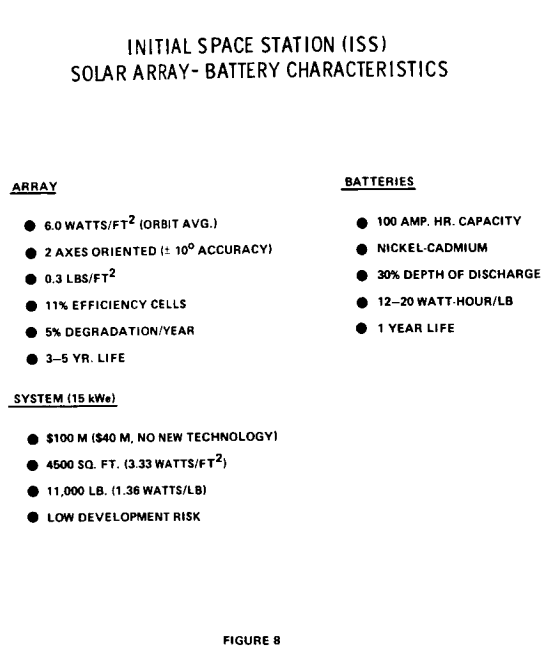

FIGURE 8

flexible roll-up arrays and increased capacity battery technology and development. An advantage of this system is its cost flexibility, enabling it to conform to varying budgetary constraints. Cost sensitivity analyses conducted in past studies have indicated that solar arrays are more sensitive to high power levels than the nuclear systems. This is due to two factors. First, the recurring costs for solar arrays are a near-linear function of array size. Secondly, the non-recurring costs increase rapidly for very large arrays due to the introduction of new technology. These factors are strong drivers toward use of a nuclear system for the GSS.

Past studies have also shown the solar array system to be the lightest by a comfortable margin. For the modular space station, however, the requirement for launching the arrays on a power module in a single shuttle payload will diminish that margin. If the batteries are kept centrally, in the power module, the supporting active cooling system with its radiators and other structures may also be charged to the system weight.

The relatively large maintenance launch weight required for the solar array system wipes out any initial weight advantage. This is largely due to frequent replacement of the batteries used for peaking and darkside operation, and an estimated three to five year replacement cycle for the array itself. Here again, the desirability of replacing the array with a nuclear reactor three to five years into the mission is clearly indicated. Just as the initial solar array became the backup to the reactor when it was added and in so doing eliminated that cost penalty, so can an advantage be realized in use of the solar array for primary power in the first three to five years of the mission, thereby eliminating the cost of replacing the reactor.

Isotope/Brayton System: It is difficult to evaluate the role of the isotope/Brayton system in the modular space station program. Those particular constraints which made the system attractive from the mission/systems integration viewpoint on the 33-foot station are lacking in the modular station program. Artificial-g requirements have been removed. Commonality with the Mars interplanetary mission module with implied writeoff of development cost has been deemphasized. In turn, significant unfavorable programmatic impacts associated with use of an isotope heat source are becoming apparent. Early commitment to a large fuel development and procurement program, involving extensive new processing facilities, is required to meet 1978 launch dates. The long lead time projected for fuel production implies a slow response to increased or decreased requirements late in the program; a significant disadvantage on the modular space station with its requirement for high flexibility in buildup and growth. A higher safety-risk-to-capability ($\frac{SR}{C}$) factor is indicated for the large isotope source as compared to the nuclear reactor.

On the other hand, with the exception of the radiator interface, the physical integration of the Isotope/Brayton system results in less impact on other station subsystems than either solar arrays or reactor systems. The external station configuration impact is minimal. The system is more amenable to IVA or shirtsleeve maintenance. The major areas of interface impact are in the ground handling, launch and recovery phases of the mission, as there must be a constant heat dump after the source is assembled. This requires extensive ground support equipment (GSE) for cooling and monitoring status in the launch, prelaunch, and recovery phases of the mission. Studies to date have indicated that credible backup heat dump modes are a problem to design. For the 33-foot station, the solution to this problem involved a meltdown of the multiple layer insulation between the heat source and shield, followed by a meltdown of the shield itself, enabling the heat source to radiate its heat directly into the subsystems compartment. The redundant heat dump problem is particularly critical for the recovery phase of the mission in which the heat source must be transported in the shuttle.

System characteristics for a nominal 15 Kwe unit are as shown in Figure 9. For higher power levels multiple units would be required, as this is about the largest system one could conceivably use.

Isotope/Brayton system costs are very sensitive to high power levels as compared to reactors, although not as sensitive as solar arrays. The system has a fairly large non-recurring to recurring cost ratio and the recurring cost is a linear function of power output. These recurring costs can be reduced by about one-third if the

MODULAR SPACE STATION
ISOTOPE/BRAYTON SYSTEM CHARACTERISTICS

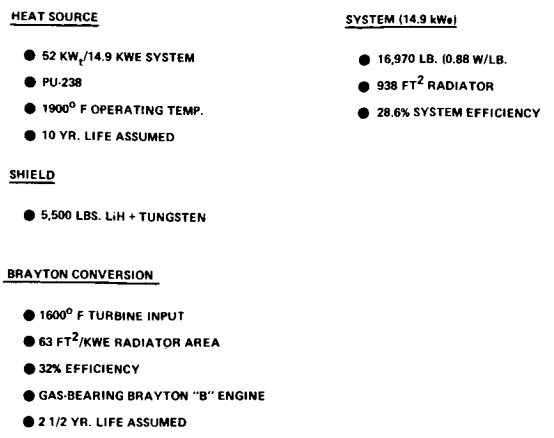

FIGURE 9

fuel can be rented and/or costs prorated over the isotope's 86-year half-life. However, as system size increases this practice becomes less credible.

Although relatively light in weight and requiring minimum maintenance launch weight, the isotope/Brayton system weight is quite sensitive to higher power levels. Again, the relationship is near-linear. The initial system weight is also sensitive to separation distance and fuel purity.

The development risks of the isotope/Brayton system are hard to assess. Although the turbine inlet temperatures run to 1600°F and the air-bearings are definitely new technology, initial performance of the conversion subsystem has been better than projected. The high (32%) cycle efficiencies demonstrated in relatively short term (2,000 hours) tests are remarkable for space-applicable systems. The endurance test results are awaited for projection of degradation rates. The disturbing factor with dynamic conversion subsystems is the number of series elements with single point failure possibilities in an individual conversion subsystem coupled with the expense involved in demonstrating the reliability and production uniformity of a statistically significant number of flight-type units. Present implementation schemes usually have two or three redundant conversion subsystems on hand as installed or stored spares. This is at best an optimistic approach for the first use of such a system in a five or ten year mission. If the system may be maintained in space, even by complete conversion system replacement, relatively significant problems, apparent late in the program, may be tolerated by earlier-than-planned replacement. However, maintenance weight-to-orbit, on-orbit replacement manhours and launch costs must be considered soft constraints.

The heat source is vulnerable to questions concerning development risk. The long term, slow response processing chain for the fuel is significant in considering fuel availability for the development program. Of greater concern is the capability to track changes in station power requirements as the program evolves. Unless large quantities could be stockpiled without prohibitive costs, the real possibility exists in having to launch a power-limited space station. If net conversion system efficiencies change, due to larger heat leaks, parasitic loads of redundant supporting subsystems, or larger-than-expected degradation in heat transfer elements or machine efficiencies, the required power would not be available from a relatively fixed fuel quantity, sized several years previously. If power requirements increase and system net efficiencies do not, a hard power level constraint exists. A backup development option should be retained to decrease the program impact in case this should happen.

The isotope heat source design, although static in nature, operates at 1600°F to 2000°F. The probability of materials problems is high. The reduced selection of materials with which to evade problems is considered a hard constraint softened only by unpredictable development times. This risk can be assessed by implementation of a representative source and endurance testing.

The isotope/Brayton system, although not as well suited to the mission requirements of the present modular space station as it was to those of the 33-foot station, is still a viable candidate for this type of long-life mission. With a reinstatement of artificial-g requirements and reemphasis of commonality with 50 years of NASA missions, its relative position could be significantly improved.

Nuclear Reactor Systems: The modular space station concept might well have been proposed to exploit the nuclear reactor's best points, namely an insensitivity costwise and weightwise to high power levels. This system, as shown in Figure 7, forms the basis for meeting the electrical power requirements of the growth version of the modular space station under Option 3.

One of the primary disadvantages of the reactor system, as shown in the previous Phase B study, was the necessity of providing a backup power system. Under Option 3, the solar array which provides primary power to the initial space station is retained and fulfills this requirement.

Figure 10 shows system characteristics for the nuclear reactor and two candidate conversion sys systems. The two systems are very similar from the integration standpoint. Weight, cost and impact on other subsystems are very near the same. The separation distance required, heavy shields, non-redundant source and safety implications require special integration consideration. The main differences are in the required operating temperature and power level of the reactor. This leads to different system lifetimes, power growth capabilities, shielding weights, and separation distance requirements.

The potential for power growth within the space station's lifetime and the potential growth within reactor technology are the main advantages reactor systems offer. The initial investment in development and support equipment is large but the delta costs for growth thereafter are small compared to the other candidates.

MODULAR SPACE STATION
NUCLEAR REACTOR SYSTEM CHARACTERISTICS

	THERMOELECTRIC SYSTEM			BRAYTON SYSTEM			
	MINIMUM*	GROWTH**		MINIMUM	GROWTH		
ELECTRICAL CAPABILITY, KWE	28	29	41.5	29	29	43.5	53.5 43.5
REACTOR OUTLET TEMP., °F	1,200	988	1,200	1,200	1,200	1,200	1,300
REACTOR LIFETIME, YEARS	5.5	8.2	4.2	10	10	8.5	5.5
REACTOR POWER KWT	880	888	845	130	127	312	367
RADIATOR AREA, FT²	1,880	3,800	3,800	2,000	2,000	2,000	2,000
REPLACEABLE SYSTEM WEIGHT, LB.	26,750	27,770	27,770	24,016	26,016	26,016	26,016
SUPPLEMENTAL RADIATOR AREA, LB.	---	2,900	2,900	---	---	---	---
WEIGHT PENALTY FOR GROWTH, LB.	---	3,920		---		2,000	

*168 TE MODULES
**192 TE MODULES

FIGURE 10

Weightwise, the nuclear reactor is at a disadvantage, being the heaviest of the three candidates. However, this is partially offset by a low weight sensitivity at the higher power levels. The requirement for keeping shuttle launchable modules to 20,000 lbs requires launching the nuclear reactor in at least two modules, thus incurring a double launch penalty. At $250/lb each launch costs $5 million. Because of its initial weight the total weight-to-orbit is higher for the reactor also, for systems under 40 Kwe. The use of the solar array for primary power on the ISS could eliminate the need for replacement of the reactor if the mission lifetime was kept at ten years; however, it is likely that if the GSS is made operational in 1984, it will function beyond the 1988 point in time and reactor replacement would have to be considered.

MODULAR SPACE STATION
POWER SYSTEM COST COMPARISON

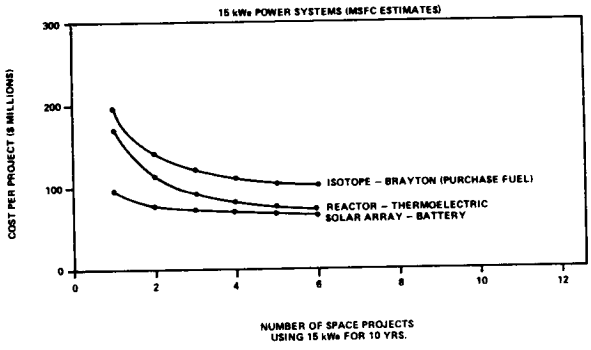

FIGURE 11

A major programmatic difference between the nuclear reactor system and the other two candidates is $(\frac{NR}{R})$ cost ratio. This ratio is much higher for the reactor, and has significant results. First, it means that for multiple applications, the total cost of using a reactor decreases in relation to the other candidates. As shown in Figure 11, at 15 Kwe no system is cheaper than the solar array, irrespective of the number of missions flown. However, as shown in Figure 12, for more than three 25 Kwe, 10-year missions, the reactor system costs less. Above 40 Kwe, the crossover occurs earlier and the reactor is cheaper from the very first mission. Secondly, a high $(\frac{NR}{R})$ ratio is desirable from the standpoint that whereas recurring costs involve large capital expenditures for materials, non-recurring costs provide jobs for people and expand technology—a preferable situation.

MODULAR SPACE STATION
POWER SYSTEM COST COMPARISON

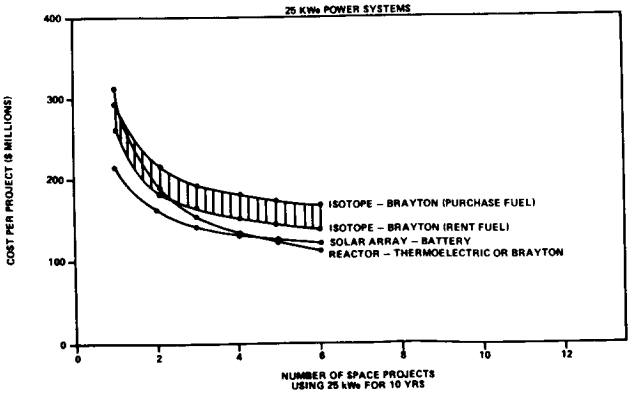

FIGURE 12

The development risks of the reactor systems vary according to the conversion system considered. Experimental and development models of the reactor have greatly contributed to mapping remaining development problems. Since remaining problems have "graceful" failure modes, the reactor would appear to be a small development risk for one to two years of operation. Due to development time available, the two year plus turn-around time in the problem-solution cycle is not as critical as when earlier station use was considered. The thermoelectric conversion subsystem appears also to have "graceful" failure or degradation modes. The temperature vs. performance vs. degradation characteristics appear to be amenable to statistical mapping so that once these trades are made, predictable performance can be expected. Although any higher efficiencies (5%) attained will be a function of success in the technology program, the flexibility of the reactor source, larger radiator area, and variations in system weight can be considered soft constraints for this subsystem.

The Brayton conversion system for the reactor source is in an anticipated development stage. If scaleup from the 2-15 Kwe machine to a 25-40 Kwe size is successful and if projected performance at reduced turbine inlet temperature is demonstrated, then comments before for the Brayton in the isotope/Brayton case are applicable here. Due to increased reactor problems at greater than 1100° - 1200°F, and due to Brayton efficiency or radiator problems below 1100° - 1200°F, the reactor and Brayton successful operation range do not overlap significantly. Higher maintenance weight-to-orbit, radiator area and cost are considered soft constraints in case a problem develops in this area.

CONCLUSIONS

The modular space station program is ideally suited to the application of nuclear power. While the impetus for this application is not present in the ISS to the degree that it was in the 33-foot station, certainly the growth flexibility and higher ultimate power levels required for the GSS support this conclusion. Many technical and programmatic advantages accrue which tend to make the overall consideration of nuclear power more attractive when growth options such as outlined here are considered.

The nuclear systems lack the experience under a variety of space flight conditions that would berequired to justify as low a development risk as for the solar array-battery system. However, contrary to the usual case, time can be considered somewhat of a soft constraint in solving the development problems of either system because of the evolving nature of the modular station itself.

ACKNOWLEDGMENTS

The authors would like to express appreciation to Mr. L. W. Brantley of George C. Marshall Space Flight Center, who contributed valuable data for this dissertation and made available his extensive library on the subject. In addition, Mr. Brantley has served as technical advisor to the Space Station Program and as such has been influential in shaping the authors' thoughts on the subject of space station nuclear power.

RADIATION ENVIRONMENT CONSIDERATIONS FOR OUTER PLANETS GRAND TOUR MISSIONS

R. Ivanoff and E. Royal
Jet Propulsion Laboratory

The planetary alignment of the solar system during the latter half of the 1970's makes it possible to utilize planetary swingbys for unmanned explorations of the outer planets. The lineup of the planets during that period will provide the rare opportunity to use this "gravity assist" swingby technique which significantly reduces flight times over the direct trajectory approach. The three planet Ground Tour missions encounter Jupiter-Saturn-Pluto (JSP) and Jupiter-Uranus-Neptune (JUN). These missions will require a spacecraft system design that provides long life reliability of up to ten years in flight with the ability to safely traverse the asteroid belt and perform multiple planet encounters in hostile environments with large uncertainties.

The sun-spacecraft distances after Jupiter flyby, will be too great to efficiently utilize the sun as a source of power, so these spacecraft must carry their own on-board generated power. Several existing Advanced System Technology projects, which had previously unrelated objectives, were coordinated and focused to a common objective to develop elements of a Thermoelectric Outer Plants Spacecraft (TOPS). This development project was sponsored by the National Aeronautics and Space Administration and has been under study at the Jet Propulsion Laboratory for the past two and one-half years.

This presentation covers some of the advanced development activities of TOPS that relate to RTG development and RTG-spacecraft system interfaces. These include development activities on the multi-hundred watt RTG unit, simulation studies, radiation mapping, shielding criteria and radiation effects testing on component parts. Emphasis will be placed on describing the natural space and RTG radiation environments, the effect this environment is expected to produce on the spacecraft and the steps being taken to assure mission success. Science instruments will monitor the interplanetary environment during the long cruise periods in addition to planetary encounter experiments that will be performed at each planet. Without proper system design the scientific experiments on the spacecraft would experience severe interferences to their measurement functions, so development activities include efforts to establish design restraints which will insure that desired interplanetary and planetary space measurements are not degraded by on-board generated RTG radiation.

(MANUSCRIPT NOT AVAILABLE)

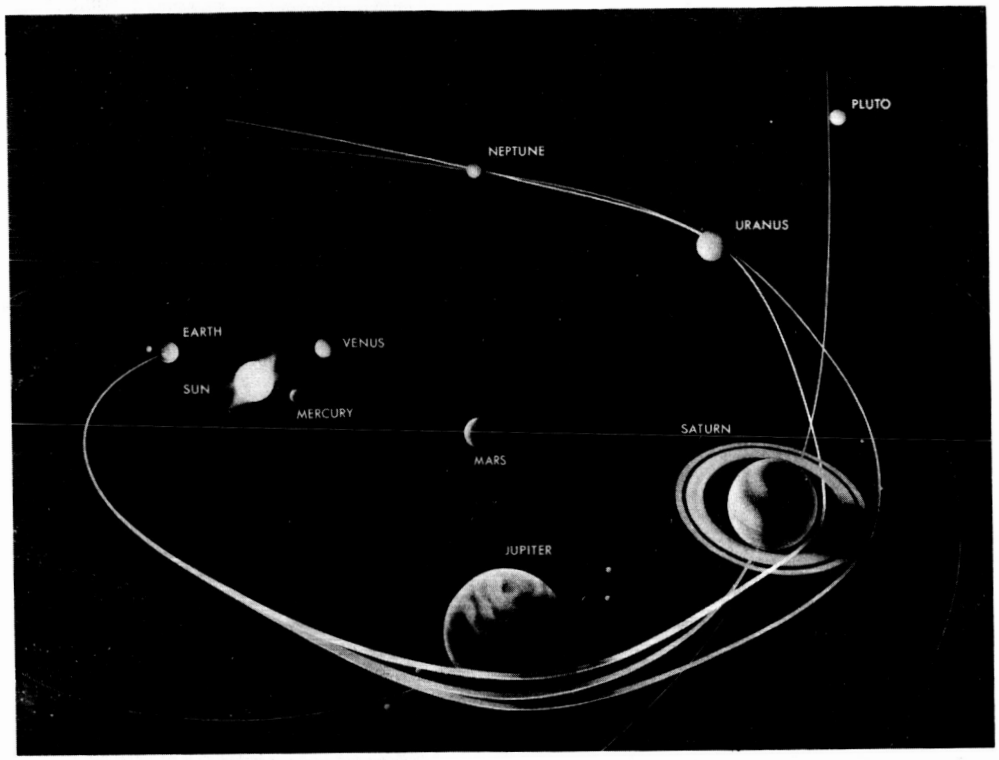

FIGURE 1. Four-Planet Grand Tour Trajectories Used in Early Mission Designs

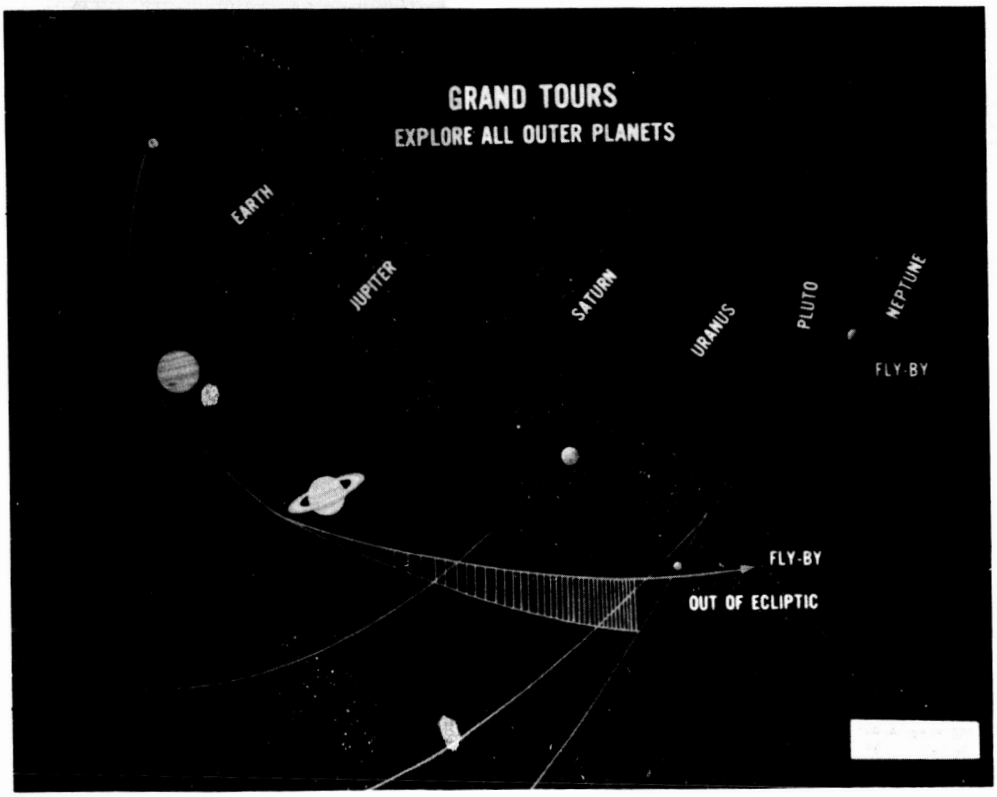

FIGURE 2. Three-Planet Grand Tour Trajectories Proposed for Outer Planet Exploration

FUNDAMENTAL REQUIREMENTS

- LONG LIFE
- LONG DISTANCE COMMUNICATION
- STRUCTURE TO INTEGRATE SUBSYSTEMS
- PROPULSION FOR MULTIPLE TRAJECTORY CORRECTION MANEUVERS
- ENVIRONMENTAL IMMUNITY
- SOLAR INDEPENDENT POWER

FIGURE 3. Some of the Fundamental Requirements of a Spacecraft Design for Outer Planet Missions

PRESENT ADVANCED DEVELOPMENT ACTIVITIES INCLUDE:

- TECHNOLOGY SELECTION FOR ENGINEERING SUBSYSTEMS
- LONG LIFE RELIABILITY CONCEPTS
- SCIENCE PAYLOAD INTEGRATION CONSIDERATIONS
- COMPUTER CONTROLLED FUNCTIONS FOR AUTOMATIC SPACECRAFT
- MAGNETICALLY CLEAN REQUIREMENTS
- SPACECRAFT CONFIGURATION
- MULTI-HUNDRED WATT RTG
- RADIATION MAPPING AND ANALYSIS

FIGURE 4. Advanced Development Activities Required for Outer Planet Missions

THERMOELECTRIC OUTER PLANET SPACECRAFT
CONFIGURATION 12L

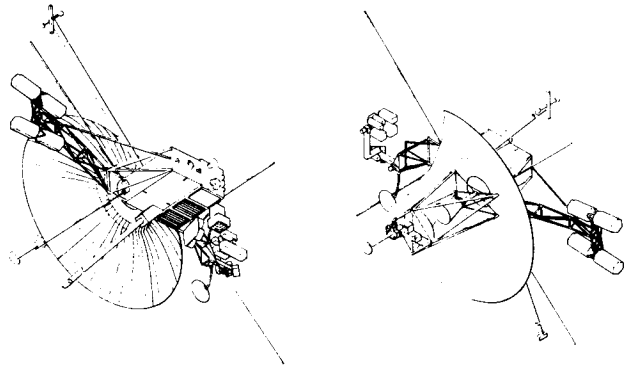

FIGURE 5. Spacecraft Conceptual Design

ENVIRONMENTAL CONSIDERATIONS FOR OUTER PLANET MISSIONS

- LAUNCH
  - ACOUSTIC NOISE, SHOCK, VIBRATION, AIR-TO-VACUUM TRANSITION AND STATIC ACCELERATION
- ON BOARD GENERATED
  - RTG RADIATION (GAMMA RAYS & NEUTRONS), EXCESS REJECTED HEAT AND MAGNETIC FIELDS
- ASTEROID BELT
  - PARTICLES AND MICROMETEROIDS
- LONG INTERPLANETARY CRUISE
  - DECREASING SOLAR CONSTANT, SOLAR FLARES AND SOLAR WIND
- PLANETARY
  - RADIATION/TRAPPED BELTS AROUND PLANETS AND PLANETARY MAGNETIC FIELDS

FIGURE 6. Environmental Considerations for Outer Planet Missions

NATURAL RADIATION ENVIRONMENT

	RADIATION	ENERGY (MeV)	PEAK FLUX (PARTICLES/cm^2/sec)	FLUENCE (PARTICLES/cm^2)
	PROTONS	1-10	4.0×10^8	8.6×10^{10}
(EARTH, JUPITER AND SOLAR)		10-100	7.0×10^6	4.9×10^{12}
		> 100	1.5×10^8	1.6×10^{12}
	ELECTRONS	3-10	1.2×10^8	5.1×10^{10}
(JUPITER AND EARTH)		10-30	2.2×10^7	2.2×10^{11}
		> 30	3.5×10^7	3.5×10^{11}

FIGURE 7. Natural Radiation Environment Produced by Solar and Interplanetary Radiation; Jupiter Trapped Radiation

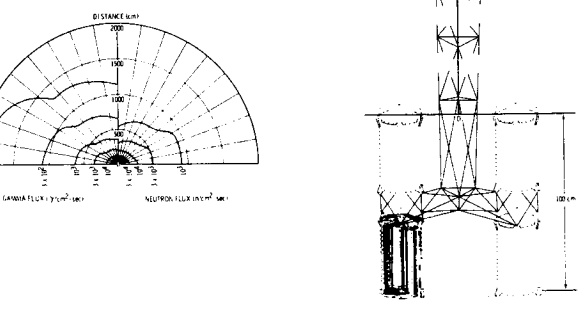

FIGURE 8. Radioisotope Thermoelectric Generator Power Source Free Field Radiation Flux Distribution

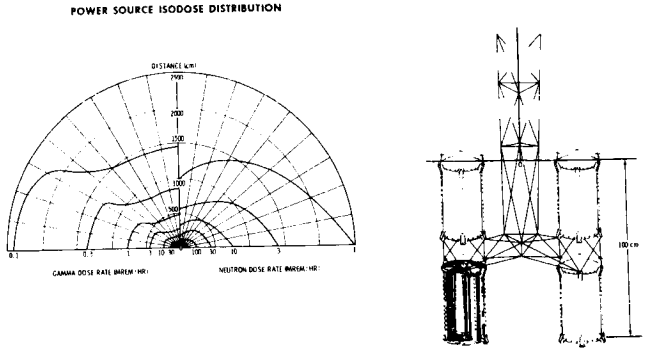

FIGURE 9. Radioisotope Thermoelectric Generator Power Source Radiation Free Field Dose Rate

CONCLUSIONS

- SPACE AND PLANETARY RADIATION CHARACTERISTICS AND MAGNITUDE
- RADIATION CHARACTERISTICS OF THE SPACECRAFT POWER SOURCES
- RESPONSE SENSITIVITY OF SCIENTIFIC INSTRUMENTS
- EFFECTS ON COMPONENTS AND MATERIALS
- SPACECRAFT RADIATION DISTRIBUTION
- DETERMINATION OF RADIATION EFFECTS ON THE SPACECRAFT SYSTEMS, COMPONENTS AND MATERIALS
  - ACCELERATED TESTING
  - DETECTOR TESTS
  - RTM TESTS

FIGURE 10. Manmade and Natural Radiation Definition and Effects Considerations

SESSION II.I.
NUCLEAR PROPULSION SYSTEMS· RADIATION ASPECTS OF VEHICLE DEFINITION

CHAIRMAN: D. SAXTON
NASA-MARSHALL SPACE FLIGHT CENTER

IMPACT OF RADIATION DOSE ON NUCLEAR SHUTTLE CONFIGURATION

C. A. Goetz and M. P. Billings
McDonnell Douglas Astronautics Company – West
Huntington Beach, California

ABSTRACT

This paper assesses the impact of nuclear radiation (from the NERVA propulsion system) on the selection of a reference configuration for each of two classes of the Reusable Nuclear Shuttle (RNS). One class was characterized by a single propellant tank, the shape of whose bottom was found to have a pronounced effect on crew radiation levels and associated shield weight requirements. A trade study of shield weight versus structural weight indicated that the minimum-weight configuration for this class had a tank bottom in the shape of a frustum of a 10°-half-angle cone. A hybrid version of this configuration was found to affect crew radiation levels in substantially the same manner.

The other class of RNS consisted of a propulsion module and eight propellant modules. Radiation analyses of various module arrangements led to a design configuration with no external shield requirements.

CREDIT

The material presented herein was generated by the McDonnell Douglas Astronautics Company – West in support of the Nuclear Flight System Definition Study conducted under contract NAS8-24714 for the National Aeronautics and Space Administration, George C. Marshall Space Flight Center, Huntsville, Alabama. Calculational techniques used in generating these data were developed under the Independent Research and Development Account No. S.O. 80205-007.

INTRODUCTION

Current interest in space nuclear propulsion is centered on the Reusable Nuclear Shuttle (RNS). Prospective missions include transportation of large payloads between low earth and synchronous orbits and between low earth and lunar orbits. Interaction with other vital components of such a transportation network is illustrated in Figure 1 for the lunar shuttle mission.

Two classes of the RNS are under consideration, these being a single-module class and a multi-module class, as shown in Figure 2. Each class has a total propellant capacity of about 300,000 pounds of liquid hydrogen. They may be distinguished as follows:

Single-module class––A single propellant tank, 33 ft in diameter (or a hybrid version using a small run tank in combination with the single main tank), placed in earth orbit by the Intermediate-21 launch vehicle

Multi-module class––An arrangement of a propulsion module plus 8 propellant modules, each of which is compatible with the 15-ft-dia by 60-ft-long cargo hold of the Space Shuttle, which transports them into earth orbit for subsequent assembly there

Radiation analyses were conducted on these concepts to identify the effects of propellant tank geometry on crew radiation levels and consequent shield weight requirements. Results from these investigations had a substantial impact on the selection of a reference configuration for each RNS class.

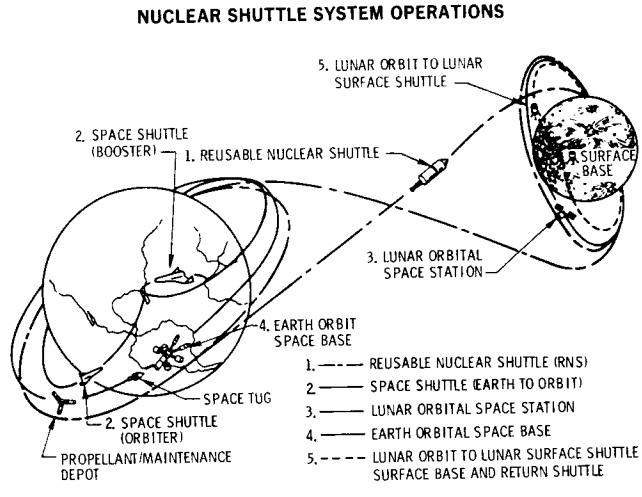

FIGURE 1. NUCLEAR SHUTTLE SYSTEM OPERATIONS

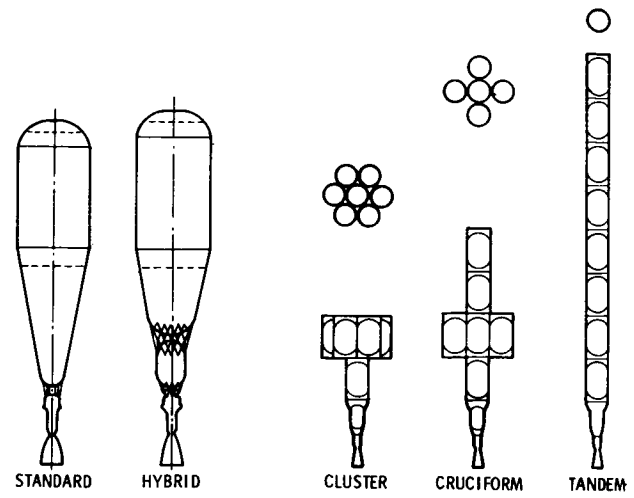

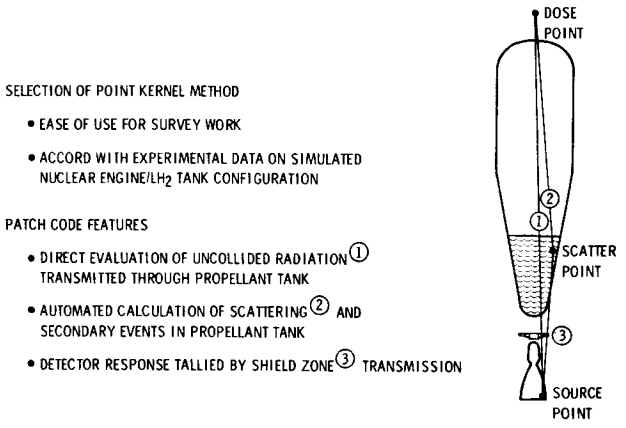

FIGURE 4. PATCH POINT KERNEL CODE

The potential influence of tank geometry on crew radiation levels arose from the fact that the propellant could provide significant reduction of crew dose due to nuclear engine radiation over the entire time period of the mission. Thus there was an incentive for effective utilization of the propellant to reduce the weight of shielding needed to meet the stipulated crew dose.

CALCULATION METHODS

The calculational techniques shown in Figure 3 were used in these analyses. Data on the engine and its radiation sources were based on the May 1969 Common Radiation Analysis Model,[1] except as modified in Reference 2. These data, together with data providing a model of each propellant tank design, were supplied as input to the PATCH point kernel code[3] (or the SOBER Monte Carlo code*) to calculate dose rate as a function of propellant level in the tank. These dose rate data were broken down into the contributions from each particular zone of a disk shield, located between engine and tank, through which the radiation had been transmitted (Figure 4).

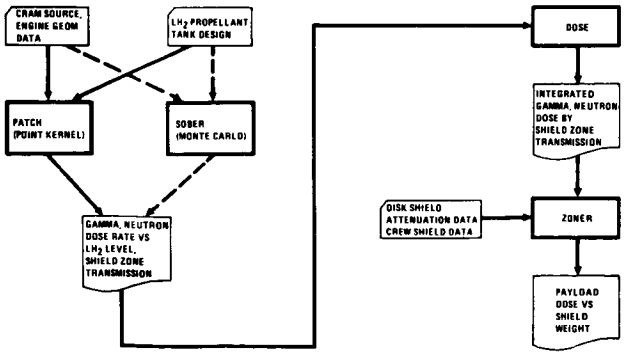

FIGURE 3. MDAC COMPUTER CODE OPERATIONS SEQUENCE

The next step in the procedure was to equate propellant *level* to drain *time* and to use the DOSE code to perform an integration of the dose rate over time. The resulting dose by shield zone was then coupled with data on shield geometry and shield material attenuation and, using the Lagrange multiplier formulation incorporated in the ZONER code, an optimum distribution of shield material was calculated for the external disk shield. The final result was payload dose as a function of shield weight.

The bulk of the dose rate analyses were accomplished using point kernel techniques. Selection of this method was based on (1) the utility of the point kernel technique for survey work and (2) the general accord shown between point kernel calculations and experimental data on simulated nuclear engine/propellant tank configurations.[4] The PATCH code (see Figure 4) provided the requisite utility and accuracy and, in addition, offered unique features of particular benefit to this study:

(1) direct evaluation of the dose from single-scatter and secondary production events in the tank, as well as the usual calculation of line-of-sight contributions,

(2) tallying of detector response by the specific shield zone through which the radiation had been transmitted,

(3) rapid determination of fluxes at scattering centers by interpolating tabular data in lieu of integration over all volume sources.

*A McDonnell Douglas adaptation of the FASTER Code[5].

EFFECTS OF CONFIGURATION ON DOSE RATE

Detailed calculations of crew dose rate, integrated dose and attendant disk shield weight requirements were performed for a number of candidate configurations for each RNS class. For the single-module configurations, this activity necessitated a continuing, intensive evaluation of results in order to develop an understanding of the effect of the tank configuration on the radiation protection requirements. Through this understanding, a family of tank configurations of interest with respect to potential reduction of shield weight were identified for detailed evaluation.

Single-Module Class

The configurations investigated for potential application in the single-module class are illustrated in Figures 5 and 6. The designs shown in Figure 5 were distinguishable solely by the shape of the tank bottom, which was either ellipsoidal (with a $\sqrt{2}$:1 ratio of radius to depth) or basically conical (with a half-angle of 8, 10, 15 or 30 degrees). The tank designs shown in Figure 6 employed baffles which retained a portion of the propellant in a configuration which enhanced its time-integrated shielding worth.

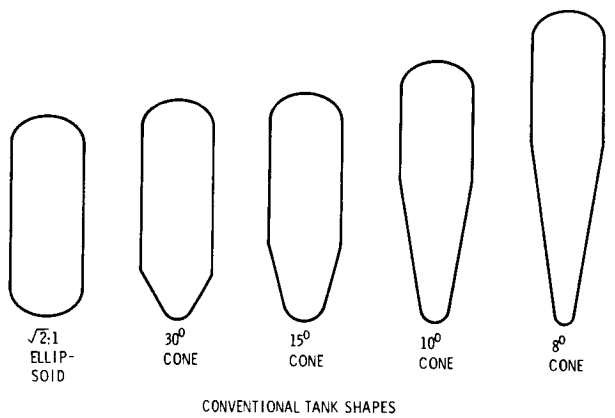

FIGURE 5. CANDIDATE LH_2 TANK CONFIGURATIONS

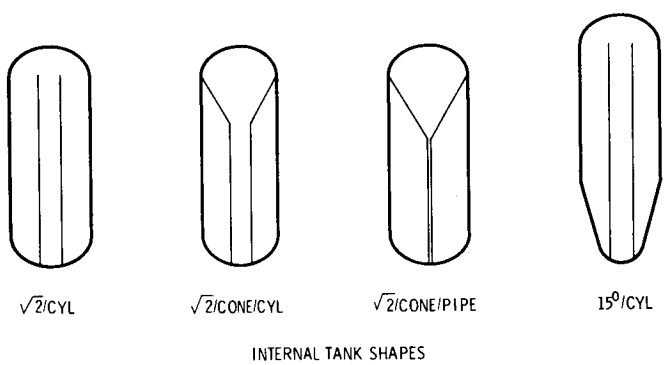

FIGURE 6. CANDIDATE LH_2 TANK CONFIGURATIONS

Tank geometrical differences were found to affect the crew dose and attendant shield weight requirements in several ways. Figure 7 exhibits one of these geometrical effects: the difference in terminal dose rate due to tank bottom shape. The data displayed correspond to a residual propellant weight of 3,500 lbs. This represents the minimum amount of liquid hydrogen reserved for final aftercooling of the engine. The shape of the tank bottom determines the level of this liquid in the tank. The narrower tank bottoms result in higher LH_2 levels and correspondingly lower direct radiation levels above the tank.

Figure 8 illustrates another important geometrical effect: differences in the rate at which the propellant is decreasing. A rapid drop rate means that less time is spent at high radiation levels. It should be noted that the configurations with the highest drop rates are the same ones which have the lowest terminal dose rates.

The configurations shown in Figure 6 represented a conscious attempt to exploit such phenomena. These so-called internal tank designs employed baffles which retained a portion of the propellant in a configuration which enhanced its time-integrated shielding worth. The idea was to simulate the behavior of the narrow-angle tank bottoms by artificially producing a fast drop rate and low radiation transmission through the inner tank near the end of engine burn. These configurations had the possible advantage of reducing overall stage length relative to the low-angle conical designs.

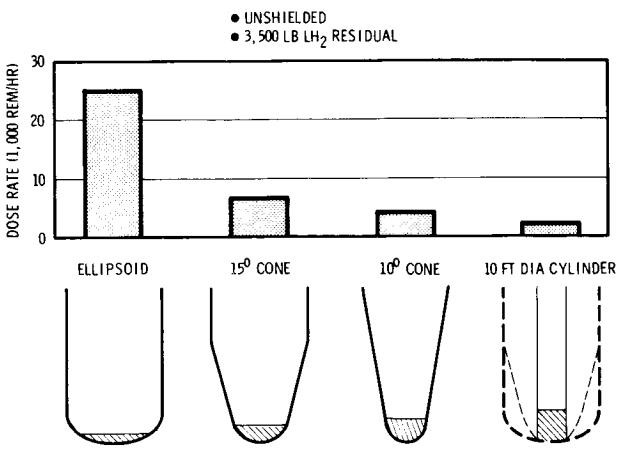

FIGURE 7. TERMINAL DOSE RATE

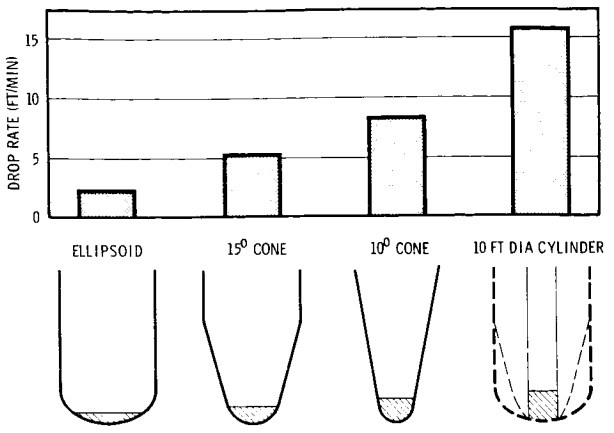

FIGURE 8. TERMINAL LH_2 DROP RATE

Comparison of Figures 9 and 10 shows the different variation with time of the dose rates for configurations with and without an internal tank. The direct dose rate represents the radiation which reaches the dose point without making any collisions in the propellant tank. The variation of this dose rate with LH_2 *level* is identical in both configurations. The variation of this dose rate with drain *time,* however, is substantially different. This difference is solely attributable to the difference in drop rates between the liquid in the central column in one case and the liquid in the unbaffled tank in the other.

TIME DEPENDENT DOSE RATES - 15-DEGREE CONE

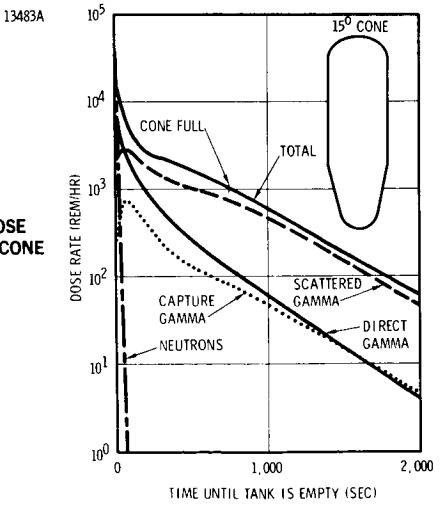

FIGURE 9. TIME DEPENDENT DOSE RATES - 15-DEGREE CONE

TIME DEPENDENT DOSE RATES - 15-DEGREE CONE WITH INTERNAL TANK

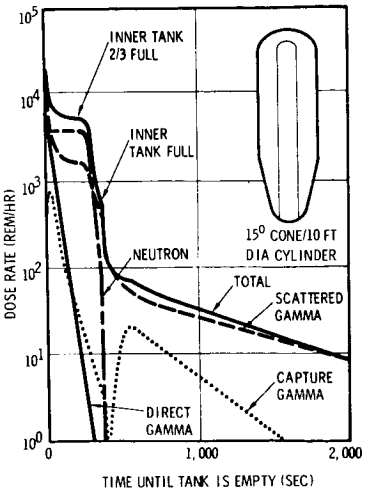

FIGURE 10. TIME DEPENDENT DOSE RATES - 15-DEGREE CONE WITH INTERNAL TANK

The advantage of the internal tank design in reducing the direct dose is partially offset, however, by scattering events. Such scattering is particularly significant during drainage of the inner tank, when the outer tank is empty (or nearly so). During this time period, radiation scattered from the walls of the empty outer tank can reach the dose point without interference from the propellant in the inner tank, except when the latter is nearly full. Hence there is a plateau in the scattered dose rate, extending over a wide range of propellant levels in the inner tank – from the nearly-full condition to the nearly-empty situation, where direct transmission through the inner tank propellant begins to dominate.

Multi-Module Class

Radiation analyses of configurations for the multi-module class RNS concentrated on the effects of module *arrangement* on crew dose rather than the effects of individual tank *shape.* The module diameters were restricted by launch considerations to 15 feet, at which value the effect of tank shape on crew radiation protection requirements was significantly diminished from that associated with the single-module class. In the survey of several candidate designs for a reference configuration for this RNS class, two key factors which affected crew radiation levels were identified:

- the 8 propellant modules should be arranged so that a minimum of two propellant modules, plus the run tank, are between the engine and crew while outboard tanks drain
- the crew dose is then due almost entirely to dose transmitted through these in-line tanks as they drain and, hence, is directly related to engine/crew separation distance.

These findings are illustrated by the dose rate data for various inboard tank arrangements shown in the following table. The indicated dose rates would be obtained throughout the period when the outboard tanks are draining, this being ~400 seconds/tank.

Number of Inboard Modules	Dose Rate Transmission Through Inboard Tanks, Rem/hr	
	Cluster	Cruciform
1 + Run Tank	16	3
2 + Run Tank	0.5	<0.1
1	~37	~9
2	~1	~0.1

RESULTS

Single-Module Class

An overall comparison of the relative shielding merits of a representative selection of tank configurations is provided by Figure 11. These results demonstrate that conventionally designed tanks which subtend large solid angles (with respect to the engine source center) require impractically large shield weights. This result is particularly evident for the ellipsoidal tank bottom configuration and, to a lesser extent, for the 30° half-angle design.

It can also be seen that the use of internal tanks is an effective means of reducing shield weight requirements. Part of this reduction is offset, however, by increased structural weight and by supplementary shield weight to reduce off-axis doses. Such weight penalites are not shown in this illustration.

The simplest and most effective means of achieving the radiation criterion is through the use of narrow-bottom tanks. Reduction of the tank bottom cone angle produces the following effects, which act in concert to reduce shield requirements:

- Lower terminal dose rate due to higher level of residual LH_2
- Decreased time of exposure to high dose rates due to faster LH_2 drop rate
- Increased separation distance
- Smaller fraction of engine leakage radiation intercepted by LH_2 tank and scattered to the crew location
- Smaller cross sectional area of external disk shield

A trade study of structural and shield weight indicated a broad minimum in total weight below a cone half-angle of about 10°. A hybrid version using a small tank in combination with the main tank showed similar effects on crew radiation levels while conferring some operational benefits in the area of propellant management. This configuration, shown in Figure 12, was selected as the McDonnell Douglas reference design for the Class 1 (or Single-Module) RNS.

DOSE VERSUS SHIELD WEIGHT
SINGLE - MODULE CLASS RNS

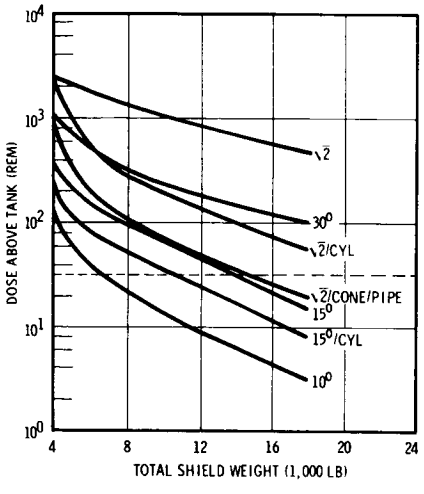

FIGURE 11. DOSE VERSUS SHIELD WEIGHT
Single - Module Class RNS

CLASS 1 SINGLE-MODULE HYBRID RNS

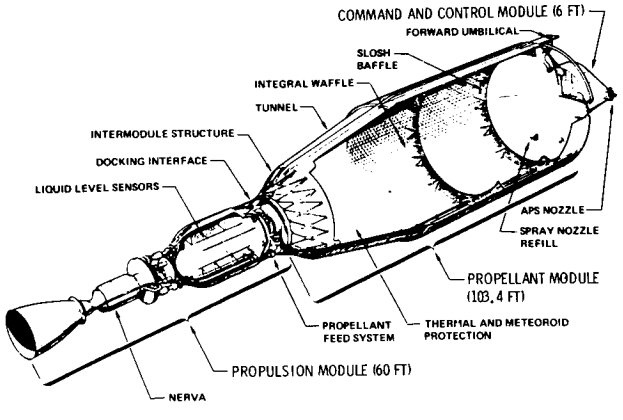

FIGURE 12. CLASS 1 SINGLE-MODULE HYBRID RNS

Figure 13 shows the variation of dose rate with time for the reference design. Figure 14 presents the minimum shield weight requirements as a function of radiation level forward of the main tank. These data reflect no credit for inherent radiation attenuation by the crew compartment structure and equipment and neglect secondary gamma radiation due to neutron capture in the disk shield (estimated at approximately 3 rem[6]).

In determining disk shield weight, a radiation criterion of 30 rem was used, based on a crew allowable dose of 10 rem per mission and a crew compartment dose attenuation factor of 3, which is representative of a modified Apollo command module.

Allowing for a 10 percent uncertainty in the calculated dose, the total shield weight needed to reduce the crew dose to 10 rem is 6,200 lb, signifying a disk shield weight of 2,900 lbs. This result is based on (1) a 3,500-lb LH_2 residual; (2) a 3-zone disk shield with radii of 25.5, 40 and 50 inches; and (3) a 160-in.-dia run tank. Table 1 compares the required shield weights for other values of propellant residual and run tank diameter.

SHIELD WEIGHT REQUIREMENTS VS DOSE

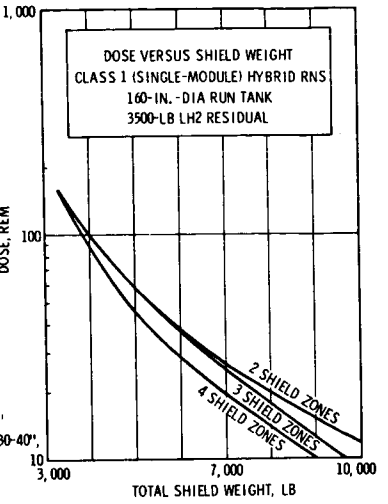

NO. OF SHIELD ZONES	SHIELD ZONE RADII
2	0-30", 30-50"
3	0-30", 30-40", 40-50"
4	0-25.5", 25.5"-30", 30-40", 40-50"

FIGURE 14. SHIELD WEIGHT REQUIREMENTS VS DOSE

TIME DEPENDENT DOSE RATES

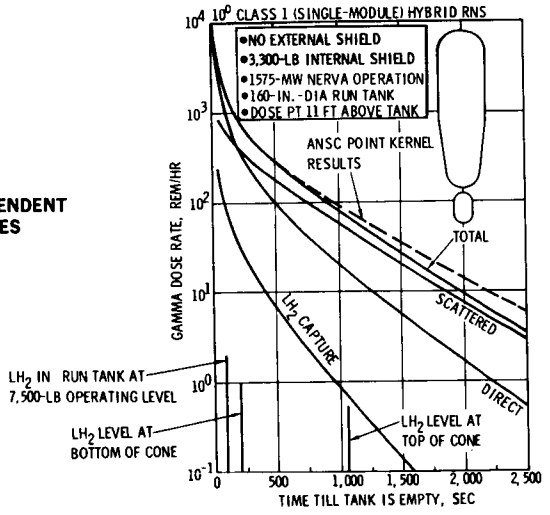

FIGURE 13. TIME DEPENDENT DOSE RATES

19625

SHIELD WEIGHT REQUIREMENTS FOR SINGLE-MODULE CLASS HYBRID RNS

RUN TANK DIAMETER, IN.	112	112	112	160	160
PROPELLANT RESIDUAL, LB	0	3,500	7,500	3,500	7,500
TOTAL SHIELD WEIGHT,* LB	6,200	5,700	5,500	6,200	5,700

*SHIELD WEIGHT TO REDUCE CALCULATED DOSE 11 FT ABOVE TANK TO 27 REM, USING A 3,300-LB INTERNAL SHIELD AND AN EXTERNAL 3-ZONE DISK SHIELD WITH RADII OF 25.5, 40 AND 50 IN.

TABLE 1. SHIELD WEIGHT REQUIREMENTS FOR SINGLE-MODULE CLASS HYBRID RNS

Multi-Module Class

Several arrangements of propellant modules, in conjunction with a propulsion module, were investigated for potential application to the multi-module class. A comparison of the unshielded doses 11 feet in advance of the forward propellant module of each of three different configurations is provided in Table 2. The difference in dose between different configurations is due to the difference in separation distances, which, as indicated, has a major effect.

19540

DOSE PER MISSION FOR MULTIMODULE CLASS RNS CONFIGURATIONS

MODULE ARRANGEMENT	CLUSTER DESIGN	CRUCIFORM DESIGN	TANDEM DESIGN
ENGINE/CREW SEPARATION	169 FT	289 FT	529 FT
GAMMA DOSE			
DIRECT	39 REM	14 REM	4 REM
INBOARD SCATTER	33	8	2
INBOARD CAPTURE	9	1	0
OUTBOARD SCATTER	6	1	0
TOTAL GAMMA	87 REM	23 REM	6 REM

*DOSE CORRESPONDING TO 3500-LB LH_2 RESIDUAL, 3300-LB INTERNAL SHIELD AND NO DISK SHIELD

TABLE 2. DOSE PER MISSION FOR MULTIMODULE CLASS RNS CONFIGURATIONS

The results in Table 2 are based on a drainage sequence in which the outboard propellant modules are drained first. The reverse situation would expose the crew to high dose rates over the drainage period of the outboard modules. Such high dose rates would result from the transmission of radiation through the empty inboard modules. As noted previously, the time-integrated crew dose is essentially due to dose transmission through the inboard propellant modules, this being accumulated during the period of drain of the run tank and the last two full inboard modules. This result is illustrated for the cluster configuration in Figure 15 and is invariant with module arrangement for the configurations indicated.

19573

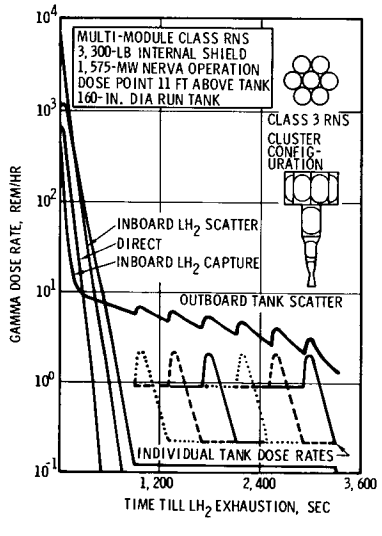

TIME DEPENDENT GAMMA DOSE RATE
CLUSTER CONFIGURATION

FIGURE 15. TIME DEPENDENT GAMMA DOSE RATE Cluster Configuration

The cruciform configuration was selected as the McDonnell Douglas reference design for the multi-module class RNS. This configuration, illustrated in Figure 16, meets the crew dose criterion without the need for external shielding.

Figure 17 shows the variation of the gamma dose rate with LH_2 drainage time for the reference design. The neutron dose rate is not shown as it is appreciable only when the propellant is nearly exhausted and is not a significant contributor to the overall dose.

Most of the dose is due to radiation which is transmitted without collision through the inboard tanks or which undergoes some scattering or capture interaction there. A recognizable but small (~ 1 rem) dose contribution is due to scatter from the structural materials of the empty outboard tanks. Most of this contribution is accumulated during the drain period of the last three inboard modules plus the run tank. When the fourth, most forward inboard module is full, it provides appreciable attenuation of this scattered radiation. Thus scatter from propellant and structural materials in the outboard modules is insignificant during the entire period of drain of the outboard tanks.

18131A

CLASS 3 MULTI-MODULE RNS

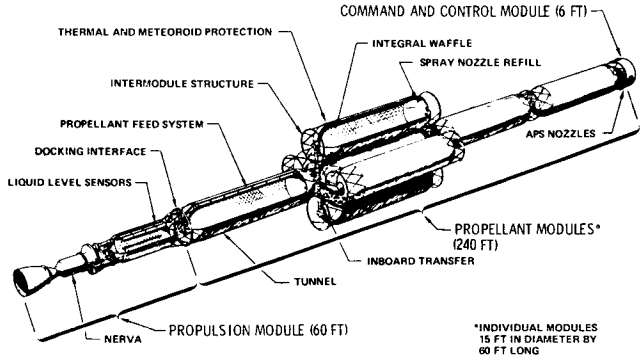

FIGURE 16. CLASS 3 MULTI-MODULE RNS

19501

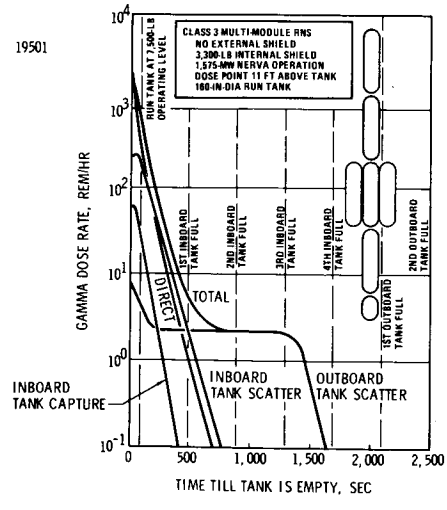

TIME DEPENDENT DOSE RATES

FIGURE 17. TIME DEPENDENT DOSE RATES

CONCLUSIONS

This study was initiated when it became evident that the RNS propellant provided potentially significant attenuation of radiation emitted by the nuclear engine. It was recognized that large shield weight savings could be realized by the effective use of the propellant in protecting the crew. Consequently shielding analyses were made to identify the effects of propellant tank geometry and drainage sequence on crew radiation levels and attendant shield weight requirements.

The results of this study clearly demonstrated that overall weight savings were possible through enlightened design of propellant tank geometry and drainage schedule. The conclusions summarized in Figure 18 provided a substantial impact on the selection of a reference configuration for each RNS class. The Single-Module design ultimately showed a reduction of several thousand pounds over the previous 15° baseline design while the Multi-Module design obviated the need for an external shield.

19539

SUMMARY OF CONCLUSIONS IN RNS SHIELDING ANALYSES

SINGLE-MODULE CLASS

- LARGE-SOLID-ANGLE CONVENTIONAL TANK BOTTOMS REQUIRE LARGE SHIELD WEIGHTS
- INTERNAL TANKS ARE PARTIALLY EFFECTIVE IN REDUCING SHIELD WEIGHT REQUIREMENTS
- SMALL-ANGLE TANK BOTTOMS OFFER SIMPLEST, MOST EFFECTIVE WAY TO CUT SHIELD REQUIREMENTS
  - LOWER TERMINAL DOSE RATE DUE TO HIGHER LEVEL OF RESIDUAL LH_2
  - DECREASED TIME OF EXPOSURE TO HIGH DOSE RATES DUE TO FASTER LH_2 DROP RATE
  - INCREASED SEPARATION DISTANCE
  - SMALLER FRACTION OF ENGINE LEAKAGE RADIATION INTERCEPTED BY LH_2 TANK AND SCATTERED TO CREW LOCATION

    SMALLER CROSS-SECTIONAL AREA OF EXTERNAL DISK SHIELD
- HYBRID (RUN TANK) DESIGN PROVIDES COMPARABLY LOW SHIELD WEIGHT REQUIREMENTS

MULTIMODULE CLASS

- INHERENT FLEXIBILITY OF CONCEPT CAN BE EXPLOITED TO ELIMINATE NEED FOR EXTERNAL SHIELD
- SEPARATION DISTANCE PLAYS A SIGNIFICANT ROLE
- MINIMUM INBOARD PROPELLANT INVENTORY SUPPLIED BY TWO PROPELLANT MODULES PLUS RUN TANK
- OUTBOARD PROPELLANT MODULES SHOULD BE DRAINED FIRST

FIGURE 18. SUMMARY OF CONCLUSIONS IN RNS SHIELDING ANALYSES

REFERENCES

1. A. D. Wilcox, B. A. Lindsey, and M. A. Capo (WANL), "NERVA-Flight-Engine Common Radiation-Analysis," RN-TM-0583, Aerojet-General Corporation (May 1969).

2. "Final Report of Shield System Trade Study," S054-023, Vol. I, Book 2, Aerojet Nuclear Systems Company (July 1970).

3. M. P. Billings, "The PATCH Point Kernel Program for Radiation Analyses in Complex Geometry," McDonnell Douglas Astronautics Company report to be published.

4. R. G. Soltesz et al, "Radiation Measurements and Analysis in a Nuclear Rocket Propellant Tank Mockup," American Institute of Aeronautics and Astronautics Paper No. 69-475, AIAA Fifth Propulsion Joint Specialist Conference (June 1969).

5. T. M. Jordan, "Synthesis of Calculational Methods for the Design and Analysis of Radiation Shields for Nuclear Rocket Systems. Vol. 9. FASTER, A FORTRAN Analytic Solution of the Transport Equation by Random Sampling," Westinghouse Astronuclear Laboratory Report No. WANL-PR-(LL)-010 (June 1967).

6. E. A. Warman, Aerojet Nuclear Systems Company, Personal Communication.

EFFECTS OF RADIATION ENVIRONMENT ON REUSABLE NUCLEAR SHUTTLE SYSTEM

A. G. Lane
Space Division, North American Rockwell

Since radiation protection for a manned nuclear rocket represents the most significant design constraint, major emphasis has been placed upon parametric tradeoff analyses of a wide spectrum of alternate tank configurations to minimize both primary and secondary, direct and scattered radiation sources emanating from the NERVA (nuclear engine for rocket vehicle application). The analytical approach utilizing point kernel techniques is described and detailed data are presented on the magnitude of neutron/gamma doses for different locations. Dose rates are presented for both engine firing and post-shutdown periods. Conical aft bulkhead geometries employing a range of included half cone-angles from 5-15 degrees and end cap radii from 25 to 125 inches were evaluated. Single-tank configurations utilizing smaller cone angles and end cap radii were found to minimize integral radiation levels, hence, stage shielding-weight penalties for shuttle missions. This is due to the greater payload separation distance, reduction of the effective energy disposition and scattering centers in the aft end of the tank, and greater depth of the liquid hydrogen propellant for radiation attenuation at any given time during the draining cycle for a fixed tank propellant capacity. Hybrid configurations employing an upper tank with a reduced cone angle and end cap radius results in low integral payload doses primarily due to the increased separation distance caused by the elongation of the larger capacity upper tank. A preliminary radiation damage assessment is discussed of possible reusable nuclear shuttle (RNS) materials, components, and subsystems, and the possible effects of the radiation environment on various phases of RNS mission operations, i.e., maintenance, rendezvous, docking, and engine disposal.

One of the major problems in designing nuclear propulsion vehicles is providing adequate shielding from the system's radiation environment. The prime mover behind the design definition of the reusable nuclear shuttle (RNS) has been the design of configurations that minimize neutron and gamma radiation levels to the man-rated payloads and radiation sensitive components and subsystems.

Since radiation protection for a manned payload represents the most serious design constraint, a major emphasis has been placed upon a parametric tradeoff analyses of a wide spectrum of alternate tank configurations to minimize primary and secondary, direct and scattered radiation sources emanating from the NERVA engine.

The discussion of tank configurations presented in this paper is primarily concerned with two promising classes of RNS configurations recently evaluated; (1) a single conical tank configuration employing aft bulkhead geometries with included half cone-angles less than 15 degrees and closing end-cap radii from 25 to 125 inches, and (2) hybrid configurations employing a separate large-capacity propellant module which includes a smaller capacity, small diameter propellant tank adjacent to the NERVA engine.

Also discussed are the possible effects of the radiation environment for a selected RNS vehicle configuration on various mission operations for a reference lunar shuttle mission.

Finally, a preliminary radiation damage assessment of candidate RNS materials, components, and subsystems for a selected candidate vehicle configuration is briefly reviewed. The damage assessment is based upon requirements for a maximum 10-hour NERVA engine operation imposed by engine design requirements.

ANALYSIS APPROACH TO TANK CONFIGURATIONS

The majority of the radiation calculations for this study were performed utilizing point kernel techniques on the IBM 360, model 65 computer system at North American Rockwell's Space Division. The point kernel techniques represent the most efficient and least costly method of preliminary analysis of the radiation environment of a wide variety of nuclear stage configurations and tank geometries. A flow chart summary of the computational methods employed in this study is shown in Figure 1.

The QAD-B and GR-34 point kernel programs, originally developed by LASL (Reference 1), were the basic tools employed in the analysis. The Space Division version of the QAD-B program is designed to calculate neutron or gamma radiation levels at detector points located within or outside a complex radiation source geometry which can be described by a combination of quadratic surfaces. The program evaluates the material thicknesses intercepted along the line-of-sight from the source point to the detector point. These material thicknesses or path lengths then are employed in attenuation functions to calculate the multigroup flux levels, dose rates, or heating rates at the detector. The attenuation function for gamma rays employs exponential attenuation with an infinite medium buildup factor. Two neutron attenuation functions are included: (1) a modified Albert-Welton function for calculating fast neutron dose rates using removal cross-sections and (2) a monovariant polynominal expression for computing neutron spectra and dose rates using infinite media moments data.

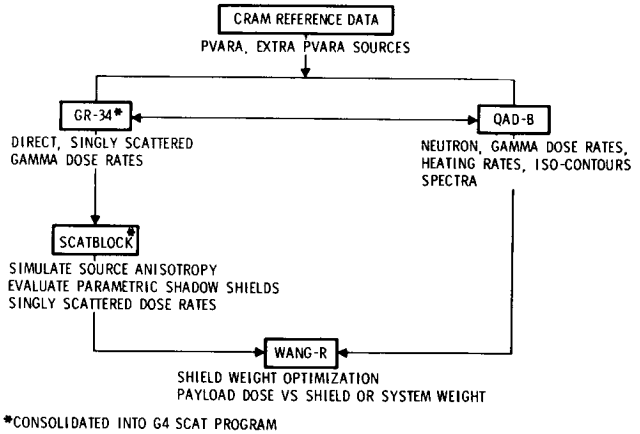

Figure 1. Computational Methodology

The Space Division version of the GR-34 program calculates the direct gamma radiation levels from a point source to a point detector as in QAD. Similarly, the attentuation function for gamma rays also employs exponential attenuation with infinite medium buildup factors. Hence, the difference between the direct radiation levels with buildup and without buildup, can be taken (in most instances) to be a somewhat conservative estimate of the scattered radiation level. However, the GR-34 program allows a calculation of the first photon or gamma ray scattering event analytically. The scattering medium for the first photon collision is described by a series of spatial points representing volume elements. Gamma scattering prediction is based on multigroup Klein-Nishina differential angular cross-sections. The source energy groups are degraded according to the Compton relationship of energy ratio versus scattering angle. A scattering event contribution is calculated for each volume element and the gamma levels at the detector point are generated by summing contributions from the first scattering event. The radiation levels may be calculated for cases either with or without the application of an infinite medium buildup factor along the scattered leg. Thus, the GR-34 is analogous to the Monte Carlo method for treating line sources until the occurrence of the first collision event.

The SCATBLOCK program, originally developed by Aerojet Nuclear Systems Company (Reference 2), has been modified by Space Division and is included as an optional subroutine within the GR-34 program. The resulting program which requires no tapes is called G4 SCAT. SCATBLOCK uses an array of scattered gamma dose rates calculated by the main program and calculates gamma kerma rates when disk shields of arbitrary location and radius are placed between the source and scatter points. This allows the calculations necessary for the design of a scatter gamma shield to be carried out parametrically for each shield configuration without the complicated problem setups and longer computer run times of the ,more general G4 SCAT or QAD-B programs.

The WANG-R is a Space Division modification of a program originally developed by Aerojet Nuclear Systems Company (Ref. 2) which is used to generate values of integral radiation doses as a function of shield and/or system weight. The principal input parameters are doses from individual PVARA (pressure vessel and reactor assembly) and from sources external to PVARA, tables of shield weight as a function of size, and matrices of transmission factors for each source as a function of shield size. Since these inputs are easily varied, parametric shield studies may be accomplished rapidly and inexpensively.

Mathematical models for the various tank propellant configurations were sized for an initial LH_2 propellant capacity of 300,000 pounds with an LH_2 residual capacity of 5000 pounds after engine shutdown for post-shutdown cooling requirements. Tank propellant drainage curves were developed on the basis of a nominal LH_2 flow rate of 91.4 pound-second^{-1} A 3300-pound internal engine shield was assumed for all calculations. The G4 SCAT point kernal program was utilized in the determination of tank-top gamma kerma rates from both PVARA and external sources.

An extrapolation of the multiregion PVARA volume source to a single point source at the core midplane, as well as the utilization of anisotropy factors for the PVARA point source extrapolations, was the general technique employed in the current analysis for PVARA source contributions to tank top integral dose. A more detailed discussion of technique may be found in Reference 3. Identical photon thirteen-group energy structures, energy spectrums, and source strengths were utilized in all calculations.

Multigroup source data for the external sources analyzed, i.e., the PDL (pump discharge line) and TCA (thrust chamber assembly) were developed from the CRAM data (Reference 4).

The multipoint source distributions in this reference were collapsed into three effective PDL sources and four effective TCA sources, respectively. Similarly, the LH_2 capture gamma sources were derived for four effective point sources.

The integral-tank top gamma doses represent the summation of each effective source contribution for the three aforementioned external sources.

The general geometry model for the various tank configurations is shown in Figure 2. The on-axis separation distance from the PVARA midplane to the tank bottom was 200 inches for all tank configurations evaluated.

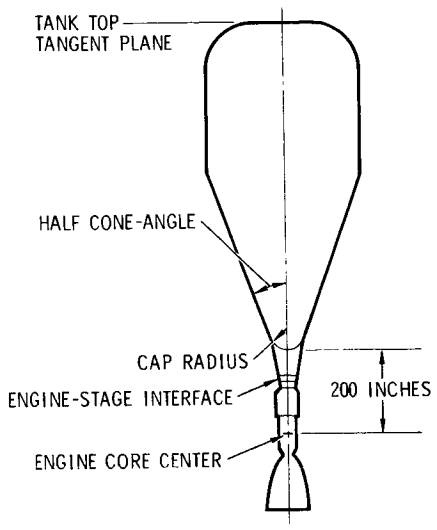

Figure 2. Tank Configurations Geometry Model

SINGLE CONICAL TANK CONFIGURATIONS

Early RNS parametric design analyses as discussed in Reference 5 led to the preliminary conclusion that the optimum single tank configuration for manned applications was one employing an aft bulkhead geometry with an eight-degree half cone-angle and an end cap radius of 25 inches.

The shield weight data utilized in the parametric tradeoff analyses was derived from this preliminary screening which considered tank top dose contributions from the PVARA source. Conical aft bulkhead configurations were evaluated that employed varying half cone-angles of 5 to 15 degrees and end cap radii of 25, 50, 75, and 100 inches.

However, a more detailed analysis of selected single-tank conical configurations was undertaken to substantiate the results of the preliminary screening analysis. The computations were performed with the G4 SCAT point kernel program for tank configurations with an initial LH_2 capacity of 300,000 pounds. More detailed drainage curves were developed based on the evaluation of tank-top gamma kerma rates at five representative propellant levels during the course of the tank drain.

Comparisons of the more detailed calculations for PVARA tank top dose with similar results obtained during the preliminary screening analysis confirmed the effectiveness of the earlier approach (Table 1).

The more detailed G4 SCAT point kernel calculations for both PVARA and external source contributions are shown in Table 2 for single tank conical configurations with aft bulkhead geometries employing half cone-angles of 8, 10, 12, and 15 degrees and end cap radii of 25, 50, 75, and 100 inches. The on-axis tank-top integral gamma dose values in Table 2 represent the summation of the PVARA and external source contributions. The aforementioned dose values are all based on the common assumptions of an initial LH_2 tank capacity of 300,000 pounds, a terminating LH_2 residual of 5,000 pounds at engine shutdown, and a 3300-pound internal NERVA shield. Similarly, the relative gamma kerma levels are displayed in Figure 3 as a function of varying half cone-angles from 8 to 15 degrees and end cap radii extending from 25 to 100 inches. Both Figure 3 and Table 2 further substantiate the results of the earlier preliminary screening analysis which indicated three reasons that single tank conical configurations with aft bulkhead geometries employing both reduced half cone-angles and end cap radii minimize integral tank top dose for a fixed propellant capacity: (1) greater source-to-tank top detector separation distance, (2) reduced effective energy deposition and scattering centers in the aft end of the propellant tank, and (3) greater depths of the LH_2 propellant column for radiation attenuation at any specified time during the tank draining cycle. For example, the single tank configuration employing an eight-degree half cone-angle and 25-inch end cap radius exhibits a source-to-detector separation distance of 561inches greater than a configuration employing a

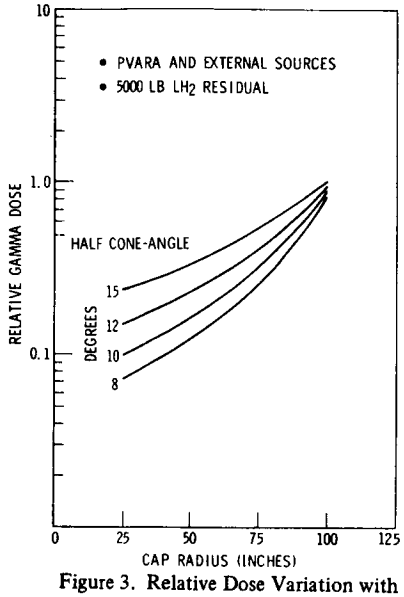

Figure 3. Relative Dose Variation with Conical Tank Geometries

Table 1. PVARA On-Axis Tank Top Integral Dose Comparisons

Aft Bulkhead Geometry					
Cone Half-Angle (degrees)	Cap Radius (inches)	LH_2 Residual (lb)	G4 SCAT Analysis (rem)(1)	Preliminary Screening Analysis (rem)(2)	Ratio (2)/(1)
8	50	7500	42.3	38.4	0.908
		5000	56.8		
		0	143.0		
8	25	7500	16.9	12.3	0.728
		5000	22.6		
		0	89.5		
5	50	7500	28.3	27.1	0.958
		5000	45.4		
		0	133.3		
15	100	7500	469.4	561.0	1.195
		5000	534.1		
		0	714.6		

Table 2. Tank Top Dose Comparison for Conical Geometries

	Cone Half-Angle (degrees)																			
	15					12					10					8				
Cap Radius (in.)	125	100	75	50	25	125	100	75	50	25	125	100	75	50	25	125	100	75	50	25
Tank Length (in.)	1212	1266	1327	1394	1464	1236	1308	1388	1475	1568	1261	1348	1448	1557	1672	1297	1407	1536	1678	1827
Gamma Dose (rem)	-	520	275	172	125	-	473	208	120	78	-	442	177	86	52	-	432	130	65	38

15-degree, 100-inch cap radius for a fixed LH_2 tank capacity of 300,000 pounds. Additionally, the depth of the LH_2 column at the end of the engine burn (5000-pound LH_2 residual) is 198 inches greater for an eight-degree half cone-angle, 25-inch end cap radius aft bulkhead geometry than a conical configuration employing a 15-degree half cone-angle, 100-inch end cap radius. This increased column depth represents approximately two photon relaxation lengths in LH_2.

Additionally, an extension of the analysis to a cap radius of 125 inches would demonstrate that the tank-top integral dose values tend to converge at this radius regardless of the half cone-angle since the three principal factors described become nearly equivalent in a practical sense. This premise is evidenced in Table 2 which shows a variation in tank length of only 85 inches (1,297 inches to 1,212 inches) at a cap radius of 125 inches over the range of half cone-angles from 8 to 15 degrees. Similarly, the depth of the LH_2 column near the termination of the tank drain tends to converge near a cap radius of 125 inches (Figure 4) for a propellant level of 7500 pounds near the end of the engine firing. Hence, the drainage rate histories are nearly equal during the time interval where the most significant portion of the total tank top integral dose is accumulated. Additionally, the geometric surface area and, consequently, the energy deposition near the tank bottom is controlled principally by the magnitude of the end cap radius for large values of cap radii, within the range of the evaluated half cone-angles.

The parametric data also illustrates the dominating influence of reduction in cap radius on minimizing the tank top integral dose. For example, it is shown in Figure 3 that the aft bulkhead geometry employing an 8-degree half cone-angle and a 25-inch end cap radius lowers the tank top integral dose. However, the aft bulkhead geometry employing a 10-degree half cone-angle and 25-inch end cap radius has about a 20-percent lower relative tank top integral dose than an aft bulkhead geometry employing an 8-degree half cone-angle and a 50-inch end cap radius although the tank lengths are approximately equal for the two configurations as shown in Table 2. This effect is principally due to the longer LH_2 column and, hence, great shielding effectiveness afforded by the smaller 25-inch cap radius during the latter stages of the tank drain cycle.

In order to determine whether an appreciable "viewing" effect around the shadow of the LH_2 column occurs in the 8-degree half cone-angle geometry employing the 25-inch end cap radius, PVARA and PDL tank top integral doses were evaluated at radial detector locations of 132.5 and 196.85 inches, respectively. Comparisons with on-axis tank integral doses are shown in Table 3 for an axial detector location 2067 inches above the core's midplane and LH_2 residual of 5000 pounds. The PVARA tank top integral doses are shown to increase from 22.6 rem on axis to 26.5 rem near the outer radius of the tank, a factor of about 1.16. Similarly, the PDL tank top integral dose varies from 6.58 rem on axis to 8.41 rem near the outer radius of the tank, a factor of about 1.28.

Table 3. Tank Top Radiation Dose Variation

Radiation Source	Integral Tank Top Dose (rem)		
	Radial Detector Location (inches)		
PVARA	0	132.5	196.85
	22.6	24.7	26.3
PDL	6.58	7.14	8.41

External disk-shield weight variations with end cap radius and half cone-angle for the single tank conical configurations are shown in Figure 5 for a tank-top integral dose criterion of 10 rem. Aft bulkhead geometries employing half cone-angles from 8 to 15 degrees and end cap radii from 25 to 100 inches were evaluated.

The external shield weights were derived from the data for the on-axis integral dose (both PVARA and external sources) shown in Table 2. The external disk shield weights are shown to vary from about 4,000 pounds for the 8-degree half cone-angle and 25-inch end cap radius aft bulkhead geometry, to about 13,000 pounds for a 15-degree half cone-angle, 100-inch end cap radius aft bulkhead geometry using a 10-rem tank top dose criterion. As expected, the external shield weight curves shown in Figure 5 have similar characteristics to their counterpart, the relative tank-top dose plots shown in Figure 3 as a function of half cone-angle and end cap radius.

COMPARISON OF RNS CONFIGURATION CLASSES

The previously discussed parametric analysis of single conical tank configurations established the basis for comparison of three classes of candidate RNS tank configurations: single tank conical, modified dual cell, and hybrid (shown in Figure 6). It has been established that the aft bulkhead geometry is the dominant factor in reduction of the tank top dose for a fixed LH_2 tank capacity, internal engine shield, and separation distance between the engine (reactor core) midplane and tank bottom.

Three tentative baseline configurations representing the three comparison classes are:

1. Single-tank conical configuration, employing an 8-degree half cone-angle and a 25-inch end cap radius
2. Modified dual-cell configuration, employing the single-tank aft bulkhead geometry of (1) with a "shortened" 50-inch radius inner cell
3. Hybrid dual-tank configuration, employing a small tank (9300 pound LH_2 capacity) that interfaces with the NERVA engine and a larger tank (290,000 pound LH_2 capacity) utilizing an aft bulkhead geometry with an 8-degree half cone-angle with a 40-inch end cap radius.

The evaluation of the tank-top integral direct and scattered gamma dose contributions from both the PVARA and external sources for the three configurations is summarized in Table 4.

Table 4. On-Axis Tank Top Radiation Dose Summary

Tank Design	8 Degree, 25-Inch R Cap, Single Tank	8 Degree, 25-Inch R Cap, Modified Dual Cell	8 Degree, 40-Inch R Cap Hybrid
PVARA direct	10.1	8.7	27.1
PVARA scattered	12.5	13.1	45.3
PVARA total	22.6	21.8	72.4
LH_2 capture	7.2	7.2	7.0
TCA direct	0.62	0.71	1.03
TCA scattered	1.03	1.13	1.54
PDL direct	3.14	2.98	3.12
PDL scattered	3.44	3.51	2.58
TPA total	(8.77)*		
	38.03 (46.80)	37.33	87.67

*Off-axis radial detector location at 132.5

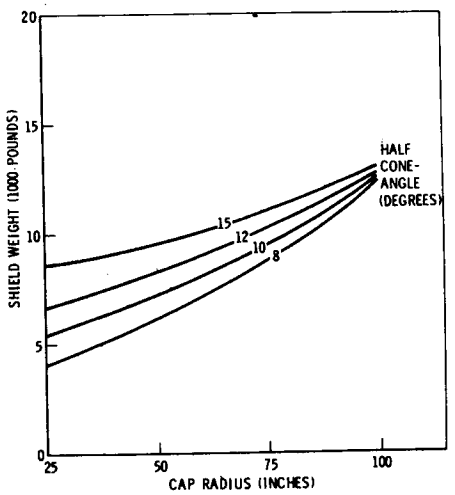

Figure 5. Shield Weight Variation for Single Tank Concial Configuration

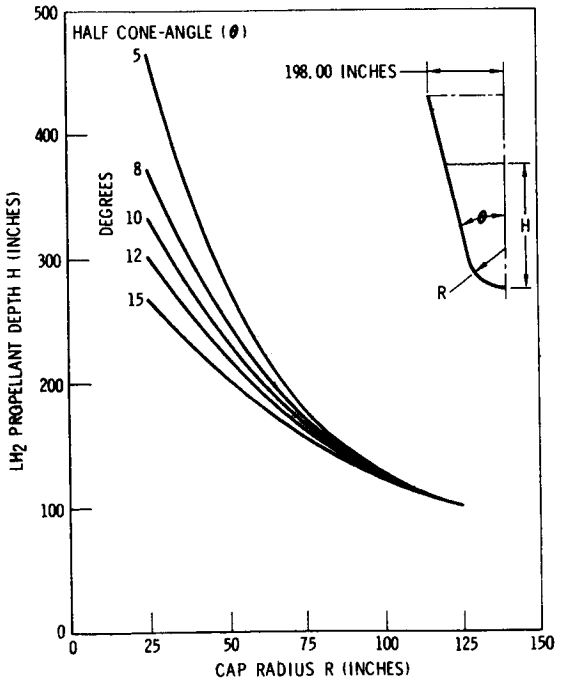

Figure 4. Residual Propellant Level for 7500-Pound Residual LH_2

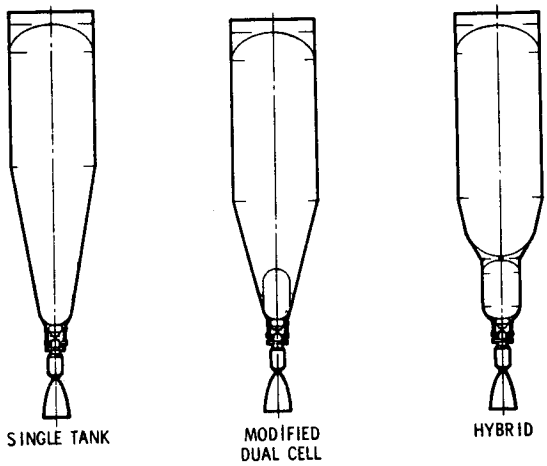

Figure 6. RNS Tank Configuration Classes

SINGLE-TANK CONICAL CONFIGURATION

The table shows the increased relative importance of the external source contributions to the total dose for the single conical tank configuration. The external source contributions represent about 43 percent of the total on-axis tank top integral dose of 38 rem. This point is illustrated in Figures 7 and 8, which depict on-axis tank-top gamma kerma rates and integral gamma doses, respectively, as a function of time prior to completion of the tank drain for the 8-degree, 25-inch conical tank geometry.

A Monte Carlo analysis of this tank configuration (Reference 6) generally confirms Space Division's assessment of the influence of half cone-angle and end cap radius on tank top radiation levels.

MODIFIED DUAL-CELL CONFIGURATION

The modified dual-cell configuration employs the 8-degree half cone-angle, 25-inch end cap radius, aft bulkhead geometry with a shortened inner cell of 50-inch radius and an "effective" column length of 427 inches from the tank bottom at the vertical midplane. The inner cell can contain 5950 pounds of LH_2. This particular dual cell design precludes any neutron dose contributions at tank top since the aft bulkhead is completely immersed in LH_2 during the engine burn to an LH_2 residual of 5000 pounds. The on-axis integral tank top doses are comparable to those obtained for the single-tank conical configuration (Table 4). Slight differences were obtained in PVARA direct and PVARA scattered contributions. The PVARA direct gamma dose is about 13 percent lower for the dual cell due to a small increase in the depth of the LH_2 column near the end of the tank drain cycle. The increase in depth at the 5000-pound LH_2 residual level is about 34 inches, or less than one-third of a photon relaxation length in LH_2. Little difference was noted in the PVARA gamma scattered dose.

Since the tank drain history for the modified dual-cell configuration parallels that of the single-tank conical configuration to the 5950-pound LH_2 level, only about 10 seconds is available for secondary gamma scattering effects in the GH_2 in the region between the outer boundary of the inner cell and the inner boundary of the outer tank wall prior to engine shutdown with an LH_2 residual of 5000 pounds. Additionally, there are fewer scattering centers available due to the drastically reduced volume of the region between the inner cell and outer tank (small cone angle and small, cap radius aft-bulkhead geometry). However, the modified dual-cell configuration has additional structural weight penalties of 1275 pounds (added complexity of the inner cell design as indicated in Reference 7). Thus, the modified dual-cell configuration offers no particular advantages in radiation shielding for RNS applications when compared to its single tank counterpart.

HYBRID DUAL-TANK CONFIGURATION

In the hybrid configuration, the on-axis tank-top PVARA integral gamma dose of about 72 rem represents about 82 percent of the total integral tank-top dose of about 88 rem (Table 4 and Figures 9 and 10).

The hybrid configuration exhibits appreciably higher PVARA direct and scattered integral gamma-dose levels than either the single-tank or modified dual-cell configurations irrespective of an increased source-to-detector separation distance of about 209 inches. However, the energy deposition and available scattering centers are greater in the aft tank for the hybrid configuration primarily due to its 77-inch end cap radius. Concomitantly, the LH_2 level in the tank is less at any given time during the engine burn and tank drain. For example, the 5000 pound LH_2 residual level is about 176 inches less in the hybrid tank than it is for the baseline single-tank conical configuration. This residual level is only about three inches greater than a single tank configuration employing the 8-degree, 75-inch end cap radius, aft bulkhead geometry. The shielding effectiveness

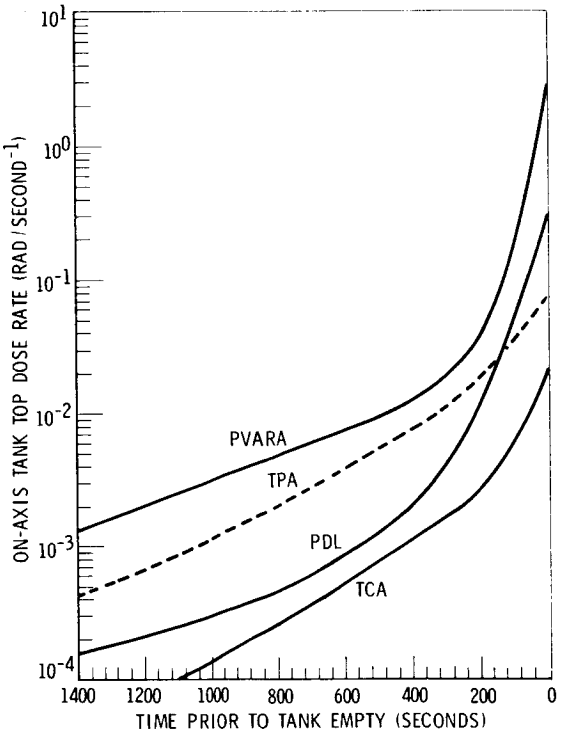

Figure 7. Concial-Tank Radiation Dose Rate Variations

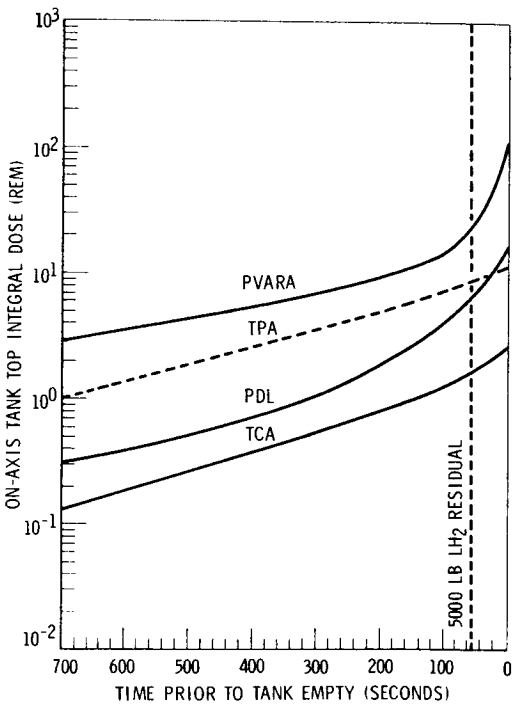

Figure 8. Conical-Tank Integral Radiation Dose Variations

of the greater depth of LH_2 column is also observed by comparison of the dose rate and integral dose curves shown in Figures 9 and 10, with identical curves for the single tank configuration shown in Figures 7 and 8.

The slightly lower tank-top dose levels for the PDL and TCA sources are attributed primarily to the larger source-to-detector separation distance in the hybrid configuration. The relative LH_2 column thickness and aft bulkhead surface geometry characteristics for energy deposition are less effective since the external sources, especially the PDL (and also the TPA if included) are located off the vertical axis of the tank configuration. Consequently, these sources do not derive the maximum benefits from the shadow shielding effect of the LH_2 column. However, since the magnitude of any single external source is considerably less than that of the PVARA source, it is a simpler design task to shield the external sources locally or to relocate the particular component or line if necessary.

Thus, the hybrid configuration employing an upper tank with a reduced cone angle and end cap radius results in relatively low tank-top integral doeses primarily due to increased source-to-detector separation distance, since the smaller aft tank adjacent to the NERVA engine is constrained by the size limitations of the space shuttle (used for delivery to orbit) and the propellant requirements for end-of-life engine disposal. The present cargo bay of the space shuttle is sized to have a clear volume of 15-foot diameter by 60-foot length. Therefore, the possible geometrical variations in the design of the small tank are limited if (1) a 9300-9500 pound LH_2 capacity is required and (2) the small tank and NERVA engine are to be launched as a unit with the space shuttle. It is concluded that further reduction of integral tank top dose might be possible by reducing the cone angle and end cap radius of the aft bulkhead of the upper tank in the hybrid configuration, thus elongating the total vehicle configuration. This, in turn would increase the source-to-detector separation distance, and could represent the achievable upper limit for minimization of integral tank top dose with the hybrid configuration under the present RNS ground rules.

However, the subtleties introduced by the coupling of the larger forward tank with a smaller capacity aft tank of larger radius should be examined in greater detail than was possible in this study.

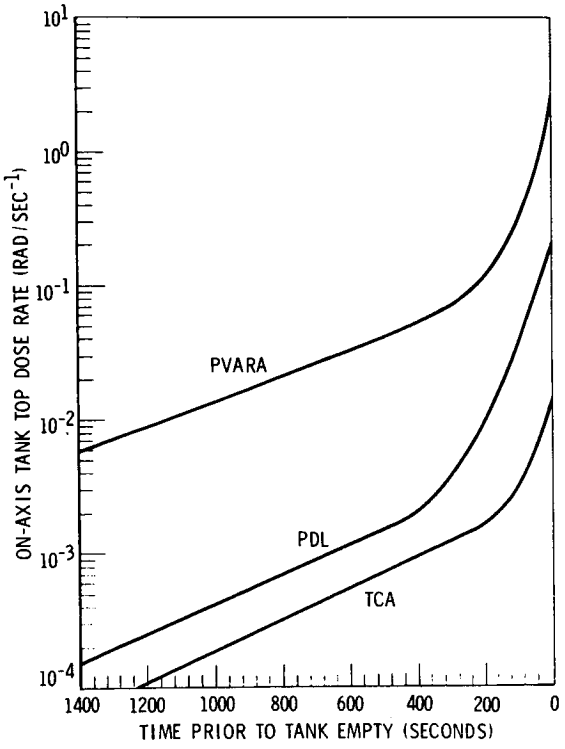

Figure 9. Hybrid-Tank Radiation Dose Rate Variations

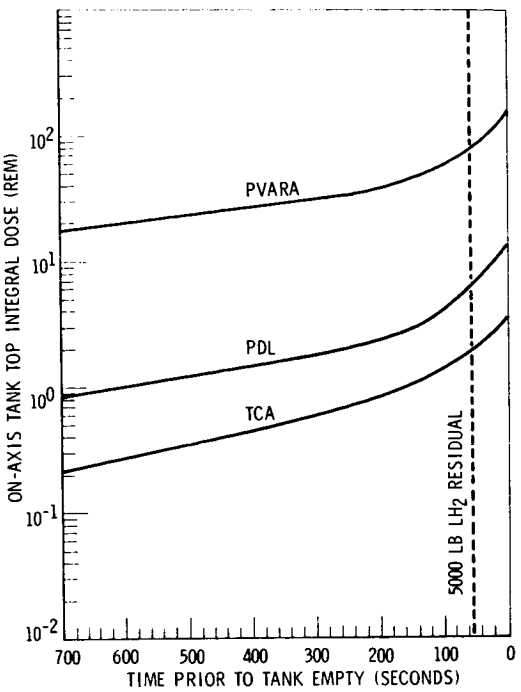

Figure 10. Hybrid-Tank Integral Radiation Dose Variations

SHIELD WEIGHT COMPARISONS TANK CONFIGURATION ANALYSIS

The external shield weights evaluation for the three tentative baseline configurations was based on a nominal 10,000-pound lead disk shield, located 81 inches forward of the core center. The baseline shield design model was taken from March 1970 CRAM data, Reference(4), and is shown in Figure 11. Parametric shield weights as a function of integral tank-top gamma dose were developed utilizing the WANGREV computer program. The external disk shield model was treated by the program in two segments, i.e., a central segment of constant 25-inch radius and varying thickness, and a peripheral section of varying thickness and varying outer radius from 25 to 50 inches. The on-axis integral tank-top dose values shown in Table 4 were utilized as initial dose levels for the computations. Comparative integral dose values as a function of external shield weight for the three tentative baseline configurations are shown in Figure 12. Since the initial integral dose values for the modified dual-cell configuration are almost identical to the single tank configuration, the shielding weights may be considered equivalent for the two configurations for all practical purposes. The curve for external disk weights versus tank top dose for the ANSC 15-degree conical baseline configuration is extrapolated from another study (Reference 8). Since the integral dose levels for this configuration were computed on the basis of a 7500 pound LH_2 residual, the external shield weights were normalized to correspond to a common LH_2 residual of 5000 pounds (Figure 12).

Assuming a payload attenuation factor of 3 (study guidelines and constraints document, Reference 9), an integral tank top dose of 10 rem would be within the allowable dose criteria of 3 rem per crew member, and 10 rem per passenger per round-trip shuttle mission. The external disk-shield weight requirements for an allowable tank top integral dose of 10 rem are summarized in Table 5 for the three tentative baseline configurations as well as the ANSC 15-degree conical configuration and ANSC results for the 10-degree hybrid configuration, both normalized to a common LH_2 residual level of 5000 pounds. Table 5 shows that the baseline single tank conical configuration and modified dual-cell configuration result in the lowest external shield weight requirement of 4050 pounds.

The Space Division hybrid configuration requires an external disk shield weight of 5900 pounds which represents an additional external shield weight penalty of 1850 pounds when compared to the single tank and

modified dual cell baseline configurations. The 10-degree hybrid configuration requires an additional 800 pounds more of external shield weight than the NR-SD hybrid configuration. The ANSC 15-degree conical configuration requires an 11,950 pound external shield based on the aforementioned study criteria. This represents a delta shield weight penalty of about 7800 pounds when compared to Space Division's single conical and modified dual-cell configurations.

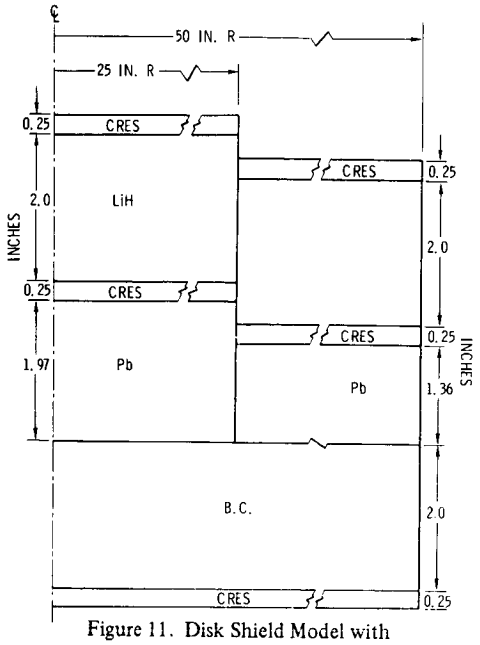

Figure 11. Disk Shield Model with Lead Gamma Shield Region

The after-shutdown gamma kerma rates (rad/hour^{-1}) following the last engine burn (EOI) are shown in Figure 13. The rates are given at a separation distance of 20 feet from the NERVA core center for three polar angles of 0, 90, and 180 degrees, respectively, for varying after-shutdown decay times.

The gamma kerma rates for after-shutdown decay times of 8 hours, 24 hours, 1 week, and 1 month (Figure 13) are summarized in Table 7. Gamma kerma rates for a nominal engine operating power level of 1575 Mw are also included in Table 7 to illustrate that the dose rates are reduced by about 3.5 to 4 orders of magnitude during the first 8-hour post-shutdown time period. Thereafter, incremental reductions reductions by factors of about 4, 9, and 5 due to natural decay are evidenced for after-shutdown decay times of 24 hours, 1 week, and 1 month, respectively, as illustrated in Figure 13 and Table 7.

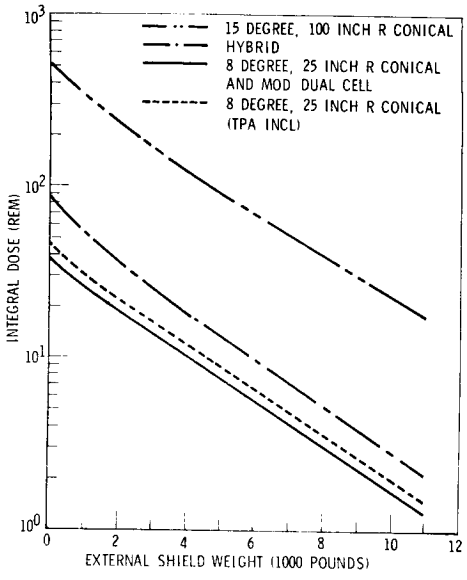

Figure 12. Baseline Shielding Weight Comparison

Table 5. Baseline External Shielding Weight Comparisons

Configuration	External Shield Weight (lb)	Delta External Shield Weight (lb)
NR-SD single conical tank 8-degree half cone, 25-inch cap radius (without TPA)	4,050	0
NR-SD modified dual cell	4,050	0
NR-SD 8-degree hybrid	5,900	+1850
ANSC 15-degree single conical tank	11,950	+7800
10-degree hybrid (ANSC)	6,700	+2650
300K lb LH_2 capacity 5000 lb LH_2 residual GRAM reference lead disk shield		

RNS MISSION OPERATIONAL CONSIDERATIONS

The preliminary assessment of the after-shutdown radiation from NERVA engine operation was conducted on a representative lunar shuttle mission (Reference 3). Summarily, the shuttle mission entails a total duration of approximately 25 to 27 days with the utilization of four NERVA engine burns during the entire mission cycle. Table 6 itemizes the elements of the mission and their duration. The four engine burns occur in the mission phases identified in the table; (1) translunar injection (TLI), 1750 seconds; (2) lunar orbit insertion (LOI), 310 seconds; (3) transearth injection (TEI), 146 seconds; and earth orbit insertion (EOI), 740 seconds.

Table 6. RNS Representative Lunar Mission

Segment Number	Segment Title	Segment Duration day	hour	min	s
1/2	Earth orbital departure (EOD) maneuver			6	44
2/3	Earth orbit departure transfer			43	39
3/4	Earth orbit departure circularization			3	44
4/5	Earth orbit departure orbit		2	08	20
5/6	Translunar injection			29	10
6/7	Translunar injection cooldown		1	09	20:00
7/8	Initial translunar flight		2	00	00
8/9	Translunar injection midcourse correction			14	31
9/10	Final translunar flight		1	18	19 19
10/11	Lunar orbit insertion (LOI)			5	10
11/12	Lunar orbit insertion cooldown			10	16 40
12/13	Lunar orbit rendezvous orbit			8	20 00
13/14	Lunar orbit rendezvous maneuver				33 20
14/15	Lunar orbit operations	17	21	31	38
15/16	Lunar orbit departure (LOD) maneuver			1	11
16/17	Lunar orbit departure transfer			59	25
17/18	Lunar orbit departure circularization			1	11
18/19	Lunar orbit departure orbit		2	46	22
19/20	Transearth injection			2	26
20/21	Transearth injection cooldown		6	40	00
21/22	Initial transearth flight		1	12	06 40
22/23	Transearth injection midcourse correction			6	58
23/24	Final transearth flight		1	10	56 22
24/25	Earth orbit insertion (EOI)			12	20
25/26	Earth orbit insertion cooldown		14	10	00
26/27	Earth orbit rendezvous orbit		13	53	20
27/28	Earth orbit rendezvous maneuver			1	05

Table 7. After-Shutdown Radiation Environment Following EOI Engine Burn

Polar Angle (degrees)	Separation Distance (ft)	Gamma Kerma Rate (rad-hr^{-1})				
			After Shutdown			
		Full Power	8 hrs	24 hrs	1 week	1 month
0	20	2.38×10^5	2.53×10^1	6.79	7.45×10^{-1}	1.51×10^{-1}
90	20	1.23×10^7	7.65×10^3	1.74×10^3	1.92×10^2	3.91×10^1
180	20	9.37×10^6	6.06×10^3	1.42×10^3	1.63×10^2	3.25×10^1

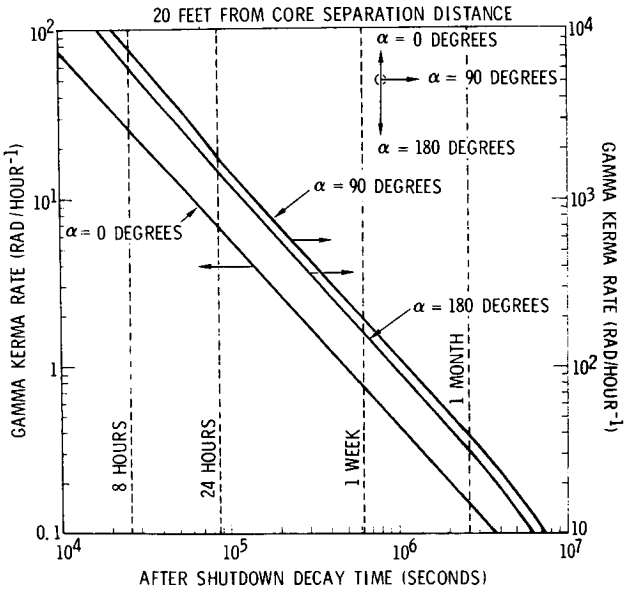

Figure 13. After-Shutdown Radiation Environment

After the fourth engine burn for EOI there is a 14-hour engine cooldown operation prior to the EO rendezvous orbit segment which has a duration of slightly less than 14 hours. After-shutdown isodose contours 24 hours after the EOI engine firing are shown in Figure 14 to further demonstrate a typical after-shutdown radiation environment in the vicinity of the NERVA engine. As in Figure 13, gamma kerma rates (rad/hour^{-1}) are given as a function of separation distance in feet from the engine core midplane with reference to a polar angle, α = 0 degrees, along the vertical axis in the forward direction.

Figure 14 illustrates that only minor stage maintenance operations (limited to the 0-15 degree quadrant forward of the engine core midplane) appear to be feasible near the engine-stage interface without additional shielding provisions up to 24 hours after the last engine shutdown cycle. This observation is predicated on the current basic criterion of a 25-rem/year allowable dose to maintenance personnel from the RNS (Reference 9).

For example, an operation involving rendezvous maneuvers with a space tug for engine removal would require rather extensive additional shielding provisions for protection of the crew, remote handling equipment, and manipulative techniques. However, if an unmanned tug vehicle were contemplated for this operation, the primary concern is possible radiation damage to its components, subsystems, and systems due to the aftershutdown gammas from the engine. Integral gamma doeses were determined for the removal operation after one and ten RNS lunar mission cycles, respectively, for a 0-degree polar angle orientation between the midplanes of the engine core and tug during the docking maneuver (as well as for a 90-degree orientation). Cumulative gamma doses of 857 rads (C) and 2.43×10^5 rads (C), respectively, were derived for the 0-degree and 90-degree orientations after one complete mission cycle.

For the engine removal after ten mission cycles, integral gamma doses of 2.14×10^3 rads (C) and 6.08×10^5 rads (C) were derived, respectively, for the 0-degree and 90-degree orientations. Thus, the 0-degree orientation of the engine and tug prior to docking affords significant radiation shielding advantages, principally due to the presence of the internal engine shield in the 0-15 degree quadrant with respect to the engine core midplane. Similarly, an additional attenuation factor of 3-4, attainable in the above quadrant if the 4,000-pound external disk shield, is included in the stage configuration. Utilizing the preferred 0-15 degree orientation between the engine and the tug during the docking maneuver, it can be concluded that the integral gamma doses are several orders of magnitude below anticipated radiation damage thresholds for most of the candidate materials and components. The above calculations assumed a separation distance of 20 feet between the engine core midplane and the location of the nearest tug component. Additionally, it was assumed that the engine removal operation was initiated 24 hours after the last engine burn (EOI) and was terminated one week later with the insertion of the NERVA engine into a 660 n mi "safe" orbit.

It may be concluded that any contemplated manned mission operations (maintenance, repair, logistics, engine removal) involving a near approach to the engine in either the radial or aft directions will dictate additional fixed shielding requirements. These fixed shielding requirements will be significantly reduced (previously shown in Figures 12 and 13 and Table 7) if such operations are performed 8-24 hours after the last engine firing. Tentatively, this doctrine does not appear to compromise presently conceived traffic models or the mission time tables for subsequent shuttle trips.

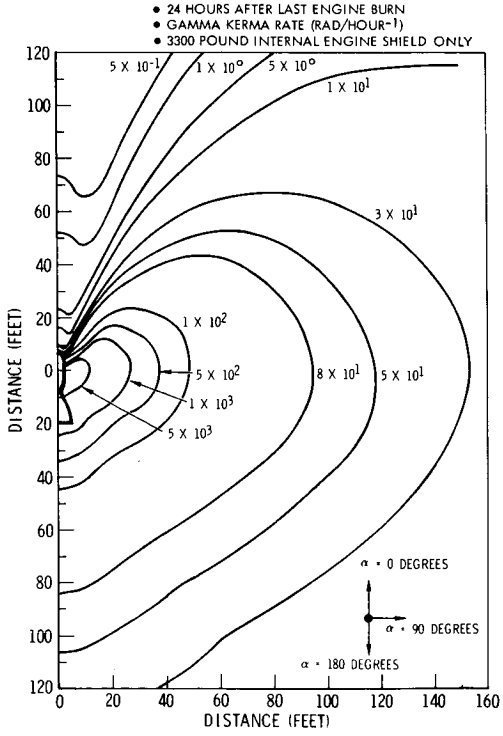

Figure 14. After-Shutdown Iso-Dose Contours

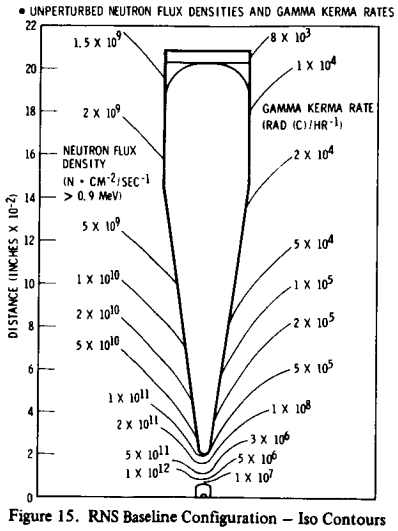

Figure 15. RNS Baseline Configuration – Iso Contours

RADIATION DAMAGE ASSESSMENT

A radiation damage assessment of candidate materials, components, and subsystems has been initiated for the single-tank conical configuration (8-degree half cone-angle and a 25-inch end cap radius). Iso-contour plots of fast neutron flux densities (E > 0.9 Mev) and gamma kerma rates are shown in Figure 15 for the single-tank conical configuration as a function of distance from the NERVA engine core midplane. Early analysis indicates that those components located in the forward bulkhead region (astrionics bay) appear to be well protected, in general, by the inherent shield design of the vehicle previously discussed in this paper. In fact, the neutron flux densities are relatively insignificant during the total engine operational cycle due to the appreciable LH_2 column and the large attenuation afforded by the internal and external shields. Similarly, integral tank-top gamma kerma rates would be about 50-75 rad (C) per hour^{-1} of engine full-power operation or about 500-750 rad (C) for ten RNS lunar missions. Several guidance, navigation and control components (horizon scanners, star trackers, RCS thruster modules, and the rendezvous radar antenna) when deployed appear to be the only components, based on the current design, that would be subjected to higher radiation levels by virtue of their location external to the periphery of the outer tank wall. A neutron fluency of 5.4×10^{13} nvt and integral gamma kerma dose of about 8×10^4 rad (C) appear possible for these components based on unperturbed neutron flux densities and gamma kerma rates from general iso-contour plots for ten RNS lunar mission cycles.

However, those components located in the tank aft bulkhead region will be subjected to appreciably higher radiation levels. In particular, the unattenuated fast neutron flux densities range from about 1×10^{11} to 5×10^{11} n-cm^{-2} second^{-1} and the gamma kerma rates from about 4×10^5 to 9×10^5 rad (C) hour^{-1} in the region between the tank bottom and the engine and stage interface. For ten RNS lunar missions, this would represent a neutron fluency of about 3.6×10^{14} to 1.8×10^{15} nvt and a gamma kerma dose of about 4×10^6 to 9×10^6 rad (C). Therefore, organic valve seals, gaskets, and organic adhesives in the insulation subsystem, etc., could be marginal in the aforementioned region. Similarly, sensors (liquid level, temperature, pressure transducers), electrical components, and lines must also be more thoroughly evaluated as part of the radiation effects test program. However, none of the aforementioned radiation levels include the additional attenuation afforded by the inclusion of an external disk shield below the engine and stage interface for manned missions.

SUMMARY AND CONCLUSIONS

The single-tank conical and modified dual-cell configurations, both employing aft bulkhead geometries with an 8-degree half cone-angle and a 25-inch end cap radius, represent the configurations with a minimum integral tank-top dose of 37-38 rem and a minimum external shield weight of about 4000 pounds on the basis of an allowable dose criterion of 10 rem at the tank top. However, the insertion of the inner cell in the modified dual-cell configuration creates an additional structural weight penalty of 1275 pounds. From a radiation standpoint, the optimum hybrid configuration exhibits a tank-top integral dose of about 88 rem. The higher integral dose for the hybrid configuration is principally due to larger dose contributions from the PVARA source arising from the geometrical constraints on the small tank adjacent to the NERVA engine. These constraints tend to limit the end cap closure to a radius of 77 to 80 inches to meet the space shuttle's dual requirements of 9300 pounds of LH_2 tank capacity for end-of-life engine disposal, and an allowable cargo volume of 15-foot diameter by 60-foot length for the space shuttle are satisfied. Consequently, further reductions in the tank-top integral dose and, in turn, external shield weight, appear possible for a fixed total propellant capacity by decreasing the aft bulkhead cone-angle and end cap radius of the large forward tank in the hybrid configuration, thereby increasing the source-to-detector separation distance for the total vehicle.

In general, single tank configurations utilizing smaller cone-angles and end cap radii were found to minimize integral radiation levels, and stage shielding-weight penalties for shuttle missions. For a fixed tank propellant capacity this is due to the greater source-to-payload separation distance, reduced effective energy deposition and scattering centers in the aft end of the tank, and greater depth of the liquid hydrogen propellant for radiation attenuation at any given time during the draining cycle.

Hybrid configurations employing an upper tank with smaller cone-angles and end cap radii result in minimum integral payload doses primarily due to increased separation distance, since the smaller aft tank adjacent to the NERVA engine is constrained by the size limitations of the earth-orbital shuttle and the mission propellant requirements.

It may be concluded that any contemplated mission operations involving a near approach to the engine and stage interface area of the RNS in either the radial or aft directions will dictate additional fixed shielding requirements. However, a preferred approach oriented toward the forward end of the vehicle will minimize shielding requirements for such operations as rendezvous, docking, maintenance, and engine disposal.

A preliminary radiation damage assessment of possible RNS materials, components, and subsystems has revealed a number of areas requiring more detailed future examination. The RNS requirement for 10-hour NERVA engine operation imposes detailed perusal of astrionics/electronics, measurement and insulation subsystems as well as materials for gaskets, seals, and adhesives. Replacement of some of the existing candidate stage materials and components with radiation hardened materials and components and/or local shielding appears to present a reasonable design approach.

REFERENCES

1. Malenfant, R.E., "QAD: A series of Point Kernel General Purpose Shielding Programs," Los Alamos Scientific Laboratory, LA-3573 (October 1966).
2. Seminar/Workshop Material on Kernel Techniques for Nuclear Rocket Propellant Tank Geometry/Shielding Analysis (U), Aerojet-General Corporation, RN-PA-0020 (8 and 19 August 1969).
3. Nuclear Flight System Definition Study, Phase II Final Report, Volume III - Systems Definition - Requirements and Systems Analysis, Space Division, North American Rockwell Corporation, SD 70-117-3 (August 1970).
4. Full Flow-Flight Engine Common Radiation Analysis Model (U), Aerojet General Corporation, RN-S-0551 (6 March 1970). (Confidential)
5. Nuclear Shuttle Definition Study - Phase III First Interim Review, Space Division, North American Rockwell Corporation, PDS-70-242 (September 2, 1970).
6. Warman, E.A. and K.O. Koebberling, Monte Carlo Analysis of North American Rockwell Propellant Tank, S100-TM04-W118 (November 1970).
7. Nuclear Shuttle Definition Study - Phase III Second Interim Review, Space Division, North American Rockwell Corporation, SD 70-644 (16 December 1970).
8. Radiation Analysis of Various Vehicles and Payloads for the Reusable Nuclear Shuttle, Aerojet Nuclear Systems Company S100-TRA06-W118-12 (August 1970).
9. Guidelines and Constraints Document - Nuclear Shuttle Systems Definition Study, Phase A, MSFC Document No. PD-SA-P-70-63, Rev. No. 2 (October 1 1970).

RADIATION ENVIRONMENTS ABOUT REUSABLE NUCLEAR SHUTTLE VEHICLES

A. O. Burford
Lockheed-Georgia Co.

Radiation environments about reusable nuclear shuttle (RNS) vehicles produced by a 1575 MW NERVA engine, in both operational and shutdown modes, are presented. Payload location environments are compared for three 300,000 pound propellant capacity RNS vehicle concepts: a single 32-foot diameter propulsion module with a 15 degree half angle ellipti-conical tank bottom containing a full height, ten foot diameter standpipe; a hybrid tank configuration of 10 degree half angle, consisting of a small propulsion module attached to a 32-foot diameter main propellant tank; and a modular vehicle employing seven propellant tanks, each 15 feet in diameter by 60 feet long.

Analyses of radiation effects to stage components near the NERVA engine will be discussed, and survivability estimates for ten missions are made. Dose rates resulting from radioactivation of the RNS are discussed, and the major radiation sources are identified. The impact of radioactivation on manned operations about the RNS is evaluated.

(MANUSCRIPT NOT AVAILABLE)

Radiation Analysis of Various Vehicle and Payload Configurations for the Reusable Nuclear Shuttle**

W. E. Preeg
Aerojet Nuclear Systems Company, Sacramento, California

Radiation analyses were performed and shielding weight requirements were estimated for various candidate vehicle and payload configurations for use with the reusable nuclear shuttle. The analyses included both Point Kernel and Monte Carlo approaches. The effects on reduced shield weight were determined for propellant tanks with pointed conical tank bottoms and for one case of a cluster of small (15 ft diameter) tanks. This later case, however, had an arrangement which had no center tank in the upper tier of tanks. This effect negated most of the gain of going to the smaller tanks. A range of shield weights is presented for various light and heavy manned payload configurations when used in conjunction with a single liquid hydrogen propellant tank, 33 ft in diameter with a 15° conical tank bottom.

I. INTRODUCTION

The importance of a minimum weight system in the nuclear rocket program requires that the maximum shielding benefit be obtained from the large liquid hydrogen propellant tank or tanks. The effects of various tank shapes and drainage patterns on the required weight of biological shielding have been examined.

The analyses were based on use of the 75,000 lb thrust NERVA* engine in a reusable nuclear shuttle between earth orbit and lunar orbit which requires a propellant tank capacity of 300,000 lbs of liquid hydrogen. The NERVA engine includes (a) an internal shield within the Pressure Vessel and Reactor Assembly (PVARA) designed to meet the requirements of protection of some of the engine components[1], and (b) provision for a mission-dependent uncooled disk shield forward of the PVARA designed to limit crew exposure during manned missions with very light payloads. A recently completed study of engine shield requirements based on a reference 33 ft diameter LH_2 tank with a 15° half-angle conical tank bottom, resulted in selection of a reference upper limit disk shield weighing 10,000 lbs.[2] This shield limits the tank top dose to 20 Rem. This is equivalent to a 10 Rem crew dose if the light payload has an attenuation factor of two. Shield weights determined for alternate propellant tank configurations were based on providing tank top radiation exposure equivalent to that predicted with the reference 15° conic tank and 10,000 lb disk shield (i.e., 20 Rem at the propellant tank top payload interface). The PVARA used in this analyses has an internal shield weighing approximately 3300 lbs.[3,4]

The transport results were obtained using two-dimensional discrete ordinates[5] to calculate the flux in the PVARA. Three-dimensional Monte Carlo calculations[6] were used outside the PVARA using the emergent flux from the PVARA as the source. Since these transport calculations require a large amount of computer time, the dependence of the tank top dose rate as a function of liquid hydrogen level for the various configurations was obtained using point kernel techniques[7]. These "drainage curves" were normalized to the Monte Carlo results at specific liquid levels. By far, the largest contribution to the tank top dose comes from the PVARA for the current engine. Therefore, for most of the transport calculations, only the PVARA source was considered.

The resulting doses for the various designs for the unshielded cases were used to estimate the shield requirements. Parameter studies with various shield thicknesses and radii were calculated with the point kernel techniques. Monte Carlo calculations were made for two cases with an external shield and for the basic configuration with no external (disk) shield.

Even though no definite payload has been defined, the attenuation of some hypothetical payloads was examined. Transport calculations for two different payloads for the 15° reference tank

**Public Release Approval: PRA/SA - SNPO-C, dated 24 November 1970.

* The Nuclear Engine for Rocket Vehicle Application (NERVA) program is administered by the Space Nuclear Systems Office, a joint office of the USAEC and NASA. Aerojet Nuclear Systems Company is prime contractor for the engine system and Westinghouse Electric Corporation is principal subcontractor responsible for the nuclear subsystem.

were performed.

II. COMPARISON OF VARIOUS PROPELLANT TANK CONFIGURATIONS

In the course of manned shielding studies performed at Aerojet in recent years, the tank top dose has decreased from several thousand Rem predicted with a hot bleed cycle engine close-coupled to a $\sqrt{2}$ elliptical bottom tank to roughly 400 Rem with the present full flow engine with a single 300,000 lb capacity liquid hydrogen reference tank with a 15° conical tank bottom. A large part of this reduction has resulted from a concentrated effort to reduce or eliminate major propellant lines and changes in the nozzle and pump discharge line which reduced the secondary gamma sources. The shape of the tank bottom has also had a large affect on the tank top dose. For example, the tank top dose from the PVARA with a 30° half angle conical tank bottom is 1680 Rem compared to 790 Rem for a 15° half angle conical tank bottom for a 190,000 lb capacity tank. Other parameters varied included the separation distance between the PVARA and tank, amount of residual liquid hydrogen and weight of internal shield.

In support of the vehicle definition studies being conducted for the Marshall Space Flight Center by Lockheed, McDonnell Douglas and North American Rockwell, Aerojet has more recently examined various tanks for the reusable nuclear vehicle. With a reusable engine, the tanks with smaller half angles become more attractive since impact of the added interstage weight (due to the longer tank length) is greatly reduced since the engine is reused many times.

Figures 1(a) and 1(b) provides a comparison of the 15° conical bottom reference tank with a 30,000 lb liquid hydrogen capacity and one with a 170,000 lb capacity. The integral tank top dose for the larger tank is about half that of the short tank, primarily because the tank top location is further from the engine. The dose rate versus liquid level has been calculated by point kernel techniques for each of the gamma ray sources as shown in Figure 2. By far, the largest contribution to the dose comes from the PVARA. Also, over half the total dose is accumulated during the last 10% of engine operation.

FIGURE 1
SINGLE TANK CONFIGUNATIONS

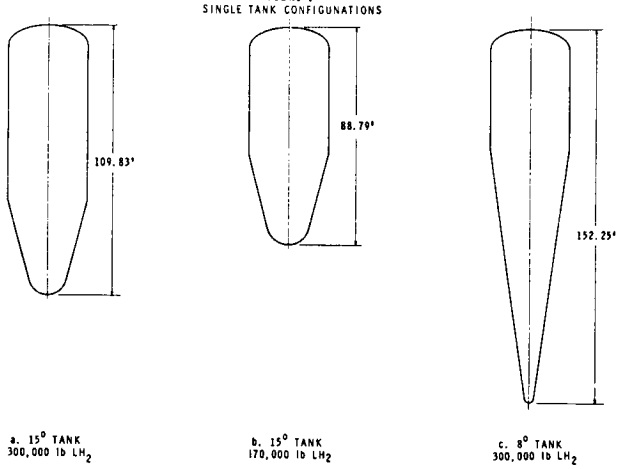

a. 15° TANK 300,000 lb LH_2

b. 15° TANK 170,000 lb LH_2

c. 8° TANK 300,000 lb LH_2

FIGURE 2

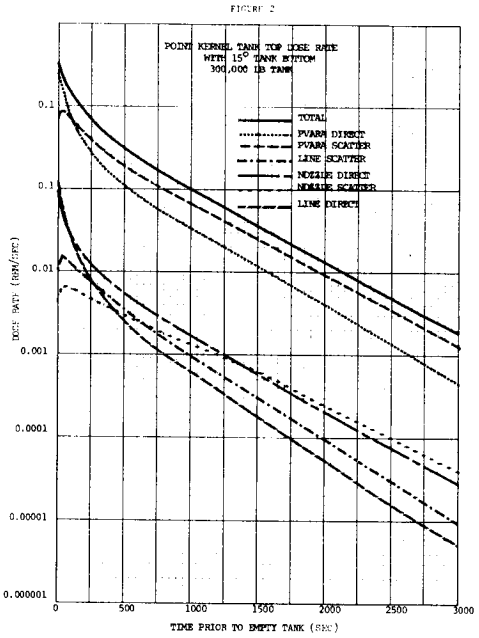

Transport calculations were made for this tank at the 7500, 38,800, and 70,000 lb liquid hydrogen levels. A comparison of the dose rates from the point kernel and transport calculations is given in Figure 3. It can be seen that the point kernel technique overpredicts the center-line dose rate but provides a good estimate of the average tank top dose rate for the case without an external disk shield. For the disk shield case, agreement is excellent both on and off axis.

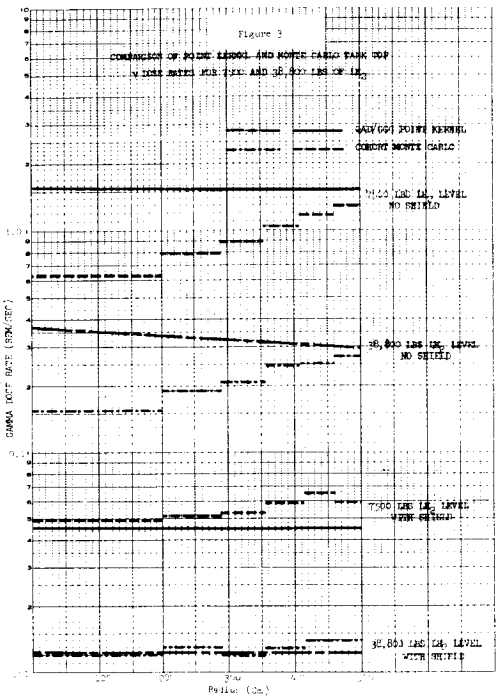

As the half angle of the tank bottom is reduced, the tank top dose is reduced by a combination of several effects. The smaller angle results in a longer tank and hence the tank top location is further from the engine. With the smaller angle, fewer particles scatter in the tank and therefore reduce the scattered contribution to the tank top dose. Also, the narrow angle results in more liquid hydrogen shielding due to a larger depth of liquid hydrogen for any given weight of propellant. Transport calculations were made for a tank with the 8° half angle tank bottom also shown in Figure 1(c). The tank top centerline integral dose from the PVARA was 33 Rem for this case compared to 210 Rem for the 15° reference tank (with no disk shield in the engine).

Several tanks with alternate drainage patterns have also been examined. A tank similar to the 15° reference tank was run with a 10 ft diameter internal cylinder or "standpipe". (See Figure 4(a)) This "standpipe" would be drained last, providing a column of a liquid hydrogen shielding. This concept was found to be effective in reducing the tank top centerline dose, but radiation levels off axis were higher than the reference tank. Also, the neutron dose which is negligible in all the other configurations, amounted to 40 Rem for the standpipe configuration.

A "hybrid" configuration consisting of a small run tank below the main tank (see Figure 4(b)) was also investigated. The small tank, which is drained last, has a liquid hydrogen capacity of about 9500 lbs. The tanks were designed such that the included half angle is 10°. The tank top centerline PVARA dose for this case was calculated to be 46 Rem. The largest factor in reducing the dose compared to the reference tank was the reduction in solid angle from 15° to 10°.

FIGURE 4

NUCLEAR SHUTTLE CONFIGURATIONS

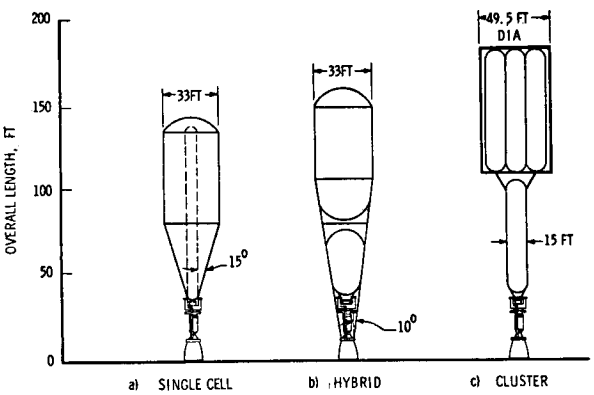

A clustered arrangement of smaller tanks that could be launched in the Earth to Orbit Shuttle (EOS) and assembled in orbit was also investigated. The multiple tank arrangement consisted of seven tanks as shown in Figure 4(c). The tank top centerline dose from the PVARA for this case was calculated to be 138 Rem. This multiple tank configuration has a void on centerline above the lower tank; a substantial fraction of the total dose was accumulated after the lower tank was filled. The tank top dose could be reduced substantially by placing a larger column of liquid hydrogen on centerline. Such an arrangement has been considered by the McDonnell-Douglas Astronautics Company. The tank top dose was greatly reduced by this arrangement.

A comparison of the centerline tank top "point kernel" dose rates versus time for the four tank configurations is given in Figure 5. From Figure 5 it would appear that the standpipe is the most attractive design from a shielding standpoint; however, it should be pointed out that the dose rate forward of tank top and the dose rate off axis are much higher than the centerline curve in Figure 5. The multiple tank arrangement has a rather high dose rate compared to the other tanks from the initial burn to a time 500 seconds prior to empty tank condition since the depth of liquid hydrogen on axis is never greater than the length of one of the tanks in the cluster. The point kernel integral dose for these configurations is given in Table 1. The amount of residual liquid hydrogen was assumed to be 7500 lbs.

Calculations were made to determine the tank top dose with a 10,000 lb external disk shield for each of the configurations. The variables of the dose along the tank top plane for the case with an external shield is quite uniform for each of the configurations except the standpipe case. Table 2 provides a comparison of the tank top doses for each configuration with the disk shield.

FIGURE 5

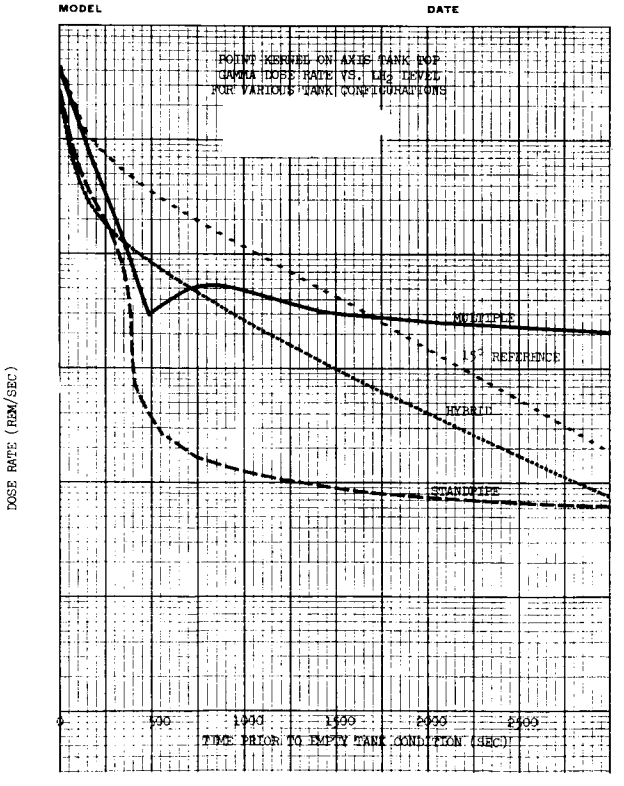

TABLE 1

COMPARISON OF POINT KERNEL CENTERLINE TANK TOP GAMMA DOSE - NO DISK SHIELD FOR ALTERNATIVE PROPELLANT TANKS

	TISSUE KERMA (Rem)					
	15° Dec. '69 Nozzle Sources*	15° May '70 Nozzle Sources**	15° Standpipe 10 Foot Diameter	10° Hybrid	10° Conic	Multiple Tanks 15 Ft. Diameter
PVARA DIRECT	169	169	5.9	30.5	74.7	77.5
PVARA SCATTER	250	250	57.9	72.0	80.7	120.6
LH_2 CAPTURE	12.5	12.5	0.5	8.8	5.0	10.4
NOZZLE ASSEMBLY DIRECT	2.5	0.8	0.3	1.5	0.8	1.0
NOZZLE ASSEMBLY SCATTER	26.0	3.7	2.7	4.5	1.1	9.2
PDL DIRECT	2.4	4.9	0.8	4.2	1.6	1.7
PDL SCATTER	5.9	4.5	18.2	4.0	1.7	4.1
TOTAL	468.2	445.4	86.3	125.5	165.5	224.5

*Based on QAD fast neutron flux with DOT leakage spectrum.
**Based on Neutron Monte Carlo nozzle analysis.
(NOTE: May '70 sources were used for alternative tanks)

III. COMPARISONS OF PAYLOAD ATTENUATION

Analyses were performed on typical payload configurations with the 15° reference tank to ascertain the payload attenuation[8]. The Monte Carlo technique was chosen for these studies because of the large effect of multiple scattering associated with complex geometries.

The payloads examined were the modified Apollo and the Mission B module. The Mission B module is representative of a heavy payload comprised of a manned space station module weighing over 80,000 lbs. The level of detail included in the mathematical model for the Monte Carlo calculations is shown in Figure 6 and Figure 7 for the Modified Apollo and Mission B module respectively. Kerma rate distributions at the various manned payload attenuation factors at different locations in the payload. The payload attenuation factors shown in Table 3 are defined as the ratio of the dose in the payload to the dose at tank top.

TABLE 2

COMPARISON OF POINT KERNEL CENTERLINE TANK TOP DOSE WITH 10000 LB LEAD DISK SHIELD FOR ALTERNATE PROPELLANT TANKS

	DOSE (REM)				
	15° REFERENCE TANK	15° STANDPIPE 10 FOOT DIAMETER	10° CONIC	10° HYBRID	MULTIPLE TANKS 15 FT. DIAMETER
PVARA DIRECT	2.2	0.1	1.7	0.7	1.0
PVARA SCATTER	15.5	2.8	3.9	1.7	7.5
LH_2 CAPTURE	0.3	---	0.1	0.1	0.3
NOZZLE ASSEMBLY DIRECT	0.2	0.1	0.3	0.8	0.2
NOZZLE ASSEMBLY SCATTER	1.3	0.7	0.1	0.4	3.1
PDL DIRECT	0.3	---	0.1	0.1	0.1
PDL SCATTER	0.7	1.3	0.1	0.1	0.6
TOTAL	20.5	5.0	6.3	3.9	12.8

REPRESENTATIVE PAYLOAD ATTENUATION FACTORS FOR VARIOUS NERVA CONFIGURATIONS

Payload Configuration	Description	Gamma-Ray Source		
		PVARA	PDL	Nozzle Assembly
	With Shadow Shield			
Modified Apollo	Crew Equipment	0.1[illegible]	0.[illegible]	0.[illegible]88
Mission B	Crew Quarter	0.[illegible]6	0.[illegible]3	0.78[illegible]
Mission B	Radiation Shelter	0.30[illegible]	0.30[illegible]	0.41[illegible]
Mission B	Apollo Equipment	[illegible]	0.01[illegible]	0.0[illegible]1
	Without Shadow Shield			
Modified Apollo	Crew Equipment	[illegible]	[illegible]	[illegible]

FIGURE 6

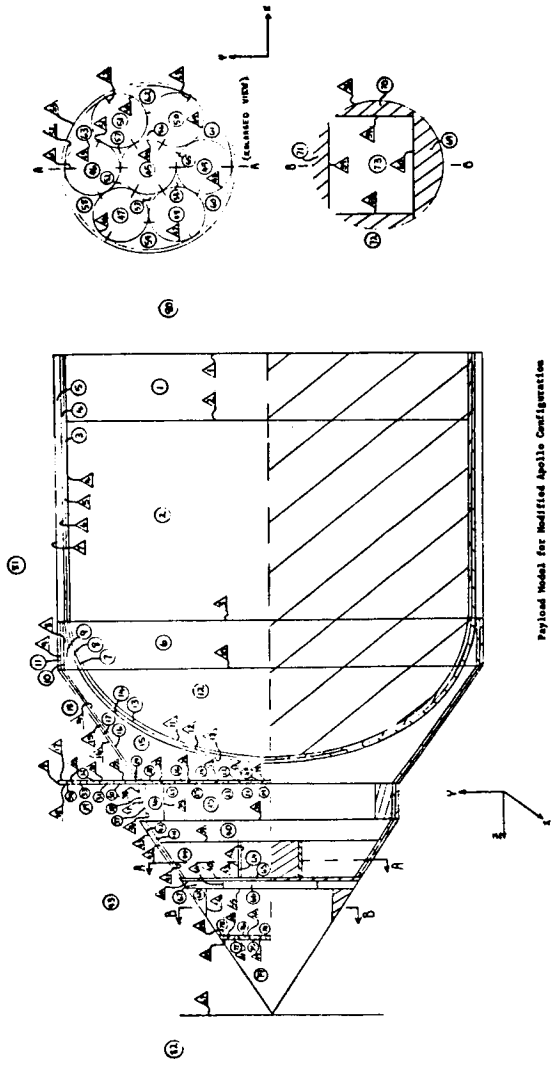

Figure 7

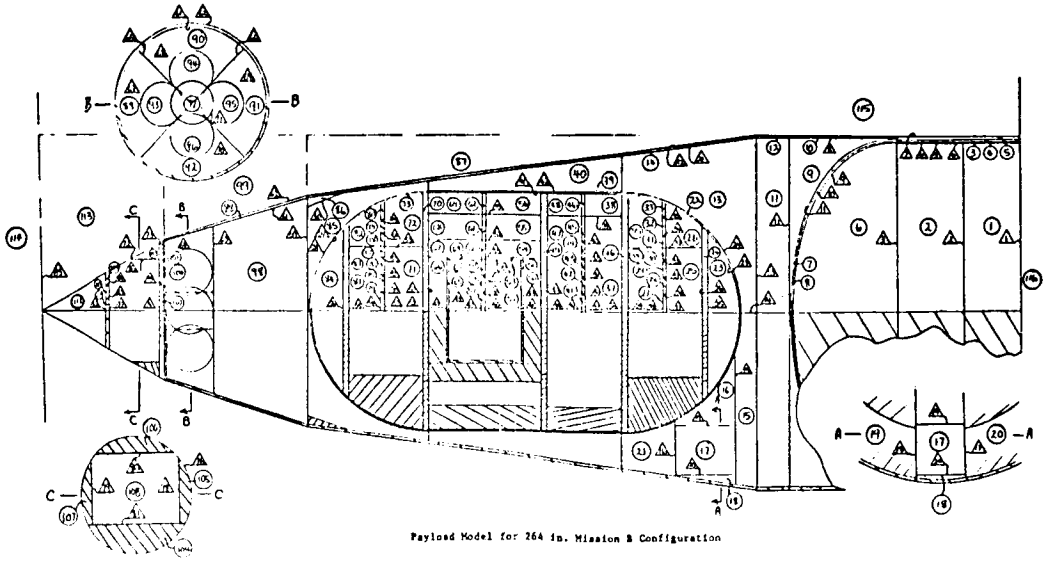

IV. SUMMARY

(a) 15° Reference Tank

Monte Carlo calculations for the 15° conical bottom reference tank confirmed the validity of the point kernel calculations used in this analysis as well as the shielding trade studies. The point kernel results should be interpreted to be a good value for the average tank top dose for a standard tank design. The agreement between the point kernel and Monte Carlo calculations with a 10,000 lb disk shield were excellent and confirmed that this shield would reduce the tank top dose to approximately 20 Rem.

(b) Alternative Tank Designs

Investigation of various tank designs has shown that the tank top dose can be substantially reduced by alternative tank configurations. The most important parameter in this study was found to be the tank bottom angle. The 8° conic resulted in a centerline tank top dose of 36 Rem compared to 246 Rem for 15° reference tank. A 10° hybrid tank configuration resulted in a tank top centerline dose of 70 Rem.

A 15° conic with an internal standpipe concept was found to be effective in reducing the centerline tank top dose. However, it was demonstrated that the shielding requirements for locations above the tank top plane or off axis resulted in no net weight saving over the reference tank.

The results of the cluster configuration examined, indicated a disk shield weight of approximately 7600 lbs would be required. It could be seen from this analysis that other cluster configurations would result in further shield weight reductions.

The results of the tank top doses and shield weights are summarized in Table 4.

(c) Payload Radiation Attenuation

A 10,000 lb engine shield is a reasonable shield configuration to assure a 10 Rem crew dose in a 16,000 lbs six-man modified Apollo command module payload, with an approximate attenuation factor of two. The large mission module payload (>100,000 lbs) with a mission module of 82,000 lbs, results in crew doses less than 10 Rem with no disk shielding at the engine. The crew in this case was located in a modified Apollo command module located at the forward end of the payload. Payloads with weights intermediate to these would have engine disk shielding requirements which would be greatly dependent on the payload mass arrangements. In no case would they be expected to require shield weights approaching the 10,000 lbs figure.

	Tank Top Gamma Tissue Dose (Rem)									
	15° Reference Tank		15° Standpipe 10 Foot Diameter		10° Hybrid		Multiple Tank 14 Foot Diameter		8° Single Tank	
	On Axis	Off Axis	On Axis	Off Axis	On Axis	Off Axis	On Axis	Off Axis	On Axis	Off Axis
Point Kernel Tank Top Dose	45	-	86	-	12	-	2	-	-	-
Monte Carlo Tank Top Dose	246	308	70	400	70	114	1	-	3	6
Disk Shield Wt To Reduce Tank Top to 20 Rem	10,000 lbs		10,000 lbs		4,000 lbs		1,000 lbs		3,000 lbs	

COMPARISON OF TANK TOP DOSE AND SHIELD WEIGHT FOR VARIOUS TANK DESIGNS

Table 4

V. ADDENDUM

This addendum is intended to provide a reference source of data pertaining to the 75,000 lbs thrust NERVA engine shielding weight as a function of allowed crew dose.

Table 5 appears in the National Academy of Sciences publication entitled, "Radiation Protection Guides and Constraints for Space-Mission and Vehicle-Design Studies Involving Nuclear Systems". These data should be replaced by Table 6 for reference purposes for the full flow 75,000 lbs NERVA engine with a reference 300,000 lbs capacity LH_2 tank. The earlier data reported in the NAS publication were for some earlier engine sources and an earlier tank configuration, which had a propellant capacity of 190,000 lbs. The newer data are applicable for the Reusable Nuclear Shuttle Mission.

TABLE 5

SHIELD WEIGHT FOR CREW DOSE OF 10 REM FOR

VARIOUS PAYLOAD ATTENUATION FACTORS

PAYLOAD ATTENUATION FACTOR	SHIELD WEIGHT (LBS)			
	INTERNAL ENGINE SHIELD	EXTERNAL ENGINE SHIELD	SHIELDING AT PAYLOAD	TOTAL
1	3300	10,000	9,000	22,300
3	3300	10,000	3,500	16,800
10	3300	7,300	-	10,600
20	3300	4,400	-	7,700
30	3300	2,900	-	6,200
50	3300	1,300	-	4,600
100	3300		-	3,300

Table 6

SHIELD WEIGHT FOR 300,000 LB LH_2 CAPACITY TANK
(CREW DOSE OF 10 REM WITH VARIABLE LEAD DISK SHIELD)

PAYLOAD ATTENUATION FACTOR	SHIELD WEIGHT (LBS)			
	INTERNAL ENGINE SHIELD	EXTERNAL ENGINE SHIELD	SHIELDING AT PAYLOAD	TOTAL
1	3300	10,000	5,500	18,800
2	3300	10,000	-	13,300
3	3300	8,700	-	12,000
10	3300	4,200	-	7,500
20	3300	1,800	-	5,100
30	3300	800	-	4,100
	3300		-	3,300

NOTES: 1. GRAPHITE ENGINE EXTENSION
2. AT PUMP DISCHARGE LINE

The tissue dose at the top of this larger tank is approximately 400 Rem with no engine disk shielding and 20 Rem with a 10,000 lbs engine disk shield.

Table 7 shows the shielding weight as a function of various possible crew exposure criteria per mission for a hypothetical payload with a factor of two payload attenuation (which includes both the material attenuation and the relatively minor geometric attenuation to a crew location approximately 11 ft forward of tank top).

Table 7

SHIELD WEIGHT FOR VARIOUS CREW EXPOSURE CRITERIA
WITH A LIGHT PAYLOAD WITH AN ASSUMED ATTENUATION FACTOR OF TWO

CREW EXPOSURE CRITERIA (REM PER MISSION)*	SHIELD WEIGHT (LBS)			
	INTERNAL ENGINE SHIELD	EXTERNAL ENGINE SHIELD	SHIELDING AT PAYLOAD	TOTAL
5	3300	10,000	5,500	18,800
10	3300	10,000	-	13,300
20	3300	7,500	-	10,800
40	3300	5,100	-	8,400
50	3300	4,200	-	7,500

*BASED ON COMPLETE DRAINAGE OF THE 300,000 LBS OF AVAILABLE HYDROGEN WITH 7,500 LBS OF LH_2 RESIDUAL FOR COOLDOWN.

REFERENCES

1. J.C. Courtney and N. A. Hertelendy, "Radiation Heating in Selected NERVA Engine Components," paper presented at this conference

2. E. A. Warman, J. C. Courtney, K. O. Koebberling, "Final Report of Shield System Trade Study," Aerojet-General Corporation, S054-023 (July 1970)

3. E. A. Warman and D. R. Rogers, "Shielding Requirements for Manned and Unmanned NERVA Missions," TRANS. AM. NUCL. SOC., 13, 441 (1970)

4. E. A. Warman, et al, "Operating Radiation Environment of Nuclear Rocket Systems," TRANS. AM. NUCL. SOC., 12, 416 (1969)

5. F. R. Mynatt, "A Users Manual for DOT," Report K-1694, Union Carbide Corp. (Feb. 1969)

6. M. B. Wells and D. G. Collins, "COHORT, A Monte Carlo Program for Calculation of Radiation Heating and Transport," RRA-T62-2 (September 1966)

7. "Seminar/Workshop Material on Point Kernel Techniques for Nuclear Rocket Propellant Tank Geometry/Shielding Analysis," Aerojet-General Corporation, RN-PA0020 (August 1969)

8. Analyses Performed by Radiation Research Associates, Fort Worth, Texas

SESSION II.2
NUCLEAR POWER SYSTEMS· SNAP REACTOR SHIELDING
CHAIRMAN: C. MC McCALLUM
SPACE NUCLEAR SYSTEMS OFFICE-NASA/AEC

The ORNL-SNAP Shielding Program

F. R. Mynatt, C. E. Clifford, F. J. Muckenthaler, and M. L. Gritzner
Oak Ridge National Laboratory

The effort in the ORNL-SNAP shielding program is directed toward the development and verification of computer codes using numerical solutions to the transport equation for the design of optimized radiation shields for SNAP power systems. A brief discussion is given for the major areas of the SNAP shielding program, which are cross-section development, transport code development, and integral experiments. Detailed results are presented for the integral experiments utilizing the TSF-SNAP reactor. Calculated results are compared with experiment for neutron and gamma-ray spectra from the bare reactor and as transmitted through slab shields.

The purpose of the ORNL-SNAP shielding program is the development of the technology for the nuclear design of radiation shields for reactor power supply systems on spacecraft. The emphasis in the program is on the development and verification of computer programs for the design of optimum shields and to predict throughout the spacecraft system the absolute spectra of radiation resulting from reactor operation.

Figure 1 shows a schematic diagram of the SNAP shielding program. The three major areas which are shown are cross-section development, transport code development and integral experiments. Five years ago the calculation of deep-penetration neutron transport in lithium hydride in a one-dimensional geometry was a challenging problem. The capabilities since that time have increased rapidly.

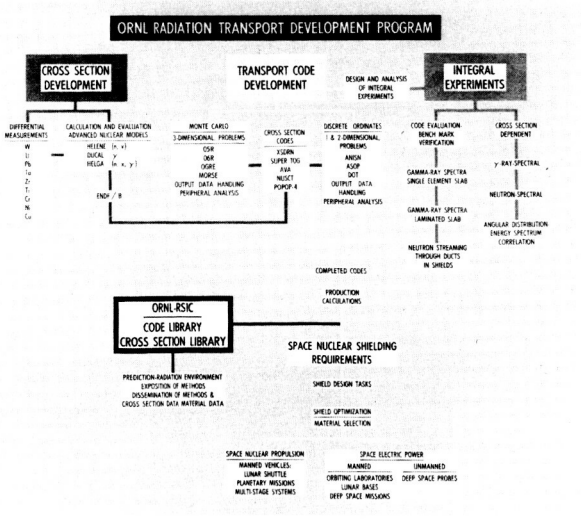

FIGURE 1.-A Schematic Description of the ORNL-SNAP Shielding Program.

The significant steps in this development include (1) the ability to calculate neutron and secondary gamma-ray transport in a coupled mode, (2) the development of the DOT (refs. 1 and 2) discrete ordinates code for deep-penetration two-dimensional transport calculations, (3) the development of a shield optimization program, ASOP (ref. 3), utilizing one-dimensional transport calculations, and (4) the development of the multigroup Monte Carlo MORSE (ref. 4) and the coupling of MORSE and two-dimensional DOT calculations for the analysis of difficult two- and three-dimensional problems.

The current development work includes MORSE-DOT coupling and the optimum shaping of shields which is a rudimentary form of multidimensional optimization. The verification of the shield design and analysis methods is effected through comparison with integral experiments. Two types of integral experiments have been performed at the ORNL Tower Shielding Facility. In the first type of experiment the measurements are of absolute gamma-ray pulse-height spectra produced from thin slabs which are exposed to a filtered neutron beam. In comparison with this experiment, the calculation of transport effects is minimized and the emphasis is placed on the calculation of the production of secondary gamma rays (refs. 5 and 6).

The second type of exeriment is more prototypical in that absolute neutron and gamma-ray spectra transmitted from slab shields placed adjacent to the TSF-SNAP reactor are compared. These comparisons test the transport calculation of neutrons and gamma rays, as well as the production of secondary gamma rays. In the comparison with integral experiments, it was soon verified that the available cross-section data for production of secondary gamma rays were grossly inadequate for most materials. This situation has now been greatly improved in that data for production of secondary gamma rays

from neutron capture as a function of neutron energy have been produced by use of nuclear model theory codes (refs. 7 and 8) and by measurements for tungsten (ref. 9) and uranium (ref. 10). Current work is directed toward the verification and improvement of data for secondary gamma-ray production due to neutron inelastic scattering.

As the techniques developed in the basic technology program have become established, they have been incorporated in an optimum-shield-design procedure which is exercised and demonstrated through detailed shield design studies. Several studies have been performed in which the reactor type and power and the radiation dose constraints are specified and an optimized shield is designed (ref. 11). Through these efforts, the techniques for shield design are being rapidly improved.

Also of interest are parametric optimization studies in which the effect of reactor size, type and power and the radiation dose constraints on the optimum shield configuration and weight have been studied. These studies, of course, incorporate considerable simplification of the geometry as compared to the more detailed design studies for a specific configuration.

Other papers by the ORNL group at this meeting will cover, in more detail, the integral experiments for secondary gamma-ray data testing (ref. 12), the use of coupled MORSE Monte Carlo and DOT calculations for three-dimensional problems (refs. 13 and 14), and the design of optimized shaped asymmetric 4π shields (ref. 15). In this paper, the status of the calculational comparisons with the TSF-SNAP integral experiments will be summarized.

The source for these experiments is the TSF-SNAP reactor shown before assembly in figure 2. The reactor is a modified SNAP-2 which was designed and constructed by Atomics International. The pressure vessel shown on the left is 9 in. in diameter, 16 in. long, and contains the uranium-zirconium-hydride fuel in 36 rods with a central stainless steel rod containing a small quantity of boron carbide. The reactor is reflected radially by beryllium and has four reflector control vanes. The coolant is NaK and the heat is removed by natural circulation to a NaK-to-air heat exchanger above the reactor. In the dry critical runs during the

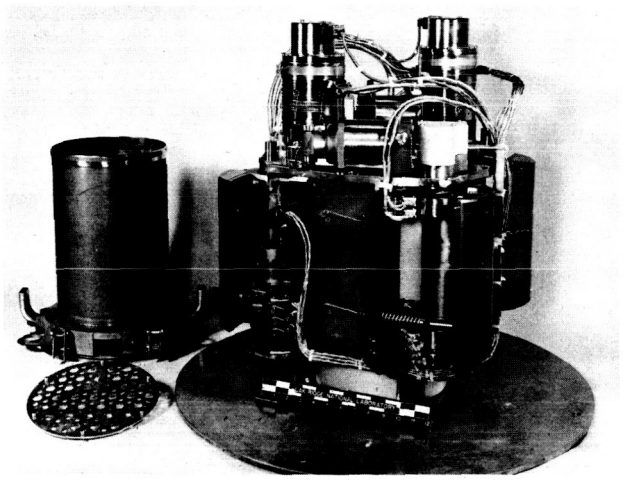

FIGURE 2.-The TSF-SNAP Reactor Prior to Assembly.

start of the reactor, the internal power distribution was measured by gamma-ray scans of the fuel elements, by copper, uranium, and gold foil activation and by activation of copper strips. Comparisons of the power distribution deduced from these measurements with 05R-Monte Carlo calculations and DOT discrete ordinates calculations show very good agreement for the radial and axial power distributions (ref. 16).

After the assembly of the reactor was completed and in its final operating stage, the first measurements which were made were of the neutron angular current leaking from the bottom of the assembly. Figure 3 shows the SNAP reactor without the heat shield suspended from its boom. The large collimator tank contains a special 2-in. by 2-in. square collimator which was designed to view only 10% of the area of the core. By moving the collimator along the track and varying the angle position, several measurements were made of the angle-dependent neutron leakage. Data from this experiment showed that except for those measurements where the collimator was vertical and viewing the outer extremity of the core and reflector, the spectral shape and intensity which were measured were very similar for each run. Comparisons of the measured absolute spectra with very detailed 05R calculations showed substantially good agreement (ref. 17).

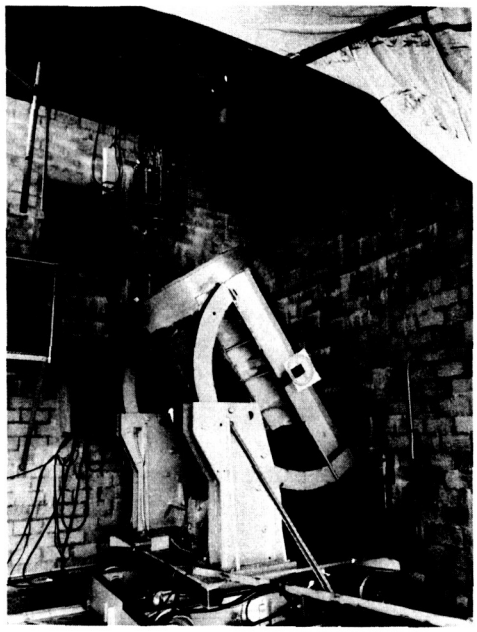

FIGURE 3.-TSF-SNAP Reactor With NE-213 Detector Collimator Used For Measurement of the Angle-Dependent Neutron Leakage.

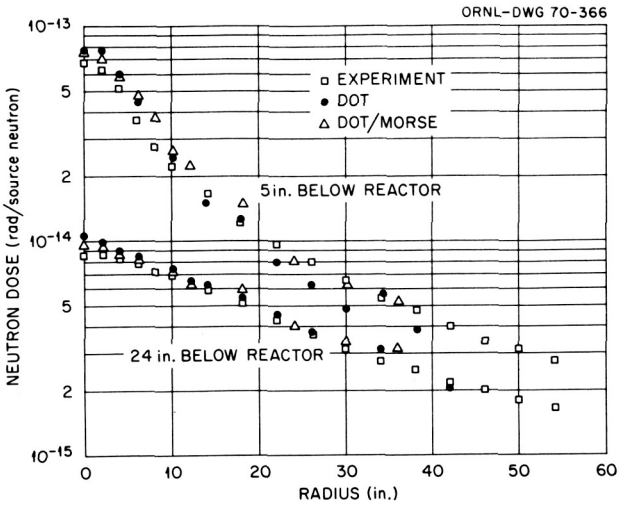

FIGURE 4.-Comparison of Calculated and Measured Radial Neutron Dose Profiles Below the SNAP Reactor.

Figure 4 shows comparison of measurements and calculations for lateral neutron dose traverses below the SNAP reactor. The measurements were made with a small Hornyak button, and the calculations were made with the two-dimensional DOT code for the reactor coupled, in one case with the SPACETRAN ray-tracing code to obtain the dose at the specified points, and in the other case the coupling at a plane just below the reactor was made to the MORSE Monte Carlo code which then determined the dose at the specified points. The agreement between the calculations and experiment is surprisingly good. In the DOT-SPACETRAN coupling, however, some ray effects can be observed for large radii on the plane close to the bottom of the reactor.

Additional neutron and gamma-ray spectral measurements for the bare reactor are included in the slab shield transmission series. The neutron and gamma-ray slab transmission measurements have been performed with large slab shields supported such that they are located directly under the SNAP reactor. Measurements have been made with the NE-213 fast-neutron scintillator and the sodium-iodide gamma-ray detector.

Figure 5 shows a list of the experiments for which calculations have been performed. There are many other experimental runs which have been made but not yet calculated. From figure 5 you can see that neutron measurements and calculations have been performed for the bare reactor, and lithium-hydride, depleted uranium, lead, tungsten powder, heavimet alloy, and laminated lithium-hydride lead-uranium slabs. More difficult gamma-ray measurements and calculations have been performed for the bare reactor, and lead, depleted uranium, heavimet alloy, tungsten powder, and laminated lithium-hydride and uranium slabs.

Figure 6 shows a scale drawing of the geometric configuration for the fast-neutron spectral measurements. The NE-213 detector is located deep in a room beneath the concrete pad. The area of the slab which it views is defined by the inner wall of the water tank. In the calculations, the leakage angular flux from a DOT calculation of the reactor is used as a boundary source for the calculation of the slab shield. The leakage angular flux from the bottom of the slab shield is then integrated with SPACETRAN code to obtain the absolute neutron flux

at the NE-213 detector. In the experiment, the pulse-height distribution from the NE-213 is unfolded with the FERDOR code and compared with the calculation at the detector point. The comparisons are always on an absolute basis with the reactor power monitored by foils during each run.

EXPERIMENTS WHICH HAVE BEEN CALCULATED

NEUTRON	GAMMA
BARE REACTOR	BARE REACTOR
6" LiH	2" Pb
12" LiH	3" Pb
1.5" U-238[a]	6" Pb
4.5" U-238	3.5" U-238
1.5" Pb	4.5" U-238
3" Pb	2" HEAVIMET
6" W[b]	6" W
12" W	6" LiH-1.5" U-238
2" HEAVIMET[c]	
1.5" U-238-6" LiH	
6" LiH-1.5" U-238	
6" LiH-1.5" Pb-1.5" U-238	
6" LiH-4.5" U-238	
6" LiH-1.5" Pb	
3" Pb-6" LiH	

[a] U-238 is depleted uranium.
[b] W is tungsten powder ($\rho \sim 6$ gm./cm.^{3}).
[c] HEAVIMET is tungsten-copper-nickel alloy.

FIGURE 5.-A List of TSF-SNAP Slab Transmission Experiments Which Have Been Calculated.

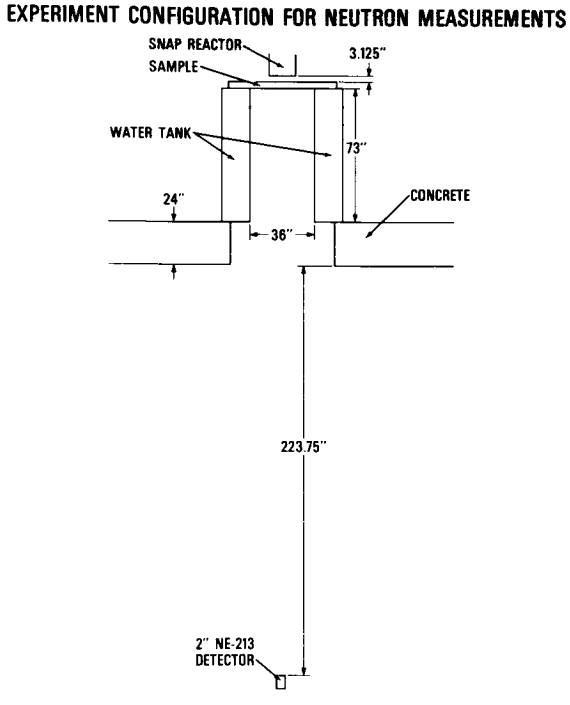

FIGURE 6.-Experimental Configuration for Fast-Neutron Measurements.

Figure 7 shows a comparison of experiment with DOT-SPACETRAN calculation and Monte Carlo 05R calculation for the fast-neutron spectra for the bare core. The agreement is very good except that the calculations are somewhat high below 1-1/2 MeV.

Figure 8 shows a comparison of DOT calculation with a recent measurement of the neutron leakage from the bare core using the Benjamin spectrometer which uses spherical hydrogen-filled detectors. The measurements were made at approximately 36 in. below the reactor core. The calculation uses DOT coupled with SPACETRAN in the usual manner, and the agreement in intensity is quite good except that the calculation is somewhat high between 600 keV and 1-1/2 MeV. Also shown is the result of scaling the NE-213 measurements to the hydrogen counter location. The agreement between the NE-213 spectrometer and the Benjamin spectrometer in the overlap energy range is excellent.

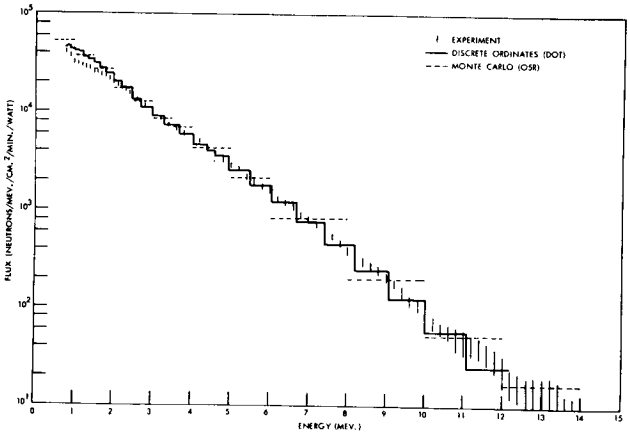

FIGURE 7.-Comparison of Calculated and Measured Fast-Neutron Spectra From the Bare TSF-SNAP Reactor.

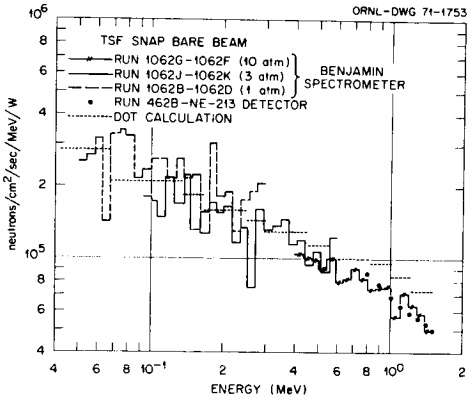

FIGURE 8.-Comparison of Calculated and Measured Intermediate Neutron Spectra From the Bare TSF-SNAP Reactor.

Figure 9 shows a comparison of measurement with DOT and 05R calculations for a 12-in.-thick slab of lithium hydride. The overall agreement is very good; however, the calculations are somewhat high below 2 MeV and somewhat low at the higher energies. The multigroup lithium cross sections used in the DOT calculation were processed prior to the availability of lithium in the ENDF/B library but used the same data as used for the ENDF evaluation. It is important that all of the neutron-producing reactions in lithium be treated in order to obtain reasonably good agreement. In this multigroup set, the secondary neutron distributions from the nonelastic reactions are assumed to be isotropic in the laboratory system. However, in the Monte Carlo calculation the angular distributions of the secondary neutrons are treated explicitly. Previous comparisons in one-dimensional sphere geometry between 05R and multigroup ANISN calculations have shown excellent agreement in lithium hydride to a depth of 90 cm (ref. 18).

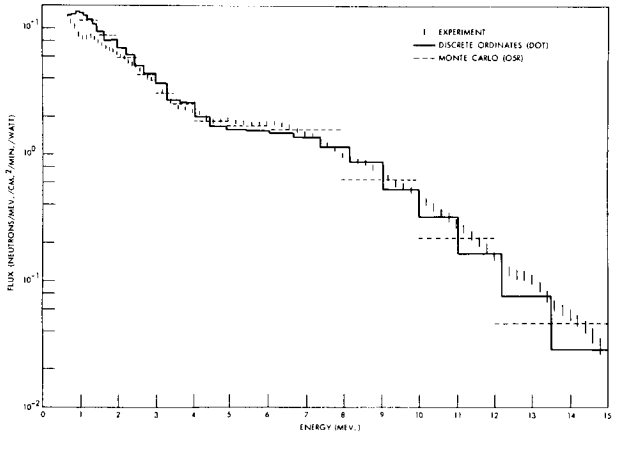

FIGURE 9.-Comparison of Measured and Calculated Fast-Neutron Spectra From a 12-in. Lithium Hydride Slab Under the SNAP Reactor.

Figure 10 shows a comparison of experiment and DOT calculation for the fast-neutron spectra transmitted through a 2-in. slab of heavimet alloy. The agreement for this case is the best for any of the metal slabs which have been calculated. For lead, the calculated spectra are consistently 15% low, and for uranium at large slab thicknesses the calculations are a factor of 2 to 2-1/2 low. This result for uranium is anomolous since comparisons of DOT calculations with experiment using the same slabs in a beam source geometry have previously shown good agreement when the fission multiplication in the slab is treated (ref. 1, page 144). Experiments are currently in progress to attempt to determine the reason for this disagreement in this case.

Figure 11 shows a scale drawing of the geometry for the gamma-ray measurements and calculations. The 5-in. sodium iodide detector is also located deep in the room beneath the concrete pad. In the gamma-ray measurements a 10-in. thickness of borated polyethylene is in the beam at all times to reduce the neutron background in the detector.

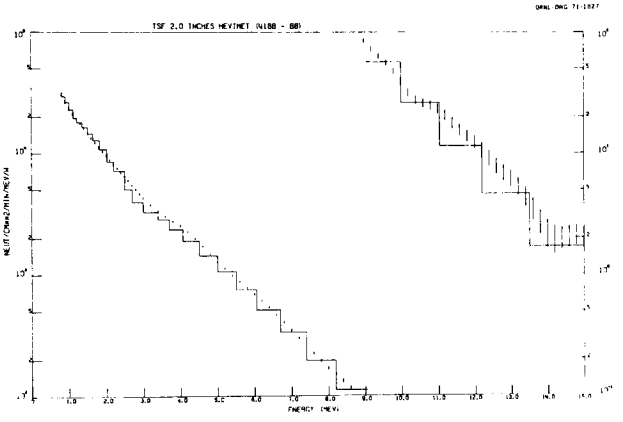

FIGURE 10.-Comparison of Calculated and Measured Fast-Neutron Spectra From a 2-in. Slab of Heavimet Under the SNAP Reactor.

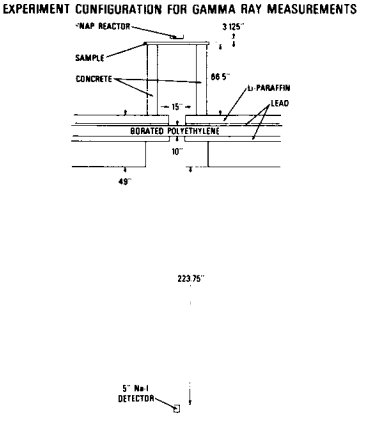

FIGURE 11.-Experimental Configuration for Gamma-Ray Measurements.

Calculations have been performed with DOT using a 27-neutron group - 60-gamma-ray group coupled library. Some of the calculations use the angular flux distribution beneath the reactor as a fixed boundary source for the slab shield calculations. In other cases, it has been necessary to calculate the reactor and shield as a single unit and include the effect of the shield on the power distribution in the reactor. The angular flux from the lower surface of the shield is integrated with the SPACE-TRAN code to determine the flux at the detector incorporating the uncollided flux attenuation of the borated polyethylene. The gamma-ray flux incident on the detector is folded with the detector response function so that the calculated pulse-height distribution is compared directly with the measurement.

Figure 12 shows the comparison of calculated and measured absolute pulse-height distribution for the bare core. The agreement below 4-1/2 MeV is excellent. Above 4-1/2 MeV, the experiment is high by almost a factor of 2. This disagreement is at present believed to be due to epithermal capture in structural materials in the reactor which are not adequately described. A comparison of dose or total energy flux would agree very well since the intensity is much greater at the lower energies.

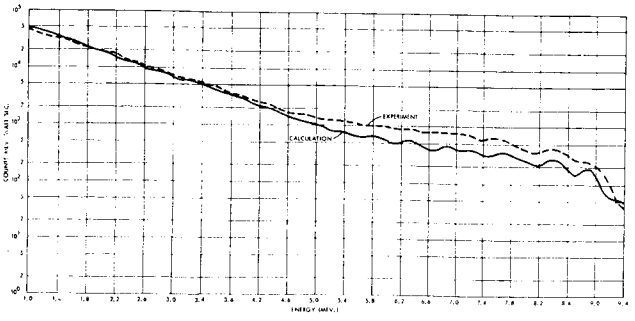

FIGURE 12.-Comparison of Calculated and Measured Gamma-Ray Pulse-Height Spectra From the Bare SNAP Reactor.

Figure 13 shows a comparison for experiment and calculation of the absolute pulse-height spectra for a 2-in. slab of heavimet placed directly under the SNAP reactor. Over most of the energy range the calculation is 20-25% low. At the higher energies above 7 MeV, the calculation is a factor of 2 low. However, the integral energy flux of the calculation and experiment agrees to within 15% due to the fact that the calculation agrees best with the experiment below 2 MeV where the intensity is the highest. This is the best comparison for any of the metal slabs.

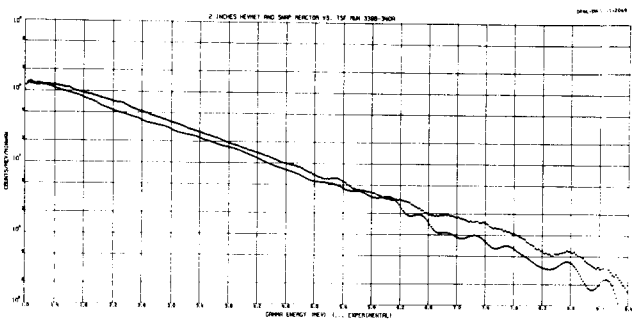

FIGURE 13.-Comparison of Calculated and Measured Gamma-Ray Pulse-Height Spectra From a 2-in. Heavimet Slab Under the SNAP Reactor.

The secondary gamma-ray production matrix used in this calculation, which included energy-dependent yields or epithermal capture, has been checked with the TSR-2 secondary gamma-ray experiment and shown to give substantially good results (ref. 19).

For the other gamma-ray shields the situation is not nearly so good. For lead, the TSR-2 gamma-ray experiments have shown that the secondary gamma-ray production data for neutron inelastic scattering is entirely inadequate. For uranium, the comparisons of calculation and measurements for the SNAP reactor experiments show that the calculations are low by about a factor of 2. This disagreement may be related to the anomaly in the neutron spectral comparisons since the TSR-2 gamma-ray experiment shows good agreement for ^{238}U foils.

In conclusion, the comparisons and calculations with the TSF-SNAP experiments have shown that the transport codes can accurately predict the neutron and gamma-ray radiation from the bare reactor. Also, the prediction of neutron transmission through shield slabs of lithium hydride, lead,and tungsten are adequately calculated. For secondary gamma-ray comparisons, the present status is not satisfactory in that relatively good agreement is only obtained for the heavimet alloy and tungsten powder assemblies.

The work presently in progress may soon resolve the difficulties experienced in neutron and gamma-ray comparisons for depleted uranium slabs, and the disagreement for lead constitutes a low priority problem in that lead has been ruled out as a likely candidate material in an actual SNAP shield.

Future experiments using the TSF-SNAP reactor will be for the verification of shield optimization by comparing measured and calculated dose derivatives and for verification of shield shaping procedures.

REFERENCES

1. MYNATT, F. R.; MUCKENTHALER, F. J.; and STEVENS, P. N.: Development of Two-Dimensional Discrete Ordinates Transport Theory for Radiation Shielding. USAEC Report CTC-INF-952, Union Carbide Corporation, 1969.
2. MYNATT, F. R.: A User's Manual for DOT. USAEC Report CCC-89, Union Carbide Corporation, 1969.
3. ENGLE, W. W., JR.: A Users Manual for ASOP, ANISN Shield Optimization Program. USAEC Report CTC-INF-941, Union Carbide Corporation, 1969.
4. STRAKER, E. A.; STEVENS, P. N.; IRVING, D. C.; and CAIN, V. R.: The MORSE Code - A Multigroup Neutron and Gamma-Ray Monte Carlo Transport Code. USAEC Report ORNL-4585, Oak Ridge National Laboratory, 1970.
5. MAERKER, R. E.; and MUCKENTHALER, F. J.: Gamma-Ray Spectra Arising From Thermal-Neutron Capture in Elements Found in Soils, Concretes, and Structural Materials. USAEC Report ORNL-4382, Oak Ridge National Laboratory, 1969.
6. FORD, W. E., III: The Use and "Testing" of Al, Fe, Ni, Cu, and Pb Secondary Gamma-Ray Production Data Sets from the POPOP4 Library. USAEC Report CTC-20, Union Carbide Corporation, 1970.
7. PENNY, S. K.; YOST, K. J.; and WHITE, J.: Calculation of Neutron-Capture Gamma-Ray Yields for Tungsten and Neutron Inelastic-Scattering Cross Sections for Iron. Transactions of the American Nuclear Society, Seattle, Washington, vol. 12, no. 1, pps. 386-388, 1969.
8. YOST, K. J.; WHITE, J. E.; and FU, C. Y.: Neutron Energy-Dependent Capture Gamma-Ray Yields for ^{238}U and ^{181}Ta. Transactions of the American Nuclear Society, Washington, D. C., vol. 13, no. 2, pps. 866-868, 1970.
9. ORPHAN, V.; and JOHN, J.: Intensities of Gamma Rays From the Radiative Capture in Natural Tungsten of Neutrons From 0.02 eV to 100 keV. Gulf General Atomic Report GA-9121, 1968.
10. JOHN, JOSEPH; and ORPHAN, V. J.: Gamma Rays From Resonant Capture of Neutrons in ^{238}U. Gulf General Atomic Report GA-10186, 1970.
11. ENGLE, W. W., Jr.: Optimization of a Shield for a Heat-Pipe-Cooled Fast Reactor Designed as a Nuclear Electric Space Power Plant. USAEC Technical Memorandum (to be published).
12. FORD, W. E., III: The POPOP4 Library and Codes for Preparing Secondary Gamma-Ray Production Cross Sections. This paper presented in this NASA document.
13. STRAKER, E. A.; CHILDS, R. L.; and EMMETT, M. B.: Application of DOT-MORSE Coupling to the Analysis of Three-Dimensional SNAP Shielding Problems. This paper presented in this NASA document.
14. BURGART, C. E.: MORSE Monte Carlo Shielding Calculations For the Zirconium Hydride Reference Reactor. This paper presented in this NASA document.
15. ENGLE, W. W., JR.: The Design of Asymmetric 4π Shields for Space Reactors. This paper presented in this NASA Document.
16. STRAKER, E. A.: Measurements of the Absolute Power and Fission Distribution in the TSF-SNAP Reactor and Comparison With Monte Carlo and Discrete Ordinates Calculations. USAEC Report ORNL-TM-2265, Oak Ridge National Laboratory, 1968.
17. CAIN, V. R.: Comparisons of Monte Carlo Calculations to Measurements of Neutron Leakage From the TSF-SNAP Reactor. USAEC Report ORNL-TM-2586, Oak Ridge National Laboratory, 1969.
18. GREENE, N. M.: Multigroup ^{6}Li and ^{7}Li Cross Sections. Paper 3.17 in Neutron Physics Division Annual Progress Report for Period Ending May 31, 1967. USAEC Report ORNL-4134, Oak Ridge National Laboratory, 1967.
19. FORD, WALTER E., III; and WALLACE, D. H.: Discrete-Ordinates Calculation of Secondary Gamma-Ray Spectra For Comparison with Tower Shielding Facility Experiments. Paper 2.22 in Neutron Physics Division Annual Progress Report For Period Ending May 31, 1969. USAEC Report ORNL-4433, Oak Ridge National Laboratory, 1969.

The Design of Asymmetric 4π Shields for Space Reactors*

W. W. Engle, Jr., R. L. Childs, and F. R. Mynatt
Oak Ridge National Laboratory

A one-dimensional shield optimization program based on the method of discrete ordinates has been developed and is used to determine material thicknesses used in asymmetric 4π shields for space power reactors. The two-dimensional discrete ordinates program DOT is used to check the design and the information generated in the DOT calculation is used as a guide in shaping the shield which may be considered a first step in two-dimensional shield optimization.

Introduction

The design of space reactor shields based on minimum weight for a specified set of dose constraints is important for obvious reasons. A one-dimensional shield optimization program, ASOP (ref. 1), has been developed and is used in conjunction with the two-dimensional discrete ordinates program, DOT (ref. 2), for the design of such shields. The next section describes briefly the ASOP optimization technique and the last section discusses the process of combining the results of two or more ASOP calculations in a 4π shield design and the significant weight savings which have been obtained using results of DOT calculations of the 4π shield.

The ASOP Technique

Most methods available for shield design or optimization based on minimum weight and specified dose constraints require analytic functions to describe the radiation transport through the shield and use complex mathematical methods to effect the weight optimization. To adequately describe the effects of spectral shifts in transition regions near interfaces and the production of secondary gamma rays the analytic function must be quite complex. Typically coefficients must be determined for each of the several sources of neutron and gamma radiation. These coefficients are usually derived from many separate transport calculations and must, or should, be reevaluated for each significant change in shield configuration. It was felt that a better, more general approach would be to include the transport calculations directly in the optimization process and, therefore, calculate precisely the radiation transport in the shield for each change in configuration.

Recent advances in technique have caused the discrete ordinates method to become widely accepted as a tool for performing deep penetration or shielding calculations. Two developments in particular made the method attractive for a shield optimization program where repetitive calculations of both neutron and gamma-ray transport are required. First the technique of space-dependent scaling (ref. 3) has significantly accelerated the convergence of the inner iterations or flux calculation, and second, the development of combined neutron and gamma-ray multigroup cross section sets (ref. 4) has made simultaneous neutron-gamma-ray calculations routine.

The optimization technique is relatively simple. If one considers the design of a shield composed of layers of different materials, the derivative of the dose at some external point with respect to the shield weight may be determined at each material interface. If the dose-weight derivatives are different at two or more boundaries, it is possible to move those boundaries such that the dose remains constant and the net shield weight decreases. If all dose-weight derivatives are equal this process is not possible and the shield weight is at least at a relative minimum. It is this condition of everywhere equal dose-weight derivatives which forms the basis of the ASOP technique.

Equations (1) and (2) describe the local approximations used in the ASOP program. First, for small perturbations the logarithm of the dose is approximated as a linear function of each material boundary position, r_i,

$$\ln D = \sum_i A_i r_i + B \quad . \tag{1}$$

Second, the dose-weight derivative at each boundary is approximated as a linear function of the position of that boundary.

$$(\Delta D/\Delta W)_i = E_i r_i + F_i \quad . \tag{2}$$

*Research sponsored by the U. S. Atomic Energy Commission under contract with the Union Carbide Corporation.

In order to determine these coefficients for each ASOP iteration an automated series of ANISN (ref. 5) calculations is performed including the initial configuration and two displacements of each movable shield boundary. The set of n+1 equations (3) may then be solved for a new set of boundary positions, r_1 through r_n. The solution attempts to maintain the dose at some design level, D^d, and also produce a configuration in which all the dose-weight derivatives are equal to λ, which is the $(n+1)^{th}$ unknown. The superscript zero denotes conditions of the initial configuration.

$$\left.\begin{aligned} A_1r_1+A_2r_2+\ldots+A_nr_n &= \ln (D^d/D^o) + \sum_i A_i r_i^o \\ E_1r_1 - \lambda &= -F_1 \\ E_2r_2 - \lambda &= -F_2 \\ \ddots & \\ E_nr_n - \lambda &= -F_n \end{aligned}\right\} \quad (3)$$

Since the new boundary positions may involve perturbations for which the approximationsin Equations (1) and (2) are not accurate, the entire process is repeated with the new r_i's as the initial configuration. Convergence of both the dose and dose-weight derivatives is usually obtained after three to five such cycles of calculation.

Asymmetric Shield Design

4π shields for space power reactors are typically asymmetric because in the interest of conserving shield weight there are relatively large differences in the crew dose requirements and in the dose requirements outside the crew quarters which allow docking manuvers or other extra-vehicular activities. If mission requirements such as power, dose constraints, and system configuration are well defined, an ASOP calculation may be performed for each of the separate dose constraints and the resulting material thicknesses combined, with some intuition, in a three-dimensional shield. The symmetry of the shield usually permits a detailed calculation with DOT in two-dimensional R-Z geometry. In general, however, mission requirements are not well defined and a set of survey calculations is performed with ASOP covering a wide range of dose rate to power level ratios. Figure 1 shows the results of such a survey for a two-cycle, tungsten-lithium hydride crew shield. Material thickness is plotted versus the dose rate to power level ratio for a crew-reactor separation distance of one hundred feet. With curves of this type for each separate anticipated dose constraint, it is possible to compute weights for a variety of shield configurations as a function of power level, dose constraints, crew-reactor separation distance, size of crew quarters, etc. Variation of shield weight may then be considered in determining the final system configuration.

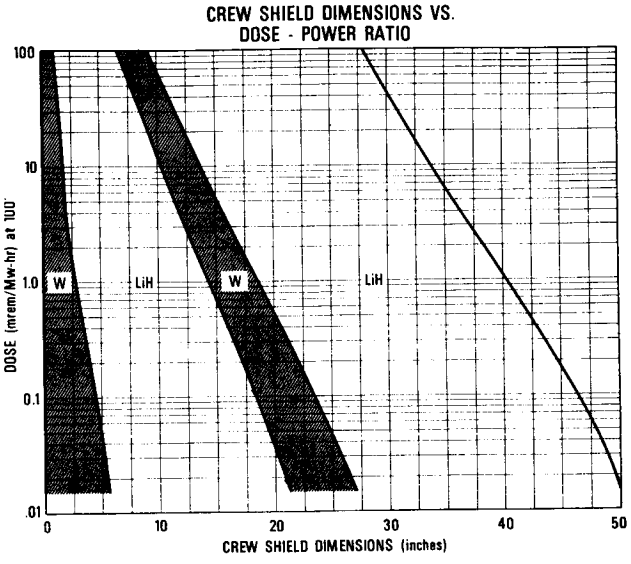

FIGURE 1.- Crew Shield Dimensions vs. Dose-Power Ratio.

The relative merits of any shield designed from several one-dimensional calculations are determined from a DOT calculation of the complete shield as mentioned previously. The DOT calculations of two specific shields will be discussed. Figures 2 and 3 show respectively neutron and gamma-ray isodose contours obtained from a DOT calculation of a tungsten-lithium hydride shield. The reactor assembly -- in the rectangular region centered at r = 0 and z = 0 -- is the zirconium hydride reference reactor similar in design to the SNAP-8. The relatively thin bands in the thickest portion of the shield are tungsten and the remainder of the shield is lithium hydride. The reactor power is 600 kWt and the dose constraints on a 100-ft radius sphere are 6 mrem/hr within the 60° cone angle of the thick portion of the shield and 100 rem/hr elsewhere. The material thicknesses were determined from ASOP calculations and the absence of tungsten

around the side and top of the reactor is due to the relatively high 100 rem/hr dose constraint. The DOT calculation indicated that the shield met or exceeded the dose constraints.

In general the isodose contours are plotted for each factor of ten decrease in dose through the shield but it is the shape of the contour, rather than the magnitude, which is important in this discussion. It should be noted that the sporadic shape of the contours near the shield surface is due primarily to mesh effects in the calculation since diagonal and curved lines must be represented by a series of rectangular steps. This effect is most pronounced when the dose gradients are very flat causing increased uncertainty in the location of the isodose lines. It appeared obvious from figure 2 that the lithium hydride at the bottom of the core could be trimmed to conform to the last neutron isodose contour without sacrificing the dose constraint within the cone angle. Because there is relatively little attenuation of gamma rays in lithium hydride the same reasoning seemed appropriate with respect to the last gamma-ray isodose contour completely contained in the last tungsten layer.

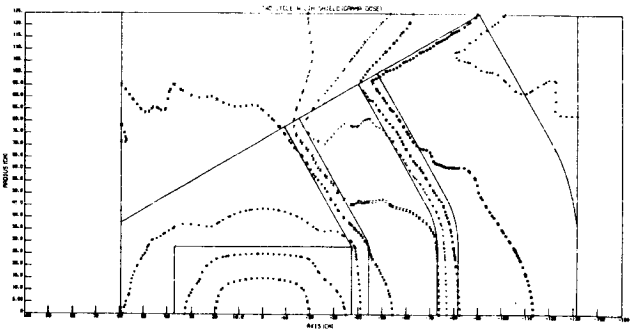

FIGURE 3.-Asymmetric Shield Configuration with a 60-deg Cone Angle - Gamma-Ray Isodose Contours.

The trimmed configuration and the resulting isodose contours are shown in figures 4 and 5. While the doses on the 100-ft sphere were slightly higher the original dose constraints were still satisfied. The shield weight was reduced from 28,000 lbs to 19,000 lbs primarily because the outer tungsten layer accounts for a significant portion of the total shield weight.

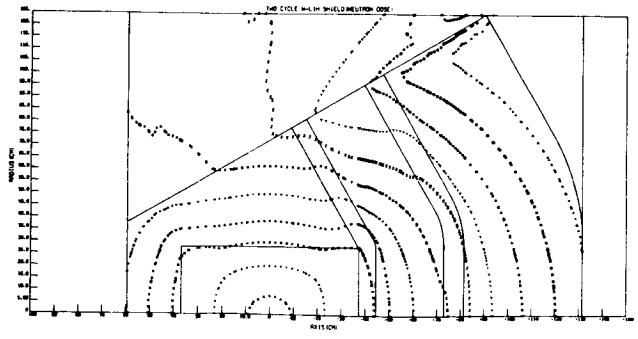

FIGURE 2.-Asymmetric Shield Configuration with a 60-deg Cone Angle - Neutron Isodose Contours.

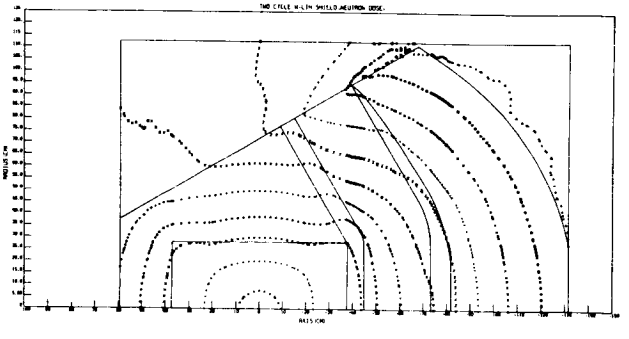

FIGURE 4.-Trimmed Asymmetric Shield Configuration with a 60-deg Cone Angle - Neutron Isodose Contours.

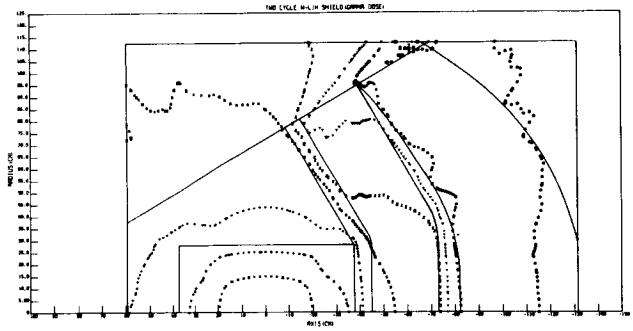

FIGURE 5.-Trimmed Asymmetric Shield Configuration with a 60-deg Cone Angle - Gamma-Ray Isodose Contours.

The second example of an asymmetric 4π shield is shown in figures 6 and 7. The reactor in this case is a small, fast spectrum core, reflected by niobium and cooled by heat pipes dispersed in the uranium nitride fuel matrix (ref. 6). The reactor power is 450 kWt. The dose constraints are 3 mrem/hr within the 90° cone angle and 300 mrem/hr elsewhere, all on a 100-ft radius sphere. The major portion of the shield is a three-cycle tungsten-lithium hydride design. Because of the high temperature of the heat pipes they could not be allowed to penetrate a lithium hydride shield. That portion of the shield at the top of the core surrounding the heat pipes was designed by ASOP from considerations of total thickness rather than minimum weight and consists of an iron-B_4C mixture followed by a BeO-B_4C mixture. The portion of the shield between the heat pipe region and the 90° cone was reduced to a two-cycle tungsten-lithium hydride configuration by ASOP because of the higher dose constraint and the fact that the inner boundaries of the tungsten layers were constrained to the positions determined for the 3 mrem/hr shield in order to avoid discontinuities.

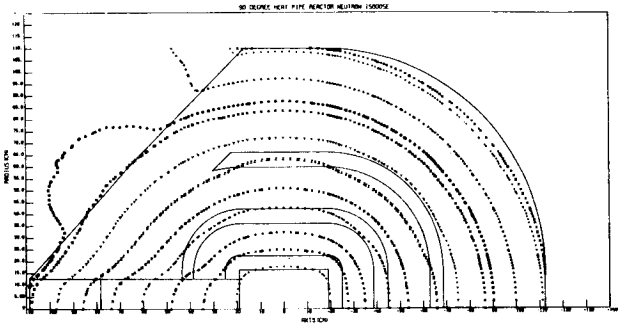

FIGURE 6.-Asymmetric Shield Configuration with a 90-deg Cone Angle - Neutron Isodose Contours.

The DOT calculation showed that the configuration did meet the design dose constraints. The isodose contours did not indicate obvious trimming of any significance however. This is attributed to the fact that the large cone angle and the wrap-around design within that cone angle cause the heaviest portion of the shield to approximate a hemisphere for which the one-dimensional ASOP calculation was quite adequate. Both the outer lithium hydride boundary and the outer tungsten boundary were trimmed slightly in the curved portion and because of the apparent direction of the gamma-ray streaming in the outer lithium hydride along the side of the core, the outer tungsten was trimmed in the side region. The resulting shield weight decreased from 28,000 lb to 25,000 lb and a DOT calculation confirmed that the design dose constraints were satisfied.

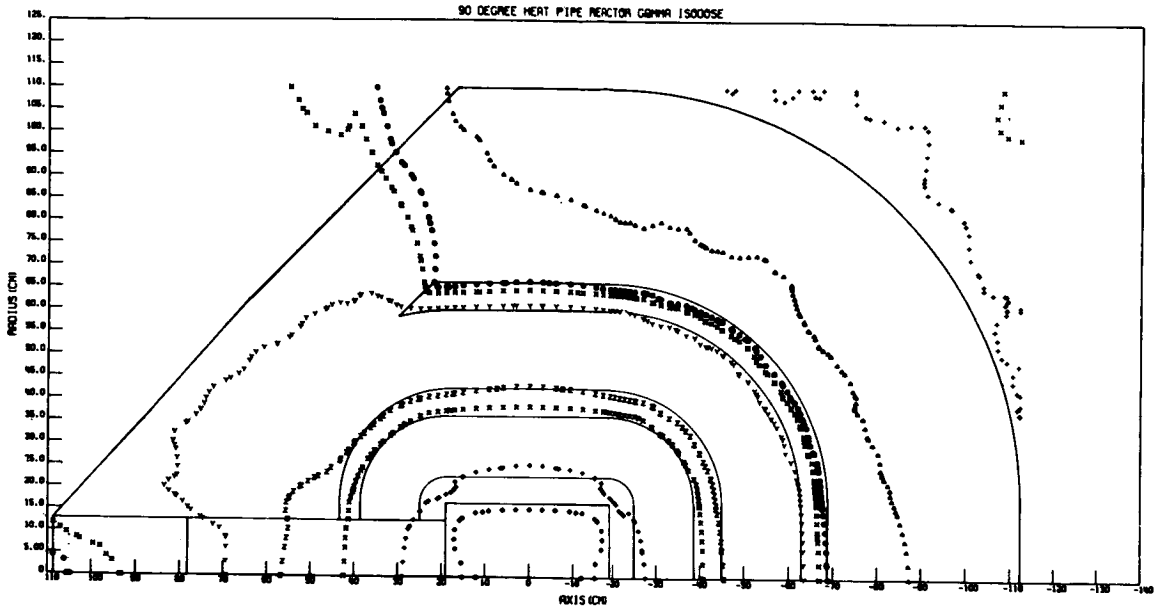

FIGURE 7.-Asymmetric Shield Configuration with a 90-deg Cone Angle - Gamma-Ray Isodose Contours.

REFERENCES

1. ENGLE, W. W., Jr.: A Users Manual for ASOP-ANISN Shield Optimization Program. USAEC Report CTC-INF-941, Union Carbide Corporation, 1969.
2. MYNATT, F. R.; MUCKENTHALER, F. J.; and STEVENS, P. N.: Development of Two-Dimensional Discrete Ordinates Transport Theory for Radiation Shielding. USAEC Report CTC-INF-952, Union Carbide Corporation, 1969.
3. ENGLE, W. W., Jr.; and MYNATT, F. R.: Trans. Am. Nucl. Soc., 11, 193, 1968.
4. MYNATT, F. R., et al.: Neutron Phys. Div. Ann. Progr. Rept., May 31, 1967, p. 52. USAEC Report ORNL-4134, Oak Ridge National Laboratory, 1967.
5. ENGLE, W. W., Jr.: A Users Manual for ANISN, A One-Dimensional Discrete Ordinates Transport Code with Anisotropic Scattering. USAEC Report K-1693, Union Carbide Corporation, 1967.
6. FRÄAS, A. P.; LaVERNE, M. E.; SAMUELS, G.; and TUDOR, J. J.: Conceptual Design of a Series of Nuclear Power Plants Employing Heat-Pipe-Cooled Reactors. USAEC Report ORNL-TM-2004, Oak Ridge National Laboratory, 1971

A PRELIMINARY SHIELD DESIGN FOR A SNAP-8 POWER SYSTEM

I. M. Karp, L. Soffer and M. R. Clark
National Aeronautics and Space Administration
Lewis Research Center
Cleveland, Ohio

A preliminary shield design for a nuclear power system utilizing a SNAP-8 reactor for space base application is presented. A representative space base configuration was selected to set the geometry constraints imposed on the design. The base utilizes two independent power packages each with a reactor operating at 600 kwt and each producing about 50 kwe. The crew compartment is located about 200 feet from each reactor and is large enough in extent to intercept a total shadow angle of 60° measured about the center line of each reactor.

Reactor dose constraints for the shield design were: (1) the dose to the crew over a 6 month mission was set at 150 mrem/day, (2) the dose along the side of either power system was set at 30 mrem/hr at a distance of 200 feet, based on considerations of exposure during repair to one power system while the other is operating, and (3) the dose constraint elsewhere around the reactor was set at 5 rem/hr at a distance of 200 feet. Personnel are not expected to be in this region during operation of the power systems except possibly for very brief periods during approach and departure from the base.

The shield design presented incorporates the results of calculations and some preliminary engineering considerations. The weight of the idealized layered lithium hydride and depleted uranium shield layout used as the calculational model was about 35,000 pounds whereas the preliminary engineering layout of the shield which includes structure, canning materials, clearance gaps between layers, etc. weighed about 41,000 pounds.

INTRODUCTION

The SNAP-8 reactor has been designed as the heat source for a space nuclear power system. Several power conversion systems compatible with the SNAP-8 reactor have been built and tested. An important component that is still required for the system is a nuclear radiation shield designed to maintain a desired set of radiation dose constraints. The purpose of a shield design, in addition to providing the desired radiation constraints, is to provide a structure that is of minimum weight and will maintain its mechanical integrity over a desired lifetime. Although minimum shield weight is desired, some trade offs between weight and good engineering design are often required. Many calculations have been made of estimates of shield weights, however, little has been presented concerning an engineered design of such a shield.

At NASA Lewis Research Center a design study is being made of an engineered flight rated shield for the SNAP-8 power system for application on a space base. Many of the engineering aspects involved in this type of shield design were considered and are discussed in Ref. 1. The present paper presents a preliminary shield designed for a specific space base configuration and a selected set of dose constraints around the power system. These constraints were based mainly on crew dose constraints recommended by the Radiological Advisory Panel of the committee on Space Medicine of the Space Science Board, Ref. 2. This design incorporates the results of calculations which involved simplified parametric optimization studies as well as more sophisticated two dimensional transport analysis and some preliminary engineering considerations.

SPACE BASE CONFIGURATION AND RADIATION SOURCES

Configuration - The space base configuration considered for this study was one investigated in a McDonnel-Douglas study, Ref. 3. The model chosen for this study is shown in Fig. 1. The space base uses two SNAP-8 power systems, each mounted at the upper end of a 200 foot long boom. The booms meet at their lower ends and make an angle of 30° with each other, so that the power systems are about 100 feet apart. The lower ends of the booms meet at the midpoint of the crew compartment which is 240 feet long. The crew compartment intercepts a total angle of 60° with each power system.

Sources - The SNAP-8 reactor and the primary coolant loop are shown schematically in Fig. 2. The reactor operates at a power level of 600 kwt and the system generates about 50 kwe. The primary coolant is NaK which removes heat from the reactor and releases this heat to an intermediate coolant in the heat exchanger.

The reactor operating at 600 kw for a desired lifetime of five years is the main source of radiation that has to be shielded. The primary coolant loop containing activated NaK and possibly some leakage fission products is also an important radiation source that has to be shielded (the primary coolant has been estimated to contain 450 curies of Na^{24}, 180 curies of K^{42}, and 0.1 percent of the volatile fission products generated by the reactor).

In addition to the shield required around these sources to maintain desired dose constraints around the power system, there has to be sufficient shield between the reactor and primary loop components (pumps, heat exchangers, expansion tanks) which are located in a region called the gallery, so that the radiation limits of the

components are not exceeded, and the intermediate coolant is not activated to a serious level.

The reactor and pressure vessel are contained within a cylindrical region (reactor cavity) which is 24 inches in diameter and 32 inches high, around which the shield is placed.

A cylindrical shaped gallery 66 inches in diameter and 24 inches high is required to contain the primary loop components.

DOSE CONSTRAINTS FROM NUCLEAR POWER SYSTEMS

Dose in crew compartment - In order to establish dose constraints, it is assumed that the mission is to be of about six months duration, and further that the crew would not be exposed to any additional radiation for the following six months. The total permissible dose as recommended by the Radiobiological Advisory Panel, Ref. 2, for this exposure-time schedule is 70 rem. This dose is sufficiently large to permit a dose to the crew from the nuclear power systems of 150 mrem/day (6.2 mrem/hr) and still leave an adequate allowance for the expected dose from natural radiation. This value of 150 mrem/day is recommended as an upper limit in Ref. 2 and by the NASA Radiation Constraints Panel, Ref. 4.

The permissible dose rate from each power system (taking into account the space base geometry) varies from 3 mrem/hr at the center of the crew compartment (200 feet away) to 4 mrem/hr at one extremity (205 feet away) and 2 mrem/hr at the other extremity (260 feet away). Fig. 3 illustrates this exclusion region of half angle 30^{o} at a nominal distance of 200 feet.

Side dose constraint - The side dose rate constraint was based on considerations of maintenance on one shut down power system while the other is operating. The total dose to be received during this operation was arbitrarily set as 1 rem. Further assuming that the repair requires about 8 hours, the equivalent dose rate at a distance of 200 feet from the side of the shield is 30 mrem/hr. This region is shown in the figure as extending from a half angle of 30^{o} to 90^{o}.

Above the shield a dose rate of 5.0 rem/hr (2.5 rem/hr from each power system) at a distance of 200 feet was set as an upper limit. This region is shown in the figure as extending from a half angle of 90^{o} to 180^{o}. The presence of personnel in this region is not anticipated except possibly for short periods during approach and departure from the base.

Coolant loop component constraints - The allowable radiation constraints to the primary coolant loop components (located in the gallery region) integrated over a lifetime of 5 years were:

10^{10} rad gamma dose and a fluence of 10^{18} neut/cm^2 of E>0.1 MeV

CALCULATIONAL PROCEDURE

In general, the method employed at Lewis Research Center for the shield design is as follows:

1. A parametric study is first made to determine the best reactor-gallery orientation, the shield materials, the number of shield layers, an estimate of their thicknesses and their arrangement around the sources.

2. A two-dimensional transport analysis is made of the shield selected in step 1 to check heating rates and dose rates within and around the shield.

3. The effects of shield penetrations and three dimensional geometry on radiation leaking out of the shield are then analyzed.

4. A fairly detailed engineering layout is made and from this another two-dimensional calculational model is constructed and further analyzed (iterations of steps 2 and 3).

The parametric study step 1 involves a multiplicity of layouts to be investigated and so requires simpler and more rapid methods of shield radiation transport calculations. Briefly, for each layout, the method involves determining the shield weight as a function of all shield layer thicknesses for the actual distribution of layers around a reactor and gallery orientation. One-dimensional transport calculations are made using the ANISN code, Ref. 5, to estimate the doses and change in doses with any change in shield layer thickness in either the radial or axial directions. These doses and weights and their changes with every shield layer thickness are input into an optimization code, D'OPEX. This code uses the method of steepest descent to determine the optimum set of thicknesses for a desired set of radial and axial dose constraints which are also input into the code. D'OPEX is the NASA Lewis extension of an Atomics International code OPEX, Refs. 6 and 7.

Some engineering design considerations are also factored into the parametric study, for example heating rates and fabricability can affect the material selection and layer arrangement.

The two dimensional analysis of the shield uses the two dimensional transport code DOT, Ref. 8, to evaluate dose and heating rates and fluxes throughout the shield. A code, MAP, Ref. 9, which utilizes the angular fluxes at the outer surface of the shield is used to calculate doses at distant detectors. The results of this phase of the analysis indicate whether any revisions to the shield are necessary (either additions to reduce doses at certain locations, or removal to increase doses or redistribution of shield to further optimize the shield weight). An iteration of the transport calculations is required to check the effects of these shield revisions.

To analyze the effects of shield penetrations and complex geometry, either a Monte Carlo approach or other methods are applied locally to the region of the irregularity to estimate the effect on radiation leakage out of a shield surface region as compared to that of the unperturbed two dimensional transport analysis. Revisions to the shield necessitated by these effects are then estimated.

The engineering layout of the shield based on the forgoing computational model includes additional materials such as structure and canning material. These additional materials, clearance gaps, and changes in the shape of some shield layers necessitated by fabrication limitations, result in the engineering layout being larger in size than the computational shield model.

RESULTS AND DISCUSSION

As seen in Fig. 3 the crew region intercepts a half angle of 30^{o} with the axis of the reactor-shield assembly.

Because for the present system, the side dose constraint is only a factor of ten greater than the crew dose constraint for each reactor, it was decided to base the shield weight optimization on a cylindrical shaped shield model rather than a shadow shaped shield model. This shape would simplify the engineering design.

Parametric Study

From the parametric study it was determined that:

1. The gallery located above the reactor (away from crew) resulted in lower shield weight.
2. Depleted uranium was to be used for gamma shield material and lithium hydride for neutron shield material.
3. Depleted uranium could not be used as the first layer (where it would be in a very high flux region) because the high fission rate produced excessive heating in the layer.
4. There was less than one percent effect on total shield weight if lithium hydride was used as the first layer instead of heavy gamma material.
5. For the thick shields required, five shield layers both radially and axially toward the crew were an optimum number; three layers were sufficient between the reactor and gallery.

For the cylindrical shaped shield, it was estimated that to obtain a dose of 4 mrem/hr at the extremity of the crew region (30^{o} position), an axial dose constraint of 1 mrem/hr (0^{o} position) and a radial dose constraint of 30 mrem/hr (90^{o} position) were required (the latter consisting of 15 mrem/hr from the gallery source and 15 mrem/hr from the reactor and secondary sources). These axial and radial constraints were used in the D'OPEX code to determine the specific layer thicknesses.

The results of the parametric study are presented in Fig. 4 which shows the various shield layers arranged around the reactor and gallery in a symmetrical two-dimensional configuration. The radial and axial layers are connected together by ellipsoids of revolution.

Two-Dimensional Analysis of Initial Shield Configuration

The two-dimensional calculations were performed in two separate parts. One calculation involved the transport of the primary coolant gamma source which was assumed to be distributed uniformly over the gallery region. The other calculation involved the transport of the reactor sources which included the generation and transport of secondary sources throughout the shield. Due to the size of the problem the spatial mesh size, angular quadrature, and scatter order, had to be relaxed from those typically used in the one-dimensional transport calculations made in the parametric study. The values used in the two-dimensional DOT calculations were as follows:

1. For the gallery gamma calculation, 15 energy groups, P-2 scatter order, S-8 angular quadrature, and 43 radial by 47 axial spatial mesh intervals. Only the top half of the configuration (above the reactor and shield midplane) was considered for this calculation.
2. For the reactor calculation, 26 neutron energy groups coupled with 15 gamma energy groups, P-2 scatter order, S-6 angular quadrature, and 43 radial by 88 axial spatial mesh intervals, were used.

Results from this initial two-dimensional shield calculation are presented in Figs. 5 and 6. Dose rates were evaluated at detectors positioned around the shield at a reference distance of 200 feet as shown in Fig. 5. The dose rate values are also presented in the figure. Dose rates in the crew compartment vary from 1.4 mrem/hr at 0^{o} to 7.7 mrem/hr at 30^{o}; along the side from 7.7 mrem/hr at 30^{o} to 41.3 mrem/hr at 90^{o}; elsewhere from 41.3 at 90^{o} to a peak value of 510 mrem/hr at 180^{o}.

The crew constraint is exceeded in the crew compartment in the range from about 15^{o} to 30^{o} and the side constraint is exceeded in the region from 70^{o} to 90^{o}. In the region from 90^{o} to 180^{o} the doses are well within the constraint of 2.5 rem/hr. These results indicated that shield revisions were necessary.

Revisions to Shield

As part of the calculations, contributions to the dose at each detector from radiation leaking out of various portions of the shield surface were determined. This information was useful to help guide where adjustments to the layered shield should best be made. Fig. 6 shows the outline of the shield surface and the portions of the surface of the DOT calculation model (labelled I - VIII) that were investigated. The figure also presents the neutron, reactor and secondary gamma, and gallery gamma dose contributions from each surface region for detectors at 30^{o}, and 90^{o}.

The high gallery gamma contribution to the 90^{o} detector from surface VIII indicated that additional shield was required along the side of the gallery. The high gallery contributions to the 30^{o} detector from surfaces VII and VIII were also due to inadequate shield along the side of the gallery. High gallery contributions from surfaces V and VI indicated that the connecting piece of uranium between the gallery side shield and outer radial uranium layer was not sufficiently thick. The reactor and shield gamma dose contribution from the surfaces II and III to the 30^{o} detector were also excessive and indicated that the connecting ellipsoids at the corners of the uranium layers needed thickening. Relatively large neutron dose contributions from surfaces VII and VIII to the 30^{o} detector, and from surface VIII to the 90^{o} detector indicated that there was appreciable scattering of neutrons by the gallery side shield. In addition to analyzing these surface contributions, plots of gamma and neutron isodose lines throughout the shield were also used to guide shield revisions.

The revisions made to the shield shown in Fig. 4 were as follows:

1. The gallery side shield thickness was increased from 2.2 cm to 3.0 cm .
2. The outer radial uranium layer thickness was increased from 2.0 cm to 2.5 cm.
3. The connecting piece of uranium between these was thickened proportionately.
4. The entire ellipsoidal corner of the outer uranium layer was thickened by an average of about 1.5 cm.

5. The uranium layer between the reactor and gallery was reduced in thickness from 5.2 cm to 4.2 cm.

A two-dimensional transport calculation of the revised shield was made and the results are shown in table I. The dose rates in the crew region now range from 0.8 mrem/hr at 0^{o} to 3.6 mrem/hr at 30^{o} and are within the permissible crew constraint everywhere. The dose rates along the side of the power system vary from 3.6 mrem/hr at 30^{o} to about 23 mrem/hr at 90^{o}, and are within the permissible side constraint. Above the gallery, in the 90^{o} to 180^{o} region the maximum dose rate is about 0.6 rem/hr, well within the desired constraint of 2.5 rem/hr.

Radiation dose levels in the gallery were calculated to be 3×10^{8} rad gammas and 2×10^{14} neuts/cm^{2}, E>0.1 Mev, over a 5 year period. These are well within the allowable constraints.

The weight of the revised shield configuration used as the calculation model is 35,000 pounds.

Engineering Design Considerations

The results of the shield analysis discussed so far were used to produce an engineered layout of the shield. In this layout, considerations of shield cooling, structural support for the entire shield, containment for the shield materials as well as fabrication of the shield layers, clearances between layers, the assembly of the entire shield, etc. were taken into account.

A simplified sketch of the engineered layout which shows some of the features of the design is shown in Fig. 7. Although some of the uranium layers are utilized as structural members, much additional steel structure is required. Shown in the figure are also the coolant ducts, control drum actuator penetrations, and about a 1/2-inch clearance gap between the removable and stationary portions of the shield. This latter feature was designed into the shield for replacement of the reactor when required. A portion of the shield which contains the reactor is removable. Thus the replacement package contains the new reactor and only a fraction of the entire shield. A sketch of this replaceable section with respect to the permanent section of the shield is shown in Fig. 8. Incidentally, although the actuator shaft penetrations enhance the radiation streaming toward the crew, their location in this position in the shield make them accessible for repair.

The structure, canning materials, and clearances, as well as some revisions in the shield layer shapes, necessitated by fabrication considerations, result in the engineering layout being larger in size and weight than the computational model of the shield. As a comparison, the engineered layout shown in Fig. 7 weighs 41,000 pounds compared to a weight of 35,000 pounds for the revised computational model.

CONCLUDING REMARKS

A preliminary shield design for a SNAP-8 nuclear power system has been evolved to meet a set of selected dose constraints for a specific space base configuration. This design incorporates results of calculations involving a preliminary parametric optimizational study, iterated two-dimensional transport analysis, and some engineering design considerations. The weight of the idealized computed shield configuration is 35,000 pounds. This compared to a weight of 41,000 pounds for an engineered shield layout.

Before the design can be finalized, the effects of shield penetrations and any changes in the shield geometry necessitated by these has yet to be determined and incorporated into the engineered layout. A calculational model of the shield based on the engineered layout has to be made and two dimensional transport calculations of this configuration performed. As the design becomes finalized finer spatial mesh size, angular quadrature, and scattering order should be used in the calculations in order to improve the accuracy of the design.

TABLE I. - DOSE RATES AROUND REVISED SHIELD CONFIGURATION

Detector θ degree	Reactor dose mrem/hr	Gallery dose mrem/hr	Total dose mrem/hr
0	0.8	---	0.8
10	1.2	0.1	1.3
20	1.9	0.3	2.2
30	2.7	0.9	3.6
40	4.1	2.0	6.1
50	5.6	3.9	9.5
60	7.3	6.3	13.6
70	8.8	9.1	17.9
80	10.3	11.4	21.7
90	11.4	11.8	23.2
120	30.	145.	175.
150	295.	225.	520.
180	360.	245.	605.

REFERENCES

1. Kaszubinski, Leonard J.; Kacher, Henry F.; and Odar, Fred: Preliminary Designs of Space Power Nuclear Reactor Shields. NASA TM X-2038, 1970.
2. Radiobiological Advisory Panel, Committee on Space Medicine, Space Science Board: Radiation Protection Guides and Constraints for Space-Mission and Vehicle-Design Studies Involving Nuclear Systems. National Academy of Sciences, 1970.
3. McKhann, G. G.; Coggi, J. V.; and Diamond, S. D.: Preliminary Design of Reactor Power Systems for the Manned Space Base. Paper WD 1296, McDonnell Douglas Astronautics Co., June 1970.
4. Space Station Task Group: Guidelines and Constraints Document Space Station Program Definition Phase B. MSC-00141, Rev. N, NASA Manned Spacecraft Center, Apr. 24, 1970.
5. Engle, Ward W., Jr.: A Users Manual for ANISN: A One-Dimensional Discrete Ordinates Transport Code with Anisotropic Scattering. Rep. K-1693, Union Carbide Corp., Mar. 20, 1967.
6. Bernick, R. L.: The OPEX Shield Optimization Code. Rep. NAA-SR-Memo-11516, Atomics International, July 13, 1965.
7. Lahti, Gerald P.: Opex-II, A Radiation Shield Optimization Code. NASA TM X-1769, 1969.
8. Soltesz, R. G.; Disney, R. K.; and Collier, G.: User's Manual for the DOT-IIW Discrete Ordinates Transport Computer Code. Rep. WANL-TME-1982, Westinghouse Astronuclear Lab., Dec. 1969.
9. Disney, R. K.; Soltesz, R. G.; Jedruch, J.; and Zeigler, S. L.: Code Description and User's Manual for the MAP Radiation Transport Computer Code. Rep. WANL-TME-2706, Westinghouse Astronuclear Lab., Aug. 1970.

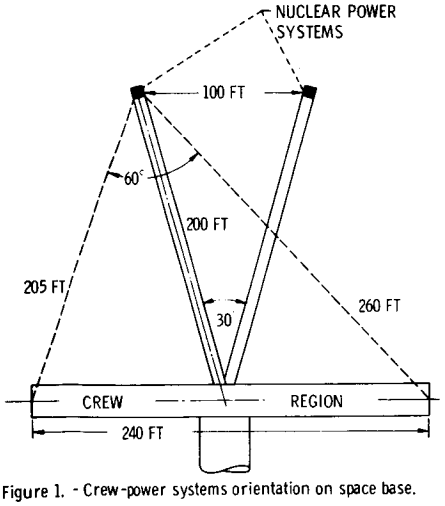

Figure 1. - Crew-power systems orientation on space base.

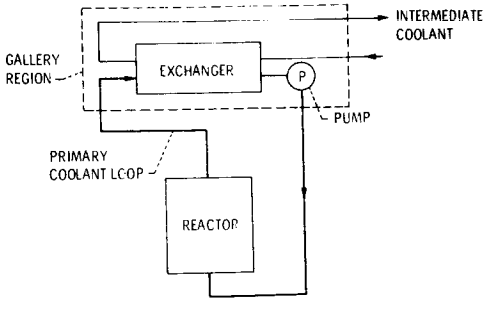

REACTOR 600 kW - 5 YR OPERATION

GALLERY { 450 CURIES Na^{24} ; 180 CURIES K^{42} ; 0.1 PERCENT OF VOLATILE FISSION PRODUCTS }

Figure 2. - Reactor and primary coolant sources.

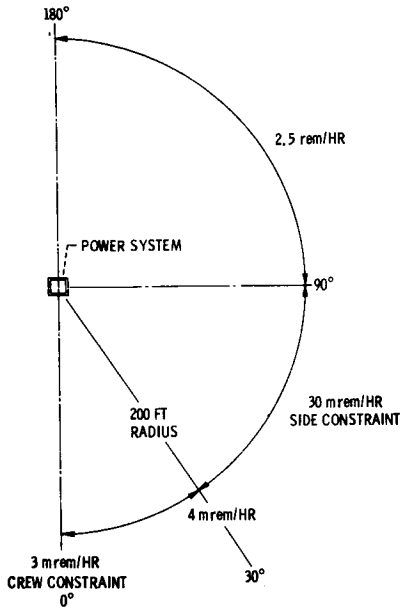

Figure 3. - Dose constraint map around each power system.

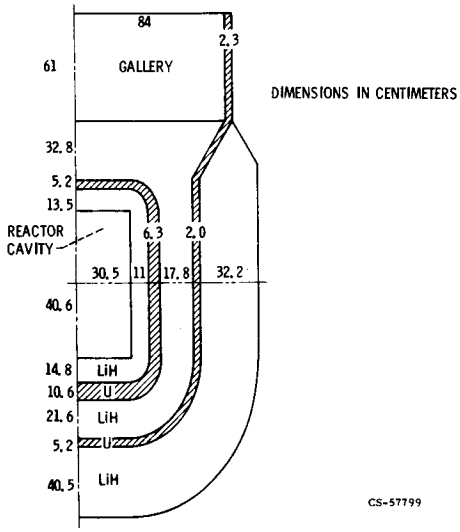

Figure 4. - Initial shield layering around reactor and gallery sources.

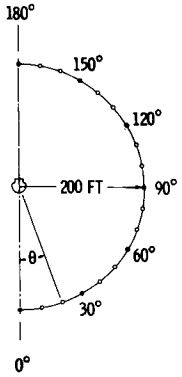

DETECTOR, θ, DEG	REACTOR DOSE RATE mrem/hr	GALLERY DOSE RATE mrem/hr	TOTAL DOSE RATE mrem/hr
0	1.4	--	1.4
10	2.9	.1	3.0
20	3.8	1.1	4.9
30	5.2	2.5	7.7
40	7.3	5.1	12.4
50	10.3	8.4	18.7
60	12.0	12.8	24.8
70	13.9	17.0	30.9
80	14.9	26.4	41.3
90	14.2	27.1	41.3
120	30.0	155.0	185.0
150	210.0	225.0	435.0
180	265.0	245.0	510.0

Figure 5. - Dose rates around initial shield configuration

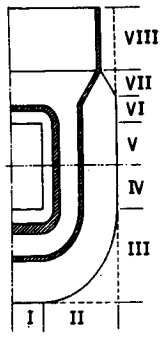

SURFACE	DOSE RATES, MREM/HR					
	30°			90°		
	REACTOR		GALLERY	REACTOR		GALLERY
	NEUT	γ	γ	NEUT	γ	γ
I	0.03	0.2	---	---	---	-----
II	.08	1.5	---	---	---	-----
III	.13	1.2	---	.1	0.6	-----
IV	.29	.8	---	1.2	5.6	-----
V	.15	.18	1.1	.8	2.8	0.2
VI	.05	.08	.5	.2	.7	.4
VII	.17	.04	.5	.1	.3	3.3
VIII	.17	.04	.4	1.2	.7	23.2

CS-57796

Figure 6. - Dose contributions to detectors at 30° and 90° from various portions of the shield surface.

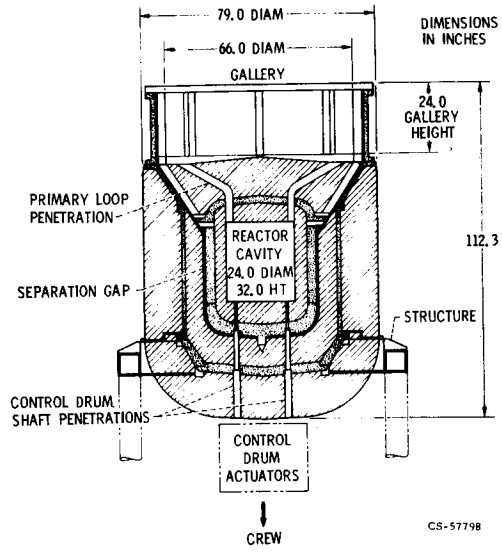

Figure 7. - Some features of the engineering layout of the shield.

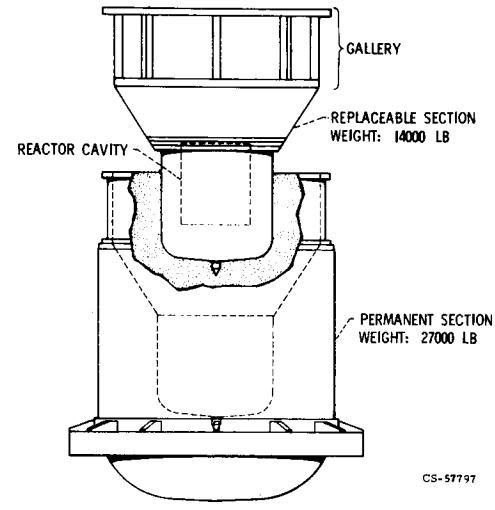

Figure 8. - Replaceable and permanent shield sections.

SNAP 8 POST-SHUTDOWN GAMMA RADIATION APPROXIMATIONS

N. R. Byrn and H. T. Smith, Teledyne Brown Engineering
H. S. Manning, NASA/MSFC

An evaluation was made of an approximate method for calculating the dose rate resulting from fission product gamma radiation after reactor shutdown. Safety analyses for advanced nuclear missions in space have used this technique for determining radiologically safe operations. This method assumes that the dose rate $D_1(r, t)$, received from a shutdown reactor is directly proportional to the residual gamma power level at that time.

To check the validity of this "power ratio" assumption, energy-dependent detector responses were calculated for normalized sources in the Perkins and King energy group structure for a SNAP 8 power system on a NASA space station. Gamma decay rates were then calculated by using an expanded, updated list of isotopic decay data, and from these, actual detector responses $D_2(r, t)$ were found for the SNAP 8 system. The two detector responses, D_1 and D_2, were then compared at several times after shutdown and at detector positions around the space station. An error of several thousand percent was found for many detectors at times greater than one year; it was also found that an increase in material attenuation produced an increase in error and that energy-dependent detector response, such as dose rates, showed greater discrepancy between D_1 and D_2 than did the energy flux.

It was concluded that these discrepancies were caused by a decrease in the proportion of high-energy gammas released at longer shutdown times. This softening of the decay gamma spectrum with time caused an increased attenuation of decay gamma energy; invalidating the power ratio assumption. Because of the complexity of the space station geometry, these conclusions were checked and verified by a point source in infinite water calculation. The results indicate that energy-dependent calculations must be made to determine decay gamma dose rates for actual reactor configurations. A simplified method for making these calculations has been devised.

This paper summarizes the results from the determination of the nuclear environment produced by the SNAP-8 reactor on the space station. The study was concerned with determination of the gamma radiation environment produced by the reactor in its shutdown mode, and its variation with respect to time elapsed after shutdown.

The general approach to this and similar shutdown reactor radiation problems, which has been in use prior to this study, involves two steps. The first step is to research the available literature and obtain data, generally in graphical form, which gives the ratio of residual shutdown gamma power to operating power, versus the two parameters of reactor operating time prior to shutdown and the time elapsed after shutdown at which one is interested in determining the radiation environment. The second step is to assume that the gamma dose rate is directly proportional to the residual gamma power level, determine the constant of proportionality, and use it to determine the gamma dose rate from the residual gamma power level found in the first step.

The accuracy of this approach depends on the accuracy of the graphs from which the gamma power ratio is found and the reliability of the assumption that the gamma dose rate is directly proportional to the residual gamma power level. Both of these matters were investigated. The investigation has yielded new power ratio curves which incorporate more recent isotopic data than had been used previously, a determination of the problems encountered, and the error incurred in relating gamma dose rate directly to residual gamma power, plus a simplified method of performing these calculations in the future.

In addition, a radiation transport analysis was made of the nuclear power system for the space station, using the Point Kernel technique to determine the radiation attenuation characteristics of the space station. The results of this portion of the study show the relative magnitude of the geometric and material attenuation, by energy group, of gamma radiation in and around the nuclear-powered space station. These results will be very useful in later investigations in that the gamma radiation environment at any of the detector positions may be quickly found for a U-235 reactor by "de-normalizing" them. i.e., by multiplying the normalized detector response in each energy group by the ratio of the actual source in that group to the source used in the normalized calculation. This process is applicable to future analysis of a U-235 reactor at any power level in both the operating and post-shutdown phases.

REVISION OF POST-SHUTDOWN POWER VERSUS TIME DATA

The General Dynamics data on post-shutdown gamma power as a function of reactor operating

time and time elapsed after shutdown (ref. 1) has proven to be a very helpful tool in performing radiation analyses on SNAP-type nuclear power systems. The original information was compiled for a NERVA-type nuclear propulsion reactor, but if the same reactor fuel is used (U-235), the data may be applied to any nuclear system. There are a few disadvantages in using this material; first, it is based on fission product data which was compiled in 1958 and 1959, and, second, the graphs contain information for reactor operating times only up to 10^4 seconds (approximately 3 hours). It was felt that a major improvement could be made to the post-shutdown gamma power data if these data were updated to include the latest fission product decay information and if results for longer reactor operating periods were incorporated. References 2 and 3 list the data in use up to 1963, with reference 3 having the more recent information, including the fission product data for 125 nuclides.

Burrell and Watts (ref. 4) supplied more up-to-date fission product data, which included a library of decay data for 200 nuclides, plus a computer program for utilizing the data. Modifications were made to the code, and an output plotting technique was written and added to it. Figure 1 shows the results of the calculation with this code in the form of total shutdown gamma power versus time after shutdown and operating time. Operating times from 1 to 1×10^9 seconds (approximately 30 years) were included in the calculations. The time after shutdown began at 1×10^2 seconds, since this was the minimum that could be used from the basic input data without extrapolation, and it was felt that periods of time shorter than this were not of interest at present.

Figures 2 through 8 display similar data, but in this case, separately for the seven Perkins and King energy groups. By presenting the data in this format, with a separate graph for each energy group rather than for each reactor operating time, the effect of operating time and shutdown time is more apparent. In this form, the results are more applicable to future calculations, as described in the next section.

EVALUATION OF POST SHUTDOWN DOSE APPROXIMATIONS

An evaluation was made of an assumption used in earlier radiation environment studies of reactors for nuclear missions. This assumption is that the dose rate received from a shutdown reactor is directly proportional to the residual gamma power level. For example, at a given time after the reactor has been shut down when the decay gamma power level is $P(t_1)$ watts, a calculation determines the dose rate at a detector to be $D_1(r, t_1)$ rads. Then, at any other time after shutdown when the decay gamma power level is $P(t_2)$ watts, the dose rate at the same detector can be found from the simple equation

$$D_1(r, t_2) = \frac{D_1(r, t_1)}{P(t_1)} P(t_2)$$

Note that the ratio of dose rate to residual power level at t becomes the constant of proportionality by which the new residual power level is multiplied. The obvious advantage of this technique for calculating decay gamma dose rates is its simplicity. Only one transport calculation need be performed; it can then be scaled to apply to any time after shutdown.

The following approach was used to check the validity of this "power ratio" assumption. As with the original assumption, only one transport calculation was made for each detector point; however, the desired information from this calculation was the dose rate as a function of energy. In particular, the doses, D_1, received from a unit source (1 MeV/sec) in each of the seven Perkins and King energy groups were calculated. Then, using the revised gamma energy release data, Γ_i, as described in the previous section, the dose at detector point r and at time t was calculated by

$$D_2(r, t) = \sum_{i=1}^{7} \Gamma_i(t)\, D_i(r) ,$$

where the summation is over the seven Perkins and King energy groups.

The doses calculated, D_1 and D_2, were then compared for several times and detector points around the space station. The discrepancy between doses seemed to depend on three different factors: time, position, and type of response. First, the error between the two methods increased greatly with increasing time since shutdown, reaching over 1000 percent for some detectors at times greater than 1 year. Also, at a fixed time, the error became larger as the amount of attenuating material between source and detector increased. Finally, the error changed at the same detector point and at the same time for different response units; for example, rads (tissue) versus rads (silicon) versus energy flux. Examples of each of these three results are given below.

For the detector located 170.7 centimeters above the center of the SNAP reactor, the tissue dose rate error between D_1 and D_2 is shown in Table 1. The percent error did not change significantly after 4×10^8 seconds.

TABLE 1. TISSUE DOSE RATE

Time After Shutdown (sec)	Percent Error
1×10^2	0
1×10^3	26
1×10^4	66
1×10^5	283
1×10^6	155
1×10^7	590
1×10^8	509
1×10^9	771
1×10^{10}	770

For 1×10^5 seconds after shutdown, typical detectors showed the discrepancy between D_1 and D_2 for dose rates in rads (tissue) per second (table 2). These detector positions are also ordered in increasing amount of attenuating material between source and detector.

For the detector located at 170.7 centimeters above the center of the SNAP reactor at 1×10^5 seconds after shutdown, the energy flux showed an error of 283 percent, while the tissue dose showed an error of 214 percent. Similarly, at 1×10^9 seconds after shutdown, the energy flux showed an error of 771 percent, while the tissue dose showed an error of 567 percent.

The physical phenomena causing the large discrepancies can be understood by examining the gamma power versus shutdown time curves (figures 1 through 8). These curves show that at early times after shutdown most of the gamma energy is coming from the higher energy gamma groups. As the time after shutdown increases, the percentage of gamma energy emitted in the higher energy groups decreases. For example, approximately one day after shutdown (10^5 seconds), the energy emitted in the highest energy group, VII, is only 0.15 percent of the total. At 10^2 seconds after shutdown, energy group VII contributed 30 percent of the total gamma energy release. As the time after shutdown approaches 10^8 seconds (approximately 3 years), only energy group II contributes significantly to the total decay gamma energy release. Group II covers the energy range from 0.4 to 0.9 MeV. In this energy group, the energy absorption coefficients for all materials are greater than those for the higher energy groups. Hence, this softening of the decay gamma spectrum with increasing time, coupled with the greater absorption coefficients for softer gammas, caused an increased attenuation of the total decay gamma energy. For detectors that are shielded from the decay gamma source, e.g., in a shutdown SNAP-8 reactor, the power ratio assumption for calculating the shutdown gamma dose would not be expected to be very accurate. In fact, the accuracy of the doses calculated by this technique should become poorer as time increases, because of the softening of the decay gamma spectra, and, as the shielding increases, because of the selective attenuation of the lower energy gammas. Also, these phenomena would cause the energy-dependent response functions to show variations.

Although the explanation of the cause of the discrepancies between D_1 and D_2 seemed plausible, the complexity of the source term and the shield geometry in the SNAP-8 reactor system required a check of the validity of the above conclusions. This check was made by calculating the dose from a normalized point source (1 MeV/sec) in each of the Perkins and King energy groups in an infinite water medium. Detectors were located at nine different radii from the point source, beginning at 5 centimeters (5 g/cm^2) and ending at 500 centimeters (500 g/cm^2). Five different responses were calculated; however, only the results of two of the response calculations will be given. These responses are the energy flux (MeV/cm^2-sec) and tissue dose rate [rads(T)/sec]. The effect of time after shutdown and shielding on the tissue dose rate is very similar to the effect on the

TABLE 2. DISCREPANCY BETWEEN D_1 AND D_2

Detector Number	Relative Number of Mean Free Paths	Percent Error
1	1.0	214
2	1.47	333
3	7.90	1,413

TABLE 3. TIME DEPENDENT DECAY GAMMA DOSE COMPARISON

Distance from Source (cm)	Response Function*	Percent Error at Time After Shutdown (sec)								
		10^2†	10^3	10^4	10^5	10^6	10^7	10^8	10^9	10^{10}
5	EF	0.0	0.52	1.11	0.91	0.33	1.13	0.82	2.49	2.49
	TDR	0.0	3.57	6.53	7.59	6.91	12.10	11.90	13.90	13.90
10	EF	0.0	0.74	1.61	1.62	0.95	2.16	1.84	3.50	3.50
	TDR	0.0	3.76	6.97	8.20	7.44	12.90	12.70	14.70	14.70
25	EF	0.0	0.69	1.59	2.83	2.17	1.25	1.32	0.89	0.89
	TDR	0.0	2.60	4.37	4.60	4.99	10.60	10.50	13.00	13.00
50	EF	0.0	7.46	16.30	23.30	18.90	29.80	29.20	26.40	26.40
	TDR	0.0	3.26	8.04	12.40	8.93	11.40	10.90	7.80	7.79
100	EF	0.0	29.90	70.90	105.00	87.20	253.40	248.80	268.10	268.10
	TDR	0.0	24.20	56.60	83.90	69.30	186.10	182.70	192.00	191.90
200	EF	0.0	78.00	242.20	379.70	297.80	3426.40	3210.50	$>10^4$	$>10^4$
	TDR	0.0	72.60	217.80	343.10	270.10	2904.20	2727.60	7885.10	7883.30
300	EF	0.0	111.10	446.70	652.50	495.90	9127.90	8589.90	$>10^4$	$>10^4$
	TDR	0.0	107.80	420.80	624.10	475.60	8396.00	7840.80	$>10^4$	$>10^4$
400	EF	0.0	134.00	673.80	819.10	608.00	$>10^4$	$>10^4$	$>10^4$	$>10^4$
	TDR	0.0	128.80	614.20	806.10	604.30	$>10^4$	$>10^4$	$>10^4$	$>10^4$
500	EF	0.0	143.00	794.70	900.80	670.00	$>10^4$	$>10^4$	$>10^4$	$>10^4$
	TDF	0.0	142.10	781.70	895.30	666.10	$>10^4$	$>10^4$	$>10^4$	$>10^4$

*Detector response are energy flux (EF) in (Mev)/(cm^2·sec) and tissue dose rate (TDR) in [rads (T)/sec].

†Results normalized to 10^2 seconds shutdown time.

other three responses. Table 3 shows that, in general, the results of the decay gamma point source support the conclusions reached above. The percent error increases with increasing time, but not monotonically. The error at 10^6 seconds after shutdown decreases because gamma group IV dominates gamma group II at this time. Thus, this higher percent of high energy gammas emitted at 10^6 seconds more closely approximates the original spectrum (at 10^2 seconds), hence the decrease in percent error between D_1 and D_2. Also, the percent error increases for more shielding, i.e., distance from the source, except at 25 centimeters. The reason for this apparent anomaly is that the build-up of dose is greater than the material attenuation until some point between 10 and 25 centimeters, causing D_2 to be greater than D_1 in this range. From 25 centimeters on, the original conclusion is valid, as expected.

Considering the original results for the SNAP-8 system and the infinite water-point source calculations, the following conclusions were reached:

- The discrepancies between D_1 and D_2 were caused by a decrease in the proportion of high-energy gammas released at longer shutdown times.
- The softening of the decay gamma spectrum with time causes an increased attenuation of decay gamma energy, invalidating the power ratio assumption.
- Energy-dependent calculations need to be made to determine the decay gamma dose rate at various times after shutdown.

Obviously, the energy-dependent calculations of the dose rate are more time-consuming than using the power ratio assumption. However, by using detector positions for which a normalized source-point kernel calculation has been made, and by using figures 2 through 8, the dose rates can be calculated as described below.

Suppose the reactor has operated at a power level of P watts for τ seconds. The conversion factor, C, for data taken from figures 2 through 8 is computed by

$$C = 6.25 \times 10^{12} \left[(\text{MeV/sec})/\text{W}\right] \cdot P\ (\text{W}) \cdot \tau\ (\text{sec})$$
$$= 6.25 \times 10^{12} \cdot P \cdot \tau\ \text{MeV}.$$

For time of shutdown, t, and for each energy group, determine the corresponding ordinate values from figures 4 through 8. If τ, the operating time, does not equal the operating times on the figures, then use logarithmic interpolation between the given values of τ. The ordinate values are the normalized shutdown gamma power, GP_i, for each of the seven energy groups. Then, for the selected detector position, r, and response, the dose rate at shutdown time, t, operating time, τ, and power level, P, is computed by

$$D\ (r,t) = C \cdot \sum_{i=1}^{7} GP_i(t) \cdot D_i(r),$$

where $D_i(r)$ is the energy-dependent detector response from the normalized source-point kernel calculations. It should be noted that the above process is valid for any shutdown reactor as long as the dose rates are determined for a normalized source (1 MeV/sec) in each of the Perkins and King energy groups.

REFERENCES

1. "Operational Safety Analysis for Advanced Nuclear Missions", General Dynamics/Fort Worth FZK-220, Vol. II, December 1964
2. Perkins, J. F. and R. W. King, "Energy Release from the Decay of Fission Products", Nuclear Science and Engineering: 3, pp. 726-746 (1958)
3. Perkins, J. F., "Decay of U-235 Fission Products", U.S. Army Missile Command, Redstone Arsenal, Alabama, Report No. RR-TR-63-11, July 1963
4. Private Communication from M. Burrell and J. Watts, NASA-MSFC, September 1970

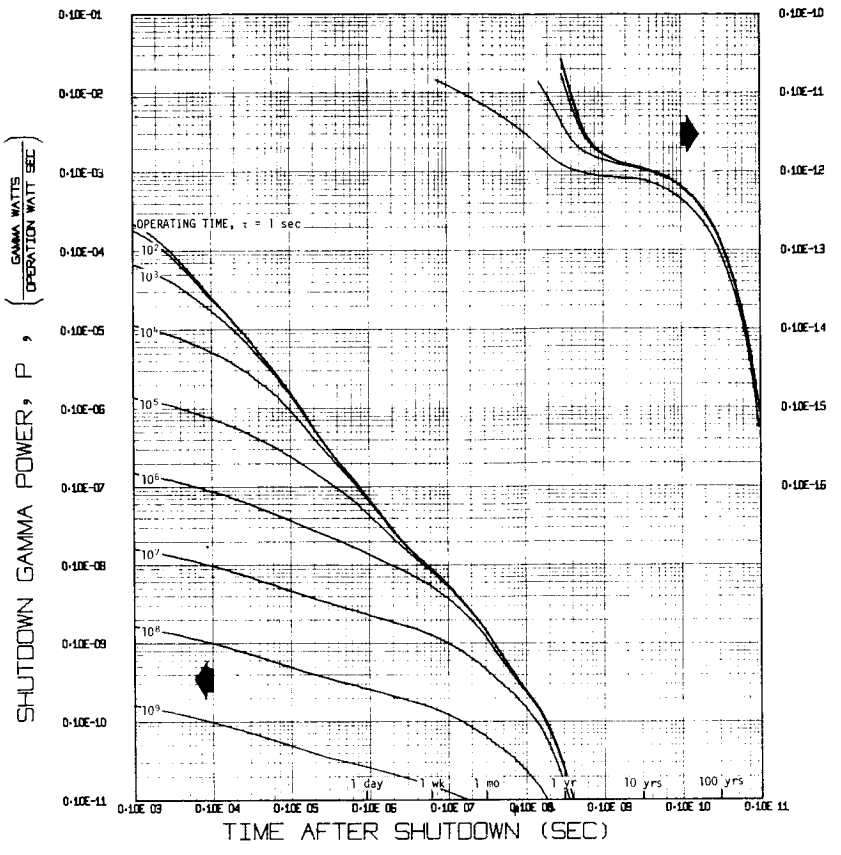

FIGURE 1. - Total shutdown gamma power level.

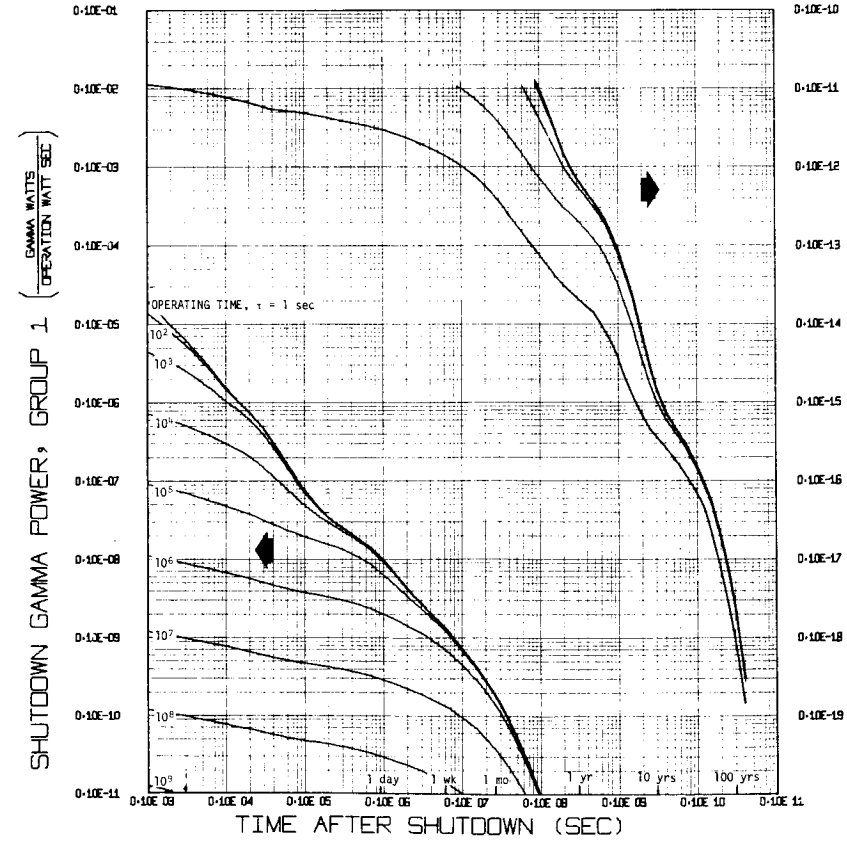

FIGURE 2. - Post shutdown gamma power level energy group (0.1 to 0.4 MeV).

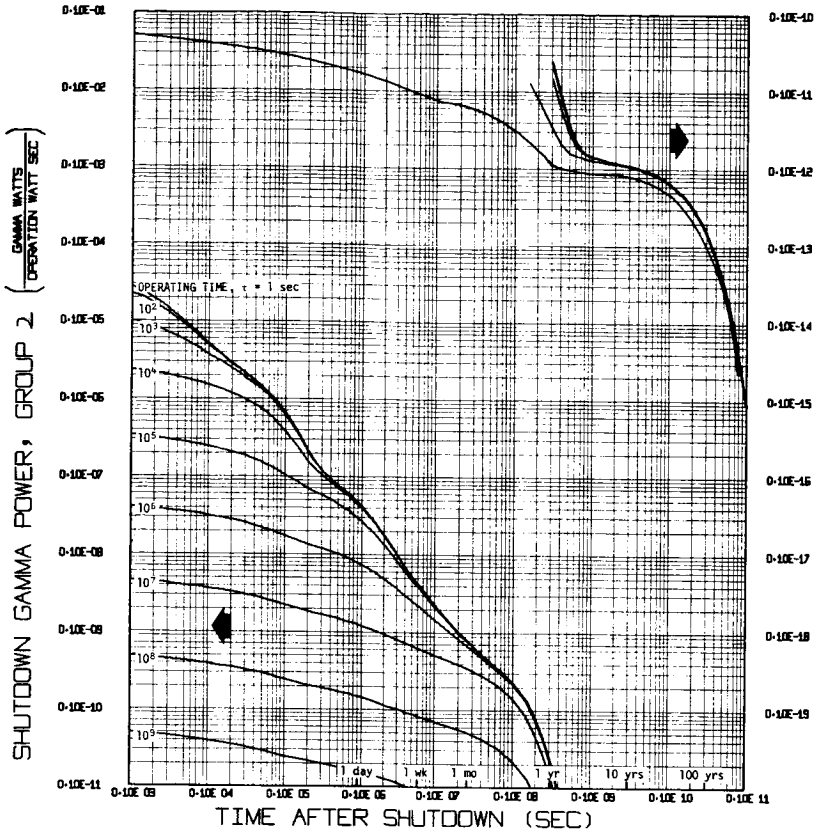

FIGURE 3. - Post shutdown gamma power level energy group (0.4 to 0.9 MeV).

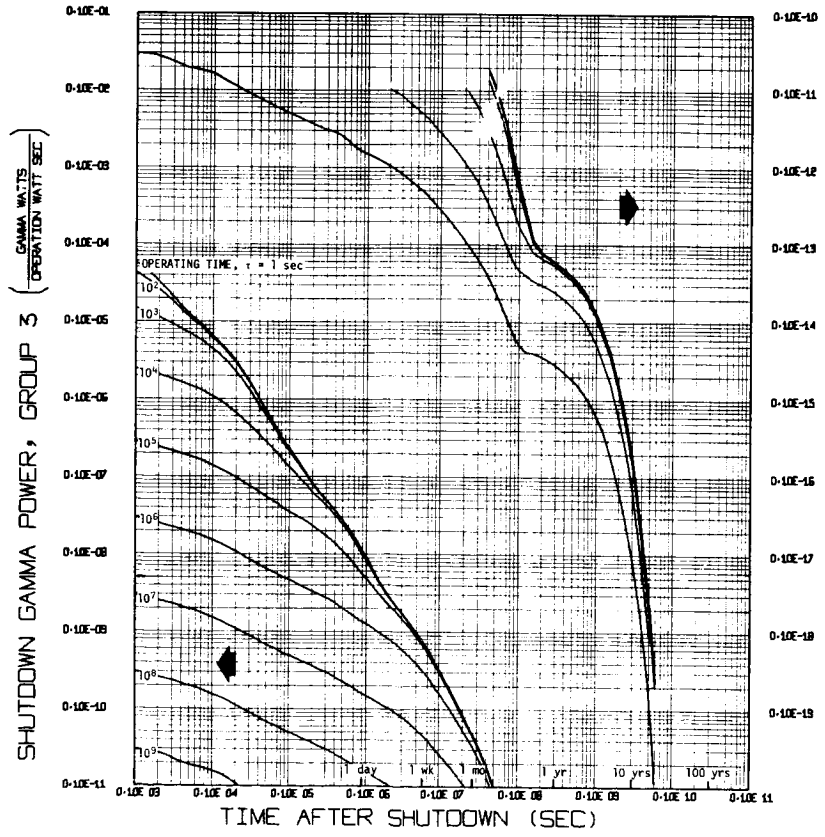

FIGURE 4. - Post shutdown gamma power level energy group (0.9 to 1.35 MeV).

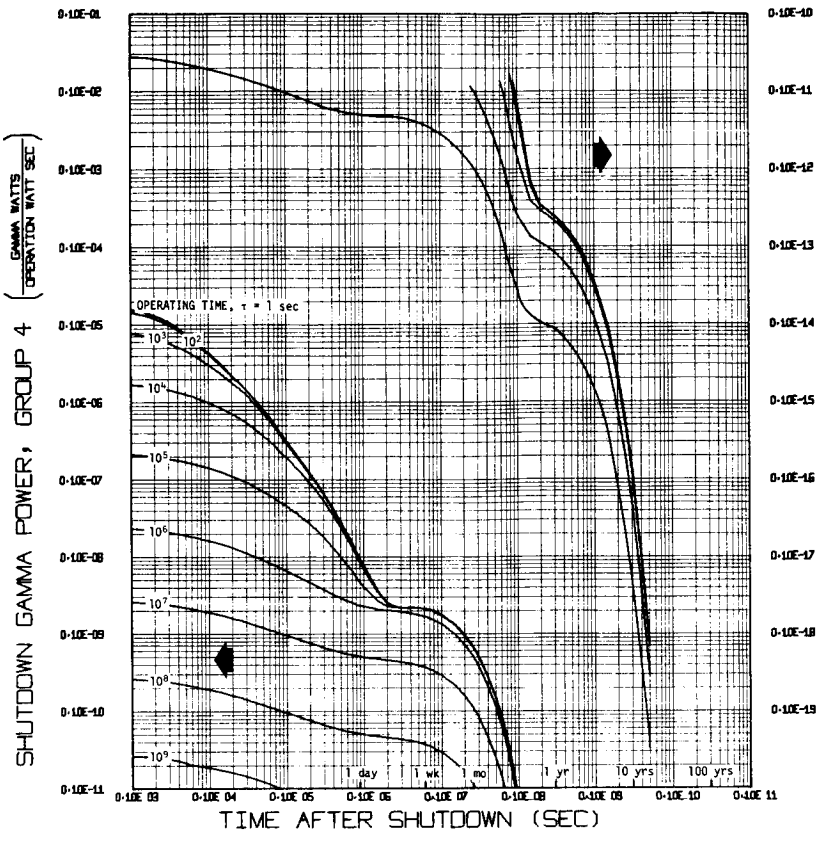

FIGURE 5. - Post shutdown gamma power level energy group (1.35 to 1.8 MeV).

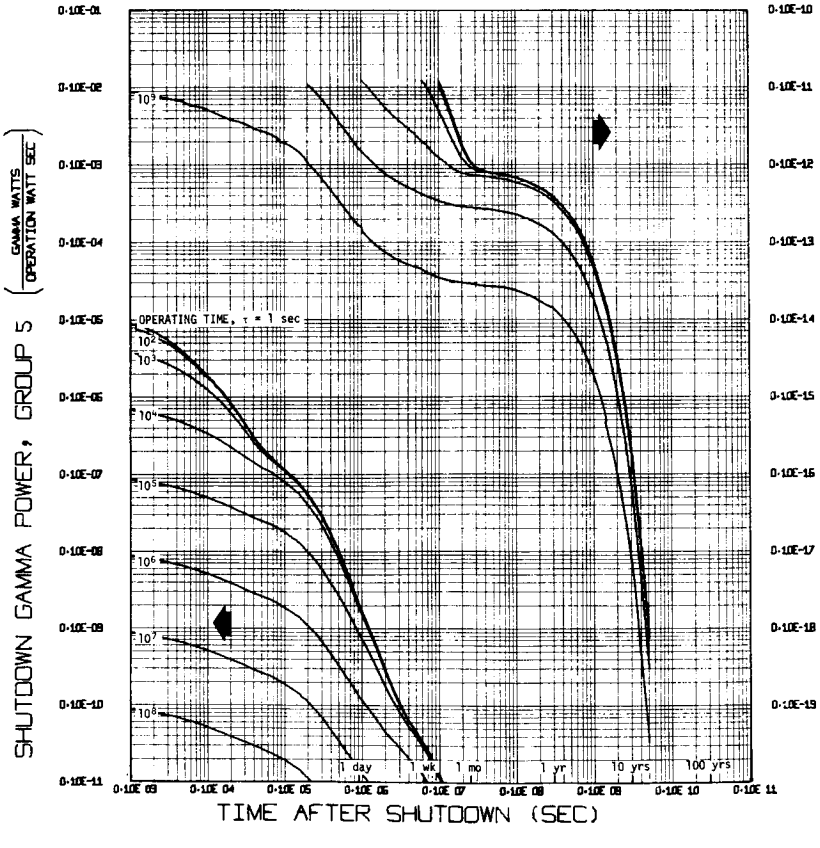

FIGURE 6. - Post shutdown gamma power level energy group (1.8 to 2.2 MeV).

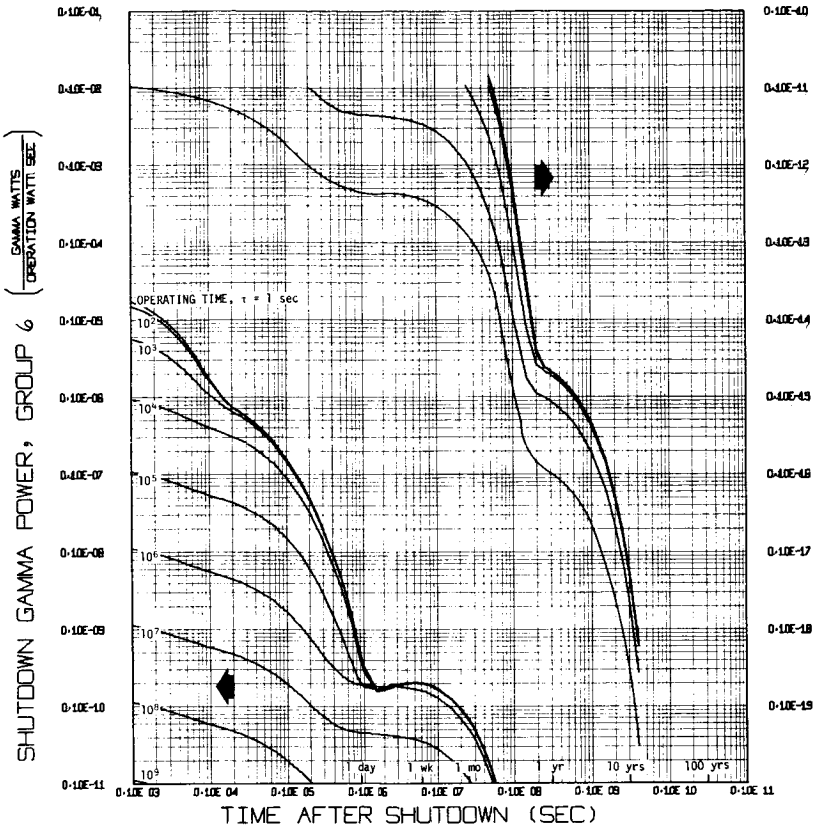

FIGURE 7. - Post shutdown gamma power level energy group (2.2 to 2.6 MeV).

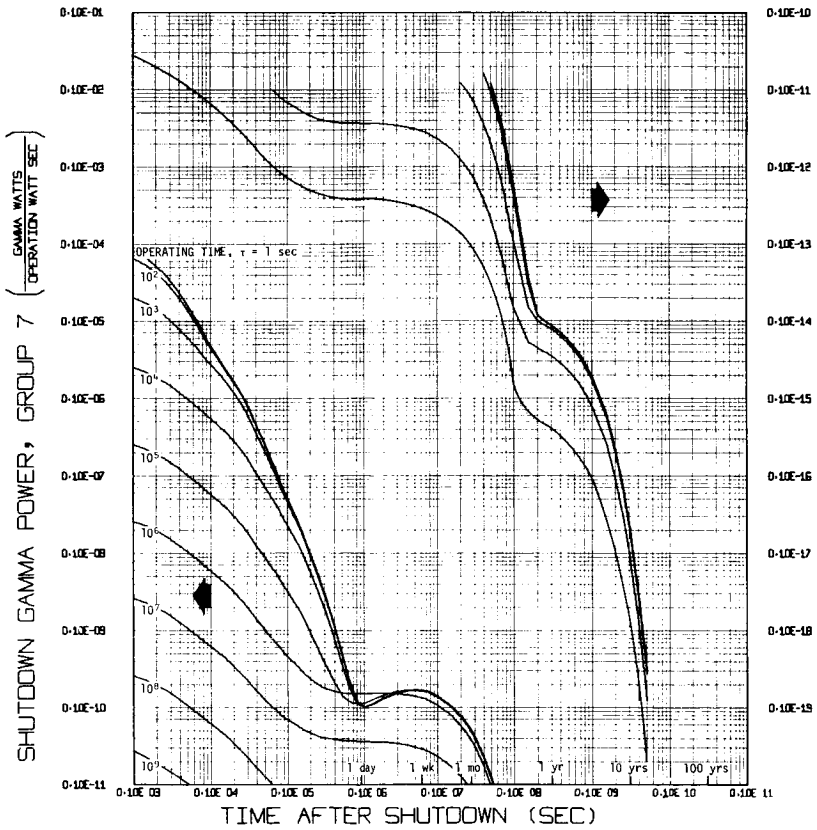

FIGURE 8. - Post shutdown gamma power level energy group (2.6 MeV to ∞).

SPACE REACTOR SHIELDING FABRICATION

FRANK H. WELCH

ATOMICS INTERNATIONAL DIVISION

NORTH AMERICAN ROCKWELL

The fabrication of ground based reactor shielding, steel, concrete, water tankage, etc., is generally simple, based upon well-known engineering data and construction experience. This is not true in the case of the reactor shielding needed for space application. The demand to provide the most efficient shielding materials has forced the nuclear engineer to consider the so-called "exotic" materials.

A new facility has been constructed at the Atomics International Nuclear Field Laboratory, funded by the Atomic Energy Commission, for the fabrication of space reactor neutron shielding by a melting and casting process utilizing one of these "exotic" materials, lithium hydride. This facility is equipped to handle lithium hydride not only under the exacting conditions dictated by the nature of the reactive, moisture sensitive material, but also under the stringent requirements of the nuclear shielding engineer for high purity, maximum density, good structural integrity, etc.

This facility, believed to provide the largest capacity in the world, is capable of producing lithium hydride neutron shields up to 8 feet in diameter weighing 10,000 lbs.

In addition, the facility contains a 1650 cubic feet nitrogen atmosphere, glove-ported room capable of handling these massive shields during a destructive examination to determine the internal characteristics of the shield after thermal and vibrational tests simulating operational conditions.

The first neutron shield fabricated in this new facility was a large, pancake shape 86 inches in diameter, containing about 1700 pounds of lithium hydride. This shield, fabricated by the unique melting and casting process, is the largest lithium hydride shield ever built.

A program of shielding materials and fabrication development has been conducted at Atomics International for about ten years funded by the Atomic Energy Commission. The ultimate goal of the program is the fabrication of a family of neutron and gamma shielding components for the reference ZrH reactor, as illustrated in Fig. 1.

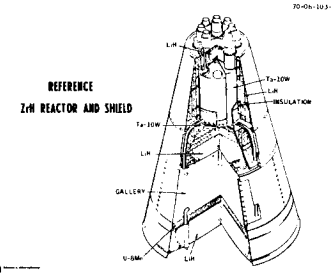

Figure 1.—Reference ZrH Reactor and Shield

This family of shields consists of uranium - 8 weight percent molybdenum and tantalum - 10 weight percent tungsten for the attenuation of gammas, and lithium hydride for the attenuation of fast neutrons.

The development of the technology for the fabrication of lithium hydride shapes as light weight, high efficiency neutron shielding for space reactor application has been the prime effort of the program. The selection of lithium hydride (LiH) as the neutron shielding material was based primarily on its high hydrogen content, stability at high temperatures, and low density.

The high hydrogen content of lithium hydride provides an effective means of shielding men and equipment against the neutrons from the reactor; the high temperature stability permits the material to be used in the high thermal environs of the reactor without melting or decomposition; and the low density (approximately three-fourths that of water) makes it attractive for use in a space system in which weight is critical. Lithium hydride is a brittle, salt-like material which is translucent and a pale-whitish blue in color. It possesses a melting point of 1267°F (686°C) and a dissociation pressure of about 20 torr at the melting point which permits the material to be melted and frozen under a slight pressure of hydrogen without degradation.

Recently a new 3600 square foot facility was completed at the Atomics International Nuclear Field Laboratory, designed specifically for the fabrication of large lithium hydride shields by a melting and casting process. This facility is equipped to handle lithium hydride not only under the exacting conditions dictated by the nature of the reactive, moisture sensitive material, but also under the stringent requirements of the nuclear shielding engineer for high purity, maximum density, and good structural integrity. The facility believed to provide the largest capacity in the world, is capable of producing lithium hydride neutron shields up to eight feet in diameter weighing 10,000 pounds.

In addition, the facility contains a 1650 cubic foot nitrogen atmosphere, glove-ported room capable of handling these massive shields during a destructive examination to determine the internal characteristics of the shield after thermal and vibrational tests simulating operational conditions.

The first neutron shield fabricated in this new facility was a large, pancake shape 86 inches in diameter, containing about 1700 pounds of lithium hydride. Figure 2 shows an artist's interpretation of the shield. Installed in a reactor-shield system, the shape would be inverted from the as-cast view and would be located at the base of the system shown in Figure 1.

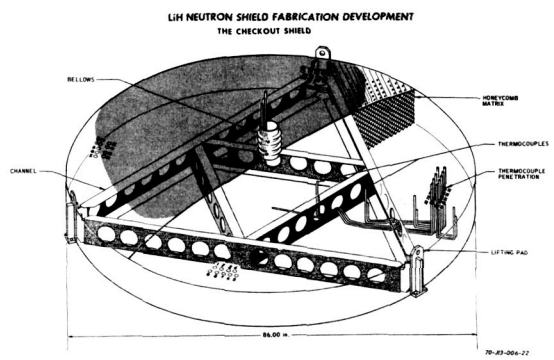

Figure 2.—LiH Neutron Shield Fabrication Development

Figure 3 illustrates the steps in the loading, melting and freezing cycle to fabricate the shield. The empty shield vessel was placed in the shield casting hardware (Figure 4), consisting of a large reservoir, a filler tube-bellows assembly, a supporting structure, and a safety vessel. The

latter is necessary in the event of an accidental spill of molten lithium hydride from a ruptured weld, etc. Figure 5 shows the empty shield vessel lifted from the safety vessel. The thermocouples are used to monitor the temperature of the lithium hydride during the cycle.

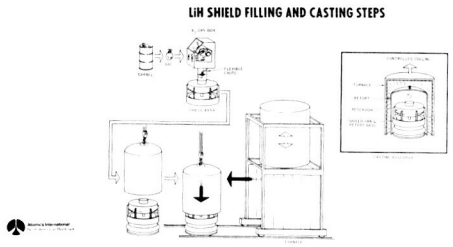

Figure 3.--LiH Shield Filling and Casting Steps

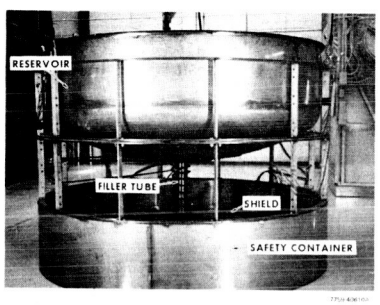

Figure 4.--Shield Assembled in the Casting Hardware

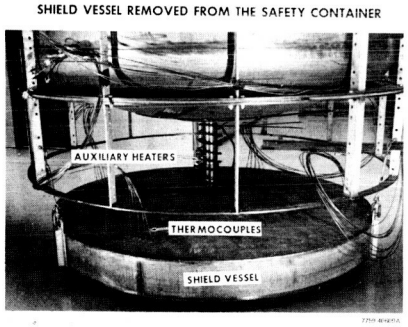

Figure 5.--Shield Vessel Removed from the Safety Container

The casting hardware-shield assembly was placed on a 10,000 pound capacity vibrator platform (Figure 6) and a nitrogen atmosphere dry box was rolled into place over the top of the reservoir. A rubber sleeve was used to connect the top of the reservoir with the bottom of the dry box. The air was purged from the reservoir and shield until the O_2 content was less than 3 percent.

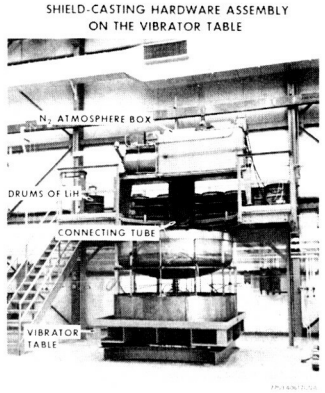

Figure 6.--Shield-Casting Hardware Assembly on Vibrator Table

The bags of LiH were removed from the sealed drums, weighed and loaded into the dry box antechamber (Figure 7). The antechamber was purged to an O_2 content of 3 percent or less and the bags transferred into the dry box where they were slit open and the lithium hydride crystals poured into the reservoir (Figure 8). After the required 1900 pounds was loaded, the reservoir was sealed and the assembly was moved to the retort base. High temperature electrical conductors were connected between the base terminals and the auxiliary heaters located around the filler tube-bellows assembly and on the bottom of the reservoir. These heaters provide the fine control necessary during the final stages of freezing. Thermocouples also were connected to their base terminals. (Figure 9).

LOADING BAGS OF LiH INTO THE DRY BOX ANTECHAMBER

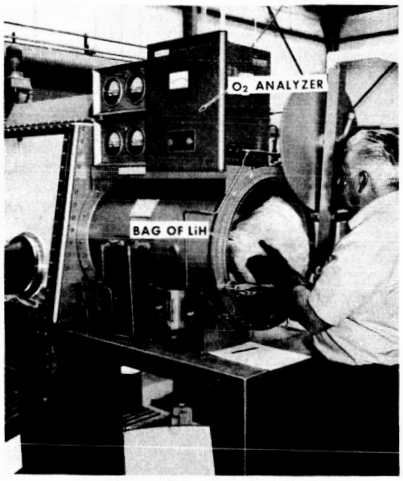

Figure 7.--Loading Bags of LiH into the Dry Box Antechamber

TRANSFERRING THE BAGS OF LiH INTO THE N_2 ATMOSPHERE BOX

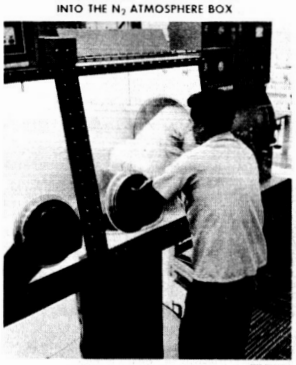

Figure 8.--Transferring the Bags of LiH into the N_2 Atmosphere Box

INSTALLING THE RETORT OVER THE SHIELD-CASTING HARDWARE ASSEMBLY

Figure 9.--Installing the Retort over the Shield-Casting Hardware Assembly

The Incoloy retort was lowered over the assembly, the retort sealed, evacuated to about 10 microns pressure, and backfilled with H_2 to 1.6 psig pressure. The furnace was elevated (Figure 10), rolled into place over the retort, and lowered onto the retort (Figure 11).

ELEVATING THE FURNACE

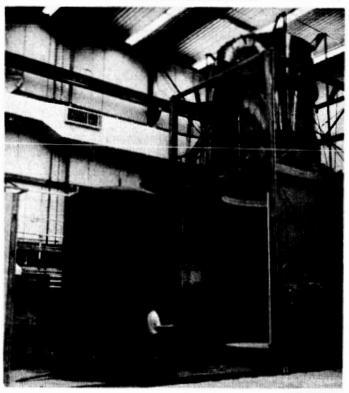

Figure 10.--Elevating the Furnace

MONITORING THE CASTING CYCLE

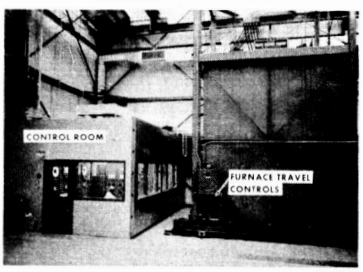

Figure 11.--Monitoring the Casting Cycle

The power to the four temperature control zones of the furnace was turned on and the retort and contents heated to about 1400°F (Figure 12). The temperatures of the shield and casting hardware, the gas flow and pressure, and the O_2 content of the H_2 were monitored throughout the cycle (Figure 13). About 30 hours were required to melt the 1900-pound charge of lithium hydride and raise the melt temperature to about 1400°F.

FURNACE TEMPERATURE CONTROL PANEL

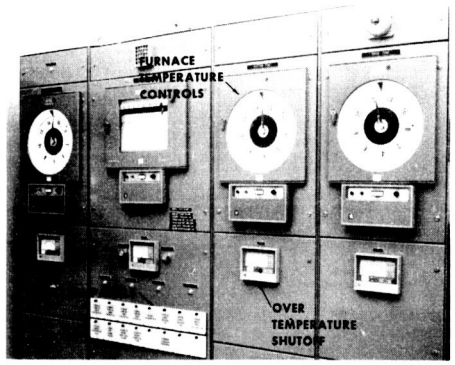

Figure 12.--Furnace Temperature Control Panel

GAS PRESSURE AND FLOW, AND AUXILIARY HEATER CONTROL PANELS CAST

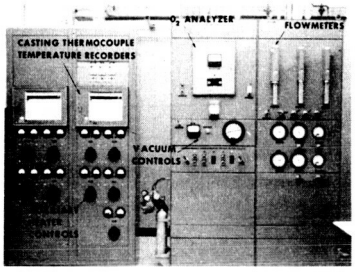

Figure 13.--Gas Pressure and Flow and Auxiliary Heater Control Panels

Cooling was accomplished by raising the furnace upwards stepwise and adjusting the furnace temperature downwards to permit the lithium hydride to freeze radially inwards and axially upwards. The lithium hydride in the reservoir and the filler tube-bellows assembly was kept hotter than the lithium hydride in the shield using the auxiliary heaters. Adjustment of the auxiliary heater power was used to force the freezing front upwards into the filler tube-bellows assembly. Seventy-five hours were required to freeze the lithium hydride in the shield.

When the assembly had cooled to about room ambient, the H_2 was evacuated from the retort, the retort backfilled with argon, and the retort unsealed and removed. The casting hardware-shield assembly was removed from the retort base, and the cast shield was lifted from the safety vessel and photographed in the same position as before the casting cycle (Figure 14). Visually the shield vessel was not found to have been distorted in any significant manner by the heating and cooling cycle.

CAST LiH SHIELD LIFTED FROM THE SAFETY CONTAINER

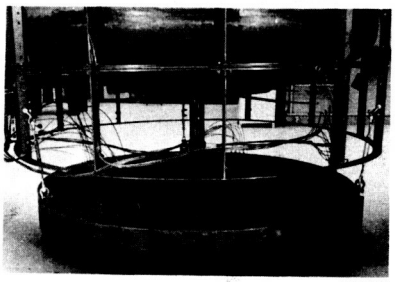

Figure 14.--Cast LiH Shield Lifted from the Safety Container

Twenty-eight radiographic exposures were made covering the entire cross-sectional area of the shield. Evaluation of the radiographs revealed that the shield was the soundest ever produced, exhibiting less than average of the normally occurring small cracks and fissures between the lithium hydride crystals.

The filler tube-bellows assembly was cut from the shield and a temporary closure of the stub made. A series of void volume measurements were made by evacuating the shield, then backfilling it to atmospheric pressure with helium from a tank of known volume and pressure, and calculating the percent void using the Perfect gas law. A void volume of 5 percent was obtained whereas the average void volume for all previous shields is about 6 percent. This measurement confirmed the visual appraisal from the radiographs.

The next steps in the normal development program would be a series of thermal cycles and vibration testing simulating near-use conditions; however, this shield was not a prototype design, but was designed and built specifically to check-out the new facility and equipment, and to investigate the difficulties which might arise in the casting of the thin, large diameter shape. The

next planned step, therefore, is a destructive examination in the Shield Examination Room. Figure 15 shows the completed shield readied for installation in the nitrogen-filled room (Figure 16).

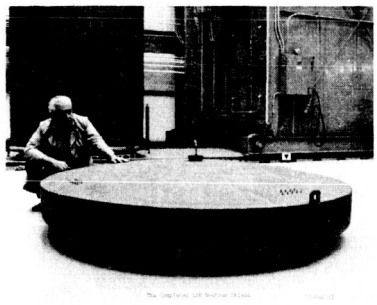

Figure 15.—The Completed LiH Neutron Shield

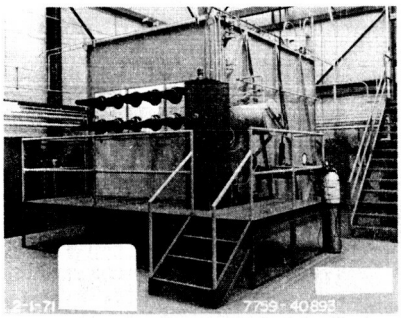

Figure 16.—The N_2-filled Shield Examination Room

Table I compares the capability of the new facility with the older, smaller facility which has been used for many years to cast numerous smaller shields. The envisioned future shield system (Figure 17) required for supplying reactor-produced electrical power for manned application will be fabricated in this large facility, although the smaller facility remains operational for the fabrication of smaller lithium hydride shielding components.

NEUTRON SHIELD
CASTING CAPABILITIES

	BUILDING 3	BUILDING 42
• RETORT ID (in.)	48	105
• RETORT HEIGHT (in.)	60	125
• SHIELD DIAMETER, MAXIMUM (in.)*	42	96
• SHIELD HEIGHT, MAXIMUM (in.)*	40	80

*MAXIMUM DIAMETER AND MAXIMUM HEIGHT CANNOT BE USED IN THE SAME ASSEMBLY

Atomics International TABLE I

Table I.—Neutron Shield Casting Capabilities

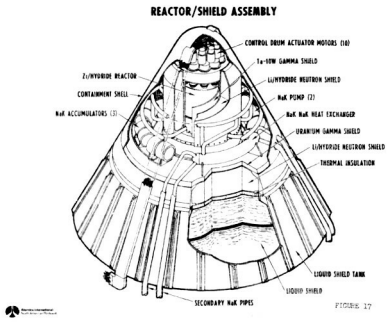

Figure 17.—Reactor/Shield Assembly

NUCLEAR REACTOR DESCRIPTIONS FOR SPACE POWER SYSTEMS ANALYSIS*

E. W. McCauley and N. J. Brown

Lawrence Radiation Laboratory
University of California
Livermore, California

For the small, high performance reactors required for space electric applications, adequate neutronic analysis is of crucial importance, but in terms of computational time consumed, nuclear calculations probably yield the least amount of detail for mission analysis study.

It has been found possible, after generation of only a few designs of a reactor family in elaborate thermomechanical and nuclear detail to use simple curve fitting techniques to assure desired neutronic performance while still performing the thermomechanical analysis in explicit detail. The resulting speed-up in computation time by three orders of magnitude, permits a broad detailed examination of constraints by the mission analyst.

INTRODUCTION

Space research in general and Space nuclear electric systems in particular are in a period of priority reassessment and technological retrenchment. Even so, new concepts and different combinations of older concepts are being put forth for possible application. In order to provide any hope of progress, the mission analyst, faced with a restricted list of missions and of vehicles, must develop a set of analyses more consistent and credible than those to date. One of the chief obstacles in his path is the state of nuclear reactor heat source data which is usually presented as a pointwise design or as a set of parametric statements so overgeneralized as to be effectively useless.

Mission analysis can hardly optimize a point, or give a reasonable estimate of specific research potential on systems where it has neither breadth nor depth of knowledge. On the other hand, the designer of the nuclear reactor heat source has insufficient information to optimize his system to the particular mission since it in turn lacks definition.

To be effective, the reactor descriptions must be presented to the mission analyst in considerable detail. However, the parametric constraints must be held to an absolute minimum or the surface to be fitted will be as full of confusing depressions as a lunar landscape.

Some years ago the Lawrence Radiation Laboratory developed a method of parallel-optimization-path reactor design for cylindrical reactors, which coupled thermo-mechanical design to multi-group neutron transport analysis to allow rapid assessment of the effects of acquired research data and potential lines of research on reactor performance. It was found practicable to rapidly convert from one type of reactor to another. Beyond this, the consistency inherent in a single pass computerized design produced configurations significantly superior to those that the same group achieved by traditional reactor design methods.

This method requires approximately 5 to 10 minutes of CDC-6600 time to produce a design point which is too long to be suitable for inclusion in mission analysis work. The neutronic routines are called 30 to 40 times in a typical iterative design sequence and require three to four orders of magnitude more computation time than the thermomechanical portion.

The obvious approach is then to attempt to eliminate the detailed neutronic analysis if possible. As a demonstration case, we have selected a heatpipe-cooled reactor type previously studied at LRL.[1] We selected the criticality-limited design region and designed a family of 12 reactors in detail at power levels of .6, 2., and 4.6 Mwth. Fueled core aspect ratios (L/D) were chosen as .8, 1.2, 1.6, and 2.0.

This paper purposely avoids extensive tables and reactor descriptions so that it may not be construed as a description of a particular reactor system, but as an approach to a particular design problem, applicable to a variety of systems, whether liquid metal convectively cooled or heatpipe cooled cores for Rankine systems, or in- core or out-of-core thermionic systems. However, it is necessary to consider some parameters and features of the system selected to demonstrate that the study was not made on an over-simplified students model.

DESCRIPTION OF THE HEAT SOURCE

The model selected was as detailed and sophisticated as any published in connection with the LRL Space Reactor Technology Program. The corresponding model here actually has its outermost radius within the fueled core radius of the SPR-4 design, yet it has been designed with a greater safety margin.

A cross section is shown in Fig. 1. Both the reactor and the heatpipe boiler sections on the ends were designed in the code. The design includes a dual control system, either of which could carry the mission to completion. The core is not represented by a simple fuel matrix but is designed

*Work done under the auspices of the U. S. Atomic Energy Commission.

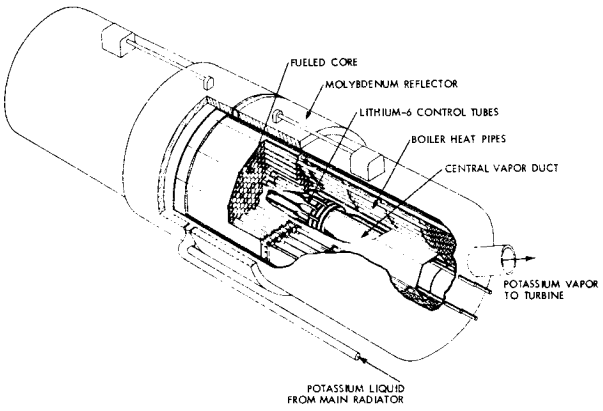

Fig. 1. Reactor Model - Double Ended Heatpipe, Integral Boiler Type

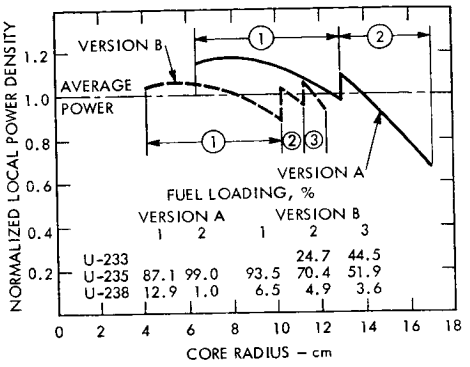

Fig. 2 Power Density Profiles

as a discrete number of fuel elements arranged in a hexagonal pattern in a discrete number of dodecagonal rows. Zonal boundaries coincide with fuel element boundaries and fuel loadings of U-238, U-235, and U-233 are varied to give radial power flattening. Material properties are temperature dependent and in cases where creep is involved, both time and temperature dependent.

Fuel elements were designed with both thermal stress and peak temperature limits. Provision was made for differential thermal expansion and burnup dependent fuel swelling. The heatpipes for each system were tailored to the reactor and optimized for the specific ase. Their design limits included peak or boiloff flux limits, and a safety margin to carry the load on failure of any single adjacent heatpipe as well as a 10% factor for power surges, 20% for transport property data scatter, and 10% for radial power variations.

The units were designed to have a maximum multiplication factor at room temperature of .96 when fully immersed in water and flooded in the absence of blowoff side reflectors. Appropriate neutron filters to accomplish this were placed between core and pressure vessel in this case. The design code could and in the past has, designed these filters into the metallic structure within the core as alloying elements or as plating.

The design code also checks zero power temperature coefficients as a function of temperature, and power coefficients for control as a function of lifetime including fuel burnup effects, production of daughter fissile species, etc.

The pressure vessel and structure were designed for each case using time and temperature dependent creep data.

The remaining figures show additional details of the system. Figure 2, previously published[2] shows the compactness and the degree of power flattening achieved by the U-233, U-235 system (version B) compared with the SPR-4 design (version A). The remaining carpet plots, Figures 3 - 10 show some of the more significant parameters of the system. In particular the readers attention is directed to the nonlinear behavior of many of the variables.

It should be obvious from the detail described above that thermionic elements could have been designed within the core instead of heatpipes, or outside the core in the boiler regions. Similar families of liquid metal cooled reactors have been designed to similar criteria and others including specific pressure drops, coolant temperature rises, etc. These have been even better behaved than the heatpipe reactors shown. They could just as easily have been gas cooled reactors for Brayton cycle applications.

This listing of the detail considered in the design is not presented with a view to convincing the reader of the credibility of this particular set of design calculations or the feasibility of this particular design concept which has been published in the past; it is presented as a demonstration that a rather complex design can be described in considerable detail employing a reasonable number of limits or weighting factors.

SHORT FORM OF THE COMPLETE SYSTEM

In place of the neutronic analysis we predicted the fuel mass using average core fuel burnup data from the twelve designs. This was purposely done in the simplest fashion by fitting second order curves through the twelve data points to produce expressions for burnup and the spacing parameter β as a function of power and aspect ratio. The details of this fitting are shown in Appendix A. Using these functionals to replace the neutronic analysis, the thermo-mechanical code portion produced fifteen additional designs at points intermediate to those of the previous detailed analysis. These fifteen cases were repeated using the full neutronic analysis and the data were compared. They agreed within a few percent in all cases. We therefore conclude that this analysis could be used for this family of reactors within the specified parameter ranges for mission studies. Running times averaged less than 1/10 second per "fitted" design.

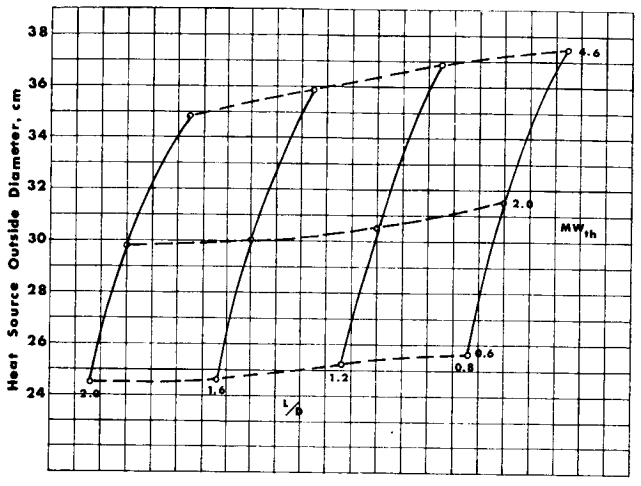

Fig. 3. Heatsource Outside Diameter

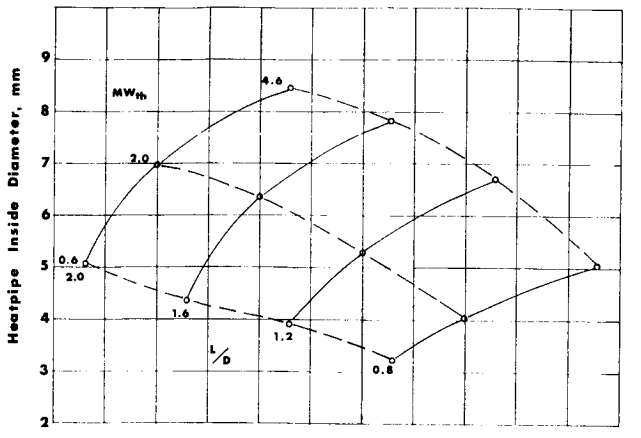

Fig. 6. Heatpipe Inside Diameter

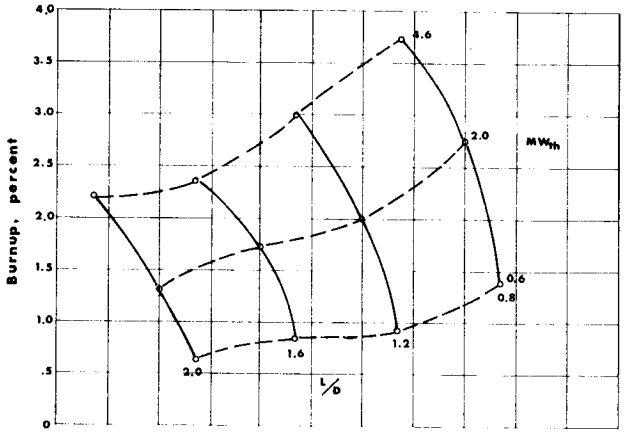

Fig. 4. Average Fuel Burnup

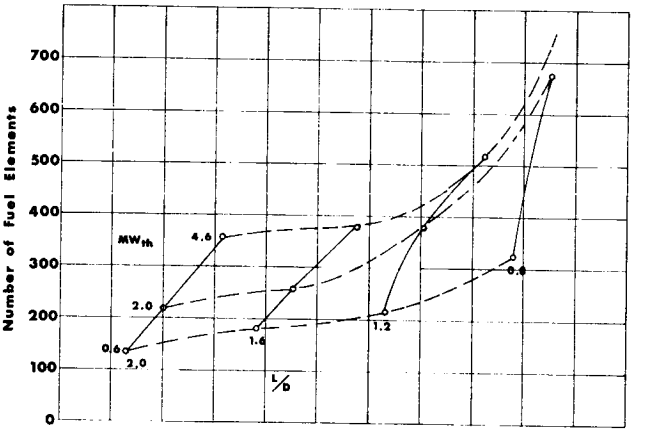

Fig. 7. Number of Fuel Elements

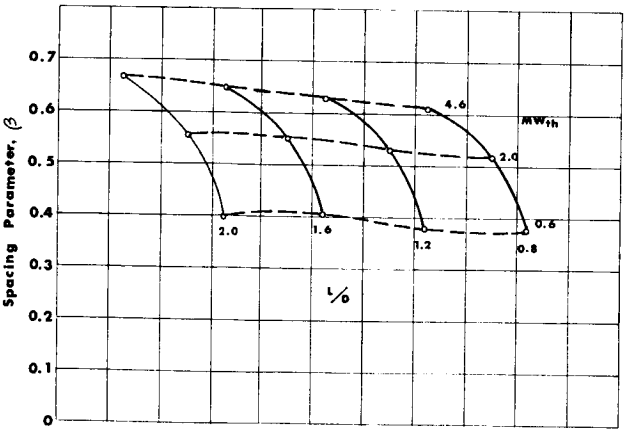

Fig. 5. Spacing Parameter, β.

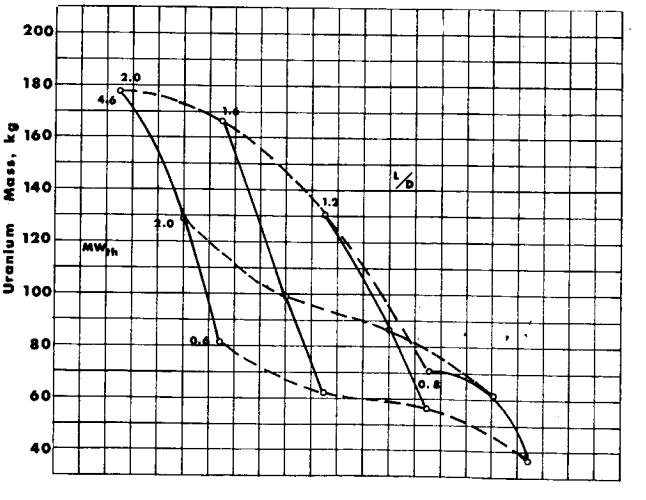

Fig. 8. Total Uranium Mass

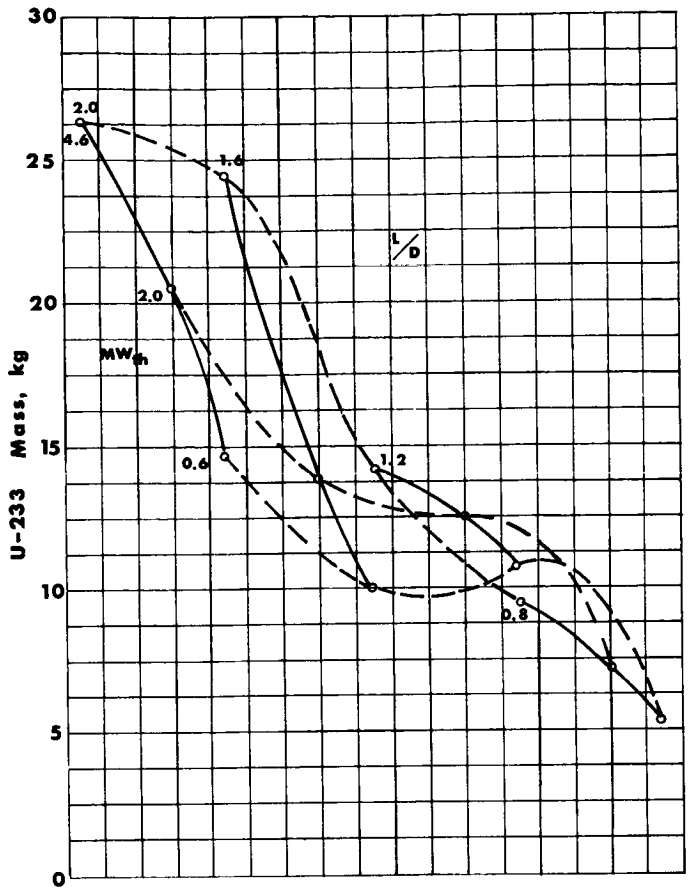

Fig. 9. U-233 Mass

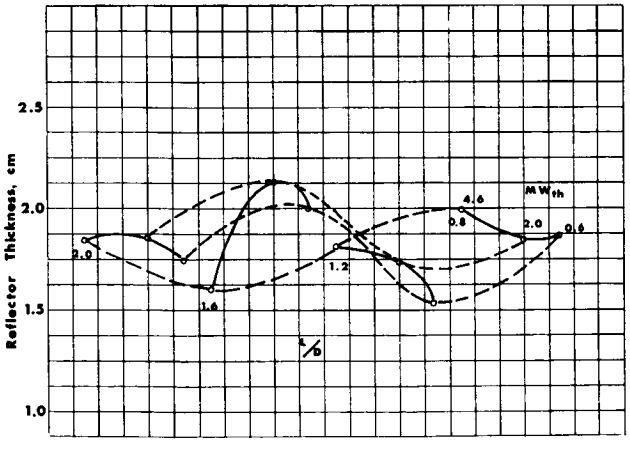

Fig. 10 Reflector Thickness

Table I shows typical results. These data were selected from the larger set as quantities of particular interest to the mission analyst, reactor physicist, and engineer. For the mission analyst fueled core radius, maximum package radius, and reactor-boiler mass were selected. For the physicist the hot-core full-power start of life and cold-core water-immersed and flooded multiplication factors are presented. For the engineer the heatpipe inside radius and a fuel element porosity parameter were selected as variables representative of areas subject to possible future constraints in view of, e.g., fabrication difficulties. The factors shown in percentages are the maximum and rms deviation of the predicted value from that established by the complete analysis. Also shown where applicable is the ratio of the maximum value of the parameter to the minimum encountered in the field, demonstrating that we were not fitting near constants. Fuel mass varied by a factor of 5.4.

Table I

Quantity(F)	Core Radius	React Radius	Mass	Keff Hot	Keff Submerged	Heatpipe Radius	β[a]
Max Dev %	2.74	2.57	5.86	2.52	2.21	.255	2.39
Rms Dev %	1.27	1.13	3.20	1.62	1.23	.12	1.13
F max/F min	1.79	1.60	5.18			2.89	1.80

[a] β is a fuel element porosity parameter representative of a design detail and is the ratio of the fuel inside radius to the outside hexagonal-flat radius.

CONCLUSIONS

As a demonstration the results indicate the promise of the method. This becomes more evident when the reactors are examined in detail. The simplicity of the fitting method selected is not meant to apply to the designs. The simplest possible representation was used to predict a complex design, to get across the point that it is neither impossible nor impractical to implicitly formulate reactor designs so that they can be meaningfully employed by the mission analyst. It is obvious that a more sophisticated set of formulae could be developed covering such parameters as reflector thickness, zone loading fraction, etc., to give even closer predictions. As an example of this, the parameter β was included above as a starting point to reduce the number of iterations in the thermo-mechanical analyses.

By using these methods, reactor analysis and reactor system surveys can be broadened in scope so as to pass from company and academic circles to interact meaningfully and credibly with the space systems analysts who must provide input data for the decision making process.

BIBLIOGRAPHY

1. Brown, N.J.; and McCauley, E.W.: Fast Reactor Design Analysis Codes, Lawrence Radiation Laboratory, Livermore, Rept. UCRL-50429 (1968).

2. Walter, C.E.; Brown, N.J; Hampel, V.E.; McCauley, E.W.; and Wilcox, T.P., Jr.; An Advanced 2000 kWth Nuclear Heat Source, Lawrence Radiation Laboratory, Livermore, Rept. UCRL-70978 (1968).

Appendix A

THE FITTED FUNCTIONALS β AND BU

In order to provide a direct path to the explicit, mechanical characterization of an implicitly critical and optimized nuclear reactor heat source of power Q and ratio L/D, it is necessary to describe the spacing parameter, β and the burnup fraction, BU as functionals. The data used are abstracted from the detailed analyses.

As is clear from Figure 5, β is a function of L/D and Q, or

$$\beta = \beta(L/D,Q) = D(Q) + E(Q)(L/D) + F(Q)(L/D)^2 \qquad 1.1$$

with

$$D(Q) = \sum_{i=0}^{2} d_i Q^i$$

$$E(Q) = \sum_{i=0}^{2} e_i Q^i \qquad 1.2$$

$$F(Q) = \sum_{i=0}^{2} f_i Q^i$$

where, for constant Q,

$$\beta\,(L/D)_Q = \sum_{j=0}^{2} g_i (L/D)^j \qquad 1.3$$

Performing the indicated least squares fit in equation 1.3, the g_i are used to fit the d_i, e_i, and f_i, respectively, of equations 1.2 thus producing the coefficients of equation 1.1. They are listed, for reference, in Table A.1.

The burnup (Figure 4) is treated in a similar manner with

$$BU = BU(L/D,Q) = A(Q) + B(Q)(L/D) + C(Q)(L/D)^2 \qquad 1.4$$

where

$$A(Q) = \sum_{k=0}^{2} a_k Q^k$$

$$B(Q) = \sum_{k=0}^{2} b_k Q^k$$

$$C(Q) = \sum_{k=0}^{2} c_k Q^k$$

and

$$BU(L/D)_Q = \sum_{\ell=0}^{2} \alpha_\ell\, (L/D)^\ell$$

The resulting coefficients of equation 1.4 are listed in Table A.2.

Table A.1

The Functional Coefficients of β

	i=0	i=1	i=2
D (d)	2.59217E-1	1.23627E-1	-1.19133E-2
E (e)	4.27773E-2	3.74926E-2	-7.96442E-3
F (f)	-8.41595E-2	-1.06819E-2	2.64808E-3

Table A.2

The Functional Coefficients of BU*

	k=0	k=1	k=2
A (a)	1.20680E-2	2.39719E-2	-3.53083E-3
B (b)	-1.07593E-2	-1.36532E-2	2.53387E-3
C (c)	3.09971E-3	2.41979E-3	-5.07874E-4

*Burn Up

SESSION II.3
NATURAL SPACE RADIATION SHIELDING
CHAIRMAN: A. REETZ, JR.
OFFICE OF ADVANCED RESEARCH AND TECHNOLOGY - NASA

GALACTIC COSMIC RAY HEAVY PRIMARY SECONDARY DOSES*

M. C. Wilkinson (Boeing), S. B. Curtis (UCLRL - Berkeley)

The free space dose rates from the various components of the galactic cosmic rays can be determined from the particle energy spectra and energy loss data. Depth-dose profiles in material shields or in body tissue are complicated by the nuclear cascade set up in the material by the incident primaries. While considerable work has been done on the proton induced particle cascade, the heavy primary secondary dose from the galactic cosmic rays, which also fragment and cascade, has not been estimated.

In this paper we present the results of a calculation which estimates the heavy primary secondary doses from cosmic ray interaction data. The incident galactic cosmic ray heavy primary spectrum is represented as the sum of helium, nitrogen (M group), magnesium (light heavy), and iron (very heavy) components. The incident iron nuclei are allowed to fragment into lesser Z secondaries, which are assumed to travel in the same direction and start with the same energy per nucleon as the interacting primary. The total emergent particle energy spectra and dose are then presented for the galactic heavy primary spectrum incident on aluminum and tissue slabs. The importance of the fragmentation parameters assumed is also evaluated.

The total dose from the heavy primaries and their secondaries is found to be reduced by only a factor of two in 20 g/cm^2 of shielding.

*Work supported by NASw-1963

We present here a method for the calculation of the secondary particles produced by heavy galactic primaries. The galactic cosmic ray spectrum consists of protons, helium and higher Z elements, all with a similar energy spectrum, but of reduced intensity with increasing Z. As these particles pass through matter, both nuclear interaction and ionization reduce the intensity and energy of the incident spectrum. While the electromagnetic interaction for the particle energies of interest are well understood, and their effects readily calculated, the nuclear interactions lead to complex cascades of secondary particles. While a great deal is known about the cascade products of proton induced reactions, the cascades induced by the higher Z elements of the galactic cosmic rays have received less attention.

The fraction of the yearly free space dose resulting from the various components of the galactic cosmic rays are shown in Table I, as determined from the particle energy spectra given in Reference 1.

In Figure 1, we show the depth-dose profiles for the helium and higher Z particle groups under two assumptions: 1) that only electromagnetic interactions attenuate the flux, and 2) that the particles suffering nuclear interaction are removed from the beam (uncollided particle dose only). The wide range between these estimates indicates a need for further analysis.

TABLE I

Component	Yearly Dose
H (Z=1)	4.6
He (Z=2)	3.5
M (6≤Z≤9)	1.9
LH (10≤Z≤14)	1.3
VH (26≤Z≤28)	1.3
TOTAL:	12.6 rads/year

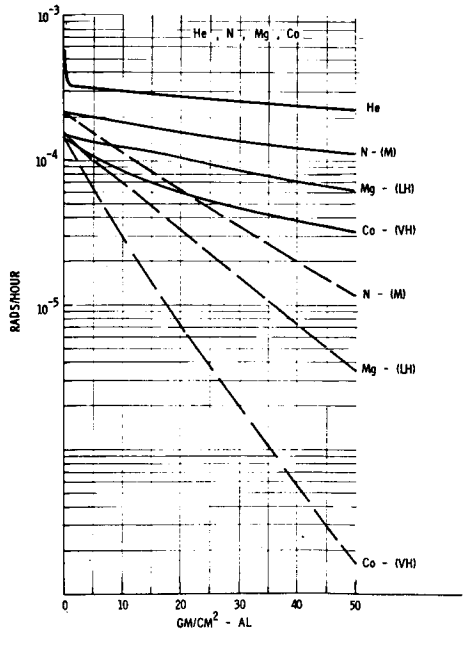

Figure 1: HEAVY PARTICLE GALACTIC DOSES

FORMULATION OF THE CALCULATION

Let $\phi_i(E,x)$ be the differential number flux of ions of type i at a point x in the absorber. Then it is easy to show that the relation between the incident flux and the flux at a point in the absorber is given by

$$\phi_i(E',x)=\phi_i(E,0)\frac{S(E)}{S(E')}$$

neglecting nuclear interactions.

If we include nuclear interactions, and change variables to energy per nucleon, T, we have

$$(1)\quad \phi_i(T',x)=\phi_i(T,0)\,x\,\frac{S(T)}{S(T')}\exp-\int_T^{T'}\frac{\mu_i(T)\,dt}{S(T)}$$

where S(T) is the stopping power of the ion of type i and energy per nucleon T. If μ_i is energy dependent, then we have simply $\exp[-\mu_i x]$ for an attenuation factor. The uncollided flux can then be determined at points of interest in the absorber.

Now ions of type i produce secondary ions of type j at points in the absorber at the following rate

$$(2)\quad \frac{d\phi_j}{dx}(T',x)=\phi_i(T,x)\frac{No}{M}\,\sigma_i(T)P_{ij}(T,T')$$

where

- $\phi_i(T,x)$ is the energy spectrum of ions of type i
- $\sigma_i(T)$ is the interaction cross section for ions of type i and energy T
- $P_{ij}(T,T')$ is the fragmentation parameter, giving the probability for an interaction of type i ions at energy T to produce a secondary ion of type j and energy T'
- N_o = Avogadro's number
- M = the atomic weight of the absorber
- $\frac{d\phi_j}{dx}(T',x)$ = the rate at which particles of type j and energy T' are being produced in the absorber at point x

Particles of type j are slowed and attenuated as they pass through the remainder of the absorber and they emerge with an energy related to their initial energy T, and remaining path length in the absorber, X-x, of

$$Rj(T)=Rj(T_f)+X-x$$

and with an intensity reduction of

$$\frac{S(T)}{S(T_f)}\exp[-u_j(X-x)]$$

The emerging flux of type j particles produced by type i primaries is then

$$(3)\quad \phi_j(T_f,X)=\frac{No}{M}\int_0^X\phi_i(T,x)\,x\,\sigma_i(T)P_{ij}(T)\,\frac{S(T)}{S(Tf)}\,x\,\exp[-u_j(X-x)]dx$$

Now we apply these basic relations to the problem of determining the final penetrating energy spectrum of the galactic heavy primaries and induced secondaries in an absorber. First, we consider a maximum Z of 26, as only a small number of higher Z particles are present in the galactic cosmic ray flux. The penetrating flux of $_{26}$Fe particles at any point in the absorber can be determined by expression (1). Once $\phi_{26}(T,x)$ is known, then the rate at which lower atomic number particles are being produced at points in the absorber can be determined bv expression (2).

The total production rate of particles of type j is given by the following sum

$$\frac{d\phi j}{dx}(T,x)=\sum_{i=j+1}^{26}\phi_i(T,x)\frac{No}{M}\sigma_i(T)P_{ij}(T)$$

where $\phi_i(T,x)$, the total flux of particles of type i, depends on both the incident flux and the accumulated secondary flux.

To determine the penetrating flux of particles, a computer program was developed to evaluate the expressions discussed numerically. This program evaluates the production rates of the secondaries at a set of thickness points in the absorber for a suitable energy grid. Then by sequential transporting the highest Z element through the absorber and determining the production rates for all lower Z elements, we obtain the final penetrating number energy spectrum.

BASIC ASSUMPTIONS USED IN THE CALCULATION

The preceding section has developed the formations used in the calculation of the secondary particles produced by the heavy galactic primaries. Now we discuss the basic assumptions used in this analysis, and some of the resulting limitations in the present calculations.

First we employ the straight ahead, or one dimensional approximation. This can be justified by use of cosmic ray interaction data as discussed in Reference 2 which shows that the heavy fragments emerging from the interaction site are strongly peaked in the forward direction. It is well known that the primary heavy particles suffer little angular deflection while passing through matter.

Second, we use the energy independent overlap cross section model used by Cleghorn, et al. (Reference 3) to fit his cosmic ray emulsion results. It was found that cross sections were essentially independent of energy in the energy range 100 MeV/nucleon to 30 GeV/nucleon. At energies below 100 MeV/nucleon, the higher Z pri-

maries have a small range, but their cross section will probably be underestimated in this energy region.

The fragmentation function, $P_{ij}(T,T')$ represents the least well known quantity required in the calculation. Since the energy dependence of the secondary fragments has not yet been described, we make the simple assumption that T=T', that is the fragments have the same velocity as the primary ion. This assumption is in agreement with an interaction model in which the heavy primary is stripped of some fraction of its mass, and proceeds on with unchanged velocity. Two sets of fragmentation parameters were then used to explore the effects of various assumptions on the final results. In the first approximation, we have used a set of fragmentation parameters which assume one $_1H$, one $_2He$, and an equal probability of higher Z fragments normalized to conserve Z in the incident heavy primary. This approximation, when coupled to the equal velocity approximation, leads to approximate conservation of energy, neglecting nuclear binding energies and pion formation. The second set of fragmentation parameters are described in the paper by Curtis in these Symposium proceedings.

Both sets of fragmentation parameters are assumed to be independent of the primary particle energy, a conclusion that is consistent with the results of Cleghorne.

Finally, the calculations have neglected the interactions of primary and secondary ions with hydrogen. While the results of Bertini's internuclear cascade calculation can be applied to this problem by a proper transformation of rest frames this has not yet been incorporated in the calculation. The results given for tissue thus neglect the fragmentation induced by hydrogen.

RESULTS

Typical results of this calculational method have been developed with the assumptions discussed. First, using the VH group heavy particle spectrum presented in Reference 1, depth dose profiles for a unidirectional beam of particles incident normally on a slab of water and aluminum are shown in Figures 2 & 3. The total tissue dose, the $_{26}Fe$ (VH) dose, and selected lower Z secondaries are shown. For H_2O, the two sets of fragmentation parameters are represented by (1) solid lines and (2) dotted lines. We see the expected rise and more gradual fall of the secondary dose components.

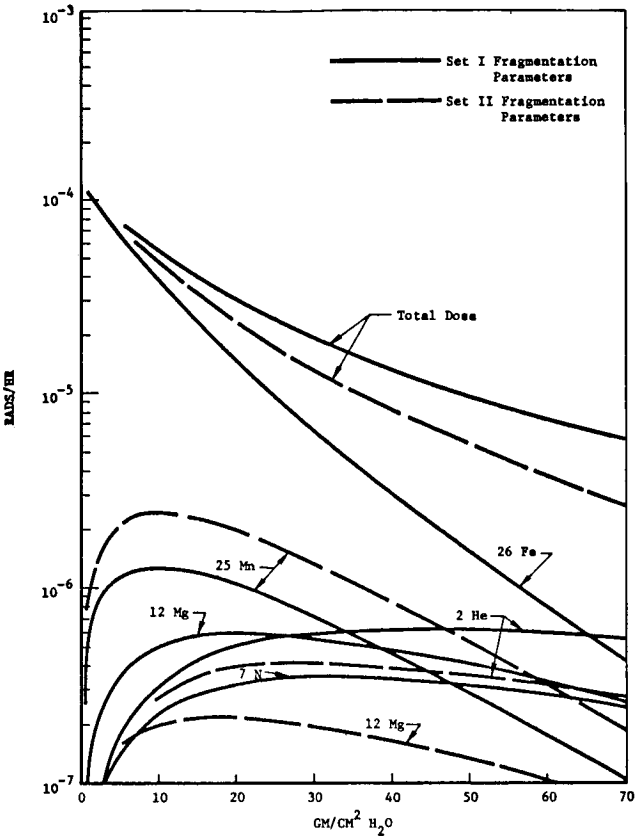

Figure 2: HEAVY GALACTIC PRIMARY VH GROUP DOSE

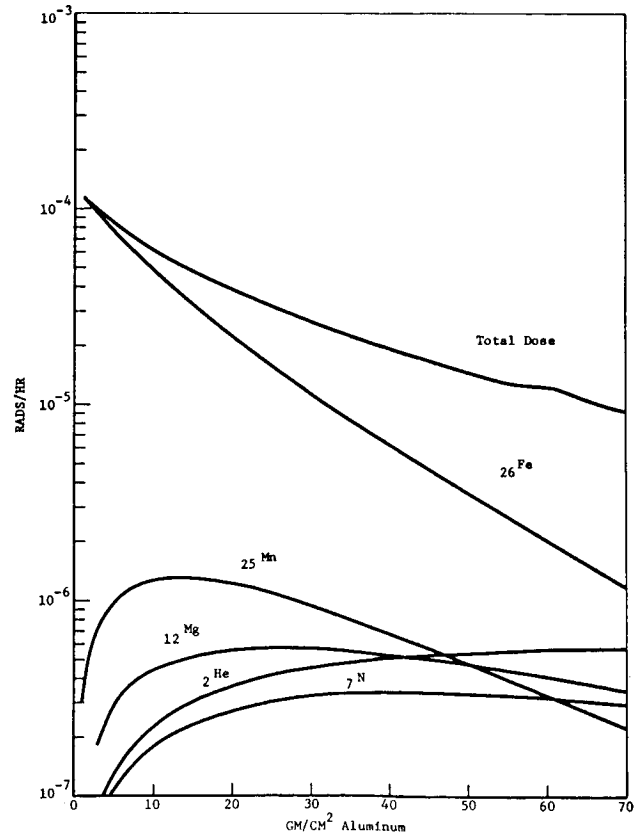

Figure 3: HEAVY GALACTIC PRIMARY VH GROUP

With the complete GCR spectra, as represented by VH, LH, M and Helium components, the results are as shown in Figure 4.

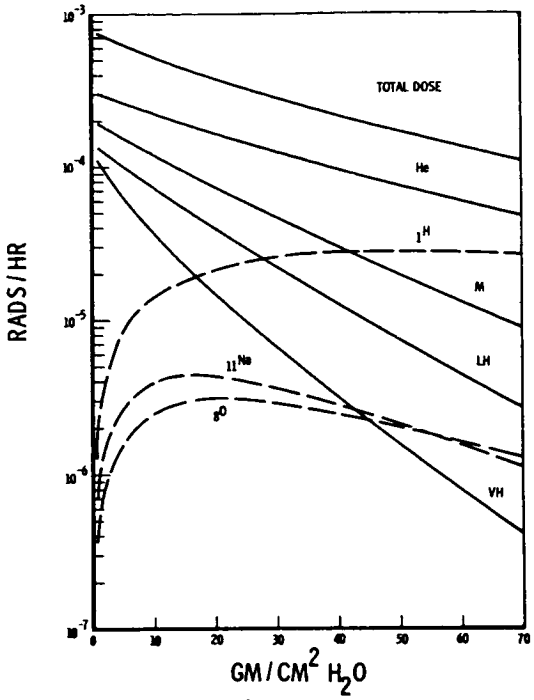

Figure 4: HEAVY GALACTIC PRIMARY TOTAL DOSE

Meyer (Reference 4) has reviewed the galactic cosmic ray data available up to 1969, and has presented an estimate of the intensity of all the heavy primary components below $_{26}$Fe. From this compilation we have calculated the total depth dose profiles in water for incident primaries $_{2}$He to $_{26}$Fe, and presented the results in Figure 5.

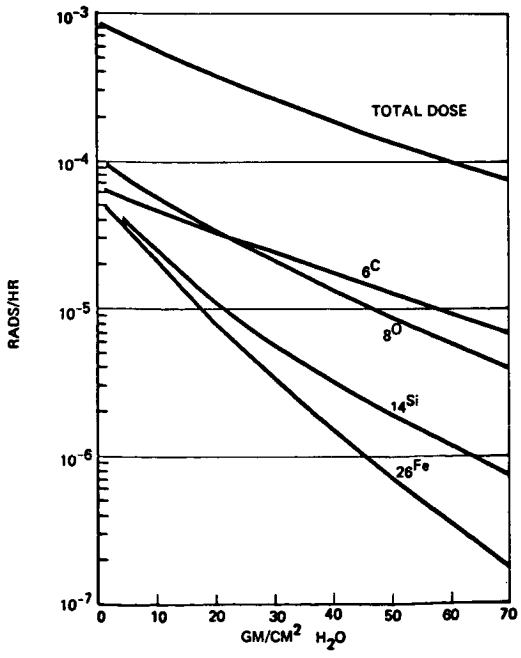

Figure 5: HEAVY GALACTIC PRIMARY TOTAL DOSE Separate Spectra, Excluding Proton Dose

CONCLUSIONS

The results presented indicate the general nature of the total depth-dose profiles we can expect in tissue and aluminum absorbers. Uncertainties in the fragmentation parameters lead to significant changes in the total dose, as well as the dose distribution among the secondary components. Further work in defining the fragmentation parameters and incorporation of the hydrogen interaction results for tissue would improve these dose estimates.

While only dose results are presented in this paper, the penetrating particle energy spectra are also calculated, and can be used to examine the LET spectra for further study of the biological implications of the galactic cosmic rays.

REFERENCES

1. S.B. Curtis and M.C. Wilkinson, "Study of Radiation Hazards to Man on Extended Missions" NASA CR-1037, May 1968

2. S.B. Curtis, W.R. Doherty, and M.C. Wilkinson, "Study of Radiation Hazards to Man on Extended Near Earth Missions", NASA CR-1469, December 1969.

3. T.F. Cleghorne, P.S. Freier, C. J. Waddington, Canadian Journal of Physics, 46, 5572 (1968).

4. P. Meyer, "Cosmic Rays in the Galaxy", Annual Reviews of Astronomy and Astrophysics, Vol. 7, Page 1, 1969.

METHODS OF SPACE RADIATION DOSE ANALYSIS WITH APPLICATIONS TO MANNED SPACE SYSTEMS

R. W. Langley and M. P. Billings

McDonnell Douglas Astronautics Company
Huntington Beach, California

ABSTRACT

The full potential of state-of-the-art space radiation dose analysis for manned missions has not been exploited. Point doses have been overemphasized, and the critical dose to the bone marrow has been only crudely approximated, despite the existence of detailed man models and computer codes for dose integration in complex geometries. The method presented makes it practical to account for the geometrical detail of the astronaut (which typically provides as much protection to the internal organs as does the vehicle) as well as the vehicle. This paper discusses the major assumptions involved and presents the concept of applying the results of detailed proton dose analysis to the real-time interpretation of on-board dosimetric measurements.

INTRODUCTION

Present state-of-the-art methods for space radiation dose analysis have been routinely used on a number of existing and proposed manned space systems. The experience gained in applying the involved analytical techniques, the extent of agreement between analytical results and experimental investigations, and the increased knowledge of the space radiation environment have resulted in reasonable confidence in the ability to predict space radiation doses to specific points in a vehicle used for manned missions. A summary of the state-of-the-art and current practices is given in reference 1; the current experimental approach and experimental results are summarized in reference 2.

The most troublesome and important space-radiation protection problem continues to be that of biological hazard, and one of the most difficult aspects of the biological hazard problem is onboard dose monitoring. The most stringent biological dose criterion is generally that associated with the internally distributed blood-forming organs (BFO) or bone marrow, and the critical radiation environment for practically all manned missions is protons, both solar protons and trapped protons. It is in the context of these generalizations that this paper is presented.

SCOPE OF PRESENT DISCUSSION

Considerable theoretical and experimental effort has gone into establishing and improving the accuracy of present methods for calculating point doses, and there seems little to be gained in further efforts along these lines at this point. Emphasis should instead be placed on improving the application of these methods to preflight and in-flight dose estimation. The two major points of this paper concern (1) astronaut self-shielding of internally distributed organs, and (2) the realistic interpretation of on-board dosimetry.

The aspect of dose analysis that in particular deserves more attention is the effective utilization of detailed astronaut (as well as vehicle) geometry. Available methods for estimating point doses are rather accurate for geometrically well-defined systems, particularly for protons. However, the application of these methods to the estimation of doses to the internally distributed organs (such as the BFO) of a mobile astronaut has not exploited the available potential for obtaining accurate dose estimates. This is because the complexity involved in the combined geometrical mockup of a vehicle and a mobile detailed man-model requires excessive time and effort to integrate over the several space and time variables involved in the dose integrations. The geometrical complexity involved can be appreciated by viewing a model or mockup of the NASA Space Station and considering a man-model described by over 2200 geometrical shapes (ref. 3). The alternative to precise "brute-force" integration that has seen widespread application is the use of gross simplifications, such as characterizing the average BFO dose by a few point doses calculated at a 5-cm depth in a phantom. Because the protection provided to the BFO by the vehicle may well be less than that provided by the self-shielding of the astronaut and because the protection provided by both is highly spectrum dependent, this degree of simplification largely negates the care normally taken with other aspects of dose analysis; for example, in specifying the quality factor and the vehicle mass distribution. The approach presented utilizes the available capability of detailed man-models and circumvents the problems of excessive effort on the one hand and excessive crudeness on the other.

Another area requiring attention is the application of the significant dose analysis capability that has been developed over the past ten years to the problem of on-board dose monitoring. The uncertainty associated with preflight dose estimation, in decreasing order of importance, is due to (1) the space environment encountered during the mission, (2) the distribution of mass providing protection, and (3) methods of radiation transport and dose analysis (ref. 4). In situ measurements, however, remove the major source of uncertainty (that associated with the radiation environment) so that the main dose uncertainties are then due to the combined mass distribution of the vehicle and astronaut. An accurate treatment of the overall geometrical arrangements of mass will therefore enhance the overall accuracy of dose estimation. It is precisely this sensitivity of dose to mass distribution

for manned space systems that makes direct dosimetric measurements impractical in real-time dose monitoring. An approach is presented for making practical use of available dose analysis tools and detailed man-models to provide a means of realistic, real-time interpretation of on-board dosimetric measurements.

REPRESENTATION OF ASTRONAUT GEOMETRY AND MOTION

The usual method of estimating dose to the BFO (for example) of a mobile astronaut has been to create a geometrical mockup of a man-model inside the space system, and to perform dose integrations about several points in the body, each of which is erroneously assumed to be at a uniform depth of 5 g/cm^2, for several man-model locations within the vehicle. This procedure represents a compromise in the spatial and astronaut time-line integrations, and makes it impractical to use both a detailed mockup of the vehicle and a detailed man-model of the type described in reference 3.

The alternative method that has been developed yields improved dose estimates by accounting for the actual organ distribution within the body, the dose distribution within the organ, and the astronaut time-line. Such a detailed integration is made practical by decoupling the mass distribution of the vehicle from the mass distribution of the astronaut. This is accomplished by using mass-distribution data generated from an existing detailed man-model to express the shielding effect of the body on critical organ dose. Typical mass distributions for the BFO are shown as curves 2 and 3 in figure 1. When fully implemented, each curve generated would be volume-averaged over some portion of the BFO; that is, each curve would represent a part of the BFO (e. g., upper limbs, lower limbs, ribs and trunk, spinal column, and skull) rather than a point, as in figure 1. Other distributed radiation-sensitive organs (e. g., the gut) could be treated similarly, and if it turns out to be important, these data should be generated for both the standing and the sitting positions. Doses to the skin and lens of the eye are essentially surface doses for which body self-shielding can be adequately estimated without the explicit use of a man-model (ref. 5).

The mass distribution data of figure 1 were generated by tracing several hundred randomly selected rays. Curve 1 is the time-averaged distribution for a simplified astronaut time-line made up of five dwell stations in the Skylab vehicle that account for most of the time, with the remainder of the time spent in uniform transit between the station locations. A more detailed time-line could be constructed from measured data like those presented in reference 6. Curve 1 was generated with the use of the SIGMA code (ref. 7). Curves 2 and 3 were generated for an isolated, standing astronaut with the MEVDP code (ref. 8), which contains the man-model of reference 3.

Such astronaut mass distribution data have been combined with the vehicle mass-distribution data in two ways. One way of combining them in a dose analysis has been to use them in the same manner that a man-model is now used; i. e., using the organ mass distribution to calculate depth doses for each ray as it is traced, and then summing the desired results. Another way, which is more efficient when integration over astronaut time-line is involved, has been to generate the time-line averaged vehicle mass distribution separately (such as indicated by curve 1, figure 1), and then obtain the final results by convoluting the mass distributions and integrating over the dose kernels and organ response (i. e., the distribution factor or other dose-modifying factors). This latter approach is illustrated in figure 2, in which the utilization of man-model geometrical mockup is shown in dashed lines to indicate that it is used only once and not in every dose analysis.

The advantages of the decoupling method over the present method are:

1. Dose estimates to such organs as the BFO are significantly more accurate and realistic.

2. Application of the available detailed man-model capability is made practical.

3. Much greater detail in dose analysis for either the final design or preliminary analysis is obtainable with a small increase in engineering effort and with reduced computer time.

4. Ability to interpret data from on-board monitoring is enhanced.

The implementation of the proposed method involves the following assumptions: (1) the effects of an astronaut's actual orientation on dose are not significant on the average, (2) the error involved in using a single reference material in the dose kernels is not significant, and (3) the vehicle mass distribution at a point is representative of a region of space (occupied by one or more organ segments, as necessary). A series of calculations indicates the validity of the first two assumptions. The third assumption is not considered restrictive, since vehicle mass distributions can be generated on the basis of a single coordinate time-line for an astronaut or as many as one coordinate time-line for each organ mass-distribution curve of interest, depending on how a specific situation affects the accuracy.

EVALUATION OF DOSE INTEGRATION TECHNIQUES

A 44-region geometrical mockup of a manned space station (ref. 9) and a simple man-model consisting of one elliptical cylinder for the head and another for the trunk were used to perform a series of calculations with the SIGMA code. Doses were calculated for a point representing the lens of the eye at a single man-model location. A surface dose was chosen to emphasize any effects of man-model orientation with respect to the vehicle. Two proton spectra were used: an exponential rigidity spectrum (P_o = 91 MV) for solar cosmic rays and an exponential energy spectrum (E_o = 94 MEV) for trapped protons. The calculations illustrate several possible approaches to dose analysis, indicate the effects of vehicle/man-model orientation, and provide a comparison between random and systematic ray-tracing. The results are summarized in table 1.

The conventional method of dose analysis corresponds to case 1, for which a combined geometrical mockup is used for both the vehicle and the astronaut, thereby maintaining a fixed specific vehicle/man-model orientation. The method of dose integration uses a systematic sectoring and ray-tracing procedure. Case 2 provides a comparison with case 1 with respect to random versus systematic ray-tracing. This is of interest because the more variables or dimensions involved in an integration, the more advantageous the Monte Carlo technique will be from a computational standpoint. Therefore, the generation of astronaut mass distributions and the dose integration for a detailed time-line using random ray-tracing (i.e., Monte Carlo integration) would significantly reduce the computation cost relative to that required for systematic ray-tracing (i.e., direct numerical integration) for the same precision. Table 1 shows that, even for a simple example with integrations employing 500 rays, Monte Carlo integration is superior; a more complex integration would show a greater advantage. Case 2 was also run, using 5,000 rays to obtain an accurate result as a basis for comparison. In this case, the solar cosmic-ray dose calculated by the Monte Carlo technique (using 500 rays) was more accurate than that obtained with systematic ray-tracing.

For dose integrations of reasonable accuracy, at least 100 rays are required (as shown later). For this many rays, there is no mathematical or practical justification for elaborately sectoring and tracing rays through sector centroids; this approach is attractive only because it corresponds to a mental construct. For systematic ray-tracing, parts of the solid angle space will always be inaccessible to rays; this is not true of random sampling. If there are thin regions or "windows," the bias used in sectoring can easily be applied to Monte Carlo integration, although this is unnecessary for all sizable space vehicles examined to date (including several configurations of MORL, MOL, Skylab, and the Space Station).

Cases 3 and 4 are similar to cases 1 and 2, except they demonstrate the use of a man-model mass distribution (defined by a histogram) applied as indicated in figure 2. The doses are slightly higher for cases 3 and 4 because of the lack of a fixed vehicle/man-model orientation. The higher doses thus obtained are to be expected because the minimum in the astronaut mass distribution is exposed to the direction of maximum flux (as well as all other directions). It is also true that the larger conservative dose is the desirable one to use except in a special (and unlikely) situation in which an astronaut's orientation is severely and reliably restricted for a significant period of time.

Case 5 indicates how little computation is involved in dose integration aside from ray-tracing computations. Once mass distributions are available, it is a trivial matter for a large computer to perform the dose integrations, and the amount of time involved is independent of geometrical complexity. The vehicle histogram used in case 5 was generated from the ray-tracing analyses performed for case 4. Therefore, the dose results from case 5 should, and do, agree with the case 4 results, in which some portions of the mass distribution data were obtained by ray-tracing instead of sampling a histogram.

Summarizing, the conclusions supported by table 1 are as follows:

1. The doses for oriented cases closely agree with those for unoriented cases, the unoriented cases giving slightly higher doses because the use of a separate man-model mass distribution exposes the minimum mass thickness to the direction of maximum flux; use of a surface dose in the examples emphasizes this effect. Because of the unlikelihood of being able to confidently predict a nonuniform astronaut orientation in most phases of the astronaut time-line, and because an unoriented man model will usually yield a slightly conservative dose, this assumption is generally desirable.

2. The use of random ray-tracing for performing dose integration or generating mass distributions is virtually always advantageous, relative to direct numerical integration, even for a one- or two-variable integration, such as the ones performed here, where the two variables are spherical angular coordinates. When the vehicle mass distribution is calculated for a detailed astronaut time-line, the use of random sampling in time and solid angle to establish the origin and direction of rays is much more efficient than the conventional systematic-sectoring procedure.

CONVERGENCE OF DOSE INTEGRATION

A general aspect of dose calculations that relates to the above discussion is the convergence of the dose estimate with the number of rays traced and the associated uncertainty in the dose estimate. The standard deviations in table 1 indicate consistent convergence, and assuming that the number of rays traced is large enough for the central-limit theorem to apply, confidence limits and corresponding dose intervals can be readily determined by using a normal distribution with the calculated variance.

The rate of dose convergence decreases as the steepness of the dose attenuation kernel increases, so that a soft solar cosmic-ray spectrum converges slower than a relatively hard trapped-proton spectrum. The McDonnell Douglas DACP code was used to investigate the statistics of a dose estimate using the idealized but realistic mass distribution of figure 3 and the 12 November 1960 solar-flare event (ref. 10). DACP performs repetitive convolutions of probability density functions by numerical integration to obtain exact statistical results, as described in reference 11.

The dose probability distributions obtained for three sample sizes (i.e., number of rays traced) are shown in figure 4. These curves represent the frequency of results that can be obtained with all possible combinations of rays, for this particular case. For 128 rays, a very good approximation to a normal distribution is obtained (i.e., the central-limit theorem applies).

Figure 5 shows the convergence in terms of confidence levels as a function of the number of rays in a sample. For example, for a 90-percent confidence level, the actual dose has a 90-percent probability of falling somewhere between the 5-percent confidence limit curve and the 95-percent confidence limit curve. These curves can be calculated by assuming a normal distribution for sample sizes greater than approximately 100 rays.

It is concluded that Monte Carlo dose integration converges as the calculated variance implies for reasonable sample sizes (greater than approximately a hundred rays). For typical mass distributions, this is true for both random and systematic ray tracing. For this example, figure 5 shows that 1,500 rays are required to obtain a dose that is 99-percent probable of being within ±1 percent of the actual (theoretical) dose. It is emphasized that for Monte Carlo integration, the statistics are essentially the same for a single point dose or for a dose calculated for a detailed astronaut time-line. This is because for typical vehicles the average mass distribution does not vary so drastically from point to point that the rate of convergence is significantly affected by including the effect of a time-line. This is in marked contrast to conventional dose analysis, which requires convergence for each of a number of point doses, which are then appropriately summed.

VALIDITY OF EQUIVALENT ALUMINUM CONCEPT

In implementing the foregoing dose evaluation technique, it is extremely advantageous to represent proton dose attenuation kernels in terms of a reference material like aluminum. While the use of equivalent aluminum seems generally to be accepted for preliminary analysis, the question often arises about its validity for detailed analysis, particularly with regard to secondary nucleon dose.

Briefly, the equivalent aluminum concept refers to the practice of performing charged-particle dose-transmission calculations through a single reference material, usually taken to be aluminum, and using these results to describe the dose transmission through any laminated arrangement of different materials. Its application simply involves modifying the actual mass density of a shield material by its relative stopping power, which is the (practically energy-independent) ratio of the stopping power of the material to that of aluminum. This relationship must be used to give accurate results for primary proton dose; expressing the material in actual areal density is not adequate.

The question of validity must be answered in terms of the environment, materials, and calculational methods relevant to the subject. Four cases, which were chosen for analysis, represent fairly extreme but reasonable arrangements of dissimilar materials that might be encountered in a manned space system. These cases were analyzed with the CHARGE code (ref. 12), which compares well with ORNL NTC code results (ref. 13). For these cases, a typical solar proton spectrum (exponential rigidity spectrum with P_o = 91 MV) was used, and the results were compared to those for an aluminum shield. This energy spectrum is soft enough for secondary nucleon dose to be dominant at shield thicknesses approaching 50 g/cm^2, thus posing a rather severe test.

The results are shown in figure 6, which also describes the shield configurations. The aluminum represents vehicle structure, the water represents tissue, the polyethylene represents stored food and waste, and the iron represents equipment. The curves, which show only a 26-percent difference at 50 g/cm^2 are surprisingly similar considering that the dose at 50 g/cm^2 is approximately 90 percent due to secondary neutrons. Similar curves for solar cosmic-ray primary proton dose and for total dose from a typical trapped proton spectrum (not shown) are represented within a few percent by a single curve, equivalent aluminum shield thicknesses up to greater than 50 g/cm^2. Little difference for the primary proton dose would be expected because the functional dependence of stopping power with particle energy is nearly the same for all materials. A large difference in total dose, however, and particularly for dose equivalent, might be expected when secondary neutron dose dominates, as it does for typical solar cosmic-ray spectra and large shield thicknesses, because neutron production and attenuation are material dependent. Fortunately, as indicated by figure 6, this is not the case.

One reason for this fortunate coincidence is that the density correction factor for proton stopping power is also approximately correct for neutron attenuation. Figure 7 shows the relative stopping power of some materials. Also shown is the approximate relationship for the macroscopic neutron removal cross section, which varies inversely as the cube root of the atomic number (except for hydrogen). Because these relationships are similar, the same material density correction factor is applicable to both phenomena for the range of material thicknesses of interest.

Another reason is that secondary neutron production in common materials is not strongly material dependent. It varies a factor of two between aluminum and lead, and differs by only 25 percent between aluminum and iron, as indicated in figure 8. For the cases shown in figure 6, about two-thirds of all neutron secondaries were formed in the first 2 g/cm^2 of aluminum The small differences among the cases at 50 g/cm^2 are due primarily to the differences in neutron production among the materials beyond 2 g/cm^2.

The conclusion drawn from these calculations is that the use of equivalent aluminum based on relative stopping power in proton dose calculations is sufficiently accurate for the detailed design of manned spacecraft. This is because the relatively small error in the dose kernel at large shield thicknesses is unimportant to the total dose because most of the dose involves transmission through only a few g/cm^2. In addition, the spread in the curves in figure 6 is only 26 percent at 50 g/cm^2, well within the uncertainty of any calculational technique when secondary nucleon dose is dominant.

It should be noted that the negligible error indicated by this comparison is in terms of total dose, the quantity of interest. The comparison given in reference 14 is presented as a function of proton energy, which resolves (calculated) variations that are insignificant in their contribution to total dose.

ROLE OF DETAILED DOSE ANALYSIS IN REAL-TIME DOSE MONITORING

Detailed dose analyses have a proper role in real-time interpretation of on-board dose-monitoring information, as well as in the more commonly applied area of preflight dose prediction. Direct on-board measurement of the dosimentric quantities of interest (i.e., critical organ dose) is not feasible, and dose analyses must be performed to accurately relate the data that can be measured to the dosimetric quantities on which mission decisions are based. The techniques discussed previously, particularly the technique for making effective use of detailed man-model geometric data, can be applied to generate the required relationship between, for example, spectrometer measurements and expected organ response.

Solar cosmic rays provide the primary impetus for establishing a dose-monitoring system that can assess the dose and dose rate that have been received and that can project the dose and dose rate to be expected (ref. 15). There is a distinct possibility of exceeding emergency doses when one considers solar cosmic-ray environments for orbital missions with inclinations greater than 40 degrees (ref. 16), or for interplanetary missions. Because operational decisions based on dose-monitoring information can result in severe restrictions or even in mission abort, it is necessary to be as definite as possible about interpreting dosimetric data in terms of actual organ dose and anticipated organ response. For practical reasons, the significant geometrical factors cannot be accounted for by direct measurement, but can be determined only by using the results of detailed calculations to properly interpret the measurements that can be made. Regardless of how carefully dose, LET, or any other similar quantity is measured at a point or at several points, either on a phantom fixed in the vehicle or on the astronaut, these data alone give only a vague indication of actual BFO dose from solar cosmic rays. The dose behind 5 g/cm^2, regardless of whether it is measured by a tissue-equivalent dosimeter with good scattering geometry or whether it incorporates other refinements, does not adequately represent actual BFO dose from solar cosmic rays (although it is not unreasonable for neutrons and gamma rays). Because of the complexity of the geometrical factors involved, a precise correlation of such measurements with actual dose or human response can be established only by detailed dose analysis. (A discussion of some of the problems and requirements of dosimetry for manned vehicles is given in reference 17; a more general survey is given in reference 18.)

For dose calculations to be made, the radiation environment at some point in the vehicle must be known. That is, the flux intensity and energy spectrum must be known; it has not been established that incident flux anisotropy is important, and an attempt to account for it in any detail would complicate things considerably. Incident flux, differential in energy, can be measured directly by a proton spectrometer or it can be inferred from depth-dose measurements in a phantom. In either case, the flux at a location can easily be described as a piece-wise representation so that doses anywhere in the vehicle or astronaunt can then be easily correlated in real time by using the parametric results of detailed calculations. Instrument design, optimum dosimetry location, and interpretation of redundant information are important considerations in the design of a dose-monitoring system, but they are not the subject of this discussion. The point of this discussion is to introduce the idea that combining the versatility of proton-dose analysis with the reality of direct measurements can alleviate some of the difficulties of dosimetry.

GENERAL TECHNIQUE FOR INTERPRETATION OF DOSE MONITORING DATA

The on-board measurements of proton spectra will provide data on the flux in several energy bands or channels at a location in the vehicle, as indicated by the histogram in figure 9. These in situ radiation-environment data can then be converted to astronaut organ dose or dose equivalent through use of a dose transfer function (DTF) that is generated by using detailed dose analysis techniques, but is expressed only in terms of the measured data, i.e., flux magnitude and energy spectrum. To minimize the error in the dose estimation, the DTF must represent these data as a continuous function. The discontinuous data can be converted to a continuous function (as indicated in figure 9) by assuming a functional representation within each channel. The form is relatively unimportant and can be a power law in energy, an exponential in rigidity, or some other form for the proton environment. It can be shown that the measured data can be quickly converted to a continuous spectrum.

For an isotropic incident flux, which is piece-wise fitted, with a spectral parameter for each channel, a total dose response can easily be obtained by applying the DTF. The DTF consists, for this example, of I+2 curves (if extrapolations outside the two spectrometer energy limits are used) where I is the number of spectrometer channels. The curves are the normalized dose per channel as a function of the spectral parameter, as shown in figure 10. If there are J dose responses (e.g., BFO dose, eye dose, etc.), the DTF for this example would be J(I+2) curves similar to the curves shown in figure 10. For the jth dose response, the dose would be given by

$$D_j = \sum_{i=0}^{I+1} \psi_i \, D_{ij} \, (\alpha_i)$$

where ψ_i is the flux in channel i, where D_{ij} is the DTF curve for channel i and dose response j, and where α_i is the spectral parameter of channel i. This same idea can as easily be applied to depth-dose measurements, rather than spectrometer measurements, since a given depth-dose curve represents a unique proton spectrum.

With this approach, the DTF can include any level of detail in its generation, without complicating its expression or use. The use of a continuous piece-wise spectrum defined by a spectral parameter simplifies the dose conversion and reduces the error that can be introduced by using a flux-to-dose conversion, which is a continuous function of energy.

The accuracy of the doses thus predicted could be improved by normalizing them to a small, battery-operated, active, personal dosimeter. That is, the BFO dose would be scaled to get the value

$$D_B = D_B^C \left(\frac{D_S^M}{D_S^C} \right)$$

where D_B is the BFO dose estimate, D_B^C is the BFO dose calculated from measured data, D_S^M is the the surface dose measured by the personal dosimeter, and D_S^C is the surface dose calculated from measured data. The value D_B could, of course, represent either accumulated dose or instantaneous dose rate, and D_B^C could be used for both an average time-line and for specific fixed locations. Since all the detailed dose analyses required to construct the DTF would be precalculated, the simple operations involved in the application of the DTF could be performed by a small on-board computer. If necessary, it is probably practical to perform the conversion by hand, using nomograms.

CONCLUSIONS AND RECOMMENDATIONS

The following conclusions have been made:

1. Accurate dose estimates require accounting for:
   a. Organ distribution within the body.
   b. Dose distribution within an organ.
   c. Astronaut time-line.
2. A practical method of implementing detailed dose analyses is to decouple vehicle and astronaut mass distributions.
3. Monte Carlo ray-tracing is generally superior to systematic sectoring.
4. The equivalent aluminum concept is adequate for proton dose kernels.
5. A DTF using spectral parameters can provide rapid, real-time, in situ dose conversion.

The following are recommended:

1. Mass distribution should be generated for radiation-sensitive organs.
2. The role of dose analysis as it relates to dose monitoring should be extended to include the described DTF technique on future manned space missions.

CREDIT

Work described in this paper was conducted by the McDonnell Douglas Astronautics Company under the Independent Research and Development Account No. S. O. 80205-009.

REFERENCES

1. Langley, R. W.: Space Radiation Protection. NASA SP 8054, June 1970.
2. Janni, J. F.; and Holly, F. E.; Editors: The Current Experimental Approach to the Radiological Problems of Spaceflight. Aerospace Medicine, Vol. 40, No. 12, December 1969, pp. 1439-1567.
3. Kase, P. G.: Influence of Detailed Model of Man on Proton Depth Dose Calculations. Proceedings of this symposium.
4. Fortney, R. E.: Flight Experiment Shielding Study (FESS) Satellite Data Analysis. Report AFWL-TR-68-108, Air Force Weapons Laboratory, April 1969.
5. Hill, C. W.; Simpson, K. M., Jr.; and Ritchie, W. B.: Physical and Biological Dose Calculations for Proton and Alpha Fluxes Incident on a Shielded Man Model. Proceedings of the Special Sessions on Radiation Transport and Biological Effects, ANS-SD-4, pp. 69-78, 1966.
6. Goodman, M.; and Middleton, W. C.: Crew Locomotion Disturbances in a Space Cabin Simulator. Journal of Spacecraft and Rockets, Vol. 6, No. 10, October 1969, pp. 1207-1209.
7. Jordan, T. M.: SIGMA, a Computer Program for Space Radiation Dose Analysis Within Complex Configurations. Report DAC-60878, McDonnell Douglas Astronautics Company, November 1967.
8. Liley, B.; and Hamilton, S. C.: Modified Elemental Volume Dose Program (MEVDP). AFWL-TR-69-68, August 1969.
9. Billings, M. P.: Optimal Shield Mass Distribution for Space Radiation Protection. Proceedings of this symposium.
10. Baker, M. B.: Geomagnetically Trapped Radiation. AIAA J., Vol. 3, No. 9, September 1965, pp. 1567-1579.
11. Yucker, W. R.: Solar Cosmic Ray Hazard to Interplanetary and Earth-Orbital Space Travel. Proceedings of this symposium.
12. Yucker, W. R.; and Lilley, J. R.: CHARGE Code for Space Radiation Shielding Analysis. Report DAC-62231, McDonnell Douglas Astronautics Company, April 1969.
13. Scott, W. W.; and Alsmiller, R. G., Jr.: Comparisons of Results Obtained with Several Proton Penetration Codes - Part II, ORNL RSIC-22, June 1958.

14. Case, R.: Techniques Used for the Calculation of Space Radiation Dose. Aerospace Medicine, Vol. 40, No. 12, December 1969, pp. 1455-1461.

15. Baker, M. B.; Santina, R. E.; and Masley, A. J.: Modeling of Solar Cosmic Ray Events Based on Recent Observations. AIAA J., Vol. 7, No. 11, November 1969. pp. 2105-2110.

Table 1

RESULTS FROM VARIOUS DOSE INTEGRATION METHODS

CASE	VEHICLE DESCRIPTION (1)	MAN MODEL DESCRIPTION (2)	METHOD OF INTEGRATION	CDC-6500 COMPUTER TIME (SEC)	DOSE (RAD) SOLAR COSMIC RAYS	DOSE (RAD) TRAPPED PROTONS	VEHICLE/MAN MODEL ORIENTATION
1	GEOMETRIC	GEOMETRIC	SYSTEMATIC	27.2	54.0 (8%)(4)	24.4 (5%)	ORIENTED
2	GEOMETRIC	GEOMETRIC	RANDOM	26.7 250.1	58.8 (6%) 59.7 (2%)(5)	24.6 (3%) 25.1 (1%)(5)	ORIENTED
3	GEOMETRIC	HISTOGRAM (3)	SYSTEMATIC	27.8	58.3 (7%)	27.6 (4%)	UNORIENTED
4	GEOMETRIC	HISTOGRAM	RANDOM	28.1	64.3 (6%)	27.1 (3%)	UNORIENTED
5	HISTOGRAM	HISTOGRAM	RANDOM	4.1	63.9 (6%)	28.3 (3%)	UNORIENTED

NOTES

(1) GEOMETRICAL MOCKUP OF 44-REGION VEHICLE.

(2) GEOMETRICAL MOCKUP CONSISTS OF TWO ELLIPTICAL CYLINDERS REPRESENTING HEAD AND TRUNK.

(3) HISTOGRAMS HAVE 100 BINS, LOGARITHMICALLY SPACED.

(4) NUMBERS IN PARENTHESIS ARE STANDARD DEVIATIONS.

(5) THESE CALCULATIONS INVOLVED 5000 SAMPLES; OTHERS INVOLVED 500 SAMPLES.

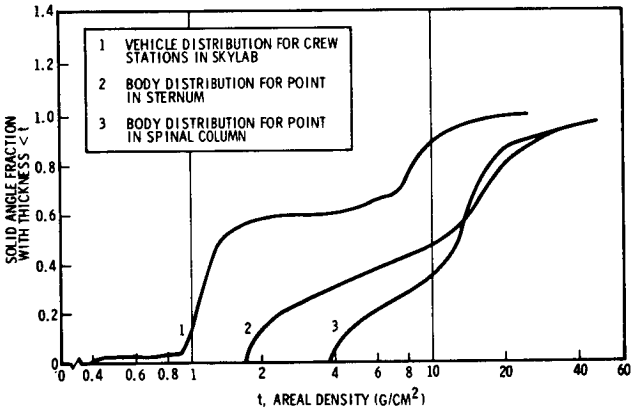

Figure 1. Typical Mass Distributions for Vehicle and Organ Segments

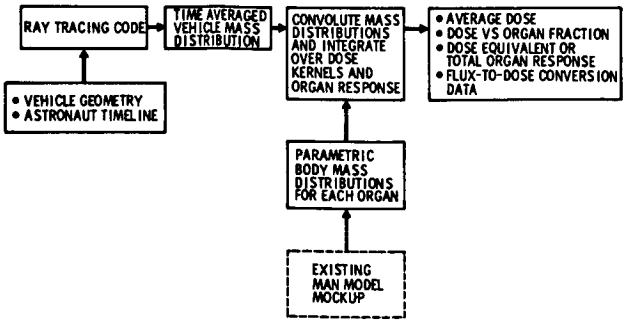

Figure 2. Technique for Dose Evaluation

16. Yucker, W. R.: Solar Cosmic Ray Hazard to Interplanetary and Earth-Orbital Space Travel. Proceedings of this symposium.

17. Holly, F. E.; and Janni, J. F.: Space Radiation Dosimetry. Aerospace Medicine, Vol. 40, No. 12, December 1969, pp. 1462-1475.

18. Sondhaus, C. A.; and Evans, R. D.: Dosimetry of Radiation in Space Flight. Radiation Dosimetry, Vol. III, Academic Press, Inc. (New York), 1969, pp. 453-521.

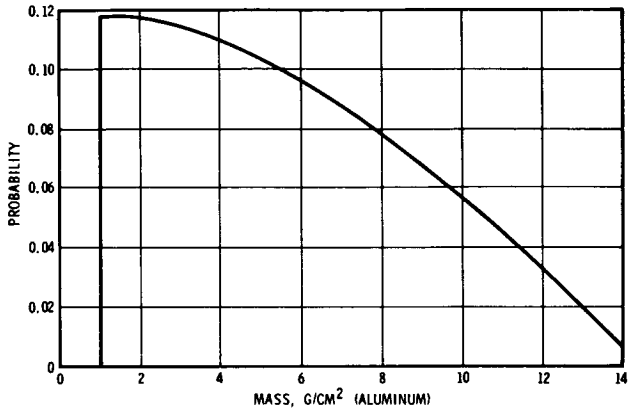

Figure 3. Mass Probability Density Function used in Statistical Analysis

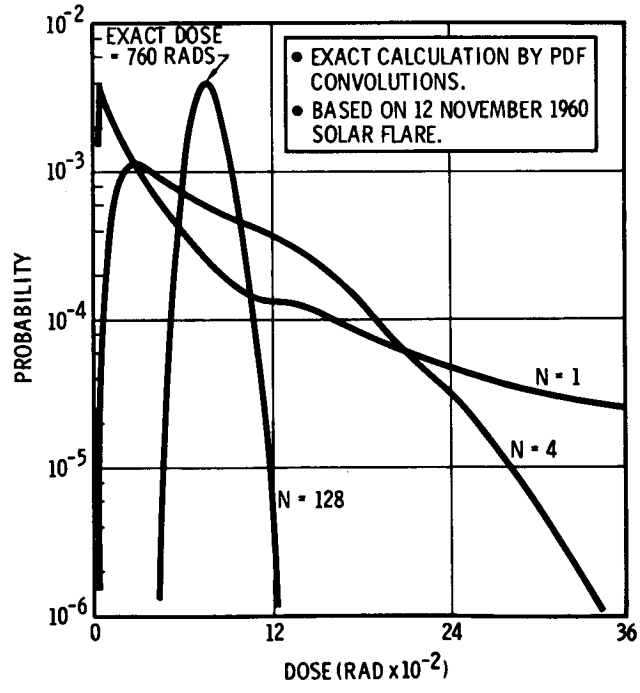

Figure 4. Dose Probability Distribution for N Random Rays

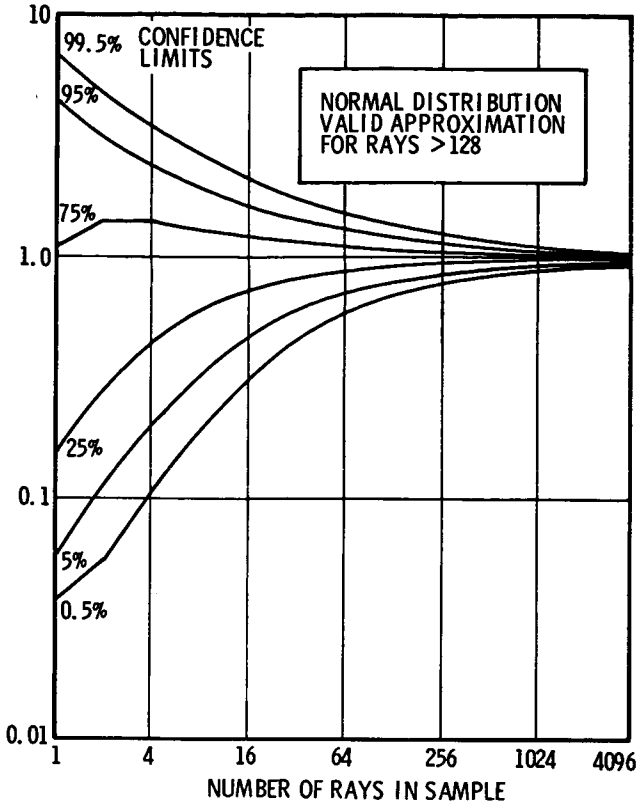

Figure 5. Confidence Intervals as a Function of Number of Random Rays

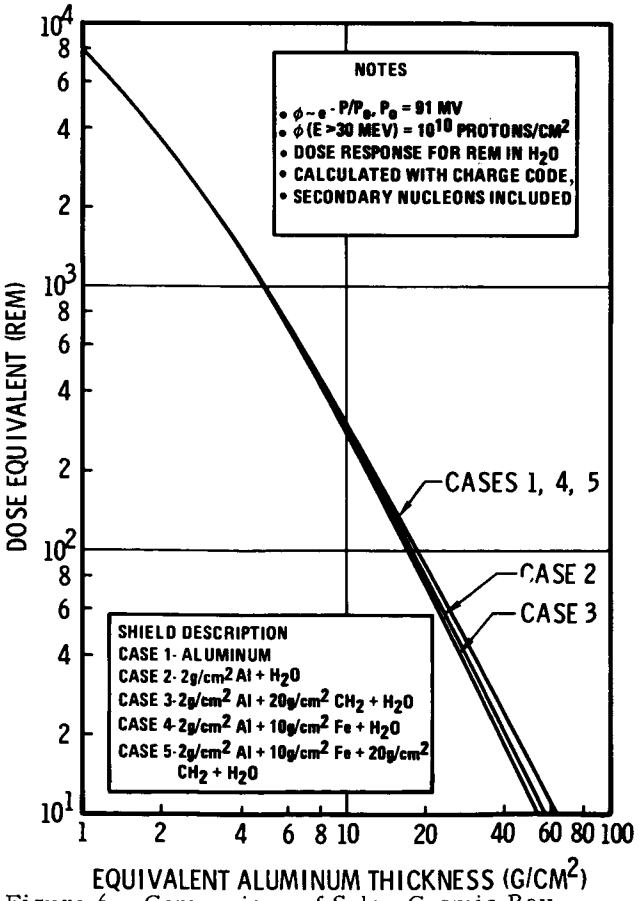

Figure 6. Comparison of Solar Cosmic Ray Dose Attenuation Kernels using Equivalent Aluminum Thickness

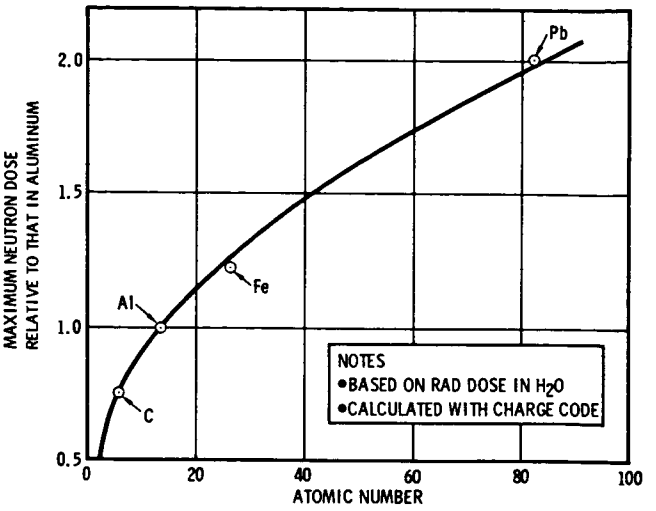

Figure 7. Relative Proton Shielding Effectiveness

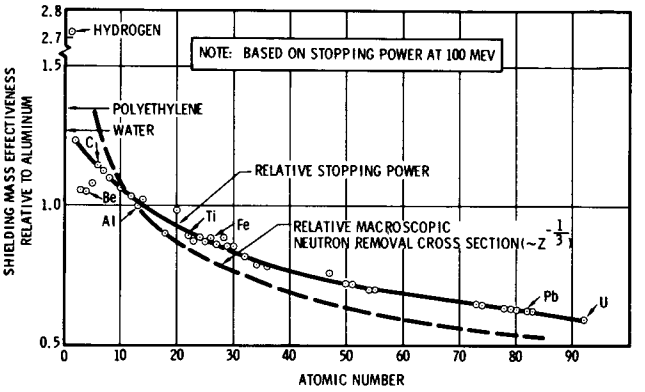

Figure 8. Secondary Neutron Dose Production as a Function of Atomic Number

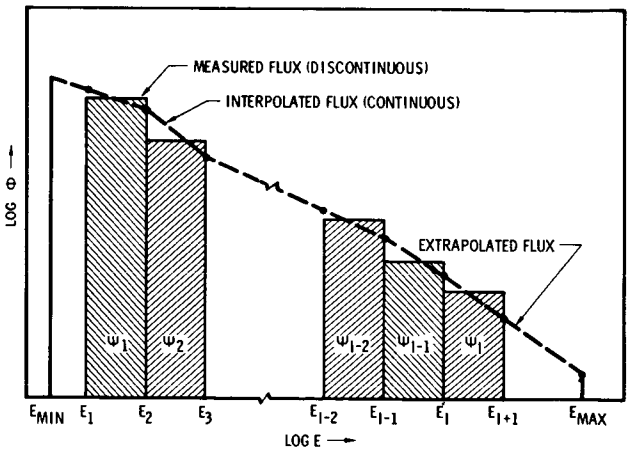

Figure 9. Flux Spectrum Representation

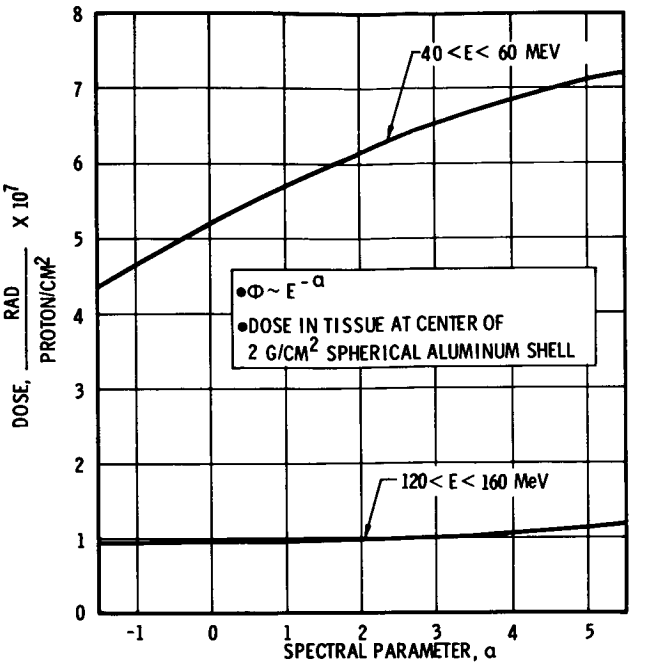

Figure 10. Example of Dose Conversion Versus Spectral Parameter

MONTE CARLO CALCULATIONS OF HIGH-ENERGY NUCLEON-MESON CASCADES AND APPLICATIONS TO GALACTIC COSMIC-RAY TRANSPORT[1]

T. W. Armstrong
R. G. Alsmiller, Jr.
K. C. Chandler

Oak Ridge National Laboratory
Oak Ridge, Tennessee, 37830

Results obtained using a recently developed calculational method for determining the nucleon-meson cascade induced in thick materials by high-energy nucleons and charged pions are presented. The calculational method uses the intranuclear-cascade-evaporation model to treat nonelastic collisions by particles with energies $\geq$ 3 GeV and an extrapolation model at higher energies. The following configurations are considered: (a) 19.2-GeV/c protons incident on iron, (b) 30.3-GeV/c protons incident on iron, (c) solar and galactic protons incident on the moon, and (d) galactic protons incident on tissue. For the first three configurations, experimental results are available and comparisons between the experimental and calculated results are given.

INTRODUCTION

Nucleon-meson transport calculations that utilize Monte Carlo techniques in conjunction with the intranuclear-cascade-evaporation model for treating nonelastic collisions were previously carried out for a variety of problems involving solar protons and other sources (refs. 1 to 3, for example). The calculational method employed for these problems is restricted to particle energies $\geq$ 3 GeV because of limitations imposed by the particular intranuclear-cascade model used (ref. 4). To enable transport calculations to be performed for galactic protons and other high-energy sources, the calculational method has been extended to higher energies by using an extrapolation model (ref. 5) to obtain the description of products from nonelastic collisions $\geq$ 3 GeV. This extrapolation method uses the differential cross sections for the production of nucleons and pions from 3-GeV nucleon-nucleus and 2.5-GeV pion-nucleus collisions as predicted by the intranuclear-cascade-evaporation model, together with energy, angle, and multiplicity scaling relations that are consistent with the sparse experimental data available for high-energy interactions, to estimate the particle production at the higher energies.

[1]This work was partially funded by the National Aeronautics and Space Administration, Order H-38280A, under Union Carbide Corporation's contract with the U. S. Atomic Energy Commission.

This recently developed high-energy transport method has been applied to compute the nucleon-meson cascade induced in thick targets for several source-geometry configurations, and the purpose of the present paper is to present some of the results obtained. The following cases are considered: (a) 19.2-GeV/c protons incident on a thick iron target, (b) 30.3-GeV/c protons incident on a thick iron target, (c) galactic and solar protons incident on the moon, and (d) galactic protons incident on tissue. For the first three cases, experimental data exist so that comparisons with the calculated results can be made in order to check the validity of the calculational method.

RESULTS

19.2-GeV/c Protons Incident on Iron

Citron et al. (ref. 6) have measured the longitudinal and lateral development of the nucleon-meson cascade induced in a thick iron target by a narrow beam of 19.2-GeV/c protons. Figure 1 shows a comparison of the experimental results, the results from the present calculations, and the results available from calculations made by others for the longitudinal development of the cascade. The cascade development is given in terms of both the star density and track intensity. For the present calculations, the star density was calculated using the cross sections for nuclear star production in emulsion given by Hess et al. (ref. 10), and the track intensity was taken to be the flux due to protons above 500 MeV and charged pions above 80 MeV.

In the experiment, the iron absorber consisted of slabs of iron of various thicknesses with air gaps between the slabs. Results for the present calculations in figure 1 are given with and without these air gaps taken into account. As indicated in figure 1, the results of the present calculations for the longitudinal development of the cascade agree reasonably well with the experimental results and with the results from other calculations.

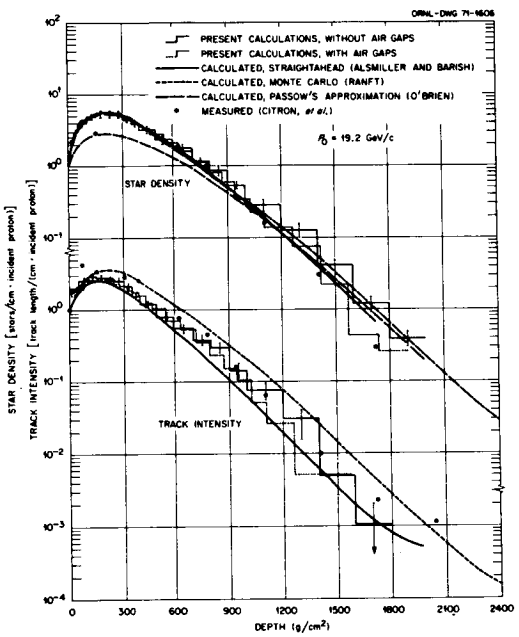

FIGURE 1.— Star density and track intensity versus depth for 19.2-GeV/c protons incident on iron. Results from the present calculations are compared with the straightahead calculations of Alsmiller and Barish (ref. 7), the Monte Carlo calculations of Ranft (ref. 8), the calculations of O'Brien using Passow's approximation (ref. 9), and the measurements of Citron et al. (ref. 6).

The lateral distribution of the track intensity at various depths has also been calculated and compared with the measurements of Citron et al. The calculated and experimental results for the lateral distributions are not in good agreement. The reason for this discrepancy is not known at present. However, as discussed later, the calculated lateral development of the cascade is in good agreement with other experimental data (ref. 11) for 30.3-GeV/c protons incident on iron. In principle, there is no reason that the calculational method should be less accurate for 19.2-GeV/c incident protons than for 30.3-GeV/c incident protons.

30.3-GeV/c Protons Incident on Iron

The lateral development of the nucleon-meson cascade induced in a thick iron target by a narrow beam of 30.3-GeV/c protons has been determined experimentally by Awschalom et al. (ref. 11). The quantity measured was the ^{18}F production in aluminum foils placed at various depths in the iron. Calculations have been carried out to determine the energy and spatial distributions of the nucleon and charged-pion fluxes for this configuration. These fluxes and available cross sections for producing ^{18}F from aluminum (ref. 1) were then used to compute the ^{18}F production as a function of distance from the beam axis. The energy dependence of these cross sections is such that, roughly speaking, the ^{18}F production can be interpreted as a measure of the nucleon and charged-pion fluxes above $\sim$ 50 MeV.

A comparison of the calculated and experimental results is shown in figure 2 for several intermediate depths in the iron. The agreement is quite good although the calculations give a consistently higher production near the beam axis. However, because of the small area and alignment of the aluminum foils used in the experiment, the experimental ^{18}F production is expected to yield an underestimate of the actual production very near

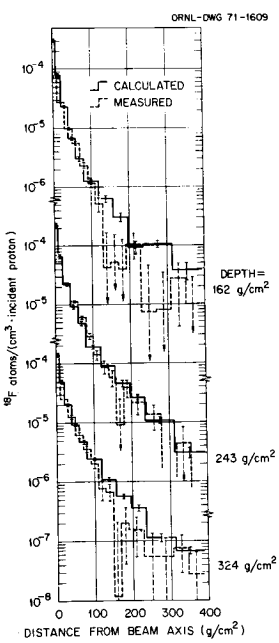

FIGURE 2.— Calculated and measured (ref. 11) lateral distribution of ^{18}F production in aluminum foils at various depths in iron for 30.3-GeV/c incident protons.

the beam axis (ref. 12). The agreement at the intermediate depths shown in figure 2 is fairly typical of the agreement obtained for other comparisons that have been made at depths ranging from 0 to 1045 g/cm^2. The laterally integrated ^{18}F production is not available from the experiment, so the calculated longitudinal development of the cascade cannot be compared with experiment for this case.

Galactic and Solar Protons Incident on the Moon

The depth-dependent radionuclide activity induced in the moon by galactic and solar proton bombardment has been calculated and compared with measurements made on Apollo 11 and 12 samples. As an example of the calculated results obtained, figure 3 shows the depth dependence of the ^{26}Al activity. The total ^{26}Al activity (i.e., the sum of the solar and galactic contributions) is shown in figure 4, together with the measured activity in two moon rocks. Additional comparisons between calculated and measured activities are given elsewhere (ref. 15).

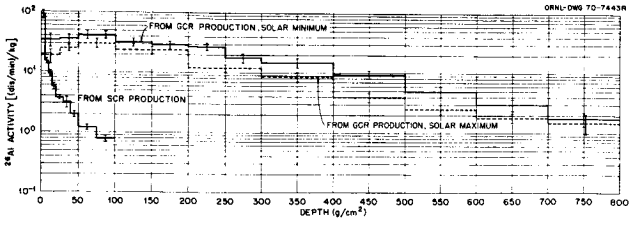

FIGURE 3.— ^{26}Al activity versus depth in moon due to solar cosmic rays (SCR) and galactic cosmic rays (GCR) at solar minimum and solar maximum.

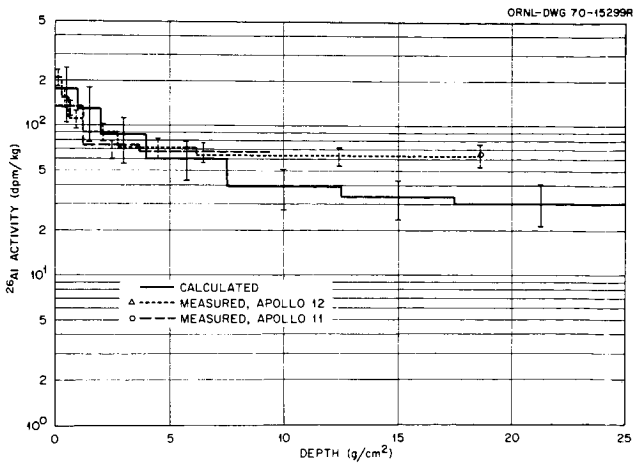

FIGURE 4.— Comparison of calculated and measured (refs. 13, 14) ^{26}Al activity induced in the moon by cosmic-ray bombardment.

The depth dependence of the neutron spectra in the moon has also been calculated. The thermal-neutron flux in the moon has been inferred from the Apollo measurements (ref. 16) and is in good agreement with the calculated flux.

The same calculational method as used here to determine the induced activity in the moon has been applied recently by Gabriel and Santoro to determine the induced activity in the soil surrounding a 500-GeV proton accelerator (ref. 17).

Galactic Protons Incident on Tissue

The absorbed dose and dose equivalent induced by galactic protons in an infinite slab of tissue 30 cm thick have been calculated using the high-energy transport code. An isotropic flux of galactic protons having a solar minimum energy spectrum (ref. 15) was taken to be incident on one side of the tissue slab. The nucleon-meson cascade in the tissue produced by incident protons in the energy range from 30 MeV to 200 GeV was calculated, and the depth dependence of the absorbed dose and dose equivalent was determined as described in reference 18. The electron-photon cascade resulting from the decay of neutral pions and the electrons and positrons from muon decay were taken into account in an approximate manner (ref. 18). The following composition (in at. %) was used for the tissue: H, 63.3; O, 25.8; C, 9.5; N, 1.4. A tissue density of

1.0 g/cm^3 was used.

The absorbed dose and average quality factor as a function of depth in the tissue are shown in figure 5. The average quality factor was computed by dividing the dose equivalent in a given depth interval by the absorbed dose in that interval. In determining the dose equivalent, the quality factors for each type of particle as a function of linear energy transfer were obtained in the same manner as described in reference 17. From figure 5, the absorbed dose for an omnidirectional (over 2π solid angle) flux incident on one side of the tissue slab is approximately 4 rad/y at all depths. For a 4π incident flux (i.e., 2π incident flux on both sides of the slab), the dose would be 8 rad/y, which is in agreement with the value of 10 rad/y quoted by others (refs. 19 and 20) for a 4π flux at solar minimum.

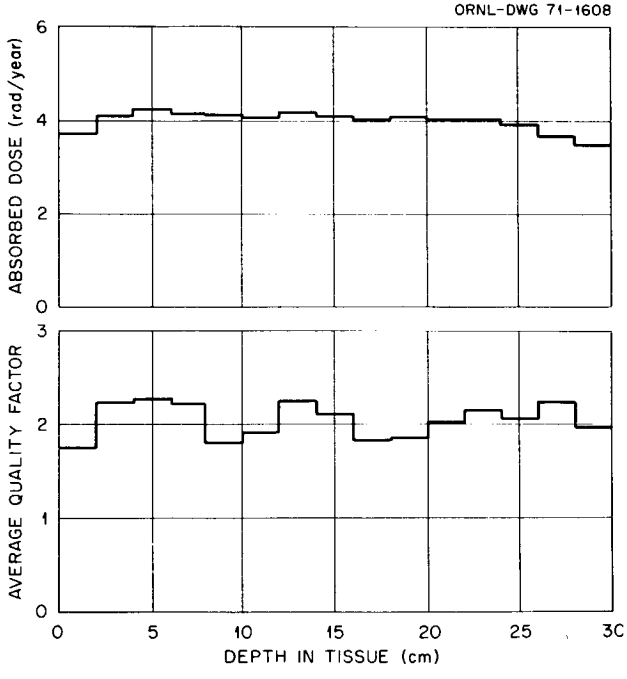

FIGURE 5.— Absorbed dose and average quality factor in tissue from galactic proton bombardment.

The contributions to the absorbed dose and dose equivalent, respectively, from various kinds of particles are shown in figures 6 and 7. The total dose is obtained by adding all of the contributions shown in the figures. The histogram labeled "primary ionization" in figure 6 gives the absorbed dose from the excitation and ionization of atomic electrons by those incident protons which have not undergone nuclear collision. The histogram labeled "secondary protons" gives the absorbed dose from the excitation and ionization of atomic electrons by protons produced from nonelastic nucleon-nucleus and pion-nucleus collisions and from the elastic collisions of nucleons and pions with hydrogen nuclei. The histogram labeled "heavy nuclei" gives the absorbed dose from particles with mass number greater than one produced from nonelastic nucleon-nucleus and pion-nucleus collisions and the absorbed dose from the recoiling nuclei produced from elastic neutron-nucleus collisions and from nonelastic nucleon-nucleus and pion-nucleus collisions. The histogram labeled "charged pions" gives the absorbed dose from the excitation and ionization of atomic electrons by both positively and negatively charged pions produced from nucleon-nucleus and pion-nucleus nonelastic collisions. The histogram labeled "photons from neutral pions" gives the absorbed dose from the electron-photon cascade produced by the photons which arise from the decay of neutral pions. The histogram labeled "electrons, positrons, and photons" gives the

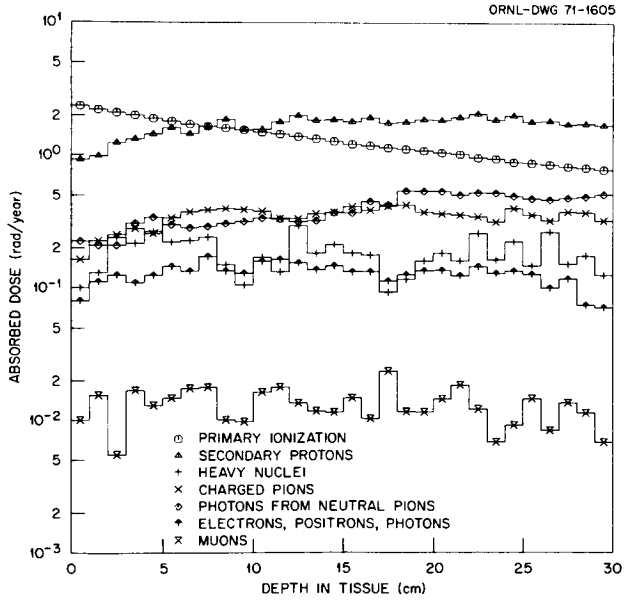

FIGURE 6.— Contribution by particle type to the absorbed dose in tissue from galactic proton bombardment.

absorbed dose from the electrons and positrons produced by muon decay and the absorbed dose from the photons produced by nucleon-nucleus and pion-nucleus nonelastic collisions. The histogram labeled "muons" gives the absorbed dose from the excitation and ionization of atomic electrons by both positively and negatively charged muons. In figure 7 the histograms have similar meanings but give the dose equivalent from these various kinds of secondary particles.

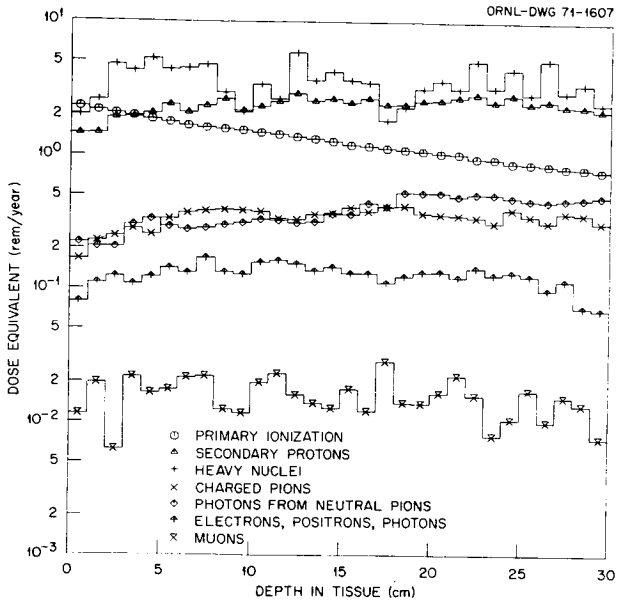

FIGURE 7.— Contribution by particle type to the dose equivalent in tissue from galactic proton bombardment.

It should be realized that only the protons in the cosmic radiation have been considered in calculating the dose. Cosmic-ray nuclei heavier than protons can contribute significantly to the dose, especially at small depths. At present, the transport code used for these calculations is not capable of transporting particles heavier than nucleons.

ACKNOWLEDGMENT

We are very grateful to M. Awschalom, T. Borak, and A. VanGinnekin of the National Accelerator Laboratory for making their preliminary data available to us prior to publication.

REFERENCES

1. ARMSTRONG, T.W.; and ALSMILLER, R.G., Jr.: Nucl. Sci. Eng., Vol. 33, 1968, p. 291.
2. ARMSTRONG, T.W.; and ALSMILLER, R.G., Jr.: Nucl. Sci. Eng., Vol. 37, 1969, p. 337.
3. ARMSTRONG, T.W.; and CHANDLER, K.C.: Calculation of the Radionuclide Production in Tissue by Solar-Flare Bombardment. Neutron Phys. Div. Ann. Progr. Rept. May 31, 1970, Oak Ridge National Laboratory Document ORNL-4592, p.89.
4. BERTINI, Hugo W.: Phys. Rev., Vol. 188, 1969, p. 1711.
5. GABRIEL, T.A.; ALSMILLER, R.G., Jr.; and GUTHRIE, M.P.: An Extrapolation Method for Predicting Nucleon and Pion Differential Production Cross Sections for High-Energy (> 3 GeV) Nucleon-Nucleus Collisions. Oak Ridge National Laboratory Document ORNL-4542, 1970.
6. CITRON, A.; HOFFMAN, L.; PASSOW, C.; NELSON,W.R.; and WHITEHEAD, M.: Nucl. Instr. Meth., Vol. 32, 1965, p. 48.
7. ALSMILLER, R.G., Jr.; and BARISH, J.: Nucl. Instr. Meth., Vol. 36, 1965, p. 309.
8. RANFT, J.: Nucl. Instr. Meth. Vol. 48, 1967, p. 261.
9. O'BRIEN, K.: Nucl. Instr. Meth., Vol. 72, 1969, p. 93.
10. HESS, Wilmot N.; PATTERSON, H. Wade; and WALLACE, Roger: Phys. Rev., Vol. 116, No. 2, 1959, p. 445.
11. Preliminary data of M. Awschalom, T. Borak, and A. VanGinnekin of the National Accelerator Laboratory, to be presented at the International Congress on Protection Against Accelerator and Space Radiation, Geneva, April 26-30, 1971.
12. Van GINNEKIN, A., National Accelerator Laboratory: private communication.
13. SHEDLOVSKY, J.P.; HONDA, M.; REEDY, R.C.; EVANS, J.C., Jr.; LAL, D.; LINDSTROM, R.M.; DELANY, A.C.; ARNOLD, J.R.; LOOSLI, H.H.; FRUCHTER, J.S.; and FINKEL, R.C.: Pattern of Bombardment-Produced Radionuclides in Rock 10017 and in Lunar Soil. Proc. Apollo 11 Lunar Sci. Conf., Geomchim. Cosmochim. Acta, Suppl.I, Vol. 2, 1970, p. 1503.
14. FINKEL, R.C.; ARNOLD, J.A.; REEDY, R.C.; FRUCHTER, J.S.; LOOSLI, H.H.; EVANS, J.C.; SHEDLOVSKY, J.P.; and DELANY, A.C.: Depth Variation of Cosmogenic Nuclides in a Lunar Surface Rock. Paper presented at the Lunar Science Conference, Houston, Texas, January 11-14, 1971.
15. ARMSTRONG, T.W.; and ALSMILLER, R.G., Jr.: Calculation of Cosmogenic Radionuclides in the Moon and Comparison with Apollo Measurements. Oak Ridge National Laboratory Document ORNL-TM-3267 (in press.)

16. O'KELLEY, G.D.; ELDRIDGE, J.S.; SCHONFELD, E.; and BELL, P.R.: Comparative Radionuclide Concentrations and Ages of Apollo 11 and Apollo 12 Samples from Nondestructive Gamma-Ray Spectrometry. Paper presented at the Lunar Science Conference, Houston, Texas, January 11-14, 1971.

17. GABRIEL, T.A.; and SANTORO, R.T.: Calculation of the Long-Lived Activity in Soil Produced by 500-GeV Protons. Oak Ridge National Laboratory Document ORNL-TM-3262 (in press.)

18. ALSMILLER, R.G., Jr.; ARMSTRONG, T.W.; and COLEMAN, W.A.: Nucl. Sci. Eng., Vol. 42, 1970, p. 367

19. ALSMILLER, R.G., Jr.: Nucl. Sci. Eng., Vol. 27, 1967, p. 158.

20. HOLLY, F.; and TRAFTON, L.: Aerospace Med., Vol. 40, #12, 1969, p. 1441.

CALCULATION OF THE ABSORBED DOSE AND DOSE EQUIVALENT INDUCED BY MEDIUM-ENERGY NEUTRONS AND PROTONS AND COMPARISON WITH EXPERIMENT[1]

T. W. Armstrong and B. L. Bishop

Oak Ridge National Laboratory
Oak Ridge, Tennessee, 37830

Monte Carlo calculations have been carried out to determine the absorbed dose and dose equivalent for 592-MeV protons incident on a cylindrical phantom and for neutrons from 580-MeV proton-Be collisions incident on a semi-infinite phantom. For both configurations, the calculated depth dependence of the absorbed dose is in good agreement with experimental data.

INTRODUCTION

Nucleon-meson cascade calculations were recently carried out for monoenergetic neutrons (60 to 3000 MeV) and protons (400 to 3000 MeV) normally incident on a semi-infinite slab of tissue (ref. 1). For several incident energies, the calculated depth dependence of the absorbed dose was compared with available experimental results (ref. 2), which were obtained using somewhat different source-geometry configurations, and substantial differences were found. It was not clear from these comparisons whether the theory was in error or whether the differences could be ascribed to the different configurations used in the calculations and experiments.

The calculations have been carried out for two configurations: 592-MeV protons incident on a cylindrical phantom, and neutrons from 580-MeV proton-Be collisions incident on a semi-infinite slab phantom. The calculated depth distributions for the absorbed dose are compared with the measured distributions of Baarli and Goebel (ref. 2) for these same configurations. The depth distributions for the dose equivalent have also been calculated.

The method of calculation used is summarized in the next section, and the results are presented and discussed in the last section.

CALCULATIONAL METHOD

The method of calculation is the same as that described previously (ref. 1), so only a brief account of the calculational method will be given here. The calculations were carried out using the Monte Carlo code NMTC (ref. 3). This code takes into account charged-particle energy loss due to ionization and excitation of atomic electrons, elastic and nonelastic nucleon-nucleus and pion-nucleus collisions, pion and muon decay in flight and at rest, and negative-pion capture at rest. The electron-photon cascade resulting from the decay of neutral pions and the electrons and positrons from muon decay are included in an approximate manner (ref. 1). At energies above 15 MeV for nucleons and 2.2 MeV for charged pions, the energy, direction, and multiplicity of particles produced in nucleon-nucleus and pion-nucleus collisions are calculated using the intranuclear-cascade-evaporation model of nuclear reactions (refs. 4, 5). Proton-nucleus collisions below 15 MeV and pion-nucleus collisions below 2.2 MeV (except for the capture of negative pions at rest) are neglected. Neutron collisions below 15 MeV are treated using experimental cross-section data (ref. 3) in conjunction with the evaporation model (ref. 5) to determine particle production from neutron-nucleus nonelastic collisions. A detailed description of the method of calculation is given elsewhere (ref. 1).

The calculations have been carried out using tissue for the phantom composition. The following concentrations were used for the tissue (in at. %): H, 63.3; O, 25.8; C, 9.5; N, 1.4. A tissue density of 1.0 g/cm^3 was used.

RESULTS AND DISCUSSION

Incident Protons

The geometry for the case of 592-MeV incident protons is shown in figure 1. The protons are incident normally on one end of a cylindrical phantom

200 cm in depth by 50 cm in diameter. The experimental spatial variation of the incident proton intensity (ref. 2) was approximated in the calculations as a Gaussian distribution with a full-width-at-half-maximum value of 30 cm.

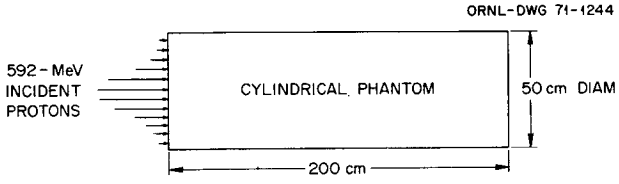

FIGURE 1.— Configuration for incident protons.

The depth dependence of the absorbed dose is shown in figure 2. The experimental absorbed dose is not given in absolute units, and thus only the shapes of the calculated and experimental distributions can be compared. Also shown for comparison in figure 2 is the absorbed dose calculated for a cylinder of infinite radius. This case corresponds to the configuration considered in the previous calculations (ref. 1), i.e., an infinitely broad beam incident on a semi-infinite slab. As shown in figure 2, the shape of the calculated distribution is in very good agreement with the experimental distribution when the cylindrical geometry used in experiment is simulated in the calculations. Therefore, for a meaningful comparison with the experimental absorbed-dose distribution it is necessary that the finite radius of the phantom be taken into account in the calculations.

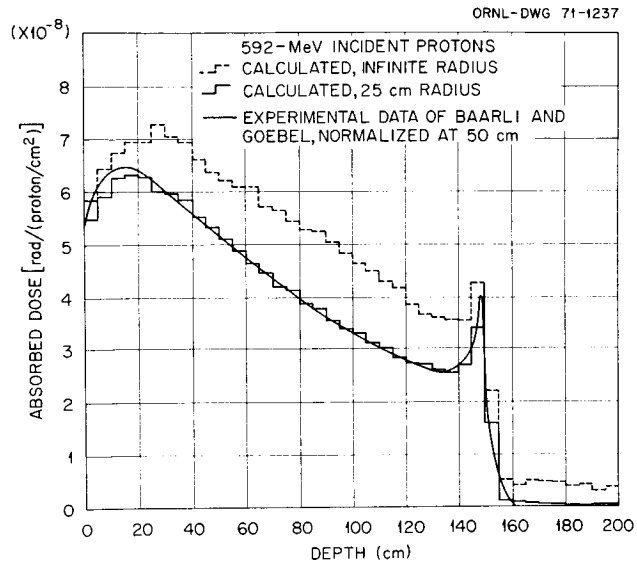

FIGURE 2.— Depth dependence of absorbed dose for 592-MeV incident protons.

The contributions to the absorbed dose and dose equivalent from various kinds of particles have also been calculated, and these are shown in figures 3 and 4 for the finite-radius geometry. The total dose is obtained by adding all of the contributions shown in the figures. The histogram labeled "primary ionization" in figure 3 gives the dose from the excitation and ionization of atomic electrons by those incident protons which have not undergone nuclear collision. The histogram labeled "secondary protons" gives the absorbed dose from the excitation and ionization of atomic electrons by protons produced from nonelastic nucleon-nucleus and pion-nucleus collisions and from the elastic collisions of nucleons and pions with hydrogen nuclei. The histogram labeled "heavy nuclei" gives the absorbed dose from particles with mass number greater than one produced from nonelastic nucleon-nucleus and pion-nucleus collisions and the absorbed dose from the recoiling nuclei produced from elastic neutron-nucleus collisions and from nonelastic nucleon-nucleus and pion-nucleus collisions. The histogram labeled "charged pions" gives the absorbed dose from the excitation and ionization of atomic electrons by both positively and negatively charged pions produced from nucleon-nucleus and pion-nucleus nonelastic collisions. The histogram labeled "photons from neutral pions" gives the absorbed dose from the electron-photon

cascade produced by the photons which arise from the decay of neutral pions. The histogram labeled "electrons, positrons, and photons" gives the absorbed dose from the electrons and positrons produced by muon decay and the absorbed dose from the photons produced by nucleon-nucleus and pion-nucleus nonelastic collisions. The histogram labeled "muons" gives the absorbed dose from the excitation and ionization of atomic electrons by both positively and negatively charged mu-mesons.

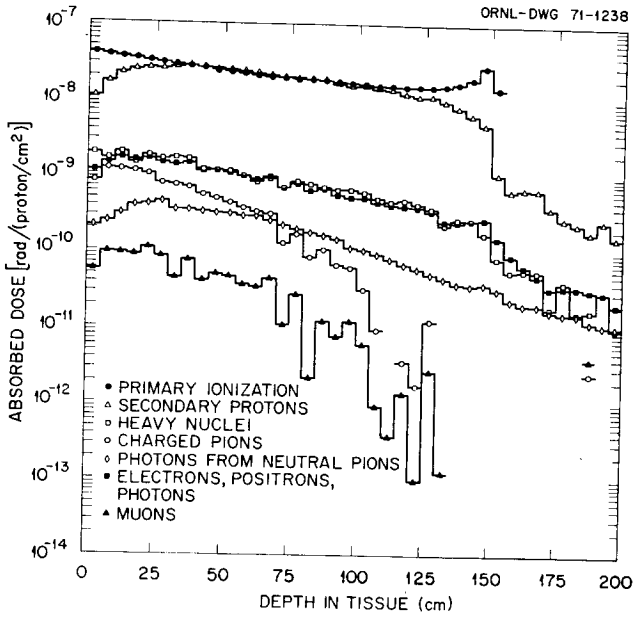

FIGURE 3.— Contribution of various particles to the absorbed dose for 592-MeV protons incident on a cylindrical phantom.

The histograms in figure 4 have meanings similar to those of figure 3 but correspond to the dose equivalent from various kinds of secondary particles. The calculation of the dose equivalent was carried out taking the quality factor to be a function of the linear energy transfer as in the previous calculations. In the case of protons, the damage curve given in reference 6, which is based on the recommendations of the National Committee on Radiation Protection and Measurements, was used. In the case of charged pions and muons, the quality factor as a function of linear energy transfer was taken to be the same as that for protons, and damage curves for charged pions and muons, constructed in a manner similar to the proton damage curve given in reference 6, were used. A quality factor of 20 was assigned to the energy deposited by all heavy nuclei and a quality factor of unity was assigned to the energy deposited by electrons, positrons, and photons.

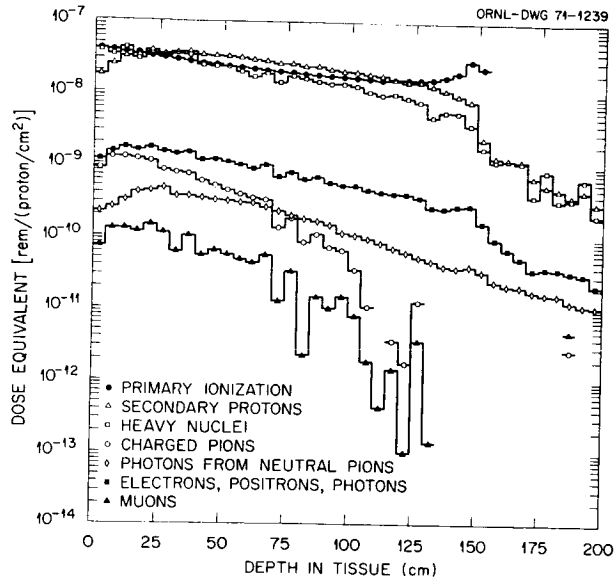

FIGURE 4.— Contribution of various particles to the dose equivalent for 592-MeV protons incident on a cylindrical phantom.

The contributions to the absorbed dose and dose equivalent by various kinds of particles have also been calculated for the case of a cylinder with infinite radius, and these results are given in reference 7.

Incident Neutrons

The experimental arrangement used by Baarli and Goebel (ref. 2) to measure the absorbed dose from incident neutrons is shown schematically in figure 5. The neutrons produced from proton-Be interactions at angles of 18° and 56° with respect to the proton beam were directed toward an absorber of tissue-like material, and the depth dependence of the absorbed dose was measured. The neutron intensity on the absorber was approximately uniform over a circular area 15 cm in radius. The energy spectrum of the incident neutrons was not measured. A "nominal" energy for the neutron beam was calculated by Baarli and Goebel assuming only elastic collisions in the target. These nominal energies are 525 MeV and 180 MeV for scattering angles of 18° and 56°, respectively (ref. 2). In the previous calculations for the depth dependence of the absorbed dose (ref. 1), all of the incident neutrons were assumed to be monoenergetic at energies of 525 or 180 MeV.

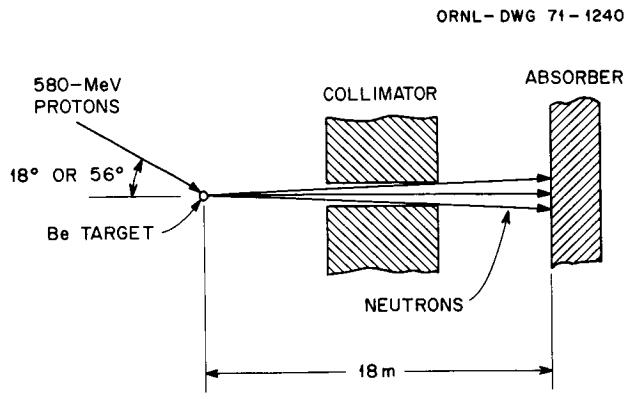

FIGURE 5.— Configuration for incident neutrons.

To obtain an estimate of the incident neutron spectrum, the energy distribution of neutrons from 580-MeV protons incident on Be was calculated using the intranuclear-cascade model (ref. 4). The results, in terms of the differential neutron production cross section, are shown in figure 6. In calculating the neutron production spectrum, the production averaged over the angular intervals from 15.5° to 20.5° and from 51° to 61° were used to represent the production at 18° and 56°, respectively. It is evident from figure 6 that representing these spectra by monoenergetic neutrons at 180 MeV and 525 MeV, as was done in the previous calculations (ref. 1), is a gross oversimplification.

The depth dependence of the absorbed dose for the case of incident neutrons is shown in figures 7 and 8. The histograms labeled "180-MeV spectrum" and "525-MeV spectrum" were calculated using the incident neutron spectra shown in figure 6. The histograms labeled "180 MeV" and "525 MeV" are taken from the previous calculation (ref. 1) for monoenergetic incident neutrons. Since the experimental results are not reported in absolute units, they have been normalized to the present calculated results at a depth of 8 cm. The measured and calculated depth dependences of the absorbed dose are in good agreement when the energy distribution of the incident neutrons is taken into account in the calculations.

The results in figures 7 and 8 have been normalized on a per-incident-neutron basis. The results could have been normalized per proton-Be interaction. Letting N be the number of neutrons incident on the absorber per proton-Be interaction,

$$N = \frac{\Delta\Omega'}{\sigma_{inel}} \int_0^\infty dE \left(\frac{\Delta^2\sigma}{\Delta E \Delta\Omega} \right),$$

where $(\Delta^2\sigma/\Delta E\Delta\Omega)$ is given in figure 6, σ_{inel} is the Be inelastic cross section for protons at 580 MeV (= 210.7 mb, from the intranuclear-cascade calculations), and $\Delta\Omega'$ is the solid angle for neutrons from the target hitting the absorber, which can be obtained from the geometry of the experiment $[\Delta\Omega' = \pi(15)^2/(1800)^2]$. The values of N are 0.95×10^{-4} and 0.29×10^{-4} for the production angles of 18° and 56°, respectively.

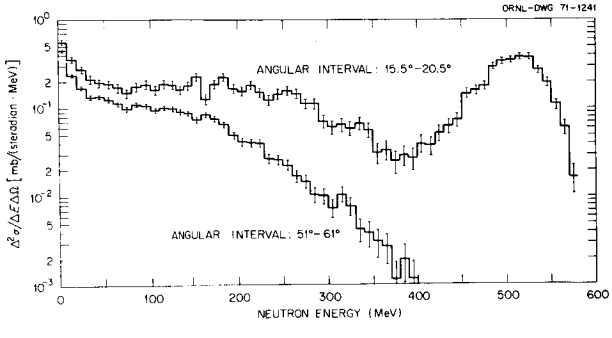

FIGURE 6.— Calculated differential neutron production cross section for 580-MeV protons incident on Be.

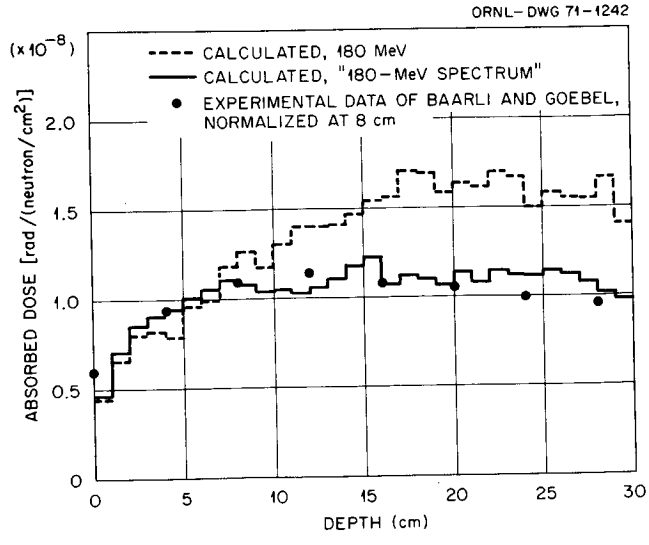

FIGURE 7.— Depth dependence of absorbed dose for neutrons incident on an infinite slab of tissue.

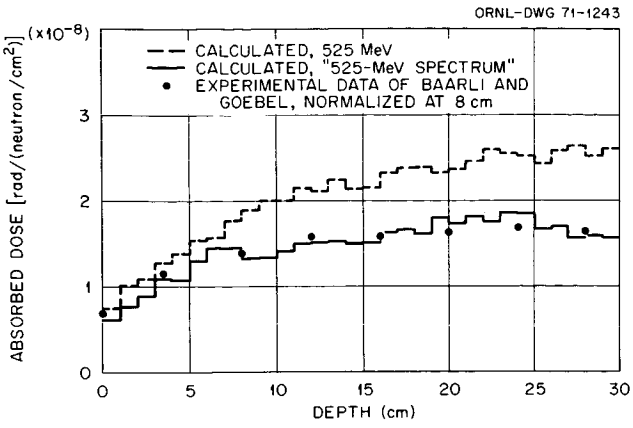

FIGURE 8.— Depth dependence of absorbed dose for neutrons incident on an infinite slab of tissue.

The contributions of various kinds of particles to the absorbed dose and the dose equivalent have also been calculated for the case of incident neutrons, and these results are given in reference 7.

In summary, the good agreement between the present calculations and the measurements indicates that the disagreement between the previous calculations (ref. 1) and measurements was a result of not taking into account some of the details of the experiment in the calculations and not due to any shortcomings of the calculational method.

[1]This work was partially funded by the National Aeronautics and Space Administration, Order H-38280A, under Union Carbide Corporation's contract with the U. S. Atomic Energy Commission.

REFERENCES

1. ALSMILLER, R.G., Jr.; ARMSTRONG, T.W.; and COLEMAN, W.A.: Nucl. Sci. Eng. Vol. 42, 1970, p. 367.

2. BAARLI, J.; and GOEBEL, K.: Properties of High-Energy Beams from a 600-MeV Synchrocyclotron. Proc. XIth International Congress of Radiology, Rome, September 1965.

3. COLEMAN, W.A.; and ARMSTRONG, T.W.: The Nucleon-Meson Transport Code NMTC. Oak Ridge National Laboratory Document ORNL-46-6, 1970.

4. BERTINI, H.W.: Phys. Rev. Vol. 188, 1969, p. 1711.

5. GUTHRIE, Miriam P.: EVAP-4: Another Modification of a Code to Calculate Particle Evaporation from Excited Compound Nuclei. Oak Ridge National Laboratory Document ORNL-TM-3119, 1970.

6. TURNER, J.E. et al., Health Physc. vol. 10, 1964, p. 783

7. ARMSTRONG, T.W.; and BISHOP, B.L.: Calculation of the Absorbed Dose and Dose Equivalent Induced by Medium-Energy Neutrons and Protons and Comparison with Experiment. Oak Ridge National Laboratory Document ORNL-TM-3304 (in press).

PRIMARY- AND SECONDARY-PARTICLE CONTRIBUTIONS TO THE DEPTH-DOSE DISTRIBUTION IN A PHANTOM SHIELDED FROM SOLAR-FLARE AND VAN ALLEN PROTONS*

R. T. Santoro, H. C. Claiborne, and R. G. Alsmiller, Jr.
Oak Ridge National Laboratory

Calculations have been made using the nucleon-meson transport code NMTC to estimate the absorbed-dose and dose-equivalent distributions in "astronauts" inside space vehicles bombarded by solar-flare and Van Allen protons. A spherical shell shield of specific radius and thickness with a 30-cm-diam. tissue ball at the geometric center was used to simulate the spacecraft-astronaut configuration. The absorbed dose and the dose equivalent from primary protons, secondary protons, heavy nuclei, charged pions, muons, photons, and positrons and electrons are given as a function of depth in the tissue phantom. Results are given for solar-flare protons with a characteristic rigidity of 100 MV and for Van Allen protons in a 240-nautical-mile circular orbit at 30° inclination angle incident on both 20-g/cm^2-thick aluminum and polyethylene spherical shell shields.

INTRODUCTION

In planning missions for manned space vehicles, it is necessary to have detailed information on the absorbed dose and dose equivalent received by the astronauts as a result of exposure to the natural radiation of space. This paper gives the results of calculations made with the nucleon-meson transport code NMTC (ref. 1) for the contributions of solar-flare and Van Allen protons to the dose distributions in a tissue phantom in a geometric model that simulates a "spacecraft-astronaut" configuration.

Calculational methods have been available for treating the transport of nucleons with energies below 400 MeV (ref. 2) for some time, but only approximate results (refs. 3-7) could be obtained for greater energies because of the lack of data on particle production from nucleon-nucleus and pion-nucleus collisions. Recently, however, calculated particle-production data for these interactions at high energies have been published (ref. 8). These data have been incorporated into the nucleon-meson transport code NMTC (ref. 1), and the results of calculations using NMTC have been shown to be in good agreement with experimental data for energies up to ∿3 GeV (refs. 9-11).

These improvements in the code permitted a more accurate representation of high-energy nucleon and pion transport and provide an accurate estimate of the contribution to the dose from charged pions and muons, as well as from the lepton component produced through muon decay. An estimate of the absorbed dose and dose equivalent from nucleons and charged mesons and their progeny was reported by Alsmiller *et al.* (ref. 12) for nucleons incident on tissue slabs. The results reported here give corresponding dose estimates for protons incident on a shielded spherical, tissue phantom.

In the following sections, the calculational methods and the spherical spacecraft-astronaut configuration are described. The incident proton spectra from both solar flares and the Van Allen belts are presented. A brief discussion of the transport calculation and the dose determinations are included. Finally, the results of the calculations are presented and discussed.

SPACECRAFT-ASTRONAUT CONFIGURATION

Depth-dose distributions were obtained for the geometric model shown in figure 1 that simulates a spacecraft-astronaut configuration. In this model, the spacecraft is considered to be a spherical shell having a fixed inner radius of 150 cm which gives a constant internal volume for all shell thicknesses. At the geometric center of the spacecraft is the astronaut who is represented by a 30-cm-diam. sphere of tissue. The composition of the tissue is shown in Table I.

TABLE I. COMPOSITION OF TISSUE

Element	Density of Nuclei (Nuclei/cm^3)
H	6.265×10^{22}
O	2.551×10^{22}
C	9.398×10^{21}
N	1.342×10^{21}

*Research funded by the National Aeronautics and Space Administration (Order H-38280A) under Union Carbide Corporation's contract with the U. S. Atomic Energy Commission.

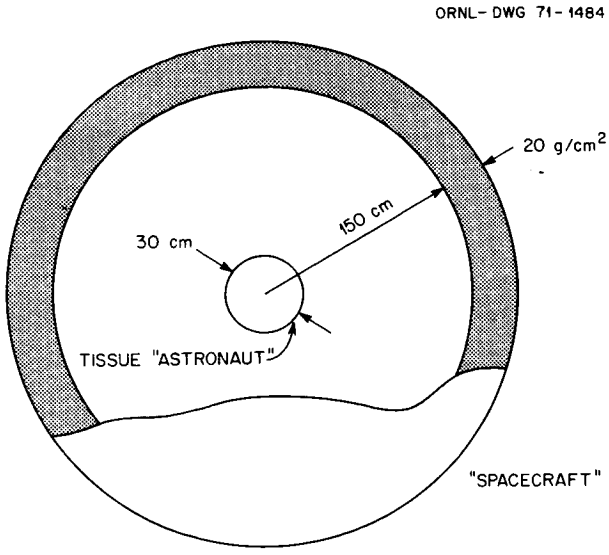

FIGURE 1. - A Schematic Diagram of the "Spacecraft-Astronaut" Configuration.

PROTON ENERGY SPECTRA

Solar-flare and Van Allen belt proton spectra are characterized by their nearly isotropic angular distributions and steep energy gradients. Since the intensity and energy spectrum vary markedly with altitude and geomagnetic coordinates in the Van Allen belts and from event to event for solar flares, it is essential in the shielding analysis of manned space flight missions that the representation of these spectra simulate those that might reasonably occur during a mission.

Solar Flares

At the higher particle energies, accurate solar-flare representations are realized when the time-integrated proton spectrum is expressed as an exponential function of magnetic rigidity; that is,

$$J(>E) = J_o \exp(- P(E)/P_o), \qquad (1)$$

where

$J(>E)$ is the omnidirectional fluence (p/cm^2) with kinetic energies above energy E,

$P(E)$ is the magnetic rigidity, and for protons $P(E) = (E^2 + 2M_p E)^{1/2}$,

M_p is the proton rest energy,

P_o is the characteristic rigidity of the flare,

J_o is an intensity parameter.

Differentiating equation 1 with respect to the kinetic energy, E, yields the differential kinetic energy spectrum

$$- \frac{dJ(>E)}{dE} = \frac{J_o}{P_o} \frac{(E+M_p)}{P(E)} \exp(- P(E)/P_o). \qquad (2)$$

The intensity is normalized such that

$$J_o = \frac{10^9}{\frac{1}{P_o} \int_{E_o}^{E_{max}} \frac{(E+M_p)}{P(E)} \exp(-P(E)/P_o) dE} \qquad (3)$$

where E_o is some lower cutoff energy in the spectrum.

Figure 2 is a plot of equation 2 for a flare of characteristic rigidity P_o = 100 MV and $J(>E_o) = 10^9$ p/cm^2 in the energy range from 30 to 3000 MeV. The energy intervals and the values indicated designate the fraction of time that protons in the given energy interval were sampled for the transport calculations.

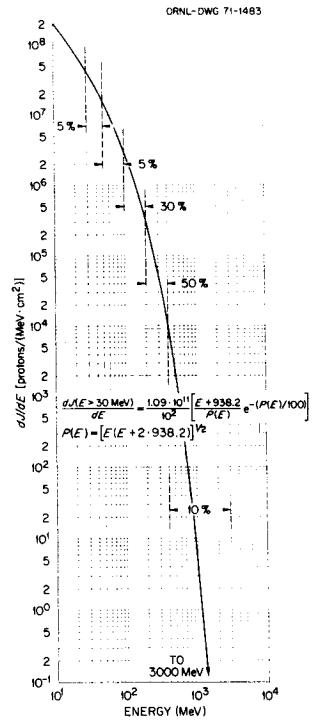

FIGURE 2. - A Solar-Flare Spectrum of Characteristic Rigidity P_o = 100 MV and Normalized to Contain 10^9 p/cm^2 With Kinetic Energy > 30 MeV.

Van Allen Belt

In the Van Allen belt, the average flux of protons above energy E that a spacecraft receives in orbit after time T is expressed by

$$J(>E) = T^{-1} \int_0^T J[(>E;B(t),L(t)]dt, \qquad (4)$$

where

$J[(>E;B(t),L(t)]$ represents the functional dependence of the omnidirectional flux above kinetic energy E in (B,L) coordinates and with time along the orbit path.

The omnidirectional flux can be approximately expressed by

$$J(>E;B,L) = J(>E_1;B,L) \times \exp[-(E - E_1)/E_o(B,L)], \qquad (5)$$

where

$J_o(>E_1;B,L)$ is the number of protons above an energy cutoff E_1, and

$E_o(B,L)$ is a fit parameter to the proton spectrum at each point in (B,L) space.

Equation 4 was solved by numerical integration using the computer code TRECO (ref. 13) developed by Vette and his coworkers (refs. 14-16), which utilizes previously determined flux maps and spectral fits of the Van Allen radiation field as input. In the code, the time dependence for J(>E;B,L) is obtained using Kepler's Laws to determine the geographic coordinates of an orbit as a function of time and transforming to the (B,L) system using a spherical harmonic expansion of the geomagnetic field. For the results given here, the AP7 flux map (ref. 16) and spectral parameters that give the best fit to the experimental data for proton energies >50 MeV were used to obtain the proton flux in the energy range $30 \leq E_p \leq 1000$ MeV. Use of this model for energies down to 30 MeV leads to a small overestimate of the flux in the 30- to 50-MeV range.

Figure 3 shows the proton flux for a 240-nautical-mile circular orbit obtained using TRECO (ref. 13) for orbit inclinations of 30°, 60°, and 90° to the equatorial plane. (At this altitude, negligible flux is obtained for a 0° orbit.) These data give the proton fluence averaged over an orbit time of one day. The larger values of the fluence observed for the 30° orbit arise from passage through the South Atlantic Anomaly. As in figure 2, the divisions on the energy scale and the values indicated between them represent the fraction of time that protons in the energy interval were sampled from in the transport calculation. The dose distributions presented in this paper were obtained using the 240-nautical-mile 30° orbit flux spectrum shown in figure 3.

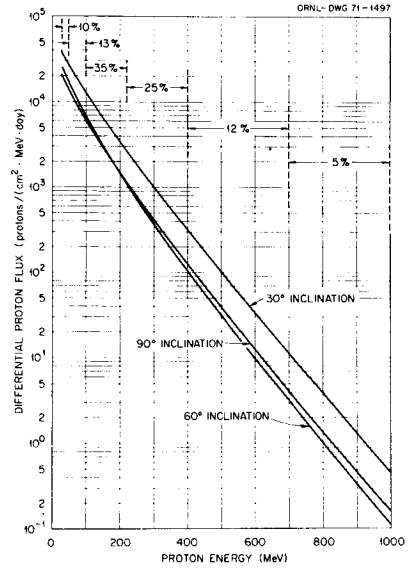

FIGURE 3. - Van Allen Belt Proton Spectra at a 240-Nautical-Mile Circular Orbit for Inclination Angles of 30°, 60°, and 90° to the Equatorial Plane. For the 30° orbit, the spectrum is normalized to contain 2.56×10^6 p/(cm^2 day) with kinetic energy > 30 MeV.

Method of Calculation

The details of the transport calculation are described by Coleman and Armstrong (ref. 1) and by Alsmiller *et al.* (ref. 12). For the results given here, the incident proton spectra were taken to be an omnidirectional fluence of 10^9 p/cm^2 for the solar flare and a time-averaged fluence of 2.56×10^6 p/(cm^2 day) for the Van Allen spectra having kinetic energy >30 MeV. The energy of the protons incident on the shield was determined by sampling from the spectrum according to the frequencies indicated in the energy bands shown in figures 2 and 3.

The incident protons, along with the secondary protons, neutrons, charged pions, and muons, were transported through the shield and tissue taking into account the energy and angular distributions of these particles. The energy loss in passage through the various media by means of excitation and ionization of the atomic electrons was treated in the continuous slowing-down approximation using known energy loss per unit distance for the charged particles (refs. 9 and 17). Heavy ions (mass > 1) were assumed to deposit all of their energy at their point of origin. Since the range of a heavy particle is short in all materials, this assumption is reasonably valid. The same assumption was made for electrons and positrons from muon decay and photons emitted through nonelastic nucleon-nucleus collisions and the decay of π° mesons. This assumption, though not entirely valid, is acceptable on the basis of the small contribution to the total dose by these particles.

For nucleons having energies >15 MeV and for pions above 2.2 MeV, the differential cross sections for nucleon and pion emission from nucleon-nucleus and pion-nucleus collisions were obtained from the intranuclear-cascade-evaporation model of nuclear reactions (refs. 8 and 18-20). This model gives the energy and angular distribution of the pions and nucleons emitted following a reaction, as well as an estimate of the energy of emitted deutrons, tritons, ^{3}He, alpha particles, and photons, and an approximate value of the kinetic energy of the recoiling residual nucleus from a nonelastic collision. The nucleon and pion nonelastic collision density was also obtained using this model. Except for capture of negative pions, proton-nucleus collisions below 15 MeV and pion-nucleus collisions below 2.2 MeV were ignored.

The intranuclear-cascade-evaporation model has been shown to be applicable at energies well below 50 MeV (ref. 21), and in all the calculations reported here the intranuclear-cascade-evaporation model was used to describe nucleon-nucleus collisions at energies >15 MeV, and the evaporation model was used to describe particle production from neutron-nucleus nonelastic collisions at energies below 15 MeV. Particles resulting from neutron-nucleus nonelastic collisions below 15 MeV were obtained using the evaporation code EVAP-4 (ref. 20) in conjunction with the total nonelastic cross-section data on the 05R master cross-section tape.*

In these calculations, the absorbed dose and the dose equivalent were computed as a function of depth in the simulated tissue astronaut. In computing the dose equivalent, the quality factor was taken to be a function of linear energy transfer. For protons, the LET curve (ref. 23) based on the recommendations of the National Committee on Radiation Protection and Measurement was used. For charged pions and muons, the quality factor as a function of LET was taken to be the same as that for protons, and the quality factor vs LET curve was constructed in a manner similar to the proton curves as described in ref. 23. A quality factor of 20 was assigned to the energy deposited by all heavy nuclei. For electrons, positrons, and photons a quality factor of unity was used.

DISCUSSION OF RESULTS

Calculations to estimate the absorbed dose and dose equivalent as a function of depth in the tissue have been carried out for solar flare and Van Allen protons incident on 20-g/cm^2-thick aluminum and polyethylene shields. The incident spectrum for solar-flare protons is given in figure 2 and the incident Van Allen proton spectrum for an altitude of 240 nautical miles at a 30° inclination to the equator is shown in figure 3. The depth-dose distributions presented here are normalized to an isotropic incident fluence of 10^9 p/cm^2 for the flare data and to a time-averaged fluence of 2.56×10^6 p/(cm^2 day) for the Van Allen protons.

Figure 4 gives the contributions to the absorbed dose when solar-flare protons are incident on the 20-g/cm^2-thick aluminum shield. The largest contribution to the dose arises from primary protons, that is, protons which have not suffered any nuclear interactions in the shield or tissue. For these protons, the dose is due entirely to excitation and ionization of atomic electrons in the tis-

*The master cross-section tape for use in the 05R Monte Carlo code (ref. 22) is available on request from the Radiation Shielding Information Center, Oak Ridge National Laboratory, Oak Ridge, Tenn. 37830

sue. The histogram labeled "secondary protons" gives the absorbed dose from the excitation and ionization of atomic electrons by protons produced by nonelastic nucleon- and pion-nucleus collisions in the shield and the tissue and from the elastic collisions of nucleons and pions with hydrogen nuclei in the tissue. The histogram labeled "heavy nuclei" gives the absorbed dose from particles with mass number greater than unity produced from nonelastic nucleon-nucleus and pion-nucleus collisions, from recoiling nuclei from elastic neutron-nucleus collisions, and from nonelastic nucleon-nucleus and pion-nucleus collisions. The histogram labeled "charged pions" gives the absorbed dose from the excitation and ionization of atomic electrons by both positively and negatively charged pions produced from nucleon-nucleus and pion-nucleus collisions. The histogram labeled "photons from neutral pions" gives the absorbed dose produced by the photons arising from the decay of neutral pions. (The assumption was made that photons were absorbed at the point of origin.) The histogram labeled "electrons, positrons, and photons" gives the absorbed dose from electrons and positrons produced by muon decay, and the absorbed dose from the photons produced by nucleon-nucleus and pion-nucleus nonelastic collisions. The histogram labeled "muons" gives the absorbed dose from the excitation and ionization of atomic electrons by both positively and negatively charged muons.

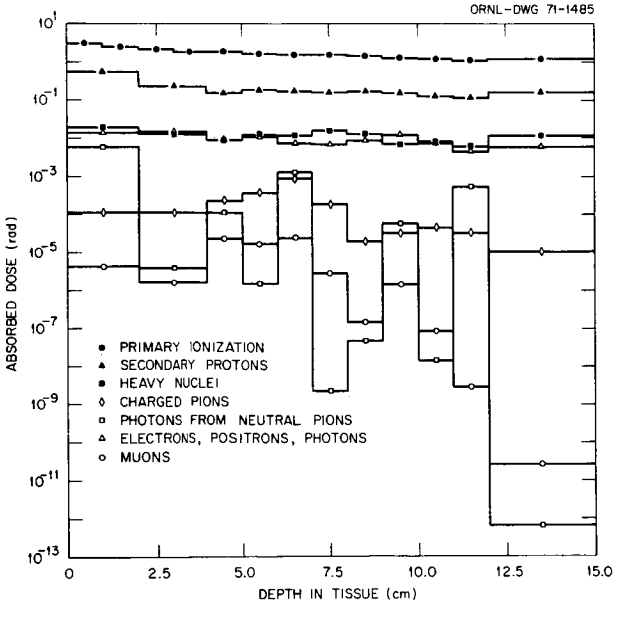

FIGURE 4. - Absorbed Dose for Various Particles Vs Depth in Tissue for P_o = 100 MV Solar-Flare Protons Isotropically Incident on a 20-g/cm^2-thick Aluminum Spherical Shell Shield.

The absorbed dose from primary-proton ionization is given as the average over each depth interval (1 cm) except for the central region of the tissue ball when the value is the average over 3 cm. For all secondary-particle contributions to the absorbed dose, the results are given as an average over the first two-centimeter and second two-centimeter depth intervals in the tissue. The remaining intervals are presented in the same manner as for the primary dose contribution.

Figure 5 shows the dose-equivalent distributions from the various particles for the solar-flare protons in the 20-g/cm^2-thick aluminum spherical shell shield. It should be noted that the dose equivalents for secondary protons and heavy nuclei are comparable (within a factor of $\sim$2). The increased contribution to the dose-equivalent results from the large quality factor (20) associated with these particles.

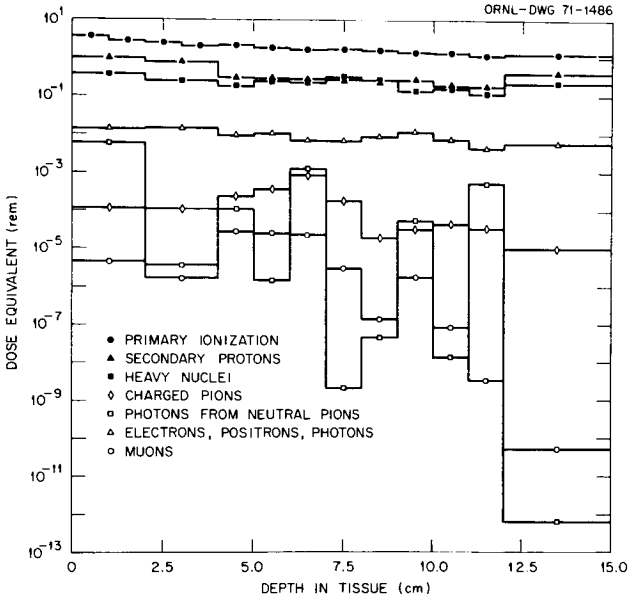

FIGURE 5. - Dose Equivalent for Various Particles Vs Depth in Tissue for P_o = 100 MV Solar-Flare Protons Isotropically Incident on a 20-g/cm^2-thick Aluminum Spherical Shell Shield.

Figures 6 and 7 show the absorbed dose and dose-equivalent distributions, respectively, from the various kinds of particles produced when the P_o = 100 MV solar flare is incident on a 20-g/cm^2-thick polyethylene spherical shell shield. Figures 8 and 9 are the absorbed dose and dose-equivalent distributions, respectively, due to primary-proton ionization and the total secondary-particle contribution to the dose for the aluminum and polyethylene spherical shell shields for the incident flare protons. These data indicate the reduction in the absorbed dose and dose equivalent realized using a polyethylene shield. This reduction is due primarily to the increased differential stopping power vs proton energy associated with polyethylene. The reduction in dose is gained at the expense of increased linear dimensions because of the additional thickness of the polyethylene shield (∿3).

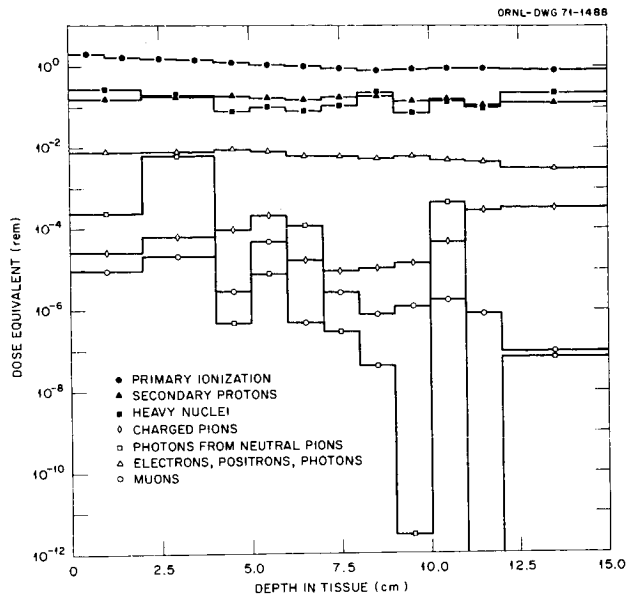

FIGURE 7. - Dose Equivalent for Various Particles Vs Depth in Tissue for P_o = 100 MV Solar-Flare Protons Isotropically Incident on a 20-g/cm^2-thick Polyethylene Spherical Shell Shield.

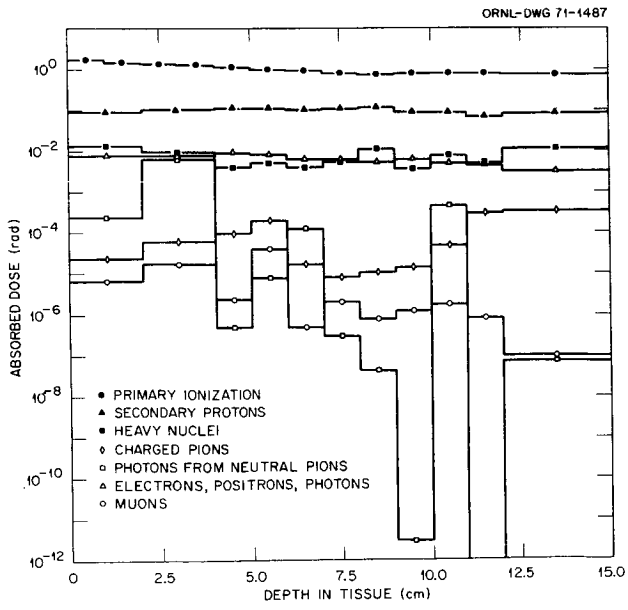

FIGURE 6. - Absorbed Dose for Various Particles Vs Depth in Tissue for P_o = 100 MV Solar-Flare Protons Isotropically Incident on a 20-g/cm^2-thick Polyethylene Spherical Shell Shield.

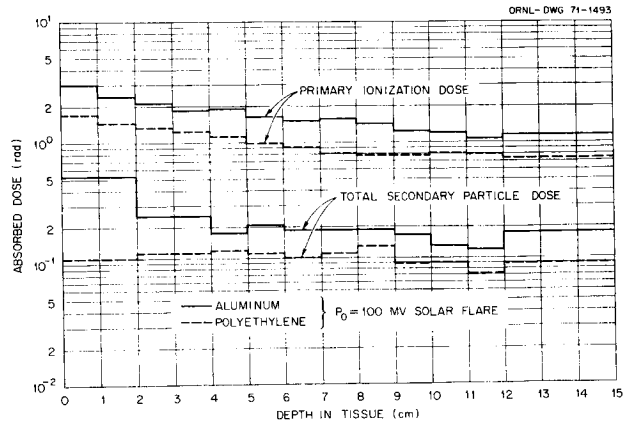

FIGURE 8. - Comparison of the Absorbed Dose Vs Depth in Tissue From the Primary-Proton Ionization and the Secondary Particles for Solar-Flare Protons (P_o = 100 MV) Isotropically Incident on 20-g/cm^2-thick Aluminum and Polyethylene Spherical Shell Shields.

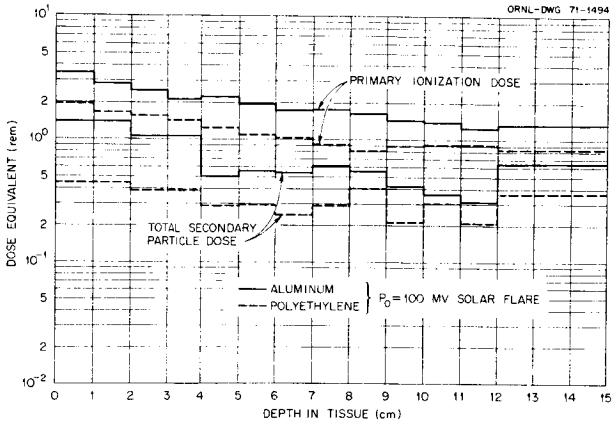

FIGURE 9. - Comparison of the Dose Equivalent Vs Depth in Tissue from the Primary-Proton Ionization and the Secondary Particles for Solar-Flare Protons (P_0 = 100 MV) Isotropically Incident on 20-g/cm^2-thick Aluminum and Polyethylene Spherical Shell Shields.

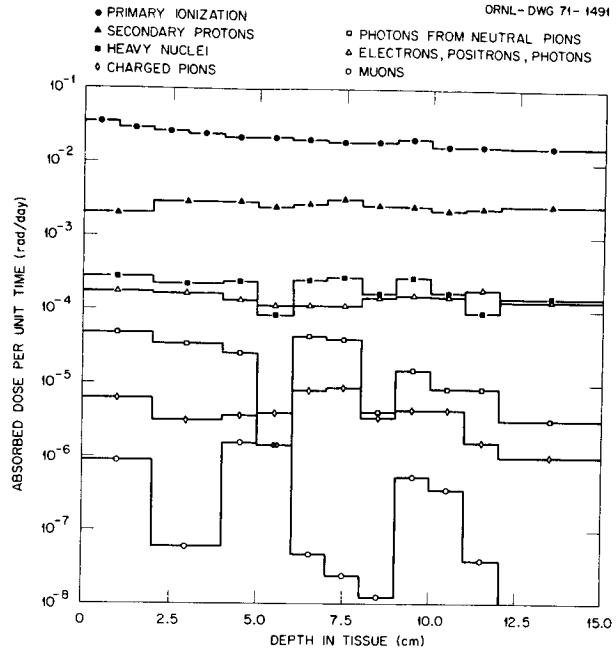

FIGURE 10. - Absorbed Dose for Various Particles Vs Depth in Tissue for Van Allen Protons (240-Nautical-Mile Circular Orbit at 30° Inclination) Isotropically Incident on a 20-g/cm^2-thick Aluminum Spherical Shell Shield.

Figures 10 and 11 show the absorbed dose and dose-equivalent distributions, respectively, vs depth in the tissue when Van Allen protons are incident on the 20-g/cm^2-thick aluminum spherical shell shield. As for the incident solar-flare protons, the principal contribution to the dose distributions is from primary-proton ionization. The dose component from secondary protons created in the shield, as well as the tissue, is down approximately one order of magnitude. In figure 11, the dose equivalent from secondary protons and heavy nuclei are comparable. The large value of the dose equivalent from the heavy nuclei component is caused by the large (20) quality factor associated with these particles.

Figures 12 and 13 give the absorbed dose and dose-equivalent distributions, respectively, vs depth in the tissue when the Van Allen protons are incident on the 20-g/cm^2-thick polyethylene shield. As in all the previous results, the largest contribution to the dose is due to the primary proton ionization.

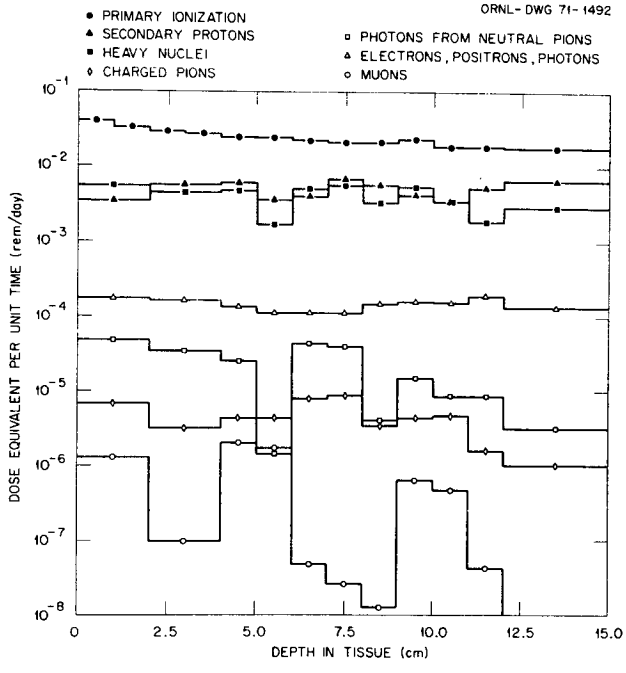

FIGURE 11. - Dose Equivalent for Various Particles Vs Depth in Tissue for Van Allen Protons (240-Nautical-Mile Circular Orbit at 30° Inclination) Isotropically Incident on a 20-g/cm^2-thick Aluminum Spherical Shell Shield.

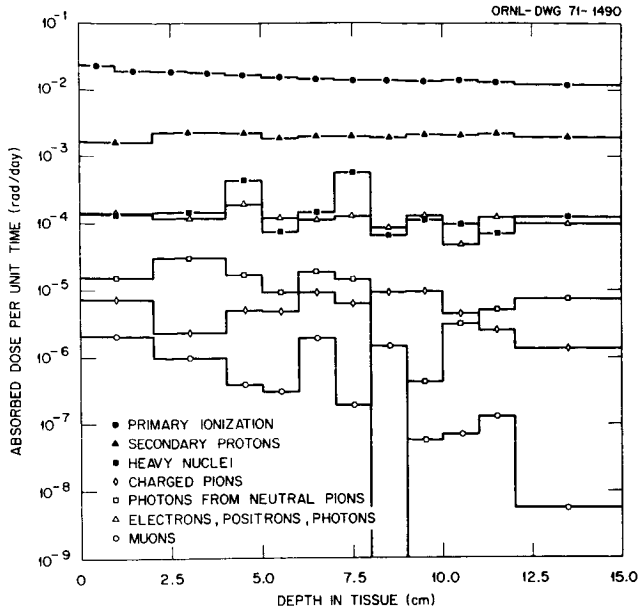

FIGURE 12. - Absorbed Dose for Various Particles Vs Depth in Tissue for Van Allen Protons (240-Nautical-Mile Circular Orbit at 30° Inclination) Isotropically Incident on a 20-g/cm^2-thick Polyethylene Spherical Shell Shield.

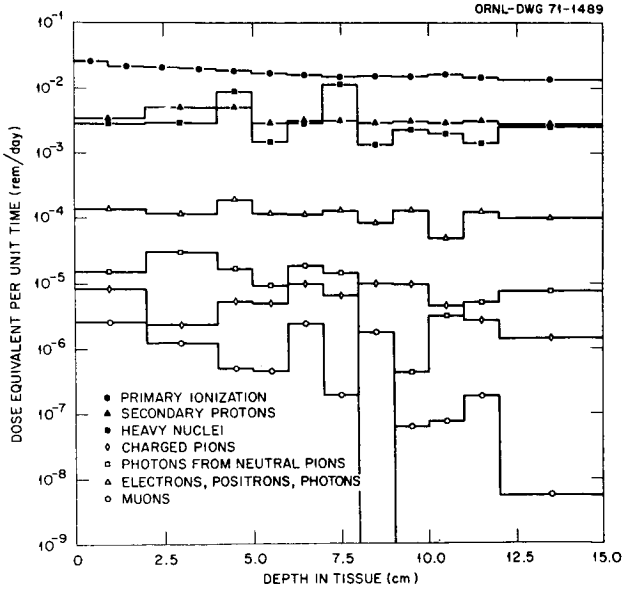

FIGURE 13. - Dose Equivalent for Various Particles Vs Depth in Tissue for Van Allen Protons (240-Nautical-Mile Circular Orbit at 30° Inclination) Isotropically Incident on a 20-g/cm^2-thick Polyethylene Spherical Shell Shield.

Figures 14 and 15, which are based on the results of figures 12 and 13, compare the primary ionization dose and the total secondary-particle dose contributions to the absorbed dose and dose equivalent, respectively. The reduced dose achieved with the polyethylene shield is from the larger differential stopping power of polyethylene compared to aluminum.

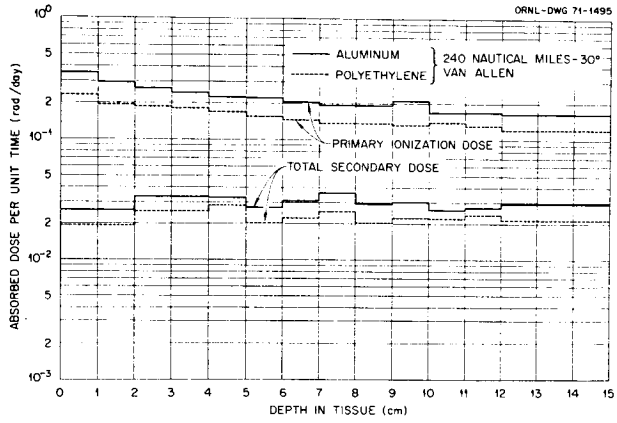

FIGURE 14. - Comparison of the Absorbed Dose Vs Depth in Tissue from the Primary-Proton Ionization and Secondary Particles for Van Allen Protons Isotropically Incident on 20-g/cm^2-thick Aluminum and Polyethylene Spherical Shell Shields.

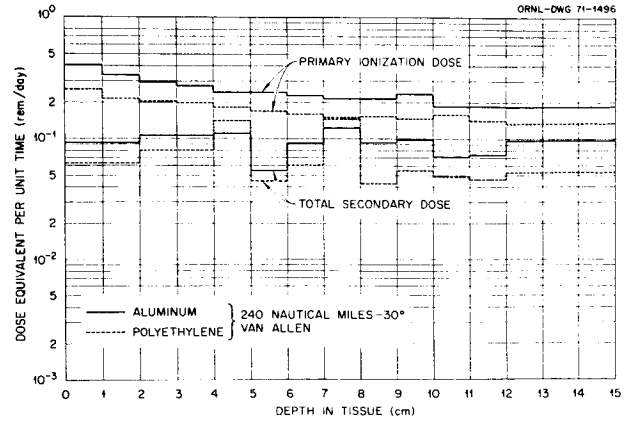

FIGURE 15. - Comparison of the Dose Equivalent Vs Depth in Tissue from the Primary-Proton Ionization and Secondary Particles for Van Allen Protons Isotropically Incident on 20-g/cm^2-thick Aluminum and Polyethylene Spherical Shell Shields.

The absorbed dose and dose-equivalent results reported here indicate clearly that for thin shields ($\lesssim$20 g/cm^2) the principal contribution to the dose from solar-flare protons in the energy range from 30 to 3000 MeV and Van Allen protons in the energy range from 30 to 1000 MeV is due to primary-proton ionization. Up to $\sim$10% of the total absorbed dose is due to secondary protons. The contributions to the absorbed dose from electrons, positrons, and photons compare with that due to heavy nuclei and are approximately two orders of magnitude lower than the primary-proton dose. The contribution to the dose equivalent from heavy nuclei is comparable to that of secondary protons. However, the contributions to the absorbed dose and dose equivalent from charged pions, photons from the decay of neutral pions, and muons are small compared to the primary-particle dose. The fluctuations in the distributions arise from generally poor statistics.

ACKNOWLEDGMENT

The authors wish to thank Dr. T. W. Armstrong for his comments and suggestions on the details of the transport calculation and analysis of these data.

REFERENCES

1. COLEMAN, W.A.; and ARMSTRONG, T.W.: The Nucleon-Meson Transport Code NMTC. Oak Ridge National Laboratory Document ORNL-4606, 1970.
2. KINNEY, W.E.: The Nucleon Transport Code, NTC. Oak Ridge National Laboratory Document ORNL-3610, 1964.
3. WRIGHT, H.A., et al.: Health Phys. Vol. 16, 1969, p. 13.
4. SNYDER, W.S., et al.: Nucl. App. Vol. 6, 1969, p. 336.
5. NEUFELD, JACOB, et al.: Health Phys. Vol. 17, 1969, p. 449.
6. ALSMILLER, R.G., JR.: Nucl. Sci. Eng. Vol. 27, 1967, p. 158.
7. SCOTT, W. WAYNE; and ALSMILLER, R.G., JR.: Comparisons of Results Obtained with Several Proton Penetration Codes. Oak Ridge National Laboratory Document ORNL-RSIC-17, 1967.
8. BERTINI, H.W.: Phys. Rev. Vol. 188, p. 1711.
9. COLEMAN, W.A.; and ALSMILLER, R.G., JR.: Nucl. Sci. Eng. Vol. 34, 1968, p. 104.
10. ARMSTRONG, T.W.; and ALSMILLER, R.G., JR.: Nucl. Sci. Eng. Vol. 33, 1968, p. 291.
11. ARMSTRONG, T.W.: J. Geophys. Res. Vol. 74, 1969, p. 1361.
12. ALSMILLER, R.G., JR.; ARMSTRONG, T.W.; and COLEMAN, W.A.: Nucl. Sci. Eng. Vol. 42, 1970, p. 367.
13. Data User's Note: TRECO, An Orbital Integration Computer Program for Trapped Radiation. National Space Science Data Center, Goddard Space Flight Center, NASA, Document NSSDC-68-02, 1968.
14. VETTE, J.I.: Models of the Trapped Radiation Environment, Volume I: Inner Zone Protons and Electrons, NASA Document SP-3024, 1966.
15. KING, J.H.: Models of the Trapped Radiation Environment, Volume IV: Low Energy Protons, NASA Document SP-3024, 1967.
16. LAVINE, J.P.; and VETTE, J.I.: Models of the Trapped Radiation Environment, Volume V: Inner Belt Protons. NASA Document SP-3024, 1969.
17. BETHE, H.; and ASHKIN, J.: Passage of Radiation Through Matter, p. 166 in Experimental Nuclear Physics, E. Segre, ed., Part II. John Wiley & Sons, New York, 1963.
18. BERTINI, H.W.: Nucl. Phys. Vol. 87, 1966, p. 138.
19. BERTINI, H.W.: Phys. Rev. Vol. 131, 1963, p. 1801; with erratum Phys. Rev. Vol. 138, 1965, AB2.
20. GUTHRIE, M.P.: EVAP-4: Another Modification of a Code to Calculate Particle Evaporation from Excited Compound Nuclei. Oak Ridge National Laboratory Document ORNL-TM-3119, 1970.
21. ALSMILLER, R.G., JR.; and HERMANN, O.W.: Nucl. Sci. Eng. Vol. 40, 1970, p. 254,
22. IRVING, D.C., et al: 05R, A General Purpose Monte Carlo Neutron Transport Code. Oak Ridge National Laboratory Document ORNL-3622, 1965.
23. TURNER, J.E., et al.: Health Phys. Vol. 10, 1964, p. 783.

SESSION II.4.
SPACE RADIATION DOSIMETRY
CHAIRMAN: T. PARNELL
MARSHALL SPACE FLIGHT CENTER

Heavy Ion Passive Dosimetry With Silver Halide Single Crystals

Charles B. Childs*
Materials Research Center
University of North Carolina
Chapel Hill, North Carolina

and

Thomas A. Parnell
NASA, George C. Marshall Space Flight Center
Huntsville, Alabama

SUMMARY

A method of detecting radiation damage tracks due to heavy particles in large single crystals of the silver halides is described. The tracks, when made visible with simple electrical apparatus, appear similar to tracks in emulsions. The properties of the crystals, the technique of printing out the tracks, and evidence concerning the threshold energy for registering particles indicates that this method may find application in heavy ion dosimetry. The method has been found to be sensitive to stopping He nuclei and relativistic M group cosmic rays. Some impurities strongly influence the "decoration" or printout of the tracks, and the effects of these impurities are discussed.

INTRODUCTION

The hazard from the heavy particle component of space radiation has been considered for some time, and interest in this component has recently increased, particularly due to reports of "light flashes" in the closed eyes of the Apollo astronauts. The particles of charge greater than one in the galactic cosmic radiation and from solar flares require special emphasis in measurement due to a number of factors: The mode of biological damage due to the densely ionizing heavy particles is different from that due to the much more abundant $Z = 1$ particles, and the radiation hazard from the heavy particles has been predicted to be very significant (ref. 1); the heavy particles must be measured in the presence of a flux of electrons and protons which is often many orders of magnitude more abundant, causing saturation in detectors sensitive to $Z = 1$ particles; due to the high energy of the cosmic ray flux, typical spacecraft shielding is not very effective, and predictions from transport calculations on the heavy particles is not very accurate due to uncertainties in fragmentation parameters. Also in a spacecraft, each crew member encounters a different shielding situation which varies with time, requiring individual heavy ion dosimeters on extended space missions.

We will discuss a technique for detecting radiation damage tracks in large single crystals of the silver halide. This method has features which make it a potentially attractive candidate for measurements on the heavy ions.

The radiation damage tracks produced by energetic heavy particles in silver halide single crystals can be made microscopically visible, and the tracks appear superficially similar to those produced by heavy primary cosmic rays in the nuclear track emulsions. The process by which these tracks are registered and made visible has been investigated for some time (refs. 2 and 3), but the method has not been generally used for heavy charged particle identification due to past inconsistencies in the printout of the tracks in different samples of crystals. Recently the study of the effects of impurities and other factors affecting track registration has advanced to the point that reproducible results now appear feasible.

In lead-doped silver chloride, the track registration is completely insensitive to electrons and recent evidence indicates that stopping protons are not registered. Stopping He nuclei and relativistic nuclei of the CNO group have been observed in the crystals. The radiation damage tracks may be erased by annealing, and the tracks may be "decorated" or printed out in a short time with simple electronic apparatus raising the possibility of a detector that will allow the heavy particle flux to be observed for a definite time period.

The ability to decorate the heavy particle tracks in silver halides depends upon the nature of the radiation damage tracks, the properties of electrons in silver halides, and impurities in the crystals. We will briefly discuss these topics, a procedure for preparation of silver chloride crystals for track detection, and summarize the experience with radiation damage tracks in lead-doped silver chloride single crystals.

PROPERTIES AND PREPARATION OF SILVER CHLORIDE CRYSTALS

Silver chloride is an ionic conductor, transparent in the visible region, and has a density of 5.56 gm/cm^3. Its index of refraction of 2.07 (5890A) increases microscope working distances by 35% compared to emulsions. It melts at 455°C. and has a hardness of 1.3 while lead has a hardness of 1.5.

Our crystals are grown by the Bridgman method in quartz crucibles 2 cm x 2 cm x 25 cm. The starting material contains only one detectable impurity, iron in concentrations less than .07 ppm. The dopant is lead which is added to the molten AgCl in the crucibles. The melt is then treated by bubbling through it a N_2-Cl_2 mixture, the crucible sealed in its Pyrex envelope, and placed in the Bridgman furnace for growth at 1 or 2 mm/hr. Samples 8 mm thick are cut perpendicular to the crystal growth axis. These samples are polished on silicon carbide polishing papers until about a 2 mm depth is removed from each of the two largest surfaces. They are then etched with a 3% KCN solution to give transparent

*Research sponsored by Advance Research Projects Agency of the Dept. of Defense (Contract SD-100), NASA Grant NGL34-003-040, and Contract NAS8-26601.

surfaces. The samples are placed on quartz plates and annealed in air at 425°C. for 12 hours, followed by cooling to room temperature at 4% per hour.

PRODUCTION OF POSITIVELY CHARGED IMPERFECTIONS BY RADIATION

The localized energy deposited by a heavy charged particle passing through the crystal may produce what Seitz and Koehler have termed "thermal spikes" (ref. 4). These spikes are regions in which some of the localized energy loss is converted into heat and the material is heated to several hundred degrees and then rapidly thermal quenched. This heating process takes place in less than 10^{-10} seconds and produces "large" concentrations of point defects which may form stable clusters during the subsequent rapid cooling. In addition, these defects can produce a disordering which causes a local volume change. This volume change plus the intense temperature gradients produce a stress field which results in plastic flow near the spike and thus forms permanent imperfections (dislocations) at distances much greater than the radius of the molten core of the spike.

Another type of spike concept has been formulated by Brinkman (ref. 5). He proposed that since the time of the molten spike is greater than the mechanical relaxation time, there is sufficient strain energy, released after density fluctuations have relaxed, to raise the temperature even higher and thus extend the period of existance of the liquid state. This temperature extension produces turbulent motion so that most of the atoms will occupy new lattice sites. Such a region which has undergone melting and resolidification is a "displacement spike."

Regardless of which model might best describe the processes involved in radiation effects in silver chloride crystals, the particle's path will be surrounded by a core of positively charged clusters of point imperfections and arrays of line dislocations which are stable at room temperature.

DECORATION OF TRACKS

Figure 1 shows the apparatus used in the laboratory for decorating tracks. The crystal is placed between blocking electrodes (E) on quartz plates (Q) and forms the major dielectric of a capacitor. The top electrode is a quartz plate covered with an ultraviolet transmitting electrically conducting thin film. That film is connected to the positive terminal of a high voltage supply (2,000 volts) which charges the pulse-forming network (P.F.N.). Above the ultraviolet transmitting electrode is a mercury flash lamp. This flash lamp is connected in series with the network and the plate of a hydrogen thyratron. The sequence of events is:

1. The high voltage supply charges the pulse-forming network and produces an external electric field on the crystal. The crystal polarizes, resulting in the surface toward the transparent electrode having negative surfaces charges.
2. When the charging cycle of about 1,000 microseconds is completed, a trigger pulse is applied to the thyratron grid discharging the network through the lamp and removing the external field on the crystal.
3. The lamp gives a 10 microsecond light pulse which forms photoelectrons at the crystal surface. These photoelectrons are then forced towards the opposite surfaces by the decaying internal polarization field.
4. Some of the electrons are trapped at the positively charged imperfections produced by the ionizing particle. These trapped electrons may then capture an interstitial silver ion, resulting in formation of silver atoms.
5. The newly formed silver atoms can capture other electrons so the process of silver atom formation continues until the particle's path is delineated by microscopic silver grains. This process continues until the silver grain size is limited by the mechanical stress in the crystal.

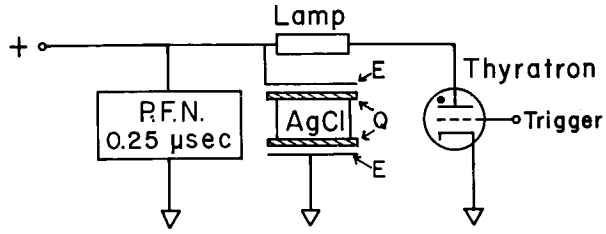

Fig. 1. Apparatus For Decorating Tracks in Silver Chloride Crystals

Since the silver grains reach a saturation size, it is possible to decorate tracks which occur after the initial decoration without affecting the original tracks.

In a crystal 5 mm thick, tracks of heavy primary cosmic rays can be made visible in 2 hours at a pulse frequency of 10^3/sec with the laboratory apparatus described above. In principle, the pulse repetition rate could be increased to around 10^5/second (limited by the electron lifetime) and the crystals decorated to saturation in a few minutes.

OBSERVATION OF TRACKS

The experience with radiation damage tracks in silver halide crystals has been too limited to allow an accurate determination of the minimum LET observable. In addition, it is yet uncertain to what extent impurities may influence the threshold for observable track decoration. We will summarize here some of the data available for silver chloride crystals.

Tracks have been observed at the surface of AgCl crystals resulting from alpha particle exposures (ref. 6). The tracks have consistent ranges of 16μ corresponding to the 5.3 MeV polonium alpha.

Tracks in the interior of lead-doped silver chloride crystals have been generated by exposing them to high energy proton and pion beams and generating "stars," and by some limited exposures of the crystals to the primary cosmic rays on balloons (ref. 2).

Figure 2 is a photograph of stars produced by 1.8 GeV/c π^- mesons which indicates tracks due to evaporation alpha particles and other heavier fragments.

Figure 3 shows the distribution of the ranges of all visible tracks from 50 stars produced by a 1.8 GeV/c π^- beam. The tracks can be attributed to He nuclei and other heavier fragments (silver evaporation He^4 nuclei of 16 MeV would have a range of 92μ). Evaporation protons from silver (8 MeV)

would have a range of 290μ, and a peak is clearly not observed there, indicating that the crystals are not sensitive to protons of 8 MeV and greater.

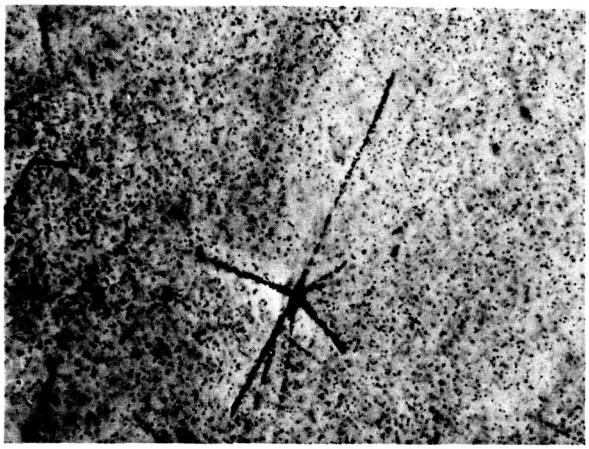

Fig. 2. A Star Produced By 1.8 GeV/c π^- Mesons.

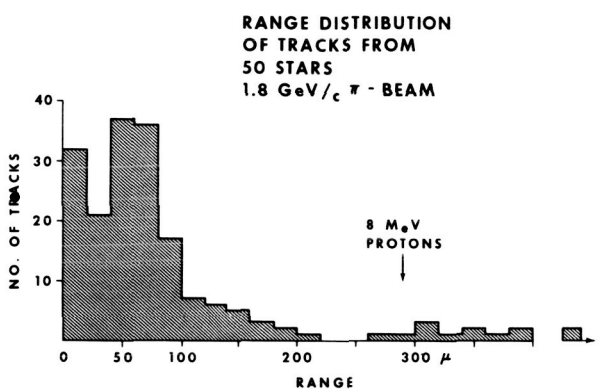

Fig. 3. Range Distribution of Tracks From 50 Stars 1.8 GeV/c π^- Mesons.

Recently we have exposed some samples of AgCl crystals dopes with 4 ppm lead to a stopping proton beam. The 70 MeV beam entered the side of a 0.5 cm x 2 cm x 2 cm crystal and stopped within the crystal. Control samples were exposed to 158 MeV protons to generate stars and check for consistency. Although tracks consistent with alpha ranges were observed, no tracks of the stopping protons were found.

Small crystals (2 cm x 2 cm) with nuclear track emulsions attached have been exposed to the heavy primary cosmic flux on balloon flights in Texas. Due to the small area-time factor, the number of observed events has been small. Figure 4 shows the tracks of two heavy primary cosmic rays in G 5 emulsions and tracks of the same particles in silver chloride crystals. The clearness of the background and the lack of delta rays in the crystals are obvious. It was also observed that the track density in the crystals varied consistently with the track width in the emulsions. In these exposures, tracks due to relativistic CNO group nuclei were observed, but no minimum ionizing He nuclei were seen.

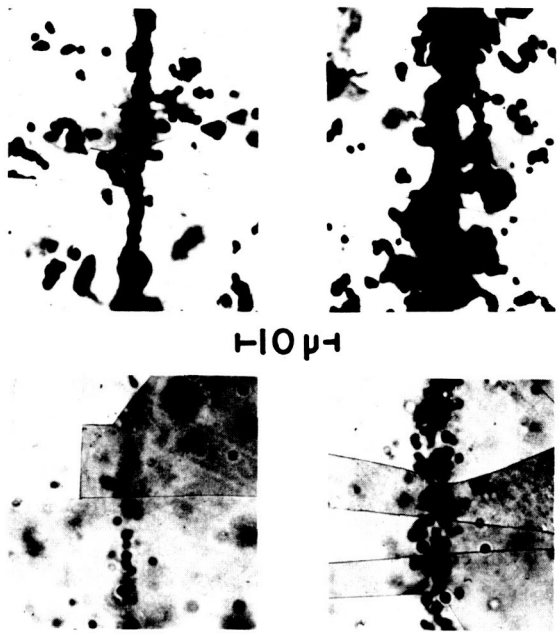

Fig. 4. Two Different Relativistic Primary Cosmic Ray Particles as Seen in G 5 Emulsions (Top) and Silver Chloride Crystals (Bottom) (ref. 8).

IMPURITY EFFECTS

It has been found that the decoration of tracks and the visible background is very sensitive to trace impurities in the crystals. For example, in crystals containing one part per million (ppm) of either iron or copper, inherent line dislocations are made visible by sweeping in electrons, but no radiation tracks are made visible. On the other hand, tracks can be made visible in crystals containing 4 ppm lead, but no dislocations are observed. One feasible explanation of this difference in impurity effect is as follows.

Before exposure to radiation, samples are cut from the crystals and annealed at 425°C. to decrease the strain introduced during growth and cutting. Since this temperature is only 30°C. below the melting point, the impurities are relatively mobile. As the samples are cooled to room temperature, the impurities settle preferentially at dislocations. So, when the samples are at room temperature, the impurities are relatively immobile and remain at the dislocations. With an impurity concentration of 1 ppm of either copper or iron, the dislocations have a positive charge so they trap electrons, leaving few if any electrons for tracks.

On the other hand, lead impurity behaves differently than iron and copper. When lead is present in about 4 ppm, it too prefers to settle at dislocations but with this difference: through complex formation, the presence of the lead leaves the dislocation regions with a negative charge. The result is that few electrons are captured by the dislocations, leaving most electrons to be captured by the positively charged imperfections produced by the ionizing particle.

While a few ppm lead are required for good track decoration, it should not exceed its room temperature soluability limit of about 8 ppm. All lead

greater than this concentration merely precipitates out of solution and increases the background as shown in Fig. 5.

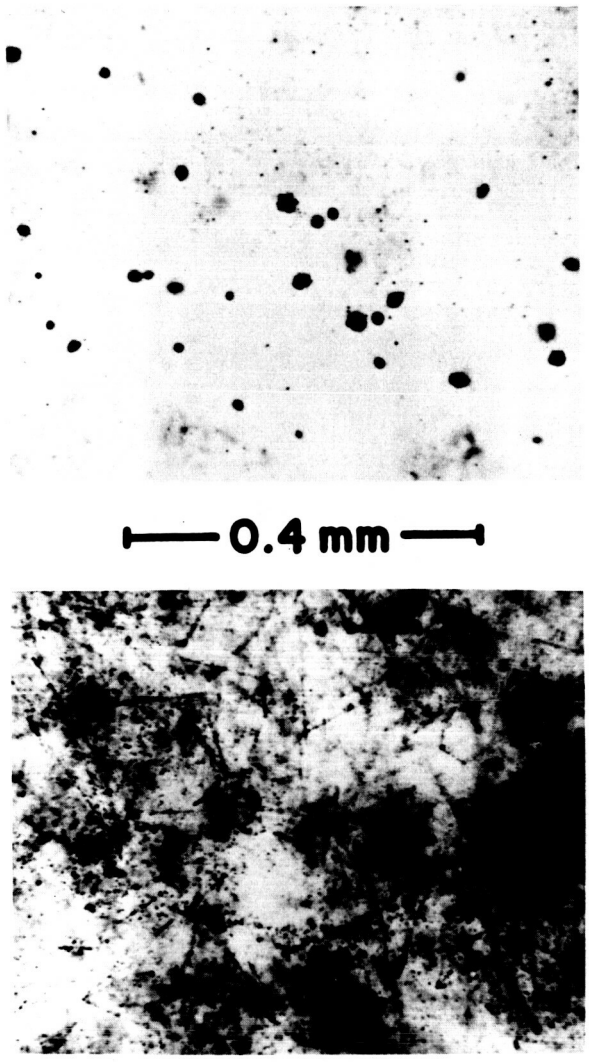

Fig. 5. Effect of Lead Concentration. Top photograph shows crystal containing 50 ppm lead after exposure to 1.5 GeV protons and decoration. Bottom photograph is crystal containing 15 ppm lead after a similar exposure and decoration.

ERASING PARTICLE TRACKS

The silver specks delineating the particle paths can be redissolved by heating the crystal to 300°C. to 400°C. Heating the crystal will cause the silver specks to dissolve and anneal out the imperfections produced by the ionizing particle. Thus with proper annealing, the crystals could be erased and reused for particle registration.

TRIGGERING CRYSTALS

Schopper (ref. 7) has proposed that it might be possible to trigger a crystal to particles having certain predetermined properties such as velocity and charge. His proposal is based on Henig's (ref. 8) studies of cadmium-doped crystals in which tracks could be made visible only immediately after exposure to particles. We are in agreement with Henig's observation since we have found that there is a cadmium ion complex relatively mobile at room temperature which would rapidly neutralize positively charged imperfections. The proposal of Schopper should be pursued with crystals containing various concentrations of cadmium and other impurities that produce a negative ion complex which is mobile at room temperature.

REFERENCES

1. TODD, P.: "Biological Effects of Heavy Ions." Second Symposium on Protection Against Radiation in Space. NASA SP-71, 1965.
2. CHILDS, C.; and SLIFKIN, L.: Bull. Am. Phys. Soc. 6, 1961, p. 52.
3. CHILDS, C.; and SLIFKIN, L.: Review of Scientific Instruments 34, 1963, p. 101.
4. SEITZ, F.; and KOEHLER, J. S.: Solid State Physics, Vol. 2, 1956, p. 307, Academic Press, New York.
5. BRINKMAN, J. A.: Journal of Applied Physics 25, 1954, p. 961.
6. SCHMITT, R.: Reunion de travail sur le enregistrement des traces de particules charges dans les cristaux, 1963, CNRS Strasbourg.
7. SCHOPPER, E.: Private Communication.
8. HENIG, G.:"Temperaturverhalten von Cadmium-dotierten Silberchlorid-Einkristallen bei Verwendung als Teilshendetektor." Institut fur Kernphysik der Johann Wolfgang Goethe-Universitat, May 1969, Frankfurt am Main.
9. CHILDS, C. B.; and SLIFKIN, L.: Brit. J. Appl. Phys. 16, 1965, p. 771.

A REAL-TIME SPECTRUM-TO-DOSE CONVERSION SYSTEM

B. J. Farmer, J. H. Johnson, and R. G. Bagwell

ADVANCED TECHNOLOGY CENTER, INC.
The Research Center for LTV Aerospace and LTV Electrosystems

A system has been developed which will permit the determination of dose in real time or near real time directly from the pulse-height output of a radiation spectrometer. The technique has been demonstrated in the laboratory using the output of a NaI(Tl) anticoincidence gamma-ray spectrometer and a beta-gamma spectrometer which was flown on Gemini XII and also in space with the electron-proton spectrometer on the Radiation and Meteoroid Satellite.

The technique involves the use of the resolution matrix of a spectrometer, the radiation energy-to-dose conversion function, and the geometrical factors, although the order of matrix operations is reversed. The usual method requires that a complete pulse-height spectrum (which is reasonably accurate statistically) be accumulated. The instrument resolution is then removed from this distribution giving the true radiation energy spectrum. This step requires the use of an inverted instrument resolution matrix or a more accurate but more time-consuming iterative process. A geometric function and the radiation energy-to-dose function must then be applied to obtain dose. This requires the use of a significant remote or on-board computer and unnecessary and time-consuming computer operations if only the dose is required.

The new technique yields a result which is mathematically identical to the standard method while requiring no matrix manipulations or resolution matrix storage in the remote computer. It utilizes only a single function for each type dose required (e.g., physical dose, biological dose) and each geometric factor involved (e.g., surface dose at a specific location inside a space vehicle). The dose functions are generated using the same resolution functions, geometric factors, and dose curves that would be used in the standard technique; however, the matrix manipulations are made only once for each function instead of each time a new pulse-height spectrum is obtained. Also, the dose may be calculated and accumulated while the data is being received, since it is not necessary to have a complete instrument spectrum before making a calculation.

For many years attempts have been made to measure physical dose (energy deposited per unit mass) in radiation fields in order to relate and predict radiation effects. For simplicity, developments have tended toward integrating devices so that a single number, dose, could be read directly from the device. Direct reading dosimeters are usually based on ionization measurements and have utilized both ionization chambers and solid state detectors. The reliability of the measurements from these devices is dependent upon the assumption that the system is wholly responsive to energy deposited, exclusive of radiation quality and/or the equivalence of the calibration and measured fields. These devices yield a single value, physical dose, which when applied to biological effect, must be converted to biological dose. Since it is generally accepted that biological dose is a function of radiation type and energy, no relationship can be established between a measured physical dose and a biological dose unless the radiation types and spectra are considered. No system is currently available which does distinguish particle type and spectra and yield a direct dose readout.

The technique to be described in this paper permits the determination of dose in real time or near real time directly from the pulse-height output of a spectrometer. The technique has been applied in the laboratory to the Beta-Bremsstrahlung Spectrometer which was flown on Gemini XII (refs. 1 and 2) and a NaI(Tl) anticoincidence gamma-ray spectrometer (ref. 3). A system based on the technique was flown on the Radiation and Meteoroid Satellite late in 1970 (ref. 4).

THEORETICAL DISCUSSION

The technique involves the use of the instrument resolution matrix, the radiation energy-to-dose conversion function, and the necessary geometrical factors, although the order of matrix operations is reversed from the standard procedure. The dose D is related to a source spectrum S by the following matrix equation:

$$D = CGS \tag{1}$$

Where C is a row matrix representing the dose per unit flux as a function of energy for a specific type of radiation and G represents the geometrical effects such as vehicle shielding. The source spectrum S is related to the pulse-height spectrum P from the radiation spectrometer by the following equation:

$$P = RS \tag{2}$$

Where R represents the response function of the spectrometer. Solving for S gives,

$$S = R^{-1}P. \tag{3}$$

Combining eqs. (1) and (3) gives,

$$D = C[G(R^{-1}P)] \tag{4}$$

It is customary to solve for D in the order of matrix operations indicated. In this order each step has physical meaning. For example, an instrument on the outside of a space vehicle would obtain a pulse-height spectrum P. The operation $R^{-1}P$ would yield S, the source spectrum outside the ship. The operation GS would yield the spectrum S' at the point where the dose is desired and the final operation CS' would yield the dose. Thus, at each step there is a physically meaningful parameter to consider. The new technique involves the calculation of a function, which when applied directly to P will yield the dose. Consider eq. (4) in which the order of matrix operations is reversed.

$$D = [(C\ G)R^{-1}]P \tag{5}$$

The product CG becomes a row matrix C' which is a dose conversion function modified to include geometric factors. The product $C'R^{-1}$ defines the pulse-height spectrum to dose conversion function F,

$$F = C'\ R^{-1} \tag{6}.$$

Then we have

$$D = FP \tag{7}$$

Thus, if dose is required immediately, the only computation required is F times the pulse-height spectrum. Perhaps the most important point, however, is that it is not necessary to have a complete pulse-height spectrum to determine the dose. One may think of F as a set of weighting values F_1, F_2 ... F_n where n is the number of pulse-height channels. Then as each pulse is analyzed the appropriate weighting value may be applied and the resulting values summed, giving

$$\sum_{i=1}^{n} F_i P_i = D \tag{8}$$

As soon as D is statistically significant, one has a reliable dose. Using the standard technique one must wait until a statistically accurate spectrum is accumulated before dose can be determined. This virtually eliminates the ability to make remote or on-board dose calculations, since a rather large computer capability is required.

BETA-BREMSSTRAHLUNG SPECTROMETER

As mentioned earlier the technique has been applied to the Beta-Bremsstrahlung Spectrometer (refs. 1 and 2) which had been flown on Gemini XII. The instrument consisted of a 3/4-inch diameter by 1/2-inch long CsI(Tl) crystal with a thin plastic scintillator behind the electron collimator. By utilizing the different decay time constants in CsI and plastic the instrument could differentiate between electrons and gammas. Examples of the response of the instrument to gamma rays and electrons are given in figures 1 and 2, respectively. These response curves indicate that the studies using this instrument represented a very severe test for the method. It is apparent, due to the complex interactions of particles in the small

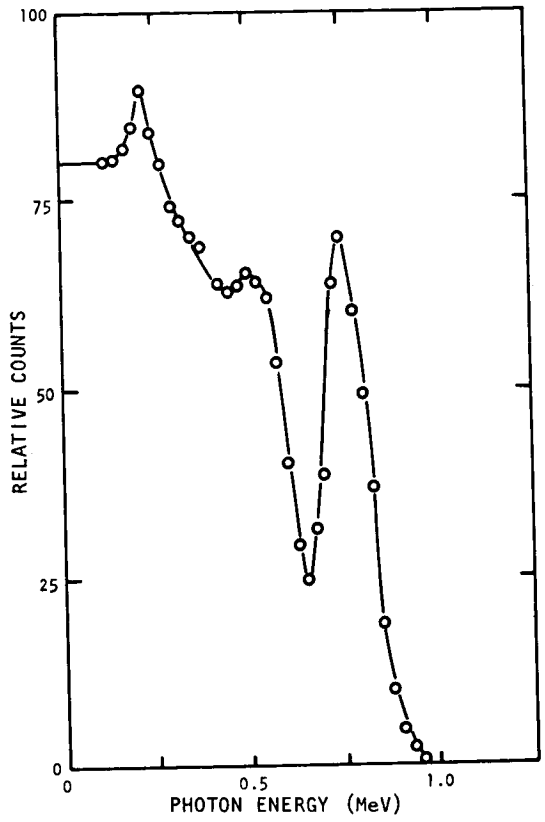

FIGURE 1. - Response of Beta-Bremsstrahlung Spectrometer to 0.83-MeV gamma rays.

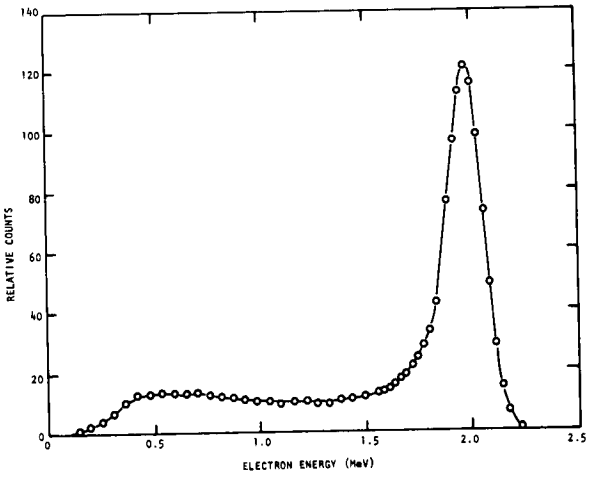

FIGURE 2. - Response of Beta-Bremsstrahlung Spectrometer to 2-MeV electrons.

crystal, that the response functions are irregular in shape and do not lend to description by analytic means. Another factor influencing the severe nature of the test was that large grid elements with energy widths of 200 keV were utilized in the computation. (This is somewhat arbitrary and can be increased to give higher resolution; however, in this test, the previously determined response matrices for electrons R_e and gammas R_γ were employed without modification). The dimensions of the response matrices were 15 x 15 with R_γ extending over the range from 0.1 to 3.1 MeV and R_e from 0.3 to 3.3 MeV. The

inversion to obtain R_e^{-1} and R_γ^{-1} was accomplished with the aid of an IBM 7090 matrix inversion routine. The energy to dose conversion values C_e and C_γ were obtained from the literature (ref. 1 and 2) and are consistent with those being used in the national laboratories. Gamma conversion to roentgen exposure dose was used to allow comparison with the R-Meter measurements. The electron conversion chosen was to rad in carbon, which is the most common absorbed dose reference. It may be noted, however, that at this point the actual dose unit is irrelevant and any one may be used to satisfy a given requirement.

The above matrices were then multiplied to give the products $R_e^{-1}C_e$ and $R_\gamma^{-1}C_\gamma$ which correspond to F_e and F_γ, respectively. Each function contained 15 terms. Inspection of these functions revealed not only an erratic nature, but some of the values were even found to be negative. This is a common characteristic of the solutions of matrix equations where the inverse is used to solve for an unknown matrix. This characteristic comes about from several causes:

(a) uncertainties in the response matrix,
(b) nature of the inverse (many large positive and negative terms),
(c) tendency of the inverse to magnify small fluctuations, and
(d) finite number of terms in the matrix (grid size).

After a detailed inspection verified the accuracies of the matrices and their inverses, and the product $R\,R^{-1}$ was shown to produce the unit matrix to within 0.1%, this technique was abandoned and an alternate approach was taken to determine F. The method is based on rewriting eq. (6) as

$$F = CR^{-1} \tag{9}$$

where the geometric factor is considered to be unity. If we multiply both sides by R, we get

$$FR = C. \tag{10}$$

This equation lends itself to a solution using a standard iterative process. We must first write R as

$$R = N\varepsilon \tag{11}$$

where ε represents the efficiency of the spectrometer and N is a normalized response matrix. Then

$$FN = C\varepsilon^{-1}. \tag{12}$$

Eq. (12) states that there exists a function (or matrix) F that when multiplied by the response matrix N, gives $C\varepsilon^{-1}$. Since $C\varepsilon^{-1}$ and N are well known, by making an intelligent estimate of F (which we will refer to as F_1) and multiplying the estimate by N, which has been suitably normalized, it is possible to compare the result with $C\varepsilon^{-1}$. The degree of agreement between F_1N and $C\varepsilon^{-1}$ is a direct measure of the degree of agreement between F_1 and F. Thus, by successively correcting F_i by the difference between F_iN and $C\varepsilon^{-1}$ and remultiplying the corrected F_i by N, an iterative method is arrived at which generates a function F_n which approaches F when $(FN - C\varepsilon^{-1}) = 0$. Since it is known that the response normalized functions N_e and N_γ are such that the pulse-height and true-energy spectra are not drastically different, the first estimate of F for each radiation was taken as the respective $C\varepsilon^{-1}$. Throughout the iterations F_iN was compared to $C\varepsilon^{-1}$ on the rms basis with the average rms difference computed after each iteration. When the average rms difference reached a minimum the computation was stopped. The function determined for the gammas had an rms difference of 1.2% while the same for the electrons was 2.6%. The resulting functions were then smoothed with a three point average routine. Plots of these functions are shown in figures 3 and 4. It is seen that these functions are smoothly varying and non-negative. This is the result of working directly with N_e and $N\gamma$ instead of their inverses.

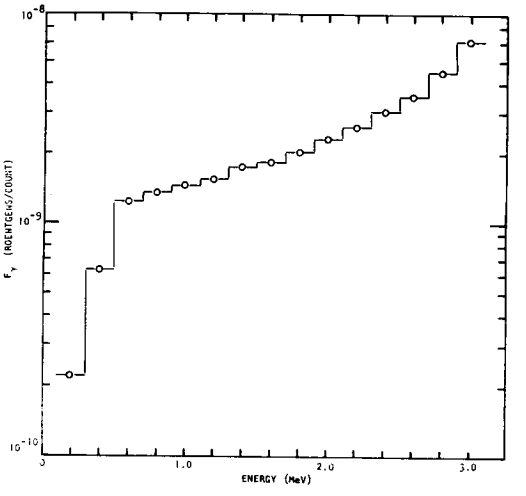

FIGURE 3. - Pulse-height spectrum-to-dose conversion fuction for gamma-rays.

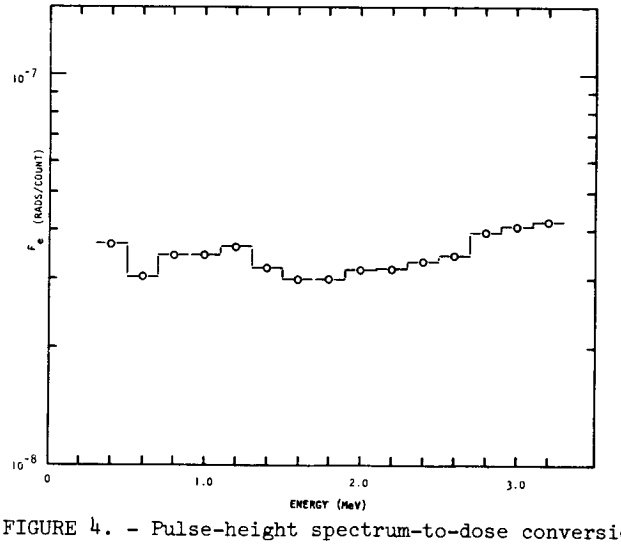

FIGURE 4. - Pulse-height spectrum-to-dose conversion function for electrons.

For electrons the experimental verification of the accuracy of the function was made using a 3-MeV Van de Graaff accelerator. The electron beam was scattered by a series of aluminum foils and allowed to pass into the air. At this point the beam was approixmately 2 inches in diameter. After passing approximately one foot through air the beam was mapped with a solid state detector and found to be uniform in intensity for a distance of 2 inches on

either side of centerline. The Beta-Bremsstrahlung Spectrometer was placed in this beam and a series of runs was taken at various energies. Using electron dose values calculated from the energy loss curves for electrons in ref. 5, the pulse-height spectrum-to-dose measurements were compared to those calculated (true dose) from the electron flux as measured with a collimated solid-state detector, the results are shown in table 1.

TABLE 1. - Pulse-height spectrum-to-dose comparisons for monoenergetic electrons.

Electron Energy (Mev)	True Dose (Rad)	Measured Spectrum-to-Dose (Rad)	Error (Percent)
0.40	7.47(-3)*	7.06(-3)	-5.5
0.50	7.06(-3)	6.93(-3)	-1.8
0.75	6.62(-3)	6.61(-3)	-0.1
1.00	6.43(-3)	6.32(-3)	-1.7
1.25	6.35(-3)	6.06(-3)	-4.6
1.50	6.32(-3)	5.85(-3)	-7.4
2.0	5.28(-3)	5.18(-3)	-1.8
2.5	3.05(-3)	2.90(-3)	-4.9

*Denotes 10^{-3}

For gammas a number of radioactive sources and a bremsstrahlung spectrum produced by a Van de Graaff Accelerator were used. Results of these measurements compared to calculated values are given in table 2.

TABLE 2. - Pulse-height spectrum-to-dose comparisons for gamma- and x-rays.

Source	Energy (Mev)	True Dose (R)	Measured Dose (R)	Error (Percent)
Cs-137	0.662	1.14(-4)*	1.04(-4)	-8.0
Mn-54	0.835	1.17(-4)	1.17(-4)	0.0
Hg-203	0.279	8.23(-5)	7.72(-5)	-6.1
Na-22	1.28	1.85(-4)		
	0.511	1.62(-4)		
		3.47(-4)	3.10(-4)	-10.7
Y-88	0.9	8.50(-5)		
	1.8	17.00(-5)		
	2.76	0.12(-5)		
		2.56(-4)	2.26(-4)	-12.0
X-Ray Spectrum	2.0	4.40(-5)	4.66(-5)	+ 6.1

*Denotes 10^{-4}

The above tests were performed to show the accuracy of the technique; however, the actual dose calculations from the F functions were made after all the data had been taken. As a next step in the studies, a real-time system was assembled (figure 5) which used the Gemini XII Beta-Bremsstrahlung Spectrometer as the sensing head. The same pulse-height spectrum-to-dose functions determined above were used for dose conversion.

In operation the linear signal from the spectrometer was pulse-height analyzed and a binary channel number produced. This binary number, along with the radiation identification binary bit, produced an address for the computer. An interrupt was produced and the computer acquired the address for processing in buffer storage. The computer then processed the radiation event in real time by adding a number representing the

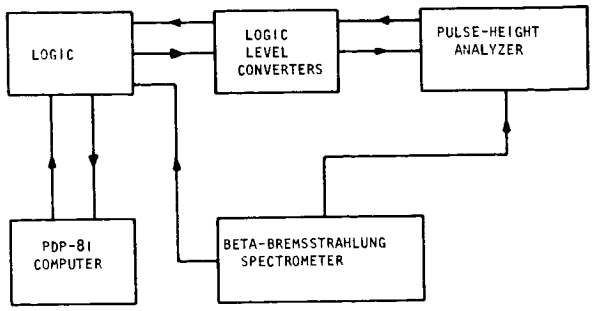

FIGURE 5. - Block diagram of real-time dose conversion system using the Beta-Bremsstrahlung Spectrometer as the sensing head.

single event dose for the particular pulse-height channel to a dose accumulator. The value in this accumulator then represented the integrated dose for the period of time the data was accumulated. In addition by properly setting the switch register of the computer, pulse-height spectra were also accumulated in the computer for comparison purposes. The pulse-height analyzer also produced a clock pulse that interrupted the computer and caused termination of the run when the end of the requested data period had been reached. The system was compensated for computer and analyzer busy time.

The gamma sources, cesium-137, cobalt-60, and sodium-22 were placed individually at various distances from the spectrometer. In addition, the spectrometer was exposed to the same cesium and cobalt sources simultaneously. Dose was integrated over a 10 second period and then displayed in rad/hr by the computer. These results were compared to the doses calculated from the known curie strength of the sources and the use of the gamma radiation levels specified in ref. 7. These levels were corrected for source strength and distance and are shown in table 3 along with the measured values. The errors shown are well within the limits anticipated considering the large grid size of the resolution matrix which was used. This system embodied the basic features of a space radiation monitoring device by providing the capability for measurements in separate or mixed radiation fields and providing both dose rate and total dose measurements.

TABLE 3. - Real-time spectrum-to-dose comparisons.

Source	Strength (Micro curies)	Calculated Dose Rate at 0.5 Meters (MR/HR)	Measured Dose Rate at 0.5 Meters (MR/HR)	Error (Percent)
Cs-136	91.2±1.0	.120	.119	-0.8
Co-60	41.2±0.8	.218	.203	-6.9
Na-22	21.3±1.0	.102	.100	-2.0
Cs-137 and Co-60	±2%	.338	.321	-5.0

LABORATORY NaI(Tl) ANTICOINCIDENCE SPECTROMETER

To further substantiate the uniqueness of the pulse-height to dose function F, a set of measurements was made using a NaI(Tl) crystal spectrometer which was surrounded by an anti-Compton coincidence annulus. The response of this system is very good as seen from the response curve for 1.28 MeV gamma rays which is shown in figure 6. The pulse-height spectrum-to-dose function F as obtained by the iterative process discussed above and the corresponding first guess, $C\varepsilon^{-1}$, are shown in figure 7.

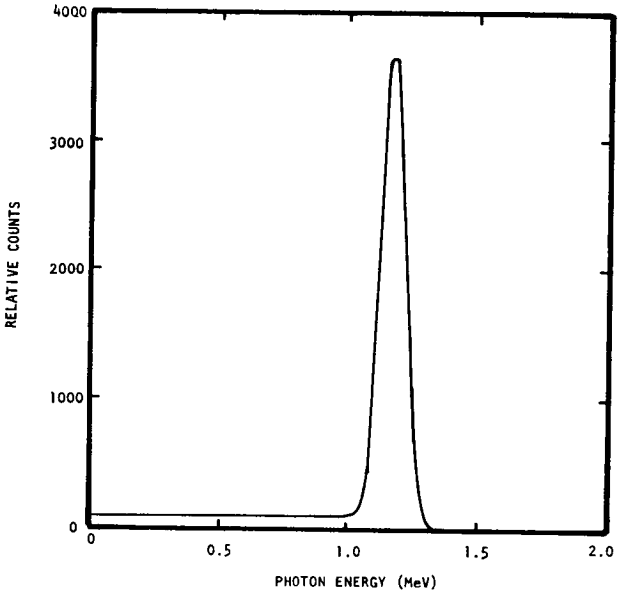

FIGURE 6. - Response of a 2" x 6" NaI(Tl) anticoincidence spectrometer to 1.28-MeV gamma rays.

As a test of F, bremsstrahlung spectra were observed from thick aluminum targets which were bombarded with monoenergetic electrons. The total dose due to each spectrum was obtained in two different ways for comparison. In one case the pulse-height spectrum P was multiplied by the pulse-height spectrum-to-dose function F, the terms then being summed to give the dose. In the other case, the pulse-height spectrum was converted to an energy spectrum as described in ref. 8. The energy spectrum was converted to a dose spectrum and the terms summed to give the total dose. Comparisons were made for photon end point energies of 1.0 and 2.5 MeV. In both cases the total dose agreed to within two percent. Figure 8 contains a plot of one of the pulse-height spectra used and the corresponding bremsstrahlung energy spectrum. This is a typical shape for the spectra used from a thick target and represents a somewhat ideal spectral shape for the type of comparison made. It is seen that there is very little distortion in the pulse-height spectrum at low energies. This is due to the rapidly increasing shape of the spectrum at low energies. This shape makes the tail contributions at low energies, due to the high energy photons, insignificant. Also, it is seen in figure 6 that F and $C\varepsilon^{-1}$ practically coincide at low energies. Thus, spectra of this shape

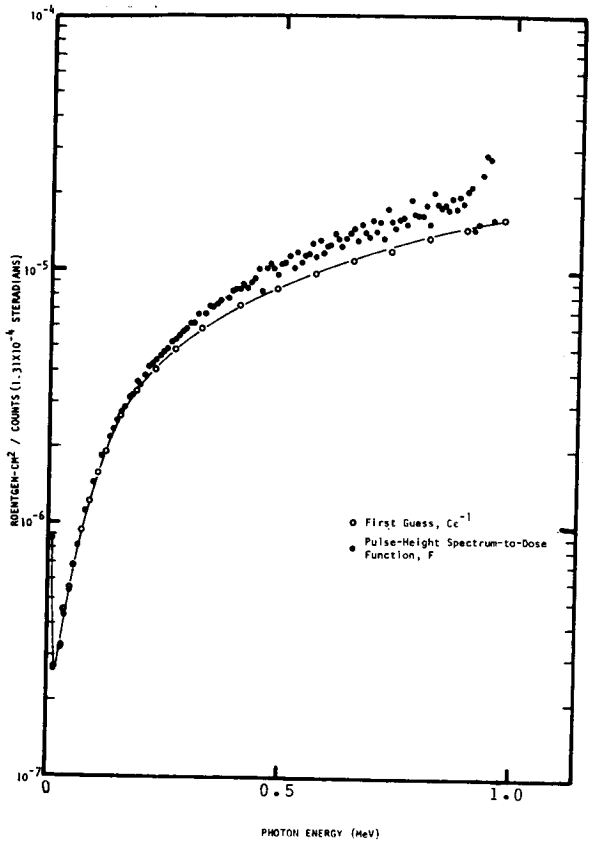

FIGURE 7. - Pulse-height to dose function and $C\varepsilon^{-1}$.

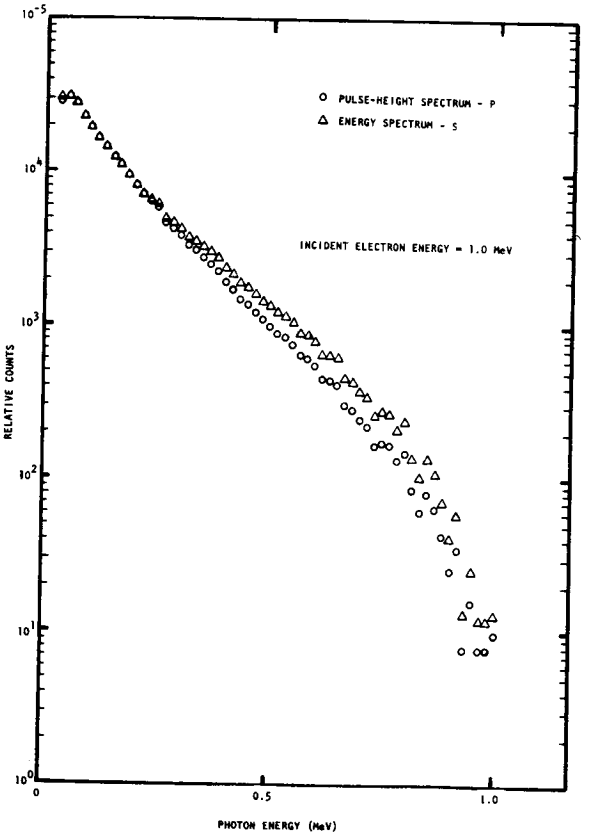

FIGURE 8. - Detector distortion produced in a typical bremsstrahlung spectrum.

test only the low-energy portion of F, since the dose contribution is weighted very heavily at low energies.

To test F over a greater range of its values and specifically in the region of higher energies, a series of hypothetical "true" spectra were smeared with N and ε to produce "theoretical" pulse-height spectra. Doses were then calculated from the curves by the two methods. This was accomplished for four cases and the total doses for each case agreed within 1%. The cases chosen are shown in figures 9, 10, 11, and 12. In each figure the "true"spectrum and the resulting"theoretical" pulse-height spectrum are shown. The cases chosen represent the most extreme cases which would be encountered. The results of these mathematical tests and those of the actual data are considered to be sufficient to establish the validity of the technique as a simple and accurate method for converting pulse-height spectra to dose.

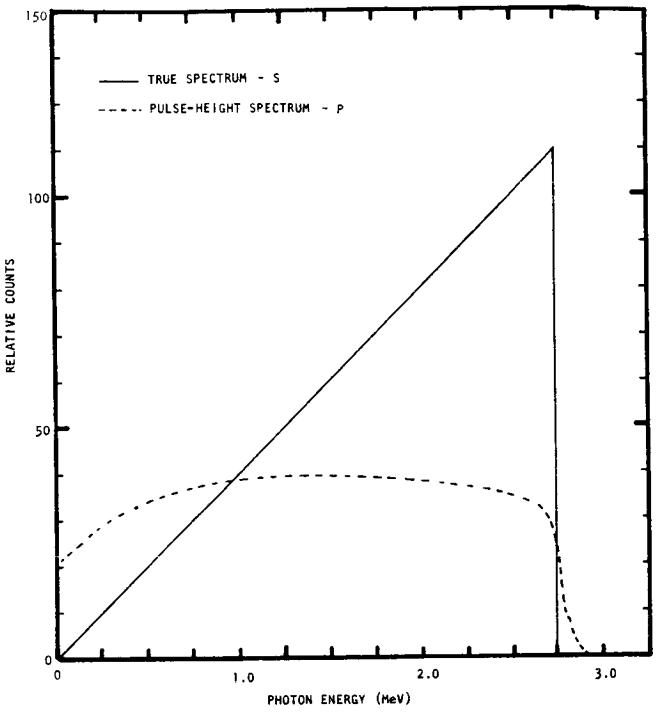

FIGURE 9. - Effect of smearing an increasing ramp with the response matrix.

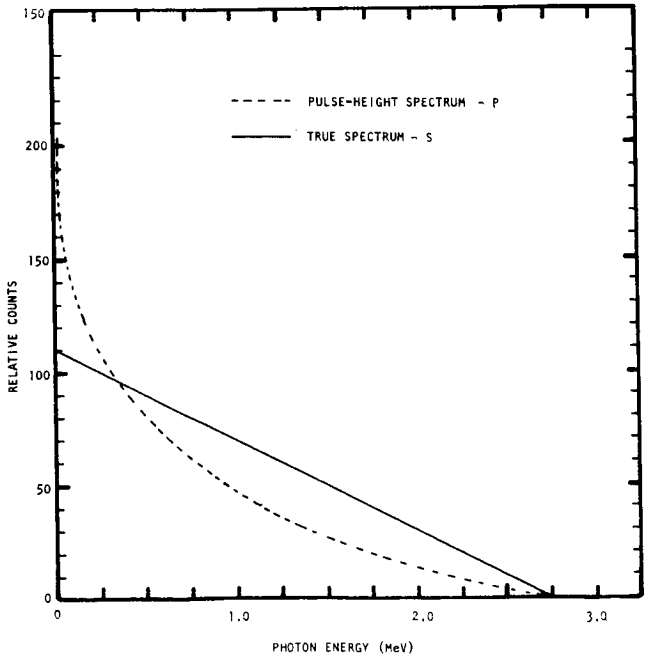

FIGURE 10. - Effect of smearing a decreasing ramp with the response matrix.

RADIATION AND METEOROID SATELLITE

The most extensive test of the pulse-height spectrum-to-dose concept was made with the proton-

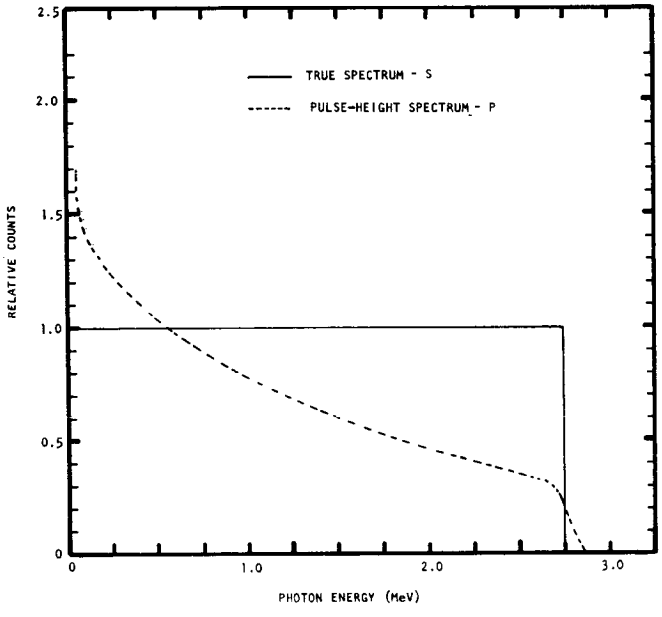

FIGURE 11. - Effect of smearing a flat distribution with the response matrix.

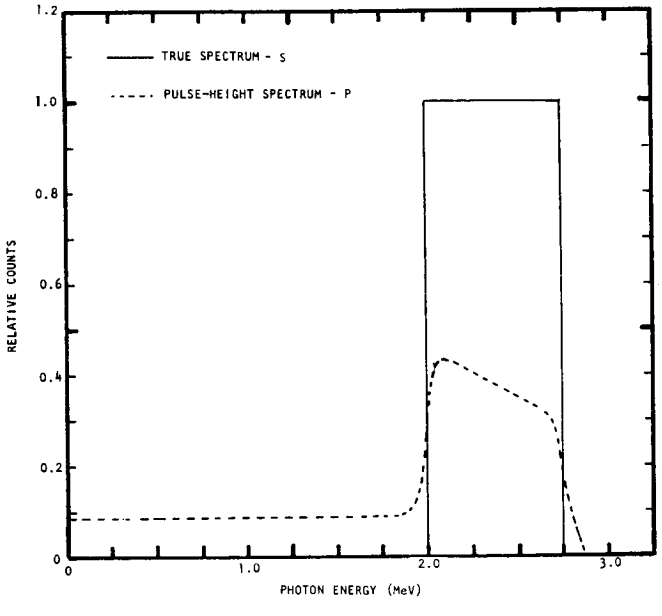

FIGURE 12. - Effect of smearing square plateau with the response matrix.

electron spectrometer on the Radiation and Meteoroid Satellite (RMS). The system is discussed in detail in the final report of the satellite program (ref. 4). A preliminary look at data obtained during the satellite mission indicates general verification of the dose-conversion system capabilities; however, the reduction of the data is in a very early state and system accuracies are yet to be determined.

CONCLUSIONS

This new technique yields a result which is mathematically identical to previous standard methods while requiring no matrix manipulations or resolution matrix storage in a remote computer. It utilizes only a single function for each type dose required (e.g., physical dose, biological dose) and each geometric factor involved (e.g., surface dose at a specific location inside a space vehicle). The dose functions are generated using the same resolution functions, geometric factors, and dose curves that would be used in the standard technique; however, the matrix manipulations are made only once for each function instead of each time a new pulse-height spectrum is obtained. Also, the dose may be calculated and accumulated while the data is being received, since it is not necessary to have a complete instrument spectrum before making a calculation. The application of this technique can be made to any monitoring system which functions as a spectrometer. Further, if any remote computations are made, the technique may be employed by the addition of software only.

REFERENCES

1. Farmer, B. J.; Chappel, N.E.; Bagwell, R. G.; and Rainwater, W. J.: "LTV Beta-Bremsstrahlung Spectrometer for Gemini XII", Contract NAS9-5765, Final Report, LTV Report No. 0-71000/7R-1, 1967.
2. Farmer, B. J.; and Rainwater, W. J.: "Study to Determine the Utility of Spectrum-to-Dose Conversion", Contract NAS9-7565, Final Report, LTV Report No. 0-71100/8R-5, 1968.
3. Rainwater, W. J.: "Derivation of a Pulse-Height Spectrum to Dose Function for a 2" x 6" NaI Crystal Spectrometer", LTV Report No. 0-71100/9R-5, 1969.
4. Farmer, B. J.; Johnson, J. H.; Bagwell, R. G.; and King, B. R.: "Radiation and Meteoroid Satellite", Contract NAS9-9195, Final Report, LTV Report No. B-95000/1CR-11, 1971.
5. Nelms, A. T.: "Energy Loss and Range of Electrons and Positrons", National Bureau of Standards Circular 583, 1957.
6. Rockwell, III, Theodore: "Reactor Shielding Design Manual", McGraw-Hill Book Co., Inc., 1956.
7. Jaeger, R. G., et al: "Engineering Compedium on Radiation Shielding", Vol. 1, New York, Springer-Verlog, 1968, pp. 21-30.
8. Rester, D. H. and Dance, W. E.: NASA CR-759, April 1967.

HIGH Z PARTICLE APOLLO ASTRONAUT DOSIMETRY WITH PLASTICS*

E.V. Benton & R. P. Henke
University of San Francisco, San Francisco
California 94117

On Apollo missions, the individual astronauts' high Z particle exposure is measured by means of Lexan polycarbonate plastic. These layers form one component of the passive dosimetry packets worn in the constant wear garment. They serve as threshold type, high Z, charged particle track detectors, recording only the very highly ionizing particles such as E < 6 MeV/amu ^{12}C, E < 45 MeV/amu ^{28}Si, E < 250 MeV/amu ^{56}Fe, etc. The detectors yield information on the particles' charge, energy, and direction of travel. This data, in turn, is used to obtain the track fluence, the stopping particle density as an integral Z distribution, and the particles' integral LET spectrum. In this paper some of the data gathered on Apollo missions 8-13 is presented.

INTRODUCTION

Recently, considerable interest has been expressed in trying to assess the radiation hazard to astronauts arising from the bombardment by energetic, multicharged particles of cosmic radiation. Although a number of investigators have been interested in this problem for some time, the observation of light flashes by astronauts on Apollo 11 and subsequent missions contributed significantly in focusing attention on this problem. Our interest in this area dates back to 1961 when we started investigating various means of measuring the multicharged particle exposure that astronauts experience in space travel. This has been accomplished on the first lunar orbiting mission, Apollo 8, and all subsequent Apollo missions by means of plastic nuclear track detectors located in the passive dosimetry packets worn by the astronauts.

* Work sponsored by NASA, Manned Space Craft Center, Houston.

MATERIALS AND METHODS

The passive dosimetry packets measuring 5.3 x 4.3 x 0.64 cm consist of a 2-mil - thick FEP Teflon bag which contains 500 mg of LiF (TLD) powder, 600μ thick nuclear emulsions, standard beta, gamma, and neutron - sensitive films, and three 190μ thick layers of type 8070-112 Lexan polycarbonate plastic (Table I). The Lexan layers (about 8 cm^2 in area) are heat sealed at the edges to insure that they remain stationary with respect to each other. The packets are worn by each astronaut in the pockets of the constant wear garment.

The Lexan plastic detectors have several features which make them well suited for heavy particle dosimetry. They are tissue equivalent. Their sensitivity range is such that they are insensitive to singly and doubly charged particles. Consequently, very long exposures of months, or even years are possible to cosmic rays without developing detector saturation.(1)

TABLE I

Sequence of layers in the passive dosimetry packet

Teflon protective pouch
Thermoluminescence pack
Black foil wrap of emulsion stack
Black paper wrap of emulsion stack
Double component film badge emulsions
G.5 emulsion
Lexan 3
Lexan 2
Lexan 1
G.5 emulsion
K.2 emulsion
NTA film
Black paper wrap of emulsion stack
Black foil wrap of emulsion stack
Label with number
Teflon protective pouch
Astronaut's garments
Astronaut's body

Perhaps the single most important and unique feature of the detectors is the character of the response as a function of the particles' LET.[2] Both in the unsensitized, and the sensitized form the response varies very rapidly with LET (see Figure 1). This property makes possible the identification of particle charge, Z, even from the relatively short trajectory segments available. The sensitivity of the unsensitized detectors has an effective threshold such that particles with LET below that of about 9 MeV/nucleon, ^{20}Ne ions are not recorded. We use the photo-oxidation technique[3] to sensitize Lexan such that particles with LET above that of about 12 MeV/nucleon, ^{16}O ions are recorded.

Examples of a calibration curve and tracks are shown in Figures 1 and 2. In Figure 1 is shown the corrected track etch rate, V_T, of 10 MeV/nucleon ^{16}O, ^{20}Ne, ^{28}Si and ^{40}Ar particles. "Corrected" signifies that the effects of UV attenuation in the detector have been removed. The open and closed points indicate the stability of the calibration from one 40 hr UV irradiation to the next. Etched tracks of 10 MeV/nucleon ^{16}O, ^{20}Ne, ^{28}Si, ^{40}Ar ions are shown in Figure 2. In all four cases the same standard UV irradiation treatment was given with etching performed in 6.25 N NaOH solution containing 0.5% Benax for 2.0 hours at 70.4°C. Four ^{16}O tracks can be seen, two of them at the approximate center of the photomicrograph.

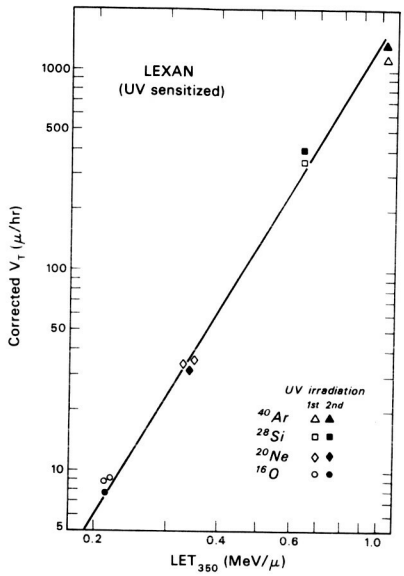

Figure 1. The corrected track etch rate, V_T (microns/hour), as a function of LET (MeV/micron) for four 10 MeV/nucleon particles in Lexan.

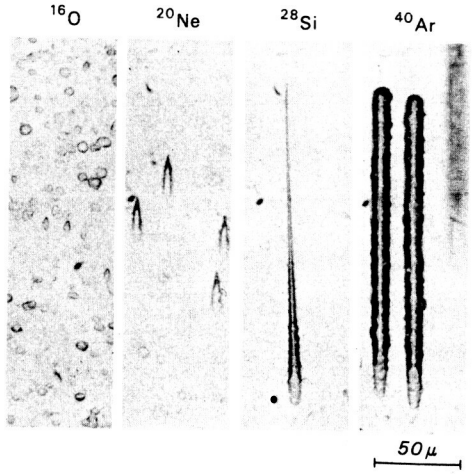

Figure 2. Tracks of four 10 MeV/nucleon incident energy particles in Lexan with etching performed in 6.25 N NaOH solution, containing 0.5 per cent Benax for 2.0 hrs at 70.4°C.

The flight detectors are UV sensitized prior to etching in the same manner as above. The processing is identical to that described above, except that the etch time is 8.0 hours. When processing flight units, calibration tracks, obtained from the Hilac, are always included in the entire processing cycle.

We have investigated a number of techniques for increasing the detector sensitivity. The nature of detector response is such that a small increase in sensitivity increases considerably the number of tracks that are recorded, and hence improves the counting statistics. The use of the UV enhancement technique increases the recorded track fluence by about a factor of 3. Also, it was found that increasing the etch time, from 2 to 8 hours for the sensitized Lexan, produces a further threefold increase in the measured track fluence. However, the extended etch time, together with the UV treatment utilized, result in a considerable deterioration of the detector surface such that many background etch-pits become visible. These in turn, significantly increase the labor required in scanning. Thus the present detector sensitivity is such that the LET required for track registration is just below that of a 12 MeV/nucleon, ^{16}O ion. A further increase in sensitivity of Lexan does not seem likely.

Tracks are located by scanning with an optical microscope usually at 200 X magnification. All detectors are scanned independently by at least two different observers. Measurements are performed at 600 X in each of the surfaces where a visible etch cone is found. Charge identification is accomplished either by measuring the particle's LET at a given residual range (for particles stopping in the detector), or by measuring the LET and its rate of change with the residual range.[1] From these observations and measurements it is usually possible to determine the particle energy, its direction of travel, and in the favorable cases make charge identification to ± 1 unit of charge.

RESULTS

Some preliminary results from Apollo 8 and 10 Missions have been published previously. A detector worn by astronaut Borman on the Apollo 8 missions was found to contain 0.62 ± 0.11 tracks/cm^2 of $Z \geq 10$ particles.[4] On Apollo 10 mission, a detector worn by Cernan yielded 1.24 ± 0.23 tracks/cm^2.[5] These two detectors were processed in the same manner (2.0 hr etch). Taking into consideration the longer exposure of Apollo 10, the data still implies that the cosmic ray heavy ion flux was somewhat higher during the latter mission. The increase in flux is presumably accounted for by the decrease in the degree of solar modulation. The Apollo 8 result is in agreement with the work of Comstock and coworkers[6] who used the Lexan Apollo 8 and 12 helmets to record $Z \geq 10$ particles. For Apollo 8 and 12 helmets, they found a track fluence of 0.56 ± 0.053 and 1.48 ± 0.15 tracks/cm^2, respectively. However, since their processing and scanning procedures differed significantly from that of ours, the agreement for Apollo 8 track fluence appears fortuitous.

In order to make track fluence intercomparisons between various missions meaningful, an effort was made to standardize as many processing parameters as possible. One,

previously unprocessed detector, from each mission was selected. All detectors were simultaneously UV irradiated, and processed at one time. Each detector was scanned, independently, by at least two different observers. Only tracks which appeared on both surfaces of the Lexan detector were recorded. This somewhat arbitrary but rigid criterion automatically insured that only primary, $Z \geq 10$ particle exposures are intercompared. It should be noted that this criteron differs from that used in references 4 and 5. In the past, all tracks of primary particles were recorded. However, the exposed detectors contain short tracks, the majority of which are energetic, proton induced recoils with $3 \leq Z \leq 8$. Without a complete charge identification of every track found, these are difficult to separate from the short tracks produced by some of the primary particles. Thus it is difficult to separate the low energy, $3 \leq Z \leq 8$ primary particles, from the same charge group of energetic secondaries.

The track fluences found in this manner, corrected for individual scanning efficiency, are shown in Table II. These numbers represent the total track fluence for the mission arising from the $Z \geq 10$ particle component. It is observed that the Apollo 8 fluence still lies significantly below that of the other missions. Therefore the increase in the heavy cosmic ray particle flux as recorded by subsequent missions, appears to be real.

The data in Table II are about a factor of 3 higher than that previously reported for the fluence of $Z \geq 10$ particles.[4,5] This arises from the fact that lower LET, $Z \geq 10$ particle tracks are now observable; it is not due to a contribution from the $Z < 10$ component. As previously stated, tracks due to $Z < 10$ particles were systematically excluded from these measurements. This means that the previously reported results[4-6] represent only a fraction of the total fluence of $Z \geq 10$ particle tracks observable with Lexan detectors etched for 8 hours.

TABLE II

Results of one detector from each flight, Apollo 8 - 13

Mission	Mission Type	Date and Duration	Detector Location	Track Fluence (Z≥10) (no./cm^2)
Apollo VIII	Lunar Orbiting	12/21/68 147 hours	W. M. Anders, LEM, ankle (3C)	2.0 ± 0.5
Apollo IX	Earth Orbiting	3/3/69 241 hours	J. McDivitt, CSM, ankle (6A)	none
Apollo X	Lunar Orbiting	5/18/69 192 hours	E. Cernan, LEM, ankle (C1)	3.4 ± 0.4
Apollo XI	Lunar Landing	7/16/69 195 hours	M. Collins, CSM, ankle (2C)	3.1 ± 0.6
Apollo XII	Lunar Landing	11/14/69 244.5 hours	R. Gordon, CSM, ankle (2C)	4.5 ± 0.8
Apollo XIII	Lunar Flyby	4/11/70 143 hours	F. Haise, LEM, ankle (3C)	2.9 ± 0.6

After charge identification of tracks, and taking into consideration the natural bias of the detectors toward registration of the higher Z particles, the density of enders (stopping particles) as an integral spectrum in charge number, Z, can be computed. An example, for Apollo 11, is shown in Table III, and Figure 3. Here, the number of stopping particles/cm^3 with $Z \geq Z_0$ are given as a function of Z_0. For all particles Z has been taken to have the even value most consistent with the track measurements. The errors indicated are those due to counting statistics. Primary particles with $6 \leq Z < 10$ are

also included. In order to eliminate low energy recoil particles, particles with Z < 6 were excluded. The stopping particle densities in Lexan can be converted to values appropriate for tissue by multiplying by the density of tissue (~ 1 g/cm^3) and dividing by the density of Lexan (1.17 g/cm^3).

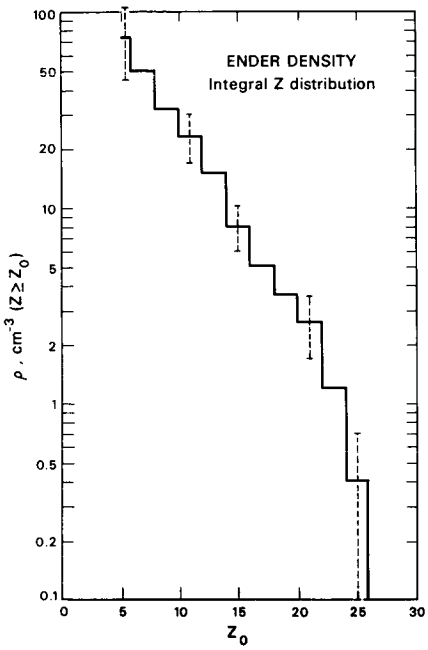

Figure 3. Stopping particle density in Lexan, $\rho(z>z_o)$ (particles/cm^3 with $Z > Z_0$) for Apollo 11 detector (2C).

Perhaps the biologically most meaningful expression of the data is a particle LET spectrum. An example, for Apollo 11, (2C) detector is shown in Figure 4. This is an integral LET spectrum giving the number of particles/cm^2 - ster. with LET > LET$_0$. The effective LET cutoff value is LET$_c$ = 0.177 MeV/μ. The errors indicated are those due to counting statistics. The LET spectra measurements with Lexan can be extended to higher LET values by either reducing the degree of detector sensitization, or by using unsensitized material. However, for lower LET values, other, more sensitive detectors must be utilized.

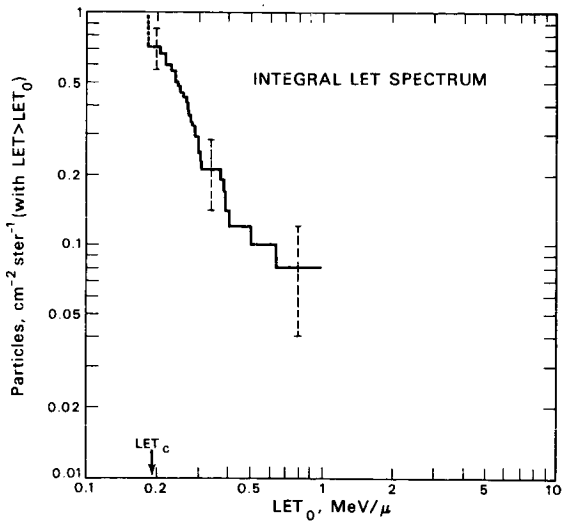

Figure 4. Integral LET spectrum, particles/cm^2-ster with LET > LET$_0$, as a function of LET$_0$ (MeV/micron) for Apollo 11 detector (2C).

SUMMARY AND CONCLUSIONS

The most interesting results and observations obtained to date with Lexan detectors can be summarized as follows:

1. Comparison of track fluences measured on Apollo 10-13 as compared with Apollo 8 mission, suggests an increase in the high Z cosmic ray flux. This increase may be due to a decrease in the degree of solar modulation.

2. Although the detectors are heavily biased toward the higher Z particles, fewer Z = 26 (Fe) particles are observed than expected as compared with lighter particles. This suggests a break up of Fe particles in passage through the spacecraft shielding. Thus the Z spectrum inside the spacecraft is shifted toward the lighter particles.

3. Only the fraction of the $Z \geq 10$ particle flux that corresponds to essentially stopping particles are recorded. These are the highest LET particles (and probably the most biologically significant) that either stop in the detector or the astronaut.

4. From these measurements, stopping particle densities in the form of integral Z distributions can be obtained.

5. High Z particle, integral LET spectra can be computed.

6. Preliminary data indicates that considerable variations exist in the recorded high Z track fluences as a function of detector location on the astronaut's body.

7. The frequency of the light flash phenomenon reported by the astronauts is considerably higher than the frequency with which the $Z \geq 10$, stopping particles are incident on tissue as recorded with Lexan. This implies that lower LET particles are at least partially responsible.

8. Tracks of the heavy ion recoil particles produced by the scattering (mostly inelastic) of protons are also observable in the Lexan detectors. Higher recoil track densities are observed on missions with trajectories that take the spacecraft through the intense regions of trapped protons. These heavy recoil particles may have a role in the light flash phenomenon since Tobias and coworkers have reported observing light flashes induced by beams of high energy neutrons.[7] It follows then the light flashes should be observable while the spacecraft is in the earth orbit, with the frequency of events being greatest in the vicinity of the South Atlantic Anomaly.

It is interesting to compare the different response to high LET particles of nuclear photographic emulsion and of plastic track detectors. In Figures 5 and 6 are shown tracks from the Apollo 8 mission.[4] In Figure 5 is shown a track of a $Z = 26 \pm 2$ particle traversing from left to right a G.5 emulsion and an adjacent plastic detector. The nearly equal lengths of the etch cones imply a fast particle. In Figure 6 is shown a track of a $Z = 23 \pm 1$ nucleus traversing from left to right a G.5 emulsion and two adjacent plastics. The observed rapid change in the lengths of the etch cones implies a slow, stopping particle. From the similarity of the two tracks in the nuclear emulsion, it is clear that in this detector a measurement of the change in the particles ionization rate (over these short ranges) is not feasible.

In order to obtain greater accuracy in the measurement of the high LET particle fluences, stopping particle densities, and LET spectra, and also to extend the measurements in both the Z and the energy, a considerably larger stack of Lexan was flown on Apollo 14. This stack was composed of some 100, 10 X 10 cm sheets of Lexan of the same batch as used on the previous missions. Positioned against the side of the spacecraft the stack remained stationary during the flight. Since the amount of data obtainable is approximately proportional to the volume-exposure time factor, this experiment should result in about a factor of 50 increase in the number of recorded tracks with a corresponding increase in the accuracy of the measured statistics.

For measurement of lower LET particles such as the $2 \leq Z \leq 9$ group or the more energetic $Z \geq 10$ group, more sensitive detectors are needed. Of the plastic detectors, cellulose triacetate, and cellulose nitrate have sensitivities which fall in this range. However, further development of these detectors is necessary, since considerably less is known of their behavior and response as compared to that of Lexan.

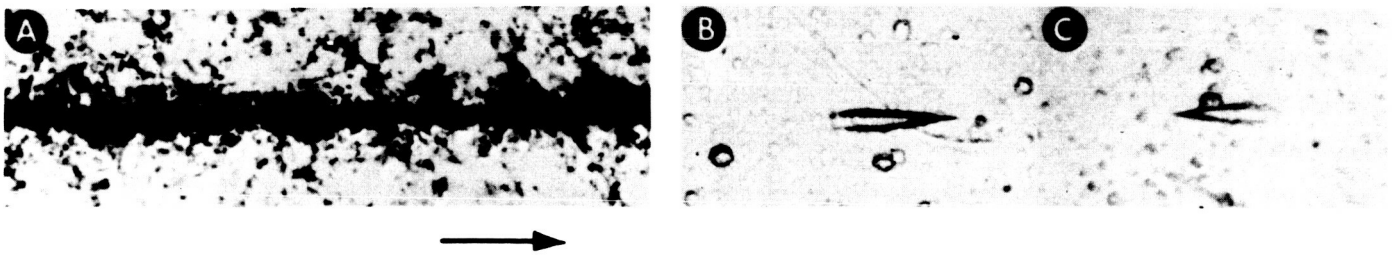

Figure 5. A track of a fast, Z = 26 ± 2 particle in a detector from the Apollo 8 mission: (a) in Ilford G.5 nuclear emulsion; (b) entrance track in adjacent Lexan sheet; (c) exit track in Lexan.

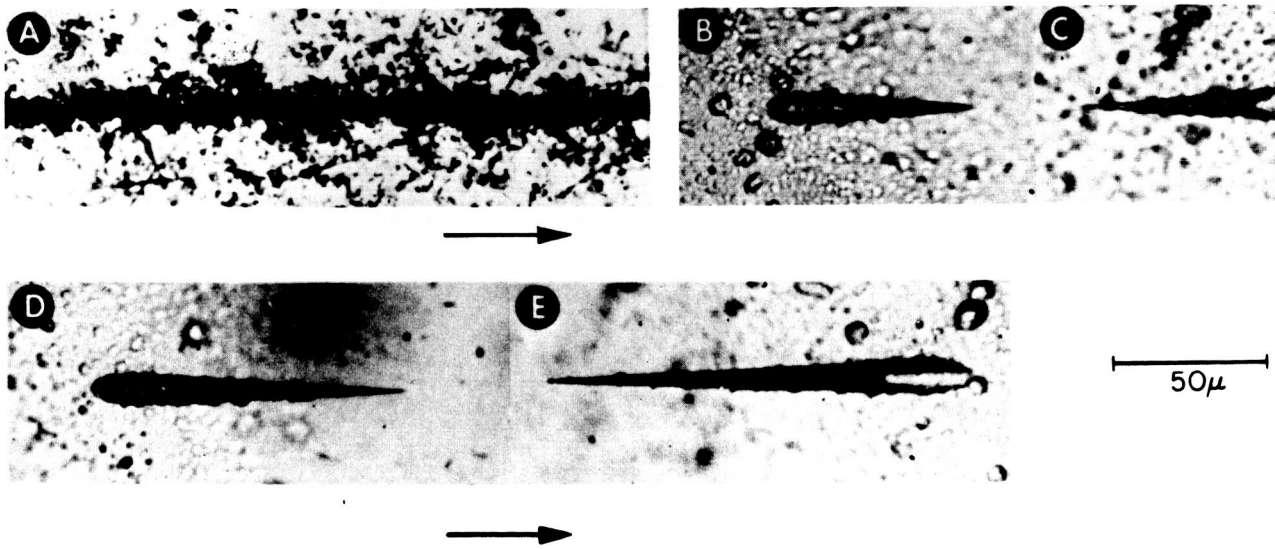

Figure 6. A track of a stopping Z = 23 ± 1 particle in a detector from Apollo 8 mission: (a) in G.5 emulsion; (b-c) and (d-e) in two adjacent plastics.

TABLE III

Stopping particle density in Lexan $\rho(z \geq z_o)$ (particles/cm^3 with $Z \geq Z_o$) for Apollo 11 detector (2C).

Z_o	$\rho(z \geq z_o)$
6	74 ± 29
8	50 ± 16
10	32 ± 9
12	23 ± 6
14	15 ± 4
16	8 ± 2
18	5.0 ± 1.4
20	3.6 ± 1.1
22	2.6 ± 0.9
24	1.2 ± 0.5
26	0.4 ± 0.3

REFERENCES

1. E. V. Benton, "A Study of Charged Particle Tracks in Cellulose Nitrate," USNRDL-TR-68-14 (1968).
2. The quantity LET as used in this paper is LET_{350}, the energy per path length of incident particle lost to electrons in energy transfer collisions of less than 350eV. Another name for this quantity is REL, the restricted energy loss rate. In the previous work, including reference (1) LET_{1000} was used. Recently we found LET_{350} to be a more realistic value.
3. R. P. Henke, E. V. Benton, H. H. Heckman, Radiation Effects, 3, 43 (1970).
4. E. V. Benton, R. P. Henke, R. G. Richmond, Radiation Effects, 3, 39 (1970).
5. E. V. Benton, R. P. Henke, Paper presented at the Seventh International Colloquium on Corpuscular Photography and Visual Solid Detectors, Barcelona (1970).
6. G. M. Comstock, R. L. Fleischer, W. R. Giard, H. R. Hart, Jr., G. E. Nichols, P. B. Price, GE Report No. 71-C-009 (1971).
7. C. A. Tobias, T. F. Budinger, J. T. Lyman, "Observations By Human Subjects On Radiation - Induced Light Flashes In Fast - Neutron, X-Ray And Positive - Pion Beams" UCRL-19868 (1970).

FLUCTUATIONS IN ENERGY LOSS AND THEIR IMPLICATIONS FOR DOSIMETRY AND RADIOBIOLOGY*

Norman A. Baily and John E. Steigerwalt
Department of Radiology
University of California, San Diego
La Jolla, California 92037

INTRODUCTION

Traditionally all of dosimetry has been based on the measurement or calculation of the average energy deposited in a small volume expressed originally by the Roentgen, a unit of exposure for x and γ-rays, and more recently and of wider applicability by the absorbed dose expressed in Rads. Both are macroscopic concepts since they presume a sufficient number of ionizing events so that statistical fluctuations of energy loss by charged particles (primary or secondary) may be ignored. In the case of very small volumes such as those of importance in radiobiology and where most effects are considered to be due to a very small number of events taking place in this volume the probability of transferring an amount of energy equal to or nearly equal to the average energy loss computed from the charged particle stopping power in most instances is very small. The energy transferred to any particular biological entity is given by a frequency distribution function which in many cases is skewed toward high energy events and therefore the most probable energy loss is considerably less than the average. This is of fundamental importance in predicting radiation damage to the individual cells, chromosomes, molecules, etc. whose cumulative effect we observe. Generally, then, the absorbed dose would only be applicable as a measure of energy delivered when large numbers of individual events are pertinent such as might be found in large masses of material or where the effect observed is due to many events.

In most instances where biological material is being studied, the individual transfers of energy from incident particles to atomic electrons are subject to wide statistical fluctuations[1-3]. In these cases, the usual concept upon which dosimetry is based (average energy loss or stopping power of charged particles) breaks down, except for the most densely ionizing particles. This is always the case when one considers volumes as small as those associated with the various biological structures of interest in fundamental radiobiology, radiation therapy, and health physics.

As a consequence in almost all cases, energy deposition in the biological volumes involved have a wide separation of the most probable and average energy losses. This state usually exists for most of the radiations currently of interest. Only in the case of very densely ionizing particles such as heavy ions can these considerations be neglected.

There are multiple reasons why this approach has persisted. First, physical determinations of statistical distributions of energy loss have been restricted to pathlengths large compared to those of biological interest and second, many have been examined using instruments which accumulated data over many pathlengths simultaneously thereby masking fundamental physical phenomena. Over the past few years, the work of Baily and his collaborators[4-6] has shown the importance of such considerations for high energy protons ($\sim$ 45 MeV).

*Partially Supported By NASA Grant No. NGL 05-009-103.

FUNDAMENTAL CONCEPTS

Despite certain discrepancies between experiment and theory which have been found for energy loss distributions due to single charged particle traversals through small volumes, a rather good representation of the experimental data is given by the theory for those energy losses occurring at and about the most probable value. The discrepancies appear as an excess of high energy events with a subsequent dearth of events lying below that of the most probable energy loss. The average energy loss obtained from theory and experiment show agreement within experimental error. Since the discrepancies mentioned are not large ($\sim$ 20% excess of high energy events), calculations made using the Blunck-Leisegang corrected Vavilov or Landau theories are sufficiently accurate to examine current dosimetry and radiobiological concepts in the light of these distributions. Major among these are: a) Linear Energy Transfer (LET) and its role in predicting Relative Biological Effectiveness (RBE) or b) the reliability of the use of the average energy deposited to describe the local microscopic dose for a small number of events. As we shall show, the energy range over which these broad distribution functions is important is fairly extensive for most charged particles. Even Compton electrons generated at conventional x-ray energies and protons generated in tissue by fast neutrons fall within the group of particles to which these statistical concepts and associated physical phenomena apply.

Perhaps, in a qualitative way, the extent of the statistical fluctuations are best illustrated by an examination of the distribution functions of the frequency with which energy losses of a given magnitude take place in a given pathlength. Fig. 1 shows such frequency distributions for various charged particles corresponding to a pathlength of approximately 1 μ of tissue. The degree of the statistical fluctuations are well illustrated by the four particles chosen. Curve A is that expected from a 50 keV electron; B from a 50 MeV proton; C from an 8 MeV alpha particle; and D from a 24 MeV stripped ^{12}C ion. The spread about the most probable energy loss is also given. This is expressed by the full width at half maximum (FWHM) as a percentage of the most probable energy loss. The ratio of the average to the most probable energy losses for the two lighter classes of particles is given in Tables I and II. These two values will coincide for very densely ionizing particles.

A number of things important to the production of radiobiological effects take place as particle charge and mass increase and similarly with decrease of particle energy. First, as shown for a heavy charged particle of energy $\sim$ 2 MeV/amu, the distribution function has a gaussian shape and is narrowly distributed about the average energy loss $\left[\Delta X \left(-\frac{dE}{dX}\right)\right]$. Second, as charge and mass decrease, the FWHM increases, but its shape is still primarily gaussian. The peak or most probable energy loss coincides with the average energy loss. Third, as the magnitude of the energy loss decreases relative to the particle's kinetic energy, the curve becomes quite skewed on the high energy end. As a consequence as this trend continues skewness increases and

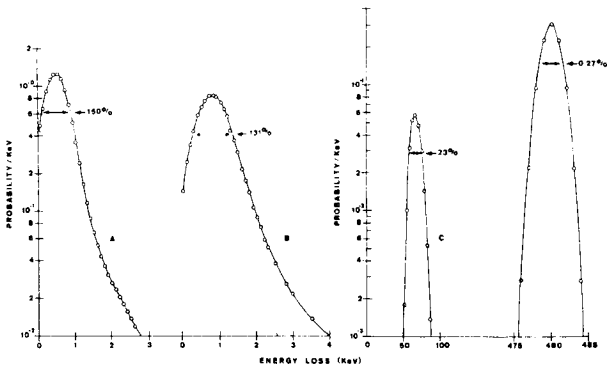

Fig. 1: Frequency distributions of energy loss by various charged particles in a tissue-equivalent medium. The pathlength used in these computations was 10^{-4} g/cm^2. Curve A is for a 50 KeV electron, B for a 50 MeV proton, C for an 8 MeV alpha particle, and D for a 24 MeV ^{12}C stripped ion. Also shown are the spreads about the most probable energy loss expressed in terms of the full width at half maximum as a percentage of the most probable energy loss.

TABLE I

A comparison of average energy loss versus most probable energy loss for protons traversing 1 micron of soft tissue (muscle).

Ep (MeV)	$\bar{\Delta}$, Average Energy Loss (KeV)	Δ_{mp}, Most Probable Energy Loss (KeV)	$\bar{\Delta}/\Delta_{mp}$
1.0	27.1	27.0	1.00
2.0	16.9	15.7	1.08
5.0	8.26	6.31	1.31
10.0	4.64	3.11	1.49
50	1.26	0.669	1.88
100	0.736	0.360	2.04
150	0.549	0.258	2.13
600	0.257	0.109	2.35

TABLE II

A comparison of average energy loss versus most probable energy loss for electrons traversing 1 micron of soft tissue (muscle).

Electron Energy (MeV)	$\bar{\Delta}$, Average Energy Loss (KeV)	Δ_{mp}, Most Probable Energy Loss (KeV)	$\bar{\Delta}/\Delta_{mp}$
0.05	0.667	0.367	1.82
0.1	0.415	0.210	1.98
0.2	0.281	0.133	2.11
0.4	0.216	0.0981	2.20
0.6	0.196	0.0886	2.22
0.8	0.189	0.0848	2.22
1.0	0.185	0.0832	2.23
2.0	0.184	0.0824	2.23
4.0	0.189	0.0843	2.24
6.0	0.193	0.0855	2.25
8.0	0.196	0.0863	2.27
10.0	0.198	0.0868	2.28

the most probable energy loss becomes increasingly less than the average. Since the ratio of these can become quite large, this is of great significance in dealing with fundamental radiobiological (and therefore the ultimate overall) effects involving single or only a small number of interactions.

A measure of this physical phenomena and its possible consequences for dosimetry can best be appreciated by noting the ratio of the average energy loss to the most probable. Tables I and II give this ratio for protons and electrons respectively over a wide range of energies for particles traversing distances approximately equal to 1 μ of tissue. It should be pointed out that this ratio, in most cases, would be even larger if shorter pathlengths were involved.

The combination of the size of the the biological material and the pattern of energy deposition which is due purely to the physics involved, prompts one to re-examine the use of macroscopic dosimetry units such as the rad asking if it is really suitable for use as a biological measure of radiation effects. Indeed if an adjustment of this unit were to be made representative of the actual probability for delivering a specified amount of energy to a small volume, we might even appear to question some of the attributes usually associated with parameters such as LET, rate effects, etc.

While we do not mean to suggest that a more proper parameter would be based on one simple number such as the most probable energy loss, we do feel that a more careful consideration of fundamental physical phenomena should be given to the associated probabilities for energy deposition before ascribing certain biological factors to various types and energies of ionizing radiation since most biological effects seem to be caused by a relatively small number of events. The requirement for having only a small number of significant events as indicated by the magnitude of the extrapolation numbers combined with the small volumes involved when considered in light of the energy deposition frequency distributions gives a high probability for many types of radiation to deliver a total effective dose considerably less than that to be expected from the macroscopic (rad) dose. The magnitude of the discrepancy will, of course, depend on the type radiation and its energy.

CONSIDERATIONS INVOLVING R.B.E.

A consideration of the actual energy likely to be absorbed in a biological structure as compared to that ordinarily specified by the absorbed dose leads one to question the validity of many values of R.B.E. reported or even to ask the question is the effect real. It is therefore of interest to examine this problem by assuming some other value of energy absorbed other than that measured or calculated by macroscopic concepts. Although an exact treatment would require a rigorous statistical treatment we have found that a simple adjustment of the dose gives values in agreement with those found experimentally by assuming that the most probable energy loss is more representative than the average energy loss. Looking at this problem then from the viewpoint of the initial experiment if the dose to the small biological volume had been specified by the actual amount of energy absorbed then many differences in R.B.E. values attributed to a true biological effect would not have been found.

To explore this hypothesis, we have assumed that the ratio of

$$\Delta_{mp}/\bar{\Delta}$$

where: Δ_{mp} = the most probable energy loss, and

$\bar{\Delta}$ = the average energy loss

is a measure of the effective dose delivered to the individual elements of which the test material is composed and that the observed effect is the accumulation of damage to these elements.

The values of the inverse quantity given in the Tables I and II show a striking parallelism to many reported R.B.E. values for these radiations. We have therefore utilized these in the manner postulated above to calculate values of the R.B.E. we would have expected to have been found. This was done by adjusting the dose ratio from which the R.B.E. was obtained by the ratio of the $\Delta_{mp}/\bar{\Delta}$ ratios of the test radiation to that of the standard radiation.

Baarli and Bonet-Maury[7] using 592 MeV protons found an R.B.E. of 0.98 for this radiation when they compared the dose for obtaining $LD_{50/30}$ survival of mice to the dose required for a similar survival level using 250 kVp x-rays. In other tests, values of 1.06 were found. Adjusting the magnitude of the dose in each case by the ratio of $\Delta_{mp}/\bar{\Delta}$ assuming a mean electron energy of 100 KeV for the 250 kVp x-ray spectra gives a value of 1.19. Since the frequency distribution of the energy depositions for 600 MeV protons is a more highly skewed distribution than would be found for the mixed electron energy spectra associated with a 250 kVp x-ray generator the answer obtained is not unreasonable. If one were to include as highly probable events those close to but greater than Δ_{mp}, we should improve the agreement. We have done similar comparisons for a group of biological experiments using various proton energies and fast neutrons. The results are shown in Table III. While these are selected references and by no means represent the bulk of the literature, no special effort was made to pick biological data to match that obtained from the physical

TABLE III

Comparison of normalized values of the ratio $\bar{\Delta}/\Delta_{mp}$ to some R.B.E. values reported for $LD_{50/30}$ survival experiments in mice and survival and proliferation of Chinese hamster cells.

Proton Energy (MeV)	Irradiation Particle and Energy	$\bar{\Delta}/\Delta_{mp}$ (normalized)	R.B.E.
	592 MeV Protons[7]		0.98, 1.06, Mice (relative to 250 kVp x-rays)
600		1.19	
	138 MeV Protons[8]		1.07, Mice (relative to ^{60}Co)
150		1.05	
	55 MeV Protons[9]		1.3 - 2.3, Mice (relative to ^{60}Co)
50		1.19	
	Fast Neutrons[10]		2.18, Chinese Hamster Cells (relative to 280 kVp x-rays)
1.0		1.97	

measurements. The correlation with our oversimplified analysis is striking particularly in view of the fact that Δ_{mp} is almost certainly too low a value to be considered as a single parameter dosimetric value.

A similar approach can be used with the data presented by Barendsen, et al.[11] for electrons and x-radiation. Assuming an average energy of 700 keV for the beta spectrum used and an effective energy of 100 KeV for the 200 kVp x-rays used, we can compare the difference in biological effects produced with the ratio of $\bar{\Delta}/\Delta_{mp}$ for electrons having these energies. The biological effects (R.B.E.'s) showed a diffetence of 12%. The difference in the energy loss ratios is also 12%.

A recent series of experiments by Čerček, et al.[12] using 380 MeV protons and ^{60}Co γ-rays obtained R.B.E. values of 1.3 - 1.4 for these protons in several biological materials. Using the data in Table I and that of Wright, et al.[13] for the fraction of dose delivered by heavy ions and pions, we would obtain a dose ratio (based on Δ_{mp}) of 1.13. If the narrowing of the frequency distribution which occurs with very densely ionizing particles was taken into account agreement would be even closer (Fig. 1). Many other examples where such agreement is found could be cited.

Examination of Table II together with the reasoning suggested would also explain the fact that in many instances, no significant changes in R.B.E. were found for L.E.T.'s as widely different as those associated with ^{60}Co and 200 kVp x-rays (0.27 KeV/μ in the case of ^{60}Co and a mean L.E.T. of 1.8 KeV/μ for a 200 kVp lightly filtered x-ray beam). In fact, with increases in photon energies up to 22 Mevp, R.B.E.'s have been found to change by only 10 to 15 per cent.

It should be realized, however, that for any meaningful application of the physical factors that we have pointed out requires a theory incorporating the probability for events of a given size in the volume of

interest corresponding to the number of events expected or required for damage or death.

Another aspect of this problem has to do with the possible requirement for deposition of a minimum amount of energy in the critical site. In an unpublished paper, Katz and his collaborators[14] have obtained very good agreement with published R.B.E. values based on cell survival curves when values of 5 to 250 KeV are used as the minimum required value of the energy deposition in the sensitive site. Frequency distribution functions automatically provide: first, the fraction of events depositing energy greater than a certain energy and second, the fraction of the total energy deposited in event sizes greater than a given value. Two typical curves of this type are shown in Figs. 2 and 3. In addition to furnishing a ready source of information which can be used in Katz's[14] or similar formulations, the data when presented in this manner serves to further illustrate the importance of taking into account possible differences in the values of $\bar{\Delta}$ and $\bar{\Delta}_{mp}$ and the associated changes in probability for events close to the average energy loss. For example, the data illustrated in Figs. 2 and 3 represent the frequency distributions for 46.4 MeV protons passing through 1.33×10^{-4} g/cm^2 of a tissue-equivalent gas (equal electron densities). The fraction of the total energy delivered to the gas by the proton in its passage through it in event sizes greater than $\bar{\Delta}$(1.56 KeV) is 60%, while the fraction delivered by events having energy losses greater than $\bar{\Delta}_{mp}$ (0.90 KeV) is 88%. Similarly, Fig. 3 shows that the fraction of events occurring with energy losses greater than $\bar{\Delta}$ is only 35%, while those occurring with losses greater than Δ_{mp} is 73%.

This type of data also lends itself to interpretations of the shape of survival curves in lieu of the simple concepts of the hit theory. Both shoulder extension and slope of the exponential portion can be analyzed using data similar to that shown.

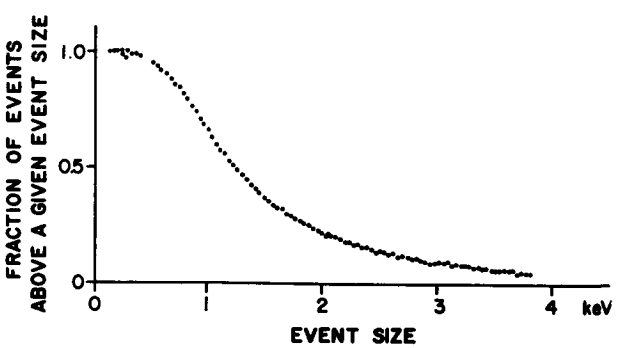

Fig. 2: Fraction of events depositing energy in amounts greater than a given size when a 46.4 MeV proton traverses 1.33×10^{-4} g/cm^2 of tissue-equivalent material.

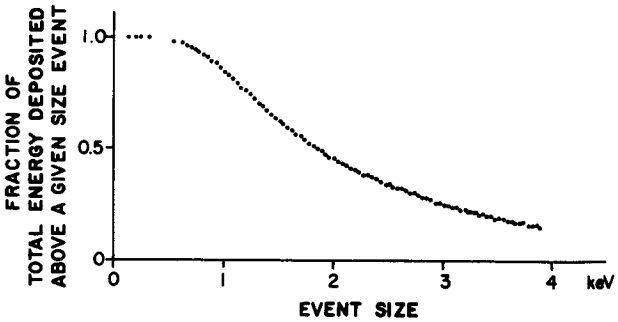

Fig. 3: Fraction of the total energy which is lost in individual events having energy losses greater than some given energy. The data was experimentally determined for 46.4 MeV protons in their passage through 1.33×10^{-4} g/cm^2 of tissue-equivalent material.

Rate effects can also be considered in the same light. For example, if the critical energy required for recording of damage corresponds to a low probability event, recovery should be more probable since the time available for it would be greater. Low dose effect data should therefore shed much light on this interesting possibility. In fact, an obvious consequence, which is, of course, observed experimentally, is the relatively larger rate effects found for low L.E.T. radiations. In terms of the distribution functions, this might be explained by the relatively lesser fraction of the dose being delivered by events having large energy depositions in instances where the critical energy required to produce the effect is considerably larger than the most probable energy loss.

DISCUSSION

The treatment presented has ignored the fact that under certain conditions many biological effects studied yield R.B.E. values considerably in excess of the ratios tabulated. This definitely shows the naivety of the approach and the need for considerable refinement or possibly a total change in concept. Further, one should not take this presentation as a basis for the elimination of all real biological differences. It is most likely that to properly account for the experimental data, a combination of real biological differences and a correct and rigorous accounting of energy deposition patterns are required.

Further, if one considers that frequency distributions having a high degree of skewness have higher probabilities for large events than do for example a narrow gaussian, irradiation by a beam having such a distribution will contribute some events although they might be rare to an effect having a threshold requirement far above Δ_{mp} or even $\bar{\Delta}$. When compared to a heavily ionizing particle beam having a narrow gaussian spread at or above this threshold, we might then find very large values of the R.B.E. The smaller the critical site the greater the apparent effectiveness of the more densely ionizing particle would become. Similar considerations were used by Rossi[15] to elucidate the probability of scoring a hit within a sensitive volume by the secondary electrons produced in irradiations using ^{60}Co gamma rays and for the secondary protons produced by irradiation with 1 MeV neutrons.

A further test of these concepts requires a theory incorporating the probability for a given size energy deposition in specific biological entities when single or relatively few events are postulated for production of an observed biological effect. This statistical treatment of the individual components would then have to be averaged over the large number of cells, chromosomes, etc. in an attempt to reproduce experimental survival curves, numbers of breaks, deletions or even overall effects on whole organs or organ systems.

CONCLUSION

Serious consideration of the physics of energy deposition seems to indicate that a fundamental change in the interpretation of absorbed dose is required at least for considerations of effects in biological systems. In addition, theoretical approaches to radiobiology and microdosimetry would seem to require statistical considerations incorporating frequency distributions of the magnitude of the event sizes within the volume of interest.

REFERENCES

1. Landau, L.: J. Phys. USSR 8, 201 (1944).
2. Vavilov, P.V.: Zh. Eksperim. i. Teov. Fiz. 32, 320 (1957) English Transl.: Soviet Phys. - JETP 5, 749 (1957).
3. Blunck, O. and Leisegang, S.: Z. Physik 128, 500 (1950).
4. Hilbert, J.W., Baily, N.A., and Lane, R.G.: Phys. Rev. 168, 290 (1968).
5. Hilbert, J.W. and Baily, N.A.: Rad. Res. 39, 1 (1969).
6. Baily, N.A., Steigerwalt, J.E., and Hilbert, J.W.: Phys. Rev. 2B, 577 (1970).
7. Baarli, J. and Bonet-Maury, P.: Nature 205, 361 (1965).
8. Dalrymple, G.V., Lindsay, I.R., Hall, J.D., Mitchell, J.C., Ghidoni, J.J., Kundel, H.L., and Morgan, I.L.: Rad. Res. 28, 489 (1966).
9. Dalrymple, G.V., Lindsay, I.R., Ghidoni, J.J., Mitchell, J.C., and Morgan, I.L.: Rad. Res. 28, 548 (1966).
10. Schneider, D.O. and Whitmore, G.F.: Rad. Res. 18, 286 (1963).
11. Barendsen, G.W., Walter, H.M.D., Fowler, J.F., and Bewley, D.K.: Rad. Res. 18, 106 (1963).
12. Čerček, L., Ebert, M., Gilbert, C.W., Haigh, M.V., Howard, A., Massey, J.B., and Potten, C.S.: Int. J. Radiat. Biol. 15, 137 (1969).
13. Wright, H.A., Anderson, V.E., Turner, J.E., Neufeld, J., Snyder, W.S.: Health Phys. 16, 13 (1969).
14. Katz, R.: Proc. of the IV Int. Congress of Rad. Res., Evian, France, 114 (1970).
15. Rossi, H.H.: Amer. J. Roentgenol., Rad. Ther., and Nuc. Med. 93, 196 (1965).

THE MEASUREMENT OF RADIATION EXPOSURE OF ASTRONAUTS BY RADIOCHEMICAL TECHNIQUES[a]

R. L. Brodzinski
Battelle Memorial Institute, Pacific Northwest Laboratories
P. O. Box 999
Richland, Washington 99352

ABSTRACT

The principal gamma-ray-emitting radioisotopes produced in the body of astronauts by cosmic-ray bombardment which have half-lives long enough to be useful for radiation dose evaluation are ^{7}Be, ^{22}Na, and ^{24}Na. The sodium isotopes were measured in the preflight and postflight urine and feces, and those feces specimens collected during the manned Apollo missions, by analysis of the urine salts and the raw feces in large crystal multidimensional gamma-ray spectrometers. The ^{7}Be was chemically separated, and its concentration measured in an all NaI(Tl), anticoincidence shielded, scintillation well crystal.

The overall sensitivity of the experiment was reduced by almost all variables such as low concentrations of excreted cosmogenic radionuclides, high concentrations of injected radionuclides, low sample sizes, long delay periods before analysis, and uncertain excretion rates. The astronaut radiation dose in millirads, as determined by this technique, for the Apollo 7, 8, 9, 10, 11, 12, and 13 missions was 330, 160, <315, 870 $\pm$ 550, 31, 110, and <250 respectively. In view of these limitations this technique would be best applied to cases of unusually high exposures, such as that encountered from solar flares.

INTRODUCTION

With the advent of space flight, it has become necessary to determine the radiation dose to man from exposure to the galactic, Van Allen, and solar flare particles. The high-energy galactic portion of the spectrum is fairly constant and has a relatively low intensity. The high intensity Van Allen radiation is of medium energy and localized in space. However, the solar radiation is not so predictable, and the flux and energy of particles from the sun can vary tremendously depending on solar activity. Since high levels of radiation exposure are possible, radiation dosimetry which will properly define radiation exposures is essential in space research programs. Dosimetry methods employed thus far, such as nuclear emulsion films, thermoluminescent dosimeters, and ionization gauges provide very useful indirect methods for estimating radiation dose but are subject to limitations. They measure only a surface exposure at a specific point(s) in the spacecraft or on the astronaut's body rather than an integral whole body exposure, and they have a limited sensitivity to large variations in particle energy. Some of the inherent limitations of these external dosimeters are avoided by using the induced radioactivity in the body of an astronaut as a measure of his radiation exposure. During a space flight, radionuclides are produced throughout the entire body of an astronaut, and the production rates are related directly to the cosmic particle flux within the body. The absolute and relative amounts of the various radionuclides bear a direct relationship to the intensity and energy spectrum of the particles which are doing the biological damage.

The radiation dose received from the cosmic particles can be determined from the quantities of induced radionuclides[1-4]. The amounts of these induced activities can be determined by direct measurement, i.e., whole body counting of the astronaut, or by indirect measurement, such as counting the radionuclides excreted in the feces and urine. The latter approach was used for evaluation of radiation activation during the course of the manned Apollo missions.

The principal gamma-ray-emitting radioisotopes produced in the body by cosmic-ray bombardment are ^{7}Be ($t_{\frac{1}{2}}$=53 day), ^{11}C ($t_{\frac{1}{2}}$=20.5 min), ^{13}N ($t_{\frac{1}{2}}$=9.96 min), ^{22}Na ($t_{\frac{1}{2}}$=2.60 yr), and ^{24}Na ($t_{\frac{1}{2}}$=15.0 hr). The primary mode of production of ^{7}Be and ^{11}C is the spallation of carbon, nitrogen, and oxygen in the body. The ^{13}N comes

[a] This paper is based on work supported by the National Aeronautics and Space Administration, Manned Spacecraft Center, Houston, Texas, under contract AT(45-1)-1830 between the USAEC and Battelle-Northwest.

principally from the spallation of nitrogen and oxygen, the ^{22}Na from the spallation of sodium, phosphorus, and calcium, and the ^{24}Na from the neutron activation of natural sodium. Of these, ^{11}C and ^{13}N are too short-lived to be measured by any method other than a direct determination, and this direct counting would have to be done as soon as possible after recovery. This is unfortunate, since these radioisotopes are produced in the largest abundance. The radionuclides ^{7}Be, ^{22}Na, and ^{24}Na are, however, sufficiently long-lived to facilitate their use in making dose estimates from measurement of their quantities in urine and fecal samples.

Other radioisotopes were also expected to be present in the bioassay samples. In addition to the aforementioned cosmogenic radionuclides, measurements of naturally present ^{40}K; normally occurring ^{7}Be, ^{22}Na, and ^{137}Cs; and ^{51}Cr and ^{59}Fe which were injected for medical studies were also made. Another radioisotope, ^{60}Co, was detected and quantitatively measured in some of the specimens. Corrections to the cosmogenic ^{7}Be and ^{22}Na must be made to account for the quantities of these radioisotopes normally occurring in the body because of fallout, food intake, and other ingestion processes. The quantities of the naturally occuring ^{40}K and the injected ^{51}Cr and ^{59}Fe in the bioassay samples could serve as biological tracers of various changes of metabolic processes during the course of a mission.

In previous studies, induced radioactivity to radiation dose relationships have been established for the radionuclides ^{7}Be, ^{22}Na, and ^{24}Na as a function of energy for proton bombardment of muscle tissue[2]. From these relationships and from the ratios in which these radionuclides are produced, the "effective proton energy" of cosmic radiation incident on an astronaut can be determined. This allows the direct estimation of the whole body radiation exposure received by astronauts from measurements of the radionuclides produced in their bodies.

EXPERIMENTAL

Preflight and postflight urine and feces and those feces specimens collected in flight were analyzed. Due to the quarantine period following lunar landing missions, all samples were not immediately available for analyses, thus allowing the short-lived radionuclides to decay. The urine specimens which were of small volume were solidified prior to analysis by the addition of $CaSO_4$ to 25 ml or less of the raw urine in order to form a standard counting geometry. Any samples of initial volume greater than 25 ml were treated by repeatedly boiling to dryness with nitric acid to destroy the organic matter present. The remaining salts were counted in large crystal multidimensional gamma-ray spectrometers[5-7] for determination of ^{22}Na, ^{24}Na, ^{40}K, ^{51}Cr, ^{59}Fe, ^{60}Co, and ^{137}Cs. The salts were then redissolved in a weak HCl solution and diluted to known volume. An aliquot of this solution was taken for neutron activation analysis to determine the concentrations of stable elements in the sample. The remainder of the solution was reduced in volume to approximately 15 ml and transferred to a 100 ml polyethylene centrifuge tube. Approximately 5 mg of Be^{++} carrier and 20 mg of Fe^{+++} carrier were added, and the solution was neutralized with concentrated NH_4OH. After centrifugation the supernatant solution was discarded. Thirty-five ml of 3 N NaOH were added to the remaining precipitate and stirred vigorously until well mixed. After centrifugation the supernatant liquid was transferred to a clear centrifuge tube, saturated with NH_4Cl, and heated in a water bath. If necessary, additional NH_4Cl was added until a $Be(OH)_2$ precipitate settled from the solution. The solution was then centrifuged, and the supernatant fraction was discarded. The resulting quantitative precipitate containing the ^{7}Be activity was counted in an all NaI(Tl) anticoincidence shielded, 7-inch diameter scintillation well crystal in the absence of all interfering activities. This was necessary in order to measure the relatively small quantities of ^{7}Be present.

Fecal samples were thoroughly mixed in their collection bags to ensure homogeneity of the specimens. A small corner was cut off each bag and aliquots were extruded into standard counting geometry containers for measurements on multidimensional gamma-ray spectrometers to measure the radioisotopes ^{22}Na, ^{40}K, ^{51}Cr, ^{59}Fe, ^{60}Co, and ^{137}Cs. Separate aliquots were wet ashed with nitric acid and hydrogen peroxide to destroy the organic matter present. The resulting salts were dissolved in dilute nitric acid, and the same procedure as above was followed for separation of the ^{7}Be activity.

A luminous material composed of ^{147}Pm microspheres mixed with a scintillator is used extensively in the spacecraft in acrylic switch tips and sighting figures used in docking maneuvers. Because of the high rejection rate of switch tips caused by promethium leaks, there is some concern about the possible presence of ^{147}Pm in the weightless space capsule environment. For the later missions, approximately 10 mg of mixed rare earths were added to the feces prior to wet ashing. These were to serve as carriers for ^{147}Pm, which could possibly have been ingested by the crew members. This rare earth fraction was separated from the beryllium fraction after the initial NH_4OH precipitation by dissolving the precipitate in approximately 8 ml of 3M HCl and adding 2 ml of 49 percent HF. Centrifugation separated the rare earth precipitate from the beryllium in the supernatant solution. The rare earth fraction was then dissolved in two parts concentrated HNO_3 and three parts saturated boric acid solution and reprecipitated with NH_4OH. After centrifugation and decantation, the precipitate was dissolved in dilute HCl; and saturated oxalic acid solution was added to precipitate the rare earth oxalates. The solution was centrifuged; the supernatant solution was decanted; and the quantitative precipitate was washed with alcohol, transferred to a 1-inch diameter stainless steel dish and counted in an end window, gas flow beta counter for the measurement of ^{147}Pm.

RESULTS

The results of the individual determinations are given in Tables I through IV. All data have been normalized to a gram of feces, a milliliter of urine, or a gram of the respective stable element as determined by a technique of instrumental neutron activation analysis[8] All data have been decay corrected to the time of splashdown of each respective mission. The results of all the radionuclide measurements in the excreta are given in the tables although only the concentrations of the cosmogenic radionuclides ^{7}Be, ^{22}Na, and ^{24}Na are of importance for the subject matter of this communication. The various samples in the tables are listed by the letters A, B, and C or LMP, CMP, and CDR to identify an individual astronaut. Those samples listed by numbers are unidentified and arbitrarily coded. The collection time for each specimen is given as Pre-, In-, or Post-flight unless more detail is known, in which case a number refers to elapsed time into the mission in hours, the letter F followed by a number indicates that number of days prior to flight, post+0 refers to the first voiding after splashdown, post+1 is the first 24 hour collection after splashdown and day 2 is the following day after splashdown.

TABLE I

RADIONUCLIDES IN FECES FROM APOLLO ASTRONAUTS

MISSION	SAMPLE IDENTIFICATION	FLIGHT PERIOD	ACTIVITY IN DISINTEGRATION/MINUTE/GRAM FECES ON DAY OF SPLASHDOWN							
			^{7}Be	^{22}Na	^{40}K	^{51}Cr	^{59}Fe	^{60}Co	^{137}Cs	^{147}Pm
7	B	PRE	1.39±0.21		5.20±0.21	19.0±0.2	0.117±0.028		0.167±0.028	
7	C	PRE	0.84±0.20		6.85±0.38	18.0±0.4				
7	S/N 2270	IN	6.0±1.2							
7	S/N 2276	IN	0.92±0.11		5.75±0.22	16.0±0.5	0.295±0.046		0.179±0.050	
7	S/N 2277	IN	0.58±0.11		8.14±0.17	20.1±0.5			0.147±0.023	
7	S/N 2278	IN	0.91±0.088	0.0089±0.0028	10.5±0.2	55.6±0.6	0.169±0.048		0.134±0.032	
7	S/N 2280	IN	0.50±0.18	0.0095±0.0029	8.82±0.25	55.1±0.5	0.122±0.055		0.090±0.032	
7	S/N 2282	IN	0.600±0.056		7.61±0.18	19.6±0.5			0.151±0.024	
7	S/N 2292	IN	1.53±0.22		4.81±0.20	53.1±0.6			0.042±0.029	
7	S/N 2299	IN	1.07±0.16		9.51±0.25	42.5±0.6	0.590±0.048		0.388±0.033	
7	S/N 2300	IN	2.10±0.22	0.0047±0.0025	3.96±0.19	16.7±0.6	0.204±0.044		0.295±0.029	
7	S/N 2312	IN	1.69±0.24		8.91±0.18	45.8±0.5	0.146±0.056		0.132±0.024	
7	A	POST	4.12±0.23	0.0052±0.0028	10.8±0.2	24.8±0.4	0.464±0.059			
7	C	POST	1.75±0.24		7.73±0.19	49.2±0.4	4.85±0.04	0.376±0.013	0.398±0.026	
8	B	PRE	2.63±0.26	0.049±0.018	5.21±0.17	3.42±0.21	0.134±0.032		0.147±0.017	
8	C	PRE	3.87±0.38		9.32±0.22	4.34±0.27	0.211±0.041	0.013±0.008	0.245±0.021	
8	1	IN	3.7±1.1		6.80±0.18	34.2±0.5	0.172±0.043		0.249±0.026	
8	2	IN	1.04±0.17		7.04±0.23	39.0±0.5	0.286±0.054		0.359±0.030	
8	3	IN	0.61±0.19	0.0043±0.0034	7.67±0.24	22.0±0.5	0.306±0.056		0.228±0.031	
8	A	POST	0.42±0.20		10.4±0.1	81.8±0.2		0.0025±0.0015	0.105±0.007	
8	B	POST	3.81±0.81	0.029±0.006	4.35±0.37	38.2±0.4	1.80±0.07			
8	C	POST	2.75±0.48	0.091±0.032	7.84±0.38	27.0±0.4	0.344±0.061		0.070±0.038	
9	1	IN			8.57±0.63	7.3±1.7	0.64±0.15	0.081±0.016		
9	3	IN	0.33±0.31		9.73±0.22	23.6±0.4	0.373±0.052	0.0065±0.0034	0.323±0.030	<107
9	4	IN			13.2±0.3	37.2±0.7	0.656±0.077		0.624±0.041	
9	6	IN			12.0±0.6	17.6±1.2	1.04±0.14		0.639±0.081	
9	8	IN	9.6±3.0		3.5±1.5		1.50±0.37	0.049±0.051		
9	LMP	168:00	1.11±0.58		10.9±0.2	36.5±0.5	0.255±0.037	0.0075±0.0036	0.216±0.025	<185
9	CMP	113:00			11.0±0.2	9.77±0.46	0.109±0.036	0.0066±0.0037	0.171±0.025	<77.4
9	CMP	190:25			11.9±0.2	10.9±0.4	0.246±0.033	0.0062±0.0033	0.161±0.024	<73.2
9	CMP	235:00	0.239±0.075		11.1±0.2	10.2±0.4	0.350±0.033	0.0099±0.0054	0.286±0.023	<24.9
10	S/N 3512	IN		0.0061±0.0052	10.8±0.2		0.144±0.037		0.174±0.021	
10	S/N 3527	IN	0.72±0.38	0.023±0.016	14.5±0.6		0.31±0.10		0.352±0.060	
11	1	IN			7.70±0.23		1.33±0.24	0.0070±0.0037	0.330±0.031	<0.038
11	2	IN			8.59±0.22			0.0067±0.0036	0.196±0.030	<0.047
11	3	IN	0.41±0.33		4.45±0.22					<0.094
11	4	IN			7.94±0.38					<0.33
12	LMP #1	IN	2.49±0.33		9.24±0.22					<0.35
12	UNKNOWN	IN	0.67±0.18		7.23±0.22				0.043±0.029	<0.1
12	LMP #2	IN	0.97±0.35		7.58±0.22			0.010±0.004		<0.4
12	LMP ZSN	IN	13.3±1.7		8.77±0.21				0.088±0.027	<0.88
12	CDR	IN	1.61±0.21	0.0054±0.0030	8.03±0.24			0.0061±0.0037		<0.36
12	CMP	79	0.83±0.14		9.15±0.22		0.30±0.15			<0.19
12	CMP	101	2.43±0.41		4.88±0.23					<0.35
12	CMP	225			7.28±0.20			0.0050±0.0030		<0.081
13	1	IN		0.0035±0.0027	18.1±0.25		4.76±0.10	0.0091±0.0037	2.759±0.034	<0.3
13	2	IN		0.0062±0.0027	13.1±0.23		4.135±0.094	0.0095±0.0035	3.580±0.034	<0.19
13	3	IN	4.07±0.53		7.02±0.51			0.021±0.009		<0.78
13	4	IN	0.503±0.059	0.0099±0.0031	19.77±0.25		4.998±0.097	0.013±0.004	1.663±0.033	<0.078
13	5	IN	1.33±0.14		11.12±0.22		0.546±0.083	0.006±0.003	0.138±0.028	<0.17
13	6	IN		0.0037±0.0027	10.07±0.23			0.006±0.003		<0.096

TABLE II

RADIONUCLIDES IN FECES FROM APOLLO ASTRONAUTS

MISSION	SAMPLE IDENTIFICATION	FLIGHT PERIOD	ACTIVITY IN DISINTEGRATIONS/MINUTE/GRAM INERT ELEMENT ON DAY OF SPLASHDOWN				
			$^{22}Na/g$ Na	$^{51}Cr/g$ Cr	$^{59}Fe/g$ Fe	$^{60}Co/g$ Co	$^{137}Cs/g$ Cs
7	B	PRE		(4.26±0.055)·10^{7}	630±150		(8.3±1.4)·10^{6}
7	C	PRE		(4.32±0.10)·10^{7}			
7	S/N 2276	IN		(3.137±0.094)·10^{7}	1410±220		(7.8±1.3)·10^{6}
7	S/N 2277	IN		(1.678±0.042)·10^{7}			(6.4±1.0)·10^{6}
7	S/N 2278	IN	0.64±0.47	(2.137±0.021)·10^{7}	410±120		(5.2±1.2)·10^{6}
7	S/N 2280	IN	1.2±0.7	(2.917±0.026)·10^{7}	810±370		(5.6±2.0)·10^{6}
7	S/N 2282	IN		(1.511±0.041)·10^{7}			(5.59±0.90)·10^{6}
7	S/N 2292	IN		(2.795±0.054)·10^{7}			(1.6±1.1)·10^{6}
7	S/N 2299	IN		(2.498±0.032)·10^{7}	3470±280		(2.42±0.20)·10^{7}
7	S/N 2300	IN	0.50±0.26	(1.859±0.071)·10^{7}	930±200		(1.40±0.14)·10^{7}
7	S/N 2312	IN		(4.771±0.057)·10^{7}	730±180		(6.6±1.2)·10^{6}
7	A	POST	5.6±3.0	(3.105±0.050)·10^{7}	3450±290		
7	C	POST		(4.159±0.037)·10^{7}	(3.609±0.032)·10^{4}	(1.956±0.068)·10^{6}	(1.461±0.096)·10^{7}
8	1	IN		(1.943±0.051)·10^{7}	880±220		(4.58±0.48)·10^{6}
8	2	IN		(6.787±0.088)·10^{7}	1380±260		(9.42±0.78)·10^{6}
8	3	IN	0.77±0.61	(1.291±0.028)·10^{7}	2230±410		(5.39±0.74)·10^{6}
9	1	IN		(4.9±1.1)·10^{6}	3090±710	(4.8±1.0)·10^{5}	
9	3	IN		(1.241±0.024)·10^{7}	1690±240	(3.2±1.7)·10^{4}	(9.51±0.88)·10^{6}
9	4	IN		(4.228±0.076)·10^{7}	1870±220		(1.95±0.13)·10^{7}
9	6	IN		(1.354±0.089)·10^{7}	3450±480		(2.13±0.27)·10^{7}
9	8	IN			9400±2900	(3.5±2.2)·10^{5}	
9	LMP	168:00		(2.325±0.035)·10^{7}	740±110	(4.2±2.0)·10^{4}	(5.20±0.61)·10^{6}
9	CMP	113:00		(6.98±0.33)·10^{6}	269±88	(4.1±2.3)·10^{4}	(4.99±0.77)·10^{6}
9	CMP	190:25		(7.26±0.29)·10^{6}	1170±160	(2.7±1.4)·10^{4}	(5.31±0.78)·10^{6}
9	CMP	235:00		(7.28±0.31)·10^{6}	1750±170	(4.1±1.4)·10^{4}	(7.47±0.61)·10^{6}
10	S/N 3512	IN	0.57±0.49		730±190	(6±4)·10^{4}	(3.41±0.42)·10^{6}
10	S/N 3527	IN	15±10		620±200		(4.65±0.85)·10^{6}
11	1	IN			9500±1700	(4.8±2.5)·10^{4}	(1.24±0.12)·10^{7}
11	2	IN				(3.4±1.8)·10^{4}	(6.29±0.95)·10^{6}

TABLE III

RADIONUCLIDES IN URINE FROM APOLLO ASTRONAUTS

MISSION	SAMPLE IDENTIFICATION	FLIGHT PERIOD	ACTIVITY IN DISINTEGRATIONS/MINUTE/ML URINE ON DAY OF SPLASHDOWN							
			^{7}Be	^{22}Na	^{24}Na	^{40}K	^{51}Cr	^{59}Fe	^{60}Co	^{137}Cs
7	A	PRE	0.105±0.015			7.10±0.02	2610±10		0.00501±0.00042	0.250±0.002
7	C	PRE	0.212±0.098			0.763±0.094	0.155±0.041			0.0096±0.0047
7	A	POST	0.72±0.20	0.0040±0.0022		3.47±0.18	123±1			0.154±0.025
7	B	POST	0.83±0.25	0.0075±0.0025		6.84±0.17	12300±100	2.79±0.03	2.79±0.03	0.407±0.025
7	C	POST	0.79±0.20			3.17±0.14	16900±100	16.7±0.1	1.00±0.02	0.166±0.023
8	A	POST	0.492±0.081			2.63±0.11	83.5±0.3	0.139±0.021	0.0037±0.0022	0.179±0.016
8	B	POST	1.16±0.13	0.0026±0.0019		2.84±0.16	1450±1	8.66±0.04	0.201±0.009	0.148±0.023
8	C	POST	1.95±0.35			7.10±0.40	9010±140	7.46±0.09	0.237±0.026	0.213±0.041
9	CMP	F-14		0.00046±0.00021		5.14±0.05				0.0526±0.0024
9	LMP	F-14		0.00051±0.00019		4.52±0.02				0.0335±0.0021
9	CDR	F-14	0.015±0.012	0.00086±0.00022		2.65±0.02				0.0352±0.0021
9	CMP	F-4	0.027±0.012			4.40±0.02	93.2±0.1	0.0162±0.0049		0.0404±0.0023
9	LMP	F-4	0.041±0.012			6.66±0.03	146±4	0.0214±0.0038	0.00053±0.00027	0.0546±0.0021
9	CDR	F-4		0.00028±0.00020		3.33±0.02	147±1	0.0095±0.0045		0.0568±0.0024
9	LMP	POST+0				3.69±0.18	119±1	0.131±0.035		0.150±0.026
9	CDR	POST+0				1.26±0.03	19.0±0.1			0.0132±0.0024
9	CMP	POST+1	0.274±0.045	0.00084±0.00073		2.90±0.06	461±40	0.058±0.016		0.122±0.008
9	LMP	POST+1				2.93±0.05	5580±50	0.0226±0.0012	0.0012±0.0010	0.0712±0.0074
9	CDR	POST+1				2.28±0.06	1570±30	0.058±0.016		0.0881±0.0085
10	CMP	PRE				2.67±0.08	1.24±0.14	0.061±0.015		0.0575±0.0093
10	LMP	PRE				2.71±0.08				
10	CDR	PRE		0.0012±0.0009		1.99±0.07		0.126±0.012		0.0160±0.0011
10	CMP	POST		0.0026±0.0010	0.06±0.03	2.62±0.06	0.315±0.083	0.0458±0.0092		0.0488±0.0006
10	LMP	POST	0.19±0.03		0.05±0.04	3.27±0.07		0.018±0.010		0.0447±0.0086
10	CDR	POST	0.04±0.03			0.421±0.044	0.626±0.088	0.0189±0.0075		0.0356±0.0068
11	CMP	PRE	0.440±0.091			2.52±0.07				0.0137±0.0087
11	LMP	PRE	0.144±0.071	0.00080±0.00069		1.55±0.05		0.067±0.026		0.0601±0.0069
11	CDR	PRE	0.208±0.069			2.62±0.05				0.0429±0.0068
11	CMP	POST	0.154±0.074	0.0010±0.0006		2.06±0.05			0.0009±0.0008	0.0072±0.0068
11	LMP	POST				1.73±0.05				0.0112±0.0066
11	CDR	POST		0.0014±0.0007		0.77±0.06				0.0196±0.0077
12	CMP	F-30				3.42±0.06		0.166±0.028		0.0708±0.0082
12	LMP	F-30				3.36±0.07		0.296±0.030		0.1046±0.010
12	CDR	F-30		0.0016±0.0006		4.02±0.05				0.0410±0.0066
12	CMP	F-15				3.38±0.06		0.257±0.028		0.1309±0.008
12	LMP	F-15				5.10±0.07		0.101±0.025		0.0868±0.0080
12	CDR	F-15								0.0472±0.0069
12	CMP	POST+0				5.72±0.21		0.259±0.098		0.1062±0.0131
12	LMP	POST+0				10.4±0.3		0.58±0.15		0.655±0.042
12	CDR	POST+0				9.12±0.27		0.59±0.11		0.402±0.036
12	CMP	DAY 2		0.0046±0.0038				0.55±0.15		
12	LMP	DAY 2				5.98±0.25		0.45±0.10	0.0098±0.0052	0.202±0.036
12	CDR	DAY 2		0.0050±0.0025		5.66±0.19				
13	LMP	F-5	0.182±0.076	0.0034±0.0009		1.80±0.072		0.095±0.028		0.0612±0.0097
13	CDR	F-5	0.283±0.074	0.0012±0.0008		2.21±0.070		0.063±0.027	0.0047±0.0013	0.0134±0.0092
13	LMP	POST+0	0.68±0.14			2.97±0.13				0.078±0.017

TABLE IV

RADIONUCLIDES IN URINE FROM APOLLO ASTRONAUTS

MISSION	SAMPLE IDENTIFICATION	FLIGHT PERIOD	ACTIVITY IN DISINTEGRATIONS/MINUTE/GRAM INERT ELEMENT ON DAY OF SPLASHDOWN			
			^{22}Na/g Na	^{24}Na/g Na	^{60}Co/g Co	^{137}Cs/g Cs
7	A	POST	1.4±0.8	20±13		
7	B	POST	4.9±1.6			
8	B	POST	1.6±1.2			
11	CMP	PRE				$(2.2\pm1.4)\cdot10^{6}$
11	LMP	PRE	0.51±0.40			$(1.07\pm0.12)\cdot10^{7}$
11	CDR	PRE				$(5.17\pm0.82)\cdot10^{6}$
11	CMP	POST	0.48±0.30		$(1.3\pm1.1)\cdot10^{6}$	$(7.2\pm6.8)\cdot10^{5}$
11	LMP	POST				$(2.4\pm1.4)\cdot10^{6}$
11	CDR	POST	0.43±0.29			$(2.04\pm0.80)\cdot10^{6}$
12	CMP	F-30				$(2.36\pm0.27)\cdot10^{7}$
12	LMP	F-30				$(1.80\pm0.17)\cdot10^{7}$
12	CDR	F-30	0.49±0.19			$(5.78\pm0.93)\cdot10^{6}$
12	CMP	F-15				$(5.22\pm0.31)\cdot10^{7}$
12	LMP	F-15				$(1.77\pm0.16)\cdot10^{7}$
12	CDR	F-15				$(1.15\pm0.17)\cdot10^{7}$
12	CMP	POST+0				$(1.45\pm0.43)\cdot10^{7}$
12	LMP	POST+0				$(1.98\pm0.12)\cdot10^{8}$
12	CDR	POST+0				$(4.51\pm0.41)\cdot10^{7}$
12	CMP	DAY 2	4.4±3.6			
12	LMP	DAY 2			$(5.7\pm3.0)\cdot10^{6}$	$(1.97\pm0.35)\cdot10^{7}$
12	CDR	DAY 2	2.2±1.1			

The average values of the cosmogenic radionuclide concentrations in each basic flight period are summarized in Table V according to the various methods of normalization. The increase in the activities from preflight to inflight and postflight periods should be indicative of the exposure to cosmic radiation. The concentrations of each radionuclide increase rather regularly for the Apollo 7 mission regardless of the method of normalization. However, the fecal data for the Apollo 8 mission are quite irregular, with only the urine data demonstrating increases in the cosmogenic radionuclides. The Apollo 9 and 13 missions show increases in the ^{7}Be concentration in the urine but demonstrate decreases in the ^{22}Na concentrations while the reverse is true for Apollo 11. Regular increases are shown for Apollo 10 and 12.

The increases in cosmogenic radioactivity from preflight levels to those after exposure to the space environment are almost certainly due to cosmic particle activation. Equating the magnitude of the increase with the radiation dose delivered by the particles is still fairly difficult, particularly when the dose is quite small as has been the case on all manned Apollo missions thus far. Concentrations normalized to the unit mass or volume of excreta are subject to variation in the biological dilution of the specimen. Concentrations normalized to the unit mass of stable element in the feces are also subject to variations in the quantities of unmetabolized elements passing through the gastrointestinal tract. Only the quantities of radionuclides in the urine normalized to the amount of stable element present can be expected to be reasonably representative of the specific activity in the whole body since the urine contains only metabolized material.

Indeed, it is necessary to make some assumptions regarding the percentages of the body burden of an element excreted in the feces or urine, the relative dilution factors of feces and urine, and the "contamination" of feces by unmetabolized elements in order to compare the data with the experimental results for proton irradiated muscle tissue[1, 2], proton irradiated radiotherapy patients [3], and neutron irradiated radiotherapy patients [4]. In this manner, the average effective proton energy incident on the astronauts and the radiation dose received by them can be estimated. The details of these calculations will be omitted here since they are given elsewhere[9-12]. The results indicate an average effective proton energy of 38-40 MeV incident on the Apollo 7 mission astronauts and <38 MeV on the Apollo 8 mission astronauts. Radiation doses of 480 $\pm$ 310, <315, 870 $\pm$ 550, <480, and <250 millirads for the Apollo 7, 9, 10, 12, and 13 missions respectively are calculated.

Since the specific activity of the cosmogenic radionuclides in the urine should be a more accurate representation of the whole body burden of induced radioactivity, the specific activity of the ^{22}Na in the postflight urine of astronauts is compared to the specific activity of ^{22}Na in the urine of radiotherapy patients who have received a known radiation dose. This comparison leads to estimated cosmic radiation doses received by the astronauts on the Apollo 7, 8, 11, and 12 missions of 330, 160, 31, and 110 millirads respectively. It should be pointed out here that the uncertainty of the data given in Table V, and hence of these results, is quite large in some instances.

DISCUSSION

In principle the relationships between induced activity and radiation dose are straightforward. The probability for production of a certain isotope in the body of an astronaut is basically a function of the energy of the proton. Similarly, the radiation dose from a cosmic proton is also a function of its energy, and therefore, the induced activity is logically related to the radiation dose. Such relationships have been empirically determined for several different situations[1-4], and it remains only to measure the quantities of induced radionuclides in a particle irradiated person to determine the dose he received.

In practice, however, the procedure is not quite as simple as that just described. A calibrated whole-body counter is required to determine the quantities of induced radionuclides, and a high sensitivity-low background instrument would be required to measure the small quantities of radionuclides induced by the low levels of cosmic radiation encountered on a normal space flight. In lieu of the availability of a suitable whole-body counter, an indirect approach such as that used in this work can be applied. The principal limitations to this method have already been touched upon above. Only a small and uncertain fraction of the induced activity is eliminated in the excreta. Thus only the

TABLE V

AVERAGE RADIONUCLIDE CONCENTRATIONS IN EXCRETA FROM APOLLO ASTRONAUTS

NORMALIZED RADIOACTIVITY IN DISINTEGRATIONS PER MINUTE

ACTIVITY	FLIGHT PERIOD	APOLLO 7	APOLLO 8	APOLLO 9	APOLLO 10	APOLLO 11	APOLLO 12	APOLLO 13
^{7}Be/g Feces	Pre	1.12	3.25					
^{7}Be/g Feces	In	1.59	1.78	1.25	0.36	0.10	2.79	0.98
^{7}Be/g Feces	Post	2.94	2.33					
^{22}Na/g Feces	Pre		0.025					
^{22}Na/g Feces	In	0.0014	0.0014		0.015		0.0007	0.0039
^{22}Na/g Feces	Post	0.0026	0.040					
^{22}Na/g Na in Feces	In	0.26	0.26		7.8			
^{22}Na/g Na in Feces	Post	2.8						
^{7}Be/ml Urine	Pre	0.159		0.014		0.264		0.233
^{7}Be/ml Urine	Post	0.755	1.20	0.055	0.077	0.051		0.68
^{22}Na/ml Urine	Pre			0.0005	0.0004	0.0003	0.0003	0.0013
^{22}Na/ml Urine	Post	0.0038	0.0009	0.0002	0.0009	0.0008	0.0016	
^{24}Na/ml Urine	Post				0.04			
^{22}Na/g Na in Urine	Pre					0.17	0.08	
^{22}Na/g Na in Urine	Post	3.2	1.6			0.30	1.1	
^{24}Na/g Na in Urine	Post	20						

specific activity of an induced radioisotope in the urine can be extrapolated to the whole body burden with a reasonable degree of accuracy.

While the efficiency of low-level sample counters is routinely several orders of magnitude higher than whole-body counters, the small fraction of the total body activity in any bioassay sample reduces the sensitivity of a specimen measurement to the point where it is little better than that of a whole-body count. To complicate the situation in this work even further, there is a large demand for aliquots of postflight urine specimens from the astronauts and typically only 10% or less of a 24-hour collection has been available for radionuclide concentration measurements. An additional complication in the case of non-lunar-landing missions (Apollo 13 excepted) was the injection of radioisotopes into the astronauts for medical studies. Although these isotopes were not the same as the cosmogenic radionuclides measured, their presence in the excreta lowered the overall accuracy of the measurements. Finally, the quarantine requirements of the lunar landing missions caused a delay in the analysis of postflight specimens which allowed substantial decay of the radionuclides present. These factors all contribute to the reduced accuracy and sensitivity of the measurements reported herein. In an effort to improve the situation, a high sensitivity combination whole-body counter and sample counter has been proposed which could be rapidly utilized after a mission (even onboard the recovery vessel) to make accurate measurements of the whole body burden of radionuclides in the astronauts. The combination of direct measurement of whole body burdens of radionuclides and the early measurement of relatively large quantities of excreta should make much more accurate dose estimates possible.

This technique for measurement of radiation dose should be perfected during routine space missions so that in the event of an unusually high exposure, such as might be expected from a solar flare, an accurate determination of the radiation dose can be obtained. This situation would be analogous to those nuclear criticality accidents[13-15] where conventional dosimetry techniques were saturated and induced radioactivity was measured to interpret the radiation dose received by the exposed individuals.

REFERENCES

1. R. L. Brodzinski, N. A. Wogman, and R. W. Perkins, "Induced Radionuclides in Astronauts," NASA-CR-73252 (1968).

2. R. L. Brodzinski, N. A. Wogman, and R. W. Perkins, "Cosmic-Ray-Induced Radioactivity in Astronauts as a Measure of Radiation Dose," Space Life Sciences 2, 69 (1969).

3. R. L. Brodzinski, N. A. Wogman, J. C. Langford, and R. W. Perkins, "Radioactivity in the Urine of Proton Irradiated Patients," Unpublished data, Battelle Memorial Institute, Pacific Northwest Laboratories, Richland, Washington.

4. R. L. Brodzinski, "Radioactivity in the Blood and Urine of Neutron Irradiated Radiotherapy Patients," Unpublished data, Battelle Memorial Institute, Pacific Northwest Laboratories, Richland, Washington.

5. R. W. Perkins, "An Anticoincidence Shielded Multidimensional Gamma-Ray Spectrometer," Nucl. Instr. and Methods 33, 71 (1965).

6. N. A. Wogman, D. E. Robertson, and R. W. Perkins, "A Large Detector Anticoincidence Shielded Multidimensional Gamma-Ray Spectrometer," Nucl. Instr. and Methods 50, 1 (1967).

7. N. A. Wogman, R. W. Perkins, and J. H. Kaye, "An All Sodium Iodide Anticoincidence Shielded Multidimensional Gamma-Ray Spectrometer for Low-Activity Samples," Nucl. Instr. and Methods 74, 197 (1969).

8. L. A. Rancitelli, J. A. Cooper, and R. W. Perkins, "The Multielement Analysis of Biological Material by Neutron Activation Analysis and Direct Instrumental Techniques," Proceedings of the 1968 International Conference: Modern Trends in Activation Analysis, Gaithersburg, Maryland (1969).

9. R. L. Brodzinski, H. E. Palmer, and L. A. Rancitelli, "The Measurement of Radiation Exposure of Astronauts by Radiochemical Techniques," April 8, 1969 Through June 30, 1969, BNWL-1183 1 (1969).

10. R. L. Brodzinski, L. A. Rancitelli, and W. A. Haller, "The Measurement of Radiation Exposure of Astronauts by Radiochemical Techniques," October 6, 1969 Through January 4, 1970, BNWL 1183 3 (1970).

11. R. L. Brodzinski, L. A. Rancitelli, and W. A. Haller, "The Measurement of Radiation Exposure of Astronauts by Radiochemical Techniques," January 5, 1970 Through April 5, 1970, BNWL 1183 4 (1970).

12. R. L. Brodzinski and W. A. Haller, "The Measurement of Radiation Exposure of Astronauts by Radiochemical Techniques," April 6, 1970 Through July 5, 1970, BNWL 1183 5 (1970).

13. "Dosimetry Investigation of the Recuplex Criticality Accident," Health Physics 9, 757 (1963).

14. R. W. Perkins and L. J. Kirby, "Radiological Chemistry Associated with the Hanford Criticality of April 7, 1962," USAEC Report HW-76823 (1962).

15. "Accidental Radiation Excursion at the Y-12 Plant," Y-1234 (1958).

PLENARY SESSION III
NATURAL SPACE RADIATION

CHAIRMAN: J. I. VETTE
DIRECTOR, NATIONAL SPACE SCIENCE DATA CENTER
GODDARD SPACE FLIGHT CENTER

THE GEOMAGNETICALLY TRAPPED RADIATION ENVIRONMENT

---A RADIOLOGICAL POINT OF VIEW---

F. Eugene Holly, Ph.D.
Air Force Weapons Laboratory
Kirtland AFB, New Mexico

The regions of naturally occurring, geomagnetically trapped radiation (Van Allen Belts) are briefly reviewed in terms of physical parameters such as; particle types, fluxes, spectrums, and spatial distributions. The major emphasis is, however, placed upon a description of this environment in terms of the radiobiologically relevant parameters of absorbed dose and dose-rate and a discussion of the radiological implications in terms of the possible impact on space vehicle design and mission planning.

These descriptions are based both upon direct measurement and calculation using the more fundamental parameters of particulate energy and flux. Comparison of such calculations with measurements emphasizes that, depending upon the location in space, that calculational techniques are extremely dependent upon detailed knowledge of either the energy spectrum or material (shielding) distribution about the dose point -- or both.

INTRODUCTION

Since Van Allen's (ref. 1) discovery of areas of geomagnetically trapped radiation in 1958, there has been a tremendous amount of attention focused upon this phenomena. Upon only a cursory examination of launch records (refs. 2-5), it is easy to identify over a hundred satellites and several times that many non-orbital vehicles, during the 10 year period 1958-1968, which contained radiation measuring instrumentation. These experimental packages ranged from emulsions and simple/geiger systems, with which the discovery of the belts and the first identifications of electrons and protons were made (refs. 1, 6, 7), to extreme complexity. Some satellites carried several dozen different experiments. Many excellent reviews concerning the trapped radiation environment have been written (refs. 2, 8-16). White's (ref. 8) is perhaps the most succinct and easily read, while those interested in a rigorous treatment may consult Hess (ref. 2). Reference 16 is a compilation of all experimental data dealing with radiological parameters.

PHYSICAL PARAMETERS

Largely due to the efforts of Vette (refs. 17, 18), the results of a large number of satellite experiments have been combined to form a model of the geomagnetically trapped radiation zones. These environmental models are available in the form of synoptic maps of flux and energy spectrums (refs. 12, 16, 17, 18, 19, 20) and use the systematic coordinates B and L or R and λ, which were developed by McIllwain (ref. 21). B is the magnetic field strength and L is a "magnetic shell" parameter relating the distance from the center of the earth through the magnetic equator to the point of interest. R is related to L through the expression $R = L\cos^2 \lambda$, and λ is the angle to the geomagnetic equator. R and λ are <u>not</u> the same as the geographic altitude and latitude and can be obtained only from the B-L system. For further discussions of these coordinate systems, the reader is referred to reference 21 and Chapter II of reference 16.

In general, the parameters which are of interest to designers and planners are those which will cause detectible influence on man or machine and these will be given the more thorough scrutiny by this writing.

<u>Protons</u>: There are distributions of high energy (10 to many hundred MeV) protons whose intensity varies with spatial location and has a maximum intensity at about L = 1.5 (L is expressed in units of earth radii). The intensity decreases to about 10^{-3} to 10^{-4} of maximum intensity at L = 3.0 with a smaller secondary maximum occuring at L = 2.2. At the position of the primary maximum, the integral flux above 34 MeV is approximately 2×10^{4} cm $^{-2}$ sec^{-1}. The spectral shape, although dependent upon spatial location, generally may be represented as decreasing exponentially, as shown in Figure 1 (ref. 16). Secondly, there are multilayers of low energy protons (0.1 to 10 MeV) surrounding the earth like "concentric skins on an onion" (ref. 8) with increasing energy toward the earth.

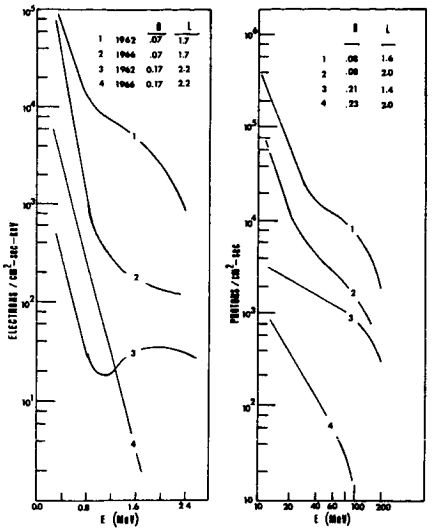

1. Typical trapped electron and proton spectrums. The difference in hardness of the 1962 and 1966 spectrums is due to the decay or loss of the artificially injected Starfish fission-electrons.

Electrons: There are two intense electron belts widely separated by a "slot" of considerably less and varying intensity. The "inner belt" maximum intensity occurs at L = 1.4 and has an integrated intensity above 0.5 MeV greater than 10^8 cm^{-2} sec^{-1} and consists of electrons with energies from a few keV to several MeV. This region is made up, primarily, of artificially injected electrons from the Starfish high-altitude nuclear explosion (1962) and does not fluctuate; however, the intensity decreases slowly with time as the electrons are lost into the atmosphere. The "outer belt", extending from L = 3 to L = 6, consists of natural electrons of lower energies and fluctuates with time. The integrated intensity above 0.5 MeV, at the maximum of this belt (L = 4.5 to L = 5), is in excess of 10^6 $cm^{-2}sec^{-1}$. Although there were no extensive spectral measurements prior to the Starfish event, the inner belt electrons were identified in 1959, and the differential energy spectrum measured at L = 1.3, B = 0.25 (ref. 7). This spectrum decreased by a factor of 20 over the energy range from 100 to 450 keV and less than 3% of the measured electrons could have had energies in excess of 1 MeV. Cladis, et. al., (ref. 22) found that, in 1960, the outer belt could essentially be characterized exponentially with a 60 keV e-folding between 50 and 700 keV, a much steeper spectrum than the inner belt. These pre-Starfish spectrums may be compared with the 1962 (ref. 23) and 1966 (ref.24) spectral determinations shown in Figure 1, which include the Starfish electrons. Qualitatively, one may conjecture that the soft component shown is natural and that the harder component is the artificial contribution.

Heavy Ions: Krimigis and Van Allen (ref.25), in 1967, first established the presence of heavy ions (helium nucleii) trapped in the geomagnetic field out to distances of 4 earth radii. The energy spectra are not unlike exponential functions and their intensity varies from 0.1 to 10% of the trapped proton component, depending upon spatial location. If, however, the intensities of both components are integrated above a common 0.5 MeV/nucleon energy, the helium to proton flux ratio is approximately 2 x 10^{-4} at L = 3.1, B = 0.19.

A composite pictorial representation of the more penetrating components of the trapped environment is shown in Figure 2. The distributions of electrons with energies in excess of 0.5 MeV are displayed on the right side of the figure and proton distributions with energies exceeding 34 MeV are shown on the left. These distributions, of course, are contours of revolution around the earth and neither the many layers of low energy protons nor the heavy nucleii are represented.

RADIOLOGICAL PARAMETERS

The mission planner or spacecraft designer, who must determine potential material damage or biological hazards, is concerned with the energy that is deposited per unit volume at points of interest which are usually located within hetrogeneous shield configurations. In such cases, an expression of absorbed dose at the point of interest is a highly useful parameter. This necessitates transport through surrounding shielding and calculation of energy deposition at a specific location. The trapped radiation environment with particle types, fluxes, and energy spectrums changing kaleidoscopically with spatial position (not to mention time) poses an extremely onerous task. This is further compounded, in the case of calculation of biological hazards, where the critical location may be influenced by spectral shape (i.e., a steep spectrum is more likely to reach an internal organ, with a low tolerance, than a soft spectrum). If the physical parameters are known in sufficient detail, these tasks may be accomplished with the aid of sophisticated computer programs; however, it is expensive and time consuming. In cases where the dose or dose-rate is needed only at selected points in space or the determination of only maximum levels is necessary, an environmental model expressed in terms of absorbed dose or dose-rate is the most practical tool. Such a model, including shield thickness as a parameter, obviates the necessity for lengthy computer calculations except where complex orbital parameters are involved or where extreme accuracy is required.

Contributions in this area have been made by the Biophysics Division of the Air Force Weapons Laboratory (ref. 16). Between July 1961 and May 1969, thirteen satellites and two suborbital probes were instrumented with combinations of instrumentation for the simultaneous measurement of both radiological and physical parameters. The dosimetric instrumentation consisted of tissue-equivalent ionization chambers, which responded with better than 90% accuracy (in mixed gamma, electron, and proton fields) from a few mr/hr to several hundred r/hr and advanced devices for the measurement of linear-energy-transfer (LET) in small volumes (refs. 16, 26, 27, 28, 29). These instruments were surrounded with varying amounts of either tissue-equivalent or elemental shields. The OV1-2 and OV3-4 satellites were typical of these vehicles and were designed for two specific purposes: (1) to provide a comprehensive synoptic dose-rate map of the trapped

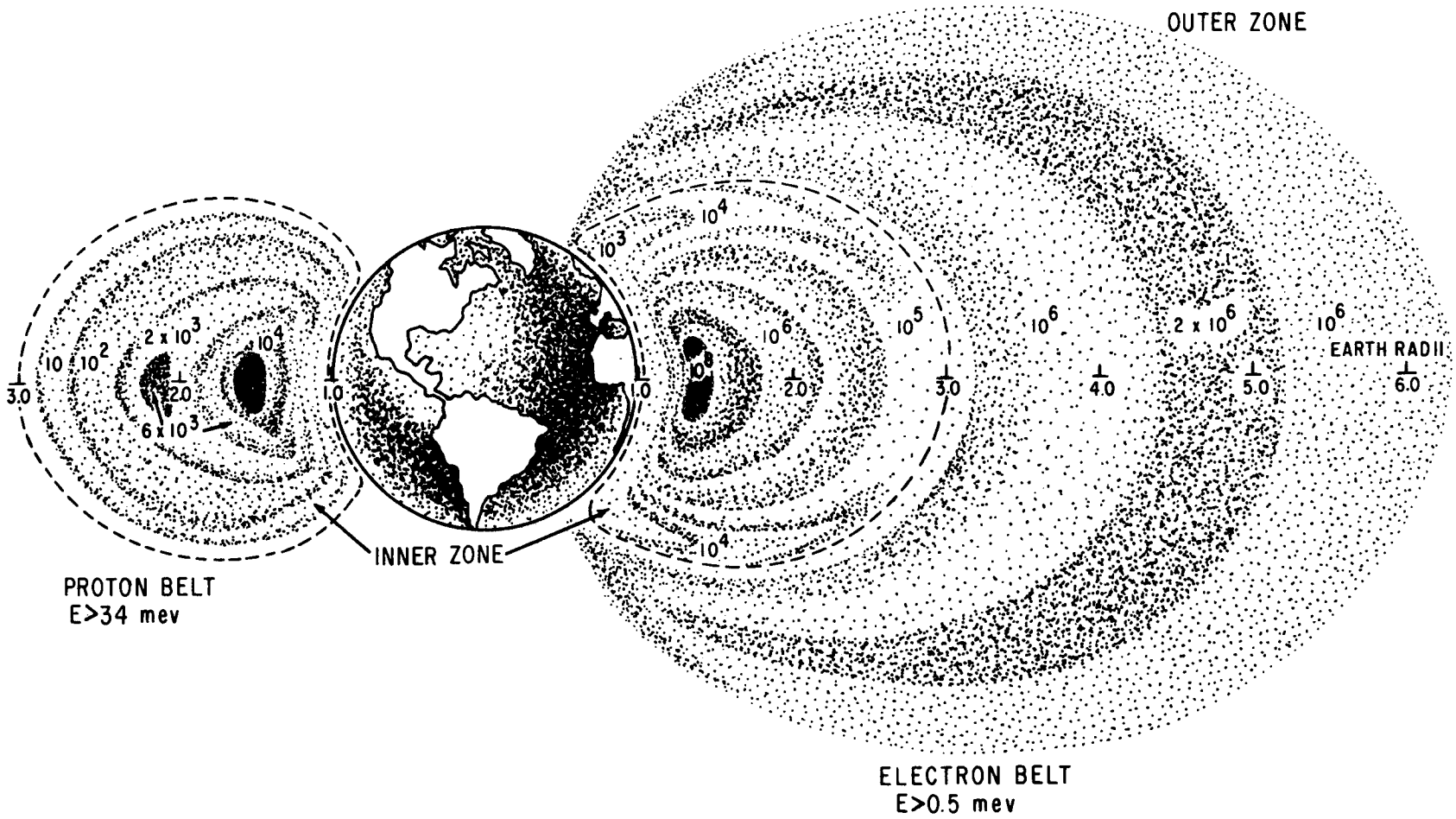

TRAPPED RADIATION ZONES

Figure 2. A model of the penetrating components of the trapped radiation environment, showing electrons on the right and protons on the left.

environment and (2) to study the effects of radiation spectra, anisotropy, and shielding hetrogeneity on the calculation of electron, proton, and bremsstrahlung doses (refs. 16, 30, 31, 32). The instrument complements of these satellites is shown in Tables 1 and 2. In addition, further data was obtained by active and passive dosimetry systems flown in a number of Gemini and Apollo missions (refs. 16, 33, 34).

Dose-rate maps based on data from four of these satellites and the Gemini flights have recently been made available by reference 16. These are in either the B, L isodose format of Figure 3; the Dose-rate, B, Iso-L format of Figure 4; or geographic projections of isodose contours at different altitudes. These are plotted in terms of dose rate beneath shielding material or in a more universally usable form of thickness of aluminum equivalent material. Table 3 gives a concise summary of the maps which are available in terms of B, L, dose-rate, and and shielding thickness ranges. Data reduction efforts currently being performed will result in the production of comprehensive synoptic dose-rate maps covering the following ranges of parameters: (1) L = 1 - 5 earth radii, (2) B = .05-0.36 gauss, and (3) 0 - 16 gm/cm aluminum equivalent thickness of shielding material (ref. 35).

TABLE 1

TYPICAL INSTRUMENTATION FOR MEASUREMENT
of
PHYSICAL PARAMETERS

Instrument	Satellite	Type of Measurement	Range
Electron Spectrometer	OV1-2	Electron flux, energy spectrums, and angular distribution	0.5 to 5.0 MeV in eight channels
Proton Spectrometer	OV1-2	Proton flux, energy spectrums, angular distribution	49 to 120 MeV in four channels
Proton Spectrometer	OV1-2	Integral proton flux between limits, angular distribution	1-20 MeV and 20-49 MeV
Omnidirectional Proton/Electron Spectromeners	OV1-2	Integral proton flux between limits	6-20, 40-80, 100-150 and greater than 100 MeV
	OV3-4		15-30, 30-55, 55-105, 105-170 and greater than 170 MeV
	OV1-2	Integral electron flux between limits	Greater than 0.3 and greater than 4.5 MeV
Charged Particle Spectrometer	OV3-4	Proton flux, energy spectrums, angular distribution	10.5 to 320 MeV in nine channels and greater than 320 MeV
		Electron flux, energy spectrums, angular distribution	0.5 to 4.8 MeV in six channels and greater than 4.8 MeV
		Heavy Particle flux, energy spectrums, angular distribution	11-300 MeV/nucleon in four channels

TABLE 2

TYPICAL INSTRUMENTATION FOR MEASUREMENT
of
RADIOLOGICAL PARAMETERS

Instrument	Satellite	Type of Measurement	Dynamic Range
Proton Dosimeter	OV1-2	Energy deposition at known depths in simple geometries	0.5 to 2 x 10^4 MeV/sec (each detector)
X-ray/Bremsstrahlung Dosimeter	OV1-2	Energy deposition from bremsstrahlung production in known shields	1.62 x 10^2 to 1.62 x 10^6 MeV per second
Tissue Equivalent ionization chamber (Tissue Equivalent shield material)	OV1-2	Absorbed dose in rads/hr at depths of 0.8, 3.2 and 8.0 gm/cm^2	0.2 to 200 Rad/hr
	OV3-4	Depths of 0.7, 2.9 and 4.7 gm/cm^2	10^{-2} to 10^3 Rad/hr
Tissue equivalent ionization chamber (Elemental shield)	OV3-4	Absorbed dose in rads/hr at depths: 0.2 gm/cm^2 Al	10^{-2} to 10^3 rad/hr
			10^{-4} to 10 rad/hr
		4.5 gm/cm^2 brass	10^{-3} to 10^2 rad/hr
LET Spectrometer	OV3-4	Linear Energy transfer at depths of 2.5 and 5.0 gm/cm^2	8 to 300 KeV/micron in 16 log channels

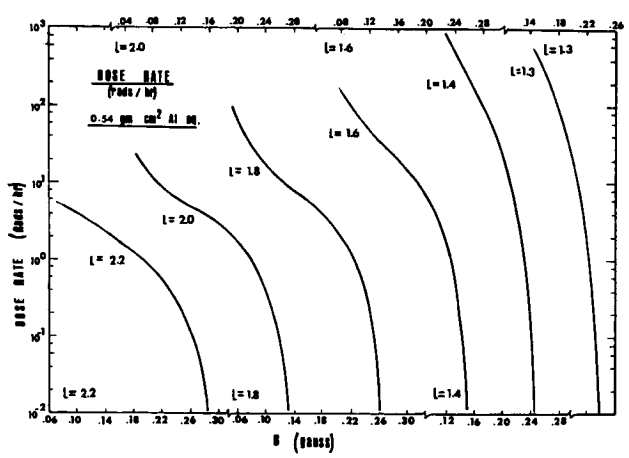

Figure 3. Typical Iso-L dose-rate profile map. The dose-rates are given in terms of amount (0.54 gm/cm^2) of aluminum equivalent material.

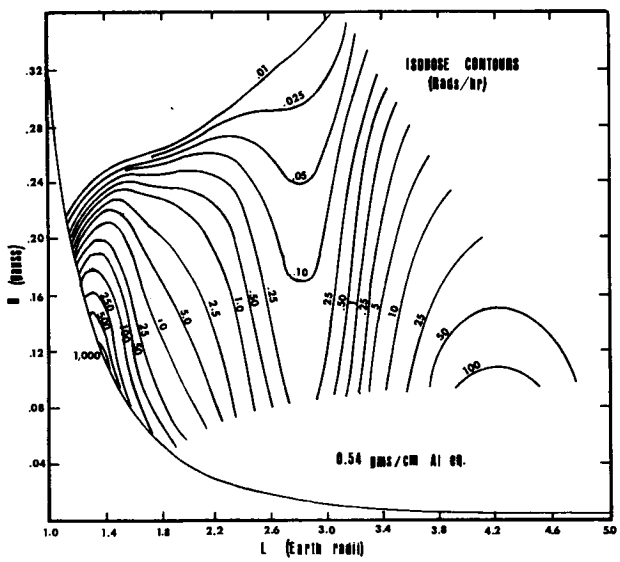

Figure 4. Typical Isodose-Rate profile map. The dose-rates are given in terms of amount (0.54 gm/cm^2) of aluminum equivalent material.

TABLE 3

DOSE-RATE MAPS PRESENTLY AVAILABLE

Shielding (gm/cm^2 Al)	Range of B (gauss)	Range of L (Earth radii)	Dose-rate Range (Rad/hr)
0.4	0.12-0.28	1.2 - 2.0	10^{-2} - 10^{2}
0.5	0.06-0.36	1.2 - 5.0	10^{-2} - 10^{3}
1.0	0.20-0.26	1.2 - 1.5	10^{-4} - 10^{0}
1.35	0.06-0.36	1.2 - 5.0	10^{-2} - 50
1.40	0.12-0.28	1.2 - 2.0	10^{-2} - 10^{2}
1.50	0.16-0.30	1.2 - 2.0	10^{-4} - 10^{1}
2.8	0.06-0.30	1.0 - 2.6	10^{-2} - 10^{1}
3.4	0.12-0.28	1.2 - 2.0	10^{-2} - 10^{1}
4.0	0.14-0.23	1.2 - 2.0	10^{-2} - 10^{1}
4.15	0.06-0.36	1.2 - 2.2	10^{-2} - 10^{3}
4.9	0.06-0.30	1.0 - 2.6	10^{-2} - 10^{1}
16.0	0.16-0.26	1.2 - 1.7	10^{-2} - 10^{1}

COMPARISON OF DOSE-RATE MEASUREMENTS WITH CALCULATIONS BASED ON PHYSICAL PARAMETERS

In those cases where extensive computer calculations using physical parameters must be performed, it is necessary to estimate the accuracy of the techniques. In order to better understand uncertainties in the transport calculations and the reliability of the available physical parameters, data from four satellites and two Gemini flights were extensively analyzed (refs. 12, 16, 19, 20, 31, 32). Data from three of the satellites included simultaneous measurements of both physical and radiological parameters and, thus, could be used to check both transport calculations per se, and dose calculations which were based on previously available data (refs 12, 17, 18). It was determined that the available physical environment was inadequate, in many cases, to accurately predict the dose-rates which were encountered. The use of simultaneously measured flux, spectrums, etc. yielded much better agreement. These data were then used to "update" the available maps and, as a check, dose-rate calculations were performed for the remaining satellite and the two Gemini flights.

The results of calculations using both the old and new environments, shown in Figure 5 and Table 4, indicate that calculations based on the old (Vette) environment underestimated the dose-rate in heavily shielded detectors where high energy (E > 80 MeV) protons contribute heavily to the dose-rate.

It was also determined (refs. 16, 31, 32) that to correctly evaluate the results of lightly shielded detectors, which are either omni-directional or do not provide "active collimation", a very sophisticated knowledge of the surrounding shielding (satellite and instrumentation) is necessary to adequately understand the data. This was also largely due to the much greater fluxes of high energy protons than had originally been estimated.

SUMMARY

Although nearly thirteen years has elapsed since the discovery of the trapped radiation environment and thousands of experiments performed, the data are insufficiently understood to accurately make estimates of radiological hazards.

Accurate calculations of doses have been possible only where precise determinations of the physical environment and spacecraft shielding were made. The only calculated results for a manned flight which were accurate to a factor of 2 were obtained using a simultaneously measured environment. In an unmanned craft on which a 1280 solid angle sectoring analysis of the shielding about the dose point was performed, the calculated and measured doses usually agreed to 50%. This latter used the new proton environment of contributions from protons with energies greater than 170 MeV.

The data from both manned and unmanned spacecraft show that the largest uncertainty is consistently in the knowledge of the radiation environment. The inner trapped region (L = 1 to 2.0) was divided into a high B and a low B region for comparison of calculation and measurement and very poor agreement was sometime found at the high magnetic field regions of the L shells, regardless of the generation of the environment used. At low magnetic field regions of the L shells, the Vette environment consistently underestimated the dose-rate by as much as a factor of 7; and the new environment, while better, yielded only a factor of 2 agreement in some regions.

The areas where manned flights occur are areas where the environmental data are most insufficient and the B-L coordinate system tends to fail. There is clearly a need for further definitions of environmental parameters.

TABLE 4

AVERAGE RATIOS OF CALCULATED TO MEASURED DOSE-RATES
for
CALCULATIONS USING THE VETTE
and
THEDE PROTON ENVIRONMENTS*

Instrument shielding (gm/cm^2 Al)	L (Earth-Radii)	Vette Environment Ratios	Thede Environment Ratios	Threshold Energy above which 50% of the dose is contirbuted (MeV)
1.4	1.3	0.48	0.48	64
	1.4	0.88	0.92	
	1.6	0.91	0.93	
	1.8	0.83	0.75	
	2.0	1.08	0.70	
3.4	1.3	0.24	0.61	94
	1.4	0.31	0.68	
	1.6	0.35	0.69	
	1.8	0.39	0.77	
	2.0	0.21	0.75	
4.0	1.2	0.25	0.63	152
	1.3	0.28	0.74	
	1.4	0.36	0.81	
	1.5	0.33	0.91	
	1.6	0.36	0.99	
	1.7	0.39	1.11	
16	1.2	0.31	0.70	190
	1.3	0.29	0.83	
	1.4	0.29	0.84	
	1.5	0.28	1.00	
	1.6	0.31	1.11	
	1.7	0.24	1.27	

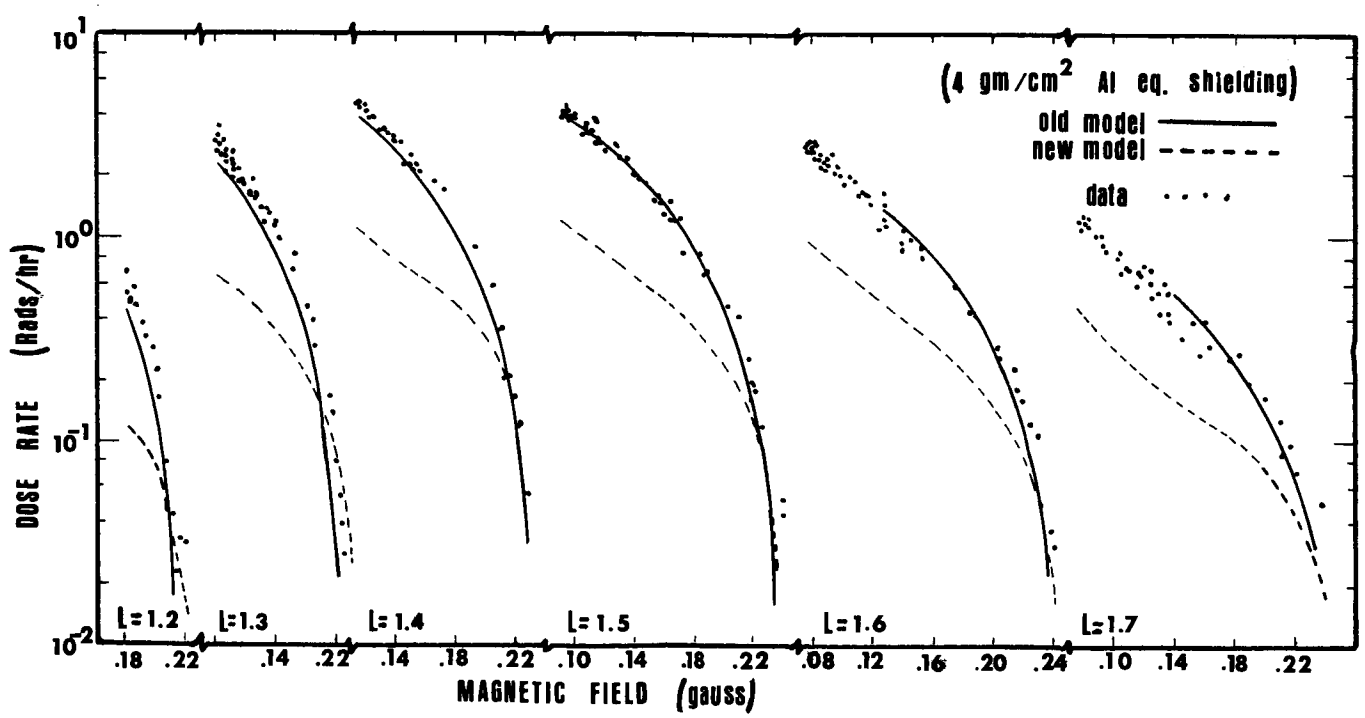

5. Iso-L dose-rate profile map for a highly shielded dose point, showing coorelation between actual measurements and calculations using both the Vette and Thede environmental models.

REFERENCES

1. Van Allen, J.A., et. al., Observation of High Intensity Radiation by Satellites 1958 Alpha and Gamma, Jet Propulsion, 28: 588-592 (1958)

2. Hess, W.N., The Radiation Belts and Magnetosphere, Bliesdell Publishing Co., Waltham, Mass. (1968).

3. Donop, W.A., Jr., Ed., TRW Space Log, Vol. 9, No. 4; TRW Systems Group, TRW Inc: (Winter 69-70).

4. Williams, D. R., Space Measurements Survey For DASA, Part II, DASA 1277, WEB No. 07.013: (Feb 65).

5. Richter, H. L., Jr., Ed., Space Measurements Survey - Instruments and Spacecraft, NASA SP-3028, T.I.D. NASA: (1966).

6. Freden, S.C. and R. S. White, Protons In the Earth's Magnetic Field, Phys. Rev. Letters, 3: 9-10 (1959).

7. Holly, F. E., et. al., Radiation Measurements to 1500 Kilometers Altitude at Equatorial Latitudes, J. Geophys. Res., 66: 1627-1639 (1961).

8. White, R. S., The Earth's Radiation Belts, Physics Today, 19: 25-38 (1966).

9. Sharp, R. D., et. al., Satellite Measurements of Low-Energy Electrons in the Northern Auroral Zones, J. Geophys. Res., 69: 2721-2730 (1964).

10. O'Brien, B. J., Review of Studies of Trapped Radiation with Satellite Bourne Apparatus, In: Space Science Reviews (C. DeJager, Ed.), D. Reidel Publishing Company, Doldrecht, Holland:415-418 (1962).

11. Shabansky, V. P., and Skuriden, G. A., Concerning the Orgin of the Earth's Radiation Belts, Foreign Translation MT-64-346.

12. McCormac, B., (Ed.), Radiation Trapped in the Earth's Magnetic Field, D. Reidel Publishing Company, Doldrecht, Holland (1966).

13. McIllwain, C. E., The Radiation Belts, Natural and Artificial, Science,142: 355-361 (1963).

14. Fillius, R. W., Trapped Protons of the Inner Radiation Belt, J. Geophys. Res., 71: 97-123 (1966).

15. Attix, F. H., and E. Tochlin, Radiation Dosimetry, Vol III, Chap. 26: 453-510, Academic Press, N.Y. (1969).

16. Holly, F. E. and J. Janni, Eds., The Current Approach to the Radiological Problems of Spaceflight, Aerospace Med., 40, 12, Sec II: 1439-1567 (Dec 1969).

17. Vette, J. I., Models of the Trapped Radiation Environment, Vol. I: Inner Zone Protons and Electrons. Vol II: Inner and Outer Zone Electrons. Vol IV: Low Energy Protons. NASA Sci. Tech. Inform. Div (1967).

18. Vette, James I., A Model Proton Environment above 4 MeV, in Radiation Trapped in the Earth's Magnetic Field, Ed. by B.M. McCormac, D. Reidel, 1966.

19. Thede, A. L., and G. E. Radke, A Correlation of Dosimetric Measurements with Charged Particle Environment of the Inner Van Allen Belt, presented at 13th Annual Meeting of the American Nuclear Society, San Diego, Calif (June 1967).

20. Thede, A.L., OV3-4 Dose Rate and Proton Spectral Measurements, AFWL-TR-68-128, Air Force Weapons Laboratory, KAFB, NM (June 1969).

21. McIllwain, C. E., Coordinates for Mapping the Distribution of Magnetically Trapped Particles, J. Geophys. Res., 66: 3681-3691 (1961).

22. Cladis, J.B., et. al., Energy Spectrum and Argular Distributions of Electrons Trapped in the Geomagnetic Fields, J. Geophys. Res., 66: 2297-2312 (1961).

23. West, H. I., et. al., Some Electron Spectra in the Radiation Belts in the Fall of 1962, Space Research V, North Holland Publ. Co., Amsterdam: 423-445 (1965).

24. Vampola, A. L. Private Communications (1967).

25. Krimigis, S. M., and Van Allen, J. A., Geomagnetically Trapped Alpha Particles, J. Geophys. Res., 72: 5779-5797 (1967).

26. Clark, B. C. Directional Sensitivity and Energy Dependance of the Gemini Dosimetry System, AFWL-TR-66-29, Air Force Weapons Laboratory KAFB, NM (May 1966).

27. Schneider, M. F., The Radiation Response of Tissue Equivalent Dosimetry Systems to 60 MeV Proton Beams, AFWL-TR-66-30, Air Force Weapons Laboratory, KAFB, NM (March 69).

28. Chapman, M. C., and Holly, F. E., An Experiment to Measure the Tissue-Equivalent Absorbed Dose (LET) and Depth-Dose Distributions Produced by Radiations in Space, In: Proceedings of the First International Congress of the International Radiation Protection Association. (W. Synder, Ed.), Pergamon Press, New York; 881-897 (1968).

29. Chapman, M. C., et. al., Development of a Cellular Absorbed Dose Spectrometer, AFWL-TR-69-76, Air Force Weapons Laboratory, KAFB, NM (Dec 1969).

30. Holly, F. E., et. Al., Results of a Space Dosimetry Experiment to Assess the Radiation Protection Calculations for Manned Space Flight, In: Proceedings of the First International Congress of Radiation Protection, Part 2 (S.S. Snyder, Ed.), Pergamon Press: 871-893 (1968).

31. Chapman, M. C., et. al., Phase I Analysis of Data Returned by the FESS Experiment from the OV1-2 Spacecraft, AFWL-TR-66-94, Air Force Weapons Laboratory, KAFB, NM (1967).

32. Fortney, R. E., Flight Experiment Shielding Study (FESS) Satellite Data Analysis - Phase II, AFWL-TR-68-108, Air Force Weapons Laboratory, KAFB, NM (Apr 1969).

33. Janni, J., Measurements of Spacecraft Cabin Radiation Distributions for the Fourth and Sicth Gemini Flights, AFWL-TR-65-149, Air Force Weapons Laboratory, KAFB, NM (Mar 67).

34. Schneider, M. F., et. al., An Active Dosimeter System to Measure Energy Deposition and Charged Particle Spectra of High Energy Inner Van Allen Belt, Solar Flare, and Galactic Cosmic Protons on Manned Spacecraft, AFWL-TR-70-29, Air Force Weapons Laboratory, KAFB, NM (Aug 70).

35. Schneider, M. F., Private Communication.

ARTIFICIAL PERTURBATIONS OF THE RADIATION BELTS

John B. Cladis

Lockheed Palo Alto Research Laboratory

A review is given of the properties of the radiation belts which have been produced by high-altitude nuclear detonations. The low-yield, Argus devices, 1, 2, and 3, and the Soviet test of 1 November 1962 injected intense electron fluxes in narrow L-shell intervals, with peaks at L = 1.72, 2.11, 2.17, and 1.77, respectively. The energy spectra of the electrons were indistinguishable from the equilibrium fission beta spectrum, and the fluxes initially decayed at rates approximately proprotional to $(\text{time})^{-1.1}$. Across L shells the electrons diffused very slowly ($\Delta[\text{full width of peak at half maximum}]^2/\Delta[\text{time}] \approx 10^{-4}$ [earth radii]^2/day). The high-yield devices, Starfish and the Soviet tests of 22 October and 28 October 1962, injected electrons over wide ranges of L -- extending from L values near the burst locations ($L \approx 1.14$ for Starfish, $L \approx 1.8$ for the Soviet tests) to $L \approx 6$. At L values near the lower boundary, the electron spectra were similar to the equilibrium fission beta spectrum; but the spectra appeared to be softer at the higher L values. The decay rates at $L \lesssim 1.25$ were in agreement with predictions based on atmospheric scattering theory; but at $L > 1.25$ the decay rates were higher, indicating the predominance of electromagnetic interactions. In addition to injecting energetic electrons, a high-altitude detonation may also cause previously-trapped particles to be redistributed. Evidence for the occurrence of such a redistribution is presented and mechanisms which may have caused the redistribution are discussed.

INTRODUCTION

Major changes in the population and redistribution of energetic particles in the radiation belts have resulted from the detonation of nuclear devices at high altitudes. In regard to radiation damage, the most important particles which have been added to the radiation belts are the high-energy electrons emitted by fission fragments undergoing beta decay. Other particles, such as the protons and electrons emitted by neutron decay, are neither significantly penetrating nor sufficiently concentrated to form damaging fluxes. Redistribution and loss of trapped particles also occur because of the interaction of the particles with electromagnetic disturbances initiated by the nuclear explosions.

In this report the characteristics of the artificially-injected electrons and an observed redistribution of the natural trapped particles by Starfish are discussed. Nearly all of the data available on the artificial belts were obtained at times after the electrons had spread approximately uniformly around the earth. It must be remembered that within about an hour or so after a burst the electron flux east of the burst is much higher than indicated by these data. If the burst is west of the South Atlantic geomagnetic anomaly, the flux is higher, not only because the "permanently"-trapped electrons are more concentrated during their initial drift motion toward the east, but also because it includes the "transiently"-trapped electrons. Transiently-trapped electrons are defined as those electrons which have mirror points so low that they become absorbed by the atmosphere, west of the anomaly, during their initial drift motion around the earth. An estimate of the early-time flux is given in the following section.

A good reference for this subject material is the Trapped Radiation Handbook (ref. 1), particularly Section 6: "History of the Artificial Belts," by M. Walt, and Section 7: "Particle Injection by Nuclear Detonations," by G. T. Davidson and R. W. Hendrick, Jr.

EARLY TIME FLUX

A model for the injection of electrons into the earth's field by high-altitude nuclear explosions, as well as a calculation of the resulting flux of trapped betas as a function of B,L, time and geographical coordinates, are given in ref 2. In figure 1 the distributions of the beta flux at early times, based on a simplified model (ref. 1), are presented. These distributions were computed by assuming that all of the electrons which finally reached the equilibrium distribution were initially in the longitudinal sector, $\Delta\varphi$. Moreover, a dipole magnetic field and an exponential energy sepctrum which approximates the equilibrium fission beta spectrum were used in this analysis. The upper figure gives the equatorial flux as a function of longitude at various times for a source at L = 1.2, and the lower figure gives the same information for a source at L = 1.6. In both figures $\Delta\varphi$ is about the width of the sector that contained the Starfish magnetic bubble (ref. 3). The flux is given in units of the equilibrium flux. In addition to the magnitude of the enhancement, it is interesting to note from these figures that the maximum value of the flux moves toward the east at a rate that is about the same as that of a low-altitude satellite. Hence, a satellite in a direct, equatorial orbit may remain in the enhanced flux for the entire time required for the flux to become uniform in longitude.

In order to estimate the early-time flux from the longitudinally-uniform fluxes given in succeeding sectors, higher factors than those shown in figure 1 are required. This is necessary because the early-time fluxes also contain the transiently-

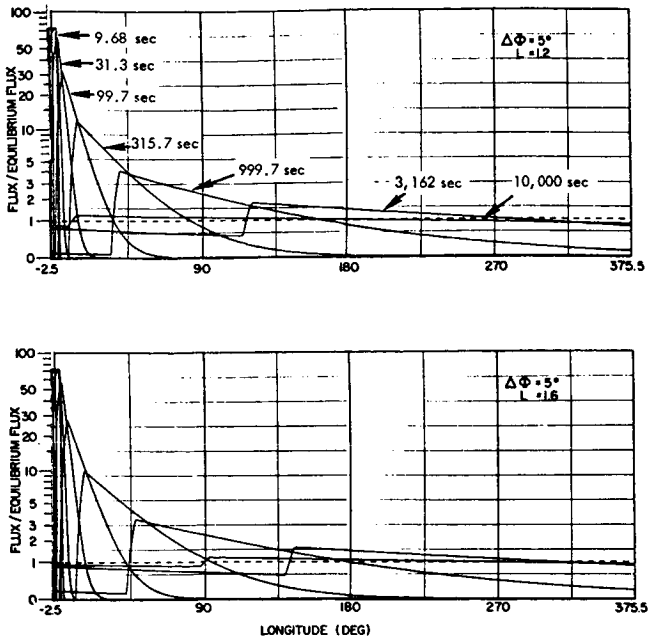

FIGURE 1.--Longitudinal distribution of injection betas at the indicated times. At t=0 the betas were assumed to be in the longitudinal sector Δφ [from Davidson and Hendrick, ref. 1].

trapped electrons, which are not included in the simplified analysis, and the electrons which are subsequently lost by scattering processes.

THE ARGUS TESTS

The Argus tests, which were conducted in the fall of 1958, were specifically designed to produce intense electron belts (ref. 4). Three devices were detonated at altitudes higher than about 200 km in the vicinity of the South Atlantic anomaly, where the injection altitude for "permanent" trapping is a minimum. The yields of the devices were in the range 1-2 kT. Information on the electron belts formed by the explosions was obtained with the Explorer 4 satellite (refs. 1, 5-7) and with sounding rockets (refs. 8 and 9). Each device produced a narrow electron shell which was approximately centered at the L value of the burst location.

Table 1 lists the locations and dates of the bursts; the L value of the maximum electron intensity; the apparent cross-L diffusion coefficient, $\Delta(\mathrm{FWHM})^2/\Delta t$, where FWHM is the full width of the shell at half maximum; and parameters of the power law decay rate. Most of the entries in this table are from the analysis of the satellite data by George (ref. 10) and Manson et al. (ref. 7). The data, as reduced by these authors, are given in figures 2-4. Figure 2 pertains to the Argus 1 shell. Figure 2a gives the time variation of the counting rate of Channel 3 (geometric factor = 0.6 cm^2, energy threshold $\approx$ 3 MeV) after corrections are made for background and the dead time of the detector. The satellite pass numbers are given at the data points. The Channel 3/Channel 1 ratios in figure 2b give a measure of the energy spectrum.

Table 1

Properties of Electron Shells Formed by the Argus Tests

Device	Date	Location	Altitude km	L Value at Peak	$\Delta(\mathrm{FWHM})^2/\Delta t$ R_E^2/day	t^{-n} decay rate
Argus 1	27 Aug. 1958	12°W 38°S	~ 200	1.72	2.0×10^{-5}	1.17
Argus 2	30 Aug. 1958	8°W 50°S	~ 250	2.11	4.1×10^{-4}	1.15 ± .03
Argus 3	6 Sept. 1958	10°W 50°S	~ 500	2.17	5.5×10^{-4}	1.09

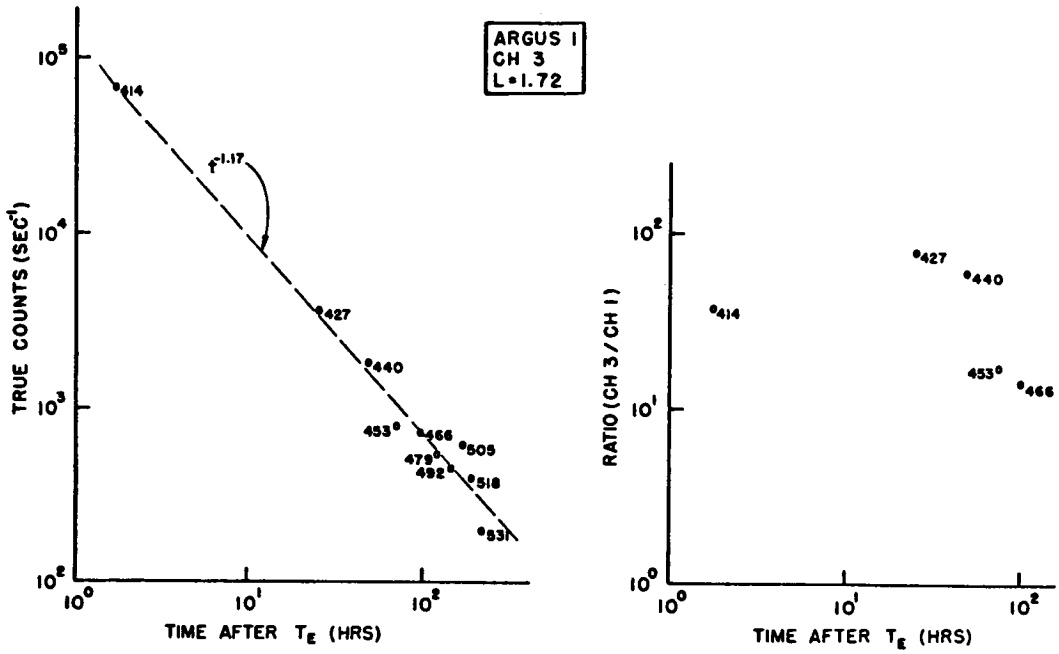

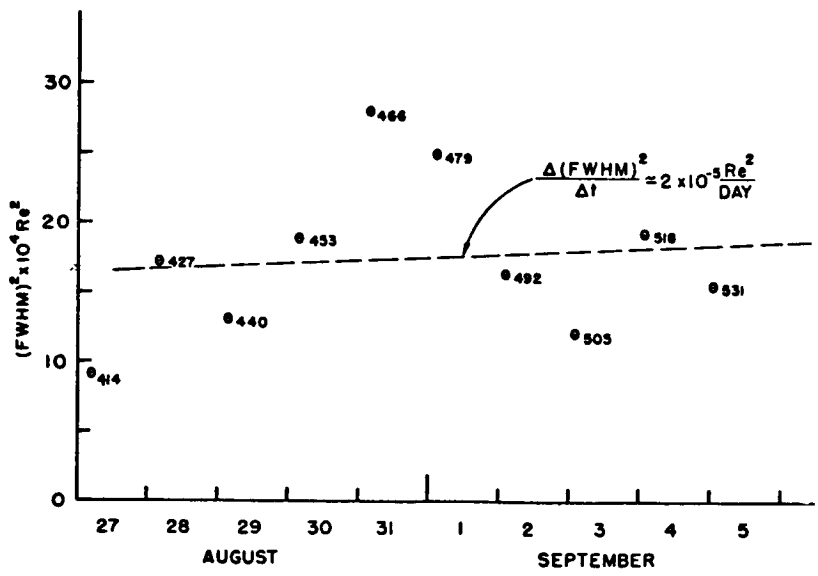

FIGURE 2.--(a) Decay; (b) Channel 3 (E > 3 MeV)/Channel 1 (E > 5 MeV) ratios; and (c) shell diffusion for Argus 1. Omnidirectional count-rates minus background are the data employed. A least squares fit to $C = C_0 t^{-n}$ yields n = 1.17. B ranges from 0.225 (Pass 414) to 0.183 gauss (Pass 531). The diffusion coefficient, $\Delta(FWHM)^2/\Delta t$, for the shell was calculated by a least squares fit to the Channel 3 data [from ref. 7].

A ratio of about 100 is appropriate for the equilibrium fission beta spectrum. (Channel 1 had an energy threshold of about 5 MeV and a geometric factor similar to that of Channel 3.) Figure 2c shows the square of the measured width of the shell at the various passes. Similar data for the Argus 2 and 3 shells are shown in figures 3 and 4. Note that the scatter of the satellite data in figure 3a is so great that a decay curve for the second event is not drawn. For this event the entry in the table, $n = 1.15 \pm 0.03$, is from the sounding rocket data which were analyzed by Cladis and Walt (ref. 9).

The satellite data, as well as the sounding-rocket data for the second event, revealed that the energy spectra of the Argus 2 and 3 electrons, in space and time, were indistinguishable from the equilibrium fission-beta spectrum. A somewhat harder spectrum of the Argus 1 electrons is indicated in figure 2b.

Pitch-angle distributions of the electrons injected by Argus 1 and 2 were measured with a directional detector (Ch 2) on the satellite. Early after Argus 1 the pitch-angle distribution changed rapidly during a rotation period of the satellite. But after about a day, the distribution was approximately normal, i.e., it was about the same as that of the natural radiation. The Argus 2 electrons were found to have a normal distribution at the time of the first measurement, 1.87 hours after the burst. The maximum directional fluxes measured at 90° to the field 1.8 hours after Argus 1 and 1.87 hours after Argus 2 were 1.5×10^6 and 5.28×10^5 electrons/cm^2·sec·ster, respectively. The corresponding widths-at-half-maximum of the pitch-angle distributions were 20° and 18°.

STARFISH

The Starfish device was detonated on 9 July 1962 at an altitude of about 400 km above Johnston Island (190.5°E, 16.7°N). On the basis of the information obtained from the Argus tests, significant trapping was not expected. Over Johnston Island the minimum injection altitude for "permanent" trapping is higher than 1000 km! However, because of the high yield (1.4 MT) of the device, fission fragments jetted across field lines (ref. 11) and injected electrons to L values of 6 or more (ref. 12). The radiation damaged several satellites which were in orbit at that time. Moreover, the duration of the radiation was much greater than expected.

The distribution of the injected electrons is still controversial as discussed by Walt in ref. 1. The satellites in orbit at the time of the burst were too low (< 1000 km) to observe the full distribution and they did not contain detectors which were designed to detect high fluxes of fission-fragment betas. It appears that the best data on the Starfish injection was obtained by the Telstar satellite, which was launched the next day after the Starfish burst. The satellite was in a good orbit (apogee, 5630 km; perigee, 955 km; inclination, 44.7°), but the data are still somewhat ambiguous because of the uncertainty in the background electron flux. The flux contours in R,λ coordinates shown in figure 5 were obtained by Newkirk and Walt (in ref. 1) from an analysis of the Telstar data taken 2 days after Starfish. These data were taken with a solid-state detector which had an energy threshold of about 400 keV (ref. 13). It was not possible to subtract the background; therefore, these fluxes include the natural electrons of energies greater than 400 keV. However, since these fluxes were observed to decay at later times and no unusual geomagnetic activity was recorded several days before the event, the background contribution may have been small.

By using the jetting-debris model described in ref. 14, a distribution of betas similar to that shown in figure 5 was computed for a Starfish-type burst. The daily fluence of the betas incident on circular-orbit satellites is shown in figure 6 (ref. 1), where the daily fluence is plotted as a function of the altitude of the satellite for various orbital inclination. Satellites in the inclined orbits receive high fluences at low altitudes, as shown in the figure, because they traverse the region of the South Atlantic anomaly.

The energy spectrum of the electrons, as discussed by Walt in ref. 1, was similar to an equilibrium fission beta spectrum at L values less than about 1.25, but it became softer toward higher L values.

The decay rate of the trapped betas was found to depend sensitively on B and L. At $L \lesssim 1.25$, the decay rate was found to be in good agreement with theoretical results (ref. 15) based on the scattering of the electrons by the atmosphere. An example of the experimental data on the decay rate and the comparison with the theoretical curves is shown in figure 7 (ref. 16). The experimental data taken at the lower altitudes are displaced downward, as shown in the figure, when corrections are made for the enhanced background of high-energy protons produced by Starfish. This background, which was observed by Filz and Holeman, ref. 17, will be discussed later. A compilation by Davidson (ref. 1) of the apparent, e^{-1} decay time, as determined from data on the decay of betas injected by various nuclear detonations, as a function of L, is shown in figure 8. The theoretical curve of Walt (ref. 29) is also shown in the figure. Note that above L values of about 1.25, the apparent loss rate is higher than that which results from collisions. In this region the increased importance of electromagnetic interactions is indicated.

THE HIGH-ALTITUDE SOVIET TESTS

In late 1962 the Soviets detonated three devices which injected high fluxes of betas into trapped orbits. The bursts occurred on 22 October, 27 October, and 1 November. Contours in R,λ coordinates of the omnidirectional flux derived from the Telstar data for the first and second events are shown in figures 9 and 10, respectively (from refs. 1 and 14). The dashed lines are extrapolations of the flux from the measured regions. Note that, as in the case of Starfish, the betas were distributed over a wide region of the magnetosphere. In each event the intensity increased sharply at the inner boundary, $L \approx 1.8$, reached a double maximum with peaks at $L \approx 1.8$ and 2.2, and decreased monotonically toward higher L values.

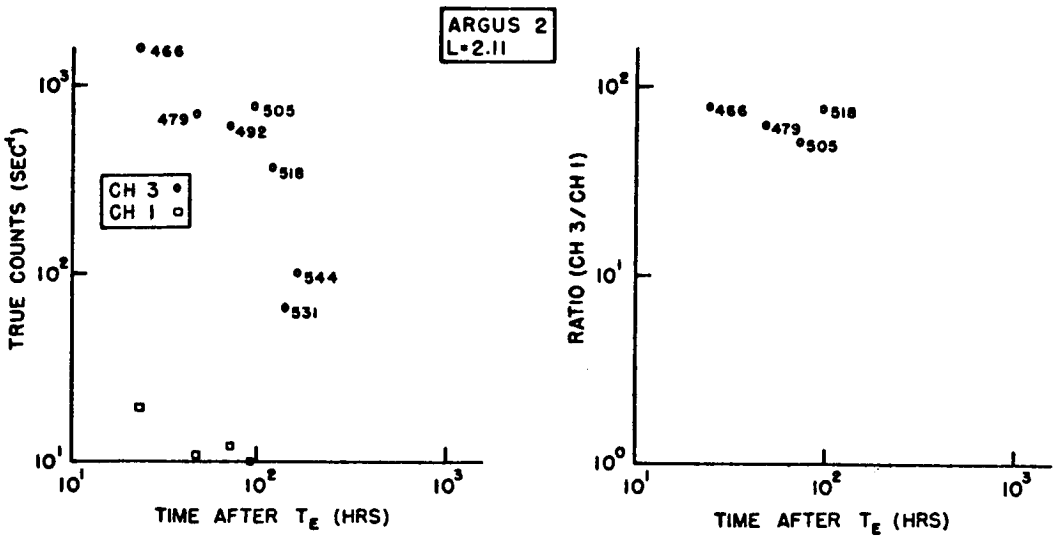

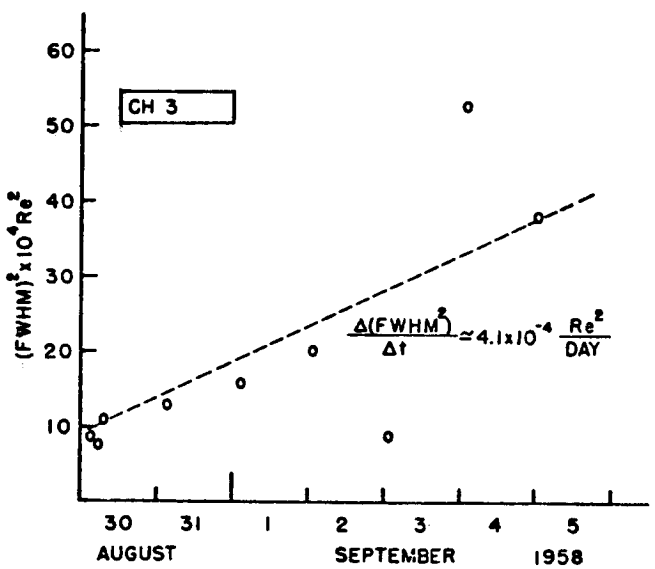

FIGURE 3.--(a) Decay; (b) Channel 3 (E > 3 MeV)/Channel 1 (E > 5 MeV) ratios; and (c) shell diffusion for Argus 2. B values range from 0.248 (Pass 466) to 0.222 gauss (Pass 531). A least squares fit to the count-rate data was not made due to the scatter of the data [from ref. 7].

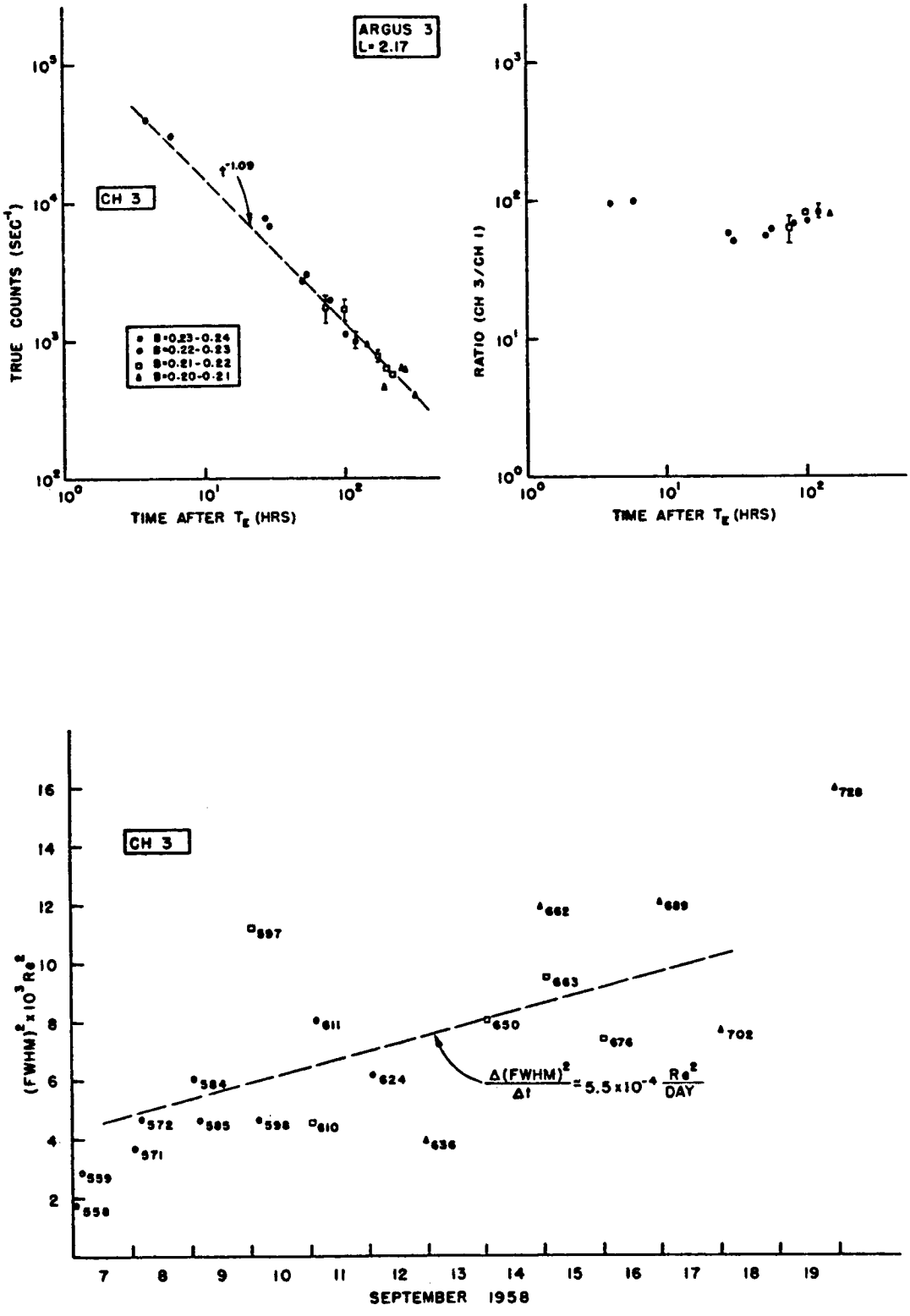

FIGURE 4.--(a) Decay; (b) Channel 1 (E > 3 MeV)/Channel 1 (E > 5 MeV) ratios; and (c) shell diffusion for Argus 3. The range of B values is indicated. The time decay of the count rate is proportional to $t^{-1.09}$ [from ref. 7].

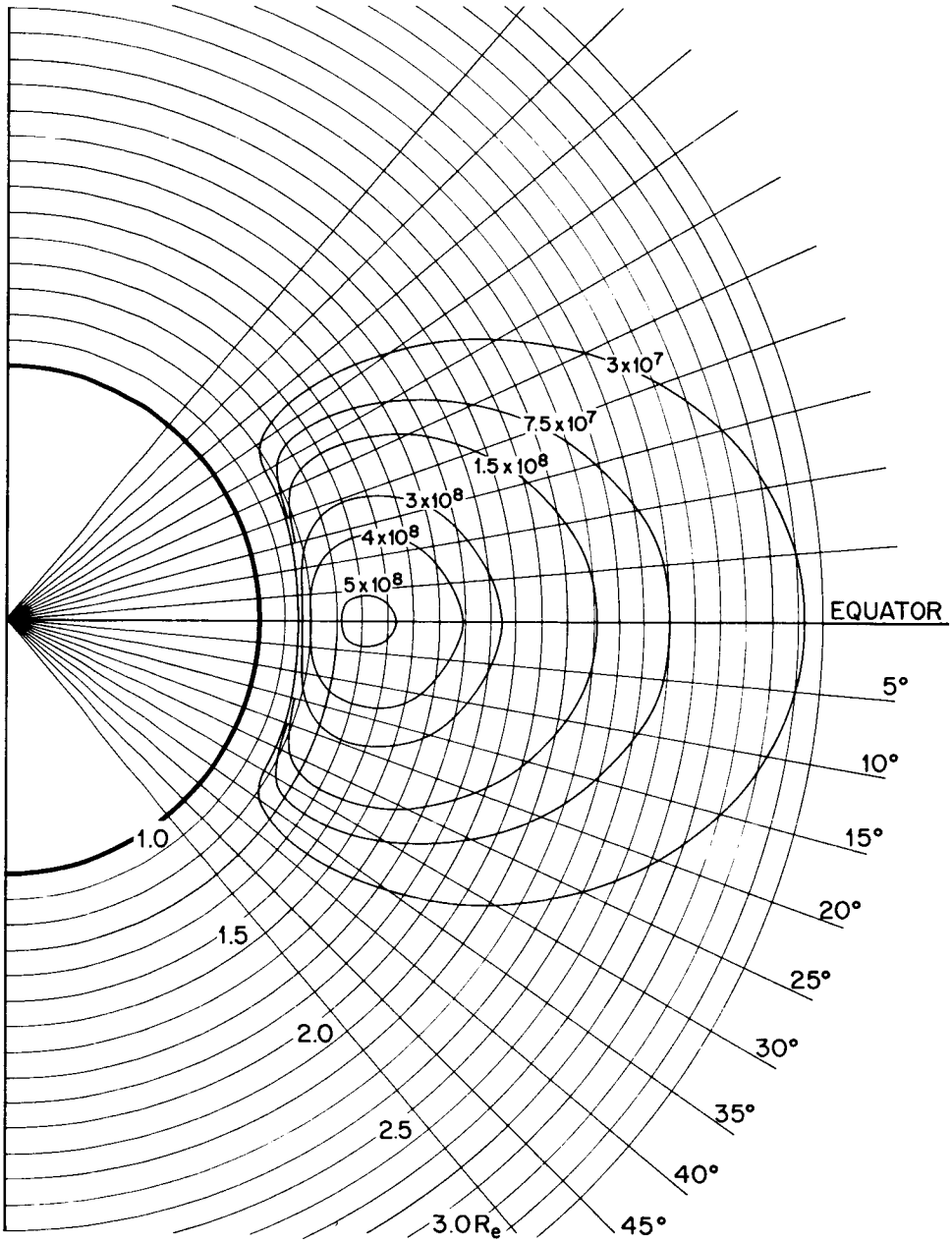

FIGURE 5.--Flux contours two days after Starfish, as determined from Telstar data by Newkirk and Walt. The numbers are the intensities ($cm^{-2}sec^{-1}$) of fission spectrum electrons required to give the observed counting rates of the Telstar solid-state detector having a threshold of about 400 keV [from Walt, ref. 1].

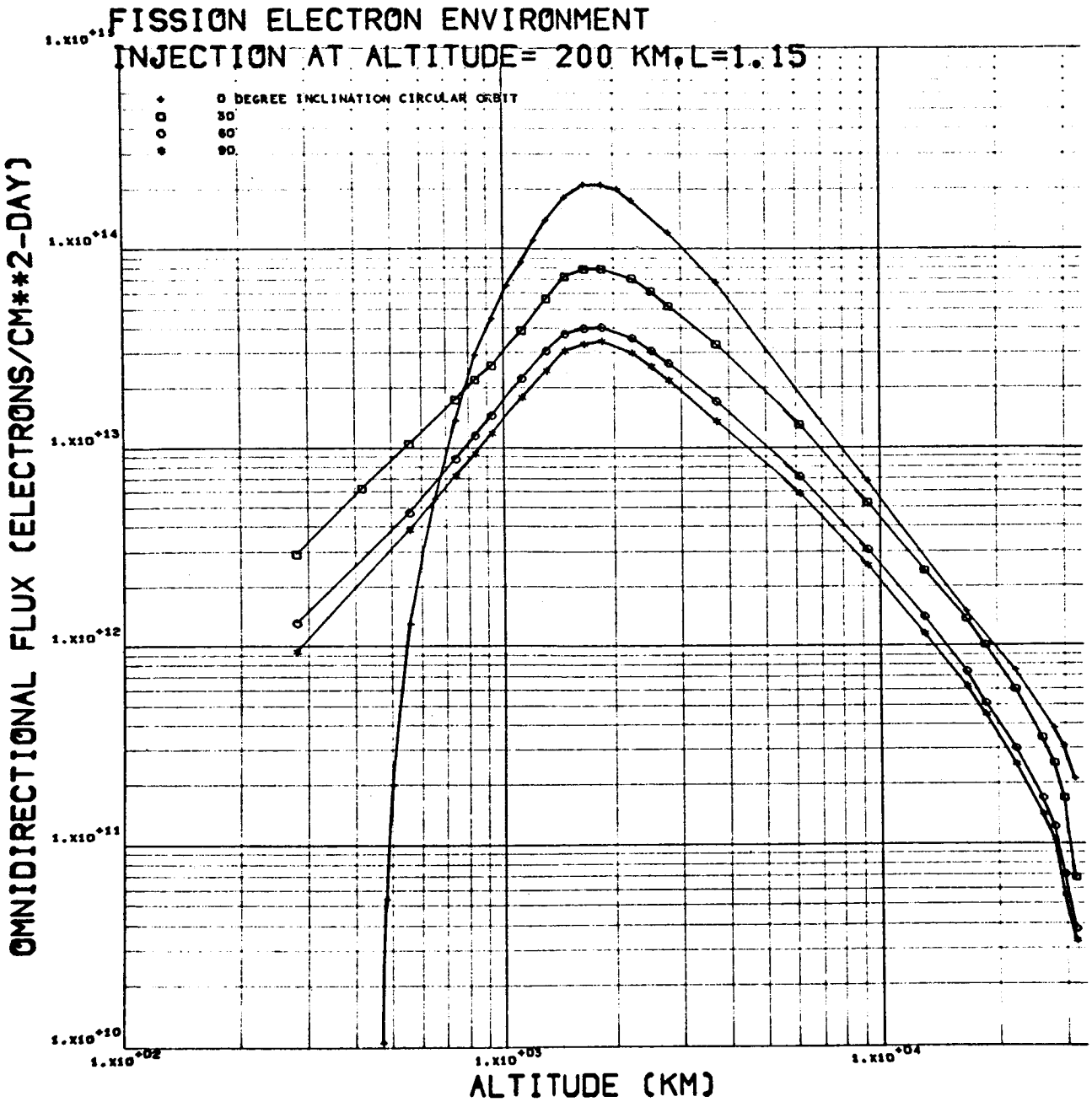

FIGURE 6.--Daily omnidirectional fluence of fission electrons incident on circular orbit satellites as function of satellite altitude for specified orbital inclinations (1-megaton fission yield) [from Crowther and Harless, ref. 1].

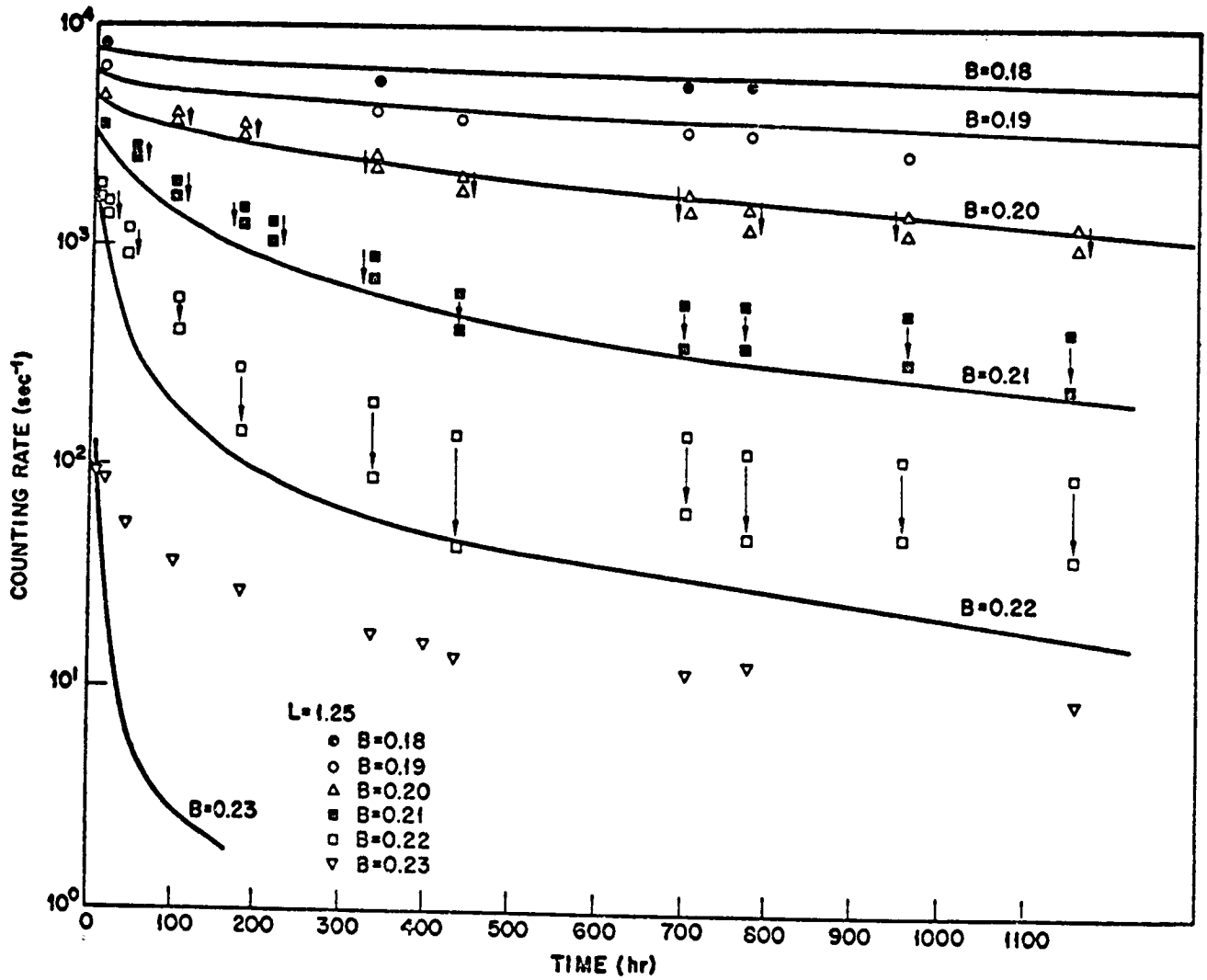

FIGURE 7.--Comparison of experimental and theoretical (solid lines) values for the time decay of the Starfish radiation belt (ref. 16). The lower sets of points for B = 0.20, 0.21, and 0.22 gauss have been corrected for the enhanced proton background observed by Filz and Holeman (ref. 17) [from Walt, ref. 1].

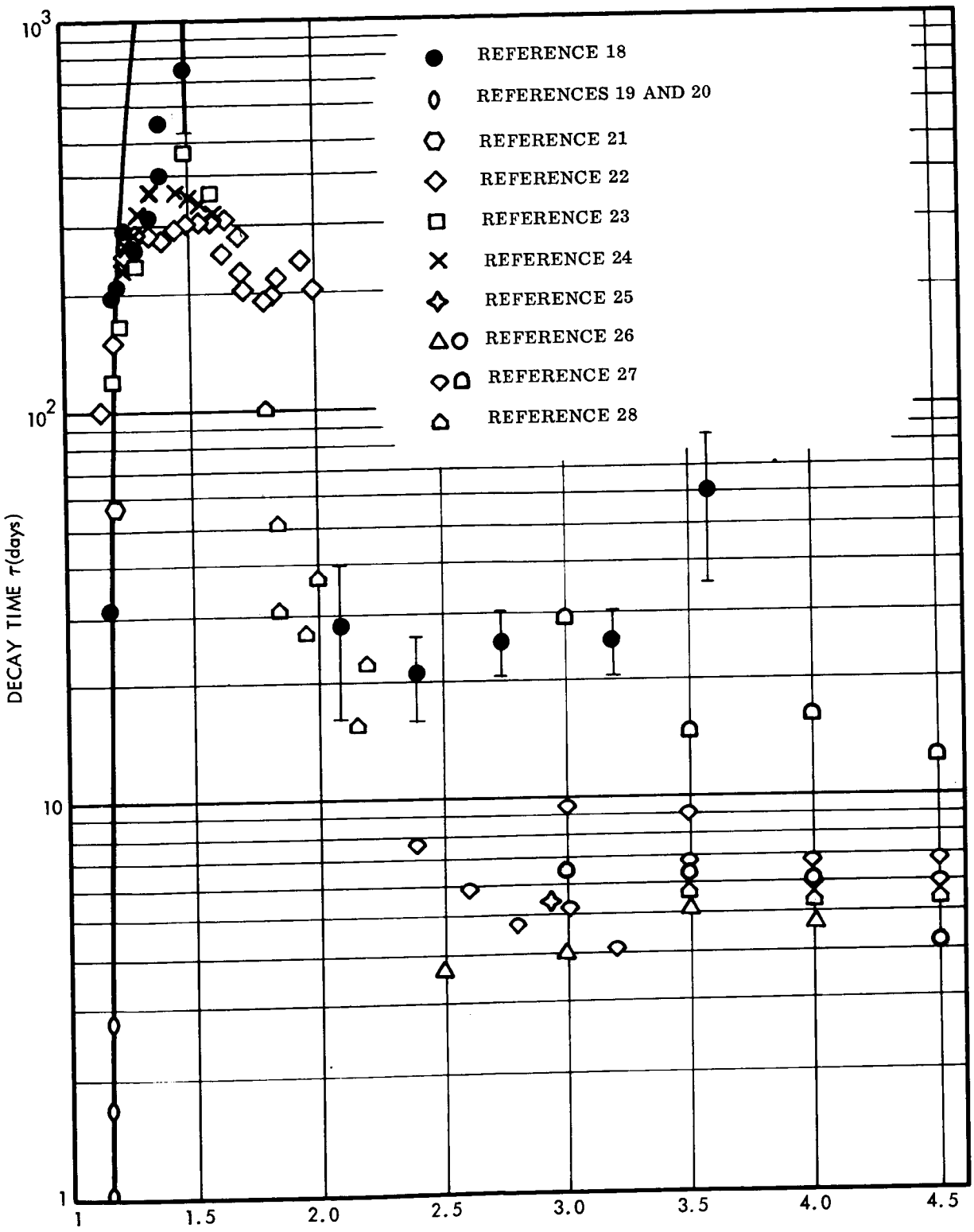

FIGURE 8.--Compilation of apparent e^{-1} decay times from experimental measurements of trapped electrons injected by nuclear tests [from Davidson and Hendrick, ref. 1].

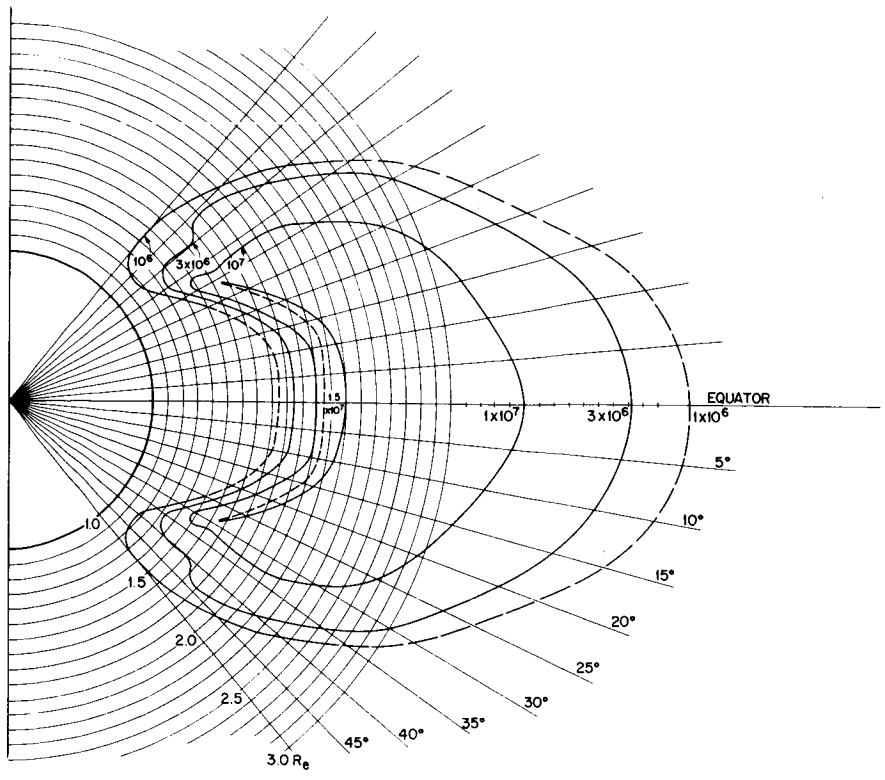

FIGURE 9.--Omnidirectional flux ($cm^{-2}sec^{-1}$) contours (Telstar data) immediately following the Russian test of 22 October 1962 [from ref. 14].

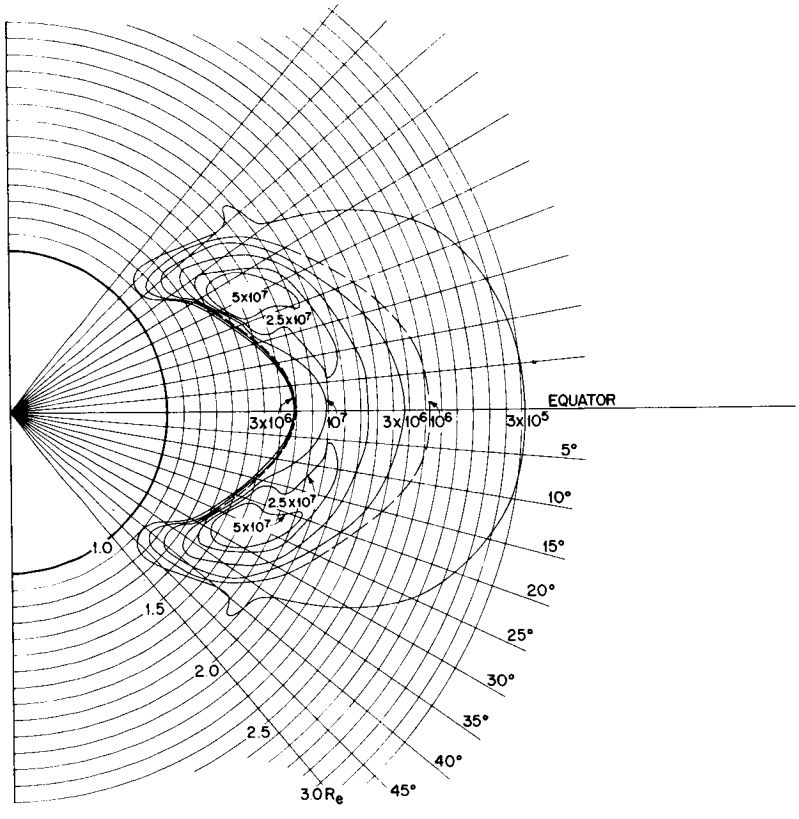

FIGURE 10.--Omnidirectional flux ($cm^{-2}sec^{-1}$) contours (Telstar data) immediately following the Russian test of 28 October 1962 [from ref. 14].

The daily fluences of betas incident on circular satellites were evaluated (ref. 1) for a distribution, derived from the jetting-debris model, which was similar to that shown in figure 9. These fluences are given in figure 11.

The 1 November event produced a narrow electron belt similar to those formed by the Argus tests. It was centered at L = 1.766 with an initial full-width-at-half-maximum of about 250 km. Two days after the test, the omnidirectional flux of electrons greater than 0.5 MeV was about 1.5×10^8/ $cm^2 \cdot sec$, as discussed by Brown (ref. 13). From observations on the increasing width of the electron shell, with time, Brown determined the cross-L diffusion coefficient to be 7×10^{-5} R_E^2/day.

The energy spectrum of the electrons injected by the 1 November event was similar to an equilibrium fission beta spectrum. However, the spectra of the electrons injected by the first and second events differed appreciably from the beta spectrum in some regions of the magnetosphere (e.g., see ref. 13).

EARLY-TIME REDISTRIBUTION EVENTS

A nuclear burst in the magnetosphere, with super-Alfvénic plasma streaming from the point of detonation and high currents along field lines, creates hydromagnetic disturbances such as shock waves, turbulence, and hydromangetic waves. Interactions of the injected betas, as well as the natural trapped particles, with these disturbances may cause the particles to be redistributed. The redistribution may occur not only by diffusion, but also by transport due to large-scale electric and magnetic fields (refs. 30 and 31).

The redistribution of emitted betas is indicated by the electron belts produced by Teak and Orange (refs. 1 and 32). These events occurred in 1958 on 1 August and 12 August over Johnston Island. Although the yields of the devices were in the megaton range, beta trapping would not normally be expected: the altitudes of the bursts were too low, with Teak at 77 km and Orange at 43 km, and the earth's field in the region of Johnston Island is high, requiring injection at altitudes greater than 1000 km. Nevertheless, Teak formed a narrow electron belt, centered at L = 1.2 with a full-width-at-half-maximum of about 110 km, which was observed for about 3 days. The maximum directional intensity, normal to the field, was about $1.4 \times 10^5/cm^2 \cdot sec \cdot ster$. Orange produced a similar belt, but of lower intensity, which was observed for about a day.

The redistribution mentioned previously of natural trapped protons by the Starfish burst was observed by Filz and Holeman (ref. 17). The experimental data of Filz and Holeman, obtained in a series of experiments with nuclear emulsions recovered from low-altitude polar-orbiting satellites, are shown in figure 12. The abrupt increase of the flux, especially at low altitudes, after the Starfish event is evident from these data. A theoretical investigation of the redistribution (ref. 33) revealed that two processes were capable of accounting for the observations. One was the interaction of the protons with the hydromagnetic waves produced by the burst. The other was the Fermi mechanism whereby the protons were accelerated along the field line by multiple reflections from a magnetic field inhomogeneity that propagated along the field line with the local hydromagnetic velocity.

Moreover, large-scale electric fields, arising from the early-time azimuthal-drift motion of the injected betas (ref. 30) would cause the betas to be convected to higher L values. This convection process, which would lower the energies of the electrons, may be responsible for the softening of the betas observed at high L values after the Starfish and the first two Soviet events.

REFERENCES

1. The Trapped Radiation Handbook, edited by J. B. CLADIS, G. T. DAVIDSON, and L. L. NEWKIRK. DASA Report No. 2546, June 1970.
2. CLADIS, J. B.; DAVIDSON, G. T.; FRANCIS, W. E.; and WALT, M.: Computation of Nuclear Irradiation Received by Satellites from Tests of High Altitude Nuclear Devices (U). DASA Report No. 2486-1 (SECRET), 1970.
3. COLGATE, S.: The Phenomenology of the Mass Motion of a High Altitude Nuclear Explosion. J. Geophys. Res., vol. 70, 1965, pp. 3161-3173.
4. CHRISTOFILOS, N. C.: The Argus Experiment. J. Geophys. Res., vol. 64, 1959, pp. 869-875.
5. VAN ALLEN, J. A.; MCILWAIN, C. E.; and LUDWIG, G. H.: Satellite Observations of Electrons Artificially Injected into the Geomagnetic Field. J. Geophys. Res., vol. 64, 1959, pp. 877-891.
6. MANSON, D. J.; GEORGE, J. A.; PAIKEDAY, J. M.; FENNEL, J. F., DELANEY, R. M.; and WEBER, A. H.: Unidirectional and Omnidirectional Flux Densities of Trapped Particles in Argus Shells and the Inner Van Allen Belt, Explorer 4 Satellite Data. DASA Report No. 2052-1, Saint Louis University, Physics Department, 1968.
7. MANSON, D. J.; FENNELL, J. F.; GEORGE, J. A.; HICKERSON, J. L.; MALDONADO, G. V.; and WEBER, A. H.: Review of Artificial Radiation Belts, Explorer 4; Unidirectional Trapped Radiation, Injun 1. DASA Report No. 2309, Saint Louis University, Physics Department, 1969.

8. ALLEN, L.; BEAVERS, J. L., WHITAKER, W. A.; WELCH, J. A.; and WALTON, R. B.: Project Jason Measurement of Trapped Electrons from a Nuclear Device by Sounding Rockets. J. Geophys. Res., vol. 64, 1959, pp. 893-907.
9. CLADIS, J. B.; and WALT, M.: Behavior of Geomagnetically Trapped Electrons Injected by High-Altitude Nuclear Detonations. J. Geophys. Res., vol. 67, 1962, pp. 5035-5054.
10. GEORGE, J. A.: Omnidirectional Fluxes; Explorer IV Satellite Data, Argus Events 1 and 2. Ph.D. Dissertation, Saint Louis University, Department of Physics, May 1966.
11. ZINN, J.; HOERLIN, H.; and PETSCHEK, A. G.: The Motion of Bomb Debris following the Starfish Test. Radiation Trapped in the Earth's Magnetic Field, edited by B. M. McCormac, D. Reidel Publishing Company, 1966, pp. 671-692.
12. ELLIOT, H.: Some Cosmic Ray and Radiation Belt Observations based on Data from the Anton 302 G-M Counter in Ariel 1. Radiation Trapped in the Earth's Magnetic Field, edited by B. M. McCormac, D. Reidel Publishing Company, 1966, pp. 76-99.
13. BROWN, W. L.: Observations of the Transient Behavior of Electrons in the Artificial Radiation Belts. Radiation Trapped in the Earth's Magnetic Field, edited by B. M. McCormac, D. Reidel Publishing Company, 1966, pp. 610-633.
14. BERG, R. A.; CLADIS, J. B.; DAVIDSON, G. T.; FRANCIS, W. E.; GAINES, E. E.; NEWKIRK, L. L.; and WALT, M.: Trapping at High L Values of Beta Particles from Nuclear Explosions (U)), vol. 1, Lockheed Missiles & Space Company Report LMSC/B039917, DASA Report 1984, Palo Alto, California, 1967.
15. WALT, M.: The Effects of Atmospheric Collisions on Geomagnetically Trapped Electrons. J. Geophys. Res., vol. 69, 1964, pp. 3947-3958.
16. WALT, M.; and NEWKIRK, L. L.: Addition to Investigation of the Decay of the Starfish Radiation Belt. J. Geophys. Res., vol. 71, 1966, pp. 3265-3266.
17. FILZ, R. C.; and HOLEMAN, E.: Time and Altitude Dependence of 55-MeV Trapped Protons, August, 1961, to June 1964. J. Geophys. Res., vol. 70, 1965, pp. 5807-5822.
18. VAN ALLEN, J. A.: Lifetime of Geomagnetically Trapped Electrons of Several MeV Energy. Nature, vol. 203, 1964, p. 1006.
19. IMHOF, W. L.; REAGAN, J. B.; and SMITH, R. V.: Long-Term Study of Electrons Trapped on Low L-Shells. J. Geophys. Res., vol. 72, 1967, pp. 2371-2377.
20. IMHOF, W. L.; and SMITH, R. V.: Longitudinal Variations of High Energy Electrons at Low Altitudes. J. Geophys. Res., vol. 70, 1965, pp. 569-577.
21. BOLYUNOVA, A. D.; VAISBERG, O. L.; GALPERIN, Yu.; POLAPOV, B. P., TEMNY, V. V., and SHUYSKAYA, F. K.: Investigations of Corpuscules on the Electron-1 and Electron-2 Satellites. Space Research, North-Holland, Amsterdam, 1966, pp. 649-661.
22. MCILWAIN, C. E.: The Radiation Belts, Natural and Artificial. Science, vol. 142, 1963, p. 355.
23. BOSTROM, C. O.; and WILLIAMS, D. J.: Time Decay of the Artificial Radiation Belt. J. Geophys. Res., vol. 70, 1965, pp. 240-242.
24. BEALL, D. S.; BOSTROM, C. O.; and WILLIAMS, D. J.: Structure and Decay of the Starfish Radiation Belt, October 1963 to December 1965. J. Geophys. Res., vol. 72, 1967, pp. 3403-3427.
25. BURROWS, J. R.; and MCDIARMID, I. B.: A Study of Beta Decay Electrons Injected into the Geomagnetic Field in October 1962. Can. J. Phys., vol. 42, 1964, pp. 1529-1547.
26. WILLIAMS, D. J.; and SMITH, A. M.: Daytime Trapped Electron Intensities at High Latitudes at 1100 Kilometers. J. Geophys. Res., vol. 70, 1965, pp. 541-556.
27. WILLIAMS, D. J., ARENS, J. F.; and LANZEROTTI, L. J.: Observation of Trapped Electrons at Low and High Altitudes. J. Geophys. Res., vol. 73, 1968, pp. 5673-5696.
28. ROBERTS, C. S.: Cyclotron-Resonance and Bounce-Resonance Scattering of Electrons Trapped in the Earth's Magnetic Field. Earth's Particles and Fields, edited by B. M. McCormac, Reinhold Book Corporation, New York, 1968, pp. 317-336.
29. WALT, M.: Loss Rates of Trapped Electrons by Atmospheric Collisions. Radiation Trapped in the Earth's Magnetic Field, edited by B. M. McCormac, D. Reidel Publishing Company, 1966, pp. 336-351.
30. CLADIS, J. B.: Dynamical Motion of Geomagnetic Flux Tube Resulting from Injection of High-Energy Particles. Earth's Particles and Fields, edited by B. M. McCormac, Reinhold Book Corporation, 1968, pp. 307-316.

32. MANSON, D. J.; FENNELL, J. F.; HOVERTER, R. T.; HICKERSON, J. L.; GEORGE, J. A.; MALDONADO, G. V.; and WEBER, A. H.: Artificial Injection of Electrons into the Geomagnetic Field by Teak and Orange, Low-Altitude Bursts of 1958. J. Geophys. Res., vol. 75, 1970, pp. 4710-4719.
33. CLADIS, J. B., DAVIDSON, G. T.; FRANCIS, W. E.; JAGGI, R. K.; NAKANO, G. H.; and OSSAKOW, S. L.: Redistribution of Trapped 55-MeV Protons by Starfish Nuclear Explosion. J. Geophys. Res., vol. 75, pp. 57-68.

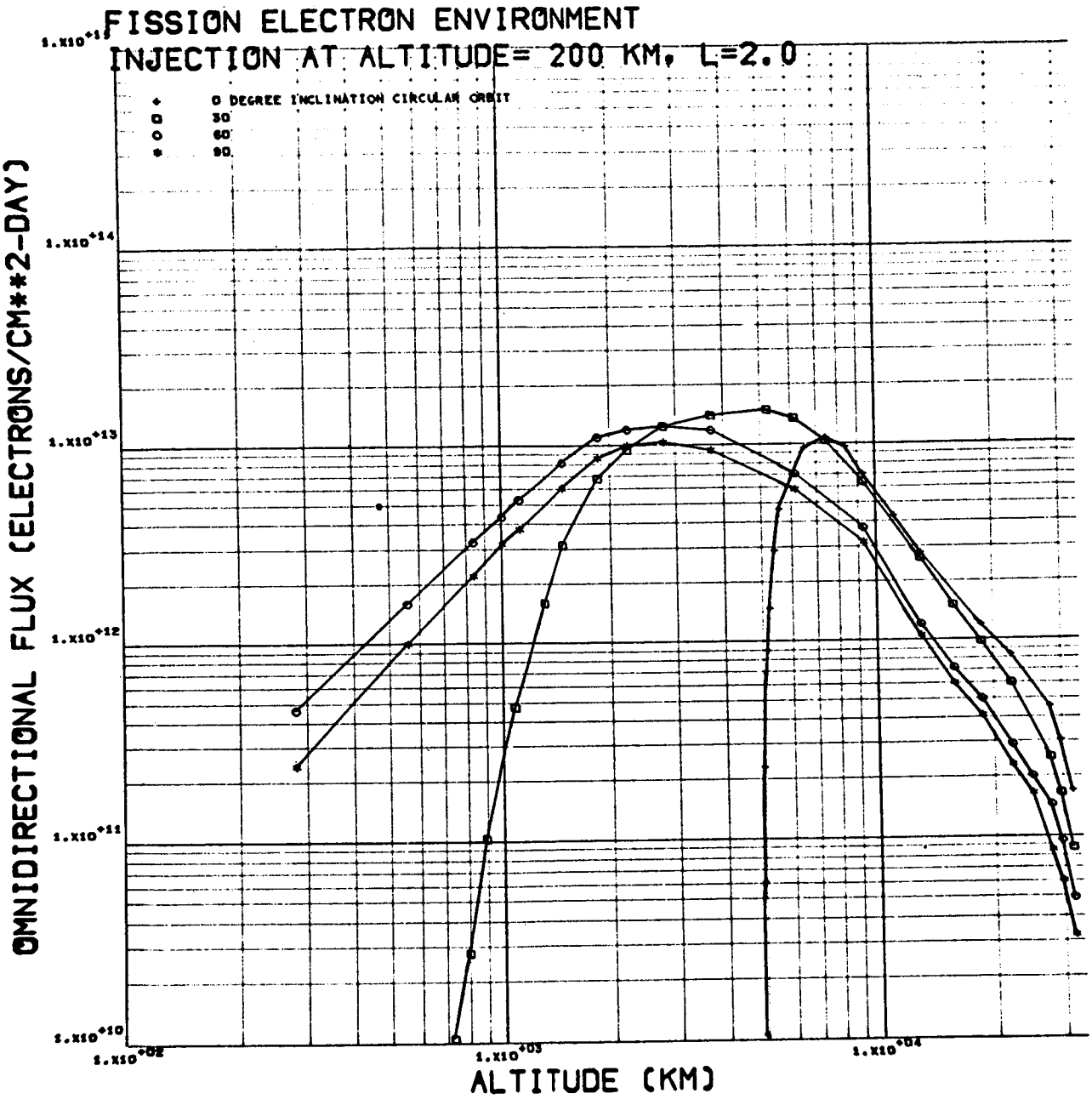

FIGURE 11.- Daily omnidirectional fluence of fission electrons incident on circular orbit satellites as function of satellite altitude for specified orbital inclinations (1-megaton fission yield) [from Crowther and Harless, ref. 1].

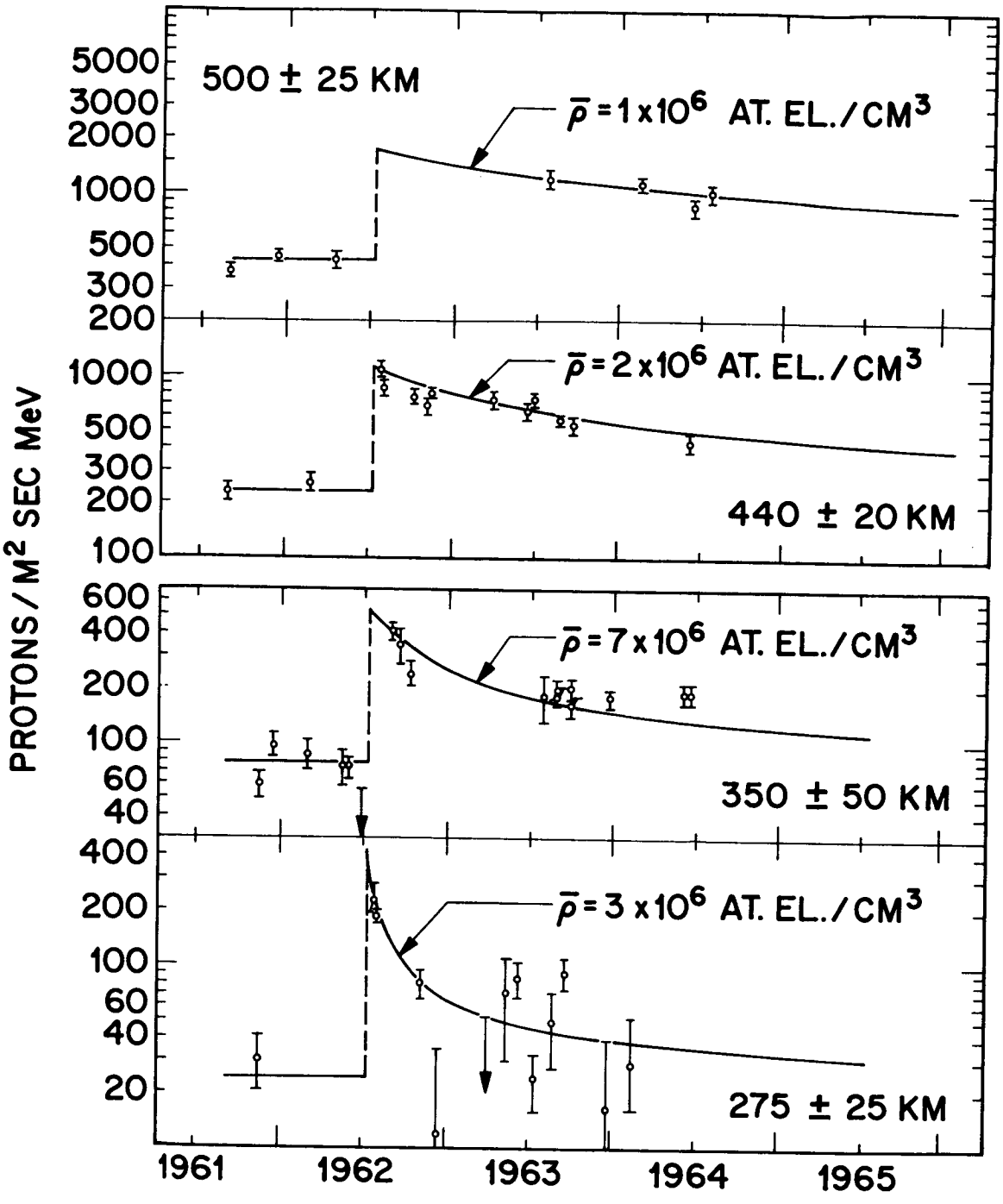

FIGURE 12.--Time variation of the 55-MeV prpton flux for altitudes of H_c = 275, 350, 440, and 500 km from August 1961 to July 1964. The solid curves drawn for the period after July 1962 are the theoretical curves based on the first data point following July 1962 [from ref. 17].

SOLAR FLARE PARTICLE RADIATION

L. J. Lanzerotti
Bell Laboratories
Murray Hill, New Jersey

I. INTRODUCTION

The sun is a source of copious fluxes of charged particles which escape into interplanetary space. These particles range in energy from the few keV solar wind particles to the several hundreds of MeV particles produced by the larger solar flares. There is even growing evidence that the sun may be a nearly continual emitter of low energy (several tens of keV) protons. This review is limited in that it concerns itself essentially entirely with the characteristics of the solar particles accelerated by solar flares and subsequently observed near the orbit of the earth.

The number of solar flares and the fluxes of energetic ($\gtrsim$ 20 MeV) solar particles observed at the earth varies in a manner similar to that of the sunspot number during the eleven-year solar cycle. This is illustrated by the data of Fig. 1 where the smoothed sunspot numbers for cycles 19 and 20 are plotted as a function of time. Also shown are histograms of the yearly integrated proton intensities for protons $\gtrsim$ 30 MeV for both solar cycles (A. J. Masley, private communication). These particle fluxes are obtained from riometer measurements of solar proton-produced PCA events in the polar-cap regions. The solar particle fluxes peaked in total intensity a year or more after the sunspot maximum during cycle 19. It remains to be seen if this same phenomenon holds during the current cycle.

This review discusses in order solar particle intensity-time profiles, the composition and spectra of solar flare events, and the propagation of solar particles in interplanetary space. The last section, dealing with the effects of solar particles at the earth, discusses riometer observations of polar cap cosmic noise absorption events and the production of solar cell damage at synchronous altitudes by solar protons.

II. INTENSITY-TIME PROFILES

Detectability Limits

The first observations of energetic particles due to solar production were the sea-level measurements of Lange and Forbush (1942), and Forbush (1946). Using shielded ionization chambers built to observe galactic cosmic rays, large enhancements in the chamber counting rates on 28 February 1942 (~1 day prior to a large magnetic storm), on 7 March 1942, and 25 August 1946 were observed. The development of the cosmic ray neutron monitor in the late 1940's and the super neutron monitor in the late 1950's and early 1960's have enabled many more solar particle increases to be observed on the ground. The neutron multiplicity monitor (Nobles et al., 1967) enables particle spectral information to be obtained from a single station.

Other pre-spacecraft observations of solar cosmic rays were made during the IGY period by polar cap radio absorption techniques (Bailey, 1957) and by balloon measurements. The balloon observations of Anderson (1958) provided the first direct identification of solar protons.

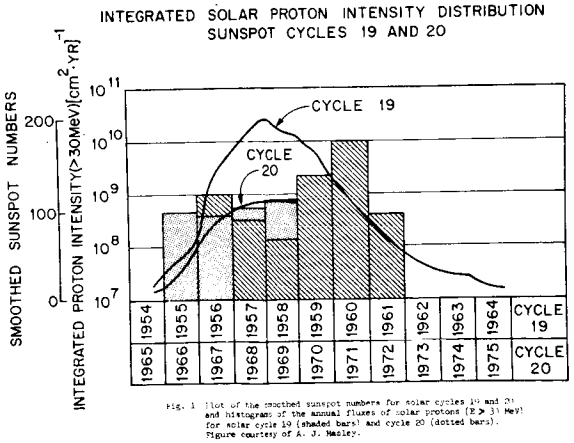

Fig. 1 Plot of the smoothed sunspot numbers for solar cycles 19 and 20 and histograms of the annual fluxes of solar protons (E > 30 MeV) for solar cycle 19 (shaded bars) and cycle 20 (dotted bars). Figure courtesy of A. J. Masley.

The neutron monitor has continued to be a valuable tool for the detection of energetic solar particles. The world-wide deployment of stations provide data for studying both the direction of incidence of the primary particles as well as their energy. An example of the difference in response to an event by super neutron monitors at two different energy (or rigidity) cut-off latitudes is shown in Fig. 2 for data measured during the 28 January 1967 solar event (Bukata et al., 1969). The vertical cut-off rigidity for the Churchill station is 1.0 GV (determined essentially entirely by the atmospheric cut-off) while that of Dallas, at mid-latitudes geomagnetically, is 4.35 GV.

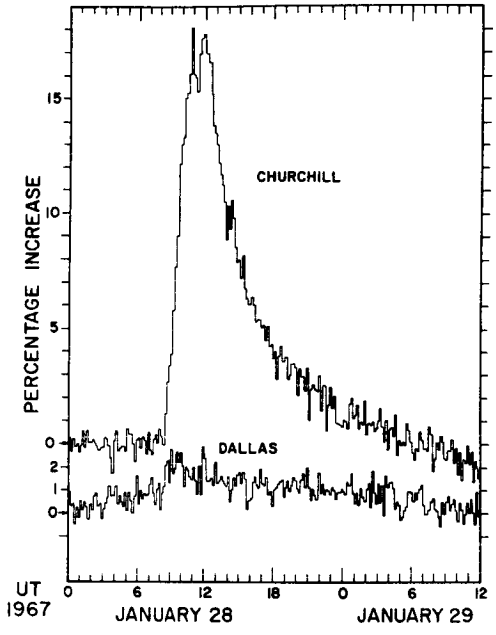

Fig. 2 Neutron monitor observations at Ft. Churchill and Dallas of the 28 January 1967 solar event

The time-intensity profile of the Churchill monitor response to the January 1967 event is quite typical of the classical, diffusive-like profiles recorded by high energy flare-particle detectors and will be discussed in more detail in Section V. In general in diffusive-like events, a rapid rise to the peak particle intensity is followed by a slower, exponential or power-law decay with time.

With the advent of instrumentation flown on spacecraft, the energy sensitivity threshold for the detection of solar particles was dramatically reduced. This reduction in the lower limit of the energy of particle detectability has continued until today measurements of 300-500 keV solar protons are routinely carried out. Accompanying this decrease in the energy sensitivity of particles that can be measured was an increase in the number of solar events that were observed. Furthermore, at the lower energies measured, the time histories of the events became complex with no simple relationships often evident between events.

The data plotted in Fig. 3 illustrates the enormous differences in the description of the interplanetary particle intensities that could be made during a one-month period depending upon the energy sensitivity limits available for analysis. The data were obtained by the solar proton monitoring experiment on the Explorer 41 satellite (C. O. Bostrom, private communication). If only the higher energy channel ($E > 60$ MeV) were available for analysis, only one large event (March 27) and a small event (March 24) would have been apparent. Although the decay times are longer, both of these events had a diffusive temporal appearance similar to the neutron monitor event of Fig. 2.

As the particle energy threshold in Fig. 3 is lowered, more solar events are detected. The event beginning on March 6 (when viewed in the $E > 10$ MeV channel) no longer has a diffusive shape. The solar fluxes in the 1-10 MeV channel of Fig. 3 are observed to remain above their background level through out the entire 31-day period plotted.

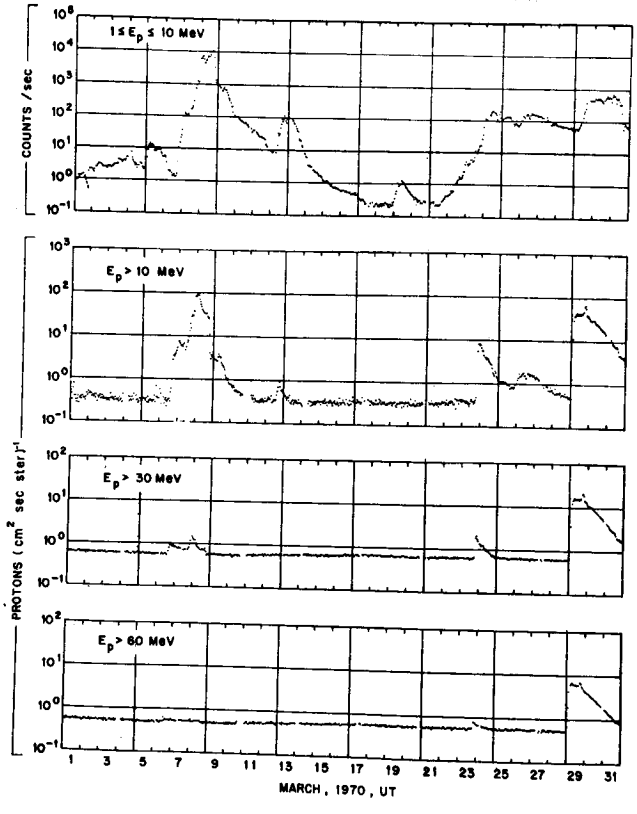

Figure 3. Solar protons measured in interplanetary space by the solar proton monitoring experiment on Explorer 41 during March 1970. Data courtesy of C. O. Bostrom.

Not all of the interplanetary particle enhancements result from discrete flare events. In general, flare-associated events occur in close association with solar X-ray and microwave emissions. Further, as noted above, the time-intensity profiles of flare-associated events tend to have a diffusive appearance. Three other types of particle enhancements, in addition to the flare-associated events considered in this paper, have been classified and discussed extensively in the literature. These are:

a) Particles associated with active centers: The onsets of these particles at the earth display no velocity dispersion and appear to be co-rotating with solar-active centers. Such enhancements have been observed to occur each solar rotation for many successive rotations (e.g., Fan et al., 1968; McDonald and Desai, 1971).

b) Recurrent events: These particle increases occasionally occur in the next solar rotation following a flare. They appear to originate from the same active region as that producing the flare (e.g., Bryant et al., 1965).

c) Energetic storm particles: Enhancements of low energy protons that appear for several hours around the time of occurrence of interplanetary shock waves (e.g., Axford and Reid, 1963; Bryant et al., 1965; Rao et al., 1967). Proton enhancements lasting for several minutes, apparently resulting from acceleration at the shock front, have been reported (e.g., Singer, 1970; Lanzerotti, 1969a, 1970a; Armstrong and Krimigis, 1970; Oglivie and Arens, 1971).

Although the three solar particle enhancements listed above are important for understanding solar processes and interplanetary propagation, they will not be elaborated upon here.

Data Organization

Although the intensity-time profiles of high energy flare particles are similar in their overall diffusive appearance, absolute differences as a function of particle energy are common. Cline and McDonald (1968) have shown that the time history of the high energy proton and electron fluxes from the 7 July 1966 solar flare is dependent upon particle velocity. This is evident in Fig. 4 where the observed-time profiles for three proton and one electron channel are plotted in Fig. 4a.

In Fig. 4b, the four particle flux channels have been normalized to their peak values and the abscissas have been transformed to represent the distance traveled from the flare occurrence.

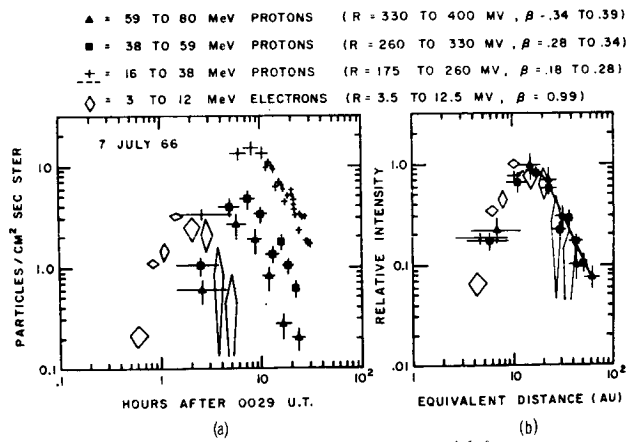

Fig. 4 (a) Profiles of the observed intensity of protons (16-38 MeV, 38-59 MeV, and 59-80 MeV) and electrons (>3 MeV) plotted versus time following the 7 July 1966 flare; (b) profiles of each particle channel relative intensity (I/I_{max}) plotted as a function of distance traveled ($x = vt$) where v is the mean velocity for each particle channel (Cline and McDonald, 1968).

Although the higher energy particle fluxes from this flare can be organized quite well by considerations of velocity-dependent travel, Lin (1970a) has shown that when electrons of energy > 45 keV from this event are included in the analysis, they show a broader curve than those in Fig. 4b. Furthermore, the E > 45 keV electrons appear to arrive earlier than the protons and electrons considered by Cline and McDonald (1968). Lin and Anderson (1967) and Lin (1970a) have interpreted this earlier arrival to low energy electron production either higher in the solar atmosphere or prior to the proton production.

III. COMPOSITION

The most recent reviews of solar cosmic ray composition are those of Biswas and Fichtel (1965) and Fichtel (1970). They discuss in detail the several counter and emulsion measurements made on balloons and rockets beginning during the maximum of solar cycle 19. The discussion here will be limited primarily to observations of solar alpha particles and electrons. Observations of higher-Z elements will be briefly outlined.

Solar Alpha Particles

The primary characteristic arising from the observations of solar alpha particles is that the ratio of the fluxes of solar alphas to solar protons appears to vary widely between individual events and even within a single event. Both of these characteristics can be seen from Fig. 5 (Durgaprasad et al., 1967). Here are plotted the proton to alpha ratios for several different events as a function of particle kinetic energy.

More recently, using satellite instrumentation, the solar alpha measurements have been extended to lower energies and the time resolution during a single event has been substantially improved (Armstrong et al., 1969; Lanzerotti and Robbins, 1970). A comparison of the intensity-time profiles of solar protons and alphas from the series of flares on 21 and 23 May 1967, is shown in Fig. 6 (Lanzerotti and Robbins, 1970). The overall appearance of the intensity profiles of the two species are similar although differences do exist. In particular, the energetic storm particle enhancement at the time of the sudden commencement (SC) on May 24 is not strongly evident in the alpha fluxes.

The detailed alpha to proton ratios throughout the May 23 event are shown in Fig. 7. Large changes in the ratios are observed, particularly at the low energies, for protons and alphas when compared as to equal energy and equal energy per nucleon

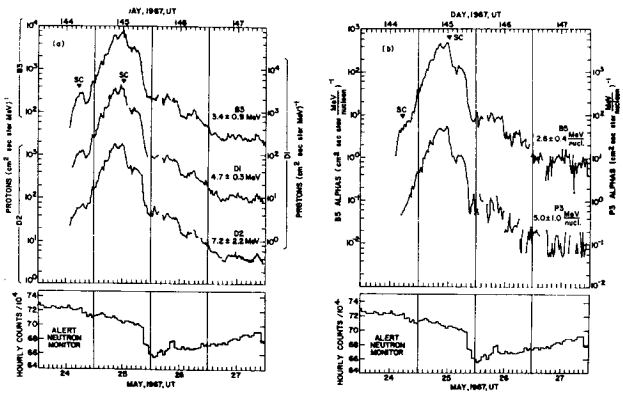

Fig. 6 Alpha particle and proton fluxes measured following the 21 and 23 May 1967 solar events. (Lanzerotti and Robbins, 1969).

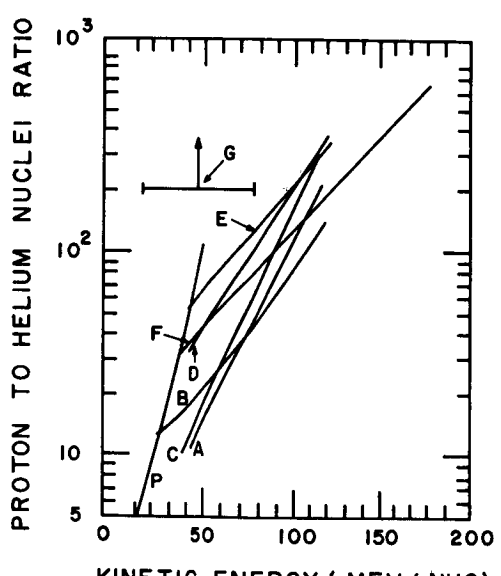

Fig. 5 Ratio of protons to helium nuclei as a function of kinetic energy per nucleon measured at different times in several solar events. The events in which the measurements were made are: A, B - 12 November 1960 (Biswas et. al., 1962); C, D, E - 15 November 1961 (Biswas et. al., 1963); F - 3 September 1960 (Biswas and Fichtel, 1964); G - 16 March 1964 and 5 February 1965 (McDonald et. al., 1965); P - 2 September 1966 (Durgaprased et. al., 1967). (From Durgaprased et. al., 1967).

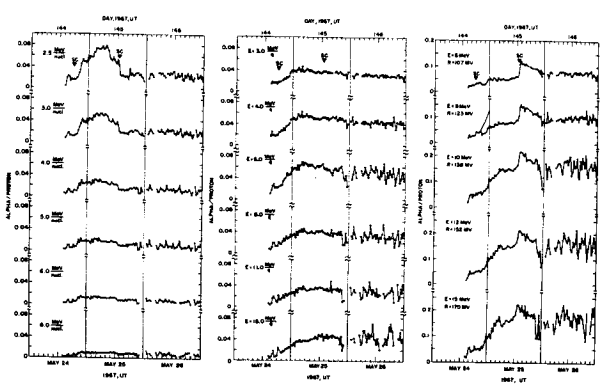

Fig. 7 Alpha particle to proton flux ratios compared as to equal particle energy, equal particle energy per nucleon (equal velocities) and equal particle energy per charge (Lanzerotti and Robbins, 1969).

(equal velocity). However, the central panel of Fig. 7 indicates that after the increases in the ratios following the May 24 sudden commencement, the ratios remain constant throughout the remainder of the event for particles compared as to equal energy per charge. Lanzerotti and Robbins (1970) have interpreted the increases in the alpha to proton ratios observed after the sudden commencement on May 24 as a source effect. They suggest that the solar particles observed prior to the SC were predominantly from flares on May 21 whereas those particles observed after the May 24 increase were from flares on May 23. They also suggested that the constancy of the ratios for equal energy per charge may indicate an important role for electric fields in low energy particle propagation and/or acceleration. Similar behavior of the alpha to proton ratios following other flare events have been noted (Lanzerotti, 1970a; Lanzerotti and Graedel; 1970).

Heavy Nuclei

Heavy solar cosmic ray nuclei ($Z \geq 3$) were first detected in nuclear emulsion stacks flown on a rocket during the 30 September 1960 event (Fichtel and Guss, 1961). The evidence gained from a number of balloon, rocket, and satellite experiments in the early 1960's indicates that the spectral forms for solar heavy nuclei and solar alpha particles are the same in any one event for particles down to ~30 MeV/nucleon (Fichtel, 1970).

A statistical study using satellite data has been made of the ratio of solar alphas to $Z \geq 3$ nuclei for a number of events in 1967-1968. The study indicates that for particles of $E > 0.5$ MeV/nucleon, the spectral behavior observed at the higher energies continues to hold (Armstrong and Krimigis, 1971). It was found that the event-integrated alpha to heavy ratio was ~20 ± 10 for most events, a value substantially smaller than the ratio of 48 ± 8 reported by Durgaprasad et al. (1968) after the 2 September 1966 event in the 12-35 MeV/nucleon range. It is also smaller than the weighted mean of 58 ± 5 determined from six large events in 1960-1969 (Fichtel, 1970).

Solar Electrons

The first direct observation of solar electrons was made from data obtained on a balloon flight by Meyer and Vogt (1962) three days after a large flare on 20 July 1959. They detected highly relativistic electrons of energy 100-1000 MeV. Non-relativistic electrons ($E > 45$ keV) were first measured in interplanetary space by Van Allen and Krimigis (1968) using an instrument flown on Mariner IV. Since that time, the time-intensity profiles of relativistic solar electrons (e.g., Cline and McDonald, 1968; Simnett et al., 1969) and non-relativistic solar electrons (Anderson and Lin, 1966; Lin and Anderson, 1967; Anderson, 1969; Lin, 1970a, 1971) have been intensively studied.

The temporal characteristics of relativistic electrons following the 6 July 1966 flares are shown in relationship to the proton component in Fig. 4. It was found that for this flare the electron and proton components could be organized in time by considerations of particle velocities alone. However, it was noted that Lin (1970a) showed that the low energy ($E > 45$ keV) electrons apparently arrived first, before the more energetic particles.

An example of a comparison of the electron intensity-time profiles for a single event is shown in Fig. 8 (Lin, 1970b, private communication; Lanzerotti, 1970a). These data, from a west limb flare, show rather similar time profiles for a wide range of electron energies. The similarities in the temporal profiles are in contrast to those observed in the case of protons (e.g., Fig. 3; see also Lanzerotti, 1970a, for proton temporal profiles measured during the same period as the electron data of Fig. 8). This could be due to a more direct propagation of electrons to the earth with less interplanetary diffusion and scattering than in the case of protons.

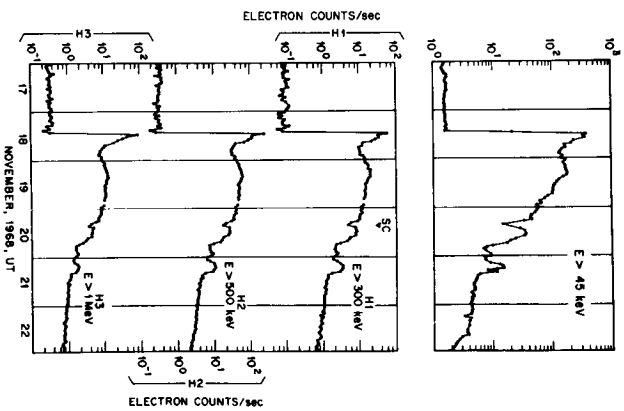

Fig. 8 Time variations of the solar electron fluxes measured following the west limb event on 18 November 1968. The $E > 45$ keV data are from Lin (1970b; private communication). The higher data are from Lanzerotti (1970a).

IV. SPECTRA

As might be expected, solar flare particle spectra have large variations in intensities and spectral shapes both between individual events as well as within a single event. Representative proton, alpha particle, and electron solar flare particle spectra are discussed separately.

Proton Spectra

The solar proton spectra, particularly for higher energies, generally steepen with time after the flare. That is, as time progresses, relatively few higher energy particles as compared to the lower energies are present. The proton energy spectra measured in several of the large events during the last decade were found to fit very well a spectral representation with a rigidity dependence. This spectral shape can be expressed as (Freier and Webber, 1963)

$$\frac{dJ}{dR} = \frac{dJ_o}{dR_o} \exp[-R/R_o(t)] \qquad (1)$$

where R = Mv/c is the proton rigidity. It was found that this spectral representation was particularly applicable during the decay phase of an event for protons of energies $\gtrsim$ 20 MeV.

Six proton energy spectra obtained during several large events of the last solar cycle are plotted in Fig. 9. These spectra exhibit the exponential-in-rigidity spectral shape (Freier and Webber, 1963). Solar cosmic ray spectra such as those of Fig. 9 are very steep compared to the galactic cosmic ray spectra (e.g., Fichtel and McDonald, 1967).

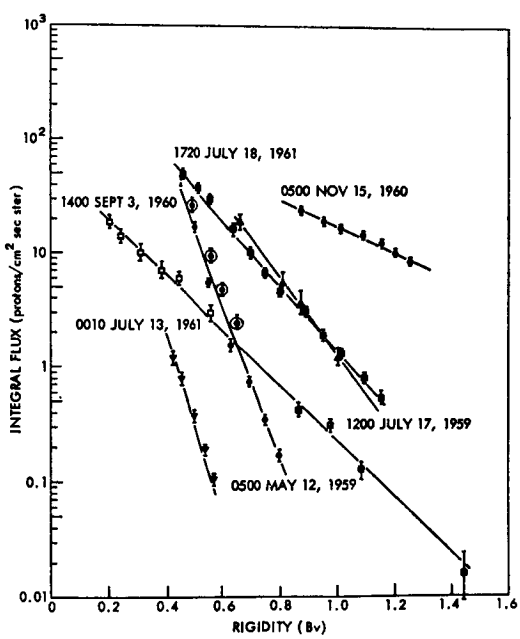

Fig. 9 Solar proton spectra measured in several solar events (Freier and Webber, 1963).

Essentially all of the solar flare particle spectra taken during the last solar cycle were obtained by rocket or balloon-based instruments. Frequently, little of the time history of an event was obtained. Hence, relatively greater emphasis appears to have been placed on the spectra of the different events. During the present solar cycle, with essentially continuous monitoring of an event's time profile and with the measurement of lower energy particles, less emphasis has been placed on the individual event spectra. This neglect of spectral emphasis partly arises, of course, because the spectra changes during an event, particularly for the events which do not exhibit a diffusive temporal profile at the lower energies (e.g., several of the events in Fig. 3). Hence, it is impossible to categorize an event simply with only one or two spectra. However, unlike the more energetic particles, and as will be discussed in Section V, the decay of low energy particles during events that do have a diffusive character appears to be energy independent. In this case, a single spectral shape would indeed describe much of the event's spectral form.

A single power-law in energy was fit by Lanzerotti (1969c) to the half-hour averaged proton spectra (E_p = 0.58 to 18.1 MeV) measured during the event plotted in Fig. 6. He found that the spectra became significantly softer during the storm particle event on May 24 and for the next two and one-half days following the SC on May 25. At both times the exponent n changed from ~1.3 to ~2.0.

The low energy proton spectra measured by Bell Laboratories' instruments on Explorers 34 and 41 near the intensity maximum of several solar flare events in the past several years are plotted in Fig. 10. The spectra are plotted on log-log scales to emphasize deviations from simple power-law relationships at these energies. In particular, the spectrum from the 2 November 1969 flare has a pronounced peak at E ~ 3.5 MeV which may signify particle propagation delays from the flare region (on the extreme west limb).

A study of the response of the world-wide network of neutron monitors to the 28 January 1967 event (see Fig. 2) has been made by Heristchi and Trottet (1971). They used the global distribution of neutron monitors as an energy spectrometer to determine a possible upper cutoff in the energy spectrum of the flare-produced protons from this event. They found an energy cutoff of $4_3 3 \pm 0.5$ GeV. This energy is 10^2 - 10^3 eV lower than that predicted by a flare acceleration model of Friedman and Hamberger (1969).

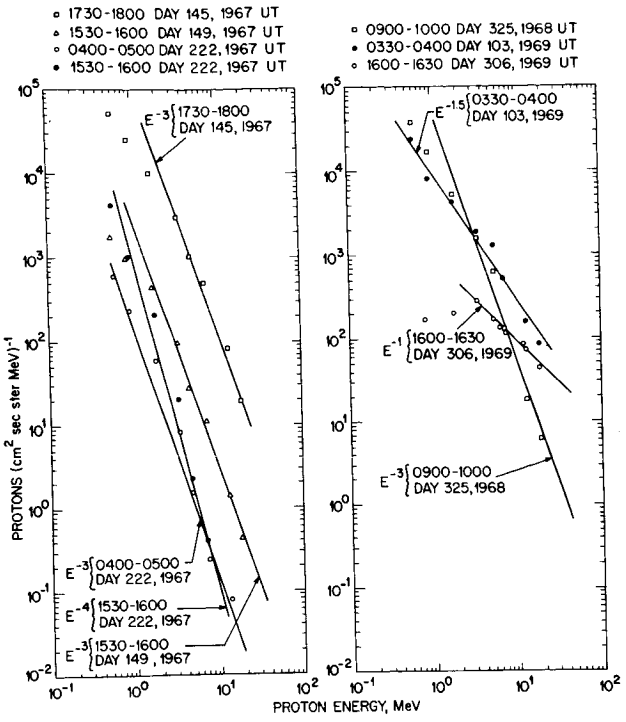

Fig. 10 Low energy solar proton spectra measured on Explorers 34 and 41 near the maximum of several solar events.

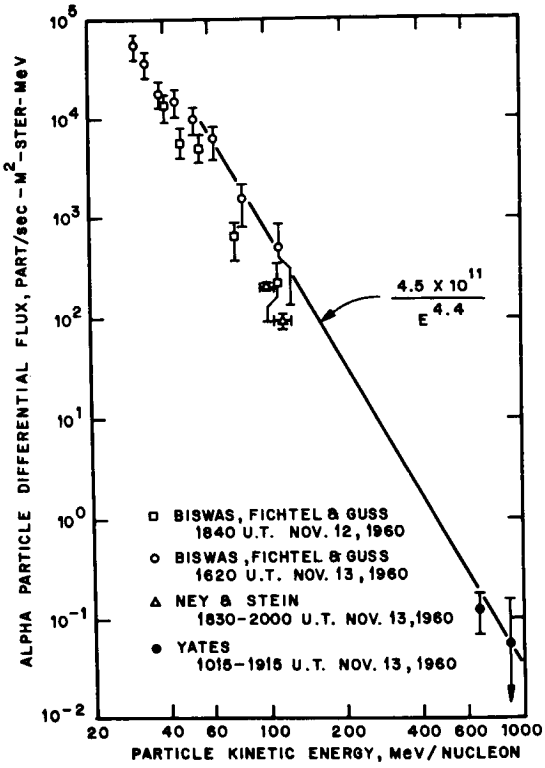

Fig. 11 High energy solar alpha particle fluxes measured by several observers following the 12 November 1960 solar event (from Yates, 1964).

Alpha Particle Spectra

High energy ($E \gtrsim 30$ MeV/nucleon) alpha particles were observed in a number of solar events to have spectra similar to those of the protons. Frequently, differential rigidity spectra (Eq. 1) were applicable to both particle species during an event, although the e-folding rigidity value R_o might at times be different for the two species (e.g., Biswas et al., 1963; Durgaprasad et al., 1968).

Solar alpha particles were studied over a very wide energy range during the 12 November 1960 solar event. The differential alpha fluxes measured between ~31 and ~100 MeV/nucleon by several workers are presented in Fig. 11 (Biswas et al., 1962; Ney and Stein, 1962). Also shown are two high energy alpha flux measurements from the work of Yates (1964) during the same event.

The flux measurements of Yates (Fig. 11), if expressed on an exponential-in-rigidity basis, would fall considerably above what would be predicted by an extrapolation of the lower energy data (Yates, 1964). Yates' measurements were challenged by Waddington and Freier (1965) as perhaps being contaminated by the high fluxes of slow protons present during the event. The controversy appears still to be unresolved (Yates, 1965); very high energy measurements of solar alpha particles need to be made during other large events.

As noted in Section III, recent years have seen an increase in the time resolution of low energy solar alpha particle observations by satellite. Studies of the changes in the alpha spectra during a single event have become feasible, although little emphasis has been placed on this aspect of the observations. Lanzerotti (1969 c) studied the power-law exponent of the alpha spectra for the May 1969 event (Fig. 6). He found that during the period between the two sudden commencements (May 24 and May 25), the alpha particle spectra were somewhat harder than that for protons; however, after the May 25 SC, both proton and alpha particle power law exponents in Eq. (2) were ~2. The low energy alpha particle spectra measured by Bell Laboratories' instruments on Explorer 34 and Explorer 41 near the maximum of several solar events of the last several years are plotted in Fig. 12. These spectra give a representative example of low energy alpha spectral shapes and intensities.

Electron Spectra

Since the number of published observations of solar electrons is substantially less than for protons, detailed information on electron spectra is less plentiful. Lin (1970a) has compiled electron spectra from four solar events in 1967 as measured by

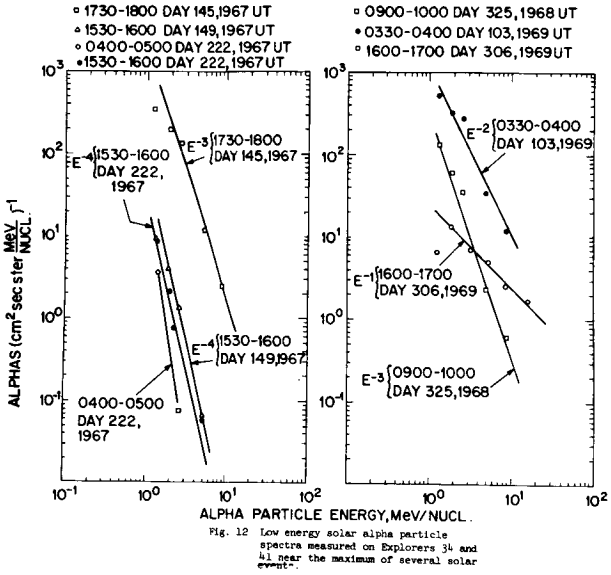

Fig. 12 Low energy solar alpha particle spectra measured on Explorers 34 and 41 near the maximum of several solar events.

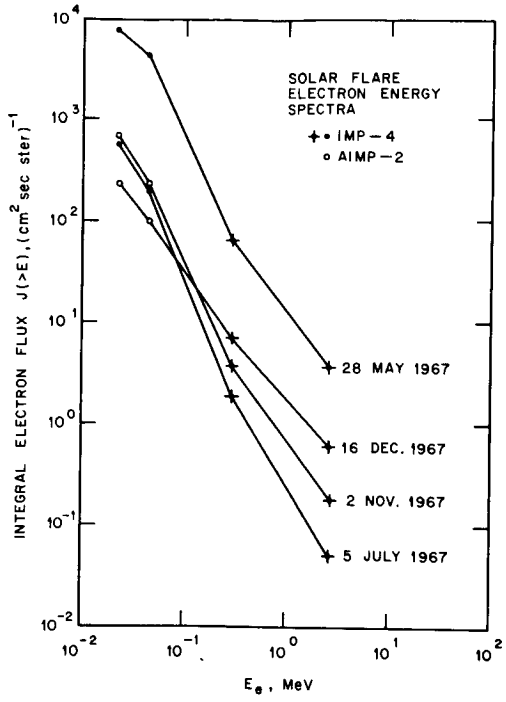

Fig. 13 Solar electron spectra measured during four events in 1967 (Lin, 1970a).

instruments on Explorers 34 and 35. These spectra are shown in Fig. 13. Lin finds that if he fits the spectra to a power law (Eq. 2), the events in Fig. 13 have exponents $n \sim 2.3\text{-}3.5$.

V. PROPAGATION

After acceleration, the flare-produced solar particles must escape from the active region and propagate through interplanetary space to the earth. Interplanetary space is permeated by the solar magnetic field. The nature of this field configuration was predicted by Parker (1960) to consist of spiral lines emanating from the sun. This prediction was subsequently confirmed by extensive satellite measurements (e.g., Ness et al., 1964). This spiral interplanetary magnetic field controls much of the propagation of the flare particles. The guiding center of the solar particles tend to follow the spiral nature of the field. However, the small-scale irregularities in the field act as scattering centers and perturb, or scatter, the particles, moving them to other field lines. Extensive theoretical work (not discussed here) has been carried out in recent years in determining the solar particle diffusion coefficients due to these random scatterings (e.g., Jokipii, 1966, 1967, 1968; Roelof, 1966, 1968; Hasselmann and Wibberenz, 1968; Jokipii and Parker, 1969).

The propagation characteristics of solar particles have been reviewed recently (Fichtel and McDonald, 1967; Axford, 1970). The first considerations of a diffusion model for solar particle propagation was that of Parker (1956) and Meyer et al. (1956). The broad considerations and the development of isotropic diffusion theory for solar particles, i.e., solutions to a diffusion equation of the form

$$\frac{\partial n}{\partial t} = r^{-2} \frac{\partial}{\partial r}\left(r^2 \kappa \frac{\partial n}{\partial r}\right), \qquad (3)$$

have been due to Parker (1963). In Eq. (3), $n(r,t)$ is the mean density of solar particles with velocity v and $\kappa = \frac{1}{3}v^2\tau = \frac{1}{3}\lambda v$ is the diffusion coefficient and is, most generally, a tensor quantity (Jokipii, 1966). τ is the mean particle "collision time" for interaction with the interplanetary magnetic irregularities and can be determined from the interplanetary field fluctuations (Jokipii and Coleman, 1968). Most commonly, solutions to Eq. (3) have assumed $\kappa = \kappa_o(T)r^\beta$ where T is the particle kinetic energy and β is time-independent.

Solutions to Eq. (3) have chiefly considered two different boundary conditions. The first of these that has been used has taken $\beta=0$ and has assumed a perfectly absorbing boundary ($n=0$) at some $r = r_b >$ 1 a.u. The solution to Eq. (3) at times $t >> r_b/\kappa_o$ after the flare yield an exponential decay for the fluxes

$$n(r,t) \sim \frac{1}{r} \sin\frac{\pi r}{r_b} \exp\left[\frac{-\pi^2 \kappa_o t}{r_b^2}\right] \qquad (4)$$

where the decay time is given as

$$\tau_D = \frac{r_b^2}{\pi^2 \kappa_o} \qquad (5)$$

This solution to the model has been utilized by Bryant et al. (1962) and Hofmann and Winckler (1962) in analyzing solar particle events. They found that the absorbing "boundary" r_b was at $r \sim 2$ a.u. Although the 2 a.u. boundary may indicate that the hydromagnetic waves producing the interplanetary irregularities are being damped out at this distance (Jokipii and Davis, 1969), Axford (1970) has maintained that an exponential decay of κ with distance r will also produce the same results.

A number of solar events have been fit by Krimigis (1965) using a solution of Eq. (3) assuming a radial dependence to the diffusion coefficient (i.e., $\beta \neq 0$) and no boundary r_b (Parker, 1963). This solution can be expressed as

$$n(r,t) \propto f(\kappa_o,\beta,T)\left[t^{3/(2-\beta)}\right]^{-1} \exp\left[-\frac{r^{2-\beta}}{(2-\beta)^2}\frac{1}{\kappa_o t}\right] \qquad (6)$$

A plot of $\ln[n(r,t)t^{3/(2-\beta)}]$ versus t^{-1} should yield a straight line for the proper choice of $\beta(<2)$. Krimigis found that for protons in the energy range 50-500 MeV, good agreement with observations was obtained for $\beta \sim 1$ and $\lambda \sim 0.1$ a.u.

Anisotropic Diffusion

The isotropic solar particle diffusion model discussed above is not able to explain several important characteristics of the solar particles observed at the earth. One of these is the direction of the non-radial anisotropy of the particles measured at the earth. The anisotropy at the beginning of events is aligned along the spiral field direction, outward from the sun (McCracken, 1963; McCracken et al., 1967). (Later in the events the anisotropy becomes much less and the direction changes to radial or nearly so (McCracken et al., 1967; Rao et al., 1969).) The second problem with isotropic models is that they can not treat the observations that show that the particle fluxes arising from flares in the eastern hemisphere of the sun tend to increase more slowly to maximum intensity than those that originate from west hemisphere flares (e.g., Fichtel and McDonald, 1967; Burlaga, 1967).

Reid (1964) has considered a solution to the east-west effect by postulating a thin diffusing shell around the sun. Particles originating from flares in the eastern hemisphere would diffuse (isotropically) across the solar surface to the spiral field lines connecting the sun to the earth and then propagate along the field lines to the earth (Fig. 14). Reid's model of diffusion across the solar surface must be combined with an interplanetary propagation model to provide a complete description of the particle event as seen at the earth. Since inclusion of the solar-surface diffusion increases the number of parameters that can be adjusted, it is likely that most diffusive-type observations could be fit with such a model. Indeed, a solar diffusing layer was one of the features included in a recent computational model for solar flare propagation (Englade, 1971).

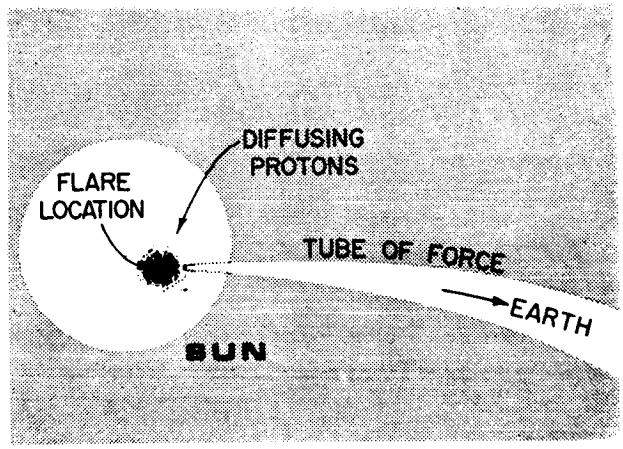

Fig. 14 Illustration depicting solar particle diffusion across the solar surface to the interplanetary flux tube linking the sun to the earth (Reid, 1964).

The consideration of an anisotropic diffusion coefficient to solve the east-west problem was first made by Axford (1965). Burlaga (1967) solved the diffusion equation considering particle diffusion transverse to the spiral interplanetary field as well as along it and neglected Reid's diffusion layer around the sun. Expressed in spherical coordinates, Burlaga solved the equation

$$\frac{\partial n}{\partial t} = \frac{1}{r^2}\left[\frac{\partial}{\partial r}\left(r^2 \kappa_{\parallel}\frac{\partial n}{\partial r}\right)\right] + \frac{1}{r^2}\frac{\partial}{\partial \mu}\left[\kappa_{\perp}(1-\mu^2)\frac{\partial n}{\partial \mu}\right] + \frac{1}{r^2 \sin^2\theta}\frac{\partial}{\partial \varphi}\left[\kappa_{\varphi}\frac{\partial n}{\partial \varphi}\right] \qquad (7)$$

where $\mu = \cos\theta$ and $\kappa_{\parallel}$, $\kappa_{\perp}$, and κ_{φ} are the components of the diffusion tensor.

Burlaga (1967) took the parallel diffusion coefficient $\kappa_{\parallel}$ to be a constant, independent of the radial position, the transverse coefficient $\kappa_{\perp}$ proportional to the square of the radial distance ($\kappa_{\perp} \propto r^2$), and an absorbing boundary at $r_b > 1$ a.u. Solving Eq. (7) with the above boundary conditions and assuming n to be independent of φ, he obtained quite satisfactory fits for a number of different flare events distributed over the solar disk. The event decay time resulting from his solution can be written as

$$\tau_D = \frac{r_b^2}{\pi^2 \kappa_{\parallel}} . \qquad (8)$$

Eq. (8) is of the same form as the decay time derived for isotropic diffusion (Eq. 5) with the isotropic diffusion coefficient κ_0 replaced by $\kappa_\parallel$.

Two examples of Burlaga's fits to particle fluxes resulting from flares at two separate solar locations are shown in Fig. 15. The angle θ_0 noted on the figure is the angle, measured from the center of the sun, between the flare location and the location on the sun of the interplanetary field line passing through the earth. Fits of the model to both the neutron monitor observations of the 23 February 1956 event and the balloon observations of E > 80 MeV protons from the 20 July 1961 event are seen to be quite good.

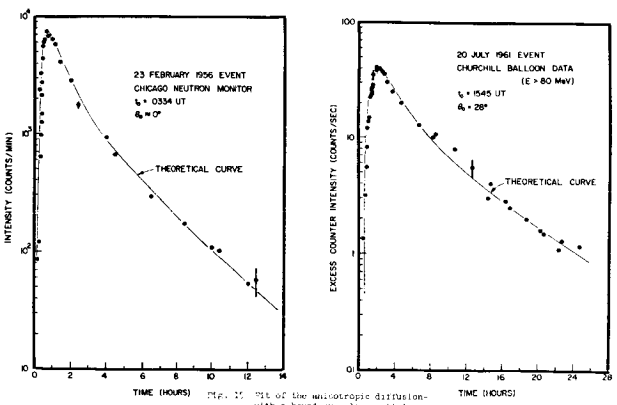

Fig. 15. Fit of the anisotropic diffusion-with-a-boundary solar particle-propagation model to an event measured by a neutron monitor and an event measured by a balloon-based detector (from Burlaga, 1967).

Low Energy Propagation

It is clear from data such as those of Fig. 3 that at lower energies solar flare particles do not often have diffusive intensity-time profiles. Substantial modulation of these low energy particles by solar wind discontinuities, shock waves, and magnetic field sector boundaries must be occurring. Although there are events where the low energy particles exhibit diffusive-type profiles, the applicability of an anisotropic diffusion model such as Burlaga's to these observations is highly suspect (Forman, 1970). Forman has maintained that the "equilibrium" anisotropy present during the decay phase of an event (McCracken et al., 1967) and the evidence that the diffusion coefficient becomes small at low energies (Jokipii and Coleman, 1968) indicate that solar wind convection, and the resulting particle energy loss, is an important mode of low energy particle propagation. (The anisotropic diffusion model of Burlaga (as well as the isotropic models) considers convection effects to be negligible for the higher energy particles, and rightly so.) Forman (1971) cites as further evidence for the importance of convection the fact that the reported decay times for both protons and alphas were essentially energy-independent for 1-20 MeV/nucleon particles after the 28 May 1967 flare (Lanzerotti, 1969a).

Forman (1971) has solved the Fokker-Planck equation first derived by Parker (1965) for particle transport including convection and diffusion:

$$\frac{\partial n(r,t)}{\partial t} + \nabla\cdot\left\{V\left(n - \frac{1}{3}\frac{\partial}{\partial T}(\alpha T n)\right) - \kappa\cdot\nabla n\right\}$$

$$= \frac{V}{3}\frac{\partial}{\partial r}\frac{\partial}{\partial T}(\alpha T n) \qquad (9)$$

Here V is the solar wind velocity, T is the particle kinetic energy, and $\alpha = (T+2Mc^2)/(T+Mc^2)$. The diffusion models discussed above all neglected the terms in Eq. (9) containing the solar wind velocity V. Forman obtained an analytic solution to Eq. (9) assuming that $\kappa_\perp = \kappa_1 r^2$, $\kappa_\parallel = \kappa_2 r$, and that there was a diffusing boundary at $r = r_b$. Forman's model predicts very well the equilibrium residual anisotropy during the decay phase of an event as observed by McCracken et al. (1967) as well as the magnitude (~14-18 hours) of the energy-independent decay time for both alphas and protons as observed by Lanzerotti (1969a).

From her solution to Eq. (9) Forman (1971) has shown that in the decay phase of the event

$$N(r,t) \propto f\left(\frac{r}{r_b}\right) r^{(V/2\kappa_2 - 1)} \exp(-t/\tau_D) \qquad (10)$$

where the decay time τ_D is given as

$$\tau_D = \frac{4r_b}{V}\frac{V/\kappa_2}{\left[j_{\eta,1}(V/\kappa_2)\right]^2} = \frac{4r_b}{V}\, g(V/\kappa_2). \qquad (11)$$

In Eq. (11) $j_{\eta,1}$ is the first zero of the Bessel function of order η. Forman has found that for r_b = 2.3 a.u. (a representative value determined from the model fits of Burlaga, 1967), τ_D has a broad maximum of ~15-17 hours for $\kappa_\parallel = \kappa_2 r$ between $\sim 3\cdot10^{19}$ and $3\cdot10^{20}$ cm^2 sec^{-1} (reasonable values for $\kappa_\parallel$ as determined from the power spectra of the interplanetary magnetic field near the earth by Jokipii and Coleman, 1968). Forman's model has recently been applied successfully to the low energy proton observations from the 7 June 1969 event (Murray et al., 1970).

The energy-independence of the decay times for both protons and alpha particles during a diffusive-type event is shown in Fig. 16 for the 13 April 1969 event (Lanzerotti and Graedel, 1970). The intensity-time profiles of the proton fluxes in the $0.56 \leq E \leq 0.60$ MeV channel is shown as an insert in the figure. This event, probably originating from a flare behind the east limb, demonstrated a diffusive-type appearance even in the lowest energy-channel measured. This was quite unlike the 28 May 1967 diffusive event where energetic storm particles greatly enhanced the lower energy proton fluxes (Lanzerotti, 1969a). Also plotted in Fig. 16 are the decay times for $E > 10$, >30, and >60 MeV protons measured by the solar particle monitoring experiment on the same satellite (Solar Geophysical Data, 1969). The decay time varied from ~28 hours at 0.58 MeV to ~19 hours at 60 MeV. Over the range 0.58 MeV to 20 MeV, the decay time decreased by only ~4 hours.

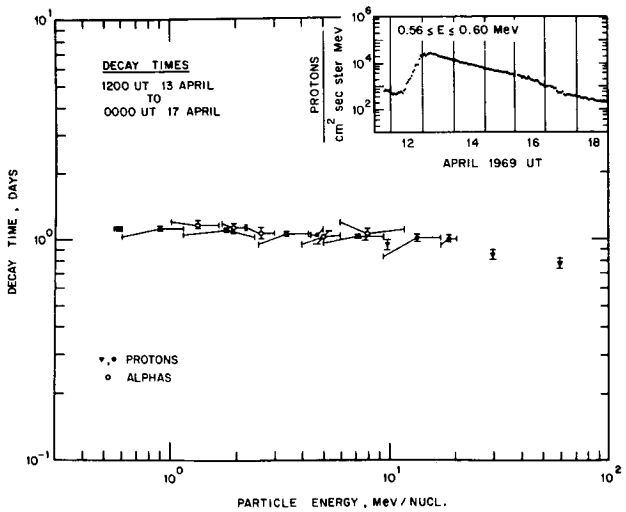

Fig. 16 Proton and alpha particle decay times following the 13 April 1969 solar event. The intensity-time profile for the $0.56 \leq E \leq 0.60$ MeV proton channel is shown as an inset to the figure (Lanzerotti and Graedel, 1970).

VI. FLARE PARTICLE EFFECTS

Two consequences of solar flare particle effects are discussed below. The first of these is the effect of energetic flare particles in producing polar-cap cosmic noise absorption and the detection of this enhanced absorption by riometer techniques. The second is the effect of solar particles, penetrating into the outer magnetosphere, on satellite solar cell lifetimes.

Riometer Absorption

The first indication of the production of enhanced ionosphere ionization by solar flare particles was the strong absorption of cosmic radio noise in the polar cap regions that Bailey (1957) correlated with the flare of 23 February 1956. Since that time, enhanced riometer absorptions in the auroral and polar cap regions during solar events have been studied as basic geophysical phenomena and as diagnostic tools for studying solar and magnetospheric processes (e.g., Bailey, 1964; Reid, 1970). Indeed, the significance of energetic storm particles was first outlined by Axford and Reid (1963) using riometer data.

Through the work of Potemra et al. (1967, 1969, 1970) good agreement has been achieved in calculating the expected riometer response from a measured incident solar flux. Potemra and his collaborators have calculated the expected total absorption A at a radio wave angular frequency ω from the formula

$$A(dB) = \int 1.16\times10^{6} \frac{n_e}{\nu_m} C_{\frac{5}{2}}\left(\frac{\omega \pm \omega_H}{\nu_m}\right) dh \qquad (12)$$

obtained from the theory of Sen and Wyller (1960). In Eq. (12) ω_H is the angular gyro frequency, dh is the increment of ionization height in 10-km units, $C_{5/2}$ is an integral function, n_e is the electron density and ν_m is the mean electron collision frequency. Using specific ionization rates due to G. W. Adams and Adams and Masley (1965) and ν_m and recombination coefficients deduced from the September 1966 event, Potemra et al. (1970) have predicted the observed absorption for high latitude riometer observations during a number of 1967 PCA events. Their calculations, using satellite measurements of the solar proton fluxes over the polar caps, are compared in Fig. 17 to the observed riometer day and night absorption measurements following the 28 January 1967 solar event. The agreement is quite good for both the day and the night observations. (It is interesting to compare these lower energy proton observations of Fig. 17 with the neutron monitor profile for the same event in Fig. 2.)

Several authors (Van Allen et al., 1964; Juday and Adams, 1969; Reid, 1969, 1970) have used the empirical relation

$$(F)^{\frac{1}{2}} = R \times A \qquad (13)$$

to relate the integral fluxes F of protons above some energy E_{min} to the riometer absorption A at a given frequency. In Eq. (13), R is a constant, dependent only upon E_{min}. Potemra and Lanzerotti (1971), using solar proton data from the synchronous equatorial ATS-1 satellite, deduced R as a function of E_{min} from the 30 MHz riometer absorption observed at Byrd during the 28 January 1967 event. (Byrd (L~7) is at

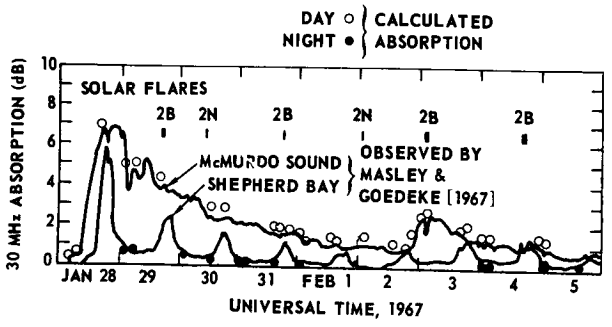

Fig. 17 Comparison of observed day and night riometer absorption and the calculated absorptions using polar cap-average solar proton data from satellite 1963-38c during the 28 January 1967 event (Potemra et. al., 1970).

nearly the same latitude as ATS-1 (L~6.4) but three hours earlier in local time.) They found Eq. (13) to be an excellent fit to the data, essentially independent of the value of E_{min}. The values of $R(E_{min})$ they found for E_{min} between 5 and 50 MeV are plotted in Fig. 18 as a function of E_{min}. Such R-values should be quite useful for the new solar proton event classification scheme (Shea and Smart, 1970).

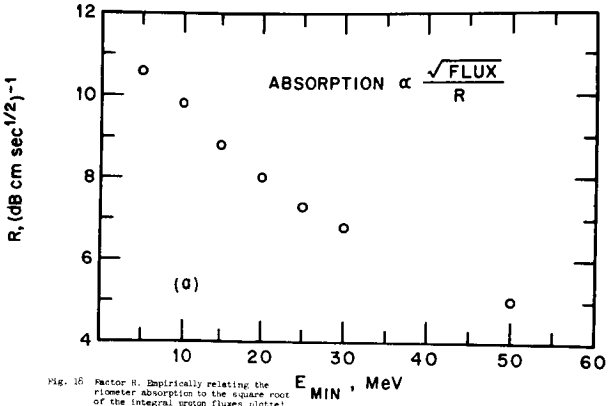

Fig. 18 Factor R, Empirically relating the riometer absorption to the square root of the integral proton fluxes plotted as a function of E_{min}, the lower energy limit on the integral fluxes. R was determined from the 28 January 1967 event (Potemra and Lanzerotti, 1971).

Solar Cell Damage

Solar protons appear to have ready access to the outer regions of the magnetosphere other than through the polar cap regions. The solar particles at synchronous altitude are observed to have essentially the same intensities and spectra as the particles in interplanetary space for protons as low as 1 MeV in energy (Lanzerotti, 1968, 1970b; Paulikas and Blake, 1969). These low energy protons could cause significant damage to unshielded solar cells on a synchronous satellite. It was pointed out by Lanzerotti (1969b) that the damage to unshielded cells from relatively low intensity solar events could dominate the normal synchronous altitude radiation (predominantly electrons) in producing damage. Indeed, anomalous, step-like changes in the short circuit current of unshielded cells in the ATS-1 solar cell damage experiment are observed in conjunction with solar flare events (Waddel, 1968).

An example of the solar proton damage to an unshielded solar cell on ATS-1 during the May 1967 events (Fig. 6) is shown in Fig. 19. The two lower bar graphs show the values of the short circuit current (in ma) measured each day for two 10 Ω-cm n-on-p type solar cells (R. C. Waddel, private communication). One cell was unshielded while the other had a 1 mil shield of 7740 glass. At the top are plotted the daily average of the integral half-hour average proton fluxes (E > 2.4 MeV) measured by the Bell Laboratories experiment on ATS-1. (No data were received on days 143, 144, and 147.)

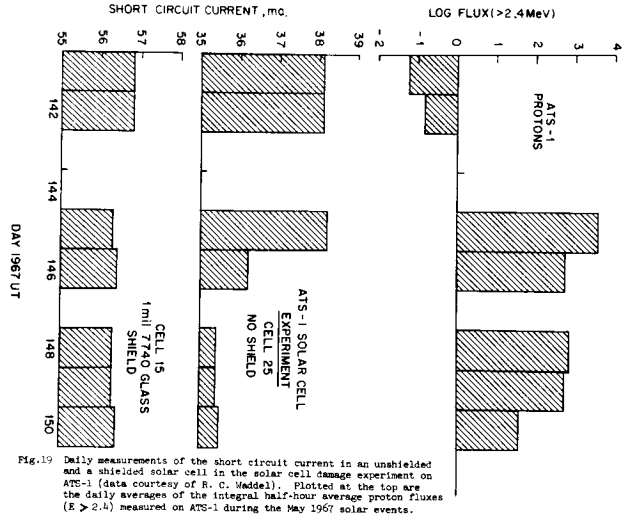

Fig.19 Daily measurements of the short circuit current in an unshielded and a shielded solar cell in the solar cell damage experiment on ATS-1 (data courtesy of R. C. Waddel). Plotted at the top are the daily averages of the integral half-hour average proton fluxes (E > 2.4) measured on ATS-1 during the May 1967 solar events.

Prior to the major interplanetary enhancement on day 145, the proton fluxes at ATS-1 were very low. The day after the large ATS-1 enhancement on day 145 the short circuit current in the unshielded cell decreased sharply whereas only a slight decrease in the current was observed in the shielded cell.

Since a 1 mil shield will stop ~0.5 MeV protons, the data of Fig. 19 are indicative that protons with energies as low as this were producing the most significant damage. This could be due both to the penetration of 0.5 MeV solar protons to the synchronous orbit as well as to the fact that the magnetosphere boundary was pushed within the ATS-1 orbit for periods of time on days 145 and 146.

Even if shields were provided for synchronous satellite solar cells, the fluxes of low energy (0.5-3 MeV) solar protons penetrating to this altitude could still play an important role in the damage considerations. This is because in the manufacturing process the shields are often not deposited uniformly over the cell surfaces, leaving a small fraction of some cells uncovered (R. C. Waddel, private communication). Such partially unshielded cells would then be subjected to unexpected damage by the low energy protons.

ACKNOWLEDGMENTS

I would like to thank the following individuals for generously providing data and comments for this review: Dr. C. O. Bostrom, Applied Physics Laboratory; Dr. R. P. Lin, University of California, Berkeley; Mr. A. J. Masley, McDonnell-Douglas Astronautics Co.; Dr. T. A. Potemra, Applied Physics Laboratory; Dr. R. C. Waddel, NASA/GSFC.

References

Adams, G. W., and A. J. Masley, J. Atmos. Terr. Phys., 27, 289, 1965.

Anderson, K. A., Phys. Rev. Letters, 1, 336, 1958.

Anderson, K. A., Solar Phys., 6, 111, 1969.

Anderson, K. A., and R. P. Lin, Phys. Rev. Letters, 16, 1121, 1967.

Armstrong, T. P., S. M. Krimigis, and J. A. Van Allen, Annals. IQSY, 3, 313, 1969.

Armstrong, T. P., S. M. Krimigis, and K. W. Behannon, J. Geophys. Res., 75, 5980, 1970.

Armstrong, T. P., and S. M. Krimigis, J. Geophys. Res., to be published, 1971.

Axford, W. I., Planet. Space Sci., 13, 1301, 1965.

Axford, W. I., Preprint, University of Calif., San Diego. August, 1970.

Axford, W. I., and G. C. Reid, J. Geophys. Res., 68, 1743, 1963.

Bailey, D. K., J. Geophys. Res., 62, 431, 1957.

Biswas, S., C. E. Fichtel, and D. E. Guss, Phys. Rev., 128, 2756, 1962.

Biswas, S., C. E. Fichtel, D. E. Guss, and C. J. Waddington, J. Geophys. Res., 68, 3109, 1963.

Biswas, S., and C. E. Fichtel, Ap. J., 139, 941, 1964.

Biswas, S., and C. E. Fichtel, Space Sci. Rev., 4, 709, 1965.

Bryant, D. A., T. L. Cline, U. D. Desai, and F. B. McDonald, J. Geophys. Res., 67, 4983, 1962.

Bryant, D. A., T. L. Cline, U. D. Desai, and F. B. McDonald, Ap. J., 141, 478, 1965.

Bukata, R. P., P. T. Gronstal, R. A. R. Palmeira, K. G. McCracken, and U. R. Rao, Solar Phys., 10, 198, 1969.

Burlaga, L. F., J. Geophys. Res., 72, 4449, 1967.

Cline, T. L., and F. B. McDonald, Solar Phys., 5, 507, 1968.

Durgaprasad, N., C. E. Fichtel, D. E. Guss, and D. V. Reames, NASA/GSFC Preprint X-611-67-324, July 1967.

Durgaprasad, N., C. E. Fichtel, D. E. Guss, and D. V. Reames, Ap. J., 154, 307, 1968.

Englade, R. C., J. Geophys. Res., 76, 768, 1971.

Fan, C. Y., M. Pick, R. Pyle, J. A. Simpson, and D. R. Smith, J. Geophys. Res., 73, 1555, 1968.

Fichtel, C. E., NASA/GFSC Preprint X-662-70-134, April 1970.

Fichtel, C. E., and D. E. Guss, Phys. Rev. Letters, 6, 495, 1961.

Fichtel, C. E., and F. B. McDonald, Ann. Rev. Astron. Astrophys., 5, 351, 1967.

Forbush, S. E.: Phys. Rev., 70, 771, 1946.

Forbush, S. E., and I. Lange: Terr. Mag., 47, 185, 1942.

Forman, M. A., J. Geophys. Res., 75, 3147, 1970.

Forman, M. A., J. Geophys. Res., 76, 759, 1971.

Freier, P. S., and W. R. Webber, J. Geophys. Res., 68, 1605, 1963.

Friedman, M., and S. M. Hamberger, Solar Phys., 8, 104, 1969.

Hasselmann, K., and G. Wibberenz, Zeit. für Geophysik, 34, 353, 1968.

Heristchi, DJ, and G. Trottet, Phys. Rev. Letters, 26, 197, 1971.

Hofmann, D. J., and J. R. Winckler, J. Geophys. Res., 68, 2067, 1963.

Jokipii, J. R., Ap. J., 146, 480, 1966.

Jokipii, J. R., Ap. J., 149, 405, 1967.

Jokipii, J. R., Ap. J., 152, 671, 1968.

Jokipii, J. R., and P. J. Coleman, Jr., J. Geophys. Res., 73, 5495, 1968.

Jokipii, J. R., and E. N. Parker, Ap. J., 155, 777, 1969.

Jokipii, J. R. and L. Davis, Ap. J., 156, 1101, 1969.

Juday, R. D., and G. W. Adams, Planet. Space Sci., 17, 1313, 1969.

Krimigis, S. M., J. Geophys. Res., 70, 2943, 1965.

Lanzerotti, L. J., Phys. Rev. Letters, 21, 929, 1968.

Lanzerotti, L. J., J. Geophys. Res., 74, 2851, 1969a.

Lanzerotti, L. J., J. Spacecraft and Rockets, 6, 1086, 1969b.

Lanzerotti, L. J., Report UAG-5, World Data Center A, 56, Feb. 1969c.

Lanzerotti, L. J., Report UAG-9, World Data Center A, 34, April 1970a.

Lanzerotti, L. J., Intercorrelated Satellite Obs. Related to Solar Events (D. Reidel Pub. Co., Dordrecht-Holland), pp. 205-228, 1970b.

Lanzerotti, L. J., and M. F. Robbins, Solar Phys., 10, 212, 1969.

Lanzerotti, L. J., and T. E. Graedel, Bull. Am. Phys. Soc., 15, 610, 1970.

Lin, R. P., and K. A. Anderson, Solar Phys., 1, 446, 1967.

Lin, R. P., Solar Phys., 12, 266, 1970a.

Lin, R. P., Report UAG-8, World Data Center A, 191, March 1970b.

Lin, R. P., Solar Phys., to be published, 1971.

McCracken, K. G., Solar Proton Manual, NASA Tech. Report R-169, 1963.

McCracken, K. G., U. R. Rao, and R. P. Bukata, J. Geophys. Res., 72, 4243, 1967.

McDonald, F. B., and U. D. Desai, J. Geophys. Res., 76, 808, 1971.

McDonald, F. B., V. K. Balasubrahmanyan, K. A. Brunstein, D. E. Hagge, G. H. Ludwig, and R. A. R. Palmeira, Trans. Am. Geophys. Union, 46, 124, 1965.

Meyer, P., and R. Vogt, Phys. Rev. Letters, 8, 387, 1962.

Meyer, P., E. N. Parker, and J. A. Simpson, Phys. Rev., 104, 768, 1956.

Murray, S. C., E. C. Stone, and R. E. Vogt, Trans. Am. Geophys. Union, 51, 798, 1970.

Ness, N. F., C. S. Scearce, and J. B. Seek, J. Geophys. Res., 69, 3531, 1964.

Ney, E. P., and W. A. Stein, J. Geophys. Res., 67, 2087, 1962.

Nobles, R. A., R. A. Alber, L. L. Newkirk, M. Walt, and C. J. Wolfson: Nucl. Instr. and Methods, 70, 45, 1969.

Ogilvie, K. W., and J. F. Arens, J. Geophys. Res., 76, 13 1971.

Parker, E. N., Phys. Rev., 103, 1518, 1956.

Parker, E. N., Ap. J., 132, 821, 1960

Parker, E. N., Interplanetary Dynamical Processes (Interscience, New York), 1963.

Parker, E. N., Planet. Space Sci., 13, 9, 1965.

Paulikas, G. A., and J. B. Blake, J. Geophys. Res., 74, 2161, 1969.

Potemra, T. A., A. J. Zmuda, C. R. Haare, and B. W. Shaw, J. Geophys. Res., 72, 6077, 1967.

Potemra, T. A., A. J. Zmuda, C. R. Haare, and B. W. Shaw, J. Geophys. Res., 74, 6444, 1969.

Potemra, T. A., A. J. Zmuda, B. W. Shaw, and C. R. Haare, Radio Science, 5, 1137, 1970.

Potemra, T. A., and L. J. Lanzerotti, submitted to J. Geophys. Res., 1971.

Rao, U. R., K. G. McCracken, and R. P. Bukata, J. Geophys. Res., 72, 4325, 1967.

Rao, U. R., F. R. Allum, W. C. Bartley, R. A. R. Palmeira, J. A. Harries, and K. G. McCracken, Solar Flares and Space Research (North-Holland, Amsterdam), pp. 267-276, 1969.

Reid, G. C., J. Geophys. Res., 69, 2659, 1964.

Reid, G. C., Planet. Space Sci., 17, 731, 1969.

Reid, G. C., Intercorrelated Satellite Obs. Related to Solar Events (D. Reidel Pub. Co., Dordrecht-Holland), pp. 319-334, 1970.

Roeloff, E. C., Thesis, Univ. of California, Berkeley, 1966.

Roeloff, E. C., Can. J. Phys., 46, 5990, 1968.

Sen, H. K., and A. A. Wyller, J. Geophys. Res., 65, 3931, 1960.

Simnett, G. M., T. L. Cline, S. S. Holt, and F. B. McDonald, Paper MO-33, International Cosmic Ray Conference, Budapest, September, 1969.

Singer, S., Intercorrelated Satellite Obs. Related to Solar Events (D. Reidel Pub. Co., Dordrecht-Holland), pp. 571-582, 1970.

Smart, D. F., and M. A. Shea, Intercorrelated Satellite Obs. Related to Solar Events (D. Reidel Pub. Co., Dordrecht-Holland), pp. 102-107, 1970.

Solar-Geophysical Data, 303 Part II, 118-123, U. S. Department of Commerce, Boulder, Colorado, November, 1969.

Van Allen, J. A., and S. M. Krimigis, J. Geophys. Res., 70, 5737, 1965.

Van Allen, J. A., W. C. Lin, and H. Leinbach, J. Geophys. Res., 69, 4481, 1964.

Waddel, R. C., NASA/GSFC Preprint X-710-68-408, October 1968.

Waddington, C. J., and P. S. Freier, J. Geophys. Res., 70, 230, 1965.

Yates, G. K., J. Geophys. Res., 69, 3077, 1964.

Yates, G. K., J. Geophys. Res., 70, 232, 1965.

The Chemical Composition and Energy Content of the Energetic Cosmic Radiation*

C. J. Waddington

School of Physics and Astronomy
University of Minnesota

A brief survey is made of our present knowledge of the composition and energy spectra of the primary cosmic radiation. The total energy carried by all forms of cosmic radiation that have appreciable penetrability into matter has been evaluated. This information, when combined with a knowledge of the rate at which the different components deposit energy in traversing matter, would permit calculations of the radiation dose that would result from exposure to the primary cosmic radiation. It is concluded that overall these radiation effects are rather small but it is emphasized that local damage can be of much greater significance.

Introduction.

Any detector or object placed outside the protection of the earth's atmosphere is irradiated by cosmic electromagnetic and corpuscular radiation that can penetrate deeply into the object. The radiation effects produced by this exposure depend critically on the physical and biological conditions involved and are one of the main topics of this conference. In this paper I present some of the data concerning the nature of this cosmic radiation that is relevant to any calculations of the magnitudes of these effects. Specifically I have summarized our current knowledge of the primary cosmic radiation and have discussed some of the factors that should be of importance. In what follows I have neglected radiation of solar origin and that present in the radiation belts, since these will be discussed by other authors.

The majority of the cosmic radiation is corpuscular in nature and is consequently subject to the effects of solar and geomagnetic modulation. Geomagnetic modulation is relatively well understood in that at any point in space within the magnetosphere, the geomagnetic field simply imposes a cut-off rigidity below which particles coming from a particular direction cannot penetrate. Solar modulation has been extensively studied as a temporal phenomena and examples of the resulting variations in particle intensities are given later. However, spatial studies have been less successful and at present we do not really know either how the intensities vary throughout the solar system, nor what they are in interstellar space. Measurements of the cosmic ray gradient have been conflicting and we have to rely on theory to calculate the demodulated spectra. Fortunately these solar modulation processes mainly affect the lower energy particles and therefore it is probable that the total energy content of the cosmic radiation is not seriously influenced by these uncertainties.

In addition to the corpuscular radiation, there are also X and γ-ray components and these will not be appreciably temporally or spatially dependent unless some cosmic cataclysm occurs, such as a nearby super-novae explosion. In what follows I will first outline our current knowledge of the composition and energy spectra and then evaluate the amount of energy carried by each component. A knowledge of the incident energy, combined with a knowledge of the absorption characteristics, permit an evaluation of the gross, or average radiation effectiveness of any particular cosmic ray component. Such an averaging approach does, of course, neglect the fact that when we consider the cosmic radiation we are concerned with particles that have a spectrum of energies and a small fraction in any component will be of extremely high energy. Indeed, in fact, a single particle may have up to 10^7 ergs. These particles, or quanta, have the potential of delivering all or most of their energy into a very small volume, producing localized radiation effects of much more serious consequence than those suggested from the overall level. A similar phenomena can be produced by the highly charged particles in the cosmic radiation, which because of the Z^2 dependence of the ionization energy loss, can also deliver a large amount of energy into a very localized volume. The effects produced by these large local radiation doses on biological or solid state systems can be much more serious than would be inferred from the values for the average doses.

X and γ-Rays.

The emission of cosmic X-rays has been observed from various point sources and as a diffuse background of galactic or metagalactic origin. High energy,

*Work supported by the Office of Naval Research under Contract N00014-67-A-0113-0021.

$E \geq 50$ MeV, γ-ray observations have generally shown that the energy spectra observed at X-ray energies either extrapolate sensibly or steepen at higher energies. It is thus not unreasonable to integrate the observed differential X-ray spectra to infinity to obtain an upper limit to the energy input. In all cases the energy intensities are rather small. Table I shows the values for the intensities above 10 KeV for the representative point sources Sco X-1 and Tau X-1 as well as for the isotropic background. Clearly, irrespective of how the energy is deposited the average radiation effects must be small although, once again, individual energetic gamma ray photons may produce large local effects.

Table I

(X-Ray Incident Energies)

Tau X-1 (Peterson (1970)).

$dN = 20\ E^{-2.3}\ dE$ photons/cm^2.sec.keV

$I(>E) = 67 E^{-0.3}$ keV/cm^2.sec.

$I(>10\ \text{keV}) = 4.6 \times 10^{-3}$ ergs/cm^2.day.

Sco X-1 (Peterson (1970)).

$I = 110\ e^{-E/4.3}$ keV/cm^2.sec.keV.

$I(>E) = 470\ e^{-E/4.3}$ keV/cm^2.sec.

$I(>10\ \text{keV}) = 6.3 \times 10^{-3}$ ergs/cm^2.day.

Diffuse Background (Schwartz (1969)).

$dN_1 = 10\ E^{-1.5}\ dE$ photons/cm^2.sec.sr.keV

for $E \leq 25$ keV.

$dN_2 = 225\ E^{-2.5}\ dE$ photons/cm^2.sec.sr.keV

for $E > 25$ keV.

$I(>E) = 20\ (5 - E_1^{0.5}) + 450\ E_2^{-0.5}$ keV/cm^2.sr.sec.

$I(>10\ \text{keV}) = 1.75 \times 10^{-2}$ ergs/cm^2.sr.day.

(A possible bump in the spectrum at 1-5 meV, Vette et al. (1970), would only raise I (>10 keV) by a few percent).

Here, as in the remainder of this paper, the energy intensities are expressed in units of ergs/cm^2.day or ergs/cm^2.sr.day. Remembering that a rad corresponds to the absorption of 100 ergs per gram of irradiated material, one could calculate the radiation effects from these energy intensities, if one knew the absorption rates as a function of energy. Of course this is a big if and represents one of the principal problems in this field.

Neutrinos.

For completeness it is appropriate to discuss neutrinos here, since they are certainly a penetrating form of cosmic radiation. Obviously their extreme penetrability implies negligible energy deposition and hence unimportant radiation effects. This is fortunate since we know very little regarding the flux of cosmic neutrinos. Burbidge (1970) has collected various estimates which suggest that probably the energy density does not greatly exceed 3 eV/cm^3, i.e. about an order of magnitude greater than that of the corpuscular cosmic radiation. (Note that for ultra relativistic particles 100 ergs/cm^2.sr. day $\approx$ 0.3 eV/cm^3.)

Charged Particles.

1) Electrons.

The true spectrum of the electrons in the cosmic radiation is somewhat controversial at the present time. Figure 1 shows the spectra reported in a recent paper, Marar et al. (1971), from which it can be seen that there are at least two plausible representations of the true spectrum at energies above 5 GeV, which differ in intensity by at least a factor of five. At lower energies the situation is equally complicated, although in this case the principal cause appears to be the effects of solar modulation rather than experimental inconsistencies. Figure 2 shows a schematic representation of the data available in this energy region. These results permit us to evaluate the incident energy carried by the electron component. The resulting energy intensity spectra for the various cases are shown in Figure 3.

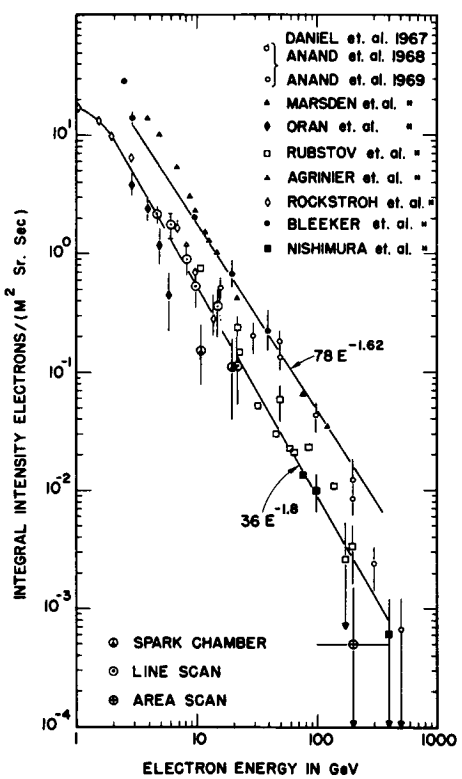

Figure 1. The integral energy spectrum of primary cosmic ray electrons above about 2 GeV, as measured by various authors. For references see the original paper by Marar et al. (1971).

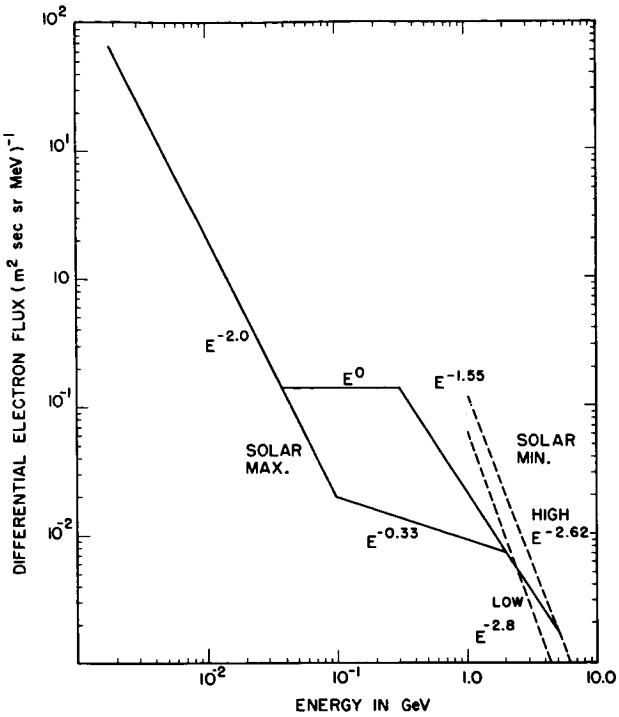

Figure 2. A schematic representation of the integral energy spectrum of low energy cosmic ray electrons as measured at times typical of minimum and maximum solar modulation.

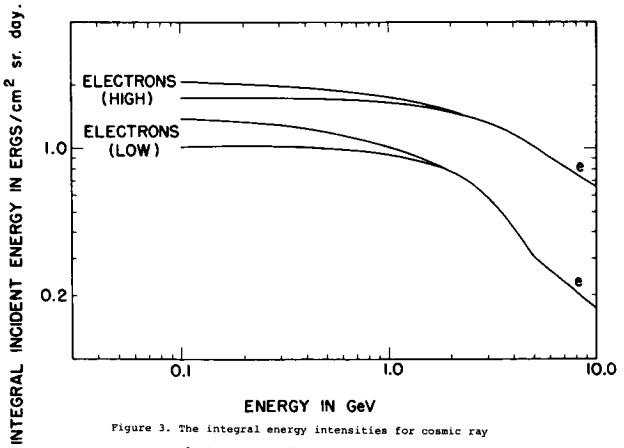

Figure 3. The integral energy intensities for cosmic ray electrons at maximum and minimum solar modulation and assuming either the high or low spectrum given in Figure 1.

2) Hydrogen and Helium Nuclei.

The energy spectra of these nuclei have been extensively studied by many workers. Figure 4 shows the differential energy spectra at times typical of solar minimum and solar maximum as recently compiled by Lezniak and Webber (1970) from selected data. At higher energies, $\geq$ 2 GeV per nucleon, the spectra of both components can be well represented as a power law in total energy with $dJ=K\ (T+m_oc^2)^{-2.5}dE$. If the kinetic energy per nucleon T, is expressed in GeV per nucleon then K=4500 for protons and 400 for α-particles. At very high energies, $\geq 10^{15}$ eV, deviations do occur from these spectra, with apparently a steepening to an exponent of about 3.0, followed at around 10^{18} eV by a flattening to the original exponent. However, the total energy carried by these energetic particles is a negligible fraction of the total.

Both components contain small fractions of isotopes other than the main one. Deuterons make up 1 or 2% of the total hydrogen component while about 10% of the helium component is probably He^3. In both cases we only know these proportions at low energies, $\leq$ 500 MeV per nucleon, but there seems little reason to expect that they would be much larger at higher energies.

3) Heavy Nuclei.

The energy spectra of the cosmic ray nuclei in the range between lithium and nickel, $3 \leq Z \leq 28$, have been studied by a large number of workers and detailed comparisons exist between these spectra and that of the helium nuclei. For example, Figure 5 is from a recent review, Waddington (1970) and shows the ratios of the helium abundance to those of various groups of heavy nuclei expressed as a function of energy. It can be seen that while there is some suggestion that at least some of these ratios are energy dependent below about 1 GeV per nucleon, it is not unreasonable to use as a working assumption the concept that all nuclei have similar energy spectra. The apparent deviations from this that are seen do not seriously affect our estimates of the total energy carried by each component. At very high energies, $\geq 10^{16}$ eV/nucleon, composition changes do occur that probably result in all the particles above $\approx 10^{18}$ eV being protons. The value assumed here for these ratios are given in Table II, together with an estimate of the mean mass number in each group. From these values we can calculate the incident energies carried by each component. As an example, the table also gives the total incident energy carried by nuclei with T $\geq$ 100 MeV per nucleon.

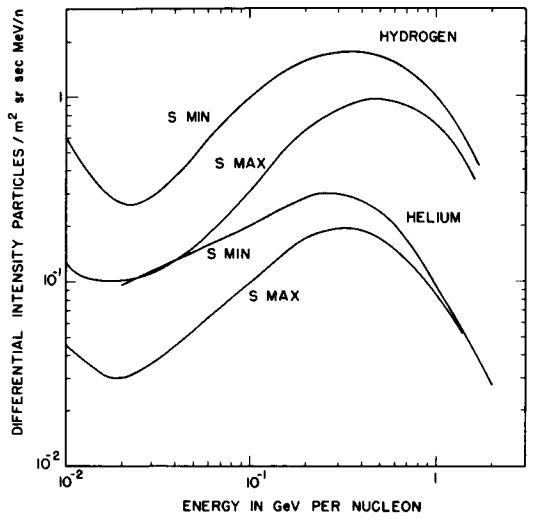

Figure 4. The differential energy spectra of hydrogen and helium nuclei below about 2 GeV per nucleon as measured by several groups. After Lezniak and Webber (1970).

that those nuclei that we believe are predominately the consequence of secondary production during interstellar propagation from the 'source' of cosmic rays to show energy dependent abundances, since we know that the nuclear parameters describing their production are energy dependent.

Energy Intensities.

The data summarized in the previous sections has been used to calculate the energy intensities, both integral and differential, carried by each major component of the cosmic radiation. The energy spectra of these intensities are shown in Figures 5 and 6. For comparison it is possibly relevant to note that the total energy intensity of cosmic ray particles at sea level and high latitudes is about 5 ergs/cm^2.sr.day, Hayakawa (1969), or 3-4% of that above the atmosphere. Although the radiation dose due to sea level cosmic rays is about 30 mrem/year, this cannot be taken as implying that the space cosmic ray dose is just 25 to 30 times greater. First of all there is the factor due to the isotropy of space cosmic rays compared to the non-isotropy of those at sea level. Secondly, and more important, is the greatly different nature of the particle

TABLE II

Charge Group		Abundance Ratio Relative to Helium	$\bar{A}$	I(>0.1 GeV/n) Ergs/cm^2.sr.day
L-nuclei	$3 \leq Z \leq 5$	1/48	9	1.53
M-nuclei	$6 \leq Z \leq 9$	1/16	14	7.07
LH-nuclei	$10 \leq Z \leq 14$	1/75	22	2.38
MH-nuclei	$15 \leq Z \leq 19$	1/600	35	0.475
VH-nuclei	$20 \leq Z \leq 30$	1/200	52	2.12
SVH-nuclei	$Z \geq 30$	$1/8 \times 10^5$	~100	1×10^{-3}
		Helium Nuclei		32.5

The abundances of individual elements are still imperfectly known, with the uncertainties generally increasing at higher charges. A recent survey by Shapiro and Silberberg (1970) probably represents the best values currently available, although several of the abundances quoted are still controversial and the values are somewhat inconsistent with the ratios quoted above. Table III shows the abundances reported by the above authors, normalized to carbon=100. These values should be regarded as being typical of those for energies between 2-5 GeV per nucleon and are uncorrected for the generally small effect of geomagnetic cut-offs on nuclei of different Z/A ratios. Physically we would expect

TABLE III

(After Shapiro and Silberberg (1970))

Abundances of Heavy Primary Nuclei at the Top of the Atmosphere

(Normalized to Carbon = 100)

Element	Z	Relative Abundance	Element	Z	Relative Abundance
Lithium	3	16 ± 2	Sulphur	16	3.5 ± 1
Beryllium	4	11 ± 3	Chlorine	17	0.5 ± 0.3
Boron	5	27 ± 3	Argon	18	2 ± 0.5
Carbon	6	100	Potassium	19	0.6 ± 0.3
Nitrogen	7	27 ± 2	Calcium	20	2 ± 0.3
Oxygen	8	86 ± 4	Scandium	21	0.3 ± 0.2
Fluorine	9	2 ± 1	Titanium	22	2.0 ± 0.5
Neon	10	20 ± 2	Vanadium	23	1.0 ± 0.3
Sodium	11	3 ± 1.5	Chromium	24	3.5 ± 1.0
Magnesium	12	21 ± 2	Managanese	25	0.9 ± 0.3
Aluminum	13	2 ± 1	Iron	26	11.3 ± 1.4
Silicon	14	15 ± 2	Cobalt	27	<0.2
Phosphorous	15	$0.6 \, {}^{+1.4}_{-0.5}$	Nickel	28	~0.2

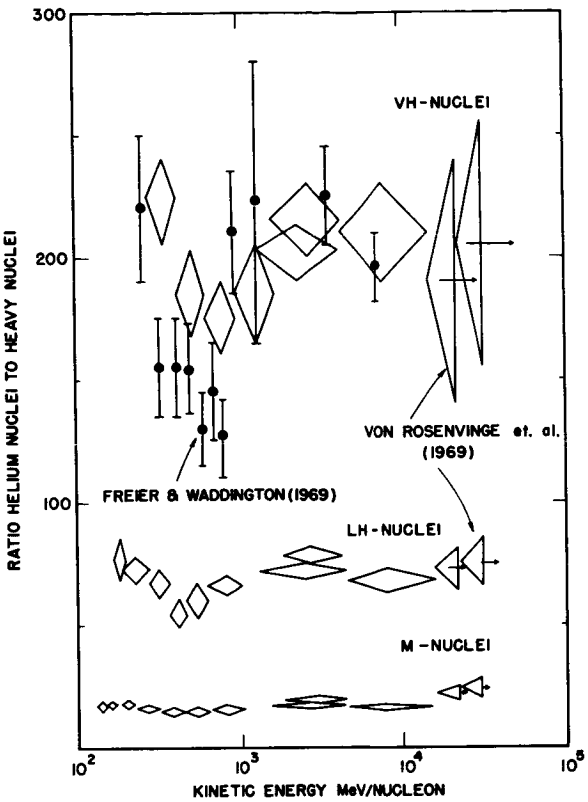

Figure 5. Measured values of the ratios of the abundance of helium to those of various groups of heavier nuclei, Waddington (1970).

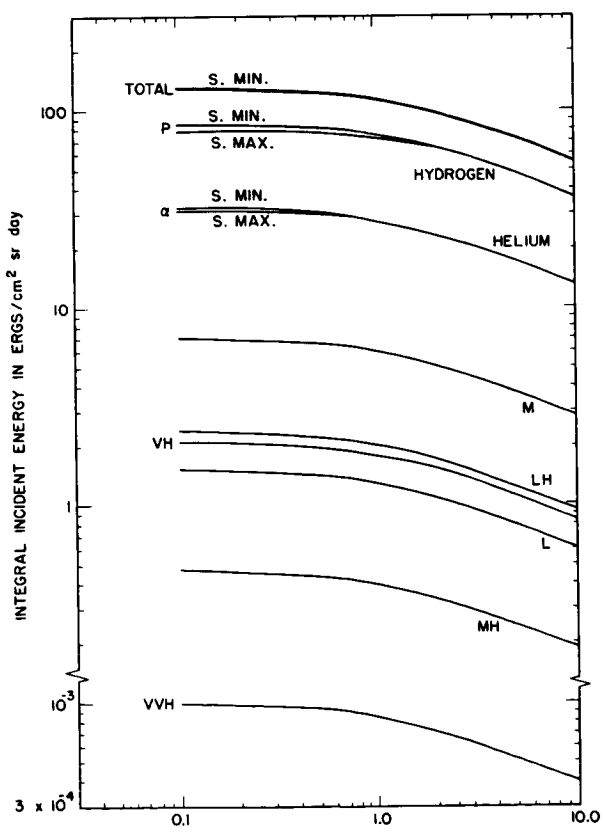

Figure 6. The integral energy intensities for cosmic ray nuclei.

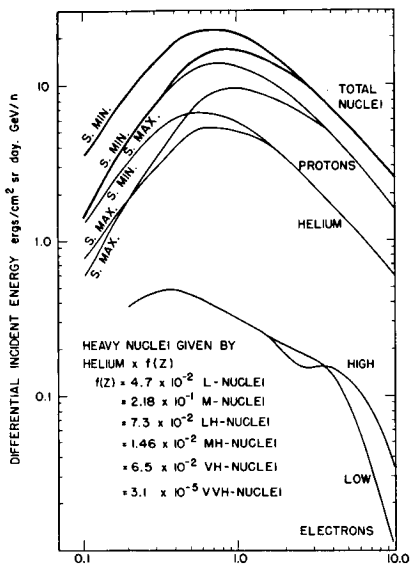

Figure 7. The differential energy intensities for cosmic ray nuclei and electrons.

radiation at the two locals. At sea level the particles are predominately muons, and the rate of energy deposition is small, while in space the deposition rate is considerably higher. This rate, which of course determines the dosage received by a sample immersed in the radiation, depends in a complex way on the charge, energy and nucleon interaction parameters of the incident particle. However, in no case can one envisage it being so high that the total energy of a component would be dissipated in traversing as little as one gram of material. Hence the average cosmic ray doses must always be very small, never exceeding a few rad/day. The localized dose, on the other hand, as pointed out before, may well be very considerable, since a single particle may release a great deal of energy in a small volume. As an extreme example, a nucleus of U^{238} having a total kinetic energy of 55 GeV has a range of 1 g/cm^2 in carbon of density 2.0 gm/cm^3. This energy is mostly dissipated by producing electrons of less than 10 keV that are absorbed within 10μm of the primary trajectory and hence in a volume of 1.5×10^{-6} cm . The energy deposited is thus equivalent to about 10^5 ergs/gm and gives a localized dose of 10^3 rads, which is sufficient to produce serious damage in many systems.

While this is admittedly an extreme example it is clear that these highly charged nuclei may well produce a line of damage. Similarly very energetic particles can produce either small volumes of damage, by nuclear interactions, or lines of damage, by production of cascades, nuclear or electromagnetic. The effects of producing these localized regions of damage in radiation sensitive systems do not appear to be well known and it seems important that further research should be undertaken to clarify our understanding of these problems.

REFERENCES

1. Burbidge, G.: Intergalactic Matter and Radiation, Invited paper presented at I.A.U. Symposium No. 44, 1970.
2. Freier, P. S.; and C. J. Waddington:Phys. Rev.,vol. 75, 1968, p. 1641.
3. Hayakawa, S.: "Cosmic Ray Physics" pub. Wiley-Interscience,1969, p.437.
4. Lezniak, J.A.; and W.R.Webber: The Solar Modulation of Cosmic Ray Protons, Helium Nuclei and Electrons, Univ. of New Hampshire preprint UNH-70-06, 1970.
5. Marar, T.M.K.,; P.S.Freier; and C.J.Waddington: J. Geophys. Res. vol. 76, March 1971.
6. Peterson: "Properties of Individual X-Ray Sources Non-Solar X and Gamma-Ray Astronomy" Ed. L. Gratton, Reidel Publ Co., 1970, p. 59-80.
7. Schwartz, D. A.: "The Spatial Distribution of the Diffuse Component of Cosmic X-Rays" Ph.D. Thesis, U of Calif.,San Diego, 1969.
8. Shapiro, M.M.; and R. Silberberg: Ann. Rev. of Nuclear Phys. vol. 20, 1970, p. 323.
9. Vette, J.I.; D. Graber; J. L. Matteson;and L. E. Peterson: Ap. J. Letters, vol. 160, 1970, p. L161.
10. von Rosenvinge, T. T.; W. R. Webber; and J. F. Ormes: Astrophys. and Space Sci., vol. 5, 1969, p. 342.
11. Waddington, C. J.: "Some Remakrs on the Composition of the Cosmic Radiation" Proc. of the Sixth Interamerican Seminar on Cosmic Rays and U of Minn. Tech. Rep. CR-150. 1970.

APOLLO MISSION EXPERIENCE*

Herman J. Schaefer
Naval Aerospace Medical
Research Laboratory
Pensacola, Florida

The preceding papers have drawn a detailed picture of the natural radiation environment in space. It is the purpose of this presentation to proceed to a discussion of the dosimetric implications for manned space missions. In other words, it is to be analyzed what the radiation field behind the heavy shielding of a manned space vehicle on a near-Earth orbital or a lunar mission will look like and how it compares with actual exposure levels recorded on the Apollo missions. In line with this objective, emphasis will shift from flux densities and energy spectra of the incident radiation to absorbed doses and dose equivalents as they are recorded within the ship preferably at locations close to the crew members.

On all missions, the Apollo astronauts were equipped with a number of different active and passive dosimeters intended for a twofold purpose. On the one hand, the astronauts should be able to carry out, at any time, in-flight readings of instantaneous radiation levels. On the other hand, accurate data on accumulated absorbed doses and dose equivalents were to be collected. From the radiation safety viewpoint, the latter data, i.e., the grand total mission doses, are of main interest. Turning to this information we see in Table I a tabulation of the grand total mission doses as they were recorded with TLD dosimeters carried by the astronauts under their space suits. Taken at face value, the picture looks very reassuring. The highest dose, encountered on Apollo XIV, remains under one rad. Another interesting fact seen from Table I is that the mission dose shows no correlation at all to mission duration, i.e., to exposure time in space. The reason for this lack of correlation is to be sought in the greatly different trajectories through the inner radiation belt as will be discussed in detail later.

If we attempt to convert the mission doses in Table I to dose equivalents, the situation becomes more complicated. Radiation exposure in space is mainly due to nuclear particles of a large variety of different kinds each, in turn, covering a broad energy spectrum. As a consequence, the Linear Energy Transfer (LET) spectrum is extremely complex. In fact, it extends from minimum ionization to values exceeding by more than a factor of 10 the highest LET obtainable from terrestrial sources.

The most accurate and sensitive LET analyzer is nuclear emulsion. In view of the very wide LET spectrum encountered in space, combinations of different emulsion sensitivities are usually applied in order to ensure sustained resolution over the full LET scale. The details of the nuclear emulsion technique as it applies to measuring the astronauts' radiation exposure have been described repeatedly throughout the past ten years when we monitored the Mercury, Gemini, and Apollo flights. Therefore, we can proceed directly to the final result of the nuclear emulsion analysis for a particular mission and present in Table II a breakdown of the total dose on the first lunar landing mission Apollo XI. It is seen that the make-up of the total exposure is indeed quite complex. Problems arise especially if one tries to establish Quality Factors (QF's) for the conversion of the various dose fractions from absorbed doses to dose equivalents.

Table I

Average Doses on Apollo Missions

Mission	Type	Launch Date	Duration, Hours	Mission Dose, millirads
Apollo 7	Earth-orbital	11 Oct 1968	260	160
Apollo 8	Circumlunar	21 Dec 1968	147	160
Apollo 9	Earth-orbital	3 Mar 1969	242	200
Apollo 10	Circumlunar	18 May 1969	192	470
Apollo 11	Lunar Landing	16 Jul 1969	195	180
Apollo 12	Lunar Landing	14 Nov 1969	245	577
Apollo 13	Circumlunar	11 Apr 1970	143	237
Apollo 14	Lunar Landing	31 Jan 1971	216	[~ 900 est.]

Table II

Components of Mission Dose on First Lunar Landing Mission Apollo XI

Component	Absorbed Dose, millirad	Dose Equivalent, millirem
Protons	150	220
Stars	15	94
Fast neutrons	~1	~12
Heavy nuclei	5	46
Electrons and gamma rays	~30	~30
Total	201	402

*The paper is based on measurements carried out as contract work for the Manned Spacecraft Center, NASA, Houston, Texas.

No special difficulties exist with regard to the proton dose. By far the largest part of the dose results from trapped protons in the radiation belt. On standard near-Earth orbital missions such as the preparatory missions Apollo VII and IX, trapped protons are encountered in repeated passes through the South Atlantic Anomaly. On lunar missions, they are encountered in two complete traversals of the radiation belt on translunar and trans-Earth injection. Since the angle of inclination of the plane of the geomagnetic equator to the plane of the coplanar orbits of the Moon and the vehicle around the Earth varies continuously on a daily and monthly cycle, the geomagnetic trajectory through the radiation belt varies from crossing to crossing. Sometimes the trajectory traverses the inner belt more peripherally, sometimes more centrally. The two crossings on the Apollo XII mission are typical in this respect as seen from Figure 1. Without carrying out any tabulation and adding of isoflux line values, one sees by inspection that the dose on the return trajectory from the Moon must have been disproportionately larger than on the way out.

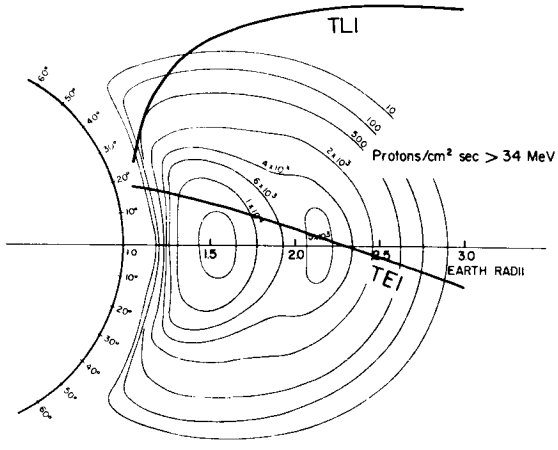

GEOMAGNETIC TRAJECTORIES OF TRANSLUNAR AND TRANS-EARTH INJECTION OF APOLLO XII MISSION Figure 1

Figure 1. Geomagnetic Trajectories of Translunar and Trans-Earth Injection of Apollo XII Mission

Energy spectrum and LET distribution of a proton flux traversing a nuclear emulsion can be established by track and grain count analysis. It was mentioned above that by flying emulsions of different sensitivities in the same pack, a sustained resolution for the entire energy scale from zero to relativistic energies can be achieved. Figure 2 shows the result of the combined evaluation of emulsions of three different sensitivities (Ilford G.5 and K.2 and Eastman Kodak NTA) in the radiation pack on Neil Armstrong's ankle on the first lunar landing mission Apollo XI. Dosimetrically the essential feature is that a substantial fraction of the total dose is produced by low-energy protons. Since these protons have short ranges the flux density depends sensitively on the local shield distribution and shows sizeable variations at locations with different slant or shadow shielding geometry within the vehicle.

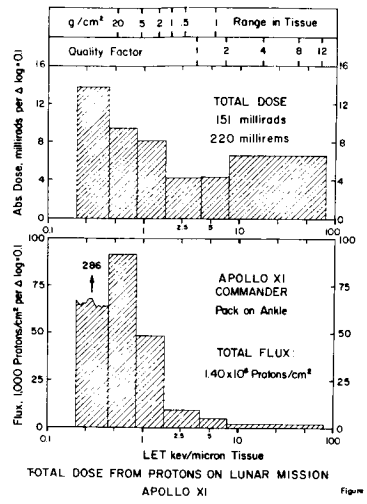

Figure 2. Total Dose from Protons on Lunar Mission Apollo XI

To what extent the shield distribution makes itself felt in directional effects of the population of enders, i.e., of protons reaching the end of their ionization ranges has been analyzed in detail on the unmanned missions Apollo IV and VI. These flights combined several traversals of the South Atlantic Anomaly with the two traversals of the core of the inner radiation belt when the vehicle swung out, on its last orbit, to an Apogee well beyond the inner belt. On Apollo VI with a total proton dose of 1.56 rad the density of enders in the emulsions reached a level which allowed a directional analysis in all three dimensions. Figure 3 shows the result of this analysis for a K.2 emulsion from one of two emulsion spectrometers flown on Apollo VI. It is clearly seen that there is a solid angle of minimum shield thickness within which eight times more proton enders arrive than within the solid angle of maximum shield thickness subtended by the heavy base of the command module and the heat shield.

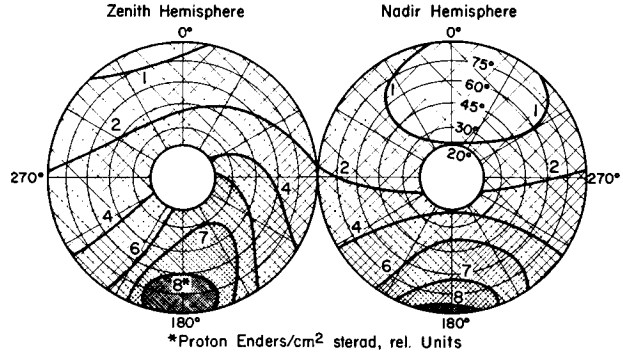

Figure 3. Directional Distribution of Proton Enders in Upper Chamber of Proton Spectrometer S/N5 Flown on Apollo VI

Radiobiologically more interesting are the large microdosimetric fluctuations of the proton dose reflecting the Poisson distribution of the fluence of low-energy protons. At first sight, one might expect that the spontaneous statistical fluctuations in the fluence of low-energy particles through small target volumes would entirely vanish in the much larger fluences of medium and high-energy protons. As far as fluences, i.e., mere particle numbers are concerned, this assumption is indeed correct. For the total dose, however, it is not. Since a low-energy proton traversing a small target volume contributes a substantially larger share to the total dose than a medium or high-energy particle, the local Poisson variations of the enders fluence show up quite strongly in the total dose. Figure 4 shows the quantitative aspects of the effect, again for the radiation pack on Neil Armstrong's ankle from which also the data presented in Figure 2 were taken. It should be emphasized that the dose distribution of Figure 4 hold for a comparatively large target volume comprising some 30 cells and that it pertains to the total dose. Since the fluctuations are exclusively due to low-energy particles they affect only the high-LET fraction of the total dose. Therefore, the corresponding Poisson variations of the dose equivalent must be substantially larger than those of the absorbed dose shown in Figure 4.

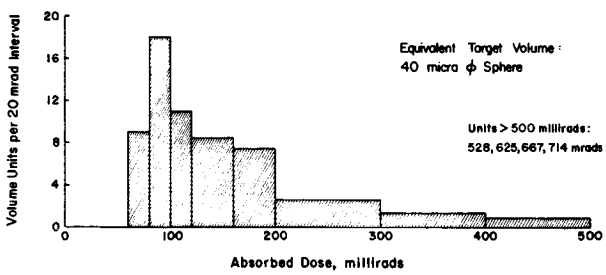

MICRODOSIMETRIC DISTRIBUTION OF PROTON DOSES IN ILFORD G.5 EMULSION ON APOLLO XI

Figure 4. Microdosimetric Distribution of Proton Doses in Ilford G.5 Emulsion on Apollo XI

It should be pointed out that the uneven distribution of the local dose due to the Poisson variations of the fluence of low-energy protons is superimposed upon the ununiformity of the energy dissipation in the microstructure of tissue due to the dense columns of ionization of the individual particles which finds its dosimetric expression in the LET. The Poisson variations of the fluence added to the latter ununiformity is bound to lead to a further increase of the biological effectiveness which is not adequately expressed in the conventional QF/LET relationship as set forth by the International Commission on Radiological Protection (ICRP). It would seem an important task to design radiobiological experimentation which would furnish quantitative data on this peculiar characteristic of proton radiation in space.

A peculiar component of any radiation exposure in space is the dose from disintegration stars in tissue. The name star stems from the characteristic microscopic appearance of nuclear disintegrations in nuclear emulsion. Well known are the spectacular multipronged stars from disintegrations of the heavy elements silver and bromine in emulsion. Obviously, they cannot occur in tissue. However, stars with smaller prong numbers originate from disintegrations of carbon, nitrogen, and oxygen atoms in the gelatin matrix. Since gelatin is a tissue-equivalent material, these stars allow a direct determination of the tissue dose from the star phenomenon. The additional star production in gelatin makes itself felt in a steepening of the slope of the integral prong spectrum in the region of $Z = 6$ to 8 according to the heaviest constituent elements of gelatin. Figure 5 shows the integral prong spectrum for Apollo XI based on a total of 1395 analyzed stars in the K.2 emulsions. The change in slope in the region of 6 to 8 prongs is clearly seen.

The star prongs represent protons and alpha particles of low energies coming to rest locally in tissue. Accordingly, the LET spectra of star particles center on rather high values. In the Bragg peaks of protons and alpha particles, the LET reaches 90 and 270 kev/micron T, respectively. Corresponding, the mean QF for the star dose is quite high and the dose equivalent substantially larger than the absorbed dose. As indicated in Table II, the star count on Apollo XI leads to an absorbed dose of 15 millirad and a dose equivalent of 94 millirem.

Closely connected to the star phenomenon is the neutron dose. Neutrons are generated in disintegration stars in the same way as protons and alpha particles. However, since neutrons themselves do not ionize, their paths do not appear as visible prongs originating in the star center hence the neutron dose cannot be determined from the star count. The bulk of the neutron dose in space is due to fast neutrons. In the hydrogen content of the gelatin of nuclear emulsion, fast neutrons release recoil protons which in turn produce short tracks that can be identified easily. Also produced are heavy recoils with extremely short ranges that disappear completely in the comparatively heavy background of emulsions exposed to radiation in space. However, since the proton recoil dose is by far the larger dose contribution, the error due to omission of the heavy recoils is small.

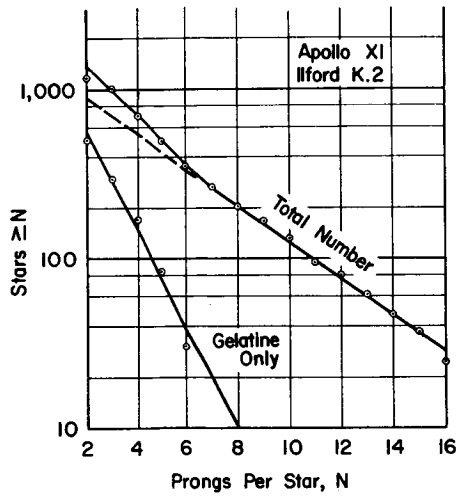

INTEGRAL PRONG SPECTRUM OF STAR POPULATION IN ILFORD K.2 EMULSIONS ON APOLLO XI

Figure 5. Integral Prong Spectrum of Star Population in Ilford K.2 Emulsions on Apollo XI

A much more serious handicap in the determination of the neutron dose results from the large population of trapped protons. Since the spectrum of these protons reaches all the way down to zero energy with a substantial flux fraction being of short range, the neutron recoil protons are masked by large numbers of true primary protons. The only clue for direct identification of a recoil proton is the test whether its track begins and ends in the emulsion. Naturally, this criterion allows only the establishment of a lower limit of the neutron dose since an unknown fraction of tracks ending in the emulsion yet entering from the outside represents recoils released in the material surrounding the emulsion. Within limitations, additional clues can be derived from the range distributions of enders and suspended tracks. However, this analysis is costly in time because it requires evaluation of large track populations for statistical significance. It is beyond the scope of this presentation to discuss the method of spectral discrimination in more detail.

Dosimetrically, the failure of the emulsion method to furnish direct clues as to the origin of low energy protons is irrelevant as long as tissue equivalence is preserved, i.e., the assurance is given that the neutron recoils entering the emulsion from the outside originate in tissue equivalent material. If this condition is fulfilled the total "proton" dose as it follows from the track and grain count analysis represents the correct sum of the doses from galactic and trapped protons and from neutrons. Expressed in terms of Table II this means that the neutron dose is underrated but the missing part, although unknown as to its magnitude, is correctly contained in both the absorbed dose and the dose equivalent of the proton component.

The last component of the mission dose to be discussed is the most difficult and controversial: the dose from galactic heavy primaries. All through the years when we flew nuclear emulsions on the Mercury and Gemini missions, we kept a wary eye on the heavy tracks that were interspersed as infrequent events among the dense populations of proton tracks. The picture changed dramatically when we examined the emulsions from the first circumlunar mission Apollo VIII and compared the counts to those from the standard near-Earth orbital mission Apollo VII. We had been aware than in deep space outside the magnetosphere flux densities of heavy nuclei should be substantially higher because the energy spectrum would extend to much lower energies in the absence of any geomagnetic cutoff. We had estimated that the flux densities should increase by about a factor of 2.5. What we actually found was a sixfold increase. Table III shows a comparison of the flux densities on the two missions. Because of the substantially higher flux density in deep space, heavy nuclei in emulsions from lunar missions are no longer occasional events, but appear quite frequently in the emulsion scan, sometimes as doublets and triplets in the same microscopic visual field at high power.

Table III

Flux Densities of Heavy Primaries on Earth Orbital Mission Apollo VII and Circumlunar Mission Apollo VIII

Z-Class	Nuclei/(cm^2 24 hrs.) Apollo VII	Apollo VIII
3-9	24.6	148
10-20	16.5	99
21-30	2.1	12.6

Radiobiologically, the higher fluxes of heavy primaries on deep space missions do not constitute the main reason for concern. As far as tissue damage is concerned the extension of the spectrum to lower energies in the absence of a geomagnetic cutoff and the associated extension of the LET spectrum to substantially higher values weigh much more heavily. Within the magnetosphere, the cutoff effect excludes low-energy primaries completely. As a consequence, the very high LET values in the terminal sections of heavy nuclei tracks near or in the Bragg peak are not encountered at all on standard near-Earth orbital missions of low inclination. Heavy nuclei enders or thindowns do reach the Earth in the polar regions, but we have never seen any on the Mercury and Gemini missions. The first thindowns appeared on the first deep space mission, the circumlunar flight of Apollo VIII.

The quantitative relationships governing flux densities of heavy primary thindowns within and outside the magnetosphere are presented in Figure 6. It shows the incident and local differential range spectra for the heaviest component of the Z spectrum, the iron group (Z = 24 to 30), for solar maximum and minimum. The local spectra show fractional flux densities of nuclei escaping nuclear collisions and spending their kinetic energy entirely in ordinary ionizations down to zero energy. In other words, the local spectra show the thindown flux densities. With regard to the attenuation geometry, one has to realize that for a parallel beam the indicated thindown flux densities would occur at depth R in a target exposed to the incident spectrum. The essential feature of Figure 6 is the two vertical lines indicating the geomagnetic cutoff ranges for 30° and 40° latitude. These cutoff values mean that the flux density is zero for both the incident and local spectrum for the entire range scale below the cutoff values. Comparing the flux densities of the incident and local spectra for a given range to the right of the cutoff ranges, one immediately sees that for the indicated sample latitudes the thindown fluxes are by more than a factor of 100 smaller than the incident fluxes. A quick estimate of thindown hit frequencies for a ten-day mission and the small target areas of the radiation packs flown on all manned missions shows an extremely small hit probability and explains why no thindown hits have been observed so far on manned near-Earth orbital missions.

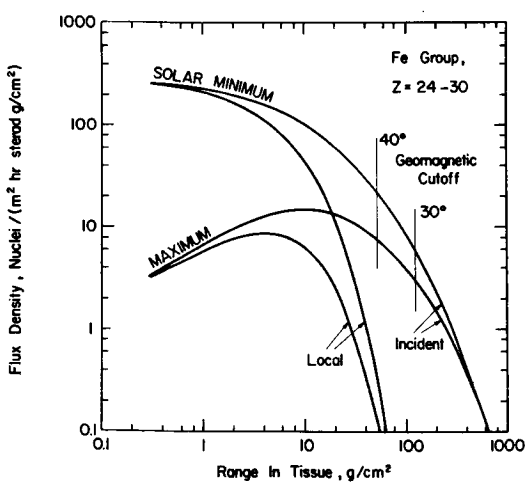

DIFFERENTIAL RANGE SPECTRA FOR IRON GROUP AT SOLAR MAXIMUM AND MINIMUM

Figure 6. Differential Range Spectra for Iron Group at Solar Maximum and Minimum

Heavy nuclei thindowns and near-thindowns constitute a radiation exposure which is well described with the term microbeam irradiation. Present knowledge in radiobiology is inadequate for a full understanding of the mode of action of this type of radiation exposure on living matter, especially as far as long-term effects from total body exposures at low dose rates are concerned. As the ICRP has stated expressly the conventional dosimetric concepts underlying the definitions of the rad and rem units are not applicable to microbeams. Satisfactory alternate methods of measuring the biological effectiveness of microbeam irradiation have not been proposed so far. Recent experiments of Tobias with alpha particle enders indicate that thindowns and near-thindowns of heavy primaries are responsible for at least two of the three different types of eye flashes experienced by the astronauts during periods of dark adaptation outside the magnetosphere on lunar missions.

In summing up the Apollo mission experience one can safely say that the natural environment of ionizing radiation in space did not impose constraints or create problems on any of the missions. While transitory radiation levels in passing through the radiation belt have reached several rads/hour accumulated doses remained well within official limits set for Radiation Workers. As no flare event of a large or medium size was encountered on any of the missions, no operational experience could be gained in that area. However, nobody is sorry about this particular issue remaining unsettled. Since we know very well that every flare event and the associated solar particle beam have their special characteristics with regard to time profile and configuration of the energy spectrum, not much could be learned anyway from a mission experiencing a major event. As far as the normal radiation environment in space is concerned, the single major source of exposure is the radiation belt. Since it dips down, in the South Atlantic Anomaly, so closely to the outer fringes of the atmosphere that near-Earth orbits of longer life times will have to encounter increased radiation levels, trapped protons will pose a problem for long or repeated duty cycles on skylabs and space platforms especially if an additional exposure from nuclear power sources has to be taken into consideration.

SESSION IV.I.
RADIOBIOLOGY: SOME HUMAN RESPONSES TO RADIATION EXPOSURE
CHAIRMAN: V.P. BOND, M.D.
(ASSOCIATE DIR. BROOKHAVEN NATIONAL LABORATORY)

A REVIEW: SOME BIOCHEMICAL EFFECTS OF HIGH LET RADIATIONS

Albert L. Wiley, Jr., M.D.

Radiotherapy Center, University of Wisconsin Medical Center
Madison, Wisconsin 53706

Abstract

The natural environment of outer space may theoretically produce a significant exposure of high LET radiation to the space traveler. The use of nuclear reactor power systems may increase this exposure.

Since biological endpoints of radiation damage are inevitably due to biochemical changes, it becomes of interest to consider the effect of high LET radiations at the biochemical level. There are qualitative and quantitative differences in the biological damage observed after exposure to high LET radiation (such as heavy ions, protons, neutrons and π^- mesons) as compared to that caused by low LET radiations (such as electrons, x-rays, and gamma rays). This review is concerned with these differences, which are ultimately reflected at the biochemical, cellular and even whole animal levels. In general, high LET radiations seem to produce biochemical damage which is more severe and possibly less reparable. Experimental data for these effects will be presented in terms of biochemical RBE's with consideration of both early and late manifestations.

An LET independent process by which significant biochemical damage may result from protons, neutrons and π^- mesons will be discussed.

Introduction

The natural environment of outer space may produce a significant exposure of high LET* radiation to the space traveler. This exposure consists of a wide variety of particles including high energy heavy ions, and perhaps some neutrons. The interaction of these particles with the space capsule may produce secondary particles such as π^- mesons which may have significant mean life and penetration ability to be of some hazard (ref. 1). The contemplated use of nuclear reactor power systems as propulsion systems may further increase the exposure, since it is probable that weight requirements will necessarily restrict the shielding so, there may be some exposure to epithermal and thermal energy neutrons.

In a review of radiobiology literature one becomes impressed by some general aspects in which there are significant differences in the biological response to high LET radiations (such as neutrons, heavy ions, protons, and π^- mesons) and low LET radiations (such as electrons and γ rays):

1. The incidence of mutations and chromosome abnormalities after high LET radiation is impressively higher than that observed after low LET radiation. The type of genetic change observed is quite variable ranging from subtle almost undetectable mutations to rather drastic endpoints such as carcinogenesis and reproductive death.

2. There is apparently a deficiency of cellular repair following radiation damage from high LET particles which is contrasted with significant or complete repair after low LET radiations (ref. 2).

3. There is relatively little oxygen dependence in the production of cellular damage with high LET radiations, contrary to a great oxygen dependence of low LET radiation (ref. 3).

From this general information, one may speculate that there are some rather significant differences between the effects of high and low LET radiations at the biochemical level. The purpose of this review, therefore, is to explore some of the currently available literature in this field (which is remarkably sparce). Also, since the purpose of a symposium is not only to exchange ideas, but perhaps to attempt to define further areas of needed research, I would like to offer some speculations and opinions.

One of the problems in discussing the biochemical effects of high LET radiation is that the biochemical effects of low LET radiation are not well understood. The term "high LET" radiation itself introduces complexities since this covers a variety of types of radiation and, as will be seen from some of the data, the physical and biological manifestations of high LET radiations are highly dependent on the energy and type of particle being discussed. However, there are some points that can be made by giving a brief summary of some of the types of biochemical experiments being done.

In attempting to describe the types of experiments that have been done with high LET radiation on biochemical processes, it seems useful to discuss these experiments in terms of biochemical RBE's*; since, although one has to be very specific in using this term, it has both fundamental and practical implications. The studies that will be

*LET can be defined as the rate of energy loss along the track of an ionizing particle with units such as KeV/micron.

*RBE = $\frac{\text{absorbed dose of standard radiation } (^{60}\text{Co or 220 KV x-rays}) \text{ required to produce a biological endpoint}}{\text{absorbed dose of test radiation required to produce the same biological endpoint}}$

discussed are those that were directed toward the study of DNA and RNA metabolism, since these macromolecules are involved in the master coding processes of the cell and, therefore, ultimately responsible for the transmission of genetic information and for cellular reproductive processes. And, there is substantial evidence that low LET radiation causes a perturbation of the functional integrity of DNA, which somehow is related to reproductive death of the cell (ref. 4).

As an introduction to some known sites of radiation damage at the biochemical level, Fig. 1 demonstrates, in a simplified manner, three processes by which DNA is ultimately related to cell function and reproduction. These processes are:

1. DNA replication, the process by which DNA duplicates itself, so that at mitosis (cell division) two genetically identical cells are produced.

2. RNA transcription, the process by which several types of RNA (messenger, ribosomal, and transfer RNA's) are formed from one of the DNA strands. These RNA's have variable lifetimes and functions within the cell and are essential intermediate molecules for transferring the DNA instructions for ultimate protein synthesis.

3. Translation, the process by which proteins are made through the appropriate assembly of a sequence of different amino acids.

This diagram is indeed oversimplified since there are many other intermediate steps involving various enzymes and energy providing compounds, but it is useful for illustration of some general sites and mechanisms of radiation damage by high and low LET radiation.

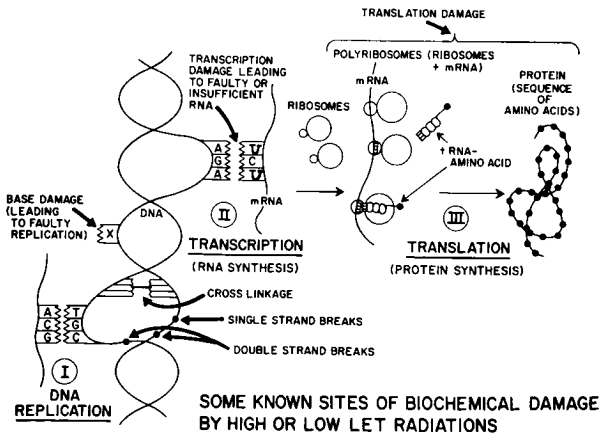

SOME KNOWN SITES OF BIOCHEMICAL DAMAGE BY HIGH OR LOW LET RADIATIONS

Figure 1: A simplified illustration of some sites of biochemical damage by high and low LET radiations.

There is considerable radiobiological data indicating that double and single strand breaks of DNA are produced by ionizing radiation (ref. 13). There is also some evidence that double strand breaks occur in DNA more frequently from high LET radiation than from low LET radiation and this is an attractive means of explaining the deficiency in repair noted for high LET radiation (ref. 14). (One example of this repair deficiency is demonstrated in cellular "survival curves" where high LET radiations have smaller or absent shoulder regions (ref. 15). These aspects of cellular radiobiology will undoubtedly be discussed in more detail in other parts of this symposium.) However, the full significance of single and double strand breaks to ultimate cell death is at present unknown, since there is also evidence that both of these lesions may be reparable (ref. 16), and even that double strand breaks may not be as well correlated with "LET" as has been assumed (ref. 17). However, it is conceivable that either double or single strand breaks, if they are not repaired, could cause drastic perturbations of either DNA replication or transcription.

There is also evidence that the bases of DNA can be significantly damaged by either high or low LET radiation (ref. 6), and this type of damage could be expressed functionally as either inhibition of replication and transcription or by causing the production of a defective quality of DNA or RNA --- and either of these types of damage could lead to various biological endpoints.

With this background we can now discuss some specific experiments on the biochemical effects of high LET radiations. One such experiment by Yatvin et al. (ref. 18), involved the study of fission neutrons as compared to x-rays on polysomes. In Fig. 1, it is seen that polysomes are messenger RNA-ribosonal RNA complexities which are involved in the transmission of information at both the transcription and translation levels. It had been shown by Curtis that fast neutrons (which in tissue produce energetic protons by elastic scatter and protons and α's by nuclear reactions with nitrogen and oxygen) that there was a significant deficit in the ability of regenerating liver to repair induced chromosome abnormalities (ref. 19). It was therefore of interest to study in this same system the DNA-RNA transcription function by studying polysomes. The details of the experiment are a little complex for this discussion, but essentially it was found that fast nertron radiation was not significantly more damaging than x-radiation --- specifically, the polysome pattern following both types of radiation showed an initial decrease, but followed by a recovery in the number of heavy aggregates at 36 hours after irradiation (implying the possibility that if the DNA-RNA transcription apparatus is damaged, then it would seem to be temporarily damaged, and "repaired" to the same extent for both types of radiation). Whenever whole animal irradiations are done, however, there are many abscopal effects to be considered and, in general, there are usually many interpretations.

As another method of looking for transcription damage following high and low LET radiation, we utilized the regenerating liver system. The system and experiments are described elsewhere (ref. 7), but, in general, these experiments were concerned with immediate and delayed damage (following fission or 2.6 MeV cyclotron neutrons as compared to x-rays) in addition to the possible cell cycle dependence of biochemical damage. Our conclusions following 2.6 MeV cyclotron neutrons, was that there appeared to be immediate inhibition of rapidly labeled RNA synthesis rate (which probably is m-RNA synthesis due to the design of the experiment in this semisynchronous system.) It is known that cell reproductive death has variable sensitivity to low LET radiation as a function of cell cycle (ref. 20), but our studies with fast neutrons seem to indicate an inhibition of RNA synthesis rates during early G_1 and early S, and G_2, while no inhibition at any stage was observed following x-irradiation. In addition, comparing either fission or cyclotron neutrons versus x-rays at one month or nine months following irradiation, we observed statistically significant depressions in the rapidly labeled RNA synthesis rate at early G_1 and early S phases following the neutron radiations, but no significant change was noted with x-rays. Our conclusions were that there appears to be both immediate and delayed inhibition of rapidly labeled RNA synthesis rates (probably reflecting inhibition of transcription) in a rather cell cycle independent manner and at low doses (300 rads) following fast neutron radiation, but not for x-ray irradiation. These results, along with other experiments to be described, are summarized in Fig. 2.

Particle Source and Type	Biochemical Parameter	RBE	Comment	Ref.
14.1 MEV neutrons D-T accelerator	DNA labeling index in bone marrow cells	1.2	Labeling done 2.5 hrs. after 90 rads	5
14.1 MEV neutrons D-T accelerator	DNA labeling index in thymocytes	1.1	Labeling done 2.5 hrs. after 10-60 rads	5
14.1 MEV neutrons D-T accelerator	DNA labeling index in intestine cells	1.8	Labeling done 2.5 hrs. after 130 rads	5
0.43 MEV proton accelerator	DNA labeling index in bone marrow cells	3.6	Labeling done 2.5 hrs. after 500 rads	5
Fission neutrons	Inhibition of DNA synthesis in pea sprouts	1.3	DNA synthesis studied 4-7 days after 1000 rads	6
Fission neutrons	Inhibition of DNA synthesis in pea sprouts	7.0	DNA synthesis studied 4-7 days after 10,000 rads	6
Fission neutrons	Immediate inhibition of RNA synthesis in regenerating mouse liver	1.2 (G_2-M)	Possible cell cycle independence of RBE (0-500) rads	7
Fission neutrons and 2.6 MEV cyclotron neutrons	9 month delay inhibition of RNA synthesis in regenerating mouse liver	1.4 (early S) 1.1-1.8 (early G_1)	Possible cell cycle independence of RBE (300 rads)	7
α particles (^{210}Po)	DNA synthesis rate in Hela cells	< 1.0	Labeling done 1 hour after radiation (0-10,000 rads)	8
1.3 MEV protons	DNA degredation in E. Coli	6.0	QUALITATIVE DAMAGE TO DNA	9
4.75 MEV protons	DNA degredation in E. Coli	2.0	" " " "	9
Fission neutrons	Change of $\frac{A+T}{G+C}$ ratio in DNA	1.4	QUALITATIVE DNA DAMAGE SHOWN	10
Thermal neutrons	Genetic effects in tomato seeds from ^{14}N (n,p) ^{14}C	1.5-3.0	" " " "	10
α and heavy ions (C,O) 10 MEV/nucleon	Transformation of DNA	2.5	" " " "	11
π^- mesons	Genetic changes of known loci in diploid yeast	1.5	" " " "	12

Figure 2: Table of Biochemical RBE's for various particles and energies.

Another whole animal experiment was done by Tsuya and Okano (ref. 5) in which the effect of fast neutrons on DNA synthesis was studied. Their procedure was to irradiate mice with various energies of fast neutrons ranging from 0.43 MeV to 1.8 MeV and then to label with ^{3}H-Thymidine approximately $2\frac{1}{2}$ hours after irradiation. Specimens were then taken from spleen, thymus, bone marrow and intestine and the rate of DNA synthesis as compared to control was determined in each of these organs. In this system the RBE for inhibition of DNA synthesis was found to vary according to cell type, and neutron energy, i.e., for bone marrow cells the RBE value for 0.43 MeV neutrons is 3.6 (at 500 rads) and was approximately 1.2 (at 90 rads) for 14 MeV neutrons. The RBE for DNA synthesis for 14.1 MeV neutrons was also found to be 1.1 for thymocytes and 1.8 for intestine cells. The value of the experiment is that it points out that biochemical RBE's are very dependent on cell type and neutron energy.

In other experiments by Tokarskaya and Kuzin (ref. 6), a reactor (which had the usual significant gamma contamination) was used to study the effect of fission neutrons on DNA synthesis in pea sprouts. The technique of this experiment was to irradiate dry seeds and to cause them to germinate several days later. The DNA synthesis rate was then compared to control and it was found, for doses of radiation from 1000 to 10,000 rads, that the inhibition of DNA synthesis rate by fission neutrons was always greater than that of the gamma irradiated seeds. The comparison between the fission neutron and gamma irradiated DNA synthesis rates was variable, but the RBE was 7-10, with gamma dose around 10,000 rads, while it was approximately 1.3 with doses around 1,000 rads. In addition biochemical analysis of the DNA after the neutron irradiation showed that neutron irradiation of 10,000 rads led to rather selective damage to the adenine base by deamination and conversion to hypoxanthine. This resulted in an ultimate shift of the AT to GC ratio in the DNA from 1.01 to 0.67. However, for 10,000 rads gamma dose, the AT to GC ratio changed from 1.01 to 0.92, so a "qualitative" RBE of .92/.67 = 1.4 was obtained. Thus from both a "quantitative" and "qualitative" point of view, neutron damage to DNA was more severe than gamma. This qualitative change seen with neutrons and not by gamma rays makes the enhanced mutation rate from neutrons in many animal and plant systems more understandable, since a change in the coefficient of specificity in DNA could easily alter transcription and thus invite mutations.

Duzin and Vainson (ref. 8) irradiated Hela cells with particles or x-rays and one hour later studied the effect on DNA synthesis rate by radioautography. They found an RBE of 1 and thus could not associate a depression in DNA synthesis rate with cell death. This correlates with the low LET results of others in that it supports the concept that the process of DNA replication may not be responsible for cell death.

Hutchinson (ref. 11) also found a "qualitative" RBE change in DNA as a function of LET when he irradiated, with various heavy ions, streptomycin-resistant pneumoccus bacteria and then extracted the DNA, which was subsequently tested for ability to transform streptomycin-sensitive pneumococus. He found that the RBE for inhibition of transforming activity rose to 2.5 when the LET was increased

to 100-500 MeV/cm^2/gm and then decreased to 1.0 again at about 3,000 MeV/cm^2/gm.

There has been only one experiment regarding the possible effects of π^- mesons* on DNA (ref. 12). This was done by Raju et al., where they studied some genetic changes of specific loci in diploid yeast cells. The RBE obtained for inducing these changes was 1.5, so again one may postulate a change in the quality of the DNA, which is reasonable when one considers that π^- mesons can modify DNA by annihilation of atoms, as well as by high LET particle tracks.

Some interesting experiments were done by Huston and Pollard (ref. 9) in which they irradiated E. Coli (prelabeled with ^{3}H-Thymidine) with several energies of protons as compared to ^{60}Co. They immediately post radiation measured the degredation of the DNA and found that 1.3 MeV protons (LET = 240 MeV/cm) was degraded much more rapidly as a function of dose than for 4.75 protons (LET = 110 MeV/cm) or ^{60}Co rays. Biochemical RBE's can thus be obtained (by dividing slope ratios) and for 1.3 MeV protons the RBE = 6, while for 4.75 MeV protons, the RBE = 2. Thus, this system again proved to be very energy dependent and those changes observed in DNA may be thought of as qualitative changes. Also, the authors raised the possibility that the results may be due to some damage at the transcription level.

As was mentioned initially, there is a great tendency in the literature to associate qualitative changes (such as cell death and mutation) with the concept of LET. There certainly is justification for this when one looks at data such as that of Barendsen (ref. 21) and Skarsgard (ref. 22) where these end points seem to be well correlated with LET changes. However, LET concepts do not completly explain some biological effects, so it also may be useful to look for other mechanisms than LET associated electron orbital ionizations, when trying to explain particle radiation effects. There is some evidence for a type of radiation damage that need not be correlated with ionization and LET associated events. This can be described by the following experiments:

Esochard (ref. 10) used thermal neutrons to irradiate tomato seeds, studied the resulting genetic mutations, and found RBE's from 1.5-3.0. His conclusion was that an important part of the enhanced RBE of thermal neutrons was due to the ^{14}N (n,p)^{14}C nuclear reaction where ^{14}N is naturally present in the plant cell (and in the DNA). He found that if ^{15}N was substituted in the plant nutrients that the enhanced RBE did not occur (since ^{15}N does not absorb thermal neutrons). Also by controlling the ^{10}B concentration in the plant, the ^{10}B (n,α)^{7}Li reaction effect was studied and by analysis, he found that the ^{14}N reaction had a larger effect per rad on RBE (since the ^{10}B reaction usually occured in the membrane or cytoplasm) and the ^{14}N is to some extent in nuclear DNA. Thus, when the ^{14}N(n,p)^{14}C reaction occurs in DNA, two types of damaging events can occur.

1. The ejected proton has an energy of 0.59 MeV and an LET of 45 KeV/μ, and this could cause double strand breaks (which, however, might be reparable.)

2. The ^{14}C atom formed has enough energy (42 KeV) to recoil and break all chemical bonds, thus leaving an empty space in the DNA strand --- the efficiency of biological systems to repair this kind of damage is unknown (and perhaps is non-existant, since only in recent history have living things been exposed to particles such as neutrons and π^- mesons, so there may have been no evolutionary development to cope with this type of lesion).

Another fascinating type of experiment by Jung and Zimmer (ref. 23) and more recently by Watt and Hughes (ref. 24) is the study of the inactivation of enzymes such as ribonuclease by very low energy (less than 100 KeV) protons. They have noted that the enzyme inactivation is highly dependent on energy as is shown in Fig. 3. The curve denoted by "S" signifies the enzyme inactivation cross section reaches a minimum at 1 KeV, but then rises again steeply below 1 KeV. The electronic stopping cross section σ_e is noted to fall and become negligible at 1 KeV, while the nuclear stopping cross section, σ_n, begins to rise at 10 KeV and thus rises in conjunction with the enzyme inactivation cross section, indicating a very strong correlation between nuclear elastic scatter (displacing a hydrogen or heavy atom from the enzyme molecule) and the biological inactivation of ribonuclease! Thus, this type of damage really had nothing to do with LET concepts (except the casual association that low energy protons do in fact provide fairly high LET's). There is of course no reason why this type of physical lesion is not induced in DNA and RNA by irradiation with various energies of neutrons, protons, π^- mesons, (and even α particles and other heavy particles) and such damage must be of real significance to the functional integrity of the macromolecule. It is known that even small changes in the hydrogen atom movement perturbs hydrogen bonds in DNA and may be responsible for tautameric shifts in base pairing and mutations (ref. 25) Thus, even a gentle elastic collision could cause major alterations in the DNA. One might argue that an LET dependent ionization type of damage is still the most significant, and this is usually hard to disprove, since the system is "saturated" with LET dependent electronic ionizations. The answer to this question will have to come from experiments like those of Jung and Zimmer and Watt and Hughes. The point is, however, (as originally implied by Platzman) (ref. 26), that ionization related damage may be much more reparable than nuclear type damage is interesting and should be vigorously pursued. It is certainly conceivable that even very small perturbations (such as the removal of a single key atom) in the DNA or RNA structure could lead to drastic endpoints, since these molecules are capable of great biochemical amplification of damage.

If nuclear interactions and reactions, therefore, are important (and it seems they might be) when evaluating biochemical responses to particle

*π^- mesons are classified as "high" LET radiation since, when they are captured by atomic nuclei (C, N,O,P, etc. in tissue), they form an unstable mesic atom which disintegrates, giving off energetic particles (heavy ions, protons, neutrons and α rays.)

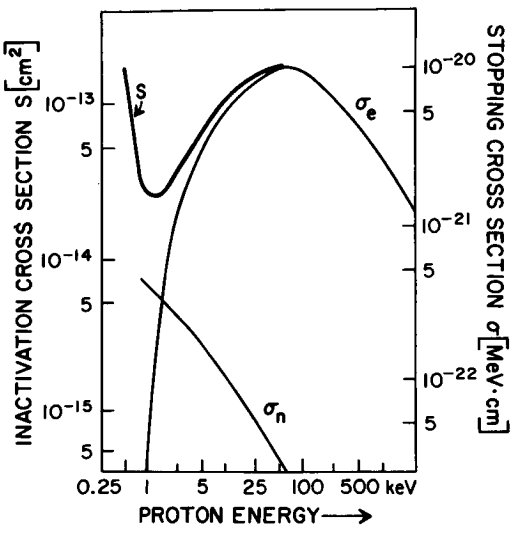

Fig. 3: Calculated stopping cross sections for electronic (σ_e) and nuclear (σ_n) processes as a function of proton energy and experimentally determined inactivation of ribonuclease cross sections (S) as a function of proton energy. (All curves were redrawn from ref. 23.)

radiation, then new avenues are opened to investigators in many fields; as an example, a better knowledge of these reactions and their biochemical effects might enable and promote the synthesis of new types of drugs ("neutron sensitizers") which might then be used to supplement the possible value of fast and lower energy neutrons in the treatment of human malignancies. (Attempts to develop such drug sensitizers for thermal neutrons (ref. 27) and low LET radiations (ref. 28) have already been made, but the results thus far are disappointing. However, the development of drugs that might utilize nuclear reactions associated with higher neutron energies, such as resonance and threshold reactions, might be rewarding.)

When discussing neutrons (which due to their neutral charge have the capability for producing an especially large number and variety of nuclear reactions), it is possible to group their reaction types into several categories, (a) elastic scatter, (b) inelastic scatter, (c) resonance absorption, (d) thermal absorption -- and all these reactions are highly and (as in the case of resonance absorption) precisely energy dependent. For biochemical purposes, their reactions can be more simply categorized into reactions which cause atomic displacements or atomic transmutations.

As theoretical examples, the mechanism and possible significance of damage to an A-T base pair of DNA by some possible nuclear interactions and reactions are described in Fig. 4, 5, or 6. The actual significance of these types of interactions and reactions is at present unproved. But, in reviewing the data of Fig. 2, one becomes impressed at the rather large energy and particle dependence of the RBE's observed, (by comparing the results of the proton-DNA degredations experiments (ref. 9), the thermal neutron effect on tomato seeds genetics (ref. 10), the fission neutron base ratio experiments (ref. 6), the immediate and delayed inhibition of RNA synthesis experiments (ref. 6, 7), and the experiments of transformation of DNA) (ref. 11). Such particle and energy dependence is highly suggestive of nuclear process cross sections. Also, in each of these cases (although there is a wide range of biological systems utilized from bacteria to the whole animal), there is direct correlation between the implied and measured functional integrity of DNA. In addition, there is great variation (from immediate to 9 months later) in the time from radiation to observations, suggesting the possibility that these findings reflect the presence of a DNA or RNA lesion(s) which might not be reparable, even over long periods of time. An interesting experiment would be to try to correlate nuclear damage (σ_n) to DNA with lack of repair (as shown by lack of a high LET s.c.* shoulder).

In closing, it is relevant to mention some ways in which the better knowledge of biochemical effects of ionizing radiation (and in particular "high" LET radiation) is applicable to problems such as manned space flight. As has been mentioned, one biological endpoint that is accentuated by "high" LET radiations is cell death and we should learn more about this endpoint by study at the molecular level. (The development of good, quick response, RBE dependent, biochemical dosimeters should also be stimulated by this type of research). Life threatening, massive cellular death, however, will occur only with large exposures; and for the lower does that are currently being recorded in manned spacecraft, perhaps this endpoint is not the most realistic hazard. A more incidious hazard which might be observed with chromic low exposures to "high" LET particles is carcinogenesis. From the data presented, it seems likely that even very small perturbations (such as perhaps a single atom displacement, transmutation, or annihilation) in DNA or even RNA (in view of Temin's recent work) (ref. 29) could theoretically be directly related to the development of an endpoint such as carcinogenesis. Thus, by further study at the biochemical level and by acquiring accurate, specific biochemical RBE's such diverse fields as space flight health physics (where this information would be very useful in assigning quality factors) and the radiotherapy of human malignancies might be mutually benefitted.

* s.c. = survival curve

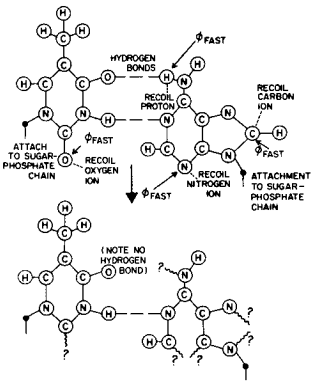

SOME POSSIBLE ATOMIC DISPLACEMENTS IN DNA (A-T BASE PAIR) RESULTING FROM NEUTRON ELASTIC SCATTERING

Fig. 4. Fast neutrons (8 fast) interacting by elastic scatter with arbitrarily chosen hydrogen, carbon, oxygen and nitrogen atoms, creating atomic voids in the DNA bases. The question marks indicate uncertainty regarding the ultimate biochemical reactions. The most probable elastic scatter is with the hydrogen atoms, producing recoil protons.

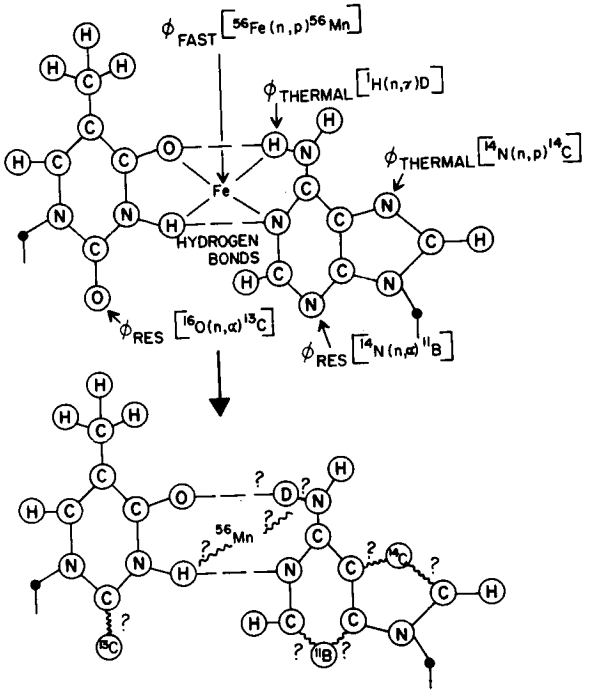

SOME POSSIBLE ATOM TRANSMUTATION REACTIONS IN DNA (A-T BASE PAIRS) RESULTING FROM THERMAL AND RESONANCE NEURON CAPTURES

Fig. 5: Fast neutrons (Ø fast), resonant neutrons (Ø res), or thermal neutrons (Ø thermal) causing nuclear reactions with various atoms and creating new elements (i.e., ^{14}C, ^{2}H, ^{13}C, ^{11}B and ^{56}Mn) which probably will cause unstable bonds with probable breakdown of the bases. (Note: Fe may be a functional part of a DNA lattice., ref. 30)

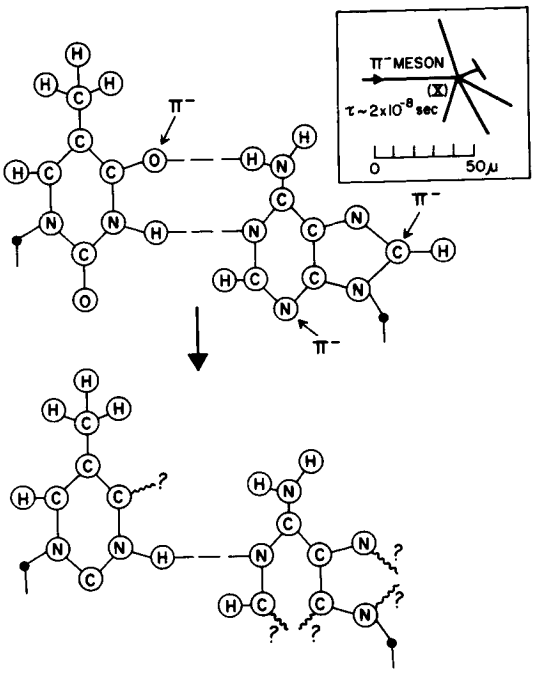

SOME POSSIBLE CHANGES IN DNA AFTER π^- ANNIHILATION OF O, N, OR C ATOMS

Fig. 7: π^- mesons capture by O, N, or C atoms causing annihilation of these atoms and ultimate chemical breakdown of the bases. The diagram in the upper right corner demonstrates how the π^- produces a "star" formation (as seen on photographic emulsion) consisting of π's, protons and heavy ions after capture by the target atoms.

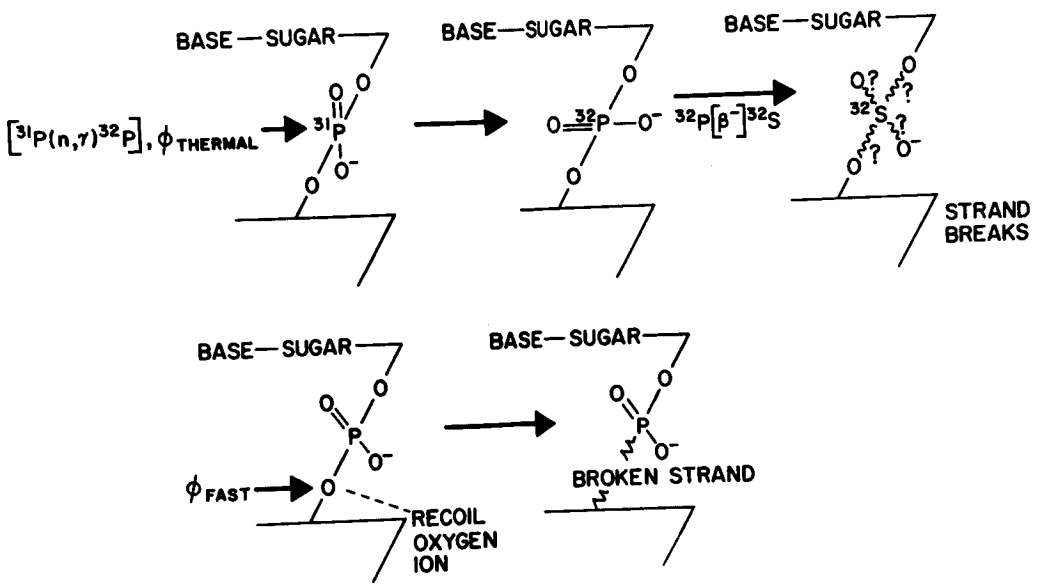

SOME POSSIBLE ATOMIC DISPLACEMENTS AND ATOMIC TRANSMUTATIONS FROM NEUTRON INTERACTIONS WITH THE PHOSPHATE LINKAGES IN DNA

Fig. 6: Fast neutron (Ø fast) and thermal neutron (Ø thermal) reactions with atoms in the phosphate linkage of DNA. The ^{31}P absorbs a thermal neutron and forms ^{32}P which is radioactive and decays to ^{32}S, which is not able to maintain proper chemical bonds and the strand breaks. The ϕ_{fast} displaces the oxygen atom, leaving an atomic void and a broken DNA strand.

REFERENCES

1. Langham, Wright H.,Editor: Radiobiological Factors in Manned Space Flight, National Academy of Sciences, National Reseach Council, Washington, D. C., Publication 1487, 1967.
2. Barendsen, G. W.; and Broerse, J. J.: Symposium on Neutrons in Radiobiology, USAEC, Conf - 691106,1969, p. 230.
3. Barendsen, G. W.:

Int. J. Rad. Biol., vol. 10, 1966, p. 317.
4. Szybalski, W.; and Opara-Kubinska, Z: Cellular Radiation Biology, Williams & Wilkins Co., Baltimore, Md., 1965, p.223.
5. Tsuya, A.; and Okano, S: J. of Rad. Res., vol. 8, no. 2, 1967, p. 53.
6. Tokarskaya, V.I.; and Kazin, A.M.: Radiobiologiya VI I, 1966, p. 1.
7. Wiley, A.L.; and Cole, L.J.: Symposium on Neutrons in Radiobiology, USAEC, Conf - 691106, 1969, p. 462.
8. Kuzin, A.M.; and Vainson, A.A., Radiobiologya, USAEC translation, UDC 612.014.481.
9. Huston, D.C.; and Pollard, E.C.: Biophysical Journal, vol. 7, no. 5, September 1967, p. 555.
10. Ecochard, R.: International J. of Rad. Biol. vol. 17, no. 5, 1970, p. 439.
11. Hutchinson, F.: Cancer Res, vol. 26, part I, 1966, p. 2045.
12. Raju, R.M.; Gnanapurani, M.; Madhvanath, U.; Stackler, B.; and Mortimer, R.: Semiannual Report, Biology and Medicine, Donner Laboratory, Univ. of Calif., Berkeley, Calif., UCRL 19420, 1969.
13. Sawada, S.; and Okada, S.: Radiation Res., vol. 41, no.1, January 1970, p. 145.
14. Alexander, P.; Lett, J.; Kopp, P.; and Itzhaki, R., Radiation Research, vol. 14, 1961, p. 363.
15. Deering, R.A.; and Rice, R.: Radiation Res. vol. 17, 1962, p. 774.
16. Kitayama, S.; and Matsuyama, A.: Biochemical and Biophysical Res. Communications, vol. 33, no. 3, 1968, p. 418.
17. Neary, G.J.: Int. J. Radiot. Biol., vol. 18,197 no. 1, p. 25.
18. Yatvin, M.B.; Mitchen, J.L., Wiley, A.L., Jr.; and Vogel, H.H.: Biochem, Biophys. Acta, vol. 169, 1968, p. 536.
19. Curtis, H.J.: Current Topics in Radiation Research, North Holland Pub. Co., Amsterdam, vol. III, 1967, p. 141.
20. Terasima, T.: and Tolmach, L.J.: Biophys. J., no. 3, 1963, p. 11.
21. Barendsen, G.W.; Walter, H.M.D.; Fowler, J.F.; and Bewley, D.K.: Radiation Res., vol. 18, 1963, p. 106.
22. Skarsgard, L.D.: The Radiobiology of Cultured Mammalian Cells, by Elkind, M.M.; and Whitmore, G.F., Gordon and Breach Science Pub., Inc., 1967, p. 421.
23. Jung, H.; and Zimmer, K.: Current Topics in Radiation Research, North Holland Publishing Co., Amsterdam, vol. II, p. 71.
24. Watt, D.E.; and Hughes, S.: Symposium on Neutrons in Radiobiology, USAEC Conf - 691106, 1969, p. 46.
25. Printz, M.; and von Hippel, P.H.: Proceedings of the National Academy of Sciences, vol. 53, no. 2, 1965, p. 363.
26. Nickson, J.J., Editor: Symposium on Radiobiology, by Platzman, R.L, John Wiley and Sons, New York, N.Y., 1952, p. 97.
27. Farr, L.E.; Sweet, W.H.; Locksley, H.B.; and Robertson, J.S.: Trans. Am. Neurol. Assoc., 1954, p. 110.
28. Bagshaw, M.A.; Doggett, R.L.S.; Smith, K.C.; Kaplan, H.S.; and Nelson, T.S.: Am. J. Roentgenol. Rad. Ther. and Nuc. Med., vol. 99, 1967, p. 886.
29. Temin, H.M.; and Mizutani, S.: Nature, vol. 226, June 1970, p. 1211.
30. Wacker, W.E.C.; and Vallee, B.L.: Biol. Chem., vol. 234, 1959, p. 3257.

EFFECTS OF X-RAY IRRADIATION ON HUMAN SPERMATOGENESIS

T.W. Thorslund and C.A. Paulsen, (University of Washington)

Direct cell kill and inhibition of mitosis have been suggested as mechanisms to explain the occurrence of absolute sterility following the irradiation of the testes. In order to obtain information on the existence and dose dependency of the mechanisms for man, a controlled study was initiated in 1963. A total of 209 normal adult non-Catholic inmate volunteers at the Washington State Penitentiary in Walla Walla participated in the experiment. Sixty-four of the men received a single mid-organ dose to both of their testes ranging from 7.5 to 400r (f = .95). The remaining men served as various control groups. Testicular function was evaluated primarily on the basis of weekly seminal fluid examinations where the response or end-point was taken to be azoospermia or complete sterility. In order to obtain direct information on testicular morphological changes, periodic unilateral testicular biopsies were also performed on a number of individuals in both the exposed and non-exposed groups.

It was deduced from the resulting length of the pre-sterile period and sterile period data that both cell kill and mitosis halting mechanisms were operating. Estimates of ED50 of 75r and 27r for cell kill and mitosis halting, respectively, were obtained. The maximum observed sterile period was 501 days with eventual recovery observed in each individual where the follow-up was complete. Thus man appears to be highly radiosensitive in regard to temporary sterility but quite radioresistant in regard to permanent sterility.

Various mechanisms suggested by animal experiments have been postulated to explain the phenomenon of absolute sterility or azoospermia resulting from irradiation of the testes.

Oakberg (ref. 1) attributes the observed depletion or total absence of germ cells in the epithelium of the seminiferous tubules to be due to direct cell kill. Under this hypothesis the length of the pre-sterile period or time to first azoospermia would be determined by the time required for the resistant cells to complete development and reach the ejaculate. The duration of azoospermia or length of the sterile period is considered to be made up of two components. The duration of the first component is equivalent in length to the age of the youngest cohort of germ cells that was not totally decimated. The second component of the sterile period is the time required for the surviving stem cells to multiply sufficiently to reach a critical density or cluster size necessary for differentiation to take place.

Jones (ref. 2) postulates that an inhibition of mitosis may be the mechanism responsible for the sterile period. Under this hypothesis the time to first azoospermia would be equivalent to the total maturation time plus the time post-irradiation required for mitosis to be halted. The duration of the sterile period is identical to the time required for the mitotic mechanism to repair itself.

The existence and dose dependency of the postulated mechanisms with respect to human beings is of obvious scientific interest and growing medicolegal importance as human exposure to radiation increases. The variability in spermatogenic kinetics observed among various species in regard to their gonadal response to dfiferent levels of radiation (refs. 3 to 5) renders any human sensitivity estimates based on animal data highly questionable.

NORMAL HUMAN SPERMATOGENIC KINETICS

In recent years a series of experiments were performed that allow one to estimate the time required for a human germ stem cell to mature and be passed into the ejaculate.

Clermont (ref. 6), Heller and Clermont (ref. 7) have devised a highly explicit model for the mode of development and timing of human spermatogenesis. The mode of development portion of the model is based on the observed ratios of germ cell types in various stages of maturation counted in biopsy specimens. The timing relationships were determined by using radioautographs of testicular sections following intratesticular injections of H^3-thymidine. The maximum transport time of the mature spermatozoa from their release from the Sertoli cell cytoplasm into the ejaculate has been determined by Rowley et. al. (ref. 8) to be no more than twenty-one days. Freund and Davis (ref. 9) observed a thousand fold depletion of sperm count at the fifth ejaculation post vasectomy. Thus the time required to evacuate ductal storage of spermatozoa is virtually equivalent to the time to the fifth ejaculation.

The minimum time required for the mature spermatozoa to reach the ejaculate under certain conditions is considered to be less than one day.

A model for the maximum time required for a maturating human germ stem cell to reach the ejaculate based on the preceding considerations is presented in a schematic manner in figure 1. This model will be utilized to test the plausibility of the various suggested disrupting mechanisms in regard to human spermatogenesis.

FIGURE 1 MODEL FOR MODE OF DEVELOPMENT AND TIMING OF HUMAN SPERMATOGENESIS

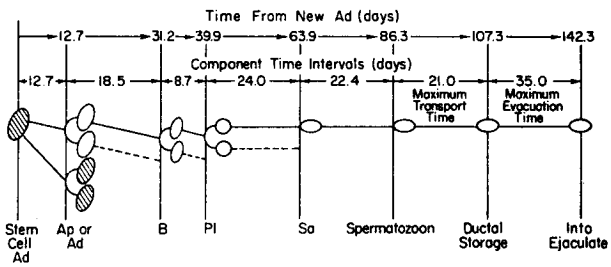

Abbreviations: Ad, A dark spermatogonia; Ap, A pale spermatogonia; B, B spermatogonia; Pl, Preleptotene primary spermatocyte; Sa, Sa spermatid.

HUMAN EXPERIMENT OF THE EFFECT OF X-RAYS

In order to obtain a reliable estimate of the existence and dose dependency of the postulated spermatogenesis disrupting mechanisms for man, a controlled experiment was undertaken in 1963. This study utilized a group of 209 healthy non-Chatholic inmate volunteers at the Washington State Penitentiary in Walla Walla. Each inmate selected for the study had to express a desire for a vasectomy. This was to be performed at the completion of his involvement in the study. The inmate and, if married, his wife both signed a written consent form authorizing all experimental procedures.

Extensive pre-irradiation sperm samples were obtained by masturbation for each inmate and sperm density estimates of ejaculate made to demonstrate normal spermatogenesis. The testes of sixty-four of the men received a mid-organ dose of X-rays ranging from 7.5 to 400.r. (f factor = .95) administered acutely by a Maximar 250 Kv unit. The remaining 145 men served as various types of controls. In addition, in order to obtain direct information on testicular morphological changes, periodic unilateral testicular biopsies were performed on a number of individuals in both the irradiated group and non-irradiated group. Weekly sperm samples were collected post-irradiation and sperm density estimates made even though the end point of central interest was azoospermia.

The number of inmates in each biopsy-radiation group and the number of these that were observed to have achieved azoospermia by 142 and by 210 days is shown in table 1. The duration in days of the pre-sterile period and the sterile period for each inmate in his biopsy-radiation group that became azoospermic is given in table 2. The question marks (?) indicate that the individual was lost for observational purposes while still azoospermic.

Table 1

DATA USED TO ESTIMATE PARAMETERS IN POSTULATED MODELS

X-Ray (r)	Number of Biopsies	Fraction Sterile by 142 Days	Fraction Sterile by 210 Days
400	0	2/2	2/2
	1	1/1	1/1
	2	2/2	2/2
100	0	5/7	7/7
	1	7/9	9/9
	3	2/2	2/2
50	0	1/8	5/8
7.5	0	0/5	0/5
0	0	0/96	0/96
	1	0/29	0/29
	2	1/18	1/18
	3	0/1	0/1

Table 2

TIME SEQUENCE OF AZOOSPERMIA AS A FUNCTION OF RADIATION AND BIOPSIES

X-Ray (r)	Number of Biopsies	Pre-Sterile Period in Days	Sterile Period in Days
0	2	38	?>509
30	0	95	182
	0	194	7
50	0	115	70
	0	160	91
	0	171	84
	0	195	21
	0	202	49
100	0	88	209
	0	107	91
	0	129	112
	0	141	112
	0	141	112
	0	152	61
	0	189	112
100	1	65	108
	1	100	421
	1	109	?>42
	1	111	?>7
	1	113	112
	1	114	232
	1	124	?>152
	1	201	?>21
	1	209	62
100	2	145	327
100	3	127	291
	3	127	501
400	0	76	147
	0	98	196
400	1	115	329
400	2	113	338
	2	116	342

The 142 day time period was selected since it represents the maximum pre-sterile period possible if the mechanism causing sterility is complete cohort decimation. This estimate is based on the observation that if an inmate masturbated only at his prescribed collection time evacuation would be accomplished in 7 x 5 = 35 days. Thus the maximum pre-sterile period is 35 + 21 + 86 = 142 days. The 210 day time period was selected since no new occurrences of azoospermia were observed after that time.

MODELS FOR THE EFFECTS OF X-RAYS

From figure 1 we note that a pre-sterile period of less than 86 days can only be explained in terms of the postulated mechanisms by assuming death of a cohort of differentiating germ cells. For two inmates azoospermia occurred at 65 and 76 days confirming the existence of that mechanism. If the pre-sterile period was greater than 142 days then complete cohort decimation did not occur. A lower limit on the dose dependency of the cohort decimation effect can be determined by assuming that if azoospermia occurs by 142 days the effect occurred. Thus the observed fraction of inmates becoming azoospermic by 142 days shown in table 1 can be utilized to estimate the ED_{50} of the effect.

A model relating the probability of total cohort decimation to the dose of X-rays can be derived under the following assumptions:

i) The probability of the most sensitive cell type being killed given a dose of X-rays of size x follows a one-hit-curve of the form

$$P = (1 - e^{-\theta x}).$$

ii) The cohort size of the most sensitive type of germ cell of an individual is a random variable N which has a poisson distribution with parameter λ.

iii) A person is azoospermic if all N of his most sensitive type of cell are killed.

Under these assumptions the probability of total cohort decimation is

$$P(x) = \sum_{N=0}^{\infty} (1 - e^{-\theta x})^N \, e^{-\lambda} \frac{\lambda^N}{N!} = e^{-\lambda e^{-\theta x}}$$

and the dose of radiation that results in 50% of the population becoming azoospermic due to cohort decimation is

$$1/2 = e^{-\lambda e^{-\theta x_{50}}}$$

or

$$x_{50} = ED_{50} = [-\ln(\ln 2) + \ln \lambda]/\theta$$

The dose required (LD_{50}) to kill 50% of the most sensitive type of germ cell can also be estimated from this model. It follows directly from the assumption of a one hit curve for cell kill that

$$1/2 = 1 - e^{-\theta x_{50}}$$

or

$$x_{50} = LD_{50} = \ln 2/\theta$$

The parameters of the model (λ, θ) were estimated from the observed data by the maximum likelihood method (ref. 10), adjusting for the probability that a testicular biopsy could also independently couse azoospermia by 142 days. The estimate of ED_{50} was found to be 74.6r with a 95% confidence interval obtained by using Fieller's Theorem (ref. 11) of 57.2 to 103.6r. In addition, it is of interest to note that this rather indirect method of estimating the LD_{50} of cell kill gives an estimate of 23.2r which is in remarkable agreement with Oakberg's estimate (ref. 12) of an LD_{50} of between 20 and 24 rad of X-ray for spermatogonia.

The longest observed pre-sterile period was 209 days with 10 out of the 32 inmates who became azoospermic having a pre-sterile period greater than 142 days. The maximum observed sterile period was 501 days where a maximum of 142 - 127 = 15 days could be explained by cohort decimation. To explain these results by the cell kill hypothesis several additional assumptions are needed. We need to assume that some stem cells are capable of functioning normally for at least 209 - 142 = 67 days post-irradiation and then die. For one individual we must assume that the total time where stem colony growth took place if 501 - 15 = 486 days and thus the number of doublings was 486/12.8 = 38 and the total restored stem cell population for an individual tubule is at least 2^{38} before differentiation took place. Neither of these assumptions appear to be very tenable.

Oakberg (ref. 13) suggests upon viewing similar results of length of the sterile period for humans based on a preliminary report by Heller (ref. 14) that differentiation of the stem cells produces non-viable daughter cells causing the stem cell population to build up slowly thus prolonging the sterile period. However, on inspection of our testicular biopsies (ref. 15) we observe a period of very low stem cell density followed by a rapid doubling of stem cells in line with the 12.8 day doubling time, which in turn is followed by the differentiation of the stem cells and eventual recovery. In the light of these results it appears reasonable to assume that mitotic division is also halted in some manner by the radiation.

If we assume that individuals have a normal distribution of log dose tolerances with regard to some mitotic division mechanism, then the probability of azoospermia given a log dose of radiation of size x is to a very close approximation

$$P(x) = \frac{1}{1 + e^{-(\alpha+\beta x)}}$$

and

$$x_{50} = ED_{50} = e^{-\alpha/\beta}$$

If we assume that a critical volume in the testes exists that has an overriding control over the mitotic division mechanism and is damaged with one hit, or if we assume that tolerances to dose have the exponential distribution, then the

$$P(x) = 1 - e^{-\theta x}$$

and

$$x_{50} = ED_{50} = \ln 2/\theta.$$

Estimates of the parameters (α, β) or (θ), for these models was obtained by maximum likelihood estimation adjusting for the probability of a biopsy causing sterility, using as data the fractions of individuals who became azoospermic by 210 days. Estimates of ED_{50} were 36.3r with a 95% confidence interval of 19.8 to 50.3r for the normal distribution of log dose tolerance model and 27.2r with a 95% confidence interval of 18.8 to 48.8r for the one hit model. The variation in the confidence intervals for these two models are minimal while the differences in the ED_{50} estimates are primarily due to different dose scales. A summary of the ED_{50} results is shown in table 3.

Simulation experiments were run on these models to verify that the asymptotic approximations used to obtain the confidence intervals were valid for the sample sizes used in the experiment. In all cases a close agreement was obtained between the observed and expected results which virtually assures the statistical validity of the stated intervals.

CONCLUSIONS

In men the occurrence and length of azoospermia or complete sterility following X-ray irradiation is made up of a number of components. It appears reasonable to assume that complete cohort decimation of some germ cell type does take place following exposure to sufficiently large doses. However, doses that are not large enough to cause total cohort decimation are still able to stop spermatogenesis by halting mitosis of the surviving stem cells for extended periods of time needed for repair. The repaired stem cells multiply until a critical cluster size is reached after which differentiation occurs followed by the reappearance of sperm in the ejaculate.

Man also appears far more sensitive to radiation than the rodent who needs almost ten times the dose to become azoospermic. The time needed for man to recover is also much longer than would be expected from animal experiments, ranging up to a year and a half after exposure. However, the evidence does point to eventual recovery even for doses of 400r.

In short, man is very radiosensitive in regard to temporary sterility periods as long as one and a half years but very radioresistant to complete sterility.

ACKNOWLEDGEMENTS

Supported in part by AEC Contracts AT(45-1)-1781 and AT(45-1)-2225 and NIH grants AM 05161 and AM 05436.

The authors wish to thank Donald J. Moore for his expert technical assistance.

Table 3

ED_{50} ESTIMATES FOR POSTULATED MODELS AND ITS 95% CONFIDENCE LEVEL

Model P(x)	Days Post Irradiation	Lower Limit	ED_{50}r.	Upper Limit
$e^{-\lambda e^{-\theta x}}$	142	57.2	74.6	103.6
$\frac{1}{1+e^{-(\alpha+\beta \ln x)}}$	210	19.8	36.3	50.3
$1-e^{-\theta x}$	210	18.8	27.2	48.8

Multifactorial Analysis of Human Blood Cell Responses to Clinical Total Body Irradiation[1]

John M. Yuhas, T. R. Stokes, and C. C. Lushbaugh

Biology Division, Oak Ridge National Laboratory, and Medical Division, Oak Ridge Associated Universities, Oak Ridge, Tennessee 37830

INTRODUCTION

Each source of information which has contributed to our knowledge of human responses to total body irradiation has characteristic advantages and disadvantages. For example, the people exposed to atomic bomb radiations in Hiroshima and Nagasaki were random samples from a presumably normal population, but estimation of the precise radiation dose that each individual received is difficult, and the confounding effects of blast and heat have made it nearly impossible to obtain an accurate dose-response relationship (1). For the analysis of data from patients given therapeutic exposures, the situation is exactly the reverse: dosimetry and clinical follow-up have been extensive, but the patients constitute a nonrandom sample whose usefulness in making extrapolations to the population at large may be seriously questioned. If precise response patterns can be determined for a variety of disease states, it may be possible eventually to combine these estimates with our knowledge of the disease processes and thereby to arrive at a rational prediction of the average radiation response of normal individuals.

Toward this end, a variety of investigators have attempted to describe the average radiation response of the patient given total body therapeutic exposures (2, 3), but none has been able to estimate the radiation response within acceptable confidence limits. This has resulted largely from the fact that therapeutic exposures are often complex combinations of total exposure, number of fractions, and time between fractions, and very few individual patients have received exactly the same combination. The individuality of clinical records prevents the construction of discrete "treatment groups" for dose-response analysis, so pooling procedures are required, such as separating patients who received their total exposure in less than 8 days from those who were exposed over longer periods (2). While this type of treatment may be adequate for gross responses, it has proved to be totally unsuitable for analysis of human blood cell responses.

Standard techniques are available (4), however, which allow the simultaneous study of the effects of total exposure, independent of the time factor, and the effects of time, independent of the total exposure factor. These multiple regression analyses have been applied successfully to the study of the effects of exposure, number of fractions, and time on such quantal responses as tumor control (5) and skin injury (6). The present report demonstrates the potential of these methods for the analysis of human blood cell responses and provides preliminary estimates of the effects of total amount of exposure and time of protraction in determining the minimum white blood cell (WBC) concentration observed after exposure of patients from four disease groups.

MATERIALS AND METHODS

More than 2700 clinical records of patients who had received single or fractionated total body exposures for a variety of diseases were collected from more than 30 participating hospitals (2). Deletion of records that contained inadequate exposure or response information reduced this number to approximately 1000. Additional requirements were imposed on the records for the purposes of the present analysis: only those records which were for the first treatment a patient received were included, since we have preliminary indications that the responses to second and later exposures differ slightly from the responses to first exposures; records for patients who received total exposures of less than 50 R were deleted due to the

[1]Research supported by the U. S. Atomic Energy Commission under contract with the Union Carbide Corporation and by the National Aeronautics and Space Administration.

questionable nature of the responses observed; records from those patients in whom the minimum concentration could not be determined with certainty were omitted [in order to be considered a true minimum, the concentration must persist for a reasonable period of time or be followed by an elevated concentration other than the occasionally observed abortive rise (7)]; and disease categories in which there were fewer than ten records were omitted. These qualifications removed all but 518 records, which were distributed among four disease categories: chronic myelogenous leukemia or CML (131 records); chronic lymphatic leukemia or CLL (200 records); lymphosarcoma or LSAR (66 records); and diseases which have no direct effects on the blood-forming tissues or NORMAL (121 patients). The NORMAL group is normal only in a relative sense and includes patients with disseminated solid tumors, as well as patients in the late stages of nonmalignant diseases of the bones, joints, and genitourinary system.

Data were stored and analyzed on a simple time-sharing computer system (Call-A-Computer, Raleigh, North Carolina), which proved entirely adequate for the requirements of this study.

RESULTS

Table I summarizes the number of patients in each disease category who were given single or multiple exposures. We were unable to obtain any data on CLL patients who had received single exposures in excess of 100 R, so a meaningful analysis of their single-exposure response curve could not be conducted.

Table I

Disease category	Single exposures	Multiple exposures
Chronic myelogenous leukemia (CML)	15	116
Chronic lymphatic leukemia (CLL)	—	200
Lymphosarcoma (LSAR)	16	50
NORMAL[a]	92	29

Numbers of patients in each of the four disease categories studied who received single and multiple total body exposures.
[a]Patients with diseases that have no direct effects on blood-forming tissues.

Table II summarizes the exposure and response data for patients from the three disease categories in which a single-exposure analysis could be performed. The mean total exposure varies among the three diseases, reflecting the differences in accepted treatment levels for each of the diseases.

Table II

	NORMAL[a]	CML	LSAR
No. of patients	92	15	16
Mean total exposure	195 R	117 R	108 R
Mean WBC at nadir	21.6%	27.7%	39.9%
Predicted tolerated exposure	19 R	18 R	34 R
Slope (WBC/E)	$-1.04 \pm .16$[b]	$-0.99 \pm .19$[b]	$-1.12 \pm .65$
Correlation coefficient	0.572[c]	0.823[d]	0.419

Exposure and response data for patients from three disease categories who were given single therapeutic exposures.
[a]Patients without diseases which have direct effects on their blood-forming tissues.
[b]$P < 0.001$.
[c]$P < 0.0005$.
[d]$P < 0.005$.

The data for each disease were fit to a variety of equations, with the most satisfactory being a simple power function,

$$\% \text{ WBC} = k\,[100]\,[E]^{\alpha}$$

where % WBC is the WBC count at the nadir as a percentage of the preirradiation levels, k is a constant, E is the midline air exposure in R, and α is the slope of % WBC on E.

Individual slopes were tested for significance by use of t-tests, and the overall correlation coefficient by use of F-ratios (4). The slopes and correlation coefficients are highly significant for the NORMAL and CML groups (Table II), but not for the LSAR group. In each case, however, the slope does not differ significantly from -1.0, indicating that with response measured as the nadir concentration of white blood cells there is no demonstrable difference in radiosensitivity among these three groups, once the tolerated exposure has been exceeded. The predicted tolerated exposure is given by

$$\text{Predicted tolerated exposure} = \text{EXP}\left(\frac{\log k - \log 100}{\alpha}\right).$$

Figure 1 gives the plot of % WBC concentration at the nadir as a function of radiation exposure for the three disease categories. The displacement of the LSAR group to a higher exposure level is not statistically significant and requires further study.

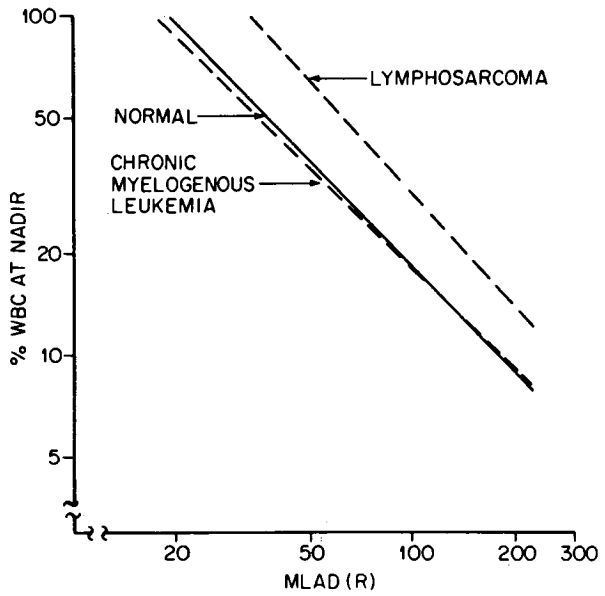

Figure 1. Percent white blood cell concentration at the nadir as a function of radiation exposure for patients with chronic myelogenous leukemia (CML), lymphosarcoma (LSAR), or without any disease which has direct effects on the blood-forming tissues (NORMAL).

For the analyses of multiple exposures we define the time of protraction as the number of days over which the exposure is given. For example, a patient who received one fraction on each of two consecutive days would have a protraction time of two days. Table III summarizes the exposure and response data for patients from the four disease categories who received multiple exposures. Mean total exposures are logically greater, since the exposures were protracted over times of 27 to 36 days on the average. As was the case with the single-exposure data, the most adequate fit proved to be a power function:

$$\% \text{ WBC} = k\,[100]\,[E]^{\alpha}\,[T]^{\beta},$$

where T is the time of protraction in days and ß is the slope of % WBC at a given E on T. The slope of % WBC on exposure does not differ among the NORMAL, CML, and LSAR groups in this multiple-exposure analysis, and it is essentially equal to -1.0, as was observed in the single-exposure groups (Table II). Theoretically, the identity of slopes in the two sets of data is expected, since by our definition the protraction time in the single-exposure studies is one day, and one raised to any power equals one. In other words, the single-exposure data should fit the multiple-exposure equation with T set equal to one. This indicates, therefore, that there are no qualitative differences between the two sets of data (single versus multiple exposure).

Table III

	NORMAL	CML	LSAR	CLL
No. of patients	29	116	50	200
Mean total exposure (E)	233 R	152 R	217 R	116 R
Mean duration of exposure (T)	27.9 days	28.9 days	32.1 days	36.9 days
Mean WBC at nadir	55.2 %	44.4 %	43.8 %	52.9 %
Predicted tolerated exposure	16 R	7 R	25 R	11 R
Slope (WBC/exposure)	$-1.07 \pm .39^{b}$	$-0.82 \pm .12^{d}$	$-1.04 \pm .22^{d}$	$-0.75 \pm .08^{d}$
Slope (WBC/time)	$0.63 \pm .24^{c}$	$0.39 \pm .10^{d}$	$0.23 \pm .18$	$0.22 \pm .06^{d}$
Multiple correlation coefficient	0.535^{c}	0.569^{e}	0.567^{f}	0.583^{e}

Exposure and response data for multiple exposures in four patient samples.
[a]Patients without diseases which have direct effects on their blood-forming tissues.
[b]$P < 0.025$. [c]$P < 0.01$. [d]$P < 0.001$. [e]$P < 0.0001$. [f]$P < 0.0005$.

The CLL group, on the other hand, demonstrates a response on exposure slope which is significantly less than -1.0, but which is not significantly different from the slopes observed for the other diseases. We are unable, therefore, to demonstrate any difference among the disease categories studied in the slope of response on exposure.

The slope of WBC concentration on time at a given exposure presents the most interesting of the results obtained from this analysis. At a given exposure the % WBC at the nadir increases as the 0.63 power of the number of days separating the first and last fractions. Figure 2 illustrates this effect for exposures of 60, 100, and 200 R given over periods of 2 to 32 days. In the CML group, the slope of WBC on time, or more loosely the recovery constant, is smaller but not significantly below that of the NORMAL group. The recovery factor for the two diseases which affect lymphatic tissues, LSAR and CLL, are each approximately one-third of that observed in the NORMAL group ($P < 0.5$ and $P < 0.05$, respectively). Figure 3 illustrates this variation in the time factor for the four groups given 100 R in 2 to 32 days.

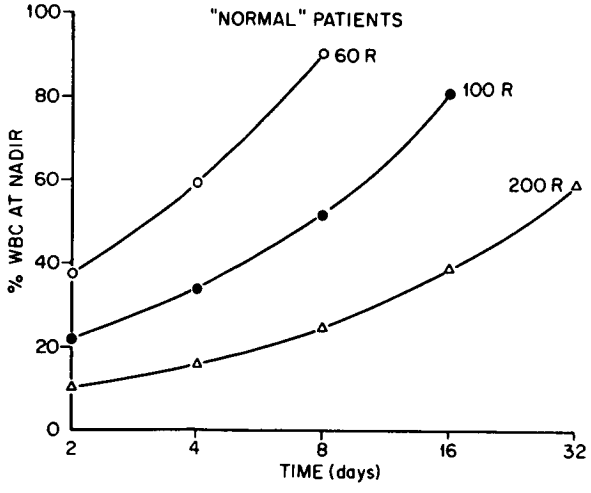

Figure 2. Percent white blood cell concentration at the nadir as a function of radiation exposures of 60, 100, or 200 R given in 2 through 32 days (NORMAL patients).

DISCUSSION

It is quite clear from the foregoing that multiple regression analyses can extract important information from complex exposure-versus-response data. It should also be pointed out exactly what this type of analysis cannot do. The data on which these analyses are based cover an exposure range of 50 to 1000 R given over 1 to nearly 100 days. Since we are dealing at present with dividing cell populations which are subject to a variety of dose- and time-dependent compensatory mechanisms, it is clear that any inferences regarding the effects of other exposure patterns must be confined to the range of exposures and times from which the equations have been derived. The analyses do not provide a means of estimating average responses to exposures less than 50 R accumulated in times in excess of 100 days.

In the present report we have considered only two variables: total exposure and time. The number of fractions in which the total exposure was delivered was deleted for two reasons: it would require more space than is available to us to discuss this factor adequately, and the number of fractions and time of protraction are closely correlated. Even with this simple two-factor analysis we have uncovered certain characteristics of the radiation response which obviously merit further study. Two observations, in particular, should be pointed out.

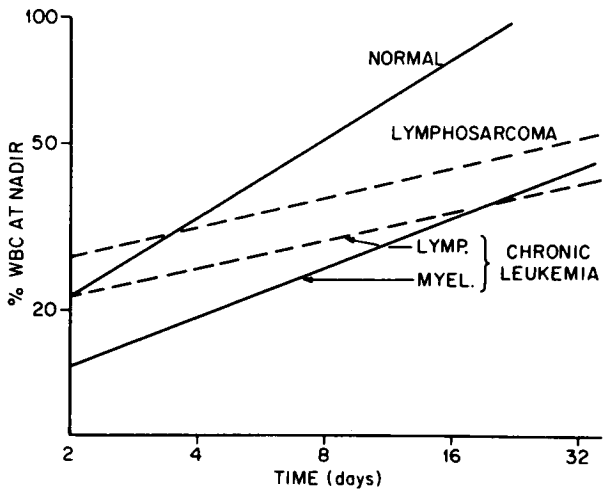

Figure 3. Percent white blood cell concentration at the nadir as a function of the time over which a 100 R exposure is protracted for patients from the four disease categories.

First, there is very little variation among the disease states in regard to the sensitivity to exposure level (cf. Tables II and III). This might appear to contradict the well-established radiosensitivity of the mature lymphocyte (8), but it should be remembered

that response in the present study does not refer to the rate at which the white blood cells disappear from the circulation. Response is measured as the lowest concentration following exposure, independent of the amount of time required to reach this nadir. The radiosensitivity of the progenitor compartments is more important in the determination of the nadir concentration than is the radiosensitivity of the mature element, and our preliminary data are compatible with a conclusion of equal radiosensitivity in the progenitor compartment of the four disease categories.

The fact that the sparing factor associated with protraction of the exposure in time varies as a function of the disease state is quite clear, at least for comparing diseases that affect the lymphatic tissues with those that do not. This corresponds to theoretical expectations (9) as well as to experimental data from lower animals (10) regarding the effects of exposure protraction on lymphatic versus nonlymphatic blood-forming tissues. We will continue to analyze this time factor in the hope of determining what, if any, correlations exist between human and lower animal responses to similar exposure regimens.

Acknowledgment.—The authors wish to thank Mrs. J. O. Proctor and M. G. Hayes for their excellent assistance.

LITERATURE CITED

1. Proceedings of the 1st Interdisciplinary Conference on Selected Effects of a General War, pp. 31-208. Defense Atomic Support Agency Information and Analysis Center. Special Report # 67, 1968.
2. Lushbaugh, C. C. In Proceedings of a Symposium on Dose Rate in Mammalian Radiation Biology, pp. 17-1 to 17-25. Division of Technical Information Extension USAEC Report No. TID-4500, 1968.
3. Lushbaugh, C. C. Radiat. Res., 27: 487-488, 1966.
4. Dixon, W. J., and F. J. Massey. Introduction to Statistical Analysis. 3rd edition. McGraw-Hill, New York, 1969. 638 pp.
5. Fowler, J. F., and B. E. Stern. Brit. J. Radiol., 36: 163-173, 1963.
6. Coutard, H. Am. J. Roentgenol. Radiat. Ther., 28: 313-331, 1932.
7. Hasterlik, R. J., and L. D. Marinelli. Proceedings of the International Conference on Peaceful Uses of Atomic Energy, Geneva, 2: 25-34, 1955.
8. Andrews, J. R. The Radiobiology of Human Cancer Radiotherapy. W. B. Saunders, Philadelphia, 1968.
9. Taliaferro, W. H., L. G. Taliaferro, and B. N. Jaroslow. Radiation and Immune Mechanisms. Academic Press, New York, 1963.
10. Gengozian, N., D. E. Carlson, and C. F. Gottlieb. Fed. Proc., 28: 582, 1969.

Pulmonary-Impedance Power Spectral Analysis: A Facile Means of Detecting Radiation-Induced Gastrointestinal Distress and Performance Decrement in Man[1]

Robert C. Ricks, C. C. Lushbaugh, Earl McDow

Oak Ridge Associated Universities

and

Edward Frome

Emory University

INTRODUCTION

It is common practice in routine physiologic monitoring of patients in intensive care units to measure respiratory rate and amplitude along with other vital signs by electronic means. In most respiratory studies the data are obtained through the use of impedance pneumography. This technique of measuring respiratory phenomena by means of electrical impedance has been previously described (refs. 1 and 2). These devices and techniques provide continuous analog and digital records of the patient's functional status and constantly updated visual displays of the data. Most often the values for the various vital sign measurements are displayed numerically on a cathode ray tube so that the nurse or physician can make assessments of pulse, respiratory rate, and temperature as often as desired without having to count the number of waves per time interval. In precarious clinical situations upper and lower bound alarms are used to alert the staff when changes occur that could require responsive action. Such systems, while serving well their purpose of continuous surveillance of the patient, produce large amounts of taped data that contain a wealth of clinical information often difficult to analyze in retrospect. Usually these data are stored until the tapes are needed for recording the data of other cases when they are erased. Little of them have been put to use in physiologic research or applied physiology because few methods have as yet been developed for reducing the data into a condensed form that provides clinically useful information beyond that of the analog trace itself.

Recently we reported preliminarily (ref. 3) a data reduction and analytical system for the electronic impedance pneumograph. This computerized analysis provides the investigator a power spectrum of the respiratory trace from the patient over a chosen time interval. Since, as is well known, respiratory rate and amplitude can be modified by direct, as well as reflex neural pathways from other systems, changes in impedance pneumograph traces are not unique for each kind of systemic stress that modifies breathing. These changes, however, can indicate that respiratory activity is being modified by external stimuli or extra-respiratory stresses. Examples include the common ear cough that results from irritation of the sensory endings of the auricular nerve by plugs of wax in the auditory meatus; altered respiratory patterns caused by sudden immersion in cold water, painful stimuli, nausea, vomiting, muscular effort, and blood pH and gas changes. These changes in respiratory amplitude and frequency are mediated through autonomic neural elements in the various organs concerned and are presumed to be primarily of parasympathetic (vagal) origin, best described as "vagal looping."

The purpose of our study was to see if pulmonary-impedance power spectral

[1]Research supported jointly by USAEC and NASA.

analysis could be used to detect the onset and course of gastrointestinal distress induced pharmacologically or by total-body irradiation; to see how typical the computed power spectra and their variances were for such well defined respiratory states as exercise induced hyperpnea, respiratory acidosis, and hyperventilation in volunteers and in patients exposed to therapeutic levels of total-body irradiation; and, if possible, to use this system to detect radiation induced decrements in physical performance to study their relation to exposure rate.

These observations could have some medical usefulness during extended manned-space missions (e.g., orbiting platforms and interplanetary expeditions) in a potentially hostile environment. The potential hazards of space radiation (proton fluxes, heavy primaries, X- and gamma-radiations, solar activity) have been previously reviewed by others (refs. 4, 5, 6, and 7). In addition to potentially high-flux space radiation, on-board power reactors will increase the environmental background and crew exposures on extended manned space missions. While the types and intensities of space radiation are well defined, if not predictable, the response of man to these ionizing events is not well known because of the absence of experimental observations. However, the general sequence of events involved in the radiation prodrome (nausea, vomiting, fatigue) are well documented for man (refs. 6, 8, 9, and 10), but the majority of quantitatively related radiation-induced changes have been studied in lower animals where psychological testing was primarily involved (refs. 11 and 12). The effects of radiation on the performance of rats subjected to swim tests, however, have shown that exposures of 300-1000 R depressed performance ability in a dose-rate dependent manner (ref. 13). Thoma and Wald (ref. 14) reviewed the clinical signs and symptoms of radiation accident victims and report that postexposure fatigue may be evident for 4 days to several months following exposures estimated to have been 240-600 rads to the total body. Fatigue was not measured quantitatively nor produced by objective testing; each victim described his own feeling of malaise.

A review of pertinent literature on human performance ability after radiation exposure has been published by Zellmer (ref. 15). Psychological testing of patients receiving total-body irradiation therapy has been reported by Payne (16) and demonstrates that no decrement occurs in man's ability to perform well-directed tests (e.g., USAF SAM rotary pursuit test and USAF SAM complex coordination test) after exposures of 15-50 R of X rays (0.95/min). Likewise, the same conclusions were reached after exposures of patients to 25-200 R given in 25 R fractions at 3.8 R/min. All individuals (ages 23-76 yr) exposed were being treated for malignancies (ref. 16).

Our studies, on the other hand, dealt with nondirected tests (bicycle ergometry) for assessing performance abilities during and after radiation exposure. While highly motivated individuals (e.g., trained astronauts) might be expected to demonstrate continued performance on well-directed duties even in the event of accidental incapacitating radiation exposures, their ability to perform nondirected (general activities) might be reduced. This is one question our investigation seeks to answer.

METHODS

Traces of pulmonary impedance were obtained before, during (in the case of exposure protraction), and after therapeutic levels of total-body irradiation of leukemic patients with ^{137}Cs or ^{60}Co gamma rays. The radiation facilities used have been previously described (refs. 17, 18, 19, and 20). Briefly, fractionated exposures of 30 R/day were carried out in a ^{137}Cs

total-body irradiator at a rate of 1.5 R/min, while protracted (30 R/day) and fractionated (10 R/day) exposures were administered utilizing a ^{60}Co total-body irradiator at the rate of 1.5 R/hr. An electronic physiologic monitoring system[2] was used to obtain the pulmonary impedance traces. Three surface (skin) electrodes were attached to the subject, one to each anterior lateral axillary line on each side of the subjects chest and over the xyphoid sternal process. The impedance of a 100 μamp current passing between the axillary electrodes is measured simultaneously with the cardiac current changes (EKG). The xyphoid electrode is the grounding circuit. This configuration of electrodes has been described previously by others using it to monitor the physiologic status of astronauts in space flight or in simulated tests (refs. 21, 22, 23, 24, 25, and 26). Impedance pneumograph traces were also obtained on a normal volunteer who ingested an emetic (ipecac); on normal unirradiated volunteers and patients (undergoing total-body therapeutic irradiation) all of whom exercised periodically on a bicycle ergometer. The voltage changes in pulmonary impedance were recorded on strip chart and on analog tape from which 4-minute data segments were selected, converted into digital form and analyzed using an IBM-1800 computer. In our system, in its present stage of development, digital data processing can be done in real time or in retrospect. After digital conversion, the data were processed with a power spectral analysis program which computed power spectral estimates and respiratory variances that were graphed automatically.

RESULTS

Selected impedance pneumograph traces obtained from a patient receiving 30 R/20 hr day at an exposure rate of 1.5 R/hr are shown in Fig. 1. The total exposure was 250 R over an 8-day period. These traces illustrate that normal, regular breathing occurred throughout all monitoring periods. The regularity of these impedance pneumographs is reflected by low-power spectra and nonvarying frequencies as shown in Fig. 2. During the entire exposure the patient, who had received no previous radiation therapy, felt well and did not develop nausea or loss of appetite. In Fig. 3 the pre- and postexposure pulmonary impedance traces are shown for a patient who received rapidly-delivered fractionated exposures of 30 R/day (1.5 R/min) on each of 5 consecutive days for a total exposure of 150 R. The pulmonary impedance traces became increasingly irregular postexposure with increasing exposure accumulation up through day 4. The effect of the last fractional dose (30 R) appears to have been suppressed by 20 mg chlorpromazine administered prior to exposure. The changes in pulmonary impedance are more easily visualized in the power spectra computed from them (Fig. 4). All 5 postexposure pulmonary impedance traces were obtained within 30 min after irradiation. Subjective levels of postexposure gastrointestinal distress experienced by the patient are shown in Table 1. These symptoms correlate well with the strip chart traces and the changes in their power spectral reductions. There is (Fig. 4) a progressive increase in the shift of pulmonary impedance waves to lower frequency and higher amplitude and power as radiation exposure accumulates. The patient reported that recovery from the postexposure nausea, reflected by these changes, occurred 2-8 hours later. The relative absence of symptoms and pathologic pulmonary-impedance patterns and power spectra also correlated, as seen in Figs. 3 and 4, for day 5. The daily pretreatment pulmonary impedance traces and their power spectra are remarkably uniform and normal, substantiating, apparently, the patient's

[2]Beckman Type R dynograph, Beckman Instrument, Inc. Palo, Alto, California.

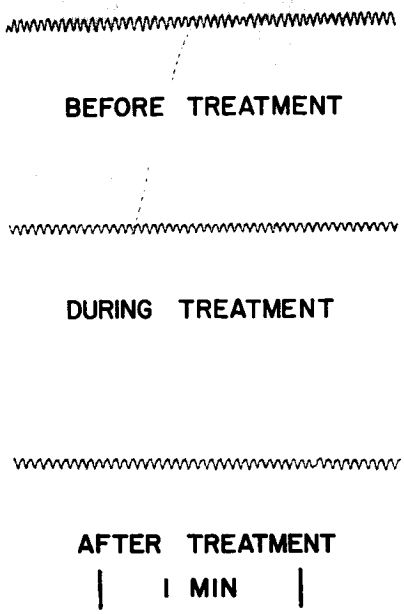

Figure 1. Strip chart tracings of pulmonary impedance recorded before, during (mid-treatment), and after treatment with 30 R daily at 1.5 R/hr.

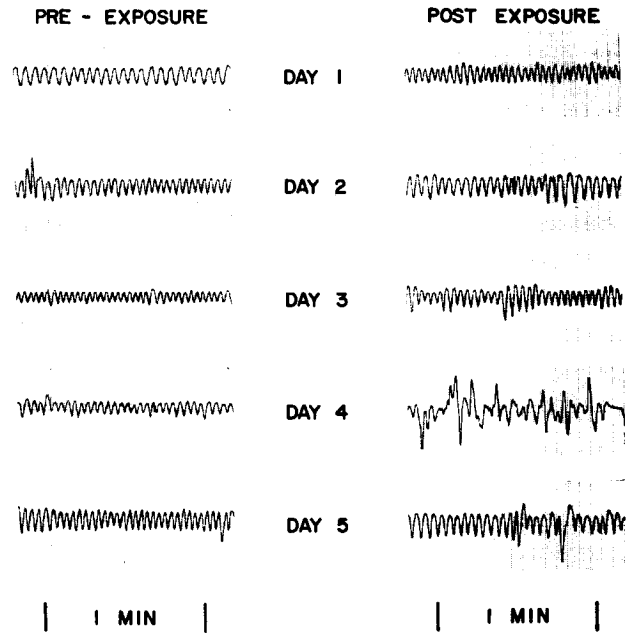

Figure 3. Strip chart tracings of pulmonary impedance following 150 R in 5 equal daily fractions at an exposure rate of 1.5 R/min.

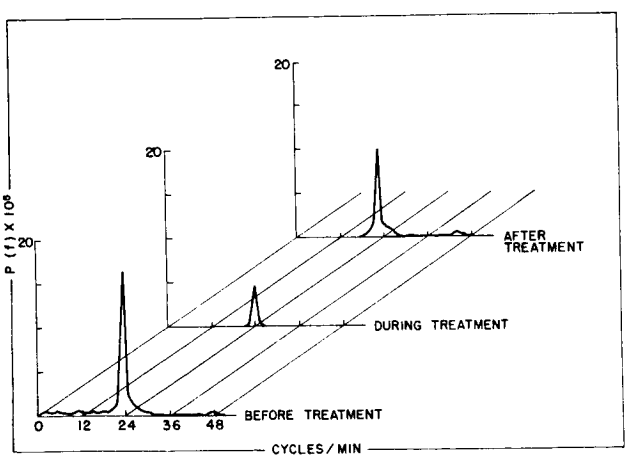

Figure 2. Graphic representation of pulmonary impedance power spectra obtained before, during (mid-treatment), and after treatment with 30 R daily for 8 days at 1.5 R/hr for a total exposure of 250 R.

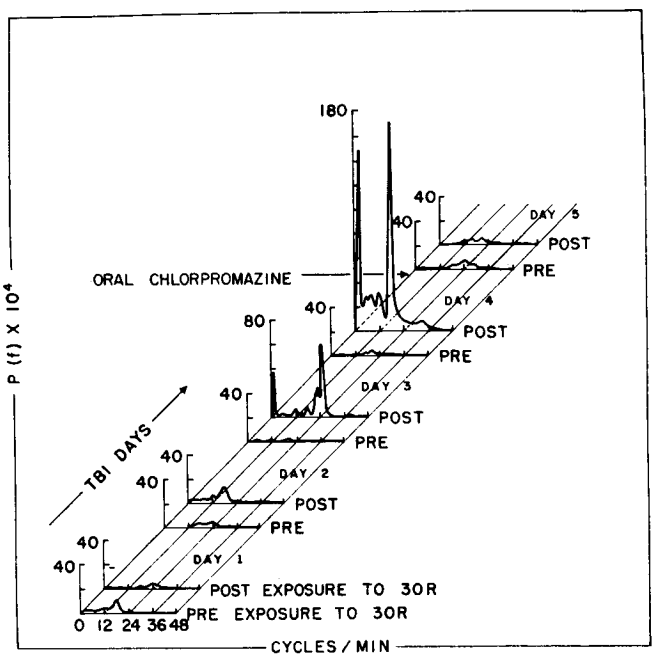

Figure 4. Graphic correlation of severity of nausea with pulmonary impedance power spectra before and 15 minutes after 20-minute exposure to 30 R (1.5 R/min on 5 consecutive days, total exposure 150 R). On the 5th day the patient was administered oral chlorpromazine (20 mg) therapy for radiation sickness.

claim that symptoms of radiation sickness were absent at those times.

TABLE I

PATIENT EVALUATION OF GI DISTRESS THAT FOLLOWED TREATMENT WITH 30 R (1.5 R/MIN) DAILY FOR 5 DAYS

Accumulated Exposure	Described GI Distress
Post 30 R	None
" 60 R	Mild
" 90 R	Moderate
" 120 R	Severe
" 150 R	Mild

The comparison of dose rate effects was enhanced by the fact that the patient who received the fractionated radiation therapy (see above) returned for additional radiation treatment but the exposure (150 R) was protracted (1.5 R/hr) over a 5-day period. Pulmonary impedance strip chart traces recorded before, during, and immediately after the therapeutic irradiation period indicate that respiratory alterations occurred prior to and early into treatment and consisted primarily of high amplitude (deep) breathing (Fig. 5). Power spectra of pulmonary-impedance wave forms (Fig. 6) reflect these findings and show that no significant pulmonary alterations occurred throughout exposure after the initial changes. No low-frequency components are present in the power spectra obtained in relation to this dose protraction, however, low frequency shifts did occur in this same patient when the exposure (150 R) was fractionated (see above). These findings are interpreted as being due to psychologically-induced nausea related to the severe nausea experienced previously by this same patient when given fractionated irradiation therapy 6 months prior. The fractionated exposure (150 R) which induced nausea in this experiment is well below the 300 rad dose (single exposure) reported by Lushbaugh, et al. (ref. 10) that resulted in a mean vomiting-onset time of 144 ± 66 min. Gerstner (ref. 9) has previously indicated that nausea and vomiting, if present, will occur approximately 6 hrs after doses below 600 rads. While this particular patient may have a low radiation-induced GI distress threshold, the dose rate influence on the human radiation prodrome is illustrated.

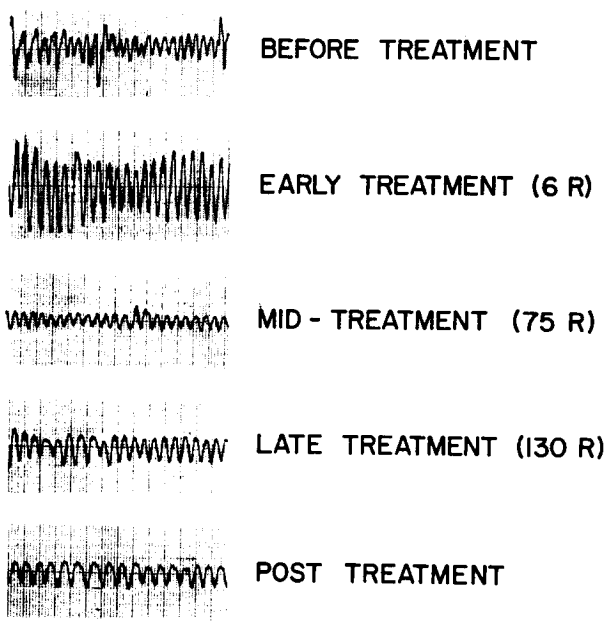

Figure 5. Pulmonary impedance tracings from patient exposed to 150 R (30 R daily) at 1.5 R/hr. Figures in parenthesis indicate accumulated R at time of pulmonary monitoring.

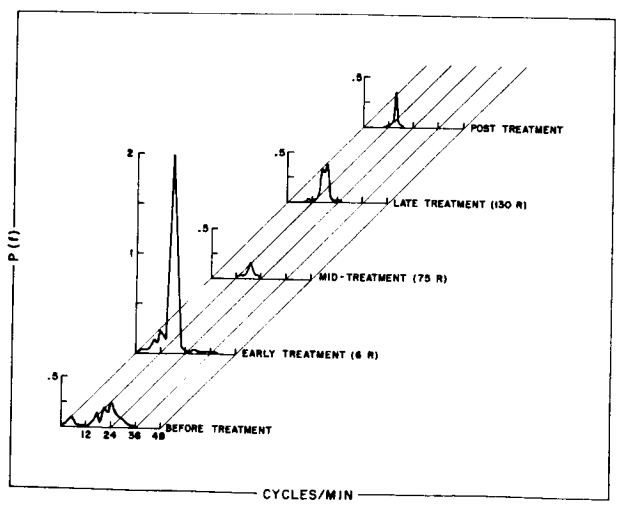

Figure 6. Power spectra of pulmonary impedance wave forms obtained at specific intervals before, during, or immediate after exposure to 150 R (30 R/day) at 1.5 R/hr. Figures in parenthesis indicate accumulated R at time of pulmonary monitoring.

In order to compare radiation and pharmacologically induced gastrointestinal distress, we obtained power spectra of pulmonary impedance wave forms from a normal male volunteer, aged 22, who was administered an emetic (ipecac). Power spectra of these pulmonary traces are shown in Fig. 7 and illustrate shifts to high-power, low-frequency components at those times when the subject experienced severe nausea (17-20 min) and when emesis occurred (49-52 and 57-60 min, respectively). These data demonstrate similar respiratory phenomena occurred (as measured by our method of analysis) in our experiments when gastrointestinal distress occurred regardless of its means of induction. The quantity of analog data obtained in this experiment encouraged us to modify the computer program to afford greater data reduction. This modification is based on the fact that the area under a pulmonary impedance power spectrum is the total variance in terms of amplitude and frequency of respiration. This single number can be computed and used as a one-dimensional expression of the level of respiratory efforts.

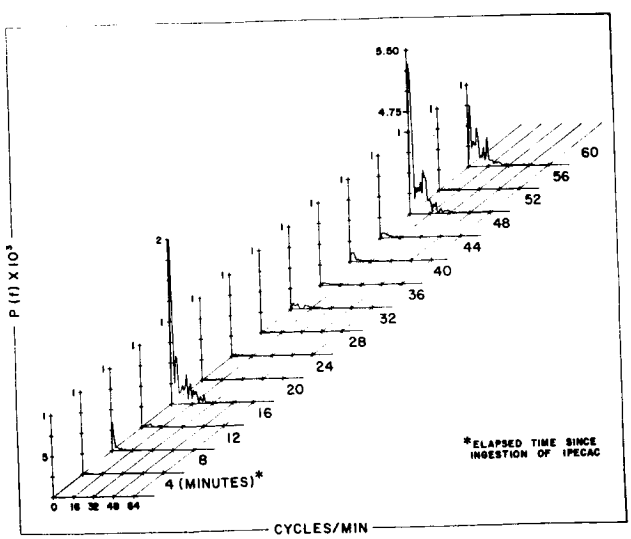

Figure 7. Power spectra of pulmonary impedance wave forms obtained over a 1 hr time period in a normal volunteer following administration of an emetic (ipecac).

When this number is plotted as it changes with time, a continuous graph is produced of the variance in respiratory effort throughout the monitoring period. This new method requires one-half the previous computing time; the output consists of two indices (a mean and the variance of the power spectrum) that can be used without graphing the individual power spectrum. In this case, the mean is the average transthoracic voltage as measured by the impedance pneumograph coupler, while the variance is directly proportional to the area under the power spectrum. The power spectrum of the pulmonary impedance wave form is not graphed in this new system unless requested by the investigator or clinician. In addition, this new method provides separate analysis of each of 4 consecutive minutes of pulmonary impedance data instead of one combined analysis of 4 minutes of data. An average mean and average variance (four 1-minute data periods /4) also is provided. We have defined the minute-by-minute variance as the continuous variance and its average over 4 minutes as the average variance.

Data obtained from the volunteer with pharmacologically induced GI distress (see above) and analyzed by the new method are shown in Fig. 8. Increased continuous variance corresponds exactly to the minute with the occurrence of severe nausea (18th min) and emesis (50th and 59th min). These changes in respiratory function are also well protrayed by the average variance which tends to smooth the data without losing fidelity. Inferences drawn from data analyzed by both the old and new methods would be the same.

We anticipated this new method would have a useful purpose in the analysis of long-term pulmonary studies and have applied it to pulmonary impedance data obtained from patients receiving total-body therapeutic irradiation, all of whom exercised on a bicycle ergometer. Figure 9 illustrates the pulmonary impedance variance obtained from a normal volunteer

before, during, and after exercising to tolerance (∿8 min) against a work load of 75 watts. Shifts in both continuous and average variance occurred during the initial phases of exercise and increased to a maximum late in the exercise period. Post-exercise variances decreased periodically returning to preexercise levels at about 35 minutes.

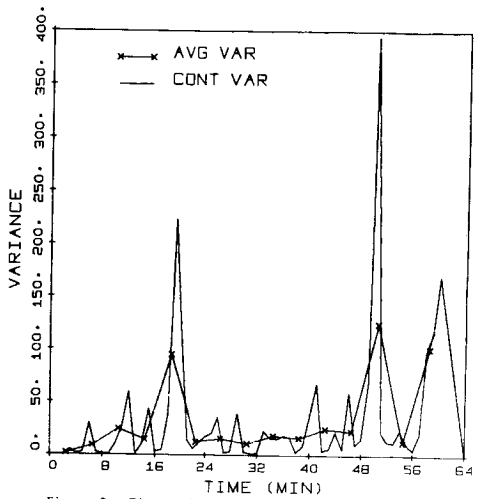

Figure 8. Time-series graph of average and continuous pulmonary impedance power spectral variances obtained over a 60 minute period in a normal subject following ingestion of ipecac.

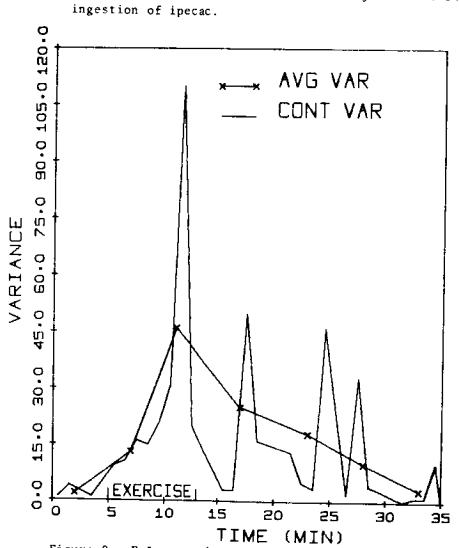

Figure 9. Pulmonary impedance variance from a normal individual obtained before, during, and after exercise on a bicycle ergometer. The exercise work load was 75 watts; pedaling speed was 60 RPM.

In order to determine the effect of total-body irradiation on performance decrement, pulmonary impedance data were obtained from selected patients receiving protracted or fractionated exposures (1.5 R/hr) and who exercised periodically before, during, and after exposure. Patients were selected on the basis of their willingness and ability to exercise and that their disease was not acutely debilitating. No aspects of radiation-induced fatigue were ever discussed with these patients. Data from two patients exposed to protracted radiation therapy (30 R/20 hr day) at a rate of 1.5 R/hr are shown in Figs. 10 and 11. Only the average variance of the pulmonary impedance power spectral data is illustrated. Increased respiratory demand during and immediately after exercise was reflected by changes in pulmonary impedance wave forms in both patients studied and closely resembled changes noted in exercising volunteers. Increased power at various respiratory rates (generally >20/min), seen as a large increase in total variance, was amplified after total-body exposures of 100-150 R. A decrement in performance ability was indicated by a greater increase in respiratory variance, after radiation, when measured at 3 and 10 days postirradiation in one patient who received 100 R (Fig. 10), and at 5 days in another patient who received 150 R (Fig. 11).

Radiation-induced performance decrement was also studied in two patients receiving fractionated exposures of 10 R daily at a rate of 1.5 R.hr and who exercised on a bicycle ergometer. The results are shown in Fig. 12. Subject A is the same individual exposed (6 months earlier) to 100 R (30 R/day) at 1.5 R/hr and who demonstrated no decrement until 3 days postirradiation. Subject B received a total exposure of 140 R (10 R/day) at 1.5 R/hr but postexposure exercise was not accomplished due to unexpected thrombophlebitis. While no postexposure performance decrement was noted, slight increases in respiratory variance did occur during exposure of both patients. The signficance of these changes is not understood at this time.

These data demonstrate that pulmonary impedance power spectral analysis is capable of detecting and predicting the onset and severity of radiation-induced gastrointestinal distress. The approach also serves

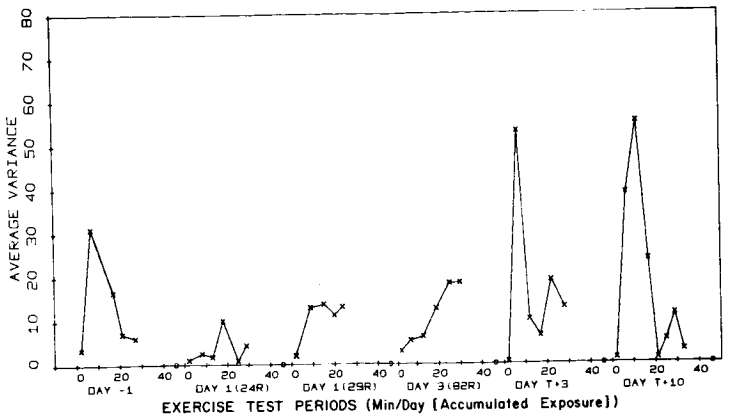

Figure 10. Pulmonary impedance variances obtained from a 62-year-old patient exercising on a bicycle ergometer before, during, and after total-body exposure (100 R) at 30 R/day (1.5 R/hr). The exercise work load was 50 watts; pedaling speed was 60 RPM. Exercise lasted 8 min for each test period.

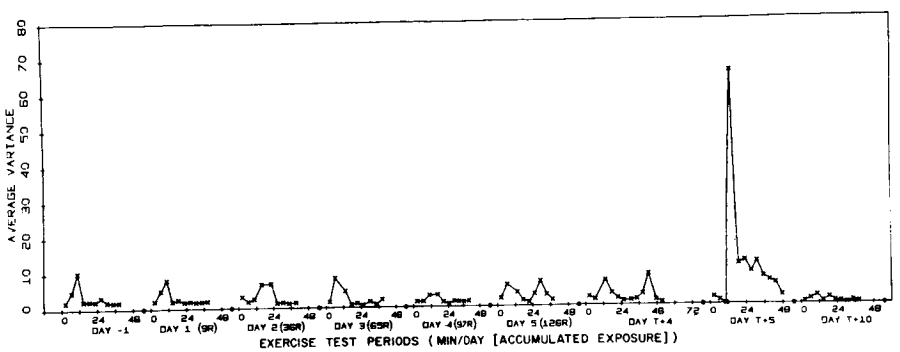

Figure 11. Pulmonary impedance variances obtained from a 65-year-old patient exercising on a bicycle ergometer before, during, and after total-body exposure (150 R) at 30 R/day (1.5 R/hr). The exercise work load was 25 watts; pedaling speed was 40 RPM. Exercise lasted 5 min for each test period.

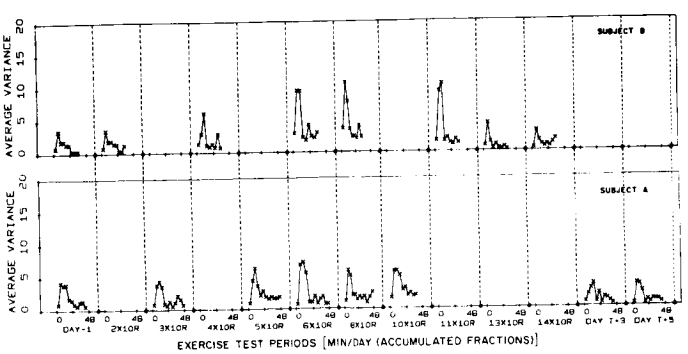

Figure 12. Treatment windows showing pulmonary impedance variance obtained from two patients before, during, and after total-body exposure to daily ^{60}Co fractions of 10 R at 1.5 R/hr. Subject A (aged 62 yr) received a total exposure of 100 R; subject B (aged 70 yr), 140 R. Each patient exercised periodically on a bicycle ergometer before and during exposure. Subject A exercised after exposure. The exercise work loads for A and B were 50 watts, 60 RPM and 40 watts, 40 RPM, respectively. Exercise lasted 5 min during each test period.

to illustrate the dose-rate influence on the human radiation prodrome and reflects the effectiveness of its chemotherapeutic control. In addition, it provides a facile means of measuring the performance decrement effects of total-body irradiation in man. The results indicate the necessity for similar studies over more extended post-irradiation time periods and a correlation of the data with biochemical changes. In experiments underway with unirradiated volunteers and with patients who receive total-body irradiation we are attempting to correlate these changes in the pulmonary impedance pneumograph during controlled exercise with levels of expired CO_2, plasma lactic acid dehydrogenase, plasma creatine phosphokinase, and plasma glutamic-oxalacetic transaminase.

SUMMARY AND CONCLUSIONS

Changes in respiratory variance revealed by power spectral analysis of the pulmonary impedance pneumogram can be used to detect and measure stresses directly or indirectly affecting human respiratory function.

When gastrointestinal distress occurred during a series of 5 total-body exposures of 30 R at a rate of 1.5 R/min, it was accompanied by typical shifts in pulmonary impedance power spectra. These changes did not occur after protracted exposure of 250 R (30 R daily) at 1.5 R/hr that failed to cause radiation sickness.

This system for quantitating respiratory effort can also be used to detect alterations in one's ability to perform under controlled exercise conditions. Performance decrement due to various stresses is difficult to quantitate because of a lack of objectivity in most tests and bias due to different levels of motivation. In our tests the end point of increased respiratory variance and the method of measuring it is too obtuse for the test subject to recognize and falsify. Increased fatigability has been reported after total-body irradiation but little is known about doses required and the time for its occurrence. Using pulmonary impedance power spectral analysis we found while observing 4 irradiated patients that increased fatigability could occur during prolonged fractionated exposures to 10 R daily and after completion of continuous exposures to 30 R/day for 5 days. The performance decrement detected by this means occurred at lower total doses than previously reported for radiation-induced fatigue and at lower exposure rates than those that cause gastrointestinal distress.

REFERENCES

1. Geddes, L. A.; and Hoff, H. E.: The Measurement of Physiologic Events by Electrical Impedance. A Review. Am. J. Med. Electron., vol. 3, 1964, pp. 16-17.
2. Geddes, L. A.; Hoff, H. E.; Hickman, D. M.; and Moore, A. G.: The Impedance Pneumograph. Aerosp. Med., vol. 33, 1962, pp. 28-33.

3. Lushbaugh, C. C.; Frome, E. L.; Davis, H. T.; and Bibler, D. S.: Power Spectrum of the Impedance Pneumograph: A Data Reduction System Producing an Analytical Parameter of Potential Clinical Usefulness. Aerosp. Med., vol. 40, 1969, pp. 425-429.
4. Langham, W. H.: Implications of Space Radiations in Manned Space Flights. Aerosp. Med., vol. 30, 1959, pp. 410-417.
5. Newell, Homer, E.; and Naugle, John E.: Radiation Environment in Space. Science, vol. 132, 1960, pp. 1465-1472.
6. Langham, Wright H.; Brooks, Phillips M.; and Grahn, Douglas (editors). Radiation Biology and Space Environmental Parameters in Manned Spacecraft Design and Operations. Aerosp. Med., vol. 36, No. 2, Section 2, 1965, pp. 1-55.
7. Odland, Lawrence T.; and Michaelson, Sol M. Space Travel: A Suggested Method for Predicting Human Response to Ionizing Radiation. Aerosp. Med., vol. 34, 1963, pp. 62-66.
8. Jenkinson, E. L.; and Brown, W. H.: Irradiation Sickness: A Hypothesis Concerning the Basic Mechanism and a Study of the Therapeutic Effect of Amphetamine and Dextro-Desoxyephedrine. Amer. J. Roentgenol. Radium Therp. Nucl. Med., vol. 51, 1944, pp. 496-503.
9. Gertsner, H. B.: Reaction to Short-Term Radiation in Man. Annu. Rev. Med., vol. 11, 1960, pp. 289-302.
10. Lushbaugh, C. C.; Comas, F.; and Hofstra, R.: Clinical Studies of Radiation Effects in Man: A Preliminary Report of a Retrospective Search for Dose-Relationships in the Prodromal Syndrome. Radiat. Res. Suppl., vol. 7, 1967, pp. 398-412.
11. Kaplan, S. J.; Gentry, G.; Melching, W. H.; and Delit, M.: Some Effects of a Lethal Dose of X-Radiation Upon Retention in Monkeys. NP 5413 (Aug. 1954).
12. Zellmer, Robert; Culver, James; and Pickering, John E.: Proton-Irradiation Effects in Primates. Radiat. Res. Suppl., vol. 7, 1967, pp. 325-329.
13. Kimeldorf, D. J.: Jones, D. C.; and Castanera, T. J.: Effect of X-irradiation Upon the Performance of Daily Exhaustive Exercise by the Rat. Amer. J. Physiol., vol. 174, 1953, pp. 331-335.
14. Thomas, G. E., Jr.; and Wald, N.: The Diagnosis and Management of Accidental Radiation Injury. J. Occup. Med., vol. 1, 1959, pp. 421-447.
15. Zellmer, Robert W.: Human Ability to Perform After Acute Sublethal Radiation. Mil. Med., vol. 126, 1961, pp. 681-687.
16. Payne, Robert B.: Effects of Ionizing Radiation on Human Psychomotor Skills. U. S. Armed Forces Med. J., vol. 10, 1959, pp. 1009-1021.

17. Brucer, M.: A Total-Body Irradiator. Int. J. Appl. Radiat., vol. 10, 1961, pp. 99-105.
18. Morris, A. C., Jr.: Measurements in a Total-Body Irradiation Facility. Int. J. Appl. Radiat., vol. 11, 1961, pp. 108-113.
19. Andrews, G. A.; Beck, W. L.; Cloutier, Roger J.; Morris, A. C., Jr.; Barclay, T. R.; Comas, Frank V.; Edwards, C. L.; and Lushbaugh, C. C.: The Low-Exposure-Rate Total-Body Irradiation Facility (LETBI). In ORAU Medical Division Research Report, 1967, ORAU-106 (1968), pp. 13-18.
20. Morris, A. C., Jr.; Barclay, T. R.; and Lushbaugh, C. C.: Physiologic Monitoring in the Low-Exposure Total-Body Irradiation Facility. In ORAU Medical Division Research Report, 1967, ORAU-106 (1968), pp. 23-27.
21. Pacela, Allan F.: Impedance Pneumography - A Survey of Instrumentation Techniques. Med. Biol. Eng., vol. 4, 1966, pp. 1-15.
22. Day, J. L.; and Lippitt, M. W., Jr.: A Long-Term Electrode System for Electrocardiography and Impedance Pneumography. Psychophysiol., vol. 1, 1964, pp. 174-182.
23. Geddes, L. A.; Hoff, H. E.; Vallbona, C.; Harrison, G.; Spencer, W. A.; and Canzoneri, J.: Numerical Indication of Indirect Systolic and Diastolic Blood Pressures, Heart and Respiratory Rate. Anestheosiol., vol. 25, 1964, pp. 861-866.
24. Geddes, L. A.: The Acquisition of Physiological Data. Int. Anesthesiol. Clin., vol. 3, 1965, pp. 379-405.
25. Montes, L. F.; Day, J. L.; and Kennedy, Lofton: The Response of Human Skin to Long-Term Space Flight Electrodes. J. Invest. Dermatol., vol. 49, 1967, pp. 100-102.
26. Day, J. L.: Review of NASA-MSC Electroencephalogram and Electrocardiogram Electrode Systems Including Application Techniques. NASA Technical Note, NASA TN D-4398, 1968.

SESSION IV.2.
SPACE OPERATIONS IN THE PRESENCE OF MANMADE RADIATION

CHAIRMAN: P.G. JOHNSON
SPACE NUCLEAR SYSTEMS OFFICE - NASA/AEC

MONTE CARLO ANALYSIS OF IN-FLIGHT NUCLEAR PROPULSION MODULE RADIATION ENVIRONMENTS

K. D. Kirby
Lockheed-Georgia Company

Monte Carlo results of radiation environments through the complex geometry of a reference nuclear propulsion module and the influence of propellant tank design parameters on payload doses are presented. The reference configuration consists of a 32-foot diameter propellant tank with a 15° half angle ellipti-conical bottom and a capacity of 176,000 pounds of liquid hydrogen and a 1575 MW NERVA engine (full flow propellant feed cycle). Tank design parameters investigated to determine their influence on payload doses are propellant tank diameter (15-32 feet), propellant tank bottom cone half angle (9°-15°), and propellant tank-payload separation distance (0-40 feet).

Radiation environments were determined throughout the reference vehicle with particular emphasis on radiation levels at the tank top. Averaged over a plane tangent to the tank top, the radiation dose for an entire drain cycle (to propellant depletion) is 2.4 rads (tissue) from neutrons and 1010 rads (tissue) from gamma rays. Gamma radiation from the Pressure Vehicle and Reactor Assembly (PVARA) was found to be the largest contributor to tank top dose, but gamma radiation from sources external to the PVARA (propellant feed lines and nozzle assembly), incident on the conical section of the tank bottom where PVARA radiation was not significant, was also determined to be an important contributor.

Utilizing the Monte Carlo technique of correlated sampling the baseline results were further analyzed to determine the influence of changes in propellant tank design parameters on payload doses. Variation in propellant tank diameter from 32 feet to 15 feet, for constant tank capacity,results in a reduction of tank top doses by a factor of 17. Increased spacecraft separation distance above the propellant tank top is an effective means for reducing doses for the larger diameter tank examined. A 40-foot separation above the 32-foot tank yields a reduction factor of 2, but the factor drops to 1.25 for the same separation above the 15-foot tank. Doses above a 176,000 pounds capacity, 32-foot diameter tank are reduced by factors of 1.7 and 3.6 if the tank bottom cone half angle is reduced from 15° to 12° and 9° respectively. Reductions in environments by these changes were due primarily to increased tank length and more rapid draining of low levels of propellant.

(MANUSCRIPT NOT AVAILABLE)

THE INFLUENCE OF RADIATION SHIELDING ON REUSABLE NUCLEAR SHUTTLE DESIGN

T.M. Littman, Program Manager
D. Garcia, Project Engineer
Space Division, North American Rockwell
Downey, California

The nuclear rocket's unique energy source affords unusually high performance while requiring special protection for manned flights. If maximum capability is to be achieved without compromising development or operating costs, stage designs must employ efficient methods for minimizing radiation shield requirement. With this objective, alternate reusable nuclear shuttle (RNS) configurations were synthesized and evaluated. Particular attention was given to design factors which reduced tank exposure to direct and scattered radiation, increased payload-engine separation, and improved self-shielding by the LH_2 propellant. The most attractive RNS concept in terms of cost effectiveness (unit payload delivery cost) consists of a single conical aft bulkhead tank with a high fineness ratio (eight-degree half cone-angle with a 25-inch cap radius). Launch is accomplished by the INT-21 with the tank positioned in the inverted attitude. The NERVA (nuclear engine for rocket vehicle application) engine is delivered to orbit separately where final stage assembly and checkout are accomplished. This approach is consistent with NERVA definition criteria and required operating procedures to support an economically viable nuclear shuttle transportation program in the post-1980 period.

The attractiveness of a space transportation system is usually measured in terms of performance, nonrecurring cost, cost effectiveness (i.e., dollars per pound of payload delivered), and development risk. Achievement of a promising design concept requires effecting a compromise between diverse factors (e.g., technology, stage geometry, launch vehicle compatibility, maintainability, and end-of-life disposal). The nuclear rocket, no exception to this logic, is unique among space propulsion systems due to the radiation field inherent to this compact, high efficiency energy source. Thus, protection of on-board personnel, sensitive equipment, other in-space personnel, and earth's population is of paramount importance. This paper is addressed generally to the task of designing a reusable nuclear shuttle (RNS) for safe, post-1980, manned space transportation while meeting the criteria of attractiveness. Of specific concern is the interaction between requirements for protecting payload-carrying personnel, launch of the stage to earth orbit, and subsystems design.

For the past 20 months, the Space Division of North American Rockwell (NR) has been conducting a Phase A study (Nuclear Shuttle System Definition Study, Contract NAS8-24975) for NASA's Marshall Space Flight Center. The study's objective is to establish conceptual definition for a 1974-technology RNS with emphasis on minimizing development and operating cost. Candidate concepts are characterized by a 33-foot diameter propellant tank launched integrally to orbit by a Saturn V INT-21 booster. Total propellant (LH_2) capacity is baselined at 300,000 pounds. The RNS is powered by a 75,000 pound thrust full-flow NERVA engine with a nominal specific impulse of 825 seconds. To provide logistics support for the RNS, the earth-to-orbit shuttle (EOS) is assumed to deliver expendables (including main propellant), engines, and stage spare parts.

A convenient method for classifying candidate RNS concepts (employing the above guidelines) is to use the Saturn V as the standard of reference. Thus, one configuration category (I) contains all single tank designs with forward and aft elliptical bulkheads. These designs permit launch of the stage as an integral unit (engine plus tank) by the currently designated NASA INT-21 baseline (Reference 1). The other category (II) employs some form of conical tank bottom and encompasses designs which may require alternate launch and operational modes. Early studies (Reference 2) indicated that the simplest Saturn-type (viz, S-II) configuration is most efficient geometrically (and weight-wise) as a propellant container; however, it is limited to unmanned missions unless a severe weight penalty is accepted in supplementary radiation shielding. This deficiency can be partially overcome by modifying the internal tank geometry to increase the effectiveness of the LH_2 propellant as a radiation shield. Such designs, designated dual cell, control the flow path of hydrogen so that a column of propellant is interjected between the tank top and engine especially during the critical period just preceding the last run engine shutdown (Reference 3). However, detail radiation field mapping has indicated that payload location is quite sensitive in such stage designs due to radiation scattering from propellant vapor and tank bottom. This effect would probably be too restrictive in designing practical manned payloads for RNS transport.

Category II configurations, the subject of this paper, tailor tank aft bulkhead geometry to minimize payload shielding requirements. This is done by (1) controlling the incident angle for radiation interception of the tank, (2) using the conical aft bulkhead to achieve dual cell benefits, and (3) taking advantage of the inverse square law to attenuate radiation beamed to the payload. These gains are achievable at the expense of reduced structural efficiency and increased operating complexity. However, radiation shielding for manned flights represents the major design driver and controlling factor in achieving best overall performance and cost effectiveness.

Stage design concepts attractiveness can be measured in terms of development cost and cost effectiveness maintaining cognizance of the design considerations. Low development cost can be attained by maximizing use of existing technology, hardware, and facilities, as well as by minimizing modifications to the launch vehicle. Cost effectiveness (in terms of unit payload delivery cost) is a function of both performance and recurring expenditures. Performance is measurable in terms of components weight which include radiation shield, structure, thermal and meteoroid protection, as well as mechanical, fluid and astrionic subsystems. Recurring cost can be subdivided into hardware and operational expenditures. The former can be minimized by simplicity of design, manufacturability, ease of Quality Assurance, and low maintenance of equipment and facilities while maintaining cognizance of component weight implications. Recurring costs include delivery of the stage, propellant, and other supplies to orbit, as well as orbital assembly and maintenance. Propellant delivery, even using the EOS at currently projected operating rates, is a major cost driver.

A number of attractive RNS design concepts have been synthesized and these are compared to illustrate how the radiation environment can be accommodated while maximizing performance and cost effectiveness for manned shuttle applications.

CONICAL AFT BULKHEAD DESIGN CONCEPTS

In the conical design, radiation attenuation to the tank top is attained by the shadow shield cone created by the aft bulkhead, depth of LH_2 column at any given point in the mission, and distance from the radiation source.

The three Category II configuration classes investigated are shown in Figure 1. One is a single tank design. A second is a modified dual cell which maximizes the column of propellant available for radiation attenuation during the critical last engine burn when the radiation dose rate is reaching its peak. The third is a hybrid or two-tank design which was conceived with the primary objective of aiding in end-of-life engine disposal while minimizing radiation dose to the payload.

The analytical approach taken was to optimize the performance of the

single tank design for the lunar shuttle mission and then assess the operational impact including the launch to orbit. Also, the single tank optimum design point has been employed to evolve attractive dual cell and hybrid concepts, aimed at improving an already acceptable overall performance.

The design issues shown in Figure 2 relate to performance and cost evaluation criteria and serve as guides in design investigations. For example, stage length is inversely proportional to the aft bulkhead cone angle and end cap radius. As stage length increases so does surface area and weight. On the other hand, the weight of the external shield required for radiation dose attenuation to the payload decreases with increase in fineness ratio of the cone. Consequently, the tradeoff yields a point of minimum total weight which denotes the stage design with the highest flight performance. Yet, to complete the tradeoff, the resulting stage geometry has to be evaluated for impact to the launch vehicle, orbital operations, and facilities in order to arrive at a realistic and attractive solution.

Other design issues that must be considered in the system evaluation include stage and engine interface and NERVA disposal requirements. As shown in Figure 2, interface design must respond to a wide range of considerations when applied to hybrid and single tank designs. These include the inherent complexities associated with mating fluid lines and electrical receptacles in earth orbit. Engine disposal also presents a wide range of design considerations when related to a hybrid stage concept. In this case, the maximum propellant capacity that can be accommodated in the EOS with the engine is 13,200 pounds. However, this results in an auxiliary tank geometry which is unattractive for radiation attenuation to the payload. Additionally, 13,200 pounds of propellant is inadequate for heliocentric orbit disposal of the engine from a low altitude earth orbit, if this is desirable. On the other hand, it is larger than necessary for safe high altitude earth orbit disposal.

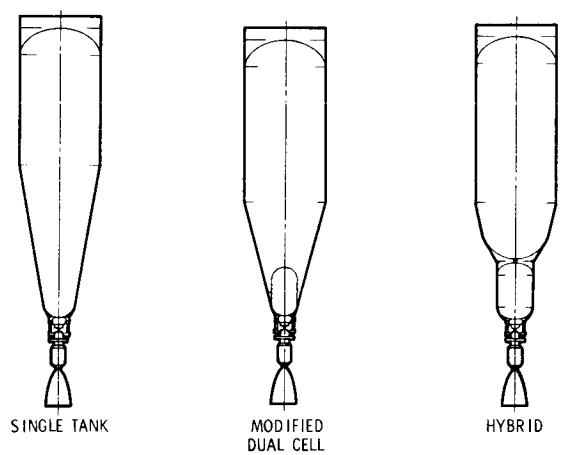

Figure 1. RNS Configuration Classes

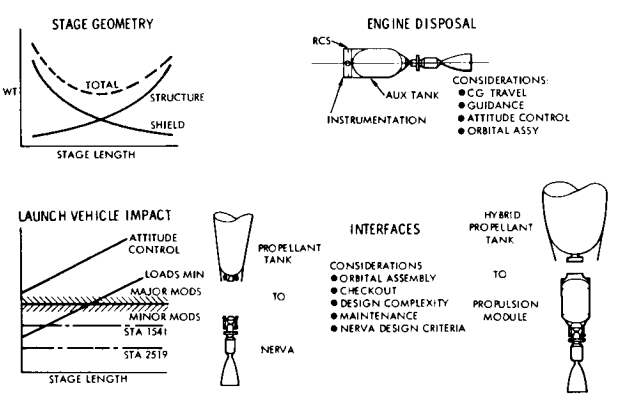

Figure 2. Design Issues

SINGLE TANK

The necessary parametric analyses were initiated by investigating the influence of aft bulkhead geometry variations on stage height and surface area. The bulkhead half cone-angle was varied from 15 to 5 degrees and the end cap radius from 125 to 25 inches. The propellant tank was sized for 300,000 pounds of LH_2 with 5 percent ullage volume. The tank configuration employed consists of three segments: forward elliptical bulkhead of 1.5 aspect ratio, cylindrical section 33-feet in diameter, and a conical aft bulkhead. The resultant stage length variation, including engine and astrionics bay, is presented in Figure 3(a). Stage length maximum variation is approximately 90 feet (190 percent) between the 5 degree half cone-angle with a 25-inch cap radius and the 15-degree counterpart with a 125-inch cap radius, accountable to both the change in half cone-angle and cap radius. The tank total surface area variation over the range of the parameters considered is less than 25 percent as shown in Figure 3(b). Since surface area can be related to weight, this result implies that a relatively small weight variation can be expected between the tank geometries under study.

This is evident in the stage weight variation as a function of the half cone-angle and cap radius shown in Figure 4(a). The weight includes forward and aft skirts with four-foot long heat blocks, foam and high performance insulation (HPI) for ground and space thermal protection, double wall meteoroid protection for three years at 0.995 probability of no impact to the tank wall, and fixed weight components consisting of auxiliary propulsion, astrionics, thrust structure, etc.

The resultant weights indicate that the maximum difference between extremes is approximately 2,600 pounds and that the majority of this weight difference is in the meteoroid and thermal protection system which responds to the surface area variation. In addition, the variation in surface area increases the heat input to the tank and, therefore, increases weight in terms of boil-off. The boil-off penalty presented in Figure 4(b) is shown to have a maximum variation of approximately 1,300 pounds between geometry extremes.

Figure 4(c) presents the external shield weight required for a tank top integral dose criterion of 10 rem. The shield weights were derived from pressure vessel and reactor assembly (PVARA) and external on-axis integral tank top dose contributions for an initial LH_2 tank capacity of 300,000 pounds. An LH_2 residual capacity of 5,000 pounds at the termination of the tank drain (for after-shutdown cooling requirements) was also assumed. The shield weights vary from approximately 2,000 pounds for the 5-degree half cone-angle and 25-inch cap radius to 13,000 pounds for the 15-degree, 100-inch cap radius design point. The reduction in tank top radiation dose and external shield weight is principally due to (1) greater source-to-tank

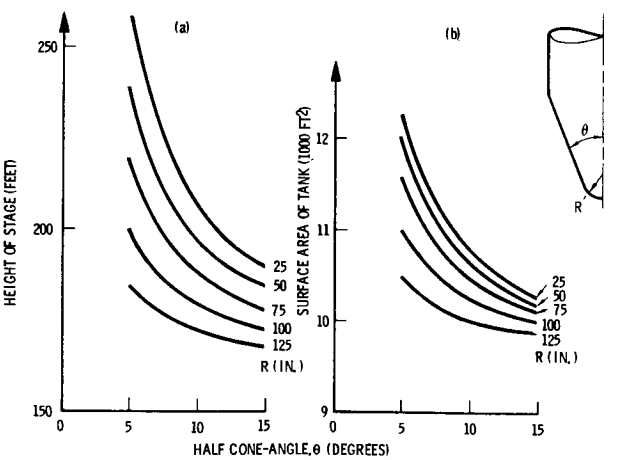

Figure 3. Stage Length and Surface Area Variations

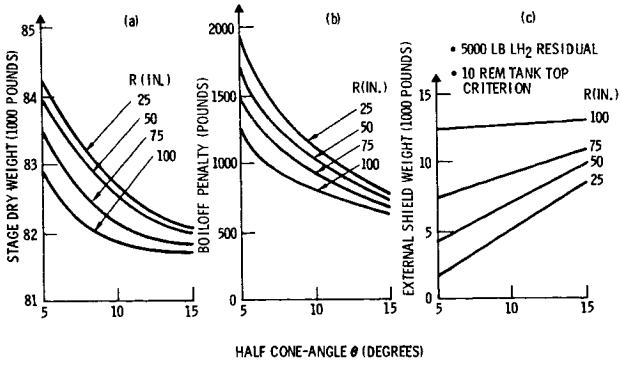

Figure 4. Stage Weight Variations

top detector separation distance (high fineness ratio tank), (2) reduced effective energy deposition and scattering centers in the aft end of the propellant tank, and (3) greater depths of the LH_2 propellant column for radiation attenuation at any given time during the draining cycle, for a fixed propellant capacity. As can be seen in Figure 4(c), the shield weight is essentially insensitive to cone angle variations at large end cap radii (≥100 inches). This is due to the very small variations in the three radiation factors at large cap radii.

The results of the parametric analyses including structure, thermal and meteoroid protection, boil-off penalties, and external shielding are expressed in Figure 5 in terms of payload weight variation with tank geometry. An 8-degree half cone-angle with a 25-inch cap radius was found to yield near-optimum performance. It is possible that performance may continue to increase somewhat beyond this point as shown by the dotted lines in the figure; however, only parametric radiation analysis has been performed beyond the noted design point and consequently the results need further verification.

The data as depicted in Figure 5 show the 8-degree half cone-angle, 25-inch cap radius configuration to have a 21,000 pound payload gain over the reference 15-degree half cone-angle x 100-inch cap radius. This payload gain results from a 9,000 pound variation in external radiation shield weight between the two designs, less a 1,300 pound increase in structure weight for the longer tank. The net weight difference of 7,700 pounds, with a lunar mission payload exchange factor of approximately 2.8 pounds of payload per pound of equivalent inert weight (fixed weights plus effective boil-off), yields the gain previously quoted. The 2.8 pounds exchange ratio is derived by letting the moon-bound payload vary with the performance mass ratio of the vehicle while maintaining the return payload constant.

The resulting single tank baseline is shown in Figure 6. The 396-inch diameter cylindrical section is 426 inches in length and the total tank length is 1,827 inches. Retaining the distance of 200 inches between the engine core center and aft end of the tank results in a 42-inch separation between NERVA and tank interface. With the 60-inch astrionics unit length added at the forward skirt, the total stage length less the engine is 1,929 inches (approximately 160 feet); and with the engine is 2,326 inches (194 feet).

Both facility size (maximum permissible height in KSC VAB) and INT-21 strength capability constraints were then imposed on the selected single tank design. The former consideration limits RNS launch configuration to 190 feet. NASA-MSFC has recently established a baseline INT-21 booster consisting of the S-IC, the S-II and a 33-foot diameter, 141-foot long payload with a biconic nose cone, and retaining the present Saturn V attitude-attitude rate control system (Reference 1). This launch configuration results in increased loading at max ($q\alpha$) over the present boost stages, requiring therefore, structural modifications. To minimize these modifications on the current S-IC's and S-II's, NASA established a lower wind criterion of 50 meter/sec maximum wind profile. This reduces the launch availability to certain months of the year.

Although the INT-21 has been ground-ruled in this study as the RNS boost vehicle, consideration can be given to integral (engine-stage mated on ground) as well as nonintegral launch as shown in Figure 7. In the latter case, the main propellant tank is launched by the INT-21 (preferably inverted to minimize aerodynamic loads including flutter) and the NERVA or propulsive module (in the case of the hybrid configuration) is launched by the EOS. The nonintegral launch requires in-orbit mating and checkout of the engine or propulsive module with the main LH_2 tank, but it must be remembered that NERVA design criteria specify engine and stage assembly and disassembly capability in earth orbit. To effect this capability the active assembly of a neuter docking system designed for the Space Station (and adapted by other space elements) has been attached to the stage thrust structure. The passive assembly of the docking system has been in turn adapted to the NERVA upper thrust structure. In this manner, orbital mating is accomplished employing the EOS, and demating, if necessary is done with the space tug.

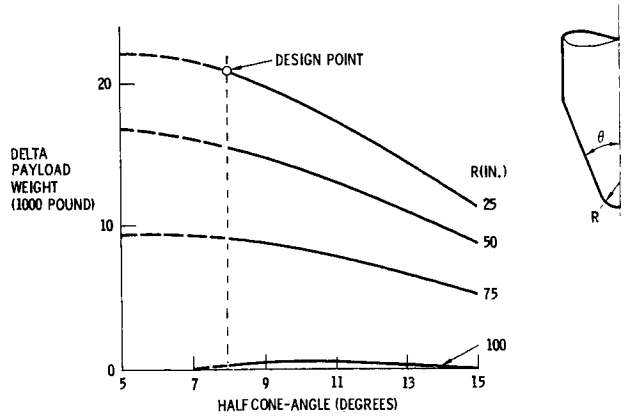

Figure 5. Design Trade-Off Map

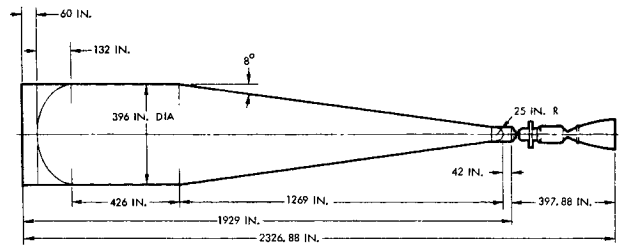

Figure 6. Single Tank Baseline Configuration

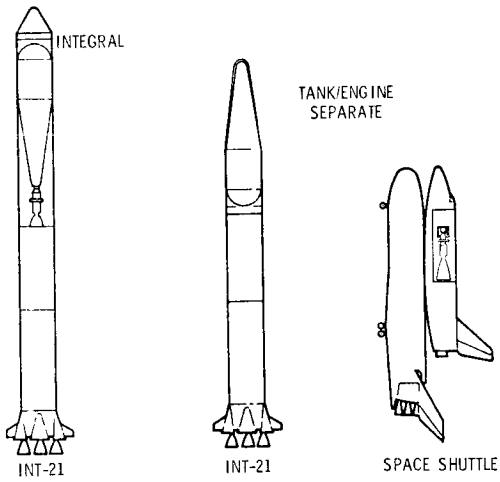

Figure 7. Alternate Launch Modes

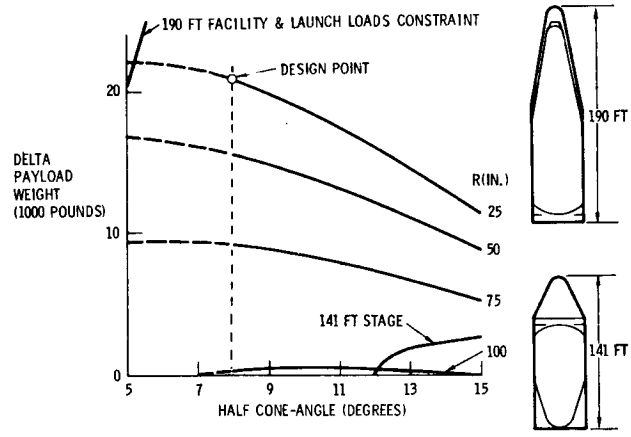

Figure 8. Design Trade-Off Map with Launch and Facilities Constraints

In employing the baseline INT-21, the acceptable size of an RNS tank with inverted launch and 8-degree, 25-inch cap radius aft bulkhead is 190 feet, as shown in Figure 8. This height capability is due to the lower combined air loads resulting from the slender 8-degree nose cone and the aft shift in center of pressure. It should be noted that the loads derived for this configuration are compatible with the 75 meter/sec wind profile (or 95 percent probability of no occurrence) corresponding to 100 percent launch time availability during the year.

The limit height of a right side up RNS launch configuration with no engine but with a nose cone, must be restricted to 141 feet and is shown in the lower right hand corner of Figure 8. The launch availability of this configuration is the same as that of the NASA baseline INT-21, that is, less than 100 percent. The data show that to preclude further modifications (and increased cost) to the INT-21 baseline, this configuration must be limited to a 12-degree half cone-angle with approximately a 90-inch cap radius. Therefore, an inverted launch of the stage is necessary to maximize payload and cost effectiveness without increasing the development cost of the baseline booster. Furthermore, only with an inverted launch of the nuclear stage less NERVA, relaxation of the wind criteria, or an off-optimum performance design concept—such as a larger half cone-angle and tank cap radius—can the impact on the booster be avoided.

MODIFIED DUAL CELL

Figure 9 depicts the configurational arrangements of the RNS using an inner cell with a capacity commensurate with the last cooldown plus residual propellant requirements, identified as 5,950 pounds. The objective is dual in nature: (1) by trapping propellant within the inner cell, propellant management during periods of zero gravity might be simplified, and (2) the resultant column of propellant could be used effectively as a radiation attenuation shield in the critical latter seconds of burn when tank top radiation dose rate is reaching its peak.

Since the single tank baseline of 8-degrees and 25-inch cap radius was shown to be optimum, the inner cell concept study was confined to that configuration only. A number of inner cells geometries were considered by varying the radius of the cylinder. The limiting upper radius is 60 inches when the bulkhead becomes tangent to the side walls of the cone.

The optimum cell geometry is based on the minimization of the algebraic sum of the tank and inner cell structure as it increases with pressure, and of shield weight as it reduces with increasing inner cell height. The pressure increase is equal to the propellant transfer line height from outer to inner cell, multiplied by the density and acceleration, and reaches a maximum when the outer cell is near depletion. Losses in and at the transfer line intake are relatively small. The results of the analysis indicated that the optimum configuration has an inner cell top radius of 50 inches.

HYBRID

The hybrid class of RNS configurations was conceived primarily to aid in engine end-of-life disposal. After the last operational flight, the auxiliary tank is filled with LH_2 and the propulsion module - consisting of the small tank, NERVA, guidance and navigation, and reaction control system - propels itself to a safe disposal orbit. Other potential benefits include ground mating of the engine with the small tank resulting in reduced orbital assembly operations, and amelioration of start-up pressurant requirements when the main tank has a large ullage.

In addition, consideration must be given to other significant design drivers that affect stage cost effectiveness. These include nuclear radiation, system weight, and EOS cargo bay compatibility for the auxiliary tank. A spectrum of hybrid configurations as shown in Figure 10 was synthesized for an initial screening prior to a more detailed tradeoff study to identify the most attractive candidate in this class. As also shown in the figure, a wide range of auxiliary tank geometries and capacities was screened on the basis of EOS cargo bay dimensional compatibility, producibility, radiation scattering, LH_2 capacity in relation to disposal capability, and interface compatibility with the main tank. Various main tank cap radii and half cone-angles were considered in the context of radiation attenuation and stage moldline symmetry.

The results of the single tank study—indicating significant weight reductions for designs with small half cone-angles and cap radii—were used to guide the hybrid design screening.

The evaluation of the most promising hybrid vehicle configurations is summarized in Table 1. The evaluation criteria include vehicle length and weight, external shield weight, and disposal capability from low earth orbit. The minimum empty vehicle weight, integral tank top radiation dose and external shield weight are seen to occur for the hybrid configuration employing a 3,000 pound capacity LH_2 auxiliary tank (8-degree half cone-angle, 25-inch cap radius). Shielding weight advantages of about 2,800 to 3,400 pounds are derived from the 25-inch end cap radius in the lower auxiliary tank of this hybrid configuration as well as the overall vehicle length of 208 feet. However, the reduced LH_2 capacity of 3,000 pounds precludes the possibility of engine disposal to a safe orbit. If the dual requirements for 9,300 pounds of LH_2 tank capacity for engine end-of-life disposal and an allowable cargo volume of 15-foot diameter by 60-foot length for the EOS are to be satisfied, one of the other three hybrid configurations listed in the table must be selected. Therefore, the hybrid configuration employing an auxiliary tank with a 7.5-degree half cone-angle and 68-inch end cap radius aft bulkhead geometry and a 7.5-degree half cone-angle, 112-inch end cap radius aft bulkhead geometry for the main tank affords the optimum selected hybrid arrangement. This configuration represents the minimum weight system while maintaining a high earth orbit NERVA disposal capability.

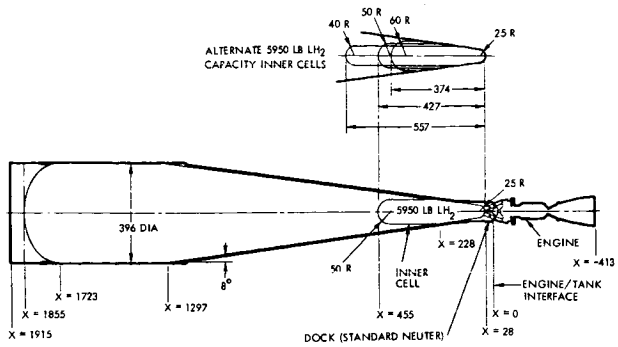

Figure 9. Modified Dual Cell Configuration

Table 1. Hybrid Configuration Evaluation

Configuration[1]	Evaluation Criteria: Disposal Capability From Low Earth Orbit	Vehicle Length (ft)	Empty Weight (lb)	Tank Top Rad Dose[2] (rem)	External Shield Weight (lb)
Main tank - 8°, 40 in. r cap Auxiliary tank - 77 in. r cyl - 9300 lb-LH_2	660 x 660 n mi 45° inclination	208	81310	88	6000
Main tank - 8°, 40 in. r cap Auxiliary tank - 8°, 25 in. r cap - 3000 lb-LH_2	660 x 660 n mi 32.5° inclination	208	79870	32	3800
Main tank - 8° 77 in. r cap Auxiliary tank - 77 in. r cyl - 9300 lb-LH_2	660 x 660 n mi 45° inclination	193	80730	107	6600
Main tank - 7.5°, 112 in. r cap Auxiliary tank - 7.5°, 68 in. r cap - 9300 lb-LH_2	660 x 660 n mi 45° inclination	186	80150	109	6600

[1] Auxiliary propulsive module compatible with EOS payload capability; Guidance Navigation and Control module required for engine disposal.
[2] 5000 lb LH_2 residual level.

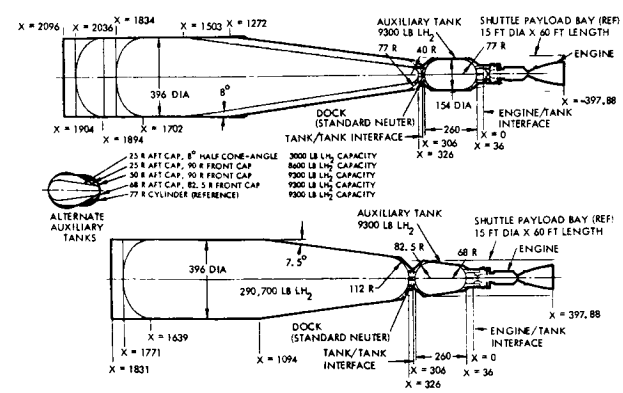

Figure 10. Hybrid Configurations

ALTERNATE CONCEPTS COMPARISON

Table 2 presents a brief summary of the most attractive design concept in each of the configuration classes considered. The burnout weight including shielding-directly relatable to payload performance and cost effectiveness-shows that the single tank design has an advantage of over 6,000 pounds over the hybrid, and 1,500 over the modified dual cell. In the case of the latter the weight difference is due to the higher tank design pressure resulting from the additional losses in feeding propellant to the top of the inner cell plus the weight of the inner cell assembly.

Over 2,500 pounds of the penalty for the hybrid are due to the higher external shield weight as shown in Table 2. The other 3,500 pounds are due to increases in stage empty weight over the single tank design. These are basically in structures, and meteoroid and thermal protection and are due to increases in surface area of both pressurized and unpressurized shells as well as a slight increase in tank design pressure due to losses accrued by transferring propellant from the main to auxiliary tank.

Of concern also is design compatibility with operational requirements, particularly those derived from earth launch of the RNS plus its logistic supplies, and orbital activities to support a program dependent on reusability to substantially reduce cost. It is particularly pertinent to determine if there are critical operational drivers which favor certain designs.

As previously indicated, the MSFC booster baseline configuration, employing Saturn V's attitude and attitude rate control mode, does not constrain the RNS length as long as the tank is boosted in the inverted position. Although this approach necessitates a separate NERVA launch with orbital mating and checkout, no requirements are imposed beyond those to support a reusable shuttle program. Furthermore, NERVA design criteria specify engine assembly and removal capability in earth orbit. Engine replacement may be necessary due to limited lifetime or unrepairable damage considerations and many common operations exist in payload mating and checkout, propellant transfer, maintenance and repair, etc., requiring development of similar in-orbit capabilities. Lastly, the limited benefit of an integral engine-tank launch (permiting ground mating and checkout) must be weighed against use of a new flight control approach–load minimum– or alternately more extensive structural design changes to the INT-21 even for the shortest conical RNS.

Like the recommended single tank concept, the hybrid design employs a separate engine launch. However, since the engine is attached to an auxiliary tank on the ground, somewhat fewer connections should be required in orbit for mating with the main tank. A preliminary assessment did not show any significant reliability benefits. A main attraction of the hybrid is the built-in auxiliary tank to permit NERVA end-of-life self-disposal. Maximum tank size is limited by EOS cargo bay dimensions and radiation attenuation requirements. Nevertheless, 9,300 pounds can be efficiently accommodated and is sufficient for a safe high altitude earth orbit engine disposal. If the disposal module is to be autonomous, it will require addition of astrionics equipment and an RCS system for flight stabilization, guidance, and control. Unless these items can be designed for installation initially with the auxiliary tank (which imposes stringent radiation-hardened and lifetime requirements), they will have to be mated in orbit just prior to disposal. This requires support by another vehicle such as the tug. With all of the other concepts, either the disposal tankage/ equipment must be delivered and mated to the engine just prior to disposal or the tug can be used to deliver NERVA to a safe location. Although the choice is not clear-cut for a normal disposal, if NERVA is inoperable the tug appears to be the only practical alternative. With this contingency as the key driver, tug disposal is recommended under all conditions, thus eliminating any significant operational benefit in the hybrid design.

One additional factor of concern is the effect of using a high fineness ratio tank with a small end cap radius. Interface studies indicate that a suitable coupling can be made without impacting NERVA requirements. Furthermore, the slender conical tank geometry should aid in zero g propellant control through migration and retention of the LH_2 at the aft end.

Payload delivery cost (cost effectiveness) is perhaps the most significant parameter in concept evaluation. The three bar charts shown in Figure 11 indicate the relative worth of the three alternate designs. As can be seen, the 8-degree single tank concept (1) is superior in terms of maximum performance and minimum payload delivery cost. On the basis of current RNS performance and cost estimates, this could amount to a savings of 10-15 million dollars per lunar shuttle flight. Although the modified dual cell (2) affords somewhat better radiation protection, it is more complex, structurally heavier, and thus more costly than the single tank design.

On the basis of the data summarized in Table 2 and Figure 11, the single tank design employing INT-21 launch of the RNS tank in an inverted attitude is clearly the most attractive configuration while meeting current standards of on-board personnel protection.

Table 2. Candidate Systems Summary Comparison

Item	Single Tank	Modified Dual Cell	Hybrid
Main tank half cone-angle - (degrees)	8	8	7.5
Main tank cap radius - (in.)	25	25	112
Auxiliary tank LH_2 capacity - (lb)			9,300
Auxiliary tank cap radius - (in.)			68
Tank top radiation dose* - (rem)	38	37	109
Tank design pressure - (psia)	27.5	28.5	28.2
Empty weight - (lb)	76,450	77,900	80,150
External shielding weight** - (lb)	4,050	4,050	6,600
Burnout weight - including external shielding - (lb)	81,930	83,400	88,180
Engine disposal			
Maximum capability	Heliocentric (limited only by EOS capability)		High earth orbit (unless extra tank added)
Inoperable NERVA	Tug	Tug	Tug
Reliability implications	No significant difference between concepts		
Recommended configuration	✓		

*5000 lb LH_2 last cooldown propellant
**10 rem criteria

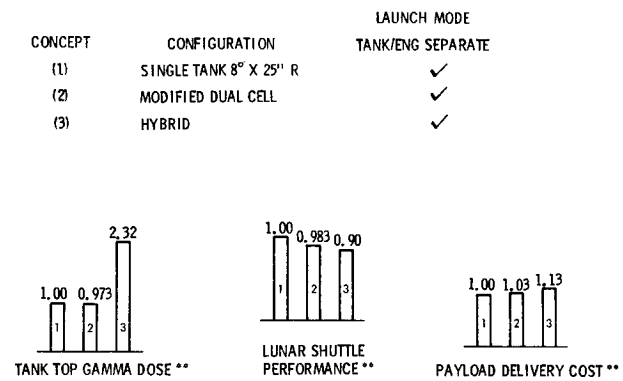

** VALUES RELATIVE TO CONCEPT (1)

Figure 11. Comparison of Alternate RNS Concepts

REFERENCES

1. Preliminary Design Loads INT-21, D5-15806 (10 August 1970)
2. Nuclear Flight System Definition Study–Phase I Report, SD 70-118 (March 1970)
3. Nuclear Flight System Definition Study–Phase II Final Report, SD 70-117 (August 1970)

RADIATION ENVIRONMENT FOR RENDEZVOUS AND DOCKING WITH NUCLEAR ROCKETS

D.R. Rogers, E.A. Warman, B.A. Lindsey

Aerojet Nuclear Systems Company
Sacramento, California

Planning for operations such as rendezvous and docking of a vehicle powered by a nuclear rocket engine with a space station requires consideration of the radiation environment produced by the engine in addition to the natural space radiation environment. This paper provides radiation environment data for the NERVA engine which may be utilized in estimating radiation exposures associated with various space maneuvers. Spatial distributions of neutron and gamma tissue kerma rates produced during full thrust operation of the engine are presented. The corresponding biological dose rates will be due predominantly to neutron contributions except within the region in space which is shadowed by the liquid hydrogen propellant. Forward of the vehicle, dose rates will depend on the characteristics of the propellant module and payload as well as those of the engine and will vary during a mission as propellant is consumed. Final rendezvous with an orbiting space station would be achieved subsequent to full thrust operation during a period of 10 or more hours duration in which impulse is delivered by the propellant used for removal of decay heat. Consequently, post operation radiation levels are of prime importance in estimating space station exposures. Maps of gamma kerma rates around the engine are provided for decay times of 4 and 24 hours after a representative firing. Typical decay curves illustrating the dependence of post operation kerma rates on decay time and operating history are included. Examples of the kerma distributions around the engine which result from integration over specific exposure periods are shown.

This paper summarizes data pertaining to the radiation environment which is produced near the NERVA* engine. The radiation environment during full thrust operation and during post-operation periods has been considered. These are presented in a format intended to make the data useful in considering the radiation exposures associated with rendezvous and docking maneuvers.

The NERVA engine employs a graphite moderated, beryllium reflected reactor which heats and exhausts liquid hydrogen propellant to develop 75,000 lbs thrust. The NERVA flight engine configuration is illustrated in Figure 1. Minimal radiation attenuation is provided for radiation emitted in directions other than along the forward centerline axis. An internal shield is included within the Pressure Vessel and Reactor Assembly (PVARA) to provide protection for critical engine system components. Some potential manned missions may require additional biological shielding. The manned mission shielding requirements depend on the characteristics of the entire nuclear stage, including the propellant module and payload as well as the engine. The engine design has provision for inclusion of an external disk shield at the location indicated in Figure 1, if additional protection is required for manned payloads. The engine is coupled to a propellant module with 300,000 lbs liquid hydrogen capacity. The payload is located forward of the propellant module.

When operating at full thrust, the reactor fission power is a little over 1500 megawatts. The radiation energy which escapes from the system is equivalent to about 1% of the total fission power. Thus, the magnitude of the NERVA engine as a source is such that radiation exposure may be an important consideration in planning rendezvous and docking maneuvers.

NERVA ENGINE WITH DISK SHIELD

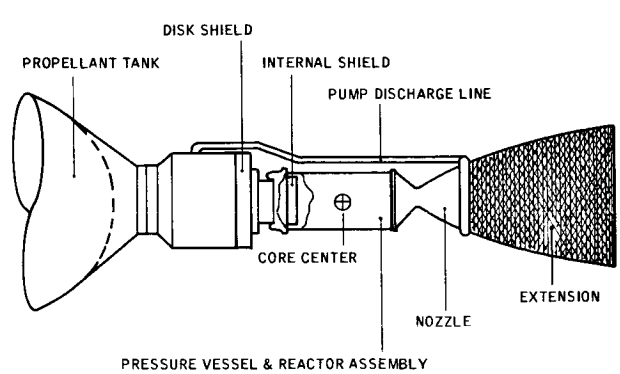

FIGURE 1

* The Nuclear Engine for Rocket Vehicle Application Program (NERVA) is administered by the Space Nuclear Systems Office, a joint office of the USAEC and NASA. Aerojet Nuclear Systems Company is prime contractor for the engine system and Westinghouse Electric Corporation is principal subcontractor responsible for the nuclear subsystem.

I. OPERATING RADIATION ENVIRONMENT

The spatial distribution of gamma radiation emerging from the engine during full power operation is shown in Figure 2. The data shown are iso-KERMA rate contours expressed in units of rads (tissue)/second. These controus provide a pictorial representation of the directional dependence of the intensity of radiation leakage from the engine. It is apparent that there is no strong dependence on direction except in a relatively small cone about the forward axis, due to the effect of the shadow shield in the forward end of the pressure vessel. The highest intensities external to the pressure vessel occur at reactor midplane where the peak value is about 3×10^5 rads/sec in contact with the pressure vessel. The radiation leakage from the PVARA in the aft or nozzle direction is only slightly less than the radial leakage, but the nozzle assembly provides some additional attenuation. In the forward direction, the gamma leakage is reduced by a factor of approximately 30 by the combined effects of the internal shield and the fuel element support plate.

Figure 3 presents the neutron leakage rates at full power conditions. The right half of this figure shows isoflux contours of fast neutrons (energies greater than 0.9 Mev) emerging from the engine in units of neutrons/cm^2-sec. The left half of the figure contains contours of KERMA rate resulting from neutrons of all energies in units of rads(tissue) per second. In the case of neutrons, intensities in the aft direction are slightly higher than to the side, because the beryllium reflector shields more effectively against neutrons than against gamma rays. The dependence of neutron leakage on direction is not strong except within the region of influence of the internal shield. If the neutron KERMA rates are compared with gamma KERMA rates of Figure 2, it is apparent that the tissue KERMA rate due to neutrons is as high or higher than that due to gamma rays at all locations. Hence, in biological dose considerations, in which the biological effectiveness of the radiation must be considered, the neutron contribution will clearly dominate. Reduction of biological dose rates through means other than distance (i.e., by shielding) is a combined neutron and gamma shielding problem. However, it is important to point out that the liquid hydrogen in the propellant tank provides a tremendous indigenous neutron shielding effect. As a result, almost all of the dose to the payload is due to gamma radiation.

Figure 2

GAMMA KERMA RATES NEAR ENGINE AT FULL POWER

UNITS: RADS(TISSUE)/SECOND

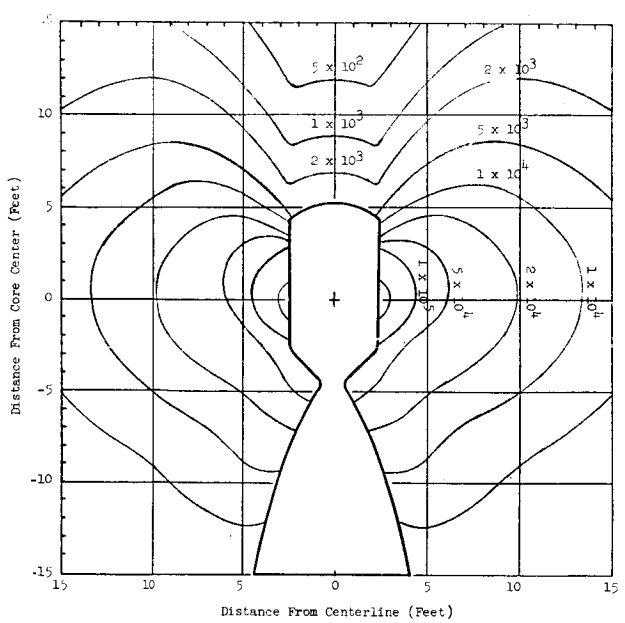

Figure 3

NEUTRON FLUXES AND KERMA RATES NEAR ENGINE AT FULL POWER

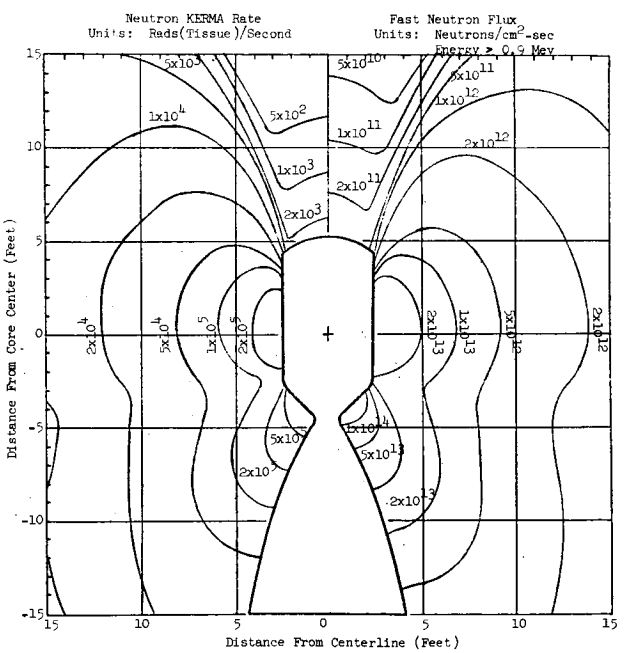

The full power operating gamma radiation environment is extended in the gamma KERMA rate map of Figure 4 to distances of approximately 200 ft from the reactor center. The Nuclear Flight Propulsion Module (NFPM) depicted in this figure includes a 33-ft diameter propellant tank with 15° half-angle conical tank bottom. These data were calculated for a minimum shield configuration; i.e., no external disk shield was included. Furthermore, the contours near the forward axis do not include any attenuation by the propellant module or payload. The actual intensities within the fairly narrow cone influenced by the propellant module will vary during the mission, increasing as the mass of liquid hydrogen remaining in the propellant tank decreases. The contours shown are representative of the limit approached as the liquid hydrogen nears total depletion at the end of the last firing. Consequently, they represent worst case limits for gamma KERMA rates experienced during a nose-on approach.

Figure 4

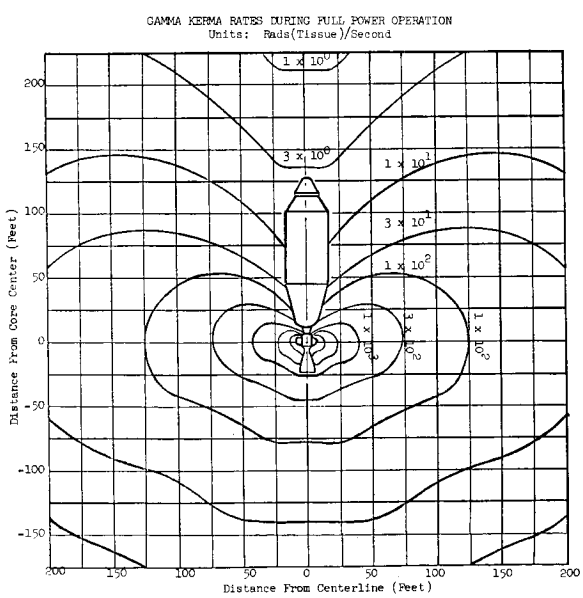

A corresponding neutron map covering the same spatial region as Figure 4 is shown in Figure 5. The fast neutron intensities were obtained with the same assumptions: the minimum shield configuration with no attenuation in regions external to the PVARA. In the area shadowed by the propellant module, this places a quite conservative upper limit on the neutron KERMA rate, because the liquid hydrogen is such an effective shield against neutrons. Even at end of burn, the liquid hydrogen required for cooldown plus the hydrogen vapor in the tank are sufficient to reduce the neutron KERMA rate to a relatively insignificant level.

Figure 5

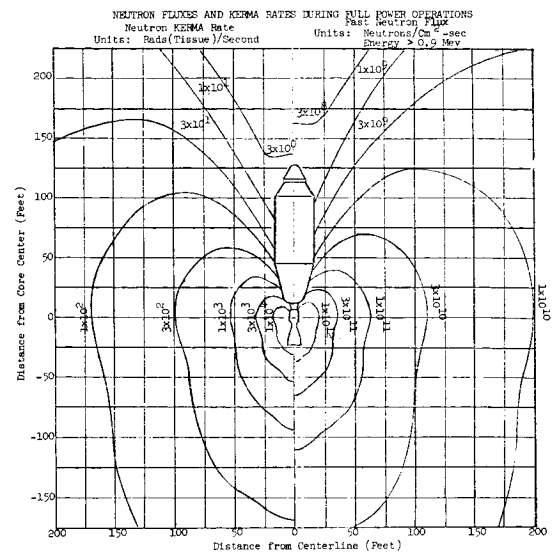

Extensive calculation of tank-top gamma KERMA rates have been performed for the reference 300,000 lb capacity 15° propellant tank, with various liquid hydrogen levels in the tank. In Figure 6, the results of some of these calculations for a point on centerline at the top of this tank are plotted as a function of residual propellant mass. The neutron KERMA rate at this location varies very rapidly with the mass of liquid hydrogen and is significant only when the tank is almost entirely drained. Since approximately five thousand pounds of liquid hydrogen are required for cooldown after the last burn, the neutron exposure above tank top is negligible compared to the gamma exposure. This is true only for the fairly narrow cone in space which is shadowed by the propellant tank.

The KERMA rates expected along the forward centerline axis can be seen to vary through about three decades depending on how much propellant is in the tank. Thus, during most of a mission, the on-axis KERMA rate is much less than the KERMA rate at the end of the last burn. As an example, the tank top KERMA rates occurring at the end of each of four burns of a typical mission (unmanned) reusable interorbit ferry) are indicated in Figure 6. The KERMA rate during a nose-on approach following the second burn is about a factor of 10 lower than for such an approach after the fourth burn. In a manned mission which includes a biological shield at the engine, the on-axis KERMA rates will, of course, be further reduced. A typical 10,000 lb disk shield at the engine would reduce the tank top KERMA rate by about a factor of 20 during most of a mission. Near the end of the last burn, when line-of-sight contributions to the tank top KERMA rate are more important relative to contributions from scattering in the propellant, the effective attenuation factor would increase somewhat. Again, the on-axis environment pertains only in a fairly narrow cone and increases rapidly toward side leakage values as the detector location moves out of the influence of the tank and/or the protection of the disk shield.

Figure 6

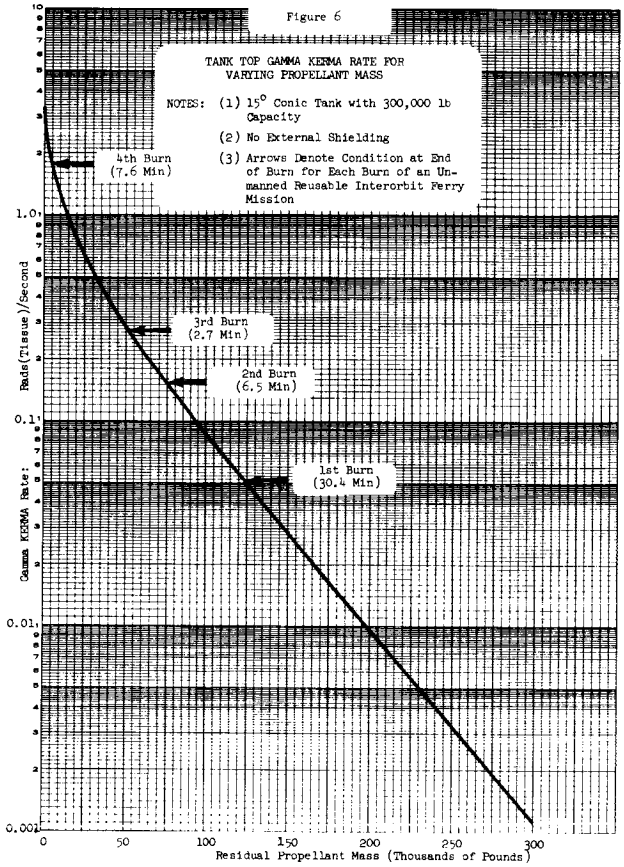

Figure 7

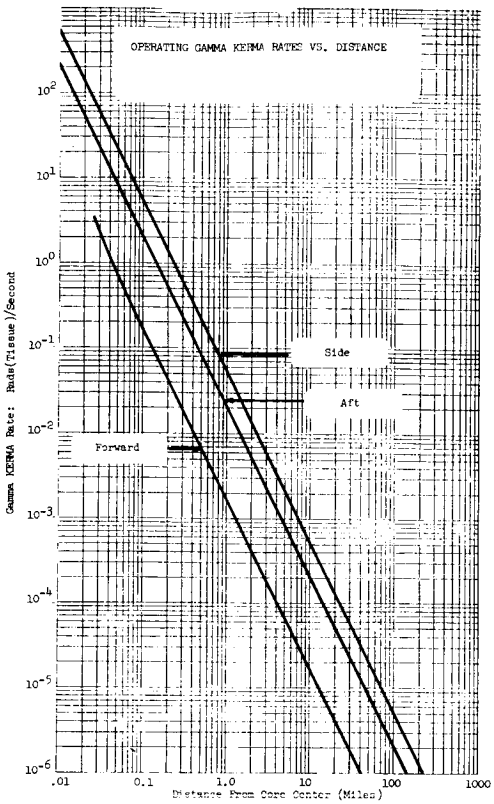

The data from the extremities of Figures 4 and 5 may be extrapolated with little error by inverse r^2 from the engine to obtain estimates of KERMA rates at greater distances. Figure 7 illustrates the $1/r^2$ extrapolation of side and aft gamma leakage data from Figure 4 out to distances of 100 miles from the engine. At 1 mile to the side, the gamma KERMA rate has dropped to 5×10^{-2} rads(tissue)/sec and at 100 miles is only 5×10^{-6} rads(tissue)/sec. The data shown for the forward direction was extrapolated from the dose rate at tank top (126 feet from reactor center) with no residual hydrogen. No payload attenuation or disk shield is included.

Extrapolated neutron KERMA rates are plotted in Figure 8. The neutron KERMA rate at 1 mile ranges from 3×10^{-1} rads(tissue)/sec in the aft direction to 1×10^{-1} rads(tissue)/sec at the side. These fall to 3×10^{-5} and 1×10^{-5} rads (tissue)/sec, respectively, at 100 miles.

Figure 8

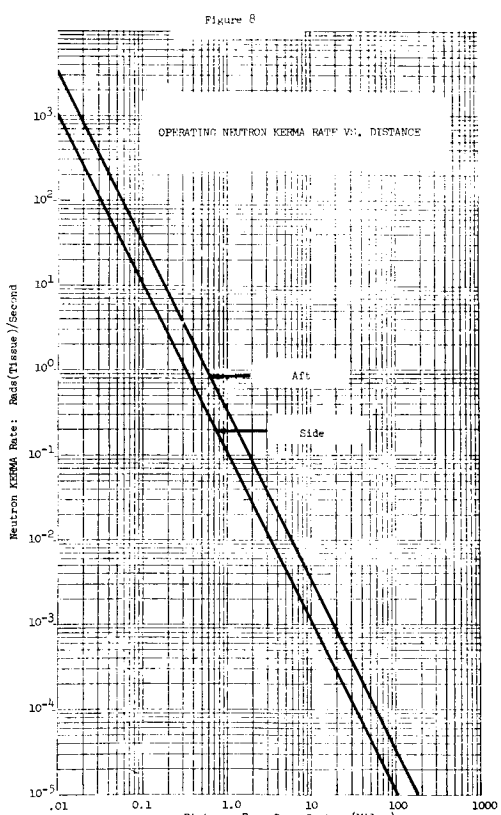

II. SHUTDOWN RADIATION ENVIRONMENT

In lunar shuttle missions, full power operation would ordinarily terminate anywhere from a hundred to several hundred miles from the space station. The subsequent maneuvering to close the distance with the station would be performed using the impulse delivered by the propellant used for afterheat cooldown. Final docking would occur after most of the cooldown impulse has been expended. This would be at least 10 hours after shutdown. The problem of estimating space station exposures during rendezvous and docking, therefore, primarily involves the post-operation radiation environment.

The magnitude of the gamma source in the engine drops rapidly after shutdown, but remains quite significant in terms of biological dose rates in the vicinity of the engine. The fission product source strength and resulting gamma intensities external to the engine are quite dependent on time after shutdown and the operating history. Post-shutdown gamma KERMA rates have been examined for representative periods of operation and decay. Figure 9 contains gamma iso-KERMA rate contours near the engine which are based on a 30-min continuous full-power firing. The data shown on the left half of the figure are KERMA rates calculated for a decay time of 4 hours after the 30-min firing. KERMA rates after an additional 20 hours or a total of 24 hours decay shown for comparison on the right half of the figure. Only gamma KERMA rates are significant because the photoneutron production in beryllium after shutdown is insufficient to result in neutron intensities which compete with the gamma rays.

FIGURE 9

GAMMA KERMA RATES NEAR ENGINE FOLLOWING 30 MINUTE FULL POWER FIRING
Units: Rads(Tissue)/Second

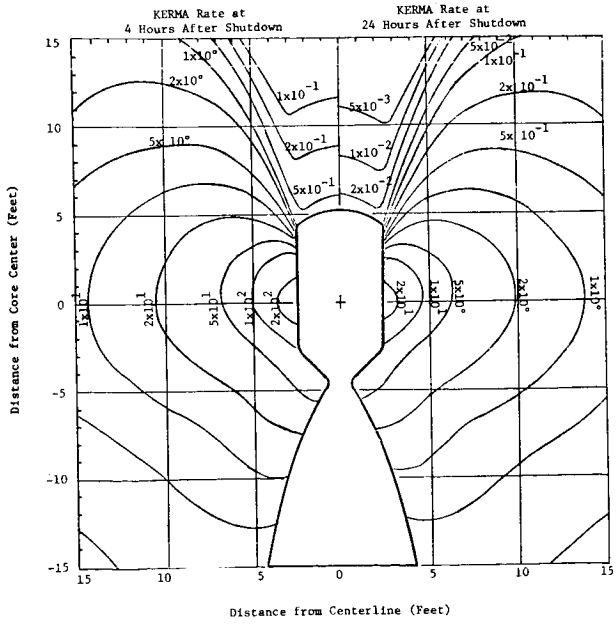

The gamma KERMA rate maps for 4 hours and 24 hours after a 30-min firing have been extended in Figure 10 to cover an area which encompasses the entire vehicle. These contours are for a minimum shield configuration (internal shield only). The levels near the forward axis do not include any propellant module or payload effects.

At 4 hours after shutdown, the KERMA rate 100 ft to the side is 1.7 x 10^{-1} rad/sec and this decays to 1.5 x 10^{-2} rad/sec at 24 hours after shutdown. On the forward axis, in the shadow of the internal shield, the KERMA rate is about 2 decades lower.

FIGURE 10

GAMMA KERMA RATES FOLLOWING 30 MINUTE FULL POWER FIRING
Units: Rads(Tissue)/Second
KERMA Rate at
4 Hours After Shutdown
Gamma KERMA Rate at
24 Hours After Shutdown

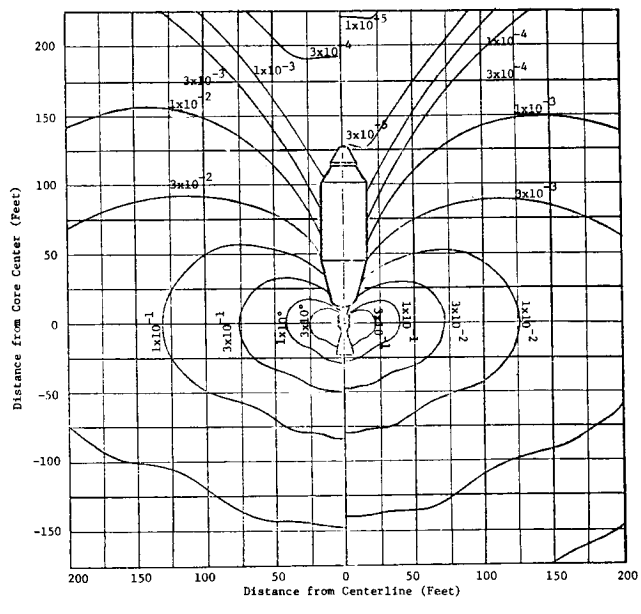

For distances beyond those covered in the previous map, the data may be extrapolated by inverse r^2. This extrapolation is shown for the forward, side, and aft directions from the engine in Figure 11 for distances out to 100 miles. At 1 mile to the side, the KERMA rate is about 5 x 10^{-6} rads (tissue)/sec at 24 hours after shutdown.

Figure 11

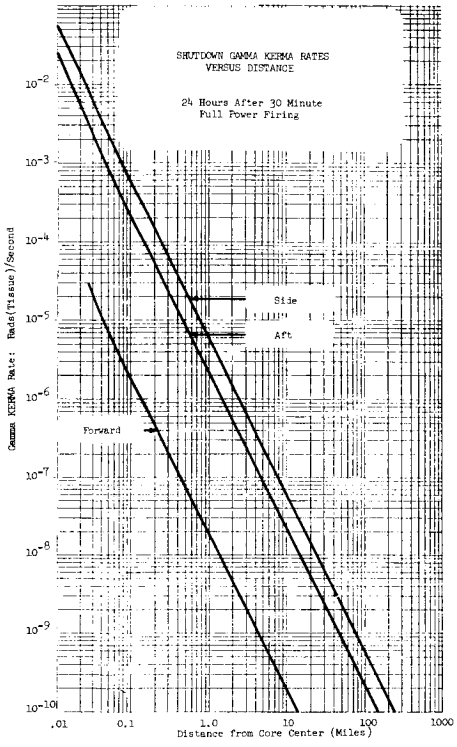

Figure 12

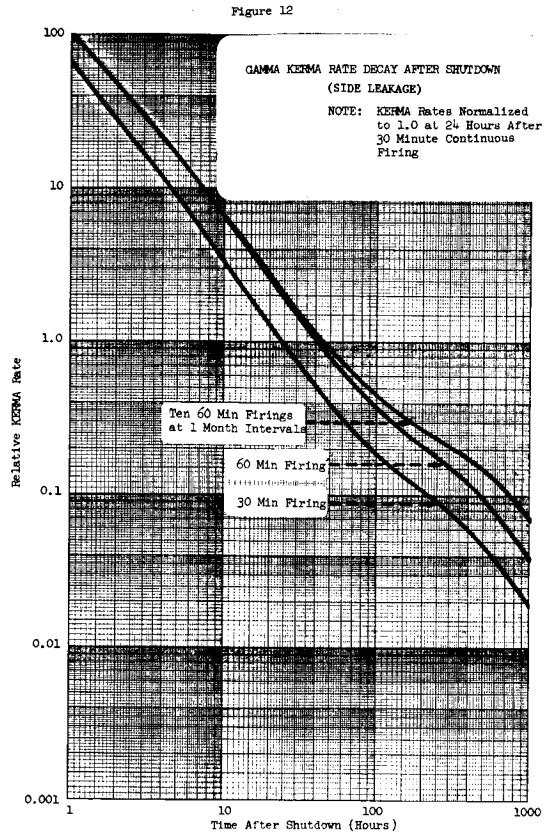

The data of Figure 12 illustrate the dependence of KERMA rate on time after shutdown for representative operating histories. The data are normalized such that the KERMA rate 24 hours after a 30-min burn is 1.0. Thus, KERMA rate data of Figures 9, 10, and 11 for 24 hours decay may be scaled to other operating and decay conditions. For example, at 100 ft to the side of the engine, the KERMA rate 1 hour after a 30-min firing is a factor of 65 greater than the KERMA rate at 24 hours or approximately 1.0 rads (tissue)/second. In Figure 12, the KERMA rates after a 30-min burn are compared with those after a 60-min burn and those following a sequence of ten 60-min operations. The latter represents the total rated lifetime of an engine. KERMA rates for other burns can be scaled from the data for 30 minutes at full power in direct proportion to the power integral for the burn so long as the decay time is long compared to the burn time.

FIGURE 13

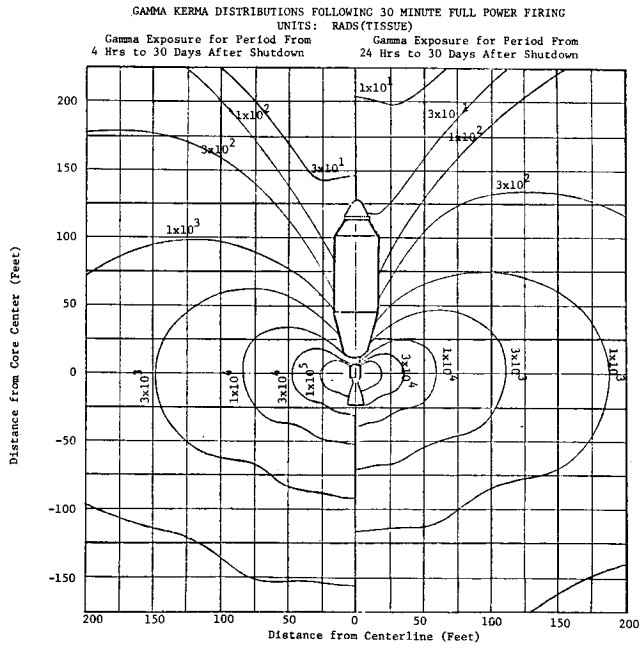

Cumulative radiation exposures may be obtained by integrating the KERMA rate versus time curve over the exposure duration. Iso-KERMA contours around the engine are shown in Figure 13 for exposures which would be accumulated during the periods from 4 hours to 30 days after shutdown and from 24 hours to 30 days after shutdown following a 30-min burn. These might represent exposures resulting during a 30-day docking, starting at 4 hours or 24 hours after termination of the firing. Data for the minimum shield configuration, consistent with Figure 10.

III. SUMMARY

In summary, the operating and shutdown radiation environment in the vicinity of the NERVA engine is presented in such a manner as to facilitate calculations of accumulated dose for rendezvous and docking maneuvers. The units of tissue rads/sec were chosen for two reasons: (1) the dose due to the stay time at any one point in traversing these maps would probably be best calculated from a per second value, and (2) the use of the tissue rad value permits one to proceed at the present maturity of mission planning by simply assuming a single conversion to rem dose based on an assumed quality factor. These data are tissue KERMA values, with no attempt to compute secondary radiation contributions in the tissue. Much larger uncertainties in radiation levels are associated with the design evaluation of a flight engine than those introduced by assumptions normally made in KERMA to dose conversion calculations.

The preponderance of the neutron levels during operation should be pointed out. If an average conversion from Rad(T) to Rem were to be based on an RBE of 7, the Rem dose from neutrons would eclipse that from gamma radiation in all but the forward direction (i.e., the region affected by the presence of the liquid hydrogen propellant tank).

Use of these data in detailed planning for specific missions will have to take into account the indigenous shielding and secondary gamma production in the approaching vehicle, while the NERVA engine is operating, and the indigenous shielding for the relatively soft gamma radiation after shutdown. For a first approximation, the operating radiation environment at less than full thrust would be in direct proportion to the full power/partial power thrust levels.

An "approach corridor" concept could be adopted in which access and egress to and from the shutdown NERVA engine would be made along the propellant tank within a band of a few feet from the tank outer surface. This would allow approach from the payload vicinity for maintenance in the tank bottom vicinity with possibly no additional shielding over and above the engine disk shield provided the stay time is very short and a combination of engine operating time and decay time did not result in prohibitively high radiation levels.

Remotely operated equipment (such as teleoperators) would be required for maintenance of most, if not all, portion of the engine, except after only short durations of operation at full power.

Cumulative exposure calculations for specific rendezvous and docking maneuvers have not been attempted herein, but enough data have been provided to allow this to be done in a relatively straight forward manner, as the details of such maneuvers with NERVA are developed.

RADIATION EXPOSURE TO THE ORBITING LUNAR STATION AND LUNAR SURFACE RELATED TO REUSABLE NUCLEAR SHUTTLE OPERATIONS

by Paul I. Hutchinson
Lockheed Missiles & Space Company
Sunnyvale, California

ABSTRACT

The radiation environment created by the Reusable Nuclear Vehicle (RNS) in performing its normal mission functions while in the lunar vicinity and the impact of that environment on the Orbiting Lunar Station (OLS) and/or the lunar surface are examined.

Trajectory data, representative of nominal lunar arrival and departure maneuvers, reflecting the unique operating characteristics of the nuclear engine, provide the basic geometry model for the evaluation of the radiation exposures. Other factors included in the evaluation are the operating source term (neutron and gamma radiation), shutdown source term (fission point gamma radiation), view angle (shielding effects of stage and engine hardware), separation distance, exposure interval, time after shutdown, and prior reactor operating history.

To permit recovery of the impulse available from the coolant flow required by the high decay heat rates at reactor shutdown, the main engine LOI burn is terminated with the RNS in elliptical orbit and the coolant impulse used to circularize the orbit and complete OLS rendezvous. This circularization maneuver may take up to 40 hours or more, depending on the percent of cooldown impulse recovery planned. Radiation exposures at the OLS were evaluated for two conditions: (1) final orbit insertion 10 km ahead of the OLS, and (2) 10 km behind the OLS assuming a 90-percent cooldown impulse recovery about 12 hours of cooling).

Radiation exposures to the OLS during the lunar orbit departure burn (TEI) were evaluated for RNS startup 10 km behind the OLS and 10 km and 20 nm ahead of the OLS. Exposures received at the OLS for these cases are higher than for the LOI burn, since the reactor operation occurs much closer to the OLS, indicating greater initial separations will normally be desirable.

Lunar surface exposures from the operating reactor were evaluated for both the arrival and departure burns and while there is little probability that manned bases would lie along the paths in which measurable exposures would be recorded, the analyses do indicate the need to consider this possibility in planning such operations.

Conclusions supported by the analyses and recommended operational constraints for the RNS are presented.

One of the recommendations contained in the Space Task Group Report to the President (September 1969) was for continued lunar exploration with significantly increased capability and flexibility. Critical to achieving the proposed goals of the program will be the establishment of an Orbiting Lunar Station (OLS) and development of a space transportation system with emphasis on low cost and maximum payload flexibility. A major element being considered for the proposed system is the Reusable Nuclear Shuttle (RNS) designed to transport men, spacecraft, and supplies between earth orbit and lunar orbit as well as to other space destinations.

The NERVA nuclear engine, presently being developed, represents a major advance in propulsion and provides the basis for the RNS concept definition and mission operation planning used in this study. Nuclear engines differ considerably from chemical engines in operating characteristics and also represent a source of ionizing radiation which must be considered when planning any operations in their vicinity. To confirm the feasibility of using the RNS for lunar shuttle operations the effects on the OLS and lunar surface were examined for normal lunar arrival and departure maneuvers.

Trajectory data and reactor operating history for lunar orbit arrival and departure developed during the Nuclear Systems Definition Study (Contract NAS 824715) and the Lunar Mission Safety and Rescue Study (Contract NAS 9-10969) provided the basis for the evaluation.

The OLS is assumed to be in 60 nm polar orbit. Current planning does not call for actual docking of the RNS with the OLS; therefore, on lunar arrival it will only be necessary to inject into orbit in the near vicinity of the OLS from which position payload exchange can be accomplished either with lunar tugs or with propulsion units contained within the payload itself.

An RNS-OLS separation distance has not been established; however, it must satisfy two conditions: (1) the RNS must not be located so as to interface with operations around the OLS such as lunar lander arrivals and departures, and (2) it should be sufficiently distant that radiation from the engine, even in the worst attitude would not restrict activities at the OLS. Two RNS positions were used in the evaluation, 10 km ahead of and behind the OLS, which should satisfy the first condition.

To minimize mission velocity requirements translunar trips will normally be scheduled to coincide with opportunities for coplanar earth departure and lunar arrival. Such opportunities occur twice each lunar month, although trip frequency would probably not exceed one every 54.6 days. Earth return opportunities permitting coplanar arrival in earth orbit will also be selected; however, to avoid extended waiting time in lunar orbit, most lunar departures will require some out-of-plane maneuvers. These departures will normally be performed

using a 3-impulse maneuver to minimize energy requirements, although single burn departures may be selected if the total plane change requirement is less than 20 degrees.

RADIATION ENVIRONMENT CREATED BY THE NUCLEAR ENGINE

The radiation environment related to normal engine operations will be most severe during periods when the reactor is operating at full power (1575 mw) and both neutron and gamma radiation are present. The intensity will depend on distance from the reactor and the presence of intervening mass such as shielding and stage and engine components. These effects are shown in Figures 1 and 2. These data were generated using the Common Radiation Analysis Model (CRAM)*. The sharp reduction in dose rate in the forward sector (0 to 15 deg) is related to the NERVA engine internal shield. Neutron dose rates assumed an RBE (radiobiological equivalent) factor of 8.

When the reactor is shutdown and the source of neutrons eliminated, the radiation environment created by the engine will be considerably diminished, consisting primarily of gamma radiation due to fission product decay in the core. Since the fission product source term is dependent on reactor operating history, time after shutdown, distance, and view angle, all these factors must be considered in the definition of the environment. Figures 3 and 4 give the dose-distance data following shutdown in lunar orbit for the first shuttle trip. Operating history assumed full power cycles of 1773 seconds and 367 seconds at leave earth and arrive moon with a 4-1/2 day coast between. The effect of view angle is presented in Figure 5. From these data it can be seen that the dose rate at 100 ft (30.48 meters) 100 seconds after shutdown is 20.5 R/sec, or more than two orders of magnitude less than the combined neutron-gamma dose rate of 3325 R/sec at the same distance during full power operation. Furthermore, at the end of the first day this rate will have dropped an additional 3 orders of magnitude.

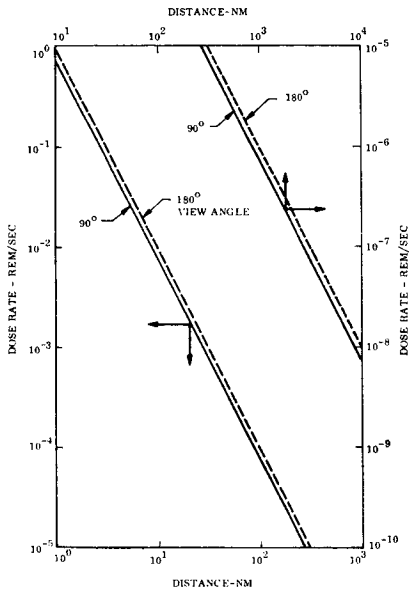

Figure 1 – Dose Rate (Neutron and Gamma) vs Separation Distance From the Operating NERVA Engine

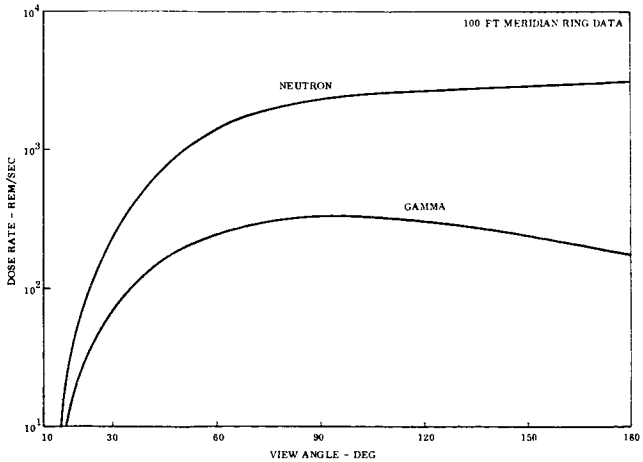

Figure 2 – Dose Rate vs View Angle for the Operating NERVA – 100 ft Meridian Ring Data

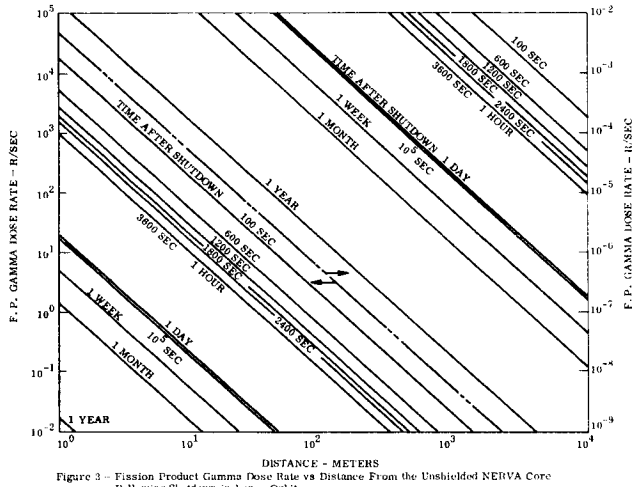

Figure 3 – Fission Product Gamma Dose Rate vs Distance From the Unshielded NERVA Core Following Shutdown in Lunar Orbit

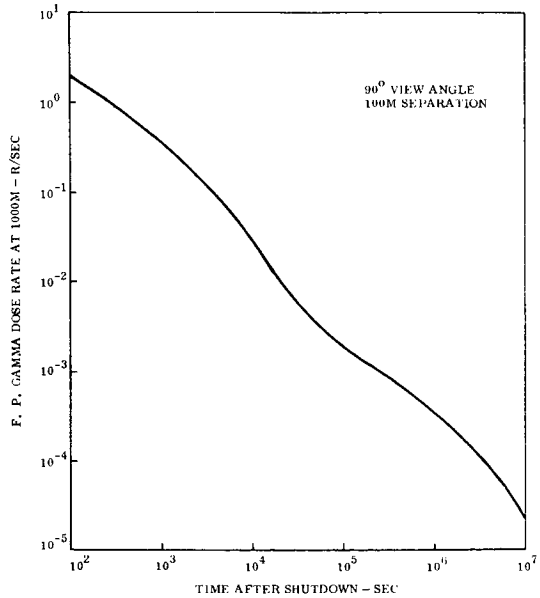

Figure 4 – Fission Product Gamma Dose Rate vs Time After Shutdown From the NERVA Core – LOI Burn

For the first 10 to 20 hours after shutdown the fission product source term will be dominated by the short-lived fission products from the last burn and not until a week or more has elapsed will the build up of greater inventories of longer lived fission products related to multiple burns have any pronounced effect on the source strength. Since the operations evaluated in this study are concerned with relatively short decay times, results based on the first trip analysis can be accepted as representative of subsequent trips as well.

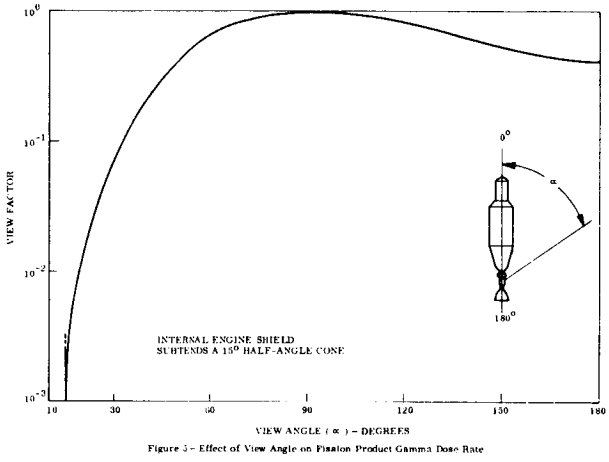

Figure 5 – Effect of View Angle on Fission Product Gamma Dose Rate

For a typical LOI burn, cooling pulse trains will last from 25 to 40 hours and consume from 1500 to 2500 lb of propellant. To minimize the impact of this coolant demand on mission performance, most of the impulse produced will be applied toward the ΔV required for orbit insertion. The effect of the delayed impulse on the trajectory at lunar orbit arrival is shown in Figure 6, in which about 12 hours of cooling impulse recovery was used. Impulse from the cooling pulses not used for ΔV must be nullified to prevent orbit perturbation. In addition to minimizing the performance impact by utilizing coolant impulse for ΔV, an added benefit is realized in that the RNS-OLS separation distance during full power operation will be greatly increased over that which would result if little or no impulse recovery was planned.

A three-impulse departure maneuver, using a 36-hour intermediate ellipse to perform a 90-deg plane change maneuver, is illustrated in Figure 7. Although the intermediate ellipse and plane change may vary for different departures, only the first burn will occur close enough to the OLS or lunar surface to be of concern from a radiation standpoint.

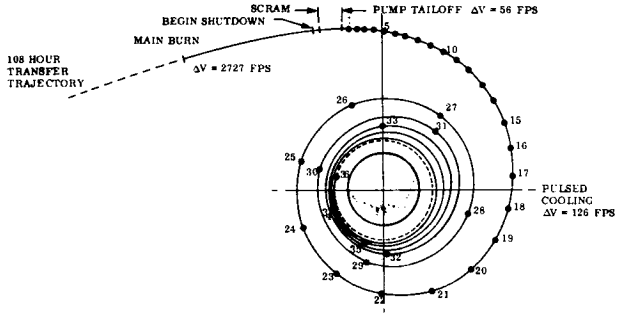

Figure 6 – Lunar Orbit Insertion Using Cooldown Pulses

EFFECT OF DECAY HEAT ON RNS PROPULSIVE MANEUVERS

In addition to the radiation environment created by the decaying fission products in the reactor core, a considerable quantity of heat is released which must be removed to prevent damage to the engine. For example, at the end of shutdown (SCRAM) for a typical LOI burn the decay heat release is about 3.7×10^5 Btu/sec which would be sufficient to vaporize core material and destroy the engine if a continuous flow of coolant was not provided. After about 5 minutes the heat release rate will have dropped to about 6.8×10^3 Btu/sec and coolant can be provided at a much lower rate. In practice, to avoid the need for continuously reducing the coolant flow throughout the cooling period, an intermittant or pulsed flow technique is employed in which engine and reactor components are held within safe temperature limits by fixed flow pulses initiated when the upper temperature limit is reached and terminated when the lower bound is reached. These pulses are fairly uniform in thrust and duration, but decrease in frequency until the decay heat rate has dropped low enough to permit cooling by radiation alone, at which time active cooling can be terminated.

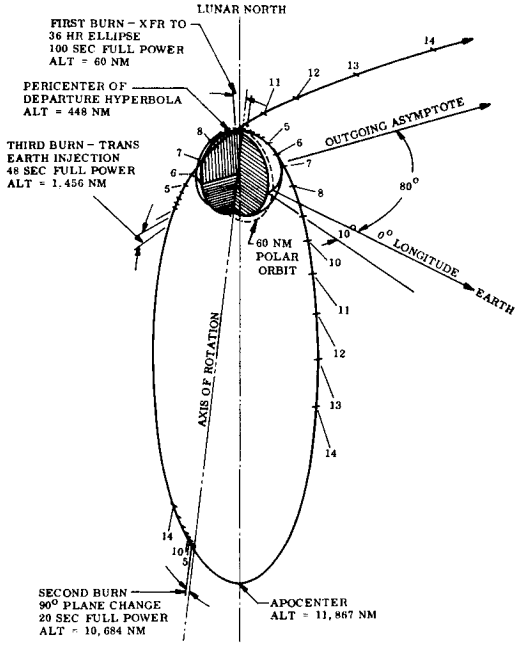

Figure 7 – Typical Three-Burn Lunar Departure With 90° Plane Change

*Full Flow Flight Engine Common Radiation Analysis Model," Aerojet General Corp., RN-S-0551, Sacramento California, 1969

RADIATION EXPOSURE TO THE OLS DURING NORMAL RNS LUNAR MISSION OPERATIONS – LUNAR ORBIT INSERTION

The integrated neutron and gamma dose levels which would be received at the OLS during RNS lunar orbit insertion were evaluated for two conditions previously mentioned; (1) final LOI 10 km ahead of the OLS, and (2) 10 km behind the OLS.

During the main engine burn the separation distance (RNS to OLS) and view angle for both cases are virtually the same and are presented in Figure 8. The total dose delivered to the OLS during the period from startup to SCRAM was computed to be 1.94×10^{-4} Rem, of which 1.44×10^{-4} Rem was attributable to neutrons and 5.03×10^{-5} Rem to gamma radiation.

Almost coincident with shutdown the view angle becomes less than 15 deg for both cases and remains so during most of the cooldown insertion. Thus, even though the RNS-OLS distance is diminishing, the protection provided by the engine internal shield effectively eliminates any radiation problem at the OLS. Separation distance and view angle for the latter half of the case in which final LOI occurs 10 km behind the OLS are shown in Figure 9. View angle for the alternate case is also shown.

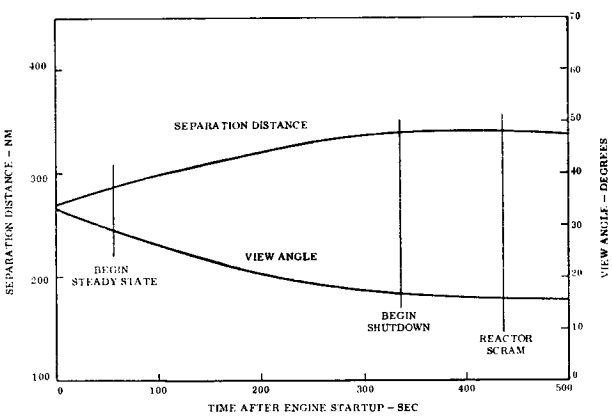

Figure 8 Separation Distance and View Angle Between OLS and RNS During LOI Burn

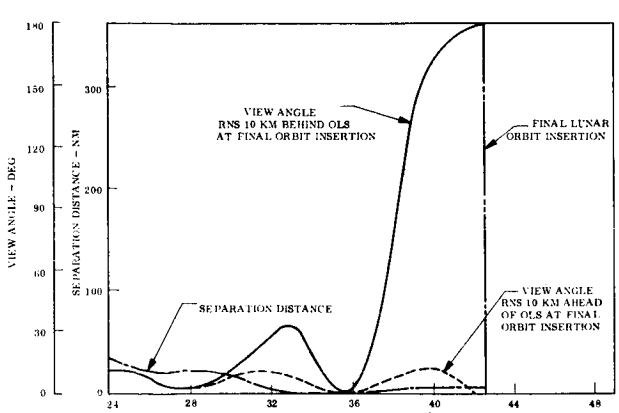

Figure 9 View Angle and Separation Distance to OLS During Cooldown Phase of RNS LOI Maneuver

For arrival 10 km behind the OLS a total fission product gamma dose of 7.03×10^{-3} Rem, roughly 36 times the dose received during the main burn, will be received at the OLS. Most of this dose will be delivered during a 20-minute interval (37,800 to 39,000 seconds) when the RNS is making a close passage with the OLS (1.5 nm) and the view angle is in the 60 to 140-deg range.

For the alternate arrival condition, 10 km ahead of the OLS, the RNS would not pass the OLS during the maneuver and would always remain oriented such that the OLS is within the engine shield cone, effectively eliminating any measurable dose at the OLS.

Increasing the separation distance at final LOI would have little effect on the fission point gamma dose if arrival behind the OLS is selected, unless the distance was increased to the point that the close passage was eliminated. It can reasonably be concluded then that unless mission conditions dictate otherwise, arrival of the RNS ahead of the OLS would normally be selected.

LUNAR ORBIT DEPARTURE

The lunar orbit departure operation may be accomplished using a single-burn or a 3-burn maneuver, depending on the amount of plane change required to satisfy the trans-earth injection (TEI) conditions. During the 3-burn departure the second and third burns will occur at such high altitudes (see Figure 7) that no effective dose will be received at the OLS.

The neutron and gamma dose received at the OLS was evaluated for three departure startup conditions; RNS 10 km behind the OLS, RNS 10 km ahead of the OLS, and RNS 37 km (20 nm) ahead of the OLS.

Separation distances and view angles for startup 10 km ahead of and 10 km behind the OLS are presented in Figures 10 and 11. Startup 37 km ahead would be similar to the 10 km ahead case except that the distances would be greater by about 15 nm.

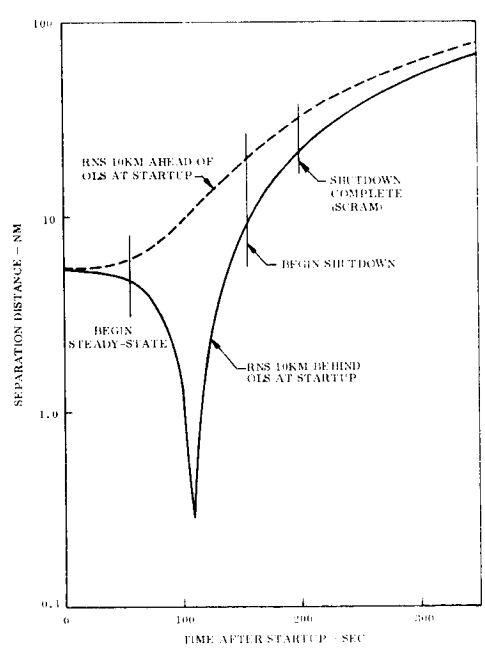

Figure 10 RNS-OLS Separation Distance During First Burn of Three-Burn Lunar Departure Maneuver

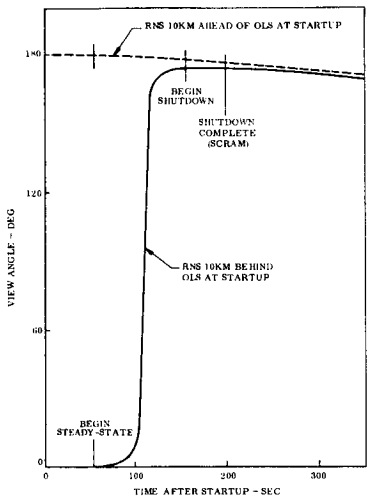

Figure 11 RNS View Angle From OLS During First Burn of Three-Burn Lunar Departure Maneuver

Integrated neutron and gamma doses at the OLS for these cases will be:

Position at Startup	Neutron Dose	Gamma Dose
10 km behind OLS	42.9 Rem	5.41 Rem
10 km ahead of OLS	2.52 Rem	0.139 Rem
37 km ahead of OLS	0.266 Rem	0.015 Rem

The high dose for the case where startup occurs 10 km behind the OLS results from the very close OLS passage (about 0.29 nm) during the reactor operating period. The benefits of even modest increases in separation distance are readily apparent from the other two cases evaluated.

The high neutron and gamma doses during engine operation for startup behind the OLS could be eliminated if the initial distance was increased to about 30 nm (56 km); however, a close OLS passage would still be required when fission product gamma rates are near maximum. Additionally, the risk of collision during the flyby would also represent an undesirable hazard.

The analyses support the conclusion that if startup near the OLS was required, a position ahead of it in orbit would be favored. A distance of at least 20 nm would be desirable. On the other hand, since the RNS requires no direct OLS support for the TEI maneuver, a more desirable condition for startup would be with the RNS beyond the lunar horizon (about 680 nm for 60 nm orbit altitudes) such that the engine burn could not be seen at the OLS and none of the low altitude operation would occur near the OLS. RNS transfer to such an orbit position can be accomplished at minimal expense in terms of ΔV during the waiting period in lunar orbit.

RADIATION EXPOSURE DURING RNS RESIDENCE IN LUNAR ORBIT

On arriving at the moon the nuclear shuttle will be divested of its outbound payload by lunar tugs or using propulsion units in the payload itself. Sometime prior to departure an earth-return payload will be delivered to the RNS and docked to it. Residence time of the RNS in lunar orbit can vary from about 4 days to as much as 30 days, during which time no NERVA engine operation will be required. During this period the RNS will maintain a nose-to-the-sun orientation, which in the worst case could result in a 90-deg OLS view angle for the entire period.

From Figure 3 it can be seen that the average dose rate would be less than 5×10^{-8} R/sec, which over the full 30 days would only result in a dose at the OLS of 0.13 Rem. From a fission product gamma radiation standpoint the 10-km separation appears more than safe. No hazards would be associated with this standby period, except in the event of an RNS system malfunction.

RADIATION EXPOSURE TO LUNAR SURFACE DURING RNS ARRIVAL OR DEPARTURE

Men or installations on the lunar surface along the RNS trajectory trace could be exposed to radiation during periods of nuclear engine operation for the lunar arrival and departure burns. The most severe arrival situation would involve a single-burn LOI maneuver in which a minimum recovery of after-cooling impulse was planned. This type of insertion would result in the lowest altitude during the burn. For evaluation, an incoming trajectory was selected for which no after-cooling impulse recovery was employed. Such an approach is represented pictorially in Figure 12. RNS altitude at the beginning of steady-state operation is about 85 nm. Neutron and gamma doses delivered to various positions along the surface track were evaluated using the separation distance and view angle data given in Figures 13 and 14.

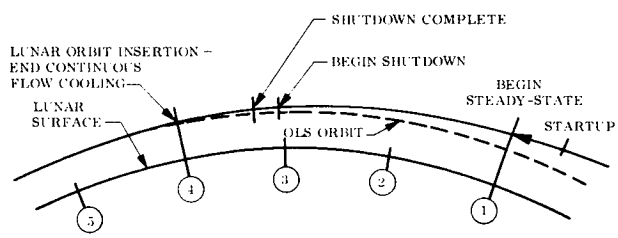

Figure 12 Relative Location of Lunar Surface Positions With Respect to RNS Incoming Trajectory – Low Altitude Approach

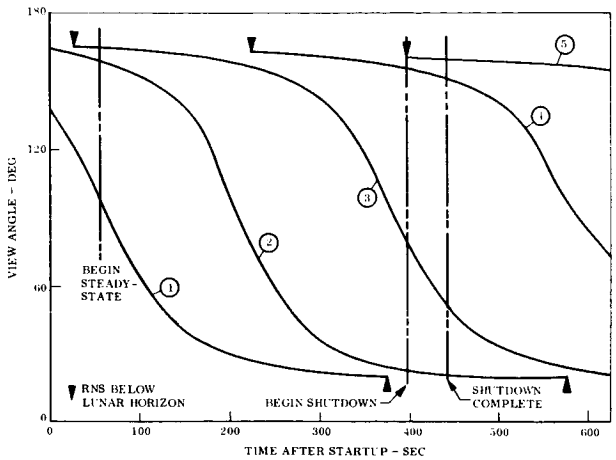

Figure 13 RNS View Angle From Indicated Surface Positions During Low Altitude LOI Burn

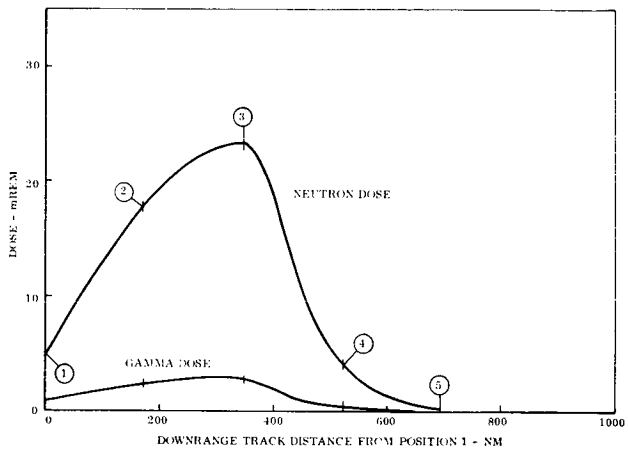

Figure 15 Neutron and Gamma Dose to Lunar Surface During Low Altitude LOI Maneuver

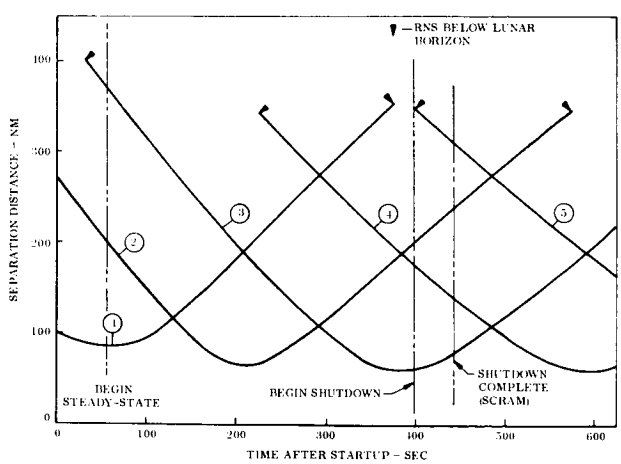

Figure 14 Line of Sight Distance to RNS From Indicated Surface Positions During Low Altitude LOI Burn

The neutron and gamma doses received along the ground track reach maximums of 2.35×10^{-2} Rem and 2.9×10^{-3} Rem at position 3, vertically below the RNS at shutdown (see Figure 15). Uprange positions 1 and 2 benefit from the change in view angle after the overflight, while downrange positions 4 and 5 benefit from increased range, and even more important are hidden by the lunar horizon during the early portion of the burn with position 5 not coming into view until shutdown is initiated.

Normal LOI burns will start at altitudes of about 125 nm and shutdown at about 95 nm, in which case the lunar surface dose will be reduced to perhaps one-third to one-half the values computed for the low altitude approach. Lunar orbit departure burns, on the other hand, would always start at 60 nm and remain low during most of the burn. For three-burn departures the first burn would rarely exceed 100 seconds duration; however, for single-burn departures burn times of 300 to 400 seconds could be required, most of which time the RNS would be at or near the 60 nm altitude. Although a specific case was not evaluated, the similarity to the low altitude arrival case suggests that the surface exposures would not be too different, although peaks might be slightly higher due to the slightly lower altitude during full power operation.

In any event, surface doses from either LOI or TEI burns do not appear high enough to be of concern unless experiments with sensitive measurement instruments were involved and then only if they happened to be located at very specific locations.

SUMMARY AND CONCLUSIONS

The analyses quite clearly support the conclusion that there is nothing in the RNS lunar operation either related to radiation or unusual operating constraints which would challenge its feasibility or practicability in supporting advanced lunar exploration. With the exception of the lunar orbit insertion maneuver, in which the engine cooldown extends the time interval for the maneuver, the nuclear and chemical shuttle operations would be nearly the same. Separation distances in orbit between the RNS and OLS will probably be established more on the basis of clearance required for other OLS operations than for control of radiation environment. Radiation exposures related to normal RNS operations at either the OLS or on the lunar surface do not reach levels high enough to be of concern, either for a single trip or for the accumulated dose from multiple trips.

INTEGRAL DOSE DURING CONSTANT VELOCITY MOTION NEAR A SPACE POWER REACTOR

H. S. Manning, NASA/MSFC

The dose rate in a rotationally-symmetric radiation field near a space power reactor is assumed to be inversely proportional to separation distance squared and directly proportional either to a constant or a constant times the sine-cubed of a polar angle. Constant velocity motion (constant speed and direction) is examined in both cases in both two- and three-dimensional geometries. The two-dimensional geometry occurs when the line of motion and the field axis of symmetry are co-planar. The dose integral in the sine-cubed region may be integrated directly, but a more useful form is obtained after a change of variable. A coordinate system rotation greatly simplifies the results. The three-dimensional problem is integrated after a change of variable. Finally, tables of normalized functions are presented and discussed.

INTRODUCTION

A key problem associated with the study of nuclear energy sources in space is the evaluation of the leakage radiation reaching the astronauts or other radiosensitive detectors. This paper discusses a solution to the problem of constant velocity motion near a space power reactor with a specific leakage radiation pattern. The term "constant velocity" is intended to be understood in the vector sense implying constant speed and constant direction.

The radiation field description was derived from material presented by Atomics International in References 1 and 2 and is illustrated in Figures 1 and 2. Figure 3 depicts an isodose contour in the (x, +y) halfplane. The radiation source is represented as a point source located at the origin O. The radiation field is assumed to be comprised of three regions. Region I represents the field due to an unshielded isotropic source or leaking through a relatively thin shield. Region III represents the field behind a thick "biological shield" of half-angle ϵ. In both regions, the shield is assumed to be of approximately uniform attenuation with azimuth angle so the dose rate is a function of distance alone. Region II represents the transition between regions I and III. Because of variations in attenuation and/or source strength, the dose rate has an azimuthal dependence. The field studied here varies as the sine-cubed of a polar angle ϕ measured from an abscissa inclined an angle δ to the x-axis.

MOTION WITHIN A SINGLE PLANE

Consider first the case where the detector moves with constant velocity along a line p contained within a nonrotating plane which also contains the x-axis. Let us first examine the case where all motion is in region II, or

$$(\epsilon - \delta) \leq \phi \leq \frac{\pi}{2} \quad .$$

Let the motion be outward along p from an initial position P_1. Then, from Figure 4,

$$r(P_1) = r_1 = \text{constant} \quad ,$$

$$\zeta = \text{constant} \quad ,$$

$$\alpha_1 = \text{constant} \quad ,$$

$$\phi = \text{constant} \quad ,$$

and

$$\frac{dp}{dt} = V = \text{constant} \quad .$$

In region II, the dose rate is

$$\dot{D}_{II} = \frac{K_1 \sin^3 \phi}{R_{II}^2} \quad ,$$

but

$$\phi = (\alpha - \zeta) \quad ;$$

thus,

$$\dot{D}_{II} = A \frac{\sin^3 \alpha}{r^2} + B \frac{\sin \alpha}{r^2} + C \frac{\sin \alpha'}{r^2} + D \frac{\sin^3 \alpha'}{r^2}$$

where

$$A = K_1 \cos 3\delta \quad ,$$

$$B = K_1 \cos \delta \sin^2 \delta \quad ,$$

$$C = K_1 \sin \delta \cos^2 \delta \quad ,$$

$$D = K_1 \sin 3\delta \quad ,$$

$$\alpha' = \frac{\pi}{2} - \alpha \quad ,$$

and

$$r = R_{II}$$

Consider the first term. Referring back to Figure 4 and introducing initial conditions,

(NOTE: MULTIPLY DOSE RATES BY 0.58 TO GET GAMMA DOSE RATE IN mrad/hr)

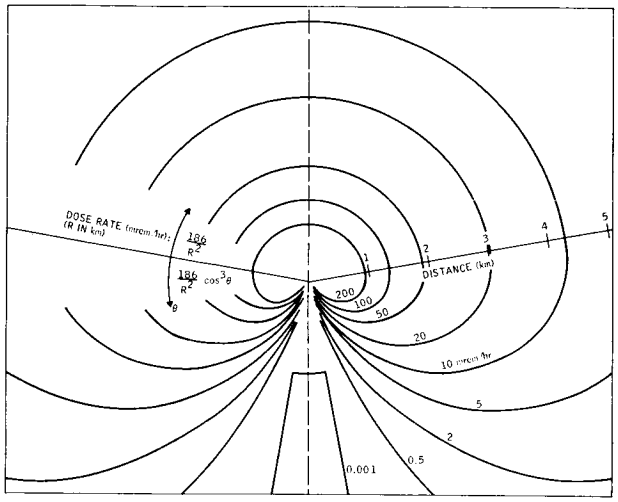

FIGURE 1. REACTOR INDUCED RADIATION FIELD ABOUT 25 kwe REACTOR-TE POWER SYSTEM

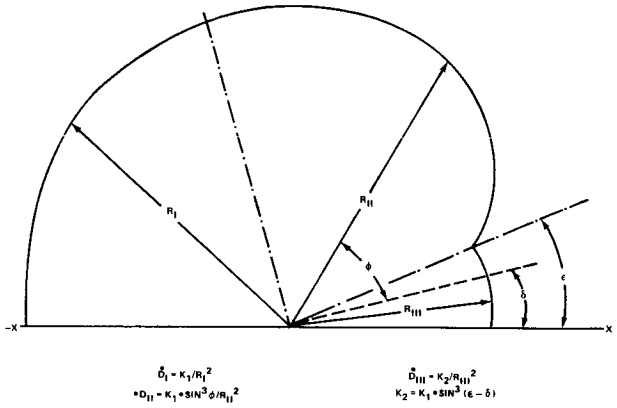

FIGURE 3. GEOMETRY OF A PLANAR ISODOSE CONTOUR

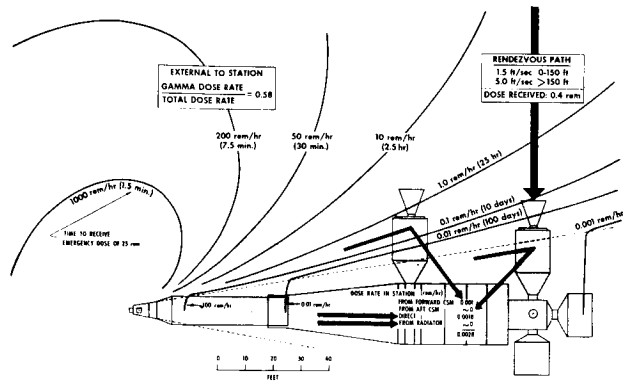

FIGURE 2. SPACE STATION RADIATION ENVIRONMENT FROM NUCLEAR REACTOR

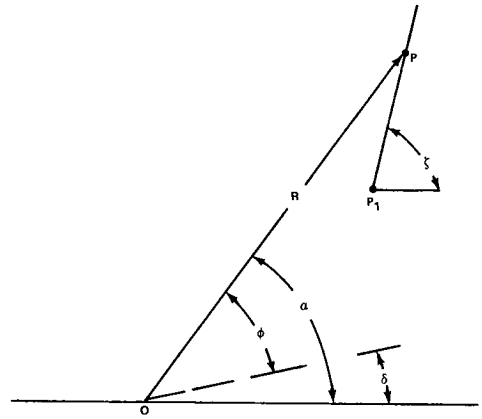

FIGURE 4. CONSTANT VELOCITY MOTION IN A PLANE

$$r \sin \alpha = r_1 \sin \alpha_1 + p \sin \zeta \quad .$$

Also,

$$r^2 = p^2 + r_1^2 + 2pr_1 \cos (\zeta - \alpha_1) \quad .$$

We now write

$$\dot{D}_{IIA} = \frac{A}{V} \frac{(r_1 \sin \alpha_1 + p \sin \zeta)^3}{[r_1^2 + 2pr_1 \cos (\zeta - \alpha_1) + p^2]^{5/2}} \frac{dp}{dt} \quad .$$

The limits for the complete integral along the line are:

$$p(1) = 0$$

and

$$p(2) = \infty \quad .$$

By integrating and inserting the limits and simplifying, the equation above eventually yields

$$D_{IIA} = \frac{A}{3r_1V} \left\{ \frac{(\sin^3 \alpha_1 + \sin^3 \zeta)}{[1 + \cos (\zeta - \alpha_1)]} + \frac{(\sin \alpha_1 + \sin \zeta)^3}{[1 + \cos (\zeta - \alpha_1)^2]} \right\} \quad .$$

CHANGE OF VARIABLE

This general form is somewhat cumbersome to handle. A more useful, if somewhat restricted, form may be obtained through a change of variable before integration. Referring again to Figure 4, we observe that

$$r \cos \alpha = r_1 \cos \alpha_1 + p \cos \zeta \quad .$$

Taking this in conjunction with the expressions above, we find that

$$r = r_1 \frac{\sin (\zeta - \alpha_1)}{\sin (\zeta - \alpha)} \quad ,$$

$$p = r_1 \frac{\sin (\alpha - \alpha_1)}{\sin (\zeta - \alpha)} \quad ,$$

and

$$\frac{dp}{dt} = \frac{\sin (\zeta - \alpha_1)}{\sin^2 (\zeta - \alpha)} \frac{d\alpha}{dt} \quad .$$

Substituting into the dose rate expression,

$$\dot{D}_{IIA} = \frac{\sin^3 \alpha}{\sin (\zeta - \alpha_1)} \frac{d\alpha}{dt} \quad .$$

The limits will be in general

$$\alpha(1) = \alpha_1$$

and

$$\alpha(2) = \alpha_2 \quad .$$

By integrating and inserting the limits, we have the complete first term,

$$D_{IIA} = \frac{A}{3r_1V} \left[\frac{3(\cos \alpha_1 - \cos \alpha_2) - (\cos^3 \alpha_1 - \cos^3 \alpha_2)}{\sin (\zeta - \alpha_1)} \right] \quad .$$

The second term of the expanded dose rate equation is

$$\dot{D}_{IIB} = \frac{B \sin \alpha}{r^2}$$

which yields immediately

$$D_{IIB} = \frac{B}{r_1V} \frac{(\cos \alpha_1 - \cos \alpha_2)}{\sin (\zeta - \alpha_1)}$$

using the limits above.

The doses D_{IIC} and D_{IID} may be evaluated using the arguments above but with the complementary angle α'. The complete dose expression can now be written as

$$\begin{aligned} D_{II} = \frac{K_1}{3r_1V \sin (\zeta - \alpha_1)} \{ & \cos 3\delta [3(\cos \alpha_1 - \cos \alpha_2) \\ & - (\cos^3 \alpha_1 - \cos^3 \alpha_2)] \\ & + 3 \cos \delta \sin^2 \delta (\cos \alpha_1 - \cos \alpha_2) \\ & - 3 \sin \delta \cos^2 \delta (\cos \alpha_1' - \cos \alpha_2') \\ & + \sin 3\delta [3(\cos \alpha_1' - \cos \alpha_2') \\ & - (\cos^3 \alpha_1' - \cos^3 \alpha_2')] \} \end{aligned}$$

This form is valid except in the case of radial motion discussed below. An additional minor constraint is that $\alpha_1 \geq \epsilon$.

This expression can be greatly simplified by performing a coordinate system rotation through an angle δ. Thus,

$$\alpha* = \alpha - \delta = \phi \quad ,$$

$$\zeta* = \zeta - \delta \quad ,$$

$$\delta* = 0 \quad ,$$

and, constraining the point P_1, to lie along the $\alpha = \delta$ line,

$$D_{II}(0, \phi) = \frac{K_1}{3r_1V} \left[\frac{\cos^3 \phi - 3 \cos \phi + 2}{\sin (\zeta - \delta)} \right]$$

where the parentheses on the left are used to indicate the angular limits. The radial case may be integrated directly from the dose rate equation. It is unaffected by the coordinate system rotation;

$$D_{II}(\phi, \phi) = \frac{K}{V} \left(\frac{1}{r_1} - \frac{1}{r} \right) \sin^3 \phi \quad .$$

The case of constant velocity co-planar motion in an inverse square field has been solved before and is included here only for completeness and notational consistency. Referring to Figure 5, we again let the motion be along a line p , and, as before,

$$r(P_1) = r_1 = \text{constant} \quad ,$$

$$\zeta = \text{constant} \quad ,$$

$$\alpha_1 = \text{constant} \quad ,$$

$$\phi_1 = \text{constant} \quad ,$$

and

$$\frac{dp}{dt} = \text{constant} = V \quad .$$

The dose rate is given by

$$\dot{D} = \frac{K}{r^2} \quad .$$

We observe that

$$\eta = \frac{\pi}{2} - (\zeta - \alpha) \quad ,$$

$$r = r_1 \cos \eta_1 \sec \eta \quad ,$$

$$p = r_1 \cos \eta_1 (\tan \eta - \tan \eta_1) \quad ,$$

and

$$\frac{dp}{dt} = r_1 \cos \eta_1 \sec^2 \eta \, \frac{d\eta}{dt} \; ;$$

thus,

$$D = \frac{K}{r_1 V} \left[\frac{\alpha_2 - \alpha_1}{\sin (\zeta - \alpha_1)} \right] \quad .$$

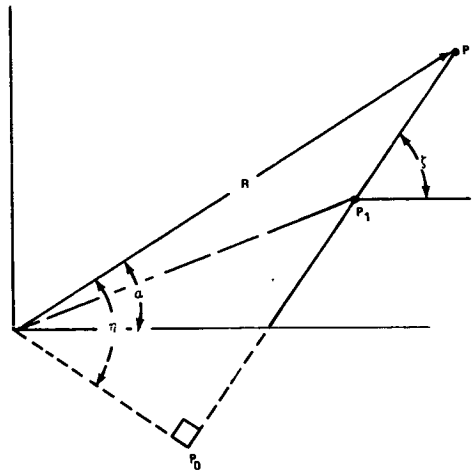

FIGURE 5. CONSTANT VELOCITY COPLANAR MOTION IN AN INVERSE SQUARE FIELD

MOTION IN THREE DIMENSIONS

If isodose contours such as in Figure 3 are rotated through 2π radians around the x-axis, a complex three-dimensional radiation field will be produced. Assume constant velocity motion along an arbitrarily oriented straight line, as in Figure 6. Again, let us first examine the case of motion within region II along the line $P_1P = p$ outward from an initial position P_1. The radiation field polar angle is again

$$\phi = \alpha - \delta \quad ,$$

and, as before,

$$\dot{D}_{II} = A \frac{\sin^3 \alpha}{r^2} + B \frac{\sin \alpha}{r^2} + C \frac{\sin \alpha'}{r^2} + D \frac{\sin^3 \alpha'}{r^2}$$

The direct integral of the cubic term has not been obtained; however, the term has been successfully integrated after performing a variable change similar to that in the restricted solution of the co-planar case.

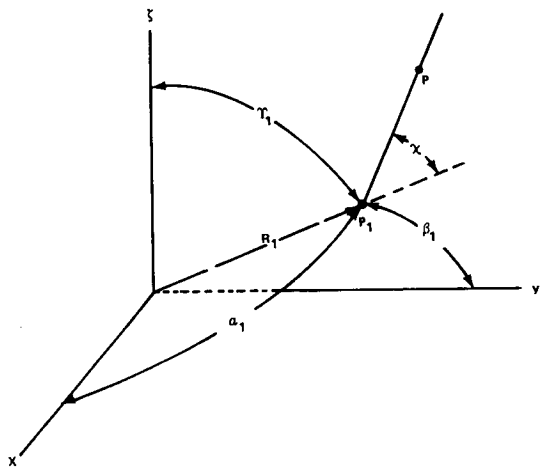

FIGURE 6. CONSTANT VELOCITY MOTION IN THREE DIMENSIONS

The radius vector to the initial point can be written

$$\bar{r}_1 = (\hat{i}\cos\alpha_1 + \hat{j}\cos\beta_1 + \hat{k}\cos\gamma_1)r_1 \quad ,$$

where $r_1 = |\bar{r}_1|$ and $\cos\alpha_1$, $\cos\beta_1$, and $\cos\gamma_1$ are direction cosines. Similarly, the vector traced by the moving point is

$$\bar{p} = (\hat{i}\cos\alpha_p + \hat{j}\cos\beta_p + \hat{k}\cos\gamma_p)p \quad .$$

Since the direction is constant, $\bar{p}/p$ is constant. The angle between these two vectors is also a constant,

$$\cos\chi = \cos\alpha_1\cos\alpha_p + \cos\beta_1\cos\beta_p + \cos\gamma_1\cos\gamma_p \quad .$$

Figure 7 illustrates the nonrotating plane containing the vectors $\bar{r}$, $\bar{r}_1$, and $\bar{p}$. This plane contains the variable angle θ between the vector $\bar{r}$ and the (x,y) plane. Consider the nonrotating plane containing the x-axis and $\bar{r}_1$ and the rotating plane containing the x-axis and $\bar{r}$. In the former, there is the constant angle α_1 and in the latter the variable angle α. If a unit sphere is constructed at the origin, these three angles become the sides of a spherical triangle. If the face angle opposite side α is called λ, then

$$\cos\alpha = \cos\alpha_1\cos(\theta - \theta_1) + \sin\alpha_1\sin(\theta - \theta_1)\cos\lambda \quad .$$

But, λ is also the angle between the planes containing POP_1 and P_1OX_1. Thus,

$$\cos(\pi - \lambda) = \left(\frac{\bar{r}_1 \times \bar{p}}{r_1 p}\right) \cdot \left(\frac{\hat{i} \times \bar{r}_1}{r_1}\right) \frac{1}{\sin\chi\sin\alpha_1}$$

and

$$\cos\lambda = \frac{\cos\alpha_p \sin^2\alpha_1 - \cos\alpha_1(\cos\beta_p\cos\beta_1 + \cos\gamma_p\cos\gamma_1)}{\sin\chi\sin\alpha_1} \quad .$$

Continuing, we simplify

$$\cos\alpha = k\cos[\theta - (\theta_1 - \psi)] \quad ,$$

where the phase angle ψ is defined by

$$\tan\psi = \tan\alpha_1\cos\lambda$$

and the modulus k is found from

$$k^2 = \cos^2\alpha_1 + \sin^2\alpha_1\cos^2\lambda \quad .$$

We note in passing that θ_1, ψ, and k are defined by initial conditions only and that $k^2 \leq 1$.

Returning to Figure 7, we may write

$$r = r_1 \frac{\sin(\zeta - \theta_1)}{\sin(\zeta - \theta)} \quad ,$$

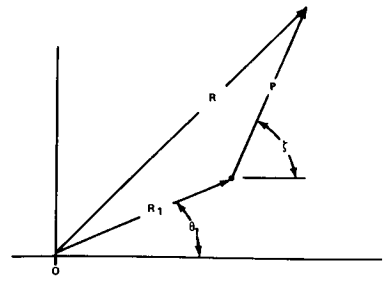

FIGURE 7. PLANE OF MOTION IN THREE-DIMENSIONAL CASE

$$p = r_1 \frac{\sin(\theta - \theta_1)}{\sin(\zeta - \theta)} \quad ,$$

and

$$\frac{dp}{dt} = r_1 \frac{\sin(\zeta - \theta_1)}{\sin^2(\zeta - \theta)} \frac{d\theta}{dt} \quad .$$

The dose rate is now

$$\dot{D}_{IIA} = \frac{A}{r_1 V} \frac{\{1 - k^2\cos^2[\theta - (\theta_1 + \psi)]\}^{3/2}}{\sin(\zeta - \theta)} \frac{d\theta}{dt} \quad .$$

Let

$$\sin^2\mu = \cos^2[\theta - (\theta_1 + \psi)]$$

and

$$\Delta = (1 - k^2\sin^2\mu)^{1/2} \quad , \qquad k^2 \leq 1$$

and the expression integrates to

$$D_{IIA} = \frac{A}{3r_1 V\sin(\zeta - \theta_1)} [k^2\Delta\sin\mu\cos\mu - (1 - k^2)F(k,\mu) + 2(2 - k^2)E(k,\mu)]_{\mu(1)}^{\mu(2)} \quad ,$$

where $F(k,\mu)$ is the incomplete elliptic integral of the first kind and $E(k,\mu)$ is the incomplete elliptic integral of the second kind. The limits of integration are indicated outside the bracket on the right.

Using the substitutions above, the second term in the expanded dose rate equation becomes

$$\dot{D}_{IIB} = \frac{B}{r_1 V \sin(\zeta - \theta_1)} \Delta \frac{d\mu}{dt} \quad ;$$

thus,

$$D_{IIB} = \frac{B}{r_1 V \sin(\zeta - \theta_1)} [E(k,\mu)]_{\mu(1)}^{\mu(2)} \quad .$$

The third term may be written as

$$\dot{D}_{IIC} = \frac{Ck}{r_1 V \sin(\zeta - \theta_1)} \sin\mu \frac{d\mu}{dt} \quad ;$$

and

$$D_{IIC} = \frac{Ck}{r_1 V \sin(\zeta - \theta_1)} (\cos\mu)_{\mu(2)}^{\mu(1)} \quad .$$

The last term is

$$\dot{D}_{IID} = \frac{Dk^3}{r_1 V \sin(\zeta - \theta_1)} \sin^3\mu \frac{d\mu}{dt}$$

which yields

$$D_{IID} = \frac{Dk^3}{3 r_1 V \sin(\zeta - \theta_1)} (3\cos\mu - \cos^3\mu)_{\mu(2)}^{\mu(1)} \quad .$$

The complete expression for the three-dimensional case could now be constructed using the components above. Regrettably, no simplifying step such as the coordinate system rotation used in the planar case has been found.

The restriction against radial motion applies here as in the planar case. However, as radial motion is necessarily co-planar with the x-axis, the special form given earlier will apply.

APPLICATIONS

Many problems involved with close-in operations near a nuclear power source can be adequately approximated by assuming constant velocity co-planar motion. The integral dose in this case can most easily be found from the expression for $D_{II}(0,\phi)$ developed above. The expression can be normalized as

$$D_{II}(0,\phi) \frac{r_1 V \sin(\zeta - \delta)}{K_1} = \frac{(\cos^3\phi - 3\cos\phi + 2)}{3} \quad .$$

This expression is tabulated as a function of the angle ϕ in Table 1. This table is organized in standard math table format and allows five significant figure values of the function to be read corresponding to three significant figure values for the angle ϕ. Linear interpolation is used for intermediate values.

TABLE 1. NORMALIZED DOSE INTEGRALS FOR A TWO-DIMENSIONAL CASE

	0	1	2	3	4	5	6	7	8	9
0.0	00000	00000	00000	00000	00000	00000	00000	00000	00000	00000
1.0	00000	00000	00000	00000	00000	00000	00000	00000	00000	00000
2.0	00000	00000	00000	00000	00000	00000	00000	00000	00000	00000
3.0	00000	00000	00000	00000	00000	00000	00000	00000	00000	00001
4.0	00001	00001	00001	00001	00001	00001	00001	00001	00001	00001
5.0	00001	00002	00002	00002	00002	00002	00002	00002	00003	00003
6.0	00003	00003	00003	00004	00004	00004	00004	00005	00005	00005
7.0	00006	00006	00006	00007	00007	00007	00008	00008	00009	00009
8.0	00009	00010	00010	00011	00011	00012	00013	00013	00014	00014
9.0	00015	00016	00016	00017	00018	00019	00020	00020	00021	00022
10.0	00023	00024	00025	00026	00027	00028	00029	00030	00031	00032
11.0	00034	00035	00036	00037	00039	00040	00041	00043	00044	00046
12.0	00047	00049	00051	00052	00054	00056	00058	00059	00061	00063
13.0	00065	00067	00069	00071	00073	00076	00078	00080	00083	00085
14.0	00087	00090	00092	00095	00098	00100	00103	00106	00109	00112
15.0	00115	00118	00121	00124	00127	00131	00134	00137	00141	00145
16.0	00148	00152	00156	00159	00163	00167	00171	00175	00180	00184
17.0	00188	00193	00197	00202	00206	00211	00216	00221	00226	00231
18.0	00236	00241	00246	00251	00257	00262	00268	00274	00280	00285
19.0	00291	00298	00304	00310	00316	00323	00329	00336	00343	00349
20.0	00356	00363	00371	00378	00385	00393	00400	00408	00416	00423
21.0	00431	00439	00448	00456	00464	00473	00482	00490	00499	00508
22.0	00517	00527	00536	00545	00555	00565	00575	00585	00595	00605
23.0	00615	00626	00636	00647	00658	00669	00680	00691	00703	00714
24.0	00726	00738	00750	00762	00774	00786	00799	00812	00824	00837
25.0	00850	00864	00877	00891	00904	00918	00932	00946	00961	00975
26.0	00990	01004	01019	01035	01050	01065	01081	01097	01112	01129
27.0	01145	01161	01178	01195	01211	01229	01246	01263	01281	01299
28.0	01317	01335	01353	01372	01390	01409	01428	01447	01467	01487
29.0	01506	01526	01546	01567	01587	01608	01629	01650	01672	01693
30.0	01715	01737	01759	01781	01804	01826	01849	01872	01896	01919
31.0	01943	01967	01991	02015	02040	02065	02090	02115	02140	02166
32.0	02192	02218	02244	02271	02298	02325	02352	02379	02407	02435
33.0	02463	02491	02520	02548	02577	02607	02636	02666	02696	02726
34.0	02756	02787	02818	02849	02880	02912	02944	02976	03008	03041
35.0	03073	03106	03140	03173	03207	03241	03276	03310	03345	03380
36.0	03415	03451	03487	03523	03559	03596	03633	03670	03707	03745
37.0	03783	03821	03859	03898	03937	03976	04016	04055	04095	04136
38.0	04176	04217	04258	04300	04341	04383	04426	04468	04511	04554
39.0	04597	04641	04685	04729	04774	04818	04864	04909	04955	05000
40.0	05047	05093	05140	05187	05234	05282	05330	05378	05427	05476
41.0	05525	05574	05624	05674	05724	05775	05826	05877	05929	05980
42.0	06033	06085	06138	06191	06244	06298	06352	06406	06461	06516
43.0	06571	06626	06682	06738	06795	06852	06909	06966	07024	07082
44.0	07140	07199	07258	07317	07377	07437	07497	07557	07618	07680
	0	1	2	3	4	5	6	7	8	9

TABLE 1. (Concluded)

	0	1	2	3	4	5	6	7	8	9
45.0	07741	07803	07865	07928	07991	08054	08117	08181	08245	08310
46.0	08374	08440	08505	08571	08637	08703	08770	08837	08905	08972
47.0	09041	09109	09178	09247	09316	09386	09456	09527	09597	09669
48.0	09740	09812	09884	09956	10029	10102	10176	10250	10324	10398
49.0	10473	10549	10624	10700	10776	10853	10930	11007	11084	11162
50.0	11241	11319	11398	11478	11557	11637	11718	11798	11879	11961
51.0	12043	12125	12207	12290	12373	12457	12540	12625	12709	12794
52.0	12879	12965	13051	13137	13224	13311	13398	13486	13574	13662
53.0	13751	13840	13929	14019	14109	14200	14290	14382	14473	14565
54.0	14657	14750	14843	14936	15030	15124	15218	15313	15408	15503
55.0	15599	15695	15792	15888	15986	16083	16181	16279	16378	16477
56.0	16576	16676	16776	16876	16977	17078	17179	17281	17383	17485
57.0	17588	17691	17795	17898	18003	18107	18212	18317	18423	18529
58.0	18635	18742	18849	18956	19064	19172	19280	19389	19498	19607
59.0	19717	19827	19937	20048	20159	20271	20383	20495	20607	20720
60.0	20833	20947	21061	21175	21290	21404	21520	21635	21751	21867
61.0	21984	22101	22218	22336	22454	22572	22691	22810	22929	23049
62.0	23169	23289	23410	23531	23652	23773	23895	24018	24140	24263
63.0	24387	24510	24634	24758	24883	25008	25133	25259	25385	25511
64.0	25638	25764	25892	26019	26147	26275	26404	26533	26662	26791
65.0	26921	27051	27181	27312	27443	27575	27706	27838	27970	28103
66.0	28236	28369	28503	28637	28771	28905	29040	29175	29310	29446
67.0	29582	29718	29855	29992	30129	30266	30404	30542	30681	30819
68.0	30958	31098	31237	31377	31517	31658	31798	31939	32081	32222
69.0	32364	32506	32649	32791	32934	33078	33221	33365	33509	33654
70.0	33798	33943	34088	34234	34380	34526	34672	34819	34966	35113
71.0	35260	35408	35556	35704	35852	36001	36150	36299	36449	36599
72.0	36749	36899	37049	37200	37351	37502	37654	37806	37958	38110
73.0	38263	38415	38568	38722	38875	39029	39183	39337	39491	39646
74.0	39801	39956	40112	40267	40423	40579	40735	40892	41049	41205
75.0	41363	41520	41678	41836	41994	42152	42310	42469	42628	42787
76.0	42946	43106	43266	43426	43586	43746	43907	44068	44228	44390
77.0	44551	44713	44874	45036	45198	45361	45523	45686	45849	46012
78.0	46175	46339	46502	46666	46830	46994	47158	47323	47487	47652
79.0	47817	47983	48148	48313	48479	48645	48811	48977	49143	49310
80.0	49476	49643	49810	49977	50144	50312	50479	50647	50815	50983
81.0	51151	51319	51487	51656	51825	51993	52162	52331	52500	52670
82.0	52839	53009	53178	53348	53518	53688	53858	54029	54199	54369
83.0	54540	54711	54882	55053	55224	55395	55566	55737	55909	56080
84.0	56252	56424	56595	56767	56939	57111	57284	57456	57628	57801
85.0	57973	58146	58318	58491	58664	58837	59010	59183	59356	59529
86.0	59702	59876	60049	60222	60396	60569	60743	60917	61090	61264
87.0	61438	61612	61786	61960	62133	62307	62482	62656	62830	63004
88.0	63178	63352	63527	63701	63875	64050	64224	64398	64573	64747
89.0	64922	65096	65271	65445	65620	65794	65969	66143	66318	66492
	0	1	2	3	4	5	6	7	8	9

Values from this table give the integral dose along a line originating on the $\phi = 0$ or $\alpha_1 = \delta$ line and proceeding outward until $\alpha - \delta = \phi$. The inclination of the line is accounted for in the normalizing constants. Integral dose accrued between the points at ϕ_1 and ϕ_2 on the same line as $[D_{II}(0,\phi_2) - D_{II}(0 - \phi_1)]$.

This allows one to correct for the small difference between $\alpha = \epsilon$, the closest the axis may be approached in region II, and $\alpha = \delta$, the abscissa of the extended field contours.

Another useful form results from constraining P_1 to lie along the $\phi = \frac{\pi}{2}$ line; thus,

$$D_{II}\left(\frac{\pi}{2}, \phi\right) = \frac{K_1}{3r_1V}\left[\frac{3\cos\phi - \cos^3\phi}{\cos(\zeta - \delta)}\right] .$$

This dose is related to the tabulated dose by

$$D_{II}\left(\frac{\pi}{2}, \phi\right) = \left[D_{II}\left(0, \frac{\pi}{2}\right) - D_{II}(0, \phi)\right] \tan(\zeta - \delta) \quad .$$

The three-dimensional problem in region II contains too many variables to allow simple parametric representation. To obtain sample results, a specific field pattern was chosen and values of the integral above were obtained. The field axis offset angle, $\delta = 8.663$ degrees, corresponds to the field illustrated in Figures 1 and 2. Generalized values of the resulting integral are shown in Table 2 as functions of the modulus k and the field angle μ defined above. The table is read in a manner similar to Table 1; thus,

$$D_{II}(k, \mu_1, \mu_2) = D_{II}(k, \mu_2) - D_{II}(k, \mu_1) \quad ,$$

where it is understood that the normalizing factor $[r_1V \sin(\zeta - \theta)/k]$ has been divided out of both sides of the expression.

TABLE 2. NORMALIZED DOSE INTEGRALS FOR A THREE-DIMENSIONAL CASE, $\delta = 8.667$ DEGREES

Range Angle μ, Degrees	Modulus Angle $\sin^{-1} k$, Degrees									
	00	10	20	30	40	50	60	70	80	90
00	0.0	0.0271	0.0620	0.1101	0.1722	0.2441	0.3172	0.3907	0.4240	0.4393
10	0.1605	0.1874	0.2218	0.2692	0.3308	0.4017	0.4743	0.5373	0.5802	0.5954
20	0.3216	0.3464	0.3784	0.4224	0.4800	0.5473	0.6162	0.6764	0.7173	0.7320
30	0.4824	0.5030	0.5302	0.5665	0.6149	0.6727	0.7328	0.7859	0.8223	0.8353
40	0.6432	0.6600	0.6764	0.6990	0.7312	0.7720	0.8165	0.8569	0.8852	0.8954
50	0.8040	0.8139	0.8161	0.8185	0.8266	0.8425	0.8639	0.8859	0.9024	0.9085
60	0.9649	0.9610	0.9499	0.9255	0.9018	0.8847	0.8763	0.8748	0.8766	0.8777
70	1.1256	1.1142	1.0782	1.0215	0.9594	0.9029	0.8592	0.8308	0.8159	0.8115
80	1.2864	1.2663	1.2027	1.1130	1.0040	0.9036	0.8214	0.7640	0.7320	0.7220
90	1.4539	1.4152	1.3250	1.1930	1.0418	0.8962	0.7728	0.6858	0.6369	0.6217

REFERENCES

1. "Joint AEC/NASA/MSFC Study of Reactor-Thermoelectric Powered Space Station," FY-1969 Summary, Atomics International.

2. Glyfe, J. D. and R. A. Johnson, "Reactor-Thermoelectric System for NASA Space Station," AI-AEC-12839, Atomics International, July 1, 1969.

BIBLIOGRAPHY

Petit Bois, G., Tables of Indefinite Integrals, Dover Publications, New York, N. Y., 1961.

Hancock, H., Elliptic Integrals, Dover Publications, New York, N.Y., 1958.

TELEOPERATORS FOR REMOTE OPERATIONS IN SPACE*

L. E. Little and F. L. DiLorenzo
Aerojet Nuclear Systems Company

INTRODUCTION

Early in 1970 a NASA Task Team was assembled to evaluate the potential application of teleoperators/robots to the integrated space program requirements. The term teleoperator as applied to space programs is generally defined as general purpose, dexterous, cybernetic, man-machine systems that augment man by extending his capabilities across distances and through physical barriers into hostile environments and amplify his energy and force capability. Teleoperators are a prime candidate to augment or possibly eliminate Extra Vehicle Activity (EVA).

EVA operations will also be limited by natural space radiation environment and will be eliminated from some operations due to manmade radiation environment. The NASA Task Team recommended the development and application of teleoperators for a variety of space tasks whose missions were broadly divided into four areas: inspection and servicing of spacecraft; construction in space; mission operations; and emergency operations.

The report described eight major classes of teleoperators, which included:

Remote Maneuvering Teleoperators (RMT)
Lunar Roving Vehicle - Unmanned Operation
Space Station/Shuttle Teleoperator
Mars Roving Vehicle
Tug
Reusable Nuclear Shuttle Teleoperator
Space Assembly Teleoperator
Planetary Support Teleoperator/Robots

One of the major classes required is the development of a teleoperator for nuclear programs. Some of the typical tasks identified by NASA for this teleoperator system were nuclear-engine replacement and maintenance, propellant transfer and refueling, cargo handling for the reusable nuclear shuttle, and the package and disposal of spent reactors.

Aerojet Nuclear Systems Company, under the direction of the Space Nuclear Systems Office, is conducting detailed analysis to:

1. Establish requirements for a Remote Nuclear Teleoperator (RNT)
2. Establish engineering concepts for the RNT
3. Establish a development and qualification plan for the RNT

The analysis has been based around the concept of the Reusable Nuclear Vehicle. The concept of the RNV involves many normal and maintenance operations in space which could require either an EVA mode or a teleoperator.

Once the propulsion system has been activated the radiation level essentially precludes any EVA operations; therefore, similar to the ground test program, any operations performed on the propulsion system will require a teleoperator. Many teleoperator concepts exist, from on-board the RNV to a flyable unit. The on-board units appear to establish large weight penalties on the RNV, so the original teleoperator concepts have been led to a flyable unit.

NERVA TELEOPERATOR PROGRAM REQUIREMENTS

System engineering documentation has been generated for both the ground and flight phases of the NERVA engine. Also, a maintainability design trade study has been completed and a maintenance concept has been formulated and published. Using this basic information, which has identified many requirements allocated to the teleoperator system, a systems analysis approach was continued to further delineate NERVA Program teleoperator requirements. Many guidelines were used in generating these functional requirements; the most important being:

No planned EVA operations in space for NERVA operations and maintenance, and

Teleoperator and NERVA engine design must be interrelated for maximum compatibility

The following specific tasks were identified for the normal and maintenance operations from the analysis:

Normal Operations

1. Install and remove external shield
2. Checkout nuclear engine (visual inspection)
3. Install or remove cargo as required
4. Remove launch support equipment
5. Disposition of spent engine

Maintenance Operations

1. Remove engine from stage, dispose/acquire, install engine to stage
2. Remove and replace engine hardware modules
3. Replace engine electronics modules
4. Support verification of maintenance actions and checkout

The teleoperator system analysis indicated (based on all ground rules, guidelines, and both normal and maintenance tasks determined from engine system analysis) that the teleoperator should consist of two or more separate parts: (1) a control unit which may be in space or earth-based; and (2) orbiting satellite teleoperators which can be maneuvered and operated by the teleoperator controller. Other requirements identified by the analysis were:

1. The teleoperator must have docking arms to attach to the engine, stage, and other devices at points to which the teleoperator must be secured as a working or transporting platform for the various tasks assigned.
2. The teleoperator must attach to the stage/

*The Nuclear Engine for Rocket Vehicle Application (NERVA) program is administered by the Space Nuclear Systems Office, a joint office of the USAEC and NASA. Aerojet Nuclear Systems Company is prime contractor for the engine system and Westinghouse Electric Corporation is principal subcontractor responsible for the nuclear subsystem.

engine, disengage and separate the engine and/or engine module/component, disengage from the stage/engine and deliver it to a point or area of disposition.

3. The teleoperator must acquire and then transport the engine and/or engine module/components from a space source to the stage/engine and attach them to the stage/engine as required, and effect their alignment, mating, and securing as required.
4. The controller must remotely checkout, control, maneuver, and secure the teleoperator slave.

FLIGHT CONFIGURATION CONCEPT

To meet the identified requirements an advanced teleoperator is required. Teleoperators of today can be built and flown but their capabilities will be limited. The remote handling technologies have been advanced to meet the "hot cell" requirements but are still considered first generation and will require advancement to meet the outer space requirements. To truly transmit man's sense of presence and instinctive control to a remote teleoperator, advancement in manipulators/controls, sensors, and display is necessary.

The present remote nuclear teleoperator concept (Figure 1) consists of a system of integral or separable space vehicles that are capable of performing the required flight preparation and maintenance tasks on the NERVA engine (Figure 2) while in earth orbit. The teleoperator is a closed-loop system with man in control at all times for surveillance and decision-making.

The concept consists of a teleoperator controller (TOC) system, a teleoperator slave (TOS) effector and, as required, a support system.

The TOC contains human operators and all subsystems necessary to control the functions of the TOS in the performance of space tasks (Figure 3). It receives data from, and transmits commands to, the TOS. The TOC is always manned but may or may not be located in space.

The subsystems consisting of actuator, sensors, control and communications appear to require the most technical advancement. Propulsion, environmental control, computers and power systems have had significant advancement in the manned space flight program.

The need is for an advanced teleoperator, and with development in the mentioned subsystems, a totally remote space teleoperator can be made available. Such things as three-dimensional television, force amplification, logarithmic force feedback, tactile sensors, light-weight, powerful actuators, and high-density communication systems, are some of the advancements which will enable a teleoperator to perform tasks which would require a man in an EVA mode plus many others.

To develop a space teleoperator, ANSC has formulated a program plan identifying the areas of advancement required and a logical approach to developing the system.

GROUND TEST CONCEPT

The time requirements for a remote nuclear teleoperator are such that a qualified space teleoperator will be required by about 1980. A development and qualification plan has identified a detailed sub-plan to advance teleoperator technologies to meet the remote nuclear teleoperator concept.

The plan identifies development of teleoperator subsystems (i.e., manipulators, controls, and sensors) utilizing a ground test configuration vehicle (Figure 4). This vehicle will be a test bed for the advancement of teleoperator technologies.

This vehicle will also be used as test support equipment (TSE) for the NERVA engine program, thus providing program-required support hardware. Conceptually, this system would consist of a prototype teleoperator slave with all space subsystems operable (except those of propulsion and environmental control, and the interface), a conveyor vehicle to provide support and maneuverability to the TOS, and the control console (representing the TOC) behind a barrier to simulate remote conditions.

CONCLUSIONS

The primary objective of the remote nuclear teleoperator study program was to define in detail a program plan which would provide a qualified operational space teleoperator system by about 1980.

The concept and philosophy presented provides a product considered to be an advanced teleoperator when compared to today's state-of-the-art. Previous studies have shown that an operational space teleoperator could be developed in two to three years, but such a teleoperator would contain today's technology and be considerably restricted in its capabilities.

The teleoperator concept was formulated to meet NERVA requirements. This concept is considered preliminary, permitting flexibility during the development period and the time at which the total integrated space program is being defined.

Considerable effort can be expended in the areas of subsystem development (e.g., actuators, sensors, communications, and controls) assuring a program of developed basic subsystems prior to final concept selection. The areas of propulsion, attitude control, and logistics can follow.

The following conclusions are made:

1. An advanced qualified remote nuclear teleoperator can be available by about 1980.
2. An integrated program for the development of a nuclear/space teleoperator is required to meet the commonality and cost-effective requirements of the integrated space plan.
3. To meet reliability and operational requirements of today's space vehicles, without EVA, a teleoperator is required to perform the planned space maintenance.
4. Teleoperator technology must be advanced to meet the requirements for a remotely operated nuclear/space teleoperator.
5. New inventions are not required, only an advancement of today's technology to develop a teleoperator to meet requirements of the nuclear/space teleoperator concept.
6. Utilization of existing facilities can meet teleoperator development and qualification requirements.
7. The design philosophy of a nuclear/space teleoperator must be one of self-repair and maintenance with modular construction.
8. Through the development of a nuclear/space teleoperator, technology can be utilized in development of planetary surface rover units and also "spinoff" applications to industrial robots for remote, hazardous operations on earth.

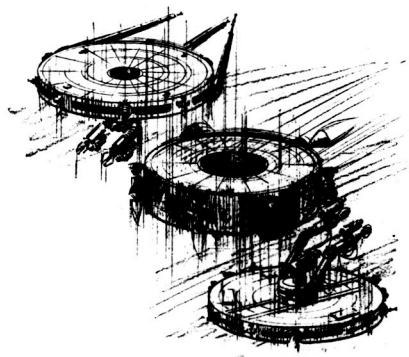

Figure 1 Teleoperator Vehicle Showing Manned Command Module With Two Unmanned Slave Units

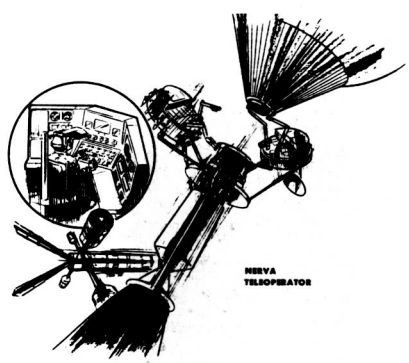

Figure 2

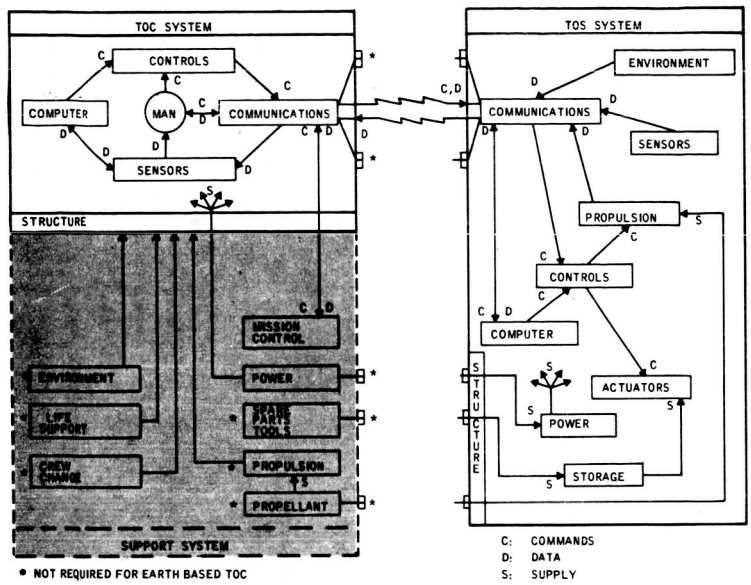

Figure 3 Teleoperator System Block Diagram Flight Configuration

GROUND TEST DEVELOPMENT VEHICLE

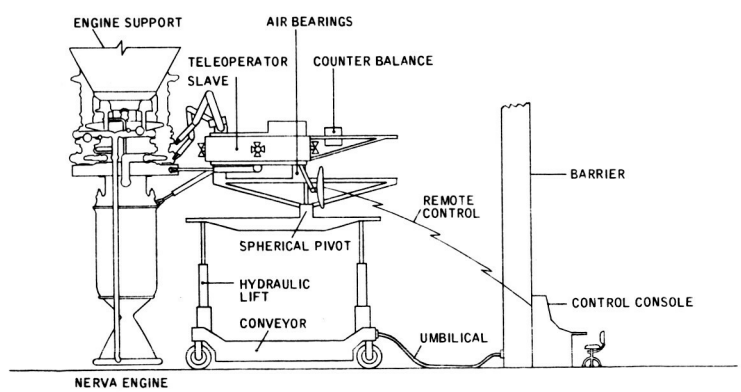

Figure 4 Ground Test Development Vehicle

Teleoperator Systems for Manned Space Missions

ALFRED INTERIAN SPACE PRODUCTS DIVISION GENERAL ELECTRIC COMPANY

In November, 1969, the President's Science Advisory Committee under the leadership of the distinguished Dr. L. DuBridge, unequivocally called for development of remote mechanical systems to augment man's capabilities in our manned space effort. A "teleoperator system" would extend man's innate intelligence and sensory capabilities to distant hostile and hazardous environments through a manipulator-equipped spacecraft and an RF link. This paper examines space teleoperator system applications in the Space Station/Space Shuttle Program, which is where the most immediate need exists and the potential return is greatest.

INTRODUCTION

As the space station and space shuttle development proceed, the necessity of applying teleoperator systems to extend man's innate intelligence and sensory capabilities to distant, hostile, and hazardous environments becomes apparent. The teleoperator system is a remote, electromechanical and visual system that utilizes video and manipulator-equipped spacecraft and an RF link to extend human capabilities across many miles in space.

The possibility of using manipulators in space environment has been suggested by space technologists for the last decade. Recent work in this area has:

1. Detailed the success of teleoperator systems on earth and described the extension of their technology to space.
2. Examined the feasibility and cost effectiveness of a ground controlled teleoperator system for refurbishing on-orbit satellites.
3. Described a teleoperator spacecraft design made up primarily of space-qualified components and with a high system reliability.
4. Described the space mission analysis and laboratory work performed to further prove feasibility and establish design criteria and concepts.

As a result of recent studies (References 1 through 4) conducted by the General Electric Company on remote manipulation, a teleoperator system concept was evolved that has many applications in the Space Station/Space Shuttle program. Three views (Figure 1) of the concept are illustrated, pictured within the volume envelope of the standard space station airlock. The system has a free flight capability with the appropriate attitude control and propulsion subsystem, and the system is controlled through the RF communication control subsystem either in the space station or in the shuttle.

The teleoperator is positioned at the worksite with sufficient accuracy and low enough drift rates to allow the manipulator arms to grasp the worksite and attach the docking legs. Of course a video subsystem is needed to see the worksite. Several cameras and an illumination subsystem are used to give the needed visual information despite the harsh visual condition in space. When properly

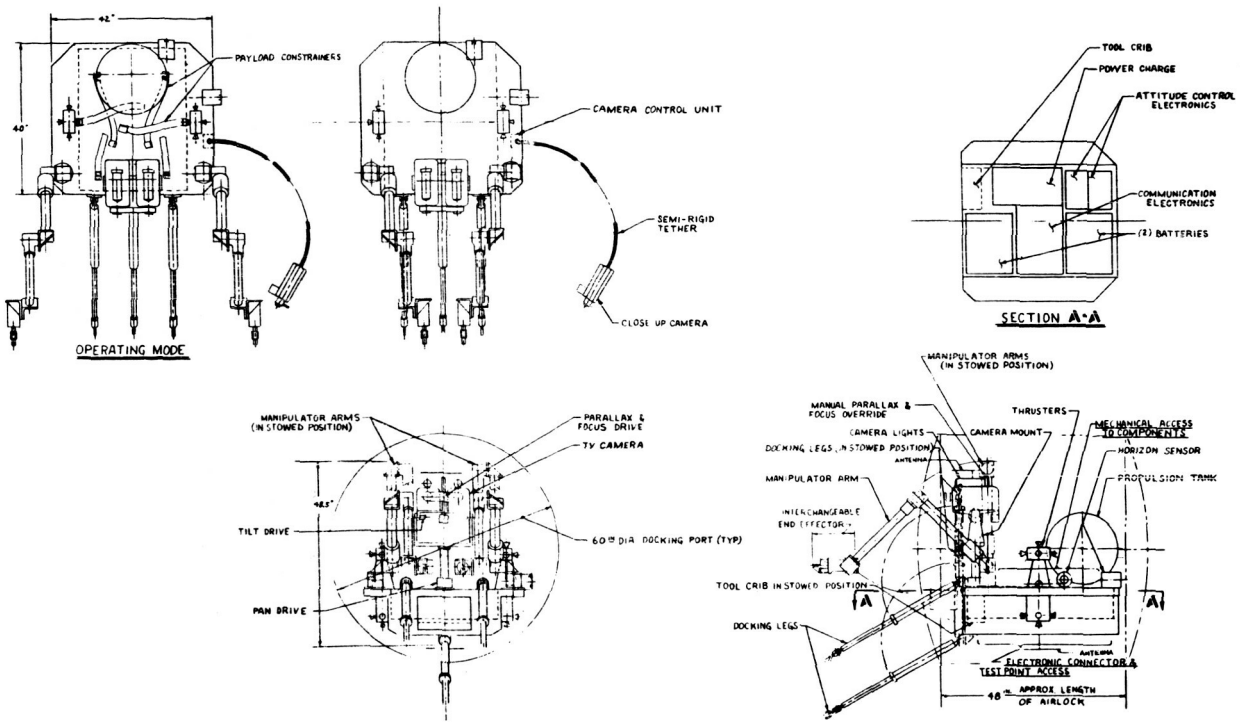

Figure 1. Baseline Teleoperator Configuration

secured to the work site the manipulator arms can perform the needed repairs or refurbishing with the use of tools and techniques previously worked out.

Estimates of the weight and power for this system are shown in Table 1.

Table 1. Space Station Teleoperator Weight and Power Summary

Subsystem	Weight (lb)	Average Power (watts)	Subsystem	Weight (lb)	Average Power (watts)
Manipulator	86.0	40	Video and Illumination	44.1	44
Docking Tethers	18.0	–			
Communications	69.0	30	Power	305.0	–
Propulsion (including fuel)	81.3	46	Structure	100.0	–
Attitude Control	40.2	35	Total	743.6	195

Several methods for station/shuttle maintenance and support are under consideration. One of these concepts would be designed around intravehicular activity, and another method would provide for maintenance through extravehicular activity and the use of special purpose mechanisms and designs.

While the current approaches do not consider general purpose teleoperators, we would like to describe their potential application and advantages. These applications will be presented first for the space station program and then for the space shuttle program.

SPACE STATION PROGRAM

On board a space station, teleoperators would support operation and maintenance of both the space station and station experiment program. A teleoperator of the type evolved from the General Electric investigation would be useful in performing inspection, maintenance, mass transfer and assembly.

Inspection

Periodic visual inspection of the exterior of the station would include a check for punctures, breaks or fouled deployment mechanisms. By taking along leak detectors, IR cameras, or contamination sensors, the teleoperator could carefully search for leaks from within the station, or from the RCS system, and for local hot spots. The environment in the vicinity of the station could also be measured in this way.

Maintenance

RCS Quadjets wear out and will have to be replaced periodically. Currently they are configured for IVA replacement, but these units could be replaced more simply from the outside of the station (Figure 2). The present technique requires large internal crew tunnels and work volumes and deployable outside covers or seals to maintain the station airtight integrity and environment in the work volume. Degraded thermal coatings could be replaced with properly coated tapes. Fouled deployment mechanisms usually operate with spring force levels of about 5 pounds and motor torques of about 200 inch-pounds. This is within the force capability of the general purpose teleoperator in the system anticipated by GE, so these devices could be overridden and deployed or undeployed by a teleoperator.

Mass Transfer

For those cases in which complete modules would not be transferred from the shuttle to the station, teleoperators could be used to transfer packaged logistics and equipment from the shuttle cargo bay to a station airlock (Figure 3). This operation would eliminate the need for docking the shuttle to the station.

Assembly

In addition to the assembly of such systems as antennas or solar arrays, a teleoperator could be used to assist in assembly of a modular space station in orbit and aid in the evolutionary operations of growing the station into a base.

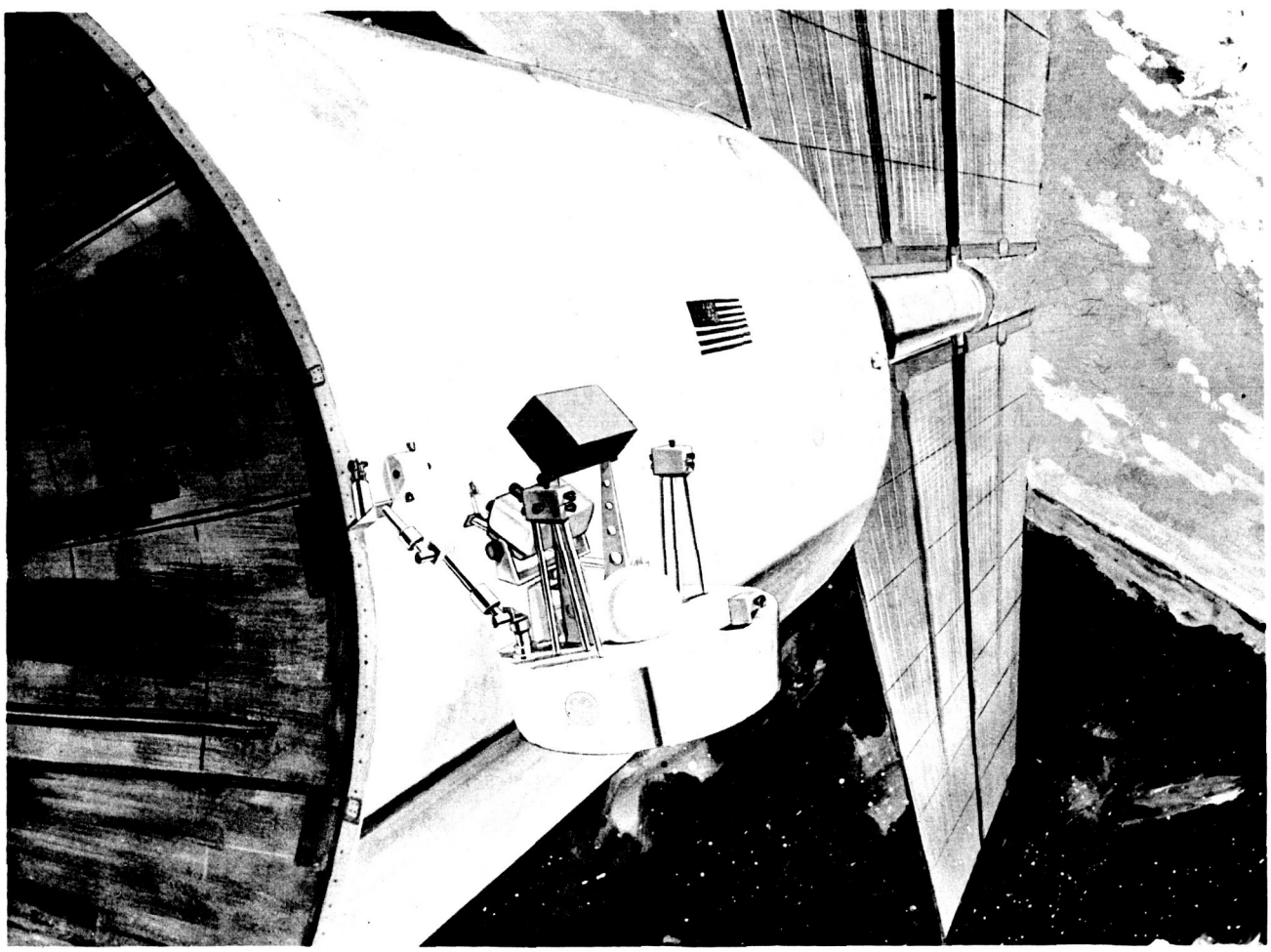

Figure 2. RCS Quadjet Replacement

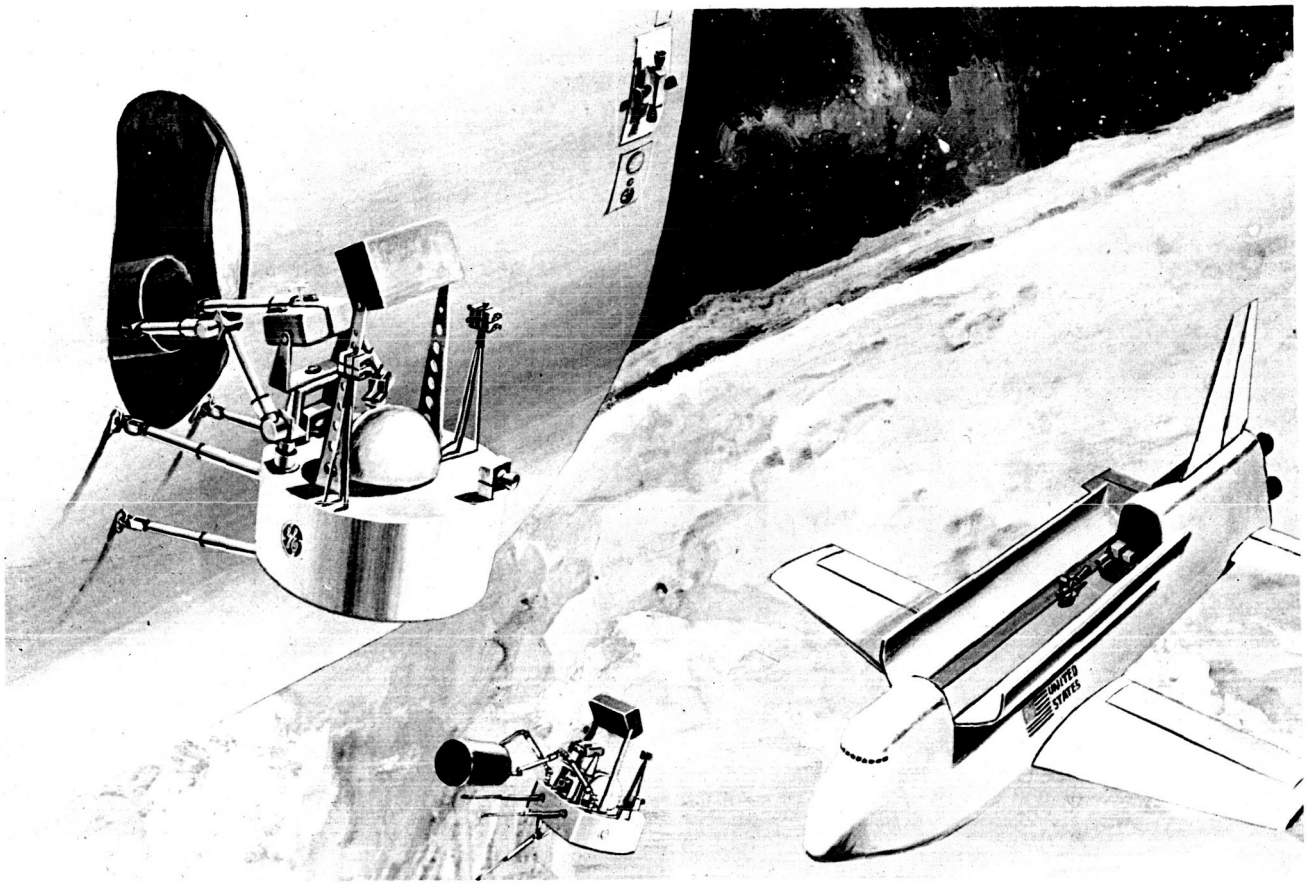

Figure 3. Logistics Transfer

EXPERIMENT PROGRAM SUPPORT

The diverse experiment program planned for the space station calls for the deployment and positioning of sensors and equipment on the station exterior. Some of these sensors will be grouped in modules that are attached to the station. Others will be part of free flight modules remote from the station. In order to accomplish this operation, use will be made of many special purpose booms, positioning devices, and special purpose subsatellites as well as frequent revisits and docking of detached modules to resupply the expendables.

Table 2 is a summary of the potential teleoperator applications that might be used in support of the experiment program. The techniques being considered are shown in the right-hand column.

Table 2. Teleoperator Applications on the NASA Space Station

Functional Program Elements		Teleoperator Applications	Technique Presently Considered
5.1 5.5A	Grazing Incidence X-Ray Telescope and High Energy Stellar Survey (X-Ray)	Film and tape retrieval and change Routine Maintenance and Servicing Refueling	Module docks to Space Station periodically. Astronauts enter module through docking port and service

Table 2. Teleoperator Applications on the NASA Space Station (Cont)

Functional Program Element		Teleoperator Applications	Technique Presently Considered
5.2	Stellar Astronomy Module	Film and tape retrieval and change Routine Maintenance and Servicing Refueling	Module docks to Space Station periodically. Astronauts enter module through docking port and service
5.3A	Advanced Solar Astronomy	Film and tape retrieval and change Routine Maintenance and Servicing Refueling	Module docks to Space Station periodically. Astronauts enter module through docking port and service
5.3B	Advanced Solar Astronomy	Film and tape retrieval and change Routine Maintenance and Servicing Refueling	Module docks to Space Station periodically. Astronauts enter module through docking port and service
5.4A	Ultraviolet Stellar Astronomy	Film and tape retrieval and change Routine Maintenance and Servicing Refueling	Module docks to Space Station periodically. Astronauts enter module through docking port and service
5.4B	Ultraviolet Stellar Astronomy Survey	Film and tape retrieval and change Routine Maintenance and Servicing Refueling	Module docks to Space Station periodically. Astronauts enter module through docking port and service
5.5B	High Energy Stellar Astronomy Survey (Gamma-Ray)	Repair of fouled deployment mechanism for detectors	Module docks to Space Station periodically. Astronauts enter module through docking port and service
5.6	Space Physics Airlock	Deployment and installation of sensors and instrumentation outside station Repair of fouled deployment mechanisms (booms)	Deployed on boom through airlock
5.7	Plasma Physics and Perturbation Investigation	Deploy Langmiur probes. Faraday cups, and cyclotron harmonic resonance mechanism (boom)	Some deployed on boom through airlock Dedicated subsatellite is presently used to deploy others

Table 2. Teleoperator Applications on the NASA Space Station (Cont)

Functional Program Element		Teleoperator Applications	Technique Presently Considered
5.8	Cosmic Ray Physics Laboratory	Photographic plate retrieval and change Resupply of liquid cryogen and plate emulsion Refueling Routine maintenance and service	Module docks to Space Station periodically. Astronauts enter module through docking port and service
5.11	Earth Surveys	Retrieve and replace film Repair fouled deployment mechanism	Module is unpressurized during operational phase and is pressurized during maintenance phase
5.12	Meterology Sub-satellite	Transport sensors, probes and instrumentation to new orbital position	Dedicated subsatellite is presently used
5.14	Man System Integration	Experiment calls for maneuvering subsatellite and teleoperators	A teleoperator system is called for
5.16	Materials Science and Processing	Deployment of processing equipment outside station during experiment operating	Space chamber is built into laboratory area for experiment operating mode
5.17	Contamination Measurements	Deploy and install sensors and instrumentation outside station	Deployed on boom through airlock
5.18	Exposure Experiments	Deploy, install and retrieve sensors and instrumentation outside station	Deployed on panel pallet through airlock and installed on outer skin of station - retrieved again using panel pallet.
5.20	Fluid Physics	Film retrieval and change Routine maintenance and Servicing Refueling	Module docks to Space Station periodically. Astronauts enter module through docking port and service
5.21	IR Stellar Survey	Resupply of liquid cryogenics Routine Maintenance and Service Refueling	Module docks to Space Station periodically. Astronauts enter module through docking port and service

Table 2. Teleoperator Applications on the NASA Space Station (Cont)

Functional Program Element	Teleoperator Applications	Technique Presently Considered
5.22 Component Test	Deploy and install equipment and instrumentation outside station	Equipment installed in space chamber in station and operated
	Conduct space welding experiment in space	Conduct space welding experiment in space chamber
5.24 MSF Engineering	Experiment calls for a maneuvering subsatellite and teleoperator	Use teleoperators
	Maintenance of isotope Brayton power system	No extensive maintenance planned

A listing is made in Table 3 of the estimated weight and volume of current techniques considered for performing experiments.

The weight and volume summary of special purpose booms and subsatellites is shown in this table but no attempt has been made to include such special mechanisms as: tunnels, structure, or gases, which will be necessary to environmentally seal-off work areas or provide access and habitability in work areas. These items are not completely defined or estimated yet but will clearly be large and heavy.

A comparison is made in Table 4 of weight and volume between current techniques for experiments and the use of a teleoperator.

Table 3. Currently Planned Techniques

Item	Weight (lbs)	Volume (ft^3)
Articulated Booms	170	120
Panel Pallet	35	120
Materials Processing Vacuum Chamber	500	72
Remote Maneuvering Satellite - FPE 5.7 & 5.12 (Mobility Package Savings)	100	–
Remote Maneuvering Satellite - FPE 5.24	80	5.0
TOTAL	885	317

Table 4. Weight and Volume Comparison

Item	Weight (lbs)	Volume (ft^3)
General Purpose Teleoperator	750	60
Other Techniques	885	317

This same teleoperator lighter and more compact would be capable of performing the maintenance missions previously described in addition to supporting the experiment program.

SPACE SHUTTLE PROGRAM

Some of the applications mentioned for the station are also applicable to the shuttle. Additional applications arise from the shuttle's ability to inject and maneuver into many different orbits. Some important applications are now being considered:

Visual Inspection

Visual inspection (Figure 4) will include the condition of the shuttle heat shield and the condition and operation of the aerodynamic control surfaces and doors prior to de-orbit and re-entry.

On-Orbit Resupply of Unmanned Satellites

The life of operational satellites may in many cases be economically extended by resupplying spent consummables such as fuel, cold gas, or batteries. Close rendezvous with the target satellite would be accomplished by the shuttle followed by deployment of the teleoperator from the shuttle, and terminal rendezvous and docking of the teleoperator to the target satellite. The teleoperator would then perform the resupply operations and return to the shuttle.

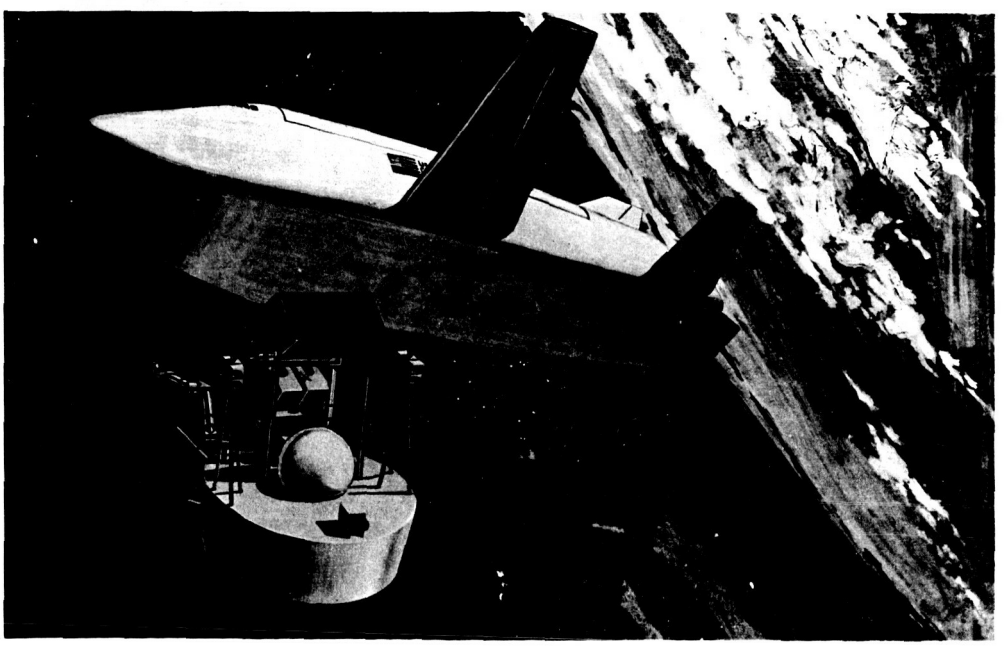

Figure 4. Inspection of Space Shuttle Re-entry Shield

On-Orbit Refurbishment or Retrieval/Deployment of Unmanned Satellites

An extension of the resupply mission would be to change satellite payloads or perform diagnosis and repair on-orbit. These missions (Figure 5) would again be performed by the general purpose teleoperator but the tasks would be greatly simplified if consideration were given to designing satellites for maintainability. The teleoperator would transfer the satellite to the cargo bay for complex tasks for operations by the astronaut crew or perhaps for return to earth.

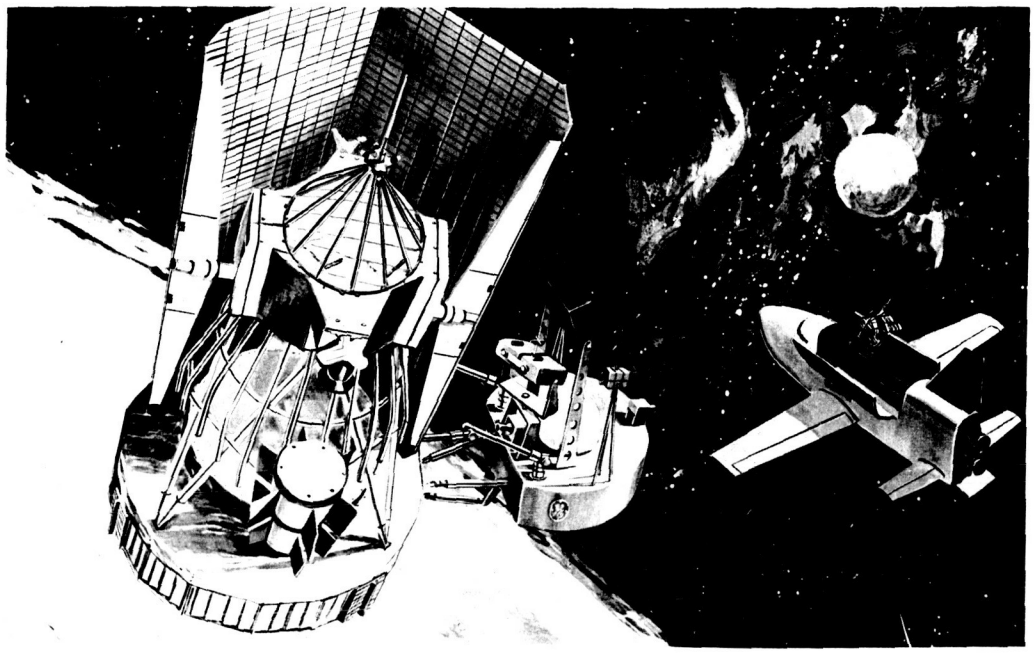

Figure 5. Satellite Retrieval

GROWTH POTENTIAL

The same teleoperator systems would play an important role in the space program of the next decade. Such studies as "The Nuclear Rocket in the Space Future," which was prepared for NASA by D. S. Gabriel, have shown that great savings can be achieved if the nuclear shuttle is made reusable. One limiting item, however, is the engine life. By replacing the engine in orbit (after approximately 10 reuses) the life of the nuclear shuttle could be greatly lengthened. This mission is illustrated in Figure 6. The radiation environment in the vicinity of the spent engine presents a hazard for man-attendance methods but is an ideal application for the mechanical teleoperator. A similar situation will exist on the space base where nuclear reactors will be used for electrical power and require replacement every two years.

Teleoperators with surface roving mobility units could be used to perform lunar or planetary surface explorations (Figure 7). These teleoperators would include many of the same subsystems as their orbiting relatives, such as: manipulators, video, power and communications. They could be deployed and controlled from lunar landing space tugs or from orbiting space stations. As teleoperators with limited artificial intelligence (robots) are developed, extensive exploration activities can be envisioned on distant planets without the detrimental effects of long transmission time delays.

Space teleoperator systems can be made ready for the first space station/space shuttle missions currently planned for about 1977. Complete on-orbit checkout and test would be performed following launch to evaluate predicted teleoperator performance in space. Based upon the results of this phase, system

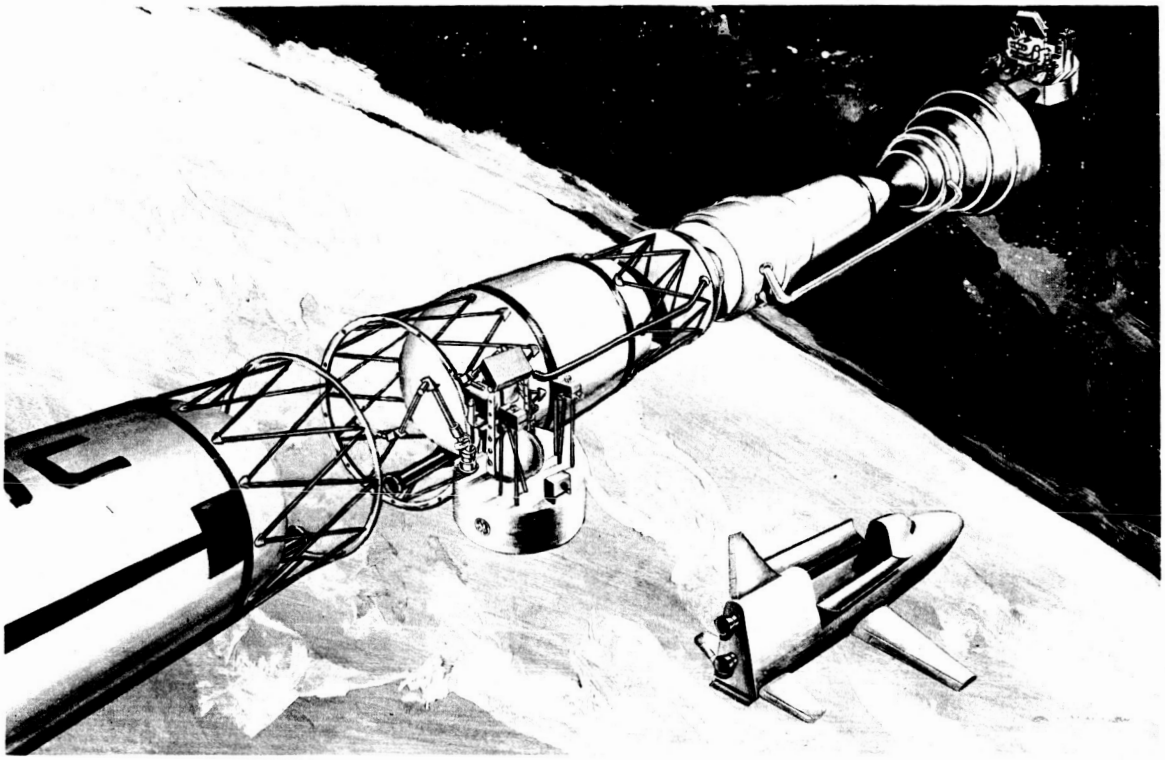

Figure 6. Nuclear Shuttle Engine Replacement

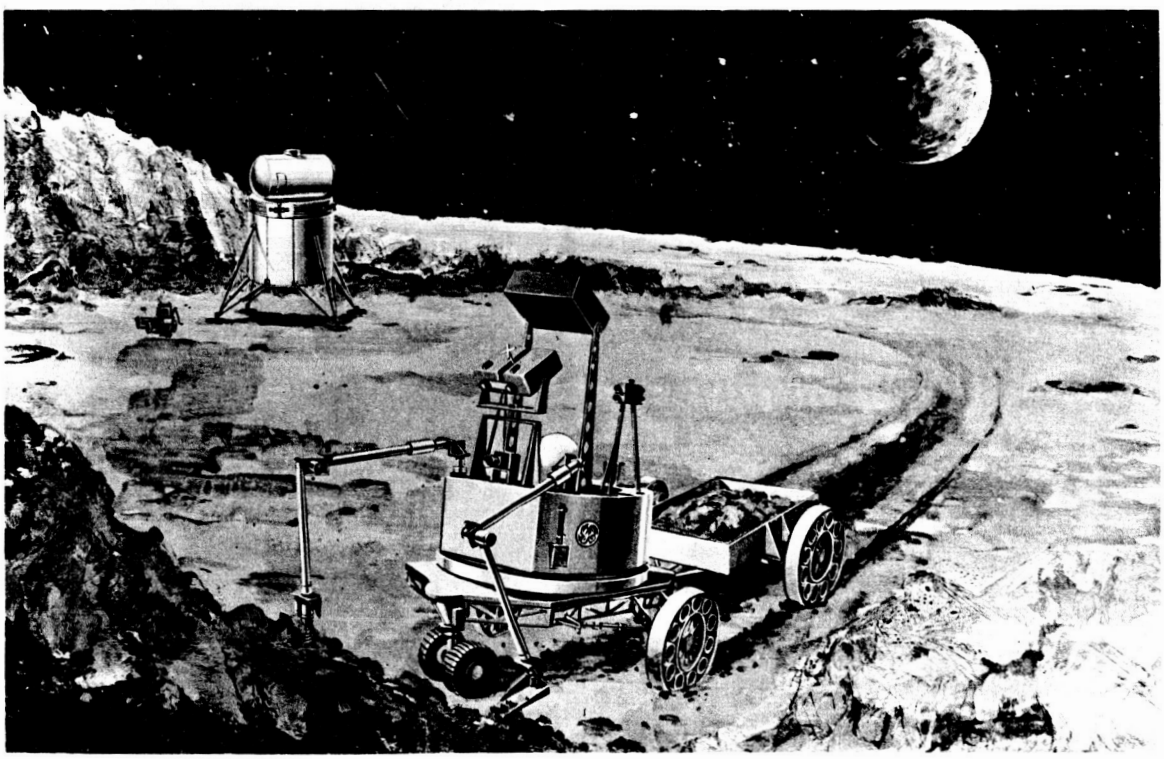

Figure 7. Teleoperations on the Lunar Surface

operating procedures, crew work schedules, and final system adjustments could be made in preparation for its operational deployment.

REFERENCES

1. "Remote Manipulator Spacecraft Systems," by A. Interian and R.H. Blackmer, General Electric Company, and W.H. Allen, National Aeronautics and Space Administration, prepared for the Twentieth Congress of the International Astronautical Federation in October, 1969.
2. "The Role of Space Manipulator Systems for Extravehicular Tasks," by R.H. Blackmer and A. Interian, General Electric Company and R.G. Clodfelter, United States Air Force, prepared for the Second National Conference on Space Maintenance and Extravehicular Activities in August, 1968.
3. "Satellite Maintenance Using Remote Manipulator Spacecraft," by A. Interian and D.A. Kugath, General Electric Company, and W.H. Allen, National Aeronautics and Space Administration, prepared for the AIAA Eighth Conference on Reliability and Maintainability, in July, 1969.
4. "A Remote Manipulator System for Space Applications," by A. Interian and D.A. Kugath, General Electric Company and W.H. Allen, National Aeronautics and Space Administration, prepared for the International Symposium on Man-Machine Systems in September, 1969.
5. "The Nuclear Rocket in the Space Future," by D.S. Gabriel, National Aeronautics and Space Administration, for the Atomic Energy Forum, 1969.

SESSION IV.3.
THERMIONIC NUCLEAR ELECTRIC SYSTEMS FOR SPACE APPLICATIONS

CHAIRMAN: E. STUHLINGER
ASSOCIATE DIRECTOR, MARSHALL SPACE FLIGHT CENTER

NUCLEAR RADIATION PROBLEMS, UNMANNED THERMIONIC REACTOR ION PROPULSION SPACECRAFT*

J. F. Mondt,+ C. D. Sawyer,# A. Nakashima≠

Jet Propulsion Laboratory
Pasadena, California

A nuclear thermionic reactor as the electric power source for an electric propulsion spacecraft introduces a nuclear radiation environment. The radiation environment effects the spacecraft configuration, the use and location of electrical insulators and the science experiments. The spacecraft is conceptually configured to minimize the nuclear shield weight by (1) a large length to diameter spacecraft, (2) eliminating piping penetrations through the shield, and (3) using the mercury propellant as gamma shield. The alumina material is damaged by the high nuclear radiation environment in the reactor. For the more ambitious (250 kwe, 30 to 40,000 hour) electric propulsion missions it is desirable to locate the alumina insulator outside the reflector or develop a more radiation resistant insulator. The net spacecraft nuclear environment is now being investigated to determine if there is a problem. It appears some experiments may require local radiation shielding.

INTRODUCTION

Some of the nuclear radiation problems which have been, or will be, encountered during the technology development of a thermionic reactor ion propulsion spacecraft (TRIPS) are described. A thermionic reactor ion propulsion spacecraft (Ref. 1) provides an electric propulsion system with the potential for delivering large payloads (Viking class-2000 Kg) to the outer planets. TRIPS consists of an in-core thermionic reactor and mercury bombardment engines configured into a propulsion system. The spacecraft configuration and the reasons for the configuration is explained.

An electrical insulator for in-core thermionic reactors is located in the high nuclear radiation environment. The effects of the nuclear environment on this insulator have been investigated in some detail. The insulator effects, how it relates to the spacecraft, and various solutions which are mission dependent is described.

The nuclear radiation shielding requirements for the power conditioner are discussed. The spacecraft arrangement is such that dual use of the spacecraft propellant is possible. The power conditioner is part of the propulsion system, and has been used as the most sensitive radiation component in designing the nuclear shield. The nuclear radiation shielding requirements also influence the spacecraft arrangement. The shielding requirement and how it affects overall propulsion system weight is also explained.

A preliminary look at the science payload environment and its possible problems are briefly described. The science payload is not well defined at this time; therefore, the environment and problems are just now being investigated.

DESCRIPTION OF SPACECRAFT

A Nuclear Electric Propulsion (NEP) spacecraft consists of an electric propulsion system, a propellant system, and a net spacecraft. The arrangement of these systems must be such as to increase reliability, reduce the weight, simplify interfaces, and maintain maximum flexibility for scientific information return. An isometric of a NEP spacecraft, identifying the major components, is shown in Fig. 1. This spacecraft configuration has a large length to diameter ratio (L/D) which reduces the nuclear shield weight and the overall propulsion system weight. This configuration also simplifies the thermal interfaces by having the high temperature components (power subsystem) all at one end of the spacecraft. The thrust subsystem and propellant system is in the center of the spacecraft, an intermediate temperature environment, and the low temperature net spacecraft at the other end of the spacecraft. The net spacecraft being at one end also allows maximum field of view, and allows the science equipment to be operational during the thrusting. This side thrust configuration, as shown in Fig. 1, has the thrust perpendicular to the long axis of the spacecraft. Therefore, the mercury propellant used for thrust is expelled away from all spacecraft components.

PROPULSION SYSTEM

The propulsion system is divided into two subsystems - power and thrust. The power subsystem consists of a primary radiator, a thermionic reactor, electromagnetic (EM) pump and (NaK) liquid metal heat rejection piping. The thrust subsystem consists of power conditioner modules, mercury ion bombardment thrusters and bus bars or power cables. The power distribution for

*This work presents the results of one phase of research carried out in the Propulsion Research and Advanced Concepts Section of the Jet Propulsion Laboratory, California Institute of Technology, under Contract NAS7-100, sponsored by the National Aeronautics and Space Administration.

+Group Supervisor #Member Technical Staff ≠Senior Engineer

NUCLEAR ELECTRIC SPACECRAFT ISOMETRIC

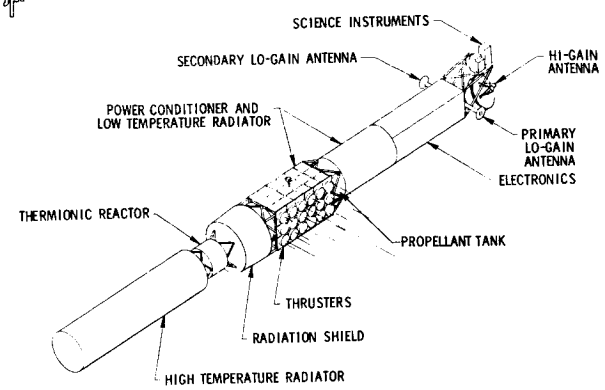

Fig. 1 NEP SIDE-THRUST SPACECRAFT

POWER BALANCE FOR 70 kwe PROPULSION SYSTEM

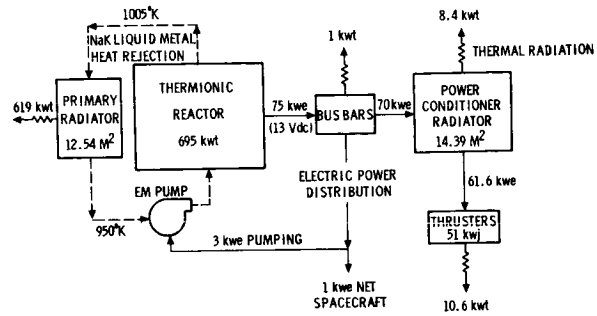

Fig. 2 70 kwe NEP POWER SCHEMATIC

a 70 kw nuclear electric propulsion system, including all components, is shown in Fig. 2. The dashed lines on the figure indicate liquid metal piping loops. The solid lines indicate electric power distribution. The accordion lines indicate heat rejected to space.

The power subsystem produces 75 kw of electric power at the thermionic reactor terminals. The reactor thermal power level is 695 kw. The thermionic reactor is cooled by liquid metal, sodium potassium (NaK), at a coolant temperature of about 1000°K (730°C). A complete power balance for the propulsion system is also shown by Fig. 2. The overall reactor efficiency is approximately 11%. The efficiency of the power conditioner is approximately 88%. The overall thruster efficiency in converting electrical energy to thrust is approximately 83%. All NEP components include a minimum of 20% redundancy at the beginning of mission life. For instance, the radiator can lose 20% of its effective area and still rejects the 619 kw thermal at design temperatures.

The primary radiator, which cools the thermionic reactor, operates at an average temperature of 700°C, has an area of 12.5 square meters (120 square feet) and rejects approximately 620 kw of thermal power to space. The radiator required to reject the heat from the power conditioner is actually larger in area than the primary radiator. The power conditioner radiator operates at an average temperature of 80°C, rejects 8.4 kw thermal, and has an area of 14.4 meters^2 (140 square feet). It is also assumed that 1 kw of electric power is used by the net spacecraft.

SPACECRAFT ARRANGEMENT

The major subsystems and their major components are shown in Fig. 3. The NEP spacecraft is shown located on the Centaur stage of a Titan 3D-Centaur launch vehicle. This configuration allows the three major spacecraft subsystems to be developed independently because of the simple interfaces. The nuclear shield, part of the power subsystem, is located between the power subsystem and the thrust subsystem. The thrusters and mercury propellants are located between the power subsystems and the power conditioner. The power conditioner has nuclear radiation-sensitive components. Radiation-sensitive components are also located in the net spacecraft which is beyond the power conditioner. The mercury propellant is used as gamma shield, as well as propellant.

The nuclear radiation levels can be divided into three main categories within the spacecraft. The power subsystem operates in the highest nuclear radiation environment. The thrust subsystem and electronics must operate in an intermediate nuclear radiation environment. Some specific payload scientific experiments will probably require a very low nuclear radiation environment.

As shown in Fig. 3, the overall length of a 70 kw propulsion system is approximately 50 feet and the spacecraft diameter is about 3 feet. This size spacecraft can be arranged very effectively on the 11-foot diameter Centaur stage. Simple easily defined interfaces between the three major subsystems of the spacecraft allows independent subsystem technology development with prototype configurations.

NUCLEAR ELECTRIC SPACECRAFT CONFIGURATION

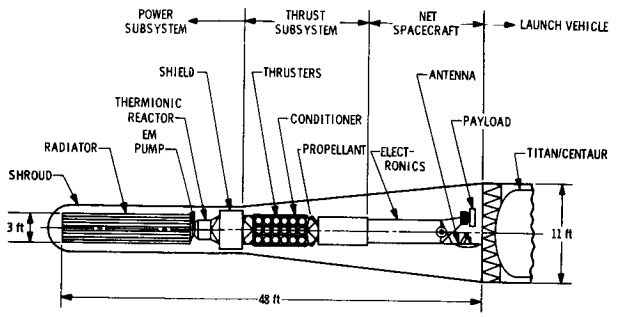

FIG. 3 SIDE-THRUST SPACECRAFT ARRANGEMENT

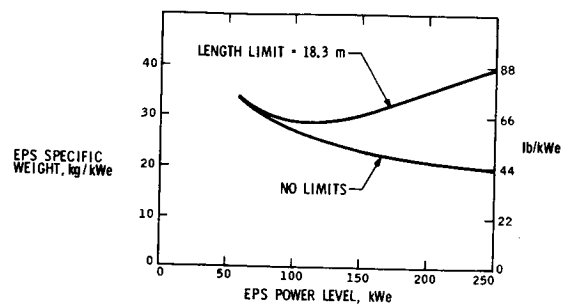

FIG. 4 EFFECT OF POWER LEVEL ON PROPULSION SYSTEM SPECIFIC WEIGHT

The NEP systems weight is very important in the performance of electric propulsion missions. The specific weight variation of this large L/D side thrust spacecraft is shown as a function of electric power output in Fig. 4. The one curve labeled, "NO LIMITS," is the minimum specific weight of the side-thrust propulsion system with no launch vehicle constraints. Given, for example, the constraint of a 60-foot maximum length Titan Centaur shroud or shuttle payload bay, then the weight variation is quite different. The weight variation with a 60-foot length limit is shown by the curve labeled, "LENGTH LIMIT," in Fig. 4. This illustrates the effect on weight of a launch vehicle constraint. The nuclear radiation constraint at the science payload will eventually be another constraint which must be examined.

The propulsion system specific weight with no limits (Fig. 4) is 25 kg/kw at 120 kw power level. With a length limit constraint, the specific weight is 28 kg/kw. An investigation based on possible constraints from radiation at the science equipment will be necessary to determine their effect on the overall propulsion system weight. The weight effect can then be used to determine the effect of science equipment radiation constraints on the overall mission performance.

LIST OF POTENTIAL NEP PLANETARY MISSIONS

2000-3000 kg

MISSION	LAUNCH DATE	THRUST MODE	POWER LEVEL kw	THRUST DURATION DA	FLIGHT TIME DA	FULL POWER HR x 10^{-3}
HALLEY'S COMET AND JUPITER ORBITERS	'83-'85	HI-LO	50-150	600	900	17
JUPITER - ORBITERS SATELLITE RENDEZVOUS	'85-'87	LO-LO	150-250	500	900	15
SATURN - ORBITERS SATELLITE RENDEZVOUS	'87-'89	LO-LO	150-250	600	1700	24
GALACTIC PROBE	'89-'91	LO-	150-250	~400	~1600	~20
URANUS - ORBITERS SATELLITE RENDEZVOUS	'89-'91	LO-LO	150-250	800	2800	37
JUPITER OR JUPITER SATELLITE SAMPLE RETURN	'90-'92	LO-LO-LO	150-250	~900	~1700	~30

FIG. 5 POTENTIAL NEP OUTER PLANET MISSIONS

POTENTIAL NEP MISSIONS

The incentive for the NEP system is the desire to explore in some detail the outer planets of our solar system. A list of potential missions with projected launch dates, power level ranges and required full power hours (FPH) is shown in Fig. 5. The assumed net spacecraft (science payload) are Viking class payloads of 2,000 to 3,000 kg. The net spacecraft would probably be designed as outer planet circular orbiters with large data return capability. The thrust mode shown in Fig. 5 as "HI" is chemical propulsion and as "LO" is electric propulsion. The full power hours (FPH) are determined by assuming full reactor power during thrust operation and 33% thermal power during coast periods of the mission.

This potential list of missions is thought of as two classes of missions based on propulsion system lifetimes. The first class includes the first four missions and requires a 15,000 to 20,000 FPH propulsion system with from 2-1/2 to 3 years of flight time. This is considered the first class of outer planet missions for which nuclear electric systems would be useful. The second class is the more ambitious mission to the more distant outer planets, and possible sample return missions from Jupiter satellites. These missions required 30,000 to 40,000 FPH propulsion systems and flight times of five to eight years. The second class of missions is considered second generation NEP systems with the capability of operating for longer times.

RADIATION EFFECTS ON INSULATOR

One of the nuclear radiation problems for the thermionic reactor ion propulsion system is the need for an electrical insulator in the high radiation environment. The electrical insulator environment and effects have been investigated in some detail. The nuclear radiation environment in the reactor is very high. The electric insulators can be located in basically three locations within the reactor. The radiation flux level is different for different locations and the insulator damage then varies with time at these locations.

The neutron flux at three different locations in a typical fast thermionic reactor is shown for different power levels in Fig. 6. The first location is designated as core center. The core center is the highest neutron flux location within the core. If the insulators are required in core, then insulators at core center receive the highest radiation dose, and are the limiting insulators. The second location is designated center of lead. This location is outside the active core, but inside the reflector. The center of lead location is in an intermediate nuclear radiation environment. The third location is designated outside reflector. The outside reflector location has 3 inches of beryllium oxide (BeO) between it and the active core. A BeO region with a density 50% of theoretical density was assumed.

The calculated flux for a 100 kwe NEP system is then 4.65×10^{13} n/cm^2 sec > 0.1 mev at core center, 2.12×10^{13} n/cm^2 sec > 0.1 mev at center of lead, and 0.246×10^{13} n/cm^2 sec > 0.1 mev outside reflector. The total accumulated neutron fluence with neutron energy (E_n) greater than 0.1 mev is the neutron flux times the full power hours.

Experimental irradiation damage of electrical insulators has been investigated by Oak Ridge National Labs and Los Alamos Scientific Lab. The insulation irradiation experiments were performed in both a thermal reactor (ETR) and a fast reactor (EBR-2). The results of these experiments are reported in Ref. 2 and 3. A summary of the insulator damage results is shown in Fig. 7. The damage is reported as volume swelling of insulator material as a function of total neutron fluence with neutron energy greater than 0.1 MeV. The percent swelling where insulator cracks are severe enough to cause insulator leaks is shown as a band in Fig. 7. The insulator samples were irradiated at 700°C, which approximates operating temperature of insulators in the thermionic reactor.

The summary of results, Fig. 7, is based on many samples of alumina material and two samples of yttria material. As shown by the figure, the alumina insulators are always leak-tight at a neutron fluence of 4.2×10^{21} nvt or less. Therefore, a useful limit for any alumina insulator-seal is 4.2×10^{21} nvt.

The two samples of yttria irradiated in the same test reactor as the alumina samples show no swelling at 3×10^{21} nvt and very little, if any, swelling at 9.8×10^{21} nvt. However, the yttria results are based on two samples and many more samples must be irradiated with similar results in order to gain confidence in these results. Also, the yttria material has lower strength than alumina. The bonding techniques and joining procedures for yttria are not well known and must be developed. The alumina is a well developed material, with well developed bonding techniques and can be reproducibly fabricated today.

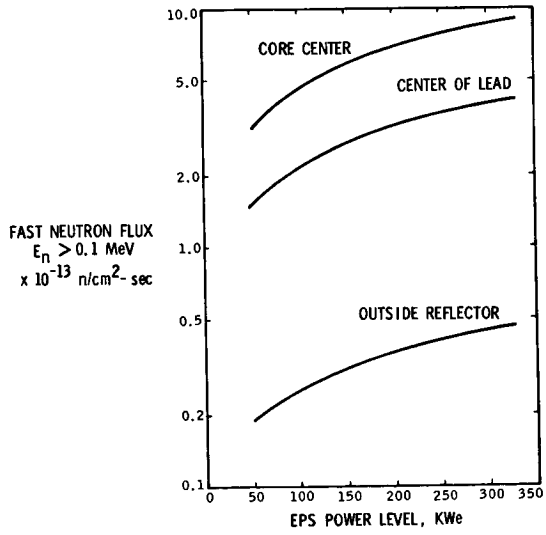

FIG. 6 FAST NEUTRON FLUX FOR DIFFERENT REACTOR LOCATIONS

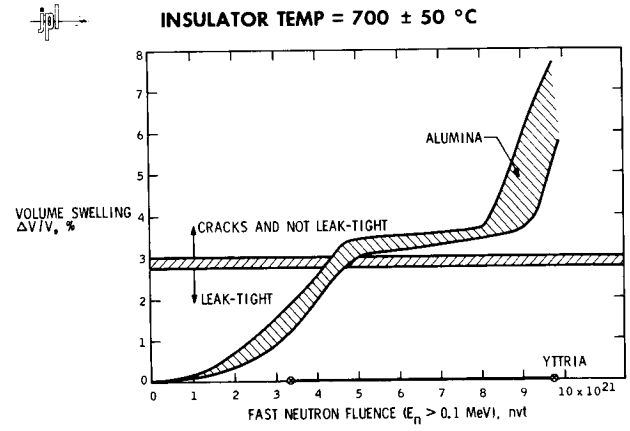

FIG. 7 INSULATOR DAMAGE AT VARIOUS FAST NEUTRON FLUENCES

The useful application limits of the alumina insulator material, based on today's technology, was determined. The insulator damage criteria, the insulator location within the reactor, and the required mission lifetimes were combined. By combining these three factors - insulator damage, mission lifetime and reactor location - the insulator technology status and its usefulness for missions can then be assessed.

The fast neutron fluence at the core center for 10,000, 20,000 and 30,000 FPH is shown in Fig. 8 for various power levels. The alumina leakage limit criteria (seal limit) is shown as a vertical band, from 4.2 to 4.7 x 10^{21} nvt > 0.1 mev. So for a 30,000 FPH mission, a fast thermionic reactor with alumina insulator-seals at core center would be limited to a power level of 75 kw electric. A mission requiring 20,000 FPH would be limited to a 150 kwe power level. A 10,000 FPH mission could use alumina insulator-seal at core-center for power levels as high as 350 kw electric.

Also shown in Fig. 8 is the one yttria sample result which would withstand the radiation environment for 30,000 FPH at core center if other properties can be developed. The yttria development requires a joining technology program, investigations of how to live within the low strength properties, and designs to accommodate the low electrical resisivity.

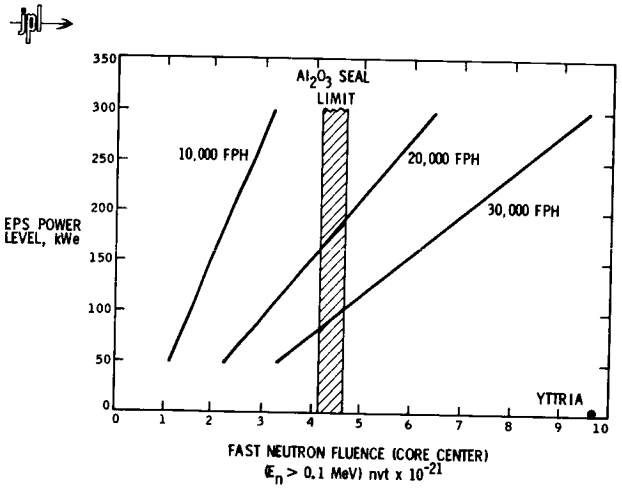

FIG. 8 FAST NEUTRON FLUENCE AT CORE CENTER FOR DIFFERENT POWER LEVELS

If the alumina insulator seal location is now restricted within the reactor, then the alumina insulator seal usefulness becomes dependent on the location. Figure 9 is a plot of NEP system power level as a function of neutron fluence after 30,000 FPH of reactor operation for three locations within the reactor. An insulator seal at core center is limited to about 75 kw electric, as also shown by the previous figure. If the insulator seal location is limited to the center of lead, then the power level can be raised to 270 kwe for a 30,000 FPH mission. With the insulator seal located outside a 50% dense 3 inch BeO reflector, there is a factor of 10 safety margin for 30,000 FPH missions up to power levels of 350 kwe. This kind of safety margin (factor of 10) is what a user looks for in the early technology phases of any program. The yttria result is still good, but as stated previously, requires a technology effort to make it useful, or to find the limiting criteria for its use.

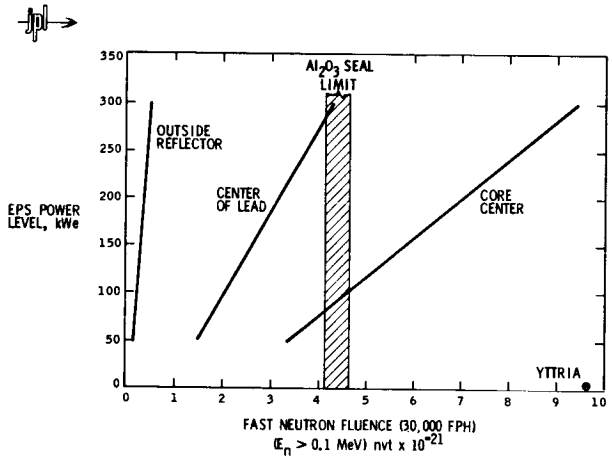

FIG. 9 FAST NEUTRON FLUENCE AT 30,000 FPH FOR DIFFERENT POWER LEVELS

NUCLEAR SHIELD INFLUENCE ON SPACECRAFT

The spacecraft (S/C) arrangement can minimize the shield weight requirement for the power conditioner. This discussion will demonstrate how nuclear radiation imposed requirements influence the spacecraft arrangement and weight. The nuclear shield is designed to limit the nuclear dose to the thrust subsystem power conditioner. The total neutron fluence is limited to 10^{12} nvt greater than 1.0 Mev and the total gamma fluence is limited to 10^{7} RAD at the power conditioner at the end-of-mission life. The neutron shield material is lithium hydride (LiH) with 20% allowance for stainless steel structure. The mercury propellant is used as the primary gamma shield. The spacecraft arrangement to shield the closest power conditioner components is shown in Fig. 10.

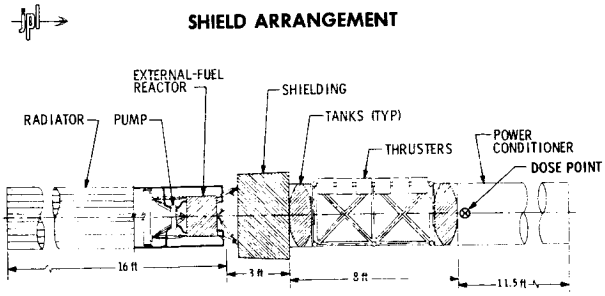

FIG. 10 SPACECRAFT ARRANGEMENT FOR SHIELDING THE POWER CONDITIONER

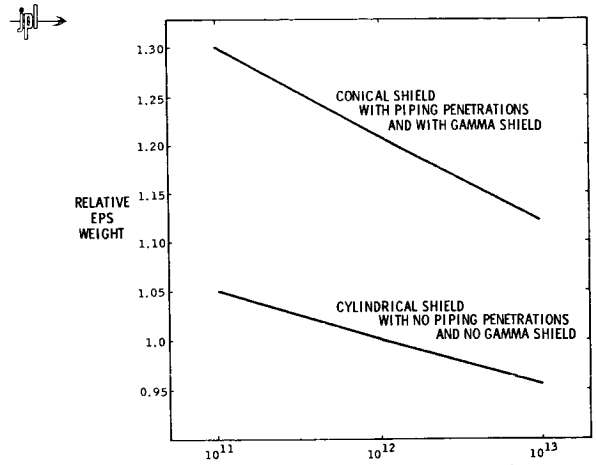

FIG. 11 EFFECT OF SHIELD CONFIGURATION AND NEUTRON FLUENCE ON PROPULSION SYSTEM WEIGHT

The shield (designated shielding and tanks in Fig. 10) is nearly the same diameter as the spacecraft. The shield thickness is fixed by the neutron and gamma fluence limits at the power conditioner, so the diameter of the shield then determines the shield weight. The shield must shadow all the equipment on the power subsystem side from all equipment on the thrust subsystem side of the shield in order to be effective. Any shield penetrations, such as liquid metal piping, will increase the shield weight. The component arrangement shown in Fig. 10 eliminates liquid metal piping penetration and therefore allows a redundant reactor coolant system without increasing the shield weight. The only penetrations through the shield or around the shield is the bus bar required for carrying the electric power from the power subsystem to the thrust subsystem.

The weight savings as a result of no piping penetration and using the mercury propellant for gamma shielding is shown in Fig. 11. The reference propulsion system's relative weight is 1.0 at a fast neutron fluence of 10^{12} nvt > 1 Mev for a cylindrical shield with no piping penetrations and mercury as gamma shielding. With a conical shield, including piping penetration and separate gamma shielding, the electric propulsion system weight is increased by 20%.

The effect of total allowable neutron fluence at the power conditioner on propulsion system weight is also shown in Fig. 11. Decreasing the allowable neutron fluence to 10^{11} nvt at the power conditioner will increase the propulsion system weight by 5%, while increasing the allowable neutron fluence to 10^{13} nvt will reduce the specific weight by 4%. This illustrates one of the radiation shielding problems and its influence on spacecraft configuration and propulsion system weight. All of the nuclear radiation factors must be eventually included before the propulsion system and spacecraft can be developed.

NET SPACECRAFT ENVIRONMENT

The net spacecraft nuclear environment for the spacecraft arrangement described above is now being defined to see if there is a radiation problem. The nuclear radiation environment must also be defined so that outer planet science experts can evaluate the effect of this radiation environment on their experiments. The neutron flux at three locations within the spacecraft has been calculated. The resultant neutron fluxes with neutron energies greater than a specified neutron energy for three locations are shown in Fig. 12. Since the NEP spacecraft science equipment and experiments cannot be defined this early, it is important to know the flux at various energies. Also, the neutron and gamma spectrum at the payload will be important to the selection of electronic equipment and science experiments.

Based on these initial calculations, the specific experiments that require very low nuclear radiation background will probably be locally shielded. The amount of local shield will be determined by the actual nuclear radiation environment from the thermionic reactor and from space radiation. The total radiation environment is an area which is now being investigated, so the allowable radiation environment from the reactor can be defined.

As shown in Fig. 12, the neutron flux greater than 1 Mev at the power conditioner (location B) is approximately 8 x 10^3 neutrons/cm^2/sec. This results in a total neutron fluence of 0.86 x 10^{12} nvt > 1 Mev for a 30,000 FPH mission as designed. The neutron flux greater than 1 Mev at the scientific experiments is then 10^2 (100) neutrons/cm^2/sec, which results in 10^{10} nvt> 1 Mev total neutron fluence at the end of a 30,000 FPH mission from the thermionic reactor. If the neutron flux at the science equipment greater than 0.1

Mev is important, then the neutron flux is 7 x 10^2 (700) neutrons/cm^2/sec, and the total nvt > 0.1 Mev would be 10^{11} at the end of a 30,000 FPH mission. The limits and radiation problems at the science equipment must be examined in detail. The effects of these limits on the NEP spacecraft and the thermionic reactor ion propulsion system technology will then be determined.

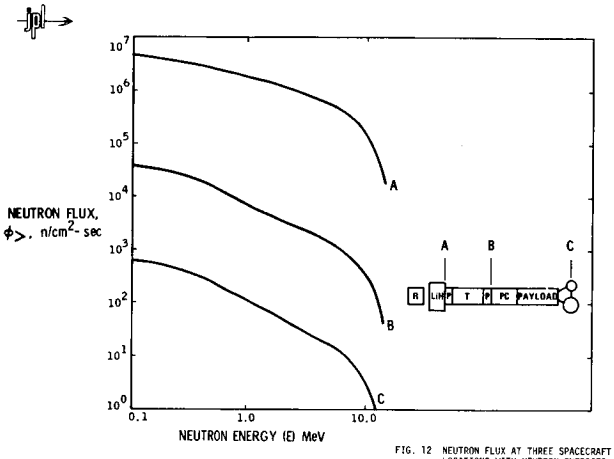

FIG. 12 NEUTRON FLUX AT THREE SPACECRAFT LOCATIONS WITH NEUTRON ENERGIES >A SELECTED ENERGY

CONCLUSIONS

The side thrust spacecraft arrangement reduces the nuclear radiation problems by making use of mercury propellant as the gamma shield and eliminating liquid metal piping penetration through the shield. The mercury propellant as a gamma shield improves propulsion system specific weight.

The alumina insulator-seals at core center are leak-tight up to a 75 kw thermionic reactor power level operating for 30,000 FPH. If the alumina insulator-seals can be located outside the axial reflector, then there is a large safety margin for NEP system power levels up to at least 350 kwe for 30,000 FPH. Therefore, the thermionic reactor technology program should investigate ways to eliminate insulator-seals at core center and also investigate new insulator-seal materials.

The neutron radiation environment at the payload is considered low enough not to cause electronic problems, but local shielding requirements for specific experiments must be investigated.

REFERENCES

1. Mondt, J. F., and Davis, J. P., "Thermionic Reactor Electric Propulsion Spacecraft for Unmanned Outer Planet Exploration," AIAA Paper No. 70-1122, AIAA 8th Electric Propulsion Conference, Stanford, Calif., Aug. 31-Sept. 2, 1970.

2. Kellholtz, G. W., Moore, R. E., and Robertson, H. E., "Effects of Fast Neutrons on Polycrystalline Alumina and Other Electrical Insulators at Temperatures From 60° to 1230°C," ORNL-4678, Oak Ridge National Laboratory, May 1971.

3. Reichelt, W. H., Ranken, W. A., Weaver, C. V., Blackstock, A. W., Patrick, A. J., and Chaney, M. C., "Radiation Induced Damage to Ceramics in the EBR-II Reactor," IEEE Conference Record, 1970 Thermionic Conversion Specialist Conference, Miami Beach, Florida, Oct. 26-29, 1970, p. 39-44.

THERMIONIC REACTOR POWER SYSTEM: EFFECTS OF RADIATION ON INTEGRATION WITH MANNED SPACE STATION*

A. J. Gietzen, C. A. Heath, and L. W. Perry

Gulf General Atomic Company

The application of a thermionic reactor power system to the modular space station is described. The nominal net power is 40 kWe, with the power system designed to be applicable over the power range from 25 to 60 kWe. The power system is designed to be launched by the space shuttle. The lifetime goal is 5 years.

The reactor contains thermionic fuel elements, in which electrical power is produced, and U-ZrH driver fuel elements. The thermionic converter design is the same as that presently being tested in the Gulf General Atomic thermionic test reactor. There are enough fuel elements in the reactor to provide a high degree of redundancy at the nominal 40 kWe design point. Reject heat from the fuel elements is removed by forced convection NaK loops to the primary radiator where it is radiated to space at about 810°K (1000°F). Electrical power output from the reactor at about 9 V is carried to a modular power conditioning system where it is processed to higher voltage for transmission to the spacecraft.

Radiation protection is provided by LiH neutron shielding and W gamma shielding in a shaped 4π configuration, i.e., the reactor is shielded on all sides but not to equal extent. Isodose contours are presented for the region around the modular space station. Levels and spectral distribution of radiation are given for later evaluation of effects on space station experiments. Parametric data on the effects of separation distance on power system mass are presented.

An alternate concept in which a reactor system is connected to the Space Station by a tether at a distance of 1 to 2.5 miles is discussed. The effect upon power system performance and shielding requirements of the tethered concept are presented.

INTRODUCTION

A recent study on design and integration of reactor power systems for extended capability Space Stations (Ref. 1) recommended a power system capability of 40 to 50 kWe. The study identified the key criteria for the power system as growth capability and the ability to adjust to varying Space Station requirements.

The thermionic reactor power system for the Space Station is designed to a nominal power of 40 kWe with a beginning-of-life capability of 55 kWe. The power output is controllable over the entire power range from zero to 55 kWe. The same fuel element design used in this system is applicable over a wide power range and has been applied in specific design studies for 25 kWe and 100 kWe systems (Refs. 2,3). The thermionic fuel element (TFE) design has evolved from over 80,000 hr of laboratory testing and 64,000 hr of testing in the TRIGA thermionic test reactor of single and two-cell fuel elements. Two complete six-cell prototype fuel elements have been fabricated and are ready for testing in the reactor.

In the in-core thermionic reactor, the electrical power is produced by direct conversion of heat to electricity within the fuel element. The TFE serves the dual role of containing the fuel in the reactor as well as performing the power conversion. In the Gulf General Atomic concept, the power from each pair of TFEs is coupled to an independent power conditioning module to become a single power production unit. The 40 kWe Space Station system contains 30 of these power production units, with 23 required for 40 kWe, to provide a modular power system with active redundancy.

The Space Station power system is described in detail in Ref. 4. This paper presents the guidelines and constraints applied to the power system design, and a general description of the overall system and of each subsystem. The shield is considered in more detail with a description of the configuration and data on dose rates, radiation spectral distribution and tradeoffs on weight and separation distance.

GUIDELINES AND CONSTRAINTS

The requirements imposed on the power system design by integration conditions include:

- Radiation dose rate at the station of 25 rem or less in a 6-month period
- Consideration of both rigid boom mounting at separation distances of 100 to 200 ft and tether mounting at 1 to 2.5 mi.
- Power system will be made up of 1 or more modules, each weighing no more than 20,000 lb.

*This work was sponsored by the U. S. Atomic Energy Commission under Contract AT(04-3)-167, Project Agreement 14.

- The power system will be confined within a 12 ft diameter by 50 ft long package.

- The nominal net power delivered to the spacecraft will be 40 kWe.

Additional design ground rules adopted for the reference power system design include:

- Design lifetime goal of 5 yr.

- Redundancy in power production units (TFE pair plus power conditioning module) of at least 25%.

- The basic fuel element design and materials the same as those presently built for testing in-pile

- Eutectic NaK coolant

- Stainless steel vessel and heat rejection system

- 1100°F reactor outlet temperature.

SYSTEM DESCRIPTION

The reference design power system (Fig. 1) consists of four major subassemblies: reactor, radiation shield, heat rejection system, and electrical power conditioning system. The reactor is made up of the reactor core containing the fuel elements and a neutron reflector which surrounds the core. Both the core and the reflector are contained within a stainless steel reactor vessel. The reactor subassembly includes the gaseous fission product storage traps and control drives.

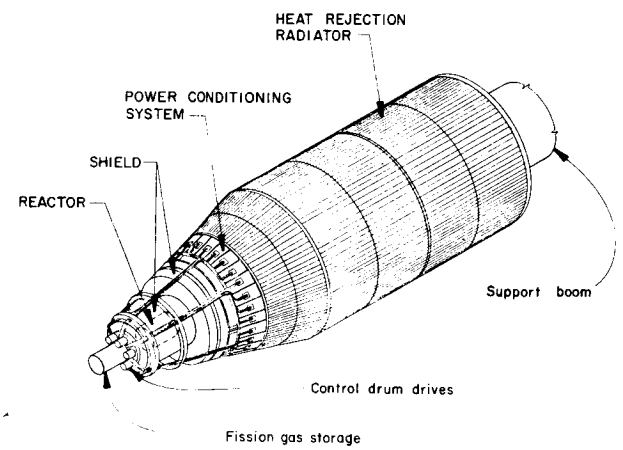

Fig. 1. Thermionic Reactor Space Station Power System

The thermal power produced in the reactor which is not converted to electricity is removed by the heat rejection system. This system consists of circulating liquid metal (NaK) loops, a heat exchanger, and a radiator. The NaK passing through the reactor becomes radioactive and would be a radiation hazard to personnel in the spacecraft if it flowed directly to the radiator. The heat is transferred to 5 radiator loops in a heat exchanger which is in a region around the reactor, shielded both from reactor and spacecraft. The radiator loops carry the heat to the radiator panels, each of which consists of 220 heat pipes making up an isothermal radiating surface.

The radiation shield protects space station personnel from nuclear radiation emanating from the reactor and from the activated reactor coolant. The reference shield is a shaped 4π shield giving a dose rate of 5 mrem/hr at 200 ft over a dose plane diameter of 130 ft. It consists of two portions; one surrounding the reactor which reduces the dose rate at the side and end of the reactor to 100 R/hr at 100 ft, and the other which provides the low dose shadow cone covering the Space Station.

The power conditioning system takes the electrical power from the reactor at approximately 10 V dc and converts it to higher regulated voltage, meeting space station requirements. Power is carried from the reactor to the power conditioning by insulated transmission lines cooled by direct radiation to space. The power conditioning system consists of 30 modules in each of which the mounting plate serves as a direct radiating heat sink for the electrical components.

The 40 kWe rating is net output capability of the system at end-of-life (EOL) after deduction of parasitic loss. The major system losses are the power dissipated in the transmission lines and power conditioning equipment, and the electrical power requirements of the electromagnetic pumps which circulate coolant.

The constraints on dose rate and dose plane diameter result in shield weights which preclude launch of the entire initial system on a single shuttle vehicle (with 20,000 lb. capacity). The system is designed to have a separable portion of the shield which can be launched with the support boom, reducing the power system module to about 12,000 lb. The station shield and boom become a permanent part of the space station. A replacement power system is easily accommodated on a single shuttle launch. The power system-station shield separation is illustrated in Fig. 2.

A summary of reference design power system parameters is given in Table 1. Descriptions of the major component assemblies are given in the following sections.

An alternate configuration for attachment to the station by a cable tether (1 to 2.5 miles) was also evaluated. This configuration (Fig. 3) offers potential advantages of reduced total system weight and minimum interaction with space station configuration and operations. Orbital mechanics and deployment techniques are being evaluated. A summary of the tethered system for a separation distance of 2 miles is given in Table 2.

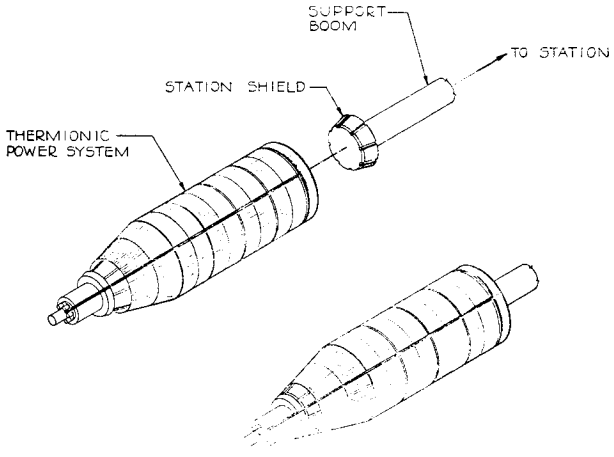

Fig. 2. Power System - Station Shield Separation

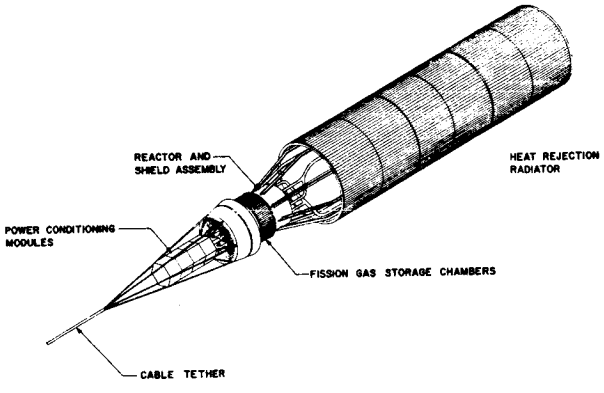

Fig. 3. Tethered Power System Configuration

TABLE 1

POWER SYSTEM SUMMARY

Net conditioned power	40 kWe
Beginning of life capability	55 kWe
Overall length	33 ft
Maximum diameter	12 ft
Power system weight (includes 4300 lb shield)	11,200 lb
Station shield and boom weight	18,900 lb
Total power subsystem weight	30,200 lb

TABLE 2

TETHERED POWER SYSTEM DESIGN SUMMARY

Net conditioned power	40 kWe
Beginning of life capability	65 kWe
Overall length	40 ft
Maximum diameter	8 ft
Power system weight	11,000 lb
Cable tether weight (approx.)	400 lb
Total power subsystem weight	11,400 lb

Reactor Design

The reactor subassembly is shown in Fig. 4. The reactor core contains thermionic fuel elements and uranium-zirconium hydride (U-ZrH) elements. The core contains 60 thermionic fuel elements (TFE) which produce the required electrical output. U-ZrH elements are added to achieve nuclear criticality. The core is surrounded by a radial reflector region containing 18 control drums which are composed of beryllium oxide reflector material with segments of neutron absorber. Nuclear control of the reactor is achieved by small rotational movements of the drums.

Each of the 60 thermionic fuel elements includes a vessel head feedthrough for passage of the electrical lead and radioactive gaseous fission products. Gaseous fission products produced within the TFEs are vented from the fuel element to prevent pressure buildup during long term operation. These gases (Xe and Kr) are vented to storage canisters filled with activated charcoal. The charcoal adsorbs the gases minimizing the containment volume required. Connection of a transmission line to each TFE is made in the region just below the gas storage chambers.

The control drives and control drum bearings use the technology developed for the U-ZrH reactor (Ref. 5). The drives are located outside the end shield where the radiation levels from the reactor are reduced and the drive motors are cooled by radiation to space.

A midplane cross section of the reactor is shown in Fig. 5. The core consists of two regions;

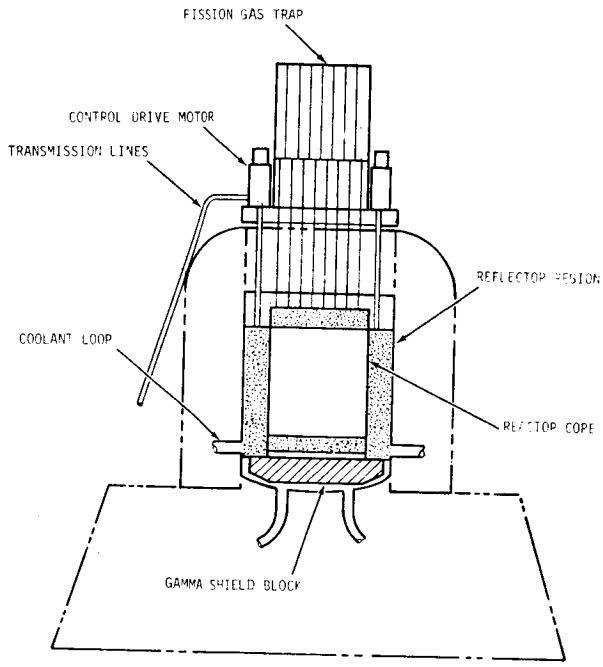

Fig. 4. Reactor Subassembly

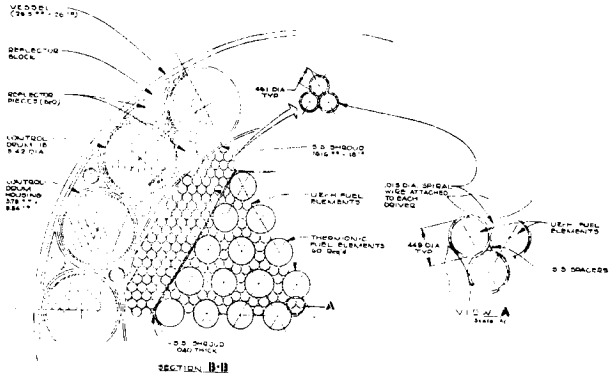

Fig. 5. Reactor Midplane Cross Section

the inner region contains both thermionic fuel elements and U-ZrH elements, and the outer region contains only U-ZrH elements. The U-ZrH elements apply the fuel technology developed for the U-ZrH reactor but are slightly smaller in diameter and operate at conditions which are less demanding than those for the U-ZrH thermoelectric system, i.e., clad temperatures 200°F lower and surface heat flux a factor of 2 lower.

The core and reflector regions are separated by a shroud which directs the incoming coolant through the reflector region before it flows back through the core. The control drums, which are contained in dry wells within the vessel, contain a segment of boron carbide neutron absorber which is rotated towards the core to shut down the reactor and away from the core to increase reactor power.

The fuel elements are supported at the top end by the vessel head and at the lower end by a grid plate (see Fig. 6). The grid plate is supported by the control drum dry wells.

A primary gamma shield is contained within the reactor vessel and is cooled by the circulating reactor coolant.

The NaK coolant enters the side of the vessel near the bottom, distributes in the small plenum area, and flows up through the reflector region to remove neutron and gamma heating energy. The coolant enters the core region through openings in the shroud, distributes in the region between the vessel head and upper end of the fuel elements, and flows down through the core. It passes through holes in the grid plate and through the shield block to the reactor outlet pipes. The coolant and vessel materials (NaK-78 and 316 SS) are the same as those in the reference U-ZrH reactor thermoelectric system.

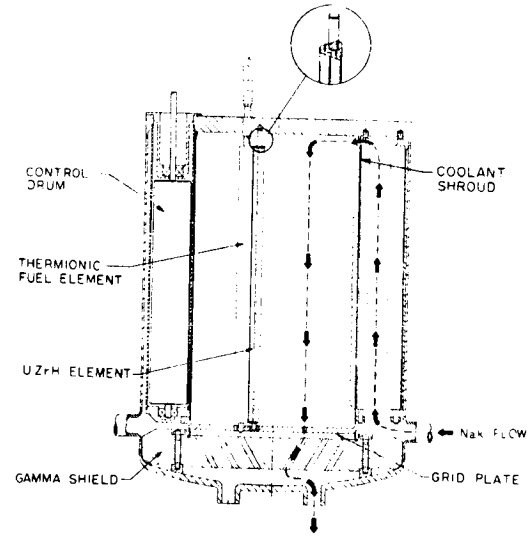

Fig. 6. Reactor Elevation Cross Section

The significant performance parameters and dimensions describing the reactor are given in Table 3. The number of TFEs required to produce the nominal output power, assuming operating conditions comparable to those of present in-pile TFE tests, is 46. The additional 14 TFEs allow operating at derated beginning of life (BOL) conditions to prolong life, and provide redundant power capability to compensate for potential TFE failures. The operating mode is such that if TFE performance degrades or failures occur, the power can be increased to maintain constant system power output. End of life (EOL) for the reactor is defined as the point at which an equivalent of 14 fuel elements have failed and the remaining 46 are operating normally.

TABLE 3

REACTOR PERFORMANCE PARAMETERS

Reactor outside diameter	26.5 in.	
Reactor length	25.0 in.	
Reactor mass	2176 lb.	
Number of thermionic fuel elements	60	
Number of U-ZrH fuel elements	813	
Number of control drums	18	
Control drum diameter	3.24 in.	
	BOL	EOL
Gross electrical output (kWe)	53	58
TFE surface heat flux, W/cm^2	25	31
Thermal power output, kW	1230	1510
Coolant inlet temperature, °F	890	960
Coolant outlet temperature, °F	1030	1100

Fuel Element Design

Two types of fuel elements are used; thermionic fuel elements in which the electrical power is produced, and U-ZrH fuel elements. The number of TFEs required for the 40 kWe output is less than required to achieve nuclear criticality on TFEs alone. The U-ZrH elements provide the additional uranium to achieve the required neutron multiplication as well as providing hydrogen for neutron moderation which enhances reactor safety.

The TFE is illustrated in Fig. 7. The TFE design has evolved through a development program which has included laboratory and in-reactor testing of experimental and prototype single cell and two-cell converters. Experimental electrically-heated converters have accumulated over 80,000 test hours with the longest single test continuing after 33,000 hours. Over 64,000 test hours have been accumulated on in-reactor converters with longest single tests of 10,000 hours on experimental converters, 7,700 hours on prototype single cells, and 6,600 hours (continuing) on a 2-cell TFE. Two 6-cell TFEs, which are essentially the same as the reference design (Fig. 7), but without the neutron reflector pieces, have been fabricated and are ready for testing in the TRIGA thermionic test reactor.

Each TFE contains 6 identical thermionic converters which convert about 11% of nuclear heat generated in them into electricity. Each fuel element produces about 1 kWe at 4 volts. Two TFEs are connected in series to a power conditioning module providing 30 independent power production units. The TFE is 1.314 in. in diameter and 25.3 in. long, including reflector pieces.

The U-ZrH element uses the same materials as the fuel elements developed for the U-ZrH reactor program but operates at lower temperatures and heat fluxes. The reactor outlet temperature is 1030°F at BOL and 1100°F at EOL. The diameter of the U-ZrH element is 0.45 in. in the TFE zone where the surface heat flux is 2.5 W/cm^2 at EOL. The diameter is 0.46 in. in the driver zone where the peak heat flux is 10 W/cm^2 at EOL.

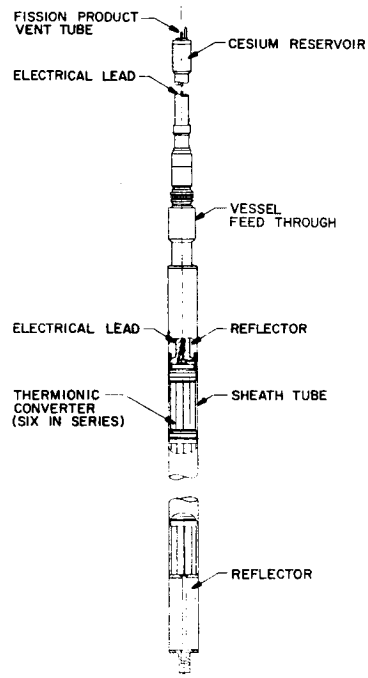

Fig. 7. Thermionic Fuel Element

Heat Rejection System Design

The heat rejection system (shown schematically in Fig. 8) consists of reactor and radiator NaK loops, a heat exchanger, and heat pipe radiator panels. The reactor loop is divided into two circuits (each having its own electromagnetic induction pump) to reduce the size of shield penetrations and provide improved flow distribution in the reactor. Reactor loop temperature at the reactor outlet is 1030°F at BOL and 1100°F at EOL. Heat is transferred from the primary reactor loop to five radiator loops in a counterflow tube-in-shell heat exchanger located around the reactor shield. Each of the radiator loops is independent and carries the heat to one of five radiator panels which are arranged in a cylindrical configuration. The heat is distributed over the surface of each panel by heat pipes using potassium as the working fluid.

The heat pipe panels are placed on the outside of the radiator loops and provide meteoroid protection for the liquid metal loops. Failure of one of the five secondary loops results in a average heat rejection system temperature increase of about 80°F at the reference operating power level. A summary of heat rejection system parameters is given in Table 4.

Power Conditioning and Transmission Lines

The power conditioning (P.C.) system consists of 30 individual modules, one for each pair of thermionic fuel elements. Each module consists of an inverter to convert low-voltage dc to square-wave ac, a transformer to increase the voltage, and a rectifier to convert the high voltage ac to dc. Analysis of the basic P.C. module circuit is given in Ref. 6. The output from some or all of the modules is fed to a common bus for transmission to the spacecraft.

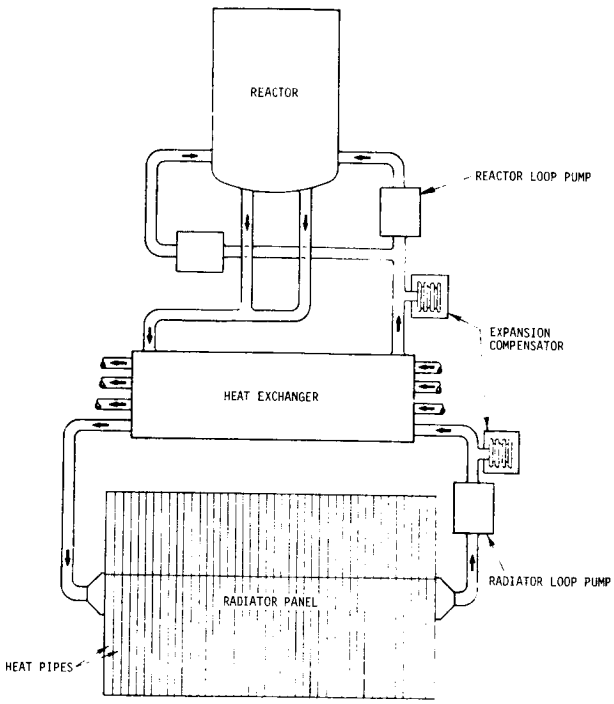

Fig. 8. Heat Rejection System Schematic

TABLE 4

HEAT REJECTION SYSTEM PARAMETERS

Radiator area	810 ft^2	
Radiator diameter	12 ft	
Heat pipe material	K in 316 SS	
Radiator weight	1990 lb	
Total heat rejection system weight	3600 lb	
	BOL	EOL
Average reactor loop temperature, °F	960	1030
Average radiator loop temperature, °F	920	990
Average radiator temperature, °F	900	975

A "direct radiating" concept is used in which heat dissipated in the P.C. components is radiated directly from the mounting plate of each module.

Transmission of the power from the reactor to the power conditioning is through four bundles of aluminum busbars which run along the outer surface of the shield and power conditioning structure and radiate the ohmic losses directly to space. All busbars in a bundle are insulated from one another to remain independent in the event of fuel element failures.

Shield Configurations

Shield designs have been prepared for the two basic concepts considered, the reactor placed on a boom attached to the space station or at the end of a long tether at a distance of 1 to 2.5 miles. The basic dose constraint of no more than 25 rem to be received at the space station during a 6-month period applies to either concept. This total dose corresponds to an hourly rate of 5.7 mrem/hr.

As shown in Table 3, the thermal power of the nuclear reactor may increase throughout the mission to compensate for any failures of the independent power modules. In order to provide adequate shielding without regard to the actual time of failure of the redundant elements, radiation protection is designed for the highest reactor power level corresponding to end-of-life conditions. In this particular case, therefore, the allowable dose rate at the space station was taken to be 5 mrem/hr at a reactor power level of 1740 kW.

Beyond the nominal requirement for the allowable dose at the space station, consideration has to be given to the radiation field in all directions around the reactor because of requirements for rendezvous and docking maneuvers, possible placement of experimental modules outside the actual space station, and other possible activities in the vicinity of the space station. The radiation dose environment around a U-ZrH thermoelectric reactor placed on a space station is shown in Fig. 9 (Ref. 1). The shield for the thermionic reactor system has been sized to provide a radiation environment equal to or less than that shown in Fig. 9.

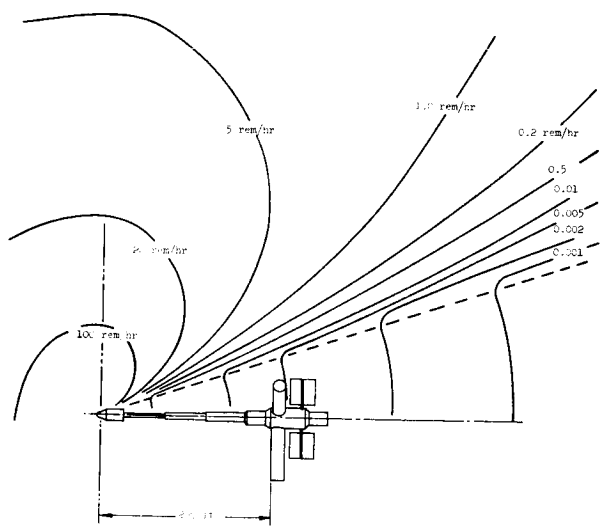

Fig. 9. Radiation Environment from Nuclear Reactor

The shield configuration for the thermionic reactor system mounted on a rigid boom is illustrated in Fig. 10. A relatively thin shield is provided at the side and top of the reactor to meet the requirement of no greater than 100 R/hr at a distance of 100 feet. A multilayer station shield is provided to shield a dose plane of 130 ft diameter at a separation distance of 200 feet. The resulting half-angle for the shield cone is 17.3°.

The intermediate heat exchanger and other liquid metal loop components have been placed adjacent to the reactor rather than in an intermediate gallery region. Elimination of the gallery permits a weight saving by reducing the diameter of the second layer of gamma shielding since it is placed closer to the apex of the shielding cone. The amount of activation of the secondary NaK passing through the heat exchanger was included in evaluating the dose rates at the space station. The secondary NaK is distributed over the area of the radiator which becomes a gamma source outside the reactor shield. This problem is considered further below.

TABLE 5

SHIELD DIMENSIONS

Boom Mounted Reactor		
Crew Shield	Tungsten	5.08 cm
	LiH	21.60 cm
	Tungsten	8.38 cm
	LiH	51.30 cm
Side Shield	Tungsten	0.63 cm
	LiH	31.00 cm
Tethered Reactor		
4π Shield	LiH	33.00 cm
Power Conditioning Shield	LiH	88.20 cm
	Tungsten	7.60 cm

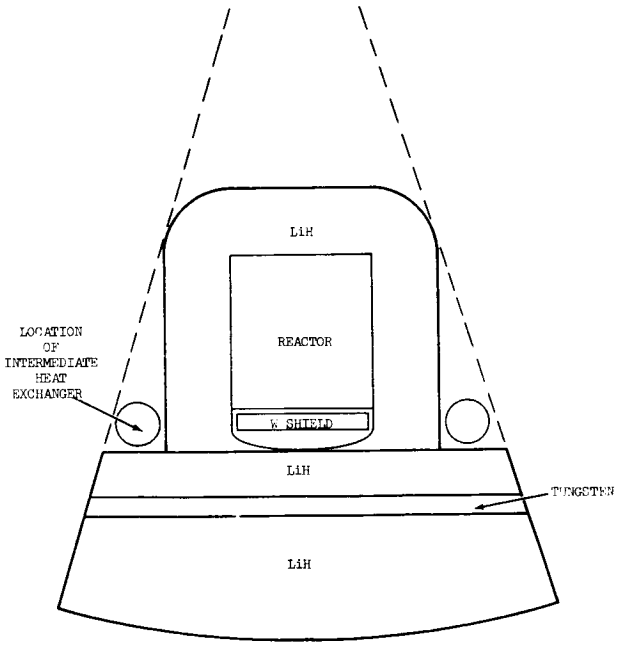

Fig. 10. Shield Configuration for Boom Mounted Reactor

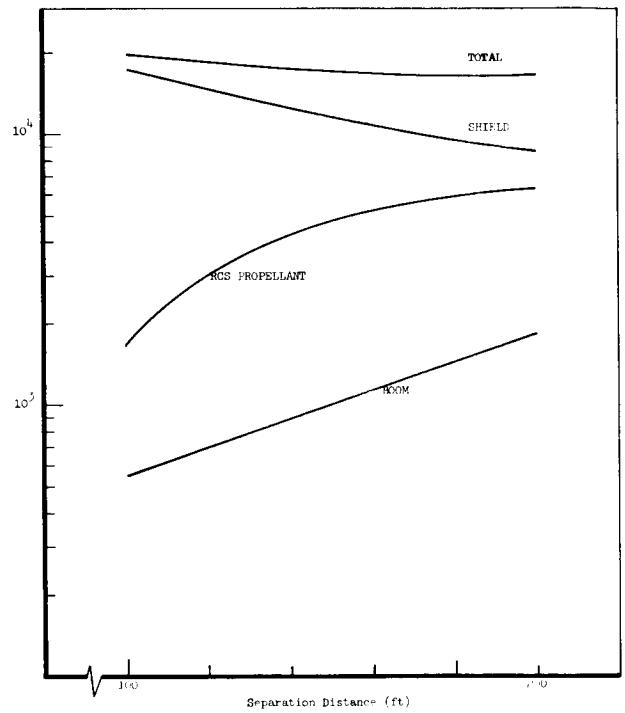

Fig. 11. Mass of Reactor Shield and Boom for Varying Separation Distance

The dimensions of the thermionic reactor shield are summarized in Table 5 for a separation distance of 200 feet and a dose plane diameter of 130 feet. Total shield mass for this configuration is 19,200 lb. (8700 kg). The effect of varying the length of the boom between the reactor and the space station is illustrated in Fig. 11. The masses of the boom and the propellant required by a reaction-control system for varying separation distances were supplied by NASA MSFC personnel (Ref. 7). The resulting total mass of shield, boom, and propellant has a broad minimum between 150 and 200 ft. separation.

The shield configuration for the tethered reactor concept is illustrated in Fig. 12 with dimensions given in Table 5. A 4π shield is provided to meet the space station dose limits at a separation of 2 miles. A thicker shaped shield at one end of the reactor protects the power conditioning equipment from direct reactor radiation and backscatter from heat rejection radiator and components. This shield is designed to reduce the dose to the power conditioning equipment to 10^6 rads of gamma rays and 10^{12} nvt of fast neutrons over a five-year operating lifetime. Total shield mass for the tethered system is 5733 lb. (2606 kg).

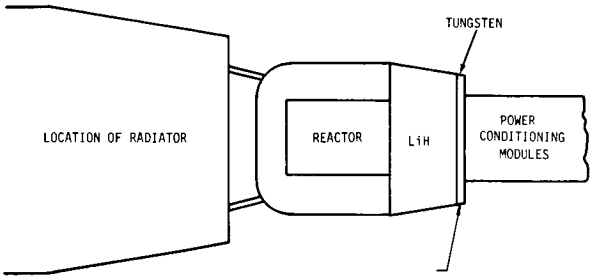

Fig. 12. Shield Configuration for Tethered Reactor System

Contributions to Radiation Dose

Nuclear radiation from the power system includes neutrons and gamma rays generated in the reactor core, secondary gammas generated by neutron interactions within the shield, and gamma rays from the coolant activated by neutron absorption in the intermediate heat exchanger. Table 6 presents the differential spectrum of neutrons and gamma rays for radiation received from primary and secondary sources in the reactor and shield, for the boom-mounted reactor system. The data is normalized to 1 mrem/hr of that particular radiation type. Although the highest values of the neutron spectrum appear in the lower energy groups, it should be noted that the major contribution to the dose comes from the fast neutrons. For example, the four highest groups, representing those neutrons with energy above 1 MeV, contribute 80% of the total dose from neutrons inside the shielded cone.

TABLE 6
SHIELDED NEUTRON AND GAMMA RAY SPECTRA

		Neutrons(1) (n/cm²-sec-eV)		Gammas(2) (photons/cm²-sec-eV)	
Group	Upper Energy (eV)	Inside Shield Cone	Outside Shield Cone	Upper Energy (eV)	Inside Shield Cone
1	1.49 + 7*	1.00 - 7	1.04 - 8	9×10^6	2.190 - 8
2	8.19 + 6	4.19 - 7	1.10 - 7	7×10^6	6.230 - 6
3	5.49 + 6	4.86 - 7	2.53 - 7	5×10^6	2.600 - 5
4	3.68 + 6	1.03 - 6	1.56 - 6	3×10^6	4.480 - 5
5	1.00 + 6	2.19 - 6	3.80 - 6	2.5×10^6	6.070 - 5
6	7.43 + 5	2.91 - 6	5.45 - 6	2×10^6	8.660 - 5
7	3.02 + 5	2.79 - 6	5.16 - 6	1.5×10^6	1.281 - 4
8	2.24 + 5	5.80 - 6	1.12 - 5	1×10^6	2.115 - 4
9	8.65 + 4	1.10 - 5	2.18 - 5	$.5 \times 10^6$	8.980 - 6
10	2.48 + 4	3.42 - 5	6.94 - 5		
11	5.53 + 3	1.04 - 4	2.16 - 4		
12	2.61 + 3	2.14 - 4	4.49 - 4		
13	1.23 + 3	4.38 - 4	9.31 - 4		
14	5.83 + 2	1.60 - 3	3.49 - 3		
15	4.79 + 1	1.39 - 2	3.12 - 2		
16	2.38	3.91 - 2	8.77 - 2		

* 1.49 + 7 equals 1.49×10^7

(1) normalized to 1 mr/hr of neutron dose

(2) normalized to 1 mr/hr of gamma dose

The secondary coolant fluid, NaK-78, is also a source of radiation to the space station when it is distributed throughout the heat rejection radiator. It is important, therefore, that the side shielding shown in Fig. 10 be thick enough to reduce the neutron activation of secondary NaK in the heat exchanger to tolerable levels. For the system design shown in Fig. 1, the total volume of NaK-78 in the secondary loop is 0.042 m^3 (1.5 ft^3). The dose received at the dose plane from the activated coolant in the radiator is shown in Fig. 13 for separation distances of 150 and 200 feet. For the reference side shield thickness of 12.2 in., the dose received at a separation distance of 200 ft is 0.17 mr/hr. It is concluded that placement of the intermediate heat exchanger in the location shown in Fig. 10 is feasible from the standpoint of dose levels from activated secondary coolant.

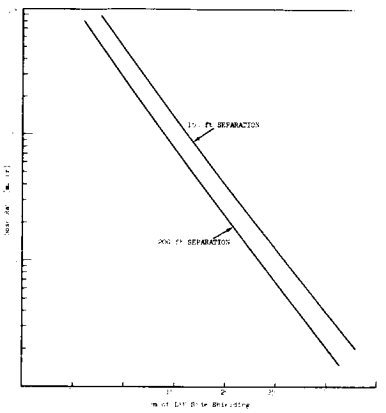

Fig. 13. Dose Received at Dose Plane from Activated Secondary Coolant

References

1. "Reactor Power System Design Document, MDC G0750, McDonnell Douglas Astronautics Company, December 1970, Vol. 1.

2. Gietzen, A. J., C. R. Fisher, and W. G. Homeyer, "25 kWe Thermionic Power System for Space Station Application," presented at IEEE 1970 Thermionic Conversion Specialist Conference, October 29, 1970, Miami Beach.

3. Gietzen, A. J., and W. G. Homeyer, "100 kWe Thermionic Power System Design," presented at IEEE 1970 Thermionic Conversion Specialist Conference, October 29, 1970, Miami Beach.

4. Gietzen, A. J., et al, Gulf General Atomic Company, "Nuclear Thermionic Space Station System Design," Report GA-10535, to be published.

5. Gylfe, J. D., and R. A. Johnson, "Reactor - Thermoelectric System for NASA Space Station," USAEC Report AI-AEC-12839, Atomics International, July 1969.

6. Gietzen, A. J., "Low Voltage Power Conditioning for a Thermionic Reactor," Gulf General Atomic Incorporated Report GAMD-9603, July 1969.

7. Brantley, L. W., NASA/Marshall Space Flight Center, private communication.

VENTING OF FISSION PRODUCTS AND SHIELDING IN THERMIONIC NUCLEAR REACTOR SYSTEMS

E. W. Salmi

Los Alamos Scientific Laboratory

Manuscript included in addendum, see page 1016.

SESSION IV.4.
NATURAL SPACE RADIATION: SOLAR COSMIC RAYS & MISSION EFFECTS
CHAIRMAN: L. LANZEROTTI
BELL TELEPHONE LABORATORIES

The Risk of Solar Proton Events to Space Missions

Martin O. Burrell

NASA/Marshall Space Flight Center, Huntsville, Alabama

SUMMARY

The total dose in rads-tissue from solar protons was tabulated for weekly time intervals, and the number of weeks which gave a dose above 25 rads behind 10 g/cm^2 of aluminum for the active 6 years of the 19th cycle were called dangerous or large event weeks. The number of such event weeks was found to be only 3 weeks for the past 20 years. Even though the chance for smaller events is examined, it was found that for any reasonable high confidence level (95%), the smaller events could be ignored. Consequently, the total particle flux for the 19th cycle was divided by a factor of 3 and determined a single large event week. Using this spectrum, the tissue dose in rads is calculated at the center of an aluminum spherical shell. To correct for geometric effects and self shielding, this dose may be reduced by a factor of about 3. To predict the probability of an event occurring, the Poisson distribution was the most logical choice. The confidence one can use in employing the Poisson process and arriving at confidence levels for the experimental value of the mean is investigated. Several examples are given for different mission lengths, and comparisons are made to other authors' results. An extension of the Poisson process is made to incorporate the concept of small sample theory and arrive at the expected distribution function which answers the following question. If x_o events are observed in time t_o, what is the probability of seeing x events in any observation time t?

INTRODUCTION

This study is concerned with the practical treatment of hazards from solar proton events outside the magnetosphere of the earth. It is not concerned with prediction of flares as such nor the long-range solar cycle indicators such as sun spots. The study of all solar proton events as such is only casually related to the problem of large dose rates inside realistic spacecraft. For example, in reference 1, there are 76 events listed from 1942 through 1963. Since 1963, there are probably an additional 24 more yielding a statistical sample of some 100 events. However, the correlation of this large sample with the events which are of real danger to space flight is very poor. For example, only 6 large events from 1950 to 1969 would have given about 85% of the total 20-year proton dose behind a thin wall of only 2 cm of aluminum. In addition, these 6 flares occurred in 3 weekly periods. Thus, 3 of these 6 large events occurred from July 10-16, 1959, 2 occurred from November 12-18, 1960, and on February 23, 1956, 1 large event was observed. The duration of an event is from 1 to 3 days. Even with this small sample, it seems that if conditions are suitable for a large event, the odds are very good that it will be followed within hours by another large event. Perhaps a time span of at least 1 week should be used to depict a total solar event, and it would be designated as the solar proton flux or dose per week. Under this definition, there are only 3 sample weeks of large solar events from about 1950 through 1969 (1,000 weeks). We are not dealing with an ordinary problem of statistical analysis, but with rare large events.

The reason that the writer has undertaken the awesome task of predicting the improbable is not by virtue of his background in solar physics or statistical analysis but because of his concern with protection of man and his radiation-sensitive equipment from space radiations for realistic spacecraft and missions. However, the reader should ask, why not leave this field of statistical astronomy to the experts. The answer is that the environmental scientists do not have to design or evaluate realistic shields for sensitive film or radiation-conscious astronauts.

The consequence of having several solar proton prediction models (which I do not wish to evaluate) has led to a wide disparity in results, especially when a reasonably high level of statistical certainty is desired. For example, at the 99% probability (percentile) level, the predicted dose behind 20 g/cm^2 of aluminum for a 1-year mission may vary by a factor of 10 or more between different writers[2]. Now this may not sound too bad considering the nature of the problem, but if a mission is planned with the requirement that the astronauts should not receive doses exceeding 100 rads skin dose with a 99% probability, and if one solar proton dose prediction model requires a shield of only 15 g/cm^2 and another model 50 g/cm^2, the radiation analyst has to make a vital decision, possibly affecting the life of an astronaut. Since no one wishes to be responsible for making a decision which could lead to dire consequences, the most pessimistic model is often chosen. This writer would not question this approach except that the desire to be on the safe side may readily get out of hand with the subsequent loss in mission capability.

A PRIMITIVE DOSE MODEL IS PROPOSED

The most direct measure of the hazard of a given solar proton event is the rads (.01 J/Kg) - tissue absorbed dose that would be measured behind various thicknesses of a typical spacecraft material such as aluminum. The simplest method is to find the point tissue dose at the center of a spherical shell of aluminum. However, due to self shielding by the astronaut (approximately a factor of 2) and spacecraft geometry as well as on-board equipment, the actual skin dose may be less by a factor of 3 or more than the point dose at the center of a spherical shell. This factor varies depending on the solar proton spectrum, the spacecraft geometry, and the location of the astronaut in the craft. This writer suggests using a factor of about 3 reduction for the solar proton point dose at the center of a spherical shell in order to estimate the likely skin dose to an astronaut in a real spacecraft of a given average thickness. (It

should be noted that this factor of 3 may be too large for a very "hard" spectrum such as seen in the trapped radiation belts, when a factor of 2.5 may be more in order.) To correct for depth dose (bone-marrow depth), a thickness of 5 cm of tissue is often employed. This is approximately equal to 6.5 g/cm^2 of aluminum in equivalent shielding effectiveness.

In order to clarify the exact assumptions which are to be employed, the following information is pertinent. The only adequate data available at this writing for solar proton predictions are from the 19th cycle (1954-64). However, there have been observations of sun spots (indicator of solar activity) for about 200 years. Based on 200+ years of observations, where the first cycle would date back to the middle of the 18th century (average cycle length is about 11 years), the 19th cycle had the highest maximum sun spot count yet recorded. In fact the average maximum sun spot count is more than a factor of 2 lower. The 20th cycle, which we are now well into (past the peak activity), has a sun spot count somewhat above this average. There has not been a large solar proton event comparable to the eight largest events of the 19th cycle (dose behind 10 g/cm^2). At this point, one may be led to believe that the 19th cycle is a fairly rare type cycle. With the present low occurrence of large solar proton events and the rather extensive sun spot counting dating back over 200 years, one might conclude that the probability of getting a solar cycle as active as the 19th is on the order of 1/20 or 0.05. This, of course, cannot be objectively demonstrated, and will not be, unless considerably more knowledge is obtained about the physics of the sun. One valid objection to the above is that the sun spot number is a poor indicator of large solar proton events. Also, the sun spot indicator may have changed during the last 50 years due to better observations, so that possibly the first 15 of the 20 observed cycles should not be used. The purpose of this paper is not to attempt to evaluate the above but to present the information for the reader's consideration. At any rate the reader may not find it difficult to believe that the use of the 19th cycle solar proton flux data may yield a pessimistic estimate of the solar proton hazard. With the above background, we can at least study the proton events characterized by the 19th cycle and infer proton events for future cycles similar to the 19th cycle.

Next we consider the observation that during the 19th cycle, the large solar proton events did occur on the whole around the most active years of the 11-year cycle, however not necessarily in proportion to sun spot count. It is generally assumed that there were only about 6 years of observed large solar proton events. Thus the following analysis is based on the so-called active 6 years (300 weeks) of the cycle. The second assumption is that it is fair and logical to lump the actual dose rates over an active week into units of total dose per week (see Introduction). This may include up to 3 proton events in a given week. Thus, instead of dealing with fundamental units of proton events, we propose to deal with observed weekly dose rates behind various aluminum thicknesses. The data available from various sources gave a total of 24 proton events worth considering. (The 30 or more events discarded gave less than 3 rads total behind 5 g/cm^2 of aluminum). The results of grouping this data into weekly time periods gave a total of 18 weeks with the frequencies of 13 weeks having 1 event, 4 weeks having 2 events, and 1 week having 3 events. Most of this data is recorded in NASA TND 4404 [3] on pages 16-23. The only major revision in reference 3 is in the use of the spectrum of A. J. Masley[4] for the November 12, 1960, flare.

One note of explanation should be made regarding the dose rates which are used in this study. They include a correction for secondary particles and thus are the sum of the primary proton dose and the secondary particles (neutrons and protons). This total dose at 20 g/cm^2 is about 20% and at 10 g/cm^2 about 10% above the primary proton dose rates.

Now we come to a very treacherous part of the analysis. How do we choose a rational and sufficient model for an event dose-week for solar protons? Table 1 is presented as a summary of the weekly solar proton doses of the 19th solar cycle which the writer will consider. The absorbed doses in rads-tissue were calculated at the center point of a spherical shell of aluminum with the shell thickness being designated as the shield.

TABLE 1: WEEKLY DOSES OF THE 19TH SOLAR CYCLE

Sample Number	Week	Year	Number of Flares	Shield (6-Year Dose) 5(906)[a]	10(251)	20(73)	Remarks
1	Nov 12 – 18	1960	2	456	83.4	17.0	Category 1 – Large Weekly Doses
2	July 10 – 16	1959	3	216	75.0	21.2	λ_1 0.01
3	Feb. 23	1956	1	92	50.0	24.8	
	Summed Dose		(6)	764	208.4	63.0	Approximately 85 Percent of 6-Year Total
	Percent of Total 6-Year Dose			84.3	83	86.3	
1	May 10	1959	1	59.3	18.3	4.4	Category 2 – Medium Weekly Doses
2	July 18 – 20	1961	2	22.0	8.2	2.4	λ_2 0.02
3	March 23	1958	1	10.9	2.5	0.4	
4	July 7	1958	1	10.5	2.3	0.4	
5	Jan. 20	1957	1	8.3	1.8	0.3	
6	Oct. 20	1957	1	4.1	1.8	0.7	
	Summed Dose		(7)	115.1	34.9	8.6	Approximately 13 Percent of 6-Year Total
	Percent of Total 6-Year Dose			12.7	13.9	11.8	
1	Aug. 22 – 26	1958	2	5.9	1.0	0.2	Category 3 – Small Weekly Doses
2	Aug. 29	1957	1	4.2	0.8	0.1	λ_3 0.03
3	Nov. 20	1960	1	3.6	1.5	0.05	
4	Aug. 3	1956	1	2.2	1.0	0.4	
5	Sept. 13	1960	1	2.9	1.2	0.5	
6	Aug. 16	1958	1	1.8	0.4	0.1	
7	July 3	1957	1	1.2	0.43	0.03	
8	July 12	1961	1	1.4	0.30	0.04	
9	April 28 – 29	1960	2	0.77	0.27	0	
	Summed Dose		(11)	23.97	6.90	1.42	Approximately 2 Percent of 6-Year Total
	Percent of Total 6-Year Dose			2.65	2.75	1.95	

a. The first number is the shield thickness in g/cm^2-aluminum. the number in parenthesis is the 6-year dose behind the shield.

The data of Table 1 have been grouped into three categories: (1) large weekly doses, (2) medium weekly doses, and (3) small weekly doses.

Category (1), consisting of only 3 weeks, gave mory than 84% of the total 6-year dose. Category (2), with 6 samples, gave about 13%, and Category (3), with 9 samples, gave less than 3% of the total dose.

The grouping which is shown is certainly not unique, and the last 2 weeks of Category (2) perhaps should be in Category (3), or perhaps the largest dose week of Category (2) should be in Category (1). The following work has attempted to provide for various combinations which the reader may wish to investigate by making the methods of approach more important than the choice of a precise set of data.

Since over 84% of the total solar proton dose is grouped into the 3 weeks of the first category, it would seem that one feasible solar proton dose model for an active week could be depicted by dividing the total 6-year dose behind the various shields by 3. Since the most active phase of the 19th cycle is about 6 years, it seems sufficient to use 300 weeks as the basic period of major solar activity. With this assumption, which will be used throughout this study, it follows that the estimated weekly expectation of a dangerous large solar proton dose would be λ_o = .01 (event/week).

In any case, the chance for an event of Category (2) or Category (3) is more likely to occur than one of Category (1) for a short exposure time. For this reason, a model will also be developed to reflect medium and small flare doses as well as large events. Thus, two solar proton dose models will be constructed and results compared in the following work.

The next part of our approach is to choose the best composite 19th cycle solar proton flare data which is available and arrive at total tissue dose in rads from primary and secondary particles at the center of spherical shells with varying thicknesses. T. T. White, et. al[6] have developed a composite model (MSC model) for the total proton flux during the 19th cycle. This model gives a larger dose for energies less than about 115 MeV than a model based on Webber's work[5]. Above 115 MeV, a composite flare model based on Webber's work (to be designated as the MSFC model) gives a larger dose. The 19th cycle composite 6-year proton spectrum which will be used in this work is the following:

$$\text{(MSC) I.}\quad J(>p) = 5.28 \times 10^{11}\, e^{-p/73} \qquad (30 \leq E \leq 115 \text{ MeV}) \qquad (1)$$

$$\text{(MSFC) II.}\quad J(>p) = 1.14 \times 10^{11}\, e^{-p/100} \qquad (E > 115 \text{ MeV}),$$

where p is the rigidity units of MV and J(>p) is the integral spectra (proton/cm^2) with energies above p. For protons, the relationship between p(MV) and E(MeV) is given by $p = \sqrt{E^2 + 1876E}$ (ref. 3, page 15).

Using the spectrum above, the best estimate of the 6-year (300 weeks) total dose (primaries and secondaries) is given in Fig. 1. From Fig. 1 and Table 1, the solar proton one-week-dose event models are constructed (Fig. 1 gives the magnitude, and Table 1 gives the fractions). Model I will be the dangerous solar event model which is represented by 3 large events over a period of 300 weeks.

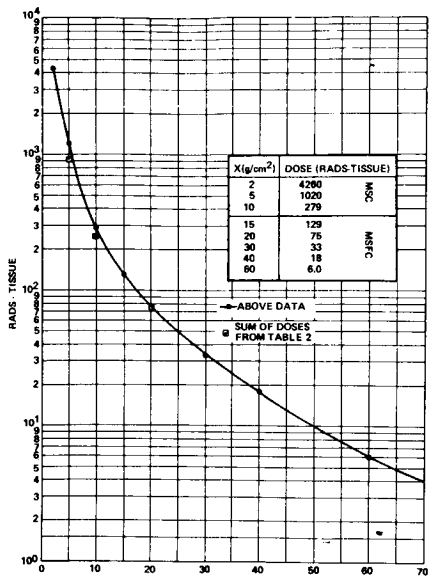

FIGURE 1: TOTAL DOSE FROM 19TH SOLAR CYCLE

The expected number of events in 1 week is given by λ_o = .01 (event/week). Model II will depict the possibility of a large, medium, or small dose in a week where the percentages of the total dose in Table 2 are used to determine the relative size of a dose week in the three groups. For the three categories of Table 1, the values λ_1 = .01, λ_2 = .02, and λ_3 = .03 are the mutually independent weekly expectations of large, medium, and small doses, respectively. Table 2 summarizes the dose models. It should be clear that the writer has presented in Table 2 only the primitive elements of a probability model. Thus the table gives the small sample estimates of the weekly expectations (λ) and the consequences (rads/week) if an event occurs according to Model I or II. It should also be made clear that the values of λ are valid only for the 300 most active weeks of a solar cycle similar to the 19th. The major unknown factor is an estimate of the chance of obtaining a solar cycle that would give total proton doses as large or larger than the 19th cycle.

The values of λ should be smaller for the so-called quiet sun (260 weeks) or else the magnitude of an event reduced to one of Category (3). Perhaps one might assume that λ = .02 (one event per year) during the 260 weeks of the quiet sun, but an event should be depicted by the D_3 column (small event) of Model II.

As a final conclusion to this section, it is of interest to recall that Fig. 1 represents the total dose versus spherical shell thickness for the 19th cycle. If for the data of Fig. 1 as described above, an effort is made to correct for the self shielding of an astronaut and the complex geometry of a spacecraft which has aluminum walls of 13.5 g/cm^2 (assume that a 5 cm depth dose corresponds to an additional aluminum thickness of 6.5 g/cm^2) then the 5 cm depth dose is estimated by dividing the dose at 20 g/cm^2 by a factor of 3. Thus one finds that the total dose from the 19th cycle was 25 rads at 5 cm tissue depth. Of course, this value is for the solar proton dose and does not account for the galactic cosmic ray dose which may range from 5 to 12 rads per year behind 20 g/cm^2 depending on how much dose is contributed by the

heavy cosmic ray particles (Z > 2). The implications of all the above are simply that since the 19th solar cycle was an example of a very active sun, and if one believes that the high energy proton fluxes received during this cycle are associated with this activity, he must be cautious in drawing certain conclusions. For example, the same astronaut above may have received from 30 to 70 rads from galactic cosmic rays during a 6-year trip whereas the above dose from solar protons at bone marrow depth was 25 rads (13.5 g/cm^2 - al. walls). Here one assumes that the galactic cosmic ray spectrum is so energetic that geometry factors are negligible for dose reduction. Thus the cosmic ray dose component may determine the limiting dose factor for long duration space travel. The purpose of the foregoing is not to minimize the importance of solar proton events but to point out that it may be quite feasible to shield against solar protons but probably impractical to consider shielding against galactic cosmic rays, and this very fact may be more important in determining man's exposure time to space outside the earth's magnetic field than the solar protons.

A PROBABILITY MODEL IS DERIVED

In this section, we shall address ourselves to the problem of choosing and using a probability density function in order to arrive at the probability of getting "x" events in "t" weeks and the associated problem of probability or percentile levels. The important question of establishing confidence intervals for the basic statistical parameters which are obtained from a small sample will be undertaken in the next section. In this section, we will be making the naive assumption that the basic statistics or population parameters (mean and variance) are well known, either by experience or apriori knowledge.

In order to derive the probability model, which seems to be the most natural outgrowth of the solar proton dose week, the process will be described in terms of probabilities $P_n(t)$ that exactly n events occur during a time interval t (weeks in our case). Thus, $P_o(t)$ is the probability of no event in the interval t and $1 - P_o(t)$ is the probability of one or more events. Next we define λ to be the mean or expectation of an event for a unit time interval. That is,

$$\hat{\lambda} = \frac{\text{no. of events}}{\text{total weeks of observation}} \qquad (2)$$

is a statistical estimate of λ. More precisely, λ is a constant which determines the density of points on the t axis. Thus for a small interval of time Δt the probability of one or more events is given by:

$$1 - P_o(\Delta t) = \lambda \Delta t + \varepsilon(\Delta t), \qquad (3)$$

where $\varepsilon(\Delta t)$ is an infinitesimal and small compared to $\lambda \Delta t$ such that

$$\lim_{\Delta t \to o} \frac{\varepsilon(\Delta t)}{\Delta t} = 0 \qquad (3a)$$

Now we make the following postulate:

Whatever the number of events during (o,t) the probability during (t, t + Δt) that one event occurs is given by $P_1(\Delta t) = \lambda \Delta t + \varepsilon_o(\Delta t)$, and the probability that more than one event occurs is given by $P_{n>1}(\Delta t) = \varepsilon_1(\Delta t)$.

These conditions are the basic assumptions of the Poisson process (Feller[7], pages 400-402). It should be clear that we are stating that for a small time interval Δt, the chance for one event is approximately $\lambda \Delta t$, and the chance for more than one event is very small compared to $\lambda \Delta t$. Since t is for a relative time scale, it is not contradictory that Δt of 1 week can be small on our time scale. The above conditions lead to a system of differential equations for $P_n(t)$. They are:

$$dP_n(t)/dt = -\lambda P_n(t) + \lambda P_{n-1}, \; n \geq 1 \quad , \qquad (4)$$

and

$$dP_o(t)/dt = -\lambda P_o(t), \; n = 0 \quad . \qquad (5)$$

From Equation (5) and $P_o(0) = 1$, we get:

$$P_o(t) = e^{-\lambda t} \quad . \qquad (6)$$

Using Equation (6) and $P_1(0) = 0$, Equation (4) can be solved for $P_1(t) = \lambda t e^{-\lambda t}$. Using the fact that $P_n(0) = 0$, (n>0), Equation (4) becomes a recursion equation and successive values of $P_n(t)$ can be found. The resulting solutions give the terms of the Poisson distribution:

$$P_n(t) = e^{-\lambda t} \frac{(\lambda t)^n}{n!} \quad . \qquad (7)$$

If the reader accepts the postulate following Equation (3), the Poisson distribution is the natural outcome. The foregoing arguments have been presented in order to minimize the illusion that the author has pulled a distribution function out of the sky. For a more rigorous treatment, reference 7 is recommended.

There are many interesting uses of the Poisson distribution in addition to the occurrence of rare events in a continuum of time. The distribution is used to approximate the binomial distribution for the case of rare events ($p < .05$). The word rare means individually rare. In a large population, several such events may occur, but the probability of occurrence of each individual event is small. For example, the number of people killed by horses in 1969. An important feature of the Poisson distribution is that for large values of the mean ($\lambda t >> 20$), the distribution approaches the normal (or Gaussian) distribution. There are many applications of the Poisson distribution given in any standard text on probability and statistics. The most common include such studies as the number born blind in a large city, radioactive disintegration, bacteria on plates, telephone traffic, etc. The remainder of this section will be devoted to a discussion of the Poisson distribution and how to apply it to our class of problems.

If a discrete variable x has a Poisson distribution, then the probability that [X = x] is given by the expression:

$$P[X = x] = \frac{e^{-m} m^x}{x!} \quad , \; x = 0, 1, 2, \ldots, \qquad (8)$$

and $P[X = 0] = e^{-m}$, since 0! = 1.

The mean (or expected value of the variable x) is given by $\mu = m$, the variance σ^2 is given by $\sigma^2 = m$, and the standard deviation is simply given by $\sigma = \sqrt{m}$. The summation equation,

$$\sum_{x=0}^{\infty} e^{-m} m^x/x! = 1 \quad , \tag{8a}$$

is satisfied. Since we are primarily interested in the time-dependent form of the Poisson, $m = \lambda t$ becomes the mean. Even though the Poisson is discrete in the variable x, it is continuous in t. For our purpose, we shall write the Poisson distribution as:

$$P[X = x] = \frac{e^{-\lambda t} (\lambda t)^x}{x!} \quad , x = 0, 1, 2, \ldots, \tag{9}$$

where t = number of weeks, x = number of events in t weeks, λ = mean number of events per week with (λt) becoming the expected or mean number of events in t weeks, and $P[X = x]$ is the probability of exactly x events in t weeks.

If one wished to find a value of x which would not be exceeded say at least 99% of the time (1% chance at most of exceeding x) for a given λt, the accumulative distribution function $P[X \leq x^*]$ is utilized. The value of x which we seek is the smallest x^* which satisfies

$$Pr[X \leq x^*] = \sum_{x=0}^{x^*} \frac{e^{-\lambda t} (\lambda t)^x}{x!} \geq P \quad , \tag{10}$$

where P = .99 for the case in question.

Since we are dealing with a discrete distribution function, the inequality is necessary, and one usually obtains a value of x^* which corresponds to a value slightly above P (.99). This discrepancy is usually circumvented by the proper use of the words "at least" and "at most."

Next, we will examine how to apply the above information to our problem of predicting the solar proton dose that would be seen on a space mission at various percentile levels. For simplicity, let us assume that if an event occurs, it is depicted by the so-called "large" event model or Model I of Table 2. Using this model, the sample statistical estimate of $\lambda_o = .01$ event/week, and for convenience, assume the duration of exposure to large solar events is 100 weeks, then the value of $\lambda t = 1.0$ for the Poisson distribution. Now assume that we wish to find the dose levels that would be exceeded 27%, 2%, and 0.1% of the time. Applying Equation (10) with P taking on the values 0.73, 0.98, and 0.999, we see that the values of x are 1, 3, and 5 events. So to find the dose at the respective levels, we multiply the doses behind the various shield thicknesses of Model I by the values of x above. The results are plotted in Fig. 2. Note that the 73.6% level corresponds in our model to the mean or expected value of the Poisson distribution function. The percentile level at the expected value is found only when λt is an integer. It becomes smaller approaching 50% as λt increases to large values. For example, when $\lambda t = 20$, the percentile at $x^* = 20$ is 55.9%.

A similar computation can be carried out using event Model II. The values of the Poisson mean become respectively $\lambda_1 t = 1.0$, $\lambda_2 t = 2.0$, and $\lambda_3 t = 3.0$ where t = 100 weeks. Tables are constructed, and the following results are found at the expected value, 98% and 99.9% level. For the

TABLE 2: MODELS OF A ONE-WEEK DOSE EVENT FOR THE ACTIVE 300 WEEKS OF THE 19TH SOLAR CYCLE

MODEL I

	N = 3* 100%** λ_o = .01†
X(g/cm^2)	D_o (Rads/Weeks)
2	1420
5	340
10	93
15	43
20	25
30	11
40	6
60	2

MODEL II

	N(Large)=3 84% λ_1 = .01	N(Med.)=6 13% λ_1 = .02	N(Small)=9 3% λ_3 = .03	3 $\sum_{i=1}$ NiDi
X(g/cm^2)	D_1 (Rads/Week)	D_2 (Rads/Week)	D_3 (Rads/Week)	Total Dose 300 Weeks
2	1195	95	15	4290
5	286	24	3.4	1032.6
10	78	7.5	0.9	281.1
15	36	3.5	0.43	132.87
20	21	2.0	0.25	77.25
30	9.3	0.80	0.11	33.69
40	5.03	0.45	0.06	18.33
60	1.70	0.15	0.02	6.18

* The N indicates the number of weeks used in dose category.

** The % gives the percent of total dose in the category.

† The "λ" gives the expectations (probability) of category for one week.

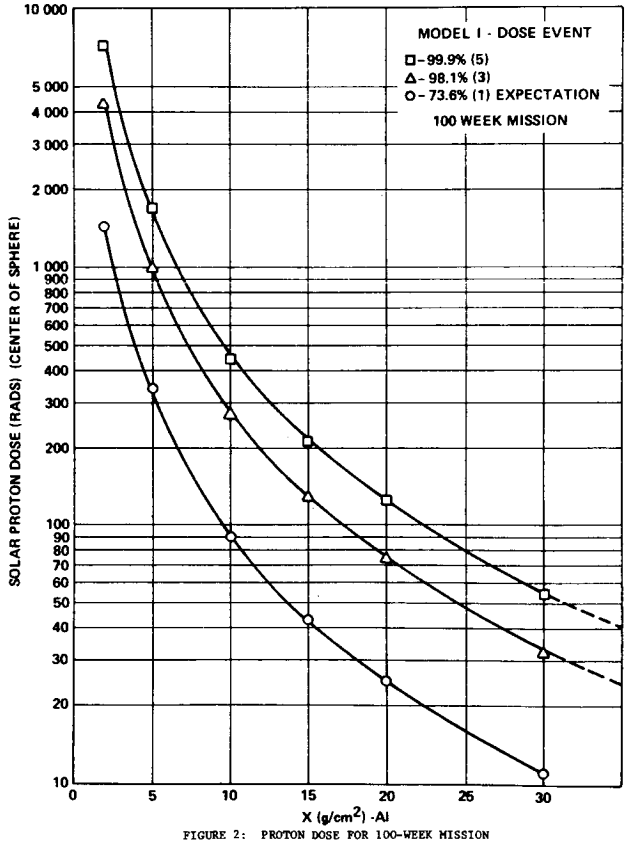

FIGURE 2: PROTON DOSE FOR 100-WEEK MISSION

large events, x = 1, 3, and 5; for the medium events, x = 2, 5, and 8; and for the small events, x = 3, 7, and 10. The percentile values at the expected or mean value levels ($x^* = \lambda t$) are 73.6%, 67.7%, and 64.7%, respectively. In order to reduce the necessity of repetition, this set of levels could be denoted as approximately 70% level. The comparison of results from these totals to Fig. 2[8] indicate very good agreement. A useful rule would be: Empirical Rule - If at a given probability level there is at least one large event, then Model I is sufficient to describe the radiation hazard. If no large event is found at the given probability level, then Model II should be used.

At this point, it might be useful to depict several curves similar to Fig. 2 for various mission times t, with λ = .01 event/week, at given probability or percentile levels. In order to do this, arrays could be constructed for various values of λt, and the number of events, x, necessary to satisfy the inequality of Equation (10) could be found for various values of $P < 1$.

Rather than provide a multitude of similar graphs, Table 3 will allow the reader to find the number of events for a range of anticipated values of λt at 9 different percentile levels from 50 to 99.9%. Table 3 was constructed by choosing a probability level, P, the number of events, N, and then finding the value of $m(-\lambda t)$ that satisfied the following equation:

$$\Pr(x \leq N) = \sum_{x=0}^{N} \frac{e^{-m} m^x}{x!} = P, \quad (m = \lambda t) \quad . \quad (11)$$

TABLE 3: VALUES OF λt TO SATISFY $\Pr(X \leq N) = P$

α	0.001	0.005	0.010	0.025	0.050	0.100	0.15	0.25	0.50
N[b] \ P[a]	99.9 Percent	99.5 Percent	99.0 Percent	97.5 Percent	95.0 Percent	90.0 Percent	85.0 Percent	75.0 Percent	50.0 Percent
0	0.0010	0.0050	0.010	0.025	0.051	0.105	0.16	0.29	0.69
1	0.045	0.10	0.15	0.24	0.36	0.53	0.68	0.96	1.68
2	0.19	0.34	0.44	0.62	0.82	1.10	1.33	1.73	2.67
3	0.43	0.67	0.82	1.09	1.37	1.74	2.04	2.54	3.67
4	0.74	1.08	1.28	1.62	1.97	2.43	2.79	3.37	4.67
5	1.11	1.54	1.79	2.20	2.61	3.15	3.56	4.22	5.67
6	1.52	2.04	2.33	2.81	3.29	3.89	4.35	5.08	6.67
7	1.97	2.57	2.91	3.45	3.98	4.66	5.15	5.96	7.67
8	2.45	3.13	3.51	4.12	4.70	5.43	5.97	6.84	8.67
9	2.96	3.72	4.13	4.80	5.43	6.22	6.80	7.73	9.67
10	3.49	4.32	4.77	5.49	6.17	7.02	7.64	8.62	10.67
11	4.04	4.94	5.43	6.20	6.92	7.83	8.48	9.52	11.67
12	4.61	5.58	6.10	6.92	7.69	8.65	9.34	10.42	12.67
13	5.20	6.23	6.78	7.65	8.46	9.47	10.19	11.33	13.67
14	5.79	6.89	7.48	8.40	9.25	10.30	11.06	12.24	14.67
15	6.41	7.57	8.18	9.15	10.04	11.14	11.92	13.15	15.67
16	7.03	8.25	8.89	9.90	10.83	11.98	12.79	14.07	16.67
17	7.66	8.94	9.62	10.67	11.63	12.82	13.67	14.99	17.67
18	8.31	9.64	10.35	11.44	12.44	13.67	14.55	15.91	18.67
19	8.96	10.35	11.08	12.22	13.25	14.53	15.43	16.83	19.67
20	9.62	11.07	11.83	13.00	14.07	15.38	16.31	17.75	20.67
21	10.29	11.79	12.57	13.79	14.89	16.24	17.20	18.68	21.67
22	10.96	12.52	13.33	14.58	15.72	17.11	18.09	19.61	22.67
23	11.65	13.26	14.09	15.38	16.55	17.97	18.98	20.54	23.67
24	12.34	14.00	14.85	16.18	17.38	18.84	19.88	21.47	24.67
25	13.03	14.74	15.62	16.98	18.22	19.72	20.77	22.40	25.67
26	13.73	15.49	16.40	17.79	19.06	20.59	21.67	23.34	26.67
27	14.44	16.25	17.17	18.61	19.90	21.47	22.57	24.27	27.67
28	15.15	17.00	17.96	19.42	20.75	22.35	23.48	25.21	28.67
29	15.87	17.77	18.74	20.24	21.59	23.23	24.38	26.15	29.67
30	16.59	18.53	19.53	21.06	22.44	24.11	25.28	27.09	30.67
31	17.32	19.30	20.32	21.89	23.30	25.00	26.19	28.03	31.67
32	18.05	20.08	21.12	22.72	24.15	25.89	27.10	28.97	32.67
33	18.78	20.86	21.92	23.55	25.01	26.77	28.01	29.91	33.67
34	19.52	21.64	22.72	24.38	25.87	27.66	28.92	30.85	34.67
35	20.26	22.42	23.53	25.21	26.73	28.56	29.83	31.79	35.67
36	21.00	23.21	24.33	26.05	27.59	29.45	30.75	32.74	36.67
37	21.75	24.00	25.14	26.89	28.46	30.34	31.66	33.68	37.67
38	22.51	24.79	25.96	27.73	29.33	31.24	32.58	34.63	38.67
39	23.26	25.59	26.77	28.58	30.20	32.14	33.50	35.57	39.67
40	24.02	26.38	27.59	29.42	31.07	33.04	34.42	36.52	40.67

a. $P = 1 - \alpha$

b. If λt lies between two entries, use N corresponding to the largest entry. Thus, if $\lambda t = 0.5$, use N = 4 at the 99.9-percent level. If λt is less than or equal to the top entry, use N = 0. Thus, if $\lambda t = 0.02$, N = 0 at the 97.5-percent level, but N = 1 at the 99.0-percent level.

The values of $m = \lambda t$, found in this manner, is the expected value or mean of the Poisson distribution which has a percentile level of exactly P x 100% for N or less events.

The top of Table 3 is headed with a row of values labeled α which denotes the probability of more than N events or simple $\alpha = 1 - P$. The probability statements using α will be made as follows: the probability is no greater than α that more than N events will be observed in t weeks. The use of α probabilities will be derived in the next section. The range of values in Table 3 should provide for the refinements needed in the following work.

CONFIDENCE INTERVALS ARE ESTABLISHED

The results of the previous section depended strongly on the choice of the parameter λ or the probability of having a large event week. In this section, we will establish the confidence we can place on the value of λ as calculated from observed sample data. One of the virtues of the Poisson distribution is that the value of the mean ($m = \lambda t$) completely determines the distribution function; i.e., $\sigma^2 = m$, whereas the mean and variance (σ^2) is needed for most distribution functions, and they are not simply related. Thus in dealing with small sampling statistics from a normal distribution, one needs to establish confidence intervals for both the mean and the variance.

In order to more clearly explain the intent of this section, an example will be given. The Poisson law arises very often in certain biological problems such as organisms distributed at random over the bottom of a lake. The number of such organisms found in a series of trial dredgings from separate small areas of the same size will follow this law. Statisticians calculate boundaries of possible outcomes from a given small sample, and these values are called confidence limits at a certain probability level for the assumed distribution function. Now, if a biologist counted 21 organisms from one of his dredgings, he could assert that he is 95% confident that the mean or expected value lies between 13 and 32 organisms per unit area assuming a Poisson distribution. Thus with only one sample and assumption of a Poisson process, it is possible to set upper and lower bounds on possible outcomes at a given probability level. From the above example, we can assert that if many dredgings are made, we expect only 5% will contain a number of organisms outside the predicted range.

Returning to the basic problem, we wish to establish the confidence interval on m, hence to find the probability

$$\Pr(m'' \leq m \leq m') \geq (1 - 2\beta)\ 100\% \quad , \quad (12)$$

where $1 - P = \beta$.

Now if P = .99 and β = .01, then

$$\Pr(m'' \leq m \leq m') \geq 98\%, \quad (12a)$$

and we are at least 98% sure that m lies between m' and m", where m has only a 1% chance of being greater than m'. We can now write the general set of equations which will determine the value of m' and m":

$$\sum_{x=0}^{x_o} \frac{e^{-m'}(m')^x}{x!} = 1 - P = \beta \quad , \qquad (13)$$

and

$$\sum_{x=x_o}^{\infty} \frac{e^{-m''}(m'')^x}{x!} = \beta \quad , \qquad (14)$$

or

$$\sum_{x=0}^{x_o-1} \frac{e^{-m''}(m'')^x}{x!} = 1 - \beta \quad , \qquad (15)$$

where x_o is observed number of events. The form of the above equation is an outgrowth of using a discrete distribution function and follows the common practice in textbooks on statistics. Solving Equations (13) and (15) for m' and m" by use of Newton's method, the upper and lower bounds on m are found for "x_o" observed events. Table 4 summarizes these results for 8 different values of β or P. Fig. 3 depicts a typical result taken from Table 4.

TABLE 4: UPPER AND LOWER BOUNDS FOR THE MEAN AT PROBABILITY OF P = (1 - β)100%

Confidence Interval	99.8 Percent		99.0 Percent		98.0 Percent		95.0 Percent	
β	0.001		0.005		0.010		0.025	
Events, X_o	Lower Bound[a]	Upper Bound	Lower Bound	Upper Bound	Lower Bound	Upper Bound	Lower Bound	Upper Bound
0	0	6.91	0	5.30	0	4.61	0	3.69
1	0.001	9.23	0.005	7.43	0.01	6.64	0.025	5.57
2	0.045	11.23	0.10	9.27	0.15	8.41	0.24	7.22
3	0.19	13.06	0.34	10.98	0.44	10.05	0.62	8.77
4	0.43	14.79	0.67	12.59	0.82	11.60	1.09	10.24
5	0.74	16.45	1.08	14.15	1.28	13.11	1.62	11.67
6	1.11	18.06	1.54	15.66	1.79	14.57	2.20	13.06
7	1.52	19.63	2.04	17.13	2.33	16.00	2.81	14.42
8	1.97	21.18	2.57	18.58	2.57	17.40	3.45	15.76
9	2.45	22.66	3.13	20.00	3.51	18.78	4.12	17.08
10	2.96	24.13	3.72	21.40	4.13	20.14	4.80	18.39
11	3.49	25.59	4.32	22.78	4.77	21.49	5.49	20.96
12	4.04	27.03	4.94	24.15	5.43	22.82	6.20	20.98
13	4.61	28.45	5.58	25.50	6.10	24.14	6.92	22.23
14	5.20	29.85	6.23	26.84	6.78	25.45	7.65	23.49
15	5.79	31.24	6.89	28.16	7.48	26.74	8.40	24.74
16	6.41	32.62	7.57	29.48	8.18	28.03	9.15	25.98
17	7.03	33.99	8.25	30.79	8.89	29.31	9.90	27.22
18	7.66	35.35	8.94	32.09	9.62	30.58	10.67	28.45
19	8.31	36.70	9.64	33.38	10.35	31.85	11.44	29.67
20	8.96	38.04	10.35	34.67	11.08	33.10	12.22	30.89
21	9.62	39.37	11.07	35.95	11.83	34.35	13.00	32.10
22	10.29	40.70	11.79	37.22	12.57	35.60	13.79	33.31
23	10.96	42.02	12.52	38.48	13.33	36.84	14.58	34.51
24	11.65	43.33	13.26	39.74	14.09	38.08	15.38	35.71
25	12.34	44.64	14.00	41.00	14.85	39.31	16.18	36.90

a. The lower bound is calculated so that β is less than the indicated value.

TABLE 4 (Concluded)

Confidence Interval	90.0 Percent		80.0 Percent		70.0 Percent		50.0 Percent	
β	0.050		0.100		0.15		0.25	
Events, X_o	Lower Bound	Upper Bound	Lower Bound	Upper Bound	Lower Bound	Upper Bound	Lower Bound	Upper Bound
0	0	3.00	0	2.30	0	1.90	0	1.39
1	0.051	4.74	0.105	3.89	0.16	3.37	0.29	2.69
2	0.36	6.30	0.53	5.32	0.68	4.72	0.96	3.92
3	0.82	7.75	1.10	6.68	1.33	6.01	1.73	5.11
4	1.37	9.15	1.74	7.99	2.04	7.27	2.54	6.27
5	1.97	10.51	2.43	9.27	2.79	9.49	3.37	7.42
6	2.61	11.84	3.15	10.53	3.56	9.70	4.22	8.56
7	3.29	13.15	3.89	11.77	4.35	10.90	5.08	9.68
8	3.98	14.43	4.66	12.99	5.15	12.08	5.96	10.80
9	4.70	15.71	5.43	14.21	5.97	13.25	6.84	11.91
10	5.43	16.96	6.22	15.41	6.80	14.41	7.72	13.02
11	6.17	18.21	7.02	16.60	7.64	15.57	8.62	14.12
12	6.92	19.44	7.83	17.78	8.48	16.71	9.52	15.22
13	7.69	20.67	8.65	18.96	9.34	17.86	10.42	16.31
14	8.46	21.89	9.47	20.13	10.19	19.00	11.33	17.40
15	9.25	23.10	10.30	21.29	11.06	20.13	12.24	18.49
16	10.04	24.30	11.14	22.45	11.92	21.26	13.15	19.57
17	10.83	25.50	11.98	23.61	12.79	22.38	14.07	20.65
18	11.63	26.69	12.82	24.76	13.67	23.50	14.99	21.73
19	12.44	27.88	13.67	25.90	14.55	24.62	15.91	22.81
20	13.25	29.06	14.53	27.05	15.43	25.74	16.83	23.88
21	14.07	30.24	15.38	28.18	16.31	26.85	17.75	24.96
22	14.89	31.41	16.24	29.32	17.20	27.96	18.68	26.03
23	15.72	32.59	17.11	30.45	18.09	29.07	19.61	27.10
24	16.55	33.75	17.97	31.58	18.98	30.17	20.54	28.17
25	17.38	34.92	18.84	32.71	19.88	31.28	21.47	29.23

Even though we have obtained confidence bounds on the estimate of $m = \lambda t$, the major interest is concerned with the upper bounds that an investigator should use when only x_o events have been observed over a "t" week time interval. Following this concept and the simple model of a large dose-event-week, we recall that only 3 such event weeks occurred over the 300 active weeks of the 19th solar cycle. Now if one wishes to find the upper bounds on this observation, he may use Table 4 in conjunction with Table 3 and arrive at the 100P% confidence level that the probability is no greater than some small value α that N'_α events will occur. Thus Table 5 is

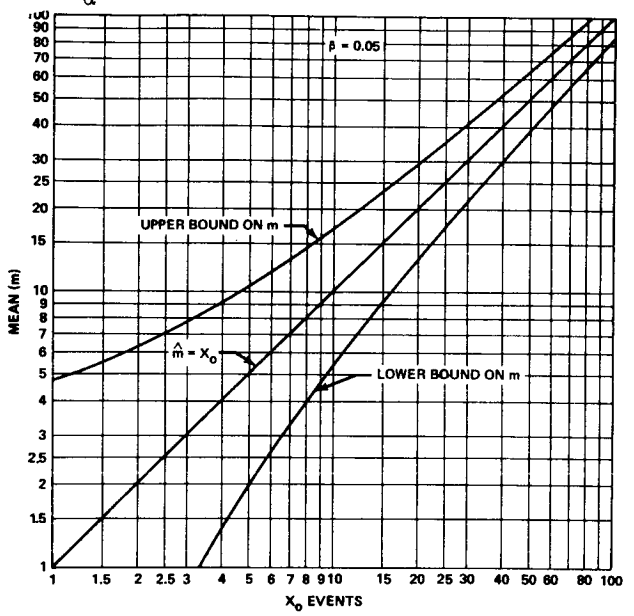

FIGURE 3: 90% CONFIDENCE LIMITS FOR POISSON

TABLE 5: THE NUMBER OF EVENTS N'_α THAT WILL BE EXCEEDED AT A PROBABILITY NO GREATER THAN α FOR THE 100-PERCENT UPPER BOUND VALUE OF THE POISSON MEAN, m', WHEN X_o = 3 OBSERVED EVENTS

m'	100P \ α Percent	0.001	0.005	0.010	0.025	0.050	0.100	0.150	0.250	0.500
13.06	99.9	25	23	22	20	19	18	17	15	13
10.98	99.5	22	20	19	18	17	15	14	13	11
10.05	99.0	21	19	18	17	15	14	13	12	10
8.77	97.5	19	17	16	15	14	13	12	11	9
7.75	95.0	18	16	15	14	13[a]	11	11	9	8
6.68	90.0	16	14	13	12	11	10	9	8	7
6.01	85.0	15	13	12	11	10	9	8	7	6
5.11	75.0	13	12	11	10	9	8	7	6	5
3.67	50.0	11	9	9	8	7	6	6	5	3

a. Example: One is 95 percent confident that the true mean does not exceed 7.75 (X_o=3), and using this value of the mean, one is certain that the probability of seeing more than 13 events during a 300 week active period is no greater than 0.050.

TABLE 6: THE NUMBER OF EVENTS N'_α THAT WILL BE EXCEEDED AT A PROBABILITY NO GREATER THAN α FOR THE 100P-PERCENT UPPER BOUND VALUE OF THE POISSON MEAN, m', WHEN X_o = 0 OBSERVED EVENTS

m'	100P \ α Percent	0.001	0.005	0.010	0.025	0.050	0.100	0.150	0.250	0.500
6.91	99.9	16	15	14	12	11	10	10	9	7
5.30	99.5	14	12	11	10	9	8	8	7	5
4.61	99.0	12	11	10	9	8	7	7	6	4
3.69	97.5	11	9	9	8	7	6	6	5	4
3.00	95.0	10	8	8	7	6	5	5	4	3
2.30	90.0	8	7	6	6	5	4	4	3	2
1.90	85.0	7	6	6	5	4	4	3	3	2
1.39	75.0	6	5	5	4	4	3	3	2	1
0.69	50.0	4	4	3	3	2	2	2	1	0

constructed.

Since the 20th solar cycle has produced no large events, it is of interest to ask if zero large events occur for a period of 300 active weeks, what are the possible upper bounds of m' and the number of events N_α' that could be expected at some small probability. (This may be a nonsense question and will be discussed in the next section.) Table 6 is constructed with this in mind. The methods used are the same as for Table 5. It is of interest to note that even though $x_o = 0$ events are observed that the 95% upper bound for the Poisson mean is m' = 3 which was the actual observed number of large events during the 19th cycle. Thus it seems that for a reasonable level of confidence (95%), the analyst would be justified if he used m' = 3 (λ = 0.01 event/week) for large events even though the solar activity for a given cycle was considerably different than the 19th cycle. Perhaps after all is said, the only conclusion that can be drawn is that the observed 19th cycle dose events could be used for any near average solar cycle, and if a cycle is predicted to be similar to the 19th cycle, then the results of Table 5 ($x_o = 3$) should be seriously considered as a possible model.

Finally, Table 7 is presented as a summary of values to use for λ (events/week) at various confidence levels. For large events, it seems that the $x_o = 0$ column is probably reasonable to use if the solar cycle is not very active. If a cycle similar to the 19th is forecast, then the column under $x_o = 3$ is perferred.

TABLE 7: VALUES FOR $\lambda' = m'/300$ (EVENTS/WEEK) FOR X_o OBSERVED EVENTS AT 100P% UPPERBOUND CONFIDENCE LEVEL

X_o / 100P%	0	3	6	9
99.9	.0230	.0435	.0602	.0755
99.5	.0177	.0366	.0522	.0667
99.0	.0154	.0335	.0486	.0626
97.5	.0123	.0292	.0435	.0569
95.0	.0100	.0258	.0393	.0524
90.0	.0070	.0223	.0351	.0474
85.0	.0063	.0200	.0323	.0442
75.0	.0046	.0170	.0285	.0392
50.0	.0023	.0122	.0222	.0322
OBS*	.0000	.0100	.0200	.0300

*OBS denotes the value of $X_o/300$

The value of λ and the dose event model to use during the remaining 270 less active weeks of a solar cycle are not obtainable from the present analysis. However, until more data is available, the best one can do is use some essentially arbitrary criteria. For example, if we believe that the chance of a large dose event week is definitely dependent on some minimal level of solar activity and this level is not approached during the quiet periods of the cycle, then it would be unreasonable to use the large event dose week even at a very low probability level such as the values shown under the $x_o = 0$ column of Table 7. Even if λ is only .002 event/week for the Poisson distribution, one sees that the chance of getting two or more large events is approximately 6% for t = 200 weeks. However, we cannot preclude the possibility of some smaller dose event occurring for the quiet period of a solar cycle. The present writer suggests using λ = .02 event/week for the quiet period but recommends that the dose model for the small dose event (D_3) of Model II (Table 2) be used. This is equivalent to expecting about one such event per year which is reasonably close to the actual observed number of events from October 1961 through July 1966.

In order to illustrate applications of the foregoing work, eight trip lengths will be considered ranging from 13 to 260 weeks (5 years), during the most active 6 years of a solar cycle which is like the 19th cycle ($x_o = 3$). In order to simplify the possible combinations, four different probability levels for the upper bound mean (λt) are used at four probability levels for the Poisson distribution. A mean (.01 t) corresponding to the actual observed (OBS) large event weeks of the 19th cycle is also given. This corresponds to the 95% level of the mean for x_o = 0 events, and this value is recommended for the average type cycle. The results of these combinations are shown in Table 8. The entries in this table give the number of large events that will be expected at a probability equal to or less than α corresponding to the Poisson mean (λt) which we are 100P% sure will not be exceeded (see footnote on Table 5). These tables are constructed in a manner similar to Table 5, however, we start with Table 7 for values of λ at various levels of percent confidence (100P).

Figures 4, 5, and 6 have been presented for values of α at .001, .01, and 0.1 for different upper bound values of the mean showing a range from the observed (approximately 50%) to the 99.9% confidence level of the mean (λt) for a 78-week mission during the active weeks of a very active cycle. Comparisons are also shown in these figures to the work of other authors[2,9,10] who have made similar computations but have used different models for prediction of the solar proton dose. An interesting aspect of the above comparison is that at the 0.1% (100 xα) level, the present work is considerably lower even for the 99.9% upper bound value of λt. However, at the 10% level, the reverse situation seems to be the case. The major difference in the methods of most of the other authors and the present work is that the size of our large event is fixed, but the number of events may be quite large, whereas in the other methods, the size of a single event may be extremely large (several times larger than the large event used in this work). These differences will be discussed in the last section.

TABLE 8: NUMBER OF EVENTS AT COMPOUND PROBABILITIES P AND α

a. t = 13 Weeks

m = λt	P × 100 \ α	0.001	0.01	0.05	0.10
0.57	99.9	4	3	2	2
0.44	99.0	3	2	2	1
0.34	95.0	2	2	1	1
0.29	90.0	2	2	1	1
0.13	OBS	1	1	1	1

b. t = 26 Weeks

m = λt	P × 100 \ α	0.001	0.01	0.05	0.10
1.13	99.9	6	4	3	3
0.87	99.0	5	4	3	2
0.67	95.0	4	3	2	2
0.58	90.0	4	3	2	2
0.26	OBS	3	2	1	1

c. t = 52 Weeks

m = λt	P × 100 \ α	0.001	0.01	0.05	0.10
2.26	99.9	8	6	5	4
1.74	99.0	7	5	4	3
1.34	95.0	6	5	3	3
1.16	90.0	6	4	3	3
0.52	OBS	4	3	2	1

d. t = 78 Weeks

m = λt	P × 100 \ α	0.001	0.01	0.05	0.10
3.39	99.9	10	8	7	6
2.61	99.0	9	7	5	5
2.01	95.0	8	6	5	4
1.74	90.0	7	5	4	3
0.78	OBS	5	3	2	2

e. t = 104 Weeks

m = λt	P × 100 \ α	0.001	0.01	0.05	0.10
4.52	99.9	12	10	8	7
3.48	99.0	10	8	7	6
2.68	95.0	9	7	6	5
2.32	90.0	9	6	5	4
1.04	OBS	5	4	3	2

f. t = 156 Weeks

m = λt	P × 100 \ α	0.001	0.01	0.05	0.10
6.79	99.9	16	16	11	10
5.23	99.0	14	11	9	8
4.02	95.0	11	9	8	7
3.48	90.0	10	8	7	6
1.56	OBS	7	5	4	3

g. t = 208 Weeks

m = λt	P × 100 \ α	0.001	0.01	0.05	0.10
9.05	99.9	20	17	14	13
6.97	99.0	16	14	12	10
5.37	95.0	14	11	9	8
4.64	90.0	13	10	8	7
2.08	OBS	8	6	5	4

h. t = 260 Weeks

m = λt	P × 100 \ α	0.001	0.01	0.05	0.10
11.31	99.9	23	20	17	16
8.71	99.0	19	16	14	13
6.71	95.0	16	13	11	10
5.80	90.0	14	12	10	9
2.60	OBS	9	7	5	5

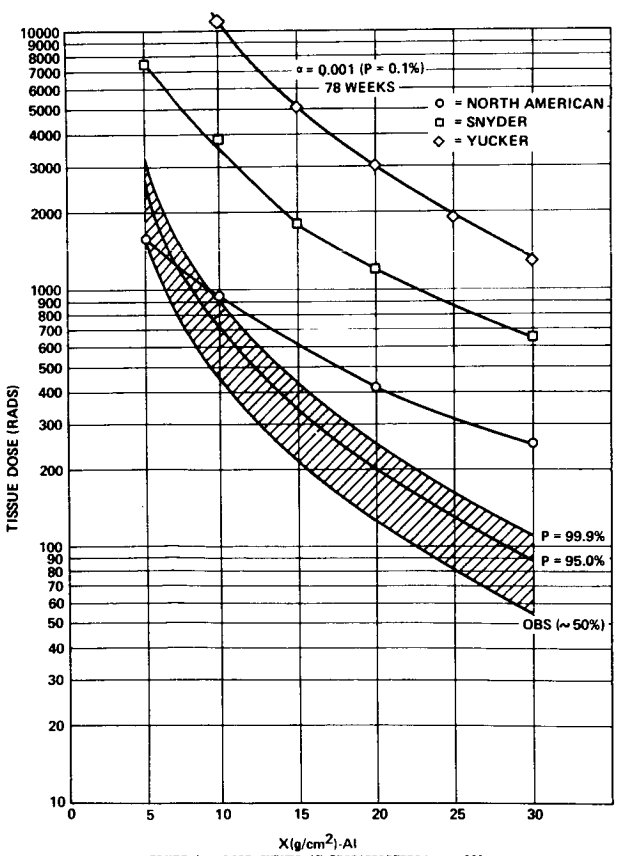

FIGURE 4: DOSE CURVES AT PROBABILITIES α = .001

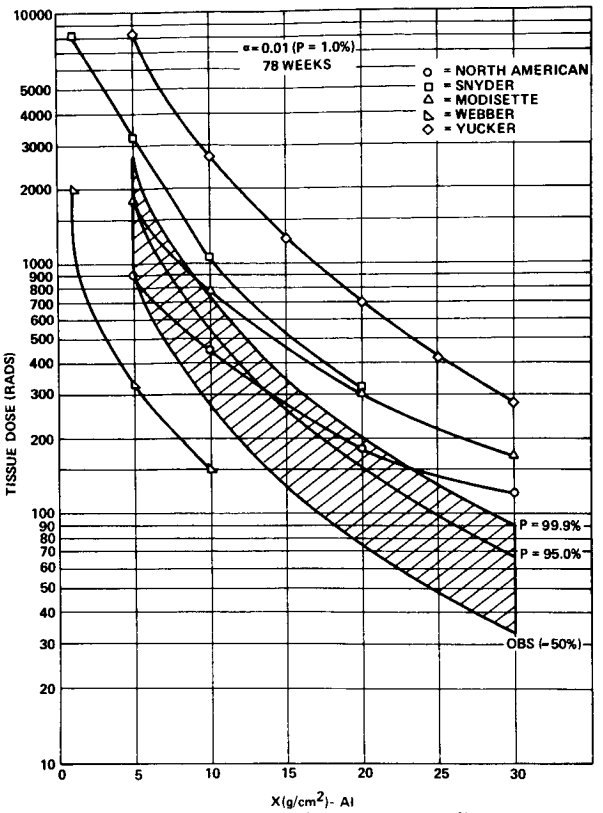

FIGURE 5: DOSE CURVES AT PROBABILITIES α = .01

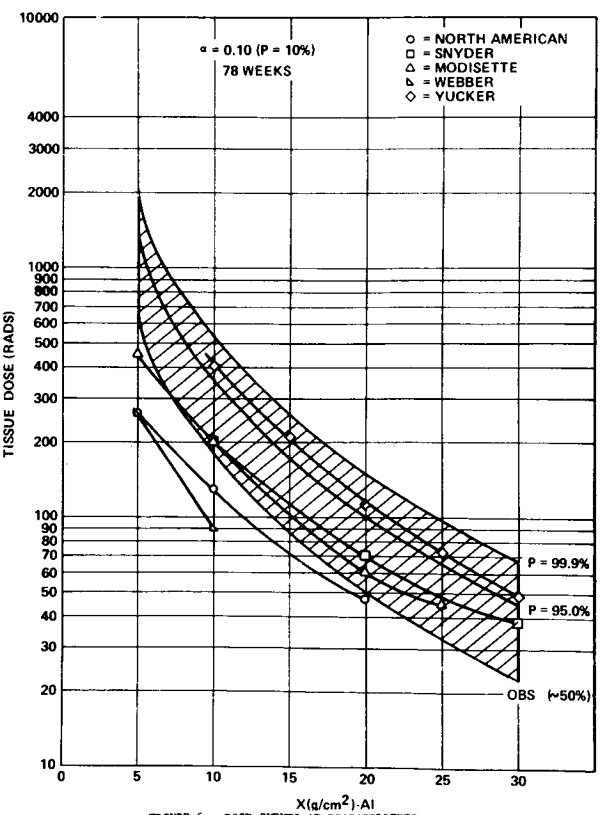

FIGURE 6: DOSE CURVES AT PROBABILITIES α = .1

A NEW PROBABILITY MODEL IS FOUND

The foregoing section seems to provide some rationale for choosing a probability function for a given set of conditions: (a) the active 300 weeks of a very active cycle such as the 19th, (b) the active 300 weeks of an average cycle, and (c) the quiet 270 weeks of any solar cycle. However, if we examine Tables 5 through 8, a question presents itself. If we choose a very high confidence level for the Poisson mean and then determine the number of events that would give a low probability α of getting a worse situation, then it seems that we are discussing a very improbable situation. That is, what is the chance of the mean being as high as the 99.9% confidence level, and if we use this mean the joint probability of seeing more than N_α' events at a probability no greater than 0.001? For example, in Table 5, we see that $N_\alpha' = 25$ events when $P = .999$ and $\alpha = .001$. At first blush, one might suspect that the chance of both conditions occurring is on the order of 10^{-6}. But care must be taken since we are dealing with cumulative distribution functions. Thus the product $(1 - P)\alpha$ does not correspond to a unique value of N_α'. This can be ascertained by examining in Table 5 the values of $(1 - P)\alpha$ corresponding to $N_\alpha' = 13$. Now, we would like to ask the question;

"If x_o events are observed in a given time, t_o, what is the probability of seeing more than N events in any observation time t?"

With this knowledge a unique value of the probability of seeing N events can be made for any period $t \leq T_o$. This question is also important because we propose to use the values of λ calculated for the total period of $T_o = 300$ weeks and might be suspect of the true probability when one applies the value of λ to a time period say of only 50 weeks. However, the reader surely agrees that the best estimate of the λ corresponds to the total sample space of the 300 most active weeks during the 19th solar cycle.

In order to provide an answer to the above, we must first ask what is the distribution of possible Poisson means if in a time t_o there are only x_o events observed. If we examine Equation (13), which gives the cumulative distribution of β as a function of the upper bound values of m for a given x_o, one sees that the derivative $(-d\beta/dm)$ yields the desired upper bound probability density function for m;

$$-d\beta/dm = f(m) = \frac{e^{-m} m^{x_o}}{x_o!} \quad . \tag{16}$$

This function is continuous in m and is the so-called gamma distribution in the variate m. The expected value of m, $E(m) = x_o + 1$; the variance, $\sigma^2(m) = x_o + 1$, and

$$\int_o^\infty \frac{e^{-m} m^{x_o} dm}{x_o!} = 1 \quad . \tag{17}$$

To summarize the meaning of Equation (16), we can state that for a given observation of x_o events, the probability of the m being in the interval m to m + dm is given by the probability equation;

$$f(m)dm = \frac{e^{-m} m^{x_o} dm}{x_o!} \quad . \tag{18}$$

See Fig. 7 for illustration of Equation (18) with $x_o = 3$.

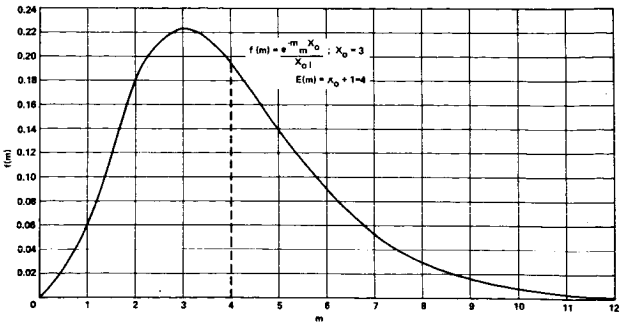

FIGURE 7: THE GAMMA PROBABILITY DENSITY FUNCTION WHEN $X_o = 3$

However, we wish to investigate the more subtle relationship that reflects the distribution of λ's for a given observation of x_o events over a period of t_o weeks. Therefore, we make the change of variables denoted by $m = \lambda t_o$; $dm = t_o d\lambda$, and our probability density function in the variate λ becomes:

$$f(\lambda)d\lambda = \frac{t_o^{x_o+1}}{x_o!} \lambda^{x_o} e^{-t_o\lambda} d\lambda \quad . \tag{19}$$

For a given value of λ, the probability of seeing exactly x events in time "t" is given by the discrete Poisson distribution function;

$$P(x) = Pr(x;\lambda t) = \frac{(\lambda t)^x e^{-\lambda t}}{x!} \quad , \; x=0,1,2,\ldots \tag{20}$$

where the probability of having a value of λ in the interval $\lambda + d\lambda$ is given by the density fuction of Equation (19) and $t \leq t_o$ (actually the case $t > t_o$ is equally valid).

Using the above definitions, the relationship we seek is given by the following:

$$Pr(x,t|x_o,t_o) = \int_o^\infty Pr(x;\lambda t) \cdot f(\lambda)\, d\lambda \quad . \tag{21}$$

Thus we are stating that for Equation (20) of the Poisson distribution, the probability of each possible λ (a spectrum of possible means) be folded into the equation and the results integrated over all possible values of λ from zero to infinity. The result is a probability density function which is the expected value of the Poisson distribution over all possible means λ. Thus,

$$Pr(x,t|x_o,t_o) = \frac{t_o^{x_o+1} t^x}{x_o!x!} \int_o^\infty \lambda^{x_o+x} e^{-(t_o+t)\lambda} d\lambda. \tag{22}$$

After integration, we obtain;

$$Pr(x,t|x_o,t_o) = \frac{t_o^{x_o+1} t^x}{x_o!x!} \left[\frac{(x_o+x)!}{(t_o+t)^{x_o+x+1}}\right] . \tag{23}$$

Now if we make the substitution $\theta = t/t_o$ and simplify, the results are the discrete distribution function in the variate x:

$$Pr(x|x_o,\theta) = \frac{(x+x_o)!}{x!x_o!} \frac{\theta^x}{(1+\theta)^{x+x_o+1}} \quad . \tag{24}$$

It can be shown that for the discrete distribution function above;

$$\sum_{x=0}^{\infty} \frac{(x+x_o)!}{x!x_o!} \frac{\theta^x}{(1+\theta)^{x+x_o+1}} = 1 \quad , \tag{25}$$

and the mean or expected value of x is given by:

$$\bar{x} = E(x) = (x_o+1)\theta \quad . \tag{26}$$

The proof of Equation (25) can be shown by resorting to hypergeometric functions, and the results of Equation (26) can be found by multiplying the summand of Equation (25) by x and after simplifying, the value $(x_o+1)\theta$ can be factored out leaving a sum that is the equivalent to that shown in Equation (25). An illustration of the density function [Equation (24)] is shown in Fig. 8 for $\theta = 1$ and $\theta = .52$.

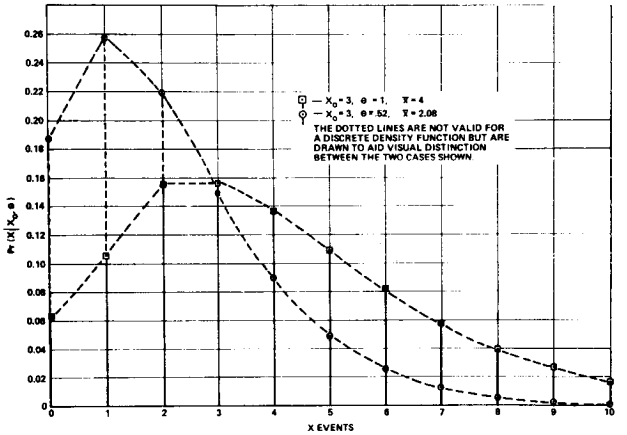

FIGURE 8: THE DISCRETE PROBABILITY DENSITY FUNCTION $Pr(x|x_o,\theta)$

This report is not intended to be a study of probability theory, and the ramifications of the above distribution function and its possible parallels in other statistical work will not be pursued.

Because of the format of Tables 5 and 8 and the manner in which we have previously made probability statements, we wish to find the probability that more than N events are seen, given x_o and θ; or

$$Pr(x>N|x_o,\theta) = 1 - Pr(x\leq N|x_o,\theta) \quad , \tag{27}$$

where $\theta = t/t_o$, x_o = number of events observed in time t_o (300 weeks), and t is the observation time during which N events are seen.

Thus, the ultimate relation which we wish to answer our probability questions is given by Equation (27) or the obvious variations associated with it. In fact, if the foregoing is valid, we may dispense with the difficulties of choosing an upper bound value of the Poisson mean at a given level and then determining the probability that N events will be exceeded at some probability α as shown in Tables 5 and 8, where the true probability is actually not known.

Using Equation (27), the number of combinations of θ, x_o, and N can readily get out of hand. For this reason, only the values of x_o observed events from 0 through 9 were used with different values of θ from 13 weeks to 300 weeks ($\theta = 1$). The values of N were extended to the point where $Pr(x>N|x_o,\theta) < 10^{-6}$. These tabulations are given in reference 8.

It is very interesting to note that when $x_o = 0$, $\theta = 1$, that the chance of seeing more than 3 events is as high as .0625. This infers that even though no events were observed during a given 300 week active cycle, we cannot be more than 93.75% confident that 3 or less events could occur in a similar cycle. Also, we see from the same above assumption that we are 50% sure that we will see more than zero events. This seems to infer a dilemma bordering on the naive statement that if you know nothing about the probability of an event, you can only be 50% sure that it can't happen; e.g. probability of life on Mars. This last statement seems to cast doubt on the usefulness of the case when $x_o = 0$.

However, it is of academic interest to investigate further the case when $x_o = 0$. For example, Equation (24) becomes:

$$Pr(x|o,\theta) = \theta^x/(1+\theta)^{x+1} \tag{28}$$

and for $\theta > 0$, we see that when $x = 0$,

$$Pr(x = 0|o,\theta) = 1/(1+\theta) \quad , \tag{29}$$

and

$$Pr(x > o|o,\theta) = \theta/(1+\theta) \quad . \tag{30}$$

The probability of seeing an event as θ approaches zero becomes very small as one would suspect for a very rare event. Now as θ increases to large values ($\theta >> 1$), the value of the probability approaches 1. This infers that if an event can happen at a given small probability, then it is almost certain that the event will occur after a sufficiently long period. Thus Equations (29) and (30) do not defy intuition in an ordinary sense but leave us with a rather insecure feeling since the number of actual observed events in time t_o is zero. However, if we examine the density function of possible values of λ [Equation (19)] when $x_o = 0$, a plausible probability density function is found;

$$f(\lambda)\, d\lambda = t_o\, e^{-t_o\lambda}\, d\lambda \quad . \tag{31}$$

Table 9 is presented as a survey of Equation (27) for $Pr(x > N|3,\theta) \leq \varepsilon$ at several values of ε and θ.

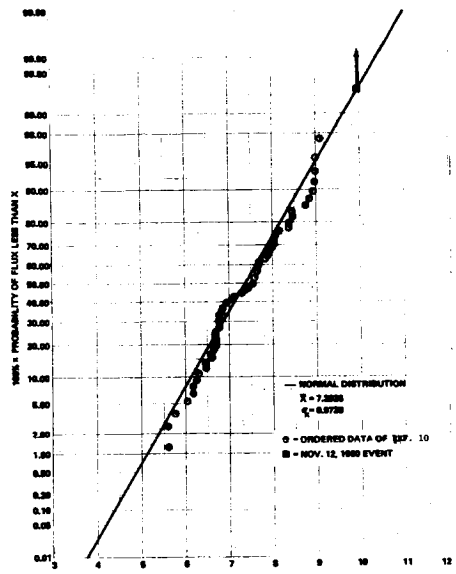

FIGURE 9: CUMULATIVE DISTRIBUTION OF LOG FLUX FOR 19TH CYCLE

A point of interest concerns the values of the results in Table 8 as compared to those in Table 9. It should be clear that the results of Table 9 do not provide the same type of probability statements as Table 8. In general, this writer feels that the results of Table 9 are more useful and to the point but others may disagree. In any case, one may ascertain which probability level of the parameter λ is more credible when using the methods of the previous section and constructing tables similar to Table 8. For example, one sees that the value of λ at the 90% level seems to yield event numbers (N) at probabilities α in Table 8 which seem to be comparable to the probabilities ϵ in Table 9.

Finally Table 10 is presented for the case when $x_0 = 0$ even though we have cast doubt on the validity of the meaning of this rather extreme case. However, it does signify a sort of boundary condition for those periods when the probability of a large event is very small as perhaps exists for the active years of an average type solar cycle.

REVIEW AND COMMENTS

In the foregoing sections, the writer has attempted to convey a method of thinking about the radiation hazards associated with solar proton events. The method of approach is felt to be more important than the actual results presented. The methods and models as developed utilize very little solar physics as such and consequently will be very unsatisfying to many physicists who have examined various aspects of the problem. There is no attempt to model or predict a solar proton spectrum, the time dependence of particle arrival, or angular distributions of the flux.

As a brief summary, the total dose in rads-tissue from solar protons was tabulated for weekly time intervals, and the number of weeks which gave a dose above 25 rads behind 10 g/cm^2 of aluminum for the active 6 years of the 19th cycle were called dangerous or large event weeks. The number of such event weeks was found to be only 3 weeks for the past 20 years.

Even though the chance for smaller events is examined, it was found that for any reasonable high confidence level (95%), the smaller events could be ignored. Consequently, we took the total particle flux for the 19th cycle and divided this spectrum by a factor of 3 and arrived at a single large event week.

Using this spectrum, one can calculate the tissue dose in rads at the center of an aluminum spherical shell (Table 2). To correct for geometric effects and self shielding, this dose should be reduced by a factor of about 3. If the space mission is planned during the quiet period of a cycle, then the small event dose curve (D_3) of Model II (Table 2) may be used with $\lambda = .02$ ($\bar{n} \simeq 1$ event/year).

To predict the probability of an event occurring, the Poisson distribution seemed to be the most logical choice. The third section was devoted to examining this conclusion and the methods of using this probability model. The fourth section was written as an effort to define the confidence one could use in employing the Poisson process and specifically arriving at confidence levels for the experimental or observed value of the mean of the Poisson distribution function. Several examples were given for different mission lengths, and comparisons were made to other authors' results.

Finally, the previous section was an extension of the Poisson process to incorporate the concept of small sample theory and arrive at the expected distribution function which answers the following question. If x_0 events are observed in time t_0, what is the probability of seeing x events in any observation time t? The results were represented by the discrete probability density function in the variate x: $Pr(x|x_0,\theta)$. Using the above function, extensive tables were tabulated in reference 8.

In the beginning of this work, the author intended to avoid commenting on the methods used by other investigators, but in order to explain the radical differences shown in Figs. 4, 5, 6, the following comments are pertinent. One of the more common procedures used is to obtain the logarithms to the base ten of the solar proton flux above 30 MeV for each of the events of the 19th cycle. This data is then plotted on normal probability graph paper, obtaining a distribution called the log normal distribution in the variable $x = \log_{10} \phi$.

This is a true normal distribution in the variate x, and there is no virtue in examining the transformed distribution in the variable ϕ which has a more complex representation. Also the values of the mean and standard deviation between the two distributions are not simply antilog related. For more details, see reference 8.

The present writer has assumed that the users of this distribution keep their statistics in the variable x which is certainly the simplest process.

From reference 10, 60 events were taken that had fluxes measured above 30 MeV.

The logarithm of these 60 entries were ordered from the smallest to the largest and the normalized cumulative sums plotted on log normal paper as shown in Fig. 9. The ungrouped data had a mean of 7.39, and the standard deviation was 0.97 as shown at bottom of the figure. The straight line in Fig. 9 depicts the cumulative normal distribution

TABLE 9: NUMBER OF EVENTS N THAT SATISFY $Pr(X>N|3,\Theta) \leq \epsilon$

WEEKS	Θ \ ϵ	.10	.01	.001	.0001	.00001
13	.0433	1	2	3	3	4
26	.0866	1	2	4	5	6
52	.1733	2	4	5	7	8
78	.2600	3	5	7	8	10
104	.3467	3	6	8	10	12
156	.5200	4	8	10	13	16
208	.6933	6	9	13	16	19
260	.8667	7	11	15	19	22
300	1.000	9	13	17	21	25

with mean of 7.39 and variance of 0.97. From examination of this fit, one might conclude that the log normal gives a reasonable representation of the data. Note that the flux for the November 12, 1960, event is plotted as a square which falls exactly on our line of best fit. This is done since actually when one obtains the cumulative distribution from a discrete set of data, the last point has the cumulative probability of 1.00, but since this cannot theoretically occur, the best choice is to place this point on the best fit line. This point which is $\log_{10} \phi = 9.9562$ corresponds to the cumulative probability of 99.6% or in terms of the standard deviation, the November 12, 1960, event is at 2.63 standard deviations above the mean. If we wished to go to the 99.9% level, then it would be necessary to take 3.09 standard deviations above the mean or a log flux of 10.4016. Now if we find the antilog of this value, we see that the flux at the 99.9% level in the log normal distribution is 2.52×10^{10} proton/cm^2 (E > 30 MeV) which is a factor of about 2.8 times larger than the November 12, 1960, event. Hence, it would seem that a flux above 30 MeV which is 3 times larger than the November 12, 1960, event would have a probability of occurring which is less than 0.001.

From the above analysis, one may be convinced that a reasonable upper bound value for a single event is at most a factor of 3 larger than the November 12, 1960, event. For the above reason this writer feels that the results obtained by some investigators for the extreme probability tails must depict a smaller probability than the estimates given. They have possibly used joint probabilities of flux and rigidity parameters which may be a factor of 10 or more smaller than those indicated by the 0.1% probability tail shown in the various reports at my disposal.

If the reader wishes to use the 99.9% probability event in the present work, he may ignore self shielding and geometry factors, a factor of 3.

TABLE 10: NUMBER OF EVENTS N THAT SATISFY $Pr(X> N|0,\Theta) \leq \epsilon$

t WEEKS	Θ \ ϵ	.1	.01	.001	.0001	.00001
13	.0433	0	1	2	2	3
26	.0866	0	1	2	3	4
52	.1733	1	2	3	4	6
78	.2600	1	2	4	5	7
104	.3467	1	3	5	6	8
156	.5200	2	4	6	8	10
208	.6933	2	5	7	10	12
260	.8667	2	5	8	11	14
300	1.0000	3	6	9	13	16

REFERENCES

1. WEDDELL, J.B.; and HAFFNER, J.W.: Statistical Evaluation of Proton Radiation from Solar Proton Events. North American Aviation, SID 66-421, May 1966.
2. FRENCH, F.W.: Solar Flare Radiation Protection Requirements for Passive and Active Shields. AIAA 7th Aerospace Sciences Meeting, Paper No. 69-15, January 1969.
3. BURRELL, M.O.; WRIGHT, J.J.; and WATTS, J.W.: An Analysis of Energetic Space Radiation and Dose Rates. NASA TN D-4404, February 1968.
4. MASLEY, A.J.; and GEODEKE, A.D.: A Complete Dose Analysis of the November 12, 1960, Solar Cosmic Ray Event. Life Sciences and Research, 1963.
5. WEBBER, W.R.: An Evaluation of the Radiation Hazard Due to Solar Particle Events. Boeing Document D2-90469, December 1963.
6. WHITE, T.T.; ROBBINS, D.E.; and HARDY, A.C.: Radiation Environment for the 1975 - 1985 Space Station Program. MSC Document MSC-00183, October 1969.
7. FELLER, W.: An Introduction to Probability Theory and Its Application. Vol. I, 1957.
8. BURRELL, M.O.: The Risk of Solar Proton Events to Space Travel. NASA TN D (to be published in early 1971).
9. SNYDER, J.W.: Radiation Hazard to Man From Solar Proton Events. J.Sci. Res., Vol. 4, 1967, p. 826.
10. YUCKER, W.R.: Statistical Analysis of Solar Cosmic Ray Proton Dose. McDonald Douglas Report MDC G-0363, June 1970.

REFERENCES

1. WEDDELL, J. B.; and HAFFNER, J. W.: Statistical Evaluation of Proton Radiation From Solar Proton Events. North American Aviation, SID 66-421, May 1966.
2. FRENCH, F. W.: Solar Flare Radiation Protection Requirements for Passive and Active Shields. AIAA 7th Aerospace Sciences Meeting, Paper No. 69-15, January 1969.
3. BURRELL, M. O.; WRIGHT, J. J.; and WATTS, J. W.: An Analysis of Energetic Space Radiation and Dose Rates. NASA TN D-4404, February 1968.
4. MASLEY, A. J.; and GOEDEKE, A. D.: A Complete Dose Analysis of the November 12, 1960, Solar Cosmic Ray Event. Life Sciences and Research, 1963.
5. WEBBER, W. R.: An Evaluation of the Radiation Hazard Due to Solar Particle Events. Boeing Document D2-90469, December 1963.
6. WHITE, T. T.; ROBBINS, D. E.; and HARDY, A. C.: Radiation Environment for the 1975 - 1985 Space Station Program. MSC Document MSC-00183, October 1969.
7. FELLER, W.: An Introduction to Probability Theory and Its Applications. vol. I, 1957.
8. BURRELL, M. O.; The Risk of Solar Proton Events to Space Travel. NASA TN D (to be published in early 1971).
9. SNYDER, J. W.: Radiation Hazard to Man From Solar Proton Events. J. Sci. Res., vol. 4, 1967, p. 826.
10. YUCKER, W. R.: Statistical Analysis of Solar Cosmic Ray Proton Dose. McDonald Douglas Report MDC G-0363, June 1970.

PROBABLE SOLAR FLARE DOSES ENCOUNTERED ON AN INTERPLANETARY MISSION AS CALCULATED BY THE MCFLARE CODE

Gerald P. Lahti and Irving M. Karp
National Aeronautics and Space Administration
Lewis Research Center
Cleveland, Ohio

The computer program, MCFLARE, uses Monte Carlo methods to simulate solar flare occurrences during an interplanetary space voyage. The total biological dose inside a shielded crew compartment due to the flares encountered during the voyage is determined. The computer program evaluates the doses obtained on a large number of trips having identical trajectories. From these results, a dose D_p having a probability p of not being exceeded during the voyage can be determined as a function of p for any shield material configuration.

The user of the code selects any number of solar flares considered to be representative of the ones that will occur during future solar active periods (these flares are generally selected from the flares that occurred during the last solar active period 1956 to 1962). The flares are assumed to occur during these periods. The dose at a distance of 1 AU from the Sun from each of these flares behind any shield configuration investigated is input to the MCFLARE code. The code accounts for the dependence of the dose received from a flare on the distance from the Sun according to a $(1/r)^{\alpha}$ variation, where r is the distance from the Sun and the exponent α can be assigned. From trajectory parameters, which are input to the computer program, the distance from the Sun as a function of time during the trip is calculated.

To illustrate the use of the code, a trip to Mars and return is calculated, and estimated doses behind several thicknesses of aluminum shield and water shield are presented.

INTRODUCTION

The protons emitted by solar flares are the most hazardous source of space radiation encountered on an interplanetary space voyage which rapidly traverses the Van Allen belts. To define shielding requirements for biological protection from solar flare protons encountered in manned interplanetary missions, a computer program MCFLARE (ref. 1) has been prepared which uses Monte Carlo methods to simulate solar flare occurrences during the trip and records the total associated biological doses for the trip behind various shield material configurations.

A set of flare events, considered to be representative of those that will occur during future solar active periods, is required. Presently, this set is selected from the flares that occurred during the last solar active period from 1956 to 1962. The flares are assumed to occur randomly during the trip. The doses behind the various shield configurations investigated have to be evaluated for each flare, at a distance of 1 AU from the Sun, by using another computer code such as one of those described in Refs. 2 or 3. (Ref. 4 presents doses from solar flare proton spectra behind two shield materials as calculated by using Ref. 2.) These dose values are input to the computer program MCFLARE. This program provides for including the dependence of the magnitude of the dose received from the flare on the distance r from the Sun. This dependence is taken to be of the form $(r_o/r)^{\alpha}$, where r_o is the distance between the Sun and the Earth, and the exponent α can be any arbitrarily selected value.

The Monte Carlo sampling procedure (analogous to particle transport Monte Carlo) is used to determine when flares are encountered on the trip, which of the input flares occur, and the total dose obtained from all flares encountered during the trip behind each shield configuration. The computer program tallies the doses obtained for a large number of trips having identical trajectories and from this, the distribution of doses incurred on the mission for each shield configuration is obtained. Each dose distribution determines a dose D_p having the probability p of not being exceeded as a function of p.

METHOD OF ANALYSIS

Any N flare events can be selected as representative of the flare activity that will occur during the space voyage. The doses from each flare at a distance of 1 AU from the Sun behind one or more shield material configurations investigated are input to the computer. Each flare is assumed to occur randomly on the average of once during the solar active period T_{ref}, which is of the order of 2000 days or $5\frac{1}{2}$ years.

Monte Carlo Method to Determine Occurrences of Flares During Trip

Inasmuch as flares are assumed to occur randomly in the solar active period, the probability of any flare occurring in the time interval dt is $(N/T_{ref})dt \equiv \mu\, dt$. Then the probability of no flare occurring for time t is $e^{-\mu t}$ and the probability of a flare occurring in dt at time t is $e^{-\mu t}\mu\, dt$.

In the Monte Carlo method, this probability of flare occurrence in the time interval dt at time t is equated to the probability of selecting a random number in an interval $d\xi$ about ξ. If a random number set uniformly distributed in the interval $(0,1)$ is selected, then the probability of selecting a random number in $d\xi$ about ξ is $d\xi$. Equating these two probabilities, one gets

$$e^{-\mu t}\mu\, dt = d\xi$$

$$\int_0^t e^{-\mu t'}\mu\, dt' = \int_0^{\xi} d\xi'$$

$$t = -\frac{1}{\mu}\ln(1 - \xi)$$

Inasmuch as both ξ and $1 - \xi$ are uniformly distributed in the interval (0,1) an equivalent expression for t which results in the same exponential distribution is

$$t = -\frac{1}{\mu} \ln \xi \qquad (1)$$

By selecting a random number from a uniformly distributed set in the interval (0,1) the time between flare events is obtained from Eq. (1).

When an event has occurred, a particular flare of one of the N is also selected by random numbers. The i^{th} flare occurs when a new random number occurs in the interval

$$\frac{i-1}{N} < \xi \leq \frac{i}{N} \qquad i = 1, 2, \ldots, N \qquad (2)$$

Dose values input to the code are calculated by using the methods of Ref. 2, or 3, for each representative flare using the solar flare proton intensity and spectral shape as observed at the Earth. The code permits an effect of the distance from the Sun on the dose (or intensity) received from a flare of the form $(r_o/r)^{\alpha}$ where r_o is the distance from the Sun to the Earth, r is the distance of the spacecraft from the Sun during the flare, and α is an exponent that is assigned.

The code evaluates r for any time during the trip by calculating the mission trajectory from input parameters describing the two transfer ellipses and the total trip time. The first ellipse is the trajectory from the Earth to the planet and the second describes the return trip.

The calculation proceeds as follows: Selecting a random number and using Eq. (1) determines the time in the mission when a flare occurs. Selecting another random number and using Eq. (2) determines the particular flare which occurs. Knowing the time in the mission (and, hence, distance from the Sun) and the particular flare, the dose received through each shield configuration is tallied. The duration of the flare event is then added to the time in the mission when the flare occurred to give the time when the event is over. From a new random number and Eq. (1), the time elapsed until the next flare occurs is calculated, and so on. This procedure is repeated until the total trip time has elapsed. The total dose from all flare events encountered on the trip is determined for each of the shields considered.

Selection of D_p

This procedure is repeated for a large number M of trips of identical trajectory. The code divides the dose range into dose intervals that are 1 dose unit wide and tabulates the number of trips $\Lambda(D)$ during which doses that lie within each dose interval are encountered. The cumulative fraction of the total trips that encounter doses less than the upper dose bound of each interval is also tabulated (this is an estimate of the probability p that a dose equal to the upper dose bound will not be exceeded). From this tabulation, for any specified p, a dose D_p which has the probability p of not being exceeded on the trip can be selected for any shield. The standard deviation of this value from the true value is shown in Ref. 1 to be

$$\sigma_{D_p} = \sqrt{\frac{p(1-p)}{M f^2(D_p)}} \qquad (3)$$

where M is the number of trips in the group investigated, and $f(D_p)$ is the dose probability density at D_p (which is calculated from the tabulated output). If $\Lambda(D_p)$ is the number of trips contained in the interval in which D_p occurs, $f(D_p)$ is approximately given by

$$f(D_p) = \frac{\Lambda(D_p)}{M}$$

If $\Lambda(D)$ is a widely fluctuating value in the vicinity of D_p, averaged values of $\Lambda(D)$ can be hand calculated from the tabular computer output; $f(D_p)$ is obtained from the averaged value of $\Lambda(D_p)$. Note that for a given p, because $f(D_p)$ is independent of the number of trips, σ_{D_p} varies inversely as $\sqrt{M}$.

To reduce the uncertainty associated with D_p for a given number of trips, the code is written so that the trips constitute a stratified sample for the time-to-first-flare selected in accordance with the exponential distribution $\exp\left[-(Nt/T_{ref})\right]$.

ILLUSTRATIVE EXAMPLE

An interplanetary trip to Mars and return has been evaluated in order to illustrate details of the method and to present some representative shield requirements for such a mission. Water and aluminum were the shield materials considered.

Selection of Flare Events

The flare occurrences during the last solar active period 1956 to 1962 are assumed to be representative of those that will occur during a future active period. Webber in Ref. 5 has compiled a record of these flares, their time-integrated proton intensities, and spectra. From these records, the 20 largest flares, based on proton intensity, were selected (the effect of neglecting the rest of the flares is small for shields considered here). These flares are listed in table I which presents the integrated flux of protons having energies greater than 30 MeV and some constants A and P_o associated with each flare. The spectral shape of each flare is assumed to vary as

$$N > E = A \exp\left(-\frac{\sqrt{E^2 + 1876E}}{P_o}\right)$$

where $N > E$ is the total number of protons per square centimeter with energies greater than E. The values of P_o were obtained from Webber's compilation, and the values of A were calculated to be consistent with flux values of $N > 30$ MeV.

It has been observed that some of the flares tend to occur in clusters. Table I indicates that such clusters occurred in August 1958, July 1959, November 1960, and July 1961. These four clusters were selected as representative of the clustered flare events that may occur and were assumed to be events of 12-, 8-, 10-, and 8-day durations, respectively. The other nine single flares were each assumed to have a duration of 2 days. During future solar active periods, each of the four clustered events and each of the nine single flare

events are assumed to occur randomly with a frequency of once during the active period (taken to be 2000 days).

TABLE I. - FLARES (FROM SOLAR ACTIVE PERIOD 1956 TO 1962)

SELECTED AS REPRESENTATIVE OF THOSE THAT WILL

OCCUR DURING FUTURE ACTIVE PERIODS

[Integral flux above 30 MeV, and spectral constants A and P_o for each flare are tabulated.]

Flare date	N > 30 MeV protons/cm^2	P_o	A, protons/cm^2	
2-23-56	1.0×10^9	195	3.4×10^9	
1-20-57	2×10^8	61	1.0×10^9	
8-29-57	1.2×10^8	56	8.6×10^9	
10-20-57	5×10^7	127	3.3×10^8	
3-23-58	2.5×10^8	64	1.1×10^9	
7-7-58	2.5×10^8	62	1.2×10^9	
8-16-58	4×10^7	64	1.7×10^9	Clustered flare event
8-22-58	7×10^7	56	5.0×10^9	
8-26-58	1.1×10^8	51	1.2×10^{10}	
5-10-59	9.6×10^8	84	1.7×10^{10}	
6-13-59	8.5×10^7	[a]48	1.2×10^{10}	
7-10-59	1.0×10^9	104	1.0×10^{10}	Clustered flare event
7-14-59	1.3×10^9	80	2.6×10^{10}	
7-16-59	9.1×10^8	105	8.9×10^9	
9-3-60	3.5×10^7	127	2.3×10^8	
11-12-60	1.3×10^9	124	8.9×10^9	Clustered flare event
11-15-60	7.2×10^8	114	5.9×10^9	
11-20-60	4.5×10^7	118	3.4×10^9	
7-12-61	4×10^7	56	2.9×10^9	Clustered flare event
7-18-61	3×10^8	102	3.1×10^9	

[a]Estimated.

Doses For Selected Flare Events

Table II presents the doses obtained behind various shield thicknesses from each of these 13 events. These doses were calculated by using the Lewis Proton Shielding Code, described in Ref. 2, and are representative of doses received at the center of a spherical crew compartment having the given shield thicknesses when the vehicle is located at a distance of 1 AU from the Sun. Table II(a) presents the rem doses behind the water shield, and table II(b) the rem doses behind the aluminum shield. The data presented in this table are input to the computer code MCFLARE.

Trajectory

The trajectory selected for the trip is one that requires 556 days for the complete mission (and happens to be one that results in near minimum vehicle weight for a departure date in 1983). The outward journey from Earth to Mars requires 280 days, then there is a 40-day stay at Mars, then a 236-day return trip during which the vehicle approaches within 0.5 AU of the Sun.

TABLE II. - REM DOSES FROM SELECTED FLARE EVENTS BEHIND VARIOUS THICKNESSES OF WATER AND ALUMINUM SHIELD AT 1 ASTRONOMICAL UNIT FROM SUN

(a) Rem dose behind water shield

Shield thickness, g/cm^2					Flare date
10	15	20	30	40	
Dose, rem					
42.10	27.76	20.79	13.03	9.03	2-23-56
1.07	.38	.19	.07	.04	1-20-57
.43	.15	.07	.03	.01	8-29-57
1.20	.65	.42	.21	.12	10-20-57
1.12	.40	.19	.07	.04	3-23-58
1.26	.45	.22	.08	.04	7-7-58
1.03	.35	.17	.07	.04	Aug. 1958 cluster
11.30	4.93	2.67	1.09	.57	5-10-59
.60	.20	.10	.04	.02	6-13-59
49.59	23.68	13.76	6.11	3.36	July 1959 cluster
.84	.46	.29	.15	.09	9-3-60
49.34	26.49	16.79	8.30	4.85	Nov. 1960 cluster
5.48	2.67	1.57	.71	.39	July 1961 cluster

(b) Rem dose behind aluminum shield

Shield thickness, g/cm^2							Flare date
10	15	20	30	40	50	60	
Dose, rem							
53.93	37.20	28.77	19.07	14.16	11.15	9.26	2-23-56
2.11	.86	.48	.24	.16	.12	.10	1-20-57
.90	.35	.19	.10	.07	.06	.05	8-29-57
1.73	1.00	.68	.38	.25	.18	.14	10-20-57
2.20	.89	.50	.25	.17	.12	.11	3-23-58
2.48	1.01	.56	.28	.19	.14	.12	7-7-58
2.12	.83	.45	.24	.17	.13	.11	Aug. 1958 cluster
18.98	9.06	5.36	2.59	1.63	1.18	.93	5-10-59
1.25	.49	.26	.14	.10	.08	.06	6-13-59
78.42	40.39	25.19	12.79	8.12	5.86	4.59	July 1959 cluster
1.22	.71	.48	.26	.17	.13	.10	9-3-60
71.89	41.17	27.59	15.09	9.87	7.17	5.61	Nov. 1960 cluster
8.57	4.49	2.82	1.44	.92	.66	.52	July 1961 cluster

Discussion of Results

Figure 1 shows the distribution of dose obtained for a large number of identical trips. The figure presents the rem dose distribution behind 20 g per square cm of water shield obtained from a computer run of 40 000 trips. The effect of distance on dose was assumed to vary as $(1/r)^2$.

In Fig. 1(a), $\Lambda(D)$, the number of trips on which a dose between D - 1 and D has been encountered, is plotted against D. A smoothed curve of this distribution $\Lambda(D)$ (obtained by averaging seven values centered about each $\Lambda(D)$) is also shown as a dashed line in this figure.

In Fig. 1(b), p(D) the probability of not exceeding any dose D is shown plotted against D

$$p(D) = \frac{1}{M}\sum_{i=1}^{D}\Lambda(i)$$

where M is the number of trips considered in a computer run. For the case of Fig. 1(b),

$$p(D) = \frac{1}{40\ 000}\sum_{i=1}^{D}\Lambda(i)$$

If D_p is defined as that dose which has a probability p of not being exceeded, then from Fig. 1(b), $D_{0.99}$ for the group of 40 000 trips, occurs in the dose interval between 93 and 94 rem and is selected as the upper bound of the interval, namely, 94 rem.

The dose probability density function f(D) is approximately equal to $\Lambda(D)/M$. At a $D_{0.99}$ of 94 rem, the value of f(D), evaluated by using the smoothed value of $\Lambda(D)$, is

$$f(D_{0.99}) = \frac{26}{40\ 000} = 0.00065/\text{rem}$$

and the standard deviation from Eq. (3) is $\sigma_{D_{0.99}} = 0.77$ rem.

There is a 97.7 percent confidence that the true dose $D^*_{0.99}$ is less than $D_{0.99} + 2\sigma_{D_{0.99}}$; is less than 95.5 rem.

Table III presents values of $D_{0.99}$ determined by using the computer code for rem doses behind various thicknesses (expressed as g/cm^2) of aluminum shield and water shield. These values are presented for both the case where the dose received from a flare event is assumed to vary as $(1/r)^2$ (considered representative of what might be a solar proton diffusion model in space) and for the case where there is no effect of distance (i.e., distance effect, g(r) = 1). Also shown in the table are the values of $\sigma_{D_{0.99}}$ associated with each $D_{0.99}$ and the corresponding values of $D_{0.99} + 2\sigma_{D_{0.99}}$.

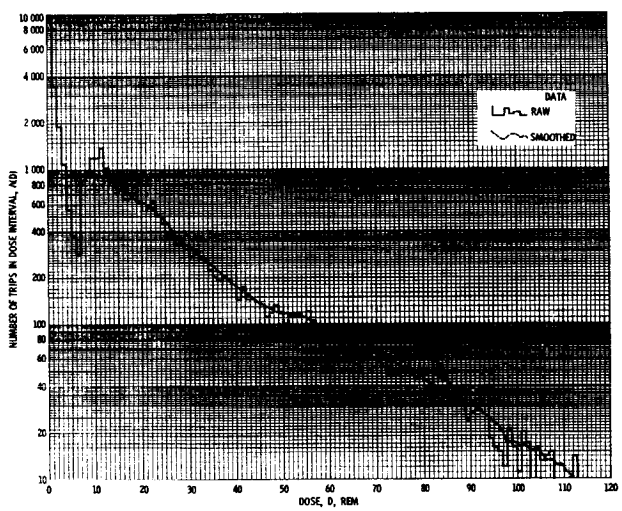

(A) NUMBER OF TRIPS ENCOUNTERING DOSES LYING WITHIN EACH DOSE INTERVAL.

Figure 1. - Distribution of trips encountering doses lying within each dose interval. Rem dose, water shield thickness, 20 grams per square centimeter; 40 000 trips; distance effect varies as $1/r^2$.

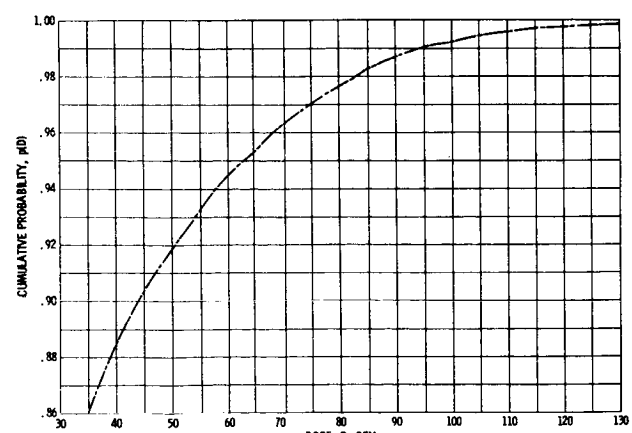

(B) CUMULATIVE PROBABILITY OF TRIP ENCOUNTERING DOSE LESS THAN D.

Figure 1. - Concluded.

TABLE III. - VALUES OF $D_{0.99}$ AND CORRESPONDING STANDARD DEVIATION BEHIND VARIOUS THICKNESSES OF WATER AND ALUMINUM DETERMINED FROM GROUP OF 40 000 TRIPS

(a) Rem dose behind water shield

Distance effect, g(r)	Quantity	Shield thickness, g/cm^2				
		10	15	20	30	40
		Dose, rem				
$1/r^2$	$D_{0.99}$	254	139	94	55	37
	$\sigma_{D_{0.99}}$	2.0	1.3	.77	.44	.31
	$D_{0.99} + 2\sigma_{D_{0.99}}$	258	141.6	95.5	55.9	37.6
1	$D_{0.99}$	165	90	63	35	23
	$\sigma_{D_{0.99}}$	1.7	1.0	.57	.25	.2
	$D_{0.99} + 2\sigma_{D_{0.99}}$	168.4	92	64.1	35.5	23.4

(b) Rem dose behind aluminum shield

Distance effect, g(r)	Quantity	Shield thickness, g/cm^2						
		10	15	20	30	40	50	60
		Dose, rem						
$1/r^2$	$D_{0.99}$	376	213	146	87	62	48	39
	$\sigma_{D_{0.99}}$	3.3	1.8	1.4	.77	.54	.42	.31
	$D_{0.99} + 2\sigma_{D_{0.99}}$	382.6	216.3	148.8	88.5	63.1	48.8	39.6
1	$D_{0.99}$	250	138	94	58	40	31	25
	$\sigma_{D_{0.99}}$	2.2	1.5	.91	.59	.31	.23	.22
	$D_{0.99} + 2\sigma_{D_{0.99}}$	254.4	141	95.8	59.2	40.6	31.5	25.4

In Fig. 2 the values of $D_{0.99} + 2\sigma_{D_{0.99}}$ are plotted against shield thickness. In Fig. 2(a), the rem dose is plotted against water shield thickness for cases of $g(r) = 1/r^2$ and $g(r) = 1$. Figure 2(b) is a similar plot of the rem dose behind the aluminum shield. From curves such as Fig. 2, one can select a shield thickness such that on a given mission, there is a probability p of not exceeding an accumulated dose D_p.

These curves indicate how much more effective water is as a shield material than aluminum for shielding against solar flare protons on the basis of grams per square centimeter of material necessary to maintain a given dose level inside the crew compartment. Also shown for this mission is that a $1/r^2$ distance effect on dose received from a flare can have an appreciable effect on shield requirements when the mission trajectory brings the vehicle to within 0.5 AU of the Sun. This result indicates a need for information regarding the effect of position from the Sun on radiation encountered from a flare.

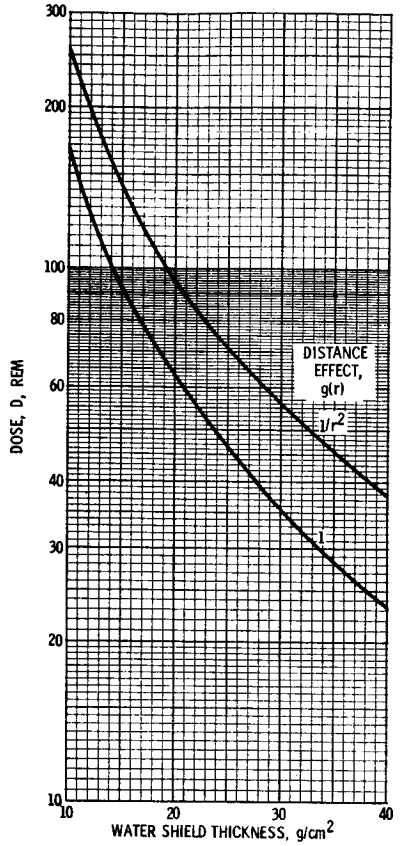

(A) REM DOSE BEHIND WATER SHIELD.

Figure 2. - Values of $D_{0.99} + 2\sigma_{D_{0.99}}$ for various thicknesses of water and aluminum shields, and for cases of distance effect varying as $1/r^2$ and no effect of distance. Number of trips, 40 000.

COMPUTER PROGRAM

Complete data input instructions for the computer program MCFLARE are presented in Ref. 1. The version of the code presented is operational on the Lewis Research Center IBM 7094-II/7044 computer system. Execution times for the examples discussed previously in this report were about 2 minutes per group of 40 000 trips. The MCFLARE code is available from the Radiation Shielding Information Center of Oak Ridge National Laboratory as code package CCC-93.

REFERENCES

1. Lahti, Gerald P.; Karp, Irving M.; and Rosenbaum, Burt M.: MCFLARE, A Monte Carlo Code to Simulate Solar Flare Events and Estimate Probable Doses Encountered on Interplanetary Missions. NASA TN D-4311, 1968.
2. Hildebrand, R. I.; and Renkel, H. E.: The Lewis Proton Shielding Code. NASA TM X-52166, 1966.
3. Kinney, W. E.: The Nucleon Transport Code, NTC. Rep. ORNL-3610, Oak Ridge National Lab., Aug. 1964.
4. Scott, W. Wayne: Estimate of Primary and Secondary Particle Doses Behind Aluminum and Polyethylene Slabs due to Incident Solar-Flare and Van Allen Belt Protons. Rep. ORNL-RSIC-18, Oak Ridge National Lab., July 1967.
5. Webber, W. R.: An Evaluation of the Radiation Hazard Due to Solar-Particle Events. Rep. D2-90469, Boeing Co., Dec. 1963.

The Significant Solar Proton Events in the 20th Solar Cycle for the Period October 1964 to March 1970

W. Atwell

Lockheed Electronics Company

Solar proton data are presented from observations by the IMP 2, 3, F and G satellites. The NASA Solar Particle Alert Network (SPAN) solar optical and radio frequency data for the period May 1967 to March 1970 are associated with the proton events observed by the IMP F and G satellites; however, missing data are supplemented with data recorded at other international observatories. From a radiation hazard standpoint, NASA is concerned with solar proton events of the order of 10^8 proton/cm^2. Radiation dose data are presented for some of the large proton events that have occurred thus far in the 20th solar cycle and are compared with some of the large proton events of the 19th solar cycle. Finally, the results of a simple parametric correlation study are presented for both the 19th and 20th solar cycles.

The author is indebted to Mrs. Louise Lui, who assisted in the reduction and computer analyses of the RF data, and Messrs. M. D. Lopez and J. W. Snyder for many stimulating discussions and helpful suggestions. The author is also appreciative for the IMP 2 and 3 solar proton data from Prof. J. A. Simpson and to Dr. J. H. King, who performed the IMP 2 and 3 time integrations. Additionally, the author is indebted to Messrs. R. Doeker, D. S. Lund and P. S. McIntosh for providing some of the optical data and whose helpful comments were invaluable.

This research was supported by NASA Contract NAS 9-10950.

For more than 25 years it has been known that the sun unpredictably emits copious amounts of high-energy particulate radiation. Since the goal of the Apollo program was to land a man on the moon and return him safely, it was thought that solar radiation might present a hazard. Consequently, in 1967 NASA developed the Solar Particle Alert Network, called SPAN. The SPAN is a worldwide network of solar optical and radio frequency telescopes used to monitor solar activity in real-time. The primary SPAN sites are located at NASA/MSC, Houston, Texas; the National Oceanic and Atmospheric Administration (NOAA), Boulder, Colorado; the Canary Islands; and Carnarvon, Australia. Supplemental sites are located at Hawaii, Teheran and Culgoora, Australia. During manned spaceflight missions SPAN observers can provide, via the Manned Space Flight Network (MSFN) communications system, the NASA Flight Safety Office with real-time information concerning impending solar radiation hazards. During non-mission periods the SPAN has provided an almost constant patrol of solar activity. Consequently, a prodigious amount of solar optical and radio frequency data has been collected during the past few years. A more detailed description of the NASA SPAN has been presented by Robbins and Reid (ref. 1).

It is the purpose of this paper to present the solar proton data as observed by the IMP 2 and 3 satellites; to present the solar proton data as observed by the IMP F and G satellites and the associated SPAN solar optical and radio frequency data supplemented with data from other observatories; to present radiation dose data from both the 19th and 20th solar cycles for various Apollo shielding configurations; to present the results of a parametric correlation study for the solar proton events in the 19th and 20th solar cycles; and to conclude with recommendations for enhancing and improving the meaningfulness of the solar data.

SOLAR PROTON EVENTS FOR THE PERIOD OCTOBER 1964 TO APRIL 1967

The IMP 2 and 3 satellites were in earth orbit during the period covered by October 1964 to April 1967. Prof. J. A. Simpson, University of Chicago, had a charged-particle, solid-state detector experiment onboard these two satellites to measure solar protons in the 0.9-190, 6.5-19, 19-90, and 90-190 MeV ranges. Dr. J. H. King, NASA/GSFC, National Space Science Data Center, plotted the 2.4 hr averaged count rates and generated event integrated fluxes at the given energies. He assumed negligible flux above 190 MeV and interpolated to

obtain event integrated fluxes above 10, 30 and 60 MeV.

Table 1 shows the solar proton events obtained from this interpolation. During this period 23 major solar proton events were recorded. The start time, time of peak intensity, end time, and event flux are given. The times are given in UT, and the integrated flux units are in proton/cm^2. The events marked by an asterisk are those cases where no significant flux was measured in the 90-190 MeV channel. Consequently, the event integrated fluxes above 30 and 60 MeV were extrapolated and are likely to be less reliable than the interpolated values of the other events (ref. 2).

These data are presented to provide a complete picture of the solar proton emissions from the commencement of the 20th solar cycle (October 1964) through March 1970. It remains to associate the optical and radio frequency data with these events.

Table 1. - IMP 2 and 3 solar proton events.

DATE	5 Feb 65	4 Oct 65	24 Mar 66	29 Apr 66*
E>10 MeV				
Start time	1912	0936	0000	1912
Peak time	0000/06	1424	0448	1912
End time	0712/09	1912/07	0936/07	0448/01
Event flux	5.90E07**	1.50E07	1.25E07	3.02E05
E>30 MeV				
Start time	1912	0936	0000	0712
Peak time	0448/06	1424	0712	1648
End time	0712/09	0712/08	0224/27	0448/01
Event flux	5.25E06	1.60E06	3.20E06	1.02E05
E>60 MeV				
Start time	1912	0936	0000	--
Peak time	2136	1648	0448	--
End time	0000/07	0224/05	0224/25	--
Event flux	1.17E06	4.25E05	9.30E05	1.99E04

Table 1. - IMP 2 and 3 solar proton events (cont'd).

DATE	3 May 66*	25 June 66*	7 July 66	14 July 66*
E>10 MeV				
Start time	0712	1648	0000	0000
Peak time	0936	2136	0936	0936
End time	0448/09	0224/28	0936/12	1648/15
Event flux	3.97E06	6.05E05	9.50E07	4.17E05
E>30 MeV				
Start time	0712	1424	0000	0000
Peak time	0936	2136	1200	0712
End time	0936/09	0224/28	0224/13	0448/16
Event flux	1.35E06	2.05E05	2.15E07	2.14E05
E>60 MeV				
Start time	--	--	0000	--
Peak time	--	--	1200	--
End time	--	--	0000/10	--
Event flux	2.70E05	3.95E04	7.10E06	7.80E04

Table 1. - IMP 2 and 3 solar proton events (cont'd).

DATE	16 July 66*	30 July 66	28 Aug 66	2 Sept 66
E>10 MeV				
Start time	0000/17	0224	1424	0224
Peak time	0712/17	1912/31	2136/29	0936
End time	0936/19	1912/02	0712/02	2136/03
Event flux	1.00E06	1.08E06	6.62E07	3.75E07
E>30 MeV				
Start time	2136	1648	1424	0224
Peak time	0712/17	1912/31	1912	0712
End time	0936/19	1424/01	0712/02	2136/03
Event flux	2.43E05	5.30E05	2.54E07	6.70E06
E>60 MeV				
Start time	--	0712/31	1424	0224
Peak time	--	1912/31	1912	0712
End time	--	1200/01	0712/02	2136/03
Event flux	2.81E04	5.10E05	1.18E07	2.83E06

Table 1. - IMP 2 and 3 solar proton events (cont'd).

DATE	3 Sept 66	13 Sept 66	20 Sept 66*	25 Sept 66*
E>10 MeV				
Start time	2136	0936	1912	1648
Peak time	2136	0448/15	0224/21	1424/26
End time	2136/10	1912/19	0712/24	1648/27
Event flux	3.35E08	2.50E07	8.80E05	3.98E05
E>30 MeV				
Start time	2136	0936	1912	1648
Peak time	0448/05	1648/14	2136	1424/26
End time	2136/10	1912/19	1424/23	1648/27
Event flux	1.10E07	1.07E07	1.49E05	1.48E05
E>60 MeV				
Start time	2136	0936/14	--	--
Peak time	0000/04	0936/15	--	--
End time	1424/04	0936/17	--	--
Event flux	2.60E05	6.25E06	1.00E04	3.36E04

Table 1. - IMP 2 and 3 solar proton events (cont'd).

DATE	27 Sept 66*	11 Jan 67	28 Jan 67	2 Feb 67
E>10 MeV				
Start time	1424	0224	0448	1912
Peak time	1648	0224/12	2136	0712/03
End time	0224/30	1912/13	2136/02	2136/13
Event flux	9.45E05	4.10E06	3.59E08	5.08E08
E>30 MeV				
Start time	1424	0224	0448	1912
Peak time	1648	0448	0936/30	0000/04
End time	0224/30	1912/13	2136/02	2136/13
Event flux	2.01E05	2.90E06	7.10E07	1.02E08
E>60 MeV				
Start time	--	0224	0448	1912
Peak time	--	0224/12	1912/31	1200/03
End time	--	1912/13	2136/02	1912/08
Event flux	1.99E04	2.50E06	2.95E07	3.13E07

Table 1. - IMP 2 and 3 solar proton events (cont'd).

DATE	13 Feb 67*	27 Feb 67	11 Mar 67
E>10 MeV			
Start time	1912	1648	1912
Peak time	0000/14	0000/28	0448/12
End time	1424/18	0712/07	1912/17
Event flux	6.97E06	4.60E07	6.90E07
E>30 MeV			
Start time	1912	1648	1912
Peak time	0936/14	0224/28	0000/12
End time	1424/18	1424/10	1648/19
Event flux	1.39E06	2.87E07	3.21E07
E>60 MeV			
Start time	--	1648	1912
Peak time	--	2136	0712/12
End time	--	1424/02	2136/14
Event flux	1.21E05	1.25E07	9.50E06

*-Events for which the flux in the 90-190 MeV channel was insignificant.

**-Exponential power of 10; 5.90E07 = 5.90x10^7.

SOLAR PROTON EVENTS FOR THE PERIOD MAY 1967 TO MARCH 1970

The IMP F (Explorer 34) satellite was in earth orbit from May 24, 1967, to May 3, 1969. This satellite carried the Solar Proton Monitoring Experiment (SPME) of Bostrom and Williams (ref. 3) and recorded approximately 32 solar proton events. The IMP G (Explorer 41) satellite was placed into earth orbit on June 21, 1969, and is still functioning properly. The IMP G satellite also contains the SPME, and both experiments record protons at the >10, >30, and >60 MeV levels.

The event integrations performed by the author are given in table 2. The table also contains the start time (UT), end time (UT), event duration (hr), peak intensity (proton/cm^2-sec-ster), time of peak intensity (UT), total integrated flux (proton/cm^2), and event integrated flux (proton/cm^2). The peak intensity is the highest hourly counting rate and includes the background flux for that hour.

Table 2. - Explorer 34 and 41 solar proton events.

DATE	23 May 67	28 May 67	6 June 67	2 Nov 67	3 Dec 67
E>10 MeV					
Onset time	2000	0700	0800	1100	1000
End time	0600/28	2400/31	1700/12	1300/04	2200/07
Duration	107	90	137	51	109
Peak intensity	1036	115	20.8	9.42	31.9
Time (peak int.)	1300/25	1100/28	1500	1800	1300
Integrated flux	1.07E09	7.40E07	9.60E07	7.50E06	2.53E07
Background flux	1.69E06	1.42E06	2.48E06	8.08E05	1.97E06
Event flux	1.07E09	7.26E07	9.35E07	6.70E06	2.33E07
E>30 MeV					
Onset time	2000	0700	0800	1100	1000
End time	2400/26	2400/30	1200/09	2 J0/03	2400/06
Duration	77	66	65	38	87
Peak intensity	32.9	27.6	5.55	1.39	11.3
Time (peak int.)	0900/25	1100/28	1500	1700	1300
Integrated flux	2.27E07	2.00E07	2.60E07	1.80E06	9.12E06
Background flux	2.60E06	2.24E06	2.35E06	1.25E06	2.95E06
Event flux	2.01E07	1.78E07	2.36E07	7.50E05	6.17E06
E>60 MeV					
Onset time	2000	0700	0800	no significant flux above background	1000
End time	2300/25	1900/30	1100/08		2400/05
Duration	52	61	52		63
Peak intensity	3.09	10.2	2.13		4.56
Time (peak int.)	0900/25	0800/28	1500		1300
Integrated flux	3.60E06	7.50E06	1.20E07		4.17E06
Background flux	1.76E06	2.07E06	1.88E06		2.14E06
Event flux	1.84E06	5.43E06	1.02E07		2.03E06

Table 2. - Explorer 34 and 41 solar proton events (cont'd).

DATE	16 Dec 67	9 June 67	6 July 68	13 July 68	26 July 68
E>10 MeV					
Onset time	0600	1000	1800	2000/12	1400
End time	2400/22	0900/14	1900/12	1800/17	0800/30
Duration	163	120	146	118	68
Peak intensity	6.45	354	5.33	54.6	0.78
Time (peak int.)	0800/18	0600/10	0200/11	2200	1900
Integrated flux	1.55E07	2.91E08	1.44E07	3.16E07	1.60E06
Background flux	2.95E06	1.63E06	2.11E06	1.71E06	9.84E05
Event flux	1.25E07	2.89E08	1.23E07	2.99E07	6.20E05
E>30 MeV					
Onset time	0600	1000	1800	0200	1300
End time	2400/20	1800/11	2400/11	1100/14	0500/29
Duration	115	75	127	34	65
Peak intensity	2.39	13.1	1.37	1.72	1.07
Time (peak int.)	2100/17	1400	1200/13	2200	1900
Integrated flux	6.39E06	1.12E07	8.28E06	1.41E06	2.29E06
Background flux	3.90E06	2.38E06	4.02E06	1.08E06	2.06E06
Event flux	2.49E06	8.80E06	4.26E06	3.30E05	2.30E05
E>60 MeV					
Onset time	0600	1000	1800	no significant flux above background	1300
End time	0500/19	0500/11	0900/11		2400/27
Duration	72	44	112		36
Peak intensity	1.30	6.13	1.15		0.98
Time (peak int.)	2100/17	1300	1200/07		1700
Integrated flux	3.10E06	3.99E06	4.58E06		1.32E06
Background flux	2.44E06	1.39E06	3.55E06		1.14E06
Event flux	6.60E05	2.60E06	1.03E06		1.80E05

Table 2. - Explorer 34 and 41 solar proton events (cont'd).

DATE	26 Sept 68	29 Sept 68	4 Oct 68	31 Oct 68	1 Nov 68
E>10 MeV					
Onset time	0900	1800	0200	0300	1100
End time	1600/28	0800/03	1600/08	1200/02	1100/04
Duration	57	87	111	57	73
Peak intensity	9.15	31.0	36.5	133	152
Time (peak int.)	1500	2300	0800	1500	0600/02
Integrated flux	6.45E06	2.89E07	3.28E07	6.57E07	1.18E08
Background flux	8.25E05	1.26E06	1.61E06	8.25E05	1.06E06
Event flux	5.62E06	2.76E07	3.12E07	6.49E07	1.17E08
E>30 MeV					
Onset time	1100	1800	0200	0300	1100
End time	2400	0800/02	0800/06	1800/01	0300/03
Duration	14	63	55	41	39
Peak intensity	0.97	19.6	6.93	10.7	12.3
Time (peak int.)	1500	2100	0500	1500	2100
Integrated flux	5.17E05	1.10E07	4.44E06	5.05E06	8.94E06
Background flux	4.24E05	1.91E06	1.49E06	1.11E06	1.06E06
Event flux	9.3E04	9.10E06	2.95E06	3.94E06	7.88E06
E>60 MeV					
Onset time	no significant flux above background	1800	0200	1000	1100
End time		1800/01	0600/05	0600/01	1300/02
Duration		49	29	21	26
Peak intensity		11.0	1.77	2.08	1.66
Time (peak int.)		2000	0400	1500	2000
Integrated flux		5.28E06	1.17E06	9.62E05	1.19E06
Background flux		1.44E06	7.87E05	5.70E05	7.06E05
Event flux		3.84E06	3.80E05	3.92E05	4.80E05

Table 2. - Explorer 34 and 41 solar proton events (cont'd).

DATE	4 Nov 68	18 Nov 68	3 Dec 68	24 Jan 69	25 Feb 69
E>10 MeV					
Onset time	0600	~1200	1000	0900	1000
End time	2300/07	2400/25	0600/13	2400/25	0700/27
Duration	90	~180	237	40	44
Peak intensity	19.6	849	152	3.47	88.7
Time (peak int.)	0900	1400	0400/06	1400	1300
Integrated flux	1.15E07	2.04E09	4.85E08	2.38E06	3.74E07
Background flux	1.30E06	2.61E05	2.79E06	5.79E05	6.17E05
Event flux	1.02E07	2.04E09	4.82E08	1.80E06	3.68E07
E>30 MeV					
Onset time	0600	~1200	1000	0900	1000
End time	0600/06	2400/23	0400/10	0500/25	2000/26
Duration	49	~132	163	21	35
Peak intensity	5.42	404	31.6	0.85	42.1
Time (peak int.)	0800	1400	0100/06	1100	1200
Integrated flux	3.37E06	4.10E08	3.99E07	6.94E05	1.48E07
Background flux	1.30E06	3.58E06	4.13E06	6.18E05	1.03E06
Event flux	2.07E06	3.54E08	3.58E07	7.60E04	1.38E07
E>60 MeV					
Onset time	0600	~1200	1000	no significant flux above background	1000
End time	0600/05	1000/21	0700/08		1700/26
Duration	26	~70	118		31
Peak intensity	2.06	96.7	5.83		24.9
Time (peak int.)	0800	1400	0100/06		1200
Integrated flux	1.16E06	6.54E07	7.85E06		7.69E06
Background flux	7.06E05	1.90E06	2.99E06		9.10E05
Event flux	4.50E05	6.35E07	4.86E06		6.78E06

Table 2. - Explorer 34 and 41 solar proton events (cont'd).

DATE	26 Feb 69	27 Feb 69	12 Mar 69	21 Mar 69	30 Mar 69
E>10 MeV					
Onset time	0700	1600	2000	0700	0400
End time	0900/28	2400/03	1500/15	0400/24	1800/12
Duration	51	105	68	70	327
Peak intensity	11.62	27.67	2.51	4.93	26.3
Time (peak int.)	1200	2200	2100	1800	1800
Integrated flux	9.63E06	2.73E07	2.34E06	5.78E06	7.70E07
Background flux	7.38E05	1.52E06	9.84E05	1.01E06	4.73E06
Event flux	8.89E06	2.58E07	1.36E06	4.77E06	7.23E07
E>30 MeV					
Onset time	0600	1600	2000	0700	0400
End time	1900/27	1100/02	1600/14	0700/23	0200/12
Duration	38	68	45	49	311
Peak intensity	4.72	9.98	1.47	1.14	13.6
Time (peak int.)	1200	2100	2100	1700	1800
Integrated flux	3.68E06	8.39E06	1.69E06	1.80E06	3.77E07
Background flux	1.12E06	2.00E06	1.32E06	1.44E06	9.15E06
Event flux	2.56E06	6.39E06	3.70E05	3.60E05	2.85E07
E>60 MeV					
Onset time	0600	1500	2000	no significant flux above background	0300
End time	1000/27	0700/01	1800/13		2400/08
Duration	29	41	23		238
Peak intensity	2.45	4.34	0.86		9.39
Time (peak int.)	0900	1900	2100		1800
Integrated flux	1.85E06	3.28E06	7.72E05		2.23E07
Background flux	8.53E05	1.21E06	6.56E05		7.00E06
Event flux	1.00E06	2.07E06	1.16E05		1.53E07

Table 2. - Explorer 34 and 41 solar proton events (cont'd).

DATE	10 Apr 69	25 Sept 69	27 Sept 69	2 Nov 69	24 Nov 69
E>10 MeV					
Onset time	1900	0900	1100	1100	1200
End time	1100/28	0700/27	0500/30	0700/09	1000/27
Duration	425	47	67	165	71
Peak intensity	1375	15.2	11.3	1317	3.75
Time (peak int.)	0300/13	1200	0300/28	1400	1700
Integrated flux	2.26E09	6.24E06	1.08E07	7.34E08	3.98E06
Background flux	6.15E06	6.80E05	9.09E05	2.04E06	1.28E06
Event flux	2.25E09	5.56E06	9.90E06	7.32E08	2.70E06
E>30 MeV					
Onset time	0300/11	0900	1100	1100	1200
End time	2400/21	1700/26	1600/28	1600/08	1400/26
Duration	262	33	30	150	51
Peak intensity	123	1.60	0.74	737	1.49
Time (peak int.)	0300/13	1100	0300/28	1300	1500
Integrated flux	2.10E08	1.19E06	8.81E05	2.23E08	2.14E06
Background flux	7.70E06	8.96E05	8.14E05	4.07E06	1.38E06
Event flux	2.02E08	2.90E05	6.70E04	2.19E08	7.6E05
E>60 MeV					
Onset time	0600/11	0900	no significant flux above background	1100	1200
End time	2400/16	2100		2400/05	1000/25
Duration	139	13		86	23
Peak intensity	16.7	0.68		201	0.86
Time (peak int.)	0300/13	1100		1300	1500
Integrated flux	2.64E07	3.57E05		4.10E07	7.28E05
Background flux	4.28E06	3.23E05		2.14E06	6.24E05
Event flux	2.21E07	3.40E04		3.89E07	1.04E05

Table 2. - Explorer 34 and 41 solar proton events (cont'd).

DATE	7 Mar 70	23 Mar 70	29 Mar 70
E>10 MeV			
Onset time	1900	1900	0200
End time	1700/10	1500/26	2400/06
Duration	71	69	215
Peak intensity	93.54	8.18	66.0
Time (peak int.)	0300/08	2200	1900
Integrated flux	5.72E07	6.52E06	8.38E07
Background flux	1.03E06	1.25E06	4.38E06
Event flux	5.62E07	5.27E06	7.94E07
E>30 MeV			
Onset time	1800	1900	0200
End time	1900/08	0500/25	0200/05
Duration	25	35	171
Peak intensity	1.52	2.09	20.8
Time (peak int.)	2400	2200	1900
Integrated flux	1.09E06	1.64E06	3.13E07
Background flux	6.82E05	1.03E06	5.03E06
Event flux	4.13E05	6.10E05	2.63E07
E>60 MeV			
Onset time	no significant flux above background	1900	0200
End time		1100/24	0200
Duration		17	97
Peak intensity		0.81	7.05
Time (peak int.)		2100	1900
Integrated flux		5.27E05	1.13E07
Background flux		4.61E05	2.63E06
Event flux		6.60E04	8.7E06

Table 2. - Explorer 34 and 41 solar proton events (cont'd).

DATE	18 Dec 69	20 Dec 69	29 Jan 70	31 Jan 70	6 Mar 70
E>10 MeV					
Onset time	1700	0400	1400	1700	1500
End time	1800/19	1200/22	1500/31	1200/04	0800/08
Duration	26	57	50	92	42
Peak intensity	1.84	8.86	4.66	24.5	7.76
Time (peak int.)	2000	0400	2400	2400	0200/07
Integrated flux	1.17E06	4.48E06	3.89E06	2.13E07	5.09E06
Background flux	3.53E05	7.74E05	6.79E05	1.25E06	6.08E05
Event flux	8.20E05	3.71E06	3.21E06	2.00E07	4.48E06
E>30 MeV					
Onset time	1700	0200	1400	1700	1500
End time	1300/19	1100/21	1500/31	2400/02	1800/07
Duration	21	34	50	56	28
Peak intensity	1.81	2.47	2.61	6.86	0.94
Time (peak int.)	2000	0300	2400	2100	1900
Integrated flux	1.03E06	1.64E06	2.69E06	5.06E06	9.60E05
Background flux	5.70E05	9.23E05	1.36E06	1.52E06	7.08E05
Event flux	4.60E05	7.20E05	1.33E06	3.54E06	2.52E05
E>60 MeV					
Onset time	1700	0200	1400	1700	no significan flux above background
End time	1200/19	1500	1400/30	2400/01	
Duration	20	14	25	32	
Peak intensity	1.12	1.17	1.26	2.35	
Time (peak int.)	2000	0200	2400	2000	
Integrated flux	6.95E05	4.86E05	1.07E06	1.63E06	
Background flux	4.98E05	3.48E05	6.22E05	7.96E05	
Event flux	1.97E05	1.38E05	4.50E05	8.30E05	

THE SOLAR OPTICAL PARAMETERS ASSOCIATED WITH THE IMP F AND G OBSERVATIONS

The solar optical parameters associated with the solar proton events observed by the IMP F and G satellites are shown in table 3. The optical parameters listed are the proton event date (the superscripts refer to the reporting station where the letter G is grouped data from several stations as reported in Solar-Geophysical Data (ref. 3), 1 is the NASA/MSC site, 2 is the Canary Islands site, and 3 is the Carnarvon, Australia site), the Mt. Wilson calcium plage area and intensity (10^{-6} of the solar disk), sunspot area (10^{-6} of the solar disk), flare start and end times (UT), flare duration (min), flare maximum (UT), flare importance, flare area either measured (m) or corrected (c) in sq deg, the heliographic location, and the McMath plage region number. The optical parameters and the IMP proton data were obtained from the Solar-Geophysical Data (ref. 3), although Mr. P. S. McIntosh provided some of the calcium plage and sunspot data.

Table 3. - Solar optical parameters

DATE	PLAGE AREA	PLAGE INT.	SUNSPOT AREA	FLARE START	FLARE END	FLARE DURATION	FLARE MAX.	FLARE IMP.	FLARE AREA	LOCATION	McMATH REGION
1967											
23 May[4G]	10000	4.0	1820*	1803	2300	297	1844	3B	18.0$_c$	N28 E26	8818
28 May[G]	10000	4.0	1050*	0527	0712	105	0546	3B	13.1$_m$	N28 W33	8818
6 June[G]	2200	3.5	70	1846	2030	104	1937	2N	4.8$_m$	S18 W58	8829
2 Nov[G]	6900	3.5	110*	0855	0916	21	0859	1B	4.6$_m$	S18 W02	9047
3 Dec	No logical flare association - probably occurred behind the west limb										
16 Dec[G]	9100	3.0	230	0247	0446	119	0256	2N	5.4$_m$	N23 E66	9718
1968											
9 June[3]	3200	3.0	70	0843	0920	37	0854	3B	21.8$_c$	S16 W06	9429
6 July[G]	8000	3.5	1000	0946	1029	43	0956	1N	1.4$_m$	N14 E89	9503
13 July[G]	3200	3.0	160	1341/12	1522/12	101	1415/12	2N	5.9$_m$	N11 W21	9499
26 July	No logical flare association										
26 Sept[G]	5300	3.0	300	0026	0105	39	0031	2B	4.7$_m$	N14 E35	9687
29 Sept[1]	4300	3.0	100*	1618	1657	39	1623	2B	10.1$_c$	N16 W52	9678
4 Oct[G]	3700	2.5	230	2348/03	0330	222	0008/04	2B	6.3$_m$	S16 W37	9692
31 Oct[G]	7000	4.0	1070*	2339/30	0133	114	0013	3B	19.4$_m$	S14 W37	9740
1 Nov[3]	5600	3.5	1000*	0835	0930	55	0842	1B	5.0$_c$	S17 W49	9740
4 Nov[3]	3000	3.5	710*	0524	0606	42	0529	1B	4.8$_c$	S14 W90	9740

a - This flare included three flares that occurred in a close time proximity (ref. 4)
* - Complex sunspot group (ref. 5)
G,1,3 - observing station code; see text

Table 3. - Solar optical parameters(cont'd)

DATE	PLAGE AREA	PLAGE INT.	SUNSPOT AREA	FLARE START	FLARE END	FLARE DURATION	FLARE MAX.	FLARE IMP.	FLARE AREA	LOCATION	McMATH REGION
1968											
18 Nov[G]	3200	3.5	650	1026	1235	129	1058	1B	1.6$_m$	N20 W90	9760
3 Dec[G]	3600	2.5	150	2116/02	2350/02	154	2202/02	3N	3.7$_m$	N18 E80	9802
1969											
24 Jan[G]	6300	3.0	60	0803	0926	83	0811	2B	9.2$_m$	N20 W09	9879
25 Feb[3]	8700	3.5	640*	0909	0949	40	0913	2N	9.4$_c$	N11 W38	9946
26 Feb[3]	10000	3.5	670*	0422	0441	19	0426	2B	8.8$_c$	N14 W46	9946
27 Feb[G]	10000	4.0	260*	1352	1511	79	1415	2B	4.2$_m$	N13 W65	9946
12 Mar[G]	3800	3.5	270*	1738	1807	29	1744	2B	4.0$_m$	N12 W80	9966
21 Mar[G]	28000	3.5	1730*	0141	0330	109	0154	2N	6.8$_m$	N19 E16	9994
30 Mar[b]	11000	4.0	1000*	~0332	0400	?	?	1N	2.6$_c$	N19 W90	9994
10 Apr[bb]	7000	3.0	120	0410	0445	35	0414	1N	0.52$_c$	N11 E90	10035
25 Sept[3]	3800	2.0	0	0709	0815	66	0730	2N	8.5$_c$	N13 W16	10326
27 Sept[G]	4800	3.5	60	0347	0545	118	0412	3B	10.45$_m$	N09 E02	10333
2 Nov[G]	4500	3.0	1070*	1102	1220	78	1138	1B	0.97$_m$	N16 W90	10385
24 Nov[3]	14000	3.0	530*	0913	1000	47	0918	2B	10.6$_c$	N16 W32	10432
18 Dec	No logical flare association										
20 Dec	No logical flare association										

b - An unconfirmed flare reported by Manila observatory
bb - An unconfirmed flare reported by Mitaka, Japan observatory

Table 3. - Solar optical parameters(cont'd)

DATE	PLAGE AREA	PLAGE INT.	SUNSPOT AREA	FLARE START	FLARE END	FLARE DURATION	FLARE MAX.	FLARE IMP.	FLARE AREA	LOCATION	McMATH REGION
1970											
29 Jan[7]	5100	3.5	820*	0932	0939	7	0932	1N	2.7$_c$	S12 W45	10542
31 Jan[1]	5100	3.5	770	1516	1630	74	1533	2B	11.1$_c$	S26 W62	10542
6 Mar	6200	4.0	160	0926	?	?	?	3B	?	N09 W90	10595
7 Mar[8]	8300	3.5	490	1601	1635	34	1610	2N	6.5$_c$	S13 E42	10618
23 Mar[1]	1800	4.0	100	1545	1600	15	1545	~F(2)	1.6$_c$	N18 W61	10638
29 Mar[3]	8700	5.0	150	0009	0225	136	0048	2N	10.72$_c$	N14 W36	10641

7 - Uccle Royal Observatory, Brussels, Belgium
8 - NOAA, Boulder, Colo.

THE SOLAR RADIO FREQUENCY PARAMETERS ASSOCIATED WITH THE IMP F AND G OBSERVATIONS

The solar radio frequency parameters associated with the solar proton events observed by the IMP F and G satellites are shown in table 4. The RF parameters listed are the proton event date (the superscripts refer to the reporting station, where 1, 2, and 3 are the same SPAN observatories as given in table 3, 4 and 5 are the ARCRL Sagamore Hill and Manila stations, respectively, and were obtained from refs. 3 and 6), the peak RF intensity and background flux (10^{-22}W/m^2-Hz), the time-integrated RF burst energy (10^{-18}J/m^2-Hz), and the energy-to-peak ratio (sec) at the three fixed frequencies of 1415, 2695 and 4995 MHz.

RADIATION DOSES FOR THE LARGE PROTON EVENTS

Webber (ref. 7) assumed that an exponential rigidity spectrum best described the solar proton event and generated flux equations based on particle rigidity P. For energies greater than 30 and 60 MeV, the characteristic rigidity, P_o, is given by

$$P_o = \frac{242.89}{\ln\left(\frac{\Phi(E>30MeV)}{\Phi(E>60MeV)}\right)}, \text{ MV},$$

where $\Phi(E>30MeV)$ and $\Phi(E>60MeV)$ are the time-integrated proton fluxes having energies greater than 30 and 60 MeV, respectively. A similar equation is obtained for protons with energies greater than 10 and 30 MeV:

$$P_o = \frac{195.78}{\ln\left(\frac{\Phi(E>10MeV)}{\Phi(E>30MeV)}\right)}, \text{ MV},$$

where $\Phi(E>10MeV)$ and $\Phi(E>30MeV)$ are the time-integrated proton fluxes having energies greater than 10 and 30 MeV, respectively.

Table 4. - Solar radio frequency parameters

DATE	1415 MHz PEAK INT.	1415 MHz BKGD.	1415 MHz ENERGY	1415 MHz ENERGY/PEAK	2695 MHz PEAK INT.	2695 MHz BKGD.	2695 MHz ENERGY	2695 MHz ENERGY/PEAK	4995 MHz PEAK INT.	4995 MHz BKGD.	4995 MHz ENERGY	4995 MHz ENERGY/PEAK
1967												
23 May[4]	85100 (1954)	102	1104.03	0.0130	5400 (1952)	220	513.08	0.0916	9858 (1948)	302	828.82	0.0841
28 May[3]	1540 (0543)	139	50.82	0.0330	1772 (0542)	223	70.44	0.0398	4691 (0545)	339	164.53	0.0351
6 June[4]	69.1 (?)				115.6 (?)				164 (?)			
2 Nov[3]	587 (0857)	96	4.81	0.0082	685 (0856)	120	2.60	0.0038	1080 (0856)	210	2.57	0.0024
3 Dec	No RF burst reported											
16 Dec[3]	200 (0252)	110	7.08	0.0354	320 (0252)	154	9.96	0.0311	440 (0252)	258	10.96	0.0249
1968												
9 June[2]	1022 (0849)	152	19.42	0.0190	986 (0851)	148	30.79	0.0312	3024 (0851)	352	53.67	0.0177
6 July[2]	415 (0946)	91	10.67	0.0257	831 (0945)	104	22.59	0.0272	2516 (0949)	189	61.64	0.0245
13 July[2]	269 (1357/12)	108	1.26	0.0047	331 (1357/12)	149	1.25	0.0038	317 (1357/12)	230	0.66	0.0021
26 July	No RF burst reported											
26 Sept[5]	839 (0031)	0	14.38	0.0171	353 (0033)	0	6.57	0.0186	699 (0030)	0	14.46	0.0207

Table 4. - Solar radio frequency parameters(cont'd)

DATE	1415 MHz PEAK INT.	1415 MHz BKGD.	1415 MHz ENERGY	1415 MHz ENERGY/PEAK	2695 MHz PEAK INT.	2695 MHz BKGD.	2695 MHz ENERGY	2695 MHz ENERGY/PEAK	4995 MHz PEAK INT.	4995 MHz BKGD.	4995 MHz ENERGY	4995 MHz ENERGY/PEAK
1968												
29 Sept[1]	358 (1620)	106	9.10	0.0254	796 (1622)	152	22.09	0.0278	2112 (1621)	91	39.74	0.0188
4 Oct[5]	229 (0043)				108 (0000)				57 (0005)			
31 Oct[3]	935 (0013)	119	78.91	0.0844	2187 (0011)	154	183.6	0.0840	3370 (0011)	268	172.41	0.0512
1 Nov[3]	1138 (0915)	116	98.69	0.0867	2603 (0913)	161	242.44	0.0914	3487 (0912)	272	285.79	0.0820
4 Nov[3]	463 (0517)	94	5.28	0.1140	1141 (0520)	151	31.33	0.0275	5652 (0523)	369	145.59	0.0258
18 Nov[2]	1097 (1031)	101	25.62	0.0234	1449 (1030)	129	65.52	0.0452	1655 (1030)	223	142.81	0.0863
3 Dec[5]					270 (2116/02)	0	7.52	0.0279				
1969												
24 Jan[5]	158 (0721)	0	10.11	0.0640	176 (0721)	0	11.83	0.0672	185 (0720)	0	7.83	0.0423
25 Feb[3]	5314 (0913)	129	35.66	0.0067	2557 (0912)	223	46.79	0.0183	4950 (0912)	300	105.63	0.0213
26 Feb[3]	779 (0425)	140	14.99	0.0192	1268 (0425)	205	25.42	0.0200	2828 (0425)	334	52.25	0.0185
27 Feb[1]	467 (1409)	92	9.94	0.0213	1369 (1409)	249	32.38	0.0237	1853 (1410)	399	53.64	0.0289

Table 4. - Solar radio frequency parameters(cont'd)

DATE	1415 MHz PEAK INT.	1415 MHz BKGD.	1415 MHz ENERGY	1415 MHz ENERGY/PEAK	2695 MHz PEAK INT.	2695 MHz BKGD.	2695 MHz ENERGY	2695 MHz ENERGY/PEAK	4995 MHz PEAK INT.	4995 MHz BKGD.	4995 MHz ENERGY	4995 MHz ENERGY/PEAK
1970												
29 Jan[3]	619 (0932)	116	0.59	0.0010	278 (0932)	161	0.51	0.0018	524 (0932)	258	1.11	0.0021
31 Jan[4]	15.5 (1516)				23.2 (1554)				46.4 (1556)			
6 Mar[3]	169 (0934)	135	0.21	0.0012	1034 (0934)	174	1.03	0.0010	413 (0934)	253	1.20	0.0029
7 Mar[4]	105 (1607)				110 (1607)				145 (1607)			
23 Mar[4]	28.8 (1547)				30 (1547)				93 (1550)			
29 Mar[3]	1400 (0040)	129	56.48	0.0403	1592 (0041)	178	86.48	0.0543	4062 (0041)	294	165.85	0.0408

Table 4. - Solar radio frequency parameters(cont'd)

DATE	1415 MHz PEAK INT.	1415 MHz BKGD.	1415 MHz ENERGY	1415 MHz ENERGY/PEAK	2695 MHz PEAK INT.	2695 MHz BKGD.	2695 MHz ENERGY	2695 MHz ENERGY/PEAK	4995 MHz PEAK INT.	4995 MHz BKGD.	4995 MHz ENERGY	4995 MHz ENERGY/PEAK
1969												
12 Mar[1]	No data				2387 (1740)	149	24.48	0.0103	2329 (1741)	376	40.99	0.0176
21 Mar[3]	528 (0153)	168	17.95	0.0340	963 (0154)	259	33.93	0.0352	2060 (0153)	411	49.02	0.0238
30 Mar[3]	5793 (0250)	68	75.88	0.0131	10845 (0250)	95	90.79	0.0084	24733 (0249)	194	140.49	0.0057
10 Apr[3]	216 (0358)	112	3.2	0.0148	408 (0357)	128	8.35	0.0205	440 (0400)	183	24.54	0.0292
25 Sept	No RF burst reported											
27 Sept[5]	98 (0401)	0	4.64	0.0473	106 (0357)	0	2.46	0.0232	86 (0426)	0	9.37	0.1090
2 Nov[2]	697 (1043)	101	52.55	0.0754	1543 (1041)	138	157.88	0.1023	1455 (1041)	229	146.45	0.1007
24 Nov[2]	1420 (0918)	108	30.18	0.0213	2031 (0918)	173	53.68	0.0264	3378 (0925)	244	84.89	0.0251
18 Dec[4]	335 (1514)	0	14.57	0.0435	70 (1515)	0	?	?	30.8 (1517)	0	?	?
20 Dec	No RF burst reported											

Table 5 shows the characteristic rigidities computed for the 20th solar cycle proton events.

Hardy (ref. 8) has generated curves for the normalized proton dose versus characteristic rigidity for various Apollo shielding configurations. Table 6 shows the radiation (skin) doses for some of the large solar proton events that occurred during the 19th and 20th solar cycles. It must be emphasized that the doses listed are accumulated over the entire event duration, which can vary from several hours to several days. However, the dose rates at the event peak may be quite high.

The proton events for which the integrated flux is in the 10^5 to 10^7 range should be considered significant and are of interest to some medical people. Radiobiological effects vary with the individuals exposed, and knowledge and understanding in this area are still somewhat limited. It is for this reason that the possible radiation threat must be considered by mission planning and hardware design personnel for space missions such as advanced lunar exploration, lunar bases, and interplanetary travel.

CORRELATION OF THE SOLAR OPTICAL AND RADIO FREQUENCY PARAMETERS

Several of the optical and radio frequency parameters given in tables 3 and 4 were correlated with the event fluxes for E>30MeV and were compared with similar correlations generated from solar data presented by Gonzalez and Divita (ref. 9) and Lopez (ref. 10). Table 7 shows the correlation coefficient for the various solar parameters for the proton events of the 19th and first half of the 20th solar cycles. The correlation coefficients for the optical data for both solar cycles are not very impressive. In fact, negative coefficients were obtained for three of the four 20th cycle optical parameters. The importance of optical solar observations cannot be over emphasized, but utilization of the optical parameters for solar proton prediction should be made only to monitor active regions and to locate the proton source from proton emitting flares.

The correlation coefficients generated from the 19th cycle RF data are reasonably good. Using a 95% confidence limit, Gonzalez and Divita (ref. 9) obtained a 0.962 correlation coefficient for the 19th cycle RF energy parameter (13 proton events). Thus far in the 20th cycle the coefficient for the RF energy is rather poor. One of the reasons for this seems to be the preponderance of limb-region events (see figure 1). There appears to be an attenuating process which limits the RF burst observed at the earth. As an example, the correlation coefficient computed for the 20th cycle RF peak intensity was 0.033. When the events that occurred near or behind the limb were deleted and the correlation coefficient was recomputed, a value of 0.757 was obtained, which is a significant improvement. Obviously, if proton prediction techniques that utilize only the RF parameters are to be used satisfactorily, then methods must be devised to incorporate the limb and behind-the-limb radio frequency data.

DISCUSSION

Solar proton data were presented thus far for the 20th solar cycle. It remains to associate the solar optical and radio frequency data with the solar proton events observed by the IMP 2 and 3 satellites. Also, it is realized that only approximately one-half of the 20th solar cycle has occurred, and an intelligible comparison of the two solar cycles cannot be fully made. However, the results obtained thus far seem to imply that methods must be devised to improve the value of the optical and RF data and to determine other parameters that can be utilized in solar proton prediction techniques. One means of improvement that has attracted attention recently is the solar x-ray parameter (see, for example, ref. 11 and 12). Kuck (ref. 12) has found that the integrated x-ray flux is more proportional to the solar proton flux than the integrated radio flux. It appears that plasma clouds in the solar corona can effectively shield the centimeter radio burst from detection near earth, but these plasma clouds do not absorb the x-ray bursts. Efforts are underway to incorporate the available x-ray peak and integrated flux data in the existing solar proton prediction programs.

It is concluded that further research in the areas of the interplanetary medium and sector boundaries, particle propagation and diffusion, and other radio, optical and magnetic observations may, and probably will, improve and enhance our understanding of solar proton emissions and other associated solar phenomena.

REFERENCES

1. Robbins, D.E.; and Reid, J.H.: Solar Physics, Vol. 10, 1969, p. 502.
2. King, J.H.: Private Communication.
3. U.S. Department of Commerce: Solar-Geophysical Data, monthly publication
4. World Data Center A, Upper Atmosphere Geophysics: Data on Solar Event of May 23, 1967 and Its Geophysical Effects, Report UAG-5, Feb. 1969.
5. Lund, D.S.; and McIntosh, P.S.: Private Communications.
6. Air Force Cambridge Research Laboratories: Geophysics and Space Data Bulletin, Quarterly Publication.
7. Webber, W.R.: An Evaluation of the Radiation Hazard Due to Solar-Particle Events, Boeing Report D2-90469, 1963.
8. Hardy, A.C.: Private Communication
9. Gonzalez, C.C.; and Divita, E.L.: Solar Proton Forecast System and Procedures Used During the Mariner V Mission, JPL Technical Report 32-1303, 1968.
10. Lopez, M.D.: Private Communication
11. Arnoldy, R.L.; Kane, S.R.; Windkler, J.R.: Astrophys. Jour., 151, 1968, 711.
12. Kuck, G.A.: Prediction of Polar Cap Absorption Events, Air Force Weapons Laboratory Technical Note WLRTH 69-8, 1969.

Table 5. - Characteristic rigidity, P_o, for the 20th solar cycle events

Event Date	P_o, MV	Event Date	P_o, MV
5 Feb 65	162	13 July 68*	43
4 Oct 65	183	26 July 68	> 400
24 Mar 66	197	26 Sept68*	48
29 Mar 66	149	29 Sept 68	102
3 May 66	151	4 Oct 68	119
25 June 66	148	31 Oct 68	105
7 July 66	219	1 Nov 68	87
14 July 66	241	4 Nov 68	159
16 July 66	113	18 Nov 68	141
30 July 66	> 400	3 Dec 68	122
28 Aug 66	317	24 Jan 69*	62
2 Sept 66	282	25 Feb 69	342
3 Sept 66	65	26 Feb 69	258
13 Sept 66	> 400	27 Feb 69	215
20 Sept 66	90	12 Mar 69	209
25 Sept 66	164	21 Mar 69*	76
27 Sept 66	105	30 Mar 69	390
11 Jan 67	> 400	10 Apr 69	110
28 Jan 67	277	25 Sept 69	113
2 Feb 67	206	27 Sept 69*	39
13 Feb 67	100	2 Nov 69	43
27 Feb 67	292	24 Nov 69	122
11 Mar 67	199	18 Dec 69	286
23 May 67	102	20 Dec 69	147
28 May 67	205	29 Jan 70	224
6 June 67	290	31 Jan 70	167
2 Nov 67*	89	6 Mar 70*	68
3 Dec 67	218	7 Mar 70*	40
16 Dec 67	183	23 Mar 70	109
9 June 68	199	29 Mar 70	220
6 July 68	171		

* - Events where there was insignificant flux above 60 MeV, consequently P_o was calculated using time-integrated fluxes for E > 10 MeV and > 30 MeV.

Table 6. Radiation skin (chest) doses for the large solar proton events of the 19th and 20th solar cycles for various Apollo shielding configurations.

EVENT DATE	INTEGRATED FLUX	CHAR. RIGIDITY P_o, MV	C/SM	SKIN DOSE (REM) LM	SPACESUIT
(19th Cycle)					
23 Feb 1956	1.0E09	195	55.00	130.00	255.00
29 Aug 1957	1.2E08	56	4.18	34.80	136.80
10 May 1959	9.6E08	84	43.20	202.56	604.80
12 Nov 1960	1.3E09	124	65.00	136.50	507.00
12 Jul 1961	4.0E07	56	1.34	11.60	45.60
(20th Cycle)					
23 May 1967	2.01E07	102	0.95	3.56	9.95
18 Nov 1968	3.54E08	141	18.41	53.45	139.83
10 Apr 1969	2.02E08	110	10.10	35.96	66.90
2 Nov 1969	2.19E08	43	5.91	79.50	281.42
29 Mar 1970	2.63E07	220	1.45	3.24	6.31

Figure 1. - Heliographic locations of solar flares for the 20th solar cycle.

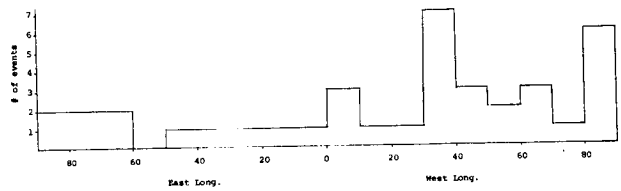

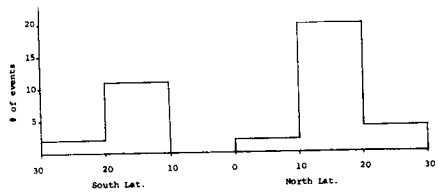

Table 7. - Correlation coefficients for several solar optical and radio frequency parameters for the 19th and 20th solar cycles.

	plage area	plage int.	sunspot area	flare imp.	rf energy	rf** energy	peak int.	peak** int.	energy peak
19th cycle	0.287	0.328	0.187	0.316	0.772	0.768	0.707	0.708	0.050
20th cycle*	-0.149	-0.077	0.068	-0.274	0.078	0.332	0.033	0.757	0.267

* - For the period May 1967 to April 1970
** - Less limb region events

TIME BEHAVIOR OF SOLAR FLARE PARTICLES TO 5 AU

J. W. Haffner
North American Rockwell Corporation
Space Division
12214 Lakewood Boulevard
Downey, California

Abstract

A simple model of solar flare radiation event particle transport is developed to permit the calculation of fluxes and related quantities as a function of distance from the sun (R). This model assumes the particles spiral around the solar magnetic field lines with a constant pitch angle. The particle angular distributions and onset plus arrival times as functions of energy at 1 AU agree with observations if the pitch angle distribution peaks near 90°. As a consequence the time dependence factor is essentially proportional to $R^{-1.7}$, (R in AU), and the event flux is proportional to R^{-2}.

I. Introduction

Solar flare particle events constitute one of the important sources of natural nuclear radiation at 1 AU from the sun. Approximately 100 such events have been observed at the earth (see Table I),[1] ranging up to $\sim 10^{10}$ protons/cm^2-event above 10 Mev. Various particle flux models have been developed describing the time and energy behavior observed at 1 AU. These models, coupled with prediction mechanisms (usually correlated to sunspot numbers) have been used to estimate the expected solar flare particle environment at 1 AU for future space missions. These techniques have also been used for missions to Mars (1.5 AU) and Venus (0.7 AU).

For missions which involve sending spacecraft far from 1 AU (e.g., the Mercury-Venus and the Outer Planet missions), the solar flare particle model developed from observations at 1 AU is not adequate. Specifically, the dependence of the solar flare particle event model on distance from the sun must be incorporated. This paper presents a simple model for incorporating this spatial dependence which agrees with the observations at 1 AU.

II. Model at 1 AU

The flux of solar flare particles observed at 1 AU is observed to rise quasi-linearly over a period of some hours to a peak value, then decay approximately exponentially over an appreciably longer period. The onset, rise, and characteristic decay times are functions of particle energy. A previously developed mathematical expression which has these characteristics is:[2]

$$\phi(>E_o, t) = \frac{A\, t\, e^{-\alpha E_o^{\,n} t}}{E_o^{\,m}} \quad \frac{\text{particles}}{\text{cm}^2\text{-hr}} \qquad (1)$$

where E_o is the particle energy(Mev)
t is the time from the arrival of the first particles (hrs)
A is a normalization factor
α, n, m } approximately constants

If the characteristics of the largest solar flare particle events are used to evaluate α, n, and m, the values obtained are approximately 0.022, 0.4, and 0.75, respectively. An attempt to incorporate the variations of these quantities due to radiation event size led to the relationships[3]

$$\alpha = A^{-0.224}$$
$$m = 16A^{-0.16}$$

where all quantities are as previously defined. Incorporation of these relationships in Equation (1) yields formulae which account for the shorter rise and decay times and steeper energy spectra for the smaller events. However, the smaller event characteristics vary so much that generalizations are difficult and attempts to account for the size-dependent characteristics are generally more trouble than they are worth.

Based on Equation (1), the following relations have been derived:

$$\phi(>E_o) = \frac{A}{\alpha^2 E_o^{\,m+2n}} \sim \frac{2100\,A}{E_o^{\,1.55}} \quad \frac{\text{particles}}{\text{cm}^2} \qquad (2)$$

$$t_{rise} = \frac{1}{\alpha E_o^{\,n}} = \frac{45}{E_o^{\,0.4}} \text{ hr}$$

$$\tau_{decay} = \frac{2.15}{E_o^{\,n}} = \frac{100}{E_o^{\,0.4}} \text{ hr}$$

$$\hat{\phi}(>E_o) = \frac{A\, e^{-1}}{\alpha E_o^{\,m+n}} = \frac{17\,A}{E_o^{\,1.15}} \quad \frac{\text{particles}}{\text{cm}^2\text{-hr}} \qquad (3)$$

$$\phi(E) = \frac{3200\,A}{E^{2.55}} \text{ particles/cm}^2\text{-Mev} \qquad (4)$$

$$\phi(E,t) = A\, t\, e^{-0.022E^{0.4}t} \cdot (0.75 + 0.0088\, t\, E^{0.4}) \quad \frac{\text{particles}}{\text{cm}^2\text{-hr-Mev}} \qquad (5)$$

These relationships have proven useful when applied to large solar flare radiation events at 1 AU. In particular, they have been applied to events for which the data was incomplete--some of the numbers in Table I were obtained this way.

These formulae have no dependence on the distance from the sun, and are therefore strictly

applicable to 1 AU only. In the following sections, modifications of these formulae to account for distance from the sun are discussed.

III. Particle Transport

In order to account for the dependence of the solar flare particle event model on distance from the sun, it is necessary to have a particle transport model. Since particle acceleration and particle transport are related during the acceleration portion of the particle event, it is desirable to go back to the solar flare itself.

A solar flare is an event observed to take place above the photosphere of the sun, generally lasting $\lesssim$ 20 minutes. The flare, which is most readily observed at the Lyman - α wavelength of ionized hydrogen ($\sim$ 1215 Å) is believed to derive its energy from the collapse of the magnetic fields associated with sunspots. Various theories have been advanced to account for the acceleration of charged particles during or as a result of a solar flare. Among these theories are betatron acceleration and shock wave acceleration. In betatron acceleration, a charged particle orbiting above a collapsing sunspot gains energy as in a laboratory particle accelerator of the same name. In shock wave acceleration the absorption of the Lyman - α photons in the inner corona produces a supersonic blast wave which accelerates the charged particles. These proton acceleration mechanisms have been investigated by Gold,[4] Wentzel,[5] Parker,[6] Weddell,[7] and others. The evidence is not conclusive for any single mechanism, and both betatron and shock wave accelerations probably contribute.

Once the charged particles have been accelerated, their propagation away from the sun is controlled by the interplanetary magnetic fields. These interplanetary fields are complex, having time and spatial dependences which are not well known. However, by making some simplifying assumptions, it is possible to obtain a spatially dependent solar flare particle model.

If it is assumed that the quiet sun interplanetary magnetic field is essentially undisturbed during the propagation of the solar flare protons, it is possible to write:

$$B = \sqrt{\left(\frac{B_r}{R^2}\right)^2 + \left(\frac{B_\theta}{R}\right)^2}$$

$$Bqv_\perp = \frac{m v_\perp}{r}$$

$$J = m v_\perp r$$

$$v_\perp = v \sin\beta$$

$$v_{||} = v \cos\beta$$

where

B is the solar magnetic field (webers/m^2)

B_r is the radial component of B (webers/m^2) (see Figure 1)

B_θ is the aximuthal component of B (webers/m^2)

R is the distance from the sun (AU)

q is the charge of the particles (coulombs)

v is the velocity of the charged particles (meters/sec)

$v_\perp$ is the perpendicular component of v (meters/sec)

$v_{||}$ is the parallel component of v (meters/sec)

β is the pitch angle (angle v makes with the guiding center line of B). Since $B_r \approx B_\theta \approx 3.5 \times 10^{-9}$ webers/m^2 (3.5 gammas) at 1 AU, B is ~ 5 gammas, and the gryroradius is $2.75 \times 10^7 \sqrt{E}$ meters, where E is in Mev. The gyroradius as a function of distance from the sun is approximately

$$r = 3.9 \times 10^7 R^2 \sqrt{\frac{E}{1 + R^2}} \quad \text{meters} \qquad (6)$$

This function is plotted in Figure 2.

Assuming the particles spiral around the magnetic lines of force, it is expected that their gyroradius will increase as their distance from the sun increases. Based upon the above equations it is expected that their pitch angle β will decrease with distance from the sun, according to the well-known relationship.

$$\frac{J q}{2 m E} = \frac{\sin^2\beta}{B} = \text{constant}$$

However, the pitch angle (β) cannot exceed 90°. If the charged particle has this limiting angle close to the sun, its pitch angle might be expected to become quite small by the time it reaches 1 AU. If a particle has a pitch angle of 90° starting at 10 solar radii, the calculated pitch angle will be $\sim 3°$ by the time it reaches 1 AU ($\sim$ 215 solar radii) according to this model. Since solar flare event particles are observed at 1 AU to be essentially isotropic after the flux peak, this simplified model is clearly unrealistic.

It is possible to obtain reasonable agreement with observations at 1 AU by making the assumption that the pitch angle is independent of distance from the sun. This accounts for the fact that particles of a given energy with small pitch angles will arrive first (as is observed), and the resultant particle angular distributions spread as functions of time. To the extent that this model appears to agree with the observations at 1 AU, it may be useful for calculating the spatial dependence of solar flare particle radiation.

The transit time (t_{tr}) as a function of particle energy and pitch angle (both assumed to be constants of the motion) is

$$t_{tr} = \frac{s}{v_{||}}$$

where s is the length of the line of magnetic flux which serves as the guiding center for the particle gyrorotation. This length(s) may be calculated from the relationship:

$$s = \int ds = \int \sqrt{(dr)^2 + (r\,d\theta)^2}$$

But since

$$\tan^{-1} \frac{r\,d\theta}{dr} = \tan^{-1} \frac{B_\theta}{B_r} = \tan^{-1} R$$

$$r\,d\theta = R\,dr$$

Therefore

$$s = \int_{r=0}^{r=R} dr \sqrt{1 + R^2}$$

$$= \frac{1}{2}\left[R\sqrt{1 + R^2} + \log\left(R + \sqrt{1 + R^2}\right)\right] \qquad (7)$$

When the distance from the sun (R) is small the two terms are approximately equal in value, but as the distance from the sun increases, the first term predominates. This function is graphically displayed in Figure 3. A reasonable approximation is:

$$s \sim R\sqrt{1 + \frac{R^2}{4}} \qquad (8)$$

If it is assumed that the pitch angle (β) of the particle is a constant of the motion, the transit time as a function of pitch angle and particle energy may be calculated. Based on Equation (7), the result is (for protons):

$$t_{tr} \quad 5.5 \times 10^3 \frac{\left[R\sqrt{1 + R^2} + \log\left(R + \sqrt{1 + R^2}\right)\right]}{\sqrt{E}\cos\beta} \qquad (9)$$

seconds

where R is in AU and E is in Mev. With only a few percent error in the region of interest (0.1 - 10 AU) this may be approximated by

$$t_{tr} \quad 1.1 \times 10^4 \frac{R}{\sqrt{E}\cos\beta}\sqrt{1 + \frac{R^2}{4}} \text{ seconds} \qquad (10)$$

Values of this function are listed in Tables II-IV, and are plotted in Figures (4) to (6). These figures show the expected dependence on proton energy (E), pitch angle (β), and distance from the sun (R). In principle, this expression may be solved to obtain any of the quantities as functions of the others. The quantity of major interest is the proton flux as a function of these parameters. This is determined by the initial proton distribution in β, assuming no protons are lost after being accelerated.

If no particles are lost after being accelerated, the total number per cm^2 per event is expected to be proportional to R^{-2} (R = distance from the sun in AU). Assuming an R^2 time-integrated spatial dependence effectively makes the solar flare particle event probability spatially independent. Any other assumption introduces the complication of a spatially dependent probability function. Since the time-integrated particle flux for a mission is essentially the product of the flux per event and the probability of that event, little, if anything, is gained by considering a spatially dependent particle event probability.

If a significant fraction of solar flare particles is lost after being accelerated, the flux per event will exhibit an $R^{-n'}$ spatial dependence where $n' > 2$ over the region where particle loss is important. The major probable loss mechanism is collision with objects in space (magnetospheres, planets, moons, etc.) Considering the relative emptiness of space this is not expected to be a major loss mechanism. Even the asteroid belt is only $\sim 10^{-6}$ opaque, which means that the solar flare particle traversing it will be small. (It may not be completely negligible, however, since the proton helical path length through the asteroid belts will be ~ two orders of magnitude larger than that of a solar photon). The probability of a solar flare particle encountering a planet, even assuming the particles are essentially confined to the ecliptic plane is $< 1\%$.

It is interesting to calculate the pitch angle which corresponds to the peak flux rate. At 1 AU the onset + rise time (time from the flare on the sun to the peak flux rate) is approximately:

$$t_{rise} \sim \frac{45}{E_o^{0.4}} \text{ hrs}$$

where E_o is the proton energy in Mev. (This relationship was obtained by averaging the values observed for the largest radiation events--smaller events often have shorter onset + rise times). Since the proton transit time (given by Equation 9) is proportional to $E^{-0.5}$, there is apparently a constant delay time to be added. A little arithmetic shows that this delay time is $860/\cos\beta$ seconds. Thus:

$$t_{rise} = t_{tr} + \frac{860}{\cos\beta} \text{ seconds}$$

This accounts for the acceleration time during which the protons do not migrate away from the sun significantly as well as the time between the arrival of the first protons of a given energy and the peak flux of these protons. It will be noted that a fairly steep proton energy spectrum has been assumed (based on observations at 1 AU), since the onset + rise time for particles above energy E_o is taken to be essentially that of particles of energy E_o.

For 1, 10, and 100 Mev protons at 1 AU, the observed onset + rise times (t_{rise}) are $\sim 1.6 \times 10^5$ seconds, $\sim 6.5 \times 10^4$ seconds, and $\sim 2.6 \times 10^4$ seconds, respectively. The corresponding transit times are $\sim 1.5 \times 10^5$ seconds, $\sim 5.2 \times 10^4$ seconds, and $\sim 1.5 \times 10^4$ seconds. These are the transit times for protons with pitch angles of $\sim 86^\circ$. It will be noted that any change of pitch angle as the protons migrate away from the sun will decrease the transit time below that observed. Thus, unless there is some mechanism which acts to increase the

pitch angles of protons as they move away from the sun, the assumption of constant pitch angle appears to be superior to any obvious simple alternative. Also noteworthy, is that beyond 2 AU solar flares on the back side of the sun can be important sources of particles.

Another interesting conclusion, valid to the extent that the assumption of a constant pitch angle is valid is that the bulk of the protons have pitch angles close to 90°. Based upon Equation (2), only ~26% of the protons above a given energy have arrived at 1 AU by the time the peak flux rate of these protons has been reached. Thus, ~74% of the protons observed at 1 AU appear to have pitch angles between 86° and 90°. Assuming a random distribution of proton velocity directions prior to acceleration, a sin β pitch angle distribution would be expected from solid angle considerations. Apparently, the acceleration mechanism favors particles with pitch angles close to 90°. This seems to favor the betatron acceleration mechanism over the shock wave acceleration mechanism. However, since the constant pitch angle assumption is merely a simplified model, any conclusions based upon it must be considered uncertain.

The maximum pitch angle determines the limits of the particle angular distribution as a function of time and energy. The particle angular distribution within these time and energy dependent limits according to this model is determined by the initial particle pitch angle distribution. However, not enough angular distribution information is available to derive statistically meaningful pitch angle distributions as functions of time and energy. When such data becomes available, its incorporation into this model is straightforward.

IV. Spatially Dependent Model

It is now possible to use the transport model to calculate the parameters of the solar flare particle radiation as functions of distance from the sun. Since the pitch angle is assumed to remain constant, so does $v_{\parallel}$ (the particle velocity parallel to the line of magnetic force which serves as the gyrorotation guiding center). The time for a particle to reach a given distance from the sun is simply proportional to the spiral path length (given by Equation 7). Thus, the time dependence of the solar flare particle flux is expected to be

$$t' \sim \frac{t}{f(R)} + t_o$$

where f (R) is given by Equation (7) and t_o is ~ 1.2×10^4 sec. It is, therefore, possible to rewrite Equations (1) to (5) incorporating R (the distance from the sun, as a parameter). The results are:[8]

$$\phi(>E_o, t) = \frac{A\,(t-t_o)\, e^{-\alpha E_o^{\,m} f^{-1}(R)\, t}}{R^2 f^2(R)\, E_o^{\,m}} \qquad (11)$$

$$\sim \frac{A\,(t-t_o)\, e^{-0.022 E_o^{0.4} f^{-1}(R) t}}{R^2 f^2(R)\, E_o^{0.75}} \quad \frac{\text{particles}}{\text{cm}^2\text{-hr}}$$

$$\int \phi(>E_o) = \frac{A}{\alpha^2 R^2 E_o^{\,m+2n}} \sim \frac{2100\, A}{R^2 E^{1.55}} \quad \frac{\text{particles}}{\text{cm}^2} \qquad (12)$$

$$t_{rise} = \frac{1}{\alpha E_o^{\,n} f(R)} + t_o \sim \frac{45}{E_o^{0.4} f(R)} \text{ hrs} \qquad (13)$$

$$\tau_{decay} = \frac{2.15}{\alpha E_o^{\,n} f(R)} \sim \frac{100}{E_o^{0.4} f(R)} \text{ hrs} \qquad (14)$$

$$\hat{\phi}(<E_o) = \frac{A e^{-1}}{\alpha f(R) E_o^{\,m+n}} \sim \frac{17\, A}{f(R) E_o^{1.15}} \quad \frac{\text{particles}}{\text{cm}^2\text{-hr}} \qquad (15)$$

$$\phi(E) = \frac{3200\, A}{R^2 E^{2.55}} \quad \frac{\text{particles}}{\text{cm}^2\text{-Mev}} \qquad (16)$$

$$\phi(E, t) = \frac{At\, e^{-0.022E^{0.4} f^{-1}(R) t}}{R^2 E^{1.75}} \left[0.75 + 0.0088 t f^{-1}(R) E^{0.4}\right] \quad \frac{\text{particles}}{\text{cm}^2\text{-hr-Mev}} \qquad (17)$$

where all symbols have been previously identified. As mentioned previously, f (R) can be approximated by

$$f(R) \sim R\sqrt{1 + \frac{R^2}{4}}$$

For R >1, this may be further approximated by $R^{1.7}$ with $\lesssim$ 15% error at 1 AU and a smaller error for $1 < R \lesssim 5$.

The relative spatial dependences of the time-integrated particle flux rate ($\propto R^{-2} \cdot f^{-2}(R)$ are shown in Figure 7. These curves show that the relative solar flare particle environment becomes severe as the sun is approached. For the largest such particle event observed at 1 AU (11-12-60), the peak and time-integrated proton fluxes above 10 Mev at Mercury (~ 0.4 AU) would be ~7.2×10^5 p/cm²-sec and ~6.3×10^{10} p/cm², respectively -- enough to affect sensitive spacecraft components. For this same event the corresponding numbers at Jupiter (~ 5.2 AU) would be 120 p/cm²-sec and 3.7×10^8 p/cm², which should cause no trouble.

It will be noted that particle loss and change of particle energy after acceleration have been neglected. If either of these changes takes place (and there is some evidence that they do), the solar flare particle environment as the sun is approached will be even more severe than here calculated. Conversely, at distances greater than 1 AU, the environment may very well be less severe than expected.

V. Conclusions

The solar flare particle event model developed to fit the observed data at 1 AU has been modified to account for the distance from the sun. This was accomplished by assuming each flare particle independently spirals around the solar magnetic field (carried frozen-in by the solar wind), while maintaining its pitch angle constant. Among the consequences of this transport model are:

(a) The majority of the solar flare particles have pitch angles close to 90^{o}. Calculated pitch angle particle distributions as a function of time agree fairly well with observations at 1 AU.

(b) The solar flare particle flux rate is quite dependent on distance from the sun ($\sim R^{-3.7}$), while the time integrated particle flux obeys the expected inverse square distance relationship (R^{-2}).

(c) The solar flare particle energy spectra are essentially independent of distance from the sun, since particle losses after acceleration are neglected. Some particle losses probably occur, leading to a softening of the energy spectra and larger flux spatial dependences than herein calculated.

This solar flare particle event model is directly applicable to missions which involve sending a spacecraft on missions in the ecliptic plane far from 1 AU from the sun. It is particularly applicable to missions to Mercury and to the outer planets. It is not intended to apply far from the ecliptic plane or past the heliosphere. Within these limits it provides an easy-to-use improvement over spatially independent models.

VI. Nomenclature

A	Normalization factor for solar flare particle event model
AU	Astronomical unit (1.5×10^{8} km)
B	Solar magnetic field strength (webers/meter^2)
B_r	Radial component of solar magnetic field strength (webers/meter^2)
B_θ	Tangential component of solar magnetic field strength (webers/meter^2)
E	Particle energy (Mev)
E_o	Particle energy limit (Mev)
J	Angular momentum of particle gyrorotation around solar magnetic field line (kg-meter^2-sec^{-1})
m	Parameter in solar flare particle event model
n	Parameter in solar flare particle event model
q	Particle charge (coulomb)
R	Distance from sun (AU)
r	Radius of particle gyrorotation around solar magnetic field line (meters)
s	Length of solar magnetic field flux line (meters)
t	Time (hrs)
t_{rise}	Onset + rise time (time from flare on sun to particle flux maximum observed at R AU) (seconds)
t_r	Particle transit time from the sun (seconds)
v	Particle velocity (meters/sec)
$v_{\parallel}$	Component of particle velocity parallel to solar magnetic field (meters/sec)
$v_{\perp}$	Component of particle velocity perpendicular to solar magnetic field (meters/sec)
α	Parameter in solar flare particle event model
β	Pitch angle of particle velocity with respect to solar magnetic field (degrees)
ϕ	Particle (proton) flux (particles/cm^2-hr-Mev)
$\int\phi$	Time-integrated particle flux (particles/cm^2)
$\hat{\phi}$	Peak particle flux rate (particles/cm^2-hr)
θ	Azimuthal angle (polar coordinate)

VII. References

1. J. W. Haffner, "Solar Cycle Effects on Mission Dose Probabilities," Report SD 69-422, North American Rockwell (July 1969).

2. J. W. Haffner, Radiation and Shielding in Space, Chapter I, pp. 29-30, and Chapter VIII, p. 258, Academic Press (1967).

3. J. B. Weddell and J. W. Haffner, "Statistical Evaluation of Proton Radiation From Solar Flares," Report SID 66-421, North American Aviation (July 1966).

4. T. Gold, "Plasma and Magnetic Fields in the Solar System," Journal of Geophysical Research 64, 1665 (1959).

5. D. G. Wentzel, "Fermi Acceleration of Charged Particles," Astrophysical Journal 137, (#1) pp. 135-146 (1963).

6. E. N. Parker, "Interplanetary Dynamical Processes," Chapter VIII, pp. 92-112, Interscience Publishers (1963).

7. J. B. Weddell, "Solar Proton Event Production by Hydromagnetic Shocks," Planetary and Space Science 13, 789 (1965).

8. J. W. Haffner, "Solar Flare Proton Propagation," Report SD 69-585, North American Rockwell (Sept. 1969).

Table I. Annual Totals for Solar Flare Radiation Event Particle Fluxes at 1 AU

Year	Number of Events ($\int\phi$>10 Mev)					Annual Totals (particles/cm^2)		
	>10^6	>10^7	>10^8	>10^9	>10^{10}	$\int\phi$>10 Mev	$\int\phi$>30 Mev	$\int\phi$>100 Mev
1956		1	1	1		2.7 x 10^9	1.1 x 10^9	3.7 x 10^8
1957	1	4	6	3		1.0 x 10^{10}	8.5 x 10^8	5.9 x 10^7
1958	1	4	2	4		1.1 x 10^{10}	1.4 x 10^9	9.6 x 10^7
1959		1	1	5		2.2 x 10^{10}	4.3 x 10^9	4.2 x 10^8
1960	3	11	1	1	1	1.3 x 10^{10}	2.7 x 10^9	3.9 x 10^8
1961	1	5	3	1		2.1 x 10^9	4.2 x 10^8	4.9 x 10^7
1962						1.6 x 10^6	2 x 10^5	1.4 x 10^4
1963	1	1	1			5.6 x 10^8	6.5 x 10^7	6.4 x 10^6
1964		1	1			1.2 x 10^8	1.2 x 10^7	1.1 x 10^6
1965		2	1			2.2 x 10^8	2.2 x 10^7	2.0 x 10^6
1966		3	2			8.1 x 10^8	1.0 x 10^8	1.0 x 10^7
1967	3	4	1	1		2.2 x 10^9	2.7 x 10^8	2.8 x 10^7
1968	1	3	4	1		2.1 x 10^9	2.4 x 10^8	2.3 x 10^7

Table II. Transit Times (Seconds) for Protons as a Function of Pitch Angle at 1 AU

Proton Energy (Mev)	Pitch Angle						
	$\beta = 0^\circ$	$\beta = 15^\circ$	$\beta = 30^\circ$	$\beta = 45^\circ$	$\beta = 60^\circ$	$\beta = 75^\circ$	$\beta = 80^\circ$
1.0	1.23 x 10^4	1.27 x 10^4	1.42 x 10^4	1.74 x 10^4	2.46 x 10^4	4.75 x 10^4	7.08 x 10^4
3.0	7.1 x 10^3	7.32 x 10^3	8.2 x 10^3	1.0 x 10^4	1.42 x 10^4	2.74 x 10^4	4.07 x 10^4
10	3.9 x 10^3	4.04 x 10^3	4.51 x 10^3	5.52 x 10^3	7.82 x 10^3	1.51 x 10^4	2.25 x 10^4
30	2.24 x 10^3	2.3 x 10^3	2.58 x 10^3	3.16 x 10^3	4.47 x 10^3	8.62 x 10^3	1.28 x 10^4
100	1.23 x 10^3	1.27 x 10^3	1.42 x 10^3	1.74 x 10^3	2.46 x 10^3	4.75 x 10^3	7.08 x 10^3
300	8.18 x 10^2	8.47 x 10^2	9.45 x 10^2	1.16 x 10^3	1.64 x 10^3	3.16 x 10^3	4.71 x 10^3

Table III. Minimum Transit Times for Protons as a Function of Energy ($\beta = 0$)

Distance From Sun (AU)	Proton Energy (Mev)					
	1	3	10	30	100	300
0.1	1.07×10^3	6.2×10^2	3.4×10^2	1.95×10^2	1.07×10^2	7.1×10^1
0.4	4.3×10^3	2.48×10^3	1.36×10^3	7.8×10^2	4.28×10^3	2.84×10^2
0.7	8.0×10^3	4.63×10^3	2.55×10^3	1.46×10^3	8.0×10^3	5.33×10^2
1.0	1.23×10^4	7.1×10^3	3.9×10^3	2.24×10^3	1.23×10^3	8.18×10^2
1.5	2.09×10^4	1.21×10^4	6.6×10^3	3.8×10^3	2.09×10^3	1.39×10^3
2.0	3.16×10^4	1.82×10^4	1.0×10^4	5.74×10^3	3.16×10^3	2.1×10^3
3.0	6.05×10^4	3.48×10^4	1.92×10^4	1.1×10^4	6.05×10^3	4.0×10^3
4.0	9.95×10^4	5.75×10^4	3.16×10^4	1.81×10^4	9.9×10^3	6.6×10^3
5.0	1.5×10^5	8.65×10^4	4.75×10^4	2.73×10^4	1.5×10^4	9.95×10^3

Table IV. Transit Times (Seconds) for 1 Mev Proton as a Function of Pitch Angle

Distance From Sun (AU)	Pitch Angle						
	$\beta = 0^\circ$	$\beta = 15^\circ$	$\beta = 30^\circ$	$\beta = 45^\circ$	$\beta = 60^\circ$	$\beta = 75^\circ$	$\beta = 80^\circ$
0.1	1.07×10^3	1.11×10^3	1.24×10^3	1.52×10^3	2.14×10^3	4.13×10^3	6.15×10^3
0.4	4.3×10^3	4.45×10^3	4.97×10^3	6.1×10^3	8.6×10^3	1.66×10^4	2.48×10^4
0.7	8.0×10^3	8.27×10^3	9.25×10^3	1.13×10^4	1.6×10^4	3.09×10^4	4.6×10^4
1.0	1.23×10^4	1.27×10^3	1.42×10^4	1.74×10^4	2.46×10^4	4.75×10^4	7.08×10^4
1.5	2.09×10^4	2.16×10^4	2.42×10^4	2.96×10^4	4.18×10^4	8.07×10^4	1.2×10^5
2.0	3.16×10^4	3.27×10^4	3.66×10^4	4.47×10^4	6.32×10^4	1.22×10^5	1.82×10^5
3.0	6.05×10^4	6.26×10^4	7.00×10^4	8.57×10^4	1.21×10^5	2.34×10^5	3.48×10^5
4.0	9.95×10^4	1.03×10^5	1.15×10^5	1.41×10^5	1.99×10^5	3.85×10^5	5.75×10^5
5.0	1.5×10^5	1.55×10^5	1.73×10^5	2.13×10^5	3.0×10^5	5.8×10^5	8.62×10^5

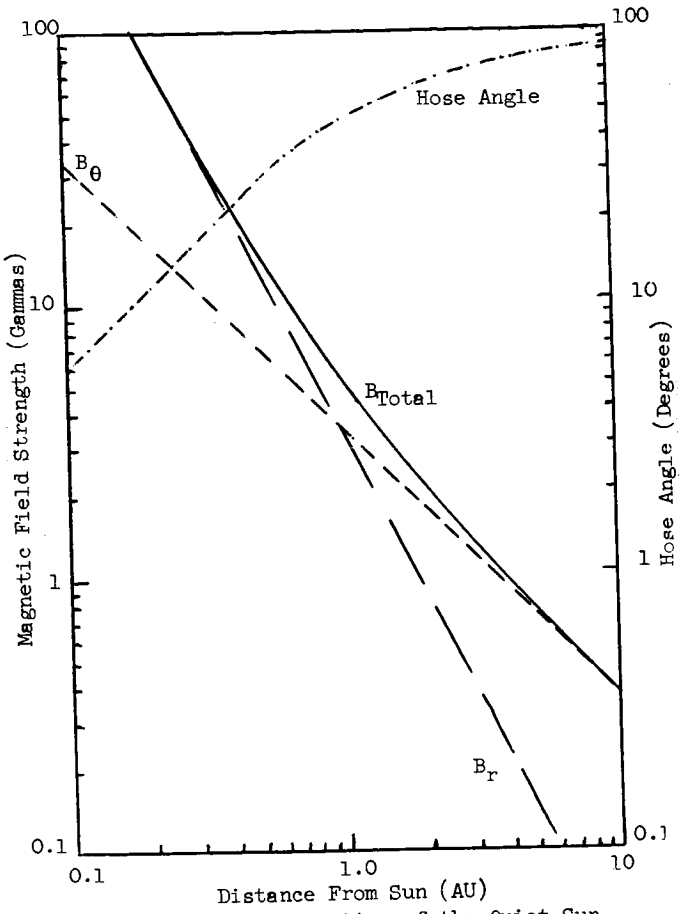

Figure 1. Characteristics of the Quiet-Sun Magnetic Field Carried Frozen in by the Solar Wind.

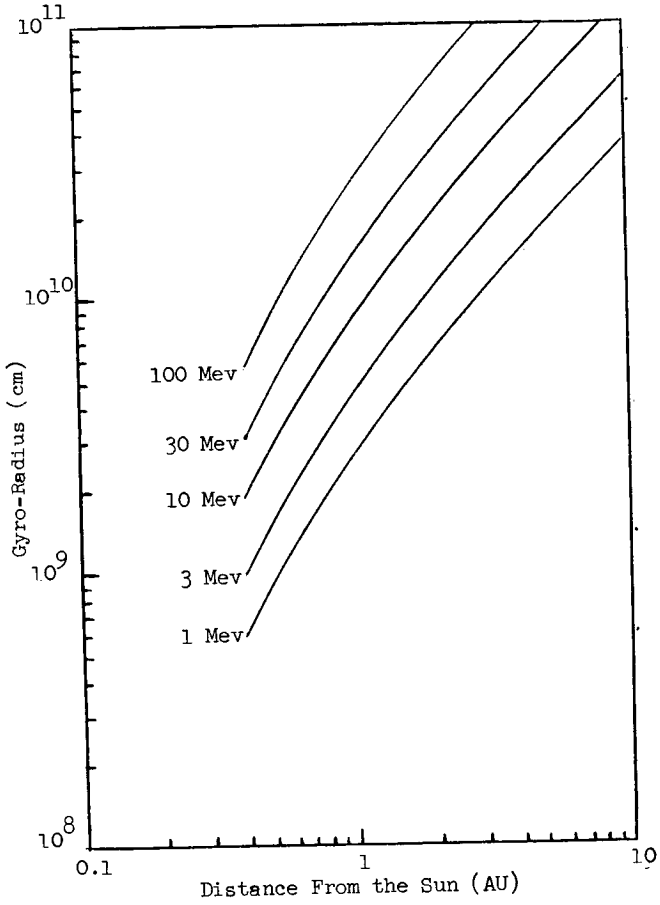

Figure 2. Proton Gyro-Radius as a Function of Distance From the Sun for Undisturbed Interplanetary Magnetic Field.

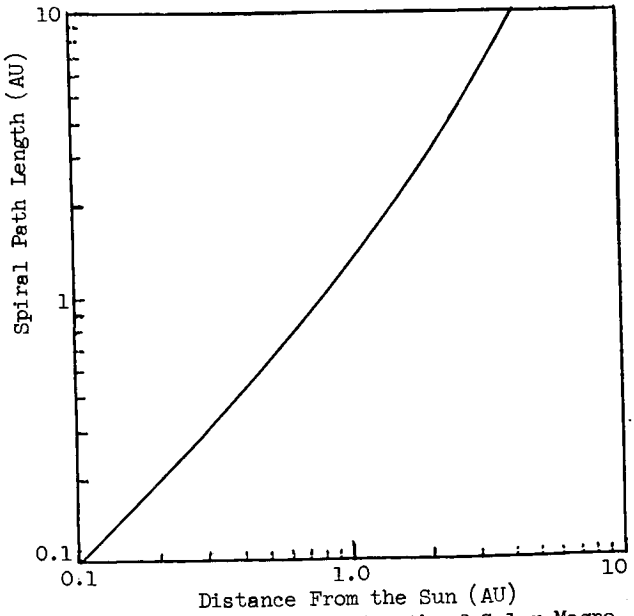

Figure 3. Spiral Path Length of Solar Magnetic Field as a Function of Distance From the Sun.

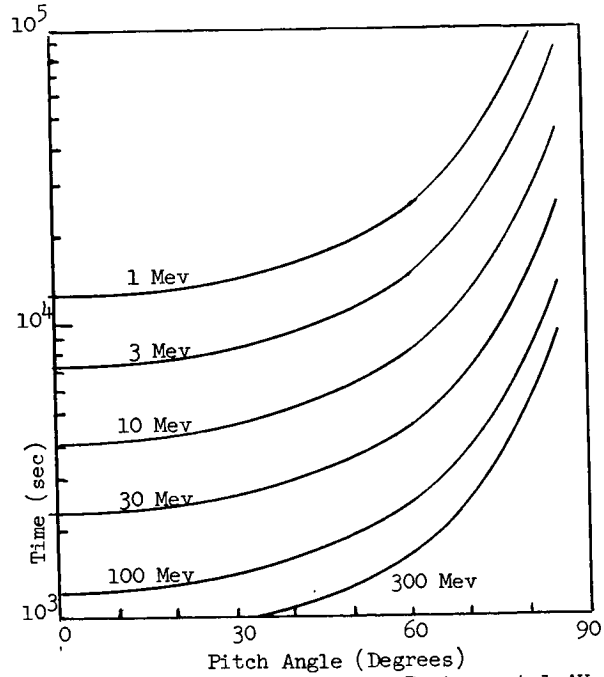

Figure 4. Transit Times for Protons at 1 AU as a Function of Pitch Angle (Assumed Constant) and Proton Energy

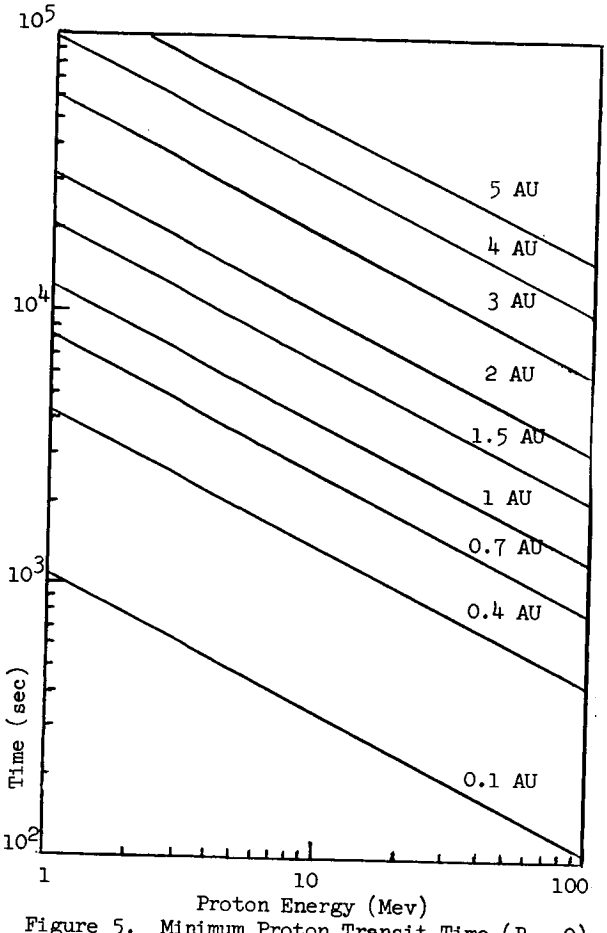

Figure 5. Minimum Proton Transit Time (B = 0) as a Function of Proton Energy and Distance From the Sun.

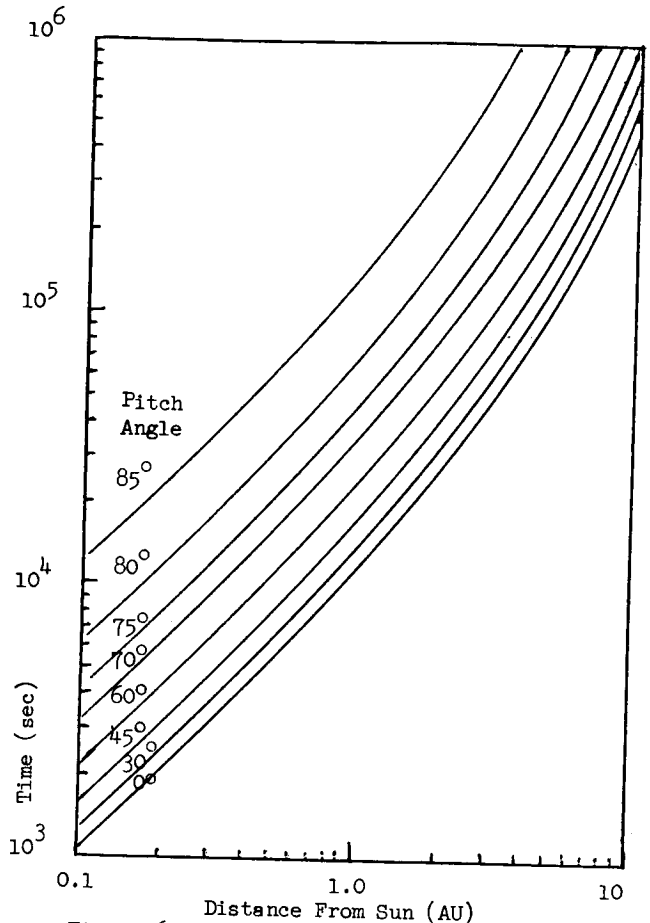

Figure 6. Proton Transit Time for 1 Mev Protons as a Function of Distance From the Sun and Pitch Angle.

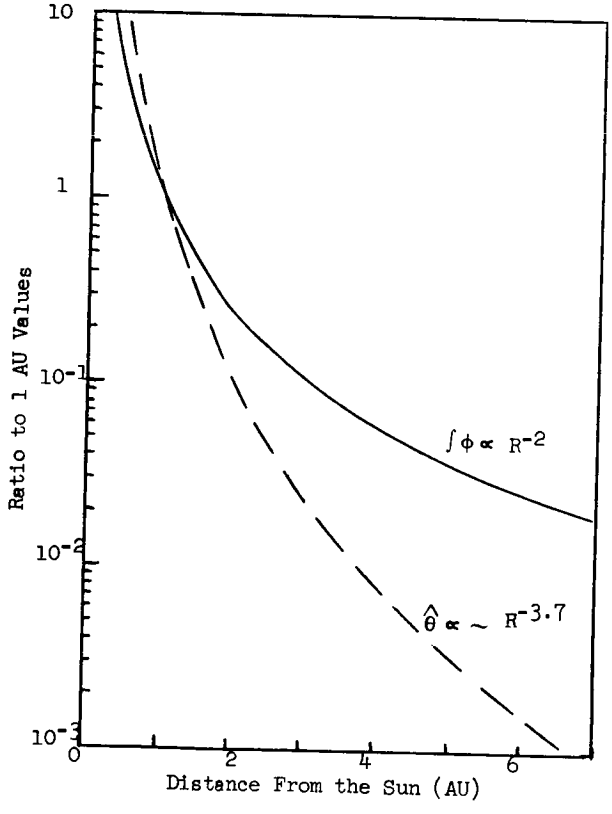

← Figure 7. Ratio of Integral Particle Fluxes ($\int\phi$) and Peak Particle Flux Rate ($\hat{\theta}$) to the Corresponding Values at 1 AU

SOLAR COSMIC RAY HAZARD TO INTERPLANETARY AND EARTH-ORBITAL SPACE TRAVEL*

W. R. Yucker
McDonnell Douglas Astronautics Company-West
Huntington Beach, California

Abstract

This paper describes a statistical treatment of the radiation hazard to astronauts due to solar cosmic ray protons. While several similar studies have been conducted in the past, objections to the use of this approach to determining shielding requirements have been raised due to the limited number of solar proton events for which data are available. More recent data are incorporated into the present analysis, including events from 1956 to 1969, in order to improve the accuracy of the predicted mission fluence and dose. The effects of the finite data sample are discussed. Also, an attempt is made to present a unified and consistent view of the solar cosmic ray proton hazard and to justify the application of a statistical approach for mission planning.

Mission fluence and dose versus shield thickness data are presented for mission lengths up to 3 years during periods of maximum and minimum solar activity; these correspond to various levels of confidence that the predicted hazard will not be exceeded.

Introduction

The occurrence of solar cosmic rays (SCR) has been recognized for almost 30 years, and accurate, detailed measurements are available from the last 14 years. Charged particles, mostly protons, but including alpha particles and small numbers of heavier nuclei, are emitted by the sun and travel through interplanetary space. The resulting hazard to manned space vehicles created by the solar cosmic rays is the subject of this paper.

Many aspects of the SCR radiation protection problem warrant continuing study. A comprehensive theoretical understanding of the origin of solar cosmic radiation has not been developed, nor is one to be expected shortly. Attempts to predict solar proton events over periods of several days have met with some success, but the long-range prediction of events is not yet possible.[1] Without adequate predictions of the occurrence and the intensity of events, prior evaluation of the radiation hazard to space travel cannot be made.

A model has been developed by Baker, et al.,[2] that predicts the total intensity of an event from spectral data measured early in the event. For earth-orbit missions, such a model would allow astronauts to abandon a mission and return to earth to avoid receiving the full dose from a dangerously large event. While the prediction is of too short a range to allow escape of the crew of a lunar or interplanetary mission, it does provide early warning of the occurrence of a large event. In this case, the mission operating plan could provide for locating the crew inside a small but relatively heavily shielded biowell to reduce the dose received, and possibly provide for premature termination of the mission to escape any additional dose from subsequent events.

Aside from the problems of evaluating the radiation source, the mission criteria for the hazard caused by the SCR environment require further refinement and more definiteness; at present, both the acceptable and incurred risks are ill-defined. The concept of allowable doses to astronauts should be considered in a much more general sense than has been common in the past. As described by Kelton,[3] the level of risk acceptable for an astronaut due to radiation exposure should be assumed to be at least as great as that accepted by persons pursuing normal occupations. Also, the dose criteria should be expressed statistically, with corresponding levels of confidence that the chosen risk to the well being of the astronauts and to the performance of the space mission will not be exceeded. This approach to specifying allowable doses is consistent with the present statistical treatment of the SCR environment; it allows the total problem of SCR hazards to be handled in a self-consistent manner and in a manner consistent with conventional mission reliability considerations.

Because long-term predictions of SCR events cannot be made, an alternative approach to space vehicle shielding design must be used. Several studies have been conducted that statistically treat the SCR events observed during the maximum portion of the 19th solar cycle, 1956 to 1961, to predict the SCR fluences expected to be encountered in the future.[4-12] In spite of the fact that a statistical approach is the only objective way to predict events that cannot be predicted from a detailed knowledge of basic causal mechanisms, the application of the results of such studies has not been universally accepted. The major objections against using these statistical results arise from the limited sample of data available on past events. It should be remembered, however; that while some aspects of SCR events for which sufficient knowledge is not now available may become known during cycles 20, 21, and subsequent cycles; the important proton event parameters (i.e., fluence distribution, frequency of occurrence, and energy spectrum) will not be determined with significantly better statistical accuracy than is now available. Thus, the long-term SCR hazard predictions for the high confidence levels appropriate for mission planning cannot be expected to improve much until data from perhaps the next 50 or 100 years have been recorded. Clearly, a rational and consistent

* Work described here was conducted by the McDonnell Douglas Astronautics Company-West under the Independent Research and Development Account No. S. O. 81205-012.

approach to the evaluation of the SCR proton hazard to space travel is needed, not only before manned interplanetary systems have been designed and operated, but also before we can reasonably expect to actually observe the somewhat extreme SCR environments we must be prepared to encounter during long missions.

One primary purpose of this report is to evaluate the statistical approach to estimating the SCR radiation hazard, using presently available data. Previous studies will be discussed, with more recent event data in mind. A second objective is to present mission-integrated fluence and dose results corresponding to various levels of confidence that the design criteria will not be exceeded on missions of up to 3 years duration.

The results of previous statistical treatments can be classified into two groups, according to the maximum possible event fluence assumed: either (1) infinite, or (2) the largest event previously observed. Most of these studies have used a statistical sampling technique to determine the distribution of mission fluences or doses. If the predictions include only event fluence values from observed events, such as those of Webber, [4] the mission fluence probability decreases rapidly to zero for fluences larger than that of the largest event. This phenomenon is unrealistic, however, since no evidence exists that no events can occur larger than any yet observed, the period of observation having been approximately 15 years.

A more reasonable approach to accounting for as yet unobserved events is to extrapolate the observed probability distribution of event fluence to include larger events with small, but nonzero probability. The accuracy of this approach depends upon the strength of the observed distribution correlation. Such an extension of the observed event data was introduced by Modisette, et al., [5] using a normal distribution in the logarithm of fluence (log-normal). That work and the study of Synder [10] produce consistent predictions, although Modisette treats the distribution of fluences and Synder treats doses. The present calculations, involving the numerical integration of compound probabilities, will be shown to lead to predicted doses about a factor of 2 higher than either of those studies, mainly due to differences in the event fluence distributions used.

Data from 84 SCR events were used in this work, 74 of which occurred during periods of maximum solar activity. Except for predictable distortions at the extremes of the sample distribution, which are inherent in any finite size sample, the event fluences follow a log-normal distribution extremely well. Because of the strength of this correlation (i.e., every data point is consistent with the log-normal function) over more than three decades of event fluence, and because of the lack of contrary evidence, the log-normal distribution must reasonably be assumed to hold for future events, as well as for those previously observed.

The frequency of occurrence of SCR events is less certain than the fluence distribution. From the data of cycle 19 alone, an average of nine events per year were observed at solar maximum. However, cycle 19 was perhaps an unusually active cycle and, as estimated by Synder, [10] assuming cycle 19 to be the most active of 20 cycles, the average frequency might be closer to five per year. This value is consistent with the data now available for cycle 20. However, the significant point is that this variation in event frequency has only a slight effect on the predicted doses for the range of confidence levels of interest, since, as Synder points out, the doses corresponding to high confidence levels are dominated by the contribution of a single large event, rather than of numerous small events. The assumption that cycle 19 is the largest of 20 cycles results in a reduction of only 40 percent in predicted does for 1-year missions during cycle 19 to those during an average cycle of five events per year, for a confidence level of 99 percent.

A calculation of the SCR proton energy spectrum, by sampling from available event data, was included in this work. As one would expect for long missions, the calculated spectrum is very close to the average spectrum of all the events used. This results from the fact that a long mission involves a significant portion of the total time during which event data have been measured. The spectrum calculated for short missions at high confidence levels departs from the average at high energies. This deviation from an average spectrum results from the dominant contribution of the largest high energy SCR event observed. Hence, the amount of deviation depends on the particular event data sample presently available. For this reason, and because of the fact that the deviation in spectrum occurs only at energies too high to significantly affect the dose behind practical shield thicknesses, the average spectrum is assumed applicable, independent of mission length and confidence level. This generalization greatly simplifies the results and their application without introducing significant error.

The data discussed thus far; the SCR proton event fluence, frequency, and energy spectrum for events during solar maximum; have been determined well enough to make reliable predictions of mission fluence and dose for missions during solar maximum. The data for solar minimum events are much less certain, since only 10 events have been observed. Because the data sample is too limited to establish a general distribution, and because there is no evidence to the contrary, the variance of the event fluence distribution and the average energy spectrum were assumed equal to the values determined for solar maximum. Thus, only the mean event fluence and the event frequency were determined from the solar minimum data. Because the predicted mission hazard is sensitive to the event fluence distribution, the solar minimum results must be considered as rough estimates. The estimated hazard during solar minimum is less than that for solar maximum by factors of 10 or greater.

Alpha particles have sometimes been observed in appreciable numbers during SCR events. However, alpha particle data are available for only a few events. Webber [7] reports proton-to-alpha particle fluence ratios varying from 1 to 100. The energy spectrum of the alpha particles appears to follow an exponential rigidity spectrum with nearly the same rigidity parameter value as that of the protons. The data shown by Webber indicate that the large proton-to-alpha ratios are correlated with very large rigidity values. These data imply an average ratio between 1 and 2. The

alpha particle data do not appear to warrant a thorough analysis of that component of the radiation hazard at this time. It would appear that the best way to handle the SCR alpha hazard is to use the solar proton rigidity spectra and fluence data described here, and to relate it to the SCR alpha environment as an estimated proton-to-alpha ratio.

Solar Cosmic Ray Data

Proton fluences measured during SCR events during the 19th and 20th solar cycles were collected; the extensive tabulation of data presented by Weddell and Haffner [9] forms the major part of the data used. Only those values reported as measured data were used, the estimated numbers being disregarded. This source provided information on events between 23 February 1956 and 23 October 1962. Data on several other events were located in the tables published by Webber [8] and by Modisette, et al., [5] which referenced the work of Bailey. [13] The fluence values for the event of 12 November 1960 were taken from the detailed study of that event done by Masley and Goedeke. [14] Data for 20th cycle events from 1966 to 1969 were taken from the work of Masley, Goedeke, and Satterblom. [15, 16]

The event integral fluence data are given in Figure 1 for particles with energy greater than 10, 30, and 100 Mev. The integral energy spectrum for each event was assumed to follow an exponential in particle rigidity. This assumption of a rigidity parameter p_o is based on correlations originally done by Freier and Webber. [17]

The integral energy spectrum is given by

$$\phi\,(>E) \;=\; A\,\mathrm{Exp}\left[\frac{-p\,(E)}{p_o}\right] \qquad (1)$$

where the rigidity p(E) of a particle with charge ze, kinetic energy E, and rest mass energy $m_o c^2$, is the momentum per unit charge and is given by

$$p(E) \;=\; \frac{1}{ze}\,\sqrt{E\,(E + 2\,m_o c^2)} \qquad (2)$$

The constants A and p_o are also given in Figure 1. They were determined separately for energies above and below 30 Mev because p_o was found to be significantly less between 10 and 30 Mev than between 30 and 100 Mev.

The events occurring during the period of minimum solar activity, September 1961 through July 1966, are noted with asterisks in Figure 1. A marked reduction can be seen in both the size and frequency of events as opposed to the events during solar maximum.

The distribution of event fluence, integral above 30 Mev, was constructed for the events given in Figure 1 by arranging the events in the order of decreasing fluence. For several events for which the fluence above 30 Mev was not available, it was estimated using Equation (1) and the fluence above 10 Mev. For this calculation, a rigidity of 75 Mv was assumed. Events for which no data are available at either of these energies were disregarded. The resulting fluence probability distribution is presented in Figure 2 for solar maximum events.

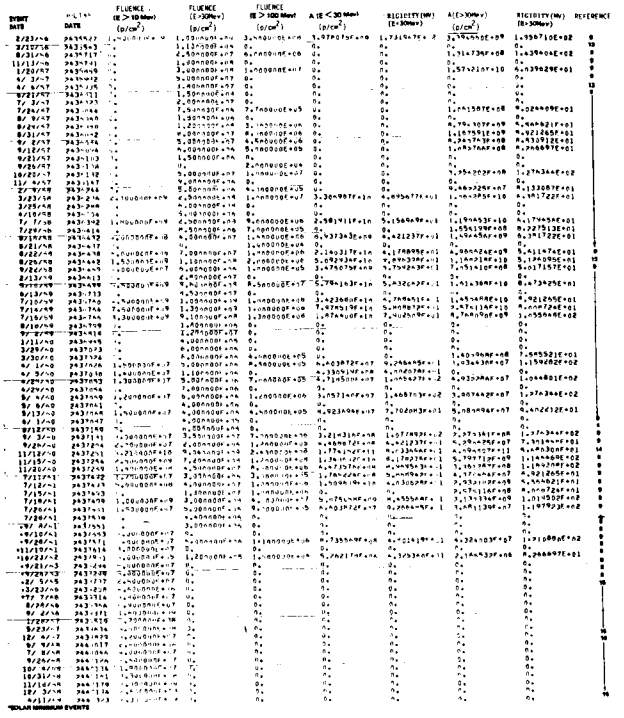

Figure 1. Basic Solar Cosmic Ray Proton Event Data

The distribution of solar maximum event fluences includes data from 72 events. Because of the finite number of data points, the distribution is necessarily distorted near both ends, including perhaps the last 5 or 10 percent of the events. The distortions manifested in the figures are typical of finite samples and do not indicate a deviation from the true distribution which has evidently reached equilibrium in Figure 2 between 10^7 and 10^9 protons/cm^2. In addition, the data for the smallest events are less reliable than for large events because it is more likely that small events occurred unrecorded before sufficiently sensitive instrumentation was available to detect them. Figure 2 exhibits these features, distorting the distribution from a log-normal, which it follows very well over two full decades in fluence, in the middle portion. Thus, there would appear to be little question about the degree of correlation when these factors are considered. The straight line shown in the figure is a log-normal distribution fit to the data points in the middle portion, between 6×10^6 and 1×10^9 protons/cm^2. For this distribution, the mean fluence is 2.7×10^7 protons/cm^2 and the variance is 1.32 in the logarithm, which corresponds to a standard deviation of a factor of 14 in fluence.

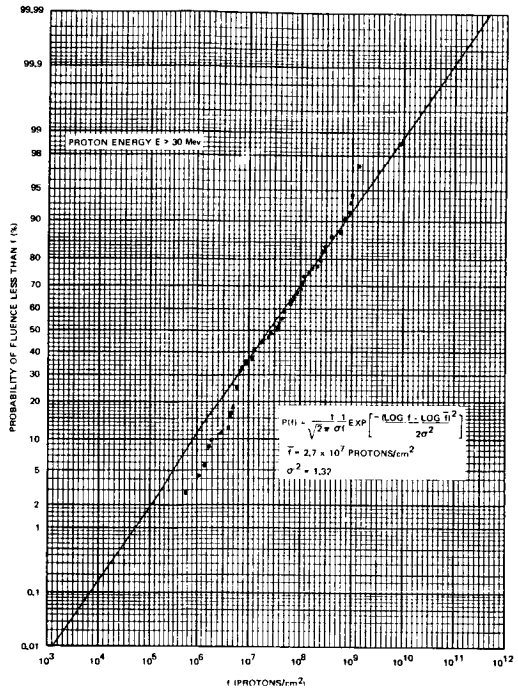

Figure 2. Distribution of Solar Cosmic Ray Proton Event Fluence During Solar Maximum

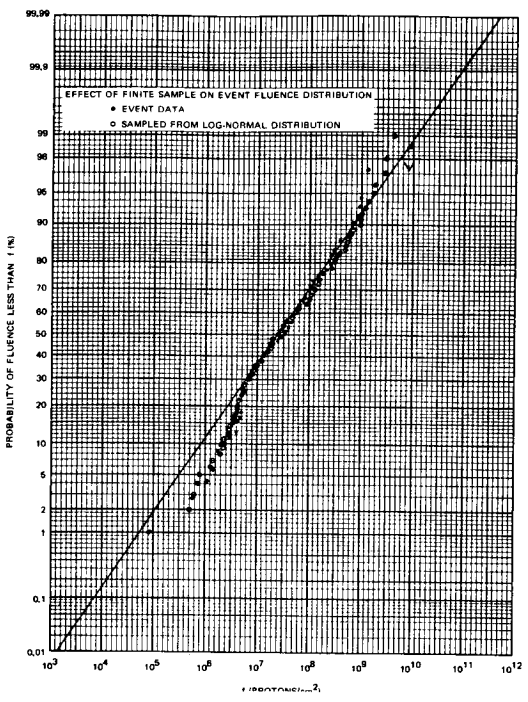

Figure 3. Effect of Finite Sample on Event Fluence Distribution

This variance is slightly larger than one would obtain if all the data points shown in Figure 2 were equally weighted in determining the log-normal fit, thus including the finite sample distortion in the fit. However, the difference in variances between the two possible log-normal distributions would lead to only a factor of 2 difference in fluence at a probability of 0.999. The detailed study by Masley and Goedeke of the 12 November 1960 event tends to support the larger variance, which was used in this study. This choice of variance is the source of the factor of two disagreement between the present results and those of Modisette, et al., and Snyder, as previously mentioned.

Figure 3 presents a clear demonstration of the distortions caused by the finite number of points in the event data sample. A similar number of fluence values were sampled randomly from this equilibrium log-normal distribution. These values, arranged by magnitude, are shown by the open circles plotted in Figure 3, which also shows the event data and the log-normal distribution previously shown in Figure 2. Clearly, the distortions in the sampled points occur at precisely the same fluence values and have the same magnitude as the distortions present in the SCR event data. Thus, the distortions in the observed event fluence distribution, which at first sight seem to indicate a failure of the log-normal distribution or to lead to large uncertainties in the proper value of the variance, are actually in agreement with the chosen equilibrium distribution.

Data from only 10 events are available to construct the distribution for solar minimum. For this reason, the derived parameters of the log-normal distribution are quite uncertain; therefore, since there is no known reason to assume otherwise, the variance is assumed equal to that for solar maximum. The mean fluence for solar minimum is 7.8×10^6 protons/cm^2.

The distribution of rigidity values, p_o, for the events of Figure 1 were constructed both for particles with energy below 30 Mev and for particles with energy above 30 Mev. The low-energy points were calculated from events for which integral fluences were available at 10 Mev and 30 Mev, and the high-energy points were calculated from data at 30 Mev and 100 Mev. Since spectral data were available for only two events, which occurred during solar minimum, no separate distribution could be constructed, and that of solar maximum is assumed to apply. The average values of the rigidity parameter p_o are 72.4 Mv below 30 Mev and 91.1 at higher energies.

Modisette, et al., found a uniform frequency of SCR event occurrence to correlate with the data of the maximum portion of cycle 19. The correlation of the data with smoothed sun-spot number, which might be a more intuitive frequency variation, was not better than with a constant frequency. Because of this result, the lack of additional data that would modify these conclusions, and the fact that Snyder showed that the results are insensitive to the event frequency, a step function was used to describe the event frequency. The average

frequency value for each half of the solar cycle was determined by the total number of events and total time span during which they were observed. The value for solar maximum is 0.0247 per day and for solar minimum, 0.00548 per day.

In summary, whatever fine structure that may exist in the periodicity of SCR proton events, the scatter of data does not allow a statistically significant resolution of them to be made. The only statistically significant frequency variation is the contrast between the average frequencies during solar maximum and solar minimum. To provide practical and reliable information in the context of mission planning, any predictable higher frequency modes must be defined rather precisely, although nothing is gained for them to be defined much more precisely than the gross parameters describing SCR activity. At this point the precision of the gross parameters (i. e., average frequency, fluence distribution, and spectral distribution) are limiting the accuracy of the predictions.

Method of Calculation

Many of the statistical studies of SCR proton dose done previously use some form of sampling from available event data. Because the calculations are restricted to tallying only from events actually observed since 1956, they are based on a small enough body of data that the upper limit in event size has almost certainly not been observed. The use of a log-normal distribution to extrapolate the mission fluence distribution removes this restriction to fluence values already observed and removes the distortions at the ends of the distribution, which are also caused by the finite sample. However, for missions longer than about 6 months, this procedure becomes uncertain because each mission history then includes a significant portion of the total number of data available, and the distorted ends of the distribution consequently tend to converge toward the center. For example, in the limit of an 8-year mission, there is only one mission history possible and therefore no distribution of fluence results. For this reason, an alternative technique, the compound probability method, was developed to calculate mission fluence distributions from the generalized log-normal event fluence distribution directly. Because relatively long missions are of primary interest, the energy spectrum to be encountered can be assumed equal to the average spectrum from all events, with a rigidity of 72.4 Mv at energies below 30 Mev and 91.1 Mv above that energy. The analysis is then performed for fluences with greater energy than 30 Mev. Data corresponding to any other energy may be readily calculated using the average spectrum.

Contributions to the mission fluence are separated according to the number of events occurring, m. The mission fluence probability distribution is given by a sum over these components.

$$P(<f,\ T) = \sum_{m=o}^{\infty} P_m(<f)\, P(m,\ T) \qquad (3)$$

The probability of encountering m events during a mission of duration T is given by the Poisson distribution as

$$P(m,\ T) = \frac{e^{-\omega T}(\omega T)^m}{m!} \qquad (4)$$

where ω is the average event frequency.

The probability that the total fluence summed over m events is less than f, $P_m(<f)$, is calculated from the distribution $P_1(<f)$, which is given in Figure 2. The probability density function g for a single event is obtained by differentiation.

$$g_1(f) = \frac{d}{df} P_1(<f) \qquad (5)$$

The density for the sum of two events is given by the product of the probabilities of single event fluence values, s and f-s, summed over all possible values of the intermediate variable s.

$$g_{2(f)} = \int_o^f ds\ g_1(s)\, g_1(f - s) \qquad (6)$$

The calculations are performed by doubling the orders of convolution

$$g_{2m(f)} = \int_o^f ds\ g_m(s)\, g_m(f - s) \qquad (7)$$

The integral distributions are then calculated from the density functions.

$$P_m(<f) = \int_o^f ds\ g_m(s) \qquad (8)$$

These distributions are interpolated to obtain probability values for all intermediate values of m at fixed fluence levels. The mission fluence distributions are then evaluated using Equation (3), obtaining for each fluence value the confidence level, or probability that the fluence will not be exceeded.

Fluence and Dose Probability Distributions

The results of the fluence probability distribution calculations for various mission lengths are presented in Figures 4 and 5, for solar maximum and solar minimum. These data represent the total probability, including missions during which no events occur. These distributions are recommended for use in determining the SCR proton fluence for mission planning.

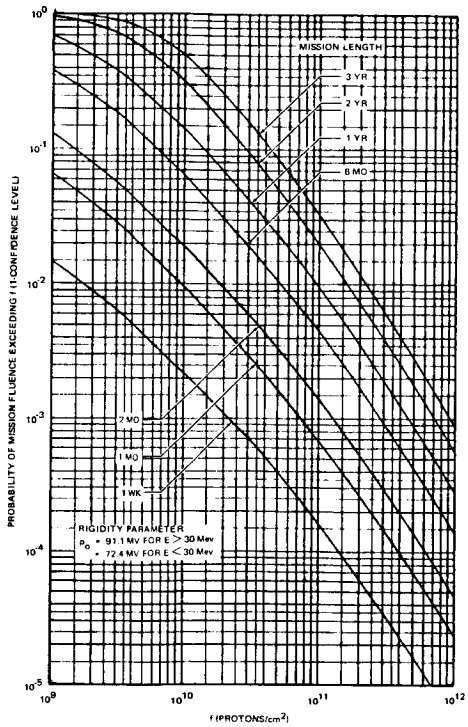

Figure 4. Fluence Distributions for Missions During Solar Maximum

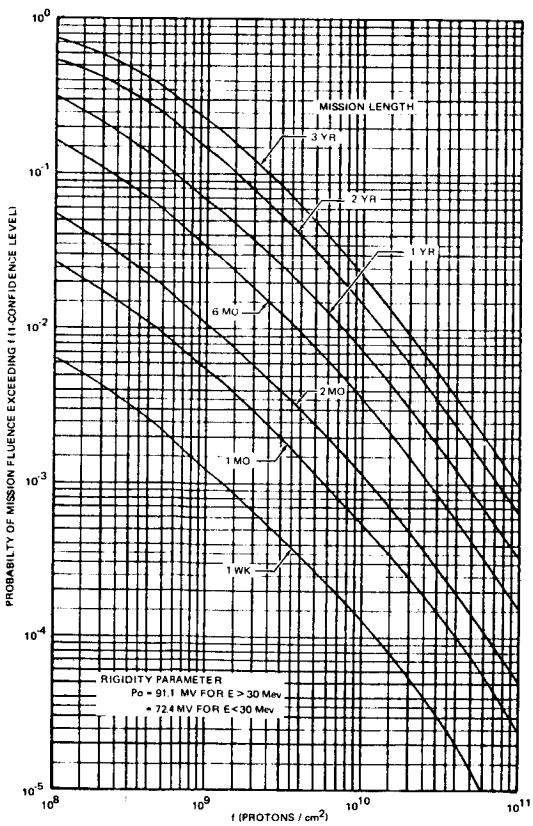

Figure 5. Fluence Distributions for Missions During Solar Minimum

The variation of these distributions with the average event frequency can be evaluated easily, since the product ωT, the average number of events during a mission, is the actual parameter used in the Poisson distribution, Equation (4). Figure 6 shows the fluence distribution for solar maximum as a function of ωT, for several levels of confidence. As discussed previously, the average event frequency has been estimated to be nine events per year (which was used in generating all data presented in this paper), or perhaps as low as five events per year. From the data given in Figure 6, this range of frequencies results in changes in the predicted fluence of less than a factor of 2 for mission durations greater than 6 months.

The dose corresponding to the fluence probability distributions was calculated as a function of aluminum shield thickness using the CHARGE code.[18] The dose curves presented are point doses to a water target at the center of a spherical aluminum shell of varying thickness. Because the proton energy spectrum has been assumed to have a shape independent of mission length, confidence level, and solar activity; all dose results can be scaled from a single calculation.

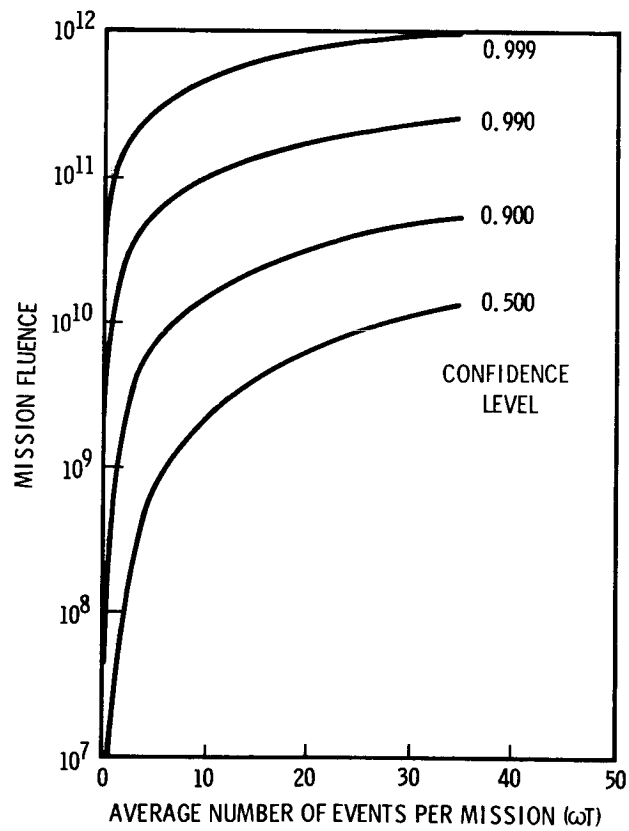

Figure 6. Combined Effect of Event Frequency and Mission Length on Mission Fluence

Figures 7 and 8 present the dose for 1-year missions as a function of shield thickness for several confidence levels, during solar maximum and solar minimum. Comparison of these two figures shows that the ratio of solar maximum dose to solar minimum dose varies with confidence level, from 10 at 0.999 to 70 at 0.500.

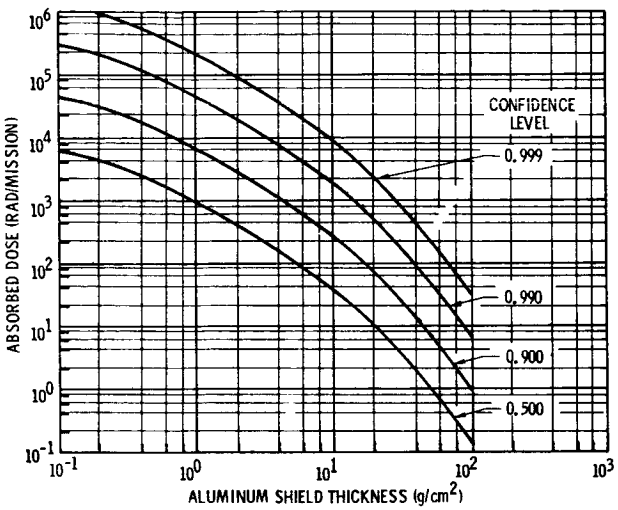

Figure 7. Solar Cosmic Ray Proton Dose for 1-Year Missions During Solar Maximum

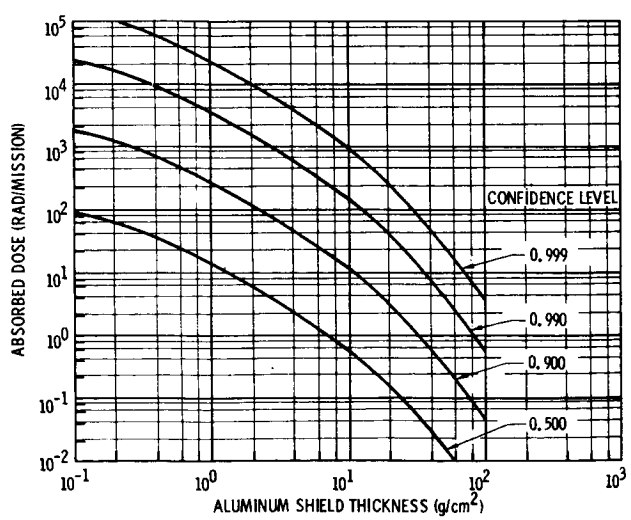

Figure 8. Solar Cosmic Ray Proton Dose for 1-Year Missions During Solar Minimum

The variations of dose with mission duration are presented in Figures 9 and 10 for solar maximum and solar minimum, respectively. These figures give the factor by which the 1-year dose must be multiplied to obtain the dose for any mission length up to 3 years. One set of curves describes each half of the solar cycle because of the single energy spectrum used. Over the range of mission durations shown, the difference between Figures 9 and 10 is only 30 percent or less. Therefore, because of the greater reliability of the solar maximum results, they can also be used for solar minimum, as a good approximation.

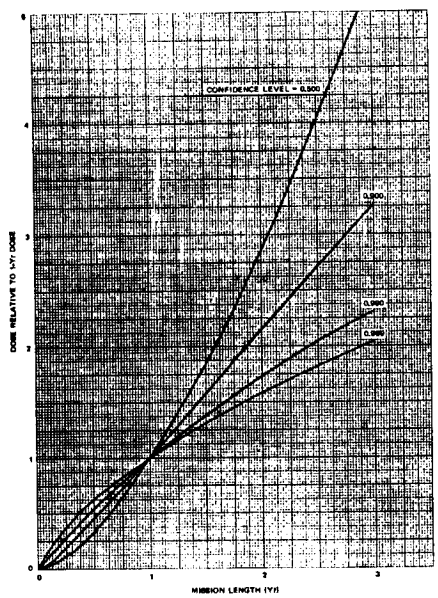

Figure 9. Variation of Solar Cosmic Ray Proton Dose with Mission Length for Solar Minimum Missions

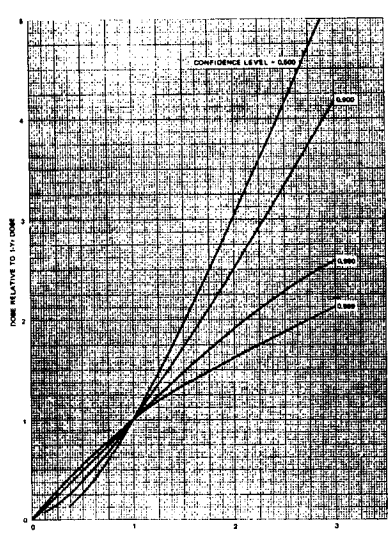

Figure 10. Variation of Solar Cosmic Ray Proton Dose with Mission Length for Solar Minimum Missions

The dose equivalent was also calculated as a function of aluminum shield thickness. The proton quality factors were taken from ICRP recommendations [19] and the dose conversion factors for the maximum neutron dose in a 30-cm slab of tissue were taken from Irving, et al. [20] and Zerby and Kinney. [21] Figure 11 presents the average quality factor, for the average SCR proton spectrum, as a function of shield thickness. The dose equivalent for various confidence levels for missions of varying length can be evaluated by using the data given in Figure 11, together with absorbed dose data presented previously.

Figure 12 presents the ratio of absorbed dose due to alpha particles to that due to protons, assuming a proton-to-alpha particle fluence ratio of unity. The alpha particle integral energy spectrum was assumed to follow an exponential in rigidity, with the same rigidity parameter as the proton spectrum, as reported by Webber. [4] The SCR alpha particle absorbed dose may be estimated using these data, the proton absorbed dose data previously presented, and an assumed proton-to-alpha particle fluence ratio. An estimate for the particle ratio was made using the distribution given by Hill, et al., [6]. Values between 1 and 2 were obtained, which indicate that the alpha particle dose is negligible in comparison with the proton dose for shield thicknesses greater than 5 g/cm^2.

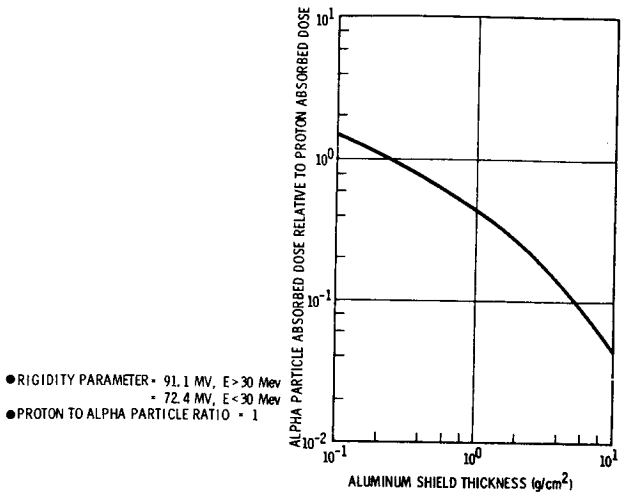

Figure 12. Ratio of Alpha Particle Dose to Proton Dose for Particle Ratio of Unity

Figure 13 shows a comparison of the results of the mission fluence distribution calculations with the results of previous studies. The present results give fluences larger than those of Modisette, et al., [5] by a factor of 2 over most of the range of probability. The results of Webber [4] are also in reasonable agreement with the present work for low confidence level values. However, at the high confidence level values of interest, the agreement is quite poor. The Webber study did not include an extrapolation to account for exceptionally large SCR events, and hence his results show a rapid increase of confidence level to unity, with a maximum event fluence of about 4 x 10^9 protons/cm^2.

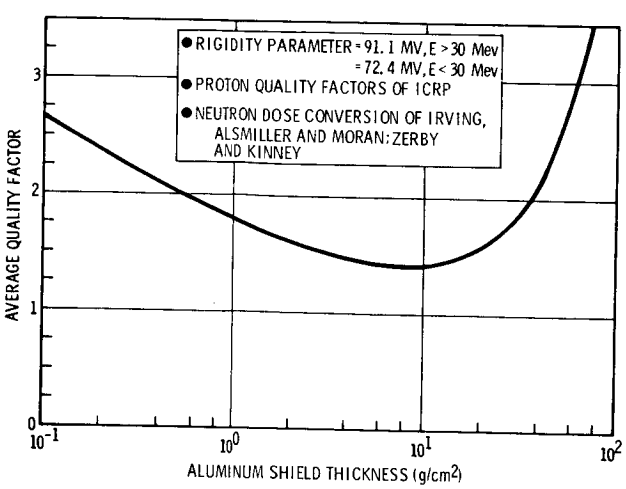

Figure 11. Average Quality Factor as a Function of Aluminum Shield Thickness

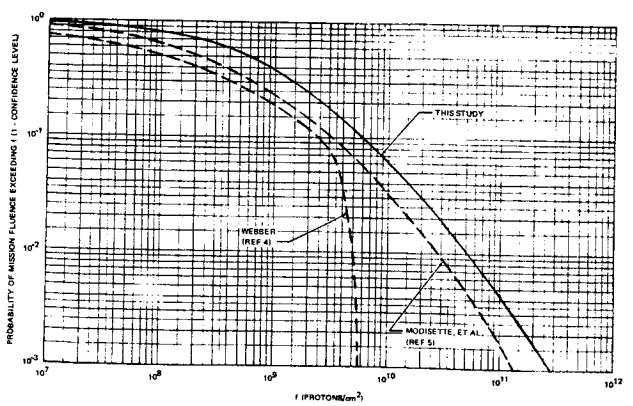

Figure 13. Comparison of Fluence Distributions for 6-Month Missions During Solar Maximum

Figure 14 shows a comparison of doses with results of Snyder[10] and Burrell, et al.,[12] for 1-year solar maximum missions and a confidence level of 0.900. The Snyder data were originally presented as dose equivalent, and were modified for purposes of this comparison using the quality factor data given in Figure 11. The Snyder dose is about a factor of 3 lower, as are the results of Burrell, et al., for shield thicknesses between 5 and 50 g/cm^2.

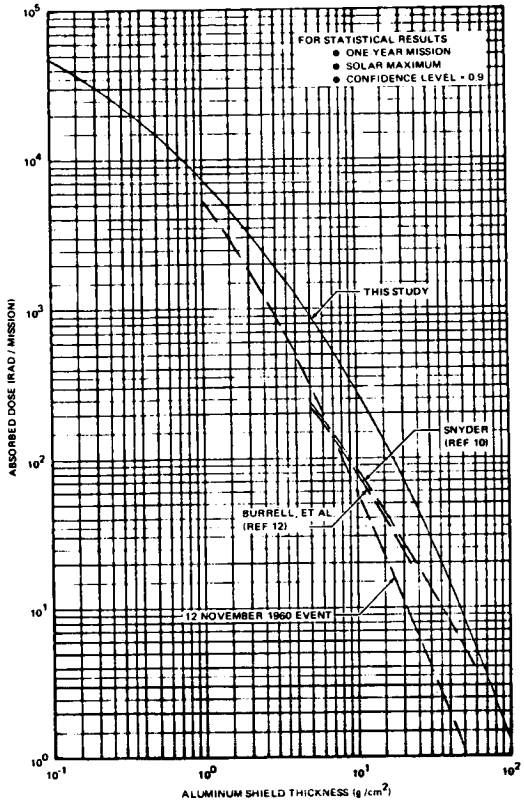

Figure 14. Comparison of Model Solar Cosmic Ray Event Doses

Figure 14 also shows the dose calculated from the largest SCR event available, that of 12 November 1960, as defined by Masley and Goedeke.[14] Dose criteria are sometimes applied using either the assumption that one large event such as this will occur per mission on short missions, or the assumption that such an event will occur with a given frequency (e.g., one per year). The figure demonstrates that such an approach has an associated confidence level of less than 0.900 for 1-year missions, and small shield thicknesses, which would increase for 30-day missions to almost 0.990. For 3-year missions, the confidence would decrease to almost 0.500. Because of the difference between the energy spectrum of the 12 November 1960 event and the average energy spectrum, these estimates are sensitive to shield thickness and the confidence would be much less at thicknesses greater than about 5 g/cm^2. Therefore, it would appear that using the statistical approach to evaluate shield requirements represents a considerable improvement over the use of a single large event, because of this large range of confidence levels associated with the single event. In fact, the degree of validity of the nonstatistical approach for a given set of conditions and assumptions, can be evaluated only by comparing it to the results of a consistent statistical analysis. There is no other known objective basis for comparison; thus, it would seem that there is little merit in this or similar nonstatistical approaches, at our present level of knowledge.

All data presented so far have been for free space (i.e., away from the influence of the geomagnetic field and mass of the earth) at one astronomical unit (AU) from the sun. In order to facilitate use of the results presented above for application to earth-orbit missions, a calculation was performed of the dose received in 200-nautical-mile circular orbits.

The orbit-averaged proton fluence was calculated from the free-space fluence presented above, for several values of orbit inclination, using the OGRE code.[22] These calculations include the reduction in fluence due to earth shadowing and the cutoff based on a detailed model of the geomagnetic field, including both the field during solar quiet, and the perturbation caused by a large SCR event. The cutoff data used are based on observations made during the 12 November 1960 event.[23] Including the geomagnetic field perturbation leads to significantly less overall reduction of the free-space proton fluence at moderate to high orbit inclinations than one corresponding to the unperturbed field during solar quiescence. Therefore the resulting dose values can be considered typical of situations involving large events (i.e., high confidence levels), but is conservative for smaller events.

The ratio of absorbed dose in orbit to that in free space is presented in Figure 15 for the solar quiet field and Figure 16 for the perturbed field, as a function of shield thickness. Because the geomagnetic field and earth shadowing effects vary slowly with altitude, these data are applicable for orbits of up to several hundred nautical miles. Since a single energy spectrum is assumed, independent of mission duration and confidence level, only a single calculation of orbit-averaged fluence is necessary for each orbit inclination.

Conclusions

Solar cosmic ray proton fluence and dose have been determined statistically from the event data available from cycles 19 and 20 (1956 to 1969). For a mission of specified duration occuring in free space near one astronomical unit from the sun, the fluences corresponding to various confidence levels have been presented. Also, corresponding dose data have been presented that allow estimating free-space and low earth-orbit shielding requirements needed to meet a specified mission dose criterion. These data are recommended as a consistent and rational approach to mission planning from the standpoint of solar cosmic ray hazards.

While the number of SCR events for which data are available is not large, enough data are available so that many conclusions about the SCR environments for future space missions can be drawn with reasonable confidence. The event

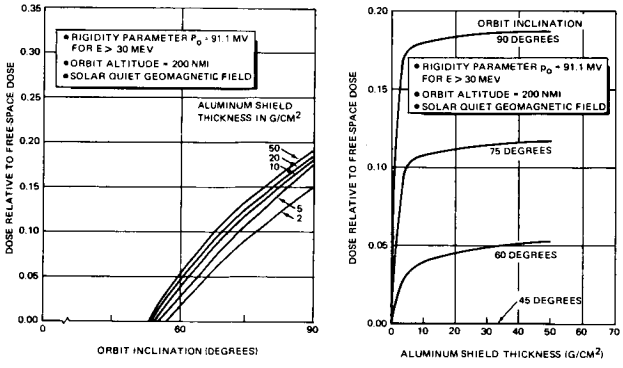

Figure 15. Variation of Solar Cosmic Ray Proton Dose with Aluminum Shield Thickness and Circular Inclination for Solar Quiet

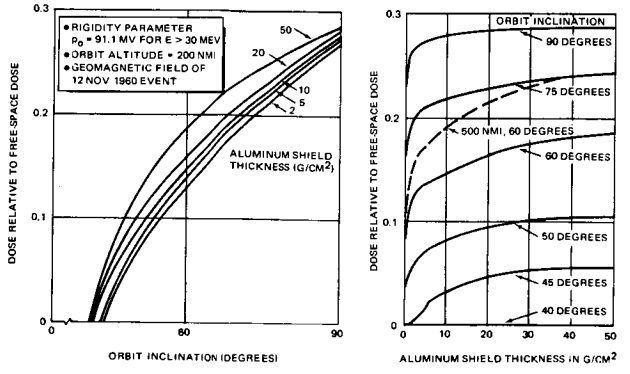

Figure 16. Variation of Solar Cosmic Ray Proton Dose with Aluminum Shield Thickness and Circular Orbit Inclination for Solar Active

fluence probability distribution and event frequency during solar maximum are determined reasonably well; their statistical quality is not likely to change for some time because of the weight of additional observations necessary to effect a significant change. The variance of the fluence distribution could be taken as slightly smaller than that used, if the data from all events were given equal weight, rather than ignoring the characteristic finite-sample tails of the observed distribution. However, this would only reduce the mission fluence by a factor of 2 for a confidence level of 0.999, which the comparisons show would lead to results nearly equal to those of Modisette, et al., and Snyder. The relatively large intensity from Masley and Goedeke analysis of the 12 November 1960 event tends to support the larger variance used.

The event frequency of 0.0247 per day may be larger than typical future values, since cycle 19 was apparently an unusually active cycle. Just how unusual it is cannot be established at this time; the correlation of SCR intensity and sunspot number is too weak to provide reliable information.(19) The data from cycle 20 alone give 0.0137 per day, or an average of five events per year. This value was arrived at by Snyder, using a binominal distribution and assuming cycle 19 to be the most active of 20 cycles (as would be indicated by average sunspot number alone). However, it has been shown in this study that the results are not sensitive to a change in frequency, because the mission fluence and dose are dominated by the contribution of a single large event. For example, the effect of the reduction in event frequency from 0.0247 to 0.0137 per day produces only about a 40 percent reduction in dose at a confidence level of 0.999 for 1-year missions.

While the fluence distribution and event frequency are quite uncertain for solar minimum, similar statistical analyses were performed as for solar maximum. However, because of the relative uncertainty in the solar minimum results, and their similarity to those for solar maximum, a justifiable approximation for mission planning is to use the solar maximum data for solar minimum with the fluences and doses reduced by a factor of 10. Similarly, the SCR alpha particle environment can be approximated by assuming Figures 4 and 5 to apply for a proton-to-alpha ratio of 1 to 2, and assuming the rigidity spectrum to be the same for alpha particles as for protons. The alpha particle dose will be negligible compared to proton dose, for shield thicknesses greater than 5 g/cm^2.

The statistical approach to the evaluation of the solar cosmic ray hazard represents a significant improvement over the use of a single model event. As demonstrated in this study, the assumption that one large event such as the one observed on 12 November 1960 will occur on a 1-year mission during solar maximum has an associated confidence level of less than 0.9 for small shield thicknesses, decreasing to almost 0.5 at 10 to 20 g/cm^2 of aluminum. For longer missions, the

confidence level decreases further. There is, in fact, little reason to use any nonstatiscal approach, since the only means available to evaluate the validity of such treatments for a given set of mission conditions is to compare it with the results of a consistent statistical analysis.

References

1. "Ionospheric Forecasting," NATO Advisory Group for Aerospace Research and Development, AGARD CP 49, January 1970.

2. Baker, M. B., R. E. Santina and A. J. Masley, "Modeling of Solar Cosmic Ray Events Based on Recent Observations", AIAA Journal, 7, 2105, November 1969.

3. Kelton, A. A., "Radiation Guidelines for Manned Space Vehicles—A Review with Recommendations," Douglas Aircraft Company, SM-47749, July 1965.

4. Webber, W. R., "An Evaluation of the Radiation Hazard Due to Solar Particle Events," The Boeing Company, D2-90469, December 1963.

5. Modisette, J. L., T. M. Vinson, and A. C. Hardy, "Model Solar Proton Environments for Manned Spacecraft Design," Manned Spacecraft Center, NASA TN D-2746, April 1965.

6. Hill, C. W., W. B. Ritchie, and K. M. Simpson, Jr., "Data Compilation and Evaluation of Space Shielding Problems: Radiation Hazards in Space," Lockheed Nuclear Products, ER 7777, Volume III, April 1966.

7. Roberts, W. T., "Probabilities of Solar Flare Occurrence," NASA TM X-53463, May 1966.

8. Webber, W. R., "An Evaluation of Solar-Cosmic-Ray Events During Solar Minimum," The Boeing Company, D2-84274-1, June 1966.

9. Weddell, J. B., and J. W. Haffner, "Statistical Evaluation of Proton Radiation from Solar Flares," North American Aviation, SID 66-421, July 1966.

10. Snyder, J. W., "Radiation Hazard to Man from Solar Proton Events", Journal of Spacecraft and Rockets, 4, 826, June 1967.

11. Lahti, G. P., I. M. Karp, and B. M. Rosenbaum, "McFLARE, A Monte Carlo Code to Simulate Solar Flare Events and Estimate Probable Doses Encountered on Interplanetary Missions," Lewis Research Center, NASA TN D-4311, February 1968.

12. Burrell, M. O., J. J. Wright, and J. W. Watts, "An Analysis of Energetic Space Radiation and Dose Rates," George C. Marshall Space Flight Center, NASA TN D-4404, February 1968.

13. Bailey, D. K., "The Detection and Study of Solar Cosmic Rays by Radio Techniques", J. Phys. Soc. Japan, 17, Supp. AI, Part I, 106, 1962.

14. Masley, A. J. and A. D. Goedeke, "A Complete Dose Analysis of the November 12, 1960 Solar Cosmic Ray Event", Life Science and Research, North Holland Publishing Company, 1963.

15. Masley, A. J. and A. D. Goedeke, "1966-67 Increase in Solar Cosmic Ray Activity", Can. Journal of Phys., 46, 1968.

16. Masley, A. J. and P. R. Satterblom, "A Discussion of Solar Cosmic Ray Activity Near Sunspot Minimum", Proceedings of the 11th International Conference on Cosmic Rays, Budapest, Hungary; McDonnell Douglas Astronautics Company, MDAC Paper WD-1070, November 1969.

17. Frier, P. S. and W. R. Webber, J. Geophys. Res., 68, 1605, 1963.

18. Yucker, W. R. and J. R. Lilley, "CHARGE Code for Space Radiation Shielding Analysis," McDonnell Douglas Astronautics Company, DAC-62231, April 1969.

19. "Permissible Dose from External Sources of Ionizing Radiation", NBS Handbook 59, 1954.

20. Irving, D. C., R. G. Alsmiller, Jr., and H. S. Moran, "Tissue Current-to-Dose Conversion Factors for Neutrons with Energies from 0.5 to 60 Mev," ORNL-4032, 1967.

21. Zerby, C. D. and W. E. Kinney, "Calculated Tissue Current-to-Dose Conversion Factors for Nucleons Below 400 Mev", Nuclear Instruments and Methods, 36, 125, 1965.

22. Baker, M. B., "Geomagnetically Trapped Radiation," Douglas Aircraft Company, SM-47635, October 1964.

23. Baker, M. B., "Geomagnetically Trapped Radiation", AIAA Journal, 3, 9, 1965.

SHORT TERM PREDICTION OF E≥10 MeV PROTON FLUXES FROM SOLAR FLARES

George A. Kuck, Capt, USAF

AIR FORCE WEAPONS LABORATORY

One problem facing the Aerospace Environmental Support Center (Det 1, 4th WW, AWS) is the prediction of ionospheric effects related to energetic proton emissions from the sun. The intensity and duration of these charged particle emissions are related to the optical, radio, and X-ray emissions from the solar flares. Radio and X-ray data give an important indication of proton production. Cm radio bursts with a high flux density and a slope reflecting greater flux values at higher frequencies are often proton productive. Examination of the data summaries has shown that the meter classification of flares as type II or type IV, even though qualitative, should be used in conjunction with the cm radio criteria. The peak intensity of the proton flux $E \geq 10$ meV correlates better with the integrated 1 to 8 Å X-ray bursts than with the integrated cm radio bursts, peak cm radio flux, or peak X-ray flux. Free-free transition theory was used to relate the X-ray flux. Free-free transition theory was used to relate the X-ray intensities recorded by different satellites with the peak proton fluxes observed at the earth.

Both the anisotropic and isotropic diffusion theories could be used to extrapolate proton fluxes for $E \geq 10$ meV for over 50% of the particle events. The isotropic diffusion theory uses a diffusion coefficient.

$$D = Mr^{\beta}$$

It was found that M and β tended to be functions of flare position on the solar disk.

A measurement of the interplanetary flux in near earth space gives a good indication of the polar cap fluxes. It was found that the 30 MHz absorption over the poles during a PCA is proportional to the square root of the integral proton flux $E \geq 11$ meV in interplanetary space.

$$J = KA^2$$

with $K = 8 \pm 2$ and J in protons/cm^2-sec-ster.

Without the moral support of the personnel assigned to the Solar Forecast Center and the Solar Forecast Facility, this report could not have been written. My thanks go to Mr. Ray Cormier of Air Force Cambridge Research Laboratories for allowing me to use his riometer data. The Vela X-ray data were kindly supplied by Dr. Kunz, Dr. Conner, and Dr. Bame of Los Alamos Scientific Laboratories. The author is solely responsible for the opinions and material presented in this report. The consent of the above-mentioned scientists to use their data does not necessarily imply their agreement with the results.

I. Introduction

One problem facing the Air Weather Service Solar Forecast Center is the prediction of ionospheric effects related to energetic proton emissions from the sun. The intensity, and duration of these charged particle emissions are related to the optical, radio, and X-ray emissions from the solar flares. Data summaries appearing in pre-published form, such as the Explorer 34 proton results in the Solar-Geophysical Data bulletins published by ESSA (ref. 1) and the Geophysics and Space Data Bulletin by AFCRL (ref. 2), have allowed the evaluation of many important parameters.

The work reported in the paper was done for an operational unit. Therefore,

the data base available to the operational solar forecaster was used. This was not the most precise data base available. Several simplifying assumptions had to be made which will become apparent in this paper. Nevertheless, the results clearly indicate that short-term proton event predictions are possible and indicate certain limitations on several current theories.

An interdisciplinary approach to PCA prediction and ionospheric forecasting allows some effects to be calculated from first principles shortly after the optical flare occurs. Solar radio and X-ray burst observations are useful in determining if protons were actually produced during the flare. These bursts also give an indication of the number of protons produced. The position of the flare on the solar disk and the solar wind velocity can be used to indicate the risetime and the peak intensity of the event in the near earth space. Using the first few proton data points, the proton intensities can be extrapolated into the future. Ground-based magnetic measurements can then be used to indicate the spatial extent of the precipitation and its uniformity. Satellite data and real time magnetic measurements can be used to update the forecasts during the event. On the basis of the extrapolated fluxes, the next step is to calculate the ionization caused by the protons using an atmospheric model and a two-ion D-region model for PCA events to obtain the electron profiles. Finally, the absorption on vertical and oblique paths can be calculated for high-frequency communication systems across the polar regions. Real time satellite and riometer measurements can be used to verify the prediction.

This paper covers several of the different phases of PCA prediction. First, the X-ray characteristics of proton producing flares are examined. Then the two theories relating to particle propagation in the interplanetary medium are investigated for their applicability. Finally, the relationships between 30 MHz riometer absorption and the exospheric proton flux are discussed. The problem of electron profiles and oblique absorption will not be covered in this report. The radio characteristics of the flare and the spatial extent of the polar cap absorption event will not be covered because they have been discussed previously (ref. 3).

II. General Discussion

In order to meaningfully predict proton fluxes at the earth before the arrival of large numbers of protons, one must use the electromagnetic characteristics of the parent flare. The simplest set of assumptions one can make about the peak proton fluxes are that (1) the peak flux is proportional to the number of particles accelerated by the parent flare, N, and (2) the transport of the particles to the earth is influenced by the interplanetary medium, P. Thus, the flux, J is just

$$J \propto N\,P \qquad (1)$$

This paper presents some experimental determinations of N and P. The actual prediction of proton production has been previously published (ref. 3).

III. Proton Acceleration and X-Radiation Flux

There are several methods of determining N, such as integrated or peak radio intensity, H-α flare classification, and integrated or peak X-ray intensity. Of these, the integrated X-ray intensity seems to be the best quantitative measure of proton acceleration. If the number of electrons accelerated during the flare is proportional to the number of protons accelerated, and if the intensity of X rays in some wavelength band is proportional to the number of electrons being accelerated, then the integrated intensity of X-radiation in that band ought to be proportional to the number of protons accelerated. For simplicity, it was assumed that the X-ray bursts had exponential rise and exponential decay time. Then

$$I_{int} = \int_{-\infty}^{o} I_{max} \exp\,(t/t_r)dt + \int_{o}^{\infty} I_{max} \exp\,(-t/t_d)dt \qquad (2)$$

$$I_{int} = I_{max}\,(t_r + t_d) \qquad (3)$$

where t_r and t_d are the exponential rise and decay times, I_{max} is the maximum X-ray intensity, and I_{int} is the integrated X-ray intensity. The use of such a simple relationship allows a forecaster to make predictions with minimum information.

The largest, most consistent X-ray data base available is the Vela X-ray data (refs. 5, 6). The 0.5 to 5 Å X-ray data were integrated using equation (3). The result of plotting the integrated X-ray intensity versus the peak 10-meV proton fluxes observed by IMP F (Explorer 33) is given in figure 1 (ref. 1). Even though these points are not corrected for propagation through the interplanetary space, the correlation is striking.

One must generalize these results shown in figure 1, to those obtainable from different sensors. This was a problem since the integrated X-ray flux presented in figure 1 was a measure of the flux deposited inside the detector after transmission through detector windows. The most commonly used assumption when determining the flux incident on an X-ray detector is that the photon spectrum is a blackbody Planckian spectrum of the form

$$W(\lambda,T)d\lambda \propto \frac{8\pi hc}{\lambda^5}\,\frac{d\lambda}{e^{hc/\lambda kT}-1}$$

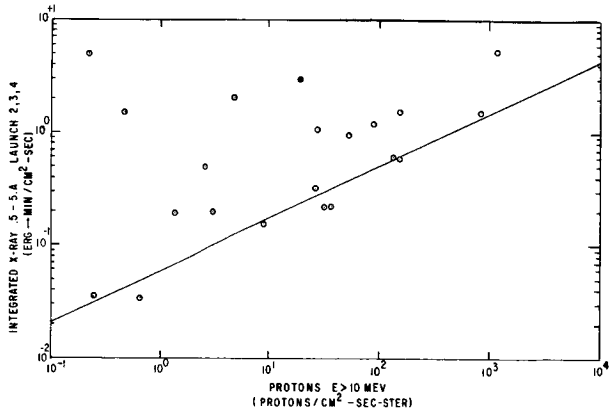

Figure 1. Integrated X-ray flux deposited in 0.5 to 5.0 Å Vela launch 2, 3, 4 detectors vs. peak proton flux (E ≥ 10 meV protons/cm^2-sec-ster). Propagation factors have not been removed.

In order to compare the data obtained from different satellites, this spectral form was folded into the different detector responses as a function of solar flare temperature. When this form was used, different detectors did not give consistent results. Figure 2 shows the flare

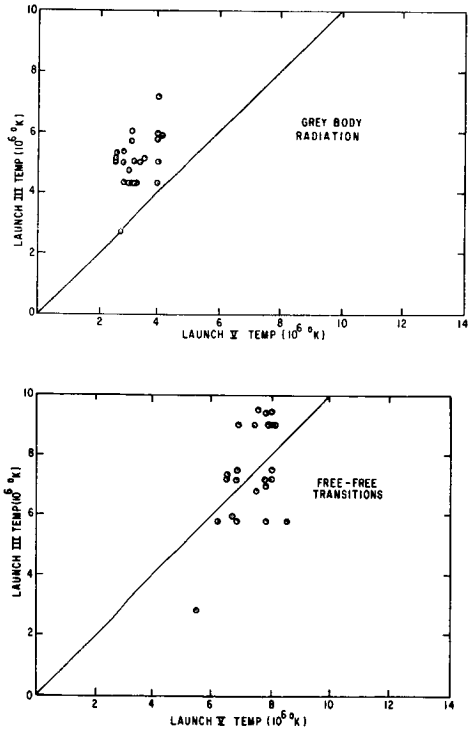

Figure 2. Solar flare temperature Vela launch 2, 3, 4 vs. solar falre temperature Vela launch 5. Figure 2a is the grey body assumption while figure 2b is the free-free transition assumption.

temperatures determined by two different methods from two distinctly different sets of satellite instrumentation. Note that the grey body assumption (fig. 2a) does not fit the data accurately. Furthermore, when the grey body assumption was employed the correlation between the 1 to 8 Å integrated X-ray flux and the peak proton flux disappeared.

The functional form of the X-ray energy spectrum which allowed the correlation between the 1 to 8 Å X-ray flux and the peak proton flux to remain and which better correlated the solar flare temperatures given in figure 2b was

$$W(\lambda,T)\,d\lambda \propto \frac{d\lambda}{\lambda^2\, e^{-hc/\lambda kT}}$$

This is the functional form obtained by assuming the X rays are produced by a Maxwellian distribution of electrons undergoing free-free transitions (i.e., bremsstrahlung) (ref. 7, 8). This assumption allowed the peak proton flux to be correlated with the 1 to 8 A X-ray flux, which is given in figure 3. Not enough data have been published at the present time to

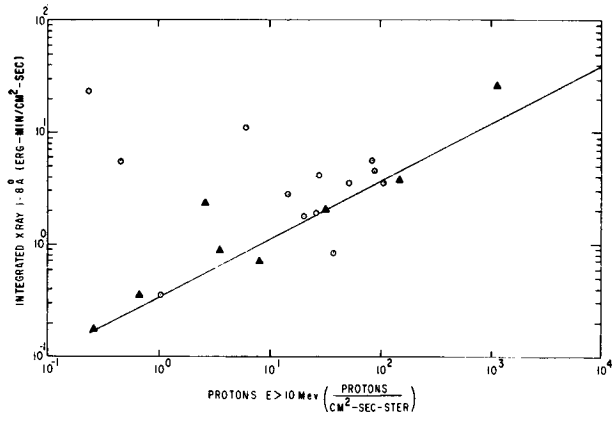

Figure 3. Integrated X-ray flux incident on a detector in the 1 to 8 Å band vs. proton flux E ≥ 10 meV. Points were derived from figure 1 using the free-free transition assumption. Triangle points were derived assuming the average proton flare temperature of 7×10^6 °K.

allow the complete verification of this analysis. However, the few points which have been obtained from Explorer 44 are presented in figure 1, but the scatter is well within that expected. The average solar flare temperature for the proton producing flares was 7×10^6 °K. This temperature was obtained from the Vela launch 2, 3, 4 sensors using free-free transition theory.

IV. Arrival of Protons

There are two theoretical frameworks within which the proton observations could be analyzed. The first is the anisotropic diffusion with boundary theoretical framework (ADB) of Burlaga (ref. 9), while the second is the isotropic diffusion theoretical framework (refs. 10, 11). Both theories have definite shortcomings. These shortcomings are illustrated in figure 4. If the theoretical models were adequate at 10 meV, one would expect systematic trends when plotting the proton risetimes against the 1/e decay times. The scatter in this diagram illustrates the problems involved in attempting to fit the experimental data. Similar plots for E > 30 and E > 60 meV protons do show more systematic results.

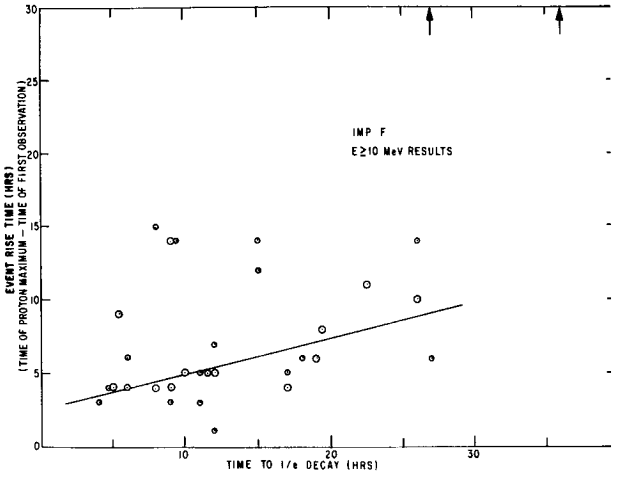

Figure 4. The time in hours it took 10-meV protons to peak as a function of the time it took for the protons to reach 1/e of their maximum value.

The anisotropic diffusion with boundary (ADB) theory assumes that the interplanetary magnetic field lines between the sun and the earth are spirals with irregularities which can effectively scatter the solar protons. The solar proton flux in this theory will be anisotropic and the flux will be greatest in the direction of the field. Beyond 1 A.U., the scattering centers change so that protons cannot be scattered back into the diffusing region once they have reached the transition region. Thus, in this model, it is assumed that there is an absorbing boundary at some heliocentric distance greater than 1 A.U. Since systematic trends did not appear in applying this theory, and since this theory has been discussed in detail (ref. 3), it will not be examined in any more detail in this paper.

One can also analyze each proton event in terms of the isotropic diffusion theory (refs. 10, 11). In this theory, the diffusion coefficient, D, is given by

$$D = Mr^{\beta} \qquad (4)$$

where r is the heliocentric radial distance in A.U., and M and β are parameters which may and often do depend upon the particle energy E. The units of $Mr^{\beta-2}$ are $(\text{hours})^{-1}$. Krimigis shows that for E < 50 meV, the parameter M does depend upon the proton energy. Thus, if one wants the time behavior for 10 meV protons, one must use a data base of 10 meV.

It can be shown that

$$t_{max} = \frac{1}{3M} \frac{r^{2-\beta}}{(2-\beta)} \qquad (5)$$

where M and β are the coefficients given in equation (2) and t_{max} is the time it takes for the protons to reach maximum intensity. Since t_{max} does depend upon the solar flare heliographic longitude, it is possible to empirically determine M and β as a function of solar flare position even though such an assumption violates the basic theoretical considerations.

Approximately 80% of the observed events could be analyzed within the isotropic diffusion framework. Figure 5 shows one of these events. This figure also shows that there is an area of agreement between the ADB theory and the isotropic diffusion theory. A certain amount of judgment was necessary in determining β from the graphs of 1/t vs. ln $It^{(3/2-\beta)}$ because of poor time resolution and uncertainties in count rates and particle backgrounds. This event also illustrates what happens when a proton event has considerable structure. Many events showed the characteristic hook at small values of 1/t. The value of β used was that value which best fit the first several values of 1/t and which also adequately fit the long time behavior at small values of 1/t.

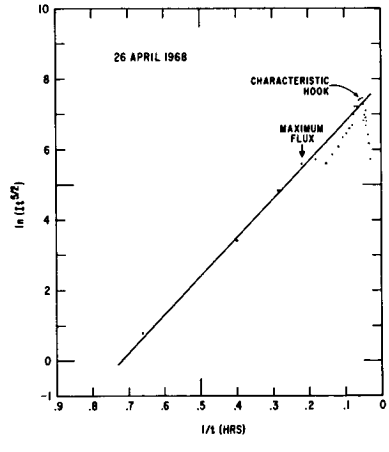

Figure 5. Intensity-time profile during 26 April 1968 event for protons E > 10 meV measured by Explorer 34. This event had considerable structure.

Figure 6 gives scatter plots of β and M as a function of Θ for 10 and 30 meV protons as a function of flare position. The Θ was determined in the ADB theoretical framework (ref. 9). Several features do stand out. The low values of β and M for Θ less than 0.25 radian are probably due to the diffusion being one or two dimensional instead of three dimensional as assumed in this analysis. There does seem to be a trend as a function of Θ for Θ > 0.5 radian. Although there is a large amount of scatter, the higher energy particles tend to have larger values of M and β than the lower energy particles.

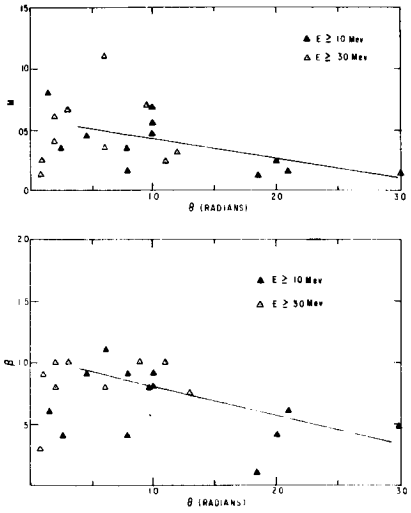

Figure 6. The diffusion coefficients, M and β as a function of flare position and the Earth-Sun Archimedes spiral angle Θ. The higher energy particles tend to have higher values of M and β.

These results can be refined. Better time resolution will lead to less scatter in the data. The better the time resolution, the easier it was to determine M and β. Data for larger values of Θ have not yet become available with the necessary count rate accuracy or time resolution.

V. Riometer Absorption

Once one has predicted the intensity of protons in interplanetary space, one can predict an upper limit to the vertical 30 MHz riometer absorption.

On the basis of theoretical calculations (ref. 12), it can be concluded that the 30 MHz riometer absorption is proportional to the square root of the incident integral particle flux for E ≥ 11 meV (ref. 13). An analysis of the Explorer 34 and Thule riometer data has helped confirm this result.

$$J = KA^2$$

where J is the flux in protons/cm -sec-ster, and A is the absorption in db of the 30 MHz riometer.

The Explorer 34 data and Thule riometer data have been examined. Figure 7 is a plot of the results for 10-meV particles One notes that these 10-meV particles scatter about the line of slope 0.5. The points tend to fall below the line at high absorption values and above the line at low absorption values. When the E ≥ 20 meV flux is plotted as the abscissa, the points at low absorption tend to fall below the line while those at high values tend to fall above the line. Thus, the square root of the absorption is directly proportional to the integral flux somewhere between 10 and 20 meV. Within the limitations of this analysis, therefore, the integral flux for E ≥ 11 meV is an experimentally verified conclusion. The constant of proportionality, K, from this curve is

$$K = 8 \pm 2$$

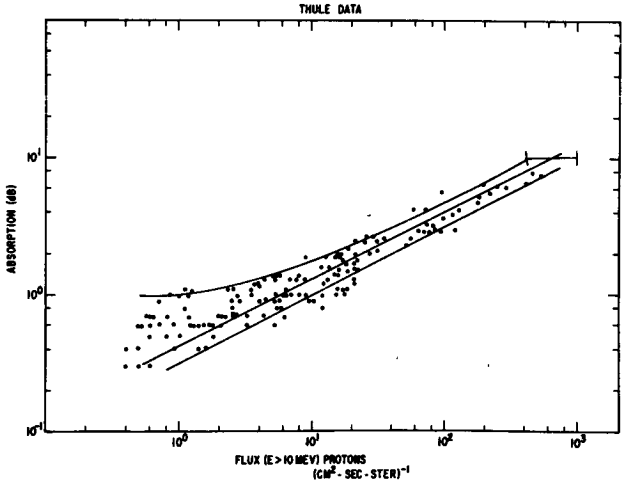

Figure 7. Riometer absorption at Thule as a function of the interplanetary proton flux (E ≥ 10 meV protons/cm²-sec-ster). If the square of the riometer absorption were proportional to the flux, the points would fall on the straight line.

VI. Summary

An interdisciplinary approach to proton event prediction allows some effects to be calculated from first principles shortly after the optical flare occurs. Solar X-ray burst characteristics are useful in determining if protons were produced in sufficient quantity to give riometer absorption. The position of the flare on the solar disk and the solar wind velocity can be used to indicate the rise-time and peak intensity of the event in near earth space. Using the first few proton data points, the proton intensities can be extrapolated into the future using previously derived values for the proton diffusion coefficients given in figure 6. Satellite data can be used to update the predictions during the event by extrapolating the fluxes as a function of time. Experimental measurements have verified some of the assumptions and theoretical predictions for 30 MHz riometer absorption. Thus, the satellite measurements can be employed to specify and predict proton fluxes and radio absorption. The approach taken in this report can be continued to give better predictions once more data become available.

REFERENCES

1. ESSA Research Laboratories: "Solar Geophysical Data," *IER-FB-281 to IER-FB-295*, 1967-1968.

2. Carrigan, A. L.; and Oliver, N. J.: Geophysics and Space Data Bulletin, IV-VI, Air Force Cambridge Research Laboratories, 1967-1968.

3. Kuck, George A.: "Proton Events in 1967-1968," *Ionospheric Forecasting, AGARD Conference Proceedings No. 49*, Vaughn Agy, Editor, Paper #9, January 1970.

4. Singer, S.: "The Vela Satellite Program for Detection of High-Altitude Nuclear Detonations," *Proc. IEE, 53, 1935*, 1965. (Also, private communications.)

5. Conner, J. P.: Private communication, Los Alamos Scientific Laboratories.

6. Blocker, N.B.; Fehlau, *et al., Vela V and VI Solar X-Ray Atlas*, Los Alamos Scientific Laboratories Document LA-4454, Vols. I, II, and other volumes in preparation.

7. Zel'dovich, Va. B.; Raizer, Yu. P.: *Physics of Shock Waves and High Temperature Hydrodynamic Phenomena*, Academic Press, N.Y., and London, 1966, Vol. 1.

8. Neupert, W. M.: "X Rays from the Sun," in *Annual Review of Astronomy and Astrophysics*, Vol 7, p. 121.

9. Burlaga, L. F.: "Anisotropic Diffusion of Solar Cosmic Rays," *J. Geophys. Res. Vol. 72*, 4449, 1967.

10. Parker, E. N.: *Interplanetary Dynamical Processes*, Interscience Publishers, New York, 1963.

11. Krimigis, S. M.: "Interplanetary Diffusion Model for the Time Behavior of Intensity in a Solar Cosmic Ray Event," *J. Geophys. Res., Vol. 70*, 2943, 1965.

12. Adams, G. W.; Masley, A. J.: "Theoretical Study of Cosmic Noise Absorption Due to Solar Cosmic Radiation," *Planet. Space Sci., Vol. 14*, 1966, p. 277.

13. Juday, R. W.; Adams, G. W.: "Riometer Measurements, Solar Proton Intensities, and Radiation Dose Rates," *Planet. and Space Sci., 17*, 1313, 1969.

SESSION IV.5
RADIATION TRANSPORT AND SHIELDING
CHAIRMAN C.E.CLIFFORD
OAK RIDGE NATIONAL LABORATORY

A MODULAR APPROACH FOR ASSESSING THE EFFECT OF RADIATION ENVIRONMENTS ON MAN IN OPERATIONAL SYSTEMS

(The Radiobiological Vulnerability of Man During Task Performance)

DEAN E. EWING, B.S., M.S., D.V.M.
MAJOR, USAF, VC

INTRODUCTION

Whether a manned system is designed for peaceful exploration or military ventures, it stands a good chance of encountering radiation environments. These environments contribute a definite hazard to these manned missions and consequently must be analyzed in regard to mission impact. This impact on man can best be assessed by use of a model designed to incorporate all of the variables having a contribution to the problem of concern.

A STATEMENT OF THE PROBLEM

A practical approach to the assessment of the vulnerability of aircrews and other personnel in operational systems has long been a difficult problem. There are various radiation environments which a system may encounter. For example, military systems may be exposed to nuclear weapons, reactors and natural space radiation. A nuclear weapon detonation gives off specific radiations of biological significance. These radiations interact with the atmosphere and are continually altered in type, number, and energy (flux and spectrum) until they impact on an object. The radiations of concern are prompt neutrons, prompt gamma rays, secondary gamma rays, and fission product gamma rays.

The space radiations of biological significance include the trapped electrons and protons of the Van Allen Belt; the protons of solar events and the galactic cosmic rays[1]. In order to assess any radiobiological problem, one must have an accurate knowledge of the flux and spectrum of the radiation impinging on the system. Radiation transport computer codes and models must be developed or adapted to obtain the most accurate and efficient method for use in specific cases.[2]

The biologically significant radiation parameters reaching man within the system must be transported through the system's materials and into the man. Various materials transport codes and models are available to obtain the most effective method for use in dose determination. These in-turn must be linked to a recently developed computerized anatomical man model to obtain dose factors at significant radiobiological points within the man in specific operational situations.[3] Data from anticipated operational situations must then be interpreted in terms of appropriate radiation dose parameters such as: total dose, dose rate, quality factor, etc. These data can then be linked to available performance response data to enable computer modeling of the probability of a performance response occurring versus time of onset.

The final outcome should be a computer model designed to assess the mission impact for personnel in operational systems exposed to radiation environments

APPROACH TO THE PROBLEM

A modular approach has been developed to provide a vehicle for interrelating the many variables inherent in a radiobiological problem encountered by an operational system. This modular design is developed within a multi-layered matrix which includes space vehicles, air breathing, systems, and ground and water based systems. The matrix is divided into three sections containing those modules which (1) define the environment, either natural or man-made, (2) transport the environment to the system, (3) transport the impinging environment through the vehicle to man within the system, (4) transport the radiation to the organ of concern within the man, (5) obtain radiobiological factors such as dose, dose rate, quality factor, etc., and (6) link these factors with the appropriate radiobiological data to properly assess the effect on man's performance capability or predict any resulting performance decrement.

THE MATRIX

Section A - Environmental Transport

The first section of the multi-layered matrix is the environmental transport section. This section deals with defining the radiation environment either natural or man-made.[4,5]

These radiation environments are as follows:

1. Man-made radiation:
   a. Nuclear Weapons
   b. Incident radiation from nuclear

power devices, primarily leakage neutrons and gamma radiation.

2. Natural Radiations:

a. The natural radiations which are relatively stable in space and time (i.e., galactic cosmic rays and magnetically trapped electrons and protons in the inner Van Allen Belt out to 3000 miles.)

b. The natural radiations which are variable with space and time, primarily solar flares and soft trapped radiations in the outer Van Allen Belt.

These sources have specific radiations of biological significance. These radiations interact with the ground, atmosphere or space and are continually altered in type, number, and energy (flux and spectrum) until they impact on an object. In order to assess the radiobiological problem, one must have an accurate knowledge of the flux and spectrum of the radiation impinging on the operational system. There are currently available several radiation transport computer codes and models. These have been surveyed to determine the most accurate and efficient combinations for use in specific cases, and have been documented using a standard format to facilitate selection of the best available code or codes for use on specific problems.[2]

Section B - Materials Transport

Section B of the matrix is designed to handle the transport of the radiation environment from its point of impingement on the system until it reaches man within the system. Various materials transport codes and models are being evaluated to obtain the most effective method for use in dose determination. These in-turn are being linked to a recently developed computerized anatomical man model to obtain dose factors at significant radiobiological points within the man in specific operational situations.[3]

Section C - Performance Response Assessment

This third section of the matrix deals with assessing mission impact for personnel in operational systems exposed to radiation environments. Data from anticipated operational radiation exposure situations will be interpreted in terms of appropriate radiation dose parameters such as: total dose, dose rate, quality factor, etc. These data will then be linked to available performance response data to enable computer modeling of the probability of a performance response occurring versus time of onset. Several models will be developed or evaluated to obtain the optimal approach for taking a radiation dose in man and linking with performance response data. Areas to be investigated include techniques for extrapolating data from animals to man; literature search including reports of accidental human exposures; reports of therapeutic human irradiation; studies of victims of the Hiroshima and Nagasaki nuclear attacks; studies of animal irradiation experiments; and theoretical papers describing the models now available for estimating radiation injury. Data from the literature will be examined to determine common factors and correlated effects, especially those which may be correlated with other effects to permit extrapolation of the results of animal experiments to the prediction of human response. This information will be summarized, input to the appropriate computer model and presented in a format for vulnerability analyses of operational systems.

PROGRESS

The Biomedical Branch of the Analysis Division of the Air Force Weapons Laboratory is primarily concerned with the vulnerability assessment of man in USAF systems; therefore, our effort to date is basically in relation to aircraft within the earth's atmosphere or the atmospheric layer of the multilayered matrix. However, it is obvious that only Section A of the matrix is significantly different among the various layers while sections B and C are virtually identical with only those differences which the various operational systems themselves contribute.

I will use USAF operational systems in the atmosphere exposed to nuclear weapons as the examples of the actual workings of the matrix, because we have done the most work and are the most knowledgable in this area.

FEASIBILITY OF THE MODULAR APPROACH

Discussing the modular approach to assessing man's vulnerability in operational systems and the multi-layered matrix we have developed, one must consider the feasibility of such an approach. In doing this, we must consider the radiation environments and a system which may potentially be exposed to nuclear weapons. Therefore, we take a weapon, let's call it a "Mark-X", and we detonate this weapon in our computer.

What sort of things do we need to know about the weapon? We need to know the type of radiation, the intensity of the radiation and the time array of delivery and the energy spectra. In order to understand these, we need to know the yield of the weapon, the type of weapon such as fission or fusion and the design of the weapon. This radiation passes through the atmosphere and consequently we need to know the surrounding environment; such things as the pressure, sensitivity, composition of the atmosphere and exponential variations. We need to know the altitude at which the weapon was detonated and then the position of the receiver such as altitude and horizontal range from the weapon.

Other factors of concern are significant interfaces such as air-ground and air-space. Air-ground, because of absorption and reflection, air-space because of leakage from the atmosphere. In addition, we need to know the burst altitude in regards to the surface and the type of air that we assume; e.g., a homogeneous atmosphere, a layered atmosphere or an exponential atmosphere. Also, we must consider whether our receiver is moving or fixed. In transporting the weapon radiation through the environment, we need to know what type of transport we are going to use, elemental cross-section data, reactions involved, build up factors and so forth. Or, in other words, we have to have sophisticated mathematical models and computer codes to obtain an accurate transport.

Upon reaching our target, other things to consider would be angle of incidence of the radiation, energy deposited, material in which the energy is deposited, accumulative errors during the transport and flux to dose conversion factors.

In considering the feasibility of section A of the matrix, we took a make believe weapon and its output in terms of prompt neutrons, prompt gammas, secondary gammas, and fission product gammas and used available computer codes to transport these outputs up to the aircraft system. Initially, we were not interested in the accuracy of our procedure, only in the feasibility. However, we did attempt to look at other overriding factors. For instance, if blast, thermal or electronics kill mechanisms were primary and destroyed the aircraft, we no longer had a radiobiology problem. Therefore, we attempted to determine kill envelopes for some of these other factors. As applied radiobiologists, we did not want to be doing vulnerability studies on purely academic situations.

The feasibility analysis of section B of the matrix, the materials transport area, resulted in discussions centering on the necessity of obtaining attenuation factors either by sectoring the system or by some other means. We elected to use the sectoring procedure.[1] That is, to use a vehicle that had been sectored into various solid angles. We did not have a sectored aircraft available so, having been in the space business for some time, we decided to use a Gemini spacecraft, on which we had good sectoring analyses. We took Gemini out of space, brought it down into the atmosphere and called it an airplane. Using Gemini's various solid angle sectors, we managed to take the impinging radiation and transport it by the use of materials transport codes to man within the system. Concerning man, we had developed, for NASA, a very sophisticated computerized anatomical man model which had several hundred solid angle sectors.[3] For the purpose of the feasibility study, we took the midline gut dose, assumed it was the vomiting dose, and transported the environment impinging on man into the midline of the gut. In using the computerized anatomical man model, we actually handle the problem as a materials transport situation.

The next step is linking the dose received by man to a performance response. This part of the matrix system is the most difficult to develop. The performance response we used for descriptive purposes was vomiting because everybody knows what vomiting is and it is one of the few performance response factors on which we have some human data. Thus, we took the dose to the midline gut and linked it with human vomiting data in such a way that we could graph the probability of the performance response occurring versus time post exposure.

We thus proved that our approach was at least feasible. In other words we can link from A through C of the matrix. However, that really doesn't solve the final problem for us. That problem being: "Is it really practical to use this modular approach in assessing man's vulnerability?" This can only be done by applying the matrix to an actual system. It happened that the Air Force was conducting studies at that time on the F-106 fighter-interceptor aircraft and were very interested in obtaining sufficient data to include man in their survivability/vulnerability analyses. They had a list of weapons that they expected the aircraft to be exposed to in a nuclear situation. We picked three of the weapons representing worst case, best case and an intermediate case situation.

In attempting to transport the weapons radiation in a more realistic manner than we had done in the feasibility study, and with a greater concern for accuracy, it became obvious that the computer transport codes available to us were not satisfactory. We had a choice of taking these codes and patching the various sections of several of the codes together or of developing an entirely new code. Development is very time consuming and expensive while adapting various sections of several codes was not a practical approach either. Therefore, we hit on a compromise wherein we developed essentially a new code but which used two other codes as basic models. One of these was a large data base code and the other a curve fit code. By using the available data base code, we were able to rebuild the curve fit code so that it was capable of doing most of those things we wanted done; such as, transporting prompt neutrons and gammas, secondary gammas, and handling fission product gammas in a realistic way with a minimum amount of computer time and with an output which could be directly input to materials transport codes. At the same time, this new code could be added to or subtracted from in a modular manner to handle other types of transport problems. Another factor, probably as important as all the rest, was that the learning time to run this code was very short.[2]

Therefore, knowing the weapon's characteristics and using the new code, we were able to properly transport the radiation from the weapons, through the atmosphere, to the aircraft system, in this case the F-106.

In the feasibility study we did not have a sectored aircraft so we used the Gemini spacecraft. The argument still remained concerning what methods to use in developing attenuation factors. Because of our experience in flying unmanned satellites in space, we fell back on an old idea; that is the radiation scanning or gamma scanning of a system to obtain attenuation factors.[1] In this whole controversy, it turns out that the only way to prove that you can take short cuts is to do it the hard way first. Therefore, we tried to obtain an F-106 and gamma scan it. There was no F-106 available to us at the time, but we could get an F-102 which has a very similar configuration, mass and distribution to the F-106. After analyzing our gamma scanning results, we determined that these factors would be fine for transporting gammas but not satisfactory for neutrons. Thus, we performed a neutron scan of the F-102 system. Using the results of these two efforts, we then were able to transport the radiation impinging on the system, through the system and to man within the system. We were then through another crucial part of the effort in establishing the practicality of our approach.

We used our anatomical man model for transporting our environment to organs of concern within the body. This model had been developed basically for transporting space radiations such as protons and electrons and we found that we had difficulty

stuffing neutrons through it. However, by proper manipulation we were able to transport the impinging radiations into the midline gut and midline brain of the man. Using our dose determinations at these points, we linked to available radiobiological research data.

Assuming the gut dose was the vomiting dose, we plotted the probability of this response occurring versus time of onset; and assuming that the brain dose was the incapacitation dose, we plotted the probability of early transient incapacitation and permanent complete incapaciation versus time of onset. This information not only allowed us to prove the practicality of our modular approach but also gave for the first time readily useable data to be applied to an operational aircraft system. While performing the above, we did one other thing which now forms the basis for our ongoing studies. At each junction within the matrix, we listed: (1) the variable encountered, (2) the assumptions we made about that variable and (3) our estimation of that variables contribution to our error.

In developing the matrix and in assessing the feasibility and practicality, of our modular approach, we had many basic problems as we worked through the program: (1) obtaining weapon information was not easy, just as it took us a decade to obtain reasonable space radiation environment data, there is quite a bit of refinement to be done to assure us that the radiation environment we are using is accurate. (2) We are still not satisfied with the transport codes that we have and we are trying to refine and update them. (3) Another concern is the atmospheric condition at the time of detonation of a weapon. Our calculations indicate that we could have an order of magnitude error if we only considered a mean spring day at 40° latitude as opposed to a typical winter day at a higher latitude. (4) The radiation impinging on a system does not impinge in a plane or perpendicular to a plane. There are many angles of incidence. These need to be considered in our procedures in order to assure that we have a handle on this possibly very important factor. (5) Radiation scanning both gamma and neutron, of systems such as the B-52 or the proposed B-1,must also be done but, hopefully, in the long run, we will be able to obtain our attenuation factors by analytical analyses of blueprints of the systems. (6) Those transport codes that we have used also need to be refined and updated. (7) The computerized anatomical model of man is excellent for handling space radiations but still unsatisfactory for handling weapons environments. Therefore, the model must be altered and adapted for this purpose.

Various dose parameters must be considered if you are going to link properly to available research data; that is, dose, dose rate, depth dose profile, quality factors and multiple exposures,to name a few, must be considered in any practical application of the model. We are fortunate in the case of dose rate in a weapons situation in that good biological research data is available to indicate that the total dose received from a weapon, delivered in less than a second, does not affect the biological response. In other words, the dose from a weapon is instantaneous and we only have a single dose rate. For reactor environments or fall-out environments, we will have to handle varying dose rates. A depth dose profile is important and our anatomical man model allows us to obtain isodose contours within the body. However, this is done at the expense of a great amount of computer time. We have managed to short cut this to some extent. If we only consider the dose to those organs which produce a given response in a specific time period, then we save a lot of time by transporting the radiation so that we obtain the dose only at those organs.

Quality factor, that area of constant controversy among radiobiologists, can best be handled in this case by linking the data of an environment similar to the actual situation. In other words, if you have a weapon output transported to your man, where impinging on the man is a particular neutron to gamma ratio , you can link with the research done with this same neutron to gamma ration, and , consequently, avoid many of the problems associated with the effect of quality factors. In section C of the matrix, where we graph the probability of response occurring versus time post exposure, we must eventually consider other variables. There are the non-performance variables such as age, whether the individual has eaten recently or not, the psychological makeup and so on. All of these will affect the shape of your curves. There are also the performance variables--early transient incapacitation, diarrhea, motor response changes, audio and visual capacity changes and so forth will affect the response and shape of the curves.

SUMMARY

A modular approach for assessing the affect of radiation environments on man in operational systems has been developed. The feasibility of the model has been proved and the practicality has been assessed. It has been applied to one operational system to date and information obtained has been submitted to systems analysts and mission planners for the assessment of man's vulnerability and impact on systems survivability. In addition, the model has been developed so that the radiobiological data can be input to a sophisticated man-machine interface model to properly relate the radiobiological stress with other mission stresses including the effects of a degraded system.

REFERENCES

1. J.F. Janni; and F.E. Holly: A Special Report - The Current Experimental Approach to the Radiological Problems of Spaceflight; Vol. 40 No. 12 Aerospace Medicine Dec. 1969.
2. H.M. Murphy, Jr.; A Users Guide to the Smaug Computer Code; Air Force Weapons Laboratory Technical Note - SAA-TN-71-2 January 1971.
3. P.G. Kase; Computerized Anatomical Model Man; Air Force Weapons Laboratory Technical Report - AFWL-TR-69-161 January 1970.
4. D.E. Ewing; A Space Radiation Monitoring System for Support of Manned Spaceflight; Procedings - XVII Congress of the International Astronautical Federation October 1966.
5. D.W. Ewing; A Space Radiation Monitoring System for Support of Manned Spaceflight; Biomedical Sciences Instrumentation Volume 4, May 1967.

OPTIMAL SHIELD MASS DISTRIBUTION FOR SPACE RADIATION PROTECTION*

M. P. Billings
McDonnell Douglas Astronautics Company-West
Huntington Beach, California

ABSTRACT

Computational methods have been developed and successfully used for determining the optimum distribution of space radiation shielding on geometrically complex space vehicles. These methods have been incorporated in computer program SWORD which uses the full capability of state-of-the-art methods for dose evaluation in complex geometry, and iteratively calculates the optimum distribution of (minimum) shield mass satisfying multiple acute and protracted dose constraints associated with each of several body organs. The unique and effective technique used to accommodate multiple constraints, eliminates the awkward discontinuities associated with the formulation of inequality constraints, and produces a result meeting mathematical tests for optimality.

INTRODUCTION

The capability to compute space radiation doses at specified points within a vehicle and shield of fixed geometry is provided by a number of computer programs, e.g., SIGMA (Ref. 1), MEVDP (Ref. 2), and LSVDC4 (Ref. 3). An additional capability is provided by techniques developed at the McDonnell Douglas Astronautics Company and incorporated in the SWORD program (Ref. 4), this being the automated computation of the optimal shield mass distribution that meets a set of radiobiological dose criteria associated with the specified vehicle configuration and mission profile. It is emphasized that this optimization function is accomplished without necessitating any simplifying assumptions regarding geometrical framework, radiation transmission evaluation, etc., that are not also commonly invoked in programs which perform dose evaluation only. In fact, SWORD incorporates the dose analysis framework of the SIGMA program referred to above. To a great extent, the capacity of SWORD to accommodate a variety of complicating factors influencing shield mass distribution is due to the efficacy, yet simplicity, of the optimization technique employed.

The role of the SWORD program in performing space radiation shielding analyses is indicated in Figure 1, together with those of other space radiation analysis programs also developed at the McDonnell Douglas Astronautics Company. Overall capabilities are summarized in Figure 2. SWORD uses basic dose transmission data, in the form of one-dimensional point kernel functions, typically calculated by the CHARGE program (Ref. 5) for the total space radiation environment defined by the OGRE program (Ref. 6) for the specified mission. These dose transmission data are applied in conjunction with ray tracing computations performed on a generalized quadric surface representation of the vehicle, to compute dose levels to specified items, usually the critical organs of crew members. The derivative of total dose from all radiation sources, with respect to the thicknesses of specified candidate shield regions located on various surfaces of the vehicle, is also computed. This dose derivative information is processed by SWORD in an iterative procedure to determine the optimal distribution of shield material among such candidate locations as wall structure, biowell for solar cosmic ray protection, and personal shields. The optimization technique employed is based on a particular formulation of the Lagrange multiplier constraint equations. Shield shaping over extended surface areas is accomplished by subdividing them into a number of smaller areas over which shield thickness is uniform. SWORD can treat the effect of (1) multiple dose constraints (separate constraints for each organ), (2) time-dependent astronaut locations (the work-rest cycle influence), (3) organ-dependent quality factors or dose distribution factors, and (4) direct and scattered neutron and gamma radiations from on-board nuclear power sources. The geometric framework, numerical integration schemes, and optimization procedures are sufficiently flexible and efficient to allow the analysis of any practical space vehicle configuration.

19533

SPACE RADIATION SHIELDING PROGRAMS

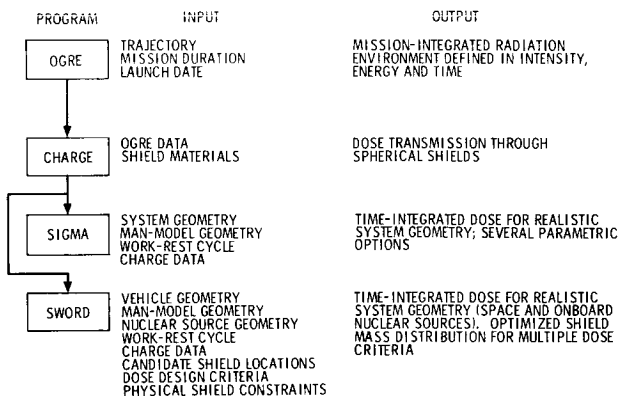

FIGURE 1

* The computational techniques described herein were developed by the McDonnell Douglas Astronautics Company under the Independent Research and Development Account No. S. O. 80205-007.

19538

SUMMARY OF SWORD CAPABILITIES

- DESCRIBES SPACE VEHICLE IN A GENERALIZED QUADRATIC SURFACE GEOMETRY
- USES TABULAR DOSE-SHIELD THICKNESS DATA FROM DETAILED SHIELDING PHYSICS CALCULATIONS
- EVALUATES MISSION-INTEGRATED CRITICAL ORGAN DOSE USING FLEXIBLE NUMERICAL ANGULAR INTEGRATION SCHEME
- CALCULATES OPTIMAL DISTRIBUTION OF SHIELD MATERIAL SUBJECT TO MULTIPLE DOSE CRITERIA
- USES EFFICIENT, ACCURATE OPTIMIZATION TECHNIQUE
- DISTRIBUTES SHIELD MATERIAL AMONG NESTED SURFACES OF VEHICLE, BIOWELL, AND PERSONAL AND PORTABLE SHIELDS
- SHAPES SHIELD THICKNESS OVER EXTENDED SHIELD SURFACE AREAS

FIGURE 2

19537

CRITICAL ORGAN DOSE EVALUATION

- GEOMETRY MODEL–GENERALIZED QUADRIC SURFACES

  $G(X, Y, Z) = A_0+A_1X+A_2Y+A_3Z+A_4X^2+A_5Y^2+A_6Z^2+A_7XY+A_8YZ+A_9ZX = 0$

- SPACE RADIATION DOSE–EVALUATED FOR EACH SOURCE AND SUMMED OVER VARIOUS TIMEWEIGHTED ASTRONAUT LOCATIONS
  - $D = \frac{1}{4\pi}\left(\frac{\Delta\theta}{3}\right)\left(\frac{\Delta\mu}{3}\right)\sum_{I_\theta} A_i \quad \sum_{M_\mu} B_m \quad K\left[\rho(\theta_i, \mu_m)\right]$
  - K(ρ) IS TABULAR, INTERPOLATED BY POWER LAW BETWEEN ENTRIES
  - $\frac{\partial D}{\partial T_i} = \frac{1}{4\pi}\left(\frac{\Delta\theta}{3}\right)\left(\frac{\Delta\mu}{3}\right)\sum_{I_\theta} A_i \quad \sum_{M_\mu} B_m \frac{\partial K(\rho)}{\partial T_i}$
  - DATA ARE SAVED FOR EACH RAY DEFINING ITS SOLID-ANGLE WEIGHT, MASS TRAVERSED, SHIELDS CROSSED, AND COSINE OF ANGLE AT EACH CROSSING
- NUCLEAR RADIATION DOSE–EVALUATED CONCURRENTLY WITH SPACE RADIATION DOSE EVALUATION USING POINT KERNEL METHOD, CALCULATING SCATTERED DOSE FOR EACH RAY TRACED IN 4π INTEGRATION AS WELL AS DIRECT DOSE

FIGURE 3

DOSE AND SHIELD MASS EVALUATION

The significance of an optimum solution to a given space radiation protection problem is dependent on a number of factors. These include: (1) the accuracy with which dose and shield mass data, and their derivatives with respect to the variables of the problems, can be determined, (2) the suitability of the variables for characterizing the shield mass distribution, and (3) the extent to which all relevant constraints are suitably imposed and satisfied.

Dose Evaluation

The procedures for dose evaluation that have been incorporated in SWORD are outlined in Figure 3. They have been adapted from the SIGMA code and are representative of the state-of-the-art of space-radiation-dose analysis. The geometric description of the vehicle structure, equipment, stores, fixed shields, astronauts, etc., is accomplished using generalized quadric surfaces which form the boundaries of homogeneous, contiguous, non-overlapping regions. Doses are evaluated at any number of points representing the locations of radiation-sensitive body organs by repetitively tracing rays from each dose point through the surrounding materials, employing the resultant data on mass distributions along each ray to determine a differential dose contribution for the path. Total, mission-integrated critical organ doses are obtained by integrating the differential dose contributions over solid angle ($d\theta\, d\mu$) about each dose point and over various time-weighted astronaut locations within the vehicle. The integration is accomplished numerically using Simpson's Rule; A_i and B_m in Figure 3 are the weighting factors associated with the particular values of the variables (θ, μ).

The specific dose transmission kernels used in an analysis are conveniently supplied in tabular form for an arbitrary number of distinct, mission-dependent sources (e.g., trapped protons, trapped electrons, bremsstrahlung, solar cosmic rays); the data are interpolated by power law between entries to obtain dose levels for various values of equivalent shield thickness. For virtually all analyses it is satisfactory to account generally for the material-dependence of the dose attenuation kernels by applying mass density scaling factors based on known radiation-interaction properties. This approach is satisfactory for secondary nucleon dose as well as for primary proton dose (Ref. 6). Since the origin of the dose attenuation kernels is irrelevant to the operation of SWORD, it is not restricted to use with a specific one-dimensional, dose-analysis computer program.

For each ray traced in the initial evaluation of mission-integrated critical organ dose, data are stored to facilitate efficient re-evaluation of the dose associated with the ray as shield thicknesses are iteratively modified. These data include the equivalent thickness of all fixed regions traversed, the solid angle weight of the ray (incorporating Simpson's rule coefficients for the particular values of polar and azimuthal angles defining the ray), the indices of all shields crossed, and the cosine of the angle at the crossing. Information is also saved regarding the neutron and gamma differential doses associated with the ray; such data represent the dose either transmitted directly from an on-board nuclear power source or single-scattered in regions lying along the ray. The scattered dose calculation is limited to scattering in regions external to the outermost shielded volume, based on the assumption that, for scattering in materials within inhabited regions to be significant, the unscattered dose would be prohibitive.

Shield System Variables

A framework defining candidate shield locations is superimposed on the basic vehicle geometry by designating that shield material be placed, as required, at a specific bounding surface of a specific region. Shield material is assumed to be uniformly distributed over such shield areas, such that a single value of the shield thickness measured along a surface normal, characterizes the mass of each such candidate shield. The relationship of shield mass and the derivative of shield mass with respect to the thicknesses are then quite simple:

$$W = \sum_I A_i t_i \; ; \quad \frac{\partial W}{\partial t_i} = A_i$$

In SWORD the areas of each shield, A_i, may be specified by input or may be estimated from data obtained during ray tracing computations associated with dose evaluation. The latter is convenient for complex shield shapes, but the former is usually more accurate.

This technique for defining shield variables is summarized in Figure 4 and illustrated in Figure 5. In the illustration, a total of seven variables have been used to define a shield system consisting of an external shell completely enclosing inhabited areas (t_1, t_2, t_3) and an internal biowell for solar flare protection (t_4, t_5, t_6, t_7). Several more shields could have been specified if, for example, it had appeared potentially rewarding to use non-uniform shield thicknesses over large areas such as those spanned by shields 1, 2 and 3. In the actual problem from which this illustration was taken, however, the location of fixed equipment along the vehicle walls was not well defined, and it was necessary to assume it to be uniformly distributed; in such a circumstance, total shield mass is best estimated by also assuming a uniform distribution of shield mass over the same areas.

19561

VARIABLES AND CONSTRAINTS

VARIABLES

- CHARACTERISTIC THICKNESS (g/cm^2) AT CANDIDATE SHIELD LOCATIONS
- THICKNESSES MEASURED ALONG SURFACE NORMALS
- SHIELD WEIGHT · THICKNESS x AREA
- TRIPLY-NESTED SHIELDS ALLOWED

CONSTRAINTS

- MAXIMUM ALLOWABLE DOSE TO CRITICAL BODY ORGANS (I.E., BFO, SKIN, EYES)
  - DOSE FOR PROTRACTED EXPOSURE COMPARED WITH MISSION-INTEGRATED DOSE (ORGAN DOSE SUMMED OVER VARIOUS TIME-WEIGHTED ASTRONAUT LOCATIONS)
  - DOSE FOR ACUTE EXPOSURE COMPARED WITH DOSE FROM A MAJOR FLARE (ASTRONAUT LOCATION MAY BE RESTRICTED DURING EVENT, I.E., TO A BIOWELL)
- MINIMUM SHIELD THICKNESS VALUES (≥ 0)
- MAXIMUM SHIELD THICKNESS VALUES CORRESPONDING TO VOLUME OR WEIGHT RESTRICTIONS AT ANY CANDIDATE SHIELD LOCATION

FIGURE 4

19532

VEHICLE CALCULATIONAL MODEL

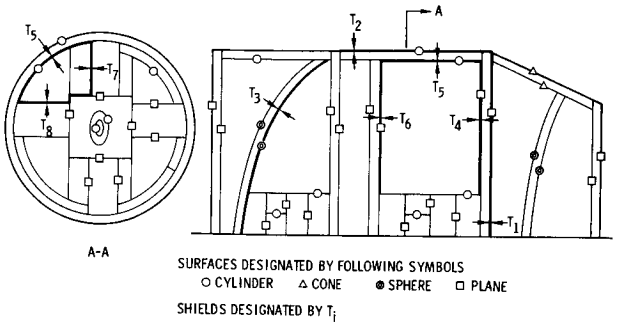

FIGURE 5

In the specification of shield variables for a given problem, two capabilities not illustrated by Figure 5 are available: (1) shields can be triply-nested (doubly-nested being illustrated), and (2) shields can be portable. Both capabilities might be employed if, for example, an astronaut wore a personal portable shield for portions of the mission, including some time in the biowell. Then the effectiveness of such a shield would be incorporated in dose and dose derivative calculations at all work and rest stations by describing the shield geometry at each man-model location, but counting its weight only once.

Constraints on Mass Distribution

Two types of constraints on shield mass distribution can be explicitly included: those dealing with maximum levels of radiation exposure and those dealing with minimum and maximum values of the variables (shield thicknesses). Several other constraints are potentially significant, but are of such a nature that they can be expressed within the overall framework; i.e., restriction to non-zero shield thicknesses, restriction of crew movement during solar flares, anisotropic radiation leakage from on-board nuclear power sources.

The constraints which can be imposed are listed in Figure 4. Those constraints pertaining to radiation exposure are expressed by allowing both acute and protracted dose criteria for each of several radiation sensitive body organs. These dose criteria are understood to be mission-integrated criteria and are compared, at each step of an optimization computation, with dose values determined by summing dose contributions for all crew stations, explicitly incorporating time factors expressing the exposure to each radiation source at each station.

OPTIMIZATION METHOD

Numerous mathematical techniques exist for computing optimal solutions to engineering problems. For many problems, the solutions can be obtained directly by solving the set of simultaneous equations for the values of the variables satisfying the constraints imposed. In other cases, and particularly for geometrically realistic shielding problems, the complexity of the functional relationships is such that the equations can only be solved by iteration on the many variables, hopefully converging on a solution that is optimum and that can be ascertained for a realistic expenditure of engineering labor and computer time.

Capabilities Required

Among the approaches to optimization of radiation shield systems, per se, those that have been reported have dealt predominantly with optimization of shields for nuclear power systems, rather than with shields for space radiations. An application of the gradient nonlinear programming technique to optimization of a divided shield system for a nuclear powered aircraft was reported in References 8, 9 and 10; the problem was considerably simplified by the assumption that the source could be adequately represented by a point source. Another approach to the same optimization problem was reported in Reference 11, in which case a restricted representation of shield system variables was used to facilitate iteration on the shield thicknesses and on the two Lagrange multipliers associated with the neutron and gamma dose constraints. A shield synthesis technique was reported for optimization of compact power reactor shields in Reference 12 and an application of the technique to optimization of proton shields was presented in Reference 13; both applications restricted shield geometry to convex shapes.

Such shield optimization approaches generally relaxed one or more important aspects in order to facilitate determination of a minimum weight solution, i.e., the detail with which the optimization problem can be characterized, the number and nature of the constraints which can be simultaneously imposed, or the accuracy of dose and dose derivative evaluations. The usual difficulty was that the optimization formulation did not have the capacity to allow for much detail in either problem geometry (basic system and shield) or design criteria. In developing SWORD, however, a determined attempt was made to avoid such simplifications; rather, a number of capabilities required of the overall program were identified as requirements to be satisfied by the optimization procedure. These included:

- Compatibility with a detailed geometric description of the vehicle, equipment, stores, etc., preferably the same generalized geometry framework now commonly employed in space radiation dose evaluation programs and with dose transmission data provided by detailed physics computations.
- A flexible system for defining shield system variables in a framework which can be superimposed on the detailed fixed geometry of the vehicle and its contents.
- Capability to accommodate multiple radiation level criteria with no a priori knowledge of their interdependence or independence. The latter implies that the design values for some constraints may necessarily be exceeded in meeting the specified values for others. Also the relative importance of each constraint should be ascertained automatically and its effect diminished automatically if it becomes an inequality constraint.
- Internal calculation of radiation levels, shield weights, and their derivatives, to minimize data handling and to permit a detailed re-evaluation of all dose and weight values as required throughout the iterative operations.
- Procedures for controlling values of the variables during iterations so as to minimize the quantity of data to be updated at each step, as this is potentially time consuming.

Candidate Techniques

Two optimization techniques potentially able to satisfy these requirements were identified. One consisted of a conventional formulation of a multiple-constraint problem using the Lagrange multiplier technique and used an iterative procedure suggested by Arrow and Hurwicz (Ref. 14); this method is outlined in Figure 6. The other method, developed and applied at McDonnell Douglas, reduced the multiple-constraint problem so that it can be handled operationally as a single-constraint problem. It used a single approximate, continuous, functional combination of the multiple constraints, which forces the result to converge to the solution for the exact original problem. This approach is outlined in Figure 7.

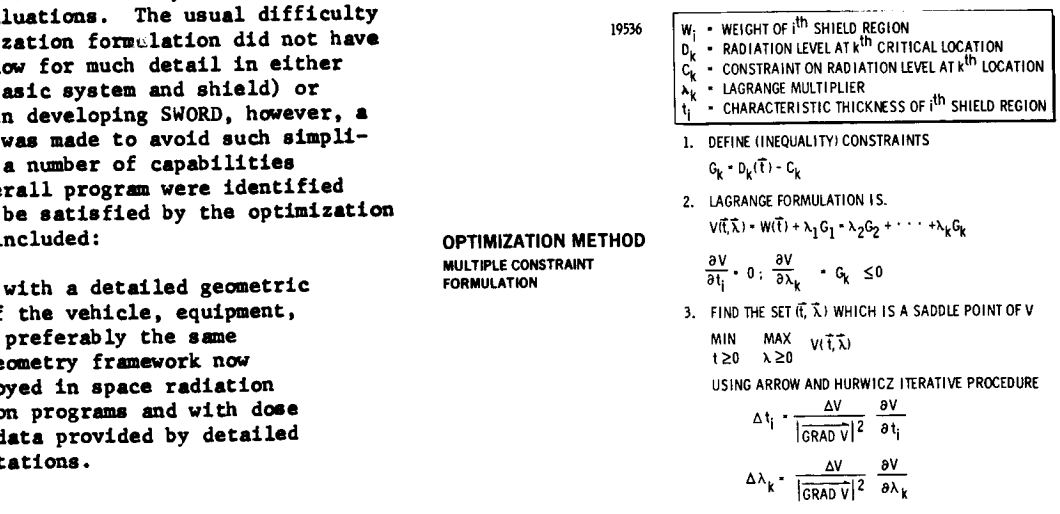

19535

OPTIMIZATION METHOD

SINGLE CONSTRAINT FORMULATION

W_i = WEIGHT OF i^{th} SHIELD REGION

D_k = RADIATION LEVEL AT k^{th} CRITICAL LOCATION

C_k = CONSTRAINT ON RADIATION LEVEL AT k^{th} LOCATION

λ = LAGRANGE MULTIPLIER

n = EXPONENT SUFFICIENTLY LARGE TO EMPHASIZE DOMINANT CONSTRAINTS

t_i = CHARACTERISTIC THICKNESS OF i^{th} SHIELD REGION

1. COMBINE CONSTRAINTS INTO SINGLE RELATIONSHIP

$$U = \left(\frac{D_1}{C_1}\right)^n + \left(\frac{D_2}{C_2}\right)^n + \cdots + \left(\frac{D_k}{C_k}\right)^n$$

2. LAGRANGE FORMULATION IS

$$V = W(\bar{t}) + \lambda U(\bar{t}); \quad \frac{\partial V}{\partial t_i} = 0$$

3. SINCE THERE IS ONLY ONE LAGRANGE MULTIPLIER (λ), FIND THE SET $(\bar{t})$ SUCH THAT

$$-\frac{1}{\lambda} = \frac{\partial U/\partial t_1}{\partial W/\partial t_1} = \frac{\partial U/\partial t_2}{\partial W/\partial t_2} = \cdots = \frac{\partial U/\partial t_I}{\partial W/\partial t_I}$$

THEREFORE, REPETITIVELY MODIFY t_m IN THE SET $(\bar{t})$ WHERE m IS SUCH THAT

$$\frac{\partial U/\partial t_m}{\partial W/\partial t_m} = \max_i \frac{\partial U/\partial t_i}{\partial W/\partial t_i} \text{ OR } \frac{\partial U/\partial t_m}{\partial W/\partial t_m} = \min \frac{\partial U/\partial t_i}{\partial W/\partial t_i}$$

FIGURE 7

Experience with these methods on a variety of shield optimization problems led to a preference for the latter, single-constraint approach. One significant advantage was due to altering only one thickness value at each step of the iterative process, because this approach then reduced the amount of data that had to be updated prior to the next step. Hence, the single constraint approach was generally more efficient. It is likely that this advantage would be attainable in the multiple constraint approach if only the few largest Δt_i were implemented at each step.

The major objection to the conventional multiple constraint formulation lay in the fact that, for shielding problems, the measure of importance of a constraint is not fairly represented by its linear distance from the criterion (as indicated in Item (1) of Figure 2). The exponential nature of the constraint functions results in the importance of each constraint being much more accurately expressed by the ratio of current value to criterion (as is utilized in the single constraint formulation). This failure to incorporate the exponential character of the function leads to severe difficulties in converging on an optimum solution. The rate of convergence is necessarily dependent on the step size (i.e., ΔV) at each iteration and this is limited by the range of (Δt_i, $\Delta \lambda_k$) over which the partial derivatives can be applied. For the linear formulation indicated in the figure, this range is quite small. While some alteration in the expression of the constraining relationships would presumably alleviate this difficulty, it was not pursued.

Rather than modify the multiple constraint formulation to achieve a more effective technique for the kinds of shield optimization analyses of interest, the activity centered instead on exploitation of the single constraint approach. This latter technique, having fewer variables, was considerably simpler to apply and, where comparisons were made of results obtained with both techniques, provided results that satisfied tests for optimality.

Optimality of Preferred Method

The capacity of the single constraint method to produce a result which not only meets the criteria at low total weight, but is truly optimum, has been demonstrated numerically. The criteria for optimality are indicated for the conventional multiple constraint formulation in Figure 6, i.e.,

$$\frac{\partial V}{\partial t_i} = \frac{\partial W}{\partial t_i} + \lambda_1 \frac{\partial D_1}{\partial t_i} + \lambda_2 \frac{\partial D_2}{\partial t_i} + \cdots + \lambda_k \frac{\partial D_k}{\partial t_i} = 0; \quad i = 1, 2, \ldots I$$

These equations can be evaluated using the set of thicknesses, t_i, provided by the single constraint method directly and using a set of multipliers, λ_k, constructed from other data determined in the analysis:

$$\lambda_k = \frac{n\lambda_i}{C_k}\left(\frac{D_k}{C_k}\right)^{n-1}; \quad \lambda_i = \frac{\partial W/\partial t_i}{\partial U/\partial t_i}$$

There obviously are a total of I values of each λ_k, these values agreeing with one another to the extent that the values of λ_i are in agreement. Since the essence of the single-constraint formulation is to align the values λ_i, the several values for each λ_k can be made to agree quite well by aligning the λ_i within a very small difference. This is accomplished by continually reducing the increment (or decrement) to each variable once all constraints have been satisfied, iterating in the neighborhood of the optimum solution until satisfactory convergence is attained. This procedure, however, can be extremely time consuming and is of almost no benefit in terms of reducing the total shield weight from the value determined with a relatively coarse optimization criterion.

Typically, the convergence of thickness values to the extent required to prove optimality doubles or triples the time required to determine a shield condition to within one percent of that optimum weight.

SAMPLE OPTIMIZATION ANALYSIS

Results from a simplified application of the SWORD program are presented in Figure 8 to illustrate some of the points made in the preceding discussion. This sample problem involves optimization of the shield system illustrated in Figure 5.

The problem included constraints on acute dose from solar cosmic rays (SCR) and on protracted dose from geomagnetically trapped radiations and their secondaries, and from neutrons and gamma rays from an on-board isotopic power system. The total number of dose constraints was six, these being separate acute and protracted dose criteria for each of three critical organs: lens of the eye, skin, and blood forming organs.

There were three man-model locations, representing crew stations in a command area, an experimental area and a living area. The command area was specified to be within a biowell for SCR protection, and all SCR exposure was assumed to be taken at this location. Two of the man-model locations were on centerline and, with the vehicle being reasonably symmetrical cylindrically, a single dose point in the man-model was used to represent the location of each of the three organs. The man-model position in the biowell, however, was sufficiently off axis that some recognition of the resultant asymmetry was required. This was accomplished by using two dose points to represent each organ, one at the appropriate depth below the surface of the skin facing the outer wall and the other 180° opposite. The time-weights associated with the biowell locations were halved to compensate for the extra dose point.

The value of making even token recognition of system asymmetry has been proven in a number of shield optimization problems. When dose can be delivered asymmetrically, as at the biowell location, it is particularly important that the dose point(s) be representative; otherwise, introduction of an appreciable bias in the discrete and discontinuous representation of critical organ location can lead to false concentrations of shield mass. Ideally, the dose would be evaluated by sampling from a continuous timeline of astronaut position within the vehicle, sampling also from the solid angle at each position along the timeline; the effects of astronaut orientation at each position might also be diminished, since these are not necessarily real. This approach to dose integration has been incorporated in a recent version of the SIGMA program, as reported in Reference 6, but is not yet incorporated in SWORD.

There were eight variables, three of which defined a cylindrically symmetric shield system enclosing all inhabited areas, and five of which defined the biowell.

Dose transmission data were furnished for a synchronous orbit mission of several months duration, these then being trapped electron and secondary bremsstrahlung dose, and SCR dose. The geometry, materials, and radiation source characteristics for the on-board isotopic power system were also defined and the direct and scattered doses computed therefrom. Only the direct dose proved to be of any significance and it had relatively little influence on the optimum shield determination, because this was dominated by SCR considerations; i.e., the acute dose criteria were the most stringent for the particular mission.

Mission-integrated critical organ doses were calculated using a relatively coarse integration grid, namely four intervals in μ (cosine of polar angle) and six intervals in θ (azimuthal angle) or a total of 21 rays for each of the twelve dose points. The 252 rays traced made a total of 382 shield crossings because of the nesting of the biowell shield within the main shield. The computer time required to perform the initial dose evaluation, in preparation for the shield optimization computation, was 21 seconds on the CDC 6500 computer. (Much more detailed integration grids can be used; problems involving up to 3000 rays have been solved.)

The optimization history for this problem is shown in Figure 8. A total of 106 iterations on weight were accomplished in 40 seconds, each iteration initially involving weight increments of up to 250 Kg, decreasing to 15 Kg as the solution converged. It can be seen that two of the constraints dominated the optimization, the domination being particularly evident when the ratios of dose to constraint value decreased to approximately 0.9 after iteration 80, and when these ratios were then raised to an exponent of 100. As noted on the figure, essentially the same result was obtained when the exponent was 4 rather than 100; there is no particular reason not to use a large value of the exponent, however, other than to avoid overflow when the ratios are large, and SWORD internally increases the value to 100 as rapidly as the values of the ratios permit.

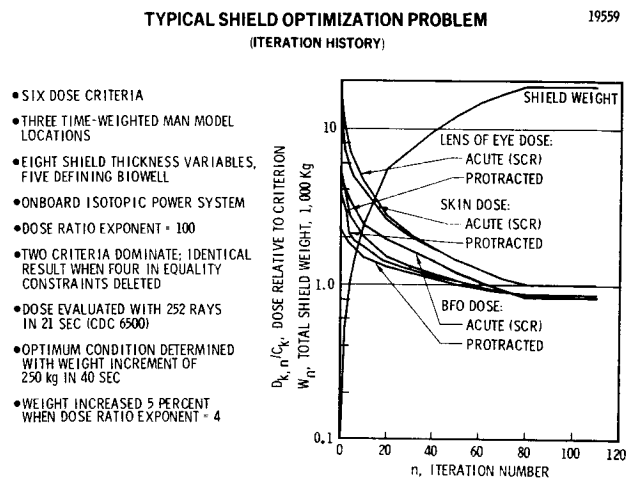

FIGURE 8

The optimization of the solution was checked at the 106th iteration by calculating the eight possible values (i.e., eight variables) of each of the six Lagrange multipliers (i.e., six dose criteria) from the several values of the multiplier determined in the single constraint solution. The set of multipliers obtained from each of the I equations was used to evaluate all I equations. Actually, each equation was divided through by A_i so that the magnitude of the remainder was referenced to the magnitude of the numbers involved, i.e.,

$$R_i = \frac{\partial V/\partial t_i}{A_i} = 1 + \frac{1}{A_i} \sum_k \lambda_{ik} G_k \stackrel{?}{=} 0$$

The iteration was then continued for another 41 steps, progressively decreasing the weight increment to 1 Kg, with these results then being compared to the optimality as evaluated after 106 steps. While the total shield weight decreased only 0.14%, the small changes in values of each of the variables led to a dramatic change in

apparent optimality: the λ_{ik} for the two significant constraints agreed within 0.4% and the maximum value of R_i for any set (λ_{ik}) was 0.001. This experience is typical and serves to illustrate that the shield mass converges much more rapidly than the variables or the multipliers, and that the convergence criterion for iteration cutoff should be based on mass (as it is) rather than on some optimization test.

CONCLUSIONS

The work reported herein was initiated when a need arose to analyze the dependence of space vehicle shield weight requirements on various system parameters. The space vehicle in question was to fly long duration missions in synchronous orbit and hence a considerable mass of supplementary shielding appeared necessary. In order for the shield parametric data to be sufficiently self-consistent that the dependence on system parameters be meaningful, it was evident that a systematic procedure was required to produce it. The optimization technique, and the implementation thereof, as described, proved to be extremely effective, both in terms of the scope of the problems which could be analyzed and optimized, and in terms of the significance of the results. Results from some production applications of SWORD were reported in References 15 and 16.

The applicability of the optimization approach embodied in the single constraining function is much broader than that reviewed here. It is certainly worthy of consideration for, and has in fact been applied to, other shielding optimization problems. It could also be effectively applied in other, non-shielding efforts, possibly with some modification of the constraining functions to best approximate the functional relationships of constrained quantities to their specific constraint values.

References

1. Jordan, T. M., "SIGMA, A Computer Program for Space Radiation Dose Analysis Within Complex Configurations", Douglas Aircraft Company, DAC-60878, November 1967.

2. Liley, B., and S. C. Hamilton, "Modified Elemental Volume Dose Program (EVDP)", Air Force Weapons Laboratory, AFWL-TR-69-68, 1969.

3. Hill, C. W., W. B. Ritchie, and K. M. Simpson, Jr., "Data Compilation and Evaluation of Space Shielding Problems", Vol. IV: LSVDC4 Program System, Lockheed, ER7777, February 1967.

4. Billings, M. P., "SWORD, A Computer Program for Space Radiation Shield Optimization in Complex Geometry", McDonnell Douglas Astronautics Company, MDC G-0362, June 1970.

5. Yucker, W. R., and J. R. Lilley, "CHARGE Code for Space Radiation Shielding Analysis", McDonnell Douglas Astronautics Company, DAC-62231, April 1969.

6. Baker, M. B., "Geomagnetically Trapped Radiation", Douglas Aircraft Company, SM-47635, October 1964.

7. Langley, R. W., and M. P. Billings, "Methods of Space Radiation Dose Analysis with Applications to Manned Space Systems", McDonnell Douglas Astronautics Company, MDAC Paper WD-1529, April 1971, or Proceedings of National Symposium on Natural and Manmade Radiation in Space, March 1971.

8. Miller, R. A., and W. Cranford, "Shield System Optimization", Convair/Fort Worth, NARF-58-24T, June 1958.

9. Miller, R. A., and W. Cranford, "Results of an Optimization Procedure", Proceedings of Seventh Semi-Annual Shielding Information Meeting (SRD), Report XDC60-6-70, October 1959.

10. Miller, R. A., W. Cranford, and R. D. Sheffield, "Recent Modifications of a Shield Optimization Method", Proceedings of Fourth Semi-Annual ANP Shielding Information Meeting (SRD), Vol. II, Oak Ridge National Laboratory, ORNL-2497, November 1957.

11. Rost, E. S., J. D. Pomeroy, and H. C. Woodsum, "Shield Optimization Code (SRD)", Pratt and Whitney Aircraft, PWAC-198, 1958.

12. Troubetzkoy, E. S., "Minimum Weight Shield Synthesis", United Nuclear, UNC-5017 (Part A), October 1962.

13. Krumbein, A. D., J. Celnik, F. R. Nakache, and E. S. Troubetzkoy, "Synthesis of Minimum Weight Proton Shields", United Nuclear, UNC-5049, February 1963.

14. Wolfe, P., "The Present Status of Nonlinear Programming", Mathematical Optimization Techniques, Chap. 11, University of California Press, 1963.

15. "MORL Concept Responsiveness Analysis, Book 1", Douglas Aircraft Company, SM-48813, November 1965.

16. "Saturn V/S-IVB Synchronous Orbit Spent Stage Study", Douglas Aircraft Company, DAC-56653, February 1968.

DEVELOPMENT AND VERIFICATION OF DESIGN METHODS FOR DUCTS IN A SPACE NUCLEAR SHIELD

R. J. Cerbone, W. E. Selph, and P. A. Read

Gulf Radiation Technology
A Division of Gulf Energy & Environmental Systems Incorporated

A practical method for computing the effectiveness of a space nuclear shield perforated by small tubing and cavities has been developed and tested.

Analysis of ducts and voids in a shield cannot be performed using the two-dimensional transport methods that are presently the most efficient means of analyzing reactor and shield problems. A three-dimensional Monte Carlo analysis is the only rigorous approach; however, it is too costly to consider in tradeoff studies. Methods are needed that will provide reasonable accuracy at a moderate cost.

Our approach to the problem is to use solutions of a two-dimensional transport code and evaluate perturbations of that solution using last flight estimates and other kernel integration techniques. In general, perturbations are viewed as a change in the source strength of scattered radiation and a change in attenuation properties of the region, and the effect of these changes is evaluated by performing last flight estimates and point kernel integrations. This method has been implemented in a new computer program called DUCT.

Calculations performed with the DUCT code have been compared to experiments conducted at the Gulf Radiation Technology Linac facility. The shield studies involved measurements on a lithium hydride assembly with a sodium filled duct and a NERVA-BATH shield mockup. Comparison has also been made with the MORSE Monte Carlo code. Overall agreement between measurements, DUCT, and MORSE has been better than 10 percent.

1. INTRODUCTION

A variety of techniques are available for estimating radiation streaming down ducts. Some of these techniques are summarized in ref. 1. The majority of the duct streaming work, both experimental and analytical, has been concentrated on void ducts whose dimensions are large compared to the radiation mean free path in the material. For these cases, the radiation incident on the mouth of the duct is the predominant source of radiation reaching the duct exit either by direct streaming or by albedo from the duct wall. Relatively simplified analyses of these two components provide answers that are in reasonable agreement with experiment for cases such as shelter entry ways or beam ports through reactor shields.

Ducts through shields in space reactors are, however, more likely to be filled either by metal or by some fluid so that radiative exchange between the duct material and the shield material becomes an important contribution to the radiation exiting from the duct. Evaluating the effect of a filled duct is therefore a more complicated process and is not amenable to an unsophisticated approach. An exact solution requires the use of a radiation transport code with a three-dimensional generalized geometry capability (a Monte Carlo code). The motive behind the work described here is to arrive at an approximate method that can be applied to iterative design studies without the large expenditure of computer time required for a series of Monte Carlo calculations.

This research was divided into four parts; namely,

1. Formulation and programming of a code for calculating the effects of shield irregularities on the space craft environment. This method consists of using the solution of a two-dimensional transport code as a starting point and making perturbations to that solution to account for shield irregularities such as coolant ducts and other shield perturbations.
2. Performance of analytical tests to determine the range of validity of the code developed in Part 1.
3. Performance of an experimental program using a geometry and material similar to real space-power shielding problems but "clean" enough to provide a good check on the analysis.
4. Extension of the experimental-analytical comparison to include neutron and secondary gamma production and transport in a NERVA-BATH shield assembly.

2. DEVELOPMENT OF THE DUCT CODE

Except for isolated irregularities, we assume that the shield can be approximated by

use of a two-dimensional model. Neglecting these irregularities, a two-dimensional calculation can be performed using a transport code such as TWOTRAN (ref. 2) or DOT (ref. 3). These codes can be made to generate a "flux tape" which is a complete listing of fluxes within a spatial energy and angle mesh specified in the calculation. The DUCT code that we have written takes these fluxes as input and solves for perturbations in the flux at specified detector points caused by the presence of irregularities in the shield. In the present form, the code only considers cylindrical ducts. In some parts of the code the 2D angular flux mesh is used in a discrete manner, in other parts, interpolations in angle are made. Spatial interpolations are made in all cases and the fixed energy grouping is used throughout.

The primary assumption attendant to the derivation of the method is that the inward-directed current passing through the surface of a duct is obtained by integrating over the angular flux predicted from the unducted 2D solution. In other words, it is assumed that changing the material in the duct region does not change the level of radiation passing into the region. Auxilliary one-dimensional transport calculations in cylindrical geometry show this to be a good approximation.

2.1 ESTIMATOR FOR THE SCATTERED RADIATION

The last collision kernel volume integral is given as

$$\varphi(E)_S = \iiint_{vE'\Omega'} \frac{\varphi(\Omega', r, Z, E')P(E'\Omega' \rightarrow E\Omega)\exp(-b(E'))}{R^2}$$

where

$\varphi(\Omega', r, Z, E')$ are flux components in phase space coordinates in cylindrical geometry centered in dv.

Ω' is direction of incoming flux, and E' is energy of incoming flux.

R is the distance from dv to the detector.

Ω is the direction from dv to the detector.

E is the energy after collision.

$P(E'\Omega' \rightarrow E\Omega)$ is the scattering cross section per steradian per cc for transitions from Ω' to Ω and E' to E. These two transitions are not independent since for a given scattering species the energy lost in a collision depends on the scattering angle. Where dv is filled with a variety of scattering species more than one E can result from a given incident E' and Ω' flux component.

$b(E')$ is $\Sigma_T(E')R$.

To simplify the evaluation of the last collision integral, group-averaged cross sections and group fluxes are used for both the incident and scattered radiation. This allows us to use the same cross-section set in the perturbation calculation as that used in the 2D transport analysis of the idealized shield.

Another simplification is to restrict the the duct shape to cylinders and divide the duct volume by planes perpendicular to the duct axis. Each of the volume elements can then be treated as an equivalent disk source. The uncollided flux from an isotropic disk source of strength S_A per unit area at a detector on the axis is given by

$$\varphi = \frac{S_A}{2}\left[E_1(\mu t) - E_1(\mu t \sec\theta)\right] ,$$

where μt is the integral of total cross sections along the axis between the two points and θ is the angle between a ray on the axis and a ray from the detector to the outer rim of the disk and the function $E_1(x)$ is given by

$$\int_x^\infty \frac{e^{-t}}{t}\,dt.$$

Using the group averaging approach the flux at a detector on the duct centerline at the exit plane is then given by

$$\varphi_S(g') = \sum_g\sum_m\sum_n P_S(g \rightarrow g', m)\, W_m \varphi_m(n, g)$$
$$*2\pi\Delta t_n\left[E_1(-\mu(g)R(n)) - E_1(-\mu(g)R(n)\sec\theta_n)\right] ,$$

where $P_S(g \rightarrow g', m)$ is the unit volume probability of scattering from group go to group g' from the mth angle to the direction of the detector. $P_S(g \rightarrow g'm)$ is given by

$$P_S(g \rightarrow g'; \theta_S) = \frac{1}{4\pi}\sum_{\ell=0}^{n} S_\ell(g \rightarrow g')P_\ell(\theta_S) ,$$

where

$S_\ell(g \rightarrow g')$ are given by the group average cross sections generated by GGC4.

W_m is the quadrature weight of the mth angle increment = solid angle/4π.

$\varphi_m(n, g)$ is the angular flux at the nth duct point in the mth angle in group g (4π x neutrons cm^{-2} $\overline{STER}^{-1}$).

$\mu(g)R(n)$ is the total number of mean free paths from the nth duct point to the detector for group g.

2.2 ESTIMATOR FOR THE UNCOLLIDED FLUX TO ON-AXIS DETECTOR

The uncollided flux from radiation passing through the duct wall is given by

$$\varphi(E)_D = \frac{\int\varphi(\Omega, r, Z, E)\bar{\Omega}\cdot\bar{n}\,dS\exp(-\Sigma_r(E)R)}{R^2} ,$$

where

$\varphi(\Omega, r, Z, E)$ are the flux components.

Ω is the direction from the surface element dS to the detector.

n is a unit vector normal to the surface increment.

r, Z are the space coordinates centered in dS. R is the distance from r, Z to the detector.

Using the same numerical approach to evaluate this integral as was used in the scattering calculations detailed above,

$$\varphi_D(g) = \sum_n \frac{\bar{\varphi}(n, g)\Delta S \cos\theta \exp(-\mu(g)R(n))}{R^2(n)}$$

where

ΔS is the duct surface area associated with the particular duct segment.

$\bar{\varphi}(n, g)/4\pi$ is the flux per steradian in the detector direction averaged over ΔS.

θ is the angle between the surface normal and a ray to the detector.

The perturbation caused by the material filling the duct is assumed to express itself as a change in the scattering intensity within that geometric region and as a change in the component which streams from the duct wall to the detector without suffering a collision. The scattered flux is thus obtained by integrating a last flight estimator over the volume based on a collision density given by the unperturbed flux times the differential angular scattering probability. The direct flux is obtained by integrating an uncollided kernel over the surface of the duct where the local source is given by interpolating the 2D fluxes. The perturbation is then obtained by comparing the results of these calculations with calculations where the volume of concern is filled with shield material.

2.3 ESTIMATOR FOR THE UNCOLLIDED COMPONENT FOR OFF-AXIS DETECTORS

Formulations have been made for calculating the uncollided component to detectors off the duct axis. It will be recalled that the basic method is capable of calculating both a collided and uncollided component on the duct axis, but for off-axis detectors it can only calculate the collided contribution. The formulation presented here permits an estimate to be made of the enhanced penetration of flux vectors whose paths lie partially within the duct and partially within the surrounding shield.

The complicated geometry is one of the major obstacles in formulating the estimator. The effective area on the duct wall that can radiate toward the detector is given by integrating over all the surface areas associated with the duct increment whose normal has a component in the detector direction

$$\int_{\Delta A} \bar{r} \cdot \bar{n}\, dA \ ,$$

where $\bar{r}$ is a unit vector in the direction of the detector and $\bar{n}$ is a unit vector normal to the tangent plane to the surface. It is assumed that the direction $\bar{r}$ is essentially the same for all points on the duct increment or that the distance to the detector is large when compared to the radius of the duct.

It is possible to evaluate the integral over the appropriate area and multiply by the flux vector to get a total "source" in the detector direction but this is inappropriate because it does not account for the varying path lengths through the duct. To account properly for the varying path lengths the surface must be split into azimuthal increments. Some trial and error cases showed that splitting the 180° band into six equal 30° increments provides a reasonable approximation of the projected area. The actual area of each increment is $\frac{\pi r}{6}\Delta t$ and the flux contribution to the detector is

$$\varphi(E)_o = \varphi(\bar{r}, E)\bar{r} \cdot \bar{n} \frac{\pi r}{6} e^{-b_1/R^2}$$

where Δt is the length increment, R is the detector-to-area increment separation distance, and b_1 is the integral of total cross section along R.

3. CALCULATIONS OF THE LITHIUM HYDRIDE SHIELD EXPERIMENT

The first test for the DUCT code was an attempt to simulate a neutron shield applicable to to the SNAP type shield. This shield consists of a lithium hydride shield with sodium coolant holes.

The shield was represented in the DOT calculation as a cylinder with radius 25.4 cm in radius, 25.4 cm high, having 22 radial intervals and 22 axial intervals. The top two and bottom two axial intervals and the outermost two radial intervals used steel cross sections; the others were LiH. An asymmetric 100-angle quadrature set with 76 downward and 24 upward angles was selected in an attempt to prevent ray effects. The spacial mesh was nonuniform, but a rule was followed that no interval be more than twice as wide as its neighbor.

The source was represented by a top boundary source in the first six downward angles. The source varied with energy group according to the measured source spectrum and with radial interval according to the measured beam profile.

In the DUCT calculations, the duct was represented by a cylinder 2.54 cm in radius completly penetrating the shield with its axis coinciding with the axis-of-symmetry of the shield. The rest of the geometry of the shield was input to the GEOM package, with the requirement that the duct be re-input as the first quadratic surface for GEOM.

DUCT calculations were run for three detector positions with shield, sodium, or void in the duct. In each case the objective is to calculate the flux crossing the duct wall or colliding within the duct and reaching the detector.

To "know" the unperturbed flux at the detector location requires that it be available from the DOT calculation. For detectors at or in the shield, simple interpolation of the DOT fluxes will

suffice. For detectors near the shield it is therefore recommended that the DOT calculation contain void intervals which themselves contain the proposed detector sites. For detectors far from the shield, surface integration of the DOT fluxes and their projection to the detector, such as is done in DASH is required to determine the unperturbed flux.

3.1 COMPARISON WITH MONTE CARLO CALCULATION

A MORSE (ref. 4) Monte Carlo calculation was performed for the experimental configuration with sodium in the duct. Detector No. 1 was represented by a point one inch from the shield on the duct axis. The scattered flux was calculated by last-flight estimation from each collision site. The source was represented by a circular beam six inches in radius with its center on the duct axis. The general O5R geometry package (GEOM) was used.

The final calculation involved 84 batches of 100 neutrons each. Each neutron started from some point in the 6-in. radius circle on the top surface of the shield. Its distance from the center of the circle was selected uniformly from 0 in. to 6 in. and its weight adjusted by

$$\text{WATE} = 2*\text{WATE}*\text{RADIUS}/\text{BEAM},$$

where RADIUS is its distance and BEAM = 6 in., to account for the fact that the circular area was not sampled uniformly. Its direction from the center of the circle was selected randomly. Its starting direction cosines were (0, 0, 1), that is, normal incidence.

The initial energy group of the neutron was selected from the 15 groups not according to the natural source energy distribution but from a biased distribution which favored the higher energy groups; MORSE adjusted its weight to compensate for the source biasing.

The path length of each flight was selected not from the natural exponential distribution but from a transformed exponential distribution which encouraged longer paths near the the favored downward direction and shorter paths near the upward direction. The parameter PATH = 0.5 was used; MORSE adjusts the weight to account for the path length biasing.

At the end of each flight path is a collision site; since absorption is not allowed, the neutron's weight is suitably multiplied by a nonabsorption probability. A last-flight estimate is then made, contributing

$$P(\theta)*\text{WATE}*\text{EXP}(-\text{ARG})/R^2$$

to the scalar scattered flux at the detector for every energy group into which the neutron could possibly scatter from its present group. Then the neutron is allowed to launch its next flight in a newly determined direction with path length selected from the transformed exponential distribution.

At the end of the 84 batches, the scattered flux and its fractional standard deviation were calculated for each energy group, the scattered flux was added to the direct flux, and the results divided by the group width in MeV. The final units of the flux were (neutrons/cm^2-MeV)/(Incident neutron-cm^{-2}). Eighty thousand, four-hundred eighty-two scattering events contributed to the flux estimates. The fractional standard deviation of the scattered flux ranged from 5 to 20 percent.

A comparison with the DUCT calculation is shown in fig. 1. In general, the agreement varies between 10 to 20 percent, with the DUCT calculations consistently higher, except for the lowest two energy groups.

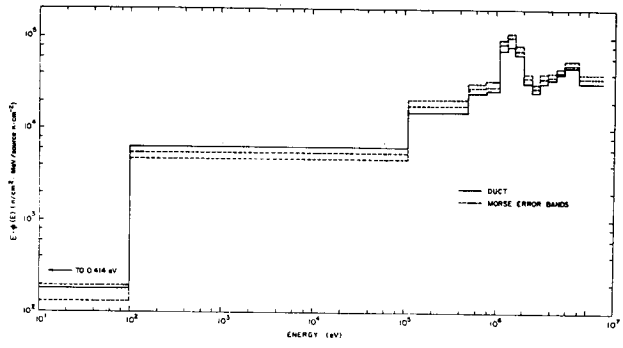

Fig. 1. Comparison between DUCT and MORSE calculated axial responses

4. EXPERIMENTAL PROGRAM

The experiments were designed to be as sensitive as possible to streaming but "clean" enough to provide a good check on the analysis.

4.1 NEUTRON SOURCE

The experimental layout for the experiments is shown in fig. 2. Photo-neutrons were produced in the tantalum-beryllium converter bombarded by 50-MeV electrons from the Gulf Radiation Technology linear accelerator. This converter has been used in several previous programs (ref. 5) at Rad Tech and provides the source spectrum shown in fig. 3. This is the spectrum measured by time of flight over 50 meters; 2.54 cm of lead and 3.144 cm of uranium were used as filters at the 16-meter station to reduce the gamma flash. This setup is for the lithium-hydride-sodium duct experiments. A similar setup was used for the BATH-NERVA shield streaming experiments with the exception that the measurements were made at 16.7 meters. Neutrons produced in the tantalum-beryllium target were then collimated to provide a circular plane beam for normal incidence on the shield assembly.

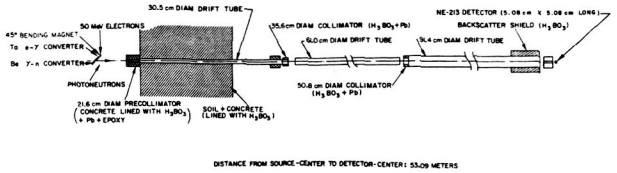

Fig. 2. Experimental layout for the lithium hydride duct *shield experiment*

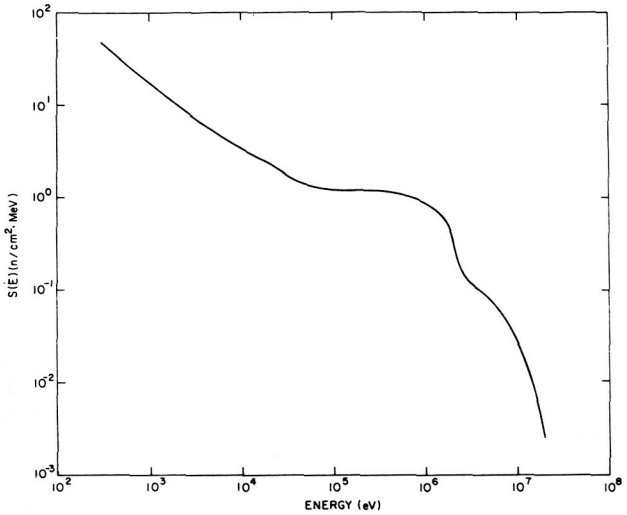

Fig. 3. Measured source spectrum for the lithium hydride duct shield experiment

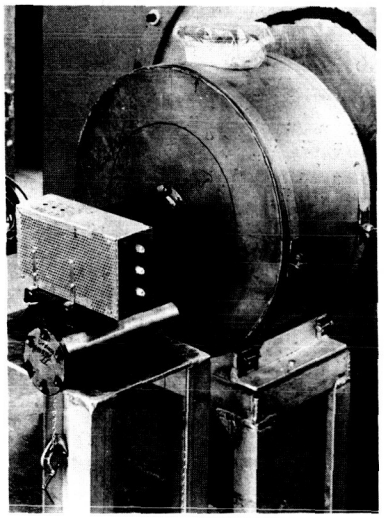

Fig. 4. Lithium Hydride Duct Shield Assembly.

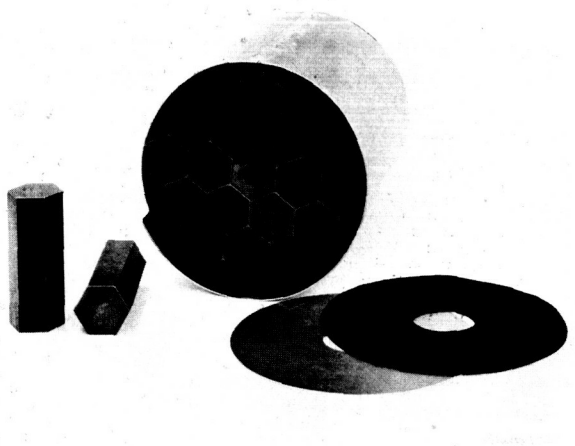

Fig. 5. Inner-BATH Shield Assembly.

4.2 SHIELD ASSEMBLIES

Two shield assemblies were studied. The first assembly was cylindrical lithium hydride assembly 50.8 cm in diameter by 25.4 cm thick with a 5.08 cm diameter axial duct. The assembly in situ at the end of the 50-meter flight path is shown in fig. 4. The duct was filled with either sodium or lithium hydride.

The BATH assembly consists of nineteen two-in. hexagonal by 11-in. long pieces, placed in an hexagonal matrix approximately 10 inches diameter by 11.1 inches long. To minimize the effect of room-return neutrons, the matrix was enclosed in a 10-in. diameter cylindrical container enclosed by a 5-in. thick shield. The shield consisted of a mixture of 50% by weight of lithium carbonate (Li_2CO_3) and polyethylene (CH_2). The inner BATH assembly is shown in fig. 5; the assembled BATH and side shield in situ at the end of the 16-meter flight path is shown in fig. 6.

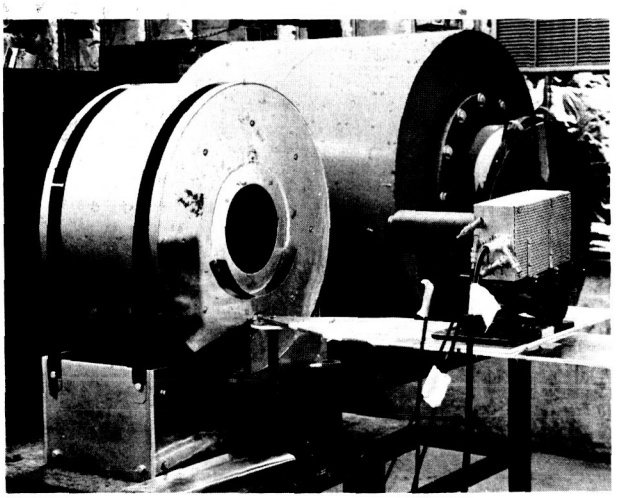

Figure 6. BATH Shield Assembly Enclosed in Outer Shield

4.3 DATA ACQUISITION

During a previous Rad Tech program (ref. 5), a new experimental method was developed for studying simultaneously fast-neutron transport and secondary gamma-ray production and transport in shields. With this method, an electron accelerator is used to produce intense 50-nsec pulses of photoneutrons. These neutrons stream down an evacuated 52-meter long drift tube to strike a shield assembly. An NE-213 detector is positioned immediately behind the shield assembly to detect both fast neutrons and secondary gamma rays produced in a shield assembly by $(n, x\gamma)$ and $(n, x\gamma)$ reactions.

A simplified block diagram of the three-parameter data acquisition system used with the NE-213 detector is shown in fig. 7. Three parameters, t, h, and x, are recorded for each detection event. The time parameter t is the time interval between the Linac pulse and the detection event; the pulse-height parameter h is proportional to the light produced in the NE-213 scintillator by neutron and gamma-ray interactions; and the pulse-shape discrimination parameter x identifies detection events as due to neutrons or gamma rays. The key features of each parameter are discussed next.

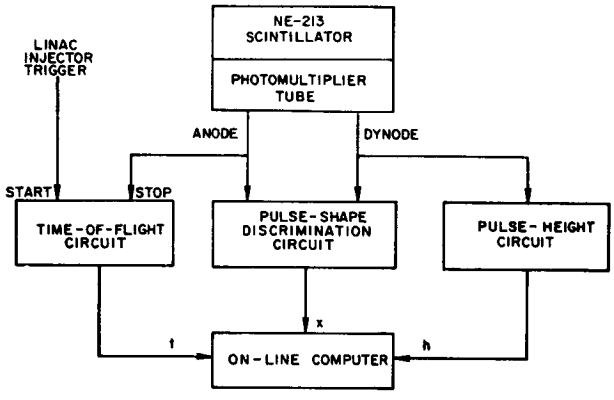

Fig. 7. Simplified diagram of the three-parameter data acquisition system

4.3.1 Time Parameter

The time parameter is related to the energies of neutrons incident on the shield assembly rather than the energies of neutrons leaking from the shield. This is true because the shield assembly is located at the end of the flight path near the detector rather than at the beginning near the pulsed neutron source as it would be for a conventional time-of-flight shielding experiment. The present geometry arrangement is also used for $(n, x\gamma)$ and (n, γ) reaction studies (ref. 6).

The time scale may be naturally divided into two regions. For short times ($t < 4$ μsec), detection events due to: (1) neutrons with energies above the detector threshold at 0.9 MeV ($t = 4.0$ μsec), and (2) gamma rays produced by $(n, x\gamma)$ reactions with threshold at 1.3 MeV ($t = 3.3$ μsec) are recorded. These events may be analyzed and interpreted in either the time domain or incident neutron energy domain. The results are completely equivalent within the abovementioned approximation.

However, for long times ($t > 4$ μsec), neutrons are not detected and only gamma rays produced by (n, γ) reactions are detected. Because these reactions may be due to uncollided neutrons, slowing-down neutrons, and/or thermalized neutrons, time and incident neutron energy cannot be uniquely related. Thus, these data are analyzed only in the long time domain. In summary, the data which are obtainable are categorized as due to:

1. Short time or fast neutrons ($E > 0.8$ MeV, $t < 4.0$ μsec)
2. Short time $(n, x\gamma)$ or inelastic gamma rays ($t < 3.3$ μsec)
3. Long time (n, γ) or capture gamma rays ($t > 3.3$ μsec).

4.4 UNFOLDING

The mathematical procedure for unfolding is carried out in the FERDOR code. The method is discussed in refs. 7 and 8. The results presented here are only the output from the FERDOR code. Each unfolded spectrum is not uniquely defined but instead gives a band of values within which the actual spectrum should lie.

The calculation of this band by FERDOR includes two contributions, one due to the statistical errors in the input pulse-height data, and the other to the suboptimal calculation of the "inverse" of the response matrix, because, in general, such errors are: (1) difficult to assess due to the indirect manner in which response matrices are produced by interpolation from calculation, and a measurement for example, and (2) difficult to propagate through the unfolding procedure. In our case, the response matrix was obtained entirely from a Monte Carlo O6R calculation performed at the Oak Ridge National Laboratory.

An excellent check on the methods described in the previous section is provided by the time-of-flight spectrum. Note that this spectrum is always measured simutlaneously by the three-parameter data acquisition system. The measured source spectrum (no shield assembly) obtained by time of flight should agree with that obtained by unfolding the proton pulse height spectra. A comparison is shown in fig. 8; the agreement is very good, which lends confidence to the unfolding procedure used here.

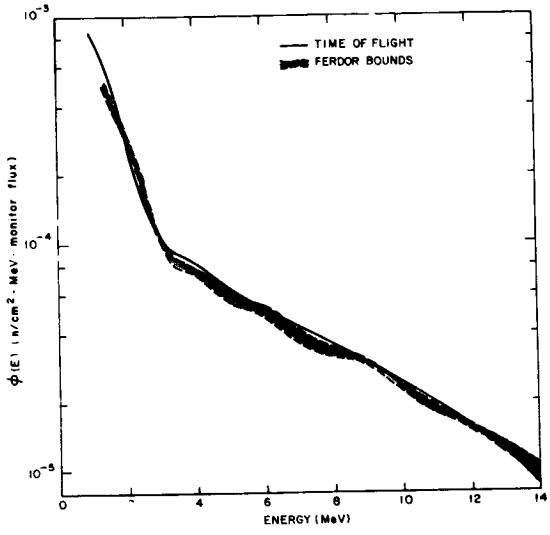

Fig. 8. Comparison between the FERDOR unfolded and time-of-flight measured source spectra

5. COMPARISON OF DUCT CALCULATION AND EXPERIMENT

Comparisons between the experimental data obtained with the lithium hydride assembly and calculations performed with the DUCT code are shown in figs. 9, 10, and 11. The calculations yielded neutron flux per MeV per source neutron; the measurements yielded neutron flux per MeV per source monitor. To compare the two on a source neutron basis, the measured results were multiplied by a source normalization factor. This factor was obtained by integrating the calculational source spectrum and the measured source spectrum over the same energy limits; namely, 2.0 MeV to 5.5 MeV, and then dividing the calculational source integral by the experimental source integral, that is

$$N_s = \frac{\left[\int_{2.0}^{5.5} \varphi(E)dE\right]_{DOT}}{\left[\int_{2.0}^{5.5} \varphi(E)dE\right]_{EXP}} = 0.674 .$$

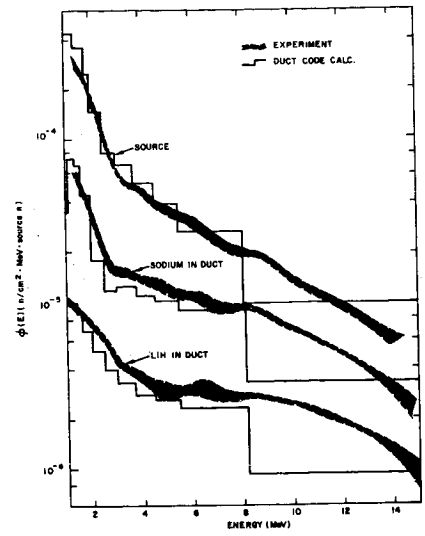

Fig. 9. Comparison between measured and DUCT calculated axial detector responses for a detector located at the duct exit

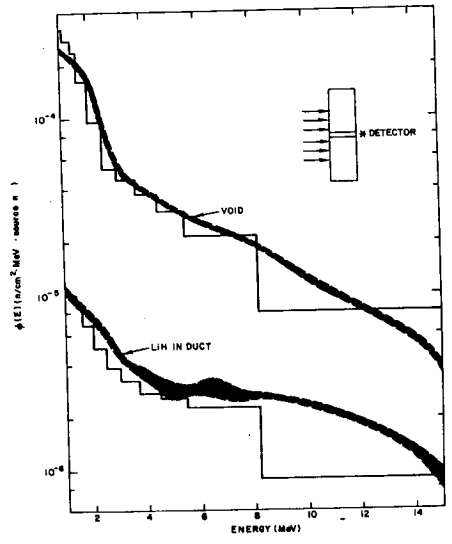

Fig. 10. Comparison between measured and DUCT calculated axial detector responses for a detector located at the duct exit

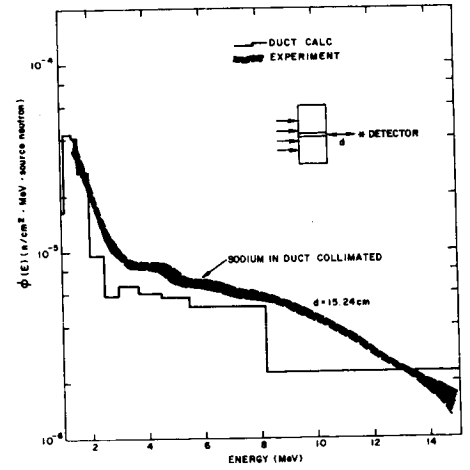

Fig. 11. Comparison between measured and DUCT calculated axial detector responses for a detector located 15.24 cm from the duct exit

This was done for the source spectrum only so that no further normalization is applied when comparing measurement with theory.

The comparison between the measured and axial detector responses is shown in fig. 9 for the sodium and lithium hydride filled ducts. Figure 10 compares the measured and calculated fluxes for void and lithium hydride filled ducts. Figure 11 compares the calculated and measured axial detector respones for a collimated detector located 12.7 cm from the duct exit. The final results for the BATH experiment-calculation comparisons are not complete at this writing.

6. CONCLUSIONS

In view of the overall agreement between measurement, DUCT and MORSE, we feel the DUCT code provides a good engineering code to claculate the effect of coolant type holes in shields. We have tested the method to its extreme limit for streaming.

The experiments were limited to neutron energies above 1 MeV; however, as noted earlier, the agreement with MORSE was very good at the low energies ($E < 10$ keV) where the fluxes tend to be isotropic lending confidence to the DUCT calculations at these energies. It is important to note that the MORSE calculation required approximately 30 to 45 minutes to achieve a 10 to 20% variance on the scattered flux estimates for a single detector position. The DUCT calculations require approximately four minutes per detector with an additional 40 to 60 minutes for the DOT calculation. However, if one were making an engineering type analysis of a shield where many duct-detector configurations are to be studied, the DOT-DUCT running time would be considerably shorter than the MORSE running time, as seen in the following table:

MORSE VS DOT/DUCT RUNNING TIMES PER DETECTOR (min)

Number of Ducts	1	2	4	6
MORSE	40	80	160	240
DOT/DUCT	64	68	72	80

We recommend that a void region be included in the DOT calculation for detectors near the shield/void region to minimize errors in extrapolating the DOT fluxes. For detectors quite distant from the shield, we recommend the use of DASH, which we plan to incorporate in the production version of DUCT.

ACKNOWLEDGEMENTS

The support of the U. S. Atomic Energy Commission under Contract AT(04-3)-167 is gratefully acknowledged.

REFERENCES

1. W. E. Selph, et al., Weapon Shielding Handbook, Chapter 5, Methods of Calculating Effects of Ducts, Access Ways, and Holes in Shields, DASA Report DASA-1891-1, January 1969.

2. K. D. Lathrop, "Theory and Use of the General-Geometry TWOTRAN Program," Los Alamos Scientific Laboratory Report LA-4432 (1968).

3. F. Mynatt, "DOT, A Two-Dimensional Discrete Ordinates Transport Code," CCC-89 K-1694, Oak Ridge National Laboratory - Radiation Shielding Information Center (1969).

4. E. A. Straker, et al., "The MORSE Code, A Multigroup Neutron and Gamma-Ray Monte Carlo Transport Code," Oak Ridge National Laboratory Report ORNL-485, September 1970.

5. L. Harris and H. Kendrick, "Time-Dependent Fast Neutron and Secondary Gamma-Ray Spectrum Measurements in Concrete," DASA Report 2401-1, Gulf General Atomic Incorporated (1969).

6. V. J. Orphan and C. G. Hoot, "Measurement of Gamma-Ray Production Cross Sections for Nitrogen and Oxygen," DASA Report DASA 2267, Gulf General Atomic Incorporated (1969).

7. W. R. Burrus and V. V. Verbinski, Nucl. Instr. Methods 67, 181 (1969).

8. V. V. Verbinski, et al., Nucl. Instr. Methods 65, 8 (1968).

APPLICATION OF THE MATRIX EXPONENTIAL KERNEL

Alfred F. Rohach
Associate Professor of
Nuclear Engineering

Department of Nuclear Engineering
and Engineering Research Institute
Iowa State University
Ames, Iowa 50010

Abstract

A point matrix kernel for radiation transport, developed by the transmission matrix method, has been used to develop buildup factors and energy spectra through slab layers of different materials for a point isotropic source. Combinations of lead-water slabs were chosen for examples because of the extreme differences in shielding properties of these two materials.

Introduction

The transmission matrix method as applied to radiation transport theory was developed by Yarmush et.al. (ref. 1). This development was applicable for uncharged particles from an infinite plane source in slab geometry. Angular distributions were approximated by angular cosine polynomial expansions and energy distributions were approximated by a group structure.

Description of the Point Kernel

As a result of the development (ref. 1), the transmission through a plane slab is

$$\underline{\phi}_{pl} = T(x)\underline{S} \tag{1}$$

where:

$T(x)$ = the transmission matrix
$\underline{S}$ = a source vector representing the source angular and energy distribution
$\underline{\phi}$ = a response vector representing the transmitted angular and energy distribution.

Recent work (ref. 2) has shown that one can obtain a point kernel from equation (1). This kernel is

$$K_{pt} = \frac{1}{4\pi x^2}\left[T(x) - xT'(x)\right]. \tag{2}$$

After application of the transmission matrix for shields consisting of two different materials, one has (ref. 1)

$$\underline{\phi} = T_2(x_2)\left[I - R_1(x_1)R_2(x_2)\right]^{-1}T_1(x_1)\underline{S} \tag{3}$$

where:

$R_i(x_i)$ = reflection matrix for material i
$x_i = a_i x$
a_i = the fraction of total thickness in material i.

By definition material one is located next to the source. In a manner similar to analyses which lead to equation (2), one can write, for the transmission matrix through two slabs,

$$4\pi x^2\,\underline{\phi}_{pt} = (I - x\frac{d}{dx}I)\left\{T_2(x_2)\left[I - R_1(x_1)R_2(x_2)\right]^{-1} \times T_1(x_1)\right\}\underline{S}. \tag{4}$$

Performing the differentiation results in

$$\begin{aligned} 4\pi x^2\,\underline{\phi}_{pt} = \Big[&T_2(x_2)\,M(x_1, x_2)T_1(x_1) \\ &- x_2T_2'(x_2)M(x_1, x_2)T_1(x_1) \\ &- x_1T_2(x_2)M(x_1, x_2)T_1'(x_1) \\ &- T_2(x_2)M(x_1, x_2)[x_1R_1'(x_1)R_2(x_2) \\ &+ x_2R_1(x_1)R_2'(x_2)]M(x_1, x_2)T_1(x_1)\Big]\,\underline{S}. \end{aligned} \tag{5}$$

where

$$M(x_1,x_2) = \left[I - R_1(x_1)R_2(x_2)\right]^{-1}.$$

At first indication this expression appears awkward for practical application; however, since the response effects from a double reflection for gamma rays can usually be neglected, one can write

$$\begin{aligned} 4\pi x^2\underline{\phi}_{pt} = \Big[&T_2(x_2)T_1(x_1) - x_2T_2'(x_2)T_1(x_1) \\ &- x_1T_2(x_2)T_1'(x_1)\Big]\,\underline{S}. \end{aligned} \tag{6}$$

Equation (5) can readily be modified to include any number of slabs of materials. Neglecting the reflection effects, one has

$$4\pi x^2\underline{\phi}_{pt} = (I - x\frac{d}{dx}I)\left[T_n(x_n)\cdots T_2(x_2)T_1(x_1)\right]\underline{S}. \tag{7}$$

Note that these expressions are matrix expressions, and the commutation property with respect to matrix

multiplication does not hold in general.

The transmission matrix is given as (ref. 1)

$$T(x) = 4C_+^{-1} e^{-\Lambda x} D(x) \tag{8}$$

where

$$D(x) = (B_+ + B_- e^{-\Lambda x} C_- C_+^{-1} e^{-\Lambda x})^{-1}$$

$$= (I - B_+^{-1} B_- e^{-\Lambda x} C_- C_+^{-1} e^{-\Lambda x} + \cdots) B_+^{-1}.$$

The matrices B_+, B_-, C_+, and C_- are functions of the material scattering and absorption properties only and not of material thickness. These operators are directly related to the radiation transport equation. Therefore the thickness occurs only in the exponential matrix which is a diagonal matrix. In most practical problems the double exponential and higher products can be neglected and equation (8) becomes the asymptotic form

$$T_\infty(x) = 4C_+^{-1} e^{-\Lambda x} B_+^{-1} \tag{9}$$

and the first derivative of T(x) becomes

$$T'_\infty(x) = -4C_+^{-1} \Lambda e^{-\Lambda x} B_+^{-1}. \tag{10}$$

Therefore equation (2) becomes

$$K_{pt} = \frac{1}{\pi x^2} C_+^{-1} (I + \Lambda x) e^{-\Lambda x} B_+^{-1}. \tag{11}$$

By similar analyses equation (6) becomes

$$\pi x^2 \underline{\phi}_{pt} = \Big(4C_{+2}^{-1} e^{-\Lambda_2 x_2} B_{+2}^{-1} C_{+1}^{-1} e^{-\Lambda_1 x_1} B_{+1}^{-1}$$

$$+ 4x_2 C_{+2}^{-1} \Lambda_2 e^{-\Lambda_2 x_2} B_{+2}^{-1} C_{+1}^{-1} e^{-\Lambda_1 x_1} B_{+1}^{-1}$$

$$+ 4x_1 C_{+2}^{-1} e^{-\Lambda_2 x_2} B_{+2}^{-1} C_{+1}^{-1} \Lambda_1 e^{-\Lambda_1 x_1} B_{+1}^{-1}\Big) \underline{S}. \tag{12}$$

Similar results can be obtained for n slabs.

Results for Multi-Layered Slabs

Results for layered combinations of lead and water are illustrated in figures 1 to 8. The choice of materials was not made for any particular shield configuration but rather to illustrate a combination of shielding material extremes. Therefore they should represent a good test for a shielding calculation. In all cases a source of 1 MeV is used.

Figure 1 shows the energy fluence build-up factor for combinations of lead slabs followed by water slabs. Figures 2 and 3 are the differential energy spectra for total shield thicknesses of five and ten mean free path lengths.

Figure 4 shows the energy fluence build-up for combinations of water slabs followed by lead slabs. As the water slabs become thicker one can note the sharp drop in the build-up factor due to even very thin slabs of lead. The shape of these curves are similar to those of Kalos (ref. 3). This effect is further illustrated in the energy spectra in figures 5 and 6. These results show the effects of the photoelectric cross section of lead. In figure 6 one can note the "filtering" effect due to the K-edge of the photoelectric cross section for lead. The effect is observable only for very thin sheets of lead.

Figure 7 illustrates the energy fluence build-up factors for a combination of three slabs of lead and water. These results show the effect of moving a lead slab through a water shield. Figure 8 shows the energy spectra for a two mean free path lead slab. This figure illustrates how effectively the lead slab removes the low energy photon build-up in the preceding water slab.

Conclusion

The point matrix kernel has been shown to be a relatively simple and effective means for calculating energy spectra and build-up factors for combinations of materials in slab geometry for a point isotropic source. This particular kernel should become an effective tool for parametric and optimization studies.

In this work only gamma ray shielding is considered; however, there is no fundamental reason why the procedure will not also work for any particles whose behavior can be described by a linear transport equation. The only distinction would be in the calculation of the particle cross sections.

ACKNOWLEDGEMENT

This work was supported by the Engineering Research Institute, Iowa State University, through funds provided by the U. S. Atomic Energy Commission.

REFERENCES

1. Yarmush, D., Zell, J. and Aronson, R., "The Transmission Matrix Method for Penetration Problems," Wright Air Development Center, Technical Report 59-772, 1960.
2. Rohach, A., "Analysis of the Matrix Point Kernel," submitted to Nuclear Science and Engineering, 1971.
3. Kalos, M., "Gamma Ray Penetration in Composite Slabs," Nuclear Development Corporation of American Report NDA-2056-10, 1957.

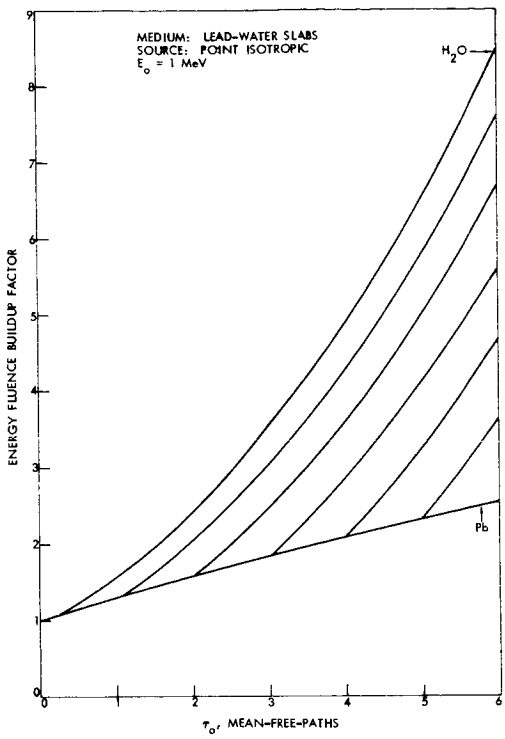

1. Energy fluence build-up factors for lead-water slabs.

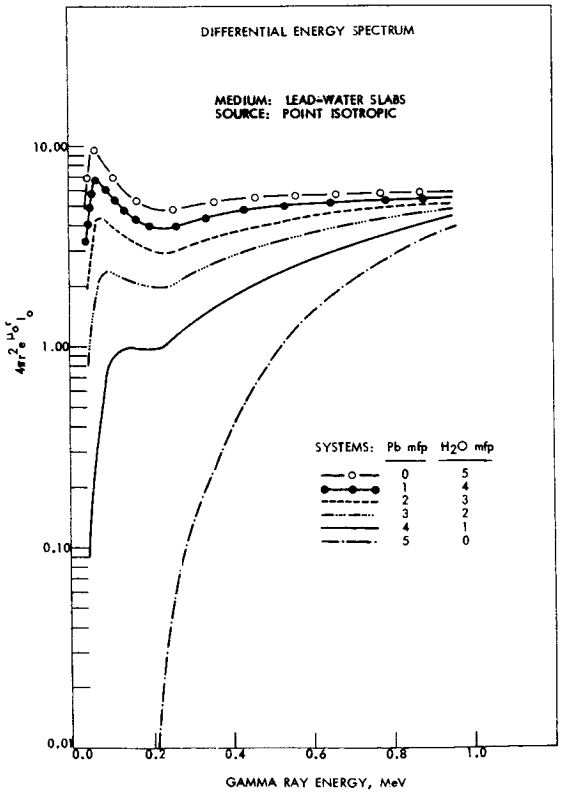

2. Energy spectra for lead-water slabs of five mean free paths total thickness.

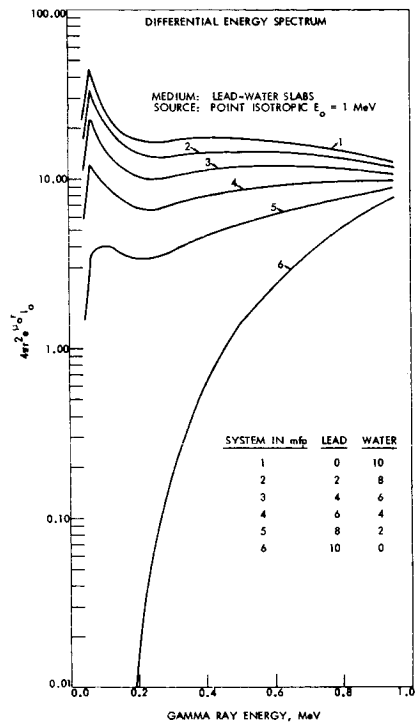

3. Energy spectra for lead-water slabs of ten mean free paths total thickness.

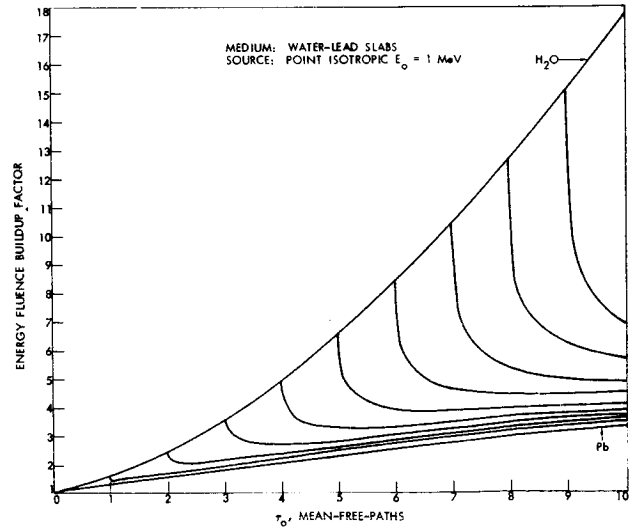

4. Energy fluence build-up factors for water-lead

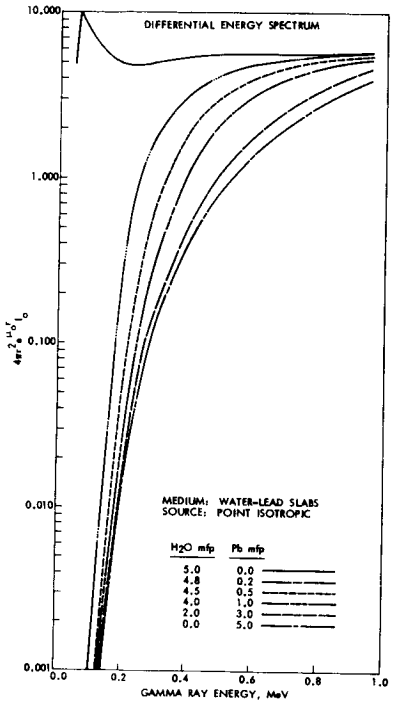

5. Energy spectra for water-lead slabs of five mean free paths total thickness.

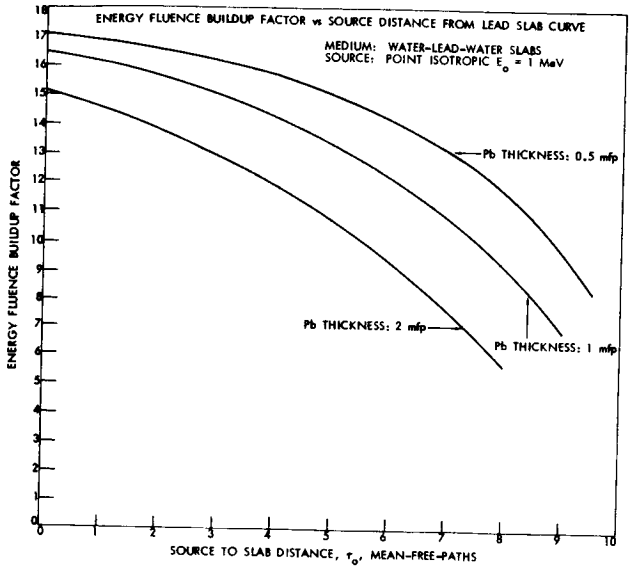

7. Energy fluence build-up factors for water-lead-water slabs.

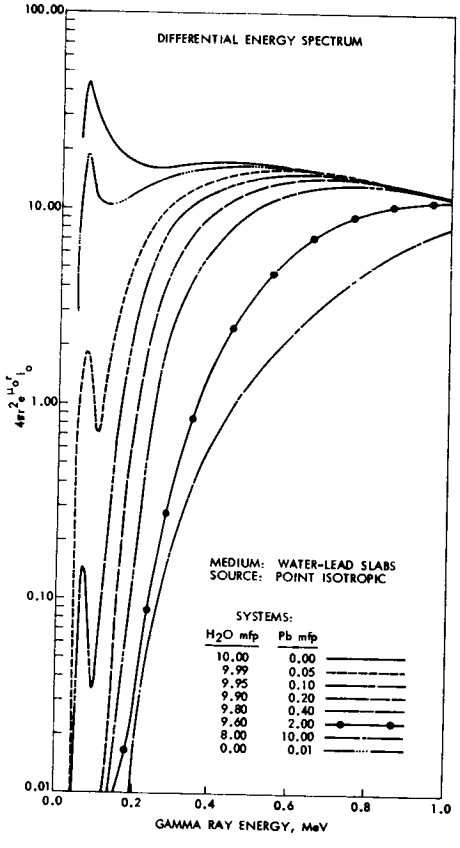

6. Energy spectra for water-lead slabs of ten mean free paths total thickness.

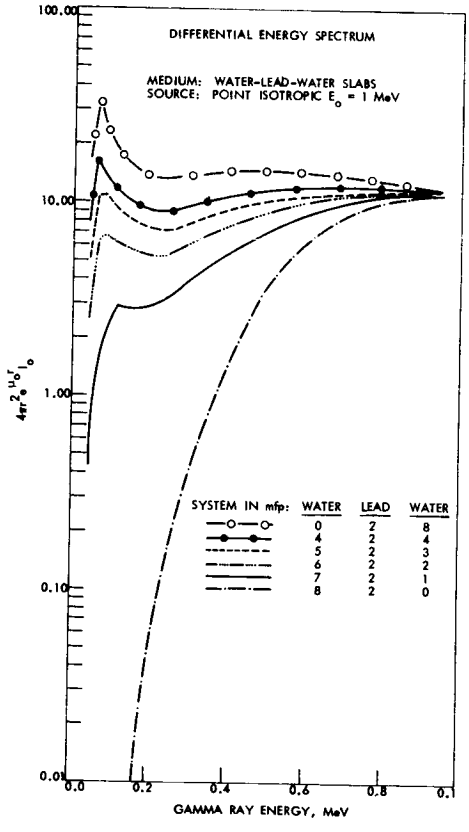

8. Energy spectra for water-lead-water slabs of ten mean free paths total thickness for a constant thickness of two mean free paths of lead.

A SIMPLE CODE FOR USE IN SHIELDING AND RADIATION DOSAGE ANALYSES

C. C. Wan
Hughes Aircraft Company

ABSTRACT

A simple code for use in analyses of gamma radiation effects in laminated materials is described in this note. Simple and good geometry is assumed so that all multiple collision and scattering events are excluded from consideration. Buildup factors may be applied to the results of this simplified analysis, when available, to arrive at improved estimates of energy deposition and attenuated intensity for actual materials.

The code proper is capable of handling laminates up to six layers. However, for laminates of more than six layers, the same code may be used to incorporate two additional layers at a time, making use of punch-tape outputs from previous computation on all preceding layers.

Spectrum of attenuated radiation may be obtained as both printed output and punch tape output as desired. This code is written in "Extended Basic" language, compatible with the GE 265 Time Sharing system.

I. Theoretical Fundamentals

Energy deposition resulting from interaction between photons (X-rays, gamma rays) and matter has been discussed in some detail in Reference (1). The basic results, obtained for simple and good geometry in a one-dimensional representation, are

Attenuated spectrum at depth x:

$$I_x(E) = I_o \cdot I(E) \cdot \exp\left[-\int_o^x \sigma(E)\, dm\right] \quad (1)$$

Energy deposited at depth x:

$$q(x) = I_o \int_o^\infty \sigma_a(E) \cdot (I_x/I_o)\, dE \quad (2)$$

where x = depth into the material, in cm.
dm = $\rho\, dx$ = differential mass depth in gm/sq cm.
ρ = density of material, in gm/cc.
E = energy level, in KeV
I_o = fluence, in cal/sq cm, incident on the surface of the first layer
$I(E)$ = spectrum of the incident radiation, function of E, normalized to unity for E ranging from 0 to infinity
$\sigma(E)$, $\sigma_a(E)$ = mass attenuation and mass absorption coefficients

To circumvent the need for a detailed definition of incident energy spectrum, Planckians expressed in terms of equivalent blackbody temperatures, in KeV units, are used as a convenient means to segregate engineering estimates of shielding and thermomechanical effects completely from specific identification of spectral contents of the primary source, i.e., bomb types, etc. Therefore, the quantity I(E) may be thought of as

$$I(E) = \sum i\, I_i \cdot P(E/E_i)$$

where I_i = fluence weighting factor for the i-th equivalent black body, with $\Sigma i\, I_i = 1$, and

$P(\xi)$ = normalized Planckian, as shown in Figure 1.

Since I_o appears in both expressions displayed above, no loss of generality will result if I_o is set equal to unity, corresponding to a fluence of 1 calorie per square centimeter. Thus a normalized dose Q(x) may be defined as

$$Q(x) = q(x)/I_o$$

which is a unique property of the material in question when subjected to an incident spectrum associated with a specific equivalent blackbody temperature, or with a particular combination of spectra associated with a number of black bodies of different equivalent temperatures. The attenuated spectrum is of course given by the ratio $I_x(E)/I_o$, or simply $I_x(E)$, since $I_o = 1$.

When materials of various thicknesses are placed one after another, either as closely spaced laminates or as a series of material layers with air spaces in between, the above computation process can be applied to each layer in succession. The attenuated spectrum from the first layer becomes the incident spectrum for the next layer, and so on. Thus, the entire series of computation may be made by means of a simple loop; the number of layers that may be accommodated becomes strictly a question of the size of machine storage available.

The mass absorption coefficients and the mass attenuation coefficients are both complicated functions of energy level, which have been tabulated by several agencies. For definiteness, the following source data are used -- these data are not always consistent with each other, but they represent the best information available at this time. Logarithmic interpolation is used throughout for establishing pertinent values associated with each energy level of concern.

(1) Photon Cross Sections from 0.001 to 100 MeV for Elements 1 through 100, Los Alamos Scientific Laboratory Report LA-3753, November 15, 1967.

(2) Analytical Approximations for X-ray Cross Sections, Sandia Laboratory, Report SC-RR-66-452, February 1967.

(3) X-ray Attenuation and Absorption Coefficients, The Boeing Company, Report D2-125065-1, September 1966.

A new edition of item (1) is in press, and will be scanned for necessary updating when published. Values to be used can be composites based on all three of the above references, a sample of which is shown on the next page, for the element copper.

For compounds, both coefficients may be approximated by proportional weighting in accordance with their atomic abundancy. Since the mass coefficients have already been referred to unit mass densities, this implies that

$$\sigma = \sum i\, A_{X_i}\, N_i\, \sigma_{X_i} \Big/ \sum i\, A_{X_i}\, N_i$$

where A_{X_i} is the atomic weight of the element X_i. The molecular formula of the compound in question is of course

$$\prod_i (X_i)_{N_i}$$

For heterogeneous mixtures of several compounds, the attenuation problem involved is far more complex than can be correctly handled by the present simplified approach. However, for an engineering estimate, it will be assumed that they behave like compounds with the same proportion of various elements by weight.

II. Description of the Code "ENEDEP"

The code written in the Extended Basic language for use on the GE-265 Time Sharing system is named ENEDEP (ENErgy DEPosition). It is capable of handling laminations up to six layers of different materials. Various combinations of source temperature (equivalent blackbody temperature) and incident fluence can be processed in series for the same material configuration. The output of this code provides:

(1) Identification of layer material by name, its density and thickness.

(2) Depth, mass depth, energy deposition per unit mass and local radiation intensity in tabular form.

(3) Attenuated spectrum at the back side of the last material layer, in tabular form and/or in punch tape form as desired to be selected by appropriate control indices.

Input data requirement, possible modification to accomodate materials with a large number of edges in their mass absorption coefficients, and a sample

problem are discussed in the following sections.

III. Input Data

Input data for executing the ENEDEP code must be presented in the following format:

1200 DATA N, M

N index for printout and punch tape input selection:

0 no attenuated spectrum information at all

1 tabulated attenuated spectrum, punched tape output optional

2 punched tape input and tabulated attenuated spectrum with optional punched tape output

M integer, denoting the number of layers, not greater than 6.

2000* DATA X(I) N(I), :

X(I) Thickness of the I-th layer, in mils

N(I) Number of printout desired in the I-th layer, integer

*2000 is a typical line number, which may be any number greater than 1200, followed by tape input containing

2010* "AAAAAAAAAA", W(I), J(I), :

"AAAAAAAAAA" alpha-numeric string of ten characters, being the name of the material of the I-th layer

W(I) Density of the material in the I-th layer, in gm/cc

J(I) Number of sets of mass attenuation and mass absorption coefficients, integer, not greater than 35

*2010 is a typical line number; for materials with no edges between 0.5 KeV and 200 KeV, there will be 22 sets of coefficients on this prepared tape; for materials with edges, add two sets for each edge.

9900 DATA S_1, P_1, S_2, P_2, ...

S_i Incident fluences, in cal/sq cm (equal to 1 for most cases)

P_i Equivalent blackbody temperature, in KeV units

The usual requirement calls for five sets of S, P combinations, namely, 1, 1, 1, 2, 1, 4, 1, 7, 1, 15. However, any other combinations pertinent to a particular problem can be used.

On the prepared tape, in addition to what is explained above under "2010", there will be other lines of material properties coefficients, specified in triplets, giving:

E(j) Energy coordinate, in KeV

F(j) Mass attenuation coefficient, σ

G(j) Mass absorption coefficient, σ_a

IV. Materials With More than Six Layers

When the material under consideration has more than six layers, the first six layers will be processed as indicated above, using an index N = 1 and obtain a punch tape output. This tape is then read into a new problem, with the following important modifications:

1200 DATA 2, 2

Only two more layers may be treated, due to storage limitation in the GE-265 Time Sharing system.

Line 9900 must be modified to read as follows:

9900 DATA S, P

S, P here must be the same set of parameters pertaining to the punch tape data being read in as tape input.

On occasions, more than 35 entries may be required to provide an adequate representation of the mass attenuation and mass absorption coefficients of one or more materials. In such cases, the dimensional statement in line 20 must be revised accordingly, an example of this may be seen in section V. Due to limitation in the size of data storage capacity, the number of layers of materials may also be adjusted. Thus a typical modification of line 20 may have the following form:

20 E(4, 42), F(4, 42), G(4, 42)

V. Sample Problem

To illustrate the usage of the ENEDEP code, a six layer laminate consisting of the following materials is analyzed:

Quartz	0.013 gm/cm^2	2	mils
Silicon	1.07 gm/cm^2	180	mils
Quartz	0.013 gm/cm^2	2	mils

Platinum	0.0022	gm/cm^2	0.04 mils
Gold	0.002	gm/cm^2	0.04 mils
Bi_2Te_3	2.0	gm/cm^2	100 mils

Due to the high Z-number associated with the materials in the last three layers, 42 entries are required for each of these layers. Therefore, the main program is modified to handle only four layers, each with provision for 42 entries. The main program would have to be recycled three times to complete the analysis required for all six layers. Input data for the first four layers used in the first cycle, results for the first four layers, input data for the fifth layer with tape input of attenuated spectrum from the first four layers, output for the fifty layer, input data for the sixth layer with tape input of attenuated spectrum from the first five layers, and output for the sixth layer are displayed in succession at the end of this paper. A summary of results for the entire range of equivalent blackbody temperature from 1 to 16 KeV is displayed in Figures 2 and 3.

VI. Concluding Remarks

A simple code for determining energy deposition dosage and attenuated fluence in material laminates induced by gamma ray radiation is presented. The average running time for one set of fluence and equivalent blackbody temperature is approximately 80 seconds (computer time). This code therefore provides a very convenient and economical tool for parametric studies in shielding problems and energy deposition analyses.

REFERENCE

1) Leipunskii, O. L., Novozhilov, B. V., and Sakhrov, V. N.: The Propagation of Gamma Quanta in Matter, International Series of Monographs on Nuclear Energy, Division X, Reactor Design Physics, Volume 6, Pergamon Press, New York, 1965.

COPPER

Z = 29; A = 63.54; ρ = 8.94: j = 28

Note: Values are given in floating point format; powers of ten are shown after the letter E.

j	Phton Energy (KeV)	Attenuation	Absorption
1	0.5000 E 00	0.1120 E 05	0.1120 E 05
2	0.6000 E 00	0.7007 E 04	0.7007 E 04
3	0.8000 E 00	0.3333 E 04	0.3333 E 04
4	0.9320 E 00	0.2237 E 04	0.2237 E 04
5	0.9320 E 00	0.1646 E 05	0.1646 E 05
6	0.1000 E 01	0.1358 E 05	0.1358 E 05
7	0.1100 E 01	0.1046 E 05	0.1046 E 05
8	0.1100 E 01	0.1100 E 05	0.1100 E 05
9	0.1500 E 01	0.5250 E 04	0.5250 E 04
10	0.2000 E 01	0.2400 E 04	0.2400 E 04
11	0.3000 E 01	0.7800 E 03	0.7800 E 03
12	0.4000 E 01	0.3500 E 03	0.3500 E 03
13	0.5000 E 01	0.1900 E 03	0.1900 E 03
14	0.6000 E 01	0.1110 E 03	0.1108 E 03
15	0.8000 E 01	0.5400 E 02	0.5383 E 02
16	0.8980 E 01	0.4100 E 02	0.4083 E 02
17	0.8980 E 01	0.2960 E 03	0.2958 E 03
18	0.1000 E 02	0.2240 E 03	0.2238 E 03
19	0.1500 E 02	0.7600 E 02	0.7580 E 02
20	0.2000 E 02	0.3300 E 02	0.3284 E 02
21	0.3000 E 02	0.1060 E 02	0.1044 E 02
22	0.4000 E 02	0.4570 E 01	0.4422 E 01
23	0.5000 E 02	0.2410 E 01	0.2268 E 01
24	0.6000 E 02	0.1490 E 01	0.1354 E 01
25	0.8000 E 02	0.7080 E 00	0.5826 E 00
26	0.1000 E 03	0.4250 E 00	0.3083 E 00
27	0.1500 E 03	0.2080 E 00	0.1083 E 00
28	0.2000 E 03	0.1480 E 00	0.6055 E-01

TABLE 1. WEIGHTED ATTENUATION AND ABSORPTION COEFFICIENTS

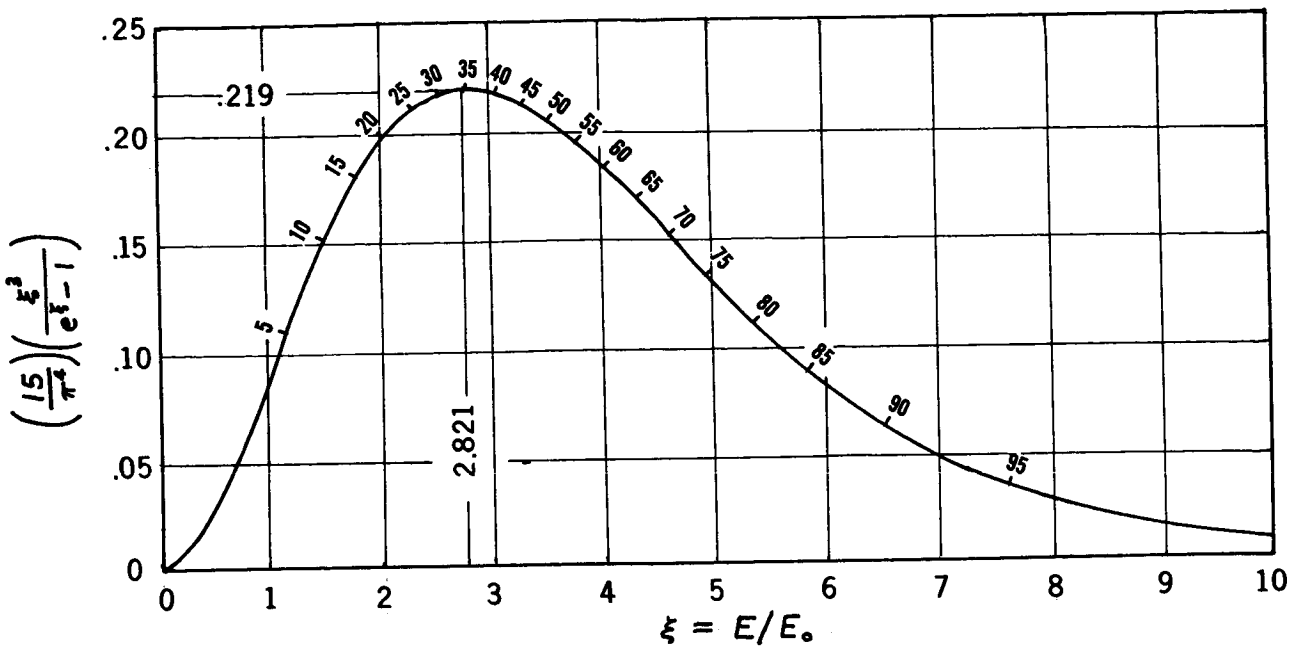

FIGURE 1. NORMALIZED PLANCKIAN

AREA UNDER CURVE = 1

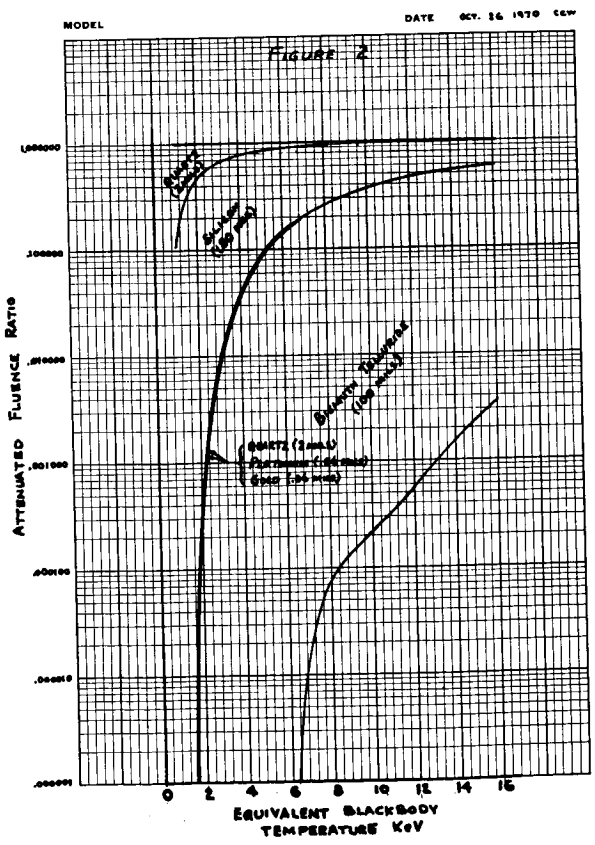

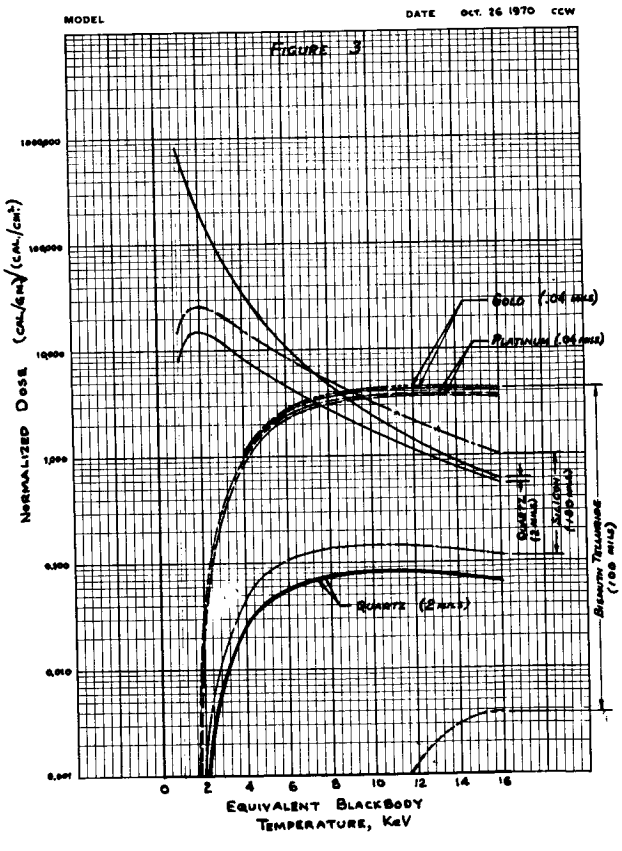

CARPET PLOT DATA FORMAT

JOSEPH M. O'BYRNE
ASSOCIATE PROFESSOR
DEPARTMENT OF MECHANICAL AND AERO-SPACE ENGINEERING
UNIVERSITY OF MASSACHUSETTS, AMHERST

Analysis and interpretation of data is the crucial phase of the decision making process. The interplay between variables must be considered as to their relative significance upon the final result, and sometimes time-sensitive decisions must be made when actual events deviate from predicted information, such as Apollo 13. As the number of variables increases past say four, the traditional method of cross-plotting tends to breakdown, and digital/analog results cannot present a sharply defined method of analysis. A graphical system is suggested. I named it "carpet plot," (since it covers anything), in which an unlimited number of complicated relationships of variables can be evaluated.

Introduction

The presentation and analysis of data involving more than two variables has traditionally been accomplished by cross-plotting data and results. An engine test is typical of this scheme, in which rpm, dynamometer load and engine temperatures are varied.

Three graphs are required, none of which define the interlationship completely, as shown in Figures 1, 2, and 3, in that one of the variables is always missing. As more variables are brought into the picture, such as spark timing, compression ratio, octane number, etc., the proliferation of graphs necessary to present the data becomes excessive, possibly increasing exponentially.

An entirely different situation exists when a fixed result can be achieved by a multiple combination of several variables. Taking a simple case, the Fourier equation for one dimensional conductive heat flow,

$$q = -KA \frac{dt}{dx} \qquad (1)$$

shows that q can be adjusted to a predetermined value by an almost infinite combination of variables. For instance, if dt is doubled for a constant K and A, dx should be doubled. If K changes by a factor of 1.4, A by 0.8, dx by 0.6, then dt can change by a factor of 1.9 and still have the same numerical value of q.

This type of problem is entirely different than the engine test type. As the system becomes more complex, and the number of variables increase and commence to interact, the difficulty of analysis increases. The carpet plot represents a new method of data presentation to simplify analysis. There is theoretically no limit to the number of variables.

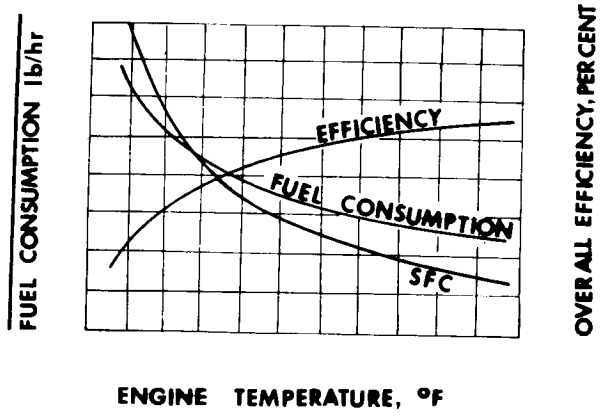

Figure 1. Plot shows the effect of dynamometer load variation on fuel consumption and other operating parameters of an internal-combustion engine

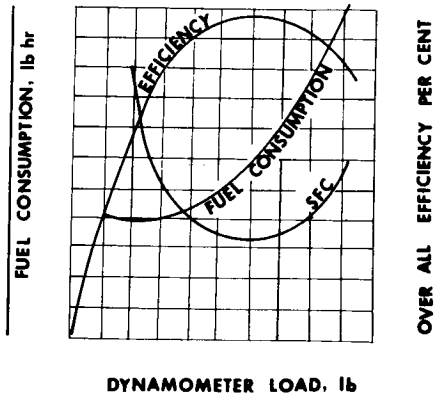

Figure 2. Plot shows the effect of engine temperature on fuel consumption and other operating parameters of an internal-combustion engine

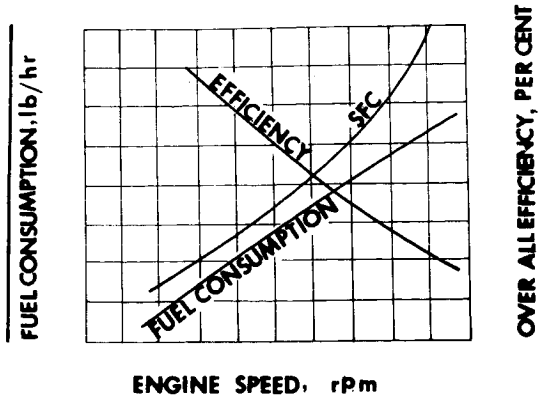

Figure 3. Plot shows the effect of engine speed on fuel consumption and other operating parameters of an internal-combustion engine.

Example of a Carpet Plot

A simple heat transfer problem was selected which could be analyzed mathematically and verified by laboratory equipment. Figure 4 shows an insulated cylinder filled with m lb. of water; its average temperature, t, is measured by six thermocouples wired in parallel. A helical cooling coil is placed in the tank, through which water flows at a mass flow rate W, regulated by an outlet valve and measured by a rotameter. A variable power heater is installed inside the tank, whose energy can be controlled by a rheostat and measured with a wattmeter.

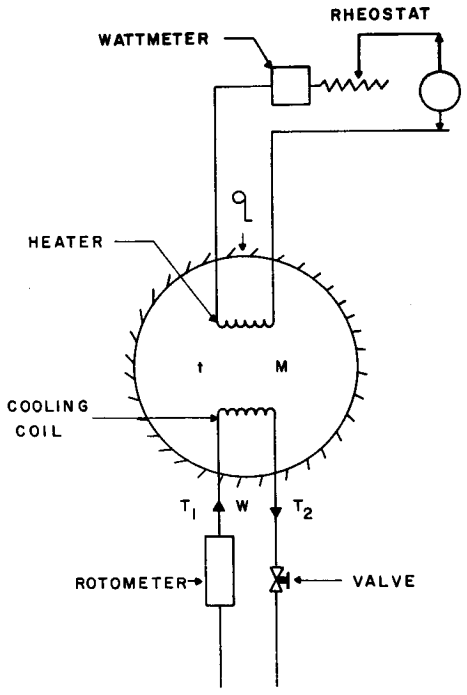

Figure 4. Schematic diagram of equipment used in a transient heat transfer experiment

With no heat application to the system, water is passed at a constant rate through the cooling coil until thermal equilibrium is reached in the tank. At time zero, the heater is turned on, and the problem is to predict the transient and steady-state values of the tank water as a function of time.

For a fixed value of W and M, various values of q were selected and the tank temperature calculated by conventional methods as a function of time, θ; a typical parametric graph is shown in Figure 5, in which the θ scale is constructed by conventional methods.

Assuming that the tank temperature is of little interest at low values of θ, Figure 6 modifies Figure 5 by ignoring the low θ values, bringing the θ values vertically into the graph, and erasing the "old" θ scale; each of the θ values are labeled.

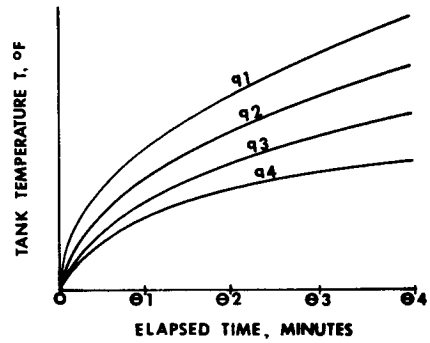

Figure 5. Traditional time-temperature plots with parametric heat loads

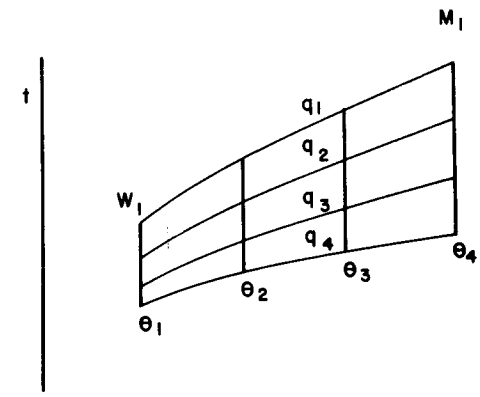

Figure 6. First step in a carpet plot technique

The graph, up to this time, has been for a constant W_1 and M_1. The carpet plot proceeds in Figure 7, in which for the same values of q and θ, a different coolant flow rate W_2 is desired. This effect is introduced by moving some convenient physical distance (3 inches, 6 inches, etc.), constructing a new time scale θ, on the traditional basis and plotting tank temperature t, as a functior of the same $q_1 - q_4$, m_1, and a constant W_2, on the "old" t scale. (The "new" W_2 plot will probably not be in a horizontal line with the W_1 graph). A significant feature of the carpet plot is that the

result, t, for all the variables uses only one scale.

For the W_2 parametric graph, the same procedure is used as previously done; bring θ into the graph, ignore small values of θ, erase the θ scale, and label the vertical θ lines; this step is shown in Figure 8.

Attention is drawn to the fact that at say the left hand bottom corner of the W_1 plane of Figure 8, a point exists for a W_1, q_4, and θ_1 value, M being a constant. Likewise the left hand bottom corner of the W_2 plane has the same q_4 and θ_1, M at the same constant. Thus, q_4 and θ_1 values are common values, and any line connecting them will have the same q_4 and θ_1. Figure 9 expands this concept to account for more points.

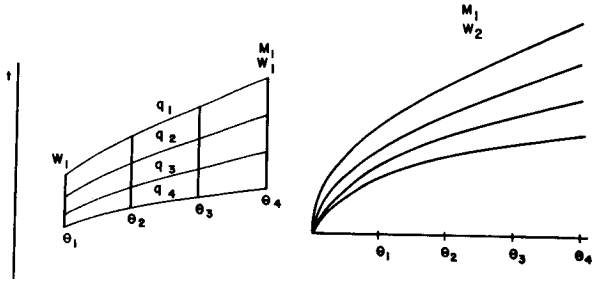

Figure 7. Extension of Fig. 6 for a different mass flow rate

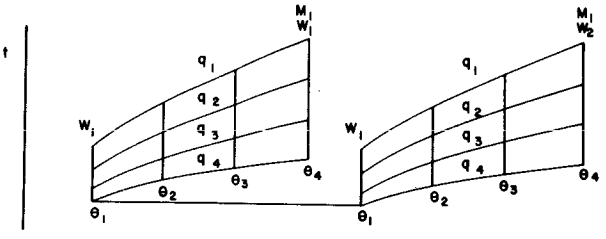

Figure 8. Common property representation for a fixed mass

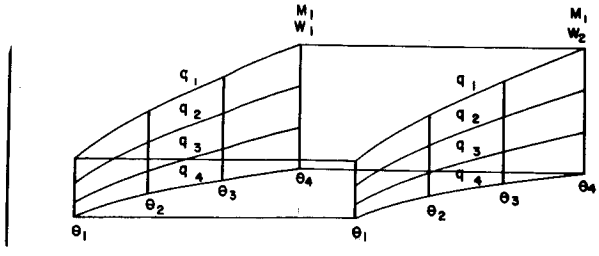

Figure 9. Extension of Fig. 8

The carpet plot takes on a 3-dimensional appearance; however, it is plotted on a flat sheet of paper and is not 3-D. It also differs from an X-Y-Z coordinate system, in that no axis is foreshortened. The stories of the box represent various q values, the ends represent various W's, and vertical slices are various values of θ.

Only two values of W are shown; in practice, at least more than three should be computed in order to establish the correct trends; the author uses four values of W as a minimum to assure that no inflections, etc., occur.

Assuming that the W_1 and W_2 planes correctly identify the tank temperature, recall that their physical separation (say 3 inches) was completely arbitrary. A plane half way between W_1 and W_2 would logically represent conditions of $W_{1\ 1/2}$; give your children the game of drawing in this interpolated plane, as shown in Figure 10, whose appearance is similar to the existing computed planes; its numerical accuracy is only a function of the artist's ability. In a similar fashion, moving 6 inches to the right of plane W_1 would logically represent a plane of W_3 conditions which can be drawn in by eye. If the interconnecting lines of common values between W_1 and W_2 are correct, and the performance of the system is assumed to be logical at higher values of W_2, then theoretically there is no limit to the extent of extrapolation and interpolation as shown in Figure 11.

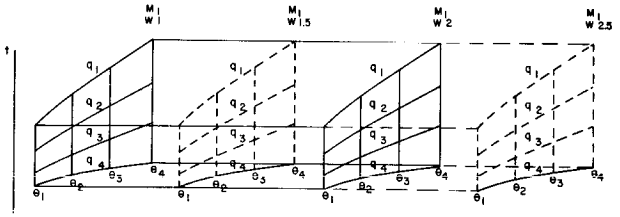

Figure 10. Technique of extrapolation and interpolation

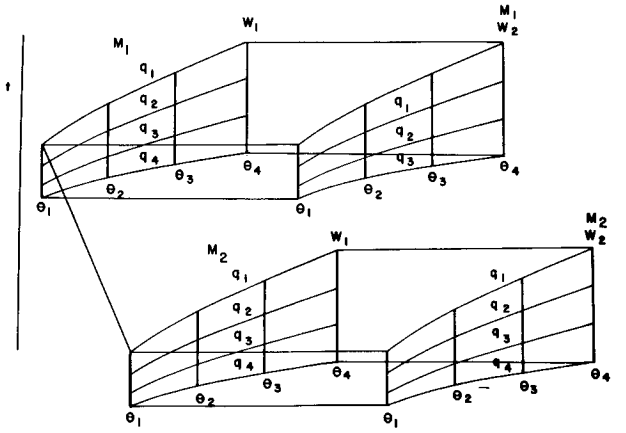

Figure 11. Introduction of a new variable into the carpet plot

To this point, the carpet plot technique has held the mass of tank water, M_1, as a constant. Let us extend the previous concepts in order to change M_1 to M_2 for the same values of θ, q, and W. The vertical location of the new M_2 plane is fixed by the temperature scale, but the horizontal location is arbitrary, as was the selection of the W_2 plane location. Basically, the problem is only to select a separation distance which will not cause overlapping of the planes. By repeating the calculations, for the same q's, W's and θ's, using a new value of M_2, Figure 11 shows the results. Only one interconnecting line between M_1 and M_2 is shown for clarity to permit interpolation and extrapolation of the M values in a fashion similar to the W values. The first objectives, presentation of coherent data for more than two variables, and logical interpolation and extrapolation of data, have been established. The variables were changed in a nested DO loop and the results computed on a CDC 3600 machine.

The next phase of utilization of a carpet plot is shown in Figure 12, which quickly shows that a tank temperature T_x will result when the system is operated with heat rate $q = q_4$, $W = W_1$, $\theta = \theta_3$ at $M = M_1$. Note that temperature at x can also be reached at $W = W_2$, $\theta = \theta_1$, $q = q_2$, an entirely different set of operating conditions. The carpet plot shows an almost infinite number of combinations. More frequently is that an operating T_x is required, and what combinations of variables will permit this T_x condition? Entering the carpet plot at the T_x value, all possible combinations can be determined rapidly and easily.

In addition to presenting every correct solution, the carpet plot will indicate every incorrect combination of variables. For instance, if temperature T_x is desired, it is perfectly obvious that M_2 cannot be used under conditions of any q, W and θ. In engineering work, the input to a data collecting or computing system is some desired performance which may change daily due to updating of information from other groups; the carpet plot permits a rapid analysis of operating conditions to achieve the result.

Another feature of the carpet plot permits an evaluation of the effect of the change in a variable upon the result. The differential equation method could be used, or the uncertainty method (1), but these techniques are extremely tedious as the number of variables increases; Figure 13 demonstrates this capability. Varying only one property, holding all others constant, the effect upon the result is shown schematically, in that dt_2 and dt_4 are about the same small magnitude, dt_1 is somewhat larger, and dt_3 far overshadows the others. The significance of this is immediately and clearly evident to a manager planning his work priorities, to define which variable should receive the major attention. In this case, it backs the previous invalid M_2 inoperative conditions for T_x, and shows that major design efforts for the system are necessary to prevent it from accidently shifting from M_1 to M_2.

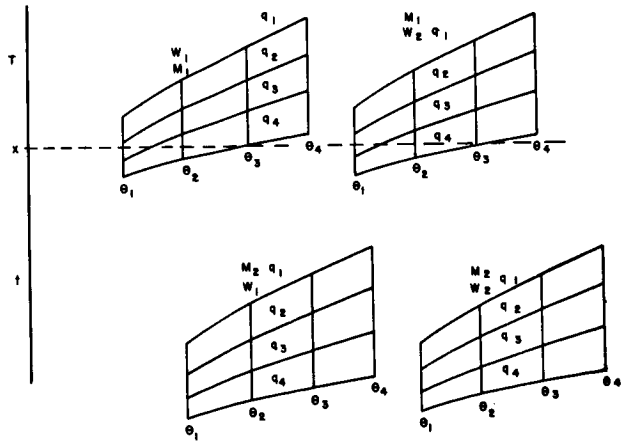

Figure 12. Method of determining all possible solutions

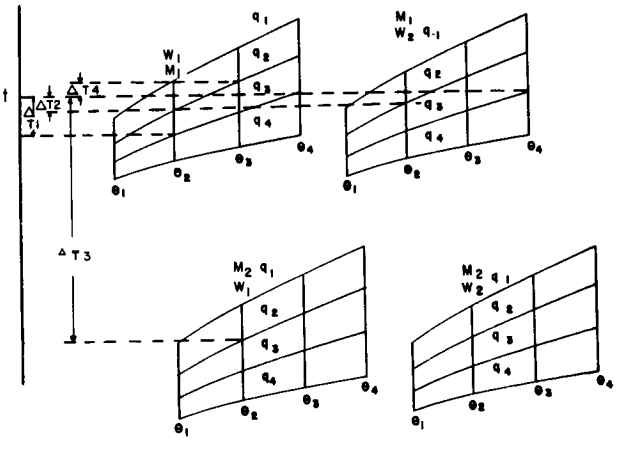

Figure 13. Relative effect upon a result with changes of a variable

Students at the University of Massachusetts proposed a detective game, in which they placed some water in the tank, then sealed it; the amount of water was not known by the writer; they set in values of power and flow rate. Access to the writer was permitted to the wattmeter, rotameter, and temperature recorder, and they posed the question: "Before the experiment ends, tell us how much water is in the tank." The appropriate heat loads and flow rates were rapidly sketched into the basic carpet plot values, and the interpolated tank water weight was established in minutes. The significance of this experiment is that the value of unmeasured and/or unknown quantities can be inferred by use of the carpet plot.

The utility of a carpet plot is unlimited. For instance, how much will the price of an automobile change as the number of coats of paint change, the color and weight of the dash padding, the quality of the spark plugs, the number of instruments, radiator size, etc. Which of the many variables is most significant?

This technique was applied to the analysis of variables associated with high performance insulation to be used on upcoming space programs such as nuclear stages in space. Only the thermal aspect was considered, but factors such as manufacturing, fabrication, cost, etc., could easily be brought into the picture. The George C. Marshall Space Flight Center has evaluated the performance of the Mars nuclear vehicle for the variables shown in Table I.

A part of this analysis is shown in Figure 14 to introduce the reader to the upcoming coordinate system. Considering only the variables of mission time, density, thickness, the weight penalty is presented in a traditional fashion; note that the remaining variables do not appear, and their effects are unknown; the information is incomplete.

Figure 15, with time scales varying, presents an almost complete version of a typical carpet plot, with a few of the variables omitted due to reproduction difficulties. Typical design parameters are immediately evident, such as no matter which of the assumed conductivities is used, large diameter tanks will have a lower weight penalty. Insulation thickness is more critical than density, and design effort in this area should be emphasized.

In conclusion, I pose the following suppose experiment to the reader, assumed to be the manager of a complex nuclear system operating in space: generate a carpet plot and ask your ten year old child some numerous questions, such as: I have designed a system for a predicted thermal conductivity, tank diameter, percent LH_2 slush, density, weight penalty, temperature levels, and manufacturing cost. Due to installation problems, the thickness, (layer density) changes from this to that. What will be the effect upon mission time? (My daughter loves to solve the 100 or so combinations of results with a school ruler.)

"A picture is worth a thousand words" applies to this technique.

References

1. Theories of Engineering Experimentation, 2nd Edition, Hilbert Schenk, Jr.
2. "Air Breathing Engines," Short Course on Air-Breathing Engine Technology, 8-12 June, 1970, Marshall Space Flight Center, Alabama.

$$WP = \frac{\rho A \Delta X}{\rho_H V}$$

$$\theta = \frac{\rho(\Delta X)^2 h_{fg}}{K \Delta T}$$

VARIABLES

1 BOUNDARY TEMPERATURES
2 INSULATION THICKNESS
3 INSULATION DENSITY
4 MISSION TIME
5 WEIGHT PENALTY
6 THERMAL CONDUCTIVITY
7 VENT PRESSURE
8 PERCENT SLUSH
9 L/D RATIO
10 DESIGN BASIS
11 VEHICLE DIAMETER

Table 1. Properties considered in the study

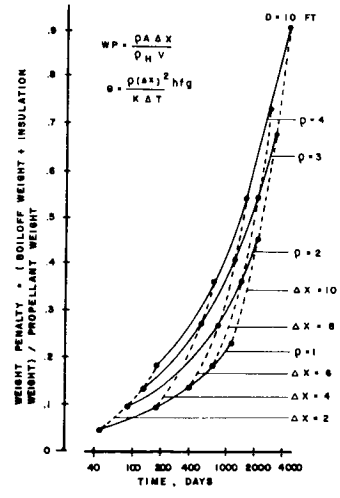

Figure 14. The effect of several variables upon the performance of a nuclear-powered space vehicle

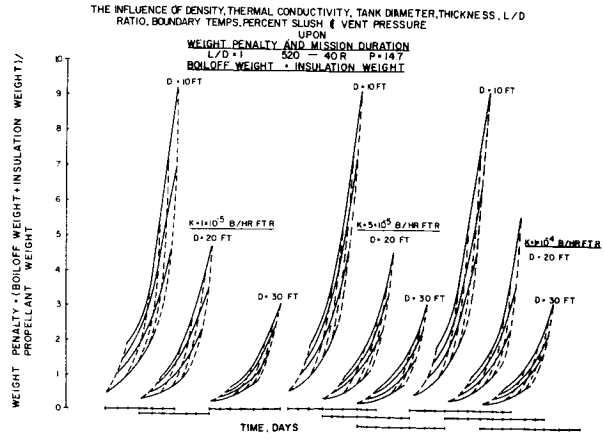

Figure 15. Extension of Fig. 14 to account for additional variables

PLENARY SESSION V
RADIOBIOLOGICAL IMPLICATIONS
CHAIRMAN: MAJ.GEN. J.W. HUMPHREYS, M. D.
DIRECTOR, OFFICE OF LIFE SCIENCES, NASA

Predicted Levels of Human Radiation Tolerance Extrapolated from Clinical Studies of Radiation Effects

C. C. Lushbaugh

Medical Division

Oak Ridge Associated Universities[1]

INTRODUCTION

Whatever the merits of the pros and cons of present day debates concerning manned space exploration, results of clinical studies of radiation effects in man himself do not support the contention that man is too radiosensitive an animal for this task. Man, other animals, electrical components, machines, etc. are all radiosensitive but have different tolerance levels that can be measured by the failure probabilities of variously performing systems. These may be immediately or only remotely important biologically or operationally. Evaluation of the space radiation hazards to man depend equally upon the accuracy of our physical knowledge of the levels and kinds of radiation that he may encounter and our biological knowledge of human radiation responses. Biologically, our knowledge is qualitatively good but not quantitatively accurate for man. Most quantitative radiobiologic estimates must be extrapolated from or with the aid of studies in animals where radiation exposures can be controlled experimentally and radiation effects quantitated by destructive techniques not applicable to clinical studies. The suitability of these animal models for prediction of the kinds and levels of human responses has been gauged by many clinical studies of victims of radiation accidents and of patients undergoing elective radiation exposure in the therapy of their disease. Unfortunately, for our purposes, there have been few radiation accidents where men have been exposed to known amounts of radiation. On the other hand, in therapeutic exposures, although the dose is well known, the radiation effects are often confused by the pre-existing disease process.

Never the less, my associates[2] and I have been directing the major part of our efforts at the Medical Division in Oak Ridge toward defining human radiosensitivity from such clinical studies of radiation effects (refs. 1 - 9). These studies were begun in 1959 when our first human total-body irradiator was constructed for radiotherapy of patients with uniform exposures to omnidirectional beams from an array of gamma ray emitting radioisotope sources. Since then, with the continuing support of the AEC and with support from NASA commencing in 1964, we have expanded these studies of human therapeutic and biologic effects of single rapidly delivered exposures with low dose

[1]The studies upon which this chapter is based have been supported since 1959 chiefly by the USAEC and augmented by NASA since 1964.

[2]Gould A. Andrews, R. M. Kniseley, C. Lowell Edwards, R. Tanida, F. Goswitz, Frank Comas, H. Vodopick, E. Balish, G. Kingdon, G. Littlefield, R. Ricks, W. Beck, T. Stokes, P. Aaron, E. Frome, E. McDow, A. Webb, A. Sipe, Mrs. Sutliff, and support staff.

rate exposure studies of protracted or fractionated radiation effects. Here we are now using another facility (Fig. 1) constructed solely for such exposures which in some instances have taken as long as ten days -- about the time for a round-trip lunar exploration. Coincidentally, the skin dose from ^{60}Co gamma rays in this low-exposure-rate total-body irradiation facility ("LETBI") accumulates with 1.5 R/hr exposures: the same rate that skin dose from protons would have, according to Dye and Wilkinson (ref. 10), in the worst week ever recorded for solar flare activity in space. As can be seen in Figure 2, derived from their study, the intestinal doses from the therapeutic and solar forms of irradiation and their respective rates of accumulation are widely divergent. The relatively small accumulated intestinal dose from solar protons offers little or no chance for untoward physiologic effects occurring from such radiation exposures in space.

We have broadened these direct therapeutic observations where possible by retrospective studies of clinical data obtained from other American and Canadian investigators and radiotherapists who kindly made these data available to this project. To obtain some basis for relating these results obtained with photons to those that might occur after exposure to high LET particles, we have been following closely the continuing studies of the ABCC staff at Hiroshima on the effects of mixed fission neutron and gamma irradiation that occurred in the Japanese atom bombings (see later).

This paper could end right here if the question to be answered for determining permissible exposures in space was only: What is the photon flux that "man" can "tolerate" and function in, while living under almost continuous exposure

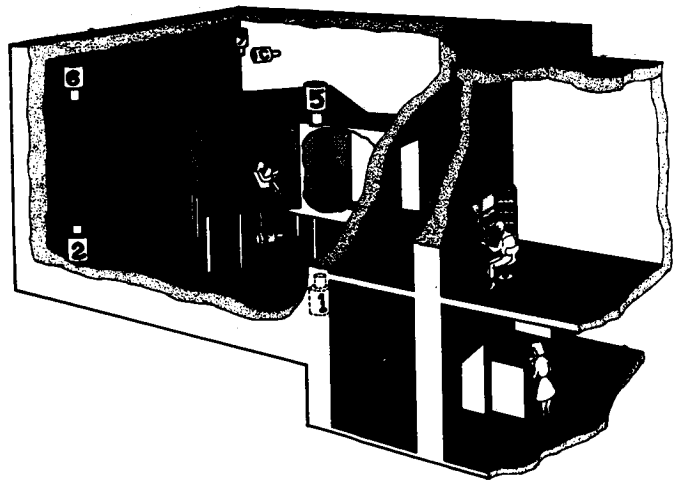

Figure 1. Cut-away diagram of the low dose-rate, total-body irradiation facility used in Oak Ridge to study the effects of protracted exposures (100 to 250 R of ^{60}Co gamma rays accumulated at 1.5 R/hr for 5 to 10 days). The location of some of the eight 26 Ci sources are shown (numbered) with the smaller trimming sources (C and F) surrounding the inner treatment room where the patient resides. The control room and data processing areas are adjacent to the 36 x 36 x 18 ft radiation containment room.

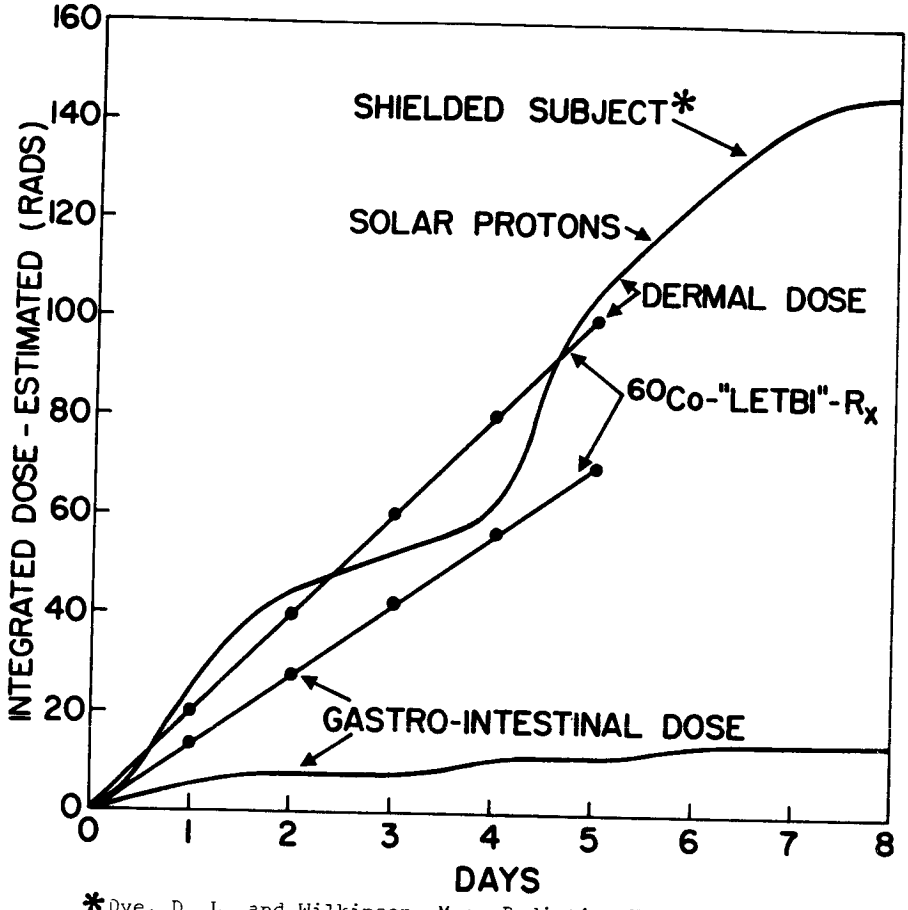

*Dye, D. L. and Wilkinson, M.: Radiation Hazards in Space, Science 147:19-25, 1 January 1965.

Figure 2. The rate of dose accumulations in the skin and intestinal tract of patients exposed to 1.5 R of ^{60}Co gamma rays/hr contrasted with those estimated for those organs of an hypothetical astronaut shielded by a space vehicle in the solar proton fluxes that occurred between 10 and 17 July 1959.

conditions? We know that patients (ours as well as others) "tolerate" total accumulated exposures of photons up to 250 R (average [estimated] bone marrow doses of 150 rads) and daily exposures at rates of 28 to 33 R at 1.5 R/hr. "Toleration" here, of course, is used by me at the subjective level; only a rare patient under these exposure conditions has shown gastrointestinal distress or complained of being sick or tired. Hematologically, however, exposures of this magnitude cause therapeutic depressions in blood leukocyte or platelet levels; percentage-depressions that would not be desirable from an occupational medicine point of view. Recently, as reported in another paper (ref. 11) in this symposium, we have demonstrated, using physiologic monitoring, that, unbeknowst to the patient being irradiated at these "tolerance" levels, he becomes exercise-intolerant or more easily fatigable even though no symptoms of the prodromal radiation syndrome or GI sickness occur. Although we believe we are defining in these retrospective and on-going studies a less-than-ten-day continuous irradiation "tolerance" level for man, we also know that many more human observations are needed before we can predict with certainty how radiosensitivity of various biologic systems change when exposures occur slowly over extremely large time periods and to relatively non-reparable high LET radiations. The late biologic consequences of irregular, numerous small exposures to high, as well as low, LET particular radiations remain our most serious problem because they are the restrictive criteria on which safe levels of occupational exposures must rest.

The word "tolerance," of course, has many definitions and many inferences that change in relation to the bodily functions being considered. The term is used by me as the biologic summation of initial response, recovery from damage, and ignorable damage remaining in the total body or a specific organ system for various periods of time. For example, the one most commonly used level of radiation tolerance for any animal species is its radiation-induced lethality expressed in terms of the exposure (R) or dose (rads) that is expected to kill 50% of that kind of animals within 30 or more days ($LD_{50/30}$; $LD_{50/60}$).

THE HUMAN LETHAL DOSE PROBLEM

There is world-wide willingness to accept the estimate that the dose that will kill the unattended normal man with 50 percent certainty within 60 days of exposure ($LD_{50/60}$) is 450 R and that the mechanism of death is damage to his hematopoietic system and defense mechanisms against infection. The degree of acceptance of this 450-R value is surprisingly high in view of its history and its lack of valid support from reported human data (ref. 12). The importance of establishing this number for man was recognized during and immediately after World War II (ref. 13). It is the obvious point of reference for relating the radiosensitivity of man to that of other mammals whose radiation sensitivity has been well established by years of extensive research - most commonly by determining precisely the LD_{50} and its confidence limits for the species (ref. 14). This number, which is reproducible experimentally in laboratories around the world for each species, has rightly become the simpliest expression for mammalian radiosensitivity. Because of the ease of its experimental determination, it has also become the end point most commonly used in radiobiological studies of relative effectiveness of various kinds of ionizing and nonionizing radiations and various kinds of radioprotective

agents and postirradiation therapy.

Just how this estimate of 450 R for man's total-body radiation tolerance was made has never been revealed publically. The assumption has been made (ref. 15) that Warren and Bowers based their estimate on lethality data obtained by the Joint Commission of the Medical Departments of the U. S. Army, Navy, and the Manhattan Engineering District in Japan during 1945. Most such accounts must be apocryphal since there was a tenfold error in the Hiroshima bomb-yield estimates that would have biased this number upwards and made it impossible to reconcile with the lower exposures in Nagasaki. These corrections, called "T65 doses" (ref. 16) are the ones now in use at ABCC in retrospective evaluation of human responses in these bombings.

Attempts to increase this estimate to 600 R, in the belief that the suggested human $LD_{50/60}$ implied a depth dose of 450 rads of photon energy, have been fought off successfully by several investigators, notably by Cronkite and Bond (ref. 17) on the basis of their observations of the hematopoietic responses of the Marshallese natives, inadvertently irradiated by fallout after a Bikini atom bomb test (ref. 18).

The LD_{50}, by definition, forms the best single measurement of the upper or acute lethal boundary of total-body radiation tolerance (see Fig. 3). There have been several attempts to check the 450-R estimate from human case histories after both accidental and intentional radiation exposures. These are tabulated in Table 1 to show how all studies have produced values lower than the original estimate and seem to indicate that 450 R is too high to be considered an estimate of midline depth-dose (absorbed radiation energy). The table also includes the results of two recent attempts to obtain

Table 1

EDUCATED GUESSES AND SOME CLINICAL AND STATISTICAL ESTIMATES OF HUMAN TOTAL-BODY RADIATION TOLERANCE

	$LD_{50/60}$	
	Exposure	Dose
A. NORMAL MAN		
1. Warren and Bowers (ref. 12)	450 R	
2. Cronkite and Bond (ref. 17)	350 rad	
3. Langham (ref. 15)	430 R	(285 rad)
4. Jablon et al. (ref. 19)	405 rem*	
B. PATIENTS		
1. Mathé et al. (ref. 20)	400 R	
2. Langham (ref. 15)	380 R	(250 rad)
3. Lushbaugh et al. (ref. 4)	370 R	(245 rad)
C. NORMAL MAN + BLAST AND BURN TRAUMA		
1. Lushbaugh and Auxier (ref. 21)	260 rem†	

*RBE for fission neutron component = 5.

†RBE for fission neutron component = 2.

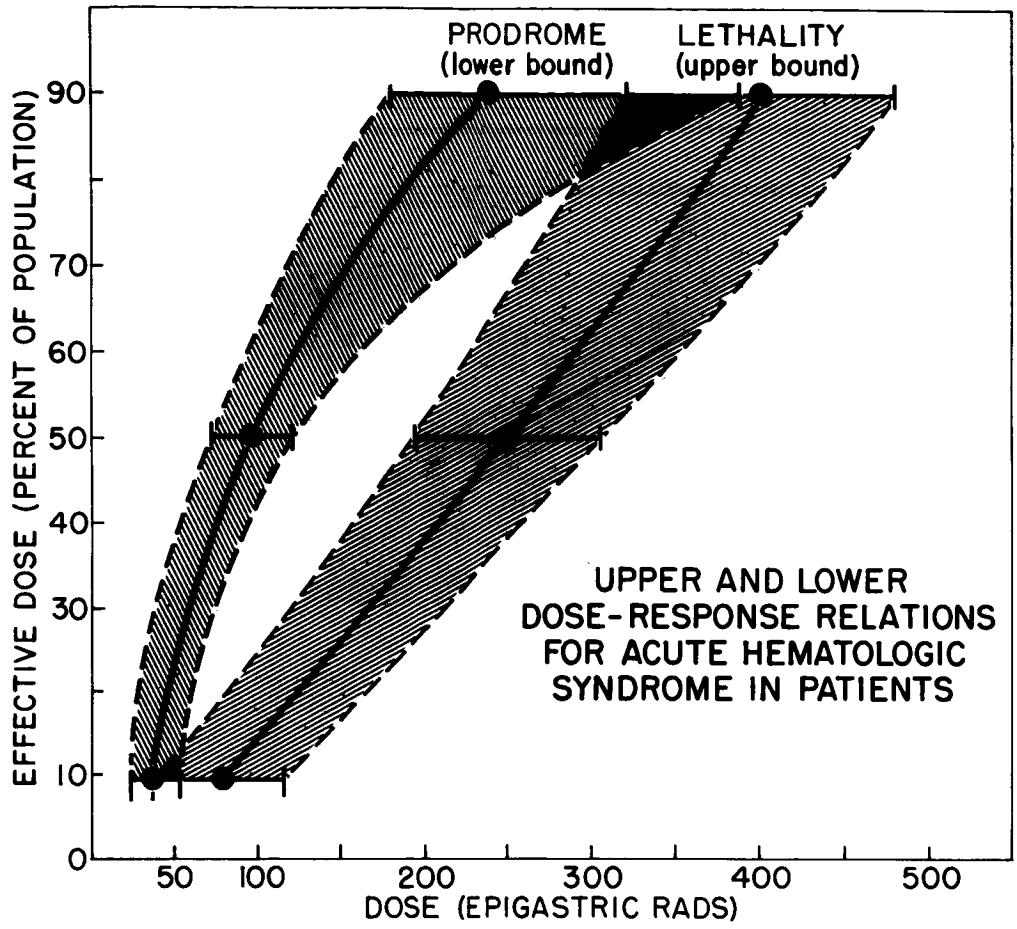

Figure 3. Acute hemopoietic syndrome is defined graphically by estimates of effective single doses for radiation-induced anorexia and lethality in patients. The probit regression lines have shaded fiducial limits. Depth dose is shown in "epigastric" rads to indicate that it is the fraction of the free field of photon radiation absorbed in the midline, midplane of the upper abdomen. This reference dose is usually 64 to 68 percent of the exposure in an average-sized man.

estimates of the human LD_{50} from the Hiroshima-Nagasaki exposures to mixed fission neutrons and gamma radiation (refs. 21 and 19). Many large animal experiments using fission neutrons, particularly those of Alpen (ref. 22) and Bond (ref. 23) and co-workers have provided a strong basis for forming the opinion that in "large" animals like man, dogs, swine, and cattle the RBE or QF for high LET radiation is 1.0 for acute hematopoietic death (ref. 15). In studies of human dermal responses to fast neutrons (refs. 24 and 25), RBE values of from 2 to 4 are needed, as in lower animals, to equate neutron dose for skin erythema with that of the reference (low LET) radiation. A QF value of 3 for high LET radiation (>3.5 keV/μ) has, however, been suggested only for damage to skin, intestines, and germinal epithelium (and not for prodromal responses, early hematologic responses, as well as hematopoietic death [ref. 15]). This recommendation seems to me to depreciate the well-known, experimentally-proven fact that sublethal cellular injury induced by high LET radiations is irreparable and as permanent as the cell in which it occurred. It would seem biologically more conservative, particularly from a safety point of view, to assume that in human tissues, including marrow, the damage caused by a dose of high LET radiation would be poorly repaired as it is in similar small animal tissues, and that hematopoietic as well as skin and intestinal crypt stem-cells would suffer equally in respect to actual dose from the same high LET radiation.

The answer to this problem is still disputable, but the more recent observations in the Japanese lend weight to the other side of the question for the first time. Lushbaugh and Auxier (ref. 21) used data from an unpublished study of the effects of various kinds of shielding upon survival in both cities in relation to the T-65 dose estimates of the free-field fluxes at the 50 percent survival points. They obtained an LD_{50} estimate of 260 rem using an RBE of 2. This estimate was expected to be low because it should reflect the additive effects of heat and blast combined with radiation-induced damage. The more recent study by Jablon et al. (ref. 19), relates the estimated individualized doses received by ∿100,000 survivors in the two cities with their clinical history of epilation and oropharyngeal hemorrhages. The human pharyngeal-epithelial and tonsillar-adenoidal barriers to infection have not been given much consideration in recent discussions of the acute hematopoietic syndrome. Yet it is an excellent objective end point for measurement. This painful, hemorrhagic sore throat is a symptom complex known as agranulocytic angina that stems from pharyngeal ulceration, bacterial invasion, granulocytopenia, and thrombocytopenia. By using this system complex as the measurable quantum of damage from total-body irradiation, any additive effect of other forms of concomitant trauma was avoided in the ABCC study. As can be seen in Table 2, the isoeffective exposures are only equal in rem when an RBE much greater than unity is used for the neutron component of the exposures. The isoeffective exposure dose (ED_{50}) of 405 rem that was found is remarkably close to the original human LD_{50} estimate. It is an even closer estimate of the exposure field strength that would be required for a mid-line human dose of 285 to 300 rads suggested as the possible human $LD_{50/60}$ by Langham (ref. 15) and Cronkite and Bond (ref. 17). The 310 rem, estimated as the isoeffective estimated dose for epilation in both cities using an RBE of 4 for neutrons, is likewise remarkably close to the widely accepted clinical value of 300 R

Table 2

FIFTY-PERCENT ISOEFFECTIVE EXPOSURE DOSES FOR HUMAN SKIN AND BONE-MARROW DAMAGE, ESTIMATED IN SURVIVORS OF NEUTRON AND GAMMA IRRADIATION IN HIROSHIMA (H) AND NAGASAKI (N)

	Neutron RBE Used	Resulting Estimates of Isoeffective Doses*	
		H	N
		(rem)	
Epilation	1	190	300
	4	→310	310←
	5	350	310
Hemorrhage	1	200	375
	4	360	390
	5	→405	405←

*Approximated from graphic data of ABCC Study by Jablon et al. (ref. 19).

of X radiation as the radiation exposure causing epilation in man. These correspondences seem to demonstrate an internal consistency in the data and their analyses that indicates, to me at least, that neutrons do have an RBE greater than 1.0 for acute hematologic, as well as for skin, effects in man. It would seem difficult to pass the ABCC study off lightly because it does not agree with large animal observations. We should not ignore Mathé's observation (ref. 20) that the man who died after neutron exposure in the Yugoslavian radiation accident had much more extensive marrow destruction than was to be expected on the basis of his estimated dose of 430 rads. There seems to be less official reluctance to accept the use of a large RBE for neutrons and other high LET radiation when late-effect end points are considered. Most fractional-cell-survival studies demonstrate well the relative irreparability of sublethal cellular damage after high LET radiation exposure and provide a firm experimental basis for assuming a large QF for such effects as genetic damage, leukemogenesis, and carcinogenesis after single exposures. When coupled with the decrease in "damage efficiency" that occurs in most biologic systems with increasing protraction or fractionation of the same total exposure, the RBE increases further (ref. 26). There is not much clinical information about high LET radiation in man other than that about the well-known effects of alpha-particle exposures in victims of radium poisoning and in uranium miners. The data under study by ABCC provides unquestionable verification for the large QF for fission neutrons for leukemogenesis and thyroid carcinogenesis (ref. 27) after single exposures.

In Figure 3 the acute hematopoietic syndrome of irradiated man is defined as the probability of of response estimates in respect to total-body photon exposures. Here, probability of lethality forms the upper bound and that of acute GI distress of the prodromal syndrome forms the lower bound of the envelope. How these dose-response relations shift when exposure is prolonged or fractionated is our continuing problem.

Retrospective studies of a large volume of clinical data extracted from hospital charts of 2000 patients given therapeutic total-body irradiation have given us dose-response relations for the symptoms and signs of the prodromal syndrome. The statistically determined single exposures that can be expected to produce these symptoms in 50 percent of the patients so exposed are shown in Table 3 along with the increased levels of the exposure required for the same incidence when the exposure period is lengthened.

When total-body exposure occurs promptly in less than one day, the effective dose for 50 percent incidence of these response (ED_{50}) are: anorexia, 147 R; nausea, 210 R; vomiting, 277 R; and diarrhea, 348 R. The log-normal frequency distribution of these responses in respect to dose indicates that

Table 3

ACCUMULATED ESTIMATED EXPOSURES* FOR

50 PERCENT INCIDENCE OF PHYSIOLOGIC SYMPTOMS

	Exposure Length (Number of Patients)		
	<1 Day (504)	<8 Days (103)	>8 Days (1083)
		(R)	
Anorexia	147	309	600?
Nausea	210	397	750?
Vomiting	277	745	>900?
Fatigue	223	400?	
Diarrhea	348	800	

*Midline upper abdominal dose (RAD = 0.66 Exposure R).

? = Guesstimate; 20 to 30 R/day is apparent threshold of dose rate.

the exposures required for their 10-percent incidence would be about one-fourth of that for a 50-percent incidence (ref. 4). The probability dose-response curves predicting the population incidence of these responses are steepest for anorexia and become progressively less steep for nausea, vomiting, and diarrhea in that order. This family-like relationship of the probability curves for the occurrence of the effects from mild to severe suggests that individual variation in ability to repair the underlying physiologic damage is progressively greater for each step in severity. If true, this analysis predicts that a radiosensitive person who shows, for example, nausea at a low dose would be more likely to show other symptoms and signs of greater damage per unit of irradiation than a radioresistant person in whom nausea did not occur without a much greater exposure. Except for the low-radiation-damage threshold of the human spermatogonia type B of about 15 rads, these gastrointestinal physiologic effects are the most radioresponsive. In the context of space exploration, these early gastrointestinal effects appear to be the most likely symptoms to occur with small exposures and therefore to be the most likely to reduce performance capabilities. Their occurrence would be improbable, however, when the exposing radiation flux was less than 20-30 R/day and the radiation was poorly penetrating, two conditions that, on the basis of previous space radiation measurements, seem to have a high probability. Nothing is known to suggest an RBE for high LET radiation for production of these physiologic effects. Although one might guess that the quality factor (QF) might be greater than three, the results of studies on the effect of dose protraction upon the size of the effective exposure dose (shown in Table 3) in 1,085 patients given small, daily total-body exposures, suggest that between 20-30 R/day are required for 30 or more days to cause these symptoms; exposures of from 10 to 20 R/day produced nausea infrequently even when these exposures were delivered rapidly at approximately daily intervals for three to four weeks; exposures of about 5 to 6 R.day were physiologically symptomless.

Although all of our statistically validated human information in this area is derived from exposures to photons, there is no reason to believe that fission neutrons delivered in small daily doses for prolonged periods to the sensitive midabdominal trigger-zone would produce damage that would ever summate in the acute onset of gastrointestinal distress. This opinion would seem correct, particularly if chronic exposures are constrained by current planning limits of 0.15 rem/day through reactor shields (ref. 15).

Recent observations obtained during the physiologic monitoring of patients in our LETBI unit during and after low-exposure rate (less than

1.5 R/day and low total daily exposure of less than 30 R/day) confirm these analyses of patients' charted histories that reveal the absence of acute GI distress under these conditions (ref. 11). They indicate, however, that increased fatigability can occur with small daily exposures of this magnitude. These studies are still too fragmentary to be considered a statistically sound basis for predicting the incidence of radiation-induced fatigue at low-exposure rates. So far, however, using bicycle ergometry, we have observed performance capability has decreased after single, prompt exposures (150 R) and after low-exposure rate, fractionated, 15 daily exposures of 10 R (150 R). These measurements, based on pulmonary impedance pneumography, seem to show that this form of performance decrement follows a cyclic-time course with a periodicity depending on the initial rate of induction of radiation damage. The long duration of the effect after one exposure could conceivably be enhanced by subsequent, remotely-spaced exposures but we are uncertain of this. This effect could be a threat to performance during long-duration space missions if small radiation exposures and muscular inactivity worked together to reduce physical strength and conditioning.

EFFECT OF MULTIPLE EXPOSURES ON LETHALITY

Almost nothing is known in truly quantitative terms about the effect of protraction or fractionation of human exposures upon the size of the isoeffective lethal dose. The Space Radiation Study Panel used an unpublished study of Focht, Nickson, and Langham in its evaluation of this problem (ref. 15) to see if clinical data obtained from the medical records of the Heublein total-body irradiation unit, Memorial Hospital, could be fitted to a Strandqvist-type of mathematical model. In this retrospective study the relative roles of the basic disease and of the protracted low-dose-rate radiation in causing death could not be determined. Whether or not a patient died during or within 60 days of his treatment was recorded only as yes or no quantal information and graphed in relation to total accumulated exposure and duration of exposure. The three graphic areas defined by exposure and time were delineated by the incidences for >90% death, 50% death, <10% death. The best fit of these data to three parallel lines for the 90, 50, and 10% probabilities of death were then computed by Langham (unpublished) using a "Strandqvist" (ref. 28) power function model:

$$\text{Isoeffective (fractionated) } LD_{50} = 345\ t^{0.26}$$

Where 345 is the assumed nominal single lethal dose in rads (midline absorbed photon energy) for a single protracted exposure to about 530 R of X radiation over one week; t is used for exposures longer than 1 week's duration and the exponent of t is the power-function or slope constant of the log-log regression line.

This model and its parameters were graphed (Fig. 4) by the author to show how this model predicts these isoeffective lethal dosage levels (90, 50, and 10%) will increase with increasing durations of exposure up to a year. The amount of repair predicted by this model for photon irradiation is remarkable. It is of interest that the power function (or slope constant) derived from the best fits was 0.26, a number remarkably similar to that factor for normal skin damage and tumor cures (ref. 28) and hematologic damage (ref. 29). As shown in the figure, this model predicts 50% survival at 18 rads/wk or ∿3 rads (marrow dose)/day/year. The slope of this regression line for increase in LD_{50}, as marrow

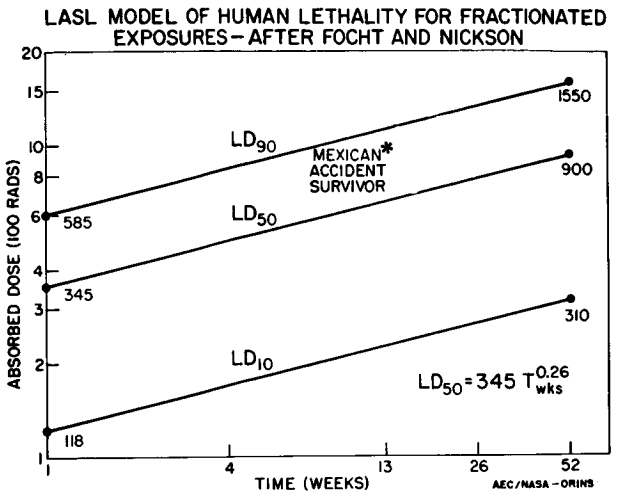

Figure 4. The Los Alamos Scientific Laboratory (LASL) model for human lethality computed from clinical total-body irradiation data of Focht and Nickson using the method of Strandqvist to determine the power function for duration of exposure in weeks.

dose is protracted, would be steeper if fatal diseases were not present in the study population. A recent study of clinical and accident data indicates that this slope may be increased as much as 2 or 3 times if the exposed persons have normal-health hematopoietic systems (ref. 29).

Low-dose-rate exposure at the rate suggested by these combined observations (about 10 R/day if the Yuhas correction of 3 is accepted) is, however, apparently not tolerable for man for a year. In fact, the events in the 1964 Mexican accident can be interpreted as demonstrating that in only 100 days of such irradiation an exposure close to that for lethality will be accumulated at ∿10 R/day (ref. 30). One of the victims in this accident was literally irradiated to death in 115 days, during which time she received an estimated 2,000 to 3,000 rem of cobalt-60 gamma radiation (15 to 25 R/day [see Table 4]). Her husband, who is still surviving at the time of this writing seven years after the accident (shown by the asterisk in Figure 4) received his daily exposures (984 to 1,717 rem in 106 days) during the night while sleeping. His wife and his mother were irradiated continuously day and night as they worked about the house where an unrecognized radiography ^{60}Co source was stored. The four deaths in this family of five were found at autopsy to be from severe hematopoietic damage that led to hemorrhage and infection. All but the survivor acted as though they had a plague-like disease. The survivor, however, had surprisingly few symptoms and signs of illness in contrast to the severe radiation-induced atrophy of his bone marrow that was subsequently demonstrated by marrow biopsy. What symptoms he had were chiefly referrable to his low-grade anemia rather than his severe leukopenia.

Table 4

1964 MEXICAN ^{60}CO RADIATION ACCIDENT

(Martinez et al., 1964)

	Exposure (days)	Estimated Exposure (rem)	Approximate Exposure Rate Ranges (rem/day)	(rem/hr)	After Survival (days)
Son	24	2940-5165	125-250	5-12	18
Wife	115	1996-2938	17-26	0.7-1	2
Daughter	99	1373-1872	14-19	0.5-0.8	30
Mother	90	1818-2897	20-32	0.8-1.3	80
Survivor* (Husband)	106	984-1717	9-16	0.4-0.6	(7+ years)

*April 1971.

In Figure 5, two ways are shown in which the dose-response relations may shift when exposure is protracted. There are: (a) a decrease in the slopes of the shifted probability lines caused by greater repair of radiation damage accumulated slowly (revealed as a greater variation in the response rates of the population); and (b) a simple displacement of dose-response envelope without a change in the slope of the lines for the probability of response. This dose-response displacement is to be expected when exposure is to high LET radiation where cellular damage is nonreparable. In Figure 6, the results are shown when the LASL study is used to predict the level of human lethality for the exposure rates of 6, 20, and 30 rads/wk. This probability estimate, shown by the solid line superimposed on those of Figure 5, supports the many observations made in mice irradiated at low-dose rates that the hematopoietic system has a remarkable ability to recover from slowly delivered photon irradiation. Recently, Yuhas, et al. (ref. 29) obtained additional evidence supporting this remarkable reparability of the normal human hematopoietic system when its exposure is made in small fractions. He derived a multifactorial regression model for human blood-cell responses to multiple as well as single total-body therapeutic exposures using approximately 2,000 clinical case histories. Individual charts were carefully selected that met strict criteria for numbers of blood examinations, dosimetry, precise diagnoses, and evidence that the individual was not in the terminal stage of his disease. The dose-response patterns of 123 single exposures and 395 multiple exposures were studied in four diagnostic groups of patients: chronic myelogenous

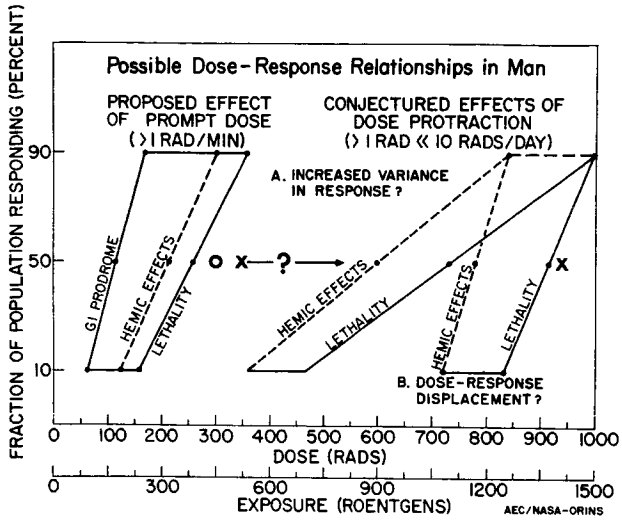

Figure 5. A graphic representation of two possible ways that clinically recognizable lower and upper dose-response probability boundaries of the hematopoietic syndrome may shift when exposure is protracted over a year.

A. Variance in the incidence of a response is increased as reparability increases as after low LET photon irradiation.

B. The dose-response envelope is displaced upwards without change in the slope of probability lines, commensurate with proliferation capacity of unhit target cells in the presence of irreparably damaged targets as after exposure to high LET particles. The prodromal synptomatology, lower bound of the prompt exposure probability envelope becomes undetectable when the daily fraction of the exposure is less than 15 R and therefore is replaced by symptoms referable to anemia or infection. (See Table 3.)

leukemia (CML), chronic lymphocytic leukemia (CLL), lymphosarcoma (LS), and nonleukemic patients with normal blood values. The percent of WBC remaining at the nadir was found to be related to a power function on total exposure and the duration of the therapy in days:

$$\% \text{ WBC} = K\,[100] \cdot [D]^{-b_1} \cdot [T]^{b_2}$$

K = a constant, required for extrapolation to the ordinate at zero dose because no effect was seen below 25 R

D = total exposure in R

b_1 = the slope of % WBC on D

T = the time of protraction in days

b_2 = the slope of % WBC on a given D or T

The slope of percent WBC on exposure was found to be essentially equal to -1.0 in all diagnostic groups (Table 5). In persons with normal marrow, percent WBC on time (T) at a given exposure (D) increased as the 0.63 power of the number of days separating the first and last fractional exposures used. In CML, CLL, and LS this exponent was found to be 0.39, 0.23, and 0.22.

Table 5

SLOPE CONSTANTS AND TESTS OF THE STATISTICAL SIGNIFICANCE OF THE YUHAS MODEL (REF. 29)

Diagnostic Group	Single Exposures b_1	Single Exposures Correlation Coefficients	Multiple Exposures b_2	Multiple Exposures Correlation Coefficients	P Value
"Normal"	1.04	0.57	0.63	0.535	<0.025
CML	0.999	0.82	0.392	0.569	<0.0001
CLL	0.91?	-	0.221	0.583	<0.0001
LS	1.119	0.42	0.231	0.567	<0.0005

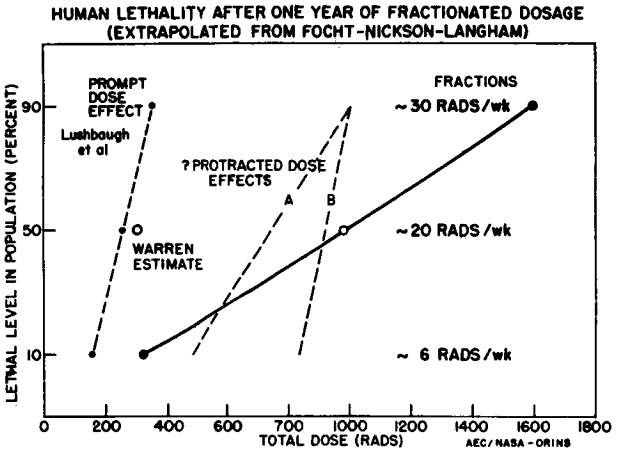

Figure 6. The conjectured effect of a year-long dose protraction upon the displacement and slope of dose-response probability regression lines (shown in Figure 5) contrasted with the prediction of the LASL model using actual data. (For further explanation, see text.)

The values for the slope constants shown in Table 5 have biological implications: The negativity of b_1 indicates that as dose increases, the percent survival of peripheral WBC decreases. The correspondence of this value for each group to 1.0 may indicate that, in the different cellular systems involved in these diseases, differences in radiosensitivity are not significant. This result is surprising in view of the widely held clinical belief that the leukocytes in CLL, for example, are much more radiosensitive than the cells comprising the WBC in CML or in "normal" persons. This apparent deviation from clinical "fact," however, can be explained by the significant differences found in the values for b_2. The larger this positive slope constant the more effective the length of exposure protraction is in increasing percent survival; according to these values, in the "normal," protection of the white blood cell level by dose protraction is three times that found in CLL and LS (see Fig. 7). In the latter groups, dose protraction should not, according to this analysis, decrease the effectiveness of the total dose as much as in the "normal" group and as, to a lesser extent, it will in the CML group. These interpretations implied by the analytical results agree well with most clinical observations and suggest, in keeping with experimental observations, that normal tissues are spared more than abnormal ones by dose protraction. This concept is in fact the rationale for fractionation and protraction of

radiation therapy of malignant tissues admidst normal ones. These observed differences in peripheral WBC survival, after the same radiation exposure, probably result more from different efficiencies of recovery mechanisms than from inately different cellular radiosensitivities in these diseases (ref. 29).

It is commonly assumed that hematologic effects reflected by changes in peripheral blood counts correlate quantitatively with lethality. This correlation, however, has not been demonstrated either clinically or experimentally. Therefore, a regression model for the effect of dose-rate upon hematologic parameters, such as blood granulocyte levels, cannot be used with much assurance as the regression model relating dose-rate and lethality. The obverse is also true. Bateman (ref. 31), however, has shown well, at least in my opinion, that dose-rate data for such end effects as human dermal responses, and lethality of mouse, rat, swine, and sheep can be fit as a linear function of the reciprocal cube root of dose rate. This empirical observation stems in large part from the way the Strandqvist model and its numerous modifications all approximate the power-function exponent of 0.33. Applying the model to the data of others where a dose-rate effect is easily demonstrable, Bateman showed that:

$$ED_{R_1} = D_{\infty} \left(1 + \frac{k}{\sqrt[3]{R_1}}\right)$$

where D_{∞} is the single dose requirement when exposure is at an infinitely rapid rate, ED_{R_1} is the isoeffective dose at some lesser rate (R_1). The size of k, the slope constant for dose-rate effect as a function of the cube root of R, seems to be related to the size of the single-exposure

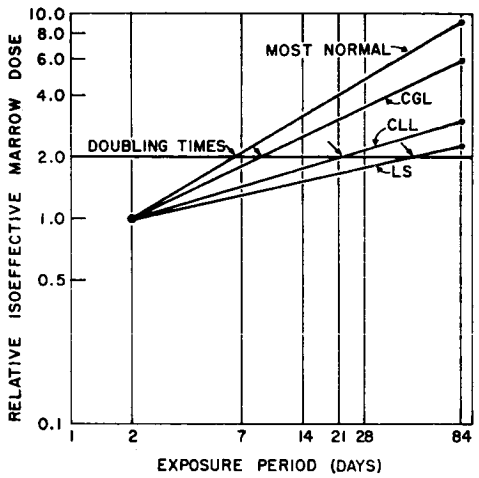

Figure 7. Graph of the rate of blood cell recovery predicted by the Yuhas multifactorial dose - WBC response model based on clinical data of total-body irradiated patients with no marrow disease ("most normal"), chronic granulocytic leukemia (CGL), chronic lymphocytic leukemia (CLL), and lymphosarcoma (LS). The data have been normalized to relative isoeffective marrow dose for two-day protraction for each set to compare the relative doubling times (straight arrows) in terms of exposure duration: 7 days, normal; 9 days, CGL; 22 days, CLL; and 42 days, LS.

dose given at conventionally rapid (therapeutic) rates. The size of k also expresses the recovery kinetics of the animal species and the cellular system involved. For example, in Bateman's study of lethality, k was 1.6 for swine, a species known to have remarkably efficient total-body repair, and 0.65 for sheep, an animal model of slow, inefficient radiation repair kinetics. Also, apparently the more radiosensitive a biologic system is (i.e., the smaller the dose is that is required to be effective) the less well it repairs the effects of this small dose; thus the size of k is variable within the same species, as it depends on the specific recovery mechanisms and kinetics of the damaged biologic system.

The Bateman model was used to construct a nomogram for human dose-rate tolerance using some of the biologic end points whose derivation and validity have been discussed above. This nomogram is shown in Fig. 8. Some of the assumptions are based on animal observations when normal human observations are not available. The extrapolations extend beyond 100 days even though the observations upon which they are based do not extend this far. They are extended to a year in the figure to correspond to the temporal requirement of deep-space exploration. Extrapolations of clinical data using the models of Strandqvist, Yuhas, and Casarett (refs. 32, 33) do not fit this reciprocal of the cube root scale of dose rate beyond one to three months after which they curve rapidly upward, away from the lines shown in the figure, indicating again perhaps the surprisingly great reparability that most tissues have of acute radiation damage induced at extremely low dose rates. Such a conclusion is, however, too optimistic for occupational radiation protection and long-mission planning guidelines since it predicts that no discernible acute responses will occur in marrow, gut, or skin below rather high dose-rate thresholds. In the absence of much objective clinical support for the quantitative relations implied by the nomogram, such reparability on the part of all men cannot be assumed. Even so, the extrapolations for the dose-rate response relation of infertility and sterility, severe hematologic effects, and hematopoietic death shown in the figure are more conservative than those of the Yuhas model, for example, as shown in Figure 7, that predict a ninefold increase in an isoeffective dose for hematologic damage to normal human marrow if exposure were fractionated over a 3-month period.

Until we obtain additional evidence that normal human marrow can actually repair as rapidly as this, the clinically conservative approach is to accept the worst predictions of the model; the doubling times of 21 to 42 days for CLL and LS, which, interestingly enough, approximate the rate that the Bateman model predicts in the nomogram (Fig. 8) by the line for "severe" hematologic response for patients.

In the dose-rate nomogram the accumulated isoeffective exposures are shown in the figure in R of photons. The encircles star, ⊛, however, along with the line for "Late Effects," which has no slope, should be considered as dose in rem. The Late Effects lines are intended to define on the nomogram the dose-rate tolerance boundary or the safe occupational upper limits for human tolerance to low-dose-rate exposure if remote and late effects, rather than prompt effects, must be considered (ref. 34). The other steeper lines in the nomograph indicate possible dose-rate effect on the size of accumulated doses for such undesirable prompt effects as the 50 percent risk of death within 60 days. Such exposures have a low probability of ever occurring in space exploration, but, as we have indicated, are the kind on which we have the most clinical information. Much more clinical information, however, is needed before the creditability of any of these lines, their slopes, and dose-rate relations can be established statistically. The nomogram does, however, support the opinion that, except for the remote possibility of some unforeseen, uncontrollably large exposure, man is more than sufficiently radioresistant to make the risks of an early acute radiation effect on one short space mission intangibly small in relation to the other non-radiation risks involved.

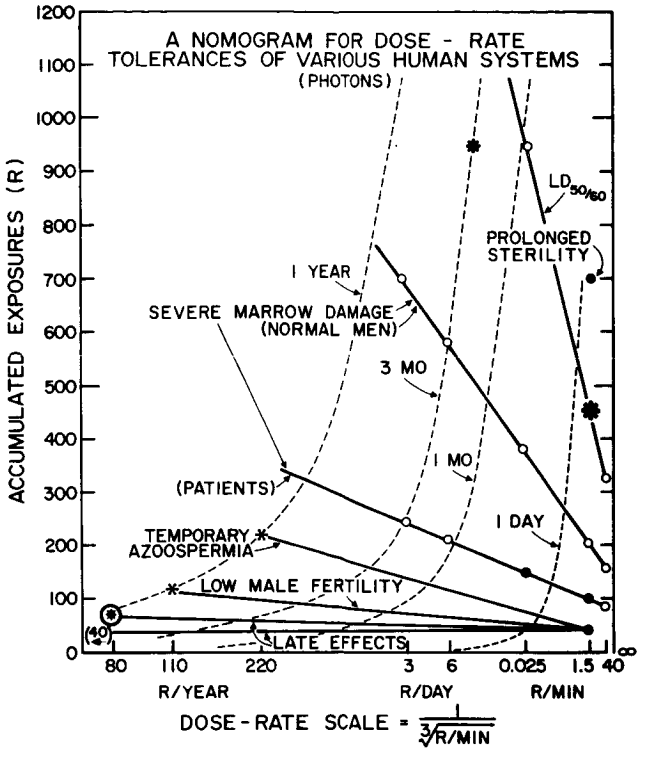

Figure 8. A nomogram predicted by the Bateman model of the effect of one-day, one-month, three-month, and one-year-long exposures on the size of accumulated exposure required to produce constant levels of several kinds of somatic damage; 60-day lethality, severe damage to normal marrow, assuming man and sheep are equally radiosensitive large animals. The smaller asterisk at ∿1000 R on the 3-month isotime line locates the Mexican radiation accident survivor (see text). The lines for severe marrow damage are extrapolated from clinical data points (solid circles) and computed points (open circles) to show damage to diseased marrow, temporary (reparable) cessation of sperm production, reduced male fertility and late effects such as increased rate of cancer induction. The largest asterisk represents the original $LD_{50/60}$ estimate for man and has a regression line with a slope constant k = 0.65 running through it. Constants (k) are assumed of 0.24 for the recovery capability of diseased and 2 x 0.24 for for normal hematopoietic systems. The lines for sterility and low fertility are based on the human data (ref. 15 [solid circles]) and canine data (small asterisks) on the one-year isotime line of Casarett and Hursh (refs. 32 and 33). The "Late Effects" lines are extracted from the Space Science Board Report (ref. 34).

REFERENCES

1. Andrews, G. A.; Lushbaugh, C. C.; Kniseley, R. M.; White, D. A.; and Friedman, B. I.: Effects of Ionizing Radiations on Hematopoietic Tissue, International Atomic Energy Agency, Vienna, 1967, p. 75.
2. Andrews, G. A.: Radiat. Res. Suppl., vol. 7, 1967, p. 390.
3. Andrews, G. A.; Comas, F. V.; Edwards, C. L.; Kniseley, R. M.; Lushbaugh, C. C.; and Vodopick, H.: Oak Ridge Associated Universities, USAEC Report, ORAU-112, 1970.
4. Lushbaugh, C. C.; Comas, F.; Saenger, E. L.; Jacobs, M.; Hofstra, R.; and Andrews, G. A.: Radiat. Res., vol. 27, 1966, p. 487.
5. Fanger, H.; and Lushbaugh, C. C.: Arch. Path., vol. 83, 1967, p. 446.
6. Lushbaugh, C. C.; Comas, F.; Edwards, C. L.; and Andrews, G. A.: Proceedings of a Symposium on Dose Rate in Mammalian Radiation Biology, UT-AEC Agricultural Research Laboratory, USAEC Report Conf-680410, 1969, p. 17.1.
7. Lushbaugh, C. C.: Advances in Radiation Biology, vol. 3, Academic Press, Inc., New York, 1969, p. 277.
8. Oakes, W. R.; and Lushbaugh, C. C.: Radiology, vol. 59, 1952, p. 737.
9. Shipman, T. L.; Lushbaugh, C. C.; Petersen, D. F.; Langham, W. H.; Harris, P. S.; and Lawrence, J. N. P.: J. Occup. Med., Suppl. 3, 1961, p. 145.
10. Dye, D. L.; and Wilkinson, M.: Science, vol. 147, 1965, p. 19.
11. Ricks, R. C.; Lushbaugh, C. C.: McDow, E.; and Frome, E.: This symposium. (In press.)
12. Warren, S.; and Bowers, J. Z.: Ann. Int. Med., vol. 32, 1950, p. 207.
13. Oughterson, A. W.; and Warren, S., eds: Medical Effects of the Atomic Bomb in Japan, McGraw-Hill Book Co., New York, 1956.
14. Bond, V. P.: Fleidner, T. M.: and Archambeau, J. O.: Mammalian Radiation Lethality, A Disturbance in Cellular Kinetics, Academic Press, New York, 1965.
15. Langham, W. H., ed.: Radiobiological Factors in Manned Space Flight, National Academy of Sciences, NRC Publication 1487, 1967.
16. Auxier, J. A.; Cheka, J. S.; Haywood, F. F.; Jones, T. D.; and Thorngate, J. H.: Health Phys., vol. 12, 1966, p. 425.

17. Cronkite, E. P.; and Bond, V. P.: U. S. Armed Forces Med. J., vol. 11, 1960, p. 249.

18. Cronkite, E. P.; Bond, V. P.; Conard, R. A.; Shulman, N. R.; Farr, R. S.; Cohn, S. H.; Dunham, C. L.; and Browning, L. E.: J. Amer. Med. Assoc., vol. 159, 1955, p. 430.

19. Jablon, S.; Fujita, S.; Fukushima, K., Ishimaru, T.; and Auxier, J. A.: Symposium on Neutrons in Radiobiology, UT-AEC Agricultural Research Laboratory and Oak Ridge National Laboratory, USAEC Report Conf-691106, 1969, p. 547.

20. Mathé, G.; Amiel, J. L.; and Schwarzenberg, L.: Ann. N. Y. Acad. Sci., vol. 114, 1964, p. 368.

21. Lushbaugh, C. C.; and Auxier, J.: Radiat. Res., vol. 39, 1969, p. 526.

22. Alpen, E. L.; Shill, O.; and Tochilin, E.: Radiat. Res., vol. 9, 1958, p. 85.

23. Bond, V. P.; Carter, R. E.; Robertson, J. S.; Seymour, P. H.; Hechter, H. H.: Radiat. Res., vol. 4, 1956, p. 139.

24. Stone, R. S.; and Larkin, J. C., Jr.: Radiology, vol. 39, 1942, p. 608.

25. Sheline, G.; Phillips, T. L.; Field, S. B.; Brennan, J. T.; and Raventos, A.: Amer. J. Roentgenol. Radium Ther. Nucl. Med., vol. 111, 1971, p. 31.

26. Field, S. B.: Radiology, vol. 92, 1969, p. 381.

27. Wood, J. W., Tamagaki, H., Neriishi, S.; Sato, T., Sheldon, W. F.; Archer, P. G.; Hamilton, H. B.; and Johnson, K. G.: Am. J. Epid., vol. 89, 1969, p. 4.

28. Strandqvist, M.: Acta Radiol., Suppl., vol. 55, 1944, p. 1.

29. Yuhas, J. M.; Stokes, T. R.; and Lushbaugh, C. C.: This symposium. (In press.)

30. Martinez G., R.; Cassab H., G.; Ganem G., G.; Guttman K., E.; Lieberman L., M.; Vater B., L.; Linares M., M.; and Rodriquez M., H.: Rev. Med. Inst. Mex. Seguro Social, vol. 3, Suppl 1, 1964, p. 14.

31. Bateman, J. L. A.: Proceedings of Symposium on Dose Rate in Mammalian Radiation Biology, USAEC Report Conf-680410, 1968, p. 23.1.

32. Casarett, G. W.; and Eddy, H. A.: Ibid, p. 14.1.

33. Casarett, G. W.; and Hursh, J. B.: Proc. Int. Conf. Peaceful Uses of Atomic Energy, Geneva, vol. II, 1955, p. 184.

34. Space Science Board: Radiation Protection Guides and Constraints for Space Mission and Vehicle-Design Studies Involving Nuclear Systems, National Academy of Sciences, Washington, D. C., 1970.

HUMAN VISUAL RESPONSE TO NUCLEAR PARTICLE EXPOSURES

C. A. Tobias, T.F. Budinger, and J. T. Lyman

Lawrence Radiation Laboratory, University of California, Berkeley, California 94720

Shortly after Roentgen's initial discovery of X rays it became known that these radiations can cause a sensation of diffuse light when they impinge on the retina of dark-adapted human subjects. When, in the course of the historic lunar Apollo 11 flight astronauts Neil Armstrong, Edwin Aldrin, and Michael Collins first experienced sensations of streaks and flashes of light it was not immediately clear that these visual phenomena were caused by radiation, as there are many modes of stimulating the visual apparatus. Visual sensations can be caused by mechanical, electric, magnetic, X-ray, and nuclear particle stimulation of the eye (1) as well as by direct brain cortex stimulation (2), and psychological states. Thus it is necessary to perform careful experiments in space and on the ground to fully account for each of the various light phenomena that have now been observed with some regularity by each of the crew members of four different lunar flights -- Apollo 11, 12, 13, and 14, and as recounted by Astronaut Philip Chapman at this Symposium (14).

Astrophysicists Fazio and others (3) have theorized that observation of light flashes in space might have been due to Cerenkov emission of light from primary cosmic ray particles. Earlier one of us predicted (4) that heavy primary cosmic ray particles traveling at any velocity could cause the appearance of light flashes due to dense ionizations and excitations in human tissue. At that time we emphasized the importance of investigating the biological effects of such particles.

Several categories of phosphenes are observed by the dark-adapted subjects in radiation exposures at ground level or in space flight. These include:

Flash: very brief white star-like events or events with short tails (comma shaped), or flashes of undiagnosed shape.

Streak: luminous, usually straight line of light, often giving a sense of rapid motion.

Supernovae (a name coined by the astronauts): bright, rapid flash surrounded by halo and minor flashes.

Luminous cloud: impression of light behind a small cloud formation or summer atmospheric electrical discharge over the horizon.

Grey phosphene: grey-blue or grey-green faintly luminous background encompassing a major portion of the visual field.

Sunrise phosphene: yellowish and rosy luminous background resembling early phases of sunrise in a clear sky.

Since none of the flash-type events has been seen by astronauts when they were in orbit under the solar radiation belt, or by us at ground level while dark-adapted in a natural cosmic radiation background, or in airplane flights up to 10,000 meters, we reasoned that relativistic singly charged particles - e.g. protons, mesons, or electrons - are unlikely to have caused the bright light flashes and streaks observed in space. These observations and the low photon yield from these particles argue against Cerenkov radiation from protons, mesons, or electrons as an important mechanism for this phenomenon. The only observation contrary to this statement of which we are aware is by D'Arcy and Porter, who have reportedly observed light flashes from μ mesons when cued with clicking sounds synchronized with the arrival of particles at an appropriately positioned coincidence counter telescope(5). (This experiment, to our knowledge, has not been substantiated by others.)

It seems more likely to us that heavily ionizing particles, including slow protons, might be capable of causing flash events when they cross the eye or some other part of the nervous system involved in the process of vision. Our first experiments were a test of the visual effects originated by very fast neutrons of 640-MeV peak energy, because these, by collision with atomic nuclei in tissue, produce heavily ionizing spallation recoils. This fast neutron beam also can generate recoil protons of sufficient energy for Cerenkov light, greater than the minimum required of about 470 MeV.

These experiments were reported in June 1970, at the International Congress of Radiation Research in Evian, France (6,1). Figure 1 of Reference 1 shows the manner in which forward neutrons from the interaction of 640-MeV protons with beryllium were utilized. Great care was taken to eliminate all stray radiation. The dark-adapted subjects reported seeing 25-50 luminous, white rapid flashes over their entire visual field when the eyes were exposed to a neutron flux from either the forward or the lateral direction. These observations established our ability to see local light events originating from ionizing events associated with nuclear interactions in the eye region. The exact location or the actual mechanism of the interaction was not established, however.

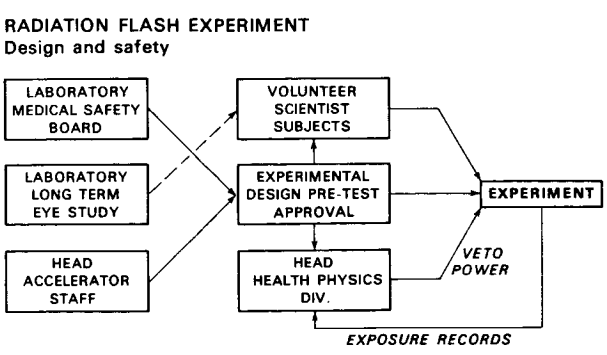

Figure 1: Design of experiments to ensure safety.

It was important to determine what contribution Cerenkov radiation made to our fast neutron beam observations, as some protons were traveling faster than the Cerenkov minimum. Fremlin, during activation analysis at neutron energies less than 8-MeV reported having seen light flashes(8). We extended our observations to fission neutrons and neutrons of energies less than 25-MeV with Bichsel at the University of Washington 60-inch cyclotron(10). The current status of these observations and other relevant experiments with X-ray and electrical phosphenes is shown in Table 1.

Radiation phosphenes fall into two distinct classes. The first class consists of local flash and streak phenomena. These include, in addition to some of the radiations encountered in space, fast neutrons of less than 25 MeV energy and neutrons of higher energy, observed at a flux density of 10^4 to $10^5 cm^{-2} sec^{-1}$. In the University of Washington exposure at neutron energies less than 25 MeV, the Cerenkov effect as the cause of light flashes is definitely excluded, since these particles and their secondaries travel much too slowly to produce Cerenkov light (10).

The second group consists of diffuse luminous clouds or greying of an otherwise dark visual field instead of highly local visual events. X-ray, electrical and magnetic phosphenes fall into this class. Eye exposure to Californium-252 at a flux density of $10^5 cm^{-2} sec^{-1}$ resulted in a persistent greying of the visual field which could have been due to phosphorescence or to distributed ionization from the abundant proton recoils. X-ray phosphenes are distinguishable from the heavy-particle phosphenes by the fact that X-ray phosphenes are not seen unless the dose rate is higher than about 24 millirads per second whereas we have seen neutron-induced phosphenes at dose rates of 0.1 millirad per second.

At this point it is important to detail the manner in which human experimentation with radiation phosphenes must be carried out. In view of the ability of radiation to induce manifold deleterious effects, including formation of cataracts and retinal degeneration, the utmost care is essential to keep doses at minimal levels. Figure 1 shows how we cope with this problem. The subjects are volunteer, mature

TABLE 1

Source	Mechanism	Flux Density	Response	Reference
Mechanical	Probably retinal membrane distortion	Finger pressure to eye ball	Diffuse, sometimes colored, visual patterns	(9)
Electricity	Induced action potential	0.3 mA	Brief, diffuse flashes, sometimes colored	(9)
Magnetic gradients	Action potential from induced EMF	1000 gauss/cm	Brief diffuse flashes sometimes colored	(9)
X-rays	Ionization and electronic excitation	$\geq$ 24 milliroentgen/sec	Diffuse light flood, left	(1,9)
Fission neutrons ^{252}Cf	Ionization by proton recoils and alpha from (n,α)	$10^5 n\ cm^{-2} sec^{-1}$	Greying of visual field. One tear-drop flash	(1,10)
Neutrons (ave. 3 MeV)	" "	$10^5 cm^{-2} sec^{-1}$	Short streaks and flashes	(8)
Neutrons (ave. 8 MeV)	" "	$10^4 - 10^5 cm^{-2} sec^{-1}$	White streaks and flashes with motion sense	(10)
μ-Mesons	Ionization or Cerenkov	Cosmic ray	Coincidences of undefined visual phenomena	(5)
Pions (1.5 BeV/c)	Ionization or Cerenkov	200 $\mu\ cm^{-2} sec^{-1}$	No visual response	(1)
Mesons, protons and cosmic particles at 10,000 meters	Ionization of Cerenkov	3,1 hr. observing periods. 35°N and 50°N	No visual response	(1)
Helium ions	Ionization	1 to 100 sec^{-1} through posterior retina	Discrete brief flashes and streaks equivalent to 1-mm image on the retina. Motion sense	(present paper)
Cosmic rays	Ionization or Cerenkov	$\sim$1 $cm^{-2} min^{-1}$ ($Z \geq 6$) light and heavy particles $\sim$ 12-25 mr/day	Various types of light flashes including long streaks	(14)

scientists,who have technical familiarity with radiation physics and radiation biology. A local responsible medical group previews the experiments, and those in charge of each accelerator facility agree to the protocol in advance. The health physicist in charge carries out independent measurements,is present during each experiment,and has veto power during any part of the proceedings. As an example of the dosages received,we were exposed during the entire high energy neutron experiments to only as much radiation dose as the general population receives from cosmic rays and natural background in the span of 2-3 days(about 1 millirad). Both principal investigators are included in a group of scientists who receive periodic eye examinations as part of a long-term study on cataract incidence in a population of radiation workers.

Helium Ion Beam

We are presenting preliminary descriptions of some very recent experiments with accelerated helium ions at the Berkeley 184-inch cyclotron, which have not been reported previously. These were designed with the hope that they would help localize the site of initial radiation interactions in the body that lead to light-flash observations and to determine the character and the efficiency of helium ion induction of visual sensations. We have earlier described the facilities at the biomedical exposure room, where monoenergetic beams of about 910-MeV helium ions are used in radiation therapy investigations (11).

Using a parallel beam of flux density of 10^6 to 10^8 particles $cm^{-2}sec^{-1}$ and a special arrangement shown in Figure 2, we adjusted the beam intensity to about 1 particle per second, representing 10^8-fold attenuation of the beam. The parallel stream of particles is restricted by an aperture 4 mm in diameter and to a maximum energy of about 240 MeV. Each particle is individually checked and recorded by means of pulse height analysis and coincidence counting. Appropriate beam tuning is used to exclude particles of unwanted properties. The position of the subject's head with respect to the particle stream is controlled by a head positioner to which is attached a tight-fitting positioning and dark-adaptation mask. The subject can be accurately aligned with respect to the beam position by means of X-ray diagnostic techniques. The depth of penetration of the particles can be changed at will by means of interposed absorbers. On a strip chart each particle is separately recorded as it arrives in time, along with any responses from the subjects, who can activate a hand-operated switch to signify visual identification of an event. A sound click can be triggered by each fast particle as it passes through the silicon detectors prior to entry into the subject; this may be used as an additional cue for the subject. Verbal instructions and reports from the subjects are recorded on magnetic tape, and closed circuit TV is used for surveillance of the subject during the experiment.

So far, the region in and around one eye of each of two subjects has been probed with a very small stream of helium ions, numbering in one experiment a total of 1500 ions for one subject (CT) and 1150 for the other (TB).

Encouraged by the earlier experiments with fast neutrons in which neutron fluences of $10^4 cm^{-2}sec^{-1}$ were used with about 25-50 visible flash events per second, we wished to establish initially whether or not a single helium ion passing through the retina of one eye could produce the sensation of a light flash. The attempt to do this in a dark adapted subject was initially unsuccessful when an intensity of only one particle per second was allowed to cross the retina for periods of two minutes. In considering the possible reasons for this initial failure it became evident that we should be concerned not only with the possibility that a helium particle can cause an action potential in one or more visual cells of the retina, but also with additional psychophysical factors that may allow or prevent conscious registration of a very small light event in a milieu of background noise in the visual cells and of electrical noise in ganglion cells, synapses, and along the optic tract to the brain. Some degree of spatial and temporal integration is probably necessary before a given pattern of neural events will emerge into consciousness at a given instant. In the field of optical studies of light perception it is already known that near the photic stimulation threshold, the eye must be fixed in the dark and that a light stimulus must have certain spatial and temporal properties before it becomes observable(12). Specifically, Van Nes et al (13) have noted that the efficiency of seeing small light flashes of narrow angular aperture depends very sensitively on the time frequency of occurrence of such flashes as well as the spatial periodicity.

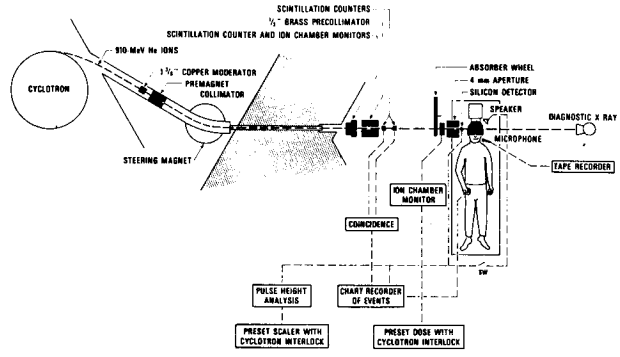

Figure 2:

Schematic of the arrangement used for human exposures. The exposures were carried out using exposure facilities developed at our Laboratory over the past several years for helium ion therapy. Special devices were added to allow exposure to individual helium ions at 0 - 250 MeV kinetic energy. The subjects wore dark-adaptation masks.

Our successful attempt at obtaining a subjective response from helium ion beams corroborates the importance of space and time summation in the response of the visual apparatus. When helium particles were allowed to cross laterally the central region of the retina of the left eye at random time intervals within an average rate of 10 per second, both subjects observed 2 to 5 flash events per second, including streaks with motion sense in the beam direction. A typical sequence of events is shown in Figure 3. At higher rates of arrival so many events were present in the visual field simultaneously that their identification became more difficult. At very high rates (> 100 per sec) only a single discrete flash was seen, and at very low rates less than 5% were recorded as visual sensations. Figure 4 gives an indication of recognition efficiencies at various particle arrival rates and reproduces particle arrivals and recognition signals from the subject in a typical 50-particle trial.

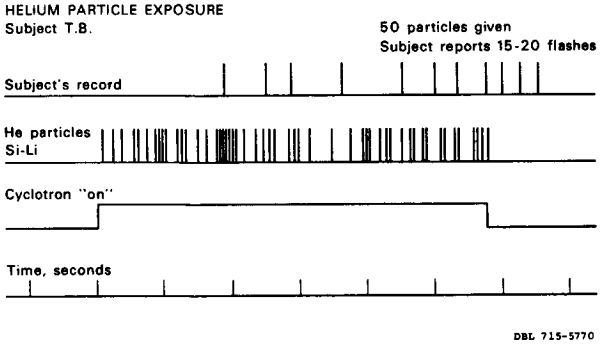

Figure 3:

A typical sequence of events in a helium ion exposure sequence. The arrival of each particle was recorded on a strip chart recorder as function of time. The subject signaled the appearance of light flash events by a manually activated switch.

When a 5 second burst of particles in a 4-mm-diameter pencil beam arrives at the retina at a random rate of 10 per second, the subject without any cues can readily identify their presence. However, a period of approximately 1 to 2 seconds appears to be necessary before clear recognition of individual events and descriptions of their characteristics became possible. From a background sea of dark grey-green fluctuation the rapid light events first emerge as faint flashes, and some time later particle events appear as brighter streaks and flashes. Some features of their structure and position can then be identified and described.

Attempts were made to enhance visual recognition of the flash events by sound clicks coincident with each particle as it passes the silicon detector and enters the head of the subject. The presence of this type of cue has made visual recognition more difficult than its absence. When helium particles entered the eye at a rate of about one per second, 4% were counted without sound clicks; in another run when sound clicks were present, no particles could be recognized (Figure 4). It is postulated that the signals from the sound clicks interfere with the central nervous system integration and conscious recognition of any visual events registered at the retina.

Oral warning or countdown at one or two seconds before the helium particle stream was turned on seemed to be helpful for the subject. Perhaps the "internal scanner" is placed on "alert" in this manner.

He IONS FLASH 240 MeV
Subject T.B.
Left eye, lateral position I, no absorber

Result of several runs

Rate	Events seen
1 per sec	4-6 per 100
10 per sec	30-40 per 100
30 per sec	20-30 per 100
>100 per sec	1 per 100

Run No. 5 No clicker

1 per sec	3 per 50

Run No. 6 Particle triggered clicker

1 per sec	0 per 50

DBL 715-5769

Figure 4:

Summary of several exposure sequences with subject TB.

The distribution of range penetrations of the helium nuclei was carefully measured before each set of exposures by means of phantom absorbers and silicon solid state detectors upstream and downstream from the absorber. With the aid of these data together with the intensity of particles and observers' reports, in various test runs it was possible to obtain some idea of the efficiency of detection of events. Events were recorded only when the central region of the retina in the posterior portion of the eye was in the beam. The size of the sensitive strip on the retina was about 8-mm on each side of the beam axis. When beams of several hundred particles were passed through the anterior portion of the eye (but behind the lens) or through the optic nerve posterior to the eye there were no flash or streak events. In this latter position, however, one observer saw a few "luminous cloud events," decaying relatively slowly in a few seconds. More work is necessary before the cloud type of event can be definitely attributed to a "neural light flash" event caused by helium ions as similar phenomenon have been observed during periods when the beam was off.

Figure 5 shows a schematic cross section of the left eye viewed from above in relation to the positions of various beams passed through it. Flash counts were attempted by the subjects at five different mean penetration distances attained by the use of absorbers. The graph indicates the depth-penetration curves as functions of absorber thickness for each of the five penetrations. The position of the eye for these could be only approximately determined from tissue stopping-power data and the subjects' reports as to the location of the light-flash events on the horizon. The frequency distribution of stopping particles is also shown.

In Figure 6 we have plotted the subjects' actual counts of light flash events when the particle rate was 10 per second against the counts of particles that penetrate to each depth. The table gives detection efficiencies for each of the five positions. It is somewhat surprising to find that particles arriving either at the center of the retina or several millimeters away are all counted at about the same efficiency of 40% to 45% by subject TB. We feel that the actual detection efficiency varies between 25% and 50% because the reliability of the experiment was not as good as indicated by these numbers. When the beam did not reach the retina (position V, Fig 6) no flash event was seen by the subject in a stream of 200 particles. During these experiments the subject did not know what particle range was being used. Apart from an oral announcement about 10 seconds before the stream of particles entered the beam line he had no cues of the times the beam was turned "on" and "off".

Streaks

Of several hundred events seen, about 25% were reported as streaks of various lengths. The subjects used a simple method to report the lengths of the streaks. They estimated what the length of the trajectory would be if it had been produced by a pencil of light at a meter distance from the eye (Figure 7).

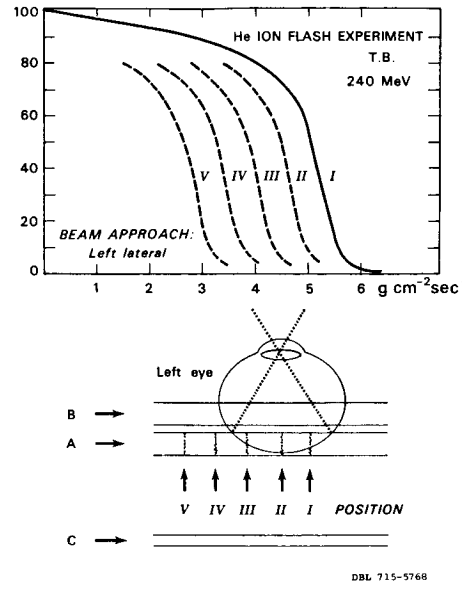

Figure 5:

The lower part of the Figure indicates beam positions A, B, and C where light flash exposures were attempted. Most events were observed in Position A. The upper curves are relative number-distance curves for the particles as determined prior to the experiment in a phantom. By insertion of appropriate absorbers, the depth of penetration was controlled to one of five penetrations (I, II, III, IV, V) in each test sequence.

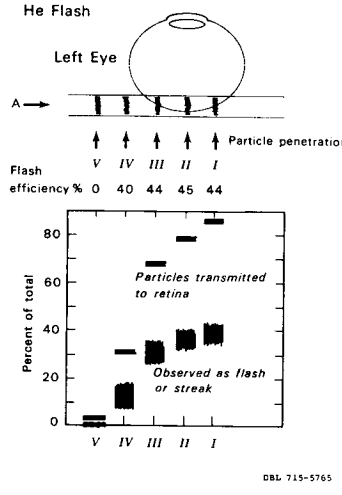

Figure 6:

The lower portion shows the percentage of particles transmitted to the retina at each of the five particle penetrations and the percentage observed as flash events. From such observations the "flash efficiency" was obtained for each exposure.

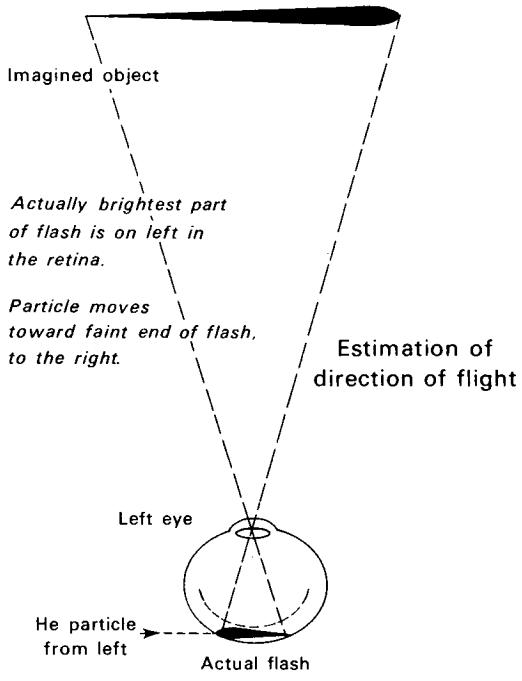

OBSERVER believes brightest part of track leading. Brightest part is on right. Hence particle is moving to right, a correct illusion.

Figure 7: DBL 715-5767

An attempt was made to explain why the observers coul attribute a direction of motion to the streaks (see text).

Persistence of the Light Flashes Observed

Most of the events observed appeared to have exceedingly brief lifetimes and left no after effect. A very few of the brighter white streaks, in the central portion of the retina did have a greenish after image, persisting for intervals of the order of 1 - 2 seconds for observer CT.

Dependence on Dark Adaptation

We have also separately shown that ability to observe the light-flash signals depends on the state of dark adaptation. In the course of the experiment and after many flashes were seen in the dark, a subject was re-exposed to room lights for 2 minutes and then dark-adapted again. His ability to see particle-induced light flashes gradually returned in a span of about 10 minutes, however, there was annoying, very persistent after image of the rectangular fluorescent light used in light adapting during this 10 minute period. In summary we have observed that helium ions, when they cross the retina, give rise to the sensation of light flashes, streaks, and "supernovae." Proton recoils and alpha particles produced by neutron interaction in the eye also give light flashes and streaks. These events are probably from ionizations and excitations in the path of the particles. The excitations are accompanied by emission of electromagnetic radiations in a broad spectrum of wavelengths. More refined work will be necessary to identify the physical events that actually initiate light sensation and the location of biological structures where primary interactions occur. It is interesting to speculate that the light-flash events may be related to some physical event in rods, perhaps initiation of action currents across membranes of the outer segments of rods. We believe that flash events may occur when several nearby rods and perhaps cones are affected simultaneously and in coincidence.

The helium flash events are not due to Cerenkov effects. Low energy helium ions, perhaps up to 50 MeV/nucleon (200 MeV) can cause flash events. It also follows that protons to about 10 MeV kinetic energy, and (in space) all heavier cosmic ray particles, probably with $Z \geq 6$, even at several hundred MeV/nucleon kinetic energy, can cause flashes.

We have also shown that the same events are seen with different efficiencies and with considerably different detail when the particle flux density changes. At very low or very high flux densities more than 90% of the flash events might be missed, whereas at an arrival rate of about 10 per second, about 40% are seen. The recognition of flash events depends on spatial and temporal integration in the nervous system. At the highest observed efficiency, about 40% of the particles passing through central regions of the retina are detected. Correlation of events observed in space with actual cosmic ray particle fluxes also depends on spatial temporal integration and it is possible that 5 to 20 times as many flash-causing events occur as the frequency actually reported by astronauts. An obvious answer to the efficiency of human detection of primary cosmic rays would be to conduct in space actual physical particle-identification studies during periods of human observation of the flashes they cause.

Most of the observed events can be accounted for by the assumption that the fast particles cause interactions in the retina particularly in the receptor layer. This is illustrated in Figure 8.

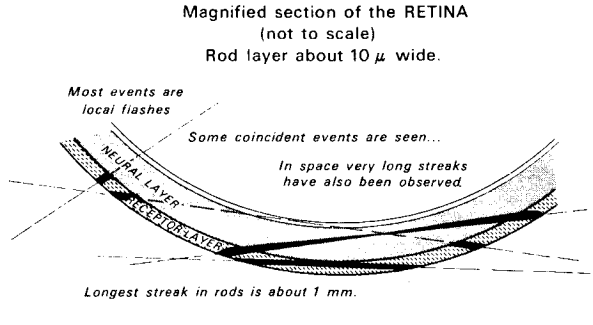

Figure 8: DBL 715-5766

A schematic section of the retina is given to illustrate how various observed events correspond to particles crossing the retina at various angles. Most events observed are local flashes. The manner in which streaks and segmented coincidences might be produced is also shown.

The receptor layer contains the outer segments of rods and cones with visual pigment.

We believe that grey or colored X-ray phosphenes are produced by diffuse interactions in the receptor layer.

Luminous cloud observations are not explained in this figure. They might be due to light that reaches the receptors from the neural layer or vitreous fluid.

From this estimation and refractive index of the vitreous humor one can estimate the length of the interaction on the retina. By this method the longest streaks had a path of about 1-mm in the retina, tangential to it, corresponding to a track length of about 5 cm, 1 meter away from the subjects When the curvature of the retina is taken into account, as well as an estimated thickness for its light sensitive part of 10 microns, it turns out that the longest unbroken straight path under these conditions is about 2 mm. We assume that only the part of a track that passes through the light sensitive layer of the retina is recorded. The depth penetration of particles is much greater than this path. It seems likely that at least the last several millimeters of a helium ion track can cause a light flash. If the retina should be sensitive to high energy helium ions as well as to low energy, we should have seen bisegmented tracks (coincidences). We have not been able to see such coincidences in any of these experiments, but more work is planned on this problem in the future. In space, quite long and intense light flashes were seen by several astronauts sometimes comprising as much as 55° aperture. In addition, about the right number of bisegmented tracks were reported to assume that many cosmic ray particles were able to elicit light sensation along several cm portion of their track.

Sense of Direction of Streaks

For a portion of the light streaks seen, the subjects reported very definite and correct sensations with respect to the direction of passage. Similar observations were reported in the low energy neutron experiments (10). Since the particles go through the retina in less than 10^{-11} second, one would not presume that normal light direction sensing mechanisms can recognize motion of the flash. At the present time the observations at hand are not sufficient to unequivocally establish for sensing the direction of travel of the particles. Nevertheless, for the purposes of discussion and further experiment, we suggest the possibility of a double optical illusion as an explanation for the recognition of direction. As we illustrate in Figure 7, the subject perceives a straight trajectory, in front of him, widening and brightening from left to right. This conveys a sense of motion in the same direction. Actually, in the retina, the track may be represented by a "thindown" due to the range distribution of its delta rays. It is assumed that more rods are affected on the left than on the right. The guess of movement to the right appears to be based on two kinds of mistaken judgement: (a) that the streak is in front not within, and (b) that it is brightest in its leading portion. Another explanation for motion sense in random directions was given by us for the neutron phosphene experience (1).

Supernovae

Each subject saw a few isolated events that had the appearance of a "supernovae", as defined by the astronauts. Such bright flashes with fuzzy margins were observed at absorber settings when most of the particles were near the end of their range, where the rate of energy is highest. The center of these events appeared to be colored blue, and in one case a brief flickering of blue and red. Similar events observed in space were brighter and larger than those observed by us, according to discussions with Apollo 14 crew. We used a variable light source of various shapes to compare the astronauts' experiences with ours.

Future experiments are planned to test the responses to interactions of accelerated particles with brain centers. Possible regions of interest are in the lateral geniculate bodies and in the occipital cortex at the calcarine and parieto-occipital fissures. Unfortunately there are no accelerated particles of ions heavier than helium available with sufficiently high penetration to test visual events caused by them. Exploitation of nuclear particles for exploring central-nervous-system function depends on constructing heavy-ion accelerators capable of accelerating particles with various atomic numbers to energies of several hundred MeV/nucleon.

The observation of light flashes in space flight and in accelerator beams has posed many scientific questions that await answer. Among these is the magnitude of deleterious effects that individual particles might cause in the retina and other regions of the nervous system (e.g., cardiac pacemakers, hypothalamus). Research has been initiated to answer some of these problems.

Acknowledgement

The authors profited by collaboration with the staff of the Manned Spacecraft Center, Houston, during recent Apollo missions, and by discussions with Professor G. Westheimer and Professor L. Stark, University of California, Berkeley.

The authors are indebted to Dr. James Born, Director of Donner Laboratory; to James Vale and the staff of the 184-inch cyclotron at Lawrence Radiation Laboratory; to H. Wade Patterson of the Health Physics Department; and for their invaluable help and technical assistance: to Edward (Pete) Dowling, Jerry Howard, Jean Luce, Frank Upham, and Robert E. Walton.

This work was jointly supported by NASA and AEC.

REFERENCES

1. TOBIAS, C.A., BUDINGER, T.F., and LYMAN, J.T.: Nature, **vol**.230, 1971, p.596.
2. PENFIELD, W.: Proceedings of Royal Society London, Series B, vol 134, 1947, p. 329.
3. FAZIO, G.G., JELLEY, J.V., and CHARMAN, W.N.: Nature, vol. 228, 1971, p. 260.
4. TOBIAS, C.A.: Aviation Med., vol. 23, 1952, p. 345.
5. D'ARCY, F.J. and PORTER, N.A.: Nature, vol. 196, 1962, p. 1013.
6. TOBIAS, C.A., BUDINGER, T. F., and LYMAN, J.T.: Potential Hazard from Heavy Particles in Long-Term Spaceflight, presented at IV International Congress of Radiation Research, Evian, France, June 28-July 4, 1970.
7. TOBIAS, C.A., BUDINGER, T.F., and LYMAN, J.T.: Lawrence Radiation Laboratory report UCRL 19868, August 1970.
8. FREMLIN, J.H.: New Scientist, vol. 47, 1970, p. 42.
9. BUDINGER, T.F.: Indirect Electrical Stimulation of Visual Apparatus, Lawrence Radiation Laboratory report UCRL 18347, 1968 (unpublished).
10. BUDINGER, T.F., BICHSEL, H., and TOBIAS, C.A.: Science, vol. 172, 1971, p. 868.
11. RAJU, M.R., LYMAN, J.T., and TOBIAS, C.A.: Radiation Dosimetry, vol. III, 1969, p. 151, F.H. Attix and E. Tochulin, ed.
12. WESTHEIMER, G.: J. Physiol., vol. 181, 1965, p. 881.
13. VAN NES, F.L., KONDERINK, J.J., NAS, H., and BOUMAN, M.A.: J.Optical Soc.Amer,,vol.57,1967,p.1082.
14. CHAPMAN, P., and PINSKY, L.: "Cosmic Ray Induced Light Flashes Observed on Apollo 14", presented, Nat.Symp. on Natural and Manmade Rad. in Space.

THE HEAVY PARTICLE HAZARD - WHAT PHYSICAL DATA ARE NEEDED?

S. B. Curtis (Lawrence Radiation Laboratory, Berkeley, California)
M. C. Wilkinson (Space Sciences Group, The Boeing Co., Seattle, Washington)

Manuscript included in addendum, see page 1007.

ON THE USE OF QUALITY FACTORS AND FLUENCE TO DOSE RATE CONVERSION IN HUMAN RADIATION EXPOSURES

C. A. Sondhaus
University of California Irvine College of Medicine

In principle, the distribution of absorbed energy in the tissues of a human exposed to ionizing radiation can either be measured more or less directly by in situ dosimetry, or it can be calculated from a knowledge of the energies and angular distributions of the particle fluences impinging on the individual or phantom. The first method can quickly and simply determine the quantity of interest: dose, without the intervening complications, approximations and uncertainties of the second method. In fact, one reason the quantity "dose" was invented was just the elimination of these intermediate steps. But direct measurement is not always possible, and it can seldom be used to obtain dose values at more than a few points within the tissues. The second, more indirect method is now developed to a degree of detail sufficient to produce a virtually complete description of the dose distribution resulting from any arbitrary combination of radiation fluence and energy. Conversion to dose by calculation, however, not only requires charged particle telescope or spectrometer data, but a computer and a program of some complexity as well, imposing even greater practical limitations than does the first method.

But a far more fundamental limitation applies in either case. The use of dosimetric data to assess the biological implications of a given exposure requires additional knowledge of the kinds and degree of effects which result, not simply from the given total amount of absorbed energy, but much more critically, from the way in which that quantity may be distributed both microsopically and macroscopically, in both space and time, from one case to another. The radiobiological uncertainties which occur at this stage are so marked and so incompletely defined that the ability to establish an exposure status still clearly lags behind the technical means of obtaining, by either of the above methods, the dose data on which to base it.

How then do we arrive at conclusions about the status of the human individual - which is, after all, what we are trying to assess - by any combination of these factors? The question is so broad and still so debatable that one can only attempt here to sum up briefly some areas in which much work has been done in the past, and to try to illustrate how imprecise are our attempts to evaluate whole body exposure, as distinct from the highly local doses so well discussed by Dr. Curtis. To paraphrase Dr. Drew, we are indeed trying here to make our technology of physical measurement serve the cause of human values - numerical ones, to be sure, but none the less human - and it is no easier here than it is elsewhere.

In Fig. 1 the familiar regulations referring to ordinary exposures are summarized; in regard to space radiation exposure they belong to an earlier and simpler age. Nevertheless, there are several assumptions implicit in these values which underlie their apparent simplicity. For example, quality factors are built in; they are not mentioned, but a QF is inherent in each rem unit used. How to decide what these QF's shall be is of course left up to the technician who must hold the personnel exposures within these levels.

More importantly perhaps, the approach used in setting these regulations is that of the critical organ or group of organs. The body is subdivided into regions or systems, and to a great extent they are treated separately. This is due not only to the kind of data available but also as much as anything else to the necessity of designing regulations which can handle both internal and external exposures. When radioisotopes are taken up by the body, of course many of them tend to concentrate in certain organs; but when an exposure is external the nonuniformity of dose distribution occurs for entirely different reasons.

In the case of space radiation exposure this nonuniformity can reach an extreme degree, not only with respect to dose distribution and LET but even to the extent of microscopically localized high doses of the kind Dr. Curtis has just discussed. In attempting to deal with such exposures we are used to a certain kind of thinking, and although we do not follow it explicitly in setting astronaut doses we still tend to think in terms of critical organs, which may not necessarily be the best approach in all cases. When we know that an effect is local, confined to the retina of the eye for example, we can certainly use this approach; but if we think that a number or set of numbers must be sought to describe the overall physiological status of an individual post-exposure, the critical organ approach can lead to contradictions.

Fig. 2 sets forth the other half of this somewhat simplistic approach, which has still been found to be practical enough for most cases. We simply make another set of rules: depending on the LET of the radiation involved, regardless of its type, we now multiply any dose by a number, the QF, and so arrive at its relative "effectiveness". This can presumably be done for any tissue location and volume in which this radiation is deposited, and doses to different regions of the body are thus multiplied by the appropriate QF's and treated almost independently.

Exposed Part of Body	*Occupationally Exposed Persons*	*Public at Large*
Whole body, blood-forming organs and gonads	5 rems/yr 3 rems/quarter*, provided the cumulated dose to age N years is less than 5 (N-18)	0.5 rems/yr
Bone, thyroid, skin	30 rems/yr 15 rems/quarter	3 rems/yr†
Hands, forearms, feet and ankles	75 rems/yr 40 rems/quarter	7.5 rems/yr
All other organs	15 rems/yr 8 rems/quarter	1.5 rems/yr

* A planned special exposure for occupationally exposed workers of twice the yearly dose is permitted when alternative techniques are either unavailable or impractical. This is 10 rems/exposure to the whole body.

† 1.5 rems/yr to children up to 16.

FIGURE 1

LET_∞ (keV/μ IN WATER)	QF
X rays and electrons of any LET	1
3.5 or less	1
3.5–7	1–2
7–23	2–5
23–53	5–10
53–175	10–20

[a]From NCRP [1954].

FIGURE 2

In practice, most records that are kept today are not broken down into these categories. Generally one is fortunate when one has a single number to describe a person's exposure. In space, we are trying to refine things somewhat further because of the different radiations and higher doses with which we are concerned, and it is here that we encounter difficulties in attempting to apply sets of numbers. The characteristics of space radiation which are of chief importance in this regard are the range of energies which occur and the change of both energy and fluence rate with time. Dr. Lushbaugh has discussed the effects of time very thoroughly; some of the other properties will be mentioned here. The situation is indeed far more complex than are those for which the ordinary MPD concepts were developed.

Fig. 3 shows what is perhaps one of the most important characteristics of heavy particle interactions; the "transition curve" and the build-up of dose to a maximum due to production of secondary radiations (1). The phenomenon has been known for some time; its effect on dose distributions is much greater than that of the Bragg Peak doses at the ends of the paths of charged particles. The transition build-up results from the production of secondary particles from two main processes: intranuclear cascades and evaporation processes, each of which vary as a function of both incident particle energy and the mass number of the target material.

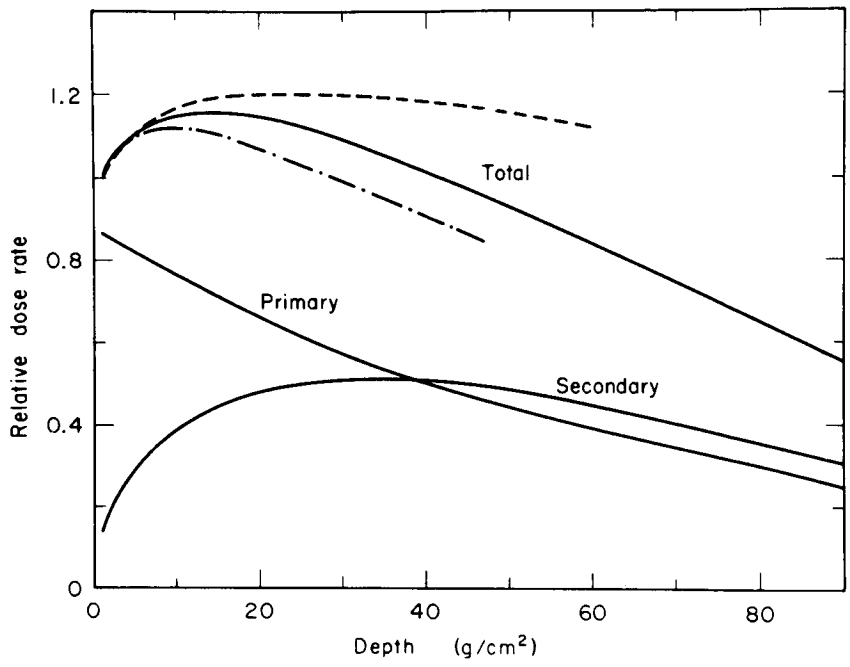

FIGURE 3

Fig. 4 illustrates one instance in which a program was designed to compute dose build-up due to these secondary processes (2). The experimental data fits the calculated values fairly well for a beam of the energy indicated (3). Fig. 5 is from another more recent program which converts flux to dose at given energies (4). These are both representative instances of the kinds of calculations that are possible. When one also folds in the energy spectrum of a solar flare, of trapped radiation, or of galactic cosmic ray charged particles, the sum of such a set of curves results in the familiar steep fall-off of dose with depth.

Quite some time ago, Dr. Schaefer very clearly pointed out that in addition to the distribution of dose on the macro scale, one should take into account the high LET at the ends of proton tracks which result either from neutron interactions or from primary proton cascades or other secondary processes. At the ends of their tracks, protons reach about a three-fold higher value of local LET than do the secondary electrons produced by electromagnetic radiation. All this is familiar ground; the problem lies in the distribution and concentration of such track ends under the conditions we are talking about.

Fig. 6, from Schaefer, illustrates the distribution of LET produced by a flux of charged particles passing through tissue (5). Three cases are shown; the first is for orthovoltage 250 KVP x-rays, showing the LET distribution of the secondary electrons produced by the gamma photons. The second is for a typical solar flare proton energy spectrum, which produces essentially the same distribution in LET as do the x-rays, and should therefore have very much the same RBE and QF, with the exception of the small portion of track enders. As Dr. Schaefer pointed out yesterday, this distribution varies between earth orbital and free space exposures. The LET distribution shown in the third case is that for the recoil protons produced by neutrons with the fission energy spectrum.

Fig. 7 shows how the use of the QF values which result from these differing LET distributions were first applied to the calculation of dose and dose equivalent for tissue for a variety of different energies. This figure, from Kinney and Zerby (6), shows first the dose and then the dose equivalent in rem for both normally incident and isotropically incident proton fluxes at five centimeters depth in tissue, as a function of proton energy. Many such curves have since been generated to estimate how rad and rem dose should vary with energy at given tissue depths under a variety of shielding conditions.

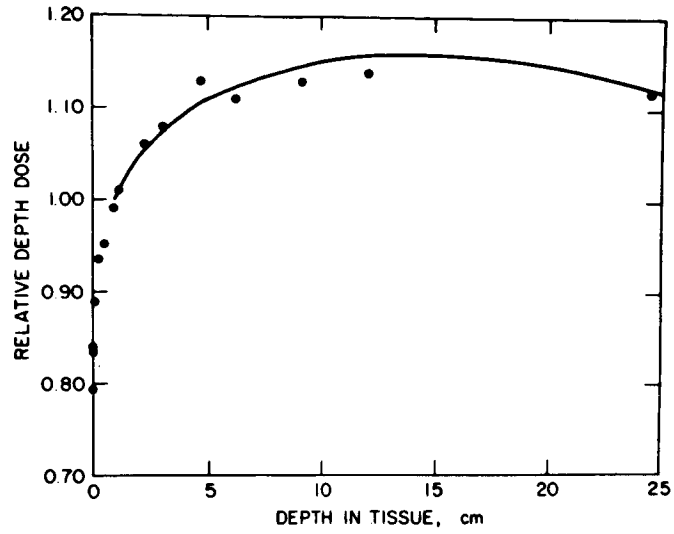

FIGURE 4

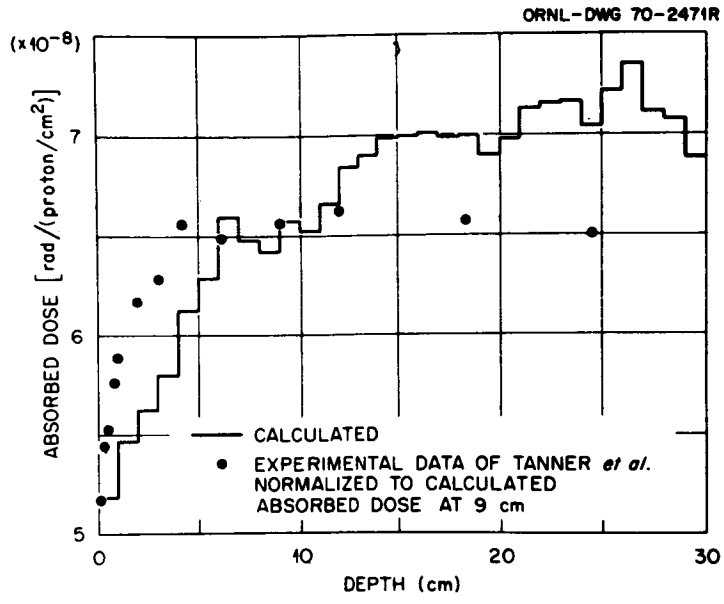

FIGURE 5

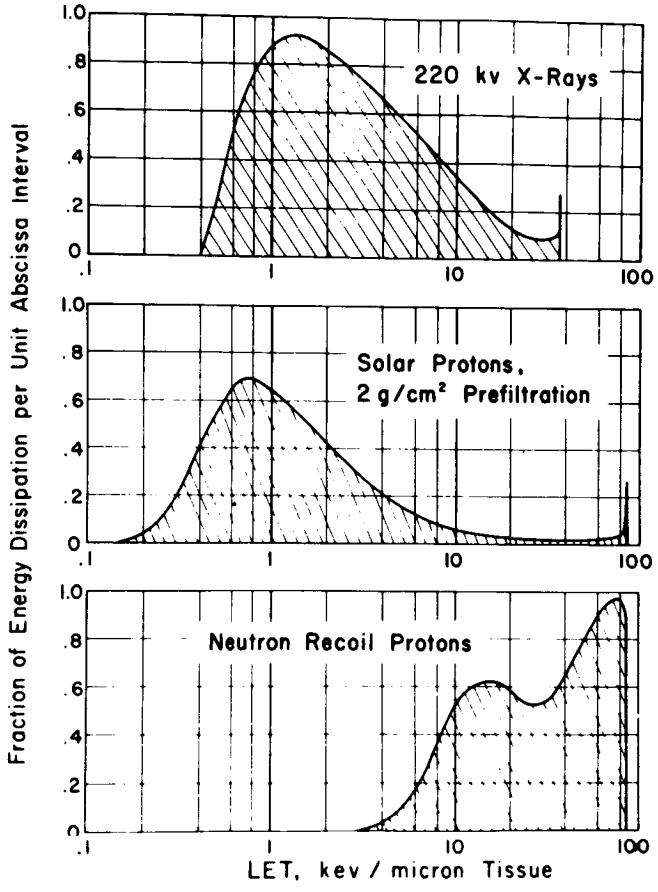

FIGURE 6

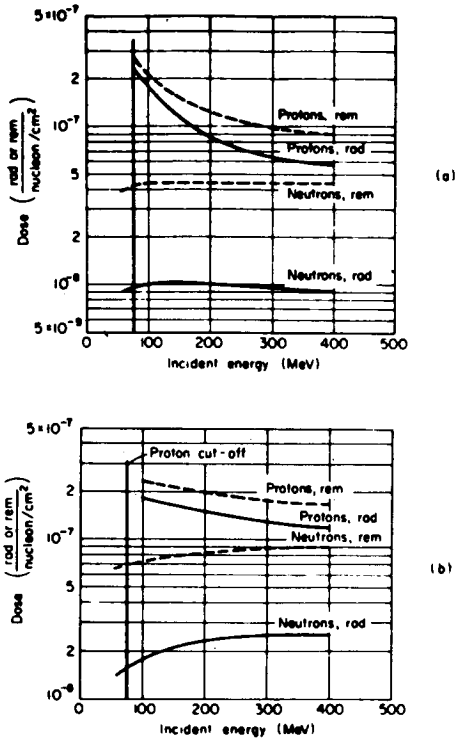

FIGURE 7

Another way to present the same data is to calculate separately the dose and dose equivalent for each type of secondary particle as a function of depth so that, for example, normally incident protons can be treated as producing ionization from both primary and secondary protons, secondary neutrons, heavy nuclei, pions, and so on. All of these sub-classes and their dose equivalents can then be added together to give a dose equivalent at any depth.

Fig. 8 shows another way in which such data have been treated (7). In this figure, the dose at the center of a water sphere whose radius varies from one centimeter to several tens of cm is calculated, and a quality factor is also calculated for its center as a function of the primary proton energy and hence, of the residual energy of protons which reach the sphere center. This quality factor is simply the number of rem per rad; again, each of the calculated values simply results in a number by which to multiply a dose which one may or may not be able to measure directly.

An important question is: how closely can any of these numbers be calculated, or applied, to the quite irregular geometry of the human? Some heroic efforts to deal with this question are currently being made. Dr. Kase will talk on this tomorrow and I will only mention it. Briefly, coordinate systems are assigned to an average human geometry, including those body elements which can be considered as separate systems which remain internally constant even though their configurations relative to each other change when seated, standing, and so on.

Using the standard Air Force man, a machine computation can then produce distributions of tissue depth surrounding any point in the body, which will indicate what percent of the total solid angle subtended by that point is shielded by a given tissue thickness. In this way the build-up factors, the attenuation, the production of secondaries and all of the other physical phenomena which intervene between flux and dose can be treated separately and summed up for the point in question.

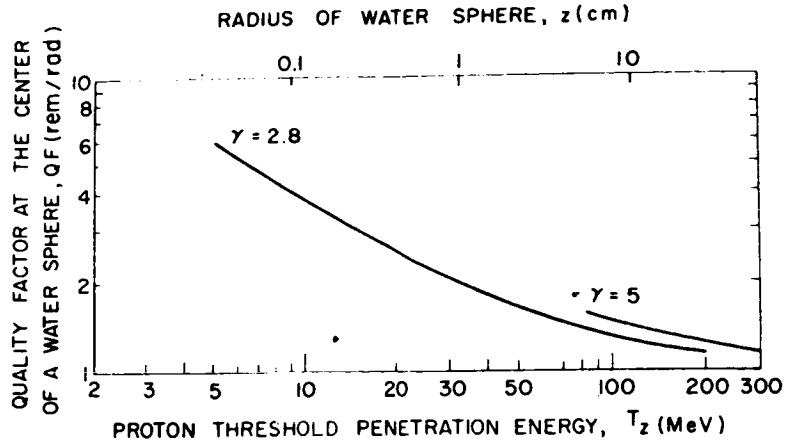

FIGURE 8

For example, in Fig. 9 the dose point is the heart; the curves compare various degrees of detail in such man models and show to what degree simplification influences the calculated tissue thickness distribution (8). In a previous study (9) a given proton spectrum, that measured on a Gemini mission, was used to determine a dose conversion factor for several points (e.g., the center of the gut in Fig. 10); that is, the number of rads per hour per 10^4 protons per square centimeter per second. One can say further that for this particular case, the greatest contribution to the dose at this particular point in this particular standard man is due to the particular calculated range of incident proton energies indicated.

What then does physical data of this kind imply in biological terms? We really do not have data which is precise enough on the biological side (particularly the human biological side, as Dr. Lushbaugh has pointed out) to match the degree of detail in the physical data; the kinds of biological data we do have are considerably more "overall" in character. For example, one can compare experimentally, as Jackson did almost a decade ago, two types of exposure in which the familiar depth dose pattern of solar flare protons is contrasted with an idealized uniform case. But, in order to do this, he had to do something physically analogous to what the computational programs have usually limited themselves to; that is, he compressed his animals literally into cylinders, into regular shapes which could be irradiated with Co-60 gamma radiation through a wedge filter, producing the dose distribution by rotation. It was of course found that the LD-50 dose for a uniform exposure could be described by a single number, but that for the non-uniform case, one had to choose some other way of characterizing the dose distribution; for example, the ratio of midline to surface dose, or the dose at some reference depth, e.g., 5 cm.

In Fig. 11, from Dr. Bond and associates at Brookhaven, another method of comparing different dose distributions is illustrated (10). Bilateral and unilateral exposure data were obtained for the dog, and the LD-50 dose for 30-day mortality was expressed as a midline air dose, as a midline tissue dose, and as an entrance and an exit dose. Since the bilateral exposure produces a symmetrical pattern with a build-up in the center, the midline LD-50 dose is 280 rads, whereas the doses at entrance and exit are somewhat less; but it is still almost a flat dose pattern. These values do not mean a compressed dog, or a cylinder, or rotation, or anything of the sort; they are simply data that were already on hand. If one now considers the unilateral case, with a midline air dose of 384 rads, it takes 337 rads at the midline, with 530 rads at entry and 168 rads at exit, to produce the same LD-50 in 30 days.

In order to arrive at some way of characterizing numerically such a difference in uniformity (Fig. 12) one very roughly divides the body into three equal regions, each containing part of the total pool of stem cells which are located in the marrow and produce the formed elements of the blood. An estimate is then made of the fraction of the total stem cell pool which is in the volume nearest to the source, the fraction located medially, and the fraction which is in the distal region. If one then estimates the average dose to each of these three parts, one can now apply the known reproductive survival curves for stem cells, making the assumption, which seems to be justified, that they are applicable in vivo. If one then calculates the fraction of each of these three parts of the marrow cell population which would be expected to go on proliferating after its respective dose, and multiplies that part of the pool population by its calculated fractional survival, then one can estimate the total relative number of surviving stem cells; this is shown in the last column. If one does the same thing for

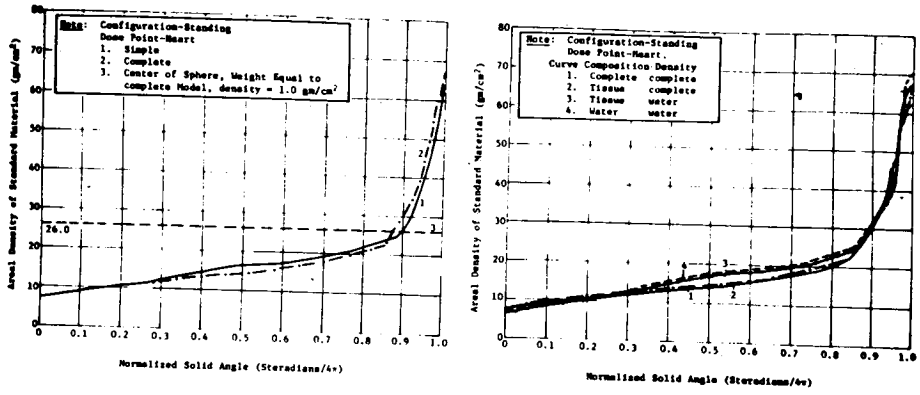

FIGURE 9

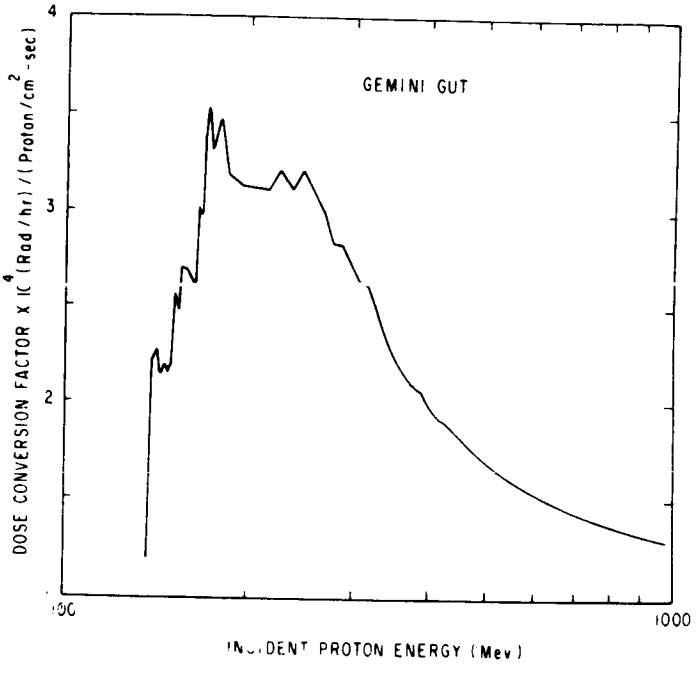

FIGURE 10

the bilateral case, which is much more uniform, one can work backwards from the dose (although as Dr. Lushbaugh says, "its in a way circular") and it can be seen that approximately the same fractional number of surviving,dividing cells results whether the exposure is uniform or not.

This analysis applies only to a regenerating tissue; in the case of a tissue which is not proliferating, of course, a different set of considerations apply. Dr. Curtis has pointed out how the Fractional Cell Lethality concept, a similar procedure applied to cells surviving high, localized particle track doses in an organ which is not proliferating, serves a somewhat similar purpose.

Figs. 11 and 12 illustrate an attempt to normalize and compare whole animal doses, and to use something similar to an FCL for the whole exposed mass of proliferating tissue (here, of course, for radiation of QF 1). As a result of this analysis, an effectiveness factor can be estimated for the non-uniform distribution compared to the uniform one; the ratio turns out to be about 0.78 in this case. In this way, a non-uniform dose distribution can be weighted by a "Distribution Effectiveness Factor" analogous to a QF, but now not due to differences in micro dose distribution, but to dose pattern differences on the gross level.

$LD_{50(30)}$ Values for Dogs and Swine Exposed Bilaterally versus Unilaterally to Megavoltage X-Radiation

Species, exposure type	$LD_{50(30)}$			
	Midline, air	*Entrance, tissue*	*Midline, tissue*	*Exit, tissue*
Dog, bilateral	319[a]	266[b]	280[b]	266[b]
Dog, unilateral	384[a]	530[b]	337[b]	168[b]
Swine, bilateral	375[a] (350–400)	272[a] (253–290)	234[a] (218–250)	272[a] (253–290)
Swine, unilateral	500[a]	584[a]	312[a]	131[a]

[a] Exposure in roentgens.
[b] Absorbed dose in rads.

FIGURE 11

Calculation of the Surviving Fraction of Stem Cells in the Dog Exposed Unilaterally to 1000-kVp X-Radiation

Body region	*Dose (rads)*	*Relative number of stem cells*	*Surviving (%) (from Fig. 1)*	*Relative number of surviving stem cells*
Proximal third	530	43	0.5	0.0
Middle third	337	31	4	1.2
Distal third	168	26	23	6.0
Total		100		7.2

FIGURE 12

In Dr. Lushbaugh's discussion it was shown that if one attempts to do something similar with man, one cannot extrapolate from all the animal data, and one cannot of course do the same kind of studies on man. But at least, for ordinary gamma radiations such as from Co-60 and Cs-137, determining a distribution of the same kind and making some assumptions based on the known percentages of the total marrow which lie at different depths, one can in principle arrive at a similar distribution effectiveness factor and compare this for cases in which, accidentally or otherwise, such non-uniform exposures have been received. There has been a fair degree of success in doing this so far. It is clearly a totally different process than just multiplying a dose distribution by a QF value, although it ideally should result in at least an equal degree of prediction confidence.

As Dr. Curtis has already shown, if one considers radiations of higher LET's, the kinds of survival curves which can be used to predict the survival of stem cell populations change in their shape as well as in their slope. It is the ratio of dose from a curve for x- or gamma radiation to that for a higher LET radiation for a given level of effect which defines the relative biological effectiveness on which all the QF's are based. There is a "multievent" shoulder on the low LET curve; as first shown by Elkind, if one divides the dose into fractions separated by a time interval long enough for recovery, by the next time a dose is given the same shoulder has reappeared. The increase in dose necessary to give the same degree of effect when a low LET dose is protracted can be explained on this basis. In the case of the straight exponential survival curve seen for high LET radiation, there is little or no recovery. The time factor is thus applicable to low LET, but not significantly to high LET exposure, just as the oxygen enhancement ratio that Dr. Curtis has mentioned also differs for high and low LET.

Another consequence of the fact that the low LET curve has a shoulder and the high LET one does not is that the ratio "RBE" is a function of the degree of effect. One therefore has a range of RBE values for any two radiations, depending upon how far down the pair of survival curves one is comparing doses. For low dose rate levels or for many small doses one is therefore comparing effectiveness at a different ratio. This generally leads to higher RBE values at low doses than have usually been obtained experimentally, where it is much easier to do an experiment by irradiating with higher doses. Caution in the use of QF's is thus necessary because of this time factor as well.

Reliable collections of animal data now exist for reasonably monoenergetic primary neutron exposures. The production of recoil protons in the tissues of rather small animals results in a fairly predictable mean LET for each of a series of energies. Experiments at these energies by several different groups of investigators using a number of endpoints have produced RBE values which follow a reasonably definite relation to LET. This "whole animal RBE" is the combined result of a number of things happening together, and it does not agree very closely with the RBE from cell survival curves, although a whole body RBE is clearly the end result of the processes that a single cell survival curve depicts for each cell type. For these small animals, one gets RBE's in the range of 5 or 6; if the animal is larger and the distribution of secondaries is different, different neutron RBE values may result.

Dr. Lushbaugh has derived a total body RBE for the human in a mixed field of gamma and neutron radiation by using Hiroshima and Nagasaki data and comparing the 60-day survival curves (11). As shown in Fig. 13, they can be superimposed as a function of horizontal range for light steel buildings, for which the most recent (T-65) dose estimates of gamma and neutron radiation yield approximately equal gamma and neutron doses in Hiroshima, but neutron to gamma ratios of about 1 to 12 in Nagasaki. Under these shielding conditions, he could then try different RBE factors for the neutron component to make the 50% survival doses match one another; in this way a human total body RBE of 2 was estimated. This should be compared with the value which he discussed earlier today, which may be about twice as high when estimated differently and with better data.

Obviously, the RBE may also depend on how one chooses the endpoint, and how confident one is that other factors are not involved, such as blast and burn damage in the case of the Japanese. One clearly cannot be as exact or as confident with the human data as is possible with cells, or even with small animal data. This is one reason the total body, approximate but presumably overcautious QF values were invented, to be distinguished from RBE's. It also should illustrate the logical inconsistency of multiplying the dose at each point in a distribution by such QF values, a practice which has unfortunately become rather widespread.

AIR-DOSE ESTIMATES FOR 50% SURVIVAL FROM ATOMIC BOMB IRRADIATION UNDER VARIOUS SHIELDING CONDITIONS

Situation[a]	50% survival distance (km)	γ Rads	n Rads	REM RBE_n 1	REM RBE_n = 2.0	
			Hiroshima			
OU	1.18	102	78	180	258	± 39%
LSF	0.73	1000	1000	2000	3000	
SRC-L	0.13	9000	10,000	19,000	39,000	
			Nagasaki			
OU	1.35	250	5	255	265	± 27%
LSF	0.76	2900	250	3150	3400	
SRC-L	0.54	6500	600	7100	8300	

[a] OU = outside, unshielded; LSF = inside light steel frame buildings; SRC-L = inside seismic reinforced concrete buildings on the lower floor.
[b] Possible error in dose estimate (Auxier, 1968).

FIGURE 13

Fig. 14 summarizes the situation that obtains if one varies yet another parameter, the area of field in a skin exposure (12). This is a collection of data from radiotherapy which shows skin tolerance in roentgens as a function not only of the number of fractions into which a given dose is divided, but also how big an area of skin is irradiated. It can be seen that there is an area factor as well as a time factor. The 2000 rad figure for a single dose that is listed, for example, in the NAS-NRC Space Radiation Study Panel Report (13) is also seen here; but fractionating the dose raises it, increasing the area lowers it, and so forth.

In summary, it can be seen that we are able by various combinations of numbers and factors to arrive at estimates of dose and dose effectiveness from values of fluence; but as yet it has not been possible to use the biological data with the same degree of precision with which one can obtain or estimate the physical data. Certainly, a QF, even properly used, is by no means the only modifying factor that one must apply to a flux-to-dose conversion; the distribution factor and the time factor are there to contend with, and the area factor as well. But above all, one must at least consider the possibility of treating a total exposure not simply on the basis of a collection of separate organs wired together, each with its own sensitivity, but by applying a separate organ approach only very judiciously as a part of the characterization of a total body exposure. It would seem that the most reasonable way one can use the human data that exists is to apply it as far as possible to the human animal as a whole(14). To conclude: the particular dosimetric problems of the space environment have been a stimulus to such efforts - but the results can clearly be useful in terrestrial human affairs.

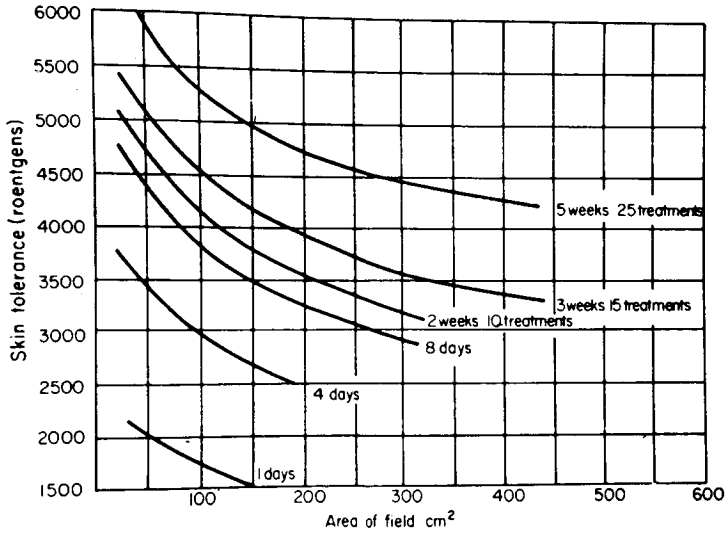

FIGURE 14

REFERENCES

1. Shen, S. P. (1963). Nuclear problems in radiation shielding in space. Astronaut Acta 9, 211.

2. Wallace, R. W., Steward, P. G. and Sondhaus, C. A. (1964). Primary and secondary proton dose rates in spheres and slabs of tissue. Proc. 2nd Symp. Prot. Against Radiations in Space, Gatlinburg, 1964 NASA-SP-71, p. 301.

3. Tanner, R. L., Baily, N. A. and Hilbert, J. W. (1967). High energy proton depth dose patterns. Radiation Res. 12, 861.

4. Alsmiller, R. G., Armstrong, T. W. and Coleman, W. A. (1970). The absorbed dose and dose equivalent from neutrons in the energy range 60 to 3000 MeV and protons in the energy range 400 to 3000 MeV. Oak Ridge Natl. Lab. Report ORNL-TM-2924 (Rev).

5. Schaefer, H. J. (1964). Local LET spectra in tissue for solar flare protons in space and for neutron-produced recoil protons. Symp. Biol. Effects Neutron Proton Irrad., Upton, N. Y. 1963, Vol. I, p. 297. IAEA, Vienna.

6. Kinney, W. E. and Zerby, C. D. (1964). Calculated tissue current-to-dose conversion factors for nucleons of energy below 400 MeV. Proc. 2nd Symp. Prot. Against Radiations in Space, Gatlinburg, 1964 NASA-SP-71, p. 171.

7. Madey, R. and Stephenson, T. E. (1964). Quality factors for degraded proton spectra. Proc. 2nd Symp. Prot. Against Radiations in Space, Gatlinburg, 1964 NASA-SP-71, p. 229.

8. Kase, P. G. (1971). This symposium, Paper VII.4.5.

9. Holly, F. E. Private communication.

10. Bond, V. P. and Robinson, C. V. (1967). A mortality determinant in nonuniform exposures of the mammal. Radiation Res. Suppl. 7, 265.

11. Lushbaugh, C. C. (1969). Reflections on some recent progress in human radiobiology. In "Advances in Radiation Biology", Vol. 3 (L. G. Augenstein, R. Mason and M. Zelle, editors), p. 277.

12. Paterson, R. (1948). "The Treatment of Malignant Disease by Radium and X-rays", Arnold, London.

13. NAS-NRC (1967). "Radiobiological Factors in Manned Space Flight", Report of the Space Radiation Study Panel. (W. H. Langham, editor). Nat'l Acad. Sci.-Nat'l Res. Council, Space Sci. Board, Washington, D.C.

14. Sondhaus, C. A. and Evans, R. D. (1969). Dosimetry of radiation in space flight. In "Radiation Dosimetry", 2nd ed., Vol. III (F. H. Attix, W. E. Roesch and E. Tochilin, eds.), Chapter 26, p. 453. Academic Press, New York.

Methods and Approaches to Dosimetry

by

Harald H. Rossi

Radiological Research Laboratories, Department of Radiology, Columbia University, New York, N.Y.

Space radiation represents by far the most difficult and most challenging task for dosimetry. It comprises not only virtually all of the radiations observable on earth but also includes various components which will not be produced in the laboratory for many years to come. High Z particles having energies of the order of tens of Gev per nucleon and protons having even higher energies can initiate an enormous variety of processes and one cannot dismiss the possibility of unknown or unexpected particles or interactions. The fact that very energetic processes are likely to be quite rare aggravates rather than simplifies the problems. A number of lines of evidence indicate that at the low dose rates normally encountered in space the high LET of energetic nuclei of large Z, and the energy releases attendant to various cascades produced by very energetic nuclei in general will be of profound importance. Consequently dosimetry must totally encompass not only an extreme dynamic range but also great differences of fluence rate.

Missions in which this kind of equipment can be deployed are likely to be few and they may well entail the requirement that the equipment has to be completely automated and operate reliably for months or even years. The fact that the equipment must be both complex and reliable means of course that it will be expensive but this may be a comparatively minor problem since the costs should still be a small fraction of the funds required for the mission. However even in the absence of financial strictures it is difficult to conceive of systems that will yield the desired information.

For the purposes of current earthbound radiation protection practice irradiation conditions are completely specified by the absorbed dose and its distribution in linear energy transfer, at all points in a suitable phantom. Although, such a determination is already quite difficult it is by no means certain that it would be adequate for space. Radiation protection standards were developed with little or no regard given to some of the radiations encountered in space and they also envisage dose limits which one might not be able to accept for astronauts. For these reasons and also because the analysis of any unexpected biological effects would require optimum physical radiation data it is highly desirable that the dosimetry system yield what might be considered to be the most complete radiological physics information. This is best expressed in terms of R(y) the time rate at which lineal energy*, y, is deposited at all locations in a human phantom and at all diameters of interest.

*The lineal energy (1) y is defined as $E/\bar{d}$ where E is the energy deposited by a charged particle and its secondaries in a tissue region of mean diameter $\bar{d}$.

The diameters of interest can in principle range from nanometers (the dimensions of macromolecules) to perhaps tens of micrometers. This latter dimension which appears to be about the maximum effective track diameter for ions of any energy(2) corresponds to the volume occupied by from ten to perhaps a hundred cells. In this connection, it might be remarked that at least one theory of radiation carcinogenesis (3) postulates that malignances arise only if several contiguous cells are injured.

At present there appear to be no methods in existence to determine energy deposition in tissue regions that are smaller than a few 100 nanometers. Between this level and the upper limit given above individual energy depositions in tissue can be experimentally determined only by simulating tissue volumes by much larger volumes of tissue equivalent gas in which proportional counting is performed. (4) Gas detectors lack the comparative simplicity, permanance and energy resolution of various solid state devices. An additional short-coming is that under certain circumstances simulation of a unit density tissue equivalent mass by a cavity filled with tissue equivalent gas is imperfect and can lead to an overestimate of energy deposition. (4,5) Nevertheless, the superior sensitivity and spatial resolution of gas detection make it the method of choice.

It is thus evident that present day technology is incapable of producing the dosimetry system ideally required and that some compromises must be made. The remainder of this presentation will be a discussion of a system which may be near the optimum compromise possible today. This apparatus has not been built and the design is largely conceptual. While the discussion will be primarily concerned with basic principles a few technical points will be made to indicate how various functions could be accomplished.

This system is designed to meet six primary objectives:

1) Determination of the dose received at various locations in the body of an astronaut. This dose to be averaged over periods of the order of 5 minutes.
2) Determination of the frequency with which high LET particles (LET > 10 keV/μm) impinge on the human body.
3) The distribution in depth of the dose due to such individual particles.
4) The LET of these particles at various depths in the human body.
5) The direction of incidence of these particles.
6) A determination of the track structure of these particles, i.e. the distribution of delta rays and other secondaries within distances comparable to the dimensions of the mammalian cell (3μm).

In addition to these primary purposes the system could provide at least on a statistical basis information on the total energy and nuclear charge of heavy particles.

These objectives are to be met by evaluation of the data produced by two sub-systems, which in the following will be termed the macro-system and the micro-system.

The macro-system is designed to yield information on points 1 through 5, the micro-system is designed to provide information on points 4 and 6. Both systems are in essence multiple ionization chambers which are normally operated in a gated pulse mode. However, when objective 1 is pursued, the macro-system operates in a pre-set time mode (in the following termed the dose mode). Both of the multiple detectors and the early electronic stages are to be contained in a hermetically sealed stainless steel drum having approximate dimensions of 20" diameter and 20" height. The optimal location with respect to a space craft would be such that the axis of this detector system coincides with the outside surface of the vehicle so that half of the detecting system sees free space with a minimum of shielding, whilst the other half sees the interior of the space craft.

Associated equipment for gas replacement and any additional electronic equipment, such as power supplies, should occupy a space that is less than two cubic feet.

The macro-system is schematically shown in Figure 1. It consists of a series of concentric cylindrical shells of tissue equivalent plastic having a total diameter equivalent to that of the human body (about 12"). The thickness of shells decreases exponentially from the center outward. The annular gaps are occupied by tissue equivalent gas at such a pressure that the width of the gap is equivalent to about 3 μm of unit density tissue. Collecting regions are established in these gaps by suspension of grids of the type shown in the drawing. The grids are secured by two simple insulators across the top and bottom of the phantom. The individual collecting regions might on the average cover about 15° of a full circle in each gap. Quite possibly the width of these chambers may vary both with respect to polar angle and with respect to distance from the center. All of the cylindrical shells are connected to a positive high voltage supply.

When the macro-system operates in the dose mode the grids are ungrounded for some period (e.g., 5 minutes) and then sequentially grounded through a digitizing network in which the accumulated charge is quantified as a corresponding number of pulses. It should be possible to obtain and store all of the numbers in a matter of milliseconds. In this mode the macro-system merely yields absorbed dose as a function of location in a phantom of the human trunk.

When the phantom is operated in the pulse mode, the principle of operation is as follows:

All tissue equivalent rings are at a positive potential and connected to a fast triggering circuit and all the grids are normally grounded. Traversal of any one gap by a high LET (> 10 KeV/μm) particle results in the liberation of 10^3 to 10^4 electrons. These are collected very rapidly and provide a signal

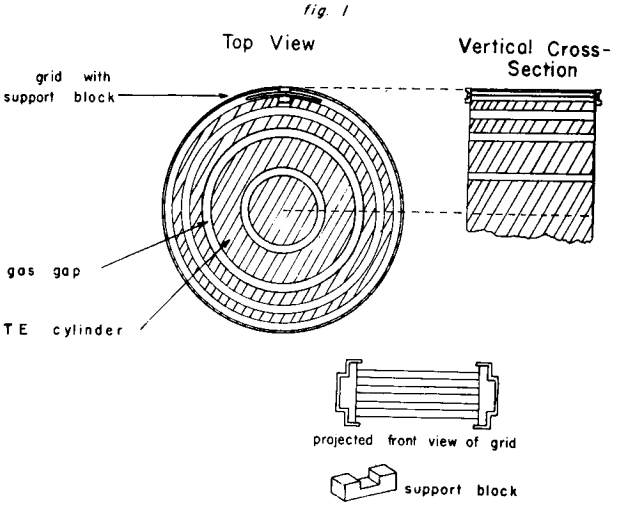

Figure 1. Schematic representation of the macro-system. Collection in various sectors of the annular gas filled regions is accomplished by grids. One of these is shown in position. Another grid together with one of its two supporting insulators is shown near the bottom.

which ungrounds all grids which then collect the much more slowly moving positive ions. After about a millisecond (to allow for ion collection) these grids are read in essentially the same manner as in the dose mode.

Large guarding scintillators above and below the ends of the cylindrical phantom can be operated in anticoincidence to assure that only particles entering nearly normal to the phantom axis can trigger the measuring cycle.

In the pulse mode only those sections in which the primary particle or any of its secondaries have passed register a signal.

In view of the very skewed distribution of particle energies it may be necessary to obtain continuous sensitivity for large but not for smaller events. This can be readily accomplished by utilization of a simple circuit which disables triggering by particles between 10 KeV/μm and, say, 100 KeV/μm for some period following each event registration.

The function of the micro-system is to provide detailed information on track structure. A pair of scintillators (or semiconductor detectors) operated in coincidence determines the direction of the incoming particle (see Fig. 2) which may traverse a number of vanes made of increasing thicknesses of tissue equivalent plastic. Strips consisting of multiple positive ion collectors are situated at some distance from these vanes. The collectors are mutually

insulated from each other and from a co-planar grounded conducting plane. The common electron collector serves again as the trigger for unfrounding of these collectors and the subsequent individual charge measurement.

This geometry permits a determination of lateral energy spread due to delta ray formation or other secondary particle production with a resolution of a few degrees. The prompt secondaries of a nuclear cascade are frequently emitted at angles of less than one degree but they are almost invariably of low LET, being protons or other light particles of very high energy. The products of nuclear evaporation having low energy (and consequently high LET) tend to be emitted isotropically.

Provided certain technical features such as an automatic gas replacement system and a variety of high speed electronic circuits are added to the elements which are shown schematically in Figs. 1 and 2 this system should be entirely feasible with present date technology and it should be well suited to automatic data transmission. It has been presented here as an example of the comprehensive and unorthodox approaches which will be needed in space radiation dosimetry.

Acknowledgement: The dosimetry system described here was developed as a result of discussions with my colleagues Dr. W. Gross and Dr. A.M. Kellerer.

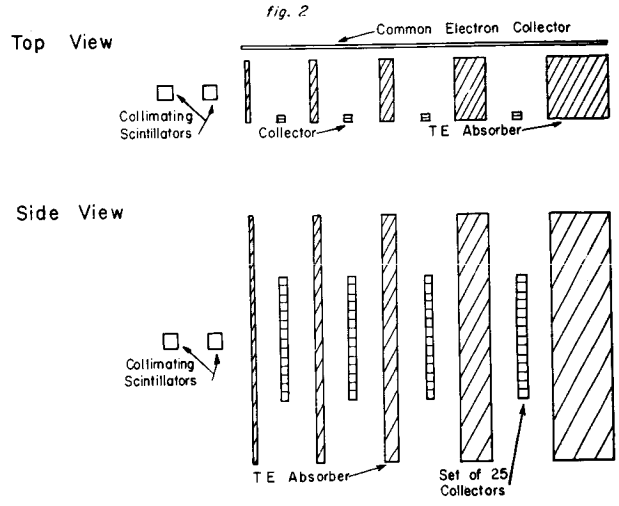

Figure 2. Schematic representation of the microsystem. High LET particles that have passed through both of the collimating scintillators traverse TE barriers of increasing thickness. The lateral energy spread is determined along strips of mutually insulated collectors.

References

1) Kellerer, A.M. and H.H. Rossi. "Summary of Quantities and Functions Employed in Microdosimetry." Microdosimetry, 2nd Symposium, Stressa, Italy, October 20-24, 1969, pp. 841-853.

2) Kobetich, E.J. and R. Katz. "Width of Heavy Ion Tracks in Emulsion." Phys. Rev. 170, pp. 405-411, 1968.

3) Failla, G. "Considerations Bearing on Permissible Accumulated Radiation Doses for Occupational Exposure." Radiology, Vol. 69, No. 1, pp. 23-28, July 1957.

4) Rossi, H.H. "Microscopic Energy Distribution in Irradiated Matter." in Radiation Dosimetry, Vol. 1, Academic Press, Inc., New York, N.Y. pp. 43-92, 1968.

5) Rossi, H.H. "Energy Distribution in the Absorption of Radiation." in Adv. in Biological and Medical Physics, Vol. 11, Academic Press, Inc., New York, N.Y., pp. 27-85, 1967.

SESSION VI.I.
NUCLEAR PROPULSION SYSTEMS: SHIELDING & RADIATION EFFECTS
CHAIRMAN: M. FLEISHMAN
SPACE NUCLEAR PROPULSION OFFICE-NASA/AEC

THE EXTERNAL GAMMA RADIATION ENVIRONMENT FROM THE KIWI, PHOEBUS, AND PEWEE REACTORS*

RICHARD E. MALENFANT

Los Alamos Scientific Laboratory
Los Alamos, New Mexico

During the past few years, ground tests of high-powered propulsion-prototype reactors by the Los Alamos Scientific Laboratory have provided several opportunities to observe the external radiation environment. Although the data may not be directly applicable to the evaluation of radiation levels for flight systems, they do provide an extensive set of results for comparison with calculations on systems similar to those which may be flown. In addition, the experience with reactor radiation fields covering square miles is considered unique. Reactor tests have been conducted in free air (the Kiwi B4D and B4E reactors) and inside of open well shields (the Phoebus 1-B, Phoebus 2-A, and Pewee 1 reactors). Measurements were taken over distances ranging from contact with the pressure vessel out to greater than 5000' both during operation and after shutdown. Separate assessments of the effects of direct beam, scatter, capture, and activation were attempted. Some measurements characteristic of each of the systems named will be presented and compared with results of calculations.

Measurements of the external radiation levels on early Rover reactor tests provided empirical information on the distribution of leakage radiation, variation of radiation levels with distance, and the shielding effects of various structures (refs. 1,2). The information was essential to provide the background for the design of further facilities to support the reactor tests, particularly in view of the complexity of the test site areas. Concurrently, techniques for analytical evaluation were being developed and applied. A comparison of some measurements on Kiwi B1A (1962) and some point-kernal calculations made by D. M. Peterson (ref. 3) for core sources only are given in figures 1 and 2. The dose points were located on an arc 127 cm in radius centered at the reactor midpoint. Energy release for the integral measurements was taken to be $\sim$ 90 MW-sec (2.95×10^{18} fissions). Agreement between calculated and measured values close to operating Kiwi size reactors has always been good. Deviations between calculated and measured gamma ray values at small angles ($<50^{\circ}$) are attributed to external scattering and to capture gamma rays from the privy roof shield shown on figure 1 below the reactor.

As the design of the reactors improved with experience, power levels and

* Work performed under the auspices of the U.S. Atomic Energy Commission.

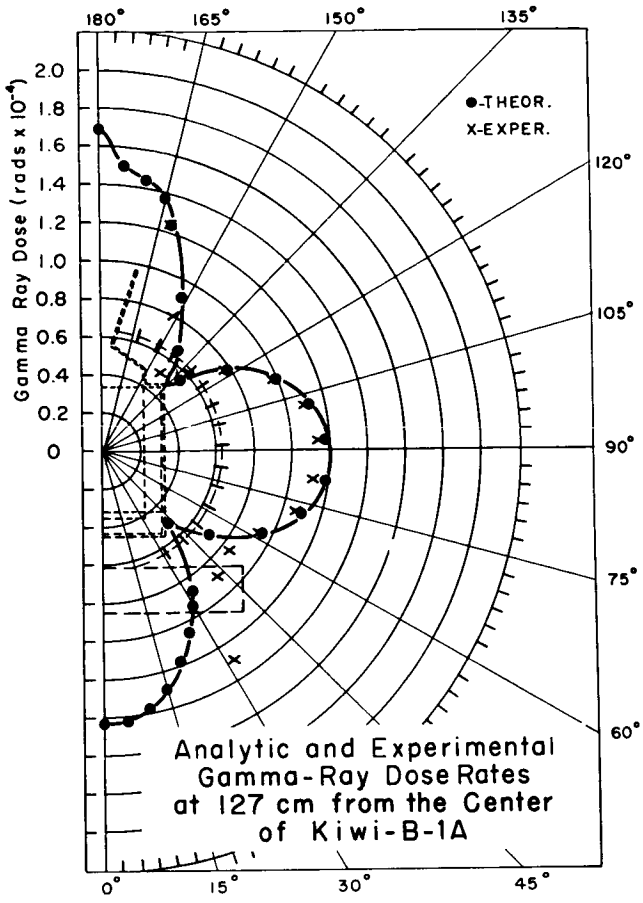

Figure 1

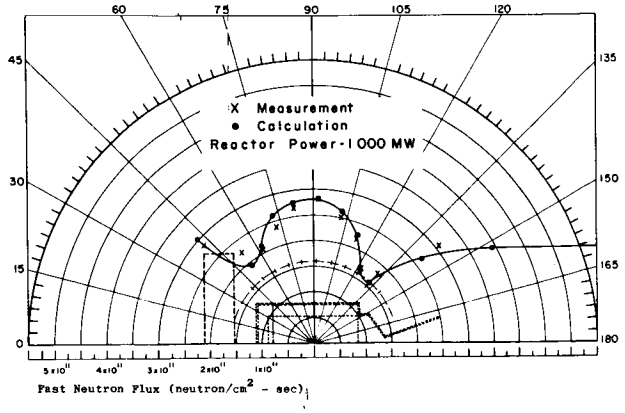

Figure 2

integrated energy releases increased. It became apparent that shielding would be required to reduce area activation and protect the structure of the test complex. Extensive measurements of operational and post-shutdown radiation levels were made during the Kiwi B4D and B4E test series (refs. 4,5,6,7) with at least one objective being the acquisition of information to design a facility shield. This was necessary because the radiation levels due to activation were fairly large (figures 3 and 4, from ref. 4), so that there would be residual radiation problems after removal of the reactor from the area where there had been high powered runs. At some decay times, radiation from activation was comparable to that from the decaying reactor.

In the radiation field arising from the decay of mixed fission products (following a $t^{-1.2}$ type law) and a few intense activation species (following $e^{-\lambda t}$ decays), there is a maximum relative contribution to the total dose from the activation product at a time equal to $\sim$ 1.7 half lives. Test site soil, asphalt, and concrete indicated decay characteristics with half-life groups near 2.5 hours, 15 hours, and 30 days. This behavior helped to distinguish between activation and contamination, even in an area illuminated by the decaying reactor.

Measurements of dose rate as a function of distance away from a shutdown reactor, as well as calculations of the operational and shutdown cases, indicated gamma ray equivalent mean-free-paths of approximately 600' (figure 5, ref. 4). Earlier measurements on operating reactors indicated a value of 1300 feet (e.g., ref. 1, p. 17). The difference has been attributed to gamma rays arising from air capture which are more penetrating than gammas associated with fission or those resulting from the decay of mixed fission products.

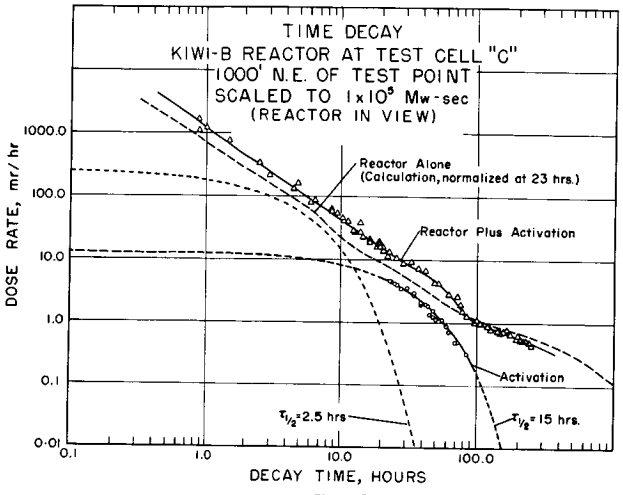

Figure 3

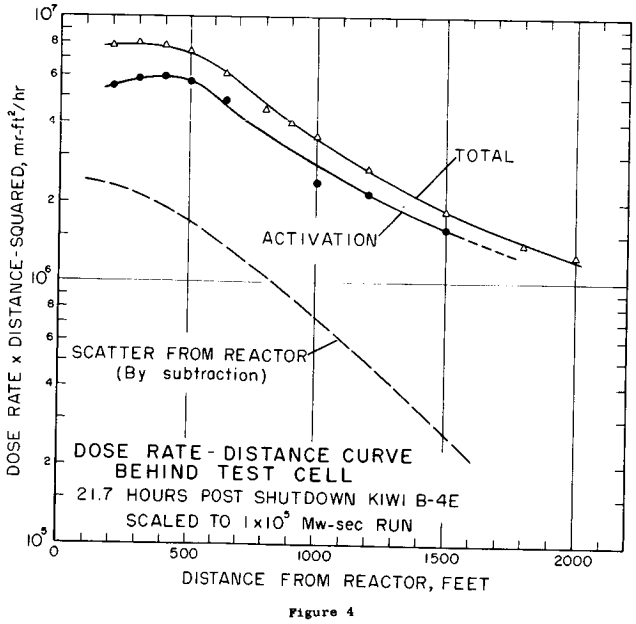

Figure 4

Following the extensive field studies and numerous calculations, the Phoebus 1 facility shield was designed and built. It was expected that radiation energy deposition in the shield, a cylindrical annulus of borated water and aluminum, would amount to 9.8 MW per 1000 MW of reactor power. Measurements at a reactor power of 1460 MW indicated an energy deposition of ~15.6 MW. Details of the shield, design and analysis of its behavior have been presented by Graves (ref. 8) and Malenfant (ref. 9).

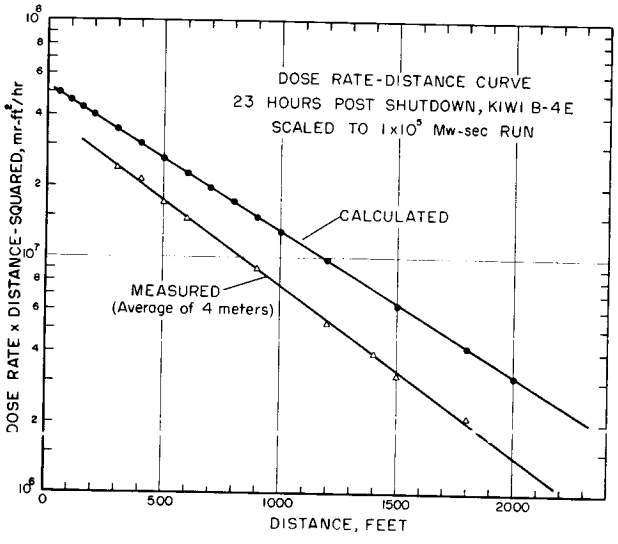

Figure 5

The Phoebus 1-B reactor was unique in many respects:

1. It was the first Rover reactor to be tested inside of a shield.
2. The Phoebus 1-B provided the most severe external radiation environment of all Rover reactors tested.
3. External radiation analysis was more extensive than that for any other LASL Rover reactor.

Phoebus 1-B was a solid core heat exchanger propulsion prototype reactor employing a uranium-graphite core 35-inches in diameter and 52-inches long. A cross-section of the reactor including characteristic dimensions is given on figure 6 (ref. 8). A model employed for various calculations is shown in figure 7 and details of its composition are provided on table 1.

Table 1

Elemental Densities and Compositions for the Reactor Mockup

Elemental Densities (g/cm^3)

Material Region	U	C	Be	Al	Nb	Fe	H	O	Na	B	Total Density (g/cm^3)
1	.214	1.234	-	-	.136	.037	-	-	-	-	1.621
2	-	1.488	-	-	-	-	.002	-	-	-	1.490
3	-	-	1.656	-	-	-	.011	-	-	-	1.667
4	-	-	-	2.700	-	-	-	-	-	-	2.700
5	-	-	-	-	-	-	.008	-	-	-	0.008
6	-	-	-	1.626	-	.333	.003	-	-	-	1.962
7	-	1.091	-	-	.776	.036	-	-	-	-	1.903
8	-	-	-	-	-	4.000	-	-	-	-	4.000
9	-	-	-	-	-	1.180	-	-	-	-	1.180
Shield borated water:					-	-	.107	.907	.010	.020	1.044
Privy roof borated water and steel balls:					-	4.800	.043	.363	.004	.008	5.218

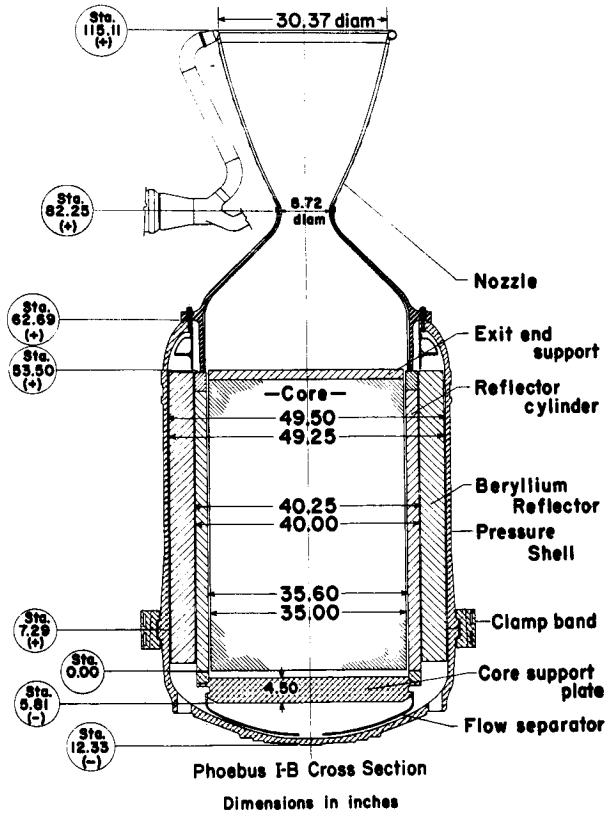

Figure 6

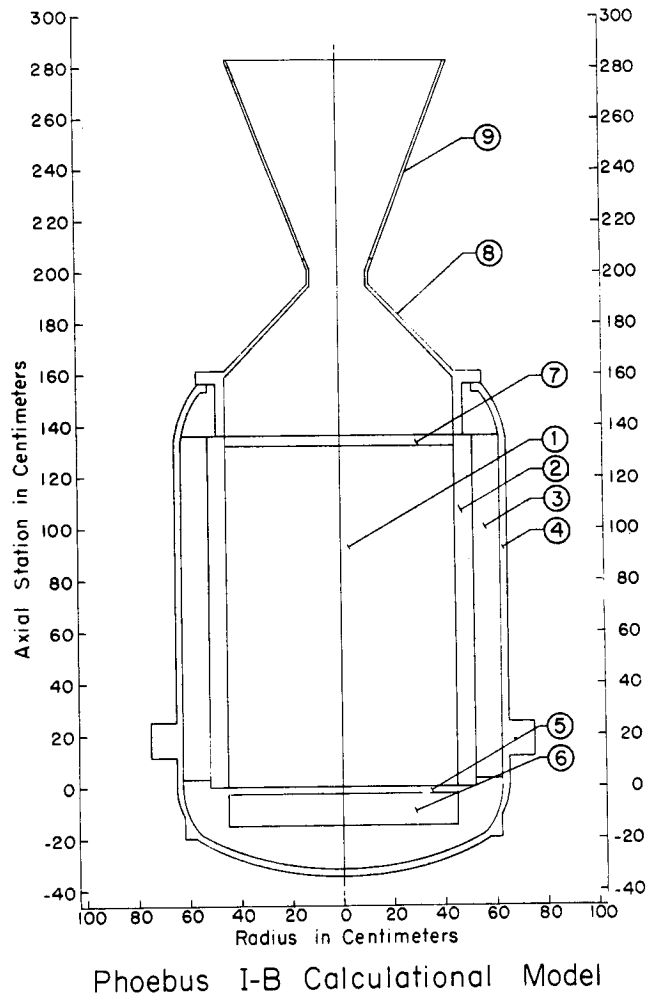

Figure 7

Figure 8 indicates the relationship of the reactor to the shield, a schematic of the shield's internal arrangement, the location of the one-inch thick supporting girdle outside the shield, and the locations of some points where detailed calculations were made for comparison with measurements. Results are indicated on table 2. (Locations on this, and subsequent tables, references the radial dimension to the core centerline and the axial dimension to the end of the fuel region near the pressure vessel dome. The positive z direction is toward the nozzle.) The analysis was performed using Monte Carlo to determine the magnitude of capture gamma sources (ref. 10), neutron transport to partition the sources among various species, and QAD point-kernal (ref. 11) calculations to determine the net effect. The calculated total values are generally within 20% of the measurements. An additional comparison between measurement and calculation is given on the shield traverse on figure 9 (ref. 8). Many additional measurements are presented in references 12 and 13.

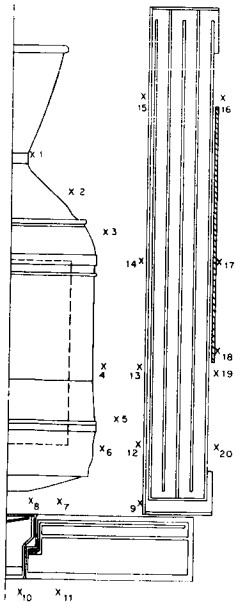

Phoebus I-B in Shield
Detector Locations Indicated

Figure 8

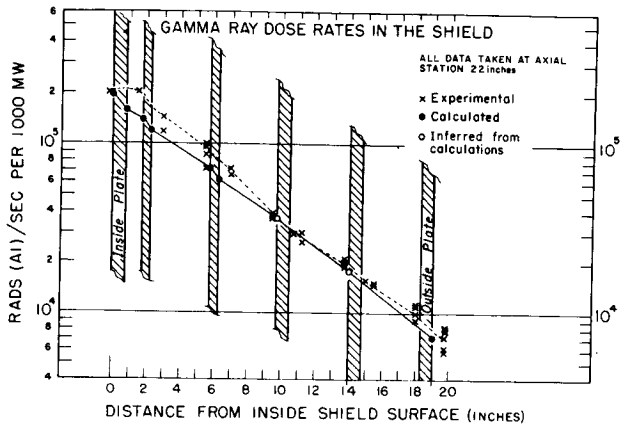

Figure 9

During the B4D and B4E tests, calculations and measurements had indicated the importance of external capture and scatter gamma rays (from the ground, test cell structures, etc.) to the dose rates under the privy roof shield. (The reactor is mounted in an upfiring position on a test car. Control rod actuators and other equipment are located in a room, the privy, under the reactor. The privy roof is a 9-foot square, 19-inch thick, shield of aluminum plates, borated water, and steel balls. The walls of the room are thin-gauge aluminum offering little shielding.) It was expected that the sides of the well shield would increase the apparent attenuation of the privy roof shield by about a factor-of-four by effectively eliminating the capture and scatter sources. Expectations were met, and the quite favorable comparisons obtained between measurement and point-kernel calculation for this location are shown in figures 10 and 11.

Table 2

Phoebus 1-B

Results of Calculations and Measurements

Location No.	Location, cm r	z	Calculation Core Gamma Rads/MW-sec	Capture Gamma Rads/MW-sec	Total Gamma Rads/MW-sec	Measurement Rads/MW-sec
1	16.5	203.9	*1.31/2	6.90/0	1.38/2	1.74/2
2	43.2	177.2	1.58/2	7.93/0	1.66/2	1.82/2
3	68.6	131.4	1.23/2	2.24/1	1.45/2	1.46/2
4	68.6	55.7	3.69/2	2.67/1	3.96/2	4.42/2
5	77.5	19.0	1.07/2	3.32/1	1.40/2	1.73/2
6	68.6	- 0.7	1.41/2	8.59/1	2.27/2	1.95/2
7	39.4	-39.1	1.79/2	5.32/1	2.32/2	1.63/2
8	8.3	-39.1	2.67/2	1.40/2	4.07/2	2.16/2
9	99.3	-39.1	6.69/1	3.17/1	9.86/1	9.46/1
10	10.2	-102.9	1.54/-1	4.75/-1	6.29/-1	
11	39.4	-102.9	2.04/-1	2.50/-1	4.54/-1	4.19/-1
12	95.1	1.7	9.39/1	2.78/1	1.22/2	1.44/2
13	95.1	56.0	2.14/2	3.53/1	2.49/2	3.05/2
14	95.1	132.2	9.03/1	2.40/1	1.14/2	1.67/2
15	95.1	244.9	2.80/1	1.02/1	3.82/1	5.83/1
16	158.9	244.6	5.72/-1	1.82/-1	7.54/-1	8.78/-1
17	161.4	131.9	1.90/0	2.57/-1	2.16/0	2.54/0
18	161.4	68.6	3.34/0	3.91/-1	3.73/0	4.63/0
19	158.9	51.6	6.53/0	8.59/-1	7.39/0	7.14/0
20	158.9	.9	4.02/0	6.78/-1	4.70/0	4.78/0

*Read 1.31/2 as 1.31×10^2.

Phoebus 2-A, with a design power level of 5000 MW, was tested shortly after Phoebus 1-B. This reactor also employed a uranium-graphite core, but one 50" in diameter and 52" long. The reflector was a beryllium cylindrical annulus 8" thick (compare with 4.5" thick for Phoebus 1 and Kiwi). A schematic of the reactor in its shield is given on figure 12 (dimensions in cm). The reactor presented calculational problems in that capture gamma rays produced outside the core assumed a greater importance relative to core gammas. A limited set of measurements made in the annular space between the reactor and shield is compared with predictions in table 3. As Phoebus 2 was the only reactor of its kind to be tested, no extensive calculations of its gamma ray environment have been made for comparison with measurements.

The Pewee reactor was designed as a fuel test device. With a power density like Phoebus 2 but 1/10 of the core volume, design power was $\sim$ 500 MW. Core length of 52" was maintained but the core diameter was reduced to $\sim$ 18.1". In order to achieve criticality and control, a 8" thick beryllium reflector was required. Like Phoebus 2, capture gamma rays were expected to be more important (relative to core gammas) than in Kiwi or Phoebus 1 type systems, again because the thick reflector attenuates core gammas at the same time that it increases neutron thermalization. A cross-section of Pewee and the location of some points of measurement are indicated on figure 13. A comparison of the calculated and measured values from an early run are given on table 4. The agreement is reasonable.

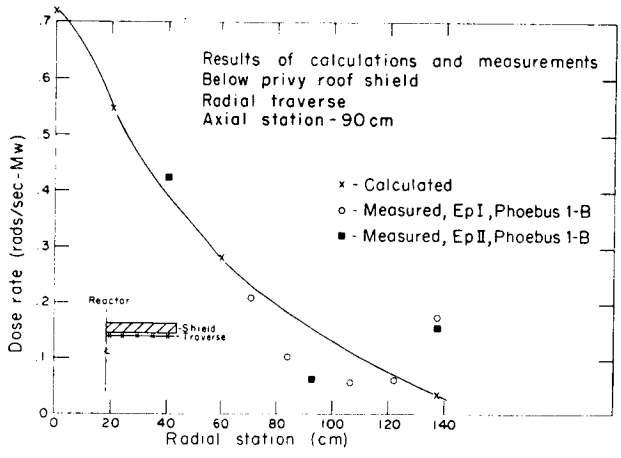

Figure 10

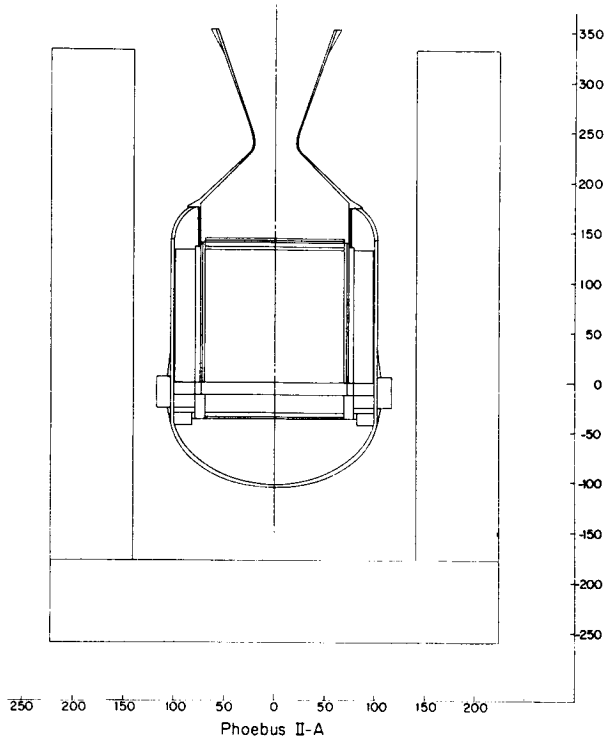

Figure 12

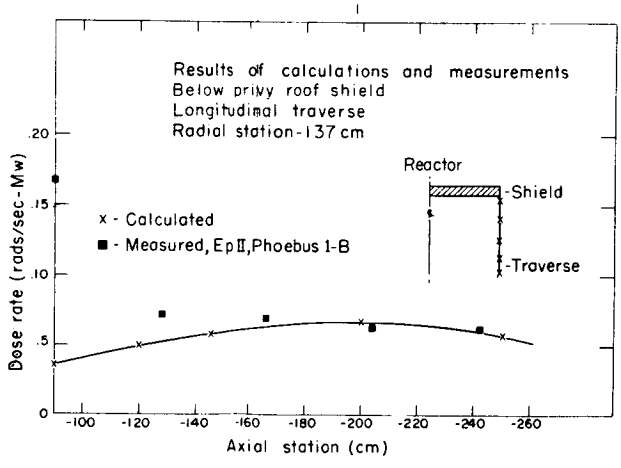

Figure 11

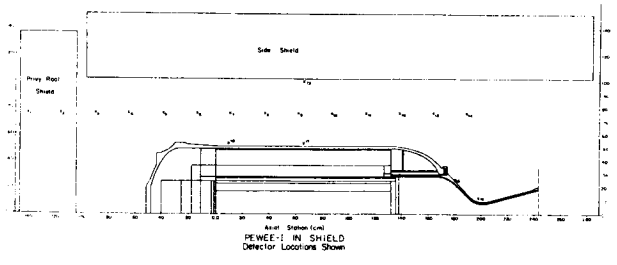

Figure 13

Table 3

A Comparison of Calculation and Measurement on Phoebus 2

Location (cm)		Calculation rads/sec @ 5000 MW	*Measurement rads/sec @ 5000 MW
r	z		
107.7	127.0	**2.2/5	4.0/5
107.7	61.0	4.4/5	7.1/5
110.0	5.1	2.4/5	4.0/5
121.2	-15.2	1.5/5	1.8/5
104.1	-58.4	2.7/5	2.2/5

* The dose rate at 5000 MW was inferred by extrapolating from passive dosimeters exposed on an early experimental operation with an energy release of ~ 32.6 MW-sec and no hydrogen flow.

**Read 2.2/5 as 2.2×10^5.

Table 4

Calculated and Measured Gamma Doses, Pewee, EP I

All Values are Tissue Rads for 6.73 MW sec

Location Number	Station, cm r	Station, cm z	Calculation Core γ	Calculation Capture γ	Calculation Total γ	Measured	Deviation Calculated-Meas. / Measured x 100
1	76.2	-141.5	1.50	41	2.3	<15	---
2	76.2	-115.6	89.2	18.0	107	100	+ 7.0%
3	76.2	- 90.1	171.	34.1	205	320	-35.9%
4	76.2	- 64.8	232.	54.6	287	410	-30.0%
5	76.2	- 39.4	531.	102.	633	500	+26.6%
6	76.2	- 14.0	832.	192.	1024	870	+17.7%
7	76.2	11.4	1285.	328.	1613	1300	+24.1%
8	76.2	36.8	1840.	441.	2281	1900	+20.1%
9	76.2	62.2	2035.	470.	2505	2200	+15.1%
10	76.2	87.6	1860.	412.	2272	2000	+13.6%
11	76.2	113.0	1319.	292.	1611	1400	+15.1%
12	76.2	138.4	743.	166.	909	840	+ 8.2%
13	76.2	163.8	453.	89.6	543	610	-11.0%
14	76.2	189.2	299.	53.3	352	430	-18.1%
15	12.7	198.1	724.	48.	772	700	+10.3%
16	26.2	180.1	651.	41.	692	660	+ 4.8%
17	53.8	66.0	3343.	914.	4257	3500	+21.6%
18	53.8	10.2	1847.	556.	2403	2200	+ 9.2%
19	99.8	66.0	1315.	270.	1585	1600	- 0.9%

Measurements of fission product decay gammas were made at the same locations following the second experimental plan of operation, EP II. Detectors were exposed for a timed period for comparison with calculation. Gamma ray source strengths for the comparison calculation were taken from reference 13. Results are compared in table 5. The lack of agreement is not understood.

Table 5

Calculated and Measured Gamma Doses, Pewee, Post EP II

~ 3 Hour Exposure ~ 4 Days Post Shutdowns

All Values are Tissue Rads

Location	Station, cm r	Station, cm z	Calculation	Measured	Deviation Calculated-Meas. / Measured x 100
1	76.2	-141.0	1.47	<15	---
2	76.2	-115.6	297.	107	+178%
3	76.2	- 90.1	625.	488	+ 28%
4	76.2	- 64.8	888.	688	+ 29%
5	76.2	- 39.4	2486.	1060	+135%
6	76.2	- 14.0	3148.	1900	+ 66%
7	76.2	11.4	5425.	3470	+ 56%
8	76.2	36.8	8006.	5170	+ 55%
9	76.2	62.2	9015.	6370	+ 42%
10	76.2	87.6	8131.	4980	+ 63%
11	76.2	113.0	5679.	3110	+ 83%
12	76.2	138.4	3468.	1630	+113%
13	76.2	163.8	2498.	1090	+129%
14	76.2	189.2	1879.	886	+112%

A thumbnail summary of the external unshielded gamma radiation environment from Phoebus 1/Kiwi B, Phoebus 2, and Pewee is given in table 6.

Table 6

A Comparison Between Phoebus 1, Phoebus 2, and Pewee

Parameters	Phoebus 1	Phoebus 2	Pewee
Characteristic Power Level	1500 MW	5000 MW	500 MW
Dose Rate, Contact with Pressure Vessel at Midplane, Measured Values (LASL Group H-8)	1.6×10^6 r/hr-MW	5.1×10^5 r/hr-MW	1.9×10^6 r/hr-MW
Approximate Dose Rate in Contact with Pressure Vessel, Full Power	2.4×10^9 r/hr	2.6×10^9 r/hr	9.5×10^8 r/hr
Characteristic Gamma Source Power	129 MW	430 MW	43 MW
Dose Rate at 50' per Watt of Gamma Source Power-Core Sources only	15 mr/hr-watt	3 mr/hr-watt	36 mr/hr-watt
Approximate Dose Rate at 50', Full Power, Core Sources only	1.9×10^6 r/hr	1.3×10^6 r/hr	1.5×10^6 r/hr

Conclusions

With the possible exception of Phoebus 2, the agreement between rather simple radiation calculations and measurements near operating propulsion prototype reactors has been quite good. Considering that uncooled metals near high power systems exhibit the ultimate in radiation damage - melting - the demonstrated ability to predict the environment during operation is very satisfying. An interesting outstanding problem is the rather persistent overprediction of dose rates post shutdown by a factor of $1\frac{1}{2}$-2.

References

1. Worman, F.C.V., et al., LA-2858, "Integral Neutron and Gamma Dose Measurements on the Kiwi B-1 Reactors," March 1963.

2. Henderson, R.W., et al., LA-2885, "Integral Gamma and Neutron Measurements on Kiwi B-4A," March 1963.

3. Peterson, D.M., "Leakage Radiation Fields from the Kiwi B-1A," TID-7653, Proceedings of Nuclear Propulsion Conference, Naval Postgraduate School, Monterey, California, Aug. 1962.

4. Malenfant, R.E. and Graves, G.A., "Ground Test Radiation Experience at the Kiwi-B-4 Tests," AIAA Paper 65-593 (1965).

5. Worman, F.C.V., et al., LA-3286, "Integral Gamma and Neutron Measurements on the Kiwi B4D-202 and Kiwi B4E-301 Reactors," March 1965.

6. Ahlquist, A.J., et al., LA-3622-MS, "Test Cell C Shielding Study, Kiwi B4D-202," Nov. 1966.

7. Sanders, F.W., et al., LA-3447-MS, "Dose Rate Measurements on the Kiwi B4D-202 and Kiwi B4E-301 Reactors," Jan. 1966.

8. Graves, G.A., "Design and Performance of a Open-Well Shield for High Power Propulsion Reactor Testing," Vol. 3, p. 859, AERE-R5773, Proceedings of the Conference on the Physics Problems of Reactor Shielding, United Kingdom Atomic Energy Authority Research Group, Harwell, England 1968. Available through British Information Services, 845 3rd Avenue, New York, N.Y. 10022.

9. Malenfant, R.E., LASL Internal Memorandum N-2-8048 Corrected (1966).

10. Watson, C.W., private communication.

11. Malenfant, R.E., LASL Report LA-3573, "QAD, a Series of Point-Kernel General-Purpose Shielding Programs," (1967).

12. Ahlquist, A.J., et al., LA-3746, "Integral Gamma and Neutron Measurements on the Phoebus 1-B Reactor," Oct. 1967.

13. Ahlquist, A.J., LA-3747, "Gamma Dose-Rate Measurements on the Phoebus 1-B Reactor," July 1968.

14. Peterson, D.M., Graves, G.A., and Seale, R.L., "Studies of U^{235} Post-Fission Gamma and Beta Radiation and of Post-Shutdown Radiation Release from Fission Operation at Constant Power," to be published as Los Alamos Scientific Laboratory Report LA-2902.

APPLICATION OF TRANSPORT TECHNIQUES TO THE ANALYSIS OF NERVA SHADOW SHIELDS

M. A. Capo and S. L. Anderson

Westinghouse Electric Corporation

Astronuclear Laboratory

A radiation shield internal to the NERVA* nuclear rocket reactor is required to limit the neutron and photon radiation levels at critical components located external to the reactor. These radiation levels are unusually severe since the reactor is designed to operate at a power level of 1511 thermal megawatts for a total time of 10 hours. The internal shield is currently being designed to meet radiation criteria developed by Aerojet Nuclear Systems Company for minimum shield weight missions. The criteria are specified in terms of the required radiation levels at a plane tangent to the dome of the nuclear subsystem and at several critical locations in the engine.

To design a minimum weight shield internal to the NERVA Nuclear Subsystem, the capabilities and limitations of the analytical techniques must be clearly understood. To further this understanding, an in-depth study was performed in which both one and two dimensional discrete ordinate techniques were applied to the analysis of several shadow shield experiments. These experiments were performed at the Westinghouse Astronuclear Experimental Facility on the PAX reactor which was modified to simulate the R-1 reactor, an upgraded version of the NRX nuclear rocket technology series of reactors tested at Nevada during the past six years.

Two significantly different shield mockups were analyzed. In one experiment, the internal shield material called BATH (a composite mixture of boron carbide, aluminum and titanium hydride) was mocked up by alternating thin sheets of titanium, Boral, aluminum and polyethylene. In another experiment a borated steel-liquid hydrogen shield was mocked up by alternating layers of borated steel and polyethylene.

The two-dimensional discrete ordinates code, DOT-IIW, was employed to calculate 16 group (11 fast and 5 thermal) neutron fluxes internal to the shield mockups. These fluxes were processed by the NAGS code to obtain photon sources throughout the assembly. Photon flux distributions were obtained by employing these sources in fixed source, thirteen group, DOT calculations. An S_8 angular quadrature was employed. Approximately 8000 mesh cells were utilized to describe the two-dimensional geometry.

One-dimensional analysis was accomplished by means of the ANISN code. Briefly, this technique employed 29 (16 neutron and 13 photon) energy groups simultaneously in one problem with the photon source generation process treated as a downscattering interaction from one of the neutron groups to one of the photon groups. Two approximations to account for transverse leakage were investigated: 1) the addition of a DB^2 correction to the energy-dependent absorption cross section, and, 2) a "void" streaming correction for geometrical regions containing no material.

Based on the comparisons between the experimental and calculated neutron and photon radiation levels, the following conclusions were noted:

1) the ability of the two-dimensional discrete ordinates code, DOT-IIW to predict the radiation levels internal to and at the surface of the shield mockups was clearly demonstrated,
2) internal to the BATH shield mockups, the one-dimensional technique predicted the axial variation of neutron fluxes and photon dose rates; however, the magnitude of the neutron fluxes was about a factor of 1.8 lower than the two-dimensional analysis and the photon dose rate was a factor of 1.3 lower,

---

* NOTE: The Nuclear Engine for Rocket Vehicle Application Program (NERVA) is administered by the Space Nuclear Systems Office, a joint office of the U. S. Atomic Energy Commission and the National Aeronautics and Space Administration. Aerojet Nuclear Systems Company, as prime contractor for the engine system, and Westinghouse Electric Corporation as subcontractor for the nuclear subsystem, are developing a nuclear propulsion system for space applications.

3) internal to the borated steel-liquid hydrogen shield mockup, the application of the DB^2 correction significantly over estimated the attenuation of the shield by as much as a factor of 30.

INTRODUCTION

A radiation shield internal to the NERVA nuclear rocket reactor is required to limit the neutron and photon radiation levels at critical components located external to the reactor. These radiation levels are unusually severe since the reactor is designed to operate at a power level of 1511 thermal megawatts for a total time of 10 hours.

The internal shield is currently being designed to meet radiation criteria developed by Aerojet Nuclear Systems Company[1] for minimum shield weight missions. The criteria are specified in terms of the required radiation levels at a plane tangent to the dome of the nuclear subsystem and at several critical locations in the engine.

To design a minimum weight shield internal to the NERVA Nuclear Subsystem, the capabilities and limitations of the analytical techniques must be clearly understood. To further this understanding, an in-depth study was performed in which both one and two dimensional discrete ordinate techniques were applied to the analysis of several shadow shield experiments.

Both one and two dimensional analysis techniques were investigated since economics and schedular considerations can necessitate the employment of the less accurate one-dimensional approach. For example, in the design of a minimum weight shield system, the need for extensive parametric studies is obvious. Yet, to perform analyses of this type with the two-dimensional discrete ordinates technique is often not feasible. In addition, situations do occur in which the employment of the two-dimensional approach is not necessary and the one-dimensional technique will suffice. Thus, it is imperative, from a practical standpoint, that the shield analyst be well aware of the capability of the one-dimensional approach for analyzing complex shield configurations. Without this knowledge, the analyst can neither apply the technique to applicable situations with any degree of confidence; nor, when forced to employ the approach, realize the possible margin of error in the analytical results.

The experiments were performed on the PAX[2] reactor which has been modified to simulate the R-1 reactor, which is the upgraded flight version (increased operating lifetime, power level, and thrust) of the previous NRX nuclear rocket technology series of reactors, tested at Nevada during the past six years.

Figure 1 is a photograph of the PAX reactor in the test cell with a mockup nozzle in place. To accomplish the experiments described in this paper, the mockup nozzle was removed from the reactor, and slab mockups of the shields were placed at the aft end of the core along with appropriate support structure.

Two different types of shield mockups were employed in the experiments. In one experiment, the NERVA internal shield material called BATH (a composite mixture of boron carbide, aluminum and titanium hydride) was mocked up by alternating thin sheets of titanium, Boral, aluminum and polyethylene. (The BATH material was chosen for use in the NERVA reactor due to its efficiency as a combination neutron-photon shield material.) The second type of shield mockup consisted of alternating layers of borated steel and polyethylene foam to simulate a borated steel-liquid hydrogen internal shield.

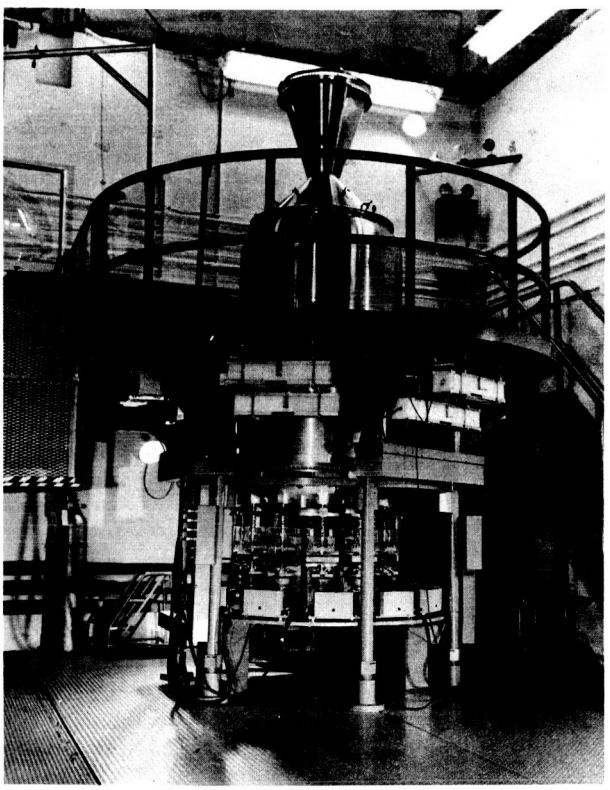

FIGURE 1
THE PAX REACTOR WITH MOCKUP NOZZLE IN PLACE

EXPERIMENTAL DETAILS

A schematic diagram of the PAX-G0C reactor assembly is shown in Figures 2 and 3. Figure 2 shows a sectional view through the reactor axis, whereas Figure 3 depicts a top view of the system. Figure 2 essentially displays a cross sectional view of the major reactor regions as mocked up in the R,Z discrete ordinate transport code analysis. Major regions are indicated by title in the figure, i.e., the reactor core, reflector, and other hardware. From Figure 3, it is observed that the shield materials were actually in the form of square slabs extending beyond the reactor radius which is illustrated by the dotted circle.

Experimental data were obtained both internal to and external to the BATH shield mockup and the borated steel-liquid hydrogen shield mockup located at the aft end of the core as shown in Figure 2. This paper discusses only the internal environment data. Additional detailed analysis is provided in Reference 2.

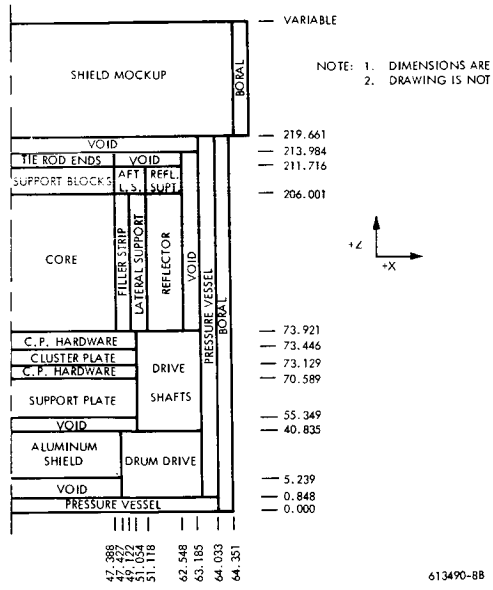

PAX-G0C REACTOR MOCKUP FOR SHIELD EXPERIMENTS
(SECTIONAL VIEW THROUGH THE REACTOR AXIS)

FIGURE 2

FIGURE 3

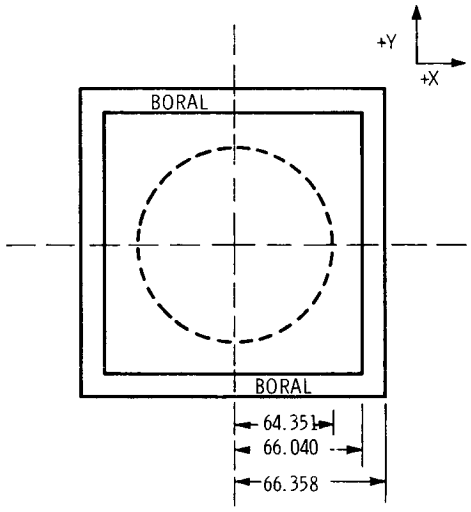

NOTE: 1 DIMENSIONS ARE IN CM.
2 DRAWING IS NOT TO SCALE.

613490-7B

PAX-G0C REACTOR MOCKUP FOR SHIELD EXPERIMENTS (TOP VIEW)

A schematic drawing of a BATH shield mockup is shown in Figure 4. The axial thickness of this mockup is about 19.5" and the mass thickness is 109 gm/cm^2. Experimental data were obtained in the ten dosimeter slots shown in Figure 4. Each dosimeter slot was $\sim$ 0.95 cm in thickness. Also shown in Figure 4 is a typical BATH module which consists of slabs of titanium, aluminum, boral and polyethylene in the proper proportions to simulate the actual BATH material composition ($\sim$ 70% aluminum, 24% titanium hydride, and 6% boron carbide by volume.)

Figure 5 illustrates the borated steel-liquid hydrogen steel mockup shield assembly consisting of alternating layers of steel and polyethylene (to simulate the liquid hydrogen). The axial thickness of this mockup is about 35 inches, but the mass thickness is only about 117 gm/cm^2. Slots were cut in the polyethylene slabs for the purpose of placing dosimeters internal to the mockups at the locations indicated.

The experimental data taken internal to the mockups was obtained in the form of radial distributions of equivalent neutron flux and photon dose rate at various axial locations within the mockup. These axial locations are defined by the dosimeter slots illustrated in Figures 4 and 5. The radiation levels internal to the mockups were obtained using passive dosimetry techniques. The neutron flux was measured by means of sulfur pellets (E>2.9 MeV), cadmium covered U-238 foils (E>1.5 MeV), and by dysprosium difference techniques (E<0.4 eV). The photon dose rate was measured with CaF_2 thermoluminescent detectors (TLD).

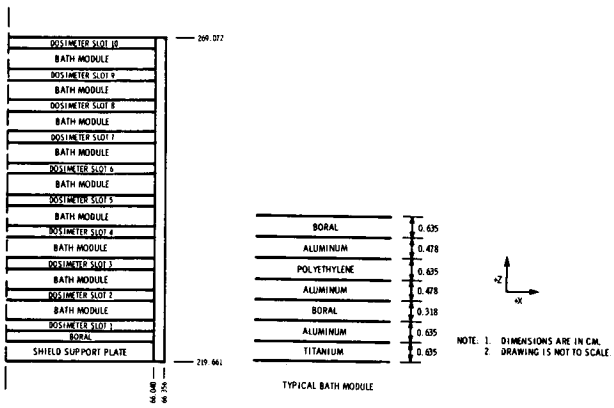

BATH SHIELD MOCKUPS USED FOR PAX-GOC EXPERIMENTS

FIGURE 4

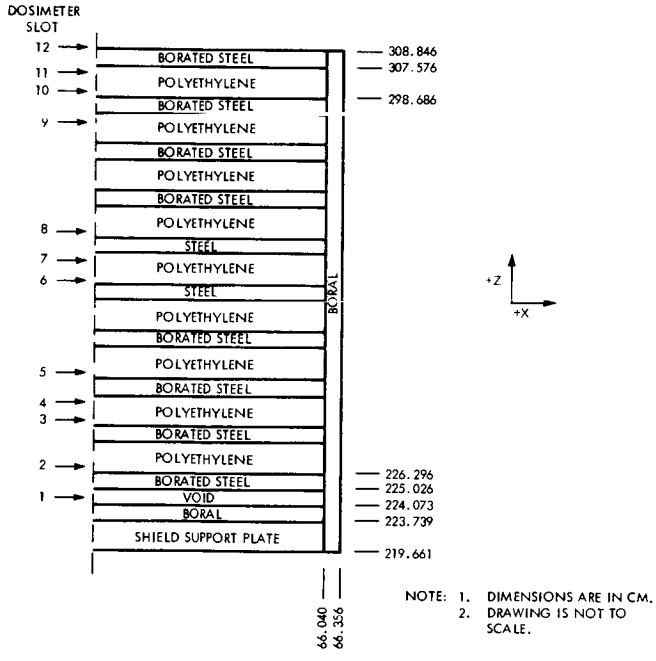

BORATED STEEL-LIQUID HYDROGEN SHIELD MOCKUP USED FOR PAX-GOC EXPERIMENTS

FIGURE 5

METHOD OF ANALYSIS

Two-Dimensional Discrete Ordinate Technique

The two-dimensional discrete ordinate analytical procedure employed to calculate the neutron and photon radiation levels internal to both shield mockups is shown schematically in Figure 6. In addition to depicting the flow of information throughout the calculation, Figure 6 illustrates the type of information derived from each computation as well as the sequence of calculations.

Basically, the neutron transport analysis was carried out in two parts utilizing the DOT-IIW S_n transport code.[3] The first part of the procedure was an eigenvalue calculation on the basic reactor assembly. The basic reactor is defined in this study as that portion of the assembly which extends from the pressure vessel dome (Z=0.00) to an axial plane located a short distance into the shield mockup (Z dependent on the shield mockup being analyzed). From the eigenvalue problem, the neutron flux distributions throughout the basic reactor assembly were obtained, as well as an angular and energy dependent boundary source, based on the angular flux distributions at the midplane of the shield support plate (Z=221.536). Using this boundary source as a coupling mechanism, a second DOT-IIW problem was employed to obtain flux distributions throughout the shield geometry. By performing the analysis in two parts, a rather large computer cost savings was realized. The eigenvalue calculations on the basic reactor required multiple (typically 5-10) outer iterations due to the criteria for source convergence. However, since the analysis of the shield geometry employed a fixed boundary source, only a single outer iteration was needed. Had the shield configurations been analyzed along with the basic reactor in a single problem, the multiple outer iterations necessary for eigenvalue convergence would, of course, have encompassed a much larger number of spatial mesh points; and the running time would have been increased accordingly. (In addition, since two BATH shield mockups were analyzed which were merely different thicknesses of the same material, it was possible to employ one boundary source for both shield geometries; and, by eliminating one reactor calculation, to effect a further cost savings. This analysis is presented in Reference 2.)

From Figure 6, it can be observed that the starting point (calculational sequence 1) is the generation of neutron cross sections. To accomplish this, the appropriate atom densities and other required data are input to the GAMB1T[4] code. GAMB1T calculates the 16 group (11 fast, five thermal), region dependent, macroscopic, P_0 transport corrected neutron cross sections for use in the discrete ordinate codes. These cross sections were weighted over region dependent 155 fine group spectra which had been generated for use in prior PAX-G0 analysis. Since the magnetic tape containing these spectra is not generally available, it would be necessary for an analyst attempting to reproduce this study to employ the GAMB1T-ANISN[5]-ANISIG[6] linkage, described in Reference 7, in his cross section generation procedure.

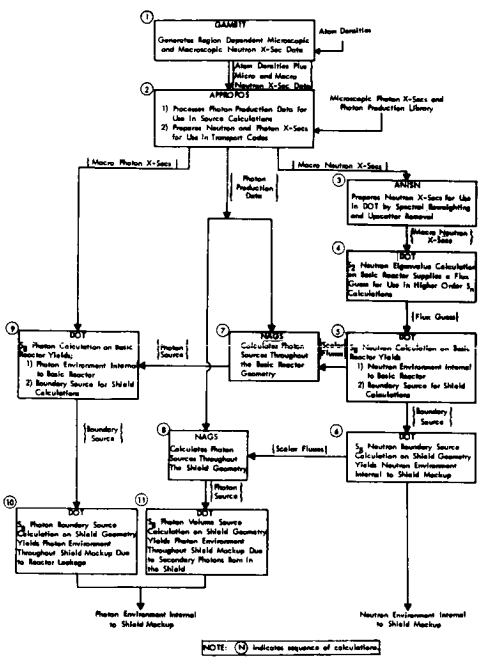

FIGURE 6

FLOW CHART FOLLOWED TO CALCULATE NEUTRON AND PHOTON ENVIRONMENT INTERNAL TO THE PAX-G0C SHIELD MOCKUPS

Although Figure 6 indicates (calculational sequence 2) that the macroscopic neutron cross sections flow through the APPROPOS[8] code, this step was unnecessary for the two-dimensional analysis. Macroscopic neutron cross sections are indeed required as input to the APPROPOS code. However, these cross sections are only used to generate data for use in simultaneous neutron-photon calculations. Analyses of this type will be discussed later in connection with the one-dimensional analysis of the PAX-G0C shield experiments. Thus, in the case of the two-dimensional analysis, the macroscopic neutron cross section output from APPROPOS was identical to the input.

Prior to application in the two-dimensional S_n analysis, the macroscopic neutron cross section output from APPROPOS[8] is input to two ANISN one-dimensional S_n transport problems - one radial and one axial problem (calculational sequence 3). First, by running a radial calculation characteristic of the reactor regions centered about the core midplane and an axial calculation including all regions located on the reactor axis, an initial flux guess for use in the two-dimensional S_n calculations was obtained. Second, the ANISN problems were employed to effect upscatter removal from the neutron cross sections By removing upscatter from the cross sections, a large cost savings is realized in the subsequent two-dimensional DOT-IIW problems. Furthermore, since the upscatter removed cross sections were weighted over the region dependent flux calculated by ANISN, it is believed that no significant loss of accuracy was incurred by employing the upscatter removed cross sections in the DOT-IIW calculations.

As was stated earlier, the neutron transport analysis employed P_0 transport corrected cross sections in a 16 energy group problem. The final eigenvalue calculation on the basic reactor configuration was preceded by a calculation which employed S_2 angular quadrature. It has been recommended[3] that a computer cost savings is achieved by running a low order quadrature DOT-IIW problem to obtain a good flux guess for the calculation employing the higher order quadrature. Using the S_2 flux guess in the S_8 problem allows eigenvalue and pointwise flux convergence in a minimum of computer time.

The boundary source to be used as input to the S_n calculations on the shield geometry was obtained from the basic reactor problem by saving, on magnetic tape, the angular flux for each of the three axial mesh intervals describing the shield support plate. The angular flux obtained in the central axial interval was then input from tape to the appropriate shield problem. In order to obtain a valid boundary source for input to subsequent calculations, it is imperative for the angular flux at the boundary source location to accurately reflect the presence of the particular shield configuration under consideration. For this reason, the basic reactor geometry was extended beyond the axial plane at which the boundary source was obtained.

The reader will recall from Figure 4 that each BATH module was constructed by laminating a series of titanium, aluminum, polyethylene, and boral plates. This configuration could not be represented as a heterogeneous shield because the mesh sizing requirements (see Reference 3) coupled with the large number of physical regions resulted in a problem whose size is beyond the capabilities of the CDC6600 computer system with 128K storage (91,000 data locations available after DOT-IIW program is loaded). Thus, it was necessary either to relax the mesh sizing requirements or to homogenize the individual BATH modules. Of these two alternatives, the latter was chosen for the analysis reported herein. In the case of the laminated borated steel-polyethylene configuration shown in Figure 5, however, each lamination was included explicitly in the shield geometry problem.

Both the experimental and analytical results internal to the various shield mockups are presented in this paper in terms of an "equivalent neutron flux" based on the response of the following detectors; sulfur pellets (E>2.9 MeV), cadmium covered U-238 foils (E>1.5 MeV), and bare minus cadmium covered dysprosium foils (E<0.4 eV). Briefly, the experimentally determined equivalent neutron flux is obtained by dividing the measured saturated activity of the given detector by a constant, C, based on an average cross section for the neutron interaction being considered. The analytical equivalent neutron flux is obtained by calculating the saturated activity and then dividing by the same constant, C, in the DOT-IIW problems. Thus, the comparisons presented in this paper are essentially based on measured and calculated activities and, for relative comparison purposes, the effective neutron interaction cross section used to determine the constant, C, is rather immaterial. (A detailed discussion of the generation and use of activation cross sections for analysis of this type is given in Reference 9).

The analysis of the photon environment internal to the various shield mockups followed a procedure which was similar and, through the source terms, intimately related to the internal neutron environmental analysis. As in the case of neutrons, the overall problem was divided into two parts; a basic reactor calculation and a shield calculation (calculation sequences 9 and 10). However, unlike the neutron analysis, a single boundary source calculation on the shield geometry was not sufficient. In addition to the boundary source calculation of leakage through the shield mockup, it was necessary to perform a fixed volume source calculation in order to account for secondary photons produced via neutron interactions in the shield itself (calculational sequence 11).

The region dependent photon cross sections employed in the internal analysis were generated by the APPROPOS code using microscopic cross section data from the GAMLEG[8] code as input. As can be seen from Figure 6, fixed volume distributed source terms for use in the analysis of the basic reactor as well as the shield mockups were calculated via the NAGS[10] data processing code. Briefly, the NAGS code combines neutron scalar flux distributions obtained from a prior neutron analysis of the geometry of interest with neutron interaction cross sections from GAMBIT and a photon production library from APPROPOS to produce a spatial and energy dependent photon source throughout the problem geometry.

All of the photon transport problems to determine the photon environment internal to the basic reactor as well as the various shield mockups employed a P_1 scattering cross section approximation with 13 energy groups and S_8 angular quadrature.

The experimentally determined photon dose rates internal to the shield mockups were reported as Mrad(C)/hr-watt. The data were obtained by calibrating the response of a CaF_2 thermoluminescent detector (TLD) with a known source of Co-60 radiation. The analytical response was obtained by converting the calculated energy flux distributions to dose rate by means of standard energy-dependent flux-to-dose conversion factors.

There are several distinct differences between the neutron and photon internal analysis which may be summarized as follows. There were, of course, basic differences in cross sections in the analysis. The neutron analysis employed P_0 transport corrected cross sections, whereas, a full P_1 cross section set was incorporated into the photon analysis. The neutron analysis of the basic reactor was an eigenvalue problem, while the photon calculation utilized a fixed distributed source based on converged neutron fluxes from the eigenvalue case. Finally, although a single boundary source computation was sufficient to obtain neutron flux distributions throughout the shield mockups, for photons it was necessary to employ, in addition to the boundary source calculation, a fixed distributed source problem to account for secondary photons born in the shield regions. Only by summing the results of the boundary source problem and the fixed source problem was it possible to obtain the total photon radiation levels internal to the shield mockups.

In the BATH shield analysis described above, 3550 mesh cells (in a 50 radial by 71 axial array) were employed in the reactor geometry, and 5350 (in a 50 radial by 107 axial array) were employed in the shield geometry, for a total of 8400 mesh cells. In the borated steel-liquid hydrogen shield analysis, 3850 mesh cells (in a 50 radial by 77 axial array) were employed in the reactor geometry, and 4200 (in a 50 radial by 84 axial array) were employed in the shield geometry, for a total of 8050 mesh cells.

One-Dimensional Discrete Ordinate Technique

Both the BATH shield and the borated steel-liquid hydrogen shield mockups were analyzed using the ANISN one-dimensional discrete ordinate transport code. The axial mesh allocation employed in the ANISN problems was identical to that employed in the pertinent DOT-IIW problem.

The analysis of the shield mockups was carried out via the simultaneous neutron-photon calculational technique incorporated into the APPROPOS - ANISN system, schematically shown in Figure 7.

As can be seen from Figure 7 the neutron cross sections employed in the analysis were obtained from the GAMBIT code, while the photon cross section data were generated by the GAMLEG code. With the exception of the reactor core, there is a one-to-one correspondence between the axial region atom densities used in the one and two dimensional codes. Cross sections for the core region were obtained by volume averaging those in the 15 radial core zones shown employed in the two-dimensional code.

As shown in Figure 7, the respective neutron and photon basic cross sections from GAMBIT and GAMLEG were input to the APPROPOS code, wherein, they were combined with photon production data to yield a single transfer matrix for use in the simultaneous neutron-photon analysis. Briefly, this technique employed 29 energy groups (16 neutron groups and 13 photon groups) with the photon source generation process treated as a downscattering interaction from one of the neutron groups to one of the photon groups. For example, if, in the calculation, a hypothetical particle scatters from energy group 16 to energy group 24, the physical analog would be the capture of a group 16 neutron with the corresponding generation of a photon with energy characteristic of group 24.

It should be noted that the cross sections utilized in the one-dimensional discrete ordinate analysis included a P_1 expansion in the scattering matrix. However, the values of the P_1 component existed for only groups 17 through 29. For the neutron groups (1 through 16), the P_1 component was input as zero. Thus, in effect, the neutron analysis employed P_0 transport corrected cross sections, whereas, the photon calculations employed P_1 cross sections. Thus, from a cross section standpoint, the one-dimensional analyses were entirely compatible with the two-dimensional calculations.

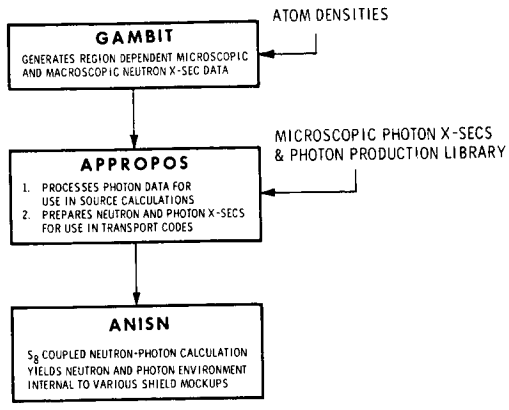

FLOW CHART FOR ONE-DIMENSIONAL ANALYSIS OF PAX-GO SHIELD MOCKUPS 613490-11B

FIGURE 7

As in the case of the two-dimensional analysis, the ANISN calculations employed S_8 angular quadrature and solutions were based on both eigenvalue and point-wise flux convergence. Likewise, both neutron and photon response functions utilized for the experimental comparisons were identical to those employed in the two-dimensional analysis.

When applying the ANISN code to perform radiation transport analysis, it is customary to include a DB^2 correction to the absorption cross sections in order to estimate the effect of transverse leakage from the slab system on the overall attenuation properties of the medium in question. In addition to this transverse leakage correction, the WANL version of the ANISN[5] code includes an option whereby a void streaming correction may be employed to account for transverse leakage in regions which contain no material.

In this study, both the DB^2 correction and the void streaming correction were employed in the analysis of the BATH shield mockup. The lateral dimensions of the slabs of material which comprised the shield mockup was utilized in the generation of these transverse leakage terms. In the analysis of the borated steel-liquid hydrogen mockup, the employment of a void streaming correction was not necessary. However, the DB^2 correction was, at first, applied. Unfortunately, when the DB^2 correction was employed, the analytical results were obviously in error. Thus, the calculation was repeated with the DB^2 correction removed. The results of this second analysis were more reasonable, but still not satisfactory. The comparison of the calculations with and without the transverse leakage correction (to be presented in the next section) point out a rather serious problem area which must be taken into account when applying the one-dimensional discrete ordinate technique to the R-1 type reactor, particularly in the areas of hydrogen plena.

RESULTS OF ANALYSIS

Before discussing comparisons in detail, it is of interest to review some data which demonstrates that, in the area of overlap, the eigenvalue calculation on the basic reactor geometry and the boundary source calculation on the shield geometry yield equivalent results. The reader will recall that the model of the basic reactor employed in the analysis extended to the midplane of the second BATH module. Thus, both the reactor calculation and the shield calculation encompassed, in part, an area which included a portion of the shield support plate, a 1/8 inch boral plate and dosimeter slots 1 and 2 as well as the aforementioned amount of the BATH mockup.

A comparison of analytical results from the basic reactor calculation with those from the BATH shield coupled calculation is presented in Figure 8. The choice of dosimeter slot 1 as the point of comparison was based solely on convenience. The ratios presented are typical of those observed from the boundary source location up to some distance into the first BATH module. As one might expect, the presence of subsequent BATH modules in the coupled calculation was reflected in the results obtained in dosimeter slot 2 and beyond. Thus, comparisons of the type presented tend to diverge in the vicinity of the second shield module.

In general, the comparisons presented in Figure 8 are quite favorable for both neutrons and photons and, thus, lend credence to the coupled calculation as a technique for analyzing complex shield systems.

FIGURE 8

COMPARISON OF RESULTS OF SINGLE CALCULATION WITH RESULTS OF COUPLED CALCULATION IN DOSIMETER SLOT 1 IN THE BATH SHIELD MOCKUP

	SINGLE CALCULATION	COUPLED CALCULATION	RATIO: COUPLED/SINGLE
SULFUR RESPONSE			
R = 0 cm	3.324(4)	3.397(4)	1.022
R = 30 cm	2.551(4)	2.606(4)	1.022
R = 60 cm	5.764(3)	5.899(3)	1.023
U-238 RESPONSE			
R = 0 cm	1.306(5)	1.345(5)	1.030
R = 30 cm	1.007(5)	1.035(5)	1.028
R = 60 cm	2.344(4)	2.416(4)	1.031
Dy RESPONSE			
R = 0 cm	2.191(2)	2.313(2)	1.056
R = 30 cm	1.846(2)	1.933(2)	1.047
R = 60 cm	1.090(2)	1.091(2)	1.001
CaF_2 RESPONSE			
R = 0 cm	1.018(0)	9.928(-1)	0.9752
R = 30 cm	7.679(-1)	7.475(-1)	0.9734
R = 60 cm	2.542(-1)	2.495(-1)	0.9815

NOTE: Numbers in parentheses refer to powers of ten.

It should be pointed out that, since these data are intended solely as a comparison of the two linked calculations, the CaF_2 response does not include the effects of secondary photons born in the shield materials. Rather, only those photons which are born within the basic reactor geometry and subsequently leak through the boundary source plane are included.

Comparisons of calculated and measured response of sulfur pellets are presented in Figures 9 and 10 as a function of axial position internal to the BATH and BSS-LH_2 shield mockups, respectively. In these and subsequent figures, the reference "0" position is located at the top of the reactor assembly as shown in Figure 2. The experimental data as well as the DOT-IIW calculated results illustrated in Figures 9 and 10 are characteristic of a traverse taken along the centerline of the two shield mockups. The analytical results obtained with the ANISN code, being one-dimensional in nature, are not representative of a unique radial position within the shield mockup.

From Figure 9, it is seen that internal to the BATH shield mockup the agreement between the measurements and the DOT-IIW calculation is excellent. No significant differences between the analytical and experimental results are observed. In addition, the results of the one-dimensional analysis indicate that, qualitatively speaking, the ANISN code predicts the falloff of the sulfur threshold flux through the BATH mockup quite well. The magnitude of the one-dimensional results are, however, lower than the two-dimensional analytical data by a factor which ranges from 1.8 in dosimeter slot 1 to 1.6 in dosimeter slot 10. These ratios are typical of the centerline to average ratios observed in the two-dimensional analysis. Hence, for this geometric situation, the one-dimensional analysis is essentially in good agreement with the two-dimensional analysis.

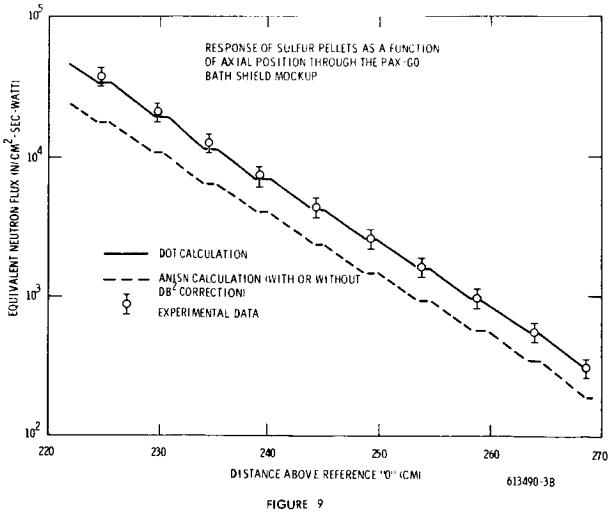

FIGURE 9

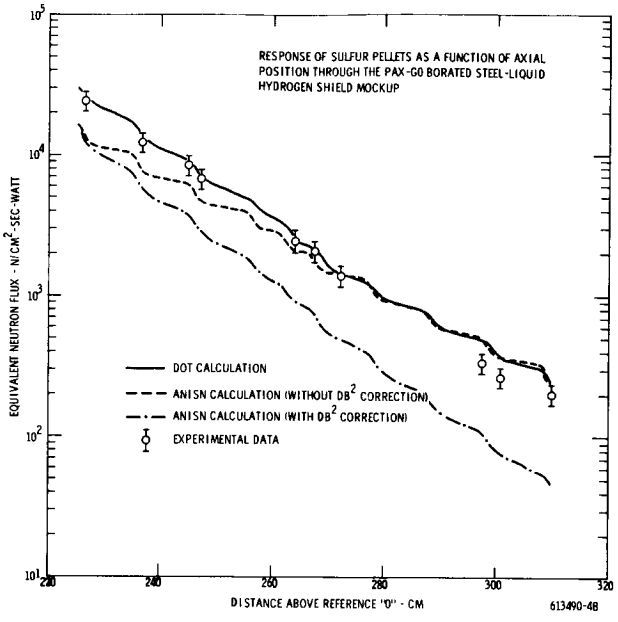

FIGURE 10

From Figure 10, it is noted that internal to the BSS-LH_2 shield mockup the agreement between the measured and DOT-IIW calculated sulfur response is, in general, quite good. However, for axial location beyond Z=280 cm a disagreement which progressively worsens with penetration distance is evident. This disagreement is apparently due to a change in the slope of the calculated attenuation curve for Z>280 cm. A slope change of this nature is not explainable on a physical basis, but may be explained in terms of a calculational deficiency.

A close examination of the calculations performed on the BSS-LH_2 mockup showed that the above mentioned anomaly was observed only for the highest neutron energy group in the calculation. It was further observed that the radius over which the anomaly occurred was governed only by the first tier of polar angles in the S_8 quadrature. Thus, the calculation near the top of the mockup and near the centerline involved an essentially uncollided transport of the forward directed flux from the boundary source plane to the top of the shield. Due to the large physical size of the mockup in question, a calculation of this type represents a severe test of the analytical approach. It is possible that, in the area of the calculational anomaly, the angular flux solutions became oscillatory in nature and the negative flux fix-up routine incorporated into the DOT-IIW code resulted in the observed slope change and the corresponding overpredictions.

Returning to Figure 10, it is noted that the one-dimensional analytical results are presented for calculations both with and without the DB^2 adjustment to the cross sections. It may be noted that when the DB^2 correction is employed the slope through the shield mockup is too steep (ANISN results underpredict measurements by a factor of 1.7 at dosimeter location 1, but by a factor of 4.0 at location 12). Conversely, the slope of the attenuation curve resulting from calculations in which the DB^2 adjustment was not employed is clearly too shallow. Thus, it is evident that the form of the transverse leakage approximation presently incorporated into the ANISN code may, in some circumstances lead to erroneous results. These erroneous results are, of course, indicative of the presence of low density regions (polyethylene) in the shield mockup. In the higher density regions (steel plates) adverse affects of the DB^2 adjustment are not observed.

It is further apparent from Figure 10 that there should be some form of transverse leakage approximation that will result in the proper slope through the mockup. The proper transverse leakage approximation might be arrived at either by making an adjustment to the transverse dimension that is used to calculate the leakage terms or by employing some form of region as well as energy dependent buckling correction. However, both of these improvements might prove to be impractical. In order to apply either an adjustment to the transverse dimension or a region dependent buckling, it is necessary to know a priori the leakage characteristics of the given system. Information of this type may be obtained only from a detailed two-dimensional analysis of the system in question.

Comparisons of the measured and one and two-dimensional calculated cadmium covered U-238 response data (E>1.5 MeV data) presented in Reference 2 displayed characteristics similar to the sulfur data described above.

Comparisons of measured and calculated response of bare minus cadmium covered dysprosium foils are presented as a function of axial location within the BATH and BSS-LH_2 mockups in Figures 11 and 12, respectively. As in the case of the sulfur data, the DOT-IIW analytical results and the measurements were obtained at the centerline of the shield system.

From Figure 11, it is of interest to note that, although the qualitative behavior of the one and two-dimensional analytical results internal to the BATH mockup are quite similar, the two-dimensional approach tends to overpredict the measurements while the results of the one-dimensional analyses agree fairly well with the experimental data. This apparent anomaly in the analytical results may be due to two competing processes which, in the one-dimensional analyses, negated one another, thus, producing the favorable results.

From the schematic diagram of the BATH shield mockup shown in Figure 4, it is clear that once the radiation leaking from the basic reactor penetrates a short distance into the shield, incident thermal neutrons have been attenuated to the point of insignificance; and the thermalization of fast and intermediate energy neutrons has become the dominant mechanism of thermal flux production. Furthermore, it may be noted that most of the thermalization in the BATH mockup is due to the presence of polyethylene. Now, it will be recalled that in the analysis of the BATH mockup, the individual BATH modules were treated as homogeneous regions. Thus, the principle thermalizing media (polyethylene) was dispersed throughout the module. Recall that in the actual experimental configuration the polyethylene was separated from the dosimeter slots and sandwiched between

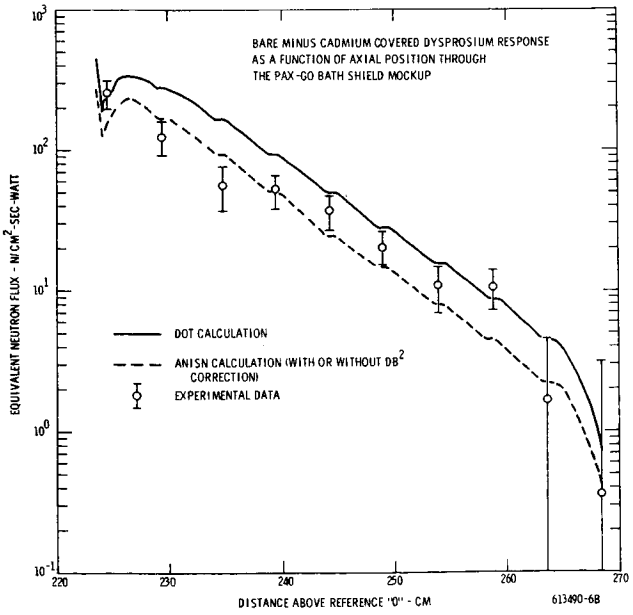

FIGURE 11

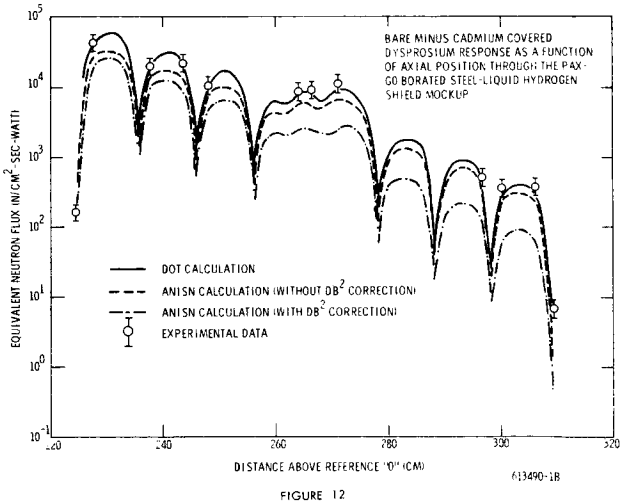

FIGURE 12

boral plates. Thus, from a calculational standpoint, the homogenization process, which not only moves thermalizing material close to the detector location but also disperses the boron poison, tends to produce an overprediction of the thermal flux within the dosimeter slots. Coupled with this overestimate of thermal flux induced by the homogenization process is the fact that the one-dimensional approach, in the slab configuration, inherently underpredicts the centerline value. It is evident, therefore that this inherent underprediction acted in conjunction with the overestimation induced by the homogenization process to produce the results shown in Figure 11. Despite this error in thermal flux calculations caused by homogenizing the BATH modules, it is evident from the qualitative behavior of the analytical results depicted in Figure 11, that the DB^2 adjustment did not have any adverse effect on the thermal flux calculations internal to the BATH mockup.

From Figure 12, on the other hand, it is apparent that, while the two-dimensional results agree quite favorably with the measurements, the one-dimensional calculations do not. The ANISN calculation which employs the DB^2 adjustment clearly underpredicts the measurement to a larger degree than does the calculation which did not include the DB^2 correction. It should be noted that the thermalization process is intimately related to the fast flux distributions within the mockup. As a result of this dependence, the transverse leakage effects observed in Figure 12 reflect changes noted in the fast flux distributions (See Figure 10) which were induced by the DB^2 adjustment.

Comparisons of calculated and measured response of CaF_2 thermoluminescent dosimeters are presented in Figures 13 and 14 as a function of axial position internal to the BATH and BSS-LH_2 shield mockups, respectively. Again, the two-dimensional analytical results as well as the experimental data are representative of a centerline traverse.

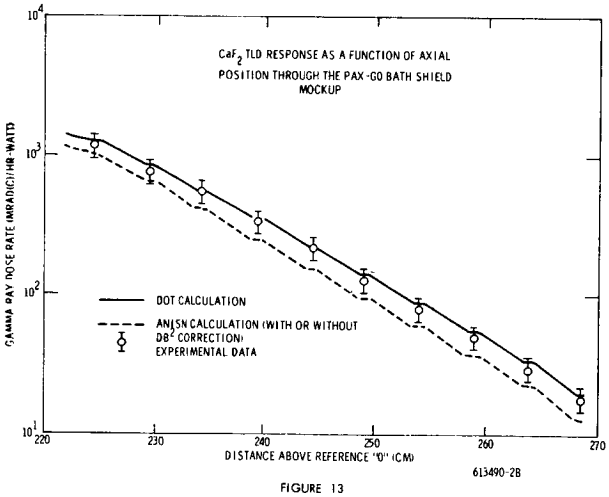

FIGURE 13

Figure 13 illustrates a comparison similar to that shown in Figure 9 in connection with the sulfur pellet data. The agreement between the two-dimensional analytical results and the measurements is excellent. The one-dimensional calculated data employing the transverse leakage adjustment reproduces the experimental gradient through the mockup with a good deal of accuracy. The analytical results are, however, low by a factor of about 1.3 throughout the mockup. As in the case of fast neutrons, the factor of 1.3 is typical of the centerline to average ratios observed in the two-dimensional analysis of the BATH shield.

From Figure 14, it is seen that the agreement between the DOT-IIW calculations and the measurements is somewhat less than desirable. At present, these differences are not completely understood. However, it is believed that the two-dimensional calculation accurately predicts the gradient of the photon dose rate across the mockup. It is further evident, from Figure 14, that although the data obtained from the ANISN calculation without the transverse leakage adjustment indicate an erroneous gradient, the overall results are not too unreasonable. On the other hand, the results obtained from the calculations in which the DB^2 correction was employed are very poor. It is interesting to note that the DB^2 correction in the polyethylene regions reduces the direct radiation component to such an extent that the secondary photons in the steel plates effect a significant increase in the photon dose rate in and around these plates. Clearly, the DB^2 correction used in ANISN cannot be employed to accurately predict the photon transport in low density media.

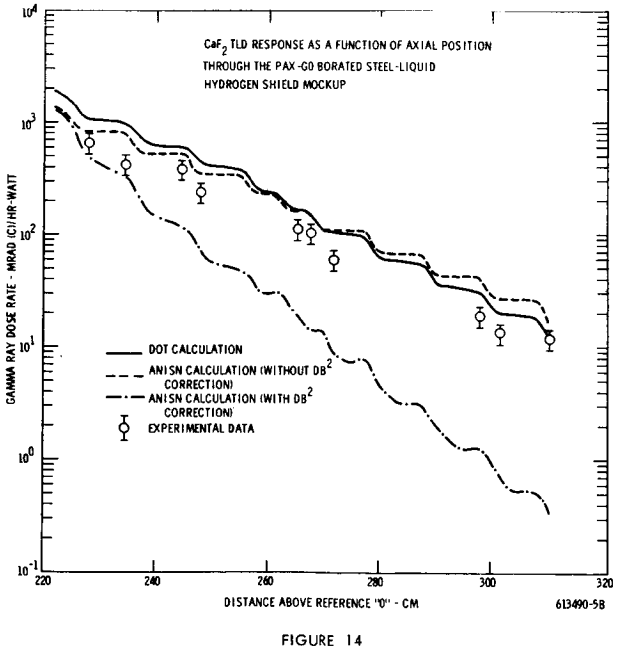

FIGURE 14

CONCLUSIONS

Based on the foregoing comparisons between the measured and calculated neutron and photon radiation levels internal to the BATH and the BSS-LH_2 shield mockups, the following conclusions were noted:

1) The ability of the two-dimensional discrete ordinates code, DOT-IIW to predict the radiation levels internal to the shield mockups was clearly demonstrated.

2) The capability and feasibility of coupling two-successive transport problems at an arbitrary "boundary source" plane was demonstrated. This boundary source feature is extremely important in that a judiciously chosen boundary source may, for a given reactor, be applied to parametric shield studies in such a way that the analysis is facilitated and the overall cost greatly reduced.

3) The one-dimensional calculation inherently underpredicted centerline radiation levels internal to the slab shields. Thus, caution should be exercised when estimating maximum or "peak" radiation levels from the results of a one-dimensional analysis. As an example of this tendency toward underprediction, recall that internal to the BATH shield mockup the ANISN analytical results were consistently lower than either the DOT-IIW calculated or experimentally measured centerline values. For fast neutrons, ANISN results were low by a factor of about 1.8 and, for photons by a factor of 1.3.

4) Problem areas attributable to the use of a transverse leakage approximation were identified in the one-dimensional analytical results. The error induced by employing the transverse leakage approximation is largest for regions in which the actual leakage is relatively large, i.e., low density regions; and, as might be expected, in regions with either large transverse dimensions or high density material these effects are somewhat mollified. Because of this transverse leakage problem, the photon attenuation of the BSS-LH_2 shield mockup was overestimated by a factor of 30.

5) The two-dimensional discrete ordinates approach has been shown to accurately predict radiation levels internal to slab mockups of shadow shields; while, at the same time, serious problem areas associated with the application of the one-dimensional S_n method to the analysis of these slab configurations have been identified. Nevertheless, for many applications the employment of the one-dimensional approach is economically attractive. Thus, further studies aimed at a better understanding of the effects of employing a transverse leakage approximation are certainly warranted.

REFERENCES

1. RN-S-0557, "Radiation Exposure Limitations for Shielded NERVA Engine Components," Aerojet Nuclear Systems Company, April, 1970.
2. WANL-TME-1912, "Nuclear Subsystem Shielding Provision Study Experiments," August, 1970.
3. WANL-TME-1982, "User's Manual for the DOT-IIW Discrete Ordinates Transport Computer Code," R. G. Soltesz, and R. K. Disney, December, 1969.
4. WANL-TME-1969, "Second Version of the GAMBIT Code," G. Collier, G. Gibson, L. L. Moran, R. K. Disney, and R. S. Kaiser, November, 1969.
5. WANL-TMI-1967, "Revised WANL ANISN Program User's Manual," R. G. Soltesz, April, 1969.
6. ANISIG User's Manual (To be Published).
7. WANL-TME-2689, "The Evaluation of the WANL Integrated Nuclear, Radiation and Shielding Standard Design Method (WISDM)," to be published.
8. WANL-PR(LL)-034, "Nuclear Rocket Shielding Methods, Modification, Updating, and Input Data Preparation," Volume 3, "Cross Section Generation and Data Processing Techniques," R. G. Soltesz, et al, August, 1970.
9. American Nuclear Society Paper Presented at the 1969 Winter Meeting, "Neutron Flux Spectra Measurements with Energy Dependent Activation Foils and Comparison with Multigroup Reaction Rate Calculations." S. Salah, W. D. Rankin, and V. S. Oblock.
10. WANL-PR(LL)-010, "Synthesis of Calculational Methods for the Design and Analysis of Radiation Shields for Nuclear Rocket Systems," Volume 7, R. K. Disney, R. G. Soltesz, and S. L. Zeigler, June, 1967.

Radiation Heating in Selected NERVA* Engine Components**

J. C. Courtney+, N. A. Hertelendy+, B. A. Lindsey+
Aerojet Nuclear Systems Company
Sacramento, California

The role of heating from nuclear radiation in design of the NERVA* engine is treated. Generally, radiation heating is more restrictive in design than material degradation considerations. Some components are subjected to very high gamma heating rates in excess of 0.5 Btu/in^3-sec in steel in the primary nozzle or 0.25 Btu/in^3-sec in aluminum in the pressure vessel. These components must be cooled by a fraction of the liquid hydrogen propellant before it is passed through the core, heated, and expanded out the nozzle as a gas. Other components that are subjected to lower heating rates such as the thrust structure and the disk shield are designed so that they would not require liquid hydrogen cooling. Typical gamma and neutron heating rates, resulting temperatures, and their design consequences are covered in this paper. The calculational techniques used in the nuclear and thermal analyses of the NERVA engine are briefly treated.

Most components in the NERVA engine (shown in Figure 1) must be designed to perform with high reliability in severe radiation environments. Radiation heating in several key components will be considered in this paper.

Generally, radiation heating is more restrictive in design than material degradation, due to the choice of material for each component.[1] The NERVA engine uses a relatively small core with a very high leakage fraction for both neutron and gamma radiation. At full power operation (75,000 lbs thrust and 1515 Mw reactor power), radiation-induced heating may exceed 0.5 BTU/in^3-sec in parts of the stainless steel nozzle, and may exceed 0.2 BTU/in^3-sec in the aluminum pressure vessel. Heating rates of this magnitude require that components be cooled by the liquid hydrogen propellant before it is passed through the core, heated, and expanded out the nozzle as a gas.

As long as the component is part of the propellant feed system or the pressure vessel and reactor assembly, liquid or gaseous hydrogen is available as a heat transfer agent. However, it is desirable that some components be designed so that they require no coolant, and thus do not influence the design of the propellant feed system. For example, the thrust structure is to be designed as an uncooled system. If a disk shield is required for some manned missions, it should be designed to operate without cooling. The thrust structure and the disk shield are located forward of the pressure vessel dome and are partially protected by a shadow shield inside the pressure vessel. Many other components forward of the dome, such as lines and valves, are already part of the liquid hydrogen propellant feed system and receive coolant during normal operation.

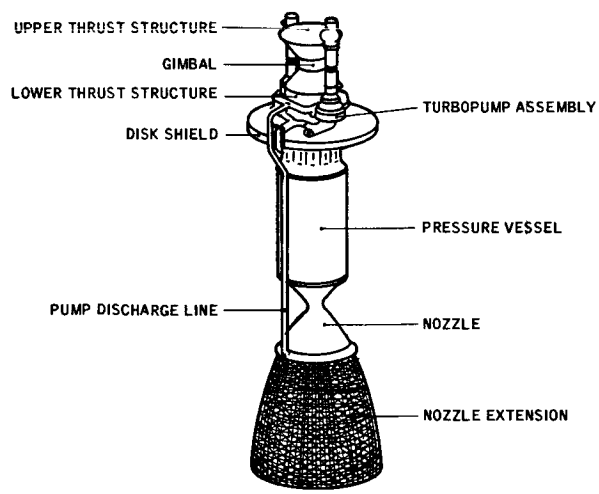

FIGURE 1
NERVA Flight Engine Configuration

*The Nuclear Engine for Rocket Vehicle Application (NERVA) program is administered by the Space Nuclear Systems Office, a joint office of the USAEC and NASA. Aerojet Nuclear Systems Company is prime contractor for the engine system and Westinghouse Electric Corporation is principal subcontractor responsible for the nuclear subsystem.

+Staff Members, Nuclear Science Section, Aerojet Nuclear Systems Company.

**Public Release Approval: PRA/SA - SNPO-C, dated 24 November 1970.

Gamma rays are far more effective than neutrons in heating metal components for the radiation leakages from NERVA. Typically, direct neutron interactions contribute about 4% of the total heating in the stainless steel nozzle. In the aluminum pressure vessel, fast neutrons contribute some 6% of the total heating opposite the core midplane. Neutrons must be considered not so much for their direct heating of metals, but because of their importance in producing secondary gamma radiation. Figure 2 presents the fraction of gamma heating in the nozzle due to secondary gammas produced in the nozzle assembly. Direct neutron heating is significant in only two components. the graphite nozzle extension and parts of the disk shield.

Heating rates in engine components presented in this paper are appropriate for the flight environment. During ground tests, additional radiation heating occurs in some components due to contributions from facility-related sources and facility scatter.[2] The components forward of the pressure vessel are designed to take advantage of the protection afforded by the internal shield in the flight environment. Special facility shielding is required to assure that these components are not overexposed in ground tests.

FIGURE 2

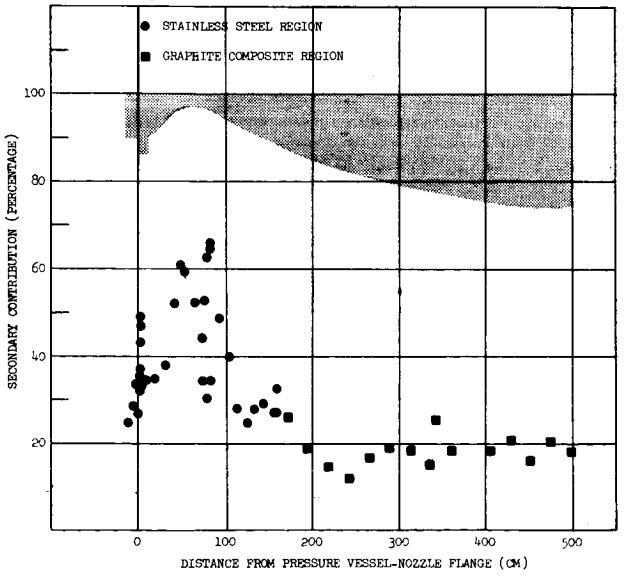

Flight environment heating rates are calculated in detail throughout the engine system using a variety of techniques. Coupled discrete ordinates-Monte Carlo techniques are used extensively. The DASH coupling code[3] has been used to bridge DOT[4] with COHORT[5] for calculations of the nozzle radiation environment and bridge DOT with DOT to calculate heating within the disk shield. Extensive point kernel calculations are used to check the predictions of the more sophisticated methods. Also, the point kernel codes, QAD[6] and GGG[7], are used to predict the facility perturbation of the ground test environment. Calculated volumetric heating rates are input to thermal analyses. Predicted temperatures are necessary for subsequent stress and reliability analyses of candidate component designs.

A numerical differencing code, CINDA[8], is used to predict temperatures throughout the components. It is used to construct and analyze mathematical models of any arbitrary one-, two-, or three-dimensional representation of physical systems governed by the Fourier equation with a source term. The user constructs a thermal analog network representing the system of interest. Nonlinear material properties and boundary conditions may be simultaneously calculated as a function of one or more independent variables. For cooled components (e.g., the nozzle), CINDA is used to calculate the steady-state temperatures using the full power heating rates. For uncooled components (e.g., the disk shield), a transient analysis is conducted to yield the temperature as a function of time.

Before the individual components are considered, it should be emphasized that the NERVA flight engine design is in the preliminary design stage. Both the engine layout and the design of individual components, hence, the heating rates, have been revised periodically. However, the techniques used to calculate radiation heating and resulting temperatures can be applied to any configuration and every attempt is made to simplify the analyses required. The particular components and data presented in this paper were selected to illustrate the analytical approach to radiation heating in the NERVA engine.

One of the most important components in the engine is the nozzle assembly. It consists of a metal primary nozzle with a graphite extension as shown in Figure 3. Currently the candidate primary nozzle materials are CRES-347 stainless steel, Hastelloy X, and ARMCO 22-13-5. The nozzle extension is to be fabricated from a fibrous reinforced graphite composite material. Because of the intense gamma heating and consequent temperature increases, the decrease in allowable stress at the convergent cone section is a major design constraint. Therefore, the primary nozzle must be cooled with a portion of the LH_2 flow from the pump discharge line. Sufficient coolant flow must be provided to assure that the bulk steel temperature is maintained below about 1050°F. Not only is gamma heating an important internal volumetric source, but the hot exhaust gases (4000°R) flow over the inside surface of the nozzle hydrogen coolant tubes. Total nuclear heating rates in the primary nozzle shown vary from 0.6 BTU/in^3-sec in the core support barrel to 0.01 BTU/in^3-sec near the nozzle extension interface. The neutron contribution is only about 4% of the total heating in the steel. For these rates, the temperatures attained in the nozzle vary from -300°F in the coolant passages to a maximum of 900°F in the nozzle wall for the designs currently under consideration.

Figure 3
THRUST CHAMBER ASSEMBLY
FOR
MONTE CARLO ANALYSIS

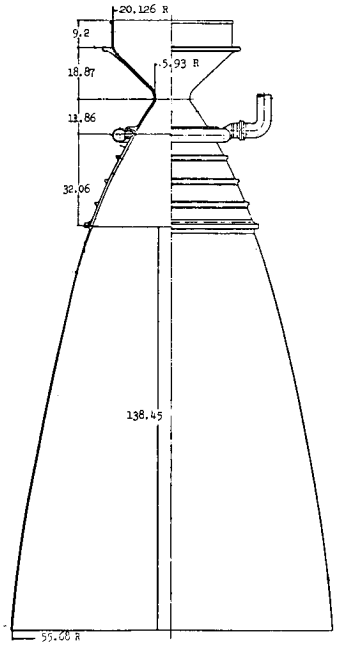

In the graphite nozzle extension, the total heating rates range from 0.002 to 0.0002 BTU/in^3-sec, with the fast neutron heating contributing about 40% to the total. The graphite composite nozzle extension is only radiatively cooled since it can tolerate higher temperatures than metals (above 3000°F) and is subjected to lower heating rates. After 60 minutes of continuous full power operation, the temperature of the graphite varies between 1850°F and 2650°F.[9]

The calculational technique used to generate steady-state nuclear heating rates is shown in Figure 4. A DOT two-dimensional discrete ordinates transport code produces a leakage tape for the lower part of the pressure vessel and reactor assembly. The DASH single event Monte Carlo coupling code is used to transport this radiation across the void between the DOT source tape and the nozzle. The COHORT Monte Carlo code is used to calculate the radiation environment throughout the nozzle assembly.[10] Subsequently, CINDA is used to calculate the temperatures in the nozzle and nozzle extension.

Next consider the results for the pressure vessel. This component consists of an Al-7075 barrel and an Al-6061 dome. The dome is attached to the barrel by a forward closure flange with 124 bolts of A-286 alloy. Peak heating rates in aluminum opposite core midplane range from about 0.26 BTU/in^3-sec on the inside surface to 0.18 BTU/in^3-sec on the outside surface. In spite of these high volumetric heating rates, the coolant flow keeps the peak wall temperature in the pressure vessel below 100°F. The temperatures attained are strongly influenced by the coolant flow allocated to the reflector region. Most of the pressure vessel steady-state temperatures are below 0°F for the current flow conditions. In the top closure flange, high density A-286 bolts attain higher temperatures than the surrounding aluminum. Typically the aluminum in the flange is about -160°F, with the bolt 13°F higher since the gamma heating rates in the bolt are about a factor of three higher than in the aluminum. To prevent fluid leakage at this closure, the bolts are prestressed upon assembly of the pressure vessel.

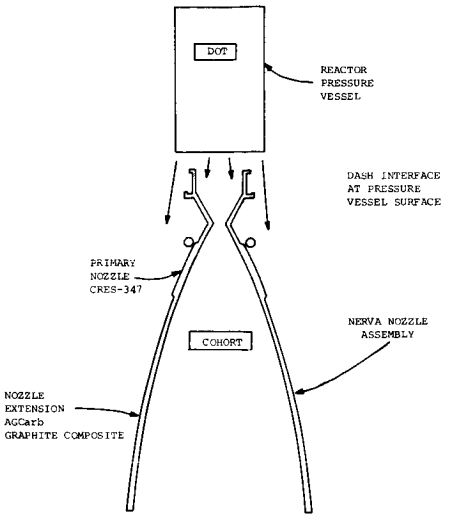

MODEL FOR CALCULATION OF THE RADIATION ENVIRONMENT
NERVA NOZZLE ASSEMBLY

Figure 4

The lower portion of the thrust structure is an aluminum cylindrical annulus with an inside radius of 19 inches and a thickness of 0.28 inches. It is attached directly to the pressure vessel. Not only does this structure transmit the thrust developed by the engine to the rest of the vehicle, but it supports part of the propellant feed system. If possible, the thrust structure should be designed so that it requires no coolant to keep temperatures below the allowable design limits. Currently two materials are under consideration for this component. The primary design uses aluminum which is limited to a maximum temperature of 300°F because above that temperature age hardening is gradually lost. An alternate design uses titanium which is limited to 700°F by the decrease in the yield stress with increasing temperature. Both designs are protected to a large extent by the shadow shield inside the pressure vessel. Heating rates in aluminum range from 3×10^{-3} BTU/in^3-sec in the lower thrust structure near the pressure vessel dome to about 5×10^{-4} BTU/in^3-sec in the upper thrust structure near the propellant tank. Peak temperature rises in the lower thrust structure are on the order of 200°F or less for an engine without a disk shield.

Since the thrust structure is uncooled, the temperature attained after a period of full power firing is strongly influenced by the initial temperature. Coatings such as Al_2O_3 can be used to keep the initial temperature below 100°F. If the thrust structure must be cooled, it will impact on the engine and introduce additional failure modes. An uncooled thrust structure design is thus favored to increase the reliability of the engine design.

The disk shield shown in Figure 5 may be required for some manned missions with light payloads. It is designed to operate as an uncooled component. Such a design permits the use of a single NERVA engine for any manned or unmanned mission. If a light payload requires additional personnel shielding, a disk shield may be added to the engine with a minimum impact on the total engine design.[11] The largest shield design considered (shown in Figure 5) is a 10,000 lb disk with regions of stainless steel, lead, borated graphite, and lithium hydride.

EXTERNAL ENGINE DISK SHIELD

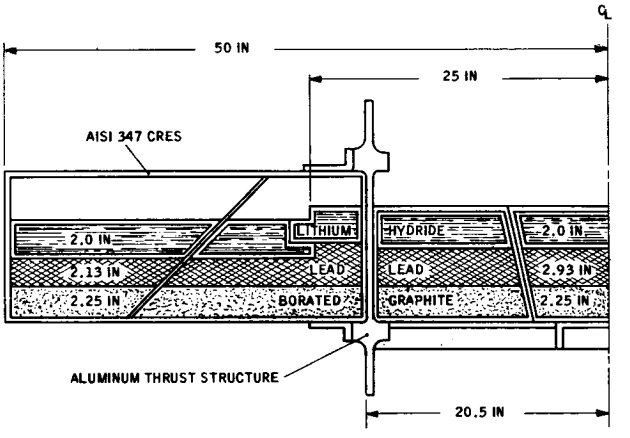

FIGURE 5

Table 1 presents the specification extreme heating rates in various regions of the shield. Neutron heating from the $^{10}B(n,\alpha)^{7}$ Li reaction is the most important source in the borated graphite. Only gamma heating is of significance in the lead. In lithium hydride the $^{6}Li(n,\alpha)^{3}H$ reaction is the most important source of heating. Fast neutron reactions are second in importance, followed by small values of gamma heating. Heating is much higher in the periphery of the shield since leakage radiation from the sides of the PVARA can "view" the disk around the internal shield.

Table 2 presents the peak temperatures for specification extreme (worst case) nuclear and thermal analyses in the disk shield for continuous firing times of 10, 30, and 60 minutes. The peak temperatures occur at the tip of the shield and decrease with decreasing radius. If some conservatism is removed by the use of nominal instead of "worst case" values for some parameters, the temperatures are lowered by at least 150°F. For instance, the lead at the outer edge of the shield remains below 600°F. Design options can also be exercised to circumvent thermal problems. For example, if the temperature is excessive in the lithium hydride, it can be removed from the outer 10 inches of the periphery of the shield.

The initial temperature of the disk is an important parameter in these calculations. It is expected that coatings such as aluminum oxide will assure that the initial temperature will not differ significantly from the ambient temperature at launch, even after a long space soak. Note that in Table 2 the initial temperatures differ in the central and peripheral portions of the shield. This is because the central portion is enclosed by the lower thrust structure and is inhibited from losing heat by radiation.

The heating rates in uncooled components near the bottom of the propellant tank, such as the gimbal assembly and the gimbal actuator, are about 1.5×10^{-3} BTU/in^3-sec in steel. The aluminum upper thrust structure is subjected to heating rates on the order of 5.5×10^{-4} BTU/in^3-sec in aluminum. For these low rates the gimbal temperature may increase 250°F, and the upper thrust structure temperature may increase by 70°F after 60 minutes of full power firing. Thus, radiation heating is not a factor in the design of such components.

REFERENCES

1. WARMAN, E. A., ROGERS, D. R., COURTNEY, J. C., DIXON, C. D., SMITH, J. R., and CONANT, J.: "Radiation Exposure Limitations for Shielded NERVA Engine Components," Aerojet Nuclear Systems Company Report RN-S-0557, April 1970.
2. WARMAN, E. A., FOREMAN, D. L., and COURTNEY, J. C.,: "Comparison of Computed and Measured Radiation Levels in NERVA Development Engine Tests," Trans. Am. Nuc. Soc., 12, 416 (1969).
3. LINDSTROM, D.G. and PRICE, J. H.: "Coupled Discrete Ordinates - Monte Carlo Technique and Applications to NERVA," Trans. Am. Nuc. Soc., 12, 952 (1969).
4. MYNATT, F. R., "A Users Manual for DOT, a Two-Dimensional Discrete Ordinates Transport Code with Anisotropic Scattering," Union Carbide Corporation, Nuclear Division, Report K-1694 (1967).
5. COLLINS, D. G. and WELLS, M. B., "COHORT - A Monte Carlo Program for Calculating Radiation Heating and Transport," Radiation Research Associates, Inc., Report RRA-T62 (1966).
6. MALENFANT, R. E., "QAD: A Series of Point-Kernel General-Purpose Shielding Programs," Los Alamos Scientific Laboratory Report LA-3573 (1967).
7. MALENFANT, R. E., RSIC Code Package CCC-75, Radiation Shielding Information Center, Oak Ridge National Laboratory.
8. LEWIS, D. R., GASKI, J. D., and THOMPSON, L. R., "CINDA-3G-Chrysler Improved Numerical Differencing Analyzer for 3rd Generation Computers," Chrysler Corporation Space Division, Technical Note AP-67-287 (1968).
9. Thermal and Fluid Flow Analysis Report, NERVA Program, Data Item S-31, Aerojet Nuclear Systems Company Report S-031-CP090290-F1 (1970).
10. WARKENTIN, J. K. and COURTNEY, J. C., "Monte Carlo Radiation Transport Analyses of the NERVA Nozzle Assembly," Trans. Am. Nuc. Soc., 13, 439 (1970).
11. WARMAN, E. A., COURTNEY, J. C., and KOEBBERLING, K. O., "Final Report of Shield System Trade Study," Aerojet Nuclear Systems Company Report S054-023, July 1970.

TABLE 1

Disk Shield Heating Rates

Nuclear Heating Rate (BTU/sec)

	Gammas (From Nuclear Subsystem)	Shield Secondaries	Neutron Absorption	Totals
Central Region 0 to 25 inch Radius				
Lower Steel Plate	1.4	0.1	0	1.5
Borated Graphite	2.1	0.1	2.0	4.2
Lead	4.3	0.3	0	4.6
Lithium Hydride	0	0	4.1	4.1
	7.8	0.5	6.1	14.4
Peripheral Region 25 to 50 inch Radius				
Lower Steel Plate	7.0	1.2	0	8.2
Borated Graphite	10.6	2.2	15.5	28.3
Lead	19.6	3.1	0	22.7
Lithium Hydride	0.2	0	14.2	14.4
	37.4	6.5	29.7	73.6
Shield Totals	45.2	7.0	35.8	88.0

TABLE 2

Disk Shield Peak Temperatures

Material Regions	Initial Temperature in ^{o}F	Specification Extreme Peak Temperatures (^{o}F) Time of Continuous Full Power Firing		
		10 Minutes	30 Minutes	60 Minutes
Central Region				
Lower Steel Plate	100	160	252	330
Borated Graphite	100	156	248	325
Lead	100	154	245	320
Lithium Hydride	100	150	240	305
Peripheral Region				
Lower Steel Plate	70	350	630	870
Borated Graphite	70	280	540	780
Lead	70	260	520	760
Lithium Hydride	70	170	390	630

SELECTION AND USE OF TLDs FOR HIGH PRECISION NERVA SHIELDING MEASUREMENTS

H. C. Woodsum

Westinghouse Electric Corporation
Astronuclear Laboratory

An experimental evaluation of Thermoluminescent Dosimeters (TLDs) was performed in order to select high precision dosimeters for a study whose purpose is to measure gamma streaming through the coolant passages of a simulated flight type internal NERVA reactor shield. The criteria for selection of the dosimeters was that they should be reproducible within ± 2% and some must have spatial resolution within ± 1.5 mm.

The experimental procedure was to expose batches of 50-100 CaF_2 and LiF chip, mini, and micro TLDs to ^{60}Co radiation by mounting these dosimeters on a rotating wheel (to minimize positional differences). ^{60}Co radiation was used since it approximates the average energy of the gammas entering the shield. The 30 Ci source was placed ~150 cm from an aluminum wheel 51.1 cm dia. by 0.079 cm thick on which dosimeters were taped. All TLDs had been annealed for 1 hour at 400°C followed by 17 hours at 80°C prior to exposure.

Reading of the TLD exposures was performed on a digital readout system. All dosimeter data was processed by the TLDEVAL code which calculates the mean, standard deviation, variance for each dosimeter and fractional standard deviation of the mean.

Based on this study, the CaF_2 chip TLDs are the most reproducible dosimeters with reproducibility generally within a few percent, but none of the TLDs tested met the reproducibility criterion of ± 2%. The microdosimeters were the least reproducible to the point of not being usable for measurements below several hundred rads. The dosimeters tested are linear with dose over the range of 1-180 rads within ± 10% and fading of dosimeters after exposure was found to be negligible within the accuracy of the measurements. The non-reproducibility of ^{7}LiF mini TLDs is not presently understood, but may be due to a combination of the following: lack of sensitivity (compared to comparable CaF_2 dosimeters), non-radiation-induced thermoluminescence, or radiation damage from previous reactor irradiations. These effects are currently under further investigation.

Since the CaF_2 chip dosimeters appear to be the only ones which approach the requirements for the combination of reproducibility and spatial resolution, attempts will be made to further improve their precision by selective use of dosimeters based on repeated calibrations and control of the effects which are known to produce non-radiation-induced thermoluminescence.

INTRODUCTION

An experimental evaluation of Thermoluminescent Dosimeters (TLDs) was performed to select high precision dosimeters for a set of experiments whose purpose is to measure gamma ray streaming through the coolant passages of a simulated flight type internal NERVA* reactor shield. The criteria for selecting these dosimeters were based on experimental requirements for reproducibility within ± 2 percent and spatial resolution within ± 1.5 mm. The TLD selection study results will be presented, followed by the experiments which led to these requirements, and, finally, some preliminary experimental data from the shield streaming measurements will be given.

EVALUATION STUDY OF TLDs AND TLD CALIBRATIONS

General Description of TLD Evaluation Experiments

TLDs were selected for the initial phase of the gamma ray streaming experiments, since they are small enough to have the potential of meeting the spatial resolution requirements, and other investigators such as ANL[1] and ANSC[2] have demonstrated their utility and accuracy for measurements of this type. TLDs are an integrating type of dosimeter, such as is needed with the source simulator used here, and considerable experience had been gained from their previous use. Several types of TLDs were available at the Westinghouse Astronuclear Experimental Facility

*The Nuclear Engine for Rocket Vehicle Application Program (NERVA) is administered by the Space Nuclear Systems Office, a joint office of the U. S. Atomic Energy Commission and the National Aeronautics and Space Administration. Aerojet Nuclear Systems Company as prime contractor for the engine system and Westinghouse Electric Corporation as subcontractor for the nuclear subsystem, are developing a nuclear propulsion system for space application.

(WANEF) and a preliminary experimental investigation was conducted to help select TLDs which would meet the reproducibility requirements as well as the spatial resolution requirements. The reproducibility criteria and spatial resolution criteria were dictated by the following shield streaming measurement experimental requirements. 1) It was desirable to have a detector which was reproducible to within 2 percent since, for the smallest duct size (0.477 cm diameter) and the thinnest shield considered (15.2 cm), the maximum effect of duct streaming was expected to be of the order of a few percent increase over the no duct case. 2) Also, in order to be able to obtain suitable spatial resolution of the streaming patterns near the openings over the smallest duct(s), dosimeters should be ideally no larger than 1/2 to 1/3 of the duct width, or perhaps 1.5 mm. Generally, however, the smaller the dosimeter, the less sensitive it is, which, in turn, reduces the signal to "noise" ratio. Thus, there is a trade-off between the spatial resolution and reproducibility.

Types of TLDs available at WANEF for use in these experiments are shown in Table 1. In order to investigate the sensitivity and reproducibility of these dosimeters, a controlled experiment was set up.

TABLE 1.

TLD TYPES AND SIZES FOR USE IN STREAMING MEASUREMENTS

Types	Shape	Size	Material
TL-028B	Chip (thin)	1/8"x1/8"x0.03"	Li^6F
TL-028A	" (thick)	1/8"x1/8"x1/16"	Nat. LiF
TL-028C	" "	1/8"x1/8"x1/16"*	Li^7F
TL-22	Tubular (mini)	1.4 mm x 12 mm	Li^6F
TL-23	"	1.4 mm x 12 mm	Li^7F
TL-31	"	1.4 mm x 12 mm	CaF_2
TL-33	Chip (thick)	1/8"x1/8"x1/16"*	CaF_2
TL-29	Tubular (micro)	0.9 mm x 6.0 mm	LiF
TL-19	"	0.9 mm x 6.0 mm	CaF_2

*Also available in thin (0.03" thick) chip with same designation.

Experimental Procedure for TLD Evaluation and Calibrations

A description of the experimental apparatus and setup for the TLD evaluation study will be presented. Batches of TLDs of the various types shown in Table 1 were exposed to ^{60}Co radiation by mounting these dosimeters on a rotating wheel (to minimize positional differences and maintain a constant radiation field on all dosimeters) placed near a fixed ^{60}Co source. The source-detector geometry is shown in Figure 1. The source used was a 30-Ci (on 9/67) ^{60}Co source capable of storage in a lead shield and remotely operable to the exposure position in a pit approximately 15' x 15' x 11-1/2' deep by the use of a manually operated, mobile gamma ray projector. The dose rate used for the calibration was taken from a calibration of the ^{60}Co source radiation field performed by use of a CO_2-filled carbon-wall ionization chamber which was previously calibrated at NBS, as described in Reference 3. The dose rate was corrected to equivalent rads (carbon) by multiplying R values by 0.869 rads (C)/R. The value obtained was 10.49 rads (C)/hr at 1.5 meters on 7/1/70.

The wheel used in this study was made of aluminum sheet 0.079 cm thick and 51.1 cm in diameter. Dosimeters were taped directly to its face at a radius of 23 cm. The TLDs were located at approximately 1.5 meters from the source and were exposed in batches of 50-100 for approximately one hour, except for the dose linearity check which required a 6-minute and 18-hour as well as a 60-minute exposure under similar conditions.

A dosimeter decay investigation was also conducted to determine the relative fading characteristics for each of the dosimeter types. Each batch of 50 - 100 dosimeters was divided into 6 equal lots following one irradiation exposure of 1 hour and were read out at approximately 0, 1, 4, 8, 24, and 48 hours after irradiation. Because of schedule difficulties, not all dosimeters were able to be read out at 8 hours after irradiation. Also, when it was determined that the micro dosimeter variability was large enough to preclude their use for the streaming experiments, the originally planned decay study was dropped for the

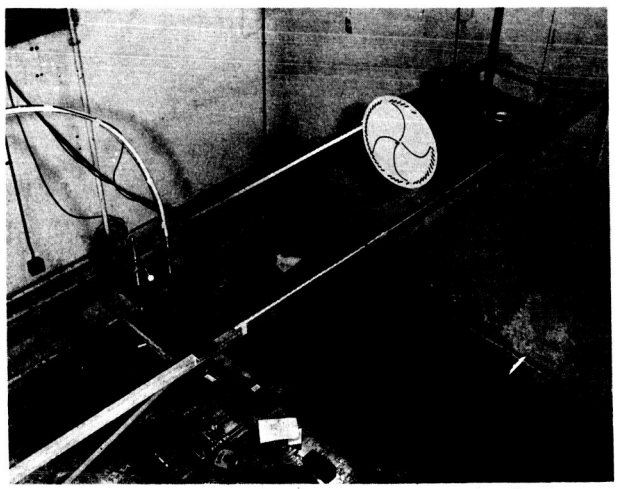

Figure 1. Experimental Configuration for TLD Evaluation Study

CaF_2 micro TLDs. The 18-hour irradiation for the LiF micro TLDs was also dropped for the same reason.

All TLDs were annealed for 1 hour at 400°C (750° F) followed by 17 hours at 80°C (176°F) in a Blue M. Co. Lab-Heat oven prior to exposure. Reading of the TLDs was performed on an EG&G Model TL-3B reader with digital readout. (Exceptions to the use of the digital reader are noted.)

All dosimeter data were processed by the TLDEVAL code which calculates the mean, standard deviation, variance for each dosimeter, and fractional standard deviation of the mean.

DISCUSSION OF RESULTS OF TLD EVALUATION STUDY

Reproducibility and Spatial Resolution

This study revealed that none of the dosimeters tested met both the reproducibility (+ 2 percent) and spatial resolution (+ 1.5 mm) criteria. The CaF_2 and LiF chip dosimeters, however, came the closest to meeting the reproducibility requirements with values ranging from + 3-6 percent (1σ). By very careful control and a better understanding of the non-random effects, it may be possible to achieve the + 2 percent criterion with these dosimeters. Based on the results of this preliminary study, however, thin (0.03" thick) ^{7}LiF chip TLDs should be substituted for the thick chip ^{7}LiF TLDs which were tested and reported here. This substitution is necessary since the thick chips give a spurious response on the digital reader for low doses and for less than 20 percent of full scale reading although the digital reader unit per se is more precise than the chart reading provided that the heater current is not too excessive. The use of thin chip LiF as well as CaF_2 TLDs, however, will necessitate the use of electron equilibrium producing material around each of these dosimeters since it has been demonstrated that their response will vary by perhaps as much as 30 percent, depending on whether the chip is placed directly on the aluminum shield or suspended slightly above it if "sufficient material" is not placed around it. "Sufficient material" for undegraded ^{60}Co radiation is approximately 380 mg/cm^2 or approximately 2/3 the range of 1.2 MeV electrons.

The LiF and CaF_2 mini dosimeters (type TL-23 and TL-31, respectively, in Table 1) are less reproducible than the chip type of TLDs. The precision for the CaF_2 type of dosimeter ranged from + 6 to 8 percent (1σ) although the size of these detectors is small enough that they could meet the + 0.15 cm spatial resolution requirement. The within-batch precision of the ^{7}LiF mini TLDs was less than that of the CaF_2 minis being in the range of + 10 to 16 percent (1σ) and reproducibility between batches was as much as 50 percent. This between-batch variability in response of the ^{7}LiF TLDs is not presently understood, but may be due to any or all of the following: sensitivity to light, sensitivity to mechanical vibrations, and radiation effects of the dosimeters from previous reactor irradiations which have been only partially annealed out by succeeding annealings and readouts. The within-batch variation is attributed largely to non-uniformity of both the contained powder and the glass containers which, by visual inspection, can be seen to be quite non-uniform. Also, the increased variability compared with the chip dosimeters is due to their decreased sensitivity. From Table 2, it can be seen that

TABLE 2.

TLD EVALUATION STUDY FOR TIS-23 WITH 30 Ci ^{60}Co SOURCE

TLD READER RESPONSE, R/RAD

	LiF			CaF_2		
	Chips (TL-02B)	Minis (TL-23)	Micros (TL-29)	Chips (TL-33)	Minis (TL-31)	Micros (TL-19)
1 Hr. Exposure	0.193 ± 4%	0.0605 ± 17.0%	4.78×10^{-3} ± 19.3%	1.07 ± 5.8%	0.396 ± 6.8%*	0.0238 ± 11.1%
6 min.	0.216 ± 4.6%*	0.0411 ± 16.1%	4.93×10^{-3} ± 25.1%	1.11 ± 3.9%	0.448 ± 6.4%	0.0702 ± 23.28%
60 min.	0.189 ± 3.7%	0.0377 ± 9.7%	3.61×10^{-3} ± 12.9%	1.05 ± 3.2%	0.409 ± 7.5%	0.0357 ± 8.21%
18 Hr.	0.200 ± 2%	0.0444 ± 8.6%	--**	1.01 ± 4.7%	0.406 ± 6.3%	0.0379 ± 12.72%
1 Hr. Exposure Read At						
0	0.191 ± 0.28%	0.0532 ± 9.0%	8.42×10^{-3} ± 22.9%	1.09 ± 4.2%	0.420 ± 5.3%	--**
1 Hr.	0.168 ± 6.8%	0.0476 ± 5.1%	8.17×10^{-3} ± 25.0%	1.04 ± 4.4%	0.371 ± 6.1%	--**
4 Hr.	0.185 ± 2.1%	0.0489 ± 18.2%	10.5×10^{-3} ± 9.8%	1.03 ± 3.1%	0.402 ± 2.3%	--**
8 Hr.	0.176 ± 4.6%	0.0517 ± 8.6%	--**	--**	--**	--**
24 Hr.	0.176 ± 4.7%	0.0526 ± 11.2%	9.24×10^{-3} ± 11.0%	1.08 ± 5.1%	0.400 ± 5.2%	--**
48 Hr.	0.187 ± 1.0%	0.0557 ± 13.9%	11.8×10^{-3} ± 38.5%	0.896 ± 5.3%	0.364 ± 11.0%	--**

*Read from chart.
**Not performed for reasons given in text.

these dosimeters are approximately a factor of 4-5 less sensitive than the LiF chip TLDs and a factor of 20-25 less sensitive than the CaF_2 chip TLDs.

The micro TLDs, while having even better spatial resolution than the mini TLDs, show even more variability and lack of precision with the within-batch variability being from 13-25 percent (1σ) for the LiF micros and from 8-23 percent (1σ) for the CaF_2 micros. The sensitivity of these dosimeters is about 50 times less than the comparable chip dosimeters. The repeatability in this case is even worse than that of the LiF minis, varying as much as a factor of 2 for between-batch irradiations. The within-batch variability is attributed to the same causes as for the mini TLDs. Since these dosimeters are even smaller and less sensitive, as expected, their non-uniformity produced variations have a larger effect. The large batch-to-batch variations are, as in the case of LiF mini TLDs, not understood. For these reasons, it is recommended that these dosimeters not be used for any precise experiment where the expected dose does not exceed ~1000 rads.

Decay Effects

Results of the dosimeter decay investigation study showed negligible fading or decay of dosimeter response from 4-48 hours after exposure, except for CaF_2 dosimeters where a 10-20 percent decrease from 24-48 hours was noted.

Light Exposure Effects

Some checks on light-produced effects were made for the chip dosimeters, which were the most reproducible obtained in this study. Specifically, an auxiliary experiment was conducted where 5 CaF_2 TLDs were exposed to fluorescent light both during and after source exposure and 5 CaF_2 chip dosimeters were covered so that light could not reach them, and a sizable difference was observed. For this case, it was noted that the TLDs which were not exposed to light read a factor of 2 higher than those exposed to light. A similar experiment with LiF TLDs showed no such effect. Thus, exposure to light is most certainly an important effect for CaF_2 TLDs.

Based on these TLD evaluation study results, the chip type dosimeters were selected for the first phase measurements of shield streaming which are described next. Since few thin chip LiF TLDs were available when these experiments were initiated, TL-033 thin CaF_2 chip dosimeters were utilized.

DESCRIPTION OF GAMMA RAY SHIELD STREAMING EXPERIMENTS

Description of Experimental Equipment and Procedures

Measurements of the gamma ray streaming through penetrations in an aluminum shield mockup using a simulated plane isotropic source of ^{60}Co radiation was undertaken in order to determine the importance of gamma ray streaming through coolant penetrations in the internal BATH shield of a flight type R-1 NERVA reactor. A ^{60}Co source was chosen for this study since its nearly monoenergetic 1.25 MeV gamma ray energy approximates the average energy of gamma rays emitted from the NERVA reactor core. Aluminum was chosen for the shield mockup material since its density and gamma ray attenuation properties closely simulate the Boron Carbide-Aluminum-Titanium Hydride (BATH) internal flight shield which is composed of 70 percent by volume aluminum.

A 40.6 cm diameter, uniform, isotropic disk source of ^{60}Co radiation was simulated by means of a mechanical source traversing system shown in Figure 2. This mechanism moves a small source back and forth across a circular area 40.6 cm in diameter. The construction of this simulator and the analytical and experimental checks to assure that this simulator system met the source uniformity criteria of + 2 percent between areas of 0.01 cm^2 will be the subject of a later paper and thus will not be discussed here. A sketch of the overall experimental geometry for the shield streaming measurements is shown in Figure 3. The shield mockup geometry is illustrated in Figure 4.

Finally, Figure 5 is a photograph of the overall assembled experimental apparatus with the shield mockup slabs and plugs in place. Duct diameters of 0.477 and 2.8 cm were investigated in the first phase of this experiment.

Aluminum boxes, as shown in Figure 6, were specially made to assure electron equilibrium in the CaF_2 chip TLDs. The boxes containing TLDs were then mounted directly on top of the shield configuration which was previously shown in Figures 2 - 4 and were exposed for one complete cycle of source traverse (~34 minutes) with the ducts plugged and with a 2.8 cm diameter duct unplugged. The results of these measurements are shown in Figure 7.

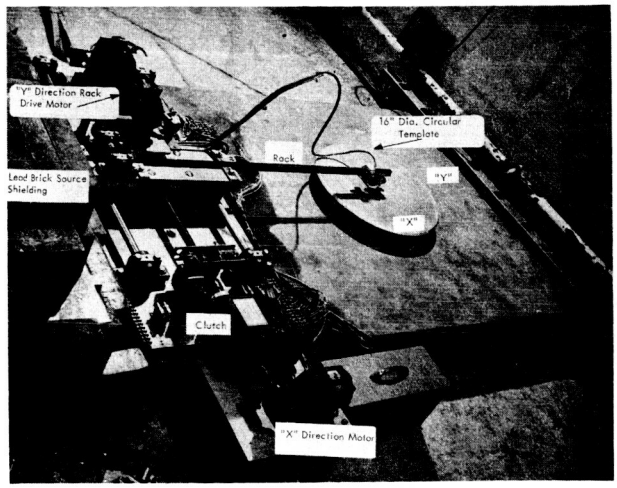

Figure 2. Plane Source Simulator Traversing System

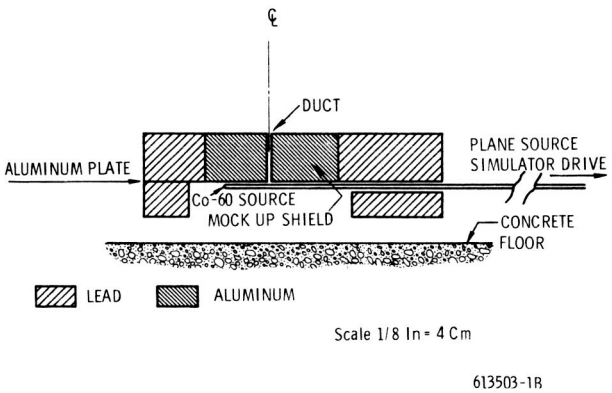

Figure 3. Sketch of Shield Streaming Experiment

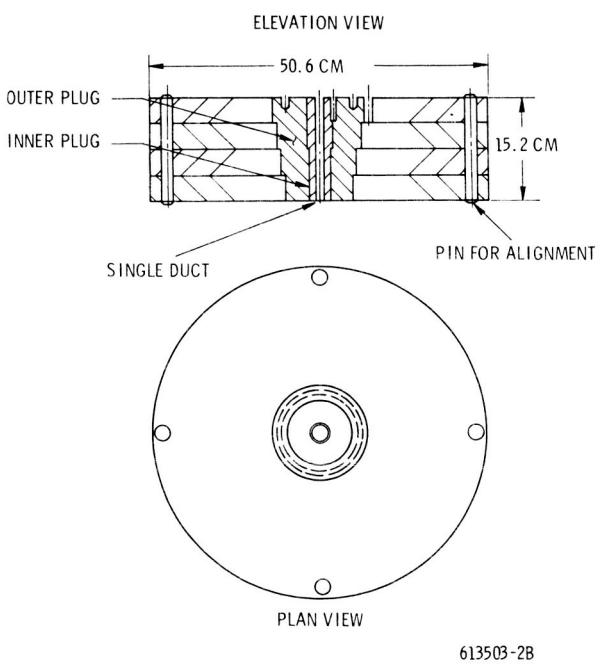

Figure 4. Shield Mockup Geometry for Shield Streaming Experiments

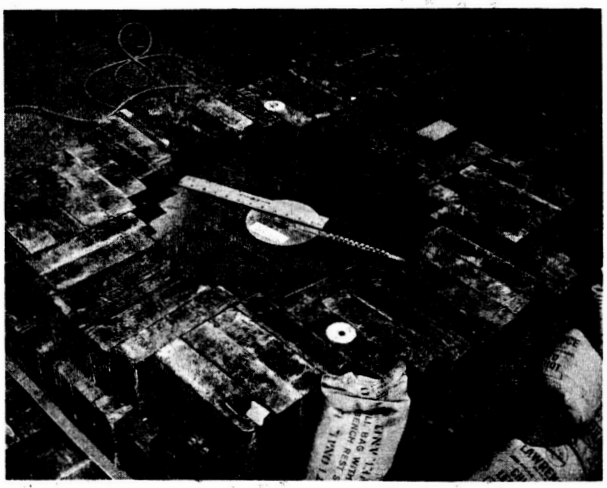

Figure 5. Assembled Shield Mockups for 2.8 cm Duct Configuration with TLDs in Place

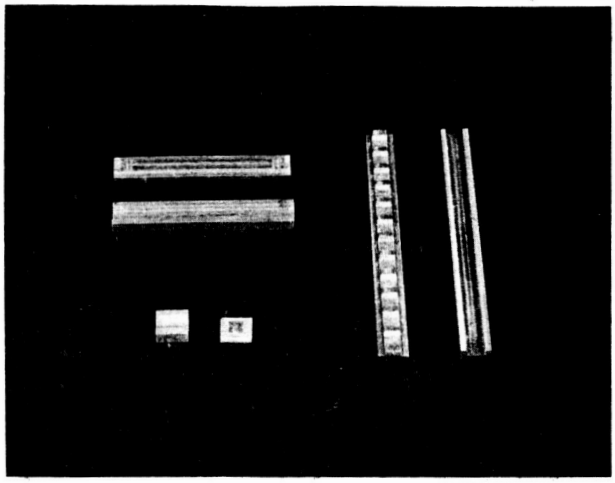

Figure 6. View of Disassembled Aluminum Boxes Made to Contain CaF_2 TLDs

required, and preliminary measurements were completed for a 2.8 cm diameter duct in 15.2 cm thick aluminum and for a 0.437 cm diameter duct in 19.0 cm thick aluminum. Based on these results, further experimental work is required to 1) more closely approach the spatial and precision requirements and 2) to resolve differences between measurements and predictions.

Results of Shield Streaming Measurements

The ratio of the measurements unplugged/plugged shows the relative streaming effect and radial distribution of the streaming. The results of the initial measurements for the 2.8 cm diameter duct indicates a ratio of about 1.40 whereas a preliminary estimate of the ratio of 1.20 was obtained based on simple line-of-sight considerations. However, more rigorous analysis, which included scattering effects, indicated that the increased ratio was probably due to floor-scattering effects and the enhanced low energy response effect of the CaF_2 dosimeters. Thus, a 0.07-inch thickness of lead was added immediately below the shield mockup and the experiment was redone. Results of this second experiment agree well with the predictions (see Figure 7). Similar measurements conducted with a 0.477 cm diameter duct in a 19.0 cm thick aluminum shield mockup showed no peaking over the duct within the accuracy of the measurements.

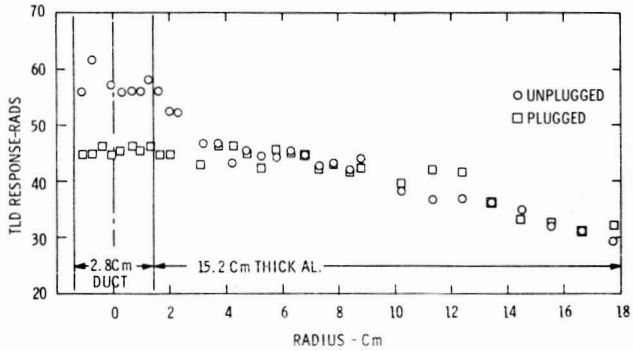

Figure 7. CaF_2 TLD Measurements on Plugged and Unplugged 2.8 cm diameter Hole in 15.2 cm Aluminum

CONCLUSIONS

An experimental evaluation of available TLDs was conducted in order to help select TLDs which would meet experimental shield streaming measurement requirements of ± 2% reproducibility and ± 1.5 mm spatial resolution. Although none of the dosimeters met both of the above criteria, LiF and CaF_2 chip dosimeters approached the reproducibility requirements (with ± 3-6%) and were about twice the spatial resolution requirements (with 3.2 mm). Thus, CaF_2 chip (rather than LiF chip dosimeters) were selected for the initial phase of shield streaming measurements because of their availability in the quantity

REFERENCES

1. ANS Transactions, Vol. 10, No. 1, 1967 Annual Meeting, San Diego, Calif., June 11-15, 1967, p. 395, "TLD Measurement of Gamma-Ray Heating with AARR Critical Assembly," G. S. Stanford, T. W. Johnson.

2. AGC-RN-S-0510, "XE-Prime Engine Final Report," Vol. III, Book 1, Test Analysis, May 1970.

3. WANL-PR(LL)-022, "Synthesis of Calculational Methods for the Design and Analysis of Radiation Shields for Nuclear Rocket Systems, Vol. 1, Radiation Measurements in a Nuclear Rocket Propellant Tank Mockup Using Simulated Liquid Hydrogen," Sept. 30, 1968.

RADIATION HARDENING OF COMPONENTS AND SYSTEMS FOR NUCLEAR ROCKET VEHICLE APPLICATIONS*

William A. Greenhow and Paul R. Cheever

GENERAL DYNAMICS
Convair Aerospace Division
Fort Worth Operation

INTRODUCTION

The Nuclear Rocket Vehicle (NRV) is an advanced space vehicle employing the NERVA engine and liquid hydrogen as fuel. The final design and ultimate selection of NRV components and systems will evolve from various technical approaches presented below.

TECHNICAL APPROACHES

As shown in Figure 1, the various procedures which can be employed in the development of NRV components and systems include: (1) experimental, (2) shielding, (3) research, (4) analytical, and (5) radiation hardening. Since all of the procedures may be employed before the NRV is a reality, the merits of each are briefly reviewed here.

Experimental

Candidate "off-the-shelf" components, such as transducers, will be tested in a combined nuclear and simulated space environment to determine the best designs for various applications and establish their safe operating limits. This approach is very costly but results in a high confidence level since the component is required to operate before, during, and after irradiation.

Shielding

The shielding approach is an extension of the experimental approach in that shielding is employed to attenuate the nuclear radiation to levels below the components recommended radiation tolerance if the component cannot be relocated in a lower radiation environment. Because of the weight penalty, the use of shields must be minimized.

Research

In some instances, materials and components unique to the NRV, e.g., reactor components, must be designed and developed. Preliminary design data, which are obtained from radiation effects tests conducted on materials and subassemblies, are integrated into prototype systems which are proof tested and modified, as required, prior to incorporating them into the NRV preliminary design.

Analytical

This technique, which is described later, requires detailed analysis of component drawings and specifications as well as establishing radiation tolerance limits for each material application. Since many NRV components are located in areas in which the predicted nuclear environment is considerably below the recommended radiation tolerance for each material contained in the component or system under consideration, their usage can be justified on the basis of this analysis.

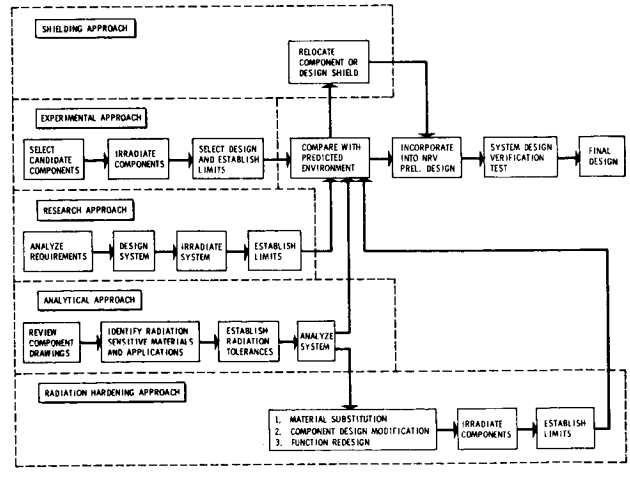

Figure 1 EVOLUTION OF RADIATION RESISTANT COMPONENTS AND SYSTEMS

*Work performed under Contract NAS8-25848 with MSFC, Dr. R. L. Gause, Contracting Officer's Representative.

Radiation Hardening

The analytical procedures provide the basis for radiation hardening studies. Those components and systems which contain radiation sensitive materials are hardened by: (1) material replacement, i.e., radiation stable materials are substituted for materials with low radiation tolerance; (2) system design modifications; or (3) redesign of functional roles of components. The modified or redesigned system is then irradiated to verify its performance in a simulated NRV environment.

RADIATION HARDENING

Analytical and radiation hardening procedures are being employed by General Dynamics for analyzing the mechanical components of the S-II and S-IVB stages of the Saturn V vehicle to determine those which might be considered suitable, or which might require modification to a sufficient level of radiation hardness, for NRV applications. The technical approach is best visualized through the following steps:

1. S-II and S-IVB drawings and specifications were examined to identify the materials prone to radiation damage and determine their locations and applications.

2. Recommended radiation tolerance limits were established for each material and application on the basis of previous test experience.

3. Each major component and subsystem was carefully analyzed, and the radiation tolerance of the basic "as designed" system was assessed.

4. Assuming the system to be located in a reasonable position on the NRV, the recommended radiation tolerance limits were compared to the predicted nuclear environment for missions requiring 10 hours of engine operation. (Radiation levels are based on ANSC nuclear flux data for the NERVA full-flow engine.)*

5. If the radiation tolerance of the basic system was less than the predicted environment, recommendations were made to radiation harden it in a multistep procedure in which (1) materials with low radiation resistance were replaced by materials having greater stability in a nuclear environment and yet can satisfy the requirements of the particular application, or (2) vulnerable components which limit its usage were replaced, or (3) a system redesign was suggested to overcome the deficiency.

6. Radiation effects test programs were designed to test modified components and systems as well as to obtain materials data for components critical to the mission whenever sufficient information was not available.

A review of stages S-II and S-IVB drawings and specifications indicated that 33 different radiation sensitive materials were employed in over 100 types of applications. Recommended radiation tolerances were established for each material application on the basis of previous radiation effects tests performed at General Dynamics and other test facilities. Table 1, which presents the recommended radiation tolerances for Buna N and the criteria employed in establishing these limits, is typical of data resulting from this analysis. In this example, the recommended limits are conservative. A high confidence level is required for the mission, and component designers must be alerted to potential problems which might result from indiscriminate usage or failure to adequately specify materials. This conservatism results from:

1. Basing recommended limits on radiation damage to the least radiation stable chemical formulation of the particular class or type of material.

2. Criteria established for mechanical properties limits. These limits correspond to radiation exposures beyond which the degradation might compromise the functional performance of the material as used.

3. Not taking advantage of improved performance which might result from operating in the space environment where oxygen is excluded unless adequate test data are available from tests conducted in a vacuum.

*NERVA Reference Data (Full-Flow) Engine, Aerojet Nuclear Systems Company Report S130-CP-090290-F1-PREL, April 1970.

Table 1

RECOMMENDED RADIATION TOLERANCES FOR BUNA N

Application	Recommended Tolerance ergs/gm(C)	Basis for Recommendation
Hoses	1×10^8	Hose Tests
Gaskets and Seals	1×10^9	25% Decrease in Elongation
Sealants	8×10^9	Absolute Elongation > 30%
Packing	1×10^{10}	Physical Deterioration
Grommets	1×10^{10}	

Material applications were arranged into four classes according to their recommended limits. Figure 2 shows the unattenuated full-flow engine gamma dose rates as well as the regions in which each class of material applications may be safely employed, assuming a 10-hr engine operation. As illustrated in Figure 2, components for a specific subsystem can be distributed from one end of the vehicle to the other, thus permitting use of materials from each class.

Table 2 summarizes the stage S-II and S-IVB systems investigated; however, it should be noted that electrical and/or electronic components were only evaluated if they were an integral part of a mechanical component, e.g., a solenoid within the actuator of a valve would be analyzed, but switching relays would not be examined.

The principles of radiation hardening can be illustrated with the 17-in. rotary shutoff valve (P/N 138025A) designed by the Whitaker Corporation for potential application as the LH_2 tank shutoff valve. The valve, which was initially designed as the LOX valve for stage S-1C of the Saturn V, was radiation hardened by the Whitaker Corporation. The modified valve assembly, which is comprised of three major subassemblies (the actuator and the upstream and downstream shell assemblies), is a spring-opened, pneumatically closed, spherical rotary shutoff valve intended for LH_2 service in a radiation field. The

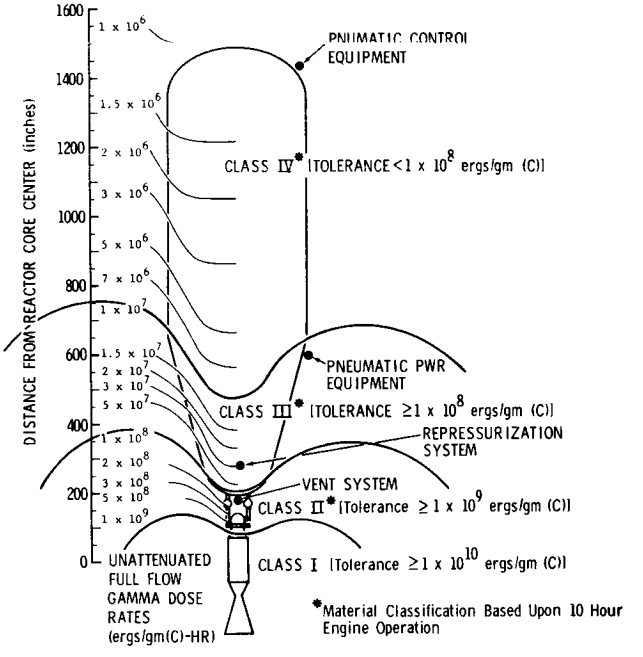

Figure 2 ASSUMED LOCATIONS OF PRESSURIZATION SYSTEM COMPONENTS

Table 2 SYSTEMS ANALYZED

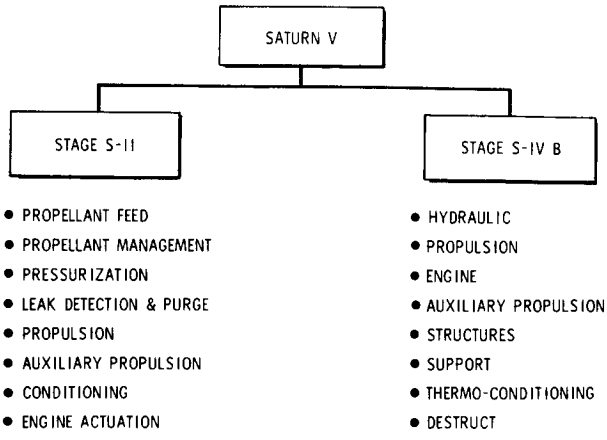

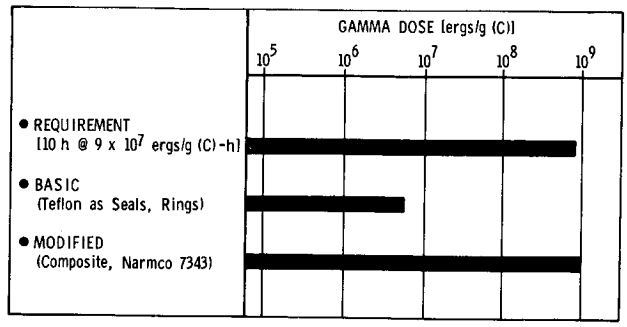

Figure 3 RADIATION TOLERANCE OF 17-INCH VALVE

valve, which has a nominal line size of 17 inches, would be flange-mounted between the LH_2 tank and the suction side of each engine turbo pump on the NRV where it would be subjected to an integrated exposure of approximately 8 x 10^8 ergs/gm(C) over a vehicle life requiring 10 hours of engine operation.

Radiation hardening of the valve for operation in the LH_2 environment was achieved primarily by replacement of the radiation sensitive materials Teflon and Rulon (reinforced PTFE). Replacement materials were (1) Kynar (vinylidene fluoride resin), (2) a composite seal of Kynar, glass, and TFE Teflon fibers, and (3) a polyurethane elastomer (NARMCO 7343). As shown in Figure 3, the valve assembly has been radiation hardened by material substitution such that its recommended radiation tolerance has been increased from 7×10^6, as limited by Teflon TFE, to 1×10^9 ergs/gm(C), which is slightly higher than the predicted exposure of 8×10^8 ergs/gm(C). The modified valve assembly is scheduled for testing later this year in a nuclear radiation environment with LH_2 flow, using the Ground Test Reactor (GTR) at the Fort Worth operation of the Convair Aerospace Division of General Dynamics.

In the radiation hardening analysis of S-II and S-IVB components, radiation sensitive material applications were identified and classified into two categories: critical and non-critical. In a critical application the mission would be compromised if the material properties degraded below the requirements of the particular application. If material substitution increases the recommended radiation tolerance to a value in excess of the predicted environment, it was recommended; otherwise, minor design modifications were suggested. The results of these analyses are typified by the data presented in Table 3.

SUMMARY

The results of the analysis of the S-II and S-IVB components, although incomplete, indicate that many Saturn V components and subsystems, e.g., pumps, valves, etc., can be radiation hardened to meet NRV requirements by material substitution and minor design modifications. Results of these analyses include: (1) recommended radiation tolerance limits for over 100 material applications, (2) design data which describes the components of each system which can be employed on the NRV and the modifications necessary to radiation harden other components, (3) presentation of radiation hardening examples of systems which will provide guidance to component designers, and (4) designing radiation effects tests to supply data for selecting materials with confidence.

Table 3 RADIATION HARDENING SUMMARY

COMPONENT	APPLICATION	MATERIAL	CRIT. APPLIC.	GAMMA ENVIRONMENT [ergs/gm (C)]		RECOMMENDATION
				PREDICTED	RECOMMENDED	
HOSE ASSEMBLY	HOSE	TEFLON TFE	YES	1×10^9	3×10^6	WELD METAL TUBING AND ELIMINATE SEALS
	SEAL	BUNA N	YES	1×10^9	1×10^9	
VALVE ASSEMBLY	SEAL	TEFLON FEP	YES	1.5×10^9	7×10^8	REPLACE WITH KYNAR
	SEAL	KEL-F	NO		1×10^9	
	SLEEVE	TEFLON TFE	NO		1×10^8	
	GROMMET	TEFLON FEP	NO		7×10^8	
	ELEC. INSULATION	SILICONE RUBBER	YES	1.5×10^9	1×10^9	REPLACE WITH MYLAR

THERMODYNAMIC AND TRANSPORT PROPERTIES OF FROZEN AND REACTING pH_2-oH_2 MIXTURES

H. G. Carter and R. E. Bullock
General Dynamics Corporation
Fort Worth, Texas

Abstract

Application of experimental state data and spectroscopic term values shows that the thermodynamic and transport properties of reacting pH_2-oH_2 mixtures are considerably different than those of chemically frozen pH_2 at temperatures below 300°R. Such differences will be significant from the standpoint of nuclear rocket design if it turns out that para- to ortho-hydrogen conversion can be catalyzed by radiation in the cold dense phase. Calculated H-S data also show that radiation-induced pH_2-oH_2 equilibration at constant enthalpy can produce a temperature drop of at least 28°R, corresponding to an ideal shaft work loss of 15% or more for a turbine operating downstream from the point of conversion. Aside from differences in thermodynamic and transport properties, frozen pH_2-oH_2 mixtures may differ from pure pH_2 on a purely hydrodynamical basis.

Significance of Possible Para-Orthohydrogen Conversion in Nuclear Rockets

Hydrogen is generally a mixture of two distinct H_2 components. A molecule of the component called "orthohydrogen" may assume quantized rotational energies that are not accessible to the component called "parahydrogen," and vice versa. The resulting disparities in energy-level populations at a given temperature imply differences in the thermodynamic and transport properties of the two types of hydrogen. Thus, for example, the enthalpies and thermal conductivities of pH_2-oH_2 mixtures differ appreciably from those of pure parahydrogen in the 36°R-500°R range, not only in absolute magnitude but also in temperature dependence. Aside from thermodynamic and transport properties, para- and orthohydrogen may differ on a purely hydrodynamical basis. The latter possibility, which has been given little attention, derives from the fact that the differences in accessible rotational energies for the two types of molecule are associated with differences in angular momenta.

The liquid hydrogen that is stored for use in nuclear rocket propulsion is usually over 99% pH_2. However, the high-temperature hydrogen gas that emerges from the nozzle of the nuclear rocket is invariably a mixture consisting of 75% oH_2 and 25% pH_2. This change in proportions results from the facts that (1) certain chemical or magnetic

reactions can convert parahydrogen to orthohydrogen when sufficient energy is available, and (2) in the presence of a suitable conversion catalyst, hydrogen tends to a pH_2/oH_2 ratio that is determined by the temperature. Catalysts which convert parahydrogen to its equilibrium proportions are available in the reactor core (in the form of H-atoms from thermal dissociation), if not elsewhere. When catalysts are present in large enough quantities that a shift in temperature is accompanied, practically instantaneously, by a shift in pH_2/oH_2 ratio to a value corresponding to the new temperature, the para-orthohydrogen mixture is called "reacting" or "equilibrating." When no such catalysts are available, the pH_2/oH_2 ratio is not affected by a temperature change, and the mixture is called "frozen." In the temperature range from $60^{\circ}R$ to $300^{\circ}R$ the specific heats of a given nominal pH_2/oH_2 mixture differ radically according to whether the hydrogen is frozen or reacting.

In nuclear rocket design, a question arises as to what type of hydrogen should be assumed to exist in the relatively cold regions between the propellant tank and the core inlet. If the hydrogen is chemically frozen throughout this region, then it obviously remains in almost pure pH_2 form, and thermodynamic and heat transfer calculations can be based on parahydrogen properties. If, on the other hand, the flowing hydrogen is catalysed by radiation or by paramagnetic surfaces, then the hydrogen may be chemically reacting over at least part of the region below the reactor core, and pure parahydrogen properties may not apply. From the standpoint of an overall design study, the effect of catalytic conversion is not limited to the values of thermodynamic and transport properties of hydrogen at a prescribed temperature and pressure. The sudden equilibration of hydrogen due to catalysis at a certain point in the flow-path can reduce the temperature by as much as $40^{\circ}R$, through a thermochemical process that is analogous to the cooling of paramagnetic salts in a decreasing magnetic field. Such "conversion-cooling" can reduce the available energy for a turbine operation or alter the dimensions of various orifices for an optimum design.

Whether hydrogen conversion in the subcore region is of design significance depends on three questions. These are: (1) does an effective mechanism for conversion actually exist in relatively cold hydrogen subject to irradiation and possible encounters with paramagnetic sites, and how much conversion can it produce? (2) What are the quantitative thermodynamic and transport properties of frozen and reacting pH_2/oH_2 mixtures? (3) What is the overall effect of conversion on a specific design? In regard to the first question, it will only be noted that data obtained during practical tests indicate that relatively cold parahydrogen can be converted by radiation, and that reasonable chemical models have been advanced to explain this effect. The third question is in the province of rocket designers. The results given here pertain only to the second question, viz., information on the basic properties of pH_2-oH_2 mixtures.

Equilibrium Orthohydrogen Fraction

The equilibrium orthohydrogen fraction at a given temperature is independent of pressure, at least for pressures in the range of nuclear rocket application and lower. For temperatures below $500^{\circ}K$ ($900^{\circ}R$) the equilibrium orthohydrogen fraction, ω_e, is given to an accuracy of 0.01% by

$$\omega_e = \sum_{j=1}^{7\,(\text{odd})} g_j\, e^{-\theta_j/T} \Big/ \sum_{j=0}^{8} g_j\, e^{-\theta_j/T} \qquad (1)$$

where j is the number of a rotational level. Even and odd values of j correspond to pH_2 and oH_2 rotational levels, respectively. The parameter θ_j represents the molecular rotational energy of a particular level divided by Boltzmann's constant. Using the spectroscopic term values cited in the definitive work of Woolley, et al. at NBS (Ref. 1), it is found that a suitable approximation is

$$\theta_j(^{\circ}K) = 85.3757\, j(j+1) - 0.065769\, j^2(j+1)^2 + 0.0000712\, j^3(j+1)^3 \qquad (2)$$

for values of j less than or equal to 8. This prescription ignores the role of vibrational excitation, which is negligible below $500^{\circ}K$. The parameter g_j in Equation (1) is a statistical weight given by

$$g_j = 3(2j+1), \quad j \text{ odd}$$
$$= (2j+1), \quad j \text{ even} \qquad (3)$$

At temperatures above $T = 500^{\circ}K$, the equilibrium orthohydrogen fraction is $\omega_e = 0.750$.

Evaluation of Equation (1) yields the dependence of equilibrium orthohydrogen fraction on temperature shown in Figure 1. It is seen that the temperature range over which ω_e varies significantly is $30^{\circ}K$ to $220^{\circ}K$, or $54^{\circ}R$ to $396^{\circ}R$.

Calculation of Enthalpy and Entropy

The calculation of enthalpies and entropies is obviated by expressing the results as ideal gas values, augmented by "real-gas" terms that arise from intermolecular reactions. The latter are obtained from an equation of state, which is usually written in the form of a temperature and density dependent for the compressibility factor $Z = pv/RT$. In obtaining the present results it has been assumed that the equation of state

$$Z = Z(T,\rho) \qquad (4)$$

is the same for either para- or ortho-hydrogen. The state equation used is that given by Wooley et al. for normal hydrogen (75% ortho). This state equation, which was based on rather old normal hydrogen data, has been compared with data reported more recently by Michels et al. (Ref. 2). Typical comparisons are shown in Figure 2. An analysis of the difference between the old and new data, which is taken as a measure of the present uncertainty in the state equation for normal hydrogen, shows that the corresponding uncertainties in enthalpy and energy of normal hydrogen are respectively only about 1 Btu/lb and 0.002 Btu/lb $^{\circ}R$. Furthermore, recent data by Hermans et al. (Ref. 3), on the difference between the second virial coefficients of para- and normal hydrogen, indicate that the use of a normal hydrogen state equation on pH_2-oH_2 mixtures will not lead to an error greater than that corresponding to the present uncertainty in the normal-hydrogen state data.

The real-gas enthalpies and entropies of a number of mixtures have been calculated using tabular data given by Woolley et al. to obtain the integrals involving Z. Ideal-gas values of the enthalpy and entropy for both frozen and reacting pH_2-oH_2 mixtures have been obtained from the θ_j and g_j defined in Equations (2) and (3).

Figure 1

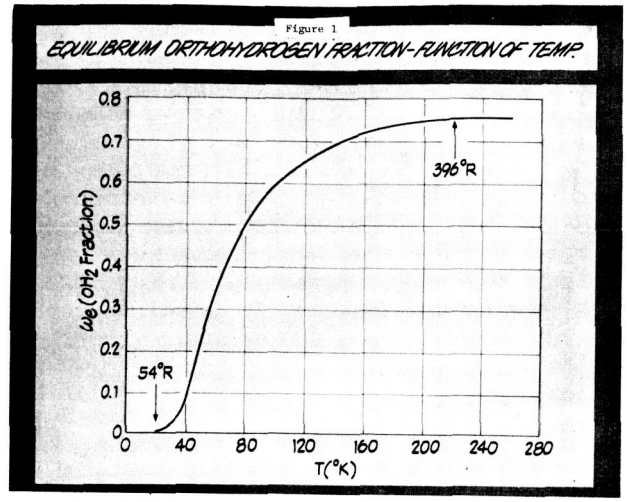

Figure 2

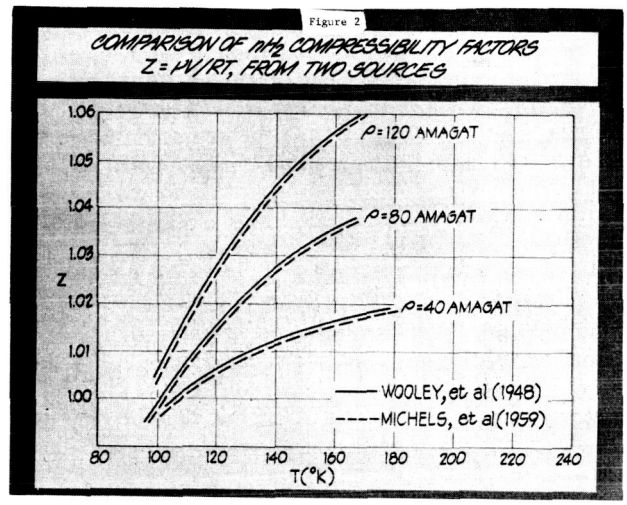

The enthalpies of frozen pH_2, frozen oH_2 and equilibrating hydrogen at 0 and 800 psi are shown in Figure 3. The corresponding specific heats, obtained by differentiation of H with respect to temperature, are shown in Figure 4. It is seen that EH_2 behaves as a mixture with an intermediate specific heat only above $100^{\circ}K$; at lower temperatures the specific heat of reacting hydrogen is appreciably higher than that of either frozen component. By contrast, the specific heat of a frozen mixture is obtained by simply calculating the average of the frozen pH_2 and oH_2 values, weighted by their respective concentrations in the mixture.

Figure 3

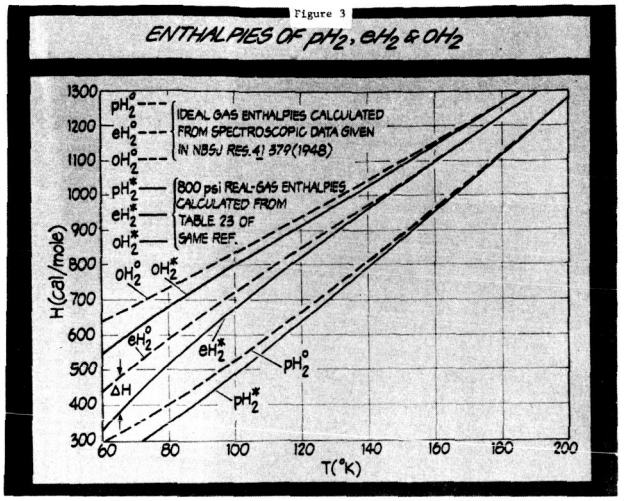

Figure 4

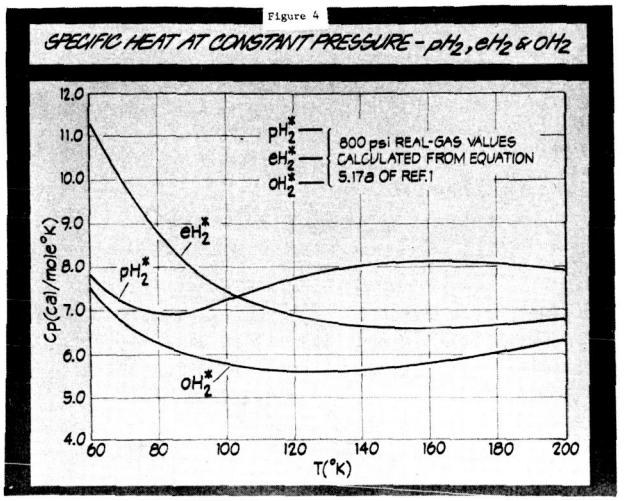

Figure 5

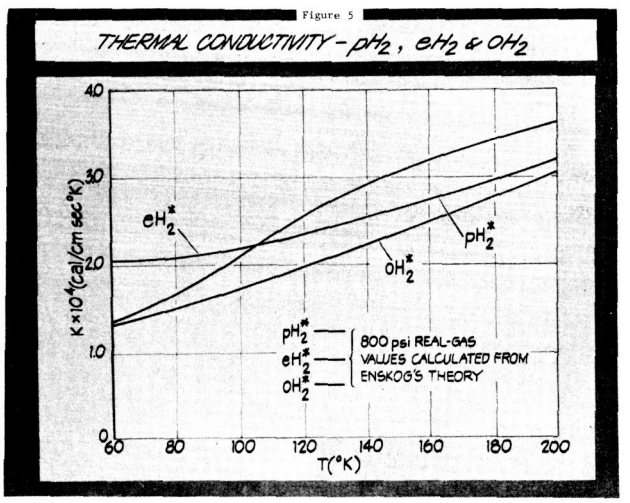

Transport Properties

The viscosity of a pH_2-oH_2 mixture is determined by transport of momentum alone, and is therefore independent of the pH_2-oH_2 composition insofar as pH_2 and oH_2 conform to the same equation of state. On the other hand, the thermal conductivity of an ideal-gas mixture of para- and ortho-hydrogen is related to the viscosity, η, by Eucken's relation

$$K_o = (9\gamma-5)C_v^o\ \eta/(4M) \qquad (5)$$

where C_v^o is the specific heat of the ideal gas, γ is the ratio of specific heats, and M is the molecular weight. The real-gas thermal conductivity K is related to K_o by the following Enskog relation:

$$K/K_o = 1 + 0.575E + 0.5017E^2 - 0.204E^3 \qquad (6)$$

where E is given by

$$E = Z - 1 + T\left(\frac{\partial Z}{\partial T}\right)_\rho \qquad (7)$$

Figure 5 shows the thermal conductivity for pH_2, oH_2 and a reacting mixture at 0 psi and 800 psi. As in the case of specific heat, the thermal conductivity depends strongly on whether a given mixture is frozen or reacting.

Cooling Due to Conversion

If a chemically frozen parahydrogen gas is suddenly exposed to a conversion-catalyst such as radiation or a paramagnetic surface, the resulting equilibration to a pH_2-oH_2 mixture is an irreversible process. Hence, the reaction cannot be isentropic even if it happens to be adiabatic. In general, the enthalpy change due to a differential conversion process is

$$dH = TdS + Vdp + \mu_1 dx_1 + \mu_2 dx_2 \qquad (8)$$

where x_1 and x_2 are the pH_2 and oH_2 mole fractions, respectively, and where μ_1 and μ_2 are the chemical potentials. In the case where no heat enters or leaves the system and the pressure is kept at a constant value, Equation (8) simplifies to

$$TdS = (\mu_1-\mu_2)dx_2 \qquad (9)$$

This increase in entropy is accompanied by a decrease in temperature, which can, for example, subsequently reduce the amount of available energy from a turbine operating between two prescribed pressures. The possible effect of such cooling is seen from the approximate H-S chart shown in Figure 6, which has been constructed from Figure 3 and calculated entropy data. When parahydrogen at 297°R is converted to 60% oH_2 at constant enthalpy and constant pressure, the temperature decreases from 297°R to 269°R. If conversion had not occurred, the energy available to a turbine operating between 975 psi and 675 psi would be 111 Btu/lb. However, it is seen that 60% conversion would reduce the available energy to 98 Btu/lb. The magnitudes of such losses depend upon the inlet enthalpy and, of course, the amount of conversion that is assumed. Figure 7 shows the percent loss in ideal energy for an assumed conversion of 60% as a function of inlet enthalpy.

Possible Hydrodynamic Differences Between pH_2 and oH_2

The difference between the thermodynamic and transport properties of parahydrogen and those of orthohydrogen are completely specified by the rotational energy levels accessible to each, at least insofar as the two modifications conform to the same equation of state. However, from the hydrodynamical standpoint, another type of difference might be worth exploring.

Parahydrogen molecules may take intrinsic angular momenta of 0, $2\hbar$, $4\hbar$, etc.; whereas orthohydrogen molecules may take intrinsic angular momenta of $\hbar$, $3\hbar$, $5\hbar$, etc. At temperatures below 180°R, over 97% of all parahydrogen molecules are in a state of zero angular momentum. For practical purposes one may say that, at these temperatures, parahydrogen is a fluid composed of molecules with no intrinsic angular momentum, whereas orthohydrogen is a fluid whose molecules have an intrinsic angular momentum of $\hbar$. Hence, on a rigorous hydrodynamical basis (Ref. 4), the equations for energy and momentum conservation, which are sufficient to describe the behavior of a parahydrogen fluid, must be augmented by an equation of angular momentum in the case of orthohydrogen. In the language of transport theory, collisions between orthohydrogen molecules involve an extra summational invarient. It is therefore conceivable that the details of such phenomena as the transition from laminar to turbulent flow might differ in the two types of fluids, independently of any effects associated with thermodynamic and transport properties.

Figure 6

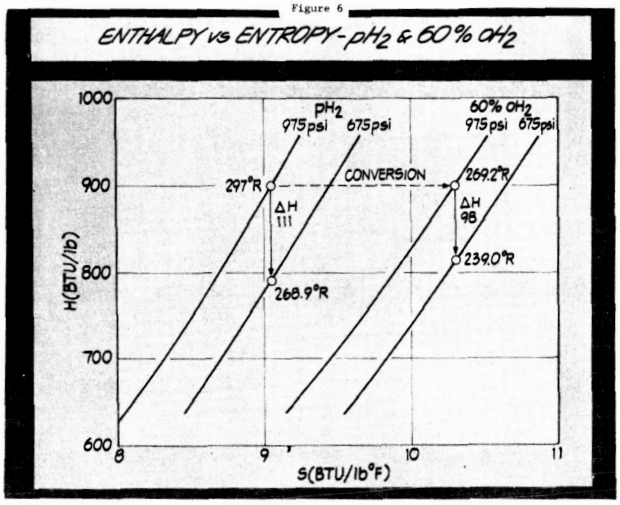

Figure 7

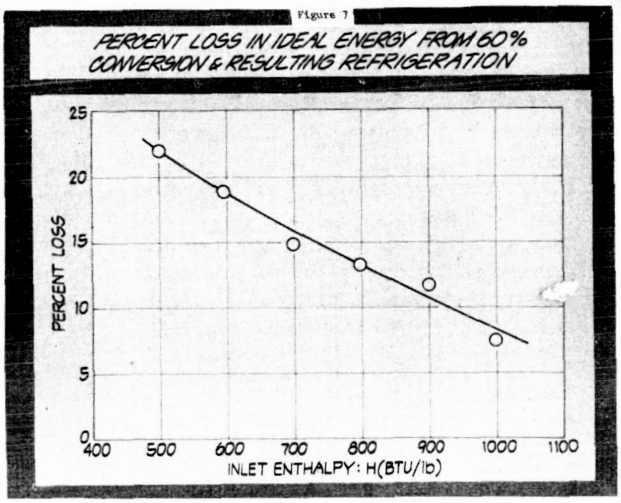

References

1. Woolley, H. W., Scott, R. B., and Brickwedde, F. G., NBS Research Paper RP1932, Volume 41, November 1948, pp. 379-475.

2. Michels, A., et al., Physica 25, 1959, pp. 25-42.

3. Hermans, L. J. F., et al., Physica 31, 1965, pp. 1567-1574.

4. Chapman, S., and Cowling, T. G., The Mathematical Theory of Non-Uniform Gases (Cambridge), 1953, p. 202.

HARDENING ELECTRONIC DEVICES AGAINST VERY HIGH TOTAL DOSE RADIATION ENVIRONMENTS

B. Buchanan, W. Shedd, S. Roosild, and R. Dolan

Air Force Cambridge Research Laboratories
Air Force Systems Command
Bedford, Massachusetts

The possibilities and limitations of hardening silicon semiconductor devices to the high neutron and gamma radiation levels (greater than 10^{16} neutrons/cm^2 (1 Mev eq.) and greater than 10^8 rads (Si) required for the NERVA nuclear engine development are discussed. A comparison is made of the high dose neutron and gamma hardening potential of bipolar, metal insulator semiconductor (MIS), and junction field effect transistors (JFET). Experimental data is presented on device degradation for the high neutron and gamma doses. Previous data and comparisons[1,2,3] indicate that the JFET is much more immune to the combined neutron displacement and gamma ionizing effects than other transistor types. Presently, hardened JFET's degrade about 50% at 10^{16} neutrons/cm^2. Theoretically they can be improved, but the resulting hardened JFET's have low breakdown voltages (less than 20 volts). Experimental evidence (5 volt threshold shift at 10^8 rads) is also presented, which indicates that p channel MOS devices, made by Hughes Aircraft may be able to meet the requirements. Electrical characteristics compromises caused by device hardening and the ability to satisfy requirements on a practical reliable basis are discussed.

Introduction: If electronic components can be made to perform their function after total doses of 10^8 rads gamma and 10^{16} neutrons/cm^2, then many shielding and cabling problems would be eliminated in electronic control systems for nuclear engines, such as the NERVA. Even though the original work more than 10 years ago on radiation effects on electronic components was directed toward radiation environments near a nuclear reactor, relatively little effort has been specifically directed toward hardening transistors to these high total dose levels. The lack of apparent effort has been partly due to great difficulty in hardening the bipolar transistor (which has been by far the most used transistor type) to these high levels.

The three principal categories of radiation damage near a reactor are displacement, ionization, and heating. (It is assumed here that the heating is accounted for in the temperature specifications). The main cause of displacement damage is fast neutrons, and the main effects which permanently degrade transistor operation are minority carrier lifetime reduction and carrier removal. A second-order effect is mobility reduction. The main cause of ionization damage is gamma radiation which results in permanent effects due to charge build-up in the oxide and photo-current generation. The extent of the transistor degradation due to displacement and ionization damage depends strongly on the transistor types.

Transistors can be classified into 2 broad types, bipolar and unipolar. The unipolar is, however, usually referred to as a field effect transistor (FET), of which there are two basic types - the Junction FET (JFET) and the Insulated Gate FET (IGFET). The IGFET is often referred to generally as an MIS (metal insulator semiconductor) and specifically as an MOS, where the insulator is an oxide. The original reason for the designation of the two classes of transistors was that the unipolar operation depends on only one carrier (majority) and the bipolar operation depends on both minority and majority carriers. The bipolar is then seriously degraded by minority carrier lifetime reduction, whereas the unipolar or field effect transistor is not. One of the two principal classes of field effect transistors, the junction field effect transistor (JFET), depends strongly on carrier removal. However, the insulated gate (MIS) is little affected by either carrier removal or lifetime changes, but is very sensitive to permanent charge build-up in the insulator caused by ionizing radiation. The bipolar and JFET suffer only minor effects due to charge build-up in the oxide passivation when compared to the MOS. This is because the active region of the MOS is adjacent to or part of the oxide layer.

Since the electrical changes in the transistor operating characteristics induced by radiation damage to materials properties vary considerably with the transistor type, it is necessary to consider "hardening" each device separately. Electronic device hardening is essentially the science of designing the device to minimize the functional dependence of the device's electrical characteristics on known radiation sensitive materials properties.

JFET Hardening: If the JFET is operated in the region of maximum transconductance, g_m, the g_m is given[4] by:

$$g_m = \frac{2Nq\mu a}{L}$$

where

- N = majority carrier concentration in the channel, either n or p
- q = the electronic charge
- μ = the mobility
- a = the channel width
- L = the channel length.

It should be noted that if the JFET is operated in a region other than for maximum g_m, the g_m has a weaker dependence on N than the linear one given by this expression. It has been shown[2,5] that the normalized neutron induced transconductance degradation for silicon JFET's is given by:

$$\frac{g_{m\Phi}}{g_{mo}} = \exp\left(-\frac{\Phi}{K}\right) = \frac{N_\Phi}{N_o}$$

where

$K = K_p = 398\ P_o^{.77}$ for a p type channel and

$K = K_n = 93\ N_o^{.82}$ for an n type channel.

Where N_o and P_o are carrier concentrations before irradiation, g_{mo}, $g_{m\Phi}$ are the maximum transconductances before and after irradiation. These relations were derived by: 1) using the above standard JFET parameter relations, 2) assuming that carrier removal in the JFET channel is the only degradation mechanism, 3) using Stein's[6,7] initial carrier removal data and assuming the exponential law, $N = N_o \exp\left(-\frac{\Phi}{K}\right)$. The theoretical g_m degradation is plotted in Fig. 1 for both n and p type channels. Since the n channel devices both theoretically and actually show less degradation and n type material has a higher mobility resulting in initially higher g_m, the results of tests on n channel JFET designs only will be reported in this paper.

The method of increasing the neutron radiation tolerance of JFET's is clearly then to heavily dope the channel. This cannot be done without some compromise, since the pinch-off voltage of the JFET must be less than the avalanche breakdown voltage and the pinch-off voltage increases with channel doping while the breakdown voltage decreases. It is fortuitous, however, that satisfying this hardening requirement actually increases the JFET gain.

The g_m and source to drain current degradation are shown in Fig. 2. Typical on resistance after $5X10^{15}$ neutrons/cm^2 is 150 ohms and after 10^{16} neutrons/cm^2 is 250 ohms. Typical leakage currents are shown in Table 1.

TABLE 1

TYPICAL LEAKAGE CURRENT CHANGES FOR JFET'S

I_{DSS} RANGE 20-48 ma

	GAMMA DOSE IN RADS			
	0	$3.7X10^6$	$2.7X10^7$	$1.6X10^8$
GATE DRAIN LEAKAGE AT 5V	$2.3X10^{-12}$	$3.4X10^{-11}$	$2.6X10^{-10}$	$2.7X10^{-10}$
	$1.4X10^{-11}$	$5.1X10^{-11}$	$1.9X10^{-10}$	$2.1X10^{-10}$
RAD 201	$2.1X10^{-12}$	$3.2X10^{-11}$	$2.4X10^{-10}$	$3.1X10^{-10}$

	NEUTRON DOSE AND GAMMA DOSE		
	0	$5X10^{15}$ n/cm^2	10^{16} n/cm^2
GATE DRAIN LEAKAGE		$1.3X10^8$ rads	$2.6X10^8$ rads
AT 10V	$3.3X10^{-12}$	$1.1X10^{-9}$	$2.6X10^{-9}$
RAD 201	$9X10^{-12}$	$1.6X10^{-9}$	$3.5X10^{-9}$

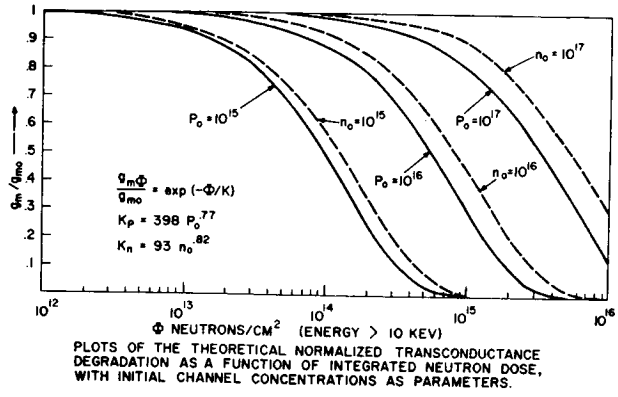

PLOTS OF THE THEORETICAL NORMALIZED TRANSCONDUCTANCE DEGRADATION AS A FUNCTION OF INTEGRATED NEUTRON DOSE, WITH INITIAL CHANNEL CONCENTRATIONS AS PARAMETERS.

AFCRL PHOTO 129-377

Figure 1

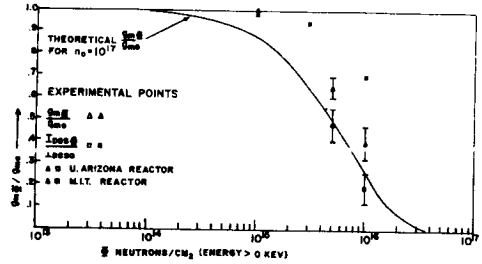

PLOTS OF THEORETICAL AND EXPERIMENTAL NEUTRON INDUCED g_m AND I_{DSS} DEGRADATIONS

Figure 2

The electrical characteristic penalty for hardening JFET's is then the resulting low breakdown voltage. Even though some increase above the bulk breakdown voltage can be achieved by grading the doping profile near the surface,[8] a breakdown voltage requirement above 40 volts cannot be satisfied simultaneously with 10^{16} neutrons/cm^2. The ionizing radiation even at the very high levels has negligible effect on the JFET.

Simplified Bipolar Hardening Relations: Using the charge control approach a simplified expression for β can be shown[9] to be

$$\beta = \frac{\tau}{t_b}$$

where τ is the minority carrier lifetime in the base and t_b is the base transit time. The base transit time is proportional to the square of the basewidth. The usual relation between the lifetime before and after a dose of Φn/cm^2 is assumed:

$$\frac{1}{\tau} = \frac{1}{\tau_o} + \frac{\Phi}{K\tau}$$

where τ_o is the lifetime before irradiation and K_τ is the lifetime damage constant. From these relations we obtain

$$\frac{\beta_\Phi}{\beta_o} = \frac{1}{1 + \Phi\tau_o/K_\tau}$$

where β_Φ and β_o are respectively the gain before and after irradiation. This is, of course, a greatly simplified expression for neutron induced β degradation, since other parameters, such as emitter efficiency are neglected. A good indication of neutron induced β degradation is given by this expression, however, which clearly points out the importance of "killing" lifetime to harden against permanent gain degradation (see Fig. 3). A plot of the simplified theoretical bipolar hardness and actual experimental points are compared to the JFET theoretical and actual hardness in Fig. 4. It should be noted that the low injection value of K_τ is used, which is compensated for in the comparison by using the high estimate for carrier removal rate. In addition to neutron damage, significant degradation occurs for ionizing radiation, especially for μ amp collector currents as is clearly shown in Fig. 5.

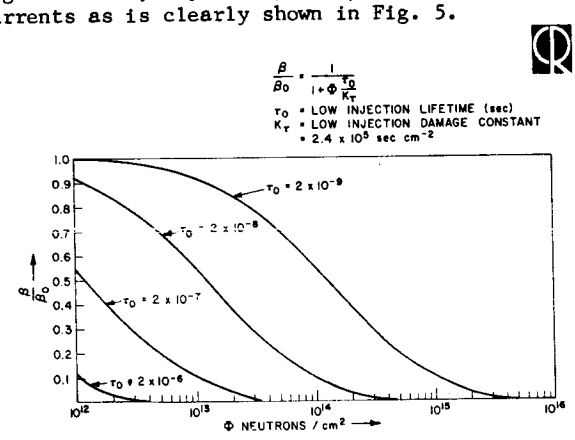

Figure 3
Plot of fractional beta degredation as a function of neutron dose.

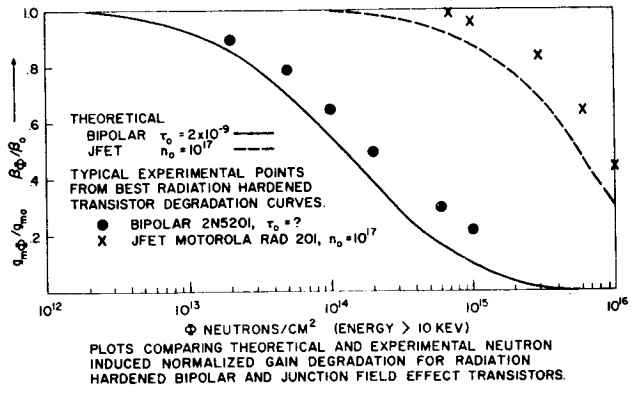

PLOTS COMPARING THEORETICAL AND EXPERIMENTAL NEUTRON INDUCED NORMALIZED GAIN DEGRADATION FOR RADIATION HARDENED BIPOLAR AND JUNCTION FIELD EFFECT TRANSISTORS.

AFCRL PHOTO 129-388

Figure 4

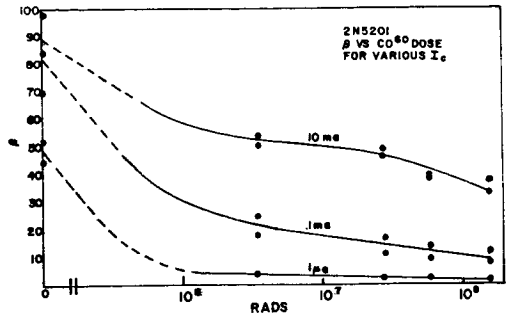

Figure 5

MIS Hardening: The effects of ionizing radiation on the transfer characteristic of a typical MOS transistor is illustrated in Fig. 6. The entire characteristic curve is seen to shift with integrated dose. The point on the curve at which the drain current I_d equals zero is referred to the "pinch off", "turn on" or "threshold" voltage V_T. Henceforth, unless otherwise noted, when reference is made to a shift in V_T, it is also meant that every point on the curve is shifted by the same amount as the threshold voltage shift. This is not true in all cases since the curve is sometimes shifted and distorted, but it is a good approximation for a simplified discussion. There is general agreement[10,11] as to the basic mechanisms that cause the threshold shifts in an ionizing radiation environment: a) the build-up of a positive space charge within the oxide by the occupation of pre-existing charge-trapping sites in the oxide and b) the creation of so called "fast surface states" at the oxide-silicon interface. Mechanism (a) seems to occur to some extent in all insulators and to be a strong feature of amorphous insulators of very low conductivity. Mechanism (b) does not seem to occur in all MIS systems. The charge build-up mechanism causes the largest threshold shifts in most cases and is much better understood than the fast surface states. The magnitude of a radiation induced threshold shift is strongly dependent on the processing of the MIS devices. The magnitude of a radiation induced threshold shift is usually an even stronger function of the bias on the MOS during irradiation. Most commercial MOS transistors show threshold shifts of 40 or more volts with a bombardment bias of less than 10 volts and a bombardment dose of approximately 10^6 rads. In addition to the regular (even though statistically varying) effects mentioned above other anomalous radiation effects, including room temperature instabilities have been reported.[10,12]

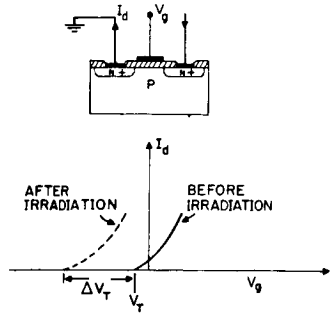

EFFECTS OF IONIZING RADIATION ON MOS CHARACTERISTIC CURVE

Figure 6

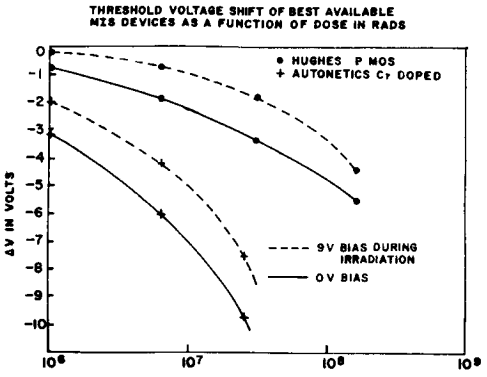

Figure 7

Since the dominant mechanism leading to threshold shifts in MOS devices is the positive charge-trapping sites in the oxide, obvious approaches to harden MIS devices are (1) either attempt to eliminate these traps in the SiO_2 or (2) attempt to find an insulator which is not afflicted by this problem. Considerable research has been devoted to approach (1). By adding various dopants to the oxide, dopants have been found which considerably reduce the threshold shifts for irradiations performed with positive gate voltages, but greatly increases the threshold shifts for irradiations with negative gate voltages. Numerous insulators have been tried to replace the silicon dioxide, which is the oxide (insulator) used in commercial MOS transistors. One such insulator, silicon nitride, showed great promise for some time of solving the problem. The nitride silicon interface was found to be much more resistant to radiation induced threshold shifts. However, offsetting this increased radiation tolerance several disadvantages were found.[11] The most notable of these is threshold shifts (instabilities) in MNS (Metal Nitride Silicon) transistors caused by a high voltage. This, combined with higher values of interface charge, makes it impractical to use a nitride-silicon interface in high field regions such as the gate of an MIS transistor.

Recently Al_2O_3 has been investigated as a replacement for SiO_2 in MIS devices. We have tested two of the RCA Al_2O_3 devices to 10^6 rads cobalt 60 gamma and the threshold voltage shifted less than 2 volts after 10^6 rads. We do not have data for higher levels because the devices developed gate to source shorts.

Results on ionizing radiation tests up to 10^8 rads are shown in Fig. 7 for new experimental radiation hardened MOS devices. The P-MOS (p channel MOS) made by Hughes appears to be the hardest MIS device at 10^8 rads. The scientific reasons for the hardness of these p-MOS devices are not clearly understood.

Even though it is generally believed that neutrons do not have an appreciable effect to the electrical characteristics of MIS devices, the fact that neutrons may have an effect should not be overlooked. Very little meaningful data exists on the radiation effects of low neutron doses on MIS devices and it is virtually non-existant at 10^{16} neutrons/cm^2. One known effect of neutrons on MIS devices is threshold shifts due to neutron induced positive charge in the oxide. This effect is due to the ionizing capability of neutrons, which is approximately 1 rad = 10^{10} neutrons/cm^2. This would give 10^6 rads at 10^{16} neutrons/cm^2, which can be neglected in comparison to the 10^8 rads from gamma for the NERVA requirement. At least two other neutron effects are possible, threshold shifts due to carrier removal and electrical characteristic changes due to neutron induced fast surface states at the interface. The reason why a threshold shift due to carrier removal, which is simply an increase in the substrate resistivity, has not been observed is probably because the substrate resistivity, ρ, of the devices tested has been too high for the effect to be noticeable. Carrier removal will have a significant effect on the threshold voltage only if the threshold voltage is strongly dependent on ρ. Brotherton[14] has determined the curve for threshold voltage V_T as a function of ρ for an n channel MOS. This curve shows that V_T is approximately independent of ρ, if $\rho > 10$ Ω-cm. Since the known effect of fast neutrons on the bulk silicon is to increase the resistivity, even very high neutron doses would therefore not be expected to cause a significant threshold shift, if the initial resistivity is greater than 10 Ω-cm. Most n channel devices are made with $\rho > 10$ Ω-cm, which explains why threshold shifts due to carrier removal have not been observed in n channel MOS's. If $\rho \ll 10$ Ω-cm and carrier removal is the only effect present, a considerable threshold shift should occur for neutron doses $> 10^{15}$ neutrons/cm^2. This fact is illustrated in the following example:

If $\rho = 1$ Ω-cm, then according to Brotherton's curve $V_T \approx 0$. One ohm-cm roughly corresponds to a p-type substrate initial doping concentration of $2 \times 10^{16} = p_o$. The doping concentration p after a neutron dose of Φ neutrons/cm^2 is given by[2]

$p = p_o \exp\left(-\frac{\Phi}{398\ p_o - 77}\right)$. Therefore, if $\Phi = 3 \times 10^{15}$ neutrons/cm^2, $p \approx 2 \times 10^{15}$ which roughly corresponds to a resistivity of 10 Ω-cm. According to Brotherton's curve the resistivity change from 1 to 10 Ω-cm would cause V_T to shift roughly from 0 to -4 volts. Similar arguments hold for p channel devices. Fortunately, if a p channel device is affected by carrier removal, the resulting threshold shifts should be in the opposite direction to ionizing induced threshold shifts.

Hardening efforts for MIS devices are then quite different from hardening efforts on bipolar and JFET devices. Whereas, bipolar and JFET hardening has stayed within the standard silicon, silicon dioxide technology, MIS hardening has involved new and different technologies. This imposes a penalty of longer term development to achieve equal reliability confidence. Other penalties which seem to be paid for MIS hardness are lack of threshold voltage control, and for MOS the use of p channel devices only.

Experimental procedure: The neutron irradiations performed to provide the data for this paper were done at the MIT nuclear reactor in the pneumatic tube facility. The temperature in this facility is approximately 42°C. The thermal neutron flux is 2.2×10^{13} n/cm^2 sec, the gamma dose rate is 1.3×10^8 R/hr and the neutron flux above 10 Kev is 1.2×10^{12} n/cm^2 sec.

Cobalt gamma radiations were performed at the AFCRL cobalt cell which delivers 1.5×10^6 Rad/hour. The MOS samples were irradiated with both positive and negative gate biases. The bipolar and junction field effect transistors were irradiated without bias applied.

The transistor electrical characteristics where measured under swept D.C. conditions on a curve tracer and under pulsed D.C. conditions when necessary to avoid annealing by electrical dissipation. The MOS threshold shift data was obtained by measuring capacitance as a function of voltage to determine the threshold voltage for each device. The electrical characterization of the devices was performed both before and after each radiation exposure.

Tentative NERVA Requirement: In a private conversation with representatives of NASA and the Aerojet Corporation, NERVA requirements for a power switch and for multiplexing were given. The radiation requirement for both was a total of 3×10^{16} neutrons/cm^2 and 7×10^7 rads gamma. The power device had a 60 volt breakdown requirement which was firm and a 5 amp current capability. The temperature requirement on the power device was -250°C to 100°C, but was considered to be flexible. The multiplexer switches were to have after irradiation 300 Ω on resistance and 10^8 Ω off resistance, with an isolation resistance of 10^6 ohms. The voltage requirements were not firm, but could be in the vicinity of 5 volts. The switching current was to be in the vicinity of 1 μ amp, with a leakage current less than 100 nano amps.

Conclusions: Theoretical and experimental information indicates that the JFET devices can meet the multiplexer requirements on a reliable reproducible basis. The power device requirements cannot be met by the JFET, however, because of the 60 volt breakdown requirement. A possibility exists that the p MOS device can meet this power device requirement. It must be cautioned, however, that the hard p MOS device is still in the experimental research stage of development and more neutron data at these high levels is needed. Further, the development of a high power device poses many more serious problems than for low power devices like those tested. It appears very doubtful that bipolar transistors can be made hard enough to meet either of these requirements. In the final analysis, however, just what constitutes an acceptable degradation (and therefore the device hardness) is determined by the circuit and systems designer.

REFERENCES

1. Snow, E. H., Grove, A. S. and Fitzgerald, D. J., Proc. IEEE, pp. 1168-85 (1967).
2. Buchanan, B., Dolan, R. and Shedd, W., "Radiation Tolerance of Bipolar and Field Effect Transistors as a Function of Lifetime and Doping", Trans. AIME, Mar 1969.
3. Shedd, W., Buchanan, B. and Dolan, R., "Radiation Effects on Junction Field Effect Transistors", IEEE Trans. on Nuclear Science, Dec 1969.
4. Dacey, G. C. and Ross, I. M., "Unipolar Field Effect Transistor", Proc. IRE, pp. 970-979, Aug 1953.
5. Buchanan, B., Dolan, R. and Roosild, S., "Comparison of the Neutron Radiation Tolerance of Bipolar and Junction Field Effect Transistors", Proc. IEEE, Jul 1967.
6. Stein, H. J., Sandia Corp., Albuquerque, N. M., Rept. SC-R-64-193, 1964.
7. Stein, H. J. and Gereth, R., J. Appl. Physics, May 1968.
8. George, W., "Optimization of the Neutron Radiation Tolerance of Junction Field Effect Transistors", IEEE Trans. on Nuclear Science, pp. 81-86, Dec 1969.
9. Gregory, B. L. and Smits, F. M., IEEE Trans. Electron Devices, Vol. ED-12, pp. 254-58, 1965.
10. Holmes-Siedle, A. G., Zaininger, K. H., "The Physics of Failure of MIS Devices under Radiation", IEEE Trans. on Reliability, Mar 1969. (Note: This reference is a very good summary of the effects of radiation on MIS devices.)
11. Snow, E. H. and Fitzgerald, D. J., "Radiation Study on MOS Structures", AFCRL-68-0045, Scientific Report No. 4, Jan 1968.
12. Stanley, A. G., "Comparison of MOS and Metal-Nitride Semiconductors Insulated Gate Field Effect Transistors Under Electron Irradiation", IEEE Trans. Nuclear Science, Dec 1966.
13. Zaininger, K. H., et al, "Radiation Effects in Complementary Devices and Circuits", Interim Technical Report No. 8, Nov 1968.
14. Brotherton, S. D., "Dependence of MOS Transistor Threshold Voltage on Substrate Resistivity", Solid State Electronics, Vol. 10, pp. 611-616, 1967.

SESSION VI.2.
RADIATION TRANSPORT AND SHIELDING: BASIC PHYSICS DATA
CHAIRMAN: C. PRESKITT
GULF RADIATION TECHNOLOGY

EXPERIMENTAL NUCLEAR CROSS SECTIONS FOR SPACECRAFT SHIELD ANALYSIS*

R. W. PEELLE†

Oak Ridge National Laboratory

Oak Ridge, Tennessee 37830

Experiments have been performed to validate and to supplement the intranuclear cascade model as a method for estimating cross sections of importance to spacecraft shield design. The experimental situation is inconclusive particularly for neutron-producing reactions, but is relatively sound for reaction cross sections and for proton spectra at several hundred MeV at medium forward angles. Secondary photon contributions are imprecisely known.

INTRODUCTION

This paper tries to outline the purpose, scope, and main qualitative results of a decade of effort for our group working on nuclear cross sections relevant to spacecraft shield design. A large share of our effort went toward the invention of experimental methods which are not discussed here.

Our crewman face in space the cosmic ray sources and, for space stations, the trapped radiation belts. We must be concerned about reactions of primaries in tissue (if $[QF]_{av.} >>1$) and about interactions in tissue of secondary neutrons and gamma rays from nuclear reactions in the spacecraft's shell. For heavy primaries, attenuation in the spacecraft may markedly influence hazard levels. The radiation problem is inherent in the manned exploration of space; its severity from an engineering point of view depends on the radiation tolerances assigned by the authorities and on the thickness otherwise required for the craft's exterior structure. If nuclear rockets or nuclear auxiliary power are used, the shield design should be studied as a unit. Radiation problems will require continuing surveillance so long as manned flight is contemplated; maintaining the underlying competence will require continued development of analysis techniques.

First-order shielding calculations are made by considering only the "continuous" energy loss by charged particles, while nuclear reaction products are ignored. The ability to continue to carry out such calculations in practical geometries is important and must be maintained. As the shield structure thickens for longer missions, more primary particles traverse a large fraction of their interaction length in the shield or in the astronaut's body, and the first approximation becomes less and less satisfactory. The knowledge of differential cross sections for nuclear interactions is needed to obtain correct results. Using current analyses, about one half the biologically equivalent (rem) dose from an 80-MV flare behind 20 gm/cm^2 of aluminum arises from secondaries produced in the shield and in tissue.[1] Unfortunately, one is so far quite unsure what LET-dependent quality factors should be utilized in making such estimates.

We accept the idea that radiation penetration studies can be done better by calculation than by experiment, provided that the necessarily huge supply of cross-section information is available. In the energy regions of interest here we assume the preferred strategy will always be to depend on calculated cross sections or at least on high-class interpolations that take into account theoretical ideas. The question for the experimenter becomes: Do the available cross-section estimation methods work well enough for the space shielding problem? If not, in what directions should one seek improvement? Answering these simple questions, an effort which must be shared with shield analysts, has been difficult because of the lack of satisfactory criteria and because of the complexity of the necessary experiments.

So far, as expected a decade ago, all higher-order methods of spacecraft shield analysis are based on cross sections provided by some intranuclear cascade model. Cascade reactions are usually followed in the model by successive evaporation of fragments until only gamma radiation is allowed by the conservation rules. To date, the cascade model receives its most productive expression in the work of Bertini[2] and in the application of the resulting model cross sections to transport calculations.[3]

Clarification of the validity restrictions on this model has been the objective for our experimental work. The model is restricted to incident neutrons or protons, and offers a little help for incident alpha particles.[4] So far, it has not led to very good estimates of gamma-ray production.[5]

The model itself assumes that the reaction within a real nucleus can be replaced in the cascade or pre-equilibrium phase by a series of nucleon-nucleon interactions and, at higher energies, meson-nucleon interactions. The cascade of successive intranuclear collisions is followed by Monte Carlo using experimental free-particle nucleon-nucleon cross sections until the cascade terminates when no more nucleons can escape the model potential which holds the target nucleus together. The model is conceptually strong at energies of several hundred MeV, but as one goes below 100 MeV it is used at risk because the binding of nucleons is no longer so small compared to the incident energy, the deBroglie wave-length of the incident particle is no longer very short, and the ignored distortions of the incident "wave" by the nuclear potential might be thought to have a strong influence. Also, Coulomb effects and differences

* Research sponsored by the National Aeronautics and Space Administration under Union Carbide Corporation's contract with the U. S. Atomic Energy Commission.

† Associate authors: F. E. Bertrand, W. R. Burrus (Tennecomp Inc.), W. A. Gibson (Tennecomp Inc.), N. W. Hill, T. A. Love, F. C. Maienschein, R. T. Santoro, R. J. Scroggs (ORTEC), J. H. Todd, V. V. Verbinski (Gulf General Atomic), J. W. Wachter, and W. Zobel.

in binding energy from one nucleus to the next start to become important. So, we must be cautious in accepting predictions of the cascade model in the region where the model was never meant to produce answers. Most of the problems with the model arise at the lowest incident energies, where there is great intensity of solar and trapped protons. Above 1 GeV, there are technical problems of what to use for the intranuclear cross sections, but this paper is not concerned with energies that high. At all energies, there is a 10% to 20% weakness that while the model deals with direct reactions, it does not allow production of deuterons etc. by such reactions even though experiments always show considerable deuteron intensity. We can hope for such an improvement in the model; no strong effort has yet been made.

STATUS OF EXPERIMENTS

Here I will concentrate on contributions by our group, but mention the other experiments which have been most influential. Table 1 outlines the main cross-section publications that have arisen from our work.

Reaction Cross Sections

Reaction cross sections give the probability of occurrence of some nonelastic nuclear reaction, and therefore are of prime importance. These cross sections are somewhat available from various physics groups for both neutrons and protons, since they are also of great importance in the optical model of the nucleus or any other reaction model. The comparisons which have been presented show the Bertini cascade model to be within experimental uncertainty (~10%) over the energy range 30 to 1000 MeV.[2,6] This success gives the cascade model a remarkably good start toward overall validity.

Table 1. ORNL Space Shielding Experiment Program

Observed	Incident Particle (MeV)	Type	Targets	Angle Range (deg)	Secondary Energy Range (MeV)	Principal Authors	Reference
dose in phantom	160	p	C,Al,Cu, Bi	0,45	N.A.	Blosser Maienschein Freestone	7
γ	16-160 59	p α	Be,B,C, O,Al,Fe	50,90, 135	0.7-10	Zobel Maienschein Todd,Chapman	9
p	160	p	Be,C,O, Al,Co,Bi	30-120	20-160	Peelle,Love Hill,Santoro	23
p	160	p	Be,C,O, Al,Cu,Co, Bi	10,45 60,135	50-160	Wachter Burrus,Gibson	12
n	160	p	C,O,Al, Cu,Co,Bi	10,45	50-160	Wachter Burrus,Gibson	12
p	450	p	Be,C,Al, Cu,Co,Pb, Bi	20,30, 45,60	120-450	Wachter Gibson,Burrus	13
n	450	p	C,Al,Co	10,20 30,45	120-450	Wachter Gibson,Burrus	13
n	14-18	p	Be,N,Al, Fe,In,Ta, Pb	0-170	1-15	Verbinski Burrus	16
p,d,T, ^{3}He,α	30-60	p	C,O,Al, Fe,Y,Sn, Au,Bi	15-160	2-60	Bertrand Peelle	24
p,d,T, α	58	α	C,O,Fe,	20-120	2-60	Bertrand Peelle	25
n	40-60	p	C,Al,Fe, Pb	0-120	5-60	Wachter Santoro,Love	18

Measurements of Dose

Observations of absorbed energy have been made from proton beams in bulk absorbers by Tanner, Bailey, and Hilbert and by Blosser and Maienschein, and in phantoms from scattered reaction products by Blosser and Maienschein.[7] These results have produced a substantial challenge to the combined calculation of cross sections and radiation transport. Since the most thorough methods involve Monte Carlo, the cost of computing integral checks in the latter case was too great to allow a complete comparison with the data. Figure 1 shows the two checks that have been performed in the work of Irving and Alsmiller.[8] Unfortunately, when such integral results do not check, it is difficult to infer what characteristics of the calculation (or experiment) is imperfect and whether indeed the disagreement is representative of practical situations.

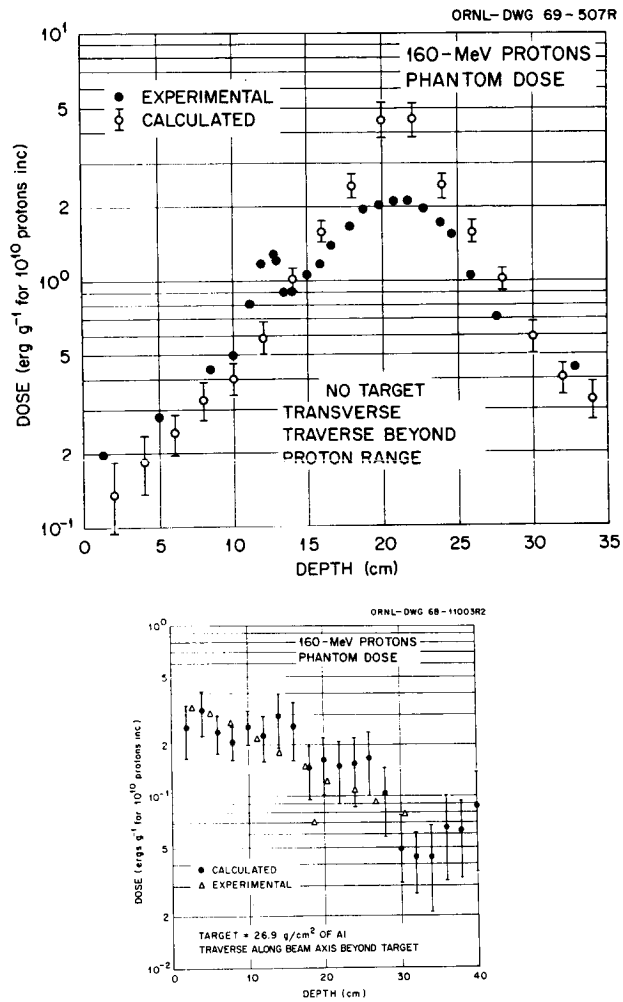

FIGURE 1.—Absorbed dose observed as a function of position in a spherical water phantom (ref 7), compared to a Monte Carlo nucleon transport calculation of Irving and Alsmiller (ref 8). For the results illustrated at the top (a), the beam was incident on the phantom in a direction perpendicular to the traverse, while in the work illustrated below (b), an aluminum target thick enough to stop the incident 160-MeV proton beam was interposed.

Gamma-Ray Spectra

Zobel and Maineschein[9] obtained photon spectra from protons in the energy range 15 to 150 MeV on typical targets. The results have not proved uniformly predictable,[4] partly because the calculated results were based on the residual energy following nculeon evaporation while many of the important excited states are collective levels excited by direct reactions. Nevertheless, current opinion holds that for flare spectra as hard as P_0 = 100 MV, gamma rays from the reactions cannot compete with the primary dose component.[10] For sufficiently soft flares of high intensity, this conclusion may not be valid.[11] Figure 2 shows a typical photon spectrum for oxygen which exhibits different structure from that calculated with the help of the cascade model. Figure 3 shows the energy dependence of the photon production cross sections observed and calculated for four target materials,

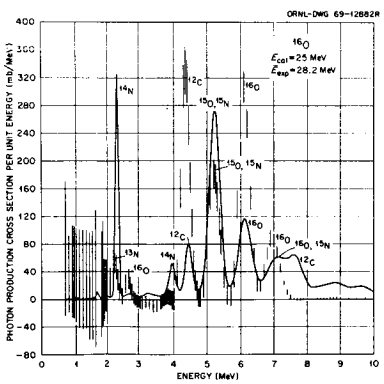

FIGURE 2.—Photon-production cross section per unit energy vs photon energy for protons on ^{16}O (ref 9). The solid line represents the cross section calculated by Shima and Alsmiller (ref 5) for 25-MeV protons and the vertical lines represent the 67% confidence limits on the experimental data for an average proton energy of 28 MeV.

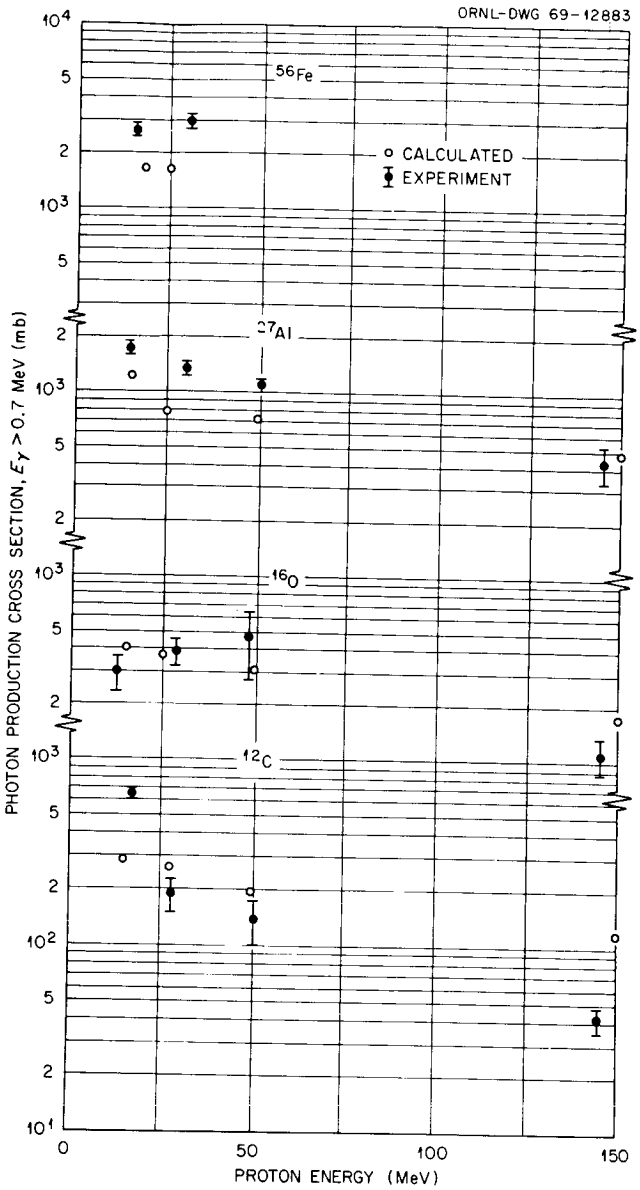

FIGURE 3.—Production cross section for photons with energy >0.7 MeV vs incident proton energy. The experimental values (ref 9) are $4\pi \times$ (mb/sr observed at 135°), though the experimental results as a function of angle were sometimes inconsistent with isotropy. The calculated values are from Shima and Alsmiller (ref 5).

Secondary Neutron Production (from protons)

Insofar as secondaries produced in the spacecraft are concerned, neutrons are felt to be the most important, and so a large fraction of our effort has been spent in neutron spectroscopy. Wachter and Gibson have observed spectra of secondary neutrons for incident 160- and 450-MeV protons for a variety of targets, some thick enough to allow a little testing of transport codes.[12,13] Agreement of this data with theory is only moderate[12,14] even after account is taken of the broad resolution of the spectrometers. Figure 4 illustrates typical results obtained at 450 MeV at forward angles for rather thin targets. Figures 5 and 6 illustrate that at

160 MeV the thick-target yields more nearly agreed with theory for bismuth than for aluminum. The source of the difficulties is not clear; theorists are understandably reluctant to modify the model until the experiments are independently confirmed, and also it is not clear from the data what modifications should be made.

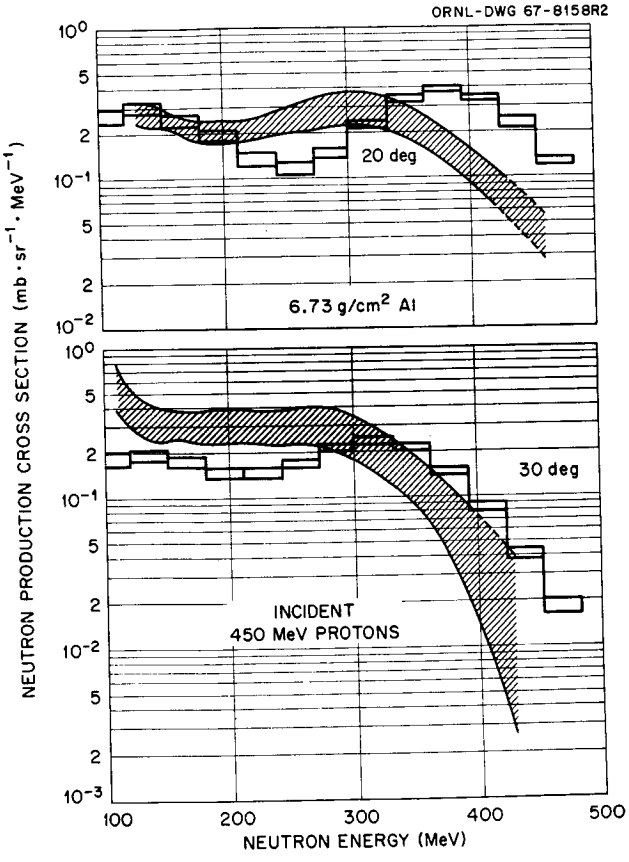

FIGURE 4.—The hatched areas are the experimental confidence intervals for the differential neutron cross sections at 20° and 30° from 450-MeV protons on aluminum (see ref 13). The histogram shows the estimated cross section from the Bertini intranuclear cascade model, smeared by the experimental resolution, for the surrounding angle intervals (ref 2c).

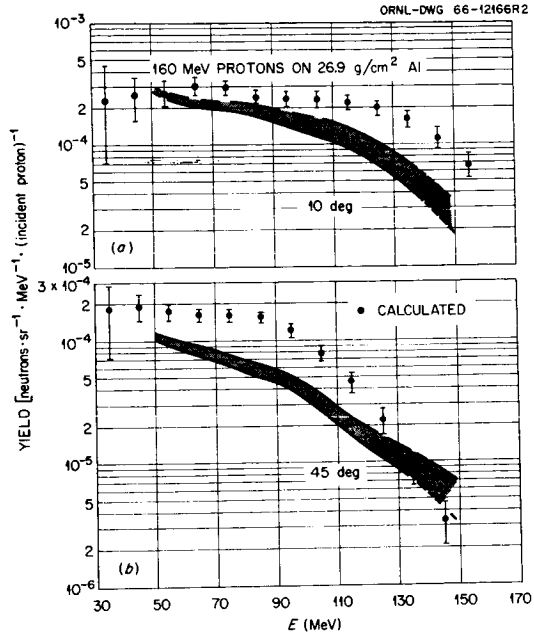

FIGURE 5.—Experimental (ref 12) and calculated neutron yields as a function of energy at 10° and 45° to a 27-g/cm²-thick aluminum target, which is thick enough to stop the incident beam of 160-MeV protons. The calculated points were obtained using the Monte Carlo transport codes of Kinney (predecessors to the work of ref 3) which employed the cross sections of Bertini (ref 2). The calculated values were smeared using a Gaussian energy resolution so that they correspond to the resolution associated with the experimental curves.

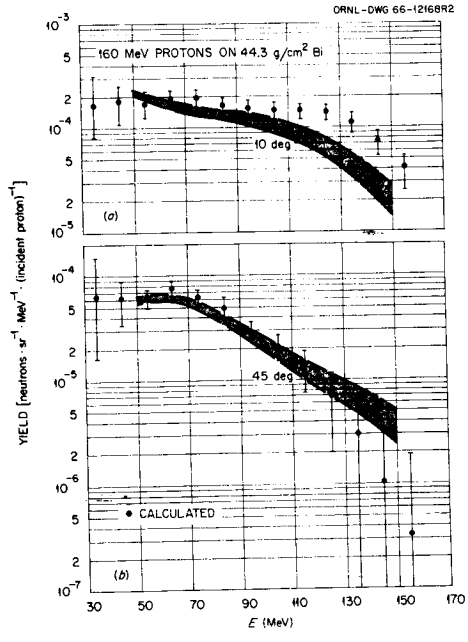

FIGURE 6.—Experimental and calculated neutron yields at 10° and 45° from a 44.3-g/cm²-thick bismuth target. (See Fig. 5 for explanation.)

Essentially no competing neutron data exists for protons in this energy range except for the measurements by Bowen et al. of neutrons at 2° from ~140-MeV protons on various targets.[15] Figure 7 is a typical example of the 140-MeV results, none of which have ever been properly explained. Not only must the peak at the high energies contain excitation of the target's isobaric analog as well as any contribution from quasifree scattering, but the continuum region (at 1/4 to 3/4 the incident energy) is underestimated by the cascade model for each target studied. Extreme forward angles are expensive to study by present Monte Carlo techniques.

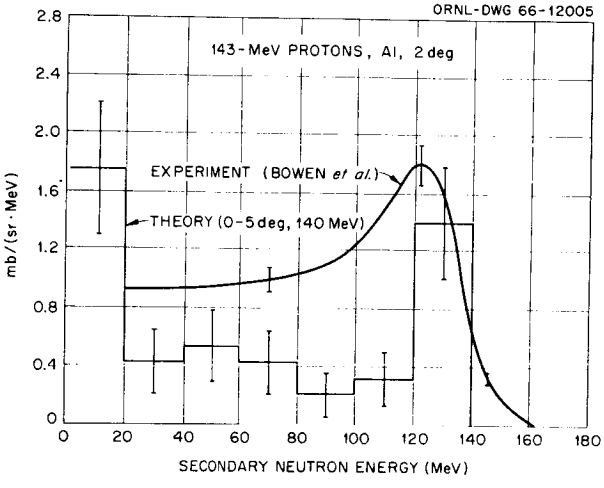

FIGURE 7.—Secondary-neutron spectrum at 2° from 143-MeV protons on aluminum. Smooth curve: experimental results of P. H. Bowen et al. (ref 15); histogram: calculated spectrum by the intranuclear cascade model (ref 2b) of neutrons emitted into the angular interval 0° to 5° from 140-MeV incident protons.

Verbinski and Burrus looked in a brief but productive experiment at neutron spectra above 1 MeV from 14- to 18-MeV protons on a series of targets.[16] Figure 8 shows the results obtained as a function of angle for an aluminum target. Some targets both lighter and heavier than Al yielded greater anisotropy. As suggested by Fig. 9, where the same results integrated over angle are compared with theory, this experiment showed that the angle-integrated spectra in this energy range are better fitted by the cascade (+ evaporation) model than by evaporation alone; the latter idea had previously been accepted. The latest interpretation of Verbinski's data by Alsmiller and Hermann[17] has shown that a simple low-energy modification of the cascade model, which takes into account the Q-value for the (p,n) reaction, is required to give the theory some validity for neutron energies near the incident beam energy.

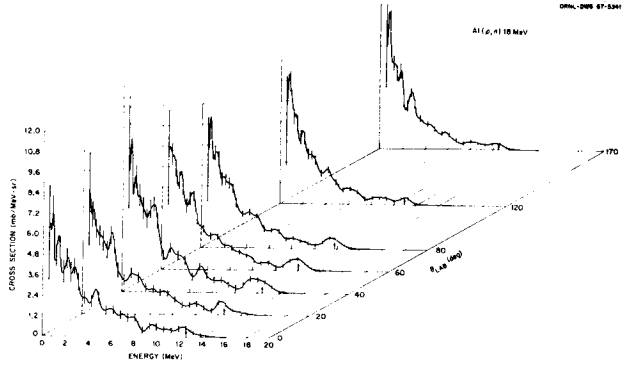

FIGURE 8.—Neutron differential cross sections vs energy and angle for $^{27}Al(p,xn)$ reactions at E_p = 18 MeV. (See ref 16.)

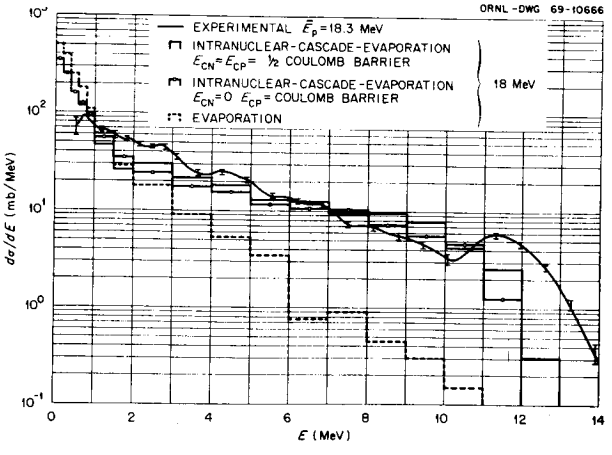

FIGURE 9.—Angle-integrated differential cross section for neutron emission from 18-MeV protons on ^{27}Al. The experimental values of Verbinski and Burrus (ref 16) are compared with the theoretical values due to Alsmiller and Hermann (ref 17).

J. W. Wachter is now analyzing the experimental results he, Santoro, Love, and Zobel obtained for neutron spectra from 40- and 60-MeV protons.[18] These data were obtained in the region where the cascade model is expected to be failing and in which marked angular distributions can be expected. These data should help greatly to clarify our ideas about reactions in this region in which the other reaction products have been studied so thoroughly (see below). Figure 10 shows preliminary results for 39-MeV protons on carbon, while Fig. 11 shows the 0° spectrum from a lead target. The peak in Fig. 11 corresponds to excitation of the isobaric analog of the target, and cannot be given by the cascade model. Similar experimental capability for measuring neutron spectra is apparently being developed at other isochronous cyclotrons, notably Texas A. and M. and University of California at Davis, and scattered results are also available showing the behavior of the peak from excitation of the isobaric analog state.

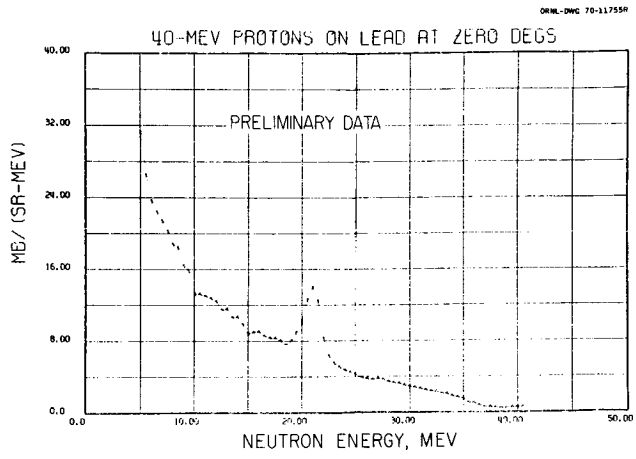

FIGURE 11.—Preliminary differential cross sections of Wachter et al. (ref 18) for neutrons at 0° from 39-MeV protons on lead.

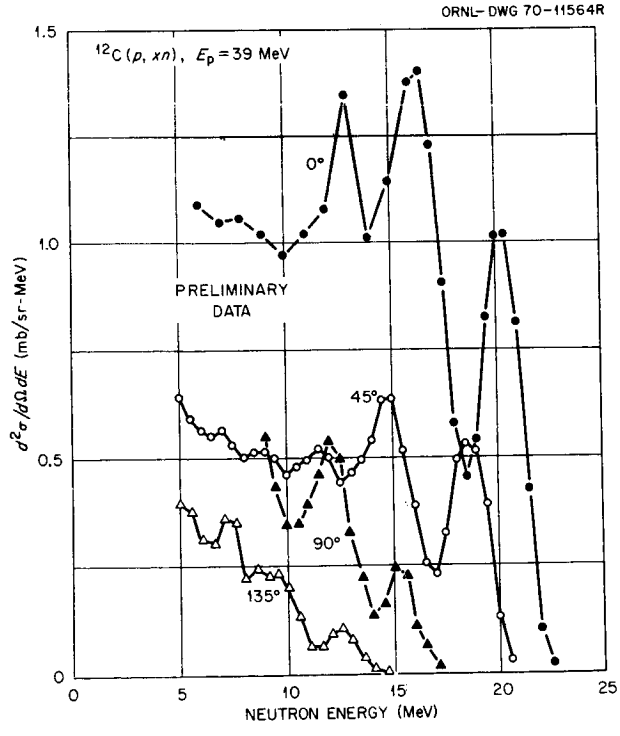

FIGURE 10.—Preliminary differential cross sections of Wachter et al. (ref 18) for differential neutron cross sections from 39-MeV protons on carbon at various detector angles.

Secondary Protons, Deuterons, Alpha Particles

Secondary proton experiments by Cladis, Hess, and Moyer[19] motivated the early development of the cascade model, and most of the nucleon data against which the model can be tested are still for protons rather than neutrons. Unfortunately, the latter are of more shielding interest, though at some hundreds of MeV the charged-particle spectra are of importance in estimating tissue dose from protons. The work of Azhgirey et al.[20] observing protons from 660-MeV protons on nuclei, though it covered only small angles, has had a strong effect on the development of the theory because it showed approximate validity of the theory in this region provided that meson production was included. (See Fig. 12.) Similar comparisons[20] for secondary energies above 800 MeV are available from the work of Corley and Wall[21] with 1-GeV protons.

At lower energies the situation becomes more confused. The results of Wachter, Gibson, and Burrus[13] from 450-MeV protons on nuclei included the proton spectra illustrated in Fig. 13. Agreement seems to improve as the angle is increased toward 60°, but consistent differences between experiment and theory appear in the 30° and 45° data.

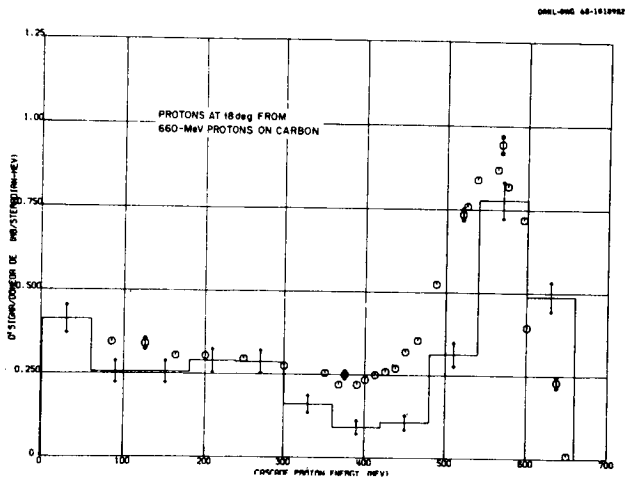

FIGURE 12.—Energy spectrum of protons emitted at a laboratory angle of 18° from 660-MeV protons on carbon. Histogram: calculated values by Bertini (ref 2c) for the angular interval 13° to 23°; circles: experimental data of Azhgirey et al. (ref 20).

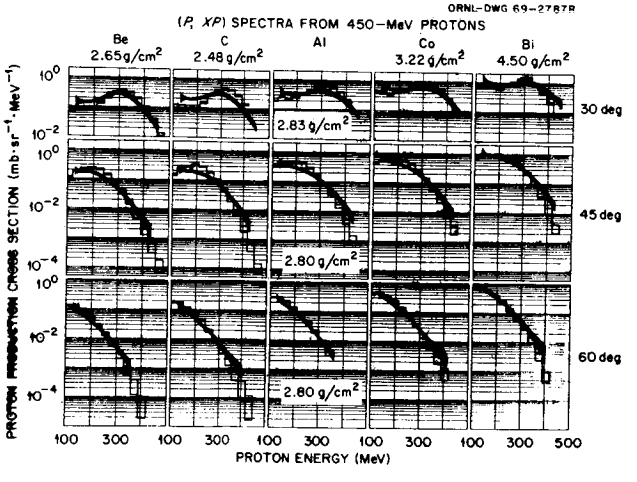

FIGURE 13.—The shaded areas are the experimental proton spectra of Wachter et al. (ref 13) for 450-MeV protons at the energies and angles indicated. The histograms give the resolution-smeared results of the Bertini cascade model (ref 2c) for appropriate angle intervals.

In the 150- to 200-MeV region real disagreements appear between various experiments. It is impossible to decide, for instance, if the quasifree scattering peak appears clearly in the data as expected from model calculations. The experimental results are generally confused by multiple-scattering effects, failure to separate explicitly the deuteron contribution, and in some cases by broad resolution. Figure 14 illustrates this discrepancy of spectral shape between the experiments of Wall and Roos[22] and those of Peelle.[23] At 60°, the experiments of Peelle and of Wachter et al.[12] (see Fig. 15) are in rough agreement with the cascade model,[2b] while the results of Roos and Wall still show maxima in the spectra. At backward angles the experimental cross section is much larger than the predicted one. We conclude that above 100 MeV the cascade model gives about the right magnitude of differential cross section except at backward angles, but the quasifree structure in the energy spectrum must remain in doubt for energies less than a few hundred MeV until more precise experiments are performed. Since the spectrum affects the energy balance, we can assume that from the evaporation phase of the reaction intensities are also in doubt.

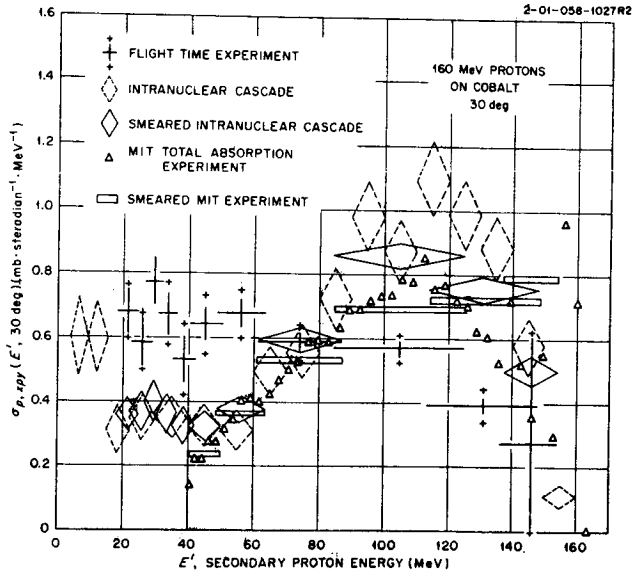

FIGURE 14.—Differential cross sections at 30° for protons from 158-MeV protons on Co. Comparisons of the flight-time data of Peelle et al. (ref 23) with the experiment of Wall and Roos (ref 22) and with the intranuclear-cascade estimates of Bertini (ref 2b) are exhibited with and without resolution smearing according to the calculated detector-response functions (of Peelle et al.).

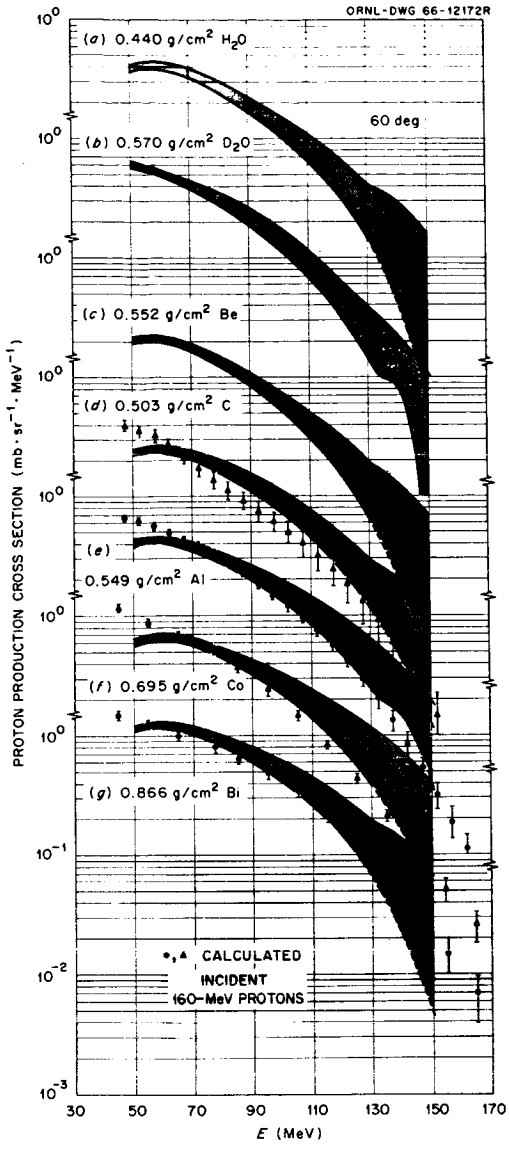

FIGURE 15.—Experimental and calculated proton cross sections (ref 12) at 60° for 160-MeV protons on a variety of elements. The points are the calculated cross sections of Bertini (ref 2b) smeared with a 15% Gaussian energy resolution so as to correspond to the energy resolution associated with the experimental results.

For the last few years results have been appearing from an exhaustive experiment by Bertrand and myself to look at complete spectra of hydrogen and helium ions from 30- to 60-MeV protons on a series of nine targets from carbon through bismuth.[24] Figure 16 illustrates the type of data available for each target, angle, and incident energy, while Fig. 17 shows some proton results from 62-MeV protons on ^{120}Sn. To state the qualitative results briefly, cross sections in the continuum regions do vary slowly with mass number (Figs. 18 and 19), alpha-particle production is not entirely explained by the evaporation model (Fig. 16), the mass 2 and 3 isotopes comprise 15% to 20% of the observed cross section and emitted energy (Fig. 19) and have spectra which completely differ from that predicted by the evaporation phase of the model (Fig. 16), at higher energies the back angle intensity is higher than estimated (Fig. 17), and the quasifree scattering peak is not seen (Fig. 20). Figure 21 illustrates the progressive shift in the accuracy of cascade model predictions at a given angle as the incident energy is lowered, while Fig. 22 illustrates that predictions of the angle-integrated spectra behave much more stably at the low energy. Some results have also been obtained for incident 59-MeV alpha particles;[25] Fig. 23 illustrates that the experimental results from the ^{54}Fe(α,xp) reaction cannot be explained on the basis of a simple nuclear evaporation model.[26]

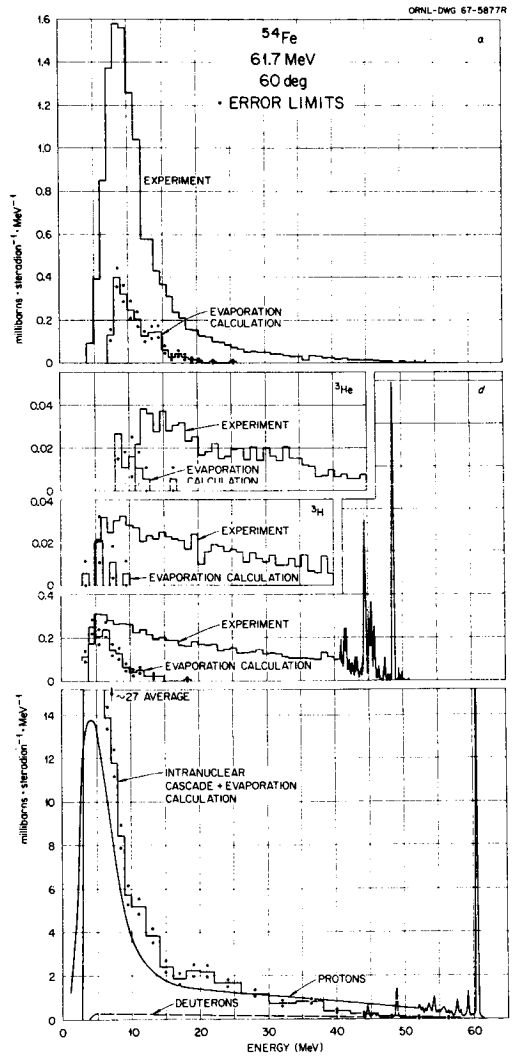

FIGURE 16.—Shown are 60° differential cross sections for hydrogen and helium particles from 62-MeV protons on ^{54}Fe (ref 24) compared with the results of Bertini's intranuclear cascade model with evaporation (ref 2). Note the shapes of the observed spectra for d, T, and ^{3}He and the relative intensities and shapes of observed and predicted alpha-particle spectra. The vertical scales differ from particle to particle.

Most of the data from this charged-particle experiment is now publicly available, but much interpretive work remains to be done. If the data can be complemented with good neutron differential cross sections in the same energy region for some of the same targets, the data base will be sufficiently complete to allow productive theoretical efforts.

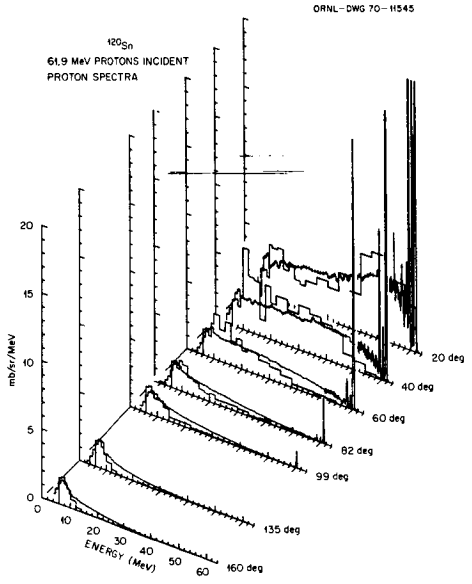

FIGURE 17.—Proton spectra as a function of angle for 62-MeV protons on ^{120}Sn (ref 24), compared to the predictions of the intranuclear cascade model (ref 2). Note that for backward angles the computed spectrum contains too few particles above the "evaporation" region.

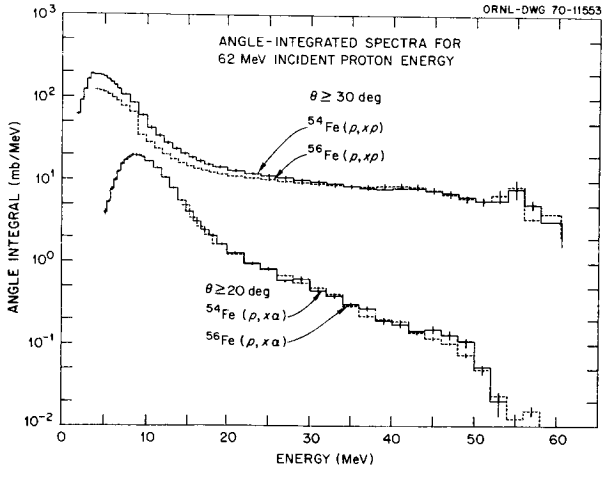

FIGURE 18.—A comparison of angle-integrated differential cross sections for protons and alpha particles from targets of ^{54}Fe and ^{56}Fe bombarded by 62-MeV protons. The results are consistent with the observed cross section being nearly independent of detailed nuclear level structure. Elastic scattering has been removed.

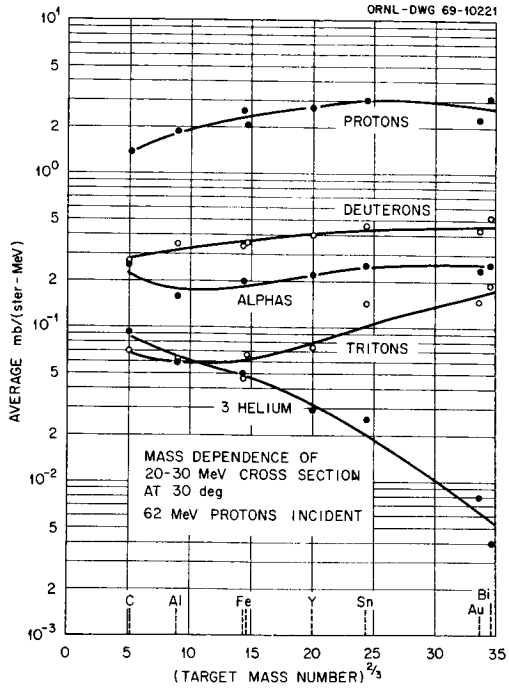

FIGURE 19.—Dependence on target mass number of the average cross sections for production by 62-MeV protons of medium energy (20 to 30 MeV) particles at 30° (ref 24). Note the relative deuteron/proton intensity, the generally smooth behavior of the cross sections, and the $T/^3He$ ratio as a function of mass number.

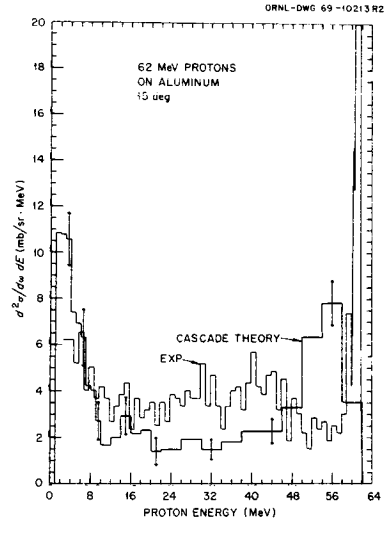

FIGURE 20.—Experimental differential proton cross section observed at 15° for 62-MeV protons on aluminum (ref 24), compared with intranuclear cascade theory (ref 2). In this energy range the theory always overestimates the quasifree scattering peak, seen here at about 54 MeV, which arises in the model from single collisions between the incident nucleon and a (moving) bound one.

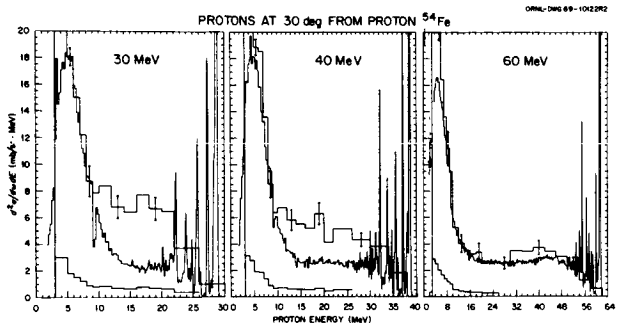

FIGURE 21.—Comparison of observed differential proton cross sections at 30° from ^{54}Fe as a function of incident energy (ref 24) compared to the corresponding predictions of the cascade model (ref 2) shown by broad-stepped histograms. (The lower histogram is 1/10 the computed cross section.)

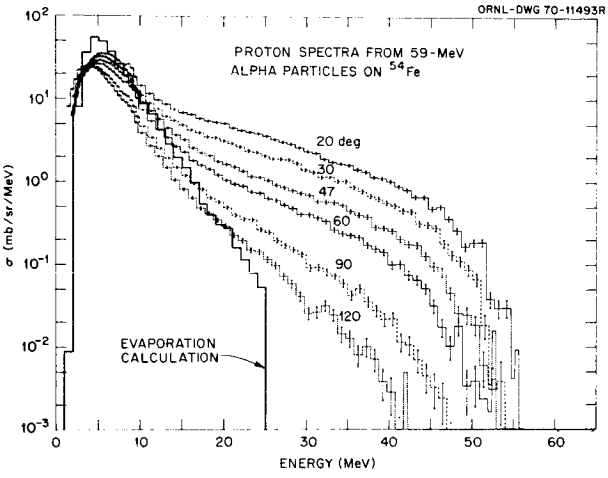

FIGURE 23.—Observed differential proton cross sections from 59-MeV alpha particles on ^{54}Fe. The evaporation calculation, using the method of Dresner and of Dostrovski (ref 26), is based on a reaction cross section of 1.7 barns; the sharp cutoff at 25 MeV is an artifice of the utilized program.

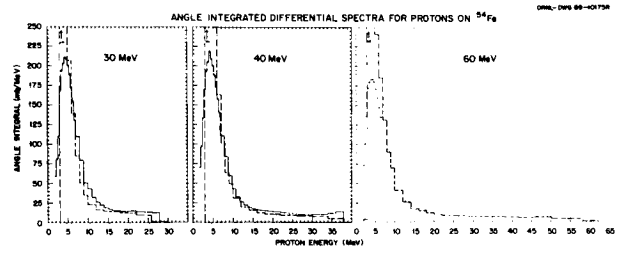

FIGURE 22.—Comparison of observed angle-integrated differential spectra from protons of various energies on ^{54}Fe (ref 24), compared with the corresponding predictions of the cascade model (ref 2). The degree of agreement is nearly independent of incident energy. Note in all cases the "evaporated" proton intensity is overestimated.

STATUS OF THE THEORY

Theory is important, since we expect to derive a complete set of usable cross sections from it rather than directly from experiment. I will try to summarize my view of the utility of present theories for computing cross sections for incident energies below 1 GeV. 1) Optical model (elastic) and distorted-wave approximation cross sections could be computed for excitation of discrete levels in residual nuclei, based on the work of many physics groups. These reactions become increasingly important for incident energies below 50 MeV as seen in Fig. 21, but they have not yet been included in shielding computations. To do so would require due respect for the detailed literature but some simplification of level schemes while keeping the main features. We do not quite know how this "collective" share of the reactions should be meshed with the rest.

2) The nuclear fragment evaporation theory itself is seldom completely valid, except for perhaps some reactions with incident heavy nuclei. In combination with the cascade theory, it has enjoyed some success. With incident particles in the 30- to 60-MeV range, the competition between alphas and protons in the Dostrovsky model now used[26] is always wrong by a factor of two or more; we do not know whether the neutron intensity shares this difficulty. Part of the difficulty lies in the unrealistic inverse cross sections used in the model, and failure to consider angular momentum may also be important.

3) The cascade model[2] gives satisfactory (∿10%) nonelastic cross sections over the whole range of interest, if the uncertainty of the literature values is taken into account. So far the model fails to predict the 10% to 15% contribution of deuterons which seem to be produced by direct reactions. For 60-MeV incident protons the model gives cascade proton spectra integrated over angle which are within about 20% of experiment, but too few cascade protons are emitted at large angles. The energy distributions of protons at moderately forward angles are similarly good at the highest energies considered here, but at low energies show too much quasifree scattering structure. We do not know for sure the behavior in the 100- to 200-MeV region. The best available comparisons for neutron spectra show disagreements larger than 30%, but so far the data are a bit inconclusive. (Comparison with a Cosmotron experiment to check neutron production in very thick samples encourages the belief that on some energy-angle average the neutron production is within 30% of the correct value.[27]) Extensive (p,2p) coincidence experiments in the physics community indicate that distortion of the incident nucleon wave by the nuclear-force field of the nucleus must be taken into account for energies below 100 MeV.[28] Since (p,2p) experiments study the intranuclear nucleon-nucleon reaction which underlies the cascade model, their conceptual results should be folded into the cascade theory. No real competitor for the intranucleon cascade theory has yet appeared, so the course must be to improve what we have. The cascade cross sections vary slowly with angle, target mass, and incident and outgoing energy, so it seems conceptually hopeful that a clever computational method could be found to reduce greatly the number of histories required for precise estimation of a broad range of results.

SUMMARY OF WORK NEEDED TO BE DONE

If man is to spend extended periods in space, more details should be worked out on the effects of nuclear reactions on his radiation environment. More experimental information should be obtained on the production of low-energy neutrons in the reactions of protons, and experiments like that of Wachter should be extended to more targets. Some additional experimental assurance on secondary gamma rays would be wise, for instance by measurement of the photon energy released by stopping 15- to 30-MeV protons in appropriate targets. Large efforts are needed to make available to the space shielding analyst improved cross-section codes which take account of the major findings of incident-proton experiments, and to continue the exploration of the consequences of these reactions for spacecraft design. Beyond the work with incident protons, experimental and theoretical exploration of the reactions of alpha particles and heavier primaries are surely in order, since the available experiments barely sample the problem and no really applicable general theory is available. The immediate problem is that current fiscal plans provide for but a small fraction of the needed effort.

The primary author wishes to acknowledge the forbearance of most of the associate authors, who had no chance to review the manuscript which depended so heavily of their long efforts.

REFERENCES

1. SCOTT, W. W.: Estimates of Primary and Secondary Particle Doses Behind Aluminum and Polyethylene Slabs Due to Incident Solar-Flare and Van Allen Belt Protons, Oak Ridge National Laboratory Document, ORNL-RSIC-18, 1967. IRVING, D. C.; ALSMILLER, R. G.; ALSMILLER, F. S.; and MORAN, H. S.: Nucl. Sci. Eng., vol. 25, 1966, p. 373.

2. BERTINI, H. W.: (a) Phys. Rev., vol. 131, 1963, p. 1801; Phys. Rev., vol. 138, AB2, 1965. (b) Phys. Rev., vol. 162, 1967, p. 976. (c) Phys. Rev., vol. 188, 1969, p. 1711.

3. COLEMAN, W. A.; and ALSMILLER, R. G., Jr.: Nucl. Sci. Eng., vol. 34, 1968, p. 104.

4. GABRIEL, T. A.; SANTORO, R. T.; and ALSMILLER, R. G., Jr.: An Approximate High-Energy Alpha-Particle-Nucleus-Collision Model, Oak Ridge National Laboratory Document, ORNL-TM-3153, 1970, to be published in Nucl. Sci. Eng.

5. SHIMA, Y.; and ALSMILLER, R. G., Jr.: Nucl. Sci. Eng., vol. 41, 1970, p. 47.

6. Private communications from E. Gross and H. W. Bertini (1970) indicate that most of the yet-unpublished data of the former for proton reaction cross sections between 30 and 60 MeV lie within 5% of the Bertini predictions (about 1/3 of the differences lie just outside of 10%).

7. TANNER, R. L.; BAILEY, N. A.; and HILBERT, J. W.,: Rad. Res., vol. 32, 1967, p. 861. BLOSSER, T. V.; MAIENSCHEIN, F. C.; and FREESTONE, R. M.: Health Phys., vol. 10, 1964, p. 743.

8. IRVING, D. C.; ALSMILLER, R. G., Jr.; and MORAN, H. S.: Nucl. Sci. Eng., vol. 37, 1969, p. 304. Comparisons against this data have also been performed by LILEY, B.; and DUNEER, A. G., Jr.: Nucl. Sci. Eng., vol. 29, 1967, p. 189.

9. ZOBEL, W.; MAIENSCHEIN, F. C.,; TODD, J. H.; and CHAPMAN, G. T.,: Nucl. Sci. Eng., vol. 32, 1968, p. 392.

10. HILL, C. W.; and SIMPSON, K. M., Jr.: Proc. Second Symp. on Protection Against Radiations in Space, NASA SP-71, 1965, p. 351.

11. PEELLE, R. W.: Proc. Special Sessions on Protection Against Space Radiation, NASA SP-169 (ANS-SD-5) 1968, p. 434 or Nuclear Reaction Cross Sections for Spacecraft Shield Design, Oak Ridge National Laboratory Document, ORNL-TM-1892, 1967, p. 8.

12. WACHTER, J. W.; BURRUS, W. R.; and GIBSON, W. A.: Phys. Rev., vol. 161, 1967, p. 971.

13. WACHTER, J. W.; GIBSON, W. A.; and BURRUS, W. R.: Neutron and Proton Spectra from Targets Bombarded by 450-MeV Protons, Oak Ridge National Laboratory Document, ORNL-TM-2253, submitted to Phys. Rev.

14. ALSMILLER, R. G., Jr.; WACHTER, J. W.; and MORAN, H. S.: Nucl. Sci. Eng., vol. 36, 1969, p. 291.

15. BOWEN, P. H.; COX, G. C.; HUXTABLE, G. B.; SCANLON, J. P.; THRESHER, J. J.; and LANGSFORD, A.: Nucl. Phys., vol. 30, 1962, p. 475.

16. VERBINSKI, V. V.; and BURRUS, W. R.,: Phys. Rev., vol. 177, 1969, p. 1671.

17. ALSMILLER, R. G., Jr.; and HERMANN, O. W.: Nucl. Sci. Eng., vol. 40, 1970, p. 254.

18. WACHTER, J. W.; LOVE, T. A.,; SANTORO, R. T.; and ZOBEL, W.: Neutron Physics Division Annual Progress Report for Period Ending May 31, 1970, Oak Ridge National Laboratory Document, ORNL-4592, p. 104.

19. CLADIS, J. B.; HESS, W. N.; and MOYER, B. J.: Phys. Rev., vol. 87, 1952, p. 425.

20. AZHGIREY, L. S.; VZOROV, I. K.; ZRELOV, V. P.; MESCHERYAKOV, M. G.; NEGANOV, B. S.; RYNDIN, R. M.; and SHABUDIN, A. F.: Nucl. Phys., vol. 13, 1959, p. 258.

21. CORLEY, D. M.: Ph.D. Dissertation, University of Maryland, 1968.

22. WALL, N. S.; and ROOS, P. R.: Phys. Rev., vol. 150, 1966, p. 811.

23. PEELLE, R. W.; LOVE, T. A.; HILL, N. W.; and SANTORO, R. T.: Phys. Rev., vol. 167, 1968, p. 981.

24. BERTRAND, F. E.; and PEELLE, R. W.: Oak Ridge National Laboratory Documents as follows: ORNL-4274, 60-MeV protons on C, Fe, and Bi,; ORNL-4450, 62-MeV protons on ^{89}Y; ORNL-4455, 62- and 28-MeV protons on ^{27}Al; ORNL-4456, 61-MeV protons on ^{56}Fe; ORNL-4460, 62- and 29-MeV protons on ^{197}Au; ORNL-4469, 62-, 39-, and 29-MeV protons on ^{54}Fe; ORNL-4471, 62- and 29-MeV protons on ^{120}Sn; ORNL-4638, 62- and 39-MeV protons on ^{209}Bi, and Neutron Physics Division Annual Progress Report for Period Ending May 31, 1970, ORNL-4592, p. 98.

25. BERTRAND, F. E.; and PEELLE, R. W.: Cross Sections for Hydrogen and Helium Particles Produced by 59-MeV Alpha Particles on ^{12}C, ^{16}O, and ^{54}Fe, Oak Ridge National Laboratory Document, ORNL-4670, to be published.

26. DOSTROVSKY, I.; et al.: Phys. Rev., vol. 116, 1959, p. 683; vol. 118, 1960, p. 781; vol. 118, 1960, p. 791. The program used is from DRESNER, L.: EVAP - A Fortran Program for Calculating the Evaporation of Various Particles from Excited Nuclei, Oak Ridge National Laboratory Document, ORNL-TM-196, 1961.

27. COLEMAN, W. A.; and ALSMILLER, R. G., Jr.: Nucl. Sci. Eng., vol. 34, 1968, p. 104.

28. RIOU, M.; and RUHLA, Ch.: Progress in Nuclear Physics, vol. 11, p. 195, D. M. Brink and J. H. Mulvey, Eds., Pergamon Press, 1970.

MEASUREMENTS OF GAMMA-RAY PRODUCTION CROSS SECTIONS FOR SHIELDING MATERIALS OF SPACE NUCLEAR SYSTEMS+

V. J. Orphan, Joseph John, and C. G. Hoot

Gulf Radiation Technology
A Division of Gulf Energy & Environment Systems Incorporated

Measurements of secondary gamma-ray production from neutron interactions have been made over the entire energy range (thermal to 16 MeV) of interest in shielding applications. A LINAC pulsed neutron source having a continuous distribution of neutron energies is used in conjunction with high-resolution Ge(Li) gamma-ray spectrometers and the time-of-flight technique. The two-parameter data (gamma-ray energy vs neutron energy) are obtained using a computer-controlled data acquisition system. Two facilities are used in the measurements. A 16-meter facility is used to measure gamma rays from resonant capture of neutrons up to 100 KeV. Gamma production cross sections from (n,xy) reactions are measured up to 16 MeV using a 50-meter facility.

The epithermal capture gamma-ray yields for both resolved gamma-ray lines and continuum have been measured from thermal energies to 100 KeV for natural tungsten and ^{238}U, two important candidate shield materials in SNAP reactor systems. Data are presented to illustrate the variation of epithermal capture gamma-ray yields with neutron energy. In the resolved resonsance region, the total observed radiated energy was within ± 15% of the known binding energy. The gamma-ray production cross sections from (n, xy) reactions have been measured for Fe and Al from the threshold energies for in-elastic scattering to ∿16 MeV. Typical Fe and Al cross sections obtained with high-neutron energy resolution (∿1% at 1 MeV) and averaged over broad neutron-energy groups are presented and compared with previous cross-section determinations made using monoenergetic neutron sources.

1. INTRODUCTION

The design of space nuclear systems, both for electric power generation and for propulsion, requires an accurate knowledge of secondary gamma-ray production cross sections over a wide neutron energy range. The necessity of optimizing shield designs for minimum weight places particularly strong demands on the precision of these cross sections. There are, in general, two different types of gamma-ray production data required: (1) gamma-ray yields from the radiative capture,(n,y) reactions, of neutrons in the energy range, thermal to about 100 keV, and (2) gamma-ray production cross sections for (n, xy) reactions of neutrons in the range, threshold for inelastic scattering to about 16 MeV. The relative importance of these two types of data in a particular space application depends, of course, on such related considerations as the material, the incident neutron flux spectrum, the geometrical configuration, the dose constraint, etc.

There is a general lack of secondary gamma-ray production data adequate for use in the analysis of radiation transport in space nuclear systems. The numerous requests (ref. 1) for this type of data testify to the current widespread deficiency.

This paper describes a program of measurements carried out at the Gulf Radiation Technology LINAC in order to provide urgently needed gamma-ray production data of the two types mentioned above. A technique for measuring epithermal capture gamma-ray yields is briefly described and typical results are shown for tungsten and depleted uranium, two important candidate shield materials for space electric power systems. Also, a method of measuring gamma-ray production cross sections for (n, xy) reactions up to 16 MeV is discussed. Representative results are shown for iron and aluminum (important structural and shield materials in space nuclear systems, such as NERVA) and these are compared with previous results in order to illustrate the advantages of the LINAC technique for obtaining gamma-ray production data.

2. EPITHERMAL CAPTURE GAMMA-RAY YIELDS

Shields consisting of a heavy metal such as ^{238}U, W, Pb or Ta, (for gamma-ray shielding) and LiH (for neutron shielding) are being considered for use in both the SNAP and thermionic electric power systems. The total capture gamma-ray yield from the heavy metal in such shields depends on both the capture cross section and the gamma-ray spectrum, i.e., the distribution of capture gamma rays as a function of gamma-ray energy. It has been shown (ref. 2) that the dose penetrating these shields is quite sensitive to the variation of epithermal capture gamma-ray spectra with neutron energy. Nevertheless, a lack of epithermal capture data has made necessary the use of thermal capture spectra in many shielding calculations even though it is known that a significant fraction of the captures take place at epithermal energies. In this section, measurements of the epithermal capture gamma-ray spectra for ^{238}U and W using a pulsed LINAC neutron source are described. Furthermore, typical results are given to illustrate the variation of spectra with neutron energy and to compare the contrast the ^{238}U and W data.

+ This work supported by the Defence Atomic Support Agency under Contract DASA 01-69-C-0083 and the U.S. Atomic Energy Commission under Subcontract No. 3032 with Union Carbine Corporation.

2.1 EXPERIMENTAL TECHNIQUE

A schematic of the capture gamma-ray facility (ref. 3) is shown in fig. 1. A LINAC target, consisting of a water-cooled tungsten alloy (fansteel) converter surrounded by a 15.3-cm-diam right circular cylinder of depleted uranium, is used to produce a pulsed source of neutrons having a continuous distribution of energies. Neutrons are moderated by a 2.54-cm-thick piece of polyethylene placed around the target. The neutrons travel down a 16-meter evacuated flight path and impinge on a 15.2-cm-diam capture sample placed at 45° to the neutron beam. The capture gamma rays from the sample are detected by a Ge(Li)-NaI spectrometer mounted on a movable carriage as shown in Fig. 1. Measurements are usually made at an angle of 90° with respect to the incident neutron beam. The energy of the neutron producing the capture gamma ray is determined by measuring the time interval between the LINAC burst and the gamma-ray event in the spectrometer; i.e., the time-of-flight (TOF) technique. An example of a TOF spectrum is shown in Fig. 2 for ^{238}U. The number of gamma rays detected by the spectrometer (counts/channel) is plotted against neutron flight time (channel number) and clearly illustrates the lower energy capture resonances in ^{238}U.

The Ge(Li)-NaI spectrometer may be simultaneously operated in three modes: (1) as a single Ge(Li) detector, (2) Compton suppression spectrometer, (3) three-crystal pair spectrometer using a computer-controlled data acquisition system. Each counting event is suitably "tagged" before storage in the computer to identify the mode in which the event is detected. The Compton suppression mode is most useful for studying lower energy capture gamma-rays from 0.1 to 3 MeV. The pair spectrometer is used to detect higher energy gamma rays, above 1.5 MeV. The simplification afforded by the pair spectrometer is illustrated in Fig.3 which shows a comparison of the tungsten capture gamma-ray spectrum measured in the singles mode (upper spectrum) and in the pair mode (lower spectrum) for neutron energies between 2.5 and 6.0 eV. The Compton background, which increases sharply with decreasing gamma-ray energy in the singles spectrum is practically eliminated in the pair spectrum. The full-energy and single-escape peaks that complicate the analysis of the singles spectrum are totally absent in the pair spectrum. The peak-to-back-ground ratio at 5164 keV is improved by a factor of 16. This simplification of complex spectra made possible by the nearly ideal single-line response of the pair spectrometer facilitates the unfolding of these spectra to obtain the intensities of continuum gamma-rays. Previous epithermal capture measurements which concentrated on the intensities of the discrete lines are of limited usefulness in shielding calculations since they do not include the large fraction (up to 95 percent) of the total capture gamma-ray intensity that appears as continuum for many elements. The spectrometer used in the present investigation makes possible the measurement of this important continuum contribution.

The experimental data are accumulated in two-parameter form (gamma-ray energy and neutron TOF) using an on-line computer. This two-parameter data is sorted off-line into gamma-ray pulse height spectra for the capture of neutrons with energies between two specified limits. Four capture gamma-ray spectra from ^{238}U measured in the pair spectrometer mode are shown in Fig. 4. The spectra are for "thermal" capture (E_n = 0.02 to 0.5 eV) and for capture in the 6.67-, 21.0- and 36.7-eV resonances. The neutron energy limits used to cover these and other low energy resonance are shown in the ^{238}U(n,y) TOF spectrum given in Fig. 2. Note in Fig. 4 the sharp variation with neutron energy of the intensities of discrete lines, especially the doublet (unresolved in our spectra) with lines at 3982 and 3991 keV and a triplet (also unresolved) with components at 4052, 4059, and 4068 keV (refs. 4,5).

2.2 DATA REDUCTION

The spectra obtained in the pair spectrometer and Compton suppression modes were unfolded (ref. 6) to remove the effects of the spectrometer response and the results were used to determine gamma-ray intensities for capture in ^{238}U. The relative number of captures in the sample as a function of incident neutron energy was calculated from the known capture cross section and resonsance parameters for ^{238}U and the measured flux shape. Detailed corrections were made for finite sample effects such as neutron attenuation, neutron multiple scattering, gamma-ray self-absorption, etc. The capture gamma-ray intensities were normalized to a previous determination (ref. 4) of the intensities of discrete lines from thermal neutron capture. Details of the data analysis and complete results for ^{238}U have been previously reported (ref. 7).

2.3 TYPICAL RESULTS FOR ^{238}U AND W

The gamma-ray intensities for capture in ^{238}U have been determined for 15 neutron energy groups spanning the range 5 eV to 100 keV. The intensities were determined for gamma-ray energy bins about 240-keV wide and include the contribution of both discrete and continuum gamma rays above about 1 MeV. Figure 5 shows, in histogram form, typical results for four energy groups. In addition to the intensities (lower curve in each plot), Fig. 5 shows the radiated energy for each gamma-ray energy bin. The calculated uncertainties are indicated on each curve. The sum of the radiated energy gives a check on the accuracy of the results. For nine of the neutron energy groups, this sum agreed with the known binding energy within $\pm$ 15%. Most of the other groups showed disagreements of the order of 20% and in these cases the results were renormalized to 97% of the binding energy, the mean value obtained from results for the first four strong resonsances in ^{238}U for gamma-ray energies greater than 900 keV.

Epithermal capture gamma-ray spectra have also been previously measured and reported (ref. 8) for natural tungsten. Results for tungsten have been reported for 10 neutron energy intervals spanning the range 1.5 eV to 100 keV. Capture gamma-ray intensities in photons/100 captures were grouped into 500-KeV gamma-ray energy bins over the energy range 1.0 to 7.5 MeV.

It is of interest to compare some of the epithermal capture gamma-ray spectra from tungsten and uranium since the shield designer often must choose between different heavy metals. Figure 6 shows a comparison of the capture gamma-ray yield distributions from depleted uranium and tungsten for two representative neutron energy intervals. The first interval spans the 6.67-eV ^{238}U resonance of the 7.65-eV ^{183}W resonance and the second interval, 0.5 keV to 1.0 keV, spans many closely spaced resonances in uranium and tungsten. As is illustrated in fig. 6, the tungsten and uranium capture gamma-ray yield distributions are quite different. Tungsten has a much harder gamma-ray spectrum for both neutron energy ranges primarily because the average neutron binding energy for natural tungsten is considerably higher than that of uranium. For instance for the 7.65-eV tungsten resonance the binding energy is 7.3 MeV while for the 6.67-eV ^{238}U resonance the binding energy is only 4.8 MeV. Note also that the magnitude of the difference in the capture gamma-ray spectra between tungsten and uranium depends on the neutron energy. The difference between the two spectra are seen in Fig. 6 to be significantly less for the 0.5 keV to 1 keV interval than for the intervals spanning the low energy resonance.

The large differences shown in this comparison demonstrate the need for the measurement of epithermal capture gamma-ray spectra for other important shield materials. In applications where a large fraction of the captures take place above thermal neutron energies, such data as described above for uranium and tungsten are essential for an accurate calculation of the secondary gamma-ray dose.

3. GAMMA-RAY PRODUCTION CROSS SECTIONS FOR (n,xy) REACTIONS

The use of moneonergetic neutron sources, usually produced with a Van de Graaff accelerator using the d-d reaction, to measure gamma-ray production cross sections results in good neutron energy resolution and accurate angular distribution studies. However, a systematic study of the energy dependence of these cross sections over a wide neutron energy range, which is required for accurate radiation transport calculations, is extremely time consuming. This is especially true if the cross section has sharp resonances which necessitate a monoenergetic measurement at many neutron energies in order to obtain the true average cross section. Furthermore, measurements with a Van de Graaff accelerator are increasingly difficult to interpret in the neutron energy range above 9 MeV, since neutrons from the d-d reaction are not monoenergetic because of deuteron breakup.

On the other hand, the use of a pulsed LINAC neutron source having a continuous distribution of energies allows gamma-ray production cross sections to be measured continuously over a wide neutron energy range in a single experimental run. The LINAC technique sacrifices neutron energy resolution to some extent but has the distinct advantage of providing a consistent set of average cross sections for a series of contiguous energy intervals spanning the entire neutron energy range of interest in most shielding calculations. Furthermore, when necessary, the neutron energy resolution of this technique as is illustrated in Fig. 11 can be made comparable or even better than that of Van de Graaff measurements.

3.1 EXPERIMENTAL TECHNIQUE

A facility for the measurement of (n,xy) cross sections using a LINAC has been described previously (ref.9). Consequently, the experimental arrangement, which is shown schematically in Fig. 7, is only briefly described in order to review the principal details of the technique. The Ta-Be target, shown in Fig. 7, produces a copious yield of high energy neutrons with a minimum of gamma flash (bremsstrahlung from electrons striking the Ta converter). The neutrons traverse a 51-meter evacuated flight path and impinge on a ring-shaped scattering sample (48.3 cm o.d. and 27.9 cm i.d.) in which gamma-ray producing reactions occur. The energy of the gamma rays is measured with an 80-cm^3 Ge(Li) detector located on the flight path axis near the sample and shadow shielded from source neutrons and gamma rays. The corresponding neutron energy is obtained by recording the time when a gamma-ray event is detected in the Ge(Li) detector relative to the LINAC pulse, i.e., by the time-of-flight technique. These two-parameter data are accumulated using an on-line computer in a manner similar to that used in the measurement of epithermal capture spectra. The Ge(Li) detector is positioned at an angle of approximately 125° to the incident neutron beam. Since the second Legendre polynomial is zero at 125°, this choice minimizes the effect of gamma-ray anisotrophy on the determination of the integrated gamma-ray production cross section from a measurement at a single angle.

The 80-cm^3(Ge(Li) detector* is sectioned to operate as a total absorption (or DUODE) spectrometer (ref. 10) as well as an ordinary Ge(Li) detector. Spectra for the two different operating modes of the detector are stored simultaneously using the same tagging features of the data-accumulation code discussed earlier in Section 2.1 for the Ge(Li)-NaI spectrometer. The principal advantages of using a total absorption spectrometer to study gamma-ray spectra from (n,xy) reactions are illustrated in Fig. 8 which shows the gamma-ray spectrum from the ^{nat}Fe(n,n'y) reaction for neutrons in the energy range, 0.8 MeV to 1.5 MeV. The upper spectrum was measured with the Ge(Li) detector in the singles mode while the lower spectrum was simultaneously measured with the detector in the DUODE mode. The improved response function of the DUODE mode of operation results in a significant decrease in the Compton distribution and it facilitates the unfolding of complex spectral data to obtain the intensity of continuum gamma rays. The principal background peak in the singles mode results from internal conversion decay of the 695-keV level in 72Ge excited by neutrons scattered into the Ge(Li) detector. Note that this background peak is almost completely absent in the DUODE spectrum. Thus, use of the DUODE has the added

* Purchased from Princeton Gamma-Tech. Inc., Princeton, New Jersey.

advantage of eliminating a principal background line nearly always present in (n,n'y) studies using Ge(Li) detectors.

The two-parameter data (gamma-ray energy, neutron energy) are usually sorted to obtain gamma-ray spectra (for both operating modes of the spectrometer) corresponding to selected neutron energy intervals spanning the energy range from the threshold for (n,xy) reactions to about 16 MeV. Gamma-ray spectra below about 3.5 MeV gamma-ray energy from the ^{nat}Fe (n,n'y) reaction measured with the Ge(Li) detector operated in the DUODE mode are given in Fig. 9. The 27 spectra which cover the neutron energy range, 0.85 MeV to 16.6 MeV, illustrate the variation of the gamma-ray spectra from (n,xy) reactions with neutron energy. Note, for example, that as the neutron energy increases, the spectra become more complex with more high energy gamma rays and an indication of a significant continuum contribution.

3.2 CROSS-SECTION DETERMINATIONS

Broad-group gamma-ray production cross sections are obtained as a function of neutron energy for discrete lines by determining the peak areas in gamma-ray spectra such as those shown in Fig. 9 for the DUODE mode or in similar spectra obtained simultaneously in the singles mode with better counting statistics. Cross sections are derived from the peak areas corrected for the variation of the neutron flux with energy, for Ge(Li) detector effiency, for neutron attenuation and multiple scattering in the sample, for gamma-ray self-absorption in the sample, for scattered neutron background, and the deadtime of the electronics'. These data-reduction procedures have been described in detail elsewhere (ref.11).

High-resolution gamma-ray production cross sections may be obtained by sorting the two-parameter data in a manner which is the reverse of that described above for obtaining broad group data. Namely, TOF spectra are generated corresponding to a narrow pulse height (gamma-ray energy interval). The procedure is illustrated in Fig. 10 which shows the gamma-ray spectrum from (n,xy) reactions in iron andthe TOF spectra generated for a gamma-ray energy interval (815 KeV $\leq E_\gamma \leq$ 873 keV) encompassing the 847-keV gamma ray from the first excited state in ^{56}Fe (spectrum A) and for an interval (902 keV $\leq E_\gamma \leq$ 960 keV) at slightly higher gamma-ray energy (spectrum B). Spectrum B provides a good approximation of the Compton background contribution from higher energy gamma rays since this background is reasonably uniform over the two gamma-ray energy intervals specified above. These data, accumulated in a 14-hour LINAC run, have more than adequate counting statistics to determine considerable structure in the 847-keV gamma-ray production cross section, especially just above the threshold energy. The neutron energy resolution is about 1% at 1 MeV and is limited primarily by the use of a 20-nsec LINAC pulse width, However, the resolution of the present measurement can be improved by almost a factor of seven by using the available minimum pulse width of 3 nsec. The difference between TOF spectrum A and spectrum B corrected as described above for broad group cross sections, has been used to determine a high resolution gamma-ray production cross section for the 847-keV gamma-ray from $^{56}Fe(n,n'y)^{56}Fe$.

3.3 HIGH-RESOLUTION CROSS SECTIONS FOR Fe and Al

Figure 11 shows the integrated high resolution cross section for the 847-keV gamma-ray obtained from $4\pi\frac{d\sigma}{d\omega}(125°)$ with a small correction ($\sim$10% just above threshold, less than 2% above 3 MeV) for anistrophy of the gamma rays. The neutron energy resolution is represented by the FWHM of the triangle shown at various energies. The error bars shown for every fifth point include only the error due to counting statistics. There is an additional estimated systematic uncertainty (primarily from the absolute flux measurement) of about 10%.

These high resolution gamma-ray production cross-section measurements are not as suitable for radiation transport calculations as are broad group average cross sections. However, the determination of high resolution cross sections facilitates a comparison between continuous values obtained with the LINAC source and those obtained with a monoenergetic neutron source at widely spaced energies. This is especially true when the cross section has a great deal of structure.

Some previous determinations of the 847-keV gamma-ray production cross section using a monoenergetic neutron source are shown for comparison in Fig. 11. The present results are significantly lower (on the average about 23%) in the energy range, $5.6 \leq E_n \leq 7.8$ MeV than the measurements of Drake et al. (ref. 12), although there is good agreement at 4.0 MeV. There is good agreement up to 4.5 MeV with the values calculated from the (n, n') cross sections by Kinney and Perey (ref. 13). The present data are in close agreement with the recent data of Dickens and Perey (ref. 14) over the range $5.35 \leq E_n \leq 8.0$ MeV but are about 20% lower than their data at 9 MeV. There is good agreement with the Texas Nuclear Corp. (TNC) data except at 14.8 MeV where their results are about a factor of two higher. However, the present data are in excellent agreement with the 14-MeV measurements of Benetsky and Frank (ref. 16) and Clayeux and Grenier (ref. 17).

The present measurement provides the gamma-ray production cross section over a wide energy range $0.86 \leq E_n \leq 16$ MeV and fills in important energy gaps, especially in the 9- to 14- MeV region where no previous measurements exist. Also, the LINAC technique is capable of resolving serious discrepancies between different measurements. This is particularly true when these discrepancies are primarily a result of sharp structure in the cross section. This situation is very well illustrated by the 847-keV gamma-ray production cross section for Fe. Figure 12 shows various monoenergetic measurements of this cross section as reported in BNL-325 (ref. 18). Note that there is nearly a factor of two discrepancy between the high and low values in the energy range shown. These large differences are primarily caused by systematic differences and by sharp structure resulting in a great sensitivity of the measured cross-section values in these Van de Graaff experiments to small uncertainties

in the beam energy and resolution. The dark stars in Fig. 12 are the present high-resolution results averaged over ∿ 0.5 MeV wide intervals. The present data are somewhat higher than the recommended curve in BNL-325 and do not indicate a fall-off around 4.5 MeV.

High-resolution cross sections have also been determined for several strong lines from the $^{27}Al(n,n'y)^{27}Al$ reaction. Figure 13 shows the gamma-ray production cross section for the 1013-keV gamma ray. Note that even though this cross section is about a factof of 5 smaller than the 847-keV Fe cross section,the counting statistics are quite adequate for these data, which were accumulated in less than 14 hours. In the region just above threshold (up to 2.2 MeV) one can compare the gamma-ray production cross section to (n,n') cross-section measurements since the 1013-keV level in ^{27}Al decays predominantly by gamma-ray emission to the ground state (ref. 19). There is good agreement with the (n, n') cross-section measurements below 1.5 MeV of Chien and Smith (ref. 20). At higher energies there is agreement with Day's value (ref.21) at 2.6 MeV and Hosoe and Susuki's value (ref. 22) near 3 MeV. In addition, there is fairly good agreement with the TNC measurements (ref. 15) between 3.6 and 4.6 MeV and the measurements of Chung et al. (ref. 23) at 3.5 MeV. As for the Fe data, there is good agreement with the measurements of Dickens (ref. 24) between 5.35 MeV and 8.5 MeV and 20 to 30% lower values than the data of Drake et al. (ref. 12) at 6.0 and 7.7 MeV. However, the present results are in close agreement with the 4-MeV value of Drake et al. In the vicinity of 14 MeV the present results lie between recent measurements at 14.1 MeV (ref. 17) and 15 MeV (ref. 25).

3.4 BROAD GROUP CROSS SECTIONS FOR Fe AND Al

Differential gamma-ray production cross sections at 125° have been determined for the principal gamma rays from (n, xy) reactions in Fe and Al. Broad group average cross sections were determinedfor 20 neutron energy groups spanning the range $0.86 \leq E_n \leq 16.7$ MeV. Typical examples of the results are given in fig. 14 for Fe and fig. 15 for Al.

Figure 14 shows plots of the cross sections for the 1408-1412-keV doublet, the 1811-keV line and the 2599-2604-keV doublet compared to several previous Van de Graaff measurements. In general, the present results are in very good agreement with the TNC data (ref. 15), the measurements of Dickens (ref.14), and two measurements (refs. 17,26) near 14 MeV. The 1408-keV and 1811-keV cross sections are lower than the measurements of Dickens above about 8 MeV. The dip in the cross section for the 1408-1412 doublet near 12 MeV is a consequence of the threshold of the $^{56}Fe(n,2ny)^{55}Fe$ reaction at 12.85 MeV, above which there is a sharp increase in the yield of the 1412-keV gamma ray.

Figure 15 shows the differential cross section for three Al gamma rays, the 1809-,2210-, and 3001-keV lines. Comparison with existing published data is also given with fair agreement. The main disagreements are with the 14.8 MeV measurements from the TNC compilation (ref. 15) which are also higher than other 14-MeV measurements shown, and with the points of Drake et al. (ref. 12), at 6 and 7.5 MeV for the 2210-keV line.

3.5 CONTRIBUTION OF CONTINUUM GAMMA RAYS

In some cases the gamma-ray production cross sections measured for discrete lines represent only a fraction of the total gamma-ray production cross section. The present results for Fe at the higher neutron energies help illustrate this point. An examination of the Fe spectra reveals a significant number of weak gamma rays whose individual gamma-ray production cross sections are too small to determine accurately but whose collective sum amounts to a significant fraction of the total gamma-ray production cross section. For instance, Drake et al. (ref. 12), have unfolded their gamma-ray spectra (measured with a NaI detector) from (n, xy) reactions in iron at 6.0 MeV and 7.5 MeV to obtain the total gamma-ray production cross section. They obtain total gamma-ray production cross sections of 3.9 b at 6.0 MeV and 4.7 b at 7.5 MeV. The total gamma-ray production cross section for 27 lines obtained in our measurement for the interval $6.03 \leq E_n \leq 7.54$ MeV is 2.2 b. This is roughly half of the total gamma-ray production cross section measured in this energy region by Drake et al., (4.3 b, the average of the 6.0 MeV and 7.5 MeV values). Thus, it is very important that the gamma-ray production cross section of the many weak lines be accounted for.

Our data are currently being unfolded in order to obtain the cross section for these weak gamma-ray lines and continuum gamma rays. Figure 16 shows the results of a preliminary unfolding using the MAZE1 code (ref. 6), of the gamma-ray spectrum Ge(Li) detector operated in singles mode) from $^{nat}Fe(n,xy)$ reactions of neutrons in the range, $6.03 \leq E_n \leq 7.54$ MeV. The gamma-ray spectrum was corrected for scattered-neutron background (about a 20% correction) and compressed by a factor of 18 prior to unfolding. The unfolded spectrum is shown in fig. 16 up to about 5 MeV gamma-ray energy along with a comparison between the original spectral data and a refolded spectrum generated from the unfolded spectrum and the detector response matrix. Note that there is good agreement between the refolded spectrum and the data. Furthermore, most of the structure in the unfolded spectrum can be associated with strong discrete gamma-ray lines from Fe. The unfolded spectrum of fig. 16 was used to calculate the gamma-ray production cross section of the sum of discrete and continuum gamma rays for 240-KeV wide gamma-ray energy intervals. A preliminary value for the total gamma-ray production cross section for the interval $6.0 \leq E_n \leq 7.5$ MeV is 4.4 b, which is in excellent agreement with the value (4.3 b) obtained from the masurements of Drake et al. Similar gamma-ray production cross sections will be determined for other neutron groups so that data which include continuum gamma rays will be available for 10 neutron energy groups spanning the range, 0.85 to 16.7 MeV.

4. SUMMARY

Techniques based on the use of a LINAC pulsed neutron source and a Ge(Li) gamma-ray detector have been described for the measurement of secondary gamma-ray production data continuously over the entire neutron energy range of interest in the shielding of space nuclear systems. Epithermal capture gamma-ray yields (including continuum gamma rays) were measured over the neutron energy range, thermal to 100 keV, and typical results for natural tungsten and depleted uranium were presented and contrasted. Measurements of gamma-ray production cross sections for (n, xy) reactions in the energy range 0.85 to 16 MeV were described. Some representative results for iron and aluminum were shown and compared to previous monoenergetic measurements in order to illustrate some of the principal advantages of the LINAC technique.

Epithermal capture gamma-ray spectra can be quite different from thermal spectra and can vary with neutron energy. Consequently, it is important that these spectra be measured for other candidate shield materials so that the designer can realistically evaluate the relative merits of each material. There are several major advantages of using the LINAC technique to study gamma-ray production cross sections for (n, xy) reactions.

1. Data are obtained in a single experimental run over a wide neutron energy range which includes the 9 to 14 MeV region where monoenergetic measurements are difficult.

2. The data are obtained in a form (namely, group-averaged cross sections) most suitable for use in radiation transport codes.

3. Coupled with Ge(Li) unfolding techniques, the use of a LINAC source provides an attractive means of obtaining the complete gamma-ray production cross section (discrete and continuum gamma rays) over the full neutron energy range of interest.

5. ACKNOWLEDGEMENTS

We are pleased to acknowledge many helpful discussions in the course of this work with V.C. Rogers, M. P. Fricke and C. A. Preskitt.

REFERENCES

1. Leona Stewart, H.T. Motz and M.S. Moore, "Compilation of Requests for Nuclear Cross Section Measurements", WASH-1144, Los Alamos Scientific Laboratory (Draft Copy; November 1969).

2. K. J. Yost and M. Solomito, "Sensitivity of Gamma-Ray Dose Calculations to the Energy Dependence of Gamma-Ray Production Cross Sections", Proc. Neutron Cross Sections and Technology Conference, NBS Special Publication 299, Vol. i, p. 53 (1968).

3. V. J. Orphan, C. G. Hoot, A. D. Carlson, Joseph John and J. R. Beyster, Nucl. Instr. and Methods 72, 254 (1969).

4. R.K. Sheline, W.N. Shelton, T. Udagawa, E.T. Jurney and H.T. Motz, Phys. Rev. 151, 1011 (1966).

5. D. L. Price, R. E. Chrien, O.A. Wasson, M.R. Bhat, M. Beer, M.A. Lone and R. Graves, Nucl. Phys. A121, 630 (1968).

6. M. Sperling, "Unfolding with the MAZE1 System, Volume 1" DASA Report Gulf-RT-10486, Gulf Radiation Technology (January 1971).

7. Joseph John and V.J. Orphan, "Gamma Rays from Resonant Capture of Neutrons in ^{238}U." Gulf General Atomic Report GA-10186 (June 15, 1970).

8. V. J. Orphan and Joseph John, "Intensities of Gamma Rays from the Radiative Capture in Natural Tungsten of Neutrons from 0.02 eV to 100 keV", Gulf General Atomic Incorporated Report GA-9121 (December 31, 1968).

9. V. J. Orphan, C.G. Hoot, A. D. Carlson, Joseph John and J. R. Beyster, Nucl. Instr. and Meth. 73, 12 (1969).

10. H. W. Kraner and R. L. Chase, "A Total Absorption Ge(Li) Gamma-Ray Spectrometer", IEEE Eleventh Scintillation and Semiconductor Counter Symposium, Feb. 1968.

11. V. J. Orphan, C. G. Hoot, and Joseph John, Nucl. Sci. Eng. 42, 352 (1970).

12. D. M. Drake, et al., Nucl. Sci. Eng. 40 294 (1970).

13. W. E. Kinney and F. G. Perey, Nucl. Sci. Eng. 40, 396 (1970).

14. J. K. Dickens and F. G. Perey, ORNL-4592, Oak Ridge National Laboratory (September 1970).

15. P. S. Buchanan, "A Compilation of Cross Sections and Angular Distributions of Gamma Rays Produced by Neutron Bombardment of Various Nuclei, "Report No. ORO 2791-28, Texas Nuclear Corporation (1969).

16. B.A. Benetsky and I. M. Frank, Proc. of International Conference on Nuclear Physics, Paris (1964) 817.

17. G. Clayeux and G. Grenier, "Spectres de Renvoi des Gammas Produits par des Neutrons de 14, 1 MeV", Report No. CEA-R-3807, CEN-Saclay (1969).

18. M. D. Goldberg, Neutron Cross Sections, BNL-325, 2nd Edition, Supplement No. 2, Feb. 1966.

19. J. H. Towle and W. B. Gilboy, Nucl. Phys. 39 , 300 (1962).

20. J. P. Chien and A. B. Smith, Nucl. Sci. Eng. 26, 500 (1966).

21. R. B. Day, Phys. Rev. 102 , 767 (1956).

22. Masano Hosoe and Shoji Suzuki, J. Phys. Soc. Japan 14, 699 (1959).

23. K. C. Chung, et al., Nucl. Phys. A115, 476 (1968).

24. J. K. Dickens, "Al(n,xy) Reactions for $5.3 \leq E_n \leq 9.0$ MeV," ORNL-TM-3284, Oak Ridge National Laboratory (January 18, 1971).

25. K. Nyberg, B. Jonsson, and I. Bergqvist, private communication.

26. F. C. Engesser and W. E. Thompson, J. Nucl. Energy 21, 487, (1967).

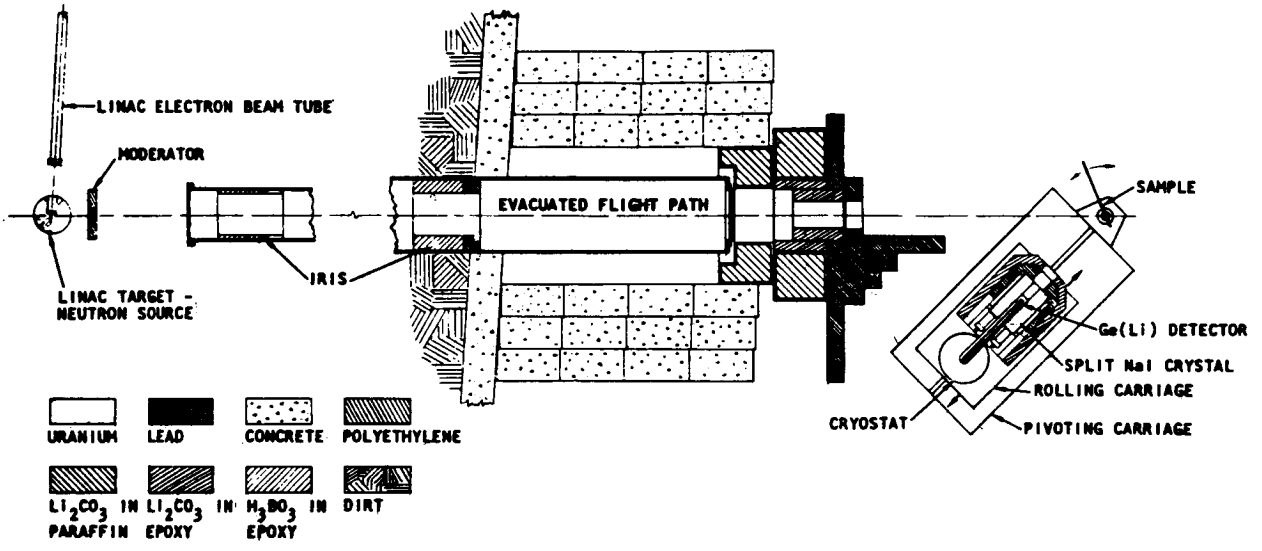

Figure 1. Schematic drawing of the capture gamma-ray facility. Details of the evacuated flight path, the beam defining collimators and the shielding arrangement are shown. To the right is the Ge(Li)-NaI(Tl) spectrometer with its shield and the movable carriage.

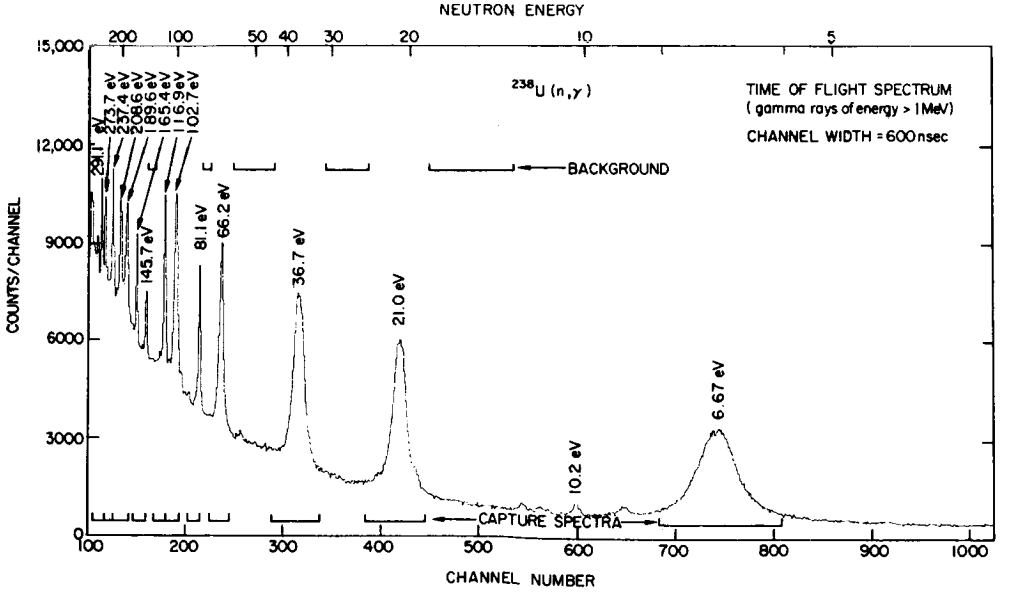

Figure 2. Neutron time-of-flight spectrum showing the low energy ^{238}U resonances. This spectrum was generated using only gamma rays that deposited at least 2 MeV in the Ge(Li) detector.

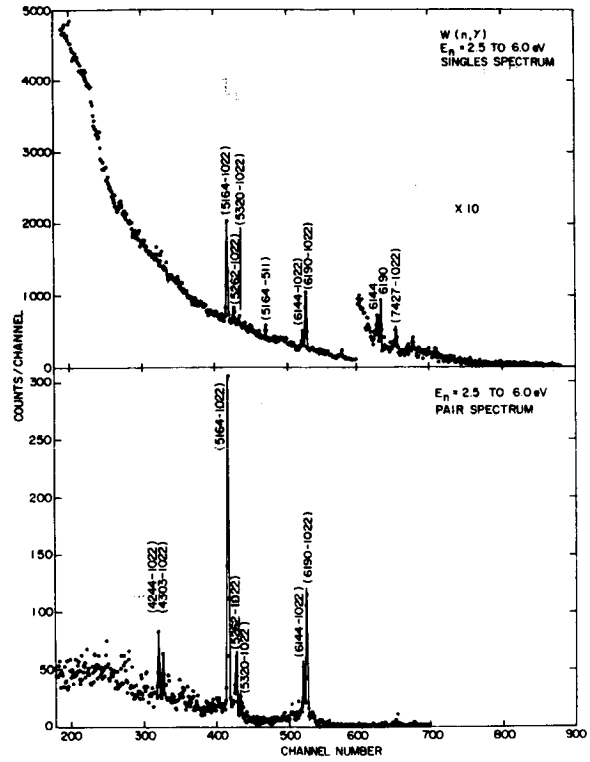

Figure 3. Comparison of capture gamma-ray spectra from tungsten obtained with singly-operated Ge(Li) detector (upper) and pair spectrometer (lower). Easy identification of peaks and high peak-to-background ratio in the pair spectrum is illustrated.

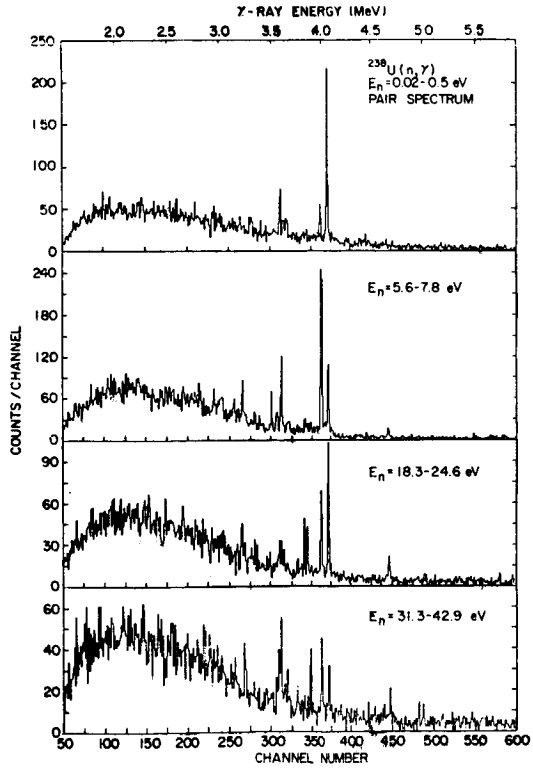

Figure 4. Comparison of measurements with the pair spectrometer of the ^{238}U capture spectra from neutrons in the energy ranges: 0.02-0.5 eV, 5.6-7.8 eV, 18.3-24.6 eV, and 31.3-42.9 eV.

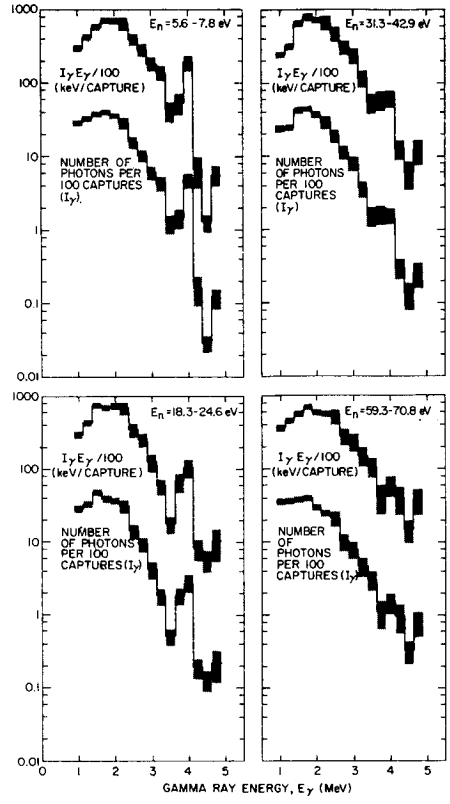

Figure 5. Intensities of capture gamma rays. The fractional radiated energy is also shown.

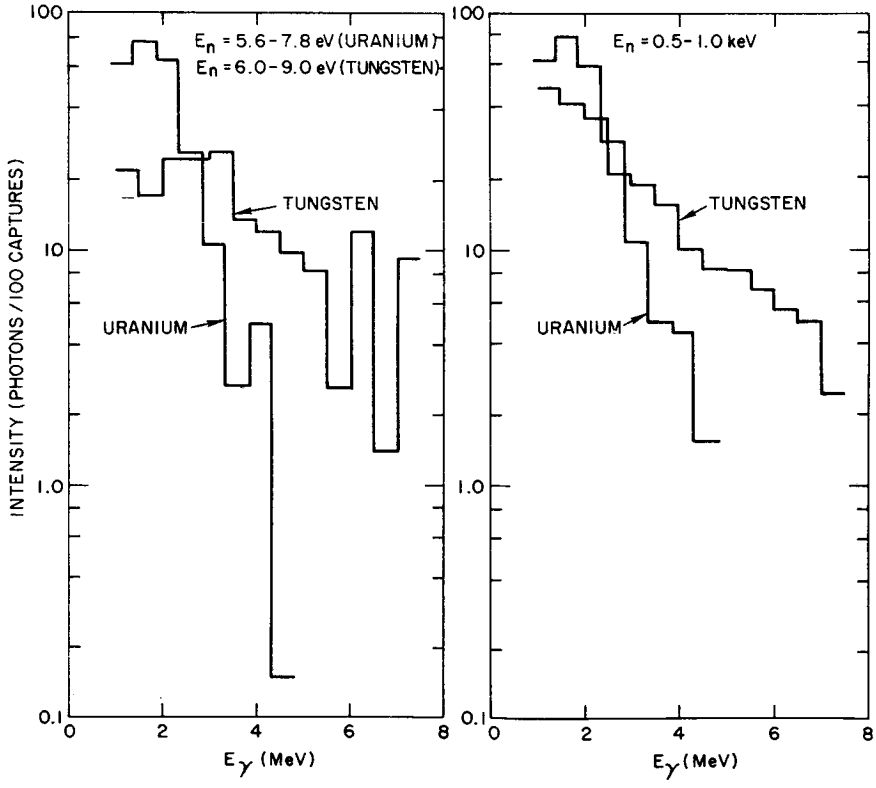

Figure 6. A comparison of capture gamma-ray intensities between uranium and tungsten for two neutron energy intervals.

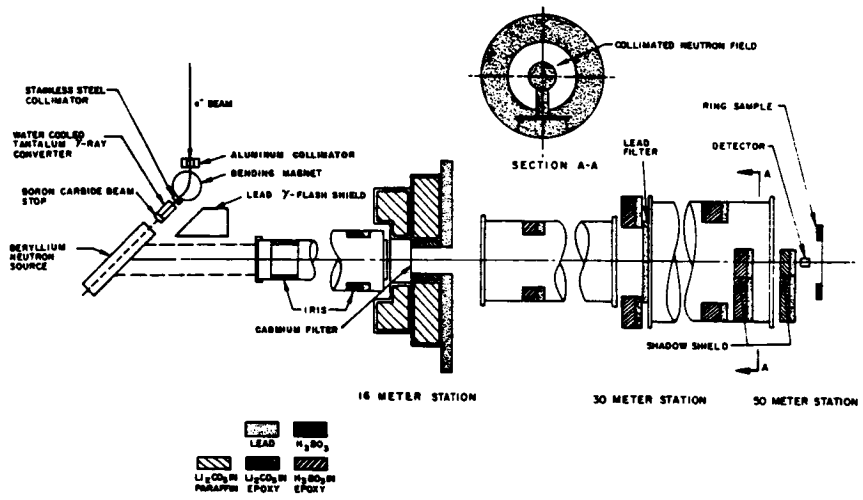

Figure 7. Schematic of the neutron flight path showing filters, irises, collimators, and shadow shields. The neutron source, the Ge(Li) detector, and the ring-shaped scattering sample are also shown.

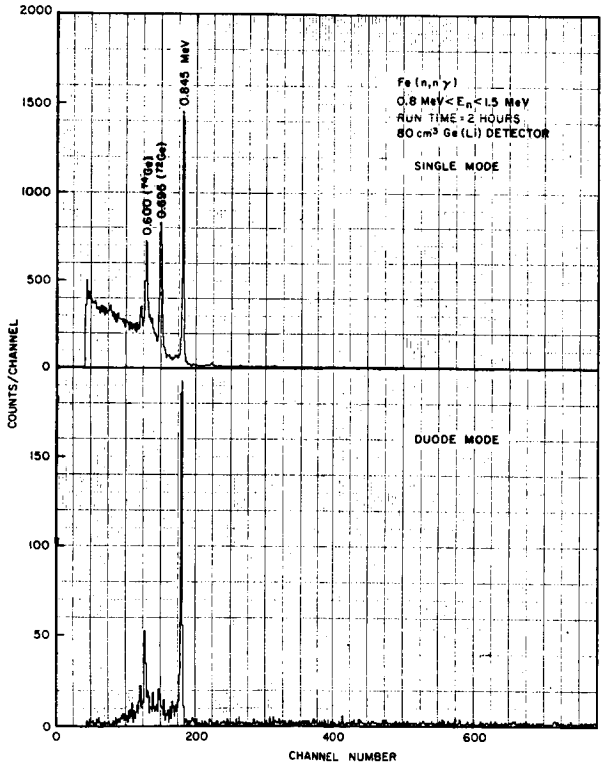

Figure 8. Gamma-ray spectrum from the $^{nat}Fe(n, n'\gamma)$ reaction for the neutron energy range, 0.8 MeV to 1.5 MeV, measured with the 80-cm^3 Ge(Li) detector in the singles mode (upper spectrum) and in the DUODE mode (lower spectrum).

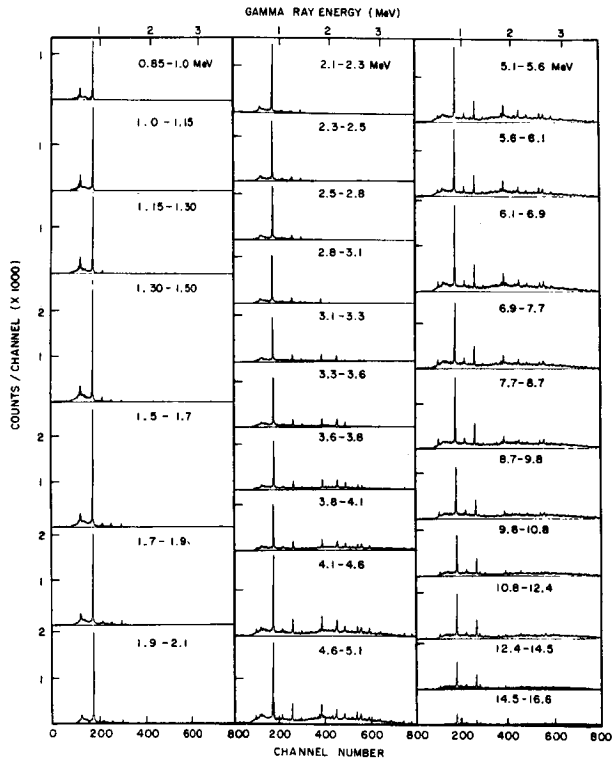

Figure 9. Gamma-ray spectra from Fe(n, xγ) reactions measured with the Ge(Li) detector operated in the DUODE mode. The variation of gamma-ray spectra with neutron energy is illustrated over the range, $0.85 \leq E_n \leq 16.6$ MeV.

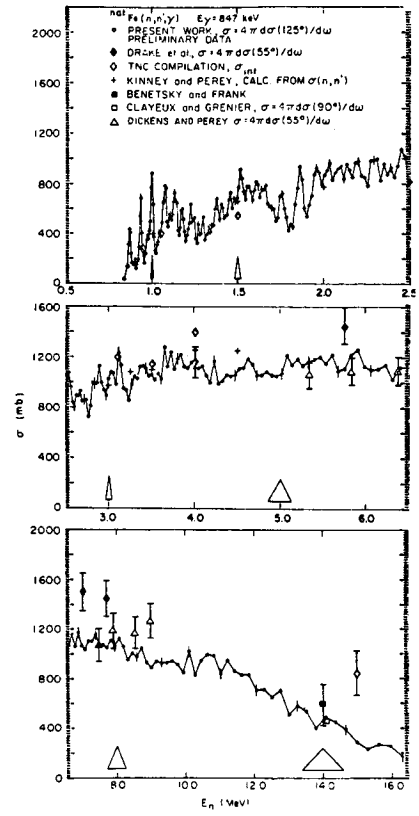

Figure 11. Gamma-ray production cross section for the 847-keV gamma ray from the ^{56}Fe(n, n'γ) reaction for neutron energy range, 0.86 MeV to 16 MeV.

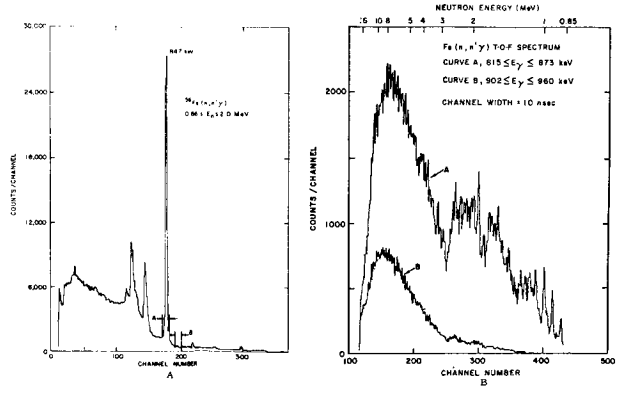

Figure 10. Gamma-ray spectrum from Fe(n, xγ) reactions (A) showing gamma-ray energy intervals for which the two time-of-flight spectra (B) were generated from two-parameter data.

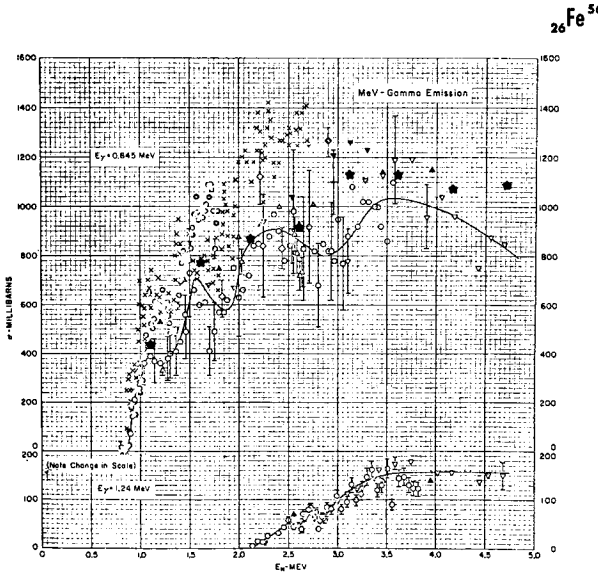

Figure 12. Comparison of present results averaged over ~ 0.5 MeV neutron energy intervals (indicated by "stars") with measurements compiled in BNL-325 (ref. 18).

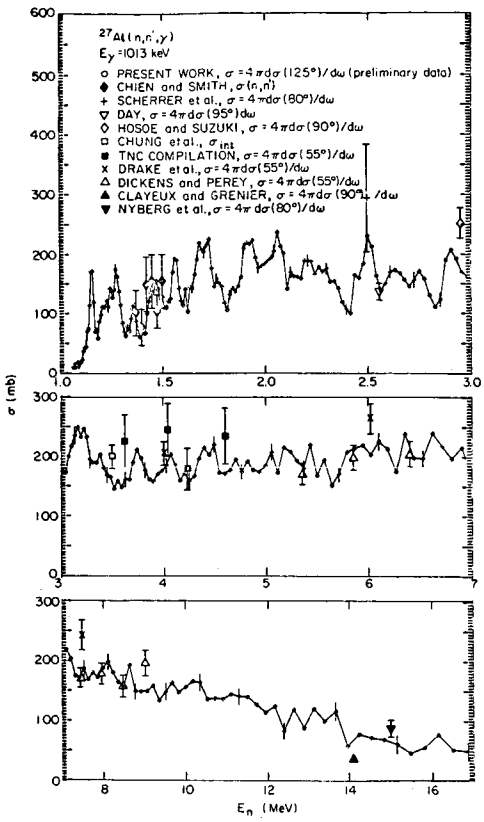

Figure 13. Gamma-ray production cross section for the 1013-keV gamma ray from the ^{27}Al(n, n'γ) reaction for neutron energy range 1.01 MeV to 16 MeV.

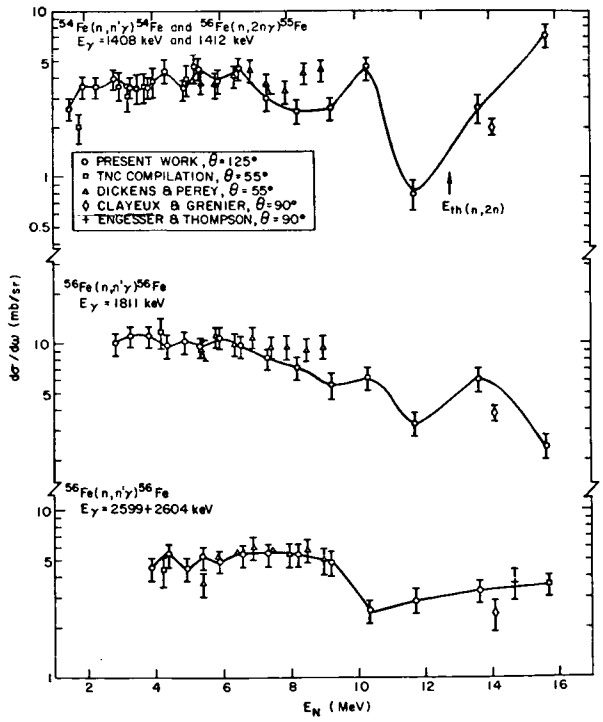

Figure 14. Differential gamma-ray production cross sections for neutron interactions with natural iron compared to previous data. The data points for the present work represent the average cross section over a neutron energy interval and are located at the midpoint of each interval. The solid line is simply a smooth curve connecting the present data points.

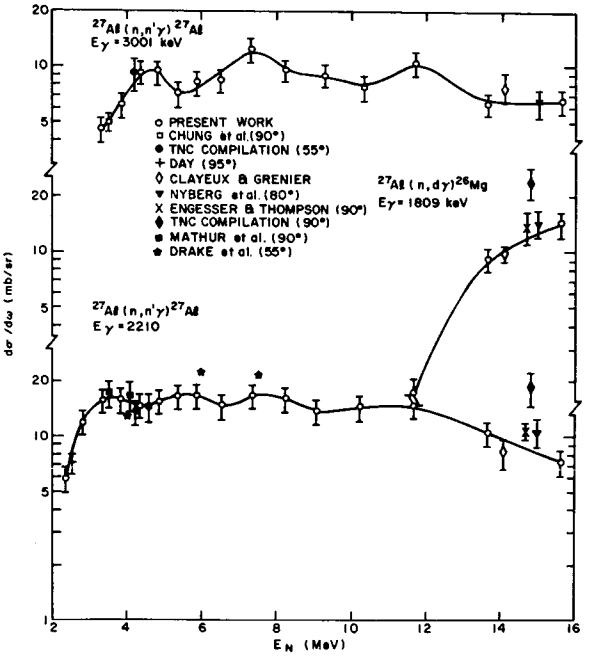

Figure 15. Differential gamma-ray production cross sections for neutron interactions with aluminum compared with previous data. The data points for the present work represent the average cross section over a neutron energy interval and are located at the midpoint of each interval. The solid line is simply a smooth curve connecting the present data points.

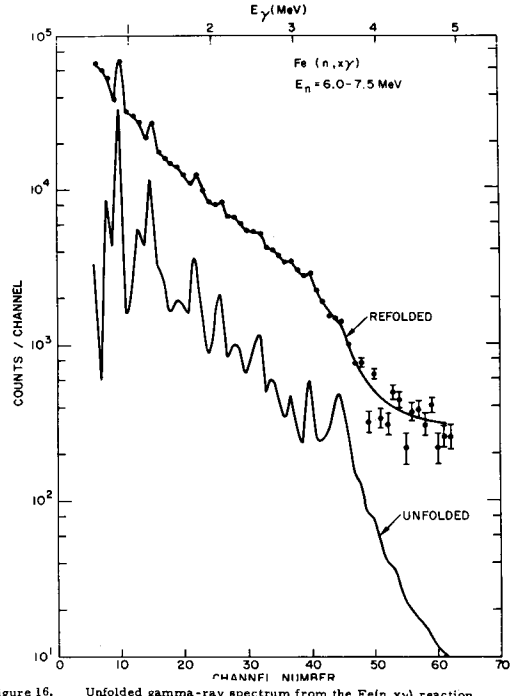

Figure 16. Unfolded gamma-ray spectrum from the Fe(n, xγ) reaction for neutrons in the neutron energy range 6.0 MeV to 7.5 MeV. The refolded spectrum is in good agreement with the original gamma-ray spectrum.

THE POPOP4 LIBRARY AND CODES FOR PREPARING SECONDARY GAMMA-RAY PRODUCTION CROSS SECTIONS

W. E. Ford, III

Oak Ridge National Laboratory
Oak Ridge, Tennessee

The POPOP4 code for converting secondary gamma-ray yield data to multigroup secondary gamma-ray production cross sections and the POPOP4 library of secondary gamma-ray yield data are described. Recent results in the "testing" of uranium and iron data sets from the POPOP4 library are given. The data sets were tested by comparing calculated secondary gamma-ray pulse-height spectra with spectra measured at the ORNL TSR-II reactor.

One of the primary considerations in the design of shields for reactors on spacecraft is the dose rate due to secondary gamma rays produced by neutron interactions in the fuel and in the structural and shielding materials. The importance of secondary gamma rays is illustrated by the calculated dose distribution shown in figure 1 for a three-cycle W-LiH shield for a SNAP-8 ZrH reference reactor (ref. 1). The design objectives were to limit the dose rate on the outer surface of the shield to a maximum value of 1.55×10^3 mrem/hr and to minimize the weight of the spherical shield. Note from the figure that before the constraint dose is obtained, the secondary gamma-ray dose rate predominates. These dose rates were calculated by coupling the transport of the neutrons and secondary gamma rays in a single discrete ordinates calculation. One of the requirements for a coupled calculation is accurate secondary gamma-ray production cross sections (SGRPXS's). To satisfy this requirement, the shield designer must have a readily accessible library of secondary gamma-ray yield data for the elements used in shield design, the means to convert the yield data to SGRPXS's in a format for use with the standard transport codes, and confidence in the accuracy of the data.

POPOP4, a FORTRAN-IV code, was written to convert secondary gamma-ray yield data as found in the literature for (n,γ), $(n,x\gamma)$, etc., reactions to any required neutron-gamma multigroup energy structure (ref. 2). If the yield data are in terms of gamma-ray intensity per neutron induced reactions, the code multiplies the converted multigroup yields by input multigroup neutron-reaction cross sections to give the SGRPXS's. [The neutron reaction cross sections are obtained from codes such as GAM-II or XSDRN (refs. 3 and 4).] POPOP4 sums the SGRPXS's for the various neutron-induced reactions to give total SGRPXS's for the nuclide of interest. Using codes such as the Sample Simple Coupling Code (ASSCC) (ref. 5), the POPOP4 cross sections are coupled with P_N neutron and gamma-ray cross-section sets for use in coupled neutron-gamma transport calculations. Discrete ordinates codes such as ANISN (ref. 6) and DOT (ref. 7) and Monte Carlo codes such as MORSE (ref. 8) use multigroup coupled cross sections produced as described above.

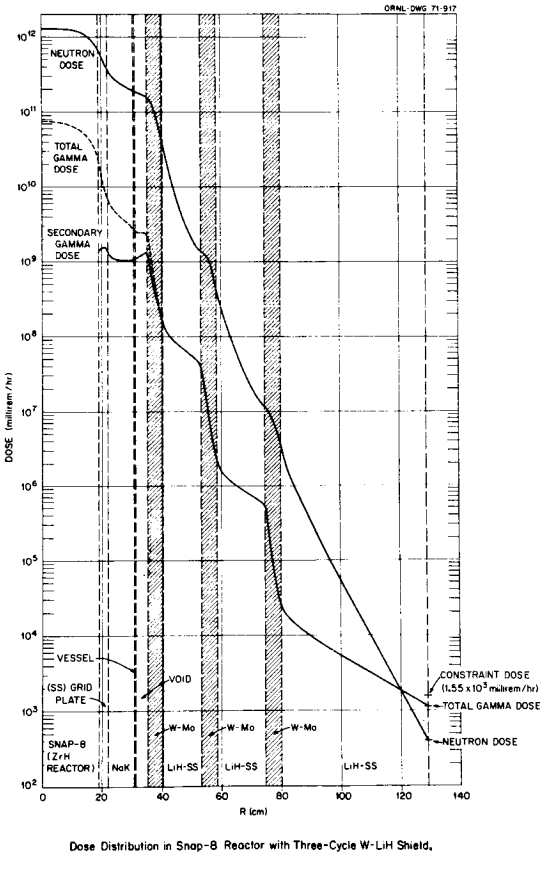

FIGURE 1.-Dose Distribution in SNAP-8 Reactor With Three-Cycle W-LiH Shield.

A compendium of neutron-induced secondary gamma-ray yield and cross-section data has been compiled for use with POPOP4. This collection of data is known as the POPOP4 library (ref. 9). Included in the library are capture and inelastic-scattering yield data sets from the United Nuclear Corporation publications (refs. 10, 11, and 12), Maerker's and Muckenthaler's measured secondary gamma-ray yields due to thermal-neutron captures in the elements found in soils, concretes, and structural materials (ref. 13), the yields for thermal-neutron captures in a large number of elements as compiled in the Nuclear Data publications (refs. 14, 15, and 16), the isotropic components of the gamma-ray production cross sections for Na, Mg, Cl, K, and Ca reported by Drake *et al.* (ref. 17), and many other (n,γ) and (n,xγ) data sets from the literature and from the private files of contributors. At present there are 223 data sets in the library for 79 elements or nuclides. The library is available on magnetic tape from the Radiation Shielding Information Center (RSIC). [POPOP4, the Sample Simple Coupling Code, and POPOP4 Library Tape Maker (ref. 5) - a code to make or update the POPOP4 library tape - are also available from RSIC.]

One of the most important objectives of the POPOP4 project is the "testing" of secondary gamma-ray yield data for use in shielding calculations. The data are tested by comparing measured secondary gamma-ray pulse-height spectra with spectra calculated using POPOP4 multigroup SGRPXS's prepared with data sets from the POPOP4 library.

A series of experiments was conducted by Muckenthaler *et al.* of ORNL's Neutron Physics Division to measure secondary gamma-ray pulse-height spectra resulting from the exposure of various slabs of reactor core, structural, and shielding materials to collimated neutron beams (refs. 13 and 18). The slabs were exposed to bare, Cd-filtered, and ^{10}B-filtered neutron beams emanating from the ORNL TSR-II reactor. A simplified illustration of the experimental configuration is shown in figure 2. Differential pulse-height spectra due to secondary gamma rays produced by neutron-induced reactions in the slabs were measured at a point 20 ft from the slabs. A borated polyethylene filter was placed between the NaI(Tl) detector and the slab to reduce thermal-neutron effects in the detector. Some materials required an additional LiH filter in front of the borated polyethylene to thermalize scattered neutrons. These experiments provided the standards for testing the data sets from the POPOP4 library.

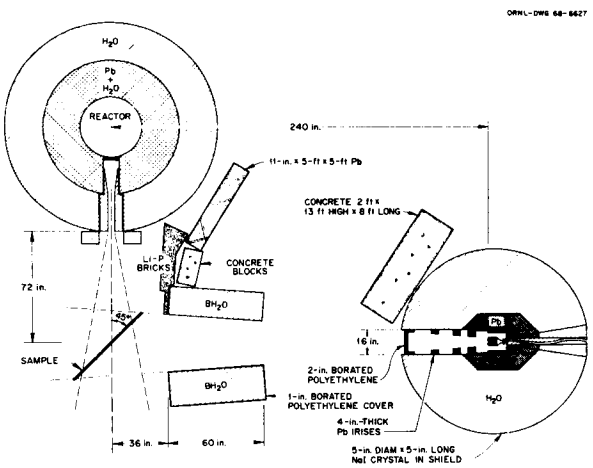

FIGURE 2.-TSR-II Experimental Configuration for Measuring Secondary Gamma-Ray Pulse-Height Spectra.

A flowchart illustrating the general procedure for calculating secondary gamma-ray pulse-height spectra is shown in figure 3. SGRPXS's were prepared by using POPOP4 to convert the yield data sets being tested to a 27 neutron - 60 gamma energy group structure and, if the data were given in terms of secondary gamma-ray yields, to combine the data with spectrally weighted, 27 group neutron reaction cross sections calculated with XSDRN or GAM-II. ASSCC was used to couple the SGRPXS's, P_3 neutron cross sections, and P_3 MUG (ref. 19) gamma-ray cross sections for the element of interest. Using multigroup representations of the TSR-II beams and the coupled cross sections as input, the one-dimensional discrete ordinates transport code ANISN was used to calculate the secondary gamma-ray angular flux emanating from the slabs. All ANISN calculations were made using a four-term expansion of Legendre polynomials and a 96th order of angular quadrature.

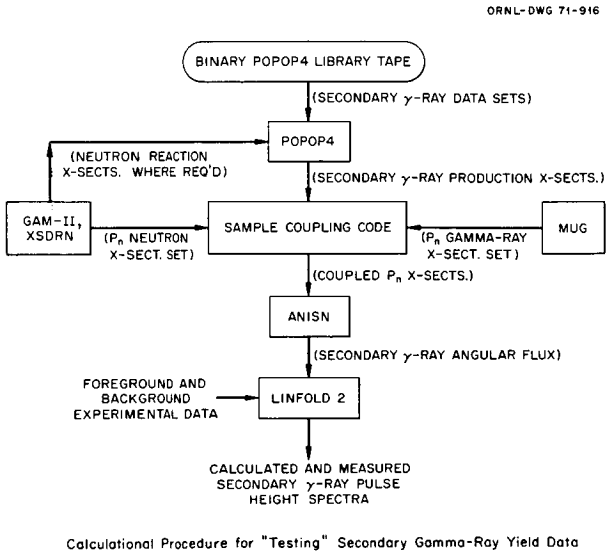

Calculational Procedure for "Testing" Secondary Gamma-Ray Yield Data

FIGURE 3.-Calculational Procedure for 'Testing' Secondary Gamma-Ray Yield Data.

The FORTRAN-IV code LINFOLD (ref. 5) was used to correct the ANISN angular flux for the geometric attenuation and for the attenuating effect of the detector neutron shield(s) - giving the intensity of secondary gamma rays striking the detector within each gamma group. One-fifth of the intensity within each group was assumed to be the intensity of five equally spaced discrete gamma energies within the group. Using Maerker's experimentally determined response functions for the NaI(Tℓ) detection system (ref. 13), the intensities of the discrete gammas were folded with LINFOLD to give the calculated spectra. Plots of the calculated and measured spectra were produced as the means for comparison.

Initial efforts in the data testing program were concentrated on the 23 Al, Fe, Ni, Cu, and Pb (n,γ) and $(n,n'\gamma)$ data sets from refs. 11, 12, 13, 14, and 16. Pictorial comparisons of the calculated and measured pulse-height spectra resulting from the exposure of slabs of these materials to the TSR-II neutron beams are shown in ref. 20. The comparisons provide a means of evaluating the validity of the data sets for various incident neutron energy ranges. Recent efforts have been directed to the testing of the U, W, and Ta data sets in the library and to the testing of a newly acquired Fe (n,γ) data set. To illustrate the testing procedure, recent results for U and Fe are described below.

Muckenthaler *et al.* measured the spectra resulting from the exposure of a 10.44 x 5.75 x 0.0304-in.-thick depleted uranium foil to the collimated TSR-II beams. Background was determined for each beam by measuring the spectra without the foil in place. The ^{235}U and ^{238}U number densities in the sample were 8.305×10^{-5} and 5.02×10^{-2} nuclei/barn cm, respectively. The foil was oriented as shown in figure 2 above. Since gamma rays are produced by the fission capture, non-fission capture, and the inelastic-scattering reactions in both ^{235}U and ^{238}U, and since the SGRPXS's depend on the resonance characteristics of the nuclides, the spectra comparisons for the foil provided an interesting challenge. XSDRN was used to calculate ^{235}U and ^{238}U P_3 neutron cross sections for the 27 neutron group structure. This calculation included the resonance self-shielding effects in both nuclides. Booth has shown that the secondary gamma-ray spectrum resulting from exposure of the foil to the Cd-filtered neutron beam minus 1.377 times the ^{10}B-filtered spectrum eliminates the effect of high-energy (fission) neutrons (ref. 21). Sample comparisons for the (Cd-1.377 ^{10}B) and bare neutron beams are shown in figure 4. The data sets used in the preparation of the SGRPXS's for the transport calculations are listed in Table I. Calculation B is a bare beam calculation which included SGRPXS's for all ^{235}U and ^{238}U neutron induced reactions <u>except</u> the ^{238}U (n,γ) reaction. SGRPXS's for all ^{235}U and ^{238}U neutron induced reactions were used in calculation D. The ^{238}U SGRPXS's for calculation D were prepared from data sets 928112, 928301, 928901, 925801, and 925804 as indicated in Table I. Calculation A is a (Cd-1.377 ^{10}B) calculation which included SGRPXS's for all reactions <u>except</u> the ^{238}U (n,γ) reaction, whereas, calculation C included SGRPXS's for all ^{235}U and ^{238}U reactions. A report describing similar tests of twelve uranium data sets from the POPOP4 library is in the final stages of preparation (ref. 25).

Measured spectra resulting from the exposure of an approximately 5-ft-square by 1/16-in.-thick Fe slab to the TSR-II beams were used as the standards for testing Fe data sets. Since the Cd-filter has a "cutoff" at 0.5 eV and a constant attenuation of 0.986 to neutrons above 1 MeV, and since the boron filter "cuts off" at approximately 10 keV and has

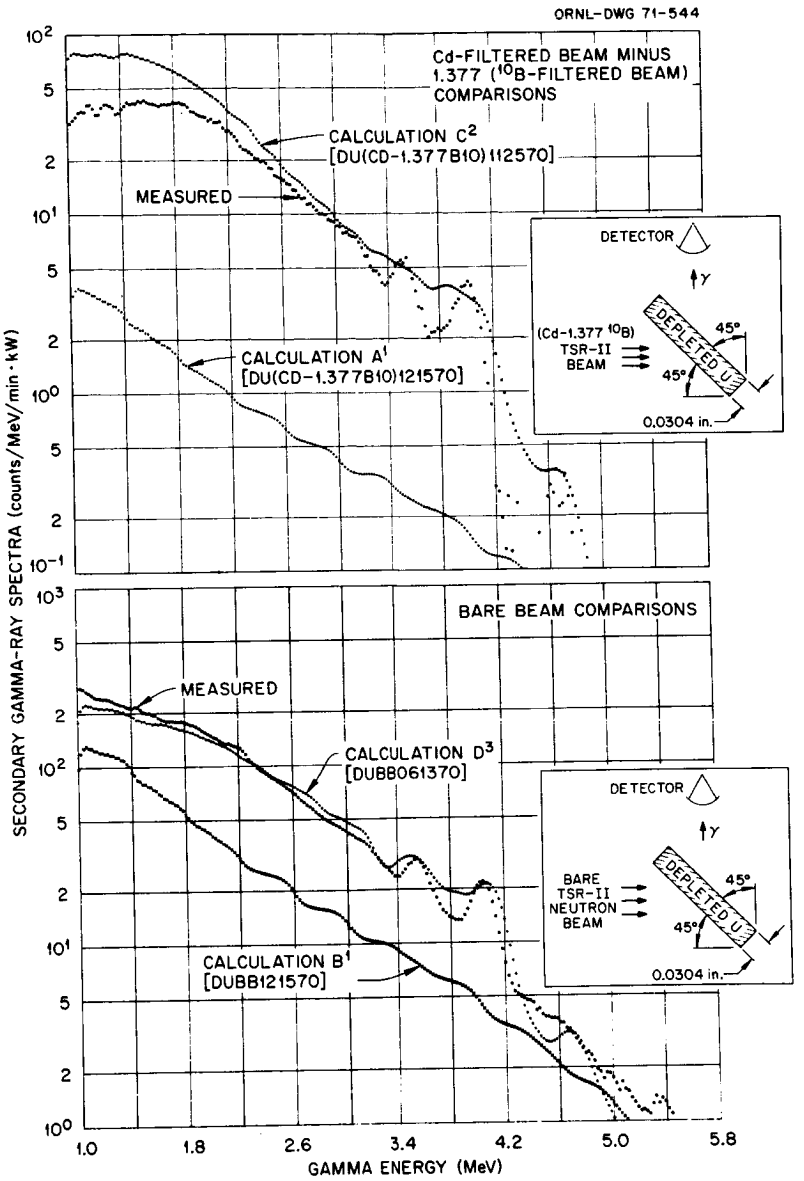

FIGURE 4.-Comparisons of Calculated and Measured Secondary Gamma-Ray Pulse-Height Spectra for a Depleted Uranium Foil.

*Ordinate caption should read Secondary Gamma-Ray Pulse-Height Spectra (counts/MeV/min.kW).

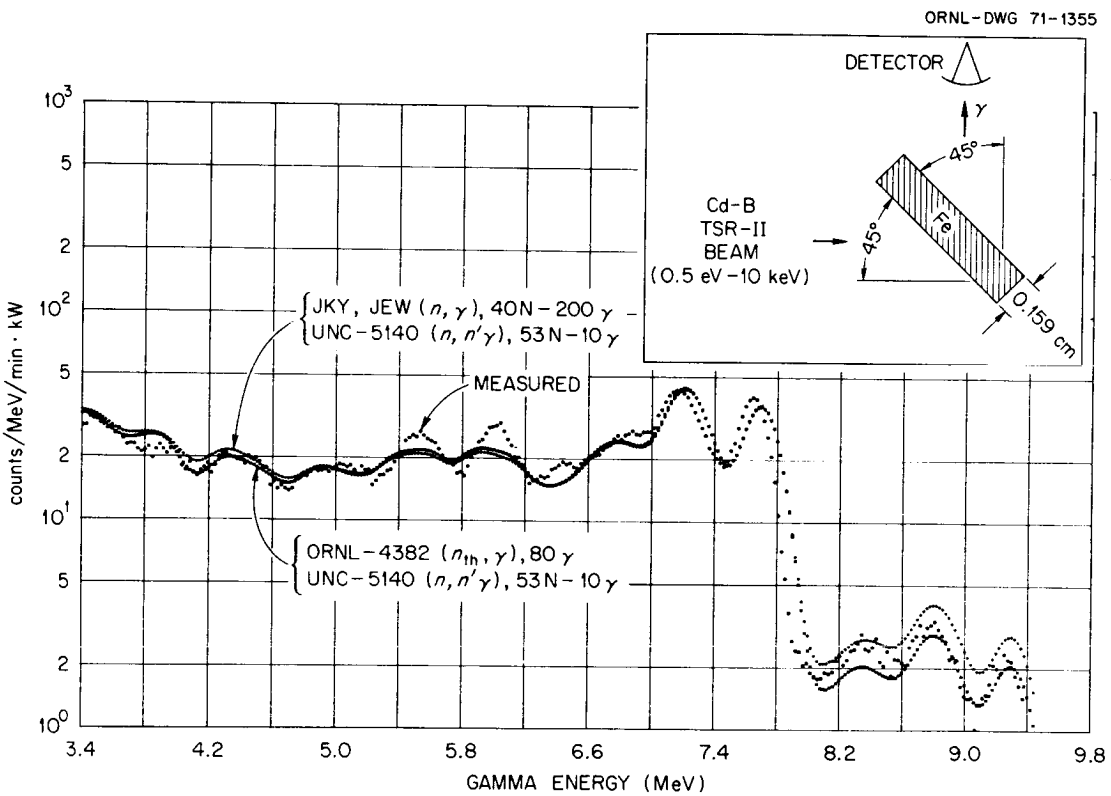

FIGURE 5.-Comparisons of Calculated and Measured Secondary Gamma-Ray Pulse-Height Spectra For an Iron Slab.

Table I. Uranium Secondary Gamma-Ray Yield Data

Data Set Identification Number†	Uranium Isotope/ Reaction	Source of Yield Data	Remarks
925101	$5/(n,\gamma)_{NF}$*	Ref. 12, p. 45	Yields given for 11 neutron groups ($3.7 \times 10^{-2} \leq E_n \leq 18.2 \times 10^6$ eV) and 13 discrete gamma energies ($0.0894 \leq E_\gamma \leq 6.42$ MeV). Data used for the $^{235}U(n,\gamma)$ reaction in all calculated spectra shown in Fig. 4.
925301	5/(n,n')	Ref. 12, p. 52	Yields given for 80 neutron groups ($1.27 \times 10^4 \leq E_n \leq 18.017 \times 10^6$ eV) and 11 gamma groups ($0.0 \leq E_\gamma \leq 6.50$ MeV). Data used for the $^{235}U(n,n')$ and (n,2n') reactions in all calculated spectra shown in Fig. 4. Assumed applicable to ^{238}U in Calculations A, B, and C.
925801	$5/(n,\gamma)_F$* and (n,2n')	Ref. 22	Thermal-neutron prompt and delayed fission capture yields given for 20 gamma groups ($0.0 \leq E_\gamma \leq 6.50$ MeV). These data assumed applicable to both ^{235}U and ^{238}U and to all incident neutron energies in Calculations A, B, and C. Data used in Calculation D for all neutron energies in ^{235}U SGRPXS and for $E_n < 1.1$ MeV in ^{238}U SGRPXS.
925804	$5/(n,\gamma)_F$	Ref. 22	Delayed part of 925801 data (t > 1 sec). Data used only in Calculation D for $E_n > 1.1$ MeV in ^{238}U SGRPXS.
928113	$8/(n,\gamma)_{NF}$	Ref. 23, pp. 51-65	Yields given for 21 neutron groups ($5.6 \leq E_n \leq 1.019 \times 10^5$ eV) and 16 gamma groups ($0.903 \leq E_\gamma \leq 4.807$ MeV). Data used in Calculation C for $^{238}U(n,\gamma)$ SGRPXS in applicable neutron energy range.
928112	$8/(n,\gamma)_{NF}$	Ref. 26	Yields given for 37 neutron groups ($0.0 \leq E_n \leq 11.08$ MeV) and 117 gamma groups ($0.0 \leq E_\gamma \leq 5.85$ MeV). Data used in Calculation C for $E_n < 5.6$ eV and $E_n > 1.019 \times 10^5$ eV. Data used in Calculation D for $E_n < 1.1$ MeV.
928301	8/(n,n') and (n,2n')	Ref. 12, p. 54	Yields given for 79 neutron groups ($0.337 \leq E_n \leq 18.02$ MeV) and 11 gamma groups ($0.25 \leq E_\gamma \leq 6.5$ MeV). Data used in Calculation D for $E_n < 1.1$ MeV.
928901	$8/(n,\gamma)_{NF}$, $(n,\gamma)_F$, and (n,n')	Ref. 24, p. 19	SGRPXS given for 15 neutron groups ($0.485 \leq E_n \leq 15.3$ MeV) and 12 gamma groups ($0.50 \leq E_\gamma \leq 6.5$ MeV). X-sects used in Calculation D for $^{238}U(n,\gamma)_{NF}$, $(n,\gamma)_{prompt\ F}$, and (n,n') reactions in applicable neutron energy range.

*$(n,\gamma)_{NF}$ is the nonfission capture reaction and $(n,\gamma)_F$ is the fission capture reaction.

†Each data set in the POPOP4 library is identified by a unique six-digit identification number.

Table II. Iron Secondary Gamma-Ray Yield Data

Data Set Identification Number	Reaction	Source of Yield Data	Remarks
260105	(n,γ)	Ref. 13, p. 67	Thermal-neutron capture yields given for 80 discrete gamma energies ($1.24 \leq E_\gamma \leq 9.30$ MeV). These data assumed applicable to all incident neutron energies in calculation labeled "ORNL-4382 ...."
260110	(n,γ)	Ref. 26	Yields given for 40 neutron groups ($0.0 \leq E_n \leq 1.0026$ MeV) and 200 gamma groups ($0.0 \leq E_\gamma \leq 10.0$ MeV). Data used in calculation labeled "JKY, JEW ...."
260301	(n,n')	Ref. 12, p. 35	Yields given for 53 neutron groups ($0.84 \leq E_n \leq 18.1$ MeV) and 10 gamma groups ($0.50 \leq E_\gamma \leq 10.0$ MeV). Data used in both calculations shown in Fig. 5.

a constant attenuation of 0.75 to neutrons above 1 MeV, the spectra from the (Cd-^{10}B) neutron beam provide a test of the epithermal Fe capture yield data (ref. 18). Two calculated spectra resulting from exposure of the slab to the (Cd-^{10}B) beam are compared with the measured spectrum in figure 5. The data sets used in the preparation of SGRPXS for the calculations are identified in Table II. Neutron cross sections for the calculations were calculated with GAM-II.

Results of these studies have proven that the conversion technique used in POPOP4 is satisfactory for the conversion of yield data to a required multigroup energy structure. Since the SGRPXS's are only as accurate as the yield data and the neutron reaction cross sections, the neutron cross sections must be properly weighted prior to being used. The growth envisioned for the POPOP4 library depends on the continued support of individuals who are willing to share their efforts with others.

REFERENCES

1. The calculation shown in figure 1 was made by R. L. Childs of Oak Ridge National Laboratory.
2. FORD, W. E., III; and WALLACE, D. H.: POPOP4 - A Code for Converting Gamma-Ray Spectra to Secondary Gamma-Ray Production Cross Sections. USAEC Report CTC-12, Union Carbide Corporation, 1969.
3. JOANOU, G. D.; and DUDAK, J. S.: GAM-II, A B_3 Code for the Calculation of Fast-Neutron Spectra and Associated Multigroup Constants. Gulf General Atomic Report GA-4265, 1963.
4. GREENE, N. M.; and CRAVEN, C. W., JR.: XSDRN - A Discrete Ordinates Spectral Averaging Code. USAEC Report ORNL-TM-2500, Union Carbide Corporation, 1969.
5. The Sample Simple Coupling Code, POPOP4 Library Tape Maker, and LINFOLD are documented in reference 20.
6. ENGLE, W. W.: A User's Manual for ANISN - A One-Dimensional Discrete Ordinates Transport Code With Anisotropic Scattering. USAEC Report K-1693, 1967.
7. MYNATT, F. R.: A User's Manual for DOT. USAEC Report K-1694 (to be published).
8. STRAKER, E. A.; STEVENS, P. N.; IRVING, D. C.; and CAIN, V. R.: The MORSE Code - A Multigroup Neutron and Gamma-Ray Monte Carlo Transport Code. USAEC Report ORNL-4585, 1970.
9. FORD, W. E., III: The POPOP4 Library of Neutron-Induced Secondary Gamma-Ray Yield and Cross Section Data. USAEC Report CTC-42, 1970.
10. TROUBETZKOY, E. S., *et al.*: Neutron Cross Sections of U^{238}, U^{235}, U^{237}, U^{239}, U^{234}, U^{236}, Pu^{239}, Pu^{240}, W, Pb, Ni, Cr, C, Li^6, Li^7, and T. United Nuclear Corporation Report UNC-5099, 1964.
11. RAY, J. H.; TROUBETZKOY, E. S.; and GROCHOWSKI, G.: Neutron Cross Sections of Nitrogen, Oxygen, Aluminum, Silicon, Iron, Deuterium, and Beryllium. United Nuclear Corporation Report UNC-5139, 1965.
12. CELNIK, J.; and SPIELBERG, D.: Gamma Spectral Data for Shielding and Heating Calculations. NASA Report NASA CR-54794 (UNC-5140), 1965.
13. MAERKER, R. E.; and MUCKENTHALER, F. J.: Gamma-Ray Spectra Arising From Thermal Neutron Capture in Elements Found in Soils, Concretes, and Structural Materials. USAEC Report ORNL-4382, 1969.
14. WAY, K., Ed.: Compendium of Thermal-Neutron-Capture Gamma-Ray Measurements, Part I. $Z \leq 46$. Nuclear Data, vol. III, nos. 4-6, pp. 367-650, 1967.
15. WAY, K., Ed.: Compendium of Thermal-Neutron-Capture Gamma-Ray Measurements, Part II. $Z = 47$ to $Z = 67$ (Ag to Ho). Nuclear Data, vol. V, nos. 1-2, pp. 1-242, 1968.
16. WAY, K., Ed.: Compendium of Thermal-Neutron-Capture Gamma-Ray Measurements, Part III. $Z = 68$ to $Z = 94$ (Er to Pu). Nuclear Data, vol. V, nos. 3-4, pp. 243-431, 1969.
17. DRAKE, M. K.; GARRISON, J. D.; and ALLEN, M. S.: Neutron and Gamma Ray Production Cross Sections for Sodium, Magnesium, Chlorine, Potassium, and Calcium. Nuclear Defense Laboratory Reports NDL-TR-89, vols. I-VI, 1967.

18. MAERKER, R. E.; and MUCKENTHALER, F. J.: Gamma-Ray Spectra Arising From Fast-Neutron Interactions in Elements Found in Soils, Concretes, and Structural Materials. USAEC Report ORNL-4475, 1970.
19. KNIGHT, J. R.; and MYNATT, F. R.: MUG - A Program for Generating Multigroup Photon Cross Sections. USAEC Report CTC-17, 1970.
20. FORD, W. E., III; and WALLACE, D. H.: The Use and 'Testing' of Al, Fe, Ni, Cu, and Pb Secondary Gamma-Ray Production Data Sets From the POPOP4 Library. USAEC Report CTC-20, 1970.
21. BOOTH, R. S.; and MUCKENTHALER, F. J.: The Total Gamma-Ray Energy Spectrum Above 1 MeV From Neutron Interactions in ^{235}U and ^{238}U. USAEC Report ORNL-TM-3060, Union Carbide Corporation, 1971 (to be published).
22. CLAIBORNE, H. C.: private communication.
23. JOHN, J.; and ORPHAN, V. J.: Gamma Rays From Resonant Capture of Neutrons in ^{238}U. Gulf General Atomic Report GA-10186, 1970.
24. NELLIS, D. O.; and MORGAN, I. L.: Gamma-Ray Production Cross Sections for ^{235}U, ^{238}U, and ^{239}Pu. Texas Nuclear Corporation Report ORO-2791-17, 1966.
25. FORD, W. E., III: The Testing of Uranium Secondary Gamma-Ray Production Data Sets From the POPOP4 Library - the 30-Mil Foil Comparisons. USAEC report (to be published).
26. YOST, K. J.; *et al.*: private communication.

NEUTRONS PRODUCED BY KNOWN ENERGIES OF IONS ABUNDANT IN SPACE

William W. Wadman III

University of California
Irvine, California

September 22, 1970

ABSTRACT

Particle accelerator radiation measurements can be applied to the present problem of calculating biological dose from radiation produced in the walls of a spacecraft by various ions in space. Neutrons, one of the products of the interactions of energetic ions with matter, are usually quite penetrating and have large values of Q.F. or R.B.E.

Ions of Helium, Boron, Carbon, Nitrogen, and Oxygen were accelerated to 10.4 MeV/nucleon and directed onto target materials of copper or Tantalum. The secondary neutron production was determined. Studies were made of the angular distribution and an inferred neutron spectrum was calculated from activities of threshold reaction detectors, although not in all cases.

The energy per nucleon of the experimental data is considerably lower than the average ion energies in space. From the literature, neutron production data for protons (hydrogen ion), deuterons (heavy hydrogen) and alpha (Helium ion) of various energies on various target materials was gathered. The first obvious fact that emerges is that neutron yield is a square function of the energy of the projectile ion.

It seems to be reasonable to assume that as the very light ion data describes various neutron yield increases with energy and increasing Z of the target, so one might expect for the light ion group. From the experimental data, neutron yields were extrapolated into the energy peak region of 300 MeV per nucleon for light ions in space. Beyond that energy, the ion energy spectrum falls off as $\propto E^{-2}$, producing a constancy in the neutron dose per ion beyond 300 MeV/nucleon. Such an extrapolation has not accounted for changes in the neutron spectra, modifications in the angular distribution in the higher energy model, or strange effects unique to very high energies per nucleon that are not now understood. It is felt that such considerations must be incorporated into a study of greater sophistication than this paper pretends.

NOTE: This work was performed under the auspices of the U.S.A.E.C.

I. Introduction

Ion beams with particles heavier than 4 a.m.u. and more energetic than 0.1 MeV/nucleon are found at only a few particle - accelerator laboratories in the world. The priority of such beam use therefore is understandably set up for primary research. Owing to a very competent crew, the UCLRL Berkeley, Heavy Ion Linear Accelerator (HILAC) was continuously improved until its original radiation shielding was no longer adequate. The Health Physics Department was assigned primary beam time to research the shielding problem. This opportunity was seized upon to simultaneously gain characteristic information of the secondary neutron radiation beyond shielding problems. Ion beams of He^4, B^{10}, B^{11}, C^{12}, N^{14}, and O^{16} were used to bombard targets of elemental Tantalum and Copper. The secondary neutron radiation was studied to determine neutron production, angular distribution from the target, and where possible, the neutron energy spectrum.

The resultant data were reduced to determine neutron production per incident 10.4 MeV/nucleon ion. At this point we were able to make a comparison to two other references using heavy ion beams. A literature search of neutron production revealed considerable data about the yields from proton and deuteron beams. A sparse amount was given about accelerated alpha (He^4) beams. That data was subsequently used as a basis for performing an extrapolation into the 300 MeV/nucleon region for heavy ions. From those results the neutron production of the various prominent free space ions was estimated and the neutron dose for the resultant flux was calculated.

II. The Experiment

The experiment incorporated a linear accelerator, a target of selected materials, beam current measuring apparatus, selected threshold detectors, detector mounting device for placing detectors at precise, predetermined positions and a power supply for secondary emission electron escape suppression.

During tune-up of the accelerator, a phosphor screen and remote controlled, local television set up were used to produce a visual picture of the beam shape and centering before running each experiment. After centering and shaping, the phosphor was removed and the beam was directed onto the target, maximized for optimum current and interrupted with an upstream Faraday cup while the detectors, mounted on the mounting ring or "Halo" as we named it, were secured in place.

A. Threshold Reaction Detectors

Materials for the threshold reaction detectors were selected on the basis of the reaction threshold, reaction cross-section and suitable half-life. These are but a part of a set of criteria set by Ringle(1) for fast neutron spectroscopy at UCLRL. Table I summarizes the properties of the threshold detectors as used in this work. For various technical reasons not all detectors were used for every experimental run.

Table 1. Threshold Detector Properties

Reaction	Calculated threshold (MeV)	Peak cross section (barns)	Product half-life	Isotope (%)	Energy of γ-ray of reactant used for data (MeV)
$^{58}Ni(n,p)^{58}Co$	1.1	0.556	71 days	67.8	0.81
$^{59}Co(n,c)^{56}Mn$	5.4	0.112	2.6 hrs.	100	0.845
$^{65}Cu(n,p)^{65}Ni$	4.1	0.035	2.6 hrs.	30.9	1.5
$^{27}Al(n,a)^{24}Na$	6.7	0.243	15 hrs.	100	1.37
$^{203}Tl(n,2n)^{202}T$	18.5	2.78	12 days	29.5	0.44

Table 1. Threshold Detector Properties (Continued)

$^{127}I(n,2n)^{126}I$	9.5	2.02	13 days	100	0.65
$^{58}Ni(n,2n)^{57}Ni$	12.4	0.25	37 hrs.	67.8	1.36

B. The Faraday Cup-Target

The target material was mounted at the back of the Faraday Cup. A ring was mounted on insulators ahead of the cup and connected via a feed-through to a high voltage connector. In this way we were able to apply a high negative potential to suppress secondary emission electrons from escaping and giving an erroneously high beam current reading. The beam current was integrated with an LRL designed beam current integrator. The charge state of the accelerated ions had to be considered to accurately state the number of beam particles stopped in the target. The Target materials were selected for their wide spread use at the accelerator and the primary reason for our studies. Elemental tantalum and oxygen-free, high conductivity copper were the two materials used as targets.

III. Data Reduction

The Threshold detectors were removed after sufficient integrated beam current was achieved, and counted in a low background counting facility. The gamma-ray spectrum of each detector was measured with a Sodium Iodide (NaI) crystal and a multichannel analyzer. That information was transferred to punched cards for computor compatible form input. The gamma-ray peaks of each of the reaction product were then stripped and reduced to an absolute disintegration rate by accounting for detector efficiency, counting geometry and peak to total ratios and abundance of the target isotope and branching ratio of the gamma-ray. The resultant disintegration rate was used along with the calculated activities of other reactions in the same position of the same run and each was corrected in terms of the saturation activity, decay, counting times for input into a program to calculate neutron spectra.

For our purposes here, the neutron spectra for these energies per nucleon, represent typical evaporation neutron spectra, and show only a moderate flux increase in the forward direction.

In later considerations, at the 300 MeV per nucleon region, one would logically expect a pronounced forward flux owing to cascade effects. In the extrapolation to 300 MeV per nucleon, the increased neutron production is recognized, the forward peaking is believed to cancel out when the isotropic nature of the incident ions is considered.

IV. Results

A. Neutron Yields

The following results were obtained and are summarized in Table II.

Table II. Neutron Yield Per Incident Particle

Beam Ion	Target Material	
10.4 MeV/nuc.	Cu	Ta
He^4	3.99×10^{-3}	2.16×10^{-3}
B^{10}	3.22×10^{-3}	3.89×10^{-3}
B^{11}	3.74×10^{-3}	---
C^{12}	2.96×10^{-3}	3.84×10^{-3}
N^{14}	2.59×10^{-3}	---
O^{16}	1.70×10^{-3}	2.52×10^{-3}

The values of neutrons per bombarding particle are integrated from data taken from the numerous angles utilized on the Halo.

The threshold detectors data were supplemented with moderated indium foils, which were quite helpful in establishing the true yield. The $Ni^{58}(n,p)Co^{58}$ reaction threshold of 1.2 MeV is only 2% of the peak cross section. With the neutron spectrum being comprised mostly of evaporation neutrons, it was felt that too much uncertainty could arise if we relied solely on the threshold detectors.

B. Anisotropy

The ion population of free space has a random direction. One would therefore assume that any high-energy or forward peaking of secondary neutrons would also be subject to such randomness. At the very low energies as achieved in this work, forward peaking is apparent in the total flux. As one observes the activities of successively higher energy threshold detectors, the forward prominence is increasingly pronounced. The prominence is greater with lighter bombarding ions and also lighter target elements.

V. Extrapolation of the Data to Space Ion Energies

A. Production Curve Models

To apply this data to the same ion types in space and to do so in a way which is both logical and realistic, we felt we should look at other experimental data on production of neutrons.

On heavy-ions, (B,C,N,O) only one report dealt with production, and one with angular spectra which could be integrated.

All other references were for He^4, $_1H^2$, and $_1H^1$. From all the references we compiled the production data according to particle type, target material and particle energy.

All data was put in terms of neutrons per bombarding particle as a function of the Energy per Nucleon of the bombarding particle. Smooth curves were drawn between the points involving the same ion and target type.

What we found was much of what we expected. Most of the curves tended to exhibit the same

shape although shifted somewhat according to ion type and target type.

B. Heavy Ion Production Curve Fitting

Using the other charge particle production data, and four points of different energy C^{12} on Ta data by Hubbard Pyle and Main(2), as models, (and some courage and lots of daring) we fit our data into the picture. By merely extrapolating out to 300 MeV per nucleon along a shape of the Copper or Tantalum curves, one arrives at values which, based on all of parameters that entered into the basic data, should be fairly realistic neutron yields.

At 300 MeV/nucleon then, one would expect the following values.

Table III. Neutron Yield Per Incident Particle

300 MeV/nuc.	Cu	Ta
He^4	7.5	4.1
B^{10}	6.1	7.4
B^{11}	7.1	- -
C^{12}	5.6	7.3
N^{14}	4.9	- -
O^{16}	3.2	4.8

It should be noted that the He^4 data might be on the low side by a factor of 2-3. Proton productions are typically an order of magnitude lower.

VI. Summary

Ions of Boron, Carbon, Nitrogen, and Oxygen which typically make up only $\approx$0.5% of the free space ion population combined, exhibit neutron yields such that they are estimated to produce nearly 5% of the total first collision dose.

As the importance of reducing the neutron fluence within the confines of space vehicles becomes increasingly important, from either personnel radiation exposure, or radiation damage to electronics components, then the data herein presented must be greatly refined. New research is required as higher ion energies become available, and spectroscopy techniques are improved, as well as when more accurate determinations of the free space ion populations are made.

Until then, calculations seem to present a most reasonable approach to estimating the radiation dose rate wothout relying upon extrapolations which extend over 1.3 orders of magnitude for answers.

VII. Acknowledgements

The author wishes to express his thanks to the UCLRL Health Physics Department, all of whom contributed greatly during the data collection and reduction; to David Pistenna+ and Walter Gundaker++ for many long hours during the accelerator and counting runs.

VIII. References

1. J. C. Ringle, A Technique for Measuring Neutron Spectra in the Range 2.5 to 30 MeV Using Threshold Detectors. UCRL-10732, Oct. 11, 1963.

2. E. L. Hubbard, R. M. Main, and R. V. Pyle. Neutron Production by Heavy Ion Bombardments Phys. Rev. 118, 2, pp. 507-514, April 15, 1960.

+Now Ph.D. M.D. at Stanford Medical School, Department of Radiology.
++Now at Bureau of Radiological Health, U. S. Dept. of Health, Education, and Welfare, Rockville, Md.

Accelerator Measurement of the Energy Spectra of Neutrons Emitted in the Interaction of 3-GeV Protons with Several Elements

W. J. Nalesnik, T. J. Devlin*, M. Merker, and B. S. P. Shen

Astrophysics Laboratory and Princeton-Pennsylvania Accelerator,
University of Pennsylvania, Philadelphia, Pennsylvania

Abstract - The shapes of the energy spectra of neutrons between 20 and 400 MeV emitted at 20°, 34°, and 90° in the bombardment of C (1.8 g cm^{-2}), Al (1.7 g cm^{-2}), Co (4.4 g cm^{-2}), and Pt (81.5 g cm^{-2}) targets by 3-GeV protons have been measured by time-of-flight techniques.

In the study of the mechanism of spallation reactions (ref. 1), in certain aspects of astrophysics and geophysics (ref. 2), and in high-energy shielding and dosimetry (ref. 3), it is often important to know the energy spectrum of neutrons emitted in spallation reactions induced by high-energy protons. This paper gives a preliminary report of our measurements of such spectra at the Princeton-Pennsylvania Accelerator. We present here neutron spectra from 20 to 400 MeV at 20°, 34°, and 90° for 3-GeV protons incident on cylindrical targets of carbon (1.8 g cm^{-2} diameter), aluminum (1.7 g cm^{-2} diameter), cobalt (4.4 g cm^{-2} diameter), and on a 0.64 cm x 0.64 cm x 81.5 g cm^{-2} thick platinum target.

Figure 1 shows the experimental arrangement. The target being bombarded is located in the internal circulating beam of the accelerator. Collimated neutral beams emerge from the target at 20, 34, and 90 degrees with respect to the direction of the internal beam. Charged particles are removed from the neutral beams by sweeping magnets. We determine neutron energy by measuring the time elapsed between the production of the neutron and its subsequent detection by a plastic scintillator placed in the beam line at a known distance from the target. The target is struck every 269 nanoseconds by a proton bunch approximately one nanosecond in width. The proton beam intensity in this operating mode is on the order of 5×10^{10} protons/second. The length of the flight path, viz. the distance between the target and the neutron detector, is limited by the accelerator shielding; this determines the lowest energies that can be measured by time of flight. The flight paths are thus 22, 37, and 44 feet at 90, 34, and 20 degrees, respectively. Since we are currently extending our results to lower energies by other techniques, only results for neutron energies greater than 20 MeV are presented here.

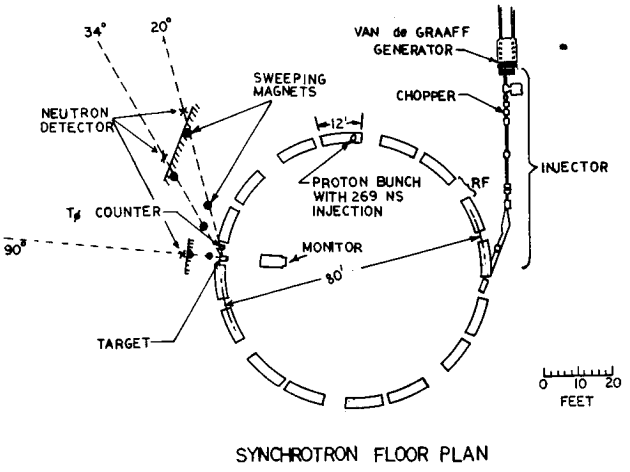

Figure 1. Experimental arrangement at the Princeton-Pennsylvania Accelerator, showing beam lines and detector locations.

* Department of Physics, Rutgers University, New Brunswick, New Jersey; on leave at CERN, Geneva, Switzerland.

The time at which a neutron leaves the target is determined by the Cerenkov detector TØ located about 2 feet from the target. The neutron detector consists of a 1 inch x 2 inch x 2 inch block of Pilot M scintillator joined to an Amperex 56 AVP photomultiplier by a lucite light pipe. This same detector is used in all three beam lines, with beam particles incident on the 2 inch x 2 inch face. The efficiency of the detector was calculated using the well-known UCRL computer code of R. J. Kurz (ref. 4) modified by Michael Hauser (ref. 5) of Princeton University. This program yields fairly good agreement with experimentally determined efficiencies up to about 150 MeV. The neutron-detector efficiency is given in Figure 2 for thresholds of 1 MeV and 2 MeV electron energy for a detector resolution of 10 %. The 1 MeV threshold was employed for the 90 degree cases, and the 2 MeV threshold for the 20 and 34 degree cases.

Each time a particle is detected, the time delay between the most recent TØ pulse and the neutron detector particle signal is measured by a time-to-amplitude converter (ref. 6). Its output, together with the neutron detector pulse height, is fed to a PDP-9 computer which records these data for each event. The computer also provides on-line display of the time-of-flight spectrum and the pulse-height distributions as a function of time-of-flight. Scalers also monitor the integral neutron detector events as well as other information for the determination of relative beam intensities.

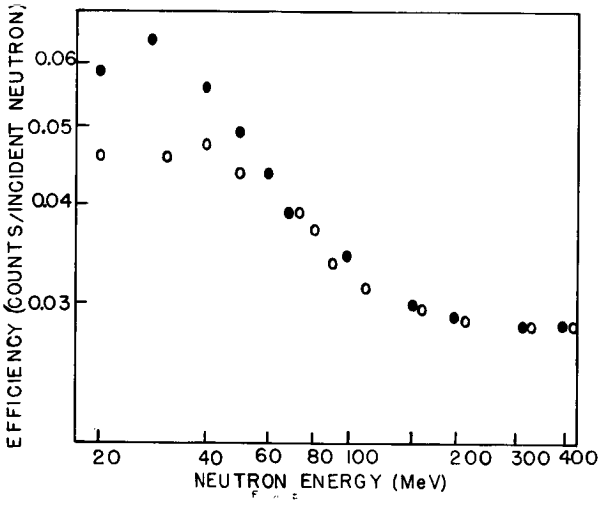

Figure 2. Neutron-detection efficiency as a function of neutron energy, calculated using the Kurz efficiency program. Filled circles are for a threshold of 1 MeV; open circles are for a threshold of 2 MeV.

Figure 3 shows a typical time-of-flight spectrum as displayed by the on-line computer. The peak on the extreme right is due to prompt gamma rays (neutral pion decays, etc.) from the target; all of these gammas have the same flight time. The gamma peak is used as the zero-point for the time determination. The width of the gamma peak at half maximum provides a measure of the time resolution of the system, which is about 2 nanoseconds.

The system is calibrated using the prompt gamma rays as follows. The accelerator is operated in the full injection mode in which there are eight circulating proton bunches per cycle. Thus, the target is struck every 33.65 nanoseconds by a proton bunch, resulting in eight spectra displaced and overlayed in the space occupied by the single spectrum produced by the 269 nanosecond injection. Knowing the distance between each of the eight gamma peaks both in real time and in time-to-amplitude converter channels enables the system to be calibrated to an accuracy of about 2%.

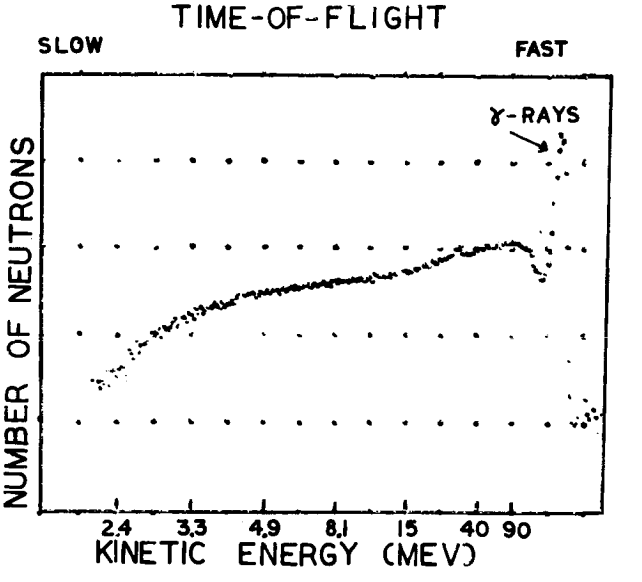

Figure 3. Typical time-of-flight spectrum as displayed by the on-line computer.

Figures 4, 5, and 6 give the relative energy spectra obtained at 20, 34, and 90 degrees, respectively. The histograms are obtained by converting the recorded flight times into energies and collecting them into bins of equal width in log E. The total count in each bin has been divided by the bin width in MeV and the detector efficiency. The error bars represent counting statistical errors only. The effects of activation gammas in the nearby wallshave recently been studied and

preliminarily indicate a contribution similar to counting statistics. Contamination of the neutral beams by charged particles has been checked with an anticoincidence scintillator shield. The present results indicate little or no charged particle contamination up to 400 MeV. Overall normalization of the neutron spectra with respect to the number of incident protons has not yet been determined at this writing.

Table 1 gives the approximate inverse-power-law exponents of the spectra shown in Figures 4, 5, and 6 for the energy intervals 20-40 MeV, 40-100 MeV, and 100-400 MeV. It can be seen that, in every case, the spectrum from 40-100 MeV is much less steep than that for either 20-40 MeV or 100-400 Mev. This effect results largely from the shape of the Kurz efficiency curve shown in Figure 3. Table 1 also shows that, in a given energy interval, the spectrum generally tends to steepen with increasing emission angle and, to a lesser extent, with increasing target mass number.

In considering Table 1 and Figures 4, 5, and 6, it should be borne in mind that, while the C, Al, and Co targets are "thin", the Pt target is not (81.5 g cm^{-2} thick).

This research was supported in part by NASA and USAEC.

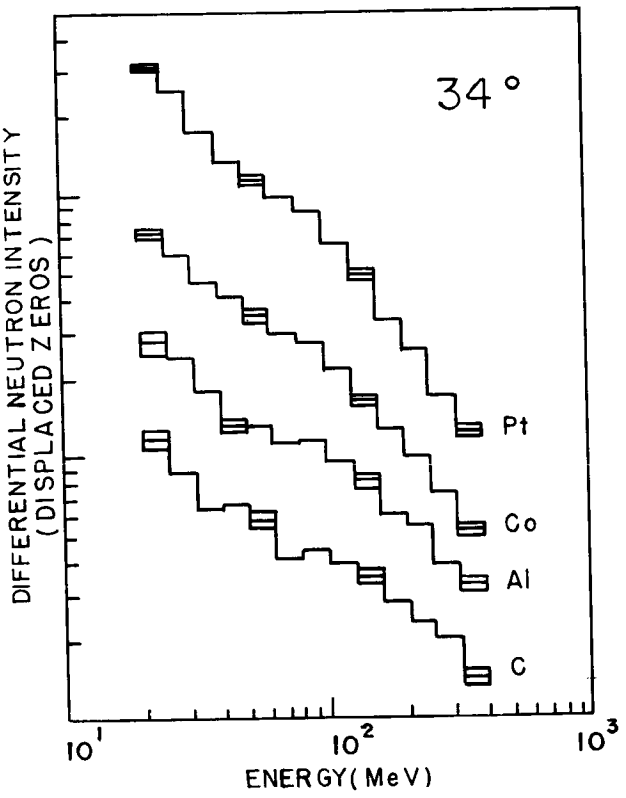

Figure 5. Same as Figure 4, at 34° emission angle.

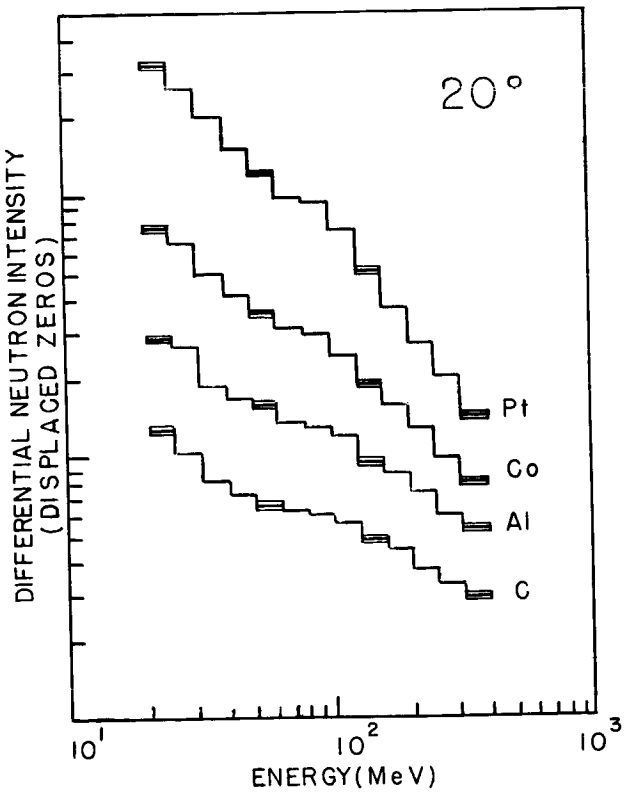

Figure 4. Measured differential neutron spectra for neutrons emitted at 20° from targets bombarded by 3-GeV protons. Representative counting statistical errors are indicated in several energy bins by triple-lined histogram segments.

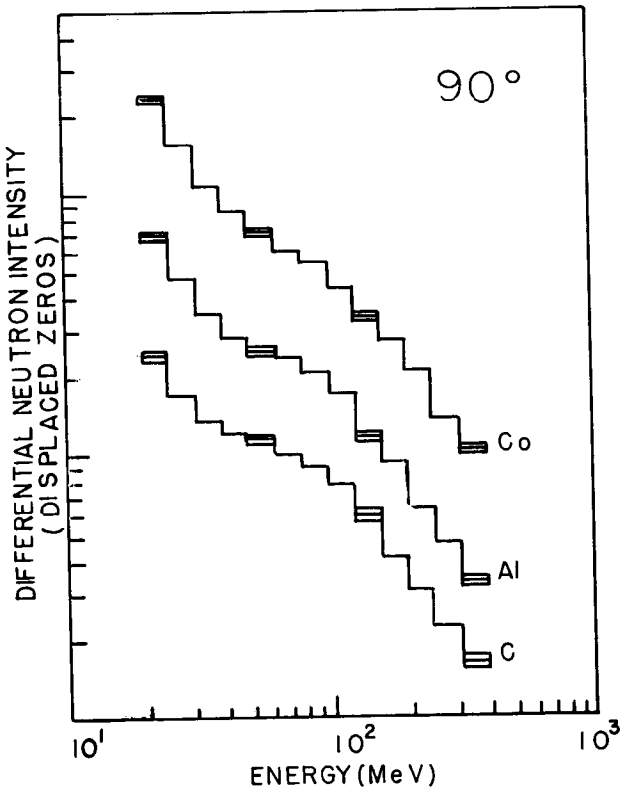

Figure 6. Same as Figure 4, at 90° emission angle.

Table 1. Approximate Inverse Power-Law Exponents of Neutron Spectra

Target	Energy Interval (MeV)	20°	34°	90°
C	20-40	0.8	1.0	1.2
	40-100	0.2	0.5	0.4
	100-400	0.6	1.0	1.3
Al	20-40	0.8	0.9	1.4
	40-100	0.4	0.3	0.4
	100-400	0.7	1.0	1.3
Co	20-40	0.8	0.9	1.4
	40-100	0.5	0.6	0.6
	100-400	1.0	1.2	1.2
Pt	20-40	1.0	1.2	
	40-100	0.6	0.7	
	100-400	1.5	1.4	

REFERENCES

1. G. Friedlander, J. W. Kennedy, and J. M. Miller, Nuclear and Radiochemistry (J. Wiley, New York, 1964), p. 316.
2. B. S. P. Shen, ed., High Energy Nuclear Reactions in Astrophysics (W. A. Benjamin, New York, 1967), p. 1.
3. B. S. P. Shen, Astronautica Acta, vol. 9, p. 211 (1963).
4. R. J. Kurz, A 709/7090 Fortran II Program to Compute the Neutron-Detection Efficiency of Plastic Scintillator for Neutron Energies from 1 to 300 MeV, UCRL-11339 (1964).
5. M. Hauser, private communication, 1971.
6. P. F. Shepard, T. J. Devlin, R. E. Mischke, and J. Solomon, N - P Charge Exchange Between 600 MeV/c and 2000 MeV/c, Princeton-Pennsylvania Accelerator Report PPAR-10 (1969).

THE CALCULATION OF NEUTRON CAPTURE GAMMA-RAY YIELDS FOR SPACE SHIELDING APPLICATIONS

K. J. Yost
Purdue University

In general, the application of nuclear models to the calculation of neutron capture and inelastic scattering gamma yields is undertaken with the following purposes in mind:

1. to calculate capture gamma-ray spectra where not even partial spectrum measurements are available. In such cases a data vacuum is filled with the understanding that if and when reliable measurements appear which seriously conflict with the calculation, the gamma yield data will be updated as required.
2. to fill in gaps in measured capture γ-ray spectra, generally in the continuum region. In such cases available experimental data are used to aid in the definition of model parameters.
3. as a part of data analysis procedures for nominally complete capture gamma measurements such as those done recently at GGA for W and U-238. This combining of advanced measurement and theoretical techniques seems to represent the optimum approach to the data acquisition problem.

The gamma-ray cascade model, DUCAL[1], developed as part of the Oak Ridge Program to generate capture and inelastic scattering gamma yields describes the cascade process in terms of parameters which either a) embody statistical assumptions regarding electric and magnetic multipole transition strengths, level densities and spin and parity distributions, or b) are fixed by experiment such as measured energies, spin and parity values, and transition probabilities for low lying states. Calculation of the latter with an appropriate nuclear model are attempted only for energies/mass regions for which either the model has been shown to apply or its predictions are judged to be closer to the truth than statistical assumptions.

With the foregoing limitations in mind, the viability of calculated yields may be considered in the light of the properties of the nuclei involved, experimental information available for the definition of model parameters, and the use for which the yields are intended. In particular, the DUCAL code has been used exclusively to generate gamma yields for neutron gamma-ray production cross sections to be input to transport codes for the calculation of integrated gamma dose at some point in a shield. As discussed in an earlier paper,[2] inaccuracies in calculated yields which lead to disrepancies in the calculated differential gamma flux do not necessarily result in significant errors in the calculated integrated dose. Errors in gamma group fluxes which are substantially compensating over several neighboring groups tend to be cancelled out in the process of folding the fluxes with the flux to the dose conversion ratio. A major consideration in the calculation of integrated dose is the conservation of gamma energy in the decay process. This the cascade model does as a matter of course.[1]

The fundamental nuclear properties are of particular significance where one attempts to calculate neutron energy dependent capture gamma yields for an element. The number of naturally occurring isotopes, their level structure, and the relative magnitudes of the binding energies of isotopes formed by neutron capture are extremely important. Changes in the capture spectrum with neutron energy associated with shifts in the relative magnitudes of capture cross sections of isotopes having different binding energies and level schemes, as in W,[3] can often be reasonably accounted for since a) the gamma cascade model conserves energy, and b) measured low lying level structure is frequently available for input to the calculation. In addition, the neutron energy dependence of the capture spectrum associated with changes in the capture state spin and parity resulting in the accessability of different sets of low lying states to E1 and M1 transitions can be accounted for to within the approximation of constant M1, E1 and E2 primary trans-

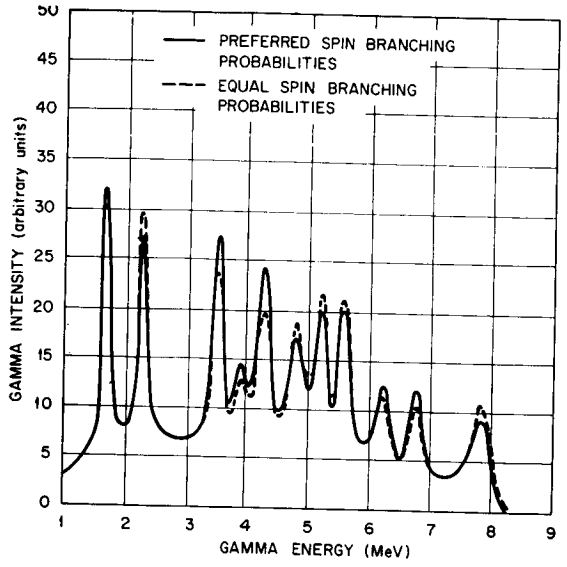

Figure 1 Comparison between fitted (——) and equal (---) dipole transition strength calculations of the caputure gamma yield for the 35 keV $^{27}A\ell$ resonance.

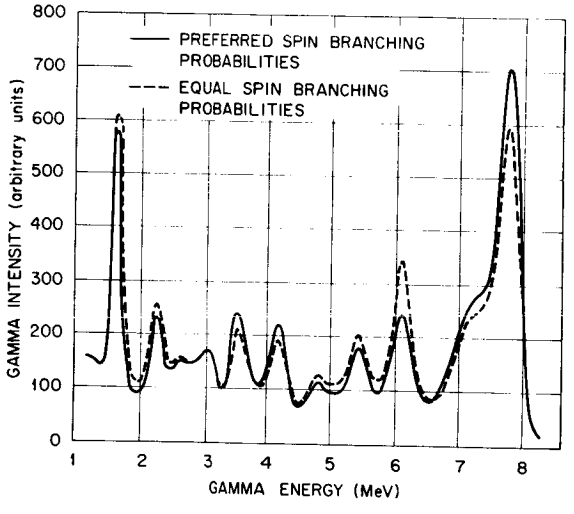

Figure 2 Comparison between fitted (——) and equal (---) dipole transition strength calculations of the capture gamma yeild for the 120 keV $^{27}A\ell$ resonance.

ition probabilities. An example is seen in the calculation of capture gamma spectra for the 35 keV 3+ and 120 keV 2^- resonances in $^{27}A\ell$ shown in figures [1] and [2]. Differences in the capture spectra represented by the dashed curves are attributable solely to the nuclear selection rules operating in conjunction with fixed M1, E1 and E2 transition strengths. In contrast, changes in the capture spectrum with capture state which depend upon more subtle wave function characteristics clearly cannot be approximated by a model.

A number of nuclear models have been implemented to aid in estimating low energy level structure and gamma decay schemes used to define corresponding parameters in the DUCAL code. These include a "unified" model which combines the Nilsson treatment of an odd particle in a deformed, rotating potential well with the Faessler-Sheline treatment of collective vibrational modes of excitation[4], and a model for odd-odd nuclei which employs products of single particle Nilsson wave functions as basis functions and the Gallagher-Moskowski coupling rules for the angular momenta of the odd nucleons.[5] In addition, a parameterization scheme to extend the applicability of the of the foregoing odd-A model has been investigated[6]. This involved an attempt to correlate values of a) a spin-dependent inverse moment of inertia corresponding to a best fit between measured and calculated level energies, and b) a deformation parameter to which the E2/M1 ratio is sensitive.

The foregoing nuclear models have been used to generate neutron energy dependent capture gamma-ray yields for tungsten, tantalum, U-238 and iron[3,7]. In each case the calculated yields have been tested against integral capture gamma yield measurements performed at the Oak Ridge Tower Shield Facility.

REFERENCES

1. Nucl. Sci. Eng., 32, 62 (1968).

2. Transactions of the Conference on Neutron Cross Sections and Technology, NBS Special Publication 299, Vol 1, 53 March (1968).

3. Trans. Am. Nuc. Soc., 12, 386 (1969).

4. Nucl. Sci. Eng., 36, 189 (1969).

5. Nucl. Sci. Eng., 41, 193 (1970).

6. Nucl. Sci. Eng., 39, 379 (1970).

7. Trans. Am. Nuc. Soc., 13, 866 (1970).

SESSION VI.3.
NATURAL SPACE RADIATION: GEOMAGNETIC TRAPPED RADIATION BELTS

CHAIRMAN: J. W. KELLER
OFFICE OF SPACE SCIENCE AND APPLICATIONS - NASA

LOW-ENERGY PARTICLE RADIATION ENVIRONMENT AT SYNCHRONOUS ALTITUDE

E. G. Shelley and S. K. Lew

Lockheed Palo Alto Research Laboratory

Low-energy charged particles in the space environment are known to be important contributors to the degradation of thermal control surfaces on satellites and may affect thin films such as cover materials used in connection with large flexible solar arrays. These particle-induced degradation effects are of particular importance in planned future satellite projects with projected lifetimes up to ten years. Early measurements in the vicinity of synchronous altitude showed that intense and highly variable fluxes of protons and electrons with energies between one and 50 keV populate this region of space. The ATS-5 satellite, launched into synchronous orbit in August 1969, was the first synchronous satellite to include instrumentation for the investigation of the plasma properties of these low-energy charged particles. The Lockheed Palo Alto Research experiment on ATS-5 measured electron and proton fluxes in the energy range from approximately one-half to several hundred keV with primary emphasis on the region below 50 keV which contains most of the plasma energy. A statistical analysis of the data, sampled over the period from September 1969 through December 1969, shows systematic variations in the average low-energy particle radiation environment at synchronous altitude with local time and magnetic activity (K_p). The existence of a systematic variation with K_p suggests the possibility of estimating the environment under various conditions of magnetic activity from the present data.

INTRODUCTION

Both laboratory simulations and in situ satellite measurements have shown that many of the commonly used low α_s/ϵ thermal control surface materials are degraded not only by solar ultraviolet radiation, but also by low-energy charged particle radiation (refs. 1-19). This is dramatically shown in figure 1 which compares the degradation rate of $Zn0$/Sil measured on several satellites. The degradation rate was significantly greater for the synchronous and deep space satellites which were exposed to much greater low-energy particle fluxes. A detailed knowledge of the charged particle environment is therefore essential to proper design of long-lived spacecraft. Prior knowledge (refs. 20 and 21) of the environment at synchronous altitude has been extremely sketchy, based primarily on measurements from satellites with highly eccentric orbits. Since these satellites are able to acquire only a few seconds of data in the region of synchronous altitude once every few days they do not provide sufficient data to define the morphology of this dynamic region.

The ATS-5 satellite, which was launched in August of 1969, was the first synchronous satellite to carry experiments capable of spectral measurements of the low-energy electrons and protons. It carried a magnetometer and several particle detectors spanning the energy range from 50 eV to 30 MeV. The Lockheed experiment was designed to perform a survey of particle fluxes of auroral energies. It consists of eleven individual detectors, each of which measures protons or electrons in a specific energy interval spanning the range from about one-half to several hundred keV. Primary emphasis was placed on the region below 50 keV which contains most of the plasma energy. Particles in this energy region have been shown to be very important in thermal control surface damage (ref. 2).

A preliminary report on the general characteristics of the particle fluxes at synchronous altitude has been given by Sharp et al. (ref. 22). It was

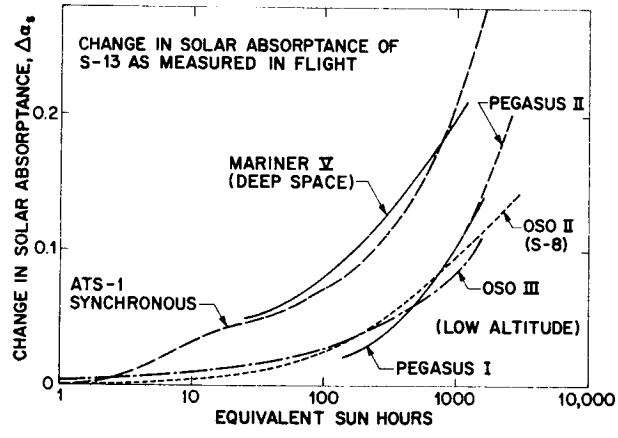

FIGURE 1.--Comparison of degradation of S-13 (ZnO/Sil) measured on several satellites. The degradation rate is significantly increased at synchronous orbit and in deep space where the particle radiation environment is enhanced (from ref. 1).

reported that large increases in the electron fluxes were observed on most nights in the vicinity of local midnight with increases of one or two orders of magnitude occurring within times ranging from a few minutes to the order of an hour and that these electron "events" were generally associated with magnetic substorms as established from auroral zone magnetograms in the vicinity of the foot of the field line passing through ATS-5. A more detailed study of the time characteristics of these electron events has also been published

(ref. 23). As reported in ref. 22, the proton fluxes were also observed to vary, but by a much smaller factor in general. A general discussion of the low-energy particle populations at synchronous orbit observed on ATS-5 has also been given by DeForest and McIlwain (ref. 24). An indication of the dramatic variations in the particle fluxes and their dependence on local time and magnetic activity is given in figures 2 and 3. Figure 2 shows the relative flux of the 6- to 18-keV electrons for two of the days included in this study. The lower and upper curves correspond to magnetically quiet and magnetically active days, respectively. During a significant part of the day the fluxes on the active day exceed those of a quiet day by about two orders of magnitude. Figure 3 shows a similar comparison for protons with energies greater than 38 keV. While the differences are not as great as those for electrons, they still differ by a factor of 5 or greater.

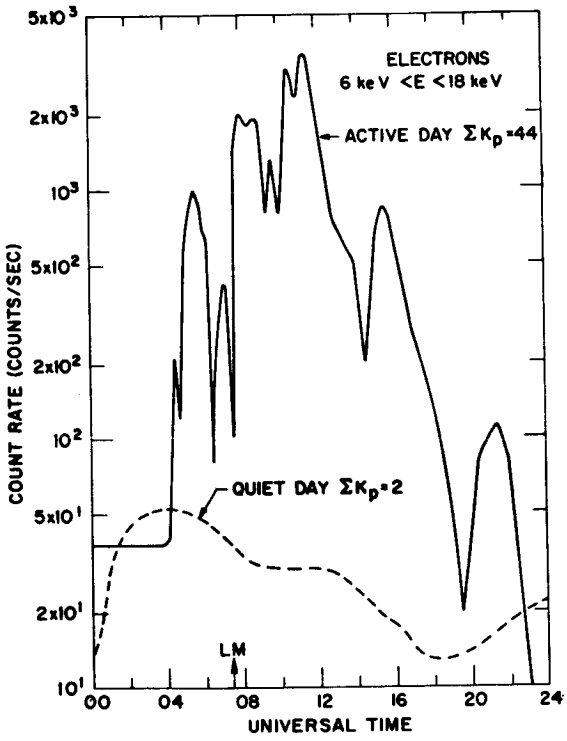

FIGURE 2.--Comparison of relative low-energy electron flux for two days of significantly different magnetic activity. Local midnight is indicated by the arrow marked LM.

In this paper, a statistical analysis of the data for 20 days spanning the period from September 1969 through December 1969 is presented. As shown in figure 4, the distribution of magnetic activity during the data samples of this study was very similar to the distribution of magnetic activity for the entire four-month period spanned by the data samples. It is therefore reasonable to treat this body of data as representative of this period. The local time dependence of four plasma parameters, electron number flux, electron average energy, proton number flux and proton average energy, was analyzed using the entire body of data. In addition, we present the results of an investigation of the dependence of these parameters on magnetic activity in several different local time sectors in the hope that this information will make it possible to extrapolate the present data to periods of differing magnetic activity.

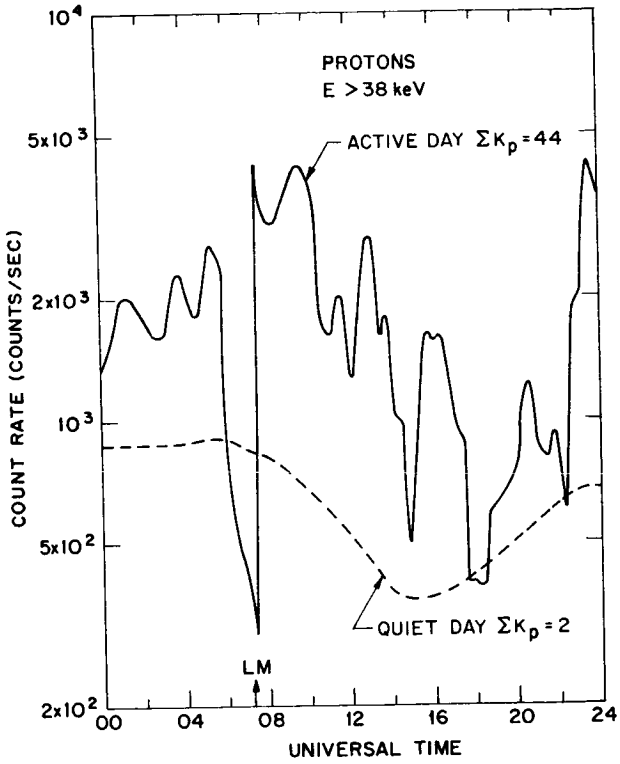

FIGURE 3.--Comparison of relative proton flux for two days of differing magnetic activity. LM indicates local midnight.

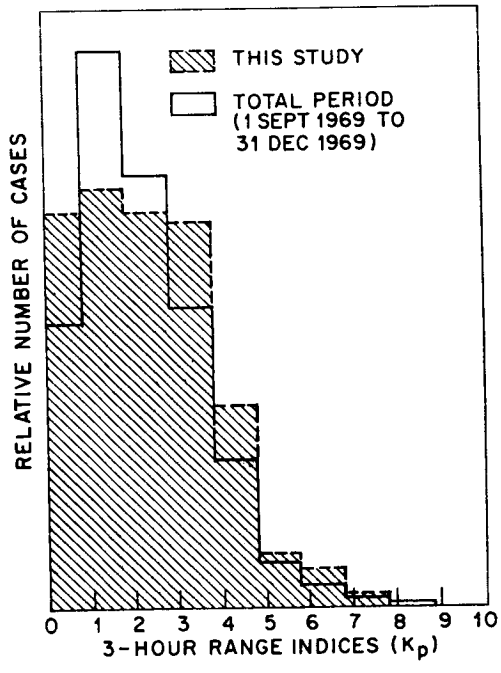

FIGURE 4.--Comparison of magnetic activity during the sample periods selected for this study with magnetic activity during the entire period from which samples were selected.

INSTRUMENTATION

The electron data presented here are from four broadband differential electron flux detectors, each consisting of a permanent magnet spectrometer which utilizes 180° deflection to achieve continuous sensitivity over a broad energy interval ($\Delta E/E \cong 100\%$). Together, the four detectors provide continuous and nearly uniform coverage for electrons over the energy range from 0.65 to 53 keV. The proton data to be presented are from three integral proton detectors with foil-determined thresholds at approximately 5, 15 and 38 keV. The minimum data sample rate for these detectors was once per telemetry sequence of 5.12 seconds. Relevant parameters for these seven detectors are given in table 1. A detailed description of the instrument and a description of the procedures used for calibration of the electron channels have been published (refs. 25 and 26).

Detector	Particle	Energy Range (keV)	Acceptance Angle (Full Angle)	Geometric Factor (cm^2-ster)
CMEA	e^-	0.65 - 1.9	$15^\circ \times 25^\circ$	1.4×10^{-5}
CMEB	e^-	1.8 - 5.4	$15^\circ \times 25^\circ$	1.0×10^{-5}
CMEC	e^-	5.9 - 17.8	$15^\circ \times 25^\circ$	1.2×10^{-5}
CMED	e^-	17.4 - 53.0	$15^\circ \times 25^\circ$	0.9×10^{-5}
CFPA	p^+	> 5	20°	3×10^{-5}
CFPB	p^+	> 15	20°	3×10^{-5}
CFPC	p^+	> 38	20°	4×10^{-4}

TABLE 1.--Detector Parameters

•For the period of the data presented here, the ATS-5 satellite was nearly stationary in geographic longitude at approximately 150°W. It was spin stabilized with spin axis approximately parallel to the earth's axis. The Lockheed experiment view direction made an angle of 11° to the spin axis, so that the detectors were sensitive to particles with pitch angles over a range of greater than 40°. This range was reduced somewhat when the spin axis was within 20° of the local magnetic field direction. The ratemeter time constants were such that the detectors averaged the flux over all pitch angles accepted. The range of pitch angles sampled varied with local time and magnetic activity, but on the average the central angle varied from about 35° near local midnight to less than 10° near local noon. It should be borne in mind that the loss cone at synchronous altitude is only about 5° full angle, so that even when the loss cone is included in the solid angle of the detectors, they are primarily sensitive to trapped particles.

DATA ANALYSIS

In order to calculate the plasma properties, such as average energy and omnidirectional-number flux, from out observations, it was necessary to make certain assumptions about the spectral and pitch-angle distributions. We assumed isotropy for both electrons and protons. This is not expected to have a large effect since, as discussed above, our detectors average over a relatively large range of pitch angles. However, because of the local time dependence of the magnetic field direction, the apparent local time dependence of the plasma parameters could be influenced by anisotropic pitch-angle distributions. That this anisotropy in our energy range is not on the average large (i.e., greater than about 2) is supported by our observations during an earlier spin mode in which the Lockheed experiment swept through all pitch angles during each spin period (ref. 22) and further by a second low-energy particle experiment on ATS-5 which had detectors at two angles (ref. 24).

The spectral model for electrons used in this analysis was as follows. The differential flux was assumed to be flat over the energy range of each of the two lower electron detectors. A function $F(E) = F_o e^{-E/E_o}$ was fit to the upper two electron channels and was used to describe the spectrum from 6 keV to 55 keV. The dependence of the calculated plasma parameters on the details of the spectral shape was tested by using other simple shapes and it was found that the results were not generally affected significantly. Similarly, the proton spectrum was assumed to be flat between the threshold energies of the lower two detectors (5 keV to 15 keV) and an exponential distribution was fit to the upper two detectors. The electron properties discussed here are for the energy range 0.65 to 55 keV and the proton properties are for energies greater than 5 keV.

With the above assumptions, the omnidirectional number fluxes (i.e., 4π times the average directional flux) and the number-density-weighted average energies for electrons and protons were calculated. Flux-weighted average energies are more appropriate for damage analysis and are generally greater than the density-weighted average energies by 10% to 50% for both electrons and protons and within the accuracy of this analysis can be assumed to be a constant 30% greater.

The plasma properties were first calculated at approximately 90-second intervals for all of the data, then averaged over one-hour periods. Each sample discussed in the following analysis and tabulated in table 2 corresponds to one of these one-hour averages.

The uncertainties in the data arising from counting statistics and other random errors are completely negligible compared with the possible systematic errors. The total systematic errors arising from all causes such as uncertainties in absolute geometric factors, spectral shapes and pitch-angle distributions were estimated at about 30% for the electron properties and 50% for the proton properties.

LT ↓ / K_p →	0^o-1^-	1^o-2^-	2^o-3^-	3^o-4^-	4^o-5^-	5^o-6^-	6^o-7^-	7^o-8^-	Total
00-03	14	8	13	12	4	4	1	0	56
03-06	15	5	15	9	4	1	3	0	52
06-09	14	11	8	15	3	2	3	0	56
09-12	11	13	10	8	9	1	2	0	54
12-15	8	13	9	13	10	2	0	1	56
15-18	8	16	12	12	4	0	0	2	54
18-21	11	18	14	10	4	0	0	0	57
21-24	11	14	11	11	9	2	0	0	58
Total	92	98	92	90	47	12	9	3	443

TABLE 2.--Number of 1-hour samples in study as a function of K_p and local time

15-6 1302-307

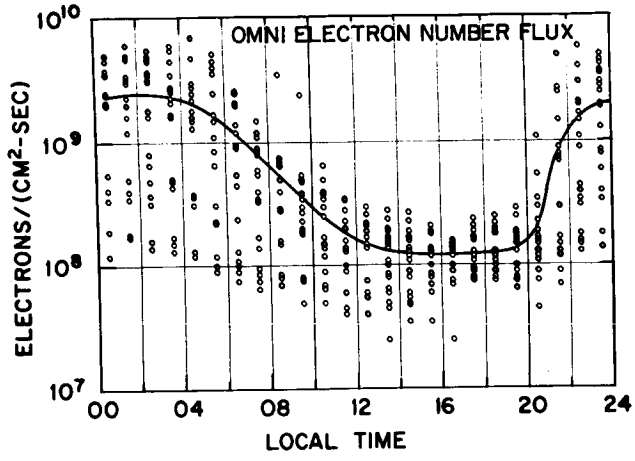

FIGURE 5.--Omnidirectional electron number flux as a function of local time. All one-hour-average samples are included. The solid curve is the average local time dependence of the flux, independent of magnetic activity.

RESULTS

Local Time Dependence

The first analysis of the data was in terms of local time dependence only, that is, there was no selection of the data on the basis of magnetic activity. In figures 5 through 8, we present the omnidirectional electron number flux, the electron average energy, the omnidirectional proton number flux, and the proton average energy, respectively. All data were included to show the variance, the solid curves give the average local time dependence. These figures are discussed separately below.

Omnidirectional Electron Number Flux (figure 5): A strong local time dependence in the overall average electron number flux is clearly evident. The average flux varies from approximately 2.5 x 10^9 electrons/cm^2-sec around midnight and early morning to 1 x 10^8 electrons/cm^2-sec near dusk. The total variation in the hourly averaged electron number flux exceeds a factor of 200; on a shorter time scale, these fluxes have been observed to vary over a range of several thousand. Another interesting observation from figure 5 is that the variation in the electron flux is much greater (~ 60X) near local midnight than around 1800 LT (~ 3X).

Average Electron Energy, Density-Weighted (figure 6): The statistical average of the electron energy has a relatively strong local time dependence. It maximizes at a value of about 13 keV near 1600 LT, approximately the time at which the electron number flux is minimum. The minimum energy, approximately 5.5 keV, occurs about 6 hours later at 2200 LT. The independent one-hour average samples of the average electron energy vary over a range from 2 keV to 22 keV. In contrast to the electron number flux, the variation in average electron energy is greatest near local dusk and smallest near local midnight.

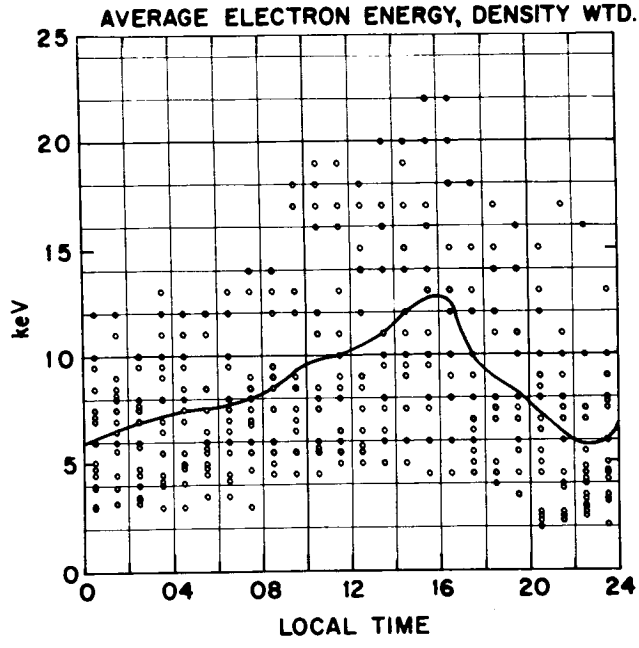

FIGURE 6.--Density-weighted average electron energy over the energy range 0.65 keV to 55 keV as a function of local time. All one-hour-average samples are included independent of magnetic activity. The solid curve is the statistical average of the electron energy as a function of local time.

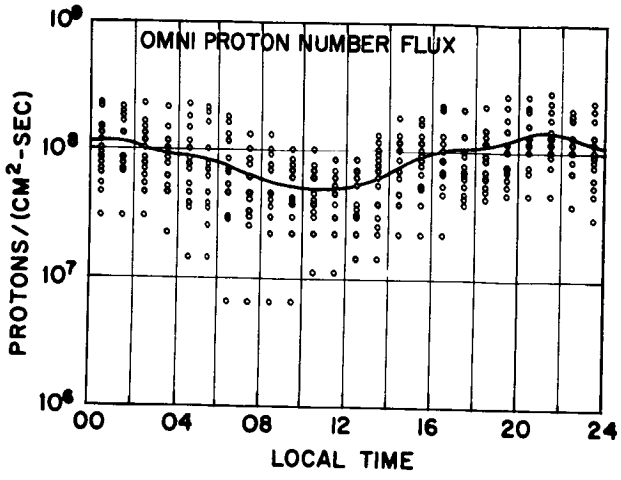

FIGURE 7.--Omnidirectional proton number flux as a function of local time for protons with energy greater than 5 keV. All one-hour-average samples are included independent of magnetic activity. The solid curve is the statistical average.

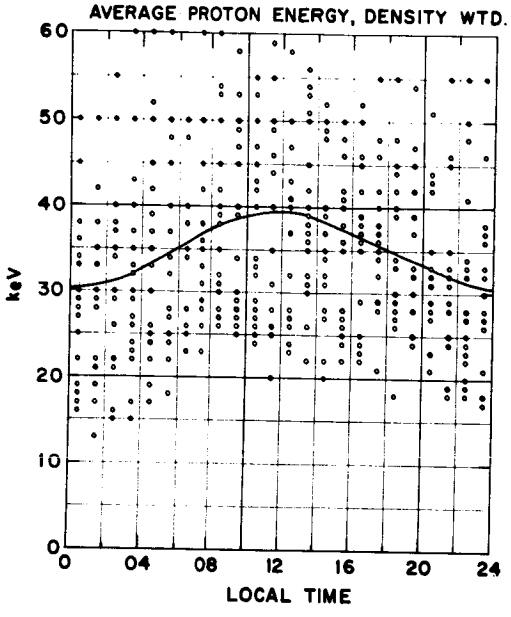

FIGURE 8.--Density-weighted average proton energy as a function of local time, $E_p > 5$ keV. All one-hour-average samples are included independent of magnetic activity. The solid curve is the statistical average dependence to the average proton energy on local time.

Omnidirectional Proton Number Flux (figure 7): The grand average proton flux is approximately 10^8 protons/cm^2-sec. In contrast to the electron flux, the apparent diurnal variation in the average proton flux is rather small (~ 3X). The local time dependence is also different, peaking about 3 hours before local midnight and reaching a minimum very near local noon. Because this variation has very nearly the same local time dependence as the systematic variation in the pitch-angle range being sampled (see the data analysis section), a significant part of this apparent diurnal variation could be explained by a pitch-angle distribution peaked at 90°. However, based on the arguments presented earlier, we estimate that at least half of this effect is a true variation in the average flux. The proton flux at a fixed local time is seen to vary by approximately a factor of 10, somewhat less than the variation observed for electron fluxes, but nevertheless highly significant.

Average Proton Energy, Density-Weighted (figure 8): The average of the proton energy is approximately out of phase in local time with the average proton flux, with the percentage variation (~ 20%) much less. The total range of the one-hour average samples is from approximately 15 keV to 60 keV with a mean of approximately 35 keV.

Magnetic Activity Dependence

An investigation of the dependence of the plasma parameters on magnetic activity was undertaken in hopes of finding relationships to make it possible to extrapolate the present data to periods of different magnetic activity. Because of the strong local time dependence of the parameters found above, the data were analyzed in 3-hour local time segments; however, where the local time effect appeared to be small these were later averaged over 6-hour segments. Table 2 shows the breakdown of the distribution of one-hour-average data samples in terms of local time and magnetic activity (K_p). This breakdown left approximately 10 samples per local time segment for each magnetic activity interval ($\Delta K_p = 1$) up to $K_p = 4$. Above $K_p = 5$, the number of samples per interval was generally 3 or less and this should be borne in mind in interpreting the results presented below.

For each of the four parameters we present a scatter plot of the parameter versus K_p for a single local time segment to demonstrate the scatter of the data. Included in these plots is a curve passing through the averages over each ΔK_p interval; the intervals are identical to those in table 2. The error bars are one standard deviation of the mean. Following each of the scatter plots is a second figure showing the average curves for each local time segment. Standard deviations are included for only a few of the points on these curves to avoid further confusion in the figures. Some "error bars" were considered necessary to indicate the significance of the fluctuations in the curves.

Omnidirectional Electron Number Flux (figures 9 and 10): The scatter in the data points within a single ΔK_p interval in figure 9 for the local time segment of zero to 0300 is typical of all of the local time segments. The average curves for all eight local time segments are included in figure 10. Several systematic effects are apparent: 1) the local time dependence is significantly less at low K_p than for high K_p; 2) the local time region from 2100 to 0600 is most sensitive to magnetic activity, but shows a saturation effect above $K_p = 3$; 3) the local time region from noon to dusk (i.e., 1200-1800 LT) is on the average unaffected by magnetic activity; and 4) the intermediate local time intervals show a slow transition in their dependence on magnetic activity from that characteristic of the midnight region to that characteristic of the afternoon region.

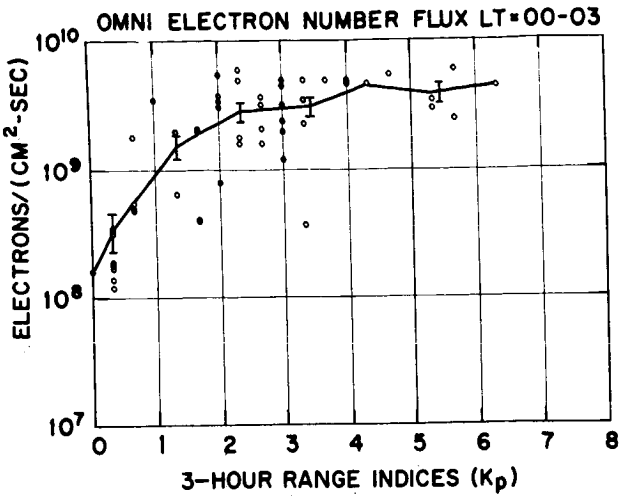

FIGURE 9.--Omnidirectional electron number flux as a function of magnetic activity (K_p) for the local time segment 0000 to 0300. The data points include all samples for this local time period. The solid curve passes through the statistical mean for each ΔK_p interval. The error bars indicate one standard deviation on the mean.

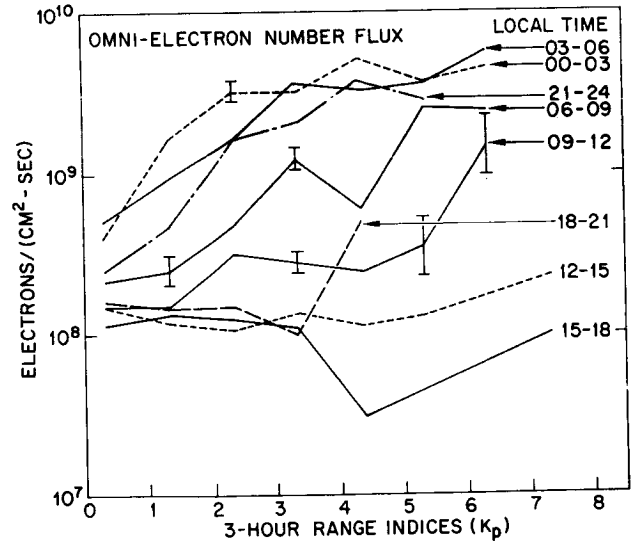

FIGURE 10.--Average dependence of the omnidirectional electron number flux on magnetic activity for each 3-hour local time segment. The error bars where given are one standard deviation on the mean.

The peaks and troughs in these curves, such as that near $K_p = 4$ on the 06-09 curve, cannot be considered statistically significant; however, the error analysis suggests that the average electron number flux can be corrected for magnetic activity within about a factor of two.

Electron Average Energy (figures 11 and 12): The scatter in the average electron data shown in figure 11 is typical for all local times except for the region 00-06 LT where the scatter is significantly less. The effect of increased magnetic activity on the average energy as a function of local time (see figure 12) is very different from the behavior observed for the electron flux. The systematic effects are as follows: 1) the local time dependence is minimal for low K_p, as was the case for the electron flux; 2) the local time region from 2100 to 0300 is least sensitive to magnetic activity; in contrast the electron flux is most sensitive in this time region; 3) in the local time region from pre-noon to dusk (0900-1800 LT) the electron energy is strongly dependent on magnetic activity up to about $K_p = 3$ or 4, followed by a saturation effect or a possible reversal (the points around $K_p = 7$ must not be given much significance since they result from only one or two samples -- see table 2). Again this contrasts with the behavior of the electron flux which was not significantly affected in this general local time region; 4) as was the case with the electron flux, the intermediate local time regions display a smooth transition in behavior between the extremes of 2) and 3) above; and 5) there is considerable evidence for a decrease in mean energy with increased magnetic activity above $K_p \simeq 5$ for most local times.

The average effect of magnetic activity on the electron average energy can be estimated from these curves with an accuracy of 20 or 30 per cent. The combined effects of magnetic activity on the electron flux and the electron average energy lead to the result that the general trend is toward increased electron energy flux with increased magnetic activity at all local times. In the vicinity of local midnight, the flux increases with little change in average energy, while in the noon to dusk region, the mean energy increases with little change in number flux. Both parameters increase in the intermediate local time regions.

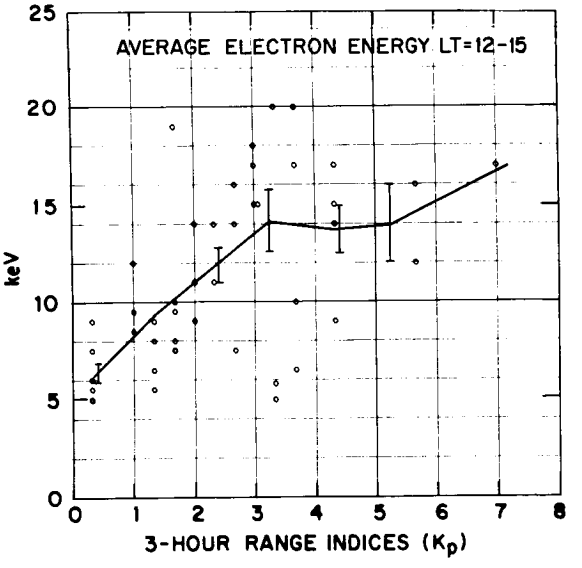

FIGURE 11.--Average electron energy as a function of magnetic activity (K_p) for the local time segment 1200 to 1500. The data points include all one-hour-average samples for this local time segment. The solid curve passes through the mean for each ΔK_p interval. The error bars are one standard deviation on the mean.

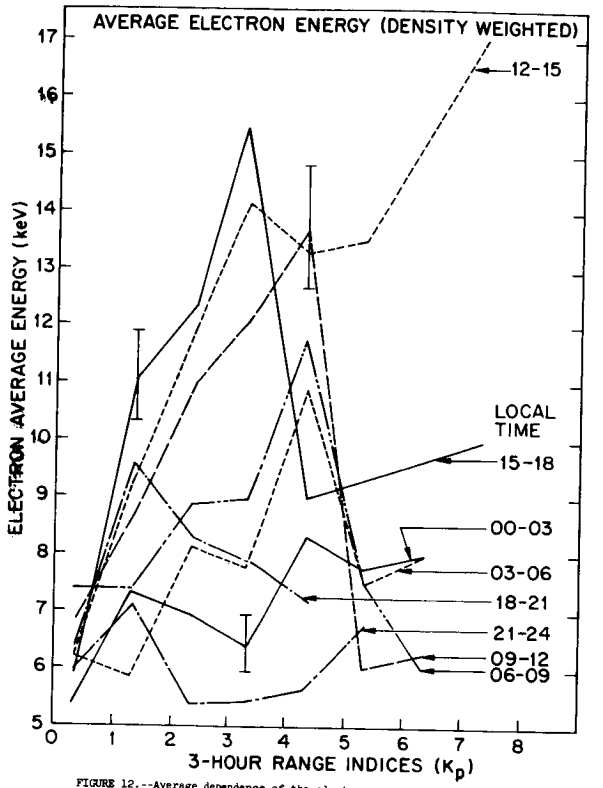

FIGURE 12.--Average dependence of the electron energy on magnetic activity (K_p) for each 3-hour local time segment. The error bars where indicated are one standard deviation on the mean.

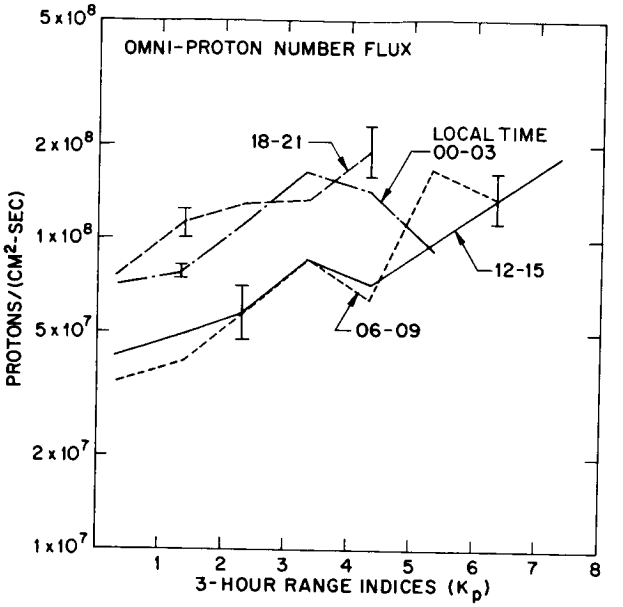

FIGURE 14.--Average dependence of proton flux on magnetic activity (K_p) for four 3-hour local time segments. The behavior of the intermediate time segment was similar. The error bars where shown are the standard deviation on the mean.

Omnidirectional Proton Number Flux (figures 13 and 14): The scatter of the data at all local times is comparable to that shown in figure 13. The relative dependence of the proton flux on K_p does not change rapidly with local time. To avoid unnecessary complications, only every other local time segment curve was included in figure 14. The proton number flux increases smoothly with increased magnetic activity in all local time segments except near local midnight where the flux maximizes around $K_p = 3$. In general the flux increases by about a factor of 2 between $K_p = 0$ and $K_p = 4$.

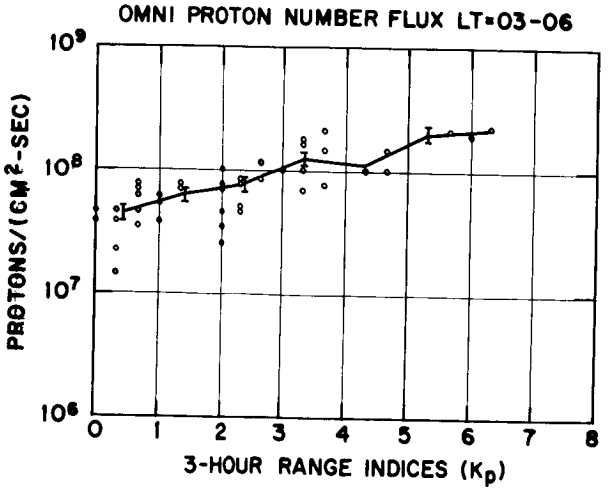

FIGURE 13.--Omnidirectional proton number flux as a function of magnetic activity (K_p) for the local time segment 0300 to 0600. The data points include all samples for this local time segment. The solid line passes through the mean for each ΔK_p interval. The error bars are standard deviations on the mean.

Proton Average Energy (figures 15 and 16): The data scatter in figure 15 is typical for all local time segments. To reduce the confusion, the data in figure 16 is averaged over 6-hour intervals in local time. At low K_p, the average energy is relatively independent of local time. As K_p increases, the average proton energy decreases nearly monotonically for all local times except near local midnight. In the region from 2100 to 0300 LT, the energy decreases with increased magnetic activity up to $K_p \cong 2$, then increases with further increases in magnetic activity. This behavior is nearly reversed from that observed for the proton flux. In general the effect is for the energy flux to remain relatively constant while both the number flux and the average energy change at all local times.

Some of the systematic variation in the plasma parameters with local time and magnetic activity demonstrated in this section can be explained qualitatively on the basis of our present knowledge of the physics of the magnetosphere; however, this is beyond the scope of the present paper. For the physical interpretation of some of the low-energy particle observations in the vicinity of synchronous altitude, see refs. 22-24 and their bibliographies.

SUMMARY

The average low-energy radiation envrionment at synchronous altitude has been shown to vary in a systematic way with respect to local time and magnetic activity. Because of this systematic behavior it may be possible to estimate the low-energy radiation environment for periods of different magnetic activity by utilizing the results of this statistical analysis. The validity of

such estimates can be established only by similar analyses of data for other periods.

Because of the great variability of the low-energy plasma it would be advisable to include particle measurements with future flight experiments on surface damage at synchronous altitude. There are some indications that particle fluxes in the loss cone may exceed the average trapped fluxes by an order of magnitude (ref. 27). This is presently under study at Lockheed by combining simultaneous plasma measurements at synchronous altitude on ATS-5 and at low altitude on OV1-18 near the foot of the field line passing through ATS-5.

ACKNOWLEDGMENTS

The authors would like to thank Drs. R. D. Sharp, R. G. Johnson and M. McCargo for their many helpful suggestions and discussions during this analysis. We would also like to thank L. F. Smith and D. L. Carr for their help in the data reduction and programming. This work was funded by the Lockheed Independent Research Program and by NASA under Contract NAS 5-10392.

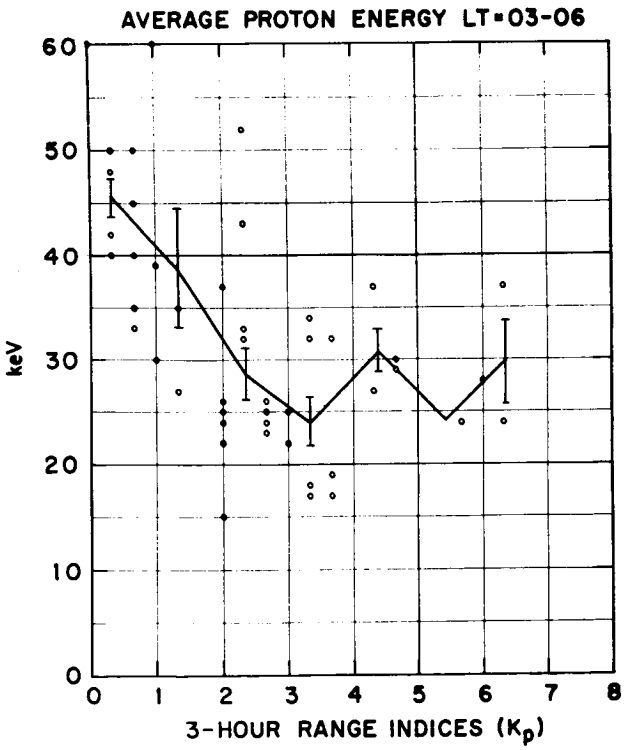

FIGURE 15.--Average proton energy as a function of magnetic activity (K_p) for the local time segment 0300 to 0600. The data points include all one-hour-average samples for this local time segment. The solid line passes through the mean for each ΔK_p interval. The error bars are standard deviations on the mean.

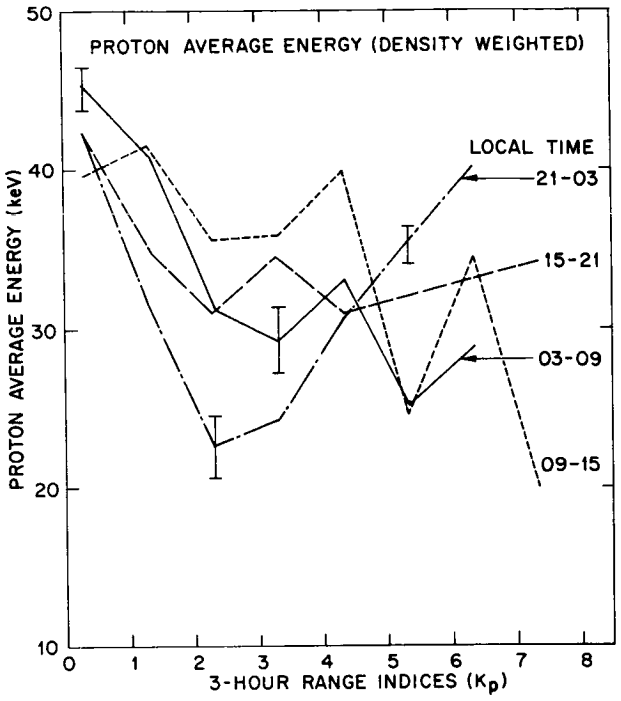

FIGURE 16.--Average dependence of proton average energy on magnetic activity (K_p). The data here were averaged over 6-hour local time segments. The error bars where shown are standard deviations on the mean.

REFERENCES

1. McCARGO, M.; GREENBERG, S.A.; McDONALD, S. L.: Quarterly Progress Report No. 1, NAS 8-26004, July 1970; No. 2, NAS 8-26004, October 1970.
2. McCARGO, M.; GREENBERG, S. A.; and DOUGLAS, N. J.: Prog. in Astronautics & Aeronautics, vol. 23, 1970, p. 189.
3. FOGDALL, L. B.; CANNADAY, S. S.; and BROWN, R. R.: Prog. in Astronautics & Aeronautics, vol. 23, 1970, p. 219.
4. HEANEY, J. B.: Prog. in Astronautics & Aeronautics, vol. 23, 1970, p. 249.
5. McCARGO, M.; GREENBERG, S. A.; and BREUCH, R. A.: NASA Ames Research Center, Final Report, NAS 2-4353, Jan. 1969.
6. GREENBERG, S. A.; MacMILLAN, H. F.; and SKLENSKY, A. F.: NASA/Marshall Space Flight Center, NAS 8-18114, Feb. 1968.
7. BROWN, R. R.; FOGDALL, L. B.; and CANNADAY, S. S.: Prog. in Astronautics & Aeronautics, vol. 21, 1968, p. 697.
8. MILES, J. K.; CHEEVER, P. R.; and ROMANKO, J.: Prog. in Astronautics & Aeronautics, vol. 21, 1968, p. 725.
9. MILLARD, J. P.: Prog. in Astronautics & Aeronautics, vol. 21, 1968, p. 769.
10. SLEMP, W. S.; and HANKINSON, T. W. E.: Prog. in Astronautics & Aeronautics, vol. 21, 1968, p. 797.
11. GREENBERG, S. A.; MacMILLAN, H. F.; and SKLENSKY, A. F.: Air Force Materials Laboratory, AFML-TR-67-294, Sept. 1967.
12. HOLLAND, W. R.: NASA/Ames Research Center, Final Report, NAS 2-3646, Dec. 1967.
13. STREED, E. R.: Prog. in Astronautics & Aeronautics, vol. 20, 1967, p. 237.
14. NEEL, C. B.: Prog. in Astronautics & Aeronautics, vol. 20, 1967, p. 411.
15. SCHAFER, C. F.; and BANNISTER, T. C.: Prog. in Astronautics & Aeronautics, vol. 20, 1967, p. 457.
16. BREUCH, R.A.: Prog. in Astronautics & Aeronautics, vol. 18, 1966, p. 365.
17. JORGENSON, G. V.: Prog. in Astronautics & Aeronautics, vol. 18, 1966, p. 389.
18. MILLER, R. A.; and CAMPBELL, F. J.: Prog. in Astronautics & Aeronautics, vol. 18, 1966, p. 399.
19. GILLETTE, R. G.; BROWN, R. R.; SEILER, R. F.; and SHELDON, W. R.: Prog. in Astronautics and Aeronautics, vol. 18, 1966, p. 413.
20. VETTE, J. I.; LUCERO, A. B.; and KING, J.H.: Vols. III and IV, NASA SP-3024, 1967.
21. HESS, W. N.; MEAD, G. D.; and NAKADA, M. P.: Prog. in Astronautics & Aeronautics, vol. 18, 1966, p. 327.
22. SHARP, R. D.; SHELLEY, E. G.; JOHNSON, R. G.; and PASCHMANN, G.: J. Geophys. Res., vol 75, 1970, p. 6092.
23. SHELLEY, E. G.; SHARP, R. D.; and JOHNSON, R. G.: Radio Science, vol. 6, 1971, in press.
24. DeFOREST, S. E.; and McILWAIN, C. E.: UCSD-SP-70-04, Sept. 1970.
25. REED, R. D.; SHELLEY, E. G.; BAKKE, J. C.; SANDERS, T. C.; and McDANIEL, J. D.: IEEE Trans. Nucl Sci., vol. NS-16, 1969, p. 359.
26. PASCHMANN, G.; SHELLEY, E. G.; CHAPPELL, C. R.; SHARP, R. D.; and SMITH, L. F.: Rev. Sci. Instr., vol. 41, 1970, p. 1706.
27. HONES, E. W., JR.; ASBRIDGE, J. R.; BAME, S. J.; and SINGER, S.: J. Geophys. Res., vol. 73, 1971, p. 63.

NATURAL VARIATIONS IN THE GEOMAGNETICALLY TRAPPED ELECTRON POPULATION

A. L. VAMPOLA
Space Physics Laboratory
The Aerospace Corporation
El Segundo, California

ABSTRACT

Temporal variations in the trapped natural electron flux intensities and energy spectra are discussed and demonstrated using recent satellite data. These data are intended to aquaint the space systems engineer with the types of natural variations that may be encountered during a mission and to augment the models of the electron environment currently being used in space system design and orbit selection (i.e., AE3 by Vette et al., refs. 2 and 3). These models, while excellent in some respects and quite satisfactory in most other respects, were generated before high resolution spectrometry data were generally available. For systems or subsystems which are particularly sensitive to radiation and respond to changes in the environment on a short time scale, these models by themselves may be inadequate for proper subsystem design or interpretation of on-orbit data. An understanding of the temporal variations which may be encountered should prove helpful. Some of the variations demonstrated here which are not widely known include: addition of very energetic electrons ($E \geq 5$ MeV) to the outer zone during moderate magnetic storms; addition of energetic electrons ($E > 1$ MeV) to the inner zone during major magnetic storms; inversions in the outer zone electron energy spectrum during the decay phase of a storm injection event; occasional formation of multiple maxima (≥ 4) in the flux vs altitude profile of moderately energetic electrons ($E \leq 1$ MeV).

This work was conducted under U. S. Air Force Space and Missile Systems Organization (SAMSO) Contract No. F04701-70-C-0059.

In the design of spacecraft systems, subsystems, and sensors, a knowledge of the radiation environment which will be encountered is essential. In the case of a particularly vulnerable sensor or biological subsystem, the configuration of the trapped radiation belts may even be a major factor in the choice of orbit. Excellent models of the average environment are available (refs. 1 and 2) but have limitations, especially their treatment of short-term spectra effects. More data are now available on what could be called "second-order" effects, and will be treated here, since for particularly vulnerable or sensitive payloads a knowledge of these "second-order" effects may be a prerequisite for proper design, functioning, or data analysis. Since we are considering short-term fluctuations in the trapped particle environment from the point of view of obtaining better criteria for system design and orbit selection, magnetospheric physics will not be emphasized here. This is perhaps just as well, since the physical processes involved in the formation of the belts are not well understood and are only indirectly relevant to our goal -- it is the final result of these processes, the radiation environment, which is used as an input to space system design.

The geomagnetically trapped natural electrons fall into two primary classes: a) the inner zone which is relatively stable and exhibits a "soft" electron spectrum (i.e., a steep differential energy spectrum with few energetic particles); and b) the outer zone which is just the converse. Here the flux intensities vary widely on a short time scale and at times the spectrum is quite hard. The outer zone includes the synchronous-orbit environment. Because of the particular importance and high usage of this orbit, the synchronous environment will be treated separately.

OUTER ZONE AND SLOT VARIATIONS

Measurements of magnetospheric electron fluxes by many investigators have shown large changes in the outer zone electron population in response to magnetic activity. For instance, Frank, in a statistical study of electrons with energies greater than 40 keV (ref. 3), showed the great variability of the total flux in the outer zone and (ref. 4) presented evidence for inward diffusion of electrons with $E > 1.6$ MeV. Williams et al. (ref. 5) showed a correlation between the magnitude of the magnetic activity and the L-value at which peak flux intensities were observed. L is McIlwain's parameter (ref. 6) and for our purposes can be taken as the geocentric radial distance, in units of earth radii, at which a particular magnetic field line crosses the geomagnetic equator. The field line of interest is the guiding center of a geomagnetically trapped particle and under appropriate circumstances can be assumed to remain constant for a particular particle while that particle executes bounce and drift motion.

Williams et al. (ref. 5) also showed that for electrons with $E > 300$ keV, the time for low altitude outer zone electron fluxes to reach equilibrium with equatorial fluxes is ≤ 0.1 day. We shall utilize this finding and assume that low altitude data is qualitatively and semi-quantitatively representative of the entire outer zone. Most of the data which will be presented was obtained by magnetic spectrometers on two low altitude (apogee < 6000 km) elliptical polar orbiting satellites, OV3-3 (1966-70A) and OV1-19 (1969-25C).

Figure 1 shows the effect of a large magnetic storm on energetic electron fluxes at $L = 4$. Unidirectional differential energy fluxes are plotted as a function of time. We see that in addition to a very large change in flux at all energies due to the storm on day 247 (January 1 = day 1), there is a significant effect due to smaller storms on days 278, 290, 302 and perhaps others. The first storm followed a relatively quiet period and hence resulted in a flux increase of about two orders of magnitude. The subsequent storms occurred during the recovery from the first and resulted in smaller relative changes. The high energy electron flux profile was less sensitive to the smaller storms than the low energy flux. Figure 2 shows the effect of the storms in the "slot". Here only the lowest energy electrons exhibit significant effects due to the later storms. However, all show a very large effect due to the day 247 storm -- as much as four orders of magnitude in the 712 keV plot. Note that the onset is very sharp and the decay is relatively fast. Plots of precipitating flux at very low altitude ($\approx$ 400 km) show the primary loss of these particles in the slot is by rapid pitch-angle scattering which lowers the mirror altitude of the particles until

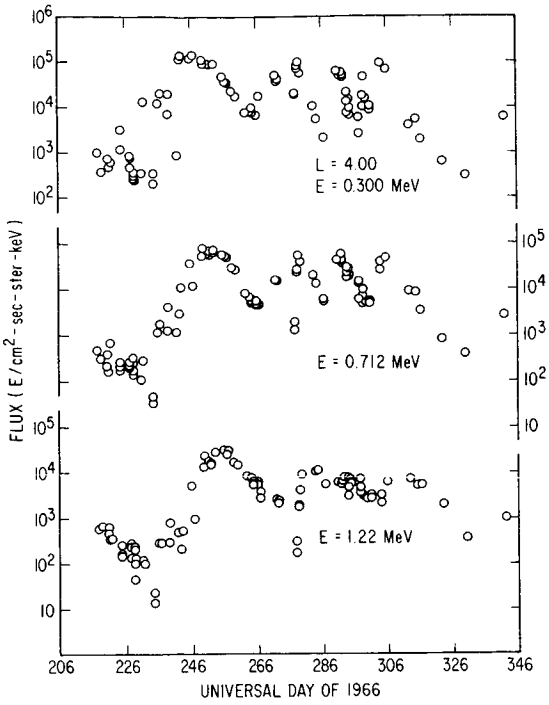

FIGURE 1. -- Electron fluxes at L = 4.0 for 1.225, .712, and .300 MeV during the period day 206 to day 346, 1966. Increases are seen on day 247, 278, 290, and 302 due to magnetic activity.

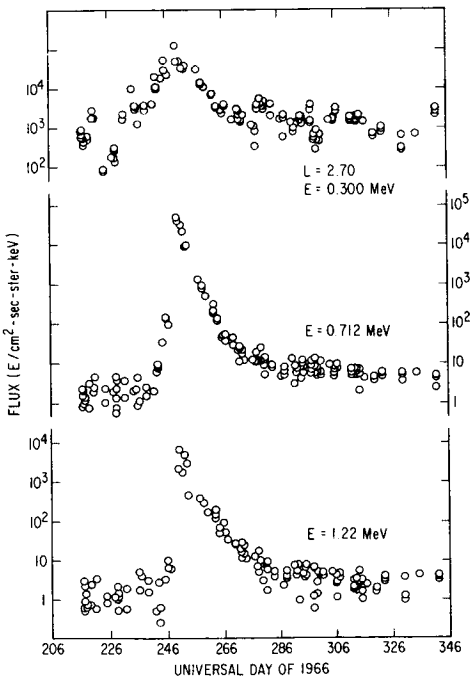

FIGURE 2. -- Electron fluxes at L = 2.7 for 1.225, .712, and .300 MeV during the period day 206 to day 346, 1966. All fluxes show a large increase due to the magnetic storm on day 247, but only the .300 MeV fluxes respond to later minor magnetic disturbances.

they are lost into the atmosphere. Figure 3 shows two examples of electron precipitation -- one with a large flux present in the slot and another with a small flux in the slot, although both exhibit significant outer zone precipitation. There is evidence that there is a continuous precipitation of particles in the outer zone at or outside of the plasmapause. Within the plasmapause, electrons are more stable except for the "slot" region.

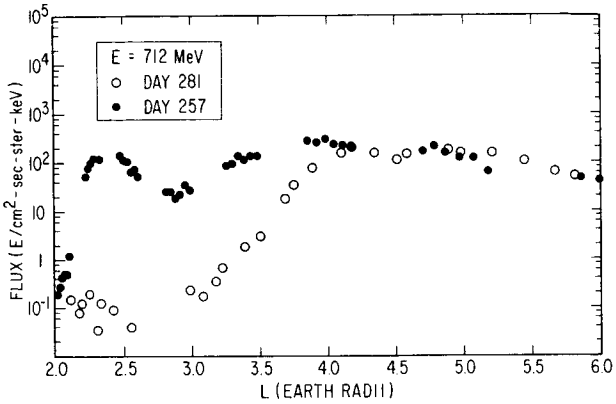

FIGURE 3. -- Low altitude precipitating fluxes for two periods. Significant fluxes are observed in the slot on day 257 but not on day 281. These fluxes are in the drift loss-cone; i.e., they will not survive a complete drift period around the earth.

We can look at the effects of a major magnetic storm from another point of view. For certain purposes, a knowledge of the electron energy spectrum is required. Often measurements are made at a couple of energy thresholds and an exponential or power law spectrum is constructed with those data points. Such a procedure can be hazardous as can be seen from Figures 4 to 6. Flux vs L for a number of electron energies is plotted for several periods preceding and following the large storm on day 247. On day 241 in Figure 4, a large null or "slot" is seen in the flux profile at all energies at L $\approx$ 3. The center of the slot appears at slightly higher L values at lower energies. Energy spectra are monotonic almost everywhere. On day 246, the outer zone is much less extensive; solar flare electrons are observed at L > 6 and the "slot" is filled with low energy electrons due to minor magnetic disturbances on days 242 and 244. Flux profiles on day 249 show a large peak at L $\approx$ 3, the

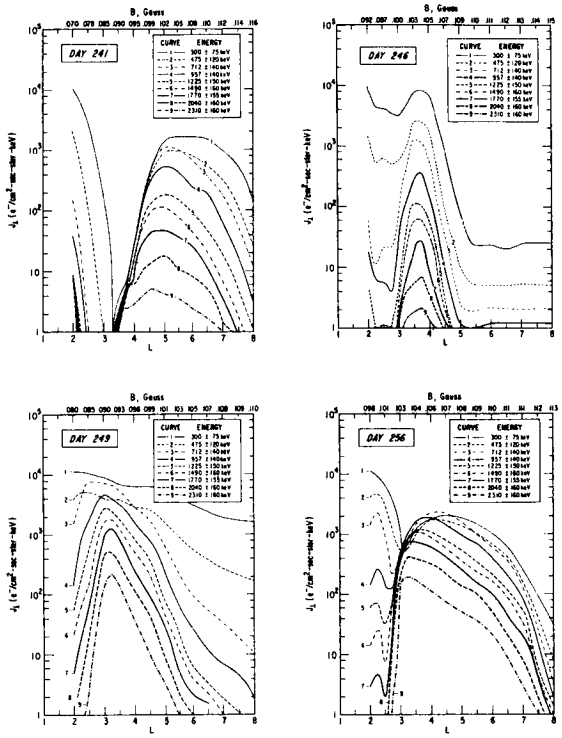

FIGURE 4. -- Plots of J_1 (electron flux with a local pitch-angle α = 90° ± 8°) vs L for nine differential energy channels for four periods prior to and after the magnetic storm of day 247, 1966. B, the magnetic field in gauss at the point of observation, is annotated for each plot. See text for discussion.

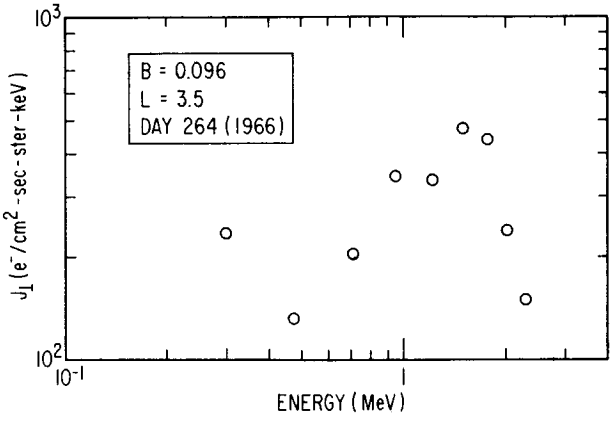

FIGURE 6. -- Differential energy spectrum of electrons at L = 3.5, B = .096 on day 264, 1966. The spectral inversion seen here demonstrates the need for caution in characterizing spectra as exponential or power-law.

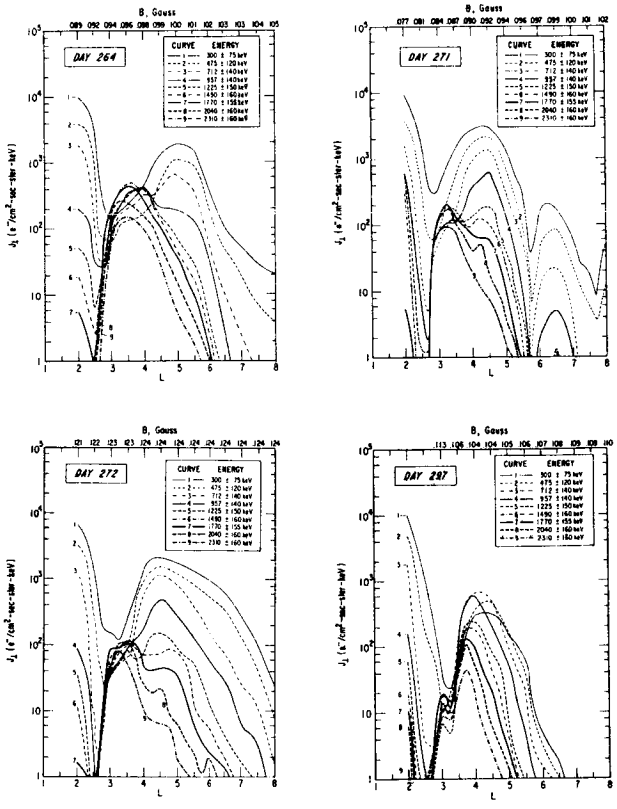

FIGURE 5. -- Plots similar to Figure 4 but for four time periods following those of Figure 4. See text for discussion.

previous location of the slot. The two lowest energy electron flux profiles indicate that some decay may have already taken place. The higher energy fluxes have increased several orders of magnitude from the previous levels. A week later, day 256, the slot is again being established at L ≈ 3. Note that due to the rapid loss there, the profile now has a small peak centered at L ≈ 2.3. Also, note that at L ≈ 3.5, a complex energy spectrum is evolving due to an effective electron lifetime which is longer for the more energetic particles. Figure 5 continues the observations through the next month. On day 264 a rather grotesque energy spectrum has evolved at L = 3.5. This sample spectrum, Figure 6, indicates the need for caution when making flux measurements at one or two energies and extrapolating. The other plots in Figure 5 show other features. On day 271, the outer zone has assumed a multiple-lobed structure. This same structure has been observed in the equatorial fluxes (H. I. West, Jr., private communication) and is probably due to an enhanced localized precipitation producing the minima. It also is possible that the maxima are discrete groups of electrons which have

been injected/accelerated in the outer regions of the outer zone. In fact, since electrons are diffused radially inward and thereby accelerated, both of the above explanations may be correct -- an occasional enhanced precipitation may cause an interruption in an otherwise continuous source of electrons which are being diffused to lower L values. The data of day 272 show that the effects are short-lived and are observable only at lower L values at higher energy, again in agreement with the inward diffusion/acceleration hypothesis. The final plot, day 297, shows a profile qualitatively similar to the initial one on day 241. A small peak near the slot is due to a magnetic disturbance on day 278. In effect, the outer zone has recovered from the large magnetic storm six weeks earlier.

We can observe the effects of magnetic storms on the higher energy particles in Figure 7. These data were obtained from instrumentation on OV1-19 during 1969. A large magnetic storm occurred on May 15. Spectra are shown at L ≈ 3.4 for one week prior to the storm, immediately after the storm, and up to three weeks after the storm. One again sees an evolution of the type seen in the 1966 storm data -- all energy fluxes are enhanced and the subsequent decay is more rapid for the lower energies. Even at 5 MeV significant fluxes of electrons appear. It would be interesting to make detailed measurements at even higher energy during a large storm to see what, if any, is the upper limit to the energy spectrum.

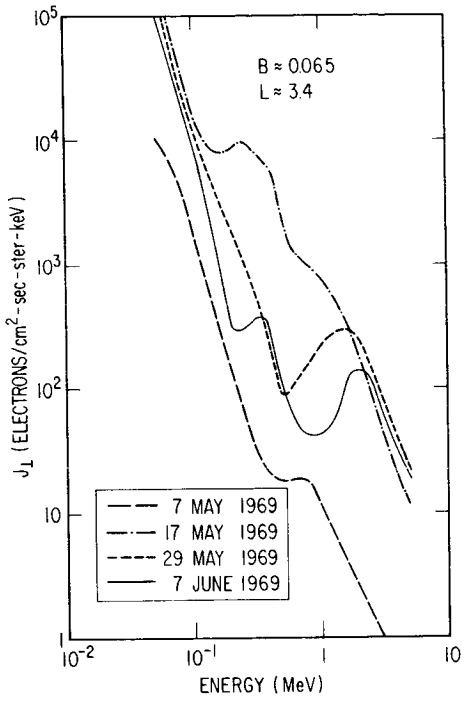

FIGURE 7. -- Energy spectra of electrons between 53 keV and 5.09 MeV at L = 3.4, B = .065 showing the effect of a magnetic storm on 15 May 1969. Significant quantities of electrons between 2 and 5 MeV are injected/accelerated.

INNER ZONE VARIATIONS

In the inner zone, the information is much less extensive. In the first place, no accurate spectral measurements of natural electrons were made prior to the Starfish nuclear detonation which obscurred the natural population. After that event, any natural flux variation would have had to be very large in absolute value in order to be observed above the artificial addition. Several years were required for the Starfish flux to decay to the point where natural fluxes could be observed. Thus most of the measurements of inner zone electrons in the period 1962 to 1966 were Starfish measurements. Secondly, the inner zone contains a large stable population of very energetic protons and these tend to obscure electron measurements. However, several reports of increases in the inner zone natural electron flux have been made (refs. 7 to 11).

Vampola (ref. 7) compared measurements in 1966 with measurements by Mihalov and White (ref. 12) in 1964 and concluded that the natural electrons in the inner zone had increased by half an order of magnitude in the two year period. Subsequent analysis of data during the 1966 period showed a large change in the inner zone flux during and following the day 247 magnetic storm. Figure 8 is similar to Figures 1 and 2, but shows the effect in the inner zone at L = 1.90. Note that there is an abrupt increase at the time of the storm and then a continuing slight increase for about a month before the fluxes begin to decay. This continuing increase is due to lower energy electrons from higher L values diffusing radially inward and becoming energized. The diffusion rate decreases at lower L values. Hence it takes longer for the fluxes to attain their peak value at lower L values. Figure 9 shows the flux vs L profile for the same time period covered in the outer zone description. The four lowest energy electron profiles show an

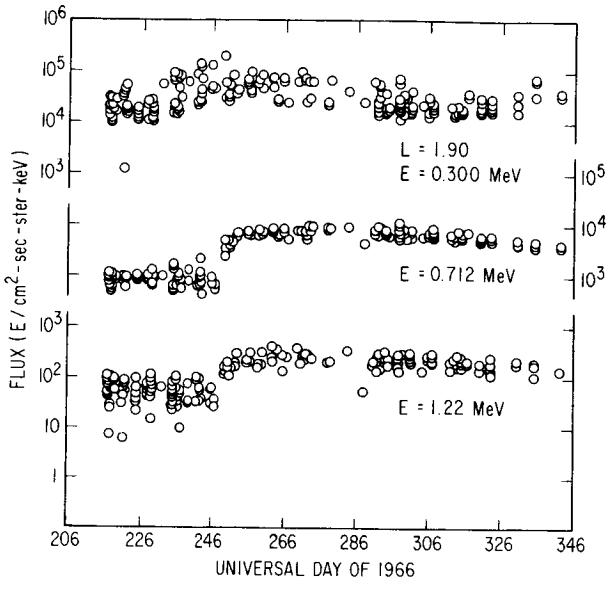

FIGURE 8. -- Plot similar to Figures 1 and 2, but in the inner zone at L = 1.9. The energetic electrons are seen to respond immediately to the magnetic storm on day 247 and then continue to slowly increase in intensity for about a month.

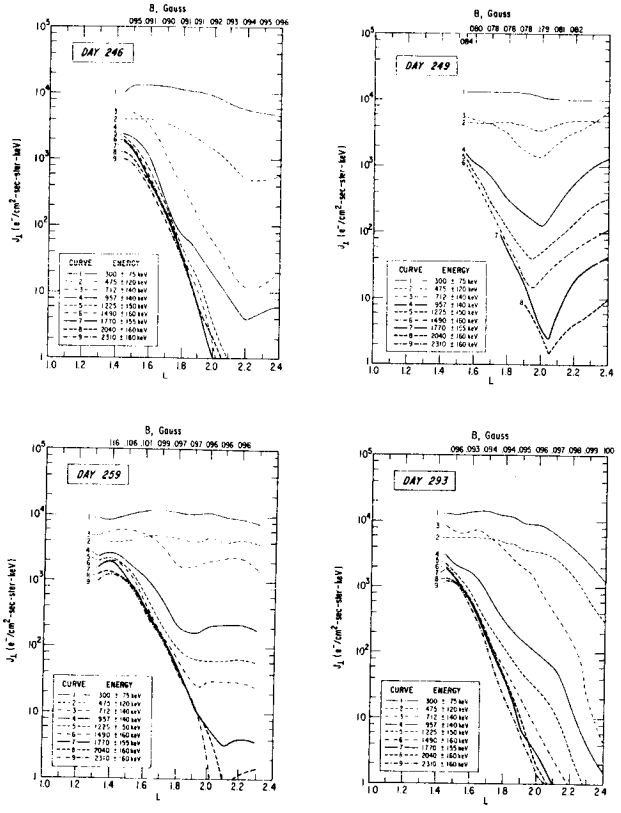

FIGURE 9. -- Plots similar to Figures 4 and 5 but covering the range $1 \leq L \leq 2.4$. Electrons are observed moving to lower L values during the time period covered. See text for discussion.

increase in flux at L ~ 2.2 on day 246. This is due to the small storms which preceded the day 247 storm. Data on day 249 show the large magnetic storm has added electrons of all energies to the inner zone. As these decay away, some also diffuse to lower L values. Data on days 259 and 293 show the evolution of this event. Data on day 293 were taken at approximately the same B (magnetic field) value and are directly comparable. One finds that at L = 1.5, there has been an increase of ≈ 15% in the 957 keV electrons and about 8% in the 1.225 MeV electrons. At L = 1.6, the corresponding figures are about 60% and 15%.

The low energy electrons have been studied extensively by Bostrom et al. (ref. 13) and show pronounced changes due to magnetic activity down to the lower edge of the inner zone. Figure 10 (from ref. 13) presents the time history of $E_e \geq .280$ MeV for L = 1.2, 1.3, 1.5, 1.8, and 2.2 during the period 1963 through 1968. Magnetic storms are indicated by the D_{st} scale. It is seen that the entire inner zone low energy electron population responds to large magnetic storms. Since we are now in the declining phase of solar activity, it can be assumed that the average level of electron flux in the inner zone will decrease. As a result, the perturbations due to magnetic storms will become much more observable.

VARIATIONS AT SYNCHRONOUS ALTITUDES

Particle detectors at synchronous altitude sample a very small region of B, L space. As a result, it is relatively easy to separate spatial and temporal effects in the electron fluxes observed. There are two principal types of variations -- diurnal and that induced by magnetic activity. During magnetically quiet times, a synchronous satellite will see a slowly varying flux intensity as it samples different local times. Due to the distortion of the magnetosphere, the electron drift shells do not remain at constant radial distance for all local times. The L value at local noon is lower than at local midnight. Since in the region of L = 6.6 (the nominal synchronous L value) the flux intensity decreases with increasing L, a satellite will see smaller fluxes of electrons at local midnight than at local noon. Fig. 11 (from ref. 14) shows this diurnal variation for several energies.

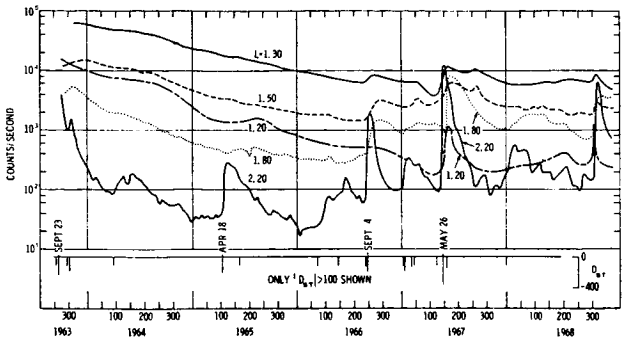

FIGURE 10. -- A history of inner zone low energy electrons ($E_e \geq$ .280 MeV) for L = 1.2, 1.3, 1.5, 1.8, and 2.2. Magnetic storms are indicated by the D_{st} scale, which shows only values of $D_{st} < -100$. The response of these fluxes to magnetic activity is pronounced (from ref. 13).

data was obtained from ATS-1 on 14 January 1967. At approximately 00:08 UT, the magnetometer output shows a reversal of the geomagnetic field. This is interpreted as a motion of the boundary of the magnetosphere past the satellite to a smaller radial distance. Simultaneous with this boundary crossing the particle counters show a loss of flux; at this point they are sampling the interplanetary medium instead of the trapped population in the magnetosphere. A similar situation existed when the data of day 246 (Figure 4) were obtained.

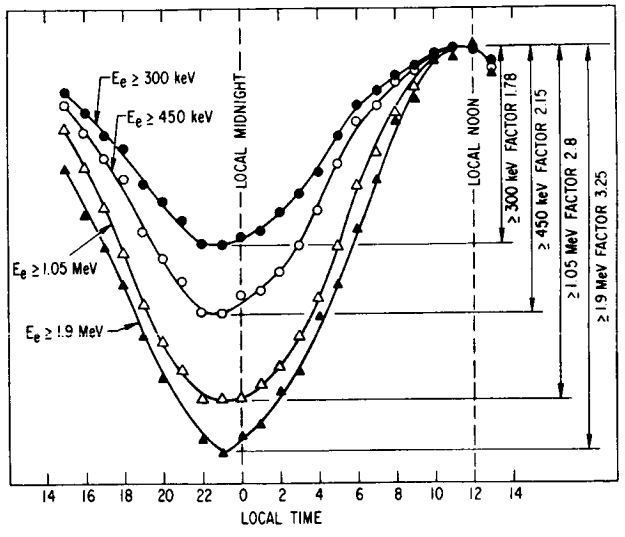

FIGURE 11. -- The diurnal variation of electrons E ≥ 300 keV, ≥ 450 keV, ≥ 1.05 MeV, and ≥ 1.9 MeV at synchronous orbit altitude as measured by ATS-1. The mean of the logarithm of the variation is plotted as a function of local time. (From ref. 14).

The mean of the logarithm of the variation of the fluxes with respect to the flux value at local noon is plotted as a function of local time. The variation is greater for higher energy electrons, which is what one would expect since these L values are near the boundary of stable trapping and the higher energy electrons, which have a larger gyroradius, are more likely to encounter destabilizing conditions near that boundary as they drift in longitude. As an example of how close the boundary is, we can exhibit Figure 12. Two electron flux channels are plotted along with a magnetometer output. The

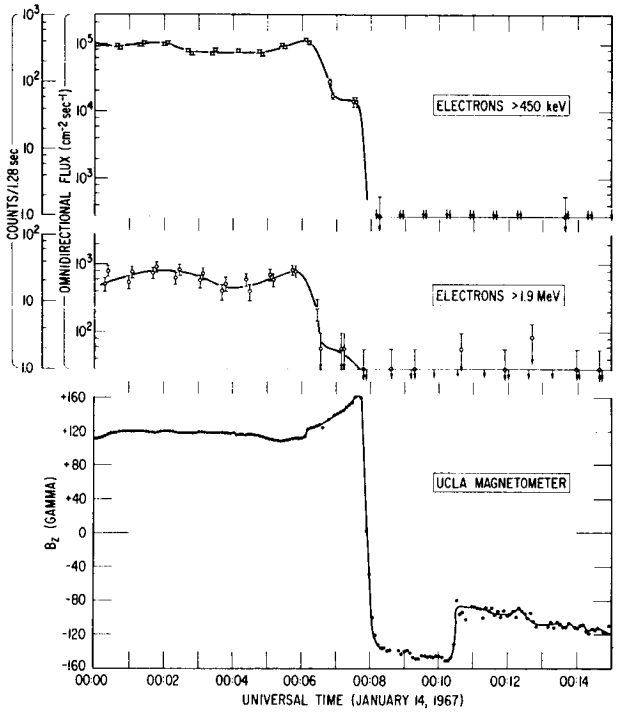

FIGURE 12. -- ATS-1 particle and magnetometer data showing an event in which the magnetospheric boundary moved inside the orbit of the spacecraft. (From ref. 15.)

The effects of magnetic activity on the flux intensities can be seen in Figure 13. Fluxes of electrons with E > 1.05 MeV and E > 1.9 MeV are shown for the time period day 340, 1966 to day 60, 1968 along with the magnetic activity index ΣK_p. The correlation between increases in magnetic activity and flux increases is quite evident. Changes of flux intensity of an order of magnitude in tens of minutes are observed on plots with shorter time scales. A comparison of the ATS-1 data with the AE3 electron environment (ref. 12) has been made and is shown in Figure 14 (from ref. 14). The AE3 prediction of the probability (P) that a flux (F) greater than a given flux (F_x) will be observed is plotted as a function of F_x for several energies. The actual observations by the ATS-1 instrumentation are also shown. The agreement is excellent except at the highest energy. The AE3 environment was compiled from data obtained during and just after a minimum in solar activity. We have seen in the first section that the outer zone energetic electron population responds to magnetic activity which, in turn, is controlled by solar activity. The ATS-1 data was gathered during the rising portion of a solar cycle just prior to the peak. Hence we would expect the ATS-1 energetic particle data to exceed the AE3 predictions, as it does.

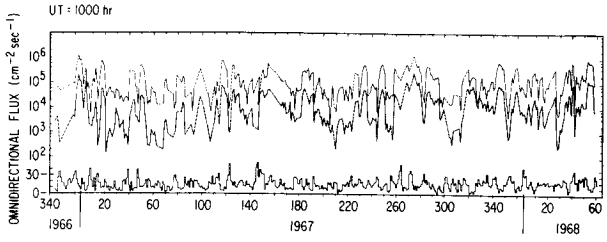

FIGURE 13. -- Flux of electrons E ≥ 1.05 MeV (upper trace) and ≥ 1.9 MeV (lower trace) for the time interval day 340, 1966 to day 60, 1968 at a local time of midnight. The daily sum of the magnetic activity index K_p is plotted at the bottom of the figure. (From ref. 14.)

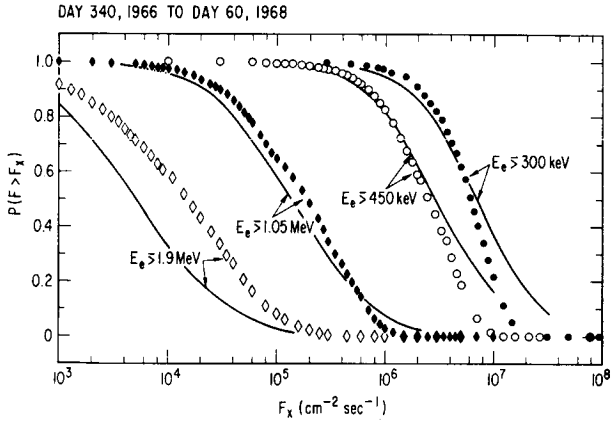

FIGURE 14. -- A comparison between electron fluxes predicted by the AE3 synchronous altitude model environment (ref. 2) and ATS-1 measured values. P(F > F_x) is the probability of observing a flux F greater than a given flux F_x. The agreement is excellent except for the highest energy electrons. (From ref. 14.)

REFERENCES

1. Vette, J. I.; Lucero, A. B. and Wright, J. A., Models of the Trapped Radiation Environment, Volume II: Inner and Outer Zone Electrons, NASA Document NASA SP-3024, 1966.
2. Vette, J. I. and Lucero, A. B., Models of the Trapped Radiation Environment, Volume III: Electrons at Synchronous Altitudes, NASA Document NASA SP-3024, 1967.
3. Frank, L. A., J. Geophys. Res., Vol. 70, 1965, p. 1593.
4. Frank, L. A., J. Geophys. Res., Vol. 70, 1965, p. 3533.
5. Williams, D. J.; Arens, J. F. and Lanzerotti. L. J., J. Geophys. Res., Vol. 73, 1968, p. 5673.
6. McIlwain, C. E., J. Geophys. Res., Vol. 66, 1961, p. 3691.
7. Vampola, A. L., Recent Measurements of Inner Zone Electron Lifetimes, COSPAR, London, 1967.
8. Freden, S. C.; Blake, J. B. and Paulikas, G. A., Earth's Particles and Fields (ed. by B. M. McCormac), Reinhold Books Corporation, New York, 1967, p. 3.
9. Pfitzer, K. A. and Winckler, J. R., J. Geophys. Rev., Vol. 73, 1968, p. 5792.
10. Vampola, A. L., Trans, Am. Geophys. Union, Vol. 49, 1968, p. 719.
11. Armstrong, J. C. and Bostrom, C. O., Trans. Am. Geophys. Union, Vol. 51, 1970, p. 393.
12. Mihalov, J. D. and White, R. S., J. Geophys. Res., Vol. 71, 1966, p. 2217.
13. Bostrom, C. O.; Beall, D. S. and Armstrong, J. C., J. Geophys. Rev. Vol. 75, 1970, p. 1246.
14. Paulikas, G. A.; Blake, J. B. and Palmer, J. A., Energetic Electrons at the Synchronous Altitude: A Compilation of Data, The Aerospace Corporation Report TR-0066(5260-20)-4, 1969.
15. Paulikas, G. A.; Blake, J. B.; Freden, S. C.; and Imamoto, S. S.; J. Geophys. Res., Vol. 73, 1968, p. 5743.

TRAPPING OF TRANSURANIUM ELEMENTS BY THE EARTH'S MAGNETIC FIELD

Justin L. Bloom and Bernard J. Eastlund

U.S. Atomic Energy Commission

The search for a transuranium element component of cosmic radiation has been carried out in high altitude balloon experiments by Price, Fleischer, Walker and Fowler. We show that the trapping of high Z elements on orbits in the Earth's magnetic field may lead to a sufficient enhancement of the intensity of particle flux to make it possible to detect these elements by satellite experiments. Calculations are presented that predict the behavior of trapped particles as a function of the predicted flux and energy distribution of high Z elements incident on the Earth's magnetic field. Techniques are suggested for the detection of such particles. In addition, the possibility of production of transuranium elements in the recently discovered pulsars are discussed.

One of the most interesting developments in nuclear physics during the past decade has been the prediction by nuclear stability theorists of the possible existence of relatively long lived nuclei with atomic number around 114--isotopes of the so-called superheavy elements. This possibility has prompted physicists and chemists to institute a search for them in (a) naturally occuring materials such as ores and meterorites and (b) as a small fraction of the cosmic ray flux. Pioneering balloon experiments by Price and Fowler (1-5) have resulted in the detection of one or two particles which may have $Z > 92$. The purpose of the present paper is to explore the possibility that transuranium and superheavy elements may remain trapped by the earth's geomagnetic field for appreciable periods of time. It is shown that if detectors are flown abroad satellites in the regions in which such a "holdup" of particles occurs the counting rates may be greatly in excess of those possible in balloon experiments. The orbits where elements of various energies would be trapped are described and a detection scheme is suggested.

It has been shown (6) that perturbations in the cosmic ray flux at the earth could be produced by pulsars. The theory that nuclear events taking place in pulsars could lead to the creation and acceleration of superheavy nuclei has also been discussed in recent papers (7,8). If these theories are correct, it is possible that nuclei with half lives as small as 10^4 years, originating from pulsars, could be detected and the sensitivity of detection increased by searching with satellite borne detectors in regions of the geomagnetic field calculated on the basis of particle trajectories.

"SUPERHEAVY" ELEMENTS

The presently popular unified theory of nuclear stability combines features of the charged liquid drop model of the nucleus (used for many years to explain nuclear fission in both qualitative and quantitative terms) and the shell model of the nucleus, by which the nuclear potential of individual nucleons can be computed--the nucleons being arranged in quantum orbitals similar to the more familiar electron orbitals which determine atomic structure (9). Out of this theory has come a set of predictions, based in part on known nuclear properties of isotopes, which indicates that the decline in nuclear stability with increasing atomic number that is observed with the known chemical elements will be reversed if so-called "superheavy" elements could be created. The hypothetical superheavy elements constitute a region of exceptional nuclear stability believed by most theorists to center around atomic number 114. The atomic number 114 is computed to be a "magic number" or closed shell of protons. Additional nuclear stability in this region is afforded by a predicted closed neutron shell of 184 neutrons.

Consequently, the isotope with atomic number 114, neutron number 184, and derived mass number of 298 is doubly magic and should be remarkably stable. "Stability" here really means resistance to decay by spontaneous fission, and this mode of decay would be overriding in the absence of any stabilizing influence of the closed nucleon shells. In the case of the half life of the isotope $^{298}114$, for example, its half life for spontaneous fission is predicted to be 10^{20} years, whereas empirical extrapolations of the spontaneous fission half lives of known transuranium isotopes would indicate that the spontaneous fission half life of $^{298}114$ should be vanishingly small. If exceptional stability toward spontaneous fission is accepted, at least in principle, then other possible modes of decay must be considered for any given isotope to determine which is controlling. The results of such a study are shown in Figure 1, which is the work of C. F. Tsang at the University of California, Berkeley (10). From the figure it can be seen that the isotope with Z=114 and N=184 is stable against beta particle decay, but has a half life of only about one year for alpha particle emission. From an overall viewpoint, the isotope with Z=110 and N=184 is optimally stable, having a net half life of the order of 10^8 years when all modes of decay are taken into consideration.

THE OCCURRENCE OF SUPERHEAVY ELEMENTS IN NATURE

Such theoretical considerations have prompted several experimental physicists and chemists to institute a search for trace quantities of superheavy isotopes in naturally occurring materials. They have followed one or the other of two lines of reasoning. First, if one assumes that superheavy elements can be created by the same nuclear processes that led to the known elements (primarily the r-process in Type I supernovae for heavy elements), then these elements should be present in exceedingly small concentrations in minerals which contain large proportions of elements chemically homologous to the superheavy element being sought, provided that the half life of the superheavy isotope or isotopes is of the order of 10^8 years--long enough to have survived the period of time that has elapsed since the creation of the elements of the earth. The search based on this hypothesis has been intensive but inconclusive (11).

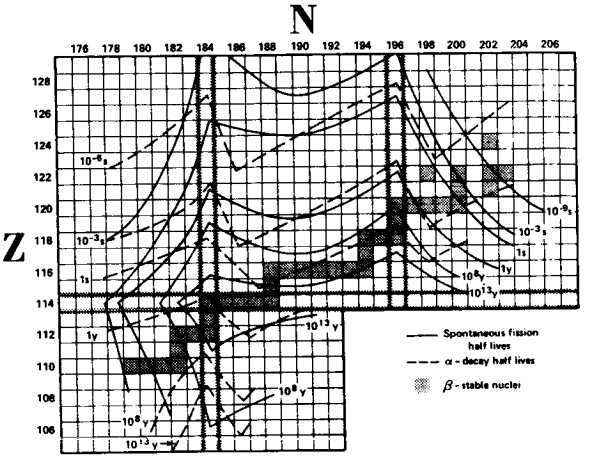

Half Life Contours for Region of Exceptional Nuclear Stability

SUPERHEAVY ELEMENTS IN COSMIC RAYS

The second possibility is that superheavy isotopes are being formed in cosmic nuclear processes of more recent vintage than the events which led to the creation of the solar system, and that cosmic rays should contain a small proportion of such isotopes. This line of thinking has been further stimulated by the remarkable work of P. B. Price, R. L. Fleischer, and R. M. Walker, and associates at the General Electric Research and Development Center and Washington University (Price is now at the University of California, Berkeley) and

P. H. Fowler and his group at the University of Bristol, England (1-5). These groups have collaborated on several occasions to measure the charge distribution of heavy cosmic rays in a series of balloon flights over the United States. The American group collects cosmic ray tracks in stacks of plastic sheets, while the British workers use nuclear emulsion sheets for recording the tracks. Since the two media are arranged contiguously in the balloon flights, a heavy cosmic ray track recorded in one medium typically will also be recorded in the other, permitting correlation of the responses observed. As shown in Figure 2, the correlation of cosmic ray atomic numbers (Z) as measured in plastic sheets, versus the values obtained for the same cosmic rays in nuclear emulsion is very good, except for one event with $Z > 100$--the most interesting event (4,5). Usually only tracks which pentrate all sheets were accepted for measurement. Measurement of the tracks produced in the sheets, has resulted in the histogram shown in Figure 3, taken from reference (5) representing the results of two balloon flights in 1968. The one event shown at Z=104 (in emulsion) is assigned a charge of 92 in Lexan and 93 in cellulose triacetate. It was registered in all three materials (the only track so to be found and examined) with essentially a uniform response and its velocity was determined to be at least 0.92c. Price et al postulate that this particle was more likely a long-lived isotope with $96 \leq Z \leq 98$ rather than with $110 \leq Z \leq 115$. That is, it probably was an isotope like ^{247}Cm or ^{244}Pu rather than a superheavy isotope. The best value assigned is $Z \approx 96, \beta \approx 0.95$, but higher and lower values cannot be ruled out completely.

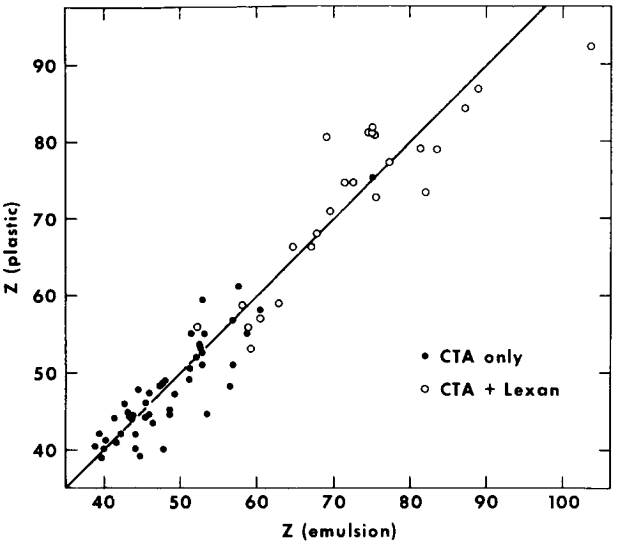

FIGURE 2

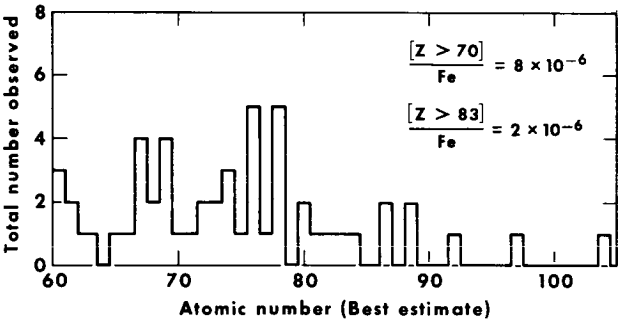

FIGURE 3

RELATIVE ABUNDANCE OF VERY HEAVY COSMIC RAYS

According to Price et al (5), of 10^{10} cosmic ray primary particles that passed through two stacks of plastic sheets and nuclear emulsion sheets, about 3×10^6 particles were in the iron group ($24 \leq Z \leq 28$). After scanning 75% of the area of these sheets, three particles with $Z > 83$ were found, indicating that less than one cosmic ray in 10^9 primaries has a charge greater than 83. Summing the data from the experiments, Price et al state that $\left(\frac{Z > 83}{Fe}\right) = 2 \times 10^{-6}$, which would indicate that cosmic rays with $Z > 83$ relative to the total primary flux would be $\frac{(2 \times 10^{-6})(3 \times 10^6)}{10^{10}} = 6 \times 10^{-10}$, also equivalent to less than one heavy particle in 10^9 primaries. Also useful is the histogram reproduced from reference (5) as Figure 4, which indicates that the

absolute flux of cosmic rays with $Z \geq 80$ is about 0.03 particle/m^2 day steradian at the top of the atmosphere.

From the data deduced above, it is apparent that efforts to determine whether the superheavy elements ($110 \leq Z \leq 126$) can be found in cosmic rays are greatly limited by using balloons to expose plastic sheets and nuclear emulsions to extremely small fluxes of heavy particles. The balloons cannot stay aloft for more than a day or two and their load-lifting capacity is restricted.

The following discussion will illuminate some of the favorable aspects a satellite experiment would have in regards to the detection of a large number of particles.

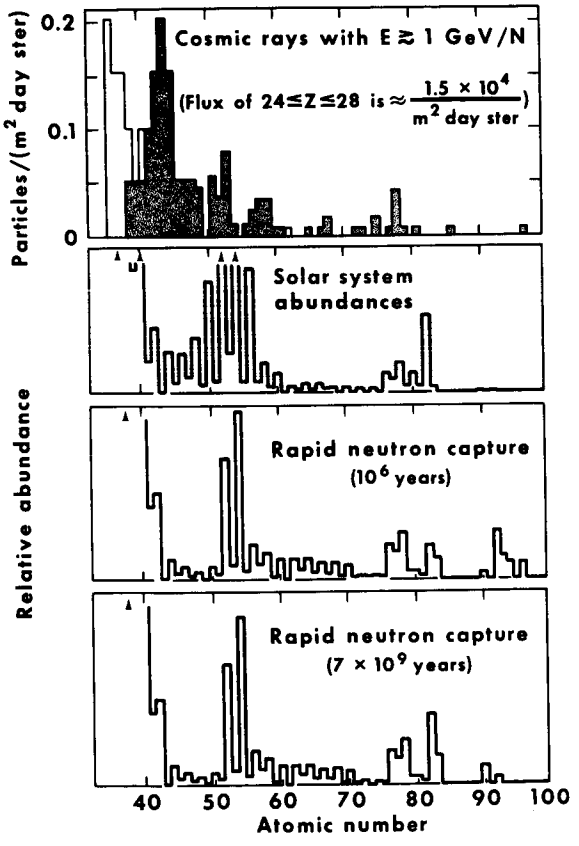

FIGURE 4

GEOMAGNETIC TRAPPING

The computation of cosmic ray trajectories in the Earth's geomagnetic field has reached a high degree of sophistication. Early work by Stoermer (12), Lemaitre and Vallarta (13) and others showed that the cosmic ray intensities, measured on earth, should be a function of location with respect to the Earth's magnetic poles. These theoretical calculations show that, depending on location, there is a "cutoff rigidity" (momentum per unit charge) which is the lowest rigidity a cosmic ray can possess and still arrive at a specific point on the earth's surface. In 1961, Gall and Lifshitz (14) proposed the temporary capture of primary cosmic ray particles on unstable periodic orbits in a dipole, as a mechanism contributing to the formation of Earth's radiation belts. The major sources of the radiation belts are now believed to be the trapping and subsequent acceleration of solar wind particles and the decay products from cosmic ray albedo neutrons. Other minor sources are solar cosmic rays (either by direct injection or via albedo neutrons) or a neutral component in the solar wind. Thus, the Gall and Lifshitz (14) paper was not the explanation of the radiation belts. However, their mathematical analysis of the unstable periodic orbits in a dipole field was correct. More recently an extensive amount of work has been done by Smart, Shea and Gall (15,16) in computation of charged particle cutoff rigidities and special orbits in which the earth's internal magnetic field is represented by a Gaussian expansion with IGRF coefficients (17) up to n=8, and the external field due to currents in the magnetopause and neutral sheet by the Williams and Mead expression (18). A class of orbits is found in these calculations in which particles of rather high rigidity, (1-10 BV) can remain in the vicinity of the earth for periods of time long compared to the bounce time between magnetic turning points. These orbits in which particles are held up for a large number of bounce periods lie typically 1 to 2 degrees below the normal cutoff latitude for particles of a given rigidity. One of these trajectories has been calculated for us by Shea and Smart, and a portion of the trajectory is illustrated in figure 5 for a superheavy element with Z=114, A=298, and an energy of 0.1 BeV per nucleon (rigidity of 1.16 BV). This particular trajectory resulted in the trapping of the particle for approximately 30 seconds, which was time for

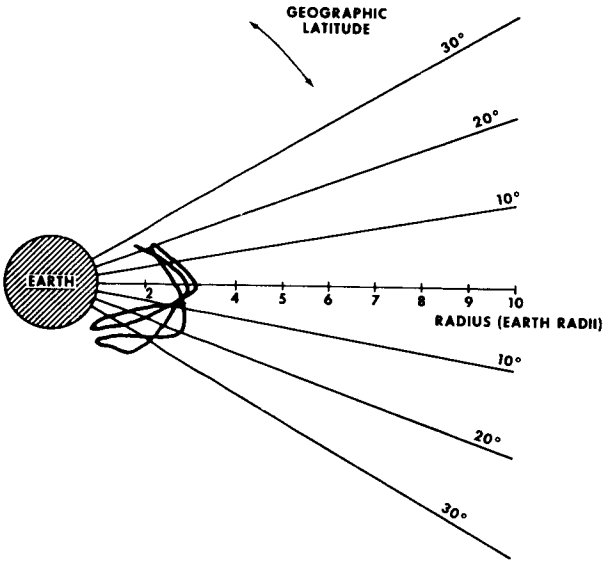

FIG.5

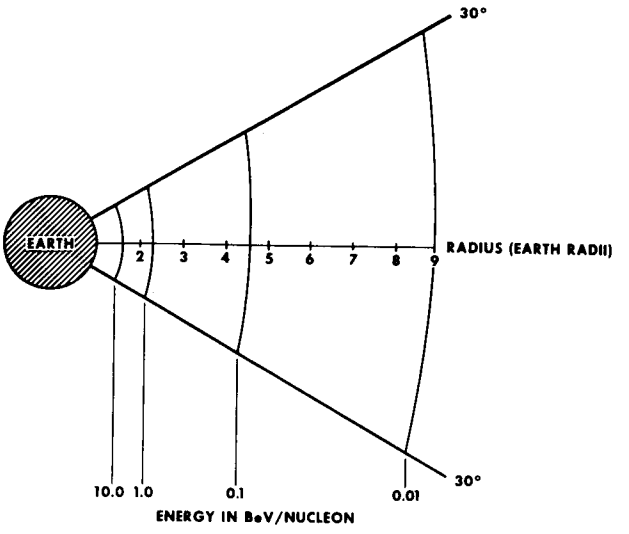

FIG. 6

four complete longitudinal orbits around the earth and 90 bounces between the latitudinal turning points. The motion occurred at a distance of approximately 3 earth radii.

While these calculations were performed with computational techniques, a general picture of the behavior of isotopes of various energies and charge to mass ratios can be obtained by approximating the earth's field as a dipole. (For high rigidity particles the earth's magnetopause and neutral sheet have little effect on the orbits). The location of the orbital regions in which isotopes may be trapped is a function of both energy/nucleon and Z/A. However, the possible range of values of energy is much greater than the range for Z/A and thus one might first look for iron say, then look for the heavier isotopes. The best orbital region for observing superheavy elements will be a function of the best estimate of the particle energy spectrum. This effect is illustrated in figure 6 where, for turning points at $\lambda = 30^{o}$, the location of the trapping regions are illustrated as a function of energy per nucleon for a superheavy isotope with Z=114, A=298. For comparison, the trapping regions for iron with Z=26, A=56,

a proton, and a superheavy element is illustrated in figure 7 for 500 MeV/nucleon particles.

Thus, we have shown, with a detailed calculation of a trajectory, that for a superheavy element, orbital regions exist in which the particle can be temporarily captured by the earth's geomagnetic field. The generalization of this effect to other isotopes has also been presented. Satellite detectors located in these regions in which particles can be temporarily trapped would be expected to provide a detection capability superior to that of balloon experiments. The degree of increase in superheavy element detection capability is a function of four factors:

(1) The possibility of an interaction between the superheavy elements and atmospheric atoms is reduced.

(2) An omnidirectional sensor located in one of these regions will detect a flux several times greater than that of an undirectional sensor. See for example, Ray (19). This enhancement in detection capability is consistent with the Liouville Theorem.

(3) These orbits, which are sometimes referred to as asymptotic to the periodic orbit, are very close to actual "trapping" regions, in which particles can remain until a scattering event removes them. Thus, if adiabaticity is violated during injection, or if an interaction occurs with any of the fluctuating electromagnetic fields in these regions, a trapped population could be formed. The detailed mechanism by which particles are trapped by the earth's geomagnetic field is still only partially understood. Thus, the enhancement of intensity of high rigidity isotopes expected in these regions would have, as an upper limit, the ratio of intensity of high rigidity protons in the radiation belts to the incoming flux of high rigidity radiation. This ratio is about 10.[4] The decay products of albdeo neutrons undoubtedly account for a significant percentage of high energy (> 100 MeV/Nucleon) trapped radiation; therefore, this ratio may be too large by a factor of ten or more. The relative fluxes of various components of the earth's radiation environment are shown in figure 8.

(4) Finally, the increased observation time possible with a satellite would make it possible to observe a larger integrated flux.

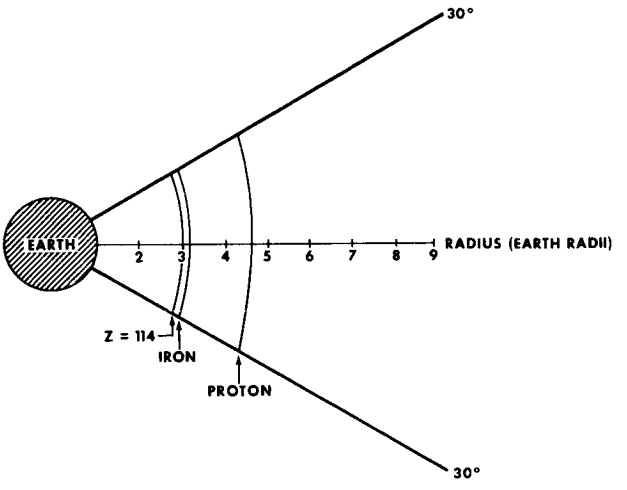

FIG. 7

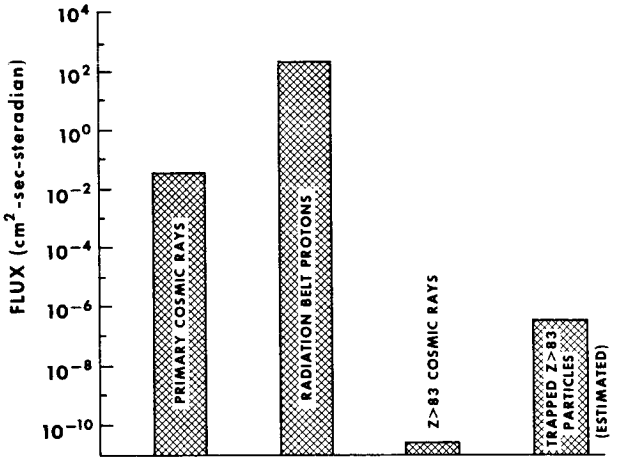

FIG. 8

The instrumentation of a satellite to detect superheavy elements and to provide for transmission of such data by telemetry to an earth station does not exist at the present time although in reference (20), a thorough description is given of cosmic ray telescopes which have been flown aboard satellites to detect particles with charges ranging up to those in the vicinity of iron. These telescopes could be used to study possible trapping regions for cosmic ray nuclei. One possibility for superheavy element detection would be to place the detector sheets in orbit with a recoverable satellite. The plastic detectors can be made insensitive to elements in the iron group or lower and thus screen out the very intense light components of the earth's radiation environment.

PULSAR SOURCES

Pulsars have been suggested as sources for at least some of the cosmic rays (7,8). These pulsars are thought to be "neutron stars" which consist primarily of a neutron "superfluid" at a density of 10^{15} gms/cm^3. The outer layers are not well understood and could consist of either an exotic crystalline solid or a gas. Thus, the mechanism for heavy cosmic ray formation could be related to some evaporative process. One such process was suggested in 1949 by M. G. Mayer and E. Teller with their "polyneutron" theory (21). If superheavy elements are formed on or near the surface of a pulsar, then the rapid rotation characteristic of these objects, through interactions with intense magnetic fields believed to be connected to the object, could provide sufficient energy to both accelerate and eject the elements from the star. P. B. Price, et al, have dismissed the pulsars as possible sources of superheavy elements because the solid portion of the crust of a neutron star is thought to consist mainly of iron. Such a conclusion may be premature as there is no direct experimental evidence on the composition of the neutron star. The only well known facts are that they are very dense, rapidly rotating objects which are releasing large amounts of energy.

An analysis of the possible contribution to the general cosmic ray flux by discrete pulsar sources has been carried out by Lingenfelter (6). His calculations included considerations of the age of the pulsars, their distance from the earth and diffusion in the interstellar medium. He finds that the pulsar PSR 1929+10, which is only 0.14 KPC from earth and is estimated to be only 6 x 10^4 years old, could be influencing cosmic ray flux at the present time.

Other, older pulsars are also found to be a possible influence on the cosmic ray flux.

CONCLUSIONS

We have attempted to show that it would be advantageous to search for temporarily trapped isotopes with satellite experiments. The particular case of superheavy elements is discussed and trajectories are shown to exist on which these particles would spend a considerable period of time. The regions defined by the trajectories have characteristics that could result in a significant enhancement of the hypothesized superheavy element component of cosmic rays, compared to that detectable in balloon experiments. While the percentage of superheavy elements in the geomagnetic trapping regions may be very small, the ability to build a detector that is insensitive to charges in the iron region or lower makes it possible to search for these elements without interference by the much more intense proton or alpha particle fluxes. The degree of increase in counting rate possible (compared to a balloon experiment) is estimated to be between a factor of 10^3 and 10^4.

A satellite search for superheavy elements is made even more attractive when one considers the possibility of discrete sources, such as the pulsars. If the lifetime of superheavy elements is less by a large factor than the estimated maximum half-life of 10^8 years, then only nearby sources could contribute to an observable flux. Furthermore, the flux from discrete sources would then approach the earth's magnetic cavity from a specific direction and trajectories followed by these particles will be a function of the orientation and detailed structure of the geomagnetic field with respect to the source. As shown in reference (6), sources as young as 10^4 years could be influencing the cosmic ray flux at the earth and thus, a satellite--borne experiment might permit detection of superheavy elements with lifetimes on the order of 10^4 years.

This idea is based, at the present time, on a number of plausibility arguments. Much more detailed calculations would be necessary before planning an actual experiment, especially since the cost of recovering a scientific payload from an orbit of several earth radii would be large.

ACKNOWLEDGEMENTS

We would like to thank P. Shea and D. Smart, of the Air Force Cambridge Research Laboratory for their contribution of Computer Calculated trajectories. R. Gall of the Universidad Nacional Autonoma and H. Sauer of the NOAA Laboratory in Boulder, both provided helpful discussions on the interpretation of the orbital calculations in terms of intensity. We also are indebted to P. B. Price of the University of California for his advice and encouragement.

REFERENCES

1. R. L. Fleischer, P. B. Price, R. M. Walker, E. L. Hubbard, Phys. Rev., 156, 353 (1967).
2. P. B. Price. R. L. Fleischer, D. D. Peterson, C. O'Ceallaigh, D. O'Sullivan, A. Thompson, Phys. Rev., 164, 1618 (1967).
3. P. B. Price et al Can. J. Phys., 45, S1149 (1968)
4. P. B. Price, R. L. Fleischer, G. E. Nichols, Acta Phys. Hung., 29, Suppl. 1, 411 (1970)
5. P. B. Price, P. H. Fowler, J. M. Kidd, E. J. Kobetich, R. L. Fleischer, G. E. Nichols, Phys. Rev., (1971).
6. R. E. Lingenfelter, Nature 224, 1182 (1969)
7. T. Gold, Nature 221, 25 (1969)
8. G. Silvestro, Lettere Al Nuovo Cimento, Vol. II, #16, page 771 (1969)
9. G. T. Seaborg, Ann. Rev. Nucl. Sci., 18, 53 (1968)
10. C. F. Tsang, Lawrence Radiation Laboratory Report UCRL-18899 (PhD Thesis), (1969)
11. G. T. Seaborg, "Do the Superheavy Elements Already Exist?" Paper delivered at American Chemical Society Annual Meeting, Houston, Texas, February 24, 1970
12. C. Stormer, Astrophysics, I, 237-274,(1930)
13. G. Lemaitre and M. S. Vallarta, Phys. Rev. 49, 719 (1936)
14. R. Call and J. Lifshitz, Proceedings of the Moscow Cosmic Ray Conference, Vol. III, International Union of Pure and Applied Physics, Moscow, page 64, 1960
15. D. F. Smart, M. A. Shea, and R. Gall, J. Geophysics, Res. 74, 4731 (1969)
16. R. Call, D. F. Smart, and M. A. Shea, Space Research 11, 1971
17. IAGA Commission 2, Working Group 4, J. Geophysics, Res. 74, 4407, (1969)
18. D. J. Williams and C. D. Mead, J. Geophysics Res. 70, 3017 (1965)
19. Ernest Ray
20. M. M. Shapiro and R. Silverberg, Ann. Rev. Nucl. Sci., 20, 323 (1970)
21. M. G. Mayer and E. Teller, 76, 1226 (1949)

Jupiter Radiation Belt Engineering Model*

Neil Divine
Jet Propulsion Laboratory

On the basis of earth observations of the HF and UHF radio emission generated near Jupiter, the presence of energetic charged particles trapped in the planet's dipole magnetic field has been inferred. For electrons, energies of the order of 10 MeV and peak fluxes of the order of 10^7 cm^{-2} s^{-1} can be derived from the data for equatorial regions about two planetary radii from the dipole. Energetic protons and lower-energy electrons and protons are also expected, but the limited data require that their fluxes be based on theory or earth analogy. Because descriptions available in the literature suggest large associated uncertainties, both nominal and limiting models for the charged-particle populations of Jupiter's belts are derived. These new engineering models describe electron and proton fluxes and their distributions in energy and position in forms suitable as space vehicle design criteria.

In the planning of missions to encounter the planet Jupiter both spacecraft design considerations and trajectory selection may be strongly affected by our understanding of the charged-particle environment trapped in Jupiter's magnetic field. These energetic electrons, and possibly protons, could be hazardous for spacecraft electronics and other sensitive subsystems. The presence of relativistic electrons has been inferred from analyses of Jupiter's radio emission. The extensive literature in this field has been reviewed recently by Carr and Gulkis (ref. 1) and by Warwick (ref. 2), from which the following brief summary is adapted.

RADIO DATA

The HF radiation, at wavelengths longer than about 7 m, is sporadic; the probability that it be observable is correlated with the sub-earth longitude on Jupiter and with the Jovicentric longitude of the first Galilean satellite, Io. The radiation's characteristic patterns in time and frequency coordinates permit conclusions to be drawn about the strength and configuration of Jupiter's magnetic field, although controversy surrounds many features of such interpretations. Nevertheless, the upper limit shown in figure 1 near 40 MHz for the radiofrequency in bursts reaching the earth implies a magnetic field strength of 14 G somewhere just above Jupiter's atmosphere, following the commonly accepted argument that the burst mechanism yields radiation at the local electron gyrofrequency. Thus, a magnetic dipole moment near 4×10^{30} G-cm^3, considerably stronger than the earth's, is implied for Jupiter. The dipole is probably centered on Jupiter (although displacements up to 0.7 radii south have been proposed; ref. 2), and inclined about 10 deg to Jupiter's axis. The interaction of this dipole with the solar wind leads us to anticipate a large magnetosphere, whose minimum extent (in the sunward direction) is about 50 Jupiter radii (ref. 1).

At wavelengths less than or near a few centimeters the UHF component shown in figure 1 is dominated by thermal emission from the disk, which need not be further discussed here. At wavelengths up to about 100 cm a non-thermal component is indicated on figure 1, having a flux density with very little dependence on time and frequency (generally less than 30%). Numerous characteristics indicate that this radiation is synchrotron radiation from relativistic electrons contained by Jupiter's magnetic field. Strong support for this hypothesis is provided by the radio brightness temperature contour maps obtained by aperture synthesis at 10.6 and 21 cm by Berge (ref. 3) and Branson (ref. 4). Most of this radiation is produced noticeably away from the disk of the planet, in a region elongated roughly parallel to the equator. In addition, up to 30% east-west linear polarization is observed. These characteristics, plus the beaming inferred from the flux density variations, confirm the synchrotron mechanism, and imply that the relativistic electrons are most abundant near Jupiter's magnetic equator. The models in the following sections have been derived from these data for use as NASA space vehicle design criteria, and are discussed more fully in ref. 5.

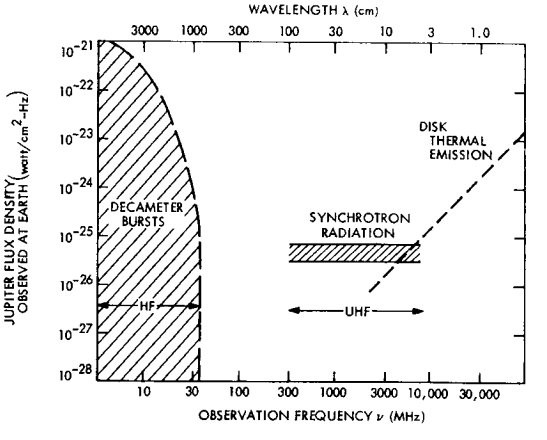

Figure 1. Schematic radio spectrum of Jupiter, adapted from Carr and Gulkis (ref. 1)

*This paper presents the results of one phase of research carried out at the Jet Propulsion Laboratory, California Institute of Technology, under Contract No. NAS 7-100, sponsored by the National Aeronautics and Space Administration.

RELATIVISTIC ELECTRONS

If the strength of the magnetic field at the UHF flux peak and the observed bandwidth are known, the characteristic electron energy can be derived from numerical formulas which summarize the results of synchrotron emission theory. As some of the required data are uncertain, only the order of magnitude of the electron energy near the UHF flux peaks has been evaluated at about 10 MeV (ref. 1). If a reasonable distribution of the source contributions along the line of sight is taken, the synchrotron theory also permits the local electron flux to be derived from the observed intensity. This can be done for the source as a whole, or in detail so that the distribution of electron flux with position is obtained.

For Jupiter's equatorial plane, figure 2 shows the results of several such derivations; the differences among them result from the application of various combinations of reasonable assumptions required in the analysis. The result credited to Carr and Gulkis (ref. 1) is simply an order-of-magnitude estimate, in which a flux of 10^7 relativistic electrons/cm^2 s occurs in a broad region of space surrounding Jupiter. The models of Branson (ref. 4) and Luthey and Beard (ref. 6) are based on the observations alone, but the poor resolution of the data is reflected by the lack of detail in their results. The model of Eggen (ref. 7) is based on earth analogy as well as on the data, but the details of this model result from the analogy and are unrealistic. The model described by Warwick (ref. 2) is based on both the data and on a physical mechanism for the population of Jupiter's radiation belts. That mechanism is the L-shell diffusion of solar wind electrons which have penetrated the outer boundary of the magnetosphere, and predicts a position distribution proportional to L^{-4} away from the observed peak within two radii of the planet.

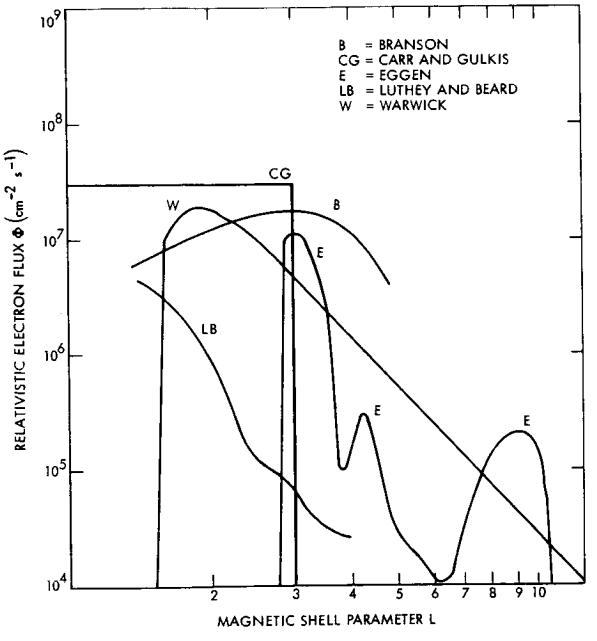

Figure 2. Flux Φ of relativistic electrons as functions of distance L from the dipole (in Jupiter radii) in the plane of the magnetic equator, as derived by the authors listed

The new engineering models reported here are plotted in figure 3 to the same scale as in figure 2, and it is intended that they bracket most of the conclusions of the authors cited above. In the figure, the central line represents the nominal values and the shaded area indicates the range of the models. In particular, the nominal model resembles the L-shell diffusion model by Warwick (ref. 2), because it was felt that the successful application of such a model to the earth's outer belt protons (ref. 8) warranted its application to Jupiter as well. For simplicity in application it is flat within 2 radii of Jupiter's dipole and proportional to L^{-4} elsewhere. The limiting models in figure 3 imply uncertainty factors of 3 at the flux peak, and larger ones elsewhere, reflecting the insecurity in the numerical details of the derivation from the limited data available.

In addition to the radial dependence just discussed, the concentration of the radiation near Jupiter's magnetic equator implies that the flux depends strongly on latitude ϕ. The engineering models include a factor proportional to $\exp(-\phi^2/10^3)$ for ϕ in degrees; this dependence cuts off near latitude 30° in a manner consistent with the brief latitude analysis presented by Warwick (ref. 2).

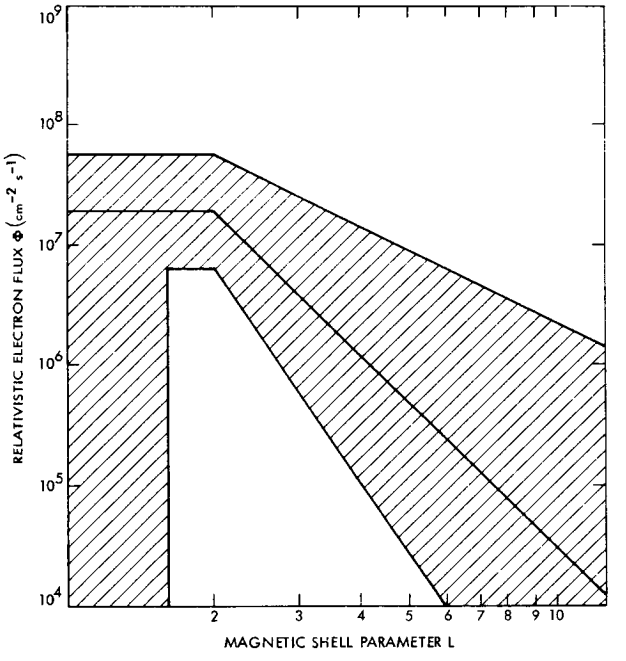

Figure 3. Flux Φ of relativistic electrons in the engineering models (same scales as fig. 2)

The electron energies, derived from the field strength and bandwidth, are near 10 MeV, but there is considerable uncertainty associated with all quantities involved. In order to achieve consistency with the features of the model adapted above from Warwick (ref. 2), the engineering models display characteristic electron energies $E_0 = 6.2 \times 3^{\pm 1}$ MeV at the flux peak, and proportional to $L^{-3\pm 2}$ elsewhere (a typical L-shell

diffusion theory dependence). Based on the synchrotron theory alone, a monoenergetic electron population would suffice to explain the observations. Nevertheless, such a distribution is probably unrealistic. The data apparently require that few low-energy electrons (ref. 9), and that few electrons above 30 MeV (ref. 4), exist near the flux peak. The differential energy distribution ($d\Phi/dE$) proportional to $(E/E_0)\exp(-E/E_0)$ is adopted for engineering purposes, because it is one of the simplest which is nearly monoenergetic (at the characteristic energy E_0) and contains an exponential term that resembles one for the earth's belts.

ENERGETIC PROTONS

There are no Jupiter data from which proton fluxes may reliably be inferred. The few published models (refs. 2, 6, 7, 10, and 11) proceed from various assumptions and derive widely divergent proton energy and flux values. Apparently the most physical discussion among the above, that of Warwick (ref. 2), applies the L-shell diffusion mechanism cited for the electrons to the trapping of solar wind protons within Jupiter's magnetosphere. The result is a number density everywhere equal to that of the electrons and identical energy characteristics, where E_0 = 29 MeV at the flux peak. In the absence of relevant data and theoretical predictions of equilibria among complex source and loss mechanisms, the uncertainties associated with the flux and energy values are arbitrarily taken as factors of 10 at the flux peak, and greater elsewhere; for the model, the lower limit is zero. The upper limit model flux and energy are independent of distance from Jupiter. These engineering models are based on the foregoing considerations, but should be considered extremely tentative.

In order to illustrate the possibly great range of proton flux values, figure 4 compares the above models with the limiting fluxes which can be trapped in Jupiter's magnetic field. The solid lines in the figure represent trapping limits, parametrized by proton kinetic energy E. The dashed lines represent the model fluxes of protons with E > 100 MeV. Although it has seldom been seriously proposed that the real flux values approach these trapping limits (see ref. 6), such fluxes are possible, do not violate any known observations or theoretical considerations, and would be severely hazardous if they were to reach spacecraft electronics.

CONCLUSIONS

Details of the engineering models for Jupiter's radiation belts based on the above considerations are presented in the Appendix. The magnetic field, securely based on the HF and UHF radio data, is strong and primarily dipolar, having field strengths near 14 G in the atmosphere, but it has few important impacts on spacecraft design directly. Although the dipole is nominally located at the center of Jupiter, it is inclined by about 10 deg and could be displaced up to 0.7 radii south of the center. The field is responsible for the containment of relativistic electrons, which are securely based on the UHF data. Their peak fluxes, near 10^7 cm^{-2} s^{-1}, and energies, near 6 MeV,

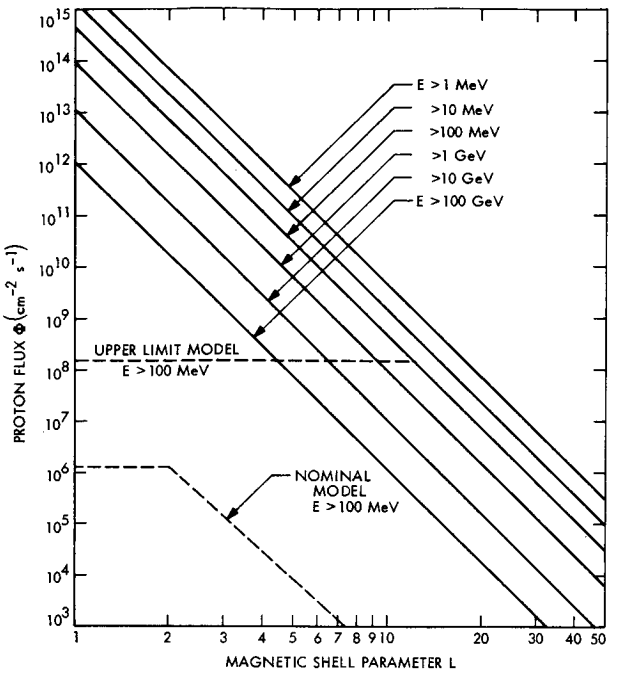

Figure 4. Flux Φ of energetic protons as a function of distance L from the dipole in the plane of the magnetic equator

could have some serious consequences for spacecraft design, particularly if their uncertain dependences of energy and flux far from the planet were relatively flat; nominally these dependences are expected to diminish rapidly with distance. The field may also contain energetic protons, for which apparently reasonable estimates and large uncertainties are presented. Even these values are severely hazardous for spacecraft electronics within two planetary radii of the dipole.

ACKNOWLEDGMENT

The assistance of Dr. James W. Warwick of the University of Colorado is gratefully acknowledged.

REFERENCES

1. Carr, T. D., and Gulkis, S.: The Magnetosphere of Jupiter, Annual Review of Astronomy and Astrophysics, vol. 7, 1969, p. 577.

2. Warwick, J. W.: Particles and Fields near Jupiter, NASA CR-1685, 1970, 123 pp.

3. Berge, G. L.: An Interferometric Study of Jupiter's Decimeter Radio Emission, Astrophys. J., vol. 146, 1966, p. 767.

4. Branson, N. J. B. A.: High Resolution Radio Observations of the Planet Jupiter, Monthly Notices of the Royal Astronomical Society, vol. 139, 1968, p. 155.

5. Anon.: 1970 October draft of "The Planet Jupiter (1970)," NASA Space Vehicle Design Criteria (Environments), to be published as NASA SP-80XX.

6. Luthey, J. L., and Beard, D. B.: The Electron Energy and Density Distribution in the Jovian Magnetosphere, Dept. of Physics and Astronomy, Univ. of Kansas, Lawrence, 1970, 19 pp.

7. Eggen, J. B.: The Trapped Radiation Zones of Jupiter, Report FZM-4789, Fort Worth Division, General Dynamics Corp., 1967, 44 pp.

8. Nakada, M. P., Dungey, J. W., and Hess, W. N.: On the Origin of Outer-Belt Protons, 1, J. Geophys. Res., vol. 70, 1965, p. 3529.

9. Gulkis, S.: Lunar Occultation Observations of Jupiter at 74 cm and 128 cm, Radio Science, vol. 5, 1970, p. 505.

10. Haffner, J. W.: Calculated Dose Rates in Jupiter's Van Allen Belts, AIAA J., vol. 7, 1969, p. 2305.

11. Koepp-Baker, N. B.: A Model of Jupiter's Trapped Radiation Belts, Report 68 SD 263, Missile and Space Division, General Electric Corp., 1968, 24 pp.

APPENDIX

Electron and proton concentrations and fluxes may be calculated from the formulas in table I for a specific position (specified by distance R and latitude ϕ with respect to Jupiter) and energy interval (between E and E + ΔE) according to the following procedure. Taking the radius of Jupiter as R_J = 71,422 km, calculate the magnetic shell parameter $L = R/R_J (\cos \phi)^2$. Evaluate the concentration parameter N_0 and the characteristic energy E_0 from two of the top eight formulas in table I, ignoring exponents following ± signs (use the pair appropriate to the particle kind, and appropriate for L less or greater than 2). Using the last formula in table I, calculate N_E, the particle concentration for energy greater than E, for both end points of the energy interval, and difference them (next-to-last formula in table I) to obtain $(\Delta E)_E$, the concentration in the energy interval of interest. Then apply the formula in the FLUX row to obtain the flux $(\Delta\Phi)_E$ in the interval; if (ΔE) is not much smaller than E, the procedure should be repeated with small intervals and the $(\Delta\Phi)_E$ values summed. Nominal interval concentrations and fluxes result, in which probably only two significant figures should be retained. Limiting ones are obtained in the same way, except that appropriate combinations of exponents following the ± signs in the expressions for N_0 and E_0 should be taken.

TABLE I. Formulas for trapped charged-particle radiation near Jupiter*

	Relativistic electrons	Energetic protons
Number density parameter for $0 \le L \le 2$	$N_0 = (6.3 \times 3^{\pm 1}) \times 10^{-4} \exp[-\phi^2/10^3]\,cm^{-3}$ (minimum $N_0 = 0$ for $0 \le L \le 1.6$)	$N_0 = (6.3 \times 10^{-4\pm 1}) \exp[-\phi^2/10^3]\,cm^{-3}$ (minimum $N_0 = 0$)
for $2 \le L \le 50$	$N_0 = \frac{5.8 \times 10^{-3}}{\exp[\phi^2/10^3]} \left(\frac{1.15}{L}\right)^{4\pm 2} cm^{-3}$	$N_0 = \frac{5.8 \times 10^{-3}}{\exp[\phi^2/10^3]} \left(\frac{1.15}{L}\right)^{4\pm 4} cm^{-3}$ (minimum $N_0 = 0$)
Characteristic energy for $0 \le L \le 2$	$E_0 = 6.2 \times 3^{\pm 1}$ MeV	$E_0 = 29 \times 10^{\pm 1}$ MeV
for $2 \le L \le 50$	$E_0 = 33\left(\frac{1.15}{L}\right)^{3\pm 2}$ MeV	$E_0 = 290\left(\frac{0.93}{L}\right)^{3\pm 3}$ MeV
Flux*† (interval distribution with energy) for $\Delta E \ll E$	$(\Delta\Phi)_E = c(\Delta N)_E$	$(\Delta\Phi)_E = c(\Delta N)_E \left\{\frac{\left[E\left(E + 2m_p c^2\right)\right]^{1/2}}{\left(E + m_p c^2\right)}\right\}$
Number density*† (interval and cumulative distributions with energy)	$(\Delta N)_E = N_E - N_{E+\Delta E}$ $N_E = N_0\left(1 + \frac{E}{E_0}\right)\exp\left(-\frac{E}{E_0}\right)$	

*For energies >1 MeV only.

†Table II gives $(\Delta N)_E$ and $(\Delta\Phi)_E$ as functions of E for $1.6 < L < 2$ and $\phi = 0$.

TABLE II. Energetic charged-particle concentrations and fluxes for individual energy intervals at the peak of Jupiter's trapped radiation belts ($1.6 < L < 2$ and $\phi = 0$)

Particle kind	Energy interval, MeV	Concentration $(\Delta N)_E$, cm^{-3}			Flux $(\Delta\phi)_E$, $cm^{-2}\,s^{-1}$		
		Minimum*	Nominal	Maximum*	Minimum*	Nominal	Maximum*
Electrons	1-3	2.2×10^{-6}	4.6×10^{-5}	6.4×10^{-4}	6.3×10^{4}	1.4×10^{6}	1.9×10^{7}
	3-10	1.9×10^{-5}	2.5×10^{-4}	1.1×10^{-3}	5.7×10^{5}	7.4×10^{6}	3.3×10^{7}
	10-30	9.8×10^{-6}	3.0×10^{-4}	1.0×10^{-3}	2.9×10^{5}	9.0×10^{6}	3.1×10^{7}
	30-100	0.0	2.9×10^{-5}	9.3×10^{-4}	0.0	8.7×10^{5}	2.8×10^{7}
	100-300	0.0	0.0	5.6×10^{-5}	0.0	0.0	1.7×10^{6}
	300-1000	0.0	0.0	0.0	0.0	0.0	0.0
Protons	1-3	0.0	2.8×10^{-6}	1.4×10^{-3}	0.0	5.6×10^{3}	2.9×10^{6}
	3-10	0.0	2.7×10^{-5}	3.7×10^{-3}	0.0	9.6×10^{4}	1.2×10^{7}
	10-30	0.0	1.4×10^{-4}	3.4×10^{-3}	0.0	8.8×10^{5}	2.0×10^{7}
	30-100	0.0	3.7×10^{-4}	3.7×10^{-3}	0.0	3.6×10^{6}	3.6×10^{7}
	100-300	0.0	8.9×10^{-5}	3.4×10^{-3}	0.0	1.3×10^{6}	5.5×10^{7}
	300-1000	0.0	0.0	3.7×10^{-3}	0.0	0.0	8.5×10^{7}
	1000-3000	0.0	0.0	8.9×10^{-4}	0.0	0.0	2.4×10^{7}
	3000-10,000	0.0	0.0	0.0	0.0	0.0	0.0

*Maximum (and Minimum) entries are interval-by-interval only, and do not yield a realistic cumulative spectrum when combined; to obtain the latter the formulas given in table I must be applied using specific values of N_0 and E_0.

"A SUMMARY OF THE OV1-19 SATELLITE DOSE, DEPTH DOSE, AND LINEAR ENERGY TRANSFER SPECTRAL MEASUREMENTS"

Captain John T. Cervini

Technology Division
Air Force Weapons Laboratory

1. INTRODUCTION.

The purpose of the radiation research satellite, OV1-19, was to make simultaneous measurements of the biophysical and physical parameters in the near earth space environment; specifically, the Inner Van Allen Belt. This region of space is of great interest to planners of the Skylab and the Space Station programs because of the high energy proton environment, especially during periods of increased solar activity. Currently, data on these radiations for both manned and unmanned space systems is inadequate. Many physical measurements of charged particle flux, spectra, and pitch angle distribution have been conducted and are programed in the space radiation environment. Such predictions are not sufficient to accurately predict the effects of space radiations on critical biological and electronic systems operating in these environments. Some of the difficulties encountered in transferring from physical data to a prediction of the effects of space radiation on operational systems are due to the following reasons:

(a) Theoretical computations of dose and linear energy transfer at depth are not precise.

(b) Shielding and mass distributions are only approximate.

(c) The proton spectra at high energies in the Van Allen Belts and in solar flares are uncertain.

The experiments aboard the OV1-19 satellite were designed to obtain accurate dose rate, depth dose, and linear energy transfer (LET) measurements. Accurate dose rate predictions are critically dependent on knowledge of the radiation environment, the shielding distribution surrounding the dose point, and radiation transport calculations. Simultaneous measurements provide knowledge of the physical spectra and the resultant dose rate behind known shielding configurations. These data may then be used to evaluate the accuracy of the transport calculations.

2. DESCRIPTION OF EXPERIMENT.

OV1-19 was launched on 18 March 1969 into an orbit with an apogee and perigee of 250 and 3125 nautical miles, respectively. The inclination of the orbit was 105°. The satellite consisted of a cylindrical center section which served as the container for the scientific payload, two faceted solar domes, and satellite support systems housed under each solar dome. The domes serve as the substrate for the solar cells which provide the primary power source for the satellite. Most of the experiments were mounted through apertures on the outer surfaces to insure unobstructed views of the environment (Fig. 1). Two of the onboard experiments are discussed here. These are the tissue equivalent ionization chambers (TEICs) and the cellular absorbed dose linear energy transfer spectrometer (CADS).

The dose rates were measured by three spherical TEICs whose sensor walls and cavity media simulate the response of muscle tissue to all ionizing radiation (ref. 1). The chambers were constructed of 0.236 gm/cm^2 of conductive tissue equivalent plastic and were filled with a tissue equivalent gas composed of methane, carbon dioxide, and nitrogen (ref. 2). TEICs of this type have successfully flown on many unmanned research satellites (ref. 3-6). A complete description of the design theory, fabrication, and calibration of these instruments can be found in reference 7. A typical TEIC sensor is shown in Fig. 2.

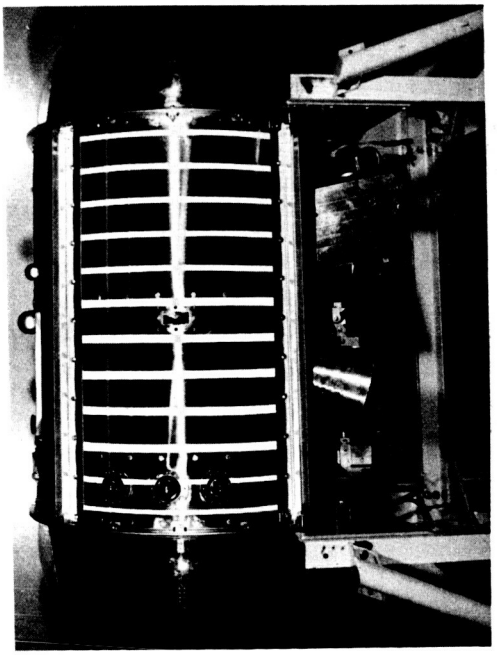

FIGURE 1. THE OV1-19 SATELLITE

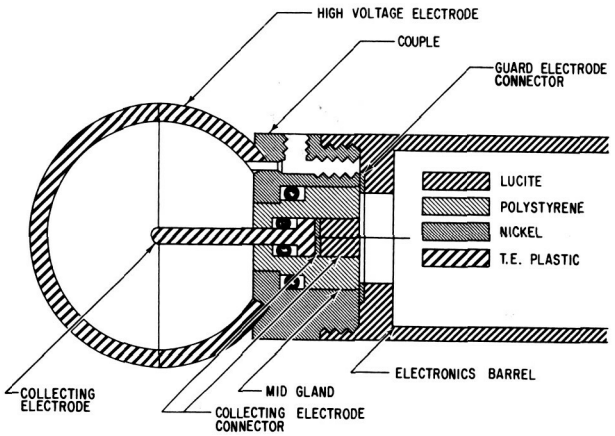

Figure 2 Tissue Equivalent Ionization Chamber Sphere and Barrel Assembly

The dynamic ranges of the OV1-19 TEICs allow measurement of dose rates from 2.0 m rad/hr to about 620 rad/hr. As shown in Table 1, each sensor was adjusted to measure the range of expected dose rates for its shielding configuration. The shields on the OV1-19 instruments were much thicker than those on any TEICs previously flown. This design was chosen so that high energy proton sources (solar flare, Van Allen Belt, and cosmic radiations) could be carefully measured since they have a much wider energy range, and far less is known about their actions on biological matter. Also, both the USAF and NASA manned space vehicles of the 1970's will have enough average shielding to "stop" all but the most energetic protons. Thus, significant dose rates, and therefore any biological effects will be caused mainly by the higher energy protons which are merely degraded or interact by nuclear collision in a non-uniform manner with the shielding

The LET spectral data discussed in this report were obtained by the CADS instrument. LET is defined as the linear rate of loss of energy per unit length, locally absorbed, by an ionizing particle traversing a material medium. It is an important quantity in that it enables a more precise definition, on a microscopic scale, of the biological effect of energy deposition due to incident radiation.

The ionization rate of the particle (and hence the LET) changes with path length and particle energy as it traverses matter; so, it is necessary to determine the LET-depth profile rather than a single point determination. Fortunately, however, the change in ionization rate is small enough that the LET does not vary significantly over a few microns of path length, so that a measurement made in a path length comparable to a micron is representative of the LET of that particle at the cellular level. The CADS is designed to conduct these types of direct LET measurements.

The CADS instrument uses the scintillation method of detection to obtain its measurements. The sensor consists of a flat plate of NE-102 scintillating material attached to a lucite light pipe, which is in turn connected to a photo-multiplier tube. The photomultiplier electrical responses are sorted and read out into various dE/dX channels, which are then processed in the analyzer (See Figs. 3 and 4). NE-102 scintillating material was used as a detector, since it closely approximates muscle tissue atomically and is readily adaptable for space flight application. It was machined into a flat plate 50 microns thick to approximate the path length across a human cell.

TABLE 1. TEIC CHARACTERISTICS

TEIC No.	Dose Rate Range (Rad/hr)	Shield Description (gm/cm^2)	Proton Energy Threshold (MEV)
3	.002 - 620	Bare	17.1
1	.005 - 150	5.0 Lucite	77.5
2	.01 - 47	12.0 Tungsten	86.6

15-49 1302-307 51°,

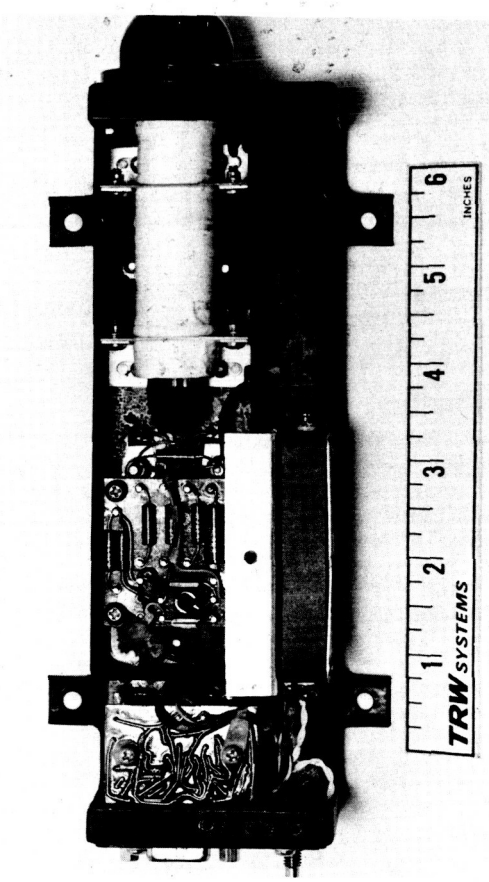

FIGURE 3. CADS SENSOR

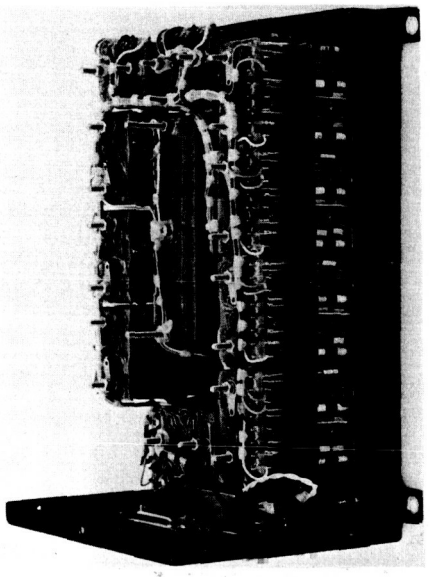

FIGURE 4. CADS ELECTRONICS

TABLE 2. CADS THRESHOLDS

Channel Number	Thresholds in MV	LET (kev/micron)
1	> 20	> .22
2	20-50	.22 - .55
3	50-75	.55 - .82
4	75-110	.82 - 1.22
5	110-160	1.22 - 1.86
6	160-230	1.86 - 2.9
7	230-335	2.9 - 4.7
8	335-480	4.7 - 8.5
9	480-700	8.5 - 19.0
10	700-1000	19.0 - 130
11	> 1000	> 130

15-52 1302-307

The CADS analyzer unit contains signal processing circuits capable of producing the following measurements:

(a) An eight channel absorbed dose spectrum from approximately 130 kev/micron

(b) The number of events having LET greater than approximately 130 kev/micron

(c) Total events, which is a measure of all pulses exceeding the threshold of the lowest channel (0.2 kev/micron)

(d) Absorbed dose rate obtained by integrating the photomultiplier tube anode current for those pulses in the range of approximately 0.2 to 0.5 kev/micron.

TABLE 2 presents the values of the thresholds of all the CADS channels, and the corresponding LET values for each of the thresholds. More complete and detailed information on the CADS operation and design can be found in reference 8.

3. PROCEDURE FOR DATA REDUCTION.

Raw data tapes collected by ground stations were digitized to make them readable to an electronic computer, and to allow all noisy data to be edited. The data on the digitized tapes were then converted from the 36-bit-per-word format to 60-bit words, compatible with a CDC 6600 computer. Programs were then written to select the desired instrument outputs from the satellite telemetry format. Since the wave train format was Pulse Code Modulation (PCM), appropriate conversions from bits to volts were incorporated. The subcommutator synchronization pulses were located and stripped off. The subcom information appeared on one of the 256 main commutator words, and contained the instrument sensor electronics temperatures as well as instrument status indicators. Temperature information was provided for the calibration of the CADS log count-rate meters which are part of the analyzer circuitry. Calibration information was then programed to allow a further reduction from volts to physical units such as dose rate and LET count-rate for the TEICs and CADS, respectively. The physical data for each revolution was then written on magnetic tape for further analysis. Ephemeris information, which determines the satellite's position as a function of GMT, was provided directly by Ent Air Force Base, Colorado. Presently, the OV1-19 data is being merged to provide isodose rate and isocount rate versus B and L as well as versus longitude and latitude. The McIlwain parameters, B and L, (Ref. 9) are computed from Hendricks and Cain's 99 term expansion of the geomagnetic field (Ref. 10), using the ephemeris data as input.

The results given here are raw dose rates and count rates reduced from the OV1-19 satellite, since a detailed analysis of all the data has not yet been accomplished. The merging of all the satellite orbits is incomplete; however, some of the preliminary information obtained during increased solar activity is presented. Data on 120 orbits of the satellite indicate that both the TEICs and the CADS instrument were operating nominally until a malfunction occurred in the multicoder of the OV1-19 telemetry system, 11 months after launch.

No further contacts were made by ground command, and all data acquisition ceased.

4. PRESENTATION OF DATA.

Preliminary data reduction techniques have allowed a review of raw physical data results. The three TEIC sensors operated as planned, as did all the CADS channels. Some problems have occurred on channel two of the CADS instrument, and we are presently checking its outputs.

Most of the data presented here are from Revs. 265 and 2551, which were recorded during increased solar activity. On 12 April 1969, a proton event was recorded by the Solar Flare Forecast Network (SOFNET). The onset occurred at 0111Z and continued in intensification until midday of 13 April 1969, when peak values of proton fluxes were measured. SOFNET reported that the Vela 4 satellite obtained integrated proton fluxes of 200 counts/sec. above 25 MEV, and 33,000 counts/sec. in the range 3-20 MEV. OV1-19 recorded Rev. 265 approximately 2 hours after the peak of the event. Figures 5 and 6 are a time history of Rev. 265 for the TEIC sensors. Figure 7 gives the McIlwain B, L coordinates as a function of UT for the same Rev. Figure 5 shows that TEIC 1 reaches a peak dose rate of 4.5 rad/hr, and 4 minutes later, TEIC 2 peaks at 2.5 rad/hr.

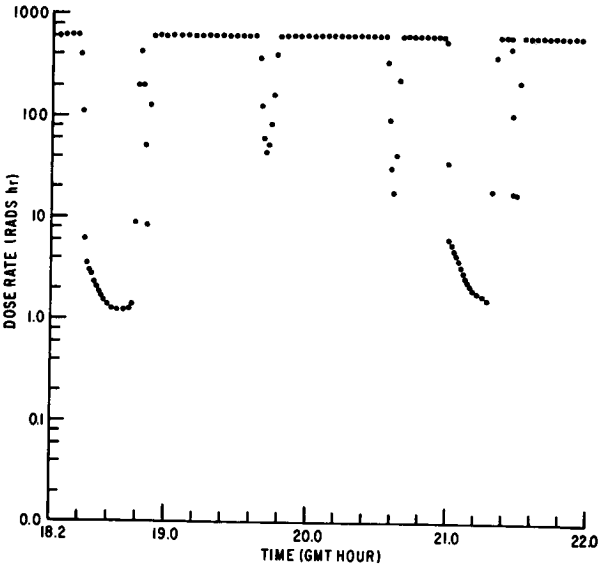

Figure 6: TEIC 3 Dose Rate vs. GMT for REV. 265

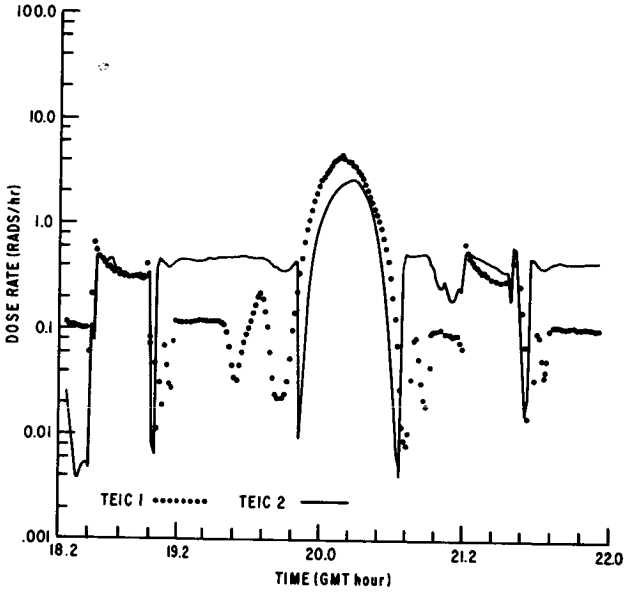

Figure 5: Dose Rate vs GMT for REV. 265

At the time TEIC 2 recorded its peak dose rate, TEIC 1 was reading 3.5 rad/hr. These measurements were taken when OV1-19 was at a high northern latitude (75°N), at an altitude of about 720NM. Data from another revolution at the same latitude and altitude indicated that TEIC 1 and TEIC 2 recorded dose rates of 2.7 and 1.3 rad/hr, respectively. These measurements occurred during a quiescent solar period, when no precipitating solar particles were present in the earth's geomagnetic field. Rev. 265 shows an increase in dose rate for TEICs 1 and 2 of about 70% and 50%, respectively, due to the presence of solar flare particles at high northern latitudes. As expected, the TEIC 3 sensor saturated at 620 rads/hr during the greater portion of both orbits (Fig. 6). Since there wasn't any shielding for this sensor, the threshold energy for protons, and to an extent electrons, was low allowing many of the lower energy particles to be absorbed in the chamber. Dose rate data during increased solar activity were also obtained on Rev. 2551 (Fig. 8). Note that both TEIC 1 and TEIC 2 initially peak at much higher values of dose rate than previously recorded. The maximum dose rate measured by TEIC 1 is now 9.2 rads/hr, and the maximum for TEIC 2 is 13.7 rads/hr. At this time, the satellite was at an altitude of 1673NM and a latitude of 33°N. Equivalent B and L values are .126 gauss and 2.17 earth radii (Fig.9). Figure 8 shows a second peak about 2 hours later. TEICs 1 and 2 now reach a maximum of 7.7 and 10.4 rads/hr, respectively. At the time of these measurements, OV1-19 was at an altitude of 3087NM, a latitude of 47°S, and a longitude of 309°E. Ten minutes earlier the satellite had reached its apogee (3125NM) at 37°S, 316°E. This indicates that the second peak of dose rate data was probably obtained above the South Atlantic Anamoly. The third and fourth peaks of Figure 8 are merely a repetition of the first two peaks at a later time in the orbit. Data was also reduced but not merged for a number of other orbits that occurred during solar flare events. The solar flare of 11 April 1969 was preceeded by a ground level neutron event that took place on 30 March 1969. This event was not recorded by our instruments; however, dose rate information was recorded 10 days after the event that were higher than the peaks of Rev. 265. TEICs 1 and 2 showed peak dose rates of 6.3 and 5.7 rads/hr for Rev. 223 which was obtained during the early hours (UT) of 11 April 1969, just prior to the April proton flare. The maximum dose rates measured during this event were 5.6 and 6.0 rad/hr on 12 April 1969 (Rev. 240). The closeness of the measurements tend to indicate that both sets of values are due to the same event. During the interval 19-21 November 1969, a class 2B solar flare was observed and on 14 December 1969 a class 3N

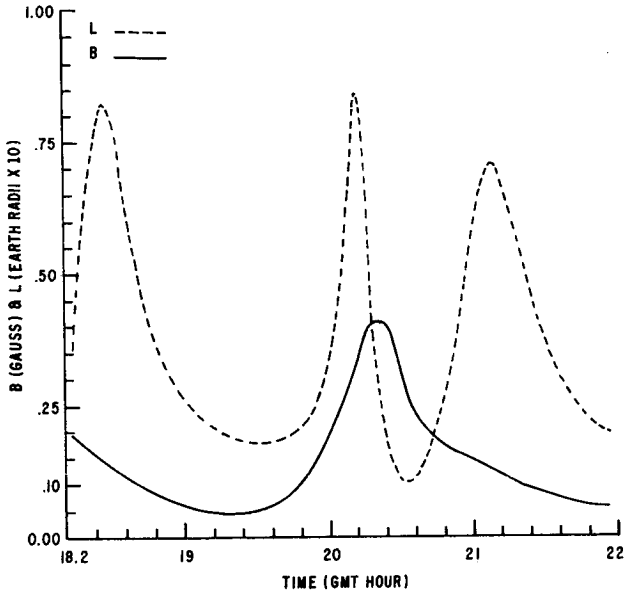

Figure 7: B, L vs. GMT for REV. 265

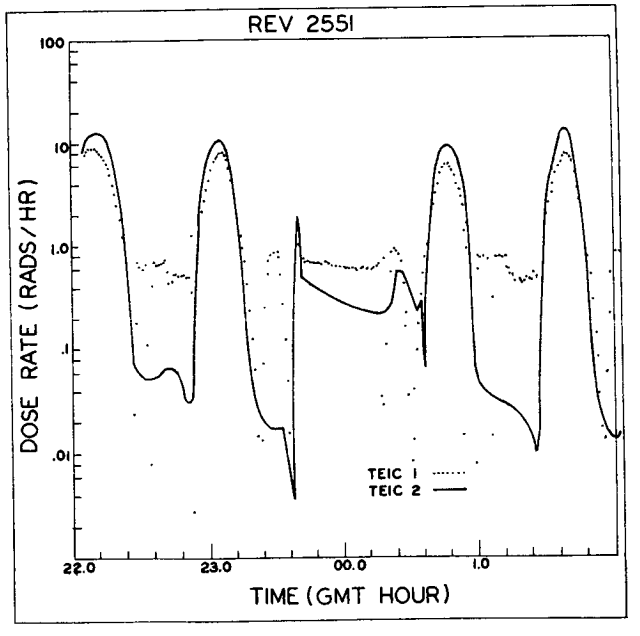

FIGURE 8: DOSE RATE vs. GMT for REV. 2551

flare took place. The dose rates for Rev. 2551 were obtained during the latter event. TABLE 3 summarizes the peak TEIC dose rates for orbits of data that occurred during the time of the four solar flare events mentioned above. Since the duty cycle of the satellite prevented continuous coverage of the sun's activity, there are many orbital gaps between the significant events. Therefore, definitive statements concerning the contribution of solar particles to the peak dose rates cannot be made at this time. The movement of apogee and perigee through the Van Allen Belts certainly has some effect on these measurements. The TEIC 1 and 2 results show that a considerable dose is received behind relatively large amounts of shielding during solar flare events. This indicates that the radiation spectrum in the near earth space environment was hardened due to an influx of protons with energies greater than 70 MEV.

TABLE 3. MAXIMUM TEIC DOSE RATES

Rev. No.	Date	TEIC 1 Max. Dose Rate*	TEIC 2 Max. Dose Rate*	
	3/30/69			Ground Level Neutron Event
208	4/9/69	5.9	5.2	
222	4/10/69	3.2	1.3	
	4/11/69			Solar Flare Event
223	4/11/69	6.3	5.5	
240	4/12/69	5.6	6.0	
249	4/13/69	3.9	2.4	
265	4/15/69	4.4	2.6	
276	4/16/69	4.2	1.6	
296	4/18/69	4.3	1.7	
---	11/19/69 to 11/21/69			Class 2B flares
2308	11/19/69	12.3	10.9	
2318	11/20/69	8.0	10.4	
2327	11/21/69	7.6	8.6	
2369	11/25/69	8.4	8.7	
2377	11/26/69	8.3	9.7	
2393	11/28/69	9.0	9.7	
2395	11/28/69	8.5	10.1	
	12/14/69			Class 3N flares
2551	12/15/69	9.2	13.7	
2555	12/15/69	7.0	10.3	
2564	12/16/69	7.7	10.1	
2572	12/17/69	6.9	10.1	

*Rads/hr

The LET spectrum measured by CADS did not show an equivalent enhancement in all channels during solar flare events. Channel 1 recorded total events above a threshold of 20 MV, which corresponds to all particles having an LET greater than .22 kev/micron. Channel 2 measured the dose rate by integrating the photomultiplier tube anode current for those pulses in the range of approximately 0.2 to 0.5 kev/micron. Channels 3 to 11 actually measure the LET spectrum, and they are our main concern. They correspond to LET channels 1 through 9. The LET outputs for Rev. 265 are given in Figures 10 through 14. Note that LETs 3 through 9 each show a well defined count rate peak which corresponds to the peak dose rates for TEICs 1 and 2 (Fig. 5). This indicates that the energy deposited per unit path length increases as the dose rate increases. However, we do not observe an equivalent peak for LET channels 1 and 2 (Fig. 10). In fact, the count rate has decreased considerably to 5 counts/sec. This may mean that we are observing a shift in the LET spectrum to higher channels due to flux increases of high energy particles. A different orbit yielded a similar pattern of behavior for these two channels. However, in reducing the LET data for Rev. 2551, channels 1 and 2 did correspond to the TEIC dose rate peaks. Further analysis is needed to correct this discrepancy. TABLE 4 shows the peak count rates for each of the LET channels. The number of counts

TABLE 4

CADS LET Channel	LET Range kev/micron	Peak Count Rate
1	.55 - .82	-
2	.82 - 1.22	-
3	1.22 - 1.86	525
4	1.86 - 2.9	475
5	2.9 - 4.7	185
6	4.7 - 8.5	135
7	8.5 - 19.0	95
8	19.0 - 130	55
9	> 130	450

decreases monotonically for each succeeding channel, except for LET channel 9 which records the count rate for particles with LET greater than 130 kev/micron. For the greatest portion of a typical orbit of data, the largest number of the counts occur in channels 1 and 2. This indicates that most of the particles sampled have LETs in the range .55 - 1.22 kev/micron. Channels 3 and 4, with LET ranges of 1.22 - 1.86 and 1.86 - 2.9 kev/micron respectively, record the next highest average count rate. Channel 9 also measures a significant number counts, and they are normally of the order of the count rate of channel 3.

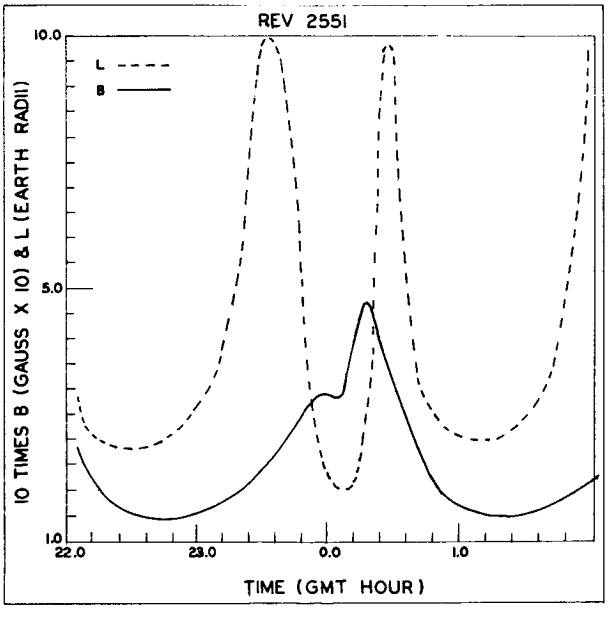

FIGURE 9: B, L vs. GMT for REV. 2551

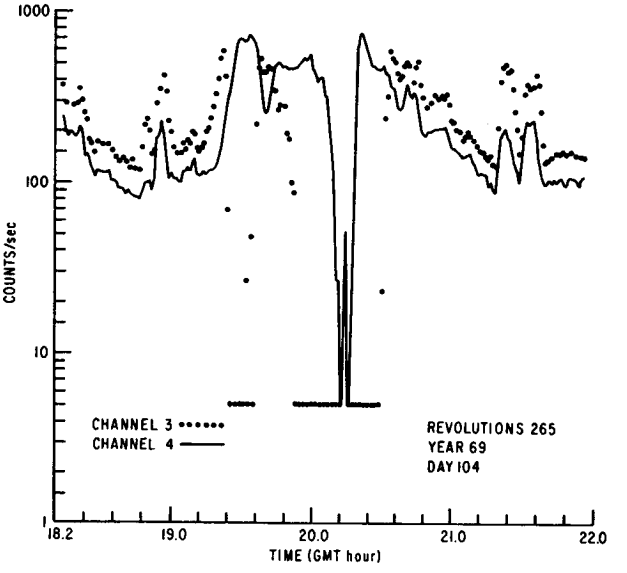

Figure 10: LET 1 & 2 (CADS Channel 3 & 4) for REV. 265

5. CONCLUSIONS.

The TEICs aboard OV1-19 show that a considerable dose rate can be expected even behind shielding whose cutoff energy is 70 MEV or higher. Most of this dose occurs due to solar flare radiation. A typical manned spacecraft provides a large amount of shielding in excess of 1.0 gm/cm^2 and the bone marrow and other vital organs are generally shielded by an additional 2.5 gm/cm^2 of surrounding tissue. Therefore, protons of high energy (> 60 MEV) are the dominant hazard to man in space. Doses from solar flares occur mainly over the polar regions. The earth's magnetic field masks out the solar flare protons almost completely in non-polar regions, where most of the Skylab missions will occur. However, if the rigidity of a flare is great enough, then the radiation belts may only partially mask out the solar flare radiation at altitudes of concern to earth orbiting manned vehicles. Also, many missions in the near future will take man outside the protection of the earth's geomagnetic field, where he will be more susceptible to the presence of a high proton environment. And, there is a great need for a more accurate description of that portion of the environment.

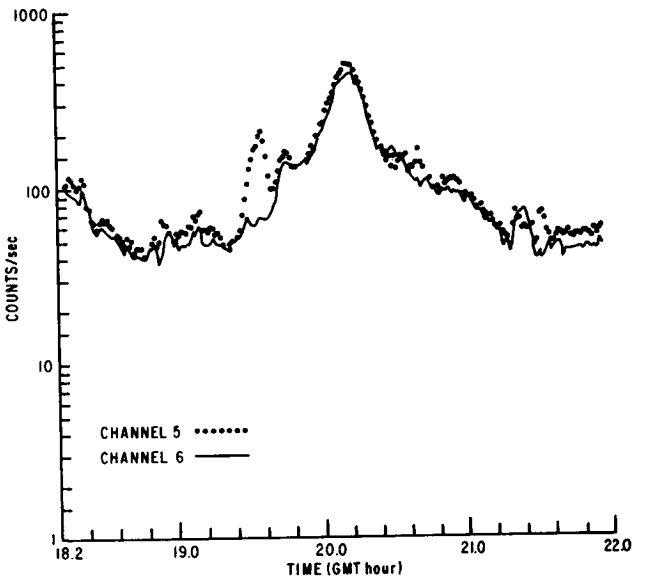

Figure 11: LET 3 & 4 (CADS 5 & 6) vs. GMT

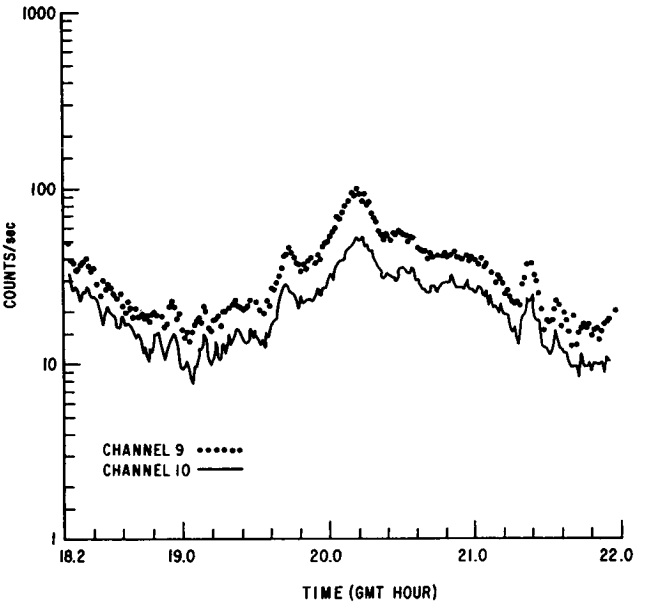

Figure 13: LET 7 & 8 (CADS 9 & 10) vs. GMT

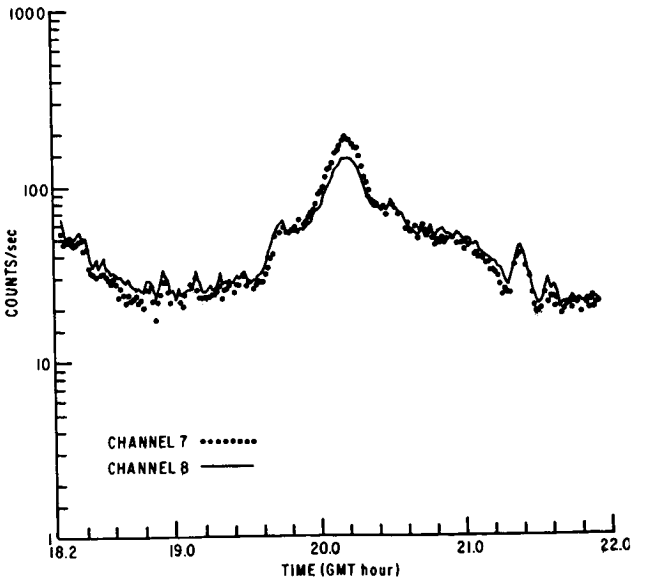

Figure 12: LET 5 & 6 (CADS 7 & 8) vs. GMT

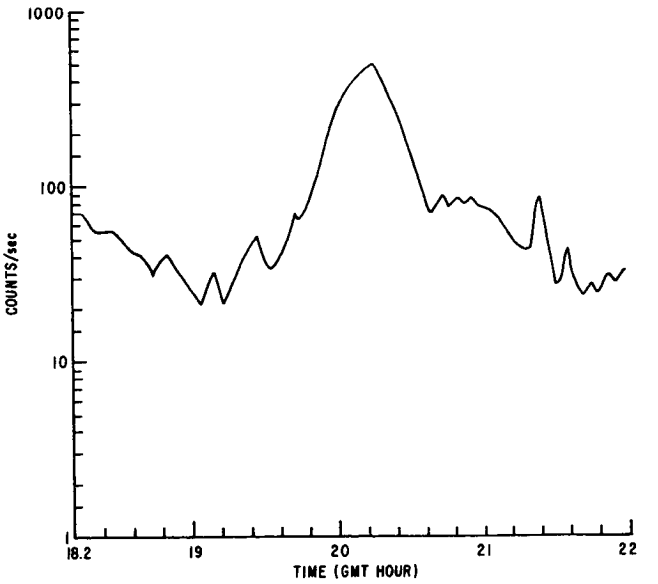

Figure 14: LET 9 (CADS 11) vs. GMT

REFERENCES

1. Schneider, M.F., Advanced Spaceborne Dosimetry Instrumentation, WL-TDR-64-96, AF Weapons Laboratory, December 1965.

2. Schneider, M.F., Calibration of Dose Measuring Ionization Chambers Using High Energy Proton Beams, WL-TR-66-30, AF Weapons Laboratory, 1967.

3. Trafton, L.M., OV1-12 Dose Rate, Spectral and Flux Measurements, AFWL-TR-69-104, AF Weapons Laboratory, January 1970.

4. Thede, A.L., OV3-4 Dose Rate and Proton Spectral Measurements, AF Weapons Laboratory, January 1969.

5. Fortney, R.E., Flight Experiment Shielding Study (FESS) Satellite Data Analysis, AFWL-TR-68-108, AF Weapons Laboratory, April 1969.

6. Janni, J.F., and Holly, F.E., "The Current Experimental Approach to the Radiological Problems of Spaceflight," Aerospace Medicine 40, December 1969.

7. Schneider, M.F., An Active Dosimeter System to Measure Energy Deposition and Charged Particle Spectra of High Energy Inner Van Allen Belt, Solar Flare, and Galactic Cosmic Protons on Manned Spacecraft, AFWL-TR-70-29, AF Weapons Laboratory, August 1970.

8. Chapman, M.C., Development of a Cellular Absorbed Dose Spectrometer, AFWL-TR-69-76, AF Weapons Laboratory, December 1969.

9. McIlwain, C.E., "Coordinates for Mapping the Distribution of Magnetically Trapped Particles," Jour. Geophys. Rsch., 66, p. 3681, 1961.

10. Hendricks, S.J., Cain, J.C., "Magnetic Field Data for Trapped Particle Evaluation," Jour. Geophys. Rsch., 71, p. 346, 1966.

SESSION VI.4.
RADIATION EFFECTS AND DOSCIMETRY
CHAIRMAN: W. ROSE
GENERAL DYNAMICS/FORTH WORTH

DESIGN CONSIDERATIONS AND TEST FACILITIES FOR ACCELERATED RADIATION EFFECTS TESTING*

William E. Price, Charles G. Miller and Richard H. Parker

Jet Propulsion Laboratory, Pasadena, California

Test design parameters for accelerated dose rate radiation effects tests for spacecraft parts and subsystems used in long term missions (years) are detailed. A facility for use in long term accelerated and unaccelerated testing is described.

INTRODUCTION

Outer planet missions require electronics and science instruments that have a useful lifetime of up to ten years. During this time, they are continuously within the gamma and neutron fields of the radioisotope thermoelectric generator (RTG), which provides electrical power to the spacecraft. Additionally, these electronics and science instruments are subjected to a number of other radiation stresses: Jovian radiation belts, solar flares, solar wind and cosmic radiation. One means of verifying the adequacy of components and of design for the ten-year useful lifetime is by accelerated testing in an adequately simulated environment. The intent is to simulate, in a short testing period, the effects to be expected in the real spacecraft mission, taking into account all of the stresses involved in radiation-cryogenic-vacuum environments.

RADIATION SOURCE CONSIDERATIONS

Jovian Radiation Belts

The Jovian radiation belt simulation testing need not be accelerated. This is because the belts may be traversed in a few hours on flyby missions. Both electrons and protons are expected to be trapped in the Jovian magnetic field, although the only direct estimates that have been made imply only an electron flux. It appears that readily available particle accelerators can simulate the Jovian fluxes in real time for both electrons and the theoretical models for protons.

Solar Flares

Solar flare rates will be lower than the Jovian radiation belts and the total doses can almost certainly be obtained by allowing 0.5 h/flare (acceleration by a factor of about 100). A twelve-hour test will conservatively simulate a ten-year mission.

Cosmic Radiation

The flux of cosmic ray particles is small and the expected damage is too low to be considered as an important area for environmental testing.

Solar Wind

The solar wind, whose effects are manifested as surface problems, has not interfered with past missions. The average flux of solar wind particles over a twelve-year period, with an assumed average energy of 3 keV, is 10^{7} protons/cm^2-s. Although at 1 AU the flux is 10^{8} protons/cm^2-s, the $1/r^2$ decrease means that at Jovian distances, the flux is reduced by a factor of 1/25. Since 3 keV protons have a range of 10^{-5} g/cm^2, if we assume a target with a thickness equal to the proton range, the delivered power density is 4.8×10^{-8} W/cm^2 at Jupiter orbit. For those components that rely on radiative cooling for their heat loss, typically unsupported thin films, too great an acceleration of the above given natural solar wind rates may lead to annealing effects in the test, which are not present in the real space environment.

The power radiated from a black body (in watts/cm^2) is equal to $(T/645)^4$ where T is the temperature in degrees Kelvin. Table 1 gives the expected equilibrium temperature of a radiatively cooled thin film, subjected to various accelerated dose rates of solar wind, calculated for various initial component temperature and power densities. In programming a test, larger accelerations (that lead to larger temperature rises) can be tolerated for systems that operate at low temperatures than for systems that operate at high temperatures, because the annealing temperature is related to the Debye temperature for the material under test. These restrictions are further relaxed when more efficient means of cooling may be employed (e.g., conductive cooling to the spacecraft for non-thin-film components).

*This paper presents the results of one phase of research carried out at the Jet Propulsion Laboratory, California Institute of Technology, under Contract No. NAS 7-100, sponsored by the National Aeronautics and Space Administration.

Table 1. Equilibrium temperature of a radiatively cooled thin film, subjected to various doses of (accelerated rate) solar wind

Acceleration, times nominal	Duration of test	Power density, W/cm^2	Initial component temperature, °K	Equilibrium temperature, °K
Earth orbit				
1	3650 days	4.8×10^{-8}	300 (earth assumed)	300
10^2	36.5 days	4.8×10^{-6}	300 (earth assumed)	300
10^4	0.36 day	4.8×10^{-4}	300 (earth assumed)	300.5
10^5	5.2 min	4.8×10^{-3}	300 (earth assumed)	308
10^6	0.52 min	4.8×10^{-2}	300 (earth assumed)	358
Mission average				
1	3650 days	4.8×10^{-9}	300 (assumed)	300
10^2	36.5 days	4.8×10^{-7}	300 (assumed)	300
10^4	0.36 day	4.8×10^{-5}	300 (assumed)	300.1
10^5	5.2 min	4.8×10^{-4}	300 (assumed)	300.5
10^6	0.52 min	4.8×10^{-3}	300 (assumed)	308
Mission average				
1	3650 days	4.8×10^{-9}	150 (assumed)	150
10^2	36.5 days	4.8×10^{-7}	150 (assumed)	150
10^4	0.36 day	4.8×10^{-5}	150 (assumed)	150.6
10^5	5.2 min	4.8×10^{-4}	150 (assumed)	155
10^6	0.52 min	4.8×10^{-3}	150 (assumed)	192
Jupiter orbit				
1	3650 days	1.78×10^{-9}	150 (assumed)	150
10^2	36.5 days	1.78×10^{-7}	150 (assumed)	150
10^4	0.36 day	1.78×10^{-5}	150 (assumed)	150.1
10^5	5.2 min	1.78×10^{-4}	150 (assumed)	152
10^6	0.52 min	1.78×10^{-3}	150 (assumed)	169

RTG Radiation

Gamma Radiation

The spectral distribution and intensity of the gamma field from the RTG, although varying with time and dependent upon the initial fuel composition and construction of the RTG capsule, have been extensively studied at JPL.

The design considerations given in this paper indicate the practical limits of acceleration of testing, and take into account costs, radiation safety needs and requirements for spatial uniformity of accelerated test fields.

The analysis is based on a generalized outer planet spacecraft configuration in which the RTG-science-instrument spacing is taken as 180 in., and the RTG electronics spacing is taken as 72 in. Actual design geometry and environmental conditions will be determined as the program proceeds. The analysis is based on the simulation of the radiation of an 8000 W (thermal) source, as was envisioned for an earlier JPL TOPS configuration. Newer configurations may have somewhat different radiation levels, but such changes will not change the conclusions of the study.

Acceleration of delivery of total dose is accomplished by increasing the dose rates delivered to the test object by either of the two methods described below, or by the use of both simultaneously.

Loading

Increasing the gamma flux by using larger amounts of nuclear material or a satisfactory nuclear species that gives the same gamma spectrum. The apparent limitations are in cost and safety necessary for large sources. A practical acceleration of X 25 (over the output of an 8000 W (thermal source) can be had for a moderate cost. The X 25 acceleration source could be used in the JPL 25-ft space simulator (see Fig. 1).

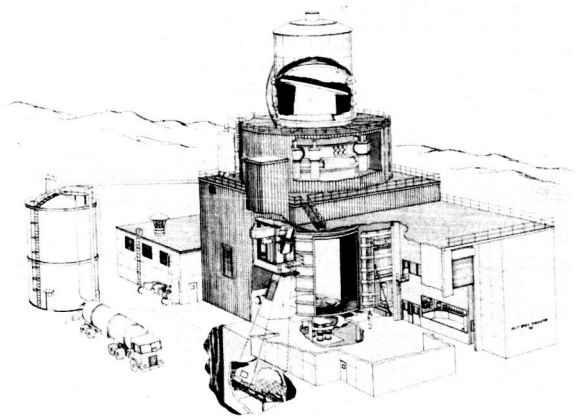

Fig. 1. JPL 25-Ft Space Simulator

An alternate loading acceleration has been designed that would use a fast decaying, but intense source of sodium-24 as the principal nuclide. This design allows a loading acceleration of X 250 at slightly more than twice the cost of the X 25 source. However, this source could not be ready for use in less than approximately eight months.

Geometrical

An increase in the gamma flux can be had by bringing the source closer to the test objects than the design value of 15 feet for the science instruments, and six feet for the electronics. When the source real or simulated, is placed closer than its normal separation distance from the test object, the field strength is increased by the ratio $15^2/d^2$ or $6^2/d^2$ for science instruments or electronics, respectively. The uniformity of the exposure from the near-face to the far-face of the test object, however, decreases as the distance d from the source to the test object decreases. Practical geometry increases are from X 10 to X 100, depending

on the size of the test object and the uniformity of flux required.

Because of the deep penetration of the gammas, the heat input per unit volume of the test object is low, and annealing is not expected to be a problem, even for a X 2500 acceleration.

Figure 2 shows the uniformity of dose (in terms of tolerance from the centerline dose) for varying distances up to 200" from the source and for test objects whose size (extent in the beam direction), is 2, 4, 8, or 16 in. The figure shows that a geometrical acceleration of X 10 may be had for a 4-inch-thick object with a uniformity of ± 6% of centerline intensity, while a geometric acceleration of X 100 yields a variation of ± 20%. Similarly, Fig. 3 shows the uniformity of dose (from centerline dose) and geometrical acceleration possibilities for electronic bay equipment, which is normally six feet from the source.

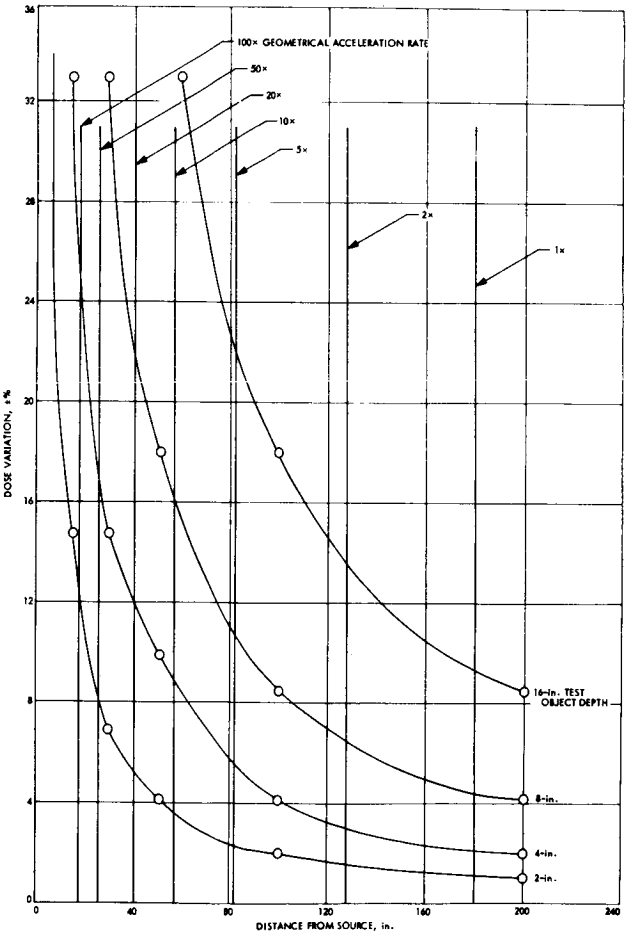

Fig. 2. Uniformity of dose as a function of distance from the source for various test objects

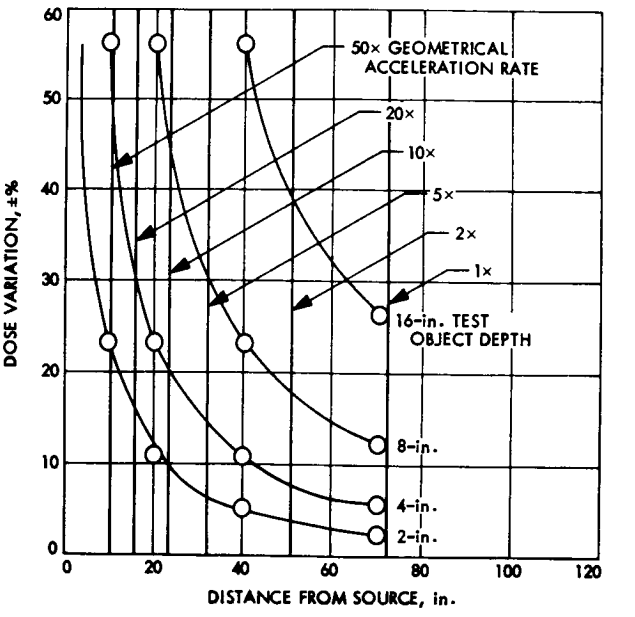

Fig. 3. Uniformity of dose as a function of distance from the source for electronic bay equipment

Neutron Radiation

It does not seem practical, at present, to make large loading accelerations for the neutron flux components of the RTG radiation. Therefore, any acceleration using isotopic sources will be dependent on increases via geometrical means. Studies are underway to determine if larger geometrical accelerations can be tolerated for neutrons than for gammas, because of the different nature of the scattering and interaction mechanisms involved.

An alternate possibility exists for accelerated neutron testing in the use of a machine accelerator as a neutron source. While this has some limitations on size of component accepted, the energy spectrum can be grossly simulated and fluxes as high as 10^{11} n/cm^2-s can be attained in small areas at JPL.

COMBINED ENVIRONMENTS AND TESTING CONDITIONS

Simultaneous application of other space environments (space vacuum, solar and ultraviolet irradiation, and control temperatures down to those of liquid nitrogen) will also be possible in the JPL facilities.

Table 2 shows a selected set of operating conditions that are available using a combination of loading and geometrical accelerations. In each case, it is possible to increase the irradiation uniformity (decrease the variation) from that presented in Figures 2 and 3 and in Table 2, to a small fraction of the given values by mounting the test objects on a rotating table, or a table that oscillates through 180 degrees, so that the two faces of test objects alternate in their exposure to the source.

Table 2. Operating conditions for accelerated testing (10-yr mission length)

Acceleration, times nominal			Required total test duration, days	Remarks
Loading	Geometrical	Total		
10	10	100	36	±12% uniformity for 8-in.-thick test object
25	10	250	14	±12% uniformity for 8-in.-thick test object
10	100	1000	3.6	±10% uniformity for 2-in.-thick test object
25	100	2500	1.5	±10% uniformity for 2-in.-thick test object
250	10	2500	1.5	
250	30	7500	0.5	

ACCELERATED RADIATION EFFECTS TESTING FACILITIES

Comparatively little work has been done to determine if long-term (years), of low level radiation environments such as encountered by spacecraft on long missions, will affect the lifetime and reliability of spacecraft parts. Most of the existing radiation effects studies have concentrated on material property studies, weapons effects, and reactor irradiations which are of little value to radiation effect studies for outer planet missions. Space radiation simulation has been done on a limited number of device types used in present day spacecraft (Ref. 1).

Accelerated testing is important to obtain data in a practical time. To be useful, however, a relationship must be established between parts testing in real time using combined environments (under varied test conditions) and accelerated testing to take the rate effects, if any, into account. Such a program of studies is indispensable for carrying out present outer planet missions. An initial simple program is described below. As the requirements become clear, additional variables may be added at the expense of increased complexity and cost.

The major object of the program described is to determine for a large number of types of parts, whether accelerated testing is a valid procedure to predict long-life, real time operation in a low level radiation field, and if so, to define for various parts and components what rate of acceleration can be tolerated in testing. Standard testing procedures must be developed and validated for the parts to be tested.

An Accelerated Radiation Effects Laboratory has been put into operation at JPL in a group of former explosive test cells. A source of radiation, 5 curies of Ir^{192}, was placed in a collimator with the radiation beam directed toward the ceiling (see Fig. 4). Circuit boards of parts and components are suspended in the cone of radiation at two or three distances from the source to obtain different radiation dose rates. Some of the parts will be non-operating and some will be operating to simulate conditions on a spacecraft (where some systems are continually in operation while others are used intermittently or only at planet encounters). There will be control specimens subject to the same environmental conditions except for the radiation, and these will be operated by the same power supplies as those powering the irradiated samples.

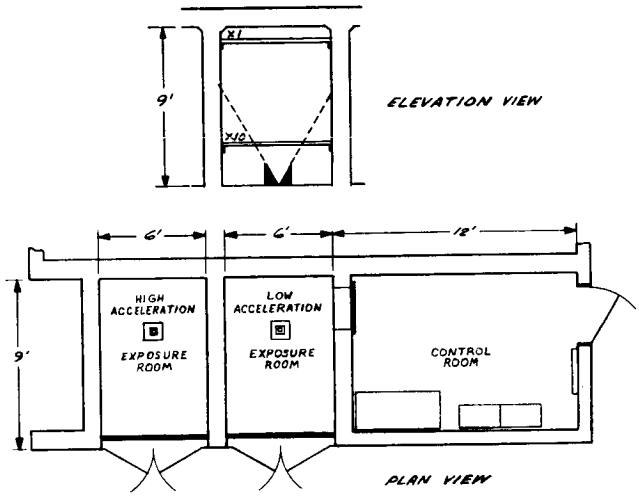

Fig. 4. JPL Accelerated Radiation Effects Laboratory

Table 3 shows the acceleration rates available with a 5 curie Ir^{192} source. To obtain a X 1 rate at the farthest distance from the source (at 2.5 meters) the radiation must be attenuated. That was accomplished using several thin lead sheets (0.033 cm each). This turns out to be a slight advantage in that a single sheet may be removed periodically to compensate for the change in dose rate due to the decay of the source (74 day half-life). However, a change to a longer-life isotope, Cs^{137} (30 year half-life), is anticipated in order to have a more stable dose rate with time at the experimental areas.

Table 3. Acceleration and Dose Rates Obtained with a 5 ci Ir^{192} Source

Distance From Source	Radiation Dose Rate	Acceleration Rate Above that at the TOPS Electronics Bay	Acceleration Rate With Attenuation by Lead Sheets
Meters	mR/hr		
2.5	456	X 4	X 1
1.5	1140	X 10	X 2.5
1.0	2750	X 24	X 6
0.75	4560	X 40	X 10
0.49	11400	X 100	X 25

A larger source is planned for an adjoining test cell which will allow accelerated testing up to X 1000, so that accelerated rates may be chosen for testing parts between X 1 and X 1000 of the radiation dose rate expected on the electronics of the outer planet mission spacecraft presently planned.

It is anticipated that the test cells will be used for long-term testing, possibly up to ten years. Therefore, the tests chosen, the test plan adopted and the environmental conditions must be planned in great detail so that useful and statistically significant data will result.

The parts which are now considered the most sensitive to radiation induced changes are semiconductor devices, since minor changes in the trapping centers and in surface ionization can produce major changes in operating conditions in these devices. Therefore, semiconductor devices of all commonly used types should be included in the test. Representative samples of various resistor types, capacitors and other active electronic components, can also be considered for long-term testing. However, past testing has shown that these device types are more radiation resistant than transistors, and they should not be included until a later phase of the long-term experiment unless they are of unorthodox construction or involve thin-film elements.

Transistors chosen from the most recent parts lists should be obtained in sufficient numbers to allow a test to be set up which has a statistical significance for the expected low rates of failure. Data analysis should include Weibull plots, since we are interested in a determination of failure predictions down to low doses and low probabilities Investigators have shown this to be a valid approach (Ref. 2).

Initial tests should be set up for times up to one year in order to determine applicable test procedures for subsequent longer term testing. Elements of the initial tests should include the following:

1. Testing at room temperature.
2. Gamma radiation exposure.
3. Powered and unpowered operating transistors in the radiation environment; and control devices in a similar, but radiation-free environment.
4. Each test group should be mounted on separate printed circuit boards to allow rapid parameter measurements.
5. The validity of removing the boards for remote measurements should be determined.
6. The test design should incorporate adequate statistical planning, so that with a limited number of specimens the most meaningful test can be carried out.

In the JPL Accelerated Radiation Effects Laboratory (AREL), the initial work is being done at the X 1 rate, because these tests take longer times. Figures 5 and 6 show the source and collimator locations in relationship to the X 1 sample locations (on the ceiling) and the X 10 location (at the table top).

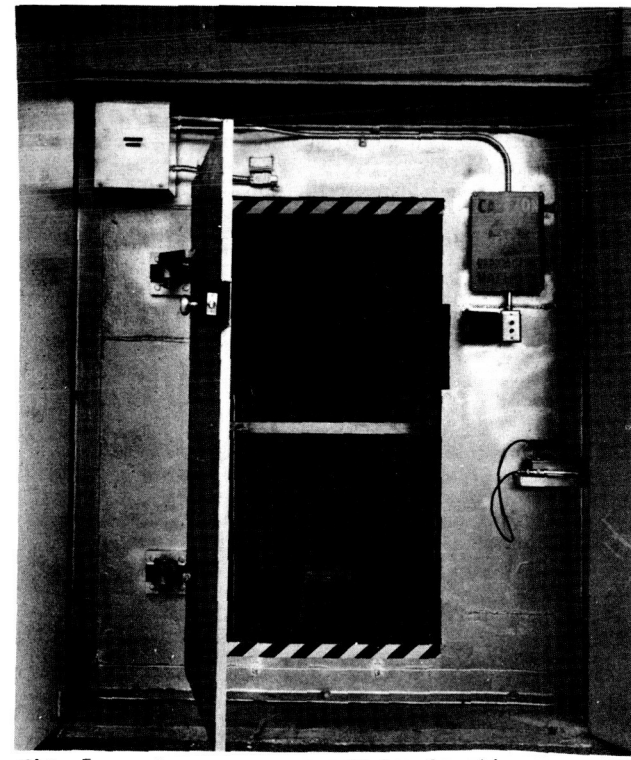

Fig. 5. Entrance to the Low Acceleration Exposure Room

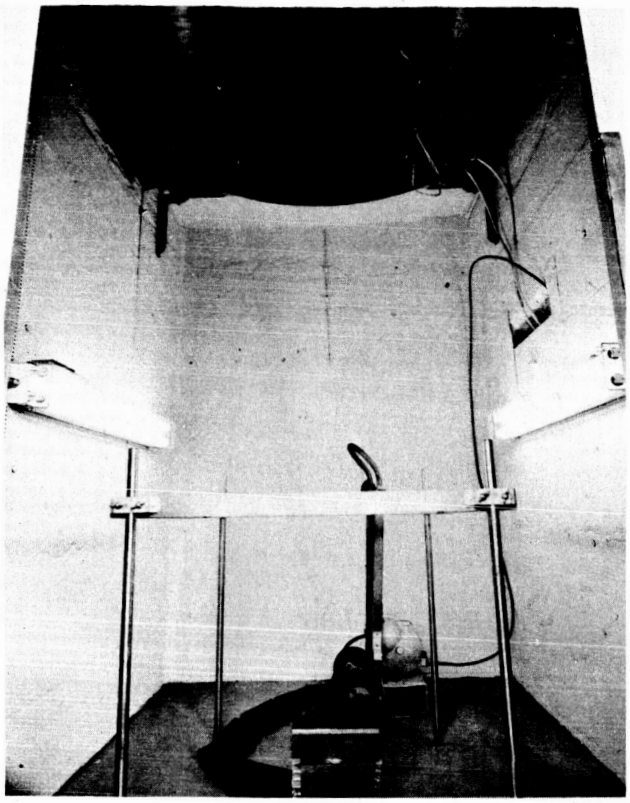

Fig. 6. Inside Low Acceleration Exposure Room

Figure 7 shows the power supplies and the test points for the integrated circuits under test and the control samples located on the wall mounting in the AREL control room. Figure 8 shows the AREL control room with the source operating mechanism, safety system and the window labyrinth for wiring feed-throughs.

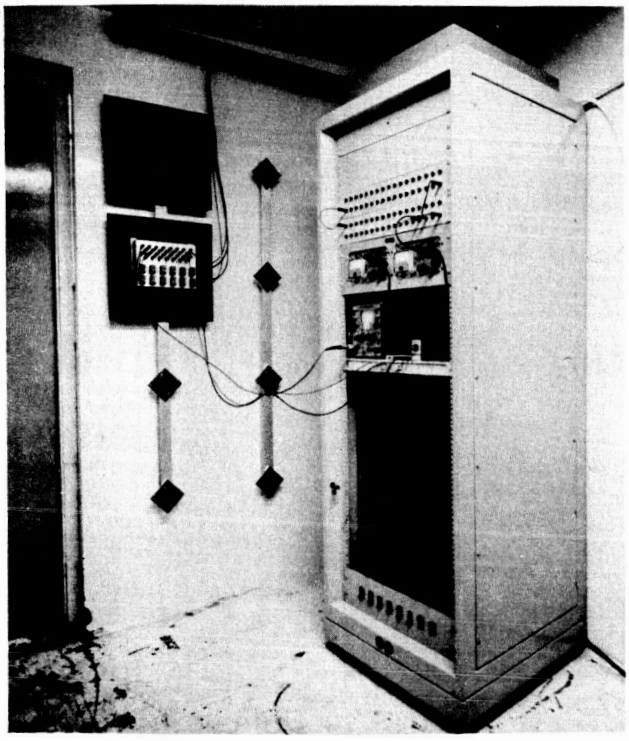

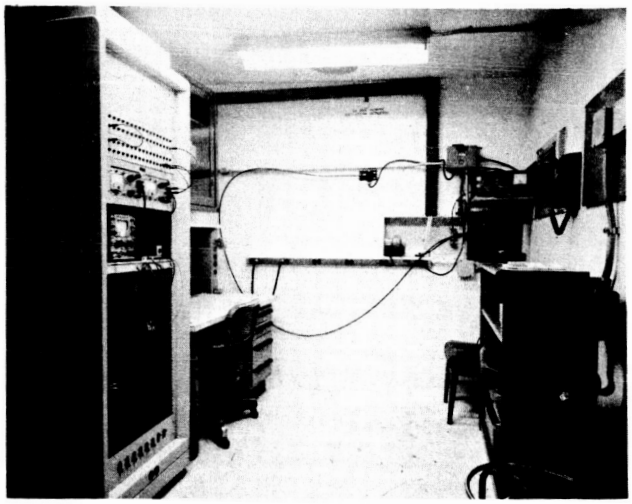

Fig. 8. AREL Control Room

CONCLUDING REMARKS

The Accelerated Radiation Effects Laboratory was constructed utilizing the design principles described in this paper and in order to confirm these principles. While the initial purpose was for testing spacecraft piece parts, the versatility allows a number of other types of experimentation to be considered, such as testing survivability of micro-organisms at low dose rates over long periods, and in vacuum. Testing of pyrotechnics and propellants is also practical in this facility and arrangements are being made to this end.

REFERENCES

1. J. E. Drennan and D. J. Hamman, "Space-Radiation Damage to Electronic Components and Materials", REIC Report #39, Battelle Memorial Institute, January 1966.

2. W. E. Horne and J. A. Folsom, "Total-Dose Survival Probability for Bipolar Transistors", IEEE Trans. on Nuclear Science, Vol. NS-17, No. 6, Pp. 167-172, December 1970.

SOLAR CELL RADIATION RESPONSE NEAR THE INTERFACE OF DIFFERENT ATOMIC NUMBER MATERIALS

E. A. Burke, J. R. Cappelli, L. F. Lowe, and J. A. Wall
Air Force Cambridge Research Laboratories (AFSC)
Bedford, Massachusetts 01730

The response of Co-60 irradiated N/P silicon solar cells was measured as a function of the atomic number of the medium adjacent to the cell and the direction of the gamma ray beam. The interpositioning of various thicknesses of aluminum between the adjacent material and the cell had the effect of moving the cell to various locations in an approximate monatomic numbered medium. Using this technique the solar cell response was determined at various distances from the interface for gold and beryllium. The results were compared with predictions based upon ionization chamber measurements of dose perturbations in aluminum and found to agree within five percent. Ionization chamber data was then used to estimate the influence of various base contact materials. The directional effect is most noticeable for gold contacts leading to a response when the beam enters the cell face which is 40% greater than for the opposite direction. The situation is reversed for beryllium which produces a response which is 17% greater when the beam enters through the base than for the reversed direction.

INTRODUCTION

The prediction of solid state device response to ionizing radiation requires a knowledge of the energy absorbed (the dose or dose rate) in active regions of the device. If the device is adjacent to materials (packaging or structural supports) with atomic numbers different than the device material and the primary radiation produces electrons with ranges that are comparable to device dimensions, ionization chamber studies indicate that the energy deposited can vary significantly from that absorbed in the absence of the surrounding materials. Methods commonly used for predicting the dose neglect the possible influence of adjoining materials. Similarly, the materials, dimensions, and encapsulation of dosimeters rarely corresponds to the test specimen so that experimental measurements can be misleading. Little experimental data exists concerning the nature and magnitude of the dose perturbations produced and as a result theoretical predictions have not been adequately tested.

The greatest amount of work on the problem of dose perturbations at interfaces has been done by those with an interest in the biological effects of radiation. They have been particularly concerned about the enhanced dose in soft tissue adjacent to bone under X irradiation. Experimental and theoretical work on this problem has been reviewed by Spiers[1].

In view of the large differences in the photoelectric cross sections for elements of different atomic number and the resultant large difference in the deposited energy it is not surprising to find dose perturbations near interfaces at x-ray energies. At gamma ray energies where the Compton cross section is dominant, energy deposition varies relatively little from one material to another and small perturbations might be expected.

The fact that significant changes in the dose can occur at gamma ray energies was first pointed out by Dutreix et al[2] and recently examined for typical device materials exposed to Co-60 gamma radiation by Wall and Burke[3]. Energy deposition profiles in aluminum adjacent to gold are shown in Fig. 1. The data was obtained using a multiple cavity parallel plate ionization chamber technique[3]. It shows that the dose in aluminum is enhanced when the gamma beam penetrates the aluminum before entering the gold. However, the dose is actually reduced below the equilibrium value for aluminum when the gamma beam is reversed. There is a strong directional effect. The effect is noticeable at a distance of 200 mg/cm^2 away from the boundary which means that it extends over typical device dimensions. For lower atomic number materials the effect is similar but somewhat reduced as shown in Fig. 2.

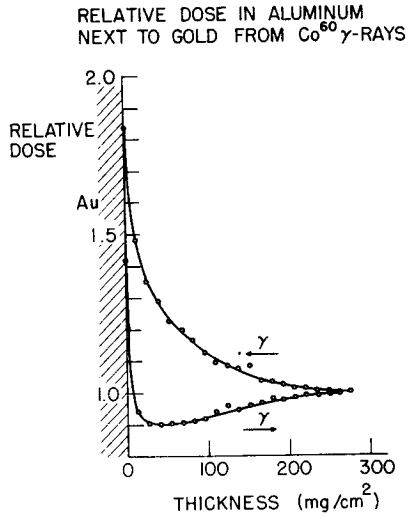

FIGURE 1. - Air Ionization Measurements of the Relative Dose in Lauminum next to Gold. Arrows indicate the direction of the gamma beam.

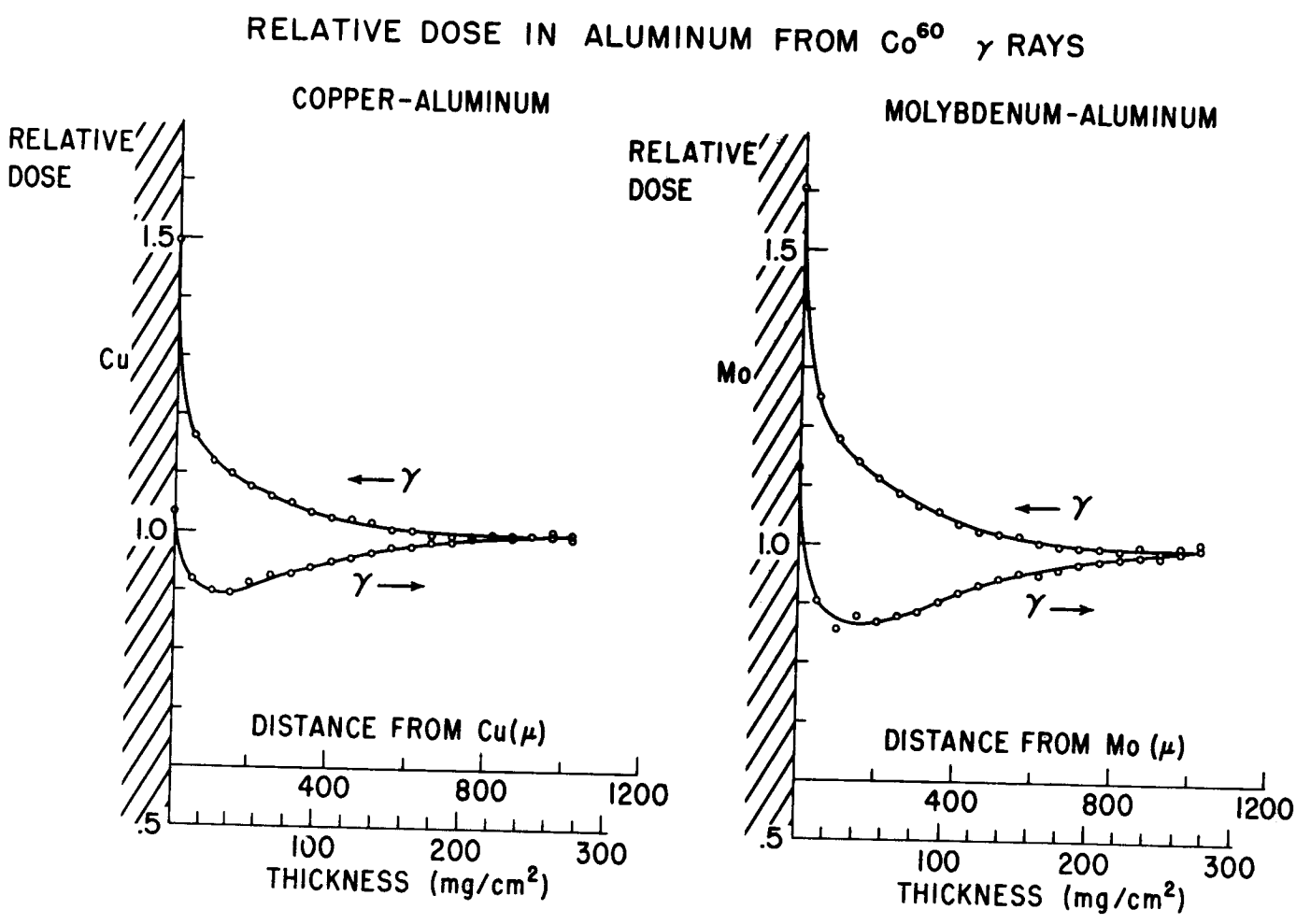

FIGURE 2. - Air Ionization Measurements of the Relative Dose in Aluminum Next to Copper and Molybdenum.

AFCRL PHOTO 120-406

Notice, however, that the minimum in the dose profile appears to be greatest for materials of intermediate atomic numbers such as molybdenum. It has also been found[3] that beryllium or carbon adjacent to aluminum reverses the effect, i. e. the aluminum dose is enhanced when the beam penetrates the beryllium first and reduced for the opposite photon direction. Finally, it has been found that micron layers of high atomic number materials produce a readily observable effect as shown in Fig. 3.

It is important to note that the results described were obtained with ionization chambers. We must be careful in assuming that other phenomena, such as electron-hole pair production in semiconductors will behave in the same way in the transition zone near an interface. If we are interested in applying ion chamber data to solid state devices it is desirable to show that the response of the latter can be predicted from the former. That was the primary objective of the work reported here.

Solar cells were selected for examining the possibility of predicting device response. The interface conditions studied were similar to those studied with ionization chambers. The results obtained indicated that ionization chamber data could be employed to predict device response. Calculations were then carried out for solar cells with base contacts of several different materials.

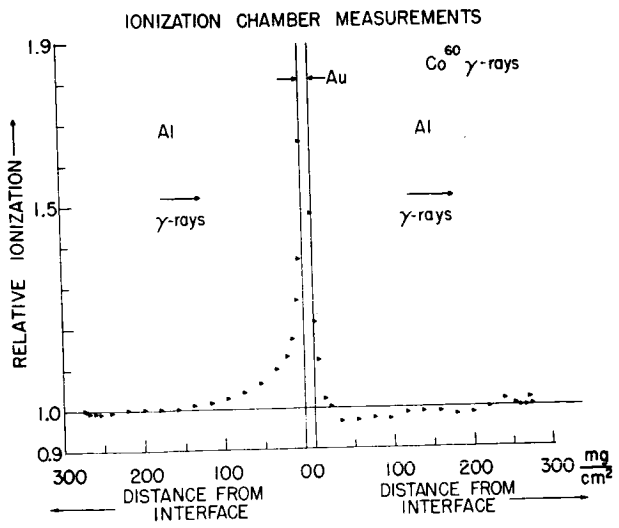

FIGURE 3. - Air Ionization Measurements of Dose Perturbations Near a Thin Gold Film.

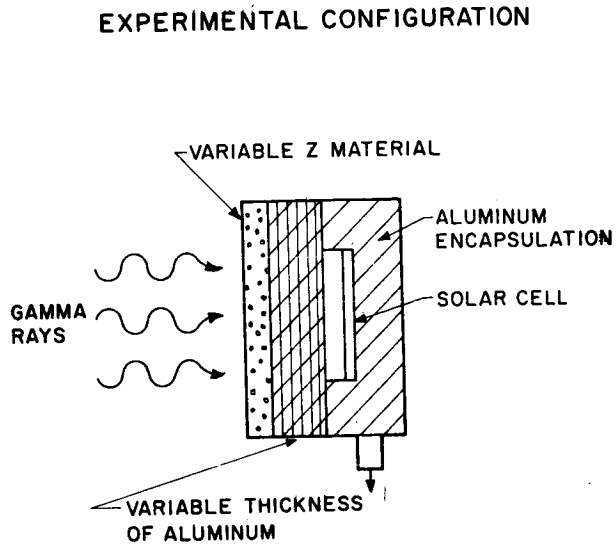

FIGURE 4. - Experimental Configuration Used in Solar Cell Measurements.

EXPERIMENTAL

The devices employed were 1 x 2 cm, N/P silicon solar cells with 0.5 μm junction depth and a 2.5 Ωcm base resistivity. The diffusion length of minority carriers in the base was determined by exposing the cells encapsulated in aluminum (to establish equilibrium dose conditions) to a Co-60 gamma source and measuring the short circuit current. The dose rate was established with a calibrated ionization chamber and the minority carrier production rate calculated assuming that 3.6 eV are required to produce an electron-hole pair[4]. Typical diffusion lengths for undamaged cells were in the vicinity of 140 μm.

The sample holder employed in the solar cell exposure is shown in Fig. 4. The cell was mounted in a recessed aluminum plate whose thickness exceeded the range of the highest energy electrons generated by Co-60 gamma radiation. In the experiments reported here the base contact was adjacent to the aluminum plate. Aluminum foils of variable thickness could be placed between the face of the cell and the gold or beryllium plates used in the interface studies. Rotation of the sample mount through 180° permitted the response to be determined for both beam directions.

A 16 kilocurie Co-60 source was employed in the irradiations. Both collimated and uncollimated photon beams yielded the same results within the uncertainty of the measurements. In order to normalize the data the cell response was measured with aluminum replacing the gold or beryllium end plate.

COMPARISON OF CELL RESPONSE WITH IONIZATION CHAMBER RESULTS

The short circuit current as a function of aluminum foil thickness was normalized to the current observed with the cell completely encapsulated in aluminum. Results are shown for both gold and beryllium end plates and for two beam directions in Figs. 5 and 6. As can be seen the response is qualitatively similar to the ion chamber results. The difference can be attributed to the solar cell thickness (0.038 cm) which represents a significant fraction of the distance over which the dose perturbation occurs. If the ion chamber results are a true indication of the dose rate the carrier generation rate will not be uniform through the cell. We can make a quantitative comparison by adopting an approach similar to that used in calculating the spectral response of solar cells[5].

For electrons in the p type base the form of the continuity equation applicable is

$$G_n - U_n + \frac{1}{q} \operatorname{div} \vec{J}_n = \frac{\partial n}{\partial t} \qquad (1)$$

where n is the excess minority carrier concentration in the base, $\vec{J}_n$ the current density, G_n and U_n are the minority carrier generation and recombination rates, and q is the charge on an electron. For steady state conditions, zero electric fields, low injection and one dimensional geometry Eq (1) simplifies to

$$G_n - \frac{n}{\tau_n} = - D_n \frac{\partial^2 n}{\partial x^2} \qquad (2)$$

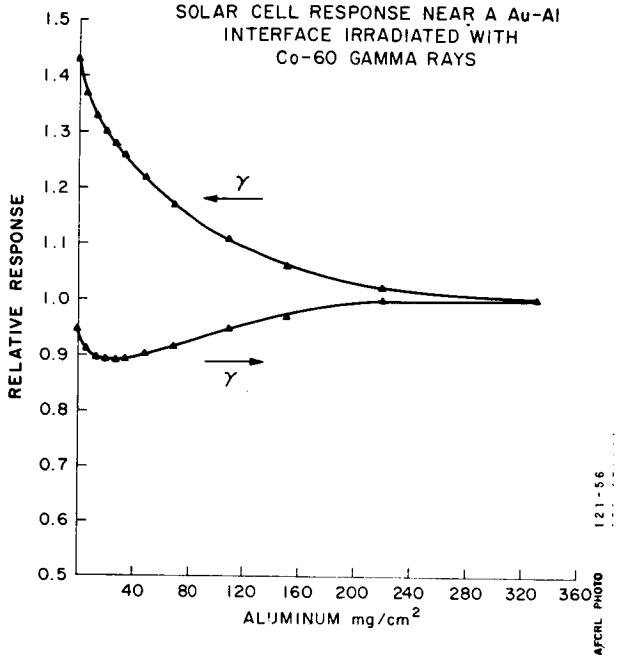

FIGURE 5. - Measured Solar Cell Response Near a Au-Al Interface.

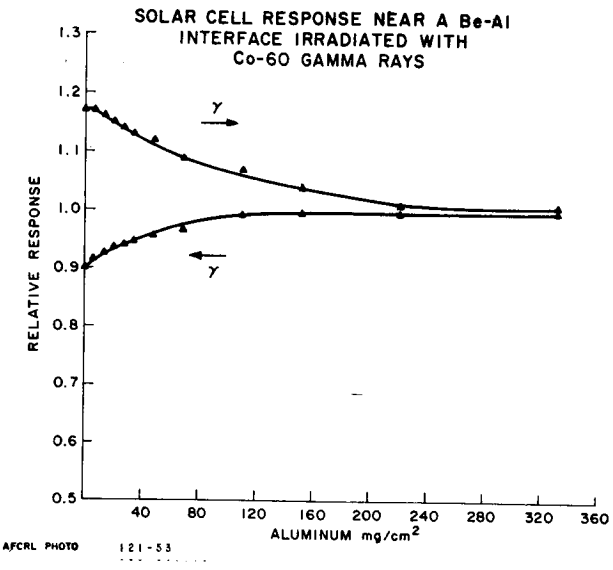

FIGURE 6. - Measured Solar Cell Response Near a Be-Al Interface.

where τ_n is the lifetime of minority carriers and D_n the diffusion coefficient. The normalized ionization chamber data can be fitted with an exponential series to within a few percent. If we assume that the generation rate is given by the same function we have

$$G_n = G_o \sum_m A_m e^{-\alpha_m (x + x_1)} \qquad (3)$$

where the values of the coefficients for beryllium, copper and gold are given in Table I, x_1 is the thickness of aluminum between the end plate and the face of the cell and x any point within the cell as measured from the cell face. The solution to Eq. 2 is

$$n = C_1 e^{x/L} + C_2 e^{-x/L} + G_o \sum_m B_m e^{-\alpha_m (x_1 + x)} \qquad (4)$$

where

$$B_m = \frac{A_m}{D_n} \left(\frac{1}{L_n^2} - \alpha_m^2 \right)^{-1} \qquad (5)$$

and L_n is the diffusion length which is equal to $\sqrt{\tau_n D_n}$. If we assume that the excess minority carrier concentration is zero at the junction and at the base contact, i.e., n = o at $x = \ell$ and x = b, then

$$C_1 = \left(e^{b-\ell/L} - e^{\ell-b/L} \right)^{-1} \cdot \qquad (6)$$

$$G_o \sum_m B_m \left(e^{-\alpha_m (x_1 + \ell) - b/L} - e^{-\alpha_m (x_1 + b) - \ell/L} \right)$$

and

$$C_2 = -\left(e^{b-\ell/L} - e^{\ell-b/L} \right)^{-1} \cdot \qquad (7)$$

$$G_o \sum_m B_m \left(e^{-\alpha_m (x_1 + \ell) + b/L} - e^{-\alpha_m (x_1 + b) + \ell/L} \right)$$

The diffusion current from the base is given by

$$J = q D_n \left. \frac{dn}{dx} \right|_{x = \ell} \qquad (8)$$

TABLE I. Coefficients for the Empirical Fit to Ionization Chamber Measurements of Energy Deposition Profiles in Aluminum Adjacent to Beryllium, Copper, and Gold.

$$\text{Relative Dose} = \sum_m A_m e^{-\alpha_m x}$$

In all cases $A_1 = 1.0$ $\alpha_1 = o$

Beam Direction High Z → Low Z

End Plate	A_2	A_3	A_4	α_2	α_3	α_4
Be	-0.159	-0.075	0	0.0213	0.137	0
Cu	-0.183	0.192	0	0.0094	0.0749	0
Au	-0.262	0.255	0.284	0.0097	0.0408	0.351

Beam Direction Low Z → High Z

End Plate	A_2	A_3	A_4	α_2	α_3	α_4
Be	0.283	-0.836	0	0.0122	0.0325	0
Cu	0.204	0.293	0	0.0172	0.334	0
Au	0.526	0.231	0.249	0.0144	0.0998	0.346

When $\ell \ll L$ the ratio of the diffusion current $J(x_1)$ to that for uniform ionization J_o, is given by

$$\frac{J(x)}{J_o} = \frac{D_n}{L^2} \frac{1}{(\beta+\alpha)} \cdot \sum_m B_m e^{-\alpha_m (x_1+\ell)} \left[\beta - \alpha e^{-\alpha_m (b-\ell)} - \alpha_m L \right] \qquad (9)$$

where $\beta = \coth (b/L)$
$\alpha = \operatorname{csch} (b/L)$

The results obtained from Eq. (9) are compared with the normalized solar cell response of a cell which had a measured diffusion length of 140 ± 15 μm in Figs. 7 and 8 for gold and beryllium the normalized results agree within a few percent. The calculated relative sensitivity of the result to the diffusion length for these cases is shown in Figs. 9 and 10.

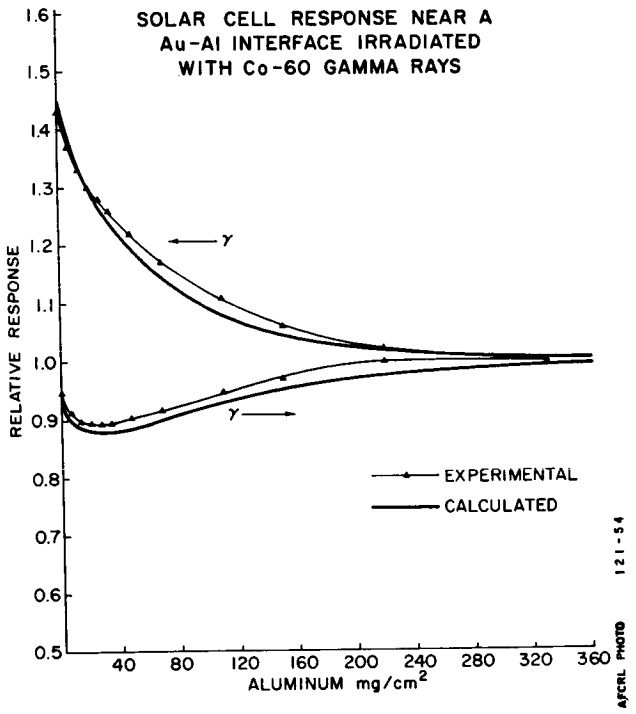

FIGURE 7. - Comparison of Measured Solar Cell Response Near a Au-Al Interface and Calculations Based Upon Ionization Chamber Measurements.

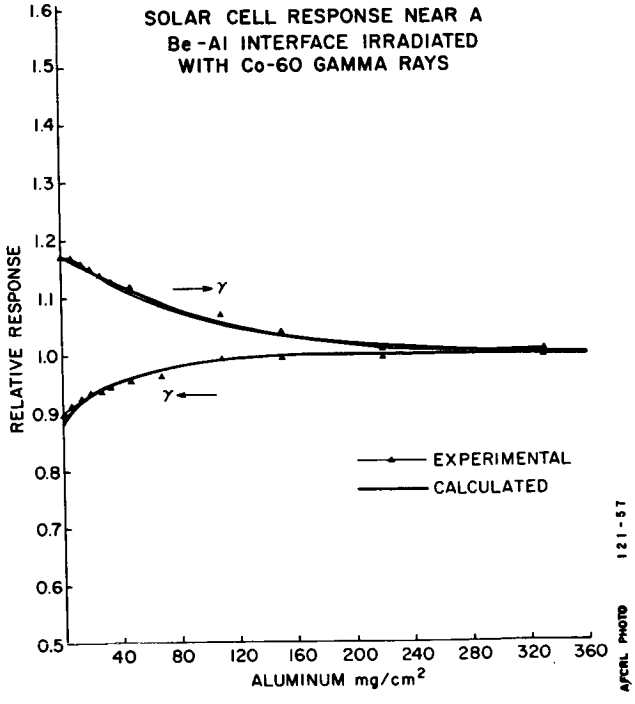

FIGURE 8. - Comparison of Measured Solar Cell Response Near a Be-Al Interface and Calculations Based Upon Ionization Chamber Measurements.

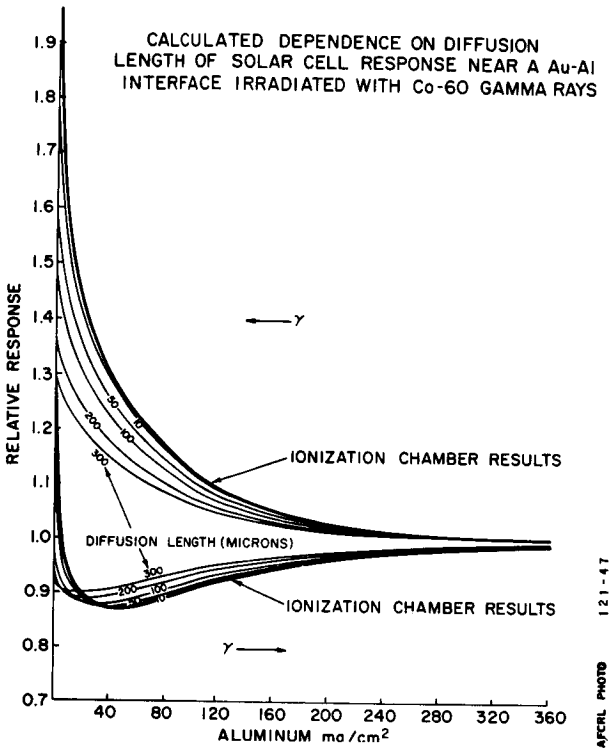

FIGURE 9. - Calculated Influence of Diffusion Length Upon Solar Cell Response Near a Au-Al Interface.

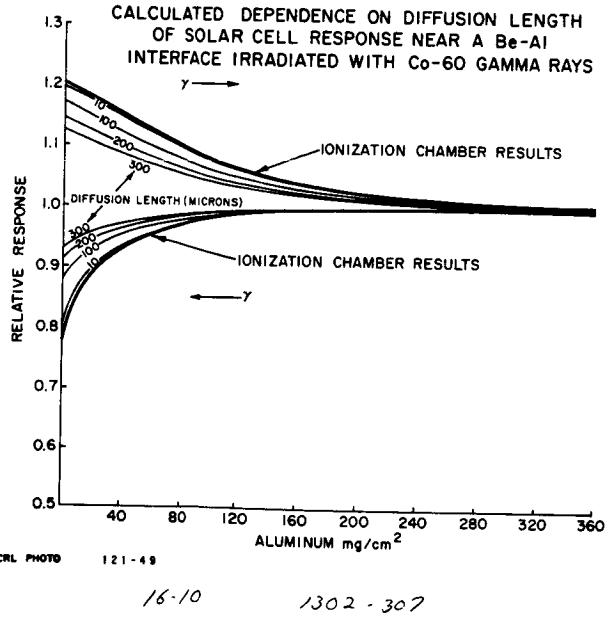

16-10 1302-307

FIGURE 10. - Calculated Influence of Diffusion Length Upon Solar Cell Response Near a Be-Al Interface.

CALCULATED SOLAR CELL RESPONSE FOR VARIOUS BASE MATERIALS

Since calculations of solar cell response based upon ionization chamber data agreed well with measurements when the interface was adjacent to the cell face, they were extended to the more realistic situation where the material was adjacent to the base contact. This requires a modification of Eq. (9) as follows

$$\frac{J(x)}{J_o} = \frac{D_n}{L^2}\,\frac{1}{(\beta+\alpha)}\cdot$$

$$\sum_m B_m e^{-\alpha_m(x_1+b-\ell)}\left[\beta - \alpha e^{-\alpha_m(\ell-b)} - \alpha_m L\right] \qquad (10)$$

In this case x_1 is the thickness of aluminum interposed between the base contact and the interface. All other quantities are the same as those employed in Eq. (9).

Calculations based on Eq. (10) are shown in Figs. 11-14. As might be expected the perturbation is largest for a thick (> 0.02 cm) gold base. When the beam enters through the cell and exits from the gold the response is 23% larger than it would be for an aluminum base contact. The reversed beam yields a result which is 12% lower than it would be for aluminum. Even 6 μm of gold produces an effect. The influence of copper and beryllium are smaller than for thick gold but readily noticeable. It is interesting to note that when the beam enters through the beryllium contact the response is approximately 12% greater than it would be for an aluminum base contact. Low atomic number elements can enhance the response if the beam traverses them before entering the device.

SUMMARY

It has been found that ionization chamber measurements of dose perturbations in aluminum adjacent to gold and beryllium can be used to predict the response of silicon solar cells near the same materials. The influence of gold, copper, and beryllium base contacts was then calculated for N/P silicon solar cells exposed to Co-60 gamma rays. Strong directional effects are evident in all cases. The response can be enhanced by both high and low atomic number materials depending upon the direction of the gamma beam. For the cells examined here the response as a function of beam direction varied as much as 40%. Ionization chamber measurements indicate that at Co-60 gamma energies (~ 1.25 MeV) the interface effects could be as large as a factor of two.

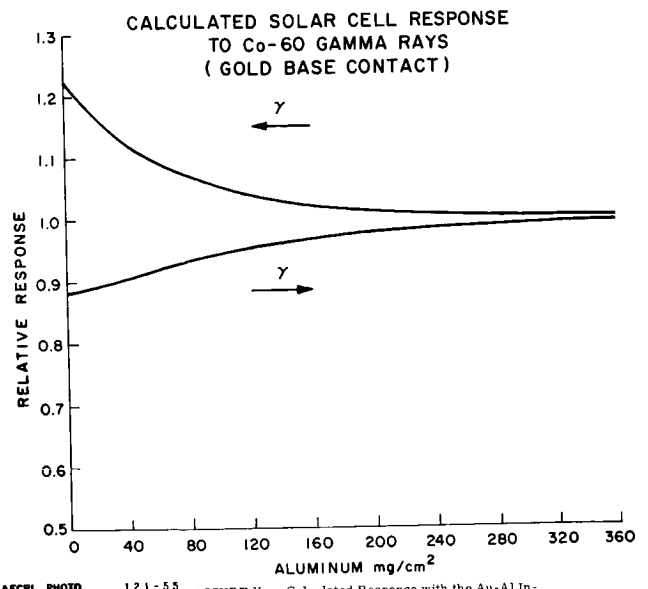

AFCRL PHOTO 121-55 FIGURE 11. - Calculated Response with the Au-Al Interface Near the Base Contact. The thickness of aluminum indicated lies between the gold and the base. Arrows indicate the beam direction relative to the cell face.

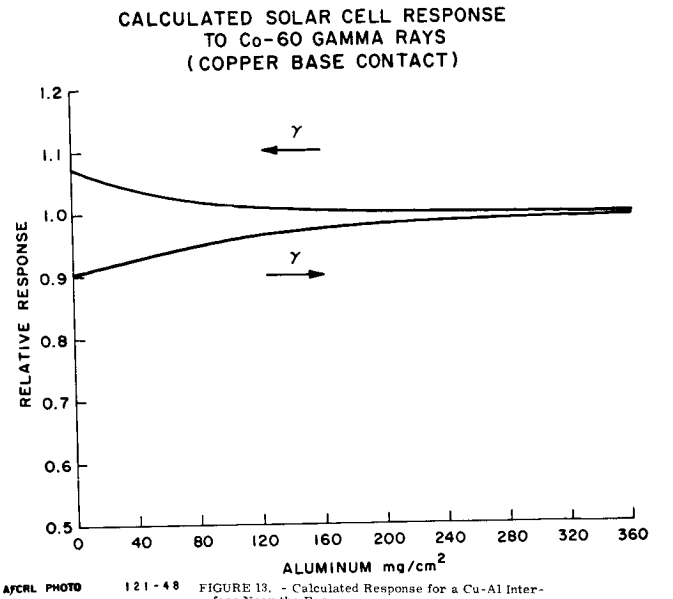

AFCRL PHOTO 121-48 FIGURE 13. - Calculated Response for a Cu-Al Interface Near the Base.

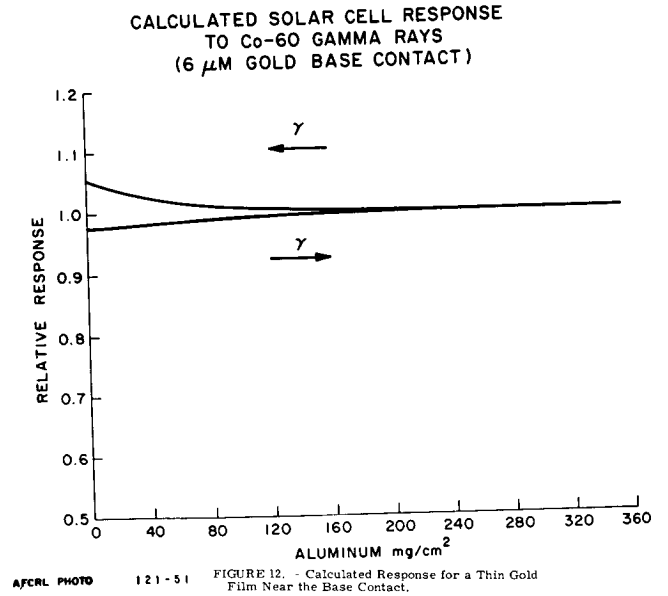

AFCRL PHOTO 121-51 FIGURE 12. - Calculated Response for a Thin Gold Film Near the Base Contact.

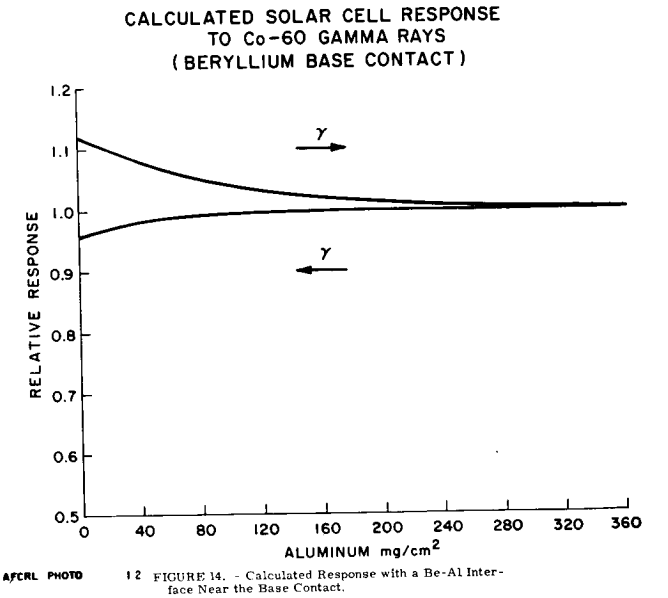

AFCRL PHOTO 12 FIGURE 14. - Calculated Response with a Be-Al Interface Near the Base Contact.

REFERENCES

1. SPIERS, F.W., in Radiation Dosimetry Vol. III, Ahix, Roesch and Tochilin, editors (Academic Press, Inc., N.Y. (1969) p 809-867.

2. DUTREIX, J. and BERNARD, M., Br. J. Radcol. 39, 205 (1966).

3. WALL, J.A. and BURKE, E. A., IEEE Trans. Nuc. Sci., NS17, 305(1970)

4. KLEIN, C. A., J. Appl. Phys. 39, 2029, (1968)

5. RAPPAPORT, P. and WYSOCKI, J. J., in Photoelectronic Materials and Devices, Larach, S., editor D. Van Nostrand Co., Inc. (1965) p. 239-275

Microscopic Observation of X-ray and γ-ray Induced Decomposition of Ammonium Perchlorate Crystals*

P. J. HERLEY**

Explosives Laboratory, Picatinny Arsenal

and

P. W. LEVY

Brookhaven National Laboratory

The x-ray and γ-ray induced decomposition of ammonium perchlorate was studied by optical, transmission, and scanning electron microscopy. This material is a commonly used oxidizer in solid propellents which could be employed in deep-space probes, and where they will be subjected to a variety of radiations for as long as ten years. In some respects the radiation-induced damage closely resembles the effects produced by thermal decomposition, but in other respects the results differ markedly. Similar radiation and thermal effects include the following: (a) irregular or ill-defined circular etch pits are formed in both cases; (b) approximately the same size pits are produced; (c) the pit density is similar, namely ca 2-40 x $10^6/cm^2$; (d) the c face is considerably more reactive than the m face; and (e) most importantly, many of the etch pits are aligned in crystallographic directions which are the same for thermal or radiolytic decomposition. Thus, dislocations play an important role in the radiolytic decomposition process.

Radiolytic decomposition produces at least three effects not previously observed with ammonium perchlorate: (a) after 10^8 rad. γ-ray irradiated crystals effervesce during solution in water; (b) the initial x-ray and γ-ray induced decomposition sites occur throughout the volume where energy is deposited. Once formed they continue to grow. In contrast, the initial thermal pits appear at the surface and grow. New pits are formed as the reaction zone proceeds inward; (c) x-ray irradiation produces highly strained crystals. The layer adjacent to the irradiated surface becomes extensively cracked and large crystals have pronounced convex curvature.

Inasmuch as the principal decomposition is restricted to certain crystallographic sites, highly mobile energy transfer mechanisms must play an important role in the radiolytic decomposition of ammonium perchlorate. Most likely, the transfer agents are electrons, holes, excitons, or possibly protons.

Pseudo-stable solids, a group of materials that includes explosives and propellents, almost always decompose when heated (ref.1,2). Also many pseudo-stable materials decompose when exposed to radiation. The decomposition occurs at "etch-pit-like" sites in certain areas of the surface and along lines associated with twins or slip systems(ref,3). The "classical" theoretical treatments on decomposition(ref.1,2) assume that the process starts at unspecified sites on both the surface and interior of the crystals. Recent measurements show that the initial decomposition actually occurs on the surface where dislocations emerge (ref 3-8). In particular, the decomposition of ammonium perchlorate originates at isolated sites and in lines along well-defined crystallographic directions associated with slip systems. As the decomposition proceeds the reaction zone, or interface, spreads across the crystal surface and then proceeds into the interior. (refs. 7,8).

The thermal decomposition kinetics of ammonium perchlorate can be greatly modified by exposing the crystals to irradiation prior to heating (refs. 9-11). The data obtained with irradiated material, analyzed by applying Avrami-Erofeev kinetics (e.g., see ref. 2), indicates that the concentration of decomposition nuclei and/or the growth rate of individual nuclei is greatly increased. Also, this material can be decomposed by exposure to radiation. However, radiolysis effects are not obvious until the crystals are exposed to at least 10^6 rad.

The investigations described above suggest that the radiation-induced decomposition of

* Research performed primarily at Brookhaven National Laboratory and supported by Picatinny Arsenal and the U. S. Atomic Energy Commission.

**Guest Scientist at Brookhaven National Laboratory, present address: Physics Department, Brookhaven National Laboratory, Upton, New York, 11973.

ammonium perchlorate should be susceptible to investigation by transmission and scanning electron microscope techniques. Most importantly, they suggest that such a study would reveal facets of the decomposition process which would be useful for evaluating the performance of propellents containing ammonium perchlorate after exposure to relatively small total doses imparted at low dose rates. Such irradiation conditions apply to propellents used in satellites which remain in orbit for long periods, and deep-space probes which are exposed to a variety of radiations from Van Allen belts, cosmic rays, solar activity, and in particular from on-board radioactivity containing power sources.

The results described below show that numerous features of the radiation-induced decomposition are revealed by electron microscope techniques. In most respects the processes observed are similar to those produced by thermal decomposition. However, in some respects the radiation-induced decomposition is quite different.

EXPERIMENTAL

Large, approximately 5 x 3 x 3 cm., single crystals of ammonium perchlorate were grown on seeds suspended in a slowly cooled and well-stirred aqueous solution (ref. 7). The crystals were large rectangular parallelepipeds with well-defined {210}, or m, and {001}, or c, faces. They are readily cleaved on the {210} and {001} planes. Measurements were made on the original external surfaces of smaller crystals, approximately 5 x 3 x 3 mm, or interior surfaces exposed by cleaving after irradiation. Handling was minimized to reduce mechanical damage and all samples were kept in desiccators as much as possible.

All transmission-electron microscope (always abbreviated TEM) studies were made with an R.C.A. Model EMU-3D electron microscope operated at 100 kV. Graphite replicas were prepared for all specimens and shadowed at 80° from the normal with germanium oxide. Scanning electron microscope (always abbreviated SEM) studies were made with a Materials Analysis Company, Model 700 instrument operated at 5 kV. Usually the sample surfaces were uniformly coated with a layer, approximately 1000Å thick, of gold-palladium alloy deposited with a device utilizing two filaments and a rotating sample mount.

Gamma-ray irradiations were made in a Co^{60} source at a dose rate of 0.66×10^6 rad/hour. During irradiation the samples were at room temperature, i.e., always less than 30°C, in air and in the dark. X-ray irradiations were made with a tungsten target, beryllium window, tube operated at 50 kV and 20 mA. Without additional filtering the dose rate was 2.45×10^6 rad/hour at the sample surface. When a 1 mm aluminum filter was used the dose rate was 8.0×10^4 rad/hour. When exposed to x rays the samples were in air and in darkness.

The process of obtaining information from transmission-electron microscope (TEM), scanning-electron microscope (SEM), and optical microscope (OM) pictures such as those in this article can be greatly facilitated by using one or more of the following "tricks".

1. To determine if any of the details on the pictures are aligned, or more specifically, if they lie along relatively straight lines, view the pictures at about 70° from the normal and rotate them slowly about the normal.

2. The appearance of many features on certain pictures will change drastically when they are viewed at 20° or 30° from the normal and rotated from 90° to 180°. Often a 180° rotation will cause a feature which originally appears to protrude to subsequently appear as an indentation.

3. To determine if an artifact is above or below the surface of a TEM picture look for specks of dirt. Usually, they appear as black dots which cast pointed unshadowed areas indicating the direction of the impinging shadowing material. Thus, one can determine if a more or less vertical surface has accumulated, or is sheltered from, shadowing material.

RESULTS

In a real sense, the major results are in the pictures and captions contained in Plates 1 thru 5. In order to demonstrate how the radiation-induced effects depend on dose the principal observations will be described, in the order they appear as the dose increases; first for gamma-ray irradiated samples and then for crystals exposed to x rays.

Gamma-ray Irradiated Crystals

1. Unirradiated Crystals: The crystals are water clear and free of inclusions and gross surface defects. Crystals etched with butanol contain approx. $2.7 \pm 2.2 \times 10^5$ pits/cm^2.

2. 10^3 to 10^5 rad: Crystals were examined after irradiations of 10^3, 10^4, and 10^5 rad. by OM, TEM and SEM. They remain water clear and radiation-related effects could not be detected on either the m or c faces. Plate 1(a) was obtained from a crystal exposed to 10^3 rad. but is typical of unirradiated samples and those exposed to 10^4 and 10^5 rad.

3. 10^6 rad: Crystals slightly opaque, i.e., milky. Surface effects were not detected by SEM. However, TEM reveals small, very flat pits on only the m face, Plate 1(b). Plate 1(c) shows a cluster of larger pits which resemble circular craters and are similar to the pits formed during the early stages of thermal decomposition (ref. 7). The pits do not appear to be aligned, i.e., they do not lie in straight lines.

4. 5.0×10^6 rad: The crystals are nearly opaque and appear milky white. Pits could not be detected by OM or SEM. However, circular pits and decoration of growth steps and/or cleavage steps with tiny pits are clearly visible in TEM pictures of only the m face.

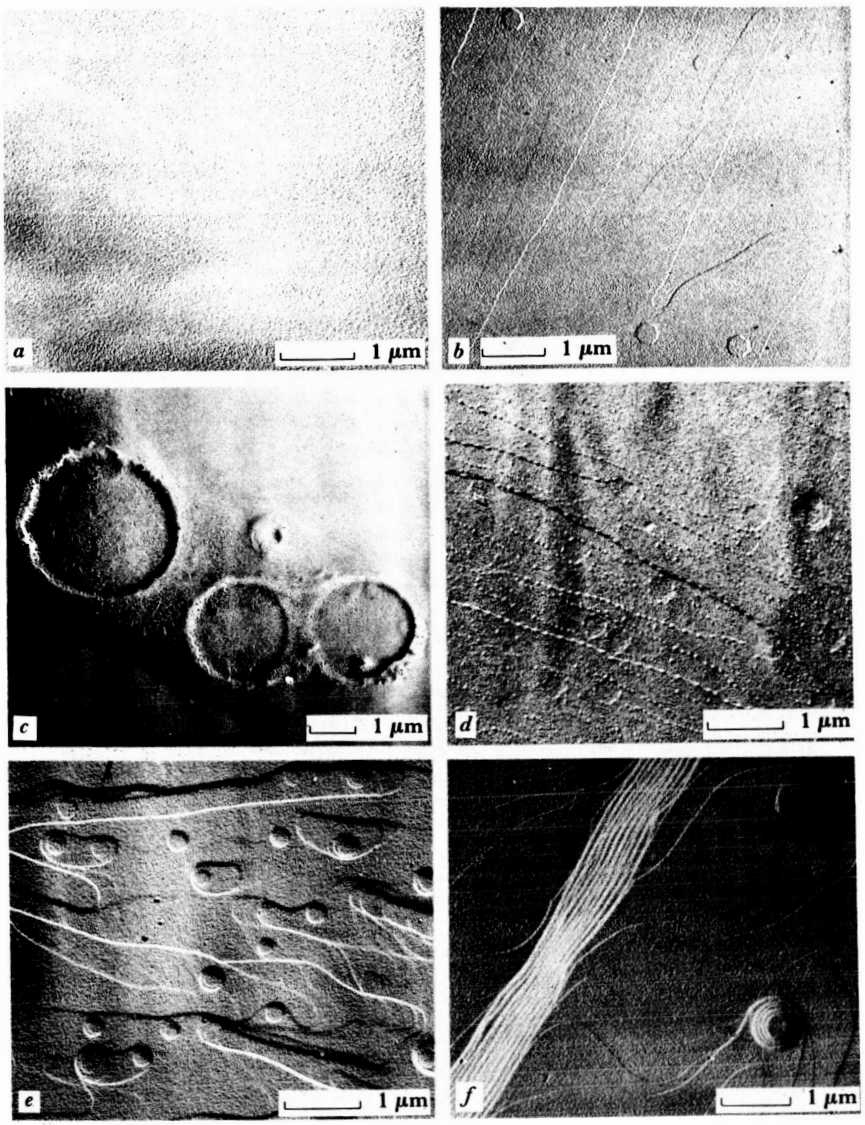

Plate 1

Plate 1. Transmission electron microscope pictures of the m face of ammonium perchlorate crystals after Co^{60} gamma-ray irradiation.

a) 10^3 rad.
b) 10^6 rad.
c) 10^6 rad. A much larger pit similar to the pits in (b).
d) 5.0×10^6 rad. Cleavage step and growth planes "decorated" during radiolytic decomposition. Similar "decoration" is produced by chemical etching.
e) 10^7 rad. At this dose the pits join or overlap to form runnels, similar to chemical etching.
f) 5.0×10^7 rad. An advanced stage of radiation-induced pitting.

5. 10^7 rad: Crystals are completely opaque and resemble white plastic. Radiation-induced decomposition is apparent on both faces, using OM or SEM. However, the TEM pictures show the most detail. Marked pitting and the formation of holes and channels occurs on the m face, Plate 1(e), which resembles the later stages of etching using ethanol.(ref. 8). At this dose decomposition features are also found on the c face. Most likely the lowest dose producing initial c face deterioration lies between 10^6 and 10^7 rad., but the dose was not precisely determined. The c-face pits are best studied by SEM and are quite dense; in some areas they appear random and do not appear to be aligned, Plate 2(a). In other areas the pits are aligned, Plate 2(b), especially along the [210] direction. These aligned pits extend across the surface for varying distances up to 1000 microns. In addition to the small pits described above, some parts of the surface, especially the m face, contain large bubbles and cavities, an example is Plate 2(c).

6. 2.5×10^7 rad: Both faces are extensively pitted. The SEM picture Plate 2(d), shows c-face pits whose concentration is approx. $2.3 \times 10^7/cm^2$. Some regions of the pits resemble those formed by thermal decomposition, in air, at 226°C, Plate 2(e). In addition, the alignment of pits originally observed at lower doses persists at this (and higher) dose rates, Plate 2(f). This should be expected since many of the pits induced by this dose must have been initiated at lower doses and have increased in size.

7. 5.0×10^7 rad: Extensive decomposition is observed on both faces. SEM pictures of the c face, Plate 3(a), show that there are approx. 4.2×10^7 pits/cm^2. Also, there are areas where the pits are aligned in distinct directions. Occasionally the pitted areas "meander" through the crystal; presumably these are grain boundaries, Plate 3(b). Note that the pits in the grain boundaries vary considerably in size both along and across the boundary zone. A TEM picture showing the interior of the c-face pit(s) is Plate 1(f). This shows the circular-layer-like structure, extending to the pit bottom, originally observed on chemically-etched crystals (ref. 8). This is perhaps the most striking observation indicating that the radiation-induced reactions closely parallel the solution chemical reactions. In particular, this similarity suggests that both reactions are ultimately related to the crystal surface-structure, i.e., the topography. At this dose small block-like particles break away from the crystal along fracture lines associated with and/or parallel to well-demarked lines of pits. One example, Plate 3(c), shows rows of pits parallel to the fracture surfaces. As suggested above, many of the details in this picture and especially the block-like character may become much more apparent if this picture is rotated 90° or 180°.

The m-face results, for this dose, are somewhat similar. Pitting occurs both randomly and aligned. The size of the pits vary considerably, some regions contain large holes and other regions contain "decorated" terraces or steps. For example, Plate 3(d) shows decorated steps with pits aligned along the [1$\bar{2}$0] direction. The aligned pits often lie along nearly parallel lines as shown in Plate 3(d). All of the observed alignments appear to lie along crystallographic planes. However, because these directions are close together, it is difficult to establish this beyond question. Occasionally mirror image pit arrangements are observed, Plate 3(d). One would expect to observe this particular arrangement if the pits are associated with dislocations produced by the "Frank-Read" mechanism. Often when crystals fracture along aligned rows of pits it is apparent that the pits, which are observed on the surface, occur at the end of hollow chimney-like tubes which extend into the solid, Plate 3(e). Often these tubes are quite evenly spaced. Plate 3(f) shows pit formation along the [120] direction and large bubbles formed in the interior. These are similar to the large pits shown in Plate 1(c).

X-ray-Irradiated Crystals

The search for x-ray induced radiation damage and/or decomposition in ammonium perchlorate utilized both hard (or filtered) and soft (or unfiltered) x rays. Doses as large as 3.5×10^6 rad, of 50 kV tungsten x rays filtered by 1 mm Al, did not produce any radiation-induced damage when the crystals were examined by OM, TEM, or SEM. However, unfiltered x rays from the same tube produced numerous effects which are described below. Inasmuch as the incident x-ray beam is attenuated as it penetrates into the crystal, one can employ a somewhat novel technique to study x-ray induced decomposition vs. dose. Namely, the crystals can be irradiated and cleaved normal to the c face and microscope studies made on both the irradiated and cleaved face.

1.6×10^7 rad: Both the m and c surfaces appear smoky and translucent and have developed cracks which could outline grain boundaries, Plate 4(a). Individual artifacts, e.g., etch pits, were not observed.

3.3×10^7 rad: A milky-white well-defined thin layer of product is formed on the m face. On the c face pits are found in isolated areas, Plate 4(b), and in some areas they are aligned. There are roughly 5×10^6 pits/cm^2 and they vary in size.

5.6×10^7 rad: On the c face the pit density at this dose is $3.5 \times 10^7/cm^2$, Plate 4(c). The pits are circular and fairly uniform in size. Most importantly, this is the lowest dose producing pits on the m face, Plate 4(d). There are approx. 2.1×10^7 circular and uniformly sized m-face pits/cm^2. In some areas on both faces the pits are aligned.

At this dose it is convenient to study the reaction at various distances from the exposed surface, using crystals cleaved parallel to the radiation beam. Place 4(e) shows both an irradiated surface and the perpendicular surface revealed by cleaving. The density of etch pits at various distances from the surface is shown in Fig. 1. Also, shown, is the x-ray intensity as a function of distance from the surface, as determined by interposing

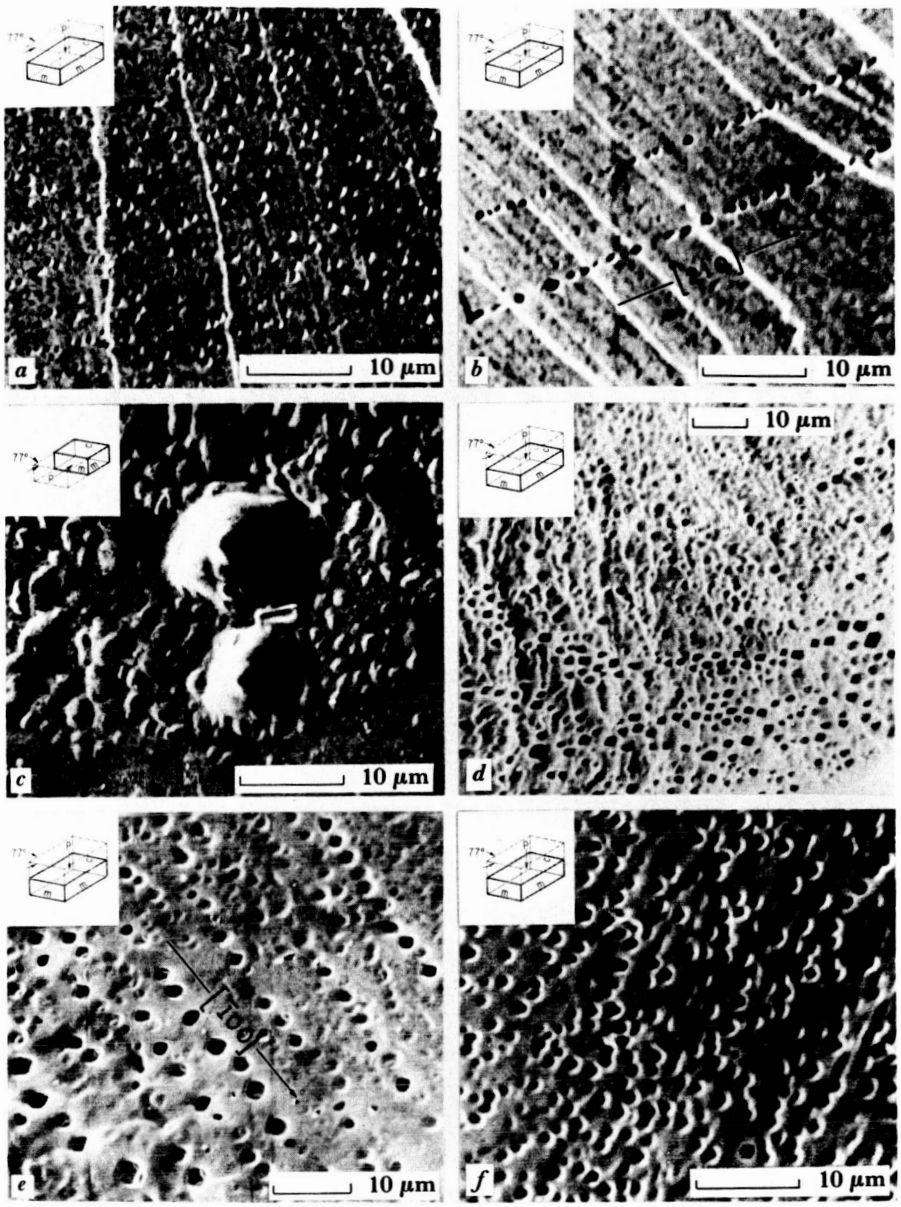

Plate 2.

Plate 2. Scanning electron microscope pictures of ammonium perchlorate surfaces after Co^{60} gamma-ray irradiation.

a) c face, 10^7 rad. Uniformly distributed circular pits.
b) c face, 10^7 rad. Marked alignment of pits in [210] direction.
c) m face, 10^7 rad. In addition to the smaller pits larger "bubbles" are formed.
d) c face, 2.5×10^7 rad. Rectangular shaped holes, resembling those found in thermal decomposition product.
e) c face, 2.5×10^7 rad. Marked alignment of the pits in the $[\bar{1}00]$ direction.
f) c face, 2.5×10^7 rad. Pit density: $2.3 \times 10^6/cm^2$.

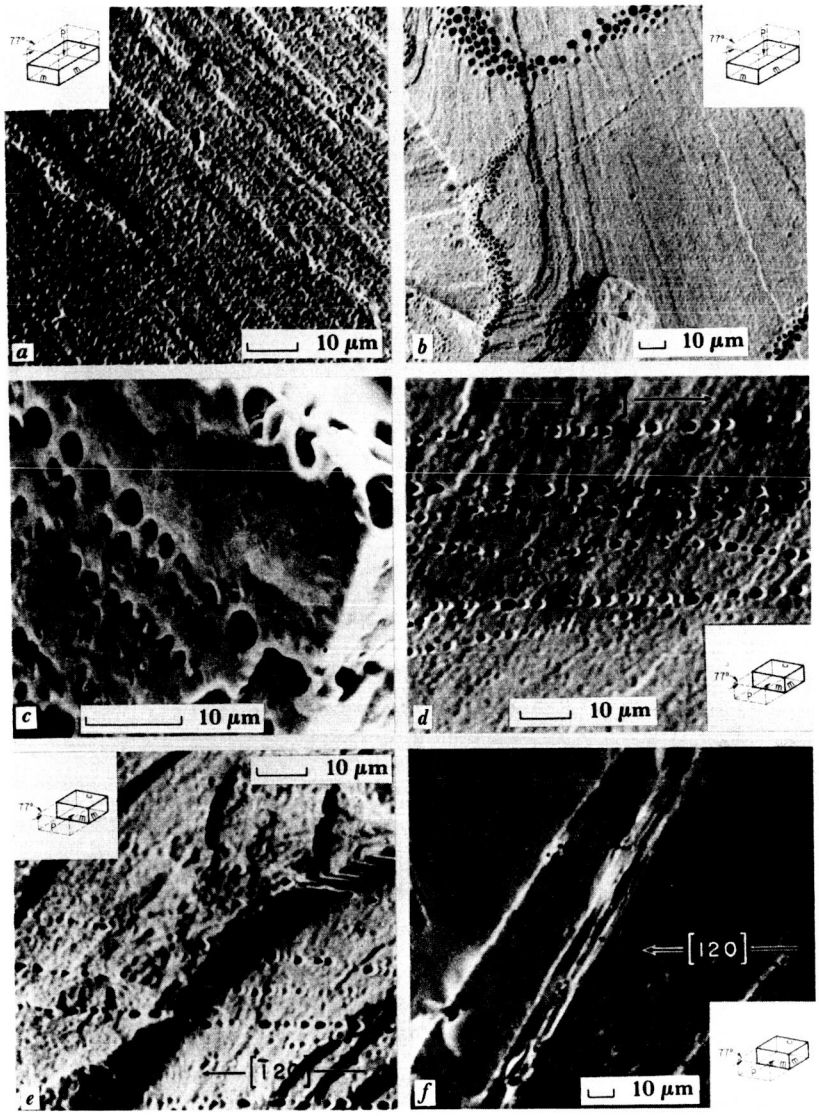

Plate 3

Plate 3. Scanning electron microscopy pictures of ammonium perchlorate surfaces after a 5.0×10^7 rad. Co^{60} gamma-ray irradiation.

a) c face. The pit density is $4.1 \times 10^7/cm^2$.
b) c face. Pitted areas "meandering" through the crystal, presumably along grain boundaries.
c) Block-like particles formed by radiation-induced pits. The crystal has fractured along intersecting pit alignments to produce the block. The block-like character may become more apparent if this picture is rotated 180°.
d) m face. Pits aligned in the $[1\bar{2}0]$ direction.
e) m face. The aligned pits occur at the ends of chimney-like tubes extending into lower layers of the solid.
f) m face. In addition to small well-aligned pits on the $[\bar{1}20]$ direction, the surface contains a larger pit similar to those shown in Plate 1(c).

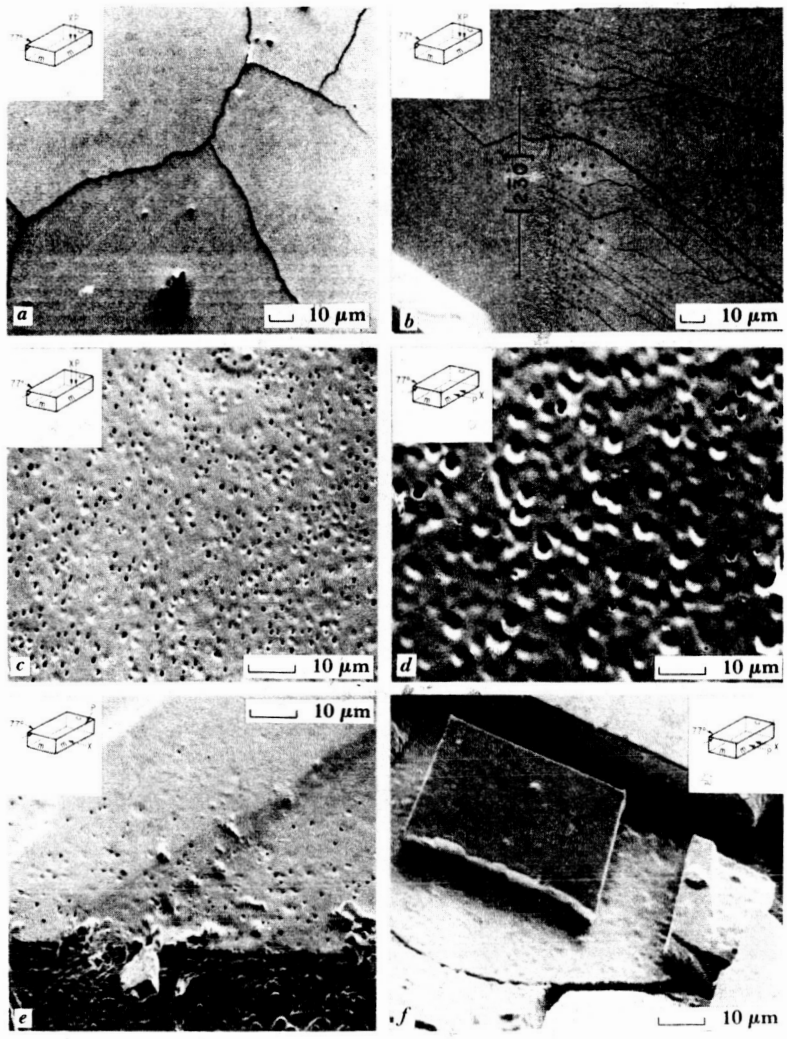

Plate 4

Plate 4. Scanning electron microscope pictures of ammonium perchlorate surfaces after 50 kV, tungsten target, and unfiltered, x-ray irradiation.

a) m face, 1.6 x 10^7 rad. Cracks form on the external surface.
b) c face, 3.2 x 10^7 rad. Initial pit formation aligned in [$\bar{2}$30] direction.
c) c face, 5.2 x 10^7 rad. Pit density: 3.5 x $10^7/cm^2$.
d) m face, 5.2 x 10^7 rad. Shallow and deep pits, density 2.1 x $10^7/cm^2$.
e) c and m face, 5.2 x 10^7 rad. After irradiation the interior m face was exposed by cleaving. Note the pit density at various distances from the irradiated surface. This c face is the same as in (c) above.
f) m face, 7.2 x 10^7 rad. Block-like product on surface with underlying cracking and pit formation.

thin Al absorbers between the x-ray tube and a detector placed at the sample position. Thus, it would appear that the x-ray intensity decreases monotonically from the irradiated surface while, in contrast, the pit density is very low at the front surface, rises abruptly to a prominent maximum, and then decreases monotonically. This somewhat surprising result is considered in the discussion section.

7.5×10^7 rad: This dose causes the surface to break up into blocks similar to those formed during gamma-ray irradiation, Plate 4(f). Also, reaction product occurs on the fracture surfaces below the loose blocks. Almost all of the external surface is covered with pits. Often the pits are markedly aligned, particularly along the [$\bar{1}$25], [350], and [241] directions on the m face, Plate 5(a).

Radiolytic Decomposition of Strained Crystals

Straining crystals prior to thermal decomposition or chemical etching produced effects which could be correlated to dislocations and related effects (refs. 7,8). Immediately below, it will be demonstrated that similar strain-related effects are observed with radiolytically decomposed ammonium perchlorate crystals. A really detailed presentation of the available data on the radiolysis of strained crystals would include observations at a variety of different doses. However, to be brief, only data obtained at one dose level, namely, 5.1×10^7 rad will be described in this paper. First, crystals compressed by squeezing the m faces prior to x-ray exposure develop broad bands of pits on the c face which lie along [120] directions, Plate 5(b). These directions are parallel to, or lie along the intersection of, prominent slip systems. Second, other areas on the same surface contain individual etch pits aligned along crystal directions previously associated with slip systems. For example, Plate 5(c) shows pits aligned along [120] and several other directions. Third, strained crystals fracture into blocks whose sides usually are low index crystal planes, Plate 5(d). The blocks separate from the original crystal along planes parallel to the original surface. Furthermore, the parallel fracture planes contain numerous etch pits similar to those formed on the original surface.

X-ray irradiation produces a high degree of strain on the crystal. Apart from the extensive cracking and block formation, pronounced curvature on large 10 x 6 x 0.5 mm m-face samples develops during an x-ray dose of 1.6×10^7 rad. Also, pronounced curvature occurs along the b axis of c-face crystals having similar dimensions and for the same x-ray dose.

DISCUSSION AND SUMMARY

The observation on gamma-ray and x-ray induced decomposition of ammonium perchlorate, described above, provides generalizations which can be grouped into two categories. First, there are many radiation effects which are similar to those occurring during thermal decomposition and chemical etching. Second, radiation induces some effects not observed during thermal and chemical treatment. These two categories will be described separately.

Radiation-Induced Effects Similar to Chemical and Thermal Effects

A. An induction period precedes the appearance of the initial decomposition. Specifically, when exposed to heat or radiation an initial heating period must elapse, or the sample must receive a specific dose, before decomposition is observed (ref. 11). For example, if a three-second etch produces well-defined pits a two-second etch may not produce any observable effects.

B. The initial radiation-induced effect, as well as the thermal and chemical effect, is the appearance of small etch pits which are aligned in some, but randomly distributed in other, areas of the same crystal.

C. The characteristics of the etch pits formed by all three stimuli are similar: the pits have roughly the same size; the pit density is comparable, namely, approx. 2-40 x $10^6/cm^2$; and the aligned pits lie in the same crystal directions no matter how produced.

D. A second, or intermediate, decomposition stage is found in all three cases when the decomposition has extended over the entire external crystal surface. Concomitantly, extensive decomposition is observed on macroscopic defects such as cleavage steps, slip systems, etc.

E. The last stage of decomposition produced by etching is characterized by blocks of undissolved crystals separated by fissures. Extensive thermal and radiolytic decomposition produces similar, apparently unaffected, blocks connected at edges or corners to form a "sponge-like" or coral structure containing rectangular voids. This structure is similar to that previously reported by Kraeutle (ref. 12).

F. In all cases decomposition on the c, or (001), face is well developed before the initial etch pits appear on the m, or (210), face. However, the final appearance of both faces is similar, except for differences imposed by the crystal structure.

Radiation-Induced Effects

When ammonium perchlorate crystals are subjected to radiation effects, described below, are observed which do not appear during thermal or chemical decomposition.

A. Crystals subjected to gamma-ray doses of 10^8rad, or larger, effervesce when dissolved in water. A similar effect was observed by Heal (ref. 13) in x-ray irradiated $KClO_4$ crystals.

B. Gamma-ray induced decomposition occurs on sites which are uniformly distributed through the crystals. X-ray induced decomposition occurs on sites thoughout the volume irradiated. In contrast, thermal and chemical decomposition starts on the surface and penetrates inward.

C. Radiation-induced strain causes several different effects. First, some curved surface cracks are formed. Second, appreciable surface cracking occurs along cleavage planes to create numerous regularly shaped blocks. Third, crystals irradiated on one

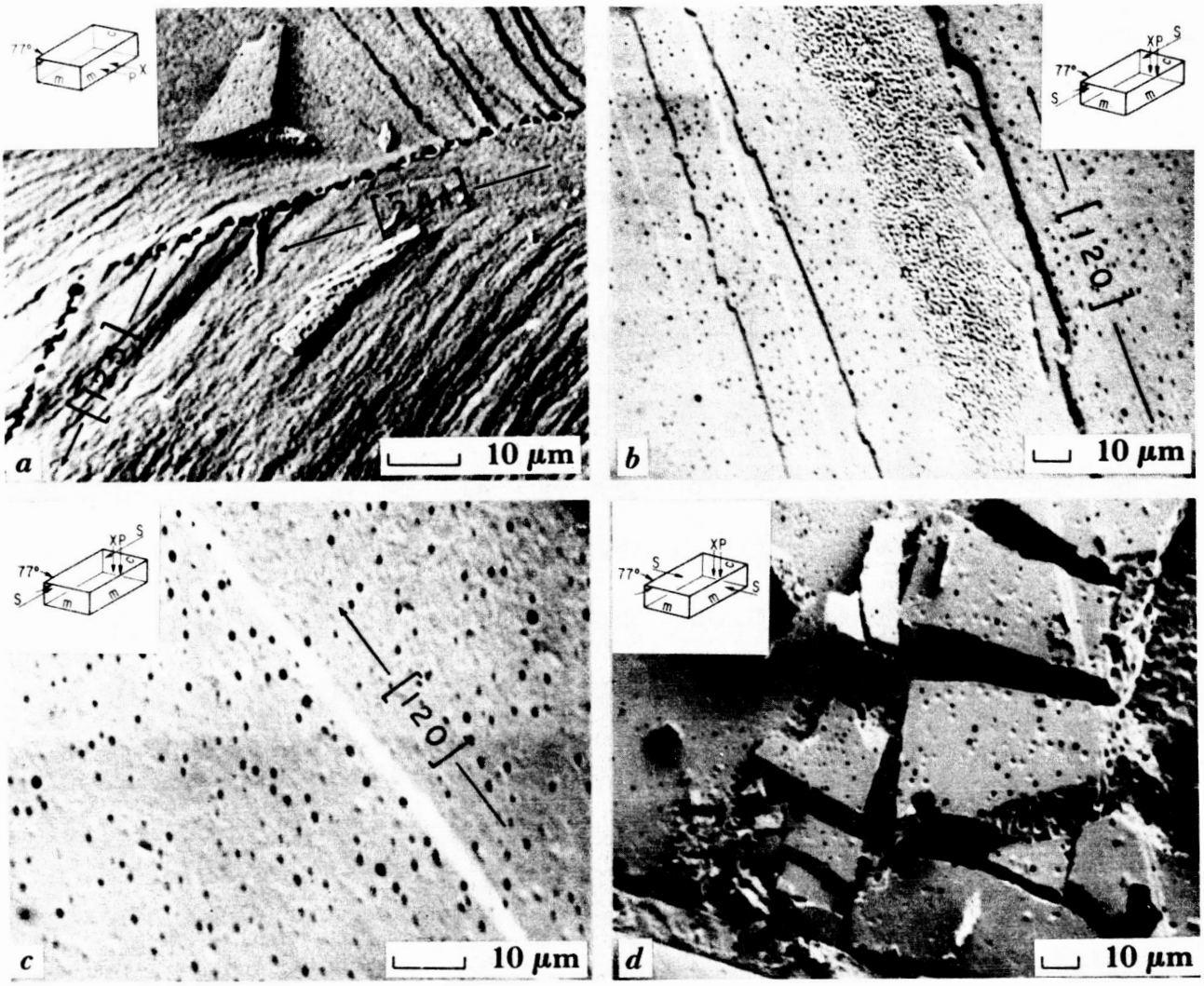

Plate 5

Plate 5. Scanning electron microscope pictures of ammonium perchlorate surface after 50 kV, tungsten target, unfiltered, x-ray irradiation.

a) m face, 7.2 x 10^7 rad. Pit alignment along the [125] and [$\bar{2}$41] directions.
b) c face, 5.1 x 10^7 rad. Region of marked activity in [120] direction. The slip planes were produced by compression on m faces.
c) c face, 5.1 x 10^7 rad. Pits aligned in [120] direction after compressing the m faces.
d) c face, 5.6 x 10^7 rad. Block-like product on strained material. Also, there is sub-surface pitting.

surface with x rays, in which case the irradiated volume is confined to a slab on the surface, develop very pronounced convex curvature.

D. One of the most interesting effects associated with radiation is the localization of the decomposition on certain sites. It has been established that the initial chemical and/or thermal decomposition sites occur where dislocations, slip systems, etc. intersect the crystal surface (ref 7). It must be concluded that the radiation-induced process on the surface also occurs at the same type of site. This particular process may be regarded as radiation-induced etching.

Decomposition in the interior of x-ray or gamma-ray irradiated crystals also occurs at sites which do not appear to be randomly distributed. Furthermore, the decomposition does not appear to be simply related to the ionization density during irradiation. This is illustrated in Fig. 1 which shows that the concentration of radiation-induced etch pits near the surface is considerably less than one would expect if the decomposition site count was proportional to the dose. A similar effect has been observed (not illustrated) on the surface of irradiated crystals which contain cleavage steps and/or similar macroscopic imperfections; namely, appreciable decomposition occurs on the steps, cracks, etc., but the area immediately around them is usually free of decomposition sites.

These observations suggest conclusions which, at this time, must be regarded as tentative. First, inasmuch as external decomposition occurs at the intersection of the dislocations and the surface, it is reasonable to expect that internal decomposition occurs at dislocation-related sites such as intersections, pinning points, etc. Second, internal decomposition occurs, almost certainly, at voids, inclusions, cracks, etc. Third, radiation-induced ionization events must occur uniformly throughout the regions reached by the incident x rays or gamma rays. Since the decomposition occurs only at specific sites, a mechanism must exist for the transfer of energy from the location of each ionization event to the site. The most likely processes are electronic and involves one or more of the usual carriers, i.e., electrons, holes, and/or excitons. This was originally proposed to explain the radiation-induced decomposition of KN_3 and NaN_3 (ref. 3). Fourth, once a decomposition site has become active, it would appear to retard the formation of additional sites in its immediate vicinity, and the area of influence, i.e., the interaction radius, is related to the pit size. In other words, it would seem that the charge and/or energy carriers mentioned above are much more likely to interact with nearby existing sites than to initiate new sites.

These ideas provide one, or several, possible explanations for the observed decomposition site distribution shown in Fig. 2. The external surface can be expected to be an efficient carrier collector, i.e., decomposition site. Thus, carriers produced within a fixed distance from the surface, perhaps a mean-free path, almost certainly cause decomposition at the surface and do not contribute to the formation of interior sites. Further from the surface it is much more likely that the carriers will interact at sites. Thus, the site concentration will be low at the surface, increase toward the interior, and then decrease as the x-ray beam is attenuated.

To emphasize that alternative explanations are possible, one other possibility will be mentioned. Because the samples are prepared by cleaving, the crystals may be more highly strained near the surface than in the interior. Thus, if the decomposition rate is reduced by the strain one would expect the site density to be low near the surface. Clearly, other surface related effects may be expected to reduce the decomposition site concentration near the surface. However, as mentioned above, the decomposition rate is observed to increase in the vicinity of strain produced slip systems.

In summary, the radiolytic decomposition of ammonium perchlorate is similar in many respects to thermal or chemically-induced decomposition. The decomposition processes are related to the defect and dislocation-related properties. However, the effects observed only with radiation suggest that electronic carriers, e.g., electrons, holes, excitons, and possibly protons play an important role in the decomposition process, whether or not the stimulus is chemical, thermal or radiation.

REFERENCES

1. Garner, W. E. Chemistry of the Solid State, Butterworth, London, 1955.
2. Young, D. A. Decomposition of Solids, Pergamon, London, 1966.
3. Dreyfuss, R. W. and Levy, P. W., Proc. Roy. Soc. A, 246, 233 (1958).
4. Thomas, J. M. and Renshaw, G. D., J. Chem. Soc. (A), 2058 (1967).
5. Thomas, J. M. and Renshaw, G. D., J. Chem. Soc. (A), 2749 (1969).
6. Thomas, J. M. Chemistry in Britain, 6, 60 (1970).
7. Herley, P. J., Jacobs, P.W.M. and Levy, P. W., Proc. Roy. Soc. A, 318, 197 (1970).
8. Herley, P. J., Jacobs, P.W.M. and Levy, P. W., J. Chem. Soc. (A) (in press).
9. Herley, P. J. and Levy, P. W. J. Chem. Phys., 49, 1493 (1968).
10. Herley, P. J. and Levy, P. W. J. Chem. Phys., 49, 1500 (1968).
11. Levy, P. W. and Herley, P. J. J. Phys. Chem., 75, 191 (1971).
12. Kraeutle, K. J. J. Phys. Chem., 74, 1350 (1970).
13. Heal, H. G. Canad. J. Chem, 31, 91 (1953), ibid, 31, 1153 (1953).

PLATE AND FIGURE CAPTIONS

The inserts provide the following detailed information on each picture:

m - m face
c - c face
X - direction of incident x rays
S - direction of applied strain
P - the view photographed

The part of the crystal removed by cleaving, usually after irradiation, is indicated by dashed lines.

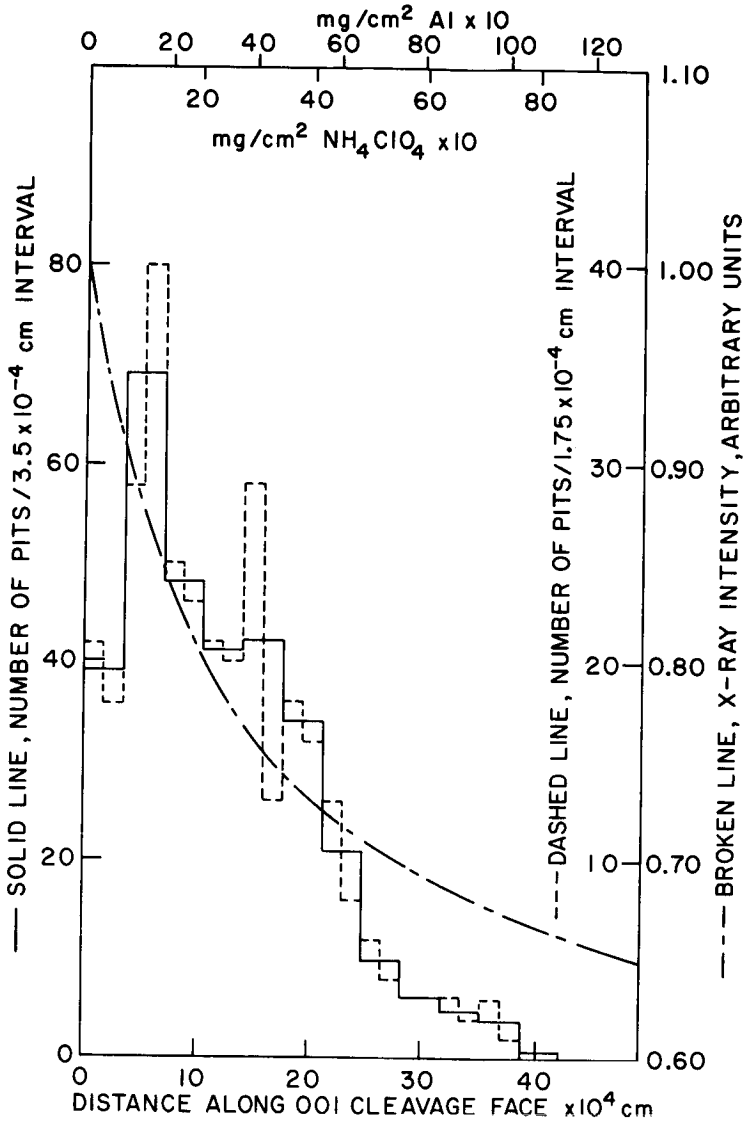

Figure 1

Fig. 1. Histographs showing the distribution of internal decomposition sites normal to the c surface of an ammonium perchlorate crystal irradiated to a total dose of 1.6×10^7 rad. with unfiltered x rays from a tungsten tube operated at 50 kV. Also shown is the x-ray intensity vs. penetration depth computed from x-ray attenuation measurements made with thin Al foils. The site concentration increases inward from the surface to a maximum and then decreases, i.e., near the surface it is not proportional to the deposited energy.

IRRADIATION EFFECTS STUDIES OF NERVA MATERIALS

J. A. DeMastry and T. P. Merrick

Westinghouse Astronuclear Laboratory

Several materials, Beryllium, CuB, BATH (Al-24 v/o TiH_2 - 6 v/o B_4C) and A-286, were irradiated at cryogenic temperatures to neutron fluences between 10^{17} and 10^{19} n/cm^2 ($E > 1.0$ Mev). Tensile properties were determined over a temperature range to evaluate the effects of irradiation on the material properties. The expected radiation damage typical of other materials was observed, a general increase in strength and decrease in ductility. The effects at LN_2 temperature (140°R) are more pronounced since radiation induced defects are not annealed out at 140°R.

Decreases in both strength and ductility of Beryllium are noted at 140°R. Mechanical strength is generally recovered at temperatures as low as 406°R for 10 minute anneals. Thermal conductivity in beryllium is decreased by almost a factor of six at 1×10^{19} n/cm^2 ($E > 1$ Mev). Both Cu 12 v/o B and Cu 24 v/o B exhibit increases in strength and decreases in elongation due to irradiation. BATH shows an increase in mechanical strength after irradiation and testing at 140°R. The A-286 alloy undergoes decreased ultimate strength and increased yield strength under the conditions studied. There were no significant changes in elongation at the temperatures studied. Comparison of test data from different reactors and the statistical techniques employed in this program are also reviewed.

The NERVA (Nuclear Engine for Rocket Vehicle Applications) Program was initiated in 1961 after the Los Alamos Scientific Laboratory had successfully demonstrated the basic principles in nuclear rocketry. The program, under the direction of the Space Nuclear Systems Office of NASA and the AEC, is being performed by the Aerojet Nuclear Systems Company as the prime contractor and Westinghouse Electric Corporation as the principal subcontractor for the nuclear subsystem development.

FIGURE 1

NERVA ENGINE

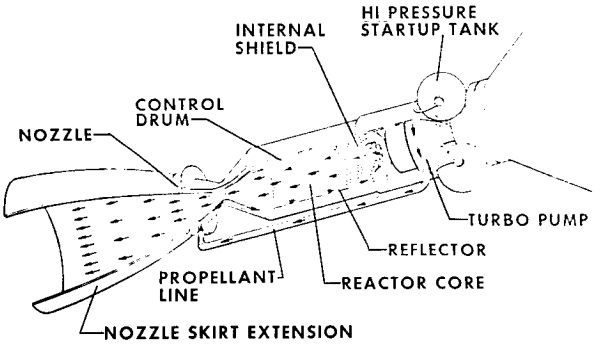

The basic operation of a nuclear rocket system is as follows. A simplified sketch of a nuclear rocket engine attached to a flight tank is shown in Figure 1. The engine delivers approximately 75,000 lbs of thrust at a specific impulse of 825 lb_f-sec/lb_m. The reactor produces 1511Mw of power and the core consists of clusters of graphite fuel elements surrounded by a beryllium reflector. The pump, which is driven by a turbine, increases the pressure of the liquid hydrogen to 1300 psia and provides approximately 91 lb/sec through the pump discharge line to the nozzle

Note:
The Nuclear Engine for Rocket Vehicle Application (NERVA) Program is administered by the Space Nuclear Systems Office, a joint office of the U. S. Atomic Energy Commission and the National Aeronautics and Space Administration. Aerojet Nuclear Systems Company as prime contractor for the engine system and Westinghouse Electric Corporation as subcontractor for the nuclear subsystem, are developing a nuclear propulsion system for space applications.

inlet plenum. The liquid hydrogen then flows through the regeneratively cooled nozzle tubes into the reflector of the reactor. After passing through the reflector and removing the radiation-deposited energy, the hydrogen enters the shield region at the forward end of the dome. The purpose of the shield is to decrease the radiation levels on the engine parts. The hydrogen passes through the reactor-fueled section and is heated to above 4000°R when it enters the thrust chamber formed by the convergent section of the nozzle. The hot hydrogen from the thrust chamber is expanded and accelerated by the nozzle, thereby producing the required thrust.

The nuclear rocket engine derives its primary advantage over chemical rocket engines from its use of the hydrogen as a propellant which results in very high specific impulse. Specific impulse (I_{sp}), which is the ratio of thrust produced to propellant flow rate, is a prime measure of a rocket engine's performance since it relates directly to the amount of propellant which must be carried to perform a mission. Since specific impulse is a function of the inverse of the square root of the molecular weight of the propellant, hydrogen with a molecular weight of two, is an ideal propellant. All chemical rocket engines combine fuel and oxidizer with resulting higher molecular weights. Thus, the nuclear rocket engine developes a specific impulse approximately double that of the best chemical rocket engine.

The high reliability requirements for the NERVA engine dictate an extensive Radiation Effects Program. Each material and component must be evaluated over a range of temperatures, fluences, and other pertinent variables to determine if performance degradation occurs. This has involved irradiation of materials and components to 1×10^{19} n/cm^2 (E > 1 Mev) at liquid nitrogen temperatures and subsequent post irradiation testing at cryogenic temperatures.

Major recent effort has focused on candidate NERVA materials and these data are being reported today. Classification as ductile or brittle is made on the basis of preliminary screening in an environment which duplicates, as nearly as possible, the NERVA application. Applicable information from literature sources and tensile test results are used in determining if the material is to be classified as ductile or brittle for NERVA use. A material is defined as "brittle" if it demonstrates a sensitivity to non-inherent flaws in such a way that it fails below its yield strength. A material is classified as "ductile" if it is insensitive to flaws that may be present. The results of the above discussed screening tests dictate the requirements for additional testing such as fracture toughness, which are currently underway. The ductile material discussed below and the other ductile material utilized in NERVA exhibit increased or relatively unaltered strengths following irradiation. Thus, unirradiated design properties are utilized in determining the stress allowables. The brittle materials are statistically evaluated for changes in fracture strength following irradiation. Testing programs are currently underway for the brittle materials reviewed in this paper and only the beryllium irradiated fracture properties are available for discussion today.

Westinghouse has employed reliability design methodology which departs somewhat from classical design approaches. A probabilistic design approach is employed whereby the material properties used in analysis are those properties identified with a 99% probability at the 95% confidence level, presuming a Gaussian distribution and considering the effects of temperature uncertainties and other potential variables. Thus, experimental statistics are employed and whenever possible, full factorial test matrices are utilized. Ordinarily, the requirement is for eight independent observations in determining the mean value for each level of a primary variable and the variance about that mean is determined with at least 15 degrees of freedom. The data is analyzed using Bartlett's Test for homogeneity of variance and the standard analysis of variance.

In selecting materials for cryogenic applications, the most important criteria are strength, ductility, and toughness. Because of this, the body-centered cubic materials which exhibit a ductile-to-brittle transition temperature

can be eliminated for purely cryogenic application since this transition temperature occurs above liquid-hydrogen temperature for most body-centered cubic materials. The materials generally used at cryogenic temperatures are the face-centered cubic materials such as the aluminum alloys, austentic stainless steel, and nickel-base alloys. In addition, certain hexagonal crystal structured materials such as beryllium, magnesium, and titanium have also been considered. The yield strength, ultimate strength, and notch strength of the face-centered-cubic materials is generally higher at cryogenic temperatures than it is at room temperatures. In most cases, the reduction of area of the fcc material is reduced by lower temperature; the total elongation may be increased, or decreased depending on the materials. Elongation at cryogenic temperature depends on grain size, degree of prior cold work, and temperature.

Theoretically, irradiations at cryogenic temperatures are expected to cause greater changes in mechanical properties than do irradiations at room temperature for the same level of fast fluence. This assumes that some of the vacancies, and interstitials produced by fast neutrons will be annealed out at room temperature; cryogenic irradiations do not produce significant annealing of fast neutron defects.

There is presently limited data available concerning cryogenic nuclear radiation effects in structural materials. Most of the data obtained to date has been developed for use in the NERVA Program. Prior studies have shown that the threshold for observable mechanical property damage is as low as 1×10^{17} n/cm^2 when irradiation temperatures are below 140°R. Since certain structural components of the NERVA system will be exposed to fluence levels of approximately 10^{20} n/cm^2 during the 10 hour lifetime, radiation damage to these components could be a serious problem.

IRRADIATION FACILITIES

Irradiation studies were conducted at the General Dynamics/Fort Worth Ground Test Reactor (GTR) which is a heterogeneous, highly enriched, thermal reactor utilizing water as neutron moderator and reflector, as radiation shielding, and as coolant. Figure 2 is a plan view of the facility and Figure 3 is a cutaway view of the irradiation test cell and the reactor tank. During operation, the

FIGURE 2. GTR RADIATION EFFECTS TESTING FACILITY

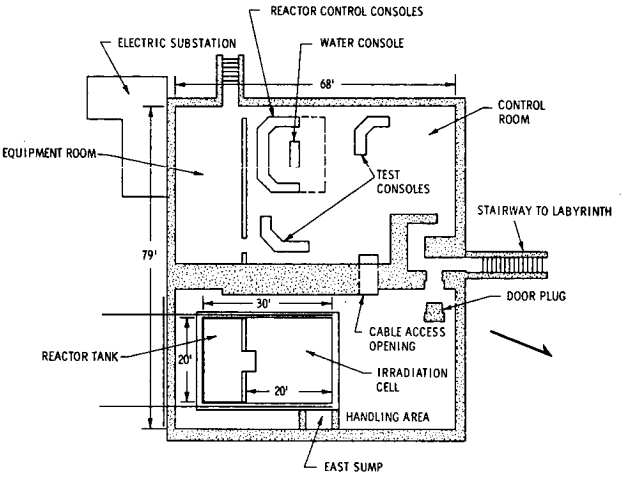

FIGURE 3 GTR TANK AND IRRADIATION TEST CELL - CUTAWAY VIEW

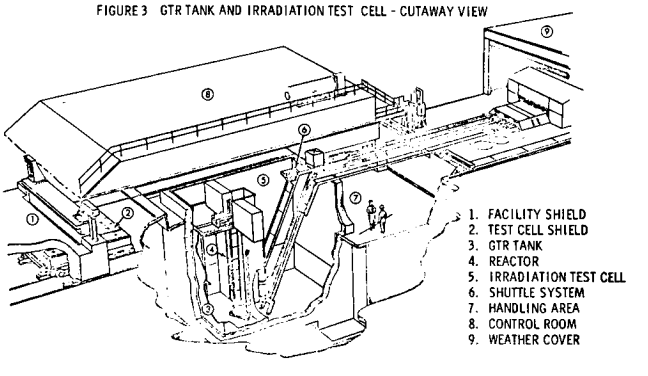

reactor is moved into the closet-like structure built into the north wall of the GTR tank. Specimens to be irradiated are located near the bottom of the test cell at the north, east, or west sides of the closet. Dewars containing the specimens to be irradiated are placed at the closet wall. The dewars are then filled with liquid nitrogen and a continuous level maintained in the dewar during the irradiation.

After irradiation, the dewars are removed from the test chamber to the General Dynamics/Fort Worth hot cells for post-irradiation examination and mechanical property studies. The liquid nitrogen level is maintained throughout transfer and storage. Specimens are never allowed to warm above liquid nitrogen temperature since such a warming would result in loss of damage due to annealing. The actual temperature of the specimens has been verified by locating thermocouples on selected specimens and monitoring the temperature throughout the irradiation, transfer, and storage phases.

Some data will also be discussed which are based on irradiation of beryllium thermal conductivity specimens in the Bulk Shielding Reactor (BSR), Oak Ridge National Laboratory (ORNL) at 200°R. Figure 4 depicts the lower end of the thermal conductivity test capsule whereby "in situ" measurements of thermal conductivity and electrical resistivity were performed. This has been intercalibrated with ORNL laboratory systems and good agreement observed.

The use of two test reactors described above, as well as the NASA Plum Brook Reactor at Lewis Research Center presents some interesting analytical problems. There are significant spectral differences between the NERVA reactor which is epithermal and these thermal water-moderated test reactors. For example, Jenkins and Williams at ORNL compared the differential flux spectra for the BSR and the NERVA radial leakage spectrum as shown in Figure 5 (normalized for E>1 Mev). As a result, a correlation coefficient (based solely on beryllium displacement calculations) was developed. These results indicate that the reflector leakage spectrum is 1.4 times more damaging than the BSR position utilized if fluence is quoted for E > 1.0 Mev.

FIGURE 4.
ILLUSTRATION OF THE LOWER END OF THE THERMAL CONDUCTIVITY-TEST CAPSULE FOR THE BULK SHIELDING REACTOR LIQUID NITROGEN-COOLED CRYOSTAT. THE SAMPLE IS 2" LONG.

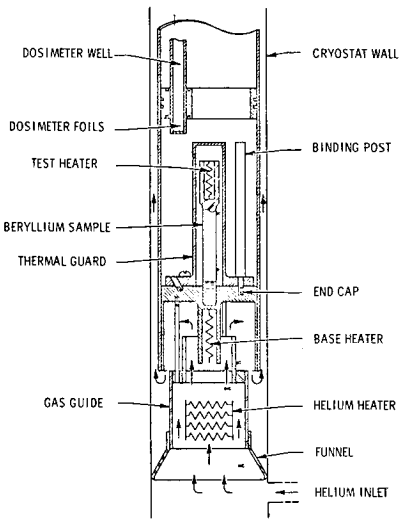

Westinghouse has performed similar machine and hand calculations for other materials and other reactors. The results indicate that a correction factor of from 1-3 is required in comparing a thermal-water-moderated reactor with NERVA.

POST IRRADIATION TESTING

Tensile tests were performed with a Model TT-D split-console Instron Tensile Test Machine having a variable-range load capacity of 20,000 lbs. Cryogenic testing was conducted in a cryostat constructed of urethane foam material; its inner and outer surfaces were coated with successive layers of siliconic adhesive and fiberglass cloth. All fracture mechanics tests were performed in the same facilities. Specimens were stored in LN_2 to prevent warming of specimens after irradiation with accompanying annealing of irradiation effects.

Beryllium thermal conductivity measurements reported today were allmade "in situ" in the apparatus described above. The results are as follows.

FIGURE 5. COMPARISON OF DIFFERENTIAL NEUTRON FLUX SPECTRUM AT BSR EXPERIMENTAL LOCATION WITH THE NSS RADIAL LEAKAGE SPECTRUM

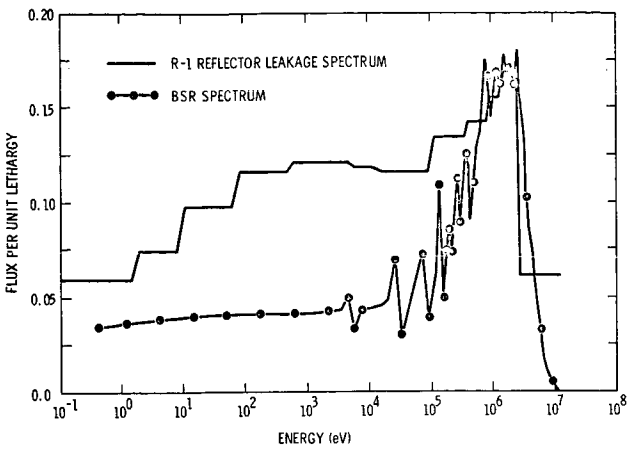

TEST RESULTS

Results of beryllium irradiation in liquid nitrogen and post-irradiation tensile testing are shown in Tables 1 and 2. Specimens tested at 140 and 273°R show decreased elongation and ultimate tensile strength. All specimens fractured prior to yielding. Almost complete recovery of mechanical properties is noted for specimens tested at 540°R for both transverse and longitudinal specimens. Recovery is also noted in material irradiated to 4.3×10^{17} n/cm^2 and tested at 406°R. Figure 7 depicts typical changes in UTS as a function of fluence at both 140°R and 540°R.

Table 3 shows the results of annealing studies to establish the time required for recovery of mechanical properties. Recovery of ultimate strength is noted at temperatures as low as 273°R after 1000 minutes. Complete recovery of ultimate strength is observed at 406°R and above for annealing times as low as 10 minutes. Ductility measured as elongation is not recovered until temperatures as high as 674°R are reached. Even at this temperature, prior irradiation ductility is not fully recovered.

TABLE 1

TENSILE TEST DATA FOR BERYLLIUM IRRADIATED AT LN_2 (140°R) TEMPERATURE TRANSVERSE DIRECTION

Test Temperature °R	Neutron Fluence 10^{18} n/cm^2 (E>1.0 Mev)	Neutron Fluence 10^{18} n/cm^2 (E<0.48 ev)	0.2% Offset Yield Strength KSI	Ultimate Tensile Strength KSI	Elongation %
140	0	0	38.2	52.3	1.51
	.46	.16	---	27.9	0
	2.4	.13	---	48.0	0
	7.5	.35	---	33.5	0
273	0	0	31.2	46.2	2.11
	.45	.16	---	50.0	0
	2.5	.13	---	48.6	0
	7.8	.35	---	49.1	0
406	0	0	32.3	49.2	2.52
	.43	.16	45.0	56.0	1.80
	2.5	.13	0	50.4	0
	8.3	.36	0	58.9	0
540	0	0	31.1	44.5	2.39
	.45	.16	30.6	43.7	2.27
	2.4	.13	34.4	40.2	1.05
	7.6	.35	33.1	45.0	2.12

TABLE 2

TENSILE TEST DATA FOR BERYLLIUM IRRADIATED AT LN_2 (140°R) TEMPERATURE LONGITUDINAL DIRECTION

Temperature °R	Neutron Fluence 10^{18} n/cm^2 (E>1.0 Mev)	Neutron Fluence 10^{18} n/cm^2 (E<0.48 ev)	0.2% Offset Yield Strength KSI	Ultimate Tensile Strength KSI	Elongation %
140	0	0	33.7	37.8	0.53
	.46	.16	---	32.5	0
	2.4	.13	---	25.0	0
	7.7	.35	---	29	0
273	0	0	38.1	48.4	1.4
	2.4	.13	---	26.1	0
	7.8	.35	---	35.7	0
406	0	0	36.0	47.6	1.41
	.44	.16	43.8	49.9	0.73
	2.5	.13	---	50.5	0
	8.1	.36	---	45.2	0
540	0	0	33.1	42.1	1.45
	.43	.16	33.5	42.5	1.43
	2.4	.13	35.3	42.2	1.02
	7.5	.35	36.0	40.0	0.52

TABLE 3

EFFECTS OF ANNEALING ON BERYLLIUM IRRADIATION AT LN_2 (140°R) TEMPERATURE ALL TESTS CONDUCTED AT 140°R

Annealing Time (min)	Annealing Temperature °R	Neutron Fluence 10^{18} n/cm^2 (E>1.0 Mev)	0.2% Offset Yield Strength KSI	Ultimate Tensile Strength KSI	Elongation %
0	140	7.1	--- ---	31.8	0
10	273	7.7	---	19.7	0
100	273	7.9	---	24.5	0
1000	273	7.4	---	30.1	0
10	406	8.4	---	31.9	0
100	406	7.8	---	26.2	0
1000	406	7.6	---	44.8	0
10	540	7.6	---	32.5	0
100	540	8.1	---	31.6	0
1000	540	7.6	---	33.1	0
10	674	7.6	39.2	39.3	.01
100	674	7.7	---	35.2	0
1000	674	7.7	39.3	41.6	0.3

Figure 6 depicts the observed beryllium fracture toughness as a function of temperature for specimens irradiated to 3×10^{18} n/cm^2 and 8.5×10^{18} n/cm^2 (E > 1 Mev). As can be seen, irradiation significantly reduces the fracture toughness of beryllium. At 8.5×10^{18} n/cm^2, the fracture toughness (K_{1C}) is reduced by 30% at 140°R.

Other studies have indicated that the above damage can be annealed out by appropriate heat treatments. No annealing has been observed below 310°R and virtually complete annealing of damage is observed at 535°R.

The next figure (Figure 8) depicts the decrease in thermal conductivity in beryllium as a function of fluence. At 1×10^{19} n/cm^2 (E > 1 Mev), its thermal conductivity is reduced by almost a factor of six. This is completely recoverable at 400-500°R.

TABLE 4
TENSILE TEST DATA (1) for Cu 12 v/o B ALLOY IRRADIATED AT LN_2 (140°R) TEMPERATURE

Test Temperature °R	Neutron Fluence 1×10^{18} n/cm^2 (E>1.0 Mev)	(E<.48 ev)	Orientation	0.2 % Offset Yield Strength KSI	Ultimate Tensile Strength KSI	Elongation %
140	0	0	L	11.5	38.0	30.4
140	0	0	L	11.8	34.1	21.7
140	2.31	0.12	L	46.2	48.8	2.74
140	2.38	0.12	L	48.4	49.3	4.15
540	0	0	L	9.4	24.1	18.4
	2.19	0.12	L	28.8	30.9	8.1
940	0	0	L	6.8	14.7	13.1
940	2.39	0.12	L	18.1	19.3	2.23
1340	0	0	L	3.8	5.6	2.59
1340	2.37	0.12	L	5.5	6.6	3.86

L - Longitudinal
(1) - Instron crosshead speed = 0.02 in/min

FIGURE 7. EFFECTS OF LN_2 (140°R) RADIATION ON BERYLLIUM TENSILE STRENGTH (LONGITUDINAL)

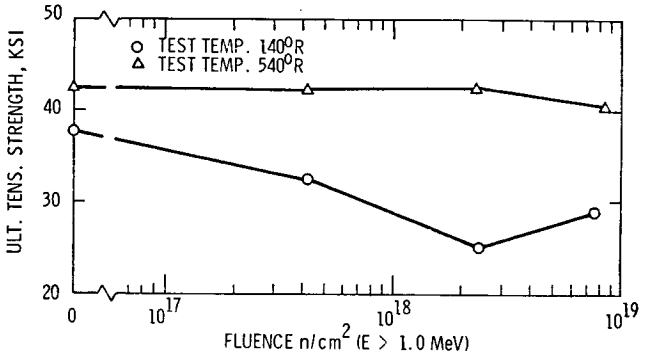

FIGURE 6. EFFECTS OF IRRADIATION ON FRACTURE TOUGHNESS

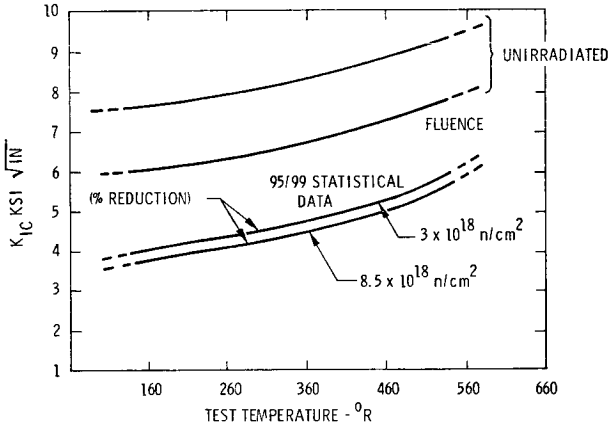

FIGURE 8. EFFECT OF RADIATION ON THERMAL CONDUCTIVITY OF BERYLLIUM

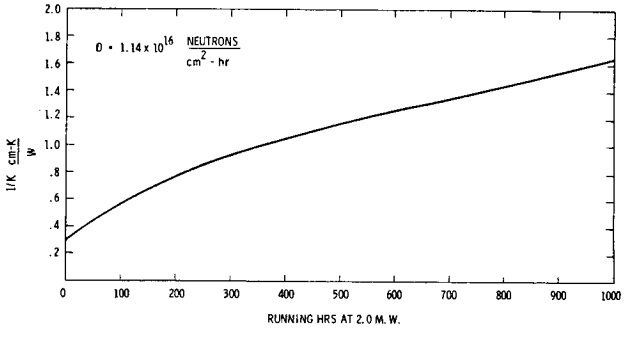

A copper-boron material is being considered for utilization as control drum vane material of the reflector assembly. Varying compositions of this alloy have been considered. Test results for two of these materials, Cu 12 v/o B and Cu 24 v/o B, are shown in Tables 4 and 5. The Cu 12 v/o B alloy exhibits large increases in yield and ultimate strength at temperatures up to 940°R. These strength increases are accompanied by reductions in elongation. The Cu 24 v/o B alloy shows much smaller increases in strength in material tested at 540 and 940°R with decreases in elongation. Material tested at 1340°R showed no effects due to irradiation at 2.36×10^{18} n/cm^2.

TABLE 5
TENSILE TEST DATA [1] for Cu 24 v/o B ALLOY IRRADIATED AT LN_2 (140°R) TEMPERATURE

Test Temperature °R	Neutron Fluence 1×10^{18} n/cm^2 (E> 1.0 Mev)	Neutron Fluence 1×10^{18} n/cm^2 (E> .48 ev)	Orientation	0.2% offset Yield Strength KSI	Ultimate Tensile Strength KSI	Elongation %
140	0	0	L	11.3	27.3	11.8
140	2.29	0.12	L	8.3	14.8	1.79
540	0	0	L	7.2	19.5	2.1
540	2.15	0.12	L	13.3	24.7	0.08
940	0	0	L	8.0	12.5	6.0
940	2.32	0.12	L	13.3	14.1	1.64
1340	0	0	L	3.6	5.5	3.82
1340	2.36	0.12	L	3.4	5.4	4.04

L - Longitudinal
(1) - Instron crosshead speed = 0.02 in/min

The BATH (Al-24 v/o TiH_2 - 6 v/o B_4C) material is to be used as a neutron shield in the NERVA reactor. The results of irradiation at LN_2 (140°R) temperatures and testing between 140 and 1140°R are shown in Table 6. Material tested at 140°R show increases in the ultimate strength and slight decreases in elongation. Testing at 340 to 1140°R produces very little change in the mechanical strength of BATH. While increasing the fluence levels at any test temperature above 140°R does not have a significant effect on the strength, it does produce changes in elongation. No pattern for this change can be noted. Both increases and decreases in elongation are noted. These changes are generally small and probably of no practical significance.

TABLE 6
TENSILE TEST DATA FOR BATH (Al-24 v/o Ti H_2-6 v/o B_4C) IRRADIATED AT LN_2 TEMPERATURE

Test Temperature °R	Neutron Fluence 10^{18} n/cm^2 (E>1 Mev)	0.2% Offset Yield Stress (KSI)	Ultimate Tensile Strength KSI	Elongation %
140	0	15.9	22.9	1.4
	2.78	-	28.9	.36
	3.4	-	34.4	.84
340	0	13.8	20.0	3.2
	2.81	20.5	22.1	1.3
	3.31	-	20.78	.72
540	0	11.9	18.8	4.89
	2.68	12.8	18.9	5.75
	3.45	12.8	18.5	2.86
740	0	11.3	14.7	7.39
	2.87	11.7	14.8	8.94
	3.21	11.4	14.8	6.55
940	0	8.9	10.6	5.36
	2.92	8.8	10.6	6.36
	3.14	9.0	10.2	8.24
1140	0	6.1	6.9	5.0
	3.04	6.1	7.1	4.3

TABLE 7
TENSILE TEST DATA FOR A-286 ALLOY IRRADIATED AT LN_2 (140°R) TEMPERATURE

Test Temperature °R	Neutron Fluence 10^{18} n/cm^2 (E > 1.0 Mev)	0.2% Offset Yield Strength KSI	Ultimate Tensile Strength KSI	Elongation %
140	0	112.0	197.3	43.3
	0.41	123.5	198.2	40.3
	2.56	147.8	201.7	37.4
	10.5	177.5	200.6	34.9
340	0	101.2	163.2	26.1
	0.41	112.6	163.7	29.6
	2.56	132.5	159.3	28.0
	10.5	139.4	153.1	22.5
540	0	96.7	152.1	26.0
	0.41	106.5	150.0	28.3
	2.56	123.3	147.0	27.0
	10.4	120.0	136.5	22.0
740	0	90.1	144.9	23.7
	0.41	101.0	143.3	24.1
	2.56	112.4	141.3	20.6
	10.4	115.2	131.2	18.5
940	0	81.2	138.5	18.9
	0.41	82.0	140.2	23.0
	2.56	88.9	132.9	21.7
	10.1	100.6	131.4	16.7

The A-286 stainless steel alloy is a prime support material for the NERVA reactor and these data are tabulated in Table 7. Irradiation at 140°R with testing from 140 to 940°R produces only slight changes in the properties of A-286 as can be seen in Figure 9. Generally, increases in the yield strength due to irradiation are noted. Increases in yield strength due to decreasing temperatures are also observable. Irradiation also causes reductions in ultimate tensile strength at most test temperatures. Slight decreases in elongation due to irradiation are noted. The reductions in elongation are not large enough to be considered a serious problem.

CONCLUSIONS

1. Irradiation to about 8.0×10^{18} n/cm^2 (E> 1.0 Mev) produces decreases in both strength and ductility of Beryllium at 140 and 273°R. The mechanical strength is generally recovered at 406°R for anneals as short as 10 minutes.
2. Beryllium thermal conductivity, at 200°R, is reduced by almost a factor of six at 1×10^{19} n/cm^2 (E>1Mev) and this is equivalent to approximately 7×10^{18} n/cm^2 (E>1 Mev) in the NERVA reflector.
3. Both Cu 12 v/o and Cu 24 v/o B show increases in strength and decreases in elongation due to irradiation.
4. BATH material shows increases in mechanical strength after irradiation and testing at 140°R. Reductions in elongation are noted. Irradiation at 140°R with testing at 340°R and above produces little effects on the properties of BATH up to fluence levels of about 3.4×10^{18} n/cm^2 (E> 1.0 Mev).
5. The A-286 alloy exhibits increased yield strength and generally decreased ultimate strength over the temperature range studied. Changes in elongation were insignificant.

FIGURE 9. EFFECT OF LN_2 (140°R) RADIATION ON A-286 YIELD STRENGTH

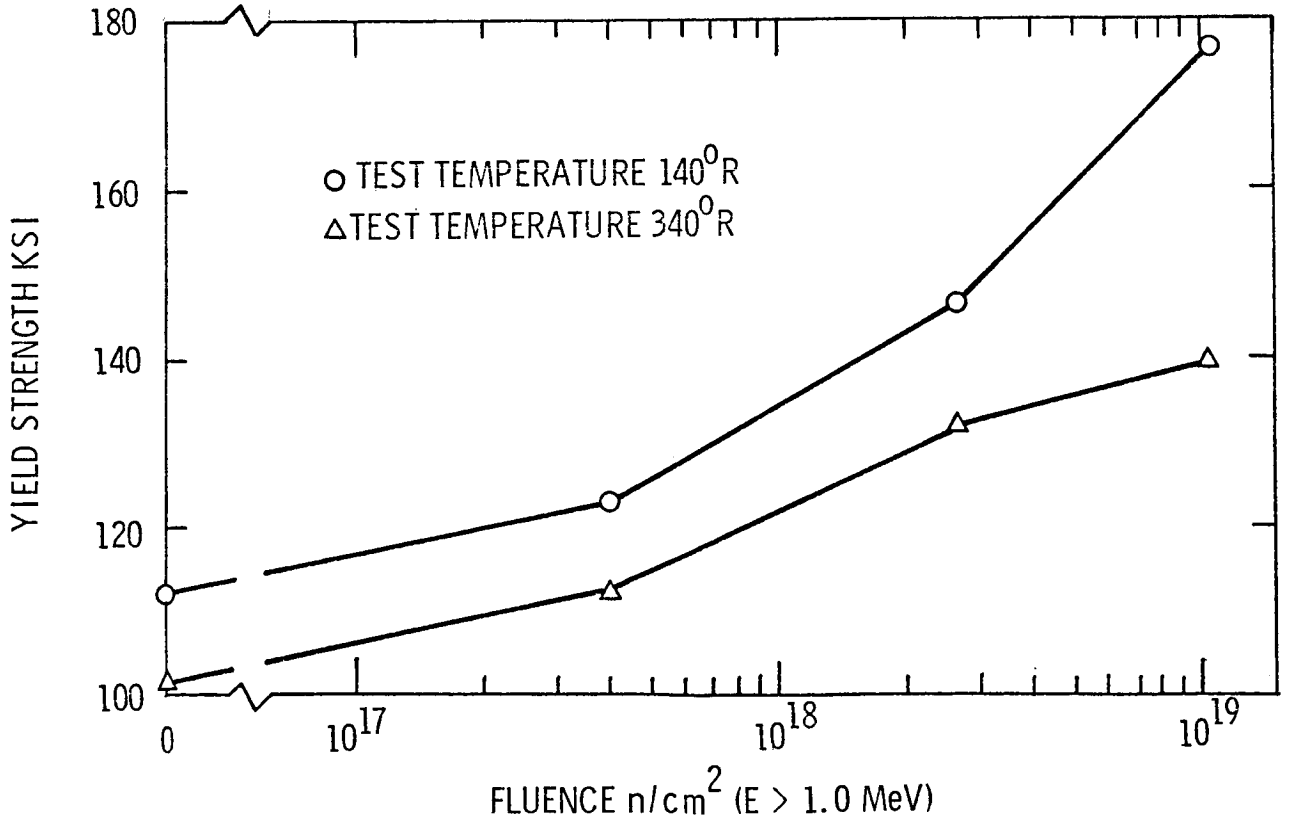

EFFECT OF CRYOGENIC IRRADIATION ON NERVA STRUCTURAL ALLOYS

C. E. Dixon[1], M. J. Davidson[2], and C. W. Funk[3]

ABSTRACT*

Several alloys (Hastelloy X, AISI 347, A-286 bolts, Inconel 718, Al 7039-T63 and Ti-5Al-2.5Sn ELI) were irradiated in liquid nitrogen (140°R) to neutron fluences between 10^{17} and 10^{19} nvt (E > 1.0 Mev). After irradiation, tensile properties were obtained in liquid nitrogen without permitting any warmup except for some specimens which were annealed at 540°R. The usual trend of radiation damage typical for materials irradiated at and above room temperature was observed; e.g., increase in strength and decrease in ductility. However, the damage at 140°R was greater because this temperature prevented the annealing of radiation-induced defects which occurs above 140°R. The more significant conclusions from these tests are:

(1) The threshold for measurable mechanical property damage in these materials at 140°R is between 10^{16} and 10^{17} nvt (E > 1.0 Mev).

(2) Room temperature annealing of tensile properties was performed prior to testing some of the alloys. Al 7039-T63 recovers about half the damage incurred at the highest exposure while the other alloys recover a smaller amount. Previous similar studies of Al 2219 showed almost complete recovery after annealing at room temperature. Aluminum components in the NERVA engine will be at temperatures above 140°R during its coast periods. Additional postradiation annealing studies are required to establish design properties after thermal cycling to various temperatures.

The high reliability requirements for the NERVA engine make it imperative that candidate material properties be determined in the particular temperature, nuclear radiation or other possible detrimental environment to which the material may be subjected. This test involves the effects of fast neutron fluences up to 10^{19} nvt on the embrittlement of several alloys (Hastelloy X, AISI 347, A-286 bolts, Inconel 718, Al 7039-T63, and Ti-5Al-2.5Sn ELI). Previous investigations in this program have shown that the nuclear radiation exposure of structural materials in the NERVA engine can impose limitations on design if ductility losses are severe. Quantitative data were obtained on engineering alloys irradiated at cryogenic temperatures at higher fast neutron fluences than in previous tests. The alloys were irradiated** in liquid nitrogen (140°R) and tensile tested at 140°R without an intermediate warmup except for selected specimens which were annealed at 540°R. The test data for each alloy are presented in tables and engineering

*The Nuclear Engine for Rocket Vehicle Application Program (NERVA) is administered by the Space Nuclear Systems Office (SNSO), a joint office of the U.S. Atomic Energy Commission and the National Aeronautics and Space Administration. Aerojet Nuclear Systems Company, as prime contractor for the engine system, and Westinghouse Electric Corporation, as subcontractor for the nuclear subsystem, are developing a nuclear propulsion system for space application.

(1) Supervisor, Materials and Processes
(2) Supervisor, Radiation Effects
(3) Manager, Materials and Processes

**This irradiation test was performed at the Ground Test Reactor of the Nuclear Aerospace Research Facility, General Dynamics, Fort Worth. These results are part of a larger test designated GTR-20C.

judgements are made of whether the design classification for these materials should be "brittle" or "ductile"* in the anticipated NERVA nuclear environment.

Hastelloy X (As-Brazed) Tensile Data (Table 1)

This material was a plate forging made from a low aluminum (0.012%) heat. It was subjected to three thermal cycles to about 1950°F and slow cooled simulating the NERVA nozzle processing heat treatment. The maximum exposure of 5×10^{18} nvt > 1.0 Mev is lower than the 1×10^{19} nvt anticipated for NERVA 10-hour service. However, the data shown in Table 1 indicate that extrapolation of properties to 10^{19} nvt can be made with confidence. The elongation decrease from 28% to 14% is significant, but the material is still considered ductile at 140°R after 10^{19} nvt > 1.0 Mev neutron fluence. The relatively large (104%) increase in tensile yield strength suggests this is a good material to use for more basic studies of radiation damage. It has been chosen for studies which will make quantitative investigations of the effects of irradiation temperature and irradiation atmosphere (GH_2 versus LN_2). The annealing studies have shown less damage recovery at 540°R than was anticipated from earlier studies made on materials irradiated to 1×10^{18} nvt.

AISI 347 Forging (As-Brazed) Tensile Data (Table 2)

This material was obtained from the NERVA technology nozzle S/N 033. The manufacturing processes included three thermal cycles to about 1800°F followed by a slow cool which slightly degraded the ductility at cryogenic temperatures; however, the unirradiated elongation of 52% is excellent, and it is considered a tough, ductile material. Its response to cryogenic irradiation is the most unusual in this group of alloys. After a fluence of 4.8×10^{18} nvt > 1.0 Mev, the tensile yield stress increased from 45 to 122 ksi (170%), but the elongation, area reduction and ultimate strength were not significantly changed. This alloy undergoes a strain-induced martensitic transformation during cryogenic tensile testing. The major part of the strain hardening is attributed to this phase transformation which appears to be insensitive to prior irradiation. AISI 347 is judged to remain ductile at cryogenic temperatures after a neutron fluence of 10^{19} nvt > 1.0 Mev.

A286 Technology Bolts Tensile Data (Table 3)

These bolts designed for the NERVA technology engines were cold-reduced and aged by proprietary processes to have a room temperature minimum yield and ultimate strengths of 180 and 200 ksi, respectively. The average elongation decreased from 16 to 10 percent after a neutron fluence of 6.5×10^{18} nvt; however, the area reduction remained unchanged at about 35%. This excellent area reduction implies good fracture toughness. These bolts are ductile at 140°R after a neutron fluence of 1×10^{19} nvt > 1.0 Mev.

Inconel 718 Tensile Data (Table 4)

These specimens from a large pancake forging after irradiation at 140°R to 4.4×10^{18} nvt > 1.0 Mev decreased their 140°R elongation from 23 to 12%, however, the area reduction did not decrease, remaining at about 30%. Inconel 718 is ductile in this cryogenic nuclear environment. A greater fraction of the damage annealed out in 100 minutes at 540°R than the other alloys except for aluminum alloy 7039-T63.

Alloy 7039-T63 Tensile Data (Table 5)

This material was obtained from a ring forging which was processed similarly to that anticipated

*The allowable stress for a "brittle" material may be less than the tensile yield strength depending upon the maximum flaw size which could be present and is determined by linear elastic fracture mechanics data and analysis. The allowable stress for a "ductile" material can be greater than the tensile yield strength at points of high stress concentration. A more detailed specification of the "ductile" or "brittle" classification as used here may be found in SNPO-C-1, "NERVA Program Structural Design Requirements".

See Appendix for the guidelines used in this program for establishing tentative ductile-brittle classifications.

for the NERVA pressure vessel. The average elongation at 140°R decreased from 12 to 5% after a neutron fluence of 5.5×10^{18} nvt > 1.0 Mev at 140°R. This material is tentatively classified brittle uder these conditions based on low elongation; however, when fracture toughness data are completed, the judgement of "ductile or brittle" according to SNPO-C-1 can be made with more confidence. After annealing for 10 minutes and longer at 540°R, the elongation damage almost completely recovered, but 50% of the increase in yield strength remained. Previous annealing studies in AA 2219-T6 had shown almost 100% of the radiation damage in all properties annealed out after a 540°R anneal. Thus, it appears that while damage annealing behavior is similar in aluminum alloys, it is not identical and extrapolation between alloy families must be made with caution.

Ti-5Al-2.5Sn ELI Tensile Data (Table 6)

These tensile specimens were fabricated from a large forging (17 in. diameter by 10 in.). The average 140°R elongation decreased from 10 to 4% after a neutron fluence of 4.9×10^{18} nvt > 1.0 Mev. This material is judged to be brittle under these conditions based on low elongation. The NERVA application for this material involves a less severe exposure (1×10^{17} nvt > 1.0 Mev) than the maximum used in this test. For NERVA applications at 10^{17} nvt, this titanium alloy is judged to be ductile. This judgement is supported by preliminary fracture toughness tests which show no decrease in 140°R plane-strain fracture toughness, K_{Ic}, after irradiation to 3×10^{17} nvt.

CONCLUSIONS

1. A neutron fluence of 5×10^{18} nvt > 1.0 Mev at 140°R does not embrittle Hastelloy X, AISI 347 or A286 (cold-worked plus aged bolts) sufficiently to change their design classifications of ductile.

2. The same neutron fluence (5×10^{18} nvt > 1.0 Mev) at 140°R degrades the ductility of Al 7039-T63 and Ti-5Al-2.5Sn enough to require a brittle classification and different design criteria for this neutron fluence at 140°R. A lower neutron fluence of 10^{17} nvt does not degrade the ductility of these two alloys significantly.

3. Annealing experiments at 540°R following irradiation at 140°R show various amounts of improvement in these alloys of the radiation damage to ductility. Al 7039-T63 completely recovers its ductility loss after annealing at 540°R.

TABLE 1

EFFECT OF FAST NEUTRON IRRADIATION
AT 140°R ON THE TENSILE PROPERTIES
OF LOW AL (0.012%) HASTELLOY X (AS-BRAZED)
FORGING AT 140°R

FLUENCE NVT > 1 MEV	ANNEAL TIME AT 540°R MIN.	0.2% YIELD STRENGTH, KSI		ULTIMATE STRENGTH, KSI		ELONGATION CHART, %		AREA REDUCTION, %		NO. SPECIMENS
		AVG	STD DEV	AVG	STD DEV	AVG	STD DEV	AVG	STD DEV	
Control	0	71.2	0.4	135.2	1.5	28.0	1.1	23.9	2.0	4
5.4×10^{17}	0	101.6	1.4	142.1	1.4	20.3	1.5	20.3	2.4	4
1.2×10^{18}	0	113.8	1.0	150.7	2.0	19.0	1.3	19.7	1.2	3
5.0×10^{18}	0	144.8	0.9	170.5	3.3	14.0	0.2	14.7	2.0	3
4.7×10^{18}	10	127.8	2.6	162.3	1.8	16.7	1.1	18.0	1.2	3
5.2×10^{18}	100	126.6	0.8	162.9	0.3	15.3	1.2	17.7	2.6	3
4.9×10^{18}	1000	124.4	2.8	161.7	2.8	17.8	1.2	17.5	2.1	3

TABLE 2

EFFECT OF FAST NEUTRON IRRADIATION
AT 140°R ON THE TENSILE PROPERTIES
OF AISI 347 (FORGING FROM NOZZLE S/N 033) AT 140°R

Control	0	45.4	2.0	176.8	1.5	51.6	6.0	46.0	13.9	4
6.2×10^{17}	0	68.0	0.8	177.2	1.1	50.2	5.1	43.6	11.1	4
1.2×10^{18}	0	86.0	4.4	178.6	0.8	50.0	4.7	40.6	9.9	4
5.8×10^{18}	0	121.9	2.2	179.4	1.3	52.4	3.3	49.0	11.5	3
5.2×10^{18}	10	106.9	6.2	180.2	0.0	51.0	3.1	50.2	7.3	3
4.7×10^{18}	100	109.8	1.4	183.1	4.2	51.7	2.6	43.9	10.8	3
5.0×10^{18}	1000	107.3	2.7	179.8	0.6	48.8	4.7	51.5	10.7	3

TABLE 3

EFFECT OF FAST NEUTRON IRRADIATION
AT 140°R ON THE TENSILE PROPERTIES
OF A-286 BOLTS (NERVA TECHNOLOGY) AT 140°R

Control	0	222.9	1.6	256.3	2.8	15.8	1.0	34.8	0.5	4
4.2×10^{17}	0	223.0	4.0	258.9	3.8	15.5	1.7	33.9	1.5	4
1.0×10^{18}	0	240.0	3.6	259.3	1.7	13.3	1.5	34.0	1.3	4
6.5×10^{18}	0	250.4	7.2	261.5	3.9	10.1	0.5	36.8	1.2	3
6.5×10^{18}	100	246.7	1.2	256.4	0.5	10.8	0.8	36.9	0.0	3
6.6×10^{18}	1000	243.3	1.9	254.8	0.5	11.1	0.8	36.1	2.3	3

TABLE 4

EFFECT OF FAST NEUTRON IRRADIATION
AT 140°R ON THE TENSILE PROPERTIES
OF INCONEL 718 (PANCAKE FORGING) AT 140°R

FLUENCE NVT > 1 MEV	ANNEAL TIME AT 540°R MIN.	0.2% YIELD STRENGTH, KSI		ULTIMATE STRENGTH, KSI		ELONGATION CHART, %		AREA REDUCTION, %		NO. SPECIMENS
		AVG	STD DEV	AVG	STD DEV	AVG	STD DEV	AVG	STD DEV	
Control	0	197.1	1.5	244.4	0.7	22.9	1.5	33.5	3.4	4
2.9×10^{17}	0	206.4	2.2	244.6	2.2	19.4	3.9	28.1	7.2	4
4.3×10^{18}	0	233.6	1.0	248.6	1.7	12.3	2.6	30.6	3.1	4
4.1×10^{18}	100	214.7	1.8	241.6	1.5	19.9	1.8	28.6	3.5	4

TABLE 5

EFFECT OF FAST NEUTRON IRRADIATION
AT 140°R ON THE TENSILE PROPERTIES
OF AA 7039-T63 (RING FORGING) AT 140°R

FLUENCE NVT > 1 MEV	ANNEAL TIME & TEMP. MIN., °R	0.2% YIELD STRENGTH, KSI		ULTIMATE STRENGTH, KSI		ELONGATION CHART, %		AREA REDUCTION, %		NO. SPECIMENS
		AVG	STD DEV	AVG	STD DEV	AVG	STD DEV	AVG	STD DEV	
Control	0	76.5	1.8	91.2	1.3	12.4	2.0	19.6	1.2	4
4.2×10^{17}	0	85.0	1.1	92.1	1.0	11.7	0.2	20.6	2.1	4
8.6×10^{17}	0	85.8	1.1	91.5	1.0	11.0	0.8	22.2	2.7	4
8.5×10^{17}	1000, 540	79.1	1.6	92.0	1.3	13.2	1.1	20.2	2.8	3
5.5×10^{18}	0	94.9	1.6	95.0	1.5	4.9	0.4	27.5	2.9	3
5.9×10^{18}	1000, 340	89.9	0.3	89.9	0.3	9.0	1.2	26.9	1.9	3
5.9×10^{18}	10, 540	85.0	1.2	90.4	1.1	11.3	0.7	23.6	2.1	3
5.6×10^{18}	100, 540	85.5	0.8	90.6	0.8	12.2	1.6	22.3	2.7	3
6.0×10^{18}	1000, 540	83.1	0.9	92.1	0.6	11.3	1.1	19.1	4.8	3

TABLE 6

EFFECT OF FAST NEUTRON IRRADIATION
AT 140°R ON THE TENSILE PROPERTIES
OF A LARGE Ti-5Al-2.5Sn (ELI) FORGING AT 140°R

FLUENCE NVT > 1 MEV	ANNEAL TIME AT 540°R MIN.	0.2% YIELD STRENGTH, KSI		ULTIMATE STRENGTH, KSI		ELONGATION CHART, %		AREA REDUCTION, %		NO. SPECIMENS
		AVG	STD DEV	AVG	STD DEV	AVG	STD DEV	AVG	STD DEV	
Control	0	175.6	1.5	185.8	2.1	10.4	2.3	29.9	3.2	4
2.3×10^{17}	0	182.4	1.8	189.5	1.1	9.1	0.9	30.4	2.6	4
8.2×10^{17}	0	187.7	1.5	195.5	1.7	7.7	1.1	29.5	5.0	4
4.9×10^{18}	0	199.1	3.3	204.4	3.1	4.1	0.5	23.2	3.4	4
5.2×10^{18}	100	192.7	1.9	200.0	1.0	6.3	0.4	27.0	1.5	4

APPENDIX*

DUCTILE-BRITTLE CLASSIFICATION

Tentative ductile-brittle classifications of reactor and engine system candidate materials have been established for design utilization, applicable to the temperature regime anticipated for NERVA operation. Factors such as form, condition, and direction of the material, as well as exposure to irradiation, gaseous and liquid hydrogen, and cryogenic temperature environments, are considered for each classification.

"Ductile" classification is based upon conservative judgement where data are available from NERVA experience or literature to substantiate the decision for all anticipated NERVA environments. "Brittle" classification is also based upon conservative judgement for the established brittle materials and, in addition, includes all materials with marginal or suspect ductility that could possibly be upgraded to "ductile" by further testing and/or experience.

Judgement is exercised by perusal of all pertinent information available and includes (but is not limited to) prior NERVA experience; available tensile ductility and notch tensile data; available fracture toughness data; and professional metallurgical expertise. This expertise is especially applied for anticipated deleterious effects of irradiation damage, high-pressure gaseous hydrogen embrittlement, cryogenic temperatures, and their combined synergistic effects.

The classifications for engine materials and reactor materials apply as the required design criterion in accordance with Paragraph 3.9 of the governing Structural Specification, SNPO-C-1. However, both the classifications and the associated temperature ranges are subject to change as new test data become available. Statistical fracture toughness testing would be required for all materials utilized for design which are classified "brittle".

*ANSC Report 2275, "Materials Properties Data Book," 15 November 1970 Supplement

A PORTABLE ABSORBED DOSE MEASURING INSTRUMENT WITH GAMMA DISCRIMINATION

W. M. Quam
W. O. Wilde

EG&G, Santa Barbara

INTRODUCTION

Dose absorbed in tissue may be measured by several types of detectors, e.g., tissue-equivalent ion chambers, Hurst proportional counters, and Rossi-type proportional counters. The latter device, designed and developed by H. H. Rossi[1], enables the experimenter to measure the spectrum of absorbed dose in LET and, with suitable electronics, the dose absorbed in tissue. These two characteristics imply that some means of discrimination of dose delivered in various LET intervals exists in this type of detector and that this capability can be applied to a relatively simple dose measuring instrument. This paper describes a suitable detector and some of the electronics necessary for its operation as a dose measuring instrument.

THE DETECTOR

The detector, shown in Fig. 1, is a sphere of tissue-equivalent plastic[2], with a single wire electrode located on a diameter of the sphere. The inside diameter of the detector described here is 2.2 inches. The sphere, together with appropriate connectors and fittings, is fastened on an aluminum base plate. A vacuum-tight aluminum cover completes the assembly. In use, the detector volume is filled to a low pressure (2 to 20 cm Hg, typically) with a tissue-equivalent proportional counting gas. The low-pressure gas in the spherical volume thus simulates a tissue cavity having linear dimensions of 1 to 10 microns. For the present design, operation at 1700 volts between the shell and the central wire is used. With this voltage gradient, ions formed in the volume are collected with a multiplication of 3 to 4 thousand.

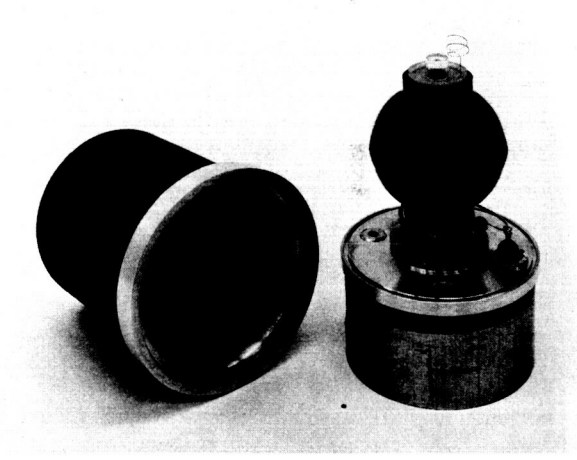

Fig. 1. Spherical Tissue Equivalent Proportional Counter

A spherical cavity with an axially arranged central wire does not collect with equal efficiency from all parts of the cavity. A solution to this problem has been pointed out by P. W. Benjamin[3]. He recommends specially shaped insulator and conductor penetrations. These recommendations have been employed in this detector; however, plastic is used for insulators and the gradient determining structures, and three-terminal construction is employed at each penetration.

The assembled detector is contained in a right circular cylinder 3.5 inches in diameter and 4.25 inches high and weighs 560 grams. Spheres with internal diameters as small as 0.5 inch or as large as 5.0 inches can be readily constructed.

The detector is a direct coupled device, i.e., it has no series coupling capacitor in its signal lead. It may thus be used as a current source with an electrometer readout, or as a pulse producing device with an a-d converter or pulse-height analyzer readout. If used as a current source, the detector produces 1×10^{-14} A per μrad/hr. This can be restated as 3.6×10^{-5} A per rad/sec or 1×10^{-8} A per rad/hr. The leakage current in the absence of high voltage is of the order of 1-2 $\times 10^{-15}$ A. The three-terminal construction prevents high-voltage leakage from appearing on the signal lead.

An internal source is usually used with detectors of this type. We have employed ^{241}Am as an alpha source for pulse-height analyzer calibration. Using this technique, the alpha peak may be adjusted to a known channel number on the pulse-height analyzer, thus providing a known keV/micron calibration per channel. This determines the overall system gain. A similar technique (with a stronger alpha source or a ^{55}Fe source) can be used to generate a known current to enable an electrometer to be calibrated.

Since the detector is a tissue-equivalent system, it responds to gamma rays, neutrons, π mesons, etc., just as tissue does. In other words, it can be calibrated to yield ergs per gram tissue or rads-tissue. If an a-d converter or pulse-height analyzer is used as a read-out, and if system gain is set with the internal alpha source, no calibration is required and rads-tissue may be determined directly.

DETECTOR USED AS A CURRENT SOURCE

A useful instrument can be constructed using the detector as a current source. With the parameters outlined before, 1700 volts and 20 cm Hg fill pressure, the detector has a sensitivity comparable to an 80-liter ion chamber, and background of 20 μrad/hr is $\sim 2 \times 10^{-13}$ A.

Figure 2 shows a block diagram of a workable system. The electrometer is an all solid-state varactor bridge device. Its input noise current is $\sim 1 \times 10^{-14}$ A. The high-voltage supply is an oscillator voltage doubler circuit. It has a special regulator so that the high voltage can be varied to adjust the system gain and still maintain good stability.

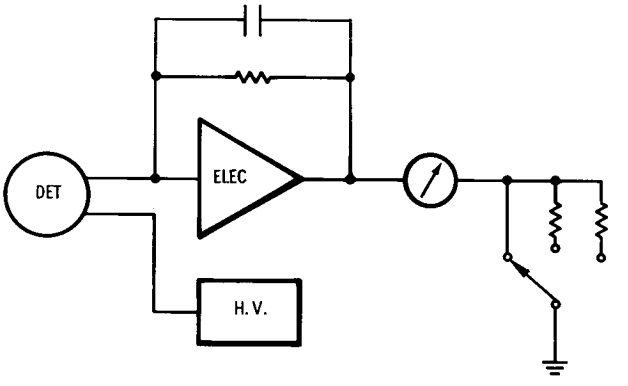

Fig. 2. Direct Coupled Absorbed Dose Measuring Instrument

Figure 3 is a photograph of a portable system following the block diagram of Fig. 2. This particular unit employs ± 18 volts for the electrometer operational amplifier and + 9 volts for the high-voltage supply. The electrometer operates well down to ± 7 volts and the high-voltage supply down to + 7 volts. Presently, simple transistor radio batteries are used with a lifetime of ~ 100 hours.

This system has full-scale ranges of 60, 600 and 6000 μrad/hr. A less sensitive instrument would require current division at the input or a lower overall detector multiplication, both of which are realizable.

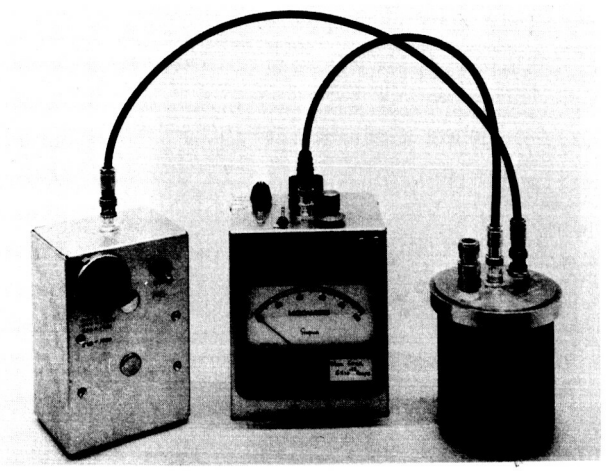

Fig. 3. Portable Battery Operated Absorbed Dose Measuring Instrument

In use, the system gain is set by turning on the internal source and adjusting the high voltage until the calibration reading is reached. The calibration may be verified by exposure to a known gamma or neutron source, or the detector output may be connected to an a-d converter or pulse-height analyzer and an independent calibration performed.

DETECTOR USED AS A PULSE SOURCE

This same detector may also be used as a regular proportional counter and thus as a source of pulses. These pulses may then be amplified in the usual manner with an FET input preamplifier, followed by a linear amplifier. Circuitry suitable for absorbed dose measurements is shown in Fig. 4. Spectroscopy uses would take the linear amplifier output and feed it into an a-d converter or a pulse-height analyzer.

Figure 4 shows a discriminator that enables a lower level to be placed on the signals fed to the meter circuit. Since pulse linearity must be preserved if an accurate dose measurement is to be obtained, the discriminator is used to control a linear gate at the amplifier output. The pulses that pass the linear gate are summed in the charge-sensitive rate-meter circuit. The rate-meter output is then proportional to the absorbed dose (rads-tissue) per unit time deposited in the detector. Such circuitry has been suggested by J. W. Baum,[4,5] and improves upon the simple rad responding instrument by addition of nonlinear electronics to produce a REM response.

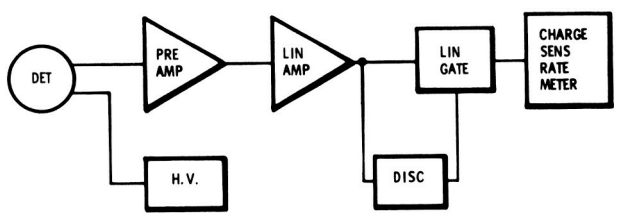

Fig. 4. Absorbed Dose Measuring Instrument With Discriminator

PULSE DETECTOR NEUTRON AND GAMMA RESPONSE

If the linear amplifier output is connected to a pulse-height analyzer, an X-Y plot such as shown in Fig. 5 is produced. The data in Fig. 5 were obtained by exposing the detector to a ^{252}Cf neutron source of ~ 0.8 micrograms at 5 cm for 40 minutes. The detector diameter was adjusted to 1 micron. The internal ^{241}Am alpha source was used to measure the system gain which was adjusted to 400 keV/micron full scale on the X axis. The usual proton "edge" may be clearly seen at ~ 90 keV/ micron. Figure 6 shows a ^{60}Co spectrum with a full-scale value of 40 keV/micron, i.e., a factor of 10 increase in gain over Fig. 5. The gamma contributions are seen to extend only to ~ 3 keV/micron. Obviously, if a linear gate were set to pass only pulses above ~ 3 keV/micron, only neutron induced events would be measured. Some percentage of the dose would be lost, of course, due to neutron induced events below the bias level.

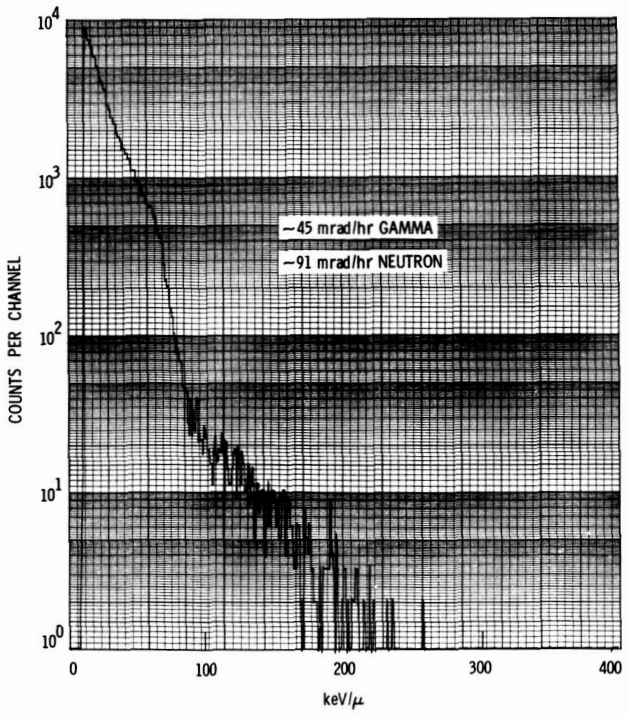

Fig. 5. ^{252}Cf Spectrum

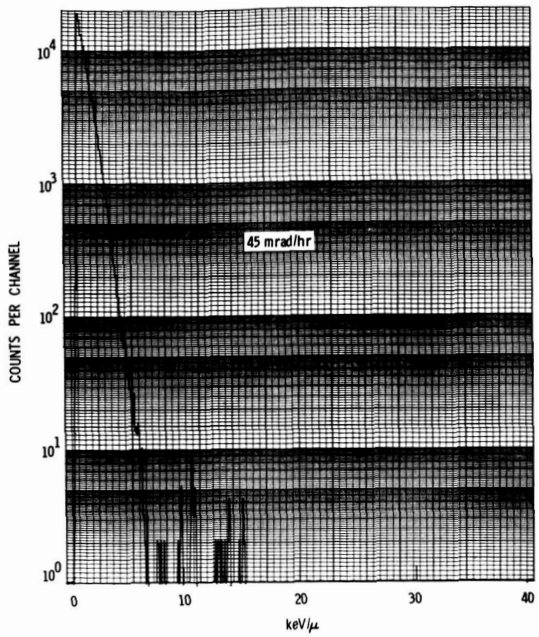

Fig. 6. ^{60}Co Spectrum

This is discussed below. System noise is shown in Fig. 7. The gain has been increased a factor of 100 over Fig. 6 and thus full scale is 0.4 keV/micron. The electronic noise is seen to become noticeable at about 0.05 keV/micron. The remainder of the "noise" is due to background activity in the detector and the room. The noise is clearly very small in comparison to the neutron dose rate and small even if ^{60}Co gammas alone are considered.

If one measures the rads-tissue per hour from ^{60}Co as registered by a circuit such as that shown in Fig. 4 versus discriminator setting, the results shown in Table 1 are obtained. It is clear that 98% of the absorbed dose is delivered at LET values of 3 keV/micron or less. Table 2 presents similar data for ^{252}Cf. Here only 50% of the absorbed dose is from events having LET values below 3 keV/micron. If a particular bias level is selected, such as 3 keV/micron, the meter reading will correspond to neutron induced events only. For the conditions of this experiment, the <u>total</u> absorbed dose rate was 133 m rad-tissue per hour

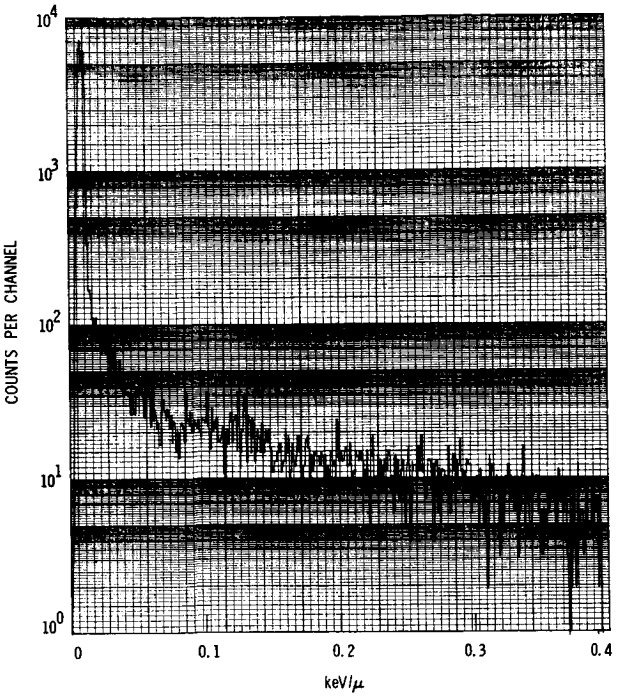

Fig. 7. Noise Spectrum

which corresponds[6] to 45 m rad-tissue per hour from gammas and 88 m rad-tissue per hour from neutrons. Thus 64 m rad-tissue per hour were measured (see Table 2) at 3 keV/micron bias level and represents about 73% of the neutron caused absorbed dose. While these data are restricted to similar source-detector configurations, a bias curve may be run for other radiation environments, the total dose measured with the direct coupled detector, and a similar analysis performed.

In conclusion, it can be seen that a simple rad-tissue responding absorbed dose-rate measuring instrument can be constructed. It uses a single wire spherical tissue-equivalent proportional counter as a current source detector. Readout is accomplished with a solid-state electrometer circuit. A further elaboration may be introduced that allows discrimination levels to be set at various levels of LET. This will provide the ability to selectively measure neutron and gamma plus neutron events. In all cases the detector size may be adjusted to be between 1 and 10 microns.

TABLE 1. CUMULATIVE FRACTIONAL ABSORBED DOSE RATE VERSUS keV/μ BIAS FOR ^{60}Co GAMMA RAYS

L, keV/μ	Absorbed Dose Rate (keV/μ ≥ L) Rad/hr	Cumulative Fractional Absorbed Dose
.322	3.83 (-3)	0.47
.483	3.46 (-3)	0.52
.638	1.75 (-3)	0.76
.685	1.75 (-3)	0.75
1.087	1.10 (-3)	0.85
1.356	0.88 (-3)	0.88
1.49	0.857 (-3)	0.88
1.89	0.579 (-3)	0.92
2.15	0.400 (-3)	0.94
2.95	0.128 (-3)	0.98
3.75	0.021 (-3)	0.99
4.55	0.018 (-3)	0.99

TABLE 2. CUMULATIVE FRACTIONAL ABSORBED DOSE RATE VERSUS keV/μ BIAS FOR ^{252}Cf

L, keV/μ	Absorbed Dose Rate (keV/μ ≥ L) Rad/hr	Cumulative Fractional Absorbed Dose
0.322	102.0 (-3)	0.23
0.483	86.2 (-3)	0.35
0.638	82.0 (-3)	0.38
0.685	78.6 (-3)	0.41
0.957	76.7 (-3)	0.42
1.36	72.9 (-3)	0.45
2.15	66.9 (-3)	0.50
3.75	62.0 (-3)	0.53
8.54	53.3 (-3)	0.60
9.53	48.8 (-3)	0.63
13.5	39.9 (-3)	0.70
16.51	34.9 (-3)	0.74
21.4	28.7 (-3)	0.78
37.3	13.5 (-3)	0.90
85.0	1.36 (-3)	0.99
164.4	0.22 (-3)	0.99

A COMPTON SCATTER ATTENUATION GAMMA RAY SPECTROMETER

W. E. Austin

General Electric Company
Space Sciences Laboratory

A Compton scatter attenuation gamma ray spectrometer conceptual design is discussed for performing gamma spectral measurements in monodirectional gamma fields from 10^2 R hr^{-1} to 10^6 R hr^{-1}. Selectable Compton targets are used to scatter gamma photons onto an otherwise heavily shielded detector with changeable scattering efficiencies such that the count rate is maintained between 500 and 10^4 sec^{-1}. Use of two sum-Compton coincident detectors, one for energies up to 1.5 MeV and the other for 600 keV to 10 MeV, will allow good peak to tail pulse height ratios to be obtained over the entire spectrum and reduces the neutron recoil background rate.

INTRODUCTION

The NASA, Marshall Space Flight Center desires to measure the gamma radiation energy spectrum created by the radiation leakage from a space nuclear propulsion reactor. The gamma ray spectrometer is to be physically located at the top of a liquid hydrogen tank with the propulsion reactor at the bottom of the tank. The purpose of the spectral and intensity measurements is to provide an accurate aid in the design of minimal weight gamma radiation shielding for various radiation sensitive payloads.

Conventional gamma ray spectrometers cannot be used for this application due to the high gamma flux intensity. The presence of a high neutron flux, composed of liquid hydrogen temperature thermal neutrons in addition to the hard neutron flux further complicates the gamma spectral measurement.

This paper briefly outlines a solution for these measurement problems resulting from a recent study contract[1]. The technique is a Compton scatter attenuation gamma ray spectrometer which basically consists of scattering a portion of the gamma flux onto an otherwise heavily shielded gamma spectral detector. The scattered gamma radiation energy spectrum may be related to the incident spectrum by the well known Compton energy shift relationship through the fixed angle of scatter. This technique may only be employed for a highly directional gamma flux, as exampled by the proposed application.

REQUIREMENTS AND PROBLEMS

The gamma field is expected to be approximately 100 R hr^{-1} with the LH_2 tank full and the reactor at full power and increasing to 5×10^5 R hr^{-1} as the tank is emptied. This is equivalent to a photon flux approximating 5×10^7 cm^{-2} sec^{-1} to 2×10^{11} cm^{-2} sec^{-1}. The pulse height analysis rate for single events is limited and the gamma interaction cross sections are such that directly exposed spectral detectors would need to be smaller than 10^{-3} grams, which is much smaller than the range of the gamma recoil electrons. Therefore, directly exposed spectral detectors are prohibited.

Another NASA requirement is that separate spectral measurements be obtained in each five second interval of the short operating time, and the data must also have reasonable statistical accuracy. To meet this requirement, the analysis counting rate must always be high, and as the gamma intensity will vary by more than three orders of magnitude, we must decrease the detection efficiency as the gamma intensity increases.

The neutron environment is not severe until the last few seconds of power as the tank is emptied. At 30 seconds prior to an empty tank, the fast neutron flux is 10^5 n cm^{-2} sec^{-1} but rapidly increases to 2×10^8 n cm^{-2} sec^{-1} as the tank is emptied prior to reactor shutdown. One consequence of the neutron environment is that small gamma spectral detectors must be employed to reduce the background rate from this source.

The gamma radiation energy range of interest is 50 keV to 10 MeV with the highest energy radiation caused by neutron scatter and capture. It is expected that the gamma spectrum intensity will vary by over four orders of magnitude from the low to high energy end of the spectrum. Thus, it is difficult to get statistical accuracy at the upper end of the spectrum during a five second interval because only 10^{-4} of the photons are above 5 MeV and the count rate and count time period are limited.

The only feasible way that we have found for performing these measurements is with a Compton scatter attenuation gamma ray spectrometer with a variable detection efficiency.

CONCEPTUAL DESIGN

Figure 1 indicates the design concept of Compton scatter attenuation. A collimator, with its axis pointing directly toward the reactor, is used to define the area of a gamma beam which strikes successive Compton scattering targets for the separate spectral detectors. The targets are located on the two wheels which are synchronized with a common axis drive. Three Compton targets are on each wheel and each can be rotated into the gamma beam by the stepping motor geared to the axis drive. A position with no target also exists, so that occasional detector background measure-

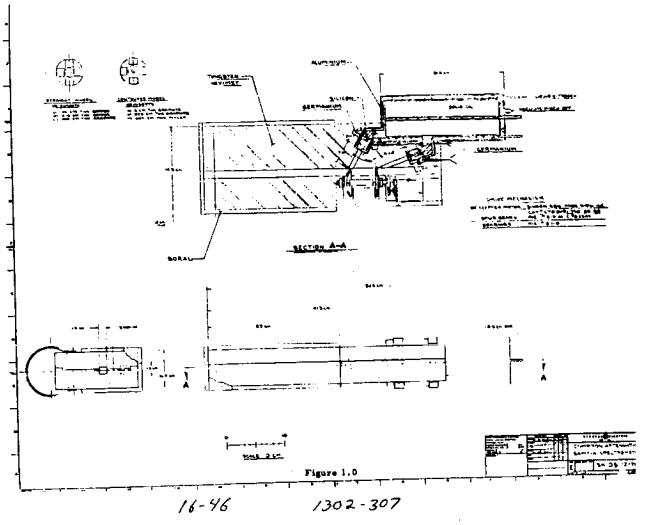

ments can be made for subtraction from the measured data. The lower wheel has carbon targets and radiation scattered through a 60 degree angle is incident on the first detector, which is designed for low gamma ray energy spectroscopy. The second wheel contains copper targets and the radiation is scattered through 20° to the second detector designed for high energy gamma ray spectroscopy. A short lead plug is inserted to remove the bulk of the low energy photons toward the second spectral detector.

We have calculated the spectral effects of non-Compton interactions in the carbon target, which include coherent scattering and pair production. These reactions are very minimal, and although coherent scattering increases the total scattering cross section at 50 keV somewhat, the energy difference to the incoherent Compton scatter is small. Coherent scattering decreases rapidly with increasing gamma energy. Pair production is high in the copper targets, which are used to increase the relative sensitivity of the second spectrometry but the 511 keV annihilation photons are below the useful range of this spectrometer and will be rejected electronically.

The Compton targets on a single wheel vary in area density by factors of 20, i.e., the carbon targets are 1.1 grams cm^{-2}, .055 grams cm^{-2}, and .0027 grams cm^{-2}. Switching from a target to the next lightest, will decrease the overall detection efficiency by a factor of 20, and for a given target the count rate will vary only by a factor of 20, and will be between 500 sec^{-1} to 10^4 sec^{-1}. The maximum counting and analysis rate is determined by inefficient sum-Compton spectrometers used as detectors, where coincident events are required between the coaxial detectors, and the singles count rate will exceed 2 x 10^5 sec^{-1} for 10^4 sec^{-1} coincident rate, and this singles rate is expected to tax the electronic circuitry, particularly the random coincidence rate and the system energy resolution. It is this singles rate that limits the coincident count rate of the system.

The tungsten shielding is a shadow shield for both neutron and gamma radiation. Photons scattered from adjacent side materials will not exceed 0.5 MeV for 90° scattering, and are more readily absorbed by the tungsten than the directly incident photons which include higher energies. Backscatter photons are even less energetic. Even so, the side shield dimensions may need to be increased beyond those shown, if massive scattering objects are close to the spectrometer.

The shield should produce a signal to background rate of 20:1 for the worst condition which is with the smallest Compton targets in view. The background rate was computed for gamma leakage through the shield interacting with the detectors and for fast neutrons producing recoil events within the detectors. Calculations using fast neutron removal cross sections from ORNL, show that the fast neutron flux is attenuated by a factor of 100 by this shield. Although the neutron radiation is not severe until the last few seconds of the anticipated measurement, it is this time period that contributes to the total gamma dose. Gamma radiation from inelastic scattering by neutrons in the tungsten is an additional source of background, but this effect is small compared to the neutron recoil interactions within the detectors. A boral shield will be used to reduce the thermal neutron flux, being almost totally opaque to the low temperature neutrons.

Two spectral detector systems are required to obtain better statistical accuracy for the high energy portion of the spectrum and additionally, because it is difficult to design small sum-Compton spectrometers with response down to 50 keV which are also capable of a response to 10 MeV. To see 50 keV, the central detector must be of a low Z material, such as silicon or glass, so that the scattered photon can escape to the surrounding secondary detector. But these materials have more energetic neutron recoil events than the heavier detector materials, such as germanium or CsI(Na), and their size must therefore be more limited. On the other hand, the range of gamma recoil electrons is approximately 0.5 grams per MeV, and thus a long and heavy detector is needed to detect most of the high energy photons. We solve this dilemma by using two spectral detectors, and we limit the photon energy incident on the low Z detector by having a 60° angle of scatter from the carbon targets on the first wheel.

Figure 2 shows the Compton energy shift relationships for various scattering angles θ. Note that for a 60° angle of scatter, the scattered energy never exceeds 1 MeV. As our expected detector peak to tail ratio is almost unity at 1 MeV, and increases for lower energies, the pulse height data for the low energy spectrometer, can be directly related to the incident spectrum by the relationship[2]

$$E_o = E' \left[1 + \alpha (\cos - \cos \theta)\right] \qquad (1)$$

where E_o and E' are the incident and scattered photon energies, α is the incident energy in relativistic units, and θ is the angle of scatter.

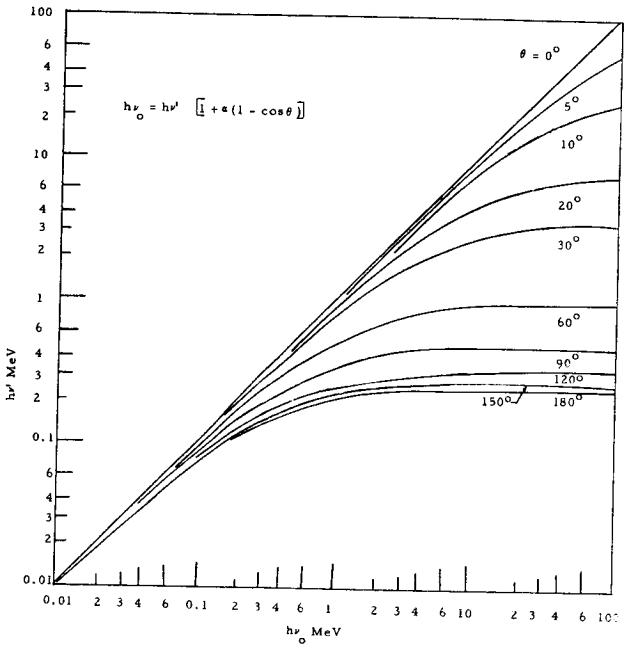

Figure 2.0. The Scattered Photon Energy $h\nu'$ as a Function of Incident Energy $h\nu_o$ and Scattering Angle θ

The low energy spectrometer would be useful for incident energies from 50 keV to 1.5 MeV corresponding to 45 keV to 600 keV for the scattered and detected radiation. Note that the energy width per channel of a pulse height analyzer is not constant due to the nonlinearity of the Compton energy shift.

As the peak to tail ratio is expected to be high, 4:1 at 600 keV and up to 60:1 at 50 keV, the data is directly reducible to a spectrum without resorting to the mathematical detector response unfolding techniques commonly used for single detector pulse height spectra. The differential Compton scatter cross section, at $\theta = 60°$, decreases with increasing photon energies, and therefore the wide angle scattering reduces the number as well as the energy of the high energy photons.

The high energy specrometer will see radiation scattered through 20°. It is expected to collect data for incident energies from 600 keV to 10 MeV. A short lead filter between the Compton target and the detector will remove most of the low energy photons and attenuate the high energy flux a moderate amount. Without the lead filter, 63% of the photons would be below 600 keV, and with the filter, only 11% of the filtered spectrum is expected to be below 600 keV, and this includes annihilation photons generated in the filter and Compton targets. Therefore, a more efficient detector may be used to increase the counting rate for the higher energy photons, and yet not be swamped with a multitude of low energy photons. This will result in a better statistical accuracy for the high energy portion of the spectrum.

The energy resolution of a Compton scatter attenuation spectrometer suffers from the nonlinear energy shift relationship. The energy resolution, ΔE_o of the incident radiation, approximates

$$\Delta E_o \cong \Delta E' \left[1 + \alpha (1 - \cos \theta)\right] + \alpha E' \sin \theta d\theta \qquad (2)$$

where $\Delta E'$ is the instrumental system energy resolution. The first term on the right is the instrumental energy resolution multiplied by the energy shift relationship. The second term results from the finite scattering angle, and is the limiting factor for the higher photon energies. The expected energy resolution is shown in Figure 3 as computed from equation (2). We also show the expected detector system resolution for fair semiconductor detectors. The horizontal dashed lines represent the NASA requirements for energy resolution.

Figure 3.0 $\theta = 60°$ Low Energy Spectrometer
$\theta = 20°$ High Energy Spectrometer

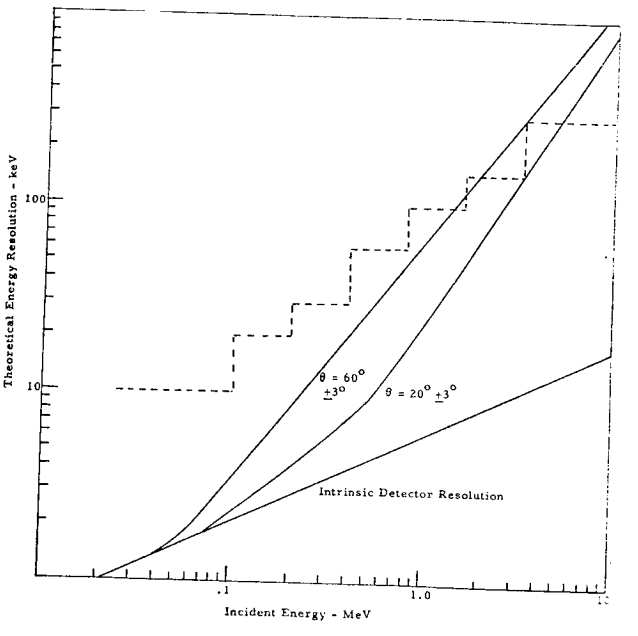

Small sum-Compton detector systems are planned for the spectrometer because this type of detector gives higher peak to tail ratios than any other type of small detector. The detected signal pulses will approach total absorption, and therefore little data reduction will be necessary to obtain the incident gamma spectrum. The alternate choice of using a single small detector and mathematically unfolding the pulse height distribution with matrices of the detector response function, is not as satisfying. In addition, the coincidence requirements for forming the sum-Compton events reduces the background due to neutron recoil events significantly.

Peak to tail ratios exceeding 100:1 have been reported[3] for various sum-Compton spectrometers. These designs were rather inefficient, i.e., only a small fraction of the incident photons results in coincident sum events, and the detectors were too large for the present purpose. We have concluded that at least the order of four percent of the photons interacting in the center detector must result in Compton events simultaneously detected in the surrounding detector, to achieve a high count rate capability without an unduly high random coincident rate.

In addition to the random coincident pulses which result in false signals, there exists a random sum rate. The latter rate is the effect of an additional event occurring in either detector during the slow coincident time period of summing, in addition to the true Compton event. These type events add to the energy of the detected event and are largely due to neutron interactions within the detectors during the last few seconds of the measurement. We have studied these effects and concluded that they are not serious for the study of environmental conditions and the proposed design, but experimental measurements should be performed to substantiate these conclusions.

The high energy sum-Compton spectrometer will additionally detect pair events created in the center detector in which either or both of the annihilation photons are recorded by the secondary detector. These events increase the detection efficiency at the higher energies of the spectrum. The peak to tail ratio for high energy photons is approximately unity, but most of the tail distribution lies relatively close to the peak energy, and in effect, deteriorates the energy resolution by broadening the peak distribution.

The solid state detectors envisioned in Figure 1 are not within the present state-of-the-art. Lithium drifting is apt to penetrate the small junctions. It is anticipated that small coaxial intrinsic germanium[4] and silicon detectors will be within the state-of-the-art within two years. For the present, experimental studies can proceed using glass scintillators for the silicon detector and CsI(Na) scintillators for the germanium detectors. The major performance difference should be in a degraded energy resolution for the completed spectrometer.

ACKNOWLEDGMENT

It is a pleasure to acknowledge the able technical monitoring of Mr. Charles Jones and Mr. Troy Ponder of the NASA, Marshall Space Flight Center, for this study.

REFERENCES

1. NASA Contract NAS8-25617.
2. Evans, R. D., American Institute of Physics Handbook, McGraw Hill.
3. Hick, H., and Peplink, R., Nuclear Instruments and Methods 68, 240 (1969).
4. Hall, R., IEE Transactions on Nuclear Science 17, 3 (1970), p 235.

SPACE RADIATION STUDIES AT THE WHITE SANDS MISSILE RANGE FAST BURST REACTOR

A. De La Paz
(Nuclear Weapon Effects Division, Army Missile Test and Evaluation,
White Sands Missile Range, New Mexico)

The White Sands Missile Range Fast Burst Reactor (FBR) has been employed in the performance of various types of space radiation tests. The FBR is operated by the Department of the Army to provide the radiation environment in support of requirements of experimenters from private industry, government agencies and their contractors. The FBR is an unreflected and unmoderated reactor employing an alloy or uranium-10 weight percent molybdenum as the fuel material. The reactor core, consisting of a stacked array of fuel rings, and the control components, including a safety block, control rods and burst rod, are all made of the same fuel material.

The FBR is operated at either an outdoor site or inside an underground reactor cell having approximately a 50 x 50 ft floor area and a height of 20 ft. Because of the size of the reactor cell, most of the experiments are conducted with the reactor in the cell. Outdoor reactor operations are conducted where large items, such as vehicles, are to be irradiated, or when the distance from the experiment to the reactor is to be large. In the usual case, where the reactor is in the cell, the experiment being studied is placed on an experimenter table through which the reactor core protrudes. A safety shield surrounds the reactor core assembly and serves to prevent movement of the experiment to a point where it could touch the reactor fuel surface. The FBR can be operated in either a burst or steady-state mode, depending on the experimenter requirements that apply.

The experiment being studied is instrumented and the necessary cabling is run from the reactor cell to the experimenter room at the reactor facility where the response of the experiment to radiation is observed, recorded and evaluated. Included with the instrumentation of the experiment is the dosimetry measurement techniques that are provided. Normally, the neutron fluence is measured by use of sulfur foils and the gamma measurements are made with calcium fluoride or lithium fluoride thermoluminescent dosimeters. Dosimetry support for experimenters using the reactor facility is provided by the Nuclear Weapon Effects Division. This support includes the foils and dosimeters and the counting and analysis necessary to obtain the required dosimetry data. The neutron and gamma output characteristics of the reactor are presented in Figures 1 and 2.

Space radiation studies conducted at the FRB include radiobiological experiments, dosimetry studies and transient radiation effects studies on electronic systems and components. Radiobiological experiments conducted using the FBR have involved the evaluation of the behaviorial response of animals subjected to the radiation environment associated with a reactor burst operation. In one category of experiments rhesus monkeys, trained to perform tasks such as maintaining a moving platform on a stable basis, are subjected to a radiation burst which gives them a dose of approximately 2500 Rads to the head. The response and performance of the animal is followed for an extended period of time. Studies of this type are being carried out at lower doses to the animal. In addition, studies have been carried out using baboons instead of rhesus monkeys. For the most part, however, radiobiological experiments are conducted with the rhesus monkeys because of the more extensive performance degradation data that can be obtained as compared to the baboons. An additional complicating factor involved with the baboons is that more elaborate measures must be taken to insure that the animal is restrained so that it cannot move in a manner such that it would alter the reactivity state of the reactor. Radiobiological experiments have also been conducted at the reactor facility with other animals; for example, dogs and laboratory rats.

Performance of space radiation studies on electronic systems and components is a major use of the reactor facility. Individual components, such as transistors or diodes, are placed in very close proximity to the reactor, approximately six inches from the core centerline, and receive the programmed radiation deposition depending on the fission yield associated with the reactor burst operation. Performance of experiments of this type is expanded to include entire electronic systems, such as missile guidance packages.

Modification of the FRB facility is planned for 1971 which will include provision for an internal irradiation cavity within the reactor core for high intensity radiation deposition of small components. In addition, the operational capability of the reactor is being upgraded to provide progressively higher radiation doses to experiments in either the burst or steady-state mode of operation.

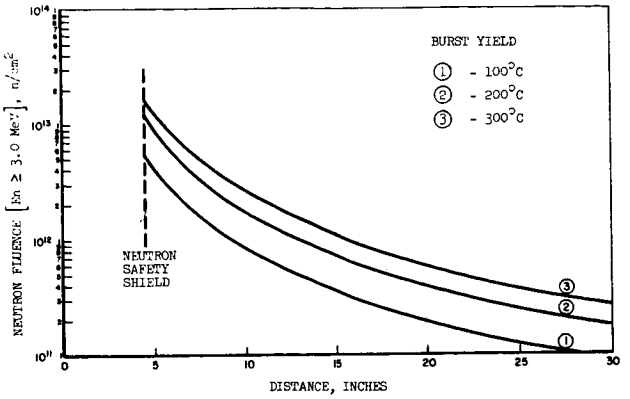

FIGURE I - NEUTRON FLUENCE AS A FUNCTION OF DISTANCE FROM THE CORE CENTERLINE

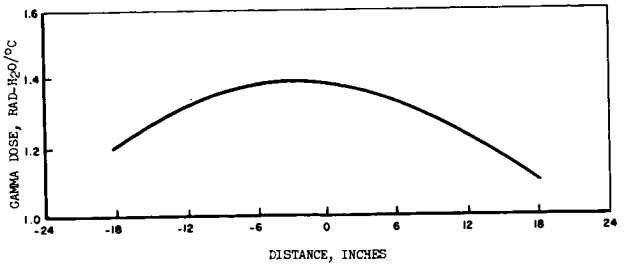

FIGURE 2. GAMMA DOSE PER °C AS A FUNCTION OF VERTICAL DISTANCE FROM CORE MIDPLANE. (FREE FIELD MEASUREMENTS AT 1 METER)

SESSION VII.I.
RADIOBIOLOGY: CLINICAL DATA FROM LABORATORY EXPERIMENTS
CHAIRMAN: COL. J. PICKERING
SCHOOL OF AEROSPACE MEDICINE, BROOKS AFB

FACTORS MODIFYING THE RESPONSE OF LARGE ANIMALS TO LOW-INTENSITY RADIATION EXPOSURE

Norbert P. Page*and Edwin T. Still+

*National Cancer Institute, Bethesda, Maryland and
+U. S. Atomic Energy Commission, Washington, D. C.

In assessing the biological response to space radiation, two of the most important modifying factors are dose protraction and dose distribution to the body. Studies are reported in which sheep and swine were used to compare the hematology and lethality response resulting from radiation exposure encountered in a variety of forms, including acute (high dose-rate), chronic (low dose-rate), combinations of acute and chronic, and whether received as a continuous or as fractionated exposure. While sheep and swine are basically similar in response to acute radiation, their sensitivity to chronic irradiation is markedly different. Sheep remain relatively sensitive as the radiation exposure is protracted while swine are more resistant and capable of surviving extremely large doses of chronic irradiation. This response to chronic irradiation correlated well with changes in radiosensitivity and recovery following an acute, sublethal exposure. Swine recover remarkably fast and develop a large and persistant radioresistance. The change in radiosensitivity of sheep after either acute or chronic sublethal exposure is basically the same, consisting of a triphasic pattern of an initial slow recovery, transient radioresistance and regression into a long-lasting period of relative radiosensitivity. The overall effect of receiving both acute and chronic exposures within a short period of time may depend upon the sequence of the exposures. In addition to protraction, spatial or body distribution is a significant factor in the response of large animals to radiation exposure.

Somatic effects of radiation are generally categorized into the familiar classification of early and late effects as utilized for terrestrial forms of radiation (1). However, space radiation exposure takes on added dimensions and complexities not normally found in conventional earth exposures that makes dose-response estimations most difficult. Certain sources of radiation are predictable with a fair degree of certainty while others are quite unpredictable. The predictable or "expected" sources include the earth's trapped radiation belts, galactic cosmic radiation, and radiation from nuclear power systems. In the category of the unpredictable are such events as solar flares, excessive exposure to the nuclear reactor in emergency repair or during rendezvous procedures, and the inadvertent or uncontrollable orbiting of a spacecraft in the earth's radiation belts. While the probability of an unpredictable exposure may be minimal for a short lunar mission, it nevertheless must be considered possible, and perhaps even probable, if the missions increase in duration and frequency.

Exposure to radiation on a space mission will likely be in the form of a more-or-less constant, low-level background of 30-50 mrads per day from galactic radiation, with moderate to high-intensity exposures occuring during transit through the earth's trapped radiation belts or from periodic, and largely unpredictable, solar-flares. Although solar flares are generally brief, and of low intensity, they may range up to a few days with peak dose-rates, of 10-20 rads per hour at the average depth of the bone marrow (2). Thus an intense solar flare lasting a day or two or several smaller flares could result in an exposure of several hundred rads to the space crew. In such a case, acute manifestations such as skin desquamation, prodromal responses, hematological depression and perhaps even lethality could result with disasterous consequences.

For space operations, certainly two of the most important factors that can modify the dose-response relationship are dose-protraction and nonuniform dose distribution to the body. The studies that we will report involved the use of large animals to explore these factors, especially as they relate to hematological depression and lethality from radiation exposure. We will employ the term "acute exposure" to refer to exposure at a high dose-rate, e.g., 450 R/hour. "Chronic exposure" will refer only to a continuous exposure at a low dose-rate. "Protraction" of an exposure is the process by which a total radiation dose is given over a longer time period. This could be accomplished by chronic exposure or by fractionation into two or more doses separated in time.

Both methods of dose protraction were used in these studies. Chronic exposure was studied with animals continuously exposed until death or by terminating the exposure after selected doses for LD50 determinations. Using the fractionated method experiments were conducted to

determine the effects of: a) fractionating acute exposures using various time intervals, b) chronic exposure followed immediately or after various time periods by acute exposures, and c) acute exposure followed immediately by chronic exposures. Figure 1 illustrates these various exposure situations.

This program was conducted at the Naval Radiological Defense Laboratory with funding provided by the Defense Atomic Support Agency and Office of Civil Defense. Unfortunately, a couple of the experiments were concluded prematurely due to the unanticipated closure of the laboratory. Since the animal management practices, dosimetry techniques, irradiation procedures and experimental design, have been previously reported (3,4) only highlights of the methodology will be repeated here.

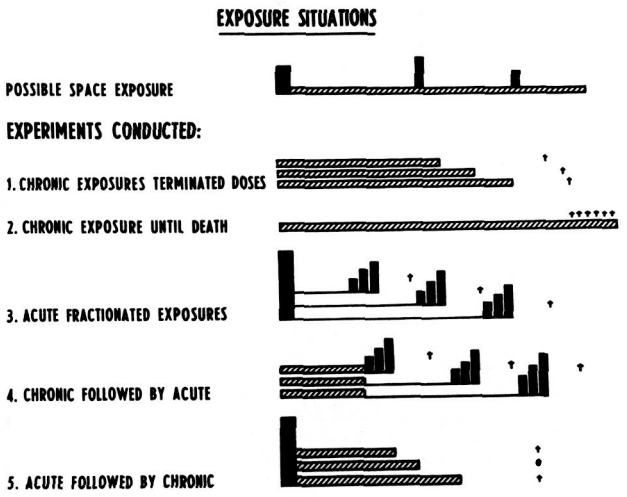

Figure 1. Experimental situations as used in the NRDL large animal experiments and their relationship to possible space exposure.

METHODS AND MATERIALS

ANIMALS

Sheep and swine were the main species used in these studies. They were selected on the basis of their being more like man than rodents in body size, depth-dose distribution, basic (or acute) radiosensitivity, metabolic rate, and lifespan. Another important consideration was our ability to obtain them in large numbers, healthy and uniform in size and age, for the entire period of the study.

The sheep were obtained at one year of age from a single source located in the Sacramento Valley of California. They were castrated-males of Columbia-Rambouillet cross-breed, weighed 35-45 kg, and measured 23-30 cm in width at the abdomen at the time they were placed on experiment.

Except for the final few lots, swine were also obtained from a single local source, with an attempt being made to reduce biological variability by a planned breeding, selection, and environmental control program. The swine were 8-12 month old, female, pure bred Durocs weighing approximately 90-110 kg at the time of irradiation.

RADIATION SOURCES AND EXPOSURE METHODS

Two types of radiation were used, cobalt-60 gamma and 1 Mvp X-rays. The cobalt-60 exposures were made at the NRDL Radiation Range, Camp Parks, California while the X-ray exposures were made with a GE Resotron, operated at 1000 KVp/3mA, producing X-rays having a HVL of 2.2 mm lead and an effective energy of approximately 300 Kev.

For the acute (high dose-rate) exposures the bilateral method of irradiation was used. For chronic (low dose-rate) irradiation, exposures were continuous for periods of up to 60 days. Since confinement in exposure boxes for such long periods was neither practical nor humane, the sheep were exposed in individual pens, 4 X 8 feet in size, situated on a gently sloping hillside, as schematically illustrated in Figure 2. This facility permitted the exposure of a large group of animals (up to 50) at the same time and same dose rate. In this configuration "uniform" whole-body exposure was dependent upon the animals' random movement in the pens since at any given time the exposure was unidirectional rather than bilateral. Food and water was provided on both sides of the pen to encourage turning of the animals during the exposure. Lithium flouride dosimeters secured to each side of groups of sheep indicated that the animal's movement resulted in equal exposure to both sides during the exposure period. Thus, both methods of exposure were effectively bilateral. Time required for servicing the pens averaged one to two hours every two days.

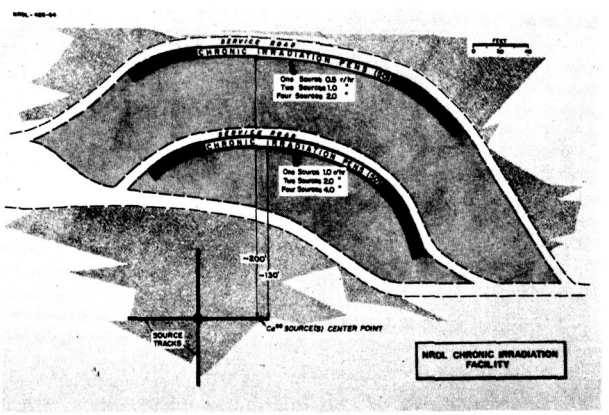

Figure 2. Schematic representation of NRDL cobalt-60 radiation range used for chronic irradiation of large animals.

DATA ANALYSIS

The method used to determine the median lethal doses (LD50's) and other parameters of mortality response was by probit analysis of the percent mortality on the natural logarithm of the radiation exposure. Dosimetric measurements were made with Landsverk, Victoreen and Phillips ionization chambers which were cross-calibrated with a National Bureau of Standards-calibrated Victoreen R-chamber. In addition thermoluminescent dosimetry (LiF) was used. The dose-rate was measured in air at the approximate midline of the exposure box or pen. The midline tissue dose, at maximum body diameter, was about 65% of the midline air dose for cobalt-60 and 60% for 1 Mvp X-ray. The radiation units expressed throughout this paper will be in Roentgens as measured in air.

RESULTS

DOSE PROTRACTION

Protraction of a given radiation dose can be attained mainly by two methods: a) by chronic exposure, i.e., lowering the dose-rate and continuously exposing the animals for a longer period of time, and b) fractionating or dividing the dose into two or more fractions with radiation-free time between exposures. Both methods were used in these studies.

A. CHRONIC EXPOSURES:

1. Terminated Exposures:

Studies to assess the effect of decreasing dose rate on dose-response (lethality) by terminating the exposures after giving predetermined doses were conducted with both sheep and swine. Table I presents the data while Figure 3 shows the correlation between the dose rates used and the LD50's that were obtained.

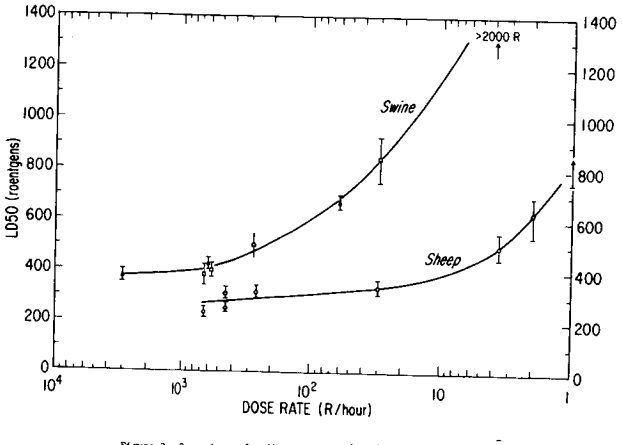

Figure 3. Comparison of radiosensitivity (LD50) of sheep and swine as related to dose-rate.

TABLE I
EFFECT OF RADIATION INTENSITY ON LD50 OF SHEEP AND SWINE

SPECIES	DOSE RATE (R/HOUR)	LD50/60 (ROENTGENS)	DURATION OF LD50 EXPOSURE (HOURS)
SHEEP	660	237 (215-257)	0.4
	450*	252 (233-276)	0.6
	450*	316 (297-335)	0.7
	261	318 (291-343)	1.2
	30	338 (313-369)	11.3
	3.6	495 (450-558)	137.5
	2.0	637 (538-698)	318.5
SWINE	651	381 (341-423)	0.6
	570*	399 (371-424)	0.7
	275	500	1.8
	30	849 (752-936)	28.3
	4	3444 (2259->5000)	861.0

Exposures were to cobalt-60 gamma or 1 Mvp X-rays*
Sheep: 35-45KG, yearling, castrated-male, Columbia-Rambouillet
Swine: 100-115 KG, 8-9 month Durocs; (NRDL - ♀ ; U.T.- ♀ and ♂)
Details of above LD50 studies can be found in references 3-8

In the sheep study the LD50's were determined within a short period of time, using sheep randomly selected from the same lots with the exception of the second LD50 at 450 R/hour, viz., 316 R. The LD50 of 316 R was determined a number of months later using sheep that appeared physically similar but from different lots. They had a slightly higher LD50 than was found previously at the same dose rate.

The results of a swine study conducted by Brown and Cragle (6) at the University of Tennessee Agricultural Research Laboratory are included in Figure 3 for comparative purposes. Those data correlate quite well with the NRDL data. It can be seen that swine show a considerable increase in LD50 as the dose rate is decreased below 600 R/hour. In contrast such a dramatic change in dose effectiveness does not occur with sheep until the dose rate has dropped below 30 R/hour.

When we consider the LD50 as a function of exposure-time (figure 4) the difference between sheep and swine are perhaps even more evident. As the exposure time is increased from 1/2 hour to 12 hours with sheep, the increase in LD50 is slight, perhaps 15-20%. Based upon the curve through the data points, protracting the exposure to 48 and 96 hours results in no more than 50 and 100% increase in the LD50.

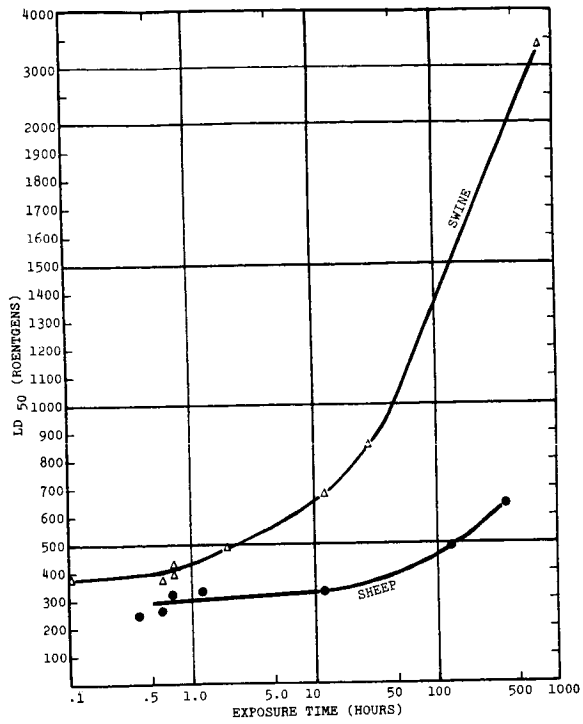

Figure 4. Comparison of radiosensitivity (LD50) of sheep and swine as related to exposure-time.

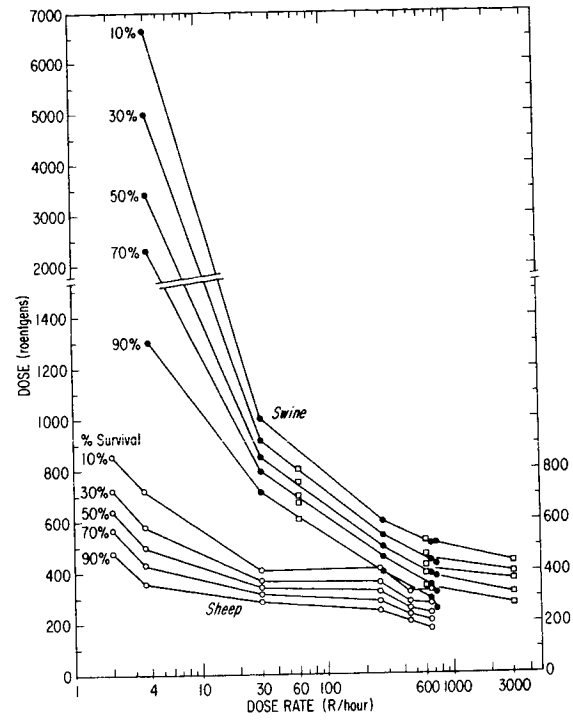

Figure 5. Percent effect dose as related to dose-rate of the exposure.

The effect of similar protraction with swine is much greater. When the exposure time is lengthened to 12, 48 and 96 hours, there is an increase in the LD50 of 75%, 100% and about 300%. Protraction of the exposure to 2 weeks results in a 4-5 fold increase in the LD50 of swine compared to 1-2 fold increase in sheep.

In Figure 5 the percent survival has been plotted as a function of the log of the dose rate. For sheep, the difference between 10 and 90% survival doses for dose rates of 30 R/hour and above was relatively constant amounting to no more than about 200 R. At 4 and 2 R/hour, the spread has doubled with a difference of 400 R. For swine the splaying out of effect curves is not obvious at 30 R/hour whereas at 4 R/hour the heterogeneity in response is enormous with well over 1000 R spread between the 10 and 90% effect doses.

2. Continuous Exposure Until Death:

These studies (9) were undertaken to determine the adaptability of a large animal to a continuous exposure at a low dose-rate, as indicated by the survival time and changes in the peripheral blood counts. The median time to death for sheep exposed continuously to cobalt-60 gamma radiation at a rate of 1.96 R/hour was 43 days. The first death occurred on day 25 after an accumulation of 1100 R; thereafter the deaths were sporadic in appearance, with no one period where a large number died. The last death was on the 60th day, after an accumulation of about 2760 R. The accumulated mortality is shown in Figure 6. Also included in this figure is the dose-response curve for sheep exposed at 2R/hour to predetermined doses. It is quite evident from the dose response curves that the dose required for a given effect is considerably less for terminated exposures, with a much greater slope to the curve.

The changes that occur in the peripheral blood cell counts are a fairly reliable indication of the injury sustained by the hematopoietic tissue following radiation exposure. In these animals, there was an almost immediate depression of the white cell count, reaching significant proportions by day 4 or after an exposure of 180 R. This early change can be attributed primarily to a decrease in the circulating mononuclear cells, for the granulocyte cells remained within the normal range for about 18 days. There is a suggestion of an abortive rise around 12-14 days. By the 25th day, both the mononuclear and granulocytic cells reached an average of 1000 or less and it was at this point that deaths began to occur. The pattern or

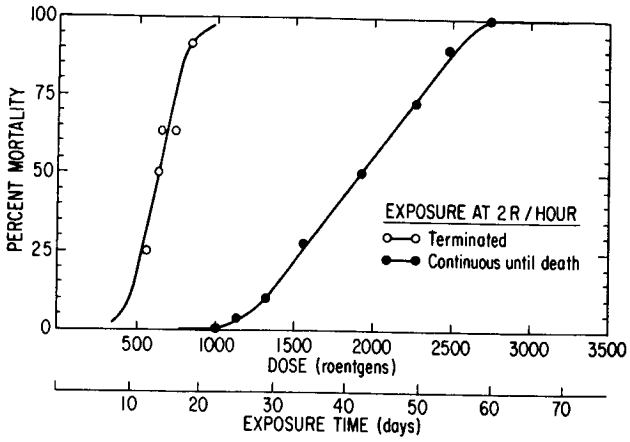

Figure 6. Dose-response curves for sheep irradiated at 1.96 or 2 R/hour.

changes in the mononuclear and granulocytic cells is shown in Figure 7. It is most evident that sheep are unable to adapt to radiation exposures continuously given at a rate of 2 R/hour.

For comparative purposes, a group of sheep were exposed to 50, 100 or 175 R at a similar dose-rate, 1.9 R/hour, with leukocyte counts made at comparable time periods. Exposure times for these animals were approximately 1, 2 and 4 days. The results obtained again showed an early decrease in the leukocyte counts, reasonably correlated with the total dose. However, since the exposures were terminated before reaching lethal levels of injury a return to nearly normal occurred by the end of the third week. These studies demonstrated the significant effectiveness of low dose-rate exposure on the hematopoietic system of sheep (10).

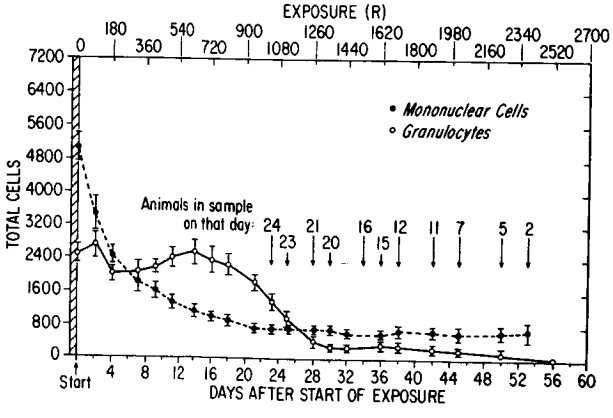

Figure 7. Peripheral leukocyte changes of sheep during continuous exposure at 1.96 R/hour.

B. FRACTIONATED EXPOSURES:

The effect of fractionation on dose response was studied using three different sets of conditions: a) acute exposures separated by various time intervals, b) chronic exposure followed by acute exposures at various time intervals and c) acute exposure followed immediately by a chronic exposure. In keeping with terminology used extensively in the literature we will refer to the first or initial exposure as the conditioning dose.

1. Acute Exposures:

In this series, large groups of sheep and swine were acutely exposed to a conditioning dose of 2/3rds of their acute single-dose LD50, i.e. 177 R for sheep and 265 R for swine. The acute LD50 was determined on subgroups of the conditioned animals at various time intervals thereafter. The results are presented in Table II and Figure 8. Immediately after the conditioning exposure (zero-time) the LD50 plus the initial dose is equivalent to the single-dose LD50. When the conditioned sheep were allowed to wait for 7 or 11 days before re-exposure, there was little change in the LD50 from that found at zero-time. However, by 16 and 20 days the LD50's were greater than that of the controls indicating an induced-radioresistance. This resistance was quite transient, and by the 24th day the animals had reverted to a sensitive stage again, remaining that way at least through the 75th day after conditioning (11).

In contrast to the slow change in radiosensitivity with time found in the sheep study, the change for swine is rapid, such that by the seventh day the LD50 was approximately the same as that of the controls. An even greater radioresistance was found with swine in that by the 16th day, the LD50 was about 165% of controls. The induced-radioresistance was still evident at 61 and 107 days (8).

In a smaller study (5), sheep were conditioned with 100 R at 450 R/hour and LD50's determined at 7 and 16 days. Although this conditioning dose was only about 1/3rd of the acute LD50, a significant amount of the injury was not repaired by one week as the LD50 was still below that of the controls. By 16 days, the LD50 was 180% of controls indicating that a dramatic radioresistance had been induced. The data for this study are included in Table III while Figure 9 contains a curve pertaining to this study. Unfortunately it was not possible to conduct studies at later time periods due to the closure of the laboratory.

TABLE II

RADIOSENSITIVITY (LD50) OF SHEEP AND SWINE AT VARIOUS TIMES AFTER A SUBLETHAL ACUTE EXPOSURE

SPECIES	SINGLE DOSE LD50	INITIAL DOSE	LD50 AT VARIOUS TIMES (DAYS) AFTER INITIAL EXPOSURE									
			0	3	7	11	16	20	24	30	45	75
SWINE[a]	399	265[b]	134	282	306	-	-	654	-	-	-	c
SHEEP	252	177	75	-	86	111	275	324	207	179	193	218
SHEEP	316	100	216	-	256	-	567	-	-	-	-	-

All exposures in Roentgens midline air dose. Radiation source - 1 Mvp X-ray
Dose rates used: Sheep - 450 R/hour; Swine - 540-600 R/hour

a Swine study conducted by Nachtwey (8)

b 240 R used for day 3 study

c LD50 after 61 days was approximately 700R; LD50 after 107 days was greater than 400 R based upon 0/9 mortality from challenge with 399 R.

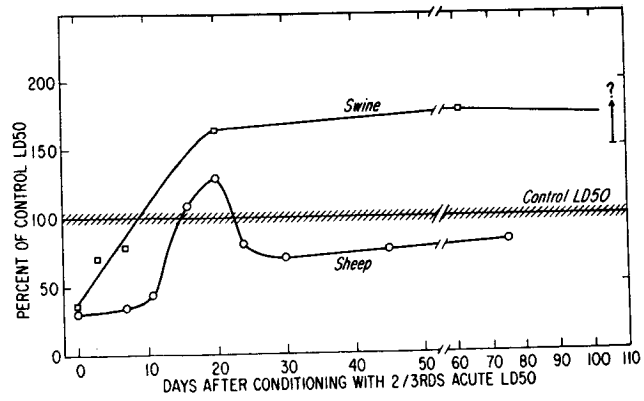

Figure 8. Changes in radiosensitivity (LD50) of sheep and swine following acute exposure to 2/3rds of their acute LD50.

1302-307

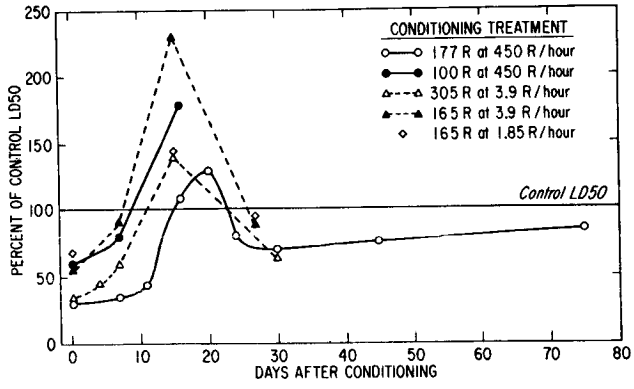

Figure 9. Temporal changes in radiosensitivity (LD50) of sheep after sublethal acute or chronic radiation exposures.

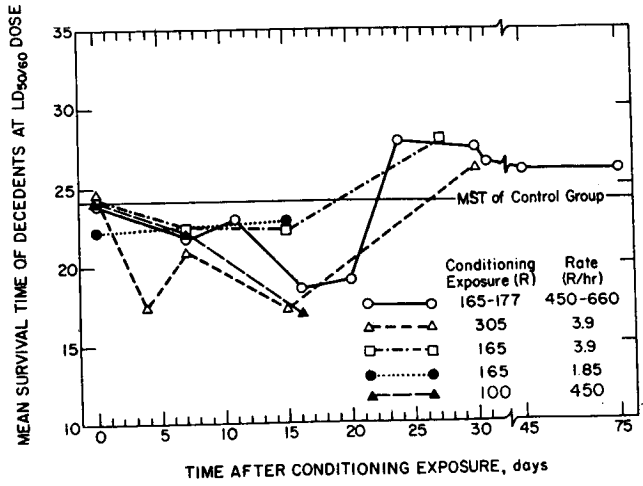

Figure 10. The mean survival time of decedents at the LD50 dose as a function of time after sublethal conditioning radiation exposures.

TABLE III

ACUTE LD50 OF SHEEP AFTER A SUBLETHAL CHRONIC RADIATION EXPOSURE

INITIAL DOSE	DOSE RATE (R/HOUR)	SINGLE DOSE ACUTE LD50	ACUTE LD50 AT VARIOUS TIMES (DAYS) AFTER INITIAL EXPOSURE					
			0	4	7	15	27	30
305	3.9	260	86	118	157	361	-	163
165	3.9	237	133	-	218	546	210	-
165	1.85	237	162	-	-	342	225	-

2. Chronic Exposure Followed by Acute Exposure:

In this study, groups of sheep were conditioned by three different radiation regimens, 165 and 305 R at 3.9 R/hour and 165 R at 1.85 R/hour. The relative radiosensitivity with time was determined using the acute single-dose LD50 again as the baseline or reference value. Immediately (zero-time) and at various time intervals following the chronic irradiation, portions of the conditioned group were exposed to graded acute exposures for LD50 determinations. The data for these studies are presented in Table III, while Figure 9 illustrates the time-related changes in radiosensitivity (LD50). The reference LD50 for the 305 R experiment was not the same as that for the 165 R experiments due to different dates, animal lots and a slightly lower dose-rate employed for the acute LD50 determinations. However, the two LD50's are not statistically different at the 95% confidence level.

The acute LD50 at the end of the 165 R exposure at 1.85 R/hour was 162 R or 68% of normal. Theoretically if the two exposures were completely additive, the LD50 would have been 72 R (237 minus 165). Thus 93 of the 165 R (56%) was repaired by the end of the chronic exposure. The other chronic studies also showed non-additivity or repair of a significant portion of the injury produced during the chronic exposure. At the end of the 165 R exposure at 3.9 R/hour, 104 R injury was present or 61 R (37%) had been repaired.

The injury repaired during the 305 R exposure amounted to 131 R. This was a slightly higher percentage recovery (43%) at 305 R than was found after 165 R. The trend toward higher recovery rates with larger doses, continued for doses of 400 and 495 R as recovery rates of 50 and 52%, respectively, where found (3). This might indicate that a specific recovery mechanism lags somewhat at the beginning and gains impetus with the greater exposure times required for the larger doses.

A consistent pattern developed in sheep allowed to rest for various periods before being subjected to acute exposures. All groups were alike in that the change in radiosensitivity (LD50) was somewhat slow for several days and remained below normal at least for the first week. This slow change or recovery phase was followed toward the end of the second week or beginning of the third week by a rapid transition into a dramatic radioresistant condition. The degree of radioresistance varied from 140 to 230 percent of normal. This radioresistance was quite transient, however, with all groups back to normal or slightly on the radiosensitive side by the 4th week.

The mean survival time (MST) of decedents at the LD50 dose was calculated by linear regression of the MST of each group on the dose received by it through the range of doses used in any particular group. The calculation of MST by this method allows a comparison of survival times normalized to a common biological endpoint, the LD50.

The survival time in the recovery experiments, appeared heavily influenced by the time interval between the sublethal conditioning exposure and the challenge LD50. In Figures 9 - 10, the derived mean survival time (MST) at the LD50 dose is graphed as a function of the time after conditioning. In all cases the MST's for animals re-exposed less than 20 days after conditioning by either an acute or protracted exposure, were considerably shorter than that of the controls. When the recovery period was greater than 20 days, the MST values were somewhat

longer than in controls and in most cases significantly longer than was seen when the recovery period was less than 20 days. The gross pathology and clinical symptomatology were not different for the specific groups. Since detailed physiological or cell kinetic studies were not conducted, one can only offer speculation to explain the nature of such findings. Death likely results from damage to several different tissues although that of the gastrointestinal tract and hematopoietic system are considered the most important in the midlethal range. Each undoubtedly has its own characteristic time course of injury and recovery. The differences observed in the survival time conceivably could reflect an alteration in tissue radiosensitivity, the capability of the stem cell constituents to respond to a second dose of radiation, or perhaps even a change in the relative contribution of various syndromes, e.g., gastrointestinal or hematopoietic, to the lethal injury.

3. Acute Followed by a Chronic Exposure:

Animals in this study (12) were acutely conditioned with 155 R cobalt-60 gamma radiation at a rate of 510 R/hour and immediately exposed to predetermined graded doses at 3.85 R/hour. The LD50 at 3.85 R/hour for the acutely conditioned sheep was 171 R. Thus the combined acute exposure plus the protracted LD50 was 326 R, compared to the single-dose acute LD50 of 314 R. Based upon previous studies, 45 - 50% recovery occurs during chronic exposure at 3.6 R/hour (3). Had a similar recovery occurred in this situation, the LD50 at 3.85 R/hour would have been greater than 300 R, about double that actually found. It can be inferred that the acute exposure has suppressed the recovery mechanisms that operate in the protracted exposure.

TABLE IV

EFFECT OF ACUTE SUBLETHAL EXPOSURE ON DOSE RESPONSE TO SUBSEQUENT CHRONIC EXPOSURE

Control LD50 at 510 R/Hour	314 R
Conditioning Dose at 510 R/Hour	155 R
Difference	159 R
LD50 of Conditioned Animals at 3.85 R/Hour	171 R
Expected LD50 Based Upon 45-50% Recovery During Exposure at 3.85 R/Hour	>300 R
Recovery Rate at 3.85 R/Hour After an Acute Exposure	7%

CONCLUSION: Acute Exposure Has Suppressed Ability To Recover During Low Dose-Rate Exposure

DISCUSSION

Of the numerous factors that can modify the dose-response relationship to space radiation, two of the most important are dose protraction and nonuniform dose distribution within the body. It is generally conceded that the reduction in dose-effectiveness observed in protracted exposure is due to recovery mechanisms that act to offset the injury as it is produced. This paper has dealt with the total of the recovery processes and has not attempted to identify the specific mechanisms involved, e.g., intracellular repair or repopulation of vital stem cells.

The two methods of protracting an exposure, i.e., by continuous exposure at lowered dose-rates (chronic exposure) or fractionating the exposure into two or more doses, were compared in these large animal experiments. It is quite apparent that the dose-response to both chronic irradiation and fractionation varies greatly between the sheep and swine. The ability of swine to survive large doses of radiation under protracted conditions was also found by Brown et al (6), using daily fractions of 50 or 100 R/day until death. The exposure was at a moderate dose-rate, about 30 R/hour; thus the actual exposure times were about 1 1/2 - 3 hours per day. In those studies swine demonstrated a remarkable ability to outlive cattle and burros. The mean accumulative lethal doses at 100 R/hour averaged 3900 R for swine compared to 3200 R for cattle and 2330 for the burro. The results at 50 R/hour were even more striking. At that rate, the mean lethal dose for swine was over 10,000 R compared to 2250 and 1510 R for cattle and burros, respectively. Thus the LD50 of 3444 R found at NRDL under chronic exposure at 4 R/hour (approximately 100 R/day) and the mean accumulative lethal dose of 3900 R found at the University of Tennessee at 100 R/day fractionated exposures are quite comparable, especially if one discounts a certain portion of the 3900 R as unnecessary or wasted radiation.

In contrast to the remarkable ability of swine to survive at 50 R/day with over half the animals alive after 200 days, none of the sheep chronically exposed at slightly less than 50 R/day survived past 60 days, with the median time of death 43 days. In effect the swine survived about 5 times as long. In going from an acute exposure to 4 R/hour continuous exposure, the ratio of chronic LD50 to acute LD50 for sheep was about 2.5%. For swine, their remarkable recovery ability again was demonstrated as the ratio of chronic:acute was nearly 9:1.

The rapid recovery and large and persistent radioresistance of swine following an acute sublethal exposure again differed from the recovery of sheep. Sheep were

slow to begin recovery and while they also progressed into a resistant state by the end of the second week, it was quite transient and by the 24th day was gone. There are data from the University of Tennessee laboratory that would tend to support the persistent radioresistance of swine. Shively et al (13) found the LD50 for swine exposed 4 months previous was 60% greater than the controls of the earlier study.

It became apparent from the dose-rate and recovery studies that swine were not the preferred animal model for extrapolation purposes. With this in mind the great bulk of the large animal studies at NRDL were conducted with sheep. Recovery or relative radiosensitivity patterns were determined after exposures to radiation at either acute or chronic exposure rates. In addition the influence of size of the exposure on subsequent recovery was assessed.

We were a little surprised with the consistency in recovery patterns of sheep after both high and low levels of injury produced at acute or chronic dose-rates. In all cases the changes in radiosensitivity (or recovery) consisted of a triphasic pattern with an initial slow phase for the first week in which no group had returned to normal by the 7th day. This was followed by an induced-radioresistance toward the end of the second week. The radioresistance phase was transient, however, and the sheep had returned to a slightly sensitive state during the third week.

While neither the dose-rate nor size of the conditioning exposure changed the basic pattern, there were differences in the extent and temporal patterns of some of the fluctuations. It would appear that recovery after acute exposure is slower than after chronic exposure. The greatest radioresistance was induced by a dose equivalent to 1/3 of the LD50, i.e., 100 R at 450 R/hour and 165 R at 4 R/hour, with LD50's 180 and 230% of the controls at 15-16 days. It was financially impossible to describe the curves at more time points as one might desire. It is probable that the 15-16 days do not represent the maximum overshot or resistance stage since no testing was done after the chronic exposures in the period of 16-27 days. In fact the 20th day was the most resistant time after the 177R acute exposure. One might speculate that an optimum dose exists for stimulating marrow cell proliferation which likely accounts for the resistance condition. If the dose is too great, the stock of progenitor cells may be reduced to a level which takes time to repopulate with minimal capability to overshoot. If the dose is too small, the stimulus for repopulation may not be as dynamic.

A significant and unexpected finding was the influence of an acute exposure to negate the usual recovery that takes place during chronic exposure. In such a situation where an acute exposure precedes a chronic exposure the doses are additive. This conceivably could be of considerable importance in assessing the effect of radiation on space travelers. Under certain conditions in which both acute and chronic exposures are received the assigning of 0.5 as a relative injury factor for chronic exposure, as suggested by the Space Radiation Study Panel (1), may not be too appropriate. Due to the potential importance of this point we feel this situation should be explored further using additional large animal species, such as the nonhuman primate and dog.

Table V summarizes the differences that we have observed in additivity of acute and chronic exposures under the various conditions as described in this paper.

TABLE V

DIFFERENCES IN ADDITIVITY OF ACUTE AND CHRONIC EXPOSURES OF SHEEP

1ST EXPOSURE	2ND EXPOSURE	EFFECT	INTERPRETATION
ACUTE (165 R at 660 R/hour)	ACUTE (0-11 days after 1st exposure)	ADDITIVE No immediate recovery 8% recovery at 7 days 20% recovery at 11 days	SLOW RECOVERY during 1st week after acute exposure
CHRONIC (165 R at 3.9 R/hour)	ACUTE (immediately and 7 days after 1st exposure)	NON-ADDITIVE 50% recovery during chronic exposure; 90% recovery at 7 days	FAST RECOVERY during chronic exposure. Nearly complete recovery within one week.
ACUTE (155 R at 510 R hour)	CHRONIC (exposure at 3.9 R/hour immediately after acute exposure)	ADDITIVE 7% recovery during chronic exposure	SLOW RECOVERY during chronic exposure which is preceded by acute exposure

Nonuniform distribution to the body can also be a significant modifier of the dose-response relationship. It is probable that space exposure will be relatively non-uniform due to variations in shielding within the space craft, and the unidirectional aspect of solar and nuclear reactor radiations. Due to body size and thus self-shielding, nonuniform exposure of man and large animals is an important consideration.

The observed ratio of midline tissue dose (MLT) to a midline air dose (MLA) is highly dependent upon the size of the animal. The following values for Cobalt-60 or x-irradiation (250-1000 kvp) were presented in a recent survey (14): .82 - .86 for dogs, .6 - .68 for swine, .58 - .65 for sheep, and .40 - .50 for cattle and burros. A factor of .65 is used by Lushbaugh, et al (15) to convert exposure dose to an epigastric rad dose for man.

With a large inhomogeneity of dose distribution, one would expect that the unilateral exposure might be considerably less effective than a bilateral exposure if the damage to bone marrow is the critical determinant for survival. The gammo and X-ray unilateral LD50's for larger animals are generally 20-30% greater than bilateral LD50's while the dog irradiated dorsally has been reported to have an LD50 approximately 50-60% higher than with bilateral irradiation (14). Bond and Robinson (16) concluded that the main factor in the decreased effectiveness of nonuniform (unilateral) exposure versus uniform (bilateral) exposure, is the relatively large fraction of stem cells surviving in areas of bone marrow receiving the lowest dose.

It would appear that shielding of only a minute but select portion of the bone marrow can have a dramatic protective effect. In a study by Cole (17) at NRDL, lead shielding, completely surrounding a single elbow of the dog for a length of 4 - 6 inches, resulted in 50% survival at 1000 R a dose 3 X greater than the whole-body LD50/30. Those animals that did die, succumbed between 6 - 8 days from what appeared to be gastrointestinal involvement. A relatively complete shielding of a single elbow was more effective than the use of a larger total amount of lead placed over all four elbows. This apparent paradox was explained on the basis of the exponential nature of cell-killing by irradiation.

The results described from these large animal studies have demonstrated that dose protraction and spatial distribution are certainly important modifying factors in determining the response to a given radiation exposure. It is quite evident that there are major differences between swine and sheep in their response to chronic exposure, pattern of recovery and relative rediosensitivity following a sublethal exposure. In attempting to extrapolate animal results to assess effects in man, selection of the appropriate animal model becomes of considerable importance. Based upon the results obtained in radiotherapy, we propose that sheep are a better model for man than is swine or small laboratory rodents. While the rhesus monkey would appear to be the choice for performance studies, he suffers greatly from being small and not as comparable in depth-dose and dose distribution to specific organs. In addition the rhesus monkey has an acute LD50 in the range of 500 - 600 R which is greater than man's.

The studies of Lushbaugh, et al (15) demonstrate that man's response to both acute and chronic radiation is reasonably close to that found with the sheep. The acute LD50 for radiotherapy patients is about 250 rads. It appears that man is slow to repair radiation-induced hematopoietic damage and remains relatively radiosensitive as the dose-rate is decreased. Using Bateman's (18) method of indexing radiosensitivity response to changes in intensity by relating the LD50 to the reciprocal cube root of the dose-rate, a slope constant for normal man was found to be quite close to that of sheep (19). Bateman's analysis of mice data in the literature and these sheep and swine data gave results of 0.65 for sheep, 0.95 for mice and 1.6 for swine. Thus, of all species analyzed by that method sheep would appear the closest to man. In addition, Lushbaugh found that fractionated, daily, acute exposures over an 8 day period had a greater effect than the same dose given chronic (continuously) over the same exposure period.

Unfortunately, data on the nonhuman primate, especially the rhesus monkey, are conflicting as to the recovery rate and their response to chronic exposure. We have more confidence in using the data obtained with sheep for assessing hematopoietic and lethality effects in man than that obtained with swine or rodents.

SUMMARY

1. While sheep and swine are basically similar in response to acute radiation, their sensitivity to chronic irradiation is markedly different. Sheep remain relatively sensitive as the radiation exposure is protracted while swine are more resistant and capable of surviving extremely large doses of chronic irradiation.
2. This response to chronic irradiation correlated well with changes in radiosensitivity and recovery following an acute, sublethal exposure. Swine recover remarkably fast and develop a large and persistant radioresistance. The change in radiosensitivity of sheep after either acute or chronic sublethal exposure is basically the same, consisting of a triphasic pattern of an initial slow recovery, transient radioresistance and regression into a long-lasting period of relative radiosensitivity.
3. The overall effect of receiving both acute and chronic exposures within a short period of time may depend upon the sequence of the exposures. At least with sheep an acute exposure appears to reduce the recovery potential for chronic exposures that follow within a short time. In such a situation the individual response to both acute and low chronic exposures are additive. In contrast the response to a chronic exposure before an acute exposure is not additive with significant recovery occurring during the chronic exposure.
4. The spatial or dose distribution within the body of a large animal is a significant factor. Unilateral or partial-body exposure is considerably less effective for a given dose than is a bilateral or total body exposure. A simple lead-cuff around a small but select portion of the bone marrow can result in significant protection.

REFERENCES

1. Radiation Protection Guides and Constraints for Space-Mission and Vehicle-Design Studies Involving Nuclear Systems, Report of the Radiobiological Advisory Panel of the Committee on Space Medicine, Space Science Board, National Academy of Sciences, p 4 (1970).
2. Radiobiological Factors in Manned Space Flight, Wright H. Langham (editor), Publication 1487, National Academy of Sciences, pp 42-43 (1967).
3. N.P. Page, E.J. Ainsworth and G.F. Leong, The Relationship of Exposure Rate and Exposure Time to Radiation Injury in Sheep, Radiation Res. 33, pp 94-106 (1968).
4. G.E. Hanks, N.P. Page, E.J. Ainsworth, G.F. Leong, C.K. Menkes, and E.L. Alpen, Acute Mortality and Recovery Studies in Sheep Irradiated With Cobalt-60 gamma or 1-Mvp X-rays, Radiation Res. 27, pp 397-405 (1966).
5. E.T. Still, J.F. Taylor, G.F. Leong, and E.J. Ainsworth, The Influence of the Amount of Initial Radiation Exposure on the Recovery Pattern in Sheep, NRDL-TR-69-97, 15 July 1969.
6. D.G. Brown and R.G. Cragle, Some Observations on Dose-Rate Effect on Burros, Swine and Cattle, Proceedings of a Symposium on Dose Rate in Mammalian Radiation Biology, Oak Ridge, Tenn., pp 5.1-5.16 (1968).
7. J.F. Taylor, N.P. Page, E.T. Still, G.F. Leong, and E.J. Ainsworth, The Effect of Exposure Rate on Radiation Lethality in Swine, NRDL-TR-69-96, 14 July 1969.
8. D.S. Nachtwey, E.J. Ainsworth, and G.F. Leong, Recovery from Radiation Injury in Swine as Evaluated by the Split-Dose Technique, Radiation Res. 31, pp 353-367 (1967).
9. E.T. Still, J.F. Taylor, G.F. Leong, and E.J. Ainsworth, Survival Time and Hematological Responses in Sheep Subjected to Continuous ^{60}Cobalt Gamma Irradiation, NRDL-TR-69-28, 9 May 1969.
10. E.T. Still, S.T. Taketa, E.J. Ainsworth, G.F.Leong, and J.F. Taylor, Hematological Response in Sheep Given Protracted Exposures to ^{60}Co Gamma Radiation, NRDL-TR-69-6, 28 January 1969.
11. N.P. Page, E.J. Ainsworth, J.F. Taylor, and G.F. Leong, Recovery of Sheep After Whole-Body Irradiation: A Comparison of Changes in Radiosensitivity after Either Acute or Protracted Exposure, NRDL-TR-69-4, 25 November 1968.
12. E.T. Still, J.F. Taylor, G.F. Leong, and E.J. Ainsworth, Mortality of Sheep Subjected to Acute and Subsequent Protracted Irradiation, NRDL-TR-69-32, 9 June 1969.
13. J.N. Shively, H.L. Andrews, A.R. Warner, Jr.. H.P. Miller, H.J. Kurtz, and K.T. Woodward, X-ray Exposure of Swine Previously Exposed to a Nuclear Detonation, Am. J. Vet. Res. 25, pp 1128-1133 (1964).
14. N.P. Page, The Effect of Dose-Protraction on Radiation Lethality of Large Animals, pp 12.1-12.23, Symposium Dose-Rate in Mammalian Radiation Biology, UT-AEC Agr. Res. Lab., Oak Ridge, Tenn., Apr. 29-May 1, 1968 (AEC Conf. - 680410).
15. C.C. Lushbaugh, F. Comas, C.L. Edwards, and G.A. Andrews, Clinical Evidence of Dose-Rate Effects in Total-Body Irradiation in Man, pp 17.1-17.25, Symposium Dose-Rate in Mammalian Radiation Biology, UT-AEC Agr. Res. Lab., Oak Ridge, Tenn., Agr. 29-May 1, 1968 (AEC Conf. - 680410).
16. V.P. Bond and C.V. Robinson, A Mortality Determinant in Nonuniform Exposures of the Mammal, Radiation Res. Suppl. 7, pp 265-275 (1967).
17. L.J. Cole, H.M. Haire, and E.L. Alpen, Effectiveness of Small External Epicondylar Lead Cuffs Against Lethal X-radiation in Dogs, USNRDL-TR-1068, 6 September 1966.
18. J.L. Bateman, A Relation of Irradiation Dose-Rate Effects in Mammals and in Mammalian Cells, pp 23.1-23.19, Symposium Dose-Rate in Mammalian Radiation Biology, UT-AEC Agr. Res. Lab., Oak Ridge, Tenn., Agr. 29-May 1, 1968 (AEC Conf. - 680410).
19. C.C. Lushbaugh, personal communication.

EFFECT OF CONTINUOUS GAMMA-RAY EXPOSURE ON PERFORMANCE OF LEARNED TASKS AND EFFECT OF SUBSEQUENT FRACTIONATED EXPOSURES ON BLOOD-FORMING TISSUE

J. F. Spalding, L. M. Holland, J. R. Prine, D. N. Farrer,* and R. G. Braun*

Biomedical Research Group, Los Alamos Scientific Laboratory,
University of California, Los Alamos, New Mexico 87544

Sixteen *Macaca mulatta* monkeys trained to perform continuous and discrete-avoidance and fixed-ratio tasks with visual and auditory cues were performance-tested before, during, and after 10-day gamma-ray exposures totaling 0, 500, 750, and 1000 rads. Approximately 14 months after the performance-test exposures, surviving animals were exposed to 100-rad gamma-ray fractions at 56-day intervals to observe injury and recovery patterns of blood-forming tissues.

The fixed-ratio, food-reward task performance showed a transient decline in all dose groups within 24 hours of the start of gamma-ray exposure, followed by recovery to normal food-consumption levels within 48 to 72 hours. Avoidance tasks were performed successfully by all groups during the 10-day exposure, but reaction times of the two higher dose-rate groups in which animals received 3 and 4 rads per hour or total doses of 750 and 1000 rads, respectively, were somewhat slower. Performance of reward and avoidance tasks was equal to control levels 60 days after termination of gamma-ray exposures, showing no residual neurological injury reflected as a decrement in motivation to perform learned tasks. Peripheral blood characteristics showed dose-dependent injury to blood-forming tissue. Radiation-induced injury in higher dose groups reached critical levels, resulting in death of three subjects. During a 60-day recovery period, peripheral blood elements returned to control levels.

During the fractionated gamma-ray exposure regime, initiated 414 days after the performance-test exposures, bone-marrow suppression was observed after each 100-rad exposure. Recovery to pre-exposure levels was observed in all groups during each 56-day recovery period between exposures. All animals in each of the four pre-test dose groups were vigorous, active, and aggressive after fifteen 100-rad fractions, and the bone marrow of each group was sufficiently resilient to maintain animals in a clinically healthy condition.

Using acute, fractionated, or protracted exposure techniques to vary dose rate, the effects of exposure to large and small doses of ionizing radiations have been studied extensively in rodents. Reference material on this subject is too voluminous to cover here. Insight gained concerning the mechanisms or kinetics of radiation injury, both transient and irreparable, has contributed significantly to the establishment of radiation standards suggested by national and international committees as being acceptable for present and future generations. Civil defense and military agencies continue to require total-dose and dose-rate effects data. Looking forward to the next decade and the future manned space program, we can expect larger numbers of space career personnel to probe deeper into space for longer periods of time. Future space missions of longer duration will entail increased risk of solar flares, greater accumulations of ambient radiation from the space environment, and possible radiation exposure from on-board nuclear power systems. In short, a new set of radiation standards, acceptable for space professions and earth-originated nuclear emergencies, is required.

Earlier investigations with mice demonstrated the following. Dose-rate affects mean survival time during continuous exposure to cobalt-60 gamma rays (ref. 1) but does not affect mean after-survival time following equal discrete gamma-ray exposures with dose rates ranging from 2.5 to 250 rads per hour (ref. 2); there is a relationship between age and radiation sensitivity with age response to high-dose-rate discrete exposure being more pronounced than to low-intensity protracted exposure (refs. 3 and 4); there is a genetic involvement in radiation-induced hematopoietic injury (refs. 5 and 6); the recovery rate of hematopoietic tissue

*6571st Aeromedical Research Laboratory, Holloman Air Force Base, New Mexico.

is independent of the size of the acute (sublethal) conditioning dose (ref. 7) or total accumulated dose from continuous exposure (ref. 8); and under given exposure conditions, it may be possible to predict residual radiation-induced injury from challenge exposure doses (ref. 9). Many of these findings may, in principle, be applicable to human response to radiation experience. Suggested guidelines for emergency radiation-exposure limits (ref. 10), based on small-animal research and human radiation-accident data, have proved overly optimistic for subhuman primates (ref. 11). Therefore, radiation-exposure experience anticipated from space and earth-bound emergency conditions must be studied on mammals more closely related to man. The rhesus monkey (*Macaca mulatta*) is more closely related to man than is the rodent and has been recommended as the best "all-purpose" laboratory primate (ref. 12). The following is a report on a continuing program to obtain radiation-exposure experience with the subhuman primate (*Macaca mulatta*).

METHODS

Sixteen rhesus (*Macaca mulatta*) monkeys, 7 males and 9 females, weighing 4.5 to 5.4 kg, were trained to perform four tasks while seated in specially designed restraint chairs (figure 1). The tasks were as follows. *Continuous avoidance.*--The monkeys were required to press a lever (on the right-hand side of the panel in figure 1) at least once every 5 seconds while a red light above the lever was on. A mild shock from the seat bars was administered automatically if the task was not performed properly. Four-minute performances were required at closely spaced intervals. *Discrete avoidance with sound cue.*--A 1000-hertz tone was emitted aperiodically from a speaker in the upper center of the performance panel (figure 1). To avoid a mild shock, the animal had to terminate the sound within 3 seconds by pressing the stimulus-response key directly below the speaker. *Discrete avoidance with visual cue.*--Seven blue lights on the performance panel were lit individually according to a preset random schedule. Monkeys were allowed 3 seconds to press the stimulus-response key to switch the light off to avoid a shock. *Fixed ratio.*--A food reward was obtained by pressing a lever at the lower left side of the panel (obscured by the monkey in figure 1) 50 times when a yellow light directly over the lever was on. One-gram banana-flavored food pellets obtained in this manner plus half an apple each day made up the total diet of the monkeys during the test period.

Twelve monkeys were positioned in performance chairs in an arc around a cobalt-60 point source at distances that would provide dose rates of 2.13, 3.19, and 4.26 rads per hour, respectively, to three groups of four animals (figure 2). Four more monkeys were positioned behind shielding to act as a control group (figure 3). Gamma-ray dose rates were mid-body air doses measured with high-energy Victoreen chambers. Thermoluminescent dosimeter implants on the front and back of each monkey were used to check total-body doses during the performance test.

One-hour work schedules included seven auditory and 28 visual discrete avoidance cues, eight 4-minute continuous avoidance sessions, and one 15-minute fixed-ratio food reward session. Six 1-hour work sessions were followed by a 6-hour rest period, during which the room was dimmed to near

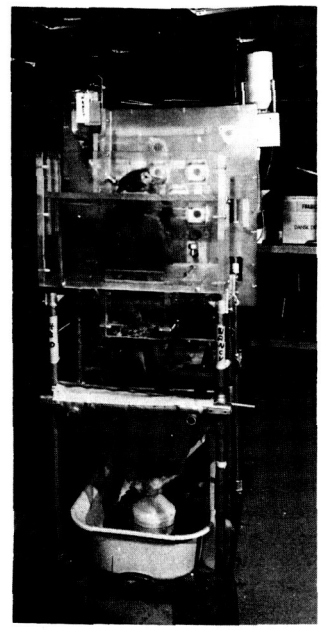

FIGURE 1.--Restraint chair showing pillory neck and waist plate. The performance panel with auditory and visual pressure disconnect plates is in front of the monkey. The continuous avoidance lever is at the lower right of the panel, but the food reward lever is obscured by the monkey. The foot rest exercise unit may be moved by foot and leg pressure.

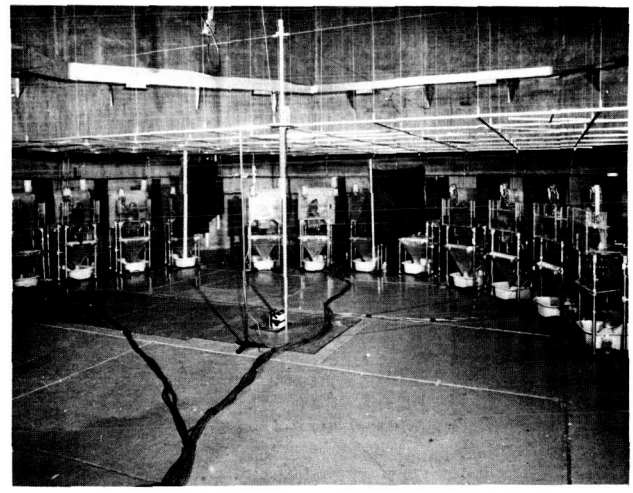

FIGURE 2.--Monkeys in performance chairs arranged in arcs around a cobalt-60 gamma-ray source (housed in tube in center of picture) at distances such that four monkeys in each of three groups would receive 2.13, 3.19, and 4.26 rads per hour, respectively.

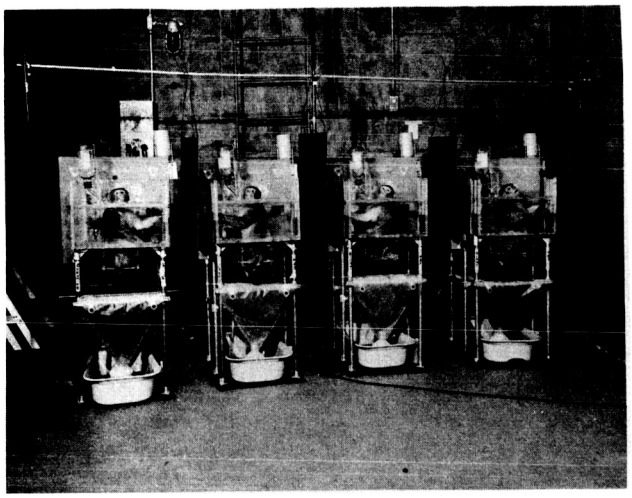

FIGURE 3.--Control monkeys arranged in performance chairs in shielded area of the source building.

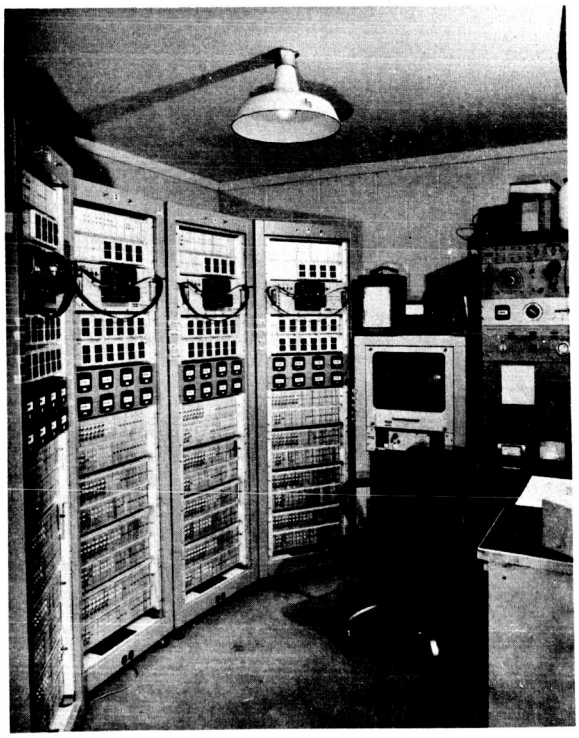

FIGURE 4.--Automated stimulus-presentation and data-collection equipment used to deliver task stimuli and to record performance data.

darkness. Animal care was performed daily during 30 minutes taken from one of the two 6-hour rest periods. Blood samples were also taken frequently. Automated stimulus-presentation and data-collection equipment was used (figure 4).

The performance test required 30 days: 10 before, 10 during, and 10 after exposure. Monkeys were transferred to comfortable cages after the test and allowed 60 days to recover from radiation injury. They were tested for possible residual effects during a second 30-day performance test without gamma-ray exposure.

Monkeys that survived the 500-, 750-, or 1000-rad gamma-ray exposure accumulated during the performance test were kept in comfortable monkey runs for 414 days to allow recovery from all repairable radiation-induced injury. After this extended recovery period, the animals in all the test groups and the control group were subjected to 100-rad whole-body gamma-ray exposures of approximately 40 rads per hour at 56-day intervals. Peripheral blood characteristics were observed before and between exposures.

RESULTS

A detailed analysis of the task-performance phase of this investigation will be published. Performance testing is discussed here primarily to show the radiation history of the animals used in the second, or fractionated-exposures, investigation. The three experimental groups performed learned tasks during the 30-day test (10 days before, 10 days during, and 10 days after gamma-ray exposure) in a like manner and did not differ from the control group. Control and irradiated groups performed all visual and auditory cue avoidance tasks with equal proficiency. The fixed-ratio, or food-reward, tasks showed a transient performance decrement beginning on the first day of gamma-ray exposure and lasting into the third or fourth day. The degree of this decrement was directly related to gamma-ray dose rate; the 2.13-rad per hour group showed the least effect, and the 4.26-rad per hour group showed the greatest.

One animal in the high-dose-rate group (1000 rads total dose) showed signs of serious radiation injury on the fifth day of the postexposure phase of the performance test and died on the eighth postexposure day. Although this animal was in a terminal stage of radiation injury, he showed no performance change until within 14 hours of death. During the 60-day recovery phase, two animals in the middle-dose-rate group (total accumulated dose of 750 rads in 10 days) died from radiation injury. The follow-up performance test after 60 days of recovery indicated that no animal surviving gamma-ray exposure had incurred irreparable radiation-induced injury measurable as a task-performance decrement. The irradiated monkeys performed all tasks at control level.

HEMATOLOGICAL OBSERVATIONS DURING AND AFTER LEARNED-TASK PERFORMANCE TESTING

Packed cell volume (PCV) values and white blood cell (WBC) counts of peripheral blood samples taken during and after the task-performance phase of this

investigation are shown in figures 5 to 8. A significant effect on PCV was apparent in all exposed groups 8 days after the cobalt-60 source was removed. The effects shown in figures 5 to 8 were dose-dependent and were greatest approximately 16 days after exposure. Recovery was rapid, and near-normal values were observed 37 days after the radiation stress was removed. The traumas of restraint and task-performance stimuli provoked an increase in WBC count in all groups during the 10-day pre-exposure test as shown in figures 5 to 8. White blood cell counts decreased within 2 days after whole-body gamma-ray exposure was started and dropped to critical levels in the two highest dose groups (750 and 1000 rads) within 8 days after the radiation source was removed (figures 7 and 8). Two animals in the 750-rad group and one in the 1000-rad group died of radiation sickness (the death of these animals was mentioned earlier). White blood cell recovery was evident in survivors by day 33 (13 days after end of exposure) and had returned to control levels 2 weeks later. Although the magnitude of injury was dose-dependent, the recovery rate appeared to be independent of dose (figures 6 to 8).

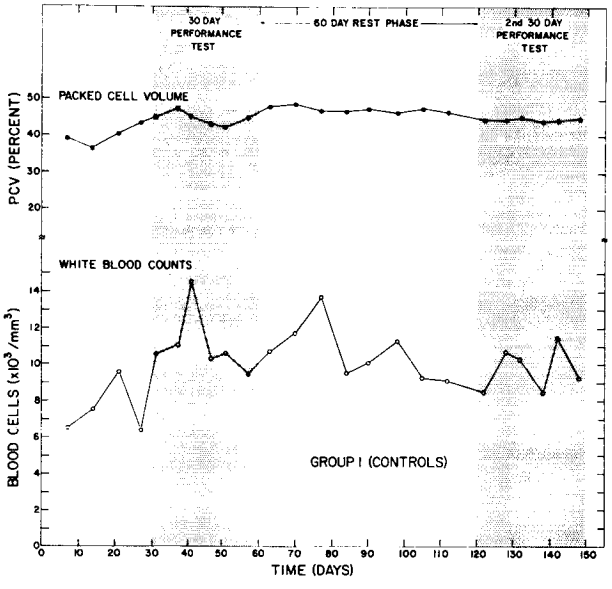

FIGURE 5.--Packed cell volume and white blood cell count plotted against time before, during, and after a 30-day task-performance test.

As might be expected, erythrocyte count (RBC) and hemoglobin (Hgb) levels paralleled PCV values. Lymphocytes, the most radiosensitive cellular element of peripheral blood, followed essentially the same injury-recovery pattern as did WBC. Lymphoid (monocytes and lymphocytes) and myeloid (neutrophils and eosinophils) ratios commonly ranged between 60 to 70 and 25 to 40, respectively. By the eighth day of exposure, these ratios were reversed with the degree of reversal being dose-dependent. Lymphoid and myeloid ratios stabilized at pre-exposure levels about 60 days after gamma-ray exposure.

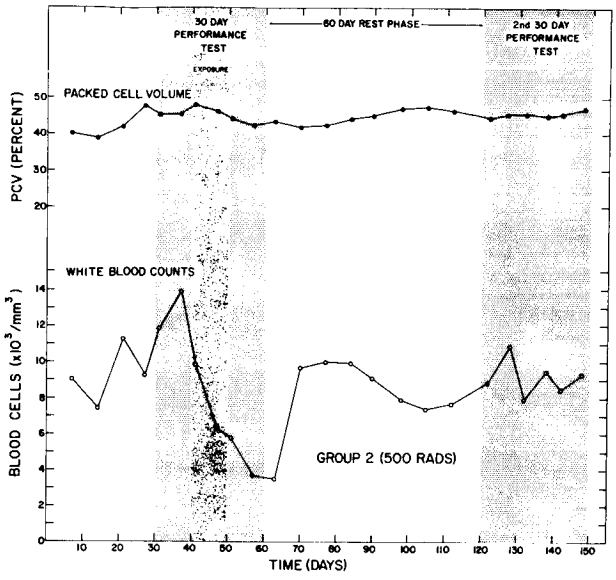

FIGURE 6.--Packed cell volume and white blood cell count plotted against time before, during, and after a 30-day task-performance test, including 10 days of gamma-ray exposure totaling 500 rads.

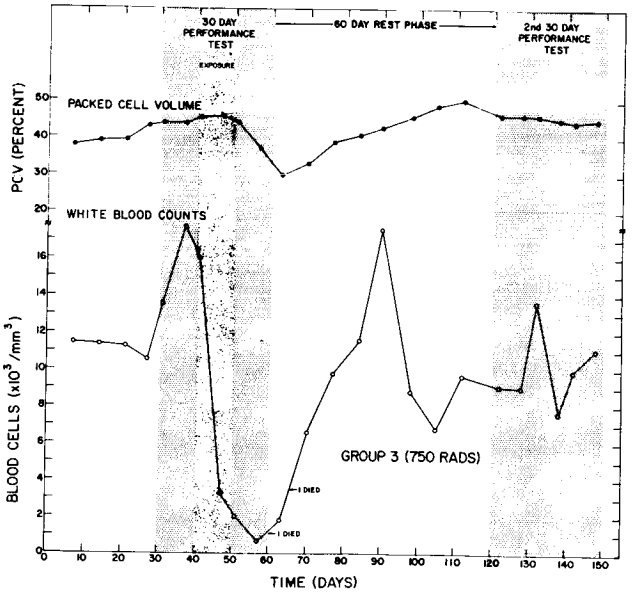

FIGURE 7.--Packed cell volume and white blood cell count plotted against time before, during, and after a 30-day task-performance test, including 10 days of gamma-ray exposure totaling 750 rads. Two animals died from radiation sickness at the times indicated on the WBC plot.

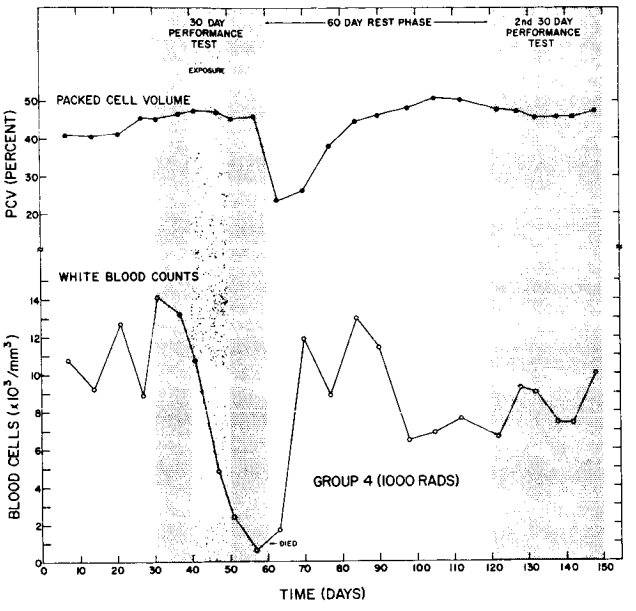

FIGURE 8.--Packed cell volume and white blood cell count plotted against time before, during, and after a 30-day task-performance test, including 10 days of gamma-ray exposure totaling 1000 rads. One animal died from radiation sickness at the time indicated on the WBC plot.

CLINICAL FINDINGS AND MORTALITY

Anorexia was present in varying degrees in all exposed animals during the first 2 or 3 days of exposure. However, all monkeys surviving the gamma-ray exposure had regained their appetites by the end of the 10-day exposure period. Exposed animals exhibited some diarrhea, and feces of those in the two higher dose groups were frequently bloody, indicating severe gastrointestinal damage. Several monkeys in the two higher dose groups showed petechiae and ecchymosis, which were most apparent on the conjuctivae and gingiva and at points of body contact with the restraining chairs. Menstrual-period cycling appeared to be unaffected by the 10-day gamma-ray stress. The three animals that died of radiation sickness suffered hematuria, and one of the two 750-rad monkeys exhibited paralysis of the right arm and left eyelid before death.

HEMATOLOGICAL RESPONSE OF MONKEYS TO 100-RAD GAMMA-RAY EXPOSURES DELIVERED AT 56-DAY INTERVALS

Peripheral blood samples taken from the saphenous vein at frequent intervals before and after each 100-rad gamma-ray exposure were analyzed for red blood cells (RBC), white blood cells (WBC), hemoglobin (Hgb), packed cell volume (PCV), and differential counts. Platelet counts were made several times but not routinely. Packed cell volume and WBC values of groups 1 through 4, respectively, are shown in figures 9 to 12. The response patterns of PCV, Hgb, and RBC to the 100-rad exposure regime were similar to each other, and lymphocytes followed the injury-recovery pattern of WBC values. Packed cell volumes ranged from 40 to 50% during the 840-day period in which the animals received fifteen 100-rad exposures. No significant differences in injury response to or recovery from the 100-rad fractions have been seen in PCV values of the four groups investigated. Thus, group 4 animals (figure 12) with 1000 rads of gamma-ray exposure 414 days before the start of the 100-rad fractionation regime appeared to have radiation resistance and recovery characteristics similar to those of group 1 (figure 9) which had no gamma-ray exposure before the fractionation study.

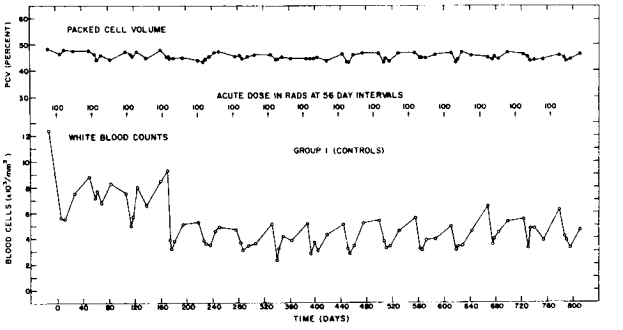

FIGURE 9.--Packed cell volume and white blood cell count of group 1 monkeys plotted against time during a fractionated gamma-ray exposure regime, including fifteen 100-rad exposures given at 56-day intervals. Group 1 monkeys had received no gamma-ray exposure prior to the fractionation series.

Lymphoid (monocytes and lymphocytes) and myeloid (neutrophils and eosinophils) ratios have fluctuated with the bone-marrow injury and recovery associated with each of the fifteen 100-rad gamma-ray fractions, but these ratios have not been scrutinized yet. White blood cells were depressed to somewhat lower levels after the first four 100-rad exposures and have maintained these lower levels (figures 9 to 12). Platelet counts done at irregular intervals on animals in all four groups were within the normal range (79,000 to 368,640) reported by Krise and Wald (ref. 13).

A major objective of this investigation is to determine the extent of radiation-induced "irreparable bone-marrow injury" using peripheral blood elements as recovery response indicators. Comparative PCV and WBC injury-recovery responses of peripheral blood from the four groups following the first and sixteenth 100-rad exposures are shown in figures 13 to 15. Packed cell volume and WBC responses from the first 100-rad exposure were extremely uniform for each of the four groups regardless of radiation history. Thus, if irreparable or residual injury remained from earlier exposures in the three exposed groups, it was not apparent in the cellular observation of peripheral blood after a single 100-rad exposure.

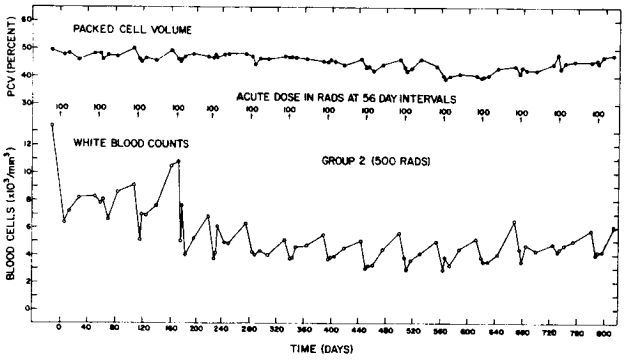

FIGURE 10.--Packed cell volume and white blood cell count of group 2 monkeys plotted against time during a fractionated gamma-ray exposure regime, including fifteen 100-rad exposures given at 56-day intervals. Group 2 monkeys had received 500 rads of gamma rays protracted over 10 days 414 days before the fractionation series.

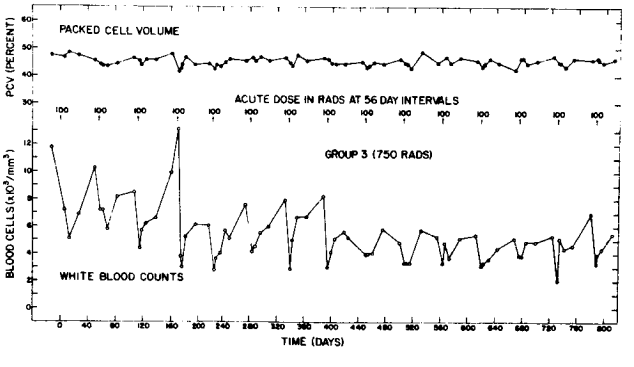

FIGURE 11.--Packed cell volume and white blood cell count of group 3 monkeys plotted against time during a fractionated gamma-ray exposure regime, including fifteen 100-rad exposures given at 56-day intervals. Group 3 monkeys had received 750 rads of gamma rays protracted over 10 days 414 days before the fractionation series.

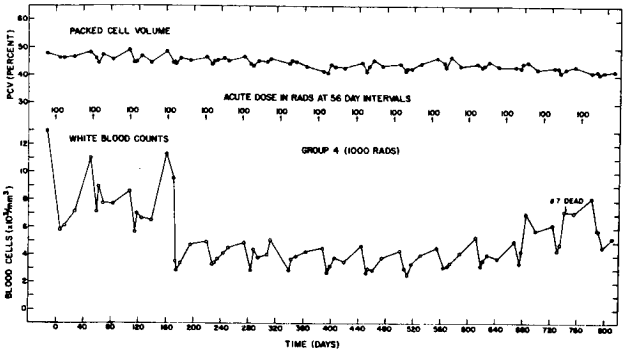

FIGURE 12.--Packed cell volume and white blood cell count of group 4 monkeys plotted against time during a fractionated gamma-ray exposure regime, including fifteen 100-rad exposures given at 56-day intervals. Group 4 monkeys had received 1000 rads of gamma rays protracted over 10 days 414 days before the fractionation series. One monkey (designated as #7) died from radiation sickness after the fourteenth 100-rad fraction.

Bone-marrow response from the sixteenth 100-rad exposure as reflected by PCV and WBC values is also shown in figures 13 to 15. The groups with radiation exposures of 500, 750, or 1000 rads 414 days before the fractionated gamma-ray study showed injury response and recovery capability comparable to that of group 1, which had not been exposed to gamma rays.

CLINICAL FINDINGS AND MORTALITY DURING FRACTIONATED GAMMA-RAY EXPOSURES

Two or three monkeys vomited during each of the 100-rad exposures, but there has been no increase in this number with additional exposures. Twenty-four days after the fourteenth 100-rad exposure, one animal in group 4 died. Symptoms were first observed only 2 days before death, and they were similar to the acute radiation death syndrome. Post-mortem examination of this monkey attributed death to generalized subcutaneous and visceral capillary hemorrhaging. The visceral organs exhibited focal hemorrhages much as would be expected in acute radiation death. The bone marrow was not depleted, and the myeloid-erythroid ratio appeared unchanged. The presence of many megakaryocytes in the marrow suggests that an adequate number of thrombocyte precursors was available. The mechanism that produced the capillary cellular permeability and resultant hemorrhage is not apparent from morphological findings.

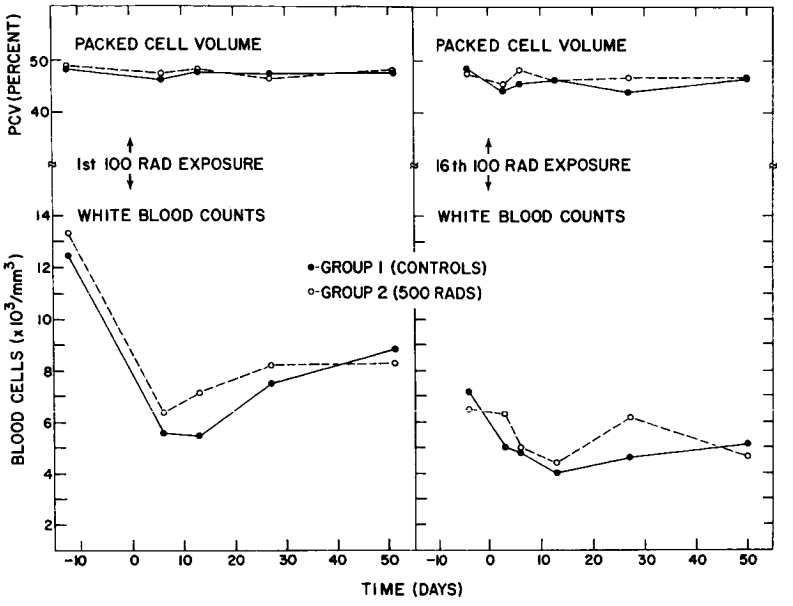

FIGURE 13.--Comparative packed cell volume and white blood cell count of group 1 (no gamma-ray exposure before fractionated exposures) and group 2 (500 rads of gamma rays before fractionated exposures) monkeys following the first and sixteenth 100-rad gamma-ray exposures.

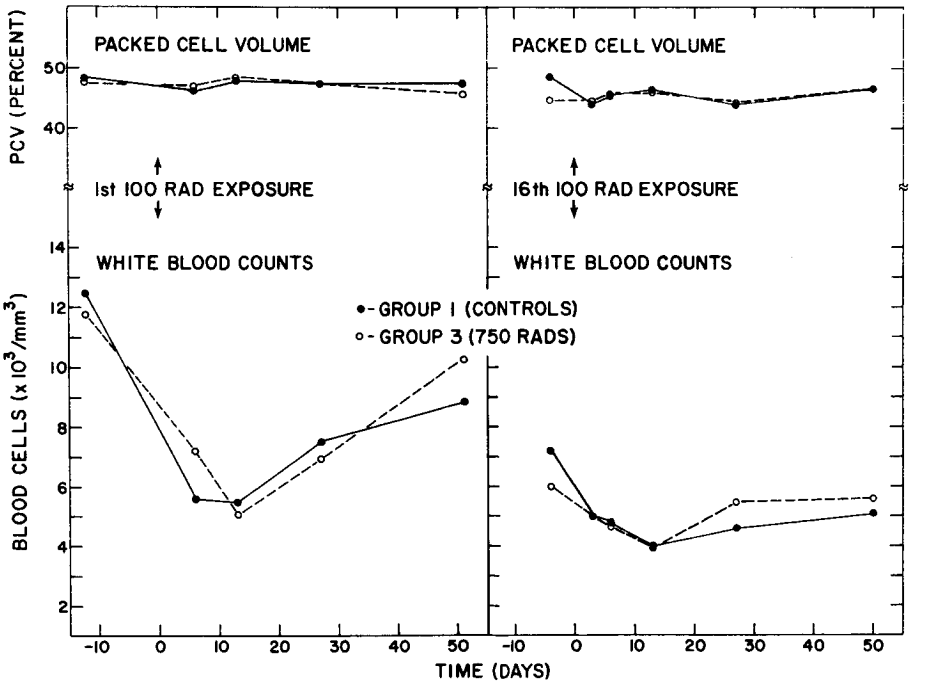

FIGURE 14.--Comparative packed cell volume and white blood cell count of group 1 (no gamma-ray exposure before fractionated exposures) and group 3 (750 rads of gamma rays before fractionated exposures) monkeys following the first and sixteenth 100-rad gamma-ray exposures.

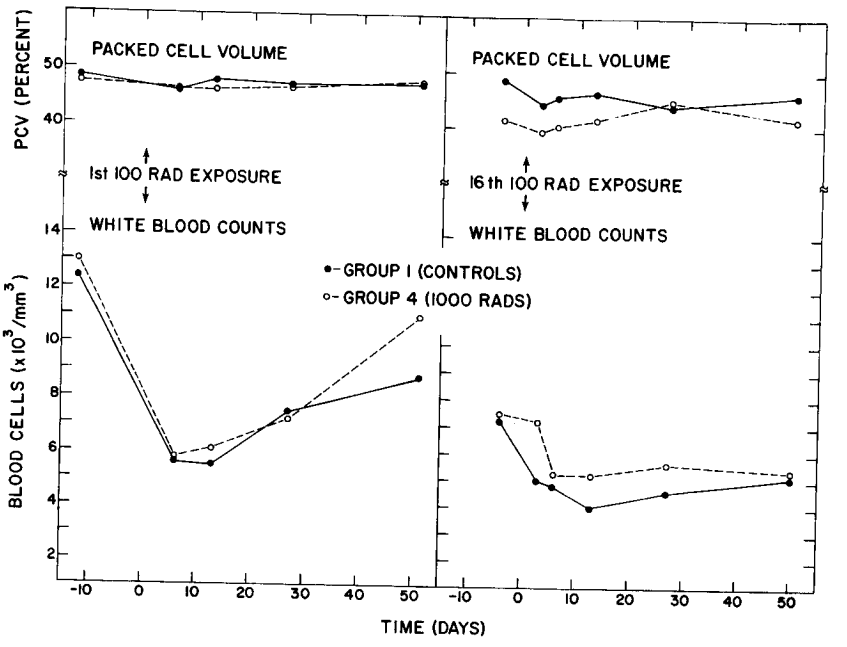

FIGURE 15.--Comparative packed cell volume and white blood cell count of group 1 (no gamma-ray exposure before fractionated exposures) and group 4 (1000 rads of gamma rays before fractionated exposures) monkeys following the first and sixteenth 100-rad gamma-ray exposures.

ACKNOWLEDGMENTS

The authors thank H. M. Wagner and R. D. Jeter for their role in training and testing the monkeys during the first phase of this program. We also thank O. S. Johnson for technical arrangements and dosimetry, N. J. Basmann, P. M. LaBauve, R. F. Archuleta, and E. A. Vigil for technical support during the entire program.

This work was performed under the auspices of the U. S. Atomic Energy Commission.

REFERENCES

1. SPALDING, J. F.; TRUJILLO, T. T.; and McWILLIAMS, P.: Health Phys., vol. 10, 1964, p. 709.
2. SPALDING, J. F.; JOHNSON, O. S.; and McWILLIAMS, P. C.: Radiation Res., vol. 32, 1967, p. 21.
3. SPALDING, J. F.; JOHNSON, O. S.; and ARCHULETA, R. F.: Nature, vol. 208, 1965, p. 905.
4. SPALDING, J. F.; and TRUJILLO, T. T.: Radiation Res., vol. 16, 1962, p. 125.
5. SPALDING, J. F.; POPP, D. M.; and POPP, R. A.: Radiation Res., vol. 40, 1969, p. 37.
6. SPALDING, J. F.; POPP, D. M.; and POPP, R. A.: Radiation Res., 1971 (in press).
7. SPALDING, J. F.; TRUJILLO, T. T.; and LeSTOURGEON, W. L.: Radiation Res., vol. 15, 1961, p. 378.
8. SPALDING, J. F.; and VAN DILLA, M. A.: unpublished manuscript.
9. SPALDING, J. F.; TRUJILLO, T. T.; and LeSTOURGEON, W. L.: Radiation Res., vol. 15, 1961, p. 754.
10. NATIONAL COMMITTEE ON RADIATION PROTECTION AND MEASUREMENTS (L. S. Taylor, ed.): Exposure to Radiation in an Emergency. National Bureau of Standards Report 29, Washington, D. C. (October 27, 1961).
11. SPALDING, J. F.; HOLLAND, L. M.; and JOHNSON, O. S.: Health Phys., vol. 17, 1969, p. 11.
12. KRATOCHVIL, C. H.: Ann. N. Y. Acad. Sci., vol. 162, 1969, p. 71.
13. KRISE, G. M., Jr.; and WALD, N.: The Normal Blood Picture of the *Macaca mulatta* Monkey. School of Aviation Medicine Report 57-130, 1957.

RELATIVE BIOLOGICAL EFFECTIVENESS OF FAST NEUTRONS COMPARED WITH X-RAYS: PRENATAL MORTALITY IN THE MOUSE

W. Friedberg, G. D. Hanneman, D. N. Faulkner

Civil Aeromedical Institute, Federal Aviation Administration
Oklahoma City, Oklahoma

and

E. B. Darden, Jr.
Biology Division, Oak Ridge National Laboratory
Oak Ridge, Tennessee

This report of work in progress is concerned with effects of fission neutrons and of x-rays on the mouse zygote.

METHODS.

Seven-week-old virgin mice were allowed a 12-hour mating opportunity beginning at 7:00 P.M. Between 1:30 and 4:00 P.M., except where indicated otherwise, the females which had mated (vaginal plug) during the night were either irradiated or sham-irradiated. At the time of irradiation the zygotes were in a pronuclear stage. Sixteen days later the mice were killed and the uteri dissected. We recorded the number of dead embryos, live embryos, and gross anomalies. Dead embryos were classified as to stage of development.

The neutron source was the Oak Ridge National Laboratory Health Physics Research Reactor, an unshielded fast reactor of the Godiva type. Neutron energies were those of a slightly moderated fission spectrum with an average energy of 1.2 MeV. The neutron-to-gamma ratio was approximately 8. Neutron absorbed doses ranged from 0.5 to 20 rads. The neutron dose rate was 2 rads/minute except for a group given a fractionated exposure at 0.05 rad/minute.

X-rays were from a General Electric Maxitron 300 operated under the following conditions: 300 kVp; 20 mA; added filtration 0.5 mm Cu plus 1 mm Al; h.v.l. 1.20 mm Cu; dose rate 66 to 68 rads/minute. X-ray absorbed doses ranged from 10 to 100 rads.

RESULTS AND DISCUSSION.

The survival curve which relates neutron absorbed dose and prenatal survival has an extrapolation number (n) of 1.3, a D_0 of 16 rads and an LD_{50} of 14 rads. For x-rays, n is 1.1, D_0 is 76 rads and the LD_{50} is 60 rads. The relative biological effectiveness of the neutrons compared with x-rays ranged from approximately 4.2 at 5 rads (neutrons) to 4.9 at D_0.

A survival curve with little or no shoulder ($n \tilde{=} 1$), as indicated by both the neutron and x-ray data, implies that prenatal death resulted primarily from a single lethal-injury event. In contrast, the presence of a shoulder ($n > 1$) would have indicated that sublethal damage to the zygote must accumulate for prenatal death to result. If our survival curves could be extended, it is possible that all the data already obtained would prove to be on a shoulder. The present curves extend down to approximately 0.3 survival; to investigate lower levels of survival would require an excessively large number of animals. Therefore, we are taking a different approach to the question of whether radiation causes sublethal damage to the zygote.

It has been observed with mammalian cells that where cell death requires an accumulation of sublethal damage (shoulder-type curve, $n > 1$), there is usually a repair mechanism. Evidence of repair is reduced lethality when the dose rate is lowered or the exposure fractionated. In a comparison of acute irradiation with a fractionated exposure at low dose rate, zygotes (in utero) were given a total neutron dose of 12 rads. One group was irradiated at 2 rads/minute from 12:43 to 12:49 P.M. and another group was exposed at 0.05 rad/minute from 10:00 to 12:00 A.M. and again from 1:30 to 3:30 P.M. Prenatal survival in the two groups was not significantly different: 60% for the acute and 57% for the fractionated low dose rate. The results suggest that embryo death after irradiation of the zygote with neutrons was a consequence of a single irreparable lethal-injury event. This is consistent with our interpretation of the neutron survival curve. A similar experiment with x-rays is planned.

More than 92% of the deaths in the irradiated (x-ray and neutron) mice occurred before day 11 in the 19-day gestation period. We calculated this from the number of resorption moles and the total number of dead embryos. A resorption mole is the amorphous remains of an embryo that died within 6 days after it implanted in the wall of the uterus. In the mouse implantation occurs about 4.5 days after fertilization of the ovum.

The number of preimplantation deaths at a specific radiation dose was estimated from the difference in number of implantation sites per pregnancy between the irradiated group and sham-irradiated controls. With neutrons the proportion of prenatal deaths that occurred preimplantation was 16% at 5 rads and 50% at 20 rads. At equivalent-lethality x-ray doses the percentages were similar. Thus, as neutron or x-ray dose was increased both preimplantation and postimplantation deaths also increased but there was a relatively greater increase in preimplantation deaths.

PROTON IRRADIATION OF STEM CELLS: RADIATION DAMAGE AND CHEMICAL RADIOPROTECTION[1]

Richard C. Riley[2], James L. Montour[3] and Clifford W. Gurney[4]

Division of Radiological Sciences, Department of Radiology and Department of Medicine
University of Kansas Medical Center, Kansas City and
Division of Radiation Biology, Department of Radiology
Medical College of Virginia, Richmond

1. Supported in part by NIH (2R01 AM 14377-02) and part by NASA (NGR 47-002-018).

2. Division of Radiological Sciences, Department of Radiology, University of Kansas Medical Center, Kansas City.

3. Department of Medicine, University of Kansas Medical Center, Kansas City.

4. Division of Radiation Biology, Department of Radiology, Medical College of Virginia, Richmond.

Although many systems for studying radiobiological effects of high energy protons are available, much work has utilized whole mammals as the test system. Cellular level studies in mammals have included characterization of hematopoietic sequelae of total body exposure. In this study the effects of high energy protons on erythropoietic stem cells (erythropoietin responsive cells) and radioprotection by chemical agents have been measured.

The facilities of the NASA Space Radiation Effects Laboratory, Newport News, Virginia, were used. Carworth Farms CF-1 mice were exposed (five in tandem) to a parallel beam of 600 MeV protons. The fluence distribution was determined by ^{11}C foil counting. The fluence, when converted to dose, was referenced to the synchrocyclotron beam monitors which were then used to administer radiation exposures. Mice were given graded doses to 300 rads to determine the dose-response curve. Other mice received saline, AET, or 5-hydroxytryptamine 10-15 minutes before irradiation.

All mice received six units human urinary erythropoietin on day 2 following exposure, 0.5 μCi ^{59}Fe on day 4, and were killed on day 7. Percent iron incorporation was then determined as a measure of the fraction of stem cells remaining. Preliminary experiments, carried out as described, show a dose-response curve similar to that obtained with 250 kV X-rays indicating an RBE of approximately one. Chemical radioprotection can be shown under these conditions for both AET and 5-HT with doses well below the LD_{50} dose. Under the conditions of these experiments AET and 5-HT are equally effective and a dose reduction factor of 2.5 is obtained.

The specification of radiation tolerance doses for manned space missions requires quantitative information from sub-lethal doses. These experiments indicate that the stem cell system can be further utilized to obtain such information.

INTRODUCTION

In recent years radiation damage and chemical radioprotection have been studied for many types of radiation using a wide variety of biological endpoints. (ref. 1,2). One of these, the stem cell system, offers the opportunity of studying cellular radiation damage in vivo. Interest in the use of the stem cell compartment of the polycythemic mouse to study radiation effects has arisen for two principal reasons. First, studies in a cellular system in vivo provide information on basic mechanisms of radiation damage which cannot be obtained from lethality studies in a population of animals. Second, since it is primarily damage to the hematopoietic system which is responsible for the acute radiation syndrome, elucidation of the kinetics of normal and irradiated hematopoietic stem cells is of critical importance in radiobiology.

The transfusion-induced polycythemic mouse

was first shown to be ideally suited for *in vivo* studies of erythropoiesis by Jacobson *et al* (ref. 3). Subsequently Gurney and his co-workers showed that hypoxia could induce polycythemia (ref. 4) and that these mice could be used to study the effect, on the stem cell compartment *in vivo*, of X-rays (ref. 5, 6), gamma rays and neutrons (ref. 7).

In these studies mice are induced to stop elaboration of red cells by first producing polycythemia. This is accomplished by confinement for three weeks in a chamber at one-half atmosphere. By the fourth day following return to atmospheric pressure, the consequence of differentiation of stem cells (maturation of erythroblasts to mature red cells) is complete and erythropoiesis is nil (ref. 4). The status of the "static" stem cell compartment can then be ascertained by measuring the erythropoietic response to a constant dose of erythropoietin. Incorporation of a tracer dose of ^{59}Fe in red cells is used as a measure of erythropoietic response which in turn reflects the status of the stem cell compartment. Thus, the effect of radiation on the stem cell compartment *in vivo* and the ability of chemical radioprotective agents to modify that effect can be measured in this system.

Our unpublished experiments have shown that 2-aminoethylisothiouronium bromide (AET) protects stem cells from X-radiation. Recently, Vittorio *et al* (ref. 8, 9), using the stem cell compartment in polycythemic mice, have reported increased iron incorporation in blood, spleen, and liver when irradiation is preceded by administration of AET or serotonin (5-hydroxytryptamine, 5-HT). Using lethality as an endpoint, Oldfield *et al* (ref. 10) demonstrated protection in mice from 440 MeV protons with mercaptoethylamine (MEA) and p-aminopropiophenone (PAPP).

Since man may be exposed to protons in a space environment at doses which, although sublethal, may still produce hematological damage, we decided to examine the response of the hematopoietic stem cell system to high energy protons. This paper records preliminary observations on the effect of 600 MeV protons on stem cells and the modifying effect of AET and 5-HT.

METHODS AND MATERIALS

Irradiation and dosimetry - Animals were irradiated with 600 MeV protons obtained from the synchrocyclotron at the NASA Space Radiation Effects Laboratory, Newport News, Virginia. Mice were exposed (five in tandem) in 2.5 cm ID plastic tubes to a parallel beam of protons. The mice were placed in a hole within a block of lucite made from four slabs 2" X 8" X 24" each (Fig. 1). Beam position was determined photographically with Polaroid film.

The fluence distribution was determined by activation of ^{12}C in a polyethylene foil by the ^{12}C (n,np) ^{11}C reaction. The ^{11}C thus formed was measured in a scintillation spectrometer calibrated with a ^{22}Na standard. Fluence was converted to dose using the data of Neufeld *et al* (ref. 11). This dose was referenced to syncrocyclotron beam monitors and thermoluminescent dosimeters. The beam monitors were then used to deliver the nominal dose and the TLD's were used to measure the dose actually delivered.

Animals - Carworth Farms CF-1 virgin female mice twelve weeks of age were placed in hypoxia chambers at one-half atmosphere for three weeks. Four days after removal from the chamber 10-12

NASA
L-71-1630

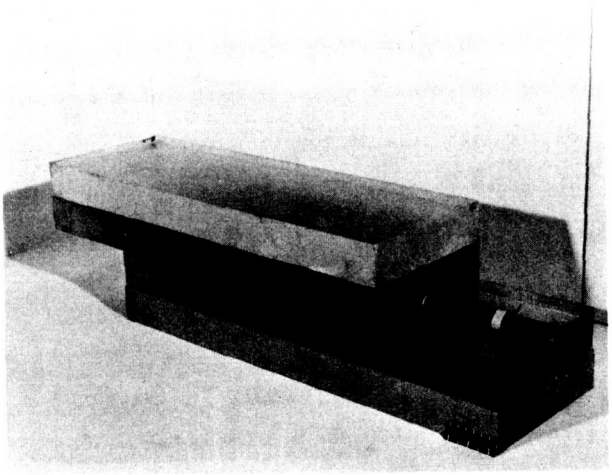

Figure 1. Proton exposure apparatus. The top half of the lucite block has been withdrawn to demonstrate the placement of the mice during proton irradiation. The beam was incident normally upon the 8 x 8 inch surface of the block. (Dark colored mice used for photography).

animals per group were exposed to specified doses of protons without injection or 10-15 minutes following intraperitoneal injection of 0.2 ml AET (360 mg/kg body weight), 5-HT (150 mg/kg body weight), or saline. The animals were housed ten per cage in shoe-box type cages and allowed Purina mouse chow and water ad libitum. On the second post-irradiation day each mouse received six units of human urinary erythropoietin subcutaneously. On day 4, they received intraperitonealy 0.5 μCi ^{59}Fe as ferric chloride. The mice were then killed on day 7 and the hematocrit, body weight, and percent iron incorporation in blood determined. Animals with hematocrits less than 55 were not included in the experiment because of the possibility of elevated radioiron incorporation due to endogenous erythropoietin production.

RESULTS

Radioiron incorporation in newly formed peripheral red cells of proton irradiated mice decreases with increasing radiation dose. Unirradiated control mice incorporate approximately 36% of the tracer dose of radioiron. Figure 2 shows the radioiron incorporation for mice irradiated with 600 MeV protons in two experiments. Values are normalized to 100% for controls. An ED_{50} of 65 rads is obtained from Figure 2. For comparison, the response of the stem cell compartment to 250 kV X-rays (ref. 12) is also shown.

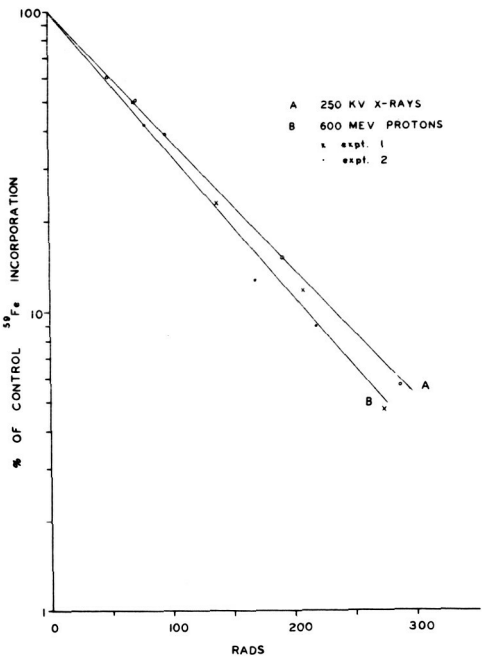

Figure 2. Iron incorporation in polycythemic mice following irradiation with protons or X-rays. Curve A: 250 kV X-rays (ref. 12). Curve B: 600 MeV protons.

Intraperitoneal injection of AET or 5-HT 10-15 minutes before proton irradiation yields higher iron incorporation than correspondingly unirradiated, untreated mice (Fig. 3). A slightly increased normalized iron incorporation in saline injected irradiated groups was observed. This was due to a slightly lower level of iron incorporation in the unirradiated, saline injected mice. Thus, the curve for saline injected mice does not differ significantly from uninjected controls.

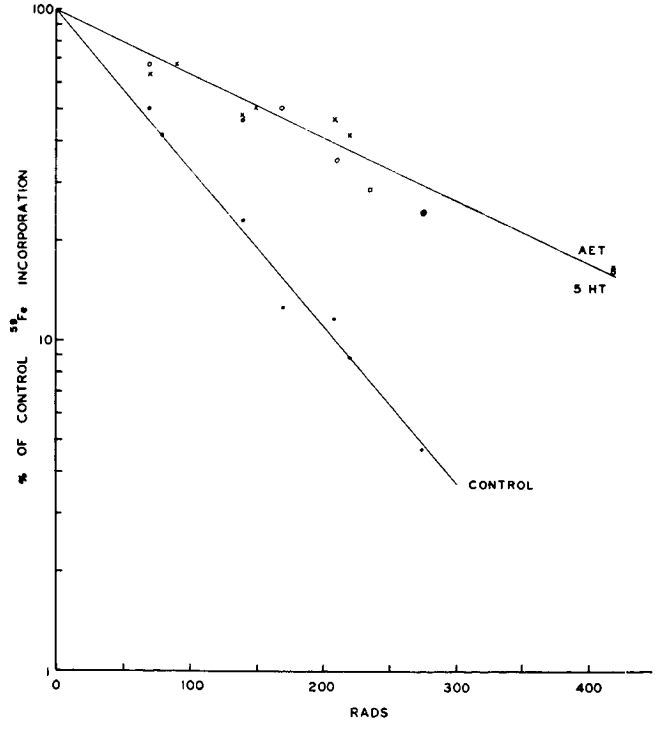

Figure 3. Modification of proton-induced radiation damage of stem cells by prior administration of AET or 5-HT. Solid circles, controls; open circles, AET; crosses, 5-HT.

DISCUSSION

From Figure 2 it is seen that 600 MeV protons are similar to 250 kV X-rays in their ability to damage the erythropoietin responsive or "stem" cell; therefore, an RBE of approximately unity can be assigned for protons of this energy in producing decreased iron uptake in hematopoietic stem cells. For this endpoint 600 MeV protons act as low LET radiation.

Both AET and 5-HT were effective in protecting the stem cell compartment from proton radiation damage. Oldfield et al (ref. 10) reported dose reduction factors (DRF) for mortality of approximately 1.5 for MEA and PAPP with both 440 MeV protons and X-rays. In our experiments with 600 MeV protons a DRF of 2.5 is obtained for iron incorporation in hematopoietic stem cells. This is comparable to the level of protection obtained in the same system by Vittorio et al (ref. 8) for ^{137}Cs gamma rays. Radioprotective chemicals are at best only slightly effective against exposure to high LET radiation. The high DRF of 2.5 obtained in these experiments further supports the observation from the dose-response curve that the major dose contribution from 600 MeV protons is low LET in nature.

Although considerable additional information is necessary to define radiation tolerance doses for space missions, this low LET behavior is significant. Low LET radiation shows a dose-rate dependence for most endpoints and part of

the damage it produces is reparable; in contrast, damage from high LET radiation is accumulated with little repair even at low dose-rates. In manned space missions the major portion of dose accumulated is expected to occur at low dose-rates. Since 600 MeV protons have been shown in these experiments to act at low LET radiation, a higher tolerance dose can be assigned for a given risk level than would be possible if the dose contribution from a high LET component were more preponderant. It appears to be possible, then, to consider the use of chemical radioprotective agents suitable for man for protection from high proton flux events.

The experiments reported here are being extended to include lower energy portions of the solar proton spectrum.

ACKNOWLEDGEMENTS

We thank Dr. C. J Shellabarger for assisting with the experiments, Miss Rita F. Straub for help with the dosimetry, and Dr. Robert T. Siegel and his staff at the Space Radiation Effects Laboratory. Special thanks are due to Dr. Stuart W. Lippincott for his advice, help and continuing interest in this work.

REFERENCES

1. Casarett, A. P.: Radiation Biology, Prentice-Hall, Englewood Cliffs, 1968.

2. Bacq, Z. M.: Chemical Protection Against Ionizing Radiation, Charles C. Thomas, Springfield, 1965.

3. Jacobson, L. O., Goldwasser, E., Plzak, L. F., and Fried, W., Proc. Soc. Exp. Biol. Med., vol. 94, 1957, P. 243.

4. De Gowin, R. L., Hofstra, D., and Gurney, C. W., J. Lab. Clin. Med., vol. 60, 1962, p. 846.

5. Gurney, C. W., Lajtha, L. G. and Oliver, R., Brit. J. Haemat., vol. 8, 1962, p. 461.

6. Gurney, C. W., Perspectives in Biol. and Med., vol. 6, 1963, p. 233.

7. Vogel, H. H., Jr., Forde, R. and Gurney, C. W., Exptl. Hematol., vol. 12, 1967, p. 66.

8. Vittorio, P. V., Watkins, E. A. and Dziubalo-Blehm, S., Can. J. Physiol. Pharmacol., vol. 47, 1969, p. 65.

9. Vittorio, P. V., Dziubalo-Blehm, S. and Amey, E. A., Rad. Res., vol. 37, 1969, p. 653.

10. Oldfield, D. G., Doull, J. and Plzak, V., Rad. Res., vol. 26, 1965, p. 12.

11. Neufeld, J., Snyder, W. S., Turner, J. E., Wright, H., Wheatley, B. M. and Wyckoff, H. O., Health Physics, vol. 17, 1969, p. 449.

12. Gurney, C. W. and Wackman, N., Nature, vol. 190, 1961, p. 1017.

RADIATION CARCINOGENESIS AND ACUTE RADIATION MORTALITY IN THE RAT AS PRODUCED BY 2.2 GEV PROTONS[1]

C. J. Shellabarger[2], R. F. Straub, J. E. Jesseph[3], and J. L. Montour[4]

Zoology Department, University of Michigan, Ann Arbor
and Medical Department, Brookhaven National Laboratory, Upton, New York[5]

1. Supported in part by NASA (NsG 214-62)
2. Present Address - Medical Department, Brookhaven National Laboratory
3. Present Address - Department of Surgery, The Ohio State University, College of Medicine, Columbus
4. Present Address - Radiology Department, Medical College of Virginia, Richmond
5. Brookhaven National Laboratory is supported by the USAEC.

The Brookhaven National Laboratory Cosmotron was used to produce 2.2 GeV protons for total-body exposure of young, female Sprague-Dawley rats. A single exposure of 42-day old rats to 92 rads of protons produced a mammary neoplastic response over a 365-day period that was qualitatively and quantitatively similar to the response produced by 158 rads of ^{60}Co gamma rays. When the two types of radiation exposures were combined they appeared to produce an additive mammary neoplastic response. Because of the qualitative similarity of the mammary neoplastic response to the 2 types of radiation and because the 2 types of radiation appeared to be additive, it was suggested that 2.2 GeV protons act by a mode of action that is similar to that of low LET radiation. Acute radiation mortality produced by a single exposure of 42-day old rats to protons was qualitatively similar in terms of mean survival time to mortality produced by ^{60}Co gamma rays. It was suggested that 2.2 GeV protons act to produce acute radiation mortality in fashion similar to that of low LET radiation. The administration of a radioprotective drug, AET, to 36-day old rats produced a small decrease in radiation mortality and a small increase in mean survival time when the drug was given before exposure to 2.2 GeV protons. This result was taken to mean that 2.2 GeV protons act at least in part as low LET radiation. Although exact RBE values could not be determined for acute mortality and carcinogenesis in the young rat, approximate values appear to be 1.4 and 1.5.

INTRODUCTION

When the 2.2 GeV proton facility of the Brookhaven Cosmotron became available for biological studies, proton carcinogenesis, the interaction of protons and gamma-rays on carcinogenesis, proton-induced acute mortality, and chemical protection against proton-induced acute mortality were studied in the rat and these proton-produced responses were compared to similar responses produced by gamma-rays or x-rays.

MATERIALS AND METHODS

Animals - Weanling, litter-mate, female, Sprague-Dawley rats were obtained from Sprague-Dawley, Inc., Madison, Wisconsin. All rats were kept at the University of Michigan until they were approximately 35 days of age when they were taken to Brookhaven National Laboratory, exposed and returned to the University of Michigan. Litter-mates were assigned to each experimental and control group so that approximately equal numbers of litter mates were placed in each group. Animals to be studied for mammary neoplasia were handled as described previously (ref. 1) for 365 days post-exposure when all animals alive were killed. All animals were examined frequently for mammary tumors and as these were found, they were removed, sectioned and given a pathologic classification. Animals used for acute mortality studies were followed for 30 days and deaths were recorded as to the nearest day post-exposure. Chemical protection studies were done by injecting 2-aminoethylisothiouronium bromide (AET), 30 mg per rat by the intraperitoneal route, 15 minutes before exposure.

EXPOSURE CONDITIONS

Protons of 2.2 GeV, produced by the Brookhaven Cosmotron were used to expose rats in exactly the

same way as described previously for mice (ref. 2) except that the inside diameter of the lucite tube holding the animals was increased to 4.5 cm and a length of 50 cm. Four rats were exposed per Cosmotron run, nose to tail, with the nose facing the stream of protons. As a check on a possible change in dose with position of the rat within the exposure tube, or change of dose with depth, rat position in the tube was recorded and checked against individual and group rat mortality. The exposure tube holding the rats was placed well within the beam of protons and parallel with the beam as determined by means of a fore and aft gun sight array and Polaroid film. The animals in the exposure tube were rotated along their longitudinal axis at 20 rpm to insure a uniform dose distribution. The Cosmotron beam pulse duration was 1 msec and the repetition rate was 25 pulses per minute. With the proton fluence employed, the instantaneous dose rate was 14 k rads/sec or an average dose rate of 350 rads/min.

Gamma-ray exposures were done at a dose rate of 14 R/min. X-ray exposures were accomplished by operating a conventional x-ray therapy machine at 250 kVp and 30 mA with 0.5 mm Cu and 1 mm Al added filtration at a dose rate of 115 R/min.

DOSIMETRY

Each proton irradiation run was monitored by use of the proton activation of the ^{12}C in a polyethylene foil via the reaction ^{12}C (p,np) ^{11}C as described previously (ref. 2). The foils were calibrated in terms of dose by means of a tissue equivalent ionization chamber (ref. 3). The foil fluence determination and the dosimetry yielded a result of 354 rads[(1)] per 10^{10} protons/cm^2.

For x-rays and gamma-rays, the exposure dose was measured in air at the dorsal-ventral midpoint of the animals with a Victoreen ionization chamber in R and these values were converted to rad values, using a physical factor of 0.95 to convert R to rads and a biological factor of 0.83 (ref. 4) to relate ^{60}Co gamma-rays to 250 kVp x-rays.

EXPERIMENTS

Carcinogenesis. Forty-two day old rats were exposed to 92 rads of 2.2 GeV protons, or 158 rads of ^{60}Co gamma-rays, or both. The gamma-ray exposure was done approximately 12 hours before the proton exposure.

Acute mortality. Forty-two day old rats were exposed to 473, 600, 661 or 729 rads of ^{60}Co gamma-rays or 354, 478, 595 or 715 rads of 2.2 GeV proton.

Chemical protection. Thirty-six day old rats were exposed to 712 rads of 250 kVp x-rays with or without prior AET, or 527, 552, 577 or 602 rads of 2.2 GeV protons with or without prior AET.

RESULTS

The mammary neoplastic response to 92 rads of proton exposure, or 158 rads of gamma exposure, or both types of radiation are presented in Table 1 along with mammary neoplastic incidence of non-irradiated litter-mate controls. It seems clear that all measures of mammary neoplasia incidence are approximately the same in response to either 92 rads of proton exposure or 158 rads of ^{60}Co gamma exposure. Although the value is somewhat uncertain the approximately equal effects of doses of 92 rads from protons and 158 rads from gammas, yield a RBE of about 1.5 using a linear dose-response relationship for each type of radiation and subtraction of control values.

When the proton exposure was combined with the gamma-ray exposure, the percent of rats with mammary neoplasia was not very informative because the dose of each radiation that was selected when combined appears to saturate this measure of mammary neoplastic response. However, the measures of total number of mammary neoplasms, or total number of mammary adenocarcinomas, or the total number of mammary fibroadenomas, when each is corrected for number of rats at risk, appear to indicate that

(1) W. H. Moore, Brookhaven calculated, for primary ionization, 332 rads and Wright et al. (Health Physics 16, 13, 1969), for total absorbed dose, 410 rads.

Table 1

Mammary Neoplasia and Mammary Neoplasms at 300 Days Post-Exposure. Exposures Done at 42 Days of Age. ^{60}Co Gamma Exposure Preceded Proton Exposure by 12 Hours. AC Refers to Adenocarcinoma and FA Refers to Fibroadenoma.

Treatment			Rats with Mammary Neoplasia		Mammary Neoplasms					
						Total		AC		FA
Radiation	Rads	N	N	%	Total	N	AC	N	FA	N
None	-	22	1	4	1	0.04	1	0.04	0	0
Proton	92	32	14	44	20	.62	4	.12	16	0.50
^{60}Co γ	158	32	16	50	23	.72	4	.12	19	.59
Proton + ^{60}Co γ	250	28	19	68	37	1.32	8	.29	28	1.00

proton irradiation and gamma-ray irradiation are very close to being additive. This result implies that the mechanism of action of the 2 types of radiation are similar.

The results of studies on acute mortality in terms of percent dead within 30 days, and the mean survival time are shown in Table 2. Within the lethal range of doses, the mean survival times are about the same for the 2 types of radiation and this implies that proton exposure or gamma-ray exposure produces acute mortality by a similar mechanism. Because the number and the range of doses of each type of radiation is small, and the sample size is not large, a value for RBE cannot be given with any high degree of confidence. However, if these data are plotted, and a visual fit of the survival curves are drawn, and the ratio of LD_{50} values is determined, the proton exposure rad for rad appears to be about 1.4 times more potent than for the gamma-ray exposure.

Table 2

Acute Radiation Mortality, Number of Animals Exposed at 42 Days of Age, Percent 30-Day Survival and Mean Survival Time in Days of Decedents.

Radiation	Rads	N	% Dead	M. S. T.
^{60}Co γ	473	9	0	-
^{60}Co γ	600	9	56	16.4
^{60}Co γ	661	9	78	17.4
^{60}Co γ	729	10	100	10.7
Proton	354	12	33	21.0
Proton	478	12	67	17.5
Proton	595	12	100	9.8
Proton	715	12	100	4.5

The data concerned with the radioprotective action of AET are shown in Table 3. Although all exposure doses used proved to be lethal in the absence of the drug, AET produced a small protective effect against mortality in the 2 lowest doses of proton exposure and the x-ray exposure. A modest increase in mean survival time was produced by AET at all proton exposure doses and the single x-ray dose. It thus appears that AET does have the capacity to protect against acute radiation mortality provoked by 2.2 GeV proton exposure.

Analysis of the position of the rat in the exposure tube by using days of survival time disclosed that survival time increased as the position was moved downstream. This increase was related to reduction in dose - produced increased survival time. This indicates that the decrease in dose received by the last rat downstream is no less than 72% of the first rat and is in agreement with interposed ionization chamber measurements where the dose decreased to 68%.

Table 3

Acute Radiation Mortality, Number of Rats Exposed at 36 Days of Age, Percent 30-Day Survival and Mean Survival Time in Days of Decedents. AET Injected by Subcutaneous Route 15 Minutes Before Exposure.

Radiation	Rads	Drug	N	% Dead	M. S. T.
X-Ray	712		10	100	5.4
X-Ray	712	AET	10	80	9.4
Proton	527		12	100	8.2
Proton	527	AET	12	75	9.7
Proton	552		12	100	7.2
Proton	552	AET	12	92	9.4
Proton	577		12	100	6.1
Proton	577	AET	12	100	9.7
Proton	602		12	100	5.3
Proton	602	AET	12	100	8.2

DISCUSSION

The results here presented are perhaps of more qualitative interest than of quantitative interest. Although only a single proton dose was tested, it is clear that 2.2 GeV protons have the capacity to accelerate the rat mammary neoplastic response and that this proton-induced mammary neoplastic response is qualitatively similar to the mammary neoplastic response to gamma radiation. This finding confirms a preliminary report (ref. 5) that indicated that the mammary neoplastic response to 2.2 GeV protons and ^{60}Co gamma-rays was qualitatively similar. Strengthening the conclusion that either proton exposure or gamma-ray exposure produces a qualitatively similar mammary neoplastic response is the finding that when the two types of exposure were combined an additive result ensued. It has been shown previously that x-rays (ref. 6) and protons (ref. 5) produce a linear dose-response. The 12-hour gap between gamma-ray exposure and proton exposure in the experimental group that received both types of exposure probably is of no biological consequence since it has been shown that the incidence of mammary neoplasia of the rat is little changed by short-term fractionation of sub-lethal total body x-ray exposure (ref. 7). It is not unreasonable to suggest, therefore, that the mechanism of action that allows proton exposure to be carcinogenic is not dissimilar to the mechanism of action that allows gamma-ray exposure to be carcinogenic. Since gamma-rays are low LET radiation, then 2.2 GeV protons should be considered to act, in a large part, as low LET radiation.

It seems clear, also, that 2.2 GeV proton exposure produces an acute radiation mortality that is qualitatively similar to that produced by gamma-ray exposure. Again, it is tempting to suggest that 2.2 GeV protons act by a mechanism that is similar to low LET radiation. Adding to this suggestion was the absence of high LET "early death" that has been reported by others who have noted a shift from marrow to gut death with high LET radiations (ref. 8).

It is generally accepted that radioprotective compounds are more effective against low LET radiation than against high LET radiation (ref. 9). Thus, the finding of a small but definite protection with AET against acute mortality as produced by 2.2 GeV protons may be taken to indicate that these protons act, at least in part, as low LET radiation.

The finding that it is possible to protect against acute radiation mortality as produced by high energy protons by prior AET treatment may be of some interest to those who are concerned with astronauts and their possible exposure to high energy protons. The data here reported are, we believe, the only direct experimental test reported on this subject, and are of some academic interest.

The interrelation between 2.2 GeV proton-produced radiation carcinogenesis and acute mortality is of some radiobiological interest. There is no *a priori* reason to expect that the relative biological effectiveness of minimum ionizing protons would be the same for tumor induction as it is for inducing mortality because the induction of a tumor must depend upon the number of cells that *are* capable of division after radiation exposure (ref. 10) while the production of acute radiation mortality depends upon the number of cells of the blood forming organs and the gastrointestinal tract that *are not* capable of division after radiation exposure (ref. 11). Thus, the finding that the relative biological effectiveness of 2.2 GeV protons was, within the limits of the two experiments, not very different on these two dissimilar biological endpoints was somewhat surprising.

Data published dealing with the biological effects of high energy protons are not extensive. Ueno and Grigoriev (ref. 12) have summarized data dealing with proton energies between 126 MeV and 730 MeV on 52 experiments in mammals including cytological changes, organ atrophy and acute mortality. They believe that a single value of RBE, 0.82 ± 0.04 can be assigned to all of these end points. On the other hand, for 2.2 GeV protons, the results are not so clear. Jesseph *et al.* (ref. 2) reported an RBE value of 0.87 for acute mortality in the mouse. Montour, *et al.* (ref. 13) using mice and spleen-thymus weight loss at 2-3 and 4-5 days after exposure and the same exposure condition and dose measurements of Jesseph *et al.*, obtained RBE values of approximately 1.0. Stoner, *et al.* (ref. 14) using mice and the same exposure conditions of Jesseph, *et al.* obtained a value of 2.5

for the repression of primary tetanus antitoxin responses, 1.5 for secondary responses and 1.5 for enhanced susceptibility to anaphylaxis. Thus, in mice, using similar exposure conditions, RBE values ranging from 0.87 to 2.5 have been reported for different end points. The approximate RBE values obtained in rats of 1.4-1.5 for mortality and carcinogenesis were well within the range reported for mice. This range of RBE values would seem to confirm a previous suggestion of Bond (ref. 15) that the RBE of 2.2 GeV protons may depend upon the criterion of biological effect under study.

Jesseph, et al. (ref. 2), Montour, et al. (ref. 13) and Stoner, et al. (ref. 14) all give reasons for interpreting their data on 2.2 GeV protons as being consistent with what would be expected from low LET radiation. The current data obtained in the rat on carcinogenesis, interaction of protons and gamma-rays on carcinogenesis, acute mortality and chemical protection against acute mortality also are consistent with low LET radiation effects. On the other hand, Jesseph, et al. suggest that as the diameter of the absorbing material is increased, it is possible that a high LET component may become relatively important although biological data on this point are too fragmentary at the present time to allow a conclusion to be reached on this point. All and all, it seems reasonable to think that 2.2 GeV protons act largely as low LET radiation but it must be admitted that the question of a high LET component must remain open.

SUMMARY

A single exposure of 42-day-old female Sprague Dawley rats to 92 rads of 2.2 GeV protons produced over 365 days an incidence of mammary neoplasia that was qualitatively and quantitatively similar to the neoplastic response to 158 rads of ^{60}Co gamma-rays. Both radiations, when combined, appeared to produce an additive neoplastic response. It was suggested that 2.2 GeV protons are approximately 1.5 times more effective than ^{60}Co gamma-rays. Acute mortality produced by 2.2 GeV protons and ^{60}Co gamma-rays was qualitatively similar and the proton irradiation appeared to be about 1.4 times more effective than gamma irradiation. A small reduction in acute mortality and a small increase in mean survival time was produced when AET was administered before 2.2 GeV proton irradiation. All of these data were interpreted as indicating that 2.2 GeV proton irradiation produces carcinogenesis and acute mortality in the rat by a mode of action that is similar to that of low LET radiation.

ACKNOWLEDGEMENTS

Many people assisted with the logistics and other aspects of these experiments includings Drs. B. Mawhinney, S. Kleinbergs, M. M. Nofal, W. H. Moore, G. M. Tišljar-Lentulis, P. Hardjosworo, V. P. Bond, E. P. Cronkite, R. W. Schmidt and W. Gross. Special thanks are due to the crew of the Cosmotron.

REFERENCES

1. Shellabarger, C. J.; Cronkite, E. P.; Bond, V. P.; and Lippincott, S. W.: Radiation Res., vol. 6, 1957, p. 501.
2. Jesseph, J. E.; Moore, W. H.; Straub, R. F.; Tisljar-Lentulis, G. M.; and Bond, V. P.: Radiation Res., vol. 36, 1968, p. 242.
3. Gross, W.; and Bell, W.: U. S. AEC Report, NYO-2740-3, 1966.
4. Cronkite, E. P.; and Bond, V. P.: Ann. Rev. Physiol., vol. 18, 1956, p. 483.
5. Shellabarger, C. J.; Schmidt, R. W.; Jesseph, J. E.; Montour, J. L.; and Straub, R. F.: Radiation Res., vol. 25, 1965, p. 239 (Abstract).
6. Bond, V. P.; Cronkite, E. P.; Lippincott, S. W.; and Shellabarger, C. J.: Radiation Res., vol. 12, 1960, p. 276.
7. Shellabarger, C. J.: Effect of Short-Term Dose Fractionation on Mammary Neoplasia Incidence in the Rat. IVth Int. Cong. Rad. Res., 1970, in press.
8. Carter, R. E.; Bond, V. P.; and Seymour, P. H.: Radiation Res., vol. 4, 1956, p. 413.
9. Alexander, P.: Protection of Macromolecules in vitro Against Damage by Ionizing Radiations. In Radiation Protection and Recovery, A. Hollaender, Editor, Pergamon Press, N. Y., 1960, p. 3.
10. Shellabarger, C. J.; and Schmidt, R. W.: Radiation Res., vol. 30, 1967, p. 497
11. Bond, V. P.; Fliedner, T. M.; and Archambeau, J. O.: Mammalian Radiation Lethality, Academic Press, New York, 1965.
12. Ueno, Y.; and Grigoriev, Yuri, G.: British J. Radiol., vol. 42, 1969, p. 475.
13. Montour, J. L.; Straub, R. F.; and Shellabarger, C. J.: Int. J. Radiat. Biol., vol. 15, 1969, p. 491.
14. Stoner, R. D.; Straub, R. F.; Moore, W. H.; and Jesseph, J. E.: Radiation Effects, vol. 2, 1969, p. 97.
15. Bond, V. P.: USAEC First Symposium on Accelerator Radiation Dosimetry and Experience, CONF-651109, USAEC, TID, 1965, p. 617.

RESPONSE OF MOUSE EPIDERMAL CELLS TO SINGLE DOSES OF HEAVY-PARTICLES

J.T. LEITH, W.A. SCHILLING, and G.P. WELCH DONNER LABORATORY AND LAWRENCE RADIATION LABORATORY, UNIVERSITY OF CALIFORNIA, BERKELEY, CALIFORNIA 94720

The survival of mouse epidermal cells to heavy-particles has been studied In Vivo by the Withers clone technique. Experiments with accelerated helium, lithium and carbon ions were performed. The survival curve for the helium ion irradiations used a modified Bragg curve method with a maximum tissue penetration of 465 microns, and indicated that the dose needed to reduce the original cell number to 1 surviving cell/cm^2 was 1525 rads with a D_o of 95 rads. The LET at the basal cell layer was 28.6 keV/micron. Preliminary experiments with lithium and carbon used treatment doses of 1250 rads with LET's at the surface of the skin of 56 and 193 keV/micron, respectively. Penetration depths in skin were 350 and 530 microns for the carbon and lithium ions whose Bragg curves were unmodified. Results indicate a maximum RBE for skin of about 2 using the skin cloning technique. An attempt has been made to relate the epidermal cell survival curve to mortality of the whole animal for helium ions.

The cell survival curves for single doses of 29 kVp x-rays, 250 kV x-rays and fast neutrons have already been defined (refs. 1 to 3) for mouse skin epithelial cells. It was felt that survival of mouse skin epithelial cells after heavy-particle irradiation would be of interest. This consideration is particularly relevant for the space environment where an astronaut might conceivably meet particles of high LET and relatively low penetration power. Indeed, the greatest radiation hazard to astronauts is exposure to particle events, with alpha particles making up a considerable fraction of the total particle flux (refs. 4 to 6). In this regard, the In Vivo epidermal cell cloning technique of Withers (ref. 1) has been used.

METHOD

A circular treatment area (25 mm diameter) on the animals ventral surface was irradiated. In this area small aluminum shields (20 mil thickness) of varying diameters were placed. Shields of 19.0, 6.4, and 2.1 mm diameter were used, and respectively, 1, 3, or 7 shields were placed within the 25 mm diameter irradiation field. Initially, the circular area was irradiated without the shields. Then, the shields were mechanically pulled into place and a large dose (i.e. 10 krad) was given to insure that cells from the periphery would not regrow into the treated areas. At intervals post-irradiation, the areas were examined for epidermal cell regrowths which could be seen as visible whitish clones. Assuming that each clone arises from a single surviving epidermal cell, the curve of cell survival/cm^2 may be obtained. If in a number of similarly treated areas the average number of surviving cells is m, the probability that 0, 1, 2, 3, etc., cells will survive will follow

a Poisson distribution with mean of m. If, in a number of equal areas (A), a fraction (f) shows regrowth after irradiation, the number of surviving clonogenic cells per unit area (S) is:

$$S = - \ln (1 - f) / A$$

By varying A, the test area, about 3 decades of a cell survival curve may be obtained.

Male, hairless mice of the CD1 strain were obtained from the Charles River Breeding Laboratories, Cambridge, Massachusetts. Mice were between 10-14 weeks of age at irradiation, and were singly housed. The animals were anesthetized for irradiation by intraperitoneal injections of Nembutal (60 mg/Kg body weight).

The helium ion exposures were performed at the Lawrence Radiation Laboratory 88'' cyclotron. Animals were individually irradiated and were positioned in a vertical manner normal to the direction of the incident helium ion beam. A large graphite shield was used so that only the circular area on the ventral surface of the animal was exposed. Photographic and miniature semiconductor diode measurements indicated that the beam intensity was homogeneous over the area irradiated. The helium ion beam had an initial energy of 40 MeV which is equivalent to a range of 90 mg/cm^2 in mylar (approximately 8% less in tissue). Mylar absorbers were placed in the beam path to produce a maximum residual range of 465 microns tissue (about 51 mg/cm^2 mylar). The single Bragg curve was modified into a family of Bragg curves occurring at different depths in tissue by placing a series of very thin overlapping mylar absorbers into the beam path. The absorbers rotated at 200 RPM through the beam to produce variable absorption with production of many Bragg curves which gave a flattened depth dose distribution. The "average" Bragg curve is shown in Figure 1. The average curve rose from a relative ionization factor of 1.1 at the surface of the skin to 2.1 at its maximum value at about 400 microns penetration. Doses were expressed at the top of the skin, and the minimum LET at this point was 28.6 keV/micron.

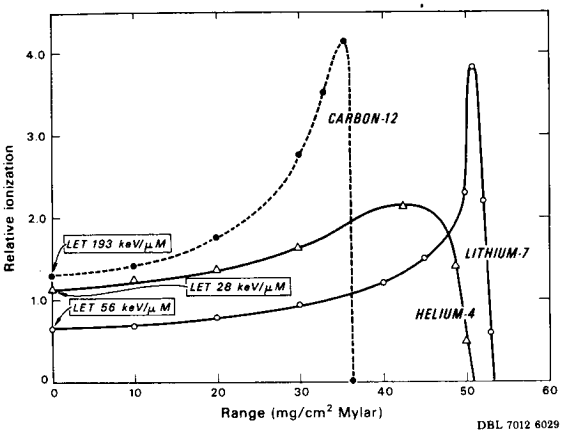

Figure 1. Depth dose curves for helium, lithium and carbon ions. The helium ion depth dose curve is formed by superimposition of separate Bragg curves which are produced by rotating varying layers of mylar absorber through the beam path with production of a resultant "average" Bragg curve which is relatively flat over its range with a well defined maximum penetration depth. Dose expressed at the top of the skin. The lithium and carbon ion curves are unmodified.

The lithium and carbon ion experiments were performed at the Lawrence Radiation Laboratory Heavy-Ion Linear Accelerator (HILAC). Initial energies of both beams were approximately 10 MeV/AMU. The lithium ion beam was degraded further in energy by interposition of mylar absorbers in the beam path. The carbon ion beam was not additionally degraded. The Bragg curves and their maximum penetration depths in mylar are also shown in Figure 1. Doses were expressed at the surface of the skin and the Bragg curves were unmodified. Doses of 1250 rads were given, with three treatment areas per mouse. Doses were measured with an integrating ionization chamber which interrupted the beam automatically after a preset dose. Average dose rate was 5000 rads per minute.

The scoring of all the epithelial survival responses was done by one observer. As pointed out by Emery et al (ref. 2), the response is quite subjective. Mice were observed from day 7 post-irradiation onward until the response could be considered complete. Ulceration of the skin appeared at different times post-irradiation with the order of appearance being carbon, lithium, and helium ions. The ulcerations appeared on about days 10, 13, and 14, respectively. Clones were observable from about day 10 onward to a maximum of about day 20. The clones differed in appearance; some being punctate, while others were more diffuse and appeared as thin sheets. Only clones which were scoreable for two or more observation periods in a row were considered positive identifications (i.e. about 4-7 days). Histological samples were taken for further identification. Due to stretching of the skin of the anesthetized animal during irradiation, the irradiation fields were often not circular but elongate. There were also scoring difficulties when extensive scab formation was seen. If there was any question as to the patency of the irradiation procedure the animal in question was excluded from the analysis. Still, as pointed out by Emery et al (ref. 2), these possible uncertainties in scoring should not shift experimental survival points by a great deal. Experiments were not subject to errors induced by fortuitous clonal regrowth via hair follicles.

RESULTS

Table I lists the surviving cells/cm^2 for each of the ions and doses.

Figure 2 shows the results obtained after irradiation for the helium ion exposures. The points fit a linear relationship of log survival to linear helium ion dose over the range of doses studied. A regression analysis of the unweighted points yields a D_o value of 95 rads, and extrapolation of the curve to zero dose produces a surviving cell number/cm^2 of 1.5×10^8. Epithelial survival curves for 29 kVp x-rays (ref. 1) and 250 kV x-rays (ref. 2) have been included for comparison purposes.

Included also in Figure 2 are the survival values/cm^2 for the single 1250 rad doses for the lithium and carbon ion irradiated animals. The points lie to the left of the helium ion or x-ray dose response curves.

TABLE I

Epithelial Cell Survival Results For Single Heavy-Particle Exposures

No. of Experimental Areas per mouse	Area (cm^2)	Dose	No. of Areas Irradiated	No. of Areas Regrowing	Average Survival Cells/cm^2
Helium Ions					
1	2.85	1625	30	20	0.251 (.21-.30)*
1	2.85	1750	30	8	0.185 (.15-.20)
3	0.317	1250	45	34	2.45 (2.14-2.76)
3	0.317	1500	84	15	1.41 (1.28-1.54)
3	0.317	1750	72	5	1.27 (1.19-1.35)
7	0.035	1250	35	12	15.1 (12.6-17.6)
7	0.035	1375	35	7	13.3 (11.4-15.3)
7	0.035	1500	35	2	11.8 (10.6-12.7)
Lithium Ions					
3	0.317	1250	78	20	1.50 (1.36-1.59)
Carbon Ions					
3	0.317	1250	75	13	1.40 (1.27-1.54)

*Numbers in parentheses indicate 95% confidence limits

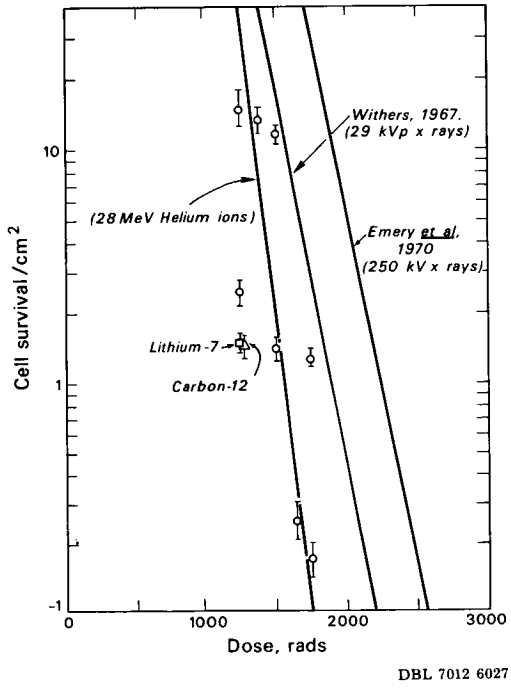

Figure 2. Survival of Epithelial cells following single doses of heavy particles. Vertical bars indicate 95% confidence limits.

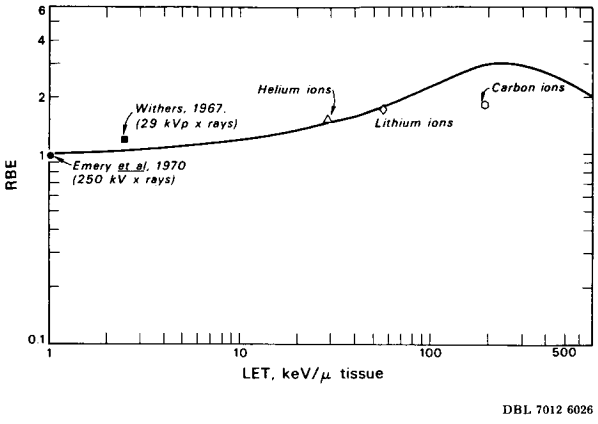

Figure 3. Schematic curve showing variation of RBE with LET from experimental data. The curve shown in for mammalian cells (ref. 7).

DISCUSSION

Results have been interpreted in terms of the estimated number of surviving cells/cm^2, assuming that each visible clone has regrown from a single cell. The heavy ions appear to have a greater effect than either 29 kVp x-rays (ref. 1) or 250 kV x-rays (ref. 2). Indeed, if one examines the doses needed to reduce epithelial cell survival to a level of 1 surviving cell/cm^2, one can obtain a tentative RBE versus LET response (Figure 3). The curve for mammalian cells has been derived from heavy ion experiments on cells in culture (ref. 7). The RBE values for x-rays (ref. 1 and 2) and the heavy ions are listed in Table II, together with other experimental values. The 250 kV x-ray work of Emery et al (ref. 2) has been used as the comparison work. Tentative doses for lithium and carbon ions have been found assuming that the cell survival/cm^2 intercept at zero dose will be the same as that found with helium ion exposure and drawing a line from this point through the observed cell survival/cm^2 extending to 1 surviving cell/cm^2 As extrapolation numbers decrease with increasing LET, the assumption that zero dose cell survival values will be equivalent for the helium, lithium, and carbon ions may be incorrect. However, the possible error from this in estimation of the 1 cell/cm^2 survival level should not be very large. The RBE-LET response curve lies below the schematized curve for mammalian cells. The data suggest that the RBE-LET response for skin reaches a plateau of only about 2 for heavy ions as compared to the value of about 3 for other mammalian systems In Vitro. Further support for a maximum RBE value of about 2 is presented by Denekamp et al (ref. 3) who show a maximum RBE of about 2

TABLE II

Researcher	Strain of Mouse	Do Rads	Y Intercept	Radiation Quality	RBE	LET_∞^{II} (keV/uM)
Emery et al (2)	Male Albino SAS/TO, 8-9 weeks of age at exposure	135	1.35×10^7	250 kV x-rays (300 rads*/ minute) III	1.0^I	1.0
Withers (1)	Inbred Albino WH/Ht, both sexes, 9-14 weeks of age at exposure	135	1.39×10^6	29 kVp x-rays (769 rads/ minute)	1.2	3.0
Leith et al	Male CD1 Hairless, random bred, 10-14 weeks of age at exposure	95	1.50×10^8	^{4}Helium (3000 rads/ minute)	1.6	28.0
				^{7}Lithium (5000 rads/ minute)	1.9	56.3
				^{12}Carbon (5000 rads/ minute)	2.0	192.8

*dose rates of treatment exposures

(All mice were anesthetized at the time of exposure)

^{I}RBE values taken as the doses needed to reduce cell survival/cm^2 to 1.0 using the data of Emery et al (2) as basis of comparison.

$^{II}LET_\infty$ denotes the total particle linear energy transfer including all secondary electrons.

III 250 kV irradiation HVL = 1.5 mm Cu

with fast neutron (mean energy 8 MeV) using the same experimental system. Expressing survival curve responses as a function of radiation dose at the epidermal basal cell layer is probably the correct way. The basal layer in our hairless CD1 mouse lies approximately 20-30 microns below the top of the ventral skin. If radiation doses were expressed as the average dose across the radiation penetration range, or as the maximum dose, which would be found close to the maximum penetration depth, the observed cell survival figures for the helium, lithium, and carbon ions would be shifted to the right (see Figure 2). Such a result does not seem probable, as one would expect some degree of greater efficiency of cell killing with higher LET particles.

RELATION OF CELL SURVIVAL TO WHOLE ANIMAL MORTALITY

Radiation of the skin of the mouse with helium ions kills a proportion of the basal cell layer of the skin. If enough of these cells are killed, this should be critical to the survival of the organism, and its fate will depend on the remaining number of surviving cells. It is of great importance to relate such whole animal mortality to the survival curves for individual cells as has been attempted for other cell systems (refs. 8 to 10). Such data is available for whole animal mortality after helium ion irradiation of the skin. In this approach a slightly different technique has been used where the animal rotates in front of the helium ion beam while enclosed in mylar holders. As the animal rotates each point on the skin will see a spectrum of Bragg curves from maximum penetration (set at 500 microns tissue) to zero penetration. Such a spectrum of curves also produces a flattened depth dose distribution very similar to Figure 1 for the helium ions. Irradiation in this fashion produces a skin damage syndrome which may be lethal to the animal. Animals that die, do so within 22-42 days post-irradiation with a mean survival time of about 29 days. The mortality response is dose-dependent, and shows an LD50/60 of 1543 rads (expressed as the dose at the top of the skin). An approximate 0.1% threshold of 1080 rads may be found from extension of the mortality response versus dose to the 0.1% mortality level. A value of 500 rads may be given for K, where K is the mortality curve probit width; i.e. the dose which causes a unit change in the probit of mortality.

If one considers the mortality response to be primarily a function of the number of surviving epidermal cells, the LD50 corresponds to about 2 surviving cells/cm^2,

Lange (ref. 11) from analysis of the Withers data (ref. 1) lists the extrapolation value for the mouse epidermal cell survival curve/cm^2 to be about 6.5. Gilbert(ref. 12) gives an equation for the relation of cell survival to whole animal mortality of:

$$\text{probit } (Pm) = (D - D_o \cdot \ln (NaE)/(D_o / B)$$

Where $LD_{50} = D_o \cdot \ln (NaE)$

and $K = D_o/B$.

As stated by Gilbert (ref. 12), the LD_{50} does not depend on the sensitivity factor (B), but is just the dose needed to reduce the sensitive cell number to a critical level. The factor Na is simply the ratio of the normal sensitive cell number to the critical number. The probit width K is not dependent on N, a, or E and is proportional to D_o.

As illustration, for the whole animal helium ion irradiations at a depth of 500 microns, the LD50 is 1543 rads, and K is 500 rads. For the epidermal cell survival curve at an irradiation depth of 500 microns, D_o is 95 rads, and E is 6.5 (ref. 11). Using the above equations, Na becomes 1.74×10^6 and B is 0.19. If one assumes that there are about 1×10^6 epidermal cells/cm^2 and that the mouse has a total surface area of about 40 cm^2, then N, the normal stem cell level is 40×10^6 cells and a then equals 4.35×10^{-2}. As comparison, the value of a for the bone marrow radiation syndrome is about 2.3×10^{-3} (ref. 12). Gilbert lists a critical level where there is 50 per cent survival of S = 1/a. For mouse cells this becomes S = $1/4.35 \times 10^{-2}$ or about 2.3×10^1 cells per animal. Again, for an animal with a surface area of 40 cm^2 this is about 0.6 cells/cm^2 surviving at the whole animal 50% mortality level. From our results, we empirically show that at the LD50 dose (1543 rads) that this should give about 2 cells surviving/cm^2, a finding not too far at odds with that calculated using Gilbert's data (ref. 12). It is interesting that Withers (ref. 1) states "10-20 cells must be capable of preventing ulceration by proliferating to cover a 1 cm^2 area.....the response of skin to irradiation is therefore critically dependent on very few cells".

REFERENCES

1. Withers, H.R.: Br. J. Radiol., vol. 40, 1967, p. 187.
2. Emery, E.W., Denekamp, J., Ball, N.M., and Field, S.B.: Radiat. Res., vol. 41, 1970, p. 450.
3. Denekamp, J., Emery, E.W., and Field, S.B.; Radiat. Res., vol. 45, 1971, p. 80.
4. Freier, P.,and Webber, W.R.: J. Geophys. Res., vol. 69, 1963, p. 1605.
5. Freier, P.: J. Geophys. Res., vol. 68, 1963, p. 1805.
6. Biswas, S.: Fichtel, C.E.; and Guss, E.: Phys. Rev., vol. 128, 1962, p. 2756.
7. Barendsen, G.W.: Walter, H.M.D.; Fowler, J.F.; and Bewley, D.K.: Radiat. Res., vol. 18, 1963, p. 106.
8. Munro, T.R.; and Gilbert, C.W: Brit. J. Radiol., vol. 34, 1961, p. 246.
9. Robinson, C.V.: Radiat. Res., vol. 35, 1968, p. 318.
10. Lange, C.S.; and Gilbert, C.W.: Int. J. Rad. Biol., vol. 14, 1968, p. 373.
11. Lange, C.S: Radiat. Res., vol. 44, 1970, p. 390.
12. Gilbert, C.W.: Int. J. Rad. Biol., vol. 16, 1969, p. 287.

LYMPHATIC INVOLUTION AND EARLY MORTALITY IN THE YOUNG CHICKEN PRODUCED BY 2.2 GeV PROTONS[1]

James L. Montour[2] and Claire J Shellabarger[3]

Radiology Department, Medical College of Virginia, Virginia Commonwealth University, Richmond, Virginia
Zoology Department, University of Michigan, Ann Arbor and
Medical Department, Brookhaven National Laboratory[4], Upton, New York

1. Supported in part by NASA (NsG 214-62)
2. Present Address - Radiology Department, Medical College of Virginia, Virginia Commonwealth University, Richmond, Virginia
3. Present Address - Medical Department, Brookhaven National Laboratory
4. Brookhaven National Laboratory is supported by the U.S.A.E.C.

Young single-comb white Leghorn cockerels were subjected to single acute doses of either 2.2 GeV protons or 250 kVp X-rays. Since young chickens exposed in the lethal range die within 48 hours of exposure, an hourly tabulation of deaths was recorded for this length of time after exposure. Animals which were exposed to sublethal doses were killed five days after exposure and their major lymphatic organs, (thymus, bursa, and spleen), removed and weighed.

In the lethal range, animals exposed to 2.2 GeV protons died sooner than those receiving similar doses of X-rays, but total mortality was similar in each case at similar dose levels. The 48 hour LD_{50} was determined to be 710 rad. Measured five days after exposure, 50% depression (ED_{50}) for lymphatic organs occurred as follows: thymus, 350 rad; bursa 500 rad; spleen 450 rad. In all case R.B.E. values were not different from unity.

The total dose from protons of this energy is comprised of a low LET portion due to dE/dx energy loss and a high LET portion due to nuclear interactions. R.B.E. values considerably below unity would be predicted on the basis of dE/dx energy loss alone. It is suggested, then, that the R.B.E. of that portion of the dose contributed by nuclear interactions is very high. If high LET interactions account for only 5% of the total dose, then these interactions could have an R.B.E. great as 7.

INTRODUCTION

Exposure of young chickens to electromagnetic radiations at dose rates above 15 R/min. results in death within 48 hours of exposure (ref. 1) with $LD_{50/48\ hour}$ values between 700 R and 1000 R. Vascular leakage, hypotension, circulatory failure, and renal failure have been the major characteristics associated with this early death. (ref. 2). This is quite different from the case in mammals where death occurs 8 - 30 days after exposure to similar doses. Inability of irradiated cells, particularly those involved in blood cell formation, to reproduce is the prime cause of death. Alterations in vascular permeability do occur in mammals, including man, after irradiation but these are generally transitory. Using the young chicken, it was possible to measure the effectiveness of 2.2 GeV protons in producing a physiologic change whose endpoint (death) was easily

determined.

Lymphatic organ weight loss in mice has been shown to be a reproducible measure of radiation dose and has been used as an endpoint for R.B.E. studies (ref. 3,4). This is also the case in the young chicken, where lymphatic organ weight loss has been used as a biological dosimeter and a measure of R.B.E. values for thermal and fission neutrons. (ref. 5).

In the experiments reported here we have used these two endpoints, early mortality and involution of lymphatic organs, to examine the relative biological effectiveness of the 2.2 GeV proton beam of the Brookhaven National Laboratory Cosmotron.

MATERIALS AND METHODS

Animals - Single comb white leghorn cockerels were obtained from Klager Hatchery, Saline, Michigan, shortly after hatching. Within 24 hours the animals were transported to the Medical Department of Brookhaven National Laboratory and housed, 50 per tier in a standard chick brooder. Purina starter mash and water were available ad libitum. Radiation exposures were performed on the third day of age. The number of animals in each experimental group is indicated in Table I and Table II. In the mortality study, an hourly tabulation of deaths was maintained for thirty hours after exposure. Animals involved in the lymphatic-involution study were killed and dissected five days after exposure. Body weights were recorded to the nearest gram and wet weights of thymus, bursa of Fabricius and spleen recorded to the nearest 0.1 mg. Because the lymphatic organs of the chick, like those of mammals, are sensitive to adrenal

Table I

Acute (30 Hour) Death Following Exposure to 250 KVP X-Rays or 2.2 GEV Protons

Dose[1]	N	Time Post Exposure In Hours*																										Fraction Killed
X-Rays		3	4	5	6	7	8	9	10	11	(12	16)	17	18	19	20	21	22	23	24	25	26	27	28	29	30	
713	40			2				1							5	8	2	1		1	1			1			22/40
808	30	1	2	2	2			2					3	3	4			1		1		1					22/30
903	30	1	2	2	7	3	1				1		1	1	2	1	2	2							2	1	29/30
Protons																											
575	16		1																					1			2/16
613	8					1																		1			2/8
647	16																										0/16
690	10					1						1										3					5/10
744	16					5	4		1																		10/16
795	16				5	5		3																			13/16
842	16	1		6		3	2																				12/16
913	16		1	12			2																				15/16
963	16			6		9			1																		16/16
1081	16			5		8			1																		14/16
1206	8	3	1		1	1		2																			8/8

1. Dose in rads

*Numbers in these columns indicate the number of animals dead during hourly intervals indicated.

Table II

Lymphatic Organ Weights Following Exposure to 2.2 GeV Protons or 250 KVp X-Rays

	Dose[1]	N	Body[2] Weight	Thymus[3]	Bursa	Spleen
Control	0	10	53	309	283	106
X-Rays	190	10	54	247	232	84
	380	10	51	158	170	52
	570	10	49	113	124	41
Protons	112	9	56	242	242	91
	188	6	54	231	267	74
	230	5	52	185	237	75
	299	5	51	143	176	71
	316	5	49	171	175	55
	344	5	50	148	196	62
	386	7	50	146	168	62
	406	5	52	150	196	56
	435	5	51	139	151	57
	437	5	51	112	151	47
	498	5	49	96	139	43
	522	5	48	98	142	48
	551	6	46	83	124	43
	576	6	47	109	140	45
	613	7	48	113	152	42
	647	5	47	85	123	34

1. Dose in rads
2. Body weight in grams
3. Organ weights in mg/100 gms. body wight

corticoid release following stress (ref. 6, 7) all animals were maintained in the exposure holders for periods equal to that of the longest exposure. Half of the control animals were sham-irradiated in the proton exposure apparatus and half in the X-ray chamber. No difference was seen between the two control groups, so they were pooled for subsequent analysis. To compensate for variations in body weights between groups, organ weights are presented as mg/100 gm of body weight.

EXPOSURE CONDITIONS

Protons - Proton exposures were carried out as previously described for mice (ref. 8, 4) and rats (ref. 9), in a lucite tube 4.5 cm in diameter and 128 cm in length. Four chicks were exposed per Cosmotron run. The exposure tube was rotated about its longitudinal axis at 20 rpm. The beam was pulsed 25/min. with a pulse duration of 1 m sec. giving an instantaneous dose rate of 14,000 rads/sec. during pulses. The integrated dose rate was 350 rads/min. from the pulsed Cosmotron beam. Dosimetry of the proton beam has been previously described. (ref. 8, 10). The doses expressed in this paper are based on: 2.82×10^7 p/cm^2 = 1 rad.

X-Rays - The source of X-rays was a standard therapy machine operated under the following conditions: 250 kVp; 15 mA; 0.5 mm Cu, and 1.0 mm Al added filtration. The dose-rate measured 60 cm from the target with a Victoreen condenser R-meter was 118 R/min. (under conditions of maximum backscatter). In order to compare the absorbed X-ray dose with that of protons, 1 R was considered equivalent to 0.95 rads. Eight or ten chicks were exposed at a time in a rotating lucite chamber 23 cm in diameter and 4 cm thick.

RESULTS

Lethality - The time distribution of deaths following exposure to either X-rays or protons is given in Table I. In the X-ray group, all animals which died, with one exception, did so in the intervals 3 - 9 hours or 17 - 30 hours after exposure. As the dose was increased, a larger percentage of the animals died in the earlier (3 - 9 hours) period. Animals which died following proton exposure did so primarily between 3 and 11 hours after exposure, regardless of dose or 30-hour mortality level. The few animals which did die in the later period were, however, in the lower dose groups. A probit plot of the accumulated 30-hour mortality is presented in Figure 1. A visual fit of the data yields a 50% mortality ($LD_{50/30\ hours}$) dose of 710 rads for both protons and X-rays. The single line in Figure 1 fit both the proton and X-ray points.

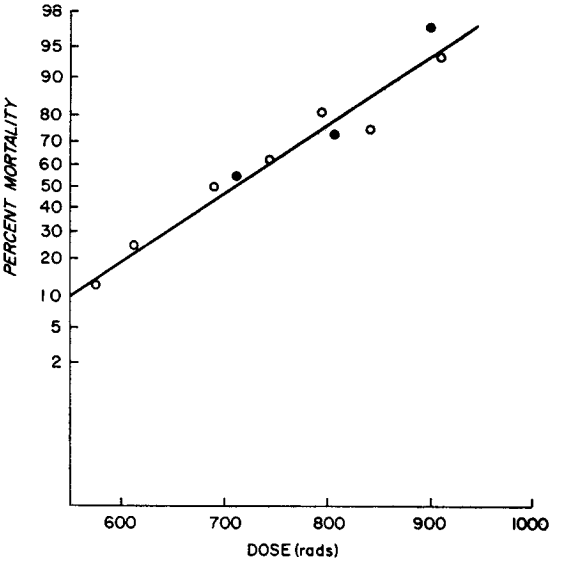

Figure 1. Thirty-hour mortality in the young chicken following proton or X-irradiation.

Lymphatic Organ Involution - Body weights and lymphatic organ weights obtained five days after exposure to sublethal doses of either X-rays or protons are given in Table II. Organ weights, as percentage of unirradiated controls are presented in Figure 2 (thymus), Figure 3 (bursa), and Figure 4 (spleen). From these figures, 50% depression (ED_{50}) values of approximately 350 rads (thymus), 500 rads (bursa) and 450 rads (spleen) were obtained for protons and nearly identical values for X-rays.

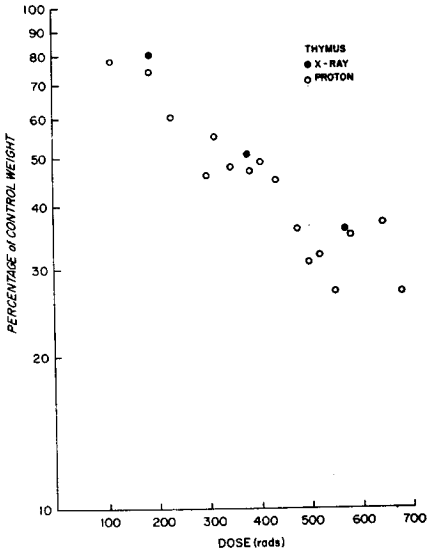

Figure 2. Thymic weights five days after proton or X-irradiation.

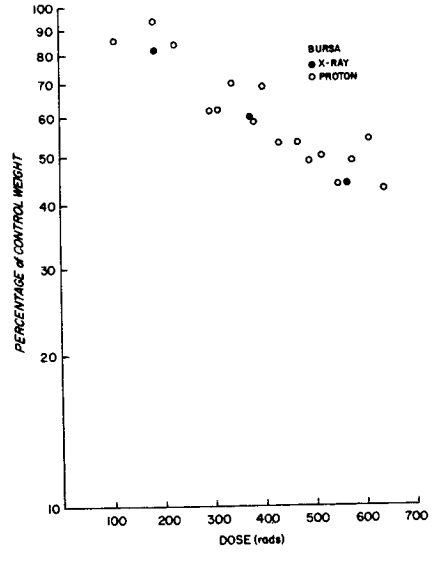

Figure 3. Bursal weights five days after proton or X-irradiation.

DISCUSSION

From Figure 1 it can readily be seen that both proton irradiated and X-irradiated chicks have $LD_{50/30\text{-hour}}$ values of 710 rads, giving an R.B.E. for early mortality of 1.0. When high LET radiations such as fission neutrons are employed, not only is the R.B.E. considerably above 1 (4.2 for early mortality, ref. 5) but the slope of the mortality curve is much steeper. For 2.2 GeV protons this is not the case. From Figure 1 it can be seen that a single slope is sufficient to describe both the proton and X-ray mortality curves. Both the R.B.E. of 1.0 and the identical slopes of the mortality curves strongly suggest that these protons act primarily as low LET radiations. The only difference seen between the proton and X-ray groups is the tendency for the proton bombarded animals to die in the earlier of the two mortality periods. Although the reasons for this are not clear, it is not suggestive of high LET exposures since our own unpublished observations indicate that neutron exposed animals die fairly uniformly throughout the 3 - 30 hour post-exposure period and do not exhibit the bimodal concentration of deaths seen with X-rays.

The weights of the thymus, bursa, and spleen five days after exposure to various doses are shown as percentages of control weights in Figure 2, Figure 3, Figure 4. These curves reflect decreases in cell populations due to both scopal (direct) and abscopal (indirect) radiation damages and subsequent recovery and repopulation. Five days after irradiation, the net result of these processes gives an approximately straight

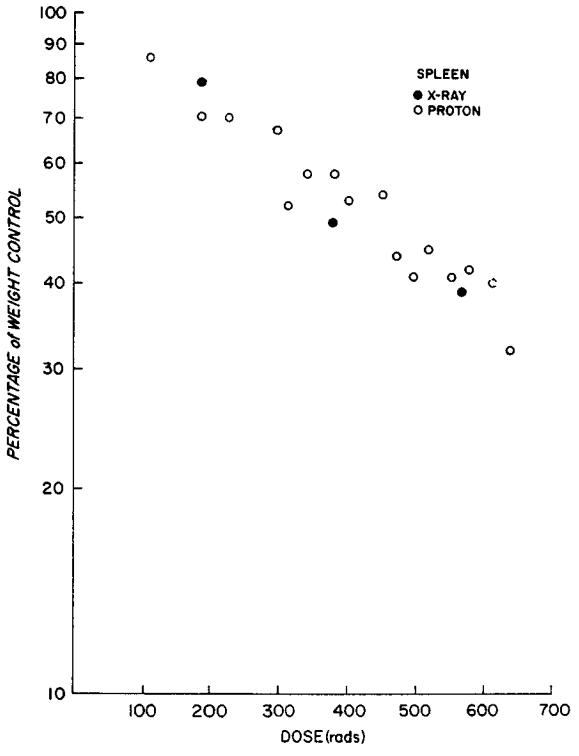

Figure 4. Splenic weights five days after proton or X-irradiation.

line dose-response relationship. The ED_{50} values of 350 rad (thymus), 500 rad (bursa) and 450 rad (spleen) are useful for determining R.B.E. values but are not indicative of cell sensitivity since considerable repair has occurred, especially at the lower doses. In each case, any line fit through the proton points could equally fit the X-ray points indicating that the R.B.E. of 2.2 GeV protons for lymphatic organ involution is indistinguishable from unity.

These experiments strongly suggest that the minimally ionizing 2.2 GeV protons act primarily as low LET radiation, but do not exclude the possibility that a small component of high LET is present.

Ueno and Grigoriev (ref. 11) have suggested that a single R.B.E. of 0.82 ± 0.04 can be assigned to all mammalian endpoints tested for protons between 126 MeV and 730 MeV. This certainly is not the case with the 2.2 GeV protons from the Brookhaven Cosmotron. R.B.E. values from 0.87 to 2.5 have been found under identical exposure and dosimetric conditions and, in the case of mouse experiments, the same strain of animals (ref. 4,8,9,12, and this paper). The R.B.E. of the 2.2 GeV protons would, therefore, appear to be dependent upon the particular biological endpoint under study.

These conclusions have certain practical implication for space flights. Since the protons act as low LET radiation, radioprotective chemicals suitable for man would be effective against high energy protons(ref. 9, 13). The effectiveness of low LET radiations is dose-rate dependent for most endpoints. The establishment of acceptable dose limits for proton exposures in space should, therefore, consider expected dose-rates as well as total doses. In addition, since the R.B.E. of protons differs for different endpoints, the tolerance dose limits must also consider what biological endpoints are critical.

ACKNOWLEDGEMENTS

The authors wish to thank Miss R.F. Straub, Drs. W. H. Moore, E. P. Cronkite, V. P. Bond, and the Cosmotron crew.

REFERENCES

1. Jacquez, J. A. and Karnofsyk, D. A.: Amer. J. Roentgenol and Rad. Therapy, vol. 64, 1950, p. 289.

2. Stearner, S. P., Sanderson, M. H., Christian, E. J., and Brues, A. M.: Am. J. Physiol., vol. 192, 1958, p. 620.

3. Harris, P. S. and Brennan, J. T.: Report LA-1410, May 1952.

4. Montour, J. L., Straub, R. F., and Shellabarger, C. J: Int. J. Radiat. Biol., vol. 15, 1969,p. 491.

5. Montour, J. L.: Radiation Res., vol. 25, 1965, p. 219.

6. Garren, H. W. and Shaffner, C. S.: Poultry Sci., vol. 35, 1936, p. 260.

7. Newcomer, W. S. and Connally, J. D.: Endocrinology, vol. 67, 1966, p. 264.

8. Jesseph, J. E., Moore, W. H., Straub, R. F., Tisljar-Lentulis, G. M., and Bond, V. P.: Radiation Res., vol. 36, 1968, p. 242.

9. Shellabarger, C. J, Straub, R. F., Jesseph, J. E., and Montour, J. L.: Radiation carcinogenesis and acute radiation mortality in the rat as produced by 2.2 GeV protons. National Symposium on Natural and Manmade Radiation in Space (1971).

10. Gross, W. and Bell, W.: U.S.A.E.C. Report NYO 2740-3 (1966).

11. Ueno, Y. and Grigoriev, Y. G.: British J. Radiol., vol. 42, 1969, p. 475.

12. Stoner, R. D., Straube, R. F., Moore, W. H., and Jesseph, J. E.: Radiation Effect, vol. 2, 1969, p. 97.

13. Riley, R.C., Montour, J.L. and Gurney, C.W.: Proton irradiation of stem cells: radiation damage and chemical radioprotection. National Symposium on Natural and Manmade Radiation in Space (1971).

Evaluation of the Hazard From Exposure to Electron Irradiation Simulating That in the Synchronous Orbit

Stuart W. Lippincott, M.D., Trutz Foelsche, Ph.D., James Montour, Ph.D., Roger Bender, Ph.D., and John Wilson, Ph.D.

Department of Radiology, Medical College of Virginia, Virginia Commonwealth University, Richmond, Virginia, NASA Langley Research Center, Hampton, Virginia, and the Department of Physics, The Citadel, Charleston, South Carolina.

The electron spectrum predicted for the synchronous orbit has been simulated to determine the effects that might occur to astroscientists exposed to such irradiation while on a prolonged space station mission in that region. Miniature pigs were exposed to monoenergetic and spectral-fractionated irradiations with 0.5 to 2.1 MeV electrons. Clinical and pathological alterations observed in biopsies were correlated with depth-dose pattern and length of post-irradiation period up to one year. With monoenergetic electrons, the lowest dose causing a recognizable lesion was 1450 rad and with increasing dose lesions appeared earlier and were more severe. At the highest dose given, 2650 rad, ulceration extending into the dermis was present by twenty-one days and required about four months for complete healing. Spectral-fractionated irradiations, in which the total dose range was essentially comparable to that of the monoenergetic series, resulted in very minimal outer dermis edema at 1790 rad and at no dose employed did necrosis of epidermis or ulceration into dermis occur.

Apart from the possibility of a solar flare, nominally only low energy electrons constitute a possible radiation hazard for astronauts and scientists spending long periods of time lightly shielded on a space station in the region of the outer belt or in the synchronous orbit. In the course of determining the maximum permissible dose for such individuals the effects of monoenergetic, spectral-fractionated, and protracted irradiations with 0.5 to 2.1 MeV electrons are being investigated in miniature pigs. Clinical and pathological alterations in the skin are being correlated with depth-dose pattern, size of area exposed, and length of post-irradiation periods. The latter have been arbitrarily divided into (a) immediate, up to thirty days, (b) intermediate, thirty to one hundred and eighty days, (c) interval, six months to three years, and (d) long-term, three to ten years. From a practical point of view it is necessary to know whether any immediate undesirable responses such as blistering, oozing, or erythema may develop, which could impair the efficiency of the astroscientists. It is also important to determine whether long-term effects such as widespread dermatofibrosis or a malignant neoplasm may arise.

Dosimetry Methods

The methodology employed has been described previously [1] so that essentially only the general procedures are herein noted. A Dynamitron was the source of electrons. A Faraday cup was used to set the intensity levels for each irradiation and to check the stability of the Dynamitron. An extrapolation ion chamber, designed for this program, was used to determine the surface dose under the same irradiation conditions as in the animal irradiations. For these irradiations the miniature pigs were covered by space suit shielding equivalent to 2.0 mm of tissue. A mockup of the pig's body simulated the tissue surrounding the ionization chamber during correlation measurements. Thermoluminescent dosimeters were used to establish the correlation of the fields measured outside the space suit to the dose measured by the extrapolation chamber placed under the space suit. During the skin irradiations a matrix of TLD's was attached to the surface of the space suit shielding to monitor the variation in radiation level over the pig's skin. A 1 cc tissue-equivalent ionization chamber was used in a constant fixed geometry to monitor the relative beam intensity during the periods of irradiation.

Spectra Simulation

The time average electron integral flux at the equatorial synchronous altitude is indicated in the following equation:

$$\psi\ (> E) = 5.2 \times 10^{7} \cdot e^{-5E}\ \frac{\text{electrons}}{\text{cm}^2\text{sec}}(*)$$

Where

E = electron energy in MeV

$(> E)$ = Flux of electrons with energy greater than E

This spectrum is plotted in Figure 1

*James I. Vette, Models of the Trapped Radiation Environment. Vol. III: Electrons at Synchronous Altitudes, Aerospace Corp., El Sequndo, Calif. NASA-SP-3024, 1967.

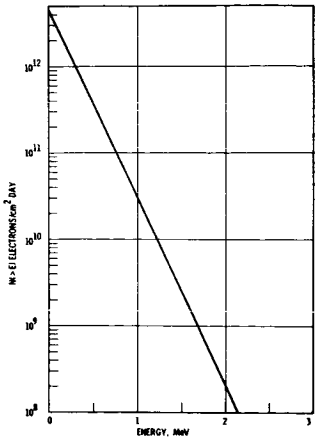

Fig. 1. Predicted electron spectrum for equatorial synchronous orbit.

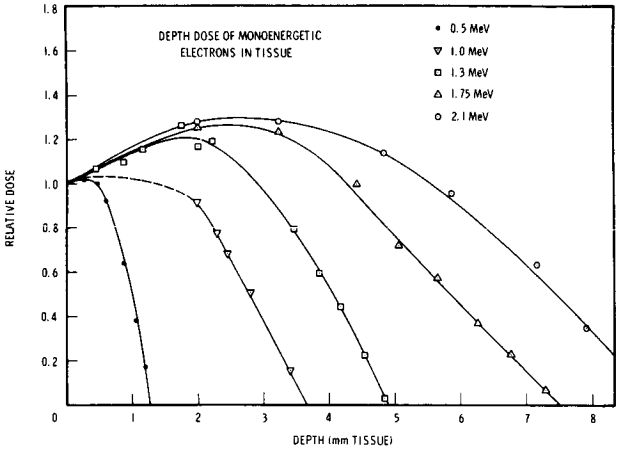

Fig. 2. Depth dose of monoenergetic electrons in tissue.

Since the space suit shielding is equivalent to 2.0 mm of tissue, electrons below 0.8 MeV cannot penetrate the space suit shielding of an astronaut and do not have to be considered.

From the depth-dose measurements taken during the first phase of the program, the penetration of a given energy electron may be accurately predicted. Figure 2 shows the characteristic penetration of electrons with energies in the region of interest taken during the first phase of the program. The data from Figure 2 may be presented in a more satisfactory manner to make interpolation between incident energies. By plotting the depths at which a given percentage of the incident dose is absorbed, a series of curves results. Figure 3 shows the relationship of absorbed dose and incident energy for 10, 50, and 90 percent of the incident dose levels. These curves exhibit a regularity that makes interpolation of depth patterns straightforward and simple.

These curves may be used to evaluate the penetration of any electron having incident energy from 0.5 to 2.1 MeV. By taking the predicted spectra of the synchronous orbit and dividing the electron spectra into small energy bins, the characteristic depth-dose relation may be calculated for each energy bin. The sum of these penetrations weighted by the number of electrons predicted in each bin then represents the total depth-dose pattern that would be expected from an electron beam whose energy spectrum is that of the synchronous orbit.

The number of electrons in each energy bin is multiplied by the value of $\frac{dE}{dX}$ in tissue for the energy of that bin from the tables of Berger and Seltzer(*) and the product then represents the absolute value of the dose-depth curve. The curves for all the energy bins are then added to get the resultant dose versus depth for the synchronous spectrum as shown in Table 1.

Table 1

Relative Dose	Depth In Tissue (millimeters)	Depth In Pig (millimeters)
1	0	0
0.67	0.5	1.5
0.42	1	3
0.25	1.5	4.5
0.13	2	6
0.04	3	9
0.01	4	12
0.006	5	15

*Additional Stopping Power and Range Tables for Protons, Mesons, and Electrons By: Berger and Seltzer NASA SP-3036

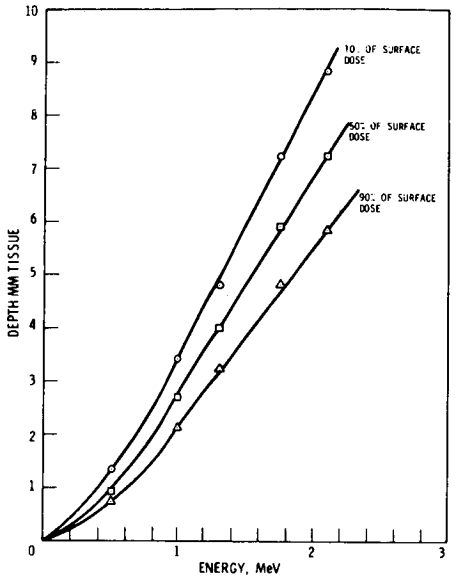

Fig. 3. Characteristics of penetration of monoenergetic electrons.

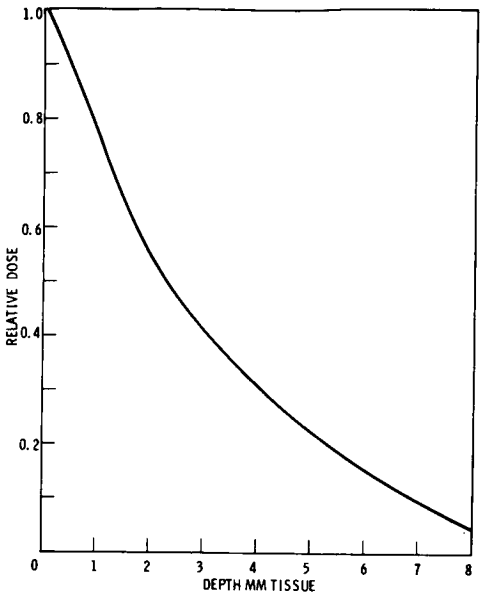

Fig. 4. Depth dose pattern from the predicted synchronous orbit spectrum.

From measurements of the skin characteristics of miniature pigs, the epidermis and dermis were considered approximately two to possibly three times thicker than the same relative layers in human skin. Thus, the relative dose desired in the target animal to simulate equivalent penetration in man occurs at the relative depths as shown in Table 1 and in Figure 4. Several monoenergetic electron energies could be selected such that the sum of their depth dose penetration curves would correspond to the predicted pattern of Table 2. A final selection of three monoenergetic electron energies was made to simulate the equatorial synchronous orbit spectrum. This selection appears in Table 3, which shows the predicted dose from the synchronous orbit spectrum, the simulation dose that would be deposited from the three monoenergetic electron irradiations, and the differences. The largest discrepancy is seen at a depth of 2 mm, where the simulation is 0.04 less than the predicted dose pattern, when normalized to 1.0 at the skin surface. The depth dose pattern that would be given by the simulation is shown in Figure 4.

During an electron irradiation the exposure was uniform to the trunk over an area 12 inches wide. The axis of rotation was approximately on a line from the head to tail, through the central mass of the animal. There is some variation in the distance from the skin surface to the exit window. To establish whether this variation made a significant change in dose deposition in relation to the 1-cc tissue-equivalent ionization chamber positioned near the exit window, the dose levels were measured as a function of distance from the window. The results, Figure 5 show that position of the central flank of the pig with respect to the exit window was not critical within $\pm$ 2 inches.

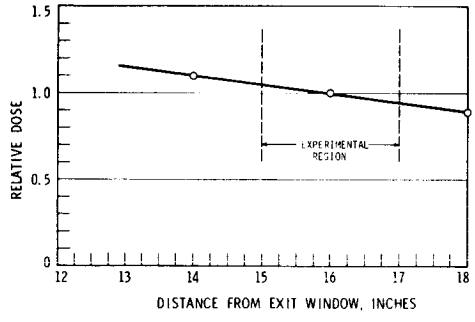

Fig. 5. Measured dose level variations with separation of the target animal from the exit window of the Dynamitron.

The procedure adopted in the first series for each pig irradiation was to make three irradiations on three successive days, with a different incident energy for each irradiation. In the second series the successive irradiations were made within 35-70 minutes. The sequence of incident energies was at random. Before each irradiation, a mockup of the pig's body surface was placed in the equivalent geometry and a relationship was established between the extrapolation tissue-equivalent ionization chamber shielded by the space suit and TLD's on the front surface of the space suit. During irradiation, the space suit shielding was placed over the pig's skin, and a matrix of TLD's was used to measure the intensity of dose over the total area being exposed.

Table 2. Depth Dose Values for Equatorial Synchronous Orbit

Relative Dose	Depth in Man (millimeters)	Depth in Pig (millimeters)	Relative Dose
27,600	0	0	1
18,600	0.5	1.5	0.67
11,700	1	3	0.42
6,990	1.5	4.5	0.25
3,550	2	6	0.13
980	3	9	0.04
340	4	12	0.01
170	5	15	0.006
55	6	18	0.002
9	7	21	-
4	8	24	-

Table 3. Comparison of the Depth Dose Pattern by the Predicted Synchronous Orbit to the Simulation by Three Monoenergetic Electron Irradiations

Depth (mm)	0	1	2	3	4	5	6	7	8	9
Predicted Dose	1.00	0.77	0.57	0.42	0.30	0.20	0.13	0.09	0.06	0.04
Simulation Dose*	1.01	0.77	0.53	0.43	0.32	0.22	0.14	0.10	0.05	0.00
Difference	+0.01	0.00	-0.04	+0.01	+0.02	+0.02	+0.01	+0.01	-0.01	-0.04

*Simulation Energies 1.0 MeV - 48% with space suit shield
1.75 MeV - 37% with space suit shield
2.1 MeV - 16% without space suit shield

To determine whether the uniformity of TLD measurements on the outside surface would correspond to a uniformity inside the shield of the space suit, a matrix of TLD's was placed inside and outside the suit and irradiated simultaneously. The results of the measurement are shown in Table 4. The uniformity represented by the measurements inside the space suit shielding shows that the measurement of dose on the surface of the space suit is a satisfactory measure of dose uniformity.

Table 4. Uniformity of Dose Deposition Inside and Outside Space Suit

MATRIX OUTSIDE

180		180		190
200	190	200	200	190
200		200		210
190	190	190	180	200
190	190	180	180	190
170		160		170

MATRIX INSIDE

150		150		160
150	170	170	170	170
160		160		170
170	180	150	180	160
170	170	160	170	170
160		150		160

The CaF_2:Mn hot-pressed chips used for this program have a thickness of 550 mg/cm^2. This represents an equivalent thickness of tissue of about 4 mm. The differences among the readings in Table 4 of the TLD measurements inside and those outside the space suit can be predicted from the depth-dose curves in Figure 2. Since the TLD chips represent a target that is thin in comparison with the range of a 2.1 MeV electron the average dose measured by the TLD should be in reasonable agreement with the dose, as measured by the extrapolation tissue-equivalent ionization chamber. This agreement was established within 10 percent for the exposures at 2.1 MeV.

The depth-dose penetration achieved in the actual irradiations of the animals is seen in Figure 6. This Figure may be compared with that of Figure 4 showing the depth-dose pattern from the predicted synchronous orbit spectrum. In general the simulation is quite good. In all cases, the quoted dose is the actual rad dosage at the skin surface.

Figure 6
Comparison of Depth Dose Penetration of Actual Irradiations

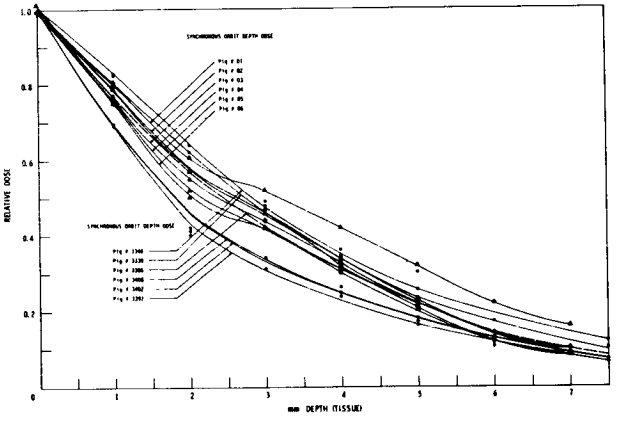

Experimental Results

Monoenergetic Trunk Irradiations

A total of eleven pigs received monoenergetic trunk irradiations at either 1.3 or 2.1 MeV with a range in doses from 245 to 2650 rad, as shown in Table 5. No gross or microscopic evidence of a reaction in the skin was observed in the first post-irradiation year (Table 8) at the following doses: 245, 312, 650, 710, 930, 1020, and 1230 rad. At 1450 and 1660 rad distinct erythema was first seen at 87 days post-irradiation while on the 102nd day it was quite marked in the former and enormous in the latter.

The erythema and pigmentation subsided slowly at both doses and disappeared completely at about 200 days. With increasing dose, reactions were noted earlier. At 1700 rad there was moistness of skin felt grossly at 29 days post-irradiation and outer corium edema seen in the biopsy at that time. Distinct erythema appeared by the 71st day and was gone by the 100th day. Biopsies on the 376th and 465th days disclosed no tissue alterations. At 1980 rad, scattered focal areas of necrosis were noted grossly at the 18th day with erythema that subsided by the 52nd day. The highest dose of 2650 rad produced the most extensive lesion with central necrosis at the 12th day and widespread ulceration extending into the dermis by the 21st day. Gradually healing took place with residual erythema and pigmentation being gone at 5 months, although scaling in the irradiated area continued up to one year.

The irradiation effects may be summarized by stating that no recognizable lesion occurred until a dose of 1450 rad was administered. As would be expected, at higher doses reactions occurred earlier and were more severe. Even with rather extensive ulcerations that occurred at the highest dose of 2650 rad, healing developed within five months.

Table 5

Monoenergetic Trunk Irradiations

Pig Number	Date Irradiated	Energy (MeV)	Average Total Dose (Rad) Rt. Side	Lt. Side
3247	9-12-68	2.1	650	
3259	9-12-68	2.1		1700
3361	1-3-69	1.3	245	312
3340	1-3-69	1.3	1980	2650
3337	7-11-69	1.3	690	760
3334	7-10-69	1.3	1660	
		2.1		1450
3338	7-19-69	2.1	1110	740
3437	7-23-69	1.3	930	710
01	2-23-70	2.1	1420	
02	2-24-70	2.1		1020
04	2-24-70	2.1		1230

Trunk Spectral Irradiations Performed in 48-72 Hour Period

Six pigs were irradiated with a spectrum of 1.0, 1.75, and 2.1 MeV within a 48 to 72 hour period as shown in Table 6. Since only one energy was available at a single exposure, it was decided to give the total dose spread out over the period noted above. While being a spectral irradiation, when all energies had been used, it was of necessity also a fractionated scheme. Subsequent to this, another experiment was run in which the time period for irradiations was compressed into 35-70 minutes. This came closer to a true spectral arrangement, but as yet still consisted of three consecutive exposures at different energies so it also represented a fractionated scheme. The dose range was selected to be similar to that of the monoenergetic trunk irradiation series, as nearly as possible, extending from 950 to 2710 rad (Table 9). No gross or microscopic evidence of a reaction in the skin was observed in the first post-irradiation year at the following doses: 950, 1020, 1300, and 1310 rad. At 1790 rad and at 2000 rad no gross reaction was seen grossly but on biopsy on the 7th day in the former and at the 35th day in the latter minimal edema of the very outer corium was seen microscopically. More frequent biopsies might have disclosed alterations but certainly, if they existed, they were insufficient to produce a lesion that could be recognized on clinical examination.

In summary, by comparison with the monoenergetic series of irradiations, only a most minimal reaction occurred and that was not until a dose of 1790 rad was given. It should be mentioned, however, that the largest single dose component in the total 1790 rad exposure was 1330 rad. In the monoenergetic series the lowest single exposure resulting in a reaction was slightly higher than that being 1450 rad. Apparently this series responded, as one might expect, as a fractionated dose response and therefore the total dose effect was quite different from that of the total dose reaction when given as a single exposure in the monoenergetic series.

Table 6. Summary of Spectrum Irradiations Performed In 48-72 Hours

Pig No.	Date (July 1969)	Energy (MeV)	Average Total Dose On Side of Pig (rad_{tissue}) Right	Left	Dose in Central Flank Area (rad_{tissue}) Right	Left	Spectrum Composite (percent)
3339	25	1.0	1,130	1,000	1,180	1,060	40
	23	1.75	1,090	1,280	1,140	1,330	44
	22	2.1	450	430	460	440	16
			2,670	2,710	2,780	2,830	100
3346	25	1.0	730	830	760	850	40
	23	1.75	850	780	900	810	42
	22	2.1	340	340	370	390	18
			1,920	1,950	2,030	2,050	100
3386	14	1.0	860	950	880	990	48
	15	1.75	660	730	710	740	37
	16	2.1	270	320	280	340	16
			1,790	2,000	1,870	2,070	101
3392	17	1.0	1,250	1,240	1,390	1,320	61
	15	1.75	600	540	650	590	28
	16	2.1	200	230	230	270	11
			2,050	2,010	2,270	2,180	100
3402	17	1.0	790	760	840	820	59
	18	1.75	360	390	380	410	29
	16	2.1	160	150	180	160	12
			1,310	1,300	1,400	1,390	100
3408	17	1.0	520	660	570	720	60
	18	1.75	300	240	320	250	27
	19	2.1	130	120	150	130	13
			950	1,020	1,040	1,100	100

Trunk Spectral Irradiations Performed in 35-70 Minutes

This series of irradiations was designed and carried out after the spectral irradiations noted previously as being performed in a 48-72 hour period as shown in Table 7. The same energies were used; namely, 1.0, 1.75, and 2.1 MeV. The time period was compressed so that individual energy irradiations were given one after another and in a total period of between 35 to 70 minutes from first to last exposure. Again, it was recognized that this also was a fractionated scheme but might better simulate the theoretical situation in which the entire spectral irradiation occurred in one exposure. In addition, intermediate doses not given in the former spectral series were administered this time to correspond more nearly to the monoenergetic series. The purpose in this was again to find out the lowest dose at which a reaction might occur.

Table 7

Summary of Spectrum Irradiations Performed in 35-70 Minutes

Pig No.	Date (Feb. 1970)	Energy (MeV)	Average Total Dose on Side of Pig (rad_{tissue})		Spectrum Composite (percent)
			Right	Left	
01	23 (L)	1.0		430	39
		1.75		385	35
		2.1		280	26
				1,095	100
02	24 (R)	1.0	390		42
		1.75	400		42
		2.1	150		16
			940		100
03	24 (L) 25 (R)	1.0	580	460	44
		1.75	550	380	40
		2.1	200	170	16
			1,330	1,010	100
04	24 (R)	1.0	810		48
		1.75	650		38
		2.1	240		15
			1,700		100
05	25 (L) 26 (R)	1.0	240	1,290	43
		1.75	390	890	44
		2.1	120	270	13
			750	2,450	100
06	25 (L) 25 (R)	1.0	950	630	53
		1.75	520	510	29
		2.1	320	180	18
			1,790	1,320	100

Six pigs were irradiated in this series in a range from 750 to 2450 rad with the largest single component being 1290 rad. It is to be recalled that the lowest dose response in the monoenergetic series occurred at 1450 rad. Twenty biopsies were performed between the third and 150th post-irradiation day. This series has currently an eight month follow-up instead of one year for comparison with the earlier (48-72 hours) spectral series. No gross clinical reaction was observed at any dose. In a biopsy on the third post-irradiation day at 2450 rad spongiosis of the epidermis was seen but no edema of underlying dermis. The epidermal spongiosis may have been an artefact.

In summary, this spectral trunk irradiation series resulted in no post-irradiation reactions, except the very minor ones at 1790 and 2450 rad. These results differ substantially from that of the monoenergetic series in which a distinct reaction occurred at 1450 rad and at all higher doses through 2650 rad. It is suggested that the dose fractionation accounts for the lack of reaction in the two spectral series, since in the latter a number of total doses given were in the range in which prominent lesions developed in the monoenergetic series.

Table 8

Summary of Monoenergetic Trunk Irradiations

Pig Number	Date Irradiated	Energy MeV	Average Total Dose Rt. Side	Lt. Side	Post-irradiation day, Dose [ ], and Histopathology Code ( )
3247	9-12-68	2.1	65u		29[650](1) 71[650](1) 177[650](1) 353[650](1)
3259	9-12-68	2.1		1700	9[1700](1) 29[1700](2) 71[1700](2) 157[1700](1) 374[1700](1) 465[1700](1)
3361	1-3-69	1.3	265	312	2[265](1) 7[265](1) 21[265](1)
3340	1-3-69	1.3	1980	2650	2[1980](1) 7[1980](1) 198[1980](5)
					21[2650](4) 263[2650](5) 353[2650](5)
3337	7-11-69	1.3	690	760	39[760](1)
					96[1660](2) 165[1660](5) 370[1660](1)
3334	7-10-69	1.3	1660		370[1660](1)
		2.1		1450	10[1450](1)
3338	7-19-69	2.1	1110	740	32[740](1)
3437	7-23-69	1.3	930	710	28[930](1)
01	2-23-70	2.1	1420		51[1420](1) 150[1420](1)
02	2-24-70	2.1		1020	150[1020](1)
04	2-24-70	2.1		1230	91[1230](1) 150[1230](1)

Histopathology code for Tables 8, 9, and 10. 1. No recognizable lesion. 2. Edema of outer dermis. 3. Epidermal necrosis. 4. Ulceration of epidermis extending into dermis. 5. Degeneration outer corium. 6. Fibrosis, dermis.

Table 9

Summary of Spectrum Trunk Irradiations Performed Within 48-72 Hours

Pig Number	Date Irradiated (July 1969)	Energy MeV	Average Total Dose Rt. Side	Lt. Side	Spectrum Composite (%)	Biopsies Post-irradiation day, Dose [ ], and Histopathology Code ( )
3339	25	1.0	1130	1000	40	35[2670](1)
	23	1.75	1090	1280	44	36[2710](2)
	22	2.1	450	430	16	
			2670	2710	100	
3344	25	1.0	730	830	40	
	23	1.75	850	780	42	
	22	2.1	340	340	18	
			1920	1950	100	
3386	14	1.0	860	950	48	4[2000](1) 35[2000](2)
	15	1.75	660	730	37	7[1790](2)
	16	2.1	270	320	16	
			1790	2000	100	
3392	17	1.0	1250	1240	61	158[2010](1)
	15	1.75	600	540	28	203[2050](1)
	16	2.1	200	230	11	
			2050	2010	100	
3402	17	1.0	790	760	59	
	18	1.75	360	390	29	
	16	2.1	150	150	12	
			1310	1300	100	
3408	17	1.0	520	640	60	35[1020](1)
	18	1.75	300	240	27	
	19	2.1	130	120	13	
			950	1020	100	

Table 10

Summary of Spectrum Trunk Irradiations Performed Within 35-70 Minutes

Pig Number	Date Irradiated	Energy MeV	Average Total Dose Rt. Side	Lt. Side	Spectrum Composite (%)	Post-irradiation day, Dose [ ], and Histopathology Code ( )
01	2-23-70 Left	1.0 1.75 2.1		430 385 280 1095	39 35 26 100	Control, non-irradiated 2-5-70 150[1095](1)
02	2-24-70 Right	1.0 1.75 2.1	390 400 150 940		42 42 16 100	7[940](1) 150[940](1)
03	2-24-70 Left 2-25-70 Right	1.0 1.75 2.1	580 550 200 1330	460 380 170 1010	44 40 16 100	4[1010](1) 150[1010](1) 150[1330](1)
04	2-24-70 Right	1.0 1.75 2.1	810 650 240 1700		48 38 15 100	4[1700](1) 112[1700](1) 150[1700](1)
05	2-25-70 Left 2-26-70 Right	1.0 1.75 2.1	240 390 120 750	1290 890 270 2450	43 44 13 100	110[750](1) 150[750](1) 3[2450](1) 8[2450](1) 15[2450](1) 95[2450](1) 150[2450](1)
06	2-25-70 Left 2-25-70 Right	1.0 1.75 2.1	950 520 320 1790	630 510 180 1320	53 29 18 100	150[1320](1) 111[1790](1)150[1790](1) 150[1320](1)

References

1. Lippincott, S.W., Bender, R., Foelsche, T., Azzam, N., Montour, J. and Rogers, C.: Arch. Path. Vol. 89, 1970 p. 416.

SESSION VII.2
RADIATION TRANSPORT AND SHIELDING: APPLICATIONS OF MONTE CARLO TECHNIQUES
CHAIRMAN: M.O. BURRELL
MARSHALL SPACE FLIGHT CENTER

Application of DOT-MORSE Coupling to the Analysis of Three-Dimensional SNAP Shielding Problems *

E. A. Straker, R. L. Childs, and M. B. Emmett
Oak Ridge National Laboratory

Many radiation transport problems can best be solved by using both discrete ordinates and Monte Carlo techniques with a coupling between the two techniques occurring at a geometry interface. A general discussion of two possible coupling schemes is given. The calculation of the reactor radiation scattered from a docked service and command module is used as an example of coupling discrete ordinates (DOT) and Monte Carlo (MORSE) calculations.

Many SNAP shielding problems involve determining neutron and gamma-ray transport in three-dimensional geometries. The solution of these problems by the application of Monte Carlo techniques alone frequently requires considerable computer time; however, many parts of the transport problem are only one- or two-dimensional and can easily be solved with discrete ordinates techniques. A convenient approach to solving the three-dimensional problem is to combine the discrete ordinates and Monte Carlo techniques, using Monte Carlo only for the transport that is three dimensional.

In coupling discrete ordinates with Monte Carlo, there is generally some difficulty associated with the compatibility of cross-section representation. This is due to the use of multigroup cross sections in the discrete ordinates codes and point cross sections in the Monte Carlo calculations. Additional problems in performing coupled neutron-gamma-ray calculations in the Monte Carlo part also arise in some cases. The use of the multigroup Monte Carlo code MORSE (ref. 1) alleviates both of these problems in that the same multigroup cross sections can be used in both the discrete ordinates and the Monte Carlo calculations, and the coupled neutron-gamma-ray transport can be solved as one problem.

In using the results of discrete ordinates calculations as a source term for a Monte Carlo calculation, it is desirable to use as much as possible of the detail that is available, or else determine the effect of ignoring the detail. In other words, the assumption of separation of energy, angular, and spatial variation of the radiation should be avoided.

*Research sponsored by the U. S. Atomic Energy Commission under contract with the Union Carbide Corporation.

In general, the source term for the Monte Carlo calculation may be distributed over a volume or may be a boundary or surface source. Both types of coupling will be discussed, and then an example will be given to illustrate a specific application.

The first case to be discussed is the coupling of results of discrete ordinates calculations [in this case, DOT (ref. 2) results] to Monte Carlo with a volume or region being unique to both calculations. The results of a DOT calculation of the fluence $\phi(r,z,E,\theta,\phi)$, a five-dimensional array defined for r,z within the volume of interest, is assumed to exist. In general, one would like to select the source term for subsequent calculations from a conditional probabilitiy distribution for particles leaving a collision as a function of each of the five variables. Because of the large array of numbers, approximations have been made in the past in which some of the variables are selected from non-conditional probabilities that are volume integrated. For example, the energy may be selected from the spectrum integrated over the volume. Likewise, the angular distribution may be assumed to be the same for all points in the volume, or for all energies. However, complete detail can be used with increased data handling and storage requirements.

The first step in coupling over a spatial region is to convert the fluence Φ to χ, the density of particles leaving a collision. This is accomplished by multiplying the fluence by the group-to-group cross section:

$$\chi(r,z,E_g,\theta,\phi) = \sum_{\theta'} \sum_{E'} \Phi(r,z,E',\theta',\phi)$$

$$\times \Sigma_s(E' \rightarrow E_g, \theta' \rightarrow \theta)$$

Then, define

$$T = \sum_{v_r} 2\pi\bar{r}\Delta r \sum_{v_z} \Delta z \sum_g \sum_\ell \sum_m wt(\ell,m)\chi(r,z,E_g,\theta,\phi)$$

where $\chi(r,z,E_g,\theta,\phi)2\pi\bar{r}\Delta r\Delta z$ is defined as the density of particles leaving a collision at r,z with energy E in group g per unit polar angle θ and azimuthal angle ϕ.

$wt(\ell) = \sum_m wt(\ell,m)$ is the solid angle segment for each polar angle θ, and

$wt(\ell,m)$ = the solid angle of each azimuthal angle ϕ for each polar angle index ℓ.

In order to select from this distribution, one must form the five following distributions:

$$R(r) = \frac{2\pi\bar{r}\Delta r}{T} \sum_{v_z} \Delta z \sum_g \sum_\ell \sum_m wt(\ell,m) \times \chi(r,z,E_g,\theta,\phi) ,$$

$$Z(z|r) = \frac{2\pi\Delta z\bar{r}\Delta r}{TR(r)} \sum_g \sum_\ell \sum_m wt(\ell,m)\chi(z,E_g,\theta,\phi|r) ,$$

$$E(E|z,r) = \frac{\Delta z 2\pi\bar{r}\Delta r}{TZ(z|r)R(r)} \sum_\ell \sum_m wt(\ell,m) \times \chi(E_g,\theta,\phi|z,r) ,$$

$$P(\theta|E_g,z,r) = \frac{\Delta z 2\pi\bar{r}\Delta r}{TE(E_g|z,r)Z(z|r)R(r)} \sum_m wt(\ell,m) \times \chi(\theta,\phi|E_g,z,r) ,$$

$$A(\phi|\theta,E_g,z,r) = \frac{wt(\ell,m)\Delta z 2\pi\bar{r}\Delta r\ \chi(\phi|\theta,E,z,r)}{TP(\theta|E_g,z,r)E(E_g|z,r)Z(Z|r)R(r)} .$$

From these conditional probability distributions one may select values for the source coordinates. With the assumption of linear variation between spatial points and angular directions the discrete values are not carried forth in the Monte Carlo calculation, but instead a continuous distribution of coordinates is selected. Care must be exercised in utilizing this type of coupling so that the transport in the overlap region is not included twice. This may be accomplished using a pure absorber in the overlap region in the Monte Carlo calculation.

Perhaps a more useful coupling technique is the coupling at a boundary of the system. For this case, similar conditional probabilities must also be formed, with some minor exceptions. Consider the coupling surface to be the outer boundary of a cylinder.

The leakage fluence, $\Phi(r,Z,E_g,\theta,\phi)$, at the top, bottom, and curved surface of a cylinder is determined as a function of energy, polar, and azimuthal angles, as well as the spatial variation on the surfaces. The leakage fluence on these surfaces designated as R_o, Z_T, and Z_B must be converted to current for the selection of the source term of the Monte Carlo calculation. Thus, there are three spatial terms - the radial variation at the top, the radial variation at the bottom, and the height variation at the outer surface of the cylinder. Define T, B, and S for the integrated leakage for the top, bottom, and side of the cylinder.

$$T = \sum_{0,R_o} 2\pi\bar{r}\Delta r \sum_{E_g} \sum_{\cos\theta>0} \cos(\theta_\ell) \sum_m wt(\ell,m) \times \Phi(r,Z_T,E_g,\theta,\phi) ,$$

$$B = \sum_{0,R_o} 2\pi\bar{r}\Delta r \sum_{E_g} \sum_{\cos\theta<0} |\cos(\theta_\ell)| \times \sum_m wt(\ell,m)\Phi(r,Z_B,E_g,\theta,\phi) ,$$

$$S = 2\pi R_o \sum_{Z_B,Z_T} \Delta z \sum_{E_g} \sum_\ell \sin(\theta_\ell) \sum_{\cos\phi>0} \times wt(\ell,m)\cos\phi\ \Phi(R_o,Z,E_g,\theta,\phi) ,$$

with total leakage TL = T + B + S.

For each of the above terms, a four-dimensional conditional probability must be determined. For example, consider the bottom surface leakage:

$$R_B(r) = \frac{2\pi\bar{r}\Delta r}{B} \sum_{E_g} \sum_{\cos\theta<0} |\cos(\theta)| \sum_m \times wt(\ell,m)\Phi(r,Z_B,E_g,\theta,\phi) ,$$

$$E_B(E_g|r) = \frac{2\pi\bar{r}\Delta r}{BR(r)} \sum_{\cos\theta<0} |\cos(\theta)| \sum_m wt(\ell,m) \times \Phi(r,Z_B,E_g,\theta,\phi) ,$$

$$P_B(\theta|E_g,r) = \frac{2\pi\bar{r}\Delta r|\cos(\theta)|}{BR(r)E_B(E_g|r)} \sum_m wt(\ell,m)$$

$$\times \phi(r,Z_B,E_g,\theta,\phi) ,$$

$$A_B(\phi|\theta,E_g,r) = \frac{2\pi\bar{r}\Delta r|\cos\theta|wt(\ell,m)}{BR(r)E_B(E_g|r)P_B(\theta|E_g,r)}$$

$$\times \phi(r,Z_B,E_g,\theta,\phi) .$$

The results for the top surface leakage and side leakage are similar.

With probability B/TL and T/TL the source would be selected from the bottom and top surface, respectively, and with probability S/TL the source would be selected from the side of the cylinder. Then, given the spatial coordinates, an energy group is chosen from E_B, and then the direction cosines are chosen for P_B and A_B.

The selection from the probability distribution given above is sometimes hindered by negative fluxes in the DOT-calculated source term. If there are no negative values, then the selection of a value x is selected from the distribution by choosing a random number R and finding j such that

$$\sum_{k=0}^{j-1} P(x_k) < R \leq \sum_{k=0}^{j} P(x_k);$$

then

$$x = \frac{[R - P(x_{j-1})]}{P(x_j) - P(x_{j-1})} (x_j - x_{j-1}) + x_{j-1} .$$

However, if some values of the distribution $P(x_j)$ are negative, then an alternate scheme is required. The random number is scaled by the sum of the absolute values of the probabilities and a selection is made. A weight correction is required which can result in negative particle weights. These negative weights in general will not severely affect the solution, but they do, of course, affect the variance of the result.

$$\sum_{k=0}^{j-1} |P(x_k)| < R*SUM \leq \sum_{k=0}^{j} |P(x_k)| ,$$

where

$$SUM = \sum_{k=0}^{Nk} |P(x_k)|$$

and

$$wate = wate* \frac{P(x_j)}{|P(x_j)|} *SUM .$$

If there is a large probability of selecting a negative weight, then the DOT source term should be recalculated.

To illustrate DOT-MORSE coupling, we have considered a problem in which the coupling is at a boundary surface. More specifically, the problem consists of calculating the radiation scattered from a docked command and service module due to the leakage radiation from a 600-kWt ZrH reactor (with its associated shielding). The problem is illustrated in figure 1. The problem which consists of determining the scattered neutron and gamma-ray dose at a detector plane due to neutrons and gamma rays leaking from the reactor power assembly has previously been investigated at Atomics International (refs. 3 and 4). A drawing of the reactor and shield assembly is shown in figure 2.

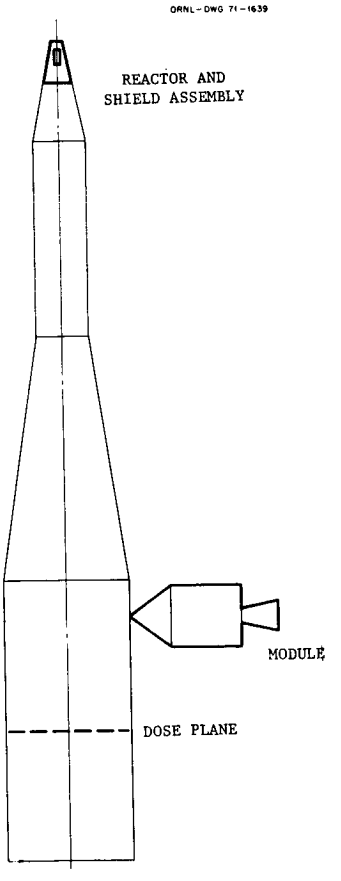

FIGURE 1.-Schematic of Reactor Power System and Docked Service and Command Module.

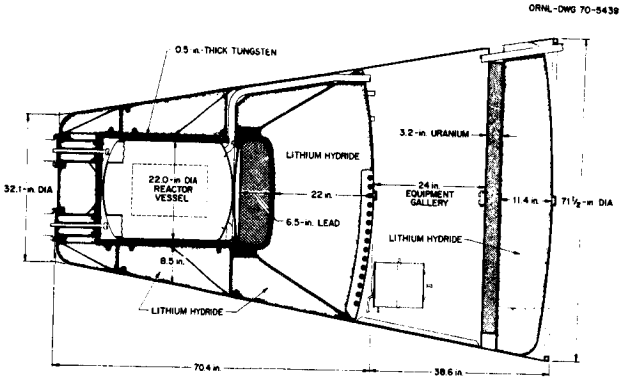

FIGURE 2.-Reactor Shield Assembly.

There are several approaches that could be used in determining the dose due to radiation scattering from the docked module. For example, one may use the boundary leakage flux obtained in a discrete ordinates calculation of the reactor and shield assembly as a source term for the Monte Carlo calculation, transport the radiation to the module, follow the transport in the service module, and estimate the dose at the detector plane. A second approach is to perform an adjoint calculation of the importance of radiation leaking from the core-shield assembly by Monte Carlo and then integrate the importance function over the source of particles leaking from the reactor assembly which was obtained in a discrete ordinates calculation. Another approach is to determine the spatial and energy distribution of the fluence at a surface surrounding the module and use this surface as the boundary for coupling the discrete ordinates results to a Monte Carlo calculation of the scattering in the service module. This last approach will be discussed.

A two-dimensional calculation of the reactor and shield assembly, as shown in figure 2, was made with the DOT (ref. 2) code. An S_8 quadrature was used to determine the energy spectra in 21 neutron and 18 gamma-ray groups. The radiation field at 15 radial locations along a plane at the top of the service module was obtained with SPACETRAN (ref. 2) using the leakage boundary fluence. SPACETRAN performs a ray-tracing calculation from each spatial mesh point to the detector point. The intensity and energy distribution of both neutrons and gamma rays was determined for each of these 15 locations. See Table I for energy group structure and fluence-to-dose conversion factors. The angular distribution of the source was determined by assuming that all the radiation was coming from the center of the reactor core located approximately 90 feet away. (The problem is not expected to be very sensitive to the small angular variation of the radiation incident on the module.) This radiation field as a function of space and energy was used as the source term for Monte Carlo.

Table I. Energy Group Structure and Fluence-To-Dose Conversion Factors

Group	Upper Energy (eV)	Fluence-to-Dose Conversion Factors (mrem/hr)/(part/cm^2/sec)
Neutrons:		
1	1.4918(+7)*	1.5000(-1)
2	1.0000(+7)	1.5000(-1)
3	6.7032(+6)	1.3700(-1)
4	4.4933(+6)	1.3200(-1)
5	3.0119(+6)	1.3100(-1)
6	2.0190(+6)	1.2500(-1)
7	1.3534(+6)	1.1600(-1)
8	9.0718(+5)	1.0600(-1)
9	5.5023(+5)	7.5700(-2)
10	3.3373(+5)	5.5100(-2)
11	2.0242(+5)	4.0100(-2)
12	1.2277(+5)	2.4500(-2)
13	4.0867(+4)	8.5000(-3)
14	1.1709(+4)	5.0000(-3)
15	3.3546(+3)	5.0000(-3)
16	7.4852(+2)	5.0000(-3)
17	1.6702(+2)	5.0000(-3)
18	3.7266(+1)	5.0000(-3)
19	8.3153(0)	5.0000(-3)
20	1.8554(0)	5.0000(-3)
21	4.1399(-1)	3.7500(-3)
Gamma Rays:		
22	1.0000(+7)	9.8000(-3)
23	8.0000(+6)	8.5000(-3)
24	7.0000(+6)	7.6000(-3)
25	6.0000(+6)	6.7000(-3)
26	5.0000(+6)	5.8000(-3)
27	4.0000(+6)	5.0000(-3)
28	3.5000(+6)	4.5000(-3)
29	3.0000(+6)	4.0000(-3)
30	2.5000(+6)	3.5000(-3)
31	2.0000(+6)	3.0000(-3)
32	1.6000(+6)	2.4000(-3)
33	1.2000(+6)	2.0000(-3)
34	9.0000(+5)	1.5000(-3)
35	6.0000(+5)	1.0500(-3)
36	4.0000(+5)	6.0000(-4)
37	2.1000(+5)	2.8000(-4)
38	1.2000(+5)	1.4000(-4)
39	7.0000(+4)	4.0000(-4)

*Read as 1.4918×10^7.

At a plane just above the module, the intensity variation was determined to be that shown in figure 3. The energy distribution, or the number in each of the 21 neutron groups and 18 gamma-ray groups, is shown as a cumulative distribution for three different radii in figure 4. These curves illustrate the distributions used for the selection of the source in the MORSE Monte Carlo calculation. By using MORSE, it was possible to determine the contribution to the scattered dose of the incident neutrons and gamma rays as well as the secondary gamma rays produced in the module.

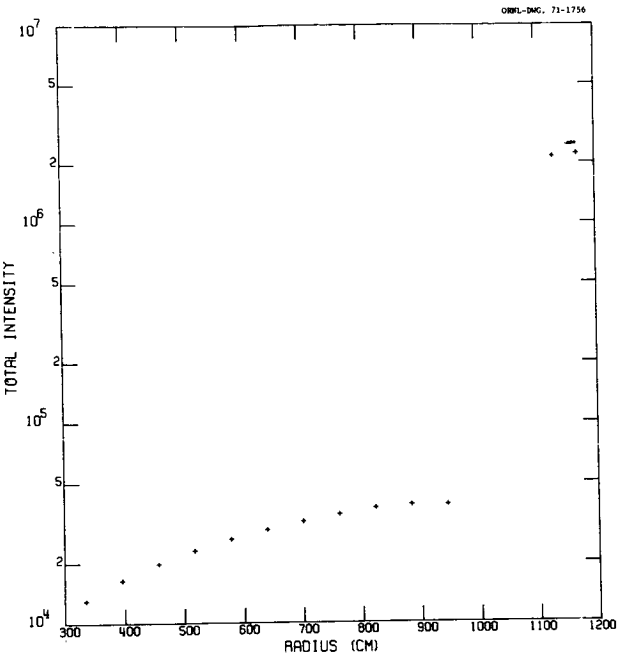

FIGURE 3.-Spatial Distribution of Radiation at Source Plane Adjacent to the Service and Command Module.

The geometry employed in the calculation is illustrated in figure 5, which shows boundary crossing events in the transport of neutrons in the module. The radial and longitudinal location of the crossing events is shown. This collision density plot is an output from MORSE and gives the boundary crossings for approximately 1000 source particles. The typed numbers give the density of the homogenized parts of the service module, and Table II gives the material composition for each region. Figure 6 shows the density of collisions of neutrons in one particular problem. The rotational symmetry of the module is taken into account in the plot, and there are few collisions in the center. The use of this type of on-line plot has been useful in determining where the events are occurring and the effects of importance sampling.

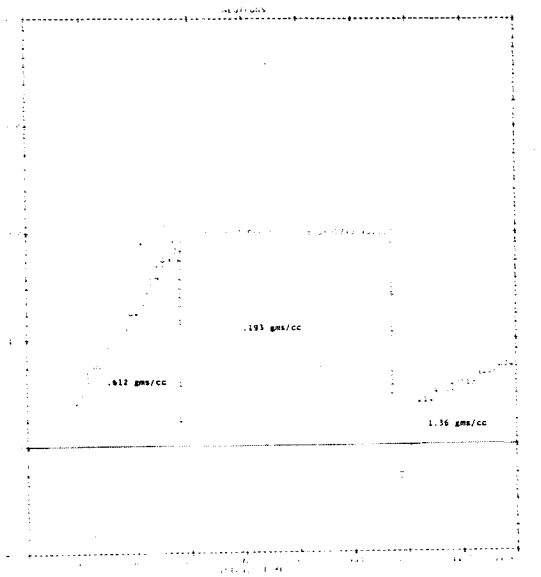

FIGURE 5.-Boundary Crossing Events From a MORSE Calculation. The density of the three material regions is given.

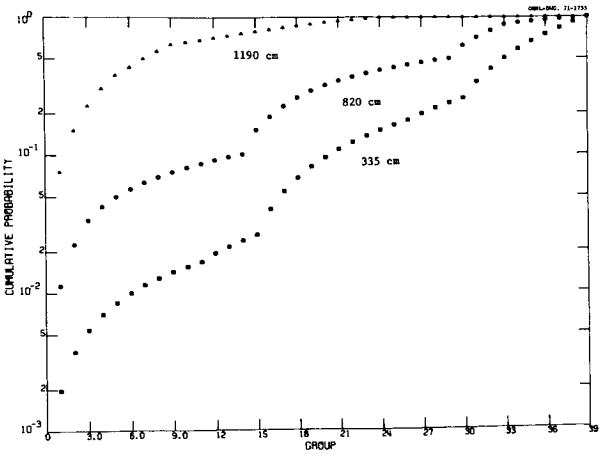

FIGURE 4.-Cumulative Probability for Energy Distribution of Neutrons and Gamma Rays at Three Locations Along Source Plane.

Table II. Material Composition for the Service and Command Module

Medium	Weight (lbs)	Density (gm/cc)	Composition (wt %)				
			H	O	Al	Ti	Fe
1	13,500	0.612	3.3	46.7	20.0	17.0	13.0
2	20,800	0.193	3.3	46.7	20.0	17.0	13.0
3	200	1.36					100.0

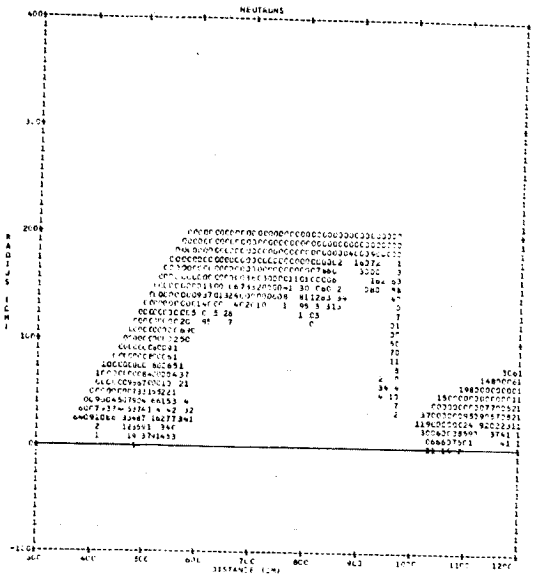

FIGURE 6.-Collision Density Plot for Neutrons Scattering in the Service and Command Module. Numbers 1-9 include the number of collisions in the intervals with 0 indicating 10 or more collisions.

The contribution of scattered neutrons and gamma rays to the dose at the detector plane (117 ft from the reactor) is shown in Table III (about 5% of the gamma-ray dose is due to secondary gamma rays produced in the service module). The total scattered dose of 0.34 mrem/hr should be compared to the direct dose of 0.70 mrem/hr (0.66 mrem/hr gamma rays and 0.04 mrem/hr neutrons). These results are compared with values calculated at Atomics International for various locations on the detector plane. There is surprisingly good agreement between the Monte Carlo and single-scattering results.

Table III. Scattered Dose at the Detector Plane (mrem/hr)

Detector Location (ft)		Neutron Dose		Gamma-Ray Dose		Total	
Along Axis	⊥ Axis	Single Scattering*	Monte Carlo	Single Scattering	Monte Carlo	Single Scattering	Monte Carlo
0	0	0.228	0.29	0.063	0.05	0.30	0.34
11	0	0.73	0.31	0.27	0.08	1.0	0.39
0	11	0.27	0.39	0.09	0.04	0.36	0.43

*With self-absorption.

As a check on the adequacy of the SPACETRAN calculated spatial distribution at the service module location, a DOT calculation with a 100-angle quadrature biased in the downward direction was made. Figures 7 and 8 show the spatial distribution at the source plane and the energy distributions. There are fairly large differences in these results compared to those in figures 3 and 4; however, the scattered dose contribution does not change more than 15%.

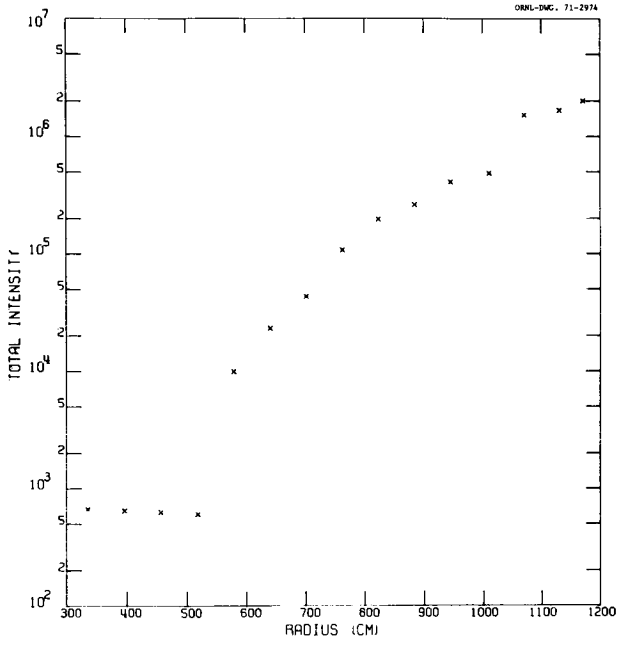

FIGURE 7.-Spatial Distribution of Radiation at Source Plane Adjacent to the Service and Command Module Calculated With a 100-angle Asymmetric Quadrature.

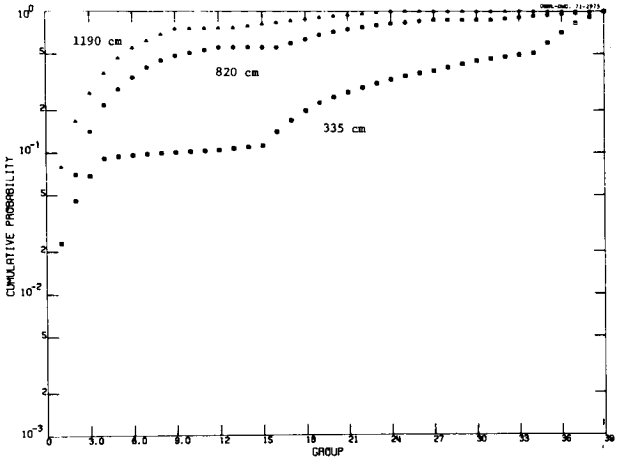

FIGURE 8.-Cumulative Probability for Energy Distribution of Neutrons and Gamma Rays at Three Locations Along Source Plane Calculated With a 100-angle Asymmetric Quadrature.

REFERENCES

1. STRAKER, E. A., et al.: The MORSE Code - A Multigroup Neutron and Gamma-Ray Monte Carlo Transport Code. USAEC Report ORNL-4585, Oak Ridge National Laboratory, 1970.
2. MYNATT, F. R.; MUCKENTHALER, F. J.; and STEVENS, P. N.: Development of TVo-Dimensional Discrete Ordinates Transport Theory for Radiation Shielding. USAEC Report CTC-INF-952, Union Carbide Corporation, 1969.
3. KESHISHIAN, V.: Shielding Analysis for NASA's Manned Orbital Space Station Using the Zirconium Hydride Reactor Power System. Atomics International Report TI-696-23-014, 1969.
4. THOMSON, R. J.: Neutron and Photon Scattering Off Command and Service Module. Atomics International Report TI-696-23-053, 1970.

Discrete Ordinates - Monte Carlo Coupling: A Comparison of Techniques in NERVA Radiation Analysis*

D. G. Lindstrom, E. Normand, A. D. Wilcox
Aerojet Nuclear Systems Company, Sacramento, California

In the radiation analysis of the NERVA Nuclear Rocket System, two-dimensional discrete ordinates calculations are sufficient to provide detail in the pressure vessel and reactor assembly. Other parts of the system, however, require three-dimensional Monte Carlo analyses. To use these two methods in a single analysis, a means of coupling was developed whereby the results of a discrete ordinates calculation can be used to produce source data for a Monte Carlo calculation. Several techniques for producing source detail were investigated. Results of calculations on the NERVA system are compared and limitations and advantages of the coupling techniques discussed.

In the analysis of the NERVA** nuclear rocket engine, a complex radiation transport problem must be solved. Since any shield design must simultaneously minimize weight and radiation level, both penetration and geometry effects are important.

ANALYSIS METHODS

Two rigorous methods have found wide application in complex radiation transport problems: discrete ordinates (S_N) and Monte Carlo. A wide range of computer codes is available for both methods.

The discrete ordinates (S_N) method can be used in one-dimensional or two-dimensional problems. It employs an iterative balance of radiation in a large number of mesh regions. Angular and energy dependence is calculated in a limited number of preselected directions and energy groups. Collision angle-to-angle and energy-to-energy transfers are determined by expansions of the scattering probability in terms of Legendre polynomials. Where these approximations can be employed, the method allows a relatively rapid evaluation of radiation transport throughout a system. If the system contains voids or regions of widely varying collision densities, two-dimensional analyses may result in anomalies called ray effects[1] in which the allowed directions do not properly intercept regions of interest. No three-dimensional representation is possible.

The Monte Carlo method may allow pointwise representation of radiation distribution in space, energy, and angle with exact kinematics to the degree to which cross section data are available. Any amount of detail must be paid for in computer time. The Monte Carlo method calculates and tabulates the fates of individual particles (or individual "particles" which may represent any number of real particles or energy quanta). If relatively few collisions occur or averages over large regions, angles, or energies are allowed, the method can be quite efficient.

APPLICATION TO NERVA

A NERVA propulsion module consists of a propellant tank and engine which includes pressure vessel and reactor assembly, shielding, nozzle, and the necessary pumps, pipes, valves, instrumentation, and controls. A typical layout is shown in Figure 1.

The pressure vessel and reactor assembly (PVARA) is the primary source of radiation. For radiation analysis purposes, it consists of a core, beryllium reflector, forward internal shield, and pressure vessel. The PVARA is essentially a two-dimensional object and can be accurately modeled in cylindrical geometry. The PVARA materials are sufficiently dense so that many mean free paths would be seen by particles before leaking from the outer surfaces of the pressure vessel. Pure analog Monte Carlo analyses of the PVARA would be very costly in computer time, especially if statistically valid radiation leakage data are needed in narrow bands of space, angle, or energy.

The portion of the engine between the PVARA and the propellant tank includes several thousand pounds of metallic components in complicated three-dimensional geometries with many void regions. In the nearly empty condition, the propellant tank and

---

*Public Release Approval: PRA/SA - SNPO-C, dated 24 November 1970.

**The Nuclear Engine for Rocket Vehicle Application (NERVA) program is administered by the Space Nuclear Systems Office, a joint office of the USAEC and NASA. Aerojet Nuclear Systems Company is prime contractor for the engine system and Westinghouse Electric Corporation is principal subcontractor responsible for the nuclear subsystem.

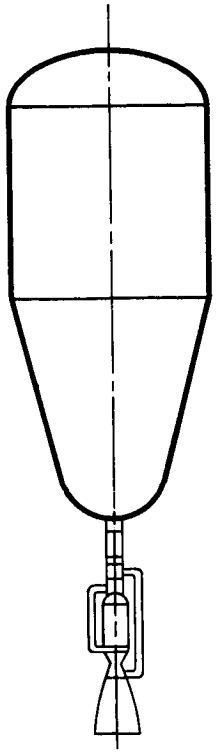

Figure 1

NUCLEAR PROPULSION MODULE CONFIGURATION

liquid hydrogen impose few mean free paths to most radiation.

A comparison of the capacities of the analytical methods and the characteristics of the system indicates that Monte Carlo is necessary for most regions but S_N may be sufficient for analysis of the pressure vessel and reactor assembly.

METHOD COUPLING

If S_N were to be used for analysis of the PVARA and Monte Carlo for most other regions of the system, a means must be devised for producing source information for Monte Carlo from S_N results. This information must be in sufficient detail for the needs of any desired analysis.

In each spatial mesh in each energy group, an angular flux can be calculated by S_N along several predetermined vectors. Each such vector can be visualized as a line from the center of an igloo to the center of a block of the igloo. Figure 2 indicates how such an igloo would describe the directions in which the angular flux could be described in a single radial band on the top surface of the reactor cylinder. The S_N fluxes are tabulated in energy, space, and angle. One could define a "particle" for each such vector in terms of the particles/second value of the tabulated flux. These vectors, if continued by Monte Carlo through a void or low density region, would not necessarily intersect regions of interest. This is comparable to the "ray effects" obtained if the S_N model contains voids. To more nearly represent the physical problem, the particle directions must be distributed uniformly over that part of the igloo that can be seen from the regions of interest.

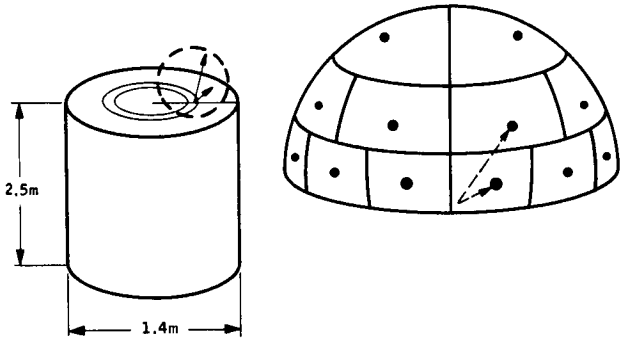

Figure 2

S_N ANGULAR DESCRIPTION

HISTOGRAM

The easiest way that particles can be produced to emerge between the vectors predicted by S_N is to sample a uniform distribution of vectors and assign to each vector that emerges through any block its share of the particles/sec value of the S_N vector in that block. This is equivalent to a histogram in angle with constant particle current within the solid angle intercepting the block. Tracing the particles evaluated in this mode results in a spatially oscillating flux at a distant surface. In particular, radiation coming from the end of the PVARA will generally be underpredicted near the polar axis and radiation from the side will be

overpredicted directly above the outer radius of the reactor.

SMOOTHING

In order to improve on the histogram results, a system of least-square curve fits in polar and azimuthal angle was devised. This results in a smoothly varying assignment of particles/sec to vectors at all angles and produces a smoothly varying flux at distant surfaces. The values at the polar axis and above the reactor radius, in general, are improved by the smoothing procedure but are limited by the extrapolation of the curve fits from the nearest S_N vector.

TAILORED QUADRATURES

The quadrature set, the set of angles defining the S_N vectors, can be tailored to a particular analysis to remove the need for extrapolating curve fits over angles of several degrees. This can improve the accuracy by providing that several of the "blocks" of a more refined igloo can be seen from the detector surface.

COMPARISON OF METHODS

A computer program was written to accept surface angular flux data from the S_N code, DOT[2] and produce the necessary fitting and sampling. This code, DASH[3,4] can also calculate the transport of the sampled vectors through a void or pure absorber.

As an example of the results from histogram, smoothed, and tailored quadrature modes, a series of calculations was performed using an S_6 quadrature set and an S_{124} quadrature set*. The results from the S_6 calculation were treated in the histogram mode and the smoothing mode. Since the S_{124} results were tailored to use very small steps in angle in the direction of interest, only the histogram mode was needed. The S_6 quadrature used a smallest polar angle of 22 degrees while the smallest S_{124} angle was 1.4 degrees.

*The quadrature order given here is that conventionally used and is not entirely consistent. The S_6 set contains 24 vectors distributed symmetrically and the S_{124} set contains 12 symmetrically distributed vectors directed downward and 94 vectors directed upward with many near the polar axis.

Figure 3* shows the dose rate in rad(c)/hr from gamma radiation leaking from the top of the PVARA to a plane 37 meters above it. A void is assumed in the 37 meters to accentuate the differences between the results of the different methods. It is seen that the S_6 histogram method predicts values well below those of the S_6 smoothed and S_{124}, which agree very well for this case. The smallest S_6 angle intercepts this plane at about 1600 cm. from the axis. The histogram mode, then, includes the assumption that the particle current over the plotted range is the same as that expected at a much larger radius. The smallest S_{124} angle, on the other hand, intercepts this plane at about 90 cm. Since the source position has a range given by the 140 cm diameter of the reactor, any such underpredictions will be masked by compensating overpredictions. Since the S_6 smoothed results are produced by a curve fit which provides an extrapolation from the vector at 1600 cm, the excellent results are perhaps fortuitous. Poorer smoothed results would be expected when the angular flux values of the different S_N vectors varied more than in this case.

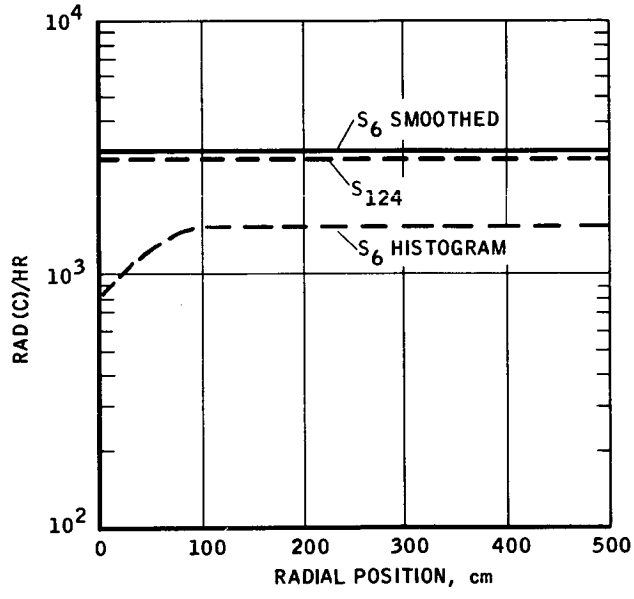

Figure 3

GAMMA DOSE RATE FROM PVARA END AT PLANE IN VOID 37 METERS ABOVE PVARA

*While these data are obtained by collecting particles in radial interval bins, they are shown here by smooth curves in order to make comparisons easier.

For a more difficult case, the radiation is considered which leaks from the side of the reactor and moves upward at a small angle with the side. The same three calculational modes were employed and transported through a void to a plane 3.4 meters above the reactor. This is approximately the location of the bottom of the propellant tank. These results are shown in Figure 4.

The detector plane in this calculation, at tank bottom, is close enough to the source locations to be intercepted by the vectors at the first two polar angles of the S_6 quadrature set. As a result, the oscillatory behavior of the histogram mode is exhibited and two peaks are seen which correspond to the two angles.

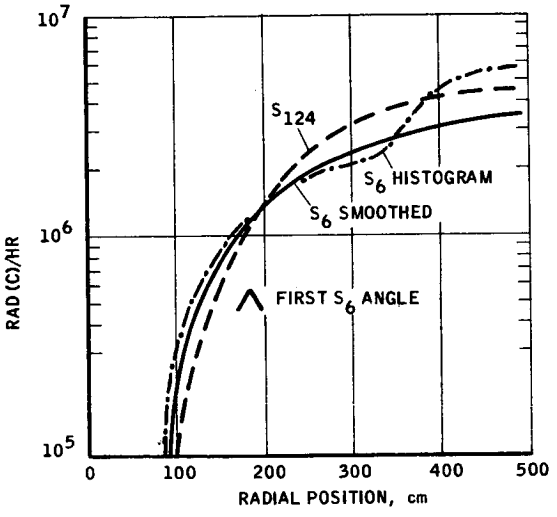

Figure 4

GAMMA DOSE RATE FROM PVARA SIDE AT PLANE IN VOID 3.4 METERS ABOVE PVARA

Considering only those particles which can strike the bottom of the propellant tank, smoothing does not significantly improve the S_6 data. This is seen to be due to the difficulty of using data from larger angles to extrapolate to angles smaller than 22° from the side of the reactor. The side leakage at small angles can be considered further by extending the particles to the plane at 37 meters as was done for the top leakage. These results are shown in Figure 5.

As in the case shown in Figure 4, these results are for angles smaller than the S_6 vector nearest the polar axis and give an indication of the accuracy of the use of S_6 quadratures for a difficult application.

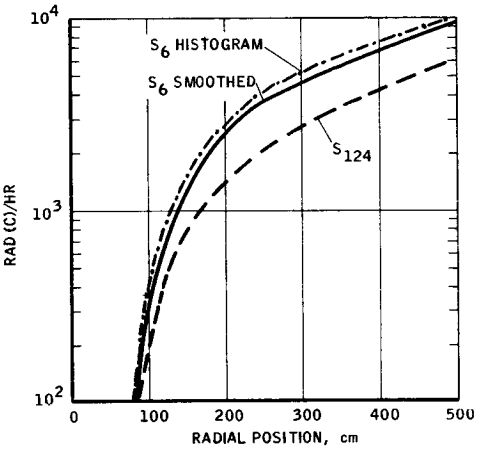

Figure 5

GAMMA DOSE RATE FROM PVARA SIDE AT PLANE IN VOID 37 METERS ABOVE PVARA

COUPLING INTERNAL TO THE S_N PROBLEM

In considering the detail of small angle results from an S_{124} calculation, it appears that the intended detail of the problem may be extreme. Some scatter was observed in flux versus angle plots from the S_{124} calculation. With regard to the approximations inherent to an S_N calculation, such detail probably is not completely reliable. The loss of strict kinematic angle-energy relationship in using expansions in Legendre polynomials causes S_N calculations to predict some results in violation of energy-angle restrictions. As an example of this, the side leakage case was considered further in order to discover the origin of small angle radiation. The outer 2 centimeters of the PVARA is the aluminum pressure vessel wall. Because of the steep angle at which radiation from inside the wall must traverse the aluminum in order to be directed toward the plane at 37 meters, the low energy gammas are strongly attenuated.

To study the effect of the wall, S_N angular fluxes from the DOT code using an S_6 quadrature set were considered in the radial interval just inside the wall. The DASH code was then used to accomplish two calculations. First, DASH was used to sample particles in the direction of the 37 meter plane, attenuate them through the wall, and

calculate their transport to the plane. This gives the dose rates at the plane from radiation which does not scatter in the wall. Second, DASH sampled particles in all outward directions into the wall and wrote these data on magnetic tape suitable for input to the COHORT Monte Carlo code. The wall was modeled in COHORT and the tape used as a source to calculate the transport of scattered gammas to the 37 meter plane. The results of these two calculations were summed* and compared with the S_6 smoothed and S_{124} calculations using angular fluxes at the outer surface of the wall. The energy spectra in a band at 400 - 500 cm on the plane are shown in Figure 6. The Monte Carlo result compares well with the S_{124} result over most of the energy range. Apparently the attenuation of the wall at very small angles cannot be properly accounted for in the S_6 calculation, resulting in a higher predicted dose rate. Probably the decoupling of angle-energy relationships in the S_N procedure hinders the assignment of scattered radiation to the lowest energy group, accounting for the steep drop in dose rate near zero energy. The peak at 6 to 7 Mev is due to sources in the reflector of the reactor.

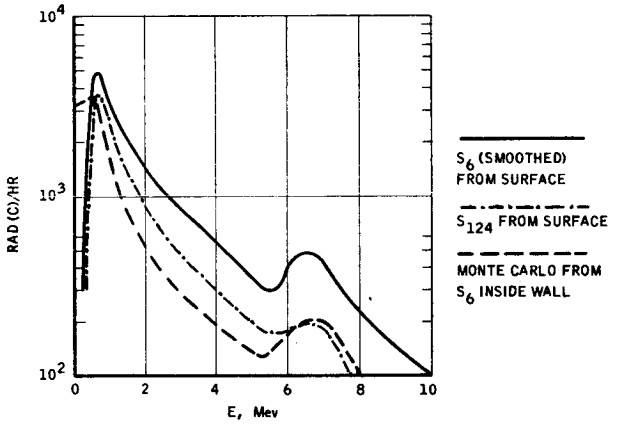

Figure 6

ENERGY DISTRIBUTION OF GAMMA RADIATION FROM PVARA SIDE IN 400-500 CM RADIAL BAND ON PLANE IN VOID 37 METERS ABOVE PVARA CENTER

*The effect of gamma sources in the wall was considered also, but did not contribute significantly to the total.

In a similar application, an S_6 DOT calculation was used to produce angular flux information between the reactor core and reflector. The particles simulated at this interface were traced through the reflector and wall regions by COHORT to a surface above the reactor, and a data tape of particle information produced. A pure Monte Carlo calculation of sources in the reflector and wall was also run using COHORT to produce a second data tape of particle information above the reactor. These data tapes were then used with a COHORT model of a propellant tank to calculate radiation levels at the top of the tank with different quantities of liquid hydrogen in the tank.

A similar set of calculations was performed using S_6 smoothed data at the outer surface of the reactor to produce a tape of particle information above the reactor. This tape was then used by COHORT to calculate radiation levels at the top of the tank with several different quantities of liquid hydrogen propellant in the tank. The results are compared for a particular hydrogen level in Figure 7. In this case, the tank has a capacity of about 180,000 lbs and is about 1/3 full. The top of the tank is about 30 meters from the top of the reactor. The results are divided into that radiation which does not scatter in the tank structure or contents (direct) and that which does scatter (scattered). These dose rates are consistent with earlier results in indicating the slight over-prediction inherent in the S_6 data. Since leakage from the side of the reactor is the primary contributor to dose rate at the tank top, it is not surprising that the relationship between surface source and core-reflector interface source results should be similar to the relationship between the S_6 and S_{124} data seen earlier.

OTHER EXAMPLES OF THE METHOD OF CODE COUPLING

The use of the method is not limited, as we have seen, to using surface angular fluxes. Nor is it limited to tracing radiation through a void. Source data can be produced at any grid within the S_N problem, axially or radially. The data can be produced in the particle source format used by many Monte Carlo codes. (It has been used with FMC, COHORT and MORSE.) It can also produce tabular source data for FASTER or additional DOT problems.

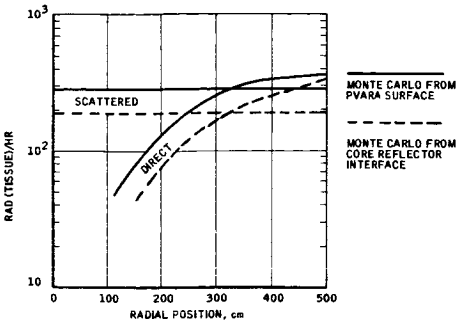

Figure 7

GAMMA DOSE RATE AT TANK TOP FROM PVARA SIDE SOURCES -- BASED ON S_6 DOT CALCULATION

ADVANTAGES OF THE METHOD OF CODE COUPLING

The method allows considerable flexibility in choice of techniques to solve many complex radiation transport problems. It allows a user to take advantage of many of the special characteristics of S_N and Monte Carlo codes. Where the detail of Monte Carlo is needed, it can be employed. Where S_N is sufficient, it can be used with significant saving in computer time. Different degrees of detail are available in S_N by using tailored quadrature sets.

Any number of samples can be produced at a problem interface. As an example of the advantage of this, consider a problem of the type in which one determines the effect of scattering in the wall on the radiation level 37 meters away. A large number of particles scattering in the wall is necessary since few of the scattered particles reach detector regions offering small solid angles to the scattering region. If the particles must originate in a pure Monte Carlo sense, where the real particles originate, few ever arrive at the scattering region of interest. Thus, a great many original particles would have to be produced in order to scatter a few in the wall.

But many scatters are necessary in the wall. Probably this problem would be prohibitively costly in computer time for all but the most liberally financed establishments. Using the S_N - Monte Carlo coupling technique, however, the problem can be quite economical. A low quadrature S_N can be run on an IBM 360/65 in an hour or less for a 10 - 20 energy group, 50 x 30 spatial mesh problem. A high quadrature problem, such as an S_{124}, may take two to three times as long. The DASH problem to produce Monte Carlo data or calculate transport through a void or pure absorber takes 5 to 10 minutes. DASH can produce any required number of source particles. A Monte Carlo problem in the wall would take a few minutes longer. The whole process takes little more time than the original S_N. Furthermore, once the S_N problem has been run and the angular flux data saved on magnetic tape, it can be used any number of times. This allows additional analyses tailored to specific needs at any later time without repeating the bulk of the calculations. Later calculations can be performed in any degree of Monte Carlo employment, from pure S_N to pure Monte Carlo, with commensurate computer costs.

The coupling method is of general applicability and can be used to produce useful source data for any Monte Carlo analysis. It is most efficient for calculating radiation environment from shielded or distributed sources. Typical applications would be in calculating fluxes or dose rates in a void, air, or complicated three-dimensional structures from reactors or shielded isotopes.

REFERENCES

1. LATHROP, K. D., "Ray Effects in Discrete Ordinates Equation," Nucl. Sci. Eng., 32, 357 (1968)

2. MYNATT, F. R., MUCKENTHALER, F. J., STEVENS, P. N., CTC-INF-95, "Development of Two-Dimensional Discrete Ordinates Transport Theory for Radiation Shielding," Union Carbide Corporation, August 1969

3. LINDSTROM, D. G. and WILCOX, A. D., "Leakage Tracing from Boundaries of Low Order S_N Solutions," Trans. Am. Nucl. Soc., 12, 401 (1969)

4. LINDSTROM, D. G. and PRICE, J. H., "Coupled Discrete Ordinates - Monte Carlo Technique and Application to NERVA," Trans. Am. Nucl. Soc., 12, 952 (1969)

MORSE Monte Carlo Shielding Calculations For The Zirconium Hydride Reference Reactor

C. E. Burgart
Oak Ridge National Laboratory
Oak Ridge, Tennessee

Verification of DOT-SPACETRAN transport calculations of a lithium-hydride and tungsten shield for a SNAP reactor has been performed using the MORSE Monte Carlo code. Transport of both neutrons and gamma rays was considered. Importance sampling was utilized in the MORSE calculations. Several quantities internal to the shield, as well as dose at several points outside of the configuration, were in satisfactory agreement with the DOT calculations of the same.

A requirement exists to provide a low radiation environment for the crew of a space station with electrical power provided by a SNAP reactor. Therefore, a shield must be designed to provide adequate protection for the crew while having the smallest possible mass.

A shadow shield consisting of lithium hydride and tungsten has been designed and optimized for a 1-MW SNAP reactor using the ASOP optimization code (ref. 1). ASOP utilizes ANISN, a well-known one-dimensional discrete ordinates code (ref. 2), in performing the optimization. Another paper presented at this symposium discusses the optimization calculations in more depth (ref. 3). Subsequent to the ASOP optimization of the shield, calculations have been performed using DOT, a two-dimensional discrete ordinates code (ref. 4), and SPACETRAN, a transport code (ref. 5) for void regions, to verify that the dose constraints were met in the ASOP shield design. The dose constraint at the bottom of the shield 100 ft from the center of the core of the reactor was 10 mrem/hr. The dose constraint 100 ft from the center of the core at the side and top of the configuration was 100 rem/hr.

Verification of the DOT-SPACETRAN calculations has been performed using the MORSE Monte Carlo code (ref. 6). This code was chosen for several reasons. First was its ability to perform transport calculations in geometrically complex configurations in two and three dimensions. Second, since this problem includes transport of both primary neutrons and secondary gamma rays, MORSE's capability of performing the coupled calculation in a single job step on the computer is quite convenient. Furthermore, the ability to use the identical multigroup cross sections makes possible the checking of the transport calculations independent of the cross sections. Also, if further investigation is required, MORSE calculations can utilize considerably more cross-section groups with little sacrifice in calculation time. The configuration considered in these calculations is shown in figure 1. This is a figure of revolution about an axis along the lower edge of the figure. (Note that plus Z and 0° is to the left, minus Z and 180° toward the crew is to the right.) The details in the core region include: region 1, the ^{235}U and zirconium-hydride core; regions 2, 3, and 4, the reflectors and poison for the control of the reactor; region 5, the stainless steel vessel; regions 8, the upper and lower stainless steel grid plates; and regions 9, the upper and lower sodium plenums. The shield is made up of lithium hydride in region 7 and tungsten in region 6.

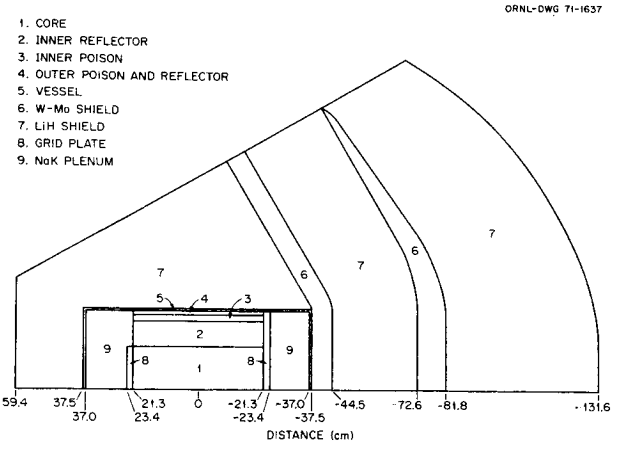

FIGURE 1.-Zirconium Hydride Reference Reactor Optimized 30° Shield.

The primary source of radiation for this problem was in region 1, the core of the reactor. A fission neutron source was distributed over the volume of the reactor according to previous DOT core calculations. The MORSE calculation was a fixed source calculation, i.e., multiplication of neutrons by fission was not allowed. However, the production of fission gamma rays was allowed.

These calculations were performed in 21 neutron groups and 18 gamma-ray groups with a P_3 expansion of the angular distribution. The DOT calculations were performed with 70 discrete angles and 4500 spatial mesh points. The MORSE calculations used the identical cross sections and the identical geometry, except for the capability of MORSE to smooth the stepped surfaces of the shield. The energy group structure, source neutron energy spectrum, and the neutron and gamma-ray flux-to-dose conversion factors are given in figures 2 and 3.

ORNL-DWG 71-1824

Neutron Group	Upper Energy (eV)	Source Spectrum (neutrons/sec)	Flux-to-Dose Conversion Factors [(mrem/hr)/neut/cm^2/sec]
1	14.918+6	1.641+7	1.50-1
2	10.000+6	3.115+8	1.50-1
3	6.7032+6	2.095+9	1.37-1
4	4.4933+6	6.948+9	1.32-1
5	3.0119+6	1.428+10	1.31-1
6	2.0190+6	2.139+10	1.25-1
7	1.3534+6	2.595+10	1.16-1
8	9.0718+5	2.763+10	1.06-1
9	5.5023+5	2.620+10	7.57-2
10	3.3373+5	2.296+10	5.51-2
11	2.0242+5	1.918+10	4.01-2
12	1.2277+5	1.422+10	2.45-2
13	4.0867+4	7.654+9	8.50-3
14	1.1709+4	0.0	5.00-3
15	3.3546+3	0.0	5.00-3
16	7.4852+2	0.0	5.00-3
17	1.6702+2	0.0	5.00-3
18	3.7266+1	0.0	5.00-3
19	8.3153+0	0.0	5.00-3
20	1.8554+0	0.0	5.00-3
21	4.1399-1	0.0	3.75-3
	2.50-2		

FIGURE 2.-Neutron Group Structure, Source Spectrum and Flux-to-Dose Conversion Factors.

ORNL-DWG 71-1825

Gamma Group	Upper Energy (MeV)	Flux-to-Dose Conversion Factors [(mrem/hr)/gr/cm^2/sec]
1	10.0	9.80-3
2	8.0	8.50-3
3	7.0	7.60-3
4	6.0	6.70-3
5	5.0	5.80-3
6	4.0	5.00-3
7	3.5	4.50-3
8	3.0	4.00-3
9	2.5	3.50-3
10	2.0	3.00-3
11	1.6	2.40-3
12	1.2	2.00-3
13	0.9	1.50-3
14	0.6	1.05-3
15	0.4	6.00-4
16	0.21	2.80-4
17	0.12	1.40-4
18	0.07	4.00-4
	0.01	

FIGURE 3.-Gamma-Ray Group Structure and Flux-to-Dose Conversion Factors.

Several quantities internal to the shield were calculated as a check on the source description. One of these quantities consisted of the average neutron and gamma-ray flux in all regions inside the stainless steel vessel. The average particle flux was calculated with MORSE utilizing a collision density estimator. Thus, the estimates far from the core or for small volumes have larger statistics. Figure 4 shows the results of this comparison between DOT and MORSE. The fractional standard deviations of the MORSE results are estimated to vary from 5% to 35%. Results are shown for both average neutron and gamma-ray fluxes. The agreement is quite good with the occasional discrepancies being attributed to the statistics involved in the MORSE calculations. The neutron results for the lower grid and lower plenum were obtained using source position biasing. Subsequently, the agreement is quite good with the statistics on the MORSE results being quite small.

ORNL-DWG 71-1823

COMPARISON OF AVERAGE PARTICLES FLUXES

Region	DOT Average Flux (particles/cm^2/sec)	MORSE Average Flux (particles/cm^2/sec)
1 (Core)		
neutrons/	5.39+13 [a]	5.50+13
gamma rays	9.43+13	9.39+13
2 (Inner Reflector)		
neutrons/	2.15+13	1.99+13
gamma rays	2.86+13	3.00+13
3 (Inner Poison)		
neutrons/	5.95+12	5.79+12
gamma rays	5.39+12	5.00+12
4 (Outer Reflector and Poison)		
neutrons/	3.47+12	3.64+12
gamma rays	2.06+12	1.94+12
8 (Upper Grid)		
neutrons/	1.36+13	2.06+13
gamma rays	1.87+13	2.36+13
8 (Lower Grid)		
neutrons/	7.83+12	7.80+12
gamma rays	9.18+12	8.31+12
9 (Lower Plenum)		
neutrons/	4.74+12	4.72+12
gamma rays	4.74+12	5.24+12

[a] Read as 5.39×10^{13}.

FIGURE 4.-Comparison of Average Particle Fluxes in the Core Region.

Another quantity considered was the average particle current leaving the core region through the top, side and bottom of the stainless steel vessel. Figure 5 shows the results of this comparison. The numbers in parentheses indicate the fractional standard deviations. The agreement again is quite satisfactory with all quantities lying within the statistics of the Monte Carlo calculation. The average neutron current leaving the bottom of the core region was obtained with source position biasing; thus, the statistics are quite small. This source position biasing was performed so that a leakage energy spectrum could be calculated with meaningful statistics in a reasonable time. This average neutron current spectrum through the bottom of the core region is shown in figure 6. The energy range shown is from 0.1 MeV to 10 MeV. The solid histogram is the result of a DOT calculation. The dashed histogram with error bars is the result of MORSE calculations. Below 370 keV, meaningful statistics were not obtained; thus, this comparison is only for fast neutrons. This comparison verifies the neutron transport in this energy range through the core and sodium plenum as it effects the transport in the shield. Any subsequent discrepancy between the MORSE and DOT results must be attributed to subsequent radiation transport between this surface and the detector. Also in future calculations it may be advantageous to use the DOT leakage current from the core as the source, and this comparison provides an added checkpoint.

ORNL-DWG 71-1826

COMPARISON OF AVERAGE PARTICLE CURRENTS

Surface	DOT Average Current (particles/cm^2/sec)	MORSE Average Current (particles/cm^2/sec)
Top		
neutrons/	0.96+12	1.02+12(.11) [a]
gamma rays	1.39+12	1.61+12(.35)
Bottom		
neutrons/	-7.01+11	-7.12+11(.03)
gamma rays	-13.6+11	-14.4+11(.21)
Side		
neutrons/	8.54+11	8.23+11(.04)
gamma rays	8.07+11	7.05+11(.18)

[a] Read as $1.02 \times 10^{12} \pm 11\%$.

FIGURE 5.-Comparison of Average Particle Currents Leaving the Core Region.

The dose at a point 100 ft from the top of the core and 100 ft from the side of the core was obtained with MORSE with a minimum of importance sampling. The dose 100 ft from the center of the core at the bottom of the configuration was a very deep penetration problem and thus required much importance sampling. Without this importance sampling the calculations of the dose at points outside the shield would have been impossible to perform. The overall attenuation of neutron dose from the center of the core to the edge of the shield was approximately 3×10^9. The attenuation through the shield alone was 2×10^8. The attenuation of gamma-ray dose from the center of the core to the edge of the shield was approximately 6×10^7. The attenuation through the shield alone was 2×10^6.

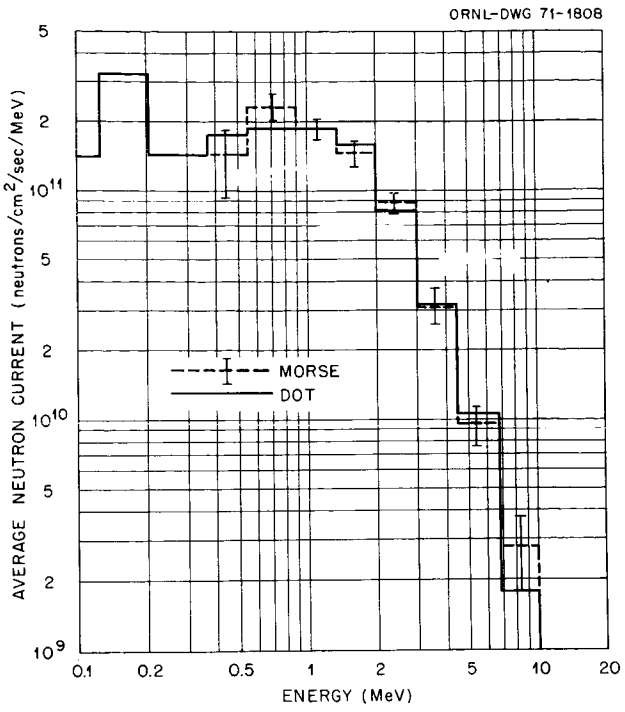

FIGURE 6.-Average Neutron Current Spectrum Through the Bottom of the Core Region.

The parameters used in the importance sampling were obtained from adjoint ANISN calculations. Also, the forward DOT calculations provided initial Russian roulette standards. The adjoint ANISN calculation was performed in slab geometry with the materials shown along the minus-Z axis of the shield; that is, core, stainless steel grid plate, sodium plenum, tungsten, lithium hydride, tungsten, and again lithium hydride. The source for the adjoint ANISN calculation was the detector response at the outermost surface of the slab. In the MORSE calculation, neutron source energy importance sampling was performed using the scalar importance calculated by ANISN in the core region. The neutron source position was biased according to the adjoint ANISN calculation. Source neutron and source secondary gamma-ray angle biasing was also performed. The importance was allowed to vary linearly from 0.01 in the backward direction to 0.99 in the forwardmost direction, that is, toward the bottom of the shield. The most important importance sampling was performed in the selection of particle-flight-path lengths. A form of the exponential transform was utilized. That is, the importance was assumed to vary exponentially along a flight path, i.e., $\exp(\beta\Sigma_t \ell)$. For the calculation of the dose at the bottom of the shield, the direction of greatest importance was assumed to be toward -z for $z > 0$ and away from a point at $z = 50$ for $z < 0$. The slopes of the exponentials, β, for each group and region were obtained by least-squares fitting the ANISN angular flux in the forwardmost direction with exponentials for a fixed number of mean-free paths. This was performed at each mesh point and then averaged over larger regions. The results of these fits may be expressed in terms of stretching parameters. These parameters can yield a good deal of insight into the particle transport in the shield. For instance, when the total response was used as a source for the adjoint ANISN calculation, path-length stretching parameters for fast neutrons were on the order of from 2 to 3 for the core first tungsten and lithium hydride regions, and on the order of 1-1/2 and less for the second tungsten region, whereas when the neutron response only was used as the source for the adjoint ANISN calculation path-length stretching parameters on the order of from 4 to 5 were calculated for all regions until the outer edge of the shield. This indicates the relative importance of neutrons to generating secondary gamma rays versus the importance of neutrons in contributing to the dose at the detector point.

Two other forms of importance sampling were also used. First, estimates were made of the dose at the bottom of the shield for only a fraction of the particle collisions occurring on the core side of the first tungsten region. When an estimate was made the weight was adjusted accordingly. Also, Russian roulette parameters were determined by observation of the number and weight of real collisions occurring in each group and in each region.

Estimation of the dose at the points outside the shield was performed utilizing a next-flight estimator. The results of these MORSE calculations and the DOT-SPACETRAN calculations are given in figure 7. The dose, 100 ft from the center of the core in mrem/hr, is given at several positions around the shield. The top dose, being the easiest quantity to calculate, yielded the best results. The DOT-SPACETRAN results fell within the statistics of the MORSE calculations. The dose falls off slightly

in proceeding from 0° to 30° due to the increased thickness of the shield. At the side of the configuration, the reflectors on the reactor and the poison control drums, as well as the increased thickness of lithium hydride, contribute in making the dose somewhat less. At 90° the first tungsten region begins to have an effect. The neutron dose appears to be reasonable, considering the statistics. The gamma-ray dose calculated by DOT falls off a factor of 2 between 85° and 95°. The MORSE results at 90° are closer to the DOT results at 95°. The dose at the bottom of the shield should be relatively flat from 150° to 180° due to the shadow shield's nature of the configuration. The MORSE neutron dose agrees quite well with that calculated by DOT. The gamma-ray dose calculated by MORSE, however, appears to be somewhat low. Two possible reasons may be: (1) the MORSE results are not yet converged to the answer, or (2) DOT results are somewhat high. The latter may be caused by some larger spatial mesh intervals in the tungsten region of the shield. In any case, the agreement appears to be quite satisfactory. After all, the attenuation is 10^6 to 10^8, or more.

ORNL-DWG 71-1917

DOSE 100 FT FROM THE CENTER OF THE CORE (MREM/HR)

	Angle	DOT Neutron Dose	DOT Gamma Dose	DOT Total Dose	MORSE Neutron Dose	MORSE Gamma Dose	MORSE Total Dose
Top	0°				1.64+5(.10)[a]	1.77+5(.16)	3.41+5(.10)
	5°	1.77+5	1.75+5	3.52+5			
	10°	1.78+5	1.77+5	3.55+5			
	15°	1.75+5	1.74+5	3.49+5			
	20°	1.45+5	1.35+5	2.79+5			
	25°	1.33+5	1.47+5	2.80+5			
	30°	1.28+5	1.40+5	2.68+5			
	80°	4.54+4	7.61+4	1.22+5			
	85°	3.39+4	7.52+4	1.09+5			
Side	90°				4.60+4(.35)	3.37+4(.15)	7.97+4(.21)
	95°	1.85+4	3.51+4	5.36+4			
	100°	6.65+3	7.23+3	1.39+4			
	165°	1.27	10.9	12.2			
	170°	1.27	10.7	12.0			
	175°	1.23	10.4	11.6			
Bottom	180°				1.35(.35)	5.90(.25)	7.25(.21)

[a] Read as $1.64 \times 10^5 \pm 10\%$.

FIGURE 7.-Comparison of the Dose of Points 100 Feet From the Center of the Core.

REFERENCES

1. ENGLE, WARD W., JR.: A Users Manual for ASOP, ANISN Shield Optimization Program. USAEC Report CTC-INF-941, Union Carbide Corporation, 1969.
2. ENGLE, W. W., JR.: A Users Manual for ANISN. USAEC Report K-1693, Union Carbide Corporation, 1967.
3. ENGLE, W. W., JR.: The Design of Asymmetric 4π Shields for Space Reactors. This paper presented in this NASA document.
4. MYNATT, F. R.; MUCKENTHALER, F. J.; and STEVENS, P. N.: Development of Two-Dimensional Discrete Ordinates Transport Theory for Radiation Shielding. USAEC Report CTC-INF-952, Union Carbide Corporation, 1969.
5. SOLOMITO, M.: SPACETRAN - A Code to Calculate Dose at Detectors at Various Distances From the Surface of a Cylinder. USAEC Report ORNL-TM-2592, Oak Ridge National Laboratory, 1969.
6. STRAKER, E. A.; STEVENS, P. N.; IRVING, D. C.; and CAIN, V. R.: The MORSE Code - A Multigroup Neutron and Gamma-Ray Monte Carlo Transport Code. USAEC Report ORNL-4585, Oak Ridge National Laboratory, 1970.

APPLICATION OF MORSE TO RADIATION ANALYSIS OF NUCLEAR FLIGHT PROPULSION MODULES

W. A. Woolson+
Aerojet Nuclear Systems Company
Sacramento, California

Several modifications and additions were made to the multigroup Monte Carlo code MORSE to implement its use in a computational procedure for performing radiation analyses of NERVA Nuclear Flight Propulsion Modules. These changes include the incorporation of a new general geometry module; the inclusion of an expectation tracklength estimator; and the option to obtain source information from two dimensional Discrete Ordinates calculations. Computations comparing MORSE and a point cross section Monte Carlo code, COHORT, were made in which a coupled Discrete Ordinates/Monte Carlo procedure was used to calculate the gamma dose rate at tank top locations of a typical propulsion module. The dose rates obtained from the MORSE computation agreed with the dose rates obtained from the COHORT computation to within the limits of the statistical accuracy of the calculations.

Several modifications and additions were made to the multigroup Monte Carlo code, MORSE[1], to implement its use as a computational procedure for performing radiation analyses of NERVA* Nuclear Flight Propulsion Modules. These changes include the incorporation of a new general geometry module; the inclusion of an expectation tracklength estimator in the analysis portion of the code; and the option to obtain source information from two dimensional Discrete Ordinates calculations to allow coupled Discrete Ordinates/Monte Carlo analyses.

A new general geometry module, patterned after the geometry routines used in the FASTER Monte Carlo program[2], was incorporated into MORSE to facilitate the modeling of complex geometric configurations. As a result of several added features of the new geometry module, the mathematical modeling of systems is made simpler than that of the 05R general geometry routines presently available with MORSE. These features, which reduce the amount computer input and hand calculation required of the user, include:

1. Simple input formats for describing commonly used geometric surfaces such as planes, cones, cylinders, and ellipsoids, along with a generalized quadratic input format.

2. Computer calculation of the ambiguity indices which describe the sign of each region with respect to the surfaces which bound it.

3. Computer check for reflected boundaries, multiple defined regions, and holes.

4. Elimination of the zone, block, sector concept for tracking particles with computer calculation of the probable region that a particle will enter upon crossing a given boundary of a region.

A new analysis routine employing an expectation tracklength estimator was added to MORSE in order to calculate the uncollided and total tracklengths within each region for each energy group. From this information the flux and flux dependent quantities can be calculated with a knowledge of the volume of the region.

Each source ray and post collision ray generated during the random walk is extended through the system until an outside boundary is encountered. The estimator will then score the expected tracklength in those regions intercepted by the ray. In material regions, the expected tracklength is the quantity

* The Nuclear Engine for Rocket Vehicle Application Program (NERVA) is administered by the Space Nuclear Systems Office, a joint officer of the USAEC and NASA. Aerojet Nuclear Systems Company is prime contractor for the engine system and Westinghouse Electric Corporation is principal subcontractor responsible for the nuclear subsystem.

+ Staff Member, Nuclear Science Section, Aerojet Nuclear Systems Company

$$\frac{We^{-\rho}\ (1-e^{-\Sigma_T S})}{\Sigma_T}$$

where W = the source or post-collision weight

ρ = total mean free paths from source or collision point to the point on the boundary of the region intercepted by the ray (ρ = 0 if source or collision point occurs in the region)

S = total length of ray in the region

Σ_T = total cross section of the region for the particle.

If the region intercepted by the ray is a void, the quantity

$$SWe^{-\rho}$$

is scored.

At the option of the user, the coordinates, direction cosines, energy group, and weight of particle at the outside boundary can be saved on tape to provide a leakage source for another Monte Carlo calculation or for discrete ordinates coupling (described later).

There are two advantages to using this type of volume detector as compared to point detectors employing last collision estimators. First, the radiation environment throughout the entire system can be calculated instead of at a few points, and secondly, the unscattered flux is estimated without the assumption of an isotropic source. On the other hand, the tracklength estimator may give large variances in regions extended from high scattering areas since the percentage of tracklengths which score is reduced.

Provisions were made in MORSE to allow input of source data generated from the two dimensional discrete ordinates code, DOT[3]. In many shielding problems, the system to be analyzed contains adjacent high/low density regions and it is economical to use S_n discrete ordinates in the high density regions and Monte Carlo in the low density regions. This situation prevails in the nuclear propulsion modules whose entire radiation environment must be calculated, i.e., both in high density regions like the pressure vessel and reactor assembly (PVARA) and external disk shield and in adjacent low density regions like the nozzle assembly and hydrogen tank.

The angular flux data from DOT is transformed to source data for MORSE by the coupling code, DASH[4]. DASH converts the DOT output to suitable source particle parameters for MORSE at specified surfaces, which may or may not be identical to DOT leakage surfaces. Furthermore, the leakage data provided by the new analysis routine added to MORSE can be transformed by DASH to source data for a subsequent DOT calculation in another region of the system if desired.

By using the same cross section group structure in MORSE that was employed in DOT, the total radiation environment calculated from the DOT-DASH-MORSE (no pun intended!) computation is based on a consistent cross section set, and has been carried out in each region by the most suitable method.

A check calculation of MORSE with the new geometry and analysis routines was performed using the DOT-DASH-MORSE computational procedure to the calculate tank top dose rate due to the gamma source from the pressure vessel and reactor assembly (PVARA) of a nuclear propulsion module employing a 75K lb thrust NERVA engine and an unshielded 176,000 lb LH_2 capacity tank with a 15° half angle conical bottom. The configuration is depicted in Figures 1 and 2.

The PVARA gamma sources[5] were input to DOT which calculated the flux within the PVARA. The leakage fluxes from the PVARA obtained from DOT were transposed to Monte Carlo source information and transported to the tally plane (Figure 2) by DASH.

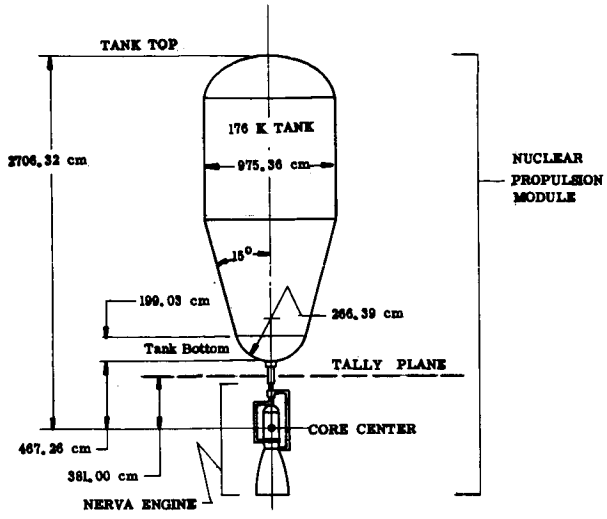

NUCLEAR PROPULSION MODULE CONFIGURATION
Figure 1

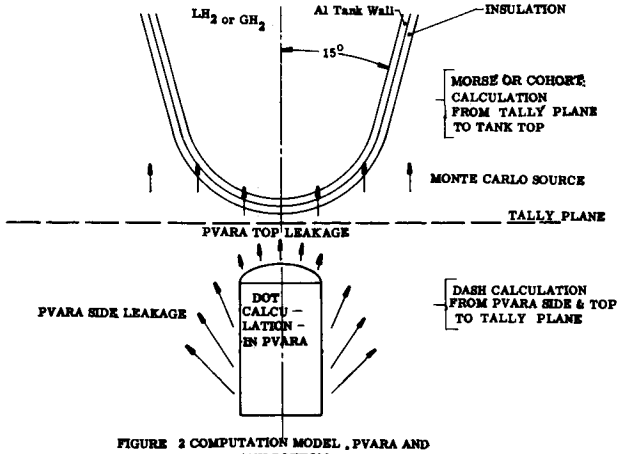

FIGURE 2 COMPUTATION MODEL, PVARA AND TANK BOTTOM

Then, MORSE performed the transport analysis from the tally plane to tank top (Z = 2706 cm). Two runs, one with the tank empty, that is, containing only gaseous hydrogen, and the other with the tank filled to 62,000 lbs LH_2, were made.

Thirteen group, P_6, cross sections for the energy range .1 Mev to 10 Mev were used in the DOT and MORSE calculations. The empty tank case was run without game biasing. However, for the case with the tank filled to 62,700 lbs LH_2, Russian roulette was played in order to prevent generating costly low weight collisions in the liquid hydrogen. Furthermore, an exponential transform was applied to bias the collision density toward the top of the liwuid hydrogen.

A similar calculation using the point cross section Monte Carlo code, COHORT[6], for the Monte Carlo portion from the tally plane to tank top was performed to check the results obtained from MORSE. This computation used last flight estimators to calculate the scattered radiation at two tank top points, one located on axis and the other at a radius of 500 cm. An expectation tracklength estimator was used to calculate the unscattered radiation. Physically, one expects little variation of the scattered radiation at tank top as a function of radius, and thus the dose at tank top locations was obtained as the sum of the unscattered radiation plus a scattered component interpolated between the two points at which the scattered radiation was calculated.

The results of the MORSE and COHORT computations for the two cases are presented in Figures 3 and 4. The results of the empty tank case show excellent agreement in the dose calculated by MORSE and COHORT, while the results for the 62,700 lb LH_2 level show a fluctuation of the dose calculated

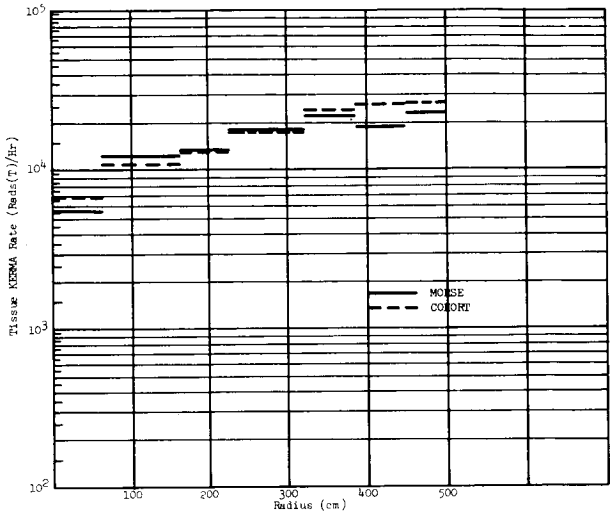

FIGURE 3. PVARA KERMA RATE AT TANK TOP WITH GH_2 ONLY

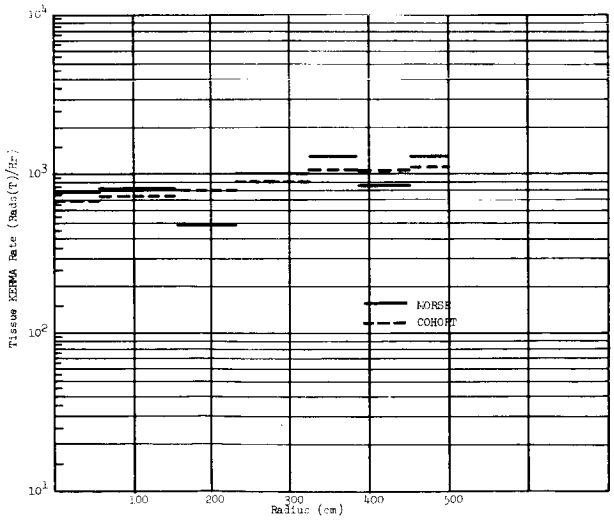

FIGURE 4. PVARA KERMA RATE AT TANK TOP WITH 62,700 LBS. LH_2

by MORSE about the dose calculated by COHORT.

In the empty tank case, scattered radiation contributes only about 15% of the total dose, thus better agreement between two Monte Carlo methods would be expected than that in the 62,700 lb LH_2 case, where scattered radiation contributes about 60% of the total dose. The fluctuation of the MORSE results for the 62,700 lb LH_2 case compared to the COHORT results occurs because of the higher variance estimator used in the MORSE computation.

A comparison of the standard deviation, computation time and efficiency of the MORSE and COHORT results is presented in Table 1. The efficiencies are comparable for the empty tank case since the increase in computation time for the COHORT run is balanced by a decrease in standard deviation. For the 62,700 lb case, the MORSE calculation was performed with one-third less computer time than the COHORT calculation. However, the standard deviation of the MORSE answers were of the order of a factor 1.5 higher than that of the COHORT results. The extra time of COHORT runs was expended mainly in estimating the scattered radiation which results in a subsequent reduction in the variance. However, the efficiency as shown in Table 1 for the 62,700 lb LH_2 runs were still comparable. This indicates that standard deviations of the order of those resulting from the COHORT calculations would obtain from MORSE calculations if the number of histories used in the MORSE runs was increased till the computer time used in the calculation was equal to that of the COHORT runs.

These Monte Carlo comparisons have shown that the use of MORSE with a tracklength estimator in a coupled Discrete Ordinates/Monte Carlo calculation can give good agreement with comparable efficiency to the point cross section code, COHORT. Several

additional features of MORSE including the ability to perform coupled neutron/gamma-ray calculations, the use of extensive source and game biasing, and the inclusion of the albedo option may make MORSE an attractive alternative to conventional Monte Carlo codes.

TABLE I

Comparison of Standard Deviation, Time of Computation, and Efficiency of the MORSE and COHORT Monte Carlo Results

Case	Standard Deviation, σ (% of answer)	Time of Computation, T (min.)	Efficiency $\frac{1}{T\sigma^2}$
γ Only			
MORSE	1%-5%	35.8	97.4-114.5
COHORT	1%-1%	50.1	99.1-150.3
γ, 100 Ibs UH_3			
MORSE	2%-4%	43.9	165-265
COHORT	1%-1%	144.8	168-216

REFERENCES

1. STRAKER, E. A.; STEVENS, P. N.; IRVING, D.C.; and CAIN, V. R.: "The MORSE Code - A Multigroup Neutron and Gamma-ray Monte Carlo Transport Code," ORNL-4585 (1970)
2. JORDAN, T. M.: "Synthesis of Calculational Methods for the Design and Analysis of Radiation Shields for Nuclear Rocket Systems," Vol. 9, WANL-PR(LL)-010 (1967)
3. MYNATT, F. R.: "A Users Manual for DOT," UCC Report K-1694
4. LINDSTROM, D.G.; and PRICE, J. H.: "Coupled Discrete Ordinates - Monte Carlo Technique and Application to NERVA," Trans. Am. Nucl. Soc., 12, 952 (1969)
5. "NERVA Flight Engine Common Radiation Analysis Model," Aerojet-General Corporation, RN-TM-0583 (May 1969)
6. WARKENTIN, J. K.; PRICE, J. H.; and WELLS, M. B.: "Users Manual for COHORT, A Monte Carlo Program for Calculation of Radiation Heating and Transport on the IBM-360," RRA-T7014 (1970)

SHIELD WEIGHT OPTIMIZATION USING MONTE CARLO TRANSPORT CALCULATIONS

Thomas M. Jordan
A.R.T. Research Corporation
Los Angeles, California

and Millard L. Wohl
National Aeronautics and Space Administration
Lewis Research Center
Cleveland, Ohio

This report outlines the theory used in FASTER-III, a Monte Carlo computer program for the transport of neutrons and gamma rays in complex geometries. The code has the additional capability of calculating the minimum weight layered unit shield configuration which will meet a specified dose rate constraint. It includes the treatment of geometric regions bounded by quadratic and quadric surfaces with multiple radiation sources which have a specified space, angle, and energy dependence. The program calculates, using importance sampling, the resulting number and energy fluxes at specified point, surface, and volume detectors.

Results are presented for sample problems involving primary neutron and both primary and secondary photon transport in a spherical reactor-shield configuration. These results include the optimization of the shield configuration.

Section 1
INTRODUCTION AND SUMMARY

The original FASTER program (ref. 1) contained a number of new techniques which provided the capability of obtaining accurate radiation levels at specified points in complex geometries. Prior use of FASTER indicated a need to broaden the overall program capabilities, automate the importance sampling, increase the computational efficiency, and revise the users manual. This revised program has been designated FASTER-III to distinguish it from earlier versions.

A specific program capability permitting the calculation of minimum weight layered unit shield configurations for mobile nuclear reactor applications, e.g., nuclear propulsion for aircraft, surface effect vehicles, and spacecraft has recently been developed. The basic Monte Carlo transport method was extended to include a calculation of partial derivatives of the radiation fluxes with respect to specified shield dimensions. These derivatives are then used to define exponential relationships used in the shield optimization procedure. This optional program feature is described more completely in Section 2.

Data preparation is simple, with very little judgment required to set up the importance sampling for most problems. The code also has a unit shield weight optimization capability.

Particularly noteworthy features of FASTER-III are the following:

(1) A calculation of optimal importance sampling parameters based on partial derivatives of the variance (Section 2.3).

(2) The acceptance of data in either fixed or variable field formats including the ANISN-DTF format for neutron cross sections.

(3) The calculation of time-dependent neutron and photon transport (using time moments and/or time intervals) including an optional exponential atmosphere.

(4) The improvement and addition of importance sampling models with the various importance sampling parameters built into the program.

Various program features are described in Refs. 2 to 6.

The application of the FASTER-III program to a shield optimization problem is discussed in Section 3. The problem involved a spherical reactor-shield configuration and included primary neutrons and both primary and secondary photons. Conclusions and recommendations are presented in Section 4.

Section 2
ANALYSIS

The techniques used in calculating optimum shield configurations and optimum importance sampling parameters are summarized below. The discussion is given in three parts: dose rate derivatives with respect to shield layer thicknesses, optimization procedures, importance parameter optimization.

2.1 Dose Rate Derivatives

The dose rate at a point detector $\underline{y}$ for a specified reactor shield configuration is written as:

$$D(\underline{y}) = \sum_{j=1}^{J} R_j \varphi_j(\underline{y}) \qquad (1)$$

where J is the total number of energy groups for both neutrons and photons (including secondaries), $\varphi_j(\underline{y})$ is the particle flux in the jth energy group, and R_j is the response function to convert from flux to dose rate. The rate of change of the dose rate with respect to a shield layer thickness is simply

$$\frac{\partial D(\underline{y})}{\partial t_l} = \sum_{j=1}^{J} R_j \frac{\partial \varphi_j(\underline{y})}{\partial t_l} \qquad l = 1, 2, \ldots, L \qquad (2)$$

where L is the total number of shield layers and t_l is the thickness of the lth layer. The equation used by the program for determining the flux is written as:

$$\varphi_j(\underline{y}) = \frac{1}{N} \sum_{n=1}^{N} \sum_{k} S^*_{jkn}(\underline{u}_{kn}) K_j(\underline{z}_{kn}, \underline{y}),$$

$$\underline{u}_{kn} = \frac{\underline{y} - \underline{z}_{kn}}{|\underline{y} - \underline{z}_{kn}|} \quad (3)$$

where N is the total number of histories tracked via the Monte Carlo method, k is the number of particle collisions, $\underline{z}_{kn}$ is the position of the kth collision of the nth history, $S^*_{jkn}(\underline{u}_{kn})$ the number of particles in the jth energy group emerging from $\underline{z}_{kn}$ in the direction $\underline{u}_{kn}$ of the detector per unit solid angle, and $K_j(\underline{z}_{kn}, \underline{y})$ represents the material and geometric attenuation kernel for particles in the jth energy group going from $\underline{z}_{kn}$ to the detector.

The partial derivative of the flux with respect to the lth shield layer thickness is simply:

$$\frac{\partial \varphi_j(\underline{y})}{\partial t_l} = \frac{1}{N} \sum_{n=1}^{N} \sum_{k} \frac{\partial}{\partial t_l} \left[S^*_{jkn}(\underline{u}_{kn}) K_j(\underline{z}_{kn}, \underline{y}) \right] \quad (4)$$

The summations are a minor part of the calculation. Therefore, the notation is simplified by concentrating on the elements in the summation

$$\frac{\partial \theta_{jkn}}{\partial t_l} = \frac{\partial}{\partial t_l} \left[S^*_{jkn}(\underline{u}_{kn}) K_j(\underline{z}_{kn}, \underline{y}) \right] \quad (5)$$

where θ_{jkn} represents the contribution to the flux in the jth energy group from the kth collision of the nth history. This equation is rewritten as

$$\frac{\partial \theta_{jkn}}{\partial t_l} = \theta_{jkn} \frac{\partial}{\partial t_l} \ln \left[S^*_{jkn}(\underline{u}_{kn}) K_j(\underline{z}_{kn}, \underline{y}) \right]$$

$$= \theta_{jkn} \left[\frac{\partial}{\partial t_l} \ln S^*_{jkn}(\underline{u}_{kn}) + \frac{\partial}{\partial t_l} \ln K_j(\underline{z}_{kn}, \underline{y}) \right] \quad (6)$$

The second term in brackets involves the attenuation kernel

$$K_j(\underline{z}_{kn}, \underline{y}) = \frac{\exp\left[- \sum_{m=1}^{M} s_m \sigma_{jm} \right]}{s^2} \quad (7)$$

where M is the total number of regions traversed from $\underline{z}_{kn}$ to the detector, s_m is the path length for the mth region traversed, σ_{jm} is the total cross section of this region for particles in the jth energy group, and s is the total distance from $\underline{z}_{km}$ to the detector, i.e.,

$$s = \sum_{m=1}^{M} s_m \quad (8)$$

A substitution of this kernel gives:

$$\frac{\partial}{\partial t_l} \ln K_j(\underline{z}_{kn}, \underline{x}) = \frac{\partial}{\partial t_l} \left[- \sum_{m=1}^{M} s_m \sigma_{jm} - 2 \ln \sum_{m=1}^{M} s_m \right]$$

$$= - \sum_{m=1}^{M} \sigma_{jm} \frac{\partial s_m}{\partial t_l} - \frac{2 \sum_{m=1}^{M} \frac{\partial s_m}{\partial t_l}}{\sum_{m=1}^{M} s_m}$$

$$= - \sum_{m=1}^{M} \left(\sigma_{jm} + \frac{2}{s} \right) \frac{\partial s_m}{\partial t_l} \quad (9)$$

The partial derivative of the partial path length s_m with respect to the shield layer thickness t_l is zero unless the mth region traversed is affected by a change in t_l. In particular, if t_l is a characteristic dimension of the region, i.e., its thickness, then

$$\frac{\partial s_m}{\partial t_l} = \frac{1}{\mu_{knm}}, \quad \mu_{knm} = \underline{u}_{kn} \cdot \underline{n}_{knm} \quad (10)$$

where μ_{knm} is the cosine of the angle measured from the surface normal $\underline{n}_{knm}$, with which the particle crosses the boundary of the region.

In the strict sense, the change of the thickness of one shield region can affect other shield regions. In particular, for a spherically symmetric reactor-shield configuration, an increase in the thickness of a shield region forces a movement of all shield regions having a larger radius. The inclusion of these effects in the above equation unnecessarily complicates the analysis and the calculations. The primary effect of changing a shield region dimension is to change the number of mean free paths which particles have to traverse in reaching the detector. Therefore, in calculating the derivatives, only the effect of the material attenuation is treated.

The derivatives at a specific boundary crossing m' then simplify to:

$$\frac{\partial}{\partial t_l} \ln K_j(\underline{z}_{kn}, \underline{y}) = - \sum_{m=1}^{M} \left(\sigma_{jm} + \frac{2}{s} \right) \frac{\partial s_m}{\partial t_l}$$

$$= - \left(\sigma_{jm'} + \frac{2}{s} \right) \frac{1}{\mu_{knm'}} - \left(0 + \frac{2}{s} \right) \frac{1}{\mu_{knm'}}$$

$$= - \sigma_{jm'} / \mu_{knm'} \quad (11)$$

where m' is the index of a region having t_l as a dimension. The partial derivatives of the particle weight with respect to the shield dimensions - the first term in brackets in Eq. (6) - are zero at the point of origin of all primary particles. For subsequent particle collisions, the derivatives are calculated using the relationship between particle weights on subsequent collisions:

$S^*_{jkn}(\underline{u}_{kn})$

$$= \frac{\sum_i S^*_{i,k-1,n}(\underline{v}_{kn}) K_i(\underline{z}_{k-1,n}, \underline{z}_{kn}) T_{ij}(\underline{z}_{kn}, \underline{v}_{kn} \cdot \underline{u}_{kn})}{p^*_{kn}(\underline{z}_{kn})}$$

$$\underline{v}_{kn} = \frac{\underline{z}_{kn} - \underline{z}_{k-1,n}}{|\underline{z}_{kn} - \underline{z}_{k-1,n}|} \tag{12}$$

where $S^*_{i,k-1,n}(\underline{v}_{kn})$ is the number of particles coming out of the previous collision point in the direction $\underline{v}_{kn}$ and in the $\underline{i}$th energy group, $K_i(\underline{z}_{k-1,n}, \underline{z}_{kn})$ is the attenuation kernel between particle collision points, $T_{ij}(\underline{z}_{kn}, \underline{v}_{kn} \cdot \underline{u}_{kn})$ is the scattering kernel for transfer of particles from group i to group j, and $p^*_{kn}(\underline{z}_{kn})$ is the probability density function used in selecting the collision point.

A straightforward substitution gives

$$\frac{\partial}{\partial t_l} \ln S^*_{jkn}(\underline{u}_{kn}) = \frac{\partial}{\partial t_l} \ln \left[\frac{\sum_i S^*_{i,k-1,n}(\underline{v}_{kn}) K_i(\underline{z}_{k-1,n}, \underline{z}_{kn}) T_{ij}(\underline{z}_{kn}, \underline{v}_{kn} \cdot \underline{u}_{kn}}{p^*_{kn}(\underline{z}_{kn})} \right] \tag{13}$$

After some manipulation, this reduces to

$$\frac{\partial}{\partial t_l} \ln S^*_{jkn}(\underline{u}_{kn})$$

$$= \frac{1}{S^*_{jkn}(\underline{u}_{kn})} \sum_i V_{ijkn} \left[\frac{\partial}{\partial t_l} \ln S^*_{i,k-1,n}(\underline{v}_{kn}) \right.$$

$$\left. + \frac{\partial}{\partial t_l} \ln K_i(\underline{z}_{k-1,n}, \underline{z}_{kn}) - \frac{\partial}{\partial t_l} \ln p^*_{kn}(\underline{z}_{kn}) \right] \tag{14}$$

where

V_{ijkn}

$$= \frac{S^*_{i,k-1,n}(\underline{v}_{kn}) K_i(\underline{z}_{k-1,n}, \underline{z}_{kn}) T_{ij}(\underline{z}_{kn}, \underline{v}_{kn} \cdot \underline{u}_{kn})}{p^*_{kn}(\underline{z}_{kn})} \tag{15}$$

The first term in brackets in Eq. (14) is the same partial derivative for collision k-1 as the partial derivative now being calculated for collision k. Therefore, it is known, either identically zero for k=0, or as determined from Eq. (14) for $k > 0$. The second term in brackets in Eq. (14) is similar to the second term in brackets in Eq. (6) and is therefore determined by Eq. (11). The last term in brackets involves the definition of the probability density function used to select the collision point $\underline{z}_{kn}$.

The probability density function for a collision point has the form

$p^*_{kn}(\underline{z}_{kn})$

$$= q^*_{kn}(\underline{v}_{kn}) \frac{A(s)a(s) \exp\left[-\int_0^s a(s')ds'\right]}{\int_0^\infty A(s')a(s') \exp\left[-\int_0^{s'} a(s'')ds''\right]ds'} \tag{16}$$

where $q^*_{kn}(\underline{v}_{kn})$ is a probability density function used to select the particle direction, $s = |\underline{z}_{kn} - \underline{z}_{k-1,n}|$ is the distance of the selected collision point from the previous collision point, A(s) is an importance factor for each region which changes discontinuously at region boundaries, and a(s) is an effective cross section which changes discontinuously at region boundaries and which may change continuously within a region.

The derivative of the logarithm of $p^*_{kn}(\underline{z}_{kn})$ involves only those terms which change when a shield dimension changes, i.e.,

$$\frac{\partial}{\partial t_l} \ln p^*_{kn}(\underline{z}_{kn}) = \frac{\partial}{\partial t_l} \left[-\int_0^s a(s')ds' \right]$$

$$- \frac{\partial}{\partial t_l} \ln \left\{ \int_0^\infty A(s')a(s') \exp\left[-\int_0^{s'} a(s'')ds'' \right] ds' \right\} \tag{17}$$

Let s_l denote the distance to a boundary involving the lth shield dimension. If the first term on the left side of Eq. (17) is affected by a change in this shield dimension, i.e. if $s > s_l$, then

$$\frac{\partial}{\partial t_l} \left[-\int_0^s a(s')ds' \right] = -a(s_l) \frac{\partial s_l}{\partial t_l}$$

$$= -a(s_l) \frac{1}{\mu_{lkn}} \tag{18}$$

where $a(s_l)$ is the effective cross section at the boundary of the shield and μ_{lkn} is the cosine the particle path makes with the outer shield normal. If there is any crossing involving the lth shield dimension, the second term in Eq. (18) will always have a non-zero derivative, i.e.,

$$\frac{\partial}{\partial t_l} \ln \left\{ \int_0^\infty A(s')a(s') \exp\left[-\int_0^{s'} a(s'')ds''ds' \right] \right\}$$

$$= \frac{A(s_l)a(s_l) \frac{1}{\mu_{lkn}} \exp\left[-\int_0^{s_l} a(s')ds' \right]}{\left\{ \int_0^\infty A(s')a(s') \exp\left[-\int_0^{s'} a(s'')ds'' \right] ds' \right\}} \tag{19}$$

Curved shield surfaces may be crossed more than once along the path between two particle collision points. Therefore, a summation of Eqs. (18) and (19) over every intersection involving the lth shield dimension is required to completely evaluate Eq. (17).

2.2 Optimization Procedures

The shield optimization calculation yields the set of shield layer thicknesses $\underline{t}' = (t_1', t_2', \ldots, t_l', \ldots t_L')$ such that the dose rate, $D(\underline{t}')$, meets the dose constraint. The Monte Carlo calculation is performed for an initial set of shield layer thicknesses $\underline{t} = (t_1, t_2, \ldots t_l, \ldots, t_L)$ and yields a set of fluxes, $\varphi_j(\underline{t})$, $j = 1, 2, \ldots, J$ and derivatives, $\partial\varphi_j(t)/\partial t_l'$, $j = 1, 2, \ldots, J$; $l = 1, 2, \ldots, L$. The assumption is made that the fluxes vary exponentially with respect to shield dimension changes in the form

$$\varphi_j(\underline{t}') = \varphi_j(\underline{t}) \exp\left[\underline{a}_j \cdot (\underline{t}' - \underline{t})\right] \qquad (20)$$

where $\underline{a}_j = (a_{j1}, a_{j2}, \ldots, a_{jL})$. It follows that

$$\frac{\partial\varphi_j(\underline{t})}{\partial t_l'} = \varphi_j(\underline{t}) \exp\left[\underline{a}_j \cdot (\underline{t}' - \underline{t})\right] \frac{\partial}{\partial t_l}\left[\underline{a}_j \cdot (\underline{t}' - \underline{t})\right]$$

$$= \varphi_j(\underline{t}')a_{jl} \qquad (21)$$

In particular

$$\frac{\partial\varphi_j(\underline{t})}{\partial t_l} = a_{jl}\varphi_j(\underline{t}) \qquad (22)$$

or

$$a_{jl} = \frac{\partial\varphi_j(\underline{t})}{\partial t_l} \Big/ \varphi_j(\underline{t}) \qquad (23)$$

The weight is also expressed as a function of the shield layer thicknesses. The weight is denoted by $W(t')$ and for spherically symmetric shields:

$$W(t') = \frac{4\pi}{3}\left\{\rho_1\left[(r_o + t_1')^3 - r_o^3\right] + \rho_2\left[(r_o + t_1' + t_2')^3 - (r_o + t_1')^3\right] + \ldots\right\}$$

$$= \frac{4\pi}{3}\sum_{l=1}^{L}\rho_l\left[\left(r_o + \sum_{m=1}^{l} t_m'\right)^3 - \left(r_o + \sum_{m=1}^{l-1} t_m'\right)^3\right] \qquad (24)$$

where ρ_l is the density of the lth shield region and r_o is the minimum shield radius.

The purpose of the optimization procedure is to minimize the weight $W(\underline{t}')$ subject to the dose rate constraint $D(\underline{t}') = D_o$ where D_o is a specified dose rate. At this optimum, a small weight perturbation in any layer causes the same dose rate change. The rate at which dose rate changes with respect to a shield weight change in the lth layer is given by

$$Q_l = \frac{\partial D(t')/\partial t_l'}{\partial W(\underline{t}')/\partial t_l'} = \text{constant}, \quad l = 1, 2, \ldots, L \qquad (25)$$

The necessary derivatives are:

$$\frac{\partial D(t')}{\partial t_l'} = \sum_{j=1}^{J} R_j \frac{\partial\varphi_j(\underline{t}')}{\partial t_l'} =$$

$$= \sum_{j=1}^{J} R_j a_{jl}\varphi_j(\underline{t}) \exp\left[\underline{a}_j \cdot (\underline{t}' - \underline{t})\right] \qquad (26)$$

and for spherically symmetric shield:

$$\frac{\partial W(\underline{t}')}{\partial t_l'} = 4\pi\sum_{i=l}^{L}\rho_j\left[\left(r_o + \sum_{m=1}^{i} t_m'\right)^2 - \left(r_o + \sum_{m=1}^{i-1} t_m'\right)^2\right] \qquad (27)$$

In arriving at the optimum shield, the total shield weight is built up in increments of weight ΔW. Each increment in shield weight is always associated with a particular shield layer thickness. At each iteration, the particular shield dimension is selected by examining the values of the shield weight quality factors, Q_l. Each factor Q_l represents the approximate change in dose rate per unit change in weight corresponding to a change in the lth shield dimension. Negative Q_l's are the most usual and correspond to shields for which an increase in weight - and shield dimensions - gives a decrease in dose rate. Positive Q_l's can occur, however, and correspond to shields for which an increase in weight also increases the dose rate.

If, at a particular iteration, the dose rate is above the dose rate constraint, the minimum shield weight increment would correspond to the least positive value of those Q_l's for which $Q_l > 0$ and for which $t_l' > t_l(\min)$, where $t_l(\min)$ is the minimum value of the lth shield layer thickness. If such a Q_l exists, the dose rate can be decreased while also decreasing the shield weight the maximum amount. If there isn't such a Q_l, the next best procedure is to find the most negative of the Q_l's for which $Q_l < 0$ and for which $t_l' < t_l(\max)$, where $t_l(\max)$ is the maximum value of the lth shield layer thickness. A change in that Q_l would give the maximum decrease in dose rate per unit increase in weight.

If the dose rate is below the specified dose rate at a particular iteration, the minimum shield weight increment would correspond to the least negative of those Q_l's for which $Q_l < 0$ and for which $t_l' > t_l(\min)$. If such a Q_l exists, the dose rate can be increased while decreasing the shield weight the maximum amount. If there isn't such a Q_l, the next best procedure is to find the most positive of those Q_l's for which $Q_l > 0$ and for which $t_l' < t_l(\max)$. A change in that Q_l would give the maximum increase in dose rate per unit increase in weight.

Assuming a particular value Q_m of the Q_ℓ's is selected through the above arguments, the corresponding shield dimension t'_m is changed by a maximum amount Δt_m where Δt_m is calculated as

$$\Delta t_m = \frac{\Delta W}{\dfrac{\partial W(\underline{t}')}{\partial t'_m}} \tag{28}$$

If this change would put t'_m outside one of its specified limits, the value of t'_m would be set to that limit, i.e., $t_m(\min) \le t'_m \le t_m(\max)$. The shield weight increment ΔW is calculated as

$$\Delta W = \frac{D_o - D(\underline{t}')}{Q_m} \tag{29}$$

subject to the constraint that $|\Delta W| < \Delta W_o$ where ΔW_o is a specified maximum shield weight increment per iteration. Note that ΔW, and therefore Δt_m, may be positive or negative depending on the value of Q_m and whether the dose rate is above or below the dose rate constraint.

Once a shield layer thickness is changed, the dose, weight, and their derivatives are re-evaluated and the entire process is repeated. The optimization would be discontinued in several ways. If the dose rate equals the dose rate constraint within the relative error of the original Monte Carlo dose rate calculation, the program will proceed to the next problem - which may be identical except with more histories to tighten the convergence of Monte Carlo calculations. Similarly, if all shield layer thicknesses have reached their minimum or maximum values, and if the optimum shield cannot be determined with these constraints, the program would again proceed to the next problem. Finally, if the dose rate and dose rate constraint are decades apart in value, the program would reevaluate the fluxes and their derivatives by Monte Carlo every time the dose rate changed by more than a specified factor during the optimization procedure.

2.3 Importance Parameter Optimization

The optimization of the importance sampling must be performed for some function, e.g., dose rate, of the energy-dependent fluxes since there is a different optimum for every initial particle energy. Therefore, assume that a minimum variance calculation of the dose rate is required where

$$\bar{D}_N = \frac{1}{N}\sum_{n=1}^{N} D_n \tag{30}$$

where N is the total number of histories and D_n is the dose rate from the nth history and $\bar{D}_N$ is the average value of the dose rate after N histories. The relative error of this dose rate is given by

$$E_N = \frac{1}{\bar{D}_N}\left[\frac{1}{N^2}\left(\sum_{n=1}^{N} D_n^2 - N\bar{D}_N^2\right)\right] \tag{31}$$

Taking the logarithm of this equation and then performing a formal calculation of the partial derivative with respect to an unspecified parameter a yields

$$\frac{\partial}{\partial a}\ln E_N = -\frac{\partial}{\partial a}\ln \bar{D}_N - \frac{\partial}{\partial a}\ln N + \frac{1}{2}\frac{\partial}{\partial a}\ln\left(\sum_{n=1}^{N} D_n^2 - N\bar{D}_N^2\right) = -\frac{\dfrac{\partial}{\partial a}\bar{D}_N}{\bar{D}_N} + \frac{\displaystyle\sum_{n=1}^{N} D_n\frac{\partial D_n}{\partial a} - N\bar{D}_N^2\frac{\partial \bar{D}_N}{\partial a}}{\displaystyle\sum_{n=1}^{N} D_n^2 - N\bar{D}_N^2}$$

$$= \frac{1}{N^2\bar{D}_N^3 E_N^2}\left[\bar{D}_N\sum_{n=1}^{N} D_n\frac{\partial D_n}{\partial a} - \left(\sum_{n=1}^{N} D_n^2\right)\frac{\partial \bar{D}_N}{\partial a}\right] \tag{32}$$

Thus the partial derivative of the relative error with respect to the parameter a is:

$$\frac{\partial E_N}{\partial a} = \frac{1}{N^2\bar{D}_N^3 E_N}\left[\bar{D}_N\sum_{n=1}^{N} D_n\frac{\partial D_n}{\partial a} - \left(\sum_{n=1}^{N} D_n^2\right)\frac{\partial \bar{D}_N}{\partial a}\right] \tag{33}$$

The dose rate from the nth history is given by

$$D_n = \sum_{j=1}^{J} R_j \sum_{k} \varphi_{jkn} \tag{34}$$

where J is the total number of energy groups, k is the number of particle collisions, R_j is the flux to dose rate conversion factor for the jth energy group, and φ_{jkn} is the flux in the jth group from the kth collision of the nth history. Since

$$\frac{\partial \bar{D}_N}{\partial a} = \frac{1}{N}\sum_{i=1}^{n}\frac{\partial D_n}{\partial a}, \tag{35}$$

the calculations required to evaluate Eq. (33) all involve the summation of terms which involve

$$\frac{\partial D_n}{\partial a} = \frac{\partial}{\partial a}\sum_{j=1}^{J}\left(R_j\sum_{k}\varphi_{jkn}\right) = \sum_{j=1}^{J} R_j\sum_{k}\frac{\partial \varphi_{jkn}}{\partial a} \tag{36}$$

The remainder of the analysis, therefore, can be concentrated on the partial derivatives of the fluxes. All other operations which must be performed are given above.

The fluxes typically depend on the detector position $\underline{y}$, so the equation for the particle flux is written as

$$\varphi_{jkn}(\underline{y}) = S^*_{jkn}(\underline{u}_{kn})K_j(\underline{z}_{kn}, \underline{y}) \tag{37}$$

The transport kernel $K_j(\underline{z}_{kn}, \underline{y})$ does not involve any importance sampling parameters so that

$$\frac{\partial \varphi_{jkn}(\underline{y})}{\partial a} = \frac{\partial S^*_{jkn}(\underline{u}_{kn})K_j(\underline{z}_{kn}, \underline{y})}{\partial a} \tag{38}$$

This equation can also be written as

$$\frac{\partial \varphi_{jkn}(\underline{y})}{\partial a} = S^*_{jkn}(\underline{u}_{kn}) K_j(\underline{z}_{kn}, \underline{y}) \frac{\partial}{\partial a} \ln S^*_{jkn}(\underline{u}_{kn}) \quad (39)$$

Without going into great detail, it turns out that the particle weight $S^*_{jkn}(\underline{u}_{kn})$ is composed of a purely analytical numerator, $V_{jkn}(\underline{u}_{kn})$ and a denominator which is the product of all the probability density functions used to select the collision points, i.e.,

$$S^*_{jkn}(\underline{u}_{kn}) = \frac{V_{jkn}(\underline{u}_{kn})}{\prod_{l=0}^{k} p^*_{ln}(\underline{z}_{ln})} \quad (40)$$

Therefore,

$$\ln S^*_{jkn}(\underline{u}_{kn}) = \ln V_{jkn}(\underline{u}_{kn}) - \ln \prod_{l=0}^{k} p^*_{ln}(\underline{z}_{ln}) \quad (41)$$

Since $V_{jkn}(\underline{u}_{kn})$ does not explicitly involve any importance parameters, it follows that

$$\frac{\partial}{\partial a} \ln S^*_{jkn}(\underline{u}_{kn}) = - \frac{\partial}{\partial a} \ln \prod_{l=0}^{k} p^*_{ln}(\underline{z}_{ln})$$

$$= - \sum_{l=0}^{k} \frac{\partial}{\partial a} \ln p^*_{ln}(\underline{z}_{ln}) \quad (42)$$

Therefore, Eq. (39) can be re-written as

$$\frac{\partial \varphi_{jkn}(\underline{y})}{\partial a} = - \varphi_{jkn}(\underline{y}) \sum_{l=0}^{k} \frac{\partial}{\partial a} \ln p^*_{ln}(\underline{z}_{ln}) \quad (43)$$

Moreover, the partial derivatives are energy-independent so that Eq. (36) becomes

$$\frac{\partial D_n}{\partial a} = \sum_k \left(\sum_{j=1}^{J} R_j \varphi_{jkn}(\underline{y}) \right) \left(- \sum_{l=0}^{k} \frac{\partial}{\partial a} \ln p^*_{ln}(\underline{z}_{ln}) \right) \quad (44)$$

The evaluation of the partial derivatives of the probability density functions can be written as

$$\sum_{l=1}^{k} \frac{\partial}{\partial a} \ln p^*_{ln}(\underline{z}_{ln}) = \sum_{l=0}^{k-1} \frac{\partial}{\partial a} \ln p^*_{ln}(\underline{z}_{ln})$$

$$+ \frac{\partial}{\partial a} \ln p^*_{kn}(\underline{z}_{kn}) \quad (45)$$

At the kth collision, the first term on the left side of Eq. (45) is known, identically zero if $k = 0$. Therefore, the analysis is completed after examining the calculation of the second term.

At this point it is necessary to identify the particular importance parameter a. Since most of the importance sampling parameters have fairly involved roles, the technique will be applied here to a set of parameters which can have a reasonably simple role. These parameters consist of the relative importance I_r of each region. Normally these parameters are all equal. However, in asymmetric problems, it turns out that some regions are much more important in terms of their scattering contributions to a detector. Therefore, these important regions have a larger value of I_r.

The region importance enters into the selection of a collision point through the following probability density function:

$$p^*_{kn}(\underline{z}_{kn}) = \frac{I_r p^*_r(s)}{\sum_{h=1}^{H} I_h P^*_h} \quad (46)$$

where r is the region in which the collision occurs (selected at random), $p^*_r(s)$ is the piecewise continuous probability density function in this region at the selected collision point (a distance s from the previous collision point), H is the total number of regions in which the collision could have occurred, and P^*_h is the integral of $p^*_h(s')$ over the partial path length in region h.

Calculating the logarithm of each side of the equation yields:

$$\ln p^*_{kn}(\underline{z}_{kn}) = \ln I_r + \ln p^*_r(s) - \ln \sum_{h=1}^{H} I_h P^*_h \quad (47)$$

The partial derivative of Eq. (47) with respect to the specific importance parameter I_g - the relative importance of region g - yields

$$\frac{\partial}{\partial I_g} \ln p^*_{kn}(\underline{z}_{kn}) = \frac{1}{I_r} \delta_{gr} - \frac{\sum_{h=1}^{H} P^*_h \delta_{gh}}{\sum_{h=1}^{H} I_h P^*_h} \quad (48)$$

where $\delta_{gh} = 0$ if region h is not region g and $\delta_{gg} = 1$.

Thus Eq. (48) is evaluated during the random selection of the kth collision point and the final term necessary to evaluate Eq. (45) and all preceding equations has been determined.

The above analysis is used to calculate the partial derivatives of the relative error of the dose rate with respect to the relative importance I_r of each geometric region, and a similar analysis is performed for the other importance sampling parameters. The result of the complete Monte Carlo calculation is a set of partial derivatives which, for the region importance, are given by

$$\frac{\partial E_N}{\partial I_r} = \frac{1}{N^2 \bar{D}^3_N E_N} \left[\bar{D}_N \sum_{n=1}^{N} D_n \frac{\partial D_n}{\partial I_r} - \left(\sum_{n=1}^{N} D_n^2 \right) \frac{1}{N} \sum_{n=1}^{N} \frac{\partial D_n}{\partial I_r} \right] \quad (49)$$

where $\partial D_n / \partial I_r$ is obtained from Eq. (44) using Eqs. (45) and (48).

After the calculation is completed, optimal values of the importance sampling parameters are

calculated by requiring that the relative error be zero - not actually achieved of course.

By a first order expansion

$$E_N' = 0 = E_N + \sum_{z=1}^{R} \frac{\partial E_N}{\partial I_z} (I_z' - I_z) \qquad (50)$$

where R is the total number of regions. A simple gradient analysis says that $I_z' - I_z$ should be proportional to $\partial E_N/\partial I_z$ so that

$$I_z' = I_z + C \frac{\partial E_N}{\partial I_z} \qquad (51)$$

where, by substitution into Eq. (50),

$$C = \frac{-E_N}{\sum_{z=1}^{R} \left(\frac{\partial E_N}{\partial I_z}\right)^2} \qquad (52)$$

where z is a general phase space coordinate

The program prints the optimum values of I_z' and other importance parameters after completing the Monte Carlo flux calculation. This analysis is performed for every response function. After more experience is obtained with the technique, the program could be modified to change these parameters internally corresponding to a specified response function.

Section 3

SAMPLE PROBLEM RESULTS

Two problems were investigated using the shield optimization capabilities of the FASTER-III program. Both problems involved a spherical reactor-shield configuration and included primary neutrons and both primary and secondary photons.

The two problems were similar except for the power level, 375 MW and 600 MW respectively. Both problems used a flat radial distribution for the primary neutron and photon source distribution. The primary photon source included an infinite operation equilibrium fission product term.

The core radii for the two problems were 82.38 and 96.38 cm respectively, corresponding to a power density of 4.53 MW/ft^3. Following the core was a 7.62 cm Be reflector; a 5 cm depleted uranium shield; three depleted uranium-borated water shield layers of 57, 15, and 15 cm thickness and 6.4, 4.6, and 2.8 gm/cm^3 density respectively; and a 117 cm borated water shield. This base line shield configuration was based on parameters obtained from SANE-SAGE calculations and subsequent calculations using the UNAMIT program, Ref. 7. The reactor-shield compositions are given in Table 1.

The primary neutron transport calculation utilized multigroup cross sections for 26 energy groups. Fifteen energy groups were utilized for both primary and secondary photons. The secondary production cross sections included both inelastic and capture gammas.

These initial configurations were each analyzed for a point detector 30 ft from the core center by following approximately 500 energy-dependent packets of primary neutrons and photons and approximately 7000 packets of secondary photons. The dose rates obtained from these calculations are tabulated in Table 2 including a breakdown by secondary source region. Each of these problems required about 28 minutes on the UNIVAC 1108 computer.

The basic calculated dose rates and dose rate derivatives were also used by the FASTER-III program to calculate the minimum weight shield configuration which would give a dose rate of 0.25 mr/hr at the specified detector point. The final shield configurations following the optimization are given in Table 3.

In both cases, the optimum shield configuration is significantly different from the base line configuration. Since the base line configuration was not generated by the FASTER-III program it is difficult to discuss many factors entering into that calculation which would account for the different optimal configuration. It is noted, however, that the base line configuration was generated using parameters corresponding to a calculated dose rate an order of magnitude below the specified dose rate constraint, Ref. 8. As such, the base line configuration used in the FASTER-III program was determined from an extrapolation of a different base line configuration.

A more critical critique can be made of the FASTER-III results independently. First it is noted that neither problem saw a significant contribution, less than a few percent, from photon sources in the core region. In fact, the 600 MW reactor dose rate from this source was about a factor of two less than it was for the 375 MW reactor. This difference is ascribed to the problem statistics since core photon sources see approximately 30 mean free paths of shield material. Therefore, it is doubtful if this dose rate component is converged within a factor of two after only 500 packets but this does not introduce a significant error since the original contribution was only two percent of the total dose rate.

The small contribution from core photon sources decreases the amount of high Z shields required around the core. Therefore, both problems gave a significant change in the first two shield dimensions during the optimization. In the 375 MW problem, the first mixture of depleted uranium-borated water (ρ = 6.4 gm/cm^3) was eliminated entirely. In the 600 MW problem, the depleted uranium and most of the first mixture were eliminated.

The main difference between the two FASTER-III calculations was the shift in the placement of lighter shield mixes towards the core for the 600 MW problem. An examination of the secondary photon dose components indicates that the contribution from the outer two shields was about 25 percent for the 375 MW reactor and almost 50 percent for the 600 MW reactor. Since these sources depend on the neutron attenuation through the closer regions and since lower effective Z materials are better neutron attenuators on a weight basis, the 600 MW problem tends to replace high effective Z material with a lower effective Z material.

The differences in the contribution from secondary sources in the outer shield regions is greater than expected for the nominal difference in the core region. Therefore, much of the difference in these sources must be ascribed to statistical variations. In fact, both problems had approximately 25 to 30 percent calculated relative error in the total photon dose rate. It should be noted that the FASTER-III program includes a number of importance sampling techniques which could be used to decrease this error. However, both

problems were run using the built-in definitions of importance parameters. Alternatively, more histories could have been used although the computer time requirements would have become excessive.

Section 4
CONCLUSIONS AND RECOMMENDATIONS

The FASTER-III program was developed to calculate neutron and photon fluxes at specified points in complex geometries. Alternatively, it can also calculate fluxes averaged over specified surfaces and volumes. The program was designed such that data preparation is simple and so that very little judgment is required to set up the importance sampling for most problems. The FASTER-III program satisfies these requirements very well.

The shield weight optimization capability included in the FASTER-III program permits the calculation of both base line radiation levels and optimal shield thicknesses all in a single computer run. However, the very large attenuation factors involved in the domonstration problems yielded some questionable results. In particular, the statistical differences in the relative contribution from various secondary source regions caused corresponding variations in the relative distributions of shield materials. Of course the statistical variations would be less in problems with less overall attenuation.

The effect of statistical differences on the shield optimization can be reduced by following more packets. However, the computer times start to get excessive if this is the only approach used. It would be more fruitful in terms of the routine application of the program to expend some effort towards altering the importance sampling.

The FASTER-III program has the capability of calculating optimal importance parameters based on partial derivatives of the variance. This feature can be used in determining better importance sampling parameters for shield optimization problems. In fact, the overall program efficiency could be improved if this feature was utilized on a wide variety of problems with the results being used to improve the built-in importance sampling models and parameters.

REFERENCES

1. Jordan, T. M.: FASTER, A Fortran Analytical Solution to the Transport Equation by Random Sampling. Vol. 9 of Synthesis of Calculational Methods for the Design and Analysis of Radiation Shields for Nuclear Rocket Systems. Rep. WANL-PR-(LL)-010, Westinghouse Astronuclear Lab., June 1967.
2. Jordan, T. M.: BETA, A Monte Carlo Computer Program for Bremsstrahlung and Electron Transport Analysis. A.R.T. Research Corp. (AFWL-TR-68-111, DDC No. AD-844258), Oct. 14, 1968.
3. Jordan, T. M.: Non-Negative Multigroup Cross Sections for FASTER. Rep. ART-19, A.R.T. Research Corp., Sept. 1968.
4. Jordan, Thomas M.; and Wohl, Millard L.: Helical Duct Geometry Routine for the Shielding Computer Program "FASTER." NASA TM X-1838, 1969.
5. Jordan, T. M.: Advanced Monte Carlo Concepts - Methods and Applications. Trans. Am. Nucl. Soc., vol. 12, no. 2, 1969, p. 945.
6. Jordan, T. M.: FASTER, A Generalized-Geometry Monte Carlo Computer Program for the Transport of Neutrons and Gamma Rays (Rev. Version). Vol. I - Summary Report. Rep. ART-42, A.R.T. Research Corp., June 1970.
7. Troubetzkoy, Eugene S.; and Wohl, Millard L.: UNAMIT-A One-Dimensional 4π Spherical Multilayer Reactor-Shield-Weight Optimization Code. NASA TM X-2048, 1970.
8. Wohl, M. L.: Private Communication, Dec. 3, 1970.

TABLE 1

SPHERICAL REACTOR-SHIELD CONFIGURATION

Element	COMPOSITIONS (10^{24} atoms/cm^3)						
	CORE	REFLECTOR	U^{238} SHIELD	MIX 1 SHIELD	MIX 2 SHIELD	MIX 3 SHIELD	H_2O+B SHIELD
H	0.01976	0.0	0.0	0.0451	0.0516	0.0580	0.0645
Be^9	0.0	0.120	0.0	0.0	0.0	0 0	0.0337
B	0.0	0.0	0.0	0.000671	0.000766	0.000862	0.000958
O	0.01184	0.0	0.0	0.0226	0.0258	0.0290	0.0
Al	0.0512	0.0	0.0	0.0	0.0	0.0	0.0
Zr	0.01744	0.0	0.0	0.0	0.0	0.0	0.0
U^{235}	0.000979	0.0	0.0	0.0	0.0	0.0	0.0
U^{238}	0.000078	0.0	0.0482	0.01446	0.00964	0.00482	0.0

TABLE 2

RESULTS OF FASTER-III BASE LINE CALCULATIONS OF REACTOR SHIELD CONFIGURATIONS AT 30 FEET FROM CORE CENTER

DOSE RATE COMPONENT	DOSE RATE CONTRIBUTIONS AT 30 FEET FROM CORE CENTER	
	375 MW REACTOR (mr/hr)	600 MW REACTOR (mr/hr)
Photon Source Region		
Core	0.009	0.004
Reflector	3.5×10^{-6}	6.3×10^{-6}
Depleted Uranium	3.2×10^{-5}	1.3×10^{-5}
Mix 1 Shield	0.018	0.026
Mix 2 Shield	0.062	0.075
Mix 3 Shield	0.017	0.063
Borated Water Shield	0.011	0.022
Total Photons	0.120 ± 0.034	0.187 ± 0.054
Neutrons	0.020 ± 0.002	0.027 ± 0.003
Total	0.140	0.214

TABLE 3

RESULTS OF FASTER-III SHIELD OPTIMIZATION
(0.25 mr/hr at 30 feet)

Quantity	375 MW REACTOR		600 MW REACTOR	
	Initial	Final	Initial	Final
Dose Rate (mr/hr)				
Photon	0.120	0.126	0.187	0.153
Neutron	0.020	0.124	0.027	0.097
Total	0.140	0.250	0.214	0.250
Shield Weight (10^3 kg)				
Depleted U	10.2	12.6	13.8	0.0
Mix 1	71.2	0.0	89.2	6.6
Mix 2	22.1	52.4	26.4	52.4
Mix 3	16.1	12.2	19.0	63.1
Water	86.7	80.3	97.7	85.3
Total	206.3	157.5	246.1	207.4
Shield Thickness (cm)				
Depleted U	5.0	6.1	5.0	0.0
Mix 1	57.0	0.0	57.0	7.0
Mix 2	15.0	57.3	15.0	48.4
Mix 3	15.0	13.5	15.0	51.4
Water	117.0	120.8	117.0	98.4

SESSION VII.3.
NATURAL SPACE RADIATION: INSTRUMENTATION & BACKGROUND EFFECTS
CHAIRMAN: H. D. HENDRICKS
LANGLEY RESEARCH CENTER

THE RESPONSE OF A 300μ SILICON DETECTOR TO MONOENERGETIC NEUTRONS DETERMINED BY THE USE OF THE MONTE CARLO TECHNICUE

M. Taherzadeh and G. Anno*

The Jet Propulsion Laboratory

The response of a 300μ thick silicon detector to an incident monoenergetic neutron beam is evaluated by the Monte Carlo method for the cases of both a shielded and a bare detector.

The result of Monte Carlo calculation, using elastic, inelastic and absorption reactions indicates that the response of the silicon detector to neutrons is basically due to the elastic scattering. In addition, the gamma rays generated in the shield of the detector will result in a response which is 3 or 4 orders of magnitude smaller than response to incident photons. The response of a bare silicon detector is calculated for neutron energies up to 6 MeV and bias energies from 50 to 250 KeV. It is found that the maximum response for a 300μ thick silicon detector is less than 4×10^{-3} c/n within this selected neutron and bias energy range. When the pulse height defect is introduced in the calculation the results at low energy neutrons were reduced.

INTRODUCTION

Nuclear radiation from an RTG used as the prime source of energy for electrical power in space science missions, can severely affect the scientific instruments or detectors aboard the spacecraft. These nuclear particles consist mainly of neutrons and gamma rays.

The neutrons and photons are emitted radially from the plutonium fuel power source with a flux level which depends upon the impurities and the age of the fuel itself. The interference between these radiations and the detectors in the science package unit, can take place via nuclear reactions. Therefore, it is necessary to identify these radiations and their effects on the detectors by a thorough analysis and evaluation of the radiation environment of the fuel and the responses that they produce in the science-experiment detectors..

In this paper, the response of a 300μ silicon detector to neutrons emitted from a plutonium dioxide fuel power source is determined. Neutrons released from the source not only interact directly with the detectors but also when detectors are shielded against primary photons additional radiation is generated by inelastic scattering and the radiative capture of the source neutrons within the shield.

RESPONSE OF A BARE DETECTOR

The response function of a 300μ bare silicon detector to neutrons can be studied by a Monte Carlo Code[1] using the probability laws of interactions and energy and angular distributions. However, in the case of a bare and a very thin detector (300μ) and low energy neutrons, the pulse height can be estimated easily via kinematical equations. This, of course, does not mean that we will be able to calculate the exact response by such a simplified scheme. Nevertheless, if we estimate the response of a silicon detector for a worst case and show it is much below the response to the primary gamma rays from the source the importance of neutrons as far as additional shielding is concerned would be reduced. Since our main interest in this analysis is the response to neutrons emanated from a PuO_2 nuclear power source, we should examine the neutron source spectrum first.

In Figure 1, the neutron flux and the flux spectrum of a typical PuO_2 fuel power source is presented. The fuel is a 2KW multihundred watt power source and emits a total of 4.59×10^4 neutrons/gmPuO_2/sec. At 50 cm away from the center of the source and at zero angle with respect to the major axis of the fuel, the total flux is 5.43×10^3 neutrons/cm^2/sec. From this flux distribution we conclude that the average neutron energy is about 2 MeV and the maximum neutron energy can be as high as 10 MeV or more but with a very small neutron abundance.

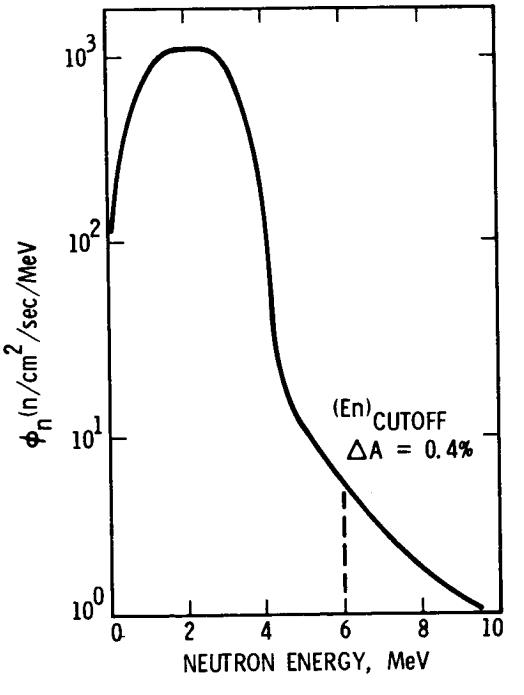

FIGURE 1. Neutron Flux Specrum of A 2KW PuO_2 Power Source (r = 50 cm and θ = 0.)

In order to limit ourselves with the number of nuclear reactions involved, we can arbitrarily set a maximum for the neutron energy so that the percent of the neutrons which will be ignored contributes an insignificant amount to the overall response of the detector. One such arbitrarily selected maximum energy is 6 MeV so that the neutrons with energies greater than 6 MeV contribution less than 0.5%.

Having selected a range of energies for the released neutrons, we can proceed to calculate the response of a silicon detector to a beam of neutrons emitted from a PuO_2 fuel power source. The total and the partial neutron cross sections as a function of neutron energies up to 6 MeV are presented in Figure 2. The reactions considered here are elastic scattering (n,n), inelastic scattering (n,n'γ), and the neutron disappearing reactions. These reactions consist of (n,α), (n,p) and the radiative capture reaction (n,γ).

The significant features of these cross sections are:

1. The (n,p) and the (n,α) reactions become important beyond a neutron energy of about 4.5 MeV, however, at these high neutron energies the neutron abundance diminishes very rapidly. For this reason reactions which are kinematically possible, but have high threshold energies such as (n,2n), are not included in this analysis, and the contribution from such reactions should be considered extremely small.

2. At low neutron energies (i.e., below 1.5 MeV), only two reactions are possible; they are elastic scattering and radiative capture.

3. In the medium range neutron energy, (i.e., between 1.5 to 5 MeV) the difference between the total cross section and the elastic scattering cross section increases with energy but never reaches 50% of the total cross section. This means, in this neutron energy range, the most important reaction is elastic scattering.

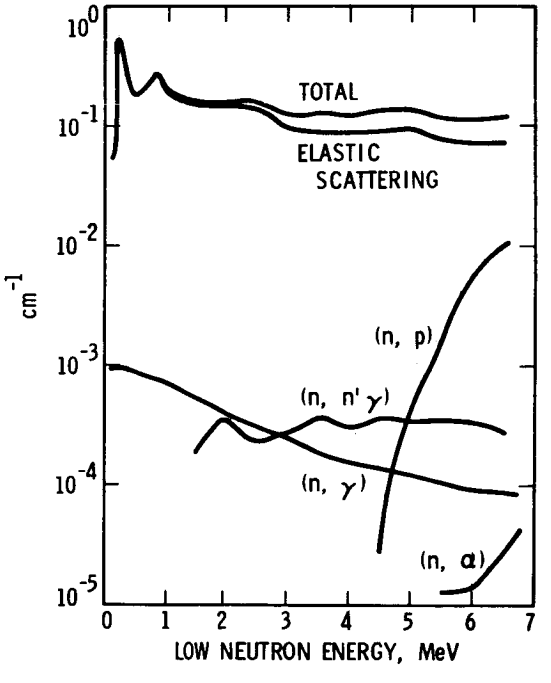

FIGURE 2. Neutron - Silicon Cross Section

Thus, the (n,p) and (n,α) reactions can be considered as a source of background while elastic scattering is by far the largest contributing reaction. The radiative capture (n,γ) and the inelastic scattering (n,n'γ) reactions have much smaller cross sections and the emitted photons escape the detector's sensitive area before depositing any energy. In Table 1, these neutron-silicon reactions are summarized with their corresponding threshold energies, Q-values, the emitted secondary particles, the neutron abundances at the threshold energies and the maximum energy and range of the outgoing particles in the silicon detector. The (n,2n) reaction is added to the list as an example of the reactions which will not be considered at all due to its high threshold energy and low neutron flux levels.

TABLE (1)
NEUTRON - SILICON REACTIONS
$(E_n)_{Max}$ = 6 MeV

	REACTIONS	$Si^{28}(n,b)R$	Q MeV	$(E_n)_{th}$ MeV	$(E_b)_{Max}$	ABUNDANCE at E_{th}	σ At 1.5 MJ barns
1)	NEUTRON DISAPPEARING	$Si^{28}(n,\alpha)Mg^{25}$	-2.7	2.66	2.68 (10μ)	13%	0
2)	NEUTRON DISAPPEARING	$(n,p)Al^{28}$	-3.9	3.66	1.81 (42μ)	8.3%	0
3)	ELASTIC SCATTERING	$(n,n)Si^{28}$	0.0	0.0	.798 (.45μ)	--	2.915
4)	INELASTIC SCATTERING	$(n,n'\gamma)Si^{28}$	0.0	0.0	--	--	3.64×10^{-3}
5)	RADIATIVE CAPTURE	$(n,\gamma)Si^{29}$	8.47	0.0	--	--	1.11×10^{-2}
6)	OTHER PARTICLE PRODUCING	$(n,2n)Si^{28}$	-8.47	8.81	--	.14%	0
7)	OTHER PARTICLE PRODUCING	$(n,np)Al^{27}$	-11.6	12.06	--	--	0

The response function of a detector medium at a given neutron energy and when pulse height defect is neglected is given by

$$R(E_n, E_B) = \epsilon_D(E_n)\, P(E_n, E_B) \qquad (1)$$

where E_B is the bias energy. The detector's efficiency function for normal incidence $\epsilon_D(E)$, is generally given by

$$\epsilon_D(E_n) = 1 - Exp\left[-\mu(E_n)t\right] \qquad (2)$$

$\mu(E)$ is the attenuation coefficient of the detector and t is the sensitive thickness. $P(E,E_B)$ is the probability that a transfer in energy to the silicon nucleus is above the bias energy E_B. The efficiency functions for (n,n), (n,p) and (n,α) reactions are presented in Figure 3 together with the total values for a 300μ silicon detector. The shape of these curves follows the total cross section because the effective thickness of the detector is small and

$$\epsilon_D(E_n) = N_D t\, \sigma(E_n) \qquad (3)$$

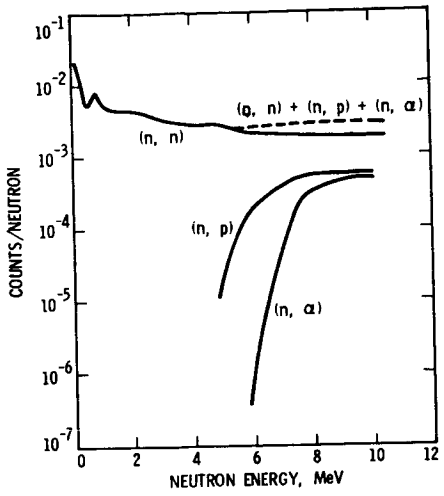

FIGURE 3. Zero Bias Efficiency of A 300μ Silicon Detector

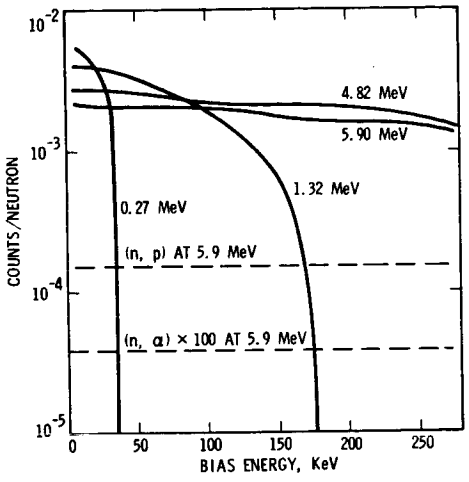

FIGURE 4. Neutron Response of A 300μ Silicon Detector

Since the energy tranferred to the silicon by neutrons is 0.133 En $\sin^2(\theta_{cm}/2)$, the maximum energy of the silicon recoil $\hat{E}_{si}$, is obtained when $\theta_{c.m.} = 180^\circ$ and the energy distribution function for the silicon nuclei after collision is $1/\hat{E}_{si}$. The probability function is given by $1 - (E_B/\hat{E}_{si})$ and the response function is

$$R(E_n, E_B) = \epsilon_D(E_n, t)\left[1 - \frac{E_B}{.133 E_{si}}\right] \quad (4)$$

In Figure 4, this function is plotted for various neutron energies and for various bias energies. The contribution from protons generated in (n,p) reactions and the contribution from α particles generated in (n,α) reactions are indeed small. At low neutron energies these charged particles do not exist and at high energies, the contribution from protons is more than an order of magnitude lower and the contribution from α particles is about 5 orders of magnitude smaller than the pulse height generated by elastic scattering of neutrons. Therefore, up to 5 MeV the major portion (~99%) of counts comes from the silicon nuclei after being struck by neutrons and at 6 MeV nearly 90% of the response is due to this reaction. The protons and particles generated within the detector are completely absorbed since the edge effects are small. Because of this they must be included in the pulse height calculation since the time interval for the ionization process is much smaller than the charge collection time interval and the deposited energy is equal to the maximum energy if it is above the bias energy.

The neutron flux from the fuel capsule can also be folded into the response function, thus, in the $(o, \hat{E}_n)$ energy interval the response of the silicon detector at E_n is

$$dR(E_n)/dE_n = \phi(E_n) A \epsilon_D(E_n) P(E, E_B) / \phi_o \quad (5)$$

A is the detector's cross-sectional area and $dR(E_n)/dE_n$ is given in $c/(n/cm^2)$/MeV. The total silicon response for a polyenergetic neutron beam with energies up to $\hat{E}_n$ is

$$R(\hat{E}_n) = \int_{(E_n)_{min}}^{\hat{E}_n} A \phi(E_n) \epsilon_D(E_n) P(E, E_n) dE_n \quad (6)$$

$(En)_{min}$ is the minimum neutron energy allowed for a given bias energy, i.e., 7.55 E_B.

Equation 4 is plotted in Figure 5 for the same neutron energies utilized in Figure 4. $R(E_n)$ is given in counts/sec for neutron energies from (E_n) min up to $\hat{E}_n$. The total counting rate at a a given maximum neutron energy depends on the bias energy. At 100 keV bias energy and at 5 MeV neutron energy the counting rate is about 20 c/sec.

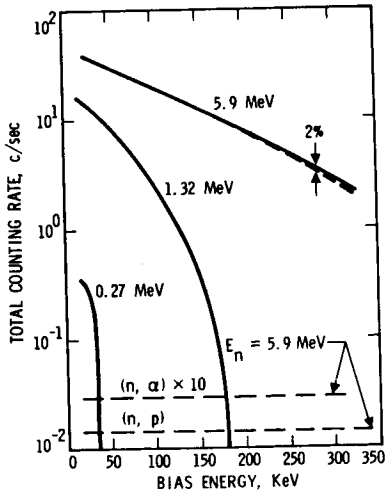

FIGURE 5. Total Counting Rate of A 300μ Silicon Detector

PULSE HEIGHT DEFECTS

The response functions which were calculated in the previous section are yet subject to another restriction namely the pulse height defect (PHD). This effect is more pronounced in the case of silicon detectors because the pulse height (PH) is mainly due to the elastic scattering of neutrons.

Neutrons transfer their energies to the silicon sensitive medium by atomic scattering and nuclear ractions rather than through an electronic ionization process. The secondary charged particles produced by the neutron interaction such as protons, alpha particles and silicon nuclei in turn transfer their energies to the medium via ionication and nuclear charge scattering. The photons generated in the (n,Y) and (n,n'Y) reactions escape the medium in most cases, thus will not deposit energy. The ionization processes contribute to the PHD. Ionization causes the displacement of electrons while nuclear charge scattering (Rutherford scattering) causes the displacement of atoms from their equilibrium position and leaves vacancies in the lattice. In Table 1, the maximum energies and ranges of the protons, alpha particles and silicon nuclei are presented. Since we have selected 300μ for the depletion depth of the detector, nearly all these charged particles remain inside. The energy transferred to the silicon is $\hat{E}_{si} \sin^2(\theta_{cm}/2)$ where $\hat{E}_{si}$ is the maximum transmitted energy. If r is the ratio of the mass of the silicon atom over the mass of the ith charged particle, namely (α,p,S_i) then

$$\hat{E}_{si} = 4 r_i E_i (1 + r_i)^{-2}$$

Since $r_{si} = 1$, $r_p = 28$ and $r_\alpha = 7$, the maximum energies are $\hat{E}_{si} = E_{si}$, $\hat{E}_{si}^{p} = .1332\, E_p$ and $\hat{E}_{si}^{\alpha} = 0.4328\, E_\alpha$. If we use the maximum energies of the charged particles for a 6 MeV neutron beam from Table 1, then the maximum transmitted energies are 798, 240 and 1170 keV for S_i,p and α particles, respectively. However, in the real case only a fraction of these energies are transmitted to the medium via non-ionizing processes, the remainder contribute to the PH.

Figure 6 presents the fraction of the PHD as a function of the charged particle energy and considers up to two neutron scatters.[4] We notice that the PHD is important only at low energies and within this range the PHD due to the silicon nuclei is much greater than the PHD due to protons or α alpha particles. For example, for a 100 keV charged particle (4.5, 4.0 and 0.75 MeV neutron energies for proton, particle and S_i, respectively) the PHD due to S_i is about 60 keV while for protons it is 6 keV and for α particles it is 12 keV.

We now can include the pulse height defects into the silicon responses presented in Figure 4.

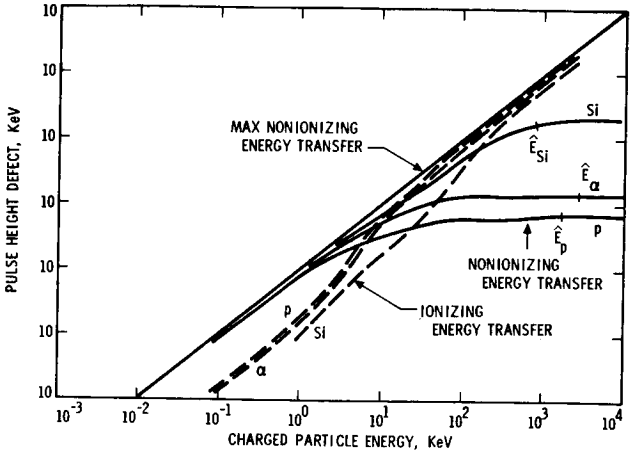

FIGURE 6. Pulse Height Defect for Silicon

For 1.32 MeV neutrons, we are concerned only with silicon nuclei which have a maximum energy of 175 keV, thus if the bias energy is set at higher values there would be no response. The PHD at this energy indicates (Figure 6) that 58% of energy is transmitted to the medium by the nonionizing processes, thus the bias energy needs to be set even lower (74 keV) if any response is desired. At high neutron energy (i.e., 6 MeV) the maximum energy of the charged particles is given in Table 1, and the PHD's are 48, 159 and 528 keV for protons, alpha particles and silicon nuclei respectively. This means protons and particles will contribute to the total response but there will be no pulse height due to the (n,n) reaction if the bias energy is greater than 270 keV.

RESPONSE OF A SHIELDED DETECTOR

Monte Carlo calculations were performed to estimate the response of a shielded 300 micron thick silicon detector to incident monoenergetic neutrons of 0.201, 1.49, and 5.18 MeV. The detector response mechanism analyzed was based on secondary gamma radiation from neutron capture (n,Y) and inelastic scattering (n,n',Y) reactions taking place both in the silicon and the 86 mil aluminum shield over the front end of the detector upon which neutrons were assumed to be normally incident.

Since the neutron interaction probabilities were small for the combined detector assembly i.e., approximately 0.03, 0.044, and 0.066 for the 5.18, 1.49, and 0.201 MeV neutrons, respectively; secondary photon sources for the shielding and detector volumes were determined assuming exponential attenuation of the incident parallel beam neutrons in the detector materials. The secondary gamma sources from the (n,γ) and (n,n',γ) reactions were assumed to be isotropic. Monte Carlo calculations were then performed to simulate the photon transport and electron transport in the detector materials and energy deposition in the 300 micron, 2.0 cm^2 silicon detector. The secondary source terms were determined using the POPOP-4 Program and source library (2)

GEOMETRY

The model which was used in the analysis is given by the configuration shown in Figure 7. As shown it is composed of three cylindrically symmetric material regions; these are the 0.03 cm x 2.0 cm^2 silicon, the aluminum holder, and the 86 mil aluminum shield. Secondary gamma ray sources were specified for the shaded portion (designated, S_1) of the aluminum shield coincident with a radial neutron beam dimension of 1.38 cm; this corresponds to the intersection at the front surface of the Al shield made by the projection of the detector holder front bevil. The calculations were performed such that secondary gamma ray sources originating in S_1, assumed to be isotropic, were biased toward the silicon detector volume, itself a secondary gamma ray source volume designated as S_2. In view of the fact that a large proportion of the secondary photon spectrum is high enough in energy to give rise to electrons (from primarily Compton interactions) whose ranges exceed the aluminum shield thickness, a biasing region on the silicon side of the aluminum shield was not specified. As the secondary sources were based on those portions of the configuration designated S_1 and S_2 in Figure 7, secondary photons originating in the holder and other portions of the aluminum shield were neglected The secondary gamma ray sources originating in the holder may not necessarily be insignificant, however, this particular analysis has been restricted to only analyzing the detector response relating to the effect of the front 86 mil aluminum shield.

SECONDARY GAMMA RAY SOURCE

This analysis considers secondary gamma ray sources which originate in the 86 mil aluminum shield and the 300 micron thick silicon detector from neutron capture (n,γ) and inelastic neutron scattering (n,n',γ). The secondary gamma ray source term is given as

$$S_r(\vec{r}, E_n, E_g) = \phi(\vec{r}, E_n) N(\vec{r}) \sigma(E_n) Y(E_n, E_g)$$

where, r = position vector, E_n = neutron energy, Eg = gamma energy, $\phi(E,E_n)$ = neutron flux, n/cm^2-sec, N(r) = atom density, atoms/cm3, $\sigma(E_n)$ = reaction cross section for gamma production, cm^2/atom and, $Y(E_n,Eg)$ = gamma yield, photons/neutron reaction.

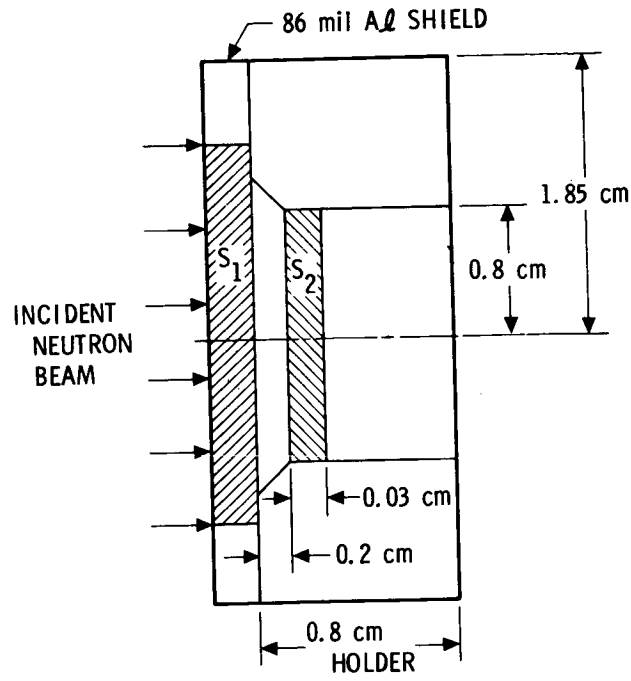

FIGURE 7. Silicon - Aluminum Configuration

The reaction product, $\sigma(E_n)\ Y(E_n,Eg)$, was computed using the POPOP-4 Program and library data. The reaction cross sections, i.e., $\sigma^{n,\gamma}(En)$ and $\sigma^{nn\gamma}(En)$ for the (n,γ) and (n,n',γ) reactions, respectively, were taken from reference (3) with the exception of $\sigma^{n,n',\gamma}$ for silicon, which was included in the POPOP-4 library data.

The (n,γ) reaction yields are based on thermal neutron reactions and are thus assumed constant over neutron energy, i.e., $Y_{n,\gamma} = Y(Eg)$ and the inelastic neutron scattering gamma rays are a function of both neutron energy and gamma energy, i.e., $Y_{n,n'\gamma} = Y(Eg,E\gamma)$.

Calculations were performed using the RAMPARTS(1) Monte Carlo program by random sampling of the secondary gamma ray source term $S_r(\vec{r}, E_n, E_g)$ over S_1 and S_2 (Figure 7) with equal weighting. Spatial sampling of $S_r(\vec{r}, E_n, E_g)$ in the cylindrical source geometry was based on assuming a constant distribution radially and azimuthally. The distribution in Z was assumed exponential, $\phi_o \exp(-N\sigma_T z)$ for which $N\sigma_T(E_n) z \ll 1$, becomes essentially linear, $\phi_o(1 - N\sigma_T z)$

Individual photon energies were selected by random sampling of the gamma ray energy spectra. Photon transport within the configuration given in Figure 7 was allowed to proceed allowing up to two collision points. Biasing of the photon transport was imposed in order to reduce the calculational varience such that the silicon was preferred with a weight of 100:1 and the aluminum shield 10:1. Consequently, the detector holder was accordingly deemphasized in this study. Further biasing of 10:1 was imposed on picking the radial dimension of the cylindrical source coordinate, and the initial direction of the photons, in order to minimize the calculational varience from the standpoint of obtaining a reasonable amount of samples in S_2 in view of the primary electron range consideration.

Primary electron sources from pair production and Compton scattering reactions of the gamma rays were simulated from which points electron transport was simulated using a Moliere type angular straggling model together with energy loss and angular deflection evaluated at 4% energy loss intervals, and allowing a maximum of up to 50 collisions for the electrons.

The secondary gamma ray sources are normalized to the total number of photons, in each of source volumes S_1 of S_2.

Results of these initial response calculations of a 300 micron silicon detector to incident neutrons are plotted in Figure 8. In general, these calculations suggest that response to neutrons, due to the generation of secondary gamma rays, are about 3 to 4 orders of magnitude below incident photons on a one-for-one basis. The channel energy bias counts per incident neutron normalized over a 2.01 cm^2 area (area of the 300μ detector) are given along with calculational error for the 3 neutron energies shown. The response values are also broken up into contributions from both neutron capture gamma (n,γ) and inelastic neutron scattering gamma $(n,n'\gamma)$ reactions occuring collectively in the aluminum 86 mil shield and 300 micron silicon detector. (For 0.201 MeV neutrons, no values are given for $(n,n'\gamma)$ reactions since this is below the threshold level for the first excited state).

The relative contribution to the response of electrons born in the aluminum shield and the silicon-born electrons to aluminum-born electrons. For the 5.18 MeV incident neutrons, silicon-born electrons are more important than aluminum shield-born electrons for the $n,n'\gamma$ reactions, i.e., 6.2:1. This can be related to the relatively large spectral gamma component at 1.5 to 2.0 MeV. The situation for 1.49 MeV neutrons is somewhat reversed, although the reversal is not as dominate. An inspection of the input spectra used suggest competition between n,γ reaction electrons in silicon and (n,n',γ) reaction electrons from the aluminum shield, with the latter being lower energies. These lower energy electrons would have smaller ranges which allow perhaps only a small proportion of them to escape from the aluminum shield and enter the silicon to add to the response, and thus disallow any possible spectral advantage as compared to the (n,γ) reactions in silicon. What is somewhat surprising for this case is why the (n,n',γ) gamma reactions are not more important in view of the essentially large single line secondary gamma component in silicon at 1.0 to 1.5 MeV.

Figure 4 gives a plot of the results for the three neutron energy cases for which these calculations were performed. The relatively large response shown for the 0.201 MeV neutron case is due primarily to the increase in the n,γ cross section, coupled with the assumed thermal neutron reaction secondary gamma yields. In fact, under these assumptions, these would be a continuing upward trend with decreasing neutron energy.

*G. Anno; ART Corporation, L. A., California

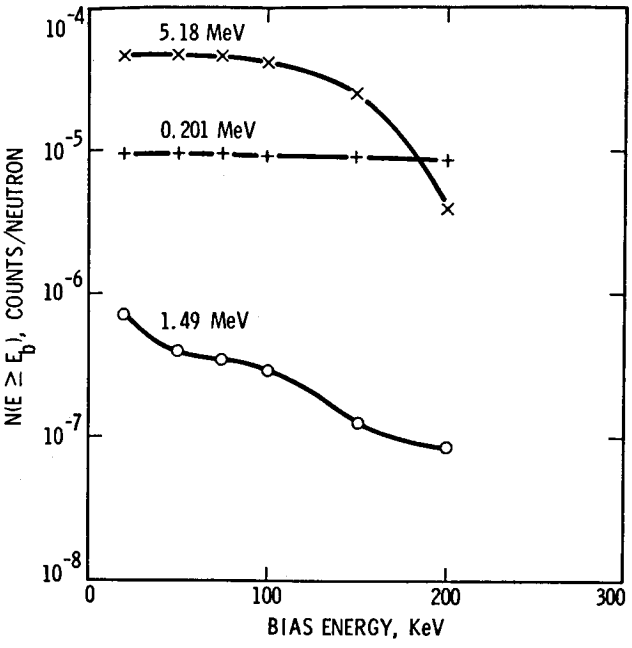

FIGURE 8

CONCLUSIONS

The following general conclusions can be made from the results.

1. In the neutron energy range of .27 to 6 MeV and 25 to 250 keV bias energy the maximum response of a 300μ silicon detector is about 4 x 10^{-3}c/n.

2. At 3 MeV neutron (or gamma ray) energy and 50 keV electron bias energy the response of the silicon detector to neutrons is about 11% of the response to the source gamma rays. (i.e., R_n = .0029 and R_γ = .025 M. Reier, JPL, 1970).

3. The contribution from the secondary particles generated in the shield is about 3 to 4 orders of magnitude smaller than the response to the source neutrons.

4. At 50 to 250 keV bias energy range and for a neutron flux emitted from a 2 KW MHW PuO_2 fuel power source the counting rate is estimated at about 31 to 5 counts/sec.

ACKNOWLEDGEMENT

The authors wish to express their appreciation to Dr. Melvin Reier of JPL for his valuable discussion during this investigation.

REFERENCES

1. T. M. Jordan, "Beta- A Monte Carlo Computer Program for Bremsstrahlung and Electron Transport Analysis," AFWL-TR-68-111, October, 1968.

2. W. E. Ford III and D. H. Wallace, "A Code for Converting Gamma Ray Spectra to Secondary Gamma Production Cross Sections" CTC-12. (May 23, 1969).

3. J. W. Ray et. al., "Neutron Cross Sections of Nitrogen, Oxygen, Aluminum, Silicon, Iron, Deuterium, and Bergllium," UNC-5139, (Nov. 1965).

Identification and Control of Spacecraft Radiation Sources of Interference to X-Ray and Gamma-Ray Experiments*

Albert E. Metzger
Space Sciences Division
Jet Propulsion Laboratory

and

Jacob I. Trombka
Laboratory for Space Physics
Goddard Space Flight Center

Apollo 15 and 16 will carry instruments for the purpose of measuring x-ray and gamma ray fluxes from the lunar surface and in cis-lunar space. The intensity levels expected are low over most of the energy range of interest, requiring that background contributions be minimized. The radiation sources on Apollo have been determined and their interference with these instruments evaluated. The results have been used as a basis for dealing with this problem and for recommendations applicable to future manned and unmanned missions.

X-ray spectrometers and gamma ray spectrometers can be used to measure fluxes of x-rays and gamma rays which originate at the surface of large objects in the solar system with little or no atmosphere such as the Moon and Mars. The gamma rays arise from two sources:

1. The radioactive decay of certain isotopes whose half-lives are comparable to the time since nucleosynthesis, principally K-40, Th-232 and U-238 and the daughter products of the last two.
2. The interaction of cosmic rays with the surface material in the form of a radiative and nucleonic cascade which distributes the energy of the cosmic ray over numbers of target nuclei.

In contrast, the dominant cause of observable x-rays to distances beyond the orbit of Mars is the Sun, whether quiet or active, which emits x-rays which will induce secondary fluorescent emission in the object they strike. The gamma ray and x-ray fluxes from the surface of the object will both contain line radiation characteristic of the originating element or isotope as well as a continuum energy distribution. The line radiation therefore contains compositional information.

Fluxes of x-rays and gamma rays also arise as the result of energetic physical interactions within the galaxy and beyond. The measurement of these fluxes has become the basis of x-ray and gamma ray astronomy. Their properties of location, intensity, line and continuum energy distribution, time variability and correlation with emissions at longer wavelengths promise to provide much information on the current state and past evolutionary processes of the universe.

Observations of celestial x-rays and gamma rays are most suitably made from satellites to avoid the effects of the Earth's atmospheric attenuation and to increase the experiment time. Observations of x-rays and gamma rays from planetary-type objects require the instrument to be on a spacecraft at, or very close to, the object. The general form of the spectral distribution for both the planetary and celestial fluxes follows an inverse exponential relationship with energy. The sensitivity of such experiments is a prime consideration. Since the fluxes are low, the inclusion of structural or other materials which contain radioactive nuclides in the spacecraft is an interference, which, if excessive, will degrade the sensitivity of the experiment. In describing the situations which have been encountered in the integration of two such experiments on a complex spacecraft, we have in mind the relevance to future experiments of this type which will be carried on manned and unmanned missions.

Apollo 15 and 16 will carry a set of remote sensing experiments in a part of one sector of the Service Module (SM) which has been designated the Science Instrument Module (SIM) (Fig. 1). These will make observations of the Moon from orbit. Three of these instruments will be spectrometers to measure fluxes of x-rays, gamma rays, and alpha particles from the lunar surface which will provide data on the abundance of certain key elements with a spatial resolution of roughly 100 km for the Gamma Ray Spectrometer and a fourth of that for the X-Ray Spectrometer. There are no significant sources interfering with the Alpha Particle Spectrometer, so we have concentrated on the X-Ray and Gamma Ray Spectrometers for this report.

The X-Ray Spectrometer consists of three collimated proportional counters pointed at the lunar surface for the measurement of secondary x-rays produced by the interaction of solar x-rays with the upper millimeter of lunar surface material. A fourth proportional counter located on the opposite side of the SM will monitor the solar x-ray flux directly to normalize the intensity of response. The counters are all sealed, thin-window detectors capable of responding to x-rays down to 0.5 KeV. The electronic system provides eight channels of

* This paper presents progress of one phase of research carried out at the Jet Propulsion Laboratory, California Institute of Technology, under Contract No. NAS 7-100, sponsored by the National Aeronautics and Space Administration.

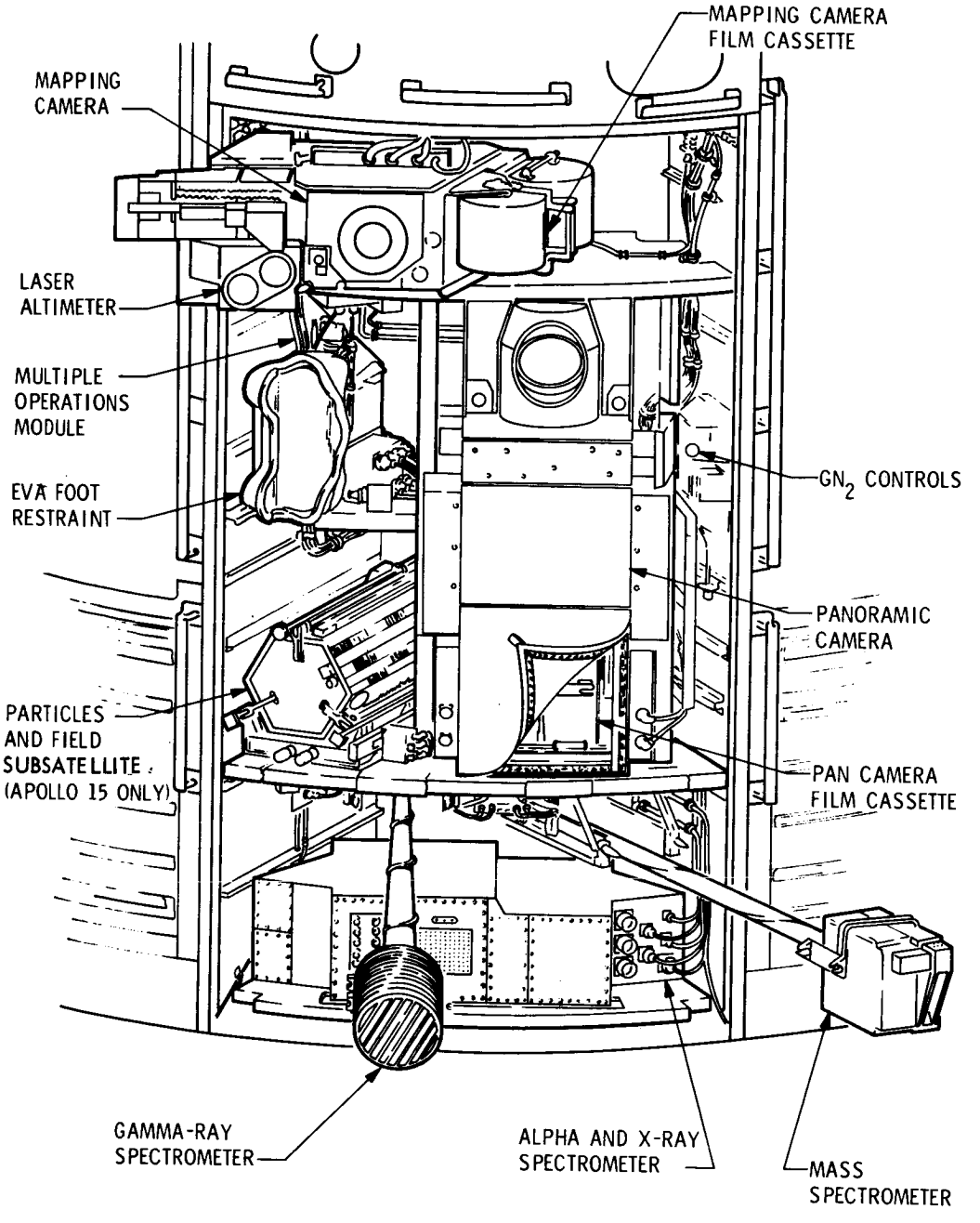

Figure 1. Location of Experiments in the SIM of Apollo 15 and 16

energy discrimination; in addition two of the lunar-directed counters will have filters to improve the resolution for characteristic x-rays of silicon, aluminum and magnesium.

The Gamma Ray Spectrometer uses a sodium iodide (NaI(Tl)) scintillator-photomultiplier tube combination as the detector. After signal amplification, a height-to-time converter and following digital electronics provide 511 channels of energy analysis which will span a nominal energy range of 0.2-9 MeV. A mantle of plastic scintillator eliminates charged particle events by detecting them in coincidence with the NaI(Tl) crystal. The detector and electronics are enclosed in a cylindrical thermal shield. The entire instrument is mounted at the end of a boom (Fig. 1) whose full extension is 25 feet. This is because gamma rays are produced by the interaction of cosmic rays with the spacecraft mass and this background interference would dominate the spectrum if the instrument were confined to the SIM even in the absence of significant quantities of natural radioactivities on the spacecraft. As it happens, significant quantities of natural radioactivities are present on the Apollo spacecraft and the boom will be essential in reducing this source of background as well as the induced component to tolerable levels.

With the Gamma Ray Spectrometer in the boom extended position, the major background component will be the induced lunar continuum with the diffuse celestial gamma ray flux making a smaller contribution. The instrumental response due to the lunar continuum has been estimated from a high altitude balloon flight experiment conducted by L. E. Peterson (Fig. 2 of Ref. 1) and the gamma ray experiment on the USSR's Luna 10 (Ref. 2), while the diffuse celestial gamma ray flux was measured initially by a Gamma Ray Spectrometer on Rangers 3 and 5 (Ref. 3); the energy region from 0.25-6 MeV was measured recently by the earth satellite, ERS-18 (Ref. 4). At energies of 1.47 MeV and 2.62 MeV which correspond to the important principal lines of K-40 and Th-232, the rates will be about 5×10^{-2} c/cm^2 sec and 2×10^{-2} c/cm^2 sec respectively over an energy range corresponding to the full resolution width of the gamma ray line. The three sigma statistical uncertainty has been taken as the limit of radioactive source contribution which could be tolerated without degrading experimental sensitivity. For 3000 seconds of data accumulation which corresponds to about 10 traversals over a lunar mare feature 500 km in diameter, the allowable levels are 1.6×10^{-3} c/cm^2 sec and 1.0×10^{-3} c/cm^2 sec for the 1.47 MeV and 2.62 MeV lines respectively. For ten hours of counting for which the spatial resolution would scale to contrast highland with mare areas, the corresponding numbers are 4.6×10^{-4} c/cm^2 sec and 3.2×10^{-4} c/cm^2 sec.

Sources of background interference to the X-Ray Spectrometer are again cosmic ray-induced radiation from the spacecraft and a backscattered lunar continuum. Cosmic ray-induced activity is minimized using electronic rejection methods. Coherent backscattered radiation from our calculations should be 1/10 that of the fluorescent component. Therefore we find that these sources of interferences do not significantly interfere with the measurement.

Minimum detectable source levels for the x-ray experiment cannot be compared with those of the gamma ray experiment. The minimum detectable x-ray activity is a function of the source strength of the induced activity rather than problems in the background. Because x-rays in the 1-6 KeV range of interest are much more easily absorbed than the more energetic gamma rays, the X-Ray Spectrometer can be operated in the SIM.

Detectable levels of gamma rays are low enough to require some care in the construction of the Gamma Ray Spectrometer itself since the closer to the detector the more effect a given radiation source will have. The photomultiplier tubes, crystal assembly, and thermal paint have been tested in a low background level counting facility. The smaller of the two tubes used in the instrument was found to produce a count rate at 1.47 MeV of 3.2 c/min equivalent to about 3×10^{-3} c/cm^2 sec at the NaI(Tl) crystal, due to the presence of photoceramic spacers high in potassium. Low potassium ceramic spacers were substituted. The crystal assembly showed a small potassium response, about 2×10^{-4} c/cm^2 sec, which was traced to the cover glass. A qualified substitute material was not available at the time so this low level of contamination was allowed to remain. The thermal paints used on the instrument are Cat-a-Lac White and Cat-a-Lac Black. Both are relatively low in potassium. Sample analyses of the two gave 0.24% by weight of potassium in the Cat-a-Lac Black, 0.008% in the Cat-a-Lac White. A calculation of the counting rate at the detector due to the paint yields 3×10^{-4} c/cm^2 sec, below, but not greatly below the 10 hr tolerance level. However, a low level facility test of an entire detector which contains 8% of the Cat-a-Lac Black by weight but about 50% of the contribution by geometry showed no indication of potassium contamination. Aluminum rather than magnesium has been used for the instrument as a whole since some alloys of magnesium contain substantial quantities of thorium.

Radiation Sources on the Apollo J Spacecraft

The problem of radiation cleanliness was discovered early in the development of the Apollo program by examining a radiation source list maintained by the Manned Spacecraft Center. It was found that hundreds of millicuries of cobalt-60 were used to measure the reaction control system (RCS) fuel content. After extensive study and debate, this serious interference was removed. Since the time that the spectrometer experiments were chosen to fly on two of the J-series missions, increasing attention has been given to radiation cleanliness. Because of the complexity of the Apollo system and its advanced state of design when the experiments were chosen for flight, the problems have been rather severe, particularly for the Gamma Ray Spectrometer. Nevertheless, significant steps have been taken to provide the necessary environment. A strong source of thorium-232 in the base plate of the guidance system in the Command Module (CM), and ten curies of promethium-147 located on the CM were removed.

The known radiation sources aboard the Apollo spacecraft at present, their activities and locations, are listed in Table 1. Much of this data has been compiled by L. Barbieri of North American Rockwell (Ref. 5). Besides reviewing material lists, experimental radiation surveys have been conducted. Two types of surveys have been carried out, integral counting surveys with both ionization chambers and scintillation detectors, as well as surveys to determine the differential energy spectra. The integral count rate survey helped to determine major sources of radiation contamination while the differential energy spectral survey determined the nature of the contaminating isotope.

Table 1. Known Radiation Sources on Apollo 15 and 16

Radioisotope	Activity	Identification and Location
	Sources Always Present	
Potassium - 40	0.7 microcuries	EPS and ECS Radiators Thermal Paint
Potassium - 40	1.5 microcuries	KOH Electrolyte-Pyro and Re-Entry Batteries
Potassium - 40	16 microcuries	KOH Electrolyte-Fuel Cells
Potassium - 40	2.1 microcuries	LM-type Battery in SM
Potassium - 40	0.003 microcuries	Mass Spectrometer Thermal Paint
Thorium - 232	5.8 microcuries	Mapping Camera Lens
Thorium - 232	microcurie range	Guidance System Heat Sinks in CM
Mercury - 203	0.1 microcuries	Gamma Ray Spectrometer
Iron - 55	1.0 microcurie	X-Ray Spectrometer
Polonium - 210	5.0 microcuries	Alpha Particle Spectrometer
	Source Jettisoned Shortly After Lift-Off	
Uranium - 238	0.1 curie	Launch Escape System Ballast Plates
	Source Jettisoned in Lunar Orbit	
Polonium - 208	1.0 microcurie	Subsatellite Particle Detector (Apollo 15 only)
	Sources on LM Descent Stage	
Plutonium - 238	$40(10)^3$ curies	Radioisotope Thermoelectric Generator on LM
Promethium - 147	200 millicuries	Landing Point Designator Paint-LM
Potassium - 40	9.2 microcuries	Five Batteries
	Sources on LM Ascent Stage	
Tritium	14.7 curies	Portable Life Support System
Promethium - 147	21.3 curies	Radioluminescent Discs in Lunar Module
Promethium - 147	0.2 curies	Self-Luminous Switch Tips in LM
Potassium - 40	3.7 microcuries	Two Batteries

Since the information concerning the elemental composition of the lunar surface resides in the discrete lines of the measured emission gamma ray spectrum, it is very important that no discrete lines in the background spectrum occur where there are significant lines in the lunar emission spectrum. Such background lines would greatly impair our ability to determine the presence of the lunar lines. The differential energy spectrum survey thus was found to be more important because it was able to establish the existence of such interference lines. We also found that it was easier to locate the source of radiation contamination by identifying the radiation sources from their characteristic line structure. Measurements of differential energy spectra require long counting times compared to an integral counting survey. Therefore a preliminary survey was made of the total Command and Service Module (CSM) and Lunar Module (LM) areas by integral counting to find obvious problem areas. Differential spectrum determinations were carried out in the regions of suspected radiation sources and detailed studies were carried out in the stowed and extended positions for the Gamma Ray Spectrometer.

Referring to Table 1, a major source is seen to be the radioluminescent discs in the LM, amounting to 21.5 curies of promethium-147. These are used to provide orientation markers during docking maneuvers. Their location is shown in Figs. 2 and 3, together with those no longer on the CM. An early mission profile called for discard of the LM after the ascent rendevous and before operation of the lunar orbit experiments. When this was revised to retain the LM after rendevous through most of the trans-Earth phase, the radiation characteristics of the Pm-147 source were investigated. Ideally, Pm-147 has only a significant low energy bremsstrahlung spectrum, but because of the high activities involved, trace contaminants contribute significantly to the background in the spectral region of interest. Figure 4 shows a pulse height spectrum of a 300 millicurie Pm-147 source measured with a 3 in. x 3 in. NaI(Tl) detector. The source is 6 in. above the crystal. The radioisotopes producing the line spectrum have not been identified but their energies can interfere significantly with the lunar gamma ray measurement. Specifically, the 1.45 MeV line in Fig. 4 falls right on top of the 1.46 MeV line of K-40. By applying geometric and source strength factors the interference of the Pm-147 on the LM can be estimated. Twenty-one and a half curies of Pm-147 would raise the minimal detectable limit of potassium from the lunar surface by about a factor of two. Besides the interference at 1.46 MeV, the presence of the LM would alter the radiation source configuration during orbital data accumulation (since it is now planned to operate the orbital experiments both before and after ascent rendevous), and decrease the effective operating time of the Gamma Ray Spectrometer by substantially increasing its dead time. Pm-147 would also increase the background level seen by the X-Ray Spectrometer. It is therefore gratifying to report that the most recent mission profile reverts back to the original plan to discard the LM shortly after rendevous.

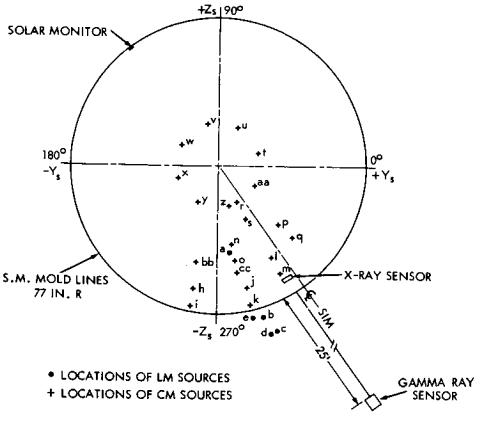

Figure 2. Location of Radioluminescent Discs

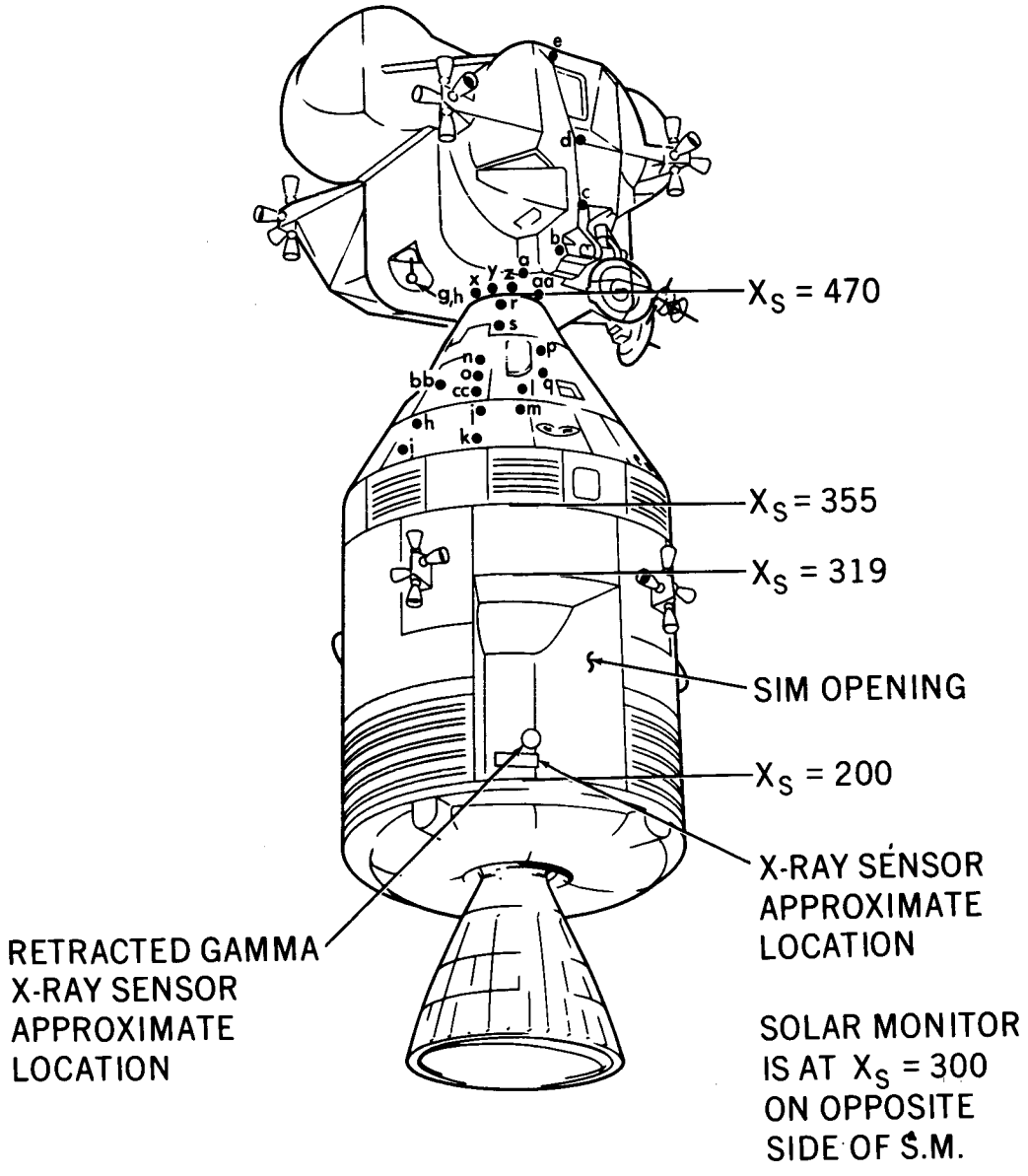

Figure 3. Relative Positions of Radioluminescent Discs and Instruments

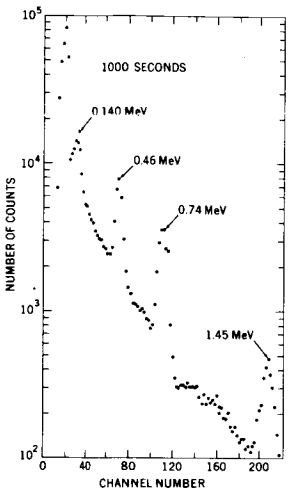

Figure 4. Pulse Height Spectrum of a 300 mc Pm-147 Source

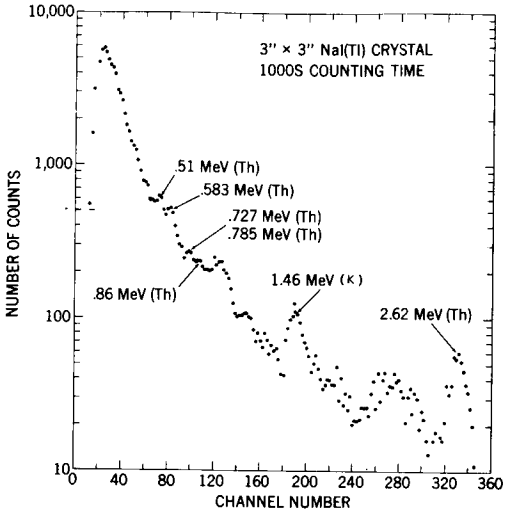

Figure 6. Pulse Height Spectrum at the Top of the SIM

When measurements around the SIM on the SM were carried out, the background appeared normal until added spectral lines were noticed near the top of the sector close to the CM. A spectrum taken on the middle plane level of the SIM is shown in Fig. 5. The K-40 line seen in this figure is the normal background. When the measurement was taken at the top of the SIM near the CM, characteristic lines of thorium were observed. These are shown in Fig. 6. It was later discovered that thoriated-magnesium solder was used in the CM and the thorium seen in the top of the sector is attributed to this source. Note that the difference in position of the K-40 line at 1.46 MeV seen in Figs. 5 and 6 is due to a change in gain between measurements.

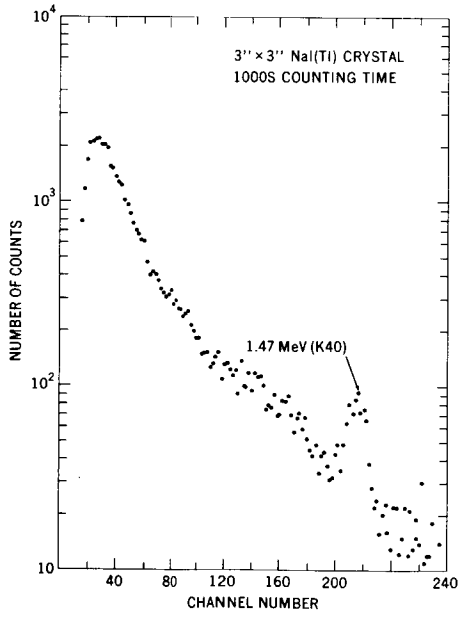

Figure 5. Pulse Height Spectrum at the Mid-Plane of the SIM

The next source of radiation interference observed in the survey was that due to the potassium in the three fuel cells. The spectrum obtained near the fuel cells is shown in Fig. 7 and has a magnitude of K-40 of about four times the normal background. The general configuration of the service module (SM) is shown in Fig. 8. Since the fuel cells are stowed in sector IV on the opposite side of the SM from the Gamma Ray Spectrometer in sector I, the spacecraft itself provides shielding from this source. In order to determine the magnitude of this shielding, a Co-60 source (E_γ = 1.17, 1.33 MeV) was used to simulate the K-40 γ source (E_γ = 1.46 MeV); the removal cross-section does not change greatly over this energy range. Measurements were made with the cobalt source in the position of the fuel cells stowed in the SM and the scintillation detector was placed in the stowed position of the gamma ray detector. The SM was in a large bay when the measurement was made. There was an empty bay with no SM present and the geometric configuration of source and detector was simulated in the empty bay. The comparison of the two spectra, i.e., with the spacecraft present and in the empty bay is shown in Fig. 9. From this figure one sees that the flux is decreased by an order of magnitude at the peak energy due to the shielding effect of the spacecraft.

The three fuel cells, each of which contains 10 kg of KOH electrolyte, are the dominant radiation source of K-40 (16μc) but there are several others. Not counting the batteries in the LM which will not affect the experiments, there are three re-entry and two pyro-batteries in the lower equipment bay of the CM as well as a larger LM-type battery in sector IV of the SM. These batteries together contain 3.6μc of K-40. Next, the Z-93 thermal control paint used on the environmental control system and electric power system thermal radiators which are widely distributed

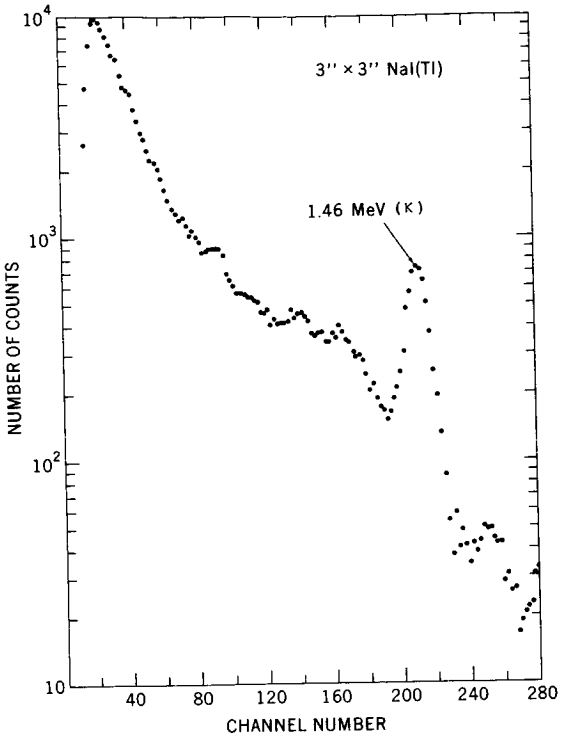

Figure 7. Pulse Height Spectrum near the SM Fuel Cells

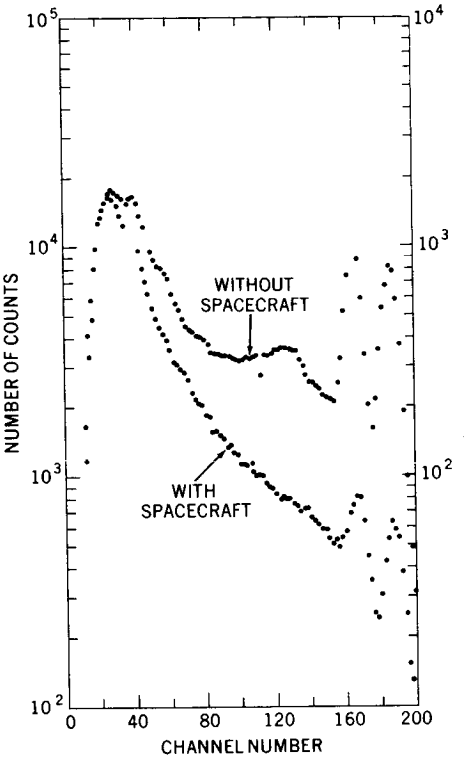

Figure 9. Spacecraft Shielding of the Fuel Cell Radiation Source

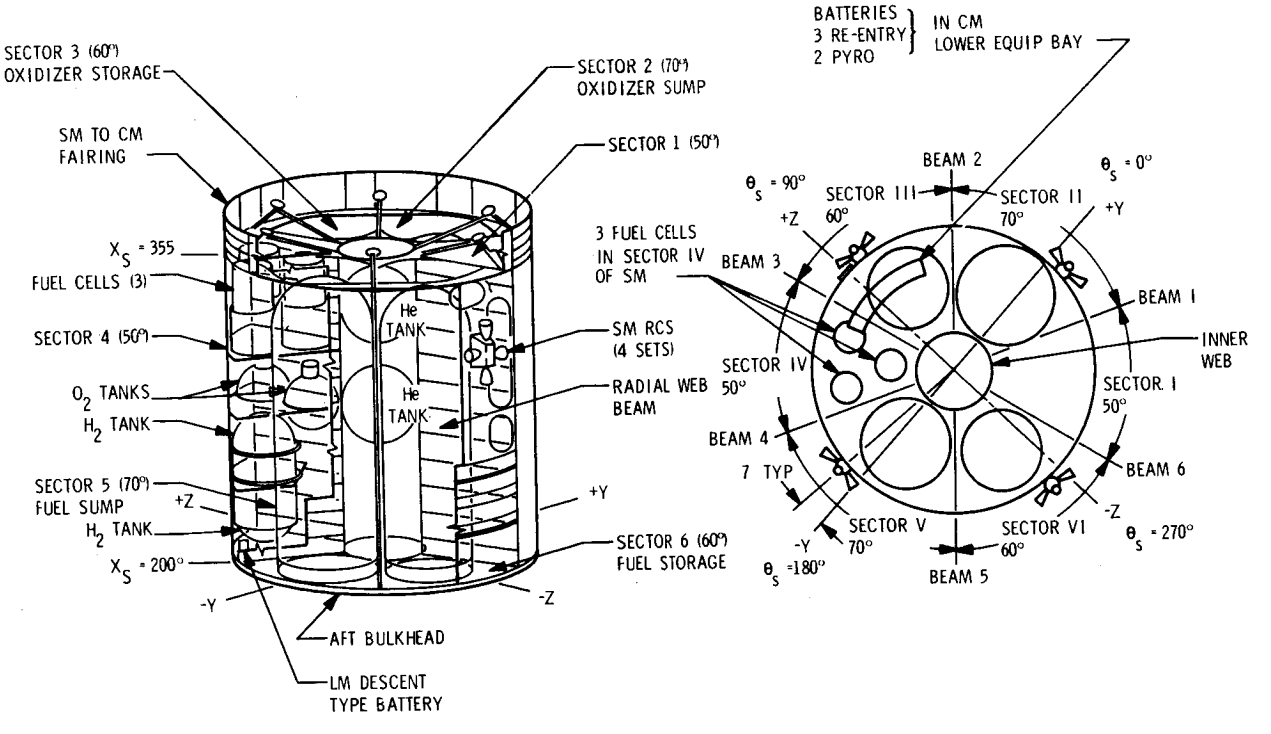

Figure 8. Apollo SM General Configuration

around the SM, contains a high percentage of potassium with a total activity calculated at 0.7μc of K-40. Summing the quantities of potassium in the fuel cells, batteries and thermal paint, the flux will exceed the 10 hr 3 sigma tolerance level at the boom extended position by a factor of 2-3 when spacecraft shielding is not considered; shielding will reduce it below the tolerance level.

One other source of potassium is worth mentioning. It was discovered relatively recently that the mass spectrometer will use a thermal control paint (MS-74) containing about 25% potassium. The Mass Spectrometer also extends out from the SIM on a boom (Fig. 1) but at a distance from the Gamma Ray Spectrometer which makes the contribution of this source negligible.

A non-negligible source is the 53 gm thorium contained in the lens of the Mapping Camera for the purpose of providing the proper index of refraction. A special survey of one such lens was made and a typical spectrum is shown in Fig. 10. This source has spectral lines which are identical to those of interest from the lunar surface. The expected flux is several times the 3 sigma tolerance value, depending in part on the degree of radioactive equilibrium reached by the daughter products. No natural spacecraft shielding is available in this case; the lens looks directly at the Gamma Ray Spectrometer when the latter is deployed. Accordingly, a tungsten shield will be provided to reduce the radiation level from the lens. This shield will cover the lens during most of the time that gamma ray spectra are being obtained.

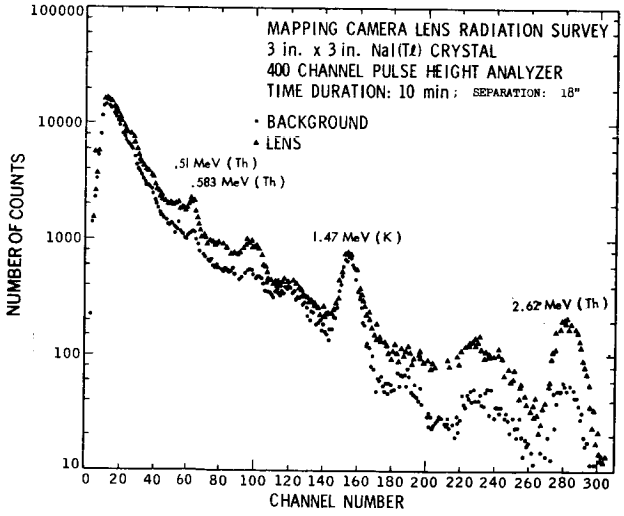

Figure 10. Pulse Height Spectrum of the Mapping Camera Lens

It remains to consider the strongest source of all on Apollo, the SNAP-27 radioisotopic thermoelectric generator which is fueled by 40,000 curies of Pu-238 and powers the ALSEP package on the lunar surface. The orbital experiment phase will not begin until after the LM has descended to the lunar surface, but because of a recent change in the event-time sequence, thermal considerations require that the instrument be powered sometime before separation of the LM. This gave rise to concern that the resultant count rate of the Gamma Ray Spectrometer might be high enough to damage the instrument. Flux measurements of Apollo 14's SNAP-fuel element have been applied to the SNAP-Gamma Ray Spectrometer spacecraft geometry to yield a maximum expected rate of 2 Kc, well within the limit of safety. Analogous data on the fuel elements for Apollo 15 and 16 will be obtained before launch for confirmation.

The remaining sources listed in Table 1 are either low in energy or intensity and pose no problem for either spectrometer.

Conclusions

The following observations may be made:

1. Distance is extremely effective in reducing source interference. Use of the inverse square relationship plus shielding allows radiation-sensitive experiments to be performed on the same spacecraft with relatively strong sources. This procedure will prove most effective for the Gamma Ray Spectrometer.

2. Early knowledge of the sources present and their characteristics can minimize the problems of radiation interference by pointing the way to early solutions; e.g., removal, alternate location or shielding.

3. A radiation source specification which defines tolerable limits of both line and continuum radiation and also lists materials to be avoided can reduce the quantity of radiation source materials used on a spacecraft. Such a specification is easier to prepare than to implement however.

4. Radiation surveys are useful in identifying sources and their characteristics. A survey of the entire CSM for Apollo 15 is scheduled.*

5. The mission profile has had a major effect on the radiation source situation in two respects; i.e., disposition of the LM and time of instrument turn-on. When such options exist and if they can be anticipated sufficiently far in advance, they should be considered in the design of the instrument and in the determination of the spacecraft-instrument configuration.

The authors are pleased to acknowledge the extensive contributions of Louis J. Barbieri and Gary Wengrow to these studies, the assistance of Richard L. Schmadebeck in performing some of the surveys and the many helpful discussions they have had with James R. Arnold.

* Note added in press: The radiation survey of the Apollo 15 CSM has revealed the fact that, contrary to our expectation, the thorium sources have not been removed from the base plate of the inertial guidance system. The base plate is 24"x24", and is mounted horizontally somewhat off axis in the direction away from the SIM. Set into the plate are a number of heat sinks made of thoriated magnesium, the combined intensity of which is presently estimated to be in the range of 30 microcuries. This is undoubtedly the source of the thorium lines seen in Figure 6. A solution to this problem is being sought.

REFERENCES

1. A. E. Metzger and J. R. Arnold, "Gamma Ray Spectroscopic Measurements of Mars", Applied Optics, Vol. 9, No. 6, June 1970.
2. A. P. Vinogradov, Yu. Surkov, G. M. Chernov, F. F. Kirnozov, G. B. Nazarkina, "Measurements of Gamma-Radiation of the Lunar Surface on the Space Station Luna-10", Geokhimiya, No. 8, Izd-vo "Nauka", 1966.
3. A. E. Metzger, E. C. Anderson, M. A. Van Dilla, and J. R. Arnold, "Detection of an Interstellar Flux of Gamma Rays", Nature 204, 766 (1964).
4. J. I. Vette, D. Gruber, J. L. Matteson, L. E. Peterson, Astrophys. J., Lett. 160, L161, 1970.
5. L. J. Barbieri, "J Missions: Nuclear Radiation Environment Due to Experiments and CSM 112", TDR 70-025, North American Rockwell Corporation, Space Division, April 1970.

A HIGH RESOLUTION SEMICONDUCTOR DETECTOR FOR APPLICATIONS IN SPACE †

Peter Alexander and Herman Shulman

Teledyne Isotopes ‡

Nuclear radiation detectors with volumes of ~1 cm^3 have been fabricated from single crystals of Germanium-Silicon alloy containing as much as 20 weight percent germanium. The properties of these detectors have been investigated and will be discussed. Tests reveal that the gamma ray photoelectric peak efficiency of an alloy detector with only 12 weight percent germanium is ~4 times that of a silicon detector of equal volume. The alloy detector will operate with excellent energy resolution at -75°C. Operation at room temperature appears to be a good possibility. Storage for long periods at room temperature does not seem to adversely affect these devices. The results of preliminary radiation damage experiments suggest that the alloy detectors possess a radiation damage resistance far greater than that of silicon.

INTRODUCTION

The superior energy resolution obtainable with semiconductor nuclear radiation detectors has made their use widespread in all fields involving gamma ray and charged-particle spectroscopy. For the purpose of nuclear spectroscopy in space, it is desirable to have a detecting device which will yield the best (lowest) energy resolution, the highest detection efficiency, and the fewest operating difficulties. In addition this detector should be light weight, rugged in construction, use little power, be able to operate at temperatures above -195°C, have room temperature storage capability, and the ability to withstand considerable damage from the high radiation zones in space. Unfortunately at present these attributes are not all combined in any one type of detector. Sodium Iodide is relatively efficient as a gamma ray detector. However, due to the relatively poor resolution of sodium iodide it becomes extremely difficult to extract accurate energy and intensity information from spectra containing more than a few lines. Conversely semiconductor detector spectra containing hundreds of lines can be accurately analyzed for energy and intensity information. The most commonly used semiconductor detector materials are germanium and silicon.

The photoelectric interaction probability for a gamma ray is roughly proportional to the fifth power of the atomic number (Z) of the stopping material. Thus, because of its low Z(14), silicon is very poor relative to germanium (Z=32), for detection of gamma rays. Silicon detectors do have an advantage over germanium detectors in that they can be operated and stored at room temperature. This room temperature operating ability stems from the larger band gap possessed by silicon (1.2 eV). The narrower band gap of germanium (0.7 eV) requires that the detector be cooled to the point at which thermal generation of carriers across the gap does not interfere with detection of the ionizing radiation. The lithium, used to compensate the impurities present in the detector, does not precipitate in silicon at room temperature as it does

†This work was supported in part by the Advanced Research Projects Agency under Contract DASA-01-70C-0040 with the Defense Atomic Support Agency and also by the National Aeronautics and Space Administration under Contract NAS 1-6654.

‡ 50 Van Buren Avenue, Westwood, New Jersey

in germanium. Such precipitation renders the detector useless.

The ideal detector for space applications would combine the high resolution, good gamma ray efficiency and large detector volume available in a germanium detector with the desirable properties of a silicon detector. These properties include room temperature operating capability, and prolonged room temperature storage capability. Such an ideal detector can, in principle, be obtained by judiciously alloying germanium and silicon in a large single crystal. Figure 1, taken from the work of Braunstein et al[1], gives the dependence of the germanium-silicon alloy band gap on the percentage of the constituents present. From this figure it becomes apparent that a silicon content of at least 15 atomic percent should be present in the alloy. At this silicon concentration the crystal has a band gap almost midway between that of germanium and silicon but has retained a large germanium concentration which will yield a high gamma ray efficiency. It may be necessary to push the silicon concentration still higher in order to produce a wider band gap and thereby permit the detector fabricated from this material to operate at more elevated temperatures.

In pure silicon as in pure germanium both interstitials and vacancies are sufficently mobile to interact with dopants and other defects so as to produce stable secondary complexes. Removal of these radiation induced complexes by annealing requires a temperature so high as to destroy the properties of the germanium and silicon which enable it to function as a detector. In the germanium-silicon alloy, the formation of complexes will be hindered not only by the low vacancy-interstitial mobility but also by the thermal annealing which may be expected to proceed at reduced temperature. If the detector bias is maintained during the annealing cycle, the resulting lithium ion drift will tend to compensate both primary and secondary damage effects. Such an "in situ" cycling procedure should enable greatly extended detector operating lifetimes.

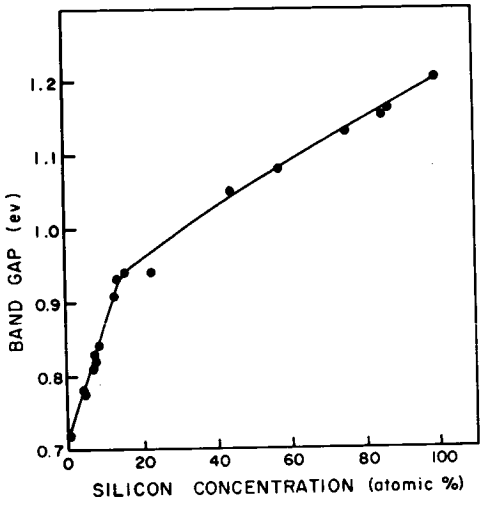

Figure 1. Variation of germanium silicon alloy band gap with silicon concentration[1].

GERMANIUM-SILICON ALLOY SINGLE CRYSTALS

It has been found that extremely high purity levels are requisite in silicon and germanium for fabrication of good detectors. The presence of such contaminants as copper, carbon or dissolved gases, particularly oxygen, in quantities as small as 1 contaminant atom in 10^9 silicon or germanium atoms is sufficient to degrade detector performance. This effect is rendered through trapping of the charge carriers and/or breakdown of the large electric field which must be applied across the detector in order to collect these carriers. The specifications

for germanium-silicon alloy crystals used for nuclear radiation detector fabrication are consistent with the crystal requirements necessary to produce good germanium or silicon detectors.

In this experiment measurements were made of those crystal parameters which most strongly influence radiation detector performance. These parameters include: minority carrier lifetime, trace oxygen content, homogeneity and degree of crystaline perfection, lithium drift mobility, and lithium diffusion constant. The measurements which define the last two quantities are detailed below.

The rate at which lithium can be drifted into germanium-silicon alloy under the influence of an applied electric field was studied, in a sample containing 10% Ge - 90% Si, as a function of temperature in the range 100°C to 160°C. The lithium drift rate is an important quantity in that it reveals how deeply a germanium-silicon alloy slice may be lithium compensated in a given time period. The drift depth measurements were performed by vacuum evaporating lithium onto the face of a germanium-silicon alloy slice, then heating at 400°C for 10 minutes in an argon atmosphere furnace, and then drifting in a silicone fluid medium maintained at the desired temperature. The progress of the n-i and i-p juntions were monitored by the copper stain technique. The change in depth of the intrinsic region was followed at a given temperature for about 12 days with a fixed applied reverse bias of 75v. Intrinsic depth versus drift time curves as measured for this alloy sample are plotted in Figure 2 for temperatures of 120°C, 140°C and 150°C. Comparison drift curves for germanium and silicon are also presented. It may be observed that the germanium-silicon alloy drifts considerably more slowly than either germanium or silicon.

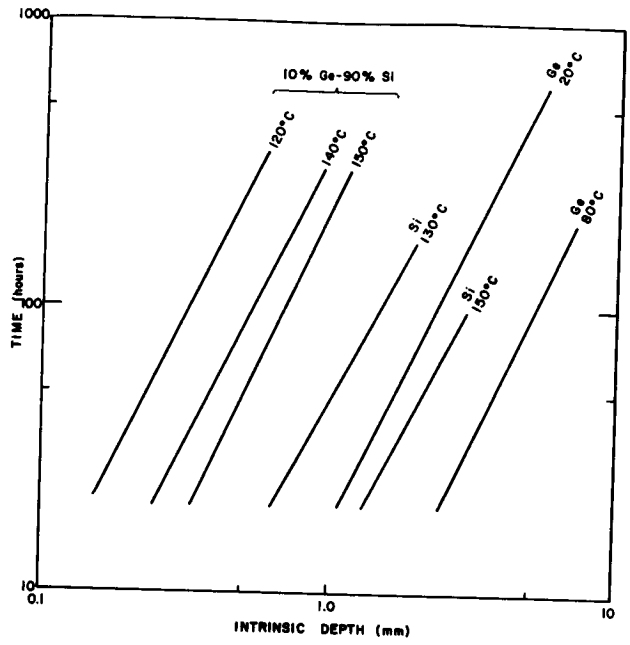

Figure 2. Lithium drift depth in germanium-silicon alloy, containing 10% Ge - 90% Si, as a function of time at various temperatures. The bias applied across the detector was 75 volts. Also plotted are comparable curves for germanium and silicon.

In order to make good semiconductor diodes it is necessary to diffuse lithium into the material to just the proper depth. If lithium is diffused too deeply, a thick "dead layer" results on the face of the detector. If lithium is not diffused deeply enough, oxidation and surface preparation will remove the lithium before it can be drifted into the material. Although the germanium-silicon alloy under study is silicon-rich, it is not at all obvious that the diffusion rate of the alloy will be expressible as some linear combination of the diffusion constants for germanium and silicon. Therefore, the diffusion of lithium in the germanium-silicon alloy is being studied as a function of temperature and Ge/Si ratio. In this study lithiated slices of both silicon and germanium-silicon alloy were heated to a preselected temperature. The slices were removed from the oven and the diffusion depth was determined by the copper stain technique.

From this data plus a knowledge of the surface lithium concentration and the acceptor dopant level, the lithium diffusion coefficient could be calculated for a particular diffusion temperature and Ge/Si ratio.

The results of the measurements described above are shown in Figure 3 where D is plotted versus the reciprocal of the absolute temperatures for pure silicon specimens, for samples from an ingot containing 10% germanium by weight, and for samples from an ingot with 16% germanium by weight. The solid line shown is based on Pell's empirical equation[2] for the diffusion constant of lithium in silicon. The data from the measurements on the alloy samples and the silicon samples agree with Pell's estimates above 500°K. Below this temperature there is departure of the data for the alloy samples from both Pell's curve and from the data for silicon. This deviation is consistent with an oxygen concentration of 10^{17} atoms/cm^3 in the base alloy. The effects of this oxygen on the diffusion constant become more pronounced as the diffusion temperature is lowered.

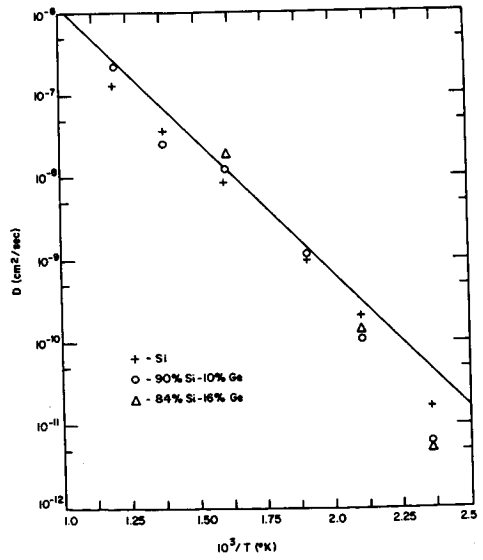

Figure 3. Diffusion constant for lithium in germanium-silicon alloy and in silicon at various temperatures. Also shown as a solid line is Pell's relation for silicon[2].

BEHAVIOR OF Ge-Si ALLOY DETECTORS

A number of gamma ray and charged particle detectors have been fabricated from germanium-silicon alloy. Due to the very low drift rate of lithium in the germanium-silicon alloy ingots, most detectors had active depths ranging from 200 to 800 μ. This depth corresponds to about 1 month of drift time and yields maximum active volumes of ~1 cm^3.

The alloy detectors deliver good gamma ray resolution at temperatures up to -75°C. At room temperature the resolution is greatly degraded due to surface leakage. A grooved or guard ring detector configuration would substantially improve this response. Typical alloy detector gamma ray resolution values range from 2 to 5 keV for ^{57}Co gamma rays. Comparable resolution is obtained using germanium detectors of the same size. At 356 keV the photopeak gamma ray efficiency of an alloy detector containing 12% Ge - 88% Si is 4 times that of a silicon detector of the same size.

Several alloy detectors have been stored for periods of up to 3 months at room temperature while exposed to the room atmosphere. In all cases it was possible to operate these devices, when they were coooled back down to -175°C, with no loss in resolution or degradation of reverse bias characteristics.

As described in reference 3, germanium-silicon alloy detectors have also been used for detection of alpha particles yielding extremely good spectral energy resolution. Application of a thin gold entrance window on the p-face of the diode yields an ^{241}Am spectrum such as that presented in Figure 4.

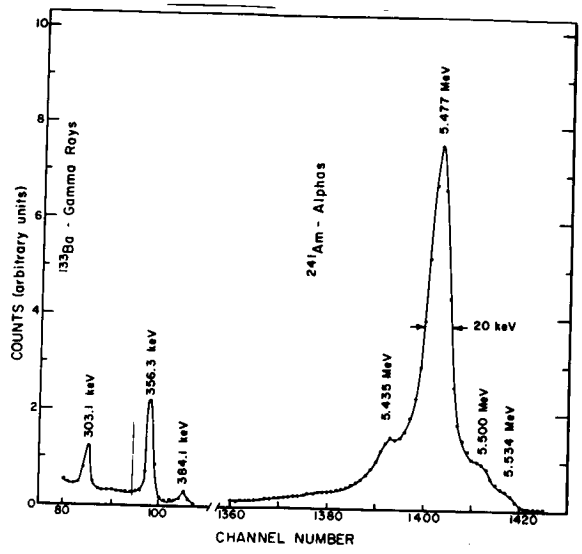

Figure 4. ^{241}Am alpha spectrum as observed with a germanium-silicon alloy detector. The ^{133}Ba gamma ray spectrum observed at the same time is used for energy calibration purposes.

RADIATION DAMAGE MEASUREMENTS

The germanium-silicon alloy detectors described in the preceding section have been employed to study the effects of gamma ray damage on detector performance. Exposure to the gamma rays was accomplished in the 3000 Curie ^{60}Co hot cell facility of the Rutgers University Reactor. Four lithium-drifted diodes were exposed to gamma radiation. Two of the diodes had been fabricated from 1000 ohm-cm boron-doped silicon, while the remaining two diodes were made from 300 ohm-cm gallium-and-boron-doped germanium-silicon alloy (88% Si, 12% Ge by weight). The four diodes were mounted on a copper plate in the vacuum space of a liquid nitrogen cooled cryostat. The diodes were maintained under vacuum and at liquid nitrogen temperature throughout the irradiation and during the post-radiation measuring period. The gamma flux to which the diodes were exposed was 1.3×10^{15} photons/cm^2 per hour, which is equivalent to a dose rate of 217 rads (Si)/sec. They were exposed for an accumulated period of 1,006 minutes, to a total fluence of 2.14×10^{16} photons/cm^2.

During the course of the above experiment measurements were periodically made of the detector: reverse-bias leakage current, reverse-bias photocurrent induced by the ^{60}Co gamma ray fluence, and resolution. The resolution of the silicon detectors was observed to degrade many times faster than the alloy detector resolution. The ^{57}Co gamma ray spectra observed with one of the germanium-silicon detectors both before and after exposure to 2×10^{16} photons/cm^2 is presented in Figure 5. A similar set of spectra for one of the silicon detectors is presented in Figure 6. The resolution of both of the silicon detectors was greatly degraded by the radiation damage while the alloy detectors were hardly affected. Post-irradiation annealing at several temperatures up to 273°K, completely restored the properties of the two alloy detectors while similar annealing caused a monotonic deterioration in the resolution of the silicon detectors. The resolution of the silicon detectors did not fully recover even after 24-hour lithium-ion drift cycle at

360°K. The reverse bias current measurements are also consistent with the above data. Additional details of these experiments will be presented in another publication.

CONCLUSION

A number of points concerning the properties of germanium-silicon alloy remain to be clarified by future experiments. Some conclusions concerning this material, based on the experiments described in this paper, are listed below.

1. Germanium-silicon alloy single crystals of detector grade can be produced with as much as 20 weight percent germanium.
2. Lithium can be drifted into these crystals to compensate them to reasonable depths.
3. Detectors of volumes ~1 cm^3 have been achieved and these yielded gamma ray resolution comparable to that of a silicon detector of similar size.
4. Alloy detectors have been found to possess a gamma ray efficiency significantly better than that of silicon detectors of comparable volume.
5. The alloy detectors work quite well at -75°C and with geometric alterations will probably function at room temperature.
6. Long term room temperature storage does not appear to harm the alloy detector.
7. The alloy detector appears to evidence a gamma ray radiation damage resistance greatly exceeding that of silicon (and implicitly germanium).
8. Annealing the alloy detector at temperatures below 300°K appears to remove the effects of the radiation damage. In silicon similar thermal treatment of gamma irradiated detectors is found to cause additional degradation.

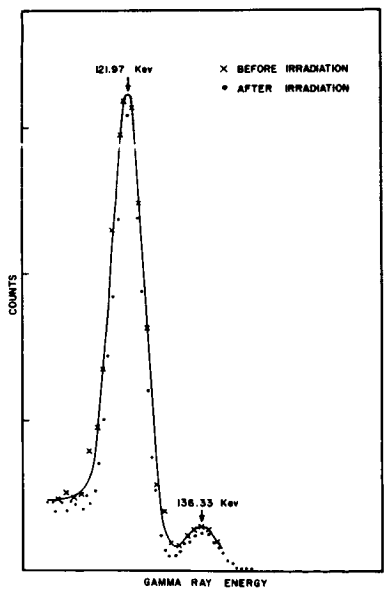

Figure 5. ^{57}Co gamma ray spectra taken with an alloy diode before and after irradiation.

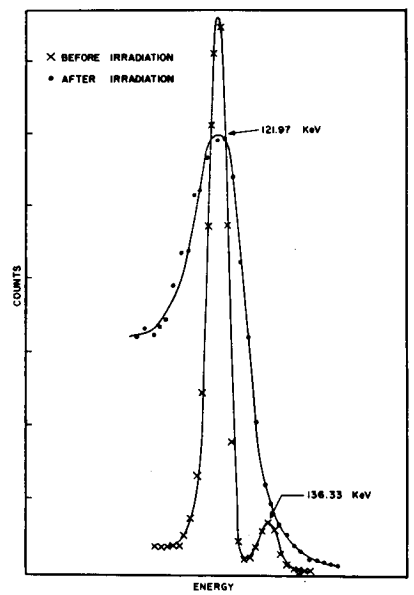

Figure 6. ^{57}Co gamma ray spectra taken with a silicon detector before and after irradiation.

REFERENCES

1. Braunstein, R; Moore, A.R.; and Herman, F: Instrinsic Optical Absorption in Ge-Si alloys, Physical Review, 109, 1958, p. 695.
2. Pell, E.M., Diffusion of Li in Si at High Temperature and the Isotope Effects, Physical Review, 119, 1960, p. 1014.
3. Alexander, P. and Shulman, H.; A Semiconductor Material Research Program., NASA-CR111793.

Radiation Effects on Science Instruments in Grand Tour Type Missions*

Richard H. Parker
Jet Propulsion Laboratory
California Institute of Technology

The extent of the radiation effects problem is delineated, along with the status of protective designs for 15 representative science instruments. Designs for protecting science instruments from radiation damage is discussed for the various instruments to be employed in the Grand Tour type missions. A literature search effort has been undertaken to collect science instrument components damage/interference effects data on the various sensitive components such as Si detectors, vidicon tubes, etc. A small experimental effort is underway to provide verification of the radiation effects predictions.

The various experimenters whose instruments are used as models have made available some of their own radiation effects experience for this study.

In response to the rare opportunity afforded by the multiplanet flyby or "Grand Tour" missions, the Jet Propulsion Laboratory has been examining mission problems and developing a practical design for an outer-planets spacecraft. The evolving spacecraft, TOPS (Thermoelectric Outer Planets Spacecraft), will be exposed to several new hazards. Two of the more difficult hazards are the requirement for long component life due to the mission duration of approximately ten years, and the subjection to Jupiter's severe trapped radiation environment. The total radiation environment includes gamma, neutron, proton, and electron fluxes. There are two dominant sources of the radiation, the Jovian trapped charged particles and the neutrons and gammas from the radioisotope thermoelectric generators (RTG). The trapped charged particles have been indirectly observed around the planet Jupiter and possibly radiation belts surround other planets. Jupiter must be used for a gravitational assist in Grand Tour type missions and, thus, the trajectory is fixed for any particular mission. The RTG is a nuclear electrical power supply which emits both gamma and neutron fluxes. It is needed for outer planets missions, because solar panel electrical power requires more kg/W than RTG power beyond ~3 AU.

Figure 1 shows the current TOPS baseline configuration (for perspective, this configuration has a 4.3 m reflector). The experiment requirements have been considered during the preliminary system design phase so that the design of the spacecraft itself permits meaningful science experiments. Configurations are under study which may further improve RTG radiation shielding of the science area. Table 1 shows representative science instruments used in the design study. Although the specific instruments for the actual mission payload have not yet been selected, the instruments listed in Table 1 form a set which adequately represents typical instrument integration problems. Table 2 is a list of radiation sensitive components being considered in this study.

The radiation problems are not equally severe. Gamma interference and proton damage are the two most critical problems and therefore will be considered in detail. The neutron fluence for the mission is expected to be about $10^{10} n/cm^2$ in the science area for the 10 year mission (ref. 1), and although interference is expected, only slight damage may occur. For example, this fluence level may be somewhat degrading to currently available components such as Si(Li) detectors in that a few percent resolution loss may occur. But this should not cause severe problems to flight instruments which generally do not require extreme resolution. Electrons are expected to contribute damage, but to a lesser degree than protons. Also, as J. Barengoltz (ref. 2) has shown, shielding would be beneficial for reducing electron damage, where as practical amounts of shielding may not adequately reduce proton damage. Thus, I will not consider electron or neutron effects.

Table 1. Representative instruments used in radiation effects study

Instrument	Principal experimenters	Institution (or mission)
Charged Particle Telescope	J. A. Simpson	(Pioneer F/G)
Cosmic Ray Detector	F. B. McDonald	(Pioneer F/G)
Imaging	TOPS	JPL
Infrared Multiple Radiometer	TOPS	JPL
Meteoroid Astronomy Detector	R. K. Soberman	(Pioneer F/G)
Micrometeoroid Detector	O. E. Berg W. H. Kinard	GSFC (Proposed for Pioneer F/G)
Plasma Probe	Wolfe Bame Bridge	(Pioneer F/G) LASL-(MVM) MIT-(MVM)
Plasma Wave	F. L. Scarf	(Proposed for Pioneer F/G)
Radio Astronomy Experiment	J. K. Alexander	(Proposed for Pioneer F/G)
Trapped Radiation Detector	J. A. Van Allen	(Pioneer F/G)
Trapped Radiation Instrument	R. W. Fillius	(Pioneer F/G)
Ultraviolet Photometer	D. Judge	(Pioneer F/G)
Vector Helium Magnetometer	E. J. Smith	(Pioneer F/G)
X-Ray Detector	K. A. Anderson G. Garmire	(Proposed for Pioneer F/G) CIT

*This paper presents progress of one phase of research carried out at the Jet Propulsion Laboratory, California Institute of Technology, under Contract No. NAS 7-100, sponsored by the National Aeronautics and Space Administration.

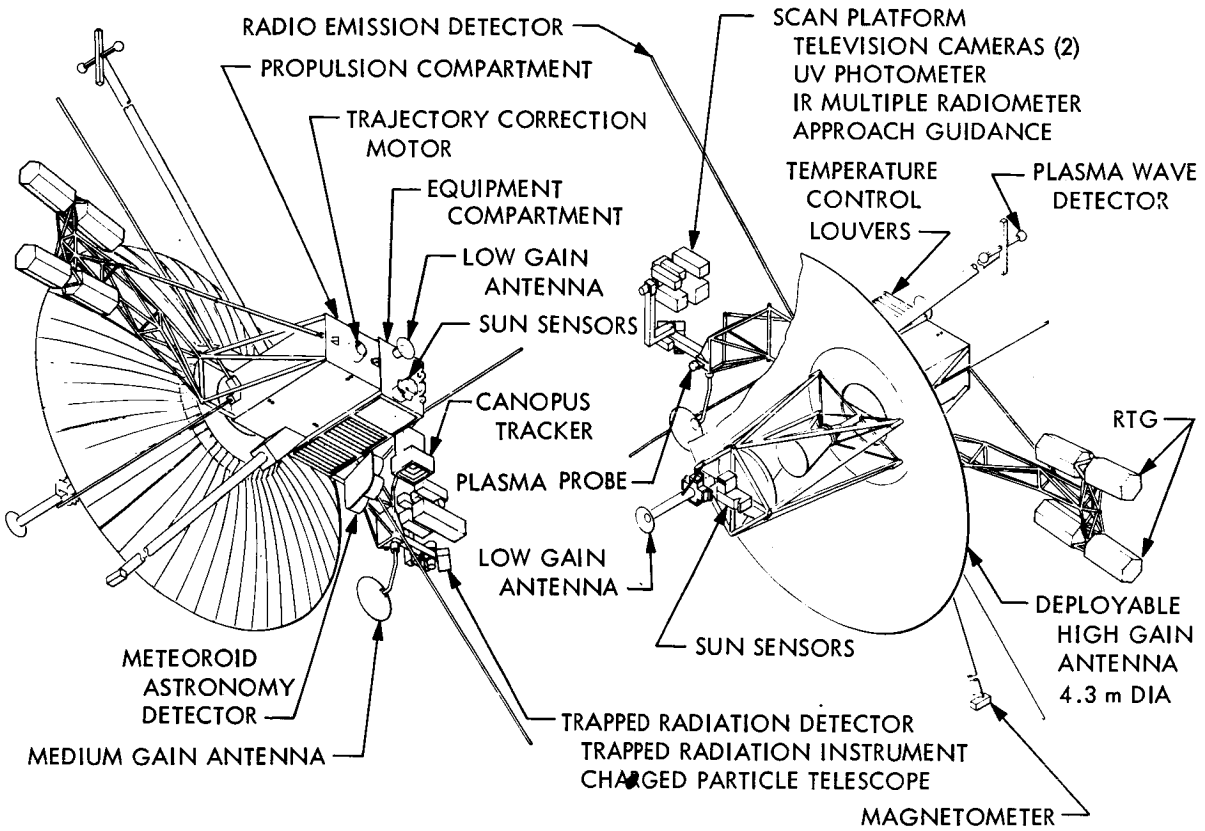

Figure 1. Thermoelectric Outer Planets Spacecraft, configuration 12L (with representative payload)

Table 2. Radiation sensitive components which limit instruments either from permanent damage or interference effects

Solid state detectors
Si surface barrier
Si(Li)
Ge(Li)
Scintillators
Na I (Tℓ)
Cs I (Na)
Plastics
Organics
GM tubes
Proportional counters
Photomultiplier tubes
Continuous channel multipliers
Vidicon tube
Emissive and optical materials for
UV (e.g., S_1O_2 etc., overlap with visible detector materials)
Visible (e.g., S20, etc., ···, > 10 types)
IR (e.g., HgCdTe; CdS, MgO, ···, > 20 types)
Electronics

Melvin Reier (ref. 3) has detailed the gamma spectrum expected from the RTG and the spectral variations, with time, impurities, and orientation, are well known. Reference 1 also establishes the design restraint gamma dose of about 300 rad in the science area for the mission. Although this dose level will not cause damage problems, interference from approximately 1600 γ/cm^2-sec of a few keV to a few MeV must be considered as a time dependent background problem. For this reason in-flight calibration is highly important to many instruments.

The University of Chicago original Charged Particle Telescope (CPT) design for Pioneer F/G, which is shown in Fig. 2, is considered to provide a typical evaluation of interference problems. The CPT instrument uses a cylindrical anticoincidence scintillator around a six element telescope. The RTG contribution to the background under various coincidence requirements is shown for both the Pioneer F/G situation (ref. 4) and the unshielded TOPS situation. By "unshielded" it is meant that the shielding effects of the electronics bay and propulsion bay are not included. Davis and Koprowski (ref. 5) have analytically shown that about one order of magnitude

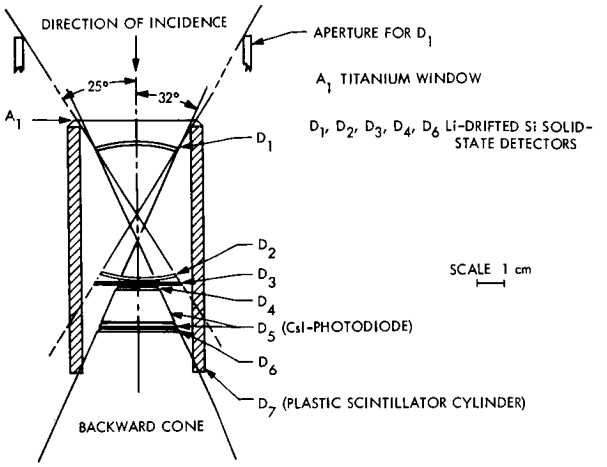

Figure 2. Charged Particle Telescope, proposed for the Pioneer F/G missions (This is a cylindrical scintillator shield around a six-element telescope.)

attenuation may be available in some areas on the spacecraft due to this shielding. This may allow instruments similar to the Pioneer F/G CPT and the Cosmic Ray Detector, to be located in regions where no additional passive shielding is required. In fact, experiment instruments as sensitive as an x-ray detector using proportional counters may be accommodated. This is possible since the projected number-flux levels without additional shielding may be as low as a few γ/cm^2-sec, most of which will be above 500 keV (i.e., above the energy region of interest to x-ray investigations) and therefore easily discriminated electronically. Background levels which would be acceptable for an x-ray instrument observing Jupiter are less than 0.04 counts/cm^2-sec (ref. 6). Figure 3 clearly shows the radiation improvement of the TOPS design which indeed should be further improved both from the revised design and reduced uncertainties using more sophisticated analysis and experimental verification of gamma number-fluxes. Additional spacecraft shielding may be provided to some instruments to reduce the radiation fluences from the RTGs. Initial instrument shielding calculations were based on unidirectional gamma and neutron fluxes from the RTG with no shielding or scattering effects due to intervening spacecraft materials. This was done as a worst case calculation to see what the limit of radiation shielding requirements might be. With the exception of the x-ray instruments (not considered in the baseline), the total shadow shield weights were less than 5 kg of tungsten or depleted uranium. The largest baseline shield was given to the Charged Particle Telescope and weighed about 2.27 kg. As Davis showed, this approach of neglecting spacecraft shielding and scattering, is pessimistic for flux magnitude calculations, but, optimistic for flux direction calculations. This means that shields will be thinner, but, must cover larger areas than unshielded calculations predict.

Table 3 shows the preliminary shield weights which are spherical surfaces that are thinned in the antenna direction, built up in the RTG direction, and made integral parts of the instrument. The specific electronic shielding (e.g., pulse amplitude discrimination, coincidence requirements, etc.), are included as well as specific geometrical configurations and experimental objectives. The x-ray detector shield weight is extremely sensitive to changes in flux levels since such a large area (~180 cm^2) must be shielded. There is a possibility that an area may be sufficiently shielded by the spacecraft electronics bay to accommodate this type of instrument without additional shielding. However, conclusive data will require radiation mapping around a prototype spacecraft.

Although the RTG radiation problem is serious, it is greatly overshadowed by the highly uncertain natural Jovian radiation environment. Many studies have been undertaken in recent years to resolve the uncertainties in the Jovian trapped radiation. Unfortunately due to the lack of experimental verification, the proton models are still highly uncertain. This will not be resolved until after Pioneer F/G results are known. The Pioneer results will not be available in time to establish spacecraft design constraints and thus we are dependent on models alone.

Table 3. Preliminary shield weights*

Experiment	Acceptable RTG fluxes	Shield weight, kg	Experiment	Acceptable RTG fluxes	Shield weight, kg
CPT	8 γ/cm^2 sec (on D1 and D2) (1500 γ/cm^2-sec on scintillator shield) 150 n/cm^2-sec	1.1	PWD	0.1 Rads/hr 3000 n/cm^2-sec	0
			RA	0.1 Rads/hr 3000 n/cm^2-sec	0
IMR	15 γ/cm^2-sec 3000 n/cm^2-sec	0.7	TRD	45 γ/cm^2-sec 150 n/cm^2-sec	0
MAD	0.1 Rads/hr 3000 n/cm^2-sec	0	TRI	45 γ/cm^2-sec 150 n/cm^2-sec	0
MAG	0.1 Rads/hr 3000 n/cm^2-sec	0	TV	0.1 Rads/hr (55,000 γ/cm^2-sec) 300 n/cm^2-sec	0
MD	0.1 Rads/hr 3000 n/cm^2-sec	0	UVP	0.1 Rads/hr 3000 n/cm^2-sec	0
PP	15 counts/cm^2-sec 300 n/cm^2-sec	~1.0	XRD	2 γ/cm^2-sec 3 n/cm^2-sec	~13.6

*The shield weights include specific experiment geometries and electronics shielding. Underlined levels are for damage, the others are for interference.

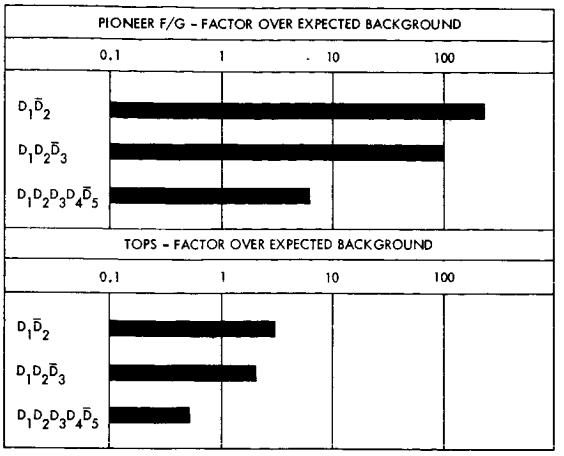

Figure 3. RTG gamma interference in the Charged Particle Telescope (the expected background is an estimate without any RTG radiation). All the detectors not indicated are in anticoincidence, e.g., $D_1\bar{D}_2 \equiv D_1\bar{D}_2\bar{D}_3\bar{D}_4\bar{D}_5\bar{D}_6\bar{D}_7$. The TOPS numbers do include the self-shielding of the spacecraft.

The best model in my opinion is the one developed by Neil Divine (ref. 7). Although, even this model has large uncertainties associated with it. Since the TOPS conservative design philosophy demands a design restraint model which includes the uncertainty and a safety margin, the design restraint levels for protons and electrons are quite severe. Table 4 shows both the electron and proton TOPS design restraint fluxes and fluences. The proton fluence levels are approximately four orders of magnitude above the nominal Divine model predictions for critical proton energies. Although the table includes particles from all sources such as the earth's Van Allen belts, solar wind, solar flares, and galactic cosmic radiation, essentially the source above 1 MeV for protons and 0.25 MeV for electrons is the Jovian trapped radiation prediction. J. Barengoltz (ref. 2) has detailed the design restraint model and what effect it will have on semiconductor devices.

In some science instruments electronics will be the sensitive components and the radiation effects on electronics obviously are inherent in all the instruments. In general, however, the damage tolerance is more restricted for science instruments and electronics which have delicate linear analog front ends as opposed to digital circuitry which in many cases can be over designed (ref. 8). Circuit design, to overcome this hazard, must be tailored to the individual instrument and this detailed work is not yet underway.

Figure 4 shows the effects on proton fluence of shielding on a Grand Tour trajectory. The weights of a sphere with radius equal to the shield thickness is shown as an indication of the weight involved. Obviously if fig. 4 represents the spectral shape even though shielding will reduce the total number fluence, the "softer" proton spectrum has more protons with energy below ~20 MeV than the unshielded spectrum. Protons in the energy region below ~20 MeV are considerably more damaging than the higher energy protons (ref. 2) and thus the shielded spectra are more hazardous than the unshielded for reasonable weight shields.

Table 4. Radiation design characteristics and restraints*

Radiation type	Energy interval (MeV unless otherwise noted)	Maximum flux (particles/ cm^2-sec)	Fluence (particles/ cm^2)
Proton	~3 keV	1.2×10^8	5×10^{15}
	1-3	3.7×10^8	5.7×10^9
	3-10	2.9×10^7	8.0×10^{10}
	10-30	3.8×10^6	9.6×10^{11}
	30-100	3.1×10^6	3.9×10^{12}
	100-300	2.4×10^7	1.6×10^{12}
	300-1000	9.1×10^7	6.1×10^9
	1000-3000	3.0×10^7	4.7×10^8
	3000-10000		2.0×10^8
	E >10000		9.9×10^7
Electron	0-0.25	4.3×10^9	8×10^{10}
	0.25-3	2.6×10^9	6.4×10^{10}
	3-10	1.2×10^8	5.1×10^{10}
	10-30	2.2×10^7	2.2×10^{11}
	30-100	3.2×10^7	3.2×10^{11}
	100-300	2.5×10^8	2.5×10^{10}

*These levels include all sources such as solar wind, GCR, solar flares and Van Allen belts. Levels above 1 MeV for protons and 0.25 MeV for electrons are essentially due to Jovian trapped radiation.

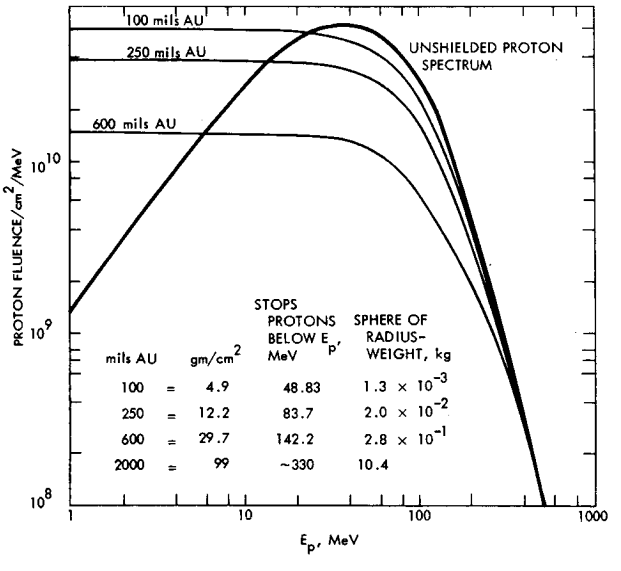

Figure 4. The effects on proton fluence of shielding on a Grand Tour trajectory (The heavy line shows the unshielded Jovian trapped proton fluence for a Grand Tour trajectory with a $3R_J$ periapsis.)

Proton damage will occur in science instruments exposed to the fluence levels required by the TOPS design restraints. This can be seen by comparing the design restraint levels to damage threshold levels for various components. Since many authors have investigated the various components, a bibliography would be excessively long. A typical example of published data however is illustrated by some work with the Si surface barrier detector. Singh and Rind (ref. 9) have obtained an empirical formula in the 5 to 40 MeV proton range. For a factor of 2 resolution degradation of the P^{210} peak width they find the fluence to be

$$\Phi = (2.94 \pm 1.20) \times 10^{10} \left(\frac{E}{E_d}\right)^{1/2} \exp\left(-7.3 \pm 2.3 \times 10^{-5} \rho\right)$$

where E is the proton energy, E_d is the energy loss in the sensitive regions (depletion region) of the detector and ρ is the original resistivity of the detector.

Thus for a 5000 μ detector irradiated by 30 MeV protons the fluence limits range from 2×10^{10} p/cm^2 to 2×10^{11} p/cm^2 for an original resistivity of ~20k Ω-cm.

Coleman, et al. (refs. 10 and 11) have looked at lower energy proton effects in the two separate experiments and together with reference 9 all of the critical energy region is covered for Si surface barrier detectors.

Figure 5 shows several proton damage thresholds for typical components. In considering these values, one must remember that experimental objectives and requirements can affect the damage threshold value of a particular component by as much as an order of magnitude. Thus, if the purpose of an experiment is to resolve two closely spaced lines, 5% or 10% resolution changes could seriously degrade the instrument. On the other hand, if one merely wants a number flux with crude energy resolution factors of 2 to 10 resolution, degradation may not be significant. For the Outer Planets Missions, the experiments are all designed for survey instruments to cover large ranges of information, but with only moderate resolution. Factors of two degradation in the resolution have been assumed as a limit for the baseline instruments.

It is apparent from Fig. 5 that most components will be affected. Presently available Ge(Li) detectors should not be considered as flightworthy on these missions unless in-flight redrifting is possible. The relatively new continuous channel multipliers are in a period of rapid development and recent indications are that at least two manufacturers expect to have significant lifetime increases available within a year. All instruments will need inflight calibration to assess the proton effects.

Experimental verification of radiation interference and, if possible, radiation damage will be quite important for science instruments as well as the entire spacecraft on Grand Tour type missions. Experiences in the Pioneer F/G radiation program have been quite enlightening and although problems still exist, one can realistically expect significant scientific results which will advance the understanding of the origin of our solar system.

The individual experimenter however must follow one or more of several options. If the instrument will survive due to lower actual levels (the probable situation) the experiment continues as planned. If his instrument is not "hard" enough to withstand the radiation, but significant data can be obtained before destruction, then he can simply monitor the instrument to destruction. A third alternative is to trade off resolution or some experimental objectives for more shielding, redundancy, harder but less desirable components in flight calibration, etc. A fourth option is to try to alter the mission such that the environment is less severe. A fifth option, and the most unpleasant, is to remove the particular experiment from the mission.

Designers of science instruments for outer planets Grand Tour missions, must consider radiation effects at all phases of the instrument development and the mission in order to be able to unfold pertinent data from radiation interference and/or radiation induced instrument degradation.

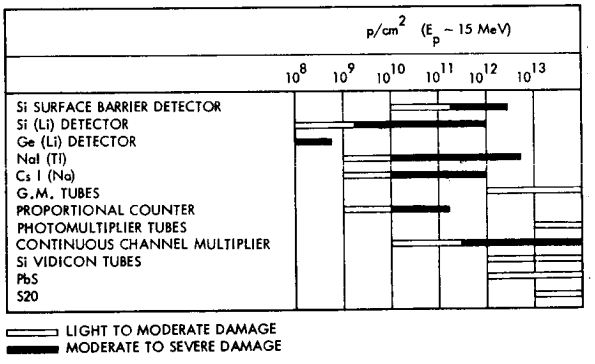

Figure 5. Science instruments' components typical damage levels (These damage levels depend strongly on the particular experimental requirements and objectives.)

References

1. Divita, E. L.: "Environmental Estimates," TOPS document 3-300, Jet Propulsion Laboratory, Pasadena, Calif., Jan. 1970.

2. Barengoltz, J.: "Jupiter Radiation Test Levels and Their Expected Impact on an Encounter Mission," (being presented at this conference).

3. Reier, M.: "The Design of a Source to Simulate the Gamma-Ray Spectrum Emitted by an RTG," (being presented at this conference).

4. O'Gallaher, J. J. and Tejero, S.: "Radiation Interference From a SNAP-27 Radioisotope Heat Source as Observed by University of Chicago Charged Particle Telescope for Pioneer F/G - Major Findings," University of Chicago, unpublished, Nov. 1969.

5. Davis, H. S. and Koprowdki, E. F.: "Nuclear Radiation Environment Analysis for Thermoelectric Outer Planets Spacecraft," (being presented at this conference).

6. Anderson, K. A. and Garmire, G.: private communications.

7. Divine, N.: "Jupiter Radiation Belt Engineering Model," (being presented at this conference).

8. Poll, R. A.: "Approaches to System Hardening," IEEE Transactions on Nuclear Science, NS-17, No. 6, p. 83, Dec. 1970.

9. Singh, J. J. and Rind, E.: "High Energy Proton Damage in Silicon Surface Barrier Detectors," NASA TN D-4528, May 1968.

10. Coleman, J. A., et al.: "Low Energy Protons Damage Effects in Silicon Surface Barrier Detectors," IEEE Transactions on Nuclear Science, NS-15, p. 482, Feb. 1968.

11. Coleman, J. A., et al.: "Effects of Damage by 0.8 MeV to 5.0 MeV Protons in Silicon Surface Barrier Detectors," IEEE Transactions on Nuclear Science, NS-15, p. 363, June 1968.

RADIATION NOISE IN A HIGH SENSITIVITY STAR SENSOR

J. B. Parkinson and E. Gordon

Aerojet ElectroSystems Company
Azusa, California 91702

PRA AESC SAMSO 2 March 1971

Abstract

An extremely accurate attitude determination has been developed by Aerojet ElectroSystems Company for space applications. This system uses a high sensitivity star sensor in which the photo multiplier tube is subject to noise generated by space radiations. The space radiation induced noise arises from trapped electrons, solar protons and other ionizing radiations, as well as from dim star background. The individual noise components have been successfully simulated for pre-flight evaluation of the star sensor performance.

The steady trapped electron and the intermittent solar proton environments for a high altitude orbit are related to solar activity. The solar activity and hence the electron and proton environments are predicted through the end of the twentieth century. The available data for the response of the phototube to proton, electron, gamma ray, and bremsstrahlung radiations are reviewed and new experimental data is presented. Prompt and delayed pulses from the faceplate/photocathode and contributions from the dynodes are isolated, and pulse height distributions are given for each.

The predicted electron and proton environments are then combined with phototube response. The average noise due to the relatively steady electron environment is of the order of 10^4 pulses per second compared with 2×10^5 pulses per second for the signal from a single 4.6 magnitude star. For a typical worst solar proton event, the noise will be 10^5 to 10^6 pulses per second, which is comparable to the signal from a nominal 4.6 magnitude star. This noise will typically last about one day. The model for the dim star background averages 3×10^4 pulses per second but varies widely.

A simulation was developed which represents the characteristics of the effect of radiations on the star sensor, including the non-stationarity of the backgrounds.

Introduction

Aerojet ElectroSystems Company has developed a high accuracy attitude determination system for space applications. The system contains a high sensitivity star sensor subject to space radiations. The object of this study is the prediction of the effects of those radiations.

Star Sensor Description

The optical portion of the star sensor collects light from stars and focuses it on the surface of a reticle. When a star image falls on a slit in the reticle, the light from that star can reach the photocathode of an EMR 541E-01 photomultiplier.

The star sensor electronics were designed for photon counting. The counting method eliminates the effects of stochastic variations in anode pulse amplitudes, i.e., there is one count for each cathode photoelectron detected. The circuitry which detects anode pulses outputs a normalized 50 nanosecond pulse for each anode pulse detected. These output pulses are counted throughout a 140 microsecond count cycle. The count value accumulated in each count cycle is transmitted to the ground for processing. The center of the star image requires about 230 microseconds to traverse the slit, so the time at which the center of the image is at the center of a slit can be determined from the count values.

When several photons reach the photocathode simultaneously, their anode pulses overlap, and there is only one normalized pulse for counting purposes. Thus when a high energy electron or proton causes the simultaneous emission of many protons, the star sensor electronics normally outputs only one normalized pulse. However, delayed photon emissions from an incident electron or proton result in several output pulses.

The counts from a star dimmer than seventh magnitude are comparable to the stochastic variations in the total background signal and such stars cannot be detected. The average contribution of stars dimmer than 4.6 magnitude is expected to be 4.2 counts per count cycle although it is much higher in the galactic plane.

Electron and Proton Environments

The trapped electron and solar proton environments are both capable of generating noise in star sensors. Both environments are affected by solar activity.

The detailed relation between solar eruptions and the solar proton and trapped electron environments is very complex, and we are not currently able to predict satisfactorily the specific causitive solar eruptions. However, estimates of the expected electron and proton fluxes can be related to expected smoothed sunspot numbers.

The expected smoothed sunspot numbers are represented by

$$\overline{R} \sim R_o + \Delta R \sin^2 \left[\pi \left(\frac{t}{10.5\,\mathrm{yr}} \right)^{3/4} \right] \qquad (1)$$

where

R_o is the expected minimum R (typically 2-10)

ΔR is the expected span of R (typically 50-200)

t is the time from solar minimum (years)

Equation 1 predicts a rise up to 6 months prematurely but is otherwise a good representation of expectancy.

The dates of certain minima and predicted minima (Reference 1) are

Beginning cycle	18	February 1944
	19	April 1954
	20	October 1964
	21	December 1974
	22	September 1985
	23	January 1997

For the parameters in Equation 1,

Cycle No.	R_o	ΔR	Estimated 6-year Mean of R Near Solar Maximum
19	6	195	150
20	8	103	85
Average	5	100	79

Cycle 21 will likely be close to average. Cycles 22 and 23 may be below average, though it is too early to predict with any confidence. For predicting cycles beyond #20, the average values can be used.

For a high altitude orbit, solar proton events may typically occur during the order of 4% a year near solar maximum. Most of the time energetic solar protons will not be encountered. The expected frequency of solar proton events larger than a given ϕ_{max} (proton/cm^2 sec) may be taken as

$$F\left(>E,\ \geq \phi_{max}\right) \sim \frac{700\ \text{proton/cm}^2\,\text{sec}}{\phi_{max}} \left(\frac{\overline{R}}{100}\right)^2 \left(\frac{100\ \text{Mev}}{E}\right)^{3/2} \qquad (2)$$

where

$\overline{R}$ is the smoothed sunspot number

E is proton energy (Mev)

F is the expected number of events per year.

For protons with energies around 50 Mev, solar proton events will generally last from 0.5 to 3 days, with one day being typical. Lower energy protons often arrive later and last for a longer total time. Duration expectancy may be scaled with $\sqrt{E}$. Total proton fluence for all events in a given period of time may be expected to be 2 or 3 times that from the expected single largest event during that period of time.

Equation 2 represents a satisfactory correlation, based on available data from Cycles 19 and 20. However, at energies less than 30 Mev, it tends to overpredict. It also tends to overpredict the number of smaller proton events. Recent data may be conveniently found in the issues of Reference 2.

For the trapped electron environment, the following model will be taken as representative of high altitude equatorial orbits:

$$\phi\left(>E\right) \sim \frac{1 \times 10^7}{\overline{R}/100}\, e^{-\frac{E}{0.21}} + 2 \times 10^6 \left(\frac{\overline{R}}{100}\right)^2 e^{-\frac{E}{0.50}} \ \frac{\text{electron}}{\text{cm}^2\,\text{sec}} \qquad (3)$$

where

R is the smoothed sunspot number

E is electron energy (mev)

A contribution to the electron flux below 0.1 Mev has been neglected.

Equation 3 represents the mean rate averaged over one day. The diurnal extremes are typically a factor of 2 higher at 0830 local time and a factor of 5 lower at 2400 local time.

Primary cosmic ray fluxes will generally range from 4 to 9 particle/cm^2 sec, varying inversely with solar activity. They may be further depressed during solar proton events. The average energy is about 3 Bev.

Photomultiplier Irradiation Results

The phenomenon of ionizing radiation interacting with a vacuum phototube device (e.g., photomultiplier) is believed to occur as follows: (1) a prompt pulse of 1 to several cathode photoelectrons equivalent followed by (2) a train of single photoelectron pulses with the rate of occurrence dying out with time (References 3 and 4). Pulse heights for the prompt pulse and also total pulses per interaction are shown in Table I, as deduced by various investigators for several vacuum phototubes and kinds of ionizing radiation.*

The prompt pulse is believed caused by Cerenkov radiation in the glass faceplate, while the delayed pulse train is thought to be caused by excitations in the faceplate and subsequent decays with emission of optical quanta. Dynode pulses are relatively few in proportion, being less than 0.1% of the total for electrons, bremsstrahlung, and gammas and likely not greater than 0.1% for protons. For very large pulse sizes (above perhaps 20 photoelectrons equivalent) the dynode pulses dominate. However, for photon counting star sensors, the dynode pulses can be neglected.

Aerojet, in cooperation with others, has performed several experiments to measure the pulse height distributions from the photocathode and dynodes of photomultiplier tubes, due to electron, bremsstrahlung, and proton radiations.** To obtain total radiation information, a photomultiplier tube may be used directly. The EMR 541E-01, with trialkali photocathode on 7056 glass (approximately S-20 response) and copper-beryllium venetian blind dynodes, is used in the star sensor. However, to separate photocathode and dynode effects, it was necessary to find a device with large separation of photocathode from the dynodes. An ITT S-412 image dissector tube, trialkali photocathode on 7056 glass (approximately S-20 response) but with silver-magnesium box-and-grid dynodes, provided 4 inches separation and was selected for the supplemental experiments. The effective photocathode area of this tube is approximately 1.8×10^6 times smaller than for the EMR 541 tubes, which further provides excellent isolation of the dynode effects. The faceplate is approximately 35% thicker. The wide separation of the aperture from the photocathode also permits direct determination of the pulse height distribution of delayed pulses without elaborate timing equipment, since prompt photocathode pulses are reduced to single-electron events.

From Sr-90/Y-90 beta and Co-60 and Ra-226 gamma testing of the image dissector, two distinct dynode-region pulse height distributions were evident. Whether the taller of two (Group A) originates from the first dynode or the aperture plate was not determined. The delayed pulse height distribution for the photocathode region was determined from beta tests. Typical spectra for these tests are shown in Figure 1.

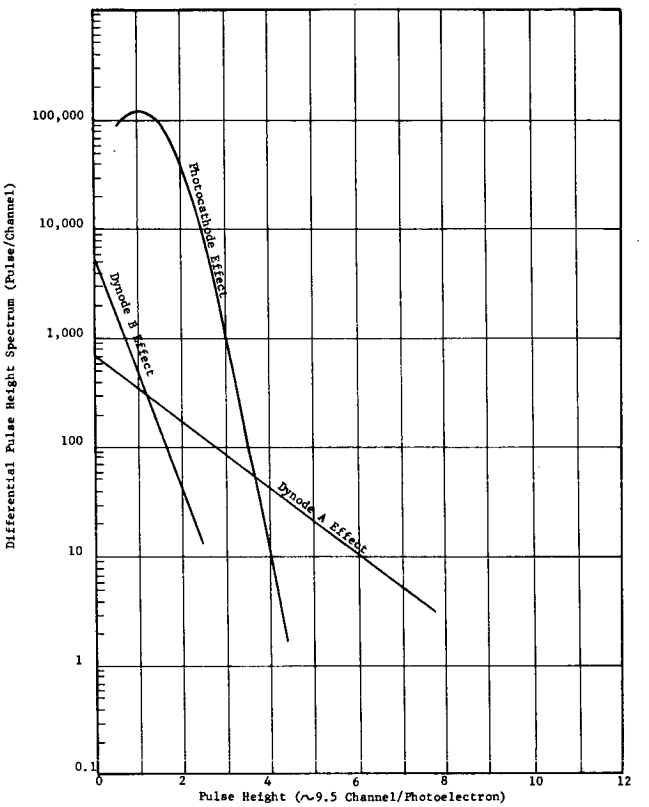

Figure 1
Pulse Height Spectrum Due To A Beta Source ($Sr^{90} - Y^{90}$)

Pulse height distributions from both photocathode and dynode regions were determined for protons at four energies from 22 to 39 Mev. A typical spectrum for these tests is shown in Figure 2. The response to protons is strongly dependent on proton energy, peaking very sharply around 34 Mev.

---

* The luminescence parameter, L, is defined as the photocathode current divided by photocathode area, peak radiant sensitivity, and dose rate.

$$L = \frac{I_c}{S(\lambda_o)\, \dot{D}\, A_c}$$

This luminescence parameter includes the Cerenkov radiation contribution.

** The excellent work and cooperation of Dr. G.F. Knoll, University of Michigan; G. Bain and C.W. Freeborn, ITT; Dr. J. Ryan, MIT Lincoln Laboratory; and L.W. Morton, Aerojet, is hereby gratefully acknowledged. (Miss Freeborn is now at Aerojet.)

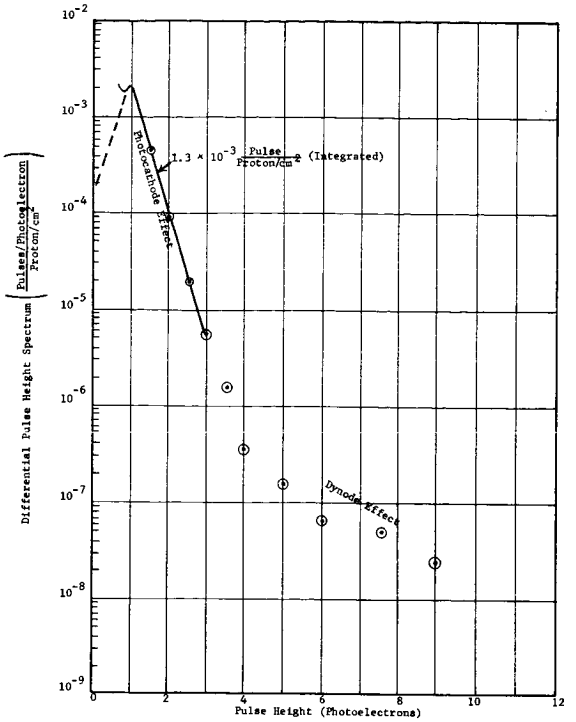

Figure 2
Pulse Height Spectrum Due To A Proton Beam (39 Mev Protons)

The photomultiplier was tested with Sr-90 bremsstrahlung and with bremsstrahlung from electrons at three energies from 0.5 to 3 Mev to determine total pulses above a minimal threshold. The prompt pulse height distribution was not measured. This information has been inferred from data from other investigators and by analogy with the distribution for delayed pulses.

Jerde, Peterson and Stein investigated the pulse height distribution for an RCA 7265 with S-20 response but a very thick soda-lime glass window. Their data for Co-60 indicate about 2.5 to 3 photoelectrons for the large-pulse height distribution, which is to be associated with the prompt pulses. (Their reported value of 10 appears applicable to only a few percent of the pulses in this distribution, and will therefore not concern us further here.) Lacking specific data for the EMR 541E-01, we shall assume the mean prompt pulse size is 3 photoelectrons equivalent. Uncertainties due to difference in faceplate thickness make this estimate somewhere between good and up to a factor of 2 too high.

Dressler and Spitzer offer measurements for the EMR 541E-01 with Co-60 indicating approximately 20% of the total pulses are prompt. Jerde, et al., report for the RCA 7265 about 3%, though their pulse height distribution data appear to indicate a somewhat larger value. Here we shall assume 20% for the EMR 541E-01.

Jerde, et al., for cosmic rays (predominately protons) report 10-20 photoelectrons per prompt pulse. This distribution was observed above 5 photoelectrons pulse size and compares well with 13.8 photoelectrons per dynode pulse observed by AGC/ITT for the image dissector. Comparing with Figure 2, the cosmic ray pulses less than 3 photoelectrons are coming predominately from the photocathode, while those greater than 5 photoelectrons are coming predominately from the dynodes. For large pulses, Cerenkov radiation would, therefore, appear to be a secondary effect with protons even up to cosmic ray energies.

For single-electron counting, Aerojet observed in the image dissector tube approximately 25% fewer pulses/rad with 39 Mev protons than with electrons and gammas. This is just about what would be expected if Cerenkov radiation is absent with protons, but all forms of ionizing radiation are equally effective in producing faceplate excitations. We hereby accept that this is true for photomultiplier tubes as well. Wolff (Reference 8) also finds that photocathode effects of image dissector tubes and photomultipliers are directly scalable with effective area.

Zagorites and Lee (Reference 5) find radiation generated currents are essentially independent of gamma and X-ray energies except around 40-100 kev, where it is probably enhanced by direct interactions with the photocathode or dynodes. Peak enhancement appears to be more than a factor of 3 but not more than an order of magnitude.

The rate of delayed pulses is reported by Dressler and Spitzer to decay in milliseconds. The effective time constant is believed to lengthen out somewhat in time due to the existence of a spectrum of excited states. For most purposes, the early-time time constant will have the greatest impact. In order to have a number to work with tentatively use $\tau = 1 \times 10^{-3}$ sec in the probability equation

$$P = Ae^{-t/\tau}. \qquad (4)$$

For most practical purposes, prompt pulses are instantaneous.

Model for Photomultiplier Radiation Response

A model pulse height distribution for the EMR 541E-01 irradiated by gamma rays, electrons and bremsstrahlung is shown in Figure 3. The models for delayed pulses and dynode pulses are based on experimental data, as described above. The assumed model for prompt pulses is, of course, dependent upon particle energy. For electron energies below about 0.5 Mev, gamma energies below about 0.8 Mev, and bremsstrahlung

generated by electrons with energies below about 1 Mev, the prompt pulses can probably be neglected.

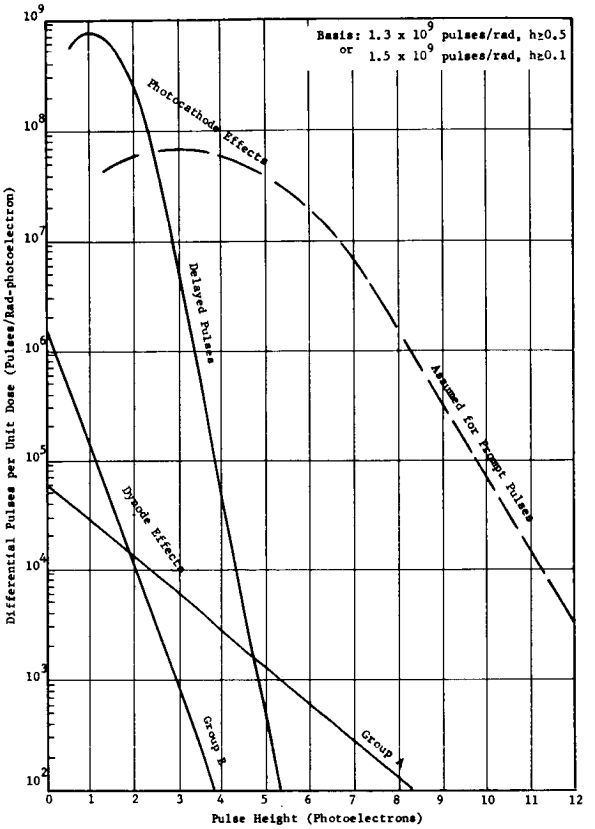

Figure 3
Pulse Height Spectra For An EMR 541E-01 Photomultiplier (Co-60 Gamma Rays)

The pulse height distributions of Figure 3 may be represented analytically:

Photocathode — Delayed Pulses

$$n(h) = 8 \times 10^8 \exp\left(-\left[\frac{h-1}{0.873}\right]^2\right) \text{ pulse/rad-photoelectron, } h < 3$$

$$= 4.2 \times 10^{12} \times 10^{-h/0.5} \text{ pulse/rad-photoelectron, } h \geq 3 \quad (5)$$

Photocathode — Prompt pulses

$$n(h) \sim 0.67 \times 10^8 \exp\left(-\left[\frac{h-3}{2.62}\right]^2\right) \text{ pulse/rad-photoelectron, } h < 9$$

$$\sim 0.35 \times 10^{12} \times 10^{-h/1.5} \text{ pulse/rad-photoelectron, } h \geq 9 \quad (6)$$

Integrated, the delayed pulses are about

1.2×10^9 pulse/rad, $h > 0.1$;

1.0×10^9 pulse/rad, $h > 0.5$;

and the prompt pulses are about

0.3×10^9 pulse/rad, $h > 0.1$ or > 0.5

Dynodes — Group A

$$n(h) = 6 \times 10^4 \exp\left(-\frac{h}{1.3}\right) \text{ pulse/rad-photoelectron} \quad (7)$$

Dynodes — Group B

$$n(h) = 1.5 \times 10^6 \exp\left(-\frac{h}{0.39}\right) \text{ pulse/rad-photoelectron} \quad (8)$$

Integrated, the total pulses are

$$N_A (>h) = 8 \times 10^4 \times 10^{-h/3} \text{ pulse/rad} \quad (9)$$

$$N_B (>h) = 6 \times 10^5 \times 10^{-h/0.9} \text{ pulse/rad} \quad (10)$$

For protons, the analytical representations are:

Photocathode — Delayed Pulses

$$N = 1.1 \times 10^9 \text{ pulse/rad} \quad (11)$$

with distribution above h = 1 given by,

$$N (>h) = 1.3 \times 10^{10} \times 10^{-h/0.75} \text{ pulse/rad} \quad (12)$$

Prompt pulses likely occur only at relativistic proton velocities (i.e., cosmic rays).

Dynode — Group A (32 Mev protons)

$$n_A(h) = 4.4 \times 10^3 \exp\left(-\frac{h}{13.8}\right) \text{ pulse/rad-photoelectron} \quad (13)$$

Dynode — Group B (32 Mev protons)

$$n_B(h) = 8.7 \times 10^4 \exp\left(-\frac{h}{4.6}\right) \text{ pulse/rad-photoelectron} \quad (14)$$

Integrated these become

$$N_A (>h) = 6 \times 10^4 \times 10^{-h/31.8} \text{ pulse/rad} \quad (15)$$

$$N_B (>h) = 4 \times 10^5 \times 10^{-h/10.6} \text{ pulse/rad} \quad (16)$$

Response to proton dose peaks sharply at 32 Mev and is about 4 Mev wide.

Alternatively, the integrated dynode responses may be represented by

$$N_A (\cdot h) = 1.8 \times 10^{-2} \times 10^{-h/31.8} \quad \text{pulse-cm}^2/\text{proton} \tag{17}$$

$$N_B (>h) = 1.35 \times 10^{-1} \times 10^{-h/10.6} \quad \text{pulse-cm}^2/\text{proton} \tag{18}$$

The above representations of dynode pulses are based on data for Ag Mg dynodes. Reed et al. data (Reference 6) indicate CuBe dynodes might be perhaps a factor of 3 less sensitive. Any such differences are overlooked here.

The prompt pulses, including dynode pulses, should be assumed to occur in 10^{-7} seconds or less. The delayed pulse rate probability decays with a time constant of 10^{-3} seconds. For sapphire, Barr and Eberhardt (Reference 9) find the time constant becomes as long as several seconds to half a minute.

Orbital Noise Prediction

The electron environment will be present almost continuously. Therefore, electron-induced noise will also be present almost continuously.

The anticipated electron environment is given by Equation 3. One component is depressed by solar proton activity, while the other is enhanced. At $\bar{R} = 100$, each component will yield about 10^{-6} rad/sec bremsstrahlung at the photomultiplier tube. The primary electrons below 5 Mev will all be stopped in the structure. The worst case for Cycles 20-21 will occur near solar minimum in 1974-1975. If it is assumed $\bar{R} \sim 10$ is representative of 1974, then noise in orbit will be generated by about 1×10^{-5} rad/sec at the photomultiplier tube.

If, from Table I, we accept 0.6 nanowatt (4100A) sec/rad cm^2 for the luminescence of the EMR 541E-01-14 faceplate ($h \geq 0.5$) and 0.07 amp/watt (4100A) peak radiant sensitivity, then the photomultiplier response will be

$$N (>0.5) = 0.6 \times 10^{-9} \frac{\text{watt sec}}{\text{rad cm}^2} \; 5 \text{ cm}^2 \times 0.07 \frac{\text{amp}}{\text{watt}} \frac{1}{1.6 \times 10^{-19}} \frac{\text{pulse}}{\text{amp sec}} \tag{19}$$

$$= 1.3 \times 10^9 \text{ pulse/rad}$$

In this case, virtually all noise generation will be by electron-gamma-delta ray (i.e., Compton electron) interaction. Since only a small percentage of incident electrons will yield delta rays exceeding the approximately 0.5 Mev gammas, the mean prompt pulse height will be only $\bar{h} \sim 1$. Since many interactions will fail to produce Cerenkov radiation, it is possible that Equation 19 overestimates the noise generation by as much as 20%.

Therefore, the predicted mean orbital noise generation is

$$\dot{N} = 1.3 \times 10^9 \frac{\text{pulse}}{\text{rad}} \; 1 \times 10^{-5} \frac{\text{rad}}{\text{sec}} = 1.3 \times 10^4 \text{ pulse/sec} \tag{20}$$

with virtually all pulses averaging $h = 1.0$. The expected number of pulses in one 140 millisecond counting interval is, therefore,

$$\bar{N} = 1.3 \times 10^4 \frac{\text{pulse}}{\text{sec}} \; 140 \times 10^{-6} \text{ sec} = 1.8 \text{ pulse} \tag{21}$$

The high energy solar proton environment will be present only a few percent of the time. Over 90% of the year, solar proton-induced noise should be negligible.

The expected solar proton environment is given by Equation 2. For a typical worst three years $\bar{R} \sim 100$. The star sensor structure, shielding, and surrounding hardware restrict protons reaching the photomultiplier to energies above 50 Mev with an effective acceptance solid angle of about 0.5 hemisphere = 0.25 sphere. For faceplate noise, the maximum solar proton environment from Equation 2 is

$$\phi_{max} \sim 700 \frac{\text{proton}}{\text{cm}^2 \text{ sec}} \left(\frac{100}{100}\right)^2 \left(\frac{100 \text{ Mev}}{50 \text{ Mev}}\right)^{3/2} \text{ per year (3 years)} = 6000 \text{ proton/cm}^2 \text{ sec (>50 Mev, omnidirectional)} \tag{22}$$

Table I

Vacuum Phototube Responses to Ionizing Radiations

Device	Radiation	Luminescence Parameter *	Mean No. of Pulses per Interaction	Prompt Pulse Size (Photoelectrons Equiv.	Investigator & Reference Numbers
Photomultipliers:					
EMR 541E-01	Bremsstrahlung	0.56			AGC
	Co-60	0.61	5		Dressler (3)
	Co-60	0.45			Wey (7)
EMR 541K-05M	Co-60	15	75		Dressler (3)
	Co-60	~38			Wey (7)
	Co-60	~12			Reed (6)
EMR 541A-01	Co-60	0.31	2		Dressler (3)
	Co-60	~0.55			Wey (7)
EMR 541A-05M	Co-60	2.0	~20		Dressler (3)
EMR 541A-05	Co-60	~6.2			Wey (7)
EMR 541A-08	Co-60	1.1	~7		Dressler (3)
EMR 541N-01	Co-60	0.12	~1.5		Dressler (3)
EMR 541N-05M	Co-60	≥2	28		Dressler (3)
EMI 6097S	Co-60, Cs-137 0.035-0.38 Mev X-rays	1.5			Zagorites (5)
Dubkont 6467	Co-60, Cs-137	3.9			Zagorites (5)
RCA 1P21	Co-60, Cs-137	0.6			Zagorites (5)
RCA 7265	Co-60		30	2.5-10	Jerde (4)
	Cosmic Rays	~1	10-30	10-20	Jerde (4)
Image Dissector:					
ITT S-412	Co-60, Ra-226 Sr-90	~1		1.3 (Dynodes)	AGC/ITT
	Protons	~0.7	~10^2	1.25 (Dynodes)	AGC/ITT
				13.8 (Dynodes)	AGC/ITT

* Units of nanowatt (λ max) sec/rad cm^2.

Combining this environment with Equation 11, the faceplate noise will be

$$\dot{N} = 1.1 \times 10^{9} \frac{\text{pulse}}{\text{rad}} \; 6000 \frac{\text{proton}}{\text{cm}^2\text{sec}} \; (0.25)\,(1.5) \times 1.8 \times 10^{-7} \frac{\text{rad cm}^2}{\text{proton}} = 4.4 \times 10^{5} \text{ pulse/sec} \tag{23}$$

where a spectrum correction factor F = 1.5 has been assumed. This rate should endure for about one day.

For the dynode pulses, it can be shown that the effective 32 Mev proton flux reaching the photomultiplier is about

$$\Delta\Phi_{max} \simeq 65 \text{ protons/cm}^2 \text{ sec} \tag{24}$$

Thus, using Equations 17 and 18, the two groups of dynode pulses will be

$$\dot{N}_A = 65 \frac{\text{proton}}{\text{cm}^2 \text{Mev sec}} (4 \text{ Mev}) \times 1.8 \times 10^{-2} \frac{\text{pulse cm}^2}{\text{proton}} \; 10^{-0.5/31.8} = 1.2 \text{ pulse/sec} \tag{25}$$

$$\dot{N}_B = 65 \frac{\text{proton}}{\text{cm}^2 \text{ Mev sec}} (4 \text{ Mev}) \times 1.35 \times 10^{-1} \frac{\text{pulse cm}^2}{\text{proton}} \; 10^{-0.5/10.6} = 8 \text{ pulse/sec} \tag{26}$$

The dynode pulses represent only about 0.03% of the total and are, therefore, negligible.

Cosmic rays will generate not more than

$$\dot{N} = 1.5 \times 10^{9} \frac{\text{pulse}}{\text{rad}} \; 9 \frac{\text{particle}}{\text{cm}^2 \text{ sec}} \times 3 \times 10^{-8} \frac{\text{rad cm}^2}{\text{particle}} \simeq 4 \text{ pulse/sec} \tag{27}$$

including prompt pulses of perhaps $h \sim 7$. Cosmic ray pulses also appear to be negligible compared to both the proton-generated and the electron generated noise.

Thus, the maximum expected orbital noise is given by Equation 23,

$$\dot{N} = 4.4 \times 10^{5} \text{ pulse/sec}$$

with virtually all pulses averaging h = 1.0. The expected number of pulses in one 140 microsecond counting interval is therefore

$$\bar{N} = 4.4 \times 10^{5} \frac{\text{pulses}}{\text{sec}} \; 140 \times 10^{6} = 61 \text{ pulses} \tag{28}$$

(For 1971-1973, these figures should be down by a factor of more than four.)

The pulse expectancies will not be entirely uncorrelated. (See Table I for the EMR 541E-01.) After a faceplate interaction, whether producing a prompt pulse or not, the rate probability of delayed pulses at time t afterwards is

$$P(t) = \frac{dN}{dt} = \frac{4}{\tau} \exp(-t/\tau), \tag{29}$$

where τ may tentatively be taken to be 1×10^{-3} sec. Equation 29 applies to both electron- and proton-generated noise. Applied to a 140 microsecond counting interval, the probability of a pulse occuring is

$$P(t) = \frac{4\,(140 \times 10^{-6} \text{ sec})}{1 \times 10^{-3} \text{ sec}} \exp\left(-t/10^{-3} \text{ sec}\right) = 0.56 \exp\left(-t/10^{-3} \text{ sec}\right) \tag{30}$$

From Equations 21 and 28, it may be seen that the expectancy of prompt pulses in a given counting interval is 0.36 and 12.2 for the average electron and expected maximum proton environments respectively. The expectancy of total pulses is 1.8 and 61 respectively.

Star Sensor Simulation

A computer program has been developed to simulate the star sensor performance. The output of the simulation program is used to provide inputs for development and qualification testing of the ground data processing. An earlier version of the simulation was used to evaluate the performance of the Kalman filter used in the attitude determination computations. The output from the star sensor simulation (star count processor) is a sequence of star sensor count values. Since the count cycle duration is 140 microseconds, almost one million of these values must be generated for every two minutes of star sensor operation simulated.

The Star Count Processor is part of a comprehensive simulation program modeling the entire satellite. Another processor in the simulation program is the Slit Crossing Processor which determines the times at which star images cross the center of a slit in the reticle. These

slit crossing times are dependent upon the reticle slit geometry, the satellite dynamics being simulated, and star positions derived from a Star Catalog Data Set containing information from Reference 10. The output from the Slit Crossing Processor is a data set of slit crossing times along with the S. A. O. catalog number of the star and its visual magnitude.

The Star Count Processor is capable of simulating a wide variety of background conditions specified by means of the input parameters discussed below. For example, the parameter EP is used as the Poisson distribution parameter for modelling the arrival of prompt pulses caused by bremsstrahlung from trapped electrons. The parameter, EP, is the expected number of count cycles (140 microsecond intervals) between arrivals of these prompt pulses. Since a Poisson process has exponentially distributed interarrival times (Reference 11), the interval between consecutive prompt pulses due to trapped electrons can be expressed as follows in terms of count cycles,

$$DTNE = -EP \ln (RU) \tag{31}$$

Where RU is a pseudorandom number generated by the computer based upon a distribution uniform on the interval (0, 1). If we let STNE' be the arrival "time" of the preceding prompt pulse due to bremsstrahlung, then the next prompt pulse arrives at

$$STNE = STNE' + DTNE$$

$$= STNE' - EP \ln (RU) \tag{32}$$

A similar logic applies to prompt pulses due to protons, either solar or cosmic, in terms of the input parameter SP, the expected number of count cycles between prompt proton-induced pulses. Hence

$$STNP = STNP' - SP \ln (RU) \tag{33}$$

As noted previously, the delayed pulses following a prompt pulse have a rate of occurrence dying out with time. This characteristic is modeled by means of the decay factors, DE and DP, for electrons and protons respectively. Then defining

RE = expected number of output pulses in any count cycle due to electrons

RP = expected number of output pulses in any count cycle due to protons

EN = an input parameter related to effect of each trapped electron

PN = an input parameter related to effect of each solar proton

Then attaching a prime to designate values of RE and RP from the preceding count cycle, we have

$$RE = (RE' + n_e \, EN) \, DE \tag{34}$$

$$RP = (RP' + n_p \, PN) \, DP \tag{35}$$

where

n_e = number of prompt pulses due to trapped electrons in the preceding count cycle

n_p = number of prompt pulses due to solar protons in the preceding count cycle

When the processing for the current count cycle begins, its index, SNC, is obtained by adding one to the previous value of the index. If the previously generated value of STNE is less than or equal to the new value of SNC, then EN is added to RE'. A new value of DTNE is generated if STNE $\leq$ SNC based on a new random number RU. The value of DTNE is then added to the current value of STNE. The process is repeated until the new value of STNE exceeds the current value for SNC. Similar logic is used for STNP with PN being added to RP.

The star background effects vary as the star sensor optical axis sweeps across the celestial sphere. Let b_o be twice the number of radians swept in 1020 count cycles and K be the number of blocks of 1020 count values which have been generated so far in this simulation. The expression

$$XS = \frac{.25}{1.25 + \sin b_o \, K} \tag{36}$$

has a maximum value of 1.0 when the sine function is -1 and a minimum value of 1/9 when the sine function is $+1$. Then the expected contribution from stars dimmer than seventh magnitude is

$$BD = BDI * XS \tag{37}$$

where

BDI = an input parameter equal to the expected contribution of stars dimmer than seventh magnitude in the galactic plane.

Contributions of stars brighter than seventh magnitude must be represented on an individual basis. Although stars dimmer than 4.6 magnitude could have been represented on the same basis as the brighter stars, it was

found that the extra computational cost was not justified. Instead, the following simplified representation was used. These intermediate intensity stars were simulated in terms of an exponential distribution of interarrival times using the quantity SD as the expected interarrival parameter and

$$SD = SDI / (0.15 + XS) \quad (38)$$

where

SDI = an input parameter 1.15 times the expected interarrival time in count cycles in the galactic plane.

The quantity SD is used in the same manner as the parameters EP and SP resulting in the equation

$$STND = STND' - SD \ln(RU) + 3 \quad (39)$$

The three is added to avoid overlap of these stars.

The intensity of the simulated star is given by

$$QD = QM / (.1 + RU) \quad (40)$$

where QM = input parameter nominally equal to one-tenth the response of the star sensor to a 4.6 magnitude star.

The timing of the slit crossing with respect to the count cycles is given in terms of another random number, Z, as follows

$$RD1 = (ZH - Z)QD \quad (41)$$

$$RD2 = QD \quad (42)$$

$$RD3 = (Z + ZH - 1.0)QD \quad (43)$$

where ZH = an input parameter equal to the half width of the slit in count cycles.

If either of the parenthetic expressions is negative, then that value of RD is set equal to zero and the deficiency is removed from RD2. With ZH equal to .82, the expression (ZH - Z) would be negative for any value of Z greater than .82. Physically, this corresponds to the situation in which the slit crossing occurs so late in the second count cycle of the set of three containing the star signal that none of the signal occurs in the first count cycle and there is a short delay before the signal starts in the second count cycle.

Conclusions

1. Vacuum phototubes are good dosimeters for both high energy electrons and bremsstrahlung radiations. This characteristic is essential to predicting sensor response to space radiation.

2. Vacuum phototube response to protons is sensitively dependent upon proton energy.

3. In the single-electron counting mode, virtually all photomultiplier pulses originate in the faceplate/photocathode. This becomes important in design shielding.

4. Star sensor response to the radiation environment of space may be readily simulated with an appropriate computer program.

REFERENCES

1. Bell, Barbara and Wolbach, John G, "Lunar Eclipses and the Forecasting of Solar Minima," Icarus 4, pp. 409-414 (1965).

2. Solar Geophysical Data, Comprehensive Reports; monthly, NOAA.

3. Dressler, K. and Spitzer, L., Jr., "Photomultiplier Tube Pulses Induced by Gamma Rays," Rev. Sci. Instr. 38, pp. 436-438 (1967).

4. Jerde, R. L., Peterson, L. E., and Stein, W., "Effects of High Energy Radiations on Noise Pulses from Photomultiplier Tubes," Rev. Sci. Instr. 38, pp. 1387-1394 (1967).

5. Zagorites, H. A. and Lee, D. Y., "Gamma and X-ray Effects in Multiplier Phototubes," IEEE Trans Nucl. Sci. NS 14, 6, pp. 190-194 (1967).

6. Reed, Edith I., Bowler, Walter B., Aitken, Charles W. and Brun, Jean Francis, "Some Effects of Mev Electrons on the OGOII (POGO) Airglow Photometers," GSFC, NASA X-613-67-132 (March 1967).

7. Wey, W. and Schrier, Joel, Hughes Aircraft Company, Private Communication.

8. Wolff, C., "The Effect of the Earth's Radiation Belts on an Optical System," Appl. Optics 5, pp. 1838-1842 (1966).

9. Barr, F. H. and Eberhardt, E. H., Final Report, "Research and Development of an Improved Multiplier Phototube," ITT/IL -Fort Wayne, Nov. 16, 1966. N67-27365, Contract NASw 1038.

10. Smithsonian Astrophysical Observatory Star Catalog, Washington: Smithsonian Inst. (1966).

11. Parzen, E., Modern Probability Theory and Its Applications, p. 262, New York: John Wiley & Sons (1960).

GE(LI) DATA REDUCTION USING SMALL COMPUTERS

W.E. MC DERMOTT
1155 T.O.S., MC CLELLAN AFB , CA.

1. INTRODUCTION

The introduction of lithium-drifted germanium detectors for use in X-ray and gamma ray spectroscopy has made it possible to measure accurately the relative abundances of radionuclides present in a mixture directly, without the use of chemical separation techniques. Events depositing differing amounts of emergy into the crystal result in pulses of varied height,which are then sorted using a pulse height analyzer. Having accumulated a spectrum, three steps are required for its analysis. The peaks in the spectrum must be found, the count rate in the photopeaks determined, and this count rate related through a knowledge of machine efficiencies to known gamma transitions to find the amount of each radionuclide present. Since 4096 channels of data are usually involved, this process has often been accomplished on a remote computer. With the introduction of small , relatively inexpensive computers it has become possible to interface these devices with the Ge(Li) detector in such a way as to allow the experimenter to maintain an interactive control not only of the experimental parameters, but also of the data interpretation. This latter approach also has the desirable advantage of providing real-time information on the progress of the experiment.

There are essentially two approaches which are used to produce an interactive system. In the first, the small computer is interfaced directly to the ADC and a portion of the computer memory provides the storage area for the data; whereas in the second, the computer is interfaced to the analyzer memory in which the data is stored. The analyzer memory thus appears to the central processor as a bulk storage device. We have pursued the latter approach.

2. ANALYZER/COMPUTER COMBINATION

The system used in this study was a commerically made 50/50 System , obtained from NUCLEAR DATA. It includes a 100 MHz ADC with 8192 resolution and a 4096 word, 24 bit analyzer memory. Also part of this system was a 12K PDP 8/I computer produced by DIGITAL EQUIPMENT CORP. Other equipment included a display scope, high speed punch/reader unit, teletype, and interface units. Machine language instructions were provided to control all major functions of the analyzer under computer control,as well as allowing acess through the computer accumulator to any memory location within the analyzer or direct access to the ADC output.

Various computing languages are available to program the PDP 8/I;including assembly languages, FORTRAN, and FOCAL (a conversational language). The assembly languages are most efficient from the point of view of speed and program size,however,programs are long and tedious to write. FOCAL requires the compiler to reside in core and is therefore wasteful of core memory. FORTRAN programs allow easier design and modification and also eliminate training operators in the assembly languages. Furthermore, FORTRAN programs are available from a variety of sources including the excellent text by Bevington (ref. 1). Our approach was to utilize FORTRAN programs with a number of FORTRAN-callable routines which provide control over the major functions of the analyzer.

3. LIMITATIONS OF FORTRAN

There are several limitations placed on the FORTRAN program by the construction of the central processor. The PDP 8/I memory is divided into 4096 word units called fields . Each field is further divided into 128 word blocks called pages. There are 32 pages in a field. The FORTRAN loader requires 3 pages in the first field (field 0), and one page each in the remaining fields. Some locations in the first page in each field are also required leaving 27 pages available in field 0 and 30 in each of the remaining fields. The FORTRAN library subroutines; including subscripting,square root,read,write,add, subtract, etc. requires another 25 pages. The exponentiation routines are not included and would require another 6 pages. Without the latter, in a 12K computer, this leaves 62 free pages or about 8K for operator programs.

4. SERVICE ROUTINES

Four service routines were written to facilitate analysis of the Ge(Li) spectrum. These are listed on Slide 1. The routines ANAL and TYME are in the same package and occupy 2 pages of core, as does each of the other routines.

5. METHODS OF ANALYSIS

The general problem in the analysis

of Ge(Li) spectra is to determine the area of the full energy photopeak after subtraction of the background, which is due to Compton interactions produced by higher energy gammas. The main portion of the photopeak is a gaussian function, modified on the low energy side by tailing. A close examination of well defined photopeaks, such as the one shown on Slide 2, also reveals the existence of a step function-like contribution, the higher level of which is again on the low energy side of the photopeak. The actual situation is not as bad as shown as the scale is semi-logarithmic.

In the case of isolated photopeaks, the photopeak area is simply what is left over after the background is subtracted so the problem reduces to a determination of the form of the background. One possible approach is to define a region on either side of the peak and draw a least square straight line through it. The photopeak is defined as anything above that line. A more pleasing solution might be to join the two regions on either side of the peak by a smooth function such as (1 - erf(x)). With a small computer, however, it is more practical to use the former method. The error resulting from using this method is about 1%.

When photopeaks are not isolated, then there is a second problem - that of determining how much of the total peak area is due to a specific gamma ray. For this it is necessary to use an expression for the individual peak shapes and an iterative procedure to minimize the weighted squared error (chisquare). The error in this type of determination is proportional to the product of chisquare and the error expected from Poisson statistics alone. Either of these types of analysis can be coded in FORTRAN and run on the 50/50 system described earlier.

6. ANALYSIS PROGRAM

A flow chart of a typical peak location and analysis program is shown on the next slide. An initial set of parameters is read in from the high speed paper tape reader. These include smoothing coefficients for the peak finding routine, gain, zero, and estimates of the peak width as a function of channel number. The teletype is then used to define the region to be analyzed, the minimum separation between isolated peaks, and the number of channels to be used in the background region. The photopeaks are then found by the subroutine FIND which examines the behavior of the smoothed first derivative of the spectrum using an algorithmn similar to that used in the GASPAN program (ref 2). When all peaks have been found, the first (highest energy) peak is checked against the second to determine if they are resolved. If so, the specified number of channels are extracted from the analyzer and the limits of the peak determined. The program looks on either side of the peak for three successive increases in the smoothed channel contents such that the difference between the first and third values are at least twice the square root of the first. The first channel in this group is taken to be the limit of the peak on that side. The remaining channels are then used to calculate a least square line to be used as the background and the resulting peak area and centroid calculated.

If the peak was found not to be isolated, then the region to be analyzed includes that second peak and any other unresolved peaks. After calculating the total peak area in the same manner as for an isolated peak, a non-linear least square fit using the functional form:

$$y = a + bx + \sum_{1}^{4} c_i \exp(- s^2(x-d_i)^2)$$

is used and the total area for each peak calculated from the area previously calculated and the relative peak amplitude. The form of the functional fit may be varied by using different calculation subprograms. The next slide shows a memory map of this program to give some idea of the size of each subprogram.

7. CONCLUSION

In conclusion, I feel that a small computer can perform the first two steps necessary in the analysis of a Ge(Li) spectrum. The last step, that of correlating the photopeak intensities and determining the amount of each radionuclide present must be taken either by the experimenter or a larger computer.

REFERENCES

1. Bevington, P.R. : Data Reduction and Error Analysis for the Physical Sciences. McGraw-Hill (1969)

2. Barnes, V.: IEEE Trans.Nucl.Sci. NS-15, no 3 (1968)

SLIDE 1 FORTRAN SERVICE ROUTINES

Name	Calling Statement	
ANAL	CALL ANAL (CTS,CHAN,N)	Load into the vector CTS, starting at CTS(1), the contents of the N analyzer locations beginning with CHAN. Convert 24 bit word to floating point.
TYME	X=TYME(T)	Load contents of analyzer channel 0 into X after converting to floating point and multiplying by the constant T.
FNDIL	CALL FNDIL (X,Y)	Find the upper channel, X, and the lower channel, Y, of the analog intensified region on the display scope.
GAUS	X = GAUS (T)	Compute EXP(- T^2). If T is greater in magnitude than 5, GAUS (T) = 0.

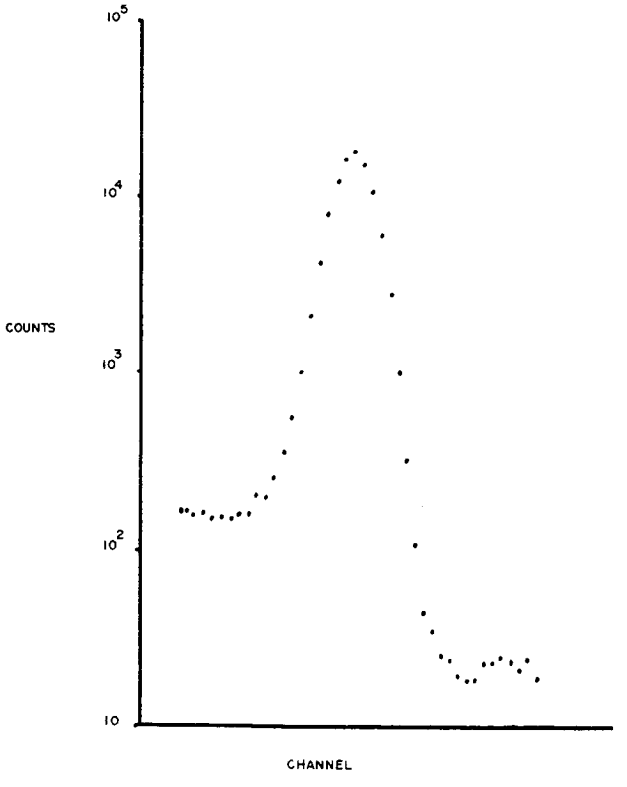

SLIDE 2

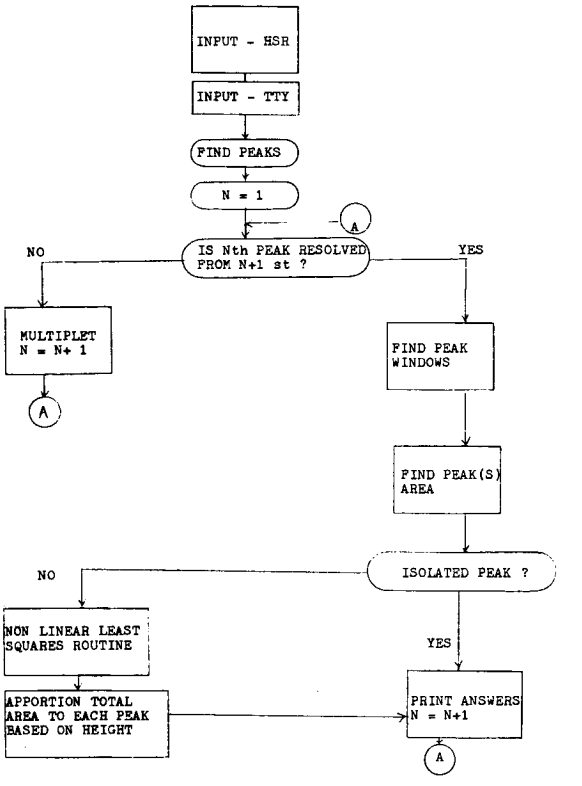

SLIDE 3

MEMORY MAP

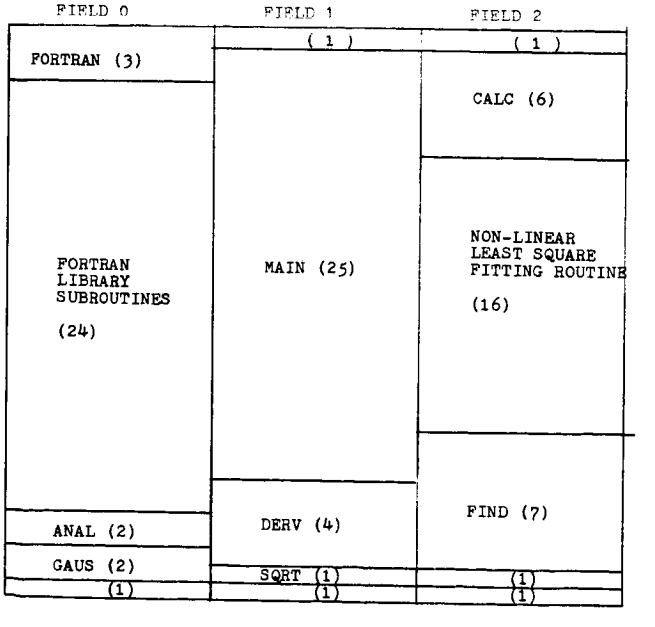

SLIDE 4

SESSION VII.4.
SPACE OPERATIONS IN THE PRESENCE OF NATURAL SPACE RADIATION (INCLUDING LIGHT FLASHES)

CHAIRMAN: R. HARTMAN
OFFICE OF MANNED SPACE FLIGHT-NASA

RADIATION PROBLEMS ASSOCIATED WITH SKYLAB

John E. Braly and Thomas R. Heaton

Martin Marietta Corporation

Skylab, an experimental space station, will orbit the earth during 1972-73. Sixty experiments will be carried out during its flight, 26 of which use some type of photographic film. In its circular orbit of 235 n mi, inclined 50°, it passes through the Van Allen belt several times a day. The expected radiation environment is too severe for some of the film on board. In addition, it was suspected that this environment would darken a borosilicate window used by the S190 experiment. Radiation tests were conducted on the various types of Skylab film to establish the total radiation dosages compatible with an acceptable level of film fogging, and on the S190 borosilicate window to establish radiation limits for an acceptable darkening level. The results verified that most of the films would be unusable when returned to earth, and that the borosilicate window would be darkened beyond allowable limit, unless additional protection was provided. The operational solutions to these problems involve protecting the film with five film vaults and protecting the window with a radiation shield. The largest vault is made of aluminum and weighs over 2000 lb (its thickest compartment wall is 3.4 in.). The window radiation shield is a light honeycomb structure which is swung away for limited astronaut viewing or when the S190 experiment is in operation. Although the shield is light weight, it is heavy enough to stop the large number of low energy electrons making up a major part of the external environment and which are potentially damaging to the window. The paper contains a brief description of the Skylab mission and some of the associated experiments. The radiation environment the spacecraft will encounter is discussed. The results of the radiation test programs on Skylab photographic film and on borosilicate glass are presented. Operational solutions to the two problems of excessive film fog and loss of transmittance through the glass are described.

SKYLAB MISSION

Skylab is an experimental space station program of the National Aeronautics and Space Administration, designed to expand our knowledge of manned earth orbital operations and to accomplish carefully selected scientific, technological, and medical investigations. This space station is to be made up of a cluster of individual modules including a Saturn IVB stage modified into an Orbital Workshop (OWS), an Airlock Module (AM), a Multiple Docking Adapter (MDA), a Saturn V Instrument Unit (IU), an Apollo Telescope Mount (ATM), and an Apollo Command and Service Module (CSM).

Flight 1 of the Skylab mission will begin with the launch from the Kennedy Space Center (KSC) of all modules except the CSM. These modules will be inserted by a Saturn V into a circular orbit 235 n mi high, inclined 50° with respect to the equator. Within the 7.5 hr lifetime of the IU, the orbital assembly will be oriented to a solar inertial (sun pointing) attitude mode, and the workshop solar array will be deployed. The ATM will be rotated 90° from the launch position, and the ATM solar arrays will be deployed. The ATM pointing control system will be activated to maintain the solar-inertial attitude. The interior of the OWS, AM, and MDA will be pressurized to 5 psia with an oxygen-nitrogen atmosphere, making it ready to accept docking of the CSM and entry of the flight crew.

Flight 2 will be launched from KSC one day after Flight 1, using a Saturn IB. A CSM with a three-man crew will be inserted into an interim orbit. The CSM will rendezvous with the orbital assembly, using the service propulsion system to boost it to the required 235-n-mi-orbit, and will dock to the axial port of the MDA, thus completing the cluster (Fig. 1). The crew will enter the workshop and complete activation of the orbital assembly for habitation. For the remainder of the Flight 2 mission, the experiment program will be conducted with emphasis on the medical experiments and evaluation of the habitability systems. The ATM experiments will be activated and their operation verified. Nominally, the CSM will deorbit on the 28th day, and splashdown is planned in the West Atlantic recovery area.

Flight 3 involves the launch of a second crew on a Saturn IV approximately 80 days after the launch of Flight 2. The orbit-insertion, rendezvous, and docking procedures will be the same as those for Flight 2. The mission will be similar to Mission SL-1/SL-2, except that it will be open ended for up to 56 days duration. In addition, more emphasis will be placed on the solar astronomy experiments. Assuming nominal mission duration and deorbit, recovery is planned in the mid-Pacific recovery area.

Flight 4 will be launched approximately 100 days after the launch of Flight 3. Its payload is the third CSM and crew. This mission will complete the planned experiment objectives, and will provide additional statistical data on the space crew's adaptability and performance over the planned 56-day mission. Recovery will be in the mid-Pacific.

EXPERIMENTS

Approximately 60 experiments, to be carried out during the 240-day lifetime of Skylab, have been divided into the six general categories of solar astronomy, science, biomedical, technology, earth resources, and crew operations. Of these, the solar astronomy, science, and earth resources

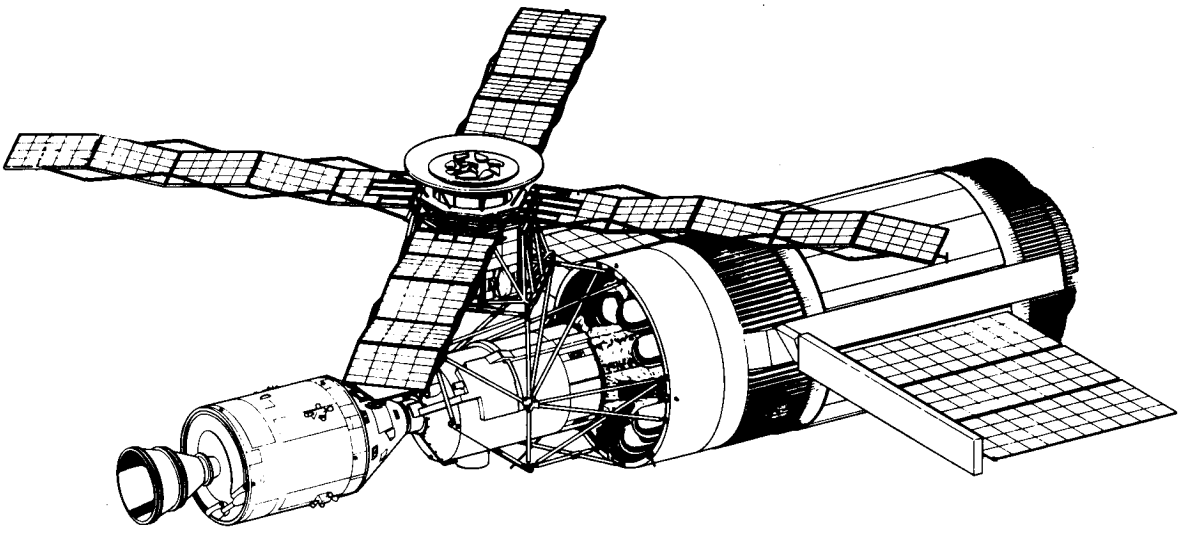

FIGURE 1.-Skylab Cluster

experiments are of most interest here because of the corpuscular radiation problems associated with them.

The solar astronomy scientific experiments comprise the payload for the ATM. These instruments are the largest, most complex ever designed for performing solar research from an orbiting spacecraft, and all but one use some type of photographic film to record their data.

The science experiments are designed to study the discipline areas of geophysics, physics of the upper atmosphere, physics of the interplanetary medium, solar studies to supplement the ATM experiments, and both galactic and intergalactic astronomy. Many of these experiments use extremely sensitive photographic film to record their data.

The earth resources experiments (EREP) are designed to support the development of sensors and applications technology, required for the design of operational spacecraft systems. These experiments are mounted both on the interior and exterior of the MDA. One EREP experiment, S190, uses a six-camera array with synchronized shutters looking through a 1.6-in.-thick borosilicate window to take pictures of the earth's surface. This window is the highest quality of any put into space to date. Even though an electroconductive coating is used on the outside surface of the glass to resistively heat it, transmittance must be at least 0.65 at a wavelength of 0.40 μm, at least 0.70 at a wavelength of 0.45 μm, at least 0.77 from 0.50 to 0.70 μm, and at least 0.63 at a wavelength of 0.90 μm.

RADIATION ENVIRONMENT

A predicted radiation environment has been calculated, using the Martin Marietta computer code PD-202, which determines positions in the trajectory at specified intervals and converts these data to the corresponding McIlwain geomagnetic coordinates (B, L) (ref. 1). The electron and proton fluxes and energy spectra are then determined from the Vette AP-1, 5, 6, 7 and AE-2, 1968, environments (refs. 2 and 3). Since the Skylab orbit repeats essentially every 24 hr, calculations were for an average daily differential spectrum (Fig. 2 and 3) and a typical daily flux history (Fig. 4). It can be seen from Fig. 4 that, in this particular orbit, Skylab passes in and out of the Van Allen belt periodically and, in fact, completely misses the South Atlantic anomaly five orbits in a day. An indication of the hardness of the proton spectrum can be seen from Fig. 5, which was generated by Martin Marietta computer code KD-205. This program uses the spectrum compiled by PD-202 and the stopping power data of Berger and Seltzer (ref. 4) to calculate the dose at the center of a sphere, of specified thickness, both in rems and in rads.

Additional doses, at various points in the cluster, have been calculated by Hill et al. (ref. 5), taking into account the specific geometry of each module and intermodule shielding. These calculations also used the spectrum generated by PD-202 and are shown in Fig. 6. Examining the values in this figure and using Fig. 4 as a rad-to-rem

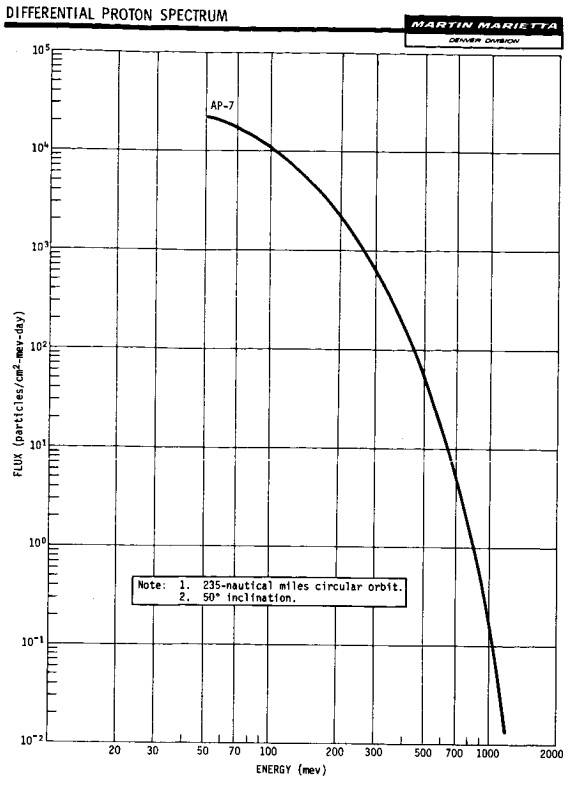

FIGURE 2.-Differential proton spectrum.

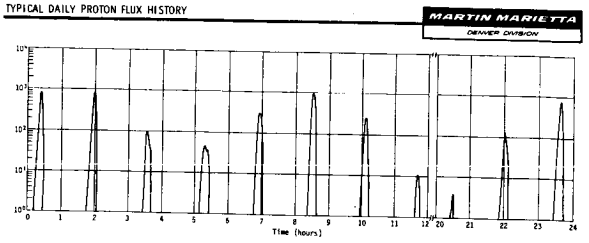

FIGURE 4.-Typical daily proton flux history.

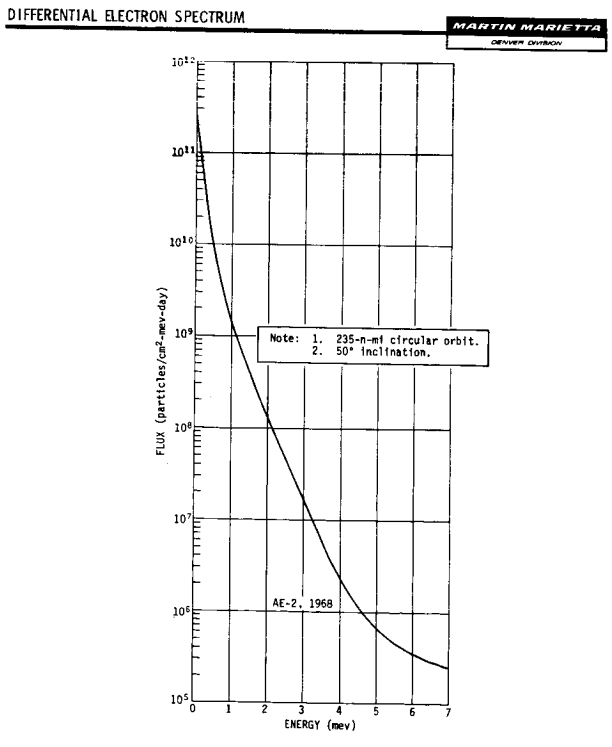

FIGURE 3.-Differential electron spectrum

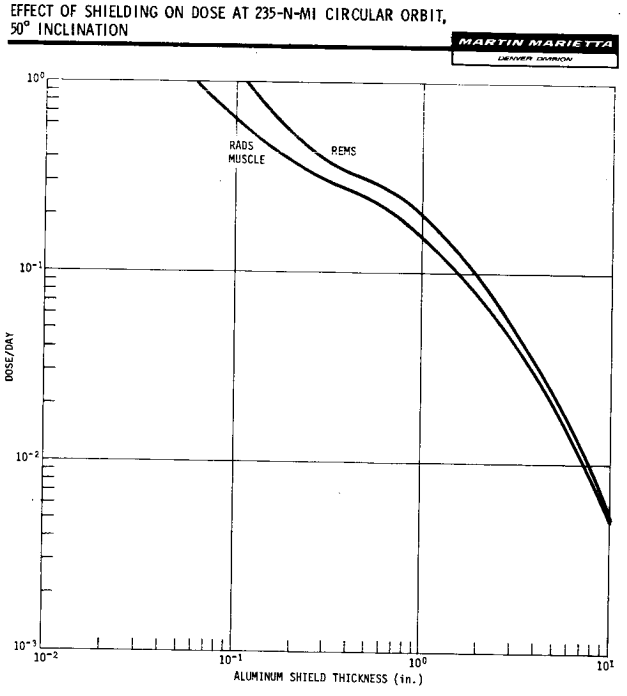

FIGURE 5.-Effect of shielding on dose at 235-n-mi circular orbit, 50° inclination.

RADIATION DOSES AT VARIOUS POINTS INSIDE SKYLAB CLUSTER

MARTIN MARIETTA
DENVER DIVISION

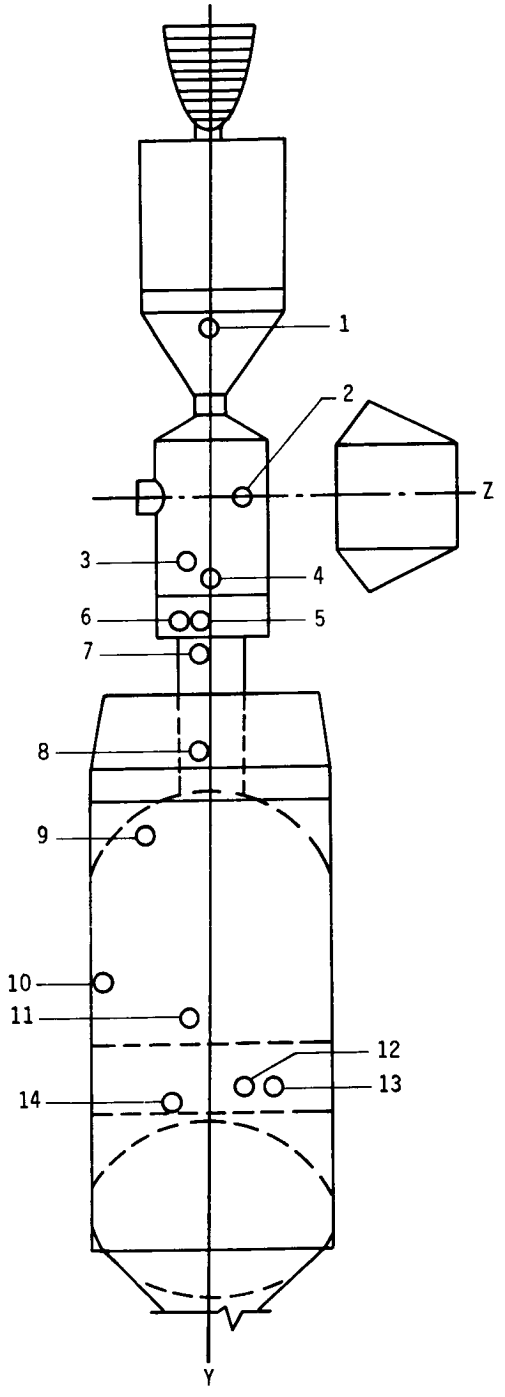

Location	Dose/Day (Rads-Air)
1	0.05880
2	0.13119
3	0.15111
4	0.15110
5	0.13936
6	0.13090
7	0.06236
8	0.05039
9	0.23846
10	0.20660
11	0.13563
12	0.12226
13	0.14284
14	0.15298

FIGURE 6.-Radiation doses at various points inside Skylab Cluster.

converter, it becomes evident that additional radiation shielding for the Skylab crewman is unnecessary because NASA's planning operational dose for a 56-day Skylab mission is 250 rems to the skin and 25 rems to the blood forming organs.

Cosmic radiation also makes up part of the radiation environment to be encountered by Skylab. Although unimportant when considering surface doses outside the orbital assembly, this environment can become significant behind very heavy shields, such as film vaults, because of the greater range of cosmic rays compared to the range of Van Allen belt protons and electrons. Burrell et al. (ref. 6), estimate that behind a 10 gm/cm^2 aluminum shield, the total cosmic ray dose at 240 n mi, 50°, will be 2×10^{-3} rads/day, or 0.4 rads to a film stored 200 days.

RADIATION TEST PROGRAMS

Photographic Film

A radiation test program was conducted by Martin Marietta's Denver Division to obtain film degradation data for establishing minimum radiation shielding requirements of the experiment and operational films to be used in the Skylab mission (ref. 7). The films were irradiated at various levels with Cobalt-60 gamma rays and then imaged in selected regions of the X-ray, ultraviolet, visible, and near infrared to simulate spectral ranges in which the films will be used. Sensitometric analysis of the processed film included Hurter and Driffield (H&D) curves, film base plus fog, gamma, and modulation plots. A series of principal investigator reviews were conducted to allow each principal investigator (PI) to render a subjective judgment of the maximum acceptable radiation dosage for the film types to be used on his experiment. This was done by visual inspection of the irradiated film samples. Results of the sensitometric analysis and PI evaluations were combined to form the Martin Marietta-recommended acceptable radiation dose levels for the various film types presented in Table 1.

Most of these films are to go into orbit in the OWS or MDA on Flight 1, even though they may be used on Flights 3 or 4. This results in the majority of the film being stored in orbit for several months (81 to 210 days). From Figure 5, the corresponding radiation dose would be 12.5 to 31.5 rads in the MDA and 9.7 to 25.2 rads in the OWS. Comparing these values with the data in Table 1, it is obvious that most of the film would be fogged beyond use before it was put into a camera, unless specific protective measures were taken.

S190 Borosilicate Window

A second radiation test program was conducted at the Lawrence Radiation Laboratory: (1) to quantify the darkening effect of electron fluence on borosilicate BK-7 glass; (2) to determine whether the electroconductive coating on the outer surface of the glass would be subject to degradation by the radiation environment; and (3) to determine if a static discharge of the trapped electrons, and resultant Lichtenberg figure, would be possible at the expected fluence levels (the latter effect was noted by the National Bureau of Standards (ref. 8) in tests performed on a similar borosilicate glass, BK-7G). Samples of the glass were exposed to a spectrum of electrons which had a maximum energy of 2.5 mev. After irradiation, the glass surface was struck with a grounded point in an effort to discharge the sample. No Lichtenberg figures were observed in any of the samples and it was assumed that the strength of the glass was unchanged since there were no cracks. However, additional tests are planned later this year to measure bending strength of an irradiated sample.

TABLE 1.-Recommended acceptable radiation dose levels for various Skylab photographic films.

Film Type	Experiment Numbers	Recommended Acceptable Rad Dose
OWS Vaults:		
S0166 (2485)	S063, S073, T025, T027	1
S0180	S190	1
	M479	2
SC-6	S019, S020	1.5
103-0, UV	S063	2
S0121 - Color	S190	2
S0246 (2424)	S190	2
S0168	M151	3
	M507, M508, M509, T013, T020, Oper.	4
2403	T025, T027	4
5242 EFB - Color	M512	8
103a-F	T027	8
I-N Spectroscopic	S190	8
3400	S190	8
3401	(Formerly considered for S190)	8
S0368 - Color	D021, Operational	8
MDA Vaults (ATM Film):		
S0114	S054, S056	8
104-01 (SWR)	S082 A & S082 B	8
3400	S052, S054	16
	S082 A & S082 B	32
S0392	H-Alpha 1	32

Transmittance was measured both before and after irradiation. The results are shown in Fig. 7 and 8, along with the required level of transmittance. Clearly, the window could not fly the entire Skylab mission of 250 days unprotected, and still be within the required specification of transmittance, since the expected external electron flux is approximately 5×10^{10} electron/cm^2/day.

OPERATIONAL SOLUTIONS

Excessive Film Fog

Prediction of the amount of radiation-induced fog that a particular film will acquire is based on a number of factors: storage location, length of time in storage, experiment (camera) location, length of time in camera, etc. The need for additional protection for a film is determined by the difference between the maximum acceptable dose (Table 1) and the dose to be received during operation of the experiment. If the dose received during storage is larger that this difference, a film vault is necessary. During the Skylab missions, even though most of the photographic film is to be launched with the workshop on Flight 1, each load is to return at the end of the flight on which it is used. Consequently, each load of film has different protection requirements, even though it is the same film used in the same experiment.

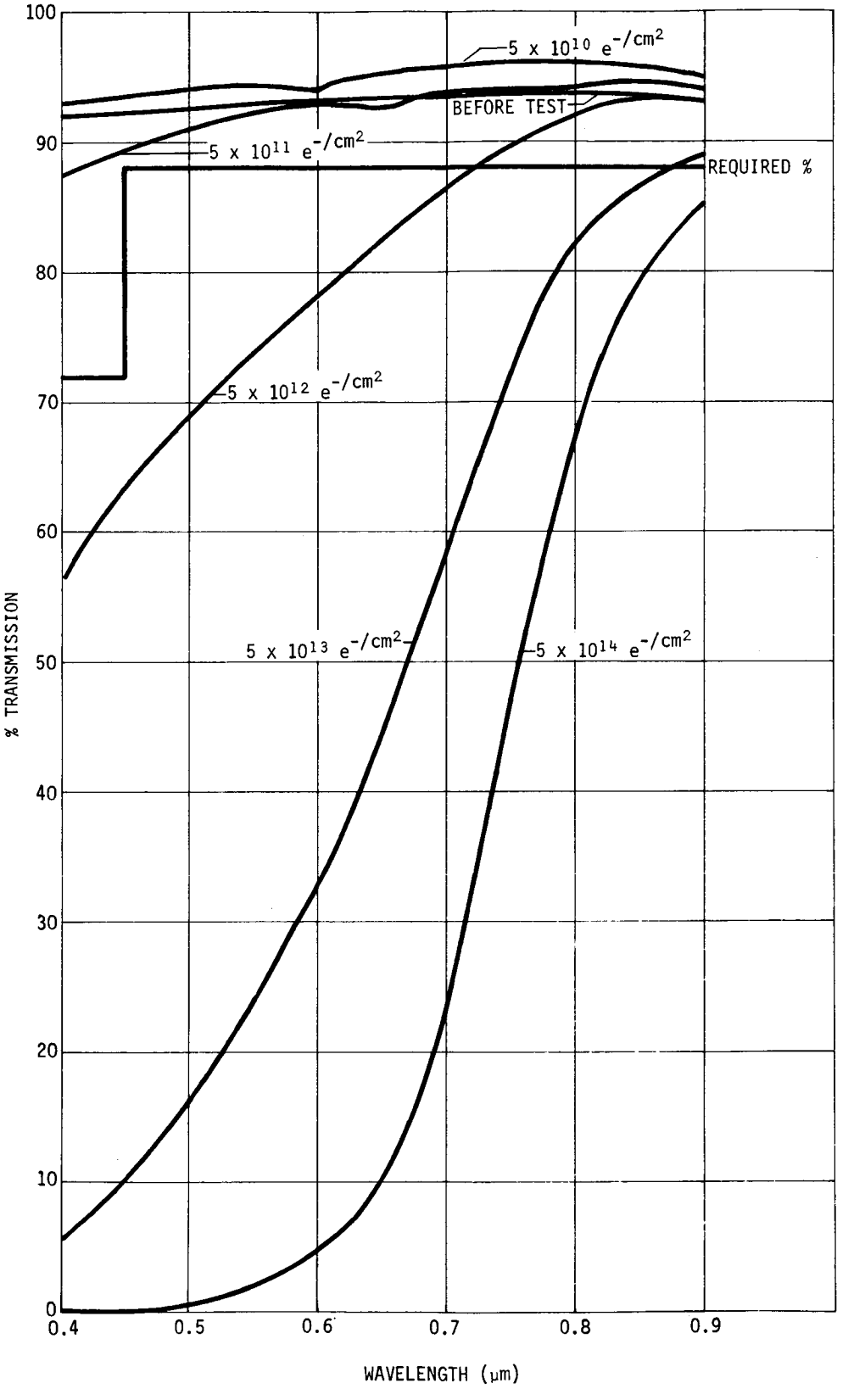

FIGURE 7.-Transmittance of irradiated uncoated samples of BK-7 borosilicate glass.

TRANSMITTANCE OF IRRADIATED UNCOATED SAMPLES OF BK-7 BOROSILICATE GLASS

MARTIN MARIETTA
DENVER DIVISION

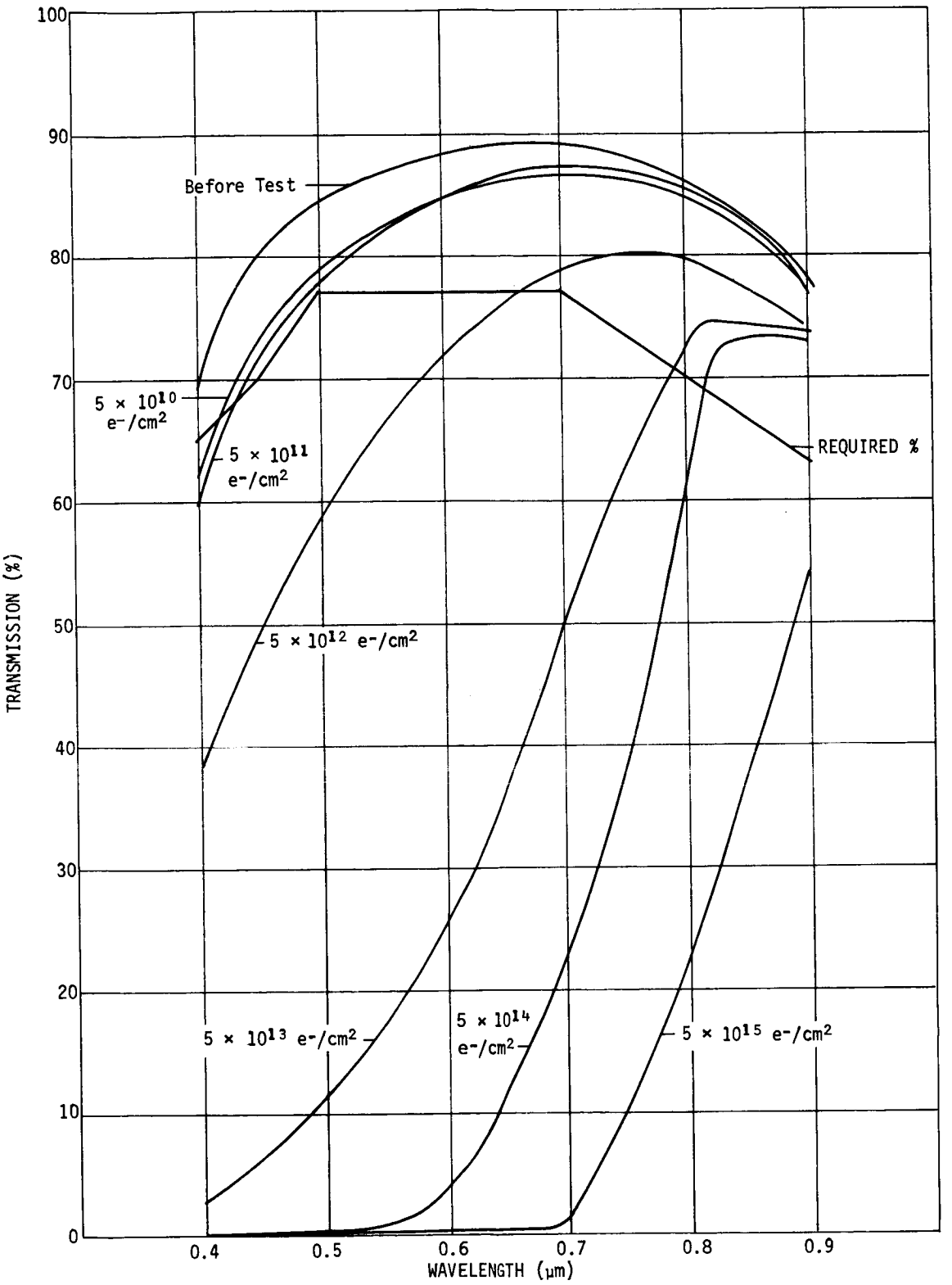

FIGURE 8.-Transmittance of irradiated coated samples of BK-7 borosilicate glass.

Taking into account these factors and the mission requirement that all ATM experiment film must be stored in the MDA, and the structural requirement that no more than 500 lb could be mounted on any one longeron, resulted in four separate film vaults in the MDA. All vaults are made of aluminum, ranging in thickness from 0.09 to 1.5 in., and weigh a total of 1545 lb empty. They were designed and built by Martin Marietta's Denver Division.

All other films are to be stored in the OWS. Since this module is capable of supporting a larger concentrated weight, only one vault with several compartments of various thicknesses was required. This, of course, is a more efficient design method, since one compartment shields the next and reduces total amount of material need. Even so, this vault weighs 2398 lb empty and requires a pallet to stand on to distribute its weight over the floor of the OWS. It is made up of four aluminum compartments whose thicknesses are 0.25, 1.9, 2.9, and 3.4 in. This vault was designed in the Astronautics Laboratory of the Marshall Space Flight Center and is being built by McDonnell Douglas' Western Division.

With the addition of these five film vaults, at a total weight penalty of almost 4000 lb, all photographic film should return with usable data.

Darkening of the S190 Borosilicate Window

Since the electron environment that the window will see is made up mostly of low energy particles, a lightweight shield is all that is needed to provide adequate radiation protection against darkening. Consequently, the current window cover design involves a honeycomb structure with 0.028-in. fiberglass face sheets. In addition to shielding the glass from radiation damage, the window cover also serves as a meteoroid shield to stop meteoroid erosion; a thermal shield to allow the window and frame heaters to stabilize the temperature of the glass (when desired for optical reasons); and a contamination shield to prevent contaminates from depositing on the window. A simple opening mechanism allows the astronaut to swing the shield away when he desires to operate the S190 experiment.

SUMMARY

An experimental space station, Skylab, is to orbit the earth during 1973 in a 235-n-mi-circular orbit inclined 50°. During its operational lifetime of approximately 238 days, three three-man crews will rendezvous with Skylab and carry out various experiments up to 56 days before returning.

The expected radiation environment Skylab will see is made up of protons and electrons from the Van Allen belt, and of cosmic rays. The large number of electrons are mostly low energy particles that result in a high surface dose, but add little to the internal dose. This high electron fluence to the outside surface of a borosilicate window used by one of the experiments could cause darkening of the glass. The dose inside Skylab (due mainly to protons), although not a problem for the astronauts, is a problem for photographic film used by some of the experiments. The dose from cosmic rays is very low and does not become significant until very heavy structures, such as film vaults, are considered.

Two radiation test programs were run to quantify maximum acceptable film fog for each type film to be used and maximum acceptable window darkening. Since the expected environment would exceed these limits, five film vaults and a removable window cover were incorporated into the Skylab design, at a weight penalty of almost 4000 lb, to insure that useful data would be returned at the end of the mission.

REFERENCES

1. McIlwain, C. W.: "Coordinates for Mapping the Distribution of Magnetically Trapped Particles." *Journal of Geophysical Research*, vol 66, November 1961, pp 3681-3691.

2. Vette, J. I.: *Models of the Trapped Radiation Environment, vol I: Inner Zone Protons and Electrons.* NASA SP-3024, 1966.

3. Vette, J. I.; Lucero, A. B.; and Wright, J. A.: *Models of the Trapped Radiation Environment, vol II: Inner and Outer Zone Electrons.* NASA SP-3024, 1966.

4. Berger, M. J.; and Seltzer, S. M.: *Additional Stopping Power and Range Tables for Protons, Mesons, and Electrons.* NASA SP-3036. National Bureau of Standards, 1966.

5. Hill, C. W.; Davis, D. N.; and Davis, J. H.: *Space Radiation Hazards to Project Skylab Photographic Film.* NASA CR-61329. Lockheed Georgia Company, June 1970.

6. Burrell, M. O.; Wright, J. J.; and Watts, J. W.: *An Analysis of Energetic Space Radiation and Dose Rates.* NASA TN D-4404. February 1968.

7. Ress, E. B.; Oldham, L. P.; and Dean, J. W.: *Skylab Radiation Film Studies.* Skylab Report ED-2002-1110. Martin Marietta Corporation, June 1970.

8. Maliston, I. H.; and Dodge, M. J.: "Effects of Space Radiation on Refractive Properties of Optical Glass." *Proceedings of the Annual Conference of Photography, Science, and Engineering.* May 1966, p 75.

TECHNIQUES FOR CALCULATING SPACE RADIATION DAMAGE TO PHOTOGRAPHIC FILM ABOARD SKYLAB

C.W. Hill and C.F. Neville
Lockheed-Georgia Company

The effect of space radiation on photographic film employed in experiments aboard Skylab is being investigated in order to minimize film vault weight and assure data survival[1]. Radiation-induced film fogging density is employed as a damage criterion in these calculations. Photographic density is computed by integrating the product of radiation flux and an energy-dependent damage function; the damage function is empirically derived from the experimental work of other investigators[2,3].

Proton damage functions are obtained for many films from experimental data of radiation-induced density for 10 to 130 MeV protons. For other films, proton damage functions are obtained by interpolation among the available damage functions using the results of Cobalt-60 tests for normalization.

Damage functions for alphas are obtained by rescaling the proton data on the basis of LET.

Damage functions for electrons are constant over the energy range 0.5 to 16. MeV and approximate the value for minimum ionizing protons. Below 0.5 MeV electron damage functions are scaled from the proton data on the basis of LET.

Damage functions for gamma rays (bremsstrahlung) are identical to those of electrons from 0.6 to 16. MeV and are relatively constant when based on the rad dose which would be delivered to air or water under charged particle equilibrium conditions. The relative sensitivity rises by factors of 7 to 50, depending on emulsion composition, at 40 keV.

Using these empirically determined damage functions, radiation fogging to Skylab film is estimated in the following manner. A mathematical model of the Skylab cluster geometry is constructed. The LSVDC4 computer program[4] calculates transport of the external radiation environment through the model embedded in the films. Recent program modifications derive proton, alpha, electron, and bremsstrahlung spectra and fold in appropriate damage functions. The computed radiation-induced fogging values are then used to estimate the adequacy of film vault shielding.

---

1 C.W. Hill, D. N. Davis, and J. H. Davis, "Space Radiation Hazards to Project Skylab Photographic Film," Lockheed-Georgia Company Report ER-10725, June 1970.

2 R. H. Herz, "The Photographic Action of Ionizing Radiations," Wiley-Interscience, London 1969.

3 E. B. Ress, L. P. Oldham, J. W. Dean, and J.E. Burghardt, "Skylab Radiation Film Studies," Martin Marietta Corporation Report ED-2002-1110, June 30, 1970.

4 C. W. Hill, W. B. Ritchie, and K. M. Simpson, Jr., "Data Comilation and Evaluation of Space Shielding Problems, "Volume IV, LSVDC4 Program Systems, Lockheed-Georgia Company Report ER-7777, February 1967.

(MANUSCRIPT NOT AVAILABLE)

FREQUENCY OF LIGHT-FLASHES INDUCED BY CERENKOV RADIATION FROM HEAVY COSMIC-RAY NUCLEI

RICHARD MADEY and P. J. MCNULTY
Department of Physics
Clarkson College of Technology
Potsdam, New York 13676

Astronauts on Apollo missions 11 through 14 have reported seeing light-flashes at a typical rate of about one per minute. We have calculated the expected frequency of light-flashes induced in the dark-adapted eye by Cerenkov radiation from the flux of heavy nuclei that exists in the region of space beyond the geomagnetic field. In order to induce a visual sensation, at least two Cerenkov photons must be absorbed in coincidence by the rhodopsin molecules in a small area of the retina served by a single optic nerve fiber. The fact that the photons must be coincident on a small cluster of rods restricts the path length of the heavy nuclei for the production of relevant Cerenkov photons to a thin layer of the nervous tissue of the retina just ahead of the rods. The expected frequency of light-flashes depends on the threshold number of photons that must be absorbed in a rod cluster. It is known that individual threshold values in the dark-adapted eye can vary by a factor of five even among young normal human subjects. The result of our calculation can be presented as a curve of the mean frequency of light-flashes versus the threshold number of absorbed photons. The results are not sensitive to variations in the path length from 5 to 15 grams per square centimeter of water-equivalent before the nucleus reaches the retina. Our calculations are based on the fluxes and energy spectra of galactic cosmic-ray nuclei helium to iron measured at a time of minimum solar modulation. The expected light-flash frequencies induced by Cerenkov radiation are consistent with the frequencies reported by the astronauts on Apollo missions 11 through 14.

Astronauts on Apollo missions 11 through 14 have reported seeing light-flashes in a region beyond the geomagnetic field when their eyes were dark-adapted (1). The mean interval between the light flashes is typically about one minute. According to physiological experience, every stimulus that is capable of exciting the visual sensory nerve fiber can produce the sensation of light (2). That part of the nervous system where light sensations can be excited comprises the retina, the optic nerve, and a part of the brain containing the fibers of the optic nerve. In addition to visible photons, types of stimuli that are known to induce light sensations include mechanical stimulation, electric currents, and X-rays (2)-(4). Pressure on the eyeball produces a pressure-image or phosphene (5). Light flashes can be induced by current discharges through the optic nerve. Collimated X-rays (3)(4)(6)-(11) have been shown to stimulate spots on the retina of the dark-adapted eye. Previously, we have given a brief report (12) of a calculation of the expected frequency of light-flashes induced in the dark-adapted eye by Cerenkov radiation from the flux of heavy nuclei that exists in regions of space beyond the geomagnetic field. In this paper, we present some of the details of this work. Fazio et al (13) have proposed that the Cerenkov mechanism may be the dominant one responsible for the light flashes observed by the astronauts. Tobias et al (14) indicate that the dominant mechanism is probably ionization.

VISUAL SENSATIONS INDUCED BY CERENKOV RADIATION

Cerenkov radiation occurs when a charged particle traverses a dielectric medium at a speed greater than the speed of light in the medium. The Cerenkov wave is conical. The apex of the cone is at the position of the charged particle. The radiation is emitted in the forward direction at an angle θ with the direction of the particle velocity. The angle θ is the half-angle of the cone. It is given by the relation

$$\cos\theta = 1/n\beta \qquad (1)$$

where n is the index of refraction of the dielectric medium at the frequency of interest, and β is the speed of the particle in units of the speed of light.

Since the Cerenkov radiation is an electromagnetic shock wave, it contains all frequency components that can satisfy Eq. (1). Per unit path length traversed by a particle of charge Ze and speed β, the number of photons with frequency ω in the interval $\Delta\omega$ is given by

$$\frac{dN}{d\ell} = Z^2 \frac{\alpha}{c} \sin^2\theta \, \Delta\omega \qquad (2)$$

Here the fine structure constant $\alpha = e^2/\hbar c \simeq 1/137$. This expression assumes that the medium is non-despersive; that is, the index of refraction is assumed to be constant over the frequency interval $\Delta\omega$ of the emitted light. Wald and Brown (15) have measured the relative absorption spectrum of human rhodopsin. The wave-

lengths at the half-amplitude points of the scotopic (rod) spectral sensitivity curve at the retinal surface are $\lambda_1 = 4.4 \times 10^{-5}$ cm and $\lambda_2 = 5.4 \times 10^{-5}$ cm. Thus, in the wavelength interval corresponding to the sensitive region of the eye, Eq. (2) becomes

$$\frac{dN}{d\ell}(\text{visible photons/cm}) = 193\, Z^2 \sin^2\theta \qquad (3)$$

Hecht et al (16) analyzed data on threshold sensitivity and showed that a fully dark-adapted human rod can be excited by the absorption of a single (5100 angstrom) visible photon. Although a rod responds to a single absorbed photon, a single rod response will not activate the optic nerve to produce a visual sensation. For vision, it is necessary that there be an N-fold coincidence of photons absorbed in a cluster of rods served by a single optic nerve fiber (17). Threshold sensation under optimal physiological conditions requires at least a two-fold coincidence and perhaps up to a 14-fold coincidence. In the experiments of Hecht et al (16), the probability is negligible that two photons would be absorbed in a single rod because of the small number of photons incident on a much larger number of rods in a cluster served by a single optic nerve. For the Cerenkov radiation from a charged particle to induce a visual sensation, there must be a coincidence of at least two photons absorbed in a small area of the retina that contains a cluster of rods served by a single optic nerve fiber. It turns out that this requirement restricts the path length to a small region in the retina for the production of Cerenkov photons that can induce a visual sensation. The fact that the Cerenkov photons must be coincident on a small area of the retina restricts the relevant path length to a thin layer of the nervous tissue of the retina just ahead of the rods. The equations that govern the production of a visual sensation by Cerenkov light can be obtained with reference to Fig. 1. Let r_o denote the radius of a small retinal area that contains a cluster of rods served by a single optic nerve fiber. The Cerenkov photons that are incident on a rod cluster are produced by a particle that traverses a path length ℓ_o just ahead of the rods. The path length ℓ_o is given by

$$\ell_o = r_o/\tan\theta \qquad (4)$$

Thus, the number M of Cerenkov photons (in the wavelength interval between 440 and 540 nanometers) incident on a rod cluster is

$$M = \int_0^{\ell_o} \left(\frac{dN}{d\ell}\right) d\ell = 193\, Z^2 r_o \sin\theta\cos\theta \qquad (5)$$

Eq. (5) may be rewritten

$$M = 193\, Z^2 \frac{(n^2\beta^2 - 1)^{1/2}}{n^2\beta^2} r_o \qquad (6)$$

The number of Cerenkov photons incident on a rod cluster is directly proportional to the radius of the cluster. A single ganglion cell serves a circular area on the retina with a diameter that corresponds to visual angle of about 20 minutes of arc (18). For a posterior

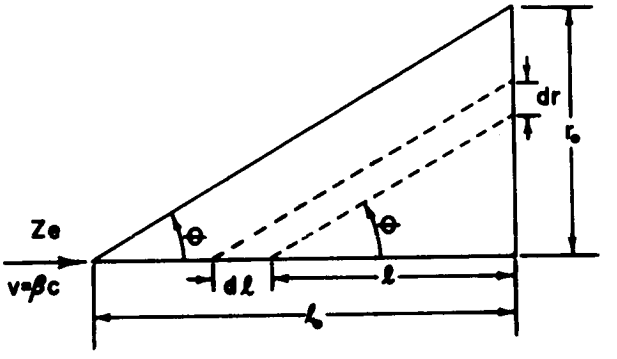

CERENKOV PHOTON PRODUCTION

FIGURE 1. Geometry for the Production of a Visual Sensation by Cerenkov Radiation from a Heavy Nucleus Traversing the Retina

nodal distance of 16.68 mm (19), a visual angle of 1 minute of arc corresponds to an image size on the retina of 4.85 microns. Thus, the radius of a circular area on the retina served by a single ganglion cell is about 48.5 microns ($= 4.85 \times 10^{-3}$ cm). For this value of r_o, Eq. (6) becomes

$$\frac{M}{Z^2} = 0.935\, \frac{(n^2\beta^2 - 1)^{1/2}}{n^2\beta^2} \qquad (7)$$

In Fig. 2, we plot the normalized number M/Z^2 of visible Cerenkov photons incident on a rod cluster as a function of the speed β of a stripped nucleus with charge Z moving in the nervous tissue of the retina just ahead of the rods. For the index of refraction n of this nervous tissue, we use 1.338. For a given nucleus of charge Z traversing the retina with a speed β, the number M of visible Cerenkov photons incident on a rod cluster is equal to the product of Z^2 and the value of the ordinate of the visible-photon production function in Fig. 2 that corresponds to the speed β. The minimum speed β_{min} at the retina of a nucleus of charge Z that can produce a specified number M of relevant Cerenkov photons can be found from this charge-normalized production function in Fig. 2. In Fig. 3, we plot β_{min} versus Z for M = 2, 5, 10, 20, 50, 100, 200, and 500. The absolute threshold speed β_{th} for the production of Cerenkov photons can be found from Eq. (1) for the limiting case $\cos\theta \to 1$; thus,

$$\beta_{th} = \frac{1}{n} \qquad (8)$$

For n = 1.338, $\beta_{th} = 0.7474$. This value for the threshold speed corresponds to a threshold kinetic energy per nucleon of 470 MeV per nucleon.

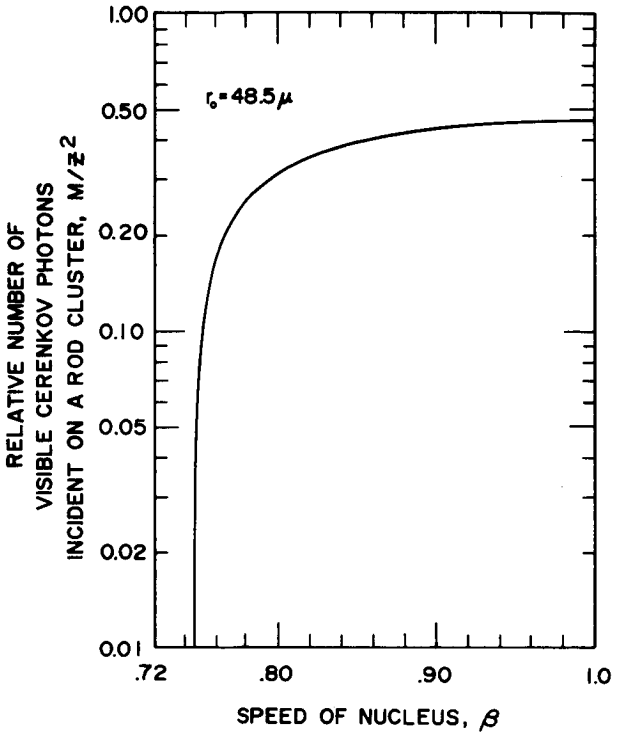

FIGURE 2. The Relative Number of Visible Cerenkov Photons Incident on a Rod Cluster versus the Speed of a Nucleus

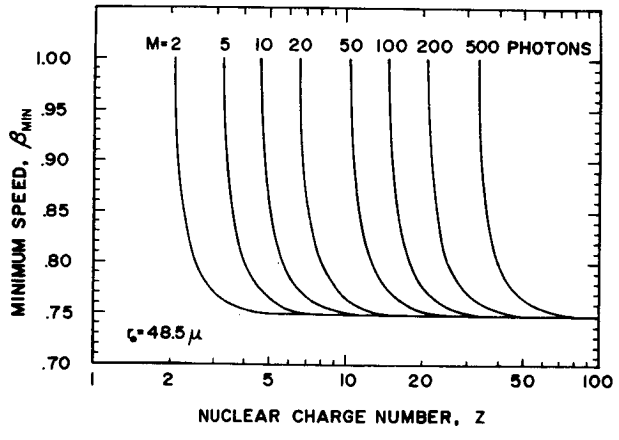

FIGURE 3. The Minimum Speed of a Nucleus for the Production of a Specified Number M of Visible Cerenkov Photons Incident on a Rod Cluster versus the Charge Number Z of the Nucleus

At least two photons must be absorbed by rhodopsin in order to induce a visual sensation. Hecht et al (16) estimated that from 5 to 20 percent of the visible (510mμ) photons incident on the retina are actually absorbed by the rhodopsin. Later estimates indicate that the probability of absorption of a visible (505 mμ) photon that interacts with a rod is about 30 percent (20)(21). Some of the photons incident on the retina interact with the cones or with material between the rods. The rod density is greatest at an angle of about 20 degrees to the right of the observer's fovea (22); in this region, about 70 percent of the area is occupied by rods. Thus, the probability of absorption by rhodopsin of visible (505 mμ) photons incident on the retina near 20 degrees is about 20 percent. If M photons are incident on the retina, the probability that exactly (M-T) photons will be absorbed is given by the binomial probability distribution:

$$P(M-T) \equiv \binom{M}{T} p^{M-T} q^{T} \tag{9}$$

where p = the probability that a photon will be absorbed, and q = 1-p = the probability that a photon will not be absorbed.

If M photons are incident, the probability that at least R photons will be absorbed is

$$Q_M(\geq R) \equiv \sum_{T=0}^{T=M-R} P(M-T) = \sum_{T=0}^{T=M-R} \binom{M}{T} p^{(M-T)} q^{T} \tag{10}$$

In Eqs. (9) and (10), the symbol $\binom{M}{T}$ denotes the binomial coefficients:

$$\binom{M}{T} \equiv \frac{M!}{T!\ (M-T)!} \tag{11}$$

These coefficients are tabulated in standard handbooks. The probability Q_M ($\geq$R) that at least R photons will be absorbed in rhodopsin is listed in Table 1 for R = 2, 5, 10, and 20 as a function of the number M of incident photons for a single photon absorption probability p= 1/5. These data are plotted in Fig. 4.

FLUXES AND ENERGY SPECTRA OF GALACTIC COSMIC-RAY NUCLEI

Comstock, Fan and Simpson (23, 24) have measured the fluxes and energy spectra of the galactic cosmic-ray nuclei helium to iron at the time of minimum solar modulation (viz, October 1964 - November 1965). Based on the reported differential energy spectra of the various nuclei, we have represented the unidirectional differential flux spectra of nuclei by an inverse power law in the total energy per nucleon E above E_1, and by a constant value in the kinetic energy per nucleon in the interval between T_o and T_1:

TABLE 1

THE PROBABILITY THAT AT LEAST R (= 2, 5, 10, and 20) PHOTONS WILL BE ABSORBED VERSUS THE NUMBER OF INCIDENT PHOTONS FOR A SINGLE PHOTON ABSORPTION PROBABILITY OF ONE-FIFTH

Number of Incident Photons M	Probability of Absorbing at Least R Photons, $Q_m(\geq R)$			
	R = 2	R = 5	R = 10	R = 20
2	0.0400			
3	0.1040			
4	0.1808			
5	0.2627	0.0003		
6	0.3446	0.0016		
7	0.4233	0.0047		
8	0.4967	0.0104		
9	0.5638	0.0196		
10	0.6242	0.0328		
11	0.6779	0.0504		
12	0.7251	0.0726		
13	0.7664	0.0991		
14	0.8021	0.1298		
15	0.8329	0.1642	0.0001	
16	0.8593	0.2018	0.0002	
17	0.8818	0.2418	0.0005	
18	0.9009	0.2836	0.0009	
19	0.9171	0.3267	0.0016	
20	0.9308	0.3704	0.0026	
30	0.9896	0.7448	0.0611	
40	0.9985	0.9241	0.2682	
50	0.9998	0.9815	0.5563	0.0009
60	1.0	0.9961	0.7868	0.0107
70	1.0	0.9992	0.9155	0.0545
80	1.0	0.9998	0.9713	0.1634
90	1.0	1.0	0.9914	0.3382
100	1.0	1.0	0.9976	0.5398
110	1.0	1.0	0.9994	0.7190
120	1.0	1.0	0.9998	0.8483
130	1.0	1.0	1.0	0.9267
150	1.0	1.0	1.0	0.9680
160	1.0	1.0	1.0	0.9872
170	1.0	1.0	1.0	0.9953
180	1.0	1.0	1.0	0.9984
190	1.0	1.0	1.0	0.9994
200	1.0	1.0	1.0	1.0

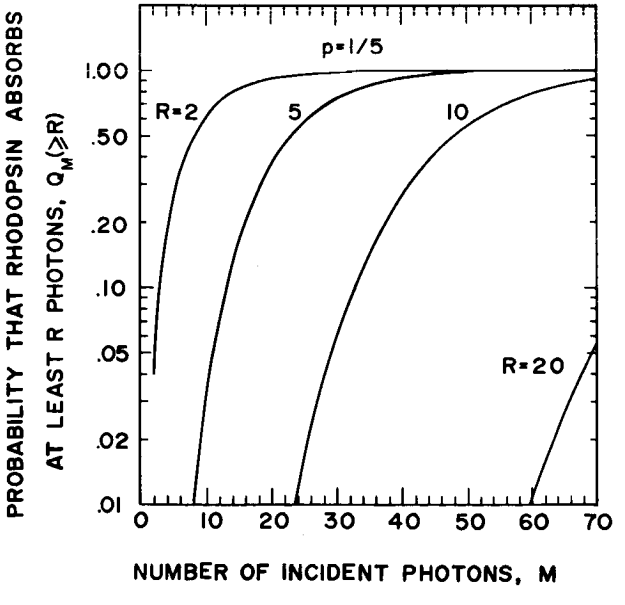

FIGURE 4. The Probability that Rhodopsin Absorbs at Least R (= 2, 5, 10 and 20) Photons versus the Number of Photons Incident on the Retina for a Single Photon Absorption Probability of Twenty Percent

$$n(E) = CE^{-\gamma} \qquad (E > E_1) \tag{12}$$

$$n(T) = C_1 \qquad (T_o < T < T_1) \tag{13}$$

where

$$E(\text{BeV/nucleon}) = T(\text{BeV/nucleon}) + 0.9315 \tag{13}$$

The spectral exponent γ has an observed value of about 2.5. The representation in Eq. (13) is valid for a kinetic energy T_o in the neighborhood of 100 MeV per nucleon. The value of the constant C_1 for oxygen, as reported by Comstock et al (23), is 5.4 nuclei/m^2-sec-sr-(BeV/nucleon) in the time interval from October to November, 1964. The values of C_1 for other nuclei come from measurements on the relative abundance of the elements in the cosmic radiation. There seems to be no significant change in the relative abundances with time even though the flux level changes with the solar cycle. Also, within the present experimental errors, the relative abundances appear to be independent of energy. The relative abundance of the nuclei in the cosmic radiation from the (IMP IV and OGO I) satellite measurements by the University of Chicago group are listed in Table 2 and plotted in Fig. 5. The coefficient C in the high-energy portion of the differential flux Eq. (12) is given by Comstock et al (23) for some of the nuclei (namely, C, O, B, Ne, Mg, Si and the Fe-Co-Ni group). These values for the coefficient C are tabulated in Table 2. For these nuclei, values for the total energy per nucleon E_1 can be found by equating Eqs. (12) and (13):

$$E_1 = (C/C_1)^{1/\gamma} \tag{15}$$

Table 2

RELATIVE ABUNDANCE OF NUCLEI IN THE COSMIC RADIATION AND PARAMETERS FOR REPRESENTING THE DIFFERENTIAL FLUX SPECTRA AT A TIME OF MINIMUM SOLAR MODULATION

Nucleus	Relative Abundance	Coefficient C_1 [p/m^2-s-sr-(BeV-nuc^{-1})]	Coefficient C [p/m^2-s-sr-(BeV-nuc^{-1})]	Total Energy E_1(BeV/nucleon)	Kinetic Energy T_1(BeV/nucleon)
$_2$He	(4.2 ± 0.6) x 10^3	228 ± 32			
$_3$Li	19.5 ± 5	1.06 ± 0.03	2.8	1.485	.554
$_4$Be	6.5 ± 2.2	0.35 ± 0.12	.94	1.485	.554
$_5$B	29 ± 6	1.6 ± 0.3	(4.3)	1.485	.554
$_6$C	100 ± 6	5.4 ± 0.3	(12)	1.376	.445
$_7$N	25.5 ± 2	1.4 ± 0.1	3.1	1.376	.445
$_8$O	100 ± 6	5.4 ± 0.3	(12)	1.376	.445
$_9$F	1.7 ± 0.2	0.092 ± 0.011	.14	1.168	.236
$_{10}$Ne	17.5 ± 3	0.96 ± 0.16	(1.4)	1.168	.236
$_{11}$Na	4.1 ± 1.1	0.22 ± 0.06	.25	1.064	.132
$_{12}$Mg	23 ± 1	1.2 ± 0.1	(1.4)	1.064	.132
$_{13}$Al	3.4 ± 0.4	0.18 ± 0.02	.27	1.183	.251
$_{14}$Si	17 ± 3	0.92 ± 0.16	(1.4)	1.183	.251
$_{15}$P	1.95 ± 1.0	0.11 ± 0.06	.18	1.170	.240
$_{16}$S	5.0 ± 1.3	0.27 ± 0.07	.40	1.170	.240
$_{17}$Cl	1.01 ± 0.29	0.055 ± 0.016	.081	1.170	.240
$_{18}$A	2.08	0.112	.17	1.170	.240
$_{19}$K	1.37	0.074	.11	1.170	.240
$_{20}$Ca	3.24 ± 0.65	0.17 ± 0.04	.25	1.170	.240
$_{21}$Sc	1.25	0.068	.10	1.170	.240
$_{22}$Ti	2.62	0.142	.21	1.170	.240
$_{23}$V	2.38	0.129	.19	1.170	.240
$_{24}$Cr	3.99 ± 1.25	0.215 ± 0.068	.32	1.170	.240
$_{25}$Mn	2.65	0.143	.21	1.170	.240
$_{26}$Fe-$_{27}$Co-$_{28}$Ni	8.15 ± 1.73	0.44 ± 0.09	(1.4)	1.589	.657

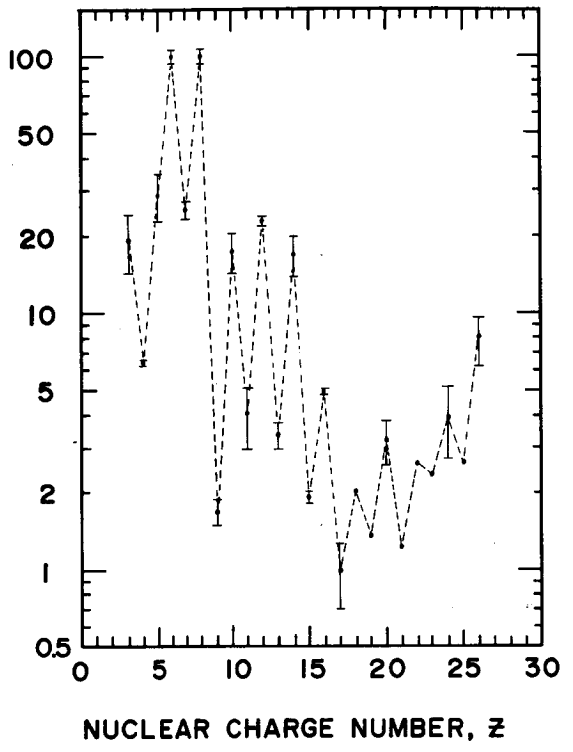

FIGURE 5. The Relative Abundance of Nuclei in the Galactic Cosmic Radiation

The values of E_1 are listed in Table 2. We have used Eq. (15) with $\gamma = 2.5$ to compute values for the coefficient C for the other nuclei for assumed (tabulated) values of E_1 and the measured values of C_1.

For $E > E_1$ (or $T > T_1$), the unidirectional integral flux spectra of the galactic cosmic-ray nuclei can be represented by the following power-law:

$$N(>E) = \int_E^\infty n(E)\,dE = \frac{CE^{-(\gamma-1)}}{\gamma - 1} \qquad (\text{for } E > E_1) \quad (16)$$

For $E_0 < E < E_1$ (or $T_0 < T < T_1$), the unidirectional integral flux spectra of galactic cosmic-ray nuclei can be represented as follows:

$$N(>E) = \int_E^{E_1} n(E)dE + N(>E_1) = C_1(E_1 - E) + \frac{C}{\gamma-1} E_1^{-(\gamma-1)} \quad (17)$$

Values of the coefficient $C/(\gamma-1)$ for integral flux spectra of galactic cosmic-ray nuclei for an integral spectral exponent $\gamma - 1 = 1.5$ at a time of minimum solar modulation are listed in Table 3. Also listed in Table 3 are unidirectional integral fluxes above a total energy of 1.4 BeV per nucleon, which is the threshold for the production of Cerenkov radiation in the retina.

Table 3

INTEGRAL FLUX SPECTRA OF GALACTIC COSMIC-RAY NUCLEI AT A TIME OF MINIMUM SOLAR MODULATION

Nucleus	Coefficient $C/(\gamma-1)$ $[p/m^2\text{-s-sr-(BeV/nuc)}^{-(\gamma-1)}]$	Flux Above Cerenkov Threshold $N(E \geq 1.40\,\text{BeV/nucleon})$ $(p/m^2\text{-s-sr})$
$_3$Li	1.88	1.04
$_4$Be	0.627	.60
$_5$B	2.87	1.58
$_6$C	8.00	4.94
$_7$N	2.07	1.28
$_8$O	8.00	4.94
$_9$F	0.091	.076
$_{10}$Ne	0.933	.78
$_{11}$Na	0.171	.43
$_{12}$Mg	0.933	.97
$_{13}$Al	0.183	.15
$_{14}$Si	0.933	.77
$_{15}$P	0.109	.091
$_{16}$S	0.267	.22
$_{17}$Cl	0.054	.045
$_{18}$A	0.107	.090
$_{19}$K	0.073	.061
$_{20}$Ca	0.168	.14
$_{21}$Sc	0.067	.056
$_{22}$Ti	0.140	.17
$_{23}$V	0.127	.11
$_{24}$Cr	0.212	.18
$_{25}$Mn	0.141	.18
$_{26}$Fe - $_{27}$Co - $_{28}$Ni	0.933	.47
		19.37

EXPECTED FREQUENCY OF LIGHT-FLASHES

To calculate the mean frequency of light-flashes expected from the Cerenkov photons associated with heavy nuclei that reach the retina, we have prepared a computer program that calculates the contribution to the light-flash frequency from each nucleus of charge number Z. For convenience, we introduce primed symbols to denote quantities at the retina. Unprimed symbols will refer to corresponding quantities in the incident spectrum. We sketch the steps involved in the calculation:

a. Find the minimum speed β'_{min} at the retina of a nucleus of charge Z as a function of the number M of visible Cerenkov photons incident on a rod cluster. This limiting speed is the solution of Eq. (7). In Fig. 6, we plot β'_{min} vs M for Z = 6, 10, 14, 20 and 28.

b. Calculate the minimum kinetic energy per nucleon T' at the retina for the production of M relevant photons:

$$T'_M = Mc^2(\gamma'_M - 1) \quad (18)$$

$$\gamma'_M = (1 - \beta'^2_M)^{-1/2} \quad (19)$$

c. Find the range (in tissue) of a proton R'_p with this kinetic energy T'_M. For this purpose, we have represented the range-energy relation by a power-law of the form:

$$R'_p = kT'^{\alpha}_M \tag{20}$$

To obtain the coefficient k and the exponent α, we use the range-energy curve for water (28). For protons in the energy interval from 100 to 1000 MeV, $k = 4.25 \times 10^{-3}$ gm/cm^2 H_2O-MeV$^{\alpha}$ and $\alpha = 1.627$; thus, for $100 < T'$ (MeV) < 1000,

$$R'_p(\text{gm/cm}^2 H_2O) = 4.25 \times 10^{-3} T'^{1.627}_M \tag{21}$$

d. Find the minimum kinetic energy per nucleon T_M in the incident spectrum for the production of M photons incident on a rod cluster. The nucleus of charge number Z and mass number A must traverse a path of length ℓ before reaching the retina. The path length in the vitreous body is typically 2.4 grams per cm^2. The nucleus must also penetrate the skin of the vehicle and possibly additional shielding material. We have carried out the calculations for typical path-lengths ℓ of 5 and 15 grams per cm^2 of water-equivalent. The range of a proton ℓ_p that is equivalent to the path-length ℓ traversed by a nucleus of charge number Z and mass number A is given by

$$\ell_p = \frac{Z^2}{A} \ell \tag{22}$$

For convenience, we calculate

$$R_p = R'_p + \ell_p \tag{23}$$

From the proton range R_p, we find the minimum kinetic energy per nucleon T_M in the incident spectrum:

$$T_M = (R_p/k)^{1/\alpha} = [(R'_p + \ell_p)/k]^{1/\alpha} \tag{24}$$

e. Calculate the minimum total energy per nucleon in the incident spectrum for the production of M relevant photons at the retina:

$$E_M(\text{BeV/nucleon}) = T_M(\text{BeV/nucleon}) + 0.9315 \tag{25}$$

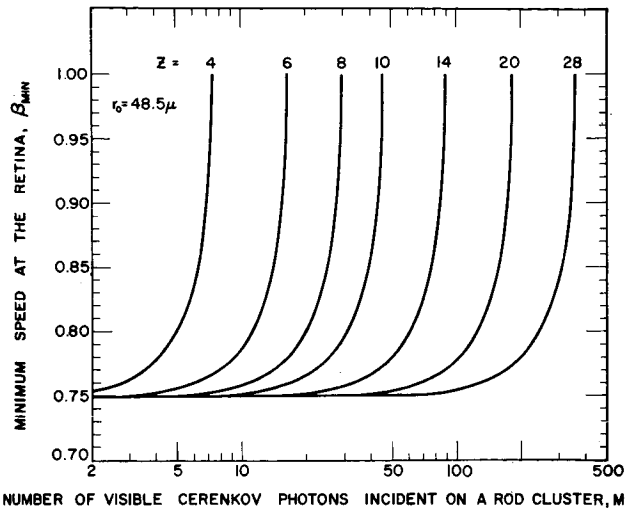

FIGURE 6. The Medium Speed of a Nuclear of Charge Number Z for the Production of M Visible Cerenkov Photons Incident on a Rod Cluster versus the Number M

f. Find the unidirectional integral flux density N_M ($> E_M$). The symbol N_M ($> E_M$) denotes the unidirectional integral flux density of a nucleus of charge Z in the incident spectrum that can produce at least M relevant photons at the retina. From Table 2, we see that the threshold value of E_M for the production of M relevant Cerenkov photons exceeds E_1 for $5 \leq Z \leq 25$.

g. Find the incident unidirectional flux density $\Delta N_{Z,M}$ of a nucleus of charge Z that produces M relevant photons at the retina:

$$\Delta N_{Z,M} = N_{Z,M-1/2}(\geq E_{M-1/2}) - N_{Z,M+1/2} - N_{Z,M+1/2}(\geq E_{M+1/2}) \tag{26}$$

h. Calculate the omnidirectional flux $\Delta F_{Z,M}$ of a nucleus of charge Z that can produce M relevant photons at the retina:

$$\Delta F_{Z,M}(\text{nuclei/minute}) = 120\,G\,\Delta N_{Z,M}(\text{nuclei/m}^2\text{-sec-sr}) \tag{27}$$

Here the factor 120 consists of a factor 2 to take into account both eyes and a conversion factor of 60 seconds per minute. The factor G (m^2-sr) is the geometric factor for the sensitive region of the retina. From a curve (29) of the relative sensitivity of the eye as a function of the angular position of the test flash with respect to the fovea, we estimate that the sensitive

region of the retina is an annulus on the surface of a sphere. For visual angles α_1 and α_2 between about 10 and 50 degrees, this sensitive annulus on the retina subtends angles β_1 and β_2 at the center of a spherical eyeball of radius R. The geometric factor G of the sensitive region of the retina for omnidirectionally incident radiation is

$$G = (4\pi)(\pi R^2)(\cos\beta_1 - \cos\beta_2) \qquad (28)$$

For R = 1.2 cm, $\beta_1 = 14^\circ$ and $\beta_2 = 70^\circ$, we obtain $G = 35.7\ cm^2\text{-sr} = 35.7 \times 10^{-4}\ m^2\text{-sr}$.

i. Use Eq. (10) to calculate the probability $Q_M(\geq R)$ that at least R photons will be absorbed if M photons are incident on a rod cluster. The probability p that the rhodopsin in a rod cluster absorbs a visible (λ=505mμ) is about 20 percent.

j. Find the contribution $c_{Z,M}(\geq R)$ to the mean frequency of light flashes induced by the absorption of at least R photons from the M relevant photons produced at the retina by the flux $\Delta F_{Z,M}$ of a nucleus of charge number Z.

$$c_{Z,M}(\geq R) = Q_M(\geq R)\,\Delta F_{Z,M} \qquad (29)$$

k. Find the total contribution $C_Z(\geq R)$ from nuclei of charge number Z to the mean frequency of light flashes induced by the absorption of at least R photons by summing over all allowed values of M:

$$C_Z(\geq R) = \sum_{M=R} c_{Z,M}(\geq R) \qquad (30)$$

The numbers in Table 4 represent the contribution from each nucleus to the number of light flashes per minute, $C_Z(\geq R)$, expected at a time of minimum solar modulation for an observer with a threshold that corresponds to the absorption of at least R (= 5, 10, and 20) visible Cerenkov photons. The light-flash frequencies in Table 4 are for a path-length of 15 grams per cm^2 of water-equivalent ahead of the retina. Since the frequencies increase slightly for a smaller path-length of 5 grams per cm^2 of water-equivalent, we note that they are not sensitive to small variations in the path-length.

l. Finally, find the mean frequency of light-flashes induced by the absorption of at least R photons by summing the contributions from each nucleus of charge number Z.

$$C(\geq R) = \sum_Z C_Z = \sum_Z \sum_{M=R} Q_M(\geq R)\,\Delta F_{Z,M} \qquad (31)$$

Table 4

THE CONTRIBUTION FROM EACH NUCLEUS TO THE LIGHT-FLASH FREQUENCY, $C_Z(\geq R)$, EXPECTED AT A TIME OF MINIMUM SOLAR MODULATION FOR AN OBSERVER WITH A THRESHOLD THAT CORRESPONDS TO THE ABSORPTION OF AT LEAST R (= 5, 10, and 20) VISIBLE CERENKOV PHOTONS. (This Calculation Assumes That Each Nucleus Traverses a Path-Length of 15 Grams/cm^2 of Water-Equivalent Ahead of the Retina)

Nuclear Charge Number Z	Frequency [(Flashes per Minute) x 10^2]		
	R = 5	R = 10	R = 20
3	---	---	---
4	---	---	---
5	68	---	---
6	1227	---	---
7	998	6	---
8	7695	247	---
9	130	14	---
10	1611	429	---
11	324	156	---
12	1805	1245	19
13	358	299	19
14	1806	1648	315
15	210	200	78
16	506	490	301
17	102	100	78
18	203	200	175
19	134	133	123
20	303	300	286
21	73	72	68
22	67	65	59
23	38	37	32
24	44	43	36
25	22	21	18
26-27-28	110	105	87
	17,833	5810	1694

In Fig. 7, we plot the number of light-flashes per minute, $C(\geq R)$, versus the threshold number R of absorbed Cerenkov photons. The upper and lower limits of each band in this figure correspond to typical path lengths of 5 and 15 grams per cm^2 of water-equivalent. It should be noted also that the curves in Fig. 7 are based upon fluxes of heavy nuclei observed at a time of solar minimum.

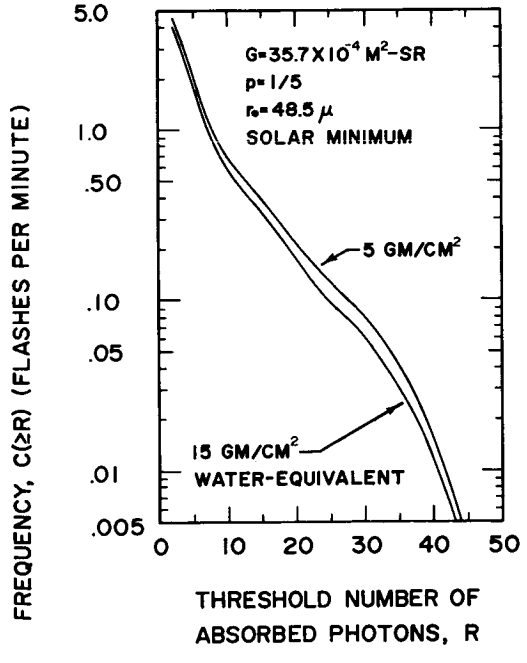

FIGURE 7. The Expected Mean Frequency of Visual Sensations Induced by the Absorption of at Least R Visible Cerenkov Photons in a Rod Cluster versus the Threshold Number R

CONCLUSION

From the results of our calculations, we can draw the following conclusions:

1. The expected frequency of light-flashes depends on the threshold number of photons that must be absorbed in a rod cluster. It is known that individual threshold values can vary by a factor of five even among young normal human subjects (30, 31). Thus, the observed frequency will depend on the physiological and psychological conditions of the observer. The calculated frequency decreases rapidly at first as the threshold number of photons increases from two to about eight; then it decreases relatively slowly in the region of eight to thirty absorbed photons; and finally it decreases more rapidly at higher values of the threshold number of absorbed photons.

2. The expected frequencies of visual sensations induced in the dark-adapted eye by Cerenkov radiation from heavy nuclei in the galactic cosmic radiation beyond the geomagnetic field are consistent with the frequencies reported by astronauts on Apollo missions. Apollo 13 astronaut Fred W. Haise reported ten flashes in five minutes; astronaut James A. Lovell reported one every two minutes; and astronaut John L. Swigert saw two flashes in about 30 minutes. The Apollo 13 observations were made at a period of maximum solar modulation.

3. The curve of the expected frequency of visual sensations induced by Cerenkov radiation is not sensitive to variations in the path length from 5 to 15 grams per cm^2 of water-equivalent before the nucleus reaches the retina.

4. The expected frequency of visual sensations induced by Cerenkov radiation decreases rapidly as the threshold number of absorbed photons increases. The observation of light-flash frequency of the order of two per minute should correspond to the absorption of a few photons and to peak efficiencies for the detection of visual sensations (16) (31-34). The steepness of the curve of frequency versus number of absorbed photons in the region of a few absorbed photons has interesting implications for studying the threshold sensitivity of the eye. A measurement of the light-flash frequency with a precision of the order of ten percent may permit a determination of the threshold number of absorbed photons. The electromagnetic radiation fields of heavy nuclei offer an alternative to weak light sources used in laboratory experiments.

ACKNOWLEDGMENTS

We thank John B. McLaughlin and K. B. Lee for their assistance with the computer programs. This research was supported in part by the Air Force Cambridge Research Laboratories and the Research Corporation.

REFERENCES

1. Science News 9 (22), 523-524 (30 May 1970).

2. W. Nagel, On the Stimulation of the Visual Apparatus by Roentgen Rays and Becquerel Rays, in Helmhotz's Treatise on Physiological Optice, edited by James P. C. Southall, Dover Publications, Inc., New York (1924), Vol. 2, pp. 22-25.

3. Leo E. Lipetz, The X-Ray and Radium Phosphenes, Brit. J. Opthal. 39, 577 (1957).

4. Leo E. Lipetz, Electro physiology of the X-Ray Phosphene, Radiation Research 2, 306 (1955).

5. Gerald Oster, Phosphenes, Scientific American 222 (2), 83 (1970).

6. W. C. Roentgen, Arch. Roentgen Ray 3, 80 (1932).

7. R. B. Tart, Am. J. Roentgenol. 28, 245 (1932).

8. A. H. Pirie, Am. J. Roentgenol. 28, 35 (1932).

9. R. R. Newell and W. E. Borley, Radiology 37, 54 (1941).

10. D. Deutschberger, Fluoroscopy Diagnost. Roentgenol. 28, 36, 100 (1955).

11. Theodore J. Wang, Visible Response of the Human Eye to X Radiation. Am. J. Phys. 35, (8), 779 (1967).

12. R. Madey and P. J. McNulty, Visual Sensations Induced in the Dark-Adapted Eye by Cerenkov Radiation from Heavy Cosmic-Ray Nuclei, presented 16 October 1970 at the Houston, Texas, meeting of the American Physical Society; Bull. Am. Phys. Soc. 15, 1671 (1970).

13. G. G. Fazio, J. V. Jelley, and W. N. Charman, Generation of Cerenkov Light Flashes by Cosmic Radiation within the Eyes of the Apollo Astronauts, Nature 228, 260 (17 October 1970).

14. C. A. Tobias, T. F. Budinger, and J. T. Lyman, Observations by Human Subjects on Radiation-Induced Light Flashes in Fast-Neutron, X-Ray, and Positive-Pion Beams, University of California Lawrence Radiation Laboratory Report UCRL-19868 (August 1970).

15. G. Wald and P. K. Brown, Science 127, 222 (1958), Human Rhodopsin.

16. S. Hecht, S. Shlaer, and M. H. Pirenne, Energy, Quanta and Vision, J. Gen. Physiol. 25, 819-840 (1942).

17. W. A. H. Rushton, Vision as a Photic Process, Ch. 15 in Photophysiology, Volume 11, edited by Arthur C. Giese, Academic Press, New York 1964).

18. C. H. Graham and N. R. Bartlett, The Relation of Size of Stimulus and Intensity in the Human Eye: II Intensity Thresholds for Red and Violet Light. J. Exp. Psychol. 24 (6), 574-587 (1939).

19. Y. LeGrand, Light, Colour and Vision. Translation of Y. LeGrand Optigue Physiologique, Vol. 2, Lumiere et Couleurs, Ed. de La 'Revue d'Optique', Paris (1948). Translation by R. W. G. Hunt, J. W. T. Walsh, and F. R. N. Hunt, Chapman and Hall, London (1957).

20. W. A. H. Rushton, J. Physiol. (London) 25, 819 (1942); 134, 30 (1956).

21. M. H. Pirenne, Spectral Luminous Efficiency of Radiation, p. 79, Ch. 4 in the Eye, Vol. 2, The Visual Process, ed. by Hugh Davson, Academic Press, New York (1962).

22. G. Osterberg, Topography of the Layer of Rods and Cones in the Human Retina, Acta Opthal., Suppl 6, (1935).

23. G. M. Comstock, C. Y. Fan, and J. A. Simpson, Abundances and Energy Spectra of Galactic Cosmic-Ray Nuclei above 20 MeV per Nucleon in the Nuclear Charge Range $2 \leq Z \leq 26$, Astrophysical Journal 146, 51 (1966).

24. G. M. Comstock, C. Y. Fan, and J. A. Simpson, Energy Spectra and Abundances of the Cosmic-Ray Nuclei Helium to Iron From the OGO-1 Satellite Experiment, Astrophysical Journal 155, 609 (1969).

25. M. Garcia-Munoz and J. A. Simpson, Galactic Abundances and Spectra of Cosmic Rays Measured on the IMP-4 Satellite, I. Helium and Medium, and the Very Heavy Nuclei (Paper OG-66), II. Li, Be, B and the Medium Nuclei (Paper OG-67), Proceedings of the Eleventh International Conference on Cosmic Rays, Budapest (1969).

26. F. W. O'Dell, M. M. Shapiro, R. Silberberg, B. Stiller, C. H. Tsao, N. Durgaprasad, C. E. Fichtel, C. E. Guss, and D. V. Reames, Paper OG-85, Proceedings of the Eleventh International Conference on Cosmic Rays, Budapest (1969).

27. W. R. Webber and J. F. Ormes, J. Geophys. Res. 72, 5957 (1967).

28. M. Rich and R. Madey, Range-Energy Tables, University of California Lawrence Radiation Laboratory Report, UCRL-2301 (1954).

29. Tom N, Cornsweet, Visual Perception, Fig. 2.4, p. 12 Academic Press, New York (1970).

30. M. H. Pirenne, Vision and the Eye, p. 61, Chapman and Hall Ltd, London, second edition (1967).

31. M. H. Pirenne, Physiological Mechanisms of Vision and the Quantum Nature of Light, Biol. Rev. 31, 194-241 (1956).

32. M. H. Pirenne and E. J. Denton, Quanta and Visual Thresholds, Jour. Opt. Soc. Am. 41, 426-427 (1951).

33. M. A. Bouman, Quanta Explanation of Vision, Documenta Opthalmologica 4, 23-115 (1950).

34. B. H. Crawford and M. H. Pirenne, Steep Frequency of Seeing Curves, J. Physiol. 126, 404-411 (1954).

DIRECT STIMULATION OF THE RETINA BY THE METHOD OF VIRTUAL-QUANTA FOR HEAVY COSMIC-RAY NUCLEI*

by
P.J. McNulty
Physics Department
Clarkson College of Technology
Potsdam, N.Y. 13676
and
Air Force Cambridge Research Laboratories+
Bedford, Mass. 01730

and
Richard Madey
Physics Department
Clarkson College of Technology
Potsdam, N.Y. 13676

The method of virtual-quanta is based on the fact that the electromagnetic field of a fast charged particle approaches the field of a plane wave as the particle speed approaches the speed of light. The electromagnetic field of a particle that passes through the retina appears to a rod in the retina as an electromagnetic pulse in time. The quantization of the components of the Fourier frequency spectrum of this pulse of electromagnetic radiation yields the virtual quanta. This method assumes that the virtual-quanta interact with the retina in the same way as ordinary photons.

We have calculated the contribution to the frequency of visual sensations induced in the dark-adapted eye by the virtual-photon field associated with the heavy-nuclei that exist in the region of space beyond the geomagnetic field. In order to determine the probability that the virtual-photon field induces a light-flash, we utilize only the portion of the virtual-photon spectrum that corresponds to the known frequency dependence of the sensitivity of human rods to visible light. The results of our calculation can be expressed as a curve of the mean frequency of light-flashes induced by the absorption of at least R virtual-photons versus the threshold number R. The contribution to the light-flash frequency from the virtual-photon field of heavy cosmic-ray nuclei is smaller than that from Cerenkov photons. We have used the flux and energy spectra of galactic cosmic-ray nuclei helium to iron measured by Comstock, Fan and Simpson.

INTRODUCTION

In the preceding paper,[1] we calculated the frequency of inducing visual sensations by Cerenkov radiation from heavy cosmic-ray nuclei traversing the retina. The results of that calculation for high detection efficiencies corresponding to states of relatively complete dark-adaption, are in general agreement with the frequencies reported by astronauts on Apollo missions 11-14. However, it has been shown that these sensations can be induced by means other than free or Cerenkov photons. Light-flashes have been induced by a number of stimuli including mechanical pressure, electric currents, X-rays, and energetic neutrons.[2-14] In the case of the energetic neutrons,[13,14] the flashes probably result from recoil protons or heavier nuclei produced in the neighboring media; more particularly, the results of Fremlin[14] seem to rule out any significant contribution from Cerenkov radiation.

In this paper we have modified the well known Method of Virtual-Quanta (MVQ) to provide a theoretical formalism for calculating the frequency of light-flashes to be expected from direct excitation of the photo-receptor elements by charged particles. The results of our calculation agree with the data of Tobias et al[13] and Fremlin[14] in the sense that one can produce visual sensations by non-relativistic particles; however, the frequency of visual sensations calculated by this method for astronauts exposed to the spectrum of galactic cosmic-ray nuclei at solar minimum is at least an order of magnitude lower than the highest rates observed. The MVQ as applied in this paper calculates only the contributions from direct excitation of the rhodopsin molecules through the exchange of virtual-quanta in a narrow energy range corresponding to optical frequencies; it should, therefore, be viewed as a minimum estimate of the

*Supported in part by funds from the Research Corporation and Air Force Cambridge Research Laboratories.
+NAS-NRC Resident Research Associate

contribution due to direct excitation.

METHOD OF VIRTUAL-QUANTA

The mechanism for the electromagnetic interaction between two charged particles is the exchange of a virtual-quantum. If the momentum transferred during the collision is small, then the exchange can be looked upon as the absorption by the target particle at rest of a virtual-quantum from the electromagnetic field accompanying the moving particle. The number and configuration of the virtual-quanta change dramatically as the speed of the incident particle approaches the speed of light. Fig.(1) is a schematic diagram showing how the magnitude of the electric field at a given distance from its charged particle source changes as the particle's speed approaches the speed of light. At rest ($\beta = 0$), the electric field at a given distance has the same magnitude in all directions; whereas for $\beta = 0.5$, the field has increased in directions transverse to the particle's motion, and it has decreased slightly in the direction parallel to the motion. This elongation of the electric field in the transverse direction increases as $\beta \to 1$. In calculating the effect on the target particle of absorbing one of these virtual-quanta, it is possible to ignore the incident particle itself and consider only the cloud of virtual-quanta that accompanies it. Weizsacker[15] and Williams[16] have developed the details of this method for charged particles moving through a vacuum. A quantum of angular frequency ω has an energy k given by the Planck-Einstein formula

$$k = \hbar\omega \qquad (1)$$

where $\hbar$ is Planck's constant divided by 2π. The energy spectrum of the photons in the equivalent pulse of virtual-quanta can be obtained directly from the frequency spectrum of the electromagnetic fields in the pulse. The differential cross-section for a given inelastic interaction (e.g. pion production, nuclear excitation, or, as in our case, excitation of a molecule) for events in which a photon of energy between $\hbar\omega$ and $\hbar\omega + d\hbar\omega$ is emitted by the incident particle and absorbed in the target system is given by the MVQ as the product of the number of virtual-quanta in the incident pulse with energies between $\hbar\omega$ and $\hbar\omega + d\hbar\omega$ and the experimental cross-section $d\sigma_Q(\hbar\omega)/d\hbar\omega$ for the analogous photon-induced interaction.

$$d\sigma_P(\hbar\omega)/d\hbar\omega = N(\hbar\omega)\,d\sigma_Q(\hbar\omega)/d\hbar\omega \qquad (2)$$

Visual sensations induced by light incident on the retina result ultimately from the absorption of individual light quanta by rhodopsin molecules that are contained in the outer segments of the rod cells. Although a rod responds to a single absorbed photon, a single absorption does not seem to be sufficient to activate the optic nerve to produce a visual sensation. The threshold for a visual sensation even under optimal physiological conditions requires from two to

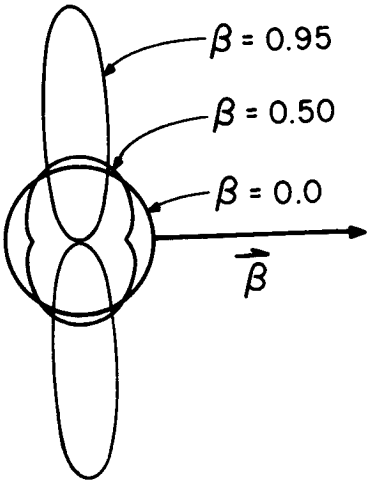

Figure 1. Magnitude of the electric field a given distance from a point source that moves with speed βc. The distance from a point on a curve to the source represents the magnitude of the field at that orientation.

perhaps as high as fourteen absorptions of photons in coincidence by rods in a cluster served by a single optic nerve fiber.[17,18] Previous exposure to light increases the threshold required for the production of light-flashes.[19,20]

The rhodopsin molecules are contained in disk-shaped sacs that are stacked at intervals of a few hundred Angstroms in the outer segments of the rod cells. The rhodopsin molecule is sensitive to light at wave lengths that are longer than distances between successive sacs and much longer than the inter-molecular distances of the medium; therefore, it is necessary to modify the MVQ to take into account the polarizability of the molecules in the rod. The virtual-quanta field polarizes the molecules of the medium which in turn change the field of virtual-quanta experienced by the rhodopsin molecule. For optical wavelengths, we can modify the MVQ to include polarization by using the characteristic macroscopic fields in a dielectric instead of the free space fields.

The expression for the number of virtual-quanta that have energies between $\hbar\omega$ and $\hbar\omega + d\hbar\omega$ has been shown[21] to be of the form

$$N(\hbar\omega) = \frac{2Z^2\alpha}{\pi\,|\varepsilon(\omega)|^2\beta^2\hbar\omega}\left[\ln\left(\frac{1.123v}{\omega a\,|1-\beta^2\varepsilon(\omega)|^{1/2}}\right) - \frac{\beta^2\varepsilon'}{2}\right] \qquad (3)$$

where α is the fine-structure constant, Z is the atomic number of the incident particle, and $v = \beta c$ is its speed; the function $\varepsilon(\omega)$ represents the dielectric permeability of the medium; the constant a is the minimum value of the impact parameter which we take equal to one Bohr radius; and $\varepsilon'(\omega)$ represents the real part of $\varepsilon(\omega)$. The number of visible virtual-quanta can be obtained by integrating Eq.(3) over the complete optical spectrum. Since the rhodopsin molecules are not equally sensitive to all photons in the visible

range, we have taken into account the rhodopsin sensitivity by replacing the actual absorption spectrum by a narrow rectangular distribution of width $\Delta\hbar\omega = 0.52$ eV centered about the energy of peak sensitivity, $\hbar\omega_0 = 2.48$ eV. All photons in this reduced optical region are assumed to have the maximum probability (20%)[22] of being absorbed by a rhodopsin molecule upon traversing the retina; photons outside of this region are assumed to have zero probability of absorption.

The number of virtual-quanta with energies in this restricted visible region that accompany a charged particle as it passes through the retina is given by

$$M = \frac{2Z^2\alpha\Delta\hbar\omega}{\pi|\varepsilon_0|^2\beta^2\hbar\omega_0}\left[\ln\left(\frac{1.123v}{\omega_0 a|1-\beta^2\varepsilon_0|^{\frac{1}{2}}}\right) - \frac{\beta^2\varepsilon_0'}{2}\right] \quad (4)$$

The dielectric permeability $\varepsilon(\omega)$ is now represented by a complex dielectric constant ε_0 which can be represented in terms of the real quantities ε_0' and ε_0'' as

$$\varepsilon_0 = \varepsilon_0' + i\varepsilon_0'' \quad (5)$$

The real and imaginary parts of the dielectric constant are related to the index of refraction n and the absorption coefficient κ by

$$n^2 - \kappa^2 + 2in\kappa = \varepsilon_0' + i\varepsilon_0'' \quad (6)$$

For transparent materials, therefore, ε_0' can be replaced by the square of the index of refraction. Absorption of visible light passing through the retina occurs primarily in the outer segments of the rod and cone cells. Individual outer segments transmit about 70% of the light incident upon them, resulting in at least 80% transmission for the retina as a whole. Taking advantage of the relative transparency of the components of the retina, the known values of n^2 were substituted for ε_0. Sidman[23] has measured the index of refraction to be 1.41 and 1.39 for the outer segments of rods and cones respectively; the extra cellular fluid which separates the outer segments in the living retina presumably has the same index of refraction as physiological saline, about 1.33.[24]

The term ε_0'' depends upon the amount of absorption in the medium. If the retina were completely transparent, ε_0'' would be zero; since the retina is only slightly opaque, it can be expected to be small. The number of visible virtual-quanta obtained from Eq.(4) is not sensitive to the exact value of ε_0'' used. A crude estimate of ε_0'' can be obtained from the relationship[21]

$$\varepsilon_0'' = \left(\frac{cN}{\omega_0}\right) d\sigma_q(\omega_0)/d\omega \quad (7)$$

where N is the number of rhodopsin molecules per unit volume in the medium. Eq.(7) can be rewritten in terms of the ratio of the transmitted light intensity I to the incident intensity I_0 as

$$\varepsilon_0'' = -(c/\omega_0 x)\ln(I/I_0) \quad (8)$$

The quantity x in Eq.(8) is the equivalent thickness of the rhodopsin molecules in the retina. Dartnell et al[25] have shown that if the outer segment of the rod is 2.5 μ in diameter, there must be $N_1 = 2\times10^8$ rhodopsin molecules in an outer segment for 30% probability of absorption for photons passing through the outer segment. If we assume a cylindrical outer segment of radius r and with a thickness of rhodopsin x we have

$$N_1/\pi r^2 x = N_0\rho/A \quad (9)$$

where N_0 is Avogadro's number, A is the molecular weight of rhodopsin ($\sim$ 40,000), and ρ is its density ($\sim$ 1.27 gm/cm^3). The value of x obtained from Eq.(9) is 2.13 μ. Substituting this value into Eq.(8) for 70% transmission through an outer segment yields $\varepsilon_0'' = 0.0133$. This value was used in Eq.(4) for our calculations.

The number of virtual-quanta M accompanying a nucleus of atomic number Z is plotted in Fig.(2) as M/Z^2 versus the velocity of the nucleus. There is a maximum value of the velocity above which less than M virtual-quanta accompany the nucleus through the layer of outer segments. The values of this maximum velocity are plotted in Fig.(3) for M = 2, 10, 20, 50 and 100. If the threshold number of photons R required for a visual sensation is greater than or equal to M then, ignoring fluctuations in M, particles moving faster than β_{max} will not produce visual sensations. When $M \geq R$, the probability that at least R out of the M incident virtual-quanta will be absorbed is given by

$$Q_M(\geq R) = \sum_{T=0}^{T=M-R} \frac{M!\,P^{(M-T)}(1-P)^T}{T!\,(M-T)!} \quad (10)$$

For the retina the probability P of absorption by a rhodopsin molecule for photons in the "visible" wavelength region defined earlier is 0.2.

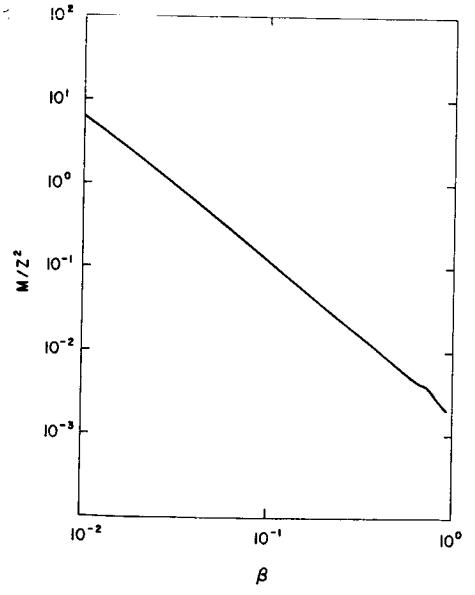

Figure 2. Plot of M/Z^2 as a function of speed at the retina.

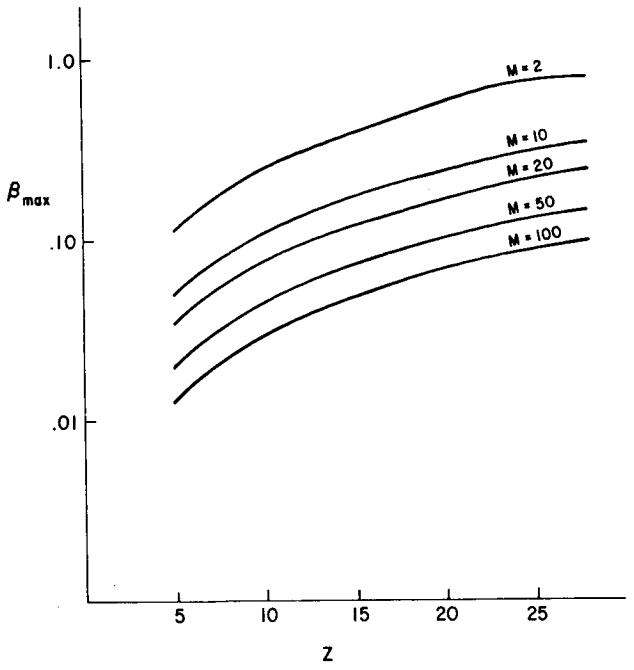

Figure 3. Maximum velocity at the retina for at least M virtual-quanta.

TABLE 1

Parameters for Representing the Differential Flux Spectra of Galactic Cosmic-Rays at a Time of Minimum Solar Modulation

Nucleus	C_1 p/m^2 -s-sr-(BeV-nuc^{-1})	C p/m^2 -s-sr-(BeV-nuc^{-1}) $^{-\gamma+1}$	T_1 (BeV/nuc)
C^{12}, O^{16}	5.4	12	.437
B^{11}	1.7	4.3	.513
Ne,Mg,Si	1.0	1.4	.207
P-Mn	1.0	1.4	.207
Fe-Ni	1.0	1.4	.207

EXPECTED FREQUENCIES OF LIGHT FLASHES

The flux and energy spectra of the cosmic-ray nuclei from boron to nickel measured by Comstock, Fan and Simpson[26] were used in calculations. Each energy spectrum was separated into kinetic energies per nucleon above and below a particular value T_1: the spectrum for that atomic number Z then being represented as

$$n_Z\ (T) = C_1 \qquad (0 < T < T_1) \qquad (11)$$

$$n_Z\ (T) = C\ (T + mc^2)^{-\gamma} \qquad (T > T_1) \qquad (12)$$

where mc^2 is the proton rest mass. The values of T_1, C_1 and C used for the nuclei included in our calculations are listed in Table 1. The value of γ used for all nuclei was 2.5. The integral flux spectra corresponding to Eqs.(11-12) can be written

$$N\ (> T) = \frac{C(T + mc^2)^{(1-\gamma)}}{(\gamma - 1)} \qquad (T > T_1) \qquad (13)$$

and

$$N\ (> T) = C_1\ (T_1 - T) + C\ (T_1 + mc^2)^{(1-\gamma)}/(\gamma - 1) \qquad (0 < T < T_1) \qquad (14)$$

To compute the mean frequency of light-flashes to be expected from direct excitations in the optical region defined earlier, we have prepared a program that calculates the contribution to the the light-flash frequency from each nucleus of atomic number Z. We sketch the steps in the program:

a. Find from Eq.(4) the maximum kinetic energy per nucleon T'_M at the retina that each cosmic ray nucleus can have and still be accompanied by M visible virtual-quanta.

b. Calculate the range in tissue R'_p of a proton with this kinetic energy. For this purpose we used the power-law[1]

$$R'_p = k\ T'^{\alpha}_m \qquad (15)$$

The values $k = 4.25 \times 10^{-3}$ gm/cm^2 H_2O - MeV$^{\alpha}$ and $\alpha = 1.627$ were used.

c. The maximum kinetic energy per nucleon T_M in the incident spectrum that a particle can have and be accompanied by M virtual-quanta after it has traversed a shielding thickness ℓ is given by

$$T_M = ((R'_p + Z^2\ \ell/A)/k)^{1/\alpha} \qquad (16)$$

d. The unidirectional flux density $N_{Z,M}(>T_M)$ of nuclei of atomic number Z with kinetic energies per nucleon greater than T_M can be obtained from Eqs.(13-14); the differential unidirectional flux of nuclei of atomic number Z that are accompanied by M visible virtual-quanta can then be written:

$$\Delta N_{Z,M} = N_{Z,M+1/2}(>T_{M+1/2}) - N_{Z,M-1/2}(>T_{M-1/2}) \qquad (17)$$

The number of nuclei of charge Z to pass through each eye per minute is obtained by multiplying $\Delta N_{Z,M}$ by

$$Y = 120\ G\ (\cos\beta_1 - \cos\beta_2) \qquad (18)$$

where β_1, β_2 and G are given in Ref. 1.

e. The number of light-flashes per minute in both eyes caused by direct excitation by cosmic-ray nuclei of atomic number Z is given by

$$C_Z\ (\geq R) = \sum_{M=R} 2\ Y\ \Delta N_{Z,M}\ Q_M\ (\geq R) \qquad (19)$$

In Fig.(4) the relative contributions to the light-flash frequency from the most abundant of the heavy cosmic-ray nuclei are given for a threshold of 10 absorbed "visible" virtual-quanta. Similar results were obtained for R = 2 and 20.

f. The total frequency of light flashes induced by at least R direct excitations of rhodopsin molecules is given by

$$C(\geq R) = \sum_{Z} \sum_{M=R} 2\, Y\, \Delta N_{Z,M}\, Q_{M}\, (\geq R) \qquad (20)$$

Fig.(5) plots the light-flash frequency as a function of the threshold R.

RESULTS AND DISCUSSION

The curve in Fig.(5) shows that the frequency of light flashes to be expected from the direct excitation of the rhodopsin molecule by the exchange of "visible" virtual-quanta is much lower than the frequencies to be expected from the absorption of Cerenkov quanta that were calculated in Ref.(1). Even if one assumes that the astronauts were completely dark-adapted and, therefore, had thresholds for visual sensations somewhere between 2 and 14 quanta, examination of Fig.(5) shows the frequency expected to be much less than the rates observed by astronauts on Apollo missions 11, 12, 13 and 14.

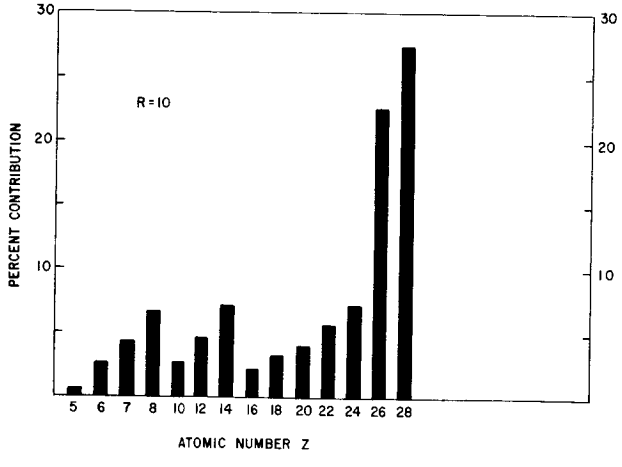

Figure 4. Relative contributions to the observed light-flash frequencies for threshold R=10.

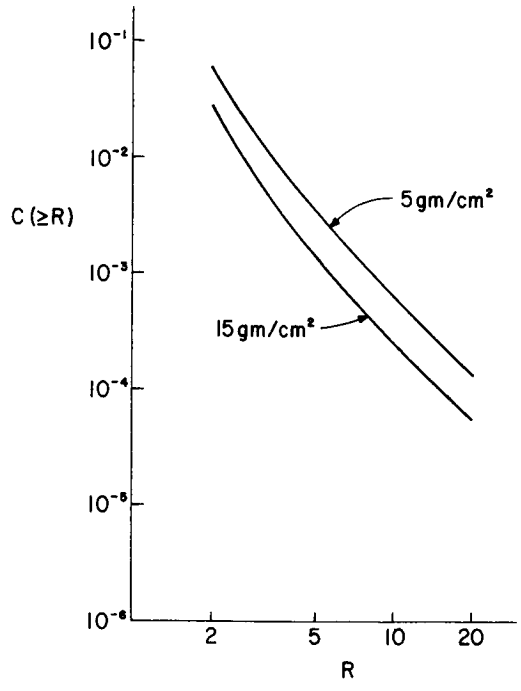

Figure 5. Counting rate versus threshold R.

The importance of the MVQ is that given the cross-section for a photon of frequency ω exciting a molecule producing an effect of interest, one can calculate the cross-section for a direct excitation of the molecule by a particle of charge Z and speed βc in which the incident particle loses energy $\hbar\omega$. For the retina we know the geometrical and coincidence requirements for visual sensations as well as the probability that each photon will excite a rhodopsin molecule; this knowledge extends, however, only over a very narrow band of photon energies. The contribution from direct excitation calculated in this paper is thereby limited to those collisions with rhodopsin molecules in which the energy lost by the incident particle corresponds to optical frequencies. The potential contribution from more energetic collisions is, therefore, ignored but could be calculated if the cross section for the analogous photo-excitations and photo-ionizations leading to visual sensations were known.

ACKNOWLEDGEMENTS

We would like to thank Mr. John B. McLaughlin for his help in writing the computer programs.

BIBLIOGRAPHY

1. Richard Madey and P.J. McNulty, Symposium on Natural and Manmade Radiation in Space, Las Vegas, Nevada, 4 March 1970, previous paper.

2. W. Nagel, In Helmhotz's Treatise on Physiological Optice, edited by James P.C. Southall, Dover Publications, Inc., New York (1924).

3. Leo E. Lipetz, Brit. J. Opthal. 39, 577 (1957).

4. Leo E. Lipetz, Radiation Research 2, 306 (1955).

5. Gerald Oster, Scientific American 222 (2), 83 (1970).

6. W.C. Roentgen, Arch. Roentgen Ray 3, 80(1899).

7. R.B. Tart, Am. J. Roentgenol. 28, 245 (1932).

8. A.H. Pirie, Am. J. Roentgenol. 28, 35 (1932).

9. R.R. Newell and W.E. Borley, Radiology 37, 54 (1941).

10. D. Deutschberger, Fluoroscopy Diagnost. Roentgenol. 28, 36, 100 (1955).

11. Theodore J. Wang, Am. J. Phys. 35,(8)779 (1967).

12. G.G. Fazio, J.V. Jelley, and W.N. Charman, Nature 228, 260 (1970).

13. C.A. Tobias, T.F. Budinger, and J.T. Lyman, University of California Lawrence Radiation Laboratory Rept UCRL-19868 (August 1970).

14. J.H. Fremlin, New Scientist, 47, 42 (1970).

15. C.F. Weizsacker Z. Physik 88, 612 (1934).

16. E.J. Williams Kgl. Danske Videnskrab. Selskab 13, No. 4, (1935).

17. S. Hecht, S. Shlaer, and M.H. Pirenne, J. Gen. Physiol. 25, 819-840 (1942).

18. W.S. Stiles, Proc. Roy. Soc. 127B, 64-105(1939).

19. G. Wald and A.B. Clark, J. Gen Physiol. 21, 93 (1937).

20. B.H. Crawford, Proc. Roy. Soc. (London) B134, 283 (1947).

21. P. Budini, Z. Zaturforschg. 7a, 722-725 (1952).

22. W.A.H. Rushton, J. Physiol. 134, 30 (1956).

23. R.L. Sidman, J. Biophs. Biochem. Cytol 3, 15 (1957).

24. G.S. Brindley, Physiology of the Retina and the Visual Pathway, p. 22, Edward Arnold Publishers, London (1960).

25. H.J. Dartnall, C.F. Goodere, and R.J. Lythgoe, Proc. Roy. Soc. A164, 216 (1938).

26. G.M. Comstock, C.Y. Fan, and J.A. Simpson, Astrophysical Journal 146, 51 (1966).

INFLUENCE OF A DETAILED MODEL OF MAN ON PROTON DEPTH/DOSE CALCULATIONS

Paul G. Kase
Martin-Marietta Corporation

Abstract

The U.S. Air Force and NASA have jointly sponsored the development of a detailed radiation shielding model of man. This model will be used to plan manned space missions in which especially sensitive human tissues could be subjected to excessive radiation. The model has two configurations -- standing and seated. More than 2500 individual elemental volumes have been used to depict the external conformation, skeleton, and principal organs. The model is briefly described and several examples of its application to mission planning are given.

Introduction

During the past decade, manned space flight has progressed from its beginning as a modern adventure, albeit with considerable supporting technology on the ground, to today's maturity. Even a flight to the moon seems rather routine to the casual observer. Future manned missions will exploit our current capability into the areas of space transportation systems, space stations, and eventually, interplanetary expeditions.

On past manned space programs -- Mercury, Gemini, and Apollo -- the flights have entailed very small radiation doses to the crews. These flights have evolved slowly from exposures to space radiation measured in minutes, to hours, and, finally, days. The next U.S. manned program, Skylab, will be launched in 1973. This precursor of larger space stations will be occupied at first for 28 days; later it will be revisited for 56 days. Much longer occupancy of permanent space stations and interplanetary vehicles will be necessary. Therefore, the astronauts of the future will encounter considerably more radiation than in previous manned space operations.

It is possible that especially radiation-sensitive organs, such as the lenses of the eyes, the gonads, or the blood-forming centers, could receive doses near or even beyond the threshold of permanent damage. Concern for this possibility has led the Air Force and NASA to jointly sponsor the development of a Computerized Anatomical Model Man, which provides the means for computing, with considerable precision, the amount of radiation from space that might penetrate to any specified location in the body.

Description of the Computerized Anatomical Model Man

The requirements for the model of man were as follows:

1) Two configurations, standing and seated;
2) Exterior conformation and dimensions corresponding to the 50th percentile Air Force man;
3) Interior detail, including skeleton and organs;
4) Accuracy - Weight within 10% of the 50th Percentile Air Force man, locations and conformation within 0.1 inch;
5) Computer compatibility - Modified Elemental Volume Dose Program (MEVDP) for the CDC 6000-series digital computer;
6) Five hundred to 1000 elemental volumes, selected from seven types of geometrical shapes incorporated in MEVDP.

The Air Force Weapons Laboratory technical monitor provided a bibliography of anatomical data and the information required for the model to interface with the MEVDP at the start of the study. These data were supplemented by literature searches, consultation with medical authorities, and observation of living subjects, cadavers, and anatomical models.

The three principal phases of model development included organizing the anatomical data from all sources into master views and sectional drawings of the 50th percentile Air Force man, transferring this information into the punched card formats required by MEVDP, and verifying that the resulting computer model was consistent with the drawings.

The first phase was accomplished by a professional artist working in consultation with medical doctors. All drawings are in a common coordinate system, half scale on a ½-inch grid. The external conformation is based on 132 standard measurements obtained during a statistical survey of over 4000 Air Force flight personnel by Hertzberg, Daniels, and Churchill.[1] Unfortunately, no statistical survey has ever been made of human skeletons and organs, especially of Air Force flight personnel. Therefore, the artist and medical consultants referred to models of the human skeleton and organs, and an assortment of human bones to proportion the interior details of the model. Over 100 scaled drawings were made during this phase of the study. Figure 1, showing the skeleton within the outline of the standing man, is a reproduction of one of these drawings.

The next phase of the study entailed transferring dimensions from the drawings, along with the composition and density of the pertinent tissues, onto punched cards in the formats required by MEVDP.[2] The seven geometrical shapes incorporated in MEVDP are shown in figure 2. Even with embedding, it was necessary to use many more elemental volumes than planned at start of the study to achieve the desired accuracy.

Finally, the model was checked -- visually by using a computer graphics option of MEVDP, and

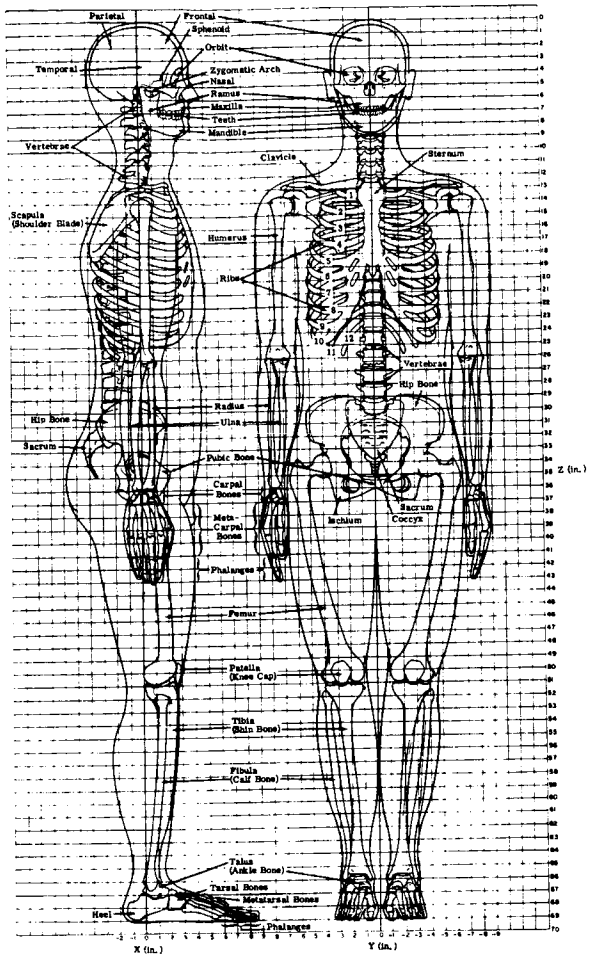

FIGURE 1.-Skeleton within standing man.

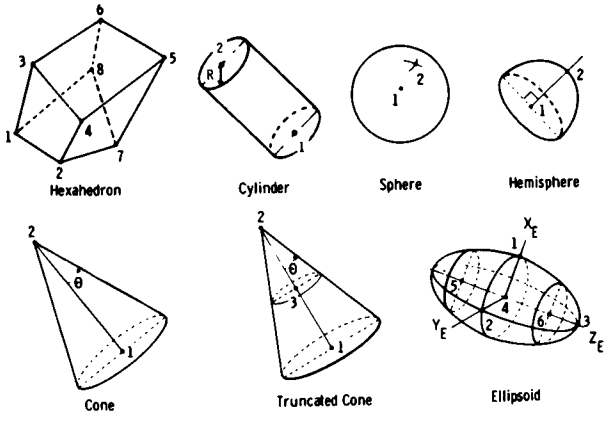

FIGURE 2.-Geometrical shapes compatible with MEVDP.

operationally on CDC and Univac computers at the Air Force Weapons Laboratory and the NASA Manned Spacecraft Center, respectively. A vertical section of the head prepared by the computer graphics option of MEVDP is compared with a sectional drawing prepared by the artist in figure 3. The agreement between the two is very good.

Chemical Composition and Density

The five chemical compositions and densities used in the model are listed in table I. The composition and density of the Radiation Standard Man due to Morgan[3] is shown for comparison as material number 6. Because of insufficient data on the specific composition of human tissues, the model falls short of its objectives in this area. However, refinements of these parameters may readily be incorporated.

TABLE 1.-Materials of the computerized anatomical model man.

Chemical Element	Fractional Composition by Weight					
	Material Number					
	1	2	3	4	5	6
	Name					
	Lung	Organ	Intestine	Muscle	Skeleton	Radiation Standard Man
	Density (gm/cm^3)					
	0.257	1.058	0.451	1.060	1.499	1.000
Hydrogen (H)	0.0980			0.1020	0.082	0.1000
Carbon (C)	0.1450			0.1230	0.423	0.1800
Nitrogen (N)	0.0380			0.0350	0.019	0.0300
Oxygen (O)	0.7070			0.7290	0.322	0.6500
Sodium (Na)	0.0015			0.0008	---	0.0015
Magnesium (Mg)	0.0002			0.0002	0.001	0.0005
Phosphorous (P)	0.0030			0.0020	0.049	0.0100
Sulfur (S)	0.0018			0.0050	0.001	0.0025
Potassium (K)	0.0026			0.0030	---	0.0020
Calcium (Ca)	0.0009				0.103	0.0015
Chlorine (Cl)	0.0020					0.0015

Geometrical Conformation

The model is actually in three sections -- the portion common to both the standing and seated configurations, and portions unique to the standing and seated configurations. These latter portions are combined with the common portion to obtain the complete configurations. The distribution of the nearly 3200 elemental volumes contained in all three portions is shown in table 2.

TABLE 2.-Distribution of elemental volumes in the computerized anatomical model man.

Body Region	Composite Shields	Individual Geometrical Shapes
Common to Both Standing and Seated Configurations:		
Head	153	772
Torso	171	803
Upper Limbs	12	58
Subtotal	336	1633
Unique to Standing Configuration:		
Genitals	9	27
Torso	50	284
Upper Limbs	68	200
Lower Limbs	94	374
Subtotal	221	885
Complete Standing Configuration	557	2518
Unique to Seated Configuration:		
Torso	12	62
Upper Limbs	70	214
Lower Limbs	86	362
Subtotal	168	638
Complete Seated Configuration	504	2271

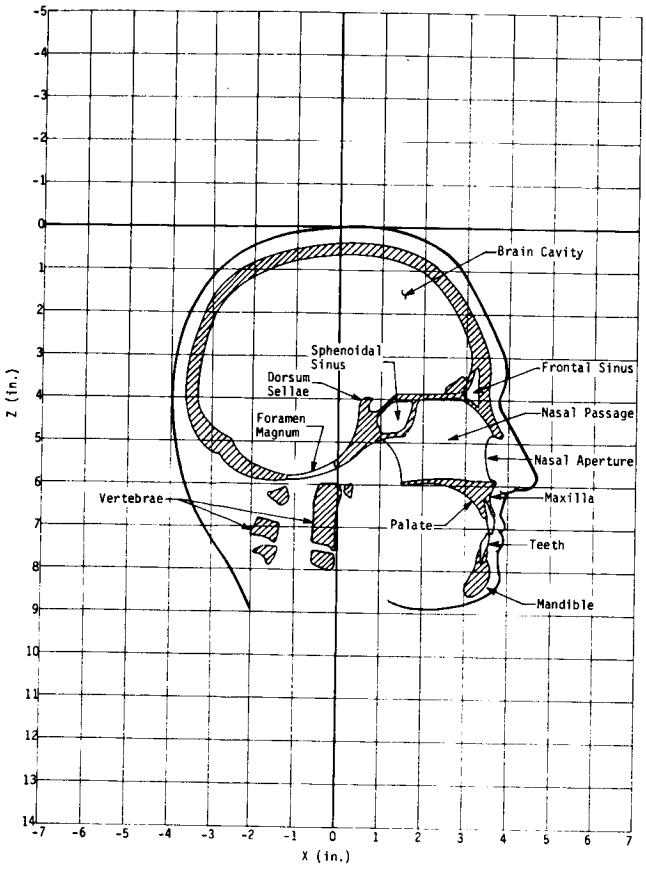

(a) As Drawn by the Artist

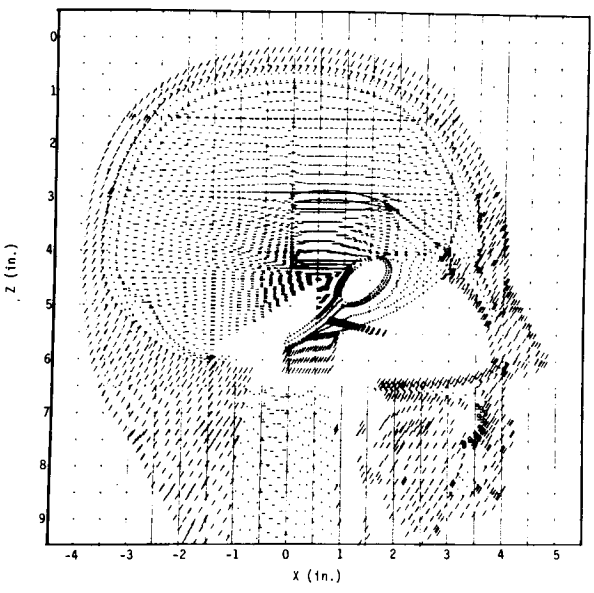

(b) As Plotted by the Graphics Option of MEVDP

FIGURE 3.-vertical selections of head.

Weight

The weights of the standing and seated model configurations are 155.5 and 150.6 lb, respectively. These weights are well within the maximum permissible error of 16.2 lb from the nominal weight of the 50th percentile Air Force man, 161.9 lb. The weights of the model elements are summarized in table 3. Note that the weight of the skeleton is in close agreement with the weights due to Morgan[3] and Long.[4] The weights of individual organs also compare favorably to weights listed by Morgan. A complete description of the Computerized Anatomical Model Man is available in the final report of the study.[5]

Application of the Computerized Anatomical Model Man to Mission Planning

The following examples show how the computerized anatomical model man could influence the conclusions of studies of missions in which radiation is a factor.

TABLE 3.-Summary of model man weight.

Body Region	Tissue	Skeleton	Organ
Common to Both Standing and Seated Configurations:			
Head	4.5	1.6	2.6
Torso	28.1	11.4	17.1
Upper Limbs	0.7	0.7	--
Subtotal	33.4	13.8	19.7
Unique to Standing Configuration:			
Genitals	0.2	--	0.0
Torso	17.6	0.9	1.5
Upper Limbs	15.8	1.5	--
Lower Limbs	44.9	5.6	--
Subtotal	78.5	8.1	1.6
Complete Standing Configuration:			
Total, Each Material	112.0	22.0	21.4
Grand Total	155.4		
% Error in Grand Total	3.9		
Unique to Seated Configuration:			
Genitals	--	--	0.0
Torso	9.4	0.2	1.4
Upper Limbs	14.4	1.5	--
Lower Limbs	49.5	6.6	--
Subtotal	73.5	8.4	1.5
Complete Seated Configuration:			
Total, Each Material	106.9	22.2	21.3
Grand Total	150.5		
% Error in Grand Total	6.9		

Note: 50th Percentile Air Force Man Weighs 161.9 lb.

The principal effect of the model man is on the mass, or areal density distribution, of the materials surrounding the location at which the dose is to be calculated. The areal density distribution results from inert materials (such as metal, plastics, glass, and propellant) that contribute to the shielding due to the spacecraft and its equipment, and living tissue (such as muscles, bones, and organs) of the astronaut and his companions. The typical distribution obtained by systematically calculating the mass of material per unit area per unit solid angle throughout all space surrounding a chosen dose point is shown in part a of figure 4. Because the order in which this histogram is arranged has no effect on the results, it is convenient to re-arrange the values in order of increasing areal density, as shown in part b of figure 4. The latter curve provides insight into ways to improve the areal density distribution of a man in a spacecraft.

Since the contribution to the radiation dose is much greater from the lower areal density region near the origin of the curve, increasing the shielding mass in this region will reduce the radiation dose. Some degree of optimization of the areal density distribution can be achieved by redistributing the mass of the spacecraft and by suitably locating and orienting the crew. However, the natural mass distribution, or self-shielding of the human body, is not ideal, especially when the astronaut is slim and tall.

At some dose locations, the areal density distribution is enhanced by the precise configuration of the complete model man, where more dense muscle and skeletal tissue may surround the dose point. In other cases, the proximity of lower density lung or intestinal tissue may have unfavorable effects. Accordingly, the use of this model will, in some instances, result in lower radiation doses, and in other instances, higher doses than would be predicted from a less precise model of man.

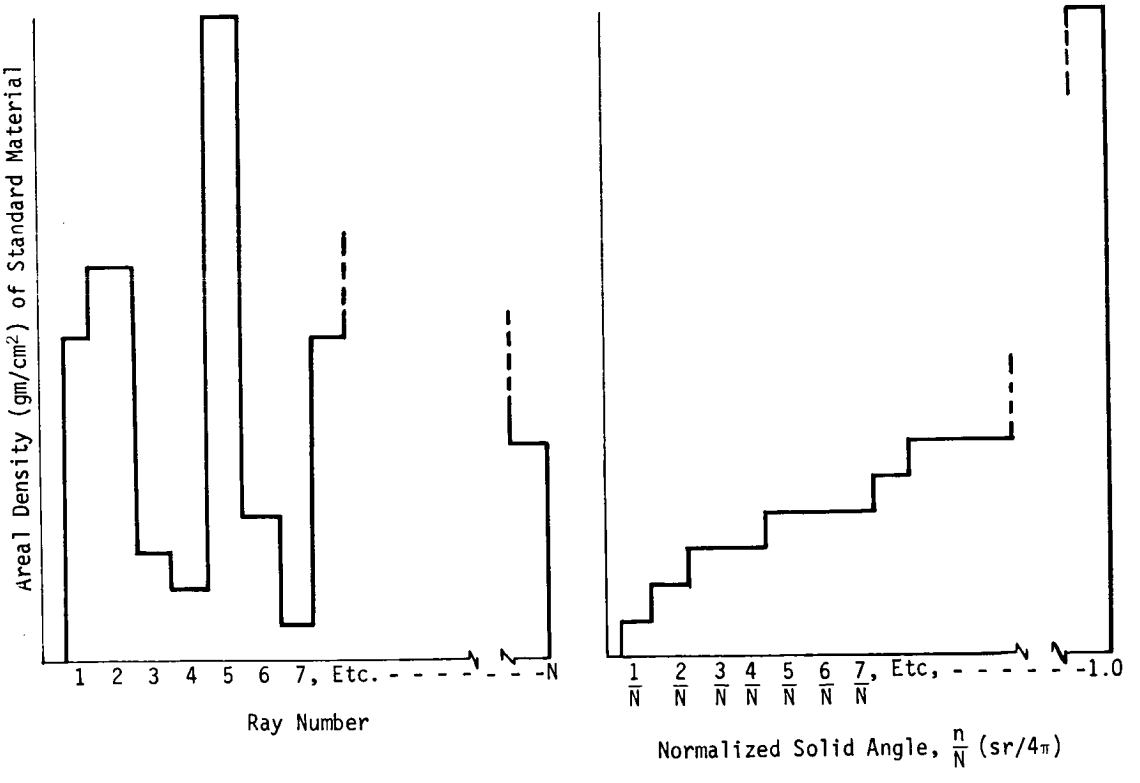

(a) Actual Distribution

(b) Reordered, Normalized Distribution

FIGURE 4.-Interpretation of areal/density distribution.

The other effects of the computerized model man on radiation analyses are largely predetermined by the combined areal density distribution of the man and his spacecraft. In sequence of calculation, the first effect is on the differential kinetic energy spectrum, shown schematically in figure 5. The incident spectrum is the uppermost curve. The effects of increasing protection against the spectrum of the radiation arriving at the dose point are also indicated.

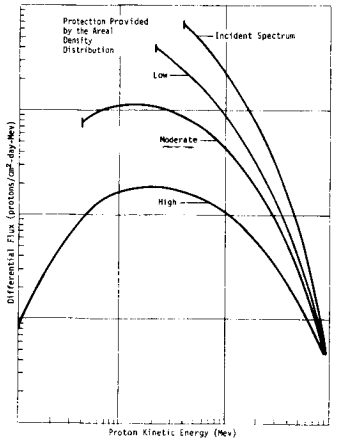

FIGURE 5.-Schematic representation of effects of area/density on differential spectrum arriving at a detector.

The total number of radiation particles that reach the dose point is obtained by integrating the differential kinetic energy spectrum. From this number, the fraction of the incident particles allowed to reach the dose point by the areal density distribution is readily calculated.

The final effect of the model is on the radiation dose absorbed by standard tissue. This has been calculated by conventional techniques from the total radiation spectrum at the dose point and from the stopping power of protons in the tissue of a radiation standard man with the composition suggested by Morgan.[3]

The first two examples of applications of the computerized anatomical model man are for a spacecraft and mission orbit similar to those planned for Skylab. The orbit is circular at an altitude of 235 nautical miles and is inclined 50 degrees. The incident radiation environment is composed of protons with energies from 4 to 5000 Mev, as defined by the Vette models of the Van Allen belt. The model of the spacecraft is a simplified version of the orbital workshop without the interior accommodations, solar panels, or attached modules that will actually be provided in the Skylab orbital assembly.

First, comparisons have been made of the radiation arriving at selected dose points in the computerized model man. The combined areal density distributions of the model man and spacecraft surrounding each dose point and the distribution due to only the spacecraft are shown in figure 6. Note that the self-shielding of the model man is of considerable benefit throughout the space surrounding the dose point. The spectra of protons arriving at the dose points are compared with the incident spectrum in figure 7, and are consistent with the areal density distributions. The remaining effects are summarized in table 4. Note from this table that the differences between the doses are small for points near the surface of the body, such as at the lens of the eye and the skin of the chest. This is to be anticipated because the greatest portion of the radiation arrives from the relatively large region of space where there is little or no intervening tissue. When the dose point is well within the interior of the body, such as in the intestine or femur, the variations of tissue composition and density have larger effects.

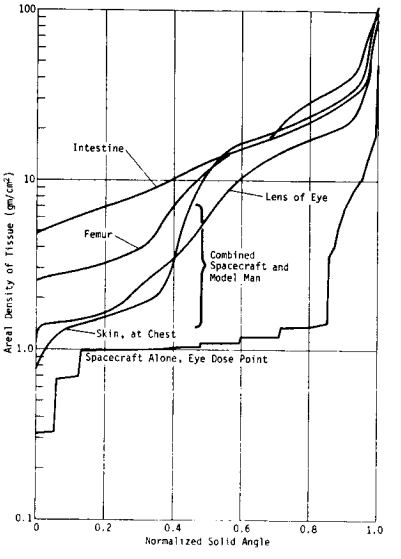

FIGURE 6.-Comparison of area/density distribution at selected dose points.

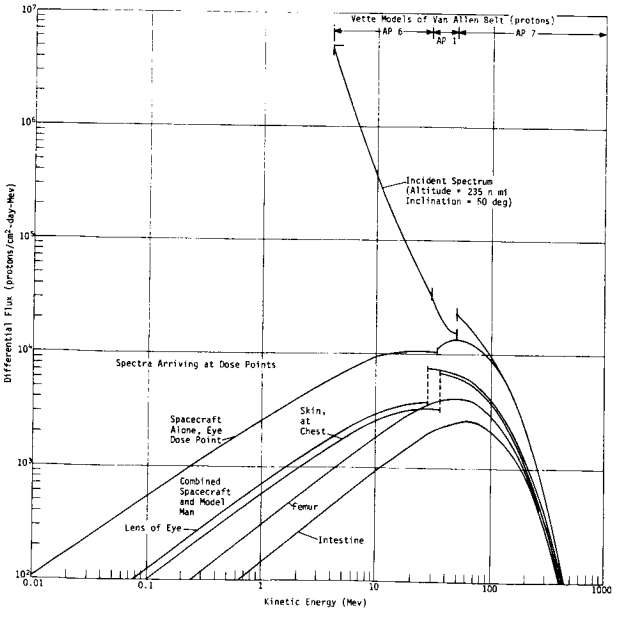

FIGURE 7.-Comparison of differential kinetic energy spectra of protons arriving at selected dose points.

TABLE 4.-Results of radiation analyses for several dose locations.

Dose Point	Minimum Areal Density (gm/cm^2)	Fraction of Incident Protons Transmitted		Radiation Dose (rad/month)
		From Exterior	From Interior	
Lens of Eye	1.218	0.067	0.54	4.55
Skin, at Chest	0.813	0.061	0.49	4.14
Intestine	4.881	0.034	0.28	1.97
Femur, Blood-Forming Center	2.552	0.047	0.38	3.09
Spacecraft Only, Point at Location of Lens of Eye if Man Were Present	0.322	0.123	1.000	10.42

A second application of the model man is to the evaluation of local shielding, or protection, such as goggles for the eyes. In this example, the goggles have lenses 2 inches in diameter and are of various thicknesses. The effects of the goggles on the areal density distribution and the differential kinetic energy spectrum at the lenses of the eyes are shown in figures 8 and 9, respectively. The fractions of the incident particles transmitted by the spacecraft and by the combined spacecraft and model man, and the resulting monthly radiation doses are plotted in figures 10 and 11, respectively.

Because the goggles provide shielding from a large region of space that would normally be open to radiation, thin glasses provide substantial protection. In fact, if the goggles were fit closer to the head than in this example, the areal density distributions near the origin of figure 8 would be considerably improved. Even so, figure 11 shows that the man's self-shielding reduces the radiation dose to less than 50% of that which would be measured by a point detector at the eye location if the man were absent.

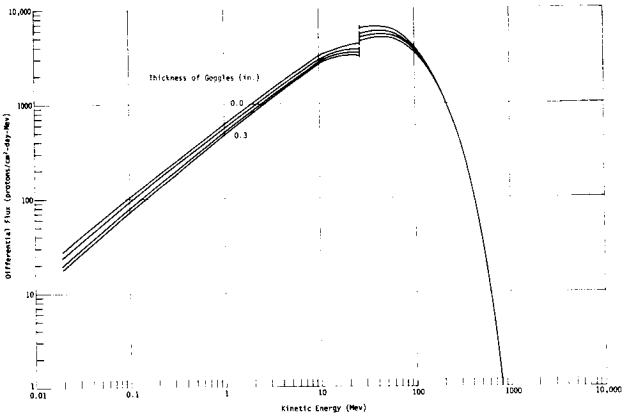

Fig. 9 Effect of Goggles on Differential Kinetic Energy of Spectra Arriving at the Lens of the Eye

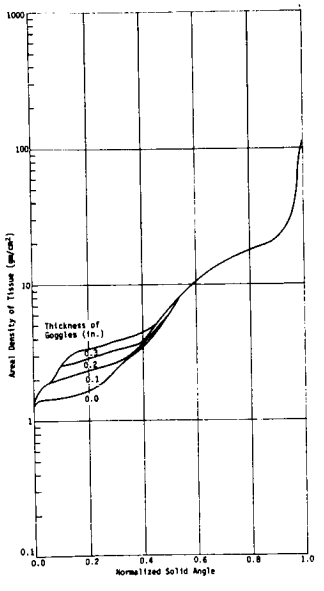

Fig. 8 Effect of Goggles on Areal Density Distribution Protecting the Lens of the Eye

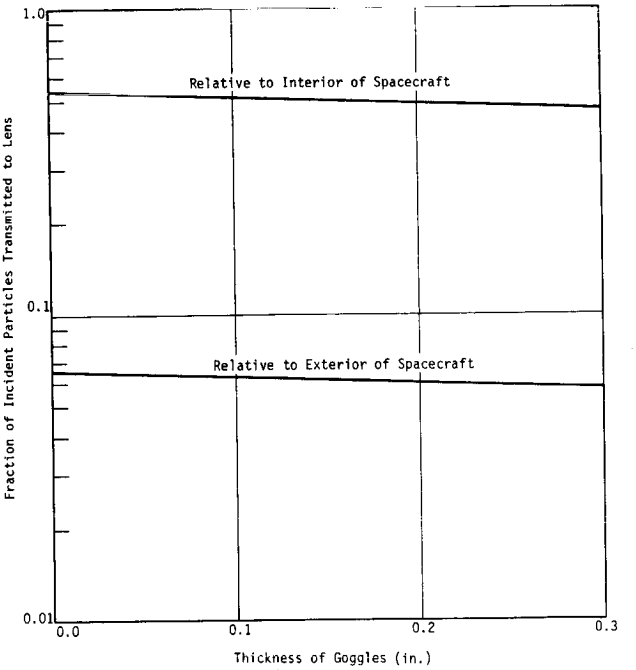

Fig. 10 Effect of Goggles on Number of Protons Transmitted to the Lens of the Eye

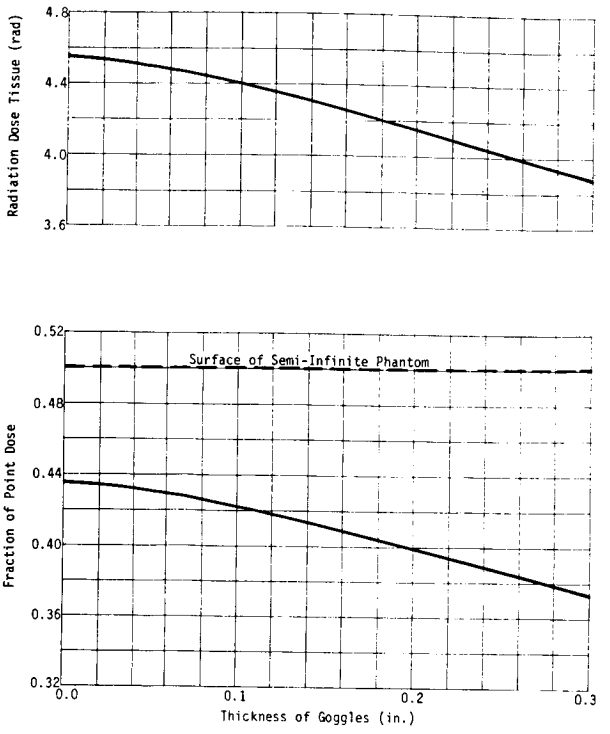

FIGURE 11.-Effectiveness of goggles in reducing the radiation dose absorbed by the lens of the eye.

The final application of the computerized anatomical model man was suggested in an interview with Dr. R. E. Benson of NASA referring to light flashes observed by the astronauts during Apollo flights 11, 12, and 13.[7] It was stated that cosmic radiation was a possible source of these flashes. To test this possibility, a calculation was made for the seated configuration of the model occupying the Apollo Block II Command and Service Module. A model of the cosmic ray environment due to Barrett[6] was assumed. To represent the conditions in cislunar space, perturbations of the environment due to the geomagnetic field were ignored. The combined areal density distribution of the seated model man and the Apollo are shown in figure 12 to range from 4.6 to 840 gm/cm^2 when the dose location is the retina of the right eye. This figure also shows that the areal density in 85% of the space surrounding the dose point is less than 50 gm/cm^2. When this areal density is combined with the Barrett spectrum, in which all particles have energies greater than 800 Mev, the spectrum at the retina appears as shown in figure 13. Though the high-areal-density region of figure 12 slows some of the particles, as shown at the lower left portion of figure 13, 96.8% of the incident particles still arrive at the retina of the eye.

According to Dr. Benson,[7] the frequencies of the light flashes observed by the Apollo 13 astronauts were as follows:

James Lovell	One every 2 minutes
Fred Haise	Ten in 5 minutes
John Swigert	Two in 30 minutes

The primary component of the cosmic radiation is the proton. In Barrett's model, the proton rate is 2.2 per second. This rate is considerably higher than reported in the article. The abundances of heavier particles are far less than protons -- only 12.5% for alpha particles and 1.6% for the total of all heavier particles. The rate of heavier particles is about two per minute, and is consistent with the observations of Lovell and Haise. It is therefore possible that these particles were the source of the light flashes.

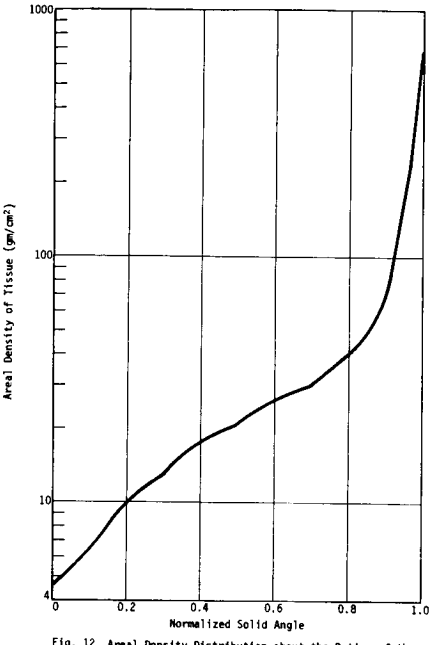

Fig. 12 Areal Density Distribution about the Retina of the Eye, Seated Configuration of the Model Man in the Apollo Command and Service Module

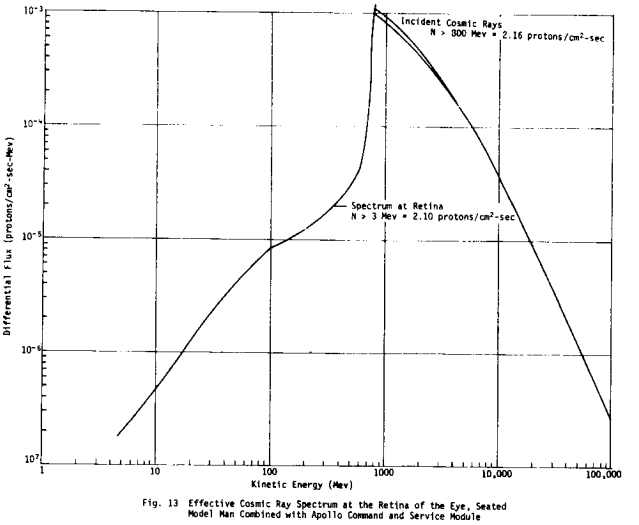

Fig. 13 Effective Cosmic Ray Spectrum at the Retina of the Eye, Seated Model Man Combined with Apollo Command and Service Module

Concluding Statement

The U. S. Air Force and NASA have jointly sponsored the development of a detailed model of the geometrical conformation, density distribution, and chemical composition of a typical astronaut. Its application is to the precise calculation of the combined areal density distribution surrounding a dose location due to the shielding provided by the astronauts and their spacecraft. From this information, radiation spectra and doses may be calculated. The results of radiation analyses employing this model could influence mission planning and operations.

Several examples of applications for the computerized anatomical model man have been discussed in this paper. Studies indicate that this model is best suited for analyses of radiation doses well within the body, where the effects of variations of tissue density and chemical composition are likely to be most significant. When the dose point is on or near the surface of the body, other effects, such as the astronauts' location and orientation with respect to the spacecraft, are probably more important.

In addition to its usefulness for depth/dose calculations, the model is appropriate for the evaluation and optimization of local protection, such as goggles or body shielding, especially when the effect of the local shielding is of the same order of magnitude as the effect of the self-shielding of the body. When the radiation is very penetrating, as in the case of cosmic radiation, the details of the spacecraft and human configurations are relatively unimportant: that is, the configurations are most influential when the most populous, lowest-energy portion of the incident spectrum is stopped.

References

1. Hertzberg, H. T. E.; Daniels, G. J.; and Churchill, E.: *Anthropometry of Flying Personnel, 1950.* WADC-TR-52-321 (AD47953), Wright Air Development Center, Dayton, Ohio, September 1954.

2. Liley, B.; and Hamilton, S. C.: *Modified Elemental Volume Dose Program (EVDP).* AFWL-TR-69-68, North American Rockwell Corporation, Los Angeles, California, August 1969.

3. Morgan, K. Z., Editor: "Report of ICRP Committee II on Permissable Dose for Internal Radiation (1959)," *Health Physics,* vol. 3. Pergamon Press, Inc., New York, New York June 1960.

4. Long, C., Editor: *Biochemists' Handbook.* D. VanNostrand Company, Inc., Princeton, New Jersey, 1968.

5. Kase, P. G.: *Computerized Anatomical Model Man.* AFWL-TR-69-161, Martin Marietta Corporation, Denver, Colorado, October 1969.

6. Barrett, P. H.; Bollinger, L. M.; Cocconi, G.; Eisenberg, Y.; and Greisen, K.: "Interpretations of Cosmic Ray Measurements for Underground," *Reviews of Modern Physics,* vol. 24, 1952.

7. "Apollo 14 Will Probe Light Flashes," *Aviation Week* and *Space Technology,* June 15, 1970.

Jupiter Radiation Test Levels and Their Expected Impact on an Encounter Mission*

J. B. Barengoltz
Jet Propulsion Laboratory

Upper limit electron and proton fluences for a Thermoelectric Outer Planet Spacecraft (TOPS) mission in a near-Jupiter environment, for use as radiation design restraints, have been extracted from the JPL engineering model of the Jovian trapped radiation belts. Considerations of radiation effects in semiconductor devices have been employed to construct simplified radiation test levels based on the design restraints. Corresponding levels, based on the nominal belt models, are found to be one to three orders of magnitude smaller. In terms of expected radiation-induced degradation in semiconductor devices, an encounter with an environment as severe as the design restraints would require hardening the system in order to guarantee high reliability. On the other hand, the nominal levels would only necessitate care in the selection of components and the avoidance of certain discrete semiconductor piece-parts.

The possible existence of prominent trapped radiation belts of energetic electrons and protons at Jupiter constitutes a serious hazard to any spacecraft in the vicinity of the planet. This radiation environment is hypothesized from the observation of apparent synchrotron emission from relativistic electrons and from analogy with Earth. A JPL engineering model (ref. 1) has been constructed based on several of the scientific models of the Jupiter trapped radiation belts, as discussed in a previous paper by Divine. In this model, the differential flux for either protons or electrons has the form:

$$\frac{d\Phi}{dE} = \frac{E\,v(E)\,N_0(L,\phi')}{E_0^2(L)} \exp\left[-\frac{E}{E_0(L)}\right]$$

where the characteristic number density N_0 is a function of the magnetic shell parameter L and the magnetic latitude ϕ', the characteristic energy E_0 is a function of L, and the speed v is a function of E.

DETERMINATION OF THE WORST CASE

In order to establish design constraint levels, the most severe environment permitted by the engineering model must be determined. Unfortunately, the functional dependences of E_0 and N_0 have large uncertainties, especially in the case of protons. The assumed dependence is constant from L = 1 to L = 2 and then decreasing according to an inverse power law. For any given trajectory, the severest dependence for N_0 is the slowest drop-off or the smallest exponent allowed by the model. Also, the largest peak (L = 2) value of N_0 is chosen. Since N_0 decreases with increasing magnetic latitude, the more severe trajectories lie in the magnetic equatorial plane. As will be shown, the selection of E_0 and its dependence for the worst case requires a consideration of the radiation damage in semiconductor devices.

RADIATION DAMAGE IN SEMICONDUCTORS

At the flux levels under consideration here, the two mechanisms for the degradation of semiconductor devices are ionization and displacement. Joule heating from induced electrical current is not a problem. Both the protons and electrons cause ionization, but the effect is long-lived only for a small class of devices, the metal-oxide-semiconductor (MOS) types, where the induced charge can be trapped. Displacement damage, or the removal of an atom from its proper lattice position, is more efficiently induced by protons than by electrons. This permanent effect, which will anneal at a temperature-dependent rate, is most harmful to minority carrier or bipolar technology devices.

For electrons, the severity of the ionization damage, which is proportional to the stopping power dE/dx shown in figure 1 (ref. 2), increases slowly with energy for energies greater than 0.7 MeV. The range curve in figure 1 (ref. 2) indicates that electrons of lower energies will not penetrate 50 mil of aluminum, a typical spacecraft wall thickness, and may be ignored. Another source of ionization from electrons, gamma bremsstrahlung production in the spacecraft wall, is negligible under these assumptions (ref. 3). The relative displacement damage as a function of electron energy (ref. 4), shown in figure 2, indicates clearly that higher energy electrons are more damaging. On the basis of both ionization and displacement damage, the worst-case characteristic energy is the highest allowed by the model.

By contrast, for protons in the energy range of interest, both the stopping power (ref. 2) in figure 3 and the relative displacement damage (ref. 4) in figure 4 decrease with increasing energy. Thus, low energy protons are the most damaging. However, the range curve (ref. 2) in figure 3 indicates that the characteristic energy

*This paper presents the results of one phase of research carried out at the Jet Propulsion Laboratory, California Institute of Technology, under Contract No. NAS 7-100, sponsored by the National Aeronautics and Space Administration.

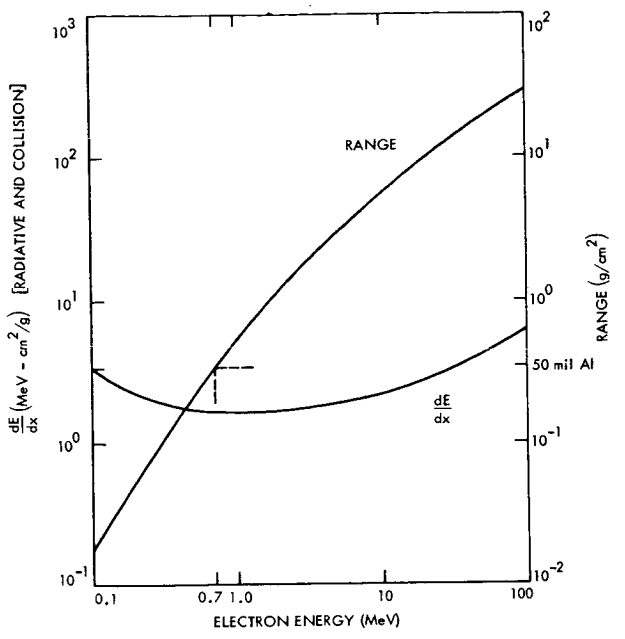

Figure 1. –Stopping power and range curves for electrons in silicon.

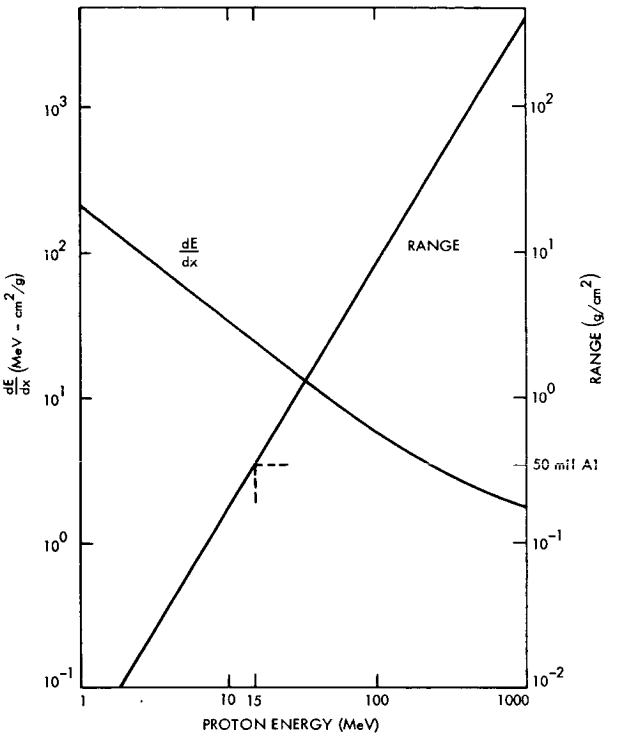

Figure 3. –Stopping power and range curves for protons in silicon.

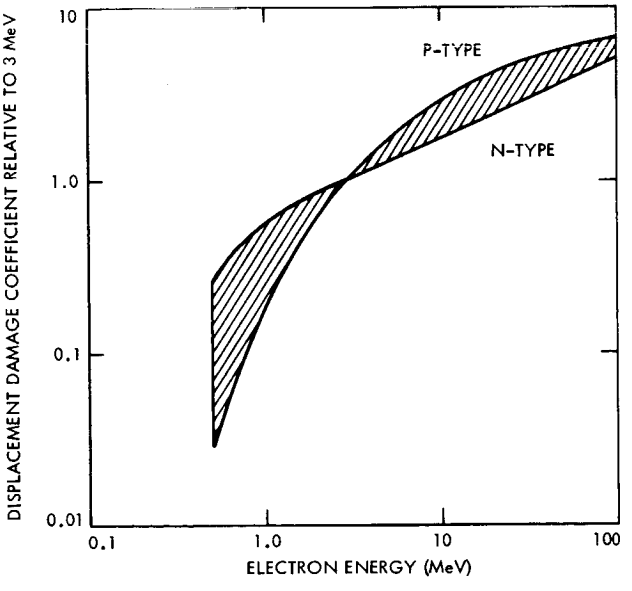

Figure 2. –Relative electron displacement damage in silicon.

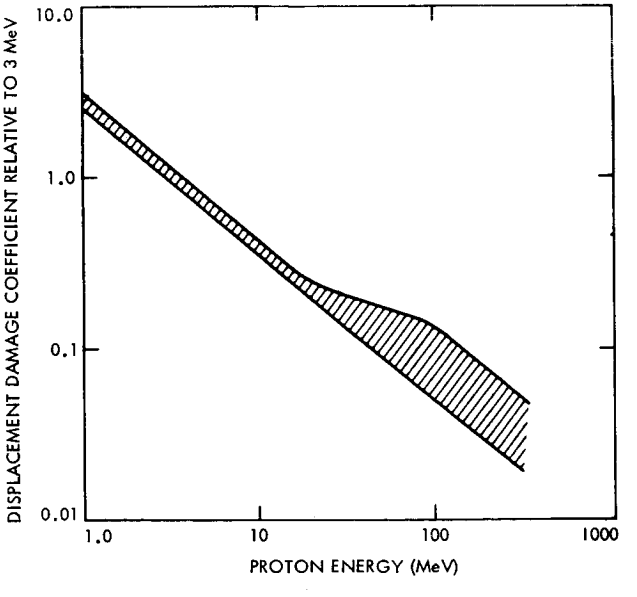

Figure 4. –Relative proton displacement damage in silicon.

must be selected large enough so that most of the protons will not be stopped by the spacecraft wall. The typical 50-mil aluminum wall will stop all protons with energy less than 15 MeV. Therefore, the worst-case characteristic energy is a compromise, the lowest value permitted by the model for which most of the protons in the spectrum will pass an assumed wall thickness.

ENERGY EQUIVALENCING

The same type of radiation effects data used to generate figures 1, 2, 3, and 4 may be used to construct relative damage functions dependent only on the particle type and energy. This procedure should be contrasted with attempts to develop equivalency in damage induced by different types of radiation, attempts which have led to inconclusive results. In energy equivalence, the requirement for testing in each predicted radiation environment remains. However, each type of exposure is reduced to a mono-energetic fluence; the relative damage function is used to collapse the energy-differential spectrum. Therefore, the test requirements avoid the serious problems of spectrum simulation. These same considerations also permit a comparison of the relative severity of environments consisting of different spectra of the same radiation type.

Although the absolute response, e.g., $\Delta(1/\beta)$, of a particular semiconductor device is strongly dependent on its electrical and physical characteristics, the relative response to a given fluence at one irradiation energy, normalized to the response at a reference irradiation energy, is reasonably device-independent. For example, in the case of transistors exposed to equal fluences of gamma radiation at different energies, for which the degradation of a particular electrical parameter is proportional to the dose, the relative damage function is proportional to the fluence-to-dose conversion factor. There is a lower limit in energy on the range of validity of the relative damage function, however, which is imposed by the effect of the device housing and geometry at low energy.

FLUENCE CALCULATIONS

Calculations of electron and proton fluences for Jupiter fly-by missions over a range of trajectories have been performed. The plane of the trajectory was taken to be the magnetic equatorial plane in each case. Upper limit and nominal fluences for some specific trajectories are listed in tables 1 and 2.

The determination of the fluences from the flux models consisted of an implicit time integration of the differential flux over the radial history of the trajectory. In the magnetic equatorial plane, the magnetic shell parameter L is equal to the radial distance from the center of the planet r, and the magnetic latitude is zero. Thus, the only time dependence in the flux is implicit in its radial dependence. Of course, it was necessary to select an arbitrary upper radial cut-off on the integration. One further assumption was made, the neglect of the radial dependence of the characteristic energy E_0, which greatly simplified the calculation by separating the radial and energy dependences. Finally, the relative damage function was used to eliminate the energy dependence, as described in the preceding section, and a mono-energetic fluence was obtained for each case.

Table 1.–Damage-weighted Jovian electron fluence (3 MeV).

MISSION NOTATION	TRAJECTORY PARAMETERS (JUPITER)		ELECTRON FLUENCE, e/cm^2	
	PERIAPSIS, R_J	DEFLECTION ANGLE, deg	NOMINAL	UPPER LIMIT
1976 JSP	1.1	136	7.4×10^{11}	7.5×10^{12}
1977 JSP	4.2	107.5	8.6×10^{10}	4.0×10^{12}
1977 JSP	5.6	85	3.7×10^{10}	2.9×10^{12}
1979 JUN	6.8	81	2.3×10^{10}	2.5×10^{12}
1979 JUN	10.3	60	6.8×10^{9}	1.5×10^{12}

Table 2.–Damage-weighted Jovian proton fluence (20 MeV).

MISSION NOTATION	TRAJECTORY PARAMETERS (JUPITER)		PROTON FLUENCE, p/cm^2	
	PERIAPSIS, R_J	DEFLECTION ANGLE, deg	NOMINAL	UPPER LIMIT
1976 JSP	1.1	136	8.2×10^{10}	5.4×10^{12}
1977 JSP	4.2	107.5	9.5×10^{9}	5.9×10^{12}
1977 JSP	5.6	85	4.1×10^{9}	5.4×10^{12}
1979 JUN	6.8	81	2.5×10^{9}	5.4×10^{12}
1979 JUN	10.3	60	7.5×10^{8}	4.9×10^{12}

Table 1 lists the calculated electron fluences for several trajectories, specified by the periapsis, in units of planetary radii, and the deflection angle between the incoming and outgoing asymptotes of the trajectory. The relative damage function for a 3-MeV reference energy was chosen to determine both nominal and upper limit 3-MeV equivalent fluences for these Jupiter-Saturn-Pluto (JSP) and Jupiter-Uranus-Neptune (JUN) missions. The results show that while the fluence decreases with increasing periapsis on the basis of both models, the upper limit fluences are quite insensitive to periapsis. It is also shown that the upper limit fluences are 1-2 orders of magnitude larger than the nominal values.

The calculated proton fluences for the same trajectories are given in table 2 in terms of 20-MeV protons. In the case of the severe proton model, the prediction of a flat radial distribution leads to fluences that are completely insensitive to periapsis. The larger uncertainties in the proton models result in a wider spread between the nominal and upper limit fluences, in the range of 2-4 orders of magnitude.

ASSESSMENT OF THE RADIATION HAZARD

At this point, the predicted proton and electron fluences should be compared with available information on the radiation sensitivity of semiconductor devices. Figure 5 indicates the fluences of 1-3 MeV electrons that will cause detectable degradation (unshaded bar) and serious degradation or total failure (shaded bar) for a few device types. The bar graph is based on a small set of data, but the large differences in radiation sensitivity of the specific devices within a category is reflected in the large uncertainties in each bar. Also noteworthy is the obvious susceptibility of MOS devices to electrons, in comparison to other device types. This contrast simply results from electrons efficiently causing ionization, to which MOS devices are most sensitive. Vertical lines are given to indicate the nominal and upper limit fluences for worst-case trajectories. It can be seen that, with the exception of discrete MOS devices, careful part selection will obviate the electron problem.

The corresponding information for 20-MeV protons in figure 6 shows that the protons are a more serious hazard. The bar graph, which is based on the results of a study (ref. 5), reflects the efficiency with which protons cause both ionization and displacement damage. Even the nominal value mission fluence would seriously damage many device types. The design of a spacecraft for survival in the upper limit proton environment requires both a complete screening of piece-parts for radiation tolerance and hardening by circuit design.

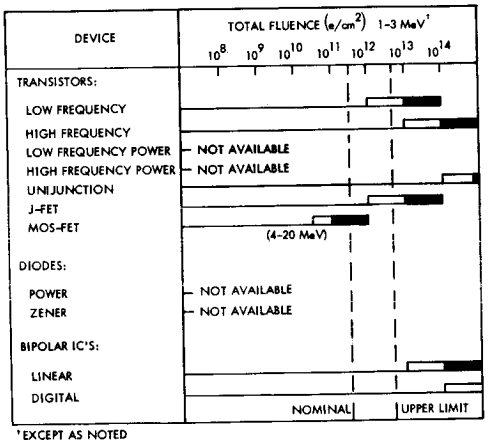

Figure 5. – Typical tolerance of semiconductor devices to electron irradiation.

CONCLUSION

Although the near-Jupiter proton and electron environment poses a serious hazard to a fly-by spacecraft, the current best estimates of this environment have large uncertainties. If some improvements in the uncertainties were obtained, especially for protons, the stringency of the test levels and parts selection requirements could be relaxed. In particular, a reduction in the uncertainty of the radial dependence of the flux would introduce a sensitivity to the trajectory and would allow a trade-off in mission planning. Efforts to improve the models in this manner are currently planned.

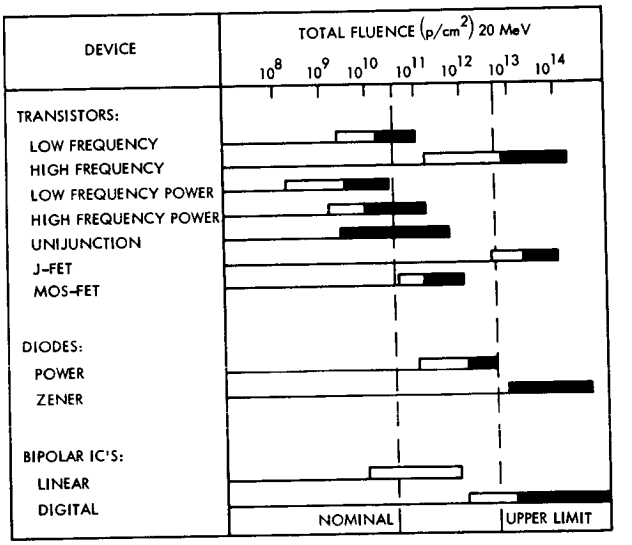

Figure 6. – Typical tolerance of semiconductor devices to proton irradiation.

REFERENCES

1. Divine, T. N.: The Planet Jupiter (1970), NASA Space Vehicle Design Criteria Monograph (to be published).

2. Berger, M. J.; and Seltzer, S. M.: NASA SP-3036, National Aeronautics and Space Administration, Washington, D. C., 1966.

3. Li, S.; and Barengoltz, J.: Jupiter's Electron Dose Calculations on MOS Structures, Space Programs Summary 37-66, Vol. III, Jet Propulsion Laboratory, Pasadena, Calif., Dec. 31, 1970.

4. Larin, F.: Radiation Effects in Semiconductor Devices, John Wiley & Sons, Inc., New York, 1968.

5. Horne, W. E.: Document D2-126203-3, Boeing Aircraft Co., Seattle, Wash., 1970.

SESSION VIII.I.
RADIATION TRANSPORT & SHIELDING: ELECTRON TRANSPORT
CHAIRMAN: R.G. ALSMILLER
OAK RIDGE NATIONAL LABORATORY

A MONTE CARLO PHOTOCURRENT/PHOTOMISSION COMPUTER PROGRAM

W. L. Chadsey and C. Ragona
The Re-Entry and Environmental Systems Division
General Electric Company
Philadelphia 19101

Abstract

A Monte Carlo computer program (POEM) has been developed for the computation of photocurrents and photoemission in gamma (x-ray)-irradiated materials. The program has been used for application to the computation of radiation-induced surface currents on space vehicles and the computation of radiation-induced space-charge environments (IEMP) within space vehicles. The program has been successfully correlated with published expirmental data.

POEM is a composite analytical-Monte Carlo computer program which calculates the photoemission from a gamma (x-ray)-irradiated slab of material. The program uses analytical routines to calculate photon flux attenuation, energy deposition and electron production within the slab, and uses a Monte Carlo routine to calculate the electron transport through the slab and the emission from the slab. The objective of using the analytical photon transport routine is to avoid the computation time-consuming complexity of a pure Monte Carlo model. When using a Monte Carlo photon transport routine, in order to produce a sufficient number of Compton scattering and photoelectric interactions to afford reasonable statistics for the initial energy-angle distributions of the electrons requires a great number of photon histories (typically several hundred thousand histories). To reduce the computation time required, an analytical routine has been incorporated in POEM to compute photon transport.

The POEM program calculates the net photocurrent within a material and the electron emission current from a material including the energy flux, energy spectrum, and angular distribution for an arbitrary incident photon spectrum. The emission can be calculated in either the direction of the incident photon flux or the reverse direction. In either case the program assumes normal incidence of the photon flux on the emitting slab, although with minor modification the program could treat an arbitrary angle of incidence. It is assumed that the time-dependence of the electron emission current is the same as the time-dependence of the incident photon flux, i.e. the model is quasistatic.

The emission calculation includes the Compton electrons, photoelectrons (K and L), and Auger electrons (L) resulting from the scattering and absorption of the primary x-ray flux. The emission calculation, at present, does not include second generation (knock-on) electrons nor the electrons produced by the scattering and absorption of fluorescent or bremsstrahlung radiation. A study is planned to investigate techniques for the inclusion of these effects, including a more rigorous treatment of the Compton scatter radiation.

I. Introduction

The description of the current density and energy-angle distribution of gamma ray or x-ray induced electron emission is required in the study of transient radiation effects on electrical systems and in the development of fast radiation detectors. A rigorous calculation of the electron emission requires both a Monte Carlo photon transport calculation of the electron source distributed throughout the irradiated matter and a Monte Carlo electron transport calculation of the intensity and energy-angle distribution of the multiple scattered electron flux at the emission surface. Because of the low quantum efficiency for the production of primary electrons (Compton, Auger, and photoelectrons) by photons, it has been experienced that a very large number of photon histories are required in the Monte Carlo photon transport calculation to produce a statistically acceptable description of the electron source. Several hundred thousand photon histories have been found necessary for a typical incident photon environment, requiring on the order of 40 minutes computation time (using the ONE-D [1] code on the GE 635 computer). The need exists for a less costly computational tool. A purely analytical electron emission model [2, 3], on the other hand, while providing an inexpensive computation of the electron emission flux, does not properly treat electron multiple scattering and so does not provide a valid description of the angular distribution of emission.

The POEM (photoemission) computer program was developed to provide a computational tool for the calculation of photon radiation-induced electron emission which would be relatively inexpensive to use but would include a proper treatment of electron multiple scattering. POEM is a composite analytical-Monte Carlo program, using analytical routines to calculate photon flux attenuation and primary electron production in the material and a Monte Carlo routine to calculate the electron transport to the surface of the material. Whereas a typical electron emission calculation required 45 minutes computation time (on the GE 635) with a pure Monte Carlo code, the same calculation requires only 3 minutes computation time with POEM, without apparent, significant sacrifice in accurancy.

POEM calculates the electron emission from a gamma or x-ray irradiated slab of material. The program assumes normal incidence of the x-ray flux on the emitting slab, although with minor modification the program could treat an arbitrary angle of incidence. The emission current, energy spectrum, and angular distribution are calculated both in the direction of the incident radiation and in the reverse direction. (Hence,

the program may be used to calculate the net primary photocurrent across any plane within the irradiated material.) It is assumed that the time-dependence of the electron emission current is the same as the time-dependence of the incident photon flux, i.e. the model is quasistatic.

The emission calculation includes the Compton electrons, photoelectrons (K and L), and Auger electrons (L) resulting from the scattering and absorption of the primary x-ray flux and (in an approximate treatment) the Compton scattered x-ray flux. The emission calculation, at present, does not include second generation (knock-on) electrons nor the electrons produced by the scattering and absorption of fluorescent or bremsstrahlung radiation. The electron transport calculation is strictly valid only for electron energies greater than the K absorption edge of the emitting material. The code seems to produce reasonable results, however, down to somewhat lower energies.

POEM has been evaluated through the comparison of computational results to published experimental data for electron emission induced by CuK_α x-radiation and Co^{60} gamma radiation, and through comparison to superflash x-ray-induced electron emission data obtained by the author. The comparisons to the published data are presented herein.

II. Program Description

II.1 Photon Transport

The radiation intensity I (photons/cm^2) at the point x of initiation of electron emission is calculated assuming a simple exponential attenuation of the intensity,

$$I(x, E_\gamma) = I_o(E_\gamma)\ e^{-\mu x} \qquad (1)$$

where $I_o(E_\gamma)$ is the incident intensity, x is the distance from the irradiated surface, and μ is the total linear attenuation coefficient. The assumption of exponential attenuation, of course, implies the complete absorption of a photon in any interaction. This is strictly true only of the photoelectric interaction. In a Compton scatter interaction, the photon recedes from the point of collision with reduced energy and altered direction. This Compton scattered radiation is treated by an approximation: rather than reducing the photon flux by decreasing the energy of each Compton scattered photon while holding the number of photons constant (which would considerably complicate the calculation), the number of photons is reduced in each Compton interaction holding the photon energy constant. Mathematically this is done by introducing a Compton attenuation cross-section σ' which is the sum of the Compton absorption cross-section σ_α and a fraction f of the Compton scatter cross-section σ_s,

$$\sigma' = \sigma_\alpha + f\sigma_s \qquad (2)$$

The total linear attenuation coefficient μ is then given by

$$\frac{\mu}{\rho} = \tau + \sigma_\alpha + f\sigma_s \qquad (3)$$

where τ is the photoelectric cross-section and ρ is the density. Values for the fudge factor f have been selected by comparisons of exponential attenuation calculations to Monte Carlo calculations.

II.2 Electron Production

The irradiated slab is divided into incremental slabs of thicknesses Δx such that $\mu\Delta x << I$, i.e. so that the photon flux variation through the zone is calculated in each zone for which there is a significant probability of escape, i.e. in each zone for which the maximum path length of the electrons produced in the zone is larger than the normal distance to the emitting surface. (Remember that the maximum electron path length is considerably greater than the extrapolated electron range range because of multiple scattering.)

The number of Compton electrons produced (per cm^2) in a zone, location x_i, by photons of energy $E\gamma$ is

$$N_c(E_\gamma, x_i) = I(E_\gamma, x_i)\left(1 - e^{-\frac{\sigma}{\rho}\Delta x}\right)$$

where $\sigma = \sigma_\alpha + \sigma_s$ is the total Compton mass attenuation coefficient and the photon intensity $I(E_\gamma, x_i)$ is given by equation (1). The initial energy-angle probability distributions of the Compton electrons are given by Klein-Nishina. (4)

The number of photoelectrons produced in the zone x by photons of energy E_γ is

$$N_\rho(E_\gamma, x_i) = I(E_\gamma, x_i)\left(1 - e^{-\frac{\tau}{\rho}\Delta x}\right)$$

where τ is the photoelectric mass attenuation coefficient. It is assumed that for all photon energies greater than the K edge the ratio of L to K photoelectrons produced is equal to the ratio at just above the K edge, i.e.

$$\frac{n_L}{n_K} = \frac{\tau(E_K - \epsilon)}{\tau(E_K + \epsilon) - \tau(E_K - \epsilon)} \qquad (6)$$

where E_K is the K edge and ϵ is an infinitesimal energy increment. The angular distribution of the photoelectrons is given by Fischer and Sauter (4), the former for low energy photelectrons ($\beta << 1$), the latter for high energy electrons ($\beta \simeq 1$).

The number of Auger electrons (L only) produced in the zone x_i by photons of energy E_γ is

$$N_A(E_\gamma, X_i) = (1 - f_K)\, N_\rho^K(E_\gamma, x_i) \qquad (7)$$

where N_p^K is the number of K photoelectrons produced and f_K is the K fluorescence yield given by.[5]

$$f_K \cong \frac{z^4}{z^4 + 30^4} \qquad (8)$$

where Z is the atomic number. The angular distribution of the Auger electrons is assumed isotropic.

The total electron initial energy-angle probability distribution for each zone of the emitter is calculated by summing for each photon energy the Compton, photoelectric and Auger distributions and then integrating over the photon energy spectrum.

II.3 Electron Transport

The transport of the electrons to the emitting surface is calculated using the POET [6] Monte Carlo electron transport program which has been incorporated into POEM. POET is a condensed history Monte Carlo program. In the condensed history Monte Carlo method, the results of multiple scattering theory are combined with Monte Carlo techniques to form a consistent approach to electron transport calculations in the media of finite dimensions. Since the large majority of electron-atom interactions involve small angel deflections and small energy loss, the condensed history random walk approach is applicable to electron transport (it is not applicable to photon transport due to the large scattering angles involved in the majority of collisions). Rather than calculate the trajectories of the electrons as they undergo each coulomb interaction, a random walk computation is performed in such a way that each step takes into account the combined effect of many collisions. The electron history is divided into logarithmically-spaced energy intervals. For each step of the random walk the path length increment traveled by the electron, corresponding to the energy loss increment, is computed using the Bethe-Moller stopping power. [7-9] By random sampling from the angular distributions calculated using the Goudsmitt-Saunderson theory [10] of multiple scatter, the direction of travel of the electron after each random walk step is obtained.

For each electron history the random walk computation is initiated by random selection of an initial location within the electron production zone (from a uniform distribution within the zone) and a random selection of the initial electron energy and velocity direction (from the computed energy-angle probability distribution for the zone). The random walk computation is continued until either the electron escapes from the emitting surface or until the residual path length of the electron is smaller than the normal distance to the distance to the emitting surface (so that in this continuous slowing down approximation the electron has zero probability of escape).

III. Comparison of Computational Results With Experiment Data

III.1 Energy Spectrum

E. P. Denisov, et. al [11] of Leningrad State University published in 1963 the results of an expirment in which the structures of the x-ray photoemission energy spectra from aluminum, titanium, chromium, and iron photocathodes were measured. The photocathodes consisted of a thin layer of the test material (thicker than the maximum exit depth of the electrons) sputtered on a planar glass substratum at the center of an evacuated, spherical collector. The energy structure of the photoemission was determined by measuring the collected current as a function of the bias potential between the photocathode and the collector. The photocathodes were irradiated by CuK_α x-rays (8 kev). The experimental results for the four photocathodes are compared to the POEM calculations of the energy structure shown in Figure 1. The experimental and calculational results are compared by adjusting the arbitrary normalizations such that the primary maxima are equal. (No attempt was made to compare the gross emission currents since these data were not published by Denisov, et. al.). The agreement of the structures of the calculated and the experimental spectra is good except for the low energy spike in the experimental spectrum, which Denisov, et.al. interpret to be the secondary electron contribution to the emission spectrum. The three peaks in the energy spectrum due to the K photoelectron, L photoelectron, and Auger electron contributions to the spectrum can be seen in both the calculated and measured spectra.

III.2 Emission Current, Angular Distribution

Ebert and Lauzon [3] of the Lawerence Radiation Laboratory published in 1965 the results of an experiment in which they measured the quantum efficiency (electrons emitted per incident photon) and the angular distribution of the gamma-ray induced electron emission from carbon, aluminum, copper, cadmium, and lead targets. Two sets of target thicknesses were used: one set of targets with thickness equal to the range of a 1.25 MeV photoelectron, and another set with thickness of one-tenth the range. The targets were irradiated by a collimated beam of 1.25 MeV gammas from a Co^{60} source. The emission current was measured by a Faraday cup; the (cumulative) angular distribution was measured by varying the solid angle subtended by the Faraday cup.

The Ebert and Lauzon results are compared to the POEM calculations for the quantum efficiency in Table 1 and for the (differential) angular distribution shown in Figure 2. The agreement in both quantum efficiency and angular distribution is excellent. The agreement in quantum efficiency is not remarkable; Ebert and Lauzon had comparable success using an analytical model to calculate quantum efficiency. What is significant is the

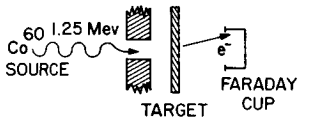

TEST CONFIGURATION

TARGET	THICKNESS (CM)	QUANTUM EFFICIENCY (ELECTRON/PHOTON) POEM	EXPERIMENT
CARBON	2.03×10^{-1}	9.68×10^{-3}	9.14×10^{-3}
	2.26×10^{-2}	2.57×10^{-3}	2.46×10^{-3}
ALUMINUM	2.27×10^{-1}	7.96×10^{-3}	7.97×10^{-3}
	1.27×10^{-2}	1.80×10^{-3}	1.99×10^{-3}
COPPER	5.24×10^{-2}	6.10×10^{-3}	6.13×10^{-3}
	5.12×10^{-3}	2.09×10^{-3}	2.04×10^{-3}

TABLE 1. COMPARISON OF POEM RESULTS WITH EXPERIMENTAL DATA OF EBERT AND LAUZON [3]

agreement in the angular distribution. Ebert and Lauzon found that calculations of the angular distribution made using an analytical model, which assumed rectilinear electron transport, were in complete disagreement with the experimental data. Here, then, is the key advantage of the Monte Carlo calculation: analytical models which cannot properly treat electron multiple scattering, but rather assume rectilinear transport, provide no valid information as to the angular distribution of photoemission.

Conclusions

Comparisons of computational results with experimental data have shown the POEM code to be quite adequate for the calculation of photon radiation-induced electron emission, at least in the limited ranges of photon energies for which test data were available for comparison. More test data, especially in the x-ray energy range, 1 keV to 1 MeV, are required for additional code verification. One shortcoming of the POEM code is its neglect of the secondary (knock-on) electrons. A study is planned of computational techniques for the inclusion of the secondary electrons in the emission calculation.

References

(1) E.T. Kennedy, "One-D: A Monte Carlo Gamma Transport Computer Program," General Electric Company, RESD, PIR-8121-111, (Sep 1966).

(2) N. Kusnezov, "Photon-Induced Charge Emission" Lockheed, B-70-69-6 (Aug. 1969).

(3) P.J. Ebert and A.F. Lauzon, "Measurement of Gamma Ray Induced Secondary Electron Current from Various Elements," IEEE Tran. Nuc. Sci. (Feb. 1966), pp. 735-741.

(4) C.M. Davisson, R. D. Evans, "Gamma-Ray Absorption Coefficients," Rev. Mod. Phy. 24, No. 2 (Apr. 1952).

(5) U.E. Condon and H. Odishaw, Handbook of Physics, McGraw-Hill, New York, (1958), pp. 7-125.

(6) E.T. Kennedy, "POET: A Monte Carlo Electron Transport Program (Vol. 1), GE TIS No. 67SD253, (April 1967).

(7) H. Bethe, Handbuch der Physik 24, (1933) p. 491

(8) C. Moller, Ann Physik 14 (1932), p. 531

(9) F. Rhorlich and B. Carlson, Phys. Rev. 93, (1954), p. 38

(10) M. Berger, in Methods in Computational Physics, ed. by B. Alder, Academic Press, New York, (1963), pp. 207-213.

(11) E.P. Denisov, V.N. Schemelev, A.N. Mezhevich, and M.A. Rumsh, "Analysis of the Energy Structure of X-Ray Photoemission From a Massive Cathode, "Soviet Physics, Solid State 6, (1965) p. 1047.

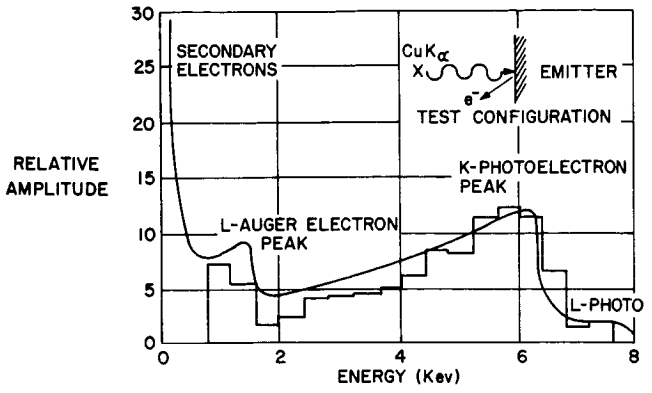

Figure 1a. Electron Emission Energy Spectrum - Aluminum --- Comparison of Calculations with Experimental Data (CuK α x-Radiation Incident on Target)

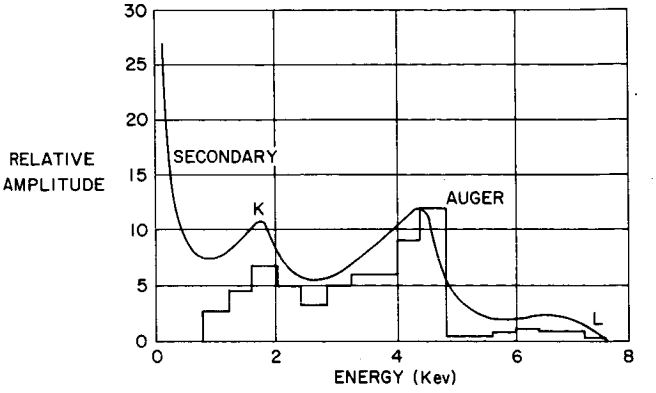

Figure 1c. Electron Emission Energy Spectrum - Chromium

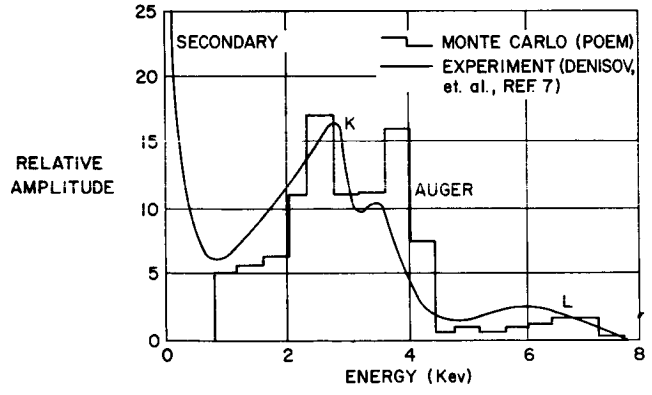

Figure 1b. Electron Emission Energy Spectrum - Titanium

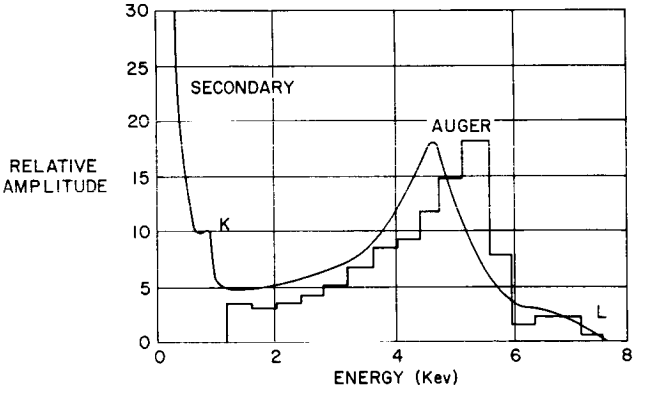

Figure 1d. Electron Emission Energy Spectrum - Iron

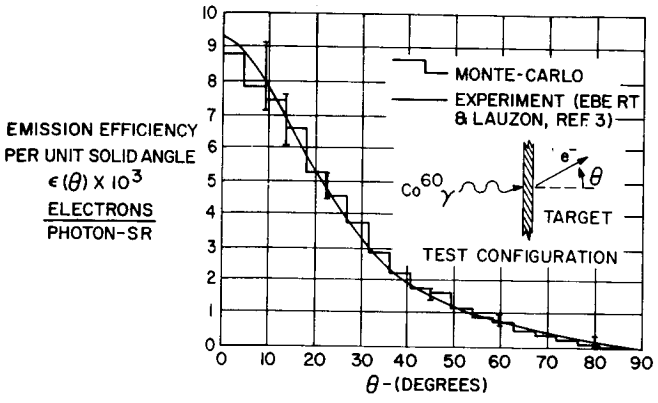

Figure 2a. Electron Emission Angular Distribution - Carbon Target (Electrons Per Unit Solid Angle Per Incident Photon) (1.25 Mev Co^{60} Gamma Radiation on Target)

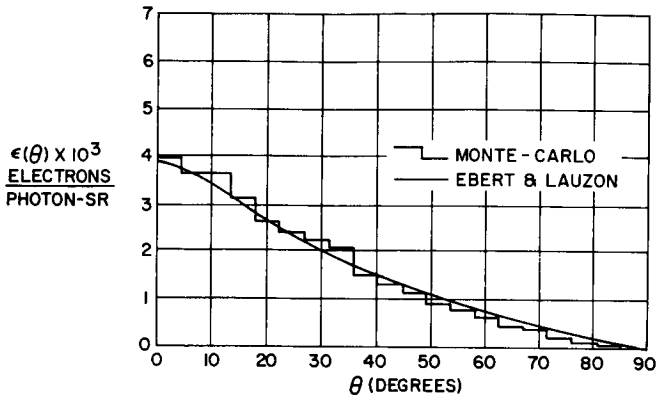

Figure 2c. Electron Emission Angular Distribution - Cooper Target

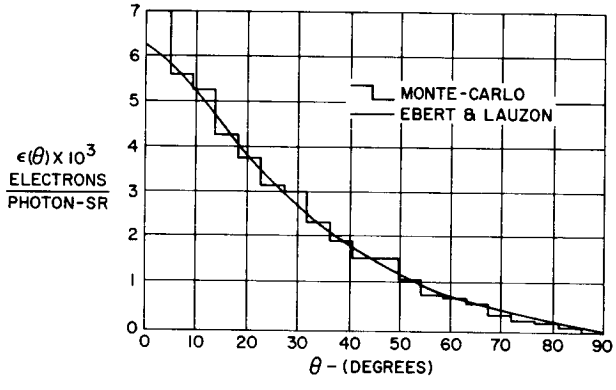

Figure 2b. Electron Emission Angular Distribution - Carbon Target

PHOTON INDUCED SECONDARY ELECTRON EMISSION

R. B. Spencer, TRW Systems Group; C. B. Smith, Norman Engineering Co.; and E. J. McGrath, Science Applications Inc.

This paper presents the results of numerical models for predicting photon induced secondary electron emission. These results are compared with recent experimental measurements made at UCLA using a Co-60 gamma ray source.

INTRODUCTION

An important consideration in the design of efficient spacecraft and missile radiation shielding is photon induced secondary electron emission. The secondary electrons may result in charge separation, thereby producing undesirable current flows and electromagnetic fields internal to the system. Basic to the prediction of such effects is a requirement to perform analyses for photon transport, electron production, and subsequent electron transport in arbitrary materials and geometries.

Electron emission from solids can be caused by high temperature, strong electric fields, and bombardment with photons and particles. Electrons emitted by primary electron bombardment are referred to as secondary electrons, and were discovered in 1902 by Austin and Starke[1] during a study of the reflection of electrons from metal. Austin and Starke observed that under certain circumstances more electrons were emitted than were incident on the material, indicating that the bombarding primary electrons ejected other electrons from the solid. Today the term "secondary electron emission" is used in a broader sense to indicate the phenomena of electron emission from solids subjected to bombardment from any type of particle or radiation. For the purpose of our study, the terms "secondary electron", and "secondary electron emission" are used with this broader meaning.

One phase of our study was a numerical investigation of the emission of secondary electrons from metals when the secondary electrons are produced by high-energy photons. A complete description of the secondary electron emission from the surface of a solid material is obtained when the number of electrons at a point in space as a function of energy is known. The function to be predicted is called the secondary electron current density and is denoted by $j_s(E,\Omega)$. The magnitude of the current density depends only on the states of interacting systems, i.e., on the properties of the primary beam and on the physical and chemical properties of the emitter, including chemical composition, crystal structure, surface conditions, and temperature. If $j_s(E,\Omega)$ is integrated over all energies and over all angles of the hemisphere surrounding an emitting planar surface, the total yield of secondary electrons is obtained. Much of the experimental work and theoretical work that has been performed in the past has been concerned with low-energy electrons (100 eV) as a source radiation. Recently, research has been directed at predicting secondary electron emission from solid materials using gamma ray sources emitting photons in the MeV energy range.

The purpose of our research is to improve the ability to predict the angular energy distributions of secondary electrons emitted from various types and thicknesses of materials exposed to photon radiation, and to develop and verify simplified calculational models for describing the phenomenon of secondary electron emission. These models provide a means of obtaining estimates of secondary electron emission produced by incident photons. The models were programmed on a digital computer to provide results for comparing with more sophisticated Monte Carlo programs and experimental results.

The computational models include one first proposed by Sawyer and Van Lint[2] and later refined by Spencer.[3] The Monte Carlo calculations were performed using the two-dimensional time dependent combined photon and electron code, TEMPER.[4]

We have performed experiments to measure the energy and angular distributions of secondary electrons emanating from several target materials.[3,5] Eight materials ($_{13}Al$, $_{22}Ti$, $_{29}Cu$, $_{42}Mo$, $_{48}Cd$, $_{73}Ta$, $_{82}Pb$ and $_{92}U$) ranging in thickness from 0.003" to 0.5" were used. The photon source used for the experiment was a 3 Ci Co^{60} source with photopeaks at 1.17 and 1.33 MeV. Pulse-height spectra (256 energy groups) of the emitted electrons were measured at 0, 10, 15, 20, 25, 30, 40, 50, and 60° to the beam forward direction for the gamma beam normal to the target.

A detection technique, proposed by Lonergan and Costello[6], which uses a transmission mounted Si semiconductor detector placed in front of a Pilot-B scintillator, was employed to discriminate against scattered incident photons. Since the semiconductor detector is only 131 microns thick, its efficiency for detecting scattered source photons is extremely low. By operating the two detectors in coincidence, the electron counts can be distinguished from

the photon counts in the scintillator. The thin semiconductor detector absorbs all electrons with energies less than about 160 keV, therefore only the high energy secondary electrons were measured for their energy and angular distributions. A complete description of the experimental measurements is given in References 3 and 5.

GENERAL SECONDARY ELECTRON EMISSION MODEL

The process of secondary electron emission consists of both the generation of the electrons and the transport, attenuation and eventual emission of the generated electrons. The concepts and details of electron transport in material have been considered using both analytical approximations and Monte Carlo numerical analysis. The majority of the electron transport theory that has been presented is based on the Boltzmann transport equation. The purpose of this paper is <u>not</u> to consider the Boltzmann equation for electrons, but rather to consider a simplified theory on which a numerical model of secondary electron emission could be based. The general secondary electron emission model described here is based on the model proposed by Sawyer and Van Lint.[2]

Figure 1 illustrates the geometry assumed in considering the general features of the secondary electron emission model. Consider a photon which is incident perpendicular to the surface of a slab target of thickness t. At a distance x before emerging from the target, the photon produces a secondary electron of kinetic energy T_i moving at an angle ϕ_i to the direction of the incident photon. The secondary electron loses energy and scatters in traveling through the remainder of the target, eventually emerging with kinetic energy T_f at an angle ϕ_f with the normal to the slab target. The purpose of the theory is to obtain an expression for the angular and energy distributions $N(T_f,\phi_f)$ of the emergent secondary electrons as a function of the target characteristics (atomic number and thickness) and the incident photon spectrum $\Phi_o(h\nu)$.

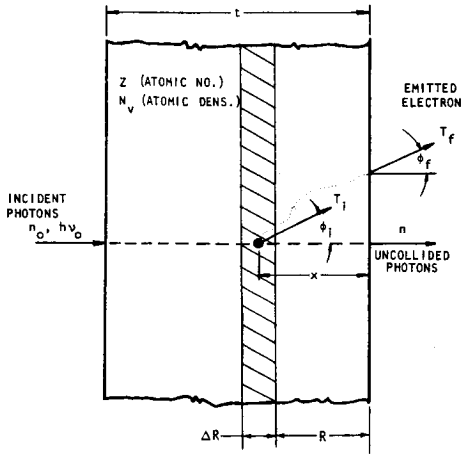

FIGURE 1. SLAB GEOMETRY FOR THIN ABSORBING SAMPLE

The total number of secondary electrons N_t generated within a thickness dx of the target, at a depth $t-x$, from photons of energy $h\nu$ is given by the product of the photon intensity at $t-x$, the electron production cross section, and the thickness dx.

$$N_t = [\text{photon intensity}]x[\text{electron production per photon per dx}]x[dx] \quad (1)$$

The number of secondary electrons of initial kinetic energy T_i within dT_i in solid angle $d\Omega'$ about initial angle ϕ_i is obtained by using the appropriate differential angular and energy electron production cross section.

$$N_{h\nu}(T_i,\phi_i)dT_i = [\Phi(h\nu,t-x)][ZN_v\frac{d\Omega'}{4\pi}\sigma(h\nu\rightarrow T_i,\phi_i)dT_i]dx \quad (2)$$

where:

$\Phi(h\nu,t-x)$ = photon intensity at $t-x$ with energy $h\nu$, photons

Z = atomic number of target material, electrons/atom

$N_v = \frac{\rho N_a}{A}$ atomic density of target material, atoms/cm^3

ρ = material density, g/cm^3

N_a = Avogadro's number = 0.6024×10^{24} atoms/g-atom

A = material atomic weight, g/g-atom

$\frac{1}{4\pi}\sigma(h\nu\rightarrow T_i,\phi_i)dT_i$ = the cross section per target electron for production of secondary electrons of energy T_i within dT_i, per unit solid angle near ϕ_i, cm^2/electron-steradian

$d\Omega' = \sin\phi_i d\phi_i d\psi$ = differential solid angle about ϕ_i, steradians

ψ = azimuthal angle of the generated secondary electrons

dx = material differential thickness, cm.

The energy spectrum of secondary electrons generated within a thin layer of thickness dx by a photon spectrum at the distance $t-x$ into the target, $\Phi(h\nu,x)$, is obtained by integrating $N_{h\nu}(T_i,\phi_i)$ over the range of energy of the incident photon spectrum.

$$N(T_i,\phi_i)dT_i = \int_0^{h\nu_{max}}\int_0^{2\pi}\Phi(h\nu,x)\,ZN_v\,\frac{1}{4\pi}\,\sigma(h\nu\rightarrow T_i,\phi_i)\cdot \sin\phi_i d\psi dh\nu d\phi_i dx\,dT_i \quad (3)$$

For a non-polarized incident photon spectrum, the secondary electron production is cylindrically symmetrical and integration over the azimuthal angle yields the following expression for the initial energy spectrum of the secondary electrons[2]

$$N(T_i,\phi_i)\,dT_i =$$

$$\frac{ZN_v}{2}\int_0^{h\nu_{max}} \Phi(h\nu,x)\sigma(h\nu\rightarrow T_i,\phi_i)\cdot \cdot \sin\phi_i dh\nu d\phi_i\,dx\,dT_i \qquad (4)$$

The transmission of a generated secondary electron to the back surface of the target can be described by a general probability function $p_e(T_i,\phi_i;\ x;\ T_f,\phi_f)$, which represents the probability per unit emerging energy T_f and solid angle Ω of escape with energy near T_f, and angle near ϕ_f for a secondary electron generated at a distance x below the surface with energy T_i and at angle ϕ_i. Including this probability function and indicating the integrations over the target thickness (t), energy of formation (T_i) and angle of formation (ϕ_i), the angular-energy distribution of emitted secondary electrons is[2]

$$N(T_f,\phi_f)dT_f d\Omega =$$

$$\frac{ZN_v}{2}\int_0^{h\nu_{max}}\int_0^{t}\int_0^{T_{i\ max}(h\nu)}\int_0^{\pi}\Phi(h\nu,x)\cdot \cdot \sigma(h\nu\rightarrow T_i,\phi_i)p_e(T_i,\phi_i;x;T_f,\phi_f)\cdot \cdot \sin\phi_i d\phi_i dT_i dx\,dh\nu\,dT_f d\Omega \qquad (5)$$

The photon intensity at each depth in the target and at each energy is related to the incident photon intensity by an exponential attenuation factor. An energy-dependent absorption coefficient $\mu_o(h\nu)$ is determined by the combined total cross sections for Compton scattering, photoelectric effect, and pair production interactions. The intensity of the energy-dependent uncollided photons at a depth t-x within the target is thus given by

$$\Phi(h\nu,t-x) = \Phi_o(h\nu)e^{-\mu_o(h\nu)(t-x)} \qquad (6)$$

where the contribution of multiple Compton scattering has been neglected.

Numerically, the energy-dependent photon attenuation and resulting photon intensity at a given target depth is calculated by means of a computer program called XRAY.[7] This code divides the incident photon spectrum into energy groups (up to 100) and obtains the energy dependent absorption cross section by means of table look-up. The total attenuation coefficients μ_o and energy absorption coefficients μ_a (for photon energies between 0.1 keV and 10 MeV) are contained on magnetic tape for about 50 of the most common elements. XRAY has the capability of handling multi-element, multi-region shields and can calculate the uncollided photon intensity, transmission factor, energy deposition, and absorbed dose in standard materials (e.g. rads Si) as a function of material depth for an arbitrary input photon spectrum.

If the assumption is made that the statistical fluctuation in the range of secondary electrons of the same initial energy is a Gaussian distribution about the mean range $\bar{R}$, the probability of escape $p_e(T_i,\phi_i;x;T_f,\phi_f)$ can be shown to be [2]

$$p_e = \frac{1}{2}\left[1-\mathrm{erf}\left(\frac{x/\cos\phi_i-\bar{R}(T_i)}{\alpha}\right)\right]\delta(\phi_i-\phi_f)\delta(T_f-\bar{T}) \qquad (7)$$

where α is the range-straggling parameter and is related to the standard deviation of the range-straggling Gaussian distribution by $\alpha = \sqrt{2}\,\delta$. The Dirac delta functions $\delta(\phi_i-\phi_f)$ and $\delta(T_f-\bar{T})$ connote, respectively, the assumptions that the final angle of emission ϕ_f is the same as the initial generation angle ϕ_i and the final energy T_f is equal to an average electron energy $\bar{T}$. $\bar{T}$ corresponds to the average range remaining to the electrons beyond the distance to the surface $x/\cos\phi_i$ for those electrons which penetrate. The first assumption presumes that multiple scattering of the secondary electrons does not, on the average, have a net effect on the direction of the generated electrons. The average energy of the emitted electrons $\bar{T}$ (all starting at the same energy T_i) is given by[2]

$$\bar{T} = \exp\left\{\frac{1.265-[1.6-0.3816\ln(\Delta R_e/0.273)]^{1/2}}{0.1908}\right\} \qquad (8)$$

for electrons with energies from 10 keV to 3 MeV. The ΔR_e in the expression for $\bar{T}$ is the increment of range from the emitting surface ($x/\cos\phi_i$) to the range R_e associated with the average energy of escape $\bar{T}$.

INVESTIGATION OF TWO SIMPLIFIED MODELS

Two simplified models were investigated in an attempt to obtain numerical results to compare with the results of experiments. The first model investigated is the model we call the "Average Angle and Energy Model" (AA model) or the "van Lint Model" since it is used essentially unmodified as proposed by Sawyer and van Lint.[2] The second model is a refinement of the AA model and gives a more realistic simulation of the secondary electron generation and emission phenomenon. We call this model the "Angle-Bin Model" (AB model). Both of these models are based on the previous equations, but differ in the details of the calculations.

Average Angle and Energy Model

The main feature of the AA model can best be described by referring to Figure 1. In this figure, the angle between the electron's initial direction and the normally incident photon is labeled ϕ_i. In the AA model, ϕ_i is taken to be the average angle, $\bar{\phi}_i$, of all the electrons produced by the photons (in a particular energy group) for the Compton scattering interaction. The $\bar{\phi}_i$ are obtained by first calculating the average energy of the recoil Compton electron

(i.e., the secondary electron). The relation for the average energy recoil Compton electron for the photons of energy group i is given by

$$\bar{T}_i = (\overline{h\nu_o})_i \frac{e^{\sigma_a}(\overline{h\nu_o})_i}{e^{\sigma}(\overline{h\nu_o})_i} \quad (9)$$

where:

$\bar{T}_i$ = the average initial energy of the recoil Compton electron for photons of energy $\overline{h\nu_o}$ (in group i).

$e^{\sigma_a}(\overline{h\nu_o})_i$ = the average Compton absorption cross section for photons of energy $\overline{h\nu_o}$ (in group i).

$e^{\sigma}(\overline{h\nu_o})_i$ = the average Compton collision cross section for photons of energy $\overline{h\nu_o}$ (in group i).

Once the average secondary electron energy $\bar{T}_i$ is evaluated, the average direction cosine of the secondary electron in terms of the average photon energy of group i can be obtained:

$$\cos \bar{\phi}_i \simeq \overline{\cos}\ \phi_i \cong \sqrt{\frac{\bar{T}_i\,(1+\alpha_i)^2}{\bar{T}_i\alpha_i^2 + 2\alpha_i(\overline{h\nu_o})_i}} \quad (10)$$

where: $\cos \bar{\phi}_i$ = the cosine of the average initial angle of the Compton recoil electron

$\overline{\cos}\ \phi_i$ = the average cosine of the initial angle of the Compton recoil electron

$\alpha_i = (\overline{h\nu_o})_i / m_o c^2$

The actual distance the electron must travel to escape, R, (assuming that the average direction of the electron does not change during its transport) is given by

$$R = X_n / \overline{\cos}\ \phi_i \quad (11)$$

where: X_n is the distance from the centerline of the appropriate ΔR to the escaping surface (shortest distance).

Numerically, this process is repeated for all of the photon energy groups and for all X_n or ΔR's comprising the target, so that the number of secondary electrons at each angle and the energies of the escaping electrons can be accumulated for small ranges of angle and energy, called "bins." The resulting accumulated secondary electron energy and angular distributions are then printed to give the final results.

Angle-Bin Model

The AB model also uses the same basic equations given previously. However, instead of using the average electron angle ϕ_i to represent the initial direction of the generated electrons, all possible angles in the forward direction are represented by dividing the quadrant into equal angle bins. The cross sections are then calculated for each angle bin.

For the Compton scattering interaction, the cross section for scattering an electron into each angle bin is obtained by integrating the differential scattering cross section over the range of angles for the particular angle bin. The average energy of the electron scattered into an angle bin is calculated using the simple average angle of the bin as $\bar{\phi}$, i.e., $\bar{\phi} = (\phi_1 + \phi_2)/2$. Numerically, the AB model is implemented by using Gaussian quadrature sets for the required integrations.

The results of the numerical calculations from the subroutine that calculates the cross sections for Compton scattering were compared with the results as calculated by Nelms.[8] The curves presented in the report by Nelms were graphically integrated to verify the numerical integrations of the Compton cross sections.

The final results of the AB model are obtained by computing the Compton scattering contribution to the secondary electron emission. Once the secondary electrons have been generated for a particular angle bin, the subsequent transmission, attenuation and emission is numerically performed in the same manner as the secondary electrons in the average angle (AA) model, except that a separate calculation is required for each angle bin.

Numerical Results

Numerical calculations were performed using the AA and AB models for a typical target configuration and using the gamma ray energy spectrum measured for the experimental source (see Figure 2). The AA and AB models were incorporated into the existing XRAY[7] program as subroutines. The XRAY program calculated the attenuated photon spectrum within the target material and then the AA and AB model subroutines were used to calculate the generation of high energy secondary electrons (initial angular and energy distributions) and the subsequent transmission, attenuation, and emission of the secondary electrons.

FIGURE 2. INCIDENT PHOTON ENERGY SPECTRUM

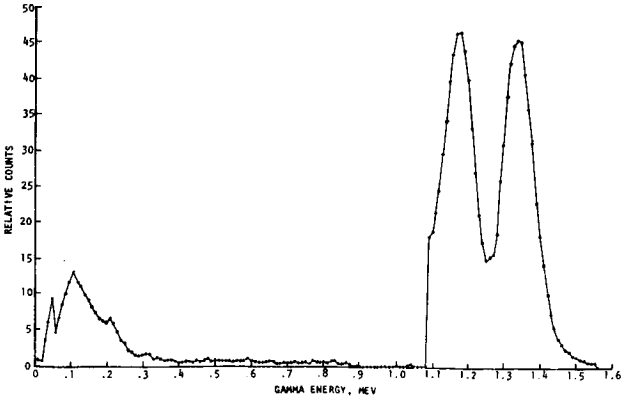

The results of the calculations for a 140 mil (0.355 cm or 3.18 g/cm^2) thick copper target (density = 8.96 g/cm^3) are shown in Figures 3 through 8. Figure 3 is the angular distribution of the emitted secondary electrons as calculated by the AA model. This figure shows the angular distribution for electrons of all energies. The range of angles represented is small (28° to 47°) because the average angle was selected for each photon energy group. For the AA model, it is not surprising that this comparatively small range of angles represented the angular distribution of the emitted secondary electrons.

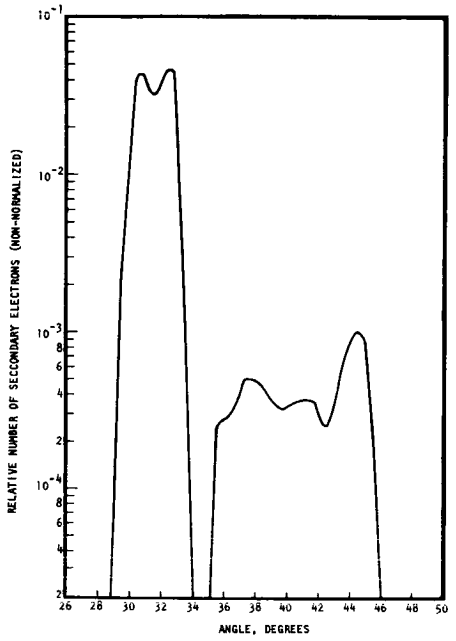

FIGURE 3. AA MODEL ANGULAR DISTRIBUTION

Figure 4 is the energy distribution of the emitted secondary electrons that was calculated by the AA model. This distribution represents the energy distribution for all secondary electrons emitted from the back surface (i.e., photon beam forward direction) of the copper target. It is expected that secondary electrons would have low energies since the attenuation of electrons produced relatively deep in the target is calculated by using range-energy relations. In addition, since the AA model considers only the Compton scattering event, and considers average angles (and the resulting average energy at that angle), energies greater than approximately 0.8 MeV are not represented in the energy distribution.

Figure 5 contains the angular energy distributions for the emitted secondary electrons as calculated by the AB model for constant angles of 10°, 20°, 30°, 40° and 50°. The striking feature of these curves is that the general shape of the incident photon energy spectrum is clearly evident for each particular emission angle. The shift to lower energy secondary electrons with increasing emission angle is also clearly seen. This shift is a result of the Compton scattering event since the closer the secondary electron is to 90° to the incident photon, the less energy is imparted to the electron. The angular distributions for both the Compton scattering and photoelectric effect cross sections were obtained for the AB model. However, the number of secondary electrons emitted as a result of the photoelectric effect was negligible compared to the number of Compton scattering electrons and thus only the Compton scattering electrons have been

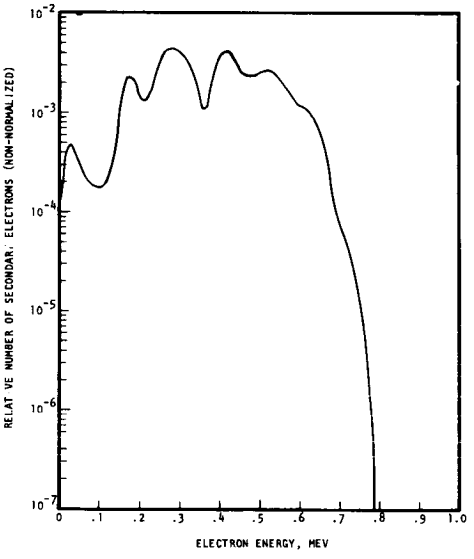

FIGURE 4. AA MODEL ENERGY DISTRIBUTION

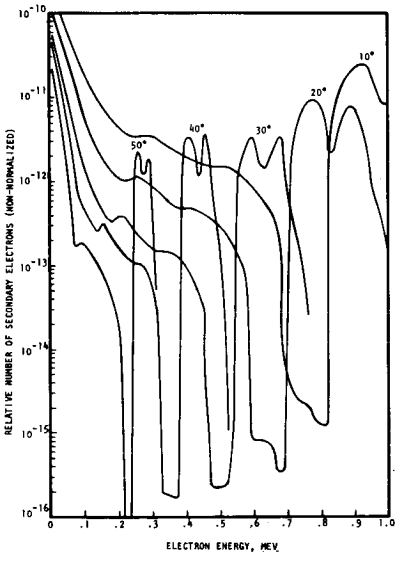

FIGURE 5. AB MODEL ANGULAR ENERGY DISTRIBUTION

plotted. This is not surprising since the photoelectric effect cross section is negligible compared to the Compton scattering cross section for the predominate range of photon energies represented by the incident gamma ray spectrum (most are around the 1.1 to 1.4 MeV range as shown in Figure 2.)

Figure 6 is a cross-plot of Figure 5 and reveals the erratic behavior of the detailed angular energy distributions for the emitted secondary electrons as calculated via the AB model. Figures 7 and 8 are the energy and angular distributions as calculated using the AB model for the secondary electrons emitted from the copper target. These distributions were obtained by integrating the angular energy distributions and the energy angular distributions of Figures 5 and 6, respectively. The similarity in shape of the AA model and AB model energy distributions (Figures 4 and 7) is clearly seen. The major difference is that the secondary electrons calculated by the AB model cover a wider range of energy. This is expected since the AA model considers only the "average" secondary electron energy for any given photon energy group, whereas the AB model accounts for the entire range of energies of the generated secondary electrons by employing angle and energy bins.

Based on the numerical results presented here, the AB model is concluded to be a more realistic method of calculating secondary electron emission. The AB model can readily indicate the detailed angular energy distributions and the energy angular distributions, as well as the angular and energy distributions of the emitted secondary electrons.

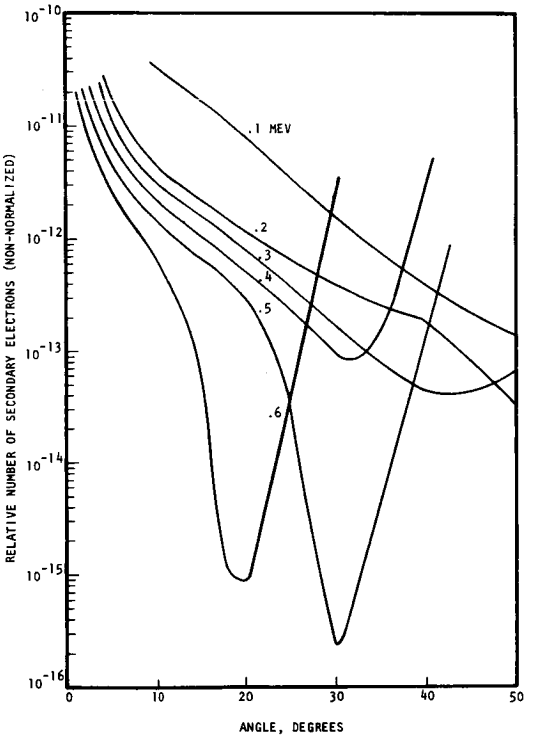

FIGURE 6. AB MODEL ENERGY ANGULAR DISTRIBUTIONS

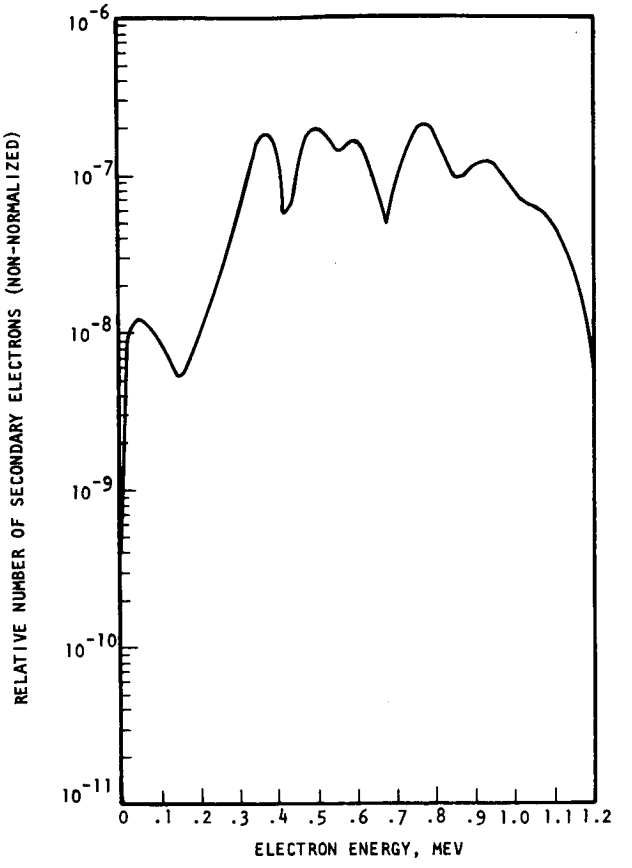

FIGURE 7. AB MODEL TOTAL ENERGY DISTRIBUTION

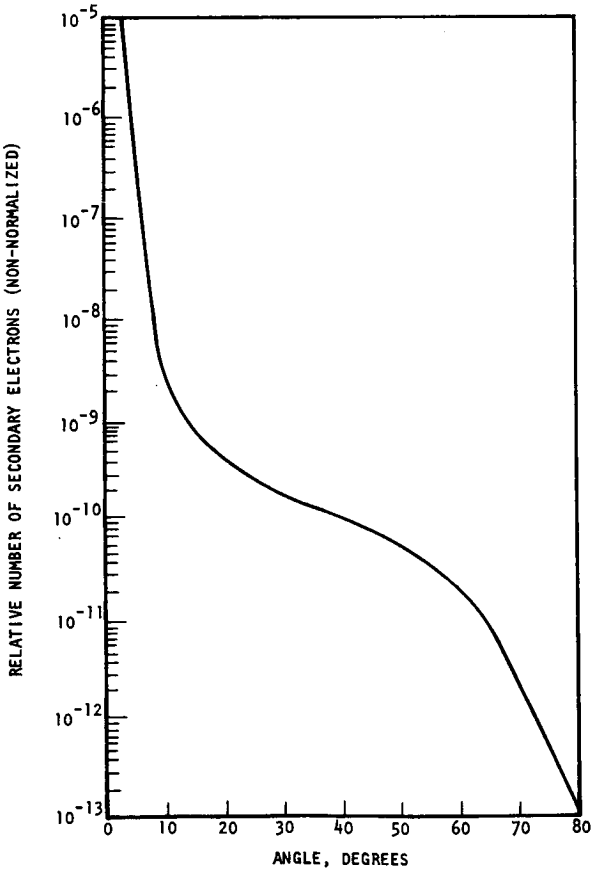

FIGURE 8. AB MODEL TOTAL ANGULAR DISTRIBUTION.

COMPARISON OF EXPERIMENTAL AND NUMERICAL RESULTS

The total angular and total energy secondary electron distributions are well suited for comparing numerical and experimental results. These distributions have many of the detailed anomalies integrated out for both the numerical and experimental results.

Figure 9 shows the AB model numerical results for the secondary electron total energy distribution of a 3.2 g/cm^2 thick copper target. Superimposed on this graph are the reduced experimental data for the same thickness copper target. The experimental data have been normalized to the numerical results at the 1.0 MeV energy point. There is generally fair agreement in the results from 0.4 MeV to 1.2 MeV. The experimental data do not possess the detailed variations that the numerical results indicate. The major reason for this relative smoothness of the experimental data compared to the numerical results is the poor resolution of the scintillation crystal detector. The calibration tests of the scintillation detector using a standard conversion electron emitter source (Cs^{137} with a 0.624 MeV conversion electron) showed that the resolution of the detector was approximately 20% (i.e., full width at half maximum), or about twice what is considered average resolution.

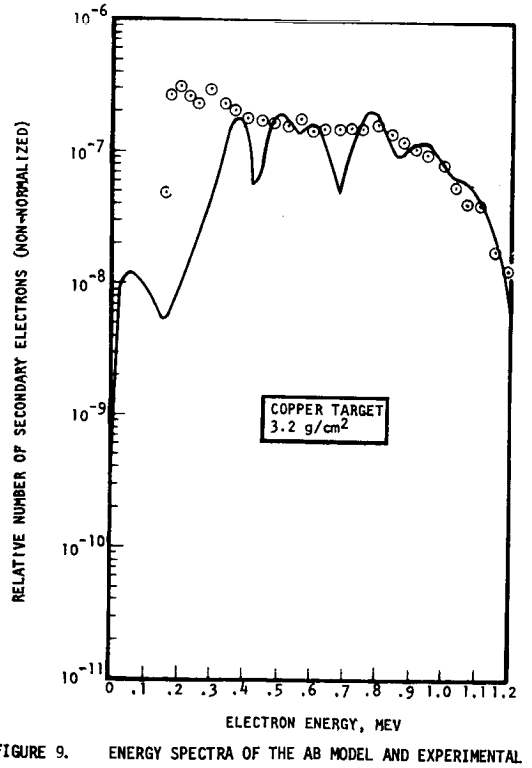

FIGURE 9. ENERGY SPECTRA OF THE AB MODEL AND EXPERIMENTAL RESULTS.

The secondary electron total angular distribution as calculated by the AB model was presented in Figure 8 for the 3.2 g/cm^2 thick copper target. This graph is shown in Figure 10 along with the reduced data for the same thickness target. The experimental data are normalized to the numerical results at the 20 degree point. The AB model results and the experimental data do not agree well for angles less than 10°. The primary reason for this is that the AB model does not account for the change in the initial angular distribution of the photon generated secondary electrons as they are scattered through the remainder of the target material. In reality, the generated electrons are highly scattered before they are emitted and, thus, the experimentally measured emitted electron angular distribution tends to be more uniform than the calculated distribution. Another reason for the difference at the low angles (<10°) is that the experimental data were subject to a high background.

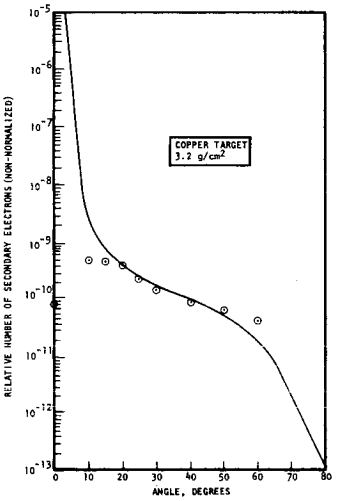

FIGURE 10. ANGULAR DISTRIBUTIONS OF THE AB MODEL AND EXPERIMENTAL RESULTS.

Comparisons with more detailed results than those obtained using the simplified AB model may indicate areas where improvements in the simplified model can be made. Several computer runs were made using the TEMPER[4] code. The TEMPER computer program was developed to solve radiation transport problems with a specified electron or photon source and to include any secondary radiations in the solution.[4] The program is well suited for the investigation of secondary electron emission since it calculates the actual energy deposition in thin samples where the secondary electrons escape from the sample. Among the more important features of the computer program are: The Monte Carlo method is used for the transport of photons and electrons; radiation sources are arbitrary functions of energy, time, space and angle; the material distributions are generalized three-dimensional volumes; and detailed angular and energy distributions are computed for volume, surface and point detectors.[4]

The TEMPER program was run for the 3.2 g/cm^2 thick copper target using two equal intensity monoenergetic photon sources at 1.17 MeV and 1.33 MeV. Figure 11 is the plot of the TEMPER numerical results for the total energy distribution of the emitted secondary electrons at the back surface of the target material. This energy distribution does not compare well with the AB model numerical results shown in Figure 9. One possible explanation for this discrepancy may be the fact that the TEMPER calculations did not have any low energy photons incident on the target and, thus, the energy distribution tended to peak at a higher energy (∿.7 MeV). The lower energy photons would tend to produce more photoelectrons with energies close to the incident photon energy.

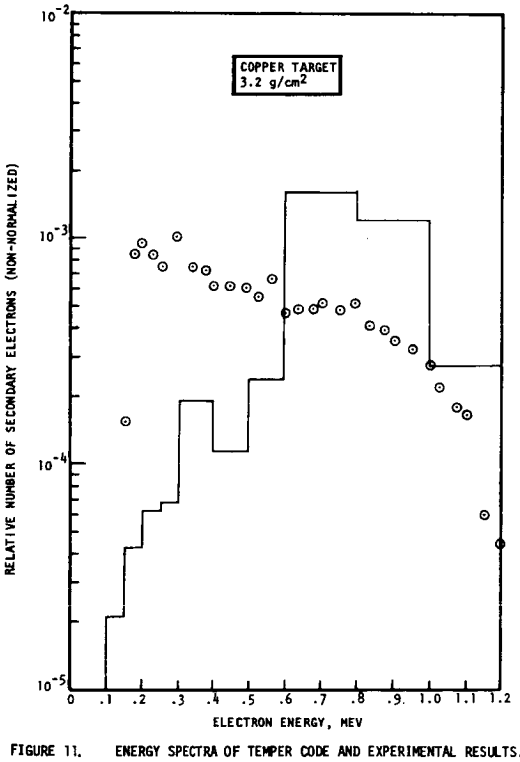

FIGURE 11. ENERGY SPECTRA OF TEMPER CODE AND EXPERIMENTAL RESULTS.

Fair agreement is found for the secondary electron total angular distributions as calculated by TEMPER and as obtained from the reduced experimental results. Figure 12 presents the TEMPER results and experimental results for the 3.2 g/cm^2 thick copper target with the experimental results normalized to the TEMPER results at 20 degrees. A slight decrease in the number of secondary electrons for angles less than about 15° is indicated from the TEMPER results. The reduced experimental results show that a relatively constant number of secondary electrons are emitted between 10° to 20° with a decrease below 10°.

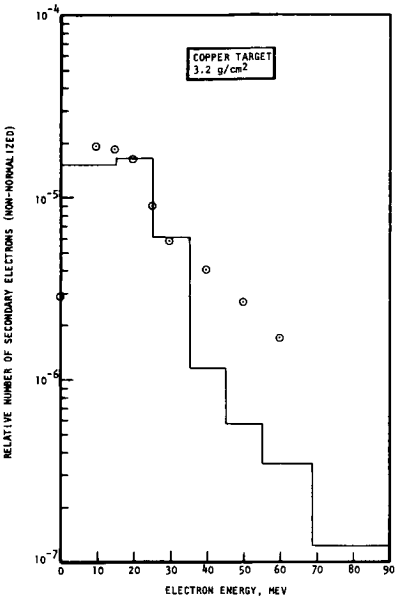

FIGURE 12. ANGULAR DISTRIBUTIONS FOR THE TEMPER CODE AND EXPERIMENTAL RESULTS.

In summary, the comparison of the reduced experimental results with the results obtained using the simplified AB model and a refined Monte Carlo code (TEMPER) indicated the following: 1) The AB model reasonably predicts the shape of the secondary electron total energy distribution for electrons with energies greater than 0.4 MeV, but this model is unsatisfactory in evaluating the shape of the angular distribution for angles less than 15°. 2) The TEMPER results indicate the general trend of the total angular distribution, but these numerical results do not compare well for the energy distribution of emitted secondary electrons.

CONCLUSIONS

An evaluation has been made of a few analytical models used for predicting the details of photon induced secondary electron emission. The results from both simplified and more sophisticated (Monte Carlo) methods have been compared with recent experimental measurements using a Co-60 gamma source and a unique detection technique for measuring the energy and angular distributions of secondary electrons. The results of the evaluation indicated that the two simplified models are useful only for idealized situations. These models did not adequately account for the detailed and complex transport of the generated secondary electrons within the target materials. The multiple and large angle catastrophic collisions that electrons can experience in traversing media must be accounted for to accurately predict the angular and energy distributions of the emitted secondary electrons. Therefore, more refined calculational procedures (e.g., discrete ordinate S_n, Monte Carlo or other analytical techniques) for dealing with the details of electron transport appear warranted.

REFERENCES

1. AUSTIN, L. and STARKE, H.,"Reflection and Secondary Emission of Kathode Rays," Ann. Physik, Vol. 9, 1902, pp. 271.
2. SAWYER, J.A., and VAN LINT, V.A.J., "Calculation of High-Energy Secondary Electron Emission," J. Appl. Phys., Vol. 35, No. 6, June 1964, pp. 1706-1711.
3. SPENCER, R.B., "Measurement of Photon-Induced High-Energy Secondary Electron Emission," Ph.D. Dissertation, University of California, School of Engineering and Applied Science, Los Angeles, 1970.
4. JORDAN, T.M., "TEMPER, A Computer Program for the Transport in Electro Magnetic Fields of Photon and Electron Radiation by Monte Carlo and Finite Difference Techniques," Report No. ART-33, A.R.T. Research Corp., Los Angeles, California, July 1969.
5. SPENCER, R.B. and SMITH, C.B., "An Experimental Investigation of Photon-Induced Secondary Electron Emission," Trans. Am. Nuc. Soc., Vol. 13, No. 1, June 1970.
6. LONERGAN, J.A. and COSTELLO, D.G., "Energy and Angular Distribution of Electrons Transmitted through Tin," Trans. Am. Nuc. Soc., Vol.12 No. 1, June 1969.
7. SPENCER, R.B., "XRAY Program User's Manual," Report No. AN031C, TRW Systems Group, Redondo Beach, California, December 1968.
8. NELMS, A.T., "Graphs of the Compton Energy-Angle Relationship and the Klein-Nishina Formula from 10 KeV to 500 MeV," National Bureau of Standards Circular 542, Washington D.C., August 28, 1953.

Electron and Bremsstrahlung Penetration and Dose Calculation

John W. Watts, Jr. and Martin O. Burrell
George C. Marshall Space Flight Center, Huntsville, Alabama

SUMMARY

Sources of high-energy electrons are encountered in space (the magnetically trapped Van Allen belt electrons) and in ground-level high-energy physics laboratories. It is important to be able to predict the damage resulting to human beings and radiation-sensitive equipment near these sources. In this report, various techniques for the calculation of electron and bremsstrahlung dose deposition are described. New energy deposition, transmission, and reflection coefficients for electrons incident on plane slabs for angles of 0, 30, 60, 75, and 89.9 deg and energies of 0.5, 1.0, 2.0, 3.0, 4.0, 5.0, 6.0, and 10.0 MeV are presented, and methods for their use in electron dose calculations are developed. A method for electron dose calculations using the "straight-ahead" approximation is also developed, and the various methods are compared and found to be in good agreement. Accurate and approximate methods of calculating bremsstrahlung dose are derived and compared. The approximation is found to give good order of magnitude estimate of dose where the electron spectrum falls off exponentially with energy. The primary weakness of both calculations is the approximation of the bremsstrahlung source angular distribution; the actual distribution is not easily determined. More work needs to be done in this area.

USE OF BERGER'S MONTE CARLO DATA IN ELECTRON DOSE CALCULATIONS

Probably the most successful attack on the electron transport problem has been by Martin Berger[1-3] using Monte Carlo methods and multiple scattering techniques. His present set of programs will take an incident beam of electrons or photons and follow both the primaries and any secondary electrons or photons produced. The output includes almost any quantity of interest depending on the program option used. Because the simulation is so thorough, the program is very complex and requires large amounts of computer time on one of the larger machines available to complete an accurate calculation. Thus, the program's primary usefulness is in generating basic data for incorporation into other programs using more simplified approaches to the problem.

Berger's program was made available to Marshall Space Flight Center (MSFC), and a number of calculations have been performed here for comparison with experimental work[4]. As a second study systematic calculations covering the energy range of from 0.5 to 10.0 MeV for a number of angles of incidence by a monodirectional beam on a plane aluminum slab were made. The geometry is shown in Fig. 1. Of particular interest were the electron energy and number transmission and reflection and the energy deposition coefficients, because they can be incorporated into an electron dose or number deposition calculation involving an arbitrary incident electron energy and angular distribution. To minimize the computer time used no photons were followed, and only enough electron histories (2500 through 7000, depending on the angle of incidence) were sampled to get good statistics for the reflection, transmission, and deposition coefficients. (A much higher number of histories would have been required to get good statistics on one of the differential quantities such as exiting energy spectrum.) The fact that secondary photons were not followed means that there is a slight underestimate both in the number of coefficients due to missing tertiary electrons produced by the photons and in the energy factors due to energy transported by secondary photons. Because over most of the energy range of interest electrons lose only a small fraction of their energy as photons, both these effects should be small. The radiative yield, the fraction of an electron's energy lost as bremsstrahlung in stopping, is 0.003324 at 0.25 MeV and 0.07721 at 10.0 MeV in aluminum[2]. This quantity should set an upper bound on the possible error induced by the limitations imposed at least for the energy factors.

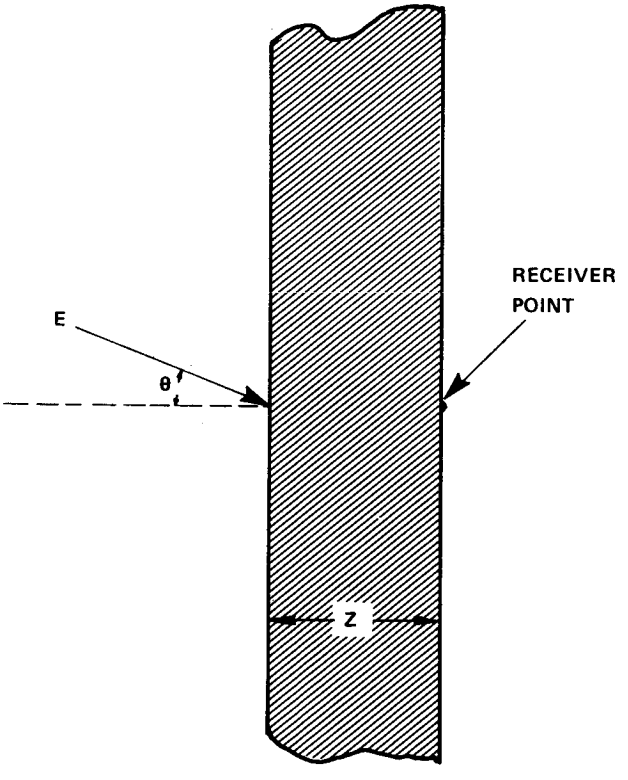

FIGURE 1: BASIC GEOMETRY USED FOR CALCULATIONS

There are several approaches for attacking a dose deposition calculation using the results tabulated by Berger's electron transport program. The most obvious is to use the internal energy spectrum and instantaneous stopping power. Two less obvious but more efficient methods - one reasonably exact and the other approximate - will be described here.

The exact calculation makes use of a quantity Berger calls energy deposition (Figs. 2 and 3), which is the average energy deposited per unit mass per electron at a given depth into a plane, infinitely thick slab by, in this case, a monodirectional beam of electrons. [This does not follow the initial model (Fig. 1) because there is material behind the receiver point.] Berger calculates the energy deposition by breaking up the slab into thin layers and keeping an inventory of energy deposited in each layer and then dividing this quantity by the incident number of initial electron histories and layer thickness. Thus,

$$\rho(E, \theta, X_j) = \frac{\sum_{i=1}^{N_j} \Delta E_{ij}}{N_0 \Delta X_j} \quad , \qquad (1)$$

where ρ is the energy deposition in MeV/g/unit current, E is the incident energy in MeV, Θ is the incident beam angle measured from the normal to the slab, X_j is the depth to the center of the jth layer, N_j is the number of electrons penetrating layer j, ΔE_{ij} is the energy in MeV deposited by the ith penetrating electron in the jth layer, N_0 is the number of initial electron histories, and ΔX_j is the thickness of the jth layer in g/cm^2. In Berger's tabulation X_j is measured in fractions of an electron pathlength at the incident energy. The electron mean pathlength is the average length of the zig-zag path followed by an electron in stopping as opposed to the mean range which is the average straight-line distance traversed. It is given by:

$$r_0(E) = \int_E^0 \frac{dE'}{S_T(E')} \quad , \qquad (2)$$

where $r_0(E)$ is the pathlength at energy E and $S_t(E')$ is the total instantaneous stopping power.

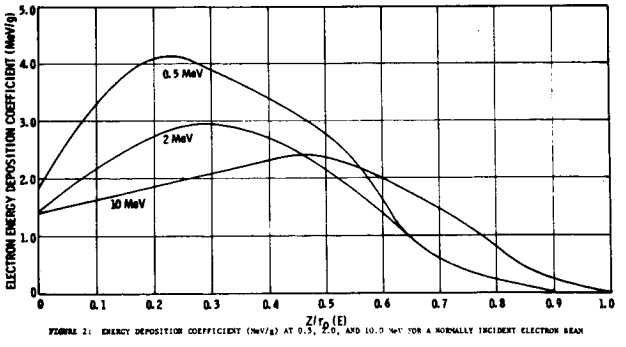

FIGURE 2: ENERGY DEPOSITION COEFFICIENT (MeV/g) AT 0.5, 2.0, AND 10.0 MeV FOR A NORMALLY INCIDENT ELECTRON BEAM

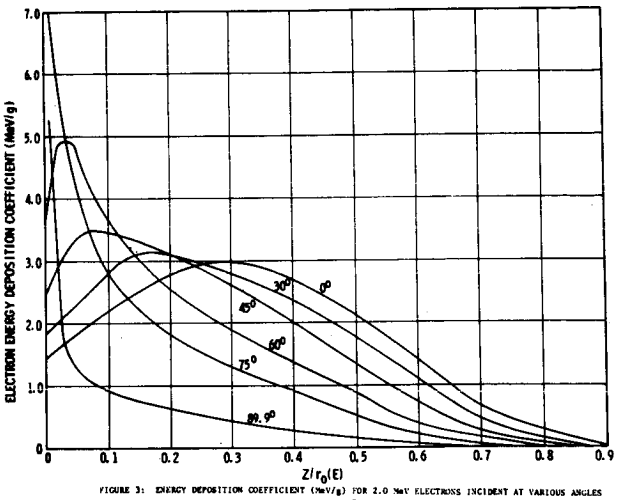

FIGURE 3: ENERGY DEPOSITION COEFFICIENT (MeV/g) FOR 2.0 MeV ELECTRONS INCIDENT AT VARIOUS ANGLES

If there is an angular and energy flux distribution given by $\Phi_o[E,\vec{\Omega}(\Theta,\phi)]$ with Φ_o electrons incident per unit at E and per unit solid angle in the direction $\vec{\Omega}$, then the incident current as used by Berger is

$$J_0(\vec{\Omega}) = \Phi_0(E,\vec{\Omega}) \cos(\theta) \quad , \qquad (3)$$

and the dose at a depth Z in g/cm^2 is given by:

$$D(Z) = K \int_{\vec{\Omega}} \int_E \rho[E,\theta,Z/r_0(E)]\, \Phi_0(E,\vec{\Omega}) \cos\theta \, dE \, d\vec{\Omega} \quad , \qquad (4)$$

where K is a units conversion constant. Dose is more often measured in rads than MeV/g, in which case K = 1.60 x 10^{-8} rads/(MeV/g).* In the case where there is a monodirectional beam incident at an angle Θ from the slab normal, Equation (4) becomes:

$$D(Z,\theta) = K \cos\theta \int_E \rho[E,\theta,Z/r_0(E)]\, \Phi_0(E)\, dE \quad . \qquad (5)$$

Another case of interest is that in which the distribution is half-space isotropic. In this case the dose is given as

$$D_{iso}(Z) = K \int_E \int_0^{\frac{\pi}{2}} \rho[E,\theta,Z/r_0(E)] \cos\theta \sin\theta \, d\theta \, \Phi_0(E) \, dE \, . \qquad (6)$$

Thus, a half-space energy deposition function may be defined by

$$\rho_{iso}(E,X) = \int_0^{\frac{\pi}{2}} \rho(E,\theta,X) \cos\theta \sin\theta \, d\theta \quad . \qquad (7)$$

*To convert rads to SI Units in joules per kilogram, multiply rads by 0.01.

This function is tabulated in Table 1. If Equation (7) is used, Equation (6) becomes:

$$D_{iso}(Z) = K \int_E \rho_{iso}\,[E,\ Z/r_0(E)]\ \Phi_0(E)\ dE \quad . \tag{8}$$

The approximate method for calculating electron dose makes use of the energy transmission and reflection factor of Berger to derive an approximation to the energy deposition function. The electron energy current transmission and reflection and number current transmission and reflection factor shown in Figs. 4 through 11 are defined as follows:

$$\begin{aligned}
T_N(E,\theta,X) &= \frac{N_T(E,\theta,X)}{J_0(\theta)} \\
A_N(E,\theta,X) &= \frac{N_R(E,\theta,X)}{J_\theta(\theta)} \\
T_E(E,\theta,X) &= \frac{\sum_{i=1}^{N_T} E_{Ti}(E,\theta,X)}{E\,J_0(\theta)} \\
A_E(E,\theta,X) &= \frac{\sum_{i=1}^{N_R} E_{Ri}(E,\theta,X)}{E\,J_0(\theta)} \quad ,
\end{aligned} \tag{9}$$

where T_N is the number transmission factor; N_T is the number of electrons passing through a slab X thick; A_N is the number reflection factor where N_R is the number of electrons reflected from a slab X thick; T_E is the energy transmission factor where E_{Ti} is the energy of the ith transmitted electron; and A_E is the energy reflection factor where E_{Ri} is the energy of the ith reflected electron.

How these factors may be used in energy deposition or dose calculations will now be considered. From conservation of energy,

$$E = E\,[A_E(E,\theta,X) + U_E(E,\theta,X) + T_E(E,\theta,X)] \tag{10}$$

or

$$1 = A_E(E,\theta,X) + U_E(E,\theta,X) + T_E(E,\theta,X) \tag{11}$$

are obtained, where $U_E(E,\Theta,X)$ is the fraction of the energy either deposited in the slab or radiated as bremsstrahlung. Since in the energy range of interest the radiated component is small, it will be assumed negligible. If a quantity $f(X',E,\Theta,X)\,dX'$ is defined, which is the fraction of the incident energy deposited between X' and X' + dX', then

$$U_E(E,\theta,X) = \int_0^X f(X',E,\theta,X)\,dX' \quad . \tag{12}$$

Using Equations (11) and (12) yields

$$\int_0^X f(X',E,\theta,X)\,dX' = 1 - A_E(E,\theta,X) - T_E(E,\theta,X) \quad . \tag{13}$$

Taking the derivative with respect to X gives

$$f(X,E,\theta,X) + \int_0^X \frac{df}{dX}(X',E,\theta,X)\,dX' = -\frac{d}{dX}\,[A_E(E,\theta,X) + T_E(E,\theta,X)] \quad . \tag{14}$$

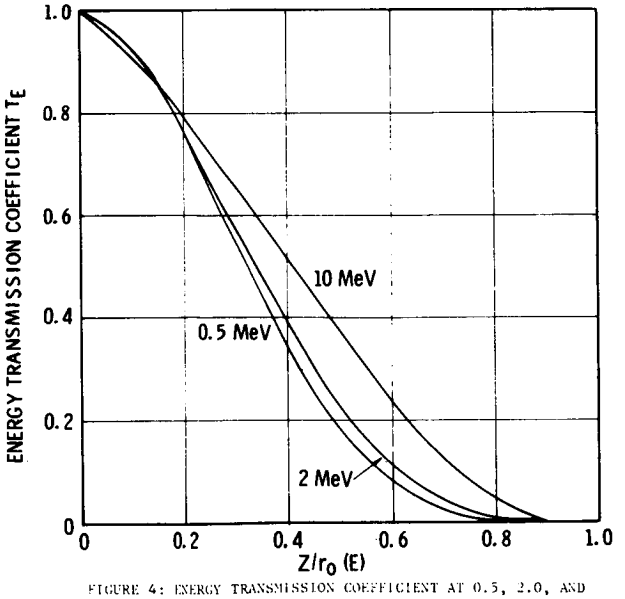

FIGURE 4: ENERGY TRANSMISSION COEFFICIENT AT 0.5, 2.0, AND 10.0 MeV FOR A NORMALLY INCIDENT ELECTRON BEAM

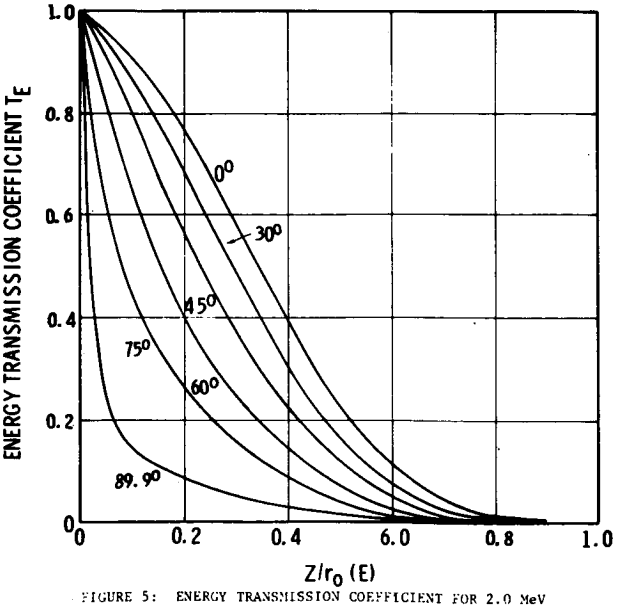

FIGURE 5: ENERGY TRANSMISSION COEFFICIENT FOR 2.0 MeV ELECTRONS INCIDENT AT VARIOUS ANGLES

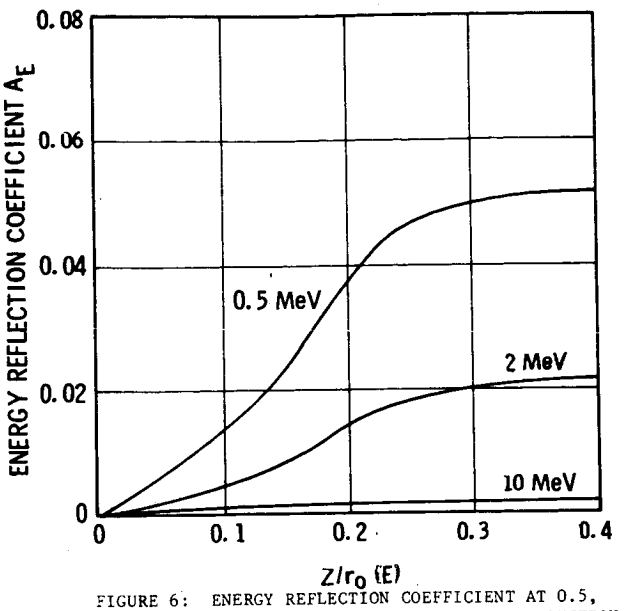

FIGURE 6: ENERGY REFLECTION COEFFICIENT AT 0.5, 2.0, AND 10.0 MeV FOR A NORMALLY INCIDENT ELECTRON BEAM

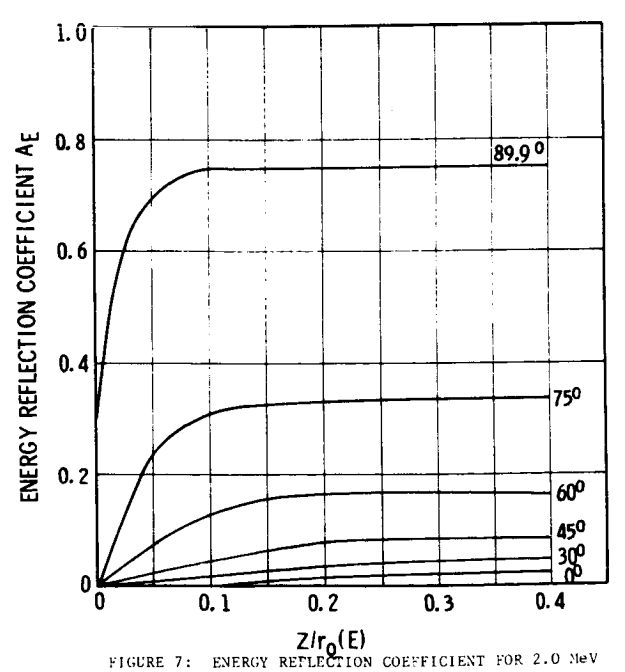

FIGURE 7: ENERGY REFLECTION COEFFICIENT FOR 2.0 MeV ELECTRONS INCIDENT AT VARIOUS ANGLES

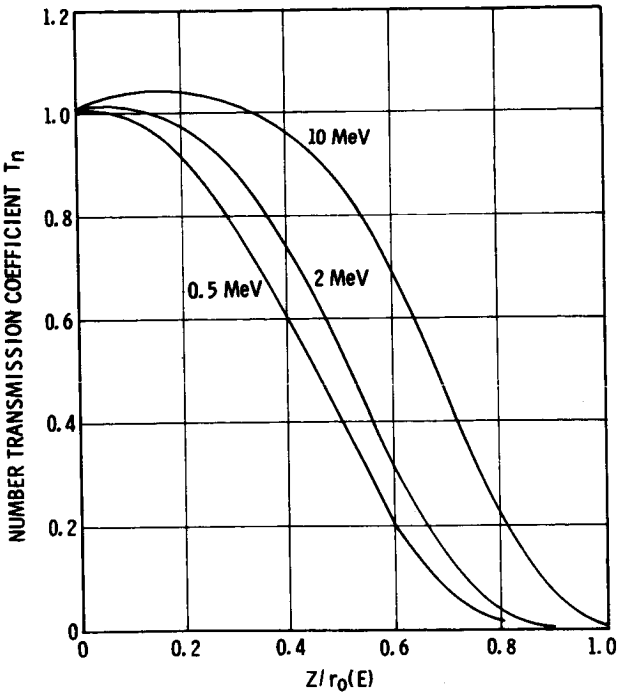

FIGURE 8: NUMBER TRANSMISSION COEFFICIENT AT 0.5, 2.0, AND 10.0 MeV FOR A NORMALLY INCIDENT ELECTRON BEAM

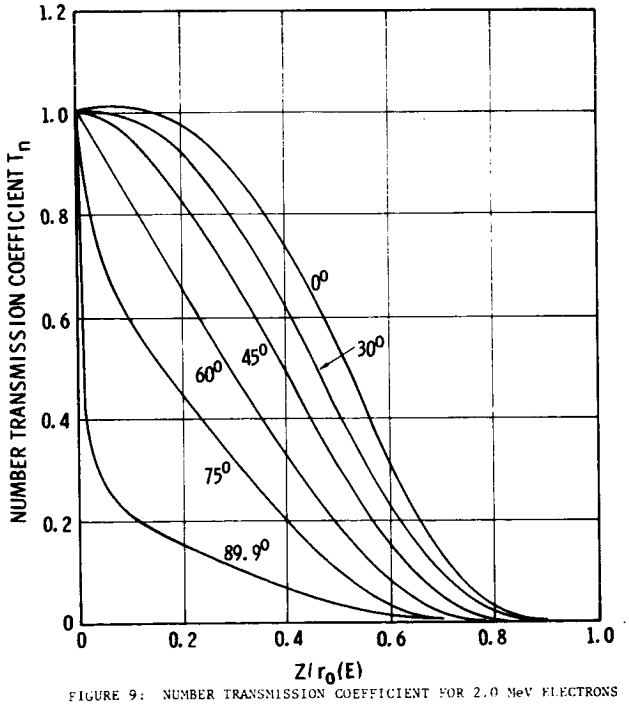

FIGURE 9: NUMBER TRANSMISSION COEFFICIENT FOR 2.0 MeV ELECTRONS INCIDENT AT VARIOUS ANGLES

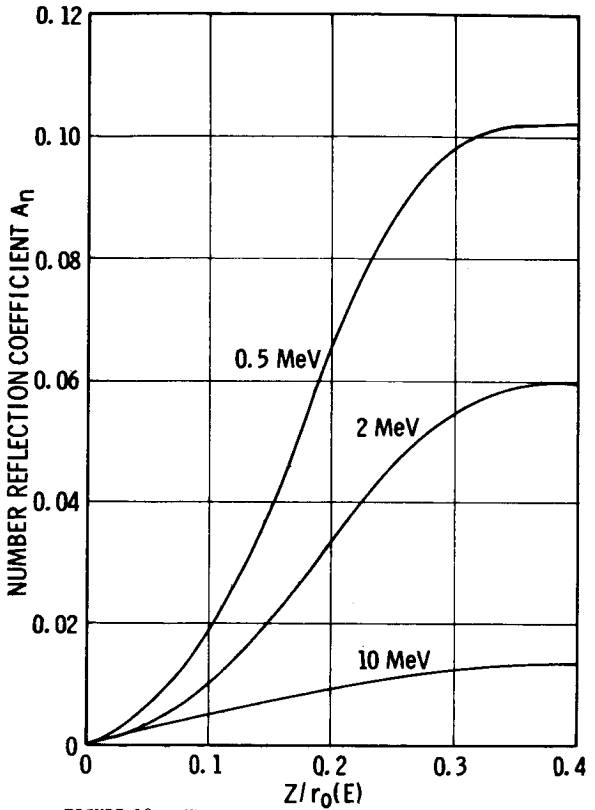

FIGURE 10: NUMBER REFLECTION COEFFICIENT AT 0.5, 2.0, AND 10.0 MeV FOR A NORMALLY INCIDENT ELECTRON BEAM

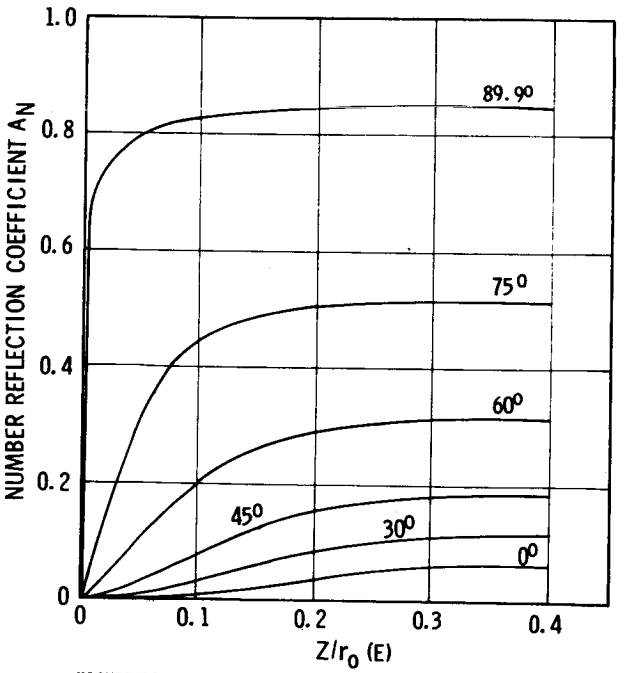

FIGURE 11: NUMBER REFLECTION COEFFICIENT FOR 2.0 MeV ELECTRONS INCIDENT AT VARIOUS ANGLES

The approximation in this method involves ignoring the integral term on the left in this equation. Since $f(X',E,\Theta,X)$ increases with increasing X (due to reflected electrons), the derivative is always greater than or equal to zero. Thus the integral is positive, and ignoring it gives a conservative estimate of $f(X,E,\Theta,X)$. It is difficult to justify this approximation except to observe that in practice it yields results comparable with those of the previously described method. It was developed because Berger's older publication presented only the transmission and reflection factors, the energy deposition factor having become available only recently.

The energy deposition function (in units of MeV/g) is given by:

$$\rho(X,E,\theta,X) = \frac{Ef(X,E,\theta,X)}{r_0(E)} \qquad (15)$$

or

$$\rho(X,E,\theta,X) \approx \frac{-E\,d}{r_0(E)\,dX}\,[A_E(E,\theta,X) + T_E(E,\theta,X)] \qquad (16)$$

It is interesting to note that $f(X',E,\Theta,X)$ for $X' < X$ always has a contribution caused by reflection from portions of the shield beyond X' but that $f(X,E,\Theta,X)$ does not. Thus it approximates the quantity needed for an energy deposition calculation in our original geometry.

Because of the definition of ρ in the derivations the material of the receiver must be the same as that of the shield. An approximate correction for estimating the dose for a different receiver can be made by multiplying the single material calculation by the ratio of the collision stopping power in the shield material at some typical energy for the exiting electron spectrum. Fortunately, the energy selected is not particularly important since the ratio of two electron stopping powers is not a sensitive function of energy except at very low energies (> 0.01 MeV). Some estimate of the accuracy of the approximation can be found by observing the variation of the ratio with energy. A particularly interesting case is that of an aluminum shield and a tissue receiver. This case, using Berger's stopping power data[3] is given in Table 2.

Taking the simple average of ratios between energies of 0.1 to 10.0 MeV yields a correction (1.30) that will be within about 3% of an exact calculation under most conceivable conditions. (For typical incident energy spectra encountered, it would be unusual for the average energy of the exiting spectrum to be less than 0.04 MeV). Thus, for an aluminum shield and a tissue receiver Equations (5) and (6) become, respectively:

$$D(Z,\theta) = 1.3\,K\cos\theta \int_E \rho[E,\theta,Z/r_0(E)]\,\Phi_0(E)\,dE \qquad (17)$$

and

$$D_{iso}(Z) = 1.3\,K \int_E \rho_{iso}[E,Z/r_0(E)]\,\Phi_0(E)\,dE \qquad (18)$$

TABLE 1: ELECTRON FLUX ENERGY DEPOSITION COEFFICIENTS (MeV/g) FOR A HALF-SPACE ISOTROPIC INCIDENT BEAM ON AN ALUMINUM SEMI-INFINITE PLANE SHIELD

INCIDENT ENERGY (MeV)	SHIELD THICKNESS (PATHLENGTHS)	0	1	2	3	4	5	6	7
	0.01	2.1151	1.8388	1.7236	1.6841	1.6654	1.6567	1.6544	1.6512
	0.03	2.1534	1.8364	1.6980	1.6611	1.6449	1.6397	1.6382	1.6372
	0.05	2.1410	1.8097	1.6726	1.6446	1.6290	1.6183	1.6140	1.6099
	0.07	2.1133	1.7840	1.6482	1.6269	1.6160	1.6148	1.6072	1.6029
	0.09	2.0838	1.7625	1.6297	1.6069	1.5999	1.5943	1.5933	1.5976
	0.11	2.0211	1.6795	1.5509	1.5095	1.4711	1.4635	1.4704	1.4684
	0.13	1.9486	1.6356	1.4837	1.4652	1.4504	1.4222	1.4041	1.4039
	0.15	1.9542	1.6299	1.4668	1.4269	1.4095	1.4239	1.4048	1.3889
	0.17	1.8698	1.6271	1.4481	1.3941	1.3847	1.4010	1.3927	1.3801
	0.19	1.8955	1.5868	1.3903	1.3376	1.3439	1.3500	1.3462	1.3506
	0.21	1.8020	1.4981	1.3542	1.3056	1.2928	1.2745	1.2780	1.2807
	0.23	1.7682	1.4329	1.3028	1.2632	1.2581	1.2417	1.2346	1.2476
	0.25	1.7289	1.3843	1.2463	1.2305	1.2192	1.2259	1.2226	1.2001
	0.27	1.6721	1.3350	1.2199	1.1777	1.1836	1.1872	1.1595	1.1788
	0.29	1.5832	1.2930	1.1661	1.1692	1.1420	1.1408	1.1312	1.1466
	0.31	1.5492	1.2267	1.1246	1.0882	1.0969	1.1041	1.0742	1.1131
	0.33	1.4704	1.1598	1.0784	1.0836	1.0735	1.0840	1.0898	1.0729
	0.35	1.4057	1.1130	1.0388	1.0351	1.0233	1.0376	1.0530	1.0419
	0.37	1.3634	1.0781	1.0206	0.9943	0.9980	1.0230	1.0058	0.9807
	0.39	1.3164	1.0411	0.9813	0.9547	0.9441	0.9551	0.9699	0.9377
	0.41	1.2093	0.9720	0.9082	0.8826	0.8778	0.8997	0.8995	0.8993
	0.43	1.0848	0.9184	0.8588	0.8378	0.8133	0.8341	0.8816	0.8775
	0.45	1.0022	0.8243	0.7744	0.7828	0.7864	0.8159	0.8054	0.8375
	0.47	0.9460	0.7738	0.7364	0.7465	0.7295	0.7477	0.7539	0.7938
	0.49	0.8892	0.7282	0.6888	0.6884	0.7006	0.7036	0.7048	0.7453
	0.51	0.8172	0.6811	0.6488	0.6307	0.6477	0.6679	0.6594	0.7232
	0.53	0.8549	0.6745	0.6252	0.5941	0.5936	0.6039	0.6301	0.6680
	0.55	0.6307	0.6320	0.5916	0.5413	0.5391	0.5531	0.5762	0.6225
	0.57	0.5520	0.4653	0.5417	0.4602	0.4884	0.5051	0.5445	0.5799
	0.59	0.4438	0.3992	0.4987	0.4224	0.4393	0.4635	0.4996	0.5380
	0.61	0.3956	0.3134	0.4259	0.3630	0.3962	0.4243	0.4466	0.4999
	0.63	0.3161	0.2719	0.2944	0.3108	0.3449	0.3597	0.3759	0.4617
	0.65	0.2496	0.2428	0.2522	0.2786	0.3101	0.3019	0.3479	0.4252
	0.67	0.2094	0.1848	0.2131	0.2323	0.2666	0.2647	0.3081	0.3730
	0.69	0.1744	0.1590	0.1869	0.1921	0.2253	0.2258	0.2643	0.3315
	0.71	0.1310	0.1248	0.1395	0.1653	0.1776	0.1981	0.2282	0.2943
	0.73	0.1031	0.0965	0.1087	0.1340	0.1513	0.1628	0.1937	0.2624
	0.75	0.0812	0.0740	0.0853	0.1014	0.1254	0.1394	0.1572	0.2139
	0.77	0.0519	0.0548	0.0722	0.0778	0.0947	0.1110	0.1320	0.1822
	0.79	0.0417	0.0355	0.0518	0.0592	0.0730	0.0859	0.1078	0.1603
	0.81	0.0274	0.0271	0.0323	0.0429	0.0581	0.0651	0.0880	0.1236
	0.83	0.0098	0.0162	0.0219	0.0295	0.0429	0.0503	0.0585	0.1045
	0.85	0.0069	0.0119	0.0115	0.0192	0.0307	0.0316	0.0424	0.0776
	0.87	0.0036	0.0060	0.0077	0.0109	0.0199	0.0253	0.0283	0.0578
	0.89	0.0031	0.0023	0.0064	0.0056	0.0225	0.0170	0.0172	0.0475
	0.91	0.0026	0.0004	0.0018	0.0036	0.0033	0.0107	0.0145	0.0306
	0.93	0.0012	0.0004	0.0018	0.0018	0.0060	0.0056	0.0110	0.0221
	0.95	0.0000	0.0004	0.0000	0.0025	0.0028	0.0050	0.0072	0.0161
	0.97	0.0000	0.0000	0.0000	0.0000	0.0004	0.0014	0.0041	0.0102
	0.99	0.0000	0.0000	0.0000	0.0000	0.0000	0.0000	0.0009	0.0060

TABLE 2: RATIO OF TISSUE COLLISION STOPPING POWER TO ALUMINUM COLLISION STOPPING POWER AS A FUNCTION OF ENERGY

Energy (MeV)	$R = \frac{dE/dX \text{ tissue}}{dE/dX \text{ aluminum}}$	$\frac{R-1.3}{R} \times 100$ (%)
0.01	1.383	6.0
0.02	1.350	3.7
0.04	1.325	1.9
0.06	1.313	1.0
0.08	1.305	0.4
0.1	1.300	0.0
0.2	1.285	-1.2
0.4	1.276	-1.9
0.6	1.272	-2.2
0.8	1.271	-2.3
1.0	1.272	-2.2
2.0	1.281	-1.5
4.0	1.301	0.1
6.0	1.317	1.3
8.0	1.329	2.2
10.0	1.340	3.0

Curve fits of $\rho(E,\Theta,X)$ have been found to be very useful for computational purposes. Fit over X of the form

$$\rho(E,\theta,X) = e^{\sum_{i=1}^{N} A_i X^{i-1}} \tag{19}$$

has been found to give satisfactory results for normal incidence and half-space isotropic incidence, two cases of special interest. Fits of the above form were made and then the coefficients were fit as a function of energy. For normal incidence the coefficients are given by:

$$\begin{aligned} A_1 &= 0.913\, e^{0.963E} + 0.021E + 0.215 \\ A_2 &= 5.0 - 0.491E \\ A_3 &= 57.573\,(E - 5.0)/(E + 29.98) \\ A_4 &= -1.6E^{0.837} \end{aligned} \tag{20}$$

and for half-space isotropic the coefficients are given by:

$$\begin{aligned} A_1 &= 0.52 + 0.09854\, E^{-1.468} \\ A_2 &= e^{-0.821E} - 1.0 \\ A_3 &= -2.5\left(e^{-1.022E} + 1.0\right) \\ A_4 &= 3.253\, e^{-0.323E} + 5.8 \\ A_5 &= -15.4375 + 1.5542E - 0.0786077E^2 \end{aligned} \tag{21}$$

Because the shape of the energy deposition function for angles near 90 deg is different from that near 0 deg, a good fit by a single functional form is difficult to achieve over the whole range of directions. Best results will probably be obtained by interpolation from the actual data or a smoothed set derived from it. The function $f(E,\Theta,X)$ derived using the reflection and transmission factors was also fit but by a different form. The fit was to the form

$$1 - T_E(E,\theta,X) - A_E(E,\theta,X) = A\left[1 - e^{(BX + CX^2 + DX^3)}\right] , \tag{22}$$

where A, B, C, and D are functions of E and Θ. Then, taking the derivative with respect to X and using Equation (14) yields

$$f(E,\theta,X) = -A\,(B + 2CX + 3DX^2)\, e^{(BX + CX^2 + DX^3)} \quad (23)$$

Fits have been derived for the two cases of special interest. For a normally incident beam (Θ = 0 deg) in the energy range 0.5 to 10.0 MeV,

$$A = \frac{0.893 + 1.682E}{1.0 + 1.665E}$$

$$B = \frac{11.0E}{11.0E + 6.0} \quad (24)$$

$$C = 4.2\exp(-0.47E)$$

and

$$D = 5.16 \ .$$

Berger has published a transmission and reflection coefficient for a cosine law source (half-space isotropic flux)[3]. In this case f_{iso} (E,X) is a relatively insensitive function of E, and satisfactory results are obtained by taking an average curve for all energies. For energy deposition,

$$A = 0.439$$
$$B = -2.08$$
$$C = -3.54 \quad (25)$$
$$D = -6.08$$

The electron pathlength $r_o(E)$ in aluminum taken from Berger[2] has also been fit by the following form:

$$r_0(E) = (1.33 - 0.019E)\left(\sqrt{0.2713E^2 + 0.0121} - 0.11\right), \quad (26)$$

which is within 2% of actual curves for energies greater than 0.3 MeV and within 5% between 0.2 and 0.3 MeV.

ELECTRON TRANSPORT USING THE STRAIGHT-AHEAD AND CONTINUOUS SLOWING DOWN APPROXIMATIONS

A method commonly used for describing the transport of protons is to assume that the particle travels through the shield along its incident direction losing energy continuously according to some stopping power law. Thus, according to the approximations, the energy and direction of the particle at any point in the shield is completely predictable. This method has the advantage of providing an energy spectrum at the internal point of interest that may be used to determine such things as secondary production sources as well as to calculate dose deposition. Its disadvantages for application to electron transport are twofold: First, electrons are more likely to be scattered from their original direction than protons, and second, electrons can suffer large energy losses in a single interaction. Thus the straight-ahead approximations should not be expected to be especially applicable. The approximations have been applied with some success, however.

Since the validity of the approximations in applications to electron transport are somewhat questionable, one would prefer to be on the conservative side in any estimate of particle energy or number. By using the extrapolated electron range rather than the mean range* for definition of other required quantities this can be accomplished. The extrapolated range is defined as shown in Fig. 12, where it can be seen that few electrons penetrate beyond this distance. A very good fit to the extrapolated range in aluminum is given by:

$$r_{ex} = R(E) = \sqrt{\frac{E^2}{a} + b^2} - b \quad (27)$$

over the energy range from 0.0 to 16.0 MeV. For R(E) in g/cm^2, E is in MeV, a is 1.92, and b is 0.11[5].

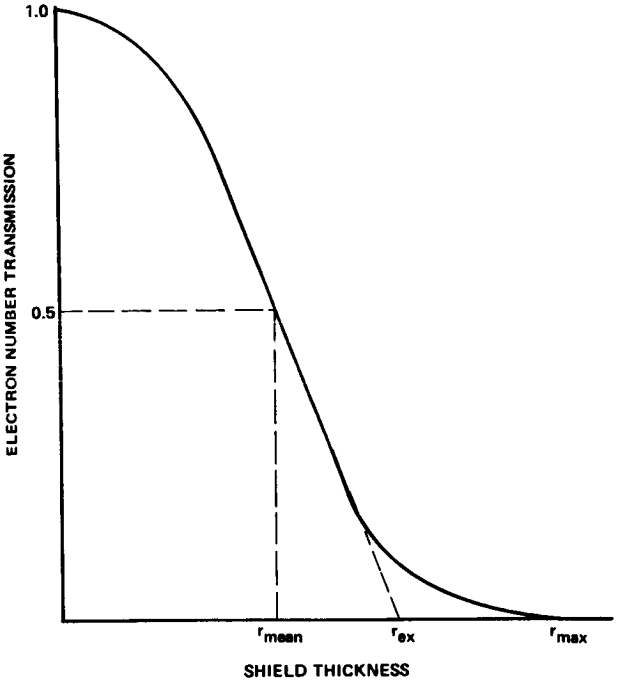

FIGURE 12: DEFINITIONS OF ELECTRON MEAN RANGE r_{MEAN}, EXTRAPOLATED RANGE r_{ex}, AND MAXIMUM RANGE r_{max}

Given the electron range, one can determine the relationship between the initial energy and the energy after passing through thickness Z of material as follows:

Since

$$R(E) = R(E') + Z \ , \quad (28)$$

where E is the initial energy and E' is the energy at depth Z,

*This mean range is not Berger's mean pathlength.

$$E = g(E', Z) = R^{-1}\,[R(E') + Z)]; \qquad (29)$$

R^{-1} denotes the inverse of the function R. Thus, using Equations (27) and (29) gives

$$E = g(E', Z) = a\sqrt{\left[\sqrt{\left(\frac{E'}{a}\right)^2 + b^2} + Z\right]^2 - b^2} \qquad (30)$$

The relationship between the external differential flux $\Phi_0(E)$ and the flux at depth Z, $\Phi_Z(E')$, is given by:

$$\Phi_Z(E') = \Phi_0\,[g(E', Z)]\,\frac{dg(E', Z)}{dE'} \qquad (31)$$

The derivative enters the equation because of change of energy E to E' units; or as one can see, lower energy electrons lose energy faster, thus changing particle densities. Using Equation (30) gives

$$\frac{dg(E', Z)}{dE'} = \frac{E'\left[\sqrt{\left(\frac{E'}{a}\right)^2 + b^2} + Z\right]}{a\sqrt{\left(\frac{E'}{a}\right)^2 + b^2}\;\sqrt{\left[\sqrt{\left(\frac{E'}{a}\right)^2 + b^2} + Z\right]^2 - b^2}} \qquad (32)$$

The electron dose deposited at depth Z is given by:

$$D(Z) = K\int_{E} \Phi_Z(E')\,\underset{\sim}{S}(E')\,dE' \qquad (33)$$

where S(E') is the instantaneous collision stopping power in the receiver. One can derive an approximation for the stopping power by using the derivative of the range

$$S(E') = -\frac{1}{\frac{dR(E')}{dE'}} \qquad (34)$$

$$S(E') = \frac{a^2}{E'}\sqrt{\left(\frac{E'}{a}\right)^2 + b^2} \qquad (35)$$

By a fortunate accident the approximate stopping power derived from aluminum extrapolated range data is a good fit to tissue collision stopping power. (Tissue is the receiver most commonly used.) The fit is within 5% of Berger's tabulated data[2] in the interval 0.15 to 4.5 MeV and within 13% from 0.08 to 10.0 MeV.

Combining the results of Equations (31), (32), (33), and (35) and simplifying the tissue dose behind an aluminum shield Z thick yields

$$D(Z) = K\int_{E'} \Phi_0\left[g(E', Z)\right]\,\frac{a\left[\sqrt{\left(\frac{E'}{a}\right)^2 + b^2} + Z\right]}{g(E', Z)}\,dE'. \qquad (36)$$

Equation (36) is derived for normal incidence. For a beam incident at angle Θ to the normal, Z is replaced in the equation by the slant distance to the dose point, Z/cos Θ, and for half-space isotropic flux the dose is given by:

$$D_{iso}(Z) = K\int_0^{\frac{\pi}{2}}\int_{E'} \Phi_0\,[g(E', Z/\cos\theta)]\,\frac{a\left[\sqrt{\left(\frac{E'}{a}\right)^2 + b^2} + Z/\cos\theta\right]}{g(E', Z/\cos\theta)}\,dE'\sin\theta\,d\theta \qquad (37)$$

COMPARISON OF THE THREE METHODS FOR DOSE CALCULATION

Typical electron spectra encountered in practical applications are exponential in nature. Figures 13 through 18 show comparisons of the three methods for spectra of the form

$$\Phi_0(E) = Pe^{-PE} \qquad (38)$$

where P varies from 0.25 to 6.0. The energy integration limits are 0.0 to 20.0 MeV. The agreement among the three methods is fairly good considering the magnitude of the attenuation that occurs. The two methods using Berger's data have significant disagreement only for high shield thicknesses and isotropic spectra. The disagreement here is probably because a significant fraction of the dose is from electrons with energies above 10 MeV where both methods are using extrapolation on the data. The disagreement between the methods using Berger's data and the straightahead method are somewhat larger, but the errors still are not so large as to cause question about the validity of any one of the three approaches.

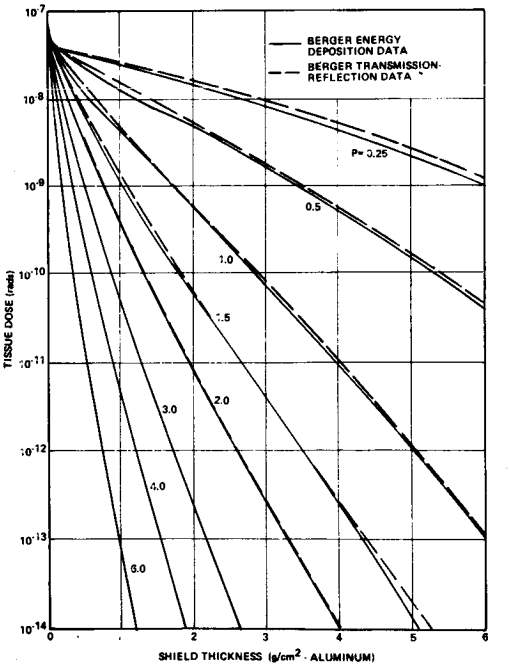

FIGURE 13: COMPARISON OF ELECTRON TISSUE DOSES CALCULATED USING BERGER'S ENERGY DEPOSITION DATA AND TRANSMISSION - REFLECTION DATA FOR A NORMALLY INCIDENT SPECTRUM OF THE FORM $\Phi_0(E) = P\exp(-PE)$ e/cm² - MeV

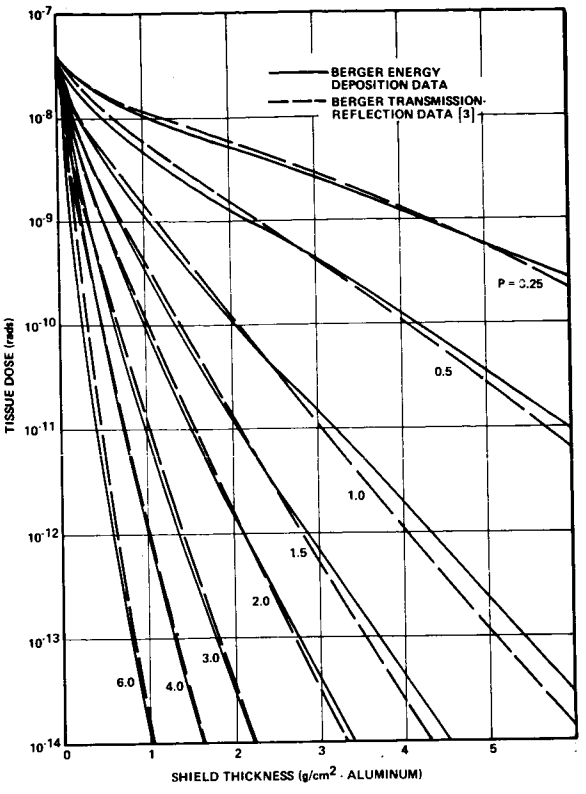

FIGURE 14: COMPARISON OF ELECTRON TISSUE DOSES CALCULATED USING BERGER'S ENERGY DEPOSITION DATA AND TRANSMISSION - REFLECTION DATA FOR A HALF-SPACE ISOTROPIC INCIDENT SPECTRUM OF THE FORM $\phi_o(E) = P \exp(-PE)e/cm^2$ - MeV

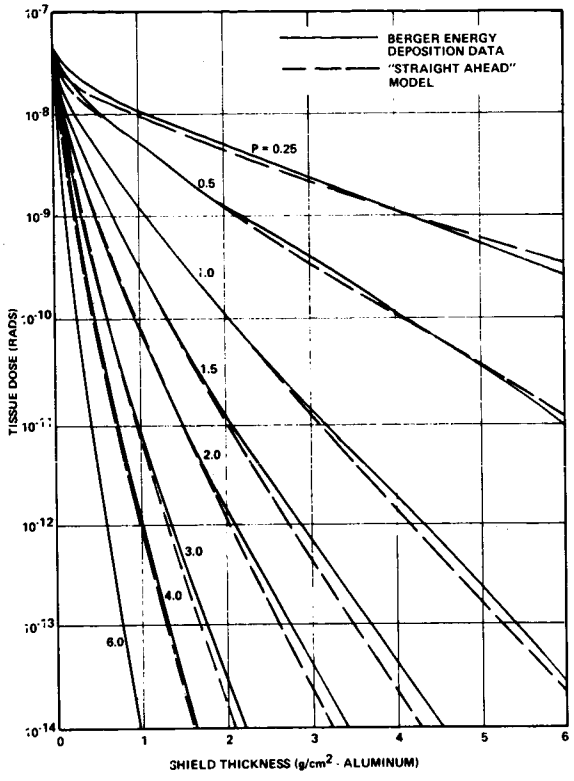

FIGURE 16: COMPARISON OF ELECTRON TISSUE DOSES CALCULATED USING BERGER'S ENERGY DEPOSITION DATA AND THE STRAIGHT-AHEAD MODEL FOR A HALF-SPACE ISOTROPIC INCIDENT ELECTRON SPECTRUM OF THE FORM $\phi_o(E) = P \exp(-PE)e/cm^2$ - MeV

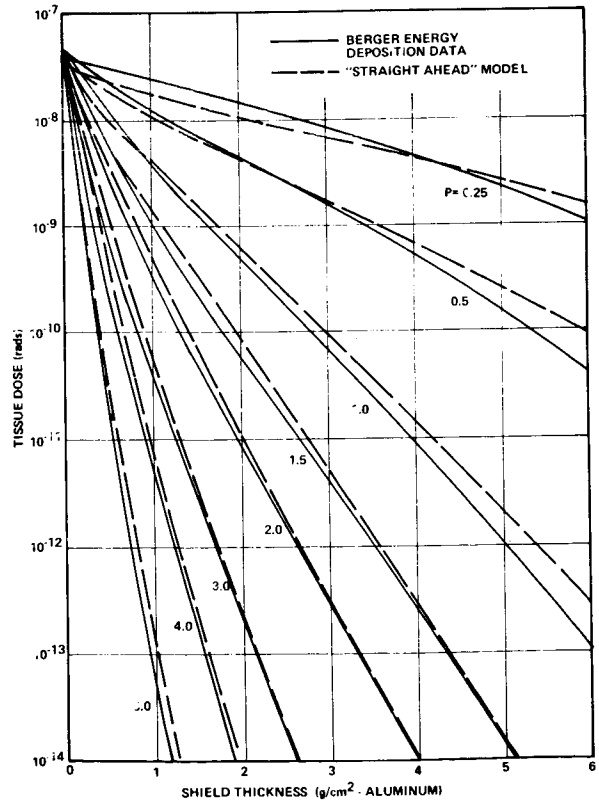

FIGURE 15: COMPARISON OF ELECTRON TISSUE DOSES CALCULATED USING BERGER'S ENERGY DEPOSITION DATA AND THE STRAIGHT-AHEAD MODEL FOR A NORMALLY INCIDENT SPECTRUM OF THE FORM $\phi_o(E) = P \exp(-PE)e/cm^2$ - MeV

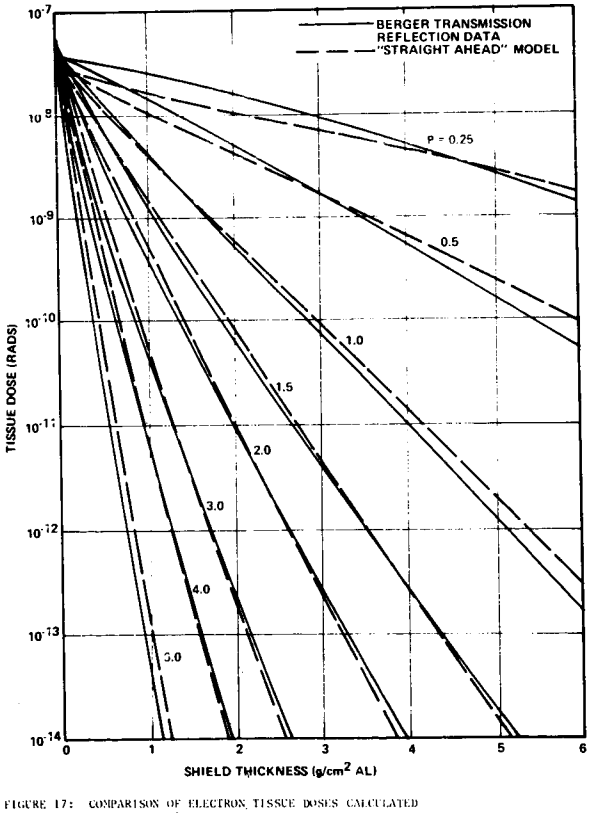

FIGURE 17: COMPARISON OF ELECTRON TISSUE DOSES CALCULATED USING BERGER'S TRANSMISSION-REFLECTION DATA AND THE STRAIGHT-AHEAD MODEL FOR A NORMALLY INCIDENT SPECTRUM OF THE FORM $\phi_o(E) = P \exp(-PE)e/cm^2$ - MeV

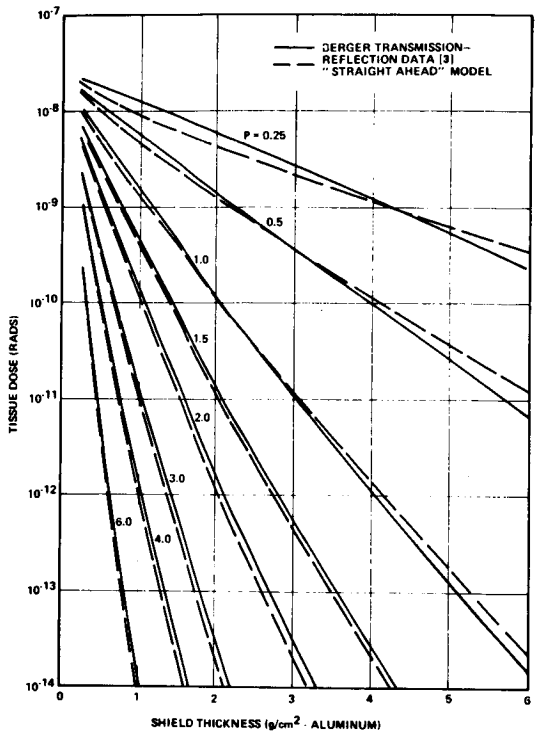

FIGURE 18: COMPARISON OF ELECTRON TISSUE DOSES CALCULATED USING BERGER'S TRANSMISSION-REFLECTION DATA AND THE STRAIGHT-AHEAD MODEL FOR A HALF-SPACE ISOTROPIC INCIDENT SPECTRUM OF THE FORM $\phi_0(E) = P \exp(-PE)$ e/cm² - MeV

BREMSSTRAHLUNG DOSE CALCULATIONS

Previously, consideration has been confined to the dose deposited by electrons; this is satisfactory for thin shields. However, when the shields are thick enough to remove a large fraction of the primary electrons, dose deposition by bremsstrahlung must be taken into account. (The point where this occurs is usually less than 3.0 g/cm^2.) To do a bremsstrahlung dose calculation one must generate a bremsstrahlung source distribution and then transport the bremsstrahlung from this source to the dose point. To generate the bremsstrahlung source distribution, one needs the electron energy and angular distribution at the source point and the bremsstrahlung production cross section.

Because the interior electron angular distribution is not easily determined and since the bremsstrahlung production cross section differentials in angle are not particularly accurate, a simplification commonly made is to use cross section differential in photon energy only and to make some assumption about the bremsstrahlung source angular distribution. (This assumption will be examined later.) In this case, the bremsstrahlung differential energy flux source or depth Z' and photon energy E_γ is given by:

$$S(E_\gamma, Z') = \int_E \int_{\vec{\Omega}} E_\gamma \sum(E_\gamma, E)\, \Phi_{Z'}(E, \vec{\Omega})\, dE\, d\vec{\Omega} \qquad (39)$$

in units of MeV/(MeV-g), where $\Sigma(E_\gamma, E)$ is the macroscopic bremsstrahlung production cross section differential in photon energy in units of photons/g-MeV-(e/cm^2) and $\Phi_{Z'}(E,\vec{\Omega})$ is the electron energy and angular distribution at depth Z in units of e/cm^2-MeV-sr.

The macroscopic cross section is given by:

$$\sum(E_\gamma, E) = \frac{N_0}{A} \frac{d\sigma}{dE_\gamma} \quad , \qquad (40)$$

where N_0 is Avagadro's number 6.02 x 10^{23} atom/mole, A is the atomic weight of the material at the source point in g/mole, and $d\sigma/dE$ is the microscopic bremsstrahlung production cross section differential in photon energy in units of photons/atom . (e/cm^2) . MeV. The microscopic cross section presently used for the MSFC calculation is given by:

$$\frac{d\sigma}{dE_\gamma} = F_E(E, E_\gamma)\, C(E)\, \frac{Z_0^2 r_0^2 P}{137 E_\gamma P_0} \left(\frac{4}{3} - 2H_0H\left(\frac{P^2 + P_0^2}{P^2 P_0^2}\right) + \frac{\epsilon_0 H}{P_0^3} + \frac{\epsilon H_0}{P^3} - \frac{\epsilon\epsilon_0}{P_0 P} + L\left\{ \frac{8H_0H}{3P_0P} + \frac{K^2(H_0^2H^2 + P_0^2P^2)}{P_0^3 P^3} + \frac{K}{2P_0P}\left[\left(\frac{H_0H + P_0^2}{P_0^3}\right)\epsilon_0 - \left(\frac{H_0H + P^2}{P_3}\right)\epsilon + \frac{2KH_0H}{P^2 P_0}\right]\right\}\right) , \qquad (41)$$

where

$$L = 2\ln\left(\frac{H_0H + P_0P - 1}{K}\right)$$

$$\epsilon_0 = \ln\left(\frac{H_0 + P_0}{H_0 - P_0}\right)$$

$$\epsilon = \ln\left(\frac{H + P}{H - P}\right) .$$

The terms H_0 and H are the initial and final total electron energies in mc^2 units given by

$$H_0 = \frac{E}{mc^2} + 1$$

$$H = \frac{E - E_\gamma}{mc^2} + 1 \ ;$$

P_0 and P are the initial and final electron momenta given by

$$P_0 = \sqrt{H_0^2 - 1}$$

$$P = \sqrt{H^2 - 1} \ ;$$

and K is the photon energy or momentum in mc^2 or mc units, respectively,

$$K = \frac{E_\gamma}{mc^2} .$$

The term Z_o is the atomic number of the source material, r_o is the classical electron radius 2.82×10^{-13} cm, mc^2 is the rest mass energy of an electron, and $F_E(E,E_\gamma)$ and $C(E)$ are two correction factors. Except for the correction factors this is formula 3BN from Koch and Motz[6], who give a complete description of the cross section. The correction factor $F_E(E,E_\gamma)$ given by

$$F_E(E,E_\gamma) = \begin{cases} \dfrac{\beta_0\left(1 - e^{-\frac{2\pi Z_0}{137\beta_0}}\right)}{\beta\left(1 - e^{-\frac{2\pi Z_0}{137\beta}}\right)} & \text{for } E < 2.0 \text{ MeV} \\ & \text{and } \dfrac{E_\gamma}{E} > 0.01 \\ 1.0 & \text{otherwise} \end{cases} \quad (42)$$

where

$$\beta_0 = \sqrt{1 - \left(\frac{mc^2}{E + mc^2}\right)^2} \quad (43)$$

and

$$\beta = \sqrt{1 - \left(\frac{mc^2}{E - E_\gamma + mc^2}\right)^2} \quad , \quad (44)$$

is the Elwert nonrelativistic coulomb correction, and the correction $C(E)$ is an empirical screening correction as shown by Koch and Motz[6]. Koch and Motz further discuss both these corrections[6].

The prime advantage of the straight-ahead approximation is that it does provide an electron spectrum at a given depth. Thus, using the result derived, for a normally incident electron beam, the bremsstrahlung source is given as

$$S_N(E_\gamma, Z') = \int_E^{E_\gamma} \sum(E_\gamma, E)\, \Phi_0[g(E,Z')]\, \frac{dg(E,Z')}{dE}\, dE \quad , \quad (45)$$

and for a half-space isotropic incident electron distribution the bremsstrahlung source is

$$S_{iso}(E_\gamma, Z') = \int_0^{\frac{\pi}{2}} \int_E^{E_\gamma} \sum(E_\gamma, E)\, \Phi_0[g(E, Z'/\cos\theta)]\, \frac{dg(E,Z'/\cos\theta)}{dE}\, dE \sin\theta\, d\theta \quad , \quad (46)$$

where Φ_o, g, and dg/dE are as defined in the third section.

The bremsstrahlung transport and dose calculation is relatively straightforward for a plane slab geometry given the source energy distribution and some source angular distribution. Using point kernel attenuation with dose buildup factors, the dose is given by:

$$D(Z) = K \int_{E_\gamma} \int_0^Z \mu_E(E_\gamma)\, S(E,Z')\, B(E_\gamma, Z, Z')\, G[\mu_m(E_\gamma)|Z-Z'|]\, dE_\gamma\, dZ' \quad , \quad (47)$$

where $\mu_E(E_\gamma)$ is the gamma ray energy absorption coefficient [7] for the receiver material; Z is the shield thickness; $B(E,Z,Z')$ is a dose buildup factor, depending on the source angular distribution chosen; and $G[\mu_m(E_\gamma)|Z-Z'|]$ is the attenuation kernel, also depending on the source angular distribution chosen where $\mu_m(E_\gamma)$ is the gamma ray mass absorption coefficient.

Much of the wide disagreement among various bremsstrahlung calculations can be traced to assumptions made about either the incident electron angular distribution expected in the problem or the angular distribution of the bremsstrahlung source. Perhaps the least conservative assumption about the source distribution that can logically be made for deep penetrations is that it is isotropic, and the most conservative assumption is that all the photons are emitted normally into the slab. In the first case the attenuation kernel is given by:

$$G[\mu_m(E_\gamma)|Z-Z'|] = \frac{E_1[\mu_m(E_\gamma)|Z-Z'|]}{2} \quad , \quad (48)$$

where E_1 is the first exponential integral and plane isotropic buildup factors are used[8]. In the second case the attenuation kernel is

$$G[\mu_m(E_\gamma)|Z-Z'|] = e^{-\mu_m(E_\gamma)|Z-Z'|} \quad , \quad (49)$$

and plane monodirectional buildup factors are used. Goldstein[7] tabulates these for infinite media, which should give a conservative estimate of the dose. These should be used cautiously, however, because they do not extend low enough in energy and extrapolation is dangerous. Figure 20 gives a comparison of these two cases for a half-space isotropic electron spectrum of exponential form incident on an aluminum shield with a water receiver (simulating tissue). Plane isotropic buildup factors were used in both calculations so that the difference observed is caused by the attenuation kernel. Actually, if correct buildup factors were used, the normal incident source case would be slightly lower.

Because of the built-in bias of using the extrapolated range in the straight-ahead approximation for calculating the source distribution, it is felt that there is no need to use the most conservative source angular distribution. Instead it is assumed that the bremsstrahlung source is half-space isotropic toward the receiver by the attenuation function given in Equation (48) multiplied by a factor of two. Still, the plane isotropic buildup factors[8] are used, making the calculation slightly more conservative. Figure 20 shows the results of an MSFC bremsstrahlung calculation for a half-space isotropic electron spectrum of exponential form incident on an aluminum shield with a water receiver (simulating tissue). Comparing Figs. 19 and 20 reveals that the MSFC calculation

(Fig. 20) is the most conservative of the three up to 4 or 5 g/cm^2. Above that depth, the monodirectional source calculation is more conservative by as much as a factor of three compared to the MSFC results.

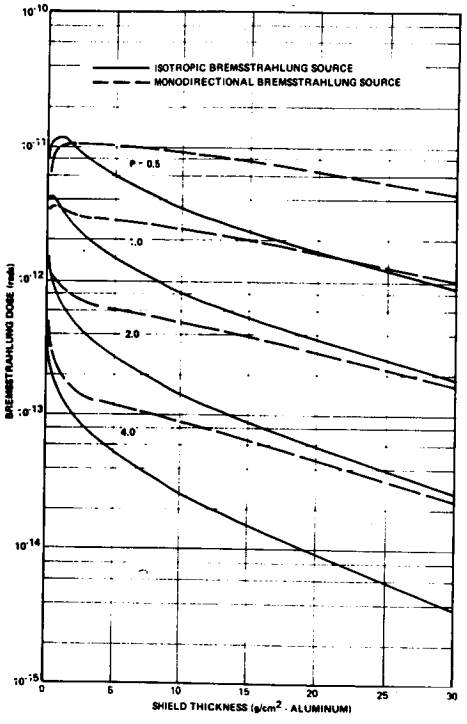

FIGURE 19: COMPARISON OF BREMSSTRAHLUNG DOSE CALCULATED ASSUMING AN ISOTROPIC SOURCE AND A MONODIRECTIONAL SOURCE DIRECTED NORMALLY INWARD FOR A HALF-SPACE ISOTROPIC INCIDENT ELECTRON SPECTRUM OF THE FORM $\phi_0(E) = P \exp(-PE)$ e/cm² - MeV

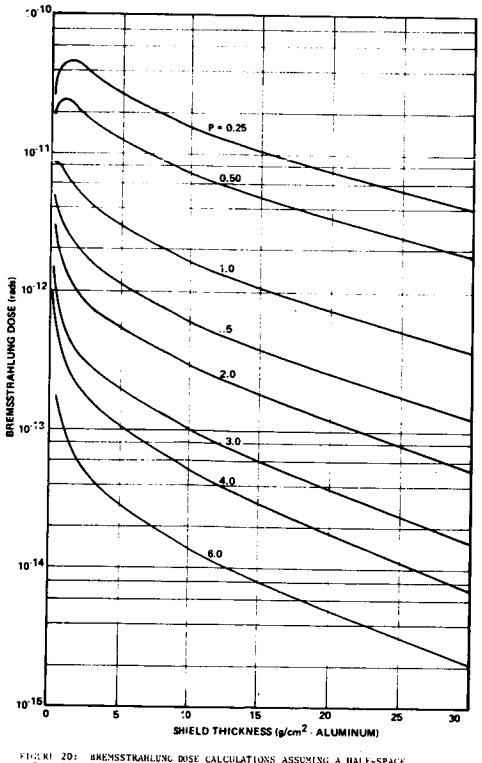

FIGURE 20: BREMSSTRAHLUNG DOSE CALCULATIONS ASSUMING A HALF-SPACE ISOTROPIC SOURCE FOR A HALF-SPACE ISOTROPIC INCIDENT ELECTRON SPECTRUM OF THE FORM $\phi_0(E) = P \exp(-PE)$ e/cm² - MeV

Since the bremsstrahlung dose calculational method described so far involved triple or quadruple numerical integration and since the functions integrated are exceptionally difficult to integrate, the calculation can be performed conveniently only on a relatively large computer. In many cases, all that is needed is a rough order of magnitude estimate useful only in determining if a problem exists. For space applications, where most of the electron spectra encountered fall off exponentially with increasing energy, a conservative estimate of bremsstrahlung dose can be calculated as follows:

First, assume that all the electrons penetrate to the source plane and that at that plane their energy is the average energy of an external electron. That is,

$$\bar{E} = \frac{\int_{\vec{\Omega}} \int_{E'} E' \Phi_0(E', \vec{\Omega})\, dE'\, d\vec{\Omega}}{\int_{\vec{\Omega}} \int_{E'} \Phi_0(E', \vec{\Omega})\, dE'\, d\vec{\Omega}} \quad . \tag{50}$$

According to Evans[9], the total source in MeV/g is approximated by

$$S = H\, Z_0\, \bar{E}^2 \int_{\vec{\Omega}} \int_{E'} \Phi_0(E', \vec{\Omega})\, dE'\, d\vec{\Omega} \quad , \tag{51}$$

where H is a constant and Z_0 is the shield material atomic number. Berger and Seltzer[3] tabulate H for a cosine law electron source as a function of incident electron energy and shield thickness. Because the variation in the table is not great, a typical value 4×10^{-4} can be used for this approximation.

Second, assume that the source plane is located at half the extrapolated range at $\bar{E}$. The bremsstrahlung dose is given by:

$$D(Z) = K\, \mu_E\, S\, B[\bar{E}, \mu_m(\bar{E}) Z^*]\, E_1[\mu_m(\bar{E}) Z^*] \quad . \tag{52}$$

For μ_E, the energy absorption coefficient in the receiver, 0.033 cm^2/g is used, which is an upper bound on the coefficient for water in the range above 0.1 MeV. The source-receiver distance is given by:

$$Z^* = Z - R(\bar{E})/2 \qquad Z > R(\bar{E})/2 \quad . \tag{53}$$

A rough fit of the buildup factor in aluminum is given by: $B(\bar{E}, \mu_m(\bar{E})\, Z^*) =$

$$1.0 + 26.47\, \mu_m(\bar{E})\, Z^* \bar{E}^{1.161} \qquad \bar{E} < 0.1 \tag{54}$$

$$1.0 + 1.827\, \mu_m(\bar{E})\, Z^* \qquad 0.1 \le \bar{E} \le 0.2016$$

$$1.0 + 1.253\, \mu_m(\bar{E})\, Z^* \bar{E}^{-0.2354} \qquad 0.2016 < \bar{E} \le 2.0$$

$$1.0 + 1.528\, \mu_m(\bar{E})\, Z^* \bar{E}^{-0.522} \qquad \bar{E} > 2.0 \quad .$$

Simplifying somewhat for an aluminum shield and a water receiver yields

$$D(Z)=2.7\times 10^{-12}\bar{E}^2 B[E,\mu_m(\bar{E})Z^*]$$
$$E_1[\mu_m(\bar{E})Z^*]\int_{\bar{\Omega}}\int_{E'}\Phi_0(E',\vec{\Omega})dE'd\vec{\Omega} \qquad (55)$$

Figure 21 shows the result of a bremsstrahlung dose calculation using Equation (55); Fig. 22 shows a similar calculation assuming a monodirectional source. As can be seen in comparisons with results of more accurate calculations, the approximation yields reasonable order of magnitude estimates that are generally conservative.

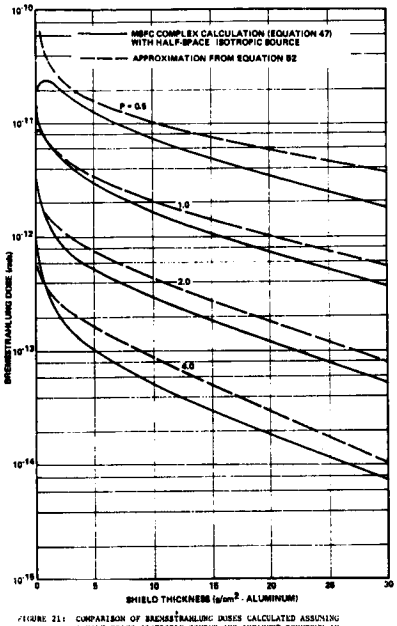

FIGURE 21: COMPARISON OF BREMSSTRAHLUNG DOSES CALCULATED ASSUMING A HALF-SPACE ISOTROPIC SOURCE AND INCIDENT SPECTRUM IN THE COMPLEX MSFC CALCULATION [EQUATION (47)] AND USING EQUATION (52). THE SPECTRUM IS OF THE FORM $\Phi_0(E) = P\exp(-PE)$ e/cm² - MeV

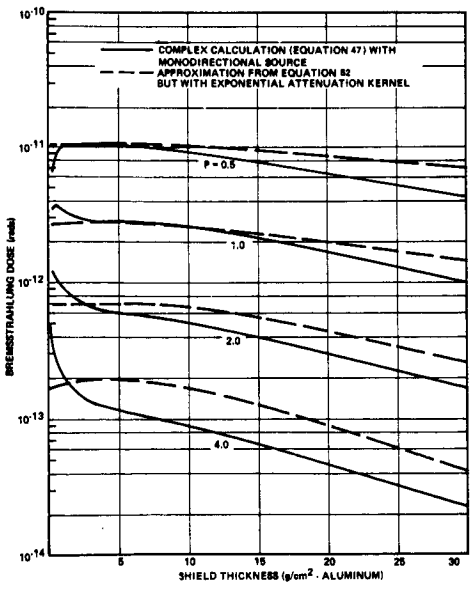

FIGURE 22: COMPARISON OF BREMSSTRAHLUNG DOSE CALCULATED ASSUMING A MONODIRECTIONAL SOURCE DIRECTED NORMALLY INWARD AND A HALF-SPACE ISOTROPIC ELECTRON SPECTRUM OF THE FORM $\Phi_0(E) = P\exp(-PE)$ e/cm² - MeV IN THE COMPLEX MSFC CALCULATION [EQUATION (47)] AND USING EQUATION (52) BUT WITH AN EXPONENTIAL ATTENUATION KERNEL

CONCLUSION

Although the results of the different electron and bremsstrahlung dose calculations developed at MSFC give results in relatively good agreement with each other, comparison with independent calculations is useful in pointing up areas of possible weakness. Wayne Scott of Oak Ridge National Laboratory has made such calculation using a Boeing program called Charge and a Douglas program called BEP as well as an older version of the MSFC program using Berger's transmission and reflection data[10]. The spectrum used was

$$\Phi_0(E) = 3.88\, e^{-0.575E-0.055E^2}\ \frac{e}{cm^2\text{-MeV-sec}}, \qquad (56)$$

which was renormalized to a total flux of unity. Table 3 gives the calculated electron dose in units of rad/h behind an aluminum shield on a tissue receiver for a normally incident beam. The MSFC results shown are for the new program using Berger's energy deposition coefficients and for the straight-ahead approximation. Both the MSFC program results are higher than the Charge and BEP results. The calculation using Berger's data is believed to be higher because the receiver had infinite backing behind it, whereas the other programs assume no backing. The straight-ahead calculation was higher because the extrapolated range was used in describing the transport.

Scott also did some spectral calculation at 0.5 and 1.0 g/cm^2 for the same incident spectrum using Charge, BEP, and Berger's Monte Carlo program, ETRAN. Figures 23 and 24 show these results plus spectra calculated with the MSFC straight-ahead program; it can be seen why the straight-ahead program yields higher doses. For the low-energy end of the spectrum consisting of particles that have lost the largest fraction of their energy and have been scattered the most, the straight-ahead program overestimates the flux by as much as a factor of three compared to ETRAN. For higher energies there is relatively good agreement with ETRAN. The overestimate of the low-energy component of the electron flux will be reflected in the bremsstrahlung calculation as an overestimate of the low-energy component of the bremsstrahlung source and in turn an overestimate of the bremsstrahlung dose, especially behind the thin shield where the low-energy bremsstrahlung has not been attenuated greatly.

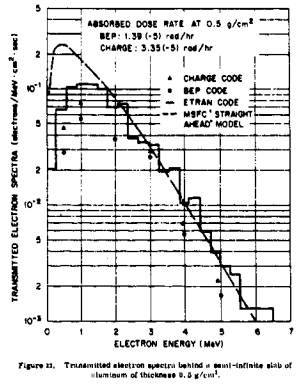

Figure 23. Transmitted electron spectra behind a semi-infinite slab of aluminum of thickness 0.5 g/cm².

In conclusion, the program using Berger's energy deposition data should be preferred for dose calculations, because in most practical problems the receiver does have effectively infinite backing and because the program is relatively easy to use. Where an electron spectrum at an internal point in a shield is needed, the straight-ahead approximation can be used to obtain a conservative estimate of the differential flux. For first-order calculations an estimate of bremsstrahlung dose can be obtained by using Equation (55) where the incident electron spectrum falls off exponentially. Where an accurate calculation is needed, Equation (47) with a half-space isotropic attenuation kernel should be used. More work needs to be done here in determining the actual source angular distribution.

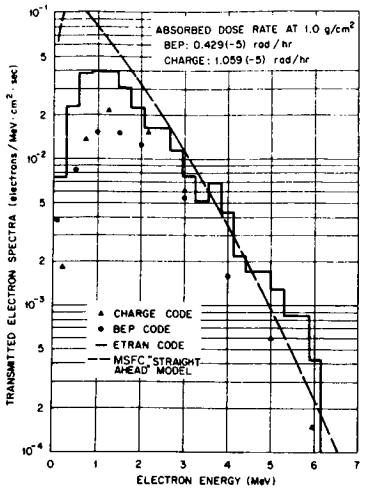

Figure 24. Transmitted electron spectra behind a semi-infinite slab of aluminum of thickness 1.0 g/cm².

REFERENCES

1. BERGER, M.J.: Diffusion of Fast Charged Particle. Methods in Computational Physics, vol. 1, Academic Press, 1963, p. 135.
2. BERGER and SELTZER: Tables of Energy Losses and Ranges of Electrons and Positrons. NASA SP-3012, 1964.
3. BERGER and SELTZER: Penetration of Electrons and Associated Bremsstrahlung Through Aluminum Targets. Protection Against Space Radiation, NASA SP-169, 1968.
4. RESTER, D.H.; DANCE, W.E.; and DERRICKSON, J.H.: Thick Target Bremsstrahlung Produced by Electron Bombardment of Targets of Be, Sn, and Au in the Energy Range 0.2 - 2.8 MeV. J. Appl. Phys., vol. 41, no. 6, May 1970, p. 2682.
5. FLAMMERSFELD, A.: Naturw, vol. 33, 1946, p. 280.
6. KOCH, H.W.; and MOTZ, J.W.: Bremsstrahlung Cross-Section Formulas and Related Data. Rev. Mod. Phys., vol. 31, no. 4, October 1959, p. 920.
7. GOLDSTEIN, H.: Fundamental Aspects of Reactor Shielding. Addison-Wesley Publishing Company, 1959, p. 237.
8. BURRELL, M.O.; and WATTS, J.W.: Plane Isotropic Buildup Factors for Bremsstrahlung Calculations. NASA-TND-4096, August 1967.
9. EVANS, R.: The Atomic Nucleus. McGraw-Hill Book Company, Inc., 1955, p. 617.
10. SCOTT, W.W.: Comparison of the Results Obtained with Several Electron-Penetration Codes. ORNL RSIC-28.

LOW-ENERGY ELECTRON TRANSPORT WITH THE METHOD OF DISCRETE ORDINATES[1]

D. E. Bartine, R. G. Alsmiller, Jr.,
F. R. Mynatt, W. W. Engle, Jr.,
and J. Barish

Oak Ridge National Laboratory
Oak Ridge, Tennessee, 37830

The one-dimensional discrete ordinates code ANISN has been adapted to transport low-energy ($\sim$ a few MeV) electrons. Calculated results obtained with ANISN are compared with experimental data for the transmitted electron energy and angular distributions for 1-MeV electrons normally incident on aluminum slabs of several thicknesses. The calculated and experimental results to date are in good agreement for a thin slab (0.2 of the electron range) but are not in good agreement for thicker slabs (0.6 of the electron range). Calculated results obtained with ANISN are also compared with calculated results obtained using Monte Carlo methods.

INTRODUCTION

The transport of low-energy (of the order of a few MeV) electrons through matter is important in the shielding of manned space vehicles that pass through the Van Allen electron belt. A code that treats this transport by means of Monte Carlo methods is available (ref. 1), but because of the poor statistical accuracy which can be obtained in some cases, a nonstatistical method of calculation is needed. To fill this need, the method of discrete ordinates has been adapted to the transport of low-energy electrons. The method of calculation is discussed in the next section, and the calculated results are presented and compared with experimental results and other calculated data in the last section.

METHOD OF CALCULATION

In principle, the discrete ordinates code ANISN (ref. 2) may be used to transport electrons by the simple expedient of introducing into the code the differential cross sections for electron-nucleus elastic collisions, electron-nucleus bremsstrahlung-producing collisions, and electron-electron collisions. In practice, however, these cross sections are quite different from those which occur in neutron transport where the method of discrete ordinates has been used extensively, and the method has shown only partial success in transporting electrons.

In the Monte Carlo treatment of electron transport, the individual electronic collisions are not considered, but rather the theories of multiple Coulomb scattering and continuous slowing down are used to group together large numbers of collisions (ref. 1). In the work reported here, the individual electronic collisions are treated except that those electron-electron collisions which result in very small energy transfers (of the order of the average ionization potential of the atom) are treated using the continuous slowing-down approximation. The equation solved is the Boltzmann transport equation with a continuous slowing-down term added:

$$\vec{\Omega}\cdot\nabla\phi(\vec{R},E,\vec{\Omega}) = P(\vec{R},E,\vec{\Omega})$$

$$+ n\int_{E}^{E_o} dE' \int d\Omega' \frac{d^2\sigma_{e\to e}(E',E,\vec{\Omega}'\cdot\vec{\Omega})}{dE d\Omega}\,\phi(\vec{R},E',\vec{\Omega}')$$

$$+ \int_{E+I'}^{E_o} \int d\Omega' \frac{d^2\sigma_{in}(E',E,\vec{\Omega}'\cdot\vec{\Omega})}{dE d\Omega}\,(\vec{R},E',\vec{\Omega}')$$

$$- n\,\sigma^T(E)\,\phi(\vec{R},E,\vec{\Omega})$$

$$+ \frac{\partial}{\partial E}\left[S(E)\,\phi(\vec{R},E,\vec{\Omega})\right], \qquad (1)$$

[1]This work was funded by the National Aeronautics and Space Administration, Order H-38280A, under Union Carbide Corporation's contract with the U. S. Atomic Energy Commission.

$$\frac{d^2\sigma_{e\to e}(E',E,\vec{\Omega}'\cdot\vec{\Omega})}{dEd\Omega} = \frac{d^2\sigma_{el}(E',E,\vec{\Omega}'\cdot\vec{\Omega})}{dEd\Omega} + \frac{d^2\sigma_{br}(E',E,\vec{\Omega}'\cdot\vec{\Omega})}{dEd\Omega} ,$$

$$\sigma^T_{e\to e}(E') = \int dE \int d\Omega \frac{d^2\sigma_{e\to e}(E',E,\vec{\Omega}'\cdot\vec{\Omega})}{dEd\Omega} ,$$

$$\sigma^T_{in}(E') = \int dE \int d\Omega \frac{d^2\sigma_{in}(E',E,\vec{\Omega}'\cdot\vec{\Omega})}{dEd\Omega} ,$$

$$\sigma^T(E') = \sigma^T_{e\to e}(E') + \sigma^T_{in}(E') ,$$

where

$\vec{R}$ = a vector denoting the position of the particle;

$\vec{\Omega}$ = a unit vector in the direction of the momentum vector;

$d\Omega$ = an element of solid angle;

E = the kinetic energy of an electron;

$\phi(\vec{R},E,\vec{\Omega})$ = the electron flux per unit energy;

E_o = the highest kinetic energy considered;

n = the atomic number density;

$P(\vec{R},E,\vec{\Omega})$ = the number of electrons per unit energy per steradian per unit volume input at R from an external source;

$\frac{d^2\sigma_{el}(E',E,\vec{\Omega}'\cdot\vec{\Omega})}{dEd\Omega}$ = the differential cross section for an electron (E') going in direction $\vec{\Omega}'$ to undergo elastic nuclear scattering (Coulomb scattering) to $(E,\vec{\Omega})$;

$\frac{d^2\sigma_{br}(E',E,\vec{\Omega}'\cdot\vec{\Omega})}{dEd\Omega}$ = the differential cross section for an electron $(E',\vec{\Omega}')$ to undergo bremsstrahlung (radiative) scattering with both nuclei and atomic electrons to $(E,\vec{\Omega})$;

$\frac{d^2\sigma_{in}(E',E,\vec{\Omega}'\cdot\vec{\Omega})}{dEd\Omega}$ = the differential cross section for an electron $(E',\vec{\Omega}')$ to undergo inelastic scattering from atomic electrons to $(E,\vec{\Omega})$, thereby producing a secondary electron with energy E'-E;

I' = an arbitrary value taken to be the minimum energy loss allowed in an inelastic electron-electron collision;

$S(E)$ = the stopping power (energy loss per unit path length) due to inelastic electron-electron collisions resulting in an energy loss smaller than I' (these collisions are presumed to be straightahead).

The differential cross sections for electron-nucleus elastic collisions and electron-nucleus or electron-electron bremsstrahlung production are taken from standard sources (refs. 3 to 5). The differential cross section given by Moller (refs. 3, 6) is used to describe electron-electron collisions which result in large energy transfers ($\geq I'$). The stopping power used to treat electron-electron collisions resulting in small energy transfers ($< I'$) is obtained in the manner outlined by Rohrlich and Carlson (ref. 7) with the density effect correction taken from Sternheimer (refs. 8, 9). The I' value used in the cases reported here is 0.0163 MeV, i.e., 100 × I where I is the average ionization potential for aluminum, 163 eV (ref. 8).

RESULTS AND DISCUSSION

Goudsmit and Saunderson have obtained an analytic expression for the angular distribution of transmitted electrons when monoenergetic electrons are normally incident on sufficiently thin slabs so that the energy degradation of the electrons may be neglected (ref. 10). Using the Goudsmit-Saunderson theory, Berger obtained the angular distribution of the transmitted electrons resulting from 1-MeV electrons normally incident on an aluminum slab of thickness 0.0287 g/cm^2 (ref. 11). The transmitted angular current of electrons calculated by Berger is represented by the histogram shown in figure 1. Also shown in the figure are the results obtained for this same case with the discrete ordinates code ANISN. In the ANISN calculation, one energy group with a range from 1.0106 MeV to 0.9894 MeV and a midpoint of 1.0 MeV were used. No energy degradation was allowed and only elastic scattering was permitted; i.e., in this calculation equation 1 with $\sigma_{in} = \sigma_{br} = S(E) = 0$ was solved. The two calculations shown in figure 1 are in excellent agreement, and thus the method of discrete ordinates can handle satisfactorily small-angle multiple Coulomb scattering.

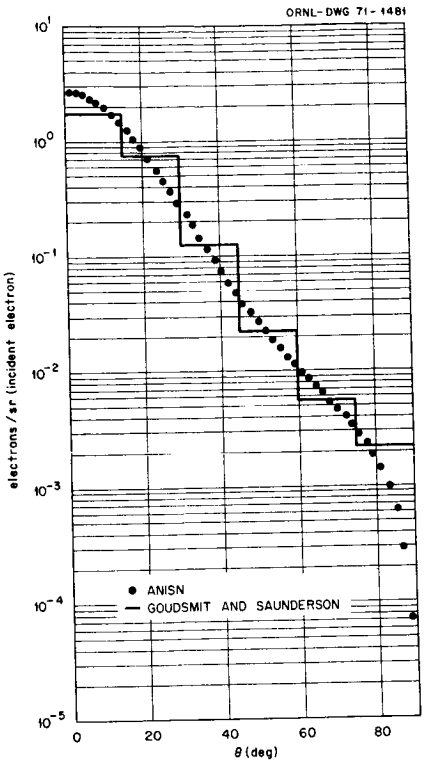

FIGURE 1.— Angular distribution of transmitted electron current for 1-MeV electrons normally incident on a 0.0287-g/cm^2-thick aluminum slab.

Rester and Rainwater (ref. 12) and Rester and Dance (ref. 13) have measured the transmitted electron current per unit energy from monoenergetic electrons normally incident on aluminum slabs of varying thicknesses. The solid histograms in figures 2, 3, and 4 show the measured transmitted electron current per unit energy for aluminum slabs of thicknesses of 0.11 g/cm^2, 0.22 g/cm^2, and 0.33 g/cm^2, respectively. Also shown in the figures are calculated results obtained with ANISN (solid curves) and calculated results obtained with the Monte Carlo transport code ETRAN of Berger and Seltzer (ref. 1). In figure 2, the agreement between the ANISN results and the experimental data is very good except at the very highest energies, and in this case, i.e., for a 0.11-g/cm^2-thick slab, the ANISN results are in slightly better agreement with the experimental data than the results given by ETRAN. In figure 3, neither ANISN nor ETRAN is in good agreement with the experimental data. In figure 4, which shows results for a relatively thick slab, 0.33 g/cm^2 (0.6 of the electron range), the Monte Carlo calculation is in very good agreement with the experimental data, while the ANISN calculation is in very poor agreement. The reason for the progressive failure of the continuous slowing-down ANISN calculation as the thickness increases is not known.

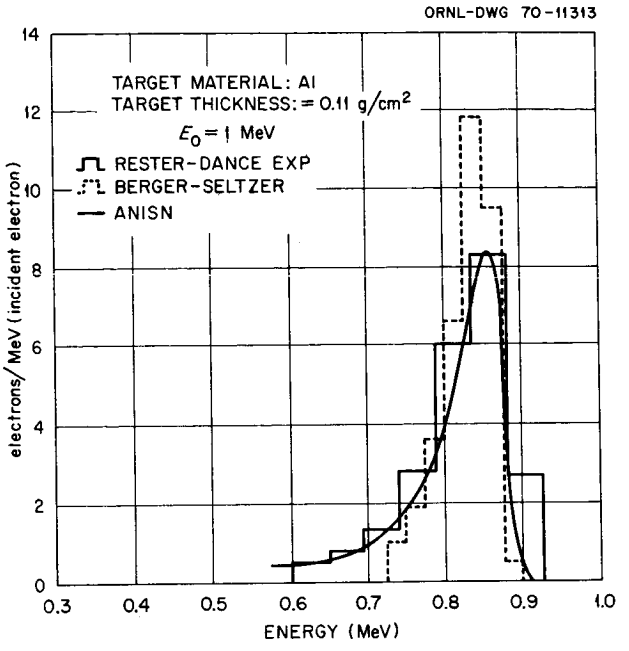

FIGURE 2.— Transmitted electron current per unit energy per incident electron for 1-MeV electrons normally incident on a 0.11-g/cm^2-thick aluminum slab.

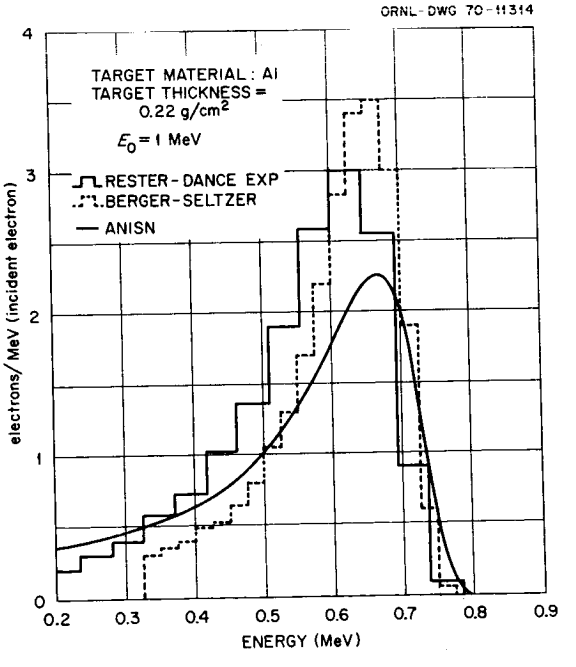

FIGURE 3.— Transmitted electron current per unit energy per incident electron for 1-MeV electrons normally incident on a 0.22-g/cm^2-thick aluminum slab.

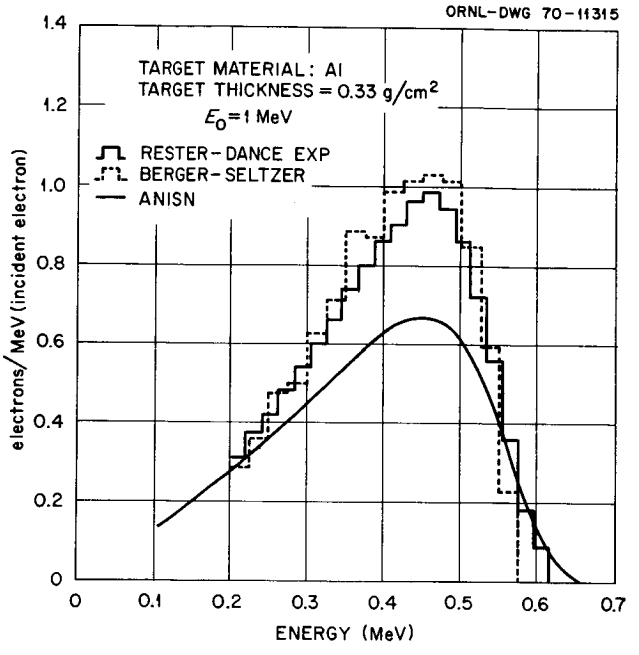

FIGURE 4.— Transmitted electron current per unit energy per incident electron for 1-MeV electrons normally incident on a 0.33-g/cm^2-thick aluminum slab.

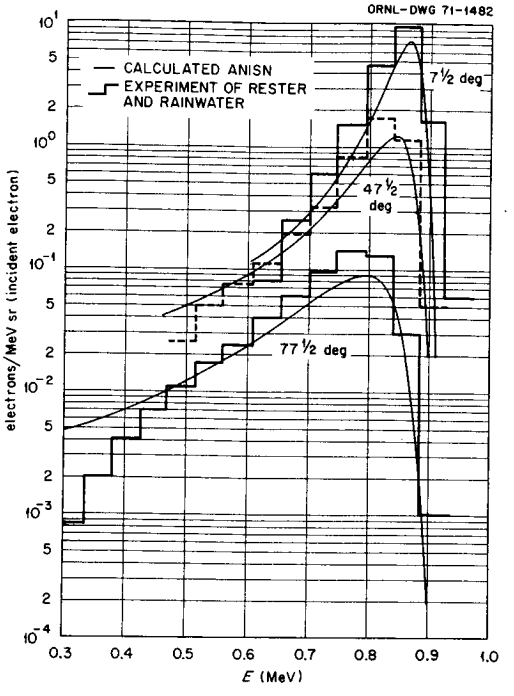

FIGURE 5.— Energy distribution of transmitted electron current at the specific angles indicated for 1-MeV electrons normally incident on a 0.11-g/cm^2-thick aluminum slab.

The calculated and measured transmitted electron current per unit energy and per unit solid angle is shown in figure 5 as a function of energy at several angles for a 0.11-g/cm^2-thick aluminum slab. The calculated results agree fairly well with the experimental data at all angles, thus indicating an acceptable energy-angle correlation.

Because of the lack of experimental data, it was not possible to present a comparison between calculation and experiment for the case of an electron spectrum incident on a slab. Using the Monte Carlo code ETRAN of Berger and Seltzer (ref. 1), Scott (ref. 14) calculated the transmitted electron current per unit energy for the case of a specific electron energy spectrum normally incident on aluminum slabs, and this theoretical calculation was compared with results obtained with ANISN. The incident electron energy distribution used in the calculations is a representation of the spectrum resulting from thermal neutron capture in ^{235}U (ref. 15). This spectrum extends to electron energies of the order of 10 MeV and is shown explicitly in reference 14.

The ETRAN results for an aluminum slab 0.5 g/cm^2 thick are shown in figure 6 as a histogram and the ANISN results are shown as plotted points. A similar comparison is given in figure 7 for an aluminum slab 1.0 g/cm^2 thick. In both figures 6 and 7 the ETRAN and ANISN results are in very good agreement. Thus, ANISN is apparently capable of treating accurately the transport of low-energy (< 10 MeV) electrons through relatively thick shields in some cases, e.g., the cases considered in figures 6 and 7, but not in all cases, e.g., figures 3 and 4.

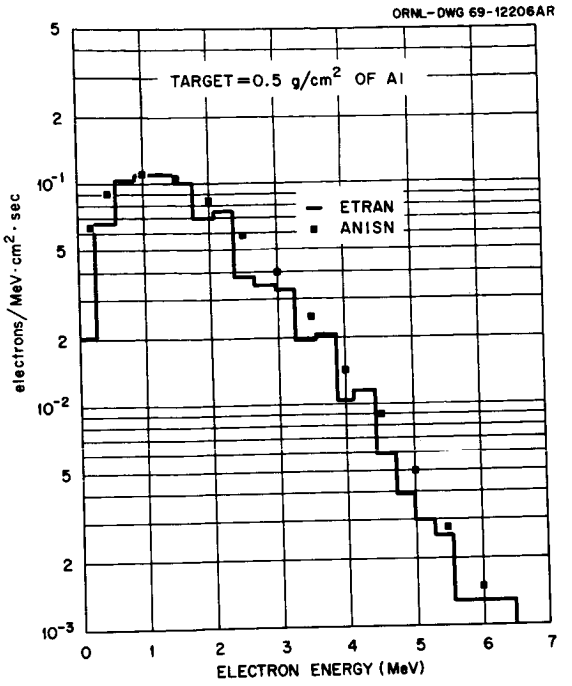

FIGURE 6.— Transmitted electron current per unit energy per incident electron for a specific energy spectrum (ref. 15) normally incident on a 0.5-g/cm^2-thick aluminum slab.

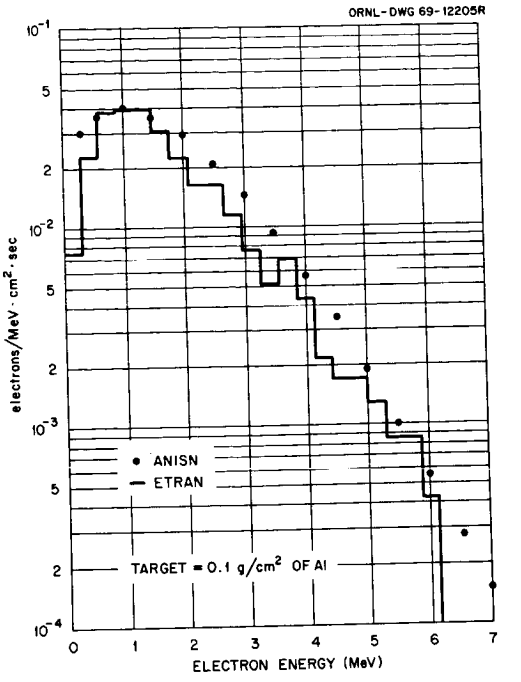

FIGURE 7.— Transmitted electron current per unit energy per incident electron for a specific energy spectrum (ref. 15) normally incident on a 1.0-g/cm^2-thick aluminum slab.

REFERENCES

1. BERGER, M. J.; and SELTZER, S. M.: ETRAN, Monte Carlo Code System for Electron and Photon Transport Through Extended Media, National Bureau of Standards Documents NBS-9836, 1968, and NBS-9837, 1968.
2. ENGLE, W. W., Jr.: A Users Manual for ANISN, a One-Dimensional Discrete Ordinates Transport Code with Anisotropic Scattering, Computing Technology Center, Union Carbide Corporation, Document K-1693, 1967.
3. ZERBY, C. D.; and KELLER, F. S.: Nucl. Sci. Eng., vol. 27, 1967, p. 190.
4. SPENCER, L. V.: Phys. Rev., vol. 98, 1955, p. 1507.
5. McCORMICK, P. T.; KEIFFER, D. G.; and PARZEN, G.: Phys. Rev., vol. 103, 1956, p. 29.
6. MOLLER, C.: Ann. Physik, vol. 14, 1932, p. 531.
7. ROHRLICH, F.; and CARLSON, B. C.: Phys. Rev., vol. 93, 1954, p. 38.
8. BERGER, M. J.; and SELTZER, S. M.: Tables of Energy Losses and Ranges of Electrons and Positrons, NASA Document NASA-SP-3012, 1964.
9. STERNHEIMER, R. M.: Phys. Rev., vol. 103, 1956, p. 511.
10. GOUDSMIT, S. A.; and SAUNDERSON, J. L.: Phys. Rev., vol. 57, 1940, p. 24; and Phys. Rev., vol. 58, 1940, p. 36.
11. BERGER, M. J.: Monte Carlo Calculation of the Penetration and Diffusion of Fast Charged Particles, p. 149 in Methods in Computational Physics, Vol. I, eds. B. Adler, S. Fernbach, and M. Rotenberg, Academic Press, New York, 1963.
12. RESTER, D. H.; and RAINWATER, W. J.: Investigations of Electron Interactions with Matter, NASA Document CR-334, 1965.
13. RESTER, D. H.; and DANCE, W. E.: Investigation of Electron Interaction with Matter, LTV Report No. 0-71000/6R-18, 1966.
14. SCOTT, W. W.: Comparisons of the Results Obtained with Several Electron-Penetration Codes, Oak Ridge National Laboratory Document ORNL RSIC-28, 1970.
15. CARTER, R. E., et al.: Phys. Rev., vol. 113, 1959, p. 280.

THE APPLICATION OF THE PHASE SPACE TIME EVOLUTION METHOD TO ELECTRON SHIELDING*

Matthew C. Cordaro, Long Island Lighting Company

and

Martin S. Zucker, Brookhaven National Laboratory

A computer-based method for treating the motion of charged and neutral particles called the Phase Space Time Evolution method (PSTE) has been developed. This technique, instead of utilizing the integro-differential transport equation and solving it by computer methods, makes direct use of the computer by employing its bookkeeping capacity to literally keep track of the time development of a phase space distribution of particles. This method is applied in this paper to a study of the penetration of electrons. In this application use is made of the continuous slowing down approximation for energy degradation and the Goudsmit-Saunderson distribution for multiple scattering. The specific problem investigated considers a 1 MeV beam of electrons normally incident on a semi-infinite slab of aluminum. Results of the PSTE calculation for this problem are compared on the basis of number transmission, energy spectrum and angular distribution as a function of penetration with existing Monte Carlo calculations and experimental results. The general agreement exhibited is good. In addition to the above, time-dependent PSTE electron penetration results for the same problem are presented. The computer time required to make the PSTE calculation discussed here was approximately 10 minutes on the CDC 6600 computer at the Brookhaven National Laboratory. This can be compared to a Monte Carlo calculation on a similar machine which requires on the order of an hour or more of computer time. As an added feature, the PSTE method generates deterministic and time dependent results during the small amount of machine time it requires.

SYMBOL MEANINGS

E	Energy
X	Position
μ_x	Cosine of the polar angle with respect to the X direction
t	Time
Δt	Time interval
v	Speed
S	Pathlength
Z	Atomic number
c	Speed of light
$m_o c^2$	Rest mass energy
ΔS_x	X displacement
ΔE	Energy interval
F	Apportioning fraction
ΔX	Position interval
ρ	Particle density
μ_i	Cosine of the polar angle of incidence with respect to the X direction
$p(\mu_x \mid \mu_i)$	Angular probability density function with respect to μ_x given an incident direction μ_i independent of incident and scattered azimuthal angle
$P_\ell(\mu)$	Legendre Polynomial of index ℓ
$G_\ell(S)$	Goudsmit-Saunderson distribution expansion terms
N	Number of scatterers per unit volume
θ_s	Polar angle of scattering relative to an arbitrary incident direction

*This work was performed under the auspices of the United States Atomic Energy Commission.

SYMBOL MEANINGS
(continued)

$\sigma(\theta_s,S)$	Coulomb single scattering cross section
$T_N(x)$	Number transmission factor
$\Delta\mu_x$	Cosine interval
$J(X,E,\mu_x,t)$	Current
E_i	Initial or incident energy
$T_N(X,E)$	Function representing energy spectrum
$T_N(X,\mu_x)$	Function representing angular distribution
$J_{X_+}(X,t)$	Transmitted current

INTRODUCTION

When traversing even a thin layer of matter, electrons engage in numerous collisions which produce in most cases small energy losses and deflections. In addition, they may undergo a relatively small number of catastrophic collisions which cause them to lose an appreciable fraction of their energy and to scatter through a large angle. The combined effect of all collisions is a complex transport process which requires an elaborate theory for description.

Monte Carlo methods of calculation have been applied to electron shielding calculations and in fact have been considered up to now the most accurate available, even though significant limitations are recognized. As with other Monte Carlo based calculations, the answers obtained can only be known with an accuracy which is governed by the statistical uncertainty inherent in the stochastic nature of the Monte Carlo method. Since individual electron slowing down case histories can be extremely complex, enormous amounts of computer time may be required to generate a statistically representative number of individual histories. This is the case even with the application of special techniques adapting Monte Carlo to the requirements of electron slowing down. Another problem with the Monte Carlo approach is that it seems suitable for handling only steady state or time independent phenomena; at least the present authors are unaware of any charged particle Monte Carlo calculations structured to take into account time dependence.

A computer-based method of treating the motion of charged or neutral particles which overcomes these difficulties has been introduced by Tavel and Zucker [1,2,3,4]. This technique, referred to as the "Phase Space Time Evolution" (PSTE) method, has been successful in the several neutron transport problems it has thus far been applied to [4]. The present paper will deal with the first application of the PSTE method to a charged particle problem, namely, electron slowing down and shielding in a semi-infinite medium.

The classical analytical approach to transport calculations usually requires the solving of an integro-differential equation subject to boundary conditions established by the problem of interest. The equation itself is a mathematical representation of the space-time evolution of a particle distribution which has been derived from the application of continuity principles in phase space. Instead of utilizing an integro-differential equation and solving it by computer techniques, the PSTE method makes direct use of the computer and employs its bookkeeping capacity to literally keep track of the time development of the phase space distribution.

The PSTE method was extended significantly beyond the approach used for neutron problems detailed in reference 4 in order to investigate the transport of electrons. This involved the addition of energy as a third dimension of the phase space and the use of multiple interaction theories for particle transport.

Defining the Three-Dimensional Digitized Phase Space

The phase space within which the flight of electrons can be traced which is shown in Figure 1 has Cartesian axes representing energy, E, position, X and cosine of the polar angle with respect to the X axis, μ_x. The values of E range from the maximum energy considered in the problem at the origin to the lowest energy of interest. The values of X can vary between any desired one dimensional spatial limit. The direction cosine, μ_x, ranges from +1 to -1.

The particle density in the phase space is stored as the number of particles per unit length in the element of phase space between coordinates X_{i-1} and X_i with energy E_K and direction cosine μ_{x_j}.

SOLVING A PROBLEM

An initial particle distribution represents the state of the phase space at time zero. The time iterative scheme used in the calculation then traces the movement of each element of phase space for one time interval Δt. As illustrated in Figure 2 during this time interval the element of phase space is first relocated in the E-X plane.

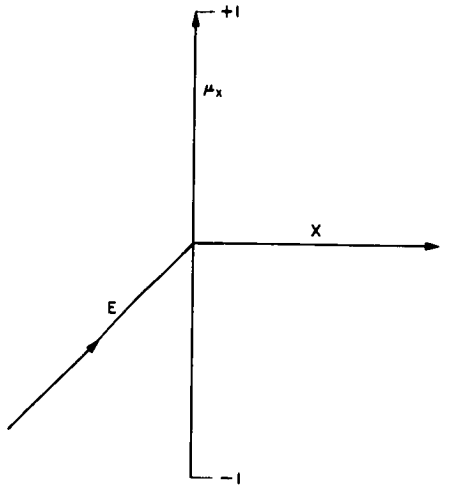

Figure 1 An illustration of the three dimensional phase space.

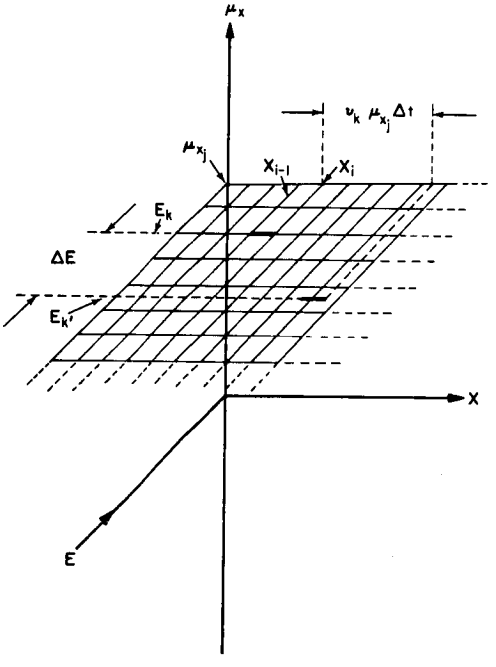

Figure 2 Movement of an element of phase space in the E-X plane.

In the calculations presented in this paper continuous slowing down theory as formulated by Rohrlich and Carlson [5], has been used to determine the energy loss of an element during Δt. Therefore, if the particles represented by an element of phase space are assumed to be traveling at an initial speed, v_K, corresponding to their initial kinetic energy, E_k, after a small time interval, Δt, their final kinetic energy, E_K', is approximately given by

$$E_K' = E_k - |dE_k/dS| v_k \Delta t \qquad (1)$$

where

$$v_k = c\left(1 - [m_o c^2/(E_k+m_o c^2)]^2\right)^{\frac{1}{2}} \qquad (2)$$

and $|dE_k/dS|$ is the stopping power given in reference 5. By using the fact that the radiative contribution to slowing down is approximately given by [6]

$$-dE_k/dS \ (ZE_k/800), \ ZE_k << 800$$

where $-dE_k/dS$ is the energy loss per unit pathlength due to nonradiative collisions, the energy loss from radiative collisions has been included in eq. (1) by multiplying $|dE_k/dS|$ by the factor $[1+ZE_k/800]$. It should be mentioned here that the PSTE method does not require the use of continuous slowing down. Straggling (energy loss fluctuations) can also be handled within the framework of this method. It was intended, however, in the present application to first see how well the method performed without this complication, which has been left for future work,

The technique employed to take into account the functional dependence on energy of dE/dS and v in eq. 1 divides the time interval Δt into many smaller intervals during which it is assumed that dE/dS and v remain constant. After each time increment the resulting final energy, E_k', calculated is used to establish the values of dE/dS and v to be used for the next smaller time step. The total pathlength traveled during Δt and the final energy after Δt are obtained by adding the contributions of all the smaller time steps.

In addition to providing the total pathlength traveled and the final energy, the iterative procedure outlined for eq. (1) also generates an average speed $\bar{v}_k$ for the time interval Δt. Once this value is available the displacement of the phase space element can be found through use of the relation

$$\Delta S_x = \bar{v}_k \mu_{x_j} \Delta t \qquad (3)$$

where μ_{x_j} is the initial direction cosine of the element and ΔS_x is its displacement after Δt. Once the X displacement has been determined the new position of the element X' is given by

$$X' = X + \Delta S_x. \qquad (4)$$

An important assumption in the determination of the X displacement is that μ_{x_j} does not change appreciably during Δt. This approximation is very good for small values of Δt. A constant μ_{x_j} during Δt is assumed mainly to avoid excessive computer time which contributes little to the accuracy of the electron PSTE calculation.

After an element of phase space has been moved in the E-X plane, it must be apportioned to the established grid lines (digitized). A moments weighting technique is used by the application presented in this paper to carry out the apportionment in energy.

The procedure followed first establishes the difference between the final energy and the end points of the energy grid interval into which the phase space element being operated upon falls. Thus, if some final energy of an element, E', falls between $E_{k'-1}$ and $E_{k'}$, these differences are $E_{k'-1} - E'$ and $E' - E_{k'}$, respectively. Once these values are found they are divided by ΔE, the energy interval between grid lines, to establish the energy apportioning fractions (moments),

$$F_{k'} = \frac{E_{k'-1} - E'}{\Delta E} \tag{5}$$

and

$$F_{K'-1} = \frac{E' - E_{k'}}{\Delta E} \quad . \tag{6}$$

A similar procedure is involved in digitizing the final position coordinate. Suppose that the original element intersects the grid line $X_{i'}$ with its end points falling on some $X_1 < X_{i'}$ and $X_2 > X_{i'}$ respectively. Then the distance $X_{i'} - X_1$ and $X_2 - X_{i'}$, divided by the increment of distance between grid lines, ΔX, are the position apportioning fractions,

$$F_{i'} = \frac{X_{i'} - X_1}{\Delta X} \tag{7}$$

and

$$F_{i'+1} = \frac{X_2 - X_{i'}}{\Delta X} \quad . \tag{8}$$

The four fractions, $F_{k'-1}$, and $F_{k'}$ representing energy apportionment and $F_{i'}$ and $F_{i'+1}$ representing spatial distribution, determine the digitization or apportionment in the E-X plane. Therefore, the number of particles per unit length contributed by the transported element having an initial particle density of $\rho_{k,j,i}$ (neglecting for the moment angular dependence)

at $E_{k'-1}$, μ_{x_j} between $X_{i'-1}$ and $X_{i'}$ is

$$\rho_{k'-1,j,i'} = \rho_{k,j,i} [F_{k'-1} F_{i'}];$$

at $E_{k'-1}$, μ_{x_j} between $X_{i'}$ and $X_{i'+1}$ is

$$\rho_{k'-1,j,i'-1} = \rho_{k,j,i} [F_{k'-1} F_{i'+1}];$$

at $E_{k'}$, μ_{x_j} between $X_{i'-1}$ and $X_{i'}$ is

$$\rho_{k',j,i'} = \rho_{k,j,i} [F_{k'} F_{i'}];$$ and

at $E_{k'}$, μ_{x_j} between $X_{i'}$ and $X_{i'+1}$ is

$$\rho_{k',j,i'+1} = \rho_{k,j,i} [F_{k'} F_{i'+1}].$$

The only operation remaining to complete the movement of the original element for Δt is its distribution in μ_x. To perform this operation the Goudsmit-Saunderson distribution [7,8] for multiple scattering was modified to provide the angular distribution of scattering referenced to the X direction independent of azimuthal angle,

$$p(\mu_x|\mu_i) = \sum_{\ell=0}^{\infty} \frac{2\ell+1}{2} \exp\left[-\int_0^s G_\ell(s')ds'\right] P_\ell(\mu_i) P_\ell(\mu_x) \tag{9}$$

where

$$G_\ell(s) = 2\pi N \int_0^\pi \sigma(\theta_s, S) \left[1 - P_\ell(\cos\theta_s)\right] \sin\theta_s d\theta_s \tag{10}$$

and μ_x and μ_i are the cosines of the polar angles of scattering and incidence, respectively, referenced to the X direction. To utilize the modified angular distribution in the PSTE calculation, the probability density given in eq. (9) is evaluated in the following way. First the interval $-1 \le \mu_x \le 1$ is divided into subintervals in such a manner that a grid line lies in the middle of each interval. The probability, therefore, of obtaining some $\mu_{x'}$ in the interval $\mu_b \le \mu_x \le \mu_a$ is given by

$$\int_{\mu_b}^{\mu_a} p(\mu_x|\mu_i) d\mu_x = \tfrac{1}{2}(\mu_a - \mu_b)$$

$$+\tfrac{1}{2}\sum_{\ell=1}^{\infty}\exp\left[\int_0^s G_\ell(s')ds'\right]P_\ell(\mu_i)$$
$$\left\{\left[P_{\ell+1}(\mu_a)-P_{\ell-1}(\mu_a)\right]\right.$$
$$\left.+\left[P_{\ell-1}(\mu_b)-P_{\ell+1}(\mu_b)\right]\right\}. \qquad (11)$$

Eq. (11) is applied to all subintervals. The probabilities generated in turn serve as weighting functions for the apportionment of the original transported element in μ_x.

Once every element in the phase space has been operated upon as outlined above, the stored results are tested against a set of terminating criteria for the problem being investigated. If these criteria are satisfied the calculation is completed. If not, another iteration is required. The final result of the PSTE calculation is a complete record of the time evolution of a particle density distribution given as a function of energy, direction and position.

Comparison of PSTE Calculations with Electron Monte Carlo and Experimental Results

To assess the validity of the results provided by the PSTE method as applied to electron transport, a comparison was made with Monte Carlo calculations and experimental results for a shielding problem which considered a 1 MeV pulse of electrons normally incident on a semi-infinite slab of aluminum. Comparisons were made on the basis of the different forms of published Monte Carlo and experimental results for this problem.

The first form of result compared is the number transmission factor. This factor, $T_N(X)$, which provides the fraction of incident electrons transmitted past X, is defined by

$$T_N(X) = \frac{1}{\Delta E\Delta\mu_x}\int_0^{E_i}\int_0^{1}\int_0^{t} J(X,E,\mu_x,t')dt'd\mu_x dE \qquad (12)$$

where the current $J(X,E,\mu_x,t)$ is given by

$$J(X,E,\mu_x,t) = \rho(X,E,\mu_x,t)v(E)\mu_x, \qquad (13)$$

E_i is the incident energy of the electrons and t is the time required for the entire pulse to essentially pass through the medium. Comparison of the PSTE generated number transmission curve with several Monte Carlo and experimental results is given in Figure 3. Penetration (X) in this case is represented as the fraction of the mean range traversed. The Monte Carlo results include calculations by Berger [9,10, 11] which use continuous slowing down in one case and straggling (energy loss fluctuation) in the other. Also shown are Monte Carlo calculations made by Perkins [12] which include the effects of straggling. The experimental points depicted include the results of experiments conducted by Rester [13] for 1 MeV electrons. Since the number transmission curve plotted as a function of the mean range traversed is approximately independent of initial energy in the neighborhood of 1 MeV, the average results of Agu et al. [14] for experiments conducted at energies below 1 MeV have also been used for comparison purposes. The agreement exhibited in Figure 3 between the PSTE and the Monte Carlo and experimental results is good. The PSTE curve, as should be expected, falls below the Monte Carlo and experimental results which considered straggling effects since, as mentioned before, this PSTE calculation utilized the continuous slowing down approximation for energy degradation. Although the experimental points of Rester lie somewhat above the PSTE curve, it should be noted that the PSTE values fall within the range of experimental uncertainty associated with these results.

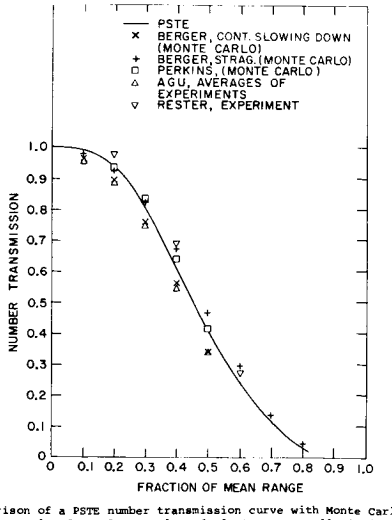

Figure 3 Comparison of a PSTE number transmission curve with Monte Carlo and experimental results for a 1 MeV pulse of electrons normally incident on a semi-infinite slad of aluminum.

The energy spectrum of transmitted electrons produced by the PSTE calculation for the problem under consideration is a critical indication of agreement with existing calculations and experimental results. The energy spectrum $T_N(X,E)$ is related to the PSTE generated current by

$$T_N(X,E) = \frac{1}{\Delta E \Delta \mu_x} \int_0^1 \int_0^t J(X,E,\mu_x,t')dt'd\mu_x \quad . \qquad (14)$$

The shapes of PSTE energy spectra for three different penetrations in terms of fractions of the mean range are compared to Monte Carlo and experimental results documented by Rester [13] in Figures 4 - 6. The Monte Carlo calculations were performed by Berger. Assuming that the total number of particles present at each penetration investigated is approximately the same for the PSTE, Monte Carlo and experimental examples, the histograms in Figures 4 - 6 have been drawn on a scale relative to the maximum of each distribution. In this way it is possible to separate an examination of the energy spectrum from other considerations. In other words, it is only intended here to investigate the relative

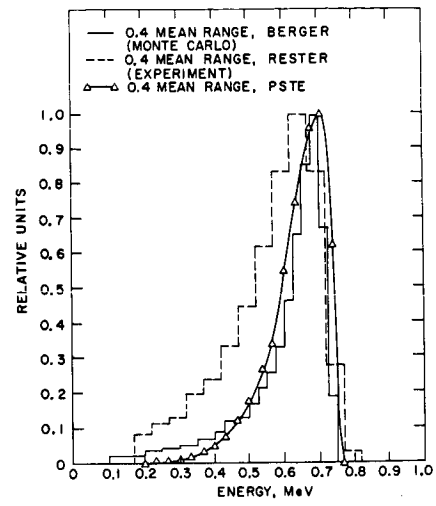

Figure 5 Comparison of the PSTE transmitted energy spectrum with Monte Carlo and experimental results at approximately .4 mean range for a 1 MeV pulse of electrons normally incident on a semi-infinite slab of aluminum.

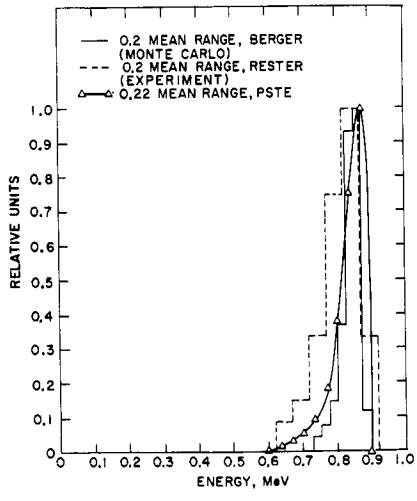

Figure 4 Comparison of the PSTE transmitted energy spectrum with Monte Carlo and experimental results at approximately .2 mean range for a 1 MeV pulse of electrons normally incident on a semi-infinite slab of aluminum.

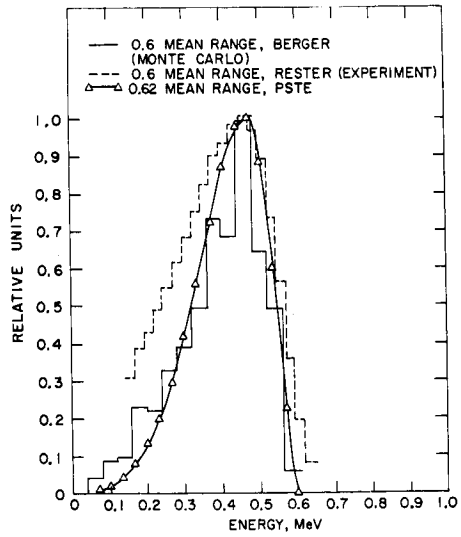

Figure 6 Comparison of the PSTE transmitted energy spectrum with Monte Carlo and experimental results at approximately .6 mean range for a 1 MeV pulse of electrons normally incident on a semi-infinite slab of aluminum.

shapes of the different energy spectra and not the total number of particles at a specific penetration (this has been done in the consideration of the number transmission factor). The good general agreement between Monte Carlo and experimental results and the PSTE calculation is well illustrated in Figures 4 - 6. For each penetration the PSTE result agrees very well with the Monte Carlo histogram. The agreement is not as good when the PSTE results are compared to the experimental values. The largest discrepancy appears at .4 of the mean range where the disparity between the Monte Carlo and experimental results is the greatest.

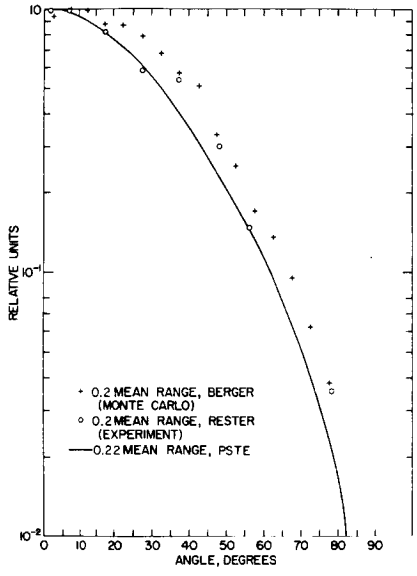

Figure 7 Comparison of the PSTE transmitted angular distribution with Monte Carlo and experimental results at approximately .2 mean range for a 1 MeV pulse of electrons normally incident on a semi-infinite slab of aluminum.

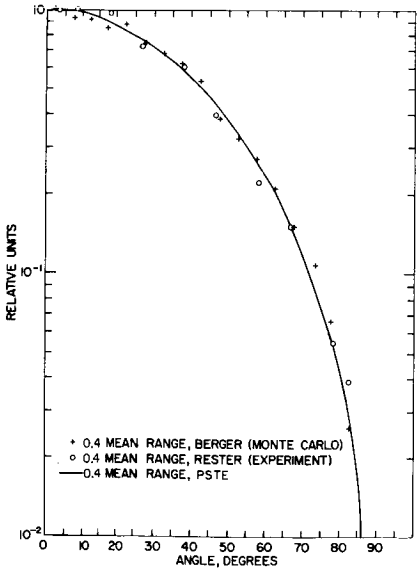

Figure 8 Comparison of the PSTE transmitted angular distribution with Monte Carlo and experimental results at approximately .4 mean range for a 1 MeV pulse of electrons normally incident on a semi-infinite slab of aluminum.

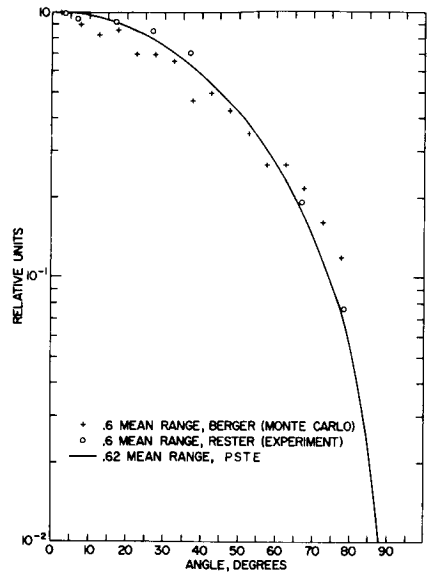

Figure 9 Comparison of the PSTE transmitted angular distribution with Monte Carlo and experimental results at approximately .6 mean range for a 1 MeV pulse of electrons normally incident on a semi-infinite slab of aluminum.

The angular distribution of transmitted electrons produced by the PSTE calculation has also been compared to Monte Carlo and experimental results. The angular distribution $T_N(X,\mu_X)$ is defined by

$$T_N(X,\mu_X) = \frac{1}{\Delta E \Delta \mu_X} \int_0^{E_i} \int_0^{t} J(X,E,\mu_X,t')dt'dE \qquad (15)$$

where $0 \leq \mu_X \leq 1$. The shapes of the angular distribution curves for the same three penetrations used in the energy spectrum investigation are compared in Figures 7 - 9. Again the curves are drawn on a scale relative to the maximum of each distribution for the same reasons outlined in the discussion of the energy spectrum. The results used for comparison are Monte Carlo calculations made by Berger and experiments conducted by Rester, the data for both being taken from publications authored by Rester [13,15]. In general there is acceptable agreement between the PSTE results and the Monte Carlo and experimental points. For all three penetrations the PSTE curve agrees very well with the experimental values. The largest discrepancy between the PSTE and Monte Carlo results occurs at the smallest and largest penetrations considered. Interestingly the greatest difference between the Monte Carlo and experimental values also occurs at these depths.

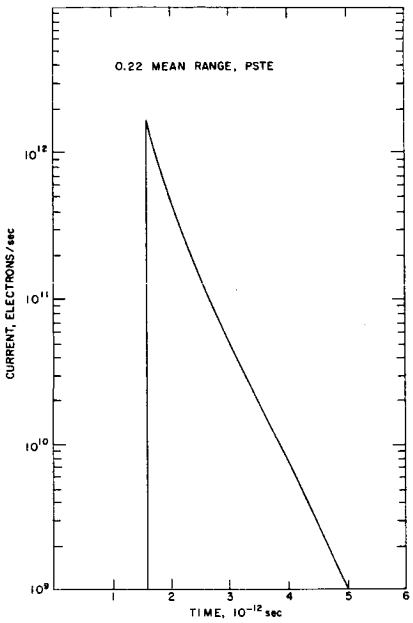

Figure 10 Transmitted current at 0.22 mean range for a 1 MeV pulse of electrons normally incident on a semi-infinite slab of aluminum resulting in an incident current of about 3.2×10^{12} electrons per second.

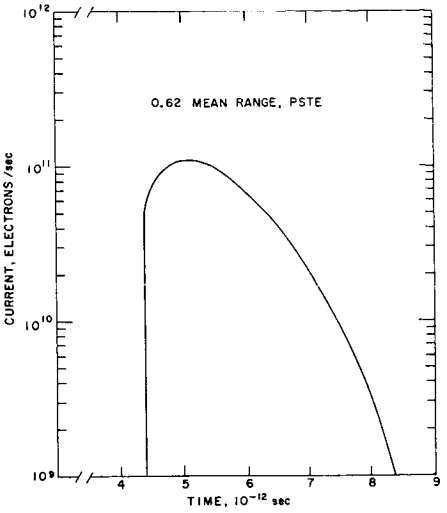

Figure 12 Transmitted current at 0.62 mean range for a 1 MeV pulse of electrons normally incident on a semi-infinite slab of aluminum resulting in an incident current of about 3.2×10^{12} electrons per second.

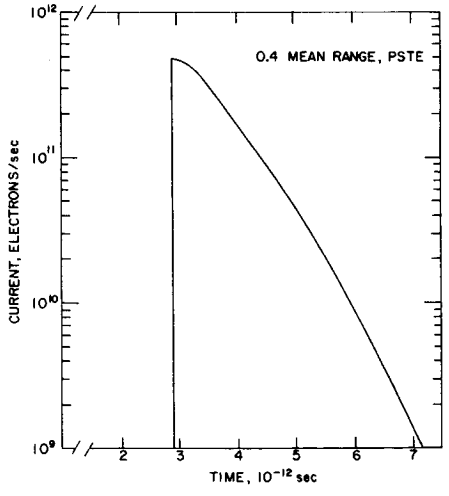

Figure 11 Transmitted current at 0.4 mean range for a 1 MeV pulse of electrons normally incident on a semi-infinite slab of aluminum resulting in an incident current of about 3.2×10^{12} electrons per second.

Time Dependent Results

One of the more significant contributions of the PSTE method is the time dependent results it provides. In Figures 10 - 12 plots of the time dependent transmitted current $J_{x_+}(X,t)$ given by

$$J_{x_+}(X,t) = \frac{1}{\Delta E \Delta \mu_x} \int_0^{E_i} \int_0^1 J(X,E,\mu_x,t) d\mu_x dE \qquad (16)$$

for the problem in question are presented. The penetrations considered are the same as those examined for the energy spectrum and angular distribution. At the small penetration (.22 mean range) the transmitted current reaches a maxmum very quickly and then decreases rapidly with time. The intermediate penetration (.4 mean range) results exhibit much of the same behavior but the current drops off at a slower rate as time increases. At the largest penetration (.62 mean range) there is a more gradual build-up to the maximum transmitted current achieved and a less rapid decrease with time than at the other penetrations. This is probably because at this depth the electrons are diffusing through medium and are characterized by relatively broad energy spectra and angular distributions.

Another way of looking at the time dependent results provided by the PSTE method is illustrated in Figure 13. Here the current as a function of position with time as a parameter has been traced by the computer. The time interval between plotted iterations is approximately 3.2×10^{-13} seconds. Essentially this figure represents a picture of the time evolution of the transmitted current in the aluminum slab. At first the current builds up rapidly and declines rapidly as the electrons enter the medium. There is also a significant reduction in the maximum transmitted current from one iteration to the other. At larger penetrations or at a later time, however, the curves representing the distribution of the transmitted current as a function of penetration become broader. This is understandable due to the fact that at later points in time the electrons are diffusing through the medium and have broad energy spectra and angular distributions. This parallels the reasoning used to describe the shape of the transmitted current curve as a function of time at the largest penetration examined (.62 mean range, Figure 12).

Advantages of the PSTE Method

One of the most attractive features of the PSTE method is the comparatively small amount of computer time it requires. For example, the PSTE calculations discussed in this paper required approximately ten minutes of computer time on the CDC 6600 computer at the Brookhaven National Laboratory. This compares to a Monte Carlo calculation for the same problem which requires on the order of an hour or more of computer time.

Another advantage of the PSTE method is that it provides deterministic results. This can be contrasted to the results of a Monte Carlo calculation which have a statiscal uncertainty associated with them dependent on the number of histories sampled.

Finally, the PSTE method generates a complete record of the time evolution of a particle density distribution. As stated previously, the authors are unaware of any successful Monte Carlo attempts at providing time dependent results for charged particle problems. It is the authors' opinion that the PSTE method is ideally suited for this application.

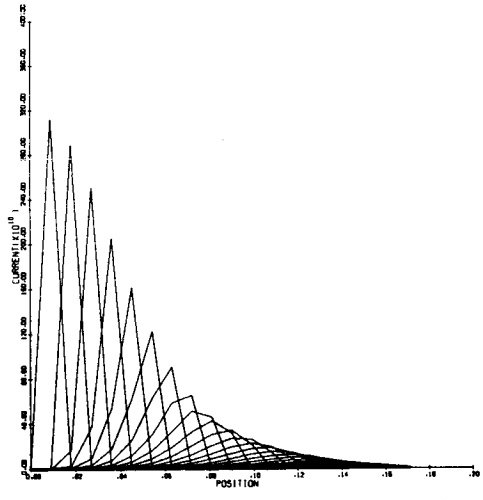

Figure 13 Time evolution of transmitted current for a 1 MeV pulse of electrons normally incident on a semi-infinite slab of aluminum resulting in an incident current of about 3.2×10^{12} electrons per second.

Acknowledgement

The material presented in this paper represents part of a thesis submitted by M. C. Cordaro in partial fulfillment of the requirements for the degree of Doctor of Philosophy at the Cooper Union. The authors wish to express their appreciation to Dr. Richard Felder for supplying a computer program to evaluate the Goudsmit-Saunderson distribution.

References

1. Tavel, M. A. and Zucker, M. S., "A Method of Solving Time-Dependent Transport Problems," Trans. Amer. Nucl. Soc. 10, 213 (1967).

2. Tavel, M. A. and Zucker, M. S., "Improvements on a New Method for Time-Dependent Neutron Problems," Trans. Amer. Nucl. Soc. 11, 557 (1968).

3. Tavel, M. A. and Zucker, M. S., "Some Quantitative Results and New Application of the Phase-Space Time Evolution Method," Trans. Amer. Nucl. Soc. 12, 158 (1969).

4. Tavel, M. A. and Zucker, M. S., "The Phase Space Time Evolution Method," Transport Theory and Statistical Physics 1, (in press).

5. Rohrlich, F. and Carlson, B. C., "Positron - Electron Differences in Energy Loss and Multiple Scattering," Phys. Rev. 93, 38 (1954).

6. Fitzgerald, J. J., Brownell, G. L., and Mahoney, F. J., Mathematical Theory of Radiation Dosimetry, Gorden and Breach, New York, 1967.

7. Goudsmit, S. and Saunderson, J. L., "Multiple Scattering of Electrons," Phys. Rev. 58, 36, (1950).

8. Goudsmit, S. and Saunderson, J. L., "Multiple Scattering of Electrons, II," Phys. Rev. 58, 36 (1940).

9. Berger, M. J., Transmission and Reflection of Electrons by Aluminum Foils, NBS Tech. Note 187, National Bureau of Standards, 1963.

10. Berger, M. J. and Seltzer, S. M., "Results of Some Recent Transport Calculations for Electrons and Bremsstrahlung," p. 437, NASA SP-71, National Aeronautics and Space Administration, 1964.

11. Berger, M. J. and Seltzer, S. M., Transmission of 1-MeV Electrons Through Aluminum, NBS 8900, National Bureau of Standards, 1965.

12. Perkins, J. F., "Monte Carlo Calculation of Transport of Fast Electrons," Phys. Rev. 126, 1781 (1962).

13. Rester, D. H. and Dance, W. E., Electron Scattering and Bremsstrahlung Measurements, NASA CR-759, National Aeornautics and Space Administration, 1967.

14. Agu, N. C., Burdett T., and Matsukawa, E., "Transmission of Electrons through Aluminum Foils," Proc. Soc. London 71, 201 (1958).

15. Rester, D. H. and Rainwater, W. J., "Coulomb Scattering of Electrons in Aluminum Without Atomic Excitation," Phys. Rev. 140, A165 (1956).

16. Cordaro, M. C. and Zucker, M. S., "A Method for Solving Time-Dependent Electron Transport Problems" Trans. Amer. Nucl. Soc. 13, 630 (1970).

17. Tavel, M. A. and Zucker, M. S., "The Phase Space Time Evolution Method, etc.," Trans. Amer. Nucl. Soc. 13, 695 (1970).

PARAMETRIC FIT TO ELECTRON TRANSPORT PROPERTIES *

J. A. Lonergan and D. C. Shreve

Science Applications, Incorporated
La Jolla, California

Empirical formulations of electron transport properties are presented. Experimental data acquired by several groups over the past few years have been gathered and organized. Parametric fits have been made to these data so that the following properties of electron transport can be represented by simple functions of atomic number and energy: transmitted electron number, transmitted electron spectra, range, backscatter coefficient, angular distribution, energy deposition, bremsstrahlung intensity and energy spectra, bremsstrahlung angular distribution and photon attenuation. Though most of the data used to derive the parametric formulas were measured in experiments, some uses have been made of results generated using well-developed Monte Carlo techniques. The formulas cover the energy ranges of interest in space shielding problems (0.1 - 10.0 MeV). These formulas were developed so they could be included in an engineering handbook addressed at the problems of electron radiation in space and its effects. The intent is to provide a simple means of calculating the radiation expected aboard a spacecraft, both on its external surface and behind arbitrary amounts of effective shielding. To satisfy the requirement that the formulas be simple, mathematical rigor based on physical interaction was replaced by convenient fits to thick target data. The formulas are as accurate as these data in most cases and can be easily evaluated without a computer. Procedures for using these formulas in practical situations are suggested.

I. INTRODUCTION

In practical problems in which it is necessary to make a quick determination of the radiation dose delivered to a point partially shielded from a radiation source, it is very useful to have an inexpensive means of obtaining reasonably accurate results. In particular, in the space environment it is often necessary to establish the dose level due to both electrons and the associated secondary photons at points inside a spacecraft. Just as frequently the initial estimate becomes the burden of an engineer or scientist whose professional interest is related to the item being placed at the point of interest and who may have only a passing familiarity with the properties of electron transport and bremsstrahlung production. Simple

* Work sponsored by National Aeronautics and Space Administration.

methods of calculating electron transport properties and bremsstrahlung production are presented in this paper. Parametric representations of both calculated and measured data are presented.

The basic guideline imposed in finding these parametric formulas is simplicity. Many comprehensive discussions of the details of electron transport exist; in particular the work of Zerby and Keller,[1] and the earlier work of Birkhoff[2] summarize the physics and some of the mathematics that describe these phenomena. However, for the purpose stated above, these works are too detailed and demanding if a dose level is the only goal of the investigation. As a means of implementing the simplicity guideline, we have made parametric fits to shielding data. For example, to fit the bremsstrahlung production property we have sought data which correlate photon output directly to the incident electron. The processes of electrons slowing down, range straggling, backscattering and photon production, and to some extent self-shielding, are gathered into one process. That is, given an electron of a certain energy, what is the probability of observing a photon of another energy at some point around a thick piece of material ? By just fitting the thick target bremsstrahlung data all the mathematical complications inherent in a rigorous analysis incorporating all the intermediate processes are avoided. With this approach we have obtained fits either from the literature of through our own efforts for a number of properties of interest.

II. ELECTRON TRANSPORT

In the following section, formulas which describe the property specified are displayed. As pointed out in the introduction, many of these formulas are the result of the efforts of other workers. We have selected these that are presented because they best represent the experimental data we have been able to compre them with.

1. Range

There are essentially two commonly used definitions of ranges, one is the extrapolated range, the other is the continuous slowing down approximation (csda) range. The extrapolated range is more easily determined from experimental data. The following expression is due essentially to Katz and Penfold[3] with some modifications by Ebert et al.,[4]

$$R_{ex}(E,Z) = 0.565\left(\frac{125}{Z+112}\right)E - 0.423\left(\frac{175}{Z+162}\right) \qquad E > 2.5\ \text{MeV} \tag{1}$$

$$= 0.38\,E^{A}\ \text{g/cm}^2 \qquad E < 2.5\ \text{MeV}$$

where

$$A = (1.265 - 0.095\ \ell n\, E)(1.7 - .273\ \ell n\, Z)$$

Here E is the electron energy in MeV and Z is the atomic number.

The continuous slowing down approximation range is more easily calculated than is the extrapolated range and has come into rather wide use because of the very convenient tabulation of this quantity by Berger and Seltzer.[5] From the data of Ebert et al.[4] and this tabulation, we have derived the following relationship between the extrapolated and csda ranges

$$(R_{ex}/R_o) = 1.21 - 0.208\ \ell n\, Z + 0.485E \tag{2}$$

2. Transmitted Number Fraction

The number of electrons penetrating to a given depth within a material is defined as the transmitted number fraction. Ebert et al.[4] have measured this quantity and have suggested the following parametric representation

$$T(E,Z) = \exp - a\left(\frac{t}{R_{ex}}\right)^{\beta} \tag{3}$$

$$a = (1 - 1/\beta)^{1-\beta}$$

$$\beta = \left[\frac{387E}{Z\,(1 + 7.5 \times 10^{-5}\, Z\, E^2)}\right]^{1/4}$$

the quantity, t, is the penetration depth in the same units as the extrapolated range.

3. Transmitted Energy Spectra

The energy spectra of electrons penetrating to a depth (t/R_o), that is, to some fraction of the continuous slowing down range, has been fit. The experimental data measured by Lonergan et al., [6] Costello et al. [7] and Rester et al. [8] were used as the base from which the following parametric representation was derived:

$$S(E, t, Z) = \left\{\exp[-(E - E_p)^2 / W^2] + \right. \qquad (4)$$
$$\left. + CE[1 + \exp((E - E_p)/W)]^{-1}\right\} N^{-1}$$

where

$$N = W\sqrt{\pi} + 1/2C\, W^2$$

$$W = 0.05\sqrt{Z}\,(t/R_o)$$

$$C = (t/R_o)^2\sqrt{Z}$$

4. Backscatter Coefficient

The backscatter coefficient is defined as the fraction of electrons incident on an infinitely thick target which are scattered in the backward direction. The following expression was derived by Tabata [9] from data he measured and is valid for $Z > 6$.

$$\eta(E, Z) = 1.28 \exp\left[-11.9\, Z^{0.65}\, x\right. \qquad (5)$$
$$\left. x\,(1 + 0.103\, Z^{0.37}\, E_o^{0.65})\right]$$

5. Angular Distribution

The angular distribution of electrons penetrating a slab after striking the slab normally has been fit in two regions. If the slab thickness is less than approximately 1/3 the extrapolated range, a gaussian distribution fits the data reasonably well:

$$\phi(E, Z) = \frac{\sqrt{\pi}}{K} \exp(-K^2\theta^2) \qquad (6)$$

where

$$K^2 = E^2 / [0.121\, t\, Z^{0.88}\, \ell n\,(t/0.00105)]$$

However, if the slab is thicker than 1/3 the extrapolated range, the distribution merges into a thickness-independent form given by

$$\phi = (0.717 + \cos\theta)\cos\theta \qquad (7)$$

where θ refers to the polar angle relative to the normal to the plane from which the electrons are emerging. It is important to note that θ is not referenced to the incident electron direction. Experimental data [7, 8] indicated that for thick targets $(t/R_{ex} > 1/3)$ the angular distribution is independent of the incident electron direction.

6. Energy Deposition

The energy deposited by electrons as they penetrate a material has been calculated for a number of cases at the Marshall Space Flight Center (MSFC). ETRAN, [10] a Monte Carlo electron transport code developed by Berger and Seltzer at NBS, was used to make these calculations. Watts and Burrell [11] of the MSFC have made parametric fits to these results for two cases. The first is for a normally incident monodirectional beam, and is given by

$$\rho_{\perp}(E, X) = \exp\left(\sum_{c=1}^{4} A_i\, X^{i-1}\right) \qquad (8)$$

where

$$A_1 = 0.913 \exp(0.963\, E) + 0.021\, E + 0.215$$
$$A_2 = 5.0 - 0.49\, E$$
$$A_3 = 57.6\,(E - 5.0) / (E + 30)$$
$$A_4 = -1.6\, E^{0.837}$$

The second case is for an isotropic incident beam,

$$\rho_{iso}(E, X) = \exp\left(\sum_{1}^{5} A_i\, X^{i-1}\right) \qquad (9)$$

where

$$A_1 = 0.52 + 0.098\,E^{-1.47}$$

$$A_2 = \exp(-0.82\,E) - 1.0$$

$$A_3 = 2.5\,[\exp(-1.022\,E) + 1.0]$$

$$A_4 = 3.25\exp(-0.323\,E) + 5.8$$

$$A_5 = -15.44 + 1.55\,E - 0.0786\,E^2$$

where X is the depth of penetration.

III. PARAMETERIZATION OF THICK TARGET BREMSSTRAHLUNG DATA

When electrons slow down, they emit bremsstrahlung radiation. In applications where the electrons are stopped, this bremsstrahlung is the only radiation which penetrates through the material, and hence is important in many space applications.

The calculation of the bremsstrahlung produced in thick targets using first principles is rather complicated due to the energy loss, straggling and angular spread of the incident electrons as they penetrate through the material. Typically, rather large computer codes which either treat the problem using Monte Carlo methods[10] or by subdividing the target into many thin sections[12] are used to calculate the bremsstrahlung intensity. These calculations are quite accurate but require considerable knowledge on the part of the person running the code and also a considerable amount of computer time.

The purpose of the present effort is to provide a fairly simple analytical expression for the bremsstrahlung radiation by parametizing the available thick target bremsstrahlung data. In the past these data have been used mainly to check the accuracy of the computer codes. We will use the data itself to try to go directly to the types of expressions that will be useful to people working in the field of space physics

1. Method of Parameterization

a) Approximation for Intensity Spectrum

Most of the thick target bremsstrahlung data have been obtained with the electron beam normally incident on the target,[6, 8, 13] and we will mainly be concerned with fitting these data. Electrons encountered in space shielding situations, however, typically do not all impinge normally on the surface of the spacecraft, so one must know the bremsstrahlung dependence on the angle of incidence of the electrons. There is a limited amount of thick target bremsstrahlung data available for electrons with non-normal incidence.[14] Examples of these data are shown in Fig. 1. Here the integrated, and partially integrated intensities for 1 and 2 MeV electrons are plotted vs. the angle between the emitted radiation and the electron beam. It is fairly obvious from these data that the γ intensity is a maximum in the direction of the incident electrons. For the Al data, it is obvious that there is some symmetry about the beam direction. We will assume that the bremsstrahlung radiation can be written as a function which is symmetric about the electron direction multiplied by an attenuation factor to account for absorption in the target

$$I(E, K, \theta, \psi) = I^{o}(\theta, K, E)\ x \qquad (10)$$

$$x \begin{cases} e^{-\mu(t - FR\cos\psi)/\cos(\psi-\theta)} : (\psi-\theta) < \pi/2 \\ e^{-\mu FR\cos\psi / \left|\cos(\psi-\theta)\right|} : (\psi-\theta) > \pi/2 \end{cases}$$

where the different attenuation factors correspond to forward going and backscattered radiation. In this equation, E is the energy of the electron, K is the energy of the photon, θ is the angle of the γ ray with respect to the beam direction, ψ is the angle between the beam direction and the normal to the target, t is the target thickness, μ is the mass absorption coefficient for the material, and FR is some fraction of the csda electron range.

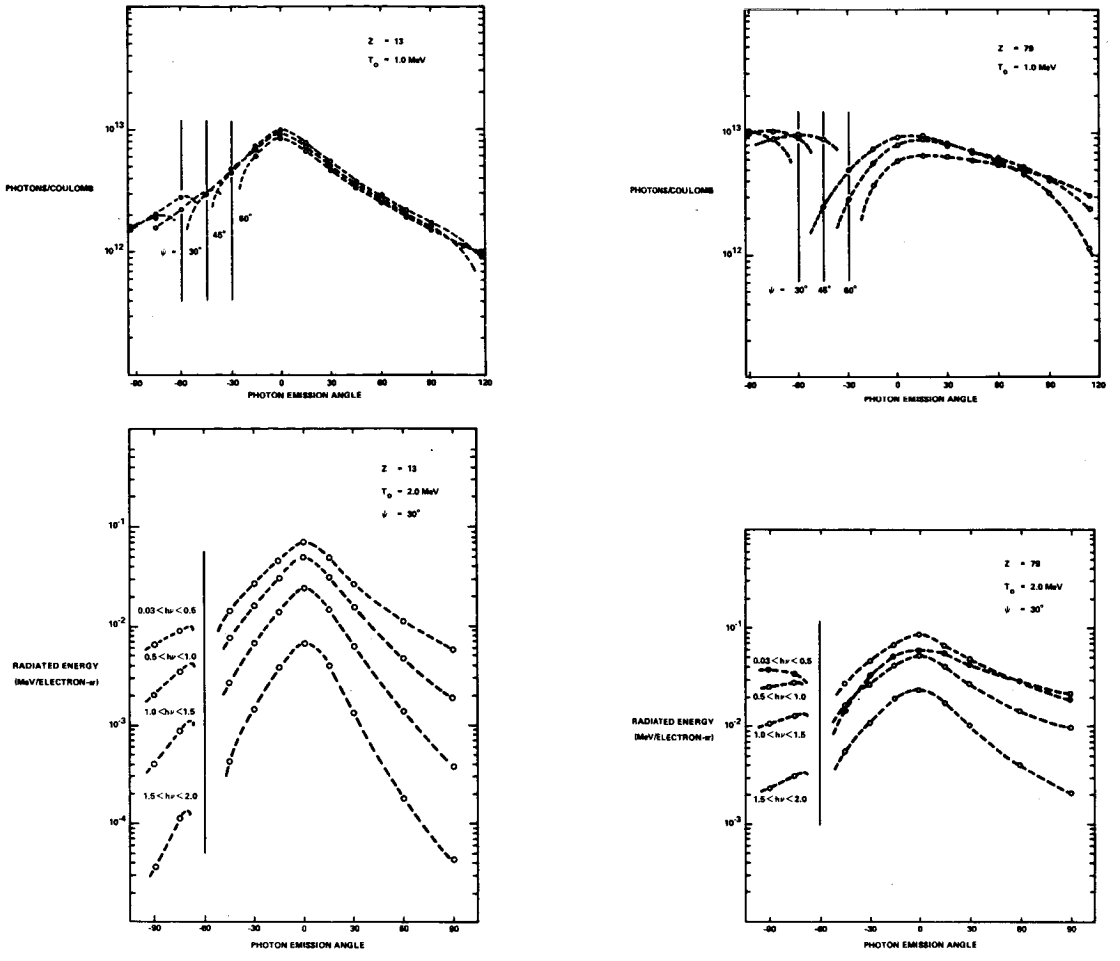

Fig. 1. Angular dependence of bremsstrahlung radiation for 1 and 2 MeV electrons incident at 30^{o} to the normal of thick Al and Au targets.

The function $I^{o}(\theta, K, E)$ which was obtained from the data shown in the previous figure, is shown in Fig. 2. A value of $F = 0.3$ was used to make the curves symmetric. The curves through the points in these figures are symmetric about 0^{o} which shows that the assumption of a source term symmetric about the direction of the electrons seems to be justified, except for the low energy Au data with the γ ray emerging at angles almost parallel to the target.

2. Fits to Individual Bremsstrahlung Spectra

The energy intensity spectra of photons emitted from a thick target at an angle θ with respect to the beam were fit by the method of least squares with a 3 parameter function of the form

$$I^{o}(E, K, \theta) = A(E, \theta) e^{-K/\left(E\, B(E,\theta)\right)_{x}} \quad (11)$$

$$x\,(1 - K/E)^{C(E,\theta)}$$

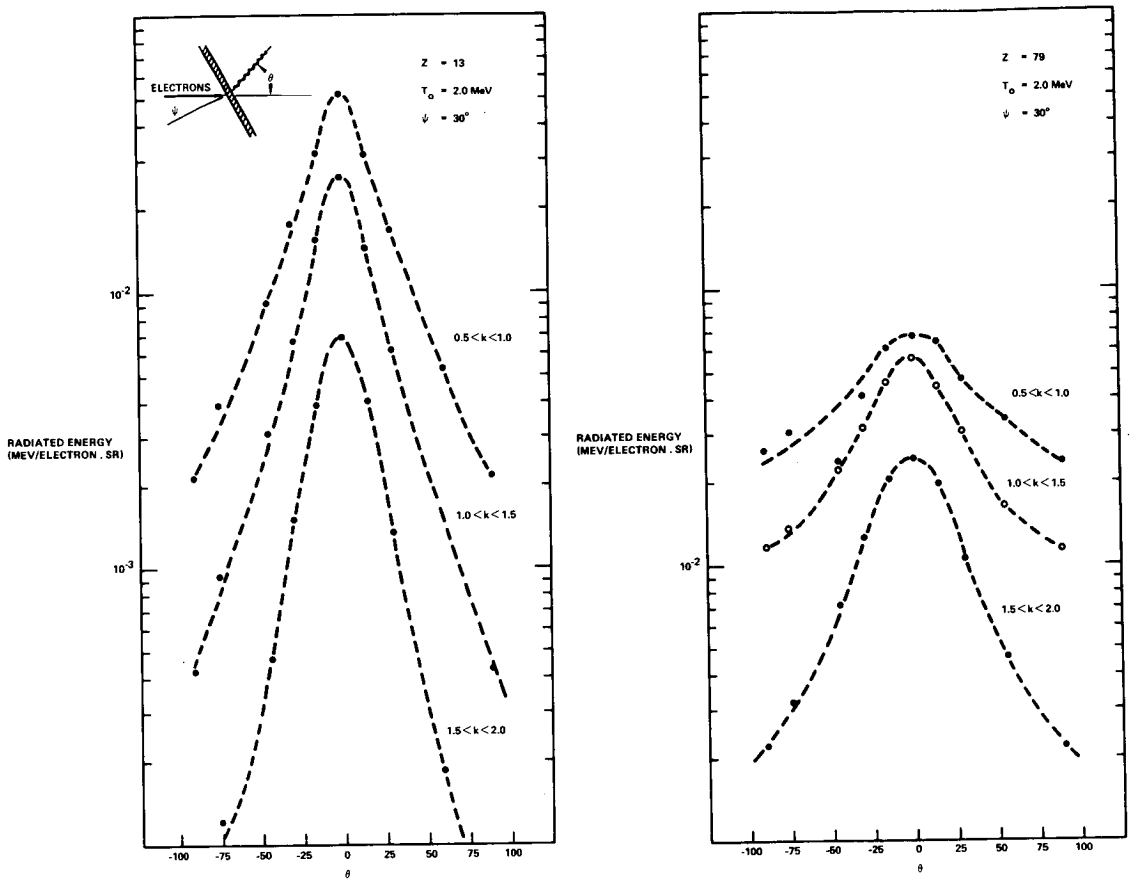

Fig. 2. Angular dependence of assumed bremsstrahlung "source" term for 2 MeV electrons incident at 30^{o} to the normal of thick Al and Au targets.

where the parameters $A(E,\theta)$, $B(E,\theta)$ and $C(E,\theta)$ were adjusted to give a best fit for each individual spectrum. This functional form was chosen because the bremsstrahlung intensity for the elements and energies considered appear to be exponentially decreasing over much of the photon energy range and falling off faster than exponential near the end point. Samples of the fits to the LTV bremsstrahlung data[8] obtained using this 3 parameter function are shown in Fig. 3. It can be seen that the fits are all reasonable; with individual points differing from the fit by less than 10%.

The parameters $A(E,\theta)$, $B(E,\theta)$ and $C(E,\theta)$ were examined as functions of the photon angle and parameterized as

$$
\begin{aligned}
A(E,\theta) &= a(E)\, e^{-(\theta/\psi_0(E))^2} + \\
&\quad + b(E) \exp\left[2\, e^{-(\theta/\psi_1(E))^2}\right] \\
B(E,\theta) &= c(E)\, e^{-(\theta/\psi_2(E))} + \\
&\quad + d(E)\, e^{\left[-(\theta/\psi_3(E))^2\right]} \\
C(E,\theta) &= 1 - (.7 - .5\, e^{-(E/E_0)^2})\, e^{-(\theta/\theta_0)^2}
\end{aligned}
\tag{12}
$$

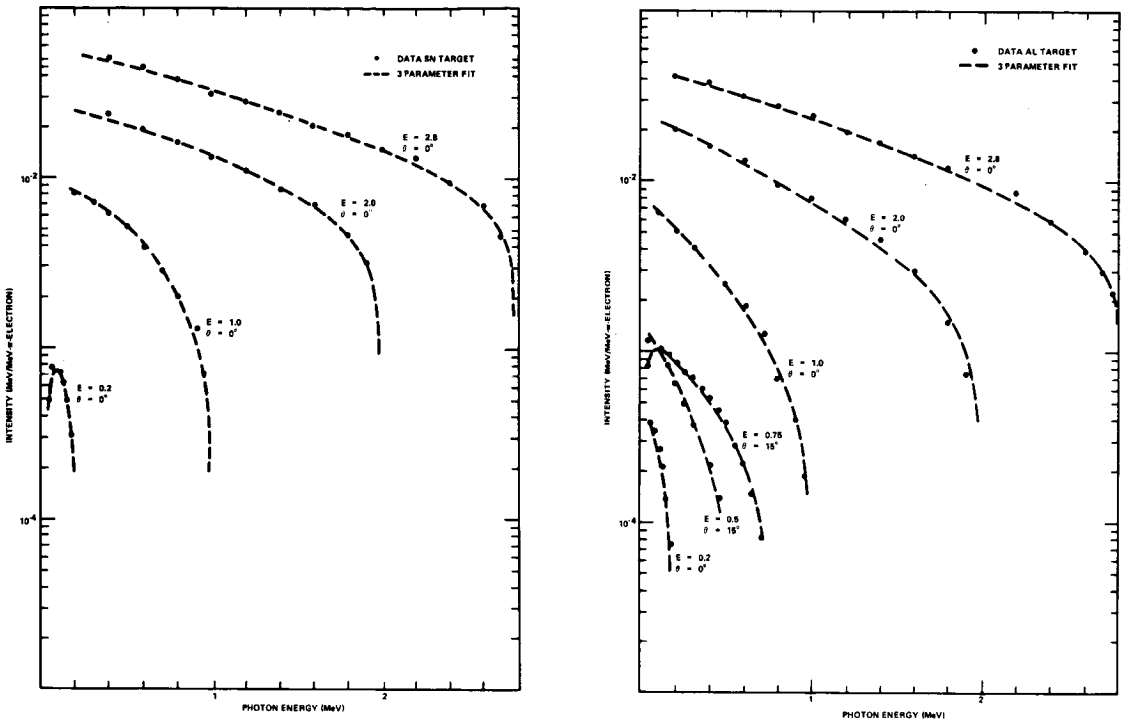

Fig. 3. Sample 3 parameter fits to thick target bremsstrahlung data on Al and Sn at .2, 1, 3, and 2.8 MeV at 0^{o}. The functional form of the curve is $F = Ae^{-K/BE}(1 - K/E)^{C}$, where A, B, and C are parameters, K is the photon energy, and E is the electron energy.

The entire distributions over both photon energy and angle were fit using the above 12 parameter function; however, only the first 8 parameters were varied for the fit.

We have at present parameterized the photon energy and angular distributions for 0.5, 0.75, 1, 2, and 2.8 MeV electrons incident on Al targets and 1, 2, 2.8, 4, and 8 MeV electrons incident on Sn targets. Samples of the fits to the photon energy and angular distributions are shown in Fig. 4. Again the fits are reasonable; with the maximum deviations of the data from the calculated curves being about 15%. It should be mentioned that the accuracy ascribed to the data by its authors is about 10% over most of the range, and 20 - 30% at the end points, so it would seem that the fits are quite adequate.

The next step in the parameterization process is to represent the 8 functions a(E), b(E), c(E), d(E), $\psi_0(E)$, $\psi_1(E)$, $\psi_2(E)$, and $\psi_3(E)$ as functions of energy for each element. Data are only available at a few values of (E), however, and the values of the 8 parameters obtained so far do not seem to follow any simple (eg. linear or exponential) pattern. The values of the parameters are given for Al and Sn in Table 1. We will generate more data at intermediate energies using the Monte Carlo calculation ETRAN-15. With this additional data we should be able to parameterize the bremsstrahlung intensity with respect to angle, photon energy and incident electron energy.

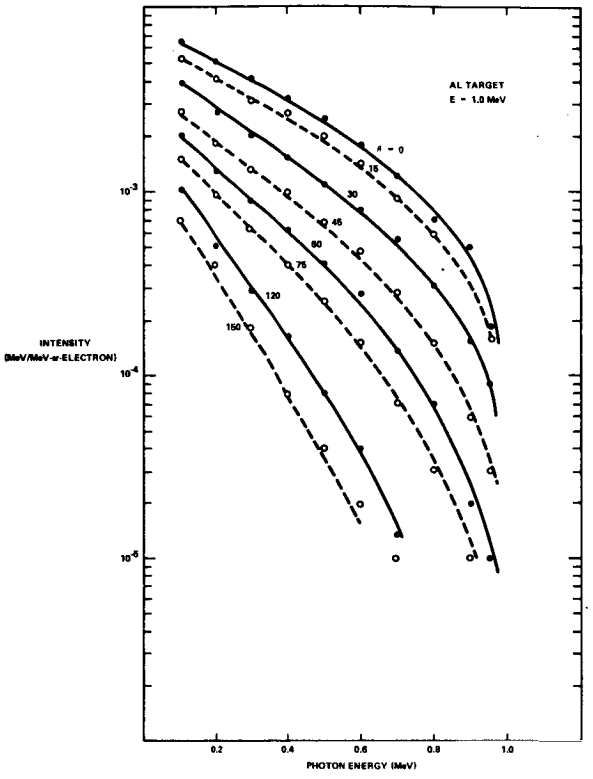

Fig. 4. Sample 8 parameter fits to photon energy and angular distribution for 1 MeV electrons on Al.

Table 1. Table of Parameters for Al and Sn Normal Electron Incidence

E (MeV)	a x10^{+3}	ψ_0 (deg)	b x10^{3}	ψ_1 (deg)	c	ψ_2 (deg)	d	ψ_3 (deg)
			Al					
0.5	0.50	35.	0.17	250.	0.70	120	0.10	60
1.0	4.86	30.7	0.48	223.	0.50	120	0.088	56
2.0	14.0	18.1	1.93	85.4	0.40	140	0.075	25
2.8	23.5	10.4	4.30	57.4	0.44	100	0.093	22
			Sn					
1.0	4.10	26.3	1.26	360.	0.53	350	0.40	66
2.0	19.2	26.3	2.43	320.	0.43	310	0.27	60
2.8	27.6	14.7	6.74	118.	0.44	230	0.12	24
4.0	63.7	12.7	7.96	136.	0.44	350	0.39	29
8.0	274.0	6.5	14.3	92.4	0.38	350	0.59	34

3. Integration Over Electron Flux

Because of the interest in space shielding calculations, we have obtained energy and angular distributions for isotropic electron fluxes. Figure 5 shows the angular distributions obtained for an isotropic 1 MeV electron source incident on unit areas of Al and Sn targets whose thicknesses are the range of 1 MeV electrons. These angular distributions are somewhat simpler than the angular distributions produced by normally incident electrons.

As was mentioned earlier, the basic bremsstrahlung data have been fit using a source term and a simple attenuation factor. If one integrates only the source term $I_o(E, K, \theta)$, one obtains angular distributions as shown in Fig. 6. These angular distributions are quite regular and can be fit with a function of the form

$$I^{o}_{iso}(\theta_\gamma, E, K) = \exp\left[A_{iso} + B_{iso} \cos\theta + C_{iso} \cos(2\theta) \right] \quad (13)$$

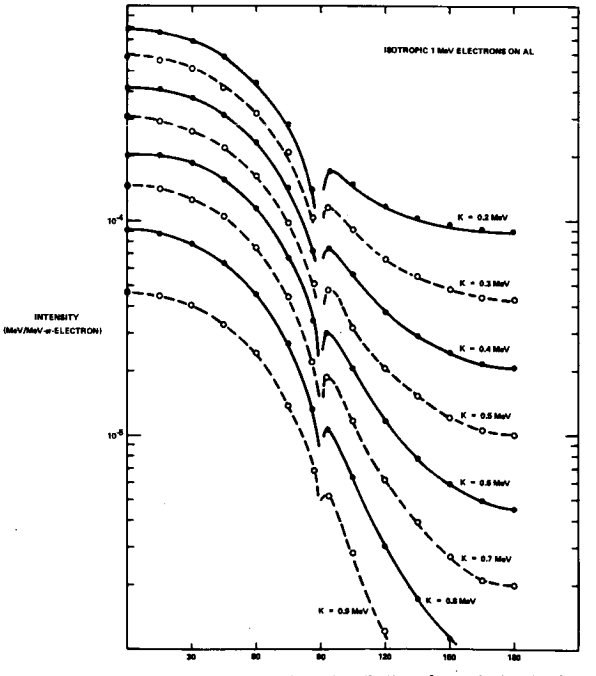

Fig. 5. Photon angular distributions for an isotropic electron source of 1 MeV electrons on one side of an Al target.

The curves through the points in Fig. 6 correspond to fits using this functional form. The functions $A_{iso}(E,K)$, $B_{iso}(E,K)$, and $C_{iso}(E,K)$ are smoothly varying functions of both K and E, but as yet, have not been fit. The values of A(E, K) for electrons on Sn are shown in Fig. 7.

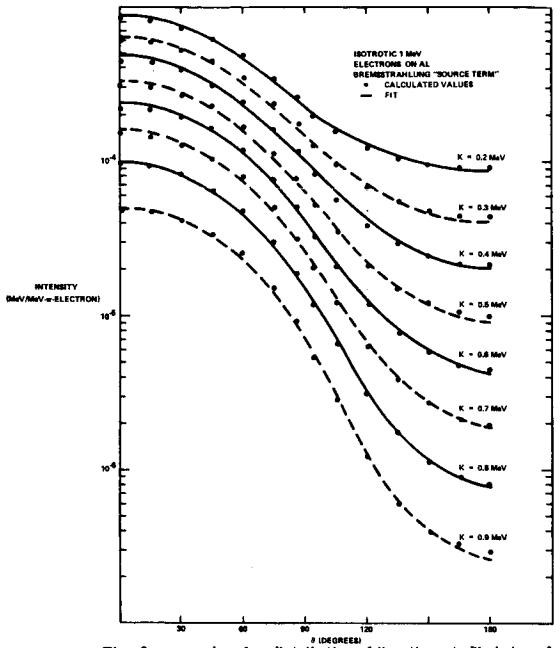

Fig. 6. Angular distribution of "unattenuated" photons for an isotropic source of 1 MeV electrons on one side of an Al target. The solid curves are least square fits using a functional form $I^{o}_{iso}(\theta, K, E,) = \exp\left[A + B\cos\theta + C\cos(2\theta)\right.$.

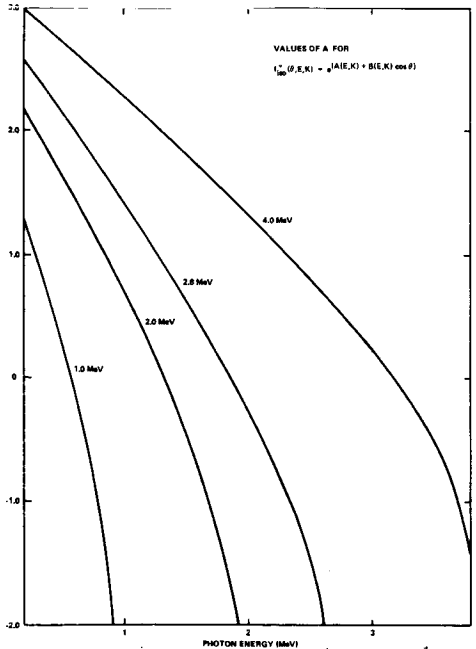

Fig. 7. Energy dependence of the parameter A used in fitting the angular distributions for the unattenuated term for an isotropic electron source on Sn at various electron energies.

4. Summary of Parametric Fits to Bremsstrahlung Data

We have obtained a parameterization of the bremsstrahlung radiation for electrons normally incident on thick targets of Al and Sn for electron energies ranging from 0.5 to 2.8 MeV for Al and 1 to 8 MeV for Sn. These bremsstrahlung distributions have been integrated over the angles of the electron incidence to obtain the photon angular distributions for isotropic electron sources. The parameterization of the radiation produced by isotropic electron sources is partially completed. These parameterizations will provide the engineer or scientist a fairly simple means of estimating the bremsstrahlung intensity inside a spacecraft for the various electron environments encountered in space.

IV. REFERENCES

1. C. D. Zerby and F. L. Keller, Nucl. Sci. Eng. 27, 190, (1967).

2. R. D. Birkhoff, Handbuch der Physik - Encyclopedia of Physics S. Flugge, ed. (Springer - Verlag, Berlin, 1958), Vol. 34.

3. L. Katz and A. S. Penfold, Rev. Mod. Phys. 24, 28, (1952).

4. P. J. Ebert, A. F. Lauzon and E. M. Lent, Lawrence Radiation Laboratory Report #UCRL-71462, December 1968.

5. M. J. Berger and S. M. Seltzer, National Aeronautics and Space Administration Report SP-3012, (1964).

6. J. A. Lonergan and C. P. Jupiter, Gulf General Atomic Report GA-8486 (Rev.), February 1968.

7. D. G. Costello, H. Weber, and J. A. Lonergan, Gulf General Atomic Report GA-9907, January 1970.

8. D. H. Rester and W. J. Rainwater, Jr., Ling-Temco-Vought Report #0-71000/8R-2, February 1968.

9. Tatsuo Tabata, Phys. Rev. 162, 336, (1967).

10. M. J. Berger and S. M. Seltzer, National Bureau of Standards Report #9837, (1968).

11. J. W. Watts and M. O. Burrell, Paper VIII - 3, National Symposium on Natural and Man-Made Radiation in Space, March 1971.

12. W. W. Scott, NASA-SP-169, (1968).

13. W. E. Dance et al., NASA-CR-58178, June 1964.

14. D. H. Rester, Ling-Temco-Vought Report #0-71100/9R-1, February 1969.

SESSION VIII.2.
NUCLEAR POWER SYSTEMS: RTG RADIATION ENVIRONMENTS
CHAIRMAN: A.C. WILBUR
AMES RESEARCH CENTER

DESIGN CONSIDERATIONS FOR COMBINED RADIATION EFFECTS FACILITIES FOR TWELVE-YEAR OUTER PLANET SPACECRAFT VOYAGES*

Charles G. Miller

Jet Propulsion Laboratory, California Institute of Technology
Pasadena, California

ABSTRACT

The design considerations influencing the choice and utility of environmental simulation methods and facilities are described, insofar as they relate to the new requirements imposed on outer planet spacecraft because of radiation environments to be expected. Possible means for duplicating the Radioisotope Thermoelectric Generator radiation environment, and for duplicating the effects of Trapped Radiation Belt environment are described, together with an assessment of radiation levels to be expected in the vicinity of an environmental testing chamber when in use.

INTRODUCTION

Spacecraft for outer-planet missions will depend on radioisotope thermo-electric generators for their electrical power, and on radioisotope heaters for compensatory thermal power. Since these will be fueled by Pu-238, the accompanying gamma and neutron radiation of the Pu-238 and of its daughter products will be interacting continually with the structure, systems and science experiments of the spacecraft during its many-year voyage. Superimposed on this slowly varying background will be solar wind impingements and short duration, but higher intensity radiation stresses--namely, proton and electron irradiation when passing through the earth's radiation belts, and when passing through Jupiter's radiation belts.

In order to predict the effect of all these radiation stresses on the spacecraft and on its components, design studies for necessary predictive simulation environment facilities and for procedures are underway at this Laboratory.

The conditions under which time-accelerated testing of the effects of chronic gamma, neutron and solar wind irradiation give meaningful results must be established. The mechanisms of damage-annealing processes for different materials must be understood in some detail, since such processes are generally time dependent and temperature dependent, both of which factors become altered in accelerated testing.

The spacecraft will pass through planetary radiation belts during its voyage, and the effect of the proton and electron irradiation will be superimposed on the on-going, chronic gamma and neutron radiation.

If there is significant alteration in the damage mechanisms in irradiated materials due to the simultaneous application of all the radiation stresses, the simulation facility should take this into account. It is practical to duplicate the complete gamma energy spectrum, the neutron energy spectrum, and the solar wind spectrum simultaneously on a specimen. It is not practical to add to this, in a cryogenic high vacuum, the very wide electron and proton spectra (1 to 100 MeV or more) that duplicate the complete radiation environment.

Such wide spectral ranges, extending to high energies, require typically linear electron accelerators and proton synchrocyclotrons. These machines do not lend themselves to combined environment testing, since they are located at separate, specialized facilities.

In order to include trapped radiation electron and proton effects in a simultaneous combined radiation effects facility, our design studies consider the validity of using lower energy electrons and protons as test fluxes. We then use an "equivalent damage" correlation for the effects to be expected from the wide range of electron and proton energies in trapped radiation belts.

The spacecraft under discussion for outer-planet trips will be designed to be usable for varying missions and purposes. The specific environments which the various outer-planet missions will encounter will have enough new features in common to justify a unified approach to the preparation of the testing facilities needed. The several different missions are depicted in Figure 1, where are shown a typical Jupiter fly-by, a Jupiter-Uranus-Neptune Mission called "JUN" and a Jupiter-Saturn-Pluto Mission called "JSP" trajectory. Each of these missions involves the use of radioisotope-thermo-electric generators for electric power; a very long (by present standards) mission-life with a corresponding high degree of reliability; and each is scheduled to pass by Jupiter, and to traverse the Jupiter trapped radiation belts.

Furthermore, most of the flights will be at a great distance from the sun with vanishingly small solar heat inputs, although the effects of the solar visible, vacuum ultraviolet, and solar wind inputs (from the early stage of the trajectory) on materials such as thermal control surfaces, will be inescapable.

All of the spacecraft in flight will be subjected to the environmental factors shown in Table I.

SIMULATION OF RADIOISOTOPE THERMO-ELECTRIC GENERATOR RADIATION

During the entire flight of the spacecraft, both gamma and neutrons are present from the on-board electric power supply: the radioisotope

*This paper presents the results of one phase of research carried out at the Jet Propulsion Laboratory, California Institute of Technology, under Contract No. NAS 7-100, sponsored by the National Aeroanutics and Space Administration.

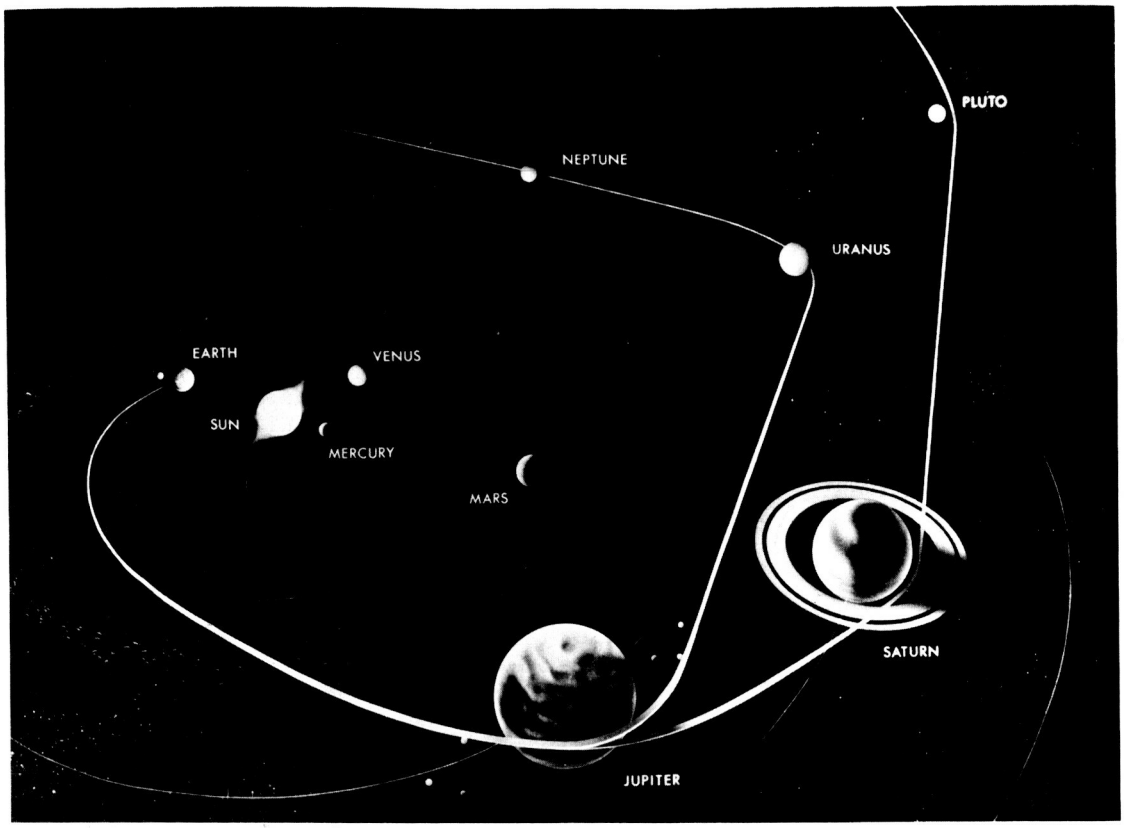

Figure 1. Typical Outer Planets Mission

Table I

Potential Combined Environment Factors
- From RTG Radiation
Gamma radiation Neutron radiation
- From Planetary Trapped Radiation Belts
High Energy Electron Flux High Energy Proton Flux
- Of Solar Origin
Visible, ultraviolet and soft X-ray
- From Conditions of Flight
Interplanetary Vacuum Space Temperature

thermo-electric generator. The effects due to the gammas and neutrons are manifested in two different ways--one effect is cumulative damage as the years go by, leading to a degradation in performance of radiation-sensitive components. The second effect is interference with operation of radiation-sensitive instruments, typically manifested as a rise in background rates of science detecting instruments.

In order to reproduce these effects, we need an accelerated source to deliver the cumulative dose to be expected in a many-year's life in a practical test time. Separately, we need a source to deliver the true rates for interference tests at the rates to be expected at various points in the trajectory.

The spectra of radiation needed for the cumulative damage studies, and for the science interference, are quite different, and are shown in Table II.

Table II

Requirements for Radiation Source Spectra		
Test	Neutron Source	Gamma Source
Cumulative Damage ($\sim 10^5$ rads)	Close Spectral Match	Spectral Insensitive
Science Interference (~100 mR/hr)	Testing not Required	Close Spectral Match

For cumulative Damage Studies, we need accelerated testing to predict the effect of the proposed 12-years' exposure, and have this testing completed in a reasonable time--well before launch. We must evaluate time-intensity reciprocity failure, which involves such factors as temperature anneal and, vacuum outgassing of protective oxygen on surface films. Such evaluations and tests are

being done in a facility described in another paper at this conference (Ref. 1). Such accelerated tests can be performed on parts and on subsystems, preferably by neutrons and gammas together.

Since the gamma damage is spectrum-insensitive, any convenient gamma source may be used, conveniently either Cobalt 60 isotope or an X-ray machine. A source in the range of 150 Ci Co-60, which constitutes 2 watts of Cobalt 60, will give cumulative damage tests in a few days' elapsed time.

An accelerated close spectral match neutron source poses a problem. The actual neutron spectrum from an RTG is an α, n spectrum of Pu-238 (alpha on impurities), peaking around 3 MeV neutrons. In examining some machine sources of neutrons, we note (Figure 2) that only the d-d reaction at low bombarding particle energy gives neutrons in the few-MeV range needed for spectral match. However, Figure 3 shows that the neutron yield is unsatisfactorily low at low bombardment energies. Another higher yield possibility, sometimes considered is the reaction d, Be. When examined in detail, however, Figure 4 shows that the d, Be reaction has much detailed structure which is unsatisfactory for interpretation of test work. Seemingly, the best material is a Cf-252 spontaneous fission source, whose spectrum is shown in Figure 5, together with the neutron spectrum of a radioisotope thermo-electric generator.

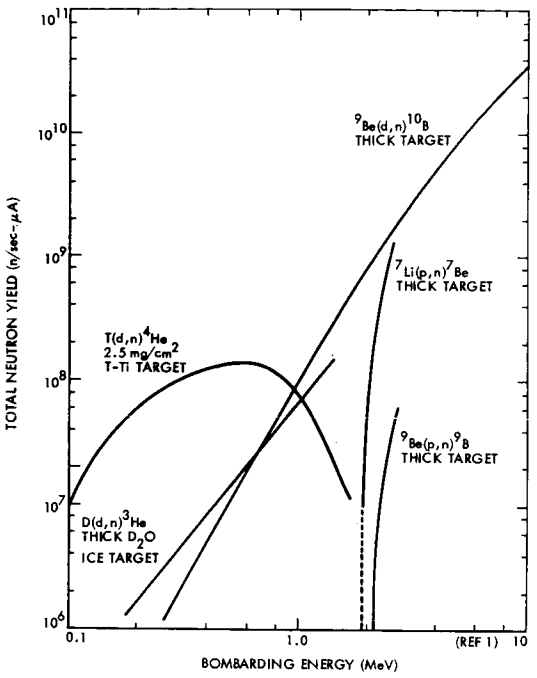

FIGURE 3 Total neutron yield per microampere of bombarding particle beam.

(From Ref. 3)

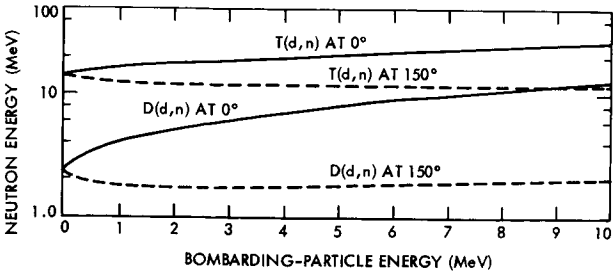

FIGURE 2 The neutron energies resulting from two accelerator produced neutron reactions vs. bombarding particle energy.

(From Ref. 3)

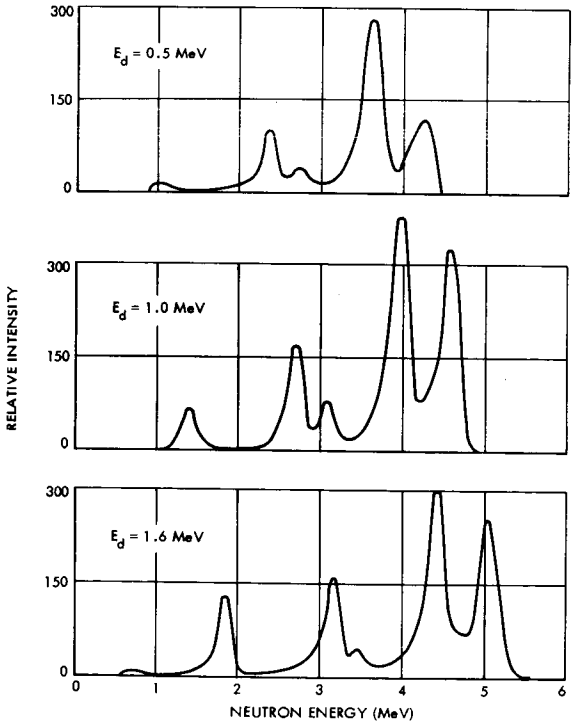

FIGURE 4 The neutron spectrum produced by deuteron bombardment of beryllium.

(From Ref. 3)

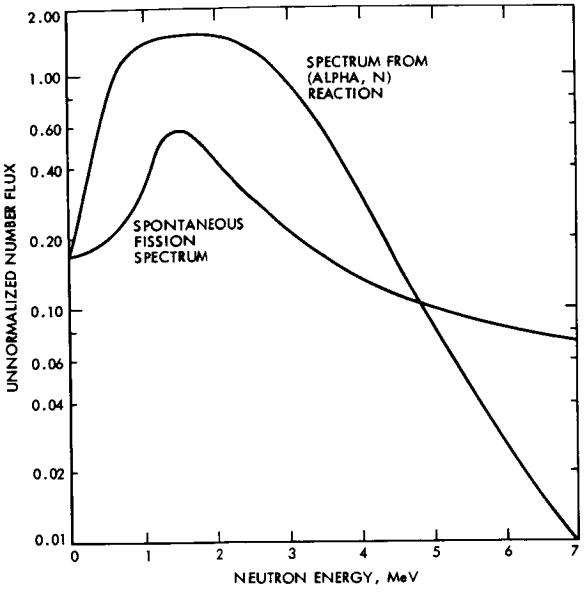

Figure 5. Comparison of Neutron Spectra

Since Cf-252 emits 2.5×10^6 spontaneous fission neutrons/second per microgram, a suitable source could consist of one milligram of this material, at a moderate cost gives 2.5×10^9 neutrons/sec (into 4π solid angle). Such a source could deliver about 2×10^5 neutrons/cm^2 sec to the surface of a 60 cm diameter sphere circumscribing the source, requiring about ten days' exposure for a mission-cumulative dose taken as 7×10^{11} neutrons/cm^2. If the requirement for depth-dose uniformity were relaxed, or the requirement were for testing small parts, a test could be conducted at the location given by a circumscribing 20 cm diameter sphere, where only one days' exposure would be required for the 7×10^{11} n/cm^2 dose.

Interference

For science interference, the neutron flux of about 200 neutrons/cm^2-sec at the science platform does not give rise to any interference. The close spectral match gamma source needed, as referred to in Table II, is available, as described in another paper at this conference (Ref. 2). This close spectral match gamma source is a combination of gamma-emitting isotopes in a form that is convenient and safe to handle. The actual source can deliver up to 100 mR/hr and requires less than a curie of isotope total. This can be handled safely in a test cryogenic vacuum and solar radiation chamber.

PLANETARY TRAPPED RADIATION BELT SIMULATION

We are here interested in sources of electrons that may be used to generate the effects of Jovian-trapped electrons, and which are usable in a combined radiation effects facility. For high energy electrons, we can consider Sr90-Y90 as a Beta source. Lutz and Newell (see Figure 6,) use this material for Van Allen Belt electron simulation. We have looked in more detail at the spectrum and find that the radiation hardens as it goes through the encapsulation of the practical source (Figure 7).

A distributed source of 11 watts of Sr90-Y90 is available to us (500 Ci), and this gives electron doses in the range of design values in one days' exposure time. Data are available for relating radiation damage caused by electrons of a given energy, to the damage to be expected at a wide range of energies, so the damage by electrons of the energies to be actually encountered in the radiation belt can be predicted. Figure 8 shows the actual data damage curve for the case of displacement damage to transistors. Similar curves showing the variation of damage with incoming energy may be generated for other components as needed.

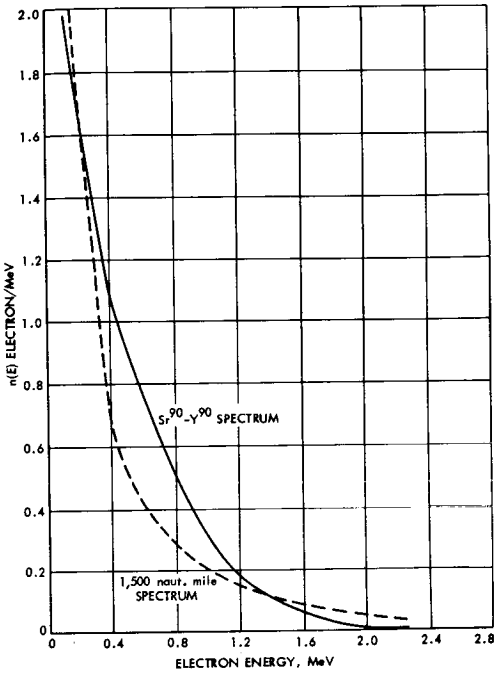

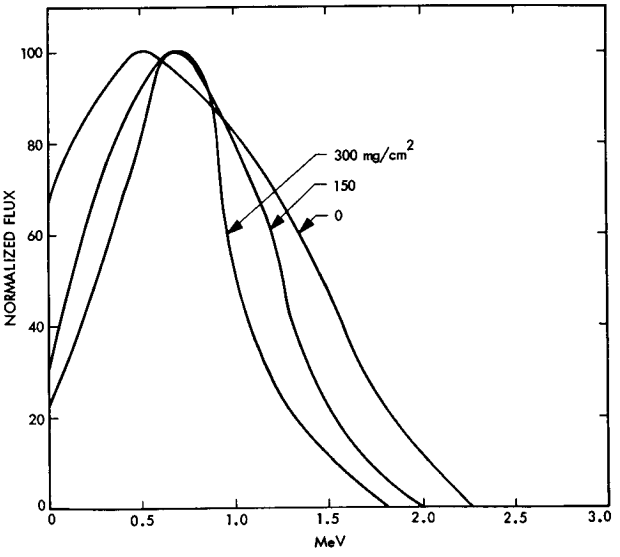

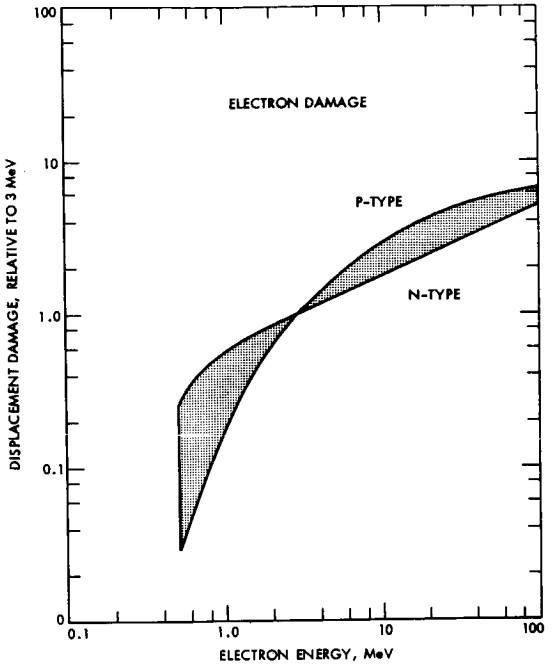

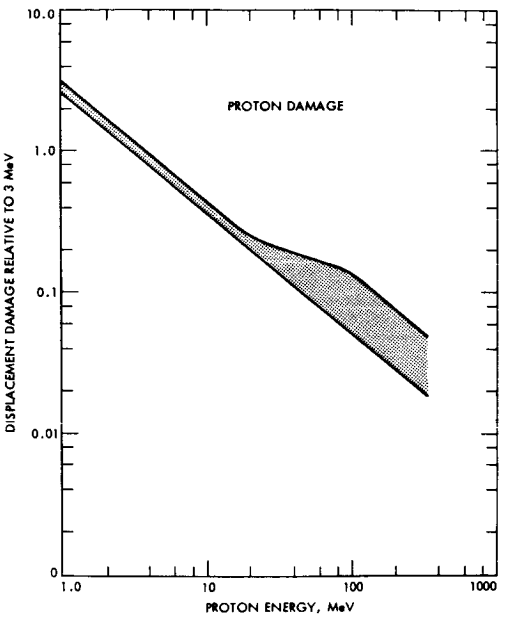

For protons, we must use a source of sufficient energy so that the protons involved will penetrate into the bodies of components. This requires well over 10 MeV energy. An important design point is that the flux be steady and not be offered in peak pulses with the attendant rate problems, as in a synchrocyclotron.

Some information on proton damage is available as shown in Figure 9, and similar curves showing the variation of damage with incoming energy may be generated for other components as needed. For such a proton generator, we envision the use of the reaction

$$He^3 + d \rightarrow p + \alpha$$

This is a mirror reaction to the well known t, d

$$H^3 + d \rightarrow n + \alpha$$

The efficiency of the process can be seen from the data in Figure 10. For comparison, we note that a d, t generator giving about 10^{11} neutrons/sec into 4π, costs about $28,000 and such a generator would serve to give over 10^{10} p/sec when using the He^3-d reaction. Such a reaction can be run in a vacuum tank, so there is no wall to stop generated protons. We are developing a dispensing target, based on the diffusion of deuterium through a palladium thimble, which is exptected to give a long life in this usage and enable tests of trapped radiation belt protons to be feasible.

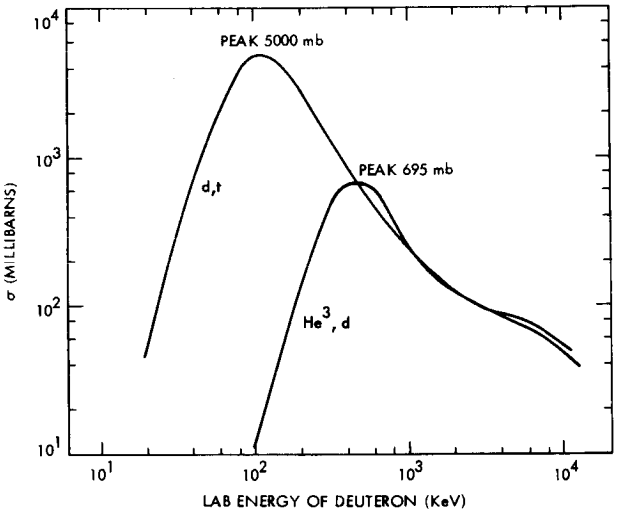

Solar Origin Radiation

Present simulation chambers are adequate for tests involving ionizing radiation insofar as space vacuum and space temperature effects are involved. It is also practical to add ultraviolet lights and solar wind sources to such simulation chambers.

Conditions of Flight

Present simulation chambers have adequate provision for maintaining the vacuum condition and for holding the shroud temperatures at space temperature simulation conditions.

A calculation has been made of the radiation levels to be expected in the vicinity of a solar simulator, when a simulated radioisotope thermoelectric generator is contained therein, along with the spacecraft full scale model. Figure 11 shows the radiation levels in mrem/hr at two selected personnel working locations in the vicinity of an environment simulation chamber.

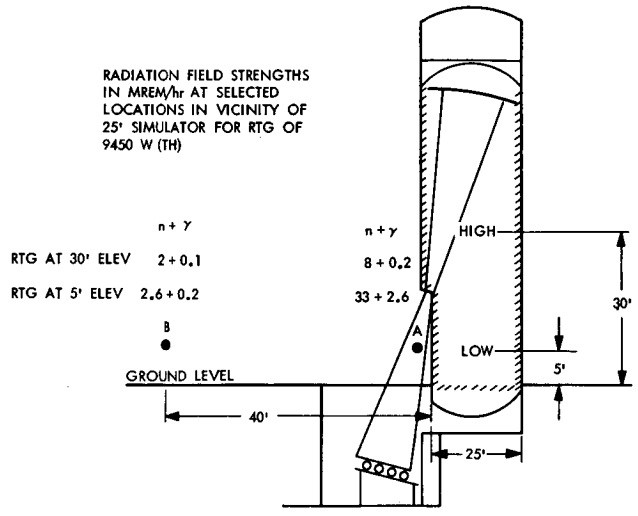

If the radioisotope thermo-electric generator of 9450 w(th) is located as shown, five feet above ground level, the field strength at the ground plane at Location A, just outside the environment chamber is 36 mrem/hr, while at the control console, Location B, the field is 2.8 mrem/hr. Alternately, if the spacecraft model occupies the upper half of the chamber, so that the radioisotope thermo-electric generator is 30 feet above the ground plane the radiation levels are 8.2 mrem/hr and 2.1 mrem/hr at the adjacent points and control console point, respectively.

Summary

The important attributes of the radiation fields needed to carry out simulated in-flight-condition testing on outer planet spacecraft have been examined. In order to carry out testing on the effects of radiation fields interfering with on-board science instruments, it is found that only the gamma field of the radioisotope thermo-electric generator must be simulated, but that a close spectral match is needed. In order to carry out tests on the cumulative damage effects of the radioisotope thermo-electric generator field on both scientific instruments, and on electronic, propulsion and guidance systems of the spacecraft, a neutron field is needed with a close spectral match and a gamma field is also needed. The gamma field for the cumulative damage tests, however, need not be of close spectral match.

In order to simulate the Planetary Trapped Radiation Belt effects, both high energy electrons and high energy protons are needed. It is practical to use beta particles from an Sr90-Y90 source to induce the effects of trapped belt electrons if the relative damage coefficients relating electron radiation damage to electron energy are known. These must be known or determined for every component under study.

In a similar fashion, protons from the He^3, d reaction, which have an energy of 16 MeV, can be generated inside a combined radiation effects facility to induce the effects of high energy trapped protons if the relative damage coefficients relating proton damage to proton energy are known. These must also be known or determined for every component under test.

It is concluded and design information is given, that all the above environments, together with other factors such as solar wind and vacuum ultraviolet can be added to presently available simulation chambers, and still have radiation levels in the vicinity of such chambers such that personnel can accomplish needed test tasks without exceeding permissable radiation exposure levels.

REFERENCES

1. W. E. Price, C. G. Miller and R. H. Parker "Design Considerations and Test Facilities for Accelerated Radiation Effects Testing" This Conference

2. M. Reier "The Design of a source to simulate the gamma-ray spectrum emitted by a radioisotope thermo-electric generator" This Conference

3. H. Berger, "Neutron Radiography", Elsevier Publishing Co., New York, 1965, pp. 14 ff.

4. C. G. Miller and V. C. Truscello, JPL TR 32-1427 (May, 1970)

5. R. F. Lutz and D. M. Newell "Use of a radioisotope as an electron source in a space environment simulation chamber", IEEE Transactions on Nuclear Science, 1967

7. S. L. Greene, Jr., "Maxwell Averaged Cross Sections for Some Thermonuclear Reactions on Light Isotopes", UCLR-70522 (May, 1967)

THE DESIGN OF A SOURCE TO SIMULATE THE GAMMA-RAY SPECTRUM EMITTED BY A RADIOISOTOPE THERMOELECTRIC GENERATOR

Melvin Reier
The Jet Propulsion Laboratory

A simulated source was designed to duplicate the gamma spectrum of a uniform cylindrical 2200-watt PuO_2 RTG containing 81% Pu^{238} and 1.2 ppm Pu^{236}. Gamma rays from the decay of Pu^{238}, Am^{241}, Pu^{239}, and the $O^{18}(\alpha,n)Ne^{21}$ reaction were catalogued in broad energy groups. Pu^{236}, which decays ultimately to Th^{228}, was treated separately, since an exact duplicate can be made by using Th^{228}. The selection of sources involves a compromise between half life, cost, and gamma-ray energy. We have chosen $Ba^{133}(T_{1/2} = 7.2y)$, $Cs^{137}(T_{1/2} = 30y)$, and $Co^{60}(T_{1/2} = 5.2y)$ which provide gamma rays to cover the spectrum from about 350 kev to 1.3 Mev. Two 46 and one 22 mc Th^{228} sources provide simulation at various times in the life of the fuel capsule up to 18 years, which covers the time span of an outer planet mission. The emission from the Th^{228} represents the overwhelming contribution of the gamma spectrum after the first few years. Therefore, the small changes in the intensity of the rest of the spectrum represent a minor perturbation on the entire spectrum. The sources, in the form of 13-inch long rods are placed in a concentric hole in a cylinder of depleted uranium which provides shielding equivalent to the self shielding of the fuel capsule. The thickness of the U^{238} cylinder (0.55 cm) was determined by Monte Carlo calculations to insure that the spectrum emerging from the simulated source closely matched that of the fuel capsule.

INTRODUCTION

It is well established that RTG's fueled by $Pu^{238}O_2$ will be used to provide instrument power on space missions where solar energy is inadequate. An obvious one is the forthcoming Outer Planets Mission.

Although the absolute number of photons per disintegration of Pu^{238} is small ($\sim 50/10^8$ for $E > 160$ kev), the gamma intensity is not negligible as we are dealing with about seventy thousand curies of Pu^{238} per source. In addition, Pu^{236}, which appears as an impurity of about 1.2 ppm decays to Th^{228}, which becomes, after about 3 years, the major source of gamma radiation. This will be discussed in greater detail shortly.

Many of the instruments aboard a space vehicle may be sensitive to this source of gamma radiation. Long-term exposure may result in radiation damage to instrumentation and electronic packages. Also, the increase in background resulting from this spurious source of radiation on sensitive detectors must be measured. For these reasons the radiation field at various positions on a spacecraft has to be mapped. The use of a fueled Multi-Hundred Watt (MHW) generator for this purpose would be wasteful. Besides, the possession of such a source imposes numerous safety, handling, and accountability problems in a laboratory. In order to avoid these difficulties, we have designed a radioactive source which reproduces the major features of the spectrum emitted by an MHW within about 20% in the radial direction and 35% in the axial direction. Using this approach we are able to represent the gamma radiation spectrum from an RTG for a cost of under $6000 while eliminating the inherent problems cited above. More importantly, the simulated source enables experiments to be conducted with an aged radiation spectrum, thus duplicating the conditions that would exist at various ages in the life of a mission.

SOURCE DESIGN

The basic philosophy of the design was to reproduce the unattenuated spectrum and then calculate the proper amount of shielding to account for the self-shielding of the fuel and subsequent attenuation of the cladding and outer jackets.

The first part of the problem is essentially a bookkeeping procedure. The following sources of radiation were included:

1. Plutonium-238 decay.
2. Gamma rays from the excited states of Ne^{21} in the $O^{18}(\alpha,n)Ne^{21}$ reaction.
3. Americium-241 decay. (Am^{241} is derived from the decay of Pu^{241}).
4. Thorium-228 decay.

Item 4 is a special (and easier) problem and will be treated separately.

The selection of sources for Items 1-3 involves a compromise between energy, half life, and ease of production. We have chosen $Ba^{133}(T_{1/2} = 7.2y)$, $Cs^{137}(T_{1/2} = 30y)$ and $Co^{60}(T_{1/2} = 5.2y)$ to cover the spectrum from about 350 kev to 1.3 Mev.

Table 1 shows the latest available data on the absolute intensity of gamma rays from Pu^{238}. A cursory examination of this table reveals that beyond about 160 kev there is nothing substantial until the region of 700 kev is reached. Although there are intense low-energy lines, they are ignored in the source design because they are enormously attenuated. The decay intensities are added up and placed in broad energy groups. The same procedure is followed for the Am^{241} and the Ne^{21} decay. The latter two give rise to an additional group around 350 kev.

The simulation of the Pu^{236} decay is relatively simple and can be done very accurately. This can be seen by an examination of Figure 1 showing the decay chain of Pu^{236}, leading ultimately to Pb^{208}. No gamma rays worthy of consideration are emitted

TABLE 1

Pu^{238} Absolute Gamma-Ray Intensities

E (kev)[a]	Photons/disintegration x 10^8	
	Reier (Ref. 1)	Lederer et al (Ref. 2)
152.71 ± 0.05	seen	1270 ± 90
200.9 ± 0.2		5 ± 1
207.6	seen	
235.9 ± 0.3?		0.01 ± 0.005
258.3 ± 0.2		0.011 ± 0.02
299.2 ± 0.2		0.07 ± 0.02
706.1 ± 0.3		0.14 ± 0.02
708.42 ± 0.20		0.38 ± 0.04
742.77 ± 0.10	6.35 ± 0.21	7.6 ± 0.7
766.39 ± 0.10	26.7 ± 0.8	33 ± 3
786.30 ± 0.10	4.98 ± 0.16	4.8 ± 0.4
805.8 ± 0.3		0.18 ± 0.02
808.25 ± 0.15	0.999 ± 0.063	1.1 ± 0.1
851.70 ± 0.10	1.64 ± 0.06	1.9 ± 0.2
880.5 ± 0.3		0.23 ± 0.03
883.23 ± 0.10	1.270 ± 0.048	1.1 ± 0.1
904.37 ± 0.15	0.072 ± 0.021	0.10 ± 0.02
926.72 ± 0.15	0.71 ± 0.04	0.83 ± 0.08
941.9 ± 0.2	0.58 ± 0.02	0.67 ± 0.07
946.0 ± 0.3		0.13 ± 0.02
1001.03 ± 0.15	1.08 ± 0.04	1.4 ± 0.2
1041.8 ± 0.3	0.20 ± 0.02	0.28 ± 0.02
1085.4 ± 0.3		0.11 ± 0.02

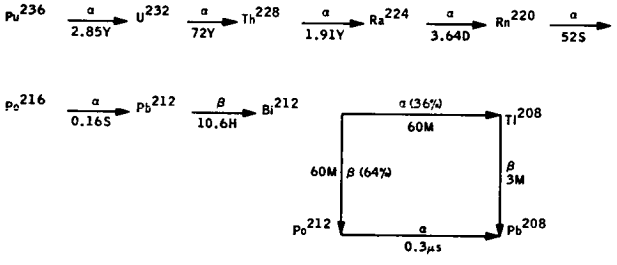

FIGURE 1. Plutonium-236 Decay Chain

until Th^{228} is reached. It then decays emitting gamma rays from Pb^{212}, Bi^{212}, and Tl^{208}, the latter producing the well-known 2.61 Mev gamma ray in 100% of the decays. Fortunately, Th^{228} is readily available and may be purchased in the desired encapsulated form. The buildup of Th^{228} is determined by solving the three linear differential equations starting with Pu^{236}. These are shown in Eq. 1-3. The activity of the Th^{228} is given by the solution, Eq. 4.

$$\frac{dN_1}{dt} = -\lambda_1 N_1 \tag{1}$$

$$\frac{dN_2}{dt} = \lambda_1 N_1 - \lambda_2 N_2 \tag{2}$$

$$\frac{dN_3}{dt} = \lambda_2 N_2 - \lambda_3 N_3 \tag{3}$$

$$\lambda_3 N_3 = \lambda_1\lambda_2\lambda_3 N_{10} \left[\frac{1}{\lambda_1 - \lambda_2} \cdot \frac{1}{\lambda_1 - \lambda_3} \cdot e^{-\lambda_1 t} + \frac{1}{\lambda_2 - \lambda_1} \cdot \frac{1}{\lambda_2 - \lambda_3} \cdot e^{-\lambda_2 t} + \frac{1}{\lambda_3 - \lambda_1} \cdot \frac{1}{\lambda_3 - \lambda_2} \cdot e^{-\lambda_3 t} \right]$$

N_{10} is the amount of Pu^{236} present at t = 0

Table II gives the amount of activity of each of the isotopes for a 2200 watt fuel source at different ages of the fuel starting with 1.2 ppm of Pu^{236}. The buildup of the Ba^{133} source with age is due to the increase of Am^{241} resulting from the decay of Pu^{241}. The Cs^{137} and Co^{60} are used mainly to simulate the decay of Pu^{238}. Their decrease with time reflects mainly the half life of Pu^{238} ($T_{1/2}$ = 86.4y). The barium, cesium, and cobalt will be packaged in a single capsule. In addition, we have ordered three separate capsules of Th^{228}, so that we will be able to reproduce the thorium activity at fuel ages of 0, 3, 5, 8, 18 years. The amount of Ba^{133}, Cs^{137}, and Co^{60} corresponds to t = 0 only. The error introduced by not using different quantities of these isotopes as the fuel ages is small since the Th^{228} activity overshadows the others within a few years.

TABLE 2

Quantity of Isotopes (Mc) For Simulated Source

Year	Ba^{133}	Cs^{137}	Co^{60}	Th^{228}
0	1.30	26.0	0.75	0
1	1.37	25.9	0.75	4.24
5	1.58	25.3	0.73	49.9
10	1.79	24.6	0.70	88.1
18	2.05	23.1	0.64	102

SHIELD DESIGN

Having selected the isotopes, the next step is to calculate a shield thickness such that the emitted spectrum is the same as that from the real source. The actual source is a 13 inch long cylinder of fuel pucks having a 2.731 cm radius, enclosed in an 0.051 cm tantalum shell, which in turn, is inserted concentrically in a graphite cylinder having a wall thickness of 3.175 cm. The fuel is a mixture of PuO_2, ThO_2, and M_O. The concentration of each element is shown in Table III. The density of the mixture is 9.17 g/cm^3.

TABLE 3

Concentration of Elements in the Fuel

Element	Weight %
Pu	68.8
Th	7.6
Mo	13.3
O	10.4

Since the real fuel is composed largely of high Z elements, depleted uranium was selected as the shield to reproduce the self-shielding of the source. The natural radioactivity of the depleted uranium and it's impurities add insignificantly to the simulated source and can be neglected. Figure 2 shows a sketch of the real and simulated source. Monte Carlo calculations were run comparing the spectrum in the radial, axial, and 45° directions of the real source with a 13 in. line source (the diameter of the capsules for the simulated source is 1/4 inch). The results in the radial direction and at 45° are very encouraging. Figure 3 shows a comparison between the real and simulated source in the radial direction. Except in the very low energy region, where the statistics are about 40%, the agreement is within about 20%. (The mismatch of the 600 to 700 kev peak from the Cs^{137} and the 700 to 800 kev peak in the real case is expected and is not considered a serious problem).

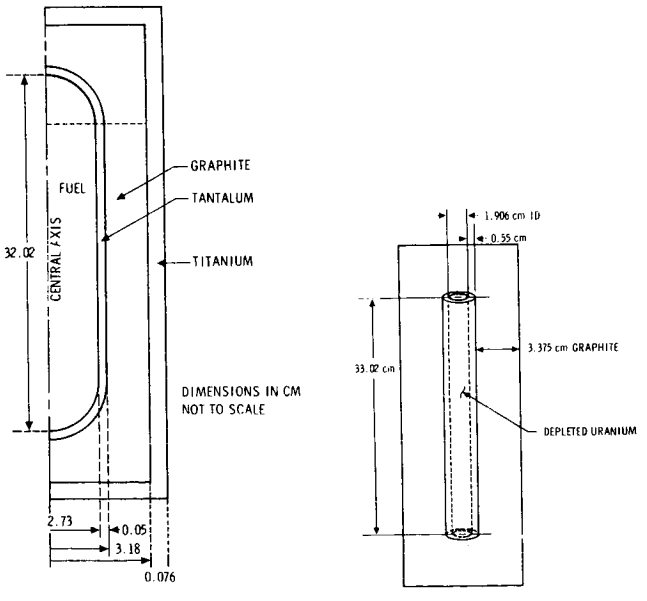

FIGURE 2. Simulated and Real Source

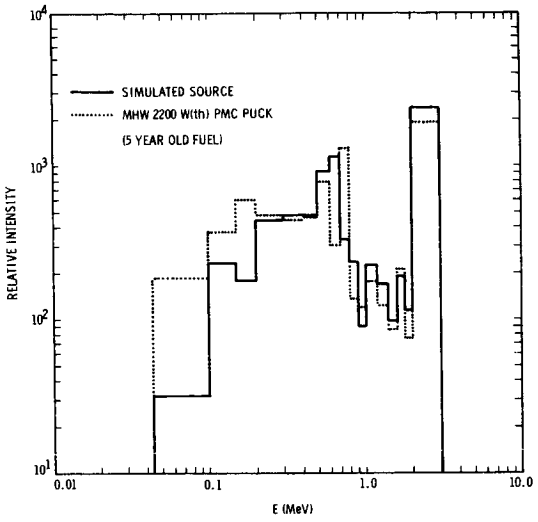

FIGURE 3. Comparison of Spectrum in the Radial Direction from the Simulated and Real Source

Because of the enormous self shielding, we were not able to simulate the radiation in the axial direction by using depleted uranium or a combination of depleted uranium and a lighter element. The best result we were able to obtain is shown in Figure 4. This uses seven cm of copper at the ends of the simulated source. A compromise had to be made between the high and low end of the spectrum. If a small medium energy source could be placed inside the end shield, the problem would be simplified and a much better match could be obtained.

It is a pleasure to acknowledge the assistance of Mr. Michael A. Dore in the computational analysis.

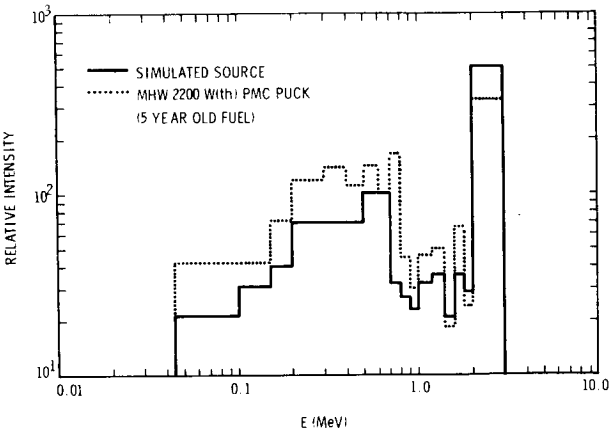

FIGURE 4. Comparison of Spectrum in the Axial Direction from the Simulated and Real Source.

REFERENCES

1. M. Reier, Nucl. Sci. & Engr. (in press).
2. C. M. Lederer, F. Asaro, and I. Perlman. Nuclear Chemistry Annual Report (1968), UCRL-18667.

Some Neutron and Gamma Radiation Characteristics of Plutonium Cermet Fuel for Isotopic Power Sources

R. A. NEFF, M. E. ANDERSON, A. R. CAMPBELL, and F. X. HAAS

Mound Laboratory, Miamisburg, Ohio*

Gamma and neutron measurements on various types of plutonium sources are presented in order to show the effects of ^{17}O, ^{18}O, ^{19}F, ^{238}Pu, age of the fuel, and size of the source on the gamma and neutron spectra. Analysis of the radiation measurements shows that fluorine is the main contributor to the neutron yields from present plutonium-molybdenum cermet fuel while both fluorine and ^{238}Pu daughters contribute significantly to the gamma-ray intensities.

Plutonium-238 has many desirable qualities for a radioisotopic heat source fuel and has been used in numerous heat sources for terrestrial, marine and space applications. The plutonium fuel has been prepared in several different forms depending on the requirements of the particular mission and the technology available at the time of fabrication. Fuel forms used in the past have been plutonium metal, alloys, and dioxide microspheres. The most recent fuel form to be used is plutonium-molybdenum cermet, (PMC), which is plutonium dioxide that has been coated with molybdenum and hot pressed into the desired shape. This paper deals with the gamma and neutron radiation emitted by the PMC fuel.

The gamma radiation can be divided into three groups; that due to radioactive decay of ^{238}Pu and other nuclides, alpha particle reactions, and fission of the plutonium. Figure 1 shows the gamma spectrum obtained with a Ge(Li) spectrometer of a 15-watt Apollo heat source fueled with plutonium dioxide microspheres. In this spectrum we can see the ^{238}Pu full energy peaks at 100, 153, and 208 keV, several peaks centered around the intense 766 keV peak, and peaks at 851, 883, 926, 942, and 1001 keV. There are some other less intense ^{238}Pu peaks which do not show up in this spectrum.

The fuel used in heat sources is nominally about 80% ^{238}Pu, 16% ^{239}Pu, and 1.2 ppm ^{236}Pu. The ^{239}Pu contributes a group of peaks around 400 keV while the main contributions from ^{238}Pu are the two intense peaks at 2614 and 583 keV due to the ^{208}Tl daughter. Other peaks from ^{238}Pu daughters which can be seen in this spectrum are the 510 and 860 keV peaks also from ^{208}Tl, the 240 and 301 keV peaks from ^{212}Pb, and the 727 and 1620 keV peaks from ^{212}Bi. However, a portion of the 510 keV peak is due to annihilation radiation following pair production from the more energetic gamma rays. About five years after chemical separation, the gamma dose rate from the ingrowth of these ^{236}Pu daughters is about equal to the dose rate from the ^{238}Pu gammas for a small encapsulated heat source. The dose rate from these daughters reaches a maximum at 18 years after separation at which time it is ~2.5 times the dose rate from the ^{238}Pu gammas.

Another source of gamma rays is fission, both spontaneous and neutron induced, which will give approximately an exponential continuum of gamma rays. For the Pioneer Program, there was some concern over the gamma rays in the 1 to 4 MeV range. We estimate that for a source the size of the Pioneer there are about 1.8×10^4 photons/sec/watt in the 1-2 MeV

*Operated by Monsanto Research Corporation for the United States Atomic Energy Commission under Contract No. AT-33-1-GEN-53.

Figure 1

HEAT SOURCE OXIDE FUEL FORM

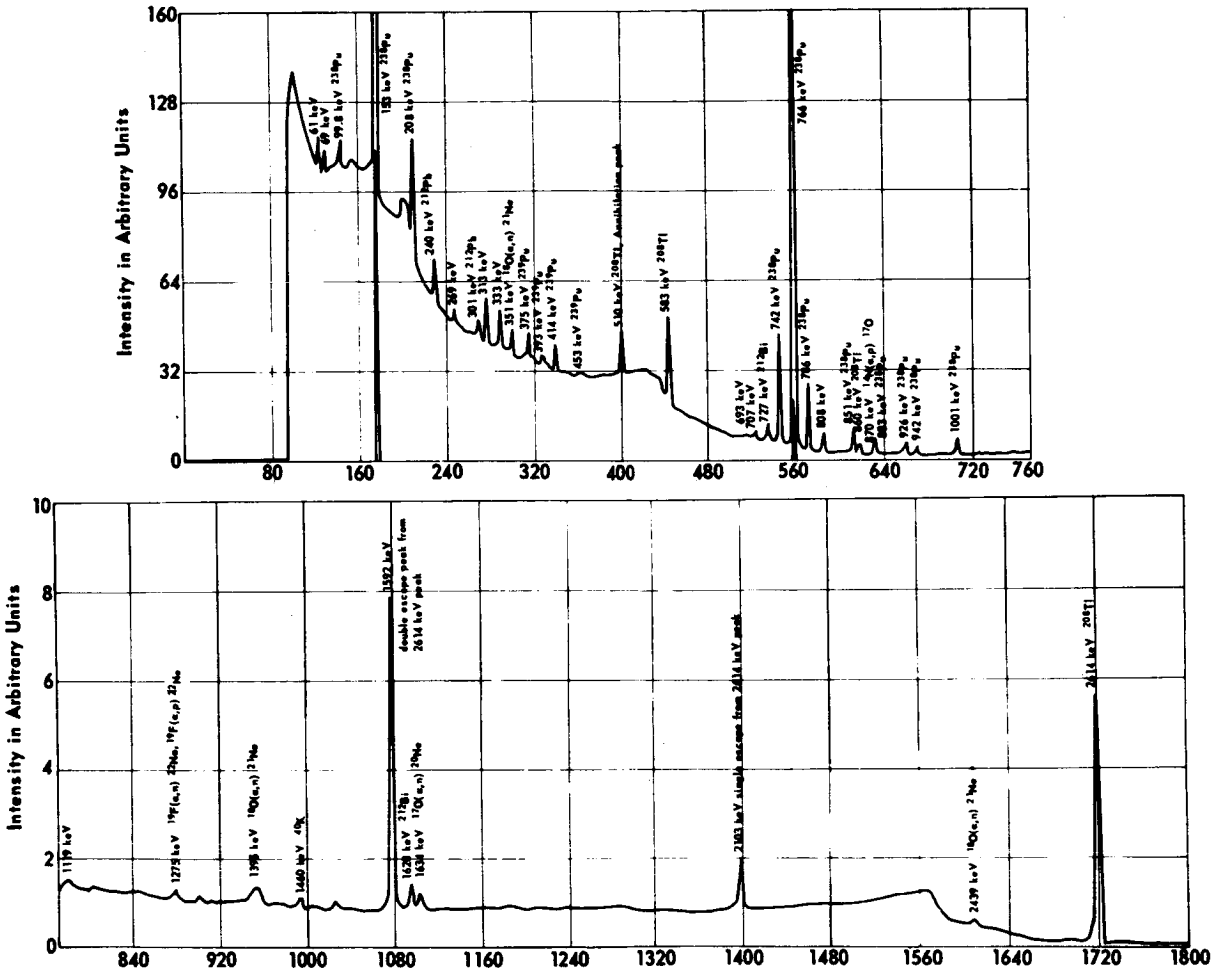

range due to fission, 6.0×10^3 in the 2-3 MeV range, and 1.9×10^3 in the 3-4 MeV range. These estimates are for bare fuel and have not been corrected for self-absorption within the source. To compare these intensities to the ^{238}Pu photopeaks, the 742, 766, and 786 keV peaks give a total of $\sim 5.1 \times 10^5$ photons/sec/watt from a bare source with no self-absorption, and the total of other ^{238}Pu gamma rays between 880 and 1085 is $\sim 5.4 \times 10^4$ photons/sec/watt.

Figure 2 shows the gamma spectra of three different plutonium sources obtained with a Ge(Li) spectrometer. The top spectrum in this figure is of a metal source containing about seven grams of ^{238}Pu. This spectrum shows the prominent ^{238}Pu peaks (some of which are labeled by energy) as well as the peaks due to ^{236}Pu daughters. Since this source is about seven years old, these peaks from ^{236}Pu daughters are relatively intense.

Figure 2

GAMMA SPECTRA OF Pu, PuF_4, and PuO_2

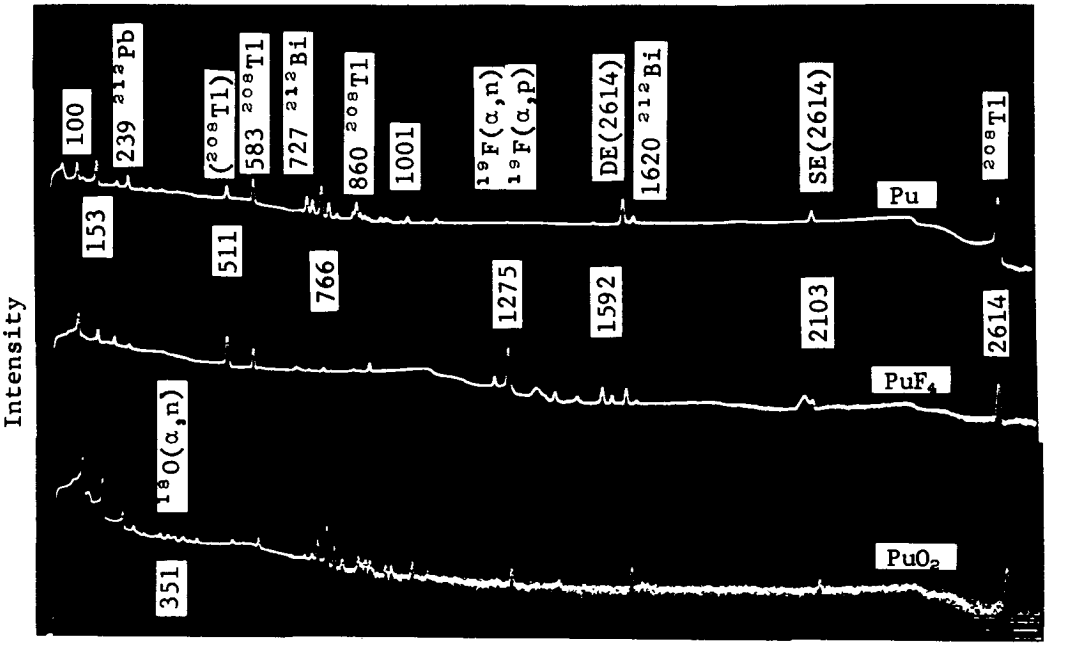

The bottom curve in Figure 2 shows the gamma spectrum of a PuO_2 source containing about 1.5 grams of ^{238}Pu. Comparing the top and bottom curves, we can see that the presence of oxygen gives only a few relatively weak gamma rays. These are at 351, 1395, and 2439 keV from $^{18}O(\alpha,n\gamma)$ reactions and at 1634 keV from the ^{17}O $(\alpha,n\gamma)$ reaction. For this oxide source, the gamma rays from the ^{236}Pu daughters are not as intense relative to the ^{238}Pu gamma rays since the material is much younger than the metal source. However, the ^{208}Tl peaks at 583 and 2614 keV are still prominent.

The gamma spectrum of a PuF_4 source containing about 0.5 grams of ^{238}Pu is shown as the middle curve in Figure 2. The contribution to the gamma spectrum due to fluorine can be seen as a very intense peak at 1275 keV due to both (α,p) reactions on ^{19}F and the decay of ^{22}Na formed by the $^{19}F(\alpha,n)^{22}Na$ reaction. There are other peaks due to fluorine at 580, 890, and 2080 keV and five additional peaks clustered around the 1275 keV peak. In normal heat source material, the fluorine content is low enough that the only significant contribution from the fluorine reactions is the peak at 1275 keV.

Since a portion of the 1275 keV peak is due to the decay of ^{22}Na formed by ^{19}F $(\alpha,n)^{22}Na$ reactions, the intensity of this peak will increase with time up to about six years (two half-lives of ^{22}Na) after the introduction of fluorine. After six years, secular equilibrium is reached and the intensity of the 1275 keV peak remains constant relative to the ^{238}Pu gamma rays. Measurements have shown that the intensity of the 1275 keV peak will approximately double over this six year period.

Since the PuF_4 source used for Figure 2 was over six years old, the spectrum readily shows the gamma rays from the ^{236}Pu daughters as well as some of the more prominent ^{238}Pu peaks.

Shown in Figure 3 is the gamma-ray spectrum of a 647-watt Pioneer capsule fueled with plutonium-molybdenum cermet. Notice the absence of structure below about 500 keV as compared to the spectra shown in Figures 1 and 2. This is due mostly to the greatly increased self-absorption for this source. We still see the ^{238}Pu group around 766 keV and the 1001 keV peak, also the ^{208}Tl peaks at 583 and 2614 keV, and the fluorine peak at 1275 keV. The peak at 2223 keV is

Figure 3

GAMMA SPECTRUM OF PF-2

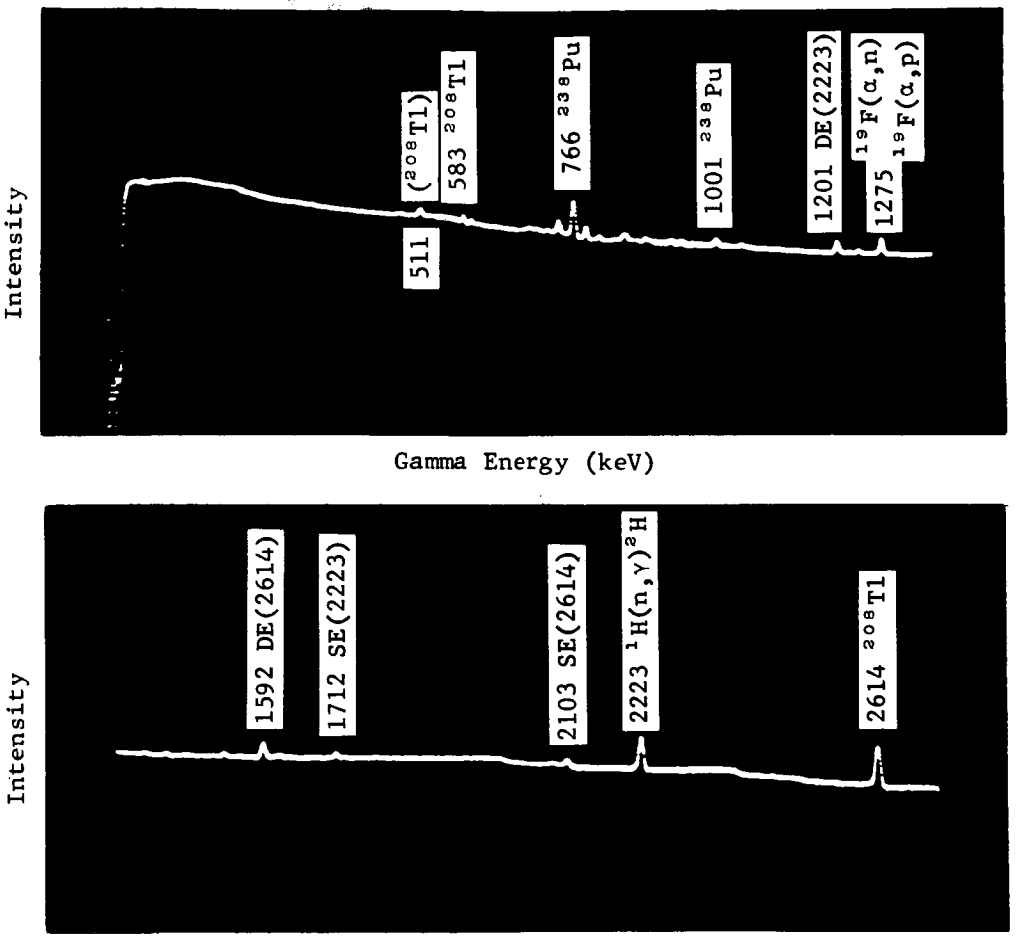

not from the source but was caused by the $^{1}H(n,\gamma)^{2}H$ reaction with the water bath the source was in during the measurements.

The neutrons from PMC fuel are contributed by spontaneous fission of ^{238}Pu, neutron induced fission of the Pu, and (α,n) reactions primarily with ^{17}O, ^{18}O, and ^{19}F. Figure 4 shows the neutron spectrum of a 15-watt plutonium metal source. About 75% of the neutrons from this source are from spontaneous fission of the ^{238}Pu while the remaining 25% are mostly due to (α,n) reactions with low Z impurities. Since the neutrons above ~5 MeV are almost all due to spontaneous fission, this portion of the spectrum was fitted to a Maxwellian distribution in order to approximate a fission spectrum. The spontaneous fission neutron yield is about 2.65×10^{3} n/sec/gram of ^{238}Pu. This value is represented by the lower curve in this figure and is the minimum number of neutrons that a ^{238}Pu source can emit. The average neutron energy for this fission curve is 2.0 MeV.

Even though PMC fuel is enriched in ^{18}O which will not undergo (α,n) reactions with the 5.5 MeV ^{238}Pu alpha particles, there are still sufficient quantities of ^{17}O and ^{18}O present to produce significant quantities of neutrons. The effects of ^{17}O and ^{18}O on the neutron spectrum are shown in Figure 5. This is the spectrum of a PuO_2 source in which the oxygen is enriched to 45.6% ^{18}O and 1.7% ^{17}O whereas natural oxygen is 0.2% ^{18}O and 0.04% ^{17}O. The data at energies greater than 1 MeV were obtained with a stilbene spectrometer while the datum point between 0 and 1 MeV was obtained from a difference calculation

Figure 4

NEUTRON ENERGY SPECTRUM OF SOURCE HP-15-2

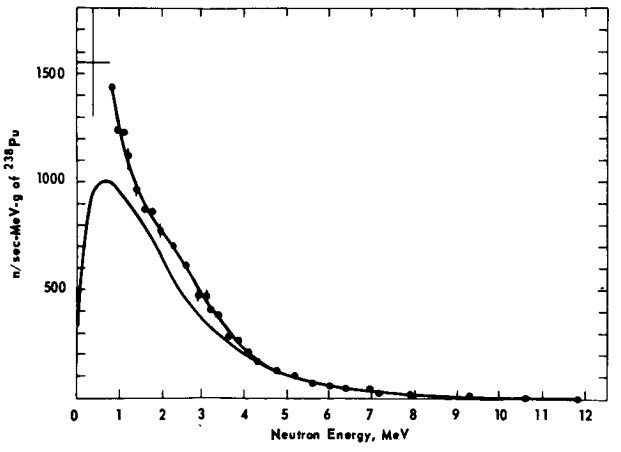

Figure 5

NEUTRON ENERGY SPECTRUM OF A ^{238}Pu-$^{18}O(\alpha,n)$ SOURCE

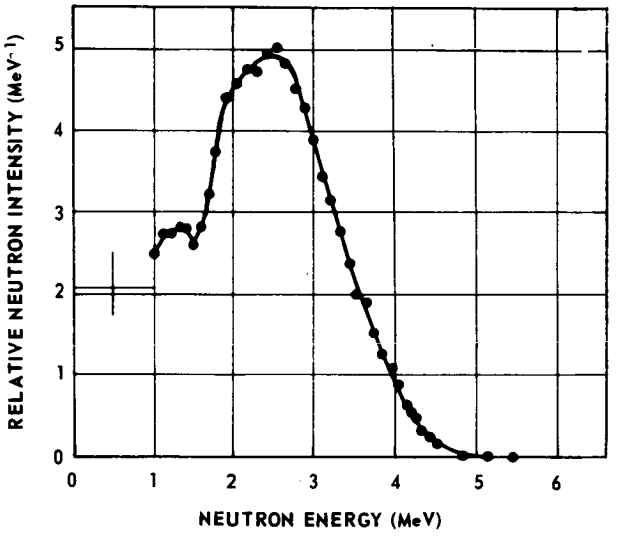

using the stilbene data and a long counter measurement. In this spectrum, we see a broad maximum around 2.5 MeV due to the (α,n) reactions with ^{17}O and ^{18}O. These (α,n) reactions yield about 1.4×10^4 n/sec/gram of ^{238}Pu in a PuO_2 source with oxygen of natural isotopic abundance and give a maximum neutron energy of about 4.5 MeV. The average neutron energy from this source is 2.1 MeV.

A similar spectrum only of a PuF_4 source is shown in Figure 6. The maximum energy the neutrons from the $^{19}F(\alpha,n)^{22}Na$ can have, using a 5.5 MeV alpha particle, is 3.2 MeV. This (α,n) reaction produces the peak at about 1.25 MeV. The average neutron energy for this source is 1.2 MeV, and the specific yield is 2.8×10^6 n/sec/gram of ^{238}Pu.

Figure 6

NEUTRON ENERGY SPECTRUM OF A ^{238}Pu-$^{19}F(\alpha,n)$ SOURCE

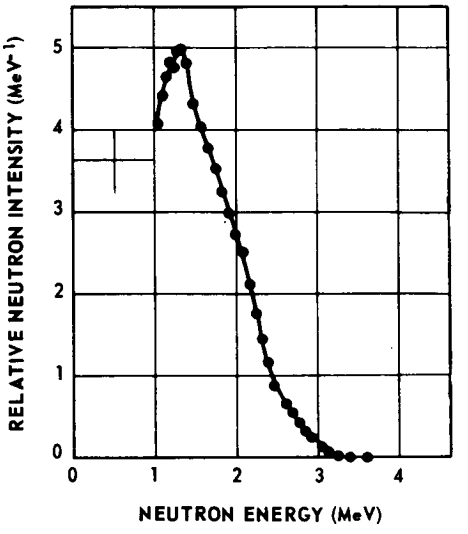

In Figure 7 we can see the effect of the neutrons due to neutron induced fission of the plutonium. The lower curve is a log plot of the data for the 15-watt metal source that was shown in Figure 4 as a linear plot. The upper curve is the neutron spectrum of a 1482 watt SNAP-27 source. Because the SNAP-27 was a natural oxygen PuO_2 source, there is a broad maximum around 2.5 MeV from the $O(\alpha,n)$ reactions. Since both of these spectra are plotted as specific yield per MeV, the spontaneous fission spectrum for the metal source also represents the spontaneous fission curve for the SNAP-27 source. At neutron energies greater than 5 MeV, the neutron induced fission spectrum is represented by the difference between the two curves. For this SNAP-27 source, the neutron yield from induced fission was ~3.7 $\times 10^3$ n/sec/gram of ^{238}Pu. This gave a neutron multiplication in this source of about 20%. The total specific yield for this source was 2.2×10^4 n/sec/gram of ^{238}Pu, and the average neutron energy was 1.9 MeV.

Figure 7

ENERGY SPECTRA OF TWO ^{238}Pu POWER SOURCES

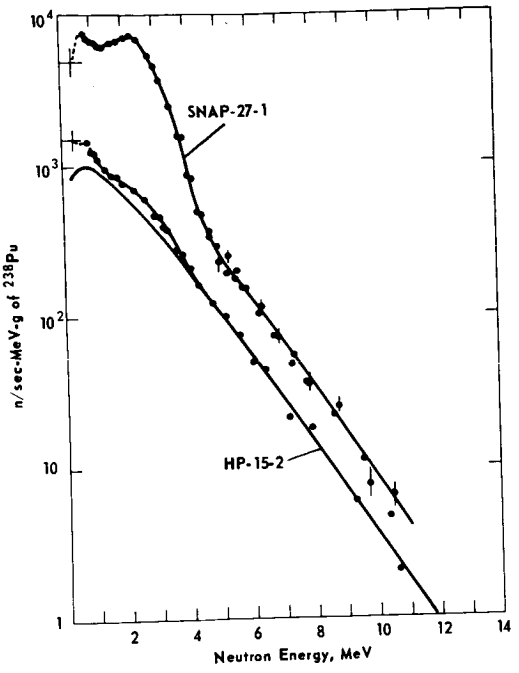

Figure 8

NEUTRON ENERGY SPECTRUM OF PIONEER CAPSULE PF-2

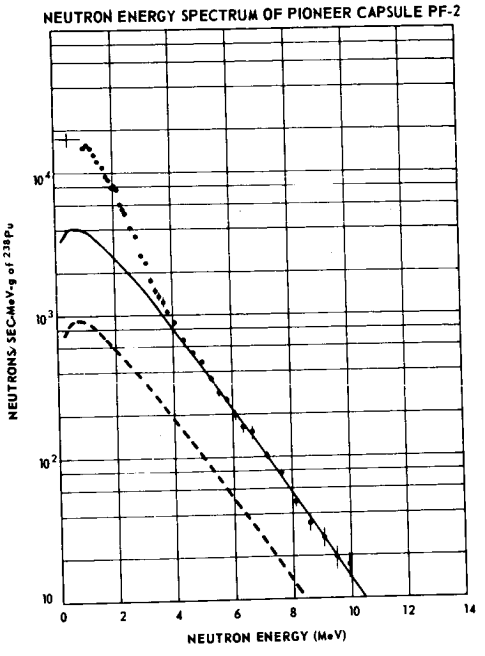

Shown in Figure 8 is the neutron spectrum of the 647-watt, PMC fueled, Pioneer capsule PF-2. The dashed line represents the spontaneous fission curve, the solid line is the sum of the spontaneous fission and induced fission curves, and the data points represent the measured neutron spectrum. The rise in the spectrum below 5 MeV is due to the presence of ^{17}O and ^{18}O which remained after the ^{16}O exchange process and to fluorine that was introduced into the fuel during the molybdenum coating process. This source had a specific yield of 3.73×10^4 n/sec/gram of ^{238}Pu. It is estimated from the spectral measurements that approximately 7% of these neutrons were due to spontaneous fission of the ^{238}Pu, 7% to O(α,n) reactions, 23% to induced fission, and 63% to the $^{19}F(\alpha,n)^{22}Na$ reaction. Neutron measurements on individual PMC discs that were stacked together to make a Pioneer capsule and on the finished capsule show an increase due to multiplication of 26%. The average neutron energy for this source was 1.3 MeV.

Table I contains a summary of the neutron data. From this table, we can see how prolific the oxygen and especially the fluorine are for producing neutrons. We can also see the effects of these two elements on the average energy and the dose conversion factors.

In summary, it is evident that the main problem, as far as lowering neutron levels in PMC fuel, is the fluorine content. Most likely, future PMC fuel will be produced using $MoCl_5$ for the molybdenum coating rather than MoF_6. This would keep all but trace amounts of fluorine out of the fuel. The small neutron contribution from ^{17}O and ^{18}O is being still further reduced through improved ^{16}O exchange methods.

For the gamma radiation, the fluorine is again a problem along with the ingrowth of ^{236}Pu daughters. It may be possible in the future to obtain fuel with a lower ^{238}Pu content or to age the fuel to allow some of the ^{236}Pu to decay before performing chemical separation.

Table 1

SUMMARY OF NEUTRON DATA

SOURCE	SPECIFIC YIELD n/sec/g ^{238}Pu	AVERAGE NEUTRON ENERGY	CONVERSION FACTORS FROM NEUTRON FLUENCE TO: DOSE EQUIVALENT	CONVERSION FACTORS FROM NEUTRON FLUENCE TO: ABSORBED DOSE
Fission*	2.6×10^3	2.0 MeV	3.3×10^{-8} Rem/n/cm^2	3.8×10^{-9} Rad/n/cm^2
$^{238}PuO_2$	1.8×10^4	2.1	3.4	4.0
$^{238}PuF_4$	2.8×10^6	1.2	3.1	3.3
SNAP-27	2.2×10^4	1.9	3.3	3.8
PF-2	3.7×10^4	1.3	3.1	3.4

*Calculated

RADIATION FROM PLUTONIUM-238 USED IN SPACE APPLICATIONS

T. K. Keenan, R. E. Vallee, and J. A. Powers [1/]

Plutonium-238 is an alpha emitter with an 87 year half-life that is produced by neutron irradiation of neptunium-237 in a reactor. Plutonium-238 has been used in all applications of space electric power using isotopes as the energy source. These applications include the SNAP-3, 9, 19, and 27 units. The SNAP-3 and SNAP-9 units were used in Navy TRANSIT satellites while the SNAP-19 was used for auxiliary power aboard a NASA NIMBUS and the SNAP-27 provided all the power for the ALSEP package left on the moon's surface by the Apollo 12 and planned subsequent Apollo landings.

The principal mode of the nuclear decay of plutonium-238 is by alpha particle emission at a rate of 17 curies per gram. Gamma radiation also present in the nuclear fuel arises primarily from the nuclear de-excitation of daughter nuclei as a result of the alpha decay of plutonium-238 and reactor produced impurities. The gamma radiation associated with the alpha decay of plutonium-238 ranges in energy from 0.044 to 1.085 MeV. Thallium-208, a subsequent decay product of the reactor produced impurity, plutonium-236, emits 0.583 and 2.6 MeV gamma-rays at a significant rate if the initial plutonium-236 content is of the order of one part per million of total plutonium.

Plutonium-238 has a spontaneous fission half-life of 4.8×10^{10} years. Neutrons associated with this spontaneous fission are emitted at a rate of 2.8×10^{3} neutrons per second per gram. Since the space fuel form of plutonium-238 is the oxide pressed into a cermet with molybdenum, a contribution to the neutron emission rate arises from (α, n) reactions with O-17 and O-18 which occur in natural oxygen and contribute approximately 2×10^{4} neutrons per second per gram of plutonium-238. This contribution can be controlled by O-16 enrichment in the fuel. Other (α, n) reactions with low atomic number impurities (principally fluorine) bring the total neutron emission rate from the plutonia molybdenum cermet to near 3×10^{4} neutrons per second per gram of plutonium-238. This contribution can, also, be reduced by proper fuel production techniques.

Plutonium-238 is an alpha emitter with a half life of 87.80 $\pm$ 0.02 years. 2/ This isotope is also a neutron emitter due to a spontaneous fission half life of $4.8 \times 10^{10} \pm 0.2$ years. 3/ There are gamma rays emitted that are associated primarily with the alpha particle decay. 99.9% of the gamma rays (5.5×10^{8} photons per second per watt) are of less than 210 kev energy and rather easily shielded. 4/ The more penetrating radiation is due to gamma rays of 766 kev present in an abundance of 3.7×10^{5} photons per second per watt of Pu-238. 4/ Other papers in this session deal with specific radiation properties of plutonium-238 as it is used in heat source applications. The purpose of this paper is to discuss the factors that affect and sometimes control the radiation characteristics of plutonium fuel used in space applications. It is intended to explain why it is difficult to produce a plutonium space fuel that has radiation characteristics of pure plutonium-238. In general, this difficulty stems from the fact that reactor production of Pu-238 and subsequent processing techniques to fuel form strongly influence the radiation properties of the space fuel form. The space heat source plutonium material 2/ is 80% Pu-238, 16% Pu-239, 3% Pu-240, 1% Pu-241 and Pu-242 and 1×10^{-4}% (1 ppm) Pu-236. There is less than 0.5 percent total other actinides. This particular composition is obtained by mixing 84% Pu-238 from Np-237 neutron irradiation with 40% Pu-238 from reactor fuel reprocessing.

Reactor Production

Plutonium-238 is AEC reactor produced primarily by the neutron irradiation of Np-237 which in turn is produced in a reactor through the burnup of uranium-235. Plutonium-238 is also produced in the reactor fuel elements.

The reactor irradiation of neptunium results primarily in neutron capture by the Np-237. Subsequent beta particle decay of neptunium-238 produces 84% Pu-238. Neutron capture by Pu-238 while it is in the reactor produces the heavier plutonium isotopes. Forty percent Pu-238 with the remainder being primarily Pu-239 is obtained by periodic reprocessing of reactor fuel, a mixture of U-235 and U-238. Since the route to Pu-239 production is more straightforward than production of Pu-238, the percentage of Pu-239 is considerably higher.

To a much lesser but still significant extent, Np-237 undergoes nuclear reactions to produce Pu-236. These reactions are neutron capture with two neutron emissions to form Np-236 which beta decays into Pu-236 and gamma ray capture by Np-237 followed by a neutron emission and a beta decay to form Pu-236. Pu-236, with a half life of 2.8 years decays to U-232, an alpha emitter with a 72 year half life. U-232 then reaches secular equilibrium with its daughter products. One of these daughter products is the 2.6 MEV gamma emitter thallium-208 which grows in at a rate such that its maximum abundance is achieved in 18 years.

In the separation of plutonium from neptunium, Pu-236 will naturally follow the plutonium stream and become an undesirable contaminant in the plutonium product. The space fuel currently being produced contains on the order of 1 ppm Pu-236. As the U-232 and, hence, Tl-208 grow in, the gamma radiation from the fuel will increase so that after five years Tl-208 contributes equally to the total hard gamma radiation from Pu-238 space fuel. After five years, the hard gamma radiation is due primarily to the thallium-208.

The 84% plutonium-238 from reactor irradiation of neptunium contains slightly less than 1 ppm Pu-236. The 40% Pu-238 material contains more than 1 ppm Pu-236. The space fuel obtained from mixing these two products results in 80% Pu-238 and approximately 1 ppm Pu-236.

There are several actions that could be taken to reduce the level of the Pu-236 impurity. Each of these affects availability or cost or else requires time. Allowing the Pu-236 to decay, followed by chemical processing to remove the daughter products is an approach but since the half life of Pu-236 is 2.8 years, this method requires the storage of material for several years. This may be feasible at some future time when there is an inventory of plutonium material, but at this time it is used almost as fast as it is produced. Another approach would be to use only the plutonium material made from irradiation of Np-237. However, 84% Pu-238 is mixed with 40% Pu-238 in order to increase the availability of Pu-238 as an 80% material. Again, at some future date when the availability of Pu-238 is considerably greater than it is now, it should be possible to use only the higher percentage plutonium-238.

Fuel Form and Chemical Processing

The current space fuel form is a cermet consisting of 83% plutonium oxide and 17% molybdenum. This fuel form will be the third form of plutonium used on space missions. Plutonium metal was the first form, used in the early 1960's when the means of disposing of the plutonium was high altitude burnup when the heat source reentered the earth's atmosphere. This fuel form did not have extraneous radiation unless light element impurities were present, in which case neutron emission could increase due to alpha capture-neutron emission (α,n) reactions between the alpha particles from Pu-238 and the impurities. The melting point of plutonium metal and the need to have a more chemically inert form of plutonium limited the use of the metal which was replaced by plutonium oxide in the form of small spherical particles (microspheres). These microspheres were made by passing plutonium oxide powder through a plasma torch, a process which produced extremely inert particles. However, these oxide particles increased the fuel neutron radiation from approximately 4000 neutrons per second per gram of Pu-238 in the metal fuel, to over 20,000 neutrons per second per gram of Pu-238. The increase in neutron activity was due to (α, n) reactions on natural oxygen. Natural oxygen consists of the O-16, O-17, and O-18 isotopes. Only the O-17 and O-18 undergo (α, n) reactions at the alpha particle energies involved. Separation of O-16 from natural oxygen have been successful to a degree and oxygen enriched in O-16 has been used to exchange the natural oxygen in Pu oxide. Attempts were made to exchange the oxygen in microspheres with oxygen-16 but these attempts were not successful, quite possibly due to the impervious,

glassy surface of the microsphere.

Microspheres are being used in the SNAP-27 (ALSEP) missions but temperatures to which the fuel was exposed under normal generator operating conditions has continued to rise. Further, it was determined that the heat source should be designed to reenter from space and impact the earth's surface without breaking open. Through this, the fuel from should remain relatively unchanged. From these criteria evolved the solid fuel, plutonia molybdenum cermet. Molybdenum was chosen since it was found to be the most compatible metal with plutonium oxide at temperatures above 1000°C. Fabrication procedures for this cermet consist of essentially two steps, coating of oxide particles with molybdenum and hot pressing the coated particles into a disc shape of greater than ninety percent theoretical density. The oxide particles are coated by the chemical vapor deposition of MoF_6 in a fluidized bed system. MoF_6 was chosen because of the control it gives over the quantity of molybdenum coated onto the particles. This fuel form has the highest neutron radiation of those discussed here. This is due to (α, n) reactions with fluorine. Fluorine has a large cross section for this reaction. Steps have been taken to limit the neutron radiation to less than 30,000 neutrons per second per gram. This level is achieved by a combination of exchanging the PuO_2 particles with O-16 prior to their being coated and bake-out of the discs following fabrication. Without these steps, the neutron radiation would be at least ten to fifteen thousand neutrons per second per gram greater.

The fluorine impurity could be eliminated by using another method for introducing the molybdenum into the fuel form. There are alternative methods for carrying out this step. Coating with molybdenum chloride is one method that is being developed. So far this method has been more time consuming and the molybdenum coat thickness more difficult to control. However, this method is being used to produce a limited quantity of fuel for thermoelectric generators to be used on a NASA Pioneer mission.

It should become increasingly less difficult to obtain plutonium fuel that is very low in or completely free from radiation producing impurities. As commercial power reactors become more plentiful, more Np-237 becomes available and the production of Pu-238 without blending with lower Pu-238 isotopic ratio material becomes more feasible. Curium-242, another by-product of commerical power reactor operation, decays into Pu-238. Recovery of Cm-242, storing it, and periodic extraction of the Pu-238 should produce essentially 100% Pu-238. Unfortunately Cm-242 will be in very short supply until the late 1970's or early 1980's and Pu-238 from this source will be coveted by those developing nuclear power for medical applications. In addition to the chloride process, there are other possible ways to reduce extraneous neutron levels. These include powder metallurgy which involves mixing very fine molybdenum powder with O-16 enriched PuO_2 followed by hot pressing to the final fuel form.

In terms of timing, it is difficult to predict the exact point in time when radiation will be at a given level. However, there are solutions for ridding the space fuel of both the gamma and neutron emitting impurities and certainly within the next few years a fuel form should be available that will satisfy both the generator designers and those who are responsible for determining the radiation levels in space.

REFERENCES

1. T. K. Keenan is a Research Scientist at the Los Alamos Scientific Laboratory
   R. E. Vallee is Manager, Non-Weapons Programs, Mound Laboratory
   J. A. Powers is Chief, Isotopes & Materials Branch, Space Nuclear Systems, AEC
2. Plutonium-238 Isotopic Fuel Form Data Sheets, MLM-1691.
3. Mound Laboratory Chemistry & Physics Progress Report: Oct.-Dec. 1970, MLM-1792.
4. C.M. Lederer, F. Asaro, I. Perlman, "Alpha Decay of Plutonium-238," Nuclear Chemistry Report of 1968, UCRL 18667, Pages 3-8.

Nuclear Radiation Environment Analysis for Thermoelectric Outer Planet Spacecraft*

H. S. Davis
Jet Propulsion Laboratory

E. F. Koprowski
ART Research Corporation

The radioisotope thermoelectric generator (RTG) nuclear radiation environment analysis of a recent design of the Thermoelectric Outer Planet Spacecraft (TOPS) is presented. The neutron and gamma-ray transport calculations were performed using Monte Carlo methods and a three-dimensional geometric model of the spacecraft. The results are compared with similar calculations performed for an earlier design.

I. INTRODUCTION

Due to the great distance between the sun and the four outer planets, a spacecraft designed to conduct outer planet missions will require a solar-independent source of electrical power. At the Jet Propulsion Laboratory, the spacecraft currently being designed for such missions is equipped with radioisotope thermoelectric generators (RTG's) and is appropriately named the Thermoelectric Outer Planet Spacecraft (TOPS).

Important inputs to the TOPS design are the RTG radiation intensities and energy spectra at radiation-sensitive scientific instrument locations. This information can be used to confirm that the radiation levels to which the instruments will be exposed are below established interference and/or damage thresholds (ref. 1). The information can also be used to estimate the effects of spacecraft configuration changes on shielding and scattering.

II. ANALYSIS

The gamma and neutron radiation transport analysis was performed using the RAMPART Monte Carlo computer code (ref. 2), a revised and expanded version of the FASTER code (ref. 3). The code treats the entire spectrum of particle energies simultaneously and makes considerable use of importance sampling.

The spacecraft design for which the radiation environment was calculated is configuration 12k. Although there are some structural differences, this newer configuration differs from the previous one, configuration 12j (ref. 4), primarily in the arrangement of the RTG's. The RTG's are mounted four in tandem in the earlier design, while pairs of RTG's are mounted side-by-side in the new design. The new configuration is the preferred one from a safety and operations point of view.

A structurally simplified form of the spacecraft which preserves the essential features of its shape and mass formed the basic input. The three-dimensional geometric model consisted of 66 plane or quadratic surfaces bounding 70 material regions of homogeneous density. The model contained the 4.3-m-diameter antenna dish, subdish, feedhorn, and hub, the electronics compartment, the propulsion bay (including the hydrazine fuel and fuel tank), and the four RTG's. The material compositions, weights, and densities for the regions defining the spacecraft, obtained from preliminary design information, are presented in table 1. The antenna dish is a homogeneous mixture of the Chromel-R mesh and the 48 aluminum ribs. For the electronics compartment, the following homogeneous composition was assumed, weight-%: plastics, 40; copper, 34; aluminum, 23; silicon dioxide, 3. The propulsion bay was approximated with a 50/50 mixture by weight of aluminum and iron.

Prior to the Monte Carlo transport analysis, the pairs of RTG's were each doubly rotated. The rotation angles orient the pairs of RTG's such that the direction of maximum RTG self-shielding (axial direction) is toward the region occupied by the science payload.

Table 1.--Material compositions for TOPS configuration 12k geometric model.

REGION DESCRIPTION	COMPOSITION	WEIGHT, kg	TOTAL WEIGHT, kg	DENSITY, g/cm^3
ANTENNA SECTION DISH	Cr	0.19		
	Ni	0.68	8.20	0.0413
	Al	7.30		
	Fe	0.03		
HUB	Al	9.55	9.55	0.0179
FEED HORN	Al	5.45	5.45	0.0875
SUB-DISH	Al	9.10	9.10	2.7
SPACECRAFT BUS ELECTRONICS CHASSIS	Al	25.9	25.9	2.7
ELECTRONICS COMPARTMENT	H	5.68		
	C	75.5		
	O	3.27	202.4	0.446
	Si	2.85		
	Cu	68.7		
	Al	46.4		
FUEL TANK	Ti	10.5	10.5	4.5
FUEL (FULL TANK)	N_2H_4	56.4	56.4	1.0
PROPULSION BAY (OTHER THAN FUEL TANK AND CONTENTS)	Al	33.4	66.8	0.132
	Fe	33.4		

*This paper presents the results of one phase of research carried out at the Jet Propulsion Laboratory, California Institute of Technology, under Contract No. NAS 7-100, sponsored by the National Aeronautics and Space Administration.

III. RTG RADIATION

The heat source used in the calculations consisted of solid solution cermet fuel disks stacked in a cylindrical, refractory metal capsule for a total loading of 1000 W(th). The fuel was assumed to be five-year-old commercial grade PuO_2 with 1.2 ppm ^{236}Pu. Two of these heat sources in-line comprise one multihundred-watt (MHW) RTG (ref. 5). The 2000-W(th) MHW-RTG is shown schematically in fig. 1. The spacecraft carries a complement of four RTG's (eight heat sources) on board; i.e., 8000 W(th). Finally, a converter jacket was simulated in order to include the shielding effect of the thermoelectric materials.

The plane between the two pairs of RTG's perpendicular to the plane in which they lie constitutes a plane of symmetry for the calculation. Using this symmetry, only half of the heat sources emitted radiation (but with double intensity) during the calculation. The remaining four heat sources were passive and served merely to absorb or scatter neutrons and gammas. This scheme makes the sampling process more efficient for point detectors located in the plane of symmetry.

The gamma source spectrum (ref. 6) was described using 21 energy groups with the Lawrence Radiation Laboratory gamma cross sections, including the photoelectric and pair production processes. Compton scattering is treated explicitly by the code. The neutron source spectrum (ref. 7) was described using 23 energy group P_0 cross sections with a transport correction for elastic scattering. Elastic scattering for the hydrazine component in the hydrazine fuel is handled explicitly in the program. The neutron spectrum was multiplied by a factor of 1.3 to simulate subcritical multiplication.

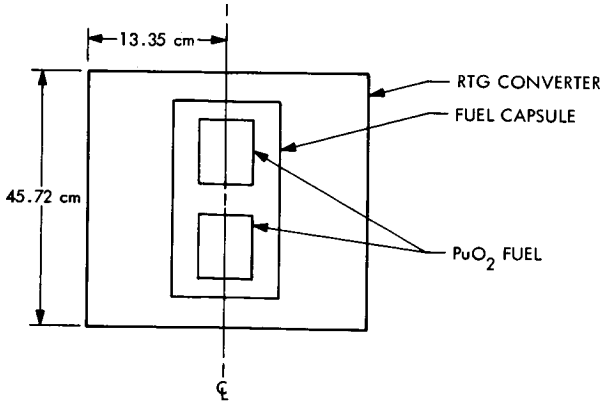

Figure 1.–Schematic diagram of 2000-W(th) MWH-RTG.

The MHW-RTG neutron and gamma leakage fluxes were calculated with the RAMPART code, using 28 point detectors at 15-deg intervals placed 50, 100, 200, and 400 cm from the RTG geometric center. Due to cylindrical symmetry, it was necessary to calculate the fluxes over only one quadrant. Figure 2 is a polar plot of the calculated "bare" MHW-RTG neutron and gamma-ray isoflux contours. Note the interesting result that the neutron and gamma-ray isoflux curves are similar in shape.

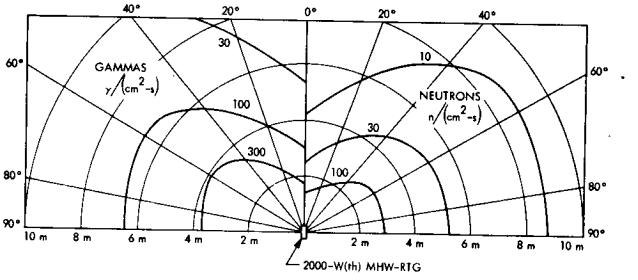

Figure 2.–Neutron and gamma-ray isoflux contours for the "bare" MWH-RTG (coordinate system origin at RTG geometric center).

IV. RESULTS AND DISCUSSION

For the spacecraft radiation analysis, a total of 38 point detectors located in the bus and in the science area were used. All but four of these detectors were placed in the plane of symmetry. The results are based on 200 history packets for both neutrons and gamma rays. The gamma and neutron intensities near the science payload were normalized to a single point, run for 800 histories, at the science payload. As in the case of the "bare" RTG, the gamma-ray and neutron isoflux contours are similar in shape. Therefore, for clarity, single lines were used in fig. 3 to map the neutron and gamma-ray isoflux contours. Note that the science payload is not located in a region of minimum RTG radiation. This condition is explained by the presence of the full tank of hydrazine fuel in the propulsion bay and by the scattering contribution from the antenna section. Nevertheless, comparison of these dose rates with those due to the "bare" RTG shows a reduction in intensity of about an order of magnitude due to the spacecraft structure. An increase in intensity of a factor of 2 to 5 for gammas and 1.5 to 2.5 for neutrons was observed for detectors lying directly behind the fuel tank when the tank was empty.

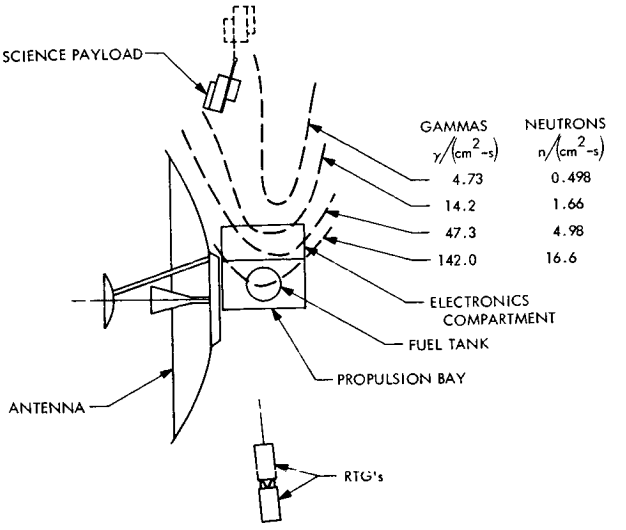

Figure 3. –Neutron and gamma-ray isoflux contours for TOPS configuration 12k.

Gamma-ray dose rates along traverses in the plane of symmetry and perpendicular to the plane of symmetry through the science payload are shown in figs. 4a and 4b. In the figures, the gamma dose rates of configuration 12k are compared with those from configuration 12j. The gamma dose rates are higher for the new TOPS configuration by about a factor of seven. Note in fig. 4b how much more quickly the "bare" RTG values are assumed in configuration 12k. This condition is due to the fact that the shielding cone of the spacecraft bus is much smaller in this RTG arrangement. The overall increase in the radiation levels throughout the spacecraft is not unexpected, since configuration 12j was optimized to provide maximum RTG self-shielding.

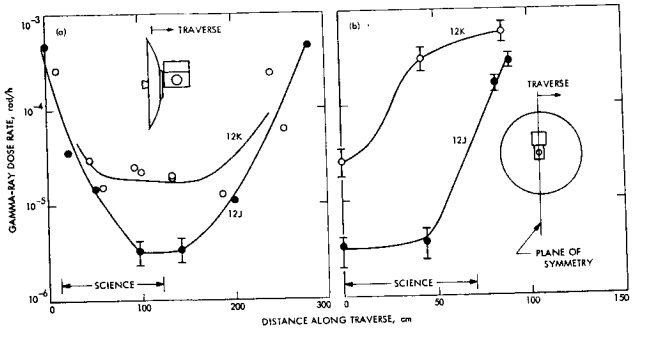

Figure 4. –Gamma-ray dose rate: (a) along a traverse in plane of symmetry at science payload; (b) perpendicular to plane of symmetry through science payload.

Figure 5 compares the differential neutron flux at the science payload with the axial RTG differential neutron leakage flux. Figure 6 makes a similar comparison for gamma radiation.

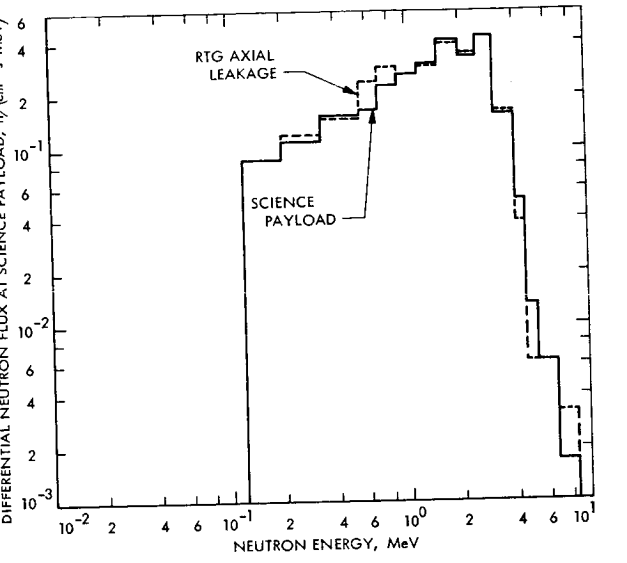

Figure 5. –Differential neutron flux vs neutron energy (data normalized at 2.6 MeV).

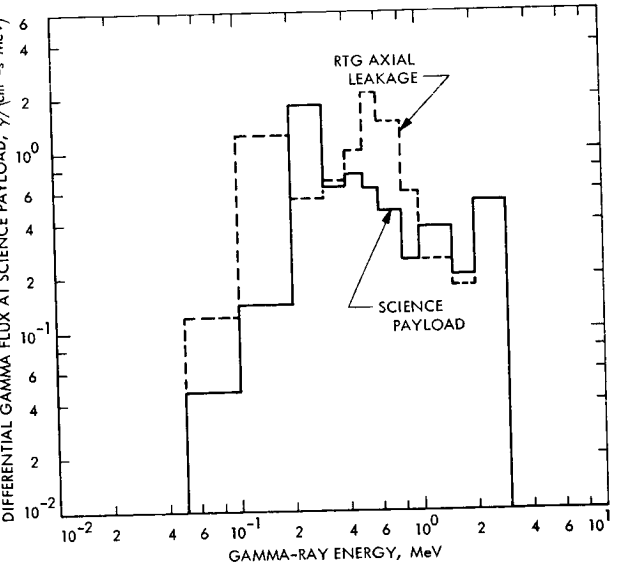

Figure 6. –Differential gamma-ray flux vs gamma-ray energy (data normalized at 2.6 MeV).

Ratios of configuration 12k scattering data to configuration 12j scattering data at the science payload are given in table 2. Standard errors are from 20 to 50% for gammas and 10 to 30% for neutrons. The table shows that higher orders of scatter are more important in the new configuration and that the effective buildup factors are twice as large. The scattering contribution from the antenna dish is lower for the new configuration mainly because the mass of the Chromel-R mesh was reduced to 0.9 kg from 3.15 kg. On the other hand, the scattering contribution from the antenna hub is larger due to the increase in solid angle as seen from the RTG's. The scattering contribution from the entire antenna section is about 30% of the total.

A TOPS radiation test model (RTM) is presently under construction at the Jet Propulsion Laboratory. The RTM construction will conform to the analytical model as closely as possible. When completed, the RTM will be used to verify experimentally the analytical results reported in this paper and to provide detailed data on the radiation environment of the science instruments.

Table 2. –Ratios of configuration 12k scattering data to configuration 12j scattering data at science payload.

	EFFECTIVE BUILDUP FACTOR	ANTENNA DISH SCATTER	ORDER OF SCATTER				
			0	1	2	3	4
GAMMAS	2.0	0.4	1.0	0.7	1.5	1.0	4.0
NEUTRONS	2.0	0.6	0.4	0.7	0.8	7.0	2.3

REFERENCES

1. Parker, R. H.: Radiation Effects on Science Instruments in Grand Tour Type Missions, this conference, Proceedings of the National Symposium on Natural and Manmade Radiation in Space, Las Vegas, Nevada, 1971.
2. Jordan, T. M.: RAMPART, A Time-Dependent, Generalized Geometry Monte Carlo Program for the Transport of Neutrons, Photons and Electrons, ART-49, ART Research Corporation, Los Angeles, Calif., 1970.
3. Jordan, T. M.: FASTER, A Fortran Analytic Solution of the Transport Equation by Random Sampling, WANL-PR-(LL)-010, vol. 9, Jun. 1967.
4. Anno, G. H.; and Wolf, F.: TOPS RTG Nuclear Radiation Environment Analysis, Trans. Am. Nucl. Soc., vol. 13, 1970, p. 535.
5. The Multihundred-Watt Radioisotope Thermoelectric Generator, developed by the General Electric Company, Space Division, King of Prussia, Pa., under A. E. C. contract.
6. Gingo, P. J.; and Dore, M. A.: Gamma Characteristics of Plutonium Dioxide Fuel, NASA TR 32-1481, National Aeronautics and Space Administration, Washington, D. C., Jun. 15, 1970.
7. Gingo, P. J.: private communication.

THE PROGRAM AT JPL TO INVESTIGATE THE NUCLEAR INTERACTION OF RTGs WITH SCIENTIFIC INSTRUMENTS ON DEEP SPACE PROBES*

Vincent Truscello, Member of the Technical Staff

The Jet Propulsion Laboratory

A major concern in the integration of a radioisotope thermoelectric generator (RTG) with a spacecraft designed to explore the outer planets is the effect of the emitted radiation on the normal operation of scientific instruments. This paper discusses the program presently being conducted at the Jet Propulsion Laboratory to evaluate these effects. The problem is being approached in both an analytical and experimental manner. The necessary techniques and tools have been developed to allow accurate calculation of the neutron and gamma spectrum emanating from the RTG. The specific sources of radiation have been identified and quantified. Monte Carlo techniques are then employed to perform the nuclear transport calculations. The results of these studies are presented.

An extensive experimental program has been initiated to measure the response of a number of scientific components to the nuclear radiation. Such devices as Geiger Muller tubes, solid state detectors and electron multipliers have been identified as being most probable for use on these missions and extremely sensitive to gamma radiation. Experiments on these devices are being conducted in the JPL radiation laboratory. The capabilities of this laboratory are discussed as well as the results of some of the experiments.

The technique used to measure the response of instruments is to irradiate them with monoenergetic radiation sources. The energy range of interest is between 275 kev to 2800 kev. Appoximately seven isotopes have been selected which provide emissions in this range. Analytical techniques have been developed which fold the measured energy response of the instrument with the calculated energy spectrum emitted by the RTG. Shielding studies are then performed to determine the thickness of shield required to reduce the spurious count level of the instrument to an acceptable level.

The final design must be qualified by irradiating the instrument with the polyenergetic spectrum emitted by the Pu-238 fuel capsule. Since actual fuel capsules are not generally available and since the spectrum from a generator will change with time due to aging of the fuel (spectrum actually becomes harder and more intense due to buildup of the daughter products of the impurity Pu-236) it becomes more practical to use simulated sources.

With the use of isotope powered generators it is now possible for NASA to conduct exploration of planets too remote from the sun to effectively use solar array power concepts. One such set of missions under consideration by the Jet Propulsion Laboratory is the outer planet grand tour missions having possible launches in the 1976 - 1979 time period. The inclusion of isotope systems on these spacecraft introduces a heretofore unconfronted problem to the Laboratory. The radioisotope used as the heat source emits both neutron and gamma radiation as a result of its natural decay. This radiation will have a significant effect on the operation of science instruments designed to measure low level particulate and short wave-length electromagnetic radiation within the interplanetary environment.

In preparation to confront this new environment, the Laboratory has directed a portion of its R&D activities to help define the exact nature of the problem and to develop technical tools and facilities to carefully study and resolve any potential interference which may exist. Over the past three years a rather extensive radiation program has evolved. The purpose of this paper is to give a brief review of the work that has been performed and to indicate the areas of study that are presently underway in the investigation

*This paper presents the results of one phase of research carried out at the Jet Propulsion Laboratory, California Institute of Technology, under Contract No. NAS 7-100, sponsored by the National Aeronautics and Space Administration.

of the RTG-science interference.

SOURCES OF RADIATION

The gamma and neutron field in the vicinity of an RTG originates primarily from the radioactivity of the Pu^{238} and associated radioactive nuclides in the heat source. Gamma rays emitted by the plutonium dioxide fuel are derived from three prominent sources: (1) Gamma radiation from plutonium isotopes and their decay products exclusive of Pu^{236}. This includes photons produced by the plutonium isotopes due to natural radioactivity, prompt gammas from fission, and the decay of fission products. (2) Gamma radiation from the radioactive decay of Pu^{236} and its daughter nucleus; and (3) Gamma radiation from alpha particle interaction with the O^{18} isotope. The interaction O^{18} (α,n) Ne^{21} produces Ne^{21} in excited states with the subsequent emission of gamma rays.

The magnitudes of these sources were compiled at JPL several years ago by Gingo and Dore (Ref. 1) based on data available in the literature at the time on the decay and emission characteristics of the various isotopes in the fuel. More recently Dore (Ref. 2) updated this information based on recent Pu^{238} experiments conducted at JPL by Reier (Ref. 3). The emission characteristics presently being used by JPL are shown in Table 1.

Table 1 Emission Characteristics of a Plutonium Heat Source

ISOTOPE: 238Pu	
Energy (keV)	γ/dis/sec (x 10^8)
1085.4	0.11
1041.8	0.20
1001.03	1.08
946.0	0.13
941.9	0.58
926.72	0.71
904.37	0.072
883.23	1.270
880.5	0.23
851.7	1.64
808.25 / 805.8	0.999
786.30	4.98
766.39	26.7
742.77	6.35
708.42	0.38
706.1	0.14
299.2	0.07
258.3	0.011
235.9	0.01
207.6 / 200.9	5.0
152.71	$1.27 \cdot 10^3$
99.84	$9.20 \cdot 10^3$
43.50	$3.80 \cdot 10^4$
17.0	$1.30 \cdot 10^7$

ISOTOPE: 239Pu	
Energy (keV)	γ/dis/sec (x 10^7)
770.0	2.0
650.0	8.0
414.0	110.0
375.0	125.0
340.0	66.0
207.0	44.0
125.0	150.0
51.6	700.0
38.6	200.0
17.0	9900.0

ISOTOPE: 212Pb	
Energy (keV)	γ/dis/sec
415.2	0.0016
300.3	0.041
238.4	0.50
176.7	0.0007
116.0	0.0054
ISOTOPE: 208Ti (36%)	
2615.0	1.00
1093.0	0.0046
861.4	0.124
763.0	0.034
584.5	0.876
510.8	0.253
486.0	0.001
277.0	0.091
ISOTOPE: 236Pu	
645.0	$2.40 \cdot 10^{-6}$
570.0	$1.00 \cdot 10^{-6}$
520.0	$1.70 \cdot 10^{-6}$
165.0	$6.60 \cdot 10^{-6}$
110.0	$1.20 \cdot 10^{-4}$
46.0	$4.70 \cdot 10^{-4}$

ISOTOPE: 212Bi		
Energy (keV)	β (64%)	α (36%)
	γ/dis/sec	
1800.0	0.0017	
1621.0	0.0247	
1512.8	0.0061	
1078.2	0.0073	
1073.0	0.001	
952.1	0.0025	
893.9	0.0058	
785.0	0.016	
729.9	0.104	
493.0 / 473.0 / 460.0 / 453.0 / 434.0	0.008	0.0042
328.0		0.00110
288.2		0.0028
288.0	0.005	
40.0	0.02	

Table 1 (Cont'd)

Spontaneous Fission and Fission Product Gammas

Group	Energy Interval (MeV)	Spontaneous	Equilibrium Fission Product γ/sec/gm-PuO_2	Total
1	6.0 - 7.0	$7.120 \cdot 10^0$	0.0	$7.120 \cdot 10^0$
2	5.0 - 6.0	$2.103 \cdot 10^1$	0.0	$2.103 \cdot 10^1$
3	4.0 - 5.0	$6.210 \cdot 10^1$	0.0	$6.210 \cdot 10^1$
4	3.0 - 4.0	$1.834 \cdot 10^2$	0.0	$1.834 \cdot 10^2$
5	2.0 - 3.0	$5.416 \cdot 10^2$	$3.446 \cdot 10^1$	$5.761 \cdot 10^2$
6	1.8 - 2.0	$1.981 \cdot 10^2$	$1.206 \cdot 10^1$	$2.102 \cdot 10^2$
7	1.6 - 1.8	$2.460 \cdot 10^2$	$2.542 \cdot 10^1$	$2.714 \cdot 10^2$
8	1.4 - 1.6	$3.056 \cdot 10^2$	$3.188 \cdot 10^1$	$3.375 \cdot 10^2$
9	1.2 - 1.4	$3.794 \cdot 10^2$	$1.594 \cdot 10^1$	$3.953 \cdot 10^2$
10	1.0 - 1.2	$4.708 \cdot 10^2$	$6.893 \cdot 10^0$	$4.777 \cdot 10^2$
11	0.9 - 1.0	$2.767 \cdot 10^2$	$1.529 \cdot 10^1$	$2.920 \cdot 10^2$
12	0.8 - 0.9	$3.084 \cdot 10^2$	$4.265 \cdot 10^1$	$3.510 \cdot 10^2$
13	0.7 - 0.8	$3.437 \cdot 10^2$	$5.837 \cdot 10^1$	$4.021 \cdot 10^2$
14	0.6 - 0.7	$3.830 \cdot 10^2$	$6.117 \cdot 10^1$	$4.442 \cdot 10^2$
15	0.5 - 0.6	$4.268 \cdot 10^2$	$5.902 \cdot 10^1$	$4.858 \cdot 10^2$
16	0.4 - 0.5	$4.755 \cdot 10^2$	$4.933 \cdot 10^1$	$5.248 \cdot 10^2$
17	0.3 - 0.4	$5.296 \cdot 10^2$	$3.770 \cdot 10^1$	$5.673 \cdot 10^2$
18	0.2 - 0.3	$5.906 \cdot 10^2$	$2.628 \cdot 10^1$	$6.169 \cdot 10^2$
19	0.044 - 0.2	$1.059 \cdot 10^3$	$2.046 \cdot 10^1$	$1.079 \cdot 10^3$
20	0.001 - 0.044	$3.248 \cdot 10^2$	0.0	$3.248 \cdot 10^2$

The neutron field from a Pu-238 heat source is mainly due to (α,n) reactions with low impurity elements associated with the plutonium oxide in the heat source. Of particular concern is the reaction with O^{18}. The smallest neutron contribution is due to the spontaneous fission of the plutonium content and to induced fission reactions. The neutron emission characteristics of a Pu-238 heat source have been studied at JPL and were reported by Taherzadeh in Reference 4. The total neutron yield from spontaneous fission was found to be 2800 n/sec per gram Pu^{238}. The number of neutrons generated from the reaction of alpha particles with impurity elements depends on the type and concentration of these impurities. Table 2 indicates an assumed concentration of impurity elements and their respective yields. The total neutron yield, excluding reactions with the oxygen associated with the PuO_2 compound, is 12,900 n/sec/gm Pu^{238} for the assumed concentration of impurities. Alpha particle reactions with O^{18} in the plutonium compound yields 19,900 n/sec/gm Pu^{238}. Both of these contributions can be decreased by reducing the impurity concentrations (particularly fluorine or by exchanging the O^{18} with O^{16}). The final source of neutrons is as a result of additional fissions induced by the available neutron flux. The yield is highly dependent upon the heat source geometry and can contribute from 15 to 30% of the total neutron field.

There is a continuing effort at JPL to maintain close liaison with the fuel production centers in order to be appraised of the exact impurities existing in the fuel. With this data highly accurate estimates of the neutron and gamma emission characteristics of the heat source can be obtained.

Table 2 Neutron Yields due to (α, n) reactions with Impurities

Impurity Elements	PPM in PuO_2	Yield/PPM (n/gm PuO_2/sec/PPM)	Yield
Li	1	4.64	4.64
Be	10	148.80	1488.00
B	20	32.80	656.00
C	500	0.20	100.00
O	11750*	0.10	1175.00
F	250	18.70	4517.50
Na	300	2.00	600.00
Mg	50	1.93	96.50
Al	400	1.08	432.00
Si	441	0.240	105.84
Others	1200	0.03	36.00
		Total	(9211.50 n/sec gm PuO_2 - 12,900 n/sec gm Pu^{238}

*Oxygen concentration due to thO_2 content

DETERMINATION OF RADIATION SPECTRUM FROM RTG

Once the gamma and neutron source strengths are established the field surrounding the RTG is determined by application of Monte Carlo transport codes to a specific geometry. The Monte Carlo code used to perform the calculations at JPL (Ref. 5) utilizes "importance functions" to achieve far better statistics than a straight Monte Carlo simulation would yield for a comparable number of particle histories. The basic technique is to sample heavily those events which are most likely to contribute significantly to the results, while only lightly sampling the others. Generally, one considers the high energy source particles to a disproportionately large extent, since they have the best chance of eventually escaping the RTG.

The neutron and gamma flux spectra from the RTG are determined for 20 energy groups ranging in energy from 1 keV to 7 MeV. The most significant complication in these calculations is the fact that the gamma spectrum will harden with time due to buildup of daughter products in the decay chain of the Pu^{236} which is present in the fuel at a level of about 1.2 ppm. The maximum radiation level occurs about 18 years after fuel processing. Figure 1 shows how the gamma spectrum from a typical fuel capsule will vary as a function of time.

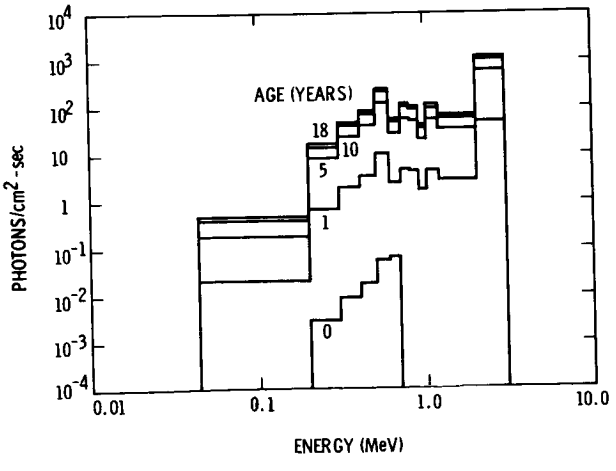

DEVELOPMENT OF SIMULATED RTG

Although JPL has developed computer techniques to accurately calculate the radiation field around an RTG, it is recognized that experiments must be performed with actual sources to substantiate any predictions made regarding the response of instruments to the radiation environment. Since actual Pu-238 fueled sources are not likely to be available on demand at JPL in order to conduct the necessary developmental activities, simulated RTG's are being designed for use. The details of this work are discussed in a paper by Reier (Ref. 6) to be given at this conference. It will suffice here to state that these sources duplicate both the geometry of an actual fuel capsule and RTG as well as the radiation spectrum emitted. This is accomplished with the use of several gamma emitting isotopes, notably Th^{228} as well as Cf^{252} to produce the neutron environment. These sources can then be used to perform full spacecraft-level radiation testing. The advantages of using this type of source are several-fold. First, it allows the radiation testing to be done easily in the developmental process, long before actual fueled generators are available; second, it can be accomplished in a safer manner and with less stringent "nuclear safe" facilities since one is using only millicurie amounts of radioactive material versus the tens of thousands of curies of the Pu 238 alpha emitting isotope; and third and most important, it allows measurements to be made with a source that represents an aged fuel. The gamma radiation spectrum and intensity change with time and reach a maximum after 18 years; it is important to reproduce this worst case situation since the missions considered by JPL for use of RTG's have lifetime approaching 10 years.

SPACECRAFT MAPPING AND TEST

Transport codes similar to those used in determining the radiation field from an RTG are used in mapping a complete spacecraft. JPL has initiated the development of techniques to construct accurate analytical models of the spacecraft. A detailed discussion on this subject will appear at this session of the conference in a subsequent paper (Ref. 7).

As part of its overall program, JPL plans to construct and test an early version of a spacecraft for the purpose of conducting radiation field mapping and instrument shielding studies. This mechanical model spacecraft is known as the Radiation Test Model or RTM and is being developed under the auspices of the Thermoelectric Outer Planet Spacecraft (TOPS) project. With this model, both γ-ray and neutron radiation levels will be obtained throughout a representative TOPS spacecraft configuration. The source of radiation will be the simulated RTGs described earlier in this paper. The objectives of this program are to:

1. Identify in detail the radiation levels at scientific instrument locations.
2. Identify radiation levels at sensitive electronic equipment locations.
3. Investigate the effects of spacecraft configuration changes on shielding and scattering.
4. Provide designers with radiation data for tradeoffs for spacecraft configuration design.
5. Provide experimental verification of existing analytic methods and establish experimental techniques.

RTG RADIATION FACILITY

In order to perform the experimental radiation program at JPL a developmental laboratory has been constructed. This facility allows spectrum measurements to be performed on simulated as well as actual fuel capsules, and enables science components and instruments to be irradiated and their response determined. A sketch of the facility is shown in Figure 2. It is an underground building located in a low population density area at JPL. The overall dimensions of the building are 67' x 16' x 9'. The walls, floor and ceiling are reinforced concrete approximately 14 inches thick. The building is about 5' below ground level.

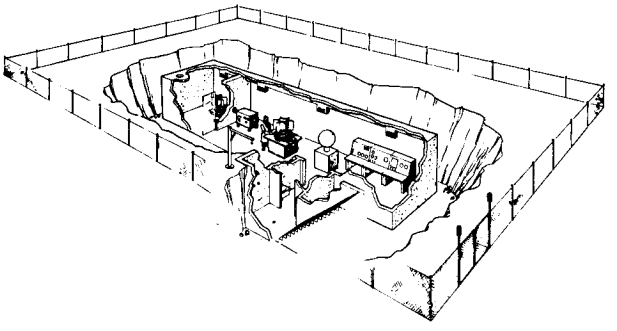

JET PROPULSION LABORATORY RADIOISOTOPE THERMOELECTRIC GENERATOR (RTG) TEST LABORATORY

This developmental laboratory is equippea with all of the necessary radiation safety monitoring equipment to handle alpha as well as gamma emitting isotopes. There are five major spectrometer systems available for spectrum measurements. These are shown in Table 3. Thus both neutron and gamma spectroscopy can be conducted. This equipment is used in conjunction with a Nuclear Data 4096 channel analyzer with tape transport for data readout.

Table 3 Spectrometer Systems

20 cm^3 Ge (Li) Gamma ray Spectrometer

7.62 x 7.62 cm NaI (Ti) Gamma ray Spectrometer

Ne -213 Organic liquid scintillation neutron Spectrometer

He -3 solid state sandwich neutron spectrometer

Thermoluminescence detection system

Several radioisotope sources are available to enable calibration of equipment and irradiation of science components. The gamma emitters available are given in Table 4. In addition, there are a number of polyenergetic sources. These include several SNAP-15A Pu^{238} metal heat sources, a PuBe neutron source, a Cf^{252} source, and an early version of a simulated PuO_2 source which was designed at JPL. This source was designed to reproduce the gamma-ray spectrum expected from a SNAP-27 fuel capsule.

Table 4 Standard Gamma Ray Calibration Sources

Radioisotope	Energy of Major γ-Ray (keV)
Am 241	59.5
Cd 109	87.7
Co 57	122 and 137
Hg 203	279.2
Cr 51	320.1
Sr 85	514
Cs 137	661.6
Mn 54	834.8
Zn 65	1115.4
Co 60	1173.2 and 1332.2
Na 22	1274.5
Ba 133	Many
Co 56	Many
Na 24	1370 and 2750
Co 57	122 and 137

GAMMA AND NEUTRON SPECTROSCOPY

An important aspect of the JPL radiation program is the ability to measure and interpret accurately the radiation fields from an RTG. In order to properly predict the response of an instrument to a polyenergetic source such as an RTG, the intensity and spectrum of the radiation must be measured quite accurately. In a previous section the equipment available to perform these measurements was discussed. The high resolution spectrometer, consisting of a Ge(Li) crystal having an active volume of 21.8 cm^3 and a resolution of about 3 keV at 1.33 MeV, has recently enabled a better definition of the radiation spectrum from a Pu^{238} heat source. This work was performed on a 1.5 W(t) SNAP 15A heat source by Reier and is documented in Ref. (3 and 8). The data given in Table 1 represents the latest measurements of the emission characteristics of Pu-238. An important outcome of this work was the development of a technique to accurately measure the concentration of Pu^{236} in a fuel capsule from the measurement of its emission characteristics. If a measurement is made of the absolute intensity of a transition of one of the daughter products of Pu^{236}, the amount of Pu^{236} in the fuel at the time the fuel was processed can be calculated. Since the Po^{212} - Tl^{208}

branching ratio is well known, an absolute measurement of the intensity of the radiation emitted during this decay (a 2.615 MeV photon is emitted for each decay) identifies the original amount of Pu^{236} present in the fuel. It is felt that by the use of this technique, a precision of 10% is easily obtainable with a sample that is several months old and has a nominal concentration of 1 ppm of Pu^{236}.

Another interesting problem which has been studied at JPL deals with interpretation of spectrum measurements. The experimentally determined spectrum of a given radiation source generally does not represent the true radiation characteristic of the source. This is mainly due to detector resolution and photon scattering within the crystal, resulting in partial energy deposition. To obtain the true radiation spectrum one employs some form of unfolding technique. Many codes are indicated in the literature for the unfolding of data obtained with a Na(I) crystal. However, until recently no such tool was available for the unfolding of the gamma-ray spectra continuum obtained with the high resolution lithium-drifted germanium gamma ray spectrometers. Such a tool is now available (Ref. 9) from work sponsored at the Jet Propulsion Laboratory. The laboratory now has available all of the necessary unfolding codes to interpret the data from gamma as well as neutron spectrometers.

DETERMINATION OF COMPONENT RESPONSE

The approach at JPL has not been merely to determine the response of science instruments to the mixed radiation field from a specific source. Instrument response is a function of both types and energy of the particle, and since the energy spectrum from any RTG depends on the geometry, materials of construction, and the age of the Pu^{238} fuel, it is more meaningful to measure this response with monoenergetic radiation sources. Seven isotopes are being used to perform these experiments. Table 5 gives the isotopes and their gamma emission energies. An extensive number of nuclear detectors which form the components of the most sensitive scientific instrument packages have been obtained for investigation. These devices are listed in Table 6.

Table 5 Monoenergetic Gamma Emitters Used for Component Response

Radioisotope	Energy (keV)
Hg 203	279
Sr 85	514
Cs 137	662
Mn 54	835
Zn 65	1115
Co 60	1173 and 1332
Na 22	1274
Na 24	2750

Table 6 Radiation detectors available for Component Response Studies

EON 6213 G-M Counter

Channeltrons (Bendix 4010, EMR)

Silicon Surface Barrier detectors

Silicon Lithium drifted detectors

Photomultiplier tubes

Pilot B plastic scintillators

Cesium Iodide (Na) crystals

Two of these devices, the GM tube and solid state detectors, have been extensively characterized at JPL and the results documented in the open literature (Refs. 10, 11, 12). Figure 3 shows the experimental results obtained for a miniature Geiger-Mueller tube, while Figure 4 indicates some of the experimental results obtained with solid state detectors of various sizes. Primarily, these devices respond to the electrons that are generated by the gamma radiation in the structure material surrounding the sensitive regions of the detectors. Significantly, it was found that the atomic number and configuration of the surrounding structure had little to do with the magnitude of the response. For example lucite and aluminum were just as effective in producing spurious counts as was a very high atomic number material such as lead. Moreover, placing absorbers both in front and back of the detector did not alter the response significantly. Thus, it was concluded that, for engineering purposes, the maximum response of a detector can be effectively measured by conducting experiments in which a thin sheet of aluminum is placed immediately in front of the detector. The aluminum need only be of a thickness equivalent to the maximum range of an electron produced by the gamma ray in question.

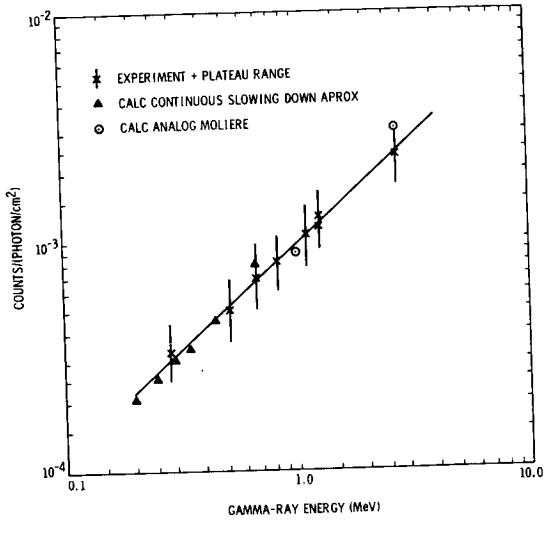

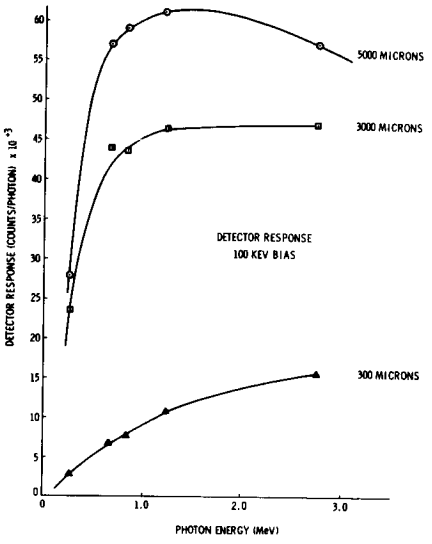

As part of the JPL overall program we are not only measuring the response of devices to radiation but in addition have developed analytical models to predict response. By comparing the results with experiments we have been able to improve our models significantly. Such models enable us to predict the performance of devices which are of different size, or configuration than the unit which has been tested and also enables predictions of devices not available for experiments. Of more importance is the fact that there is a complete class of experiments which are extremely difficult to perform and for which analytical models are preferred. These are experiments to determine the response of devices to monoenergetic neutrons. A clean field of neutrons without accompanying gamma rays is not possible. Since detectors are generally more sensitive to gammas than to neutrons, an accurate understanding of the response to neutrons is very difficult. Of course time-of-flight techniques in which the gamma response is differentiated from the neutron response is possible but extremely expensive. Thus, at JPL, we have initiated an analytical program to determine the response of devices to neutrons. This will be accompanied with a low level experimental program to substantiate our model. Some initial work which has been accomplished to date in this area was reported by Taherzadeh at this conference (Ref. 14).

INSTRUMENT RESPONSE AND SHIELDING ANALYSIS

Once the spectrum of radiation impinging on an instrument from a polyenergetic source is established, it is possible from basic monoenergetic response data to determine the total response of an instrument. With this and a knowledge of allowable response levels, the required thickness of shield to reduce the response to a tolerable level is quickly determined.

The spurious count rate of a science instrument is determined from the expression

$$C = \sum_{i=1}^{20} \xi_i \cdot \eta_i \cdot S_i \cdot A$$

where

C is the total spurious counting rate (Counts/sec)

A is the sensitive area of the detector (cm^2)

S is the spectrum of radiation at the instrument (photons/cm^2 -sec)

N is the relative sensitvity to monoenergetic photons (counts/photon)

ξ is the relative attenuation of the shield (photons out/ photons in)

The calculations are typically done in 20 energy groups. With knowledge of the maximum allowable counting rate for a given instrument, the thickness of shield can be determined from the above expression. Numerous shielding studies have been conducted at JPL by Dore on various spacecraft configurations and reported in the literature (Ref. 13). Typical scientific packages which have been studied to date at JPL are shown in Table 7. The table indicates the type of sensors employed in these instruments.

Table 7 Typical Science Instruments

Experiment	Sensitive Detectors	Number	Sensitive Area	Thickness (in microns)
Charged particle telescope	Li-drifted S. S	1, 1, 2, 1	3.8 cm^2, 4.9 cm^2, 7.1 cm^2, 1.9 cm^2, 7.1 cm^2	500, 1500, 1000, 1000, 1000
Plasma probe	Channeltrons or PM's	40	1.2 cm^2	---
Trapped radiation experiment	PM tube Solid-state detectors (Totally depleted)	1 2 1	1 mm^2 500μ x 1000μ in diam 0.7853 mm^2	100 500 1000
Trapped radiation detector	G. M. tubes (EON 6213) Solid-state detector	3 1	1 cm^2 11 cm^2	--- 32μ
X-ray Telescope	Proportional counters	7	133 cm^2	---
UV Photometer	Channeltron (CEM 4010) Geiger (EON 6213)	1 1	1.2 cm^2 1.0 cm^2	--- ---

REFERENCES

1. P. J. Gingo and M. A. Dore, "Gamma Radiation Characteristics of Pluton-Dioxide Fuel," JPL Technical Report 32-1481, NASA.

2. M. A. Dore, "Gamma-ray Source Characteristics of PuO_2," Trans. Am. Nucl. Sec., 13, 537 (1970).

3. M. Reier, "Absolute Gamma Ray Intensity Measurements of a SNAP 15A Heat Source," Nuclear Science and Engineering (in press).

4. M. Taherzadeh, "Neutron Emission Characteristics of a PuO_2 Source," Trans. Am. Nucl. Soc., 13, 537 (1970).

5. T. M. Jordan, "Beta--A Monte Carlo Computer Program for Bremsstrahlung and Electron Transport Analysis," AFWL-TR-68-111, October, 1968.

6. M. Reier, "The Design of a Source to Simulate the Gamma-Ray Spectrum Emitted by a Radioisotope Thermo-electric Generator," Transactions of the National Symposium on Natural and Man-made Radiation in Space, March, 1971, (To Be Published).

7. H. Davis and E. Koprowski, "Nuclear Radiation Environment for Thermo-electric Outer Planet Spacecraft," "Transactions of the Natural and Man-made Radiation in Space, March, 1971, (To Be Published).

8. M. Reier, "Spectral Analysis of Gamma Radiation from a SNAP 15A Source," Trans. Am. Nucl. Soc., 12, 478 (1969).

9. J. J. Steyn, "Code Cugel--A Code to Unfold Ge(Li) Spectrometer Polyenergetic Gamma Photon Experimental Distributions," NUS-692.

10. R. Campbell, "The Response of Miniature G-M Tubes to Monoenergetic Gamma Radiation," Trans. Am. Nucl. Soc., 13, 533 (1970).

11. M. Reier, "The Response of a Shielded 300-Micron Silicon Detector to Gamma Rays," Trans. Am. Nucl. Soc., 13, 534 (1970).

12. T. D. Jones et al, "The Response of Selected Totally Depleted and Lithium-Drifted Silicon Detectors to Monoenergetic Gamma and Neutron Radiation," Trans, Am. Nucl. Soc., 13, 539 (1970).

13. M. A. Dore, E. L. Noon, "RTG/Radio-isotope Heater Shielding for Sensitive Science Instruments on Spacecraft," Trans. Am. Nucl. Soc., 13, 539 (1970).

14. M. Taherzadeh, "The Response of Solid State Detectors to Monoenergetic Neutrons Determined by the Use of the Monte Carlo Technique," Transactions at the National Symposium on Natural and Man made Radiation in Space," Mar., 1971, (To Be Published).

SESSION VIII.3.
ATMOSPHERIC AND SUPERSONIC TRANSPORT RADIATION ENVIRONMENT
CHAIRMAN: J. MCLAUGHLIN
AEC HEALTH AND SAFETY LABORATORY

EVALUATION OF 2 POSSIBLE FURTHER DEVELOPMENTS OF THE UK IN-FLIGHT RADIATION WARNING METER FOR SSTS

I J Wilson and R C Eustace
Radiation Measurement Section
UKAEA/AWRE Aldermaston, UK of GB

Various radiation measurements have been made to investigate 2 possible further developments of the present hybrid ionisation and neutron detection system of the Dose-Equivalent Ratemeter commissioned for the SST Concorde, namely

(i) A reduction of the mass of the moderator from that of the Anderson-Braun neutron-remmeter assembly, and

(ii) the inclusion of a response to the nucleon flux responsible for the tissue-star component of the total dose-equivalent rate by means of a high atomic number material as a nucleon-neutron converter within the moderator.

Radiation situations at SST cruising altitudes (~20 km) due to solar proton flares were simulated approximately both in the stratosphere and on the ground. Actual stratospheric situations due to galactic cosmic radiation with a limited range of Quality Factor values (2-4) were encountered during slow ascents by balloons to 36 km from Aire-sur-Adour (France). Synthetic situations obtained from high and low energy accelerator radiations were used to obtain radiation distributions having a larger range of Quality Factor values ($1\frac{1}{2}$-9) than experienced in the stratosphere. The measurements made in these simulations related to the Directly Ionising, Neutron and Tissue-Star components of Dose-Equivalent Rate.

The stratospheric and high energy accelerator experiments taken together with results from both radioactive and machine neutron sources indicated 2 conclusions. Firstly that, due to the restricted range of neutron spectra encountered in the stratosphere, a significant and welcome reduction of the mass of the moderator by 4 kgm could be made, provided the moderator is clad with cadmium or some other slow neutron absorber. Secondly, that to achieve a tissue-star response with a lead insert would result in a nett increase in moderator-assembly weight of $5\frac{1}{2}$ kgm. Hence the lead insert proposal was abandoned, while the potential moderator reduction is being exploited.

A reduced moderator geometry compatible with the existing electronics package was derived; its oversensitivity with respect to the Anderson-Braun neutron remmeter was determined for a number of fast neutron energies. Two different methods of correcting the oversensitivity - a slow neutron absorber within the moderator and a reduced sensitivity boron trifluoride counter - were tested. As a result, a new - reduced weight - version of the In-Flight Radiation Warning Meter for the SSTs can now be designed in detail.

Reasons for the Experiments

The balloon-borne experiments at Aire-sur-Adour in the autumn of 1969 were a recent phase in the continuing British programme of stratospheric radiation research and development for the Concorde - described by Wilson (Ref.1). At ground level, we are unknowingly enjoying the benefits of a radiation shield provided by the atmosphere, which is equivalent to a 1 metre (~1 yard) thickness of lead. But the cosmic radiation shield for a Concorde flying at a height of ~17 km (~11 miles) is equivalent to only about 8 centimetres (3 inches) of lead!

The background cosmic radiation - mostly protons of 10000 MeV (million electron volts), produces a stratospheric dose-equivalent-rate which differs with latitude and varies with the 11 year solar activity cycle. The maximum dose-equivalent-rate was measured in 1964 at Fort Churchill, Canada, during the International Quiet Sun Year, and reported by Fuller and Clarke (Ref. 2).

Maximum Cosmic Radiation Dose-Equivalent-Rates at Concorde Cruise Altitudes (these will only be met on polar and northerly transatlantic flights)

Ionisation (Chambers and Geiger Counters)	1.1 milli-rem/hr
Neutron (Instruments and Activation)	0.6 milli-rem/hr
Tissue Star (Nuclear Emulsions + Microscope)	0.5 milli-rem/hr
Total	2.2 milli-rem/hr
Maximum Cosmic Radiation Dose-Equivalent/flight	= 5 milli-rem, Passengers
Maximum Cosmic Radiation Dose-Equivalent/Year	= ~1.0 rem, Crew
(Maximum Permissible Dose-Equivalent/Year	= 5 rem Radiation Worker)

The International Commission on Radiological Protection has stated that there is 'No need for personal dosemeters where the annual dose-equivalent is not greater than 3/10 maximum permissible, provided the radiation environment is monitored'.

The global (i.e world-wide) average dose-equivalent-rate due to cosmic radiation at Concorde cruising altitude will be about 1 milli-rem/hr (probably less) which is unlikely to present any operational problems!

However, Solar Proton Flares do pose a problem - Buley (Ref. 3), see Figs 1 and 2. It is estimated that on about 1 occasion per year, averaged over a solar activity cycle of 10-12 years solar outbursts of high energy protons (1000 MeV) will cause dose-equivalent rates greater than 100 milli-rem/hr in the Concorde cruising altitude band at northerly latitudes. Thus, only one northerly flight in several thousand such flights will be affected. On these very few occasions the Concorde will make a normal, controlled descent to increase the atmospheric shielding. As the atmospheric tenth-value attenuation layer for solar flare protons is about 40-50 gm/cm^2, a descent to an altitude of about 14-15 km (45000 - 50000 ft), which is well above the subsonic flight levels, should suffice to reduce the dose-equivalent-rate to less than 100 milli-rem/hr. (Solar proton flares are expected to have no effect on the operations of supersonic passenger aircraft at tropical or equatorial latitudes.)

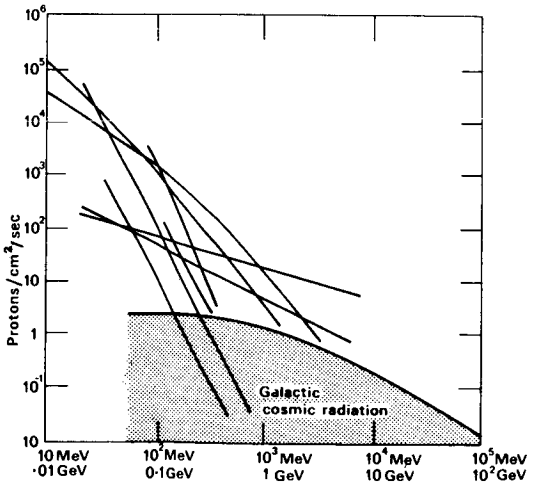

FIGURE 1. ASSORTED INTEGRAL ENERGY SPECTRA OF SOLAR FLARE PROTON AND COSMIC RADIATIONS.

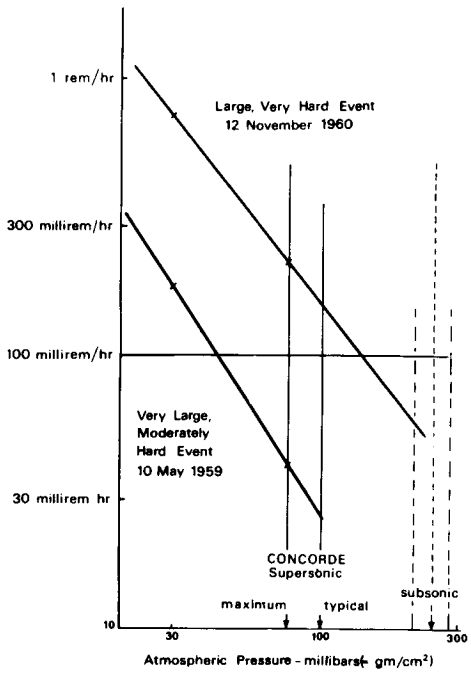

FIGURE 2. ESTIMATED SOLAR PROTON FLARE DOSE-EQUIVALENT RATES IN THE STRATOSPHERE.

Neither ground nor satellite systems can give radiation warnings sufficiently reliable or exact to be useful for the flight management of supersonic airliners. Thus, an In-Flight Radiation Warning Meter was specified for Concorde: it has been described by Benbow (Ref. 4). The present instrument is a hybrid device based on the Fort Churchill results, plus information on Solar Proton Flares in the last 2 solar cycles:-

Direct Ionisation (Low LET -- Low QF)	
Geiger Counters	
Neutrons	(Medium LET -- Medium QF) likely to contribute the major component of dose-equivalent during a solar proton flare.
Anderson-Braun moderator plus Boron Trifluoride Tube	although a smaller moderator was thought to be adequate for the restricted range of stratospheric neutron spectra.
Tissue-Stars	(High LET -- High QF)
Instrumental Scaling Factor	an indirect measurement of this component was thought to be possible by the use of a high atomic number material - such as lead - within the moderator.

[LET = Linear Energy Transfer, QF = Quality Factor]

The electronic package of the instrument utilizes silicon microcircuits and devices with components tested to military environmental requirements, and uses 9 to 11 watts from the aircraft 115v 400 Hz power supply. The Geiger counter (ionization) and boron trifluoride tube (neutron) pulses are brought together to drive a single ratemeter which gives a 4 decade logarithmic indication of total dose-equivalent-rate at a display unit separate from the electronic package but linked by a multi-signal cable. For simplicity of readout by SST aircrew personnel of 'the radiation level', the meter scale is marked in 20 equispaced divisions. The 4 decades are indicated by coloured quadrants - the first and second (0.1-10 mrem/hr) being coloured green to indicate safe ambient ranges, the third (10-100 mrem/hr) being orange for an alert range, and the fourth (100 mrem/hr - 1 rem/hr) being red for the action range. There are orange and red signal lamps corresponding to the orange and red dose-equivalent rate ranges: also, there is an audio signal when the dose-equivalent-rate exceeds the threshold of the red (action) range, 100 mrem/hr. Dose-equivalent integration is performed by a register in which each digit represents 1 mrem: this register will continue to function without loss up to a dose-equivalent-rate in excess of 10 rem/hr. While the weight of the electronics package plus display unit is only $3\frac{1}{2}$ kgm/8 lb, the weight of the Anderson-Braun moderator assembly is $8\frac{1}{2}$ kgm/18 lb: hence the interest in a smaller moderator.

The very reason for the Warning Meter, the unpredictability of the infrequent large solar proton flares, makes the validation of smaller and modified moderator assemblies during an actual solar proton flare virtually impossible prior to regular Concorde flights. Simulation with high energy accelerators is usually difficult and limited: normally the radiation is delivered in short intense pulses, the particle beams are of restricted cross-sectional area, and the common shielding material concrete is not equivalent to air because it contains both elements with higher atomic masses than air, and hydrogen (which moderates neutrons). The alternative is to make use of the various situations due to cosmic radiation to be found at different stratospheric altitudes. Some simulation of the range of solar proton flare situations within the Concorde cruising altitude band 16-19 kms (10-12 miles), is available with cosmic radiation at progressively higher altitudes.

Actual Stratospheric Exposure

French colleagues provided balloon flights to heights of 36 km (22 miles) (where the air pressure is only $\frac{1}{2}\%$ of that at ground level) from their excellent balloon launching site at Aire-sur-Adour in the south of France. Unlike nearly all other balloon experiments which need a quick ascent and a long float, a slow ascent and a short float was required. The primary aim was not to measure the stratospheric radiation environments, but to use the various radiation situations for the comparison of instruments with different moderator assemblies - one standard Anderson-Braun moderator assembly and 3 modifications obtained by-

I Removing the inner parts of an Anderson-Braun moderator to produce a hollow moderator having a reduced moderator wall thickness

II Cladding such a hollow moderator with cadmium to remove the resulting enhanced slow neutron response

III Including a lead insert within such a cadmium-clad hollow moderator to give an indirect 'tissue-star' response - see Fig.3 for the principle.

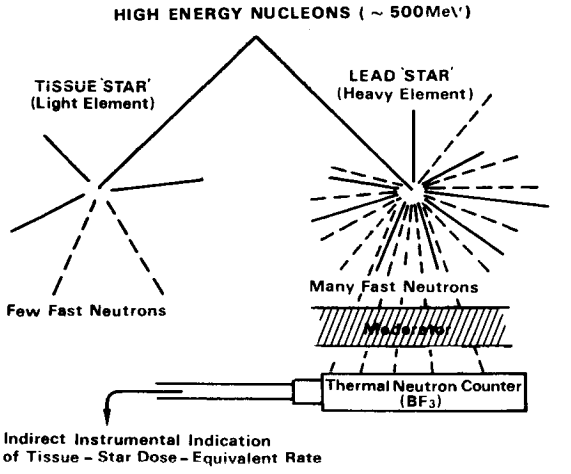

FIGURE 3. INDIRECT TISSUE-STAR RESPONSE

In the actual experimental assembly the lead was incorporated within the polythene outer moderator (the inner moderator etc. having been removed) as a sleeve around the boron trifluoride tube. The fast neutrons from the disintegrations of lead nuclei by high energy nucleons (protons, neutrons) were moderated by the polythene and reflected back through the lead to the boron trifluoride tube.

The secondary aim of the balloon experiments was to obtain an independent demonstration of the range of radiation situations encountered in the stratosphere. Recombination ionisation chambers, described by Wilson (Ref 5), were flown in an attempt to obtain some measure of the variation with altitude of the stratospheric quality factor at the place and time of the balloon flight. On the basis of nuclear emulsion and similar data obtained from polar balloon flights during the Quiet Sun period, as reported by Davison (Ref. 6), the stratospheric quality factor had been estimated as varying from 2 to $4\frac{1}{2}$ between 20 and 36 km, respectively - see Fig. 4. The maximum quality factor value encountered at Aire-sur-Adour would have been somewhat less. In the event it was not possible to derive any information relating to the variation with altitude of the stratospheric quality factor from the ionisation chamber results. (However, the neutron count rate and ratio profiles themselves qualitatively demonstrate the range of stratospheric radiation situations.)

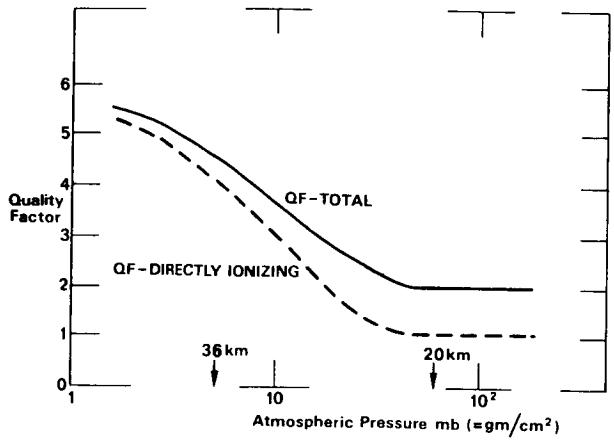

FIGURE 4. ESTIMATED STRATOSPHERIC QUALITY FACTORS.

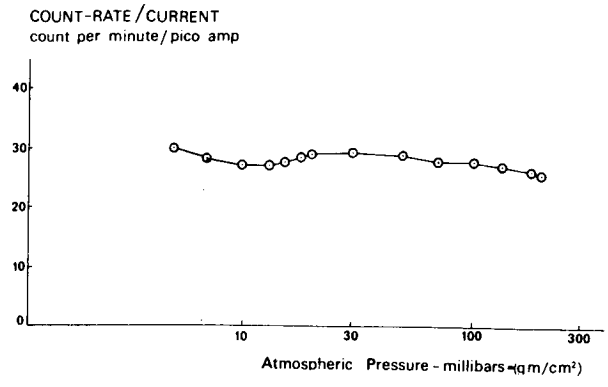

FIGURE 5. IONIZATION (Comparison of Geiger Counters with Ionization Chambers)

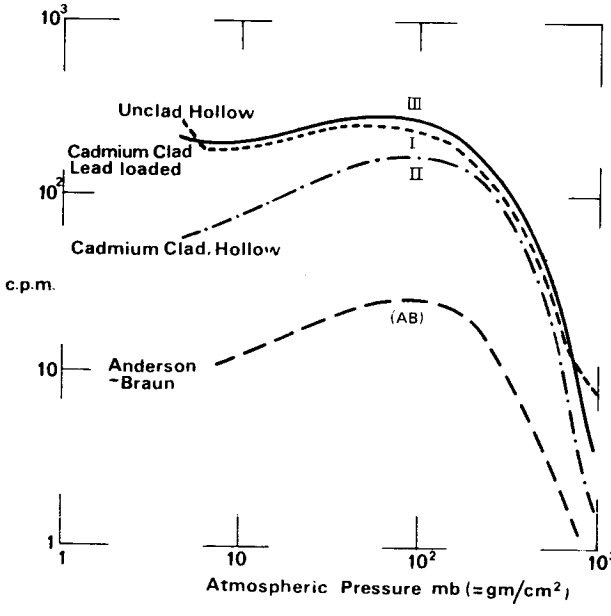

FIGURE 6. STRATOSPHERIC NEUTRON COUNT-RATES.

The technical details of the counting equipment have been described by Benbow (Ref. 7).

The way that the count-rate from the Geiger counters varied with altitude was very nearly the same as the variation of the current output of ionisation chambers also flown from Aire at the same time - see Fig. 5. This provides yet another demonstration of the validity of using a compact and simple Geiger counter system for the ionisation channel of the Concorde In-Flight Radiation Warning Meter in place of a more bulky and more involved ionisation chamber system.

The results from the neutron counters were also as had been expected - see Fig. 6. The hollow moderator needed cadmium cladding to remove the enhanced response due to the slow neutrons from the other moderators in the balloon flight package - see curves I and II. (In a Concorde there will be some 110 tons of moderator - about 100 tons of fuel and about 10 tons of passenger and crew). Nevertheless the count-rate from the cadmium-clad reduced moderator was greater than that from the standard Anderson-Braun moderator (due to its internal partial neutron absorber) - see curves AB and II. The presence of an insert of lead within a cadmium-clad moderator caused an enhanced response due to the copious secondary neutron production - see curves II and III of Fig. 6.

Two important conclusions became apparent from comparison of the curves of Fig 6. The first conclusion comes from considering the ratio of the response of the cadmium-clad hollow moderator with that of the Anderson-Braun - see Fig. 7 (the results of the two flights, shown by circles and crosses respectively, are in agreement). The important feature here is that over the whole altitude range, the ratio of the count-rates from these two moderator assemblies was essentially constant. The stratospheric value of this ratio was confirmed by similar values obtained with 4 different laboratory radiation sources: at Aldermaston both radioactive (α-Be) and machine (D-D and D-T) neutron sources, - and at the Rutherford High Energy Laboratory, scattered protons etc, transmitted through graphite were used to give some simulation of the stratospheric situation.

The first conclusion is that a reduction in the moderator for the In-Flight Meter could be made provided that it is clad in cadmium or some other slow neutron absorber. Aircraft operators and constructors seek equipments that perform their tasks reliably over a wide range of conditions with the minimum of weight - not an easy combination, as will shortly be illustrated. As the moderator accounts for the majority of the weight of the present instrument, the possibility of reducing the moderator weight by about half, to some 4 kilograms, is most welcome.

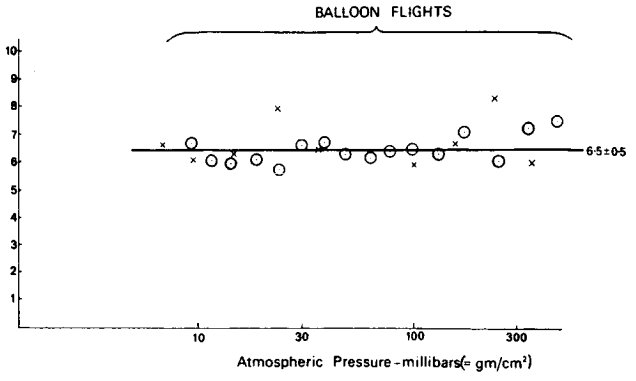

FIGURE 7. NEUTRON COUNTING RATIO: HOLLOW MODERATOR (Cadmium clad) /ANDERSON-BRAUN

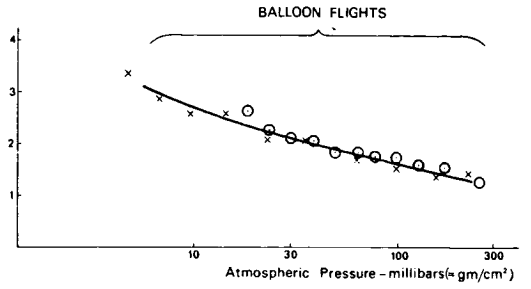

FIGURE 8. TISSUE-STAR COUNTING RATIO: LEAD INSERT/HOLLOW MODERATOR (both Cadmium clad)

The second conclusion comes from considering the ratio of the response of the cadmium-clad moderator loaded with $7\frac{1}{2}$ kilograms of lead to that of the hollow cadmium-clad moderator, the 'Lead Effect' - see Fig. 8 (the results of the two flights, shown by circles and crosses respectively, are in agreement). In this case the important feature is the steady increase of the effect with reduction of overlying air-mass (pressure) i.e with increasing altitude. The stratospheric values of this ratio are well in excess of those obtained with the 4 neutron sources used to simulate stratospheric neutrons: this indicates that the stratospheric 'Lead Effect' is not due to a modified response to neutrons external to the moderator. It is a genuine effect due to neutrons being produced within the moderator by the disintegration of lead nuclei as a result of high energy particle (nucleons etc) bombardment. This was confirmed by subsequent accelerator experiments (described later) some of which gave 'Lead Effects' greater than that experienced in the stratospheric balloon flights (see Fig. 9). In respect of the NIMROD-graphite simulation, it should be remembered that the majority of galactic cosmic radiation protons have energies in excess of those scattered through 90° from a 7 GeV proton beam: thus the difference between the balloon and NIMROD results.

High energy particles also cause the disintegration of light nuclei such as C, N and O and are thus the cause of 'tissue-stars'. The 'tissue-star' component of the total dose-equivalent-rate due to cosmic radiation at Concorde cruising altitude has been estimated from the Fort Churchill results as being equal to 80% of the neutron dose-equivalent-rate. To achieve an 80% enhancement of the neutron count-rate for cosmic radiation at an altitude of about 20 km, a lead insert of 6 kilograms would be needed. (Theoretical reasons indicate that 5 kilograms of uranium should do the same job, and also deal with some of the excess neutron sensitivity of the reduced moderator.)

The consequence of these conclusions is that either the In-Flight Radiation Warning Meter could be made lighter but without a 'tissue-star' response (as at present), or a 'tissue-star' response could be incorporated together with a reduction in the moderator mass to give an instrument of somewhat greater weight than at present: this is the sort of dilemma that developers of aircraft instruments often encounter. As the existing instrument already met the requirements for an In-Flight Radiation Warning Meter, only developments giving a significant weight reduction were of practical interest. Hence, although the balloon experiments showed that a 'tissue-star' response could be obtained by a simple reliable means, such a development is ruled out on the grounds of excessive weight.

Simulated Stratospheric Exposure and Other High Energy Accelerator Experiments

The set of moderators used in the balloon flights were also exposed in a number of environments found around the NIMROD (7 GeV proton) and NINA (5 GeV electron) accelerators in order to obtain experience in a range of high energy radiation situations differing from the graphite simulation of the stratosphere. To facilitate comparisons, details and results of all 12 experiments are tabulated together - see Fig. 9. The 'cadmium ratio' is the ratio of the count-rate response of the cadmium-clad hollow moderator to that of the unclad hollow moderator: this was normally less than one, indicating the presence of slow neutrons. The 'hollow ratio' is the ratio of the count-rate response of the cadmium-clad hollow moderator to that of the Anderson-Braun moderator: in situations comparable to the stratosphere, the value of this ratio lay within the restricted range 5-7. The 'lead ratio' is the ratio of the count-rate response of the cadmium-clad moderator containing the $7\frac{1}{2}$ kgm of lead to that of the cadmium-clad hollow moderator: the values of this ratio varied from 0.8 to 8. For experiment one, the balloon flights, the extremes of the ranges of values already indicated in Figs. 6, 7 and 8 are summarised.

Experiment	Radiation Source	Shielding	Overall Average Quality Factor	'Cadmium Ratio'	'Hollow Ratio'	'Lead Ratio'
1	Galactic Cosmic	5-500 gm/cm^2 Air	(4$\frac{1}{2}$-2) [a]	0.15-0.65 [b]	6.5±0.5 [b]	3-1.5 [b]
2	D-D	None	(9)	0.92	5.9	0.80
3	Am-Be	None	7.4	1.00	6.4	0.79
4	D-T	None	7.8	0.98	5.8	0.90
5	D-D	None	(9)	0.90	4.6	0.83
6	Am-Be	None	7.4	1.00	5.0	0.78
7	D-T	None	7.8	0.92	4.5	0.98
8	NINA, 2.5 GeV electrons	Thick concrete + iron	3.8	-	6.6	-
9	NIMROD, 7 GeV protons Unanalysed 90° scatter	$\frac{1}{2}$ m graphite	3.3	0.54	5.4	0.93
10	Unanalysed 90° scatter	2 m concrete	4.8	-	5.1	1.1
11	1.0 GeV π^+ (and 0.5 GeV p)	0.3 m concrete	1.6	1.08 [c]	3.9	4.0 (4.3) [c]
12	1.0 GeV π^+ (and 0.5 GeV p)	None	2.3	-	4.3	7.4 (8.0) [c]

a) Fort Churchill, Canada - Quiet Sun

b) Aire-sur-Adour, France - Active Sun

c) See comments in text regarding the anomalous aspects of experiments 11 and 12.

FIGURE 9. SUMMARY OF EXPERIMENTAL DETAILS AND RESULTS.

Experiments 2-7 inclusive were the simulations done at Aldermaston: in 2, 3 and 4 the cylindrical moderators, in their balloon flight configuration were irradiated normally with respect to their flat top surfaces - an irradiation situation similar to that experienced in the stratosphere. The 'hollow ratio' values of experiments 2-4 indicate that the Am-Be neutron spectrum can be used to represent the stratospheric neutron spectrum in simulation tests with moderators. In experiments 5, 6 and 7 the cylindrical moderators were irradiated normally with respect to their curved side surfaces, one moderator at a time. As the cadmium ratios for experiments 2-4 approximate to one, neutron scatter between the moderators in the flight configuration can be eliminated as a factor in the comparison of the results of 2-4 with those of 5-7: this is confirmed by the fact that the 'hollow ratio' values from experiments 5, 6 and 7 are all a constant 78% of the corresponding values from experiments 2, 3 and 4 respectively. Thus compared with the Anderson-Braun moderator, the cadmium-clad hollow moderator has an angular response which differs from isotropic by ± 12%. Although the 'lead ratios' for experiments 2-7 are all less than one, there is some indication of neutron enhancement with the D-T irradiations (experiments 4 and 7). Experiment 8 utilised a location behind one of the beamstops of the 5 GeV electron synchrotron, NINA, at the Daresbury Nuclear Physics Laboratory. At the Rutherford High Energy Laboratory, a graphite wall was erected for experiment 9 in a shield-tunnel facility at right angles to one of the external beams from the 7 GeV proton synchrotron NIMROD, at a distance of about 15 meters from the scattering

target. The dimensions of the wall were about $1\frac{1}{2}$m x $1\frac{1}{2}$m x $\frac{1}{2}$m thick, providing a 'beam' of about $1m^2$ cross-sectional area. As the atomic number and mass of carbon are comparable with, but less than those of nitrogen and oxygen, it was considered that the graphite wall ($\sim$100 gm/cm^2) would approximate to the Concorde's maximum cruise altitude ($\sim$80 gm/cm^2). Experiment 10 was above the concrete top shielding of a different proton beam over another scattering target. In experiments 11 and 12 a pion beam was used: the anomalous 'cadmium ratio' obtained from 11 indicated that the cadmium generated neutrons instead of absorbing them and hence the 'lead ratios' for experiments 11 and 12 have been adjusted. As there was every indication that all neutrons detected during experiments 11 and 12 were produced within the moderator-assemblies (i.e no external neutron flux) these experiments must be regarded as unrepresentative.

The Quality Factor values for the stratosphere were derived from Ref. 6. The Quality Factor values for experiments 3/6, 4/7, 8, 9, 10, 11 and 12 were derived from measurements made with the AWRE portable LET spectrometer by B Day - see Ref. 8: the Quality Factor value for experiments 2/5 was interpolated from other measurements by B Day. Estimated values of Quality Factor are bracketed in Fig. 9.

The experimental results indicate that:

(a) An Am-Be neutron source can be used to represent the stratospheric neutron spectrum for the purpose of moderator tests.

(b) The cadmium-clad, hollow (i.e reduced wall thickness) moderator is a valid replacement for the Anderson-Braun remmeter in the context of the restricted range of stratospheric neutron spectra; but its sensitivity is considerably enhanced (see Figs 7 and 9).

(c) From the 'Lead Ratios', the relative stratospheric incidence of tissue-stars for a solar proton flare will be less than that for cosmic radiation, and hence for the purpose of the Concorde In-Flight Radiation Warning Meter an instrumental scaling factor will be adequate to deal with the approximately 20% tissue-star component of stratospheric dose-equivalent-rate during a solar proton flare.

The Reduced Moderator

Preliminary tests with a moderator of 17 cm/6.7" diameter having the same wall thickness as the previous hollow moderator (but without the internal cavity) and having the same length 24.5 cm/9.7", demonstrated that as expected it had the same relative neutron energy response as the hollow moderator and was a little less sensitive, but still significantly more sensitive than the Anderson-Braun assembly. However, computed sensitivities of moderators of different sizes as functions of neutron energy such as reported by Stevenson (Ref. 9) indicate that significant further reduction in moderator size should be possible before the minimum moderator adequate for the stratospheric environment would be obtained. Reduction of moderator size would also remove some of the over-sensitivity referred to above. The remaining over-sensitivity can easily be removed by including sufficient cadmium (or compound of lithium or boron) with the enriched boron trifluoride proportional counter within the moderator. A simple calculation indicated that the substitution of natural boron trifluoride in place of the usual counter filling of enriched boron trifluoride would remove nearly all of the over-sensitivity.

In the development of the reduced moderator version of the In-Flight Radiation Warning Meter some instrumental considerations had to be borne in mind. The electronics package had been

(a) Designed and built within a 15 cm/6" diameter case in the confident theoretical expectation that a moderator of about this diameter (and length) would be demonstrated as adequate for the stratospheric radiation environment

and

(b) Built and tested to general aircraft and particular SST specifications: hence the reduced moderator development should provide the same count-rate sensitivity with the same electronic operating conditions as the Anderson-Braun assembly in order to avoid expensive re-design, re-building and re-testing of the electronic circuitry.

In addition to the 2 general conditions (a) and (b) indicated above, the replacement moderator also had to be compatible with both the aircraft makers' requirements of overall instrumental dimensions, and the need to maintain a certain minimum neutron path length to the internal boron trifluoride tube through the moderator in all directions. These considerations resulted in a reduced moderator of dimensions, 15 cm/6" diameter and $20\frac{1}{2}$ cm/$8\frac{1}{4}$" length, which when clad with cadmium weighs $4\frac{1}{2}$ kgm/10 lb (ie comparable with the electronic package.)

The sensitivity of this reduced moderator was compared with that of an Anderson-Braun assembly for a number of fast neutron energies in the range $\sim$0.1-15 MeV by normal irradiation of the curved surfaces of the moderators. As expected, the sensitivity ratio varied slightly with neutron energy and, for the neutron energies of most significance in the stratosphere, had a value of $3\frac{1}{2}$-4, see Fig 10. The deviation of the angular response of the reduced moderator from isotropy is typically $9\frac{1}{2}$% but with an extreme value of -20% corresponding to the case where neutron irradiation is of the flat moderator face through which the boron trifluoride counter tube is inserted.

Cadmium sleeves (20 milli-inch thick) with different degrees of perforation were mounted in turn upon the boron trifluoride counter tube and the resulting count-rate sensitivity of the reduced moderator was determined as a percentage of that for the unsleeved situation. Both whole counter tube sleeves and active length only sleeves were investigated: the results are given in Figure 11.

Source of Neutrons	Count Rate Ratio or Response of Reduced Moderator to that of an Anderson-Braun Assembly			
	Unmodified	5 cm/2" Fe	10 cm/4" Fe	15 cm/6" Fe (or Polythene)
D-D	4.1	4.7	5.7	6.3
Am-Be	3.5	-	-	3.8 Polythene
D-T	3.2	4.6	5.2	5.7

FIGURE 10. COMPARISON OF CADMIUM-CLAD REDUCED MODERATOR WITH AN ANDERSON-BRAUN ASSEMBLY FOR NEUTRONS ~ 0.1—15MeV

% Area		% Sensitivity	
Cadmium	Perforation	Whole BF_3 Tube Sleeve	Active Length Only Sleeve
0	100	100	100
10	90	-	81
20	80	54	64
30	70	41	53
40	60	31	42
50	50	25	34
60	40	20	26
70	30	14	19
80	20	10	12
90	10	6	5
100	0	2	2

FIGURE 11. EFFECT ON SENSITIVITY OF PERFORATED CADMIUM SLEEVE AROUND BORON TRIFLUORIDE COUNTER TUBE

The sensitivity of the reduced moderator with a natural isotopic mixture boron trifluoride proportional counter tube of the same dimensions and filling pressure as the usual enriched counter tubes was determined as 31% of that of the reduced moderator with an enriched tube. In respect of both pulse amplitude and resolution the natural isotopic mixture counter tube compared favourably with the enriched isotopic mixture counter tubes.

A theoretical estimate was made of the cadmium thickness necessary around an enriched boron trifluoride counter tube to achieve the required sensitivity fraction of 25-29% (i.e $1/4 - 1/3\frac{1}{2}$). As the cadmium slow neutron absorption cross-section does not follow the usual inverse neutron velocity relation, an effective absorption cross-section was obtained for an assumed Maxwellian slow neutron energy distribution of temperature about 300°Kelvin (absolute). The transmission of slow neutrons, assumed to be isotropically incident on a cadmium-plated boron trifluoride counter tube, was obtained using a tabulation of the second exponential integral $-E_2(x)$, where x = the slow neutron mean free path. Cadmium thicknesses of 44 micrometers/1.7 milli-inches (25% transmission) and 38 micrometers/1.5 milli-inches (29% transmission) were indicated for the enriched isotopic mixture boron trifluoride counter tube.

A simulation of cadmium plating was obtained using indium foils as sleeves over the whole boron trifluoride counter tube. It had been theoretically estimated from consideration of the effective 300°K slow neutron absorption cross-sections, atomic mass numbers and densities that 21 milli-inches of indium would be equivalent to 1 milli-inch of cadmium. Using this equivalence factor, the indium simulation experiment indicated cadmium thicknesses of 38 micrometers/1.5 milli-inches (25% transmission) and 30 micrometers/1.2 milli-inches (29% transmission) for the enriched isotopic mixture boron trifluoride counter-tube - see Fig. 12.

Indium Sleeving Over Whole BF_3 Counter Tube

Thickness (milli-inch)	0	5	10	15	20	25	30
% Count Rate	100	62	47.5	39	32.5	28.3	25

NB 1 milli-inch cadmium equivalent to 21 milli-inch indium

Cadmium Plating

Tube	Nominal Cadmium thickness (milli-inch)	% Count Rate		% Count Rate	
		With Cd on Stock	Without Cd on Stock	With Cd on Stock	Without Cd on Stock
Enriched	0	-	100		
Enriched	1.0	48	51.8		
Enriched	1.3	35.5	37.3		
Enriched	1.5	21.0	22.7		
Natural	0	-	30.8	-	100
Natural	0.1	24.6	26.8	79.8	86.9
Natural	0.2	22.4	24.4	72.5	79.1

FIGURE 12. EFFECT OF INDIUM SLEEVING AND CADMIUM PLATING ON BORON TRIFLUORIDE COUNTER TUBE SENSITIVITY

Guided by the results of theory and experiment, both the enriched and the natural isotopic mixture boron trifluoride counter tubes were plated with appropriate thicknesses of cadmium: the sensitivity fraction results are given in Fig. 12. It should be noted that (a) so as not to risk the reliability of the boron trifluoride counter tubes their mounting-stocks were not immersed in the plating solution, and (b) the cadmium plating thicknesses are only nominal, being equated with the measured cadmium thicknesses on flat test plates in the same solution for the same time and at the same current density. As the mounting-stocks of the counter tubes are also inserted within the moderator, the cadmium-plated tubes were tested for sensitivity both with and without a cadmium sleeve over their unplated stocks. The cadmium-plating experiment, in reasonably good agreement with theory and the indium simulation, indicated that a sensitivity fraction in the range 25-29% could be met by either:

a cadmium thickness of about 35 micrometers/1.4 milli-inches over an enriched isotopic mixture filling boron trifluoride counter tube
or
a cadmium thickness of about $1\frac{1}{2}$ micrometers/0.05 milli-inches over a natural isotopic mixture filling boron trifluoride counter tube.

As the natural isotopic filling boron trifluoride counter tube has no disadvantages and requires only a very slight adjustment of its sensitivity (the required cadmium thickness corresponds to about a tenth of the usual 'flashing' of cadmium employed as a protective finish) and may be acceptable without sensitivity adjustment, it appears to be a commendably simple solution to the reduced moderator over-sensitivity problem. This solution can be restated as a prediction - that the indication of stratospheric dose-equivalent-rate obtained from a cadmium-clad reduced moderator plus natural isotopic filling boron trifluoride counter tube (perhaps with a 1-2 micrometer finishing of cadmium) should be essentially the same as that from the earlier, Anderson-Braun version of the In-Flight Radiation Warning Meter (see Figs. 13 and 14 which are to the same scale): this prediction should be verified by flight testing.

SUMMARY AND COMMENT

In the course of the work described in this paper the fact that Geiger counters can give an adequate indication of the dose-equivalent-rate of the directly ionizing component of stratospheric radiation was demonstrated yet again. Although providing the In-Flight Radiation Warning Meter with a tissue-star response was shown to be technically possible, this development was not pursued because the weight increase that would have resulted was not considered justified for a ~20% component of dose-equivalent rate (an instrumental scaling factor will continue to be used for the stratospheric tissue-star dose-equivalent-rate). It has now been demonstrated that an adequate indication of the stratospheric neutron dose-equivalent-rate can be obtained from a simple moderator-detector comination of significantly less weight than the Anderson-Braun neutron remmeter but with the same count-rate sensitivity: a new reduced-weight version of the Concorde In-Flight Radiation Warning Meter can now be engineered (see Fig. 14).

The topics of this paper are but part of the British programme of work dealing with the radiological protection of supersonic passenger aircraft: this will be reviewed by Fuller and Day in a paper to be presented later this year at a CERN International Congress - see Ref. 10.

ACKNOWLEDGEMENTS

The work described in this paper was done under contracts for the Ministries of Technology and Aviation Supply, and for the British Aircraft Corporation by members of the AWRE Radiation Measurement Section with the technical support of the AWRE Nuclear Instrumentation Section. The balloon flights at the 'Centre de Lancement de Ballons', Aire-sur-Adour, were arranged by Dr R Kaiser of the 'Centre des Recherches Nucleaires' (CRN) in collaboration with Dr Miro and Dr Deltour of the 'Centre d'Enseignement et de Recherches de Medecine Aeronautique' (CERMA). The experiments around NIMROD and NINA were made possible by radiation protection staff of the Science Research Council at the Rutherford High Energy and Daresbury Nuclear Physics Laboratories respectively.

FIGURE 13. SST IN-FLIGHT RADIATION WARNING METER: ANDERSON-BRAUN VERSION

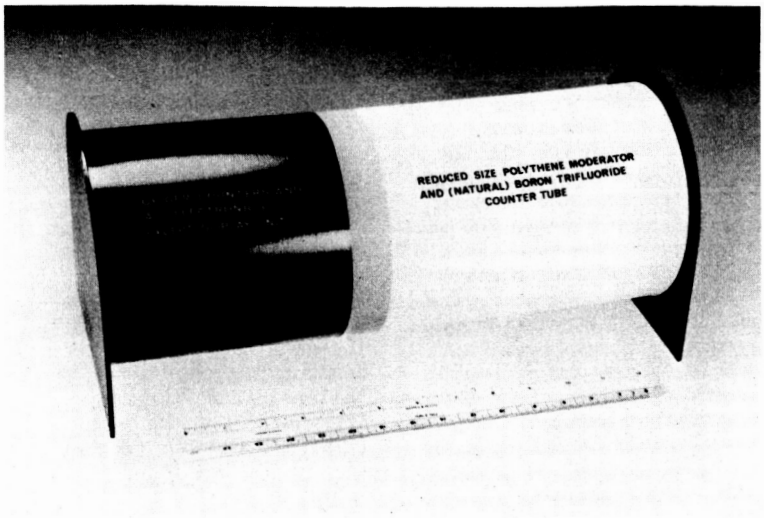

FIGURE 14. SST IN-FLIGHT RADIATION WARNING METER:

MODEL OF PROPOSED NEW REDUCED MODERATOR VERSION

REFERENCES

1 "Radiation and Supersonic Flight", I J Wilson, Science Journal May 1966.

2 "The Radiological Dose to the SST Concorde from Galactic Cosmic Rays", E W Fuller and N T Clarke, UKAEA/AWRE Report O-64/68, December 1968.

3 "Provision of Solar Flare Radiation Information in Support of Supersonic Transport Operations", L E Buley, ICAO, Aerospace Medicine, Vol. 40, No. 10, October 1969.

4 "A Solar Flare Monitor for Concorde", T G Benbow, 5th International Aerospace Instrument Symposium, Cranfield, March 1968.

5 "A Recombination Ionization Chamber as a Sensitive, Three Channel LET Indicator for Stratospheric Use", I J Wilson, 2nd Microdosimetry Symposium, Stresa (Italy), 20-24 October 1969.

6 "The Cosmic Ray Environment of Supersonic Aircraft", P J N Davisson (thesis), University of Bristol, 1967.

7 "Radiation Experiments High Above France", T G Benbow and I J Wilson, AWRE News, April 1970.

8 "A Portable LET Spectrometry System for the Calibration of the Concorde Radiation Meter", B Day, UKAEA/AWRE Report O-57/69, 1969.

9 "Neutron Spectrometry from 0.025 eV to 25 GeV", G R Stevenson, Rutherford Laboratory Report RHEL/R154, 1967.

10 "Radiological Protection in SST Aircraft" E W Fuller and B Day, International Congress on Protection against Accelerator and Space Radiation, CERN, Geneva, April 1971.

AN EXPERIMENTAL MEASUREMENT OF GALACTIC COSMIC RADIATION DOSE IN CONVENTIONAL AIRCRAFT BETWEEN SAN FRANCISCO AND LONDON COMPARED TO THEORETICAL VALUES FOR CONVENTIONAL AND SUPERSONIC AIRCRAFT

Roger Wallace and Michael F. Boyer

Lawrence Radiation Laboratory
Berkeley, California 94720

ABSTRACT

By utilizing beta-gamma and NTA photographic emulsions and thermoluminescent dosimeters, measurements of radiation dose have been made in conventional jet aircraft between San Francisco and London. These direct measurements are in fair agreement with computations made using a program which takes into consideration both basic cosmic ray atmospheric physics and the focusing effect of the earth's magnetic field. These measurements also agree with those made at supersonic jet aircraft altitudes in RB-57 aircraft. It is concluded that both experiments and theory show that the doses received at conventional jet aircraft altitudes are slightly higher than those encountered in supersonic flights at much higher altitudes when the longer time of exposure at the lower altitudes is taken into consideration.

A. COSMIC RAYS

The polar route from Los Angeles* to London is significant in two respects concerning cosmic radiation. First, it is a relatively long flight (about 12 hours) giving it greater time at latitude, and secondly, its flight path goes to very high magnetic latitudes.

Incoming cosmic rays are deflected away by the horizontal component of the earth's magnetic field. Thus, all energies of cosmic rays can hit the top of the atmosphere over the magnetic poles, but only high energy particles can hit the top of the atmosphere over the equator. This so-called "latitude effect" caused by the shape of the earth's magnetic field is shown in Fig. 1. The result is that the latitudes least affected by the earth's magnetic field are those above 50°. For this reason concern about radiation levels is centered on those flights which take a polar flight path. The San Francisco to London route is one of these.

There are essentially two types of cosmic radiation which are encountered by commercial aircraft: galactic cosmic rays and solar cosmic rays. (Several good reviews of these are available, Peters,[1] Waddington,[2] and a complete treatment of space physics, LeGalley and Rosen.[3])

*Although the airmail letters carrying the dosimeters were sent from Berkeley, California to Hammersmith, U.K., the vast majority of the accumulated dose was received between Los Angeles and Heathrow Airports, since all San Francisco to London planes go through Los Angeles on both east and west bound flights.

1. Galactic Cosmic Radiation

Under normal conditions the largest fraction of ionizing radiation in the altitudes used by transport aircraft (30,000-80,000 feet) is due to the secondary radiation produced when galactic cosmic rays strike the upper layers of the atmosphere. These galactic cosmic rays originate in not completely understood processes from various sources in the galaxy. Recent experiments with satellites and high altitude probes have substantiated this theory. The energy density of the galactic primary cosmic rays in free space is of the order of one electron volt per cubic centimeter. This is comparable to the energy density of starlight, the energy contained in the galactic magnetic fields, and the energy due to turbulence throughout the galaxy. Galactic cosmic ray particles have energies that are too high to be contained in our solar system and they must therefore be generated by a source outside our solar system.[4]

When these galactic cosmic ray particles reach the earth's orbit, four processes have already occurred: (1) "initial acceleration followed by diffusion through the galaxy;" (2) "possible post acceleration;" (3) "modulation by the solar wind;" (4) "momentum selection by the solar magnetic field."[4] The galactic cosmic rays produce secondary radiation in the upper atmosphere which is then encountered by commercial aircraft. These secondaries produce the major biological dose received by passengers and crews. The atmospheric secondaries are conveniently described in the following categories: (1) chemical composition and charge composition; (2) energy distribution; (3) distribution in latitude due to the earth's magnetic field and in altitude due to the shielding provided by the air.

At the top of the atmosphere the particle flux due to cosmic rays is about 85 percent protons, 13.5 percent alpha particles, and 1.5 percent heavier nuclei. The entire atmosphere from sea level to outer space is a shield of 1031 g/cm^2. The primary flux is attenuated rapidly by this shield, and at an altitude of 65,000 feet, or a shielding thickness measuring from the outside in of 60 g/cm^2, 50 percent of the original protons, 25 percent of the original alphas, and 3 percent or less of the original heavier nucleons still remain uncollided, as seen in Fig. 2. The total ionization level at 65,000 feet is larger than at the top of the atmosphere due to the buildup of secondaries from collisions of the primary cosmic rays with the oxygen and nitrogen nuclei of the air.[5] This effect is illustrated by Fig. 3.[6]

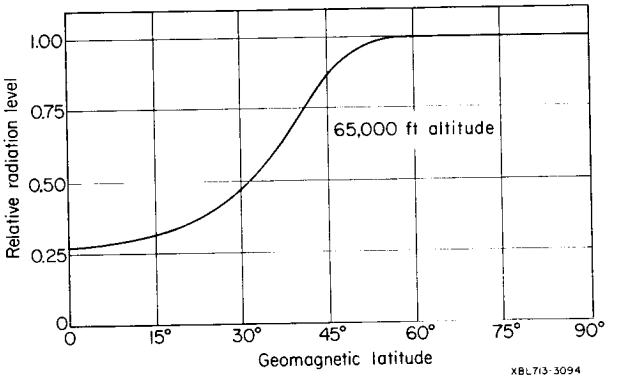

Fig. 1. Latitude dependence of galactic radiation level in the lower stratosphere showing the relative radiation level at 65,000 feet. (From Schaefer.)[5]

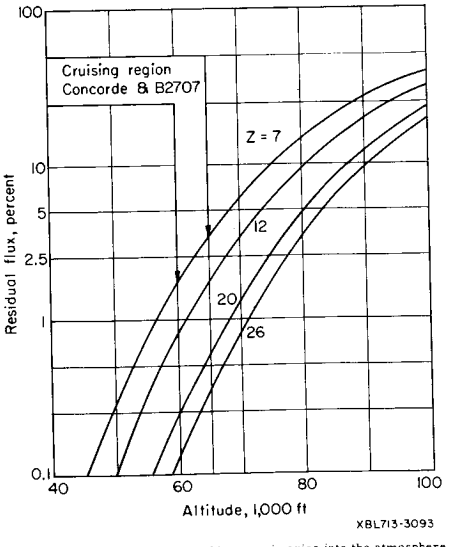

Fig. 2. The depth of penetration of heavy primaries into the atmosphere showing the residual flux versus altitude.

The heavy ions (Z > 2) left at these altitudes are not present in large numbers. Experiments with a high energy (> 10 MeV/atomic mass unit [AMU]) heavy ion particle accelerator should be conducted in order to answer the question of their biological significance. The neutrons are produced by nuclear collisions in the atmosphere. The energy spectrum of these neutrons in the atmosphere has been measured. The shape of the neutron spectrum is constant at all levels in the atmosphere below 100 g/cm^2 or 17 km, as seen in Fig. 4.[8] Near the top of the atmosphere the flux varies with solar activity by a factor of 2, and latitude by a factor of 10, as detailed in Ref. 9. The neutron flux also varies with altitude reaching a maximum at about 17 km (100 g/cm^2) (see Fig. 5). After taking into account the various measurements and calculations available, the following table seems to represent the best estimates of the galactic cosmic ray neutron flux. (See Table I.)

Table 1. Galactic cosmic ray neutron flux and dose rate in relation to altitude

Altitude (feet)	Flux density: Observed at 41°N (n/cm^2. sec)*	Flux density: Estimated at 90°N (n/cm^2. sec)†	Dose rate: at 41°N (μrad/hr)‡	Dose rate: at 90°N (μrad/hr)‡
0	5.4×10^{-3}	5.9×10^{-3}	4.3×10^{-2}	4.7×10^{-2}
10,000	4.0×10^{-2}	5.0×10^{-2}	3.2×10^{-1}	4.0×10^{-1}
20,000	1.6×10^{-1}	2.4×10^{-1}	1.3	2.0
30,000	5.0×10^{-1}	7.5×10^{-1}	4.0	6.0
40,000	7.9×10^{-1}	1.2	6.3	9.4
50,000	1.1	1.8	8.8	14.5
60,000	1.1	2.0	8.8	16.7
70,000	1.0	2.7	8.0	21.5
80,000	0.9	3.9	7.4	31.8

(from Patterson, et al)[10]

*Experimental data from HAYMES.[11]

†The values observed at 41°N were multiplied by factors from LINGENFELTER[9] to obtain the estimated values for 90°N latitude.

‡Values in rads were calculated with flux density-to-dose conversion factors given in Handbook 63 of the National Committee on Radiation Protection and Measurements of the U. S. National Bureau of Standards.[12]

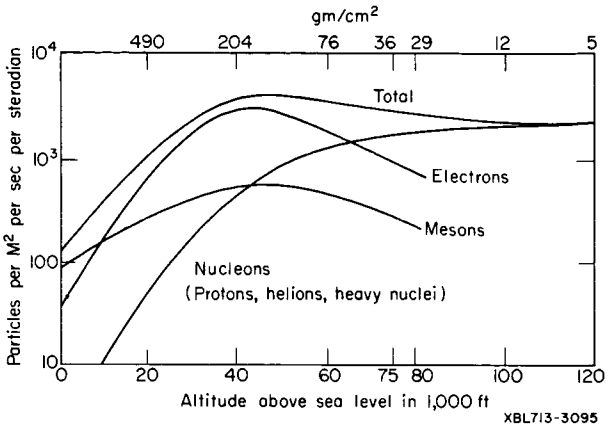

Fig. 3. Altitude profile of particle transition of cosmic ray beam in the atmosphere giving the composition at various altitudes.

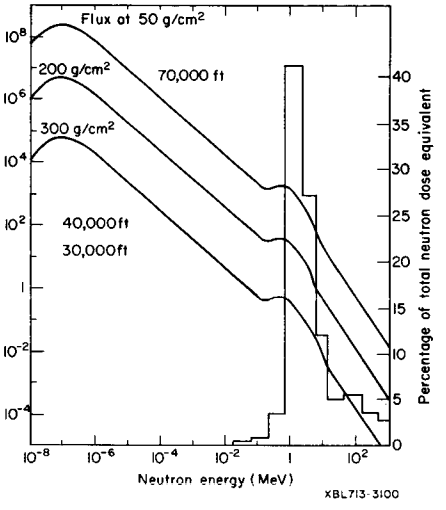

Fig. 4. Combined galactic cosmic ray neutron energy spectrum (from Patterson, et al Ref. 10) and the distribution of the dose equivalent resulting when the spectrum is multiplied by the values of RBE given in Handbook # 63 of the National Committee on Radiation Protection and Measurements of the U. S. National Bureau of Standards.[12] (from Upton, et al.)[7]

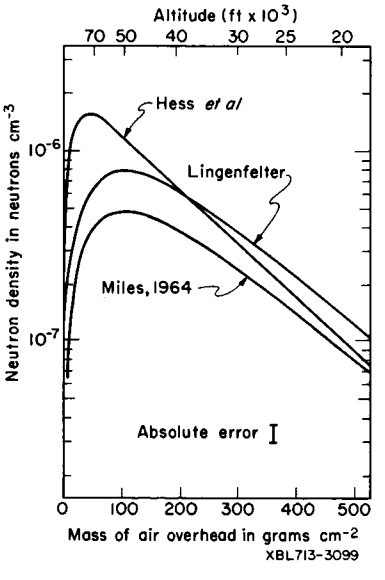

Fig. 5. Galactic cosmic ray neutron flux in relation to altitude.

2. Solar Cosmic Radiation

As previously stated, under normal conditions the solar contribution to the cosmic ray spectrum is minor compared to that of galactic origin. Occasionally, however, the sun erupts with an explosive disturbance or "solar flare" which sends large numbers of x-rays and charged particles into space. The solar flares occur with a wide range of intensities and the probability of occurence follows the 11-year cycle of solar activity fairly closely. Low-energy solar flare events, even of large magnitude, are of relatively little consequence at lower levels of the atmosphere, or at low latitudes. Concern, however, is generated by the possibility of a flare of magnitude similar to that of February 23, 1956. Figure 6, from Foelsche et al., shows the relative importance of such a large flare. The dose in rem/h at various altitudes in this flare is estimated to have been as follows:

Altitude ft:	65,000	50,000	40,000	30,000
km:	20	15	12	9
Dose equivalent in rem/h				
Upper limit:				
Feb. 1956	2.9	1.8	1.0	0.45
Lower limit:				
Feb. 1956	0.45	0.2	0.1	0.025

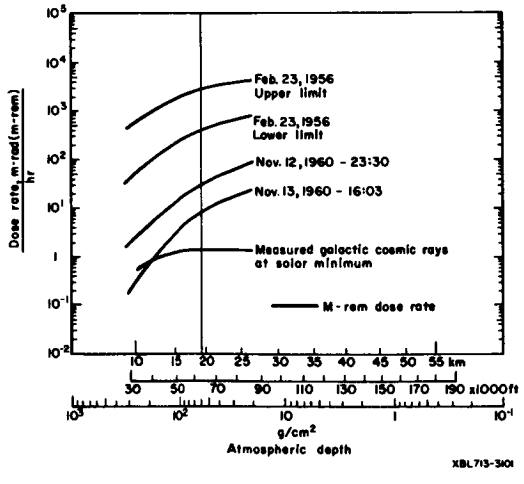

Fig. 6. Dose rates during the large solar events of February 23, 1956 (maximum phase), and November 12, 1960, at 1840, 2330, and 1603 (Nov. 13) universal time.

(from Foelsche, et. al.)[13]

Figure 6 shows dose equivalents which are higher than comparable earlier dose estimates. This calculation of greater penetration of biologically effective components is due mainly to energetic neutrons resulting from nuclear interactions of high energy primaries and secondaries. These neutrons then have a much greater probability of deep penetration, since they have no charge and are not slowed by ionization.[13] (For a detailed discussion of how these curves are derived see Ref. 13.)

C. THE EXPERIMENT

The dosimetric measurements were made by emulsions of three types sealed in plastic packets. These packets were sent by air mail back and forth from Berkeley, California to Hammersmith (London), England, until a dose sufficiently above background had accumulated. Although there were some small variations in the contents of certain packets, all were basically the same. Pieces of polyvinyl-chloride (0.6 mm thick) were cut to the size of a regular business envelope (10 cm × 23 cm). The packet was compartmentized and sealed with a radio-frequency plastic welder. Each packet contained β-γ films, NTA films, one 600μ emulsion, and occasionally CaF_2 thermal luminescent detectors (TLD). Before sealing, the entire packet was flushed with dry nitrogen gas to reduce photographic fading of the latent image by decreasing the relative humidity and decreasing the atmospheric oxygen in contact with the emulsion.[15]

Each packet contained four β-γ films. Two of these films were unexposed, the third film was pre-exposed to 20 mr, and the fourth film was pre-exposed to 100 mr of radium x-rays. One NTA film was pre-exposed to 20 mrem and the other to 100 mrem of PuBe neutrons.

From a schedule obtained from the post office and considering the number of available flights, it is reasonable to assume that at least 80% of the packets made the trip by the polar

route, rather than landing in New York. Polar flights from San Francisco to London always go via Los Angeles on a flight profile approximately like that seen in Fig. 7. They usually go over the southern part of Hudson Bay, Baffin Island, and the southern third of Greenland. Each flight is flown over the predicted "least time" route based on the latest weather predictions. Some flights may be considerably south of Greenland, occasionally as far south as Atlanta, although this is rare. These variations probably don't affect the galactic cosmic ray dose since they take longer at a lower dose rate, which has a compensating effect on the integrated dose. The solar flare dose, if any, would be reduced by a larger factor by the lower magnetic latitude. Since few flares occurred during this experiment, these relatively rare and self-compensating route variations have little effect on our results.

Calculations made at Boeing Aircraft Co. indicate that one should expect about 5 mr/round trip.[16] Since the lower limit of sensitivity for the film is around 10 mr, each packet was sent on about five round trips. Unfortunately, there were no large flares and only one small flare during the experiment. Three groups of packets completed five round trips.

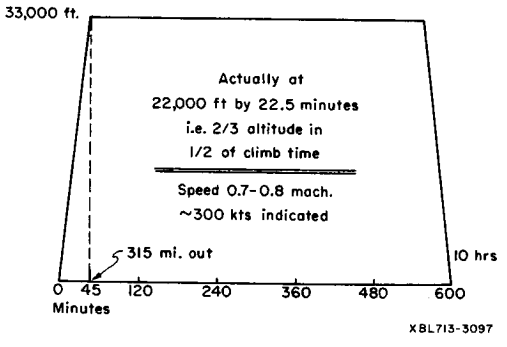

Fig. 7. Flight profile of a typical flight between Los Angeles and London from TWA.

D. BACKGROUND RADIATION

Realizing that from the time the film is sealed until it is developed, it spends more time at sea level than at altitude, it is necessary to estimate the dose of ionizing radiation which is accumulated during the time not spent in the aircraft. Approximately 3 mr were accumulated by each film when it was not at flying altitude.

E. ANALYSIS OF β-γ FILM DATA

In interpreting the data there were two experimental factors which needed special mention. First, these films, all from the same emulsion number, were packaged, exposed, and developed in three different groups; and secondly, the time which elapsed from loading to development in the three different groups was different, even though the time which each group spent in the air was essentially the same. The total dose gathered on these films represents about 2052 hours of exposure at altitudes as calculated from the flight profile in Fig. 7.

The average additional dose from cosmic rays of all flights from December, 1969, to July, 1970, was 12.5 ± 4 mr/round trip with a lower limit of 8.3 mr/trip and an upper limit of 16.1 mr/round trip.

The experience which has been gained over many years in reading this type of film indicates that the data is reasonable. It may not be possible to attach dosimetric significance to the measurements of any one film, but, in view of the large total number of hours which the film spent in the air, the average is probably significant.

Although no large solar flares occurred during the experiment, an attempt was made to correlate enhanced solar activity with those packets which showed a higher dose. This was only mildly successful.

F. THE TLD's[18,19]

The TLD's (thermoluminescent dosimeters) were CaF_2. Each reading is actually an average of three dosimeters contained in a small plastic disk. All reading and calibrating of these dosimeters was done at the Lawrence Radiation Laboratory, Livermore, under the direction of D. E. Jones and R. E. McMillan, of the Hazards Control Group.

Due to their greater sensitivity (down to 0.1 mrad) TLD dosimeters were sent on only one round trip before being read. Of special interest is the TLD sent on the 30th of May. It was in the air when the first proton event in 45 days occurred. Unfortunately, on this particular day a TLD was not sent via JFK and so no comparison could be made between the polar and lower magnetic latitude routes. However, the measurement during the flare was clearly above the other measurements.

A description of the flare of May 30, as given by ESSA, is as follows:

> "The proton event was associated with an imp IN* in Class M flare at 30/0240 Z, again in region 760. The 1-8A x-ray burst associated with this flare had a peak flux of only 0.04 erg per sq cm per cm per sec but a total duration of 6 hours. Protons were first detected by the ATS-1 satellite at about 30/0800 Z and were of the order of 350 and 16 particles per sq cm per sec in the 5 - 21 and 21 - 70 MeV channels respectively. Associated riometer absorption at 30 MHz was 1 Db or less."

What is the meaning of the dose during the flare, compared to average conditions? If the readings for the four previous days from the polar route are averaged together using the amounts over the 4.0 mrad background one gets an average of 1.925 mrad/round trip. We assume that half of this dose was accumulated during each flight direction or that on a no-flare trip the extra amount of radiation from flying is about 1 mrad. There was an increase of about 50% per round trip due to the flare.

G. THE BOEING CALCULATIONS

The Boeing calculations[16] were made by a code originally programmed by Stanley Curtis (now at Lawrence Radiation Laboratory, Berkeley, California), which gives tissue doses due to galactic cosmic radiation during subsonic and supersonic flight for times of minimum solar activity and average solar activity. The results of the twelve city pairs, which were chosen for analysis, are shown in Table II for minimum solar and in Table III for average solar conditions.

Table. II. Results of Boeing's calculations for dose in mrem obtained when flying between various city pairs for solar minimum conditions.

City Pair	Block time* (BT) -hrs-	Subsonic Flight-35000 mrad/ BT-h	mrad/round trip	mrad/600 BT-h
Paris-Anchorage	9.45	0.240	4.54	144
Los Angeles-Paris	11.15	0.239	5.33	144
Anchorage-Hamburg	8.95	0.239	4.27	143
Chicago-Paris	8.35	0.237	3.96	142
New York-Paris	7.45	0.234	3.48	140
Montreal-Paris	7.05	0.232	3.27	139
New York-London	7.05	0.232	3.27	139
San Francisco-N. Y.	5.45	0.210	2.29	126
Los Angeles-N. Y.	5.25	0.201	2.11	121
Los Angeles-Washington	4.95	0.195	1.93	117
Los Angeles-Chicago	3.95	0.186	1.47	112
Sydney-Acapulco**	17.45	0.131	4.57	79
		Supersonic Flight 60-64000		
City Pair	Block time (BT) -hrs-	mrad/BT-h	mrad/round trip	mrad/600 BT-h
Paris-Anchorage	3.25	0.608	3.95	365
Los Angeles-Paris	3.85	0.594	4.57	356
Anchorage-Hamburg	3.05	0.594	3.62	356
Chicago-Paris	2.85	0.574	3.27	344
New York-Paris	2.65	0.553	2.93	332
Montreal-Paris	2.45	0.546	2.67	328
New York-London	2.45	0.545	2.67	327
San Francisco-N. Y.	2.05	0.422	1.73	253
Los Angeles-N. Y.	1.95	0.390	1.52	234
Los Angeles-Washington	1.85	0.368	1.36	221
Los Angeles-Chicago	1.55	0.338	1.05	202
Sydney-Acapulco**	6.25	0.173	2.16	104

* Time in the air ** Two stopovers SOLAR MINIMUM CONDITIONS

*IN - A size and intensity evaluation. In this case area 2.1 - 5.1 sq deg with normal intensity.

Table III. Results of Boeing's calculations for dose in mrem obtained when flying between various city pairs for solar average conditions.

City Pair	Block time* (BT) -hrs-	Subsonic Flight-35 000 mrad/BT-h	mrad/round trip	mrad/600 BT-h
Paris-Anchorage	9.45	0.215	4.07	129
Los Angeles-Paris	11.15	0.215	4.79	129
Anchorage-Hamburg	8.95	0.214	3.84	129
Chicago-Paris	8.35	0.213	3.56	128
New York-Paris	7.45	0.210	3.13	126
Montreal-Paris	7.05	0.209	2.94	125
New York-London	7.05	0.209	2.94	125
San Francisco-N. Y.	5.45	0.190	2.07	114
Los Angeles-N. Y.	5.25	0.183	1.92	110
Los Angeles-Washington	4.95	0.177	1.75	106
Los Angeles-Chicago	3.95	0.169	1.34	102
Sydney-Acapulco**	17.45	0.126	4.40	76

City Pair	Block time* (BT) -hrs-	Supersonic Flight 60-65 000 mrad/BT-h	mrad/round trip	mrad/BT-h
Paris-Anchorage	3.25	0.486	3.16	292
Los Angeles-Paris	3.85	0.481	3.70	289
Anchorage-Hamburg	3.05	0.478	2.92	287
Chicago-Paris	2.85	0.464	2.64	278
New York-Paris	2.65	0.449	2.38	269
Montreal-Paris	2.45	0.443	2.17	266
New York-London	2.45	0.442	2.17	266
San Francisco-N. Y.	2.05	0.351	1.44	211
Los Angeles-N. Y.	1.95	0.329	1.28	197
Los Angeles-Washington	1.85	0.313	1.16	187
Los Angeles-Chicago	1.55	0.288	0.89	173
Sydney-Acapulco**	6.25	0.166	2.08	99

*Time in the air ** Two stopovers SOLAR AVERAGE CONDITIONS

In this calculation the computer utilizes geographical coordinates of the cities, altitude-distance flight profiles and block times. The program then changes these to geomagnetic latitudes and longitudes and pressure altitude as it follows the aircraft on a great circle route. At 0.1 hour intervals, the ionization density (ion pairs per cm^3 per sec per atm of air) is converted to an equivalent tissue dose rate in mrads per hour with all the appropriate conditions taken into account. The dose rate is then integrated and accumulated over the entire flight.

In particular, note that the direct Los Angeles - Paris flight is 5.33 mrad/round trip and that the same trip made by way of New York is 5.59 mrad/round trip. In general, while more southerly routes have a lower hourly dose rate, due to the larger area of the earth in the equatorial and temperate zones, the flight routes are longer and more time is spent in these lower dose rate regions. Thus, there is a compensating effect which tends to make doses on polar flights almost the same as those on lower latitude flights. There is a similar compensating effect of altitude. Subsonic flight at 35,000 ft takes about 3 times as long as supersonic flight over the same route at 65,000 ft. Since the dose rate is about 3 times higher at 65,000 ft relative to 35,000 ft these effects cancel. In fact the doses in the subsonic 35,000 ft flights are about 20% higher than in the supersonic range, and are undoubtedly given to far more people.

J. MEASURED COSMIC RAY NEUTRON SPECTRUM

One of the 600 μ emulsions was scanned for proton recoils, and these in turn converted to the neutron spectrum in Fig. 8.

The emulsions were read using the random-walk method described by Lehman. Using this method, 1150 proton recoil tracks were measured in the emulsion, which is approximately 2 cm × 2 cm × 600 μ in size. This data is then introduced into a computer program which determines the track-length energy. The number of tracks per energy interval DN/P*DE is then plotted versus energy. (See Fig. 8.) The error bars are also determined in the program. From this a smooth proton spectrum is drawn.

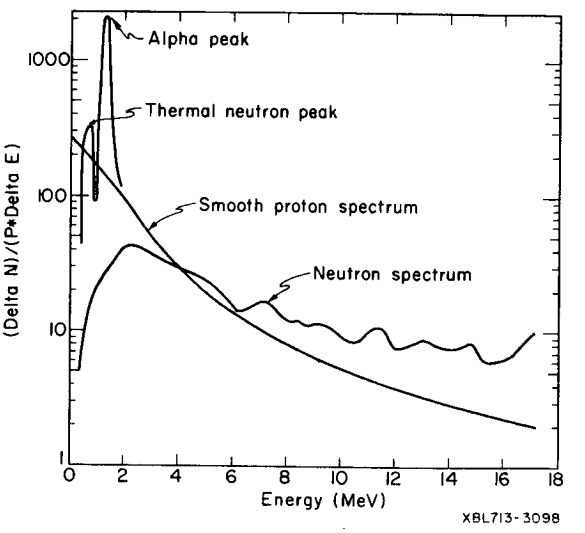

Figure. 8. Cosmic Ray neutron spectrum obtained by measuring proton recoil track lengths in the 600 micron emulsion 1150 tracks were scanned in obtaing this spectrum.

The two peaks at the low end of the proton spectrum are produced systematic effects. They are caused by nitrogen in the emulsion (an $[n_{th}, p]$ reaction) and alphas from thorium and radium impurities.

Points from the smooth proton spectrum are then introduced into another program which determines the neutron spectrum. (See Fig. 8.) A second plot of this neutron spectrum was made with a linear scale. (See Fig. 9.) Then using the expressions in Table IV[20] an integral rem dose was calculated for each energy interval. This rem spectrum was then plotted with the linear neutron spectrum for comparison. (See Fig. 9.)

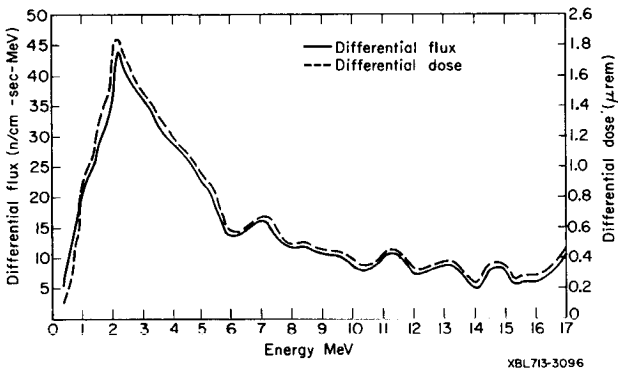

Figure 9. Comparison of Energy Spectra

K. CONCLUSIONS

The average of the experimental measurements was:

β-γ film	12.5 mr/rd trip average
TLD's	2.0 mrad/rd trip average
Boeing calculations	5.5 mrad/rd trip average

One reason for the larger β-γ film reading is that the film has a wider response to a wider γ spectrum than the TLD. This is especially true in the low energy end of the spectrum. Also, the background correction subtracted from each dosimeter is a different percentage of the total reading in each case. The β-γ film dose represents all radiation received from cosmic rays and radioactive x-ray background while on the ground, as well as while in the air. The TLD dose represents only what is gained in the air since the controls were not kept in our low level cave, but themselves received the full sea level cosmic ray and background γ exposures. The Boeing calculations represent the dose obtained from cosmic rays only while flying.

If the same background correction of 4 mrad used for the TLD's is subtracted from the β-γ film, then the average cosmic ray dose for the film is lowered to about 8.5 mr. This would then be in good agreement with the calculation. The question to resolve is whether the dosimeter or the calculation is more accurate. The strongest tendency is to place more faith in the TLD's. First, they show very consistent readings at about 10% of the minimum measurable dose of the films and judging from their response to the one solar flare which they encountered, their response seems to be internally consistent. Secondly, they were under much closer control than the film, since they made only one round trip. The film spent many weeks being exposed and perhaps fading. The chance of encountering some unexpected phenomenon on one trip is much less likely with the TLD than it is with the films which made five trips.

Table IV. Analytic expressions for dose equivalent vs neutron energy

Energy range (MeV)	$n\text{-}cm^{-2}\text{-}sec^{-1}$ equivalent to 1 $mrem\text{-}h^{-1}$
$< 10^{-2}$	232
$10^{-2} - 10^{0}$	$7.20\ E^{-3/4}$
$10^{0} - 10^{1}$	7.20
$> 10^{1}$	$12.8\ E^{-1/4}$

This experiment indicates that further work should emphasize the use of the TLD's. The Boeing calculations are probably quite realistic. The total dose on 35,000 subsonic flights is about 20% higher than on 65,000 ft supersonic flights.

The neutron dose also requires further consideration. Making the measurement over the shortest possible time period seems to be the key to this problem. At the same time as the measurement is being made a careful check on the amount of fading taking place during the measurement must be made.

A more complete description of this experiment can be found in UCRL-20052, A Measurement of Cosmic Radiation Dose: Jet Aircraft Polar Route San Francisco to London, by Michael F. Boyer (M.S. Thesis, 1970).[22]

ACKNOWLEDGMENTS

We would like to express our appreciation to the staff of the Lawrence Radiation Laboratory, Berkeley, for their guidance and encouragement; in particular, those in the Health Physics Department -- Lloyd Stephens and Jerry Miller for their day-to-day advice, Ellen Cimpher for typing the paper, and Josephine Camp, Dorothy Hadley, and Olga Fekula for their assistance in processing and reading emulsions. Thanks to the Hazards Control Department at Livermore, in particular, Don Jones and Robert McMillen, for their work with the TLD's.

We wish to thank Dr. J. F. Fowler and his staff at Hammersmith Hospital, London, England, for their unfailing constancy in getting all our dosimeters to make round trips.

REFERENCES

1. B. Peters, The Nature of Primary Cosmic Radiation, Progress in Cosmic Ray Physics, 1, 191 (1952).

2. C. J. Waddington, The Composition of the Primary Cosmic Radiation, Progress in Nuclear Physics, 8, (1960).

3. Donald P. Le Galley and Alan Rosen, editors, Space Physics, John Wiley and Sons, Inc., New York, 1964.

4. F. B. McDonald, Review of Galactic and Solar Cosmic Rays, in the Second Symposium on Protection Against Radiation in Space, from the Proceedings of a conference held in Gatlinburg, Tennessee, October 12-14, 1964.

5. Herman J. Schaefer, Public Health Aspects of Galactic Radiation Exposure, Nasa Joint Report, March, 1968, NAMI-1033.

6. T. Foelsche, The Ionizing Radiations in Supersonic Transport Flights, in the Second Symposium on Protection Against Radiation in Space, from the Proceedings of a conference held at Gatlinburg, Tennessee, October 12-14, 1964. NASA SP-71, pp 287-299.

7. A. C. Upton, et al, (ICRP Task Group), Radiobiological Aspects of the Supersonic Transport, Health Physics, 12, 209-226 (1966).

8. W. N. Hess, H. W. Patterson, R. Wallace, and E. L. Chupp, Cosmic Ray Neutron Energy Spectrum, Phys. Rev., 116, 445 (1959).

9. R. E. Lingenfelter, Production of Carbon ^{14} by Cosmic Ray Neutrons, Rev. Geophysics, 1, 35-55 (1963).

10. H. W. Patterson, et al., The Flux and Spectrum of Cosmic Ray Produced Neutrons as a Function of Altitude, Health Physics J. 2, 1, 69-72 (1959).

11. R. C. Haymes, Fast Neutrons in the Earth's Atmosphere. 1. Variation With Depth, J. Geophys. Res., 69, 841-852 (1964).

12. National Committee on Radiation Protection and Measurements, Protection Against Neutron Radiation Up to 30 Million Electron Volts, Handbook 63, National Bureau of Standards, Washington, D. C. (1957)

13. T. Foelsche, et al, Measured and Calculated Radiation Levels Produced by Galactic and Solar Cosmic Rays in SST Altitudes and Precaution Measures to Minimize Implications at Commercial STT-Operations, NASA Langley Research Center, Langley Station, Hampton, Va., RIF:FAUSST 7.3.3.02, March 3, 1969.

14. Preliminary Report and Forecast of Solar Geophysical Activity, Space Disturbance Forecast Center, ESSA, Boulder, Colorado.

15. Robert A. Dudley, Dosimetry with Photographic Emulsions, in Radiation Dosimetry, edited by Frank H. Attix and William C. Roesch, Academic Press, New York and London, pp. 325-388 (1966).

16. City Pair Dose Calculations, Boeing Document D6 A11467-1 .

17. Personal communication with H. Wade Patterson, Health Physics Department, Lawrence Radiation Laboratory, Berkeley, July, 1970.

18. Frank H. Attix, ed., Luminescence Dosimetry, U. S. Atomic Energy Commission, Div. of Technical Information, April, 1967.

19. Proceedings of the Second International Conference on Luminescence Dosimetry, 1968. Sponsored by USAEC and held at ORNL, CONF-680920.

20. Richard L. Lehman and Olga M. Fekula, Semiautomatic Scanning of Proton-Recoil Tracks in Nuclear Emulsion, UCRL-11321 (March, 1964).

21. W. S. Gilbert et al., 1966 CERN-LRL-RHEL Shielding Experiment at the CERN Proton Synchrotron, UCRL-17941, Sept. 1968, p. 120.

22. Michael F. Boyer, A Measurement of Cosmic Radiation Dose: Jet Aircraft Polar Route, San Francisco to London, Lawrence Radiation Laboratory Report UCRL-20052, August 5, 1970, (M.S. Thesis).

RADIATION MEASUREMENTS AND DOSES AT SST ALTITUDES

Trutz Foelsche

NASA Langley Research Center
Hampton, Virginia

A brief survey of results up to 1970 of an experimental and theoretical study of biologically important radiation components and dose equivalents due to galactic and solar cosmic rays in the high atmosphere, especially at SST altitudes, is presented.

The dose equivalent rate for the flight personnel flying 500 hours per year in cruise altitudes of 60,000-65,000 feet (18-19.5 km) in high magnetic latitudes turned out to be about 0.75-1.0 rem per year averaged over the solar cycle, or about 15-20 percent of the maximum permissible dose rate for radiation workers as established by the International Commission on Radiological Protection (ICRP) for peacetime operations (5 rem per year).

The gross of passengers, who do not encounter major solar events, would be exposed only to the low level galactic cosmic rays. Such exposure would amount to some mrem per North-Atlantic trip and is therefore negligible. Very rarely, groups of passengers, who happen to be passing through the impact zone of a rare giant solar event such as that of February 23, 1956, would be exposed to 0.45 rem, provided the airplane descends to subsonic altitudes at the beginning of the event and continues its flight at the lower altitudes. This exposure, 0.45 rem, is 90 percent of the permissible limit for individuals of the general population (0.5 rem per single year). At cruise altitude, the maximum permissible limit would have been surpassed. The suggested evasion measure of descending to lower altitudes is therefore sufficient to avoid overexposure of passengers in such rare cases.

I. INTRODUCTION

There has been continuing concern about the radiation safety in airplanes such as the SST. The high-altitude commercial airplanes, as they are envisioned for the future, will cruise at altitudes of 60,000 to 65,000 feet (18-19.5 km). At such altitudes, only about 6 percent (about 60 g/cm^2) of the mass of the atmosphere is left above the airplane, which may grant little protection against space radiation such as galactic and energetic solar cosmic rays. In fact, the nuclear reactions of the cosmic rays within this upper 6-percent of the atmosphere produces many secondaries, including the particularly biologically effective neutrons whose net biological effect may exceed that of the primaries.

In the following the author may review what we know of this problem - mainly as it concerns the radiation exposure of the crew and passengers at SST and lower altitudes - and what evasion measures might have to be taken during times of energetic and intense solar particle events.

II. DATA SOURCES

Our understanding is based to a large extent on Langley high-altitude experiments with high-altitude balloons and airplanes measuring cosmic rays and their variations with solar activity, from 1965 to the present, over a large part of the solar cycle (refs. 1 and 2).

Figure 1 is a brief review of these data sources. Through the 4 years from 1965 to 1968, 20 balloon launches, five each year, were conducted by Langley from Fort Churchill, Hudson Bay, Canada. From 1968 to the present, about 300 U2 and RB57-F flights from London, England; Maine, USA; and Eielson AFB, Alaska, have been made. The latter in cooperation with the Air Force and FAA. We owe particular thanks to the Air Force for its generous cooperation. Spot checks in lower latitudes were conducted with balloons from Heiderabad, India, and from Pallestine, Texas. Furthermore, five latitude scans with RB57-F's from Eielson AFB, Alaska, to Albuquerque, New Mexico, and down to the equator were made. A complete latitude scan at 35,000 feet was conducted by participating in the 65-hour globe-circling flight over both poles with a Boeing 707 airplane in 1966.

We note that most flights were made in high magnetic latitudes. The reason is that we are mostly interested in maximum doses and these occur at latitudes above $\approx \pm 50^{\circ}$, which contain the North Atlantic and Canadian routes and possibly routes from Moscow to the U.S.A. Below 50° magnetic latitude, the doses fell off rather rapidly because the magnetic field of the Earth deflects the cosmic ray particles at the lower latitudes. The dose rates decrease by about a factor of 6 toward the equator, according to our measurements. Thus, precautionary measures would not be necessary on the Pacific and Southeast Asian routes.

Additional relevant data include ground experiments and extensive theoretical analyses made at Oak Ridge National Laboratory in an 8-year study (refs. 3-8) and at Langley (refs. 9-13) applying the developing dose calculation methods to the accumulated spectral data on solar events, especially those of the highly active solar cycle 19 (1954-1964) and extending the Oak Ridge Laboratory methods to higher energies.

III. MAXIMUM PERMISSIBLE DOSES

Before reporting on measurements and relevant results, it may be well to recall the biological doses which are internationally accepted as maximum permissible doses (MPD's) for peacetime operations and their definitions.

In figure 2, applicable MPD's, as established by the ICRP, are briefly summarized.

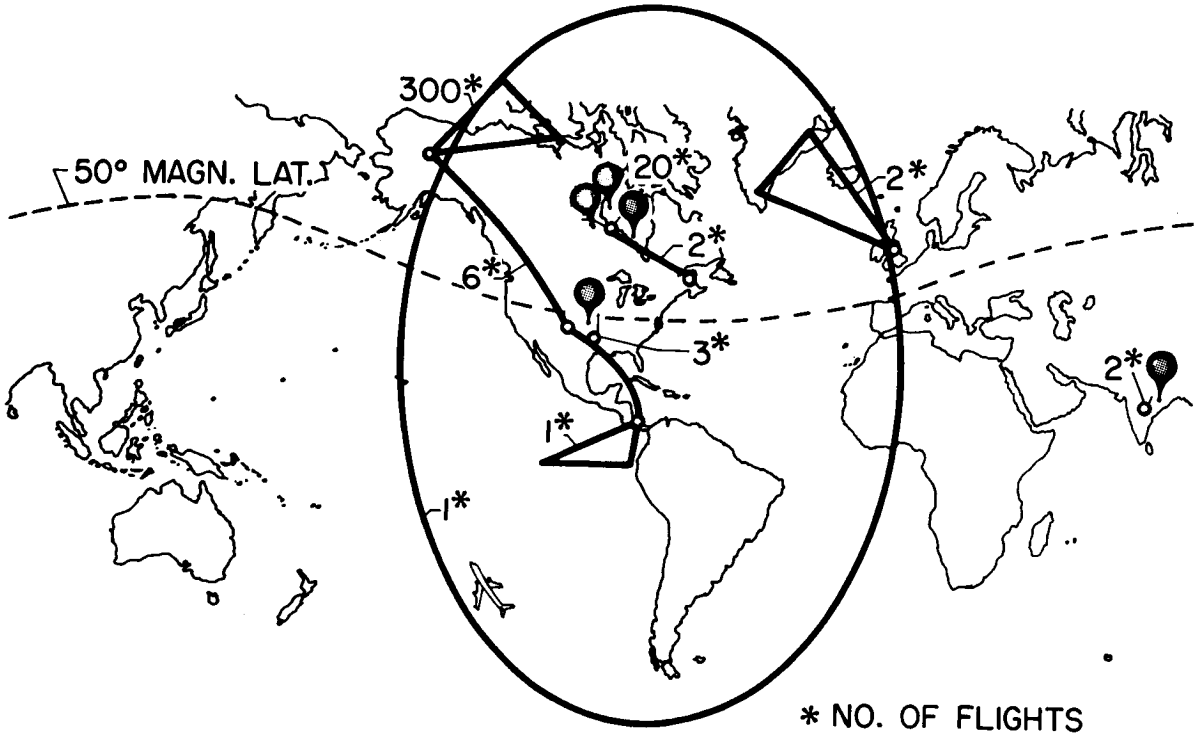

HIGH ALTITUDE RADIATION MEASUREMENTS
1965 - 1971

The doses are given in rem, which stands for "roentgen equivalent man" and is different from rad which measures only the energy absorbed per gram. For a given amount of absorbed energy, heavily ionizing nuclei and neutrons do much more biological damage than X-rays or electrons or other lightly ionizing particles. When the dose is corrected for this increased biological effectiveness, we have the rem. For example, for fast neutrons as we encounter them in high altitudes, the dose equivalent or rem is about 10 times their absorbed dose.

We note in figure 2 that the average MPD for radiation workers is 10 times higher (5 rem per year) than the MPD for individuals of the general population in a single year (0.5 rem per year). The reason is that radiation workers are a small group of adults. The general population encompasses children, including infants - even the fetus in pregnant women - who are much more sensitive to radiation. In fact, the guidelines for the general population are even more restrictive. "Total of 5 rem to age 30" means that in the average to age 30 only 0.167 rem per year is permissible. Thus, 0.5 rem is not allowed for every year.

MAXIMUM PERMISSIBLE DOSES (MPD'S)

RADIATION WORKERS: WHOLE BODY	$\frac{5 \text{ rem}}{\text{yr}} = \frac{0.6 \text{ mrem}}{\text{hr}}$
POPULATION: INDIVIDUAL	$\frac{0.5 \text{ rem}}{\text{yr}}$ (TOTAL OF 5 rem UP TO AGE 30)

For high altitude flight, we equate the crew or flight personnel to the radiation workers because they are adults; and we equate the passengers to the general population. Thus, we may note the following two numbers:

For the crew	5 rem per year on the average over long periods, say 10 to 30 years, are permissible
For passengers	Maximum 0.5 rem per year in single years, or one time in a single year, is considered permissible.

IV. MEASUREMENTS AND DERIVATION OF THE DOSE EQUIVALENT RATES WITHIN THE ATMOSPHERE

The following describes the measurements which were made and how the dose equivalent rates were obtained from measurements and theoretical calculations. As mentioned before, one of our main concerns has been the contributions of the fast secondary neutrons to the dose equivalent rate in SST altitudes, which were unknown in wide limits. Figures 3 and 4 illustrate the problem.

Figure 3 shows, schematically, the incoming galactic and solar light and heavy nuclei, which interact in nuclear collisions with the air atoms, mainly in the first 30 g/cm^2 of air that is above 80,000 feet. In their collisions, the primary particles produce secondaries which, on their part, again produce secondaries in further nuclear collisions, and so forth. Figure 3 shows only the produced neutrons and shall indicate that the produced neutrons penetrate relatively freely, that is, without substantial energy loss, deeply into the atmosphere. Being neutral particles, they lose no energy by ionization. The neutrons have a mass which is by a factor of about 15 lower than that of the air atoms O and N and lose, therefore, also little energy at elastic collisions. In fact, at low energy solar events ($E \leq 200$ MeV/nucleon) essentially only a neutron increment is found in SST altitudes, because the charged primaries come to rest by ionization or are fragmented in nuclear interactions - their charged secondaries coming to rest by ionization in higher altitudes.

NEUTRONS IN AIR

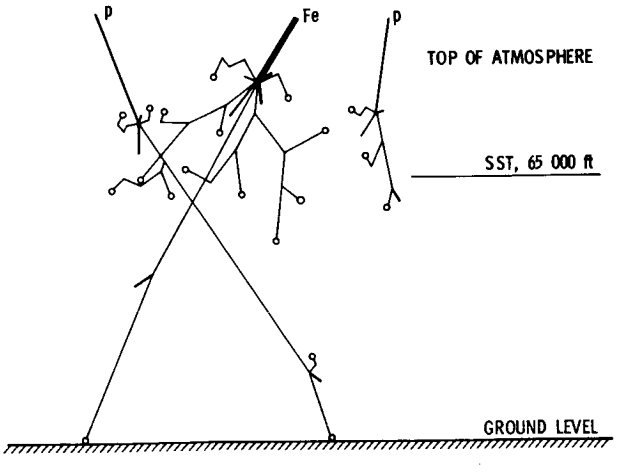

NEUTRONS IN TISSUE

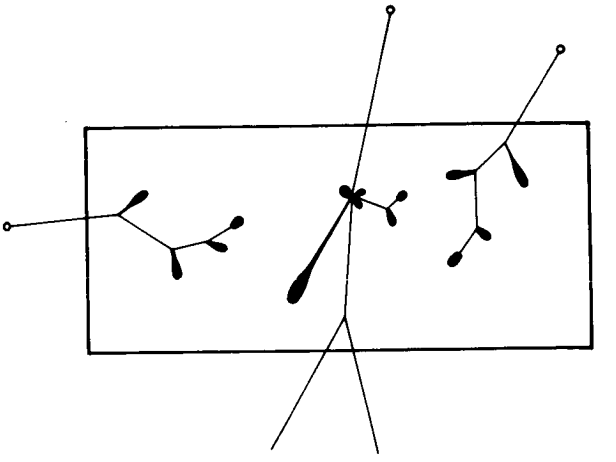

Within the hydrogen containing tissue of man's body, however, the neutrons are most biologically effective, as indicated in figure 4. In tissue they are strongly absorbed in losing, on the average, half of their energy in every elastic collision with protons (H); which protons, in turn, are charged and produce the heavily ionized recoil tracks, being highly biologically damaging. In the midst of figure 4, a so-called "star" or nuclear interaction with a C, N, or O atom of tissue is indicated with prongs of heavier (biologically effective) and lighter fragments.

Because of their possible importance and the large uncertainty of fluxes and energy spectra, the neutrons were measured separately in the Langley program with a special neutron spectrometer developed and maintained by Dr. R. Mendell, New York University. The detection of neutrons with this instrument is based on discrimination of pulse shapes in a liquid scintillator surrounded by a plastic scintillator, the latter for exclusion of charged particles (refs. 14 and 15).

Besides neutrons - protons, mesons, and photon-electron cascades penetrate to SST altitudes. To determine the doses produced by these more lightly ionizing particles, a tissue equivalent ion chamber which was designed and built by AVCO, Oklahoma, and supplemented with a recorder and maintained by Dr. R. R. Adams, Langley Research Center, was used in the flight experiments. The neutron spectra and tissue absorbed dose were measured with these instruments. They were first suspended in free air and then inside spherical phantoms of tissue equivalent material representing man's body, to derive the dose equivalents in extremities (small tissue sample represented by the sensors) and in the depth of the body.

From the neutron spectrum, the absorbed dose rate (rad) and dose equivalent rate (rem) due to neutrons have been calculated by using the flux-to-dose conversion and quality factors defined by the ICRP for neutrons up to 10 MeV energy, and extended by Oak Ridge National Laboratory to neutrons and protons up to 400 MeV. It must be mentioned here that the spectrometer measures only the neutron spectra in the energy range 1–10 MeV. These measurements were used to normalize the total spectra from 0.1–400 MeV obtained by J. W. Wilson (ref. 13) who succeeded in developing a nuclear cascade and transport computer code for incident protons up to 10 GeV (see also ref. 10). The neutrons 10–400 MeV produced by galactic cosmic rays have been found to contribute substantially (about 40 percent) to the neutron dose equivalent rate in high altitudes.

Besides by neutrons, highly biologically effective stars are produced in tissue by primary and secondary charged particles, in particular, protons at SST altitudes. Their contribution to the dose equivalent rate is calculated by taking into account the measurements in tissue equivalent emulsions of Davison (ref. 16).

The total dose equivalent rate is obtained by subtracting the absorbed doses due to neutrons and due to charged-particles-produced stars from their dose equivalents (rem - rad) and adding the ion chamber dose which measures both the absorbed dose due to lightly and heavily ionizing or damaging particles (the latter neutrons, stars). The dose equivalent rate derived in this way is due to all lightly ionizing primaries and secondaries and due to neutrons and charged-particles-produced stars in tissue.

Heavy primary hits or penetrations and heavier fragments than protons produced in nuclear interactions with air are neglected. According to measurements of Yagoda (ref. 17) and also unpublished measurements in the course of the Langley program, the fluxes of heavy primaries and of energetic heavy fragment are practically zero in 60,000 to 65,000 ft altitude (> 60 g/cm^2 air shielding). The same result with respect to heavy nuclei have theoretical estimates of H. Schaefer (ref. 18).

IV. MAXIMUM EXPOSURE OF SST OCCUPANTS AND COMPARISON WITH MPD's

To obtain the maximum exposure of SST occupants and compare these with the MPD's, some of our results on galactic and solar cosmic ray dose rates in SST and subsonic altitudes and at high latitudes will now be presented. We begin with:

1. Galactic cosmic ray dose rates

Galactic cosmic rays are of low intensity; however, they are always present. Their intensity varies by a factor of about 2 in the high-energy range and a factor of about 4 in the low-energy range during the 11-year sunspot cycle.

In figure 5, the circles show the measured dose rates as a function of altitude. The scale is on the right-hand side and is given in rads - not corrected for biological effectiveness. This dose rate is nearly constant above SST altitude in the year 1967. The squares show the fast neutron flux measured separately. The scale is on the left-hand side.

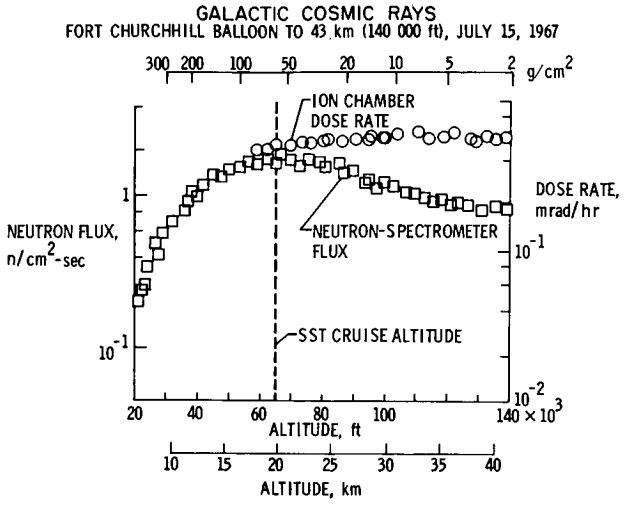

One recognizes that the neutron flux has a maximum just at SST altitudes.

Figure 6 shows the biological dose rates of dose equivalent rates in mrem per hour derived from these measurements.

Consider first the light lines labeled 1965. The dashed curve shows the contribution mainly of the lightly ionizing particles; the dotted line shows the contribution rem-rad of the neutrons; and the x's show the contribution rem-rad of the stars produced by charged particles which are the sites of nuclear reactions, with extensive local damage to the cells (as the stars produced by neutrons). We may mention that the dose equivalent rate due to neutrons, as derived from our measurements and calculations, is about four times higher than that estimated in the ICRP task group report of 1966 (ref. 19).

The light solid line is the total dose equivalent rate as function of altitude, which indicates again a maximum at SST altitude. It may be noted that the curve is labeled 1965. That was near sunspot minimum of the solar cycle, when the galactic cosmic ray flux is a maximum. The average over the 11-year solar cycle would be less – about as shown by the heavy line. The average dose rate is about 1.2 mrem/hour at SST altitude.

We obtain, thus, the following results: If the crew flies 500 hours/year in cruise altitude, their average dose rate due to galactic cosmic rays would be about 500 x 1.2 mrem/year = 0.6 rem/year or only about 12 percent of their maximum permissible dose rate.

The gross of passengers, who may cross the North Atlantic only a few times a year, not encountering solar events, would be exposed in 2 hours at cruise altitude to only about 3 mrem, which is negligible in comparison with 500 mrem or 0.5 mrem, which is their permissible limit.

BODY DEPTH DOSES FROM GALACTIC COSMIC RAYS

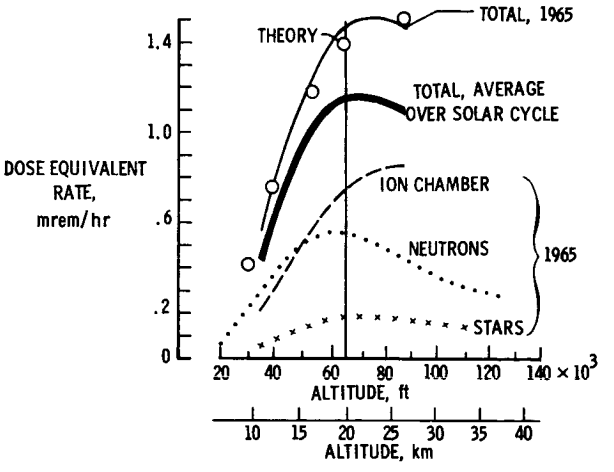

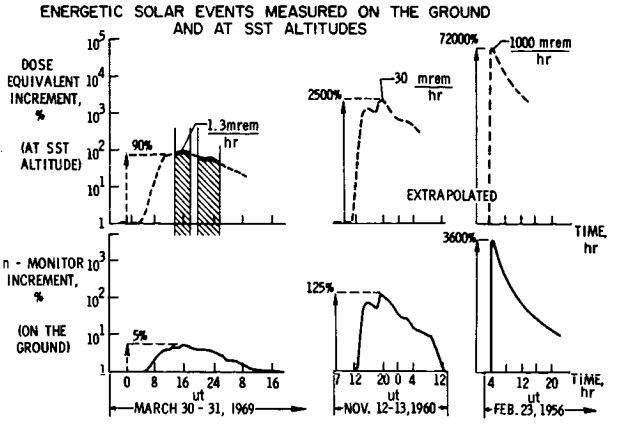

The circles labeled "theory" on the total dose curve for 1965 were calculated starting from the known cosmic-ray spectrum in space, using the mentioned Langley developed computer program, to determine the dose at various depths in the atmosphere. The fairly good agreement with the measurements suggests that such a computer code may be useful to monitor the dose rate in SST's with fair accuracy from the primary spectra measured, for example, in synchronous satellites far out in space, without having instruments onboard the SST's.

2. Solar cosmic ray doses

Solar cosmic rays or solar particle events, accompanying some - but not all - flare outbursts on the sun, are transient particle showers (duration 8-24 hours); however, in some cases, they may have 1000 times higher intensity than galactic cosmic rays.

In figure 7 the two curves on the left correspond to a high-energy event of very low intensity that occurred on March 30-31, 1969. The intensities (ordinates) are plotted against time in hours (abscissa).

The neutron monitor on the ground showed only a 5-percent increase over its background; the latter due to the steady flux of galactic cosmic rays. Our airplane flying at SST altitude, however, showed about a 90-percent increase in biological dose rate or nearly 20 times as much. The factor 20 is somewhat obscured by the log scale on the ordinate, however, the log scale is needed to present in the same figure the much higher increments observed in 1956 at a very intense high-energy event.

The event on the right is the famous giant event of February 23, 1956, which is the largest event observed for at least 30 years. Instead of 5 percent, an increase of 3600 percent on the ground, or 36 times galactic cosmic-ray background was observed. No measurements at altitude could be made in 1956; however, if we use the same factor of about 20 that we found for the smaller flare, we get an increase of 720 times that of March 1969, which represents a dose rate of 1000 mrem/hour or 1 rem/hour at the beginning of the event.

Since the dose that would be accumulated during, say, 2 hours at cruise altitude is apparently above the permissible limit for passengers, it is very important to confirm this high dose rate in any possible way. We started with the fluxes and spectrum above the atmosphere in space which were estimated by Meyer, Parker, and Simpson from ground measurements over a wide latitude range at that time (refs. 20-22) and applied our computer program mentioned earlier.

The prompt spectrum supplemented by estimates of other authors (ref. 12) is presented in figure 8 right.

Figure 9 shows the result of these dose calculations for different altitudes. The maximum dose equivalent rate for February 1956 at SST altitude is found between 3 rem/hour and 0.5 rem/hour, which is in fair agreement with figure 5. The large difference between the upper and lower limit is mainly due to the uncertainty in the lower energy part of the prompt spectrum (< 1 BeV) which could not be measured in 1956.

We have made similar dose calculations for the most significant of the 60 solar events of the particularly active solar cycle 19 starting with the energy spectra in space composed from balloon, rocket, satellite, riometer, and scattering network data. The second largest event was that of November 12-13, 1960, which is seen at two different times in figure 9. The dose equivalent rates are only in the order of 30-50 mrem/hour at altitude.

On the basis of these measurements and calculations on solar events, we may again first draw conclusions on the average exposure of the crew from solar cosmic rays assuming, conservatively, that the crew passed through each major event of cycle 19 in its maximum phase. The result is given in figure 10.

One sees that the contribution of all major events, except that of February 1956, is very low. If one includes the February 1956 event, one obtains an upper limit of 0.3 rem/year as the average

contribution per year from solar events of one cycle. Of course, in none of the single years was the maximum permissible dose rate of 5 rem/year for the crew reached, even if the airplane were to stay in cruise altitude during the events. In adding the previously given galactic cosmic-ray average dose rate of 0.6 rem/year, we arrive at 0.9 rem/year from solar plus galactic cosmic rays. This is the average over the solar cycle and is only 15 to 20 percent of the maximum permissible exposure for radiation workers. We should add here, for correctness, that this exposure on high latitude routes is nevertheless somewhat higher than the actual exposure of 90 percent of the radiation workers in the nuclear industry, which is of the order of only 10 percent of the MPD for radiation workers.

FLARE-PARTICLE SPECTRA

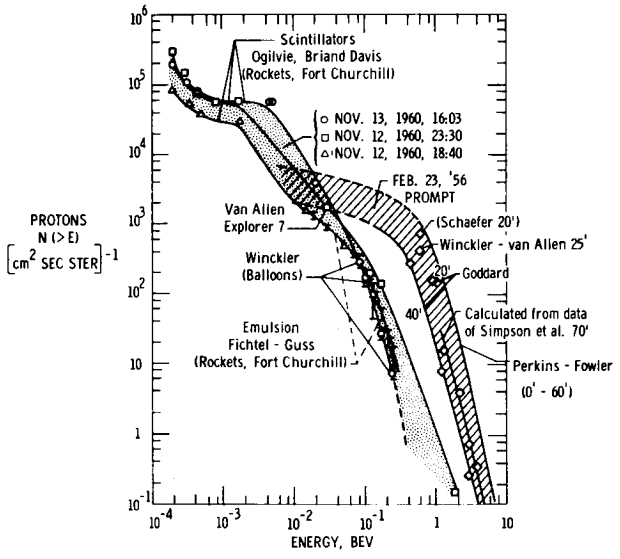

The numbers 20', 25', ... are the minutes after solar cosmic ray onset, observed on earth 0350.

CALCULATED SOLAR FLARE DOSES

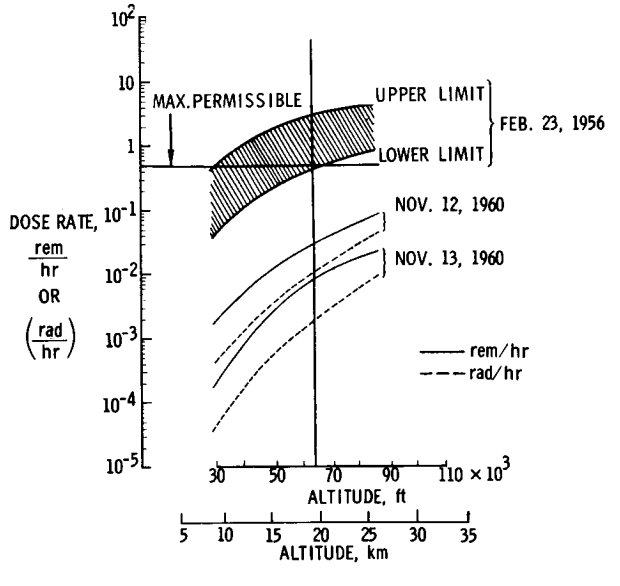

GALACTIC AND SOLAR COSMIC RAYS AVERAGED OVER 10-YEAR DUTY

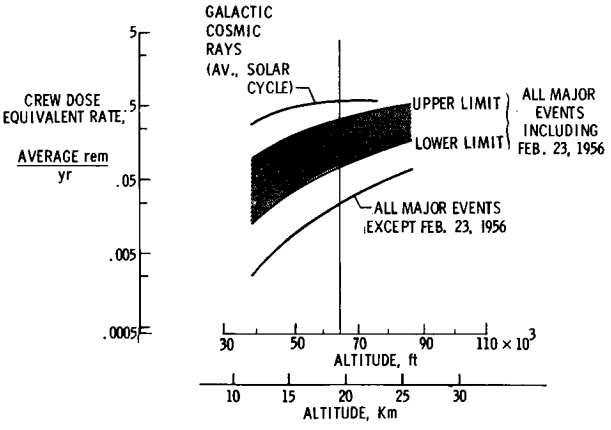

We come now to the most important result so far, namely, that to the best of our knowledge, the permissible exposure of passengers is exceeded if the SST flies at its cruise altitude during such giant events as that of February 1956. This would be contrary to the internationally accepted radiation protection guidelines.

On the other hand, fortunately, atmospheric attenuation is sufficient so that, by timely descent to subsonic altitude during such events, the conservatively high estimated accumulated dose would have been below 0.5 rem, or below the MPD for passengers. We see in figure 9 that the maximum dose rate at 30,000 feet altitude would have been 0.45 rem/hour. This is the dose rate at the peak of the event - of about 10 minutes' duration. This dose rate fell off very fast in the first hours (as in all highly intense energetic events observed so far). The accumulated dose for the first 3 hours, about the maximum time that the SST would remain at subsonic altitude, would not be more than 0.45 rem. Thus, such an evasion measure is sufficient to keep the dose within safe limits in such rare cases.

Furthermore, it appears that in all the other of the approximately 60 solar events such evasion would not have been necessary in order to comply with the requirement to stay below the maximum exposure limit of 0.5 rem, because the maximum dose rate even for the November 12, 1960, event was only on the order of 30-50 mrem/hour at SST altitude. Since it is desirable to hold any exposure as low as possible, one may descend also in such cases, that is, if a level of 50 mrem/hour or even less is reached. Even when evasion in such cases is included, solar cosmic radiation will only in rare cases interfere with the normal operation of the airplanes, since only three more events comparable in size and energy to the November 12 event were observed in the highly active cycle 19.

A design requirement for evasion to subsonic altitude is that the airplane has sufficient subsonic flying capability to reach the next airport from every point of its route. The latter capability was specified for the American SST and is probably specified for the Concorde and the Russian SST for safety reasons. It may be emphasized that an in-flight radiation warning and monitoring system is required to minimize evasion measures or interference with the normal operation of the SST planes. Other precautionary measures such as delaying flights or rerouting the airplanes to lower latitudes in case active regions on the sun are about to erupt would interfere considerably more with the economical operation of high-altitude aircraft, since as yet, even experienced forecast centers cannot predict if and when such regions erupt and if high-energy particles are produced with high intensity. Only very rare intense high or medium energy events require evasion measures. Giant events comparable to that of February 23, 1956, have occurred only one to two times per 11 year cycle in the past three decades.

V. SUMMARY ON RADIATION EXPOSURE AND SAFETY MEASURES

We may now finally summarize the obtained results on radiation exposure and safety measures (see fig. 11).

1. The maximum exposure of the crew due to galactic and solar cosmic rays, as listed in the upper half of the table, is found to be 0.75-1.0 rem/year averaged over the solar cycle or 15 to 20 percent of the maximum permissible dose rate for radiation workers. This is, of course, also the exposure of passengers who fly as often as the crew on high latitude routes such as, perhaps, executives of airlines, who are presumably adults and would take no significant radiation risk either.

2. The gross of passengers, who do not encounter major solar events, would only be exposed to the low-level galactic cosmic rays. Such exposure would amount only to some mrem per trip and is therefore negligible. A small group of individual passengers, passing such rare giant solar event as that of February 1956, would be exposed to maximum 0.45 rem, which is 90 percent of their permissible limit per year, if the airplanes descend in time and continue the flight at subsonic altitudes during the event.

From the preceding considerations, we come to the following conclusions:

1. If the suggested precautionary measure of timely descent or other evasion measures can be taken in case of giant solar events, radiation appears to pose no hazard to the health and safety of passengers and crew in commercial SST flight - assuming, of course, the validity of the present internationally accepted exposure limits, especially for pregnant persons, for which case there still exists some uncertainty.

2. If a radiation monitoring system exists which indicates to the pilots in time when to descend to subsonic altitudes, and if the pilots can reach the next airport at subsonic altitude, cosmic radiation will only in very rare cases interfere with the normal operation of high-altitude aircraft.

	EXPOSURE	PERCENT OF MPD'S
CREW: (>55° MAGNETIC LATITUDE, AVERAGE OVER SOLAR CYCLE)	0.75 TO 1 rem/yr	15 TO 20% OF MPD FOR RADIATION WORKERS
PASSENGERS: GROSS	NEGLIGIBLE	
INDIVIDUALS (WITH EVASIONS, FEB. 1956)	< 0.45 rem/yr	< 90% OF MPD FOR POPULATION, ONE TIME IN 10 yr

DOSE EQUIVALENTS FOR SST OCCUPANTS

REFERENCES

1. Foelsche, T.; Mendell, R.; Adams, R. R.; and Wilson, J. W.: Measured and Calculated Radiation Levels Produced by Galactic and Solar Cosmic Rays in SST Altitudes and Precaution Measures to Minimize Implications at Commercial SST Operations. Preprint from Proceedings of FAUSST VII Meeting, Paris, France, March 3, 1969. Available on request from NASA Langley.
2. Foelsche, T.; and Wilson, J. W.: Results of NASA SST Radiation Studies Including Experimental Results on Solar Flare Events. Minutes of the Standing Committee on Radiobiology Aspects of the SST. FAA, Washington, D.C., April 10-11, 1969. Available on request from NASA Langley.
3. Bertini, H. W.: Preliminary Data From Intranuclear-Cascade Calculations of 0.75-, 1-, and 2-GeV Protons on Oxygen, Aluminum, and Lead, and 1-GeV Neutrons on the Same Elements. ORNL-TM-1996, U.S. Atomic Energy Comm., Dec. 1967.
4. Kinney, W. E.: The Nucleon Transport Code, NTC. ORNL-3610, U.S. Atomic Energy Comm., Aug. 1964.
5. Kinney, W. E.; and Zerby, C. D.: Calculated Tissue Current-to-Dose Conversion Factors for Nucleons of Energy Below 400 MeV. Proceedings of the Second Symposium on Protection Against Radiation Hazards in Space, Gatlinburg, Tenn., NASA SP-71, 1964.
6. Turner, J. E.; Zerby, C. D.; Woodyard, R. L.; Wright, H. A.; Kinney, W. E.; Snyder, W. S.; and Neufeld, J.: Calculation of Radiation Dose From Protons to 400 MeV. Health Physics 10, pp. 783-808, 1964.
7. Irving, D. C.; Alsmiller, R. G.; Kinney, W. E.; and Moran, H. S.: The Secondary-Particle Contribution to the Dose From Monoenergetic Proton Beams and Validity of Current-to-Dose Conversion Factors. Second Symposium in Protection Against Radiation in Space, Gatlinburg, Tenn., NASA SP-71, pp. 173-176, 1964.
8. Armstrong, T. W.; Alsmiller, R. G.; and Barish, J.: Calculations of the Radiation Hazard at Supersonic Aircraft Altitudes Produced by an Energetic Solar Flare. Nuc. Sci. and Eng., vol. 37, no. 3, pp. 337-342, Sept. 1969.
9. Foelsche, T.: Radiation Exposure in Supersonic Transports. Paper No. 49, and comments, 14 IATA Symposium, April 17-21, 1961.
10. Foelsche, T.: Radiation Exposure in Supersonic Transports. NASA Technical Note D-1383, August 1962.
11. Foelsche, T.; and Graul, E. H.: Atompraxis 8, pp. 365-379, October 1962.
12. Foelsche, T.: The Ionizing Radiations in Supersonic Transport Flights. Second Symposium on Protection Against Radiation in Space, Gatlinburg, Tenn., October 12-14, 1964, NASA SP-71, pp. 287-299.
13. Wilson, J. W.; Lambiotte, J. J.; Foelsche, T.; and Filippas, T. A.: Dose Yield Functions in the Atmosphere Due to 0.1 to 10 GeV Protons With Application to Solar Cosmic Rays. NASA TN D-6010, Nov. 1970.
14. Mendell, R. B.; and Korff, S. A.: Fast-Neutron Detector With Discrimination Against Background Radiation. Rev. Sci. Instr. 34, pp. 1356-1360, 1963.
15. Mendell, R. B.; and Korff, S. A.: Fast Neutron Flux in the Atmosphere. J. Geophys. Res., vol. 68, pp. 5487-5495, 1963.
16. Davison, P. J. N.: Radiation Dose Rates at Supersonic Transport Altitudes. Abstract of Final Report on M.O.A. Grant PD /34/017, Royal Aircraft Establishment (Farnborough),1967.
17. Yagoda, Herman: Cosmic Ray Monitoring of the Manned Stratolab Balloon Flight. GRD Res. Notes No. 43 (AFCRL-TN-60-640), Air Force Res. Div., Sept. 1960.
18. Schaefer, Hermann J.: Public Health Aspects of Galactic Radiation Exposure in Supersonic Transport. NAMI-1033, NAVAL Aerospace Medical Institute, March 1968.
19. Radiobiological Aspects of the Supersonic Transport ICRP Task Group Report. Health Physics, Pergamon Press, 1966, vol. 12, pp. 209-226.
20. Meyer, P.; Parker, E. N.; and Simpson, J. A.: Solar Cosmic Rays of February 1956 and Their Propagation Through Interplanetary Space. Phys. Rev., vol. 104, no. 3, Nov. 1, 1956, pp. 768-783.
21. Van Allen, J. A.; and Winckler, J. R.: Spectrum of Low-Rigidity Cosmic Rays During the Solar Flare of February 23, 1956. Phys. Rev., vol. 106, no. 5, June 1, 1957, pp. 1072-1073.
22. Winckler, J. R.: Cosmic-Ray Increase at High Altitude on February 23, 1956. Phys. Rev., vol. 104, no. 1, Oct. 1, 1956, p. 220.

"DOSE AND LINEAR ENERGY TRANSFER SPECTRAL MEASUREMENTS FOR THE SUPERSONIC TRANSPORT PROGRAM"

CAPT RICHARD B. PHILBRICK

Technology Division
Air Force Weapons Laboratory

The Air Force Weapons Laboratory (AFWL) in conjunction with the Federal Aviation Administration is flying radiation monitoring systems on board aircraft provided by the Air Weather Service. The purpose of the package, called the High Altitude Radiation Instrumentation System (HARIS), is to measure the radiation hazard to Supersonic Transport passengers from solar and galactic cosmic rays. The HARIS was fabricated by Solid State Radiations, Inc., and includes gaseous linear energy transfer spectrometer, a tissue equivalent ionization chamber and a geiger meuller tube.

The HARIS is flown on RB-57F aircraft at 60 000 feet from Eielson Air Force Base, Alaska. During solar active periods, crews of the 58th Weather Reconnaissance Squadron are on alert to launch the aircraft during solar flares. Notification for launches and the proper alert status are provided by the Solar Forecast Center located in the North American Air Defense Command Chyenne Mountain Complex in Colorado.

Data from the HARIS are reduced at the AFWL to give rad and rem dose rates measured by the package during the flights. Results presented include ambient data obtained on background flights, altitude comparison data and solar flare data.

The Air Force Weapons Laboratory (AFWL) is conducting a theoretical and experimental program in defining the radiation hazards to man at high altitudes and in space. Experimental efforts have included tissue equivalent ionization chambers (TEICs) for dose measurements and linear energy transfer (LET) spectrometers for energy deposition measurements. Particle spectrometers are also flown to define the physical environment (Ref 1).

In 1965, the AFWL and the Federal Aviation Administration (FAA) agreed to measure the biophysical aspects of the radiation environment encountered by passengers and crews at the high operating altitudes of the Supersonic Transport (SST). The objective of the program is to provide operational data for the Advisory Committee on Radiation Biology Aspects of the SST[1] so that they can recommend appropriate actions to protect the passengers and crews of the SSTs.

To be operati nally relevent, the data must be obtained at the altitudes associated with SST operation - approximately 60,000 feet. Background data taken during solar ambient periods are required and must be obtained at high geomagnetic latitudes, as well as normal latitudes. Measurements must be taken during energetic solar particle events at high geomagnetic latitudes. To measure these events, the program must continue through the upslope, top and downslope of the current solar cycle.

Operational Approach

The AFWL/FAA instrument is called the High Altitude Radiation Instrumentation System (HARIS) and will be discussed in more detail later. It is designed to fly on the RB-57F aircraft of the 58th Weather Reconnaissance Squadron (58th WRS), 9th Weather Reconnaissance Wing, Air Weather Service (AWS). The RB-57F can fly higher than 60,000 feet and can remain at this altitude in excess of five hours if necessary. The HARIS was first flown on background missions near Kirtland AFB, New Mexico (the location of the 58th WRS) in September of 1966.

Initially, the package was mounted beneath the navigator's seat, causing undersirable shielding for the sensors. In February 1968, the HARIS was relocated in the upper pressurized compartment of aircraft (see Fig 1) resulting in shielding much closer to that envisioned for SST passengers and crews. The shielding above the sensors on the RB-57F is 0.5 gm/cm^2 aluminum as opposed to an estimated 3.5 gm/cm^2 for the SST.

[1]Formerly the Standing Committee on Radiation Aspects of the SST.

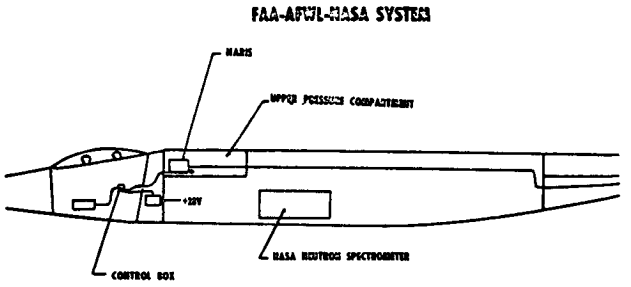

Fig. 1

Kirtland Air Force Base is at 35° geographic latitude and about 45° geomagnetic latitude. This is too far under the earth's magnetic belts to receive significant changes in dose rates from energetic solar charged particle events. In March 1968, one RB-57F and two flight crews of the 58th WRS were deployed to Eielson AFB, Alaska (near Fairbanks, geomagnetic latitude 65° N) to stand alerts for solar flares. At that time the operational portion of the program was given the nickname Operation Cold Flare by USAF. From Eielson, the aircraft can fly as far north as 75° geomagnetic.

Under the initial plan, alert conditions and launch requests were relayed from AFWL to the 9th Weather Reconnaissance Wing Command Post and then to Eielson. The requests were based on information from the Solar Forecast Center (SFC)[2] at the North American Air Defense Command Cheyenne Mountain Complex. The complexity of life support procedures of the RB-57F makes launches fairly slow. On the highest alert condition launches were required no more than three hours after notification.

This system proved too slow in launching the aircraft after flares dispite an increase in support to two aircraft and three flight crews. The launch time was too long and the alert chain too cumbersome. The data gained from proton events in February, March and April of 1969, showed that only very high energy protons - greater than 100 Mev - contributed to the dose rate at SST altitude. The vast majority of such particles come very quickly, so they arrive before the aircraft can be launched.

In an effort to shorten the response time, FAA requested USAF to provide more support for the program. The AWS increased support for the program in June of 1970, to three aircraft and five crews, resulting in a vastly improved alert posture. Under the highest alert condition, an aircraft can reach 60,000 feet one hour after notification. In addition, the alert conditions and launch notifications are sent directly to Eielson by SFC.

Figure 2 shows the current routes used by the aircraft launched to measure solar flares. The shorter Lima route is used by the initial aircraft flying with a reduced fuel load so that it can reach SST altitude more quickly. The longer Mike route is flown by follow-on aircraft and on background missions. Route flown previous to June 1970 was similar to the Mike route.

Instrumentation

The HARIS[3] was developed by Solid State Radiations, Inc. (SSR), Los Angeles, California, under contract to the FAA. AFWL prepared the specifications for the package and monitored the technical aspects of the contract. Four nearly identical instrument packages were fabricated in all. Included in the system are a linear energy transfer spectrometer (LETS), a tissue equivalent ionization chamber (TEIC), a geiger counter (GMT) and a digital recorder.

The choice of sensors was based on the radiation environment at 60,000 feet. The field is a conglomeration of protons, neutrons, electrons, gamma rays, heavy particles and photons. Establishing the physical spectrum would be impractical so the sensors measure the dose rate directly. The TEIC measures the total ionization in the chamber which can be directly related to dose.

The LETS measures the ionization from each individual particle track and can thus establish the quality factor for the radiation. The damage done by an ionization track can increase out of proportion to the number of ions if the track is sufficiently thick. Thus, the total ionization must be multiplied by a parameter (called the quality factor) which takes into account the ionization per unit distance or linear energy transfer (LET). The quality factor can vary with the type of cells being considered but a curve has been established which should allow for any effect (Fig 3, Ref 3).

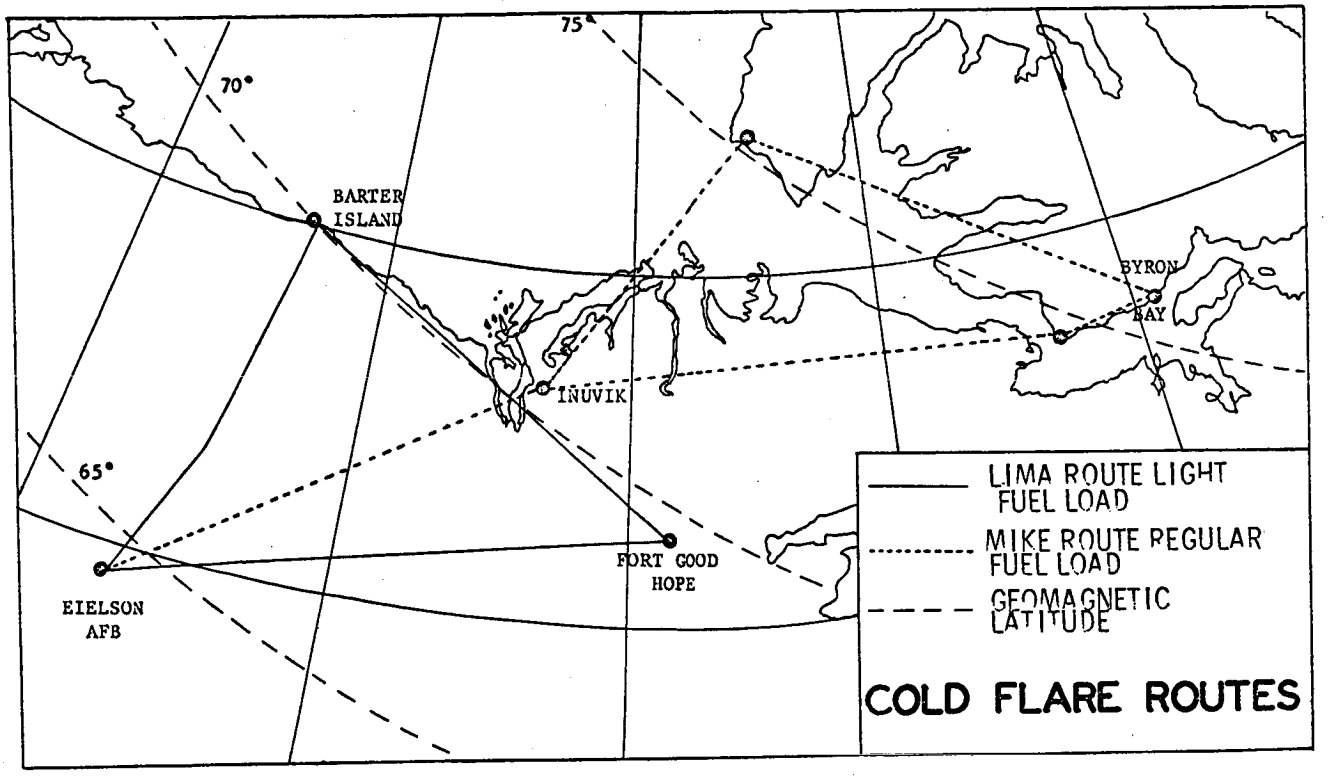

Fig. 2

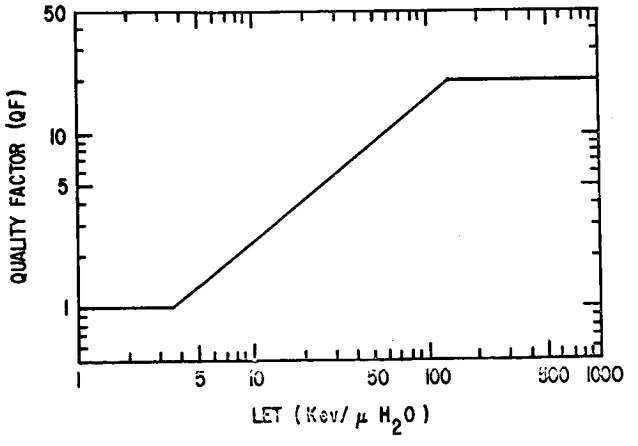

Fig. 3

The geiger counter is used to show consistency in changes in dose rates indicated by the other sensors. Digital readout is used to simplify data reduction.

The LETS is a spherical chamber two inches in diameter with a 3.5 mm lexan wall. It is filled with methane to a pressure giving a path length through the chamber diameter equivalent to four microns of tissue. The anode is a central needle with a high voltage applied between it and the evaporated aluminum coating the inside of the sphere. This voltage is regulated through the use of an Am^{241} alpha source in a side arm counter.

---

[2]SFC is a part of the 4th Weather Wing. AWS

[3]A more complete discription of the HARIS is available in Ref 2.

The alpha particles traverse a diameter of the chamber and will deposit a known energy. The voltage can be corrected up or down through the use of these calibration pulses, thus, allowing for changes in the gas pressure or consistency.

Events measured by the LETS are sorted by a ten channel pulse height analyzer according to their LET. The channels increase in width by a factor of two with the channel one lower boundary at .2 Kev/micron and the channel ten upper boundary at 200 Kev/micron. The LETS is accurate in measuring dose rates from about 1.0 mrem/hr to about 2 rem/hr.

The ionization chamber has a moderately tissue equivalent lexan wall 3.2 mm thick. It is the same size as the LETS to allow intercomparison of results. The filling gas is tissue equivalent, pressurized to three atmospheres absolute. The digital readout is logarithmically related to the dose. The TEIC will measure from about 0.3 mrad/hr to about 25 rad/hr.

The digital recorder writes the data on tape every two mintes. Twenty seconds of each cycle is allowed for the electronics to return to normal after the four-second readout period. Then the sensors accumulate data for 96 seconds.

Physically the HARIS is 12" x 8" x 12" and weighs 25 lbs. It draws .5 amp at 28 v DC.

Calibration Procedures for the HARIS

Certain calibration and monitoring procedures have been applied to the HARIS on a routine basis since the summer of 1968. These include internal alpha spectrum analysis and alpha pulse monitoring, gamma calibration and a neutron constancy check. The spectrum from the LETS Am^{241} alpha pulses is examined and the shape of this spectrum along with analysis of the alpha pulses themselves can reveal the relative degradation of the LETS.

HARIS instruments are calibrated on the Cs^{137} gamma range at AFWL before and after deployment to Eielson AFB. These exposures are used primarily to calibrate the TEIC, but they are also a good check on the LETS.

At Eielson, the LETS and TEIC are in turn exposed to a 100 millicurie Am-Be neutron source. These exposures are used as a constancy check and are made, if possible, before and after individual flights. All available check point voltages, as well as the cycle time of the digital tape recorder are monitored.

In addition to the routine checks, proton and neutron calibrations have been performed on the LETS and TEIC to check their response to these particles. In general the sensors respond adequately if they are handled properly.

Data Reduction Procedures

The HARIS digital tape recorder writes the data with bits incorrectly spaced to be used on a computer. A tape to tape converter is used to rewrite the data on a tape which can be read by a Control Data Corporation (CDC) 160a computer. The 160a changes the format of the data and writes it in standard record lengths which can be read by the CDC 6600 computer at AFWL.

The CDC 6600 punches the raw data on cards, as well as in a printout so that erroneous records can be removed. Finally, the flight position and time information is merged with the raw data which is reduced on the 6600 using a standard program. The program prints rad and rem dose rates, GM tube count rates and standard deviations along with position, altitude and time for each reading.

Data from all the sensors can vary greatly given the two-minute recording intervals. To smooth out the variations, the data are averaged over ten record (20-minute) periods. These periods are advanced five records (10-minute) at a time so that each data frame is effectively reduced twice.

The TEIC dose rate is derived by interpolating between the calibration curves obtained for the sensor before and after deployment to Eielson AFB.

To reduce the ten channels of LETS information, a number of counts is first subtracted from each channel readout. These are "background" counts which originate in the instrument from two sources. The first source is internal conversion electrons from the Am^{241} alpha source. The second source is spurious pulses from the electronics of the instrument. "Background" counts are likely to change with time, therefore, the spectrum to be subtracted is established by running the instrument at sea level in the aircraft before the flight.

A rad dose rate is extracted from this spectrum using standard techniques. To obtain a rem dose rate, the spherical shape of the sensor must be allowed for. Rossi's triangle unfolding technique (Ref 4) is used to redistribute the counts in a new spectrum from which the rem dose rate can be

obtained.

The TEIC rad dose rate is more reliable than the LETS rad dose rate as a result of uncertainties in the "background" mentioned above. This "background" is concentrated in the lower channels of the LETS readout. The TEIC rad dose rate is used to modify the LETS rem dose rate readout. The lower four channels of the LETS all have a quality factor of one and the fifth channel has a factor of 1.2. The TEIC dose rate, minus the dose rate for the upper five channels of the LETS, is used as the dose rate for the lower five channels. This method eliminates use of the less reliable channels in the final rem dose rate readouts.

Data From Background Missions

Flights made during solar ambient periods generally show rem dose rates right at the bottom of the effective measurement range of the LETS. The error likely at this extreme is quite large - as much as 40 percent for the rem dose rate. The TEIC rad measurement is more accurate with a probable error of 20 percent.

The average measured dose rates to date are .45 mrad/hour and .96 mrem/hour. Considering only measurements from November of 1968 to date, the dose rates have varied only slightly with the solar cycle. The lowest average dose rate measured was in the summer of 1969 at .40 mrad/hour and .85 mrem/hour. The correct average measured rate (January 1971) is .50 mrad/hour and 1.03 mrem/hour.

Data From Solar Flares

HARIS data have been accumulated for solar proton events which occured on the following dates: 25 and 27 February 1969, 30 March 1969, 11 - 16 April 1969, 2 November 1969, 24 January 1971. No huge increases over background were measured for any of these flares. However, it should be noted that the measurements were not taken during the ground level neutron peak of these events except in the case of the 30 March 1969 flare. The specific results from each event are listed here:

25 February 1969: Five and one-half (5 1/2) hours after the flare the instrument measured a rad dose rate of .54 mrad/hour and a rem dose rate of 1.1 mrem/hour. The ambient rates at this time were .42 mrad/hour and .90 mrem/hour.

27 February 1969: (No ground level increase) Six hours after the flare the dose rate was 0.5 mrad/hour and 1.2 mrem/hour.

30 March 1969: This is the only case to date where measurements were taken during the ground level neutron peak. Here the data are presented in graph form (Fig 4).

11 - 16 April 1969: There was no ground level increase during this period but VELA >25 Mev proton counts increased substantially. Measurements taken during this period show no substantial increase.

2 November 1969: Thirteen (13) hours after the flare the rad dose rate measured was 0.55 mrad/hour and the rem dose rate was 1.25 mrem/hour.

24 January 1971: Data from this event are presented in Figure 5. The dose rates given are preliminary as the HARIS instruments are still deployed at Eielson so that post-deployment calibrations have not been performed. Such calibrations should not change the readings more than ten percent, however.

REFERENCES

1. Janni, J., Holly, F.E., et. al., "The Current Experimental Approach to the Radiological Problems of Spaceflight," Aerospace Medicine, Vol 40, No 12, December 1969.

2. Katzenstein, H., Zatzick, M., et al., "Final Report on High Altitude Radiological Instrumentation System," Solid State Radiations Report No. 1F2900-67 (1967).

3. Madey, R., and Stephenson, T., "Quality Factors for Degraded Proton Spectra," In: Second Symposium on Protection Against Radiations in Space (A. Reetz, Jr., ed.), NASA SP-71: 229-234 (1964).

4. Rossi, H., "Microscopic Energy Distribution in Irradiation Matter," In: Radiation Dosimetry, Chapter 2 (F. Attix and W. Roesch, eds.), Academic Press, 43-90 (1968).

5. Fichtel, C., Guss, D., and Ogilvie, K., "Details of Individual Solar Particle Events," In: Solar Proton Manual, Chapter 2 (F. McConald, ed.), NASA TR-169 (1963).

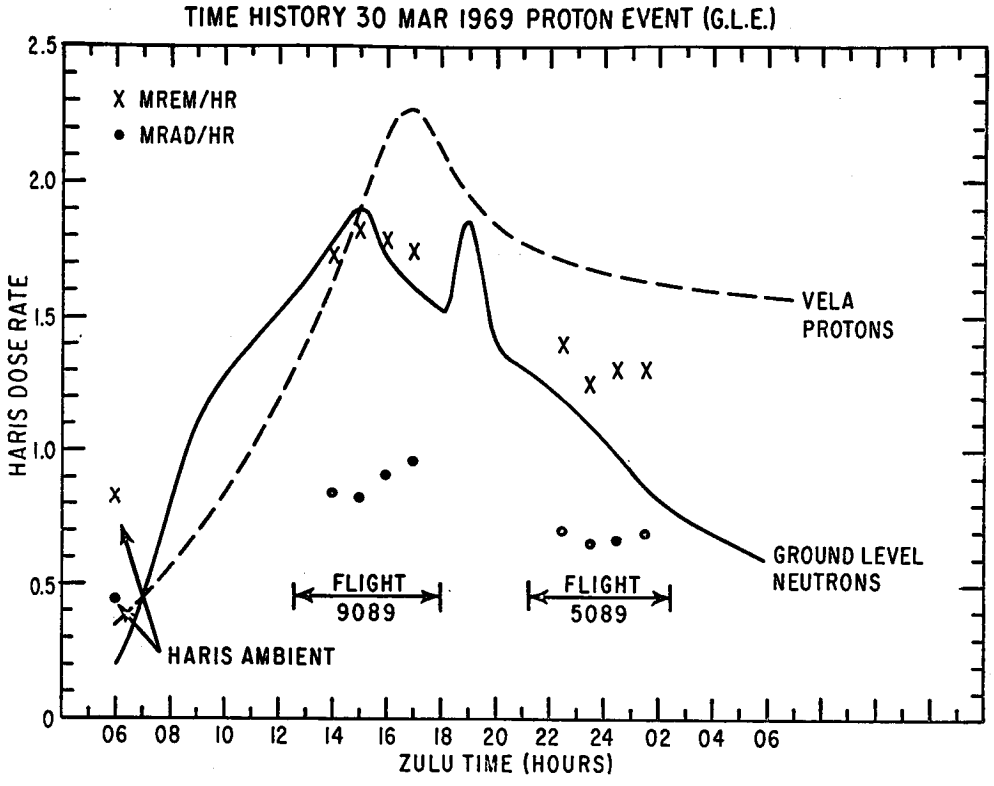
TIME HISTORY 30 MAR 1969 PROTON EVENT (G.L.E.)
X MREM/HR
• MRAD/HR
VELA PROTONS
GROUND LEVEL NEUTRONS
FLIGHT 9089
FLIGHT 5089
HARIS AMBIENT
HARIS DOSE RATE
ZULU TIME (HOURS)

Fig. 4

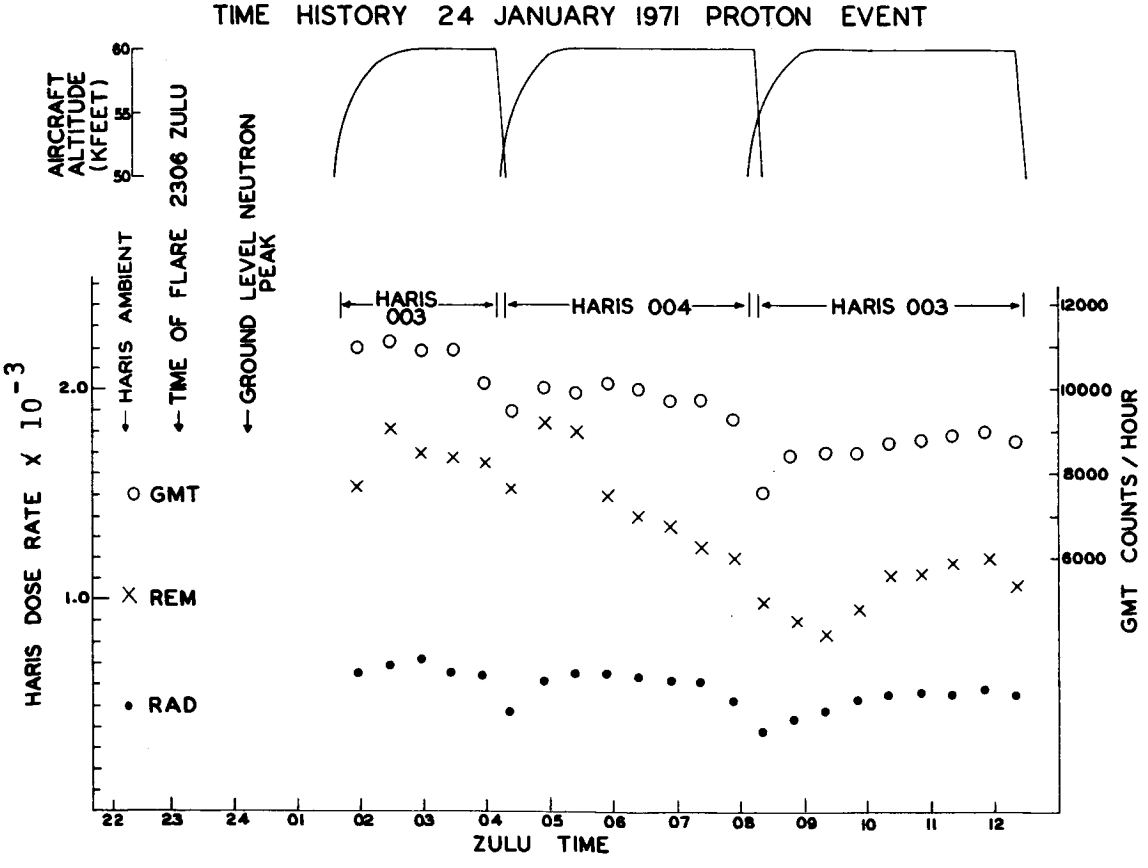
TIME HISTORY 24 JANUARY 1971 PROTON EVENT
AIRCRAFT ALTITUDE (KFEET)
HARIS AMBIENT
TIME OF FLARE 2306 ZULU
GROUND LEVEL NEUTRON PEAK
HARIS 003
HARIS 004
HARIS 003
GMT
REM
RAD
HARIS DOSE RATE X 10⁻³
GMT COUNTS / HOUR
ZULU TIME

EXPERIMENTAL DETERMINATION OF COSMIC-RAY CHARGED PARTICLE INTENSITY PROFILES IN THE ATMOSPHERE

W. M. Lowder, P. D. Raft, and H. L. Beck

Health and Safety Laboratory, U. S. Atomic Energy Commission
New York, N. Y.

Absolute cosmic-ray free air ionization and charged particle fluxes and dose rates throughout the atmosphere have been measured on a series of balloon flights that commenced in 1968. Argon-filled ionization chambers equipped with solid-state electrometers, with different gas pressures and steel wall thicknesses, and a pair of aluminum-wall GM counters have provided the basic data, which are supplemented by measurements with air-filled and tissue equivalent ionization chambers and a scintillation spectrometer. Detailed laboratory experiments together with analyses of the theoretical aspects of the detector responses to cosmic radiation indicate that these profiles can be determined to an overall accuracy of ±5 percent.

Data from various balloon flights at 53°N and 42°N geomagnetic latitude provide ionization profiles consistent with our earlier results in the lower atmosphere, but 20 percent lower than comparable data obtained by the California Institute of Technology. No explanation has yet been found for this discrepancy, although a quantitatively similar one was previously noted by the University of Minnesota group. Our results indicate a total charged-particle free-air ionization (dose rate) at 53°N latitude of 6.3 I (9.5 μrad/hr), 114 I (170 μrad/hr), and 290 I (436 μrad/hr) at 10,000, 35,000, and 65,000 ft., respectively. These data are approximately minimum values for the 11 year solar activity cycle.

The ionization and flux data are compared with the analytical calculations of O'Brien, with generally satisfactory agreement between theory and experiment.

I. INTRODUCTION

Many measurements of total ionization and omnidirectional particle flux of cosmic-ray secondaries in the atmosphere have been conducted over the past four decades, and these have contributed much to our understanding of the properties of the incoming primary radiation and its interaction with the atmosphere. In addition, the atmosphere has provided us with a unique high energy physics laboratory, where experiments can be conducted at particle energies beyond the capabilities of any ground-based laboratories. An opportunity is thus provided to design experiments to test the predictions of theories of high-energy radiation transport in low-z media.

The HASL balloon program of cosmic-ray measurements, commenced in 1968, was designed to provide accurate data on charged particle ionization and flux throughout the atmosphere. Two applications were envisaged: (1) to provide basic information relevant to the potential exposure of aircraft crews and passengers to ionizing radiation, and (2) to provide critical tests for analytical calculations of the properties of cosmic radiation throughout the atmosphere, particularly those being conducted here by O'Brien (refs. 1 and 2). In this paper, we summarize our results to date, critically compare them with earlier data, and discuss their relevance to theory.

II. EXPERIMENTAL PROGRAM

Our initial cosmic-ray measurements at ground level (0 to 12,000 feet) in the continental United States were made to estimate this source of radiation exposure of the whole population. A high pressure argon ionization chamber was utilized, and its gamma-ray response was corrected for by means of concurrent measurements with a gamma scintillation spectrometer. The results obtained in 1965, primarily in Colorado, were reported by Lowder and Beck (ref. 3), and a recheck of these data in 1968 yielded essentially the same results.

These ionization profiles were extended to altitudes above 12,000 ft. by a series of balloon flights conducted beginning in 1968 with the cooperation of the United States Air Force balloon team at Goodfellow Air Force Base in San Angelo, Texas, the NCAR Scientific Balloon Base in Palestine, Texas, and the University of New Hampshire. The flights to be discussed are listed in Table I, along with the instrumentation included in each flight package. The basic instrument in each flight was a pressurized argon ionization chamber for total charged particle ionization determination. On two flights, a specially designed dual Geiger tube package was included, to provide particle flux data. Other types of ionization chamber are being flown, and the University of New Hampshire scintillation spectrometer has provided much information on charged particle and photon fluxes. However, the analysis of these results is not yet complete, and we restrict our attention here to the argon chamber and Geiger counter data.

TABLE I

HASL BALLOON FLIGHTS, 1969-70

Date	Site	Geom. Lat.	Ionization Chambers: Gas (atm.)	Wall (g/cm^2)	Volume (ℓ)	Other Instrumentation
5/27/69	Durham, N. H.	54°N	9.0 Ar	1.1 Fe	2.8	UNH scintillation spectrometer
11/16/69	Palestine, Tex.	42°N	(1) 9.2 Ar	0.5 Fe	2.8	UNH scintillation spectrometer
			(2) 27.5 Ar	2.7 Fe	2.8	
4/9/70	Sioux City, Ia.	52°N	(1) 22.9 Ar	1.1 Fe	2.8	-
			(2) 0.9 TE	0.5 Fe	8.2	-
4/16/70	Sioux City, Ia.	52°N	22.9 Ar	1.1 Fe	2.8	dual GM counters
6/7/70	Palestine, Tex.	42°N	22.9 Ar	1.1 Fe	2.8	UNH scintillation spectrometer + dual GM counters

III. IONIZATION MEASUREMENTS

The ionization measurements were carried out with pressurized argon ionization chambers similar to those used in the long series of measurements conducted by the group led by H. V. Neher at the California Institute of Technology. Basically, they are hemispheres of type 304 stainless steel welded together to form 7 or 10 inch diameter spherical shells. The collecting electrode is a 0.75 inch diameter steel sphere mounted on a rigid steel tube attached to a triaxial metal-to-ceramic seal welded to the outer shell. The gas filling is ultra-high-purity argon. Chambers with various wall thicknesses and filling pressures were fabricated, to permit study of the effect of these parameters on the inferred free air ionization. Our "standard" chamber has been one filled to 23 atmospheres surrounded by 55 mil (1.1 g/cm^2) steel walls.

The output current from the chamber is measured with a HASL designed solid-state electrometer using a MOSFET (metal-oxide-semiconductor field-effect transistor) as the input element. This electrometer is an improvement over one described by Negro, Cassidy, and Graveson (ref. 4), with the high input impedance and low leakage current capability required by this type of measurement. The voltage output of this electrometer is recorded on-board by a Rustrak strip-chart recorder.

Figure 1 shows one of the ionization chamber systems mounted in its flight package.

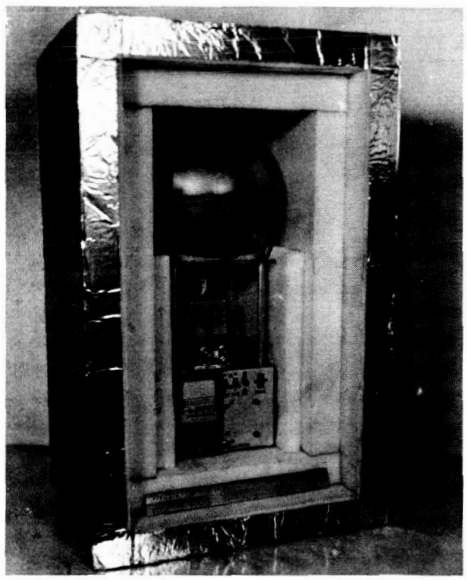

Figure 1. HASL pressurized argon ionization chamber mounted in balloon flight case.

The absolute calibration of the response of these chambers is complicated by the absence of any known "standard" cosmic radiation fields to check our laboratory or armchair calibration procedures. These procedures can be divided into four steps:

(1) calibration of the output of the data recorder in terms of the output voltage of the MOSFET electrometer,
(2) calibration of the output voltage of the electrometer in terms of input current from the ionization chamber,
(3) calibration of the output current of the chamber in terms of ion pairs produced per cm^3 of filling gas reduced to STP,
(4) conversion of absolute ionization (STP) within the chamber to absolute ionization in free air.

Each of these steps is discussed in detail by Raft, Lowder, and Beck (ref. 5), taking into account the experience gained from previous experimental programs of a similar nature. We concluded there that the treatment of these ionization chambers as essentially argon cavities in an air medium is basically correct. Any significant deviation from this circumstance would manifest itself as discrepancies among the free air ionization values inferred from the responses of chambers with differing wall thicknesses or gas fillings. Our calibration is essentially identical to that used by the Caltech group, and should yield comparable ionization values.

The ionization data from the flights listed in Table I are summarized in Table II. The two Sioux City flights are combined, as the three argon chambers yielded essentially identical results. Also indicated are the data from the Colorado ground measurements in 1965 and 1968. The conversion factor indicated at the bottom of the table permits the conversion of the charged particle ionization data to free air dose rate units. Particular note should be taken of the fact that these data all pertain to a period near solar activity maximum in the 11 year cycle, when the cosmic radiation intensity is near minimum.

Although it is always hazardous to compare different sets of cosmic-ray measurements displaced in space and time, the latitude effect is clearly discernable at altitudes above 35,000 ft., as is the significant profile change at a single location (Palestine) for two flights separated by seven months. It is impossible to ascertain whether this latter phenomenon represents a long-term trend, or is the result of particular conditions pertaining on the dates of the flights.

TABLE II

IONIZATION AND AIR DOSE RATE PROFILES, 1969-70

Atm. Depth (g/cm^2)	Altitude (feet)	Ionization (I)* Durham (5/69)	Sioux City (4/70)	Palestine (11/69)	Palestine (6/70)	Colorado ('65, '68)
20	87,200	285	-	195	165	-
50	67,900	290	282	232	201	-
75	59,500	280	266	230	206	-
100	53,500	254	248	214	197	-
150	45,100	198	198	183	166	-
200	39,100	155	156	136	128	-
250	34,400	110	112	109	97	-
300	30,500	78	80	76	73	-
350	27,100	54	55	55	52	-
400	24,000	38	38	38	37	-
450	21,300	28	28	28	27	-
500	18,800	20	21	19	20	-
550	16,400	15	15	14	15	-
600	14,300	11	11	9.8	10.5	12:
700	10,400	6.5:	7.1	5.9	6.5	7.2
800	6,900	4.3:	4.9	4.3	4.2	4.3
900	3,800	3.3:	3.3:	-	2.8	2.9
1033	0	-	-	-	-	2.1

*"I" = ion pairs/cm^3/sec/atm. air at STP; 1I = 1.50 μrad/hr.

The low-altitude data is in reasonable agreement with our ground measurements, particularly those from the June 1970 Palestine flight which we believe to be the most reliable at great depths. The higher values for the Colorado data at 600 and 700 g/cm^2 may be due to the latitude effect and to the fact that the 1965 data were obtained near cosmic radiation intensity maximum of the 11 year cycle.

No significant differences between the ionization values inferred from chambers with different wall thicknesses and filling gas pressures have yet been noted. This tends to indicate that the distortion of the free air radiation field produced by the chamber has little effect on the observed ionization. Future flights should enable us to quantitate whatever small effects that may exist.

IV. PARTICLE FLUX MEASUREMENTS

The Geiger tube package consists of one tube mounted vertically and the other horizontally with the ratemeter outputs recorded by on-board Rustraks synchronized with those indicating the ionization chamber responses. The Geiger tubes are 7.0 cm long and 19 cm diameter, with 30 mg/cm^2 Al walls. The calibration of these counters has been described by Keppler (ref. 6) and we have adopted his results. The detection efficiency for

charged particles is 0.96, and for photons is < 0.01 from 0.05 to 1 MeV, increasing to 0.1 at 6 MeV. The geometry factors are such that the geometric mean of the count rates of the two counters is ten times the omnidirectional particle flux for $\cos^n\theta$ distributions of the incoming particles with n ranging from 0 to 3. The detector calibration is thus essentially independent of atmospheric depth, since the angular distribution of the incident particles closely satisfy these conditions throughout the atmosphere.

The inferred particle fluxes obtained on two flights in 1970 are given in Table III. The Sioux City flight data (52°N) were obtained nearly two months earlier than the Palestine data (42°N), but the two profiles agree closely at depths greater than 200 g/cm². The divergence at lesser depths reflects the latitude effect.

The observed counting rates of the Geiger tubes include some photon-initiated counts that would produce an overestimate of the charged particle flux. It is well known that the photon flux in the atmosphere is of the order of ten times the electron flux (e.g., see ref. 7), and that the electrons make up the bulk of the charged particle flux throughout most of the atmosphere. Anderson's data (ref. 7) indicates that most of the photons are between 10 and 1000 keV in energy, implying a detector efficiency of less than 1 percent for this component. Thus, the photon contribution to the flux measurement is < 10 percent.

We can relate the measured particle flux data to the ionization results for the same flights to estimate the mean specific ionization per particle as a function of atmospheric depth. These figures are also shown in Table III, and indicate a nearly constant value for this parameter of ~100 ion pairs/cm (STP air) between 20 and 500 g/cm² (correcting for photons). This result is somewhat unexpected, particularly at the highest altitudes where a significant contribution from high specific ionization particles might be anticipated. There is no evidence for this on either flight.

The sea level figures given in Table III are derived from the flux value given by Rossi (ref. 8) and the sea level ionization value estimated by Lowder and Beck (ref. 3).

TABLE III

CHARGED PARTICLE FLUX AND SPECIFIC IONIZATION, 1970

Atm. Depth (g/cm²)	Particle Flux (cm^{-2} sec^{-1})* 52°N	42°N	Mean Specific Ionization (ion pairs/cm)
20	2.63	1.72	95
50	2.72	2.19	95
70	2.68	2.25	94
100	2.49	2.17	93
150	2.05	1.81	92
200	1.48	1.40	91
250	1.04		96
300	0.76		96
350	0.52		98
400	0.37		102
450	0.28		96
500	0.20		100
550	0.16		93
600	0.13		82
1033	(0.025)		(85)

*Uncorrected for photon counts, which amount to < 10 percent of the total (see text).

V. COMPARISON WITH OTHER EXPERIMENTS

The standard data on cosmic-ray ionization in the atmosphere have long been the results obtained by the Caltech group over several decades (see e.g., Neher, ref. 9). Our ground level results (ref. 3) were observed to disagree with comparable measurements by this group, and this disagreement now extends to all altitudes. George's data (ref. 10), obtained in January 1968 on airplane flights over the southwestern United States, can be directly compared to our Texas results in 1969 and 1970, and this comparison indicates a 20 percent discrepancy extending from 200 g/cm² depth to sea level (ref. 5). A discrepancy of about the same magnitude has been noted by Winckler (ref. 11) between his results and comparable Caltech data. There may exist some subtle error in the ionization chamber calibration procedures used by the various groups, and experiments are now planned to resolve this uncertainty. Barring any unexpected systematic errors of this type in our calibrations, which the redundancy built into our procedure as well as agreement with other data render highly unlikely, we believe the ionization results reported here to be accurate to ~5 percent.

The particle flux data are comparable to those obtained by Anderson (ref. 7) and others. However, the overall accuracy is somewhat poorer than that estimated for the ionization results, partly due to the uncertainty in the correction for photon counts as well as the poorly known angular distributions of the incident particles.

Further balloon experiments are being planned to provide more data at various latitudes and near solar activity minimum. The results from the various types of ionization chambers, as well as the anticipated laboratory intercomparisons, should resolve most existing uncertainties in the data and provide additional information on the properties of the atmospheric radiation field.

VI. COMPARISON WITH THEORY

At this symposium, O'Brien (ref. 1) has compared his calculated ionization values near cosmic-ray intensity maximum with the appropriate Caltech data. More recent calculations permit a comparison with our data near cosmic-ray intensity minimum. The ionization profiles at 42°N latitude are shown in Figure 2 and the charged particle flux profiles at the same latitude are given in Figure 3. Measured and calculated dose rates at four important altitudes are given in Table IV, along with the calculated tissue dose rate from all components. The agreement between theory and experiment is in general surprisingly good. The observed differences can be readily understood on the basis of the transport approximations introduced into the calculations, particularly the non-transport of the electromagnetic cascade energy from the point of neutral pion decay and the assumption of zero upward directed flux near the top of the atmosphere. Both effects would tend to pile up the absorbed energy near the Pfotzer maximum. At great depths, where these effects are minimal, the discrepancy becomes small. We regard the experimental data as providing strong evidence for the validity of the theory, within the limitations of the necessary approximations introduced.

ACKNOWLEDGMENTS

Various members of the Instrumentation Division, HASL, particularly Vincent Negro and Norman Latner, have provided invaluable assistance in the development of the balloon flight instrumentation.

The successful record of balloon flights was made possible by the close cooperation of the several groups involved, i.e., University of New Hampshire (Prof. E. Chupp, Project Director; D. Forrest, A. Mammay, L. Orwig, A. Sarkady); Detachment 31, Sixth Weather Wing (MAC), U. S. Air Force, Goodfellow A.F.B., San Angelo, Texas (Col. E. B. Lewis, Commander); and the NCAR Scientific Balloon Base, Palestine, Texas.

Major Thomas Gross, USAF, attached to AEC Division of Biology and Medicine, has provided necessary liaison to the HASL-USAF flight program.

REFERENCES

1. O'Brien, K.: The Physical Theory of One-Dimensional Galactic Cosmic-Ray Propagation in the Atmosphere. National Symposium on Natural and Manmade Radiation in Space, March 2-5, 1971.
2. O'Brien, K.: J. Geophys. Res., vol. 75, 1970, p. 4357.
3. Lowder, W. M.; and Beck, H. L.: J. Geophys. Res., vol. 71, 1966, p. 4661.
4. Negro, V.; Cassidy, M.; and Graveson, R. T.: IEEE Trans. Nucl. Sci., vol. NS-14, 1967, p. 135.
5. Raft, P. D.; Lowder, W. M.; and Beck H. L.: USAEC Report HASL-234, August 1970.
6. Keppler, E.: Mitteilungen aus dem Max-Planck-Institut Für Aeronomie, Nr. 20(5), Springer Verlag, Berlin, 1965.
7. Anderson, K. A.: Phys. Rev., vol. 123, 1961, p. 1435.
8. Rossi, B.: Rev. Mod. Phys., vol. 20, 1948, p. 537.
9. Neher, H. V.: J. Geophys. Res., vol. 72, 1967, p. 1527.
10. George, M.: J. Geophys. Res., vol. 75, 1970, p. 3693.
11. Winckler, J. R.: J. Geophys. Res., vol. 65, 1960, p. 1331.

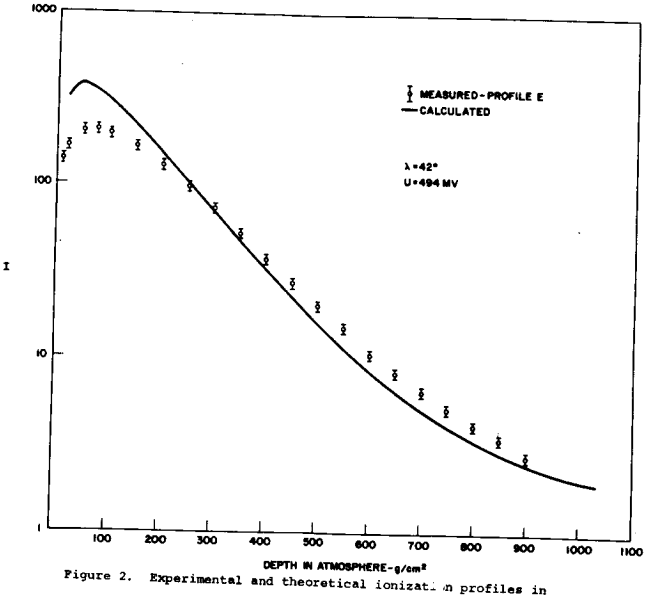

Figure 2. Experimental and theoretical ionization profiles in the atmosphere, Texas, 1970.

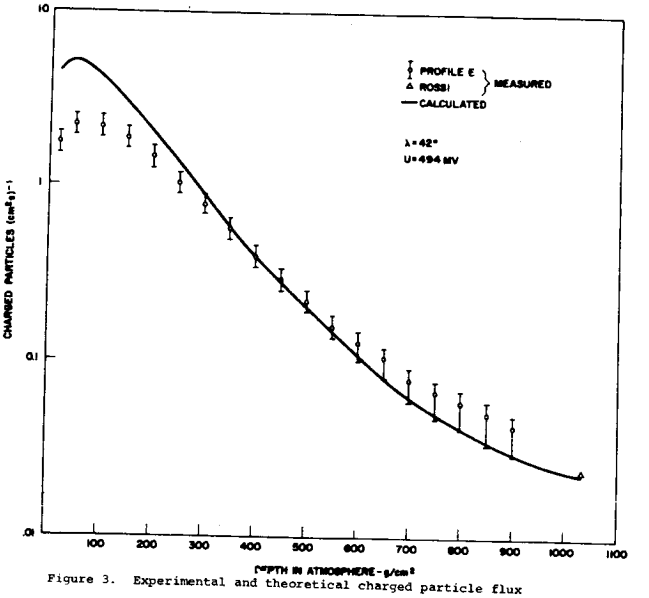

Figure 3. Experimental and theoretical charged particle flux profiles in the atmosphere, Texas, 1970.

TABLE IV

COMPARISON OF MEASURED AND CALCULATED DOSE RATES NEAR SOLAR MAXIMUM

Altitude	Charged Particle Air Dose Rates		Total Tissue Dose Rates
	Measured (μrad/hr)	Calculated (μrad/hr)	Calculated*
Sea Level	3.1	3.0	3.0
10,000 ft.	9.5	8.7	11
35,000 ft.	170	180	210
65,000 ft.	436	611	800

*Dose rates calculated for 5 cm depth in tissue slab.

SOME GAMMA-RAY SHIELDING MEASUREMENTS MADE AT ALTITUDES GREATER THAN 115,000 FEET USING LARGE Ge(Li) DETECTORS*

G. T. Chapman, R. P. Cumby, J. H. Gibbons

and

R. L. Macklin

Oak Ridge National Laboratory
Oak Ridge, Tennessee

and

H. W. Parker

Space Sciences Laboratory
G. C. Marshall Space Flight Center
Huntsville, Alabama

A series of balloon-flight experiments at altitudes greater than 115,000 feet has been conducted to gain information relative to the use of composite shields (passive and/or active) for shielding large-volume, lithium-drifted, germanium (Ge(Li)) detectors used in gamma-ray spectrometers at these altitudes. The measurements were made in the gamma-ray energy region 60 keV $\leq E_\gamma \leq$ 2 MeV and clearly illustrate the necessity of using a dense gamma-ray shield protected by an active charged-particle shield for effective shielding of these detectors in the primary cosmic-ray environment. Data showing the pulse-height spectra of the environmental gamma radiation as measured at 5.3 and 3.8 gms/cm^2 residual atmosphere with an unshielded diode detector is also presented.

INTRODUCTION

The purpose of the work reported in this paper was to study the effectiveness in the primary cosmic-ray environment of a composite gamma-ray detector shield incorporating both active and passive shielding material to reduce the background in a proposed gamma-ray spectrometer[1] for astrophysical measurements. In addition, it was desired to ascertain the reliability of using lithium-drifted, germanium (Ge(Li)) diodes as gamma-ray detectors in both balloon-flight and orbital experimentation.

DESCRIPTION OF THE INSTRUMENTS AND SHIELDS

The required shielding for the proposed spectrometer was determined initially by Monte Carlo and other computational methods at ORNL with the assistance of members of the Mathematics and Neutron Physics Divisions. A mock-up of the calculated shield was built for balloon-flight tests as shown on the right in fig. 1. Basically the shield was a composite of active and passive elements designed to either detect a background-producing event or to physically prevent undesired radiation from reaching the spectrometer. The outer shield consists of a scintillating plastic (NE-103) region on the outside both to detect charged particles and, by using a thickness of four inches of this hydrogeneous material, to moderate the high energy neutrons which born as a result of the charged-particle interactions or which enter the shield from the outside. The scintillations which occur in the plastic at the time of the interaction are detected by the photomultiplier tubes and are used to provide signals to "gate off" the analysis of all pulses from the gamma-ray detector for 8 μsec after the interaction.

*Research sponsored jointly by USAEC under contract with the Union Carbide Corp., and by Marshall Space Flight Center, NASA, Huntsville, Alabama.

Thus, the gamma rays reaching the detector during this period are not recorded on the supposition that they are probably the results of the interaction.

Most of the neutrons which enter the shield from the outside or are born in the shield as a result of charged-particle interactions are moderated to a sufficiently low energy to be stopped in a 1/2-in.-thick layer of LiF immediately inside the plastic. Low-energy neutrons are captured in the ^{6}Li with the subsequent emission of an alpha particle ($^{6}Li(n,\alpha)t$) rather than a gamma ray as with other common thermal-neutron shielding material; i.e., $^{10}B(n,\alpha)^{7}Li^{*} \rightarrow {}^{7}Li + \gamma(478\ keV)$. Fast neutrons, which penetrate both the lithium and lead with little difficulty, are often elastically scattered in the plastic and produce anticoincidence signals by virtue of the ionizations produced by the recoil proton. Thus gamma-ray pulses resulting from neutron interactions in the detector or inner shield are further reduced.

Since gamma rays easily penetrate the plastic and lithium due to their low density, it is necessary to include a high-Z material in the shield to attenuate this radiation. Lead was used for the mock-up, but it is proposed that bismuth be used in the final shield because of its relatively high threshold for neutron inelastic scattering compared to lead[2]. This gamma-ray shield as well as all other passive components of the configuration are placed inside the thermal-neutron and active plastic shields to reduce the neutron interactions and subsequent gamma-ray production in these materials. A total thickness of two inches of lead was used in the balloon measurements. Finally, the mock-up includes a 1/4-in.-thick layer of stainless steel to suppress the fluorescent radiation which originates in the lead (K x-ray at $\simeq$ 88 keV).

This mock-up of the shield was tested at ORNL by Rodda, Macklin, and Gibbons[3] with a pulsed-neutron source generated by the 3 MV Van de Graaff accelerator. The shielded detector as shown in fig. 1 was exposed to 1.7-MeV neutrons (a typical energy for evaporation neutrons) with the plastic anticoincidence shield operated in the passive mode and then with shield operated in the active mode. Time-of-flight techniques were used to separate the prompt gamma-ray spectra from the delayed spectra. The results showed a reduced neutron sensitivity for this detector compared to NaI(Tl), a reduction of about one order of magnitude in the observed number of inelastic scattering events in the Ge(Li) detector due only to the passive plastic shield, and an additional reduction of another order of magnitude in these events with the plastic shield operating in the active mode.

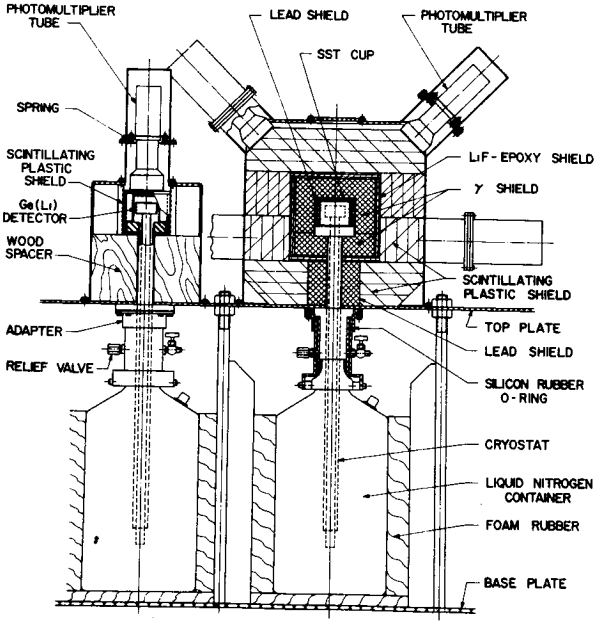

Fig. 1

During the first two balloon flight of the series, the pulse-height spectra of the environmental gamma radiation were obtained with the use of the detector shown on the left in fig. 1. The Ge(Li) detector in this configuration was unshielded except for the 1/8-in.-thick aluminum of the container and a 1/4-in.- thick plastic anticoincidence shield. In both configurations, the 25-cc Ge(Li) detectors were thermally coupled to a reservoir of liquid nitrogen (LN_2) by means of a long vacuum-sealed cryostat. A vacuum-tight adapter collar was used to prevent excessive boil-off of the LN_2 at high altitudes and both instruments were rigidly mounted in a stable frame for support and protection during the flights.

MEASURED PULSE-HEIGHT SPECTRA OF THE ENVIRONMENTAL GAMMA RAYS

The pulse-height spectra of natural gamma radiation as measured with the unshielded diode at 116.5- and 125.8 kilofeet are shown in fig. 2. The spectrum measured at 125.8 kilofeet was obtained with the anticoincidence shield (A/C) inoperative and probably includes some pulses produced by electrons - especially in the low energy region. Both spectra show distributions corresponding to E_γ^{-2} (E_γ = gamma-ray energy) below about 600 keV. Above this energy there is a strong indication that the distribution changes to E_γ^{-1}. This is not inconsistent with the findings of Perlow and Kissinger[4] who argue that the spectrum of natural gamma radiation in the atmosphere is primarily the result of two sources: (1) bremstrahlung radiation resulting from electrons produced by the decay of μ-mesons (see also ref. 5) which gives rise to the E_γ^{-1} component, and (2) photons degraded in energy by multiple Compton scattering to

ORNL DWG. 71-1844

Comparison of the Experimental Values of the 511 keV Photon Flux in the Atmosphere

Reference	Date of Flight	Pressure (g/cm^2)	Detector	Intensity (gammas cm^{-2} sec^{-1})
1	May–June 1964	a	1¾-in.-diam by 2-in.-high NaI (no anticoincidence shield)	0.34
1	June–July 1964	a	Same	0.40
2	May 2, 1961	6	2-in.-diam by 2¼-in.-high NaI, ⅛-in.-thick NE-102 plastic anticoincidence shield	0.31 ± 0.03
3	December 1966 to April 1968[b]	3.7	3-in.-diam by 3-in.-high CsI, ½-in.-thick NE-102 plastic anticoincidence shield	Varied from 0.16 ± 0.02 to 0.21 ± 0.02
4	May 5, 1968	4.7	22-cc Ge(Li) with a 2.25-in. NaI anticoincidence shield with opening to collimate incoming vertical radiation	0.47
This work	November 4, 1967	5.3	20-cc Ge(Li) with ¼-in.-thick NE-103 plastic anticoincidence shield	0.48 ± 0.03
This work	May 29, 1967	3.8	Same	0.38 ± 0.09

[a]Taken from curves published by the experimenter based on data taken to about 10 g/cm^2. Values quoted here were read from the curve at 5 g/cm^2.

[b]Reported variation of the intensity during this period.

[1]Robert Rocchia, *Gamma Radiation in Space and in the Atmosphere*, CEA report R-2939 (1966).

[2]L. E. Peterson, *J. Geophys. Res.* 68, 979 (1963).

[3]E. L. Chupp, D. J. Forrest, P. J. Lavakare, and A. A. Sarkady, *Bull. Am. Phys. Soc.* 13, 1399 (1968).

[4]E. A. Womack and J. W. Overbeck, *Bull. Am. Phys. Soc.* 13, 1398 (1968).

TABLE 1

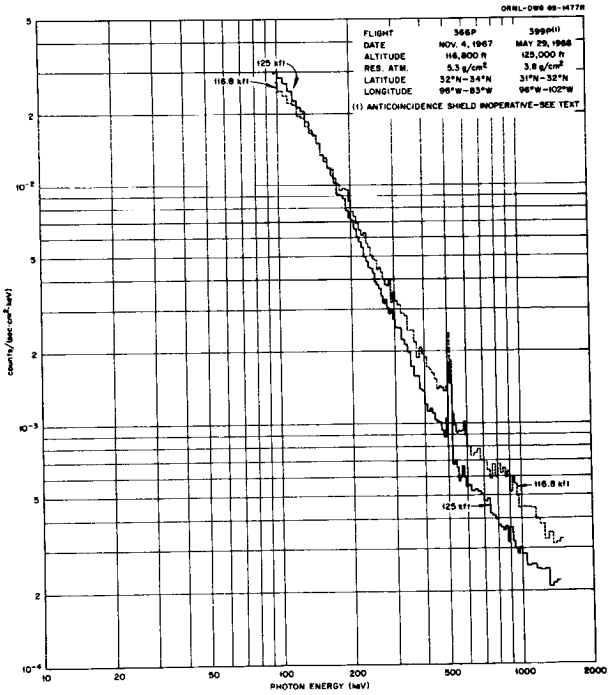

Fig. 2

produce the E_γ^{-2} component. The only distinct monoenergetic gamma ray present in the data is the 511-keV annihilation photon. The values of the intensities of this photon as reported by other experimenters[5-8] are compared to the values derived from these data in Table 1. There is a spread of a factor of three in these reported measurements. This variation, which is larger than would be expected from the altitude differences, may reflect in part temporal variations in the cosmic-ray intensity at the time of the measurements.

ALTITUDE DEPENDENCE OF THE DATA

Representative of the balloon flights in this series is the one launched on May 12, 1969 at the NCAR Balloon Facility in Palestine, Texas. Fig. 3 shows the time-altitude profile for the flight. The balloon ascended at an average rate of 650 fpm to a float altitude of 124 kilofeet. It remained at this altitude for about 13 hours. From about 5000 feet until termination of the flight, the following data were recorded.

1. Pulse-height spectrum of pulses in the Ge(Li) diode detector not associated with pulses in the plastic shield.

2. Integral count-rate of all pulses in the Ge(Li) diode detector not associated with pulses in the plastic shield.

3. Integral count-rate of all pulses in the Ge(Li) diode detector.

4. Integral count-rate of all pulses in the plastic shield above a bias levels at ~ 500 keV.

The count rate for all data channels remained essentially constant after reaching float altitude as illustrated in fig. 4 which shows the count rate as a function of time for all pulses occurring in the Ge(Li) detector. Each of the data channels showed similar constancy.

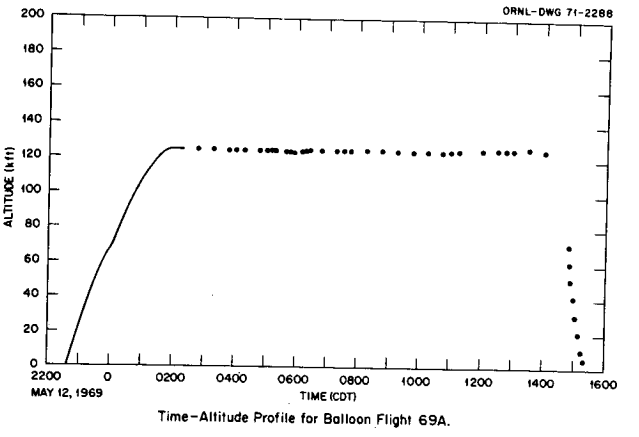

Time-Altitude Profile for Balloon Flight 69A.

Fig. 3

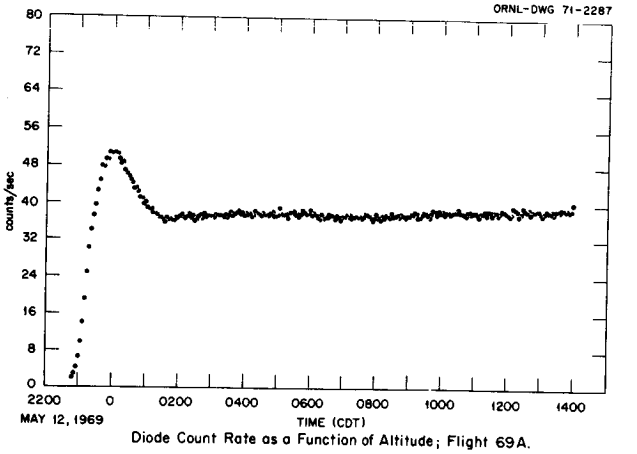

Diode Count Rate as a Function of Altitude; Flight 69A.

Fig. 4

Fig. 5 shows the same data as fig. 4 except that the count rate is now shown as a function of atmospheric pressure. The data between about 500 gms/cm^2 and 150 gms/cm^2 is well represented by exponential law

$$I(P) \sim e^{-P/Po}$$

with P_o = 158 gms/cm^2. The peak counting rate occurs at about 50 gms/cm^2 in the atmosphere. Rocchia[5] has shown that the production of photons at 511 keV in lead peaks at about 83gms/cm^2 (atmosphere) whereas the production of photons in air reaches a maximum at about 100 gms/cm^2. We speculate, then that the data shown in fig. 5 may reflect, in part, a production of photons in the shield. Fig. 6 shows the count rate in the plastic shield at two bias levels - 150 keV (low bias) and 500 keV (high bias). The analysis of pulses in the Ge(Li) detector was gated off by all pulses greater than the 500-keV level. These data show maxima at 100 gms/cm^2 and follow an exponential law, as before, with a P_o of 187 gms/cm^2 and 194 gms/cm^2 for the high-biased and low-biased data respectively. There is a difference in count rate of only about 10% at the maxima of the curves. The anticoincidence rates between the Ge(Li) detector and the plastic shield at the two bias levels are shown in fig. 7. There is no significant difference in these count rates, indicating that the diode rate was indeed being biased by good pulses in the plastic rather than noise pulses. Since these data represent pulses that are not associated with events in the shield, they must represent the natural gamma radiation and possibly neutral particles which leak through the shield and interact in the detector. Again, these data are described by an exponential law with P_o = 175 gms/cm^2 and with the maximum count rate occurring at 100 gms/cm^2.

Rocchia's[5] measurements of the atmospheric photon count rate as a function of atmospheric pressure shows P_o = 170 gms/cm^2 with the maximum count rate at 95 gms/cm^2. Consequently, it is felt that the pulses accepted from the Ge(Li) detector as a result of these gating pulses are indeed correlated with true atmospheric photons and do not originate in the shield.

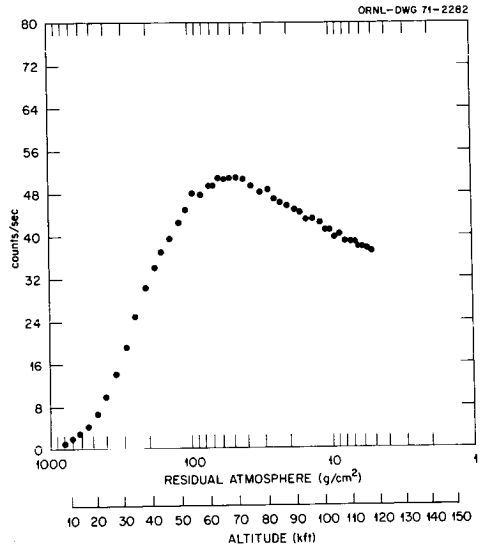

Diode Count Rate as a Function of Altitude; Flight 69A.

Fig. 5

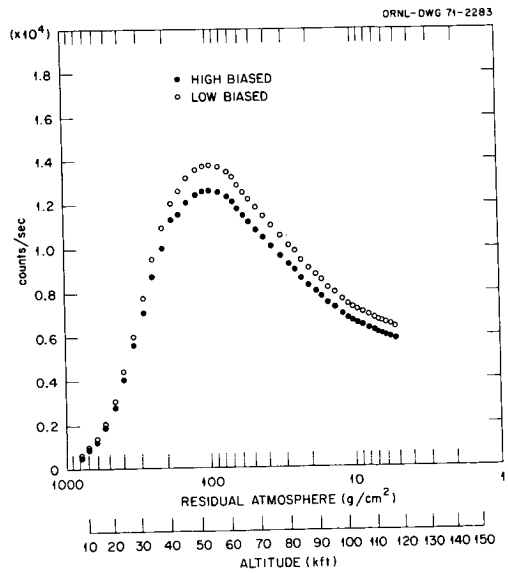

High-Biased and Low-Biased Plastic Count Rates; Flight 69A.

Fig. 6

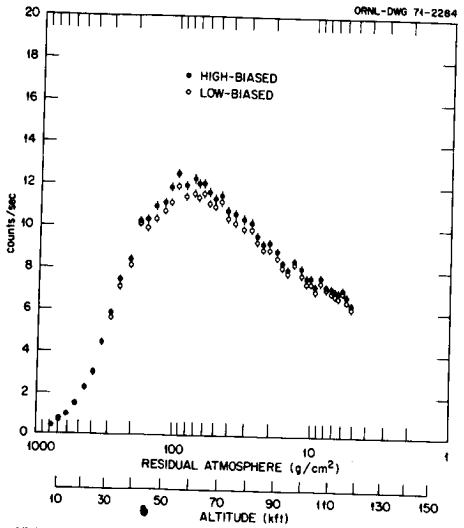

High-Biased and Low-Biased A/C Rates vs Altitude; Flight 69A.

Fig. 7

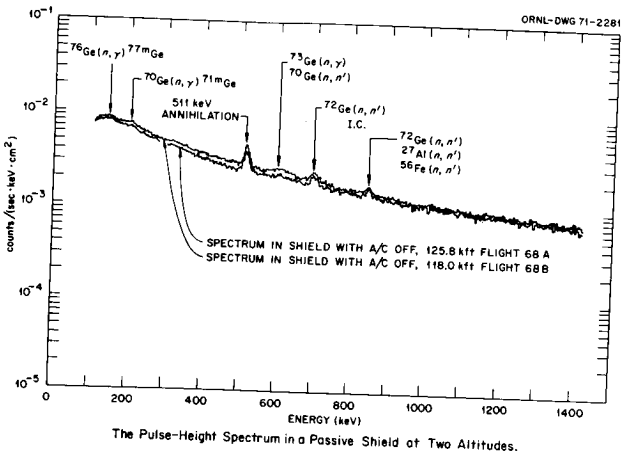

The Pulse-Height Spectrum in a Passive Shield at Two Altitudes.

Fig. 8

MEASURED ENERGY SPECTRA

During the series of balloon flight, measurements were made of effects on the energy spectrum when various shield parameters were changed. In flights 68A and 68B, the spectra inside the shield were obtained at 125.8 KFT and at 118.0 KFT respectively with the anticoincidence shield inoperative. These data are shown in fig. 8. There are prominent gamma-ray peaks through out the pulse-height spectrum. The reaction which produce the lines are:

138 keV	$^{74}Ge(n,\gamma)^{75m}Ge$ (48 sec)
198 keV	$^{70}Ge(n,\gamma)^{71m}Ge$ (20 msec)
511 keV	Annihilation
600 keV	$^{74}Ge(n,n'\gamma)^{74}Ge$
696 keV	$^{72}Ge(n,n'\gamma)^{72}Ge$ (422 nsec IC transition)
845 keV	$^{72}Ge(n,n'\gamma)^{72}Ge$

The lines at 138 keV and 198 keV have been observed by Womack[6] in a measurement similar to these and the lines resulting from neutron-inelastic-scattering events in the detector were reported by Rodda, et al.[3]. To see the effectiveness of LiF thermal-neutron shield, flights 67B and 68B were made at approximately the same altitude with the LiF removed from the shield during flight 67B. The results are shown in fig. 9. There is a constant reduction in the intensity over the whole energy range with the LiF in the shield. This is attributable to the reduction by the Li of thermal neutrons in the shield and the subsequent reduction of high-energy capture gamma rays. On the other hand, the relative intensities of the gamma-ray peaks are not significantly reduced. This would be expected if these peaks are the result of fast-neutron interactions in the detector as discussed above. Although Rodda[3] did detect thermal-neutron-capture gamma rays in the germanium at 600, 695 and 870 keV and possibly at 967 keV, the continued prominence of these lines with the LiF shield in and the elimination of the peaks in these data with the anticoincidence shield active as discussed later led us to conclude that lines in these data are indeed the results of the interactions of fast neutrons born during cosmic-ray events in the plastic shield.

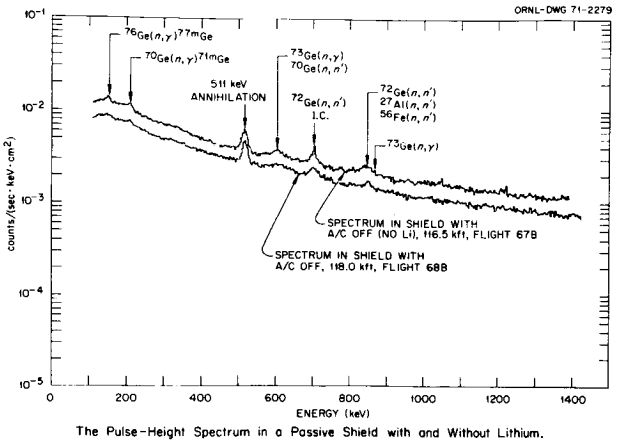

The Pulse-Height Spectrum in a Passive Shield with and Without Lithium.

Fig. 9

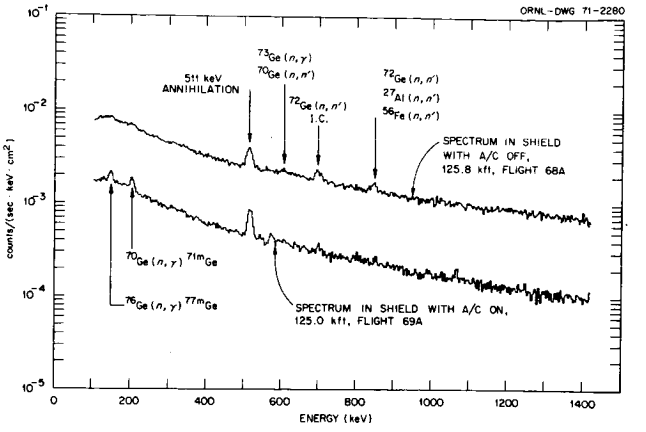

The Pulse-Height Spectrum in an Active and Passive Shield at 125 kft.

Fig. 10

The effectiveness of the total shield with the anticoincidence shield active is presented in the final set of data shown in fig. 10. These data were obtained at essentially the same altitude for comparison. The most distinctive difference in the two spectra is the virtual elimination of the gamma ray peaks by the use of the active plastic shield. The lines at 139 keV and 198 keV, which are due to neutron capture in germanium isotopes and the subsequent transition from long-lived isomeric states, do appear to be enhanced in the total-shield data. This may be explained, at least in part, by the fact that the life-time of both the isomers involved is sufficiently long to persist beyond the 8-μsec anticoincidence gate time. The overall reduction in the intensity of the spectrum is due to the elimination from the gated pulse-height spectrum those photons which are born during or within 8 μsec after a shower occurs.

CONCLUSIONS

The shielding of sensitive gamma-ray detectors for use in gamma-ray spectrometers in the primary cosmic-ray environment is a complex undertaking. Calculations suffer from the lack of adequate input data and the necessity of using complex geometries in realistic shields. Balloon-flight measurements, such as the one described here, to test specific shield designs may be the most reliable approach. The studies reported here have indicated that the use of a sufficiently thick external active shield such as scintillating plastic is almost essential to effectively stop charged particles and aid in the thermalization of neutrons. Plastic serves well in this capacity since it is hydrogeneous and not subject to induced long-lived activity by the neutron and charged particle interactions. A high-density material of sufficient thickness to overcome the effects of the gamma-ray "build-up factor" in the material must be used to attenuate the gamma radiation which results from cosmic-ray interactions on

which enter the shield from the outside. The use of a thermal-neutron shield between the plastic and the inner shield was shown to be desirable in preventing capture gamma rays in the shield. With the exception of gamma rays from long-lived isomers in germanium and annihilation radiation, the shield described here utilizing a sufficiently long anticoincidence gate time has reduced the unwanted peaks in the background spectrum to an almost insignificant level. As proposed for the final shield design but not discussed here, an inner anticoincidence shield immediately adjacent to the detector is desirable especially for the suppression of Compton-scattered photons from events in the detector. For example, it is estimated that a 1-in.-thick layer of NaI(Tℓ) inside the shield discussed here would reduce the background continuum to less than 10^{-5} counts per (sec. keV cm^2) for energies greater than 500 keV. This is almost a factor of ten lower than the best published, totally active shield[6] for this energy region with which we are familiar.

ACKNOWLEDGMENTS

The work reported here required the cooperation of too many people to recognize individually. We would especially like to thank the NCAR people at Palestine, Texas who handled all the launches, tracking and recovery operations for this series of flight. They all worked long hours, lost much sleep, and traveled many miles to ascertain that everything possible was done to assure the success of each flight and the safe recovery of the "package".

REFERENCES

1. G. T. Chapman, R. P. Cumby, H. J. Gibbons, R. L. Macklin, R. Nutt and H. W. Parker Proceedings, Fifth AFCRL Scientific Balloon Symposium, p. 47, AFCRL-68-0661, Dec. 1968.

2. R. L. Macklin, Neutron Induced Background Effects in Gamma-Ray Spectrometers for Use in Space, ORNL-TM-2675, August 12, 1969.

3. J. L. Rodda, Jr., R. L. Macklin, J. H. Gibbons, Nucl. Instr. and Methods 74 (1969) 224-228.

4. G. J. Perlow and C. W. Kissinger, Phys. Rev. Vol. 84, No. 3, p. 572, Nov. 1, 1951.

5. Robert Rocchia, Gamma Radiation in Space and in the Atmosphere, CEA-R-2939.

6. E. A. Womack, Jr., A Search for Cosmic Nuclear Gamma Ray (Thesis), MIT, June, 1969.

NEUTRON SPECTRAL MEASUREMENTS IN THE UPPER ATMOSPHERE[1]

W. Zobel
T. A. Love
J. T. Delorenzo
C. O. McNew

Oak Ridge National Laboratory
Oak Ridge, Tennessee 38930

An experiment to measure neutrons in the upper atmosphere has been performed on a balloon flight from Palestine, Texas, at an altitude of about 32 km. The experimental arrangement is discussed briefly, and results of a preliminary analysis of the data for neutrons in the energy range 3 to 30 MeV are given.

The decay of neutrons, produced by the interaction of cosmic rays in the atmosphere and subsequently leaving it (so-called "cosmic-ray albedo neutrons"), was suggested initially by Singer (ref. 1) as a mechanism to explain the observed protons in the Van Allen belt. Hess et al. (ref. 2) had measured the spectrum of neutrons in the atmosphere, and these measurements were used as the basis for subsequent calculations designed to test the "Cosmic-Ray Albedo Neutron Decay" (CRAND) theory (refs. 3-5). Additional measurements of neutrons (refs. 6-9) at high altitudes appeared to confirm the spectrum to about 20 MeV since calculated extrapolations from these measurements agreed with the calculated leakage flux of Newkirk (ref. 4) and Lingenfelter (ref. 5) which use the measurements of Hess et al. (ref. 2). Note that the experiments referenced in 6-9 arrive at the "spectrum" by assuming a spectral shape and converting it into the measured quantity, either pulse-height spectra (refs. 6-8) or count rate (ref. 9).

Calculations of the proton injection into the belt from CRAND neutrons by Dragt et al. (ref. 10) using Lingenfelter's estimate for the neutron source, indicated, however, that the CRAND source is too small by a factor of 50 for particles with energies greater than about 20 MeV. Later measurements of the proton spectrum in the belt for protons above 10 MeV appear to confirm this discrepancy (refs. 11-12). While a recent paper by Farley et al. (ref. 13) goes far toward resolving the discrepancy, it too uses Lingenfelter's spectrum with the observation that experimental verification of this spectrum for energies above 10 MeV is lacking.

It is unfortunately true that the measurements by Hess et al. were performed with counters which had minimal sensitivity in the energy region from roughly 10 to 100 MeV. It is in this very region that the greatest discrepancies are observed. A program was therefore started in 1966 at the Oak Ridge National Laboratory to reduce the uncertainty in the neutron spectrum at high altitude in the energy region from 2 to 60 MeV, the upper limit being chosen because of the availability of detector calibration facilities to this energy, and the lower limit following from the experimental scheme employed. The data-gathering program culminated in a balloon flight on 17 June 1969 from Palestine, Texas. The device floated at an altitude of 31,950 ± 200 m (corresponding to about 9 g/cm^2 residual atmosphere) for about 9-1/2 hours. This paper will describe the instrument used and give the results of a preliminary analysis of the data obtained from this flight.

The heart of the spectrometer is a liquid scintillator (Nuclear Enterprises Inc. NE-213) in which neutron interactions are detected by measuring the light pulses produced by recoil protons. Gamma-ray interactions in the scintillator result in pulses which can be separated with pulse-shape discrimination (PSD) techniques. Since incident charged particles can give rise to pulses similar to those from neutron interactions in the detector, the latter is enclosed in a plastic scintillator "mantle" of NE-110 (Nuclear Enterprises, Inc., San Carlos, California). The output from this

[1]Research funded by the U. S. Atomic Energy Commission under contract with Union Carbide Corporation; flight costs and telemetry support provided by the NASA Office of Space Science and Applications and the George C. Marshall Space Flight Center.

"mantle" is usually put in anticoincidence with the output from the liquid scintillator, thus preventing any counts due to events which trigger both detectors. The arrangement used is shown in figure 1. The NE-213 is contained in an aluminum can which is mounted on an RCA Type-8575 photomultiplier tube. The mantle is also viewed by an 8575 tube. At the bottom of the assembly can be seen the preamplifier used with the NE-213 detector and the high-voltage power supplies for both tubes. The can shown on the left is 1/16-in.-thick aluminum, used as a pressure vessel to maintain the assembly at ground pressure to eliminate high-voltage sparking. The aluminum can was then surrounded by about 1-1/2 in. of foam insulation to maintain proper operating temperature in the assembly.

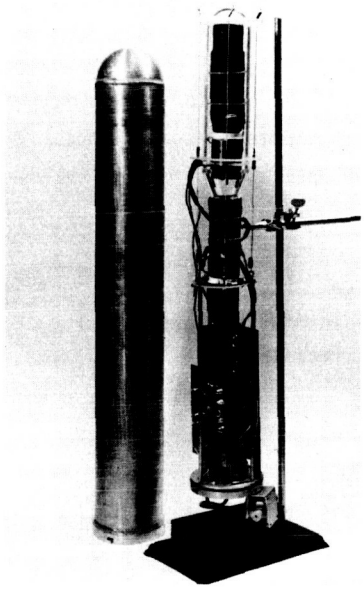

FIGURE 1.– Detector Assembly.

In order to reduce locally produced background, we decided to lower the detector assembly after launch about 90 ft below the gondola on which were mounted the electronics and batteries as well as miscellaneous support equipment. Since it was impractical to retract the detector assembly to the gondola prior to landing, the foam insulation was in turn contained in a 16-gauge sheet-steel can designed to take the landing impact. Proof of the effectiveness of this arrangement was obtained when we recovered the equipment and it showed no deterioration in performance.

A block diagram of the electronics used in this experiment is shown in figure 2. Two functions must be distinguished: pulse-shape discrimination, and pulse-height analysis.

As can be seen from figure 2, the pulse-height analysis was conventional. The major item of note here is that the discriminators had their thresholds adjusted so that the pulse height to be analyzed was determined by the threshold of the zero-crossing discriminator.

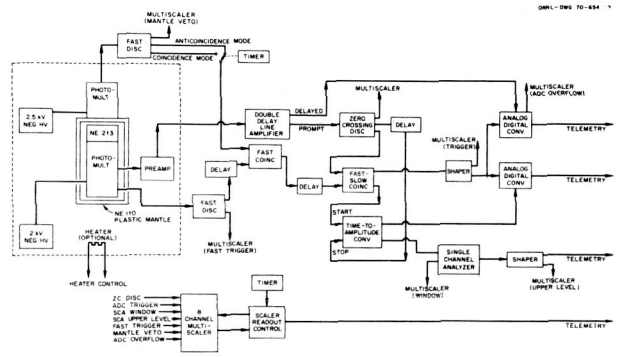

FIGURE 2.– Block Diagram of the Electronics.

The pulse-shape discrimination was based on the difference in the base-line crossing time of the amplifier output pulses due to the different relative amounts of slow light output from proton and electron recoils. The crucial feature of such a scheme lies in the proper adjustment and stability of the timing involved. The time of an event was determined by the input signal to the fast discriminator connected to the NE-213 photomultiplier, and this signal eventually was used as the start signal to the time-to-amplitude converter (TAC). The TAC stop signal was provided by the zero crossing discriminator after an arbitrary delay chosen so as to put the desired signals into the middle of the TAC range.

The TAC output was also digitized in a separate analog-to-digital converter (ADC); in addition, a single channel analyzer used the TAC output to set a bit in the telemetry whenever the TAC signal exceeded a predetermined level corresponding to pulses due to incident neutrons. For each event, then, the output to the telemetry consisted of the output from the two ADC's and two flags, one to identify the PSD ADC and the other to distinguish neutrons from gamma rays. A separate telemetry channel carried the information from the 8-channel multiscaler shown; yet another telemetry channel, not shown, carried housekeeping information such as pressures, voltages, and temperatures.

A preliminary analysis of the data has been performed, based on the hardware-set bias for the pulse-shape discrimination. A pulse-height spectrum of the events so ascribed to incident neutrons is shown in figure 3. While a few pulses can be seen extending to about channel 230 (corresponding to ~ 50 MeV incident neutrons), most of the spectrum lies below channel 130, or about 30 MeV.

The analysis performed on these data makes use of the calibration of a similar NE-213 detector by Verbinski et al. (ref. 14) and a spectrum unfolding scheme due to Burrus (ref. 15). The calibration of the detector was extended to about 40 MeV (ref. 16), and a slightly different version of the unfolding code (i.e., FERD rather than FERDoR) was employed. The results of this analysis are shown in figure 4. Also shown on the figure are the results of the group at New York University (ref. 8) in the 2 to 10 MeV energy range.

Several points must be made in connection with this figure. The first and most important is that it is still preliminary; for example, no attempt has been made to estimate in any detail the required correction for locally produced background neutrons. A very crude, zeroth-order calculation indicates that such a correction should not amount to more than 25% of the total number of counts observed, but no detailed calculation to determine the spectral shape of this correction has yet been

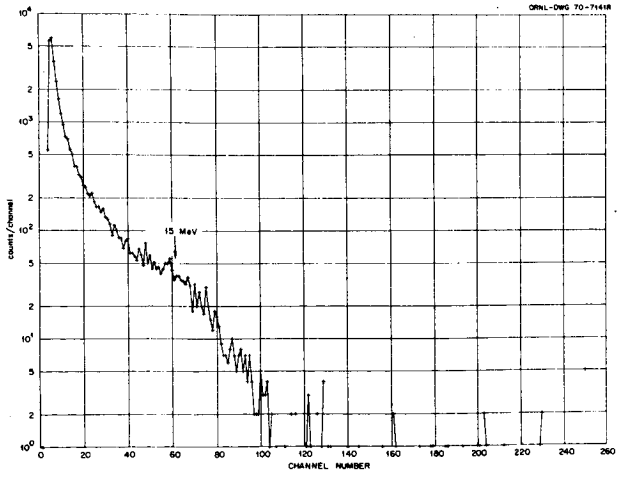

FIGURE 3.– Pulse-Height Spectrum from Neutron Events.

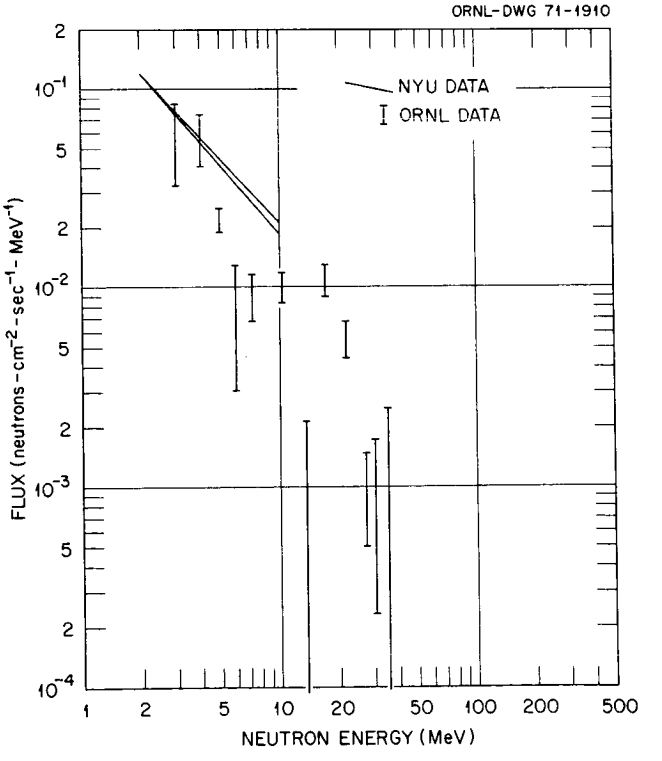

FIGURE 4.– Neutron Energy Spectrum at ~ 9 g/cm^2 Between 95.5° - 100.7° W, and 31.3° - 31.8° N.

performed. A second point to note is that the analysis procedure results only in the determination of a 68% confidence interval within which the result can be expected to lie. It is for this reason that no data points are shown but only the limits of this confident interval. The width of the interval is due not only to the statistical deviations expected from the input data but also includes the uncertainties associated with the unfolding process except those associated with the response matrix. For the comparison with the NYU data it must be remembered that their data were obtained during a period of solar minimum, whereas our data were taken during solar maximum. One would, therefore, expect their results to lie above ours, by perhaps 25%.

A comparison with the calculations of Lingerfelter is best accomplished by comparing our results with his in the form of an integral over a common energy region. Part of his calculations yield 0.106 neutrons-cm^{-2}-sec^{-1}-MeV^{-1} for the integrated flux from 3.16 to 10 MeV at 8 g/cm^2 residual atmosphere for 40° geomagnetic latitude (ref. 17). Our preliminary data, integrated from 3 to 10 MeV for 9 g/cm^2 residual atmosphere at about 41° latitude give an upper limit of 0.155 and a lower limit of 0.142 neutrons/cm^{-2}-sec^{-1}-MeV^{-1}.

Further analysis of the data, as well as an attempt to calculate the neutron spectrum to be expected, is in progress.

We wish to gratefully acknowledge the vital contribution to the project made by Mr. H. W. Parker and his associates from George C. Marshall Space Flight Center, who furnished and operated the telemetry equipment, and, of course, the invaluable cooperation of the personnel at the NCAR Scientific Balloon Facility, Palestine, Texas, who conducted the launch, flight, and recovery operation. Mr. R. H. Baldry, formerly with the Laboratory, designed and supervised construction of the necessary interfacing to the telemetry equipment. Thanks are also due Dr. R. B. Mendell of New York University for making available their data prior to publication, and to Dr. R. E. Lingenfelter for use of his unpublished results.

REFERENCES

1. SINGER, S. F.: Phys. Rev. Letters, vol. 1, 1958, p. 171, 181.
2. HESS, W. N.; PATTERSON, H. W.; WALLACE, R.; and CHUPP, E. L.: Phys. Rev., vol. 116, 1959, p. 445.
3. HESS, W. N.: Phys. Rev. Letters, vol. 3, 1959, p. 11.
4. NEWKIRK, L. L.: J. Geophys. Res., vol. 68, 1963, p. 1825.
5. LINGENFELTER, R. E.: J. Geophys. Res., vol. 68, 1963, p. 5633.
6. MENDELL, R. B.; and KORFF, S. A.: J. Geophys. Res., vol. 68, 1963, p. 5487.
7. HAYMES, R. C.: J. Geophys. Res., vol. 69, 1964, p. 841.
8. MENDELL, R. B.: private communication.
9. Boella, G.; ANTONI, G. D.; DILWORTH, C.; PANETTI, M.; SCARSI, L.; and INTRILIGATOR, D. S.: J. Geophys. Res., vol. 70, 1965, p. 1019.
10. DRAGT, A. J.; AUSTIN, M. M.; and WHITE, R. S.: J. Geophys. Res., vol. 71, 1966, p. 1293.
11. IMHOF, W. L.; and REAGAN, J. B.: J. Geophys. Res., vol. 74, 1969, p. 5054.
12. FARLEY, T. A.; TOMASSIAN, A. D.; and CHAPMAN, M. C.: J. Geophys. Res., vol. 74, 1969, p. 4721.
13. FARLEY, T. A.; TOMASSIAN, A. D.; and WALT, M.: Phys. Rev. Letters, vol. 25, 1970, p. 47.
14. VERBINSKI, V. V.; BURRUS, W. R.; LOVE, T. A.; ZOBEL, W; HILL, N. W.; and TEXTOR, R.: Nucl. Instr. Methods, vol. 65, 1968, p.8.
15. BURRUS, W. R.; and VERBINSKI, V. V.: Nucl. Instr. Methods, vol. 67, 1969, p. 181.
16. COHEN, L. D.; LOVE, T. A.; SANTORO, R. T.; WACHTER, J. W.; and ZOBEL, W.: Calibration of an NE-213 Detector with 40-MeV Neutrons. Neutron Phys. Div. Ann. Progr. Rept. May 31, 1969, Oak Ridge National Laboratory Document ORNL-4433, 1969, p. 108.
17. LINGENFELTER, R. E.: private communication.

THE PHYSICAL THEORY OF ONE-DIMENSIONAL GALACTIC COSMIC-RAY PROPAGATION IN THE ATMOSPHERE

Keran O'Brien

Health and Safety Laboratory, U. S. Atomic Energy Commission, New York, N. Y.

An essentially analytical theory of atmospheric cosmic-ray propagation is developed on the basis of a phenomenological model of hadron-nucleus collisions. This model correctly predicts the sea-level cosmic-ray nucleon, pion and muon spectra, the cosmic-ray ionization profile in the atmosphere, and neutron flux and density profiles in the atmosphere. It is concluded that the large scale properties of atmospheric cosmic-rays can be accurately predicted on the basis of a purely nucleonic cascade as a result of which all secondaries are mediated by pion production.

Implications for energy independence of cross sections, the recent 70 GeV results from Serpukhov, and nucleonic relaxation rates in the atmosphere are discussed.

INTRODUCTION

This paper attempts to establish the physics on which the large-scale, time-averaged, one-dimensional properties of galactic cosmic-rays in the atmosphere depend.

The point of departure for this theory is a phenomenological model of high energy nucleon-nucleus collisions which can be applied to analytical transport theory. Particle spectra, fluxes, densities and ionization calculated from the theory yield good agreement with measured values indicating the adequacy of the nuclear model and of the supporting cosmic-ray and geophysical data. All comparisons are on an absolute basis.

Preliminary results of this work have already been reported comparing calculations and measurements of various components of cosmic-ray ionization in the lower atmosphere (<2.5 km elevation) at a geomagnetic latitude of 51° (ref. 1).

ATMOSPHERIC MODEL

The atmosphere is assumed to be a flat slab 1033 g/cm^2 thick with a constant scale height of 6.7 km. It is assumed to be composed of a single nuclear species with an atomic weight of 14.48, atomic number of 7.31, and an ionization potential of 86.8 volts. Because oxygen and nitrogen are so close in the periodic table, this simple assumption yields the correct nuclear data. The density of the atmosphere is

$$\rho = r/H \qquad (1)$$

where

ρ is the density in g/cm^3,
r is the depth in the atmosphere in g/cm^2, and
H is the scale height in cm.

Since the mean free path for decay of a charged particle is

$$\lambda_q = \frac{(P_q c)}{(m_q c^2)} \; (c\tau_q \rho) \qquad (2)$$

where

λ_q is the mean free path for decay in g/cm^2 of a particle of type q,
m_q is the mass of the particle in MeV/c^2,
P_q is the momentum in MeV/c,
c is the velocity of light, and
τ_q is the mean life in the rest frame, in seconds,

we have the useful result that

$$\lambda_q = P_q c r / C_q, \qquad (3)$$

where

$$C_q = m_q c^2 H / c\tau_q.$$

THEORY OF THE ATMOSPHERIC NUCLEONIC CASCADE

The Boltzman Equations

In this paper, atmospheric cosmic-ray fluxes will be obtained as analytic solutions to an approximate form of the Boltzman equations. The Boltzman equations for the nucleonic cascade in the atmosphere are

$$B_q \varphi_q(r,E,\vec{\Omega}) = S_{qj}, \qquad (q = p,n,\pi : j = p,n), \qquad (4.1)$$

$$B_\mu \varphi_\mu(r,E,\vec{\Omega}) = S_{\mu\pi^\pm},$$

$$B_\alpha \varphi_\alpha(r,E,\vec{\Omega}) = S_{\alpha\beta}, \qquad (\alpha = \gamma,e : \beta = \gamma,e,\pi^\circ,\mu),$$

$$B_q = \vec{\Omega} \cdot \nabla + \sigma_q + \frac{C_q}{P_q c r} - \frac{\partial}{\partial E} k_q \qquad (q = p,n,\pi,\mu,e\gamma), \qquad (4.2)$$

$$S_{qj} = \int_{4\pi} d\vec{\Omega}' \int_E^\infty dE_B \; \sigma_{qj} \; F_{qj}(E_B \to E, \vec{\Omega}' \cdot \vec{\Omega}') \cdot \varphi_j(r,E_B,\vec{\Omega}') \qquad (4.3)$$

$(qj = np,\ pn,\ \pi n,\ \pi p,\ \mu\pi^\pm,\ e\mu,\ \gamma\pi^\circ,\ e\gamma,\ \gamma e),$

$$\sigma_\mu = C_p = C_n = C_e = C_\gamma = k_n = k_{\pi^\circ} = k_\gamma = 0,$$

where

r is the depth in the atmosphere in g/cm^2,
E is the particle kinetic energy in MeV,
$\vec{\Omega}$ is the unit vector in the direction of particle travel,
φ_q is the particle flux of type q per second per steradian at a depth r with a direction $\vec{\Omega}$,
σ_q is the total cross section for absorption of a particle of type q in cm^2/g,
σ_{qj} is the cross section for the production of particles of type q from collisions with, or decay by, particles of type j in cm^2/g,
k_q is the stopping power of a charged particle of type q in air, in MeV cm^2/g, and
F_{qj} is the number of particles per MeV per second per steradian at E and Ω resulting from a collision with or decay by a particle of type j at E_B and $\vec{\Omega}'$.

The subscript π implies application to all pions, charged and neutral. The subscript $\pi^\pm$ implies application to the charged pions, and π° to neutral pions only.

Nucleon-Nucleus Collisions

In eq. (4) it has been assumed that atmospheric cosmic-rays propagate by means of the nucleonic cascade in an exponential atmosphere [see Fig. 1 of O'Brien (ref. 1)]. Thus all other secondaries result from nucleon-nucleus collisions. The following reactions are considered.

$$\begin{aligned}
&p + \text{air} \to \nu_p p + \nu_n n + \nu_{\pi^\pm} \pi^\pm + \nu_{\pi^\circ} \pi^\circ \\
&n + \text{air} \to \nu_p p + \nu_n n + \nu_{\pi^\pm} \pi^\pm + \nu_{\pi^\circ} \pi^\circ \\
&\pi^\pm \to \mu + \nu \\
&\pi^\circ \to 2\gamma \to \text{electromagnetic showers} \\
&\mu \to e + 2\nu \to \text{electromagnetic showers}
\end{aligned} \qquad (5)$$

where ν_j are the multiplicities of j type resulting from the collision of a nucleon with a nucleus of air. The influence of kaon production has earlier been shown to have a small influence on ionization, and it is neglected here, at a considerable saving of computer time (ref. 1).

The nucleon-nucleus reactions of eq. (5) will be considered at high energies only, because the mathematical form of the approximation to the Boltzman equation to be obtained is only applicable at energies above about 0.1 GeV*.

It is required (a foreseen mathematical result motivates the choice of the function) that

$$G_{qj} = I_q \frac{E_B^{\ell}}{E^n} U(E_B - \eta_q)$$
$$G_{qj} = 2\pi \int_0^{\pi} d\theta \sin\theta \, F_{qj}(E_B \to E, \Omega) \qquad (6)$$
$$\Omega = \cos\theta$$

where

G_{qj} is the secondary production spectrum of type q particles integrated over the solid angle,

I_q is an arbitrary constant depending on q,

ℓ and n are arbitrary constants which must be the same for all j,q, and

$U(x)$ is the Heaviside function $[U(x < 0) = 0, U(x \geq 0) = 1]$,

η_q is a lower energy limit below which secondary particle production is cutoff.

The formula for G_{qj} is certainly very crude, however it is suitable to represent the behavior of the partial inelasticities and multiplicities associated with high energy nucleon-nucleus collisions. Inelasticities are known to vary quite slowly with energy, and to become essentially constant at energies of a few 10's of GeV (ref. 2). If $n = \ell + 1$, then G_{qj} can be rewritten in terms of a constant partial inelasticity, K_q, for the production of a type q particle

$$G_{qj} = (1 - \ell) K_q \frac{E_B^{\ell}}{E^{1+\ell}} U(E_B - \eta_q) \qquad (7)$$

Hagedorn and Ranft (ref. 3) have calculated K_q using the statistical model for p-p collisions at 12.5, 18.8, 30 and 300 GeV/c and it would be quite convenient to use these results for K_q. However, Alsmiller and Barish (ref. 4) have shown that the secondary production spectrum, G_{qj}, softens with increasing atomic weight as a result of the intranuclear cascade. This effect has been simulated in eq. (7) by making K_q a function of atomic weight (ref. 5). This is, unfortunately, at the expense of the conservation of energy in high atomic weight nuclei, although for air, energy is conserved reasonably well. The intranuclear cascade conserves energy as G_{qj} softens, by the emission of low energy particles but these low energy particles are not important to deep penetration calculations at high energies. Values of K_q interpolated from among the values obtained earlier are given in Table I (ref. 5).

Table I. - Partial inelasticities for proton-air collisions.

q	K_q
p	0.211
n	0.211
π^+	0.180
π^-	0.112
π^o	0.180
K^+	0.034
K^-	0.022
K^o	0.034

Experimental values of partial inelasticities in the energy range 0.1 to 20 TeV have been obtained in nuclear emulsion from the Brawley and I.C.E.F. emulsion stacks (ref. 2). The quantities measured were; K_{ch}, the energy that goes into new charged particles, and hence

$$K_{ch} = K_{\pi^+} + K_{\pi^-} + K_{K^+} + K_{K^-}; \qquad (8)$$

K_γ is the energy that goes into photon production, and so

$$K_\gamma = K_{\pi^o}; \qquad (9)$$

K_o is the energy that goes into long lived neutral particles. It is assumed that these are neutral kaons. This is a small number, and any error that may arise here is unimportant to the study. The energies involved in the measurement are high compared to the largest rest masses involved and thus they may be neglected.

*Low energy nucleon transport (<0.1 GeV) is chiefly neutron transport. Low energy neutron and electromagnetic shower transport are treated only very roughly here due to the limitations of the transport theory to be described. It is intended in the near future to apply the S_n method to this problem, and treat it much more generally. The analytic theory presented here is if less general, quite accurate at high energies, quite simple and rather transparent.

In Table II, the predictions of O'Brien (ref. 5) (which in conjunction with eq. (7) will be referred to as the power law model hereafter) is compared with these data, and with the predictions of other nuclear models.

These other nuclear models have all been compared against, and in some cases based upon, accelerator target yields, mostly at small angles and at high secondary momenta. The well known CKP model (ref. 6), the Trilling model (ref. 7), the extrapolation model (ref. 8), and the TRB model (ref. 9) are considered. Ranft and Borak (ref. 9) have modified the formulae used by Trilling (ref. 7), and this is referred to as the TRB model.

Table II. - Partial inelasticities at very high energies.

	Experimental[α] (0.1-20 TeV)	Statistical[β] model (300 GeV)	Power Law[α] model (=)	TRB[c] model (20 GeV)	Extrapolation[β] model (200 GeV)	Trilling[β] model (=)	CKP[β] model
K_{ch}	0.31± .06	0.364	0.303	0.23	0.166	0.21	0.38
K_γ	0.16	0.186	0.157	0.14	0.084	0.09	-
K_0	0.03	0.035	0.029	-	-	0.01	-
Total	0.50±0.07	0.585	0.489	-	-	0.31	-

α nuclear emulsion.

β hydrogen.

c air, kaons neglected.

β aluminum, kaons neglected.

The considerable variation is occasion for surprise. The statistical model, the power law model which is an adaption of it, and the CKP model are in agreement with the cosmic-ray emulsion measurements, though all the models appear to agree within a factor of two. This is probably a consequence of the fact that most of the accelerator target data, and much of the physical interest, is at small forward angles and at large secondary momenta, and this does not determine K_q precisely enough.

The secondary particle multiplicities of the power law model depend on the value chosen for ℓ. Since eq. (7) has an "infrared" divergence, it it not suitable for total particle yields. However, shower particles in an emulsion produced by high energy nucleons have finite lower energy limits of 80 MeV for mesons and 500 MeV for protons (ref. 10). The power law model yields as the multiplicity of particles above a lower limit Γ

$$\nu_q(E_B) = [(1 - \ell)/\ell]K_q[(E_B/\Gamma)^{\ell} - 1].$$

Using the data of Meyer et al. (ref. 11), the best value of ℓ, in the least squares sense, was chosen. The procedure is described in a somewhat more expanded way in O'Brien (ref. 5). In Table III, the predictions of shower particle production by various nuclear models are given. The power law result is not really a prediction but a fit. Since the statistical model and the extrapolation model cannot be manipulated without the proper computer codes, their reported total charged particle production is given in place of the shower particle multiplicities. As the Trilling model does not give back emitted particles correctly (ref. 7) it has been omitted from consideration here.

Some of the differences in Table III are certainly due to differences in the target nucleus and in the lower energy limit. But it is clear that the power law model agrees with the experimental data as well as the other models.

Multiplicities and inelasticities are averaged quantities related to hadron-nucleus collisions. Matters are different when one considers the form of G_{qj} predicted by the various models. Figure 1 exhibits $G_{\pi^{\pm}p}(E_B, E)$ for E_B equal to 10 and 100 GeV protons incident on air calculated using the power law and TRB prescriptions, and the CKP prescription for protons on hydrogen. The CKP and TRB models agree at high secondary momenta, but differ elsewhere. The greater sophistication of the TRB model can be seen in the graph. For instance, the inflection point at $G_{\pi^{\pm}p}(100, 18)$ corresponds to the transition from energetic pions resulting from isobar decay to low energy pions emitted isotropically in the center of mass. The power law model overestimates pion production at high secondary momenta but underestimates at low secondary momenta.

In Fig. 2, secondary proton production predictions $G_{pp}(E_B, E)$ are exhibited for protons on air, again for E_B equal to 10 and 100 GeV. The relative crudity of the power law model is clear. It underestimates proton production at high secondary momenta and overestimates at low secondary momenta. It is probably more significant for the cascade

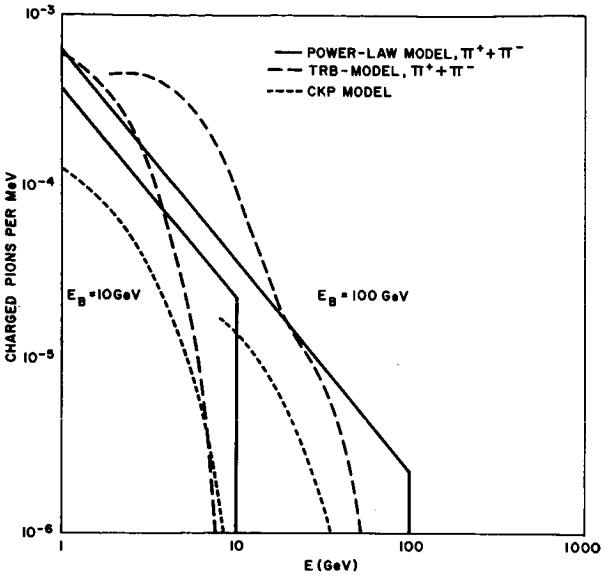

Fig. 1. Three models of charged pion production spectra from proton-air collisions.

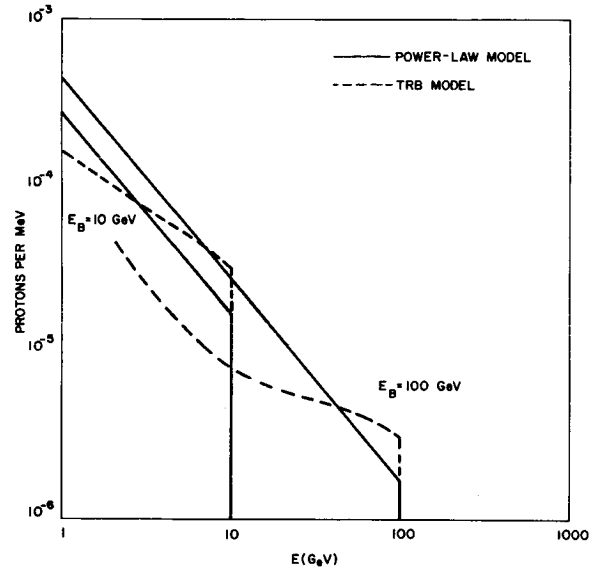

Figure 2. Two models of proton production spectra from proton-air collisions.

calculations to follow that the power law model should be right on the average, than it should be right at some particular secondary energy or angle.

The reaction cross sections used in the calculation to follow are assumed to be constant and geometric, i.e. $\sigma=\pi r_0^2 L/A$, $r_0=1.28\ A^{\frac{1}{3}}$ F, where L is Avogadro's number. This assumption is valid for low energy nucleon-nucleus collisions for atomic weights from less than 12 to greater than 64 (ref. 12), and it is used in what follows for all energies and hadrons.

APPROXIMATE SOLUTION TO THE BOLTZMAN EQUATIONS

Hadrons and Muons

A solution will be obtained for a sort of "Green's function", that is for incident nucleons homogeneous in energy and angle, of unit strength per steradian, the integral of which over the cosmic-ray primaries yields atmospheric cosmic-ray fluxes per steradian per second.

Making the "straight-ahead" approximation

$$F_{qj} = G_{qj}\ \delta\ \frac{(1 - \vec{\Omega}' \cdot \vec{\Omega})}{2\pi} \qquad (11)$$

and eq. (4.3) becomes for the hadron component

$$S_{qj} = \int_E^{E_o} dE_B\ \sigma\ G_{qj}(E_B, E)\varphi_j(r, E_B, \Omega) \qquad (qj = np, pn, \pi n, \pi p) \qquad (12)$$

where σ is the geometric reaction cross section in cm^2/g, and for the muons (ref. 13)

$$S_{\mu\pi^\pm} = \frac{m_{\pi^\pm}/m_\mu}{2\pi}\ \frac{C_{\pi^\pm}}{P_{\pi^\pm}\ r}\ \varphi_{\pi^\pm}[r(m_{\pi^\pm}/m_\mu)E_B, \Omega] \qquad (13)$$

where Ω is the cosine of the zenith angle of the incident radiation and E_o is the energy of the incident nucleon.

The Boltzman operator of eq. (4.2) for the muon component is then

$$B_\mu = \Omega\ \frac{\partial}{\partial r} + \frac{C_\mu}{P_\mu\ r} - \frac{\partial}{\partial E}\ k_\mu. \qquad (14.1)$$

The neutron operator is

$$B_n = \Omega\ \frac{\partial}{\partial r} + \sigma \qquad (14.2)$$

The remainder are all simplified by the omission of charged particle stopping

$$B_p = \Omega\ \frac{\partial}{\partial r} + \sigma \qquad (14.3)$$

$$B_\pi = \Omega\ \frac{\partial}{\partial r} + \sigma + \frac{C_\pi}{P_\pi\ r} \qquad (14.4)$$

This omission is not important for secondaries above about 1 GeV (ref. 14). Compensation for this can roughly be made with the use of the Heaviside function of eq. (7), as will be shown.

Separating the primary nucleons from the secondaries produced in the atmosphere

$$\varphi_q = \varphi_{iq} + \varphi_{sq} \qquad (15)$$

Table III. - Shower particle multiplicities.

E (GeV)	Experimental[a]	Power Law[a] model	Statistical[b] model	Extrapolation[c] model	TRB[b] model	CKP[b] model
12.5	3.8	5.0	3.0	5.5	3.8	4.9
20	5.3	5.9	3.8	-	4.3	5.5
30	7.3	6.8	4.8	-	5.0	6.1
200	12	12	-	6.9	10	9.8
300	13	13	8.5	-	12	11
1000	17	17	-	-	20	15

[a] nuclear emulsion.

[b] hydrogen, total charged particle yield.

[c] aluminum, total charged particle yield, kaons neglected.

[b] air, kaons neglected.

[b] hydrogen, total charged pion yield.

where

φ_{iq} is the flux of primary nucleons, and

φ_{sq} is the flux of secondary nucleons.

This leads to 3 differential equations

$$\left[\Omega \frac{\partial}{\partial r} + \frac{C_\mu}{P_\mu r} - \frac{\partial}{\partial E} k_\mu\right]\varphi_{s\mu} = \frac{m_{\pi^\pm}}{2\pi m_\mu} \cdot \frac{C_{\pi^\pm}}{P_{\pi^\pm} r} \varphi_{s\pi^\pm}\left(r, \frac{m_{\pi^\pm}}{m_\mu} E_B, \Omega\right) \tag{16.1}$$

$$\left[\Omega \frac{\partial}{\partial r} + \sigma\right]\varphi_{iq} = 0 \qquad (q = p, n) \tag{16.2}$$

$$\left[\Omega \frac{\partial}{\partial r} + \sigma + \frac{C_q}{P_q r}\right]\varphi_{sq} = \sum_{j=p,n} \int_E^{E_{max}} dE_B \, \sigma(1 - \ell) K_q \cdot \frac{E_B^\ell}{E^{1+\ell}} U(E - \eta_q) \qquad (q = p,n,\pi) \tag{16.3}$$

Equation (16.1) is written in integral form and reduced to quadratures (ref. 15). A 51 point set was found necessary for the integral over space and 7 for the integral over angle.

The solution to eq. (16.2) is

$$\varphi_{iq} = \exp(-r/\sigma\Omega) \tag{17.1}$$

Passow (ref. 16), and Alsmiller (ref. 17) have shown that the solution to an integro-differential equation of the form of equation (16.3) with constant cross section for incident nucleon flux of energy E_o and zenith direction Ω is

$$\varphi_{sq} = \frac{\sigma^a}{\left(\sigma + \frac{C_q}{P_q r}\right)} (1 - \ell) K_q \left(\frac{E_o^\ell}{E^{1+\ell}}\right) \cdot \cdot U(E_o - \eta_v) \left[\frac{r}{\Omega B(E_o, E)}\right]^{\frac{1}{2}} \cdot \cdot I_1\left[2\sqrt{(r/\Omega) B(E_o, E)}\right] \tag{17.2}$$

$$B(E_o, E) = \sigma \sum_{t=n,p} (1 - \ell) K_t \cdot \cdot \{\ln E_o - \ln[EU(E - \eta_t) + \eta_t U(\eta_t - E)]\},$$

$$(v = p,n: \; q = p,n,\pi)$$

Equation (17.2) differs slightly from the form obtained by Passow (ref. 16) and Alsmiller (ref. 17) by the inclusion of the decay term in the solution. The reason for this lies in the fact that $C_n = C_p = 0$, that $G_{\pi j}$ does not appear under the integral of eq. (16.3), and that pion production and absorption is purely local so that the energy independence of the cross section required by the solution can be relaxed.

The remaining parameter, η_q, is a lower energy limit beneath which secondary particles of type q are suppressed. Thus, $\eta_\pi = E_o$, and $\eta_n = 0$. To compensate for the neglect of proton stopping, η_p is set equal to 500 MeV.

The neglect of charged particle stopping, the straight ahead approximation, and the constant geometric cross section make eq. (17) increasingly shaky as secondary particle energies go below 1 GeV and fails completely by 100 MeV. At high energies, eq. (17) should become and remain quite accurate as long as ℓ and σ can be treated as constants. It may seem that the neglect of hadron production by incident pions should fail at high energy since $\lambda_{\pi^\pm}$ (eq. 3) can become very long. However, as argued by Adair (ref. 18), any pion which interacts with a nucleus can be treated as an absorption. This arises because of the combination of the relatively low pion inelasticity with the steepness of the nucleonic energy spectrum. Only rarely will a pion be emitted from a pion-nucleus collision with an energy near to that of the incident nucleon (see Fig. 1 for the predictions of CKP and TRB at high secondary energies). The steepness

of the energy distribution then causes the number of pions resulting from pion-nucleus collisions to be small compared with those produced directly in nucleon-nucleus collisions.

The restrictions on the form of G_{qj} imposed by the power law model would seem a priori to be the most serious limitation on the use of eq. (17). It is then worth pointing out that eq. (17), suitably modified, has been applied to accelerator beam measurements in iron for proton energies from 1 to 18 GeV (refs. 5, 19), and an 8 GeV pion beam on tin (ref. 20) with excellent results.

Once it is established that the parameters underlying the power law model are correct and that the cross sections are correct, more general methods can be used and many of the approximations made here to stay within the bounds of Passow's mathematical framework (refs. 16, 17) can be abandoned. The relative ease and transparency of Passow's approximation make it of value in itself however.

Photons and Electrons

Electromagnetic shower propagation is not so problematic as nucleon transport. Essentially exact Monte-Carlo treatments exist and have been tested against experimental data (ref. 21, 22). These calculations are difficult to carry out over the range of depths and energies required, and as the goal at this time is the establishment of sufficient conditions to determine the atmospheric flux, the propagation of the electromagnetic cascade is treated very primitively.

Since the mean life of the neutral pion is 0.91×10^{-16} s, $\frac{C\pi^o}{Pr}$ is huge compared with $\sigma(C_{\pi^o} = 3.3 \times 10^{10}$ GeV) it decays immediately into 2 photons. The muon decay probability is very much less (C_μ = 1.1 GeV) and is of significance only below about 10 GeV. Energy deposition is calculated from the assumption that the total energy of the neutral pion produced per gram of air (from eq. 17.2) is absorbed at the point of production, and 1/3 the total energy of the decaying muon (from eq. 16.1) is absorbed at the point of decay.*

*However, at this time, an attempt is being made to apply the electromagnetic shower code CASCADE (ref. 22) to this problem to improve the treatment of this important component of atmospheric cosmic rays.

This assumption will deteriorate inversely as geomagnetic latitude. As the geomagnetic cutoff rises toward 17 GV, the neutral pion production spectrum will become harder, and as the radiation length of air is of the same order of magnitude as the nucleonic collision mean free path, neglect of transport will become increasingly serious. However at higher latitudes, the error will be seen to be tolerable.

SOLAR AND TELLURIAN MODIFICATION OF THE GALACTIC COSMIC-RAY SPECTRUM

Solar Activity and the Interplanetary Medium

It is well known that variations of solar activity, through the agency of the solar wind modulates the cosmic-ray spectrum found at the earth's orbit. This modulation is a consequence of cosmic-ray transport through the interplanetary medium and it is formally the same as that which would be produced by a heliocentric electric field having a magnitude at the earth's orbit of about 100 MV at solar minimum and about 1000 MV at solar maximum (ref. 23, 24).

The electric field model is a useful computational tool for representing solar effects as the potential is the only adjustable parameter. This representation is for convenience only. It is not asserted here that a heliocentric potential of this size exists and is responsible for solar modulation.

The electric field model of the modulated cosmic-ray flux is (ref. 25)

$$n(E) = n_o(T) \left[\frac{P(E)}{P(T)}\right]^3 \left[\frac{W(T)}{W(E)}\right], \qquad (18)$$

$$T = E + ZU$$

$$P(x) = \frac{1}{c}\sqrt{x^2 + 2A\, m_p\, c^2\, x},$$

$$W(x) = x + A\, m_p . c^2$$

where

n_o is the unmodulated galactic spectrum of atomic weight A, and atomic number Z, per steradian per cm^2 per s per MeV, having an energy of E MeV, and

U is the solar potential in MV.

For the calculations to follow, the unmodulated spectrum is taken from Freier and Waddington (refs. 24, 26) below 10 GeV per nucleon. Above that energy the

spectrum is taken from Peters (ref. 27) with which it has a smooth overlap.

Calculations of atmospheric ionization will be made and compared with some of the measurements performed by Neher (ref. 28). These measurements have been analyzed to yield the incident proton cosmic-ray spectrum. This is compared to the predictions of the electric field model for U = 200 MeV in Fig. 3. The measurements were performed during the course of several months in 1965, and are near a solar minimum, but a minimum not as deep as that of 1954 (ref. 28), so the value of U is reasonable. The agreement is quite good, and this spectrum will be used for the ionization calculations to follow. Some neutron calculations will require different values of U. These will be taken, where possible, from Freier and Waddington (ref. 26).

In Fig. 4 the cutoffs for the eastern and western horizons and the zenith, from Lemaitre and Vallarta (ref. 30) are shown along with the values obtained by Richtmeyer et al. (ref. 29) as a function of geomagnetic latitude. It is evident that the assumption of isotropy of the radiation near cutoff is not justified at latitudes below 40° to 45°.

This, in combination with the assumptions made with respect to electromagnetic shower transport, will probably cause the calculations based on an isotropically incident spectrum to fail at low latitudes. Consequently, at this stage in the development of the calculations the experimental comparisons will be limited to higher latitudes.

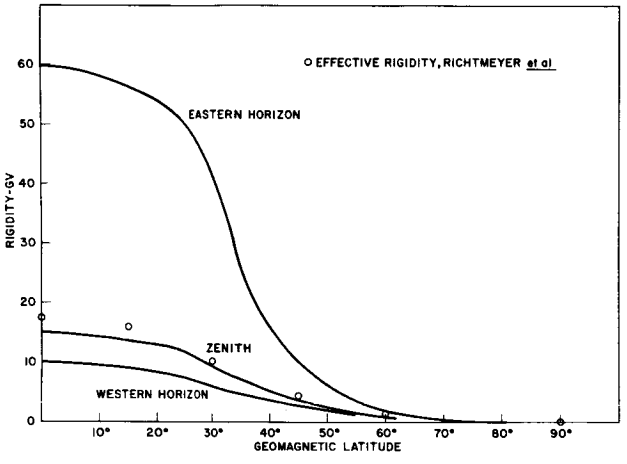

Fig. 3. The East-West variation of geomagnetic cutoff rigidity as a function of geomagnetic latitude compared with the effective cutoff rigidity for an isotropic detector.

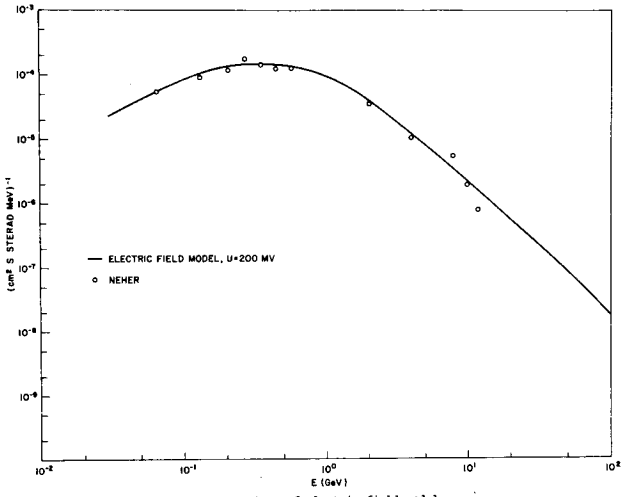

Fig. 4. Comparison of electric field model calculations of the incident cosmic-ray proton spectrum with Neher's measurements.

The Earth's Magnetic Field

The magnetic field of the earth deflects incoming cosmic-rays depending on their rigidity and angle of incidence, so that for each angle of incidence there is a critical rigidity below which the incoming particle cannot interact with the earth's atmosphere. In the calculations which follow, a single cutoff rigidity will be applied. The primary spectrum will be assumed unchanged in angle and energy above the cutoff, and vanish below it. Richtmeyer et al. (ref. 29) have calculated the effective cutoff rigidity seen by an isotropic detector exposed to the primary spectrum at the top of the atmosphere and this cutoff will be used here.

COMPARISON WITH EXPERIMENT

Sea-Level Particle Spectra

The first step in producing integral quantities such as ionization or neutron density is the calculation of the differential energy angle particle distributions.

As a test of eq. (17), the vertical component of the cosmic-ray spectra has been calculated for a geomagnetic latitude of 57°. Equation (17) with $\Omega = 1$ and $r = 1033$ g/cm^2, was integrated over the source spectrum. Seventy percent of the source spectrum was assumed to be composed of free protons, and 30 percent of bound neutrons and protons all having

the energy distribution given by eq. (18), with U = 200 MV. For geomagnetic purposes bound nuclei were treated as bound, but for the purpose of atmospheric transport treated as free i.e., an α particle is assumed to behave exactly like 2 free neutrons and 2 free protons. In Fig. 5, the calculated vertical component of the cosmic-ray nucleon spectrum of one charge state (neutrons or protons) is compared with the experimental sea level proton spectrum of Brooke and Wolfendale (ref. 31) and the sea level neutron spectrum of Ashton and Coats (ref. 32).

At this atmospheric depth, eq. (17) predicts nearly equal numbers of neutrons and protons, and so both experimental and theoretical data were combined. Agreement is very good over 4 decades of energy and 10 of intensity.

The calculated vertical component of the sea level pion spectrum is compared in Fig. 6 with the measurements of Brooke et al. (ref. 33). Agreement is good over most of the range of comparison.

The sea level muon spectrum for a zenith angle of 0° is shown in Fig. 7 compared with measurements by Owen and Wilson (ref. 34), Holmes et al. (ref. 35), Gardener et al. (ref. 36) and Hyman and Wolfendale (ref. 37). Agreement with experiment is quite satisfactory over the range from about 1 to about 1000 GeV. All measurements and calculations were for 57° geomagnetic latitude.

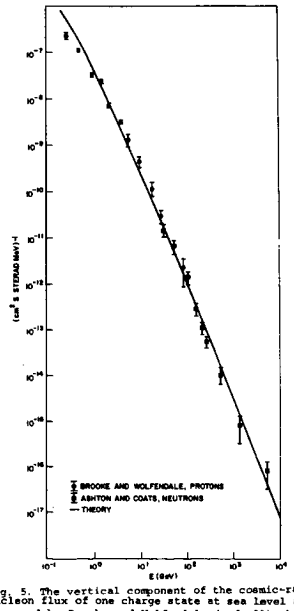

Fig. 5. The vertical component of the cosmic-ray nucleon flux of one charge state at sea level as measured by Brooke and Wolfendale (ref. 31), by Ashton and Coats (ref. 32), and as calculated.

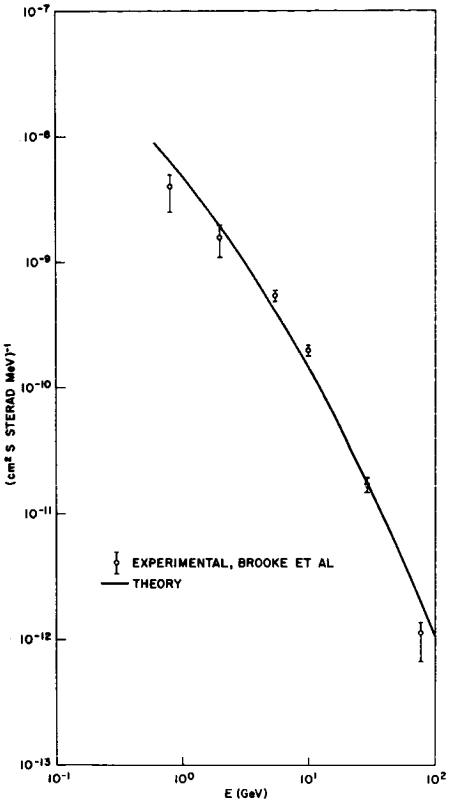

Fig. 6. The vertical component of the cosmic-ray pion flux as measured by Brooke et al. (ref. 33), and as calculated.

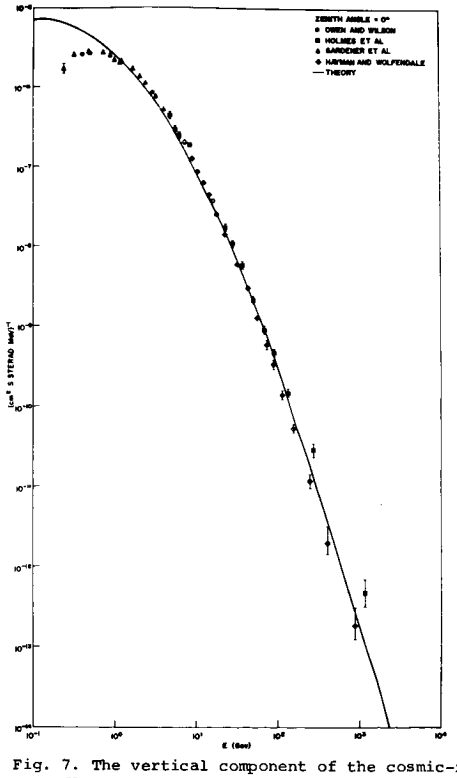

Fig. 7. The vertical component of the cosmic-ray muon flux as measured by Owen and Wilson (ref. 34), Holmes et al. (ref. 35), Gardener et al. (ref. 36), and Hayman and Wolfendale (ref. 37), and as calculated.

In Fig. 8, the sea-level muon spectrum is calculated for a zenith angle of 75° and compared with the measurements of Stefanski et al. (ref. 38). The lowest experimental point is above the maximum cutoff for this latitude, 52° (see Fig. 4).

As has been observed earlier, the assumptions that lead to eq. (17) become increasingly shaky below about 1 GeV. This affects all the charged particle distribution, including the muon energy distribution which of course depends on the pion distribution, and can be seen clearly in Fig. 5, 6, and 7, where the calculated fluxes rise above the measured fluxes in every case.

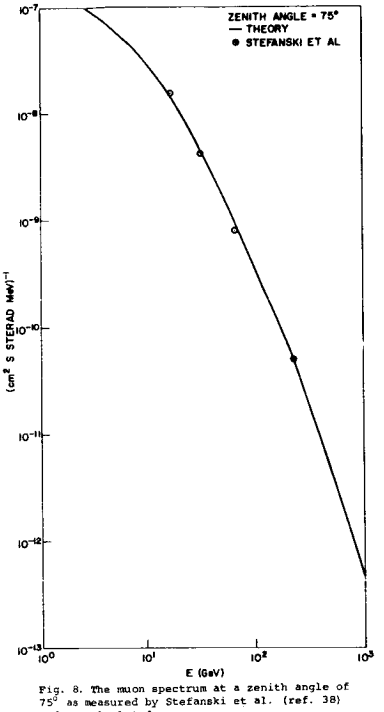

Fig. 8. The muon spectrum at a zenith angle of 75° as measured by Stefanski et al. (ref. 38) and as calculated.

Cosmic-Ray Ionization in the Atmosphere

Ionization from protons, pions and muons is calculated by multiplying the energy distributions by the appropriate stopping powers as described earlier (ref. 1). The lower energy limit for the proton, charged pion and neutral pion energy distributions is 100 MeV, below which the theory fails. The muons are allowed to slow down to 10 MeV, below which very little is contributed to the ionization.

It was found necessary empirically tc use an upper limit of 10^4 GeV to include all significant contributors to the ionization.

In Fig. 9, the calculated ionization (in units of I, the number of ion pairs per cm^3 of NTP air) at a geomagnetic latitude of 55° is compared with the measurements of Neher (ref. 28), and later data as reported by George (ref. 39) down to 600 g/cm^2. To complete the curve, the results of Lowder and Beck (ref. 40) from 600 g/cm^2 to sea level measured at 51° geomagnetic latitude at about the same time are included.

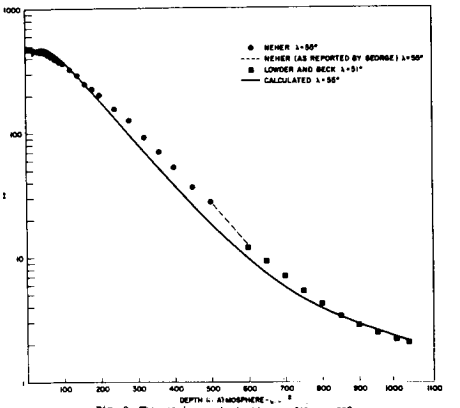

Fig. 9. The cosmic-ray ionization profile at 55° as measured by Neher (ref. 28) and by Lowder and Beck (ref. 40), and as calculated.

Over-all agreement is seen to be within 20% with the exception of the region near 600 g/cm^2, where the disagreement is nearer 40%. The comparison is absolute it must be emphasized. The composition of the total ionization is shown in Fig. 10. Because the secondary fluxes interact differently with the atmosphere each component has a noticeably different profile. The kink in the electron curve about 850 g/cm^2 is a consequence of the transition from shower production originating in neutral pion decay at low depths to shower production resulting from muon decay at larger depths.

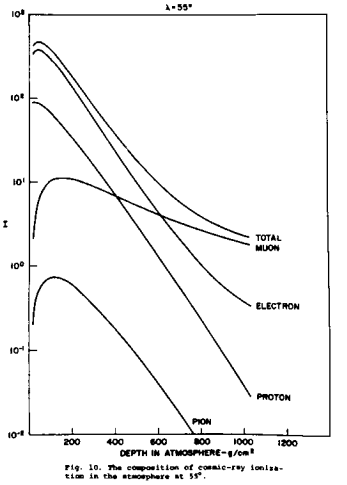

Fig. 10. The composition of cosmic-ray ionization in the atmosphere at 55°.

A similar comparison is shown in Fig. 11, where the calculation is carried out at 44°, and the data again are taken from Neher (ref. 28). To complete the curve, the data of George (ref. 39) are included from 188 g/cm² to sea level. The disagreement is typically 20% with higher values at near 800 g/cm² and 50 g/cm². The latter is probably a result of the departure of the incident primary cosmic-ray flux from isotropy, and the hardening of the photon production spectrum that results from the higher average cutoff (see Fig. 4). George's (ref. 39) measurements were carried out during 1968 near a solar maximum, and hence the additional modulation, if removed, would make the disagreement worse.

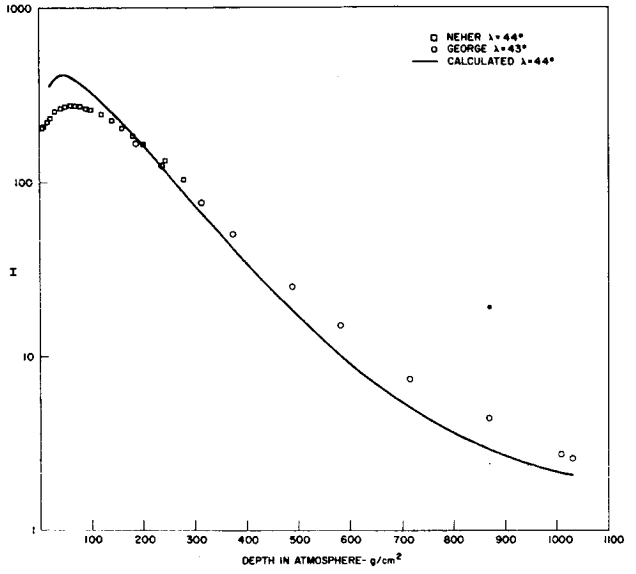

Fig. 11. The cosmic-ray ionization profile at 44° as measured by Neher (ref. 28) and by George (ref. 39) and as calculated.

Cosmic-Ray Neutrons in the Atmosphere

The lower energy limit of the cascade calculations described above is 100 MeV, and the agreement with measurement indicates that this cutoff which is forced on the calculations by the limitations of the analytical theory, is adequately high. This is a consequence of charged particle stopping which limits the number of charged particles at low energies. Neutrons are uncharged however, and extend all the way down to thermal energies. In order to account for neutron fluxes below 100 MeV, the cosmic-ray neutron spectrum reported by Hess et al. (ref. 41) at sea level and 44° geomagnetic latitude has been patched onto the calculated differential spectrum at 100 MeV. This approach is rather rude, and fails at small depths as it cannot account for the diffusion hardening which takes place near a vacuum boundary.

This is clearly seen in Fig. 12, where the neutron flux measurements of Boella et al. (refs. 42, 43), and Yamashita et al. (ref. 44) are compared with calculations. At depths greater than 200 g/cm² the agreement is really rather good. The lack of isotropy of the incident flux near cutoff and the absence of diffusion hardening lead to an overestimate at small depths. The measurements of Boella et al. (ref. 42) and Yamashita et al. (ref. 44) are both ground level measurements rather than free air measurements, but yet are seen to fall on the curve. The effect of the air ground interface on the calculations has not been evaluated.

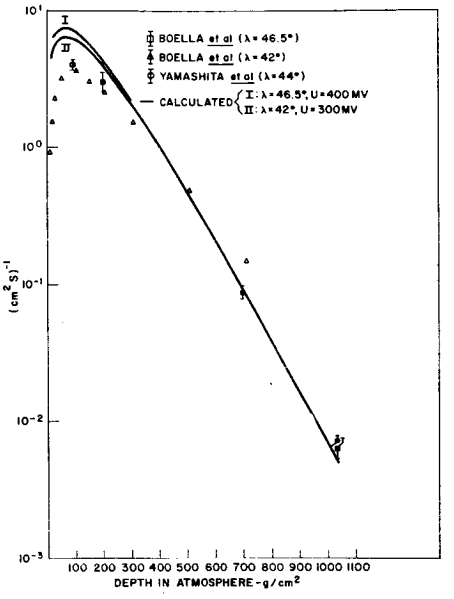

Fig. 12. The cosmic-ray neutron flux in the atmosphere as measured by Boella et al. (ref. 42), Boella et al. (ref. 43), and Yamashita et al. (ref. 44), and as calculated.

In Fig. 13, the neutron density measurements of Yuan (ref. 45) and Gold (ref. 46) have been compared with calculations on the same basis. Again, the agreement between calculations and measurements is good except at small depths, with the exception of the ground level value of Gold (ref. 46). Gold (ref. 46) recognizing that his values were quite high compared with balloon measurements in free air (ref. 47) attributed this to the interface with the ground, to which the neutron density appears much more sensitive than the neutron flux.

Yuan's data appear to have a markedly different slope from the measurements. This can also be seen in Boella et al. (ref. 43) on Fig. 12. This effect may be a consequence of operating near the threshold of instrument sensitivity since

the calculation is in good agreement with the deeper measurements, all the way down to sea level both in Fig. 5 and 12. Such an effect will lead to rather long reported relaxation lengths.

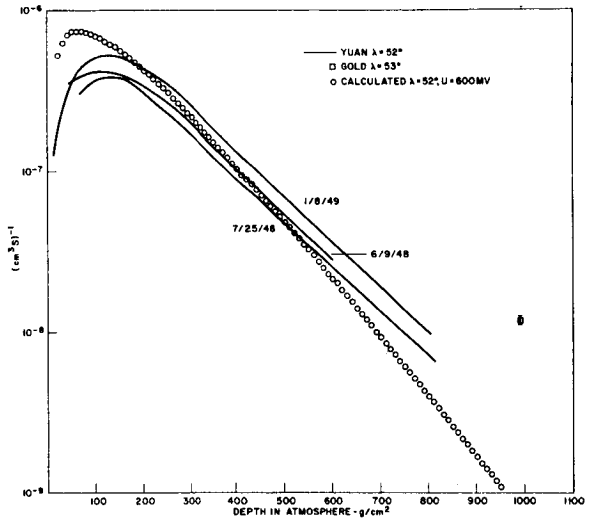

Fig. 13. The cosmic-ray neutron density in the atmosphere as measured by Yuan (ref. 45), and Gold (ref. 46), and as calculated.

Figure 14 shows the data of Miles (ref. 48). In this case a general underestimate appears below 200 g/cm^2. The identical calculations can be applied to the data of Haymes (ref. 49) and Soberman (ref. 50) which have been converted to neutron density and adjusted by Miles (ref. 48) for differences in latitude and time so that comparison with his own results might be made. Above 100 g/cm^2, the data of Soberman (ref. 50) in Fig. 15 are seen to be in excellent agreement with calculation. At smaller depths, the neglect of leakage, which was not taken into account in the low energy model, causes the calculation to be too high. Although much more scatter appears in the measurements of Haymes (ref. 49), agreement is clearly reasonably good except again at small depths.

DISCUSSION

Analytical calculations of the secondary energy distribution of cosmic-rays in the atmosphere, cosmic-ray ionization, and neutron flux and density have been performed. The model of nucleon-nucleus collisions on which the calculations depend is based on the constant partial inelasticities of Table I, and constant geometric reaction cross sections. The transport calculations assume a purely nucleonic cascade, and consider (eq. 5) only protons, neutrons, pions, electrons and photons.

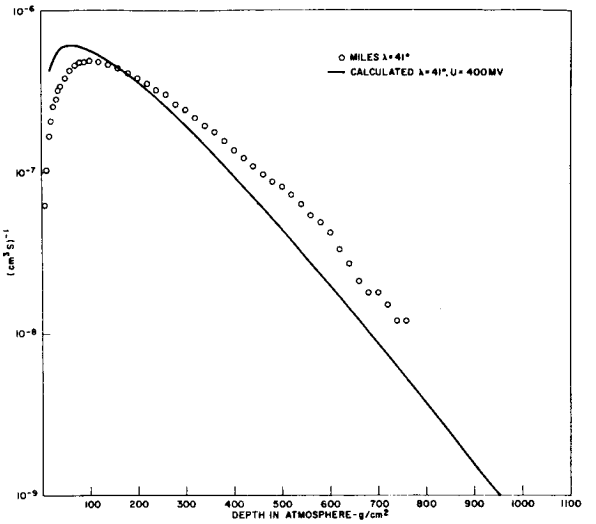

Fig. 14. The cosmic-ray neutron density in the atmosphere as measured by Miles (ref. 48), and as calculated.

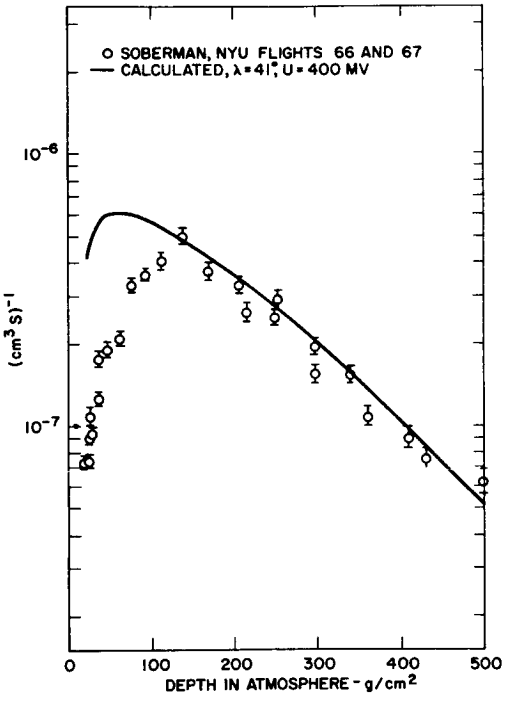

Fig. 15. The cosmic-ray neutron density in the atmosphere as measured by Soberman (ref. 50), and adapted by Miles (ref. 48), and as calculated.

In particular; the muon ionization and the high zenith angle energy distributions calculated on the basis of $\pi^{\pm} \rightarrow \mu$ decay, are in agreement with measurement (Fig. 8) and support the conclusion of Stefanski et al. (ref. 38) that there is no other important contribution to the muon flux below 300 GeV such as would account for the Utah muon measurements (ref. 51).

Ranft and Borak (ref. 9) observe that the measurements of negative pions at 70 GeV of Bushnin et al. (ref. 52) are in strong disagreement with the TRB model of hadron nucleus collisions and with the statistical model of strong interactions (ref. 3). The extrapolation model disagrees by an order of magnitude with the same data (ref. 8). If the measurements are correct, they cannot imply a change in the appropriate partial inelasticities. As has been shown the power law model used in the calculations of the fluxes in figs. 5-8 is in agreement with these models. Thus a large error in the assigned values of ν_j or K_j would lead to quite large errors in the differential nucleon, pion and muon fluxes starting somewhere between 30 and 70 GeV. However, the measurements are only at small angles ($\leq$ 15 milliradians) and high secondary momenta (> 45 GeV/c), and it is possible that average quantities such as multiplicity and inelasticity are not much affected by what happens in this region.

It has been suggested that nucleon-nucleon and meson-nucleon cross sections may vanish at infinite energy (ref. 53). These calculations, performed with constant cross sections, indicate that hadron-nucleus cross sections are essentially constant and geometric out to 10^4 GeV. For instance, a 10% perturbation of the nucleon-nucleus cross section will cause a change in the nucleonic flux in the region of 10^3 - 10^4 GeV of 150%. This would put theory and experiment out of agreement in Fig. 5. But, such a discrepancy could be accounted for in terms of errors in the primary spectrum used, or errors in the sea level measurements. Much larger changes in the cross section however, would lead to very big changes in the sea-level flux which would not be reconcilable with the data.

In these calculations, all hadron-nucleus cross sections are equal and geometric. It is known that pion-nucleon cross sections are 2/3 of the nucleon-nucleon cross sections (ref. 53). As Adair (ref. 18) points out, pion-nucleus and nucleon-nucleus cross sections will differ by less than this as a consequence of the intra-nuclear cascade. He calculates the ratio to be 0.77. Ranft and Borak (ref. 9) obtain 0.83 from published experimental data. The effect on pion and muon spectra of a 20% error in the reaction cross section would be much less than in the nucleon case, as pions are locally produced, and locally absorbed.

Apparently one-dimensional nucleonic cascades depend only weakly on the angular and energy behavior of the secondary production spectra, but strongly on the partial inelasticities, multiplicities and cross sections. The calculation described here which is based on a straight ahead power law approximation to the doubly differential production spectrum yields good agreement with the sea level differential fluxes of nucleons, pions and muons with the cosmic-ray ionization at all depths in the atmosphere, and with the neutron fluxes and densities in the atmosphere.

Lastly, it may be observed that in Figs. 12, 13, and 14, the neutron calculations appear to relax more rapidly than some sets of measurements. Yet in the Fig. 5, and the sea level values of Fig. 12, this would appear to represent experimental error, possibly a consequence of operating near the threshold of experimental sensitivity. Too rapid a relaxation rate of the nucleon spectrum would also result in the calculated pion spectrum of Fig. 6 to be too low, which it is not, as the pions are produced locally from nucleon-nucleus collisions.

The neutron attenuation is not actually exponential although its departure from exponentiation is not large (ref. 54). In Table IV, relaxation lengths obtained from the neutron density calculations at $\lambda = 41^\circ$ and with U = 400 MV are compared with Miles (ref. 47). Agreement is poor, but the calculated neutron densities agree well with Haymes (ref. 49) and Soberman (ref. 50) when they are reduced to the same conditions and are never less than half of Miles (ref. 49). In addition, Simionati deFritz and Cicchini (ref. 54) have measured cosmic-ray neutron attenuation lengths in air at 25° (ref. 55) as a function of atmospheric depth which are included for comparison. In this case agreement is quite close, and this suggests that exponential relaxation lengths are not well determined by experimental attenuation data, as relaxation rates are not constant with height and the true variation is marred by poorer quality at greater depths and at lower intensities.

The success of the preceding calculations rests primarily on the phenomenological model of hadron-nucleus collisions presented here. The description of the exclusively nucleonic cascade combined with the neglect of kaons is a simplification with which more sophisticated and expensive calculations may dispense. Other, more obvious, approximations are being discarded as the study progresses.

Real improvement on the forms of the doubly differential production spectra must probably await progress in studies being carried out at Oak Ridge and elsewhere. The adequacy of the power law nuclear model for calculations of this type is clear from the results shown here, and the average properties, particularly the partial inelasticities and cross sections, as applied to air, appear to be well established.

Table IV. - Comparison of calculated neutron attenuation lengths for $\lambda = 41^{\circ}$ and U = 400 MV with measurements.

Atmospheric depth (g/cm^2)	Calculated (g/cm^2)	Measured (g/cm^2)
300	149	155[a]
500	129	125[a], 165±20[b]
1033	113	115[a]

[a] $\lambda = 25^{\circ}$ (ref. 54).

[b] $\lambda = 41^{\circ}$ (ref. 47).

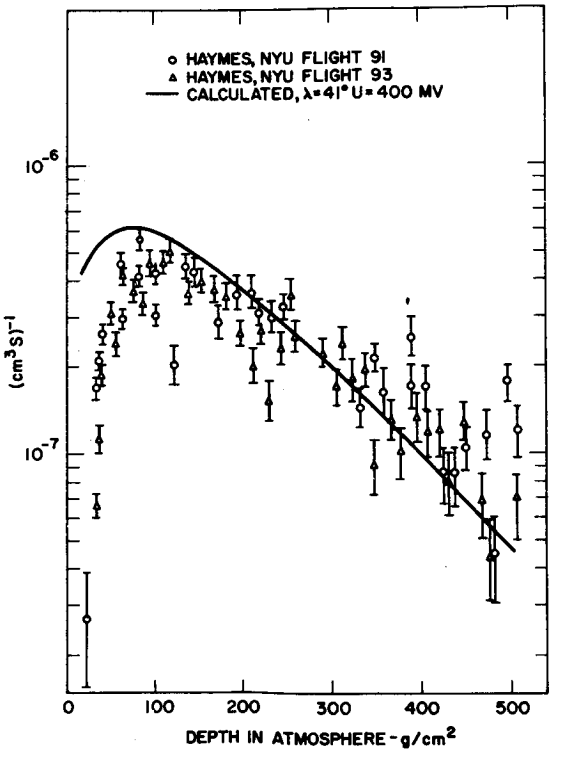

Fig. 16. The cosmic-ray neutron density in the atmosphere as measured by Haymes (ref. 49) and adapted by Miles (ref. 48), and as calculated.

REFERENCES

1. O'Brien, K.: J. Geophys. Res., vol. 75, 1970, p. 4357.
2. Fujimoto, Y.; and Hayakawa, S.: Cosmic rays and high-energy physics, in Encyclopedia of Physics, 46/2, Springer-Verlag, Berlin, 1967, p. 115.
3. Hagedorn, R.; and Ranft, J.: Nuovo Cimento Suppl., vol. 6, 1968, p. 169.
4. Alsmiller, R. G., Jr.; and Barish, J.: ORNL-3855, 1965.
5. O'Brien, K.: Nucl. Instr. and Meth., vol. 72, 1969, p. 93.
6. Cocconi, G.; Koester, L. J.; and Perkins, D. H.: UCRL-10022, 1961, p. 167.
7. Trilling, G.: Lawrence Radiation Laboratory Report, UCID-10148, 1966.
8. Gabriel, T. A.; Alsmiller, R. G., Jr.; and Guthrie, M. P.: ORNL-4542, 1970.
9. Ranft, J.; and Borak, T.: Improved nucleon-meson cascade calculations, FN-193,1100.0, National Accelerator Laboratory, 1969.
10. Camerini, U.; Davies, J. H.; Fowler, P. H.; Franzinetti, C.; Muirhead, H.; Lock, W. O.; Perkins, D. H.; and Yekutieli, G.: Phil. Mag., vol. 42, 1951, p. 1241.
11. Meyer, H.; Teucher, M. W.; and Lohrmann, E.: Nuovo Cimento, vol. 28, 1963, p. 1399.
12. Bertini, H. W.: Phys. Rev., vol. 188, 1969, p. 1711.
13. Alsmiller, R. G., Jr.; Alsmiller, F. S.; and Murphy, J. E.: ORNL-3289, 1963.
14. Alsmiller, R. G., Jr.; Alsmiller, F. S.; and Barish, J. B.: ORNL-3854, 1967.
15. Kronrod, S. A.: Nodes and Weights of Quardrature Formulas, Consultants Bureau, New York, 1965.
16. Passow, C.: Phenomenologische Theorie zur Berechnung einer Kaskade aus schweren Teilchen (Nukleonenkaskade) in der Materie, Desy Notiz A. 2.85 (1962), Deutches Elektronen Synchrotron, 1962.
17. Alsmiller, F. S.: ORNL-3746, 1965.
18. Adair, R. K.: Phys. Rev., vol. 172, 1968, p. 1370.
19. Armstrong, T. W.; and Alsmiller, R. G., Jr.: The nucleon-meson cascade in iron induced by 1 and 3 GeV protons, in ORNL-RSIC-25, ANS-SD-9, Shielding Benchmark Problems, A. E. Profio, ed., Oak Ridge National Laboratory, 1970.
20. O'Brien, K.: Nucl. Instr. and Meth., vol. 86, 1970, p. 217.
21. Zerby, C. D.; and Moran, H. S.: ORNL-3320, 1962.
22. Beck, H.: USAEC Report HASL-213, 1969.
23. Gleeson, L. J.; and Axford, W. I.: Can. J. Phys., vol. 46, 1968, p. S937.
24. Freier, P. S.; and Waddington, C. J.: Space Science Reviews, vol. 4, 1965, p. 313.
25. Ehmert, A.: Proceedings of the International Conf. on Cosmic Rays, Moscow 1959, vol. 4, 1960, p. 140.
26. Freier, P. S.; and Waddington, C. J.: Proceedings of the Ninth International Conf. on Cosmic Rays, London 1965, vol. 1, 1966, p. 176.
27. Peters, B.: Cosmic-rays, in Handbook of Physics, eds. E. U. Condon and H. Odishaw, McGraw-Hill, New York, 1958, p. 9.
28. Neher, H. V.: J. Geophys. Res., vol. 72, 1967, p. 1527.
29. Richtmeyer, F. K.; Kennard, E. H.; and Lawritsen, T.: Introduction to Modern Physics, (5th Edition), McGraw-Hill, New York, 1955, p. 566.
30. Lemaitre, G.; and Vallarta, M. S.: Phys. Rev., vol. 50, 1936, p. 493.

31. Brook, G.; and Wolfendale, A. W.: Proc. Phys. Soc., vol. 83, 1964, p. 843.
32. Ashton, F.; and Coats, R. B.: J. Phys. A (Proc. Phys. Soc.), vol. 1, 1968, p. 169.
33. Brooke, G.; Meyer, M. A.; and Wolfendale, A. W.: Proc. Phys. Soc., vol. 83, 1964, p. 871.
34. Owen, B. G.; and Wilson, J. G.: Proc. Phys. Soc., vol. 68, 1955, p. 409.
35. Holmes, J. E. R.; Owen, B. G.; and Rodgers, A. L.: Proc. Phys. Soc., vol. 78, 1961, p. 505.
36. Gardener, M.; Jones, D. G.; Taylor, F. E.; and Wolfendale, A. W.: Proc. Phys. Soc., vol. 80, 1962, p. 697.
37. Hayman, P. J.; and Wolfendale, A. W.: Proc. Phys. Soc., vol. 80, 1962, p. 110.
38. Stefanski, R. J.; Adair, R. K.; and Kasha, H.: Rev. Letters, vol. 20, 1968, p. 950.
39. George, M.: J. Geophys. Res., vol. 75, 1970, p. 3693.
40. Lowder, W. M.; and Beck, H. L.: J. Geophys. Res., vol. 71, 1966, p. 4661.
41. Hess, W. N.; Canfield, E. H.; and Lingenfelter, R. E.: J. Geophys. Res., vol. 66, 1961, p. 665.
42. Boella, G.; Degli Antoni, G.; Dilworth, C.; Gianneli, G.; Rocco, E.; Scarsi, L.; and Shapiro, D.: Nuovo Cimento, vol. 29, 1963, p. 103.
43. Boella, G.; Degli Antoni, G.; Dilworth, C.; Panetti, M.; Scarsi, L.; and Intriligator, D. S.: J. Geophys. Res., vol. 70, 1965, p. 1019.
44. Yamashita, M.; Stephens, L. D.; and Patterson, H. W.: J. Geophys. Res., vol. 71, 1966, p. 3817.
45. Yuan, C. L.: Phys. Rev., vol. 81, 1951, p. 175.
46. Gold., R.: Phys. Rev., vol. 165, 1968, p. 1411.
47. Miles, R. F.: J. Geophys. Res., vol. 69, 1964, p. 1277.
48. Miles, R. F.: Thesis, California Institute of Technology, 1963.
49. Haymes, R. C.: Phys. Rev., vol. 116, 1959, p. 1231.
50. Soberman, R. K.: Phys. Rev., vol. 102, 1956, p. 1399.
51. Bergeson, H. E.; Keuffel, J. W.; Larson, M. O.; Mason, G. W.; and Osborne, J. L.: Phys. Rev. Letters, vol. 21, 1968, p. 1089.
52. Bushnin, Y. B.; Denisov, S. P.; Donskov, S. V.; Dunaitsev, A. F.; Gorin, Y. P.; Kachanov, V. A.; Khodirev, Y. S.; Kotov, V. I.; Kutyin, V. M.; Petrukhin, A. I.; Prokoshkin, Y. D.; Razuvaev, E. A.; Shuvalov, R. S.; Stoyanova, D. A.; Allaby, J. V.; Binon, F.; Diddens, A. N.; Duteil, P.; Giacomelli, G.; Meunier, R.; Peigneux, J.-P.; Schlupmann, K.; Spighel, M.; Stahlbrandt, C. A.; Stroot, J.-P.; and Wetherell, A. M.: Phys. Letters, vol. 29B, 1969, p. 48.
53. Wetherell, A. M.: Selected Topics in Particle Physics, ed., J. Steinberger, Academic Press, New York, 1968.
54. Simionati deFritz, N. A.; and Cicchini, A. A.: Nuovo Cimento, vol. 40B, 1967, p. 220.
55. McNish, A. G.: Terrest. Magnetism Atmospheric Elec., vol. 41, 1936, 37.

SESSION VIII.4.
SPACE RADIATION DOSIMETRY
CHAIRMAN: M.D'AGOSTINO
GRUMMAN

ADVANCED DOSIMETRY SYSTEMS FOR THE SPACE TRANSPORT AND SPACE STATION

MAJOR LOUIS F. WAILLY
U S Air Force Academy

CAPT MARION F. SCHNEIDER
Air Force Weapons Laboratory

DR. BENTON C. CLARK
Martin Marietta Corporation
Denver, Colorado

Instrumentation to measure the operationally significant high energy radiations encountered in future manned spaceflight is of fundamental importance in ensuring astronaut safety, system survivability, and ultimate mission success. This paper describes advanced dosimetry systems concepts that will provide automated and instantaneous measurement of dose and particle spectra. Proposed are systems to measure dose rate from cosmic radiation background to >3600 rads/hour. Charged particle spectrometers, both internal and external to the spacecraft, to determine the mixed field energy spectra and particle fluxes for both real time on-board and ground based computer evaluation of the radiation hazard are described.

New and advanced automated passive dosimetry systems consisting of thermoluminescent dosimeters and activation techniques are proposed for recording the dose levels for twelve or more crewmembers. This system will allow automatic on-board readout and data storage of the accumulated dose and can be transmitted to ground after readout or data records recovered with each crew rotation.

The United States Space Station/Space Shuttle Program to be flown in the late 1970's and early 1980's will be constrained to operate in the hostile energetic radiation environments surrounding and constantly impinging on near earth space. The very high energies of many of these radiations and the relatively thin shielding of the Space Station/Space Shuttle will expose crews, critical biological and electronic experiments and systems to a constant bombardment of charged and neutral particles, and X-rays. The real time and time historical profiles of these radiations must be monitored on-board all spacecraft. Special problems are associated with the monitoring of space radiations that prohibit the use of presently available ground based systems. The space hardware must measure a much wider range of energies and particle types in operational situations that would never be demanded of an earth based system. This dictates that the hardware be highly complex, yet due to weight, power, volume, and recording and readout limitations imposed by spaceflight, many additional constraints will be associated with the space radiation monitoring instrumentation. In addition, space hardware must be specifically hardened to environmental specifications not usually considered in earth based operations. In this report are described a unique family of active and passive radiation sensors and electronics that will adequately monitor the radiation threat to Space Station and Space Shuttle crews and on-board systems. All instruments described in this report can be fabricated from existing state of the art radiation detection technology.

SUMMARY OF EXPECTED RADIATION ENVIRONMENTS AT SPACE STATION/SPACE SHUTTLE OPERATING ORBITS

The Space Station/Space Shuttle flights will encounter two general types of radiations that will be of dosimetric and spectroscopic concern to their operations. Classed according to origin these are:

1) Naturally Occurring Radiations
2) Manmade Radiations

The naturally occurring radiations of operational interest are 1) the trapped electrons and protons of the Van Allen Belts; 2) energetic solar flare protons and alpha particles; and 3) protons, alpha particles, and multicharged heavy nuclei of galactic cosmic rays. The general geophysical characteristics of these radiations are well known (Ref. 1 through 11). The naturally occurring Van Allen Belt electrons have been measured with energies from a few kev to over 4.5 Mev. Protons of the Inner Van Allen Belt are observed to extend from below 10 Mev to over 600 Mev. Solar flare particles reach near earth space with energies from a few Mev to well over a Bev, depending on the nature of the accelerating mechanisms on the sun. Solar flare particle events are as of this writing unpredictable and are considered by many as the greatest hazard to manned spaceflight operations in near earth space. Cosmic rays range from below 0.1 Bev to over 10^{11} Bev. For the energy range of 500 Mev to 20 Bev, cosmic ray protons have been observed to follow the spectral law:

$$J(E) = \frac{0.3}{1 + E^{1.5}} \quad \frac{\text{particles}}{\text{Cm}^2 - \text{Sec.}}$$

(Ref. 13).

The manmade radiations encountered in spaceflight are: 1) the artificial fission spectrum

trapped electrons of the Inner Van Allen Belt, 2) potential nuclear reactor sources associated with the Space Shuttle and Space Transport, and 3) other on-board radioactive sources required to operate spacecraft and on-board experimental systems. The current fluxes of electrons in the earth's artificial radiation belts were created in 1962 by United States and Soviet high altitude nuclear weapons detonations that produced high fluxes of trapped fission spectrum electrons, (Ref. 14). These were superimposed on the natural electrons already present in the Van Allen Belts in 1962. A typical series of artificial electron spectra of the Van Allen Belts are shown in Figure 1 (Ref. 14). The flux levels of artifically injected electrons in the earth's radiation belts are subject to constant decay (Ref. 15) and at this writing have become comparable to the natural electron fluxes. If no further electrons are artifically injected into the radiation belts, by the time that the Space Shuttle is flown, these so called "Starfish Radiations" will be of little concern to operations. However, Figure 2 (Ref. 16) predicts that the flux levels at 400 Km from a nuclear weapon of 4 Megatons will be at least 10^8 electrons/Cm^2-Sec. (1.0 < E < 2.0 Mev). With electron fluxes of this magnitude possible, hardware designed for the Space Station/Space Shuttle must include contingency procedures to measure artificial electron fluxes of this nature in the event of hostile action. It is uncertain at this time if nuclear reactors will be flown on the Space Station or Space Shuttle. In the event that they are flown, specific sensors to monitor the neutron and gamma components of reactors must be developed. High neutron fluxes such as produced by reactor operations are not ordinarily encountered in spaceflight. The intensity of neutrons produced in the earth's albedo, in the spacecraft mass, or directly from the sun are negligible compared to the primary charged particle radiations or to the neutron fluxes that would be produced in a spaceborne reactor. The flight of a nuclear reactor in

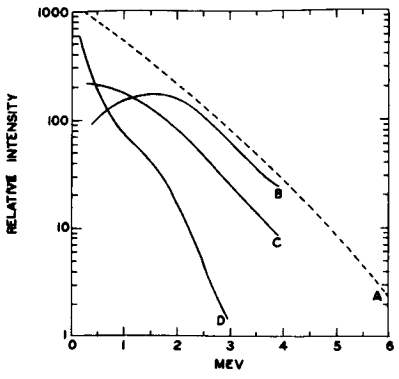

Figure 1. Selected Electron Energy Spectra for the Starfish Electrons. Curve A is the Equilibrium- Fission Spectrum, Curve B is Measured at L= 1.25, Curve C is Measured at L= 1.34, and Curve D is Measured at L= 1.57. All Measurements Dec. 1962.

conjunction with any future manned space mission would increase the radiation exposure as well as result in the need for a larger array of radiation monitoring instruments. The type and number of on-board radiation sources that may be used on the Space Platform and associated flights cannot be accurately determined at this early date, however, if we take the present Apollo and Skylab Programs as representative spaceflights, there are many beta and gamma emitters that the crew could come into contact with. In most cases though, the on-board sources on either of these present space programs are of very low energy or activity or are located at a great enough distance or behind sufficient shielding that they provide negligible doses to the crew or other critical systems. The types of on-board sources flown to date can easily be monitored by instruments already designed to measure the natural space radiations.

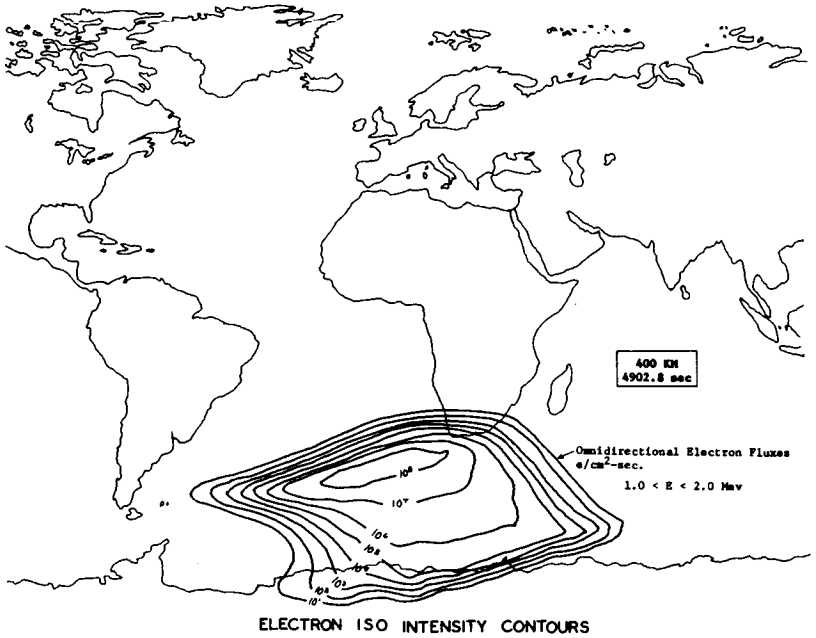

Figure 2. Predicted Artificial Electron Fluxes in the South Atlantic Anamoly.

The expected dose levels from the natural and manmade trapped radiations in the Van Allen Belts has been calculated, (Ref. 17) for selected orbital altitudes and inclinations using different possible shields from 0.0001 grams/cm^2 to 10 grams/cm^2. Table 1 summarizes these calculations.

TABLE 1

Dose Calculations for Selected Shielding Depths (g/cm^2 aluminum) and Various Orbital Parameters for the Space Platform, Doses in Rad/day.

Orbital Parameters		Shielding Thickness (Uniform Cylindrical)					
Altitude	Inclination	.0001	0.4	1.0	2.0	5.0	10.0 (g/cm^2)
320 Km.	55°	3 x 10^5	3.30	.65	.13	.022	.006
320	70°	2.5 x 10^5	2.72	.53	.10	.017	.0045
320	90°	2 x 10^5	2.47	.47	.086	.015	.004
480	55°	10^6	2.02	3.94	.74	.17	.09
480	70°	10^6	16.7	3.10	.57	.13	.07
480	90°	10^6	14.3	2.70	.51	.12	.067

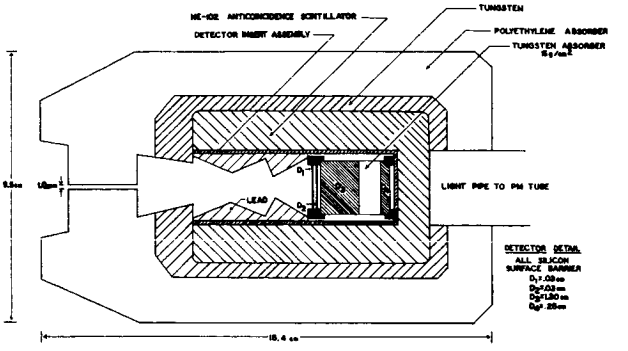

ELECTRON, PROTON, ALPHA, AND MULTICHARGED PARTICLE DIRECTIONAL SPECTROMETER TELESCOPE

SPACE RADIATION MONITORING SYSTEMS

Instruments described in this report are classified as either external or internal to the Space Platform. The external sensors measure the flux and spectra of energetic electrons, protons alpha particles, and higher Z multicharged particles. Both directional and omnidirectional detectors are required to define the physical characteristics of space radiations. The second group of instruments proposed are internal to the space vehicle. They measure both dose and particle energy plus linear energy transfer spectra. This class of instruments are in some cases mounted in the spacecraft, or may be when required worn on the astronauts' person for monitoring internal or external to the spacecraft.

Directional and Omnidirectional Charged Particle Spectrometers

It is possible with recent advances in micro and integrated circuitry to combine both directional electron and proton measurements into a single system. We have flown and examined the results of many other charged particle spectrometers designed since 1961. Based on performance in flight of the various instruments, the use of multidetector solid state sensors provides the most accurate and reliable Space Platform directional electron and proton measurements. We propose the use of the multiple charged particle telescope arrangement shown in Figure 3, to conduct directional measurements of charged particles both in the Van Allen Belts and from solar flare particles. This telescope assembly was modified by the authors from an original solid state space radiation monitoring system developed by Ref. 18. Extensive changes in detector design were performed by the authors following flights of the instrument on unmanned Air Force Van Allen Belt satellites over the past several years. These include new state of the art, solid state detectors, the inclusion of an additional anticoincidence scintillator to prevent unwanted particles from entering the sides and back of the detectors, and the replacement of the original beryllium electron collimator with polyethylene which is more suitable for manned spaceflight. The electronics of this system have been completely revised to include the best available energy discriminators, low noise power conversion system, and signal conditioning amplifiers. The electronic block diagram for this system is shown in Figure 4. This solid state system is designed to achieve a high level of refinement in particle type and energy analysis, a narrow angular acceptance cone (less than 6°), and excellent time resolution. This provides outstanding charged particle resolution in any earth orbit to be flown by the Space Station or Space Shuttle. Readily measured are high levels of radiation including relativistic solar flares, natural and artificial trapped Van Allen Belt particles and cosmic rays. In its present configuration this system measures the following particle types and energy ranges.

Electrons:	0.25 to 0.60, 0.70 to 0.80, 1.0 to 1.2, 1.5 to 1.8, 2.5 to 3.0, 4.3 to 4.8, and greater than 4.8 Mev.
Protons:	10.5 to 15, 15 to 24, 24 to 40, 40 to 56, 56 to 80, 80 to 113, 113 to 150, 150 to 200, 200 to 320, and greater than 320 Mev.
Alpha Particles:	11 to 30, 30 to 70, 70 to 113, 113 to 300, and greater than 300 Mev.
Heavy Nuclei:	Two groups with ranges in Tungsten of 0.25 to greater than 20 g/cm^2.

The solid state directional telescope is designed to be mounted external to the space vehicle. It may be mounted close to the main body of the structure or on a boom. This system will provide the essential particle identification, energy discrimination, and pitch angle distributions for trapped particles, as well as solar flare and cosmic ray particle fluxes required for evaluation by

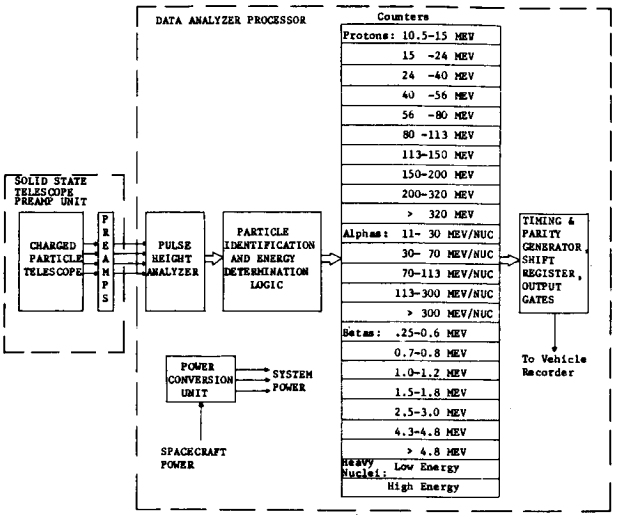

Figure 4, Directional Multicharged Particle Spectrometer System Block Diagram.

on-board or ground based computers to provide internal dose data or radiation hazard data during extra vehicular activity.

In addition to measurements of the directional properties of space radiations, it is required that the omnidirectional energy spectra and fluxes of particles be well known to allow for a complete evaluation of the operational hazards. The omnidirectional spectrometer has been flown extensively in the past decade to measure the earth's Van Allen Belt radiations. The authors propose that at least one omnidirectional spectrometer system be flown on the Space Platform. Two basic systems have been designed and either may be used depending on the orbit flown. One omnidirectional system employs $1mm^3$ or $2mm^3$ solid state detectors shielded by hemispheres of varying thickness to provide the desired energy cutoff. A minimum of eight (8) individual sensors varying in thickness from 0.112 g/cm^2 to 50 g/cm^2 will define the spectral range of interest. Typical sensors for this omnidirectional system are shown in Figures 5 and 6. The electronic block diagram for the omnidirectional system is displayed in Figure 7. This system has been successfully breadboarded in the laboratory and employs the best available state of the art integrated microcircuits throughout. The energy and particle ranges measured by this spectrometer are:

Electrons:	Five Energy Levels:	0.37 to 1.0, 1.0 to 2.2, 2.2 to 4.0, 4.0 to 9.5, and greater than 9.5 Mev.
Protons:	Eight Energy Levels:	10 to 20, 20 to 34, 34 to 50, 50 to 72, 72 to 120, 120 to 170, 170 to 200, and greater than 200 Mev.
Alpha Particles:	Eight Energy Levels:	34 to 75, 75 to 125 125 to 190, 190 to 275, 275 to 470, 470 to 600, 600 to 1000, and greater than 1000 Mev.

TYPICAL OMNIDIRECTIONAL HIGH ENERGY ELECTRON, PROTON, AND ALPHA PARTICLE SPECTROMETER SENSORS

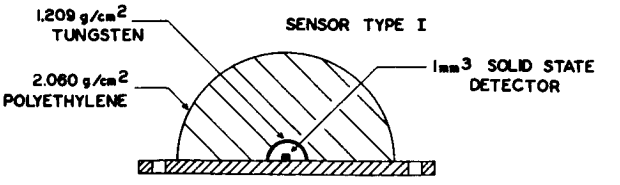

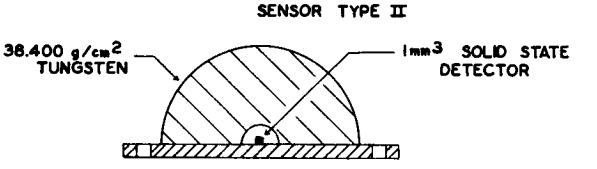

Figures 5 and 6.

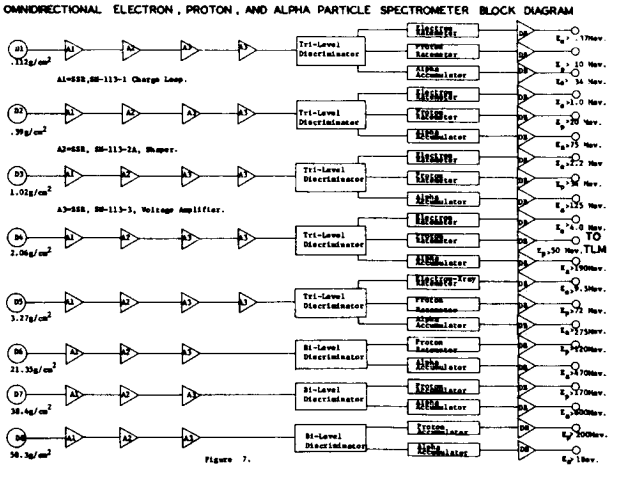

Figure 7.

This omnidirectional spectrometer functions well in the presence of relatively high fluxes of particles due to the small geometric factors of the sensors. If the expected fluxes of particles are low, sensors such as shown in Figure 8 after a design proposed in Ref. 19, would be more suitable. This instrument employs either 0.5 cm^2 or 1 cm^2, 2000 micron fully depleted silicon detectors instead of the previously described $1mm^2$ or $2mm^2$ detectors and allows for a much larger geometric factor when low particle fluxes are encountered. The electron sensor for this system employs 217 small radial collimators in the shielding material to prevent electron saturation. Comparative weights and dimensions of the two systems are approximately the same. The omnidirectional spectral range measured by this spectrometer is also the same as previously described. If a hemispherical shield design is employed great care must be taken to insure that the sensors are mounted on plates whose thickness over the 2π solid angle at the backside considerably exceeds the thickness of the sensor hemispherical shielding. If a hemispherical design is flown, it is likely to be hard-mounted to the external of the spacecraft where the primary structure shielding can be taken advantage of on the backsides of the detectors. An alternative system would be the full spherical shields over the sensors as shown in Figures 9 and 10. These may be boom mounted so that a full 4π steradian instead of a 2π steradian measurement can be conducted. Where the spacecraft shielding is very thin, the heavier 4π detectors might be also mounted directly to the spacecraft without notable effect on the shielding of the sensors. This eliminates difficulties encountered with mounting the heavier sensors on a boom.

OMNIDIRECTIONAL ELECTRON SPECTROMETER SENSOR

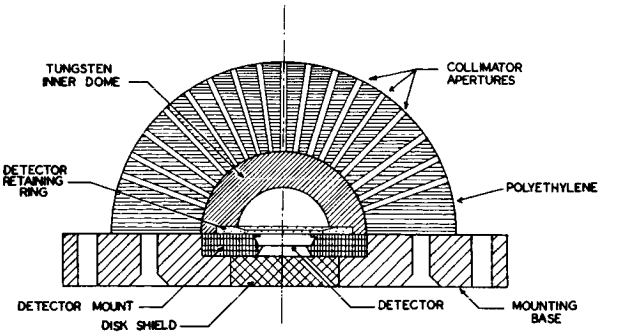

Figure 8b.

SPHERICAL 4π OMNIDIRECTIONAL SENSOR

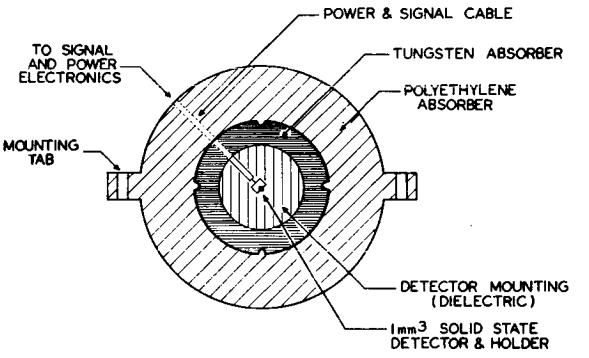

Figure 9.

OMNIDIRECTIONAL PROTON SPECTROMETER SENSOR

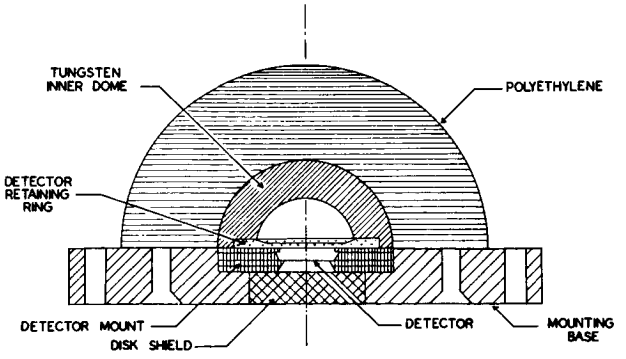

Figure 8a.

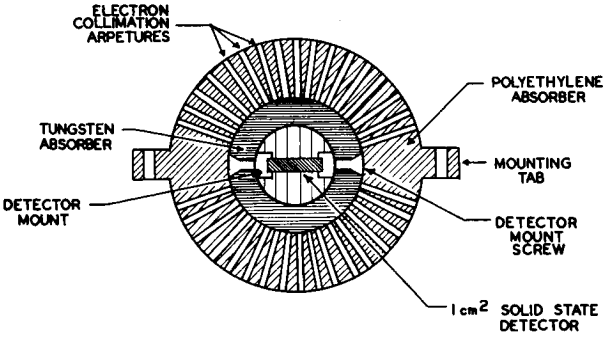

Figure 10. Spherical 4π Omnidirectional Electron Sensor

PARTICLE WARNING SYSTEMS

Since the Space Station may operate in solar flare environments and artificially injected electrons external on-board warning systems to alert the astronauts of the onset of such unexpected radiations, as well as insure the turn on of other required radiation monitoring instruments will be very important. Such a warning system would of necessity have two separate functions: 1) to detect the presence of energetic (E > 30 Mev) protons in the absence of significant high energy (E > 2 Mev) electrons and 2) detect appreciable increases in the electron fluxes in the earth's Van Allen Belts over the quiescent or natural background levels. Figure 11 indicates a conceptual solar flare and artificial electron enhancement detection system for use on the space station. This system as shown in Figure 11 has separate sensors from the omnidirectional spectrometer. However, the cost of the instrument could be greatly reduced by employing several of the lower energy omnidirectional charged particle spectrometer sensors previously described with a separate electronics system.

Large time of flight neutron spectrometers are under development by White, (Ref. 20). This system uses liquid scintillation detectors in a time of flight arrangement as shown in Figure 12 to measure the very low primary solar and earth albedo neutron fluxes. This system is a satellite consisting of its own self contained signal conditioning and processing electronics. The use of this system on the Space Station would greatly increase the range and resolution of particle measurements. With this type of device it may be possible to predict in advance the arrival of solar protons by measuring the prompt neutron spectrum from the sun. This system is currently being developed for flight test this year and should be fully operational for possible use in conjunction with the Space Station/Space Shuttle. This system could be attached to the Space Platform or flown in co-orbit with it. The neutron spectrometer would be incorporated as part of the solar flare warning system when the flux of neutrons reaches a pre-determined level. Such levels are as of this writing unknown. It is hoped that flights of this system before the Space Station/Space Shuttle will establish the solar neutron flux levels associated with proton events. If this is done, it is likely that the shape of the proton spectrum, as well as the particle flux emitted in a solar flare can be determined from measurements of the neutron fluxes in advance of the arrival of particles.

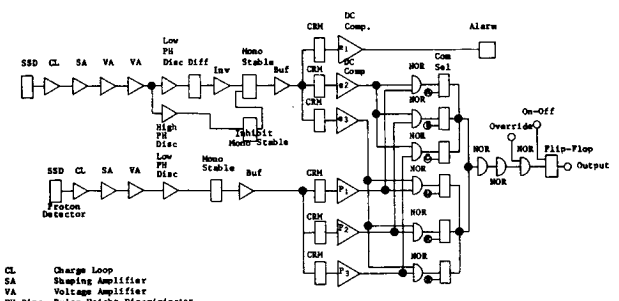

CL Charge Loop
SA Shaping Amplifier
VA Voltage Amplifier
FH Disc Pulse Height Discriminator
NOR Dual Input NOR Gate
CRM Count Rate Meter (Capable of 10^5 counts at 5V.)
SSD Solid State Detector
DC Comp DC Level Comparator

Figure 11. Solar Flare/High Intensity Electron Detector Functional Block Diagram

INTERNAL SPACECRAFT DOSIMETRY AND SPECTROSCOPY

Portable Radiation Monitor

The maximum allowable radiation doses to an astronaut for a 30-day mission have been defined for the Space Station (Ref. 21) and are presented in Table 2. Although the unavoidable mission-related doses to the astronauts are expected to be more than an order-of-magnitude below this, situations could arise in which one or more astronauts must receive doses near the acceptable maxima. Situations in this category include: extravehicular activity (EVA) during passage through the magnetic anomaly, repair or maintenance of equipment containing or in proximity to radiation sources (SNAP units, instrument radioisotopes, possibly a nuclear reactor), and solar flare proton events. In such cases, the radiation safety of the astronauts who assume the extra risk can only be assured by an "active" (i.e., read-out in real time) dosimeter carried on the astronaut's person. The criteria for such a device are as follows: 1) it must be self-contained, small, and portable, 2) total dose should be accumulated up to at least 100 rad, 3) dose-rate should be indicated so that the astronaut can take steps to minimize his exposure, 4) it should be accurate at low dose-rates, viz., so that it can record a dose of only 2.5 rad accumulated over a span of 24 hours (order of 0.1 rad/hour), 5) accuracy is critical at maximum dose-rates, viz., maximum dose of 75 rad reached in only a couple of minutes (order of 2000 rad/hour), 6) can measure surface doses (0.4 g/cm^2), 7) relays dose and dose-rate information to the central radiation monitoring system, and 8) measures the true radiation absorbed dose in a mixed field (protons, electrons, X- and gamma rays, neutrons, heavy charged particles).

TABLE 2

Radiation Exposure Limits* for Space Station Crew (30-Day Mission) for Ancillary Reference Risks.

Depth		Dose
Skin	(0.01 Cm)	75 REM
Eye	(0.3 Cm)	37 REM
Marrow	(5.00 Cm)	25 REM

*See Reference 21.

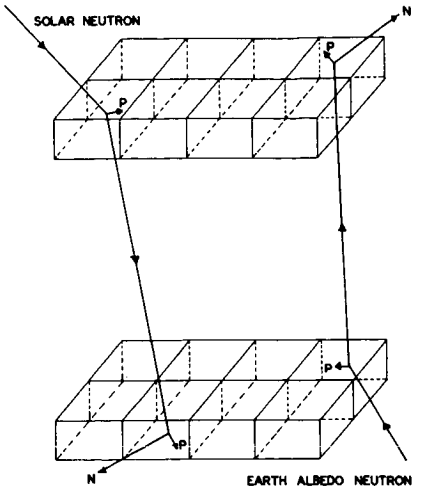

Figure 12. Large Time of Flight Neutron Spectrometer

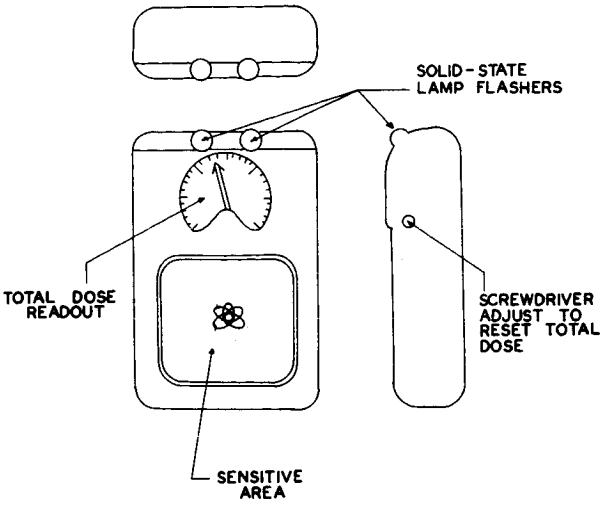

Figure 13. Astronaut Radiation Monitoring Instrument (ARMI).

To satisfy the above requirements, an Astronaut Radiation Monitor Instrument (ARMI) has been designed using presently available technology and techniques.

The device is similar in size, weight, and basic operating principle to the Personnel Radiation Dosimeter (PRD) used on Apollo flights (Ref 22) but incorporates several improvements and added features, including advanced circuitry, better collection geometry for the ionization chamber sensor, human-engineered total dose read-out, dose-rate indication, and telemetered output. The ARMI device is portrayed in Figure 13. It is intended to be small and streamlined to easily be accomodated in a pocket in the astronaut's spacesuit or underwear garment. At the same time, it is large enough to be easily held and manipulated with a gloved hand. Accumulated dose is read out to the astronaut via a meter having a pseudo-logarithmic scale divided into three color-coded sections: green, 0 to 1 rad; yellow, 1 to 10 rad; red, 10 to 200 rad. The radiation level is indicated by two solid-state lamps whose flash frequencies are directly proportional to dose-rate. Two flashers extend the observable dose-rate range by having one lamp flash at only one-tenth the rate of the other. Thus, at the upper dose-rate limit of 3,600 rad/hour, one lamp will pulsate at 10 pulses/second while the other lamp appears fully on at 100 pulses/second. On the other hand, at a lower dose-rate, say 36 rad/hour, the lamps will flash at rates of one-tenth and one pulse/second, respectively. Such indications are sufficient to enable the astronaut to minimize his exposure through adjustment of location, position, and/or shadow shielding. Monitoring of the astronaut's accumulated dose by other crew members and by ground control is accomplished by transmitting a low-power pulse from the ARMI to suitably-located receivers in the Space Station each time another 0.01 rad dose has been accumulated. Since several ARMI's may be in use simultaneously, the pulse from each unit will be uniquely coded in waveform for identification. Received pulses are then processed at the central radiation safety monitoring subsystem and accumulated dose information stored and displayed for each ARMI in operation. The subsystem also will contain computing circuitry for determining dose-rate by measuring the time between successive 0.01 rad pulses. It also will compute and display the remaining permissible exposure time from the ARMI accumulated dose and dose-rate information plus a maximum permissible dose manually entered by the radiation safety officer.

The radiation-sensing element in the ARMI is a parallel-plate tissue-equivalent ionization chamber whose gas volume is shielded from one face of the instrument by only 0.4 g/cm^2 of material (outside housing plus one electrode). The parallel-plate geometry and small interelectrode gap allows a collection efficiency of over 95% in a field of 3,000 rad/hour with only a 10 V bias. The ionization current from the chamber is integrated by an electrometer circuit which operates in the "recycling coulometer" mode. Figure 14, is the block diagram outline of the circuit operation. The circuit is accurate over 4 1/2 decades of dose-rate, covering 0.1 to 3,000 rad/hour. All circuitry is of the low-voltage, micropower type recently developed for battery-powered instruments. The total dose-readout is a mechanically-advanced pointer, so that no standby power is required to maintain a reading. This, the chief power drain occurs during each recycling pulse, when the pulse must be flashed and transmitted. Sufficient long-life mercury batteries are sealed into the unit to provide four months of operating life. Thus, the ARMI is always "ON" and alert. It is not required that the astronaut activate a switch for its use, although if desired, the mechanical pointer can be reset to zero using a screwdriver adjustment. This allows the device to be used repeatedly by different astronauts.

Ultra-Sensitive Dosimeter

A compact (six-inch diameter) tissue-equivalent dosimeter has recently been developed (Ref. 23) for measurement of dose-rates below 1 rad/hour, with sensitivity down into the tens of microrad/hour. Such a dosimeter could serve as an accurate monitor of cosmic ray doses and inside levels of penetrating Van Allen Belt protons and electron bremsstrahlung. This instrument is light-weight, low-power, and fully flight-qualified.

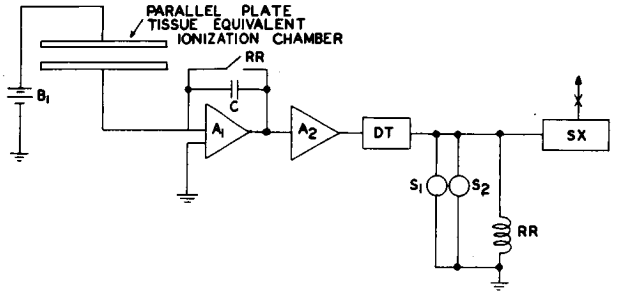

Figure 14. Electronic Block Diagram of the Astronaut Radiation Monitoring Instrument .

Determining the Quality Factor

Assessment of radiation hazard to an astronaut requires knowledge not only of the absorbed dose, but as well as the time course of delivery, the distribution of dose throughout the body (especially as pertains to the gastro-intestinal and blood forming organs), and the specific ionizing power (linear energy transfer, LET) of the radiation. Proper allowance for all of the above factors is, in itself, an exceedingly difficult task. The physical measurements alone are quite formidable in the space environment. Indeed, due to the many uncertainties involved, the best policy remains to prevent all avoidable exposures to ionizing radiation. Nonetheless, as pointed out previously, some exposure is unavoidable, and in addition, emergency actions may require additional exposures. Active and passive dosimetry and radiation monitoring systems are mandatory. The full evaluation of the effect of an exposure likewise requires data on the depth-dose distribution and LET spectra. Ideally, these would be measured on-board, during exposure. This is very impractical, however, since depth-dose distributions require large phantoms containing multiple dosimeters and no space-qualified instruments have as yet been flown for extended missions in space for measuring the LET spectra in mixed radiation fields. Concerning the latter problem, several instruments may hold promise for providing at least partial solutions to the LET problem: 1) the AFWL has recently developed a LET spectrometer for measuring proton and alpha LET spectra (Skylab Experiment D008), 2) the Rossi spherical proportional counter (Ref. 24) has been ruggedized, sealed, and flown with some success on high-altitude aircraft (Ref 25), and 3) a multiplying ionization chamber with electronic analysis of the mean square fluctuation of output has been demonstrated (Ref.26) for semi-quantitative determination of quality factor due to LET differences in mixed neutron-gamma ray fields.

Two additional combination dose and linear energy transfer spectrometer sensors have considerable promise for flight internal to the Space Platform. One system consists of a triaxis solid state detector telescope arrangement to measure the lower energy (higher LET components) of radiation entering the Space Station. The other system consists of thin scintillating tissue equivalent plastic plates less than 25 microns thick or small less 100 micron diameter spheres to measure the linear energy transfer spectrum as well as the dose rate received internal to the spacecraft.

The charged particle telescope shown in Figure 15 consists of four solid state detectors arranged to accept protons, alpha particles, and other multicharged heavily ionizing particles. The system employs a thin, less than 20 micron, planar dE/dX detector and a 0.5 cm stacked silicon surface barrier detector. An annular detector and a 2000 micron totally depleted surface barrier detector are included to perform system anticoincidence. The electronic block schematic for this system is displayed in Figure 16. The solid state spectrometer measures particles with dE/dX from 3.5 to 100 Kev/micron. The deployment of this system in a tri-axis arrangement will provide an average or omnidirectional LET spectrum interior to the spacecraft. However, spectral data are limited to charged particles. We would propose in the interest of cost that this system be made semi-portable for use in any desired location in the spacecraft. The sensor could be attached to one of a number of hard-mounted inputs at various station locations and the signals processed by a central electronics system and relayed to ground and/or on-board computers for analysis and display.

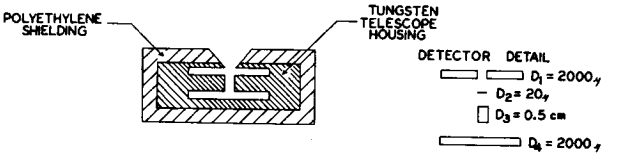

SOLID STATE DETECTOR LET SENSOR

Figure 15.

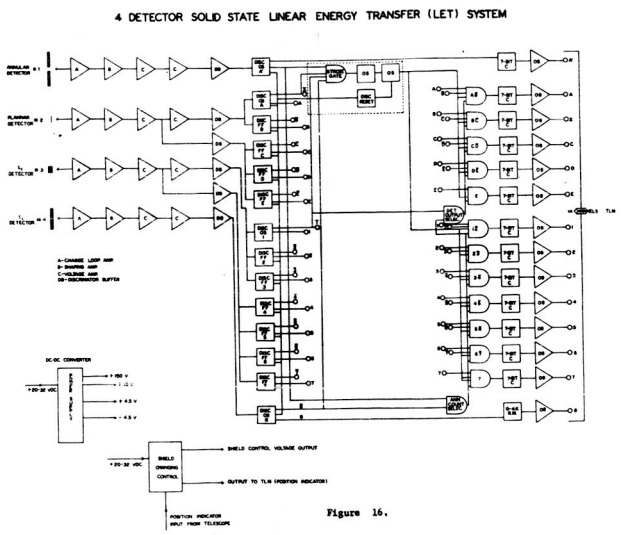

Figure 16.

location measurements. LET measurements are made in eleven channels from .22 Kev/micron to greater than 130 Kev/micron. This range could be easily extended on the high end by minor electrical modifications to the system. The microscintillators are by virtue of their tissue equivalenty excellent mixed field detectors but lack the excellent charged particle pulse resolution of the previous solid state detector system.

As an alternative to considering the inclusion of phantoms or LET spectrometers, it may be sufficient for protection purposes to conduct suitable studies of these factors on the ground. The radiation fields from the on-board radiation sources can be characterized very thoroughly by appropriate ground studies. Space radiation is presently well understood qualitatively, which places limits on possible depth-dose and LET distributions. By incorporating results of the on-board radiation environment spectrometers (omnidirectional and unidirectional) as previously described, it may be possible to quite satisfactorily estimate quality factors directly from a knowledge of the type of exposure and measured level in rad.

The scintillating dose system has been developed and flown (Ref 27). It consists of either of two basic sensors. One sensor, Figure 17, employs a less than 25 micron NE-102 scintillating plate to measure the dE/dX of all particles producing ionization in the plate. This sensor can be used in either a 2π or highly collimated shield to provide omnidirectional or directional data on the radiation received by the crew. The other sensor employs small, less than 100 micron, spheres to provide the desired LET measurements. This latter system can also be either a directional or omnidirectional device depending on the degree of collimation chosen around the sensor. This system can (as suggested by Ref 26) be employed to measure cellular hit frequency to provide additional radiobiological data of interest to the crew and biological experiments and on-board systems. The two scintillating systems share common, signal conditioning electronics shown in Figure 18. Either of the microscintillating LET systems can have semiportable sensors for multi-

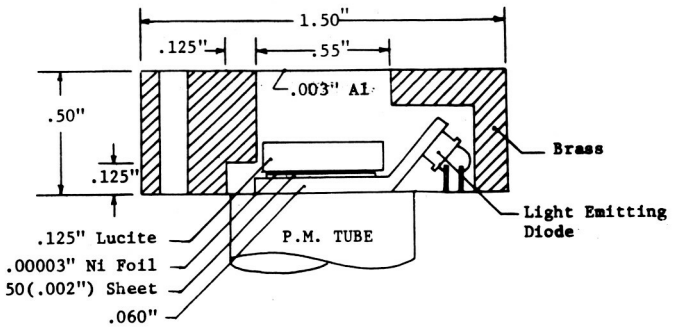

Figure 17. Thin Plastic Scintillating Plate Linear Energy Spectrometer Sensor.

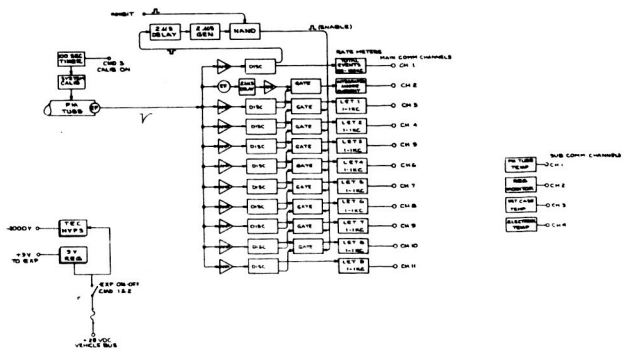

Figure 18. Microscintillator LET Electronic Block Diagram

PASSIVE DOSIMETRY SYSTEMS

Thermoluminescent Dosimetry Space Package

The need for a space radiation dosimeter which would be sensitive to charged particle radiations and also be responsive to thermal and fast neutrons has been the goal of scientific investigators for the past decade. New packaging techniques and greater sophistication of electronic instrumentation have increased the probability of securing a dosimeter with required sensitivity and adequate energy response. The ideal dosimeter is suitably accurate over a wide neutron energy spectrum and at the same time responsive to radiations such as gamma, high energy betas, protons, alphas, and X-rays of various energies.

If this dosimeter is to be utilized in the space program, additional points of interest must be considered. This instrument is rugged but light in weight, has no sharp edges or protruding connectors, and is small enough in size to fit comfortably into a special pocket on the astronaut's space suit. Astronaut identification and calendar date coding during readout are necessities for accurate data storage. All the above have been incorporated into the TLD system, Figure 19, which is proposed as a bio-radiation space package which meets the requirements for extended durations of planned space missions.

The TLD Space Package contains either two or three envelopes made of borosilicate glass. The filaments are nicrome ribbon which are finished and spot welded to the heating electrodes. The filament and TLD rough finishes, combined with the retainer clip tension, provide a large resistance to the TLD chip (Lithium fluoride bars). The glass envelopes shown in Figure 19 may be as small as 5/16" in diameter and 3/4" in length, which makes the complete dosimeter package less than 1 1/2" x 2" x 3/4". The filaments and identification code terminals are flush mounted receptacles as shown in the single glass envelope dosimeter, Figure 20.

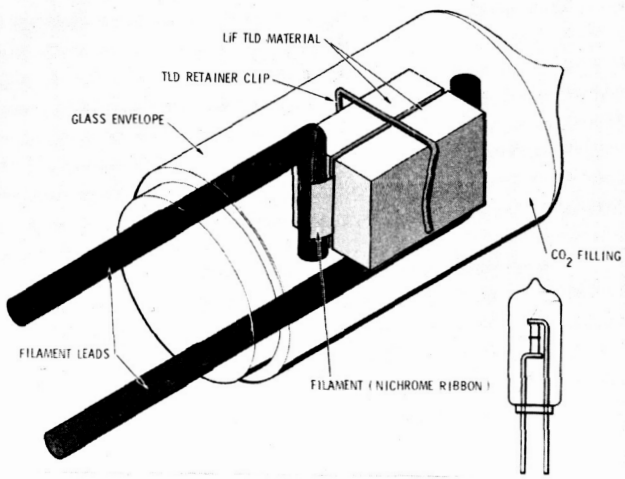

LITHUM FLUORIDE THERMOLUMINESCENT DOSIMETER

Figure 20.

During extended space flights such as those in conjunction with the use of a Space Platform, data processing readout and storage capability necessitates an integrated system as indicated by Figure 21. By use of the bio-radiation packet and onboard readout system, the irradiation exposures

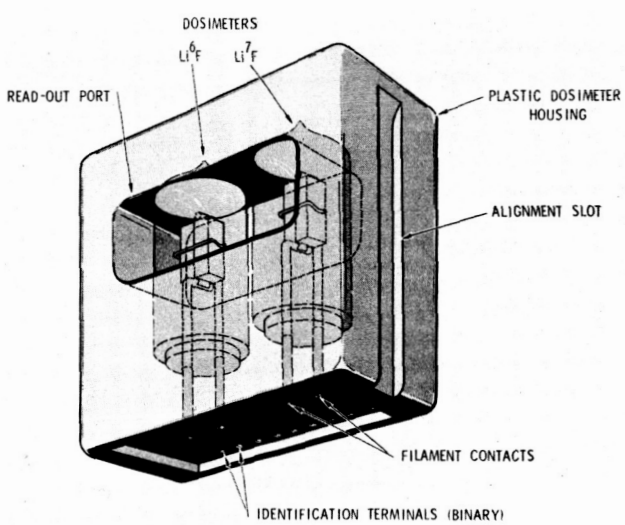

THERMOLUMINESCENT DOSIMETER SPACE PACKAGE

Figure 19.

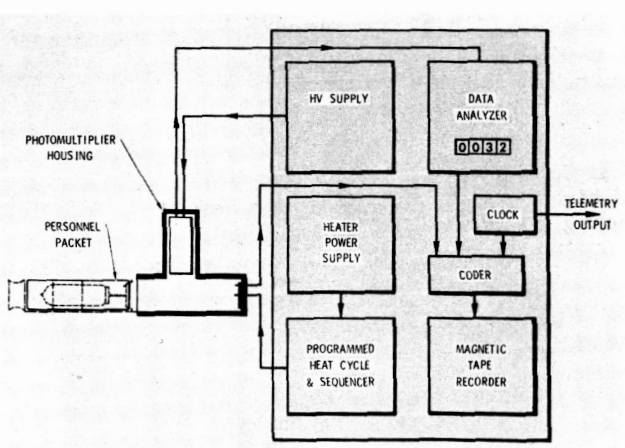

DATA PROCESSING READOUT AND STORAGE

Figure 21.

caused by any of the anticipated sources can be automatically calculated, visually read out, recorded, dated, and personally coded for each astronaut by the identification coder. The Programmed Heat Cycle and Sequencer will provide the astronauts with a newly activated, ready to use dosimeter capable of measuring all expected radiation exposures.

Responses from both thermal and fast neutrons have been studied by E. Tochilin and et. al., (Ref 28). Since the ^{6}LiF has an extremely high cross section for thermal neutrons (945 barns) and ^{7}LiF has a negligible cross section, one can measure simultaneously gamma and neutron exposures. (Ref 29) This dosimeter functions as a satisfactory system since the TLD's have a response that is relatively independent of storage time (at cabin or crew area temperature) between exposure and readout. The accuracy for dose determination is greater than 93%. Additional dosimeters contained within 5 centimeter thick tissue equivalent shields could be placed as monitors throughout the work area such that data need not be extrapolated as one compares read out parameters with the guidelines expressed by the Radiobiological Advisory Panel Committee on Space Medicine 1970 (Ref 30).

Foil Activation Counting With A Liquid Scintillator

Foil activation analyses for determining both neutron energies and neutron fluxes as described by H. M. Murphy (Ref 30) have been standard laboratory procedures for the past two decades. However, during the recent years great advancements have been made in the equipment and instrumentation relative to scintillation counters. Since certain metallic foils are responsive to a specific neutron energy range, an array of foils is used to detect the energies of interest. Two methods for counting are proposed; first, the foils may be returned following a space flight and counted as indicated above in ground based laboratories; or secondly, liquid scintillation counting vials could be fabricated prior to flight with the fluors plus foils which had been sealed and prepared for counting. As the foils are exposed to an unknown neutron flux they are read out immediately to give not only an integrated dose but also dose rate. The latter assumes capability for counting in a space laboratory or modification of existing experiments to accomodate such samples by vial exchange mechanisms activated in the event of a solar flare, in maintenance periods should a nuclear reactor malfunction, or for extra-vehicular activities during the passes near or through the magnetic anomalies (especially if high altitude nuclear detonations were initiated during the space flight). Having the scintillation counting vials prepared prior to launch has one great advantage over the returning of foils to ground based laboratories for counting since one can register the maximum number of counts from the activation process before they have had a chance to decay. Computer programs will have to be a part of the readout system to subtract the decay events such that new exposures may be expressed and current dose rates displayed on the visual screen. Generally, after the activated foil has decayed greater than five half lives, counting efficiencies and statistics are extremely low.

Rather than the use of a liquid fluor in the scintillation vial one may substitute a solid scintillator and in this way give more "ruggedness" to the system. However, at this time, the liquid scintillation process appears to be the most promising.

Modification of Discharge Ionization Chamber

With the increased demand for biomedical instrumentation and space suit complexity, one strives to reduce the size and weight for the essential items which are proposed to be contained on or within the astronaut's space suit or working garments. The pocket type dosimeter, Figure 22, has been modified to 1/3 its original length and weight without loss of accuracy. A readout system is proposed to be incorporated into the bench type console unit within the space laboratory such that the astronauts will have access to the reader on periodic checks. Since the reader system will be a necessity for radiation exposure determination, a record of this information will be automatically stored on tape with a date and astronaut identifier posted during readout. Two dosimeters of this type should be included within the space suit at all times. The combined size of coupling two of the modified dosimeters would be smaller than one of the present units. The only changes in design for the modified dosimeter are the removal of the optics and placing them in the console readout system with the coding and clock mechanisms. The sensitivity and maximum accumulated dose indicated by the readout system are comparable to the presently used dosimeter which is designed for maximum full scale readings to match the mission profile.

Using the same reader and charger system, the astronauts have similar dosimeter cartridges to measure not only gamma plus faster neutrons but also units to determine thermal neutron exposures or gamma plus X-ray exposures. The feature which permits differentiation among types of radiation is the wall material of which the ionization chamber is made. For example, to develop a dosimeter which is insensitive to neutrons but sensitive to gammas, one would include an ionization chamber wall material in which the elemental hydrogen content is less than two percent. The insulating material surrounding the ionization chamber is also to be nonhydrogenous. The Skylab Pocket Type Dosimeters have a full scale reading of 5 rads but this may be redesigned to read 25 rads, 50 rads or higher if required.

By including the two bio-radiation type dosimeters (TLD and small ionization chamber) plus the on-board liquid scintillation counting system for neutron dose analyses, one has many of the parameters needed to calculate not only the radiation absorbed dose in man but also valuable data to assess radiation effects on other spacecraft systems.

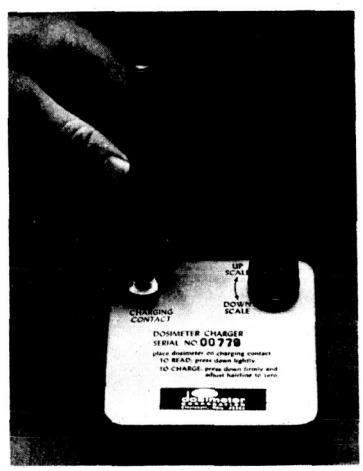

Figure 22. Discharge Ionization Chamber and Charger

REFERENCES

1. Hess, W.N., The Radiation Belts and Magnetosphere, Bliesdell Publishing Co. Waltham, Mass., 1968.

2. O'Brien, B.J., Review of Studies of Trapped Radiation with Satellite Bourne Apparatus, Space Science Reviews (C. DeJager ed.), Reidel Publishing Co., Dordrecht, Holland, 415-418, 1962.

3. White, R.S., The Earth's Radiation Belts, Physics Today, 19: 25-38, 1966.

4. McIllwain, C.E., The Radiation Belts, Natural and Artificial, Science, 142: 355-361, 1963.

5. Fillius, R.W., Trapped Protons of the Inner Radiation Belt, Journal of Geophysical Research, 71: 97-123, 1966.

6. Vette, J.I., Models of the Trapped Radiation Environment, Volume I, Inner Zone Protons and Electrons, Volume II, Inner and Outer Zone Electrons, NASA SP-3024, 1966.

7. Webber, WR., Time Variations of Low Rigidity Cosmic Rays During the Sunspot Cycle, Progress in Elementary Particle and Cosmic Ray Physics, Vol. 6, (Wilson and Wouthuysen editors.) North Holland Publishing Co., Amsterdam, 1962.

8. Carmichael, H., High Energy Solar Particle Events, Space Science Reviews, 1: 28-61, 1962.

9. Frier, P.S. and Webber, W.R., Exponential Rigidity Spectrums for Solar Flare Cosmic Rays, Journal of Geophysical Research, 68: 1605 - 1629, 1963.

10. Linsley, J., Evidence for a Primary Cosmic Ray Particle with Energy of 10^{20} ev, Physical Review Letters, 10: 146-148, 1963.

11. Ormes, J.F. and Webber, W.R., Measurements of Primary Proton and Helium Spectra and Their Modulations Using Balloon Borne Cerenkov Scintillation Counter, Proceedings of the Ninth International Conference on Cosmic Rays, London, 1965.

12. Winckler, J.R., Primary Cosmic Rays, Radiation Research, 14: 521-539, 1960.

13. Neher, H.V., and Anderson, H.R., Cosmic Rays at Balloon Altitudes and the Solar Cycle, Journal of Geophysical Research, 67: 1309 - 1313, 1962.

14. West, H.I., et al., Spectra and Fluxes of Electrons Trapped in the Earth's Magnetic Field Following Recent High Altitude Nuclear Bursts, AFCRL Report, Interm Results of Radiation Measurements from Air Force Satellite 1962 BK 1963.

15. Bostrom, C.O., and Williams, D.J., Time Decay of the Artificial Radiation Belts, Journal of Geophysical Research, 70: 240-242, 1965.

16. Wiley, R., Private Communications, 1971, Calculations from Air Force Weapons Laboratory High Altitude Weapons Particle Injection Codes.

17. Hopkins, K., Private Communications, 1971, Computations from Air Force Weapons Laboratory Space Radiation Transport Codes.

18. Rinehart, M., Solid State Space Radiation Monitoring System, Final Report to the Air Force Weapons Laboratory, Kirtland Air Force Base, New Mexico, Philco Ford Corp., Under Contract AF29600-3498, 1965.

19. Burton, B.S., Design and Construction of an Electron Proton Spectrometer, Air Force Weapons Laboratory Technical Report, TR-65-186, August 1966.

20. White, R.S., Design of a Large High Resolution Time of Flight Spectrometer to Measure Neutrons, University of California at Riverside Final Report to the Air Force Weapons Laboratory under Contract F29601-69-C-0029, 1969.

21. Radiation Protection Guides and Constraints for Space Mission and Vehicle Design Studies Involving Nuclear Systems, National Academy of Sciences Special Publication, 1970.

22. Warren, C.S., and Lill, J.C., et. al., Radiation Dosimetry on the Gemini and Apollo Missions, Journal of Spacecraft, Vol. 5, p-207, 1968.

23. Lay, L.B., Private Communications, AVCO Corporation, Tulsa, 1971.

24. Rossi, H.H., and Rosenzweig, W., Radiology, Vol. 64, p-404, 1955.

25. Philbrick, R., Air Force Weapons Laboratory, Private Communications, 1971.

26. Bengtsson, L.G., Estimation of Dose Equivalent from Proportional Counter Current Variation, Annual Report on Research Project NYO-2740-6, 1969.

27. Chapman, M.C., et. al., Development of a Cellular Absorbed Dose Spectrometer, Air Force Weapons Laboratory Technical Report No. AFWL-TR-69-76, Kirtland AFB, New Mexico, December 1969.

28. Wingate, C.L., and Tochlin, E., and Goldstein, N., Responses of Lithium Fluoride to Neutrons and Charged Particles, Luminescence Dosimetry, USAEC, Oak Ridge, Tennessee, p-421-434, 1967.

29. Tochilin, E., and Shumway, B., Dosimetry of Neutron and Mixed Neutron Gamma Fields, Radiation Dosimetry, Vol. 3, Chapter 22, Academic Press Inc., New York, 1969.

30. Radiation Protection Guides and Constraints for Space Mission and Vehicle Design Studies Involving Nuclear Systems, Space Science Board, National Academy of Sciences, 1970.

31. Murphy, H.M., Summary of Neutron and Gamma Dosimetry Techniques, Air Force Weapons Laboratory Technical Report AFWL-TR-66-111, Kirtland AFB, New Mexico, 1967.

OPERATIONAL RADIATION INSTRUMENTATION AND FLIGHT CREW DOSIMETRY FOR THE SKYLAB PROGRAM

J. V. Bailey and R. E. English
NASA-Manned Spacecraft Center

A. The operational radiation instrumentation for the Skylab Program was derived from the Apollo systems. The personnel radiation dosimeters the radiation survey meter and the Van Allen Belt dosimeter will be used with minimum modification. A new instrument, a proton-electron spectrometer, will be fabricated for use on the Saturn Workshop. The instruments are fully described. The NASA management scheme for establishment of the operational radiation instrumentation system is described. The space environment section of the flight mission rules are a part of the operational solution to the space radiation problems. The Apollo rules are reviewed and preliminary considerations for Skylab mission rules are presented.

B. Radiation Source Summary:

Astronaut space radiation exposure will originate primarily from proton and electron components of the South Atlantic anomaly. Radiation exposure also will arise from cosmic and solar particles with engergies above the geomagnetic cutoff, and neutrons originating from atmospheric and spacecraft primary interactions. In addition to the space radiations, a number of pre- and postflight experiments have been proposed which will add significantly to astronaut exposure. Among the proposed experiments are whole body neutron activations for body composition determinations, x-ray scanning to determine bone mineral changes, and injections of radioisotopes for metabolic studies.

(MANUSCRIPT NOT AVAILABLE)

EXPERIMENTAL ACTIVE AND PASSIVE DOSIMETRY SYSTEMS FOR THE NASA SKYLAB PROGRAM

CAPT MARION F. SCHNEIDER, JOSEPH F. JANNI, AND GLENN C. AINSWORTH

Technology Division
Air Force Weapons Laboratory

Active and passive dosimetry instrumentation to measure absorbed dose, charged particle spectra, and linear energy transfer spectra inside the command module and orbital workshop on the NASA Skylab Program in 1972 have been developed and tested.

The active dosimetry system consists of one integral unit employing both a tissue equivalent ionization chamber and silicon solid state detectors. The instrument measures dose rates from 0.2 millirad/hour to 25 rads/hour, linear energy transfer spectra from 2.8 to 42.4 Kev/micron, and the proton and alpha particle energy spectra from 0.5 to 75 Mev. The active dosimeter is equipped with a portable radiation sensor for use in astronaut on-body and spacecraft shielding surveys during passage of the Skylab through significant space radiations. Data are transmitted in real time or are recorded by on-board spacecraft tape recorder for rapid evaluation of the radiation levels.

The passive dosimetry systems consist of twelve (12) hard-mounted assemblies, each containing a variety of passive radiation sensors which are recoverable at the end of the mission for analysis. The passive dosimeters consist of calcium and lithium fluoride thermoluminescent dosimeters, special discharge ionization chambers, activation foils, Ilford G.5 and K.2 nuclear emulsions and plastic heavy particle track dosimeters. The passive dosimeters record the total mission dose from 5 millirads to 5000 rads and the linear energy transfer spectra from 0.20 to >85 Kev/micron.

Instrumentation to measure the radiobiologically significant high-energy radiations encountered in manned spaceflight is of fundamental importance in ensuring astronaut safety and ultimate mission success. Since the discovery of the Van Allen Radiation Belts in 1958, and the advent of our knowledge of solar flare charged particles, it has been recognized that manned operations in near earth space would require a very careful consideration of these emissions. To date, manned space operations have not encountered dangerous radiation levels either because of the absence of high-energy solar flare particles, the avoidance of the highest fluxes of trapped particles in the earth's magnetosphere, or the relatively short duration of the missions where radiations were encountered. However, on future long-term missions the avoidance of such encounters will not always be possible and a very comprehensive measurement of radiation levels received by the crew must be realized. In this paper are described specially designed, active and passive dosimetry systems that will measure and record the radiobiologically significant radiations encountered in future manned spaceflight. Described specifically are instruments to be flown on the Skylab Programs, the first US. Space Station.

The most important radiations to be monitored in future extended long-term missions, like Skylab and the Orbital Space Stations, are solar flare, Van Allen Belt and primary cosmic protons with energies greater than 30 Mev. These particles exist in a complex and often unpredictable array of fluxes and spectra. For manned operations, the energy spectra and depositions of these particles must be measured at specific locations of astronaut activity.

Numerous ground-based experiments show that the degree of radiation effectiveness in impairing the functions of biological systems is determined principally by the two following parameters:

a. the locally absorbed radiation dosage,

b. the locally delivered linear energy transfer spectrum of the absorbed radiations (ref. 1).

The highly heterogeneous shielding afforded the astronauts by spacecraft and body self-shielding will cause high-energy protons to degrade in a very complex manner. This produces a significant depth dose gradient over the astronaut's whole body. The doses will also vary from astronaut to astronaut depending on shielding locations most frequented by him. Figure 1, after Schneider, (ref. 2) shows a measured variation of depth dose with shielding in the earth's inner Van Allen Belt measured on the Gemini 4 spacecraft.

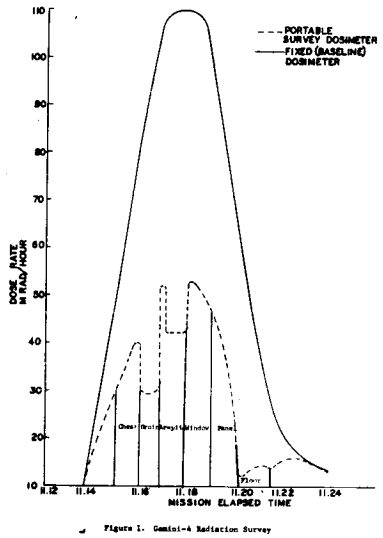

Figure 1. Gemini-4 Radiation Survey

An idealized picture of the theoretical depth dose behind 2.0 grams/cm^2 shielding for the Van Allen Belt and a typical relativistic solar flare as a function of a number of critical organ depths is shown in Figure 2 (Langham, ref. 3). It is emphasized that such depth dose gradients as these have not been measured for Skylab or the Apollo Command Module. Adequate space radiation dosimetry systems must lend themselves to the measurement of a large enough number of body points so that a depth dose gradient can be constructed. Also, dosimetry systems must record the average surface (skin) dose, and allow for the conduct of these measurements over short time periods to detect large changes in the radiation field. For example, on the Gemini flights the authors observed a rise of three orders of magnitude in the radiation levels in the spacecraft within a few minutes as the vehicles entered the Van Allen radiation belt.

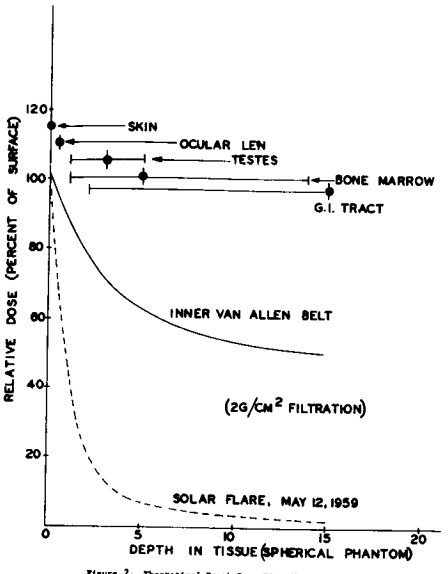

Figure 2. Theoretical Depth Dose Distribution for Critical Organs in Space Radiations

In order to indicate how the radiation dose is modified for radiations of different linear energy transfer, we examine Figure 3. Here, the variation of radiation RBE with LET values for mammalian tissues and crystalline lens cellular destruction and division is observed. We note also the recommended radiation protection values of relative biological effectiveness (RBE) as a function of LET, as defined by the 1967 United States National Radiation Protection Subcommittee, M-4 (ref. 4). There are wide variations in the RBE values for different radiation effects. For mammalian tissue damage the RBE is constant at a value of 1.0 for LET values of 3.5 kev/micron and less. The experimental RBE curve then shows a nonlinear rise to values of up to 5.0 for a LET of 100 kev/micron. The recommended RBE Subcommittee values of RBE vary from 1.0 at 3.5 kev/micron up to 20 at 100 kev/micron. The RBE Subcommittee established radiation protection values of RBE as a function of LET are generally higher and allow for larger safety factors than the observed experimental values.

The best use of the RBE-LET relationships is made by applying them to the various radiation effects on critical centers in the body such as the formation of cataracts in the eyes, gastrointestinal, skin and bone marrow damage, etc. As in the case of dose, this also requires measurement or simulated measurement of the LET at various depths. Especially important are measurements at depths where low-energy secondary radiations may significantly build up.

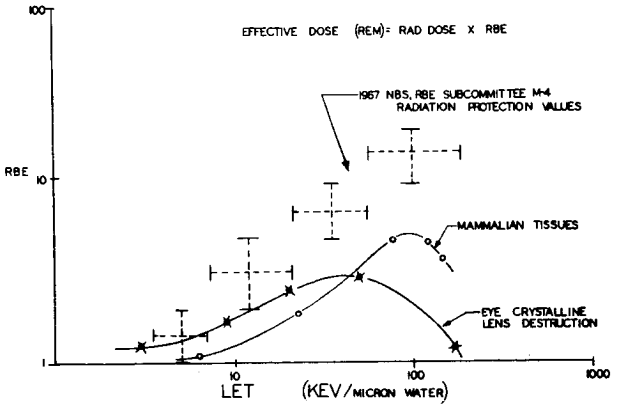

Figure 3. Effective Dose (REM) = Rad Dose X RBE

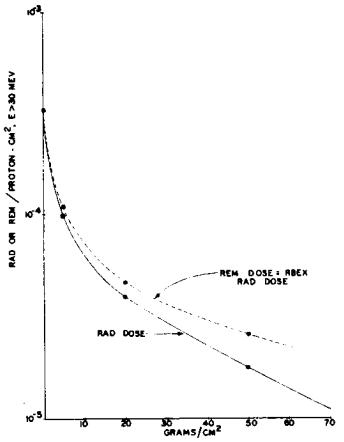

Figure 4. Calculated Rad and REM Dose as a Function of Shield Thickness for a Typical Inner Van Allen Belt Spectrum

For heterogeneous mixture of corpuscular radiations such as exist in the earth's radiation belts, in solar flares, and in galactic cosmic radiations, a wide spectrum of LET values may exist at various depths. The LET spectra must be measured and combined with the radiation surface doses and depth doses to give the REM dose.* The dose measurement problem in its most fundamental form reduces to one of determining the fraction of the dose (energy) delivered in each energy interval at the shielding depth of interest.

The LET spectrum in a spacecraft, such as Skylab, increases to higher dE/dX values as larger numbers of nuclear particles have their energy reduced closer to zero and as the number of secondary and recoil nuclei increases with increased shielding. The predicted effect of increased LET and RBE values with increasing shielding depth is clearly indicated in Figure 4 (Scott, ref. 5). Referring to this figure, the rem dose is calculated to increase to a factor of two over the rad dose at less than 50 grams/cm^2 of shielding, indicating that the LET values have increased greatly. This is a result of a wide variety of lower energy radiations, mostly secondary and degraded primary protons, secondary neutrons, and recoil nuclei produced in primary slowdown through heavier shielding. It is, therefore, important that the LET spectrum be determined where more than a first estimate of dose is required.

* REM Dose = RBE X Rad Dose. Where RBE is obtained from observed RBE versus LET relationships.

An adequate dosimetry system must be capable of conducting the following minimum measurements of the radiation field inside of the spacecraft:

a. the astronaut whole-body average surface dose levels,
b. the depth dose gradient at critical astronaut body organs (gastrointestinal tract, eyes, etc.),
c. the dose as a function of differently shielded spacecraft locations where the astronaut may be operating,
d. the instantaneous dose rates and depth dose rates delivered to the astronaut,
e. the accumulated or total mission doses and depth doses at the spacecraft shielding and body self-shielding locations previously mentioned,
f. the LET spectra at the same locations, where possible.

The above measurement must be conducted in the earth's Van Allen radiation belts and during irradiation from solar flare and primary cosmic charged particles, and from manmade trapped or onboard radiation sources.

Not only must an idealized dosimetry system be able to conduct these measurements, but it must also meet the criteria of small weight and size, be highly ruggedized, and have portable sensor elements. The systems must also have a wide radiation response range and excellent long-term accuracy. The radiation levels must further be determined where possible in a test material that has radiation reaction properties that closely match human

muscle tissue, i.e., the instrumentation must be able to measure the tissue equivalent dose levels from mixed radiation fields over an obviously wide range of energies. The active and passive dosimetry systems developed by the authors and described in the following sections of this report will be flown on the Skylab. They meet the above suggested criteria in the most accurate, reliable, and inexpensive manner currently possible with today's state of the art radiation detection methods.

Each active dosimeter system contains one tissue equivalent ionization sensor equipped for portable as well as fixed mounted operation combined in close proximity with a low energy charged particle spectrometer to measure LET spectra. With this instrument the astronaut can measure the dose, depth dose, and LET simultaneously and instantaneously inside a manned spacecraft. The radiation measurements are processed automatically by self-contained signal-conditioning electronic systems for recording by spacecraft telemetry.

Multisensor passive dosimeters at five (5) fixed mounted locations of minimum to maximum shielding have been developed and will be flown in the command module. Each passive dosimeter contains the latest state of the art ground based systems to measure total dose and LET spectra. The electronic and mechanical design of each subsystem is discussed in detail in the following sections. The spacecraft mounting locations of the active dosimeter and the five passive dosimeters are shown in Figure 5.

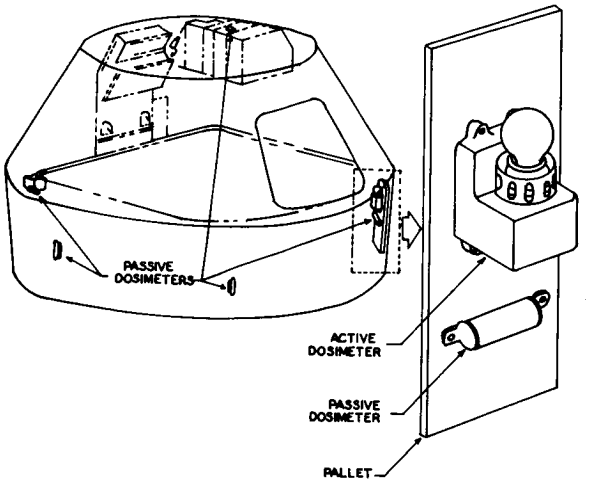

Figure 5. Active and Passive Dosimeter Locations in Command Module.

ACTIVE DOSIMETER SYSTEM DESCRIPTION

Tissue Equivalent Ionization Chamber System:

The active dosimeter described in this report involves the use of ionization chambers operated on the Bragg-Gray principle. This principle relates the ionization of a gas in a cavity contained in a medium to the absorbed dose in that medium. Ionization current in a gas cavity contained in a medium is related to the absorbed dose rate in the medium by the following linear equation:

$$E_m = S_m W J_{gas}$$

where: E_m = energy absorption in the medium in electron volts/gram sec

S_m = mass stopping power of the wall material relative to the gas

W = average energy in ev required to form

J_{gas} = ionization current in ion pairs/gram sec

According to Fano (ref. 6), if the gas and the surrounding medium in an ionization chamber are of identical atomic composition, the cavity may be large without disturbing the flux of secondary particles. More precisely this principle dictates that in a medium of given composition exposed to a uniform flux of primary radiation, the flux of secondary radiation is also uniform and independent of the density of the medium, as well as of the density variations from point to point.

The cavity ionization principle, therefore, permits a determination of energy absorption in a solid medium from the measured ionization in a small gas-filled cavity. This principle is the basis for the development of the advanced dosimetry system discussed in this report.

Since the biological damage resulting from ionizing radiation, in general, occurs in human tissue, the wall material of the ionization chamber that forms the medium in which the dose is measured should be tissue equivalent. The tissue usually chosen for this purpose is muscle tissue. The energy deposition is determined by the cross sections of each of the many chemical constituents making up tissue to the total radiation field encountered by that material. The cross sections are themselves dependent on the energy and type of radiation striking the tissue material. This means that the material of the ionization chamber walls must be as

closely matched in atomic composition to the atomic composition of human muscle tissue for the chamber to be tissue equivalent to the particle flux entering the spacecraft. That is, the material making up the walls should have cross sections and stopping powers for all possible encounterable radiation that are very closely matched to standard muscle tissue. Shonka (ref. 7) has developed a series of plastic resins that are ideally suited for this purpose. These are the plastics that were chosen for the Skylab Ionization chamber sensors. A comparison of Shonka plastic to the standard muscle composition as defined by the International Committee of Radiological Units ICRU (ref. 8) is shown in Table I. To avoid the necessity for making energy dependence corrections to the dose, it is measured directly in our dosimetry system by using Shonka sensor material previously described. This allows an unperturbed tissue response to be realized at all points of interest for all possible radiations. Fano's principle requires that to have an ionization chamber cavity of reasonably large volume capable of measuring the dose in a tissue equivalent medium, the gas should be matched atomically to this medium. A suitable nonexplosive tissue equivalent gas comprising methane, carbon dioxide, and nitrogen in the proportions shown in Table II is employed inside the chamber.

Table I

ICRU MUSCLE COMPOUND AND SHONKA CHEMICAL COMPOSITION

Element	Atomic Number	ICRU Muscle Percent by Weight	Shonka Plastic Percent by Weight
H	1	10.20	10.25
C	6	12.30	76.05
N	7	3.50	3.50
O	8	72.90	5.19
Na	11	0.08	0.08
Mg	12	0.02	0.02
P	15	0.20	0.20
S	16	0.50	0.50
K	19	0.30	0.30
Ca	20	0.007	0.007

Table II

TISSUE EQUIVALENT GAS COMPOSITION

Element	Composition by Weight (percent)
C	45.6
O	40.8
H	10.1
N	3.5

Observations of the gamma and neutron sensitivity of a tissue equivalent ionization chamber using this filling gas have indicated that it is stable to $\pm$ two percent over a nine month period; demonstrating that negligible changes in the filling gas occur through diffusion or absorption losses in the cavity wall during the period of measurement. Since the relative mass stopping power of the wall to gas is unity, the Bragg-Gray relation reduces to $E = WJ_{gas}$.

The radiation produced ionization chamber current is conditioned by the following electrical subsystems which comprise the complete tissue equivalent ionization chamber system. These systems are manufactured in a flight-ready configuration by the AVCO Electronics Division/Tulsa.

a. Sensor and Preamplifier
b. Operational (Signal Conditioning) Amplifier
c. Power Supply
d. Temperature Monitor

The tissue equivalent ionization chamber sensor consists of two electrodes. One is an 0.0625-inch-thick Shonka Type A-150 tissue equivalent plastic sphere described previously with an inner diameter of 2.188 inches. This spherical shell acts as the high voltage electrode for the ionization chamber system. The other ionization collecting electrode is a thin cylindrical probe 0.05 inch in diameter and 0.747 inch long centered within the spherical outer electrode. The collecting electrode is connected directly to the grid of a Raytheon CK 8520 electrometer. The CK 8520 preamplifier, Figure 6, collects and amplifies the instantaneous ionization current formed in the tissue equivalent cavity

operates in the triode connected floating grid mode. Experiments show that the triode connected electrometer has the following relationship between the grid and plate currents.

$$i_p = (s \log_{10} i_g + q)^{3/2}$$

where: i_p = the plate current

i_g = the grid current

s = a proportionality constant dependent on the cathode temperature and the tube geometry

q = dependence of plate current on current on cathode temperature, the tube geometry, the grid to cathode potential, the plate voltage, and amplification factor (which is in turn dependent on the tube geometry).

For an optimum filament current of 10 milliamperes at 1.50 volts and a plate voltage of 6.5 volts, the above relationship for an 8520 electrometer has the following form:

$$i_p = (4.43 \log_{10} i_g + 94.5)^{3/2}$$

The plate current of an 8520 electrometer varies with the log of the grid current over eight decades or orders of magnitude of the grid current. Thus, this system can be used to measure radiation induced currents from 5.0×10^{-15} amperes to over 10^{-7} amperes. This wide range of current values allows for the measurement of all known levels of ionization resulting from cosmic rays, solar flare particles, or the trapped Van Allen particles that might be encountered on manned space missions.

The plate current, which is typically several hundred microamperes in magnitude, is input for the final signal conditioning amplifier that connects with the spacecraft telemetry system.

The signal-conditioning amplifier displayed connected with the sensor and preamplifier is shown in Figure 7. The signal conditioning amplifier subsystem changes the CK 8520 electrometer plate current (typically a few hundred microamperes) to a 0.0 to 5.0 volt dc level compatible with spacecraft telemetry. It is a Fairchild SN 52709 high-gain operational amplifier constructed on a single-silicon chip using special planar epitaxial processes. It features high-input impedance, low offset, large input common mode range, and high output swing under load. The system is a low power device drawing less than 300 milliwatts maximum power and less than 150 milliwatts as operated in the tissue equivalent ionization chamber system. Additionally, the operational amplifier is highly stable with temperature over the range -55°C to 125°C, as a result of excellent internal temperature compensation.

The signal conditioning subsystem is designed with both gain and bias adjustments. These adjustments are used to set the dc level and slope of the input current versus output voltage curves before flight of the instrument.

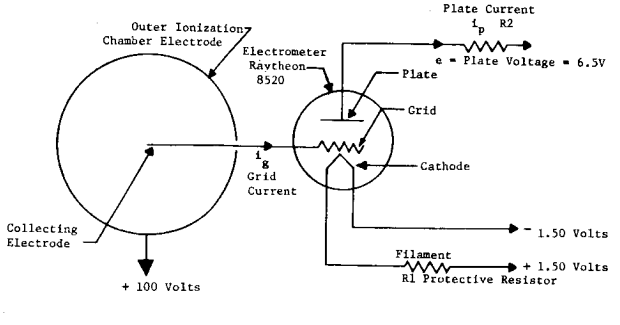

Figure 6. Tissue Equivalent Ionization Chamber Sensor and Preamplifier

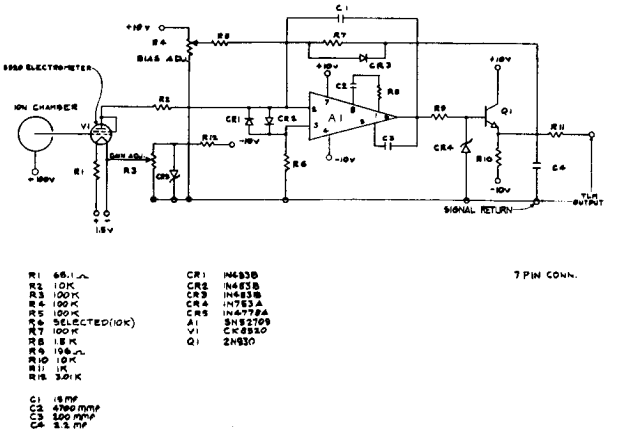

Figure 7. Tissue Equivalent Ionization Chamber Sensor, Preamplifier and Amplifier

The electronic conversation unit (power supply) subsystem for the TEIC is a standard dc to dc converter with series input regulation and hard diode protection. The dc to dc converter supplies high voltage for the ionization chamber high-voltage electrode, electrometer plate and filament voltages, and the driving voltages for the signal conditional amplifier and temperature sensor.

The flight configuration of the tissue equivalent ionization chamber sensor, Figure 8, is constructed of three walls. The inner wall consists of the high-voltage, tissue-equivalent Shonka plastic 2.31-inch outer diameter sphere covered with a second wall of 0.0625-inch thick epoxy coating to electrically isolate the inner conductive sphere from the third or outer wall. The outer wall is the hermetic seal for the two inner walls. It consists of a 0.025 $\pm$ 0.005-inch thick aluminum sphere. These three concentric spheres are attached to a cylindrical (also triple walled) barrel assembly housing the inner collecting electrode and the Raytheon CK 8520 preamplifier electrometer. The outer aluminum housing for the cylindrical barrel is machined in a single assembly with one of the hemispheres of the sensor. This assembly is hermetically sealed by press fit arrangement at the hemispherical interface shown in Figure 8.

The tissue equivalent ionization chamber electronic subsystems exclusive of sensor and preamplifier are packaged in hermetically sealed steel containers. The signal conditioning amplifier and temperature sensor subsystems are packaged in one container and the power supply is housed in the other container. Electrical interconnections between modules are made with special teflon insulated wire approved for flight on the Skylab Program.

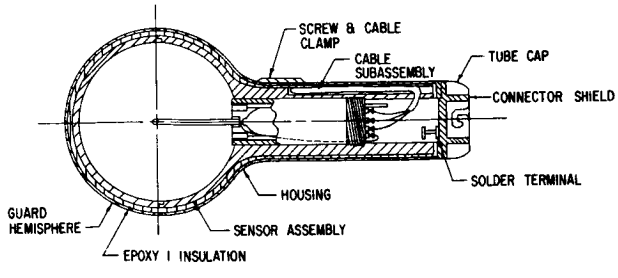

Figure 8. Multiple Wall Sensor Assembly

LINEAR ENERGY TRANSFER (LET) SPECTROMETER SYSTEM DESCRIPTION

The linear energy transfer (LET) spectra of space radiations are in general extremely complicated and difficult to measure activity. This is evidenced by the previous lack of such devices on manned spacecraft. Sensors have been developed in ground-based experiments (Rossi, ref. 9) to measure the LET spectrum employing low-pressure proportional counters. The Air Force Weapons Laboratory designed and tested similar types of space hardened gaseous proportional counters for use on satellite flights and high altitude aircraft flights to measure the anticipated LET spectra encountered in spaceflight. Instruments of this type have, however, had only very limited success in spaceflight. Limitations were due to problems involved with maintaining stable gas pressures and compositions in the low-pressure environment of space for extended periods and the poor resolution of such devices. The numerous difficulties encountered by attempts to use proportional counters in space to measure the LET spectrum are avoided on Skylab by the use of solid state semiconductor detectors. These devices are commercially available in long life, high reliability versions that can be obtained in almost any variety of detector thickness.

The LET spectrum for radiation penetrating the wall of the spacecraft indicates the quality or the relative biological effectiveness (RBE) of the radiation. The lower energy protons have high LET and a correspondingly high RBE. For example, protons of energies less than 14 Mev have LET greater than 3.5 kev/micron in water or muscle, and RBE greater than 1. Assuming 2 gm/cm^2 aluminum as representative of the spacecraft wall thickness at which the active dosimeter will be mounted and tested, trapped protons having external energies $40 < E < 46$ Mev are those which will have energies < 18 Mev inside the spacecraft. These are most easily measured by determining their total energy deposition in the solid state detectors. The same detectors can also measure alpha particles up to 75 Mev entering the spacecraft. The proton and alpha particle counts and energies measured by the method of total energy deposition are coverted to LET spectra using range, energy, and (dE/dX = LET) tables generated by the author, Janni (ref. 10). The relative $\frac{dE}{dX}$ versus E

responses for silicon and standard muscle tissue are uniquely defined and are shown in Figure 9. The $\frac{dE}{dX}$ values for the two materials are related by a well known mathematical function over the energy range which will make conversion from $\frac{dE}{dX}$ in silicon to muscle a straightforward process. The total counts in the intervals 0.5 to 18.5 Mev and greater than 18.5 Mev are also normalized for the tissue equivalent ionization chamber dose rate readings for baseline data in the depth dose radiation surveys with the portable tissue equivalent ionization chamber.

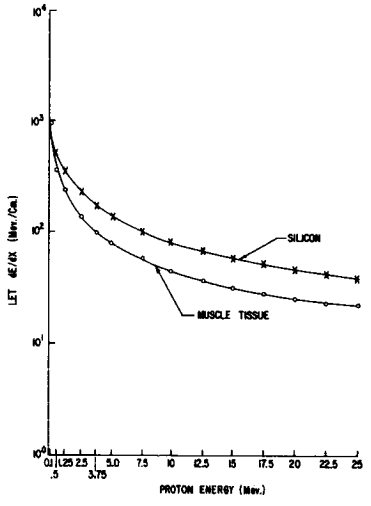

Figure 9. Stopping Power as a Function of Proton Energy

The LET system described in this report consists of two lithium drifted silicon solid state detectors operated as a charged particle telescope in near proximity to the tissue equivalent ionization chamber to record and to measure the energy of protons and alpha particles entering the spacecraft. The LET detectors designed by the authors are manufactured by Nuclear Semiconductors Inc. The first (entrance) solid state detector shown in Figure 10 is 2000 microns thick to provide the desired energy analysis of the high linear energy transfer components (lower) proton and alpha particle energies of the radiation environment entering the spacecraft. The second or anticoincident detector is 1000 microns thick. These two detectors are shielded with tungsten such that the protons and alpha particles enter them almost entirely from one plane so that they can be analyzed. The 2000-micron detector of the charged particle telescope measures the proton energies between 0.5 Mev and 18.5 Mev in five energy increments: 0.5 to 2.0, 2.0 to 6.0, 6.0 to 10.0, 10.0 to 14.0, and 14.0 to 18.5; and alpha particles between 18.5 and 75 Mev. The corresponding LET ranges are protons: 16 to 42.4 kev/micron, 6.8 to 16 kev/micron, 4.5 to 6.8 kev/micron, 3.5 to 4.5 kev/micron, 2.8 to 3.5 kev/micron, and < 2.8 kev/micron alpha particles: 10.4 to 32 kev/micron.

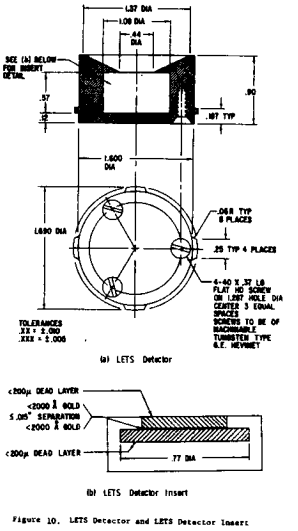

(a) LETS Detector

(b) LETS Detector Insert

Figure 10. LETS Detector and LETS Detector Insert

Original design plans for this system called for a four detector type telescope consisting of an additional thin (less than 20 microns) planar solid state detector and an annular solid state detector in the telescope arrangement shown in Figure 11. The four-detector system would extend energy measurements down to 0.1 Mev for protons and would expand the range of proton LET measurements to 93 kev/micron. Additional high LET multicharged particle measurements resulting from cosmic rays and recoil particles are readily possible with this larger system. The electronic block diagram for the four-detector system is shown in Figure 12. The basic electronic subsystems for the four-detector arrangement are analagous to those described later for the two-detector LET system. This system will not be flown because of telemetry and manufacturing cost constraints. Instead the two-detector LET system will be employed in the Skylab active dosimeter.

The LET electronics to shape, analyze, select, and telemetry condition the charged particle pulses produced in the solid state detectors, are displayed in block form in Figure 13. These are as follows:

a. Detectors, preamplifier, shaper, and voltage amplifiers
b. Analyzer buffer amplifiers
c. Analyzers (Discriminators)
d. Analyzer logic
e. Delayed strobe
f. MOSFET counters (seven-bit stair steps)
g. Ratemeter
h. Telemetry buffer amplifiers
i. Power supply

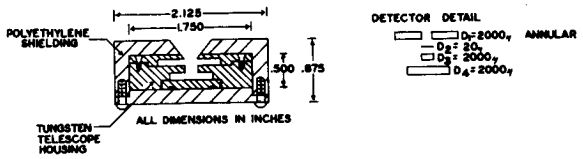

FOUR DETECTOR SOLID STATE LET TELESCOPE

Figure 11.

4 DETECTOR SOLID STATE LINEAR ENERGY TRANSFER (LET) SYSTEM

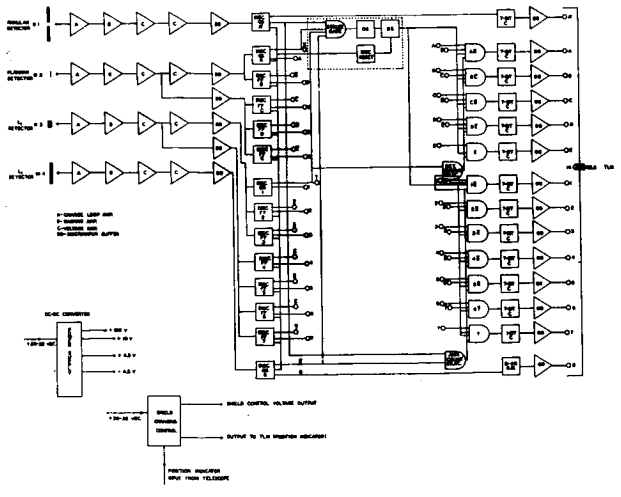

Figure 12.

The charge signals originating in the solid state detectors are converted to voltage signals by special charge loop preamplifiers A1 (see Figure 13). These amplifiers have a sensitivity of approximately 10 millivolts/Mev of energy loss in the silicon solid state detectors. The voltage pulses from the charge loops are processed by the shaper amplifiers A2 shown in the same figure. This amplifier develops a gain of 10 and has 0.5 x 10^{-6} second equal integration and differentiation. The signal is finally amplified by specially designed X10 voltage amplifiers A3.

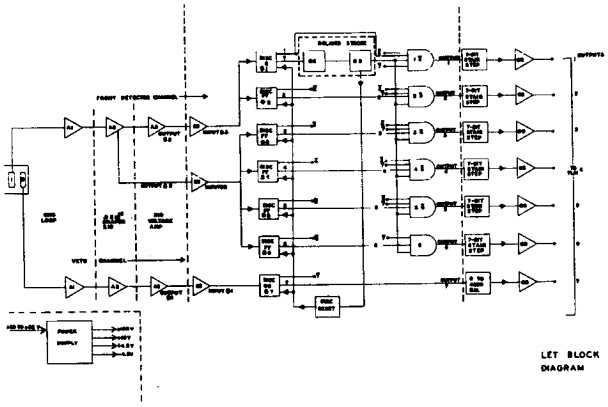

Figure 13.

The detailed electrical schematics for the detectors, preamplifiers, shaper amplifiers, and voltage amplifiers are shown in Figure 14.

The pulse height analyzers (discriminators) select the shape and amplified voltage pulses according to their amplitude into distinct energy channels. The pulse height analyzers are integrated circuits, RCA type CD2203s. Electrical schematics of the discriminators are displayed in Figure 15.

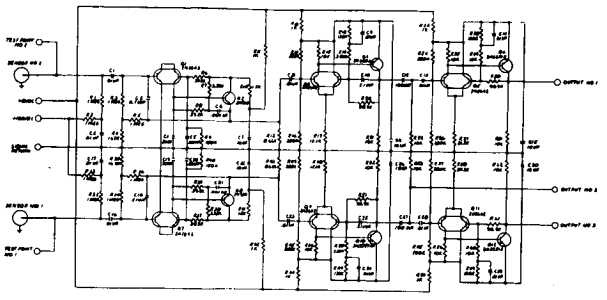

Figure 14. Schematic Detectors and Preamplifiers

Integrated circuits A8 and A9 comprise the delayed strobe shown in Figure 15. A9 generates pulse inversion for the delayed strobe while A8 is a double one-shot (the first one-shot has a 3 microsecond delay and the second has a 7 microsecond delay). This pulse action by the delayed strobe resets the discriminators and logic circuitry of the LET system so that they are in the ready-to-count condition. Since count rates of the order of no greater than 200 per second on the Skylab mission are anticipated, this is satisfactory.

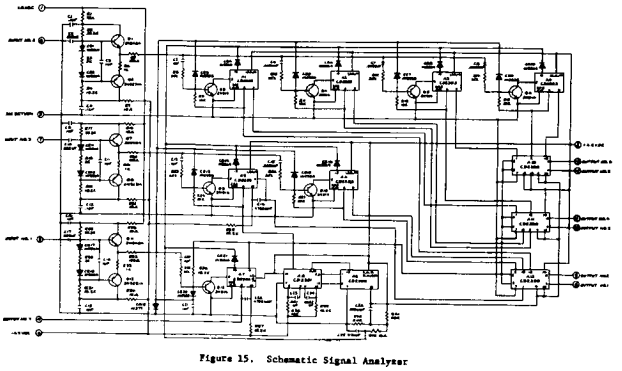

Figure 15. Schematic Signal Analyzer

The MOSFET (Metal Oxide Silicon Field Effect Transistor) counters are shown in Figure 16. They are RCA CD4004T MOSFET counters in ladder adder R-2R networks. These counters are output for the six energy analyses channels of LET detector.

The ratemeter for the LET system in Figure 16. is the output of the anticoincidence (second) detector. It transfers particle count rate received into a steady 0.0 to 5.0 volt dc level. It is the only nonlinear ramp type output that the LET system has. The ratemeter is a semilogarithmic device that is set so that 0.0 to 4000 counts/minute are recorded on a 0.0 to 5.0 vdc scale.

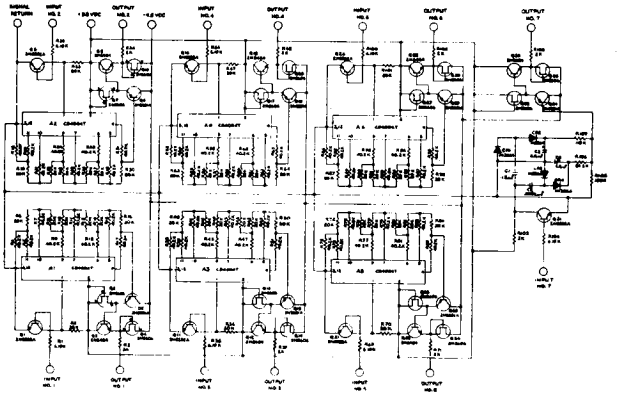

Figure 16. Schematic Counter and Output

The LET power supply system in Figure 17. supplies voltages to operate all other electronic subsystems just described. The power supply is designed to operate from a dc input of 28 + 4 or -8 volts of unregulated spacecraft power.

The power supply regulator is the integrated circuit component A1, a National Semiconductor LM100 transistor.

The LET electronics described in this report are packaged in four separate module subsystems. Each module corresponds to one of the major electronic systems and is hermetically sealed in steel cannisters of the same type of design as those used in the tissue equivalent ionization chamber electronics.

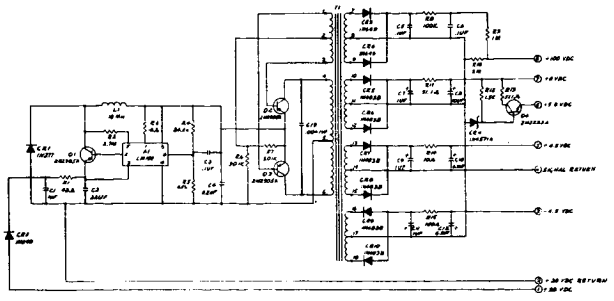

Figure 17. Schematic, Power Supply

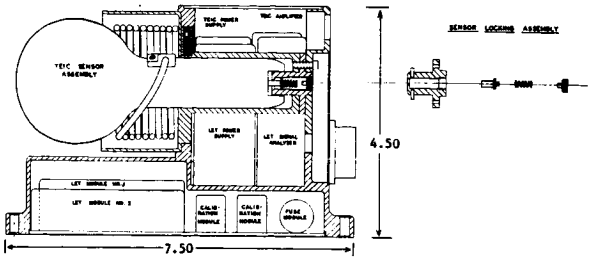

Figure 19. Active Dosimeter Module Mounting Sensor Locking Assembly Side Views

The tissue equivalent ionization chamber and LET electronics are mounted into a single, small 135 in^3 package with modules shown in Figures 18 and 19. The tissue equivalent ionization chamber is locked into the mounting case but can be removed to a length of over 6.5 feet for cabin and astronaut on-body surveys. During the Skylab mission fourteen (14) selected astronaut on-body and spacecraft shielding locations will be surveyed by the crew for Van Allen Belt, and cosmic ray encounters. The LET detector total counts will be normalized to a fixed location dose as base line date during the surveys.

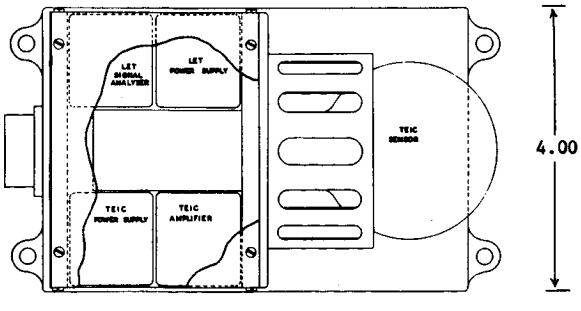

Figure 18. Active Dosimeter Module Mounting - Top View

The Skylab active dosimeter has nine electrical output signals.

The following description of each output channel, parameter sampled and sample rate is given:

Channel	Parameter Samples	Sample Rate
$TEIC_1$	TEIC dose rate	every 0.8 sec
LET_2	Proton energy, ΔE_1	every 0.8 sec
LET_3	Proton energy, ΔE_2	every 0.8 sec
LET_4	Proton energy, ΔE_3	every 0.8 sec
LET_5	Proton energy, ΔE_4	every 0.8 sec
LET_6	Proton energy, ΔE_5	every 0.8 sec
LET_7	Proton anticoincidence	every 0.8 sec
LET_8	Alpha particle count	every 0.8 sec
$TEIC_9$	Temperature sensor	every minute

The output impedences of each of these channels ranges between 2000 and 5000 ohms for compatibility with a greater than 1-megohm spacecraft telemetry.

The nine data outputs of the active dosimeter are decommutated after transmission from the spacecraft commutator to ground and placed on magnetic tape as a function of time. The data are in 550 bits per inch BCD format. The telemetry output voltage cannot exceed +5.0 VDC nor drop to less than -0.5 VDC. Continuous coverage is also employed where possible. When full coverage by ground stations is not possible, the output can be stored on an on-board tape recorder and relayed as soon as possible thereafter to ground facilities. The use of an on-board tape recorder having a data storage capacity of 90 minutes is used for full coverage in a 200-mile orbit around the earth. The data for an entire revolution are then dumped to one ground

station and placed on one tape. The resulting data are continuous in time. This greatly simplifies data processing.

ACTIVE DOSIMETER PERFORMANCE AND TEST DATA

The tissue-equivalent ionization chambers are calibrated with gamma radiations from the isotopes of Cobalt-60 and Cesium-137. Calibration is conducted on NBS certified radiation ranges to ensure the radiation response of the instruments. The radiation response as a function of output voltage is displayed in Figure 20. The radiation range is 0.2 millirad/hr to 25 rad/hr using an 0.0 to 5.0 volt telemetry range. It is possible by expanding the telemetry range to measure dose rates of 10^3 rad/hr. The response times of the tissue-equivalent ionization chambers are determined by timing their performance under irradiation by the sources described above. The following response time data have been generated for the tissue equivalent ionization chamber.

Radiation Level	Rise Time (sec)	Decay Time (sec)
2.9 mrad/hr to 1.05 rad/hr	0.525	1.40
10.0 mrad/hr to 5.7 rad/hr	0.480	1.50
0.5 rad/hr to 16.5 rad/hr	0.21	.45

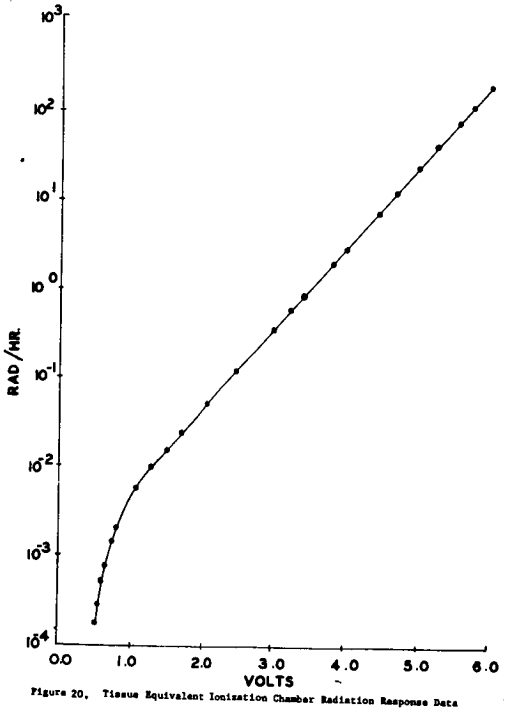

Figure 20. Tissue Equivalent Ionization Chamber Radiation Response Data

The rise time is defined as 90 percent of the lowest radiation value indicated, and the fall time is 110 percent of the lowest radiation level. The instrument is stable with temperatures between 0° and 120°F. For temperatures between -40° to 160°F, the instrument will not drift by more than 5 percent from its radiation response at room temperature.

Three types of tests are employed in calibrating the LET system. These are:

a. radiation sources
b. precision pulser
c. cyclotron irradiation

Americium-241 alpha particles of energy 5.476 Mev are used to activate the first two LET data channels 0.5 to 2.5 and 2.5 to 6.0 Mev. The alpha source cannot be employed after final assembly of this system because the entire LET is hermetically sealed. Therefore, functional and prelaunch testing is conducted with strontium-90 beta rays.

A precision 1 micro-micro farad capacitor is mounted to each input of the preamplifiers to conduct tests with an electronic pulser. The capacitors are mounted to the first input pin of the preamplifier. The capacitors are connected through a coaxial cable system to pins in the system's power and signal connector. Pulses from a precision pulser are applied to the preamplifier inputs. The test pulse has a rise time of approximately 10^{-8} seconds and a decay time of about 3×10^{-4} seconds. Each solid state detector produces approximately 4.5×10^{-4} coulombs of charge for each Mev liberated in it. Using the simple relation $V = Q/C$ the pulse amplitude X, that is equal 45 millivolts. This is easily measurable. Pulses equivalent to 1.5, 4.0, 7.5, 12, 15, and 50 Mev are used to test the six LET channels.

Measurements have been conducted at the Texas A&M University and Oak Ridge National Laboratory cyclotrons using degraded proton beams to ensure that the proper energy detection and pulse discrimination were achieved by the LET electronics. The results of these irradiations with protons of 60, 30, 25, 20, 15, 12, 9, and 5 Mev indicated satisfactory operation of the LET's system. The LET electronics system is insensitive to within 1% for temperatures between -40°F and +160°F.

PASSIVE DOSIMETRY SYSTEMS

The passive dosimetry portion of the Skylab radiation monitoring systems determine the radiation intensities at five fixed shielding locations within the Apollo command module, and seven similar locations in the Orbital Workshop. These intensities will be a function of the space radiation environment exterior to the spacecraft, mission length, orbital variables, and dosimeter location within the command module. The passive dosimetry units will be located at points approximating maximum, minimum, and intermediate shielding each containing the following dosimeters: lithium fluoride and calcium fluoride thermoluminescent dosimeters, a quartz fiber ionization chamber, nuclear emulsions, plastic polymers, and gold and iridium foils. The individual components making up each Skylab passive dosimeter unit are discussed in the following paragraphs.

Each dosimeter unit for Skylab includes a series of small rugged individual dosimeters housed in a sealed aluminum cannister. A diagram of the aluminum mounting containers and each of the individual dosimeters within the small cylindrical container are shown in Figure 21. Figure 22 shows the aluminum cannister construction teflon shock mounts, and the mounting arrangement of the individual dosimeters. The cannister and the end mounts are anodized aluminum. The O-ring is circular in shape and is constructed of Teflon. Since the passive dosimeters do not require any electrical power or telemetry connections there are no electrical plugs or feed-throughs.

Several types of radiation detectors are housed within the aluminum container. The selection of the dosimeter material was strongly influenced by the volume and weight limitations which are associated with spaceflight. Each passive dosimetry unit, including all contents and the aluminum container, will weigh only 0.37 pounds. The weight restrictions do not allow the more standard technique of successively varied and increased shield thickness about each dosimeter to be used. For this reason, the inherent charged particle response of the various individual dosimeters will be used to evaluate the particle type and energy cut-off. Only one clacium fluoride thermoluminescent dosimeter will be shielded. The dosimeters selected for use are each discussed in the following paragraphs.

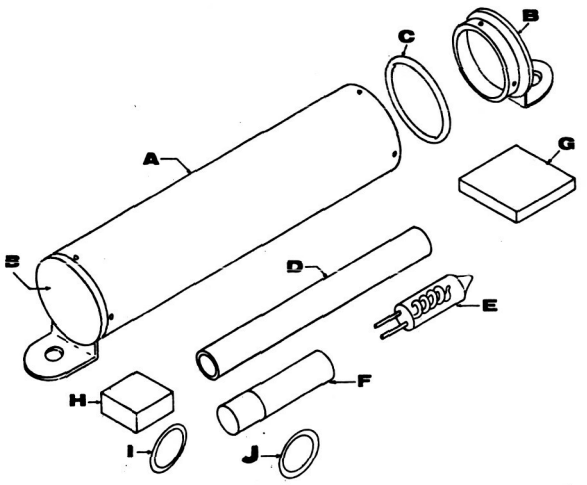

FIGURE 21 Complete Dosimeter Unit (Graphic Anatomy)

A. Aluminum Dosimeter Unit Housing
B. Aluminum Dosimeter Unit Housing End Plate
C. Teflon Seal
D. Ionization Chamber, Pocket Dosimeter
E. Thermoluminescent Dosimeter
F. Thermoluminescent Dosimeter Shield
G. Polymer Dosimeter
H. Nuclear Emulsion Dosimeters (Types K-2 and G-5)
I. Gold Foil
J. Iridium Foil

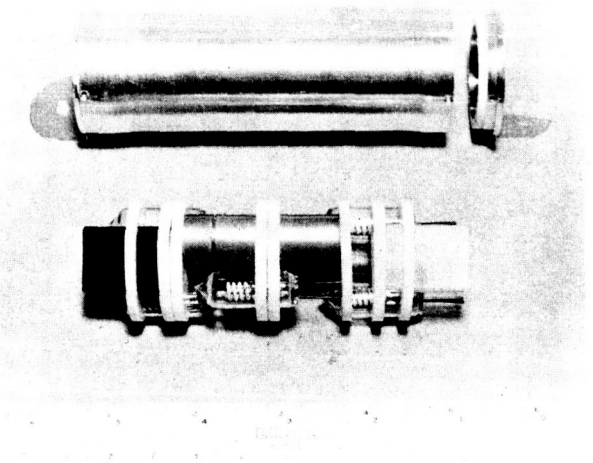

Figure 22. Passive Dosimeter Container Showing Mounting Locations of Individual Sensor Elements.

Thermoluminescent Dosimeters:

Several types of thermoluminescent dosimeters are commercially available, but only the glass enclosed lithium fluoride and calcium fluoride types manufactured by EGG (Durkee, ref. 11) are used. When a thermoluminescent material is irradiated, electrons become trapped at lattice imperfections within the crystalline solid. This trapping is relatively stable at temperatures on the order of 70°F, but the addition of large amounts of thermal energy causes the electrons which were trapped within the imperfections of the solid to be thermally agitated, allowing them to combine with charge carriers of the opposite sign. Visible light is emitted in this process which can be correlated with the amount of absorbed energy that has been deposited within the material. Calcium fluoride and two isotopes of lithium fluoride will be flown in the Skylab passive dosimeter systems. These materials are evenly coated on a heating element sealed within a glass container similar in construction to a small vacuum tube. The coating of the powder on an ohmic heater allows a known quantity of heat to be applied to this powder, and also provides a very high degree of reproducibility in the system. The powder must be heated in a vacuum or a pure inert gas atmosphere to eliminate spurious luminescence peaks which would otherwise occur. The vacuum technique also eliminates errors caused by inaccurate weighing, chemical change, or handling. The emitted light is blue-green and is measured post flight by using a photomultiplier tube and an associated electronics system to determine the intensity of the light emission. This dosimetry system is quite sensitive and can record total doses as low as 10 millirads approaching accuracies of 10 percent. The percent accuracy improves rapidly as the total dose increases and is about 5 per percent at 50 millirads. A shield will be used on one of these dosimeters in each cannister to provide charged particle cut-off points at reasonably well defined energies.

Two different lithium isotopes will be used to determine the contribution of secondary thermal neutrons to the total dose. Because the Li^6 isotope has a very low neutron cross section, the difference between the readings of the Li^6 and Li^7 types of lithium fluoride is interpreted as the thermal neutron dose. The Edgerton, Germeshausen, and Grier thermoluminescent dosimeters and associated shields will be used, and have the following common designation: lithium fluoride dosimeter - EGG TL-12, calcium fluoride dosimeter - EGG TL-21, and shield - EGG TL-32.

Nuclear Emulsions:

Practical methods of obtaining comprehensive information on the Linear Energy Transfer (LET) using passive dosimeters are limited to the use of nuclear emulsions. The most severe problem associated with the use of emulsions on long duration missions is that of track fading with time. A variety of emulsions are available and some have more severe fading characteristics than others. Emulsions of the Ilford G-5 and K-2 types are very suitable and have been chosen for use on Skylab. The dose fading is considerably less for the G-5 emulsion than for the K-2 types. However, this fading will not introduce particle losses greater than 30 percent for missions of one month.

The G-5 emulsion is considerably more sensitive than the K-2 emulsion. Using a combination of these two emulsions allows resolution of proton and alpha tracks of low energies which would be saturated in the G-5 emulsion alone but which still may be cleanly detected in the K-2 emulsion. This arrangement also allows discrimination of electrons from protons and alphas over the LET range 0.2 kev/micron to >85 kev/micron. This is accomplished by post flight microscopic examination of the individual particle tracks in the developed emulsions. The track count and grain density are then used to establish the atomic number of the charged particle, and the straggling and scattering of the tracks may be used to differentiate electrons from the heavier protons and alphas.

After a statistically significant number of particle tracks have been counted over a broad range of energy deposition values, an integral spectrum can be determined. This is then differentiated to obtain a differential spectrum. The tissue dose is required for comparison with active dosimeter data. The tissue dose is established by assuming the track population in the emulsion is the same as would have existed in an equivalent volume of tissue.

The tracks from protons and helium nuclei are very similar and the majority cannot be distinguished. However, a differential LET distribution for these Particles can be determined, and the tissue dose can still be found. The tissue-equivalency problems associated with the use of these emulsions are circumvented in this manner.

A large amount of bremsstrahlung would register in the emulsions as an increased electron population. The greater majority of such secondary electrons are readily identifiable.

Emulsions which have grains and grain spacing much larger than nuclear track emulsions are not capable of producing individual tracks. An increase in the optical density as a function of incident radiation intensity for those types of emulsions allows them to be used as dosimeters. Although this method has been widely used in health physics applications, there are still calibration and processing uncertainties as well as serious tissue equivalency problems with the use of such emulsions in unknown radiation fields. Because the LET cannot be determined, densitometric emulsions cannot be directly corrected to tissue response as can nuclear track emulsions. For these reasons, densitrometric emulsions are not included in the Skylab passive dosimeters, and only the Ilford G-5 and K-2 nuclear track emulsions will be used. The nuclear emulsions will be processed and analyzed for the authors by Dr. Herman J. Schaefer of the Naval School of Aviation Medicine.

Plastic Polymers:

Several plastic polymers are capable of recording the heavy ion component of the galactic cosmic radiation. These detectors have a number of characteristics that make them particularly appropriate for this application. They are light, rugged, compact, insensitive to temperature and humidity changes, have no latent image fading at ordinary temperatures, and are straightforward to process. Since protons and electrons are not registered, the heavy ions can be detected without being masked by an associated proton or electron population. This method allows classification of multicharged particles by their rate of energy loss.

The polymers as flown on Skylab consist of a sandwich of three layers of different polymers, each having a well-defined sensitivity. A particle traversing this system will leave tracks in some polymers and not in others. Counting tracks in each of the polymers gives the flux of particles above some known value of LET. By subtracting the fluxes recorded in adjacent materials, the flux of particles in a given broad range of LET can be obtained. The resolution of such a system depends upon the number of polymers used, and at least three polymers are required to provide adequate information concerning the heavy particle contribution for mission radiation.

Activation Foils:

Dosimetry by means of activation foils suffers from two primary difficulties. First, activation foils are relatively insensitive to radiations of low level and are not capable of measuring low doses; and second, the information contained in an activation foil decays away with the passage of time. Nevertheless, two types of activation foils are suitable for use in the Skylab passive dosimeter units to provide an evaluation of the neutron fluences. These are small gold and iridium foils which are being included because of their very low volume and weight.

A small gold activation foil will be used to provide information concerning the thermal neutron detector having an effective cross section of 98.9 barns with a half life of 2.7 days (Murphy, ref. 13). The large cross section tends to offset the radioactive decay resulting from the 2.7-day half life. The thermal neutron detectability within one half life is about $10^6 n/cm^2$. Except for the resonance at 5 ev, gold is not an epithermal or high energy neutron detector. With modern counting equipment and proper care, gold activation equivalent to one rad of thermal neutron fluence can still be counted after 10 half lives.

Iridium is the second activation foil which will be used and is sensitive over a broader neutron energy band than gold. Two isotopes of iridium will be used to detect thermal as well as higher energy neutrons; both isotopes will be contained within the same foil. The $_{77}Ir^{191}$ isotope is 38.15 percent abundant and under neutron irradiation goes to $_{77}Ir^{192}$ via two metastable states. The $_{77}Ir^{193}$ isotope is 61.5 percent abundant and has a neutron capture cross section of 110 barns; the product nucleus is $_{77}Ir^{194}$. The effective

neutron capture cross section for naturally occurring iridium containing both the $_{77}Ir^{191}$ and $_{77}Ir^{193}$ isotopes is 453 barns, with 385 barns (Lederer, ref. 13) being contributed by the 38.5 percent abundant $_{77}Ir^{191}$.

Other types of activation foils are not being included in the passive dosimetry experiment because their combination of half life and neutron cross section make them unsuitable.

Quartz-fiber Ionization Chamber:

Operation of the quartz-fiber dosimeters is well known. They consist of a sensitive chamber, a quartz-fiber electrometer, and a charging system. This response time is determined by the capacitance between the various parts of the chamber.

Response times of dosimeters of this type are generally quite rapid and are more than adequate to record the slowly accumulating dose anticipated on the Skylab mission. Dose fading is usually not negligible in such dosimeters and may be as large as 1 percent per day; however, the dosimeters selected for this flight are manufactured by the Dosimeter Corporation, Cincinnati, Ohio, and have leakages much less than this.

Analysis Considerations:

In order that the passive dosimeters record primarily the radiation dose during the length of the flight, and not the background accumulation which is caused by the galactic cosmic radiation which penetrates to the Earth's surface, the flight passive dosimeters will be installed in the spacecraft three days prior to launch. The standard use of ground control dosimeters configured identically to the flight units will be used. The flight dosimeters will be recovered as soon as possible after splashdown and returned to the AFWL for analysis. Prompt recovery is important because of the dose fading characteristics of several of the individual dosimeters. Recovery within two days after splashdown is programmed.

REFERENCES

1. Janni, J. F. and Holly, F. E.; Chapter IV "Space Radiation Dosimetry" Aerospace Medicine Vol 40, No. 12, December 1969, pp 1462-1475.

2. Schneider, M. R., and Janni, J. F.; "Experiment D-8, Radiation in Spacecraft, Gemini-4," First Manned Spaceflight Symposium, p 171, Wash DC, 1965.

3. Langham, W., Chapter III, "Biological Effects of Ionizing Radiation," Aerospace Medicine, Vol 36, No. 2, p 32, 1965.

4. United States National Radiation Protection Subcommittee, M-4 Report, 1967.

5. Scott, W. W.; Estimates of Primary and Secondary Particle Doses Behind Aluminum and Polyethylene Slabs Due to Incident Solar Flare and Van Allen Belt Protons, RSIC-18, Oak Ridge National Laboratory, Tennessee, July 1967.

6. Fano, U., Radiation Research, Vol I, p 237, 1954.

7. Shonka, F. R., et al; Proceedings of the Second United Nations International Conference on the Peaceful Uses of Atomic Energy, 21, p 184, 1958.

8. "Report of the International Commission on Radiological Units and Measurements (ICRU)," National Bureau of Standards Handbook 78, 1959.

9. Rossi, H. H., and Rosenzweig, O.; Radiology, 64, No. 3, pp 290-299, March 1955.

10. Janni, J. F., Calculations of Energy Loss, Range, Pathlength Straggling, Multiple Scattering, and the Probability of Inelastic Nuclear Collisions for 0.1 to 1000 Mev Protons, AFWL TR-65-150, Air Force Weapons Laboratory, Kirtland AFB, New Mexico, September 1966.

11. Durkee, R. K., et al; Energy and Rate Dependence Studies, EG&G Technical Report S-237-R.

12. Murphy, H. M., Summary of Neutron and Gamma Dosimetry Techniques, AFWL Technical Report AFWL TR-66-111 (1967).

13. Lederer, C. M., Holtauclen, J. M., Perlman, I.; Table of Isotopes (Sixth Edition), John Wiley & Sons, Inc., New York (1967).

DOSIMETRY FOR RADIOBIOLOGICAL STUDIES OF THE HUMAN HEMATOPOIETIC SYSTEM[1]

W. L. Beck, T. R. Stokes, and C. C. Lushbaugh

Oak Ridge Associated Universities

INTRODUCTION

At present, physical measurements of radiation exposure field fluxes are considerably more accurate than retrospective biologic estimates of the radiation dose in any particular exposure incident. However, wide individual variation in clinical response to radiation exposure often creates an apparent disagreement between physical and biological dose estimates. This disparity is largely caused by biologic variations in radiosensitivity and systemic repair but is also the result of individually different depth-dose distributions owing to body size differences or orientation geometry occurring during otherwise equal exposures.

Medical appraisal of the range of human biological variation in hematologic responses is needed, but has not been made because dosimetric information about the real depth doses to the bone marrow of individual patients is not available. The wide spatial distribution of bone marrow in the human skeleton makes the determination of the total averaged dose or any local bone marrow dose difficult and at present requires an empirical approach. This study was performed to devise a system for estimating individual bone marrow doses in therapeutic radiation exposures of leukemic patients. These measurements are needed to make dose-response correlations and to study the effect of dose protraction on peripheral blood cell levels. Such correlations are basic to medical management of irradiated persons since the bone marrow is one of man's most important radiosensitive tissues; lethality within 60 days of acute exposures from 200 to about 1000 R usually results from hematopoietic failure. Some studies (refs. 1 and 2) have shown that in selected patient populations the human $LD_{50/60}$ may approach a low of 250 rads average body-dose, but confidence in these estimates is poor.

During extended space explorations there may be little risk of receiving such sizeable doses acutely but there is a real chance of accumulating doses to the marrow that may be biologically significant. True correlation and variation of human hematologic responses to total-body irradiation (TBI) are sorely needed to help in establishing workable limits for these occupational exposures during missions in outer space. While the studies we have made were primarily intended for clinical uses, the data obtained is applicable to some of the dosimetric and shielding problems of space medicine.

In the Oak Ridge Associated Universities (ORAU) Medical Division program of therapeutic TBI, three irradiators with different exposure rates are in use: the ORAU low-exposure-rate total-body irradiator (LETBI) and medium-exposure-rate total-body irradiator (METBI), and the University of Tennessee-AEC Variable Dose Rate Irradiation Facility (VDRIF). Each of these irradiators was specifically designed to produce a uniform field of high-energy-gamma radiation for total-body exposures of large animals and man.

[1]Research supported jointly by U.S. AEC and NASA.

THE IRRADIATORS

The LETBI facility consists of a large outer room (Fig. 1B) in which a smaller exposure room (Fig. 1A) is centrally positioned. Eight cobalt-60 sources of 16 Curies each are located in the outer room and they irradiate the treatment room from all sides. This arrangement provides a radiation field uniform to within ±10% in the living volume (16×16×8 ft) occupied by the patient. Treatments given at an average exposure rate of 1.5 R/hr have ranged from 3 to 8 days duration to provide total protracted exposures up to 250 R. During exposure the patient is free to move about the exposure room while being irradiated for 18 to 22 hr per day. This facility is described in more detail by Andrews, et al. (ref. 3).

A model of the METBI facility is shown in Fig. 2. The control room is connected by a curved hallway to the 8×8×8 foot treatment room. Eight cesium-137 sources of 500 Curies each, located in the walls, irradiate the centrally suspended treatment bed. The radiation field in the 2×2×6 foot volume occupied by the patient on the bed is uniform to within ±5% of the 1.5 R/min exposure rate in the volume center. Exposure times here range from a few minutes to a few hours for total exposures of 20 to 350 R. A complete description of this facility has been published by Brucer (ref. 4).

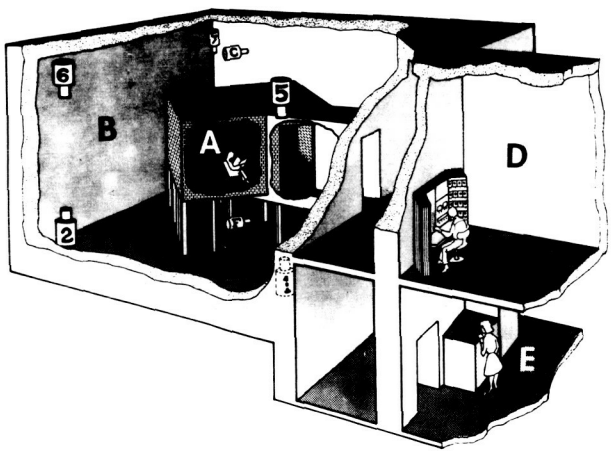

Figure 1.—Cutaway drawing of the low-exposure-rate total-body irradiation facility (LETBI) showing:
(A) Centrally positioned radiation exposure/living room.
(B) Concrete shielded radiation containment room.
(D) The remote control room for operation of the ^{60}Co sources (only sources No. 1,2,5,6,7, C and F are shown), radiation exposure level supervision, nursing and physiologic surveilance of the patient.
(E) The on-line and data processing room.

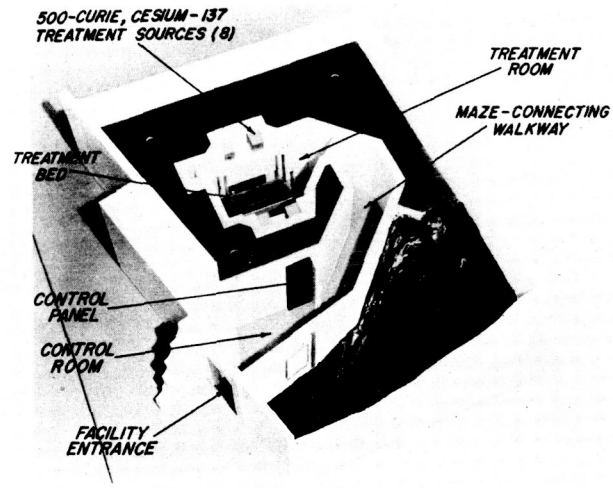

Figure 2.—Cutaway model of the medium-exposure-rate total-body irradiation facility (METBI).

The floor plan of the third irradiator (VDRIF) used in this therapy program is shown in Fig 3. Six cobalt-60 sources of 7700 Curies each are arranged in a rectangular array with 20 ft between adjacent sources. Exposures are done with the patient lying on his side on a hospital stretcher in the center of the source array. During patient therapy five sources are used to provide exposure over the stretcher at a rate of 40 R/min ±5%. To minimize the radiation hazard to hospital attendants, who might be required to aid the patient in case of equipment failure, we do not use source No. 1, which is nearest the entrance to the exposure room. A more complete description of this irradiator is given by Checka, et al. (ref. 5).

The radiation characteristics and dimensions of these irradiators are summarized in Table 1.

TABLE 1

RADIATION CHARACTERISTICS AND DIMENSIONS OF THREE TOTAL-BODY IRRADIATORS

FACILITY	SOURCES	RADIATION (Gamma)	EXPOSURE VOLUME	EXPOSURE RATE TREATMENT VOLUME	MODE OF EXPOSURE	SOURCE TO CENTER EXPOSURE VOLUME
LETBI	8 ^{60}Co	1.25 MeV	16×16×8' (room)	1.5 R/hr (±10%)	Multilateral	19.5'
METBI	8 ^{137}Cs	0.662 MeV	6×2×1' (above bed)	1.5 R/min (±5%)	Multilateral	5.8'
VDRIF[a]	5† ^{60}Co	1.25 MeV	6×2×1' (above bed)	40 R/min (±5%)	Bilateral	10' (Sources 3,4) 22.5' (Sources 2,5,6)

*This irradiator belongs to the UT-AEC Agricultural Research Laboratory.
†VDRIF has 6 sources, but only 5 are used during therapy to patients.

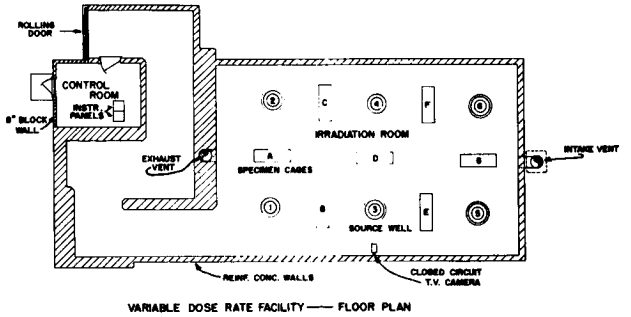

Figure 3.—Floor plan of the University of Tennessee-Atomic Energy Commission (UT-AEC) Agricultural Research Laboratory Variable Dose Rate Irradiation Facility (VDRIF). Source positions are indicated by No. 1-6.

THE PHANTOM

An Alderson Rando phantom (ref. 6) was used as a patient analogue. This standard-man-sized phantom is constructed of isocyanate rubber, equivalent to tissue in interactions with ionizing radiation. A human skeleton and density-adjusted lungs are contained within the otherwise solid phantom. The phantom is sliced into transverse sections 2.5 cm thick with holes of 5 mm diameter arranged in a 3×3-cm grid to provide positions for thermoluminescent dosimeters (TLD). When not in use as dosimeter sites, the holes are filled with removable plugs of tissue-equivalent material.

Each of the 137 dosimeter sites located within the bone-marrow loci, identified from radiographs of the 34 transverse sections of the phantom, contained an individually calibrated TLD during periods of irradiation similar to the exposure of the patients.

DOSIMETERS

Extruded lithium fluoride dosimeters[2] (1.4×1.4×7 mm) were used to make all measurements within the phantom. These dosimeters are well suited for this application because of their small size, energy independence, approximately tissue equivalence, sensitivity, reusability, and ease of handling. They have a linear response from 10^{-2} to 10^{3} rads and a slightly supralinear response from 10^{3} to about 5×10^{5} rads when radiation damage becomes a limiting factor. In our laboratory we found the response of freshly calibrated dosimeters to be reproducible with a standard deviation of the order of 1-2% when exposed under calibration conditions. Repeated measurements in the same position in the phantom rarely disagree by more than 5%. We have previously reported details for calibrating, annealing (processing for reuse), and analyzing these dosimeters (ref. 7).

MARROW DOSE CALCULATIONS

Since the active marrow is not uniformly distributed within the body in a simple, well-defined volume, it was necessary to know the spatial distribution of the marrow to determine average marrow dose. The distribution of active marrow for normal adults as estimated by Ellis (ref. 8) is expressed as the percent of the total amount located in a particular anatomical marrow compartment, e.g., the ribs or skull. The distribution of the dosimeters in the marrow compartments defined by Ellis was not proportionate to the amount of marrow therein. For example, 19% of the 137 dosimeters were located in ribs which contained only about 8% of the total active marrow. Therefore, average total dose to marrow had to be calculated by first determining the average dose for a specific compartment and then using its percentage of total marrow as a weighting factor. Table 2 lists the average compartment dose and its range per 100 R of exposure from each of the three irradiators. Table 3 summarizes the average marrow dose calculations.

TABLE 2

MARROW COMPARTMENT AVERAGE DOSE IN RADS/100 R

	IRRADIATORS					
	LETBI		METBI		VDRIF	
Marrow Compartment	Average Dose	Range	Average Dose	Range	Average Dose	Range
Head	82	73-89	78	71-85	68	61-74
Upper Limb Girdle	69	58-75	66	58-73	78	70-82
Sternum	75	73-77	69	65-71	77	74-77
Ribs	63	46-76	68	62-72	75	70-84
Vertebrae	58	47-75	65	59-80	70	63-78
Sacrum	45	41-46	54	50-56	75	67-83
Lower Limb Girdle	52	44-62	59	52-71	72	63-77

TABLE 3

CALCULATIONS OF AVERAGE BONE-MARROW DOSE IN RADS/100 R

		LETBI		METBI		VDRIF	
Bone Marrow Compartment	Percent Active Bone Marrow	Average Dose	Weighted* Factor	Average Dose	Weighted* Factor	Average Dose	Weighted* Factor
Head	13.1	82	1074	78	1022	68	891
Upper Limb Girdle	6.4	69	442	66	422	78	499
Sternum	2.3	75	173	69	159	77	177
Ribs	7.9	63	498	68	537	75	593
Vertebrae	28.4	58	1647	65	1846	70	1988
Sacrum	13.9	45	626	54	751	75	1043
Lower Limb Girdle	26.1	52	1357	59	1570	72	1879
Totals	98.1†		5820		6277		7070
Average Weighted Dose‡		59		64		72	

* Weighted factor = average dose × percent bone marrow.
† Average weighted dose = Σ weighted factors ÷ total percent active bone marrow.
‡ Total percent is 98.1 because 1.9% of the marrow is located in the heads of the humeri where no measurements could be made.

[2]Dosimeter available from Harshaw Chemical Company, Cleveland, Ohio.

The compartment dose estimates in Table 2 indicate that the marrow dose distribution is different in each of these irradiators. The most unexpected result is that the LETBI ^{60}Co gamma irradiator produces a smaller marrow dose than the METBI ^{137}Cs gamma irradiator. The other irradiator (VDRIF) produces the largest marrow dose as would be expected on the basis of relative penetrability of the gamma rays involved. This apparent paradox between the LETBI and METBI doses can be explained only on the basis of the distance the radiation travels in the body to the deep-seated marrow sites. In the VDRIF about 80% of the radiation is incident at 90° to the long axis of the body and passes through the body's least thickness, the anterior-posterior diameter. This geometry provides the minimum radiation-path length to all marrow sites and therefore the largest average depth dose.

In the METBI facility the ^{137}Cs gamma rays are incident on the body's long axis at angles from 78-90° and they penetrate the body at an angle of approximately 30° to its larger lateral (side to side) diameter. The average length of radiation path in this geometry, somewhat greater than in the VDRIF, and the lower energy radiation explain the smaller marrow dose from the METBI exposures. However, other depth dose studies (refs. 9 and 10) have shown a less than 5% difference in average marrow dose from ^{137}Cs and ^{60}Co gamma rays under equal exposure geometries.

In the LETBI the exposure geometry is complicated by the patient's freedom to move about the large exposure room. We have calculated the angle of incidence for two typical positions of the patient; when he is standing near the room center, the average angle of incidence is about 70°; lying on the bed, the average angle of incidence is only about 25°. If we make the assumption that the average angle of incidence is the average for these two positions, or about 45°, then by simple geometry the length of the radiation path is 40% greater in this geometry than it would be for radiation incident at 90°. Because of this geometry, the LETBI average marrow dose is the lowest of the three irradiators studied.

The large dependence of average marrow dose on the angle of incidence of radiation is shown also by the study of Clifford (ref. 11), who measured this average dose in a rotating phantom first exposed at 90° and then at several angles down to 15° with the long axis of the body. Radiation energies of 60, 100, 212, and 660 keV were used. His results indicate that average dose to the marrow is reduced by a factor of two for exposures at 15° compared with 90° for all radiation energies. In addition, he also shows that marrow dose for 90° exposures varies by only about ±10% over the energy range from 60 to 660 keV and is maximum at about 100 keV.

Since the LETBI and METBI facilities produce essentially omnidirectional fields, we can compare the marrow dose estimates in LETBI of 0.59 and METBI of 0.64 rads/R with that predicted from Clifford's measurements (integrated over the angular region of 0° to 90°) of 0.62 rads/R. This agreement is surprisingly good considering that his estimates were based on measurements in only eight positions in his phantom and were primarily intended for evaluation of potential hazards of radiations from atomic weapons for civil defence planning.

The International Commission on Radiological Protection (ICRP) (ref. 12) has defined the active marrow dose as the appropriate radiation criterion for relating not only short-term hematopoietic effects but also certain late somatic biological effects to radiation exposures. To simplify its calculations to estimate marrow dose, the ICRP determined that the active marrow is located at an average depth of 5 cm. To test the validity of this simplification, we determined the average 5-cm dose to the phantom in each of the three irradiators.

The circumferential 5-cm depth line was defined in each of the 34 phantom sections and divided by radii at every 30°. The depth dose at the intercepts of the radii and the 5-cm depth line was determined by interpolation of the depth-dose data obtained from dosimeters located in surrounding grid positions. These were averaged for each section and then weighted by the mass of the section to obtain the overall average 5-cm depth dose. The comparisons of these dose estimates with the average marrow doses are shown in Table 4.

TABLE 4

COMPARISON OF ESTIMATED DOSE TO BONE MARROW WITH AVERAGE BODY DOSE AT 5-cm DEPTH

	Average Active Bone-Marrow Dose (in rads/100 R)	Average 5-cm Depth Dose (in rads/100 R)	Ratio $\frac{\text{5-cm Depth Dose}}{\text{Marrow Dose}}$
LETBI	59	68	1.15
METBI	64	66	1.03
VDRIF	72	73	1.01

These data indicate that the 5-cm dose approximates the average marrow dose quite closely in the ^{137}Cs gamma-ray field (METBI) and the high-flux ^{60}Co gamma-ray field (VDRIF) where the incident radiation is principally at right angles to the stationary body. The agreement, while adequate, is not as good for the low-exposure-rate cobalt irradiator (LETBI) where the incident radiation is from both above and below a standing patient and where the angles change as the patient sits down, reclines, or walks about, changing his geometric relationship to each source.

These results also suggest that a dosimeter, capable of indicating simultaneously dose rate and total accumulated dose, located in the center of a 5-cm radius sphere of tissue-equivalent material could be used to approximate the astronaut's average marrow dose received during space flight. The dose-rate signal from this dosimeter could also be used to indicate when maximum shielding from unidirectional exposures, such as solar flares, is needed and to indicate what vehicle orientation provides the maximum shielding.

This study also shows clearly that average dose to the marrow is strongly dependent on the length of the radiation path in the body. It is therefore obvious that for equal exposure conditions, a very large person will receive a relatively smaller dose to the marrow than a very small person. To determine how large this variation due to body size will be, we are extending these studies to determine body self-shielding factors for a particular individual rather than the idealized 70-kg man. The exposure rate from a small radioactive source is first measured in air and then at the center point of phantoms of different sizes by a high-sensitivity whole-body counter containing an array of eight 5×4-in. sodium iodide crystals. The ratio of the counts from within the phantom to the counts in air can be used to indicate the body's self-shielding factor. The results of this study are still incomplete but the feasibility studies indicate that this experimental approach has merit. From these studies we should obtain correction curves relating average marrow dose to self-shielding factor for each of our irradiator geometries and type of source. The self-shielding factor for each individual or patient could then be obtained by having him swallow a less than 1.0-microcurie radioactive source, then counting him in the whole-body counter when the source is located at the center of the patient's body.

Accurate dosimetric information relevant to the biological effects under study are essential for improving the reliability of established human dose-response relations. This is particularly true when the effects considered are the changes in peripheral

blood-cell levels. These studies are limited to medical exposures because changes in the blood-cell levels are related to the preirradiation levels. For these reasons, we are seeking to obtain truly adequate dosimetry information from which we can deduce dose-response relations which will aid in space mission planning, management of radiation accident victims, and will improve the usefulness of TBI therapy of disseminated diseases.

REFERENCES

1. Lushbaugh, C. C.; Comas, F.; and Hofstra, R.: Radiation Res., suppl. 7, 1967, pp. 398-412.
2. Lushbaugh, C. C.; Comas, F.; Edwards, C. L.; and Andrews, G. A.: USAEC Report CONF-680410, 1968, pp. 17.1-17.23.
3. Andrews, G. A.; Beck, W. L.; Cloutier, R. J.; Morris, Jr., A. C.; Barclay, T. R.; Comas, F. V.; Edwards, C. L.; and Lushbaugh, C. C.: USAEC Report ORAU-106, 1967, pp. 13-18.
4. Brucer, M.: Int. J. Appl. Radiation Isotop., vol. 10, 1961, pp. 99-105.
5. Checka, J. S.; Robinson, E. M.; Wade, Jr., L.; and Gramly, W. A.: Health Phys. (in press).
6. Alderson, S. W.; Lanzl, L. H.; Rollins, M.; and Spira, J.: Amer. J. Roentgenol. Radium Therap. Nucl. Med., vol. 87, 1962, pp. 185-195.
7. Beck, W. L.; Callis, E. L.; and Cloutier, R. J.: USAEC Report CONF-680920, 1968, pp. 976-989.
8. Ellis, R. E.: Phys. Med. Biol., vol. 5, 1961, pp. 255-258.
9. Facey, R. A.: Health Phys., vol. 14, 1968, pp. 557-568.
10. Jones, A. R.: Health Phys., vol. 12, 1966, pp. 663-671.
11. Clifford, C. E.; and Facey, R. A.: Health Phys., vol. 18, 1970, pp. 217-225.
12. Recommendations of the International Commission on Radiological Protection (Adopted September 17, 1965), ICRP Publication 9, New York Pergamon, 1966.

BIOLOGICAL EFFECTS OF AMBIENT AND ON-BOARD RADIATION ON TRADESCANTIA DURING PROLONGED FREE FLIGHT*

A. H. Sparrow and L. A. Schairer
Biology Department, Brookhaven National Laboratory, Upton, New York

A special clone of hybrid origin of the common roadside plant, spiderwort, or Tradescantia, has been successfully flown in Biosatellite II. In the two-day flight, plants responded to combined gamma radiation and weightlessness by developing abnormal nuclei (resulting from disturbed spindle function), an increased rate of pollen abortion and increased loss of reproductive integrity in stamen hair cells. Chromesome aberration and somatic mutation rates showed effects attributable to space flight factors. In order to confirm and extend these results and perhaps to define the mechanisms responsible, another experiment of longer duration is being developed.

The Tradescantia test system is particularly adaptable to this type of experimentation because it is easy to grow over a wide range of environmental conditions, flowers continuously throughout the year, is heterozygous for flower color (thus permitting easy detection of somatic mutations), has only 12 large chromosomes making it suitable for cytological analyses and has a high radiosensitivity. While new clones possessing more stable pollen and more sensitive somatic genetic markers are being developed and tested, the original Tradescantia clone 02 is being used extensively in ground-based studies designed to establish optimal environmental conditions for extended flights. By growing the plants at low light intensity and low temperatures (50 to 55°F) mitotic cycle time is doubled and the resultant increased radiation exposure per mitotic cycle doubles the somatic mutation rates. This lower temperature and increased sensitivity have several advantages; (1) a smaller, safer on-board radiation source can be used; (2) the more sensitive system would serve as an ideal detector of ambient space radiations and further serve to establish their relative biological effectiveness and (3) plants growing at lower temperatures would survive for extended periods of time, e.g., on deep space probes, and they would require less light, water and nutrients.

Representative dats will be given showing the response of several end points to chronic gamma irradiation at rates from 0.75 to 12 R/day as well as RBE values for x-rays and 13.4 and 0.43 MeV monoenergetic neutrons. RBE values for 0.43 MeV neutrons for various end points were found to range from about 10 to 166.

---

* Research supported by NASA (Purchase Order A-44246A) and by the U.S. Atomic Energy Commission

MANUSCRIPT NOT AVAILABLE

HAIR RADIOACTIVITY AS A MEASURE OF EXPOSURE TO RADIOISOTOPES

W. H. STRAIN, W. J. PORIES, R. B. FRATIANNE AND A. FLYNN

Cleveland Metropolitan General Hospital

and

Case Western Reserve University

ABSTRACT

Measurement of hair radioactivity appears to be a suitable method for monitoring systemic exposure to radioisotopes and certain types of manmade radiation. This concept has developed from a suggestion we made in 1963 that the strontium-90 content of hair affords a nondestructive method of estimating the body burden of this radionuclide. Since many radioisotopes accumulate in hair, this tropism has been investigated by comparing the radioactivity of shaved with plucked hair collected from rats at various time intervals up to 24 hrs. after intravenous injection of ca 5 uCi of the ecologically important radioisotopes, iodine-131, manganese-54, strontium-85, and zinc-65. The plucked hair includes the hair follicles where important biochemical transformations are taking place. The data indicate a slight surge of each radioisotope into the hair immediately after injection, a variation of content of each radionuclide in the hair, and a greater accumulation of radioactivity in plucked than in shaved hair. These results have application not only to hair as a measure of exposure to radioisotopes, but also to tissue damage and repair at the hair follicle.

In 1963, we (ref. 1) suggested that the strontium-90 content of hair provided a nondestructive method of estimating the body burden of this radioactive fission product. Sternberg (ref. 2), had previously noted that strontium-90 injected in pregnant guinea pigs was distributed to hair as well as to the embryos. Our results from studies on rats were quickly confirmed by Della Rosa et al. (ref. 3), who investigated beagles. Their data indicated that the strontium-90 content of beagle hair could be used to estimate directly the radionuclide concentration of the diet and plasma,

and indirectly the remodeling labeled portion of the skeletons. Late in 1964, Moeller et al. (ref. 4) reported that the strontium-90 content of human hair seemed to correlate with the levels of the radionuclide in the diet. This initial report was expanded by Magno et al. (ref. 5), who showed that there were some irregularities between the mean levels of strontium-90 in the diet, and in the hair collected from children living in five installations participating in U.S. Public Health Service Institutional Diet Sampling Program.

The accumulation of other radioisotopes in the hair of several species has been studied by various investigators. Cesium-137 (ref. 6) has been shown to be present in Alaskan Eskimo hair as a result of fallout, but correlation with body burden has not been definitely established. Iron-59 (ref. 7), sulphur-35 (ref. 8), and zinc-65 (ref. 9) have also been shown to accumulate in human hair. Among the first radioisotopes to be studied in this way, were selenium-75 in dog hair (ref. 10), and iodine-131 (ref. 11,12) in rat hair. Other radioisotopes investigated in rat hair include cobalt-58 (ref. 13), vanadium-48 (ref. 14), and zinc-65 (ref. 15,16).

The mechanisms by which radioisotopes, especially of trace elements, accumulate in hair and other tissues are important to us. We are investigating the metabolism of trace elements with radioisotopes to develop new diagnostic procedures, to evaluate tissue damage from toxic excesses, to develop new therapies for burn and wound healing, and to study particulate pollutants. Accordingly, we have explicated the tropism of various radionuclides for rat hair by comparing the radioactivity of clipped with plucked hair at various time intervals after intravenous injection of ecologically important radioisotopes. The plucked hair includes the hair follicle where important biochemical transformations are taking place. The radionuclides employed were iodine-131 (T/2, 8D), manganese-54 (T/2, 300D), strontium-85 (T/2, 64D), and zinc-65 (T/2, 245D).

METHODS AND RESULTS

The procedure used for measuring the accumulation of radioisotopes in rat hair was an elaboration of a previously described method (ref. 17). The radionuclides studied included sodium iodide-I-131, manganous-Mn-54 chloride, strontium-Sr-85 chloride, and zinc-Zn-65 chloride. Commercial preparations of these radioisotopes with high specific activity were diluted with normal saline so that 1.0 ml of each solution contained ca 5 μCi. Both young adult and old retired breeder male Sprague-Dawley rats were used, so that age effects could be investigated. Eight rats were injected in a tail vein with 1.0 ml of each radioisotope, and then divided into two groups of four animals each so that adequate quantities of hair could be harvested. Samples of hair ranging in weight from 0.20 to 0.50 mg were plucked with tweezers or shaved with animal clippers from the back of each rat at intervals of 1,2,4,6,12, or 24 hrs. These hair samples were weighed to 1 mgm, counted in a deep-well gamma scintillation counter, and the specific activity calculated. Between intervals of sample collection, the rats were housed individually in stainless steel cages provided with food and water ad lib. A 1.0 ml aliquot of each radioisotope solution was diluted to 100 ml, and 1.0 ml of this diluted solution was counted simultaneously with the hair samples to

provide a standard that was corrected for decay to calculate retention of injected dose per gram of hair.

The results are shown graphically in figures 1-5, in which the mean values and range of the percent retention of each radioisotope per gram of hair are plotted against time on semilogarithmic paper. As is evident from these graphic representations, the patterns of accumulation are similar for all radionuclides. The plucked hair with follicle always retained a higher percent of radioisotope per gram of hair than the shaved hair. The effect of age is to reduce slightly the rate of accumulation of each radioisotope in hair, as is illustrated by the comparison of data on the accumulation of strontium-85 in shaved hair of young adult and old breeder male rats, in figure 5. Standard errors and analyses of significance have not been included because these values probably cannot be applied to the hair samples, and would mask certain peculiarities if they were routinely used.

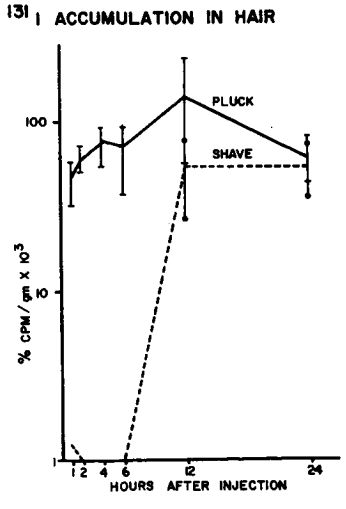

Figure 1. Comparison of iodine-131 retention in plucked and shaved rat hair following intravenous injection of ca 5 μCi of sodium iodide-I-131 in normal saline. The large differences between the radioactivity of plucked and shaved hair suggest that radioiodine accumulates rapidly in the hair follicle, and enters the hair shaft slowly from the follicle.

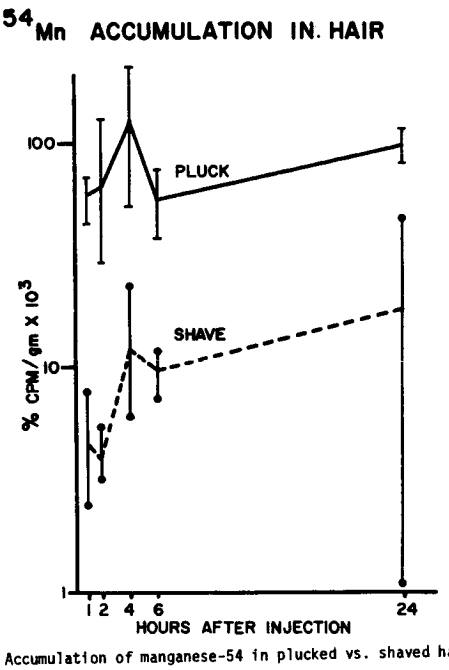

Figure 2. Accumulation of manganese-54 in plucked vs. shaved hair, following intravenous injection of ca 5 μCi of manganous-Mn-54 chloride, shows an initial slight surge of the radioisotope into both kinds of hair.

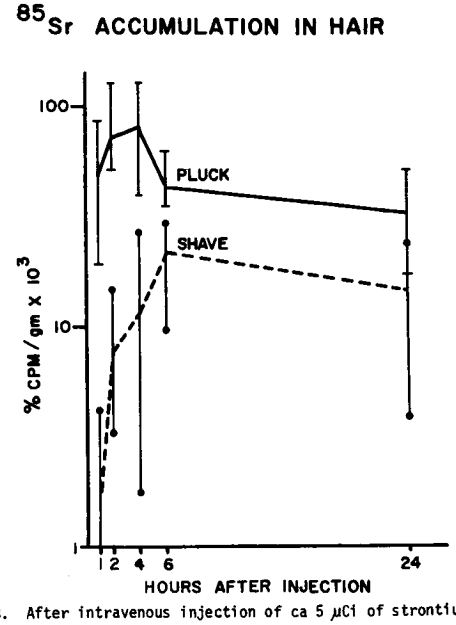

Figure 3. After intravenous injection of ca 5 μCi of strontium-Sr-85 chloride into rats, plucked hair shows a surge of the radioisotope, but shaved hair does not. This suggests that the radionuclide accumulates rapidly in the hair follicle, and passes slowly into the hair shaft from the follicle.

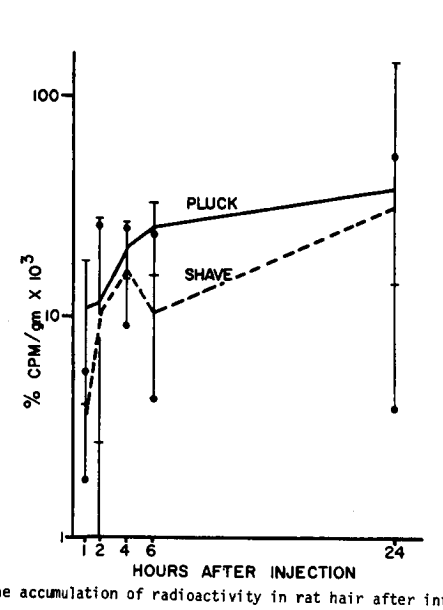

Figure 4. The accumulation of radioactivity in rat hair after intravenous injection of ca 5 μCi of zinc-Zn-65 chloride is slower than of the other radioisotopes, and the difference in radioactivity of plucked and shaved hair is small. Although the rate of accumulation of zinc-65 is slow initially, hair and bone become, and remain, the tissues with the highest specific activity after eight days.

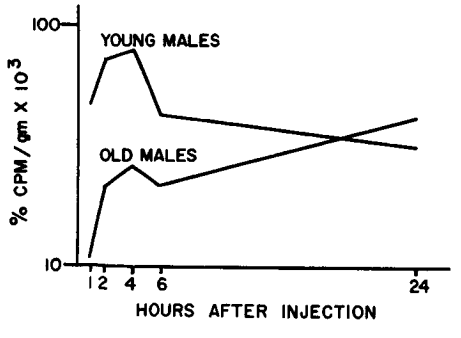

Figure 5. Comparison of uptake of strontium-85 in plucked hair from young adults and old retired male breeder rats indicates a faster rate of accumulation of radioisotope in the hair by the younger animals.

DISCUSSION

The curves showing the large ranges and mean values for the accumulation of the four radionuclides in plucked and shaved hair bring out similarities and differences. The large ranges probably relate to the mixture of hair in growing, transitional, and resting stages which are obtained by the sampling procedure. Iodine-131, manganese-54, and strontium-85, but not zinc-65, show a surge of radioactivity into the hair immediately after injection. This surge is followed by an ebbing out from the hair tissue which suggests that the hair levels reflect both the rise and fall in blood levels and something about the biochemistry of the hair follicle. There are significant differences in the retention patterns of manganese-54 (figure 2) and strontium-85 (figure 3) between plucked and shaved hair which indicate that the rate of uptake is much greater for strontium-85 than for manganese-54. As shown by the differences in the curves for the radioactivity of plucked and shaved hair in figure 1, iodine-131 seems to accumulate rapidly in the hair follicle and is then slowly transferred to the hair shaft. Zinc-65, in contrast, enters the hair follicle less rapidly than the other radioisotopes, and, apparently, is transferred rapidly to the hair itself, as shown in figure 4. The absence of a surge and ebb response may be related to the information of stable ligands of zinc with the sulfhydryl groups which are abundant in hair.

The effect of age on the uptake of radioisotopes is brought out in figure 5 which shows a comparison of uptake of strontium-85 by the hair of younger adult with that of old retired breeder male rats. Strontium-85 is particularly suitable

for this comparison since it is the only radionuclide of the four which seems to be transferred easily from hair follicle to hair shaft. As is evident from the two curves, the accumulation of strontium-85 is much less in the hair of the older than of the younger animals.

Hair growth proceeds through three stages designated as anagenesis, catagenesis, and telogenesis (ref. 18). In anagenesis, there is active growth of hair from the follicle, but there is little information on the biomechanisms for producing keratin, the protein of hair which has such a high sulfur content. Keratin synthesis presumably takes place in the hair follicle, and incorporation of labeled sulfur amino acids, such as cystine-S-35, in hair is so prompt that injection of small amounts of this radiolabeled amino acid into an animal provides a way of measuring hair growth (ref. 19). The incorporation of most inorganic elements in hair is usually explained as an excretion, but there is no real information on possible mechanisms of the excretion. Presumably, the excretion takes place in the hair follicle, where some of these elements from ligands with sulfhydryl and other chelating groupings of keratin. The iodine content of hair, however, is the highest of any body tissue other than thyroid, and, apparently, the iodine is present entirely as inorganic iodide (ref. 11,12).

Determination of hair radioactivity has potential as a method of diagnosing inadvertent exposure to radioisotopes or radiation which produces radioisotopes in the body (ref. 20,21). Additional investigations are needed to establish the best methods of sampling and handling hair and related tissues, and of developing statistical relationship. Statistical analysis does not seem appropriate for the present studies because of the short cycle of hair growth in the rat of about 28 days. It is difficult to distinquish the stage of a cycle without a biopsy of the skin which would invalidate further work. Since the hair cycle is very much longer in man, as much as three years, and some head hairs persist for many years, hair analysis seems much more appropriate for man.

Exposure to high levels of radionuclides usually produces burns and traumatic injuries. The specialized tissues of the hair follicle and sebaceous glands are stimulated by injury to form migrating epithelium which will cover the injured surface (ref. 22). Since we (ref. 23) and others (ref. 24,25) have found that oral zinc therapy promotes healing of burns and wounds in man, there is need for an understanding of the biochemistry of hair follicles and hair formation. Accordingly, investigations on the accumulation of stable and radioactive forms of the elements in hair may provide additional information for the repair of burns, trauma, and critical injuries. These studies are sorely needed because of the lack of programs to furnish such basic information.

REFERENCES

1. Hopkins, B.J.; Tuttle, L.W.; Pories, W.J.; and Strain, W.H.: Science, vol. 139, 1963, p. 1064.

2. Sternberg, J.: Strahlentherapie, vol. 45, Sonderband IV, 1960, p. 73.

3. Della Rosa, R.J.; Gielow, F.; and Peterson, G.: U.S.A.E.C., Document UCD No. 108, 1963, p. 37; Nature, vol. 211, 1966, p. 777.

4. Moeller, D.W.; Baratta, E.J.; and Leonard, I.E.: Public Health Rep., vol. 79, 1964, p. 1030.

5. Magno, P.J.; Baratta, E.J.; and Leonard, I.E.: Health Physics, vol. 12, 1966, p. 1493.

6. Beasley, T.M.; and Palmer, H.E.: Health Physics, vol. 11, 1965, p. 454.

7. Weintraub, L.R.; Demis, D.J.; Conrad, M.E.; and Crosby, W.H.: Amer. J. Path., vol. 46, 1965, p. 121.

8. Haley, H.B.; and Williamson, M.B.: J. Cell. Comp. Physiol., vol. 55, 1960, p. 234.

9. Strain, W.H.; Lankau, C.A., Jr.; and Pories, W.J.: Nature, vol. 204, 1964, p. 490.

10. McConnell, K.P.; and Dreamer, A.E.: Proc. Soc. Exp. Biol. Med., vol. 105, 1960, p. 1970.

11. Leblond, C.P.; Endocrinology, vol. 54, 1954, p. 104.

12. Brown-Grant, K.; and Pethes, G.: J. Physiol., vol. 152, 1960, p. 474.

13. Strain, W.H.; Berliner, W.P.; Lankau, C.A., Jr.; McEvoy, R.K.; Pories, W.J.; and Greenlaw, R.H.: J. Nucl. Med., vol. 5, 1965, p. 664.

14. Gilbert, I.G.F.; and Taylor, D.M.: Biochem. Biophys. Acta, vol. 31, 1956, p. 545.

15. Ballou, J.E.; and Thompson, R.C.: Health Phys., vol. 6, 1961, p. 6.

16. Palmer, H.E.; and Beasley, T.M.: Health Physics, vol. 13, 1967, p. 889.

17. Strain, W.H.; Danahy, D.T.; O'Reilly, R.J.; Thomas, M.R.; Wilson, R.M.; and Pories, W.J.: Trans. Amer. Nuclear Soc., vol. 8, 1965, p. 332.

18. Montagna, W.; and Ellis, R. (ed.): Biology of Hair Growth, Academic Press, New York, 1958.

19. Munro, D.D.: Arch. Dermat., vol. 93, 1966, p. 119.

20. Van Dilla, M.A.; and Engelke, M.J.: Science, vol. 131, 1960, p. 830.

21. Cohn, S.H.; Love, R.A.; and Gusmano, E.A.: Science, vol. 133, 1961, p. 1362.

22. Eisen, A.Z.; Holyoke, J.B.; and Lobitz, W.E.: J. Invest. Derm., vol. 25, 1965, p. 145.

23. Pories, W.J.; Henzel, J.H.; Rob, C.G.; and Strain, W.H.: Lancet, vol. i, 1967, p. 121.

24. Husain, S.L.: Lancet vol. i, 1969, p. 1069.

25. Larsen, D.L.; Maxwell, R.; Abston, S.; and Dohrkovsky, M.: Plastic Reconstr. Surg., vol. 46, 1970, p. 13.

LIST OF ATTENDEES
(Name, Affiliation and Mailing Address)

H. Aceto
College of William and Mary
Space Radiation Effects Laboratory
Williamsburg, Virginia 23185

G. C. Ainsworth
Air Force Weapons Laboratory
Kirtland Air Force Base, New Mexico

P. Alexander
Teledyne Isotopes
39 Rose Avenue
Woodcliff Lake, New Jersey

R. E. Alexander
NASA Headquarters
9407 Stuart Avenue
Manassas, Virginia 22110

R. G. Alsmiller, Jr.
Oak Ridge National Laboratory
150 N. Seneca Road
Oak Ridge, Tennessee

G. H. Anno
ART Research Corporation
12251 Darlington Avenue
Los Angeles, California

T. W. Armstrong
Oak Ridge National Laboratory
613 W. Hardwicke Drive
Knoxville, Tennessee

W. Atwell
Lockheed Electronics Company
535 NASA Boulevard
Webster, Texas 77598

W. E. Austin
General Electric Company
99 Anthony Wayne Drive
Wayne, Pennsylvania 19087

N. A. Baily
University of California, San Diego
La Jolla, California

J. V. Bailey
NASA Manned Spacecraft Center
3942 Wagon Road
Dickinson, Texas 77534

J. Barengoltz
Jet Propulsion Laboratory (233-201)
4800 Oak Grove
Pasadena, California 91103

D. Bartine
Oak Ridge National Laboratories
819 Patton Ferry Road
Kingston, Tennessee 37763

D. K. Barton
EG&G Inc.
680 Sunset Road
Las Vegas, Nevada

F. R. Basque
Aerojet Nuclear Systems Company
P. O. Box 13070
Sacramento, California

J. J. Baum
Analog Technology Corporation
3410 E. Foothill Boulevard
Pasadena, California

G. V. Beard
Associated Western Universities
136 E. So. Temple
Salt Lake City, Utah

H. L. Beck
U. S. Atomic Energy Commission
376 Hudson Street
New York City, N.Y.

W. L. Beck
Oak Ridge Assoc. Universities
274 East Drive
Oak Ridge, Tennessee 37830

E. V. Benton
University of San Francisco
Physics Department
San Francisco, California 94117

C. A. Berry
Medical Research and Operations
NASA Manned Spacecraft Center
Houston, Texas 77058

M. P. Billings
McDonnell Douglas-WD
6212 W. 82nd Street
Los Angeles, California 90045

J. B. Blake
Aerospace Corporation (120/1825)
P. O. Box 95085
Los Angeles, California 90045

J. L. Bloom
U. S. Atomic Energy Commission
11600 Georgetowne Ct.
Rockville, Md. 20854

A. L. Bond
Los Alamos Scientific Laboratory
3006 El Camino Avenue
Las Vegas, Nevada

V. P. Bond
Brookhaven National Lab
12 Cedar Lane
Setauket, New York

G. B. Bradshaw
Gulf General Atomic
1320 Puterbawgh Street
San Diego, California

J. Braly
Martin Marietta Corporation
5850 Bell Flower Drive
Littleton, Colorado 80123

R. L. Brodzinski
Battelle-Northwest
423 Sierra
Richland, Washington

N. J. Brown
Lawrence Radiation Laboratory
955 Via Seville
Livermore, California

B. L. Buchanan
Air Force Cambridge Research Laboratory
Baldwin Road
Carlisle, Mass.

T. Budinger
Lawrence Radiation Laboratory
Berkeley, California

C. E. Burgart
Oak Ridge National Laboratory
Oak Ridge, Tennessee 37830

T. C. Burke
AIAA
1728 Loch Lomond
Las Vegas, Nevada 89102

M. O. Burrell
NASA Marshall Space Flight Center
Rt. 4, Rainbow Drive
Madison, Alabama 35758

Mary Ann Capo
Westinghouse Astronuclear Laboratory
1221 Berkshire Avenue
Pittsburgh, Pennsylvania

R. T. Carpenter
U. S. Atomic Energy Commission
Washington, D.C. 20545

H. G. Carter, Jr.
General Dynamics/Fort Worth
7405 Llano
Fort Worth, Texas

R. J. Cerbone
Gulf Radiation Technology
P. O. Box 608
San Diego, California

J. T. Cervini
Air Force Weapons Laboratory
512A Kentucky Street SE
Albuquerque, New Mexico 87108

W. L. Chadsey
General Electric (VFSTC)
Re-Entry and Environmental Systems Division
P. O. Box 8555
Philadelphia, Pennsylvania 19101

G. T. Chapman
Oak Ridge National Laboratory
114 Canterbory Road
Oak Ridge, Tennessee

P. K. Chapman
NASA Astronaut Office
NASA Manned Spacecraft Center (Code CB)
Houston, Texas 77058

C. Childs
University of North Carolina
Apt. 18-I: Sharon Heights Apts.
Chapel Hill, North Carolina

J. B. Cladis
Lockheed Research Laboratory
15 Bear Gulch Drive
Portola Valley, California 94025

C. E. Clifford
Oak Ridge National Laboratory
Rt. 7
Concord, Tennessee

R. L. Clothier
Aerojet Nuclear Systems Company
9512 Tonkin Drive
Orangevale, California

W. A. Coleman
Science Applications, Inc.
5942 Erlanger Street
San Diego, California

J. Conant
Aerojet Nuclear Systems Company
Box 59
Tesuque, N.M.

M. Cordaro
LILCO
175 E. Old Country Road
Hicksville, New York 11801

J. C. Courtney
Aerojet Nuclear Systems Company
10831 Coloma Road
Rancho Cordova, California

O. L. Curtis
Northrop Corporation Labs
4 Pony Lane
Rolling Hills, California

S. B. Curtis
Radiobiological Institute T.N.O.
151 Lange Kleiweg
Rijswijk, The Netherlands

M. D. D'Agostino
Grumman Aerospace Corporation
Bethpage, New York 11714

H. S. Davis
Jet Propulsion Laboratory
519 Paulette Place
La Canada, California 91011

J. R. Davolio
Aerojet Nuclear Systems Company
10819 Dunbar
Rancho Cordova, California

A. Delapaz
White Sands Missile Range
10220 Montwood
El Paso, Texas 79925

C. A. DeLorenzo
Aerojet Nuclear Systems Company
2616 Burton Avenue
Las Vegas, Nevada 89102

R. Detterman
Atomics International
120 Colt Lane
Thousand Oaks, California 91361

B. Dietrick
Aerojet Nuclear Systems Company
Nuclear Rocket Development Station
Jackass Flats, Nevada

A. Dikansky
L. A. County Engineering
1401 N. Poineettia Place
Los Angeles, California

F. L. Dilorenzo
Aerojet Nuclear Systems Company
327 Garden Court
Roseville, California

N. Divine
Jet Propulsion Laboratory
1130 N. Verdugo #12
Glendale, California 91206

C. E. Dixon
Aerojet Nuclear Systems Company
959 Mammoth Way
El Dorado Hills, California

J. E. Donnelly
Westinghouse Astronuclear Laboratory
Jackass Flats, Nevada 89023

R. C. Drew
Office of Science and Technology
Executive Office of the President
Washington, D.C.

A. B. Driscoll
Central Research Labs, Inc.
Red Wing, Minnesota 55066

B. Eastlund
U. S. Atomic Energy Commission
12312 Village Square Terrace
Rockville, Md. 20852

G. W. R. Endres
Battelle-Northwest
1206 Mahan
Richland, Washington 99352

W. W. Engle, Jr.
Oak Ridge National Laboratory
104 Paint Rock Road
Kingston, Tennessee 37763

P. B. Erickson
NASA-AEC Space Nuclear Systems Office
801 South Mallard
Las Vegas, Nevada

D. E. Ewing
Air Force Weapons Laboratory
633 Monroe N.E.
Albuquerque, New Mexico 87110

E. M. Faelten
TRW Systems
1412 Butler Avenue #14A
West Los Angeles, California 90025

B. J. Farmer
Advanced Technology Center Inc.
512 E. Arkansas Lane #15
Arlington, Texas

L. G. Faust
Battelle-Northwest
P. O. Box 999
Richland, Washington 99352

G. J. Fishman
Teledyne-Brown Engr. Company
416 Julia Street, Apt. 119
Huntsville, Alabama

M. R. Fleishman
NASA-AEC Space Nuclear Systems Office
21000 Brookpark Road
Cleveland, Ohio 44135

T. Foelshe
NASA-Langley Research Center
604 Old Landing Road
Yorktown, Virginia

W. E. Ford, III
Union Carbide Corporation
245 Landoak Lane
Concord, Tennessee 37720

D. C. Frick
EG&G Inc.
1733 Ophir Drive
Las Vegas, Nevada

W. Friedberg
Federal Aviation Administration
7805 N.W. 26 Street
Bethany, Oklahoma

J. Froechtenigt
Martin-Marietta Corporation
5860 N. Canyon Drive
Littleton, Colorado 80123

M. J. Gaitanis
U. S. Atomic Energy Commission
8807 Bells Mill Road
Potomac, Md.

D. Garcia
North American Rockwell
1261 Pine Edge Drive
La Habra, California

S. J. Gerathewohl
Federal Aviation Administration
5208 Albemarle Street
Washington, D.C. 20016

E. Gordon
Aerojet Electro Systems Company
974 Ottawa Drive
Claremont, California

D. Grahn
Argonne National Laboratory
Argonne, Illinois 60439

D. Gray
Aerojet Nuclear Systems Company
3821 Turf Circle
Las Vegas, Nevada

W. A. Greenhow
General Dynamics/Fort Worth
3703 Gene Lane
Haltom City, Texas

J. C. Gregory
Teledyne Brown Eng.
621 Franklin Street
Huntsville, Alabama

G. Guenther
University of Alabama
1209 Governors Drive
Huntsville, Alabama 35801

J. W. Haffner
North American Rockwell Space Division
16390 Colegio Drive
Hacienda Heights, California

D. J. Hamman
Battelle Memorial Institute
505 King Avenue
Columbus, Ohio 43201

W. J. Hare
USAF-Aerospace Research Labs
Wright-Patterson AFB, Ohio

R. W. Harman
Analog Technology Corporation
3410 E. Foothill Boulevard
Pasadena, California

M. S. Harris
Air Force Office of Scientific Research
4118 Summit Place
Alexandria, Virginia

R. A. Hartman
NASA Headquarters (MM)
Washington, D.C.

A. J. Haverfield
Battelle-Northwest
P. O. Box 999
Richland, Washington 99352

C. A. Heath
Gulf General Atomic
6127 Syracuse Way
San Diego, California

R. D. Heimbach
Air Force Weapons Laboratory (SA)
Kirtland AFB, New Mexico 87118

H. D. Hendricks
NASA-Langley Research Center
15 Marldale Drive
Hampton, Virginia 23366

A. E. Hey III
Grumman Aerospace
Bethpage, New York 11714

F. E. Holly
Air Force Weapons Laboratory
Kirtland AFB, New Mexico

D. Holzman
Aerojet Nuclear Systems Company
4149 Buchanan Drive
Fair Oaks, California

K. C. Hopkins
Air Force Weapons Laboratory
Kirtland AFB, New Mexico 87117

J. W. Humphreys Jr.
NASA Headquarters (MM)
Washington, D.C.

P. Hutchinson
Lockheed Missiles & Space Company
5362 Eileen Drive
San Jose, California

A. Interian
General Electric Company
Valley Forge Space Technology Center
P. O. Box 8555
Philadelphia, Pennsylvania 19101

R. G. Ivanoff
Jet Propulsion Lab.
4800 Oak Grove Drive
Pasadena, California

M. T. Johnson
Westinghouse Astronuclear Laboratory
P. O. Box 10864
Pittsburg, Pennsylvania 15236

P. G. Johnson
NASA-AEC Space Nuclear Systems Office
U. S. Atomic Energy Commission
Washington, D.C. 20545

T. M. Jordan
ART Research Corporation
1570 S. Bundy Drive
Los Angeles, California

E. H. Judkins
Savanah River
P. O. Box 6103
North Augusta, South Carolina 29841

I. M. Karp
NASA-Lewis Research Center
21000 Brookpark Road
Cleveland, Ohio 44130

P. G. Kase
Martin-Marietta Corporation
11865 West 22nd Place
Lakewood, Colorado 80215

J. W. Keller
NASA Headquarters (SL)
Washington, D.C. 20546

V. Keshishian
Atomics International
4545 Willis Avenue
Sherman Oaks, California 91403

K. D. Kirby
Lockheed-Georgia Co.
891 Richard Street
Marietta, Georgia

M. Klein
NASA-AEC Space Nuclear Systems Office
U. S. Atomic Energy Commission
Washington, D.C. 20545

R. L. Kloster
McDonnell Douglas Corporation
13237 Greenbough Drive
St. Louis, Missouri 63141

G. A. Kuck
Air Force Weapons Laboratory
2058B Crossroads Pl. SE
Albuquerque, New Mexico 87110

J. Lacetera
Nuclear Effects Laboratory, Dept. of Defense
8415 Bellona Lane
Towson, Md. 21204

L. C. Laciny
McDonnell-Douglas
P. O. Box 516
St. Louis, Missouri 63166

G. P. Lahti
NASA-Lewis Research Center
229 Wayne Drive
Berea, Ohio 44017

A. G. Lane
North American-Rockwell
9121 Vons Drive
Garden Grove, California

R. W. Langley
McDonnell Douglas
7322 W. 90th Street
Los Angeles, California 90045

G. C. Langner
EG&G Inc.
P. O. Box 809
Los Alamos, New Mexico

L. J. Larzerotti
Bell Laboratories
Murray Hill, New Jersey 07974

J. C. Law
AVCO Corporation
10700 E. Independence
Tulsa, Oklahoma 74115

L. B. Lay Jr.
AVCO Electronics
Box N Admiral Station
Tulsa, Oklahoma 74115

J. Leith
Lawrence Radiation Laboratory
2045 Hey Boulevard
El Cerrito, California

J. T. Leh
Colorado State University
2017 West Lake
Fort Collins, Colorado

P. W. Levy
Brookhaven National Laboratory
Upton, New York 11973

C. F. Leyse
Aerojet Nuclear Systems Company
Rt. 3, Box 534
Placerville, California 95667

P. E. Lindquist
Hughes Aircraft
4201 Via Marina
Marina Del Rey, California

D. G. Lindstrom
Aerojet Nuclear Systems Company
8131 Capitola Avenue
Fair Oaks, California

Stuart Lippincott
Medical College of Virginia
1200 East Broad Street, Box 87
Richmond, Virginia

L. Little
Aerojet Nuclear Systems Company
P. O. Box 13070
Sacramento, California

J. A. Lonergan
Science Applications Inc.
P. O. Box 2351
La Jolla, California 92037

W. M. Lowder
U. S. Atomic Energy Commission
376 Hudson Street
New York, N.Y. 10014

L. F. Lowe
Air Force Cambridge Research Laboratory
7 McMahon Road
Bedford, Ma. 01730

Max Luming
Hughes Aircraft Company
Space & Communications Group
Building 366/C1081
El Segundo, California

C. C. Lushbaugh
Oak Ridge Assoc. Universities
Box 117
Oak Ridge, Tennessee

R. Madey
Clarkson College
Potsdam, New York 13676

L. Maggio
Grumman Aerospace
48 Highland Down
Shoreham, New York 11786

R. E. Malenfant
Los Alamos Scientific Laboratory
P. O. Box 1663
Los Alamos, New Mexico

H. S. Manning
NASA-Marshall Space Flight Center
2110 Fulton Drive
Huntsville, Alabama 35810

B. F. Maskewitz
Radiation Shielding Information Center
Oak Ridge National Laboratory
113 Patomac
Oak Ridge, Tennessee 37830

A. S. Mays
Lockheed Research Laboratory
P. O. Box 225
Palo Alto, California 94302

E. W. McCauley
Lawrence Radiation Lab
1733 Beachwood Way
Pleasanton, California

W. E. McDermott
USAF-LVSP, Attn. NYNI
McClellan Air Force Base, California

J. E. McLaughlin
U. S. Atomic Energy Commission
AEC/Health and Safety Laboratory
376 Hudson Street
New York, N.Y. 10014

D. R. McMorrow
Philco-Ford
3939 Fabian Way
Palo Alto, California

P. McNulty
Air Force Cambridge Research Labs. (PHE)
Bedford, Mass 01730

E. O. Meals
Idaho Nuclear Corporation
2935 Fieldstream
Idaho Falls, Idaho

T. P. Merrick
Westinghouse Astronuclear Laboratory
6174 Boxer Drive
Bethel Park, Pennsylvania

A. Metzger
Jet Propulsion Laboratory
4800 Oak Grove Drive
Pasadena, California

C. G. Miller
Jet Propulsion Laboratory
4800 Oak Grove Drive
Pasadena, California

E. W. Miller
Space Nuclear Systems Office-Cleveland
20946 Northwood Avenue
Cleveland, Ohio 44126

R. P. Minx
Environmental Protection Agency
2369 Longview Drive
Woodbridge, Virginia

P. S. Mittelman
Magi
180 S. Broadway
White Plains, New York 10605

J. F. Mondt
Jet Propulsion Laboratory
4800 Oak Grove Drive
Pasadena, California 91103

J. L. Montour
Medical College of Virginia
Box 31
Richmond, Virginia

W. J. Nalesnik
University of Pennsylvania
Dept. of Physics
Colgate University
Hamilton, New York 13346

P. E. Neal
Aerojet Nuclear Systems Company
4721 Marconi #15
Carmichael, California

R. A. Neff
Mound Laboratory, MRC
5553 Forest Bend Drive
Dayton, Ohio

J. M. Neill
Gulf Radiation Technology
P. O. Box 608
San Diego, California 92112

R. M. Nelson
U. S. Atomic Energy Commission
4445 Denia Cr.
Las Vegas, Nevada

K. O'Brien
U. S. AEC-Health & Safety Laboratory
30 Dover Terrace
Monsey, New York 10952

J. M. O'Byrne
University of Mass.
163 Northampton Road
Amherst, Mass. 01002

V. J. Orphan
Gulf Radiation Technology
2377 Newcastle Avenue
Cardiff, California 92007

N. Z. Osborne
NASA-Manned Spacecraft Center (TG-7)
Houston, Texas

N. P. Page
National Cancer Institute
702 W. Edmonston Drive
Rockville, Mo. 20852

J. A. Palmer
U. S. Air Force Academy (DFP)
Colorado Springs, Colorado

R. H. Parker
Jet Propulsion Laboratory
1154 S. Oakland Avenue
Pasadena, California

J. B. Parkinson
Aerojet Electro Systems Company
2039 Norwalk Avenue
Los Angeles, California 90041

T. A. Parnell
NASA-Marshall Space Flight Center (S&E/SSL)
Marshall Space Flight Center
Alabama 35812

G. A. Paulikas
Aerospace Corporation
P. O. Box 95085
Los Angeles, California 90045

C. A. Paulsen
University of Washington
School of Medicine U.S. Public Health Service Hospita
P.O. Box 3145
Seattle, Washington

R. W. Peelle
Oak Ridge National Laboratory
P. O. Box X
Oak Ridge, Tennessee

R. B. Philbrick
Air Force Weapons Laboratory (SYA)
Kirtland AFB, New Mexico 87117

J. F. Piccolo
EG&G Inc.
680 E. Sunset Road
Las Vegas, Nevada

J. E. Pickering
School of Aerospace Medicine
Brooks AFB, Texas

R. K. Plebuch
TRW Systems
28563 Blythewood Drive
Palos Verdes, California

W. F. Preeg
Aerojet Nuclear Systems Company
870 Shasta Circle
El Dorado Hills, California

B. Pregel
New York Academy of Sciences
50 Rockefeller Plaza Suite 1009
New York, New York 10020

C. A. Preskitt
Gulf Radiation Technology
8705 La Jolla Scenic Drive
La Jolla, California

W. E. Price
Jet Propulsion Laboratory
4615 Hampton Road
La Canada, California 91011

R. K. Purves
St. Josephy's Hospital
3333 E. Central
Wichita, Kansas

W. M. Quam
EG&G Inc.
P. O. Box 98
Goleta, California 93017

A. Reetz, Jr.
NASA Headquarters (RX)
Washington, D.C. 20546

M. Reier
Jet Propulsion Lab.
4800 Oak Grove Drive
Pasadena, California

R. C. Ricks
Oak Ridge Associated Universities
Box 117
Oak Ridge, Tennessee

R. C. Riley
University Kansas Medical Center
Kansas City, Kansas 66103

M. C. Rinehart
Philco-Ford
2447 Benjamin Drive
Mountain View, California

D. R. Rogers
Aerojet Nuclear Systems Company
6913 Mercedes Avenue
Citrus Heights, California

A. F. Rohacb
Iowa State University
Department of Nuclear Engineering
Ames, Iowa 50010

W. B. Rose
General Dynamics/Fort Worth
4001 Sacita Drive
Ft. Worth, Texas

S. G. Rosen
U. S. Air Force Rocket Propulsion Laboratory
(LKOA)
Edwards Air Force Base, California 93523

H. H. Rossi
Columbia University
630 W. 168th
New York City, N.Y.

E. L. Royal
Jet Propulsion Laboratory
5230 Veronica Street
Los Angeles, California

S. Russak
Martin Marietta Company
5800 S. Kearney
Englewood, Colorado

E. W. Salmi
Los Alamos Scientific Laboratory
2920 Arizona
Los Alamos, New Mexico

A. Sanders
ART Research Corporation
3739 Sheridge Drive
Sherman Oaks, California 91403

A. C. Sanderson
Westinghouse Astronuclear Laboratory
5654 Florida Avenue
Pittsburg, Pennsylvania

H. W. Sankey
Penberthy
6701 Maynard So.
Seattle, Washington 98108

D. R. Saxton
NASA Marshall Space Flight Center
1011 Cole Drive
Huntsville, Alabama

H. J. Schaefer, Ph 1
Naval Aerospace Medical Research Laboratory
Pensacola, Florida 32512

L. A. Schairer
Brookhaven National Laboratory
29 Bay Road
Brookhaven, New York 11719

N. M. Schaeffer
Radiation Research Assoc.
3550 Hulen Street
Fort Worth, Texas

E. J. Schneeil
Grumman Aerospace Corporation
28 Harvard Lane
Commack, New York

M. F. Schneider
Air Force Weapons Laboratory
9800 Dorothy Place NE
Albuquerque, New Mexico

R. E. Schreiber
Los Alamos Scientific Laboratory
1300 20th
Los Alamos, New Mexico

F. C. Schwenk
NASA-AEC Space Nuclear Systems Office
U. S. Atomic Energy Commission
Washington, D.C. 20545

J. F. Scoles
GE/Knolls Atomic Power Laboratory
18 Haviland Drive
Scotia, New York

W. E. Selph
Gulf Radiation Technology
RFD N20
Del Mar, California

W. M. Shedd
Air Force Cambridge Research Laboratory
L.G. Hanscom Field
Bedford, Mass 01720

C. J. Shellabarger
Brookhaven Nat Lab
Upton, New York 11973

D. C. Shreve
Science Applications Inc.
P. O. Box 2351
LaJolla, California 92037

E. G. Shelley
Lockheed Research Laboratories
3251 Hanover
Palo Alto, California

G. J. Sieren
NASA-Marshall Space Flight Center
4010 Dobbs Drive, S.E.
Huntsville, Alabama

E. C. Smith
Hughes Aircraft Company
2725 Firethorne Avenue
Fullerton, California 92631

H. T. Smith
Teledyne Brown Engineering Company
M.S. 5 Research Park
Huntsville, Alabama 35807

R. E. Smith
Los Alamos Scientific Lab
3101 Hastings Avenue
Las Vegas, Nevada 89107

C. A. Sondhaus
University of California
Irvine College of Medicine
Irvine, California

J. F. Spalding
Los Alamos Scientific Laboratory
154 El Rayo
Los Alamos, New Mexico

K. Stewart
U. S. Air Force
Space and Missile Systems Organization
Hq Samso, LAAFS, AF Unit Post Office
El Segundo, California

E. T. Still
Atomic Energy Commission
10113 Kinvoss Avenue
Silver Spring, Md 20901

A. J. Stosick
Aerojet Nuclear Systems Company
811 Coronado Boulevard
Sacramento, California 95825

W. H. Strain
Case-Western Reserve
3395 Scranton Road
Cleveland, Ohio 44109

E. A. Straker
Oak Ridge National Laboratory
995 W. Outer Drive
Oak Ridge, Tennessee

D. J. Strobel
U. S. Air Force
SAMSO (SVGN)
Norton AFB, California

P. Strom
Atomic Energy Commission
P. O. Box 1
Jackass Flats, Nevada

E. Stuhlinger
NASA-Marshall Space Flight Center
3106 Rowe Drive
Huntsville, Alabama

M. Taherzadeh
Jet Propulsion Laboratory (198-220)
4800 Oak Grove,
Pasadena, California

S. T. Taketa
NASA-Ames Research Center
3295 Lindenoaks Drive
San Jose, California

R. L. Tanner
University of Tennessee
450 North Avon Road
Memphis, Tennessee 38117

R. K. Thatcher
Batelle Memorial Institute
3318 Braidwood Drive
Columbus, Ohio 43220

J. R. Thomas
The Boeing Company
6226-122nd S.E.
Bellevue, Washington 98006

T. Thorslund
University of Washington
U.S. Public Health Service Hospital
P.O. Box 3145
Seattle, Washington

C. A. Tobias
Lawrence Radiation Laboratory
363 Donner Lab Univ Calif
Berkeley, California

V. Truscello
Jet Propulsion Laboratory
1429 Descanso Drive
La Canada, California

C. D. Turner
AF Cambridge Research Laboratories
Bedford, Mass.

R. Vallee
Monsanto
619 S. Bourbon
Blancheiter, Ohio

A. L. Vampola
Aerospace Corporation
2400 E. El Segundo Boulevard
El Segundo, California

M. A. Van Horn
General Electric Company
G.E. Space Division
P. O. Box 8661 CCF#8
Philadelphia, Pennsylvania 19101

J. I. Vette
Goddard Space Flight Center (Code 601)
Greenbelt, Md 20771

J. Vorreiter
NASA-Ames Research Center
937 Aster Court
Sunnyvale, California 94086

J. Vreeland
Sacramento State College
P. O. Box 254
Sacramento, California

C. J. Waddington
University of Minnesota
School of Physics
Minneapolis, Minnesota 55455

W. W. Wadman III
University of California
P. O. Box 4085
Irvine, California 92664

L. F. Wally
USAF Academy
Box 203
USAF Academy, Conn.

J. A. Wall
Air Force Cambridge Research Laboratories
L.G. Hanscom Field
Bedford, Mass. 01730

R. Wallace
University of California
Bldg. 72
Lawrence Radiation Laboratory
Berkeley, California 94720

C. C. Wan
Self-employed
2207 W. 35th Street
San Pedro, California 90732

E. A. Warman
Aerojet Nuclear Systems Company
P. O. Box 13070
Sacramento, California

J. W. Watters
USAF Academy
6301 J Street
Colorado Springs, Colorado

J. W. Watts
NASA-Marshall Space Flight Center
400 Chateau Drive, Apt. 614D
Huntsville, Alabama

F. H. Welch
Atomics International
North American Rockwell
11983 Elnora Place
Granada Hills, California

K. T. Wheeler Jr.
Colorado State University
719 S. Washington Apt. 118
Ft. Collins, Colorado 80521

A. C. Wilbur
NASA-Ames Research Center
Moffett Field, California 94035

A. L. Wiley
University of Wisconsin Medical Center
% Dept. of Radiation Therapy
Madison, Wisconsin 53706

Maurice Wickinson
The Boeing Company
12801 S.E. 186 Place
Renton, Washington

V. E. Winter
Programmed and Remote Systems
4701 Alpine Place
Las Vegas, Nevada

W. O. Wetmore
Aerojet Nuclear Systems Company
P. O. Box 13070
Sacramento, California

M. L. Wohl
NASA Lewis Research Center
13499 Trenton Trail
Middleburg Heights, Ohio

H. C. Woodsum
Westinghouse Astronuclear
592 Farview Drive
Greensburg, Pennsylvania 15601

W. A. Woolson
Aerojet Nuclear Systems Company
396 Parkfair
Sacramento, California 95825

K. J. Yost
Purdue University
116 Knox Drive
W. Lafayette, Indiana

J. M. Yuhas
U. S. Atomic Energy Commission
Biology Division, Bldg. 9207
Oak Ridge National Laboratory
Oak Ridge, Tennessee 37830

W. Zobel
Oak Ridge National Laboratory
P. O. Box X
Oak Ridge, Tennessee 37830

P. Zigman
Environmental Science Assoc.
770 Airport Boulevard
Burlingame, California

F. Zwicky
California Institute of Technology
2065 Oakdale Street
Pasadena, California

ADDENDUM

The addendum consists of a special report by Dr. P. K. Chapman, and two papers by Drs. S. B. Curtis and E. W. Salmi which arrived too late to be included in the main section of the Proceedings.

Dr. Chapman's remarks were delivered as part of Session IV.1; Dr. Curtis' paper was presented in Plenary Session V on Radiobiology; and Dr. Salmi's paper was presented in Session IV.3.

OBSERVATIONS OF COSMIC-RAY INDUCED PHOSPHENES ON APOLLO 14

P.K. Chapman*, L.S. Pinsky*, R.E. Benson*
and T.F. Budinger+

INTRODUCTION

Phosphenes, which may be defined as visual sensations in the absence of light entering the eye, are readily observed by dark-adapted subjects. The flashes and streaks produced by transient pressure on the eyeball (for example, by rubbing the eyes in the dark) are a familiar experience. It has been known for more than seventy years that X-rays of the head can produce diffuse flashes. Small pulses of electric current through the head produce displays which have been described as "lightning behind clouds". Recently, the experiments of Tobias et al (which were reported at this symposium and which have now been confirmed by other investigators) have shown that discrete flashes can be produced by a variety of nuclear particles, of widely varying energy, if they pass through the eyeball.

During a study of radiation hazards associated with flight at high altitudes and in spacecraft, Tobias[1] suggested in 1952 that "a dark adapted person should be able to 'see' very heavily ionizing single tracks as a small light flash". In the early 'Sixties, D'Arcy and Porter[2] carried out experiments which demonstrated a statistical correlation between sea-level cosmic radiation, primarily μ-mesons, and phosphenes observed by dark-adapted subjects. Tobias' prediction was strikingly confirmed during the flight of Apollo 11 in July, 1969, when Aldrin and Armstrong reported seeing flashes in lunar orbit, with their eyes closed or the spacecraft cabin darkened. All lunar crews since then have observed these flashes, so consistently that there can be no doubt that they are due to external stimuli, the obvious source being cosmic rays, rather than to some form of physiological stress. Nearly all the phosphenes reported by astronauts in the vicinity of the moon have been star-like flashes and narrow streaks, similar to those generated by accelerated particles in terrestrial experiments. Typically, about one flash per minute is seen in space.

Phosphenes have never been reported by astronauts in Earth orbit. Conrad[3] has stated that the flashes he saw on Apollo 12 were so bright that he could not have missed them if they had been present during his Gemini missions, V and XI. A possible explanation is that the phenomenon is caused by particles of such low energy that the magnetosphere of the Earth forms an effective shield, but this is inconsistent with at least one proposed mechanism, Cerenkov radiation from high-energy particles traversing the vitreous humor. Furthermore, the effect was not observed by the two lunar crews prior to Apollo 11. In particular, Lovell saw flashes on Apollo 13, but not on Apollo 8. The consensus appears to be that the flashes are readily observable, but only if one is alerted to look for them. The question of their observability in Earth orbit will be resolved at the next opportunity, which probably will not occur during the remaining Apollo missions, as they spend too little time in the vicinity of the Earth.

Apart from the intrinsic interest of this phenomenon, it is important to find the cause in order to determine whether a hazard may be present during long-duration (e.g., interplanetary) missions. By conventional radiation measurement standards, the whole-body dose due to cosmic radiation is quite low during most space missions, unless a major solar flare is encountered, but the biological interactions of the high-energy, high Z (HZE) particles common in space are not well understood. Further investigation is required to determine realistic human tolerance levels for extended missions and to evaluate the need to provide special spacecraft shielding.

The Cerenkov Hypothesis

Soon after the Apollo 11 mission, Fazio and Jelley[4] suggested that the flashes observed might be due to Cerenkov radiation generated by primary cosmic-ray particles passing through the vitreous humor of the astronauts' eyes. Since the electric field of a charged particle cannot propagate faster than the speed of light in the vitreous humor, it emits a conical electromagnetic shock wave, quite analogous to the sonic boom of a supersonic aircarft, if it is moving at a velocity $\beta=v/c > 1/n$, where n is the refractive index of the medium, ~ 1.34 in the present case. The shock front forms an angle

$$\theta = \cos^{-1}(n\beta)^{-1} \qquad [1]$$

to the direction of motion of the particle. For the fastest particles, this amounts to $\sim 41°$ in the eye. If the particle has charge Ze, the number of photons produced per centimeter, within the visual range 0.35-0.55 μ, is given by[5]

$$N \simeq 470\ Z^2 \sin^2\theta \qquad [2]$$

* NASA Manned Spacecraft Center, Houston, Texas
+ Lawrence Radiation Laboratory, Berkeley, Calif.

As the particle passes through a surface (e.g., the retina), a contracting annulus of light is thus produced, which is seen as a single flash because the process lasts about 0.1 nanosecond. For normal incidence, the illumination in the observed spot is easily shown to be

$$L = \frac{N}{2\pi \tan \theta} \simeq 38 \frac{Z^2}{r} \sin 2\theta \quad \text{photons/cm}^2 \quad [3]$$

where r is radial distance away from the point where the particle impacts the surface. Away from the fovea, the human retina contains about 13 million rods/cm^2, so the illumination may also be written

$$L = x/r \quad \text{photons/rod} \quad [4]$$

where the characteristic distance

$$x \simeq 0.03\ Z^2 \sin 2\theta \quad \text{microns} \quad [5]$$

may be taken as a rough estimate of the size of the perceived spot. For a relativistic stripped iron nucleus (Z=26), this gives a radius of about 20μ, corresponding to an apparent angular diameter of some 4 arc minutes. According to Ricco's Law[6], the threshold for vision should then be independent of the size of the spot depending only on the total number of photons contained in it. By integration of [3], out to a radius x, this is given by

$$M = Nx \cot \theta \simeq 7 \times 10^{-4} Z^4 \sin^2 2\theta \quad [6]$$

The fraction of light reaching the retina which is absorbed in dark adapted rods is [7] ∿0.2. However, the Cerenkov light contained in a spot of radius x is generated while the particle traverses a distance x cot θ. Since this is much less than the thickness of the retina, any perceived small spot caused by Cerenkov radiation is produced while the particle is actually traversing retinal cells (the photosensitive segments of the rods being on the outer side of the retina, next to the choroid), not while it is in the vitreous humor. The efficiency factor, determined from optical measurements, is therefore somewhat doubtful. To an adequate approximation, the number of absorbed photons is taken as

$$M' = 1.5 \times 10^{-4} Z^4 \sin^2 2\theta \quad [7]$$

For brief flashes subtending small angles, the measured visual threshold for thoroughly dark-adapted subjects corresponds[6] to about 10 photons absorbed by the rods. For relativistic particles, [7] then implies that point Cerenkov flashes will not be observed for Z < 16. If it is assumed that the uncertainties in the calculation produce an order of magnitude uncertainty in the coefficient of Z^4, the lower bound on Z becomes 9. In practice, this is not very important, since it is known that iron group nuclei (Z=24 to 28) predominate amongst the heavy (Z>10) cosmic rays[8]. According to [7] a relativistic stripped iron nucleus should produce a star-like flash which is of an intensity about one order of magnitude above the scotopic treshold.

Eq. [2] indicates that HZE particles produce about $200Z^2$ photons/cm while traversing the vitreous humor. If the average path length in the eye is taken as 15 mm, a fast iron nucleus can thus generate as many as 200,000 photons in the eyeball, but only a very small fraction of them are concentrated in the area of the retina around the point where the particle penetrates. The rest are scattered over much of the retinal surface, giving a very faint illumination which may produce a visual sensation, but not of the star-like type characteristic of observations in space. It is possible that particles of much lower charge can produce Cerenkov flashes, but it is expected that these would be of the diffuse, "summer lightning" type.

This analysis allows the following conclusions to be drawn concerning star-like Cerenkov phosphenes:

1) Since the photosensitive outer segments of the rods are considerably longer than the path length of the particle involved in generating the flash, it can produce a percentible sensation even if it is coming from behind the eye, after penetrating the pigmented epithelium forming the outer surface of the retina. Since shielding by the head is negligible for these high-energy particles, there should not be a marked difference in the frequency of these flashes, depending on the orientation of the observer's head with respect to the source of the particles. It is therefore doubtful whether the Cerenkov hypothesis can be tested by looking for an anisotrophy in the effect in lunar orbit, where the cosmic-ray flux is anisotropic because of shielding by the moon.

2) These flashes are produced only by heavy cosmic rays. At the top of the Earth's atmosphere, the flux of particles having Z > 10 and sufficient energy to produce Cerenkov radiation in tissue is ∿1/m^2-sterad-sec.[9] In lunar orbit, where approximately 2π steradians are shielded by the moon, a heavy particle should pass through one eye or the other about once every four minutes. The rate may dobule during transit to or from the moon. In view of uncertainties in the actual flux, this is in reasonable agreement with the observed frequency.

3) Since the intensity of the spot is so small, the flash should be observed by scotopic vision only. The spot should therefore be colorless.

4) For the same reason, since the proportion of rods over cones increases away from the fovea, there should be a tendency for star-like flashes to concentrate in the peripheral field of vision. A particle passing through the fovea would not produce a percentible flash at all.

5) Since the intensity is not much more than an order of magnitude above the scotopic threshold, extensive dark-adaption is required in order to see these flashes. The light adapted eye would require at least 15 minutes of total darkness before they became visible. This is a sensitive test of whether Cerenkov radiation is responsible for the star-like phosphenes observed on lunar missions.

Observations on Apollo 14

On previous missions, observations of phosphenes had been entirely informal. Prior to Apollo 14, the crew was briefed on what their predecessors had seen, the phosphene phenomenon was discussed in general terms, and interest in the degree of dark adaption required to see the flashes are expressed. These discussions with the crew led to the development of a common language for describing different types of flash and to a single protocol for making the observations.

During trans-lunar coast, the crew looked for flashes before each sleep period, after the spacecraft cabin had been darkened. They reported their observations on awakening, and described three types of event: a) star-like flashes, b) streaks, and c) cloud-like flashes ("summer lightning"). This was the first lunar mission to report diffuse displays.

At the beginning of one sleep period the Command Module Pilot (Roosa) shone a flashlight in his eyes, to ruin his dark adaption. He reported seeing flashes "in less than a minute" after the flashlight was turned off.

These results prompted a dedicated, formal session of observations during trans-Earth coast, which began at 1343 CST, February 8, 1971, when the spacecraft was 115,000 nautical miles from Earth. The spacecraft cabin was configured for total darkness, although slight light leaks around the window shades were reported when the sun shone directly on them -- the spacecraft was in the Passive Thermal Control ("barbecue") mode at the time. However, each crew member tried to keep his eyes closed throughout the observations.

The Commander, Alan Shepard, was in the left couch, looking up; the Lunar Module Pilot, Edgar Mitchell, was in the right couch, looking up; and Roosa was below them in the Lower Equipment Bay, also looking up. The experiment was started by having each crew member stare directly into a flashlight until thoroughly light-adapted.

For the first 16 minutes, no events were reported. There were indications from the Aeromed sensors that at least two crew members were becoming drowsy. On query from the CapCom in Houston, the crew confirmed that they had seen no events and expressed their feeling that this was very unusual. Very shortly thereafter, Mitchell reported the first event. The session was continued for a further 30 minutes and a total of 48 flashes were reported.

Observations were reported via the downlink by saying "Mark" as soon as a flash was seen, followed by a short description including the type of event, which eye it was seen in, position in the visual field, and any other pertinent information. The 48 events in this session were all of the previously reported type, with the addition of some "double stars" (two stars in one eye).

Mitchell illuminated his eyes again at the 24-minute mark in the session, dark-adapted for 12 minutes, and then repeated this procedure. Care was taken to avoid exposing the other crew members eyes to the flashlight while Mitchell was light-adapting.

Figure 1 gives a breakdown of the events by observer, type, and eye in which the flash was seen. "Stars" and "flashes" are similar phenomena, "flash" denoting a spot of larger apparent size. If "streaks" are assumed to be caused by particles moving tangentially in the retina, they would be expected to be relatively infrequent, and in fact the ratio of spots to streaks observed was 3:1.

Figure 2 shows the number of events reported in each eye by each crew member. Note that all three are biassed towards the right eye, although Mitchell had the impression just after the session that he had seen more in the left than the right eye. All the crew members felt sure of their ability to distinguish which eye the flash occurred in.

		STREAK	STAR	FLASH	CLOUD	DOUBLE
L M P	RIGHT EYE	2	4	6		
	LEFT EYE	2	1	1	2	
	BOTH EYES				1	
	NOT REPORTED	1		1		1
	TOTAL 22	5	5	8	3	1
C D R	RIGHT EYE	1	1	5	1	2
	LEFT EYE	2		2		
	BOTH EYES					
	NOT REPORTED					
	TOTAL 14	3	1	7	1	2
C M P	RIGHT EYE	1		5		
	LEFT EYE	1				1
	BOTH EYES					
	NOT REPORTED			3	1	
	TOTAL 12	2	0	8	1	1
TOTAL 48		10	6	23	5	4

FIGURE 1

	TOTAL	RIGHT EYE	LEFT EYE	BOTH EYES	NOT REPORTED
L M P	22	12	6	1	3
C D R	14	10	4	0	0
C M P	12	6	2	0	4
TOTALS	48	28	12	1	7

FIGURE 2

Analysis of the times of occurrence of flashes reported by Mitchell after light-adapting yields what seems to be a random distribution. Figure 3 is a timeline plot of these events. It is clear that it is not necessary to be dark adapted to see these phosphenes. On event (a streak) occurred only 51 seconds after beginning dark adaption.

Figure 4 is a histogram showing the distribution of intervals between successive events (not broken down by observer), in ten-second bins. The theoretical (Poisson) distribution function having the same mean is shown for comparison. A χ^2 test yields a probability of fit of the data to the theoretical distribution of 19%, so it is concluded that the flashes do in fact occur at random times.

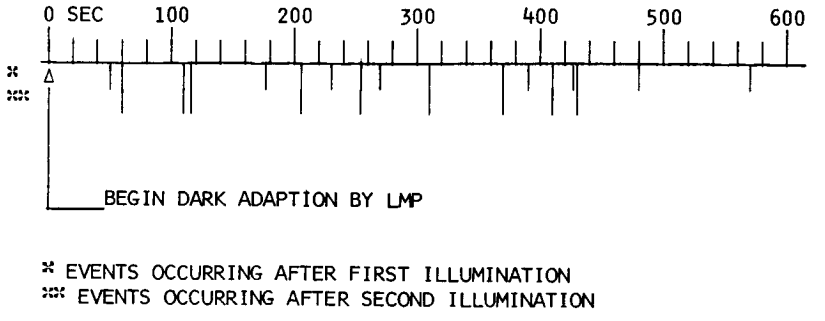

FIGURE 3

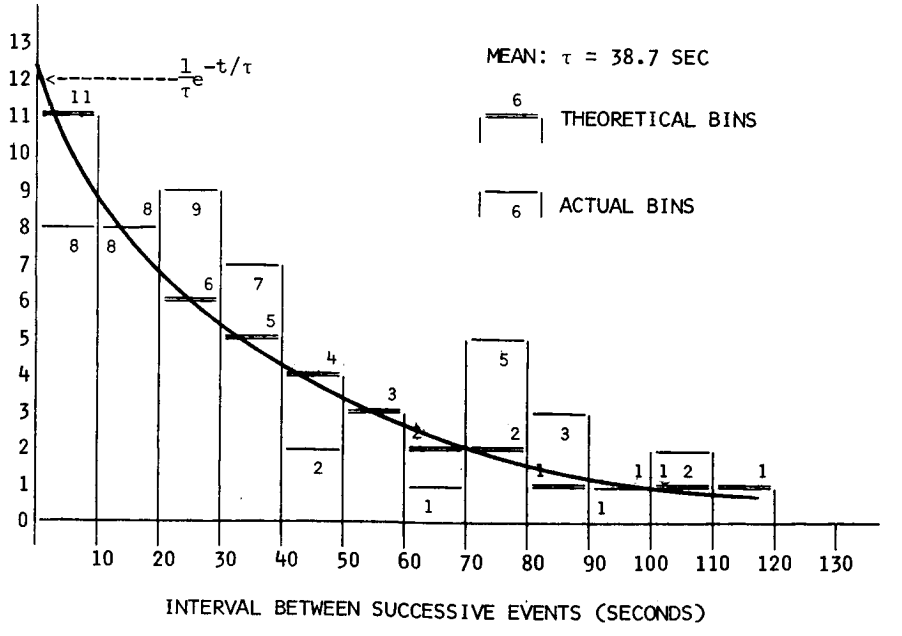

FIGURE 4

There was only one report of color in the flashes during the entire mission. This was a double star seen by Mitchell during the formal session, which he described as "white with a blue cast", like a blue diamond".

At the end of the observation session, Roosa commented that both the frequency and brightness of the events were much lower than he had experienced during informal observations. His position in the LEB may have contributed to this phenomenon. However, both Mitchell and Shepard felt that the flashes they had seen earlier in the mission were much brighter (especially when they woke up during a sleep period), although they could not say whether they had been more frequent.

During debriefing in the Lunar Receiving Laboratory, after the mission, all three crew members were positive that it was possible to tell which way a "streak" was moving. This was surprising, in view of the exceedingly brief time taken by a cosmic-ray particle to traverse the eyeball. However, recent experiments[10] have revealed similar sensations of movement in the streaks produced when accelerated particles are injected tangentially to the retina. It seems probable that the impression of movement is due to a characteristic variation in the width of a streak, along its length, due to variation in the rate of loss of energy of the particle. This may provide evidence that streaks, at least, are produced by relatively low energy particles, for which Cerenkov radiation is not a factor, but the observations are not definite enough as yet to allow firm conclusions on this point.

Conclusions

The observations of cosmic-ray phosphenes on Apollo 14 were very simple, required no equipment, and were carried out on a time-available basis. They provided the first quantitative data on the statistics of this phenomenon, but by far the most significant result was the discovery that it is not necessary to be dark-adapted to see flashes. This is strong evidence that some, and probably most, of the flashes are produced by mechanisms other than Cerenkov radiation.

It is probable that many of the flashes are due to direct ionizing interactions in the retina. This conclusion is supported by experiments of Tobias and his associates, in which flashes were observed by subjects exposed to low-energy neutron beams. Neutrons, being uncharged, of course cannot produce Cerenkov radiation directly, and the beams employed were energetically incapable of producing charged spallation products of sufficient velocity.

The sensitivity of the retina to light increases monotonically during dark adaption, with a break in the slope corresponding to the shift from photopic to scotopic vision. It is known[11] that sensitivity to electrical phosphenes does not follow this pattern -- in fact, there is a peak in sensitivity within a minute after dark adaption begins. The dark adaption curve for particle phosphenes is quite unknown at present, although terrestrial experiments with accelerators should be capable of providing this information. It would be useful to carry out such experiments using subjects with different degrees of dark adaption and beams of sufficiently low intensity to provide countable numbers of flashes. In general, the shape of the dark adaption curve may be diagnostic of the type of phosphene involved.

More detailed experiments are planned for upcoming Apollo missions. Because the frequency of flashes is relatively low compared to dark-adaption time-constants, many trials are required to obtain reliable information on the shape of the dark-adaption curve. Light-tight goggles will be carried on all future missions, to standardize the dark adaption process.

In lunar orbit, comparison of the observed frequency of flashes between the day and night sides of the moon should allow determination of the role, if any, of solar cosmic rays in producing these phosphenes. On later missions, the experiments may include equipment to determine the energy, charge, direction and position of the track relative to the head of a particle producing a visible flash. These experiments should produce definitive data, including confirmation that the flashes are produced in the eye, rather than in the visual ganglia or cortex. When the opportunity arises, observations in Earth orbit may provide additional data on the magnetic rigidity of the particles involved.

Acknowledgement

The authors wish to thank the crew of Apollo 14, Alan Shepard, Edgar Mitchell and Stuart Roosa, for their cooperation in investigating cosmic ray phosphenes in space.

References

1. Tobias, C.A., Journal of Aviation Medicine 23, 345 (1952)

2. D'Arcy, F.J., & Porter, N.A., Nature 196, 1013 (1962)

3. Conrad, C., Jr., private communication.

4. Fazio, G.G., & Jelley, J.V., internal report, Smithsonian Astrophysical Lab., Cambridge, Mass. (1970).

5. Jackson, J.D., Classical Electrodynamics, Wiley, N.Y. (1962), p. 495

6. Pirenne, M.H., loc cit, p.131.

8. Price, P.B., et al, Phys. Rev. Lett. 21, 630 (1968)

9. Ginzburg, V.L., & Syrovatskii, S.I., The Origin of Cosmic Rays, Pergamon, N.Y., (1964), p. 13

10. One of the authors (TFB) was a participant in these experiments.

11. Budinger, T.F., Lawrence Radiation Lab. Report UCRL 18347 (1968), unpublished.

THE HEAVY PARTICLE HAZARD - WHAT PHYSICAL DATA ARE NEEDED ?

S.B. Curtis*
Lawrence Radiation Laboratory, Berkeley, Calif. 94720
and
M.C. Wilkinson
Space Sciences Group, The Boeing Company, Seattle, Wash. 98124

It is impossible at present to evaluate adequately the radiation hazard from heavy galactic cosmic rays to astronauts on extended missions. Both physical and biological data are sorely needed for the proper assessment of the risk on missions lasting a year or longer outside the earth's magnetosphere.

The physical data required fall into three main categories:

1. Spectral Characteristics. From the relative abundance of the high Z nuclides and the limited data already obtained at solar minimum in the low energy region, it is clear that the flux of very high LET particles (above 2×10^3 MeV cm^2 / g) will be predominantly low energy ions ($<$ 500 MeV/nucleon) in the iron group ($26 \leq Z \leq 28$). Thus, it is important to determine the shape of the low energy portion of the spectrum during the next solar minimum ($\sim$1976), when galactic fluxes reach their maximum values.

2. Nuclear Interaction Parameters. Although ionization will be the main energy loss process for the heavy ions, a considerable fraction will also undergo nuclear collisions, fragmenting into particles of lower charge but perhaps greater range than the primary particle. Because the mean free path for interaction ($\sim$15 g/cm^2) is on the order of the probable shielding available for critical body organs (the eye, brain), it is necessary to know the secondary production characteristics in order to make a reasonable estimate of particle fluxes within the body organs in question. Results of a computer code are presented in which two different assumptions for the fragmentation parameters and their Z dependence (experimentally unknown at present) have been made.

---

* Presently on leave of absence at the Radiobiological Institute TNO, 151 Lange Kleiweg, Rijswijk Z.H., The Netherlands.

3. Track Structure. The spatial distribution of ionization surrounding a high energy, high Z ion plays an important role in determing the ultimate biological damage. Knowledge of track structure will help to predict biological effects and may be crucial in the all-important extrapolation from animals to man. A rough theory for calculating the dependence of the energy density in water as a function of distance from the track trajectory will be reviewed. Limited biological data at much lower energies suggest that the height of the shoulder of this curve (which is proportional to Z^2/β^2, not total LET) may be closely correlated to biological damage.

Data in the first category above must be obtained by spacecraft flying outside the magnetosphere during solar minimum and instrumented to measure the low energy portion of the high Z galactic component. The data in the second and third categories can be most reliably and readily obtained in earth-based laboratories (along with the necessary biological data). The requirement here is an accelerator of ions in the iron group up to the region of 300-500 MeV/ nucleon.

A convincing case has been made that on recent Apollo missions, astronauts have experienced within their eyes, and probably via direct retinal excitation, the effects of the passage of high energy heavy galactic cosmic rays (ref. 1). It remains to be determined the extent of any lasting, deleterious effects produced by such ions over a continuous extended exposure. At the present time, there are no data on the biological effects of such high LET penetrating radiation on man or animals. The reason for this, of course, is that no accelerator exists at present which can produce beams of heavy ions with sufficient penetration to attempt the type of biological experiments necessary for the proper evaluation of this hazard. There is much to learn before we can be sure that astronauts on very long missions, that is, missions of a year or longer, will be safe from the continuous bombardment of these high LET particles.

In this paper we will not deal with the biological research that must be done to study the long term effects of such radiation, but instead will discuss the physical data necessary for an adequate evaluation of the problem.

The research falls into three main categories, each of which is interesting in its own right. These are presented in Table 1.

First, there is the radiation environment itself - what is the flux of these high energy, heavily ionizing ions; how many might be expected to hit

PHYSICAL DATA REQUIRED

RADIATION ENVIRONMENT OF HIGH ENERGY HEAVY IONS

- Fluxes
- Energy spectra (emphasis on energies < 500 MeV/nucleon)
- Solar modulation

NUCLEAR INTERACTION PROPERTIES

- Cross sections in aluminium and water (tissue)
- Fragmentation parameters

TRACK STRUCTURE

- Radial energy density
- Track core size
- Correlation of structure to biological effects

a spacecraft on, say, a Mars mission ? Of particular interest is the energy region just below 500 MeV/nucleon, where the penetration is still sufficient to be of concern and where the ionization (that is the LET) will also be high.* Solar modulation is important since these lower energy particles are affected more than those of higher energy by the modulation mechanism. Long manned missions may be planned for solar inactive years to decrease the probability of encountering giant solar-particle events. If so, the galactic fluxes encountered will be near maximum.

Secondly, we must study the nuclear interaction properties of the particles involved in the materials of the spacecraft and the bodies of the astronauts themselves. No data are presently available on the cross sections of heavy ions in the 1 GeV/nucleon range in aluminum and water or tissue. The total non-elastic cross sections can be estimated with fair accuracy, but we must also know the fragmentation parameters associated with the various particle reactions. The fragmentation parameter for a given secondary particle type is either the probability of emission of the secondary, if less than unity, or the average number of secondaries per interaction, if greater than unity. Also, how is the energy shared as the two nuclei break up ? Does the resulting fragment continue with the same velocity, or is there significant change in the energy per nucleon of the emerging heavy particle ?

These questions must be answered before a clear idea can emerge of the penetration characteristics of the heavy ions. Only then will it be possible to make accurate predictions of the fluxes of high Z ions at organs which may be critical in that they might accumulate enough damage to impair normal function.

Finally, there is the field of track structure. Here the interest is in the spatial distribution of energy deposition by the heavy ions as they slow down in tissue. What is the extent of the core of such an ion ? What is its "radius of destruction" ? Is the important physical parameter its LET or dE/dx, or does the diffusive character of the "electron penumbra" decrease its biological effectiveness to less than that of a lower energy ion at the same dE/dx? These are all questions which bear directly on the biological effects of these ions. Since laboratory experiments may be performed with animals which have cells or cell nuclei with different sizes than the equivalent cells in man, it may be important to know as much as possible about the physical distribution of energy density around a heavy ion track in order to extrapolate results from animals to man.

We now review briefly some of the things we already know in these areas.

Integral Number-LET Spectra

Considerable data have been obtained from satellites and balloons on the fluxes and energy spectra of heavy galactic particles during the last solar minimum period; that is, during the period of maximum galactic fluxes - 1964-66 (ref.2).

* For orientation, a 500 MeV/nucleon iron nucleus has a residual range of 10 g/cm^2 of water and an LET of 2000 MeV cm^2/g (200 keV/μ).

In figure 1 we show the integral spectra not as a function of the energy or energy per nucleon as is usually presented, but as a function of the dE/dx or LET of the particles, which has more biological relevance. We note that the particles in the iron group ($26 \leq Z \leq 28$) dominate the spectra at very high LET (>1000 MeV cm^2/g) and also that the data is scanty - the solid curve stops at 5000 MeV cm^2/g corresponding to an energy of 100 MeV/nucleon. The dashed lines at high LET for each component are just guesses which are consistent with the low energy spectral behavior of the lighter components we know more about - protons and alpha particles. The dotted line at high LET was calculated assuming a sharp low-energy cut off in the iron spectrum at 100 MeV/nucleon. We conclude that more data are needed on the spectra of the very heavy, i.e. iron group ions, in the energy region just below 300 MeV/nucleon (residual range in water: 4-5 g/cm^2) during the next solar cycle minimum (1975-77). Since these particles are strongly affected by solar modulation mechanisms, it would also be of interest to determine when and to what extent the low energy fluxes of these heavy ions decrease during the cycle.

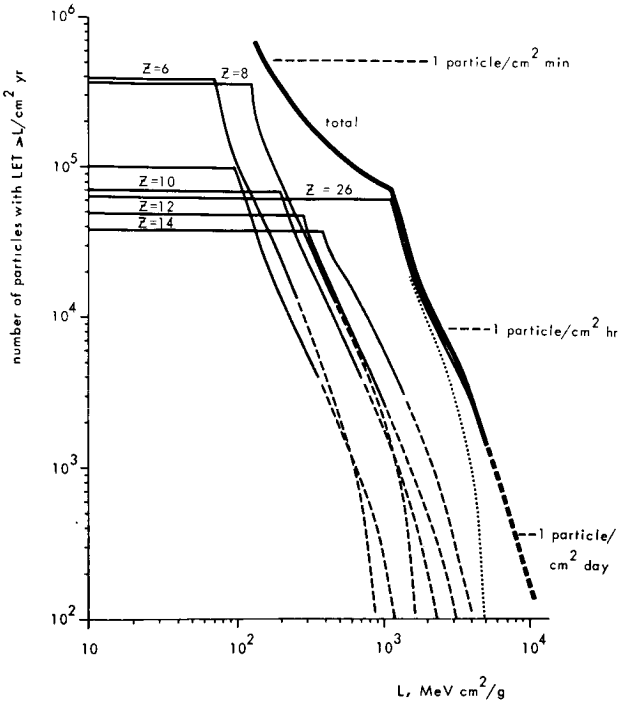

Figure 1. Integral number-LET spectrum for the galactic cosmic rays behind no shielding at solar minimum. The contribution of the various Z groups are also shown. The dotted line was obtained assuming a sharp low-energy cut off of 100 MeV/nucleon to the iron spectrum. The dashed lines represent regions where the data are lacking.

Nuclear Fragmentation

For high energy heavy ion-nucleus interactions, we have only cosmic ray data to give us any feeling for the cross sections and types of secondaries involved. In figure 2 we show a compilation of

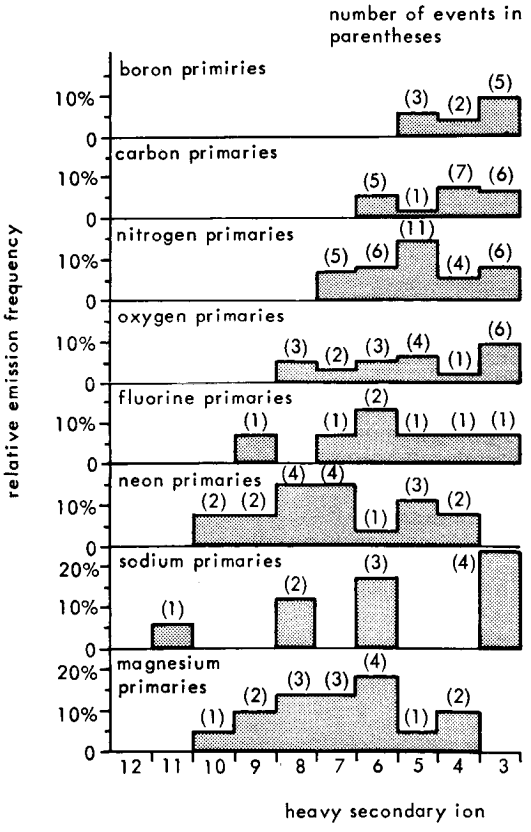

Figure 2. Compilation of experimental data for fragmentation parameters of heavy ions on the light elements (excluding hydrogen) in nuclear emulsion. The data come from rather old cosmic ray studies on balloons by the Bristol group (refs. 3 and 4).

data gathered from nuclear photographic emulsion on the fragmentation parameters in the light elements of the gelatine, i.e. carbon, nitrogen and oxygen. This was all the emulsion data in the literature a few years ago and was taken from the old compilations of the Bristol group (refs. 3 and 4). Now recent balloon flights could undoubtedly yield more data of relevance here, but the heavy elements in the emulsion (silver and bromine) will always give a certain amount of contamination trouble and considerable scanning would be required to get good statistics on each incident ion. Of lesser importance is the fragmentation in materials of which the spacecraft itself is made, for instance aluminum.

In the Space Physics Group at Boeing, a computer code has been developed to calculate the resultant fluxes and dose behind various shielding thicknesses for any incident galactic particle spectrum or combination of spectra. The results and details of the calculation have been presented earlier in this symposium (ref.5) and will not be repeated here, except to show the two sets of fragmentation parameters selected and the results of the dose rate calculations using the different sets. Figure 3 shows the two sets used. In set I, a constant probability for emission as a function of secondary Z is assumed, such that total charge is conserved. In set II, we try to reflect the possibility that fragments with Z close to two and close to the Z of the primary particle might be more probable than intermediate Z secondaries. In figure 4, the results of the dose rate as a function of depth for the iron group spectrum using the two sets are shown as the upper solid and dashed lines. There is a factor of two difference at 60 g/cm^2 of water. Also shown are representative curves of the secondary dose rates from the product secondary fragments. These are just representative curves since there are actually twenty-five such secondary curves plus the uncollided iron curve contributing to the total.

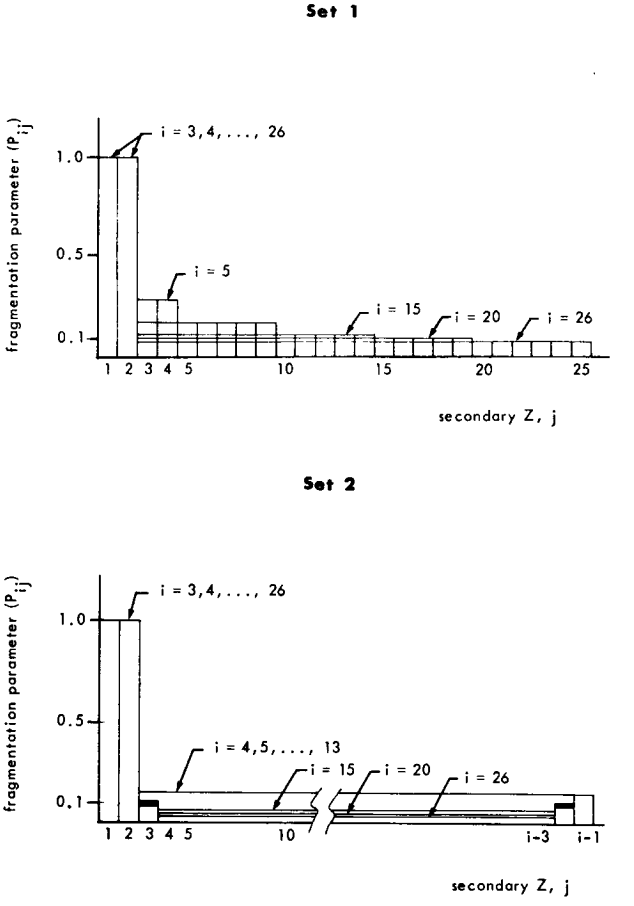

Figure 3. Two sets of fragmentation parameter secondary Z dependence assumed in the Boeing computer program mentioned in the text. Set I assumes a constant dependence on secondary Z plus charge conservation. Set II reflects the possibility that secondary ions with Z just less than the primary Z and secondary ions with Z close to that of α particles might be more probable than intermediate Z secondaries.

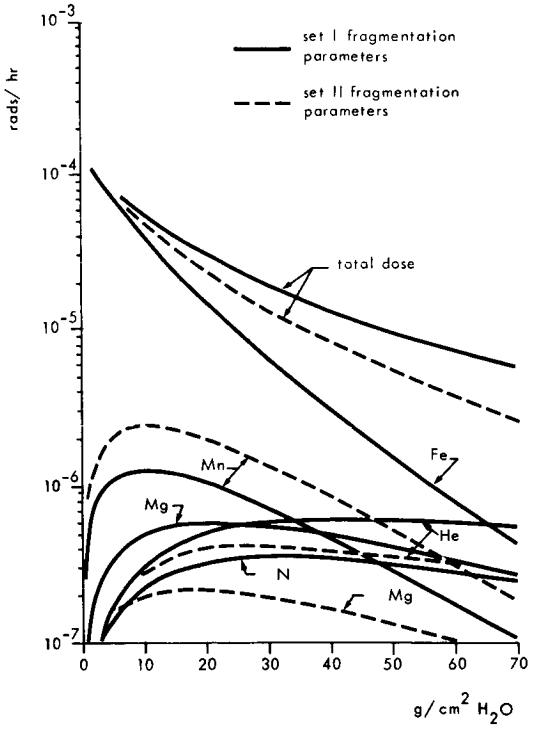

Figure 4. Dose rates as a function of depth from galactic cosmic rays of the iron group including secondary production as calculated by the Boeing code. Total dose rates as well as representative values from the secondary contributions are presented. The solid lines result from the Set I fragmentation parameters and the dashed result from the Set II fragmentation parameters presented in Figure 3. Note a difference of a factor of two in the total dose rates at 60 g/cm^2 of water.

We conclude that a better knowledge of the fragmentation parameters for such heavy ion breakups is essential. At the same time, of course, this will provide us with more insight into nuclear structure and the way energy is shared in high energy nucleus-nucleus collisions, an area of interest to the nuclear physicist.

Track Structure

The physical distribution of energy deposition (ionization density) along the trajectory of a charged particle has been an area of increasing interest in recent years. One way of approaching this problem is by defining an average energy density $\rho_T(r)$ as a function of distance from the track trajectory. The integral of $2\pi r \rho_T(r)$ over distance from the trajectory yields the average dE/dx or LET_∞ :

$$LET_\infty = 2\pi \int_0^\infty \rho_T(r)\, r\, dr$$

The distance r is the perpendicular distance from the track trajectory. It is easier to study the quantity $\rho_T(r)$ at large distances, say greater than 50-100 Å, than at small distances. At large distances, the only electrons present have come from the so-called "close collisions" and can be treated with the familiar Rutherford expression for free electrons. Two rather crude theories (refs. 6 and 7), which will not be discussed here, yield a dependence of $\rho_T(r)$ going as Z^2/β^2 of the particle in question and falling as a function of r as $1/r^2$ up to distances which are still small compared with the range of electrons with maximum transferable energy. As we approach this range, of course, the function falls off much more rapidly. One estimation of the dependence of ρ_T on r for an iron nucleus of energy 500 MeV/nucleon is shown in figure 5. Here the ordinate is ρ_T, the "dose" in units of 100 ergs/g. Dose is in quotes here because it is not a dose in the strict sense of the word. It can be considered an average dose over distances along the track large enough so that dE/dx has meaning, that is, long compared to distances where the fluctuation of energy loss plays an important role. The dependence of this quantity at small distances is an open question at present. It is assumed to rise steeply because we know that the total integral must equal the total dE/dx, and subtraction of the tail contribution from the total leaves a large portion of the energy to be deposited in the core, at least one-half the energy. Hence the core is undoubtedly very important in producing biological effects. This nonuniformity of energy deposition implies that the average dose deposited by such particles or their total LET may

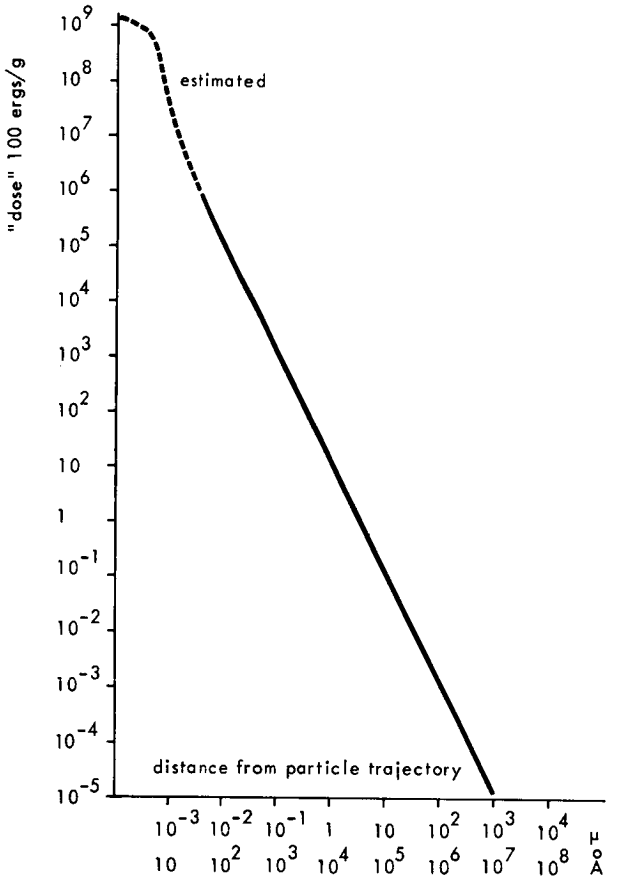

Figure 5. Estimation of the dependence of the energy density on distance from the particle trajectory of a 500 MeV/nucleon iron ion. The ordinate is not a true dose but can be considered an average dose over distances along the track long compared to distances where fluctuations of energy loss are important.

have little relevance to the evaluation of the hazard from these high-energy heavy ions.

There is evidence at much lower energy that the quantity Z^2 / β^2 is a more relevant quantity than LET_∞ to describe biological effects (ref.8). It is well known that hypoxic cells are more radioresistant than oxygenated cells. The Oxygen Enhancement Ratio (OER) is a measure of this difference in radiosensitivity for a particular type of radiation. An OER of 2.7 as measured in human kidney cells for X-ray irradiation, for instance, means that 2.7 times the dose is needed to produce the same effect on hypoxic cells as on well-oxygenated cells. If for a different type of radiation, the difference in radiosensitivity is less, the OER is lower. For an OER of unity, there is no difference in the radiosensitivity of oxygenated and hypoxic cells.

In general, the OER is closer to unity for radiations of high LET than for those of low LET. This is shown for two sets of experimental data in fig. 6a for the system of human kidney cells in tissue culture. The two sets of data differ in that the solid squares were obtained with high-energy heavy ions ($\sim$ 7 MeV/nucleon) all at the same velocity (ref.9), and the open circles were obtained with alpha-particles at different velocities (ref.10). We note that there is no overlap of the data. If, however, we plot the data against Z^{*2}/β^2 instead of against LET_∞, we obtain the results in figure 6b. Here Z^* is the charge of the particle, taking into account charge pick-up of the ion as it slows down. The data overlap to a much greater extent and are consistent with lying on the same curve. Thus we conclude that at least for this biological system and endpoint, Z^{*2}/β^2 is a more relevant physical quantity to plot the biological results against. This correlation should be checked with other endpoints and, in particular, should be checked with high-energy heavy ions of importance in the galactic cosmic rays, where the "electron penumbra" is greater in extent, thus diffusing part of the energy deposited over a greater distance. The "close in" shoulder of the curve, as seen in fig.5, rises as Z^2/β^2, so for high Z^2 the shoulder will also be large. Core effects are extremely important because of the very high energy density in the core and it is even possible that new inactivation processes will come into play which are entirely absent at lower energy densities.

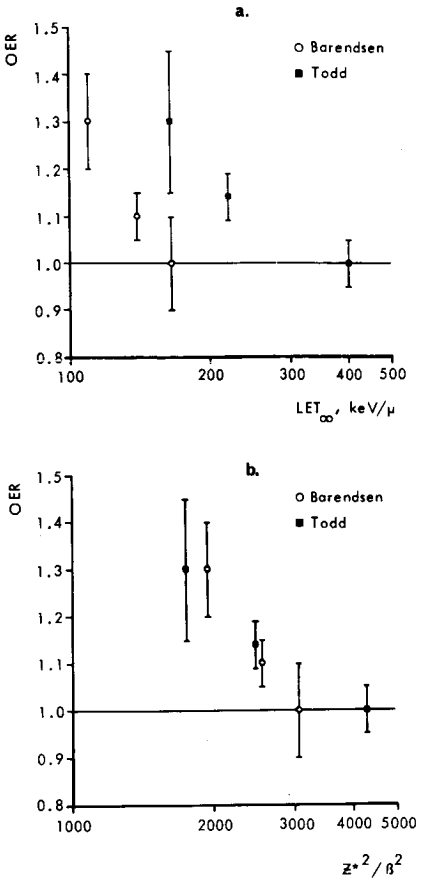

Figure 6. **a.** OER of human kidney cells (in vitro) from heavy ions at ~7 MeV/nucleon (solid squares) and from low energy alpha particles (open circles) plotted against LET_∞. **b.** Same data as in a. plotted instead against Z^{*2}/β^2, where Z^* is the effective charge of the ion (including charge pick-up) and β is the ratio of the velocity of the particle to that of light.

Conclusion

We have mentioned several areas where physical data are needed in order to evaluate adequately the potential hazard of high-energy heavy ions in the galactic cosmic radiation to long manned missions outside our magnetosphere. The first, more data on the lower energy portion of the differential energy spectrum of the iron group, can be obtained in appropriately instrumented satellites during the next period of solar inactivity 1975-1977. The other two areas, nuclear interaction parameters in tissue and aluminum and the structure of the energy deposition along the trajectory of the tracks, appear to require an accelerator which accelerates ions of the iron group up to at least 300-500 MeV/nucleon. This information, along with the necessary biological information concerning the extent of damage and functional impairment to various critical organs, is necessary before we can confidently send manned expeditions to explore the near planets or establish bases for extended exploration of the moon.

REFERENCES

1. TOBIAS, C.A., BUDINGER, T.F., LYMAN, J.T.: Preceding paper, this symposium, 1971.
2. See review by MEYER, P., Ann. Rev. of Ast. and Astrophys., vol. 7, 1969, p. 1.
3. FOWLER, P.H., HILLIER, R.R. and WADDINGTON, C.J.: Phil.Mag. vol. 2, 1957, p. 293.
4. RAJOPADHYE, V.Y. and WADDINGTON, C.J., Phil. Mag. vol. 3, 1958, p. 19.
5. WILKINSON, M.C. and CURTIS, S.B.: this symposium, 1971.
6. BUTTS, J.J. and KATZ, R.: Rad. Res., vol. 30, 1967, p. 885.
7. CURTIS, S.B.: unpublished, 1970.
8. CURTIS, S.B.: Charged Particle Tracks in Solids and Liquids, The Inst. of Physics and the Physical Society, Conf. Series No. 8, 1970, p. 140.
9. TODD, P.W.: Med. Coll. Va. Q., vol. 1, No. 4, 1966, p. 2.
10. BARENDSEN, G.W., KOOT, C.J., KERSEN, G.R. van, BEWLEY, D.K., FIELD, S.B. and PARNELL, C.J.: Int. J. Radiat. Biol., vol. 10, 1966, p. 317.

VENTING OF FISSION PRODUCTS AND SHIELDING IN THERMIONIC NUCLEAR REACTOR SYSTEMS*

E. W. Salmi
Los Alamos Scientific Laboratory
University of California
Los Alamos, New Mexico 87544

Most thermionic reactors are designed to allow the fission gases to escape out of the emitter. There exist several design variations to allow the gas to escape from the reactor core. The final disposition of the gas has several interesting problems. If the gas is put into a chamber, its volume is too large to be contained in the shield. Fortunately the fission gas do not pose a radiation problem at 100 ft. Because of the long half-life the fission gases could prevent any close approach to the reactor after it has been shut down.

The fission gases could instead be stored in an absorption trap. An absorption trap is usually assumed to require very low temperatures, however, experimental data indicate that reservoirs at several hundred degrees C can be useful.

Another scheme is to simply allow the fission gases to escape. Again, because of the low activity of the fission products, this method should pose no radiation hazards.

INTRODUCTION

A thermionic reactor has an interesting radiation problem generally not associated with other nuclear systems, that is, the disposal of gaseous fission products. Almost all designers of thermionic reactors assume that the gaseous fission products must be removed from the core. This assumption is due to the very high operating temperatures of the fueled emitter in a thermionic diode. In order to illustrate the problem an idealized (not real) schematic of an emitter is shown in Fig. 1. This hypothetical emitter consists of a heavy (~ 1-mm-thick) tungsten cladding surrounding the fuel which usually consists of UO_2 or UC. If UO_2 is used, a void amounting to ~ 10% of the fuel volume is created in the fuel after prolonged high-temperature operation. A typical set of operating conditions is shown in Table I.

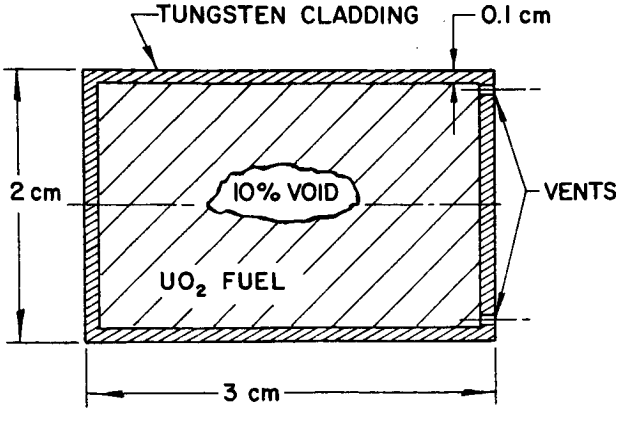

Fig. 1. Hypothetical tungsten-clad fuel emitter.

TABLE I. TYPICAL EMITTER OPERATING CONDITIONS

Emitter surface temperature, °C	1700
Emitter center-line temperature, °C	2500
Fuel power density, W/cm^3	50
Total fissions/cm^3 after 10^4 h	7.1×10^{19}
^{235}U burnup, %	~ 0.24
Final gaseous fission-product pressure, psi	~ 1000
Time to 2.5% creep of cladding, h	10

Experiments have shown that at an operating temperature of ~ 1700°C almost all gaseous fission products, e.g., xenon and krypton, escape from the solid fuel and accumulate in the central void. After 10,000 h of operation the gaseous fission product pressure in the void would be ~ 1000 psi. This high pressure would induce high hoop stresses in the tungsten cladding with resultant creep and eventual shorting of the emitter to the collector. The required creep time until shorting occurs is ~ 10 h. Obviously, this is unsatisfactory. Most emitter designs are affected by this difficulty and therefore allow the fission gases to escape. The design of emitters which would permit such escape before the cladding swells presents some problems. Solutions to these difficulties have apparently been found, but are not the subject of this paper.

RELEASE OF FISSION PRODUCTS FROM THE REACTOR

The fission products from the reactor core can be released by several methods. Two are illustrated in Fig. 2, which shows a typical thermionic fuel element of the flashlite design. The fission gases, on leaving the fueled emitter, enter the emitter support. In Method A, shown in the lower half of

*Presented at the National Symposium on Natural and Manmade Radiation in Space, Las Vegas, Nevada, Feb. 1971. Work performed under the auspices of the U. S. Atomic Energy Commission.

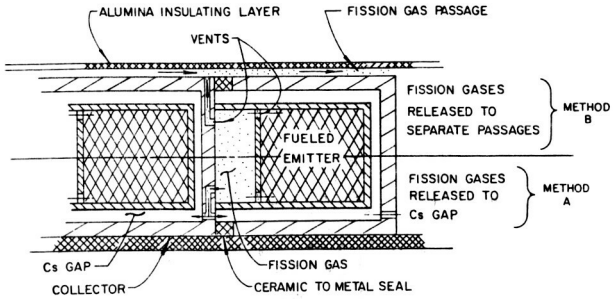

Fig. 2. Typical thermionic fuel element and possible methods of fission-gas release.

the illustration, vents are leading from the support structure to the cesium gap. The cesium gaps of the individual diodes are then connected by separate vents throughout the length of the fuel rod.

In Method B, illustrated in the upper half of Fig. 2, the vents bypass the cesium gap and lead to separate fission-gas passages outside the collector in the Al_2O_3 insulating region. These passages also extend throughout the full length of the fuel rod.

Fission Gases Enter the Cesium Gap - Method A

Both methods have their disadvantages. Experiments with Method A show that the gaseous fission products degrade the electrical power output of the diode even after only a short operating time: the presence of xenon or krypton in the cesium vapor at more than 10 or 20 Torr can increase the electrical resistivity across the cesium vapor gap and thereby reduce the electrical power output. Also, the presence of foreign gases increases the thermal conductivity across the gap, which, in turn, results in a reduction of the emitter temperature. The final result is the fact that only a very small fraction of the gaseous fission products can be retained in the cesium vapor space.

Fission Gases Bypass the Cesium Gap - Method B

Method B offers the advantage of not restricting the fission-product pressure to 10 or 20 Torr. This pressure restriction can influence the fission gas storage problem outside the reactor core. There are some disadvantages to the method. The small passages running through the alumina outer sheath might contain cracks connecting the collector and the outer sheath. The gaseous fission products are not purely xenon and krypton but also contain many other elements. In particular, cesium fission products are about 70% as numerous as the xenon and krypton products. Therefore, cesium at high pressure is present in any cracks in the separate venting system. With approximately 10 V possible across the small passage, there may be electrical shorting between the collector and the outer sheath resulting in very low electrical power output of the fuel element.

Another disadvantage of Method B is the presence of many ceramic-to-metal seals in the fuel element (Fig. 2). Should any of these break, the high-pressure gaseous fission products could enter the cesium vapor gap and reduce or terminate the power output. Because of this latter possibility and because of the large number of seals, the separate venting system should preferably be limited to the 10- or 20-Torr pressure regime. From these considerations, a separate fission-gas venting system does not appear to offer major advantages.

FISSION-GAS STORAGE PROBLEMS

Assume that the fission products, after venting, are finally stored in an outside reservoir. Fission products that may be gaseous at an emitter temperature of ~ 2000°C are listed, together with their atomic percentages, in Table II. Note that the rare gases represent ~ 12% of the fission products while the total high-temperature gases amount

TABLE II. GASEOUS FISSION PRODUCTS AT 2000°C AND THEIR PART OF TOTAL GAS RELEASE

Fission Products	Amount of Species, At. %
Kr and Xe	12.2
Br and I	2.5
Rb and Cs	9.0
As, Se, Te	4.3
Total	28.0

to almost 30%. In assessing whether all these gaseous products can escape from the emitter, some understanding of the escape mechanism may be useful. A microphotograph of UO_2 fuel after several thousands of hours of operation at ~ 2000°C is shown in Fig. 3; the dark spots are voids and the gray material is UO_2. Many dark spots have a lenticular shape and seem to have developed a trail through the UO_2.

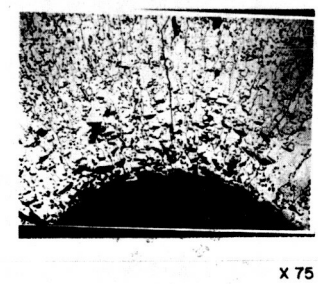

Fig. 3. Microphotograph of UO_2 fuel after prolonged operation at 2000°C.

According to fission-product escape theory voids are formed during operation, move up the temperature gradient through the fuel, sweep up the gaseous fission products, and eventually deposit the gases in the center of the fuel. In other words, the fission products do not have to diffuse long distances. This would imply that all fission products with a substantial vapor pressure at ~ 2000°C could be swept up by the lenticular voids and escape from

the fuel as readily as either xenon or krypton. Experimental data on these problems at present are not abundant.

The postulated escape mechanism out of the emitter can be considered to have a half life, which has been estimated to be about one week to one month for all fission products that can escape. The value of one week is used throughout this study.

After the high-temperature gaseous fission products escape from the emitter they may condense on cool surfaces both inside and outside the reactor. The escaped products can be bled through various filters or absorption beds, which could either react with or condense these products into a relatively small volume located within the reactor radiation shield. The rare gases, however, may not be trapped by these devices and may require some other method of disposal. To illustrate the problem, consider Table III which shows the results of a few simple calculations. A 100-kWe thermionic reactor with

TABLE III. GENERATION OF RARE GASES IN TYPICAL FUEL EMITTERS

Reactor thermal power, MW	1
Fissions produced during 10^4 h	1.1×10^{24}
Total number of xenon and krypton atoms	2.6×10^{23}
Gas volume at STP, liter	9.8
Gas volume at 20 Torr and 600°C, liter	1.2×10^3
Diameter of equivalent sphere, m	1.32

10% efficiency would have a thermal power of 1 MW. In 10,000 h of operation there would have been 1.1×10^{24} fissions. Assuming that 12% of the fission products are rare gases, there would be 2.6×10^{23} atoms of xenon and krypton or 0.44 mole. At standard temperature and pressure the gas volume would be 9.8 liters. However, in most reactor system designs a large radiator operates at ~ 600°C in the immediate vicinity of the reactor so that a large volume at room temperature may be difficult to locate. Also, as mentioned earlier, a rare-gas pressure greater than ~ 20 Torr may not be acceptable because of restrictions imposed by the thermionic diodes. Assuming the two worst conditions, i.e., a pressure of 20 Torr and a temperature of 600°C, the gas volume becomes 1190 liters rather than ~ 10 liters. A sphere of this large volume would have a diameter of 132 cm or of nearly 4.5 ft. Such a gas volume is almost an order of magnitude larger than the reactor and obviously could not be accommodated inside the reactor radiation shield.

POSSIBLE SOLUTIONS TO STORAGE PROBLEM

Three solutions to the fission-product storage problems exist:

- Remove the gaseous products from the main shield to a special shielded tank.
- Absorb the gases in a charcoal trap.
- Let the fission gas escape to space.

Remove the Gases to a Special Shielded Tank

In examining this method, the question of the existing radiation level arises immediately. To investigate the problem an example was postulated. Assume again a 1-MW thermal reactor and a half-life of one week for gaseous fission products to leave the emitter and calculate the activity of the various fission products. Decays per second as a function of operating time are plotted in Fig. 4. The top curve shows the fission-product activity remaining in the reactor; the middle curve plots the activity of the fission products which escape from the emitter but are assumed to be collected in a trap; and the bottom curve shows the activity of the rare gases which have escaped from the emitter and are assumed not to be caught in the trap.

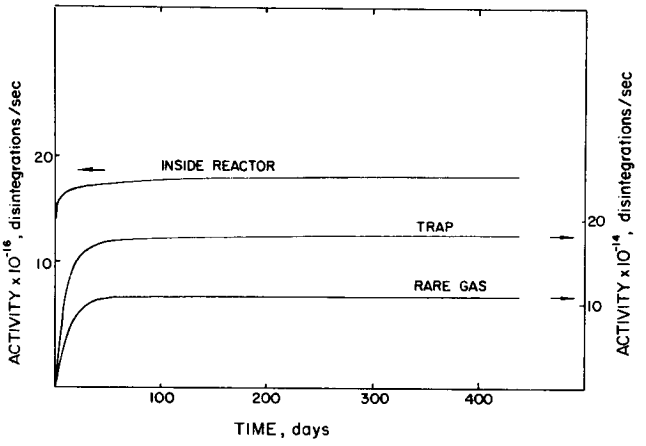

Fig. 4. Activity of various fission products as a function of reactor operating time.

The curves show that a steady state is achieved after two months of reactor operation. The activity in the trap would be 1.8×10^{15} disintegrations/sec or ~ 50,000 Ci. However, this trap was assumed to be small and located within the reactor shield. The rare gas value is 1.1×10^{15} disintegrations/sec which represents 30,000 Ci. To calculate the roentgens this source represents, the activity and decay schemes of the various isotopes of xenon and krypton were investigated. More than 90% of the activity of the rare gases is due to ^{133}Xe and ^{135}Xe (Fig. 5). In each case there is a metastable state; however, a detailed investigation of the decay chain shows that the metastable states contribute little to the activity. The ^{133}Xe is about six times more active than ^{135}Xe; however, the 81-keV γ-ray is strongly internally converted and because of the high absorption cross section it may be readily absorbed in a gas container wall. The main contribution to the outside γ-radiation therefore probably comes from ^{135}Xe. If one assumes that the β-rays do not leave the fission-gas container, and taking into account the internal conversion of the γ-rays, this rare-gas source would produce about 500 R/h at one meter or ~ 500 mR/h at 100 ft.

In some directions around a reactor power supply this radiation level is acceptable; however, in the direction of the crew compartment it is excessive. The activity calculations assumed an escape lifetime from the emitter of one week. Because the two

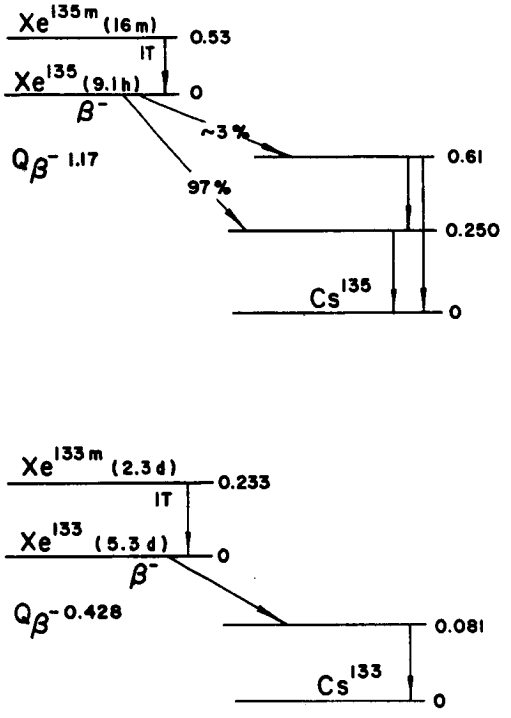

Fig. 5. Decay schemes for ^{133}Xe and ^{135}Xe.

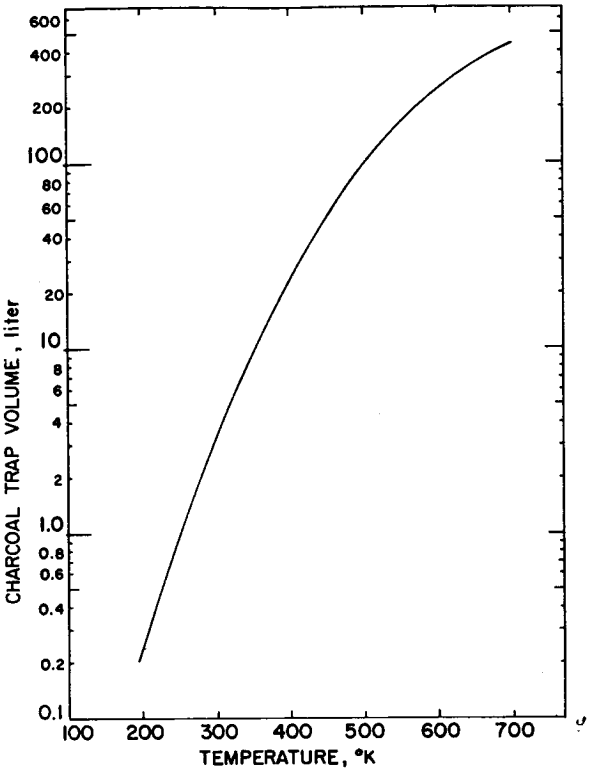

Fig. 6. Amount of xenon absorbed in charcoal as a function of temperature.

isotopes of greatest interest, ^{133}Xe and ^{135}Xe, have half-lives of 9 h and 5.3 days, respectively, the large uncertainty in the value of the escape lifetime can significantly affect the calculated radiation level. Experimental investigations of escape rates out of emitters are required before a satisfactory value can be assigned to the radiation level. In any case, the storage of fission gases in a lightly shielded gas chamber can pose design problems.

Absorption in a Charcoal Trap

Normally, absorption traps are thought to operate at very low temperatures; however, at pressures of 20 Torr a charcoal trap can be useful even at moderate temperatures. For the example of a 1 MW thermal reactor, the volume of charcoal required to store the xenon and krypton at 20 Torr can be calculated as a function of temperature.[1] As shown in Fig. 6, this charcoal volume is considerably smaller than the original volume of 1.2×10^3 liters without charcoal as shown in Table III. At a temperature of 100°C the charcoal volume is about 15 liters. Although 15 liters is not a trivial volume to shield, it may represent a compromise solution. At 100°C, the use of heat pipes may prove feasible for controlling the charcoal trap temperature.

The two methods discussed above of handling fission gases have their disadvantages. If the charcoal-trap temperature rose appreciably, the fission-gas pressure could increase and pose a hazard to reactor operation. On the other hand the lightly shielded gas-chamber system could pose a radiation hazard after reactor shutdown. Figure 7

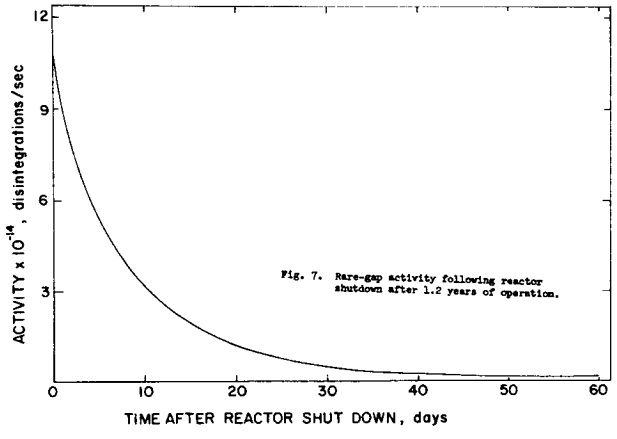

Fig. 7. Rare-gap activity following reactor shutdown after 1.2 years of operation.

shows the rare-gas activity expected following reactor shutdown after 1.2 years of operation. The curve shows that after one month the activity has fallen by a factor of 100. At this time the activity is due mainly to ^{85}Kr which has a ten-year half-life. Although this activity is small compared to the previously cited values, it is a 5-R/h radiation source at a distance of 1 m. With a ten-year half-life it does not disappear suddenly. If poorly shielded, it might pose a hazard for any crew working near the reactor after shutdown.

Escape of Gases to Outer Space

Values for fission gases escaping to space have been calculated, Table IV, and show that the number of rare-gas atoms escaping per second would be 7.5×10^{15}. These escaping atoms have an activity of 1.5×10^{10} disintegrations/sec, which represent 0.5 Ci leaving the reactor per second. Although at first glance this value seems high, the radiation hazard is actually small. Assume that the gases are emitted by an orifice to form a radioactive cloud filling 2π radians. As the cloud expands, the atom density at a distance of 1 m from this low-density expanding radioactive cloud, the radiation dose would be $\sim 10^{-8}$ R/h and certainly should pose no radiation hazard.

TABLE IV. ACTIVITY OF RARE GASES RELEASED TO SPACE

Atom escape rate, atom/sec	7.5×10^{15}
Activity of escaping atoms, disintegration/sec	1.5×10^{10}
Radiation leaving reactor, Ci/sec	0.5
Atom density at 1 m, atom/cm^3	1.5×10^{7}
Atom mean free path, km	200
Dose rate a 1 m from cloud, R/h	$\sim 10^{-8}$
Moles of ^{85}Kr released per year, mole/yr	7×10^{-3}
1975 projection for ^{85}Kr release, mole/yr	~ 500

Another aspect of this method of disposal of fission gases is simply that radioactivity is being released. The isotope that is worrisome is the long-lived ^{85}Kr. This 1-MW reactor would release about 7×10^{-3} moles of ^{85}Kr per year. This value must be contrasted with other sources of ^{85}Kr. At present, the ^{85}Kr obtained from the reprocessing of power reactor fuel elements is allowed to escape out of the air vents. No attempt is made, at present, to prevent their escape. Assuming that 100% of the ^{85}Kr is released, the escape rate in a few years is projected to be about 500 moles per year. By contrast, the 1-MW reactor is only a very small source.

Conclusions

This study led to the following conclusions:

- Release of rare-gas fission products to space is desirable, and
- Their release does not constitute a safety hazard.

If however, for some reason, the gases should not be released to space, design variations are possible to store the rare-gas fission products and to solve the associated radiation problems.

REFERENCE:

1. "Gas-Cooled Fast Breeder Reactor," GA-9359, Quarterly Progress Report, Feb. 1 - April 30, 1969.

"The aeronautical and space activities of the United States shall be conducted so as to contribute . . . to the expansion of human knowledge of phenomena in the atmosphere and space. The Administration shall provide for the widest practicable and appropriate dissemination of information concerning its activities and the results thereof."

—NATIONAL AERONAUTICS AND SPACE ACT OF 1958

NASA SCIENTIFIC AND TECHNICAL PUBLICATIONS

TECHNICAL REPORTS: Scientific and technical information considered important, complete, and a lasting contribution to existing knowledge.

TECHNICAL NOTES: Information less broad in scope but nevertheless of importance as a contribution to existing knowledge.

TECHNICAL MEMORANDUMS: Information receiving limited distribution because of preliminary data, security classification, or other reasons.

CONTRACTOR REPORTS: Scientific and technical information generated under a NASA contract or grant and considered an important contribution to existing knowledge.

TECHNICAL TRANSLATIONS: Information published in a foreign language considered to merit NASA distribution in English.

SPECIAL PUBLICATIONS: Information derived from or of value to NASA activities. Publications include conference proceedings, monographs, data compilations, handbooks, sourcebooks, and special bibliographies.

TECHNOLOGY UTILIZATION PUBLICATIONS: Information on technology used by NASA that may be of particular interest in commercial and other non-aerospace applications. Publications include Tech Briefs, Technology Utilization Reports and Technology Surveys.

Details on the availability of these publications may be obtained from:

SCIENTIFIC AND TECHNICAL INFORMATION OFFICE

NATIONAL AERONAUTICS AND SPACE ADMINISTRATION

Washington, D.C. 20546